Proceedings of WHEC-2022

Bridging Continents by H_2

WHEC-2022

23rd World Hydrogen Energy Conference

Onsite and Online

June 26-30, 2022

Istanbul Congress Center, Istanbul, Turkey



Editors:
Ibrahim Dincer
Can Ozgur Çolpan
Mehmet Akif Ezan

www.whecistanbul.org
info@whecistanbul.org

ISBN: 978-625-00-0843-0

Foreword ..... **IV**
Committees ..... **VII**
General Information ..... **vii**
Acknowledgment of Support ..... **IX**
Plenary Speakers ..... **XI**
Keynote Speakers ..... **XVI**
Invited Speakers ..... **XX**
Proceedings **1**
Track 1. Hydrogen Production: Thermochemical and Photonic Methods 1
Track 2. Hydrogen Production: Electrolysis 151
Track 3. Hydrogen Production: Biological Methods and Biohydrogen 299
Track 4. Hydrogen Production: Nuclear 350
Track 5. Hydrogen Separation and Purification 370
Track 6. Hydrogen Storage 436
Track 7. Fuel Cells: PEMFC 647
Track 8. Fuel Cells: SOFC and other types 827
Track 9. Integrated Hydrogen Energy Systems 889
Track 10. Power to Gas 1110
Track 11. Hydrogen Safety 1161
Track 12. Codes, Standards and Regulations 1209
Track 13. Hydrogen Strategies and Policies 1230
Track 14. Hydrogen Industry, Commercialization and Marketing, Applications 1277
Track 15. Hydrogen Economy, Logistics, Infrastructure 1344
Track 16. Environmental Impact and Sustainable Development 1431
Track 17. Social Dimensions 1485

MESSAGE FROM CONFERENCE CHAIRMAN



Due to the unexpected COVID-19 pandemic, the entire humanity has faced many devastating challenges. As a consequence, we had to postpone our 23rd WHEC from July 2020 to June 2022 with the hope that we will successfully organize the conference. Its format will this time be hybrid to cover both onsite and online presentations along with the exhibitions in both manners.

WHEC is a unique scientific event, as initiated by Prof. T. Nejat Veziroglu and his Colleagues back in 1974, and it aims to bring all researchers, scientists, academicians, and professionals working in the field of hydrogen energy systems, ranging from production to storage and end-use options, such as fuel cells for a common goal to hydrogen civilization. This time I have the privilege to chair this conference which provides both online and onsite platforms for contributions to the development and enhancement of hydrogen energy systems; as well as a place to interact with researchers from all around the world to gain a better understanding of the use of hydrogen energy systems for a sustainable future. Much like past WHECs, WHEC-2022 does not only provide an outlook on the current research activities, but also helps in shaping the future of hydrogen energy technologies.

Furthermore, Istanbul, as an ancient city that connects two continents of Asia and Europe, has always been strategically very important, and hosting such a conference in Istanbul will attract researchers from every part of the world to promote hydrogen energy systems and share their innovative ideas and future plans. Moreover, one has to keep in mind that Turkey is dedicated to increase the share of renewables in its energy supply and consider hydrogen energy systems as potential solutions. In conjunction with this, Turkey has expanded its research, innovation, and technology development activities to produce, store, and use hydrogen in an affordable, reliable, safe, clean, and sustainable manner. Given these activities as well as the financial investment and dedication to hydrogen energy systems in Turkey, Istanbul is undoubtedly the perfect host city for this event. Under the shelters of the prestigious International Association for Hydrogen Energy (IAHE) and Turkish National Hydrogen Association, we are now ready to host you for the 23rd WHEC in Istanbul and make it a success story with the strongest online and onsite participations. In this regard, I would like to take this opportunity to warmly thank everyone who has contributed to this success story.

Enjoy the Conference and enjoy your stay in Istanbul.

Prof. Dr. Ibrahim Dincer

Conference Chairman, WHEC-2022

President, National Hydrogen Association

MESSAGE FROM HONORARY CHAIRS



Welcome to the 23rd World Hydrogen Energy Conference (WHEC-2022) held from 26-30 June 2022 in Istanbul, Turkey.

Fossil fuels (i.e., petroleum, natural gas and coal), which meet most of the world's energy demand today, are being depleted fast. Also, their combustion products are causing global problems, such as global warming, climate change, ozone layer depletion, acid rain, oxygen depletion and pollution, which pose a great danger for our environment and, eventually, for life on our planet. Many engineers and scientists agree that the solution to these global problems would be to replace the existing fossil fuel system with the Hydrogen Energy System. Hydrogen is the lightest, most efficient, and cleanest fuel. Its use will produce no greenhouse gases, no ozone layer depleting chemicals, no acid rain ingredients, no oxygen depletion, and no pollution.

Around the world, there is extensive Research and Development work on Hydrogen Energy. Internal combustion engines are being modified for hydrogen fuel. Many types of fuel cells – to convert hydrogen efficiently to electricity – are being developed. Hyundai, Toyota, Honda, and Mercedes started selling hydrogen fueled cars. Many bus companies are selling hydrogen fueled buses. Siemens is selling hydrogen fuel cell powered submarines. Hydrogen fueled appliances based on catalytic combustion have been built. There is research and development work on hydrogen hydride refrigeration and air conditioning systems. Aircraft manufacturers are working on hydrogen fueled subsonic and supersonic transport planes.

Scientists and Engineers from many countries of the world will gather at the 23rd WHEC-2022 Conference to present their papers covering the recent advances in hydrogen energy and technologies. All these will no doubt speed up the conversion to a hydrogen economy eliminate global environmental problems and provide the humankind with higher living standards. I congratulate the organizers of this conference and wish all the participants a very fruitful meeting and pleasant days in the historic capital of two world empires, Istanbul, Turkey.

T. Nejat Veziroğlu

Honorary Chair, 23rd WHEC-2022

Founding President, International Association for Hydrogen Energy

MESSAGE FROM HONORARY CHAIRS



Welcome to the 23rd World Hydrogen Energy Conference.

The demand for hydrogen is predicted to increase fivefold by 2050, driven primarily by the transport, maritime and aviation sectors, according to the recent Global Energy Perspective report developed by Energy Insights, the global market intelligence and analytics group of McKinsey & Company. This report predicts the role of electricity in the global consumption of energy to grow from approximately 20% today to 40% by 2050. Renewable energy is predicted to account for 80 to 90% of the global electric power generation by 2050.

As a result, green hydrogen is predicted to account for approximately 28% of the electric power demand by 2050. Despite creating additional electric demand, dispatchable electrolyzers will permit the integration of intermittent renewable energy sources resulting in more resilient and sustainable energy systems. Green hydrogen is predicted to serve as an energy storage for electric power generation. Gas turbines and compression-ignition, internal combustion engines converted to hydrogen can provide additional flexibility when integrated with power-to-power smart grids, especially stand-alone microgrids.

Finally, three fundamental enablers will be needed for the development of our hydrogen economy: the timely deployment of infrastructure and supply chain; cost reduction from technology advancement and manufacturing scale-up; and government support and targeted actions.

I wish you Godspeed in your endeavors for a bright and sustainable future.

John W. Sheffield, Ph.D.

President – International Association for Hydrogen Energy

ORGANIZING COMMITTEE

HONORARY CHAIRS

T. Nejat Veziroglu
John Sheffield

CONFERENCE CHAIR

Ibrahim Dincer

EXECUTIVE ORGANIZING COMMITTEE

Can Ozgur Colpan
Inci Eroglu
Aysel Kanturk Figen
Filiz Karaosmanoglu
Adnan Midilli
Murat Ozturk
Bestami Ozkaya
Ramazan Solmaz
Ayfer Veziroglu
Emre Veziroglu

ORGANIZING COMMITTEE

Technical Co-Chairs

Can Ozgur Colpan
Mehmet Akif Ezan

Track Coordinators

Canan Acar, Coordinator of Track 1. Hydrogen Production: Thermochemical and Photonic Methods
Ankica Kovač, Coordinator of Track 2. Hydrogen Production: Electrolysis
İlgi Karapinar, Coordinator of Track 3. Hydrogen Production: Biological Methods and Biohydrogen
Rami El-Emam, Coordinator of Track 4. Hydrogen Production: Nuclear
Adolfo Iulianelli, Coordinator of Track 5. Hydrogen Separation and Purification
Tayfur Ozturk, Coordinator of Track 6. Hydrogen Storage
Selmiye Alkan Gursel, Coordinator of Track 7. Fuel Cells: PEMFC
Meng Ni, Coordinator of Track 8. Fuel Cells: SOFC and other types
Yusuf Bicer, Coordinator of Track 9. Integrated Hydrogen Energy Systems
Benedetto Nastasi, Coordinator of Track 10. Power to Gas
Tahir A.H. Ratlamwala, Coordinator of Track 11. Hydrogen Safety
Nader Javani, Coordinator of Track 12. Codes, Standards and Regulations
Adnan Midilli, Coordinator of Track 13. Hydrogen Strategies and Policies
Yilser Devrim, Coordinator of Track 14. Hydrogen Industry, Commercialization and Marketing, Applications
Wei-Hsin Chen, Coordinator of Track 15. Hydrogen Economy, Logistics, Infrastructure
Farrukh Khalid, Coordinator of Track 16. Environmental Impact and Sustainable Development
Can Ozgur Colpan, Coordinator of Track 17. Social Dimensions

Conference Planning Coordinators

Yusuf Bicer, Communications Coordinator
Mehmet Karakilcik, Financial Coordinator
Adnan Midilli, Sponsorship and Exhibitions Coordinator
Kaan Baltacioglu, Social Media Co-Coordinator
Huseyin Turan Arat, Social Media Co-Coordinator

Graduate Student Volunteers

Yagmur Nalbant Atak
Sera Ayten Cetinkaya
Tacettin Disli
Beyza Dursun
Anıl Erdogan
Feride Cansu Iskenderoglu
Aykut Korkmaz
Fatih Sorgulu

INTERNATIONAL ADVISORY BOARD

Frano Barbir, Croatia & USA
Juan Carlos Bolcich, Argentina
Eniya Listiani Dewi, Indonesia
Ibrahim Dincer, Canada
Gibril S. Eljrushi, Libya
Inci Eroglu, Turkey
Chiara Fiori, Italy
Patrick Hallenbeck, Canada
David Hart, Switzerland
Yun Hang Hu, USA
Ioan Iordache, Romania
Terry Kimmel, Canada
Vladimir Linkov, South Africa
Zong Qiang Mao, China
Cesare Marchetti, Italy
Elisa Marrasso, Italy
Matthew M. Mench, USA
Paulo Emílio de Miranda, Brazil
Nazim Muradov, Azerbaijan & USA
Byeong Soo Oh, South Korea
Alexander Y. Ramenskiy, Russia
Jacques Saint-Just, France
John W. Sheffield, USA
Giuseppe Spazzafumo, Italy
Detlef Stolten, Germany
Andrei V. Tchouvelev, Canada
Hirohisa Uchida, Japan
Ayfer Veziroglu, USA
Emre A. Veziroglu, USA

INTERNATIONAL SCIENTIFIC COMMITTEE

Angelo Basile, Italy
Sema Baykara, Turkey
Fanglin (Frank) Chen, USA
Marcos Vera Coello, Spain
Debabrata Das, India
Umit B. Demirci, France
Nedjib Djilali, Canada
Daniel Fruchart, France
Jürgen Garche, Germany
Maximilian Gorensek, USA
Makoto R. Harada, Japan
Alfredo Iranzo, Spain
Arunachalanadar M. Kannan, USA
Ilgi Karapinar, Turkey
Kevin Kendall, UK
Umit O. Koylu, USA
Gurkan Kumbaroglu, Turkey
E. Caglan Kumbur, USA
Xianguo Li, Canada
Hongtan Liu, USA
Matthew M. Mench, USA
Greg F. Naterer, Canada
Meng Ni, Hong Kong – China
Sandro Nizetic, Croatia
Ken-ichiro Ota, Japan
Tayfur Ozturk, Turkey
Bestami Ozkaya, Turkey
Vicenzo Palma, Italy
Sumer Sahin, Turkey
Oumarou Savadogo, Canada
David S. Scott, Canada
P Joseph Sebastian, Mexico
S. A. Sherif, USA
Patrick Takahashi, USA
Armen Trchounian, Armenia
Alexander Vorontsov, Russia
Chao-Yang Wang, USA

FORMAT OF THE CONFERENCE

WHEC-2022 will include both inspiring technical programs as well as enjoyable social events. The technical part of the WHEC-2022 will include sessions where plenary, keynote, invited and general speakers will deliver talks on their work and research in hydrogen energy. The conference will also include several specialized sessions and panel discussion sessions. There will also be numerous poster sessions where the poster presenters will have an opportunity to directly discuss their research outcomes with the conference participants. The social events will include a welcome reception, a gala dinner, and an optional tour of historical places. The conference will also include many other opportunities to socialize and connect with participants. The conference will offer both onsite and online presentations and exhibitions. The official language of the event is English. All papers must be presented in English. There will not be simultaneous translations.

PRESENTATIONS

Papers are to be presented in “Oral” or “Poster” Sessions. Speakers are requested report to the session chair 10 minutes before the start of the session. During the Oral Sessions each speaker is allocated for her/his presentation an estimated time of 12 minutes + 2-3 minutes for questions and answers. All posters will be shown on digital boards. Onsite presenters should be near the digital boards for taking any comments or questions at the break following the session scheduled in the conference program. Both online and onsite presenters should include an e-mail address on the poster. We will ask the participants to ask the questions by e-mail or via the conference website to the online presenters. Online participants may post questions to onsite participants via the conference website. So, we kindly encourage onsite/online poster presenters to visit the conference website regularly to follow up on the possible questions. There will be technical assistant in each room in case you have technical issues.

PUBLICATIONS

WHEC-2022 conference proceedings will be available for download right after the conference. The short papers of the authors who presented their papers in the conference will be included. The authors will have a chance to extend their papers and submit extended versions of their papers to special issues in prestigious journals associated with the conference. The selection and invitation process of the special issues will start after the conference ends. The authors will be informed of this process via e-mail.

The support received from the following sponsors is highly appreciated:

Main Sponsors

REPUBLIC OF TURKEY
MINISTRY OF ENERGY AND
NATURAL RESOURCES

TENMAK
TURKISH ENERGY, NUCLEAR AND
MINERAL RESEARCH AGENCY

TURKISH AIRLINES
A STAR ALLIANCE MEMBER

Platinum Sponsors

BAU
Bahçeşehir University

FuelPositive
Fuel For A Mindful World

INOGEN
ENERJİ TEKNOLOJİLERİ
ENERGY TECHNOLOGIES

Gold Sponsors

ENERJİSA ÜRETİM

TEMSA
MOTORLU ARAÇLAR

Sabancı Üniversitesi

ÜSKÜDAR BELEDİYESİ

Silver Sponsors

Kawasaki
Kawasaki Gas Turbine Europe GmbH

TEKSIS

WHTC 2023 İNHİ

Bronze Sponsors

BCS MÜHENDİSLİK

Fakir
HAUSGERÄTE

İTÜ

Sistem
ALÜMİNYUM

Westfälische Hochschule

Other Sponsors

KUTEM

OZ
Energy

TeknoVak
INDUSTRIAL FURNACE SYSTEMS INC.

WHEC-2022

23rd World Hydrogen Energy Conference

PLENARY SPEAKERS



Kazunari Domen

The University of Tokyo/Shinshu University

domen@chemsys.t.u-tokyo.ac.jp

PHOTOCATALYTIC WATER SPLITTING FOR LARGE SCALE SOLAR HYDROGEN PRODUCTION

Water splitting to hydrogen and oxygen using particulate photocatalysts is one of the potential candidates to produce green hydrogen at low cost and on a large scale. To achieve solar hydrogen production based on such systems in a near future, there are several problems that need to be solved, such as development of efficient and durable photocatalysts, cost effective reactors, efficient hydrogen separation systems, ensuring safety issues, and so on. In this talk, recently developed photocatalysts, water splitting reactors and hydrogen separation systems being developed in our project will be introduced. In addition, safety issues of the total solar hydrogen production system based on particulate photocatalysts for water splitting will be discussed.



Stuart Hawksworth

Head of Centre for Energy, HSE, UK &
President of International Association for
Hydrogen Safety, HySafe

SafetyStuart.hawksworth@hse.gov.uk

SAFETY OF HYDROGEN IN THE ENERGY SYSTEM

This presentation will give an overview of the activities of the International Association for Hydrogen Safety (IAHYSAFE) and their impact in the hydrogen safety space. It will also provide an overview of current hydrogen safety projects and how their outputs will be applied in Regulations, Codes and Standards. The presentation will then:

- describe current priorities addressing transport, heat, and power applications in the hydrogen
- discuss future technical challenges in hydrogen safety and the importance of addressing them to enable future progress and innovation in hydrogen technologies.
- discuss broader challenges around education and training in hydrogen safety as uptake in technologies grows.

The presentation will draw on inputs such as IAHYSAFE Research Priorities Workshop.



Bruce E Logan

Penn State University, USA

blogan@psu.edu

GREEN HYDROGEN PRODUCTION USING BIOMASS IN NEXT GENERATION MICROBIAL ELECTROLYSIS CELLS AND IMPAIRED WATER IN NOVEL WATER ELECTROLYZER SYSTEMS

The promise of widespread use of H_2 for heavy duty transport and many other applications will depend on developing both green (no net carbon dioxide emissions) and inexpensive methods to produce H_2. The US DOE has set a goal of 1:1:1 (1 kg for $1 USD, within 1 decade) for green H_2. In this talk I examine two of the main methods being examined by the DOE: microbial electrolysis cells (MECs), and novel water electrolyzer systems (WEs). My laboratory is developing next-generation MECs based on using zero-gap architectures incorporating an anion exchange membrane and a vapor gas phase cathode chamber for electrochemical H_2 evolution. We have recently achieved an order of magnitude increase in volumetric production rates. MECs have the advantage of using a favorable anode reaction (biomass utilization by exoelectrogenic bacteria) and therefore they have lower power requirements than WEs. WEs can achieve much higher current densities than MECs but they currently require ultra-pure water, and the cost, process intensification, and potential impacts of brine production for making this water could impact overall WE costs. Therefore, we are looking at novel architectures and materials that could enable the use of impaired (slightly salty) water in WEs. One approach is to use thin film membranes, such as those used for reverse osmosis (RO) desalination. RO membranes are $1/10^{th}$ the price of proton exchange membranes (PEMs), they can withstand high pressures, and unlike PEMs there is no use of PFAS chemicals to make RO membranes. Another WE approach is to use a vapor phase anolyte for water splitting to minimize salt crossover to the anode that can result in unwanted reactions such as chlorine gas production. Innovations in MECs and WEs such as those presented here have great promise to provide new and green methods of H_2 generation in many different locations around the world.



Peter Strasser

Technical University of Berlin, Germany

pstrasser@tu-berlin.de

ELECTROCATALYSIS OF HYDROGEN TECHNOLOGIES

Electrified solid-liquid interfaces of catalytic materials orchestrate the conversion of free electrons to molecular bonds and back. That is why they play such a key role for the performance of electrochemical energy conversion devices such as water electrolyzers and hydrogen fuel cells.

This talk will highlight advances, challenges and prospects in the quest and development of ever improved electrocatalysts and electrodes for hydrogen-based electrolysis and fuel cell technologies.

WHEC-2022

23rd World Hydrogen Energy Conference

KEYNOTE SPEAKERS



Shannon Bragg-Sitton

Idaho National Laboratory, USA

shannon.bragg-sitton@inl.gov

THE ESSENTIAL ROLE OF NUCLEAR-GENERATED CLEAN HYDROGEN IN ACHIEVING A NET-ZERO ECONOMY

We are faced with an unparalleled challenge as we plan our future energy systems. Various studies have painted a rather bleak future, calling on all of us to take action to change our habits to reduce temperature rise, or to face the dire consequences to our ecosystems and way of life. All of this comes as we are also working to provide many communities greater access to electricity, clean water, and other resources that many of us in developed nations take for granted every day. Those communities can't be denied the opportunity to improve their quality of life, which means that energy demands will continue to increase, even as developed nations flatten or reduce energy demands through energy efficiency measures.

In light of these challenges, numerous decarbonization commitments have been announced by nation states, municipalities, and private companies, with many seeking to decarbonize the electricity sector by 2035 and to achieve net-zero emissions economy-wide by 2050. Traditionally, electricity generation and management and meeting energy demands for industry and transportation are considered independently. As we seek to achieve net-zero, we need to reassess energy demands, and energy carriers. When we consider overall energy use, only one-third is in the form of electricity. Additional energy demands are in the form of heat or steam for industrial processes, as well as transportation. These sectors are much harder to abate, and electrification may not be the best option—hydrogen, when produced without concurrent emissions, is an enabler to many clean energy solutions. Reducing environmental emissions at an affordable cost, while maintaining grid reliability and resilience, will require all clean energy resources available. That means coordinating the use of nuclear, renewables, and fossil fuels with carbon capture to meet growing demands for electricity, industrial applications, and mobility.

The DOE Office of Nuclear Energy (DOE-NE) Program on Integrated Energy Systems (IES) is led by researchers at Idaho National Laboratory (INL) and work is conducted in partnership with an array of other DOE laboratories, industry, and academia. The primary focus of IES research is to assess the technical and economic potential of IES to enhance the flexibility and utilization of nuclear reactors working alongside renewable generators to meet an array of energy demands—thereby maximizing the utilization of clean energy resources across all energy sectors. Various energy applications and product streams beyond electricity are being evaluated, ranging from generation of potable water to production of hydrogen and hydrogen-based products such as fertilizers, synthetic fuels, steel, and various chemicals. This presentation will highlight the wide array of R&D being conducted across multiple DOE-funded programs to develop and deploy nuclear-based IES that will be key to achieving our net zero goals. By working with key collaborators in the nuclear industry, analytical studies are now becoming a reality in nuclear-generated hydrogen demonstration projects.



Xianguo Li

University of Waterloo, Canada

Xianguo.Li@uwaterloo.ca

THE DEGRADATION AND DURABILITY OF HYDROGEN PEM FUEL CELLS

Hydrogen PEM (proton exchange membrane) fuel cells have made significant technical progress and have reached early stage of commercial applications. However, cost reduction and durability improvement, the two interrelated technical challenges, are required for widespread commercial adoption. In this presentation, the degradation mechanism leading to the durability reduction is summarized, including thermal degradation, chemical degradation, and mechanical degradation; efforts for their analyses and simulations are described, interactions between the different degradation mechanisms are outlined for accelerated degradation. Various test protocols for the accelerated stress tests (ASTs) will be previewed, and methods to mitigate the various degradation mechanisms will be discussed. Finally, some of our own efforts in the field will be shared. The current effort will be presented with the objective of achieving low cost, highly performing and durable hydrogen fuel cells with high power density. To achieve this technical target, it is necessary to combine the efforts in the development of low cost, highly performing and durable fuel cell materials, fuel cell manufacturing/processing techniques and design optimization, with a good understanding of fundamentals and command of applied aspects for the technology development, involving phenomena at the nano-, micro-, and macro-scales.



Hirohisa Uchida

Tokai University / KSP Inc., Japan

uchida@se.kanazawa-u.ac.jp

HYDROGEN STORAGE BY HYDROGEN STORAGE ALLOYS – FUNDAMENTALS AND APPLICATION

With the development of FC technology, hydrogen technology is spreading rapidly. The development and establishment of large-scale hydrogen generation, transportation and storage technology are very important issues. In the growing awareness of the global environment, clean hydrogen from renewable energy is attracting high attention. However, on the other hand, hydrogen production from fossil fuels such as LNG and lignite is also practical at present. For example, Japan, which aims to realize a hydrogen society, plans to produce a large amount of hydrogen from Uruguay's LNG, and from Australian lignite and transport it to Japan using tankers. A large amount of hydrogen on land is mainly stored as liquid hydrogen or high-pressure hydrogen gas.

As a project of Japan's Ministry of the Environment, we have developed a mass production technology of nanostructured FeFi hydrogen storage alloy and succeeded in reducing the price to one-third compared with those of conventional alloys. As a result, renewable energy such as wind or solar energy can be stored easily with hydrogen, and output/input fluctuation can be controlled well using the developed alloy.

In this lecture, at first, the basic reaction mechanisms between hydrogen gas and metal, and then the surface or bulk process controlling the rate of hydrogen absorption/storage will be explained. In applications of hydrogen storage alloys, the reaction rate is determined by the surface process and heat transfer factors depending upon density of alloy in a tank and materials contacting alloy. Secondly, the application of hydrogen storage alloys will be mentioned; (1) the application of the exothermic / endothermic heat reaction that occurs during hydrogen absorption / desorption reactions to agriculture and fish breeding, and (2) the renewable energy storage and fluctuation control by the nanostructured FeTi alloy will be reported.

WHEC-2022

23rd World Hydrogen Energy Conference

INVITED SPEAKERS



Frano Barbir

Faculty of Electrical Engineering, Mechanical Engineering and Naval Architecture (FESB), Center of Excellence for Science and Technology – Integration of Mediterranean Region (STIM), University of Split

fbarbir@fesb.hr

COMMON MISCONCEPTIONS ABOUT HYDROGEN AND HOW TO DEBUNK THEM

Hydrogen is now in a focus of interest, not only in EU, and mass deployment of hydrogen from production to applications is being planned on the highest level. However, there are still skeptics that need to be convinced that hydrogen is not only a viable but the key technology for full or deep decarbonization of energy supply. Some people, even experts, usually focus just one aspect, such as efficiency or storage size or perceived danger, and jump to conclusions without considering a wider picture. Common misconceptions about hydrogen typically include:

- Hydrogen is not an energy source. Indeed, hydrogen is an energy carrier like electricity.
- Hydrogen is (mainly) produced from fossil fuels (natural gas). That is true today, however in a decarbonized energy system hydrogen will be produced exclusively from renewable energy sources
- There is no hydrogen infrastructure. That is true today, it needs to be built. There was no infrastructure when the first cars appeared or when the first power plants were built.
- There is no hope for hydrogen fuel cell electric vehicles – BEV are so much better. This is true for light vehicles and relatively short distances. Hydrogen storage onboard is at least two times lighter than the batteries and hydrogen refueling takes a fraction of time that batteries charging takes.
- It is inefficient to produce hydrogen and then to convert it back to electricity. Compared to batteries that is inefficient indeed. However, for storing large amount of energy for relatively long time (seasonally) we do not have a better option.
- Hydrogen is bulky. Compared to gasoline or diesel hydrogen is indeed bulky. However, car manufacturers managed to fit bulky hydrogen tanks in vehicles without sacrifices
- Hydrogen does not create pollution, but its use will produce huge amounts of water. Use of hydrogen, combustion or electrochemical conversion creates exactly the same amount of water as it was used for its generation.
- Hydrogen is extremely flammable and explosive, thus dangerous. Many safety studies and use records have shown that hydrogen is not more dangerous than other fuels.

Hydrogen should not be judged by these individual properties, but by its ability to decarbonize those energy sectors that would be hard to decarbonize otherwise.



Wei-Hsin Chen

National Cheng Kung University, Taiwan

chenwh@mail.ncku.edu.tw

OPERATION AND SYSTEM OPTIMIZATION FOR HYDROGEN PRODUCTION AND SEPARATION

Over the last several decades, hydrogen has been considered as a promising green fuel to substitute fossil fuels for heat and power generation. In recent years, the development of hydrogen technology and economy has attracted a great deal of attention because it is a promising route to achieve deep decarbonization of the global energy system. Hydrogen is a non-carbon fuel; therefore, no air pollutants are emitted when hydrogen is burned. Meanwhile, hydrogen is a potential energy carrier, so it can be delivered to the appropriate places for its usage. In recent years, significant progress in proton exchange membrane fuel cell (PEMFC) has been made. Accordingly, hydrogen can be applied in the transportation sector through the applications of PEMFC. On account of a foreseeable hydrogen-based society in the future, hydrogen production and separation with high-efficiency routes become a crucial task in the implementation of hydrogen technology. In this study, a number of operation and system optimization methods for hydrogen production from thermochemical methods (such as gasification, catalytic partial oxidation, and autothermal reforming) and for hydrogen separation using palladium membranes will be illustrated. The introduced optimization methods include the Taguchi method, response surface method (RSM), and Nelder-Mead method. From these methods, the influences of operating conditions (e.g., temperature, steam-to-carbon ratio, oxygen-to-carbon ratio, and GHSV) on hydrogen yield and recovery can be figured out. The performances of the optimization methods will also be addressed.



Francesco Ganda

International Atomic Energy Agency (IAEA)

Vienna International Centre, Austria

WORLDWIDE NUCLEAR HYDROGEN DEVELOPMENT PLANS AND HYDROGEN-RELATED SERVICES OFFERED BY THE IAEA

An overview will be provided of plans by several countries related to the development of nuclear hydrogen.

In addition, a high-level description will be provided of the tools and services offered by the IAEA to all Member States, including techno-economic assessment tools and models, recent nuclear hydrogen related publications, a new coordinated research project on “Role of Nuclear Cogeneration within the Context of Sustainable Development”, and technical and consultancy meetings related to the field of hydrogen.



Yun Hang Hu

Department of Materials Science and Engineering, Michigan Technological University, USA

yunhangh@mtu.edu

THERMO-PHOTO CATALYTICAL HYDROGEN PRODUCTION

The critical issues of fossil fuels are their limited natural sources and their contribution to the increase of atmospheric greenhouse gases. To solve those issues, hydrogen is being developed as a promising alternative fuel. Furthermore, solar energy is the largest energy source and technologies are being developed to exploit solar energy efficiently. Visible-light photocatalytic splitting of water to hydrogen is attractive, but its efficiency is poor due to insufficient driving force. In recent years, Prof. Hu's group demonstrated a new strategy by introducing thermal energy as kinetic energy to increase the driving force for the visible light photocatalytic process, leading to 100 times increase in efficiency. Actually, this created a new type of catalysis, "Thermo-Photo Catalysis". In this talk, he will discuss the thermo-photo catalytic hydrogen production from water with emphasis on the reaction mechanism and the synergetic effect of thermal/photo energies.



Nafiz Arica

Bahcesehir University, Turkey

nafiz.arica@eng.bau.edu.tr

ARTIFICIAL INTELLIGENCE IN SUSTAINABLE ENERGY

Artificial Intelligence (AI) has a significant impact on achieving sustainable development goals. Shaping many sectors, AI is one of the most important technologies in the transformation of the energy sector for sustainable development. Intelligent software is used in many areas from energy production to supply and demand management, from integration of renewable resources to price estimation. As sustainable energy is predicted to become the essential provider of global energy demand, the role of AI is paramount in accelerating, maintaining, and expanding this adoption on which civilization is run on clean and dependable energy with minimal impact on the environment. In this presentation, the applications of Artificial Intelligence, especially for sustainable energy purposes, how AI techniques outperform the classical models, and the future directions will be discussed.



Michaela Kendall

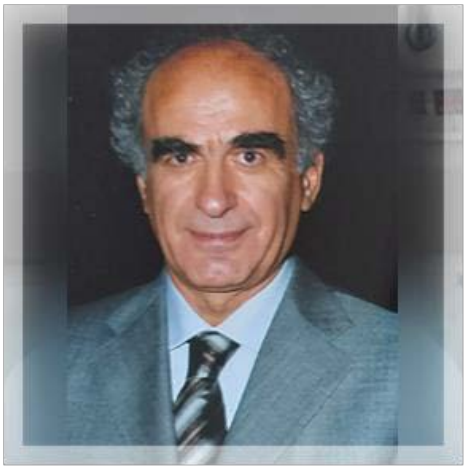
Adelan, UK

THE UK HYDROGEN STRATEGY AND TECHNOLOGY SUPPLY CHAINS

In 2017, Dr Kendall published the first UK Fuel Cell and Hydrogen Strategy devised by colleagues that created the Midlands Hydrogen and Fuel Cell Network, a regional trade association representing the pioneers of the early hydrogen economy. In August 2021, Minister Kwarteng published the second Hydrogen Strategy committing to a 5 GW hydrogen production target for the UK; only 8 months later, the target doubled to 10 GW.

The UK Hydrogen Strategy has been in the making for several decades, and the history of fuel cells and hydrogen globally is depicted in the Adelan book “Hystory”. The story is one of remarkable serendipity and chance for such an important topic as low carbon energy, driven by pioneering characters inspired by international events and coincidences. The UK is a key nation in the innovation narrative, but other countries namely the USA and China have been much more successful at clustering expertise, supporting infrastructure investments, commercializing technologies, and creating momentum in the growing global hydrogen economy. Turkey played an incredibly important role in the story of hydrogen by hosting the UN Hydrogen Centre in Istanbul, forming a global nucleus of scientists, engineers, businesses, and international agencies to build critical networks that remain today, especially in Europe.

This talk will examine the history of hydrogen to predict the net-zero technologies and fuels of the future. Important top-down lessons have been learned to date related to the role of hydrogen technology policy, early market clustering, market barriers, accelerating scale-up, and investment bottlenecks. Reflecting on past successes and failures will support the creation of a more resilient global hydrogen economy from the ground up.



Saim Özkar

Department of Chemistry

Middle East Technical University, Turkey

sozkar@metu.edu.tr

NOBLE METAL NANOCATALYSTS FOR HYDROGEN GENERATION FROM THE HYDROLYSIS OF AMMONIA BORANE

Ammonia borane (AB) is the most promising solid hydrogen storage materials, and its catalytic hydrolysis is the best way of releasing H_2 at ambient conditions. Noble metal nanoparticles (NPs) are the most active catalysts providing high TOF for hydrogen generation from the hydrolysis of AB. However, high price of the precious noble metals hampers their large-scale applications in catalysis. Achieving high catalytic performance with the smallest amount of metal is critical for any catalytic applications of noble metals. While continuous efforts have been devoted to improve the catalytic activity of non-noble metals in hydrolytic dehydrogenation of AB, an immense challenge is the enhancement of utilization efficiency and thus, ultimately lowering the cost of noble metal catalysts. The following approaches can be used for increasing the catalytic efficacy of noble metal nanocatalysts. (i) Reducing the particle size from macroregime to nanoregime increases the surface area and thus, the number of active sites. For example, using the colloidal NPs can increase the catalytic activity tremendously compared to the bulk metals. However, colloidal NPs are unstable and tend to aggregate to larger particles, which greatly hampers their recyclability/reusability and catalytic performance. (ii) Adding a suitable ligand into the suspension can stabilize the colloidal NPs though the activity may decrease as well. (iii) Another way of stabilizing noble metal NPs is to support them on the surface of solid materials such as metal oxide or carbonaceous materials whereby catalytic activity is expectedly enhanced by the large surface area. The catalytic activity and stability of supported noble metal NPs depend on the particle size distribution, surface area of support, and strength of metal-support interaction. Selecting suitable supports is of paramount importance in obtaining NPs which are stable and still catalytically active. (iv) Downsizing the NPs can also increase the catalytic activity of supported noble metal nanocatalysts. (v) Using reducible oxide as support is found to enhance the catalytic activity of noble metal NPs significantly. (vi) Increasing the lifetime and reusability of nanocatalysts can certainly help to improve the atom efficiency of noble metal nanocatalysts. (vii) Making the NPs magnetically separable significantly improves the reusability of noble metal nanocatalysts. The results on rhodium and platinum nanoparticles will be discussed for each approach to demonstrate that the catalytic efficiency of noble metal nanocatalysts in hydrolytic dehydrogenation of ammonia borane can be increased by a suitable combination of all the available methods.



Joris Proost

Division of Materials and Process Engineering, Université catholique de Louvain (UCLouvain), Belgium

joris.proost@uclouvain.be

CRITICAL ASSESSMENT OF THE PRODUCTION SCALE REQUIRED FOR FOSSIL PARITY OF GREEN ELECTROLYTIC HYDROGEN

Hydrogen produced from renewable electricity through Power-to-Hydrogen can facilitate the integration of high levels of variable renewable electricity into the energy system. An electrolyser is a device that splits water into hydrogen and oxygen using electricity. When electricity is produced from renewable energy sources, electrolytic hydrogen can be considered to be green. Key green hydrogen production technologies, mostly PEM and alkaline electrolysers, are still further maturing, both in technical (efficiency), economical (CAPEX), and durability (lifetime) performance. Nonetheless, we will show in this contribution how fossil parity for green hydrogen, i.e., a Total Cost of Ownership (TCO) similar to grey H_2 coming from CO_2 intensive SMR processes, can already be achieved today. Moreover, this can be realised at a scale which corresponds to the basic units of renewable electricity generation, i.e., a few MW.



Karen Quackenbush

Fuel Cell and Hydrogen Energy Association (FCHEA)

CODES AND STANDARDS FOR HYDROGEN ENERGY SYSTEMS

Codes and standards enable widescale commercialization of hydrogen energy systems. FCHEA facilitates industry participation to ensure that developing requirements reflect industry best practices and facilitates harmonization of technical requirements throughout national and international codes and standards. This presentation will describe current efforts and explore the importance of interdisciplinary collaboration on technical requirements for hydrogen energy systems in emerging markets.



S.A. Sherif

Department of Mechanical and Aerospace Engineering, University of Florida, USA

LIQUID HYDROGEN STORAGE IN MICROGRAVITY

Cryogens such as liquid hydrogen are frequently stored over long periods of time particularly in space applications. The operating conditions of cryogenic storage systems are strongly influenced by several factors including heat leak. Cryogens are stored at temperatures close to their respective boiling points. As a result, any addition of energy could lead to the vaporization of a portion of the liquid cryogen. In the absence of gravity, gaseous cryogens could form a vapor bubble, the shape and location of which are not known a priori. The boil-off losses associated with the storage, handling, and transportation of cryogens can result in severe losses. Heat leak causes an increase in the internal pressure of the dewar. Several mechanisms influence the size and position of the vapor bubble in the dewar. Understanding these mechanisms is important to designing storage vessels under optimum conditions and also to the development of cryogenic transfer systems. The work upon which this presentation partially reports aimed at investigating some of the fluid physics observed in a cryogenic dewar under microgravity. The objective is to quantify changes in the storage pressure and temperature and the amount of boil-off observed in a typical dewar under microgravity conditions.



S. Vasudevan

CSIR-Central Electrochemical Research Institute

Karaikudi, India

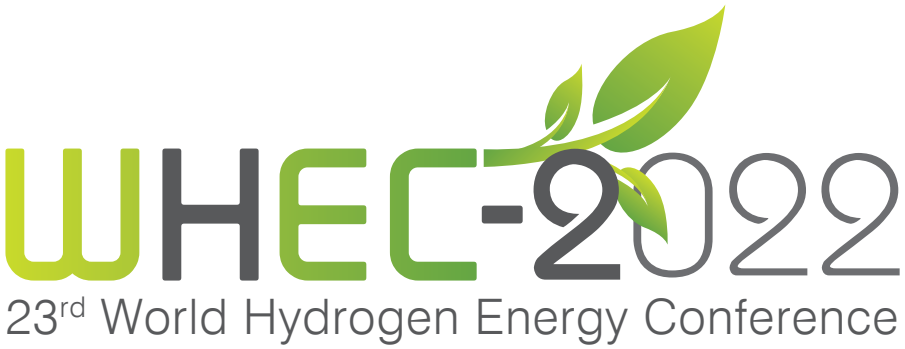
HYDROGEN PRODUCTION BY ELECTROLYSIS TO CLEAN REALITY

Alternative energy sources like solar, wind, thermal, ocean, geothermal, thermonuclear, hydrogen etc., are being considered as possible sources of energy to meet the growing demand. However, none of these energy sources except hydrogen has all the desirable qualities to replace petroleum and natural gas. For example, some are only intermittently available; others are available away from the consumption centers and cannot be used as fuel for transportation. Therefore, out of the above alternative energy sources, hydrogen is considered the best option, which could form the link between the new energy sources and the user. Hydrogen is the clean fuel and when used as a fuel, produces only water. In the hydrogen energy system, it is envisaged that hydrogen will be produced from non-fossil energy sources and will be used in every application where fossil fuels are used today. Over the last decade there have been increasing research efforts to investigate the various aspects of the hydrogen energy systems like production, storage and transport and its applications.

Generation of hydrogen via electrolysis is a well-known and established technology. There are two main types of electrolyser [Alkaline and Proton Exchange Membrane (PEM)] and both are well proven and long-lived. Electrolysis has been traditionally based on an alkaline technology, but Proton Exchange Membrane (PEM) electrolysers are now coming to the forefront. However, due to the high cost of both electricity and material, only a small proportion (4 -5%) of the worldwide hydrogen production comes from electrolysis. Yet electrolyser costs are expected to drop within the few years as a consequence of standardization, mass-production, and a greater competitiveness. The demand for clean-produced hydrogen and its storage potential spell enormous possibilities for renewable electrolysis in the future. Even non-renewable electrolysis is bound to play an important role in the short-term as a source of moderate amounts of hydrogen for small fuelling stations and domestic applications.

In future low-carbon economics, electrolyser technology could provide a central solution to meeting both the power management needs of the electricity sector and the needs of the transport and industrial sectors for low/zero carbon fuels. Electrolytic hydrogen could thereby displace large proportions of non-electricity fuel consumption. Hence, the new market potential for electrolyser dwarfs the existing market potential and on a global scale it is truly vast.

In this talk some of the important and recent developments in the electrochemical alternatives with newer materials for hydrogen generation are discussed. The talk also covers hydrogen-based technologies developed at CSIR-CECRI.



PROCEEDINGS

Track 1. Hydrogen Production: Thermochemical and Photonic Methods
Track 2. Hydrogen Production: Electrolysis
Track 3. Hydrogen Production: Biological Methods and Biohydrogen
Track 4. Hydrogen Production: Nuclear
Track 5. Hydrogen Separation and Purification
Track 6. Hydrogen Storage
Track 7. Fuel Cells: PEMFC
Track 8. Fuel Cells: SOFC and other types
Track 9. Integrated Hydrogen Energy Systems
Track 10. Power to Gas
Track 11. Hydrogen Safety
Track 12. Codes, Standards and Regulations
Track 13. Hydrogen Strategies and Policies
Track 14. Hydrogen Industry, Commercialization and Marketing, Applications
Track 15. Hydrogen Economy, Logistics, Infrastructure
Track 16. Environmental Impact and Sustainable Development
Track 17. Social Dimensions

WHEC-2022

23rd World Hydrogen Energy Conference

TRACK 1. HYDROGEN PRODUCTION: THERMOCHEMICAL AND PHOTONIC METHODS

TRACK 1. HYDROGEN PRODUCTION: THERMOCHEMICAL AND PHOTONIC METHODS

#11 ASSESSMENT OF HYDROGEN PRODUCTION SYSTEMS BASED ON BIOGAS CATALYTIC REFORMING WITH CARBON CAPTURE	4
#29 AMMONIA DECOMPOSITION OVER Ru-COATED METAL STRUCTURED CATALYSTS FOR CO_x-FREE HYDROGEN PRODUCTION	7
#42 EXPERIMENTAL INVESTIGATION OF A PHOTOELECTROCHEMICAL REACTOR FOR HYDROGEN PRODUCTION AND WASTEWATER TREATMENT	10
#58 IMPROVING CATALYTIC ACTIVITY OF SUPPORTED PRECIOUS METAL CATALYSTS FOR HYDROGEN PRODUCTION BY HYDROTHERMAL CONVERSION PROCESSES	13
#81 THERMODYNAMIC ANALYSIS OF BIOGAS-TO-SYNGAS CONVERSION WITH DRY OXIDATIVE REFORMING AND CH_4 RECYCLING USING ASPEN HYSYS	17
#82 H_2-ENRICHED SYNGAS PRODUCTION BY ALGAE-PLASTIC WASTE CO-GASIFICATION USING ASPEN PLUS	20
#83 MODELING CATALYST POISONING DURING METHANE REFORMING FOR THE PRODUCTION OF HYDROGEN	23
#84 MECHANISTIC KINETIC MODELING FRAMEWORK FOR THE CONVERSION OF WASTE CRUDE GLYCEROL TO VALUE-ADDED HYDROGEN-RICH GAS	26
#85 APPLICATION OF DFT AND MACHINE LEARNING TO PREDICT OPTIMUM OPERATING CONDITIONS FOR METHANE PYROLYSIS USING MOLTEN METALS FOR CARBON-FREE HYDROGEN PRODUCTION	29
#130 PHOTOCATALYTIC GLYCEROL REFORMING ON GOLD - COPPER NANO METALLIC TiO_2	31
#138 NOVEL DESIGN CONCEPT FOR THERMOLYSIS REACTOR IN THE THERMOCHEMICAL COPPER-CHLORINE CYCLE OF HYDROGEN PRODUCTION	34
#158 CHEMICAL KINETICS OF TWO-STEP THERMOCHEMICAL DECOMPOSITION OF H_2S OVER NICKEL SULFIDE	38
#162 APPLYING ARTIFICIAL INTELLIGENCE ON STEAM GASIFICATION OF WASTE PLASTIC TO GENERATE HYDROGEN	41
#174 DESIGN OF GREEN HYDROGEN PRODUCTION SYSTEM IN CONTEXT OF COLLABORATIVE INTERNATIONAL ONLINE LEARNING (COIL)	44
#177 TECHNICAL AND ECONOMIC ASSESSMENT OF A SOLAR HYDROGEN PRODUCTION PLANT IN A PERUVIAN MINING COMPANY	46
#199 PHOTOELECTROCHEMICAL WATER SPLITTING: SHORT REVIEW ON CURRENT DENSITY AND STABILITY OF PHOTOELECTRODES	48
#202 THERMODYNAMIC ANALYSIS OF BIOGAS-TO-METHANOL CONVERSION WITH CH_4 RECYCLING USING ASPEN HYSYS	51
#208 ENHANCED HYDROGEN-RICH SYNGAS PRODUCED BY DEVELOPED PLASMA REFORMER SYSTEM	54
#219 PERFORMANCE OF MICROWAVE AND CONVENTIONALLY HEATED REACTOR SYSTEMS IN STEAM REFORMING OF ETHANOL OVER NICKEL IMPREGNATED MESOPOROUS CARBON	57
#244 PSEUDO-DYNAMIC MODELING AND OPTIMIZATION OF HEAVY PARAFFIN DEHYDROGENATION PROCESS FOR SELECTIVE OLEFIN AND HYDROGEN PRODUCTION IN CONVENTIONAL REACTORS	59
#272 STATIONARY METHANOL STEAM REFORMING TO HYDROGEN FUEL FOR FUEL-CELL FILLING STATIONS	62
#284 EXPERIMENTAL INVESTIGATION OF A Fe_2O_3 CARBOTHERMIC REDUCTION CYCLE FOR HYDROGEN PRODUCTION	65
#287 ON-SOLAR SIMULATOR DATA FOR KINETIC STUDIES OF CdSZnS-Pt WATERS SPLITTING	68
#291 ECONOMICALLY VIABLE LOW TEMPERATURE HYDROGEN PRODUCTION USING ALUMINUM-WATER SPLITTING METHODS	71
#311 UTILIZATION OF Al_2O_3 AND MgO AS STRUCTURAL PROMOTERS OF Fe INTO 2 AND 3 STEPS CHEMICAL LOOPING HYDROGEN PROCESS: PURE AND GREEN H_2 PRODUCTION	74
#319 GLYCEROL STEAM REFORMING FOR THE PRODUCTION OF HYDROGEN OVER REMARKABLY ACTIVE AND STABLE PEROVSKITE SUPPORTED Ni CATALYSTS	77

#381 COMBINED AUTOTHERMAL AND SORPTION-ENHANCED REFORMING OF OLIVE MILL WASTEWATER FOR THE PRODUCTION OF HYDROGEN: THERMALLY NEUTRAL CONDITIONS ANALYSIS	80
#383 HYDROGEN PRODUCTION VIA STEAM REFORMING OF GLYCEROL OVER Ce-La-Cu-O TERNARY OXIDE CATALYSTS	83
#396 SODIUM FORMATE FORMATION VIA IN-SITU CATALYTIC HYDROGEN PRODUCTION FOR DECARBONIZATION	86
#400 HYDROGEN AND METHANE PRODUCTION FROM ANAEROBICALLY DIGESTED WATER PLANT BY HYDROTHERMAL GASIFICATION	89
#415 A THERMODYNAMIC EVALUATION OF BORON BASED THERMOCHEMICAL HYDROGEN PRODUCTION CYCLE	92
#420 A NOVEL SOLAR ENERGY DRIVEN THERMOCHEMICAL HYDROGEN PRODUCTION SYSTEM INTEGRATED WITH ELECTRIC VEHICLE CHARGING STATION	96
#421 CFD SIMULATION AND ANALYSIS OF A NOVEL PHOTOELECTROCHEMICAL HYDROGEN GENERATING REACTOR DESIGN	99
#424 PHOTONIC REACTORS FOR HYDROGEN PRODUCTION AND WASTEWATER TREATMENT IN UNDERGROUND AND UNDERWATER APPLICATIONS	102
#430 SYNTHESIS OF SnS_2 PHOTOCATALYST FOR PHOTOCATALYTIC HYDROGEN PRODUCTION	104
#433 PROGRESS OF 5 m^3/h H_2 PRODUCTION TESTING FACILITY THROUGH IODINE-SULFUR THERMOCHEMICAL WATER-SPLITTING METHOD	107
#1512 PHOTOCATALYSIS vs PHOTOVOLTAICS: WHY NOT MAKE IT A SYMBIOSIS?	110
#1515 PROMOTION OF COPPER-ZINC CATALYST WITH Sm AND Gd FOR STEAM REFORMING OF METHANOL	113
#1527 KINETIC CHARACTERIZATION OF Pt/Al_2O_3 CATALYST FOR HYDROGEN PRODUCTION VIA METHANOL AQUEOUS-PHASE REFORMING	116
#1537 Ni-BASED CATALYSTS FOR CO_2 REFORMING OF GLYCEROL TO H_2	119
#1545 SHAPE DEPENDENT ELECTROCATALYTIC HYDROGEN EVOLUTION BY COPPER-ANTIMONY SULFIDE	122
#1546 CATALYTIC HYDROGEN EVOLUTION BY USING DIFFERENT CARBON-BASED NANOCOMPOSITE AT SOFT INTERFACES	125
#1548 APPLICATION OF DIFFERENT CATALYSTS IN BIOMASS GASIFICATION IN UPDRAFT/DOWNDRAFT FIXED BED REACTORS	128
#1561 THE EFFECT OF THERMAL OXIDATION TIME IN AIR AND ARGON ATMOSPHERE ON PEC EFFICIENCY OF HEMATITE (Fe_2O_3) PHOTOANODE	131
#1584 PRODUCTION OF HYDROGEN-RICH SYNTHESIS GAS BY GASIFICATION OF WASTE MATERIALS IN A ROTARY KILN REACTOR	134
#1586 $Cd_xZn_{1-x}S$ WITH BULK-TWINNED HOMOJUNCTIONS AND RICH SULFUR VACANCIES FOR EFFICIENT PHOTOCATALYTIC HYDROGEN PRODUCTION	137
#1601 SOLAR-LIGHT-DRIVEN PHOTOCATALYTIC HYDROGEN EVOLUTION *IN SITU* DEPOSITED Pt ON PEROVSKITE TYPE OXIDES	141
#1605 NICKEL-BASED GRAFTED CATALYSTS FOR DRY REFORMING OF METHANE THROUGH HIGH-THROUGHPUT EXPERIMENTATION	144
#1633 GREEN HYDROGEN PRODUCTION FOR ESKIL OIZ HEATING	147

WHEC-2022
23rd World Hydrogen Energy Conference
June 26-30, 2022 - Istanbul

#11

ASSESSMENT OF HYDROGEN PRODUCTION SYSTEMS BASED ON BIOGAS CATALYTIC REFORMING WITH CARBON CAPTURE

* *Calin-Cristian Cormos, Ana-Maria Cormos, Letitia Petrescu, Simion Dragan*
Babes-Bolyai University, Faculty of Chemistry and Chemical Engineering, Arany Janos 11, Cluj-Napoca, Romania

*Corresponding author e-mail: calin.cormos@ubbcluj.ro

ABSTRACT

Hydrogen is considered one of the most promising energy carriers for the future. Increasing the share of renewable energy and large-scale deployment of carbon capture, utilization, and storage (CCUS) technologies are also important for reducing the greenhouse gas emissions to combat climate change actively. This work is aimed to evaluate the hydrogen production by biogas catalytic reforming processes equipped with CO_2 capture feature. The size of evaluated designs is 100,000 Nm^3/h hydrogen with purity higher than 99.95% (vol.). The assessed carbon capture options involved conventional gas-liquid absorption and innovative chemical looping cycle using iron oxide as an oxygen carrier. The evaluated schemes were modeled and simulated using the process flow modeling software ChemCAD. The mass & energy balances were used to quantify the key plant performance indicators. As the results show, the chemical lo”oping option is very promising in term of increasing the overall energy efficiency (61.02% vs. 54.53%) and the carbon capture rate (95 vs. 70%) as well as reducing specific CO_2 emissions (29.42 kg/MWh vs. 206.89 kg/MWh) than the reactive gas-liquid absorption.

Keywords: Hydrogen production, Biogas catalytic reforming, Carbon capture, Utilization and storage (CCUS).

INTRODUCTION

The need to develop low carbon energy systems is of paramount importance to actively combat global warming by reducing greenhouse gas emissions (mainly CO_2). Along this line, hydrogen-based energy conversion systems attract much interest in last years as they involve no CO_2 emission at the point of use. The reduction of fossil CO_2 emissions can also be achieved by Carbon Capture, Utilization and Storage (CCUS) technologies. Renewable energy sources are also important for the future low carbon economy. To promote the transition for low carbon economy, the European Union enforced the energy and climate package which set quantifiable targets for the member countries [1].

Biogas production and utilisation got significant attention as a renewable energy source and an energy-efficient way of converting various wastes into energy. This article is evaluating the biogas conversion via catalytic reforming into hydrogen coupled with two carbon capture technologies. Since the biogas has a substantial content of CO_2, the catalytic reforming was done in dry (see Eq. (1)) or semi-wet (see Eq. (2)) conditions according to the chemical reactions:

$$CH_4 + CO_2 \Leftrightarrow 2CO + 2H_2 \quad (1)$$

$$CH_4 + H_2O \Leftrightarrow CO + 3H_2 \quad (2)$$

Semi-dry reforming conditions are better in order to avoid side reactions (e.g., carbon deposition on the catalyst). Dry reforming can also be seen as a CO_2 utilisation method in which CO_2 captured from different energy-intensive applications (e.g., heat and power production) can be used to react with natural gas [2]. The syngas produced by biogas reforming is then subject of pre-combustion CO_2 capture by two reactive gas-liquid and gas-solid methods:

1. Reactive gas-liquid absorption using alkanolamines; Methyl-DiEthanol-Amine (MDEA) was considered as an illustrative example in this analysis. The main reaction involved in syngas decarbonisation is the following [3]:

$$CO_2 + MDEA + H_2O \Leftrightarrow MDEA^+ + HCO_3^- \quad (3)$$

2. Iron-based chemical looping cycle involves utilisation of three looping Circulating Fluidized Bed (CFB) reactors which convert the syngas into hydrogen simultaneously with CO_2 capture. The following chemical reactions take place [4]:

- Fuel reactor:

$$CO + H_2 + Fe_2O_3 \Leftrightarrow CO_2 + H_2O + 2Fe \quad (4)$$

- Steam reactor:

$$3Fe + 4H_2O \Leftrightarrow Fe_3O_4 + 4H_2 \quad (5)$$

- Air reactor:

$$2Fe_3O_4 + 1/2O_2 \Leftrightarrow 3Fe_2O_3 \quad (6)$$

CONCEPTUAL DESIGNS, MAIN DESIGN ASSUMPTIONS, SIMULATION AND THERMAL INTEGRATION ASPECTS

The following hydrogen production concepts were investigated: Case 1: Biogas catalytic reforming without carbon capture; Case 2: Biogas catalytic reforming with pre-combustion carbon capture by gas-liquid absorption (MDEA); Case 3: Biogas catalytic reforming with pre-combustion carbon capture by iron-based chemical looping cycle. Fig. 1 presents the conceptual layout of biogas catalytic reforming with pre-combustion carbon capture used for hydrogen production.

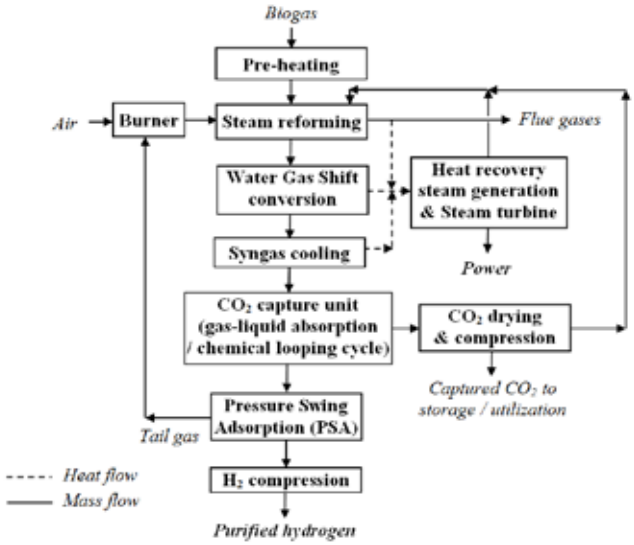


Fig. 1. Conceptual layout of hydrogen production via biogas reforming with carbon capture

The evaluated concepts were modeled and simulated using ChemCAD software. The main design assumptions are presented in Table 1 [3]. All evaluated concepts were subject of detailed thermal integration analysis (using pinch methodology) for optimization overall plant energy efficiency. As an illustrative example, Fig. 2 presents hot and cold composite curves for Case 3: Hydrogen production by biogas reforming with iron-based chemical looping cycle.

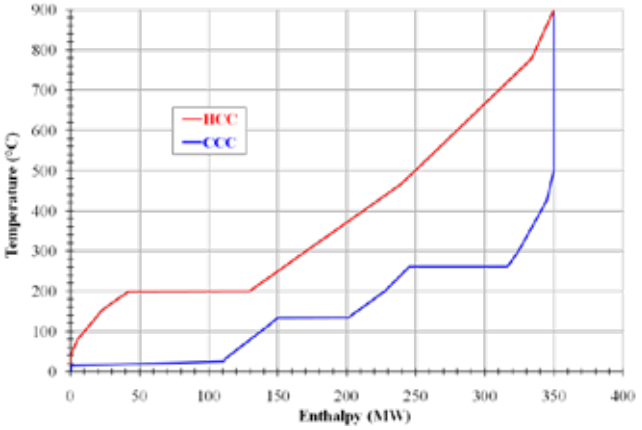


Fig. 2. Hot and cold composite curves for iron-based chemical looping design (Case 3)

Table 1. Main design assumptions of evaluated biogas catalytic reforming concepts

Plant sub-system	Design parameters
Biogas composition (% vol.)	67% CH_4, 30% CO_2, 2% N_2, 0.1% O_2, 0.9% H_2O; Prior desulfurized by ZnO guard bed
Reforming island	Ni-based catalytic reforming reactor; Operating pressure: 30 bar; Pressure drop: 1 bar Reformer outlet temperature: 900°C; Thermal operational mode: heat exchanger
Water gas shift conversion	Two catalytic reactors; Pressure drop: 1 bar / reactor; Thermal operational mode: adiabatic
CO_2 capture by reactive gas-liquid absorption	MDEA aqueous solution 50% wt.; Absorber / desorber columns: 30 / 20 stages Solvent regeneration: thermal; CO_2 removal efficiency: 90%
CO_2 capture by iron-based chemical looping	Oxygen carrier: Fe_2O_3; Fuel reactor: 700 - 750°C; Steam reactor: 725 - 800°C Air reactor: 900 - 1,000°C; Pressure drop: 1.5 bar / reactor; Reactor type: Gibbs free energy
Hydrogen purification unit	Capacity: 100,000 Nm^3/h; Purity: > 99.95% (vol.); Plant delivery pressure: 60 bar
CO_2 conditioning unit	Delivery pressure: 120 bar; Drying solvent: TEG; Quality specification (% vol.): CO_2 > 95%; CO < 2,000 ppm; O_2 < 10 ppm; H_2O < 250 ppm; H_2S < 100 ppm; other gases < 4%

RESULTS AND DISCUSSION

The mass and energy balances were used to quantify the main performance indicators (see Table 2). The introduction of carbon capture step involves an increase of ancillary energy consumption due to CO_2 capture and conditioning units. For gas-liquid absorption, the CO_2 capture energy penalty is about 3.2 net energy percentage points. For chemical looping case, the overall energy efficiency is higher even compared to non-capture design (Case 1) due to higher energy conversion efficiency of the looping cycle. In terms of capture rate and specific CO_2 emissions, the chemical looping is also more promising than gas-liquid absorption (95% vs. 70% and 29.42 kg/MWh vs. 206.89 kg/MWh respectively).

Table 2. Overall key performance indicators of evaluated hydrogen production systems via biogas catalytic reforming

Main plant data	Units	Case 1	Case 2	Case 3
Biogas thermal energy (A)	MW_{th}	552.85	552.85	516.50
Gross power output (B)	MW_e	24.12	12.55	23.52
Ancillary power consumption (C)	MW_e	5.25	11.01	8.33
Net power output (D=B - C)	MW_e	18.87	1.54	15.19
Hydrogen thermal output (E)	MW_{th}	300.00	300.00	300.00
Net power efficiency (D/A * 100)	%	3.41	0.27	2.94
Hydrogen thermal efficiency (E/A * 100)	%	54.26	54.26	58.08
Cumulative plant energy efficiency ((D+E)/A * 100)	%	57.67	54.53	61.02
Carbon capture rate	%	0.00	70.00	95.00
Specific CO_2 emissions	kg CO_2/MWh	652.17	206.89	29.42

CONCLUSIONS

The presented work evaluates via computational tools various hydrogen production concepts based on biogas catalytic reforming with and without carbon capture. Two carbon capture technologies were assessed: reactive gas-liquid absorption using alkanolamines (MDEA) and iron-based chemical looping cycle. The quantifiable results show that the innovative chemical looping concept is very promising in delivering higher cumulative plant energy efficiency (about 61%) and carbon capture rate (95%) and reduced specific CO_2 emissions than the reactive gas-liquid absorption.

REFERENCES

1. European Commission. 2014. A policy framework for climate and energy in the period from 2020 to 2030. Brussels, Belgium.
2. Zhang G, Liu J, Xu Y, Sun Y. 2018. A review of CH_4 CO_2 reforming to synthesis gas over Ni-based catalysts in recent years (2010-2017). International Journal of Hydrogen Energy 43:15030-15054.
3. Szima S, Cormos CC. 2019. Techno - economic assessment of flexible decarbonized hydrogen and power co-production based on natural gas dry reforming. International Journal of Hydrogen Energy 44:31712-31723.
4. Fan LS. 2010. Chemical looping systems for fossil energy conversions. Wiley-AIChE, Hoboken, New Jersey, USA.

WHEC-2022
23rd World Hydrogen Energy Conference
June 26-30, 2022 - Istanbul

#29

AMMONIA DECOMPOSITION OVER Ru-COATED METAL STRUCTURED CATALYSTS FOR CO_x-FREE HYDROGEN PRODUCTION

[1,2] *Kee Young Koo,* [1] *Hyo Been Im,* [1] *Dahye Song,* [1*] *Unho Jung*
[1] Hydrogen Research Department, Korea Institute of Energy Research (KIER), 152 Gajeong-ro, Yuseong-gu, Daejeon 34129, Republic of Korea
[2] Advanced Energy and System Engineering, University of Science and Technology (UST), 217 Gajeong-ro, Yuseong-gu, Daejeon, 34113, Republic of Korea

*Corresponding author e-mail: uhjung@kier.re.kr

ABSTRACT

Ammonia decomposition reaction produces green hydrogen without CO_x emission and has a simple process without post treatment like water-gas shift reaction unlike the conventional natural gas reforming reaction. At the point of end use, ammonia has been considered as a promising hydrogen carrier due to a high volumetric energy density and gravimetric energy density. Liquid hydrogen makes it difficult to handle and store due to cryogenic temperature (-253°C) and boil-off loss (2-3% per day), while ammonia is feasible to liquefy at room temperature (8-10 bar) and utilize established infrastructures for storage and transport. Herein, we present the results about the catalytic performance of Ru-coated metal structured catalysts (monolith, foam) in ammonia decomposition. Metal structured catalyst has been highlighted as an alternative to ceramic pellet catalyst which causes some problems such as pressure drop, low thermal conductivity, and slow response in fixed bed reactor. We tested the metal structured catalysts at various temperatures (550-700°C) and gas hourly space velocities (GHSV = 3,000-10,000 h^{-1}) in ammonia decomposition reaction. It was confirmed that the monolith catalysts with large geometric surface area showed a high NH_3 conversion at low temperature below 650°C, while the foam catalysts showed good catalytic performance at high GHSV.

Keywords: Ammonia decomposition, Hydrogen, Ru catalyst, Metal structured catalyst

INTRODUCTION

There is currently a growing need to move away from a carbon-based economy dominated by fossil fuels to a sustainable hydrogen-based economy due to acute environmental problems such as air pollution, global warming, and fine dust. Interest about not only hydrogen fuel cell electric vehicles (FCEV) but also CO_x-free hydrogen production picks up. Hydrogen is an eco-friendly fuel that emits only water when burned but handling safety and solving storage and transportation problems are crucial. In particular, hydrogen requires expensive storage tanks at very low cryogenic temperatures (-253°C) for liquefaction and there is no qualified hydrogen supply infrastructure. As an alternative, ammonia with a higher hydrogen storage density per unit volume than liquefied hydrogen is drawing attention as a hydrogen carrier. It can be easily liquefied under the conditions of room temperature and an operating pressure of 8-10 atm. In addition, ammonia is currently imported/exported or locally distributed via well-established infrastructures around the world, and can be stored in large amounts [1,2]. Furthermore, when ammonia is decomposed, it only produces nitrogen and hydrogen, which are not harmful to the environment; this means that its products are eco-friendly. Ammonia decomposition reaction has a simple process without post treatment like water-gas shift reaction unlike the conventional natural gas reforming reaction. However, ammonia is a toxic substance, and safety issues must be resolved [3]. In this study, CO_x-free hydrogen was produced over metal structured catalysts via ammonia decomposition reaction. Owing to an excellent heat and mass transfer properties, the metal structured catalyst such as monolith and foam can be replacing the ceramic pellet catalysts in typical chemical processes. Since a metal structured catalysts provide a large geometric reaction surface area to reaction volume (S/V) and increase the heat transfer rate per unit volume of process flow (US/V), it enables a compact reactor design [4]. Moreover, the radial concentration and temperature gradient as well as pressure drop can be minimized by the well-behaved uniform flow of the metal structures through the regular channel [5]. However, there is a key challenge to address the detachment of catalyst coating layer on the metal substrate due to the difference in the thermal expansion coefficient between the ceramic catalyst layer and metal substrate. Herein, we coated the Ru/Mg-Al oxide catalyst uniformly on the surface of FeCralloy monolith and foam using a proprietary KIER coating technique based on precipitation method and evaluated the catalytic performance in the ammonia decomposition for CO_x-free hydrogen.

MATERIALS AND METHODS

FeCralloy (Fe:72.8, Cr:22, Al:5, Y:0.1, Zr:0.1wt%) monolith and foam were used as metal structured carriers. The diameter of monolith was 22 mm, the height was 20 mm, and the cell density was 600-1000 cpi (cells/in^2). The foam

with 6.35 mm thickness and porosity of 20 and 40 ppi was used by cutting round in diameter of 22 mm. Metal structured carriers were rinsed with acetone and then pre-calcined at 900°C to form Al_2O_3 layer on the metal substrate. The Ru/Mg-Al oxide-coated metal structured catalysts were prepared by the proprietary KIER coating technique based on precipitation method [6]. Magnesium nitrate ($Mg(NO_3)_2 \cdot 6H_2O$, Aldrich), aluminum nitrate ($Al(NO_3)_3 \cdot 9H_2O$, Aldrich), and Ruthenium(III) nitrosyl nitrate solution ($Ru(NO)(NO_3)_x(OH)_y$, Aldrich) were used as metal precursors. For comparison, commercial Ru/Al_2O_3 pellet catalyst (3mm x 3mm, AlfaAesar) was used as a reference. The Ru content, surface area, metal dispersion and surface morphology of prepared metal structured catalysts were analyzed by ICP-MS, BET, CO-chemisorption, and SEM. The NH_3 decomposition test was carried out in a 1-inch Inconel tubular reactor under reaction conditions of T = 550-700°C and GHSV = 3,000-10,000 h^{-1}. The catalysts were reduced at 600°C for 3 h under 10%H_2/N_2 before the reaction. The effluent consisted of H_2, N_2, and NH_3 and the residual NH_3 concentration was analyzed using a gas analyzer by tunable diode laser absorption spectroscopy (TDLAS).

RESULTS AND DISCUSSION

Table 1 summarizes the Ru content, Ru dispersion, and Ru metal particle size of metal structured catalysts and pellet catalyst. The geometric surface area of monolith and foam affected the characteristics and Ru loading amount. In particular, compared to the pellet catalyst, the amount of Ru metal used in the metal structured catalyst was about 1/10 or less based on the same reaction volume, and a very small amount of Ru was uniformly coated on the metal substrate. The surface morphology and shape of Mg-Al oxide support layer and Ru metal particles were observed by SEM analysis. Thin plate-like shaped Mg-Al oxide support layer was formed evenly on the metal substrate while nano-sized Ru metal particle was highly dispersed on the surface of Mg-Al oxide layer (Not shown here). It was noted that the proprietary KIER coating method allows the uniform coating of catalysts on the various metal substrates regardless of the geometric shape.

Table 1. Characteristics of Ru-coated metal structured catalysts and pellet catalyst

Catalyst		Ru content (wt%)[a]	Ru content (g)	Ru dispersion (%)[b]	Ru particle size (nm)[b]
Monolith	**600 cpi**	0.036	0.0024	19.3	6.92
	800 cpi	0.020	0.0015	12.5	10.7
	1000 cpi	0.025	0.0023	15.7	8.53
Foam	**20ppi**	0.021	0.0012	16.0	8.37
	40ppi	0.030	0.0014	13.2	10.1
Pellet catalyst		0.40	0.016	34.6	3.9

(a) Determined by ICP-MS. (b) Estimated from CO-chemisorption at 50°C.

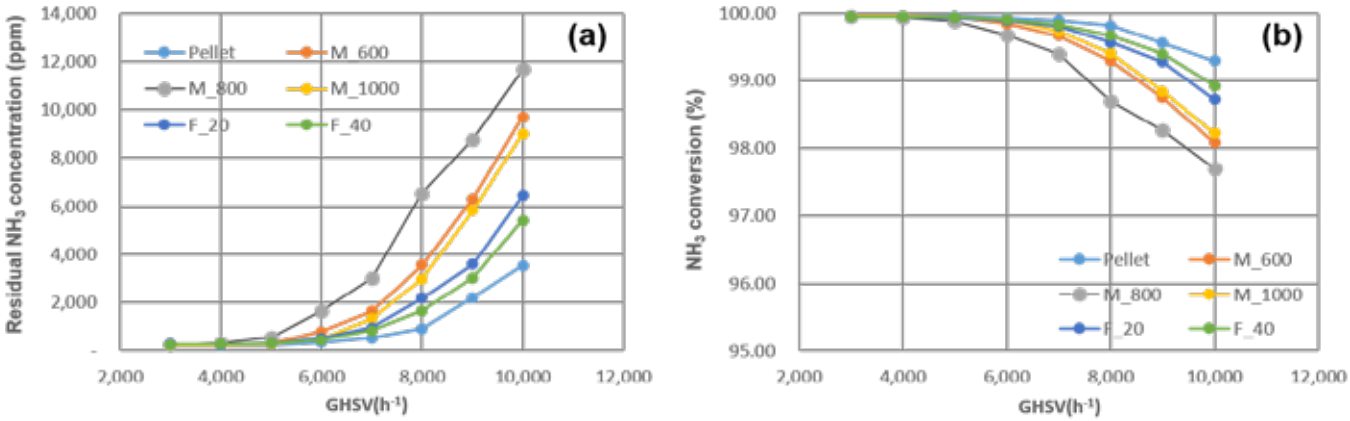


Fig. 1. (a) Residual NH_3 concentration and (b) NH_3 conversion of metal structured catalysts and pellet catalyst in NH_3 decomposition reaction (reaction condition: T_{cat} = 700°C, GHSV = 3,000-10,000 h^{-1})

The Ru/Mg-Al oxide coated metal structured catalysts were tested in the ammonia decomposition at 550 - 700°C. As increasing the reaction temperature, the unreacted residual NH_3 concentration decreased while the metal structured catalysts had the same NH_3 conversion as the pellet catalyst at over 650°C. It was confirmed that the monolith catalysts with large geometric surface area showed a high NH_3 conversion at low temperature below 650°C (Not shown here). Fig. 1 shows the unreacted residual NH_3 concentration and NH_3 conversion of metal structured catalysts and pellet catalyst corresponding to a change in the reaction gas flow rate at 700°C. Since the increase of GHSV causes a mass transfer limitation owing to an increased diffusion resistance, the unreacted residual NH_3

concentration increases [7]. Moreover, the heat transfer is important from heat source to catalyst bed due to the fact that the required reaction heat increases greatly with increasing GHSV in endothermic reactions like ammonia decomposition. It was confirmed that the foam catalyst exhibits better catalytic activity than the monolith catalyst at high GHSV owing to good heat transfer.

CONCLUSIONS

CO_x-free hydrogen was produced via ammonia decomposition over Ru/Mg-Al oxide-coated metal structured catalysts. Ru/Mg-Al oxide catalyst could be coated uniformly on the metal substrate by KIER coating method regardless of the geometric shape of metal structured catalysts. Nano-sized Ru metal particles were highly dispersed on the surface of thin plate-like shaped Mg-Al oxide support layer. The geometric surface area of metal substrate and Ru content have a significant effect on the catalytic activity in the ammonia decomposition reaction. The metal structured catalysts showed similar NH_3 conversion to the pellet catalyst at temperatures above 650°C even though the amount of Ru metal was below 1/10. Furthermore, the foam catalyst showed better catalytic performance than monolith catalyst at higher GHSV due to enhanced heat transfer.

ACKNOWLEDGEMENT

This work was supported by the Korea Institute of Energy Technology Evaluation and Planning (KETEP) and the Ministry of Trade, Industry & Energy (MOTIE) of the Republic of Korea (No. 20183010042020).

REFERENCES

1. Christensen CH, Johannessen T, Sørensen RZ, and Nørskov JK. 2006. Toward an ammonia-mediated hydrogen economy? Catalysis Today. 111:140-144
2. Lan R, Irvine JT, and Tao S. 2012. Ammonia and related chemicals potential indirect hydrogen storage materials. International Journal of Hydrogen Energy 37:1482-1494.
3. Koo KY, Im HB, Song D, and Jung UH. 2019. Status of COx-free hydrogen production technology development using ammonia. Journal of Energy & Climate Change 14: 34-42.
4. Sirijaruphan A, Goodwin Jr JG, Rice RW, Wei D, Butcher KR, Roberts GW, and Spivey JJ. 2005. Metal foam supported Pt catalysts for the selective oxidation of CO in hydrogen. Applied Catalysis A: General 281: 1-9.
5. Roh HS, Lee DK, Koo KY, Jung UH, and Yoon WL. 2010. Natural gas steam reforming for hydrogen production over metal monolith catalyst with efficient heat-transfer. International Journal of Hydrogen Energy 35:1613- 1619.
6. Koo KY, Eom HJ, Kwon SC, Jung UH, and Yoon WL. 2017. Ru-coated metal monolith catalyst prepared by novel coating method for hydrogen production via natural gas steam reforming. Catalysis Today 293-294: 129-135.
7. Koo KY, Eom HJ, Jung UH, and Yoon WL. 2016. Ni nanosheet-coated monolith catalyst with high performance for hydrogen production via natural gas steam reforming. Applied Catalysis A: General 525: 103-109

WHEC-2022
23rd World Hydrogen Energy Conference
June 26-30, 2022 - Istanbul

#42

EXPERIMENTAL INVESTIGATION OF A PHOTOELECTROCHEMICAL REACTOR FOR HYDROGEN PRODUCTION AND WASTEWATER TREATMENT

*[1,2]Murat Emre Demir, [1,3]Ibrahim Dincer
[1]Clean Energy Research Laboratory, University of Ontario Institute of Technology, Faculty of Engineering and Applied Science, 2000 Simcoe Street North, Oshawa, Ontario L1H 7K4, Canada
[2] Faculty of Naval Architecture and Ocean Engineering, Istanbul Technical University, Maslak-Sariyer, Istanbul, 34469, Turkey
[3] Yildiz Technical University, Faculty of Mechanical Engineering, Istanbul, 34349 Turkey

Corresponding author e-mail*: medemir@itu.edu.tr

ABSTRACT
In this study, a novel photoelectrochemical reactor for hydrogen and clean water production is designed, constructed, and experimentally investigated. TiO_2 photocatalyst is used in a photoelectrochemical (PEC) reactor, which cleans the water via Fenton-like process and produces hydrogen. A novel dual anode structure is used in the experiments. The TiO_2 nanoparticle deposited photoanode induces electro currents for hydrogen production and produces hydroxyl ions, which assist the removal of chemical oxygen demand (COD) process. The second anode is a stainless-steel plate, which is used as a sacrificial anode to electrogenerated iron ions for the Fenton process. It is aimed to reduce the anode cell half potential and energy consumption by replacing oxygen evaluation with the iron oxidation process. The overall energy and exergy efficiencies of the system are 81% and 80% respectively. After 40 minutes of the operation time of the PEC reactor under 2.3V and 60°C of cell potential and temperature, the reactor produces 22.6 mg of hydrogen and removes 87% of the COD.

Keywords: Hydrogen, Electrolysis, Photoelectrochemistry, Effluent treatment, Titanium dioxide, Fenton reagent, Energy, Exergy, Efficiency

INTRODUCTION
Energy and fresh water are one of the most vital issues for society, international politics, and the environment. The finite existence of these elements emerges the need for sustainable solutions. Consequently, reactors become popular that produce hydrogen as the energy carrier simultaneously with the wastewater treatment process. Simultaneous hydrogen production-wastewater treatment reactors can be built via biological, electrochemical, photochemical and hybrid (combining one or more these processes). The electrochemical processes can provide high hydrogen purity. However, these reactions require relatively high electrical potential, which increases the production costs of hydrogen. One way to reduce the energy need in the electrolyzer is by replacing the anodic reaction of the O_2 generation with an alternative reaction that requires less energy. It could be achieved by anodic oxidation of iron via electrogeneration. Fenton reaction in a PEM electrolyzer was tested only once in the literature before (Navarro-Solís, Villalba-Almendra, & Alvarez-Gallegos, 2010). Promising results were obtained for the decolorization of water. However, photocatalysts assisted the photoelectron-Fenton process in a PEM electrolyzer has not been studied for both hydrogen production and water treatment before. In this study, a PEC reactor for simultaneous wastewater treatment and hydrogen production is used. A novel dual anode structure is used in the experiments. The TiO_2 nanoparticle deposited photoanode induces electro currents for hydrogen production and produces hydroxyl ions, which assist the removal of chemical oxygen demand (COD) process. The second anode is a stainless-steel plate, which is used as a sacrificial anode to electrogenerated iron ions for the Fenton process. It is aimed to reduce the anode cell half potential and energy consumption by replacing oxygen evaluation with the iron oxidation process. Under different conditions, hydrogen output and COD reduction rates of the designed system are examined. Thermodynamic system analyzes are carried out and the system performance is evaluated both energetically and exergetically.

EXPERIMENTAL SET-UP AND PROCEDURE
The photo-electrochemical system for simultaneous wastewater treatment and hydrogen production system consists of a PEC reactor, light source, power source, flowmeter, liquid column (manometer) and a quartz glass case. The Photo-electrochemical reactor experiments are tested under the solar simulator (artificial light) illumination. The experimental configuration is presented in Fig. 1(a) and the basic reaction mechanism takes place in the PEC reactor is demonstrated in Fig. 1(b). The photoelectrochemical reactor consists of a SS sacrificial anode, a PtB- IrRuOx coated Nafion membrane, SS cathode and TiO_2-coated photoanode. Due to its strong moisture resistance, reactor casing material is selected as high-density polyethylene (HDPE). In addition, HDPE is also resistant to most of the chemicals, flame retardant and machinable. This device has two parallel anode plate, unlike traditional PEM electrolyzer setups. Since the TiO_2 deposition limits the electrogeneration of iron ions, the reactor is equipped with a

stainless-steel anode. The titanium dioxide-coated photoanode is placed almost adjacent to the quartz glass to ensure that a sufficient amount of Ultraviolet light hits the photoactive layer. Like in the typical PEM electrolyzer, a sacrificial anode is placed near the proton exchange membrane.

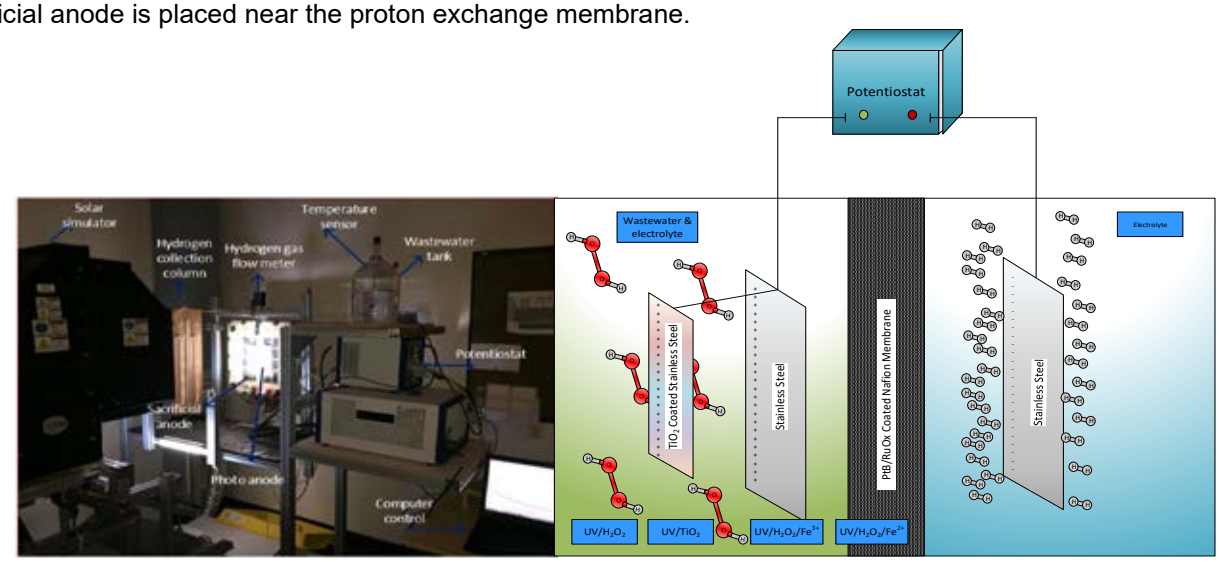


Fig 1. (a) The experimental setup, (b) The reaction mechanisms

In this study, Gamry 3000 high-performance Potentiostat/Galvanostat/ZRA is used, which has a maximum electrical potential and current of ±32 Volts and ±3 A respectively. In order to provide additional supply to the potentiostat, Gamry Reference 30K Booster is connected to the potentiostat which raises the current limit up to ±30 Amps with compliance limits of +20 and -2.5 V. Characterizations of photoanodes are performed with the potentiostat in various modes including linear voltammetry, cyclic voltammetry, potentiostatic, galvanostatic and open circuit potential. The potentiostat is also used for supply and record electrical input to the reactor. Also, analytical methods are used to determine chemical oxygen demand, decolorization and electro-generated iron ions are introduced. Open and colorimetric closed reflux methods measure the COD. Mercury (II) sulfate, sulphuric acid, potassium dichromate used as the digestion solution, while sulphuric acid and silver sulfate is used as the sulphuric acid reagent. Iron concentration and decolorization assessments are performed based on spectrophotometric methods.

ANALYSIS

The reactions of an anode and cathode of a PEM electrolyzer for water splitting can be given as follows:

$$H_2O \rightarrow O_2 + 2H^+ + 2e^- \quad (1)$$

$$2H^+ + 2e^- \rightarrow H_2 \quad (2)$$

This reaction requires 1.23V theoretically in acid mediums. However, the true cell voltage is higher such as 1.8-2.0 V. Hydrogen production is directly linked to the features of the O_2 evolution at the anode side. One of the methods to reduce the energy requirement in this process is replacing the anodic reaction of the oxygen generation with the oxidation of iron ions electrochemically (Navarro-Solís et al., 2010). The theoretical energy demand of the reaction is $\Delta G^0 = 74.2\ \mathrm{kJ/mol}$, which is 162.9 kJ/mol less than the oxygen evaluation reaction in water electrolysis. The Fenton type reactions take place with the presence of H_2O_2 and iron ions in an acidic medium. Hydrogen peroxide reacts with the iron catalyst and generates hydroxyl radicals. (Ghiselli, Jardim, Litter, & Mansilla, 2004) where the addition (or generation from Fe^{2+}_{aq}) of Fe^{3+}_{aq} increases the radical chain mechanism. Any process that speeds up the reduction of ferric ions to ferrous can be used for the reaction chain as a catalyst. This is accomplished electrochemically in electro-Fenton processes. A method to speed up this reaction is through Ultraviolet/V light irradiation (Machulek, Quina, & Gozzi, 2012). The ultraviolet light can also be applied in the mechanism of H_2O_2 decomposition through photochemical reactions for the production of hydroxyl radicals (Bensalah, Chair, & Bedoui, 2018). The performance evaluation of PEM electrolyzers can be made via several criteria. Among them, energy efficiency is one of the most commonly used assessment methods. One of the definitions of energy efficiency for the electrolyzer is the ratio of total energy consumption by the electrolyzer to the potential amount of heat released by the combustion of the produced hydrogen. Further information on the theoretical background, experimental setup, results, and interpretation can be found in the thesis study. (Demir, 2018). For the PEC system, energy and exergy efficiencies are defined as follows:

$$\eta_{PEC} = \frac{\mathrm{HHV}_{H_2}\dot{m}_{H_2}}{W_{in}}\ ,\ \psi_{PEC} = 1 - \frac{\sum \dot{E}x_d}{\dot{E}x_{in}} \quad (3)$$

RESULTS AND DISCUSSION

Fig. 2(a) shows the KHP degradation and hydrogen production in the PEC reactor after 40 minutes of operation. 17.6 mg of hydrogen is produced at the end of the photoelectrochemical reaction at 20°C and it increases to 22.6 mg at 60°C. Moreover, the temperature also has a positive effect on the COD removal process. The COD removal efficiency of the system rises from 44% to 87% with the increasing temperature from 20°C to 60°C. Furthermore, the performance of the PEC reactor is also tested in the decolorization aspect. The textile wastewater with 0.0014 M Reactive Black 5 dye is treated in the PEC reactor for 5 hours, and at the end of each one hour, 10 ml of sample treated water is collected and pictured. The highest color change is observed in the first 3 hours then it decolorization process slows down. Fig. 2 (b) shows the change in absorbance values during the 5 hours operation of the PEC reactor. Since the excess iron ions generation occurs in the reactor, which does not react with hydrogen peroxide, a yellowish colored solution is formed (yellow for Fe^{3+} and light green for Fe^{2+}) and the absorbance values are obtained higher than expected. Hence, to see the impact of Fenton type reactions on the wastewater, iron ions are precipitated in higher pH levels with NaOH to form $Fe(OH)_2$. The optical transmittance of the treated sample is increased considerably during the operation time of 5 hours.

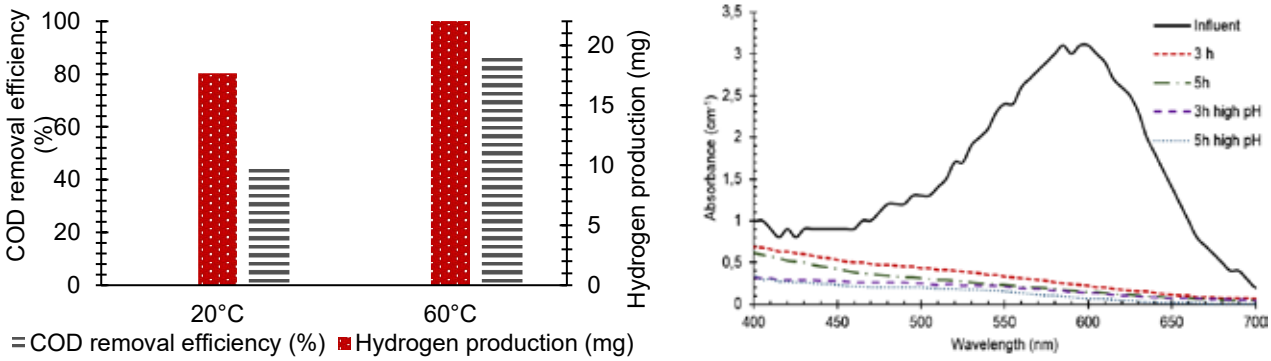


Fig. 2 (a) KHP degradation and hydrogen production in the PEC reactor under different temperatures. (b) Optical absorbance of textile wastewater (RB5 solution) in the PEC reactor during 5 hours of operation.

The overall energy and exergy efficiencies of the PEC system under 40˚C and 1.5 V cell potential are calculated as 81% and 80% respectively. As the solar energy input of the system is too large and the light to hydrogen conversion efficiency is relatively low, any small change in solar irradiance dominates the energy and exergy efficiency definitions. In order to better understand the system performance, solar input of the system is not included in these calculations and modified efficiency definitions results are obtained and presented instead.

CONCLUSIONS

Some concluding remarks are extracted from this study as follows:

- The overall energy and exergy efficiency of the PEC system under 1.5 V of cell potential, 40°C of operating temperature, and 600 W of solar irradiance are calculated as 81% and 80% respectively.
- The maximum hydrogen production rate of the PEC system is obtained as 33.9 mg/h at 2.3 V of cell potential and 60°C operating temperature.
- The COD removal efficiency of the PEC system rises from 44% to 87% with the increasing temperature from 20°C to 60°C.
- The hydrogen production rate of the PEC system rises from 26.7 mg/h to 33.9 mg/h with the increasing temperature from 20°C to 60°C.

ACKNOWLEDGEMENT

The authors acknowledge the support by the Natural Sciences and Engineering Research Council of Canada and Turkish Academy of Sciences (TÜBA).

REFERENCES

1. Bensalah, N., Chair, K., & Bedoui, A. (2018). Efficient degradation of tannic acid in water by UV/H2O2 process. *Sustainable Environment Research*, *28*(1), 1–11.
2. Demir, M. E. (2018). *Experimental investigation of an integrated solar driven wastewater treatment system for trigeneration applications*. University of Ontario Institute of Technology.
3. Ghiselli, G., Jardim, W. F., Litter, M. I., & Mansilla, H. D. (2004). Destruction of EDTA using Fenton and photo-Fenton-like reactions under UV-A irradiation. *Journal of Photochemistry and Photobiology A: Chemistry*, *167*(1), 59–67.
4. Machulek, A., Quina, F. H., & Gozzi, F. (2012). Fundamental Mechanistic Studies of the Photo-Fenton Reaction for the Degradation of Organic Pollutants. *Organic Pollutants. Intech Publisher Inc., Rijeka*, 271–292.
5. Navarro-Solís, I., Villalba-Almendra, L., & Alvarez-Gallegos, A. (2010). H2 production by PEM electrolysis, assisted by textile effluent treatment and a solar photovoltaic cell. *International Journal of Hydrogen Energy*, *35*(20)

WHEC-2022
23rd World Hydrogen Energy Conference
June 26-30, 2022 - Istanbul

#58

IMPROVING CATALYTIC ACTIVITY OF SUPPORTED PRECIOUS METAL CATALYSTS FOR HYDROGEN PRODUCTION BY HYDROTHERMAL CONVERSION PROCESSES

*Sibel Irmak
Pennsylvania State University, Agricultural and Biological Engineering Department, 227 Agricultural Engineering Building, Shortlidge Road University Park, PA 16802 USA

Corresponding author e-mail*: sji5137@psu.edu

ABSTRACT

Development of highly active and robust catalysts for hydrothermal conversion of biomass-derived compounds to hydrogen is the most effective way for economically feasible hydrogen production. Precious metal catalysts have been known to be active catalysts for hydrogen production. Since precious metals are expensive these catalysts are widely used in the supported form for recycling.

In the present study, following strategies were applied to increase and improve activity of supported Pt catalysts to be used in hydrothermal conditions for hydrogen production from organic-rich biomass-derived feeds: (i) integrating non-expensive metals into catalyst system, (ii) using different precursors for metals, and (iii) evaluating various carbon supportive materials with enhanced properties. The catalysts were prepared by wet impregnation method that followed by chemical reduction and thermal activation processes.

The results showed that use of different precursors for Pt did not change activity of the catalysts. Co-deposition of W or Ni with Pt showed promising activity. Catalytic performance of the catalyst considerably improved by changing the type of carbons used as support for metal deposition. However, each carbon studied brought its own drawback that indicates there is a need to develop new carbons with unique properties to maximize catalytic activity of the supported metal catalysts.

Keywords: Precious metal supported catalysts, Carbon, Hydrogen, Biomass.

INTRODUCTION

The main challenge for upscaling of hydrothermal conversion technologies for large scale hydrogen gas production is the lack of catalysts that show high activity in hydrothermal conditions. Although research efforts have been made so far significantly improved catalytic activity of supported precious catalysts towards hydrogen [1-2], activity and selectivity of these catalysts are still needed to be improved further for advancing the utility of hydrothermal gasification technologies for hydrogen gas production.

The reason for low activity of the supported precious catalysts in hydrothermal conditions is the deactivation of the catalysts because of following reasons: oxidation of catalyst surface, leaching/sintering of metals from the support or aggregation/poisoning of the metal particles [3]. Following strategies can be applied to improve catalytic activity of the catalysts and lower the deactivation process: ●using a carbon-based catalyst support with enhanced properties for better catalytic action (mechanical strength, high porosity, high surface area, thermal stability, multiple active sites, etc.) [4], ●using different precursors for metals for effective deposition, ●integrating non-expensive metals into precious metal catalyst system to increase resistance of metals to sintering, leaching, poisoning, and carbon deposition [5], and ●doping a heteroatom (e.g., N ad S) into carbon network to improve the stability of deposited metal particles [6]. First three strategies were investigated to improve catalytic performance and stability of the carbon supported Pt catalysts in the present work. The catalysts were evaluated for gasification of simple biomass model compound, glucose, for hydrogen gas production by aqueous-phase reforming (APR) as one of the hydrothermal gasification processes. APR has the potential to produce hydrogen from biomass-derived compounds in aqueous medium under mild reaction conditions (225-265 °C and 2.7-5.4 MPa) that reduces the cost of the procedure [2, 7-9].

MATERIALS AND METHODS

Preparation and characterization of the catalysts: The metal particles were deposited on various carbon supports (graphene, single-walled carbon nanotube and activated carbon in monometallic and bimetallic compositions by wet impregnation. All catalysts were prepared in the total of 8% metal content. Bimetallic catalysts were made of 4% precious metal (Pt) and 4% non-precious metal (W) content. Following precursors were used for preparation of metal nanoparticles: H_2PtCl_6, $PtBr_2$, $PtCl_2$, $NiCl_2$, and $(NH_4)10W_{12}O_{41}$ that are all soluble in water. The metal precursor(s) were dissolved in water and mixed with carbon support at room temperature, magnetically stirred for 30 min and sonicated for 10 min. Then, $NaBH_4$ solution were added drop by drop to reduce the metals on the carbon support.

The solid fraction was heated under flowing H_2 gas at 300°C in a tube furnace. Liquid fraction was kept for determination of undeposited metal contents. Size and distribution of the metal particles were determined by transmission electron microscopy (TEM). X-ray diffraction and BET surface area measurement were also performed to determine important information on structure and physicochemical properties of the catalysts. Actual concentrations of metal nanoparticles deposited on the support were determined by inductively coupled plasma (ICP) using liquid fraction collected after $NaBH_4$ treatment.

Evaluation of the catalysts for hydrogen gas production: Hydrogen gas production activity of the catalysts were evaluated by APR of glucose solution (7.5 g/l). The gasification experiments (APR) were carried out in a Parr 4520 benchtop 600 ml stainless steel reactor equipped with magnetic drive stirrer and a temperature control system. 350 ml glucose solution and 0.1750 g catalyst were placed in the reactor. The air in reactor was purged with argon inert gas before APR. Gasification was performed at 250°C for 1.5 h. After 1.5 h APR process, the reactor was quickly cooled down to room temperature using an ice-water bath. This step took several minutes. Then, the gas mixture produced was collected into a gas burette filled with water to determine the volume of the gas mixture produced.

Analysis of gaseous products: Gas products were characterized using a gas chromatograph with thermal conductivity detector (TCD) (Thermo Scientific Trace 1300). Argon was used as carrier gas. The column was Carboxen 1010 plot fused silica capillary (30mx0.53mm). Triplicate gas mixture (250 µl) was injected into GC with 1:3 split injection mode. The GC was programmed at 40°C for 3 min, increased at 20°C/min to 230°C and maintained at this temperature for 10 min. Inlet and detector temperature were 230°C and filament was at 360°C. The column flow and reference flow were 40 ml/min and 5 ml/min, respectively. The standard gas mixture was composed of acetylene, ethylene, ethane, methane, carbon monoxide, carbon dioxide and hydrogen.

RESULTS AND DISCUSSION

Evaluation of different carbon materials as catalyst supports for platinum metal particles: Catalytic performance of single-walled carbon nanotube (CNT), graphene and activated carbon supports were compared. Despite graphene supported Pt catalyst produced least volume gas mixture, the composition of the hydrogen in this mixture were the highest and not diluted with other gases in the same extent as in other catalysts (Table 1).

Table 1. APR of glucose using different carbon supported Pt catalysts

Carbon support	Gas mixture produced (ml)		Gas Composition (ml)[1,2]		
		H_2	CO_2	CO	CH_4+ C_2H_2
CNT-single walled	568 ±13	298 ±14	215 ±12	29.6 ±1.3	25.4 ±3.7
Graphene	373 ±15	322 ±19	19.9 ±2.5	30.6 ±3.1	n.d.
Activated carbon	594 ±10	308 ±10	255 ±12	25 ±6.1	10.4 ±5.1

[1] The calculation made using ideal gas equation: n_{total}=PV/RT. P=1 atm, T=300 K, V= volume of gas mixture produced. $n_{hydrogen}$ = n_{total} * hydrogen composition/100. [2] n.d. not detected

Production of lower gas mixture in graphene support is attributed to extensive stacking between graphene layers. Van der Waals interactions between surfaces lead to graphene sheets to stack on top of each other and surface area between graphene layers becomes inaccessible. This reduces number of active sites in the catalyst structure. If stacking the graphene layers could be lowered in some extent, the activity would considerable increased.

Evaluation of different Pt precursors: H_2PtCl_6, $PtBr_2$ and $PtCl_2$ precursors were deposited on graphene support at the same conditions. Although the size of Pt particles deposited on graphene support were different, the catalytic activities of the catalysts were similar (Fig. 1). The sizes and distributions of Pt particles on graphene were relatively small with uniform and narrow dispersion in $PtCl_2$ compared to the catalysts prepared with other precursors. The presence of different halogens (Cl and Br) in different quantity in the precursors might affect the morphology of the Pt nanoparticles [10].

Integrating non-expensive metals into Pt metal catalyst: The metal particles were deposited on graphene in monometallic (Pt and W) and bimetallic compositions (Pt-W). The particle size of the metal particles became larger when the catalysts were prepared in bimetallic composition. Integrating non-precious metal, W particles into Pt particles on graphene support created a positive synergy and the catalytic performance of the catalyst significantly enhanced (Fig. 2).

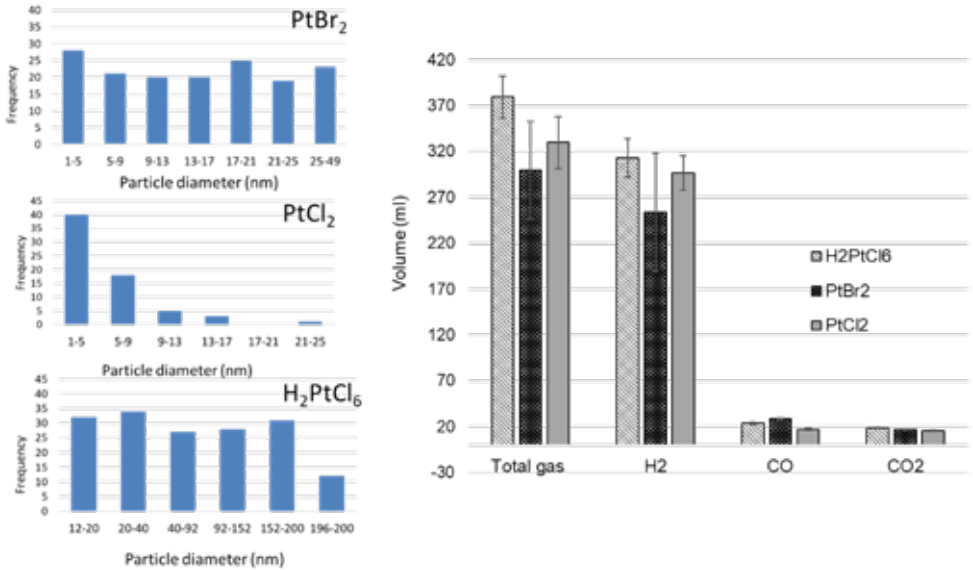


Figure 1. Particle size distributions of the catalysts prepared with different platinum precursors and gasification performance of the catalysts.

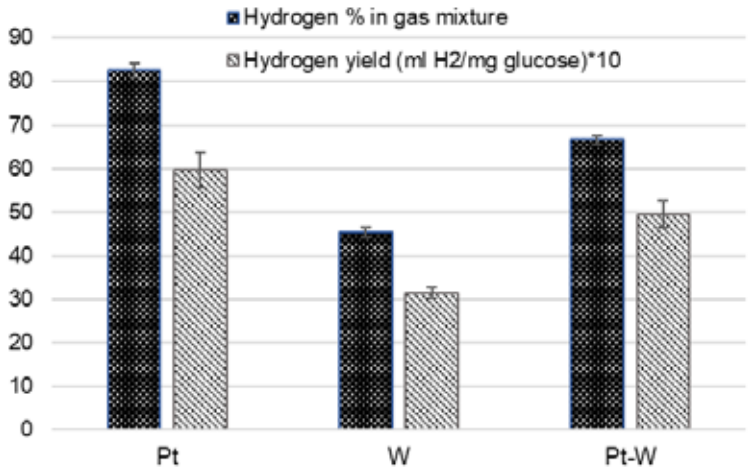


Figure 2. Comparison of gasification performance of the graphene supported Pt catalysts with W catalysts.

CONCLUSIONS

Graphene showed promising catalytic performance as catalyst support for hydrogen gas production. However, extensive stacking between graphene layers should be reduced to improve activity further by increasing surface area. This can be done by partial oxidation of the graphene layers by various treatments. Co-deposition of non-expensive W and low quantity of Pt on modified graphene support could result in highly active and robust catalysts.

REFERENCES

1. Meryemoglu B, Hesenov A, Irmak S, Atanur OM and Erbatur O. 2010. Aqueous-phase reforming of biomass using various types of supported precious metal and Raney-nickel catalysts for hydrogen production. Int.J. Hydrogen Energy 35:12580-12587.
2. Davda RR, Shabaker JW, Huber GH, Cortright RD, Dumesic JA. 2002. Aqueous phase reforming of ethylene glycol on silica-supported metal catalysts. Appl.Catal. B: Environ. 43:13-26.
3. Ren N, Yang Y-H. Shen J, Zhang Y-H, Xu H-L, Gao Z, Tang Y. 2007. Novel, efficient hollow zeolitically microcapsulized noble metal catalysts. J. Catalysis 251:182-188.
4. Meryemoglu B, Irmak S, Hesenov A, and Erbatur O. 2012. Preparation of activated carbon supported Pt catalysts and optimization of their catalytic activities for hydrogen gas production from the hydrothermal treatment of biomass-derived compounds. Int. J. Hydrogen Energy 37:17844-17852.
5. Tanksale A, Beltramini JN, Dumesic JA, Lu GQ. 2008. Effect of Pt and Pd promoter on Ni supported catalysts-A TPR/TPO/TPD and microcalorimetry study. J. Catal. 258:366-377.

6. Sharma PP, Wu J, Yadav RM, Liu M, Wright CJ, Tiwary CS, Yakobson BI, Lou J, Ajayan PM, Zhou XD. 2015. Nitrogen-doped carbon nanotube arrays for high-efficiency electrochemical reduction of CO_2: On the understanding of defects, defect density, and selectivity. Angew. Chem. Int. Ed. 54:13701-13705.
7. Cortright RD, Davda RR and Dumesic JA. 2002. Hydrogen from catalytic reforming of biomass-derived hydrocarbons in liquid water. Nature 418:964-967.
8. Huber GW, Shabaker JW, Evans ST, Dumesic JA. 2006. Aqueous-phase reforming of ethylene glycol over supported Pt and Pd bimetallic catalysts. Appl. Catal. B 62:226-235.
9. Irmak S. and Ozturk I. 2010. Hydrogen rich gas production by thermocatalytic decomposition of kenaf biomass. Int. J. Hydrogen Energy 35:5312-5317.
10. Borges L, Lopez-Castillo A, Meira D, Gallo J, Zanchet D, Bueno J. 2019. Effect of the Pt precursor and loading on the structural parameters and catalytic properties of Pt. Chem.Cat.Chem. 11:3064-3074.

WHEC-2022
23rd World Hydrogen Energy Conference
June 26-30, 2022 - Istanbul

#81

THERMODYNAMIC ANALYSIS OF BIOGAS-TO-SYNGAS CONVERSION WITH DRY OXIDATIVE REFORMING AND CH_4 RECYCLING USING ASPEN HYSYS

*Pali Rosha and *Hussameldin Ibrahim*
Clean Energy Technologies Research Institute, Process Systems Engineering, Faculty of Engineering and Applied Science, University of Regina, 3737 Wascana Parkway, Regina, SK, Canada

*Corresponding author e-mail: hussameldin.ibrahim@uregina.ca

ABSTRACT

Syngas synthesis from biogas through the dry oxidative reforming route was studied using an Aspen HYSYS simulator. This study dealt with the biogas-to-syngas conversion process's feasibility; initially, the simulation outcomes concerning O_2 effects in dry oxidative reforming, followed by their parametric optimization w.r.t. temperature and O_2/CH_4 ratio, were studied. The simulation outcomes of reported work revealed that the CH_4 conversion influenced primarily by O_2 injecting, particularly at lower temperature range. At all temperatures, CO_2 conversion was found to be less in dry oxidative reforming when compared to dry reforming, but the conversion rate improved at 0.20 O_2/CH_4 ratio. Further, the CH_4 recycling loop showed positive effects in CH_4 conversion and CO_2 emission reduction. For model validation, the simulated outcomes were compared with the previous experimental study in biogas reforming was carried out using pure nickel nanoparticles. Overall, the study infers that the dry oxidative reforming integrated with CH_4 recycling can be an enviro-friendly route for syngas production.

Keywords: Biogas, hydrogen, CH_4 recycling, Hydrocarbon reforming, Aspen HYSYS.

INTRODUCTION

Fossil fuels are a more significant threat to energy security since they are finite in quantity; however, once the Earth's oil is depleted, there will be no energy security without green energy technologies. Moreover, the environment is being severely affected by the excessive use of non-renewable energy resources, such as petrol, diesel, coal, and natural gas. In this regard, focusing on renewable energy resources, various researchers have contributed to produce biomass-derived renewable (biodiesel, biogas, hydrogen, syngas, etc.) fuels [1]. Various techniques currently produce syngas; likewise, catalytic reforming, pyrolysis, and gasification using different feedstocks [2]. In addition, all these techniques above require a vast amount of energy during operation and emit carbon dioxide (CO_2), contributing to climate change.

Syngas as a gaseous fuel is that form of energy source, which isn't gift naturally. The catalytic reforming strategies presently available consist of steam reforming, dry reforming, and partial oxidation. Dry reforming, which makes use of CH_4 and CO_2 as reactants, is an effective approach to make use of greenhouse gases. This approach usually needs excessive energy because of its endothermicity, proscribing its suitability to put in force industrially [3]. Moreover, the catalyst deactivation has additionally emerged as extreme difficulty in dry reforming reactions; thus, to boom reforming catalysts' operational balance, various oxide supports, and promoters had been efficiently investigated with the aid of using diverse researchers [4]. A detailed literature survey reviewed Pakhare et al. stated that non-noble catalysts provide better catalytic activity; however, higher coke formation makes it unsuitable for long-time stability [5]. Thus, to lessen energy input and coke formation on the catalyst in the dry reforming process, one such technique, i.e., dry oxidative reforming, has been proposed by various researchers [1,6]. Dry oxidative reforming utilizes CH_4 and CO_2 as reactants, as well as O_2 as an oxidant to limit catalyst carbon deposition and initiate exothermic reactions.

Few experimental studies are available in open platforms investigating the influence of O_2 addition in terms of reactant (CH_4 and CO_2) conversion and product (H_2 and CO) yields [7, 8]. However, the literature lacks a simulation study that needs to be done for better process understanding and optimizing the parametric conditions. The thermodynamic-based simulation studies are necessary as they provide a footprint to predict performance parameters required for reactor design. In the presented work, the injecting O_2 together with CH_4 and CO_2 into the Gibbs reforming reactor has been completed to get advantages of the reaction exothermicity in the dry reforming. Emphasis was given to the CH_4 recycling loop in the simulation flowsheet and the effect of O_2 addition in dry reforming reactions. Findings of a few reported studies have been referenced inside the text for result validation.

MATERIALS AND METHODS

Aspen HYSYS software was employed as a process simulator, and for optimization purposes, the Peng-Robinson fluid package was used. The assumptions considered were: (1) Biogas with 0.6 CH_4 and 0.4 CO_2 content, and oxidant O_2 in the range between 0-0.20 as for CH_4 volumetrically; (2) Calorific value of CH_4 is 55.5 MJ/kg; (3) Reforming reaction runs were at 1 bar and temperature (range: 450-700°C); (4) 0.1 bar pressure drop in the Gibbs reactor, heater, and cooler; (5) Purely thermodynamic-based study, thus, no catalyst-related aspects taken into account. A

detailed process layout is shown in Fig.1. It incorporates a mixer (M), heater (H), Gibbs reactor, cooler (C), compressor (CR), and component splitter (CS). The streamlines of CH_4 and CO_2 were initially mixed through a mixture; then, O_2 was added by varying O_2/CH4 ratio. All reactant streamlines were passed into the mixture before the heater. Subsequently, this high-temperature stream was fed into the Gibbs reactor to get a syngas product stream. The cooler was used to reduce the enhanced temperature of CH_4 (unreacted); following this, and the unreacted CH_4 is ready for reuse.

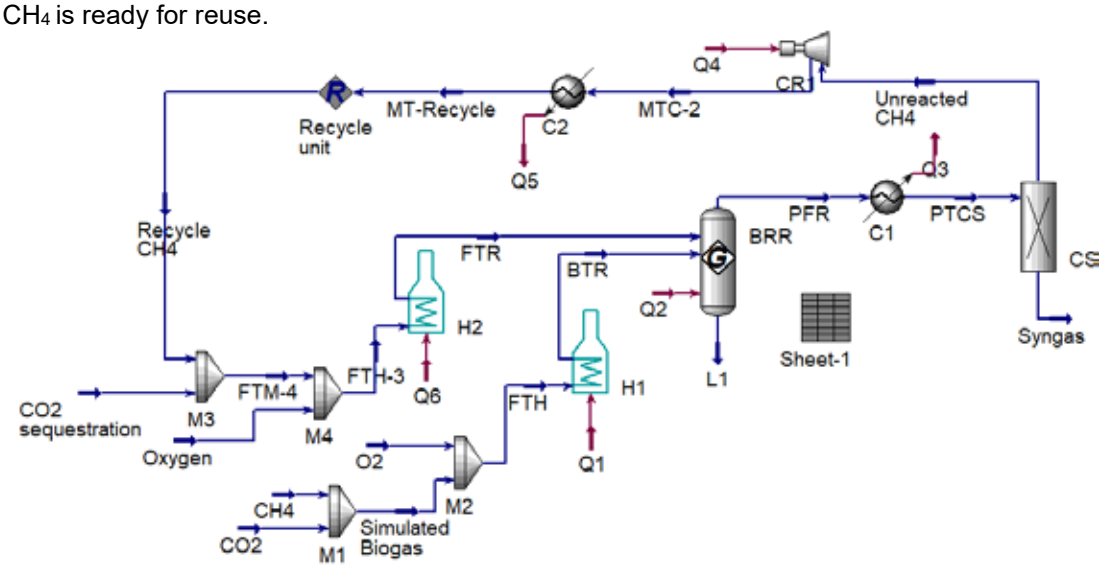


Fig. 1. Process flow diagram for syngas production

RESULTS AND DISCUSSION

EFFECT OF O_2 ADDITION

Table 1 depicts the O_2 effects in terms of reactant (CH_4 and CO_2) conversions, H_2 production, and product (H_2/CO) ratio. Results indicated that as the temperature increases from 450 to 700°C, the reactant conversion enhances. At 450°C, in dry reforming, the maximum CH_4 conversion attained was 6.5%; after that, at 500, 550, 600, 650, and 700°C of temperature, the conversion values were 12.3, 21.2, 32.9, 45.7, and 56.2%, respectively. This enhancement in conversion values was due to increased reaction temperature, which shifts reaction equilibrium to product (H_2 and CO) side [9]. After adding O_2, an improved CH_4 conversion was noticed, stating that the O_2 affects positively on the conversion rate. Contrary, it was also observed that CO_2 conversion reduced in dry oxidative reforming than dry reforming. This statement is consistent with the reported study, which mentioned that exothermic reactions are more dominated at lower temperatures [10]. On the other side, in dry oxidative reforming, the H_2 production and H_2/CO ratio followed an upward trend at all temperature ranges when compared to dry reforming. Further, upon comparing the potential of temperature and O_2 to enlarge H_2 production, it was identified that the lower temperature of 500°C utilized O_2 co-feeding more effectively than all other temperatures.

Table 1. Simulation outcomes summary w.r.t. A=CH_4 conversions; B=CH_4 conversion; C=H_2 production; D=H_2/CO ratio

	O_2/CH_4 =0				**O_2/CH_4 =0.10**				**O_2/CH_4 =0.15**				**O_2/CH_4 =0.20**			
Temp. (ºC)	A	B	C	D	A	B	C	D	A	B	C	D	A	B	C	D
450	6.5	15.5	0.06	0.55	11.6	1.2	0.08	1.13	14.3	-4.7	0.10	1.45	14.3	-4.7	0.10	1.45
500	12.4	27.1	0.11	0.63	17.7	12.4	0.15	0.96	20.6	5.8	0.17	1.14	20.6	5.8	0.17	1.14
550	21.2	42.7	0.21	0.71	27.3	28.6	0.26	0.92	30.4	22.0	0.28	1.03	30.4	22.0	0.28	1.03
600	33.0	60.8	0.35	0.79	40.2	48.2	0.41	0.95	43.7	42.0	0.44	1.02	43.7	42.0	0.44	1.02
650	45.7	77.8	0.51	0.87	54.6	67.5	0.59	0.99	58.6	62.0	0.63	1.05	58.6	62.0	0.63	1.05
700	56.3	90.1	0.65	0.94	67.6	82.5	0.77	1.04	72.3	78.0	0.81	1.09	72.3	78.0	0.81	1.09

EFFECT OF CH_4 RECYCLING

Table 2 presents the CH_4 recycling effects on CH_4 conversion and H_2 production. As discussed previously, the reactant conversion and product yield values increase or decrease owing to the increment and decrement in

conversion values. Further, the reuse of unreacted CH_4 showed positive CH_4 conversion and H_2 production effects. Specifically, at 500°C, the CH_4 conversion was 21.7%; after using the recycling loop, 38.6% of CH_4 conversion value and 0.308 kg mole/h of H_2 production rate were observed. It is clear from the simulation outcomes that reusing unreacted CH_4 enhances CH_4 conversion and H_2 formation.

Table 2. Simulation outcomes summary regarding CH_4 recycling in terms of CH_4 conversions and H_2 production

Temp. (ºC)	CH_4 conversion (%)		H_2 production (Kg mol/h)	
	without recycling	with recycling	without recycling	with recycling
450	15.4	33.8	0.10	0.25
500	21.7	38.7	0.17	0.31
550	31.6	46.4	0.29	0.41
600	45.0	56.9	0.45	0.54
650	60.2	68.8	0.64	0.71
700	74.0	79.6	0.82	0.87

CONCLUSIONS

It is concluded that CH_4 conversion is primarily influenced by O_2 addition, particularly at lower temperatures. However, CO_2 conversion was lower in dry oxidative reforming over all temperature ranges compared to dry reforming. Moreover, the CH_4 recycling showed positive effects on the reactant conversion values. In summary, the simulated study indicates that the dry oxidative reforming process was found to be an eco-friendly route for renewable syngas production. It is also recommended that a detailed experimental study be required to incorporate recycling units better to understand the process in terms of industrial implementation.

REFERENCES

1. Rosha P, Dhir A and Mohapatra SK. 2018. Influence of gaseous fuel induction on the various engine characteristics of a dual fuel compression ignition engine: A review. Renewable Sustainable Energy Reviews 82:3333-49.
2. Rosha P, Rosha AK, Ibrahim H, and Kumar S. 2021. Recent advances in biogas upgrading to value added products: A review. International Journal of Hydrogen Energy 46(41): 21318-21337.
3. Song Y, Liu H, Liu S and He D. 2009. Partial Oxidation of Methane to Syngas over Ni/Al_2O_3 Catalysts Prepared by a Modified Sol−Gel Method. *Energy & Fuels* 23 (4):1925-30.
4. Zhao A, Ying W, Zhang H, Ma H and Fang D. 2012. Ni–Al_2O_3 catalysts prepared by solution combustion method for syngas methanation. Catalysis Communications 17: 34-38.
5. Pakhare D and Spivey J. 2014. A review of dry (CO_2) reforming of methane over noble metal catalysts. Chemical Society Reviews 43: 7813-37.
6. Connor AMO and Ross JRH. 1998. The effect of O_2 addition on the carbon dioxide reforming of methane over Pt/ZrO_2 catalysts. Catalyst Today 46: 203-10.
7. Rosha P, Mohapatra SK, Mahla SK and Dhir A. 2019. Hydrogen enrichment of biogas via dry and autothermal-dry reforming with pure nickel (Ni) nanoparticle. Energy 2019; 172: 733-39.
8. Rosha P, Singh R, Mohapatra SK, Mahla SK and Dhir A. 2018. Optimization of hydrogen enriched biogas by dry oxidative reforming with nickel nanopowder using response surface methodology. Energy & Fuels 32(6):6995-7001.
9. Goula MA, Charisiou ND, Papageridis KN, Delimitis A, Pachatouridou E and Iliopoulou EF. 2015. Nickel on alumina catalysts for the production of hydrogen rich mixtures via the biogas dry reforming reaction: influence of the synthesis method. International Journal of Hydrogen Energy 40:9183-9200.
10. Amin NAS and Yaw TC. 2007. Thermodynamic equilibrium analysis of combined carbon dioxide reforming with partial oxidation of methane to syngas. International Journal of Hydrogen Energy 32(12):1789-98.

WHEC-2022
23rd World Hydrogen Energy Conference
June 26-30, 2022 - Istanbul

#82

H_2-ENRICHED SYNGAS PRODUCTION BY ALGAE-PLASTIC WASTE CO-GASIFICATION USING ASPEN PLUS

Pali Rosha and * *Hussameldin Ibrahim*
Clean Energy Technologies Research Institute, Process Systems Engineering, Faculty of Engineering and Applied Science, University of Regina, 3737 Wascana Parkway, Regina, SK, Canada

*Corresponding author e-mail: hussameldin.ibrahim@uregina.ca

ABSTRACT

Fluidized bed gasification is considered one of the most well-known methods in the thermochemical conversion route for renewable fuel production. Several experimental studies were reported in the open literature on downdraft gasification using different biomass feedstocks. In this study, an initiative was made to assess the feasibility of co-gasifying algae-plastic waste mixtures using an Aspen Plus simulator. Simulation results demonstrated that the algae-plastic waste co-gasification enhances H_2 content in the gaseous product distribution. The effect of gasifier temperature is more prominent in energy-efficient product formation; moreover, plastic loading enhanced H_2 production to a greater extent. At the same time, CO_2 formation increased due to more carbon conversion after improving O_2 content in the gasifier. Hence, the findings can produce energy-efficient renewable fuel that simultaneously addresses the waste disposal concern. Also, the study can serve as a guideline for future experimental studies.

Keywords: Co-gasification, Algae, Plastic waste, Hydrogen, Aspen plus.

INTRODUCTION

Currently, a significant portion of the world's energy demands is fulfilled by fossil (coal, oil, and natural gas) fuels. Furthermore, the overuse of fossil fuels as energy sources causes destructive environmental impacts, i.e., acid rain, global warming, natural resource depletion, air pollutants, and so on [1]. In this context, the biomass-to-energy sector is growing worldwide, as biomass waste is already a surprisingly large energy source [2]. Biomass wastes are predominantly municipal solid wastes, agricultural residues, wood, and so on, being investigated worldwide as a potential renewable energy resource [3]. Moreover, microalgae-based renewable fuels provide substantial opportunities to satisfy the worldwide energy requirement, offering zero-carbon solutions and permitting CO_2 mitigation from the open environment [4]. Contrary, the increased worldwide energy demand led to increased waste disposal issues. Generally, plastic wastes are hard to process because of their heterogeneity, quality, and composition [5].

Literature reveals that gasification is the most prominent biomass-to-energy conversion process, offering higher efficiency with minor environmental effects [6, 7]. The produced gaseous effluent comprises H_2, CO, CO_2, and CH_4, while syngas (H_2 and CO) are readily processable to produce green chemicals and/or fuels [8]. Syngas formed via gasification offers lower calorific value, which limits its applicability in terms of power generation [9]. It is expected that the syngas heating value can be improved with the co-gasifying approach, such as algae-plastic waste co-gasification [10]. H_2 is counted as an energy-efficient alternative fuel, energy carrier, and vector; it has the highest calorific value (119.9 MJ/kg) when compared to other fuels [3]. H_2 is likewise probable to contribute almost 34% of the total renewable energy supply of 69% by 2050 [11]. In addition, the usage of blended biomass might also additionally increase H_2 proportion in the product stream of gasifier; as extensive quantity of literature mentioned that the H_2-enriched feedstock may be an H_2 donor to the H_2 low biomass [12, 13].

In the reported study, the main focus is to examine H_2 production by co-gasification route using algae and plastic waste mixture as a feedstock. Concerning novelty, this study seems to be the first study of its kind that presents a simulation for H_2-enriched gaseous fuel production through co-gasification algae-plastic waste mixture using Aspen plus simulator that have not been reported yet elsewhere. The use of computer simulation yields a better understanding of the overall system and is a handy tool in support of design. It is anticipated that the model will help understand the general process's behavior without undertaking laborious, high-cost involved time-consuming experiments. Aspen Plus is essential software for chemical process design and can be used to simulate the gasification systems of solid feedstocks [24, 25]. Han et al. [25] worked on the gasification reduction zone with a chemical restricted equilibrium model to offer the overall performance statistics of the incorporated biomass to the liquid system. The version became efficiently proven with experimental statistics of downdraft gasification, with high-quality accuracy on principle bio-syngas compositions. Tavares et al. [26] said that steam (gasifying agent) improves H_2 content and improved gaseous product calorific value when compared with air. This simulation takes a look at investigating the feasibility of co-gasifying algae and plastic waste combinations using Aspen Plus simulation software.

MATERIALS AND METHODS

Aspen PLUS software was employed as a process simulator, and for optimization purposes, the PR-BM fluid package was used. In this simulation model, the assumptions considered were: (1) Feedstock feed rate was 100 kg/h at 30°C and 1 bar; (2) Steady-state process; (3) Major volatile components are H_2, CO, CO_2, H_2O, and CH_4; (4) Ash as an inert material. The process performance was assessed w.r.t. LHV (lower heating value), CCE (carbon conversion efficiency), and ER (equivalence ratio). Fig.1 shows the complete layout of the process flowsheet. Initially, algae-based biomass stream was passed through the dryer to reduce moisture content. Then, a splitter block was employed to separate dry (DTS) feed and moisture. The ash was separated from the mixed (MTC) stream using a cyclone block, and, after that, the volatile matter was fed to the partial oxidation block followed by a gasification block.

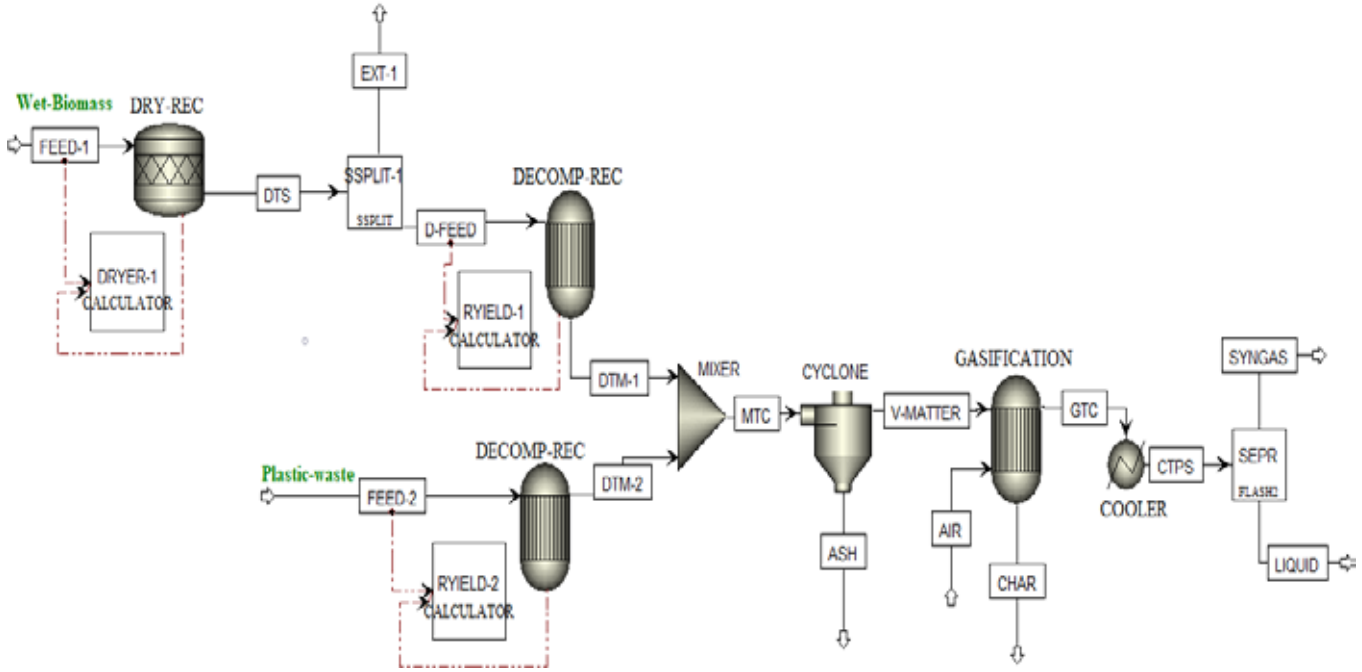


Fig. 1. Process flow diagram for H_2-enrcihed gaseous fuel production

RESULTS AND DISCUSSION

TEMPERATURE EFFECTS ON SYNGAS COMPOSITION, LOWER HEATING VALUE, AND CARBON CONVERSION EFFICIENCY

Table 1 presents the gaseous product distribution w.r.t. H_2, CO, CO_2, and CH_4 at temperatures between 550 and 900°C. Results revealed that the H_2 proportion increases with rising temperature from 550 to 900°C, whereas CO_2 content was found to be decreased w.r.t temperature. It was observed that the lower heating value and carbon conversion efficiency improved with a rise in temperature up to 850°C and, after that, been constant at higher temperatures (>850°C). These improved values enhance H_2 and CO production at the given temperature range. Simulation results demonstrated that the rise in equivalence ratio showed adverse effects w.r.t. H_2 and CO content in the product effluent.

Table 1. Simulation outcomes summary w.r.t. product distribution, lower heating value, and carbon conversion efficiency

Temp. (°C)	H_2 (%)	CO (%)	CO_2 (%)	CH_4 (%)	Lowe heating value (MJ/Nm^3)	Carbon conversion efficiency (%)
550	18.70	6.05	15.90	2.79	3.78	37.29
600	21.56	11.12	13.30	1.83	4.39	43.79
650	23.43	17.70	9.76	1.14	5.17	54.15
700	24.45	24.34	6.08	0.70	5.96	66.41
750	24.99	29.39	3.25	0.43	6.56	76.98
800	25.30	32.35	1.59	0.27	6.91	83.77
850	25.50	33.84	0.76	0.17	7.09	87.36
900	25.66	34.13	0.58	0.07	7.11	87.74

H_2 ENRICHMENT USING CO-GASIFYING TECHNIQUE

Table 2 highlights the effect of temperature and composition of feedstock on product distribution and lower heating value. The higher temperature favours H_2 production at all algae-plastic waste mixed feedstocks. In the co-gasification process, the thermal energy provided to the plastic waste is larger than the covalent bond strength energy; thus, the bond breakage occurs, and the plastic waste decomposes, which may include mostly H_2. The presence of plastic results in H_2 enrichment, along with decrement in CO and CO_2 using co-gasification.

Table 2. Simulation results w.r.t. product distribution and lower heating value by varying plastic waste content from 0 to 10%

Temp. (°C)	H_2 (%)			CO (%)			CH_4 (%)			CO_2 (%)			Lower heating value (MJ/Nm^3)		
	0	5	10	0	5	10	0	5	10	0	5	10	0	5	10
550	18.7	20.0	21.2	6.1	5.9	5.7	2.8	3.2	3.6	15.9	15.0	14.1	3.8	4.0	4.3
600	21.6	23.0	24.4	11.1	10.8	10.5	1.8	2.1	2.3	13.3	12.6	11.8	4.4	4.6	4.8
650	23.4	24.9	26.4	17.7	17.2	16.7	1.1	1.3	1.4	9.8	9.2	8.7	5.2	5.3	5.5
700	24.5	26.0	27.5	24.3	23.6	22.9	0.7	0.8	0.9	6.1	5.7	5.4	6.0	6.1	6.2
750	25.0	26.6	28.1	29.4	28.5	27.6	0.4	0.5	0.5	3.3	3.1	2.9	6.6	6.6	6.7
800	25.3	26.9	28.5	32.4	31.3	30.4	0.3	0.3	0.3	1.6	1.5	1.4	6.9	7.0	7.0
850	25.5	27.1	28.7	33.8	32.8	31.7	0.2	0.2	0.2	0.8	0.7	0.7	7.1	7.1	7.2
900	25.7	27.2	28.8	34.1	33.4	32.4	0.1	0.1	0.1	0.6	0.4	0.3	7.1	7.2	7.3

CONCLUSIONS

It is concluded that gasifier temperature plays an important role in energy-enriched product formation; however, higher equivalence ratio not showing noteworthy effects. An elevated temperature at optimal equivalence ratios facilitates gasification reactions, casing large tar cracking. Moreover, carbon conversion efficiency enhanced in the initial phase because of the synergy of temperature and air oxidant. In the co-gasification process, simulation results revealed that the feedstock composition varies the product distribution. The findings can produce energy-efficient renewable fuel through a co-gasification route that simultaneously addresses the waste disposal issue. Also, the study can serve as a guideline for future experimental studies.

REFERENCES

1. Marwaha A, Rosha P, Mohapatra SK, Mahla SK and Dhir A. 2019. Biodiesel production from Terminalia bellerica using eggshellbased green catalyst: An optimization study with response surface methodology. Energy Reports5:1580-1588.
2. Chien FS, Kamran HW, Albashar G and Iqbal W. 2021. Dynamic planning, conversion, and management strategy of different renewable energy sources: A Sustainable Solution for Severe Energy Crises in Emerging Economies. International Journal of Hydrogen Energy 46(11):7745-7758.
3. Rosha P, Rosha AK, Ibrahim H and Kumar S. Recent advances in biogas upgrading to value added products: A review. International Journal of Hydrogen Energy 46(41): 21318-21337.
4. Abdel-Shafy HI and Mansour MSM. 2018. Solid waste issue: Sources, composition, disposal, recycling, and valorization. Egyptian Journal of Petroleum 27(4):1275-1290.
5. Daioglou V, Faaij APC, Saygin D, Patel MK, Wicke B and Van Vuuren DP. 2014. Energy demand and emissions of the non-energy sector. Energy & Environmental Science 7(2):482-498.
6. Serrano-Ruiz JC, Luque R and Sepúlveda-Escribano A. 2011. Transformations of biomass-derived platform molecules: from high added-value chemicals to fuels via aqueous-phase processing. Chemical Society Reviews 40:5266-5281.
7. Mastellone ML, Zaccariello L and Arena U. 2010. Co-gasification of coal, plastic waste and wood in a bubbling fluidized bed reactor. Fuel 89:2991-3000.
8. Rosha P, Mohapatra SK, Mahla SK and Dhir A. 2018. Biogas reforming for hydrogen enrichment by ceria decorated over nickel catalyst supported on titania and alumina. International Journal of Hydrogen Energy 43:21246-21255.
9. Nipattummakul N, Ahmed II, Kerdsuwan S and Gupta AK. 2010. Hydrogen and syngas production from sewage sludge via steam gasification. International Journal of Hydrogen Energy 35(21):11738-11745.
10. Rathnayake D, Ehidiamhen PO, Egene CE, Stevens CV, Meers E, Masek O and Ronsse F. 2021. Investigation of biomass and agricultural plastic co-pyrolysis: Effect on biochar yield and properties. Journal of Analytical and Applied Pyrolysis 155:105029.
11. Nanda S, Rana R, Zheng Y, Kozinskia JA and Dalai AK. 2017. Insights on pathways for hydrogen generation from ethanol. Sustainable Energy & Fuels 1:1232-1245.
12. Ghorbannezhad P, Park S and Onwudili JA. 2020. Co-pyrolysis of biomass and plastic waste over zeolite- and sodium-based catalysts for enhanced yields of hydrocarbon products. Waste Management 102:909-918.
13. Huber GW, Iborra S and Corma A. 2006. Synthesis of transportation fuels from biomass: chemistry, catalysts, and engineering. Chemical Reviews 106:4044-4098.

WHEC-2022
23rd World Hydrogen Energy Conference
June 26-30, 2022 - Istanbul

#83

MODELING CATALYST POISONING DURING METHANE REFORMING FOR THE PRODUCTION OF HYDROGEN

[1] *Michael Fabrik,* [1*] *Amgad Salama,* [1*] *Hussameldin Ibrahim*
[1]Faculty of Engineering and Applied Science, University of Regina, 3737 Wascana Parkway, Regina, Saskatchewan, Canada

*Corresponding author e-mail: hussameldin.ibrahim@uregina.ca

ABSTRACT

A one-dimensional simplified heterogeneous reactor model is used to simulate both steam methane reforming and dry methane reforming (i.e., using methane and carbon dioxide) under hydrogen sulfide poisoning conditions – a key challenge to this method of hydrogen production. The proposed simulation utilizes the Temkin sulfur adsorption isotherm of Alstrup et al. [1] and a Maxted-type catalyst activity expression. The reactor model is solved using the finite volume method, and the complete simulation is written and optimized in MATLAB. The simulation is validated against the numerical results of Rout & Jakobsen [2] and the experimental data of Koningen & Sjörström [3]. It was found that the deactivation order for methane reforming, based on the results of Koningen & Sjörström, was $n = 1$ versus the order of $n = 3$ proposed by Rostrup-Nielsen [4]. Discussion is provided concerning differences in expected deactivation orders observed both in this study and in other investigations, and potential influences of sulfur coverage isotherms on estimated deactivation order.

Keywords: Catalyst deactivation, Sulfur poisoning, Hydrogen, Methane reforming, Reactor simulation

INTRODUCTION

It is well-understood that greenhouse gases are contributing to climate change, instigating unfavorable environmental changes and threatening natural disasters. One potential solution is the utilization of steam-methane reforming along with dry methane reforming (utilizing carbon dioxide instead of steam) for use in hydrogen, fuels, and chemical production. Both steam methane reforming and dry methane reforming have been well studied and thoroughly modeled in literature [5]. However, reforming catalyst sulfur poisoning is not frequently explored, with only a sparse collection of reactor modeling studies being available [6].

Methane reforming is generally described by the following stoichiometric equations:

$$\mathrm{CH_4 + 2H_2O \rightleftharpoons 4H_2 + CO_2} \quad (1)$$

$$\mathrm{CH_4 + H_2O \rightleftharpoons 3H_2 + CO} \quad (2)$$

$$\mathrm{CO + H_2O \rightleftharpoons H_2 + CO_2} \quad (3)$$

With methane dry reforming (being a combination of equations 2 and 3) expressed as:

$$\mathrm{CH_4 + CO_2 \rightleftharpoons 2H_2 + 2CO} \quad (4)$$

Catalyst sulfur coverage can be calculated as the ratio of the mass of sulfur adsorbed versus the empirically-determined catalyst sulfur capacity (representing the total mass of sulfur adsorbed at 100% surface coverage) [7]:

$$\theta_{\mathrm{S}} = \frac{w_{\mathrm{S}} M_{\mathrm{H_2S}}}{S_{\mathrm{p}} \rho_{\mathrm{p}}} \quad (5)$$

Of particular importance is the model for saturated sulfur coverage. A simplification of the adsorption isotherm presented by Alstrup et al. [1] is given by Rostrup-Nielsen [4]:

$$1 - \theta_{\mathrm{s}} = 0.293 \exp\left(-\frac{4300}{T}\right)\left(\frac{P_{\mathrm{H_2S}}}{P_{\mathrm{H_2}}}\right)^{-0.3} \quad (6)$$

Lastly, translation of sulfur coverage to residual catalyst activity is given by Rostrup-Nielsen [4], based on a Maxted-type representation of catalyst activity under poisoning conditions [8]:

$$r_{\mathrm{A}} = r'_{\mathrm{A}} * (1 - \alpha\beta\theta_{\mathrm{s}})^{n} \quad (7)$$

In this expression, α represents the number of adsorbed sulfur atoms per nickel atom at surface saturation while β represents the number of nickel atoms deactivated per adsorbed sulfur atom. With $\alpha = 0.5$ and $\beta = 2.0$, the catalyst's nickel active surface area coverage is taken as proportionate to the sulfur coverage of the catalyst.

MODELING & SIMULATION

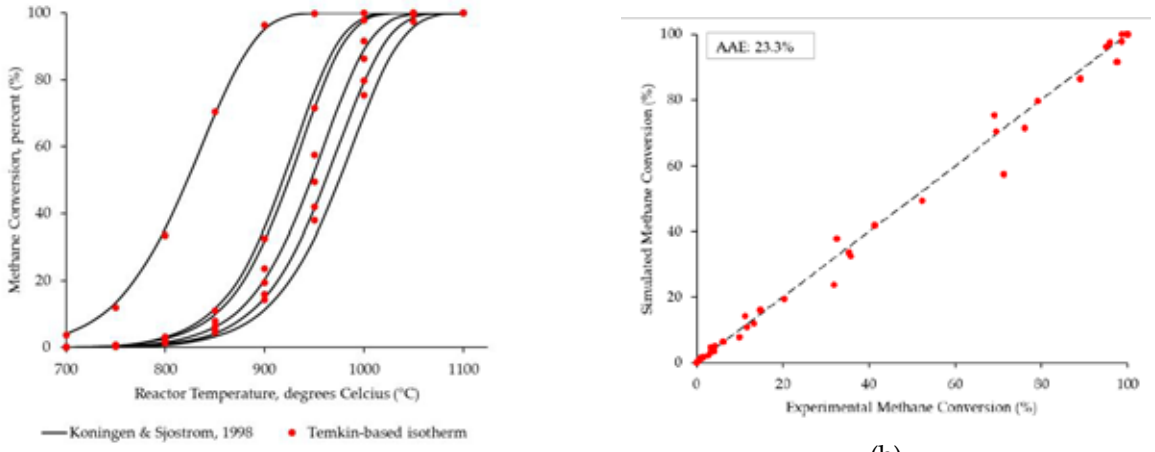
A simplified heterogeneous reactor model is developed following the approach outlined by Rout & Jakobsen [2], but instead using a finite volume framework programmed in MATLAB. Utilizing the reaction rate expressions of Xu & Froment [9], validation of the reactor modeling program was done against the numerical results of Rout & Jakobsen [2], finding good agreement with respect to temperature profile and methane conversion.

Assessment of the experimental data presented by Koningen & Sjörström [3] requires first that the data be shown to satisfy a *quasi-uniform poisoning* condition. This condition identifies when the catalyst particle is small enough to assume that internal sulfur coverage gradients are negligible, and that the computed sulfur coverage at the catalyst surface is essentially the same as what is found throughout the catalyst particle. Taking the catalyst pellet center sulfur concentration to be 90% that of the pellet surface concentration at saturation (to evaluate a worst-case scenario), saturation time was found to be 0.2 seconds – implying that catalyst pellet poisoning was quasi-uniform. This, along with broad agreement with other kinetic criteria [10], provided sufficient justification to proceed with the use of a simplified heterogeneous approach. The expression for quasi-uniform poisoning saturation time is given as:

$$t_{\mathrm{sat,D}} = N_{\mathrm{D}}/N_{\mathrm{S,sat}} = \left(D_{\mathrm{eff}}\frac{\left(C_{\mathrm{H_2S,s}} - C_{\mathrm{H_2S,c}}\right)}{r_{\mathrm{p}}}\right)\Big/\left(\frac{S_{\mathrm{p}}\rho_{\mathrm{p}}}{M_{\mathrm{H_2S}}}\right) \tag{8}$$

RESULTS AND DISCUSSION

Simulated methane conversion compared well against Koningen & Sjörström [3], having an average absolute error of 23.3% - with underprediction of methane conversion observed at lower H_2S concentrations and overprediction observed at higher concentrations (see Figure 1). Notably, these results are only possible for a deactivation order of $n = 1$, versus the order of $n = 3$ presented by Rostrup-Nielsen [4]. However, methanation studies have suggested deactivation orders ranging from 1 to 2 [11, 12], to as high as 4.3 [13]. It is also worth considering the impact of different models for sulfur coverage on modeling residual catalyst activity at high H_2S concentrations. For example, utilizing the chemisorption isotherm presented by Wise et al. [14], which predicts lower sulfur coverage than Alstrup et al. [1], may result in a predicted order of deactivation of $n = 2$.



(a) (b)

Figure 1: Direct comparison of simulated versus reference methane conversions from Koningen & Sjörström [3] (a), and overall parity plot between simulated versus reference methane conversions. Data based on H_2S feed concentrations of 0 ppm, 25 ppm, 50 ppm, 100 ppm, 200 ppm, and 300 ppm, respectively.

CONCLUSIONS

The principal conclusions of this study are:

- A simplified heterogeneous fixed-bed reactor model was developed and validated to simulate the influence of hydrogen sulfide poisoning for methane steam and dry reforming. A quasi-uniform poisoning criteria (along with conventional criteria to verify kinetic control of methane conversion) was applied to verify it was appropriate to simulate the data of Koningen & Sjoström [3] using this approach.
- Assuming an order of deactivation of $n = 1$, good agreement was obtained between simulated and literature values for methane conversion under H_2S poisoning. An average absolute error of 23.3% was observed, with underprediction at lower H_2S feed concentrations and overprediction at higher concentrations.

- While the order of deactivation differs from what is directly presented for steam-methane reforming, it is inline with similar studies conducted for methanation. Further, variations in what is used to predict sulfur chemisorption may also significantly affect what is predicted for the order of deactivation.
- It is recommended that additional experimental work be completed to permit modeling of both sulfur chemisorption and residual activity for methane reforming catalysts, particularly at lower temperature operation (i.e., below 800°C) where they are most vulnerable to poisoning. It would also be interesting to see how such studies compare with sulfur poisoning studies conducted for other syngas processes.

REFERENCES

1. Alstrup I, Rostrup-Nielsen JR and Roen S. 1981. High-Temperature Hydrogen Sulfide Chemisorption of Nickel Catalysts. Applied Catalysis 1:303-314.
2. Rout KR and Jakobsen HA. 2015. A numerical study of fixed bed reactor modelling for steam methane reforming process. Canadian Journal of Chemical Engineering 93:1222-1238.
3. Koningen J. and Sjostrom K. 1998. Sulfur-deactivated steam reforming of gasified biomass. Industrial & Engineering Chemistry Research 37:341-346.
4. Rostrup-Nielsen JR. 1984. Sulfur-Passivated Nickel-Catalysts For Carbon-Free Steam Reforming Of Methane. Journal of Catalysis 85:31-43.
5. Fabrik M, Salama A and Ibrahim H. 2021. State-of-the-art in methane-reforming reactor modeling: challenges and new insights. Reviews in Chemical Engineering 000010151520200038.
6. Sadooghi P and Rauch R. 2015. Experimental and modeling study of hydrogen production from catalytic steam reforming of methane mixture with hydrogen sulfide. International Journal of Hydrogen Energy 40:10418-10426.
7. Christiansen LJ and Andersen SL. 1980. Transient Profiles In Sulfur Poisoning Of Steam Reformers. Chemical Engineering Science 35:314-321.
8. Maxted EB. 1951. The Poisoning of Metallic Catalysts. In Advances in Catalysis, Vol. 3. Edited by Frankenburg WG, Komarewsky VI, Rideal EK, Emmett PH and Taylor HS. New York, Academic Press.
9. Xu JG and Froment GF. 1989. Methane Steam Reforming, Methanation And Water-Gas Shift. 1. Intrinsic Kinetics. AIChE Journal 35:88-96.
10. Levenspiel O. 1999. Chemical reaction engineering. New York, Wiley.
11. Erekson EJ and Bartholomew CH. 1983. Sulfur Poisoning of Nickel Methanation Catalysts. 2. Effects of H2S Concentration, CO And H2O Partial Pressures and Temperature on Deactivation Rates. Applied Catalysis 5:323-336.
12. Fitzharris WD, Katzer JR and Manogue WH. 1982. Sulfur Deactivation of Nickel Methanation Catalysts. Journal of Catalysis 76:369-384.
13. Rostrup-Nielsen JR and Pedersen K. 1979. Sulfur Poisoning of Boudouard and Methanation Reactions on Nickel Catalysts. Journal of Catalysis 59:395-404.
14. Wise H, McCarty J and Oudar J. 1985. Sulfur and Carbon Interactions with Metal Surfaces. In Deactivation and poisoning of catalysts. Edited by Oudar J and Wise H. New York, Dekker.

WHEC-2022
23rd World Hydrogen Energy Conference
June 26-30, 2022 - Istanbul

#84

MECHANISTIC KINETIC MODELING FRAMEWORK FOR THE CONVERSION OF WASTE CRUDE GLYCEROL TO VALUE-ADDED HYDROGEN-RICH GAS

[1] Anita Odoom, [1] Michael Fabrik, [1] Amgad Salama, [1*] Hussameldin Ibrahim
[1]Faculty of Engineering and Applied Science, University of Regina, 3737 Wascana Parkway, Regina, Saskatchewan, Canada

*Corresponding author e-mail: hussameldin.ibrahim@uregina.ca

ABSTRACT

The kinetics for crude glycerol autothermal reforming over 5% Ni/CeZrCa catalyst were studied using previous experimental work. An overall power law model was developed for autothermal crude glycerol reforming, with a frequency factor of 4.3×10^{10} (mol/min)/g_{cat}, an activation energy of 8.78×10^{4} kJ/mol, and orders of reaction for crude glycerol, water, and oxygen of 1.04, 0.54, and 1.78, respectively. The power law model featured an average absolute error (AAE) of 5.8%. Additionally, mechanistic models describing autothermal crude glycerol reforming were also developed for three primary sub-reactions: steam reforming of crude glycerol, total oxidation of crude glycerol, and carbon dioxide methanation. An Eley-Rideal (ER) type expression best described steam reforming of crude glycerol, featuring an AAE of 9.7%. A Langmuir Hinshelwood Hougen Watson (LHHW) type expression best described total oxidation, presenting an AAE of 14.6%. Lastly, carbon dioxide methanation was best represented by an ER type expression, featuring an AAE of 5.8%.

Keywords: Glycerol, Hydrogen, Kinetics, Reactor modeling, Autothermal reforming

INTRODUCTION

Net-zero emission fuels production, representing one of three key pillars (along with net-zero emission electricity and hydrogen production) to addressing greenhouse gas emissions, offers a fast route to decarbonizing otherwise difficult to manage use cases like commercial aviation, mechanised agriculture, and heavy construction. In the latter two cases, diesel fuel may be substitute with biodiesel – a fuel produced by the transesterification of animal fats and plant-based oils to produce fatty acid ethyl esters (FAEEs). However, glycerol ($C_3H_8O_3$) is produced as an unwanted and low-value co-product of transesterification. What is proposed as part of this study's overall program is the conversion of co-product glycerol into synthesis gas via autothermal crude glycerol reforming, where a supply of hydrogen can be generated for use in downstream biodiesel upgrading processes like hydrodeoxygenation.

A number of other investigators have considered glycerol reforming [1-3], but – to our present awareness – there does not seem to be a mechanistic analysis of the reforming of crude glycerol. Accordingly, kinetic data generated through the experimental work of Ghani et al. [4] was used to derive mechanistic rate expressions for the autothermal reforming of crude glycerol over 5% Ni/CeZrCa catalyst.

MATERIALS AND METHODS

Briefly, the experimental data of Ghani et al. [4] was derived for a representative crude glycerol mixture comprising of pure glycerol, methanol, potassium palmitate (i.e., soap), oleic acid (i.e., free fatty acid), and sodium and potassium chloride (i.e., ashes). Integral reactor tests were conducted under conditions ranging between 773 to 923 K, 0.05 to 0.20 oxygen-to-carbon ratio, 1.6 to 3.6 steam-to-carbon ratio, and space velocities between 12.71 and 158.23 g_{cat}.min/mol_C. Integral reactor tests were conducted to determine the rate of reaction under each condition. While a rudimentary power law model was developed, it remains desirable to propose and scrutinize mechanically postulated rate expressions in order to gain insights concerning the potential reaction steps involved in autothermal crude glycerol reforming. Following an approach similar to that of Liu & Lawal [3], the autothermal reforming of crude glycerol was subdivided into three (3) independent reactions: glycerol steam reforming, glycerol oxidation, and CO2 methanation.

Overall Autothermal Reforming Reaction	$C_{2.5}H_7O_2 + 0.7H_2O + 0.65O_2 \rightarrow 2CO_2 + 0.5CH_4 + 3.2H_2$	(4)
Glycerol Steam Reforming	$0.8C_{2.5}H_7O_2 + 2.4H_2O \rightarrow 2CO_2 + 5.2H_2$	(5)
Glycerol Oxidation	$0.2C_3H_8O_3 + 0.65O_2 \rightarrow 0.5CO_2 + 0.7H_2O$	(6)
CO_2 Methanation	$0.5CO_2 + 2H_2 \leftrightarrow 0.5CH_4 + H_2O$	(7)

For the sake of simplicity, crude glycerol was written out as pure glycerol in both the derived mechanistic rate expression as well as for the reversible and irreversible power law rate expressions.

Glycerol steam reforming was found to best match an Eley-Rideal type mechanism describing molecular adsorption of glycerol to the catalyst, followed by dissociation to ethylene glycol and formaldehyde, which then undergo reaction with gas-phase steam to produce carbon dioxide and water. In the case of total oxidation of glycerol, an LHHW mechanism featuring the molecular adsorption and surface oxidation of glycerol was found to be successful. Lastly, in the case of CO_2 methanation, it was found that an Eley-Rideal mechanism describing the methanation of surface-adsorbed carbon dioxide by hydrogen provided the best performance. The mechanisms are described in Table 1 below, and in the rate expressions that follow.

Table 1. Summary of successful glycerol reforming mechanisms

Glycerol Steam Reforming	Glycerol Total Oxidation	CO_2 Methanation
$0.8C_3H_8O_3 + S \leftrightarrow 0.8C_3H_8O_3$	$0.2C_3H_8O_3 + S \leftrightarrow 0.2C_3H_8O_3.S$	$0.5CO_2 + S \rightarrow 0.5CO_2.S$
$C_3H_8O_3.S \leftrightarrow C_2H_6O_2.S + CH_2O.S$	$0.65O_2 + S \leftrightarrow 1.3O.S$	$2H_2 + S \rightarrow 2H_2.S$
$C_2H_6O_2.S + H_2O \leftrightarrow 1.5CO_2 + 4.2H_2 + S$	$0.2C_3H_8O_3.S + 1.3O.S \leftrightarrow 0.5CO_2.S + 0.7H_2O.S$	$0.5CO_2.S + 2H_2 \rightarrow CH_3OH.S$
$CH_2O.S + 0.2H_2O \leftrightarrow 0.5CO_2 + H_2 + S$	$0.2C_3H_8O_3.S + 1.3O.S \leftrightarrow CH_2O_2.S + S$	$CH_3OH.S \rightarrow 0.5CH_4 + H_2O + S$
	$CH_2O_2.S \leftrightarrow 0.5CO_2.S + 0.7H_2O$	
	$0.5CO_2.S \leftrightarrow 0.5CO_2 + S$	

Rate Expression for Glycerol Steam Reforming

$$r_4 = k_0 e^{-\left(\frac{E_a}{RT}\right)} \times \left[\frac{\left(\frac{[A]^{0.8}[B]^{2.4}}{[E]^{1.5}[F]^{4.2}} - \frac{[F][E]^{0.5}}{K_{p(eq)}}\right)}{\left(1 + K_1[A]^{0.8} + \frac{K_W[A]^{0.8}[B]^{2.2}}{[E]^{1.5}[F]^{4.2}} + \frac{K_C[E]^{1.5}[F]^{4.2}}{[B]^{2.2}}\right)}\right] \quad (8)$$

Rate Expression for Glycerol Total Oxidation

$$r_2 = k_0 e^{-\left(\frac{E_a}{RT}\right)} \times \left[\frac{\left([A]^{0.2} - \frac{[E]^{0.5}[B]^{0.7}}{K_{p(eq)}[C]^{0.65}}\right)}{\left(1 + K_3[C]^{0.65} + K_6[E]^{0.5}[B]^{0.7} + K_B[E]^{0.5} + \frac{K_w[E]^{0.5}[B]^{0.7}}{[C]^{0.65}}\right)}\right] \quad (9)$$

Rate Expression for CO_2 Methanation

$$r_1 = k_0 e^{-\left(\frac{E_a}{RT}\right)} \times \left[\frac{\left([E]^{0.5} - \frac{[D]^{0.5}[B]}{K_{p(eq)}[F]}\right)}{\left(1 + K_{3(ads)}[D]^{0.5}[B] + \frac{K_{1(ads)}[D]^{0.5}[B]}{([F]^2)}\right)}\right] \quad (10)$$

RESULTS AND DISCUSSION

The models described here were the most successful in predicting the rate of each respective reaction. The glycerol steam reforming model featured an average absolute error (AAE) of 9.7%, with total oxidation having an AAE of 14.6% and carbon dioxide methanation presenting an AAE of 5.8%. Further, these models were also successfully tested against thermodynamic scrutiny criteria [5].

Power law rate expressions, in addition to the mechanistic expressions, were derived for each of the three reactions and compared favourably against other results found in literature. Activation energy in glycerol steam reforming was 89.1 kJ/mol, versus 103.4 kJ/mol [6] and 43.4 kJ/mol [7] for nickel-ceria catalyst, and 63.3 kJ/mol [2] for cobalt-nickel-alumina catalyst. Further, activation energies for the total oxidation and CO_2 methanation reactions were calculated to be 88.8 kJ/mol and 88.6 kJ/mol, respectively, versus the predicted 116.4 kJ/mol and 87.8 kJ/mol activation energies [8] predicted for each respective reaction over lanthanum oxide catalyst using methane.

CONCLUSIONS

The main findings of this study are as follows:

- The intrinsic kinetics of crude glycerol autothermal reforming (ATR) was studied over Ni/CeZrCa catalyst at conditions of 773 – 923 K at atmospheric pressure, steam-to-carbon ratio of 2.6, and oxygen to carbon ratio of 0.125. The intrinsic kinetic data provided by Ghani et al. [4] was not limited by heat or mass transfer, and

conditions were assumed to be far from equilibrium. The kinetics were studied following a power law approach as well as by proposing a number of kinetic mechanisms following the LHHW and Eley-Rideal frameworks.

- For steam reforming, it was found that the Eley-Rideal models best described the reaction rate, with ER 4 ultimately being chosen as the preferred model following thermodynamic scrutiny, possessing an AAE of 9.7%. This model reflected a rate-limiting reaction between adsorbed intermediate and steam.
- The most suitable model for total oxidation was found to be the power law model. Generally, LHHW-based mechanistic rate expressions performed better than those based on an Eley-Rideal style mechanism. The mechanistic model considering the molecular adsorption of crude glycerol was found to be the best mechanistic description, with an AAE of 14.6%.
- Lastly, the CO_2 methanation reaction was best described by an Eley-Rideal type mechanism considering the adsorption of carbon dioxide, presenting an AAE of 5.8%.

REFERENCES

1. Sundari R and Vaidya PD. 2012. Reaction Kinetics of Glycerol Steam Reforming Using a Ru/Al2O3 Catalyst. Energy & Fuels 26:4195-4204.
2. Cheng CK, Foo SY and Adesina AA. 2010. Glycerol Steam Reforming over Bimetallic Co-Ni/Al2O3. Industrial & Engineering Chemistry Research 49:10804-10817.
3. Liu YJ and Lawal A. 2015. Kinetic study of autothermal reforming of glycerol in a dual layer monolith catalyst. Chemical Engineering and Processing: Process Intensification 95:276-283.
4. Ghani AA, Torabi F, and Ibrahim H. 2017. Kinetics of hydrogen production by the autothermal reforming of crude glycerol over modified nickel supported catalyst. Journal of Environmental Chemical Engineering 5:5827-5835.
5. Vannice MA. 2005. Kinetics of Catalytic Reactions. New York, Springer.
6. Adhikari S, Fernando SD and Haryanto A. 2009. Kinetics and Reactor Modeling of Hydrogen Production from Glycerol via Steam Reforming Process over Ni/CeO2 Catalysts. Chemical Engineering & Technology 32:541-547.
7. Pant KK, Jain R and Jain S. 2011. Renewable hydrogen production by steam reforming of glycerol over Ni/CeO2 catalyst prepared by precipitation deposition method. Korean Journal of Chemical Engineering 28:1859-1866.
8. Nguyen TH, Lamacz A, Krzton A, Ura A, Chalupka K, Nowosielska M, Rynkowski J and Djega-Mariadassou G. 2015. Partial oxidation of methane over Ni-0/La2O3 bifunctional catalyst II: Global kinetics of methane total oxidation, dry reforming and partial oxidation. Applied Catalysis B: Environmental 165:389-398.

WHEC-2022
23rd World Hydrogen Energy Conference
June 26-30, 2022 - Istanbul

#85

APPLICATION OF DFT AND MACHINE LEARNING TO PREDICT OPTIMUM OPERATING CONDITIONS FOR METHANE PYROLYSIS USING MOLTEN METALS FOR CARBON-FREE HYDROGEN PRODUCTION

[1] Lord Ugwu, [1] Hussameldin Ibrahim, [2] Yasser Morgan*
[1]Clean Energy Technologies Research Institute (CETRI), Process Systems Engineering, Faculty of Engineering and Applied Science, University of Regina, 3737 Wascana Parkway Regina, SK, S4S 0A2, Canada.
[2]Software Systems Engineering, Faculty of Engineering and Applied Science, University of Regina, 3737 Wascana Parkway Regina, SK, S4S 0A2, Canada.

*Corresponding author e-mail: hussameldin.ibrahim@uregina.ca

ABSTRACT

The production of hydrogen from various feedstock involves the catalyzation of various reactions for the generation of the desired product. Experimental studies provide an understanding of the reaction mechanism and the nature of the reactants and products of the reaction. Computational studies involving DFT provide even greater insights into these reactions. The pyrolysis of methane over various catalysts requires an efficient means of screening catalysts for the reaction. The reaction is an endothermic reaction that is associated with a high demand for energy to drive the reaction. A process associated with a reduced demand for energy and increased yield of hydrogen will make the pyrolysis reaction more efficient and more industrially applicable. A combination of DFT and ML provides a means of establishing catalytic descriptor-based predictions for the reaction. The prediction of the relaxation energies of doped group 10, 11 and 12 transition elements from their initial structures with the adsorbate ions at the different stages of the reactions provides a predictable path for the calculation of the Turnover Frequency of the reactions, suggesting the preferred catalyst for the reaction. This study seeks to establish a model for predicting catalytic activity in methane pyrolysis reactions at various operational conditions.

***Keywords*:** Heterogeneous catalysis, hydrogen, density functional theory, machine learning, pyrolysis

INTRODUCTION

Global demand for energy continues to increase, and hydrogen becomes a promising fuel to power our industrial machines [1]. Hydrogen can be produced by water electrolysis, thermochemical and biological methods. Among these, the biological process can be the most favourable because it requires less energy. The method of electrolysis of water requires a lot of energy and hence cannot be a viable alternative. Notwithstanding, it is often used when hydrogen is required in a highly pure form. Steam reforming, a type of thermochemical method, is often used to produce hydrogen and steam reforming of methane is most commonly done. Steam–methane reforming (SMR) is the current industrial method of choice for hydrogen production. However, the SMR process still suffers disadvantages from reactant properties and thermodynamics conditions of the reaction, which include insufficient catalytic activity, low long-term stability of reactant (methane), high production cost and high energy consumption, mostly due to the handling of large amounts of CO_2 co-produced [2].

With the growing need for hydrogen production, and the need to adopt a process that is sustainable and environmentally friendly, it becomes necessary to upgrade some of the existing industrial processes used for hydrogen production for effective management of raw materials such as methane while adopting technologies that are environmentally sustainable. Furthermore, catalysts with higher activity and stability necessary to control the reaction routes and also efficient reaction conditions such as temperature, pressure, feeding rate, type of reactor etc., have to be improved upon for efficient hydrogen production [2][3].

The pyrolysis of methane over molten metals provides an opportunity for carbon dioxide-free hydrogen production while co-producing solid carbon that has several industrial applications.

MATERIALS AND METHODS

This work involves ab initio investigation of molten metals as catalysts for the heterogeneous catalysis of hydrogen production via methane pyrolysis. It has been reported that metals that are active catalysts for methane (Ni, Pt, Pd, Cu, Ag, Au), when dissolved in Bi, an inactive low–melting temperature, produce stable molten metal alloy catalysts for pyrolysis of methane into hydrogen and carbon [4][5].

$$CH_{4\,(g)} \rightarrow 2H_{2\,(g)} + C_{(s)} \qquad \Delta H^0 = 75\,\frac{\text{kJ}}{\text{mol}} \qquad (1)$$

Experimental reports indicate the deactivation of solid catalysts, while the insoluble carbon would float to the surface in molten alloy systems in the reactor[4]. Hence the aim of this work is to simulate the structural and chemical properties of molten alloy systems of varying concentrations of active and inactive metals using ab initio molecular dynamics (MD) code of Car-Parrinello (CP) implemented in Quantum Espresso.
The specific objectives being carried out in the study include:

- Determine the kinetic and wavefunction cutoffs for the separate metal and metal alloy systems.
- Perform variable cell relaxation for separate active (Ni, Pt, Pd), inactive (In, Ga, Sn and Pb) and molten metal alloy systems containing different concentrations.
- Determination of density of states (DOS), projected DOS, D-band etc., to characterize the metal systems.
- Calculate the pair distribution functions, the local concentrations, and Bader charges for the constituent metal atoms as one approaches the surface of the liquid.
- Calculate the activation parameters for the dissociative adsorption of methane using a nudged elastic band (NEB)
- Calculate the adsorption energies of the adsorbate on the catalyst surface.
- Correlation of parameters such as concentrations with turn over frequency (TOF)
- Simulate the effect of temperature and pressure on the molten catalyst systems for the pyrolysis of methane.
- Predict catalytic performance and optimum operating conditions using machine learning models

REFERENCES

1. Giddey S, Badwal SPS, and Kulkarni A. 2013. Review of electrochemical ammonia production technologies and materials. International Journal of Hydrogen Energy 38, 14576–14594.
2. Chen L, Qi Z, Zhang S, Su J, and Somorjai GA. 2020. Catalytic hydrogen production from methane: A review on recent progress and prospect. Catalysts.
3. Angeli SD, Turchetti L, Monteleone G, and Lemonidou AA. 2016. Catalyst development for steam reforming of methane and model biogas at low temperature. Applied Catalyst B Environment. 181, 34–46.
4. Upham DC *et al.* 2017. Catalytic molten metals for the direct conversion of methane to hydrogen and separable carbon. Science (80-100).
5. Palmer C *et al.* 2019. Methane Pyrolysis with a Molten Cu-Bi Alloy Catalyst. ACS Catalysis.

WHEC-2022
23rd World Hydrogen Energy Conference
June 26-30, 2022 - Istanbul

#130

PHOTOCATALYTIC GLYCEROL REFORMING ON GOLD - COPPER NANO METALLIC TiO_2

[1*] *Ramazan Yıldırım,* [1] *Pınar Özdemir*
[1]Department of Chemical Engineering, Boğaziçi University, 34342, Istanbul, Turkey

*Corresponding author e-mail: yildirra@boun.edu.tr

ABSTRACT

The photocatalytic reforming of glycerol was studied on gold-copper (Au-Cu) loaded titanium dioxide (TiO_2) photocatalyst with the aim of utilizing glycerol, which is the main by-product of biodiesel production, to produce hydrogen using solar energy. 0.2 wt. % Au, 1 wt.% Cu as well as 0.2% Au and 0.8 wt.% Cu containing photocatalysts were tested. The monometallic and bimetallic photocatalysts were synthesized by deposition precipitation with urea (DPU) and sequential deposition precipitation with urea (S-DPU) respectively and calcined in air at 400°C for 4h. Then the photocatalysts were tested in a photoreactor, equipped with 300 W xenon lamp, at ambient condition using 20 wt.% aqueous glycerol mixture. 0.2 wt.% Au loaded on TiO_2 produced H_2 with 1085 µmol/h.gcat production rate, which is comparable to that of 1 wt.% platinum (Pt) loaded on TiO_2. Then, it was concluded that Au/TiO_2 could be a more economical alternative for Pt considering that it produced the same results even thought its loading was five times lower.

Keywords: Glycerol, Au/TiO_2, Hydrogen production, Photocatalysis, Photocatalytic reforming

INTRODUCTION

The increasing world energy demand, which is supplied by fossil fuels, creates new challenges like global warming and climate change due to the emission of greenhouse gases; these challenges initiated worldwide search to find alternative and sustainable energy production processes from the renewable natural resources such as biomass, sun, wind, geothermal reservoirs, and tidal waves [1, 2]. The glycerol, as the main by-product of biodiesel production (10% of total yield) [3], can be also used as an alternative source for hydrogen production via photocatalytic process, and increase the feasibility of biodiesel production from renewable biomass. Additionally, some valuable products of glycerol such as dihydroxyacetone, glyceraldehyde, glyceric acid, hydroxypyruvic acid, and glycolic acid, which are used in food, cosmetics, and pharmaceutical industries, can be also produced more feasibly via the photocatalytic reforming [3, 4]. This way, the glycerol can be utilized in a simpler and more economical process that run under ambient conditions, than the high energy consuming conventional ways like stream reforming, fermentation, and esterification [4-6].

In literature, photocatalytic glycerol reforming has been conducted on especially TiO_2 nanopowder with precious or non-precious metals such as platinum (Pt), palladium (Pd), gold (Au), ruthenium (Ru) or copper (Cu), nickel (Ni), zinc (Zn) so as to get higher H_2 yield [4, 6]. Even though the mostly used monometallic photocatalyst Pt/TiO_2 is the most active, it suffers form O_2 and CO poisoning and more expensive than alternative ones like Au or Cu loaded TiO_2 [4, 7]. In this regard, Au and Cu were used as a mono and bimetallic catalyst on TiO_2 due to their nearest working function values and plasmonic effects under visible light condition to reduce the cost, prevent the oxygen and carbon monoxide poisoning and enhance H_2 production.

EXPERIMENTAL

1 wt.% Cu/TiO_2 and 0.2 wt.% Au/TiO_2, monometallic catalysts were prepared using DPU. 1.1 10^{-3} M aqueous solution of $CuCl_2$ (or $HAuCl_4.3H_2O$) in distillated water were added into 5 g of TiO_2 and 100 mL distillated water mixture. After stirring $CuCl_2$ (or $HAuCl_4.3H_2O$) solution with TiO_2 in 100 mL distillated water, 0.42 M urea aqueous solution was added into the suspension and stirred for four hours at 70°C in order to decompose urea and rise pH to 7-8 interval. Then, the catalyst samples were washed, centrifuged three times, dried overnight at 100°C and finally calcined at 400°C for 4 hours in air [8, 9]. The bimetallic 0.2 wt.% Au-0.8 wt.% Cu/TiO_2, on the other hand, were prepared using S-DPU methods. First the copper was deposited on TiO_2 as previously explained DPU procedure above. Then the catalyst sample was centrifuge, dried and calcined at 400°C for 4 hours in air. After that, all steps were repeated for Au deposition on Cu/TiO_2. Both DPU and S-DPU methods were conducted in dark condition to prevent the effect of light on gold and copper particles [10, 11]. For comparison, 1 wt.% Pt on TiO_2 was also prepared via incipient-to-wetness impregnation of tetraammineplatinum(II)nitrate and calcined in air at 400°C for 4h.

H_2 production from glycerol were conducted in a semi batch photocatalytic reaction system in which argon (Ar) was used as inert-carrier gas with the flow rate of 30 mL/min. 1.0 g_{cat}/L was suspended in 500 mL reaction solution (20 wt.% glycerol and 80 wt.% distillated water). The photoreactor was irradiated by Luzchem 300 W Xe lamp. Determination of H_2 production rate was carried out via a gas chromatograph system.

RESULTS AND DISCUSSION

Au/TiO_2 which was the best performed catalysts was characterized by SEM to investigate distribution and size of gold nanoparticles on TiO_2. In SEM images, the shiny and spherical gold nanoparticles were 40-50 nm size clusters. There can be also smaller gold particles on TiO_2, however they could not be visible in the range of SEM. Although there are some agglomerations of gold in only certain areas, the samples generally have well distributed and large number of gold nanoparticles.

The reflectance – wavelength values of each catalyst were measured using UV-VIS spectroscopy by Kubelka-Munk method to calculate direct band-gap energy; the band gap of samples (about 2.97 eV) was quite close to TiO_2 indicating that Au, Cu or Au-Cu loading on TiO_2 did not have any effect on band gap.

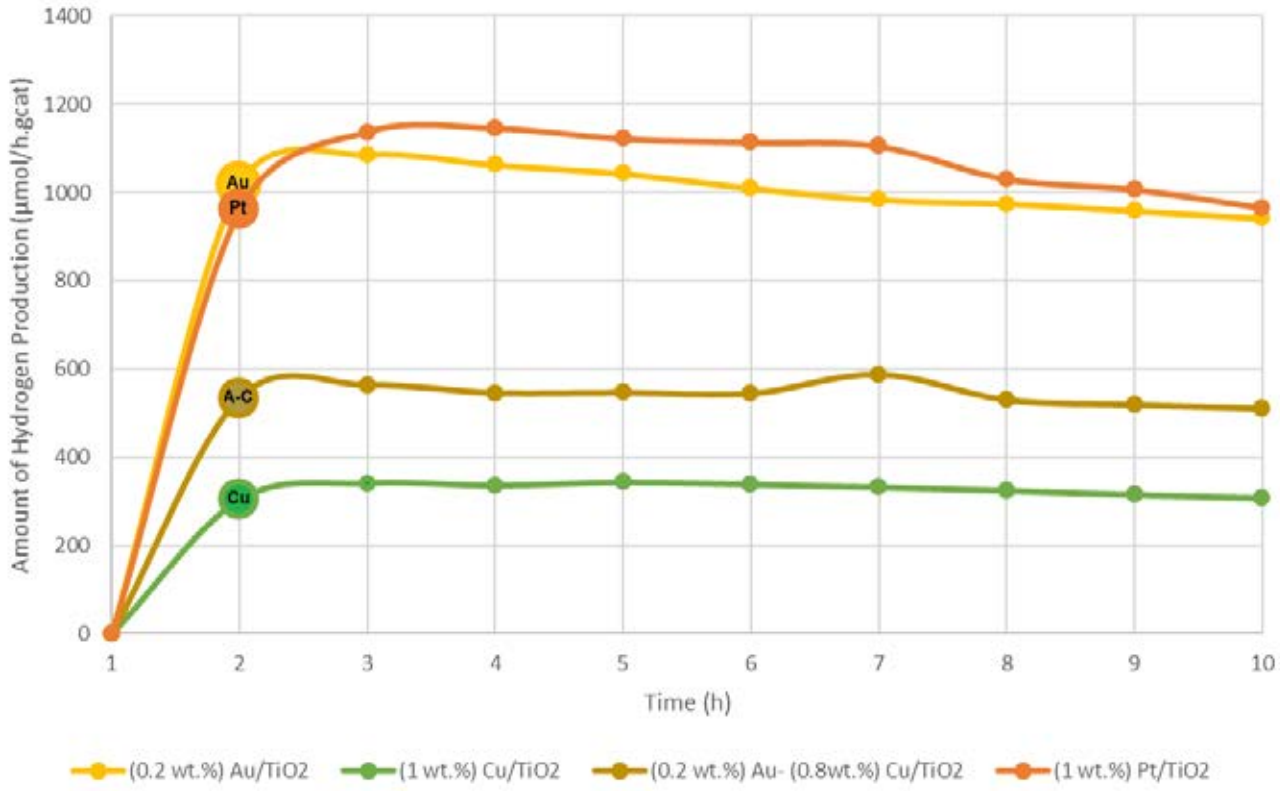


Figure 1. H_2 production rate of (0.2 wt.%) Au, (1 wt.%) Cu and (0.2 wt.%) Au-(0.8 wt.%) Cu loaded TiO_2 catalysts

It can be easily seen from Figure 1 that 0.2 wt.% Au/TiO_2 is active as much as 1 wt.% Pt/TiO_2 for H_2 production with the maximum of 1085 µmol/h.gcat. Having almost the same level of H_2 production in two catalysts, even though Au loading is five times lower than Pt, may be attributed to the plasmonic effects of gold nanoparticle on H_2 evolution [12]; this may increase the feasibility of using Au considering that Pt is more expensive and more sensitive to O_2 and CO [4, 7]. As Figure 1 also indicates, Cu/TiO_2 has the lowest level of H_2 production while Au-Cu containing bimetallic catalyst, tested under same ambient condition with Au/TiO_2 and Cu/TiO_2, performed in between only Au or Cu containing catalysts with the maximum H_2 production of 587 µmol/h.gcat. Since the copper is much cheaper than Au and Pt, it may be considered as a potential catalyst even though the H_2 production rate on this metal in glycerol reforming.

CONCLUSIONS

In this study, photocatalytic glycerol reforming under ambient condition was examined on Au, Cu and $Au-Cu/TiO_2$ catalysts. Glycerol, the main by-product of biodiesel, was utilized as a raw material here instead of sacrificial agent. 0.2 wt.% Au/TiO_2 has the best performance with the maximum 1085 µmol/h.gcat hydrogen production rate which is almost the same with the production rate of 1 wt.% Pt/TiO_2. This makes Au/TiO_2 as a suitable candidate in terms of both cost and catalyst performance for the glycerol photocatalytic reforming. Although 1 wt.% Cu/TiO_2 and 0.2 wt.% Au-0.8 wt.% Cu/TiO_2 give lower hydrogen production rates, the performance is still considerably high such that Cu can be also considered as an alternative catalyst for this purpose.

ACKNOWLEDGEMENT

This work is financially supported by TUBITAK, through Project No: 217M52834342

REFERENCES

1. Desai B. G. A. 2019. Tale of Two Eras (1973 – 2014): World energy scene 40 years after the energy crisis. Current Science 116: 521-523.
2. Kalyanasundaram K. 2013. Dye-sensitized Solar Cells. Lausanne, EPFL Press.
3. Guo L., Sun Q., Marcus K., Hao Y., Deng J., Bi K., & Yang Y. 2018. Photocatalytic glycerol oxidation on AuxCu–CuS@TiO2 plasmonic heterostructures. Journal of Materials Chemistry A 6: 22005–22012.
4. Rahim S. A. N Md., Lee C. S., Abnisa F., Aroua M. K., Wan Daud W. A., Cognet P., & Pérès Y. 2020. A review of recent developments on kinetics parameters for glycerol electrochemical conversion – A by-product of biodiesel. Science of the Total Environment 705: 135-137.
5. Luo N., Zhao X., Cao F., Xiao T., & Fang D. 2007. Thermodynamic Study on Hydrogen Generation from Different Glycerol Reforming Processes. Energy & Fuels 21: 3505-3512.
6. Puga A. V. 2016. Photocatalytic production of hydrogen from biomass-derived Feedstocks. Coordination Chemistry Reviews 315: 1-66.
7. Dodekatos G., Schünemann S., & Tüysüz H. 2018. Recent Advances in Thermo-, Photo-, and Electrocatalytic Glycerol Oxidation. ASC Catalysis 8: 6301-6333.
8. Saadetnejad D., & Yıldırım R. Photocatalytic hydrogen production by water splitting over Au/Al-SrTiO3. 2018. International Journal of Hydrogen Energy 43: 1116-1122.
9. Zanella R., Giorgio S., Henry C. R., & Louis C. Alternative Methods for the Preparation of Gold Nanoparticles Supported on TiO2. 2002. The Journal of Physical Chemistry B 106: 7634-7642.
10. Gomez-Cortes, A., Diaz G., Zanella R., Ramirez H., Santiago P., & Saniger J. M. Au-Ir/TiO2 Prepared by Deposition Precipitation with Urea: Improved Activity and Stability in CO Oxidation. 2009.The Journal of Physical Chemistry C 113: 9710-9720.
11. Sandoval A., Louis C., & Zanella R. Improved activity and stability in CO oxidation of bimetallic Au–Cu/TiO2 catalysts prepared by deposition–precipitation with urea. 2013. Applied Catalysis: Environmental 140-141: 363-377.
12. Xiao N., Li S., Li X., Ge L., Gao Y., & Li N. 2020. The roles and mechanism of cocatalysts in photocatalytic water splitting to produce hydrogen. Chinese Journal of Catalysis 41: 642-671.

WHEC-2022
23rd World Hydrogen Energy Conference
June 26-30, 2022 - Istanbul

#138

NOVEL DESIGN CONCEPT FOR THERMOLYSIS REACTOR IN THE THERMOCHEMICAL COPPER-CHLORINE CYCLE OF HYDROGEN PRODUCTION

[1*] *Ehsan Armoudli,* [1] *Ofelia A. Jianu*
[1] Mechanical Automotive and Materials Engineering, University of Windsor, 401 Sunset Avenue, Windsor, Canada

*Corresponding author e-mail: armoudl@uwindsor.ca

ABSTRACT

Hydrogen is considered one of the most promising solutions for renewable energy storage and decoupling generation from demand for large-scale implementation in the near future. The copper-chlorine (Cu-Cl) cycle for clean hydrogen production is known to be the most feasible thermochemical cycle due to its low energy requirements. Nonetheless, there are difficulties in scaling up and enhancing the efficiency of the Cu-Cl cycle for its commercialization. One of the most challenging sections to design is the thermolysis reactor in which the decomposition of copper oxychloride ($CuO.CuCl_2$) into molten CuCl(l) and O_2(g) occurs at approximately 530 °C. To address this challenge, this study presents a novel design concept for the thermolysis reactor in a 4-step Cu-Cl cycle with the principal objective of improving the temperature distribution on the reactant side. The results of the flow and heat transfer analysis of the reactant side in the heat exchanger showed a decrease of 61% in temperature standard deviation in the upward direction, which shows an improved temperature distribution.

Keywords: Thermochemical Cu-Cl cycle for hydrogen production, Continuous thermolysis reactor, Molten salt heat exchanger, Solar salt.

INTRODUCTION

Decoupling the generation from the demand is a well-known solution to address the challenges involved with uncertainty and fluctuations in implementing renewable sources. Hydrogen is one of the most reviewed mediums to carry on the decoupling. The thermochemical Cu-Cl cycle for hydrogen production is mentioned to be the most promising method in more than 200 thermochemical cycles studies by McQuillan et al. [1] due to its comparably low heat requirement. Wang et al. [2] investigated the Cu-Cl cycle in terms of heat quantity, heat grade, thermal efficiency, engineering challenges, and hydrogen production cost, and concluded that its overall efficiency is between 37 and 54% by having the lowest temperature requirement among all cycles, similar cost, and it has the ability to line up with a variety of low-temperature sources with lower technical challenges. There are three main variations of the Cu-Cl cycle, 3-step, 4-step, and 5-step [3], which are sharing the main components of electrolysis, thermolysis, and hydrolysis reactors [2]. Based on a comparison done by Ishaq and Dincer [1], the 4-step cycle has the highest energy and exergy efficiencies of 41.9, and 75.7, respectively. However, the thermolysis reactor is mentioned to be the most critical component in the cycle as it has the highest maximum heat requirement of 194.5 kW, a required temperature of 450-530°C, and a maximum exergy destruction rate with a value of 112.2 kW [3], [4]. Furthermore, transporting corrosive products with such a high temperature is a challenging task. Wajda and Gabriel [5] asserted that the Cl_2(g) controls the decomposition of $CuO.CuCl_2$, and represented a design for the thermolysis reactor to scale up the total cycle for a pilot industrial site. Using CuCl(s) as the reactant, they showed that their reactor with dual electrical heaters can decompose 2 kg of CuCl between 3.5-4 hours. Daggupati et al. [6] found that the release of O_2(g) begins at 380°C and speeds up considerably at temperatures higher than 500°C. Naterer et al. [7] suggested that by generating a reduced pressure inside the reactor, the $CuO.CuCl_2$ decomposition is spontaneous at 480°C, despite the difficulty in controlling the reaction. It is suggested that in the temperature range of 500-530°C the decomposition is spontaneous and below 500°C the reverse reactions will occur. Abdulrahman [8] investigated the thermal scale-up analysis of a multiphase continuous stirred tank (CSTR) that is heated by a half jacket as the thermolysis reactor. In another study by Abdulrahman [9] a heat transfer analysis for a scale-up thermolysis reactor with an internal helical heating tube was investigated. They concluded that the molten CuCl acts as a better heating fluid compared to helium gas and using an internal heating tube is more effective than a half-pipe jacket in transferring heat. Despite all of these efforts in paving the way for commercializing the Cu-Cl cycle, previous reactor designs showed the generation of unwanted substances such as CuCl(g) and Cl_2(g) due to non-uniform distribution of temperature in the reactant which resulted in forming condensed CuCl(s) crystalline and caused blocking and clogging of the reactor tubes [5]. This abstract represents the pathway to design a novel thermolysis reactor that aims to address the following challenges:

- The significant temperature gradient between the surface and bottom of the reactant due to the proximity of the electrical heaters to the bottom caused the temperature to increase over 600°C near the bottom.
- The insufficient temperature on the surface of the reactant for the adequate decomposition of the salt.

- Crystalline formation with a thickness of up to 4 mm inside the reactor is caused by high CuCl vapor pressure.
- Scale-up difficulties due to using batch reactors and problems related to handling the materials.
- Trapping and condensation of oxygen vapor before exiting the molten salt upper surface.
- Production of intermediate chemicals in the reactor.

A primary CFD study of the involved heat exchanger inside the reactor is presented to show to the feasibility of the design.

DESIGN APPROACH AND METHODOLOGY

Temperature variation inside the reactant is crucial in achieving the desired reaction since at temperatures over 450°C, $CuCl_2$ starts to decompose into CuCl(s) and Cl_2(g) [3]. The generated Cl_2(g) reacts with the CuO over 450°C and the generation of O_2 will speed up between 500-530°C.After 550°C, CuCl(l) is vaporized and condensed on the cooler walls and tubes. It can block the outflow of materials, generates partial pressure of oxygen inside the reactor, and negatively effect the heat transfer and thermal performance of the reactor [5]. Consequently, temperature margins, are considered as the main constraints for this design. The proposed reactor consists of three main components: a screw pump and junctions, heat exchanger chamber, and molten salt chamber. Key features of the proposed reactor along with their reasoning are presented in Table 1. Fig. 1 shows the reactor design concept.

Table 1. Key features of the reactor and their reasoning.

Feature	Reasoning
Upward flow of materials	The density of the involved materials in the reaction is ranked as $\rho_{O_2} < \rho_{CuCl} < \rho_{CuO.CuCl_2}$[2]. To prevent the contamination of the O_2(g) in the molten bath, assist its extraction, and have a controllable continuous flow of material, the reactant is pushed in the upward direction. This scheme, along with the next features, enables the effective handling of solid, liquid, and gaseous phases.
Heating temperature increases upward	Considering the density difference, the molten salt is on top of the solid reactant. Therefore, to decrease the thermal resistance, temperature increases as the particles flow upward. In this way, the molten bath is developed at the top of the overall volume of reactant, where the temperature is higher. Generation of O_2(g) increases at higher temperatures which are located at the top surface. This further facilitates the removal of the O_2(g) with minimum traveling through the molten bath.
Screw pump for material handling	To enable a controllable continuous delivery, reaction, removal, and flow of solid material into the reactor, a horizontal screw pump is used. It also provides a seamless flow of material that prevents the product heel between the working cycles.
Oxygen removal port	The oxygen removal port is located at the top of the heat exchanger chamber where the O_2(g) is generated. This prevents sudden surge in O_2(g) partial pressure due to the proximity of the port to the location that the majority of O_2(g) is produced.
Use of conjugate heat transfer by implementing a cross flow heat exchanger	$Cl_2(g)$ and $CuO(s)$ are extremely reactive. Hence, the only available direct heating technique can be provided by inert gases, which are found to be ineffective [11]. Therefore, conjugate heat transfer is used by introducing circuits of bended pips that form a cross-flow heat exchanger inside the reactor. Solar salt is considered as the heating fluid. Thermal resistance is minimized by increasing the heat exchanger aspect ratio and injecting the reactants as near as possible to heating interfaces.
Variable height gate for molten CuCl removal	To control the speed and completeness of the reaction a variable height gate is used to connect the heat exchanger chamber to the molten salt chamber. This gate is used to change the residence time of the molten salt in the heat exchanger chamber.
Molten salt chamber	Molten salt overflows the gate after the required residence time. The molten salt chamber provides a vertical flow of reactant to feed the next step in the cycle which is the heat recovery from the CuCl molten salt.
Nitrogen injection and removal ports	To have a complete reaction and avoid unwanted substances, inside the reactor should be free of any gaseous that can react with the reactant and products. Therefore, N_2(g) is injected into the reactor to purge the remaining gaseous inside.

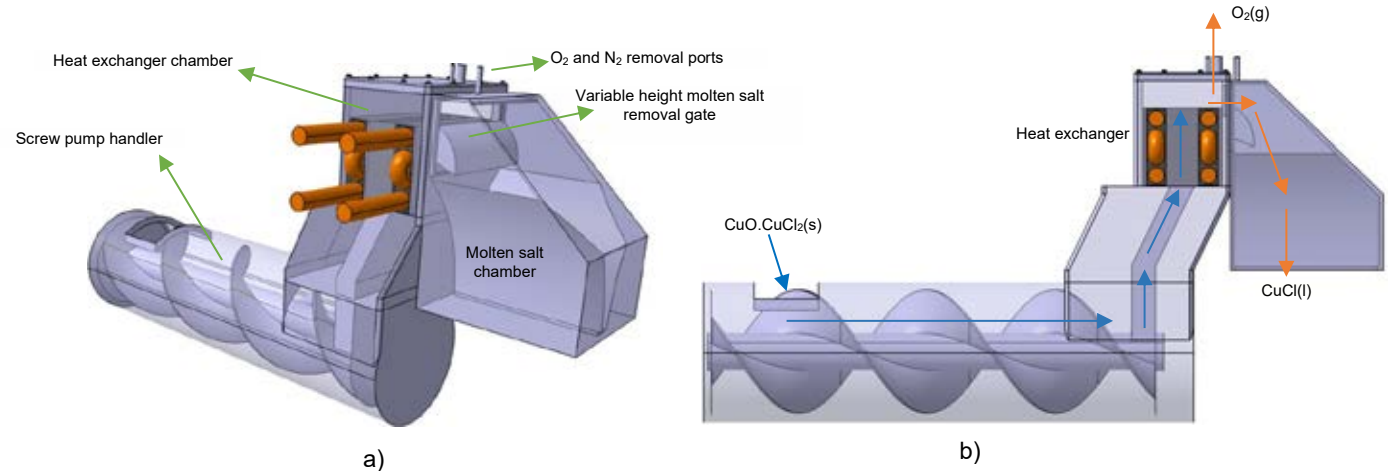


Fig. 1. a) Components of the reactor; b) flow of material inside the reactor.

RESULTS AND DISCUSSION

Fig. 1a shows the reactor and Fig. 1b shows the reactant and products as they move upward in the reactor. A CFD analysis of the heat exchanger has been conducted to assess the temperature distribution of the reactant inside the reactor. It is assumed that reactant will enter the heat exchanger chamber with 430°C and $CuO.CuCl_2$(s) is substituted by CuCl in the numerical model due to its unknown thermal conductivity and dynamic viscosity. Fig. 2 shows the temperature contours inside the reactant. The temperature standard deviation is a measure to show the dispersion which is 58.27°C at the heat exchanger entrance, 35.14 at the middle section, and decreases to 22.49°C at the heat exchanger outlet. This shows an improvement of 61% in temperature distribution along the channel. To further improve the temperature distribution, a study should be performed to improve the heat exchanger design inside the reactor.

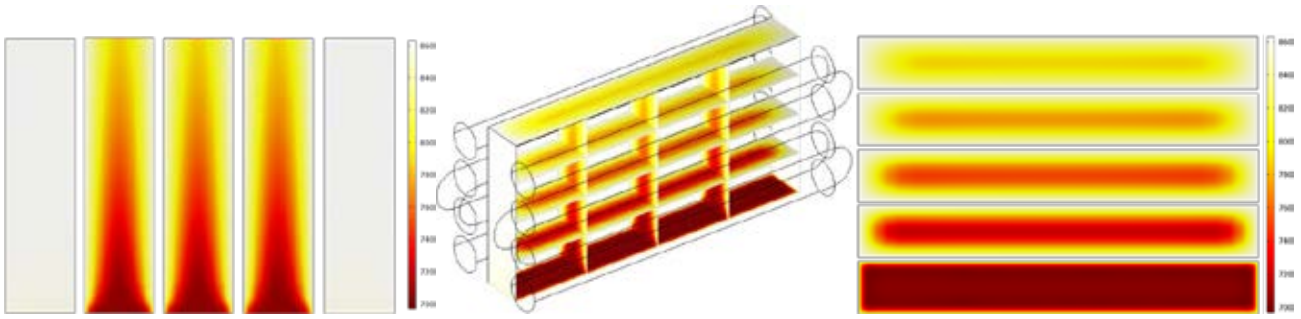


Fig. 2. Temperature distribution of the reactant inside the heat exchanger

CONCLUSIONS

The thermolysis reactor is one of the most critical components of the CuCl cycle and addressing its challenges helps the scale-up process of the CuCl cycle, substantially. With the proposed design, the main objective to improve the temperature distribution inside the reactant was achieved. To do so, an upward flow of reactant was considered, which is powered by a screw pump, and the heating is provided at the heat exchanger by using a circuit of solar salt as the heating fluid. This combination enables the easy removal of O_2(g) and CuCl(l) as well as providing the highest temperature at the top section of the heat exchanger which results in optimum heating of the reactant and avoiding the generation of unwanted substances. A numerical model was developed for the involved heat exchanger to assess the temperature distribution inside the reactant channel. It was shown that the temperature standard deviation decreases by 61% in the upward direction, from 58.27°C to 22.49°C. To further assess the feasibility of this design, separate studies should be done on designing an optimum heat exchanger and assessing the dynamic of other components of the reactor.

REFERENCES

1. McQuillan, B. W., Brown, L. C., Besenbruch, G. E., Tolman, R., Cramer, T., Russ, B. E., ... & Lewandowski, A. (2010). High efficiency generation of hydrogen fuels using solar thermo-chemical splitting of water (solar thermo-chemical splitting for H2). GA-A24972. Prepared under Solar Thermochemical Hydrogen Grant No. DE-FG36-03G013062 for the US Department of Energy and F03-STCH2-002 for the University of Nevada Las Vegas Research Foundation, General Atomics.

2. Z. Wang, G. F. Naterer, and K. Gabriel, “Multiphase reactor scale-up for Cu–Cl thermochemical hydrogen production,” Int. J. Hydrogen Energy, vol. 33, no. 23, pp. 6934–6946, 2008.
3. H. Ishaq and I. Dincer, “A comparative evaluation of three Cu-Cl cycles for hydrogen production,” Int. J. Hydrogen Energy, vol. 44, no. 16, pp. 7958–7968, 2019.
4. F. Razi, I. Dincer, K. Gabriel, “Thermal management of a new integratedcopper-chlorine cycle for hydrogen production. Energy Convers. Manag. 212,112629, 2020.
5. T. Wajda and K. Gabriel, “Thermolysis reactor scale-up for pilot scale Cu-Cl hybrid hydrogen production,” Int. J. Hydrogen Energy, vol. 44, no. 20, pp. 9779–9790, 2019.
6. V. N. Daggupati, G. F. Naterer, K. S. Gabriel, R. J. Gravelsins, Z. L. Wang. “Equilibrium conversion in Cu–Cl cycle multiphase processes of hydrogen production,” Thermochimica Acta. 2009 Dec 10;496(1-2):117-23.
7. G. F. Naterer et al., “Clean hydrogen production with the Cu–Cl cycle–progress of international consortium, I: Experimental unit operations,” Int. J. Hydrogen Energy, vol. 36, no. 24, pp. 15472–15485, 2011.
8. M. W. Abdulrahman, “Similitude for thermal scale-up of a multiphase thermolysis reactor in the Cu-Cl cycle of a hydrogen production,” World Acad. Sci. Eng. Technol. Int. J. Electr. Comput. Energ. Electron. Commun. Eng., vol. 10, no. 5, pp. 567–573, 2016.
9. M. W. Abdulrahman, “Heat transfer analysis of a multiphase oxygen reactor heated by a helical tube in the Cu-Cl cycle of a hydrogen production,” World Acad. Sci. Eng. Technol. Int. J. Mech. Aerospace, Ind. Mechatron. Manuf. Eng., vol. 10, no. 6, pp. 1018–1023, 2016.
10. C. Zamfirescu, I. Dincer, and G. F. Naterer, “Thermophysical properties of copper compounds in copper–chlorine thermochemical water splitting cycles,” Int. J. Hydrogen Energy, vol. 35, no. 10, pp. 4839–4852, 2010.
11. G. F. Naterer, K. Gabriel, Z. L. Wang, V. N. Daggupati, and R. Gravelsins. "Thermochemical hydrogen production with a copper–chlorine cycle. I: Oxygen release from copper oxychloride decomposition." International Journal of Hydrogen Energy 33, no. 20 (2008): 5439-5450.

WHEC-2022
23rd World Hydrogen Energy Conference
June 26-30, 2022 - Istanbul

#158

CHEMICAL KINETICS OF TWO-STEP THERMOCHEMICAL DECOMPOSITION OF H_2S OVER NICKEL SULFIDE

*Asma Al Blooshi,[1] Ahmed Al-Hajaj,[1&3] Mohammad Abu Zahra,[1&3] and Giovanni Palmisano,[1&3] Khalid Al-Ali,[*1,2&3]*
[1] Department of Chemical Engineering, Khalifa University, P.O. Box 127788, Abu Dhabi, United Arab Emirates
[2] Center for Catalysis and Separations, Khalifa University, P.O. Box 127788, Abu Dhabi, United Arab Emirates
[3] Research and Innovation on CO_2 and H_2 (RICH) Center, Khalifa University, P.O. Box 127788, Abu Dhabi, United Arab Emirates

*Corresponding author e-mail: khalid.alali@ku.ac.ae

ABSTRACT

The conversion of Hydrogen Sulfide into H_2 and Sulfur ($H_2S \rightarrow H_2 + S$) is beneficial from both environmental and energy perspectives. The two-step thermochemical decomposition of H_2S is considered one of the most promising technologies for Hydrogen production. This work investigates the chemical kinetics of the two-step thermochemical decomposition of H_2S using Nickel Sulfide and studies the key parameters that affect the overall cycling process and H_2S conversion efficiency. Gas-phase and surface-phase kinetics of the two-step thermochemical decomposition of H_2S models were developed in CHEMKIN software. The formulated model results were found to be consistent with the experimental results.

Keywords: Solar thermochemical cycle, H_2S splitting, Hydrogen, Nickel sulfide

INTRODUCTION

Most oil and gas reservoirs in the United Arab Emirates (UAE) are sour, enriched with a high amount of hydrogen sulfide (H_2S) and sulfur species. H_2S is a highly hazardous gas that has serious poisoning effects on industrial processes or human health if exposed at concentrations above 100 ppm. The conventional approach to dispose of this noxious gas is the Claus process, which is not an economically viable method due to the high cost of the chemical process that results in the formation of SO_2, a further environmental containment. H_2S production is expected to increase due to the discovery of sour gas reservoirs and heavy oil refining.

Various strategies for converting H_2S into Hydrogen and Sulfur have been investigated in literature through a variety of technologies. These involve thermal decomposition, thermochemical, electrochemical, and photochemical methods. Owing to the thermodynamic limitations of H_2S dissociation by thermal decomposition reactions, extensive research has been investigating more practical methods for generating higher H_2 equilibrium concentrations at lower temperatures. Higher conversion efficiencies at lower temperatures were found to be achieved using closed-loop thermochemical decomposition cycles. This involves breaking up the overall reaction into a sequence of kinetically favorable reactions with at least one separation step to fully decompose the H_2S into H_2. Kiuchi et al. in [1], demonstrated splitting the H_2S dissociation into two intensive steps; First, sulfiding of a metal or metal sulfide by H_2S to liberate the hydrogen and then calcining the higher metal or metal sulfide to decompose into sulfur and the original metal or metal sulfide.

$$M_xS_y + zH_2S \rightarrow M_xS_{y+z} + zH_2 \quad (1)$$

$$M_xS_{y+z} \rightarrow M_xS_y + zS \quad (2)$$

The main objective of this research work is to develop multistep chemical kinetics of the two-step Thermochemical decomposition of H_2S using Nickel Sulfide. The kinetic model was simulated to examine the key parameters that affect the overall cycling process and H_2S conversion efficiency, including temperature, residence time, catalyst time stability, and the behavior of adsorbed species on active catalyst sites during sulfurization/ regeneration transient steps.

MATERIALS AND METHODS

The kinetic model was developed using CHEMKIN® software to investigate the kinetics of the gas-phase of species that might interact during the chemical reaction without a catalyst. Similar to the gas-phase kinetic model, surface-phase kinetic was also simulated in CHEMKIN® software to understand the kinetics of hydrogen sulfide on Nickel surface. Both model simulations include the inlet gases, a CSTR reactor, and an outlet source.

RESULTS AND DISCUSSION

The kinetics of the H_2S splitting gas-phase chemical reaction was developed using CHEMKIN® software. The validity of the kinetic model was compared with two experimental studies obtained by Binoist in [2] and Hawboldt et al. in [3].

Figure 1 represents the comparison between the developed gas-phase kinetic model and the experimental result of Hawboldt et al. and Bionoist.

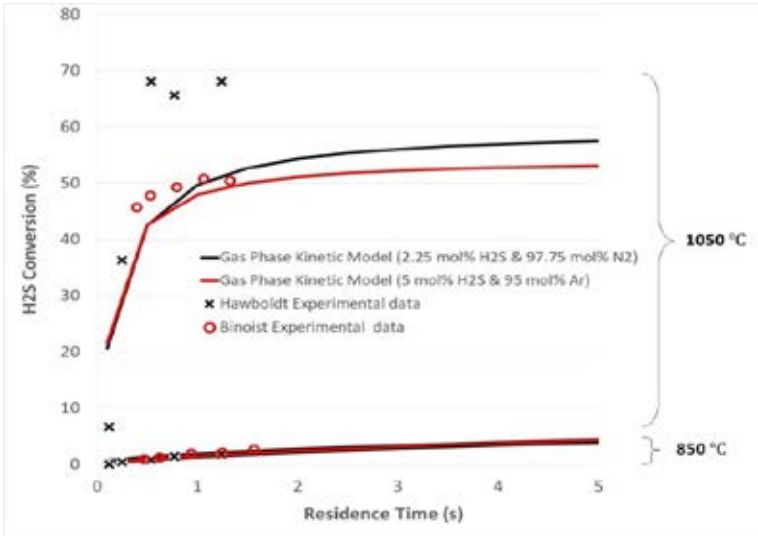


Figure 1. Comparison between the experimental result of Hawboldt et al. (H_2S: 2.25 mole%, N_2: 97.75 mol%) & Binoist (H_2S: 5 mole%, N_2: 95 mol%) with the Gas Phase Kinetic model.

Figure 1 clearly demonstrates that the model reasonably well predicts the gas-phase kinetic behavior for the system without catalysts. It can be noted that the H_2S conversion increases with both the residence time and temperature. The H_2S conversion at 5 s residence time were 4% and ~55% at 850°C and 1050°C, respectively. However, the gas-phase H_2S conversion is kinetically not significant below 850°C.

To understand the kinetics of hydrogen sulfide on Nickel sites, a surface-phase kinetics model was also developed and simulated in CHEMKIN® software using a transient solver. The experimental results obtained by Osasuyi in [4] were used as a benchmark in validating the model competence. Figure 2 reflects this comparison at three different temperatures of 150°C, 300°C, and 500°C. As shown, at 150°C, the H_2S decomposition reaction is hardly successful due to the reaction kinetics and mass transfer limitations accompanying the heterogeneous reaction with Ni_3S_2. Moreover, from 300 to 500°C temperature levels, the total H_2S conversion is displayed at an early stage of the reaction for a very short-lived period.

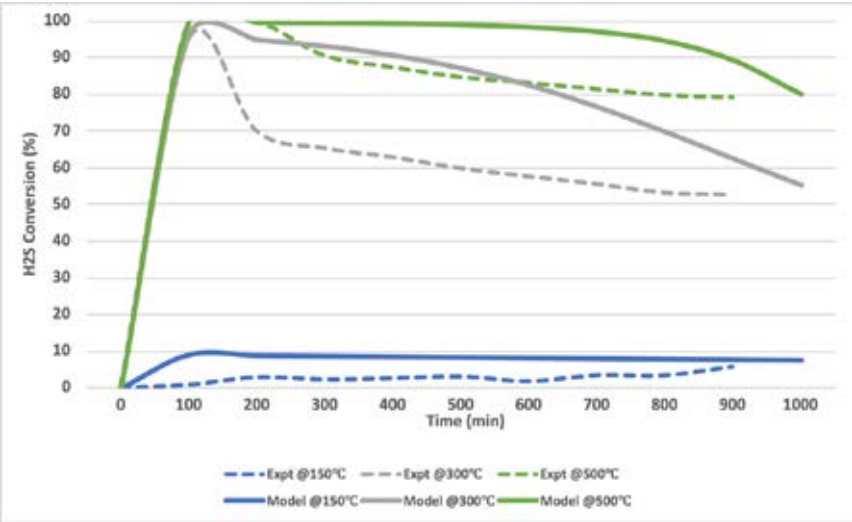


Figure 2. Osasuyi experimental results vs. Surface Phase Kinetic Model results

The deviation between the kinetic model from experimental results is because the surface phase kinetic model considers the sulfur formation as a single site attachment on Nickel sites, whereas in reality, there could be additional complex reaction routes like the formation of S_2-S_8, which is not considered in the model but encountered by the experimental results.

The predictive capability of the model is further explored by analyzing the site fraction of H_2, higher and lower Nickel Sulfides, and Sulfur at a temperature range of 150 to 800°C.

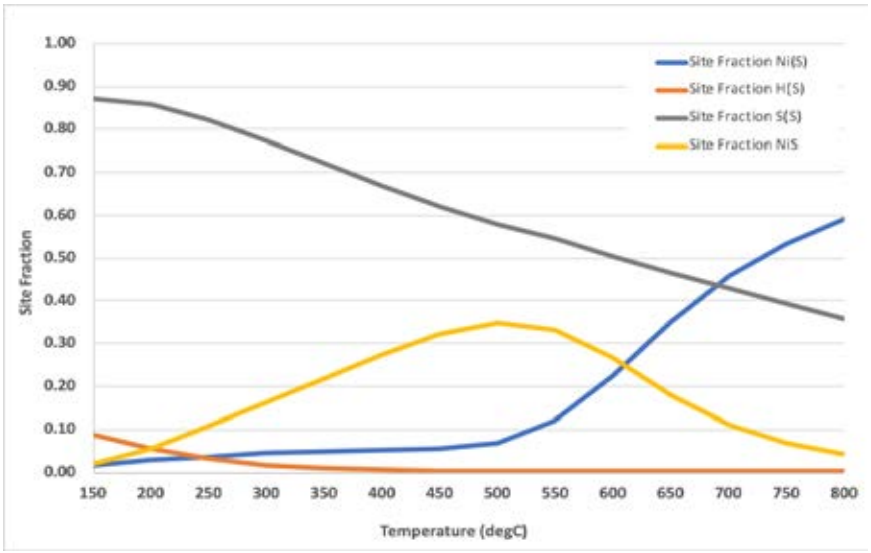


Figure 3. Site fraction of H(S), lower and higher Nickel Sulfide Ni(S) & NiS, and Sulfur S(S) at a temperature range of 150 to 800°C

Figure 3 represents the steady-state solutions of site fractions and clearly explains the H_2S decomposition behavior on the Nickel surface as temperature increases from 150°C to 800°C. As temperature progresses, the sulfur atoms on the Nickel surface desorbs, freeing up vacant positions on the Nickel surface for H_2S adsorption. As the reaction proceeds and more sulfur atoms are desorbed, a bulk transformation of the Nickel Sulfide to a higher stable Sulfide state eventually occurs. This sulfidation phenomenon is exothermic in nature; however, this takes place up around 500°C, while the regeneration step can happen at a higher temperature above 700°C.

CONCLUSIONS

The gas phase and surface phase kinetics of the two-step thermochemical decomposition of H_2S was simulated in CHEMKIN software. The predictive capability of the model was explored by using the experimental data obtained by Binoisit in [2], Hawboldt in [3] and Osasuyi in [4]. The formulated model results were found to be consistent with the experimental results. However, the model can be further developed by encountering additional complex reaction routes like the formation of S_2-S_8. The model will be used to select suitable reactor type and design parameters that is the key aspect for developing and optimizing the chemical process system.

REFERENCES

1. Kiuchi H,Iwasaki T, Nakamura I and Tanaka T. (1980). Thermochemical Decomposition of H_2S with Metal Sulfides or Metals. ACS Symposium Series.
2. Binoist M, Labègorre B and Monnet F. (2003). Kinetic Study of the Pyrolysis of H_2S, Ind. Eng. Chem. Res. 42:3943-3951.
3.Hawboldt KA, Svrcek WY and Monnery WD. (1997). Kinetic Modelling of the Modified Claus Plant Front End Furnace. Proceeding of the 47th Annual Laurance Reid Gas Conditioning Conference
4. Osasuyi, O., Quang, D. V., Basina, G., Al Wahedi, Y., Abu Zahra, M. R., Palmisano, G., & Al-Ali, K. (2021). Reversible Metal Sulfide Transition in a Two-Step Thermochemical H2S Splitting. Industrial & Engineering Chemistry Research.

WHEC-2022
23rd World Hydrogen Energy Conference
June 26-30, 2022 - Istanbul

#162

APPLYING ARTIFICIAL INTELLIGENCE ON STEAM GASIFICATION OF WASTE PLASTIC TO GENERATE HYDROGEN

[1] Serap Özmen, [1] Peter T. Clough*
[1]Cranfield University, Cranfield, Bedfordshire, MK43 0AL, UK

*Corresponding author e-mail: s.ozmen@cranfield.ac.uk

ABSTRACT

Global warming is a major environmental threat, and the demand of renewable energy sources has been increased significantly. Hydrogen has been proposed as a key future energy carrier for the low carbon energy systems owing to its cleanliness and high-energy yield. Meanwhile another significant global threat is plastic pollution and waste plastic management is a major concern in many countries. Consequently, hydrogen production from waste plastic has become one of the most demanding research topics. One of the most promising techniques to produce hydrogen from waste plastic is gasification. However, there is a lack of understanding for the plastic gasification process since the plastic samples are mostly used as a side feedstock with biomass and coal for the gasification studies. In this study, Artificial Neural Network (ANN) modelling will be employed to provide insights of plastic gasification process. Different types of plastics will be gasified under different reaction conditions within a lab scale fluidized bed reactor and the data will be collected to train the ANN model with the data collected from literature. Thus, the impact of the input materials on the hydrogen production will be investigated.

Keywords: Plastic gasification, Hydrogen production, Artificial neural network, Process modelling, Waste to hydrogen

INTRODUCTION

Plastic pollution and waste management have been identified crucial challenges to tackle in recent years as the global production of plastic increases. One of the cornerstones to deal with this problem is the thermal conversion of the plastic waste via gasification through which, syngas is produced as a main product. Among the species found in syngas, hydrogen is the most desirable fraction since it has been found as the key energy carrier since it has the highest energy content per unit mass among all fuels [1,2]. Meanwhile to enhance this process for the production of syngas with high H_2/CO ratios, steam is commonly chosen as the gasifying agent, promoting the reforming and water-gas shift reactions [3].

Various modelling methods have been commonly used for the gasification processes such as kinetic modelling, black box modelling and computational fluid dynamics (CFD) modelling. However, ANN modelling has gained popularity in the applications related to renewable energy systems since it does not contain any energy or mass equations unlike the traditional mathematical models. ANN modelling approach is a generic nonlinear regression model which learns the mapping from the input data onto the output with high prediction accuracy. Currently, ANN modelling is widely used for process simulation, pattern recognition and signal processing and it is the most popular and reliable computation technique in the chemical engineering applications due to its accuracy, precision time and low cost [4].

Several other methods such as pyrolysis and in-line and dry reforming have been practiced for the production of hydrogen as well among which gasification plays an advantageous role due to its flexibility in the usage of plastics with alternative composition or blended with other feedstocks. Many research studies have co-blended plastics with biomass and coal, which are the most common feedstocks for gasification processes, in order to increase the hydrogen concentration in the syngas [5]. Consequently, there is a lack of understanding on the relationships between the inputs and outputs to and from a reactor for the gasification of waste plastics. The aim of this research is to investigate the artificial intelligence prediction of the characteristics of catalytic steam gasification for waste plastic within a fluidised bed reactor for hydrogen production. This will provide insights into the operation of gasifiers and contributes to the knowledge on the impacts of input materials on the yield of hydrogen.

METHODOLOGY

The primary work package included the chemical characterisation of the plastic materials and the design, setup and operation of a lab-scale fluidised bed system suitable for catalytic steam gasification. Following this, the application of ANN for the prediction of the concentration of H_2 in the syngas is assessed. These predictions will be based on the literature data and the experimental data collected from steam gasification of various types of plastics under different conditions such as reaction temperature, flow rate of plastics, catalyst/plastic ratio, steam/plastic ratio.

Reactor design

For the experimental study, a lab-scale fluidised bed reactor system was designed, procured, and installed. The system includes a fluidised bed reactor, a radiation heating system (to control the temperature of the reaction), mass flow controllers (to control the gas and steam flow rates to the system), a data logger for the thermocouples (to read the temperature at different locations in the system), tar collection bottles and a gas analyser (to define the gas concentrations which are H_2, CO_2, CO and O_2 in the syngas). Also, a software called Agilent VEE was employed to control the process and collect the data outputs. The process flow diagram of the system and an image of the system can be seen in Fig. 1.

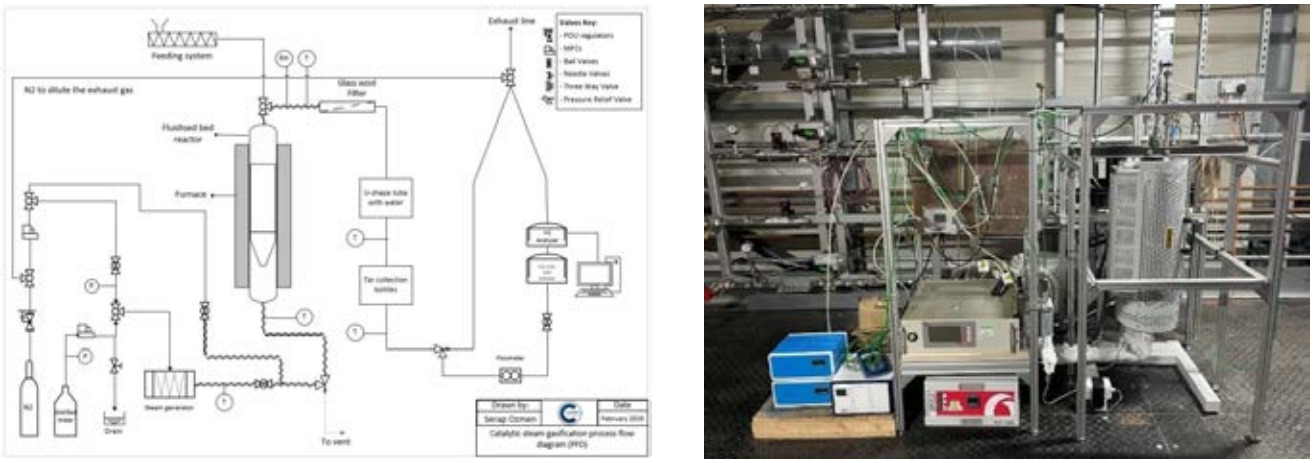


Fig. 1. Process flow diagram of the system (left), An image of the rig setup for plastic gasification experiments (right)

Furthermore, to overcome the difficulties of the feeding of the plastic samples into the reactor, a novel solid feeding system was designed. A linear actuator was employed to control the feeding rate of the plastic samples into the reactor.

Characterisation of plastic samples

The instruments which will be employed to determine the characteristics of the plastic samples and gas products are:

- Thermogravimetric analysis (TGA) for proximate analysis
- Gas Chromatography/ Mass Spectroscopy (GC/MS) to identify the different substances within the plastic samples
- Calorimetry (Bomb calorimeter) (CV) to measure low heating value of plastic samples
- Brunauer, Emmett and Teller (BET) to measure the surface area of materials and to explain the physical adsorption of gas molecules on a solid surface
- Barrett-Joyner-Halenda (BJH) to calculate the pore size distributions and volume of pores

ANN modelling

A prediction model was created on MATLAB trained with data collected from literature until the experimental data collection was completed. The data were analysed and pre-processed to make them suitable for the model. The independent variables such as the type and characteristics of the plastic and reaction conditions such as temperature, catalyst type, catalyst/plastic ratio, steam/plastic ratio, etc. will be called 'input data' while the dependent variable which is hydrogen volume concentration in the syngas will be called 'output data'. To analyse the data, Pearson's correlation coefficients (PCC) and distance correlation coefficients (DCC) were calculated. Feed-Forward Neural Network (FFNN) was employed with different model structures (number of layers and hidden layers) and different training functions to find the best model according to the different performance functions. To validate the model, different datasets collected from literature was used as an unseen data.

RESULTS AND DISCUSSION

For the initial steam gasification experiments, 0.1g of Polypropylene (PP) was used as a feedstock and 12 g of sand was used as a bed material without any catalyst. The test was run at 850 °C with 60% of steam and 40 % of Nitrogen as carrier gas with 25.79 ml/s total gas flow rate. The results show that 0.0026 mol CO, 0.0011 mol CO_2 and 0.0569 mol H_2 was produced with 82% hydrogen conversion. Once the novel feeding system will be added to the system, the amount of plastic used in the tests will be increased significantly.

In terms of ANN modelling, the structure of the model and the training algorithm was defined based on the performance of the model by using mean square error and regression results. Highlighted in Table 1, Levenberg-Marquardt algorithm (TRAINLM) is the best training algorithm for the model with the existing data. It can also be seen that there is no major difference with the results of single- or two-layers structure. Although there are limited data to train the model (as the data collected from the literature), the performance results of the model are quite promising.

Table 1. Performance results of the prediction model based on different training algorithms and different structure of the network

	Single layer		**Two layers**	
Training algorithm	MSE	Regression	MSE	Regression
TRAINLM	0.002	0.986	0.001	0.988
TRAINBFG	0.002	0.979	0.003	0.974
TRAINRP	0.003	0.976	0.003	0.978
TRAINGDA	0.011	0.904	0.005	0.963

Moreover, the Regression Learner app within MATLAB was employed to compare the performances of different machine learning algorithms. While the best algorithm is Gaussian Process Regression (R squared: 0.72), ANN still has a better performance.

CONCLUSIONS

The thermochemical degradation processes to convert waste plastic into fuels are promising methods not only it helps to decrease the dependence on fossil fuels but also it helps to mitigate the plastic pollution and plastic waste management. In this research ANN modeling will be used to contribute to the knowledge on the relationship between the input materials (type of plastic, reaction temperature, steam/plastic ratio, catalyst/plastic ratio, etc.) and the hydrogen yield within the steam gasification process.

REFERENCES

1. Baykara SZ. 2018. Hydrogen: A brief overview on its sources, production, and environmental impact. International Journal of Hydrogen Energy 43(23):10605-10614.
2. Mastellone ML and Arena U. 2008. Olivine as a tar removal catalyst during fluidized bed gasification of plastic waste. AIChe Journal 54(6):1656-1667.
3. Lazzarotto IP *et al.* 2020. The role of CaO in steam gasification of plastic wastes recovered from the municipal solid waste in a fluidized bed reactor. Process Safety and Environmental Protection 140:60-67.
4. Yucel O, Aydin ES and Sadikoglu H. 2019. Comparison of the different artificial neural networks in prediction of biomass gasification products. International Journal of Energy Research 43(11):5992-6003.
5. Lopez G, *et al.* 2018. Recent advances in the gasification of waste plastics A critical overview. Renewable and Sustainable Energy Reviews. 82:576-596.

WHEC-2022
23rd World Hydrogen Energy Conference
June 26-30, 2022 - Istanbul

#174

DESIGN OF GREEN HYDROGEN PRODUCTION SYSTEM IN CONTEXT OF COLLABORATIVE INTERNATIONAL ONLINE LEARNING (COIL)

[1] *Enzo Ochoa,* [2] *Patricio Alarcon,* [3] *James Gonzales,* [4] *Abrahan Malpartida,* [5] *Marlis Campos,* [6] *Gabriel Bancayan,* [7] *Luis Machaca,* [8] *Daniel Tafur,* [9] *Ignacio De-La-Puente,* [10] *Jose Gamarra,* [11] *Hector Bravo,* [12] *John Sheffield,* [13] *Stewart Bauserman,* [14] *Johnny Nahui,* [15*] *Jose Ramos-Saravia*
[1,2,3,4,5,6,7,8,9,15] University of Engineering & Technology, Department of Energy & Mechanical Engineering, Jr. Medrano Silva 165 (Barranco), Lima, Peru
[10, 14] National University of Engineering, Lima, Peru
[11] National University of San Agustín, Arequipa, Peru
[12, 13] Purdue University, West Lafayette, Indiana, USA

Corresponding e-mail: enzo.ochoa@utec.edu.pe

ABSTRACT

This work is about the collaboration between Purdue University (Purdue) and University of Engineering & Technology (UTEC). Both are educational institutions located in the USA and Peru, respectively. This work presents the results of the implementation of a Collaborative Online International Learning (COIL) Program. Students from different engineering careers and cultures participated in the development of a COIL Project on the hydrogen production by water splitting using high temperature heat from a concentrating solar plant. Students formed working groups to carry out the different research activities. It was found that the objective of the COIL Project were achieved in a short period of time, evidencing the academic growth of the students and, at the same time, students gained international experience.

Keywords: Collaborative Online International Learning (COIL) Program, Transformative pedagogy, Green hydrogen.

INTRODUCTION

The short experience in international collaboration activities of a university may represent a barrier in its academic growth. Currently, online international intercultural collaborative programs could contribute to solving this problem. This work presents the results about the experience of students from different disciplines, culture, and nationality around the development of the COIL Project "Hydrogen production by water splitting using thermochemical cycles powered by Solar Concentration Power Plant for a mining industry in Peru". These students belong to Purdue (USA) and UTEC (Peru). The main goal of this work is to show the results of the implementation of a COIL Program to facilitate the transformative pedagogy [1–3] for students from Purdue and UTEC through the development of an academic project.

METHODOLOGY

The implementation of the COIL Program took into account the following activities: (a) videoconference meetings with the participation of students and professors from Purdue and UTEC universities; with the support of the zoom platform and computer applications (powerpoint, google drive, Homer Pro, System Advisor Model and Aspen Plus), (b) formation of working groups with students from different interdisciplinary careers, and (c) research in charge of the different working groups on the production of green hydrogen using thermochemical cycles supported by concentrating solar plants for a mining industry in Peru.

RESULTS

The results of the COIL approach in the development of the project "Hydrogen production by water splitting using thermochemical cycles powered by Solar Concentration Power Plant for a mining industry in Peru" include: (i) calculation of the hydrogen consumption of the truck fleet of transportation of material from the mining industry, (ii) sizing of the hydrogen production plant through water fractionation supported by a concentrating solar plan, and (iii) sizing of the concentrating solar plant.

CONCLUSIONS

Conclusions of the implementation of the COIL program are the following:

- The COIL program presents great potential for the exchange of knowledge and experiences in an international and intercultural framework, in addition to knowing different teaching methodologies, and expanding the network of contacts with students from other countries.

- The objectives of the COIL Project were achieved in a relatively short time thanks to the synergy of the effort of the work teams working in cellular mode,
- The disparity of the effort and intellectual contribution of each student from work teams was evidenced. For the next edition of the COIL Program, we recommend that the participants could be chosen through a selection process, where the candidate must have interest in COIL-Project' subject, while demonstrating a solvent time management and predisposition to work in independent groups,
- Good results were achieved without the need to travel.

ACKNOWLEDGEMENT

We appreciate the support of Purdue's Office of Globalization and UTEC's Office of Internationalization.

REFERENCES

1. https://www.rsisinternational.org/3ICMRP-2016/332-337.pdf. Accessed on December 12, 2021.
2. http://www.campusengage.ie/wp-content/uploads/2019/06/Transformative-TL-Quillinan-et-al.-2019.pdf. Accessed on December 12, 2021.
3. https://ulir.ul.ie/bitstream/handle/10344/7458/MacPhail_2018_Transformative.pdf. Accessed on December 12, 2021.

WHEC-2022
23rd World Hydrogen Energy Conference
June 26-30, 2022 - Istanbul

#177

TECHNICAL AND ECONOMIC ASSESSMENT OF A SOLAR HYDROGEN PRODUCTION PLANT IN A PERUVIAN MINING COMPANY

[1] Enzo Ochoa, [2] Patricio Alarcon, [3] James Gonzales, [4] Abrahan Malpartida, [5] Marlis Campos, [6] Gabriel Bancayan, [7] Luis Machaca, [8] Daniel Tafur, [9] Ignacio De-La-Puente, [10] Jose Gamarra, [11] Hector Bravo, [12] John Sheffield, [13] Stewart Bauserman, [14] Johnny Nahui, [15*] Jose Ramos-Saravia
[1,2,3,4,5,6,7,8,9,15] University of Engineering & Technology, Department of Energy & Mechanical Engineering, Jr. Medrano Silva 165 (Barranco), Lima, Peru
[10, 14] National University of Engineering, Lima, Peru
[11] National University of San Agustín, Arequipa, Peru
[12, 13] Purdue University, West Lafayette, Indiana, USA

Corresponding e-mail: jramos@utec.edu.pe

ABSTRACT

The basic engineering of a hydrogen production plant has been developed. In this work, the results of the technical and economic assessment of a green hydrogen production plant with renewable energy in Peru, is presented. The hydrogen production plant employs a water splitting technology based on thermochemical cycles [1-2] powered by a concentrating solar plant and a photovoltaic power plant. This plant includes a hydrogen storage and hydrogen transportation systems to replace diesel fuel (1,15 millions of liters per year) by hydrogen within a truck fleet from a mining company in Peru.

Keywords: Green hydrogen, Green mining, Concentrating solar plant, Replacement of diesel by hydrogen, Renewable energy, Sulfur-iodine thermochemical cycle.

INTRODUCTION

Based on the demand of a Peruvian mining company, we estimated a consumption of 1,15 million liters of diesel per year, which represents an emission of 2 870 tons (CO_2). In this work, the deployment of a hydrogen production plant is proposed to replace the diesel fuel consumed by the mining trucks fleet.

The hydrogen production plant employs a water splitting technology based on thermochemical cycles [1 -2] powered by a concentrating solar plant and a photovoltaic power plant. A concentrating solar plant meets the demand for high temperature heat to the thermochemical cycles and the photovoltaic power plant provides electricity to the different hydrogen compression processes for the hydrogen storage and transport systems.

In this work, the results of a technical and economic assessment of a green hydrogen production plant with renewable energy in Peru are presented.

METHODOLOGY

The following activities were carried out:

- Identify the mining truck model that consumes the most diesel fuel.
- Characterization of the hydrogen demand of the mining trucks fleet.
- Sizing of the hydrogen storage system.
- Analysis and simulation of the thermochemical process.
- Sizing of the solar concentrating thermal plant.
- Sizing of the photovoltaic power plant.
- Technical and economic assessment of the hydrogen production plant.

RESULTS

The technical and economic assessment of a green hydrogen production plant with renewable energy in Peru has the following results:

- The hydrogen demand accounted for 3,02 tons/day for the 14 mining trucks.
- It could be necessary the deployment of a green hydrogen production plant for 3,02 tons/day (running 6

hours per day) to replace the diesel fuel (1,15 million of liters per year). The CAPEX of the project is about 4,3 million dollars.

- An 8,4 MW_{th} concentrating solar plant was designed
- A 6,47 MW_e photovoltaic solar power plant was designed

CONCLUSIONS

It is concluded that:

- It is technically feasible to use hybrid solar concentrating and photovoltaic plants to produce hydrogen by thermochemical water splitting technique at a large scale, supplying green hydrogen on-demand.
- The SI (sulfur-iodine) reaction process uses two operation modalities: discontinuous operation based on solar energy availability and continuous operation. The discontinuous section working for about 6 h/day, includes mainly the SO3 decomposition at 850°C and storage of the produced SO2. While the other modality comprises the rest of the process working 24h/day.
- The costs of the main and auxiliary equipment of the plant were estimated and the results show that this project is not economically feasible. This suggests that some adjusts should be made on the plant's design to process and transport it efficiently.
- The implementation of a green hydrogen plant could decarbonize the mining company's operation in around 2870 tons of CO2 per year.

ACKNOWLEDGEMENT

We appreciate the support of Purdue's Office of Globalization and UTEC's Office of Internationalization.

REFERENCES

1. Liberatore M, Lanchi A, Giaconia A and Tarquini P. 2012. Energy and economic assessment of an industrial plant for the hydrogen production by water-splitting through the sulfur-iodine thermochemical cycle powered by concentrated solar energy. International Journal of Hydrogen Energy 37(12):9550–9565.
2. Sattler C, Roeb M, Agrafiotis C and Thomey D. 2017. Solar hydrogen production via sulfur based thermochemical water-splitting. Solar Energy (2017), http://dx.doi.org/10.1016/j.solener.2017.05.060

WHEC-2022
23rd World Hydrogen Energy Conference
June 26-30, 2022 - Istanbul

#199

PHOTOELECTROCHEMICAL WATER SPLITTING: SHORT REVIEW ON CURRENT DENSITY AND STABILITY OF PHOTOELECTRODES

[1] Dinko Brezak, [1] Doria Marciuš, [1] Ankica Kovač*
[1] University of Zagreb, Faculty of Mechanical Engineering and Naval Architecture, Zagreb Croatia

*Corresponding author e-mail: dinko.brezak@fsb.hr

ABSTRACT

Direct conversion of water to hydrogen via solar energy encounters multiple obstacles in practical operation - the most important ones being low current density and short-term stability. If photoelectrochemical water splitting is expected to ever compete with a solar panel system in tandem with electrolyzers, it is necessary to develop photoelectrodes with higher current densities using certain nanostructures and a combination of materials that meet a wide range of requirements. The limited stability of photoelectrodes becomes more pronounced with the rise of their efficiency and in photoelectrochemical water splitting is one of the biggest challenges hindering the commercialization of this technology. For this reason, it is of utmost importance to find materials that could fulfill both aforementioned requirements to bring the photoelectrochemical water splitting to the level of competitiveness. This review seeks to provide insight into what has been researched so far, as well as to propose the perspective future directions for the technology development regarding mentioned drawbacks.

Keywords: Photoelectrodes, Photoelectrolysis, Efficiency, Stability

INTRODUCTION

Environmental change, greenhouse gas pollution and depletion of fossil fuel supplies have motivated the scientific community to explore alternative ways of energy production and usage. Hydrogen as a carrier and reservoir of energy has proven to be a potential solution for the energy transition to renewable energy sources. When combusted, it creates only water as a by-product, which makes it safe for the environment. Hydrogen can be produced in multiple ways, of which one of the most desirable ways is water electrolysis. Combining solar panels and electrolyzers enables renewable energy production without emitting harmful gas emissions. The photoelectrochemical (PEC) method of splitting water (WS) simplifies things even more by 'inserting solar panels' into the electrolyzer. This reduces the construction complexity and allows direct hydrogen production from solar energy without the intermediate conversion of solar energy into electricity [1].

A material that can both utilize solar energy and enable a chemical reaction of water decomposition has many requirements to fulfill, which generally necessitates compromise and optimization [2]. Some of the demands for photoelectrode material are bandgap, bandgap limits, absorption of broad solar spectra, high efficiency, long life cycle, low electron-hole recombination, nontoxicity, stability in acidic and alkali environment, low-cost and earth-abundant. As some of the mentioned requirements are mutually opposed, multilayer structures are used, where every layer assuages a certain aspect [3]. The aim of this research is to investigate perspective photoelectrodes that placate the most mentioned requirements with an emphasis on higher current densities and stability as ultimately, these two parameters are crucial for the commercialization of this technology.

PHOTOELECTRODE MATERIALS

Titanium dioxide (TiO_2) is the first material used for PEC WS and thanks to its one-dimensional structure is still one of the most promising materials for photoelectrodes. The main drawbacks are wide band gap (3 eV) which causes poor solar light utilization, and easy recombination of charge carriers, holes and electrons. To improve the active catalytic area, modification of surface morphology is essential. Band structure modification is required to reduce photogenerated charge recombination and surface sensitization is for improving light absorption. Tubular morphology improves TiO_2 photocatalytic ability, but it doesn't solve the wide band gap. The most common methods for synthesizing TiO_2 nanotubes (NT) are a hydrothermal method, template and electrochemical anodization method, latter being most prominent as it ensures highly oriented NTs. Tubular morphology improves TiO_2 photocatalytic ability, but it doesn't solve the wide band gap. Reducing the bandgap is accomplished through element doping and by self-doping of Ti^{3+}. With TiO_2 color changes, bandgap can be reduced from 3eV to 1eV [4].

By forming heterojunctions with various materials, electron hole recombination can be reduced. Homojunction interfaces are beneficial for the charge carrier separation due to similar characteristics on two sides of homojunction. TiO_2 has two typical photoactive phases, anatase and rutile, and by combining these two phases and creating homojunction we achieve fewer recombination centers for charge carriers [5]. Co-doping with anions and modification with different nanoparticles (NP) result in broadening the absorption region for visible light and the reduction of band gap energy [6]. Oka et al. [7] investigated π-conjugated polymer as a pure organic semiconductor film, polythiophene,

characterized with a crystalline polymer well filled with grain morphology. It is prepared with a facile polymerization method and achieves decent current density and high durability. Photoanodes based on zinc oxide (ZnO) as a transitional metal oxide have strong stability, excellent electron mobility and convenient conduction band position [8]. Yu et al. [9] studied organic semiconductors that are ideal for PEC WS for their superior charge transfer characteristics, easy sustainability of energy levels and low production costs. They reported stable organic semiconductor photoanodes with a high performance consisting of n-type non-fullerene, which is passivated with nickel foils, p-type polymers, layered double hydroxide and gallium indium (GaIn) eutectic as model materials [9]. In [10] researchers studied photoanodes based on alloy containing elements from groups III and V in the periodic table (III-V). These photoelectrodes spatially and functionally decouple the light harvesting from the electrolysis part of the device and that reduces the cost, liquidates parasitic light absorption and enhances the stability without compromising efficiency. The monolithically combined PEC cell was produced by an epitaxial lift-off method and inversely grown InGaP/GaAs transfer to a robust Ni-substrate. The resultant photoanode exhibits stability of over 150 hours and solar-to-hydrogen (STH) efficiency of 9% [10]. Another promising candidate for a photoanode material is hematite (α-Fe_2O_3). Its main disadvantage is difficult charge recombination suppression but has high efficiency. Thick hematite films constructed by highly ordered and attached hematite mesocrystals (MC) and the formation of plenteous interfacial oxygen vacancies delivers high current densities, great collection efficiencies and charge separation, short depletion widths, and a large fraction of depleted regions in hierarchical structures [11]. He et al. [12] developed highly efficient photoelectrode by sandwiching photothermal cobalt (II, III) oxide (Co_3O_4) layer between an electrocatalysts sheet FeOOH/NiOOH and a$BiVO_4$ photoanode film. Deposited Co_3O_4 layer shows excellent photothermal effect in the near-infrared region and raises the photoanode temperature in situ, leading to improved charge transfer, expanded light absorption and fast water oxidation kinetics [12].

PHOTOELECTRODE COMPARISON AND DISCUSSION

In Table 1. Comparison of different photoelectrodes and their characteristicsTable 1, previously mentioned photoanode characteristics are summarized with their current densities, stability, preparation method and applied bias voltage.

Table 1. Comparison of different photoelectrodes and their characteristics including stability and current density

Photoanode	Electrolyte	Bias	Reference electrode	Stability	Current density	Preparation method	Ref.
TiO_2-NT/NiS	Na_2S and Na_2SO_4	0 V_{RHE}	Ag/AgCl	Over 30 min.	7.68 mA/cm^2	Electrochemical anodization	[4]
TiO_2-R/A	Na_2SO_4	0.6 V_{SCE}	Saturated calomel electrode	Over 2 hours	1.7 mA/cm^2	Hydrothermal	[5]
C, N-TiO2/NiS/CdS/ZnS	Na_2S and Na_2SO_3	0 V_{RHE}	Ag/AgCl	Over 30 min.	18.79 m A/cm^2	Anodization	[6]
TiO_2-Bi_2Se_3	Na_2S and Na_2SO_3	1.23 V_{RHE}	Ag/AgCl	Over 6 hours	1.76 mA/cm^2	Hydrothermal	[13]
Polythiophene	NaOH	0 V_{RHE}	Ti mesh	Over 12 hours	0.75 mA/cm^2	Facile polymerization	[7]
Cross-linked ZnO/CdS/BiOI	-	1.1 V_{RHE}	Ag/AgCl	Over 2 hours	9.12 mA/cm^2	Solvothermal	[8]
Organic semiconductor LDH/Ni/eu@nfOP	-	1.23 V_{RHE}	Ag/AgCl	Over 10 hours	15.1 mA/cm^2	Passivation	[9]
Inverted tandem InGaP/GaAs	KOH	0 V_{SCE}	Saturated calomel electrode	Over 150 hours	11.7 mA/cm^2	Epitaxial lift-off	[10]
Ti-Fe_2O_3 MCs	NaOH	1.23 V_{RHE}	Ag/AgCl	-	3 mA/cm^2	Solvothermal and spin coating	[11]
NiOOH/FeOOH/ Co_3O_4/$BiVO_4$	KPi	1.23 V_{RHE}	Ag/AgCl	Over 4 hours	6.34 mA/cm^2	Deposition	[12]

TiO_2-rutile/anatase (R/A) photoanode is prepared by in situ growth method. Mismatched heterojunction interfaces are mostly full of defects that affects electron-hole recombination. TiO_2-R/A homojunction on the other hand has extreme band bending and improved surface area, which consequently improves transmission and charge separation [5]. Mollavali et al. [6] achieved the highest photocurrent of 18.79 mA/cm^2 in the presence of sacrificial agent/electrolyte (Na_2S and Na_2SO_3). A stable photo response was possessed by multi-metal chalcogenide (CD) heterojunction, and it acts as an electron reservoir that traps photogenerated electrons and separates electron-hole pairs. In [13] TiO_2 metal oxide photoelectrode was sensitized with semiconductor Bi_2Se_3 that has a narrow band gap which improves light response and generates transport of charge carriers. A 3D cross linked heterostructure

ZnO/CdS/BiOI NR arrays has been prepared by solvothermal strategy. Photoanode achieves a high photo conversion efficiency of 3.49% and long-term stability over 6000 seconds [8].

CONCLUSIONS

Investigated photoelectrodes by various researchers so far showed a promising but challenging future for PEC technology. The greatest achieved stability of photoelectrode (150 hours) is still nowhere near the time (10,000 hours) needed to justify commercialization and mass production. Another obstacle is low current density, as present maximum measured current density with the presence of sacrificial agents amounts to 18.8 mA/cm^2 as shown in Table 1. For comparison, photovoltaic panels achieve around 45 mA/cm^2 current density and have a lifespan of around 25 years (200,000 hours). For that reason, to make PEC technology competitive with photovoltaic-electrolyzer (PV-E) tandem devices, more research should be conducted and one of the possible potential directions could be in utilizing perovskite structures who showed excellent photoactive properties.

ACKNOWLEDGEMENT

The authors thank the Croatian Science Foundation, which finances the project UIP-2020-02-7332 Advanced methods of green hydrogen production and its transportation, within which research was conducted, and the results of which are presented in this work.

REFERENCES

1. Hamdani IR and Bhaskarwar AN. 2020. Recent progress in material selection and device designs for photoelectrochemical water-splitting. Renewable and Sustainable Energy Reviews 138:110503.
2. Marwat MA, Humayun M, Afridi MW, Zhang H, Karim MRA, Ashtar M, Usman M, Waqar S, Ullah H, Wang C and Luo W. 2021. Advanced Catalysts for Photoelectrochemical Water Splitting. ACS Applied Energy Materials 4:12007-12031.
3. Ros C, Andreu T, Morante JR. 2020. Photoelectrochemical water splitting: a road from stable metal oxides to protected thin film solar cells. Journal of Materials Chemistry A 8:10625-10669.
4. Arifin K, Yunus RM, Minggu LJ, Kassim MB. 2021. Improvemenent of TiO_2 nanotubes for photoelectrochemical water splitting: Review. International Journal of Hydrogen Energy 46:4998-5024.
5. Huang X, Zhang R, Gao X, Yu B, Gao Y, Han ZG. 2021. TiO_2-rutile/anatase homojunction with enhanced charge separation for photoelectrochemical water splitting. International Journal of Hydrogen Energy 46:26358-26366.
6. Mollavali M, Falamaki C, Rohani S. 2018. Efficient light harvesting by NiS/CdS/ZnS NPs incorporated in C, N-co-doped-TiO_2 nanotube arrays as visible-light sensitive multilayer photoanode for solar applications. International Journal of Hydrogen Energy 43:9259-9278.
7. Oka K, Nishide H, Winther-Jensen B. 2021. Completely Solar-Driven Photoelectrochemical Water Splitting Using a Neat Polythiophene Film. Cell Reports Physical Science 2:100306.
8. Han J and Liu Z. 2021. Optimization and Modulation Strategies of Zinc Oxide-based Photoanodes for Highly Efficient Photoelectrochemical Water Splitting. ACS Applied Energy Materials 4:1004-1013.
9. Yu JM, Lee J, Kim YS, Song J, Oh J, Lee SM, Jeong M, Kim Y, Kwak JH, Cho S, Yang C, Jang JW. 2020. High-performance and stable photoelectrochemical water splitting cell with organic-photoactive-layer-based photoanode. Nature communications 11:5509.
10. Varadhan P, Fu HC, Kao YC, Horng RH, He JH. 2019. An efficient and stable photoelectrochemical system with 9% solar-to-hydrogen conversion efficiency via InGaP/GaAs double junction. Nature communications 10:5282.
11. Zhang Z, Karimata I, Nagashima H, Muto S, Ohara K, Sugimoto K, Tachikawa T. 2019. Interfacial oxygen vacancies yielding long-lived holes in hematite mesocrystal-based photoanodes. Nature communications 10:4832.
12. He B, Jia S, Zhao M, Wang Y, Chen T, Zhao S, Li Z, lin Z, Zhao Y, Liu X. 2021. General and Robust Photothermal-Heating-Enabled High-Efficiency Photoelectrochemical Water Splitting. Advanced Materials 33:2004406.
13. Subramanyam P, Meena B, Suryakala D, Subrahmanyam C. 2021. TiO_2 Photoanodes Sensitized with Bi_2Se_3 Nanoflowers for Visible–Near-Infrared Photoelectrochemical Water Splitting. ACS Applied Nano Materials 4:739-745.

WHEC-2022
23rd World Hydrogen Energy Conference
June 26-30, 2022 - Istanbul

#202

THERMODYNAMIC ANALYSIS OF BIOGAS-TO-METHANOL CONVERSION WITH CH_4 RECYCLING USING ASPEN HYSYS

*Pali Rosha, * Hussameldin Ibrahim*
Clean Energy Technologies Research Institute, Process Systems Engineering, Faculty of Engineering and Applied Science, University of Regina, 3737 Wascana Parkway, Regina, SK, Canada

*Corresponding author e-mail: hussameldin.ibrahim@uregina.ca

ABSTRACT

The methanol synthesis from syngas derived through dry reforming of biogas was studied using an Aspen HYSYS simulator. Studies revealed that hydrocarbon reforming is a practical approach to produce energy-efficient renewable fuels. In this simulation study, an initiative was made to utilize biogas for renewable methanol production using Aspen HYSYS simulator. In the biogas dry reforming process, it was observed that the reactant (CH_4 and CO_2) conversions are largely favoured at elevated temperature (900°C) and ambient pressure (1 bar). Moreover, at optimal parametric conditions, i.e., 200°C (temperature) and 100 bar (pressure), the methanol production rate of 24.7 kg/h was assessed. However, the variation in syngas product distribution was observed w.r.t. temperature and pressure in the water gas shift reactor. Hence, based on the above observations, it can be stated that the biogas-to-methanol process is eco-friendlier, and might be used to mitigate greenhouse gases.

Keywords: Biogas, Syngas, CH_4 recycling, Renewable methanol, Aspen HYSYS.

INTRODUCTION

The conversion of biomass-to-renewable fuels is currently growing worldwide, as biomass waste is already a surprisingly large energy source [1]. The worldwide scientific fraternity has explored various renewable (biodiesel, biogas, hydrogen, syngas, and so forth) fuels using technological approaches [2]. It is worth mentioning that today's research mainly focuses on bio-energy to replace existing conventional fuels. Various hydrocarbon (dry reforming, steam reforming, partial oxidation) reforming routes have been investigated successfully in the last couple of decades for syngas production. Dry reforming is the only one, which consumes two major greenhouse (CH_4 and CO_2) gases; moreover, CH_4 and CO_2 are the main constituents of biogas.

Lately, researcher attention has shifted to bio-methanol production using renewable biogas as a feedstock [3, 4]. In this context, strategies that join biogas and syngas to produce value-added chemicals and/or fuels have recently attained prominence. Syngas, mainly composed of H_2 and CO, serve as essential sources of bio-methanol. At present, methanol comes from conventional fuels using reforming routes; interestingly, literature states that other carbon sources, consisting of CO_2 and biomass, could be effectively utilized for bio-methanol production [5]. In this context, producing syngas from biogas may gain researcher attention. Few scattered simulation studies exist in an open platform on methanol synthesis, likewise, with tri-reforming to optimize the parametric conditions of the overall process [6, 7].

Considering this, it is a right time to utilize biogas for methanol production using dry reforming process. Moreover, for a complete understanding of the biogas-to-methanol conversion process, a detailed simulation study needs to be done first. The use of computer simulation yields a better experience of the overall system and is a handy tool supporting design. This Aspen Hysys-based simulation study seems to be the first study that presents a bio-methanol simulation via dry reforming of biogas. It is anticipated that the model will help understand the general process's behavior without undertaking laborious, high-cost involved time-consuming experiments.

MATERIALS AND METHODS

An Aspen HYSYS simulation software was employed as a process simulator, and for optimization purposes, the Peng-Robinson fluid package was chosen. The assumptions considered were: (1) Simulated (0.6 CH_4 and 0.4 CO_2) biogas was fed at 30°C and 1 bar; (2) The 0.1 bar of pressure drop is assumed in heaters and coolers; (3) A thermodynamic-based study, hence, no catalyst-related aspects are consideration; (4) Impurity-free biogas. A detailed process layout w.r.t. biogas-to-methanol conversion process is shown in Fig.1. The biogas (clean) was initially entered into the pre-heater (H1) at 1.1 bar and 30ºC. The H1 was used to increase the temperature of the biogas stream in the temperature between 700 and 1000ºC. The produced high-temperature stream was then passed into the Gibbs reactor for conducting reforming reactions. The unreacted CH_4 was compressed in the compressor (CR1), and the temperature of unreacted CH_4 was reduced to 30ºC using a cooler (C2). The FTH-2 stream was fed to the heater (H_2) followed by FTR into the Gibbs reactor. The water gas shift reactor product stream was fed to the

component splitter (CS-2); following this, the syngas (STM-5) and H_2 (HTM-5) coming from the prior processes were sent to the mixture (M4) to make H_2/CO ratio suitable for the methanol synthesis process.

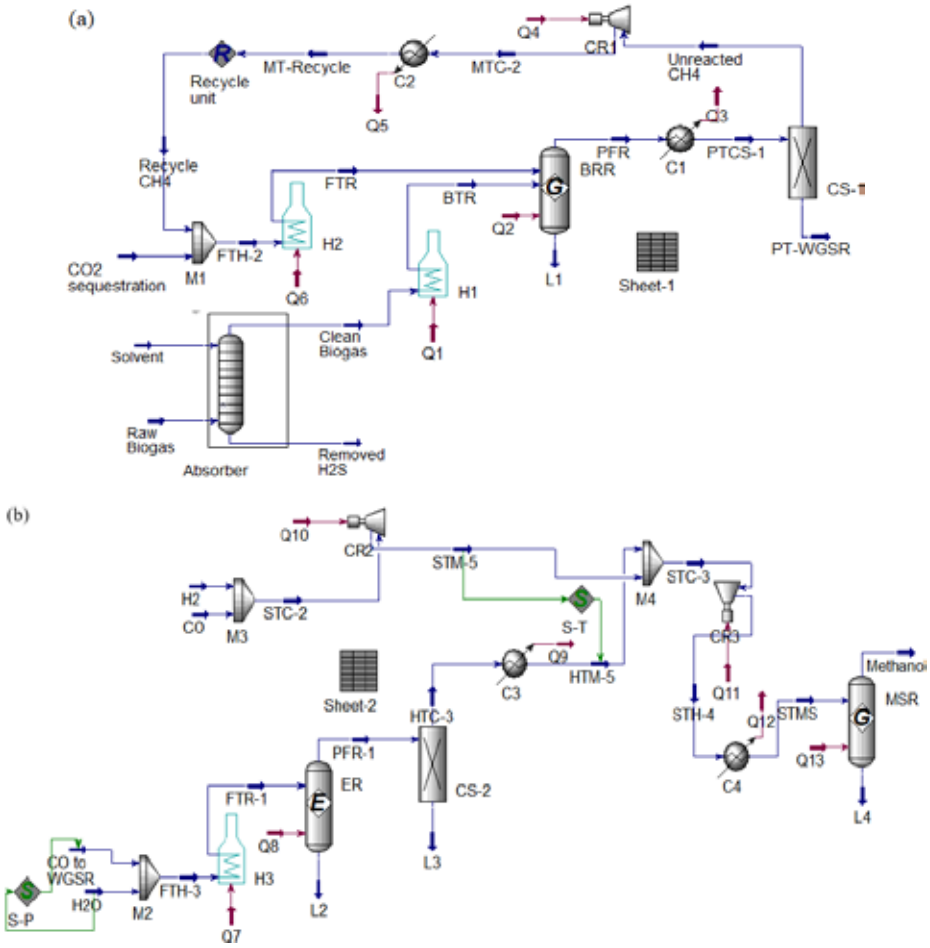


Fig. 1. Schematic layout of biogas-to-methanol conversion unit (a) Biogas dry reforming; (b) Methanol production

RESULTS AND DISCUSSION

EFFECT OF RECYCLING OF UNREACTED CH_4

Table 1 depicts the unreacted CH_4 effects in terms of CH_4 conversions and H_2 production at different temperatures. Results demonstrated that conversion of CH_4 and productivity of H_2 increase with increasing temperatures (700 to 1000°C). It was attributed to the dry reforming endothermicity, which shifts reaction equilibrium towards the product side [8]. After that, recycling of unreacted CH_4 showed positive effects in terms of CH_4 conversion and H_2 productivity. However, at elevated temperatures (>900°C), the recycling loop showed a negligible influence due to higher CH_4 conversion when compared to the lower temperature. Table 2 depicts the results of water gas shift reactions in terms of reactor conversion and product (H_2/CO) ratio. Results showed that the reactor conversion and H_2/CO ratio decrease with increasing temperature (150 to 400°C). It was due to the exothermicity of the water gas shift reaction, resulting in more favorable at lower temperatures [9].

Table 1. Simulation result summary of biogas dry reforming w.r.t. CH_4 conversion and H_2 production

Temp. (°C)	CH_4 conversion (%)		H_2 production (Kg/h)	
	Without recycling	With recycling	Without recycling	With recycling
700	56.3	90.2	1.32	2.34
750	62.6	84.9	1.49	2.39
800	65.3	84.0	1.57	2.42
850	66.2	83.6	1.60	2.42
900	66.5	83.5	1.61	2.42
950	66.6	83.5	1.61	2.43
1000	66.6	83.6	1.61	2.43

METHANOL SYNTHESIS

Table 3 highlights the results of the methanol production at different temperatures and pressure. Results showed that lower reactor temperature and high-pressure offer maximize methanol production rates. Since methanol production reaction is exothermic; thus, according to the Le Chatelier-Braun effect, the temperature must be maintained as low as possible to obtain maximum methanol yield [10]. Simulation results indicated that a minimum reactor temperature of 200°C and pressure of 100 bar should be needed to get the maximum methanol proportion rate.

Table 2. Results of waste gas shift reactor in terms of conversion and product ratio

Temp. (°C)	CH_4 conversion (%)	H_2/CO ratio
150	96.65	1.983
200	94.07	1.97
250	90.74	1.954
300	86.85	1.934
350	82.62	1.913
400	78.26	1.891

Table 3. Methanol production by varying temperature and pressure in kg/h

Temp. (°C)	80 bar	85 bar	90 bar	95 bar	100 bar
200	24.49	24.56	24.62	24.67	24.71
225	21.91	22.27	22.61	22.95	23.31
250	18.84	19.31	19.75	20.15	20.53
275	14.76	15.35	15.91	16.43	16.92
300	10.17	10.80	11.41	11.99	12.54

CONCLUSIONS

The study reveals that biogas-to-methanol conversion might be a sustainable solution to meet worldwide energy demands. It was noticed that CH_4 and CO_2 conversions are more favorable at elevated temperature (900°C) in the dry reforming of biogas. Meanwhile, a 0.585 kg mole/h rate of methanol was achieved at parametric conditions of 200°C and 30 bar. However, the variation in syngas composition was observed regarding temperature and pressure in the water gas shift reactor. Hence, it can be stated that the biogas-to-methanol conversion process could be utilized to mitigate greenhouse gases.

REFERENCES

1. Chien FS, Kamran HW, Albashar G and Iqbal W. 2021. Dynamic planning, conversion, and management strategy of different renewable energy sources: A Sustainable Solution for Severe Energy Crises in Emerging Economies. International Journal of Hydrogen Energy 46(11):7745-7758.
2. Rosha P, Dhir A and Mohapatra SK. 2018. Influence of gaseous fuel induction on the various engine characteristics of a dual fuel compression ignition engine: A review. Renewable Sustainable Energy Reviews 82:3333-49.
3. Awe OW, Zhao Y, Nzihou A, Minh DP and Lyczko N. 2017. A review of biogas utilisation, purification and upgrading technologies. Waste Biomass Valorization; 8:267-283.
4. Ryckebosch E, Drouillon M and Vervaeren H. 2011. Techniques for transformation of biogas to biomethane. Biomass and Bioenergy 35:1633-1645.
5. Kothandaraman J, Kar S, Goeppert A, Sen R and Prakash GKS. 2018. Advances in homogeneous catalysis for low temperature methanol reforming in the context of the methanol economy. Topics in Catalysis; 61:542-559.
6. Zhang Y, Cruz J, Zhang S, Lou HH and Benson TJ. 2013. Process simulation and optimization of methanol production coupled to tri-reforming process. International Journal of Hydrogen Energy 38:13617-13630.
7. Dwivedi A, Gudi R and Biswas P. 2017. An improved tri-reforming based methanol production process for enhanced CO_2 valorization. Int J Hydrogen Energy 42:23227-23241.
8. Park JH, Yeo S, Kang TJ, Shin HR, Heo I and Chang TS. 2018. Effect of Zn promoter on catalytic activity and stability of Co/ZrO_2 catalyst for dry reforming of CH_4. Journal of CO_2 Utilization 23:10-19.
9. Chen WH and Chen CY. 2020. Water gas shift reaction for hydrogen production and carbon dioxide capture: A review. Applied Energy 258:114078.
10. Sun Y, Ritchie T, Hla SS and McEvoy S. 2011. Thermodynamic analysis of mixed and dry reforming of methane for solar thermal applications. Journal of Natural Gas Chemistry 20:568-576.

WHEC-2022
23rd World Hydrogen Energy Conference
June 26-30, 2022 - Istanbul

#208

ENHANCED HYDROGEN-RICH SYNGAS PRODUCED BY DEVELOPED PLASMA REFORMER SYSTEM

[1] Ahmed Alharbi, [1] Naif Alqahtani, [1]Abdullah Alkhedhair, [1] Abdullah Alabduly, [1] Ahmed Almaleki, [1] Mustafa Almadih, [1] Miqad Albishi, [1] Abdullah Almayeef*

[1]King Abdulaziz City for Science and Technology (KACST), P.O. Box 6086, Riyadh 11442, Saudi Arabia

nqahtani@kacst.edu.sa; akhoder@kacst.edu.sa; alabduly@kacst.edu.sa; aalmaleki@kacst.edu.sa; malmadih@kacst.edu.sa; malbishi@kacst.edu.sa; amayeef@kacst.edu.sa

* Corresponding author e-mail: ahalharbi@kacst.edu.sa

ABSTRACT

The wide use of internal combustion engines significantly affects the environment, human health, and global warming due to their exhausts, while spark ignition engine is considered as one of the main pollution sources globally. Therefore, in order to create a clean environment, achieve higher efficiency, and comply with strict regulations aimed at protecting the globe, many methods have been used to enhance SI engine performance and reduce emissions. Possible solution for emission reduction is the use of alternative fuels such hydrus ethanol or synthesis gas under lean conditions. In this study, a developed design of plasma fuel reformer was used to enhance generation of hydrogen-rich synthesis gas mixing with gasoline. Four modifications of the anode design, two modifications of the swirl ring, and two cathode materials were tested to decide the most efficient configuration of the plasma torch assembly in terms of syngas (or hydrogen) yield. The experimental results revealed that the anode design with smooth funnel shape of the gas inlet anode 1 in ring 1 at air:fuel flow rate of 30:5 was the most effective in terms of hydrogen concentrations in the reformate syngas, by about 46% increment comparing to plasmatron old design.

Keywords: plasma, fuel reforming, syngas production, plasma torch

INTRODUCTION

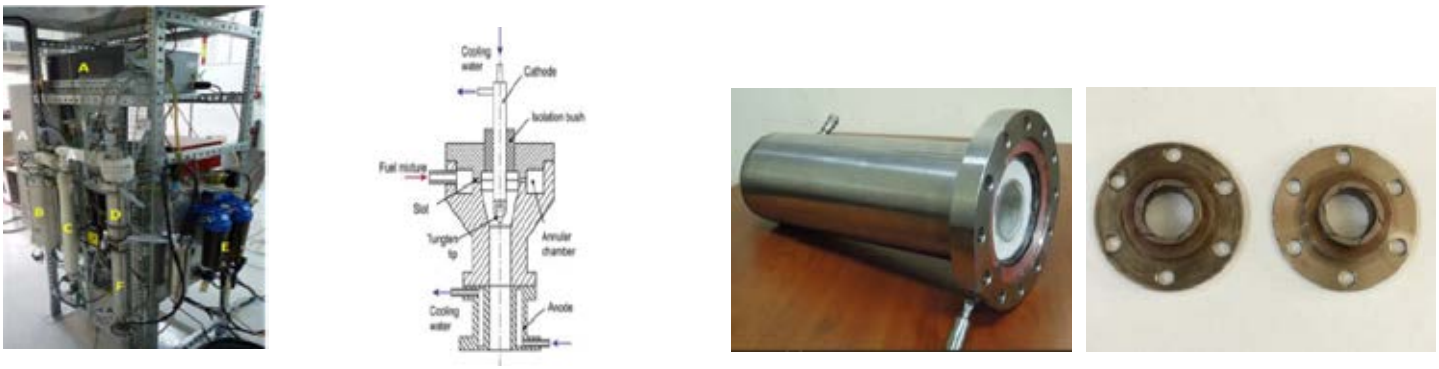
One way in the technology to reduce pollutant emissions from internal combustion engines (ICs) is to reform hydrocarbon fuels. This technology involves reacting engine fuel with oxygen and/or water as an oxidizer. So that the final product after the reaction is a synthetic gas consisting of a mixture of hydrogen (H2) and carbon monoxide (CO). In-vehicle fuel reform systems can significantly reduce nitrogen oxide (NOx) and emissions for a combustion engine when hydrogen-rich synthetic gas is added to the internal combustion unit [1-6]. Synthetic gas from fuel reforming technology can also be used as a fuel cell source for automotive applications, such as auxiliary power units (APUs) for heavy vehicles and marine transportation [7-10]. Hydrocarbon fuel reform applications use plasma technology as a heat source through reaction. The plasmatron, consisting of a cathode and anode, produces a plasma torch. First, the plasmatron heats the mixtures, which are fuel, air, and gaseous vapor, to high temperatures due to the high energy density produced by the plasma. Second, the ionization and reaction of the components of the gas mixture to produce hydrogen-rich synthesis gas [11]. This study is concerned with the development of plasma-assisted fuel reform for internal combustion engines to reduce emissions. Early studies [12 -16] have shown the production of hydrogen-rich syngas and the reduction of NOx emissions when fueling engines with syngas mixtures. In this study, we investigated the effect of changes in the shape of the anode, cathode material, and plasmatron inlet flow characteristics on the performance of the fuel reforming process. The optimum configuration of the plasmatron with the highest hydrogen yield was identified and used for further operation [12-13]

MATERIALS AND METHODS

The plasma system developed and tested in the experimental series was part of a fuel re-former used in conjunction with a spark ignition (SI) engine test system. The purpose of the reformer is the production of hydrogen-rich syngas as an admixture to hydrocarbon fuels to feed the SI engine. Fuel reformation occurs in a controlled mixture of air, gasoline vapor and steam at atmospheric pressure. The interaction between the constituents of the fuel mixture is initiated by energy of the plasma arc inside the discharge chamber; then, the fuel reforming proceeds to completion when the components exit the discharge tubular reactor. Fig 1a depicts the fuel reforming system employed in this work.

The swirling ring is shown in Fig 1c. Fig 1d shows a picture of the quartz-lined post-discharge reactor with thermal insulation, which was made of mineral wool, water-cooled, and a shell and flange made of stainless steel. In the experimental series, the hydrogen content in the reformate syngas was the main indicator of successful modification of the plasma system. The hydrogen content was measured during each modification of the plasma system configuration. Additionally, the voltage and power output were evaluated during these modifications. The plasma system modifications were the anode geometry, the emitting material of the cathode, and the swirling ring geometry. Four anodes with various

dimensions and cross sections were made and then used as modifications. All anodes were made of low-carbon steel, type AISI 1020. Differences in dimensions consisted of variations in the gas channel diameter. Differences in cross sections consisted of stepped or straight pattern variations of the gas channel. These variations are shown in Fig 2a. The anodes were replaced in sequence within the dis-charge chamber to compare the resulting plasma system performance.Two copper cathodes with different emitting materials of the insert tip were prepared as modifications. The first emitting tip was made of hafnium metal of 99.8% purity. The second tip was made of lanthanated tungsten alloy, as shown in Fig 2b.



(a) (b) (c) (d)

Fig 1. a: View of the test bench showing the following components: (A) power supply, (B) steam generator, (C) air heater, (D) reactor, (E) gas filters, and (F) cooler. b: The discharge chamber of the plasmatron and discharge unit of the plasma converter. (c) The swirling rings of the discharge chamber. (d) Quartz-lined post-discharge reactor with water-cooled shell and flange.

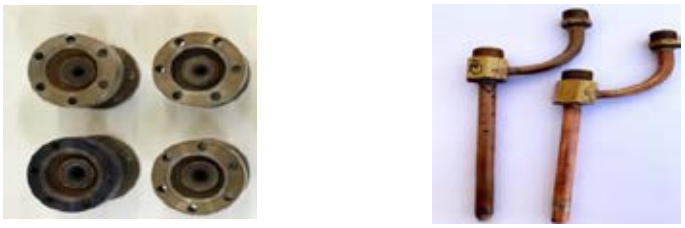


Fig 2. (a) Four anodes with various dimensions and cross sections. (b) Two copper cathodes with different emitting materials.

RESULTS AND DISCUSSION

Two series of comparative tests were performed using a hafnium metal cathode tip and an EWLa2 alloy tip. The individual test series consisted of three consecutive reforming runs with air-fuel ratios of 30: 5, 27: 4.5 and 24: 4 g / min, each lasting 15 minutes. Steady-state discharge voltages were determined during testing at 500 mA DC in the range of 3.6 to 3.7 kV for both types of cathode chips. lanthanated tungsten alloy cathode tips were much preferred for the reformer over those made of hafnium metal. Further experiments were performed in this regard using EWL a2 alloy chips. Four series of tests were performed on different dimensions of the anode under the two vortex ring conditions of the Ring 1 and Ring 2 designs. Experimental results for anode 1 using rings 1 and 2 are shown in Fig 5a and 5b. Initially, the system was in steady state for the first few minutes when the fuel-air mixture began to form in the reactor. Steady-state discharge voltages were set to approximately 4kV and 500mA DC using the anode in the first and second experiments. Syngas production began in the first 15 minutes and the experiment was performed at 24: 4 g / min with a constant air-fuel ratio of 6. The ratio for the next 15 minutes was 27 / 4.5 g / min and the ratio for the last 15 minutes was 30/5 g / min. The highest proportion of syngas in both experiments was H_2 compared to CO and CO_2. For Ring 2, hydrogen reached 21%. In the case of ring 1, it reached 24% due to the difference in the dimensions of the vortex ring. Ring 1 design has a depth width of 0.5 x 1 mm. At 6%, CO_2 share represents the lowest share of syngas. From the start to the end of all experiments with Ring 2, CO_2 was almost completely reduced compared to Ring 1 under 6% conditions. In particular, the increased pressure when the system was closed increased the voltage discharge at the end of the experiment.

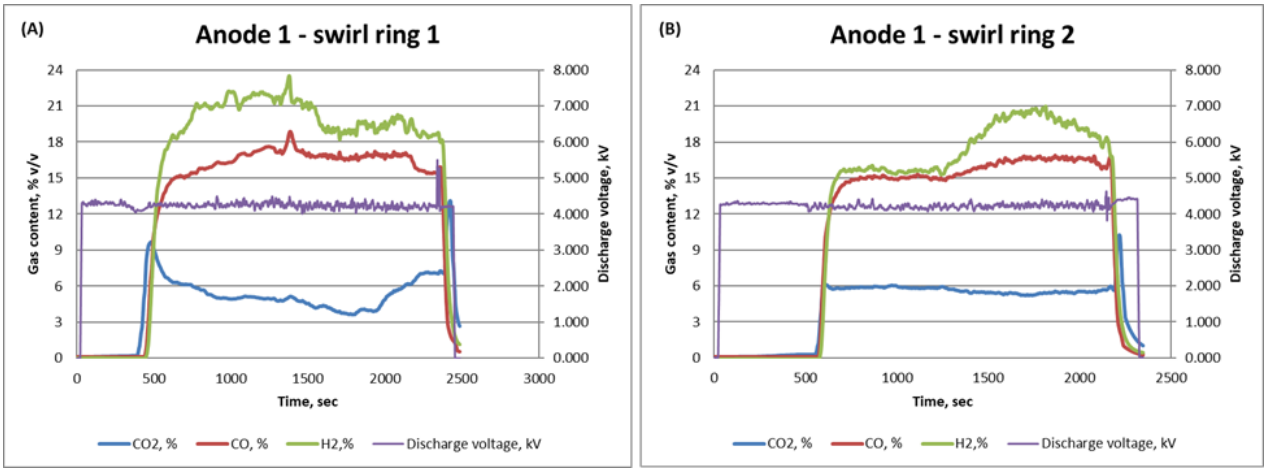


Fig 5. Comparison between ring 1 and ring 2 with anode 1.

CONCLUSIONS

The aim of this study is to investigate the increase in hydrogen-rich syngas produced by plasma reformer system and its effect on nitrogen oxides emissions and fuel consumption in internal combustion engines. An improved plasmatron design carried out consisting of four anode, two swirling rings and two cathode (hafnium metal and Lanthanated) to study the effect on producing hydrogen-rich synthetic gas. It was found that the highest hydrogen percentage in the synthetic gas is 24% (comparing to 13% with old plasmatron design) at anode 1, swirling ring 1 and the best type for cathode is Lanthanated tungsten material due to more resistance to corrosion during the fuel reforming process.

REFERENCES

1. Conte, E.; Boulouchos, K. Influence of Hydrogen-Rich-Gas Addition on Combustion, Pollutant Formation and Efficiency of an IC-SI Engine; SAE Technical Paper Series; SAE International: Warrendale, PE, USA, 2004; doi:10.4271/2004-01-0972.
2. Tully, E.J.; Heywood, J.B. 2003. Lean-Burn Characteristics of a Gasoline Engine Enriched with Hydrogen Plasmatron Fuel Reformer; SAE Technical Paper Series; SAE International: Warrendale, PE, USA, doi:10.4271/2003-01-0630.
3. Quader, A.A.; Kirwan, J.E.; Grieve, M.J. 2003. Engine Performance and Emissions near the Dilute Limit with Hydrogen Enrichment using an On-Board Reforming Strategy; SAE Technical Paper Series; SAE International: Warrendale, PE, USA,; doi:10.4271/2003-01-1356.
4. Sobyanin, V.; Sadykov, V.; Kirillov, V.; Kuzmin, V.; Kuzin, N.; Vostrikov, Z.; Smirnov, E.; Sorokin, A.; Brizitskiy, O.; Terentyev, V.; et al. 2005. Syngas as a fuel for IC and diesel engines: efficiency and harmful emissions cut off. In Proceedings of the International Hydrogen Energy Congress and Exhibition, Istanbul, Turkey.
5. Kirwan, J.; Quader, A.; Grieve, M. 1999. Advanced Engine Management Using On-Board Gasoline Partial Oxidation Reforming for Meeting Super-ULEV (SULEV) Emissions Standards; SAE Technical Paper 1999-01-2927; SAE International: Warrendale, PE, USA, doi:10.4271/1999-01-2927
6. Lindstrom, B.; Karlsson, J.; Ekdunge, P.; De Verdier, L.; Häggendal, B.; Dawody, J.; Nilsson, M.; Pettersson, L. 2009. Diesel fuel reformer for automotive fuel cell applications. Int. J. Hydrog. Energy 2009, 34, 3367–3381, doi:10.1016/j.ijhydene.02.013.
7. Bromberg, L.; Cohn, D.R.; Rabinovich, A.; Heywood, J. 2001. Emissions reductions using hydrogen from plasmatron fuel converters. Int. J. Hydrog. Energy, 26, 1115–1121, doi:10.1016/s0360-3199(01)00049-0.
8. Samsun, R.C.; Prawitz, M.; Tschauder, A.; Pasel, J.; Pfeifer, P.; Peters, R.; Stolten, D. 2018. An integrated diesel fuel processing system with thermal start-up for fuel cells. Appl. Energy, 226, 145–159, doi:10.1016/j.apenergy.2018.05.116.
9. Kang, I.; Bae, J. 2006. Autothermal reforming study of diesel for fuel cell application. J. Power Sources, 159, 1283–1290, doi:10.1016/j.jpowsour.2005.12.048.
10. Bensaid, S.; Specchia, S.; Federici, F.; Saracco, G.; Specchia, V. 2009. MCFC-based marine APU: Comparison between conventional ATR and cracking coupled with SR integrated inside the stack pressurized vessel. Int. J. Hydrog. Energy, 34, 2026–2042, doi:10.1016/j.ijhydene.2008.11.092.
11. Bromberg L.; Cohn, D.R.; Rabinovich, A.; Alexeev, N.; Samokhin, A.; Hadidi, K.; Palaia, J.; Margarit-Bel, N. 2006.Onboard Plasmatron Hydrogen Production for Improved Vehicles; PSFC JA-06-3; MIT Plasma Science and Fusion Center: Cambridge, MA, USA.
12. Alharbi, A.A.; Alenazey, F.S.; Migoun, A.N.; Dmitrenko, Y.M.; Zhdanok, S.A. 2016. Reducing Pollution Emissions by Adding Syngas Generated by a Plasma-Assisted Gasoline Converter in the Intake Manifold of a Gasoline Engine with Electronic Fuel Injection System. Heat Transf. Res. 47, 1073–1082, doi:10.1615/HeatTransRes.2016016579.
13. Alharbi, A.A.; Binjuwair, S.A.; Alshunaifi, I.A.; Alkhedhair, A.M.; Alabduly, A.J.; Almorat, M.S.; Albishi, M.S. 2019. NOx Emission Reduction Using Hydrous Ethanol-Gasoline Blend with Syngas in SI Engine. J. Environ. Prot., 10, 1278–1298, doi: 10.4236/jep.2019.1010076.

WHEC-2022
23rd World Hydrogen Energy Conference
June 26-30, 2022 - Istanbul

#219

PERFORMANCE OF MICROWAVE AND CONVENTIONALLY HEATED REACTOR SYSTEMS IN STEAM REFORMING OF ETHANOL OVER NICKEL IMPREGNATED MESOPOROUS CARBON

*Merve Sarıyer, *Naime Aslı Sezgi, Timur Doğu*
Middle East Technical University, Department of Chemical Engineering, Ankara, Turkey

*Corresponding author e-mail: sezgi@metu.edu.tr

ABSTRACT

Hydrogen production via steam reforming of ethanol reaction was investigated over nickel impregnated commercial mesoporous carbon catalyst (10Ni-MC) in conventionally and microwave heated reactor systems. The characterization results of the catalyst revealed that according to UIPAC classification, nickel impregnated mesoporous carbon showed Type IV isotherm with H2 hysteresis. Highly stable product distributions for steam reforming of ethanol were obtained with the 10Ni-MC catalyst. With an increase in the reaction temperature, the hydrogen yield and the hydrogen concentration were increased in both reactor systems. Higher hydrogen yield and higher concentration of hydrogen were observed in the microwave heated reactor system compared to the conventionally heated reactor system.

Keywords: Hydrogen, Ethanol steam reforming, Microwave heating, Mesoporous Carbon, Nickel

INTRODUCTION

The need for clean and renewable energy sources or carriers has been growing due to the necessity of sustainable and environmentally friendly energy. Hydrogen, a non-toxic, clean, and renewable energy carrier can be considered a potential energy carrier. Ethanol produced from the fermentation of wastes such as corn cobs and sugar beets is one of the most promising sustainable resources for the on-board production of hydrogen via steam reforming reaction. The steam reforming of ethanol involves two main reactions: the steam reforming of ethanol (SRE) and water gas shift reactions (WGSR).

$$C_2H_5OH + H_2O \leftrightarrow 2CO + 4H_2 \qquad \text{(SRE)}$$

$$CO + H_2O \leftrightarrow CO_2 + H_2 \qquad \text{(WGSR)}$$

A conventionally (CONV) heated reactor system is generally used to heat the catalytic bed in the reaction system. Recently, many researchers have focused on improving a new heating reactor system as a process intensification method for different reactions. Microwave (MW) heating reactor system arises as a new heating method. Moreover, recent research studies have revealed that microwave heated reaction system provides more stable reactor performance, higher yield and conversion, and lower coke formation than the conventionally heated reaction system [1,2].

The selection of the catalyst in the microwave reactor applications is critical. Only if the material has a high dielectric loss tangent value can the catalyst bed be heated by microwave. The high dielectric loss tangent value of carbon-based materials provides high microwave absorption capacity. Moreover, the metal particles are good microwave absorbers due to the shape of the metal crystals on the catalyst surface and pores. Due to the sharper parts and corners of the metal crystals, the catalyst can absorb microwaves quickly. The carbon-based catalyst and these metal particles are the reason of the hot spot formed in the catalyst bed, which enhances the reaction rate, the conversion of reactant, the yield and mole percentage of the desired product.

MATERIALS AND METHODS

Commercial mesoporous carbon (MC) was used as a catalyst support, and 10 % nickel was incorporated into mesoporous carbon using an impregnation method. Activity tests of the 10Ni-MC catalyst for the steam reforming of ethanol reaction were performed ~~by~~ using both microwave heated and conventionally heated reactor systems at 500°C and 600°C under atmospheric pressure with a feed H_2O/C_2H_5OH ratio of 1:1 by volume. Weight hourly space velocity (WHSV) of the reaction gas mixture was 4.8 h^{-1} in all 5-hour activity tests. In all experiments, 0.15 g of catalyst is charged to the reactor. The hydrogen production system has been described in detail in our previous publication [1].

RESULTS AND DISCUSSION

XRD pattern of the 10Ni-MC catalyst revealed the presence of metallic nickel and the characteristic peaks of the carbon. According to IUPAC classification, nickel impregnated mesoporous carbon catalyst showed Type IV

isotherms with H2 hysteresis loops. Its surface area and mean pore diameter values were 241 m^2/g and 10.6 nm, respectively.

In all activity tests, the complete conversion of ethanol was achieved. The comparison of the mole percentages of hydrogen and methane at 500°C at the conventionally heated and microwave heated reactor systems is shown in Figure 1. After reaching the steady-state at 500°C and 600°C in the microwave heated system, a more stable product distribution was achieved than the electrically heated reactor system. The hydrogen yield at 500°C in the CONV heated reactor was 51 %; on the other hand, the hydrogen yield in the MW heated reactor was 78 % for the SRE reaction. Moreover, with an increase in the temperature to 600°C, the hydrogen yield values in the CONV and MW heated reactors increased to 78 % and 86 %, respectively. Higher hydrogen yield was observed in the MW heated reactor at the SRE activity tests at both temperatures.

Moreover, in the microwave heated reactor system at 500°C and 600°C, there was a decrease in the mole percentage of methane. The mole percentage of the hydrogen increased with microwave heating compared to the conventionally heated reactor system (Fig.1). The hot spots on nickel particles are responsible for the increase in the hydrogen yield, the mole percentage of hydrogen, and the decrease in the mole percentage of methane because higher temperatures favor the steam reforming of ethanol reaction and methane reforming reaction.

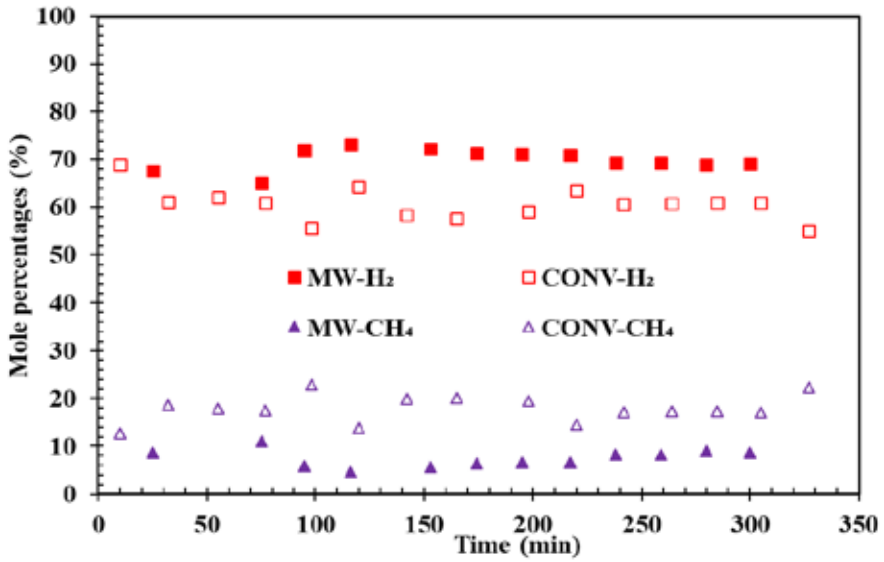


Fig.1 The comparison of H_2 and CH_4 mole percentages in MW and CONV reactors at 500°C

CONCLUSIONS

The activity results in the microwave heated reactor system have shown that highly stable product distributions were obtained in the steam reforming of ethanol reaction. The hydrogen yield and hydrogen mole fraction were increased with an increase in the reaction temperature. Higher hydrogen yield and higher mole fraction of hydrogen were observed in the microwave heated reactor system compared to the conventional heated reactor system. Nickel-loaded mesoporous carbon-supported catalyst gave good catalytic activity in the microwave heated reactor system due to the high microwave absorption capacity of the carbon-supported materials.

ACKNOWLEDGEMENT

Financial supports of Middle East Technical University Research Funds and TUBA are gratefully acknowledged. The authors also thank the Central Laboratory and Chemical Engineering Department of METU for the characterization analyses.

REFERENCES

1. Sarıyer, M., Bozdağ A.A., Sezgi N.A., Doğu T. 2019. “Performance Comparison of Microwave and Conventionally Heated Reactors for Sorption Enhanced Reforming of Ethanol over Ni Impregnated SBA-15” Chemical Engineering Journal, 377,120138.
2. Gunduz, S., ve Dogu T. 2015. “Hydrogen by Steam Reforming of Ethanol over Co–Mg Incorporated Novel Mesoporous Alumina Catalysts in Tubular and Microwave Reactors” Applied Catalysis B: Environmental 168–169, 497–508.

WHEC-2022
23rd World Hydrogen Energy Conference
June 26-30, 2022 - Istanbul

#244

PSEUDO-DYNAMIC MODELING AND OPTIMIZATION OF HEAVY PARAFFIN DEHYDROGENATION PROCESS FOR SELECTIVE OLEFIN AND HYDROGEN PRODUCTION IN CONVENTIONAL REACTORS

[1] *M. Dehdashti,* [2*] *M. Farsi,* [3] *M. Binazadeh*
[a] Department of Chemical Engineering, School of chemical and Petroleum Engineering, Shiraz University, Shiraz 71345, Iran

*Corresponding author e-mail: farsi@shirazu.ac.ir

ABSTRACT

Hydrogen has emerged as a clean novel energy carrier. Catalytic dehydrogenation of hydrocarbons such as paraffin is a reliable method for hydrogen production. In this study, a radial flow conventional tubular fixed bed reactor is pseudo-dynamically modeled and the operating conditions are optimized using genetic algorithm to maximize olefin and hydrogen production. The model accuracy is validated by industrial data and the model output is optimized using multi-objective genetic algorithm method. Validated model reveals that paraffin conversion and selectivity are enhanced by 3.6% and 0.12% in the optimized process compared to the conventional process, respectively.

Keywords: Heavy paraffin dehydrogenation, Radial flow conventional tubular reactor, Pseudo-Dynamic model, Genetic algorithm

INTRODUCTION

Greenhouse-gas (GHG) emissions and its consequent climate change have raised international concerns [1]. According to 2021 British petroleum's (BP) annual statistical review of world energy [2], global consumption of fossil fuels have risen exponentially from 1965 until 2019. Renewable and clean energy sources are being developed to ensure industrial growth while reducing the hydrocarbon fuel consumption. Hydrogen is a promising and clean energy source [3]. Amidst numerous ways of hydrogen production, catalytic dehydrogenation of hydrocarbons and specifically heavy paraffin is focus of this paper. Dehydrogenation is a chemical process that separates hydrogen from an organic molecule. This process is usually used to convert alkanes to olefins which are much more reactive and therefore precious [4].

Several studies have simulated heavy paraffin dehydrogenation process. Zahedi *et al.* have reported the dynamic model of an industrial dehydrogenation reactor and compared the results with industrial reactor's data [5]. Saeedizad *et al.* studied reversible and irreversible reactions of the overall dehydrogenation of heavy paraffin and the conversion of Paraffin to olefins over deactivating $Pt - Sn - Al_2O_3$ catalyst [6]. They obtained kinetic parameters using non-linear estimation methods and they also showed that the catalyst erosion is even more dependent on temperature than the main reactions. The modeling of a dehydrogenation reactor and optimization by NSGA-II method was represented by Bayat *et al.* and the rate of production as a function of reactor radius was reported [7]. Finally Frantsina *et al.* introduced the results of comparative analysis on three cycles of heavy paraffin in presence of a Pt catalyst in their study [8]. To date there is no published study on dynamic modeling of hydrogen production via dehydrogenation of heavy paraffin in conventional reactors. In this paper, a radial flow conventional tubular fixed bed reactor is pseudo-dynamically modeled and the respective operating conditions are optimized using genetic algorithm to maximize olefin and hydrogen production.

MODEL DESCRIPTION

A pseudo-dynamic mathematical model of a radial flow fixed-bed conventional tubular reactor was prepared. Dominant reactions in dehydrogenation of heavy paraffin are shown in Figure 1(a). Reaction rates and optimized Kinetic parameters were taken from Zahedi *et al.* [5] and Vafajoo *et al.* [9] which are shown in Table 1. Governing equations reported in Table 2 include mass and energy balances, Ergun equation for pressure drop, and catalyst deactivation equation. All balance equations dependent to radius were numerically solved using Backward Euler method. Main assumptions of the model are: (a) all gas mixtures are assumed to be ideal, (b) external reactor wall is assumed to be insulated, (c) gas mixtures move radially inside the reactor therefore radial velocity is variable, (d) there is no mass and heat transfer between catalyst particles, (e) molecular diffusion is ignored compared to bulk flow, and (f) pressure drop only occurs radially. The differential element along the radius of the reactor is shown in Figure 1(b).

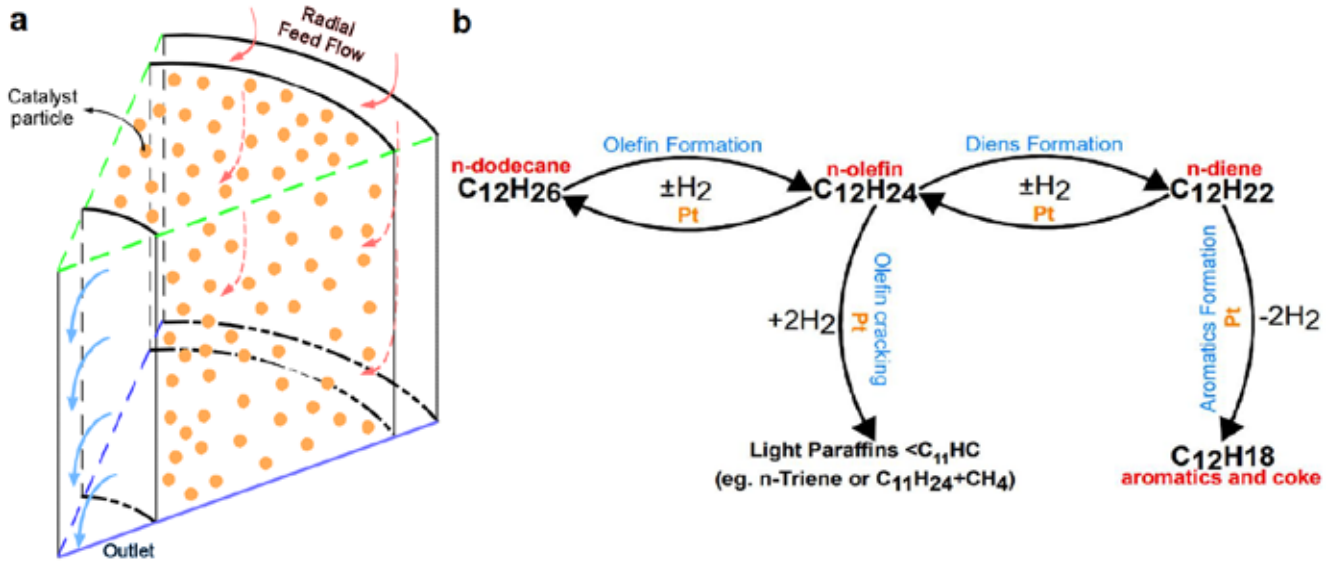


Figure 1. (a) A Differential element of conventional tubular reactor, (b)Dominant reactions in dehydrogenation of heavy parraffin

Table 1. Reactions and Reaction rates

Reactions	Reaction rates	
$C_{12}H_{26} \leftrightarrow C_{12}H_{24} + H_2$	$\frac{k_1 K_p (P_p - {P_O P_H}/{K_{E_1}})}{(1 + K_p P_p + K_o P_o + K_D P_D + K_A P_A + K_H P_H)^2}$	(1)
$C_{12}H_{24} \leftrightarrow C_{12}H_{22} + H_2$	$\frac{k_2 K_O (P_O - {P_D P_H}/{K_{E_2}})}{(1 + K_p P_p + K_o P_o + K_D P_D + K_A P_A + K_H P_H)^2}$	(2)
$C_{12}H_{22} \rightarrow C_{12}H_{18} + 2H_2$	$\frac{k_3 K_D P_D}{(1 + K_p P_p + K_o P_o + K_D P_D + K_A P_A + K_H P_H)^2}$	(3)
$C_{12}H_{24} + 2H_2 \rightarrow < C_{11}HC (C_{11}$ or $C_{11}H_{24})$	$k_4 P_O$	(4)

Table 2. Governing equations

Paraffin mass balance	$(N)_i = (N)_{i+1} + (\rho_b a(-r_1))_{i+1} \times \Delta r$	(5)
olefin mass balance	$(N)_i = (N)_{i+1} + (\rho_b a((r_1 - r_2 - r_4)))_{i+1} \times \Delta r$	(6)
Diene mass balance	$(N)_i = (N)_{i+1} + (\rho_b a((r_2 - r_3)))_{i+1} \times \Delta r$	(7)
Aromatics mass balance	$(N)_i = (N)_{i+1} + (\rho_b a(r_3))_{i+1} \times \Delta r$	(8)
Light paraffins mass balance	$(N)_i = (N)_{i+1} + (\rho_b a(r_4))_{i+1} \times \Delta r$	(9)
Hydrogen mass balance	$(N)_i = (N)_{i+1} + (\rho_b a((r_1 + r_2 + 2r_3 - 2r_4)))_{i+1} \times \Delta r$	(10)
Energy balance	$(T_g)_i = {(T_g)_{i+1} + (A_c \rho_b a \sum_{j=1}^{n} r_j (-\Delta H_{f,i} (\frac{J}{mol})) \times \Delta r)}/{F_t C_{Pg}}$	(11)
Ergun equation	$(P)_i = (P)_{i+1} + (150 \frac{(1-\varepsilon)^2 \mu u_g}{\varepsilon^3 d_p^2} + 1.75 \frac{(1-\varepsilon) u_g^2 \rho}{\varepsilon^3 d_p}) \times \Delta r$	(12)
Superficial velocity of gas component i	$u_{g_i} = (F_{t_i} \times MW_m \div \rho_m \div 1{,}000)/(A_c)$	(13)
Catalyst Deactivation	$t = \frac{1 - a_c^{(1-n-{E_d}/{E_A})}}{k_{d0}(1 - n + {E_d}/{E_A})}$	(14)

RESULTS AND DISCUSSION

Steady-state and pseudo-dynamic simulations have been performed on model and the model is validated by Bistoon petrochemical complex (BPC) LAB plant data [10] with less than 5% error. Olefin production rate along the radius of the reactor in 1st, 10th, 20th and 29th days are compared in Figure 2. Olefin is considered to be the desirable product of process and its yield decreases with time due to the coke formation and subsequent catalyst deactivation process. Radial temperature profile during 29 days of operation is demonstrated in Figure 3. As the overall process of heavy paraffin dehydrogenation is endothermic, temperature decreases along the radius of the reactor but the amount of

this decline in temperature decreases by time due to the catalyst deactivation and subsequent reduction of paraffin conversion.

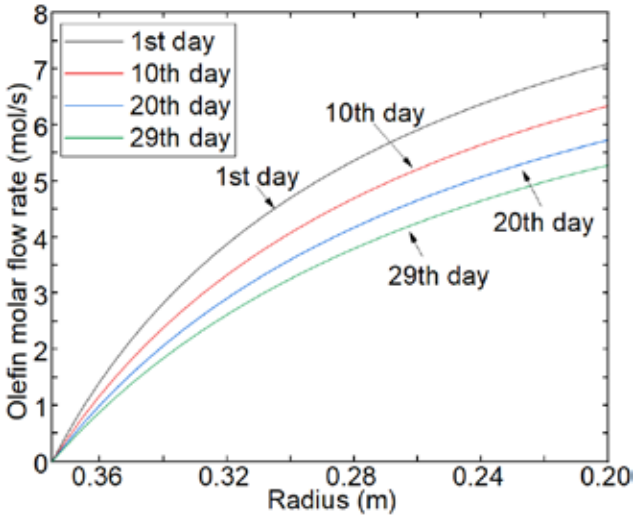


Figure 2. Olefin production rate in designated times

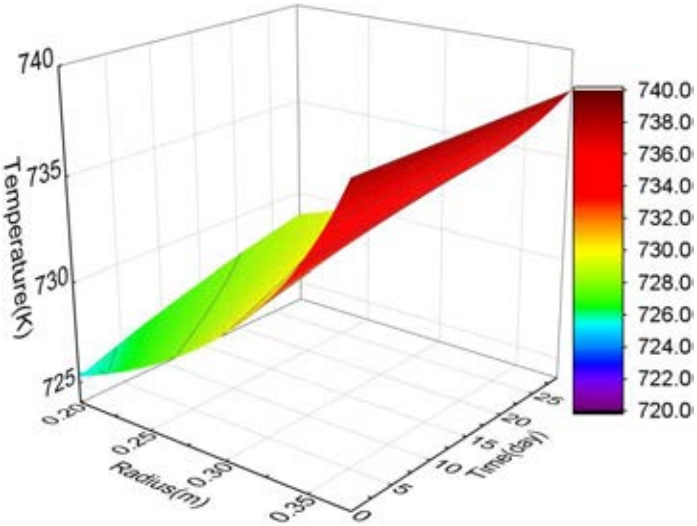


Figure 3. Radial temperature profile for 29 days

CONCLUSIONS

Steady-state and pseudo-dynamic simulations are performed on a pseudo-dynamic mathematical model of a radial flow fixed-bed conventional tubular reactor. Model validation proves the simulation accuracy. A multi-objective optimization is performed using genetic algorithm method to increase yield of the reactor. It is shown that paraffin conversion and selectivity are potentially enhanced by 3.6% and 0.12% in the optimized process compared to the conventional process, respectively.

REFERENCES

1.Zecca, A. and L. Chiari, Fossil-fuel constraints on global warming. Energy Policy, 2010. 38(1): p. 1-3.
2.https://www.bp.com/en/global/corporate/energy-economics/statistical-review-of-world-energy/downloads.html. Accessed on november 2, 2021.
3.Basile, A., et al., Hydrogen Production, Separation and Purification for Energy. Vol. 89. 2017: IET.
4.Wittcoff, H.A., B.G. Reuben, and J.S. Plotkin, Industrial organic chemicals. 2012: John Wiley & Sons.
5.Zahedi, G., H. Yaqubi, and M. Ba-Shammakh, Dynamic modeling and simulation of heavy paraffin dehydrogenation reactor for selective olefin production in linear alkyl benzene production plant. Applied Catalysis A: General, 2009. 358(1): p. 1-6.
6.Saeedizad, M., S. Sahebdelfar, and Z. Mansourpour, Deactivation kinetics of platinum-based catalysts in dehydrogenation of higher alkanes. Chemical Engineering Journal, 2009. 154(1-3): p. 76-81.
7.Bayat, M., Z. Dehghani, and M.R. Rahimpour, Dynamic multi-objective optimization of industrial radial-flow fixed-bed reactor of heavy paraffin dehydrogenation in LAB plant using NSGA-II method. Journal of the Taiwan Institute of Chemical Engineers, 2014. 45(4): p. 1474-1484.
8.Vafajoo, L., et al., Kinetic Parameters Optimization and Modeling of Catalytic Dehydrogenation of Heavy Paraffins to Olefins. Petroleum Science and Technology, 2014. 32(7): p. 813-820.
9.Bistoon Petrochemical Complex, IFP Manual, 2007.

WHEC-2022
23rd World Hydrogen Energy Conference
June 26-30, 2022 - Istanbul

#272

STATIONARY METHANOL STEAM REFORMING TO HYDROGEN FUEL FOR FUEL-CELL FILLING STATIONS

[1] *Athanasios A. Tountas,* [2] *Geoffrey A. Ozin,* [*1,3] *Mohini M. Sain*
[1] University of Toronto, Faculty of Engineering, Department of Chemical Engineering and Applied Chemistry, 200 College St., Toronto, Canada
[2] University of Toronto, Faculty of Arts & Science, Department of Chemistry, 80 St. George St., Toronto, Canada
[3] University of Toronto, Faculty of Engineering, Department of Mechanical and Industrial Engineering, 5 King's College Circle, Toronto, Canada

*Corresponding author e-mail: m.sain@utoronto.ca

ABSTRACT

Renewable hydrogen (H_2) carriers such as methanol (MeOH), dimethyl ether (DME), oxymethylene dimethyl ethers (OMEs) and conceivably ammonia (NH_3) can be reformed back into H_2 and are fundamental chemical conversions for the long-term viability of the H_2 economy due to their higher densities and ease of transportability compared to H_2. MeOH is an especially important carrier as it is a simple C1 chemical that can be produced from green solar-PV-generated H_2 and direct-air-captured CO_2 with a current commercially practical solar-to-fuel efficiency of 10% from renewable solar energy. MeOH steam reforming (MSR) in stationary systems next to H_2 fuel-cell filling stations can eliminate the need for on-board mobile reformers and the former systems can be more robust in terms of attaining strict H_2 product specifications and MeOH is a safe, lossless and a compact medium for long-term H_2 storage. Both thermal- and photo-catalysts are viable options for achieving stable, long-term performance of stationary MSR systems.

Keywords: fuel-cell vehicle filling stations, methanol steam reforming, hydrogen transport and storage, stationary reformer, liquid hydrogen carriers

INTRODUCTION

Much research has focused on the MeOH steam reforming (MSR) to produce H_2 and CO_2 with minimal selectivity and yield to carbon monoxide (CO) [1]. CO must remain at low to trace levels to avoid poisoning the noble metal catalysts (platinum (Pt), palladium (Pd) *etc.*) that are applied in fuel-cell stacks. Using H_2 in mobility applications such as fuel-cell vehicles can increase fuel efficiency to 80% or higher, or approximately double the efficiency of state-of-the-art internal combustion and compression ignition engines. H_2 for transport also avoids the shortcomings of Li-ion batteries with the former having superior range and faster filling times for short and long-haul transport. However, auxiliary equipment such as on-board reformers for mobile applications can increase the complexity of the fuel system. Alternatively, we propose reforming liquid hydrogen carriers at stationary installations such as H_2 filling stations so that H_2 can be stored safely and at high density and released as needed for filling fuel-cell vehicles.

The MSR and MeOH decomposition reactions are endothermic (Eq. (1) and (2)) and as such require heat be applied to the system to drive them to completion. Another important reaction is the water-gas shift (WGS) reaction (Eq. (3)) that can be used to generate further H_2 while simultaneously eliminating CO.

$$CH_3OH + H_2O \rightarrow 3H_2 + CO_2 \qquad \Delta H_{298K} = +49.6 \text{ kJ mol}^{-1} \qquad (1)$$

$$CH_3OH \rightarrow 2H_2 + CO \qquad \Delta H_{298K} = +90.6 \text{ kJ mol}^{-1} \qquad (2)$$

$$CO + H_2O \rightarrow CO_2 + H_2 \qquad \Delta H_{298K} = -41.3 \text{ kJ mol}^{-1} \qquad (3)$$

The catalysts needed for reforming MeOH are widely known and available [1] and coupling them with a suitable reactor can allow for a proof-of-concept demonstration. A microchannel reactor is one type of prospective MSR reactor that has excellent heat transfer characteristics and suitable flow properties in the catalyst bed to avoid 'hot spots' and 'dead zones', respectively. It also allows for high conversion of feed MeOH and steam being of the plug-flow type. The moderate operating temperature of 200–300°C can be achieved using a hot oil heat transfer fluid and a low operating pressure favours the forward reaction by Le Chatelier's principle.

The gas specifications for fuel-cell operation are provided in ISO 14687-2 [2]. It should be noted that these specifications are conservative and "reflect the priority of automobile OEMs to minimize risks of damaging very expensive pre-commercial fuel cell demonstration vehicles" [3]. Multiple grades of hydrogen may be accommodated in the future.

A system demonstrating this conversion technology must be scalable to prototype and pre-commercial/commercial scales. To achieve this, the following technology criteria ought to be accounted for: cost, safety, selectivity to intended products, H_2 yield, ease of optimization, low operational sensitivity, and relevant capacity.

DISCUSSION OF MEOH VS. NATURAL GAS AS A HYDROGEN SOURCE

There is a two-fold nature to the hydrogen sourcing challenge, there is the need to trade off fuel cell performance and durability against the cost of delivering adequate quality hydrogen to the consumer [3]. MSR is distinguished from steam methane reforming (or SMR) in that it avoids many shortfalls of the latter that and can be made from renewables. Methane can also be sourced from biogas *via* anaerobic digestion although not at the scale needed for the hydrogen economy and is typically used as a fossil fuel.

MSR eliminates sulphur and ammonia that are present in natural gas

MSR avoids all sulphur compounds (such as H_2S etc.) and NH_3 found naturally in natural gas streams. Sulphur's effect on fuel-cells requires it to be maintained at ppb levels. Catalyst poisoning when exposed to sulphur compounds has been found to increase with time of exposure. Like sulphur, NH_3 contamination is cumulative. The effect of CO (discussed more latter) is displaced by H_2S meaning that although the kinetics of CO are faster, H_2S has a higher adsorptive strength and over time suppresses CO adsorption making H_2S worse for the catalyst overall. Detection of sulfur compounds also requires "extremely sensitive analytical equipment and careful monitoring of fuel quality along the entire fuel chain from production to dispensing" [3].

MSR avoids many inert gases present in natural gas

MSR avoids helium and other hydrocarbons contamination and dilution naturally present in natural gas streams. Helium is difficult to detect and can be present at 100s of ppmv in natural gas. A cumulative inert amount of ~300 ppmv is recommended for fuel-cell operation to avoid sensor and stack malfunction. Competing technologies such as SMR and water electrolysis both entrain or produce inert gases. Air is typically entrained during SMR, and water electrolysis can also produce trace amounts of inert O_2, that require to be kept below the threshold.

The MSR process is less complex overall than SMR

An example of a SMR process for hydrogen is shown in Fig. 1. Major differences are that the MSR can be operated at lower reforming temperature of 200–300°C compared to 750°C for SMR. MSR still requires WGS, water separation, and PSA, but can more easily compress liquid MeOH prior to the reforming step than natural gas. A lower WGS step temperature is preferred as the equilibrium yield to CO increases with temperature and as such the MeOH reforming temperature is more compatible with WGS. Moderate pressures of 8–10 atm were modelled as a good target pressure at a steam/carbon ratio (S/C) of 4 for SMR and is expected to be similar for MSR [3].

Removing contaminants and quality of H_2 product gas needed

As mentioned previously, ISO 14687-2 details the H_2 gas specification needed for fuel-cell durability. CO (0.2 ppmv specification) is seen as limiting species to remove, higher removal leads to lower H_2 recovery and lower overall fuel efficiency. Attempting to maintain low CO contamination can affect the H_2 purity as N_2 can 'break-through' in the PSA process if present at high concentrations prior to PSA. Because MSR starts with a liquid MeOH feed it can be designed to avoid any entrained air during the process (as opposed to SMR) and is an advantage of this route. This highlights the challenge of maintaining all inert gases (He, HCs, O_2, water, N_2, Ar etc.) at low to trace levels prior to PSA. CO_2 is easily removed from PSA.

Easing the CO specification will increase the overall efficiency. In an analysis carried out by the DOE assuming relatively high fuels cost ~US$ 7.73 $MMBTU^{-1}$ the CO purification only affects the H_2 cost 4.4% over an order of magnitude change (0.1–100 ppmv CO) [3]. A slightly dated (2015) but still relevant DOE target for hydrogen fuel cost at the station is US$ 1.5 kg_{H2}^{-1}.

INTERESTING CATALYST SYSTEMS

Stage 1: Thermal Catalysts:

Many thermal catalyst systems have been proposed as seen in the following references [1,4]. Typically, a good MeOH synthesis catalyst would also act as a good reforming catalyst under different conditions. However, the traditional copper-based, copper zinc-oxide alumina (CZA) catalyst, used successfully for decades for MeOH synthesis, presents challenges due to its short-term stability under MSR conditions. Catalysts that avoid the dispersed copper phase based on Pd and ZnO have shown improved durability under operating conditions [4].

Another approach that could be explored is to decompose MeOH into CO and H_2 directly on standalone Pd catalyst and shift the CO out of the system in a downstream WGS step. This approach has not been significantly documented in the literature.

Stage 2: Photocatalysts

A ZnO material demonstrates photoactivity for MeOH reforming under dark or thermal-only conditions with MeOH-water vapour and under UV light with MeOH-only and MeOH-water vapour [5]. In unpublished results, direct UV-assisted MeOH decomposition and thermal MSR is not as favoured as UV-light-assisted MSR. The analytical technique UV electron paramagnetic resonance (UV-EPR) confirmed the production of UV induced electrons/defects upon irradiation. The electron reduces the Zn(II) to Zn(I) and light provides photogenerated electron and holes for MSR.

The benefit of using ZnO is that it avoids the metallic Cu or Pd phase of thermal catalysts that tend to sinter due to the hydroxylation of the ZnO phase. By using ZnO alone and allowing it to slowly hydroxylate, it is conceivable that the material could be regenerated in a thermal reconditioning step to remove the water in the structure. Such a technique of operating two reactors in parallel (on online and one regenerating) is used throughout the chemical and petrochemical industries and addresses and simplifies the unavoidable catalyst deactivation typical under MSR conditions.

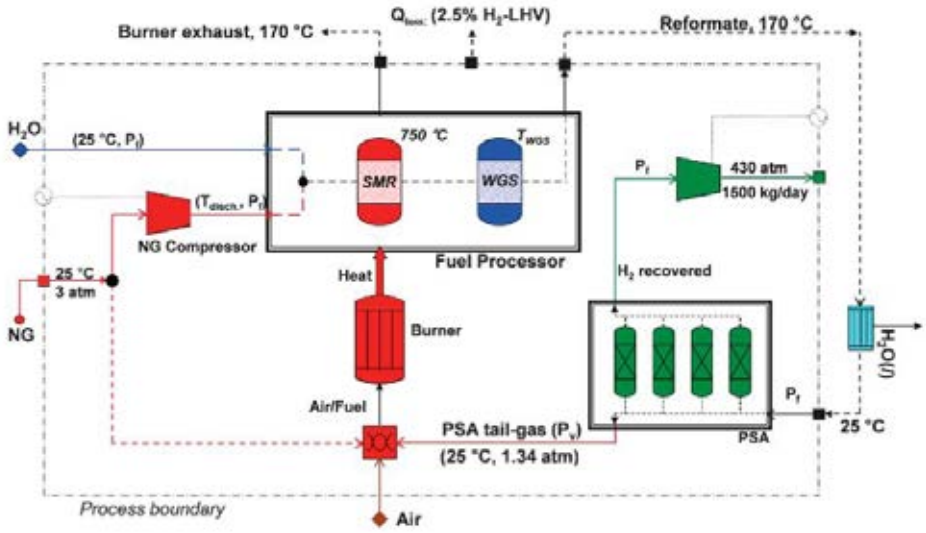


Fig. 1 Example of SMR process and auxiliaries that would be similar to a MeOH-based system [3]

ACKNOWLEDGEMENT

We thank J. Tjong of Ford Motor Canada for financial support.

REFERENCES

1. Li D, Li X and Gong J. 2016. Catalytic Reforming of Oxygenates: State of the Art and Future Prospects. Chem. Rev. 116:11529–11653.
2. Arrhenius K, Alexandersson A, Yaghooby H, Engelbrektsson J, Stromberg N. 2015. Analysis of hydrogen quality. Teknikbevakning Bransleceller.
3. Ohi, JM, Vanderborgh N and Voecks G. 2016. Hydrogen Fuel Quality Specifications for Polymer Electrolyte Fuel Cells in Road Vehicles. Safety, Codes Stand. Progr. U.S. Department of Energy. 1–72.
4. Kappis K, Papavasiliou J and Avgouropoulos G. 2021. Methanol Reforming Processes for Fuel Cell Applications. Energies. 14:1–30.
5. Tountas, AA. 2021. Solar Methanol: From Process Engineering and Photoreactor Development to Materials Discovery and Photocatalysis. University of Toronto - Ph.D. thesis.

WHEC-2022
23rd World Hydrogen Energy Conference
June 26-30, 2022 - Istanbul

#284

EXPERIMENTAL INVESTIGATION OF A Fe_2O_3 CARBOTHERMIC REDUCTION CYCLE FOR HYDROGEN PRODUCTION

[1*] *Lina Maria Varon Cardona,* [1,2] *Beethoven Narváez-Romo,* [3] *Marcelo Mourão* [1] *José Roberto Simões-Moreira*
[1]Renewable and Alternative Energy Systems Laboratory (SISEA), Escola Politécnica at University of São Paulo, São Paulo, Brazil
[2] Grupo de Energía y Termodinámica, Facultad de Ingeniería Mecánica, Universidad Pontificia Bolivariana, Medellín, Colombia
[3] Department of Metallurgical and Materials Engineering, Escola Politécnica at University of São Paulo, Brazil

*Corresponding author e-mail: varon@usp.br

ABSTRACT

The use of thermochemical water-splitting cycles to produce hydrogen gas is considered a promising low-carbon technology if they are powered by solar energy. This work presents an experimental study of a two-stage thermochemical cycle for hydrogen production. It is based on the carbothermic reduction of iron ore (Fe_2O_3) and the re-oxidation of it with steam, being the whole process powered by concentrated solar energy. Samples studied were self-reducing pellets The first stage of the proposed cycle consists in the reduction of hematitic iron oxide into its own metal at temperatures above 1173 K. The second phase of the cycle consists of iron metal oxidation by steam, which produces hydrogen gas. The rate of hydrogen gas production was measured using the gas chromatography methodology. After carbothermic reduction the samples showed a high specific surface area of 35.05 m^2/g measured by the BET method.

Keywords: Hydrogen production, Solar fuels, Carbothermic reduction, Iron oxide (Fe_2O_3), Catastrophic swelling,

INTRODUCTION

The use of renewable energies and renewable materials in industrial processes are the path to a low-carbon society. A well analyzed to hydrogen production process is based on a two-step cycle of metallic oxides, in which the solar thermal energy is used to decompose a metallic oxide into a reduced form of the metal and oxygen gas. Next, the reduced metal is reoxidized with steam, generating hydrogen gas. In this work, it is proposed a two-step thermochemical cycle to produce CO and H_2 based on the carbothermic reduction of self-reducing pellets of iron ore (Fe_2O_3) and charcoal followed by the oxidation of the reduced iron produced in the reduction step by steam.

The metal oxide must react with carbon at relatively low temperatures, ideally under 1273 K, and it should be abundant, recyclable, and available at a low cost. The iron oxide meets those requirements [1-3]. The first step is the carbothermic reduction which is endothermic and produces a CO and CO_2 gas mixture at a higher content of carbon monoxide. The second step is the oxidation of the reduced iron with steam producing a steam and H_2 gas mixture. Iron ore reduction by solid carbon takes place as they are brought in contact and heated above the equilibrium temperature between the oxide and the metal (Eq. 1), and the oxidation step, the reaction is exothermic and the final principal species are hydrogen and iron oxide (Fe_3O_4) (Eq.2).

$$Fe_2O_{3(s)} + 3C_{(s)} \leftrightarrow 2Fe_{(s)} + 3C_{(g)}, \quad (1)$$

$$Fe_3O_{4(s)} + H_2O_{(g)} \leftrightarrow Fe_2O_{3(s)} + H_{2(g)}, \quad (2)$$

The oxidation reaction occurs at temperatures between 823 and 1173 K [4]. These temperatures are lower than those needed in direct decoupling cycles and therefore, the amount of energy supplied to the system is lower. During the first stage of the tested cycle, a porous metal with a high specific surface is formed, which has advantage of a high reaction kinetic rate that makes the second step cycle reaction more efficient.

MATERIALS AND METHODS

A commercial pellet feed with a particle size of less than 0.150 mm was used as the iron ore for the experiments. The charcoal was obtained from a raw rice carbonization process. The carbonization was performed by heating a certain amount of rice to 973 K during 2 hours. The self-reducing pellets were manually pelletized ranging from 1.5 to 2.0 cm in diameter. The reduction step was performed by using an electrical resistance vertical furnace. The sample holder is tied by a nickel-chromium wire connected to an analytical balance. The reduction experiments were performed isothermally at 1223 K in an inert atmosphere established by nitrogen gas flowing during 120 minutes.

The schematic representation for the iron oxidation step is presented in Fig. 1. Steam and nitrogen gas are fed into the reactor cavity at 270 °C. The sponge iron samples are placed in the cavity and the temperature is monitored with a K-type thermocouple.

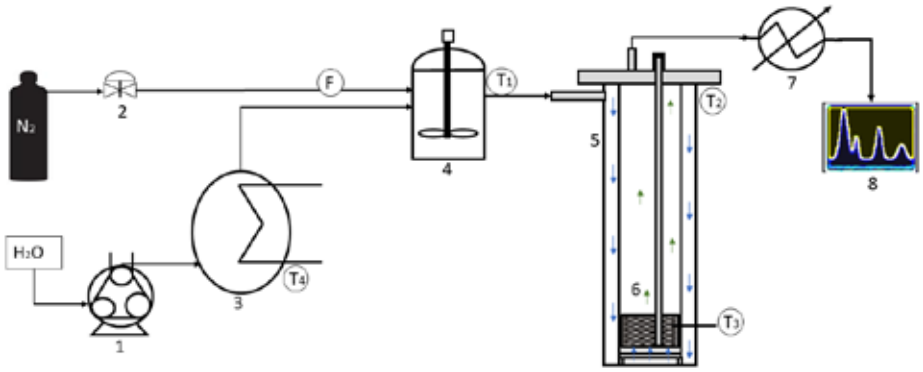


Fig. 1. Schematic diagram of experimental setup used for Oxidation step. 1) peristaltic pump, 2) pressure regulating control valve, 3) water evaporator, 4) Mixer and pre-heater, 5) reactor, 6) iron samples, 7) condenser, 8) as chromatograph.

The experiments were performed isothermally at 1023±5K, for 50 minutes. Nitrogen flow (1.5 mL/min) and the steam were injected as shown in Fig. 1. The steam was generated by dripping a controlled amount of water (0.04 mL/s) in a stainless-steel chamber heated by using a electrical resistance plate at 523 K. The reactor output was connected to a gas chromatograph Nexis GC-2030, with split injection of gaseous samples and TCD detector. The products were separated by a carboxen 1010 plot column (30 m), which uses N_2 (99.999%) as the carrier gas. A chromatogram analysis of the gases was carried out at every 3.75 min until finishing the test.

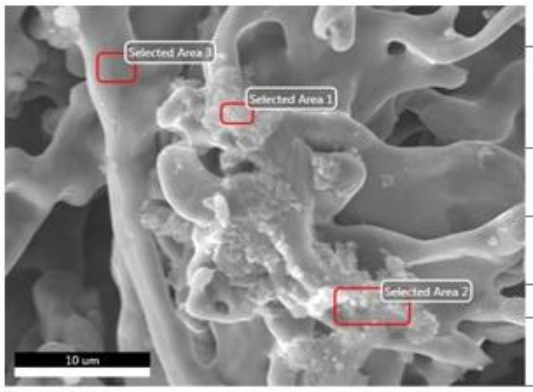
The oxidized samples were characterized by a scanning electron microscopy using a FEI microscope model Inspect f50 equipped with an EDS detector. The phases in the samples were characterized by an X-ray diffraction analysis using a Philips X'PERT MPD equipment. The sample surface area was estimated by nitrogen adsorption isotherms using the BET method, using a Micromeritics equipment, model ASAP 2020.

RESULTS AND DISCUSSION

Carbothermal reduction: After reduction of iron ore and rice charcoal to 1173 K for 120 min, the material had a spongy appearance, with a shape characterized by catastrophic swelling, showing a significant increase in volume. After the treatment, the sample lost 25.85 wt.% of its initial weight. It is observed that the weight loss can be attributed to the output of oxygen from the iron ore that reacts with the fixed carbon contained in the charcoal. Due to the carbonization conditions of rice, there are no losses by volatile material. Which did not need to be taken into account. The mass balance showed a 39.81 wt.% weight loss of the self-reducing pellets. However, for the conditions of temperature and time, the reduction was not complete. As can be seen in Fig. 2, charcoal (C) particles are still detected and the presence of ash in the composition of the analyzed (area 1 and 2).

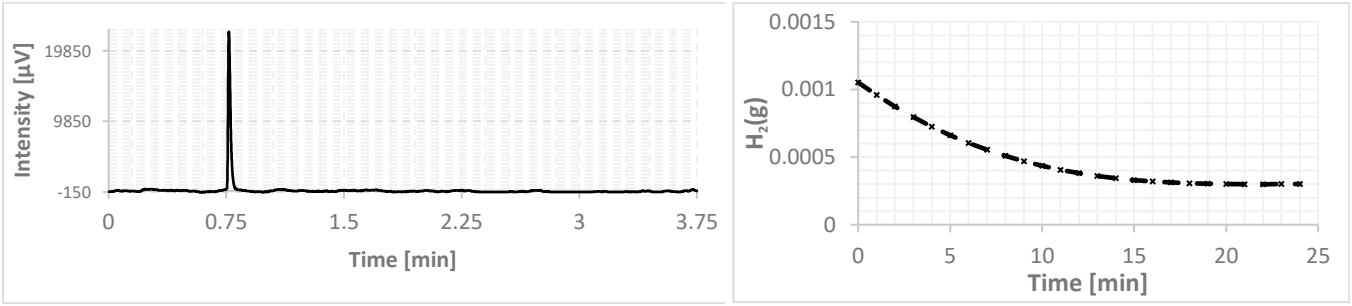
The sponge iron samples obtained in this work had a specific surface area of 35.05 m^2/g measured by the BET method. This is an exceedingly high value compared to the specific surface area of sponge iron obtained by conventional processes, for which, a typical value of 1 m^2/g of DRI has been reported for Schutze [5] or 16.26 m^2/g reported for Guo [6]. The microstructure of the tested sample was observed in a scanning electron microscopy (SEM), which revealed a structure formed by iron filaments throughout the sample. Nearly all the iron grew from the oxide in the form of whiskers. In the results of X-ray diffraction analysis can be seen that practically all the material was converted to metallic iron during the reduction, with an almost negligible presence of wustite.

Iron Re-Oxidation: In spite of the gas chromatograph being in-line connected to the reactor outlet, gas samples were collected every 3.75 min. Fig.3a) shows the results of one of the analyzes performed with gas chromatography. It can be seen that for a retention time of 0.767 min, a peak associated with gas hydrogen was generated, as expected, only this gas was identified. At the same time that the sample shows a mass gain due to the conversion of iron to magnetite and wustite, the release of hydrogen in its gaseous form also occurs. Fig. 3b) shows that there is a high initial rate of H_2 release, which decelerates rapidly as the oxidation process occurs. There was a high rate of H_2 formation at the beginning of the process, followed by a decreasing rate, thus, 60.27% of the total produced was released during the first 13 min. after the oxidation started. This behavior was explained in greater detail in previous works [7]. In the results of the X-ray diffraction analysis, it can be observed that practically all the material was transformed into Fe_3O_4 during the oxidation, with less presence of FeO and Fe_2O_3.



	Area1		Area 2		Area3	
Element	Weight %	Atomic %	Weight%	Atomic %	Weight%	Atomic %
C	42.41	77.22	24.00	57.20	3.49	13.98
O			2.59	4.63	1.39	4.16
Na			0.55	0.68		
Al	0.24	0.19	0.14	0.15		
Si	0.13	0.10	0.05	0.05		
P	0.18	0.13	0.13	0.12		
S	0.05	0.03				
Fe	56.99	35.35	72.54	37.18	95.12	81.86

Fig. 2. Energy-dispersive X-ray spectroscopy (EDS), macrophotography of the pellet composed of iron ore and rice charcoal after being subjected to 1173 K for 120 minutes and Chemical composition corresponding.



a) b)

Fig. 3. a) Chromatogram obtained in the oxidation of iron at 1023 K, b) Hydrogen production in the oxidation step of iron at 1023 K

CONCLUSIONS

This work presents an experimental investigation of a reduction-oxidation thermochemical cycle for the production of hydrogen and carbon monoxide gas (syngas), each at different stages of the cycle. This type of cycle works at lower temperatures than those commonly used, due to the presence of a reductant from biomass such as rice coal. The high iron surface area obtained in this work favored the production of H_2, allowing the possibility for the cycle to be optimized in relation to the time of the iron oxidation step, interrupting the oxidation process as it decelerates.

ACKNOWLEDGEMENT

We gratefully acknowledge support of the RCGI – Research Centre for Gas Innovation, hosted by the University of São Paulo (USP) and sponsored by FAPESP – São Paulo Research Foundation (2014/50279-4 and 2016/09509-1) and Shell Brazil. The first author thanks FAPESP for the personal financial support - Grant No. 2018/12224-4. The second author thanks FAPESP for the personal financial support - Grant No. 2020/08211-4, as well as the Colombian Administrative Department of Science, Technology, and Innovation -Minciencias - (COLCIENCIAS grant 1.087.046.934-728/2015).

REFERENCES

1. Wei, G., Zhao, W., Huang, Z., Yi, Q., He, F., Zhao, K., Zhao, Z. (2019). Synthesis gas production from chemical looping gasification of lignite by using hematite as oxygen carrier. Energy Conversion and Management, 185, 774-782.
2. Stehle, R. C., Bobek, M. M., Hooper, R., Hahn, D. W. (2011). Oxidation reaction kinetics for the steam-iron process in support of hydrogen production. International Journal of Hydrogen Energy, 36(23), 15125-15135.
3. Wang, H., Sohn, H. Y. (2011). Effects of firing and reduction conditions on swelling and iron whisker formation during the reduction of iron oxide compact. ISIJ international, 51(6), 906-912.
4. Rydén, M., Arjmand, M. (2012). Continuous hydrogen production via the steam–iron reaction by chemical looping in a circulating fluidized-bed reactor. International Journal of Hydrogen Energy, 37(6), 4843-4854.
5. Schütze, W. R. (1999). HBI–Hot Briquetting of Direct Reduced Iron Technology and Status of Industrial Application, Maschinenfabrik Köppern GmbH & Co. KG, Hattingen, Germany.
6. Guo, D., Hu, M., Pu, C., Xiao, B., Hu, Z., Liu, S., Zhu, X. (2015). Kinetics and mechanisms of direct reduction of iron ore-biomass composite pellets with hydrogen gas. International Journal of Hydrogen Energy, 40(14), 4733-4740.
7. Varon L.M, Narita C.Y, Mourão M., Simões-Moreira J.R. (2021) Experimental verification of a two-stage thermochemical cycle for hydrogen production. International Journal of Energy Research. Online ISSN:1099-114X. doi.org/10.1002/er.7259.

WHEC-2022
23rd World Hydrogen Energy Conference
June 26-30, 2022 - Istanbul

#287

ON-SOLAR SIMULATOR DATA FOR KINETIC STUDIES OF CdSZnS-Pt WATERS SPLITTING

[1] Tayseir Mohammed and [1,2,] Konstantinos Kakosimos,*
[1]Chemical Engineering Department, Texas A&M University at Qatar, PO Box 23874, Doha, Qatar
[2]Chemical Process & Energy Resources Institute, Centre for Research & Technology Hellas (CPERI/CERTH), Greece

Corresponding author e-mail: k.kakosimos@qatar.tamu.edu

ABSTRACT

Water splitting via solar energy to generate hydrogen represents a promising energy resource to address the emission and the environmental climate change. Cadmium Sulfide (CdS), with its specific characteristics, attracts significant attention as a promising photocatalyst for water splitting. However, most experimental studies do not provide adequate data to perform kinetic studies and develop kinetic models that are necessary for reactor and process design. Therefore, in this study, the binary photocatalyst CdS-ZnS/Pt was employed for water splitting using simulated solar energy to produce Hydrogen. In addition, it was necessary to design and fabricate a fully automated experimental lab-apparatus (cylindrical reactor with 70 mm ID and 10 mm depth; top-down illumination) to conduct unattended and long-duration experiments while collecting data continuously. At first, the crystallinity of the catalyst, the particle size distribution of the particles, and the band gap of the catalyst were checked given their critical role in the hydrogen evolution rate. The XRD results verified the hexagonal structure (of CdS), the FESEM images showed particles' size from 150 nm to 2 μm, and the solid state UV-Vis yielded a band gap of 2.3 eV. Toward the collection of the kinetic data, various ranges of the catalyst loading, the concentration of the sacrificial reagent, the temperature, and the light intensity were studied. In parallel, the photo-deposition of Pt cocatalyst proved as another critical factor; herein conducted for 30 min under 1-sun intensity. The so far data showed that the optimum hydrogen evolution rate at one-sun is 37 μmol/h or (2507 μmol/g.h) at 50^{O}C and 0.2 M ascorbic acid. At completion, the experimental dataset will be one of the few appropriate ones for kinetic studies' and comprehensive design of photocatalytic reactors.

Keywords: Kinetic data, Experimental, PhotoReactor, Water splitting

INTRODUCTION

Fossil fuels are still the main energy resource around the world causing multiple environmental challenges with many associated with the global warming. Hydrogen, with its high energy content, is considered a promising renewable and sustainable energy source of the future [1]. Different techniques have been proposed for hydrogen production such as photocatalytic, photoelectrochemical, thermal and biological [1, 2, 3]. The advantages of using photochemical and electrochemical over the other techniques is the direct utilization of solar energy with higher yields but at ambient pressure and temperature [4]. Photocatalytic solar energy conversion with high efficiency and at large scale will have a significant impact on the economy, environment and energy [5]. For this reason, one of the most active research topics is on the development of technologies for water splitting using solar energy and a semiconducting catalyst [6, 7, 8]. However, the challenges scaling these technologies are also many [9]. The photochemical techniques depend on photocatalysts' efficiency to drive the chemical changes but also involve multiple physical processes (photon's absorption, electrons production, carrier diffusion and transport, and mass transfer of reactant and products [10]. The main emphasis in the literature is to synthesize innovative materials with ideal conduction band, narrow bandgap, and at low-cost [11, 12]. As an example, CdS with a narrow bandgap (2.4 eV) and negative flat band potential (-0.9 V vs. NHE) is one of the widely used components of photocatalysts [2, 13, 14]. However, the overall hydrogen production depends on the contribution of all parameters affecting the chemical and physical process. Despite that, most of the research focuses on the materials regardless of the need to improve the overall photocatalytic process, including the reactor design as well as the mechanism of the reaction. The lack of comprehensive hydrogen evolution reaction kinetics studies is also prominent in this field. In this work, emphasis is on conducting a thorough experimental campaign on the photocatayitic hydrogen evolution reaction and the effect of external factors on the mechanism and kinetics. The generated data, upon completion, can be used to predict hydrogen rate, as a function of photocatalyst loading, reagent concentration, light intensity, and temperature, and to describe the reactions kinetic model.

MATERIALS AND METHODS

Materials

Cadmium acetate dihydrate (98%) purchased from Aldrich, Sodium Sulfide nonahydrate (98%) acquired from ACROS ORGANICS. Zinc Acetate dihydrate (99%) obtained from Aldrich, Chloroplatinic Acid hydrate (99.99%) obtained from

Merck, PVP from Fluka Analytical (average MW 40,000), Sodium borohydride (98%) purchased from Aldrich, Ascorbic Acid (L+ 99.7%) purchased from BHD. All the chemicals were used without further purification.

Synthesis of Photocatalyst

Cadmium Sulfide was synthesized in our lab by mixing approximately 0.1 M Cadmium Acetate and 0.1 M Sodium Sulfide in 1:1 molar ratio, under continuous stirring for 30 min at room temperature; the yellow precipitate was filtered and washed with deionized water several times; and the product was then subjected to high-temperature treatment at 600 °C under N_2 atmosphere for 3 h.

The CdSZn photocatalyst was synthesized using our reported procedure [2], in more details CdS powder was used in suspension of water under continuous stirring, 0.1 M of Zinc Acetate was added drop wise to produce CdSZnS photocatalyst. 0.2% Pt nanoparticles was used as cocatalyst to produce CdSZnS/Pt photocatalyst.

Hydrogen Evolution Reaction

The synthesized CdSZnS/Pt photocatalyst was transferred to the reactor (Fig. 1) for hydrogen evolution reaction, Ascorbic Acid was used as sacrificial reagents. The water splitting reactions were conducted at different catalyst loading (5-15-20 and 25mg), various concentrations of Ascorbic Acid (0.2-0.3M), different temperatures (40-50-60^{O}C) and light intensities (~500, 1097, 1500 and 2000 W/m^2). The CdSZnS/Pt suspension was kept under stirring while the reactor temperature was controlled by a heat exchanger. The photoreactor was purged with Argon for 30 min before each experiment in order to remove oxygen from the system. The photocatalyst was illuminated (with the ScienceTech UHE16 Solar Simulator using a Xenon-arc lamp) for 30 min for Pt nanoparticles photodeposition at the surface of the catalyst, then the illumination was paused to inject the sacrificial reagent in dark and allow adsorption to reach equilibrium. The hydrogen evolution reaction was carried out under Argon atmosphere (~54 ml/min flow) to prevent the photo-corrosion and dissolution of the photocatalyst. The pressure within the reactor was maintained at around 50 mbar using an back flow pressure controller. The evolved hydrogen gas was continuously monitored using a residual gas analyzer (Hiden Analytical RGA) calibrated before each experiment with a 50 µl pure H_2 bolus injection which corresponds to partial pressures similar to the ones during the experiments. Finally, the photoreactor system was shielded by four opaque acrylic windows to prevent personnel exposure to the UV irradiation.

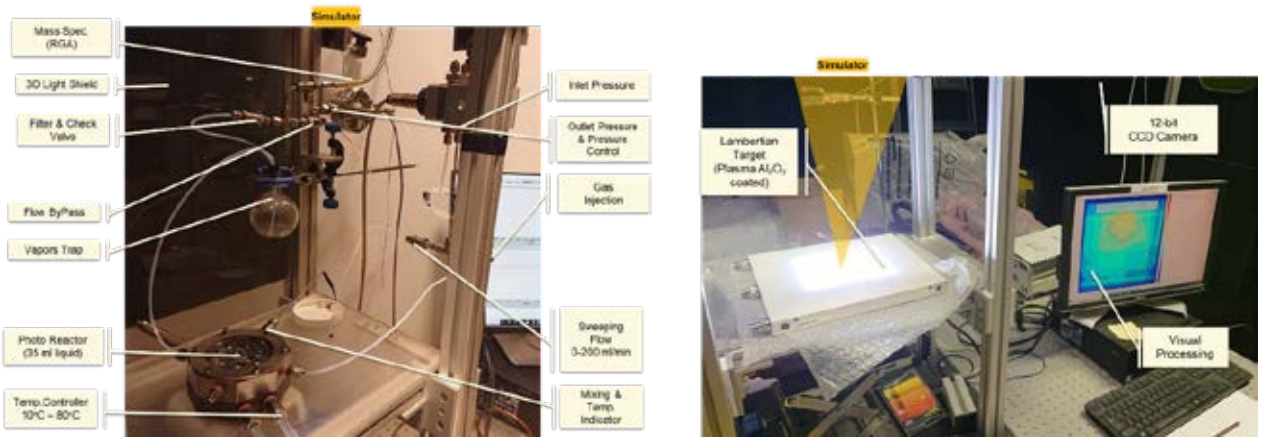


Fig. 1. Photo of the photoreactor system (left) and an example of the light intensity measurement and calibration (right).

PRELIMINARY RESULTS AND DISCUSSION

Effect of Photocatalyst Loading

To study our photoreactor's capacity under specific temperature and light intensity different loadings of photocatalyst suspension were loaded. At 40^{O}C and with 0.2M of Ascorbic Acid, the hydrogen specific evolution rate (µmol/g.h on Table 1) achieved the maximum at 15 mg photocatalyst loading. However, with 0.3M of Ascorbic Acid the optimum photocatalyst loading was at 20 mg. On the other hand, the hydrogen evolution rate (µmol/h) for 0.2M Ascorbic Acid continuously increased for increasing photocatalyst loading from 5 to 25 mg while reached a maximum at 20 mg for 0.3M concentration. In all cases tested so far, the hydrogen production is stable for at least six hours indicating a fair stability of the photocatalyst.

Effect of Temperature

So far, the effect of temperature on hydrogen production was tested at three values 40, 50 and 60^{O}C and only for 0.2M Ascorbic Acid. The hydrogen production showed the highest value at 50^{O}C (2507µmol/g.h) which indicates the significant role of temperature.

Table 1: Hydrogen production at different photoatalyst loadings and ascorbic acid concentrations.

Catalyst. Loading [mg]	Hydrogen Evolution [μmol/g.h] (or [μmol/h]) Ascorbic Acid 0.2M	Ascorbic Acid 0.3M
5	794 (4)	1210 (6)
15	1754 (26)	1565 (24)
20	1508 (30)	1768 (35)
25	1329 (33)	401 (10)

CONCLUSIONS

Numerous parameters are essential for the hydrogen evolution reaction the ones related directly to the semiconducting properties of the photocatalyst that are typically studied in the literature. The interpretation and understanding of these parameters are critical to achieve a sustainable and economically viable photochemical water splitting. In this work we reported the preliminary results of photocatalyst loading and temperature on the hydrogen evolution using a specific chemical system and demonstrated the importance of collecting continuous data and at various conditions. Data that will be used for the development of kinetic models and subsequently for photoreactor design.

ACKNOWLEDGEMENT

This publication was made possible by an NPRP award [NPRP12S-0228-190188] from the Qatar National Research Fund (a member of the Qatar Foundation), and co-funded by the Qatar Shell Research and Technology Center.

REFERENCES

1. Karimi Estahbanati M, Feilizadeh M, Iliuta MC. An intrinsic kinetic model for liquid-phase photocatalytic hydrogen production. AIChE Journal. 2019;65(11):e16724.
2. Vagia EC, Muradov N, Kalyva A, et al. Solar hybrid photo-thermochemical sulfur-ammonia water-splitting cycle: Photocatalytic hydrogen production stage. International Journal of Hydrogen Energy. 2017; 42(32):20608-20624.
3. Wang X, Peng W. Photocatalytic hydrogen generation with simultaneous organic degradation by composite CdS–ZnS nanoparticles under visible light. International Journal of Hydrogen Energy. 2014;39.
4. Colmenares JC, Luque R. Heterogeneous photocatalytic nanomaterials: prospects and challenges in selective transformations of biomass-derived compounds. Chemical Society reviews. 2014;43 3:765-78.
5. Hisatomi T, Takanabe K, Domen K. Photocatalytic Water-Splitting Reaction from Catalytic and Kinetic Perspectives. Catalysis Letters. 2015;145(1):95-108.
6. Jing D, Guo L. A Novel Method for the Preparation of a Highly Stable and Active CdS Photocatalyst with a Special Surface Nanostructure. The Journal of Physical Chemistry B. 2006;110(23):11139-11145.
7. Yao W, Song X, Huang C, et al. Enhancing solar hydrogen production via modified photochemical treatment of Pt/CdS photocatalyst. Catalysis today. 2013;199:42-47.
8. Li H, Liu L, Wang Z, et al. Optimizing the precursor of sulfur source for hydrothermal synthesis of high performance CdS for photocatalytic hydrogen production [10.1039/C8RA00250A]. RSC Advances. 2018;8(21):11489-11497.
9. Tojo F, Ishizaki M, Kubota S, et al. Histidine Decorated Nanoparticles of CdS for Highly Efficient H2 Production via Water Splitting. Energies. 2020;13(14):3738.
10. Takanabe K. Photocatalytic water splitting: quantitative approaches toward photocatalyst by design. ACS Catalysis. 2017;7(11):8006-8022.
11. Rufus IB, Ramakrishnan V, Viswanathan B, et al. Rhodium and rhodium sulfide coated cadmium sulfide as a photocatalyst for photochemical decomposition of aqueous sulfide. Langmuir. 1990;6(3):565-567
12. Ismail AA, Bahnemann DW. Photochemical splitting of water for hydrogen production by photocatalysis: A review. Solar energy materials and solar cells. 2014;128:85-101.
13. Song L, Zhang S. A novel cocatalyst of NiCoP significantly enhances visible-light photocatalytic hydrogen evolution over cadmium sulfide. Journal of Industrial and Engineering Chemistry. 2018;61:197-205
14. Wenderich K, Mul G. Methods, mechanism, and applications of photodeposition in photocatalysis: a review. Chemical reviews. 2016;116(23):14587-14619.

WHEC-2022
23rd World Hydrogen Energy Conference
June 26-30, 2022 - Istanbul

#291

ECONOMICALLY VIABLE LOW TEMPERATURE HYDROGEN PRODUCTION USING ALUMINUM-WATER SPLITTING METHODS

[1*]Jayaraman Kandasamy, [1] Rasiha Nefise Mutlu, [1,3] Esra Eroğlu, [2] Mehmet Karaca, [3] Hande Toffoli[1] İskender Gökalp
Middle East Technical University, 06800, Ankara, Turkey
[1]Department of Mechanical Engineering
[2] Department of Aerospace Engineering
[3] Department of Physics

*Corresponding author e-mail: jayaraman_mit@yahoo.com

ABSTRACT

Hydrogen can be produced as a thermochemical by-product from the reactions involving metals such as Na, Al, And Fe with water in tbe gas or liquid phase. The effectiveness of the splitting of hydrogen from water molecule can be increased using activators or catalysts. The faster chemical reaction rate is demanding to meet the industry needs. The process controlling should be implemented in this reaction, since metal reaction with water is exothermic in nature. In this work, cylindrical aluminum wires are activated using a NaOH solution and hydrogen production rate is studied experimentally as a function of several parameters including temperature and wire diameter. To provide an atomistic insight into our experimental results, first-principles total energy calculations were carried out using density functional theory (DFT). Activation barriers calculated by DFT are compared with experimental results and validate our theoretically proposed reaction mechanism.

Keywords: Hydrogen generation, Aluminum activation, Density functional theory, Clean energy.

INTRODUCTION

The deficit of organic non-sustainable fossil fuels and growing global ecological problems has increased interest in hydrogen technologies with renewable power sources. Safety issues related to hydrogen storage and transportation hamper the effective use of hydrogen in various energy applications. Aluminum is the energy carrier that can be potentially used to produce hydrogen due to its inherent high energy density, pollution-free energy release, lightweight and its recyclable technology. The aluminum could react with oxygen in the water, but it has been prevented by the inert alumina formed on the outer skin. Sarou-Kanian et al [1] studied the low temperature reactivity of aluminum nano-powders with liquid water. Zhuk et al [2] explained the commercial possibility and awareness of the hydrogen production using aluminum and its alloys. They examined the combined cycle of steam turbine (heat engine), electrochemical generator, and air-aluminum fuel cells, with the aluminum-steam combustion as a starting stage. Wang et al [3] reported the aluminum-based hydrogen production methods, their limitations and challenges for commercialization. They explained the Al–water reaction with assistance of alkalis, in neutral conditions, at elevated temperatures, hydrogen production from aluminum–alcohol reactions, and the concept for cogeneration of hydrogen and electrical energy. In this work, we investigate the aluminum activation using NaOH concentration using experiments and DFT model is applied for estimating the activation barriers. The estimated activation energy barrier from the experiment is compared with DFT theoretical results.

METHOD

The cylindrical pure (99.86 %) aluminum wire with a diameter of 0.6 mm is used. The aluminum wire is immersed in a 4M NaOH solution in a typical burette system at three constant temperatures (298 K, 323 K and 343 K) and monitor the volume of the produced H_2 gas until the wires are fully consumed. The temperature of the solution is controlled by a sensor immersed in the solution. The sensitivity of the hydrogen volume evolution measurements is estimated to be +/- 0.2 ml. The initial weight of the aluminum wires is 51.5 mg (+/- 0.001).

In an attempt to understand the mechanism of the hydrolysis reactions, a DFT model of the reactions was constructed. First-principles total energy calculations were carried out within a plane-wave DFT framework using the Vienna Ab Initio Simulation Package (VASP) [4]. Calculation parameters were chosen for describing the quantum mechanics of the system [5]. Long-range attractive van der Waals (vdW) interactions were modeled using the DFT-D3 correction [6,7]. Due to its macroscopic dimensions, the Al wire was modeled by a mildly oxidized Al(111) surface. A reaction mechanism wad proposed that involves the consecutive dissociation of water molecules. Following the determination of the optimized geometric structures of the reactants and products of each step, the activation barriers were calculated using the climbing image variant [8] of the nudged elastic bands (CI-NEB) method [9]. To validate our theoretical model, a simple Arrhenius analysis was performed, and the global activation barrier of the

experimental reactions was estimated. This result was then compared to the activation barrier of the theoretical rate-limiting step.

RESULTS AND DISCUSSION

The experimental reactions for Al hydrolysis in NaOH solutions is commonly represented as follows,

$$2Al + 2NaOH + 6H_2O \rightarrow 2NaAl(OH)_4 + 3H_2 \quad (R1)$$

$$2NaAl(OH)_4 \rightarrow 2NaOH + 2Al(OH)_3 \quad (R2)$$

The resultant H_2 gas evolution is recorded under different experimental conditions for the determination of the optimal conditions. The effect of NaOH concentration and solution temperature are considered in this study, as represented in Figure 1(a). It is noticed that higher temperatures lead to enhance the production rate of the H_2 gas. by comparing the 4H duration of the reaction at 25℃ and 70℃, it requires about 20 minutes for completing the reaction, i.e., the whole wire is consumed. As the surface area of the wire decreases due to reaction in progresses, the hydrogen evolution rate shows a downward trend until the reaction is finished.

We estimate the activation energy barrier (E_a) and hydrogen evolution rate (k) of the experimental reactions using an Arrhenius model. Using the hydrogen evolution rates at the three temperatures as represented, the Arrhenius plot for lnK vs 1/T is drawn from hydrogen evolution rate vs time (Fig. 1(b)). The activation energy is calculated from Arrhenius relation that gives the dependence of the rate constant k for chemical reactions on temperature:

$$ln\ k = ln\ ko + E_a/RT \quad (1)$$

where k is the rate constant at T, E_a is the activation energy, R is the ideal gas constant (8.3145 J/(mol K),T is the temperature, A is the collision frequency factor. E_a can then be calculated from the slope of the plot lnK vs 1/T. The factor n in model influences the deviation from a straight line in the ln(k) vs 1/T plot. The calculated activation energy is 35.06 kJ/mol. In the DFT model, the initially oxidized Al wire is represented by an Al(111) surface linked with three oxygen atoms as seen in Figure 1(a). We design a set of reaction steps that involve the consecutive dissociation of three H_2O molecules, followed by the adsorption of two OH- groups that is captured from the NaOH solution. In the final reaction steps, an $AlOH_4$ group is formed and released into the solution. This mechanism is summarized in Eq. R_3-R_6.

$$2Al + 3O + H_2O \rightarrow Al_2O_2(OH)_2 \quad (R_3)$$
$$Al_2O_2(OH)_2 + H_2O \rightarrow Al2O(OH)_4 \quad (R_4)$$
$$Al_2O(OH)_4 + H_2O \rightarrow Al_2(OH)_6 \quad (R_5)$$
$$Al_2(OH)_6 + 2OH \rightarrow 2Al(OH)_4^- \quad (R_6)$$

The initial, transition and final states of each of the reaction steps and also the calculated activation barriers are illustrated in Figure 1(c). It is seen that the reaction limiting step is R_3 with an activation barrier of 61.75 kJ/mol. Each step has a larger activation barrier than the earlier step that is mainly due to the decreasing accessibility of the central Al atom. In the third step, the H_2O molecule could not form a bond with the vicinity of surface atoms and its dissociation is therefore largely unassisted. The calculated values of activation energy barrier agree well with reported ones [10-12]. The product of the last step is the $AlOH_4$ group, detaches that leaves behind a surface vacancy. Though, the subsequent reactions are taking place around the edges of these craters since they present low coordination sites. These gaps are then expected to further grow as reaction proceeds to form larger crater. This is endorsed from SEM images, as shown in Figure 1(d) of an Al wire immersed in 4M NaOH solution for 30 minutes.

CONCLUSIONS

The activation of aluminum particles in NaOH solutions and their reactions with water are investigated in a joint experimental and theoretical framework. Ab initio activation barriers of a four-step surface reaction mechanism was compared with the experimentally estimated barrier. Given the difficulties associated with determining the actual reactions steps in any experimental setup, the agreement between the experimental and theoretical activation barriers is considered as acceptable. These results validate the proposed reaction mechanism involving the mixture of dissociation of water molecules and direct surface adsorption of free OH^- radicals from the solution. Hence, the optimum combinations exist between the particle size, NaOH concentration and reaction temperature to maximize the hydrogen reaction rate and yield, that will be considered in the future work.

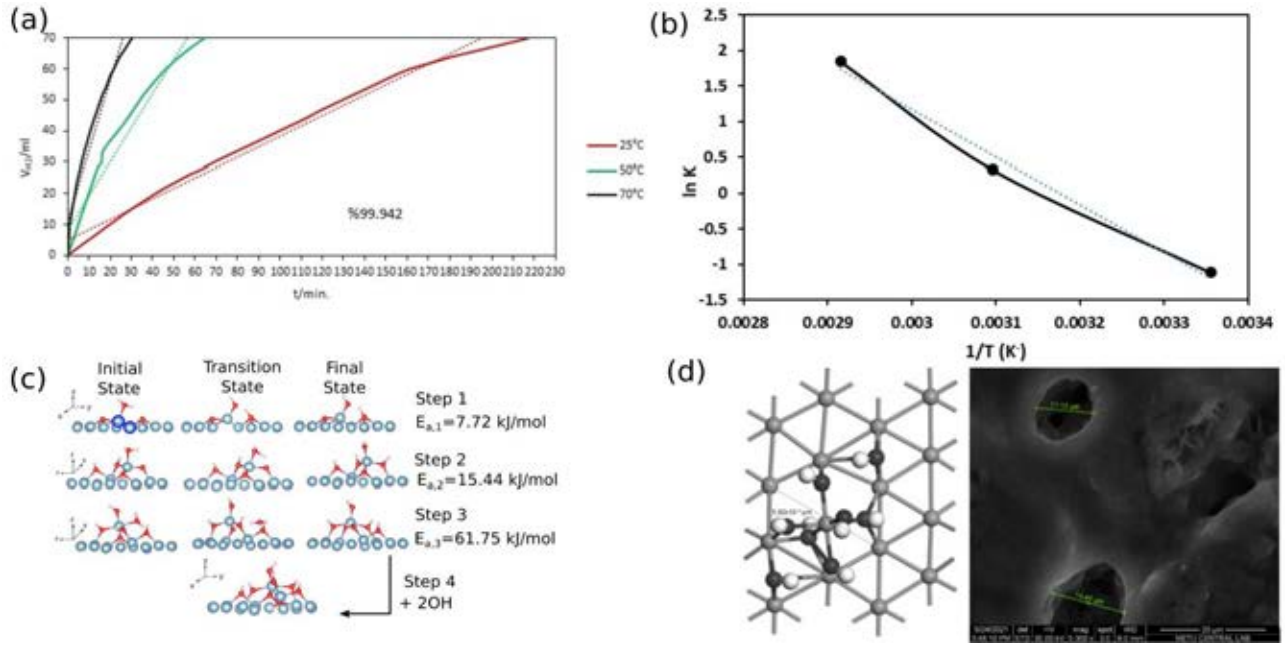


Figure 1: (a) The volume of produced hydrogen for a 99.942 % pure Al wire with an initial diameter of 0.6 mm. Red, green and black curves correspond to reactions taking pace at 25 C, 50 C and 70 C, respectively. The dashed lines are linear fits for better clarity. (b) The Arrhenius plot used to estimate the experimental activation barrier. (c) The DFT model. The top, middle and bottom panels correspond to the first, second and third steps of the reaction that are detailed in Equations R_3-R_6. The bottom panel represents the final system after the final direct adsorption of the 2 OH^- groups. The two Al atoms in the first image circled in blue are the two Al atoms participating in the reactions. Red, white and blue spheres represent oxygen, hydrogen, and aluminum atoms, respectively. The point of view, denoted by the Cartesian axes inserts, is rotated to provide the clearest view. (d) Top view of the Al surface with some adsorbed H2O molecules and the SEM images of the wire surface after 30 minutes of exposure to a 4M NaOH.

ACKNOWLEDGEMENT

This work is financially supported by the Scientific and Technological Research Council of Turkey (TÜBITAK), Grants No: 118C291 and 118C287.

REFERENCES

1. Sarou-Kanian V, Ouazar S, Escot Bocanegra P, Chauveau C, and Gökalp I. 2007. Low Temperature Reactivity of Aluminium Nanopowders with Liquid Water. Proceedings of the European combustion meeting.
2. Zhuk AZ, Sheindlin AE, Kleymenov BV, Shkolnikov EI, Lopatin MY. 2006. Use of low-cost aluminum in electric energy production. Journal of Power Sources 157:921926.
3. Wang HZ, Leung DYC, Leung MKH, and Ni M. 2009. A Review on Hydrogen Production using Aluminium and Aluminium alloys, Renewable and Sustainable Energy Reviews 13:845–853.
4. Hafner J. 2008. Ab-initio simulations of materials using VASP: Density-functional theory and beyond. J. Comput. Chem. 29: 2044–2078.
5. Perdew JP, Burke K, Ernzerhof M. 1996. Generalized Gradient Approximation Made Simple. Phys. Rev. Lett. 77:3865–3868.
6. Grimme S, Antony J, Ehrlich S, Krieg H. 2010. A consistent and accurate ab initio parametrization of density functional dispersion correction (DFT-D) for the 94 elements H-Pu. J. Chem. Phys., 132:154104.
7. Carrasco J, Klimeš J, Michaelides A. 2013. The role of van der Waals forces in water adsorption on metals. J. Chem. Phys., 138(2):024708.
8. Jonsson H, Mills G, Jacobsen KW. 1998. Classical and Quantum Dynamics in Condensed Phase Simulations, Singapore, :385–404.
9. Henkelman G, Uberuaga BP, Jonsson H. 2000. A climbing image nudged elastic band method for finding saddle points and minimum energy paths. J. Chem. Phys.113, 9901–9904.
10. Lu YH, Chen HT. 2015. Hydrogen generation by the reaction of H_2O with Al_2O_3-based materials: A computational analysis. Phys. Chem 17(10):6834-6843.
11. Wei X, Dong C, Chen Z, Xiao K, Li X. 2016. A DFT study of the adsorption of O_2 and H_2O on Al (111) surfaces. RSC Adv. 6(61):56303-56312.
12. Reber AC, Khanna SN, Roach PJ, Woodward WH, Castleman Jr AW. 2010. Reactivity of aluminum cluster anions with water: origins of reactivity and mechanisms for H_2 release. J. Phys. Chem. A, 114(20):6071-6081.

WHEC-2022
23rd World Hydrogen Energy Conference
June 26-30, 2022 - Istanbul

#311

UTILIZATION OF Al_2O_3 AND MgO AS STRUCTURAL PROMOTERS OF Fe INTO 2 AND 3 STEPS CHEMICAL LOOPING HYDROGEN PROCESS: PURE AND GREEN H_2 PRODUCTION

[1*] *Martina Damizia,* [1] *Benedetta de Caprariis,* [1] *Maria Paola Bracciale,* [1] *Francesco Anania,* [2] *Livio D'Alvia,* [2] *Zaccaria Del Prete,* [1] *Paolo De Filippis*

[1] SAPIENZA University of Rome, Department of Chemical Materials Environment Engineering, Via Eudossiana 18, Rome
[2] SAPIENZA University of Rome, Department of Mechanical and Aerospace Engineering, Via Eudossiana 18, Rome

*Corresponding author e-mail: martina.damizia@uniroma1.it

ABSTRACT

The use of H_2 as alternative fuel in the transportation sector is one of the most promising solutions to reduce global warming. Chemical looping hydrogen processes (CLH) allow the production of high purity H_2, suitable for powering PEM fuel cells. This work focuses on the production of pure and renewable H_2 by CLH process using iron as redox material and ethanol as renewable reductant. To scale up the technology, the thermal stability of Fe for repeated redox cycles is a key point and still needs improvement. The addition of structural promoters can be an effective solution. Experiments at 3 different reaction temperatures (675°C-750°C) are conducted to evaluate the effect of the addition of Al_2O_3 and MgO on Fe_xO_y redox performances. The particles' thermal stability is evaluated for 10 redox cycles. The results show that the presence of Al_2O_3 led to a completely deactivation of iron oxides after few cycles at all the conditions due to the formation of Hercynite ($FeAl_2O_4$), which cannot be oxidized by water. However, introducing an air oxidation step in the system (3 steps CLH) makes this material suitable for this application. The addition of MgO guarantees stable H_2 yields at the lowest temperature tested (675°C, E=35%).

Keywords: Hydrogen, Chemical looping, Structural promoters, Water splitting, Iron oxide

INTRODUCTION

Nowadays, H_2 is considered an ideal fuel as its combustion yields only water. However, H_2 does not exist in nature in its molecular form but it is extracted from other compounds such as fossil fuels, water and biomass using different technologies. In order to obtain a totally clean H_2 also the H_2 production should derive form a CO_2-neutral process.

Chemical looping hydrogen processes (CLH) allow the production of pure H_2 by water splitting, exploiting the redox properties of transition metals. The 2 steps CLH process consists by two spatially and temporary separated phases. First, the reduction step, in which the metal oxide is reduced to the metallic form at the expense of the fuel oxidation by the lattice oxygens of the metal oxide into CO_2 and H_2O. Then, in the water oxidation step, in which the reduced metal is oxidized by steam to produce pure H_2 and to restore the metal oxide, which are ready for the subsequent reducing step. The process can also involve a 3-steps configuration, in which the oxidation step with steam is followed by an oxidation step with air. Generally, the 3 steps CLH is adopted to minimize the heating costs of the plant by exploiting the heat released by the oxidation of the metal oxide with air to heat the process units.

The main advantage of the CLH is the feasibility to produce directly pure H_2 able to be fed to Proton Exchange Membrane fuel cells usable in the automotive sector, without any additional purification units. Furthermore, if a renewable fuel and an environmentally safe metal are used, H_2 can be obtained in a completely green way.

The aim of this work is to produce pure and green H_2 by chemical looping technology using Fe-based particles and bioethanol as renewable fuel, making the pure H_2 production stable for a high number of cycles. The carbon formation during the reduction step and the decay of the reactivity of the Fe are the primary limitations of the proposed system. The carbon formation, caused by the utilization of a carbonaceous fuel in the reduction step, is one of the main issues for the development of this process undermining the purity of the hydrogen and the particle reactivity. If the carbon deposition occurs, carbon can react with water during the steam oxidation step producing CO by gasification reaction. For PEMFC applications the concentration of CO must be lower than 10 ppm to avoid the deactivation of the Pt-based catalyst of the cell. Furthermore, a fraction of solid carbon can remain on the particles surface during the cycle contributing to the particle' s deactivation. In author's previous works, a relationship between the amount of ethanol fed in the reduction and the purity of H_2 obtained in oxidation was demonstrated. Specifically, the reduction degree of Fe_xO_y is directly linked to the amount of ethanol fed; the carbon deposition takes place when carbon is not needed for the iron oxide reduction; in fact, avoiding the complete reduction to Fe, the lattice oxygen atoms are able to convert solid carbon into CO and CO_2

To improve the resistance at high temperature of the Fe_xO_y/Fe, Al_2O_3 and MgO are added as promoters (60 wt.% Fe_2O_3- 40 wt.% Al_2O_3, 60 wt.% Fe_2O_3- 40 wt.% MgO). These two materials are widely used in the field of heterogeneous catalysis as support, but they also offer a catalytic activity to many chemical reactions. The samples were already tested by the authors in isothermal cycles (675°C)[1]; the results showed that both MgO and Al_2O_3 actively participate in the process offering their catalytic activity on the ethanol cracking reactions but also reacting with Fe forming spinel structures.

The aim of this work is to evaluate the redox performance of 60Fe40Al (60 wt.% Fe_2O_3- 40 wt.% Al_2O_3) and 60Fe40Mg(60 wt.% Fe_2O_3- 40 wt.% MgO) into a 2 steps CLH process at 3 different temperatures (675°C,700°C and 750°C) in order to find the optimal operative conditions which maximize both the H_2 yields and the stability of the redox material. The experiments are also conducted on pure Fe_2O_3 to better understand the effect of promoter's addition on particle's reactivity. The sample 60Fe40Al is also tested into a 3 steps CLH (reduction-steam oxidation-air oxidation) in order to prevent the formation of the spinel with Fe and make possible the use of this material in the process.

MATERIALS AND METHODS

Fe-based particles synthesis and bench scale plant details.

The Fe-based particles are synthesized by coprecipitation method from the nitrate metals salts and then calcined with air in a muffle furnace at 350°C for 2 h and 900°C for 2 h. The amount of the structural promoter added is constant and equal to 40 wt.%. Tests are conducted in a fixed bed reactor at 3 different reaction temperature (675°C, 700°C, 750°C) maintaining the pressure constant at 1 bar. The fixed bed is constituted by 1 gram of Fe-based particles with particle's diameter of 150 μm < d_p < 300 μm. The bench scale plant is described in detail in the author's previous works[1,2]. The 2 steps CLH tests are conducted feeding alternatively ethanol in the reduction step and water in oxidation with a constant flowrate of 4 mL/h, in the presence of Argon as carrier gas (250 mL/min). In the 3 steps CLH experiments air is also fed to the reactor with a constant flowrate of 500 mL/min.

RESULT AND DISCUSSION

Influence of Al_2O_3 and MgO addition into 2 and 3 steps CLH as a function of temperature (675°C, 700°C, 750°C)

The experiments related to the determination of the optimal amount of ethanol consist into 1 redox cycle in which different amount of ethanol are fed in reduction (5.7-1.9 mmol EtOH/g_{Fe2O3}). The optimal amount is defined as the amount for which no CO is detected in the water oxidation step. This parameter is strongly connected to the accessibility of the iron active sites, to the surface area of the sample and to the kinetics of the reduction reactions at the tested temperatures. For the samples tested in all the temperature range studied the optimal amount of ethanol is equal to 1.9 mmo/g_{Fe2O3}.Table 1.0 summarizes the results obtained with the sample 60Fe40Al at 700°C.

Table 1: Determination of the optimal amount of ethanol fed for the sample 60Fe40Al at 700°C.

Ethanol Fed (mmol/g_{Fe2O3})	H_2 (NL)	CO (NL)
5.7	0.081	0.021
3.8	0.031	0.008
1.9	0.023	0.000

After the determination of the optimal amount of ethanol stability tests (10 redox cycles) are conducted. Figure 1. reports the process efficiency (E) of each sample for 10 consecutive redox cycles at all tested temperatures. E is calculated as the ratio of the amount of H_2 produced during the oxidation step and the maximum amount of H_2 that can be produced by the sample, considering the complete reduction to Fe and the complete oxidation to Fe_3O_4. Looking at the results collected in Figure 1.0, the promoter addition significantly affects the Fe reactivity and stability at each tested temperature[3]. The decrease in H_2 yields during the cycles registered for the sample of pure Fe_2O_3 (Figure1.0 A) confirms the low thermal stability of this material. Increasing the reaction temperature from 675°C to 750°C the deactivation is favored. The addition of MgO is promising: the process efficiency is kept constant to 35% for all the cycles without any significant variations with temperature. The results obtained with the sample 60Fe40Al confirms the issue in coupling Fe/Al into 2 steps CLH. The sample deactivation occurs at each operative conditions tested and at higher temperature it becomes more evident. These results suggest that the hercynite ($FeAl_2O_4$) formation occurs at each temperature and that its production is favored at high temperatures. Figure 1.0 D report the E (%) of the 3 steps CLH experiments with the sample 60Fe40Al.Based on the results obtained the introduction of an air step in the process seems to be the only way to use this material for H_2 production by water splitting. In this case the process efficiencies are constant for 10 consecutive redox cycles. In fact, according to literature results, $FeAl_2O_4$ can be oxidized and converted to Fe_2O_3 and Al_2O_3 only by air [4].

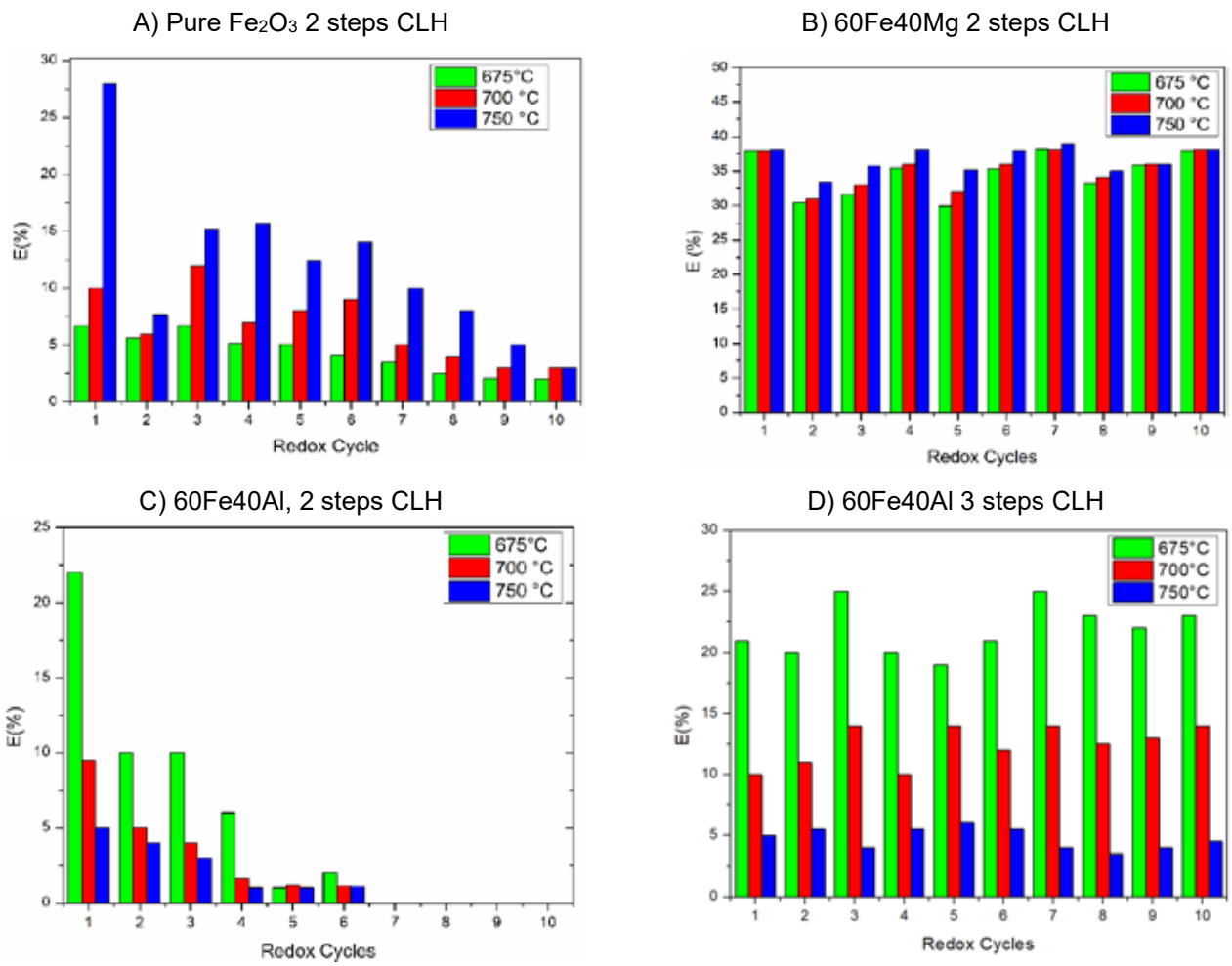


Figure 1: Process Efficiency for 10 consecutives redox cycles, 2 steps CLH: A) Fe_2O_3, B) 60Fe40Mg, C) 60Fe40Al. Process Efficiency for 10 consecutive redox cycles, 3 steps CLH: D) 60Fe40Al.

CONCLUSIONS

The directly production of pure and green H_2 by CLH process is studied focusing the attention on the effect of adding Al_2O_3 and MgO in the redox cycle of iron. The redox activity is evaluated at 3 different temperatures in order to find the optimal value using bioethanol as renewable reductant. The results demonstrated that the presence of MgO confers to the Fe/FeO couple a better reactivity and stabilty without any significant variation in the temperature range studied. Otherwise, the addition of Al_2O_3 led to a fastly deactivation into 2 steps CLH due to the formation of $FeAl_2O_4$. The deactivation is significantly affected by the reaction temperature becoming more evident at higher temperatures. However, the addition of an air oxidation in 3 steps CLH is fundamental to convert $FeAl_2O_4$ into Fe_2O_3 and Al_2O_3 allowing the successful utilization of this material with a constant process efficiency for 10 cycles.

REFERENCES

1. de Caprariis B, Damizia M, De Filippis P, Bracciale MP. The role of Al2O3, MgO and CeO2 addition on steam iron process stability to produce pure and renewable hydrogen. Int J Hydrogen Energy 2021; 46:39067–78. https://doi.org/10.1016/J.IJHYDENE.2021.09.135.
2 De Filippis P, D'Alvia L, Damizia M, de Caprariis B, Del Prete Z. Pure hydrogen production by steam-iron process: The synergic effect of MnO2 and Fe2O3. Int J Energy Res 2020. https://doi.org/10.1002/er.6117.
3. Voitic G, Hacker V. Recent advancements in chemical looping water splitting for the production of hydrogen 2016. https://doi.org/10.1039/c6ra21180a.
4. Yüzbasi NS, Kierzkowska A, Müller C. Development of Fe2O3-based, Al2O3-stabilized Oxygen Carriers using Sol-gel Technique for H2 Production via Chemical Looping. Energy Procedia 2017;114:436–45. https://doi.org/10.1016/J.EGYPRO.2017.03.1186.

WHEC-2022
23rd World Hydrogen Energy Conference
June 26-30, 2022 - Istanbul

#319

GLYCEROL STEAM REFORMING FOR THE PRODUCTION OF HYDROGEN OVER REMARKABLY ACTIVE AND STABLE PEROVSKITE SUPPORTED Ni CATALYSTS

[1*] Igor Luisetto, [2] Anastasios I. Tsiotsias, [2] Nikolaos D. Charisiou, [2] Andreas Beka, [3] Kyriaki Polychronopoulou, [2*] Maria A. Goula
[1] ENEA Research Center, Department of Energy Technologies, Process and Energy Systems Engineering Laboratory, Casaccia, Via Anguillarese, 301, 00123, S.M. di Galeria, Rome, Italy
[2] Laboratory of Alternative Fuels and Environmental Catalysis (LAFEC), Department of Chemical Engineering, University of Western Macedonia, GR-50100 Kozani, Greece
[3] Department of Mechanical Engineering, Khalifa University of Science and Technology, Abu Dhabi, P.O. Box 127788, UAE

*Corresponding author e-mail: mgoula@uowm.gr (Maria A. Goula); igor.luisetto@enea.it (Igor Luisetto)

ABSTRACT

The glycerol steam reforming (GSR) reaction for hydrogen production, was investigated over Ni catalysts supported on perovskite-type oxides ($Ni/BaZrO_3$, $Ni/CaZrO_3$ and $Ni/SrZrO_3$) synthesized via the auto-combustion method. The prepared catalysts were characterized via XRD and H_2-TPR, showing a high phase purity (limited formation of alkaline earth carbonate impurity phases) and reducibility. Catalytic activity evaluation revealed that $Ni/CaZrO_3$ (CaZ-Ni7) and $Ni/SrZrO_3$ (SrZ-Ni7) were remarkably active for the conversion of glycerol towards gaseous products, yielding high amounts of H_2 and preventing its consumption via side-reactions, like CO_x hydrogenation. $Ni/BaZrO_3$ (BaZ-Ni7) was found to be less effective for the gasification of glycerol, providing an overall lower H_2 yield. $Ni/SrZrO_3$ (SrZ-Ni7) was shown to be the best-performing and most resilient catalyst, exhibiting a remarkably stable performance during 20h time-on-stream at 600 °C, as it outperforms many of the employed catalysts in the literature. The produced gas has a very high H_2/CO ratio (> 20) and thus, could be fed into fuel cell stacks without extensive downstream processing.

Keywords: Glycerol steam reforming, Hydrogen production, Nickel catalysts, Perovskite oxides, Catalytic stability

INTRODUCTION

Biofuels, and especially biodiesel, are being portrayed as an attractive alternative to petrol-based fuels in a decarbonized economy [1]. The production of biodiesel proceeds through the transesterification of triglycerides found in plant-derived oils, a process which inevitably produces large amounts of crude glycerol as a by-product (> 10 vol%) [1]. As an alternative to its costly refinement process, crude glycerol can be directly gasified into H_2 and CO_x, through a process known as glycerol steam reforming (GSR) reaction, which can theoretically yield 7 mols of H_2 per mol of converted glycerol [1-3]. Ni-based catalysts are typically used in this reaction, due to the known ability of Ni to split C-C bonds in organic molecules and O-H bonds in water, favouring the production of H_2, all the while being considerably cheaper to noble metal alternatives (e.g., Rh) [1-3]. However, Ni has the disadvantages of being particularly prone to deactivation via coke deposition and of promoting the hydrogenation of CO_x, thereby consuming part of the produced H_2 [1,2,4]. Ni-perovskite systems are known to be remarkably stable towards carbon deposition, while they exhibit a very strong metal-support interaction, that can disfavour CO_x hydrogenation (e.g., methanation) [5]. Moreover, $Ni-CaZrO_3$ has already demonstrated superior stability during the dry reforming of methane [6]. Taking all this into account, this work reports on the application of Ni catalysts supported on alkaline earth perovskites ($BaZrO_3$, $CaZrO_3$ and $SrZrO_3$) for the glycerol steam reforming.

MATERIALS AND METHODS

The perovskite catalysts were prepared via the auto-combustion method. Stoichiometric amounts of metal nitrates and glycine were dissolved in d-H_2O and used as fuel. A gradual increase in temperature to approx. 250 °C was employed to ignite the auto-combustion. The rapid flame propagation that followed ended in few minutes, producing very fine and voluminous powders, which were calcined at 800 °C (CaZ-Ni7 and SrZ-Ni7) or 950 °C (for BaZ-Ni7) for 5 h to remove carbonaceous impurities. To prepare the reduced catalysts, their calcined counterparts were reduced at 800 °C for 1 h. Following the synthesis, the supports, calcined and reduced catalysts were characterized via XRD and H_2-TPR.

The steam reforming of glycerol was performed in a continuous flow stainless-steel fixed-bed reactor (ID= 14 mm) under two experimental protocols. The first one was employed to investigate the catalytic activity as a function of reaction temperature, (400-750 °C), while the reactant gas mixture consisted of 73% H_2O, 4% $C_3H_8O_3$ and 23% He (20 v.v. % of $C_3H_8O_3$ in d-H_2O). The second protocol was designed with the aim of examining the stability of the catalysts during 20h time-on-stream, performed at 600°C. More severe conditions were chosen, so as to promote carbon deposition. The reactant gas mixture in this case consisted of 63% H_2O, 7% $C_3H_8O_3$ and 30% He (31 v.v. % of $C_3H_8O_3$ in d-H_2O). For both experimental protocols used, the Weight Hourly Space Velocity (WHSV) equalled 50,000 ml g_{cat}^{-1} h^{-1}, while a prior in situ catalyst activation step was performed using a pure H_2 flow at 800 °C for 1 h. Liquid products were analyzed vai GC-MS and gaseous products via GC with a TCD detector.

RESULTS AND DISCUSSION

XRD patterns of the prepared MeZ (BaZ, CaZ and SrZ) perovskites (Fig. 1) reveal the formation of the respective perovskite phase ($BaZrO_3$, $CaZrO_3$ and $SrZrO_3$) with a remarkable phase purity. For the calcined MeZ-Ni7 catalysts (BaZ-Ni7, CaZ-Ni7 and SrZNi-7), no clear NiO reflections can be observed, which is an indication of a high solubility of Ni^{2+} ions in the perovskite lattice and/or the amorphous nature of supported NiO. Following reduction, the reduced catalysts (BaZ-Ni7 red., CaZ-Ni7 red. and SrZNi-7 red.) exhibit the emergence of the Ni^0 (111) reflection at approx. 44.4° 2θ (Fig. 1d) except for SrZNi-7 red., where the Ni^0 (111) reflection overlaps with a perovskite reflection. This is attributed to the formation of Ni^0 nanoparticles on the perovskite surface, which can be considered as partly exsolved, due to the initial solubilization of part of Ni^{2+} cations into the perovskite lattice [5]. The crystallite size of metallic Ni was calculated via the Scherrer equation as 30 nm and 25 nm for reduced BaZ-Ni7 and CaZ-Ni7 respectively. The reducibility of the perovskite catalysts was also examined via H_2-TPR, which revealed the presence of three reduction peaks (α, β and γ). α and β peaks observed for BaZ-Ni7 and CaZ-Ni7 were attributed to the reduction of NiO in the surface and sub-surface of the perovskites, whereas the γ peak found for CaZ-Ni7 and SrZ-Ni7 was ascribed to the reduction of Ni^{2+} solubilized into the perovskite lattice and therefor to the exsolution process [5,6].

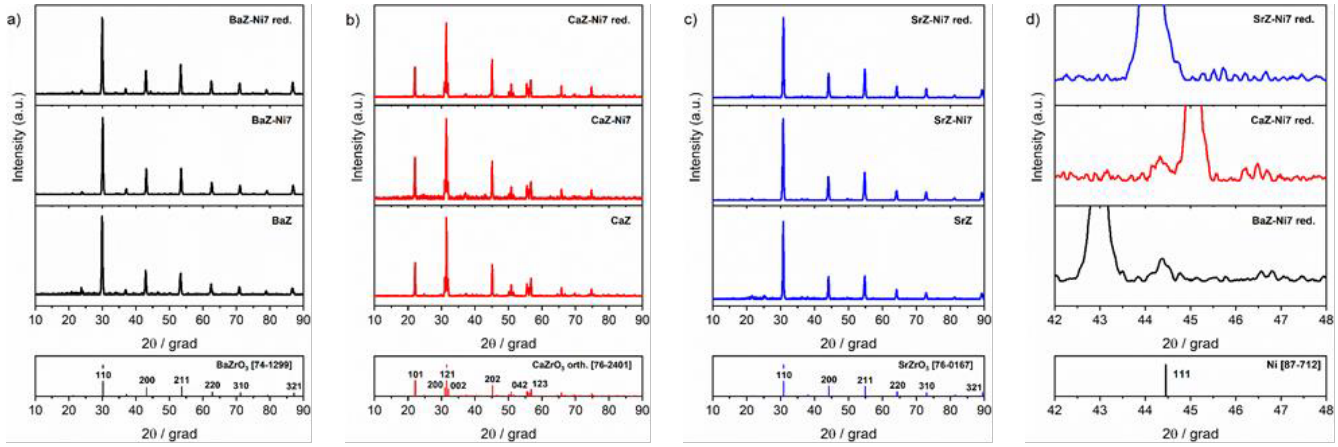


Fig. 1. X-ray diffraction patterns of calcined MeZ perovskite, calcined and reduced MeZ-Ni7 catalysts: (a) BaZ and BaZ-Ni7; (b) CaZ and CaZ-Ni7; (c) SrZ and SrZ-Ni7. (d) Patterns for 2θ = 42-48° showing the Ni^0 (111) peak for the reduced MeZ-Ni7 catalysts.

Fig. 2a-c presents the evolution of GSR catalytic activity as a function of reaction temperature. It can be observed, that CaZ-Ni7 and SrZNi-7 can offer superior catalytic performance to BaZ-Ni7 in terms of total glycerol conversion, as well as glycerol conversion to gaseous products (Fig. 2a). These two catalysts are also better in terms of H_2 selectivity and yield, with the H_2 yield being close to the theoretical maximum of 7 mols of produced H_2 per mol of fed glycerol (Fig. 2b). Moreover, the H_2/CO ratio is very high for CaZ-Ni7 and SrZNi-7 at the 550-650°C temperature range (Fig. 2c), which is well suited for fuel cell applications, where CO acts as a poison [1]. Liquid by-products of glycerol (e.g., acetol, acetone etc.) are only produced at temperatures below 550°C for CaZ-Ni7 and SrZNi-7 (Fig. 2d), whereas for BaZ-Ni7 they can be produced up to the final temperature of 750°C.

Fig. 2e-f presents the evolution of GSR catalytic activity at a constant temperature of 600°C as a function of reaction time during 20h time-on-stream under more severe reaction conditions. As expected, the lower water to glycerol feed ratio (WGFR) acts to lower the gasification of glycerol and the H_2 yield [4]. SrZ-Ni7 is more resilient to this harsher reaction conditions and presents a superior catalytic performance to many of the catalysts studied in the literature [1-4]. This can be attributed to the partly exsolved nature and strong metal-support interaction of the supported Ni nanoparticles, which act to hinder carbon deposition and preserve the structural integrity of the catalyst [5,6].

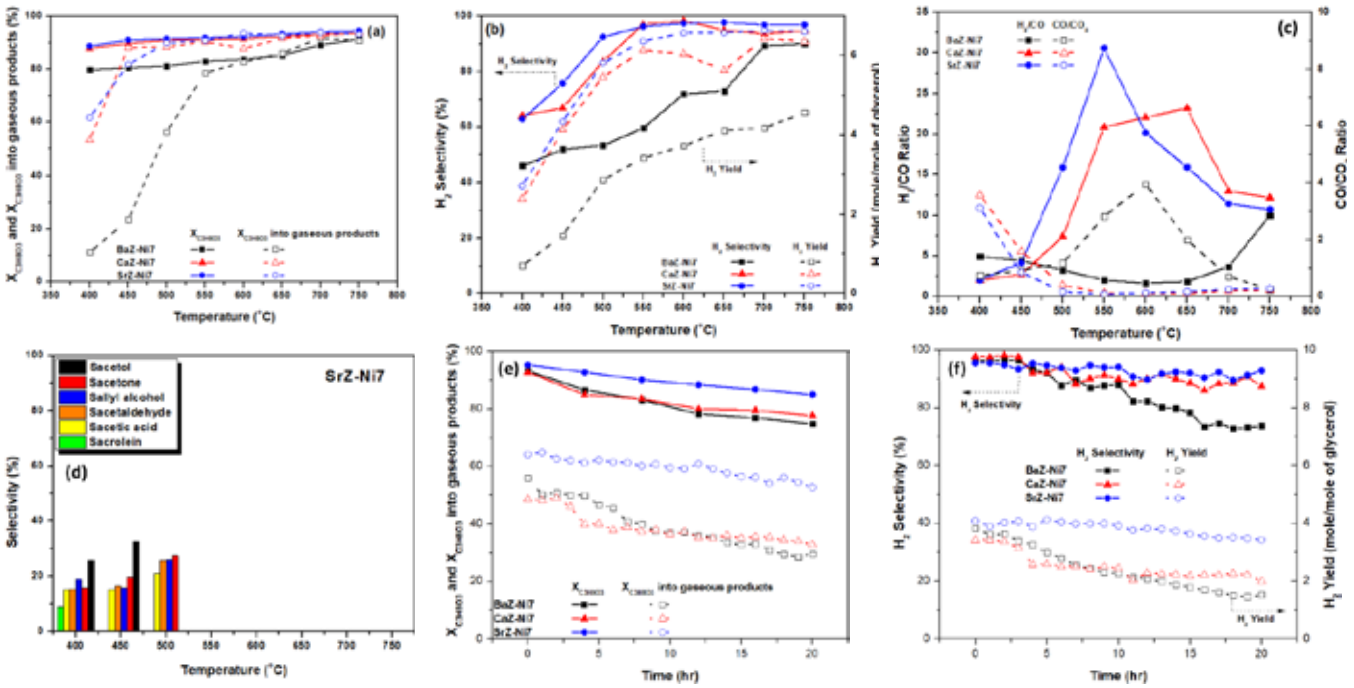


Fig. 2. Experimental Protocol #1: (a) Total glycerol conversion along with glycerol conversion into gaseous products, (b) H_2 selectivity and yield, (c) H_2/CO and CO/CO_2 molar ratio and (d) liquid products selectivity for the SrZ-Ni7 catalyst as a function of reaction temperature. Experimental Protocol #2: (e) Total glycerol conversion along with glycerol conversion into gaseous products and (f) H_2 selectivity and yield as a function of reaction time.

CONCLUSIONS

This study reported on the auto-combustion synthesis of alkaline earth perovskite supported Ni catalysts for the steam reforming of glycerol. The high structural purity of the prepared catalysts and the strong metal-support interaction induced via the exsolution of initially solubilized Ni^{2+} cations acted to enhance the catalytic activity and stability. The Ni/$SrZrO_3$ (SrZ-Ni7) catalyst provided a stable catalytic performance and H_2 yield under harsh conditions, rivaling other catalysts in the literature and demonstrating its potential for industrial implementation.

ACKNOWLEDGEMENT

We gratefully acknowledge that this research has been co-financed by the European Union and Greek national funds under the call “Greece – China Call for Proposals for Joint RT&D Projects” (Project code: T7DKI-00388).

REFERENCES

1. Charisiou ND, Polychronopoulou K, Asif A and Goula MA. 2018. The potential of glycerol and phenol towards H_2 production using steam reforming reaction: A review. Surface and Coatings Technology 352:92-111.
2. Papageridis KN, Siakavelas G, Charisiou ND, Avraam DG, Tzounis L, Kousi K and Goula MA. 2016. Comparative study of Ni, Co, Cu supported on γ-alumina catalysts for hydrogen production via the glycerol steam reforming reaction. Fuel Processing Technology 152:156-175.
3. Charisiou ND, Italiano C, Pino L, Sebastian V, Vita A and Goula MA. 2020. Hydrogen production via steam reforming of glycerol over Rh/γ-Al_2O_3 catalysts modified with CeO_2, MgO or La_2O_3. Renewable Energy 162:908-925.
4. Charisiou ND, Siakavelas G, Tzounis L, Dou B, Sebastian V, Hinder SJ, Baker MA, Polychronopoulou K and Goula MA. 2020. Ni/Y_2O_3–ZrO_2 catalyst for hydrogen production through the glycerol steam reforming reaction. International Journal of Hydrogen Energy 45:10442-10460.
5. Kousi K, Tang C, Metcalfe IS and Neagu D. 2021. Emergence and Future of Exsolved Materials. Small 2006479.
6. Dama S, Ghodke AR, Bobade R, Gurav HR and Chilukuri S. 2018. Active and durable alkaline earth metal substituted perovskite catalysts for dry reforming of methane. Applied Catalysis B: Environmental 224:146-158.

WHEC-2022
23rd World Hydrogen Energy Conference
June 26-30, 2022 - Istanbul

#381

COMBINED AUTOTHERMAL AND SORPTION-ENHANCED REFORMING OF OLIVE MILL WASTEWATER FOR THE PRODUCTION OF HYDROGEN: THERMALLY NEUTRAL CONDITIONS ANALYSIS

[1,2*]P. Cerqueira, [1,2]M.A. Soria, [1,2]L. M. Madeira
1. LEPABE, Department of Chemical Engineering, Faculty of Engineering, University of Porto, Rua Dr. Roberto Frias s/n, 4200-465 Porto, Portugal.
2. ALiCE - Associate Laboratory in Chemical Engineering, Faculty of Engineering, University of Porto, Rua Dr. Roberto Frias, 4200-465 Porto, Portugal

*Corresponding author e-mail: up201505213@up.pt

ABSTRACT

In this work a thermodynamic study and an energy analysis are performed on the autothermal and sorption-enhanced reforming of olive mill wastewater (OMW), to produce green hydrogen. The thermodynamic equilibrium compositions are calculated by using the Gibbs free energy minimization method. The effect of different parameters is assessed for the different reactor configurations. The results show hydrogen yields close to the theoretical maximum for the sorption-enhanced autothermal reforming of OMW whilst operating in thermally neutral conditions.

Keywords: *Thermally neutral; Sorption; Autothermal; Olive mill wastewater; Hydrogen*

INTRODUCTION

Hydrogen is a crucial industrial chemical. Its production has grown in recent years due to its potential to be used in fuel cells to produce energy, whilst avoiding CO_2 emissions [1]. As of now, the production of hydrogen is still largely dependent on fossil fuels. A possible alternative is the use of renewable biofuels via steam reforming [2]. One such potential biofuel, which carries economic weight, is olive mill wastewater (OMW). By resorting to the steam reforming of this waste product (Eq. 1), hydrogen can be obtained, reducing the organic load of the effluent, while simultaneously turning its treatment into a profitable endeavour. Further gain, in terms of hydrogen yield and purity, can be reached through process intensification. Carbon dioxide sorption (e.g., with CaO) can be employed to reach sorption-enhanced reforming (SER), a method which reduces emissions and favourably shifts the equilibrium of the reactions (thus improving reactor performance or allowing to reach the same performance under more moderate conditions) (Eq. 2) [1]. Partial oxidation of OMW with oxygen can also be used, simultaneously, to reach autothermal reforming (ATR), which has the potential for thermally neutral operation (Eq. 3) [3].

$$C_xH_yO_z+(2x-z)H_2O \rightarrow (\frac{y}{2}-z+2x)H_2+xCO_2 \quad \Delta H^0_{298}> 0 \qquad (1)$$

$$CO_2+CaO \leftrightarrow CaCO_3 \quad \Delta H^0_{298}=-179\ kJ\cdot mol^{-1} \qquad (2)$$

$$C_xH_yO_z+\frac{(x-z)}{2}O_2 \rightarrow xCO+\frac{y}{2}H_2 \quad \Delta H^0_{298}< 0 \qquad (3)$$

The goal of this work is to determine, from the thermodynamic point of view, thermally neutral operating conditions and maximize hydrogen production for the sorption-enhanced autothermal reforming (SE-ATR) of OMW, a novel approach to OMW treatment.

METHODOLOGY

The thermodynamic model was developed using the Aspen Plus® V11.0 software. To achieve the equilibrium composition of the chemical species at a given pressure and temperature, a non-stoichiometric method was utilized, namely the minimization of the Gibbs free energy [4]. Different reactor configurations were considered, namely, traditional reforming (TR), SER, ATR, and SE-ATR. The conditions assessed were as follows: temperature (300-900 °C), pressure (1-20 bar), steam to carbon molar ratio (S/C: 0.6-16.0), for the sorption-enhanced configurations the calcium oxide to OMW molar ratio (CaO/OMW: 0-8.0) and for the autothermal configurations, the oxygen to OMW molar ratio (O_2/OMW: 0-6.0).

RESULTS

The thermodynamic study for the TR and SER provided the optimal operating conditions. Maximum hydrogen yields were obtained for P=1 bar, T= 500-600 ºC, high S/C ratios, and for the sorption-enhanced configuration for *CaO/OMW* = 7.0. Coke formation is avoided in these conditions as well. For the TR, 98% of the maximum theoretical

H_2 yield (calculated based on reactions stoichiometry) was obtained for S/C = 16.0, whilst for the SER the same hydrogen yield was obtained for S/C = 4.0 only.
With the results obtained in the thermodynamic study, the energy balance was performed for ATR and SE-ATR. Fig. 1 a) shows that as the level of *O_2/OMW* increases, the OMW partial oxidation will provide larger amounts of energy (as it is exothermic) at the expense of a diminished hydrogen yield (yH_2). Fig. 1 b) highlights the decrease in energy requirement per mole of H_2 formed for the two configurations. Fig. 2 a) shows the effects the S/C ratio and temperature have on the yield of hydrogen for thermally neutral conditions. Together with Fig. 2 b) it is possible to observe that high hydrogen yields can be obtained (94% of the theoretical maximum) for low quantities of O_2/OMW and S/C = 2.0, a much lower amount than what was observed for TR and SER.

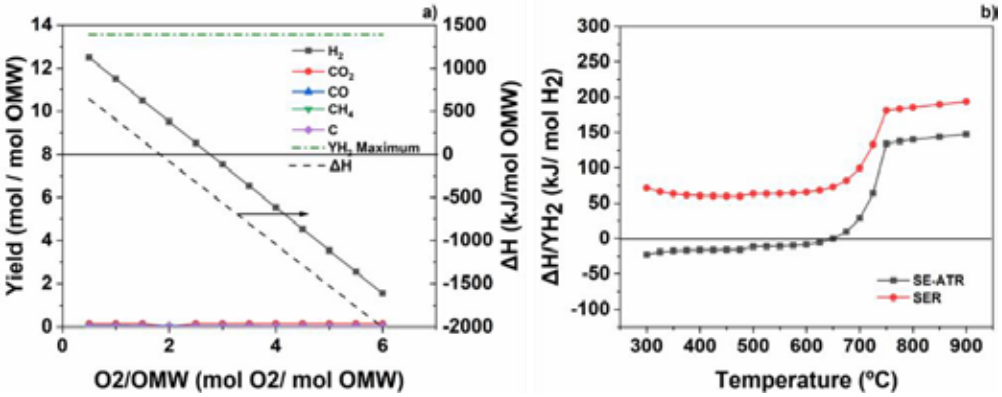


Fig. 1 Effects of O_2/OMW on the yields of the reaction products and on the heat-duty for the SE-ATR (a) and effect of temperature on the spent energy per mole of hydrogen produced for the SER and the SE-ATR configurations (b); P= 1 bar, S/C =4.0 mol H_2O/mol C, CaO/OMW = 7.0 mol CaO/mol OMW; T = 600°C (a), O_2/OMW = 2.0 mol O_2/mol OMW (for SE-ATR) (b).

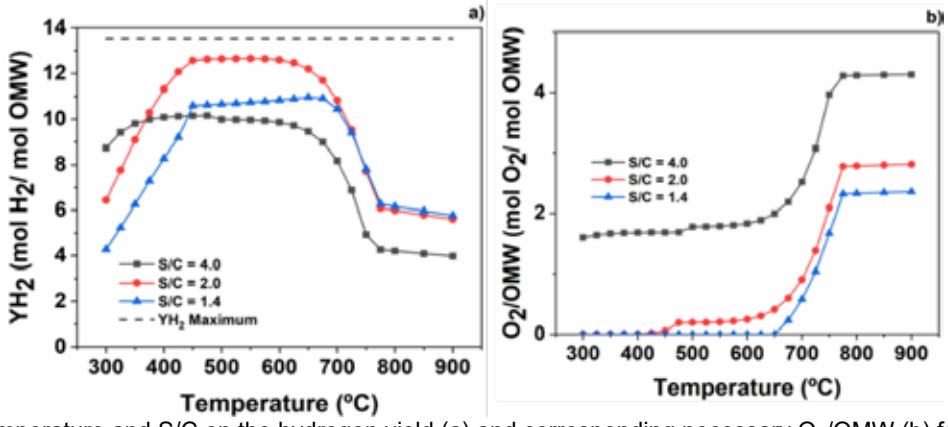


Fig. 2 Effect of temperature and S/C on the hydrogen yield (a) and corresponding necessary O_2/OMW (b) for the SE-ATR for thermally neutral operation; P= 1 bar.

CONCLUSIONS

Full conversion of OMW was reached. The autothermal reforming configurations produce less hydrogen compared to their non-autothermal counterparts, but a decreased energy requirement per mole of hydrogen is observed. The autothermal configurations can operate at thermally neutral conditions. For the ATR, the thermally neutral operation requires a high amount of oxygen, which reduces the hydrogen yield. For SE-ATR, the exothermal sorption reaction provides nearly enough energy for the process to be thermally neutral by itself. With the addition of a controlled amount of oxygen into the reaction medium thermally neutral conditions are reached without significant hydrogen loss and much less steam requirements, which is quite significant from the economics point of view.

ACKNOWLEDGEMENTS

This work was financially supported by LA/P/0045/2020 (ALiCE), UIDB/00511/2020 and UIDP/00511/2020 (LEPABE), funded by national funds through FCT/MCTES (PIDDAC) and by the Project NORTE-01-0247-FEDER-39789, funded by the European Regional Development Fund (ERDF) through the Programa Operacional Regional do Norte (NORTE 2020). This work was also funded by the project HyGreen&LowEmissions (NORTE-01-0145-FEDER-000077), supported by Norte Portugal Regional Operational Programme (NORTE 2020), under the PORTUGAL 2020 Partnership Agreement, through the European Regional Development Fund (ERDF). P. Cerqueira acknowledges the Portuguese Foundation for Science and Technology (FCT) for the PhD grant (2021.04726.BD).

M. A. Soria thanks the Portuguese Foundation for Science and Technology (FCT) for the financial support of his work contract through the Scientific Employment Support Program (Norma Transitória DL 57/2017).

REFERENCES

[1] S.Z. Abbas, V. Dupont, T. Mahmud, Modelling of high purity H-2 production via sorption enhanced chemical looping steam reforming of methane in a packed bed reactor, Fuel, 202 (2017) 271-286.
[2] F. Sabri, M. Bakhtiari, H. Ibrahim, Robust power-law kinetic model for the autothermal reforming of glycerol over metal oxide catalysts, Reaction Kinetics Mechanisms and Catalysis, 123 (2018) 543-557.
[3] Y.S.M. Camacho, S. Bensaid, G. Piras, M. Antonini, D. Fino, Techno-economic analysis of green hydrogen production from biogas autothermal reforming, Clean Technologies and Environmental Policy, 19 (2017) 1437-1447.
[4] M.A. Soria, C. Mateos-Pedrero, A. Guerrero-Ruiz, I. Rodríguez-Ramos, Thermodynamic and experimental study of combined dry and steam reforming of methane on Ru/ ZrO2-La2O3 catalyst at low temperature, International Journal of Hydrogen Energy, 36 (2011) 15212-15220.

WHEC-2022
23rd World Hydrogen Energy Conference
June 26-30, 2022 - Istanbul

#383

HYDROGEN PRODUCTION VIA STEAM REFORMING OF GLYCEROL OVER Ce-La-Cu-O TERNARY OXIDE CATALYSTS

[1] Angeliki Latsiou, [1] Nikolaos D. Charisiou, [2,3] Aasif A. Dabbawala, ,[2,3*] Kyriaki Polychronopoulou, [1*] Maria A. Goula
[1] Laboratory of Alternative Fuels and Environmental Catalysis (LAFEC), Department of Chemical Engineering, University of Western Macedonia, GR-50100 Kozani, Greece
[2] Department of Mechanical Engineering, Khalifa University of Science and Technology, Abu Dhabi, P.O. Box 127788, UAE
[3] Center for Catalysis and Separation, Khalifa University of Science and Technology, Abu Dhabi, P.O. Box 127788, UAE

*Corresponding author e-mail: mgoula@uowm.gr (Maria A. Goula); kyriaki.polychrono@ku.ac.ae (Kyriaki Polychronopoulou)

ABSTRACT

In the work presented herein, Ce-La-xCu-O catalysts with different Cu contents were synthesised using the conventional microwave (MW) method and an enhanced microwave method where air cooling (AC) during heating was applied. The catalytic materials were then studied for the steam reforming of glycerol (GSR). It was revealed that the synthesis methods (MW and AC) had an effect mainly on the degree of Cu incorporation into the Ce-La-O fluorite lattice, leading to one or two phases system. GSR tests revealed that the Ce-La-10Cu-O (AC) catalyst showed the highest glycerol conversion, conversion to gaseous products and yield of H_2 (5.3 mol/mol of glycerol) and deactivated at slower rate. The improved performance of the AC catalyst can be correlated to a more homogeneous Cu incorporation into Ce-La-O mixed oxide thus forming more accessible active sites to reactants which overall impact on the catalytic performance.

Keywords: Ce-La-Cu oxides; ternary oxides; Glycerol steam reforming; hydrogen production

INTRODUCTION

Crude glycerol is the main by-product of the transesterification process; it may be used for H_2 production through the process of steam reforming [1-3]. Transition metal catalysts, especially Ni, have been shown to process excellent intrinsic activity in steam reforming reactions, but as is well understood, they tend to deactivate as they are susceptible to carbon deposition and the sintering of metal particles. Bimetallic catalysts can improve metal dispersion as well as catalyst resistance towards deactivation. Another important component to consider is the modification of the support as it can have an important effect on the metal-support interactions, active phase dispersion, reducibility of the active metal, and the acid/basic properties which can control side reactions. A ubiquitous supporting material is CeO_2, because it promotes the Water Gas Shift (WGS) reaction, the dissociation of water and the reforming of methane, due to its basic character and ability to store/release lattice oxygen [4]. La_2O_3 is another promoter often used in catalytic reactions because it offers thermal stability and has the ability to store/release oxygen [5]. For the work presented herein we synthesised Cu-based catalysts by incorporating Cu in a La-modified CeO_2 matrix. In particular, Ce-La-xCu-O, (x = 3, 5, 7, 10, 20) catalysts were synthesized through the sol-gel method coupled with microwave (MW) radiation. Apart from this method (MW), we also prepared Cu-based catalysts using an enhanced MW method, where simultaneous air cooling (AC) is applied during heating. The materials were extensively characterized using XRD, Raman spectroscopy, SEM, TEM, H_2-TPR, NH_3 and CO_2-TPD, and XPS to probe the microstructure, surface and redox properties and the Cu/La doping into the ceria matrix.

MATERIALS AND METHODS

More information regarding this section can be found in ref [5]. Ce-La-Cu-O catalysts with different Cu contents were synthesized through the sol-gel method under two different conditions; (a) stand-alone conventional microwave heating and (b) enhanced microwave approach. The experiments were carried out in MARS-6 microwave system with 0-1800 W ± 5 power output. The catalysts were thoroughly studied in terms of their structural, morphological, redox, surface basicity, surface composition and catalysis performance employing XRD, Raman spectroscopy, SEM, TEM, H_2-TPR, NH_3 and CO_2-TPD, and XPS. The experimental work for GSR was performed in a continuous flow fixed-bed reactor at atmospheric pressure. Catalytic activity and selectivity were assessed in the temperature range of 400 - 750 °C. Catalytic stability was assessed at 600 °C. The Weight Hourly Space Velocity (WHSV) used was 50,000 mL g^{-1} h^{-1}. The liquid products were analysed via a combination of Gas Chromatography (Agilent 7890A) and Mass Spectroscopy (Agilent 5975C). The gaseous products were determined via an Agilent gas chromatographer (7890A).

RESULTS AND DISCUSSION

XRD patterns of the calcined (500 °C for 6 h) conventional microwave (MW) and enhanced microwave (AC) Ce-La-xCu-O catalysts are presented in Fig. 1 (left hand side). For all the metal oxides and regardless of the Cu composition (3-20 at%), the main peaks at 28.5°, 33.1°, 47.5° and 56.0° diffraction angles can be assigned to the

crystal planes (111), (200), (220) and (311), respectively, of the ceria (CeO_2) cubic fluorite structure. It is important to note that the characteristic peaks belonging to the lanthanum (III) oxide (La_2O_3) are absent in both types of microwave oxides (conventional MW and enhanced AC), suggesting a rather homogeneous Ce-La-O solid solution in which the La^{3+} cations replace the Ce^{4+} cations in the ceria lattice structure. Also, the position of the diffraction peaks for the Ce-La-xCu-O samples appear shifted towards lower 2theta values as compared to pristine CeO_2 (not presented here) which also signifies the incorporation of the larger La^{+3} (1.10 Å) ions into the lattice of CeO_2 and the subsequent lattice expansion, as anticipated. Furthermore, the substitution of Ce^{4+} in CeO_2 lattice with aliovalent cations leads to the creation of oxygen vacant sites (O_v) [4].

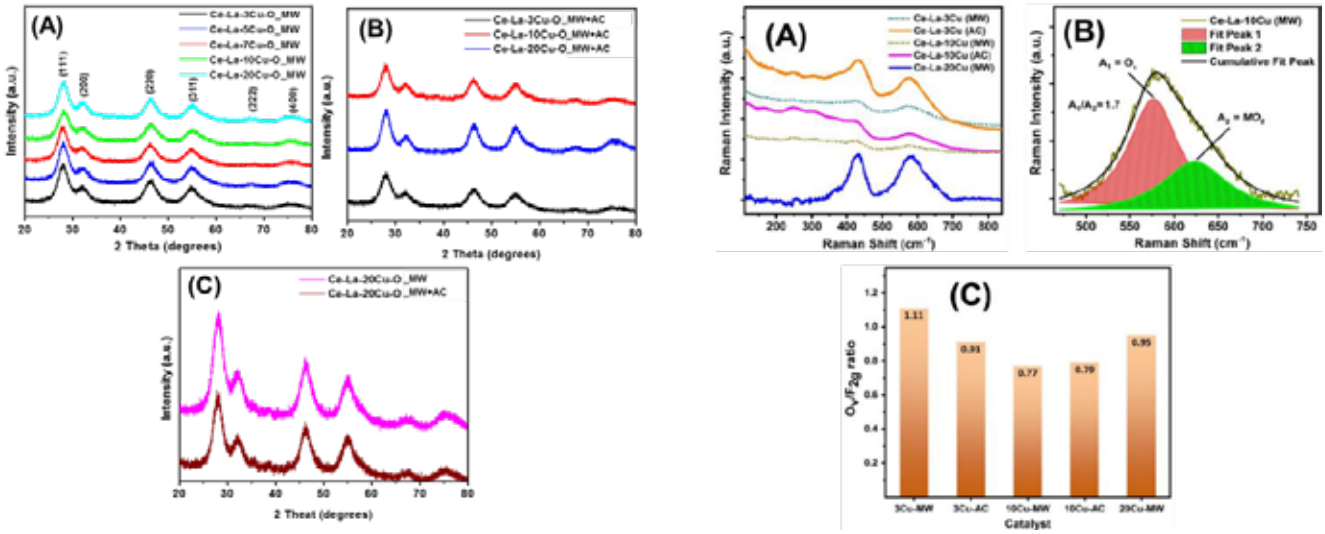


Fig. 1. Left hand side: (A) XRD patterns of the microwave prepared Ce-La-xCu-O oxides, x=3, 5, 7, 10, 20 at%; (B) XRD patterns of the air-cooled microwave prepared Ce-La-xCu-O oxides, x=3, 10, 20 at%; (C) XRD patterns of the Ce-La-20Cu-O oxide prepared using conventional and enhanced (air cooled, AC) microwave methods. Right hand side: (A) Raman spectra of Ce-La-xCu-O oxides, x=3, 10, 20 at%; prepared using conventional (MW) and enhanced (AC) microwave methods; (B) Deconvoluted Raman spectrum obtained over the Ce-La-10Cu-O MW oxide in the 500-700cm^{-1} region (defects); (C) O_v/F_{2g} intensity ratio for Ce-La-xCu-O oxide catalysts.

The Raman shift studies were conducted on calcined catalysts (500 °C/6h) in order to monitor the metal-oxygen bond environments and to evaluate the impact of La^{+3} and Cu^{+2} cations incorporation to the CeO_2 cubic lattice. For a critical comparison between the two methods, the Raman spectra of the oxides prepared through MW and AC methods and containing Cu at different concentration levels (3-20 at%) are presented in Fig. 1 (right hand side). It is known that CeO_2 exhibits a characteristic Raman band at 464 cm^{-1}, which corresponds to the vibration mode F_{2g} of the ceria lattice. The two main peaks in the Raman spectra of the Ce-La-Cu-O oxides shown in Fig. 1A are located at 433 and 580 cm^{-1} (ceria is reference oxide, not presented). The first peak can be linked to the F_{2g} vibrational mode in the fluorite lattice of the ceria-related phase and is shifting towards lower wavelength value (blue shift), caused by the lanthanum (III) doping, compared to the undoped ceria. La^{3+} substitutes Ce^{4+} in the lattice leading to a concomitant oxygen departure followed by creation of oxygen vacancies (O_v), changing the electronic structure of the oxide [5].

The stability of all catalysts was evaluated during time-on-stream experiments, for a total of 12 h. Total glycerol conversion and the conversion of glycerol towards the gaseous products are shown in Fig. 2A, while the H_2 selectivity and H_2 yield are presented in Fig. 2B. It is obvious that all catalysts experience a loss in their ability to convert glycerol during the first few hours of the experiments although X_{C3H8O3} remained rather high. The Ce-La-10Cu (AC) catalyst, despite experiencing a similar drop, from 91% to 74%, i.e., was somewhat more active. The loss in the ability to convert glycerol to gaseous products was significantly more pronounced; the drop from the first to the last measurement was 57-26% for the Ce-La-3Cu (MW), 60-27% for the Ce-La-5Cu (MW), 67-30% for the Ce-La-7Cu (MW), 67-33% for the Ce-La-10Cu (MW) and 55-22% for the Ce-La-20Cu (MW). For the Ce-La-10Cu (AC) X_{C3H8O3} (gaseous) dropped from 68% to 34%. The significant decrease in catalytic performance with time clearly suggests the deactivation of catalysts, which primarily occurs due to the carbon deposition arising from various secondary reactions and/or metal particle sintering. However, from Fig. 2B, it is quite obvious that although all catalysts retain stable S_{H2} values, these depend on the Cu content and preparation method. For example, during the 4th hour of time-on-stream, S_{H2} followed the order: Ce-La-10Cu (AC) (72%) > Ce-La-10Cu (MW) (68%) > Ce-La-7Cu (MW) (67%) > Ce-La-5Cu (MW) (60%) > Ce-La-3Cu (MW) (57%) > Ce-La-20Cu (MW) (56%).

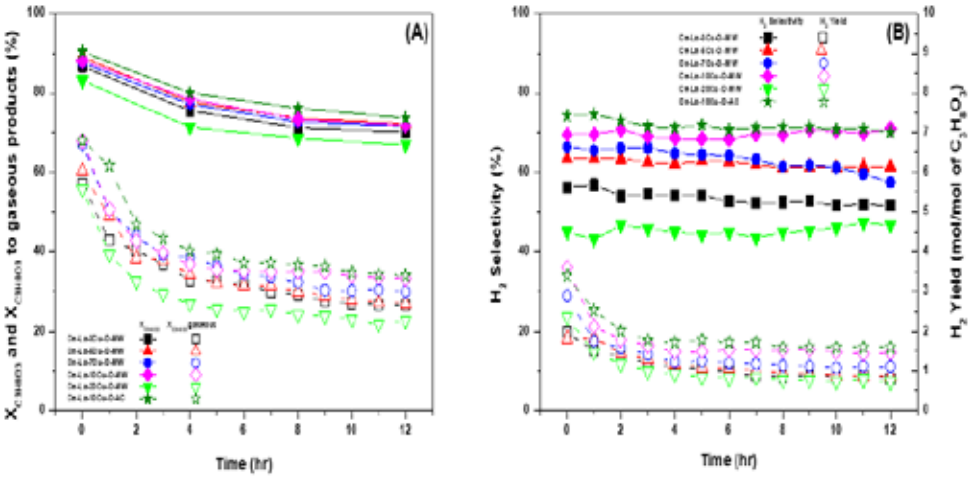


Fig. 2. (A) Total $C_3H_8O_3$ conversion and $C_3H_8O_3$ conversion into gaseous products, (B) H_2 selectivity and yield for all catalysts (time-on-stream experiments)

CONCLUSIONS

Ce-La-xCu-O catalysts with different Cu contents were rapidly synthesized through sol-gel method under two different microwave conditions; (i) conventional microwave heating (MW) and (ii) enhanced microwave (AC) condition, where simultaneous air cooling was applied while heating. It was shown that the Ce-La-10Cu-O (AC) catalyst was more active and deactivated at slower rate because of a more homogeneous Cu incorporation into Ce-La-O mixed oxide, which helped form more accessible active sites to reactants.

ACKNOWLEDGEMENT

We gratefully acknowledge that this research has been co-financed by the European Union and Greek national funds under the call “Greece – China Call for Proposals for Joint RT&D Projects” (Project code: T7DKI-00388).

REFERENCES

1. Charisiou ND, Italiano C, Pino L, Sebastian V, Vita A and Goula MA. 2020. Hydrogen production via steam reforming of glycerol over Rh/γ-Al_2O_3 catalysts modified with CeO_2, MgO or La_2O_3. Renewable Energy 162:908-925.
2. Charisiou ND, Siakavelas G, Tzounis L, Dou B, Sebastian V, Hinder SJ, Baker MA, Polychronopoulou K and Goula MA. 2020. Ni/Y_2O_3–ZrO_2 catalyst for hydrogen production through the glycerol steam reforming reaction. International Journal of Hydrogen Energy 45:10442-10460.
3. Charisiou ND, Sebastian V, Hinder SJ, Baker MA, Polychronopoulou K and Goula MA. 2019. Ni Catalysts Based on Attapulgite for Hydrogen Production through the Glycerol Steam Reforming Reaction. Catalysts 9:650.
4. Polychronopoulou K, Charisiou ND, Siakavelas G, AlKhoori AA, Sebastian V, Hinder SJ, Baker MA and Goula MA. 2019. Ce-Sm-$_x$Cu cost efficient catalysts for H_2 production through the glycerol steam reforming reaction. Sustainable Energy & Fuels 3:673-691.
5. Polychronopoulou K, Dabbawala A, Sajjad M, Singh N, Anjum DH, Baker MA, Charisiou ND and Goula MA. 2022. Exploring the potential of Ce-La-Cu-O oxide towards hydrogen production via steam reforming of glycerol: an experimental and DFT study. Applied Surface Science. Accepted for publication, https://doi.org/10.1016/j.apsusc.2022.152798

WHEC-2022
23rd World Hydrogen Energy Conference
June 26-30, 2022 - Istanbul

#396

SODIUM FORMATE FORMATION VIA IN-SITU CATALYTIC HYDROGEN PRODUCTION FOR DECARBONIZATION

[1]Özge Coşkuner, [2]Umit Bilge Demirci,* [1]Aysel Kantürk Figen*
[1]Yıldız Technical University, Department of Chemical Engineering, İstanbul, Turkey
[2]Institut Européen des Membranes, IEM – UMR 5635, Univ Montpellier, ENSCM, CNRS, Montpellier, France

*Corresponding author e-mail: umit.demirci@umontpellier.fr (U.B. Demirci), akanturk@yildiz.edu.tr (A. Kantürk Figen)

ABSTRACT

Hydrogenation strategies, in which hydrogen and boron hydrides are used as hydrogen and heat carriers, draw attention to reducing the carbon footprint and creating a sustainable hydrogen-boron-carbon cycle. An alternative strategy to achieve the goal of the European Green Deal is the synthesis of synthetic fuels such as methanol (CH3OH), methane (CH4), and formic acid (HCOOH) from greenhouse gases.

Within this scope, the study is focused on sodium formate formation via in-situ hydrogen production for decarbonization, especially formic acid production. For this purpose, sodium borohydride ($NaBH_4$) is used as a hydrogen and heat carrier. Cobalt-catalyzed hydrolysis of $NaBH_4$ takes place, and the reaction is accelerated in the presence of CO_2. As a result, sodium formate (NaHCOO) and an HCOO group containing borate $B(OH)_2(OOCH)$ are obtained.

Keywords: Carbon dioxide reduction; Formate; Hydrolytic conditions; Sodium borohydride

INTRODUCTION

It has been reported that the amount of anthropogenic CO_2, which increases in the atmosphere and causes global warming, was 316 ppm in 1960 and reached 417 ppm in 2021 [1,2]. To prevent a further increase and limit global warming to 1.5°C [3], it is necessary to reduce the amount of CO_2 entering the atmosphere and investigate the methods of removing it from the atmosphere if possible. According to literature, CO_2 can be used as a cheap and abundant carbon source to produce valuable chemicals such as methanol, formic acid, and methane via hydrogenation [4,5].

Borohydrides are the materials with the highest gravimetric H_2 density. As a type of borohydrides, Alkali metal borohydrides are well-known for their high reductive properties [6] and their ability to be used for CO_2 hydrogenation [7-13]. The transfer of H^- of BH_4^- to CO_2 is highly favorable and competitive with H_2 formation [14]. As metal borohydride, $NaBH_4$ is also used for the hydrogenation of CO_2. Wartik and Pearson reported the formation of sodium triformatomonohydroborate ($NaBH(OOCH)_3$) when 3 equiv of CO_2 reacts with 1 Equiv $NaBH_4$ in dimethyl ether at 25°C. On the other hand, sodium methoxyformato(oxo) borane ($NaBO(OCH_3)(OOCH)$) was obtained, where 2 Equiv CO_2 reacted with 1 equiv of $NaBH_4$ above room temperature in solvent-free media. In their study $NaBO(OCH_3)(OOCH)$ was converted to sodium formate and methanol by hydrolysis [7,8]. Knopf and Cummins studied the same reaction under a pressure of 20.7 bar CO_2 in the presence of acetonitrile at 25°C [9], confirming $NaBH(OOCH)_3$ as the hydrogenation product. The formation of formate anion has also been reported as the main product of the CO_2 hydrogenation with $NaBH_4$ in an ethanol-water mixture by Zhao et al. [10].

In our previous study [11], we reported the CO_2 hydrogenation by $NaBH_4$ in an aqueous solution with a nickel catalyst. In this study, we focused on the cobalt-catalyzed hydrolysis of $NaBH_4$ in the presence of CO_2 at ambient conditions. The hydrogenation also was carried out in the absence of catalyst following the same procedure. In addition, the structural properties of the hydrogenation products and the effect of the catalyst on the hydrogenation process were investigated.

EXPERIMENTAL

Materials

$NaBH_4$ (Acros Organics, Fisher Scientific; 98%) and cobalt chloride ($CoCl_2$) (Sigma Aldrich) were used as received. Deionized ultra-pure water (Milli-Q grade; resistivity > 18 MΩ cm) and carbon dioxide CO_2 (Linde; 5.0) were used.

Method

The hydrolysis of 120 mg of $NaBH_4$ was performed in the presence of 26.7 mg $CoCl_2$ and CO_2, following the protocol of our previous work [11]. $NaBH_4$ was mixed with $CoCl_2$ in an argon-filled glove box (MBraun M200B; H_2O and O_2 < 0.1 ppm). The hydrolysis was realized in a fume hood and a three-necked round bottom flask used as a hydrolysis reactor. The reactor was connected to the CO_2 gas line (1.05 bar), and it was filled with 50 mL of water. CO_2 was bubbled in the water for 10 min. After the step, the $NaBH_4$-$CoCl_2$ mixture was poured into the flask. While the hydrogenation was performed rapidly, it contributed to CO_2 effervescence, and the solution became milky. The flow

of CO_2 was stopped when the effervescence stopped, and then the solution returned to its transparence. The reaction was completed in 10 minutes. A clear solution with black particles was obtained. The solution was centrifuged for 10 min at 5400 rpm to remove the in situ formed Co particles. The solid product obtained from the reaction is denoted as CB-1. We repeated the hydrolysis mentioned above experiment in the absence of a Co catalyst and the solid hydrogenation product denoted as CB-2.

Characterization

The hydrogenation products were investigated by Fourier Transformed Infrared (FTIR) spectroscopy (ThermoFisher, Germany, NEXUS instrument equipped with an attenuated total reflectance (ATR) accessory; wavenumber range of 4000-600 cm^{-1}); powder X-ray diffraction (XRD; PANalytical X'pert Pro diffractometer) and scanning electron microscopy (SEM; Zeiss EVO® LS 10). The elemental content of CB-1 is also investigated by Inductively Coupled Plasma Mass Spectrometry (ICP-MS; Agilent 7800 ICP-MS).

RESULTS AND DISCUSSION

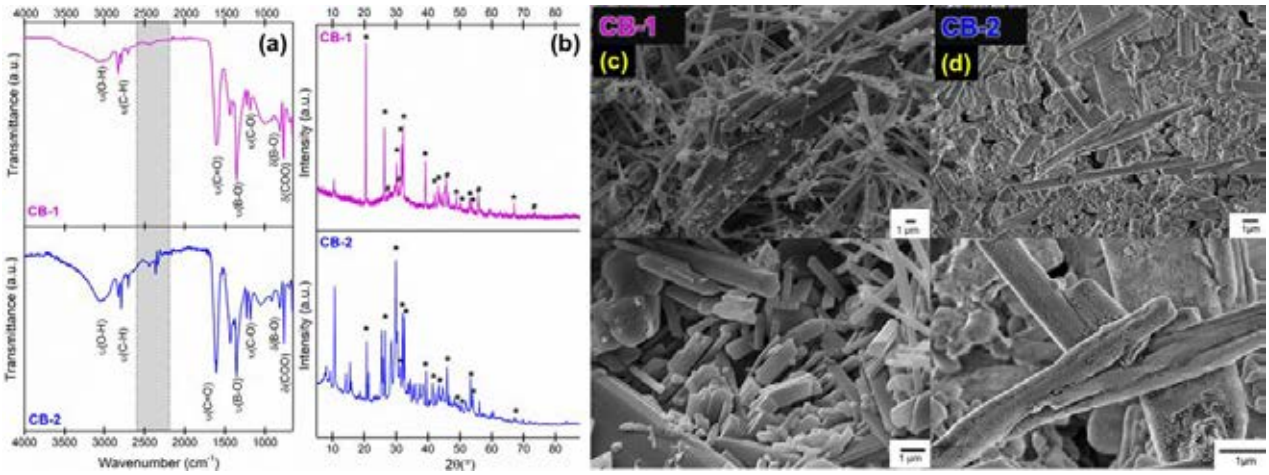


Figure 1. The comparable FTIR spectra (a) and XRD patterns (b); SEM images of CB-1 (c) and CB-2 (d)

The hydrogenation products analyzed by FTIR spectroscopy are given in Figure 1. The FTIR spectra of the products are investigated comparatively. The bands of both products observed at the wavenumber ranges are attributed to the following bonds: O-H (stretching 3600-2870 cm^{-1}), C-H (stretching 2870-2640 cm^{-1}), and B-O (stretching and deformation 1450-650 cm^{-1}). Moreover, the peaks are attributed to C-H deformation (CB-1 and CB-2 1046 cm^{-1}), C=O stretching (CB-1 and CB-2 1610 cm^{-1}), C-O stretching (CB-1 1345 cm^{-1}; CB-2 1350 cm^{-1}), COO deformation (CB-1 760 cm^{-1}; CB-2 758 cm^{-1}) [9, 15-17] and B-O-C (CB-1 1184 cm^{-1}; CB-2 1175 cm^{-1}) [9, 18]. The presence of O-H and B-O bands in both products shows the products' borate structure [15,16]. Also, the results are comparable to NaHCOO [17]. The FTIR spectra of CB-1 and CB-2 were very compatible with the hydrogenation product of our previous study [11]. It can be observed that there is no B-H band in the structure of the hydrogenation product we obtained in our previous study and the CB-1 product in this study. However, a B-H band between 2600-2200 cm^{-1} was found in the structure of the hydrogenation product CB-2, which was carried out in a catalyst-free environment [19]. This shows that the BH_4^- conversion is completely realized with the hydrogenation carried out in the presence of a catalyst.

The XRD patterns of CB-1 and CB-2 were also given in Figure 1. Most of the diffraction peaks (indicated by a star) of the products are ascribed to the structure of NaHCOO (ref. 00-011-0724). The diffraction peaks (indicated by number sign) of CB-1 are also ascribed to NaCl (ref. 00-001-0996) [20]. The excluded broad peaks below 20°, between 25-35° and 40-50° belong to the amorphous phase [11], and based on the XRD and FTIR analysis results, we assume the formation of crystalline and/or amorphous $B(OH)_2(OOCH)$.

The elemental content of CB-1 was investigated by ICP-MS analysis to observe Co content in the structure. The results show that the sample has 6.28±0.63% B, 22.26±0.96% Na and 0.573±0.063% Co elemental content by weight.

The hydrogenation solids were visualized by SEM (Figure 1). The solids consist of needle-like crystals of mixed sizes. CB-1 crystals' have lengths varying from 0.5 µm to 11.8 µm and a thickness in a range 0.24-of to 0.8 µm. CB-2 have a thickness from 0.3 µm to 12.3 µm and length from 0.6 µm to 2 µm.

CONCLUSIONS

In conclusion, the study proves that CO_2 could hydrogenate in an aqueous $NaBH_4$ solution at ambient conditions and NaHCOO is obtained as the chemical conversion product of CO_2. The hydrogenation product CB-1 is a mixture of NaHCOO, $B(OH)_2(OOCH)$, and NaCl. The usage of cobalt catalyst in the process provides the total BH_4^- conversion.

ACKNOWLEDGMENT

This work was supported by TUBITAK (project n° 218M181) and CAMPUS FRANCE PHC BOSPHORUS (project n° 42161TB).

REFERENCES

1. Letcher TM. 2021. Global warming- a complex situation. In Climate Change: Observed Impacts on Planet Earth. Ch. 1. Edited by Letcher TM. Amsterdam, Elsevier.
2. https://climate.nasa.gov/vital-signs/carbon-dioxide/ (accessed November 11, 2021).
3. Mundaca L, Ürge-Vorsatz D and Wilson C. 2018. Demand-side approaches for limiting global warming to 1.5 °C. Energy Efficiency 12:343-362.
4. Olah GA, Prakash GKS and Goeppert A. 2011. Anthropogenic chemical carbon cycle for a sustainable future. Journal of the American Chemical Society 133:12881–12898.
5. Gulzar A, Gulzar A., Ansari MB, He F, Gai S and Yang P. 2020. Carbon dioxide utilization: A paradigm shift with CO2 economy. Chemical Engineering Journal Advances 3:100013.
6. Nakaromi Y and Orimo S. 2008. Borohydrides as hydrogen storage materials. In Solid-State Hydrogen Storage. Ch. 15. Edited by Walker G. UK, Woodhead Publishing.
7. Wartik T and Pearson RK. 1955. A New Type of Substituted Borohydride. Journal of American Chemical Society 77:1075.
8. Wartik T and Pearson RK. 1958The reaction on of carbon dioxide with sodium and lithium borohydrides. J. Inorganic Nuclear Chemistry 7:404-411.
9. Knopf I and Cummins CC. 2015. Revisiting CO2 reduction with NaBH4 under aprotic conditions: synthesis and characterization of sodium triformatoborohydride. Organometallics 34:1601-1603.
10. Zhao Y, Zhang Z, Qian X, Han Y. Properties of carbon dioxide absorption and reduction by sodium borohydride under atmospheric pressure. Fuel 142:1-8.
11. Coşkuner Ö, Castilla-Martinez CA, Sonzogni O, Petit E, Demirci UB, Kantürk Figen A. 2022. Sodium borohydride hydrolysis-mediated hydrogenation of carbon dioxide, towards a two-step production of formic acid. International Journal of Hydrogen Energy.
12. Dovgaliuk I, Hagemann H, Leyssens T, Devillers M, Filinchuk Y. CO2-promoted hydrolysis of KBH4 for efficient hydrogen co-generation. International Journal of Hydrogen Energy 39:19603-8.
13. Fletcher C, Jiang Y, Amal R. Production of formic acid from CO2 reduction using potassium borohydride at ambient conditions. Chemical Engineering Science 137:301-7.
14. Grice KA, Groenenboom MC, Manuel JDA, Sovereign MA, Keith JA. Examining the selectivity of borohydride for carbon dioxide and bicarbonate reduction in protic conditions. Fuel 150:139-45.
15. Jun L, Shuping X, Shiyang G. 1995. FT-IR and Raman spectroscopic study of hydrated borates. Spectrochimica Acta Part A: Molecular and Biomolecular Spectroscopy 51:519–532.
16. Kanturk A, Sari M, Piskin S. 2008. Synthesis, crystal structure, and dehydration kinetics of $NaB(OH)_4 \cdot 2H_2O$, Korean Journal of Chemical Engineering 25:1331–1337.
17. Charlton TL, Harvey KB. 1966. Infrared absorption of single crystals of anhydrous sodium formate. Canadian Journal of Chemistry. 44: 2717–2727.
18. Shawgi N, Li S, Wang S. 2017. A Novel method of synthesis of high purity nano plated boron carbide powder by a solid-state reaction of poly (vinyl alcohol) and boric acid. Ceramics International 43:10554–10558.
19. Harvey KB, McQuaker NR. 1971. Infrared and Raman spectra of potassium and sodium borohydride. Can J Chem 49:3272-81.
20. Bao N, Miao X, Hu X, Zhang Q, Jie X, Zheng X. 2017. Novel synthesis of plasmonic Ag/AgCl@TiO2 continues fibers with enhanced broadband photocatalytic performance. Catalysts 7:117.

WHEC-2022
23rd World Hydrogen Energy Conference
June 26-30, 2022 - Istanbul

#400

HYDROGEN AND METHANE PRODUCTION FROM ANAEROBICALLY DIGESTED WATER PLANT BY HYDROTHERMAL GASIFICATION

[1,2]*Fatma Gamze Bodur,* [1*] *Tülay Güngören-Madenoğlu,* [3]*Güven Özdemir,* [1]*Nalan Kabay,* [1]*Levent Ballice*
[1]Ege University, Engineering Faculty, Department of Chemical Engineering, Bornova-Izmir, Turkey
[2]Ege University, Graduate School of Natural and Applied Sciences, Biotechnology Division, Bornova-Izmir, Turkey
[3]Ege University, Science Faculty, Department of Biology, Bornova-Izmir, Turkey

*Corresponding author e-mail: tulay.madenoglu@ege.edu.tr

ABSTRACT

Previously, water hyacinth (*Eichornia crassipes*) was anaerobically digested with anaerobic sludge in batch system at varying total solid (TS) contents of 3.3 and 4.3% and at 35°C. In this study, high organic content of the digested biomass was evaluated in hydrothermal gasification in batch reactor system at different temperatures (200-500°C) to produce biofuels and biochemicals. Hydrothermal gasification was performed in sub- and super-critical water (T_c=374°C, P_c=221 bar) conditions. Prevailing products are biochemicals (glycolic acid, formic acid, acetic acid, furfural, 5-methyl furfural, phenols etc.) at lower temperatures (200-300°C) while biofuels (especially hydrogen and methane) are produced at higher temperatures (400-500°C). Nearly 63% of the feed was converted to gas and aqueous products at 500°C.

Keywords: Hydrothermal gasification, Water hyacinth, Hydrogen, Methane

INTRODUCTION

Water hyacinth is a free-floating aquatic weed those spreads very rapidly and causes damage to aquatic life. Besides the harmful properties of this plant, it provides wastewater reclamation by removing pollutants such as toxic organic compounds and heavy metals [1]. These plants are usually burned or dumbed into landfills causing green house gas emissions. Uncontrolled growth of aquatic plants is problematic in many countries such as India, Pakistan, France, Italy, Portugal, Spain and South America [2]. Recently, surface of the Asi River in Turkey has been covered by water hyacinth plants [3]. High organic content of water hyacinth can be evaluated in energy production. Anaerobic digestion (AD) is the most used method for biogas and fertilizer productions from aquatic plants. Usage of digestate as fertilizer is not suitable because of low capacity for application in agriculture, different pollutions like heavy metals and organic compounds, danger of infection, legal problems, and transportation distances [4]. Digestate can also be converted into biofuels and biochemicals via hydrothermal gasification (HTG). Simultaneous production of hydrogen and methane rich gas can be accomplished with HTG process. Main advantages of HTG are to gasify biomass without drying, fast degradation and less formation of coke and CO gas. Former application of AD process also provides pumpable biomass slurry for continuous HTG process. AD process can be used as a kind of pre-treatment method for better dissolution of lignocellulosic structure of aquatic plants that will be further degraded in HTG with higher yields without requirement of catalyst usage. Final solid residue can also be evaluated as bio-adsorbent, catalyst support and fertilizer. Usage of a hybrid process integrating AD and HTG is a novel method for producing biofuels and biochemicals with net zero waste.

MATERIALS AND METHODS

In a previous study, water hyacinth was anaerobically digested with anaerobic sludge at different TS contents (3.3% for D1 and 4.3% for D2) and at 35°C. D1 represents only anaerobic sludge while D2 includes both sludge and water hyacinth. Remaining digestate were used as feedstock for hydrothermal studies. Proximate analysis of digested biomass solution after anaerobic digestion was given in Table 1.

Table 1. Proximate analysis of digested biomass solution after anaerobic digestion

Run Code	D1	D2
TS (Total Solid, %)	6.1	6.7
VS (Volatile Solid, %)	60.1	61.8
TC (Total Carbon, %)	26.8	29.1

Digested biomass solution with a volume of 15 mL was used in all hydrothermal studies. Hydrothermal studies were performed between 200-500°C (pressure range of 0-340 bar). Only studies at 500°C represents the super-critical condition, others are sub-critical conditions. Experimental conditions for hydrothermal studies were given in Table 2.

Table 2. Experimental conditions for hydrothermal studies

Run Code	D1T200/ D1T300/ D1T400/ D1T500	D2T200/ D2T300/ D2T400/ D2T500
Gasification Temperature (°C)	200/300/400/500	200/300/400/500
Gasification Pressure (bar)	0/80/150/340	0/80/150/340
Mass of TS in feed (g)	0.915	0.927
Mass of VS in feed (g)	0.549	0.572

Digested biomass solution was put into batch reactors with a volume of 100 mL. Reactor was purged for 15 min with nitrogen gas and placed into heaters that provide constant heating rate of 6 K min^{-1}. After reaching gasification temperature, reactor was heated for 1 h when the reaction reached the equilibrium conditions. At the end of this time, reactor was rapidly cooled by fans and then submerged in cool water. The volume of gas products was measured by water-displacement method. They are analyzed by gas chromatography (GC). Inside of the reactor was washed with water and then filtered to separate aqueous product and solid residue. Before analysis, aqueous products were stored in a refrigerator at 4°C.

Analysis of gas products: Composition of the gaseous products (H_2, CO_2, CO and C_1-C_4 hydrocarbons) was analyzed by Agilent HP 7890A model GC equipped with 3 detectors (FID-TCD-TCD) and serially connected 7 columns. Technical features and operating conditions of GC were given in previous work [5].

Analysis of aqueous products: Total organic carbon (TOC) and inorganic carbon (IC) contents of aqueous phase were analyzed by a TOC analyzer (Shimadzu TOC-V_{CPH}, Japan). The amounts of carboxylic acids, aldehydes, ketones, furfurals and phenols present in the aqueous solutions were analyzed by Shimadzu LC-20A model High Performance Liquid Chromatography (HPLC, Japan). Technical features and operating conditions of TOC and HPLC systems were given in previous work [5].

Analysis of solid residue: The TOC content of solid residue was analyzed by SSM-TOC analyzer (Shimadzu TOC-V_{CPH}, Japan).

RESULTS AND DISCUSSION

Carbon gasification efficiency (CGE in g C in gas/g C in digestate), carbon liquefaction efficiency (CLE in g C in aqueous/g C in digestate) and residue (RE in kg C in residue/kg C in digestate) were calculated as given in our previous work [5]. Gas products were not obtained at 200°C. Gas composition and product efficiencies were given in Figs.1 and 2, respectively.

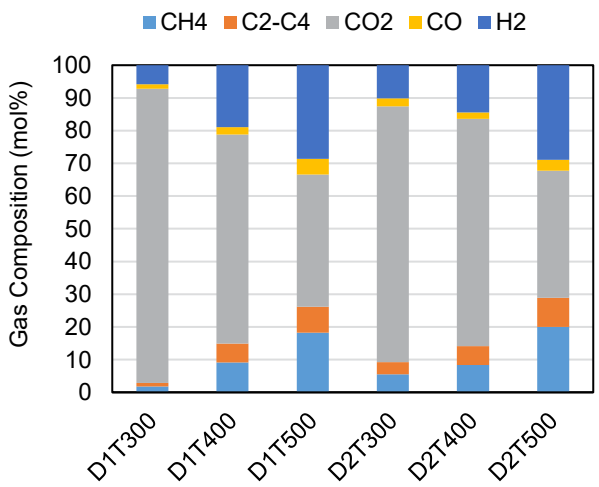


Fig. 1. Gas composition

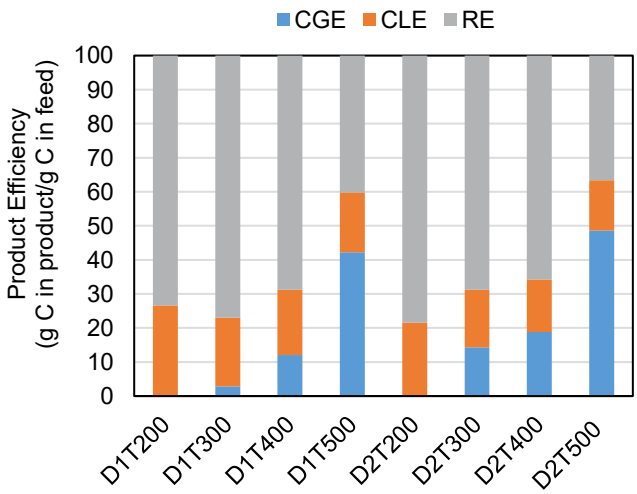


Fig. 2. Product efficiencies

Main composition of gas product was carbon dioxide, hydrogen, and methane. As the temperature increased from 300 to 500°C, share of the hydrogen and methane in the gas mixture increased while carbon dioxide decreased. Nearly half of the gas was composed of hydrogen (29 mol%) and methane (20 mol%) at 500°C for sample D2 which has higher VS and TS (Fig.1). These findings are better than that obtained in a previous study (15 mol% H_2 and 25 mol% CH_4) with sewage sludge at 500°C [6]. Product was composed of aqueous and residue parts at lower temperatures and nearly 63% of the feed was converted to gas and aqueous products at 500°C (Fig.2). Carbon content and composition of aqueous phase were given in Figs.3 and 4, respectively.

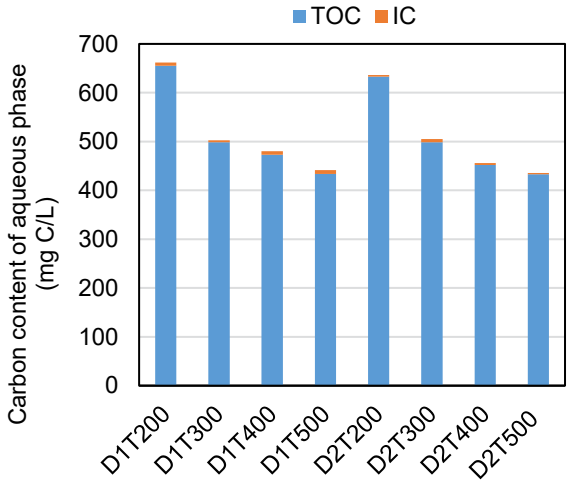


Fig. 3. Carbon content of aqueous phase

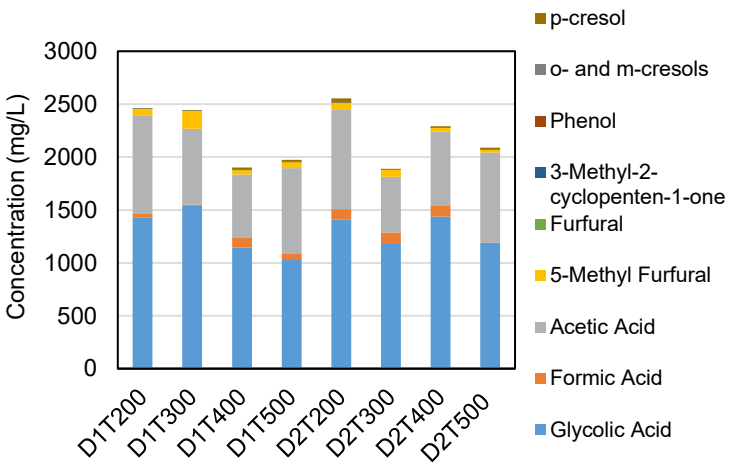


Fig. 4. Composition of aqueous phase

The TOC content of the aqueous product was relatively higher at 200°C since the degradation rate was lower. The IC content of the aqueous phase was extremely low at all conditions (Fig.3). Aqueous phases were mostly composed of carboxylic acids such as glycolic acid, formic acid and acetic acid which are the main degradation products of furfural or 5-HMF (Fig.4). Carboxylic acids are temperature-resistant and not converted to gas products. Phenols (phenol and cresols) are the main degradation products of the lignin structure and found quietly low in aqueous phase.

CONCLUSIONS

Consecutive application of AD and HTG gasification processes provides evaluation of anaerobically digested water hyacinth as biofuel and biochemical source. The AD process accelerated the dissolution rate of lignocellulosic structure of the aquatic plant and resulted in high conversion to gas and aqueous products.

ACKNOWLEDGEMENT

We gratefully acknowledge the financial support provided by Ege University, National Research Project Grants-BAP-ONAP (Project No: FOA-2021-22343). This research work is the continuation of our previous research work supported by SAN-TEZ (Project No. 0330.STZ.2013-2). We are grateful to IZSU Çiğli Advanced Biological Wastewater Treatment Plant, Izmir for giving us waste sludge for biogas production. We are grateful to Profs M.Yüksel and M.Sağlam for their great efforts to establish the infrastructure in the Chemical Technologies laboratories where this research study was carried out. We would like to thank Assoc.Prof.Dr. A. Gunes for providing us water hyacinth seedlings and MSc student G. Öztep for previous anaerobic digestion studies. We would like to thank Mr. Gürsel Serin for supporting the mechanical work.

REFERENCES

1. Gülgün B, Keskin N, Aktaş E, Köse H. 2010. Su Sümbülü Bitkisi (Eichornia crassipes) ve Atıksu Arıtımında Kullanımı, Ziraat Mühendisliği, Sayı:354:48–53.
2. https://ec.europa.eu/environment/nature/pdf/IAS_brochure_species.pdf. Accessed on February 13, 2022.
3. https://www.aa.com.tr/tr/cevre/asi-nehrini-isgal-eden-1000-ton-su-sumbulu-temizlendi/2437493. Accessed on February 13, 2022.
4. Alburquerque JA, Fuente C, Ferrer-Costa A, Carrasco L, Cegarra J, Abad M, Bernal MP. 2012. Assessment of the fertiliser potential of digestates from farm and agroindustrial residues. Biomass and Bioenergy 40:181–189.
5. Madenoğlu TG, Sağlam M, Yuksel M, Ballice L. 2013. Simultaneous effect of temperature and pressure on catalytic hydrothermal gasification of glucose. Journal of Supercritical Fluids 73:151–160.
6. Amrullah A and Matsumura Y. 2018. Supercritical water gasification of sewage sludge in continuous reactor. Bioresource Technology. 249:276–283.

#415

A THERMODYNAMIC EVALUATION OF BORON BASED THERMOCHEMICAL HYDROGEN PRODUCTION CYCLE

[1*] Onur Oruc, [2,1] Ibrahim Dincer
1 Faculty of Mechanical Engineering, Yildiz Technical University, Besiktas, Istanbul, Turkey
2 Faculty of Engineering and Applied Science, University of Ontario Institute of Technology, Oshawa, Ontario, Canada

*Corresponding author e-mail: onur.oruc@std.yildiz.edu.tr

ABSTRACT

In this study, thermodynamic analyses and simulations are performed via using the Aspen Plus software to examine the Boron based thermochemical hydrogen production cycle in detail. There are four main reactions in the cycle and one of them is performed in electrolyzer. Therefore, the cycle requires heat, electricity and water to obtain hydrogen. The electrolyzer efficiency is around 60%, and the overall cycle exergy efficiency varies between 70%-85%.

Keywords: Boron cycle, Hydrogen production, Thermochemical water splitting

INTRODUCTION

There are several ways to produce hydrogen. One of the cleanest and popular hydrogen generation technique is that thermochemical water splitting and hydrogen generation cycles. Thermochemical hydrogen production techniques came to the fore in the 1970s [1]. Water can be split into oxygen and hydrogen at over 2500 K temperature [2]. Thermochemical hydrogen production cycles can be divided into pure and hybrid production cycles. Hybrid cycles need electrical energy and heat , on the other hand, pure cycles require only heat [3]. There are several studies regarding boron-based thermochemical cycle that evaluates the energy and exergy efficiency of the cycle [4,5].

The boron based thermochemical cycle consists of four main reactions to generate hydrogen. One of the four reactions is the electrolyzing of magnesium chloride. In this study, the reactions of the cycle are modeled and investigated using Aspen Plus and EES thermodynamically.

MODELING

The Boron based thermochemical cycle consists of four necessary reactions to produce hydrogen and oxygen. The reactions can be summarized as follows:

$$3MgCl_2 \rightarrow 3Mg + 3Cl_2$$
$$3Mg + B_2O_3 \rightarrow 2B + 3MgO$$
$$3MgO + 3Cl_2 \rightarrow 3MgCl_2 + 1.5O_2$$
$$2B + 3H_2O \rightarrow 3H_2 + B_2O_3$$

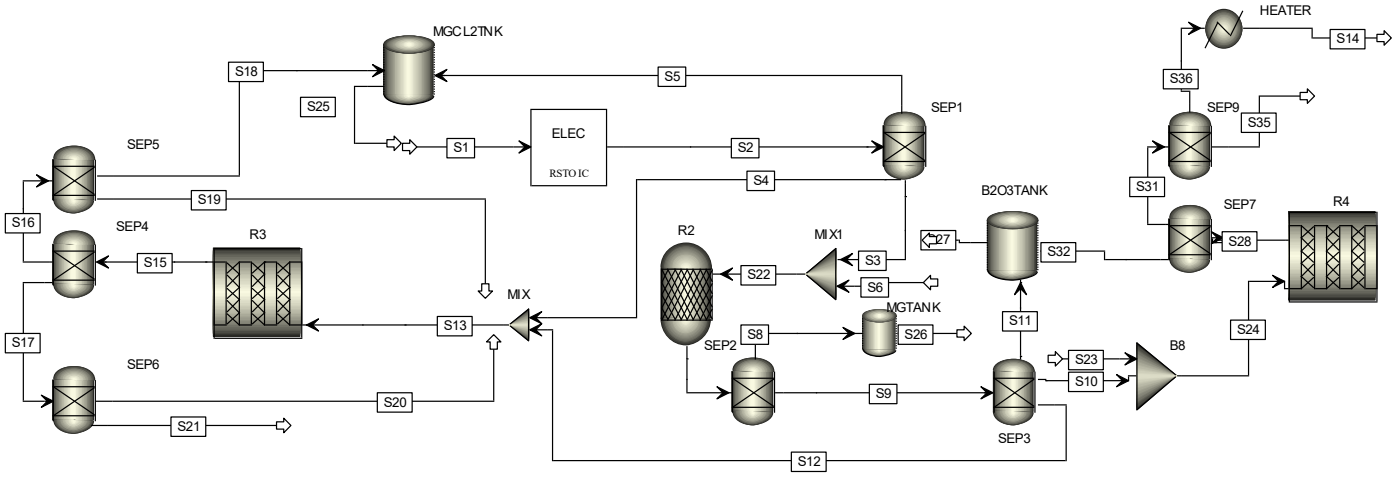


Fig. 1. AspenPlus flowsheet of Boron based thermochemical hydrogen production cycle

The cycle is required water, heat and electricity to perform. The heat source can be nuclear, renewable, or any kind of heat supply. One reaction required electrolyzer to obtain magnesium and chloride. The other reactions can be occurred without electricity. The AspenPlus flowsheet of the cycle is shown in Fig.1.

RESULTS AND DISCUSSION

The characteristic of the electrolyzer is shown in Figure 2. When the modeling is compared with the experimental data, it can be said that it is in full agreement. It is calculated that the efficiency of the electrolyzer is around 60%, respectively by considering the cycle operating conditions.

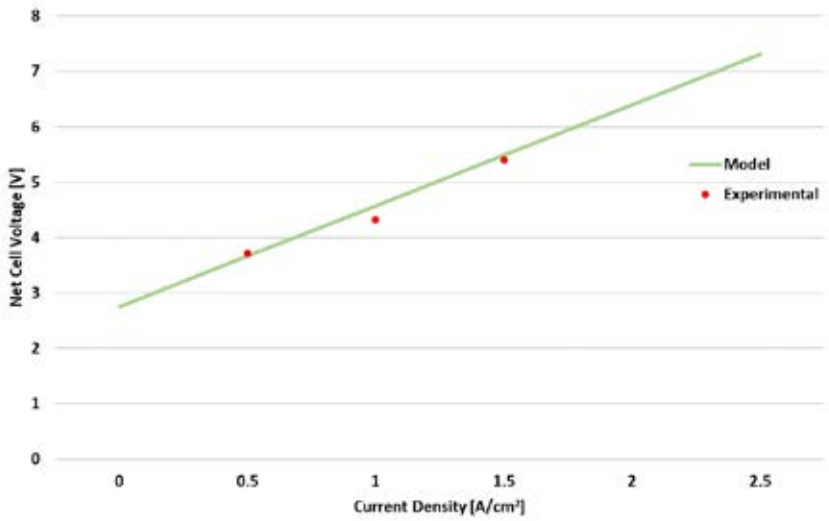


Fig. 2. The effect of current density on the net cell voltage

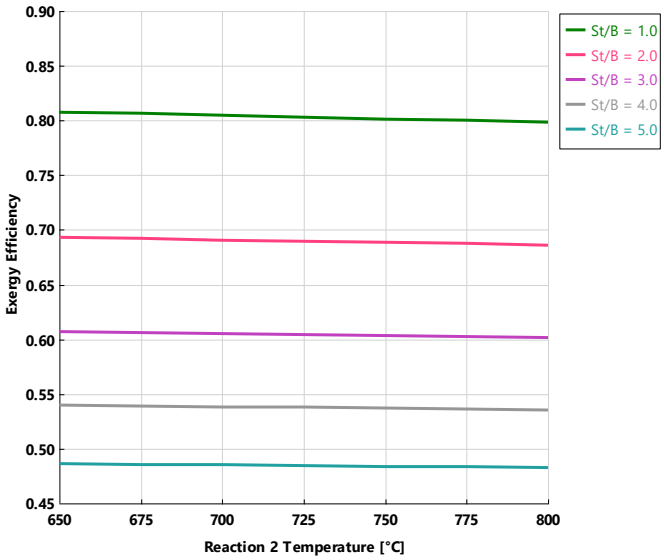


Fig.3. Variation of exergy efficiency with the change of reaction (Boron Production) temperature at different St/B molar ratios

The variation of the exergy efficiency of the cycle according to the Steam/Boron ratio and the reactor temperature in the boron production reaction is seen in Figure 3. The highest cycle efficiency is obtained when the steam/boron ratio is 1.0. The variation of exergy efficiency of MgO chlorination reaction according to temperature and steam/boron ratio is given in figure 4. Similarly, the highest exergy efficiency is obtained when the steam/boron ratio is 1.0 and the temperature is 470°C.

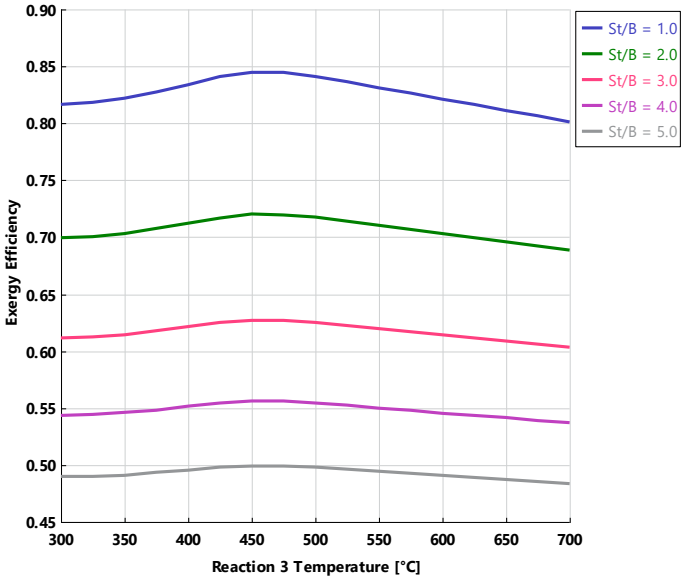


Fig.4. Variation of exergy efficiency with the change of reaction (MgO Chlorination) temperature at different St/B molar ratios

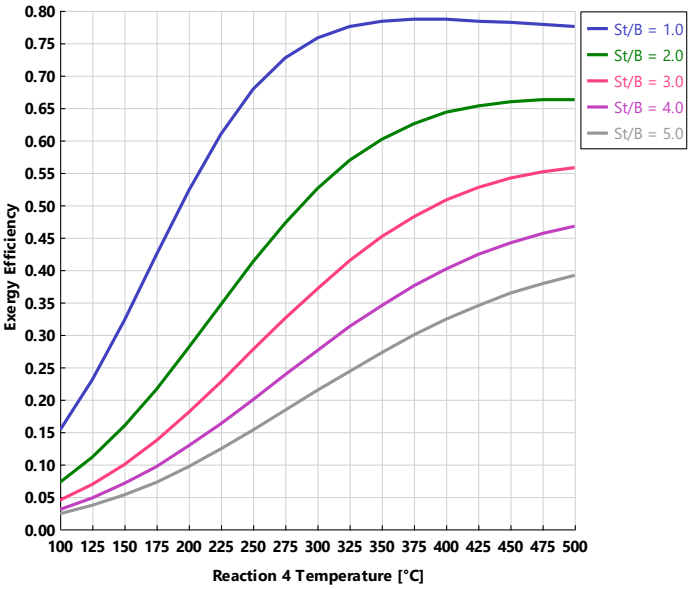


Fig.5. Variation of exergy efficiency with the change of reaction (Boron Hydrolysis) temperature at different St/B molar ratios

In Figure 5, the variation of exergy efficiency of the hydrolysis reaction according to temperature and steam/boron ratio is given. The highest efficiency can be obtained when the steam/boron ratio is 1.0 and the temperature is 350 °C for the analysis and assessment.

CONCLUSIONS

In this study, the Boron based thermochemical cycle is analyzed thermodynamically. The main findings can be found below.

- The first reaction of the boron-based thermochemical cycle is the $MgCl_2$ electrolysis process. As a result of the modeling studies carried out in EES with electrochemical modeling, the electrolysis process has an efficiency in the range of 60% - 65%.
- The exergy efficiency of the cycle varies between 70% - 85%.
- The reason for the higher efficiency of the boron-based thermochemical cycle compared to the other cycles is that it requires low heat and low temperature. In addition to these, the reactions that make up the cycle have kinetically high yield values.

REFERENCES

1. Beghi GE. A Decade of Research on Thermochemical Hydrogen at the Joint Research Centre - ISPRA. Hydrogen Systems, Elsevier; 1986, p. 153–71. https://doi.org/10.1016/B978-1-4832-8375-3.50022-9.
2. Baykara S. Experimental solar water thermolysis. International Journal of Hydrogen Energy 2004;29:1459–69. https://doi.org/10.1016/j.ijhydene.2004.02.011.
3. Oruc O, Dincer I. Assessing the potential of thermo-chemical water splitting cycles: A bridge towards clean and sustainable hydrogen generation. Fuel 2021;286:119325. https://doi.org/10.1016/j.fuel.2020.119325.
4. Balta MT. Thermodynamic performance assessment of boron based thermochemical water splitting cycle for renewable hydrogen production. International Journal of Hydrogen Energy 2020:S0360319920313719. https://doi.org/10.1016/j.ijhydene.2020.04.056.
5. Yılmaz F, Balta MT. Energy and exergy analyses of hydrogen production step in boron based thermochemical cycle for hydrogen production. International Journal of Hydrogen Energy 2017;42:2485–91. https://doi.org/10.1016/j.ijhydene.2016.04.017.

WHEC-2022
23rd World Hydrogen Energy Conference
June 26-30, 2022 - Istanbul

#420

A NOVEL SOLAR ENERGY DRIVEN THERMOCHEMICAL HYDROGEN PRODUCTION SYSTEM INTEGRATED WITH ELECTRIC VEHICLE CHARGING STATION

[1*] *Faran Razi*, [1] *Ibrahim Dincer*

[1] Clean Energy Research Laboratory (CERL), Faculty of Engineering and Applied Science Ontario Tech University 2000 Simcoe Street North, Oshawa, Ontario, L1H 7K4, Canada

*Corresponding author e-mail: faran.razi@ontariotechu.net

ABSTRACT

Due to excessive emissions contributed by transportation sector, electrification of vehicles has become extremely essential. In this regard, battery electric vehicles are a promising solution however, a downside to electrification is its impact on power grid. To reduce pressure on power grid, utilization of renewable energy sources is essential. Thus, this paper presents a novel idea of a solar energy based integrated system where a thermochemical hydrogen production system is combined with an electric vehicle charging station. The hydrogen produced through the thermochemical process is utilized for electricity generation through a proton exchange membrane fuel cell. The thermal energy requirements of the thermochemical cycle are fulfilled by both solar thermal energy and internal heat recovery while the electrical energy requirements of the entire system are met though solar photovoltaic energy.

Keywords: Solar energy, Hydrogen, Fuel cell, Charging station, Cu-Cl cycle.

INTRODUCTION

Transportation sector is one of the major sources of environmental pollution due to excessive greenhouse gas emissions as a result of combustion of hydrocarbon-based fuels. To prevent the environmental degradation through road transport, electrification is considered as an extremely promising option. However, this puts an additional pressure on the power grid to provide the electricity to charge electric vehicles (EVs). Thus, exploitation of renewable energy can potentially address this issue. Solar energy is an extremely important source of both thermal and electrical energies and can thus be exploited by either directly using it via photovoltaic (PV) panels for electricity generation or by utilizing it as a thermal energy source to supply heat to various power generation systems. In addition, hydrogen is one of the cleaner fuels and an excellent energy carrier and can be converted into electricity via fuel cell technology. Copper-chlorine (Cu-Cl) thermochemical water-splitting process is one of the most environmentally benign pathways of producing green hydrogen. Several systems have been proposed in the literature that suggest the integration of solar energy with either Cu-Cl cycle for hydrogen production or directly with EV charging stations. In this regard, a solar PV energy based EV charging station was proposed by Fathabadi [1] and a hybrid solar energy and fuel cell-based EV charging station was investigated by Fathabadi and He [2] where hydrogen was produced through water electrolysis. In addition, a solar and geothermal energy based trigeneration system was developed by Siddiqui et al. [3] where hydrogen production was considered through a Cu-Cl cycle. However, based on the literature review, there are no studies that consider the integration of Cu-Cl cycle with a fuel cell system to supply electricity for EV charging station. Thus, in the present study, a novel renewable energy-based Cu-Cl cycle is coupled with a proton exchange membrane (PEM) fuel cell system. Another novelty of this study is that both the electrical and thermal energy requirements of the system are met via solar energy by incorporating a solar tower and PV panels. Thus, the specific objectives of this study include: (i) to develop a new solar energy-based thermochemical hydrogen production system integrated with a fuel cell system to produce electricity for an EV charging station, (ii) to thermodynamically model and investigate the cycle through energy and exergy approaches to evaluate the overall performance of the system, and (iii) to recover waste heat from the Cu-Cl cycle to supply thermal energy within the cycle to improve the overall system efficiencies.

SYSTEM DESCRIPTION AND ANALYSIS

This study proposes a solar energy driven power generation system as schematically represented in Figure 1. The present system comprises a four-step Cu-Cl water-splitting cycle for hydrogen production, a solar tower to provide the required thermal energy for the cycle, a multi-stage hydrogen compression system, a hydrogen storage system, solar PV panels to supply electrical energy to various system components, a PEM fuel cell for converting hydrogen into electricity, a battery storage system, and an EV charging station. The Cu-Cl cycle is incorporated with internal heat recovery which reduces the thermal energy requirements of the cycle. The PV panels not only fulfils the electricity requirements of the integrated system but also supplies excess electricity to be stored in the battery storage system to be used during nighttime when sufficient hydrogen is not available to be converted into electricity by PEM fuel cells. The total number of fuel cells are taken as 10. The Cu-Cl cycle constitutes four main processes namely hydrolysis, thermolysis, electrolysis, and drying. The details of the chemical reactions and operating temperatures of the various steps in the cycle are given elsewhere [3].

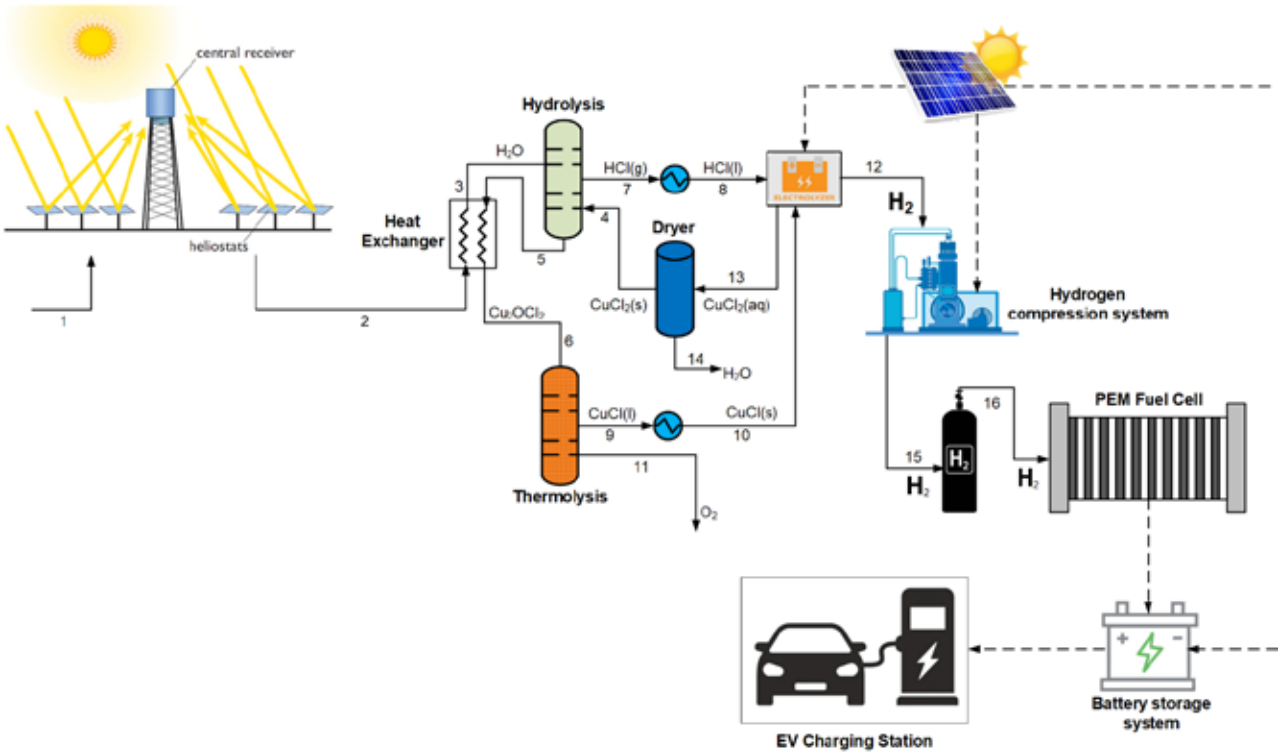


Fig. 1. Schematic illustration of the proposed integrated system for electricity generation

The solar radiation intensity is considered for the chosen location of Cochrane, Ontario for which the annual solar radiation intensity is 336 W/m^2 [4]. The heliostat mirror dimensions are taken as 2.25m × 2.25m, the number of heliostats are taken as 135, and the heliostat efficiency is taken as 80%. The PV panel area is taken as 1250 m^2 and the PV module efficiency is taken as 20%. The overall energy and exergy efficiencies of the system are defined as follows:

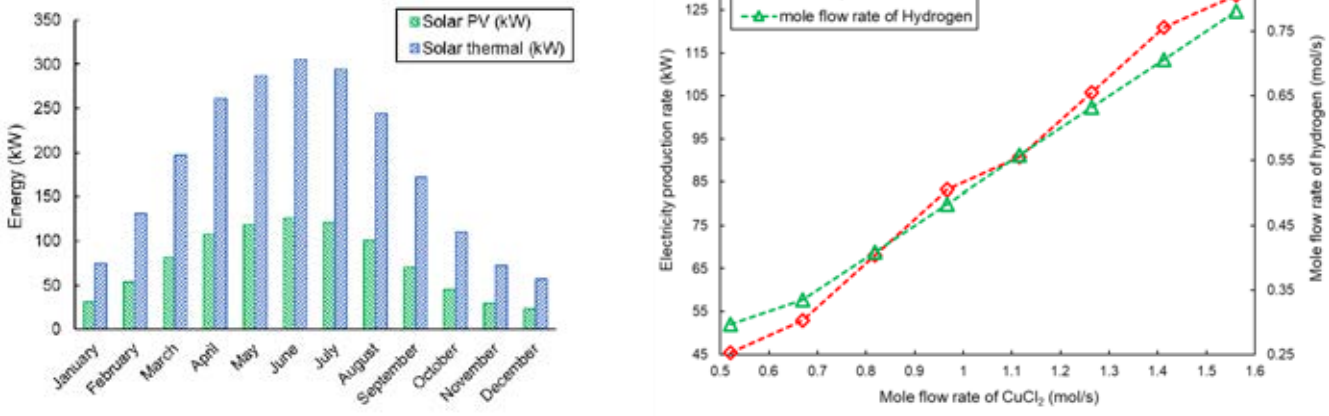
$$\eta = \frac{\dot{W}_{PEM.FC}+\dot{W}_{PV}-\dot{W}_{elec}-\dot{W}_{HCS}}{\dot{Q}_{solar,Thermal}+\dot{Q}_{solar,PV}} \quad (1)$$

and

$$\psi = \frac{\dot{W}_{PEM.FC}+\dot{W}_{PV}-\dot{W}_{elec}-\dot{W}_{HCS}}{\dot{Q}_{solar,Thermal}\left(1-\frac{T_0}{T_{sun}}\right)+\dot{Q}_{solar,PV}\left(1-\frac{T_0}{T_{sun}}\right)} \quad (2)$$

RESULTS AND DISCUSSION

The system is modeled using both Engineering Equation Solver and Aspen-plus software. The total thermal energy produced by the solar tower is estimated to be 184 kW while the total electrical energy produced by PV panels is evaluated to be 75.6 kW. The hydrogen produced by the Cu-Cl cycle is 0.448 mol/s. Each fuel cell is modeled to produce 7.56 kW with 10 fuel cell units eventually producing a total electricity of 75.6 kW. The electricity consumed by the electrolyzer and hydrogen compression system is 22.12 kW and 15.16 kW, respectively. The system results in an overall energy efficiency of 18.8% and an exergy efficiency of 18.99%. Figure 2a shows the solar thermal and electrical energies available to be produced during the 12 months of the year. The highest thermal and electrical energies can be obtained during June and July while the lowest corresponding values can be achieved during November and December due to the highest and the lowest solar radiation intensities in the respective months. Figure 2b shows the effect of the input mole flow rate of cupric chloride on the production mole flow rate of hydrogen and electricity production rate of fuel cells. The flow rate of cupric chloride is found to linearly increase the hydrogen and electricity production rates. At a flow rate of 0.52 mol/s of cupric chloride, the hydrogen flow rate is evaluated as 0.297 mol/s and the electricity production rate is estimated as 45.36 kW while increasing the input cupric chloride flow rate to 1.56 mol/s causes the hydrogen and electricity production rates to increase to 0.781 mol/s and 128.52 kW, respectively.



(a) (b)

Fig. 2. (a) Solar thermal and electrical energy production during various months of the year and (b) effect of cupric chloride mole flow rate on hydrogen and electricity production rates

CONCLUSIONS

In this study, a novel solar energy driven thermochemical hydrogen production system integrated with a PEM fuel cell-based electricity generation system is proposed and its performance is investigated. The system is found to operate at energy and exergy efficiencies of 18.8 and 18.99%, respectively. The Cu-Cl cycle produces hydrogen at a rate of 0.448 mol/s while the total electricity produced by the fuel cells is 75.6 kW The mass flow rate of cupric chloride in the Cu-Cl cycle is found to influence the hydrogen production rate and consequently the total electricity production through fuel cells.

NOMENCLATURE

$\dot{Q}$	Heat rate, kW
T	Temperature, ºC
$\dot{W}$	Work rate, kW
Greek Letters	
η	Energy efficiency
ψ	Exergy efficiency
Subscripts	
elec	Electrolyzer
FC	Fuel cell
HCS	Hydrogen compression system
Acronyms	
Cu-Cl	Copper-chlorine
EV	Electric vehicle
PEM	Proton exchange membrane
PV	Photovoltaics

REFERENCES

1. Fathabadi H. 2017. Novel solar powered electric vehicle charging station with the capability of vehicle-to-grid. Solar Energy 142:136–143.
2. He F. and Fathabadi H. 2020. Novel standalone plug-in hybrid electric vehicle charging station fed by solar energy in presence of a fuel cell system used as supporting power source. Renewable Energy 156:964–974.
3. Siddiqui O., Ishaq H., and Dincer I. 2019. A novel solar and geothermal-based trigeneration system for electricity generation, hydrogen production and cooling. Energy Conversion and Management 198:111812.
4. https://www.nrcan.gc.ca/maps-tools-and-publications/tools/modelling-tools/retscreen/7465%0A. Accessed on March 7, 2022.

WHEC-2022
23rd World Hydrogen Energy Conference
June 26-30, 2022 - Istanbul

#421

CFD SIMULATION AND ANALYSIS OF A NOVEL PHOTOELECTROCHEMICAL HYDROGEN GENERATING REACTOR DESIGN

[1] Ali M. M. I. Qureshy and [1] Ibrahim Dincer*
[1] Clean Energy Research Laboratory, Faculty of Engineering and Applied Science, Ontario Tech University, 2000 Simcoe Street North, Oshawa, Ontario L1G 0C5, Canada.

*Corresponding author e-mail: ali.ismael@ontariotechu.net

ABSTRACT

This study presents a novel photoelectrochemical apparatus configuration for producing hydrogen to maximize the light harvested by the photoelectrode. The new design of the photoelectrode can receive the maximum amount of light energy at any angle of sunlight. Two trapezoidal photoanode and cathode are immersed in potassium hydroxide alkaline solution. The photoanode, cathode, and Nafion membrane are positioned in the potassium hydroxide solution in the new reactor design. The multiphysics simulation of the novel photoelectrochemical reactor configuration for hydrogen production is conducted. The energy and Navier-Stokes equations of the photoelectrochemical apparatus design are solved for the hydrogen bubbles and the solution flow using CFD software. The fluid flow simulation results confirm that this new design can completely clean the adhered bubbles over the surface of the electrodes due to the unique configuration that leads to an exceptional flow distribution.

Keywords: Multiphysics simulation, Hydrogen production, Novel photoelectrode, Photoelectrochemical reactor, Photonic energy

INTRODUCTION

Recently, the use of fossil fuels increased to meet the energy demand leading to an increase in the carbon dioxide concentration (CO_2) that affects global climate change [1]. Therefore, clean energy sources must be used to address climate change issues. Hence, hydrogen is one of the most potential energy sources for the future due to its cleanliness. Various sustainable energy sources could be utilized for green hydrogen production, such as solar energy, wind energy, geothermal energy, biomass energy, and nuclear energy. Photoelectrochemical (PEC) is one of the most promising applications for green hydrogen production [2]. The energy of the light source can generate electricity when it hits the photoelectrode to dissociate the water molecules for producing hydrogen at the cathode side [3]. The excess electrons in the valence bands are excited by the photonic energy to reach the conduction bands leaving holes that need new electrons to be balanced [4]. The generated electron holes will oxidize water molecules to generate oxygen along with hydrogen ions. Hydrogen ions react with the transported electrons on the cathode surface to generate hydrogen.

Researchers have listed the most critical parameters that affect the performance of PEC reactors. Bubble coverage is one of those parameters that can significantly affect PEC reactors' performance [5]. The hydrogen bubbles tend to stick on the cathode surface as an increasing hydrogen generation rate. These adhering bubbles can reduce the active area, increasing the cathode's ohmic losses and decreasing the associated current density. Thus, this study concerns developing the flow distribution to be able to clean the cathode's surface from any adhered bubbles.

METHOD AND ANALYSIS

The photoelectrochemical reactor can split water into oxygen and hydrogen using light energy. The PEC process entails a light source, two electrodes (one of them photoelectrode or two photoelectrodes), membrane, and solution electrolyte. The photoelectrode is responsible for generating electrons using light energy. The light energy can move the excess electrons in the photoelectrode from the valence electrons' bands to the electrons' conduction bands. The light energy must overcome the energy bandgap of the photoelectrode material. Figure 1. shows the proposed PEC device with two novel electrodes and a Nafion membrane. The current photoelectrochemical cell is studied to develop the fluid flow analysis through presenting the temperature plan, streamlines, velocity contours, and hydrogen volume fraction. All governing equations of the electrolyte can be written at transient conditions in 2D of the coordinates r and z [6].

Continuity equation:

$$\frac{\partial \rho}{\partial t} + \frac{1}{r}\frac{\partial (r\rho v_r)}{\partial r} + \frac{\partial (\rho v_z)}{\partial z} = 0 \quad (1)$$

Momentum equations:

$$\rho\left(\frac{\partial v_r}{\partial t} + v_r\frac{\partial v_r}{\partial r} + v_z\frac{\partial v_r}{\partial z}\right) = -\frac{\partial p}{\partial r} + \rho g_r + \mu\left(\frac{1}{r}\frac{\partial}{\partial r}\left(r\frac{\partial v_r}{\partial r}\right) - \frac{v_r}{r^2} + \frac{\partial^2 v_r}{\partial z^2}\right) + F_s \quad (2)$$

$$\rho\left(\frac{\partial v_z}{\partial t}+v_r\frac{\partial v_z}{\partial r}+v_z\frac{\partial v_z}{\partial z}\right)=-\frac{\partial p}{\partial z}+\rho g_z+\mu\left(\frac{1}{r}\frac{\partial}{\partial r}\left(r\frac{\partial v_z}{\partial r}\right)+\frac{\partial^2 v_z}{\partial z^2}\right)+F_s \quad (3)$$

$$F_s=\nabla[\sigma(I+(-n\,n^T))\delta] \quad (4)$$

$$\delta=6|\varphi(1-\varphi)||\nabla\varphi| \quad (5)$$

$$\rho=\rho_1+(\rho_2-\rho_1)\varphi \quad (6)$$

$$\mu=\mu_1+(\mu_2-\mu_1)\varphi \quad (7)$$

Energy equation:

$$\rho C_P\left(\frac{\partial T}{\partial t}+v_r\frac{\partial T}{\partial r}+v_z\frac{\partial T}{\partial z}\right)=\frac{k}{r}\frac{\partial}{\partial r}\left(r\frac{\partial T}{\partial r}\right)+k\frac{\partial}{\partial z}\left(\frac{\partial T}{\partial z}\right)+2\mu\left(\frac{\partial v_r}{\partial r}\right)^2+2\mu\left(\frac{v_r}{r}\right)^2+2\mu\left(\frac{\partial v_z}{\partial z}\right)^2+\mu\left(\frac{\partial v_z}{\partial r}+\frac{\partial v_r}{\partial z}\right)^2+\nabla q^r \quad (8)$$

$$\nabla q^r=\int_0^\infty \alpha_\lambda\left(4\pi I_{b\lambda}-\int_{4\pi} I_\lambda\, d\Omega\right)d\lambda \quad (9)$$

Interface equation (level set):

$$\frac{\partial\varphi}{\partial t}+v_r\frac{\partial\varphi}{\partial r}+v_z\frac{\partial\varphi}{\partial z}=\gamma\left(\frac{\partial\varphi}{\partial r}+\frac{\partial\varphi}{\partial z}\right)\left(\varepsilon_{ls}\left(\frac{\partial\varphi}{\partial r}+\frac{\partial\varphi}{\partial z}\right)-\varphi(1-\varphi)n\right) \quad (10)$$

where $n=\frac{\nabla\varphi}{|\nabla\varphi|}$ (11)

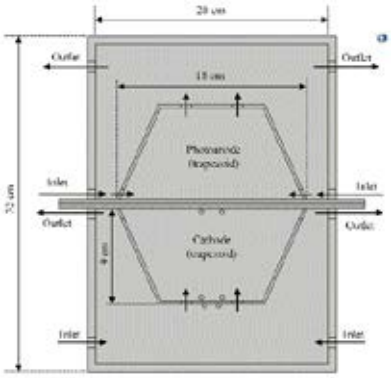


Fig. 1. The proposed PEC reactor with two novel electrodes.

RESULTS AND DISCUSSION

The fluid flow modeling of the novel PEC device is conducted to eliminate the issue of the sticky bubbles on the cathode surface. COMSOL packages are employed to simulate the hydrogen evolution process in the PEC devices. The PEC device is considered as a 2D configuration due to the symmetry of the design and to reduce the cost of the computational process. The current case study is simulated at a transient condition to evaluate the hydrogen evolution process with time. The mesh independence test is conducted to determine the best mesh size. By solving the above governing equations of the PEC device, the velocity surface, streamlines, and hydrogen volume fraction are calculated. The simulation results of the electrolyte flow confirm that the velocity distribution can remove any adhered bubbles from the cathode surface. As shown in Fig. 2 through the velocity surface and streamlines, the electrolyte flow has high values adjacent to the cathode surfaces to prevent hydrogen bubbles from not sticking on the metal surface. Moreover, the hydrogen gas volume fraction is presented at three different times in Fig. 3. It is clearly obvious that hydrogen bubbles are completely moving to the outlet of the cathode chamber due to the flow distribution of the new PEC design.

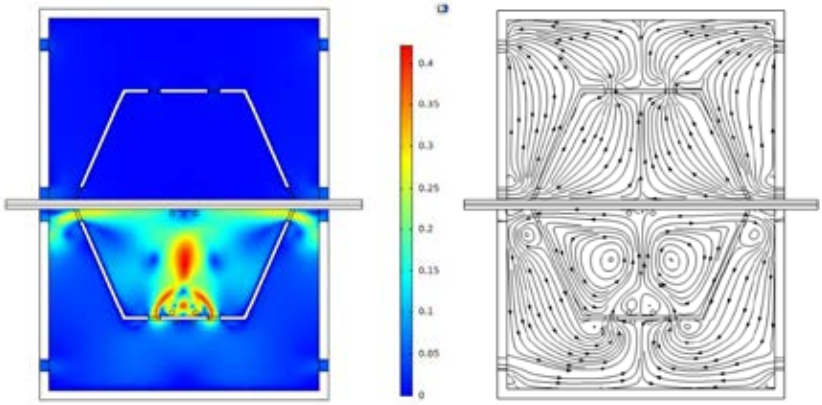


Fig. 2. Velocity surface and streamlines of the electrolyte of the novel PEC device.

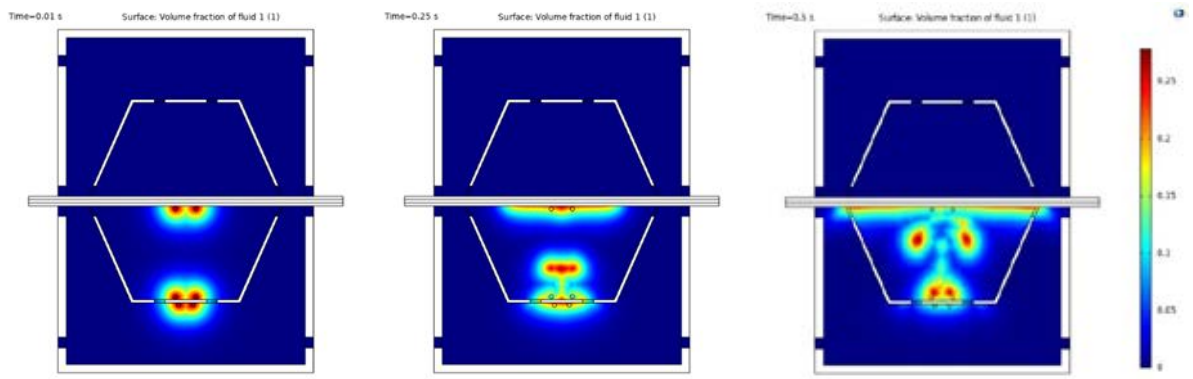


Fig. 3. The volume fraction of hydrogen for the novel PEC device at different times.

CONCLUSIONS

A CFD study of a novel PEC reactor device for sustainable hydrogen production is conducted. The energy and Navier-Stokes equations of the new PEC device are solved by the COMSOL tool. The physical flow characteristics of the flow are evaluated to define the velocity surface, streamlines, and hydrogen gas volume fraction. The results of the current PEC design indicated that the flow could generate enough circulations to prevent hydrogen bubbles from not sticking on the cathode surface. This PEC design can keep the cathode resistance at the lowest level due to cleaning its surface from any adhering bubbles. Moreover, the present PEC design is easier than earlier designs to fabricate, manufacture, build, assemble, and disassemble.

NOMENCLATURE

e^-	Electron	r	Radius, m
g_r	Gravitational acceleration component in r-direction,m/s^2	t	Time, s
g_z	Gravitational acceleration component in z-direction, m/s^2	T	Temperature, K
H^+	Hydrogen proton	v_r	Velocity component in r-direction, m/s
p^+	Electron hole	v_z	Velocity component in z-direction, m/s
q^r	Radiative solarbeam, W/m^2		

Greek Letters

α_λ	Spectral absorption coefficient	ρ	Fluid density, kg/m^3
δ	Membrane material thickness, m	σ	Conductivity losses, S/m
β	Thermal expansion coefficient, 1/K	ν	Frequency, s^{-1}
$d\Omega$	Solid angle	φ	The level set function
μ	Viscosity dynamic-based, kg/ms		

Superscripts

r	radiative factor

Superscripts

PEC	photoelectrochemical

REFERENCES

1. IEA. Global Energy Review 2020. OECD; 2020. https://doi.org/10.1787/a60abbf2-en.
2. Sivula K, van de Krol R. Semiconducting materials for photoelectrochemical energy conversion. Nat Rev Mater 2016;15010:16010. https://doi.org/10.1038/natrevmats.2016.10.
3. Dai Y, Yu J, Cheng C, Tan P, Ni M. Engineering the interfaces in water-splitting photoelectrodes-an overview of the technique development. J Mater Chem A 2020;8:6984–7002. https://doi.org/10.1039/d0ta01670e.
4. Guo L, Chen Y, Su J, Liu M, Liu Y. Obstacles of solar-powered photocatalytic water splitting for hydrogen production: A perspective from energy flow and mass flow. Energy 2019;172:1079–86. https://doi.org/10.1016/j.energy.2019.02.050.
5. Vogt H, Balzer RJ. The bubble coverage of gas-evolving electrodes in stagnant electrolytes. Electrochim Acta 2005;50:2073–9. https://doi.org/10.1016/j.electacta.2004.09.025.
6. Qureshy AMMI, Dincer I. Multi-component modeling and simulation of a new photoelectrochemical reactor design for clean hydrogen production. Energy 2021;224:120196. https://doi.org/10.1016/j.energy.2021.120196.

WHEC-2022
23rd World Hydrogen Energy Conference
June 26-30, 2022 - Istanbul

#424

PHOTONIC REACTORS FOR HYDROGEN PRODUCTION AND WASTEWATER TREATMENT IN UNDERGROUND AND UNDERWATER APPLICATIONS

[1,2*] *Dogan Erdemir,* [1,3] *Ibrahim Dincer*
[1]Ontario Tech University, Clean Energy Research Laboratory, Oshawa, ON, Canada
[2] Erciyes University, Department of Mechanical Engineering, Kayseri, Turkey
[3] Yildiz Technical University, Department of Mechanical Engineering, Istanbul, Turkey

*Corresponding author e-mail: erdemir@erciyes.edu.tr and dogan.erdemir@ontariotechu.ca

ABSTRACT

This study investigates the potential use of photocatalysis and photoelectrochemical reactors in underground and underwater applications for hydrogen production and wastewater treatment. The solar photons are transmitted by fibre optic cables. At the end of the present study, it is observed that the efficiency of the system is limited to the low efficiency of photocatalysis and photoelectrochemical reactors. Today's fibre optic technology provides a satisfactory performance for solar transmission. The biggest obstacle for the proposed system is the cost of fibre optic cables. It may be more suitable for the defence industry and space technology applications.

Keywords: Hydrogen; wastewater treatment; sustainability; underground energy systems; underwater energy systems.

INTRODUCTION

One has to note that hydrogen, as an energy carrier, energy storage medium, fuel, and feedstock, is undertaken now a ground-breaking technology for sustainable future. Today, hydrogen systems have already taken placed in many sectors, and it is expected that hydrogen-powered systems will be more commonly deployed in the near future with the extension of the hydrogen economy all around the world.

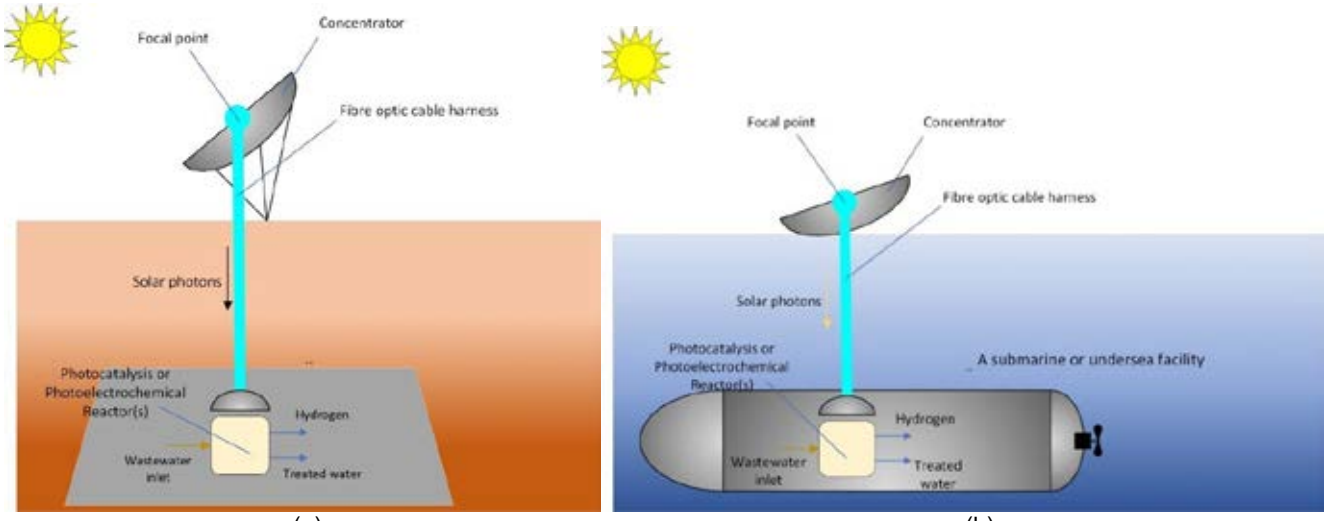
Underwater and underground facilities, vehicles and hence systems are considered critical for from research activities to defense industry, from energy applications to environmental research. Hydrogen is one of the most effective fuel and power source for underwater and underground applications as using hydrogen is a process that is air-independent propulsion. Sezgin et al. [1] have reviewed the use of hydrogen in the underwater application. They have emphasized that proton exchange membrane (PEM) fuel cells can be used as the power source. Also, as hydrogen storage options compressed, and metal hydride based H_2 storage techniques are suitable for small to medium submarines. On the other hand, there are various attempts for combining hydrogen production and wastewater treatments. Photocatalysis and photoelectrochemical reactors are used for this purpose. While photocatalysis is a light-driven process where chemical reactions occur under the presence of a catalyst, photoelectrochemical cells produce hydrogen along with photocurrent upon absorption of light. Aydin et al. [2] have reviewed the hydrogen production methods with wastewater treatment. Finally, the use of the fibre optic cables in the solar-driven system is not actually a novel aspect. Kribus et al. [3] have studied the potential use of optical fibers for solar thermal power generation. They have concluded that the use of fibre optic cables in concentrated solar power (CSP) systems is feasible at under specific conditions. They have additionally emphasized that the cost of optical fibre is the key cost driver for the proposed system.

Hydrogen-driven systems are now expected to be an essential option for underwater and underground systems due to their unique advantages: silent operation, environmentally friendly process, high efficiency, and low thermal dissipation. Photocatalysis and photoelectrochemical methods have a significant potential for hydrogen production along with wastewater treatment. The solar input for photocatalysis and photoelectrochemical reactors can be provided by fibre optic cables for the locations where do not have direct solar access such as underground and underwater. This study offers a unique system for hydrogen production and wastewater treatment with photocatalysis and photoelectrochemical for underground and underwater applications with carried solar photos via fiber optic cables.

MATERIALS AND METHODS

Fig. 1 depicts the schematics for the proposed systems. In order to receive solar input intensity, a dish concentrator is included in the system. Solar trackers can be included in the proposed system. The solar input is collected by a fibre receiver and carried to the location where photocatalysis and photoelectrochemical reactors are located. A fibre optic distributor is used for distributing solar photons to the reactors. Wastewater is sent to the reactor for hydrogen production and water treatment. The produced hydrogen is used for power generation in the PEM fuel cells. Stationary dishes with two-axis solar trackers can be used in the underground system. In the underwater systems, while floating dishes can

be used, foldable structures such as the submarine periscopes can also be used. Similar to the underground system, solar photons collected by fibre optic receivers are carried to the location where reactors are located via optical fibre cables. Thus, hydrogen is produced along with the wastewater treatment.



(a) (b)

Fig. 1. The system layouts for the proposed system a) underground application and b) underwater application

RESULTS AND DISCUSSION

The main challenge in the use of the proposed system is the cost of the fibre optic cables, especially for higher capacities, since they require a larger diameter cable harness. However, when the investment costs of the underwater and underground technologies are considered, it can be an acceptable level, especially for the defence industry applications such as submarines. The efficiency of the proposed system is limited to the low efficiency of photocatalysis and photoelectrochemical reactors. Today's photocatalysis and photoelectrochemical technologies offer up to 5-6% hydrogen production efficiency. Also, generating hydrogen from wastewaters is not a common method yet. However, the use of photocatalysis and photoelectrochemical methods for hydrogen production and wastewater treatment is a promising technique due to their potential lower carbon footprint impacts. Today's fibre optic technologies serve a tremendous performance to carry the sunlight. So, there are no significant losses in solar photon transmission in the fibre optic cables. Consequently, although today's photocatalysis and photoelectrochemical technologies do not offer high performance, they will probably offer better performance for hydrogen production and wastewater treatment in the near future. When the increasing need for silent operation, environmentally friendly process, high efficiency, and low thermal dissipation for underwater and underground applications is taken into consideration. The proposed system can play a significant role in those applications for hydrogen production and wastewater treatment.

CONCLUSIONS

This paper has dealt with the potential use of photocatalysis and photoelectrochemical hydrogen generating reactors in underground and underwater applications with a wastewater treatment option where the solar photons are transmitted by fibre optic cables with a satisfactory performance for solar transmission. Due to an increased efficiency and enhanced use of hydrogen, such systems offer a great potential for applications in defence and space industries.

REFERENCES

1. Sezgin B, Devrim Y, Ozturk T and Eroglu I. 2022. Hydrogen energy systems for underwater applications, International Journal of Hydrogen Energy, https://doi.org/10.1016/j.ijhydene.2022.01.192
2. Aydin MI, Karaca AE, Qureshy AMMI, Dincer I. 2021. A comparative review on clean hydrogen production from wastewaters, Journal of Environmental Management, Vol. 279. 111793. https://doi.org/10.1016/j.jenvman.2020.111793
3. Kribus A, Zik O and Karni J. 2000. Optical fibers and solar power generation. Solar Energy, Vol. 68, 5, pp. 405-416.

WHEC-2022
23rd World Hydrogen Energy Conference
June 26-30, 2022 - Istanbul

#430
SYNTHESIS OF SnS_2 PHOTOCATALYST FOR PHOTOCATALYTIC HYDROGEN PRODUCTION

*Alaaddin Cem Ok, *Cevat Sarıoğlu*
Marmara University, Faculty of Engineering, Metallurgical and Materials Engineering Department, TR34722, Istanbul, Turkey

*Corresponding author: cevat.sarioglu@marmara.edu.tr

ABSTRACT

Hydrogen could be generated from both renewable and non-renewable sources of energy. Using nonrenewable energy sources to produce hydrogen will result in greenhouse CO_2 gas emissions and cause global warming. Photocatalytic systems for generating hydrogen from solar energy have a great deal of potential to solve the global warming problem because of the totally renewable green source of sun and water. Because of its superior properties, such as a proper and narrow bandgap, better chemical stability, non-toxic, photo-corrosion resistance, and suitable optimum conduction and valance band potentials, the tin disulfide (SnS_2) photocatalyst has great potential to be used for producing H_2 from the splitting of water via solar energy. In this study, SnO_2 powders were successfully thermally sulfurized to SnS_2 powders at 500°C for 24 hours under an Argon (Ar) atmosphere. The XRD analysis verified the hexagonal SnS_2 crystals. UV-vis spectroscopy was used to determine the band gap value of the generated powder, which is 2.24 eV.

Keywords: Tin disulfide, Photocatalyst, Solar energy, Water splitting, Hydrogen production

INTRODUCTION

Hydrogen can be solution for climate crisis as stated by the latest decision taken by the European Parliament and of the Council on 30 June 2021. Hydrogen is one of the leading sources of renewable energy as an alternative to fossil fuels. Hydrogen may be produced from both renewable and nonrenewable sources of energy. However, using non-renewable energy sources in hydrogen production will cause greenhouse gas emissions and cause global warming. The production of H_2 by splitting water with solar energy as a renewable energy source through photocatalytic and photo-electrochemical methods has great potential to be alternative energy source to satisfy the need for energy of the world [1-3]. Photocatalysts are semiconductor materials that are activated by light energy and initiate a series of electrochemical reactions. Many photocatalytic semiconductor materials have been studied, such as metal oxides, metal nitrides, oxy-nitrides, metal sulfides, and organic materials. Metal oxides (e.g., TiO_2) have suitable band structures that provide the thermodynamic requirements for splitting water, and they are resistant to photo-corrosion. However, they are active under ultraviolet light, which constitutes 4% of the solar spectrum due to its wide band gap value, and because of this they have very low efficiency, which limits their uses [4,5]. On the other hand, metal sulfide (CdS, ZnS, CdZnS, SnS_2) photocatalysts have suitable band gaps (2.3-3.2) and valence and conduction band levels to harvest the visible light region of the solar spectrum. In this way, they have the advantage of possessing greater efficiency of H_2 by splitting water as compared to metal oxides (TiO_2). Due to their low oxidation ability, sacrificial electron donors (SO_3^{-2}) as an oxidation reaction for photocatalytic H_2 production were used [4,5]. Amongst metal sulfides SnS_2 has an optimum band gap value of 2.3 eV. Because of this, it has a high potential to have a high H_2 production efficiency. [6,7,8] In the literature, there is a limited number of research on the SnS_2 photocatalyst. The research has done in this paper to fill this gap.

Within the scope of this study, it is aimed to synthesize SnS_2 photocatalyst to produce H_2 with high efficiency by splitting water via solar energy. SnS_2 will be synthesized by the thermal sulfurization method since it is simple and affordable to synthesize SnS_2.

EXPERIMENTAL

Synthesis of tin disulfide (SnS_2)

Tin disulfide (SnS_2) powder has been synthesized from tin oxide (SnO_2) nano-powders (≤100nm average particle size obtained from sigma Aldrich) by sulfurization using 99.9% pure sulphur powder in a Protherm hot-wall tube furnace at 500°C.

As indicated in Fig. 1, 100 mg of SnO_2 powder was put in an alumina crucible and placed in the center of the heating zone at 500 °C, while the crucible containing elemental sulphur was placed outside of the heating zone at a temperature between 180-200 °C. The system was flashed with argon gas for 40 minutes before the furnace was heated. The furnace reached 500 °C by heating at a rate of 10 °C/min and was kept constant at this temperature for 24 hours under

the flow of Ar gas. The rate of Ar gas flow was set to 0.15 liters per hour. At the end of 24 hours, the furnace was switched off and the powder was left to cool in the furnace to room temperature.

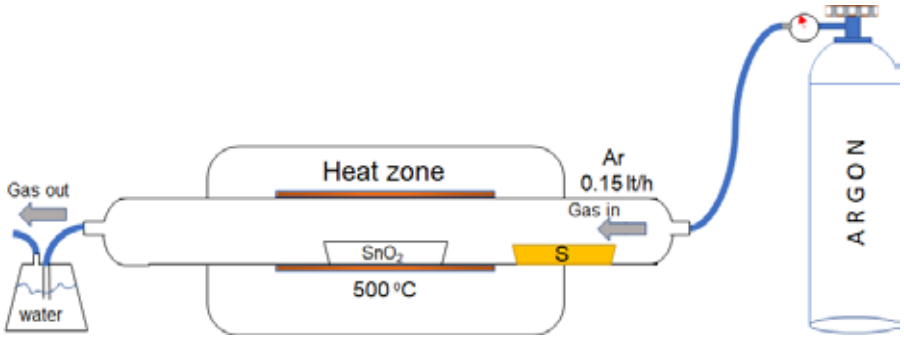


Fig. 1. Schematic representation of a tube furnace for the thermal sulfurizing of SnO_2 powder at 500°C for 24 hours.

Characterisation of Powders

X-ray diffraction measurement technique was used to identify the present phases and crystal structures of produced powder samples using a Bruker D2 Phaser. Scan was performed between $10° \leq 2\theta \leq 90°$ using Cu-Kα radiation of wavelength 1.5406A°.

UV-vis spectrophotometry tests were performed to measure the band gap values of synthesized powders in the wavelength range of 300-900 nm.

RESULTS AND DISCUSSION

An image of pristine SnO_2 and thermally sulfurized powder at 500 °C for 24 hours in an Ar atmosphere can be seen in Fig 2. Due to the yellow color of SnS_2, sulfurization of SnO_2 powder, which is white (Fig 2a), to SnS_2 resulted in a powder with yellow tones (Fig 2b), as expected [9].

An XRD analysis was carried out before and after thermal sulfurization to confirm the formation of the SnS_2 phase. Normalized XRD pattern of SnO_2 and SnS_2 powders given in Fig 3. The diffraction peaks clearly prove the existence of a SnS_2 phase having a hexagonal crystal structure with lattice parameters a= 3,645 b=3,645 c= 11,802 A° (PDF 01-089-2357). The major peaks of SnS_2 were detected at 15.13°, 32.13°, 41.87° 50.05° and 52.5°. These peaks correspond to the (002), (102), (104), (110), and (112) planes of hexagonal structure, respectively. This repeatable (2 times) results indicated that 24 hours thermal sulfurization needed to obtain fully sulfurized SnO_2 powder under Ar flow at 500 °C .



Fig. 2. Photograph SnO_2 powder a) Before sulfurization b) After sulfurization at 500°C for 24 hour

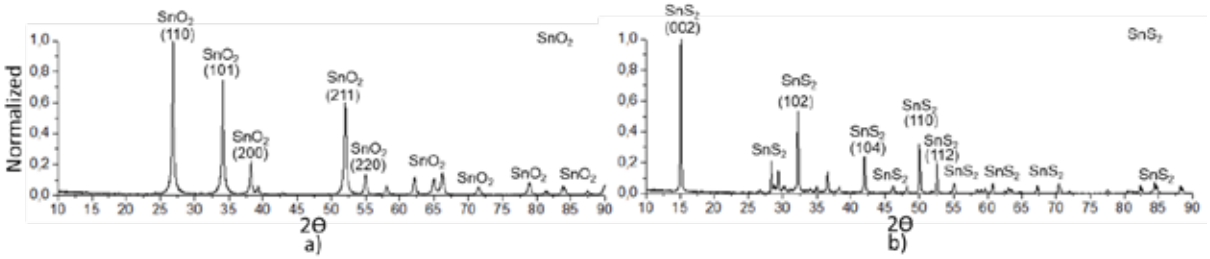


Fig. 3. XRD patterns SnO_2 powder a) Before sulfurization b) After sulfurization at 500°C for 24 hours.

The band gap value (Eg) of the produced SnS_2 powder was determined by measuring the powder spectrum absorption using UV-Vis absorption spectroscopy. In Fig. 4, the UV-Vis reflectance spectra and Tauc plot can be seen. The Eg value of SnS_2 powders was calculated by applying the Kubelka-Munz theory and drawing a Tauc plot to the data obtained from the UV-vis spectrometer measurement [10]. According to the Tauc plot, SnS_2 powder has an indirect band gap of around 2.24 eV, which is within the expected range of earlier reported values in the literature [6–9].

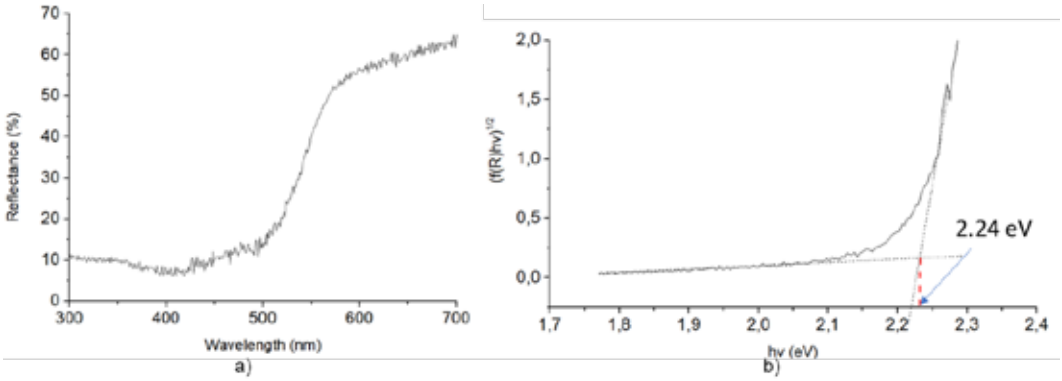


Fig. 4. a) UV-Vis diffuse reflectance spectra of SnS_2 b) Tauc plot for determine the band gap of SnS_2

CONCLUSION

SnS_2 powders were successfully synthesized from SnO_2 powders in a tube furnace at 500 ^oC for 24 hours under the Ar atmosphere, and fully sulfurized SnS_2 phases were confirmed via XRD analysis. The band gap value of the produced powders was determined as 2.24 eV of indirect band gap. With 2.24 eV band gap, SnS_2 is considered to be an ideal choice for photocatalytic water splitting amongst the metal sulfides. The characterization of the photoelectrochemical behaviour of SnS_2 and the measurement of H_2 gas production efficiency by splitting water with the presence of a sacrificial agent such as SO_3^{-2} will be carried out in the future.

ACKNOWLEDGEMENT

This study was supported by Marmara University through the unit of scientific research project (BAPKO) (Project No: FEN-C-YLP-130319-0072).

REFERENCES

1. Ismail AA and Bahnemann DW. 2014. Photochemical splitting of water for hydrogen production by photocatalysis: a review. Solar Energy Materials and Solar Cells, 128, 85-101.
2. Van de Krol R and Grätzel M. 2012. Photoelectrochemical hydrogen production (Vol. 90). New York: Springer.
3. . Dincer I and Joshi AS. 2013. Solar based hydrogen production systems. Oshawa: Springer.
4. Di T, Xu Q, Ho W, Tang H, Xiang Q, and Yu J. 2019. Review on metal sulphide-based Z-scheme photocatalysts. ChemCatChem, 11(5), 1394-1411.
5. Zhang K and Guo L. 2013. Metal sulphide semiconductors for photocatalytic hydrogen production. Catalysis Science & Technology, 3(7), 1672-1690.
6. Gedi S, Minnam RVR., Kotte TRR, Park C and Kim, WK. 2021. Fundamental Aspects and Comprehensive Review on Physical Properties of Chemically Grown Tin-Based Binary Sulfides. Nanomaterials, 11(8), 1955.
7. Su R, Besenbacher F, and Hutchings G. 2016. Alternative Materials to TiO_2. In Heterogeneous Photocatalysis. Edited by Colmenares JC, Xu YJ. Springer, Berlin, Heidelberg.
8. Sharma K, Patial S, Singh P, Khan AAP, Saini V, Nadda AK., Hussain MC, Nguyen VH, Nguyen CC, Nguyen TBH, Kim YS, Le QV and Raizada P. 2022. Strategies and perspectives of tailored SnS_2 photocatalyst for solar driven energy applications. Solar Energy, 231, 546-565.
9. Park JC, Lee KR, Heo, H, Kwon SH, Kwon JD, Lee MJ, Jeon W, Jeong SJ and Ahn JH. 2016. Vapor transport synthesis of two-dimensional SnS2 nanocrystals using a SnS_2 precursor obtained from the sulfurization of SnO_2. Crystal Growth & Design, 16(7), 3884-3889.
10. Landi JS, Segundo IR, Freitas E, Vasilevskiy M, Carneiro J, and Tavares, CJ. 2022. Use and misuse of the Kubelka-Munk function to obtain the band gap energy from diffuse reflectance measurements. Solid State Communications, 341, 114573.

WHEC-2022
23rd World Hydrogen Energy Conference
June 26-30, 2022 - Istanbul

#433

PROGRESS OF 5m^3/h H_2 PRODUCTION TESTING FACILITY THROUGH IODINE-SULFUR THERMOCHEMICAL WATER-SPLITTING METHOD

[1] Bo Ling, [1] Yong He, [1] Jinxu Zhang, [1] Yanqun Zhu, [1] Zhihua Wang*
[1]Zhejiang University, State key laboratory of Clean Energy Utilization, 310027, Hangzhou, P.R. China

*Corresponding author e-mail: wangzh@zju.edu.cn

ABSTRACT

The Iodine–Sulfur (IS) thermochemical water-splitting cycle is regarded as one of the most promising hydrogen production methods with the advantages of high efficiency, low cost and zero carbon emissions. Several research institutions have done extensive studies in this field. The CEU initiated the IS research in 2004 and constructed a pilot-scale facility made of industrial structural materials with the design rate of 5 m^3/h in 2019. In this paper, the pilot-scale facility is briefly introduced, and the results of preliminary continuous test is shown.

Keywords: Thermochemical hydrogen production, Iodine sulfur cycle, Pilot-scale facility

INTRODUCTION

Hydrogen, as a clean and environmentally-friendly energy carrier, has attracted worldwide attention. Comparing all types of hydrogen production methods, the Iodine–Sulfur (IS) thermochemical water-splitting cycle is the most promising one. Since 1980s, several research institutions, such as the General Atomics Corp (GA), Italian National Agency for New Technologies (ENEA), Japan Atomic Energy Agency (JAEA) and Institute of Nuclear and New Energy Technology of Tsinghua University (INET) et al., had attempted to construct and operate the IS system [1-4]. The State Key Laboratory of Clean Energy Utilization (CEU) of Zhejiang University in China initiated the IS research in 2004. Then a bench-scale facility using glass with hydrogen production rate of 50 L/h was built in 2015. After that, a pilot-scale facility made of industrial structural materials with the design rate of 5 m^3/h (IS-5m^3 system) was built in 2019. A preliminary continuous experiment was carried out in September of 2021.

SYSTEM DESCRIPTION

The IS-5m^3 system includes three sections: Bunsen reaction section, HI decomposition section and H_2SO_4 decomposition section. After a series of anti-corrosion experiments, TC4 was chosen for Bunsen reaction section and HI decomposition section, while Hastelloy C276 and SiC were chosen for H_2SO_4 decomposition section. The photographic images of the whole system, the HI decomposer and H_2SO_4 decomposer are shown in Fig. 1.





Fig. 1. The photographic images of the whole system, the HI decomposer and H_2SO_4 decomposer

RESULTS AND DISCUSSION

In September of 2021, the continuous test of the closed IS cycle was carried out. The initial molar ratio of H_2SO_4:HI:I_2:H_2O was set to be 1:2:2:12. The test lasted for about 4 hours with the hydrogen production rate of 80 L/h and the oxygen yield of 40 L/h, as shown in Fig. 2.

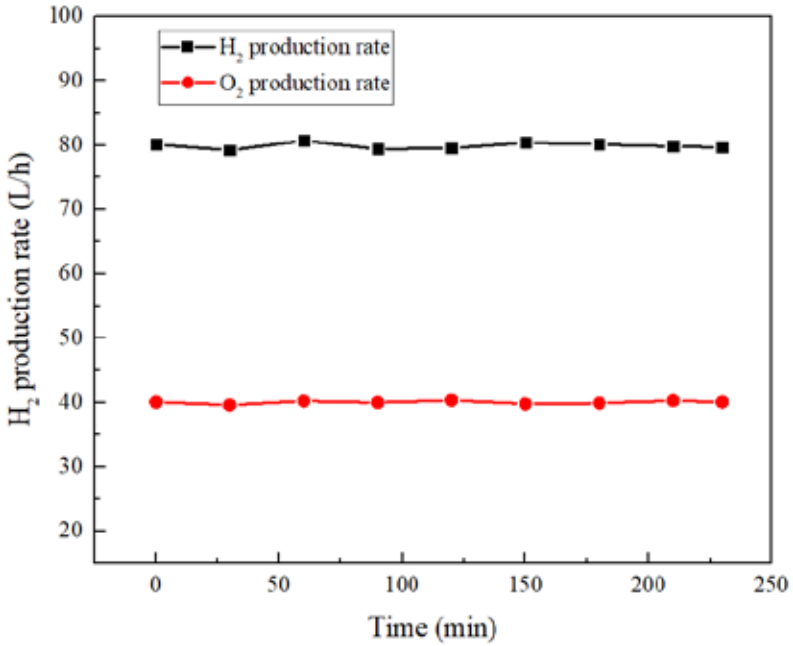


Fig. 2. The hydrogen and oxygen production rate of continuous test

CONCLUSIONS

The continuous test verifies the feasibility of the IS process and the stability of major industrial structural materials. A further modification on this system is now underway. Higher hydrogen gas yield and longer operation time are expected to happen soon.

REFERENCES

1. Norman JH, Besenbruch GE, Brown LC, O'Keefe DR, Allen CL. February 1977-December 31, 1981. Thermochemical water-splitting cycle, bench-scale investigations, and process engineering. Final report.
2. Liberatore Raffaele, Caputo Giampaolo, Felici Claudio, Spadona Annarita. 2010. Demonstration of hydrogen production by the sulphur- iodine cycle: realization of a 10 NL/h plant, 18th world hydrogen energy conference. Garmany: Essen.
3. Hiroki N, Yu K, Nobuyuki T, Hiroaki T, Jin I, Seiji K, et al. 2021. Hydrogen production using thermochemical water-splitting Iodine-Sulfur process test facility made of industrial structural materials: Engineering solutions to prevent iodine precipitation. International Journal of Hydrogen Energy 46:22328-22343.
4. Zhang Ping, Wang Laijun, Chen Songzhe, Xu Jingming. 2018. Progress of nuclear hydrogen production through the iodine-sulfur process in China. Renewable and Sustainable Energy Reviews 81(Part 2):1802-1812.

#1512

PHOTOCATALYSIS VS PHOTOVOLTAICS: WHY NOT MAKE IT A SYMBIOSIS?

[1*] *Paul Hazemann,* [1] *Cedric Brochier,* [1] *Laure Peruchon,* [2] *Eric Puzenat*
[1] Brochier Technologies, Villeurbanne, France
[2] IRCELYON, Université UCBL Lyon1, CNRS, UMR 5256, Villeurbanne, France

*Corresponding author e-mail: paul.hazemann@brochiertechnologies.com

ABSTRACT

Photocatalytic reforming of biomass-sourced molecules is a promising method for green hydrogen production from solar energy. Current photocatalysts cannot use the entire solar spectrum efficiently, and an alternative approach is to couple photovoltaics with LED technology to convert the highest solar spectrum fraction into a monochromatic light. Such a process has yet to be energetically optimized to be competitive with conventional heliophotocatalytic processes, and numerous parameters can be tuned such as LED current intensity, carbohydrate concentration, temperature, or catalyst amount. In this study, it has been shown that these parameters significantly affect the hydrogen production rate, and their optimization is necessary to maximize energy-to-hydrogen efficiency and so the hydrogen production cost. It was however observed, using the H2A tool, that the optimum of energy efficiency is not necessary the optimum of hydrogen production cost and a careful cost analysis should be carried out to design the best industrial operating point.

Keywords: Photocatalysis, Reforming, TiO_2, Woven optical fiber

INTRODUCTION

The development of new technologies to make renewable intermittent energy available and affordable is necessary to face global warming. Photocatalysis is a promising method to convert solar energy into solar fuels such as hydrogen [1] (Figure 1.a). The main challenge is to find a photocatalyst able to use efficiently the entire solar spectrum, which is still at the research stage. But even in that case, this technology would be in direct competition with photovoltaics. An alternative approach is to take assets of both these methods, by coupling them using an efficient and fast-growing technology, LEDs (Figure 1.b). This innovative concept has however to be cleverly engineered to maximize the hydrogen yields and costs and make it competitive with conventional heliophotocatalytic or electrocatalytic processes.

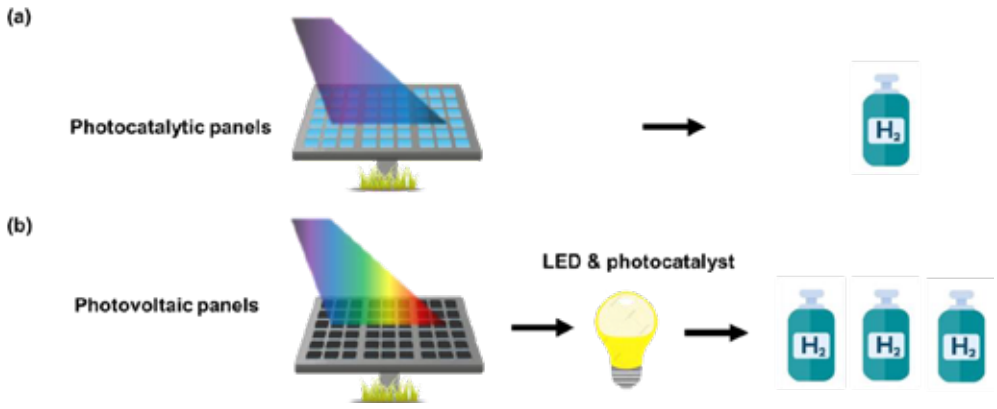


Fig. 1. Conventional heliophotocatalysis (a) against photovoltaic-coupled photocatalytis (b) for solar fuels production

H2TEX project aims at developing an optimized photoreactor for carbohydrate reforming, using LED-powered UVTEX® photocatalytic textiles from BrochierTechnologies [2], [3]. This technology has the advantage to maximize the contact between light, catalyst, and reagents, but also to minimize the photoreactor land occupation since textiles can be superimposed in the reactor to operate in three dimensions.

While some studies have characterized the effect of different operating parameters on H_2 production rate via carbohydrate photoreforming [4]–[8], no quantitative link between them and the overall efficiency & cost of the process have been established. This step is yet mandatory to evaluate the potential of this technology compared to other hydrogen production methods, but also to determine on which part of the process research should focus on [9]–[11].This study quantifies experimentally the effect of several operating factor that can be tuned to maximize the

H2TEX process efficiency, and evaluate their impact on the final hydrogen price considering feedstock expenditures, OPEX and CAPEX evolutions.

MATERIALS AND METHODS

Photocatalytic data have been recorded using a semi-batch photoreactor containing 200 mL of a glycerol/water solution, with various volume ratio from 1 to 50%vol. The reactor temperature was varied between 10 and 45°C using thermostated water recirculating in a double wall. UVTEX® textiles (Figure 2) were coated with a commercial P-25 TiO_2 catalyst using dip coating and spraying methods, on which a platinum based cocatalyst is photodeposited. A LEDENGINE UVA LED operating between 100 and 900mA was used as a light source. Technico-economic analysis has been carried out using the H2A tool v3.2018, considering a daily H_2 production of 50 000kg and feedstocks & energy prices from 2016.

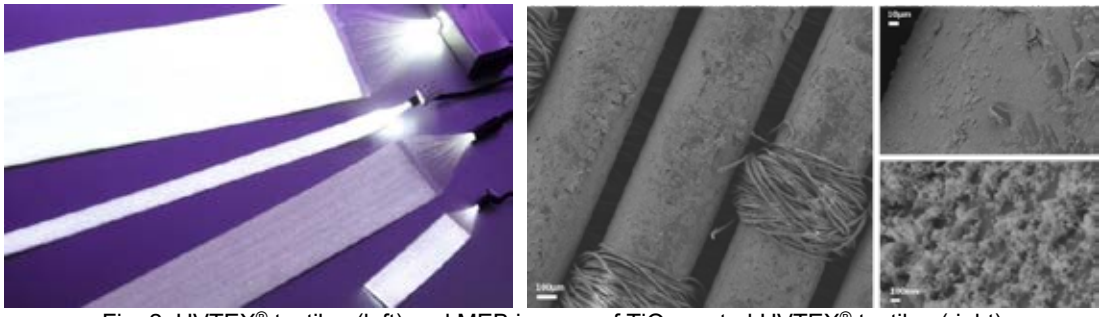


Fig. 2. UVTEX® textiles (left) and MEB images of TiO_2 coated UVTEX® textiles (right)

RESULTS AND DISCUSSION

As reported for different carbohydrates [4], [8], glycerol concentration has a positive effect on H_2 production rate which follows a Langmuir-Hinshelwood profile. Since energy consumption (*i.e.,* renewable electricity) accounts for more than half of the hydrogen cost with the reference case (Figure 3a), the increase of glycerol concentration decreases significantly the H_2 production cost by improving the process efficiency.

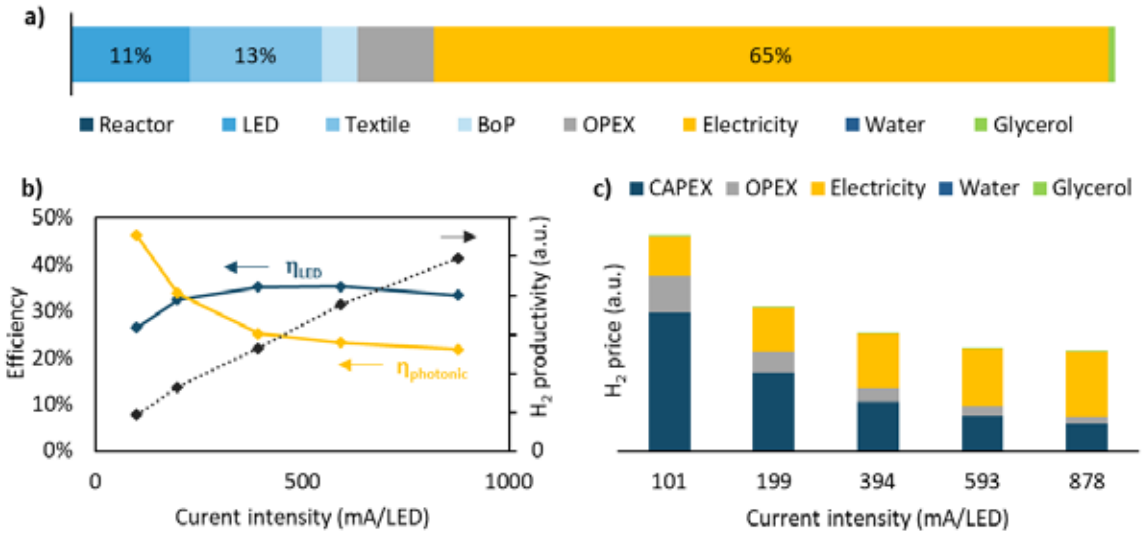


Fig. 3. (a) Hydrogen cost structure, effect of current intensity on (b) LED efficiency, photonic yield, H_2 productivity and (c) cost

The effect of catalyst loading and temperature are also in line with literature [4], [5], [12] since these two parameters can be well described using Beer-Lambert and Arrhenius laws respectively. Considering the relatively low amount of catalyst involved in the photocatalytic textile and assuming that heat is recovered from LED cooling, the energy consumption is globally reduced when increasing catalyst mass and temperature, and so is the cost.

The most interesting result concerns the light intensity effect: its increase induces an increase of the H_2 production rate, but not in a perfectly linear manner as illustrated on Figure 3b. The increase starts to slow down at high intensities, which traduces lower electric to hydrogen yields. This is first linked to the LED efficiency, that diminishes

slightly at high current intensities due to the Shockley behavior [13], but mostly because electrons/holes recombinations are accelerated at high intensities [14]. Yet, H2A analysis shows that despite an increase of the electricity consumption, higher current does not significantly impact the hydrogen production cost: CAPEX is also reduced in the same time due to a higher rate of amortization (Figure 3c). Thus, the optimum of efficiency does not necessary correspond to the optimum of cost, and a carreful price analysis should be performed to evaluate a photocatalytic process viability or its optimum operational point.

CONCLUSIONS

LED-powered photocatalytic reforming is a promising route for hydrogen production since the process efficiency can be significantly increased by optimizing catalytic parameters such as photocatalyst loading, temperature, light intensity or reagents concentration. This optimization can significantly reduce the H_2 production cost since renewable electricity accounts for more than half of the total cost in most of cases. Yet, it should be noted that the optimum of cost is not necessary the optimum of efficiency: an optimum between H_2 production rate and efficiency should be determined to minimize the overall hydrogen production cost, which is today the main obstacle to its deployment.

ACKNOWLEDGEMENT

Auvergne-Rhône-Alpes Region and Bpi France are acknowledged for the financial support of the H2TEX project.

REFERENCES

1. I. Dincer et C. Acar, « Review and evaluation of hydrogen production methods for better sustainability », *International Journal of Hydrogen Energy*, vol. 40, nº 34, p. 11094-11111, sept. 2015, doi: 10.1016/j.ijhydene.2014.12.035.
2. C. Indermuhle, « Textile lumineux pour le traitement de l'eau par photocatalyse », 2015.
3. P.-A. Bourgeois *et al.*, « Characterization of a new photocatalytic textile for formaldehyde removal from indoor air », *Applied Catalysis B: Environmental*, vol. 128, p. 171-178, nov. 2012, doi: 10.1016/j.apcatb.2012.03.033.
4. J.-M. Herrmann, « Heterogeneous photocatalysis: fundamentals and applications to the removal of various types of aqueous pollutants », *Catalysis Today*, vol. 53, nº 1, p. 115-129, oct. 1999, doi: 10.1016/S0920-5861(99)00107-8.
5. J. Rodriguez, « Production d'hydrogène par photocatalyse et conversion électrochimique dans une pile à combustible. », 2013.
6. N. Wu, « Enhanced TiO2 photocatalysis by Cu in hydrogen production from aqueous methanol solution », *International Journal of Hydrogen Energy*, vol. 29, nº 15, p. 1601-1605, déc. 2004, doi: 10.1016/j.ijhydene.2004.02.013.
7. M. Bowker, L. Millard, J. Greaves, D. James, et J. Soares, « Photocatalysis by au nanoparticles: Reforming of methanol », *Gold Bull*, vol. 37, nº 3-4, p. 170-173, sept. 2004, doi: 10.1007/BF03215209.
8. C. R. López, E. P. Melián, J. A. Ortega Méndez, D. E. Santiago, J. M. Doña Rodríguez, et O. González Díaz, « Comparative study of alcohols as sacrificial agents in H2 production by heterogeneous photocatalysis using Pt/TiO2 catalysts », *Journal of Photochemistry and Photobiology A: Chemistry*, vol. 312, p. 45-54, nov. 2015, doi: 10.1016/j.jphotochem.2015.07.005.
9. C. A. Rodriguez, M. A. Modestino, D. Psaltis, et C. Moser, « Design and cost considerations for practical solar-hydrogen generators », *Energy Environ. Sci.*, vol. 7, nº 12, p. 3828-3835, 2014, doi: 10.1039/C4EE01453G.
10. B. A. Pinaud *et al.*, « Technical and economic feasibility of centralized facilities for solar hydrogen production via photocatalysis and photoelectrochemistry », *Energy Environ. Sci.*, vol. 6, nº 7, p. 1983, 2013, doi: 10.1039/c3ee40831k.
11. M. R. Shaner, H. A. Atwater, N. S. Lewis, et E. W. McFarland, « A comparative technoeconomic analysis of renewable hydrogen production using solar energy », *Energy Environ. Sci.*, vol. 9, nº 7, p. 2354-2371, 2016, doi: 10.1039/C5EE02573G.
12. S. M. Ould-Mame, O. Zahraa, et M. Bouchy, « Photocatalytic degradation of salicylic acid on fixed TiO 2 - kinetic studies », *International Journal of Photoenergy*, vol. 2, nº 2, p. 59-66, 2000, doi: 10.1155/S1110662X0000009X.
13. W. Shockley, « The theory of p-n junctions in semiconductors and p-n junction transistors », *The Bell System Technical Journal*, vol. 28, nº 3, p. 435-489, juill. 1949, doi: 10.1002/j.1538-7305.1949.tb03645.x.
14. D. F. Ollis, E. Pelizzetti, et N. Serpone, « Photocatalyzed destruction of water contaminants », *Environ. Sci. Technol.*, vol. 25, nº 9, p. 1522-1529, sept. 1991, doi: 10.1021/es00021a001.

WHEC-2022
23rd World Hydrogen Energy Conference
June 26-30, 2022 - Istanbul

#1515

PROMOTION OF COPPER-ZINC CATALYST WITH Sm AND Gd FOR STEAM REFORMING OF METHANOL

You-Sheng Lin, Kuen-Song Lin, Wang-Ting Hong, Yun Ko, Abrar Hussain, Yun-Cheng Hsieh*
Department of Chemical Engineering & Materials Science, Yuan-Ze University, Taoyuan City, Taiwan.

*Corresponding author e-mail: kslin@saturn.yzu.edu.tw

ABSTRACT

Steam reforming of methanol (SRM) is a chemical reaction in which methanol and water vapor are decomposed through a catalyst, thereby producing gas rich in hydrogen and other substances. The $CuO/ZnO/Al_2O_3$ catalysts have been synthesized, X-ray diffractometer (XRD) and temperature programmed reduction (TPR) (<200°C) have been used to characterize reduction property and catalyst structure. The catalyst was filled into the packed reactor, and the gas composition after the SRM reaction was analyzed by a gas chromatograph (GC-TCD) (WHSV=10 h^{-1}). The research shows that the catalyst activity of $CuO/ZnO/Sm_2O_3/CeO_2$ and $CuO/ZnO/Gd_2O_3/CeO_2$ promoters modified Cu-Zn catalysts have been improved, with conditions as the T_{95} is at 250°C, and the value of Y_{H2} is close to 3.0. Compared with promoter doped $CuO/ZnO/Al_2O_3$ catalyst, bare Cu-Zn catalyst (T_{95}: 240°C, Y_{H2} < 2.7) have been considered as limited efficacy of SRM reaction. In this study, the hydrogen production from SRM reaction have been applied in self-made U-shaped tube filled reactor (filled with 2.5 g of catalyst) combined with fuel cells, which can produce 20W of electricity successfully.

Keywords: Copper-Zinc catalyst, SRM, Samarium, Gadolinium, Hydrogen.

INTRODUCTION

In order for the SRM reaction to produce hydrogen-rich gas (HRG), the quality of the catalyst is the primary key. In the literature, $CuO/ZnO/Al_2O_3$ catalysts are mostly used for steam reforming of methanol (SRM) reaction. Methanol is liquid form at normal temperature and pressure, it is easy to store and transport, and has low sulfur content (< 5 ppm), which is not easy to poison the catalyst. The methanol steam reforming reaction uses methanol decomposition to generate CO, and then reacts with water vapor and CO to obtain CO_2 and H_2. In this experiment, different promoters (Promoter): samarium (Sm) and gadolinium (Gd) are added to the base of copper, zinc, and aluminum to modify the catalyst, which is expected to reduce reaction temperature (T_{95}) (conversion rate > 95%), reducing carbon monoxide (CO) concentration in the product, and increasing hydrogen yield (F_{H2}). Moreover, the reaction temperature (200 - 350 °C) of SRM is similar to the proton exchange membrane fuel cell (PEMFC) (80 - 120 °C), and the generated hydrogen can be directly supplied to the PEMFC without additional heating. Therefore, SRM is often regarded as the liquid fuel of PFEMC hydrogen source [1,2]. The difference between the $CuO/ZnO/Al_2O_3$ catalyst and these catalysts with promoters is the adsorption capacity of methanol. In this study, copper-zinc catalysts with high activity and high durability were prepared by adding different co-activators, the influence on the catalytic activity was discussed as well [3,4]. Among of them, the precious metal additions have been considered as an outstanding method to improve the SRM [5]. Moreover, the economic value of CuO/ZnO SRM system have been attracted scientists' attentions, base on the design of multi-tubular reactor [6]. Finally, the best experimental conditions were found, and the recombines were made from them.

MATERIALS AND METHODS

Co-precipitation (CP) and homogeneous precipitation (HP) preparation process of catalyst precursor is as follows; take 1000 mL of deionized water (DI water), and add appropriate amount of $Cu(NO_3)_2$. Nitrate precursors such as $2.5H_2O$, $Zn(NO_3)_2.6H_2O$, $Al(NO_3)_3.9H_2O$, etc., are stirred to dissolve and uniformly dispersed in the solution. (1) Co-precipitation process: dropwise with 0.5N sodium carbonate aqueous solution, control its pH value between 7-8 and continue stirring for 2 hours, and maintain the temperature at 70°C. (2) Homogeneous-precipitation process: Add urea aqueous solution, start to heat up to 90°C, and maintain at 90°C, so that the pH value rises to 7-8. After 2 hours, the fully stirred aqueous solution was filtered to remove the precipitate, and then the precipitate was washed with DI water to ensure no chlorine residue. The precipitate was dried in an oven at 70°C, taken out and ground into fine powder. Then calcined at 400°C for 4 h. Heating rate: 3°C/min.

RESULTS AND DISCUSSION

Figure 1(a) shows the TPR spectra of CP and HP-XM catalysts, which can have demonstrated the Cu^{2+} - Cu^0 reduction temperature (Tr) of calcinated catalysts. It can be seen that the lye concentration is postive with the Tr of HP-catalyst, which is explaining the tends of HP-0.5M (Tr = 210°C) and HP-3M (Tr = 222°C). However, HP-1M have showed some plus signal in TPR spectra. Compared with HP and CP catalysts, the reduction temperature of HP is slightly lower, and the reducibility of the catalyst: HP-0.5M > HP-1.5M = CP > HP-2M > HP-1M > HP-2.5 M > HP-3M.

Figure 1(b)shows the XRD patterns of CP and HP-XM catalysts. The effects of different lye concentrations and different methods on catalyst particles are discussed. The main peak pf copper oxide and zinc oxide have demonstrated at 38.8°, which was used as the benchmark to compare the size of copper particles. Among four samples, it can be found that the characteristic front of HP-0.5M copper is broadened, which described the tend of size decreasing of Cu nanoparticles.

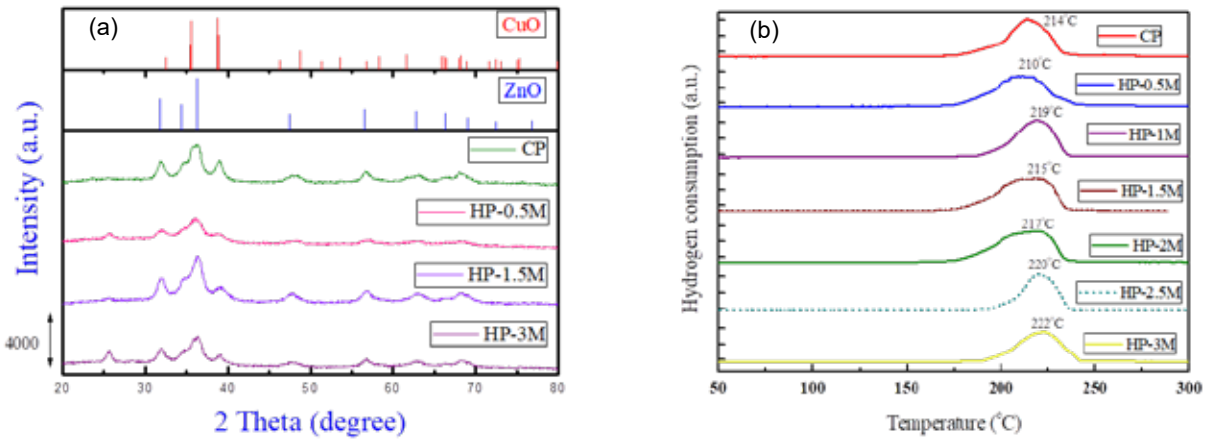


Figure 1 (a) XRD patterns and (b) TPR spectra of catalysts prepared by HP and CP methods.

In this study, the Sm_2O_3, CeO_2 and Gd_2O_3 have been indicated as promoters of copper-zinc catalyst. The electron orbitals of Sm and Gd are [Xe]6s24f6 and [Xe]4f75d16s2, respectively, it is easy to grab an electron with other elements. The reduction temperature has been depended on the type of metal oxide and the force between the metal and the support. Therefore, the effect of the support force on the reduction properties of CuO was obtained by TPR analysis. Figure 2 (a) shows the TPR spectrum of Cu/RE-Zn catalyst, the higher reduction temperature of CuZnAlSm and CuZnAlGd (227°C) than CuZnAl catalyst (210°C). However, CuZnGdCe and CuZnSmCe showed shifted tends than CuZnAl, which was below 200°C. Figure 2(b) XRD pattern of Cu/RE-Zn catalyst. After the two promoters of Sm and Gd are added, the specific peaks of CuZnAl catalyst can hardly observe the characteristic peaks, and only a very broad peak can be seen when 2 Theta = 30° - 40°.

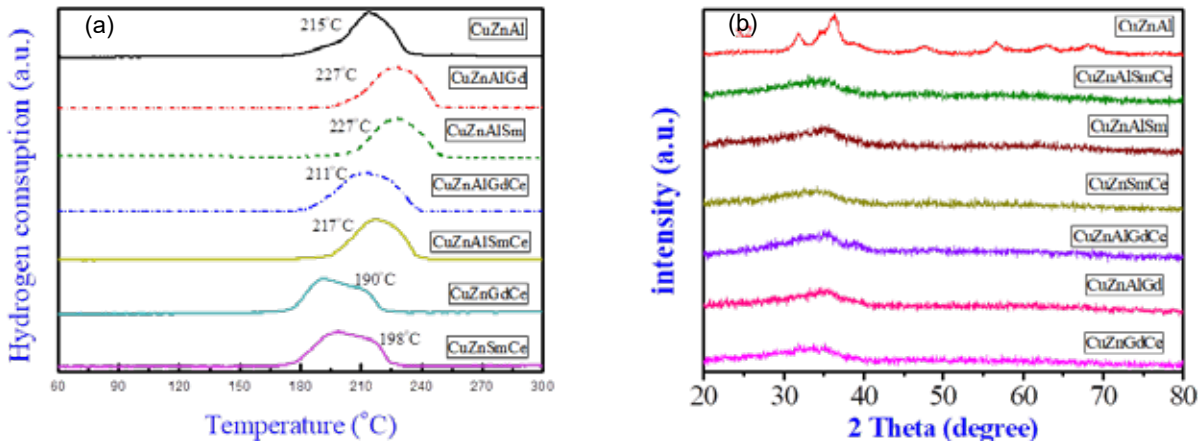


Figure 2 (a) TPR spectra and (b) XRD patterns of CuZnAl with Gd/Sm/Ce catalysts.

Figure 3(a) is the activity test of Cu/RE-Zn catalyst, the most important test data of activity test. First, take 0.5 g of catalyst and place it in a quartz tube with an inner diameter of 4 mm, and feed water and alcohol (S/C=1.1). In the SPM reaction, flow rate was WHSV = 10 h^{-1}, and no carrier gas was added, the reaction temperature range was 180 - 270°C, and the test was performed every 3 °C. Figure 3(b) is a graph showing the comparison between methanol conversion and hydrogen yield. The two catalysts, CuZnGdCe and CuZnSmCe, have the best reactivity, and the conversion rate of methanol is more than 90% at 240°C. Based on this, the addition of the promoter has an increasing effect on the hydrogen yield, illustrating the potential for application in fuel cells. Therefore, the order of reactivity is CuZnGdCe = CuZnSmCe > CuZnGdAl > CuZnSmAl > CuZnAlCeSm > CuZnAlCeGd.

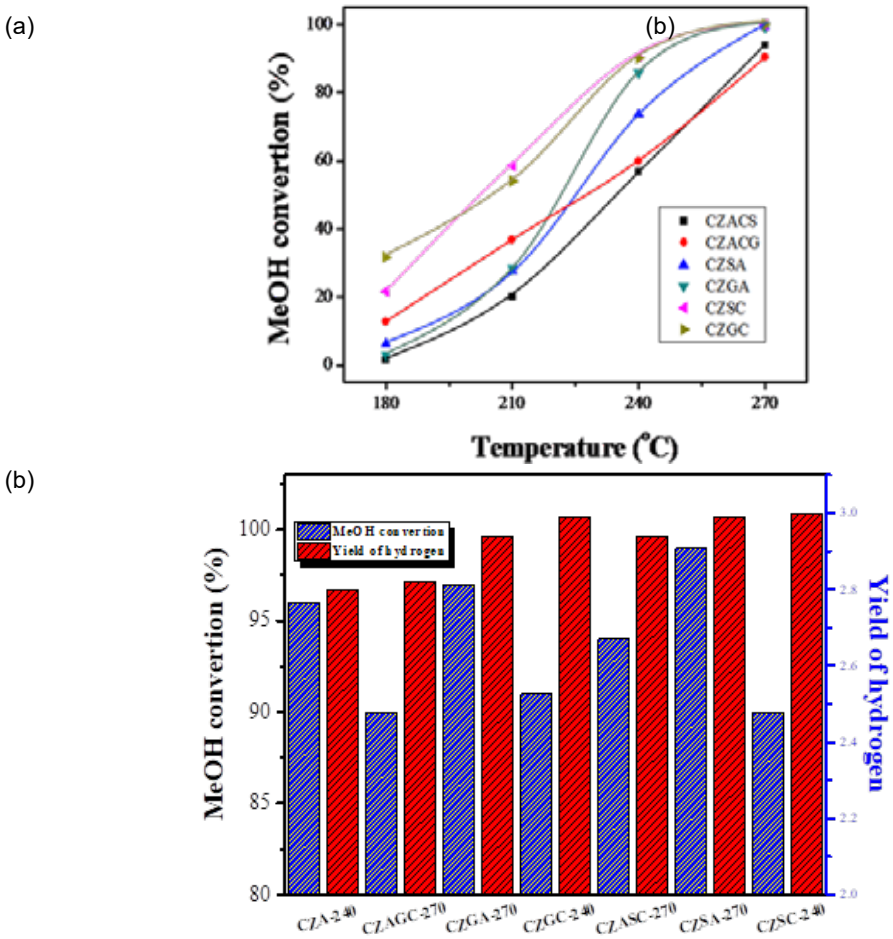


Figure 3 (a) Activity test and (b) methanol conversion and hydrogen yield of CuZnAl with Gd/Sm/Ce catalysts.

CONCLUSIONS

In this research, different preparation methods and the promoter additions have been used to modify the catalyst, the influence of modification on the reaction performance of the catalyst was studied. The catalyst was filled into the self-made reactor to carry out the system combined with the fuel cell. Compared with the traditional CP method, the catalyst prepared by the HP method has smaller catalyst particles and better uniformity. When the concentration of urea is 1.5M, it has performed the best reactivity in this study. It can be seen from the XRD results that the addition of Gd_2O_3 and Sm_2O_3 can increase the dispersion of copper-zinc catalysts, because it is known from the spectrum that in addition to a wide peak in the middle of 2 theta = 30° - 40°, other Cu, Zn, and rare earths The special micro-peaks of the metal could not be found at all, which was an amorphous state. In this experiment, the methanol vapor reformer is combined with the fuel cell system. It is found that the performance of the reactor is determined by the heat transfer efficiency. The heat transfer performance is good, in addition to making the catalyst play its role, it can more effectively produce 24W of electricity.

REFERENCES

1.Choi Y and Stenger HG. 2002. Fuel cell grade hydrogen from methanol on a commercial $Cu/ZnO/Al_2O_3$ catalyst. Applied Catalysis B: Environmental 38(4):259-269.
2.Bravo J, Karim A, Conant T, Lopez GP, and Datye A. 2004. Wall coating of a $Cu/ZnO/Al_2O_3$ methanol steam reforming catalyst for micro-channel reformers. Chemical Engineering Journal 101(1-3):113-121.
3.Agarwal V, Patel S, and Pant KK. 2005. H_2 production by steam reforming of methanol over $Cu/ZnO/Al_2O_3$ catalysts: transient deactivation kinetics modeling. Applied Catalysis A 279(1-2):155-164.
4.Liu Q, Jin H, Hong H, Sui J, Ji J, and Dang J. 2011. Performance analysis of a mid- and low-temperature solar receiver/reactor for hydrogen production with methanol steam reforming. International Journal of Energy Research 35:52-60.
5.Cifuentes A, Soler L, Torres R, and Llorca J. 2022. Methanol steam reforming over $PdZn/ZnAl_2O_4/Al_2O_3$ in a catalytic membrane reactor: An experimental and modelling study. International Journal of Hydrogen Energy 47(22): 11574-11588.
6. Zhu J, Araya S S, Cui X, and Kær SK. 2022. The role of effectiveness factor on the modeling of methanol steam reforming over $CuO/ZnO/Al_2O_3$ catalyst in a multi-tubular reactor. International Journal of Hydrogen Energy 47(14): 8700-8715.

WHEC-2022
23rd World Hydrogen Energy Conference
June 26-30, 2022 - Istanbul

#1527

KINETIC CHARACTERIZATION OF Pt/Al_2O_3 CATALYST FOR HYDROGEN PRODUCTION VIA METHANOL AQUEOUS-PHASE REFORMING

[1,2] *Paranjeet Lakhtaria,* [1,2] *Paulo Ribeirinha,* [1,2,3] *José Sousa,* [1,2*] *Adélio Mendes*

[1] LEPABE - Laboratory for Process Engineering, Environment, Biotechnology and Energy, Faculty of Engineering, University of Porto, Rua Dr. Roberto Frias, 4200-465 Porto, Portugal

[2] ALiCE - Associate Laboratory in Chemical Engineering, Faculty of Engineering, University of Porto, Rua Dr. Roberto Frias, 4200-465 Porto, Portugal

[3] Departamento de Química, Escola de Ciências da Vida e do Ambiente, Universidade de Trás-os-Montes e Alto Douro, Quinta de Prados, 5000-801 - Vila Real, Portugal

*Corresponding author e-mail: mendes@fe.up.pt

ABSTRACT

Methanol aqueous-phase reforming (APR) is a simpler and more energy-efficient process compared to traditional gas-phase reforming. Methanol APR is considered to be a potential technology for providing *in-situ* hydrogen (H_2) production, mainly for H_2-powered fuel cell technology. The performance evaluation of a Pt/Al_2O_3 catalyst in methanol APR under various operating conditions is reported. Studies were conducted at various temperatures, pressures, methanol concentrations, and residence times to evaluate APR performance. An increase in methanol conversion was observed with increased operating temperature and decreased system pressure. It was also noted that higher methanol concentration in the feed had an adverse effect on APR performance.

Keywords: Aqueous-phase reforming, Methanol, Hydrogen production, Catalyst, Pt/Al_2O_3

INTRODUCTION

As the world tackles the challenges of global warming, energy decarbonization, and CO_2 emission caused mainly due to the usage of fossil fuels, H_2 has emerged as a promising energy vector [1]. However, an inexpensive infrastructure for H_2 storage and transportation is yet to emerge [2]. Therefore, *in-situ* H_2 production from renewable resources (*e.g.* alcohols) is an economical and efficient perspective to overcome the aforementioned challenges. Among other alcohols, methanol can be considered the most advantageous H_2 carrier with the highest H/C ratio and in the liquid state at room temperature [3]. Apart from widely accepted methanol steam-reforming (MSR) [4], methanol APR is an emerging competitive approach for H_2 production [5]. Methanol APR provides multiple advantages, namely elimination of vaporization of methanol solution, single-step process, and minimized carbon monoxide formation from water-gas shift (WGS) reaction compared to MSR. APR can produce H_2 and CO_2 at temperatures between 200 °C - 250 °C and in the pressure range of 1.5 MPa - 5.0 MPa [6]. However, reforming and WGS reactions are kinetically favored by higher temperatures. Methanation side reaction is also thermodynamically favored in methanol APR operating conditions. Additionally, system pressure plays a vital role in APR performance since APR is a multi-phase system with reaction kinetics often controlled by the diffusion of products through an aqueous phase. Therefore, it becomes necessary to evaluate the effects of operating conditions on methanol APR for optimal performance. The purpose of this study is to further explore methanol APR kinetics characteristics to propel much-needed research on novel catalysts and reactor design. In this work, we report the performance of a Pt/Al_2O_3 catalyst under various operating temperatures, operating pressures, residence times, and feedstock concentrations in methanol APR.

EXPERIMENTAL

An in-house designed set-up was used to evaluate catalyst performance in APR under different operating conditions. A commercial Pt/Al_2O_3 (5 wt. % Pt) catalyst supplied by Sigma-Aldrich was placed in the mid-section of a fixed-bed reactor mixed with equal amounts of glass beads. The reactor was placed vertically in a temperature-controlled oven. The catalyst was reduced *in-situ* at 300°C for 2 h in a flowing H_2/N_2 (1:1) atmosphere. Afterward, the reactor was purged with N_2 gas (50 mL·min^{-1}) for 30 min to remove the adsorbed H_2. Aqueous methanol solutions, with concentrations of 5 wt. % and 55 wt. % of methanol was fed to the reactor in an upwards direction by an HPLC pump, with weight hourly space velocity (WHSV) between 0.1 h^{-1} - 21.2 h^{-1}. All these experiments were performed with N_2 co-feeding of 30 mL·min^{-1}. The outlet stream from the reactor was cooled down in a condenser at *ca.* 0°C to separate liquid-phase effluents and gaseous products. The formed gaseous products were measured with online gas chromatography. A back pressure regulator was used to regulate the operating pressure of the reforming reaction. The catalytic performance in methanol APR under various operating conditions was evaluated in terms of methanol conversion (%) as shown in Eq. (1). Herein, n denotes the number of moles, M_{in} is the inlet methanol stream, and M_{out} is the outlet methanol stream.

Methanol conversion (%) = 100 x ($n\,M_{in} - n\,M_{out}$) / $n\,M_{out}$ (1)

RESULT AND DISCUSSION

Effect of temperature

Fig.1 shows the methanol conversion as a function of WHSV at temperatures of 190°C, 210°C, and 230°C with an operating pressure of 3.2 MPa and 6.0 MPa for (a) 5 wt. % and (b) 55 wt. % methanol solution respectively. 6.0 MPa operating pressure was applied to keep 55 wt. % methanol solution in the liquid phase.

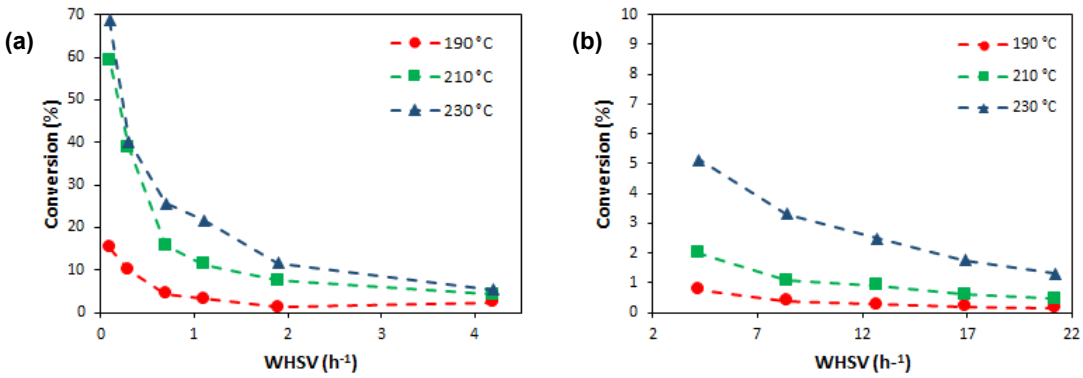


Fig. 1. Methanol conversion vs residence time in APR for (a) 5 wt. % and (b) 55 wt. % methanol aqueous solution at operating temperatures of 190°C, 210°C, and 230°C. Operating pressure of (a) 3.2 MPa and (b) 6.0 MPa, and 5 wt. % Pt/Al_2O_3.

As Fig. 1 depicts, an increase in methanol conversion was observed with increasing temperature and decreasing WHSV. However, methanol conversion did not increase significantly when using high methanol concentration (55 wt. % of methanol). With increased methanol concentration and WHSV, the contact time between reactants and catalyst decreased, which adversely affected methanol conversion [7]. For lower operating temperatures, the reforming reactions are inhibited and catalyst deactivation due to carbon depositions becomes a possibility [8].

Effect of pressure

Fig.2 shows the effects of operating pressure on methanol conversion at an operating temperature of 230°C. For 5 wt. % methanol APR, the inhibited reforming reactions at higher operating pressure can be caused by the high partial pressures of the products and unavailability of active sites (caused by high H_2 concentration on catalyst surface) [6], [9]. The catalyst was more sensitive to changes in system pressure near the bubble point pressure, as the conversion stays nearly constant beyond 4.0 MPa. The effect of operating pressure was negligible on the conversion when using high methanol concentration (55 wt. %). Even methanol reforming performed below the bubble point pressure (gaseous phase) did not yield conversions higher than methanol APR (Fig.2). This is indicative that reforming reactions are affected more by feed concentration than operating pressure.

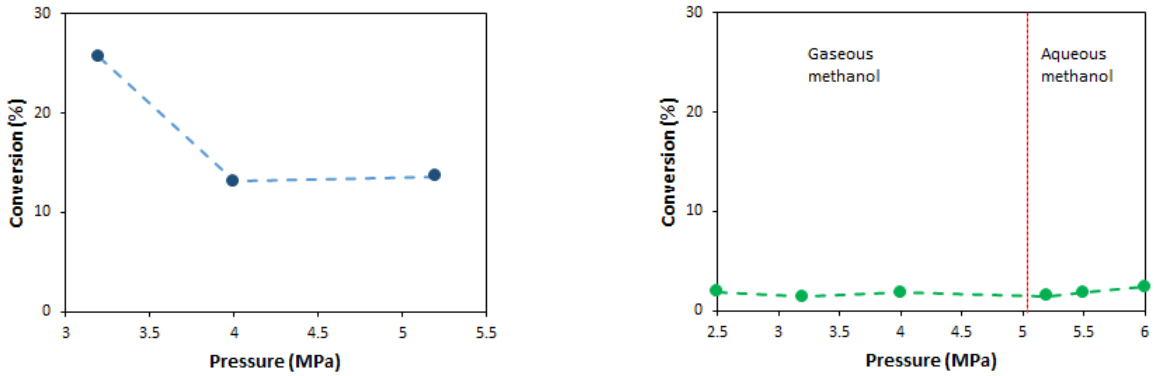


Fig. 2 Methanol conversion as a function of pressure for (a) 5 wt. % and (b) 55 wt.% methanol aqueous solution. Operating temperature of 230°C, residence time of (a) 0.7 (h^{-1}) and (b) 12.7 (h^{-1}), and 5 wt. % Pt/Al_2O_3.

CONCLUSIONS

Kinetic characterizations were performed for methanol APR over Pt/Al_2O_3 catalyst using two different feedstock concentrations at various temperatures, pressures, and residence times. Methanol conversion increased with increasing temperature and decreasing operating pressure for methanol (5 wt. %) APR. However, these effects were not prominent for 55 wt. % methanol APR. At all operating temperatures and pressures for this concentration, the highest conversion achieved was 6 %, indicating that APR performance was inhibited by high methanol concentration. For decreasing residence times, reforming reactions were inhibited for both methanol concentrations.

ACKNOWLEDGEMENT

This research was financially supported by the European Union's Horizon 2020 research and innovation programme under grant agreement No 875081 (project EMPOWER). This work was financially supported by LA/P/0045/2020 (ALiCE), UIDB/00511/2020 and UIDP/00511/2020 (LEPABE), funded by national funds through FCT/MCTES (PIDDAC).

REFERENCES

1. Oliveira AM, Beswick RR and Yan Y. 2021. A green hydrogen economy for a renewable energy society. Current opinion in Chemical Engineering 33:100701.
2. Abe JO, Popoola API, Ajenifuja E and Popoola OM. 2019. Hydrogen energy, economy and storage: Review and recommendation. International Journal of Hydrogen Energy 44:15072-15086.
3. Bepari S and Kuila D. 2020. Steam reforming of methanol, ethanol and glycerol over nickel-based catalysts-A review. International Journal of Hydrogen Energy 45:18090-18113.
4. Iulianelli A, Ribeirinha P, Mendes A and Basile A. 2014. Methanol steam reforming for hydrogen generation via conventional and membrane reactors: A review. Renewable and Sustainable Energy Reviews 29:355-368.
5. Lakhtaria P, Ribeirinha P, Huhtinen W, Viik S, Sousa J and Mendes A. 2021. Hydrogen production via aqueous-phase reforming for high-temperature proton exchange membrane fuel cells-a review. Open Research Europe 1:81.
6. Davda RR, Shabaker JW, Huber GW, Cortright RD and Dumesic JA. 2005. A review of catalytic issue and process conditions for renewable hydrogen and alkanes by aqueous-phase reforming of oxygenated hydrocarbons over supported metal catalysts. Applied Catalysts B:Environmental 56:171-186.
7. Shabaker JW, Davda RR, Huber GW, Cortright RD and Dumesic JA. 2003. Aqueous-phase reforming of methanol and ethylene glycol over alumina-supported platinum catalysts. Journal of Catalysis 215:344-352.
8. Cortright RD, Davda RR, and Dumesic JA. 2002. Hydrogen from catalytic reforming of biomass-derived hydrocarbons in liquid water. Nature 418:964-967.
9. Shabaker JW and Dumesic JA. 2004. Kinetics of aqueous-phase reforming of oxygenated hydrocarbons: Pt/Al_2O_3 and Sn-modified Ni catalysts. Industrial & Engineering Chemistry Research 43:3105-3112.

WHEC-2022
23rd World Hydrogen Energy Conference
June 26-30, 2022 - Istanbul

#1537

Ni-BASED CATALYSTS FOR CO_2 REFORMING OF GLYCEROL TO H_2

Ozge Selcuk, Ahmet K. Avci
Department of Chemical Engineering, Bogazici University, Bebek 34342, Istanbul, Turkey

*Corresponding author e-mail: avciahme@boun.edu.tr

ABSTRACT

Dry reforming of glycerol is a recently emerging pathway for making H_2. The route is promising due to the consumption of glycerol, a side product of biodiesel synthesis, with CO_2, a major greenhouse gas. This study aims to develop Ni-based catalysts for providing insight into the role of support material on activity towards glycerol dry reforming. In this respect, Ni/La_2O_3, Ni/ZrO_2 and Ni/La_2O_3-ZrO_2, all loaded with 5% Ni by mass, are synthesized. The catalysts are tested at 750°C, molar inlet CO_2-to-glycerol ratio (CO_2/G) between 1-5 and residence time of 0.25 mg min NmL^{-1}. The results clearly showed that Ni/La_2O_3-ZrO_2 was more active than the single-oxide supported counterparts. The catalyst showed superior durability with only 12% loss in CO_2 conversion after the 72-h time-on-stream stability test. On the other hand, Ni/ZrO_2 and Ni/La_2O_3 were completely deactivated at the 47th and 63rd h of the stability tests, respectively. Superior activity and stability of the Ni/La_2O_3-ZrO_2 is attributed to the fine dispersion of the Ni nanoparticles and durability against coke deposition.

Keywords: Catalyst, CO_2, Glycerol, Hydrogen, Reforming

INTRODUCTION

Biodiesel is conventionally synthesized by the trans-esterification of animal-based or vegetable oils in the presence of methanol or ethanol, yielding glycerol as a side product which typically accounts ~10% by mass of the resulting mixture. This fraction, however, causes a notable surplus of glycerol when the scale of biodiesel production is considered. Unless valorized into useful products, surplus glycerol will elevate the cost of biodiesel synthesis. Among several options of valorization, catalytic transformation of glycerol to hydrogen (H_2) receives increasing interest. This transformation is carried out typically by reforming glycerol with steam. However, recently, replacing steam with CO_2 is considered with the motivation of making H_2 through a carbon-negative path, *i.e.,* by consuming CO_2 (*i.e.,* a greenhouse gas) and glycerol (*i.e.* waste of biodiesel synthesis).

$$C_3H_8O_3 + CO_2 \rightleftharpoons 4CO + 3H_2 + H_2O \qquad \Delta H° = 292 \text{ kJ/mol} \qquad (1)$$

The overall Reaction (1) can be considered as the combination of glycerol decomposition (2) and the reverse water–gas shift (RWGS, (3)):

$$C_3H_8O_3 \rightarrow 3CO + 4H_2 \qquad \Delta H° = 251 \text{ kJ/mol} \qquad (2)$$

$$CO_2 + H_2 \rightleftharpoons CO + H_2O \qquad \Delta H° = 41 \text{ kJ/mol} \qquad (3)$$

Despite its reformate H_2-content is less than that obtained from the steam reforming route, glycerol dry reforming (GDR) is receiving increasing interest in the recent years, with the Ni–based catalysts being the most studied ones [1]. It is commonly reported that the performance of the Ni-based catalysts is dictated by the support material [1]. While some of them showed promising activities, quantified by glycerol conversion to gaseous products, Ni-based catalysts generally deactivated rapidly primarily due to coking and/or sintering of the active species [1]. Recently, Ni supported by Al_2O_3-ZrO_2-TiO_2, a ternary oxide, is reported to deliver CO_2 and glycerol conversions close to the pertinent thermodynamic limits and superior stability [2]. In an effort to provide further insight into the roles of the support, the present study aims enriching the expanding GDR literature by screening of numerous single and binary metal oxide supported Ni catalysts for their activities quantified both by CO_2 and glycerol conversions.

MATERIALS AND METHODS

Catalyst Synthesis

Research grades (purity: >99.99%) of La_2O_3 (Sigma-Aldrich), ZrO_2 (Alfa-Aesar) and La_2O_3-ZrO_2 (Daiichi Kigenso Kagaku Kogyo) were used as the support materials. All the catalysts used in this study were prepared by incipient wetness impregnation of the aqueous solution of $Ni(NO_3)_2.6H_2O$ (Sigma-Aldrich) onto the pertinent porous support as described in detail elsewhere [2]. Nominal value of the Ni loading is fixed to 5% by weight in all catalysts.

Catalytic performance experiments

The experiments were conducted in a down-flow quartz tubular packed bed reactor placed inside a three-zone furnace. Catalyst bed consists of 10 mg catalyst supported by a quartz wool plug. Flow of liquid glycerol was set to deliver 4 NmL min^{-1} of glycerol. Inlet flow of CO_2 was determined based on CO_2/G and the balance gas N_2 flow rate was set according to the feed ratio to obtain a constant total flow rate of 40 NmL min^{-1}. Liquid effluents were retained inside cold traps before online gas chromatograph (GC) units. Two GC units were used to detect products and determine their compositions. Further details of reactant dosing, flow reaction and product analysis systems can be found in [3].

Catalytic experiments were carried out at 750 °C, CO_2/G=1-5 and residence time=0.25 mg_{cat} min NmL^{-1}. Duration of the catalytic activity tests was fixed at 5 h. The first data was taken 30 min. after the start of experiment, then the rest were taken every following 45 min. Catalytic activity was quantified by CO_2 conversion (X_{CO2}) and glycerol conversion to gaseous products (X_G) calculated using Eqs. 4 and 5, respectively:

$$X_{CO_2}(\%) = \frac{F_{CO_2,in} - F_{CO_2}}{F_{CO_2,in}} \times 100 \quad (4)$$

$$X_G(\%) = \frac{2F_{H_2} + 4F_{CH_4} + 4F_{C_2H_4} + 6F_{C_2H_6}}{8F_{G,in}} \times 100 \quad (5)$$

In Eqs. 4 and 5, $F_{i,in}$ (mol min^{-1}) is the molar flow rate of species i fed, F_i (mol min^{-1}) is the molar flow rate of i in product stream. Glycerol conversion was calculated *via* elemental H balance, which includes all detectable species containing H-atom in the gas phase. In addition to the catalytic experiments, blank tests involving reactor packing with only inert α-Al_2O_3 and quartz wool were conducted to figure out homogeneous (non-catalytic) reactions.

RESULTS AND DISCUSSION

Thermodynamic Analysis

In order to determine equilibrium conversions of CO_2 and glycerol and yields of products, thermodynamic analysis was carried out by the Gibbs free energy minimization technique at the current operating conditions in CHEMCAD 7.1.4 suite. The results are presented in Table 1 in the form of product yields, CO_2 conversion, and glycerol conversion. No liquid organic products, and solid carbon were predicted in the product stream.

Table 1. Product yields (moles product/moles glycerol fed) and reactant conversions at thermodynamic equilibrium

CO_2/G	Y_{H2}	Y_{CO}	Y_{CH4}	Y_{C2H4}	Y_{C2H6}	X_{CO2} (%)	X_G (%)
1	3.49	3.40	0.03	0	0	43.0	88.6
2	3.17	3.78	0.01	0	0	39.3	80.0
3	2.90	4.07	0.01	0	0	35.7	73.0
4	2.67	4.30	0.01	0	0	32.7	67.1
5	2.48	4.50	0.00	0	0	30.1	100.0

Catalytic Activity Experiments

Two single oxide supported catalysts, Ni/La_2O_3 (Ni/L) and Ni/ZrO_2 (Ni/Z), and binary oxide supported catalyst, Ni/La_2O_3-ZrO_2 (Ni/LZ), are comparatively tested for their CO_2 conversions reported in Fig. 1. The results clearly show that Ni/LZ catalyst is more active than any of the single-oxide supported catalysts in the entire range of operating conditions. It is also observed that CO_2 conversions are the highest between CO_2/G=3-4. The common decrease in catalytic activity at CO_2/G=1, the lowest range of feed ratio, can be attributed to coke formation which is likely to occur due to the lack of CO_2 that acts as a gasifying agent [2]. Moreover, formation of steam, another coke gasifying agent, via RWGS (Reaction 3) is less promoted at CO_2-lean conditions. This pattern is observed predominantly on Ni/L which fails to show any activity at CO_2/G=1. Despite its poor activity at CO_2-lean conditions, the fast increase in CO_2 conversion on Ni/L at CO_2/G >2 can be attributed to the removal of coke species by means of oxygen vacancies provided by La_2O_3. Molecular level evidences of these findings are in the course of being obtained by detailed characterization studies including TGA, SEM imaging and RAMAN spectroscopy.

Glycerol conversion to gaseous products of the screening catalysts, on the other hand, have complex response to the CO_2/G ratio and this behaviour is seen in Figure 1. Blank experiments carried out at CO2/G=1-5 (details not shown here) give glycerol conversions between 49-51%, which is more than half of the catalytic glycerol conversions reported in Figure 1. The same experiments, however, did not show any activity towards CO_2. In this regard, CO_2 conversion is used as a more reliable metric for monitoring catalytic response.

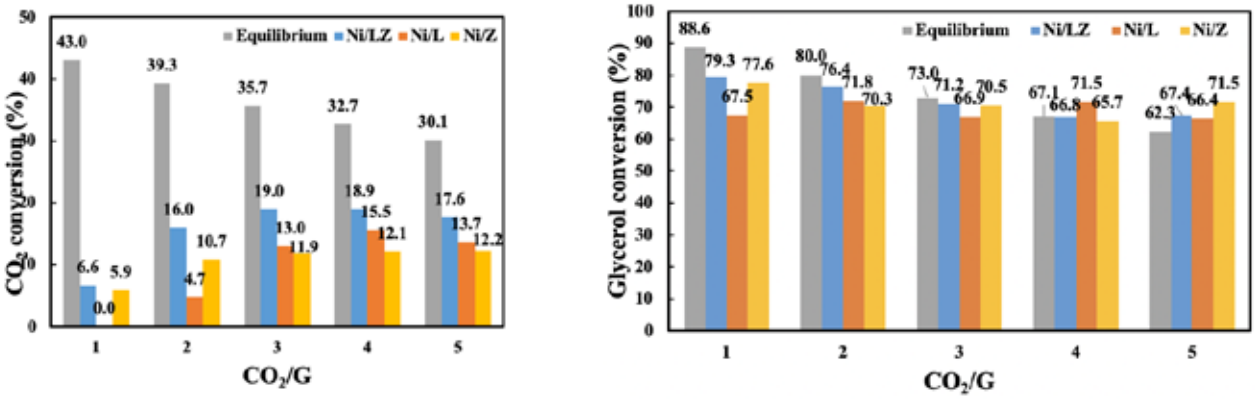


Fig. 1. CO_2 (left) and glycerol (right) conversions obtained on Ni-based catalysts

In addition to activity screening, 72 h time-on-stream experiments are performed at 750°C and CO_2/G=2 for providing insight about stability performance of prepared catalyst. According to findings, Ni/LZ has exceptional behavior with only 12% activity loss. However, Ni/L and Ni/Z are completely deactivated at the end of 47th and 62nd h of the stability experiments. Superior stability of the Ni/LZ catalyst can be associated to the fine dispersion of the Ni nanoparticles and its resistance against coke deposition. These possible mechanisms are currently under investigation by means of molecular level characterization of the catalyst samples before and after the reaction tests.

CONCLUSIONS

The goal of this study was to develop active Ni-based catalysts for GDR. The results clearly showed that Ni/La_2O_3-ZrO_2 was more active than the single-oxide supported counterparts in the complete span of the operating conditions. The catalyst also showed superior durability with only 12% loss in CO_2 conversion after the 72-h time-on-stream stability test. Superior activity and stability of the Ni/La_2O_3-ZrO_2 is attributed to the fine dispersion of the Ni nanoparticles and durability against coke deposition.

ACKNOWLEDGEMENT

Financial support was provided by TUBITAK (117M163) and by Bogazici University Research Fund (BAP–13880).

REFERENCES

1. Bac S, Keskin S, Avci AK. 2020. Recent advances in sustainable syngas production by catalytic CO_2 reforming of ethanol and glycerol. Sustainable Energy & Fuels. 4: 1029-1047.
2. Bac S, Say Z, Kocak Y, Ercan KE, Harfouche M, Ozensoy E and Avci AK. 2019. Exceptionally active and stable catalysts for CO_2 reforming of glycerol to syngas. Applied Catalysis B: Environmental 256:117808.

WHEC-2022
23rd World Hydrogen Energy Conference
June 26-30, 2022 - Istanbul

#1545

SHAPE DEPENDENT ELECTROCATALYTIC HYDROGEN EVOLUTION BY COPPER-ANTIMONY SULFIDE

[1*] *Emre Aslan,* [2] *Faruk Özel,* [3] *İmren Hatay Patır*
[1] Selcuk University, Department of Biochemistry, 42030, Konya, Turkey
[2] Karamanoglu Mehmetbey University, Department of Metallurgy and Materials Engineering, Karaman 70200, Turkey
[3] Selcuk University, Department of Biotechnology, 42030, Konya, Turkey

*Corresponding author e-mail: emreaslan89@gmail.com

ABSTRACT

The chalcostibite electrocatalysts are using towards energy conversion processes including hydrogen evolution reaction (HER) due to its excellent properties as low-cost and high activity. Herein, the ternary chalcostibite copper-antimony sulfides in different shapes and as nanodot (D-$CuSbS_2$) and microrod (R- $CuSbS_2$) were synthesized by hot-injection approach. These chalcostibite materials were firstly investigated on the electrocatalytic HER in alkaline media. Microrod shape of catalyst displayed enhancing catalytic activity of HER in alkaline conditions when compared to spherical shape of catalyst. This result may be explained by efficient charge separation efficiency of 1D materials, which is microrod shape.

Keywords: Electrocatalytic hydrogen evolution, Copper-antimony sulfide,

INTRODUCTION

The demands of sustainable and environmental-friendly energy sources are inevitably increasing because of the growing of population and solding current fuels. Hydrogen is the most promising energy source due to the high energy capacity, unlimited availability, clean and sustainable properties [1]. Recently, the studies of hydrogen evolution reaction (HER) have been showed that water splitting is the most appropriate way to produce hydrogen on a large scale [2]. During the past decades, electrocatalytic hydrogen evolution has been substituted among energy conversion processes including sustainable energy technologies developed with the aim of reducing global energy crisis [3]. So, it has been intensively focused on the discover of electrocatalysts with low cost and high activity for hydrogen production [1]. Despite noble metal-based electrocatalysts (especially platinum-based) have been preferred due to its excellent activity during the HER, these materials could not use because of their structural properties such as high cost and low abundance [2,4-6]. Cu-based Transition metal chalcogenides (TMCs) have been alternatively developed as an alternative to noble-metal electrocatalysts for HER because of its noble-metal-like electronic structures. Thereby, it has been thought that copper sulfides may have suitable for water splitting applications owing to its unique anisotropic structure, rapid electron transfer pathways and small optical band gaps [1,7-10]. Ternary chalcostibite copper-antimony sulfide ($CuSbS_2$ or CAS) which is one of four forms (Cu_3SbS_4, $CuSbS_2$, Cu_3SbS_3, and $Cu_{12}Sb_4S_{13}$) of the ternary copper antimony sulfide (CuxSbySz) system is a copper-based semiconductor multicomponent chalcogenide [11]. Among these phases, the photovoltaic properties of $CuSbS_2$ as a solar absorber has attracted much attention in solar energy conversion and optoelectronic applications due to its appropriate bandgap of 1.5 eV [12,13], hole mobility of 49 $cm^2 (Vs)^{-1}$, a high absorption coefficient $\cong 10^5\ cm^{-1}$ [13-16], tunable hole concentration in a range of 10^{16}-10^{18} cm^{-1} [17-19].Therefore $CuSbS_2$ has been proposed as earth abundant, low toxicity and environmental friendly materials for sustainable and cost-efficient photovoltaics [20-23].

Herein, we have reported that electrocatalytic hydrogen evolution for the first time in alkaline conditions by the different shape of $CuSbS_2$ (nanodot and microrod), which were prepared by a simple hot-injection method as reported previously [24]. It has been determined that the electrocatalytic activities of these $CuSbS_2$ were enhanced by changing shapes. It has been observed 474 mV and 508 mV overpotential values in which are using R-$CuSbS_2$ and D-$CuSbS_2$, respectively, at the current density at 10 mA cm^{-2}. The microrod electrocatalyst exhibited high electrocatalytic activity than its spherical form by efficient charge separation efficiency of R-$CuSbS_2$ which has 1D structure.

MATERIALS AND METHODS

The HER catalysts were dispersed in the ethanol solution. The dispersed solution was added to the glassy carbon electrodes with drop casting method. Prepared electrodes were used for the electrocatalytic HER in the oxygen-free alkaline solution (1.0M KOH). Linear sweep voltammetry (LSV) measurements were performed from 0 to-0.5 V (vs. RHE) with 10 mV/s. Cyclic voltammetry measurements were carried out from -0.3 to -0.2 V (vs. RHE) with different scan rates (10–90 mV/s).

RESULTS AND DISCUSSION

The electrocatalytic HER experiments of copper-antimony sulfides were carried out in the anaerobic 1M KOH solution by using three electrode cells with glassy carbon electrode, Ag/AgCl and Pt as working, reference and counter

electrodes, respectively. The electrocatalytic activities of R-$CuSbS_2$ and D-$CuSbS_2$ were determinated by linear sweep voltammetry (LSV) and cyclic voltammetry (CV) methods. The measured potentials vs. Ag/AgCl were converted to the reversible hydrogen electrode (RHE) scale according to the Nernst equation:

$$E_{RHE} = E_{Ag/AgCl} + 0.059\ pH + E^{o}_{Ag/AgCl}$$

where E_{RHE} is the converted potential vs. RHE, $E^{o}_{Ag/AgCl}$ = 0.1976 at 25°C, and $E_{Ag/AgCl}$ is the experimentally measured potential against Ag/AgCl reference [25]. Catalytic activities of R-$CuSbS_2$ catalysts were also compared to D-$CuSbS_2$. The overpotential values are observed 474 mV and 508 mV in which are using R-$CuSbS_2$ and D-$CuSbS_2$, respectively, at the current density at 10 mA cm^{-2} (Fig 1a). R-$CuSbS_2$ has been displayed the lowest overpotential.

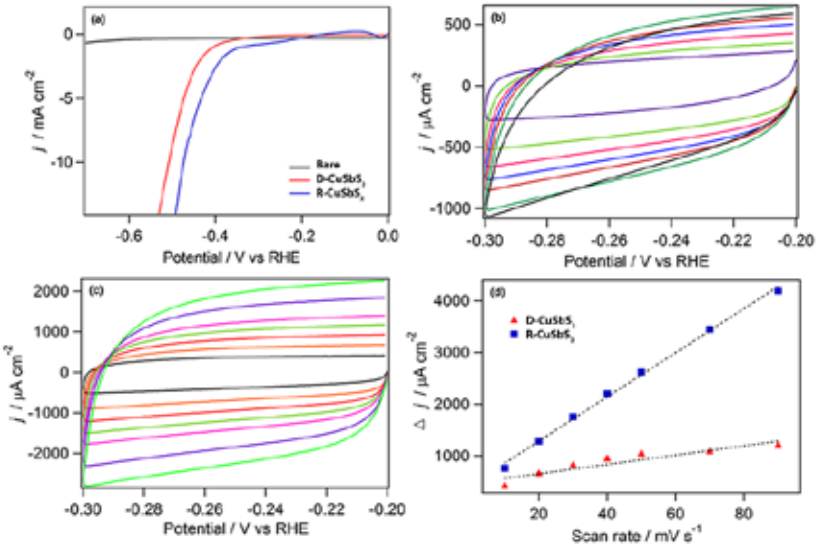


Fig 1. (a) Polarization curves, cyclic voltammograms of (b) D-CuSbS2 and (c) R-CuSbS2, (d) plots of (Cdl) linear fitting of the capacitive currents of catalysts for the electrocatalytic HER in alkaline media.

Measuring the electrochemical capacitance, different scan rates (10, 20, 30, 40, 50, 70, 90 mV/s) were carried out by sweeping between -0.3 and -0.2 V vs. RHE (Fig. b ve c). Double-layer capacitance (C_{dl}) was calculated from cyclic voltammetry method, where no faradaic processes were detected. The effective active sites of R-$CuSbS_2$ and D-$CuSbS_2$ catalysts can be determined from C_{dl}. C_{dl} values are also related to effective active sites. The observed capacitive current differences were plotted as a function of specific capacitances and scan rate, and then C_{dl} were found out by the slopes of the linear fitting (Fig. d). C_{dl} values of the R-$CuSbS_2$ and D-$CuSbS_2$ catalysts were founded as 42.67 mF and 8.97 mF, respectively, which are having harmony with overpotentials of catalysts. Consequently, it was revealed that, R-$CuSbS_2$ exhibit larger C_{dl} than D-$CuSbS_2$, which asserted more active site area for the HER [26]. Electrocatalytic activities related to shapes of these catalysts which might be explained by efficient charge separation efficiency of 1D materials.

CONCLUSIONS

It was carried out electrocatalytic hydrogen evolution reaction (HER) by using different shapes of copper-antimony sulfide in alkaline media for the first time, which are using towards energy conversion processes including due to its excellent properties as low-cost and high activity. It was found out that the electrocatalytic activity of $CuSbS_2$ may enhanced by changing of shapes. The microrod shape of $CuSbS_2$ exhibited high electrocatalytic activity than spherical shape of $CuSbS_2$ owing to the efficient charge separation efficiency of 1D structure. These results may use different energy conversion applications such as photocatalytic HER, solar cell and supercapacitors.

REFERENCES

1. Xu, F., Lu, J., Luo, L., Yu, C., Tang, Z., Abbo, H. S., ... & Yin, S. (2019). Cu2s-Cu3p Nanowire Arrays Self-Supported On Copper Foam As Boosting Electrocatalysts For Hydrogen Evolution. *Energy Technology*, *7*(4), 1800993.
2. Flores-Lasluisa, J. X., Quílez-Bermejo, J., Ramírez-Pérez, A. C., Huerta, F., Cazorla-Amorós, D., & Morallón, E. (2019). Copper-Doped Cobalt Spinel Electrocatalysts Supported On Activated Carbon For Hydrogen Evolution Reaction. *Materials*, *12*(8), 1302
3. Xu, F., Yu, C., Qian, G., Luo, L., Hasan, S. W., Yin, S., & Tsiakaras, P. (2019). Electrocatalytic production of hydrogen over highly efficient ultrathin carbon encapsulated S, P co-existence copper nanorods composite. *Renewable Energy*.

4. Xu, G.R.; Hui, J.J.; Huang, T.; Chen, Y.; Lee, J.M. Platinum nanocuboids supported on reduced graphene oxide as efficient electrocatalyst for the hydrogen evolution reaction. J. Power Sources 2015, 285, 393–399. [CrossRef]
5. Kemppainen, E.; Bodin, A.; Sebok, B.; Pedersen, T.; Seger, B.; Mei, B.; Bae, D.; Vesborg, P.C.K.; Halme, J.; Hansen, O.; et al. Scalability and feasibility of photoelectrochemical H2 evolution: the ultimate limit of Pt nanoparticle as an HER catalyst. Energy Environ. Sci. 2015, 8, 2991–2999. [CrossRef]
6. Raoof, J.B.; Ojani, R.; Kiani, A.; Rashid-Nadimi, S. Fabrication of highly porous Pt coated nanostructured Cu-foam modified copper electrode and its enhanced catalytic ability for hydrogen evolution reaction. Int. J. Hydrogen Energy 2010, 35, 452–458. [CrossRef]
7. Huang, J., Zhao, S., Chen, W., Zhou, Y., Yang, X., Zhu, Y., & Li, C. (2016). Three-dimensionally grown thorn-like Cu nanowire arrays by fully electrochemical nanoengineering for highly enhanced hydrazine oxidation. *Nanoscale*, *8*(11), 5810-5814.
8. Yang, L., Xie, L., Ren, X., Wang, Z., Liu, Z., Du, G., ... & Sun, X. (2018). Hierarchical CuCo 2 S 4 nanoarrays for high-efficient and durable water oxidation electrocatalysis. *Chemical communications*, *54*(1), 78-81.
9. Jaramillo, T. F., Jørgensen, K. P., Bonde, J., Nielsen, J. H., Horch, S., & Chorkendorff, I. (2007). Identification of active edge sites for electrochemical H2 evolution from MoS2 nanocatalysts. *science*, *317*(5834), 100-102.
10. Zhang, X., & Xie, Y. (2013). Recent advances in free-standing two-dimensional crystals with atomic thickness: design, assembly and transfer strategies. *Chemical Society Reviews*, *42*(21), 8187-8199.
11. Rath, T., MacLachlan, A. J., Brown, M. D., & Haque, S. A. (2015). Structural, optical and charge generation properties of chalcostibite and tetrahedrite copper antimony sulfide thin films prepared from metal xanthates. *Journal of Materials Chemistry A*, *3*(47), 24155-24162.
12. Welch, A. W., Zawadzki, P. P., Lany, S., Wolden, C. A., & Zakutayev, A. (2015). Self-regulated growth and tunable properties of CuSbS2 solar absorbers. *Solar Energy Materials and Solar Cells*, *132*, 499-506.
13. Rabhi, A., Kanzari, M., & Rezig, B. (2009). Optical and structural properties of CuSbS2 thin films grown by thermal evaporation method. *Thin Solid Films*, *517*(7), 2477-2480.
14. Colombara, D., Peter, L. M., Rogers, K. D., Painter, J. D., & Roncallo, S. (2011). Formation of CuSbS2 and CuSbSe2 thin films via chalcogenisation of Sb–Cu metal precursors. *Thin Solid Films*, *519*(21), 7438-7443.
15. Septina, W., Ikeda, S., Iga, Y., Harada, T., & Matsumura, M. (2014). Thin film solar cell based on CuSbS2 absorber fabricated from an electrochemically deposited metal stack. *Thin Solid Films*, *550*, 700-704.
16. Colombara, D., Peter, L. M., Rogers, K. D., & Hutchings, K. (2012). Thermochemical and kinetic aspects of the sulfurization of Cu–Sb and Cu–Bi thin films. *Journal of Solid State Chemistry*, *186*, 36-46.
17. Ornelas-Acosta, R. E., Shaji, S., Avellaneda, D., Castillo, G. A., Roy, T. D., & Krishnan, B. (2015). Thin films of copper antimony sulfide: a photovoltaic absorber material. *Materials Research Bulletin*, *61*, 215-225.
18. Choi, Y. C., Yeom, E. J., Ahn, T. K., & Seok, S. I. (2015). CuSbS2-sensitized inorganic–organic heterojunction solar cells fabricated using a metal–thiourea complex solution. *Angewandte Chemie International Edition*, *54*(13), 4005-4009.
19. Vinayakumar, V., Shaji, S., Avellaneda, D., Aguilar-Martínez, J. A., & Krishnan, B. (2018). Copper antimony sulfide thin films for visible to near infrared photodetector applications. *RSC advances*, *8*(54), 31055-31065.
20. Loranca-Ramos, F. E., Diliegros-Godines, C. J., González, R. S., & Pal, M. (2018). Structural, optical and electrical properties of copper antimony sulfide thin films grown by a citrate-assisted single chemical bath deposition. *Applied Surface Science*, *427*, 1099-1106.
21. Yamada, Y., Yano, K., Xu, Q., & Fukuzumi, S. (2010). Cu/Co3O4 nanoparticles as catalysts for hydrogen evolution from ammonia borane by hydrolysis. *The Journal of Physical Chemistry C*, *114*(39), 16456-16462.
22. Zou, Y., & Jiang, J. (2014). Colloidal synthesis of chalcostibite copper antimony sulfide nanocrystals. *Materials Letters*, *123*, 66-69.
23. Yan, C., Su, Z., Gu, E., Cao, T., Yang, J., Liu, J., ... & Liu, Y. (2012). Solution-based synthesis of chalcostibite (CuSbS 2) nanobricks for solar energy conversion. *RSC Advances*, *2*(28), 10481-10484.
24. Yıldırım, M., Kocyigit, A., Sarılmaz, A., & Ozel, F. (2019). The effect of the triangular and spherical shaped CuSbS 2 structure on the electrical properties of Au/CuSbS 2/p-Si photodiode. *Journal of Materials Science: Materials in Electronics*, *30*(1), 332-339.
25. Wang, L., Lee, C.Y., Schmuki, P., Solar water splitting: preserving the beneficial small feature size in porous alpha-Fe2O3 photoelectrodes during annealing, J. Mater. Chem. A 1 (2013) 212–215.
26. Sarilmaz A., Genc E., Aslan E., Ozen A., Yanalak G., Ozel F., Hatay Patir I., Wang, L., Lee, C.Y., Schmuki, P., Photocatalytic hydrogen evolution via solar-driven Water splitting by CuSbS2 with different shapes, Journal of Photochemistry and Photobiology A: Chemistry, 400, (2020) 112706.

WHEC-2022
23rd World Hydrogen Energy Conference
June 26-30, 2022 - Istanbul

#1546

CATALYTIC HYDROGEN EVOLUTION BY USING DIFFERENT CARBON-BASED NANOCOMPOSITE AT SOFT INTERFACES

[1] Emre Aslan ,[2]Imren Hatay Patir*
[1]Selcuk University, Faculty of Science, Department of Biochemistry, Konya, Turkey
[1]Selcuk University, Faculty of Science, Department of Biotechnology, Konya, Turkey

*Corresponding author e-mail: imrenhatay@gmail.com

ABSTRACT

Efficiency increment of hydrogen evolution reaction (HER) is great challenge in the literature. Nanocomposite based catalysts are significant drawn attention due to the increasing active sites for hydrogen evolution. Herein, it is reported that in situ electrodeposition of metallic nanoparticles on multi-walled carbon nanotube or reduced graphene oxide by using organic sacrificial electron donor decamethylferrocene (DMFc) at liquid/liquid interfaces. The nucleation and catalytic reactions have been tracked by using 4-electrode voltammetry and biphasic reactions. The catalytic activities of metallic nanoparticles on carbon-based nanocomposites are founded as higher activities than that of non-metallic nanocomposites for biphasic catalysis.

Keywords: Hydrogen evolution, Liquid/liquid interface, Electrodeposition

INTRODUCTION

Providing sustainable energy in an affordable and eco-friendly manner is one of the challenges in the literature. Hydrogen is regarded as ideal energy carrier and good alternative to the fossil fuels due to the pollution-free, energy efficiency, recyclability and sustainability. Catalytic hydrogen evolution by water splitting gives a promising solution to growing demands for clean and sustainable energy. Platinum group metals (PGMs) are well-known and efficient catalyst for the HER. Although developing PGM-free catalyst, their catalytic activities did not reach the PGM catalysts up to now. Because of this disadvantage, efficient and durable PGMs are still under investigation. Electrocatalytic reactions are generally performed on the solid electrodes. Energy conversion reactions such as oxygen reduction, CO_2 reduction and H_2 production reactions can be carried out at soft liquid/liquid interfaces. Hydrogen evolution reaction (HER) can be figured out by different organic electron donor molecules like osmocene, decamethylosmocene, decamethylruthenocene and decamethylferrocene (DMFc) [1]. DMFc is most used sacrificial molecules and its reaction rate can be increased by using different catalysts [1]. However, these catalysts are generally used as synthesized. Recently, in situ electrodeposited electrocatalysts have been investigated for the hydrogen evolution reaction at liquid/liquid interfaces. Our group have been reported that catalysis of HER at water-1,2-dichloroethane (DCE) interface by in situ electrodeposited Pt, Pd, Cu and Cu/CNT catalysts [2-4]. The electrodeposition at liquid/liquid interfaces is generally carried out by using Pd. For example, research group of Dryfe is investigated the Pd electrodeposition at the water/DCE interface. Structural, morphological and electrochemical characterizations of the electrodeposited Pd nanoparticles have been investigated at templated and bare soft interfaces [5-8]. Herein, the using templates were supplied to control the electrodeposition of Pd. Electrodeposition begins at the soft interface with nucleation of particles, and then the particles are growth on the templates.

Carbon based materials like carbon nanotubes, graphene, or fullerenes, can be improved the catalytic activity because of increasing surface area, active sites as well as supplying electrical contact between donor molecule and catalyst surface [9]. We have been aimed to increase catalytic activity of free-standing Pd nanoparticles at water/DCE interface. There is no study reported that hydrogen evolution by using in situ electrodeposited CNT/Pd catalyst at the liquid/liquid interfaces.

Herein, in situ electrodeposition of CNT/Pd have been reported for both electrochemical characterization and catalytic HER at the water/DCE interface by using organic sacrificial agent DMFc. The catalytic activity of CNT/Pd is also compared to only Pd. The nucleation and catalytic activities are followed by 4-electrode voltammetry and chromatographic techniques with biphasic reactions. The obtained results were providing comparable results for different non-noble metallic or non-metallic composites.

MATERIALS AND METHODS

4-electrode voltammetry experiments have been carried out by using the cell having 1.53 cm^2 geometric area (two Ag/AgCl reference electrode and two Pt counter electrode in the organic and aqueous phases) with or without catalyst precursor. Biphasic hydrogen evolution experiments were carried out in headspace vials having 11 mL volume with stirring conditions in the absence and presence of Pd or CNT/Pd. the whole experiments have been performed under the anaerobic conditions in glovebox. The evolved hydrogen amount has been measured by gas chromatography

(Shimadzu, GC 2010 Plus, using thermal conductivity detector (TCD) and argon carrier gas), after biphasic reactions. Galvani potential difference is determined by using tetraethylammonium cation (TEA^+) [10,11].

RESULTS AND DISCUSSION

Obtaining and electrochemical characterization of Pd nanoparticle and CNT/Pd nanocomposite were tracked by using 4-electrode voltammetry technique. Firstly, blank voltammogram was obtained by using only supporting electrolyte in both phases and potential window was determined between -0.2 V and 0.3 V. Then, organic sacrificial agent DMFc was added to DCE phase to observe assisted proton transfer from water to organic phase, which can be explained small current increasing and potential shifting at the positive potential edge [12]. Both DMFc and $(NH_4)_2PdCl_4$ were added to organic and aqueous phases, respectively, were displayed a nucleation loop and robust current increasing, which is based on the formation of Pd nanoparticles [2]. When both $(NH_4)_2PdCl_4$ and CNT added to aqueous phase in the presence of DMFc in the organic phase, there is no nucleation loop due to the larger capacitive current, which related to adsorption of CNT at the water/DCE interface.

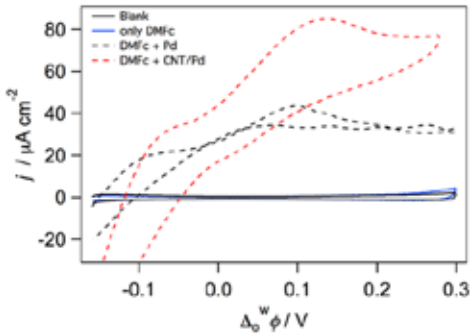


Figure 1. The nucleation of Pd and CNT/Pd at the water/DCE interface.

The catalytic activity of CNT/Pd nanocomposite is also investigated by biphasic reactions, which is also known as shake-flask. This technique is based on chemical polarization of interface with distribution of common ion TB^- both liquid phases. The catalytic HER was carried out by chemically controlled Galvani potential difference at water/DCE interface. In the absence of catalyst, reaction rate is very slow, and the amount of evolved hydrogen reached only 0.8 μmol after 24 hours of shaking. Using only CNT in the aqueous phase, HER rate is a little increased, which might be originated from metallic impurities in the CNT [4]. When Pd precursor and/or CNT added to aqueous phase, evolved hydrogen amount was increased dramatically. These results show that Pd and CNT/Pd occurred by in situ electrodeposition during the HER and they were catalyzed the HER at water/DCE. Gas chromatogram of HER is given in the figure 2 and it shows that electrodeposited Pd and CNT/Pd catalyzed HER efficiently. After 30 min of shake-flask experiments, Pd and CNT/Pd were produced 2.8 and 4.2 μmol hydrogen, respectively.

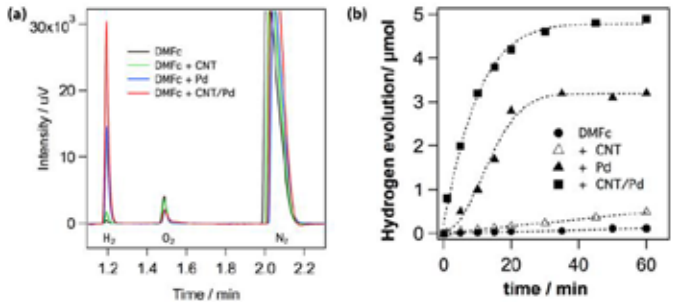


Figure 2. (a) Gas chromatograms of biphasic HER after 20 min both in the absence and presence of CNT, Pd or CNT/Pd catalysts. (b) Time dependent evolved hydrogen amount

The HER mechanism at the water/DCE interface is proceeded by proton coupled electron transfer (PCET) mechanism. Herein, electrons from DMFc injected to the CNT/Pd and protons adsorbed on the Pd nanoparticles is reduced into hydrogen gas. The role of CNT is that the electrons “pooled” in the CNT are highly mobile along the CNT “electron superhighway” [13]. CNT-based catalysts show also more catalytic activity than that of rGO-based once because 1D properties of CNT increase the charge carrier ability than 2D graphene-based materials. The obtained experimental data by using nanocomposite catalysts for the HER were given the comparable results with the non-metallic composites.

CONCLUSIONS

This work reported that catalytic hydrogen evolution reaction at the water/DCE interface by *in situ* spontaneous electrodeposited CNT/Pd nanocomposite for the first time. While nucleation is monitored by 4-electrode voltammetry, catalysis of HER is followed by biphasic reactions. HER activity of Pd is enhanced by using CNT/Pd nanocomposite due to the high electron transport efficiency of CNT. This activities differences between free Pd and CNT/Pd may be originated from preventing the aggregation of Pd nanoparticles by using CNT. This study paves the way a new approach for catalysis by using in situ spontaneous electrodeposited nanocomposite catalysts instead of as synthesized catalysts.

REFERENCES

1. Peljo P., Scanlon M. D., Olaya A. J., Rivier L., Smirnov E., Girault H. H., 2017. Redox Electrocatalysis of Floating Nanoparticles: Determining Electrocatalytic Properties without the Influence of Solid Supports, The Journal of Physical Chemistry Letters, 8, 15, 3564-3575.
2. Nieminen J. J., Hatay İ., Ge P., Mendez M. A., Murtomaki L., Girault H. H., 2011, Hydrogen evolution catalyzed by electrodeposited nanoparticles at the liquid/liquid interface, Chemical Communications, 47, 5548-5550
3. Aslan, E., Patir, I. H. and Ersoz, M., 2015, Cu nanoparticles electrodeposited at liquid-liquid interfaces: a highly efficient catalyst for the hydrogen evolution reaction, Chemistry - A European Journal, 21 (12), 4585-4589.
4. Aslan, E., Akin, I. and Patir, I. H., 2016, Enhanced Hydrogen Evolution Catalysis Based on Cu Nanoparticles Deposited on Carbon Nanotubes at the Liquid/Liquid Interface, ChemCatChem, 8 (4), 719-723.
5. Dryfe R. A. W., Simm A. O., Kralj B., 2003, Electroless Deposition of Palladium at Bare and Templated Liquid/Liquid Interfaces, J. Am. Chem. Soc. 125, 43, 13014-13015
6. Platt M., Dryfe R.A.W., Roberts E.P.L., Electrodeposition of palladium nanoparticles at the liquid–liquid interface using porous alumina templates, 2003, Electrochimica Acta, 48, 3037-3046.
7. Platt M., Dryfe R.A.W., Roberts E.P.L., 2004, Structural and electrochemical characterisation of Pt and Pd nanoparticles electrodeposited at the liquid/liquid interface, Electrochimica Acta, 49, 3937-3945.
8. Platt M. and Dryfe R.A.W., 2005, Structural and electrochemical characterisation of Pt and Pd nanoparticles electrodeposited at the liquid/liquid interface: Part 2, Phys. Chem. Chem. Phys., 7, 1807–1814.
9. Peng S., Li L., Han X., Sun W., Srinivasan M., Mhaisalkar S. G., Cheng F., Yan Q., Chen J., Ramakrishna S., 2014, Cobalt sulfide nanosheet/graphene/carbon nanotube nanocomposites as flexible electrodes for hydrogen evolution, Angew. Chem. Int. Ed. 53, 12594-12599.
10. Akin, I., Aslan, E. and Hatay Patir, I., 2017, Enhanced Hydrogen Evolution Catalysis at the Liquid/Liquid Interface by NixSy and NixSy/Carbon Nanotube Catalysts, European Journal of Inorganic Chemistry, 2017 (33), 3961-3966.
11. Ozel, F., Aslan, E., Sarilmaz, A. and Hatay Patir, I., 2016, Hydrogen Evolution Catalyzed by Cu2WS4 at Liquid-Liquid Interfaces, ACS Applied Materials & Interfaces, 8 (39), 25881-25887.
12. Hatay, I., Su, B., Li, F., Partovi-Nia, R., Vrubel, H., Hu, X., Ersoz, M. and Girault, H. H., 2009, Hydrogen evolution at liquid-liquid interfaces, Angewandte Chemie International Edition, 48 (28), 5139-5142.
13. Aslan, E., Akin, I. and Patir, I. H., 2016, Highly Active Cobalt Sulfide/Carbon Nanotube Catalyst for Hydrogen Evolution at Soft Interfaces, Chemistry - A European Journal, 22 (15), 5342-5349.

WHEC-2022
23rd World Hydrogen Energy Conference
June 26-30, 2022 - Istanbul

#1548

APPLICATION OF DIFFERENT CATALYSTS IN BIOMASS GASIFICATION IN UPDRAFT/DOWNDRAFT FIXED BED REACTORS

[1]Özgün Tezer, [2]Nazlıcan Karabağ, [3,4]Atakan Öngen, [5*]Azize Ayol
[1] Dokuz Eylul University, The Graduate School of Natural and Applied Sciences, Department of Environmental Engineering, 35160, Buca, Izmir, Turkey
[2] Istanbul University-Cerrahpaşa, Department of Environmental Engineering, Istanbul, Turkey
[3] Istanbul University-Cerrahpaşa, Department of Environmental Engineering, Istanbul, Turkey
[4] Istanbul University-Cerrahpaşa, Environmental and Earth Sciences Application and Research Center, Istanbul, Turkey
[5] Dokuz Eylul University, Department of Environmental Engineering, 35160, Buca, İzmir, Turkey

*Corresponding author e-mail: azize.ayol@deu.edu.tr

ABSTRACT

This study aims to investigate the effects of different catalysts on biomass gasification. Two different types of red mud (RM1, RM2), white mud (WM), and aluminum - nickel alloy were used as catalysts with biomass mixture for the lab-scale gasification studies by using an updraft and a downdraft fixed bed reactors. Green waste (GW), sewage sludge (SS) and olive pomace (OP) were used as feedstock. The results showed that the highest concentration of H_2 (47 vol.%) was observed in mixed sample with 0.05 L/min dry air at 900°C in updraft gasifier. In downdraft gasifier, max. H_2 concentration was measured for mixed sample at 800°C while 0.1 L/min dry air was applied. In general, it has been observed that RM increases the H_2 gas in the syngas between 1-7 vol.% at 900°C in updraft gasifier. In the downdraft reactor, on the contrary, H_2 concentration in the syngas decreased by 2-6% with the addition of RM. However, when aluminum - nickel alloy was added to the samples, syngas production drastically increased and its H_2 content was found more than 65% for both reactors. This study presents the research results on the catalytic effects on the syngas composition in detail.

Keywords: Gasification, Hydrogen, Biomass, Catalyst, Renewable energy

INTRODUCTION

Energy security and environmental pollution are two major concerns worldwide. The negative effects of fossil fuels on the environment have accelerated the research need for renewable resources such as biomass, which is a sustainable and valuable fuel source. In recent studies, it has been stated that more importance is given to energy and hydrogen production from biomass, since biomass is more advantageous than fossil fuels in terms of carbon emissions and carbon density (Al-Zareer et al., 2018). In addition, gasification as a thermochemical conversion process involving various chemical reactions, heat, and mass transfer is considered as one of the most promising methods for the use of biomass. H_2 produced by biomass gasification is a clean energy source. However, the enrichment of hydrogen is a great concern. The usage of catalysts might be an important alternative to increase the hydrogen yield in biomass gasification. Chai et al. (2020) have found that catalysts can affect H_2 production. New catalyst with high catalytic activity is to be developed to improve hydrogen production. Nickel catalysts are widely used in biomass gasification due to their low cost and high activity for C-C bond breaking. Alumina-based materials (Al_2O_3) are often used as supports due to their chemical and physical stability and suitable mechanical properties (Alvarez et al., 2014). In this study, the catalytic performance of different catalysts for biomass gasification was evaluated in terms of improving syngas quality and increasing H_2 gas content and its effect on tar formation. RM and aluminum-nickel alloy showed a more effective catalytic performance for gasification at high temperature and low agent flow rate. This experimental study can be considered as a preliminary study to improve the performance of a large-scale gasification plant operation.

MATERIALS AND METHODS

In this study, GW, SS and OP was used as biomass mixture. GW samples were taken from Manisa Metropolitan Municipality while SS samples were provided from Cigli Wastewater Treatment Plant in Izmir. OP samples were taken from a chemical plant working on olive oil soap located in Izmir, Turkey. In the gasification experiments, a biomass mixture consisting of GW, SS and OP samples was prepared as fuel. 25g was taken from each sample and a total of 75g sample was fed to the reactor system. Dry air was used as the gasification agent at different flow rates (0.05-0.1-0.2 L/min) The gasifier temperatures were used as 700°C, 800°C, and 900 °C.. RM1, the waste product of an aluminum processing plant for catalytic tar/tar removal was used as a low-cost catalyst. RM2 and WM catalysts are commercially used muds and aluminum - nickel alloy was provided from Merck. The photographs of the biomass samples and catalysts were given in Figure 1 and Figure 2.



a b c d

Figure 1. Biomass samples, (a) Raw GW, (b) Dried GW, (c) SS, (d) OP



a b c d e

Figure 2. Catalysts, (a) RM1, (b) Commercial RM2, (c) Dried commercial RM2, (d) Commercial WM, (e) Dried commercial WM,

The characterization studies on GW, SS and pomace OP were carried out in Department of Environmental Engineering, Sludge Laboratory at Dokuz Eylul University. pH, electrical conductivity (EC), salinity, dry solids content (DS), volatile solids content (VS), loss of ignition (LOI), higher heating value (HHV), total nitrogen (TN), total phosphorus (TP), thermogravimetric analyses (TGA) were done.

The reactors having a maximum 3 L of volume are designed as updraft and downdraft fixed bed systems and constructed from high temperature resistant AISI 310 S stainless steel. They were operated at different amounts of biomass at different temperatures and gasifying agent's flow-rates. The outer wall of the reactors was covered with a ceramic jacket. The syngas produced in the reactors are circulated in the reactors several times and then passed through the cyclone and taken to the cooler. Updraft fixed bed reactor system were set up in Dokuz Eylul University (DEU), Izmir while the downdraft system was installed in Istanbul University-Cerrahpasa (IUC), Istanbul, Turkey. The biomass mixture samples were gasified by adding different amounts of catalysts. Syngas measurements were done by MRU brand VARIOluxx model online gas analyzer and ABB brand syngas analyzer in DEU and IUC, respectively. These analyzers contain O_2, CO, CO_2; CH_4 and H_2 sensors and calculate the calorific value of the produced gas.

RESULTS AND DISCUSSION

In the characterization studies, VS of GW was found as 79.7% while it was determined as 48% and 74% for SS and OP, respectively. Ultimate and proximate analysis of biomass samples were given in Table1. GW and OP have higher VS and calorific value than SS.

Table 1. The physico-chemical properties of biomass samples

Ultimate Analysis (wt.%)				Proximate Analysis (wt.%)			
	GW	SS	OP		GW	SS	OP
C	38.88	32.23	47.57	Moisture	6.80	6.54	8.97
H	5.59	5.02	6.40	Volatile Solids	79.71	47.53	73.98
N	1.90	2.14	1.65	Fixed Carbon	7.73	12.84	12.83
S	0.12	0.70	0.12	Ash	12.56	39.63	13.19
O (by difference)	40.86	20.37	31.06	Bulk Density, kg/m3	25	365	600
				LHV, MJ/kg	15.95	12.65	17.32

In the gasification experiments, the max. H_2 concentration varied between 41 vol. % and 47 vol.% in updraft gasifier. In the downdraft gasifier, the max. H_2 concentration vary between 36 vol. % and 41 vol.%. Max. H_2 (47%) was observed in the syngas with using 0.05 L/min dry air and at 900 °C. When RM1 and RM2 were added to the mixed sample, the max. H_2 concentration was obtianed between 33% and 50 vol.% in updraft gasifier and between 30% and 37 vol.% in downdraft gasifier. Max. H_2 (50%) was observed using RM1 and RM2 with using 0.05 L/min dry air

and at 900 °C in updraft gasifier. The H_2/CO ratio was found between 2-4 for biomass mixture. In the catalyst added mixed sample, this ratio was ranged between 1.6 and 6. The calorific values of syngas were recorded between 8-13 MJ/m^3 in mixed samples with RM1, RM2, WM and aluminum – nickel alloy catalysts. When aluminum - nickel alloy was added to the samples, syngas production drastically increased and its H_2 content was found more than 60% for both reactors.

CONCLUSIONS

In this experimental study, gasification of the mixture sample formed by different biomass sources was done. The effects of different catalysts as RM1, RM2, WM and aluminum- nickel alloy on syngas formation was investigated by using fixed bed updraft and downdraft gasifiers. The max. H_2 and CH_4 concentrations were achieved approximately as 47 and 8 vol.% in updraft gasifier. These values are observed 50 vol.% and 5 vol.% for RM1 (7.5 g) added mixed sample. When 15g RM2 was used as catalysts, the max. H_2 and CH_4 concentrations were obtained in updraft gasifier 50 vol.% and 4 vol.%, respectively. Compared to the H_2 content produced without the catalyst addition, an increase of 3 vol. % H_2 concentrations were determined. As the amount of RM1 increased in the biomass mixture, a lower concentration of H_2 gas was formed. It was observed that the calorific value of the syngas slightly decreased when RM1 was added in the same conditions. When WM was added as a catalyst, syngas with the highest calorific value was found. The max. calorific value was determined approximately 13 MJ/m^3. In this study, the effects of different catalysts usage were determined to improve the syngas performance in biomass gasification. The detailed results of the experimental studied will be debugged for the achieving higher syngas efficiency.

ACKNOWLEDGEMENT

This study was funded by TÜBİTAK-ÇAYDAG “Sustainable Energy Recovery from Treatment Plant Sludge, Green Wastes, and Olive Pomace via Gasification Process: Investigation of Beneficial Usage Alternatives of Gasification Products” Research Project (under grant #119R029).

REFERENCES

1. Alvarez J, Kumagai S, Wu C, Yoshioka T, Bilbao J, Olazar M and Williams PT. 2014. Hydrogen production from biomass and plastic mixtures by pyrolysis-gasification. International Journal of Hydrogen Energy, 39(21), 10883-10891.
2. Al-Zareer M, Dincer I and Rosen MA. 2018. Influence of selected gasification parameters on syngas composition from biomass gasification. Journal of Energy Resources Technology, 140(4).
3. Chai Y, Wang M, Gao N, Duan Y and Li J. 2020. Experimental study on pyrolysis/gasification of biomass and plastics for H2 production under new dual-support catalyst. Chemical Engineering Journal, 396, 125260.

WHEC-2022
23rd World Hydrogen Energy Conference
June 26-30, 2022 - Istanbul

#1561

THE EFFECT OF THERMAL OXIDATION TIME IN AIR AND ARGON ATMOSPHERE ON PEC EFFICIENCY OF HEMATITE (Fe_2O_3) PHOTOANODE

[1,2] *Fatma Betül Yılmaz,* [1*] *Cevat Sarıoğlu*
[1]Marmara University, Faculty of Engineering, Department of Metallurgical and Materials Engineering, 34854, İstanbul, Turkey
[2]Marmara University, Graduate School of Natural and Applied Sciences, 34722, İstanbul, Turkey

* E-mail: cevat.sarioglu@marmara.edu.tr

ABSTRACT

Fe thin films electrodeposited on FTO substrate were thermally oxidized to hematite. The photocurrents values, indication of H_2 production efficiency in PEC cell were improved by optimizing thermal oxidation parameters of undoped hematite photoanode such as oxidation atmospheres (air and argon), oxidation temperatures (450 and 550°C) and oxidation time. The effect of these parameters on the photocurrents measured in PEC cell in hematite photoanode were characterized by using LSV (the linear sweep voltammetry), Mott Schottky and, EIS analyses. The effect of oxidation time on photocurrents were studied. Photocurrents first increased and reached the maximum values and then decreased with oxidation time in both argon and air atmospheres at 450°C and 550°C. The photocurrents measured at 0.6 V vs. SCE for hematite at 450°C and 550°C in argon atmosphere were greater compared to the photocurrents measured in hematite synthesized in air. The highest photocurrent of 0.56 mA/cm^2 at 0.6 V vs. SCE was measured for the hematite synthesized in argon atmosphere at 450°C with oxidation time of 96 hours.

Keywords: Hematite, Photoanode, Water splitting, PEC, Thermal Oxidation.

INTRODUCTION

Today, climate change whose effects are clearly visible by increasing greenhouse gases has become a global problem and dealing with it requires taking global action. The EU plays an active role in climate change set a target to reduce carbon emissions by at least 55%, by 2030, compared with 1990 levels [1]. Thus, renewable energy is essential for reducing carbon dioxide emissions that mainly occurred by fuel fossil and for satisfying the increasing clean energy demand. Photoelectrochemical (PEC) water splitting which converts solar energy directly into chemical energy is promising renewable energy source.

Hematite has attractive properties for use in photoactive semiconductor materials due to the significant light absorption (ideal bandgap with a 2.0-2.2 eV), its abundance, non-toxicity and its maximum theoretical STH efficiency of 16% with a photocurrent of 12.6 mA/cm^2 [2]. In previous studies, hematite showed a low performance (highest known photocurrent value ~6 mA/cm^2 at 1.23 V vs. RHE [3]) compared with theoretical value because it has some limitations such as its poor electrical conductivity, low hole diffusion length and high overvoltage requirement despite its promising properties [2].In the literature, it has been investigated that the photoelectrochemical performance of hematite was affected by changing synthesis conditions such as atmosphere (oxygen partial pressure), temperature and time [4-7]. Chnani et al. studied the parameters of thermal oxidation of Fe thin film i.e. time, temperature and rapid heating-cooling under ambient air and they reported that the increasing temperature and time had a positive effect on the photocurrent [4]. Smart et al. used first-principal calculations to predict the polaron concentration in hematite depending on synthesis conditions such as temperature and oxygen partial pressure. As a result of this study, they proposed that the electron concentrations of undoped hematite increase dramatically when the synthesis temperature is increased, or the oxygen partial pressure is decreased [5].

In this paper, the photoelectrochemical performances of undoped hematite photoanode were studied by optimizing thermal oxidation parameters such as time, temperature, and atmosphere. In addition to literature, the first time the effect of the oxidation time in argon atmosphere was investigated.

MATERIALS AND METHODS

First, the FTO substrates were carefully cleaned by ultrasonic rinsing in acetone, ethanol, and deionized water for depositing homogenous films. Then, Fe thin films were prepared on FTO by electrodeposition that was carried out in a two-electrode setup cell in a galvanostatic mode by using Bio-Logic galvanostat. During the deposition process, the distance between an FTO substrate (working electrode) and a platinum wire (counter electrode) was kept at about ~1.5 cm. The time for deposition was 50 s and the current density was 5 mA/cm^2. After electrodeposition, thermal oxidation of Fe thin film samples was performed in a Protherm tube furnace to study the effect of different synthesis conditions for hematite. The synthesis parameters were oxidation temperatures (450℃ and 550℃), oxidation atmospheres (air and argon) and oxidation times. In oxidation in Ar atmosphere, the system was flushed with Ar (1.5 L/min) for 30 minutes

before switching on the furnace. The heating rate was 10℃/min for all samples. At the end of the oxidation, the samples were left to cool in the furnace to room temperature. More details about the oxidation process are given in the following Table 1.

Table 1. The details of the oxidation process for the samples

Atmosphere	Temperature	Time
Air	450℃	5 h
		24 h
		68 h
	550℃	15 min
		30 min
		5 hour

Atmosphere	Temperature	Time
Argon	450℃	48 hour
		96 hour
		192 hour
	550℃	5 hour
		24 hour
		48 hour

After oxidation, all samples were connected to the copper wire using conductive paint for making photo-electrodes. Photoelectrochemical experiments (I-V, EIS and, Mott Schottky) were performed in a three-electrode system using a saturated calomel electrode as the reference electrode, a platinum wire as the counter electrode and a hematite photoanode as the working electrode. The measurements were conducted in 0.1 M sodium hydroxide electrolyte using a potentiostat (Bio-Logic VSP) and carried out under AM1.5G solar irradiation from an Abet solar simulator (100 mW cm^2).

RESULTS AND DISCUSSION

Photocurrents measured for hematite in the argon atmosphere at 450ºC with various oxidation times (48, 96 and 196 hours) were plotted in Fig. 1a. Photocurrent measured at 0.6V vs. SCE first increased and reach the maximum value of 0.56 mA/cm^2 at 96 hours and then decreased at 192 h. The similar trend was found for hematite formed in air, Fig. 1b [8]. Maximum photocurrents measured at 0.6V vs.SCE for argon and air atmosphere were 0.56 mA/cm^2 and 0.38mA/cm^2 respectively. The highest photocurrent density value of 0.56 mA/cm^2 for argon atmosphere was 1.5 times of the best photocurrent density obtained in air for 24h at 450°C (0,38 mA/cm^2) in Fig. 1. In agreement with the literature, the results showed that decreasing oxygen partial pressure in argon atmosphere increased the PEC performance of hematite annealed at 450°C for 96h.

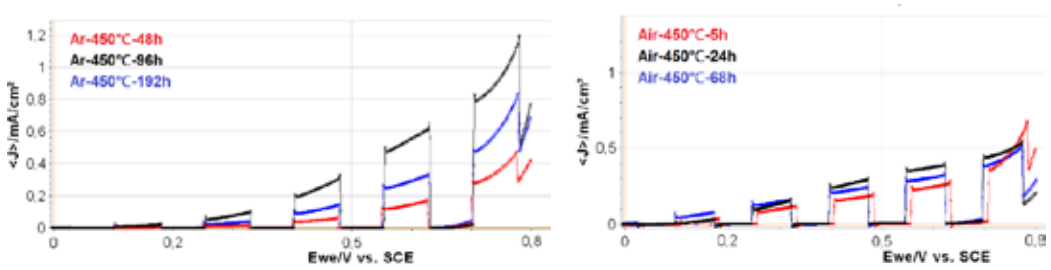


Figure 1. LSV under the light condition of hematite photoanodes oxidized for (a) 48h, 96h and 192h in argon (b) 5h, 24h and 68h in air atmosphere at 450 ℃

According to Fig. 2, increasing the oxidation temperature from 450°C to 550°C improved the photocurrent at the initial potentials but as potential increased further the photocurrent decreased in both air and the argon atmosphere. The photocurrent measured at 0.6V vs. SCE in argon atmosphere at 450ºC was significantly greater than the photocurrent measured at 550ºC, Fig. 2a. Unlike argon atmosphere, the best photocurrents of samples oxidized at 450°C and 550°C were similar in air in Fig. 2b and photocurrent measured at 0.6V vs. SCE was 0.32-0.38 mA/cm^2 range for both at 450°C and 550°C in air.

The defect concentration (Nd) and flat-band potential (Vf) obtained from the Mott Schottky measurement for the samples oxidized under argon atmosphere at 450ºC for different oxidation times, Fig. 3 was given in Table 2. The hematite annealed for 96 h in argon atmosphere, exhibited the highest defect concentration compared to others. EIS impedance results indicated similar results. The electrical conductivity was the highest for the hematite synthesized in argon at 96 hours. As a result, the photocurrent of the sample synthesized at 450ºC in argon has the highest value because of its high conductivity and high defect concentrations.

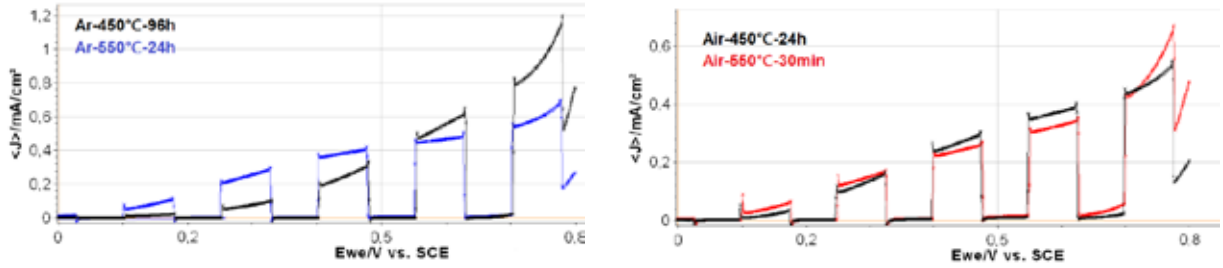


Figure 2. LSV under the light condition of hematite photoanodes oxidized under a) argon and b) air atmosphere at 450 and 550 ℃

Table 2. Mott Schottky analysis data of the samples oxidized in argon atmosphere at 450℃ under the light conditions

Sample	Frequency	Flat band potential	Donor Density
Ar-48h	1 kHz	-0,824 V	$0.583x10^{21}cm^{-3}$
Ar-96h	1 kHz	-0,806 V	$1.114x10^{21}cm^{-3}$
Ar-192h	1 kHz	-0.771 V	$0.332x10^{21}cm^{-3}$

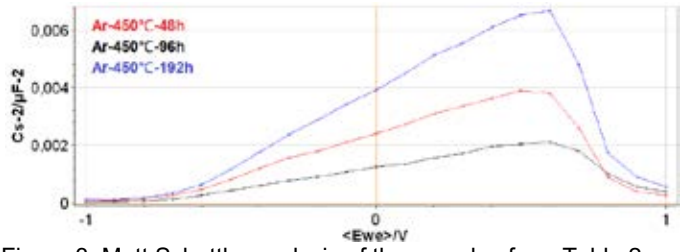


Figure 3. Mott Schottky analysis of the samples from Table 2

CONCLUSIONS

- The photocurrent changes with oxidation time. The photocurrent first increased and reached the maximum and then decreased with increasing oxidation time for the hematite synthesized in both argon and air at 450°C and 550°C. The highest photocurrents were found at 24 hours at 450°C and 30 minutes at 550°C in air while that was found at 96 hours at 450°C and 24 hours at 550°C in argon atmosphere.
- The photocurrent measured at 0.6 V vs. SCE for hematite at 450°C in argon atmosphere was the highest (0.56 mA/cm^2) with the highest defect concentration and conductivity compared to the photocurrents measured in hematite synthesized in air.

ACKNOWLEDGEMENT

This research was supported by Marmara University through Coordination Scientific Reearch Project (BABKO) with project no: FYL-2022-10336.

REFERENCES

1. Official Journal of the European Union. 2021. Regulation (EU) 2021/1119 of the European Parliament and of the Council, L 243/1-L 243/17
2. Sivula K, Formal FL. and Gratzel M. 2011. Solar water splitting: progress using hematite photoelectrodes. ChemSusChem 4:432-449.
3. Jeon TH, Moon G, Park H and Choi W. 2017. Ultra-efficient and durable photoelectrochemical water oxidation using elaborately designed hematite nanorod arrays. Nano Energy. 39:211-218.
4. Chnani A, Kurniawan M, Bund A and Strehle S. 2022. Nanometer-thick hematite films as photoanodes for solar water splitting. ACS Appl. Nano Mater. 5(2):2897-2905.
5. Smart TJ, Chen M, Grieder AC, Baltazar VU, Bridges F, Li Y and Ping Y. 2021. The critical role of synthesis conditions on small polaron carrier concentrations in hematite- A first-principles study. J. Appl. Phys. 130:245705-11.
6. André LMF, Waldemir M, Carvalho JR and Flavio LS. 2015. Enhanced water oxidation efficiency of hematite thin films by oxygen deficient atmosphere. J. Mater. Res. 30:3595-3604.
7. Makimizu Y, Yoo J, Poornajar M, Nguyen NT, Ahn HJ, Hwang I, Kment S and Schmuki P. 2020. Effects of low oxygen annealing on the photoelectrochemical water splitting properties of a-Fe2O3. J. Mater. Chem. A 8:1315-1325.
8. Hiralal P, Yarahmadi SS, Bayer BC, Wang H, Hofmann KG, Wijayantha and Amaratunga GAJ. 2011. Nanostructured hematite photoelectrochemical electrodes prepared by the low temperature thermal oxidation of iron. Solar Energy Materials and Solar Cells 95:1819-1825

WHEC-2022
23rd World Hydrogen Energy Conference
June 26-30, 2022 - Istanbul

#1584

PRODUCTION OF HYDROGEN-RICH SYNTHESIS GAS BY GASIFICATION OF WASTE MATERIALS IN A ROTARY KILN REACTOR

[1*] *Anđelina Bubalo,* [2] *Danica Maljković,* [1] *Dražen Vouk*
[1] University of Zagreb, Faculty of Civil engineering, Water research department, Kačićeva ulica 26, 10 000 Zagreb, Croatia
[2] Dok-ing Energo Ltd., Research and development, Slavonska avenija 22, 10 000 Zagreb, Croatia

*Corresponding author e-mail: andelina.bubalo@grad.unizg.hr

ABSTRACT

The problem of today is the increasing disposal of waste materials and the increasing depletion of natural resources. Therefore, the European Commission is adapting further regulations on waste management to the principles of the circular economy. Gasification of waste materials has not yet been established as one of the methods of waste utilisation, but a considerable number of studies on the subject point to a number of advantages of this method while reducing greenhouse gas emissions. One waste whose disposal is a global problem is sewage sludge (SS). In addition to SS, plastic waste is also a major issue due to the growing problem of microplastic contamination. In this work, the following wastes were used for gasification: SS from the wastewater treatment plant (WWTP) Zagreb and mixed plastic wastes (MP) originating from one of the waste collectors on the territory of the Republic of Croatia. Gasification was carried out in a rotary reactor. SS was gasified at temperatures of 1100°C and MP at temperatures of 900°C. The syngas produced from SS has a lower heating value (LHV) of 6.1 MJ m^{-3} and a volume fraction of H_2 in the syngas of 22.94%, while the syngas produced from gasification of MP has a better LHV of 14.4 MJ m^{-3} and a volume fraction of H_2 of 48.56%.

Keywords: Gasification, Sewage sludge, Mixed plastic waste, Syngas, Hydrogen

INTRODUCTION

Under European Union law, the disposal of organic waste is increasingly prohibited. In addition, much is being done to reduce the use of fossil fuels, and the possibilities of converting energy from a diversified waste stream into fuel gas and/or electricity are increasingly being considered. In addition to energy recovery, gasification also offers the advantages of less waste to dispose of, less harmful impact on water and air, and lower disposal costs.

Sewage sludge (SS) is a waste that is a problem in many countries around the world. However, due to its high organic matter content, the use of dry SS as an alternative solid fuel in gasification processes is increasingly being investigated. Plastic waste is a complex waste that is inadequately recycled. Much of the non-recyclable plastic waste must be disposed of in an appropriate manner. The disposal of this type of waste is becoming increasingly important, especially because of the increasing pollution that can be caused by microplastics. Gasification produces the following gases in particular: Hydrogen and Carbon Monoxide. The solid residues are mainly collected as inorganic ash. The use of hydrogen as an energy carrier and environmentally friendly fuel is on the rise.

In this work, gasification of waste materials was carried out in a rotary reactor on a semi-industrial scale. The gasification reactor was designed and built by Dok-ing Energo Ltd. Two experiments were conducted with two types of wastes. The wastes used were SS and mixed plastic (MP). The composition of syngases from two types of waste was determined and their heating value was determined. The aim of this work is to investigate the possibility of obtaining hydrogen-rich syngas from waste materials, the disposal of which is a challenge.

MATERIALS AND METHODS

The SS samples used in this study were from the Zagreb WWTP (1.2 million PE with secondary treatment stage), after anaerobic digestion and dewatering (with approximately 33% DM), collected in December 2021. The samples were collected in plastic containers and brought to the laboratory. The SS was then dried at 105°C for 24 hours. The moisture content of the dried SS was 2 wt.%. The lower heating value (LHV) was determined by the method HRN EN 15170:2010 and was 7.15 MJ kg^{-1} (DM). The dry SS was subjected to a grinding process to obtain particles of approximately equal size.

The MP waste was supplied by a company that collects waste in the Zagreb region. The moisture content of the MP waste was 0.05 wt.%. The heating value (LHV) of MP was also determined according to the method HRN EN

15170:2010 and was 28.3 MJ kg^{-1} (DM). The MP waste was delivered as shredded and ready for the gasification process.
Gasification of waste materials was carried out in a pilot plant consisting of the following units (Fig. 1)

1. Dosing system
2. Drying system
3. Main gasification reactor with rotary kiln
4. Syngas purification system with cyclone and wet scrubbers (scrubbing liquid - water)
5. Solid residue storage system

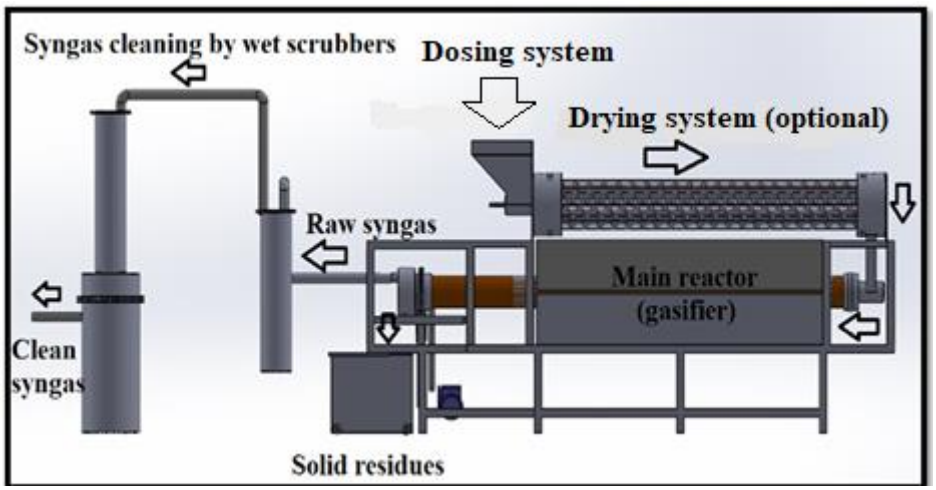


Figure 1 Gasification pilot plant with rotary kiln

The first experiment was performed with 10 kg of waste SS gasified at a temperature of 1100°C in a low-oxygen atmosphere (max. 5% oxygen per volume). Air was used as the gasification agent.

The second experiment was performed with 4.3 kg of MP waste gasified at a gasification temperature of 900°C, also in a low-oxygen atmosphere (max. 5% oxygen per volume). And again, air was used as the gasification agent.

The syngas produced passes through a purification gas system consisting of a cyclone and a scrubber. After purification, the composition of the produced syngas was determined using a syngas analyzer from the company MRU (vario luxx -syngas analyzer).

RESULTS AND DISCUSSION

The analysis of the synthesis gas obtained from SS and MP is shown in Fig. 2. The composition of the syngas obtained by gasification of SS has significantly lower fractions of hydrogen compared to the syngas obtained from MP. The nitrogen content is the largest fraction in the syngas obtained from SS, which affects the reduced heating values of the syngas, as can be seen in Fig. 3. (left). Fig. 3 (right) shows the presence of the acid gas H_2S in the syngases after treatment.

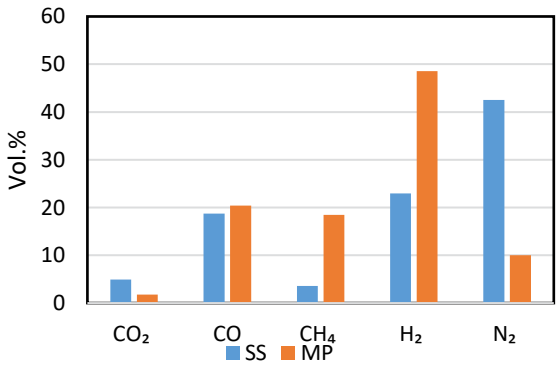


Figure 2. Composition of syngas from SS and MP

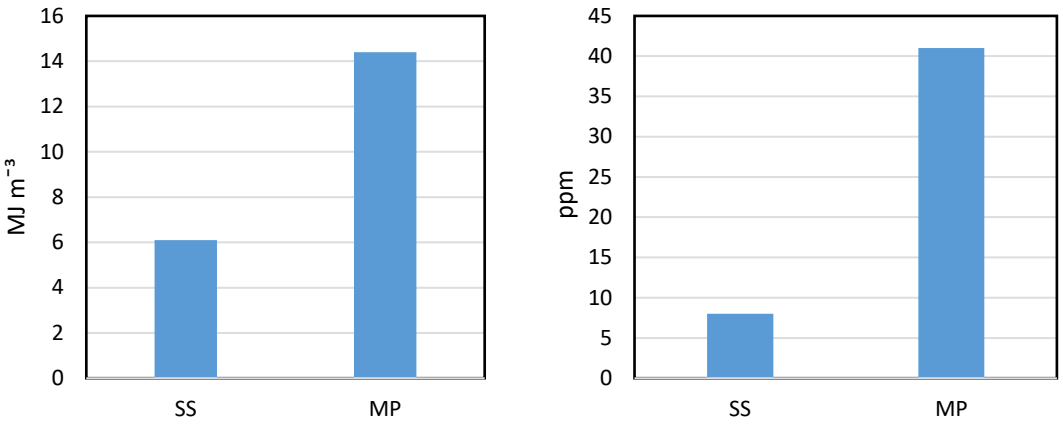


Figure 3. Comparison of LHV value of syngas from gasification of SS and from MP (left)
Presence of the acid gas H_2S in the syngases (right)

CONCLUSIONS

Gasification of waste materials SS and MP was carried out in a semi-industrial plant with a rotary reactor. In both cases, a significant amount of hydrogen predominates in the syngas. The waste material MP with a higher initial heating value (LHV) also resulted in a higher heating value (LHV) of the syngas.

ACKNOWLEDGEMENT

This work has been fully supported by Croatian Science Foundation under the project “IP-2019-04- 1169 – Use of treated oily wastewater and sewage sludge in brick industry – Production of innovative brick products in the scope of circular economy”. The authors thank the company Zagrebačke otpadne vode d.o.o. Zagreb for providing the necessary quantities of raw sludge.

WHEC-2022
23rd World Hydrogen Energy Conference
June 26-30, 2022 - Istanbul

#1586

$Cd_xZn_{1-x}S$ WITH BULK-TWINNED HOMOJUNCTIONS AND RICH SULFUR VACANCIES FOR EFFICIENT PHOTOCATALYTIC HYDROGEN PRODUCTION

[1] İsmail Boz, [2] Mohammed Alfatih Hamid, [3] Yaşar Zengin*
[1] Boğaziçi Üniversitesi, Faculty of Engineering, Chemical Engineering Department, Bebek, Istanbul, Turkey
[2] Istanbul University-Cerrahpaşa, Faculty of Engineering, Chemical Engineering Department, Avcilar, Istanbul, Turkey
[3] Istanbul University-Cerrahpaşa, Faculty of Engineering, Chemical Engineering Department, Avcilar, Istanbul, Turkey

*Corresponding author e-mail: Alfatiham874@gmail.com

ABSTRACT

Photocatalysts containing rich sulphur vacancies and bulk-twinned homojunctions have showed good prospects for solar hydrogen production. In this work, we synthesized photocatalysts composed of bulk-twinned homojunction $Cd_xZn_{1-x}s$ solid solutions along with rich sulphur vacancies to promote charge transfer and prevent the recombination. The photocatalysts were prepared via a simple hydrothermal method and then characterized by X-ray diffractometer to study the phase purity and crystallographic structure. UV-vis spectra were also carried out to investigate the optical properties. The achieved $Cd_xZn_{1-x}s$ photocatalysts exhibited a high solar hydrogen production activity in comparison with the sulphur vacancies free or non-twinned $Cd_xZn_{1-x}S$ solid solutions.

Keywords: Photocatalysts, Visible light, Hydrogen production

INTRODUCTION

Photocatalysis, which refers to the induction of spontaneous and efficient reactions at ambient temperatures under sunlight radiation, has been given so much attention. Because of its possibility to set up the best possible alternative energy systems with the ability to transform environmentally friendly, adequate, and secure solar energy into other forms such as electrical and chemical energy [1].

After Honda and Fujishima demonstrated that water can be split on a TiO_2 electrode into hydrogen and oxygen, over the past few decades. A lot of effort has been put into the development of semiconductor-based photocatalytic materials, especially metal oxides, and metal sulfides. Due to the wide bandgap of metal oxides, their photocatalytic activity is observed in the UV region, which accounts for about 4% of the received solar energy and thus renders the whole process unfeasible [2]. Metal sulfides have conduction bands composed of d and sp orbitals, while the valence bands are composed of S 3p orbitals, which are much more negative than O 2p orbitals. Therefore, the conduction band positions of the photocatalysts in this group are negative enough to reduce water to hydrogen and have narrow band gaps that respond appropriately to the solar spectrum. Despite the photocatalytic activity under visible light, Metal sulfides possess many challenges like degradation and fast recombination of holes and electrons [3] [4].
The photocatalytic performance of metallic sulfides can be improved through more efficient light absorption and reduced hole-electron recombination, both properties dependent on the bandgap energy and the crystal structure [5]. Recently, $Cd_xZn_{1-x}S$ nanocrystals used as the solid solutions of Cadmium sulfide CdS and Zinc sulfide ZnS have aroused interest because of their suitable bandgap, improved stability against photocorrosion, and redox capabilities of charge carrier [6]. However, the photocatalytic performance of pure $Cd_xZn_{1-x}S$ is still limited due to fast charge recombination, which is unfavorable for the more widespread use of this photocatalyst. Therefore, to overcome the above difficulties, wurtzite/zinc-blende (WZ/ZB) homojunction was developed as an alternative to $Cd_xZn_{1-x}S$ solid solutions with higher photocatalytic performance for hydrogen production. By virtue of staggered gab (type II) band alignment between WZ and ZB, bulk photoexcited electrons and holes can be well separated and transported to the photocatalyst surface.

On the other Hand, modulating the photocatalytic properties via defect engineering has been considered an effective approach. Vacancies are intrinsic impurities presented in crystals, perform as adsorption sites to enhance charge transportation and restrain the recombination of photoexcited electrons and holes [7].

In this work, photocatalysts composed of WZ/ZB twinned $Cd_xZn_{1-x}S$ solid solutions with rich sulphur vacancies (TV-$Cd_xZn_{1-x}S$) were synthesized. Compared to non-twined $Cd_xZn_{1-x}S$ and twined without sulphur vacancies (T-$Cd_xZn_{1-x}S$), the TV-$Cd_xZn_{1-x}S$ solid solutions are endowed with enhanced photocatalytic performance under visible light, achieving the optimal photocatalytic performance of 850 μmol/h.g in Na_2S/Na_2SO_3 solution.

MATERIALS AND METHODS

Materials

All the chemicals used in this study were analytical grade with high purity and commercially on hand as follows: Cadmium acetate dihydrate (Alfa Aesar), Zinc acetate dihydrate (ACS reagent), Thioacetamide (Alfa Aesar).

Synthesis of $Cd_xZn_{1-x}S$ solid solution

The $Cd_xZn_{1-x}S$ nanocrystals were synthesized as stated by a previous approach with some modifications [7]. Typically, 50 mmol Cadmium acetate dihydrate and Zinc acetate dihydrate was dissolved in 100 mL deionized water. Then, desired amount of thioacetamide was added to the above mixture and stirred for 20 min. After that, the suspension was further stirred for 20 min before it was transferred to a 200 mL Teflon autoclave and kept at 180 °C for 24 h. After being cooled to room temperature, the product was washed two times with deionized water and once with ethanol. Finally, the obtained product was dried at 75 °C for 6 h in a vacuum oven.

Characterization

The powder XRD patterns were collected on a Rigaku D/Max-2200 diffractometer supplied with a Cu X-ray tube (Cu Kα radiation, λ = 0.154 nm). The data sets were acquired over the 2θ range of 10−80°. The light absorption properties of the samples were conducted on Ocean optics model USB-4000 spectrophotometer. Spectra were recorded in the 280-1000 nm range using halogen and deuterium lamps as light sources.

RESULTS AND DISCUSSION

Fig.1. (a-b) shows the UV-Vis absorption spectra of the prepared $Cd_xZn_{1-x}S$ samples. Since the solid solution of $Cd_{0.1}Zn_{0.9}S$ is in Zinc-blend crystal arrangement, its absorption edge remains in the blue region (<400 nm) in the visible light spectrum. As expected, in the $Cd_{0.9}Zn_{0.1}S$ sample, the absorption edge shifts towards the red region (>500 nm) due to the high content of CdS compounds (Wurtzite/Zinc-blende). It is also seen that the absorption edge of the $Cd_{0.5}Zn_{0.5}S$ sample containing equal molar ratios of Cd and Zn corresponds to ~480 nm in the visible light spectrum. The crystal structure and phase purity of the prepared samples were investigated by X-ray diffraction (XRD). Fig. 1. (c-d) The characteristic diffraction peaks from the CdS are located at 2θ = 24.99°, 26.60°, 28.36°, 36.87°, 44°, 48.19°, 51.68°, 52.29°, 53.29°, 54.83°, 58.73°, 67.33°, 70.50°and 76.18° correspond to the planes (100), (002), (101), (102), (110), (103), (200), (112), (201), (004), (202), (203), (210), and (105) planes of Wurtzite, respectively. It is matched with the crystal structure [ICDD PDF 80-0006]. In addition, the characteristic diffraction peaks of the ZnS are located at 2θ = 28.5, 33.1, 47.4, 56.3, 69.4 and 76.7 correspond to the planes (111), (200), (220), (311), (400) and (331), respectively. It is matched with the crystal structure [ICDD PDF 65-1691]. Characteristic diffraction peaks of $C_{0.5}Z_{0.5}S$ were detected at 2θ = 25.8, 27.5, 29.3, 31.85, 45.6, and 54.185, unlike the characteristic peaks of CdS and ZnS in the literature. The 100's peak at 2θ =27.5 of $Cd_{0.5}ZnS$ has a high angle side (2θ =26.5) with the 100's peak of CdS and a low angle with respect to the 100's peak of ZnS (2θ =28.5) showed slip. With the increase of Cd content, the XRD diffraction peaks of $Cd_xZn_{1-x}S$ gradually and continuously shifted from the dominant of Wurtzite phase to the dominant of Zinc-blende phase. These results show that the synthesized catalysts are not a simple physical mixture of CdS and ZnS, but a solid solution of $Cd_{0.5}Zn_{0.5}S$ is formed.

Solid solutions of $Cd_xZn_{1-x}S$ generally produce much higher photocatalytic H_2 than ZnS and CdS alone. It is predicted that the activity can be improved by varying the Cd/Zn molar ratio of $Cd_xZn_{1-x}S$ (x = 0.1, 0.3, 0.5, 0.7 and 0.9) solid solutions. It can be seen from Fig. 2. that the $Cd_{0.9}Zn_{0.1}S$ photocatalyst provides hydrogen production at a relatively low rate of approximately 50 µmol/h.g. On the other hand, in the $Cd_{0.7}Zn_{0.3}S$ sample, where the Zn molar ratio is 30%, the amount of photocatalytic H_2 production increased significantly and was calculated as 720 µmol/h.g per hour.

In the presence of $Cd_{0.5}Zn_{0.5}S$ photocatalyst synthesized equimolarly, the highest H_2 production rate was reached with 850 µmol/h.g. Afterwards, the photocatalytic activity decreased significantly when the molar ratios of cadmium were less than 50%. In the presence of $Cd_{0.3}Zn_{0.7}S$ photocatalyst, the amount of H_2 production as a result of the photocatalytic reaction was 677 µmol/h.g; In the presence of $Cd_{0.1}Zn_{0.9}S$ photocatalyst, it was determined as 75 µmol/h.g. WZ/ZB twinned $Cd_{0.5}Zn_{0.5}S$ solid solutions with rich sulphur vacancies have the highest photocatalytic performance. Compared to non-twined $Cd_{0.5}Zn_{0.5}S$ with 234 µmol/h.g and twined without sulphur vacancies with 368 µmol/h.g.

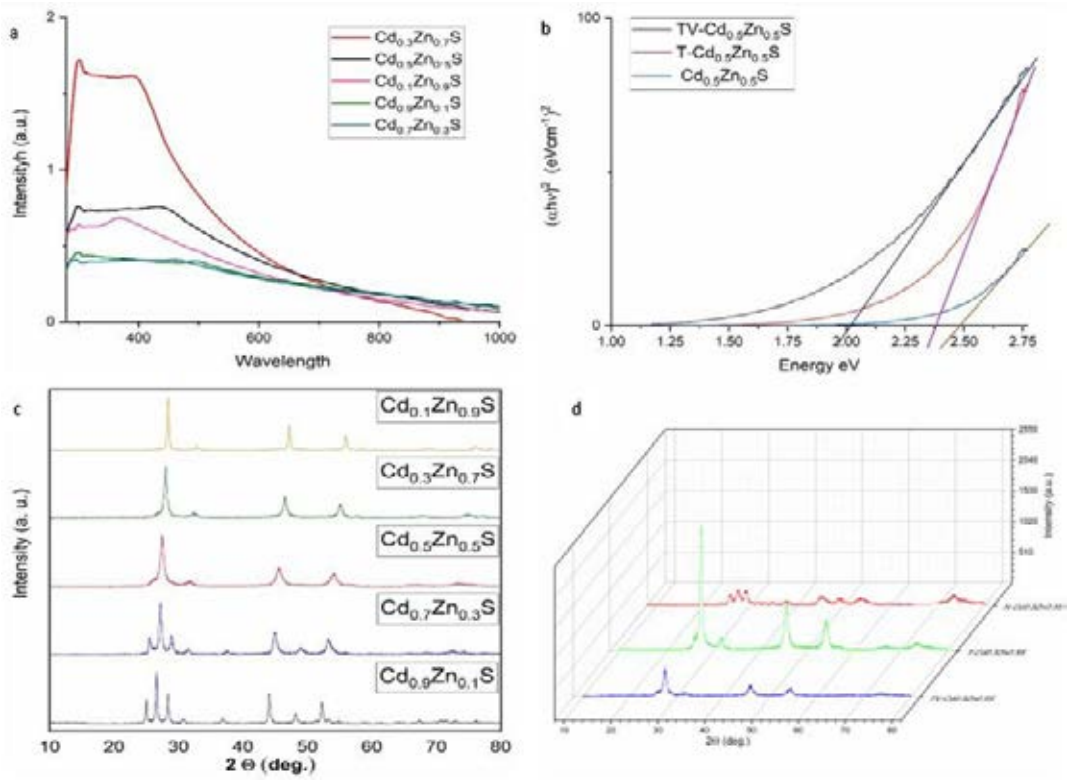


Figure 1 (a-b) UV–vis absorption spectra of $Cd_xZn_{1-x}S$ and Tacu plots of X-$Cd_{0.5}Zn_{0.5}S$ and (c-d) XRD patterns.

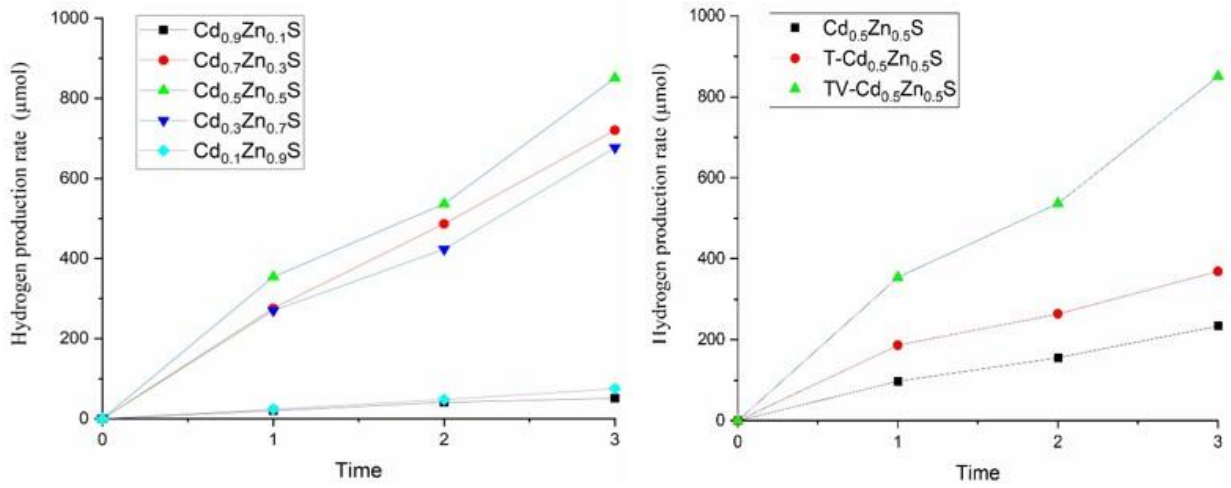


Figure 2 H_2 production rate of $Cd_xZn_{1-x}S$ photocatalysts.

CONCLUSIONS

In summary, the photocatalytic hydrogen production of $Cd_xZn_{1-x}S$ solid solutions can be enhanced by improving optoelectronic properties with binary Wurtzite and Zinc-blende phases obtained by changing Cd/Zn molar ratios and controlling the reaction conditions. Due to the fact that the solid solution of $Cd_{0.5}Zn_{0.5}S$ has an optimum band gap and a middle position of the conduction band, the visible light absorption, photogenerated electron-hole pair separation is improved, resulting in more efficient H_2 production. The enhanced photocatalytic performance of TV-$Cd_{0.5}Zn_{0.5}S$ can be ascribed to the twinned solid solutions and the presence of rich sulphur vacancies.

REFERENCES

1. Liu, Z., Zhang, J. and Yan, W. 2018. Enhanced Photoelectrochemical Water Splitting of Photoelectrode Simultaneous Decorated with Cocatalysts Based on Spatial Charge Separation and Transfer. *ACS Sustainable Chemistry and Engineering* 6: 3565–3574.
2. Yi, F. *et al.* 2022 .Electronic and thermal transfer actuating memory catalysis for organic removal by a plasmonic photocatalyst. *Chemical Engineering Journal*, 427:132028.
3. Takanabe, K. and Domen, K. 2011 .Toward visible light response: Overall water splitting using heterogeneous photocatalysts.

Green, (5–6): 313–322.
4. Liu, M. *et al.* 2011. Energy & Environmental Science Twins in $Cd_xZn_{1-x}S$ solid solution. Highly efficient photocatalyst for hydrogen generation from water 4: 1372-1378.
5. Pinaud, B. A. *et al.* 2013 .Technical and economic feasibility of centralized facilities for solar hydrogen production via photocatalysis and photoelectrochemistry. *Energy and Environmental Science*, 6(7): 1983–2002.
6. Zhao, S. *et al.* 2015 . A non-noble metal MoS_2-$Cd_{0.5}Zn_{0.5}S$ photocatalyst with efficient activity for high H_2 evolution under visible light irradiation. *Journal of Materials Chemistry A*. 41: 193–199.
7. Yu, K. *et al.* 2020 .CdZnS nanorods with rich sulphur vacancies for highly efficient photocatalytic hydrogen production', *Chemical Communications* 56: 7765–7768.

WHEC-2022
23rd World Hydrogen Energy Conference
June 26-30, 2022 - Istanbul

#1601

SOLAR-LIGHT-DRIVEN PHOTOCATALYTIC HYDROGEN EVOLUTION *IN SITU* DEPOSITED Pt ON PEROVSKITE TYPE OXIDES

[1*] *Ali Keles,* [1] *Talha Kuru,* [2] *Emre Aslan,* [3] *İmren Hatay Patır*
[1] GKE Energy R&D Center,48200, Mugla, Turkey.
[2] Selcuk University, Department of Biochemistry, 42030, Konya, Turkey
[3] Selcuk University, Department of Biotechnology, 42030, Konya, Turkey

*Corresponding author e-mail: a.keles@gke.com.tr

ABSTRACT

Hydrogen generation through photocatalytic splitting of water, which is known as hydrogen evolution reaction (HER), is an attractive method of converting the solar energy generated from renewable sources into chemical energy stored in molecular hydrogen. perovskite oxides hold promise as functional materials for the water splitting due to its excellent properties as low-cost and high activity. Herein, platinum photodeposited onto $MTiO_3$ (M: Ba and Sr) perovskites ($MTiO_3$-Pt) have been investigated on the photocatalytic hydrogen evolution under solar light irradiation in the presence of triethanolamine (TEOA) and Eosin Y as electron donor and photosensitizer, respectively. Photocatalytic hydrogen evolution activities take place in the order of SrTiO3-Pt> BaTiO3-Pt> SrTiO3> BaTiO3.

Keywords: Photocatalytic hydrogen evolution, Perovskites, Titanates

INTRODUCTION

Hydrogen evolution from water splitting with highest mass energy density and its rich reserves is pursued as an ideal clean energy system due to the lessen the reliance on fossil fuels [1]. Since the pioneering work of photodecomposition of water onto Pt/TiO_2 electrodes by Honda and Fujishima (1972), tremendous efforts have been proposed mostly for the development of photo/catalysts that are activated with UV–visible light spectrum [2]. Besides, proton reduction and water oxidation reactions are required to excess overpotentials; thus, catalysts with appropriate band position and also the bandgap design are major point for overall water splitting systems [3]. $SrTiO_3$ and $BaTiO_3$ perovskite-type oxides can be used as an alternative to mostly used TiO_2 because of suitable band positions, opticaland crystallographic properties for the efficient photochemical energy conversion reactions [4, 5]. These perovskites have been widely used for the photocatalytic hydrogen evolution systems due to their structural flexibility, suppression of photocorrosion and physicochemical stability [4].For example, numerous valuable studies have been recently reported by using different kind of perovskite based catalysts such as NiO-$SrTiO_3$ [6], $BaTiO_3$/ZnO [7], Rh-doped $SrTiO_3$ [8], g-C_3N_4 coated $SrTiO_3$ [9], Cr/N-codoped $SrTiO_3$ [10], Cu–$SrTiO_3$ [11], TiO_2/$BaTiO_3$ [12], $BaTiO_3$/$SrTiO_3$ [13], Co_3O_4/CdS/$SrTiO_3$ [14], $SrTiO_3$/Bi_2S_3 [15], Al/$BaTiO_3$ [16], Mo doped $BaTiO_3$ [17], NiS/g-C_3N_4/$SrTiO_3$ [18], La,Rh-doped $SrTiO_3$ [19].

Herein, we have reported that Pt have been *in situ* generated on the $MTiO_3$ (M: Ba and Sr) by reduction of H2PtCl6 from excited electrons during the photocatalytic reaction. Then, the effect of the photodeposited Pt on $MTiO_3$ (M: Ba,Sr) ($MTiO_3$-MoS_x)were systematically investigated for the photocatalytic HER by using triethanolamine (TEOA) as a sacrificial electron reagent and EY as a sensitizer.

MATERIALS AND METHODS

The photocatalytic hydrogen evolution experiments were performed in a 135 mL sealed tightly with a rubber septum Pyrex flask in the anaerobic glovebox system. Commercially available Eosin-Y dye and triethanolamine were used for photosensitizer and electron donor, respectively. Triethanolamine (TEOA) (5%) and Eosin-Y (0.33 mM) solution (20 mL solution volume) were prepared in the other flasks and bubbled with nitrogen to remove oxygen, then took in the glove-box. Firstly, catalysts were taken Pyrex flask and then, both electron donor solution (TEOA) and dye (EY) were added the flask in the glovebox. Before the photocatalytic experiments, the mixing solution with TEOA, (EY) and $MTiO_3$ were sonicated about 10 minutes to homogenize the solution. After this procedure, well-dispersed mixture was stirred spiritedly under the visible light source at 25±2°C temperature. The headspace gas was analyzed hourly to determine amount of produced hydrogen with gas chromatograph.

RESULTS AND DISCUSSION

The hydrogen production rates of $MTiO_3$ (M= Ba and Sr) by EY sensitization have been investigated in aqueous TEOA solution at pH 9. The HER rate found out as the 0.82 $mmolg^{-1}h^{-1}$ and 0.55 $mmolg^{-1}h^{-1}$ for BaTiO3 and SrTiO3, respectively. No hydrogen production is observed in the absence of dye molecule or sacrificial electron donor.

Photocatalytic hydrogen evolution activities of $MTiO_3$ have also been studied under long time visible light irradiation (8 h) in the presence of EY solution. Figure 1a indicates that the hydrogen production rate for EY/ $MTiO_3$ photocatalytic system shows almost steady increase over 8 h solar light irradiation. The total amount of H_2 after 8 h have been turned out to be 2.16 $mmolg^{-1}$ and 2.24 $mmolg^{-1}$ by using BaTiO3 and SrTiO3, respectively. in the TEOA and EY solutions. The HER rates of $MTiO_3$ (M= Ba and Sr) have been increased by in situ photodeposited Pt co-catalyst reducing H2PtCl6 during the photocatalytic HER. When the effect of Pt co-catalyst loading on $MTiO_3$ have been investigated, the HER activities of $BaTiO_3$-Pt and $SrTiO_3$-Pt were increased about 6.8 and 7.6-fold compared to bare $BaTiO_3$ and $SrTiO_3$, respectively. It can be seen that $SrTiO_3$-Pt was shown the highest photocatalytic HER performance as 16.96 mmol g^{-1}, while $BaTiO_3/MoS_x$ was produced 14.59 mmol g^{-1} hydrogen for 8 hours of photocatalytic reaction. Photocatalytic hydrogen evolution activities were changed in the order of $SrTiO_3$-Pt> $BaTiO_3$-Pt> $SrTiO_3$> $BaTiO_3$.

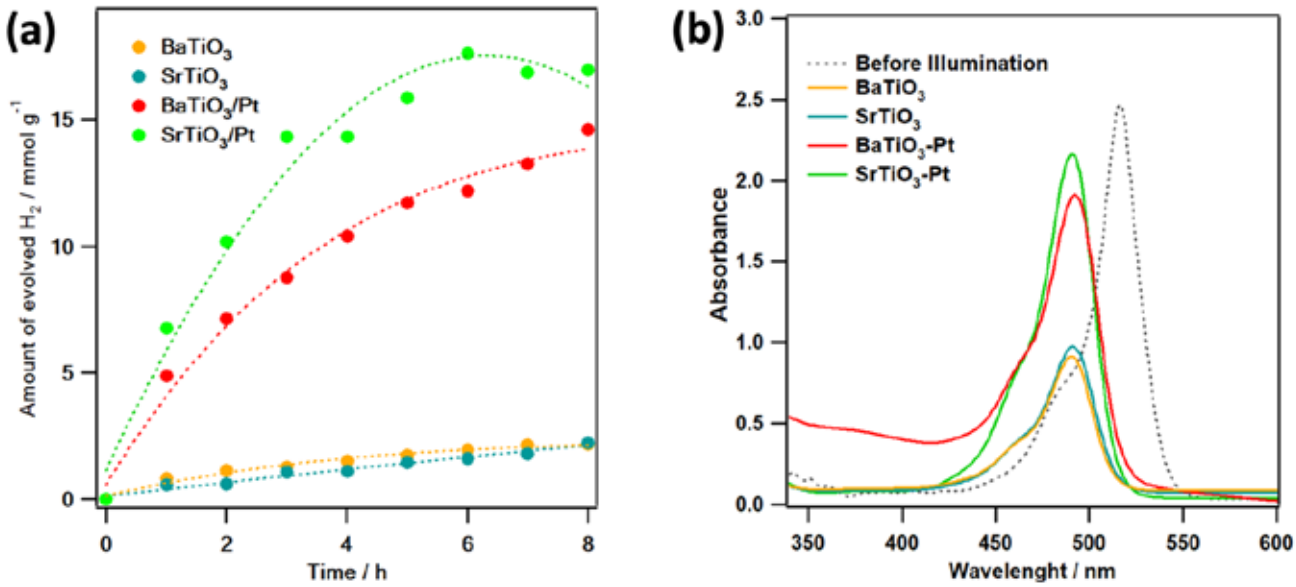


Fig 1. (a) Photocatalytic HER activities of MTiO3 and MTiO3/Pt, (b) UV-Vis absorption spectrums of the EY dye solutions before (black dashed line) and after (black solid line) photocatalytic HER

The photocatalytic stability of HER can be explained by the degradation of the EY dye. The degradation of dye molecule was determined by UV-Vis absorption spectroscopy technique as shown in Figure 1b. Also, the shift of the characteristic absorption peak EY (from 520 nm to 490 nm) with gradually intensity decrease is observed in the UV-Vis spectra after 8 h photocatalytic reaction, indicating that the sensitizer EY could degraded in this photocatalytic system [20, 21]. The peak shift can be explained by the removal of some bromine atoms from EY and the degradation of the dye as a result of possible formation of fluorescein-like species [22-24].

CONCLUSIONS

The highly crystalline perovskite particles $MTiO_3$ are utilized for solar-light-driven photocatalytic hydrogen evolution from water splitting by dye sensitization due to their wide band gaps. Photocatalytic HER activities of $MTiO_3$ are enhanced by loading Pt, which is obtained by photodeposition of H_2PtCl_6 reduction, as a non-noble metal co-catalyst. The HER rates of $SrTiO_3$/Pt and $BaTiO_3$/Pt have been increased approximately 6.8 and 7.6-fold, respectively, when compared to their pristine $MTiO_3$ forms.

REFERENCES

1. R. He, J. Hua, A. Zhang, C. Wang, J. Peng, W. Chen, J. Zeng, Molybdenum disulfide–black phosphorus hybrid nanosheets as a superior catalyst for electrochemical hydrogen evolution, Nano letters, 17 (2017) 4311-4316.
2. A. Fujishima, K. Honda, Electrochemical photolysis of water at a semiconductor electrode, nature, 238 (1972) 37-38.
3. B. Dong, J. Cui, Y. Qi, F. Zhang, Nanostructure Engineering and Modulation of (Oxy) Nitrides for Application in Visible-Light-Driven Water Splitting, Advanced Materials, 33 (2021) 2004697.
4. M. Ganapathy, Y. Hsu, J. Thomas, C.T. Chang, V.J.J.o.M.S. Alagan, Co-catalyst free SrTiO3 nano-cube for efficient photocatalytic hydrogen production, (2021) 1-13.
5. T. Chen, J. Meng, S. Wu, J. Pei, Q. Lin, X. Wei, J. Li, Z. Zhang, Room temperature synthesized $BaTiO_3$ for photocatalytic hydrogen evolution, Journal of alloyscompounds, 754 (2018) 184-189.
6. Y. Fo, M. Wang, Y. Ma, H. Dong, X. Zhou, Origin of highly efficient photocatalyst NiO/SrTiO3 for overall water splitting: Insights from density functional theory calculations, Journal of Solid State Chemistry, 292 (2020) 121683.

7. X. Zhou, S. Wu, C. Li, F. Yan, H. Bai, B. Shen, H. Zeng, J. Zhai, Piezophototronic effect in enhancing charge carrier separation and transfer in ZnO/BaTiO3 heterostructures for high-efficiency catalytic oxidation, Nano Energy, 66 (2019) 104127.
8. M.G.C. Zoontjes, K. Han, M. Huijben, W.G. van der Wiel, G. Mul, The effect of Rhδ+ dopant in SrTiO3 on the active oxidation state of co-catalytic Pt nanoparticles in overall water splitting, Catalysis Science & Technology, 6 (2016) 7793-7799.
9. X. Xu, G. Liu, C. Randorn, J.T.S. Irvine, g-C3N4 coated SrTiO3 as an efficient photocatalyst for H2 production in aqueous solution under visible light irradiation, International Journal of Hydrogen Energy, 36 (2011) 13501-13507.
10. H. Yu, S. Yan, Z. Li, T. Yu, Z. Zou, Efficient visible-light-driven photocatalytic H2 production over Cr/N-codoped SrTiO3, International Journal of Hydrogen Energy, 37 (2012) 12120-12127.
11. D.-N. Bui, J. Mu, L. Wang, S.-Z. Kang, X. Li, Preparation of Cu-loaded SrTiO3 nanoparticles and their photocatalytic activity for hydrogen evolution from methanol aqueous solution, Applied Surface Science, 274 (2013) 328-333.
12. H. Li, Y. Song, J. Zhang, J. He, Turbulence enhanced ferroelectric-nanocrystal-based photocatalysis in urchin-like TiO2/BaTiO3 microspheres for hydrogen evolution, Nanoscale Advances, 3 (2021) 5618-5625.
13. X. Liu, X. Shen, B. Sa, Y. Zhang, X. Li, H. Xue, Piezotronic-enhanced photocatalytic performance of heterostructured BaTiO3/SrTiO3 nanofibers, Nano Energy, 89 (2021) 106391.
14. Z. Chen, J. Pan, J. Mei, Q. Yu, P. Wang, P. Wang, J. Wang, C. Song, Y. Zheng, C. Li, Ternary Co3O4/CdS/SrTiO3 core-shell pn junctions toward enhanced photocatalytic hydrogen production activity, Journal of Environmental Chemical Engineering, 9 (2021) 104895.
15. M. Ganapathy, Y. Hsu, J. Thomas, L.-Y. Chen, C.-T. Chang, V. Alagan, Preparation of SrTiO3/Bi2S3 Heterojunction for Efficient Photocatalytic Hydrogen Production, Energy & Fuels, 35 (2021) 14995-15004.
16. L. Guo, C. Zhong, J. Cao, Y. Hao, M. Lei, K. Bi, Q. Sun, Z.L. Wang, Enhanced photocatalytic H2 evolution by plasmonic and piezotronic effects based on periodic Al/BaTiO3 heterostructures, Nano Energy, 62 (2019) 513-520.
17. P. Xie, F. Yang, R. Li, C. Ai, C. Lin, S. Lin, Improving hydrogen evolution activity of perovskite BaTiO3 with Mo doping: Experiments and first-principles analysis, International Journal of Hydrogen Energy, 44 (2019) 11695-11704.
18. X.-L. Luo, G.-L. He, Y.-P. Fang, Y.-H. Xu, Nickel sulfide/graphitic carbon nitride/strontium titanate (NiS/g-C3N4/SrTiO3) composites with significantly enhanced photocatalytic hydrogen production activity, Journal of Colloid and Interface Science, 518 (2018) 184-191.
19. Y. Kageshima, T. Kawanishi, D. Saeki, K. Teshima, K. Domen, H. Nishikiori, Boosted Hydrogen-Evolution Kinetics Over Particulate Lanthanum and Rhodium-Doped Strontium Titanate Photocatalysts Modified with Phosphonate Groups, Angewandte Chemie International Edition, 60 (2021) 3654-3660.
20. P. Kush, K. Deori, A. Kumar, S. Deka, Efficient hydrogen/oxygen evolution and photocatalytic dye degradation and reduction of aqueous Cr(vi) by surfactant free hydrophilic Cu2ZnSnS4 nanoparticles, Journal of Materials Chemistry A, 3 (2015) 8098-8106.
21. X. Zhang, Z. Jin, Y. Li, S. Li, G. Lu, Photosensitized reduction of water to hydrogen using novel Maya blue-like organic–inorganic hybrid material, Journal of Colloid and Interface Science, 333 (2009) 285-293.
22. R. Abe, K. Hara, K. Sayama, K. Domen, H. Arakawa, Steady hydrogen evolution from water on Eosin Y-fixed TiO2 photocatalyst using a silane-coupling reagent under visible light irradiation, Journal of Photochemistry and Photobiology A: Chemistry, 137 (2000) 63-69.
23. K. Kimura, T. Miwa, M. Imamura, The radiolysis and photolysis of methanolic solutions of eosin. I. The γ-radiolysis of neutral and alkaline solutions, Bulletin of the Chemical Society of Japan, 43 (1970) 1329-1336.
24. M.K. Gonce, E. Aslan, F. Ozel, I. Hatay Patir, Dye-Sensitized Cu_2XSnS_4 (X= Zn, Ni, Fe, Co, and Mn) Nanofibers for Efficient Photocatalytic Hydrogen Evolution, ChemSusChem, 9 (2016) 600-605.

WHEC-2022
23rd World Hydrogen Energy Conference
June 26-30, 2022 - Istanbul

#1605

NICKEL-BASED GRAFTED CATALYSTS FOR DRY REFORMING OF METHANE THROUGH HIGH-THROUGHPUT EXPERIMENTATION

[1,2] *Gokhan Celik,* [2*] *Magali Ferrandon,* [2*] *Massimiliano Delferro*
[1] Department of Chemical Engineering, Middle East Technical University, Ankara, 06800, Turkey
[2] Chemical Sciences and Engineering Division, Argonne National Laboratory, Lemont, IL, 60439, USA

*Corresponding author e-mail: delferro@anl.gov, ferrandon@anl.gov

ABSTRACT

High-throughput synthesis of Ni-based catalysts was performed by organometallic liquid grafting using a robotic arm. Monometallic catalysts contain Ni, whereas bimetallic catalysts contain a promoter metal such as B, Mg, V, Mn, Fe, Co, Cu, Zn, or Sn, supported on inorganic metal oxides such as magnesia, alumina, titania, silica, or ceria. The catalytic performance results showed that the support-metal-promoter choice affect catalyst activity, stability, syngas composition, and type and nature of carbon species formed under reaction conditions. Among 95 catalysts studied, NiFe/MgO and NiFe/Al_2O_3 catalysts are the most active and stable. In addition, the synthesized catalysts were characterized using several characterization methods including, but not limited to, N_2 physisorption, chemisorption, X-ray diffraction, vibrational spectroscopy, and imaging techniques. Characterization results show that (i) the best performing catalysts have metallic sites that are highly dispersed, uniform, and resistant to sintering at 800 °C, (ii) reduction profile of catalysts supported on alumina exhibits important structure-activity relationships, and (iii) distinct carbon species formed on specific sites, affecting the stability. Our findings demonstrate that organometallic grafting is a successful technique for synthesizing catalytic materials with highly dispersed and uniform sites that lead to promising catalytic performance for dry reforming of methane.

Keywords: Hydrogen, Dry Reforming, Methane, Grafting, Carbon dioxide

INTRODUCTION

Dry reforming of methane, Eq. (1), is a catalytic chemical transformation where CO_2 and CH_4, two greenhouse gases, are converted into CO and H_2, a gas mixture known as syngas, which can be used to produce value-added chemicals and fuels. [1,2] The reaction holds an enormous potential for net positive utilization of CO2 into chemical building blocks through hydrogen economy.

$$CH_4 + CO_2 \leftrightarrow 2CO + 2H_2 \qquad \Delta H^0_{298} = 247\ \mathrm{kJ/mol} \qquad (1)$$

Several precious metals including Ru, Rh, Pd, and Pt and transition metals including Fe, Co, and Ni supported on inorganic metal oxides catalyze dry reforming of methane. Yet, endothermic nature of the reaction and high operating temperatures required for meaningful transformation rates lead to catalyst deactivation due to carbon deposition. Precious metals perform better against carbon deposition; but they are expensive and not abundant. Therefore, Ni emerges as an attractive reforming catalyst owing to its wide availability and low cost. Yet, Ni-based catalysts are prone to deactivation by carbon deposition and agglomeration under the reaction conditions.

It was reported that Ni catalysts with small particles sizes (small nanoparticles to single atom catalysts) [3,4] and easier reducibility [4,5] perform well for dry reforming of methane and alleviate the carbon deposition issue by preventing methane decomposition to carbon [4]. Conventional techniques for synthesizing catalysts such as impregnation lead to ill-defined active sites and large Ni nanoparticles. If a control at the atomic level is achieved, homogeneous distribution of metals in a close proximity to Ni may cause an ensemble effect and result in unique catalytic performance. [6] 30 In addition, presence of a secondary metal helps with some of the catalyst attributes and may enhance the ensemble effect.

Among the techniques for synthesizing catalysts, surface organometallic chemistry (SOMC) is a powerful bottom-up synthesis technique. [7] In SOMC, liquid organometallic precursors can be grafted on dehydroxylated metal oxides creating isolated metal sites or highly-dispersed uniform nanoparticles upon heat treatment. Such nanoparticles lower the energy of the surface and increase their interaction with the support, resulting in enhanced resistance to sintering under reaction conditions. [8]

In this study, by means of high-throughput synthesis and testing, we've [9, 10] synthesized bimetallic catalysts supported on different metal oxides to improve catalytic performance of Ni-based catalysts by grafting a submonolayer of promoters to enhance interactions between the metal and promoter-modified support. Specifically, nickel-containing bimetallic catalysts with different secondary metals (boron, zinc, manganese, cobalt, vanadium, copper, iron, magnesium, and tin) over six different metal oxide supports (silica, alumina, titania, ceria, and magnesium oxide) were synthesized via SOMC. The synthesized catalysts performance was obtained over dry reforming of CH_4.

EXPERIMENTAL

Experimental studies consist of catalyst syntheses, characterization (pre-reaction or post-reaction), and catalytic performance tests. For catalyst syntheses, a high throughput automated synthesis platform placed in a N_2-filled glovebox was used. The robotic arm was programmed to perform basic actions such as dispensing solids and liquids as well as stirring.

Catalysts were synthesized using a stepwise surface organometallic chemistry (SOMC) technique as shown in Fig. 1. After depositing organometallic precursors of promoters to partially dehydroxylated inorganic metal oxide supports to obtain approximately 50% of a monolayer coverage, calcination was performed in static air at 450 °C for 2 h. Then, the resulting solid material was suspended in toluene for grafting of organonickel precursor (bis(N,N'-di-t-butylacetamidinato)nickel(II)) in toluene to obtain sub-monolayer coverage. Before each reaction, samples were reduced under hydrogen at 800 °C.

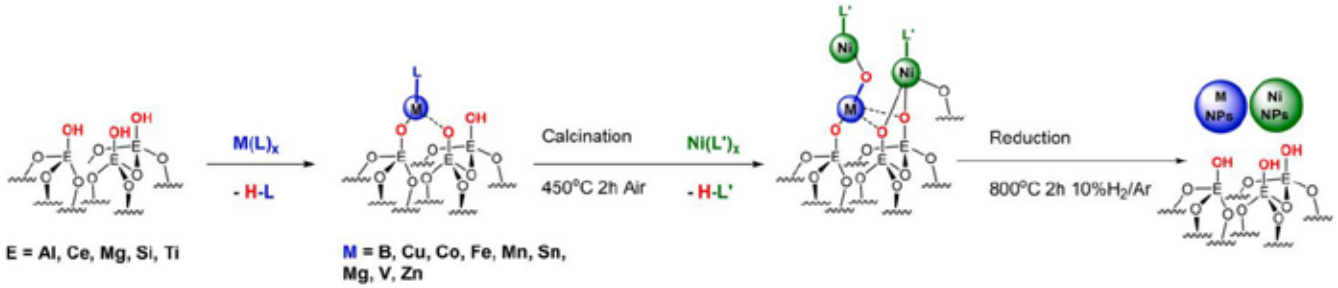


Fig. 1. High-throughput multi-step catalyst synthesis schematic via surface organometallic chemistry (SOMC) process [9]

Catalytic activity experiments were performed using a high-throughput system consisting 16 channels of fixed-bed reactors. Prior to each reaction, catalysts were pre-reduced under H_2 at 800 °C. Activity experiments were performed as temperature scans between 650 – 800 °C, followed by a stability test for 24 h at 800 °C at a gas hourly space velocity (GHSV) of 3200 h^{-1}. The exhaust composition was obtained with a gas chromatography.

The synthesized catalysts were characterized using inductively coupled plasma atomic emission spectroscopy (ICP-OES), X-ray photoelectron spectroscopy (XPS), temperature programmed reduction in H_2 (H_2-TPR), X-ray diffraction (XRD), Thermogravimetric Analyses coupled with a mass spectrometer (TGA-MS), Raman spectroscopy and electron microscopy imaging techniques.

RESULTS AND DISCUSSION

All the samples are first reduced under hydrogen and tested for dry reforming of methane for an equimolar CH_4 and CO_2. To assess the catalytic performance better, conversions obtained over bimetallic catalysts, i.e. NiX/M_2O_3, were divided with that obtained over monometallic Ni/M_2O_3. The top right quadrant of Fig. 1a. shows that bimetallic samples perform much better than their monometallic counterpart. To examine undesired carbon formation on the samples and composition of the reformed gas, Fig. 1b. shows H_2/CO ratio with respect to C balance. The higher H_2/CO ratio was attributed to occurring of methane cracking and Boudouard reactions, whereas the lower ratio was attributed to CO_2 reduction to CO with a subsequent C deposition on the samples. Fig. 1c. shows the stability test of the 10 best performing samples for 25 hours. NiFe/MgO and $NiFe/Al_2O_3$ are the most active and stable catalysts combinations for dry reforming of methane with a conversion very near to the thermodynamic limits. In addition to catalytic activity experiments, the present talk will also discuss characterization results and how they are related to the observed catalytic performance.

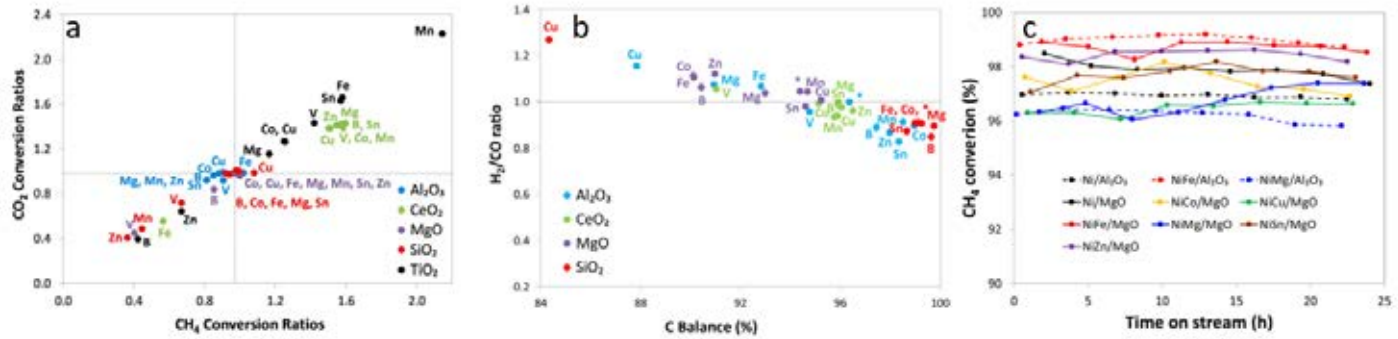


Fig. 2. (a) CO_2 conversion ratio to CH_4 conversion ratio of NiX/M_2O_3 to Ni/M_2O_3, (b) The ratio of H_2/CO to total carbon balance for some of the NiX/M_2O_3 to Ni/M_2O_3 catalyts, and (c) thermal stability runs of selected bimetallic catalysts. Reaction Temperature= 800 °C, CH_4:CO_2 = 1:1, and GHSV = 3200 h^{-1}. [9, 10]

CONCLUSIONS

Through extensive experimental studies including characterization and high-throughput syntheses and catalytic performance testing, $NiFe/Al_2O_3$ and NiFe/MgO bimetallic catalysts were identified to be the best performing samples for dry reforming of methane. The high performance of these samples was attributed to the presence of highly dispersed, uniform, and reducible Ni active sites, formed by the state-of-the-art top-down synthesis technique SOMC. In addition, characterization studies over pristine and post-reaction samples shed a light on the underlying chemistry of the catalytic surface reactions involved in dry reforming of methane and different carbon-induced deactivation modes.

REFERENCES

1. Pakhare D and Spivey JA. 2014. A review of dry (CO_2) reforming of methane over noble metal catalysts. Chemical Society Reviews 43:7813–7837
2. Dry ME. 2002. The Fischer–Tropsch process: 1950–2000. Catalysis Today 71:227–241
3. Mortensen PM and Dybkjær I. 2015. Industrial scale experience on steam reforming of CO_2-rich gas. Applied Catalysis A: General 495:141–151
4. Akri M, Zhao S, Li X, Zang K, Lee AF, Isaacs MA, Xi W, Gangarajula Y, Luo J, Ren Y, Cui Y-T, Li L, Su Y, Pan X, Wen W, Pan Y, Wilson K, Li L, Qiao B, Ishii H, Liao YF, Wang A, Wang X, and Zhang T. 2019. Atomically dispersed nickel as coke-resistant active sites for methane dry reforming. Nature Communications 10:5181
5. Cao Y, Lu M, Fang J, Shi L, and Zhang D. 2017. Hexagonal boron nitride supported mesoSiO$_2$-confined Ni catalysts for dry reforming of methane. Chemical Communications 53:7549–7552
6. Yu M, Zhu K, Liu Z, Xiao H, Deng W, and Zhou X. 2014. Carbon dioxide reforming of methane over promoted $Ni_xMg_{1-x}O$ (1 1 1) platelet catalyst derived from solvothermal synthesis. Applied Catalysis B: Environmental 148–149:177–190
7. M.K. Samantaray, E. Pump, A. Bendjeriou-Sedjerari, V. D'Elia, J.D.A. Pelletier, M. Guidotti, R. Psaro, J.-M. Basset, Chem. Soc. Rev. 47 (2018) 8403–8437, https://doi.org/10.1039/C8CS00356D.
8. Mavrokefalos CK, Kaeffer N, Liu HJ, Krumeich F, and Cop´eret. 2019. Small and Narrowly Distributed Copper Nanoparticles Supported on Carbon Prepared by Surface Organometallic Chemistry for Selective Hydrogenation and CO_2 Electroconversion Processes. ChemCatChem 12 (1):305–313
9. Ferrandon MS, Celik G, Delferro M. 2020. Multimetallic catalysts for methanation of carbon dioxide and dry reforming of methane. US Patent: US20220040677A1
10. Ferrandon MS, Byron C, Celik G, Zhang Y, Ni C, Sloppy J, McCormick RA, Booksh K, Teplyakov AV, and Delferro M. 2022. Grafted nickel-promoter catalysts for dry reforming of methane identified through high-throughput experimentation. Applied Catalysis A: General 629:118379

WHEC-2022
23rd World Hydrogen Energy Conference
June 26-30, 2022 - Istanbul

#1633
GREEN HYDROGEN PRODUCTION FOR ESKIL OIZ HEATING

[1*]Yasin Öğütcü, [2"]Bahattin Tanç
Iskenderun Technical University, Energy Institute, Energy Systems Engineering, Hatay, Turkey

*Corresponding author e-mail: yasinogutcu.96@gmail.com

ABSTRACT

Energy need is a major concern than ever before. The increasing demand and developing technology in every field within the industry have increased the demand for energy. Therefore, the gradual depletion of fossil fuels, which has been used as an energy source, pushed people to seek new energy sources. Energy from fossil fuels was polluting the environment depending on the amount reducing the resources since it was consumed from the volume of the limited resource. The energy source of the future is seen as alternative energy sources, as they can be adapted to any area where energy is needed, from transportation to lighting. Among these, gas that contains the highest energy is hydrogen and can be produced by renewal. It comes to the fore in the choice of energy source. As Green Hydrogen, the production of hydrogen with solar energy and the use of the produced hydrogen in heating the Industrial Zone have been studied theoretically. As a result, hydrogen can be produced with zero emission with a solar power plant to be built in the vicinity of the OIZ, which is planned to be built in Eskil, and the heating of the OIZ can be provided with Green Hydrogen.

Keywords: Energy, Green Hydrogen, Solar Energy, Heating, Hydrogen Production

INTRODUCTION

It has been decided to establish an OIZ (Organized Industrial Zone) in 3 more districts of Aksaray, including Eskil [1]. In order to produce the hydrogen that will be used in the heating of the Organized Industrial Zone as "Green Hydrogen" with zero emission, the establishment of a photovoltaic facility in the Eskil salt lake basin has been theoretically foreseen and studied.

MATERIALS AND METHODS

In order to generate electricity from the sun, a region has been selected in the salt lake basin near the Organized Industrial Zone. Konya region and Tuz Gölü basin are in the most productive region class for the production potential in the photovoltaic field [2-3].

RETScreen application is an application where you can simulate the production and management of clean energy on the mapped Earth. The location of the solar power plant planned to be produced for the Organized Industrial Zone is shown in Figure 1. [4]. According to the data received from RETScreen, the amount of sun received by the region is shown in Figure 2. [5]

When we evaluate the data obtained from the RETScreen application on a monthly basis, Table 3 shows values such as air temperature, relative humidity, precipitation rate, amount of sunlight received, and atmospheric pressure of the selected region [5].

There are two methods to produce hydrogen after the energy is produced. These are burning hydrogen or giving electricity. There are four main groups to produce hydrogen with electricity obtained from the sun as a method. There are [6]:

1) photovoltaic (PV)
2) photo electrochemical
3) photo biological
4) solar thermal energy

Figure-3 shows schematically how hydrogen is produced with solar energy. [8-9].The hydrogen that is desired to be produced as Green Hydrogen with zero emission can be produced by the photovoltaic method. The electrical energy obtained from the sun's rays is given to the water and the water is electrolyzed. Thus, the hydrogens in the water can be separated and stored.

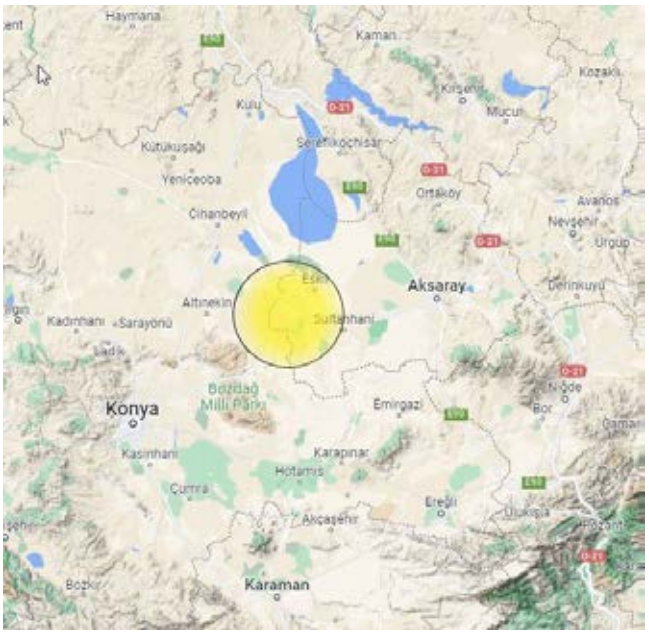


Figure 1. Planned Area of OIZ and Solar Power Plant

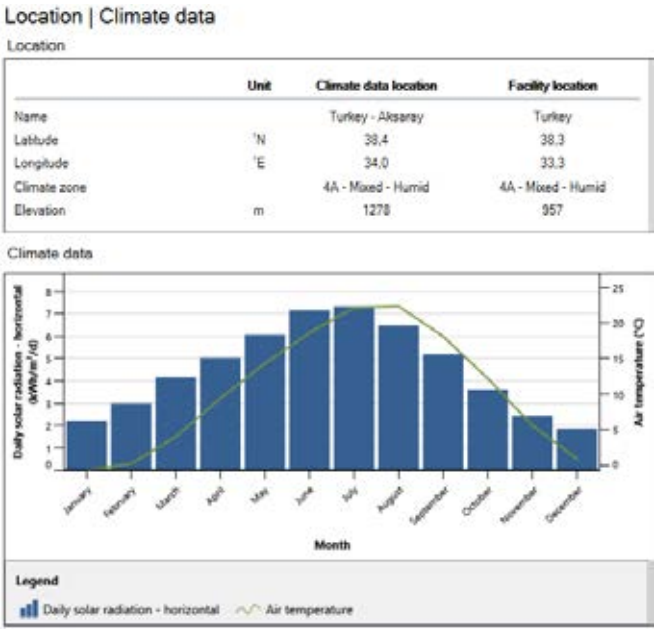


Figure 2. Location of the Power Plant and Energy Efficiency

Table 3. Energy Production of the Power Plant on a Monthly Basis

	Heating design temperature	-4,8							
	Cooling design temperature	26,8							
	Earth temperature amplitude	23,0							
Month	Air temperature	Relative humidity	Precipitation	Daily solar radiation - horizontal	Atmospheric pressure	Wind speed	Earth temperature	Heating degree-days	Cooling degree-days
	°C	%	mm	kWh/m²/d	kPa	m/s	°C	°C-d	°C-d
January	-0,7	77,4%	39,37	2,22	87,2	3,6	-1,5	580	0
February	0,2	73,8%	33,60	2,98	87,1	3,9	-0,1	498	0
March	4,0	66,8%	35,96	4,17	87,0	3,9	4,1	434	0
April	9,4	61,0%	43,50	5,04	87,0	3,6	9,9	258	0
May	14,3	55,4%	41,23	6,07	87,1	3,1	15,2	115	133
June	18,6	47,3%	26,70	7,16	87,1	3,4	20,0	0	258
July	22,1	38,5%	7,75	7,33	87,0	4,0	23,9	0	375
August	22,3	34,9%	4,65	6,48	87,1	3,8	24,2	0	381
September	18,1	37,9%	10,50	5,20	87,3	3,2	19,4	0	243
October	12,2	52,1%	32,55	3,62	87,5	3,2	12,3	180	68
November	5,6	66,9%	42,60	2,43	87,4	3,3	4,8	372	0
December	0,9	76,4%	46,19	1,87	87,3	3,5	-0,1	530	0
Annual	**10,6**	**57,3%**	**364,60**	**4,56**	**87,2**	**3,5**	**11,1**	**2.967**	**1.459**

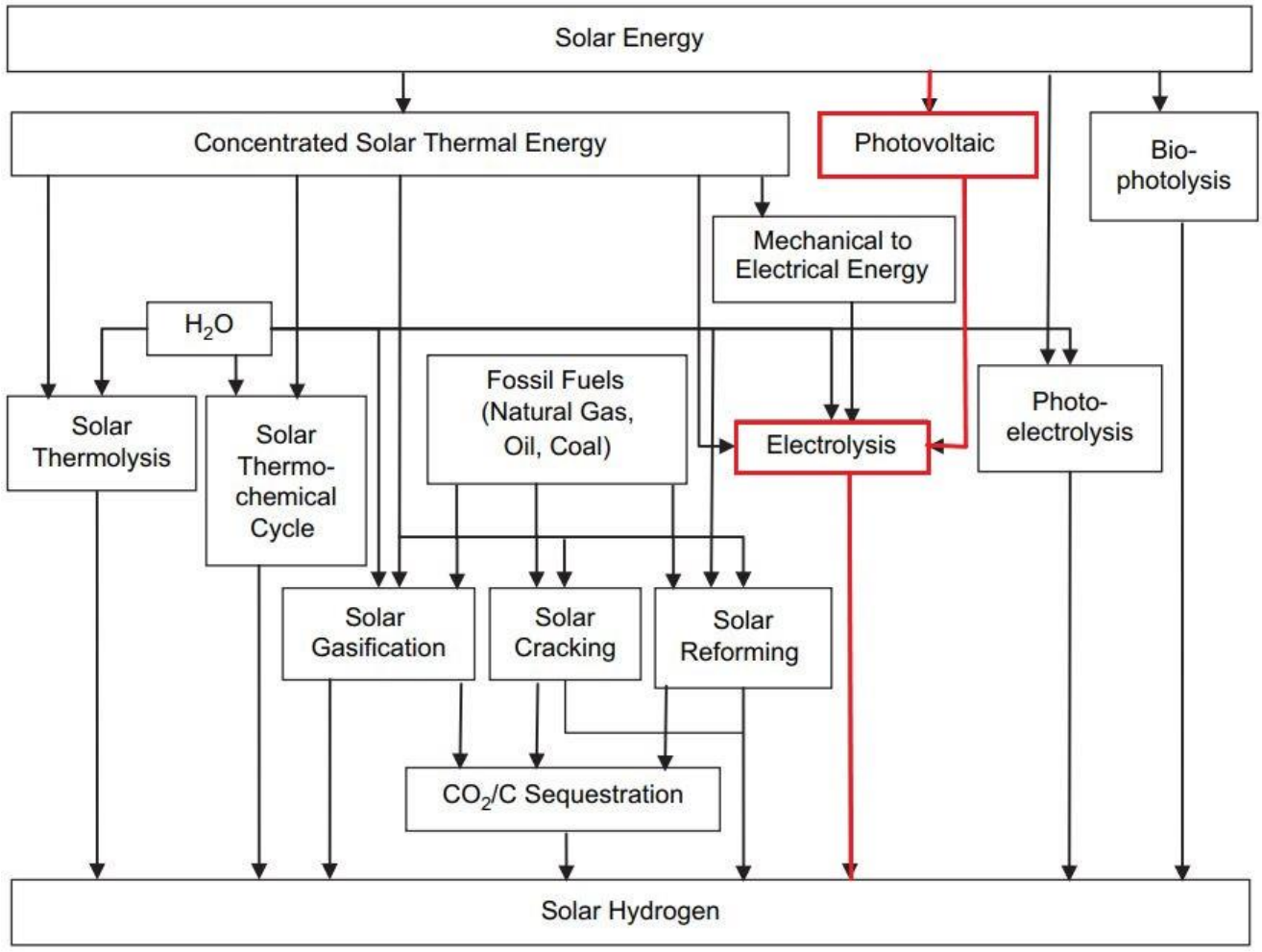


Figure-3. Energy Production Scheme of the Designed Solar Power Plant Area

The reaction that takes place at the electrode, that is, the anode, where the oxidation reaction takes place:

$$2H2O+ \rightarrow O2 + 4H+ + 4e- \quad (1)$$

The reaction that takes place at the electrode, the cathode, where the reduction reaction takes place:

$$4H2O+ 4e- \rightarrow 2H2 + 4OH- \quad (2)$$

It separates water into its components by electrolysis with its formulas. In the last step of the plant, hydrogen is transferred in liquid form or directly to the organizing area. Thus, an environmentally friendly and efficient energy source is used for the heating need in the region. [9]

RESULTS AND DISCUSSION

The need for heating of the Organized Industrial Zone, which is planned to be built, can be supplied with alternative energy sources. The need for heating of the region can be met by providing hydrogen production with photovoltaic production with zero emission value as Green Hydrogen. As Green Hydrogen, the need for heating of the region can be met by providing hydrogen production with photovoltaic production with zero emission value.

It is very important for the campus to have open areas exposed to the sun, especially on the Konya-Aksaray border. This indicates that it is convenient and positive to produce hydrogen from the Sun. Possible relocation of the organized Industrial zone will affect the location of the photovoltaic plant to be established around the plant. The plant efficiency will not change significantly due to the high amount of sunshine in the region, but the distance of the suitable land to the Industrial Zone will be an important item for the transportation of hydrogen.

REFERENCES

1. https://www.trthaber.com/haber/ekonomi/aksarayda-3-yeni-organize-sanayi-bolgesi-kuruldu-658036.html Accessed on May 06, 2022
2. Mosca, L., Jimenez, J. A. M., Wassie, S. A., Gallucci, F., Palo, E., Colozzi, M., ... & Galdieri, G. (2020). Process design for green hydrogen production. International Journal of Hydrogen Energy, 45(12), 7266-7277.
3. Karayel, G. K., Javani, N., & Dincer, I. (2021). Green hydrogen production potential for Turkey with solar energy. International Journal of Hydrogen Energy.
4. https://www.google.com.tr/maps/dir//36.842046,30.599106/@36.842046,30.599106,17z?hl=tr Accessed on May 06, 2022
5. https://www.nrcan.gc.ca/maps-tools-and-publications/tools/modelling-tools/retscreen/7465 Accessed on May 02 , 2022
6. Yilanci, A., Dincer, I., & Ozturk, H. K. (2009). A review on solar-hydrogen/fuel cell hybrid energy systems for stationary applications. Progress in energy and combustion science, 35(3), 231-244.
7. Joshi, A. S., Dincer, I., & Reddy, B. V. (2010). Exergetic assessment of solar hydrogen production methods. International Journal of Hydrogen Energy, 35(10), 4901-4908.
8. Steinfeld, A. (2005). Solar thermochemical production of hydrogen—a review. Solar energy, 78(5), 603-615.
9. Caglar, A. (2000). Possible use of biomass materials by pyrolysis method.

WHEC-2022

23rd World Hydrogen Energy Conference

TRACK 2. HYDROGEN PRODUCTION: ELECTROLYSIS

TRACK 2. HYDROGEN PRODUCTION: ELECTROLYSIS

#13 ENHANCED WATER OXIDATION REACTION BY NICKEL OXIDE NANOROD ARRAYS ELECTROCATALYST	154
#19 THE USE OF NANOSTRUCTURED NICKEL-MOLYBDENUM OXIDE AS AN EFFICIENT AND LOW-COST ELECTROCATALYST FOR THE HYDROGEN EVOLUTION REACTION IN THE ACIDIC MEDIUM	158
#22 QUALIFYING TESTS AND ECONOMIC ANALYSIS OF ELECTROLYZERS FOR GRID SERVICES	161
#68 NICKEL COBALT OXIDE NANOCUBES AS AN EFFICIENT ELECTROCATALYST FOR HYDROGEN EVOLUTION IN ALKALINE SOLUTION	165
#70 MODELING OF H_2O AND CO_2 ELECTROLYSIS IN A MOLTEN CARBONATE ELECTROLYZER	167
#72 INVESTIGATION OF ELECTRICITY, HYDROGEN AND CLEAN WATER PRODUCTION WITH RENEWABLE ENERGY SYSTEM INTEGRATED ONTO A SHIP: MOBILE ENERGY PRODUCTION ON A SHIP	170
#74 PARABOLIC TROUGH SOLAR COLLECTOR INTEGRATED WITH SOLAR POND FOR ELECTRICITY AND HYDROGEN PRODUCTION BASED ON SOLAR ENERGY	173
#78 HYDROGEN PRODUCTION FLAT PLATE SOLAR COLLECTOR INTEGRATED WITH PV-T	177
#94 CRITICAL ASSESSMENT OF THE PRODUCTION SCALE REQUIRED FOR FOSSIL PARITY OF GREEN ELECTROLYTIC HYDROGEN	180
#109 ANALYSIS OF EXPERIMENTAL APPLICATION OF PERMANENT NEODYMIUM MAGNETS IN ALKALINE ELECTROLYZER FOR GREEN HYDROGEN PRODUCTION	183
#127 AISI 442 AND 446 FERRITIC STAINLESS STEELS AS A SUPPORT FOR BIPOLAR PLATES IN PROTON EXCHANGE MEMBRANE WATER ELECTROLYZERS	186
#128 CHEMICALLY STABILISED SHORT SIDE CHAIN AQUIVION® MEMBRANES FOR OPERATION IN WATER ELECTROLYSIS	189
#150 H_2BASQUE – TECHNOLOGIES FOR BOOSTING THE HYDROGEN ECONOMY IN THE BASQUE COUNTRY: GREEN HYDROGEN PRODUCTION	192
#156 ACTIVITY OF BINARY NON-PRECIOUS METAL OXIDE-BASED ELECTRODE FOR OXYGEN EVOLUTION REACTION IN ACID	194
#157 SOEC AS ENABLER OF HIGHLY EFFICIENT HYDROGEN & E-FUEL PRODUCTION	197
#167 A NOVEL HYDROGEN ECONOMY BASED ON ELECTROCHEMICAL CELLS INTEGRATED WITH FOSSIL FUEL ASSETS AND WASTEWATER RESOURCES	200
#180 PREPARATION AND ANALYSIS OF MEMBRANE ELECTRODE ASSEMBLIES FOR PEM WATER ELECTROLYSERS BASED ON LASER-GENERATED IRIDIUMOXIDE NANOPARTICLES AS ELECTROCATALYSTS FOR THE OXYGEN EVOLUTION REACTION	204
#183 ELECTRODEPOSITION OF A Ni-Mo ALLOY CATALYST WITH OPTIMIZED Mo-CONTENT FOR HYDROGEN EVOLUTION REACTION IN AEM-ELECTROLYSIS	207
#187 UPSCALING HIGH PERFORMANCE 3-D ELECTRODES FOR ALKALINE WATER ELECTROLYSIS TOWARDS NEAR-INDUSTRIAL CONDITIONS	210
#205 ACTIVITY OF ELECTRODEPOSITED RHODIUM IN ACIDIC AND BASIC WATER ELECTROLYSIS	213
#209 MEMBRANE ELECTRODE ASSEMBLIES FOR PEMWE BASED ON GLASS FIBRE REINFORCED PFSA/SSPS COMPOSITE MEMBRANES	216
#218 ELECTROCHEMICAL PERFORMANCE OF 3-D PRINTED ELECTRODE GEOMETRIES IN VIEW OF ENHANCED GAS EVACUATION DURING ALKALINE WATER ELECTROLYSIS	219
#224 EXPERIMENTAL RESEARCH ON 100-BAR HIGH PRESSURE DIFFERENTIAL PROTON EXCHANGE MEMBRANE ELECTROLYZER	222
#231 ELECTROCATALYTIC AMMONIA OXIDATION COUPLED WITH HYDROGEN PRODUCTION - MOVING TOWARDS A CARBON-NEUTRAL WATER TREATMENT CYCLE	225
#250 POWDER METALLURGY: AN EFFICIENT AND SCALABLE PRODUCTION PROCESS OF ELECTRODES FOR THE GIGAWATT ELECTROLYSIS INDUSTRY	228
#251 INVESTIGATION OF ELECTROLYTE FORCED FLOW FOR ALKALINE WATER ELECTROLYSIS USING COMPUTATIONAL FLUID DYNAMICS	231

#307 A NUMERICAL ENERGY AND EXERGY ANALYSIS OF THE EFFECT OF PHASE CHANGE MATERIALS ON A PHOTOVOLTAIC THERMAL COLLECTOR FOR HYDROGEN PRODUCTION IN NORTH CYPRUS	234
#308 Ir-DECORATED Pt NANOPARTICLES AS A BIFUNCTIONAL CATALYST FOR OXYGEN EVOLUTION AND REDUCTION REACTIONS	237
#344 GREEN HYDROGEN FOR AMMONIA PRODUCTION – A CASE FOR THE NETHERLANDS	240
#382 HIGH-PRESSURE PEM WATER ELECTROLYSIS BASED ON HYDRAULIC SINGLE CELL COMPRESSION	243
#391 EXTERNAL EFFECTS ON THE HIGH FREQUENCY EIS RESPONSE OF A PEM ELECTROLYSIS CELL	246
#393 EFFICIENCY OF THE PRODUCTION PROCESS AND MANAGEMENT OF GREEN HYDROGEN THROUGH SIMULATION AND BALANCE OF PLANTS (BOF)	249
#434 PARAMETRIC ANALYSIS OF BIOMETHANOL PRODUCTION UNIT USING BIOMASS GASIFIER AND HIGH-TEMPERATURE ELECTROLYZER	252
#1449 A HIGH-PERFORMANCE ELECTROLYSIS CELL PROMISES MORE COST-COMPETITIVE RENEWABLE HYDROGEN	255
#1469 ENHANCING THE ELECTROCATALYTIC HYDROGEN EVOLUTION ACTIVITY OF BARE COPPER ELECTRODES THROUGH ULTRAFAST FEMTOSECOND LASER NANOSTRUCTURING	258
#1481 THIN FILM COATING OF PLATINUM ON 3D PRINTED POLYMERIC ANODE ELECTRODES FOR PEMWE	261
#1487 IMPROVING HYDROGEN EVOLUTION CATALYTIC ACTIVITY OF 2D CARBON ALLOTROPE BIPHENYLENE WITH B, N, P DOPING: DENSITY FUNCTIONAL THEORY INVESTIGATIONS	264
#1517 IRIDIUM-RUTHENIUM CATALYST ON SPUTTER-ETCHED MEMBRANE FOR PROTON EXCHANGE MEMBRANE WATER ELECTROLYZERS	267
#1538 EXERGETIC ANALYSIS OF A SOLAR ENERGY-BASED HYDROGEN PRODUCTION SYSTEM	269
#1543 UNDERSTANDING RESEARCH EVOLUTION IN HYDROGEN PRODUCTION FROM WATER ELECTROLYSIS: A BIBLIOGRAPHIC STUDY	272
#1573 DEVELOPMENT OF Pt-Cr COATED SS316L ELECTRODES FOR PEM ELECTROLYZERS BY SELECTIVE LASER MELTING METHOD	275
#1576 A NEW EXPERIMENTAL INVESTIGATION ON HYDROGEN PRODUCTION OF NaCl, KCl AND $CaCl_2$ SOLUTIONS THROUGH CHLORALKALI REACTOR	278
#1578 FLOW CHANNEL EFFECT ON PERFORMANCE OF PEM WATER ELECTROLYSIS	281
#1594 EFFECT OF MOLYBDENUM OXIDE ADDITION TO METAL-SUPPORTED ZEOLITE CATALYST FOR REVERSE WATER GAS SHIFT REACTION	284
#1598 ON THE POTENTIAL OF COUPLING SOLAR CHIMNEY AND WIND ENERGY TO PRODUCE HYDROGEN AS GREEN-TO-GREEN SYSTEM	287
#1627 ENERGY PERSPECTIVE AND ANALYSES OF SEAWATER ELECTROLYZER FOR SEA VEHICLE	290
#1629 THE EXPERIMENTAL STUDIES ON ELECTROLYSER MODE OPERATION OF UNITIZED REGENERATIVE PEM FUEL CELL	293
#1637 TAKE YOUR ENERGY USING SERVI DUT PEKMEZİ (MULBERRY MOLASSES): A NOVEL ELECTROACTIVE FILM FOR WATER ELECTROLYSIS	296

WHEC-2022
23rd World Hydrogen Energy Conference
June 26-30, 2022 - Istanbul

#13

ENHANCED WATER OXIDATION REACTION BY NICKEL OXIDE NANOROD ARRAYS ELECTROCATALYST

[1] *Khadijeh Hemmati,* [2] *Omran Moradlou,*[1,3*]*Alireza Z.Moshfegh*
[1] Department of Physics, Sharif University of Technology, P. O. Box 11155-9161, Tehran, Iran
[2] Department of Chemistry, Alzahra University, P. O. Box 1993893973, Tehran, Iran
[3] Institute for Nanoscience and Nanotechnology, Sharif University of Technology, P. O. Box 14588-8969, Tehran, Iran

*Corresponding author e-mail: moshfegh@sharif.edu

ABSTRACT

Water splitting for hydrogen generation is an interesting strategy in energy technology. Hence, developing cheap and robust electrodes have received great attention in recent years. In this research, we fabricated nickel oxide (NiO) Nanorod Arrays structure coating as an anode that has a strong bonding with the Ni foam (NF) substrate to prepare NiO/NF. The electrode was prepared by using the hydrothermal method (in a temperature of 100°C and reaction time of 12 h) in a solution containing nickel nitrate and urea under the optimized experimental conditions. The electrochemical performance of the fabricated electrode was investigated in alkaline solution of 1 M KOH and revealed that only +450 mV is required to achieve a current density of 100 mA cm^{-2} for water oxidation showing an efficient electrocatalyst. The enhanced performance of the developed electrode for water splitting can be related to the morphology of the nanorod structure, high ordered array structure and high adhesion of NiO nanorod arrays on nickel foam substrate.

Keywords: Water oxidation, NiO, Nanorod array

INTRODUCTION

Splitting of water into H_2 and O_2 is one of the most efficient approaches for generation of high-purity H_2 fuel [1,2]. Due to the sluggish kinetics of the oxygen evolution reaction (OER) at the anodic electrode surface in an overall water-splitting cell, which is resulting from the four-step this reaction, the development of effective electrocatalysts for these systems is still considered as a bottleneck [1,3]. Therefore, finding the economical and efficient electrocatalysts with low overpotentials to overcome the sluggish kinetics is necessary to deliver high current density. The electrocatalysts based on precious metal oxides such as IrO_2 and RuO_2 are the best choice for OER [3,4]. Unfortunately, large-scale applications of these materials are limited because of their scarcity and high price. Recently, an attractive alternative to these noble metal materials as OER catalysts is introduced by using nickel-based electrocatalysts in the different forms such as oxides, nitrides, phosphides, etc. [5]. Morphology is an important factor that directly affects the degree of catalytic activity of the compound and is able to create a high surface area with many active sites to expose in the electrolyte that results in high performance in the water-splitting processes [5,6]. Considering this goal, in this work, we report an OER electrode fabricated with a NiO nanorod arrays on nickel foam, in which they have been vertically grown on porous Ni foam as conductive support. The prepared OER electrode exhibits high current density of 100 mA cm^{-2} at overpotential of +450 mV in 1M KOH at the room temperature. Furthermore, the array-nanostructured electrode showed an efficient charge transfer with a small impedance arc and it resulted in the high OER performance.

MATERIALS AND METHODS

The materials nickel nitrate hexahydrate ($Ni(NO_3)_2{\cdot}6H_2O$), urea ($CO(NH_2)_2$) and absolute ethanol were purchased from Merck (Germany). In order to synthesize NiO nanorod arrays on Ni foam, the simple hydrothermal method was applied. Typically, 0.5 g of $Ni(NO_3)_2{\cdot}6H_2O$ and 0.2 g of urea were dissolved in 12.0 mL of di-ionized (DI) water and stirred for 30 min to prepare a clear and homogeneous solution. Ni foam with dimensions of (3 × 1 cm^2) was cleaned via sonication in acetone and ethanol for 15 min and then, it was annealed at 500°C in Ar atmosphere to fully remove the surface native oxide layer. The well-cleaned Nickel foam as substrate and the solution obtained were transferred into a 15 mL cylindrical Teflon located in a stainless-steel autoclave. The autoclave was maintained at 100°C for 12 h and then cooled down to room temperature naturally. After the hydrothermal process, the deposited thin film (green color) was rinsed 3 times with DI water and pure ethanol via sonication and then dried in oven for 6 h at 80°C. Then, the sample was placed at the middle of a tube furnace and annealed at 450 °C under a constant flow of 200 standard cubic centimeters (sccm) Ar for 1 h at a heating rate of 2 °C /min. Finally, the furnace was cooled down to room temperature for removing the sample.

CHARACTERIZATIONS

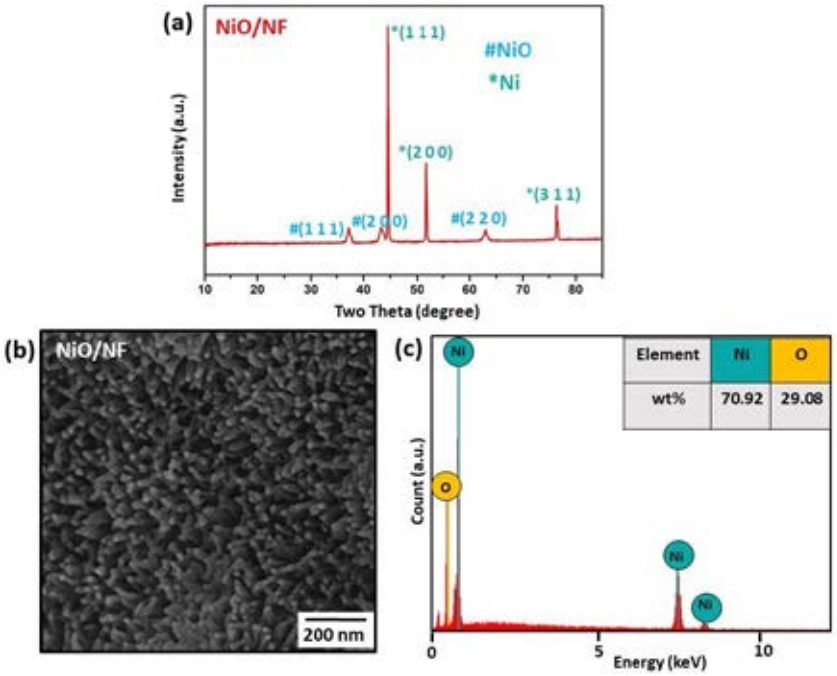
The morphology and composition of samples were characterized by field emission scanning electron microscopy (FE-SEM) Mira 3-XMU model equipped with an energy dispersive spectroscopy (EDS). In order to study the crystal structure, the X-ray diffraction (XRD) patterns were recorded in a range from 10° to 80° with 0.02° per step using an X'Pert MPD X-ray diffractometer with Copper Kα (λ=1.5410 A˚) radiation at 40 kV and 40 mA.

ELECTROCHEMICAL TESTS

The electrochemical performance was tested by a three-electrode galvanostat/potentiostat (Autolab PGSTAT302). All measurements were carried out in a three-electrode glassy cell which contained with 1 M KOH aqueous solution, the fabricated NiO Nanorod NiO/NF, platinum wire, and an Ag/AgCl electrode as working, counter and reference electrodes, respectively. The effective working electrode area in the electrolyte was approximately 1 cm^{-2}. The working electrode (NiO/NF) was cycled 50 times by CV until reaching a stable polarization curve. OER polarization curve measurements were performed by linear sweep voltammetry (LSV) at a scan rate of 50 mV s^{-1}. Electrochemical impedance spectra (EIS) were measured at an overpotential of +270 mV from 0.1 Hz to 100 KHz frequencies.

RESULTS AND DISCUSSION

A) XRD/SEM/EDS analysis: XRD pattern of NiO/NF nanorod arrays after its annealing at 450°C is shown in Fig. 1a. The peaks at the 2θ= of 37.21˚, 43.23˚ and 62.87˚ were originated from (111), (200) and (220) planes of the prepared NiO structure, respectively. As illustrated in the Figure, all the peaks marked (#) are indexed to NiO (JCPDS 47-1049) and the other peaks which have been marked with (*) are ascribed to Ni metal associated with the Ni foam substrate. The morphology and composition of the NiO/NF nanorod arrays were investigated by FE-SEM and EDS analysis, respectively. According to the FE-SEM image (Fig. 1b), we have found that the array structure with a perfect rod shape was formed during the hydrothermal treatment. The nanorods were typically 100–200 nm in length and their diameters ranging from 10 to 15 nm. The nanorods were vertically aligned on the Ni foam substrate and forming an array structure. EDS analysis (Fig. 1c) of the NiO nanorod arrays only revealed the peaks of Ni and O which further confirms that the as-fabricated NiO nanorod is of high purity. The obtained results by EDS is in good agreement with the XRD result where no other impurity peaks were observed.



. Fig. 1. (a) XRD pattern, (b) FE-SEM image, and (c) EDS analysis of NiO/NF nanorod arrays

B) Oxygen evolution reaction: In order to evaluate the oxygen-evolution reaction performance of the electrode based on NiO/NF nanorod arrays, we first evaluated the OER activity of the as-prepared catalysts in 1M KOH electrolyte at room temperature (25°C) by using electrochemical measurements including LSV and EIS. So, the NiO/NF nanorod arrays electrode and pristine NF (for comparison) were applied as working electrodes. Fig. 2a shows LSV polarization curves of the NF and NiO/NF nanorod arrays electrodes. The NiO/NF nanorod arrays exhibited a good OER activity, requiring overpotential of +450 mV to deliver current density of 100 mA cm^{-2}, which is smaller than that of NF (+839 mV). The whole coverage of the NF and strong adhesive of nanorod arrays on the NF substrate facilitate the charge transfer between the electrode/electrolyte as revealed by the results from EIS measurements (Fig. 2b). EIS curve depicts that the charge-transfer resistance of the NiO/NF nanorod arrays electrode is ~1.0 Ω, which is significantly smaller than that of pristine NF (~80 Ω), confirming its easier charge transfer ability.

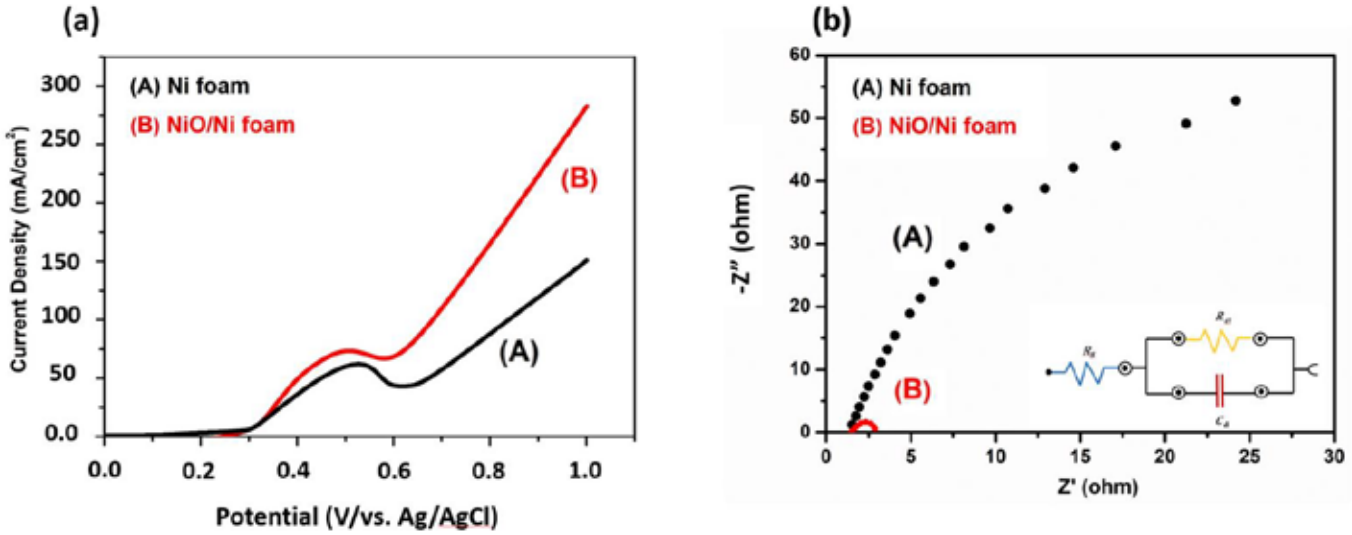


Fig. 2. (a) Polarization curves of the Ni foam (A) and NiO/NF nanorod arrays (B), and (b) EIS Nyquist plots of the Ni foam (A) and NiO/NF nanorod arrays (B) catalyst measured at the potential of 0.5 V vs. Ag/AgCl.

CONCLUSIONS

In summary, this study has developed an economic and simple OER electrocatalyst based on the NiO nanorod arrays deposited on nickel foam (NiO/NF) for efficient and stable water splitting process. The prepared NiO nanorods possess a large surface area, which yields an easier charge transfer and numerous active sites. The NiO/NF catalyst exhibited an excellent electrochemical behavior in water splitting which requires a low overpotential of ~450 mV to deliver a high current density of 100 mA cm^{-2}, in alkaline media at room temperature. The results clearly revealed that the simply prepared of high oriented NiO/NF array structure and low cost with efficient activity can be applied for H_2 production via water splitting, supercapacitors, and other electrochemical devices.

ACKNOWLEDGEMENT

Financial support by the Iran National Science Foundation (INSF) through Research Project under No 99019385 is gratefully acknowledged.

REFERENCES

1. Lu, X. and Zhao, C., 2015. Electrodeposition of hierarchically structured three-dimensional nickel–iron electrodes for efficient oxygen evolution at high current densities. Nature Communications, 6, p.6616.
2. Barough, V., Iranizad, E.S., Bayat, A. and Hemmati, K., 2018. Synthesis of binder-free MoSe2 nanoflakes as a new electrode for electrocatalytic hydrogen evolution. Journal of Electroanalytical Chemistry, 823, pp.278-286.
3. Qiu, B., Cai, L., Wang, Y., Lin, Z., Zuo, Y., Wang, M. and Chai, Y., 2018. Fabrication of nickel–cobalt bimetal phosphide nanocages for enhanced oxygen evolution catalysis. Advanced Functional Materials, 28(17), p.1706008.
4. Roger, I., Shipman, M.A. and Symes, M.D., 2017. Earth-abundant catalysts for electrochemical and photoelectrochemical water splitting. Nature Reviews Chemistry, 1(1), p.0003.
5. Vij, V., Sultan, S., Harzandi, A.M., Meena, A., Tiwari, J.N., Lee, W.G., Yoon, T. and Kim, K.S., 2017. Nickel-based electrocatalysts for energy-related applications: oxygen reduction, oxygen evolution, and hydrogen evolution reactions. ACS Catalysis, 7(10), pp.7196-7225.

6. Faraji, M., Yousefi, M., Yousefzadeh, S., Zirak, M., Naseri, N., Jeon, T.H., Choi, W. and Moshfegh, A.Z., 2019. Two-dimensional materials in semiconductor photoelectrocatalytic systems for water splitting. Energy & Environmental Science, 12(1), pp.59-95.

WHEC-2022
23rd World Hydrogen Energy Conference
June 26-30, 2022 - Istanbul

#19

THE USE OF NANOSTRUCTURED NICKEL-MOLYBDENUM OXIDE AS AN EFFICIENT AND LOW-COST ELECTROCATALYST FOR THE HYDROGEN EVOLUTION REACTION IN THE ACIDIC MEDIUM

[1*] *Mahmoud Rammal*, [2] *Sasha Omanovic*
Department of Chemical Engineering, McGill University, 3610 University St., Montreal, Quebec H3A 0C5, Canada

Corresponding author email: mahmoud.rammal@mail.mcgill.ca

ABSTRACT

Due to its favorable chemical and structural properties, nanostructured nickel-molybdenum oxides produced through an environmentally benign solution combustion method were investigated as possible cathode materials for the hydrogen evolution reaction in an acidic electrolyte. Ni-Mo-oxides of different compositions were employed, leading to the identification of the equiatomic stoichiometric sample ($NiMoO_4$) as the best performing electrode composition for the HER. The promising performance of this material could be linked to the synergistic effect that is induced through the combination of metal oxides in a binary form. While the activity of $NiMoO_4$ is slightly inferior to the state-of-the-art 20% Pt/C, when the cost of the material and the stability aspect are considered, $NiMoO_4$ emerges as the more economically viable option.

Keywords: Hydrogen, mixed-metal oxides, electrocatalysis, synergism, acidic electrolyte

INTRODUCTION

H_2, in combination with renewable energy systems (wind/solar/hydro), is a viable, long-term option to counter the fossil fuel dilemma. Indeed, H_2 can be produced using the surplus of renewable energy in a zero-emission process by water electrolysis. Currently, most industrial applications employing water electrolysis to produce H_2, utilize alkaline electrolyzers since the mild alkaline environment allows the use of cheap electrode materials like Ni and Fe, but they suffer from large power requirements and poor stability [1]. In contrast, polymer-electrolyte-membrane (PEM)-based electrolyzers offer a significantly higher current efficiency, are compact and modular, and enable the internal compression of gases [2]. However, due to the aggressive acidic environment, PEM electrolyzers require expensive metals as electrode materials (e.g., Pt, Ir, Ru, Pd), which limits the widespread use of those electrolyzers.

The goal is to bring the PEM technology closer to commercialization by using inexpensive and durable electrocatalysts. This research seeks to develop bimetallic Ni-Mo-oxide nanostructures to achieve, at a low cost, high electrocatalytic activity and long-term stability that approaches that of Pt. The rationale follows a three-pronged approach: (1) Ni and Mo can induce a synergistic effect, thus enhancing the cathode activity in HER (intrinsic effect), (2) metal oxides have been proven to be stable under extremely acidic conditions in several electrochemical applications and are, thus, excellent candidates for PEM electrolyzers, and (3) nanostructures provide a remarkably high specific surface area and increased surface energy, thus also yielding higher intrinsic and extrinsic electrocatalytic activity.

The $NiMoO_4$ family has been used, traditionally, in industrial catalysis. However, its electrochemical affinity has been, thus far, mainly limited to supercapacitor applications [3]. Also, the harsh, highly corrosive environment of the PEM electrolyte (acidic environment) has discouraged its use in PEM-simulated conditions due to instability concerns and limited conductivity [4]. Different methods can be employed to produce $NiMoO_4$; however, most of the currently used wet chemical methods generate toxic chemical waste leading to environmental toxicity and non-biodegradable products, while physical methods necessitate massive energy requirements. In this study, we propose an environmentally-friendly solution combustion method using agar as a fuel agent.

EXPERIMENTAL

Synthesis of metal-oxides

A stoichiometric amount of nickel nitrate ($Ni(NO_3)_2 \times 6H_2O$) and ammonium heptamolybdate tetrahydrate ($(NH_4)_6Mo_7O_{24} \times 4H_2O$) were dissolved separately in ultrapure water (resistivity >18 MΩ cm). The solutions were stirred for 30 minutes and subsequently mixed together. An appropriate amount of agar was added, at a high temperature, to dissolve agar and induce gelation. After the formation of the gel, the solution-containing beaker was equilibrated at room temperature, after which it was placed in an oven to remove the water content. The dried gel was, then, placed in a preheated furnace at an appropriate temperature to obtain the oxide structures through a

highly exothermic combustion reaction. NiO, MoO_3, and different Ni-Mo-oxide compositions were prepared using the same method except for changing the amount of the precursor salts. A commercial 20% Pt/C was employed as a control HER electrocatalyst in the electrochemical measurements.

Electrochemical measurements

The electrochemical measurements were conducted in 0.5 M H_2SO_4 using a three-electrode electrochemical cell. The working electrode consisted of a glassy carbon electrode (GCE) covered with a thin layer of the electrocatalytic material, while a platinum wire and a saturated calomel electrode (SCE) were used as the counter and reference electrodes, respectively. The working electrode was prepared by mixing the produced electrocatalytic material with an appropriate amount of water and ethanol to enhance dispersion. Subsequently, carbon black was added to the catalyst ink to increase the conductivity of the electrocatalytic layer. Then, a 20 µL aliquot of this suspension was dropped on the mirror-polished GCE (surface area: 0.283 cm^2) and dried at room temperature. The performance of the synthesized electrocatalyst was screened using a short term chronoamperometry (1000 seconds) experiment carried out at an overpotential of -0.55 V. Subsequently, an LTP (linear Tafel plot) was performed in the overpotential range from 0.55-0 V to obtain the Tafel slope and other electrochemical performance indicators. The potentials reported in this study were converted to RHE (reversible hydrogen electrode).

RESULTS AND DISCUSSION

Effect of composition and morphology characterization

The effect of the composition of Ni_xMo_{1-x}-oxide (x = 0.0, 0.2, 0.4, 0.5, 0.6, 0.8, 1) towards the HER is presented in Fig. 1. It is notable that the pure oxides (NiO and MiO_3) exhibit a negligible activity for the HER. As the oxide components are combined, an increase in the hydrogen activity is notable, which reaches a maximum (ca. 190 mA/cm^2) at $NiMoO_4$. The increase in the performance of the material can be attributed to several factors (composition, electrochemical surface area, particle size, electronic configuration, to name a few). The determination of the electrochemical surface area is hindered by using carbon black as a conductive additive, which confounds the computation of a reliable active surface area.

Selected SEM images of the synthesized materials are presented in Fig. 2. Since the HER is a heterogeneous reaction occurring at the surface of the electrocatalyst, a small particle size would, theoretically, entail a higher specific surface area, which would result in improved performance. However, this is not the case here, since the smallest particle size is associated with $Ni_{0.8}Mo_{0.2}$-oxide (2-3 nm) which performs relatively poorly towards the HER, as seen in Fig. 1. The BET surface area and pore volume of the synthesized materials were determined, as shown in Fig. 3. The maximum surface area and pore volume are observed for $Ni_{0.8}Mo_{0.2}$-oxide (110 m^2/g, 0.25 cm^3/g) which is markedly higher than those of the best-performing $NiMoO_4$ (26 m^2/g, 0.10 cm^3/g); however, this sample exhibits comparatively lower electrocatalytic HER performance, indicating that the surface area is not the determining factor in the observed HER activity.

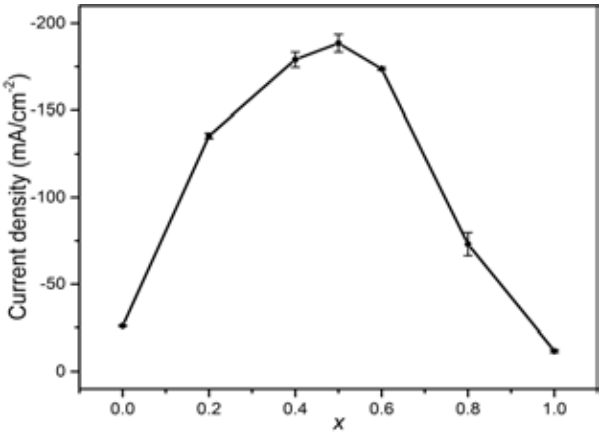


Fig. 1. *Extrinsic* electrocatalytic activity of the Ni_xMo_{1-x}-oxide (x = 0.0, 0.2, 0.4, 0.5, 0.6, 0.8, 1) in 0.5 M H_2SO_4 at an overpotential of -350 mV vs. RHE.

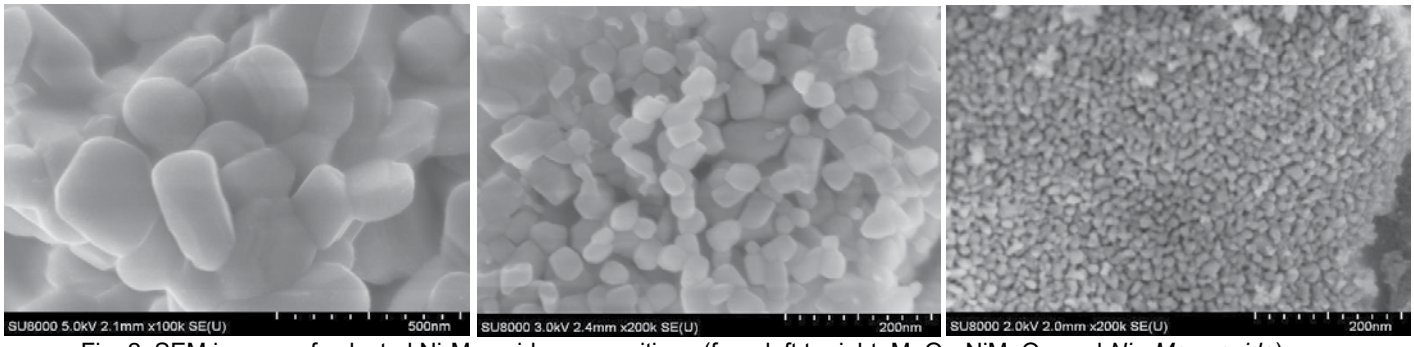


Fig. 2. SEM images of selected Ni-Mo-oxide compositions (from left to right, MoO_3, $NiMoO_4$, and *$Ni_{0.8}Mo_{0.2}$-oxide*).

XRD measurements were also performed (not shown here), illustrating the existence of different phases as a function of compositions. The predominant phase in $NiMoO_4$ is β-$NiMoO_4$, which has been proven to be more kinetically active in various chemical applications, compared to its α-$NiMoO_4$ counterpart. In addition to the positive influence of the β-

phase, it can be purported that the high activity of $NiMoO_4$ is also related to the optimal electrical configuration that stems from the synergistic effect that is elicited upon combining Ni and Mo [5]. Different theories have been proposed to explain this phenomenon, among which the most notable is the spill-over theory.

Long-Term Stability

The long-term stability of the most electrocatalytically active material ($NiMoO_4$) is compared to that of the state-of-the-art 20% Pt/C, as portrayed in Fig. 4. Despite the large overpotential at which the experiment is conducted (-350 mV vs. RHE), the performance of $NiMoO_4$ is stable after 24 h. The satisfactory stability of $NiMoO_4$ can be attributed to the favorable surface chemistry of mixed metal oxides due to their electron-filled *s* shells. On the other hand, the activity of 20% Pt/C drops precipitously in a linear fashion. The decay in performance of 20% Pt/C is likely due to the underpotential deposition phenomenon – commonly observed for bulk Pt [6].

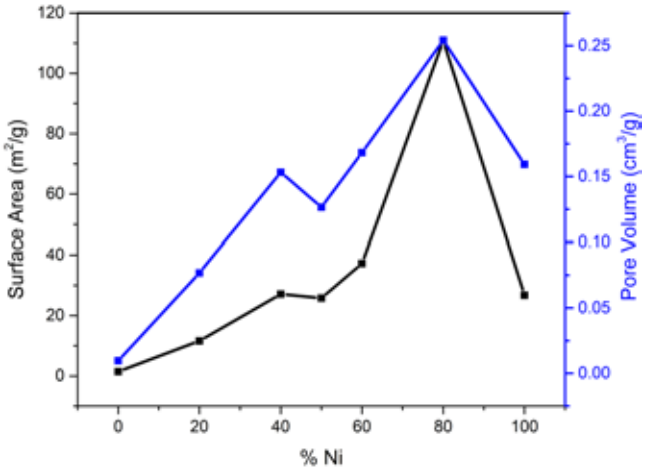


Fig. 3. The variation of surface area and pore volume as a function of nickel content.

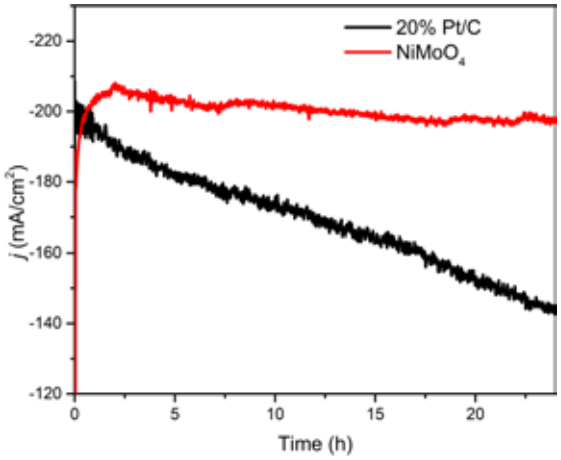


Fig. 3. Long-term stability of $NiMoO_4$ at an overpotential of -350 mV vs. RHE and the commercial 20 % Pt/C recorded at an overpotential of -250 mV vs. RHE.

CONCLUSIONS

Nanostructured Ni-Mo-oxides of several compositions were employed in the hydrogen evolution reaction in the acidic medium. The best-performing oxide composition exhibited a Ni:Mo ratio of 1:1 ($NiMoO_4$), with an HER current density of
190 mA/cm^2 at an overpotential of -350 mV vs. RHE. Different characterization techniques were employed to relate the electrocatalytic activity to the physicochemical properties of the materials, showing that an optimal electronic configuration brought about by alloying Ni and Mo is responsible for the high HER electrocatalytic activity of $NiMoO_4$.

REFERENCES

1. Ray, C. and T. Pal, *Recent advances of metal–metal oxide nanocomposites and their tailored nanostructures in numerous catalytic applications.* Journal of Materials Chemistry A, 2017. **5**(20): p. 9465-9487.
2. Ursua, A., L.M. Gandia, and P. Sanchis, *Hydrogen Production From Water Electrolysis: Current Status and Future Trends.* Proceedings of the IEEE, 2012. **100**(2): p. 410-426.
3. Xu, R., et al., *A high-performance pseudocapacitive electrode material for supercapacitors based on the unique NiMoO4/NiO nanoflowers.* Applied Surface Science, 2019. **463**: p. 721-731.
4. Faber, M.S. and S. Jin, *Earth-abundant inorganic electrocatalysts and their nanostructures for energy conversion applications.* Energy & Environmental Science, 2014. **7**(11): p. 3519-3542.
5. Navarro-Flores, E., Z. Chong, and S. Omanovic, *Characterization of Ni, NiMo, NiW and NiFe electroactive coatings as electrocatalysts for hydrogen evolution in an acidic medium.* Journal of Molecular Catalysis A: Chemical, 2005. **226**(2): p. 179-197.
6. Bessarabov, D. and P. Millet, *PEM water electrolysis*. Vol. 1. 2018: Academic Press.

WHEC-2022
23rd World Hydrogen Energy Conference
June 26-30, 2022 - Istanbul

#22
QUALIFYING TESTS AND ECONOMIC ANALYSIS OF ELECTROLYZERS FOR GRID SERVICES

[1] Regine Reissner, [1]Jörg Bürkle, [2]Stéphanie Crevon, [2]Valérie Seguin, [3]Valerian Klemenz, [3]Tanaka Mandy Mbavarira, [3]Christoph Imboden*
[1]German Aerospace Center (DLR), Institute of Engineering Thermodynamics, Pfaffenwaldring 38, 70569 Stuttgart, Germany
[2] CEA, Energy Systems and Demonstration Lab, 17 Rue des Martyrs, 38054 Grenoble, France
[3] Lucerne University of Applied Sci. and Arts, Inst.of Innovation and Technology Management, Technikumstr. 21, Horw, Switzerland

*Corresponding author e-mail: regine.reissner@dlr.de

As part of the European project QualyGridS, drafts for standardized testing protocols for electrolyzers to perform electricity grid services are defined and elaborated. These protocols are designed to be used by alkaline and proton exchange membrane (PEM) electrolyzers up to the Megawatt scale. The protocols are being submitted for standardisation. Testing results using these protocols on a state-of-the-art PEM electrolyzer system of 50 kW with 1500 cm^2 area stack are presented with considerations of the influence of balance of plant (BOP) components. System behaviour of 50 kW and Megawatt PEM electrolyzers are compared to determine the influence of their scale in performance and response time. An economic analysis has been conducted in the scope of the project. Today's situation has been analyzed in a first part: the objective was to identify the best way to combine H_2 supply for a primary value stream and provision of grid services. A second part of the analysis studied the potential future evolutions that could change the current picture.

Keywords: PEM electrolyser, grid service, dynamics

INTRODUCTION

The potential of water electrolyzers (WE) to provide different services to the grid has been widely discussed in the literature [1-3] as well as initially demonstrated in pilot projects in the EU [e.g. 4]. The electrolysers are capable to generate hydrogen for different applications, as flexible loads are connected and disconnected when demanded by electricity distributors (Transmission System Operators (TSO), Distribution System Operators (DSO) and peer-to-peer operators) and gas grid operators. Thus, flexibility is defined as the modification of injection (through generation) to the grid and/or withdrawal (through consumption patterns) from the grid, in reaction to an external signal in order to provide a service within the energy system [5]. For electric grids, it implies covering certain parameters like amount of power modulation, duration, rate of change or response time. Flexibility is going to be increasingly needed in the EU due to widespread introduction of renewable energy sources (RES) in the electric grid in such a way that non-dispatchable generation will replace the traditional generation. In this context, the benefits from flexibility in the demand side may lead to key achievements such as: (i) being able to increase the amount of RES in the system, (ii) avoiding or delaying network reinforcement; (iii) systems operators being able to successfully match generation and demand.

Some of the gaps for further market penetration of electrolyzers operating on renewable electricity are the precise analysis of performance requirements, definition of standardized tests for qualification of electrolysers and development of business models combining various electrolyzer uses. These issues are addressed throughout the QualyGridS project [6].

SCIENTIFIC APPROACH

Based on existing electricity grid services in the European countries with the published prequalification procedures and typical operation patterns testing protocols for electrolysers were worked out. The grid services are grouped based on the recommendations of ENTSO-E, however there are still differences between the countries. Recently some changes of the services were seen based on the EU Commission Regulation 2017/1485 [8] giving guidelines for transmission system operation.

Testing protocols from our project QualyGridS try to unify the variations in the grid services throughout Europe to make sure that an electrolyzer passing these tests will be capable of doing grid services in all countries that offer this service. With specific tests for given grid services as well as basic characterizations identifying the most relevant capabilities for this application parameters like dynamics and stability are tested.

An example of such a unified testing protocol for FCR (Frequency control reserve) is given in Figure 1. FCR requires the fastest power variations of the different services available in many countries and can achieve interesting remuneration rates.

The testing protocols were applied to a 50 kW electrolyzer operated at DLR (Fig. 2). This PEM electrolyzer manufactured by Hydrogenics uses a 6-cell 1500 cm^2 area stack and can be run up to 2 A/cm^2. Stack and system concept are built in an equivalent way as for the 1.5 MW PEM electrolyzer operated at Uniper in Reitbrook, Hamburg. However, the 50 kW electrolyzer can be considered rather as a test bench for the large area short stack and it is by no way an optimized system for an electrolyzer with 7.5 Nm^3/h hydrogen production.

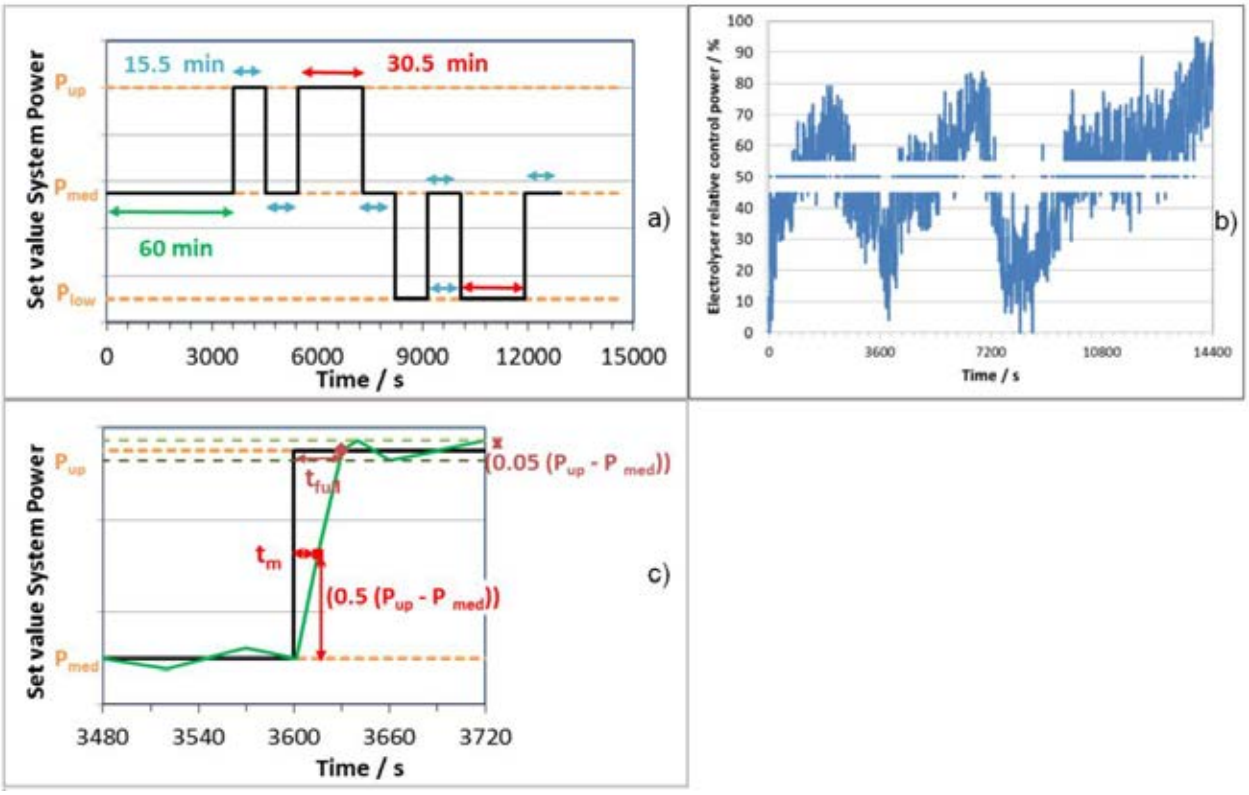


Fig. 1: QualyGridS suggested unified FCR testing protocols and evaluation. a) Testing protocol part 1 derived from prequalification procedures; b) Testing protocol part 2 derived from a real case of grid frequency input; c) Evaluation of activation times and stability. Pass criteria: t_m. ≤ 15 sec, t_{full} ≤ 30 sec, stability ≤ 0.05 (P_{up}-P_{med})).



Fig. 2: process room (left) with stack and operation room (right) with HMI (Human machine Interface) and DI water processing of 50 kW experimental electrolyser used at DLR

RESULTS AND DISCUSSION

The reaction of the stack power to the step power change request will be given in the presentation. While the stack behaviour is comparable at all scales and highly dynamic the system architecture, control strategies, volumes and dynamics of components have a strong influence on the ramping rates and the stability of the total power consumption. In comparison a startup ramp from hot standby of the 1.5 MW electrolyzer is shown. FCR requests a maximum duration of the ramp of 30 seconds. This is achieved by the full size electrolyzer but not by the experimental smaller electrolyzer. The reason for the slower behaviour of the smaller system is the setup of the BOP components: pressure control is slower, ramp speed of the rectifier is limited and the safety conditions for the system prevent it from faster changes. However the 1.5 MW system is not designed for very fast changes of power. Hydrogenics has with the same stack technology also set up a 2.5 MW electrolyzer in Markham, Canada, that follows the grid's power request within seconds [7].

Similarly alkaline electrolyzer systems are tested in the project and it could be shown that with the right systems setup they can just as well achieve the necessary dynamics and stability to perform grid services.

The economic analysis of electrolyzers performing grid services was set up in several stages: in a first stage 2017 economic data of grid services in Europe were collected and a few attractive grid services were selected. An assessment of the potential revenue for a water electrolyzers that could come from the participation to grid services was made considering the situation of today with the best way to combine H_2 supply for a primary value stream and to provide grid services [9]. Dynamic simulations with optimization of the operating strategy and of the size of the system were performed.

A second part of the analysis studied the potential future evolutions that could change the current picture. Simulations were done on prospective scenarios, highlighting notably the potential impact of electricity prices evolution on the results.

CONCLUSIONS

Similar grid services can be characterized by a generic testing protocol that should qualify an electrolyzer for a given grid service in most European countries trading this service. The requirements about dynamics of power ramping, stability and precision of reaching a given power, duration of keeping the new power level as well as power capacity if no aggregation is possible are characterising the different services. PEM and alkaline electrolyser systems have shown the capability of fulfilling the requirements of the services with proper adaptation of the system BOP. More services for which there is no clearly defined market and no prequalification procedures available will request similar performances of the electrolysers so that with the test results on the most popular services and some basic characterisation data of the system one can decide on the electrolyzer's capability. Providing grid services can contribute to an increased income of the electroyzer.

ACKNOWLEDGEMENT

This project has received funding from the Fuel Cells and Hydrogen 2 Joint Undertaking under grant agreement No 735485. This Joint Undertaking receives support from the European Union's Horizon 2020 research and innovation programme and Hydrogen Europe and N.ERGHY. This work is also supported by the Swiss State Secretariat for Education, Research and Innovation (SERI) under contract number 17.00009.

REFERENCES

1. Troncoso E, Newborough EM, 2011. Electrolysers as a load management mechanism for power systems with wind power and zero-carbon thermal power plant. International Journal of Hydrogen Energy 36: 120-134.
2. Guinot B, Montignac F, Champel B, Vannucci D, 2015. Profitability of an electrolysis based hydrogen production plant providing grid balancing services. International Journal of Hydrogen Energy.40: 8778-8787.
3. Marcuello P. 2014. Improvements to Integrate High Pressure Alkaline Electrolysers for Electricity/H2 production from Renewable Energies to Balance the Grid. Publishable summary report ELYGRID project. http://www.elygrid.com/wp-content/uploads/2015/09/D1-2-Publishable-summary-ELYGRID_PU.pdf.
4. Element Energy, E4Tech. 2014. Development of Water Electrolysis in the European Union. Final Report, pp.5. https://www.fch.europa.eu/sites/default/files/study%20electrolyser_0-Logos_0_0.pdf. Accessed December 8, 2019 Accessed on December 8, 2019.
5. EURELECTRIC. 2014. Flexibility and Aggregation. Requirements for their interaction in the market. https://www.usef.energy/app/uploads/2016/12/EURELECTRIC-Flexibility-and-Aggregation-jan-2014.pdf. Accessed on December 8, 2019.
6. https://www.qualygrids.eu. Accessed on December 8, 2019.
7. https://www.energy.gov/sites/prod/files/2018/08/f54/fcto-h2-scale-kickoff-2018-7-del-core.pdf. Accessed on December 10, 2019

8. COMMISSION REGULATION (EU) 2017/1485 of 2 August 2017 establishing a guideline on electricity transmission system operation. https://eur-lex.europa.eu/legal-content/EN/TXT/?uri=CELEX%3A32017R1485. Accessed on December 8, 2019.
9. Klemenz V, Mbavarira TM, Imboden C. 2019. Offering water electrolyzers' flexibility to European grid service markets. 3rd Europen Grid Service Markets Symposiuem 3-4 July 2019, Lucerne Switzerland. https://gsm450601838.files.wordpress.com/2019/07/g0404-paper.pdf

WHEC-2022
23rd World Hydrogen Energy Conference
June 26-30, 2022 - Istanbul

#68

NICKEL COBALT OXIDE NANOCUBES AS AN EFFICIENT ELECTROCATALYST FOR HYDROGEN EVOLUTION IN ALKALINE SOLUTION

[1] *Hossein Faraji,* [2] *Khadijeh Hemmati,*[1] *[*]Kavoos Mirabbaszadeh*
[1] Department of Energy Engineering and Physics, Amirkabir University of Technology, 14588 Tehran, Iran
[2] Department of Physics, Sharif University of Technology, P. O. Box 11155-9161, Tehran, Iran

*Corresponding author e-mail: mirabbas@aut.ac.ir

ABSTRACT

The use of hydrogen as a promising approach to meet the impending climate change and global warming has attracted a lot of attention. Electrolysis of water is one of the best ways to produce pure H_2. However, implementing water electrolysis for large-scale applications requires robust and efficient electrocatalysts that can sustain water splitting without corrosion. Here, we reported 3D nanocubes grown on Nikel foam ($NiCo_2O_4$/NF) by a hydrothermal method that can act as an efficient hydrogen evolution reaction (HER) electrocatalyst in alkaline solution (1M KOH). We have achieved a unique structure that exhibits exceptional HER activity (overpotential of 38 and 166 mV to drive current densities (j) of 10 and 100 $mA.cm^{-2}$). Such superior HER catalytic performance can be derived from the rough feature of the edges and synergistic effect between Ni and Co atoms and exposure to many active sites on the nanocubes. This discovery significantly helps us to design and synthesize low-cost and highly efficient electrocatalysts for large-scale hydrogen production from water electrolysis.

Keywords: $NiCo_2O_4$/NF, Nanocubes**,** Hydrothermal, Hydrogen Evolution Reaction.

INTRODUCTION

Hydrogen is considered as one of the most promising energy carriers due to its applications in reducing the global energy crisis [1]. Some methods to produce hydrogen are coal gasification, steam reforming methane, electrochemical water-splitting, etc [2]. Hydrogen generated by water electrolysers with renewable energy inputs, like wind and solar power, is a clean energy carrier due to no harmful by-products and zero-pollution emission [3]. Electrochemical water-splitting reaction ($2H_2O \rightarrow O_2 + 2H_2$) consisting of two half-reactions (oxygen evolution reaction (OER) anode $2H_2O\ (l) \rightarrow O_2(g) + 4H^+\ (aq) + 4e^-$ and hydrogen evolution reaction (HER) cathode $2H^+\ (aq) + 2e^- \rightarrow H_2\ (g)$) [4]. The benchmark and commercially electrocatalysts are platinum group metals (PGMs) with high catalytic activity, leading to low overpotentials to derive high current densities. However, using these materials at an industrial scale is not cost-effective due to their scarcity and high cost [5]. In recent years, significant research has been done to design and development of Earth-abundant-based electrocatalysts with good catalytic performance. Among many nonprecious metal alloys, sulfides, selenides, oxides, and phosphides, Ni and Co-based oxides are highly desirable in developing of efficient HER electrodes for the realization of hydrogen economy [6].

MATERIALS AND METHODS

In this work $NiCo_2O_4$/NF nanocubes have been developed by hydrothermal method. To gain more insight in the characterization of the developed electrodes, ex-situ studies of the catalyst were performed by using X-ray diffraction (XRD), field emission scanning electron microscopy (FE-SEM). All electrochemical characterizations were investigated by a standard three-electrode system in 1M KOH.

RESULTS AND DISCUSSION

FESEM images demonstrated the uniform formation of 3D nanocubes of Ni and Co on Ni foam with highly rough edges. (Fig. 1a and 1b). Such unique homogeneous nanocubes structure provides a large surface area and thereby enabling an outstanding electrocatalyst performance [7, 8]. The X-ray diffraction (XRD) analysis revealed the product is the phase of cubic $NiCo_2O_4$ (JCPDS 00-020-0781) (Fig. 1c). To determine the electrocatalytic performance, we used the Linear Sweep Voltammetry (LSV) technique with a scan rate of 20 mV s^{-1}. (Fig. 2a) exhibits a superior catalytic activity of 3D nanocubes $NiCo_2O_4$/NF compared to previous work, only requires an overpotential of 36 mV to achieve current density of 10 $mA.cm^{-2}$. For more evaluate the electrocatalytic activity of electrode, electrochemically active surface area (ECSA) (Fig. 2b) was assessed by the measuring double-layer capacitance (C_{dl}). The Nyquist plots (Fig. 2c) from Electrochemical impedance spectroscopy (EIS) measurement shows the charge transfer resistance (R_{ct}) for the prepared electrode is small and indicated the fast reaction kinetics for HER.

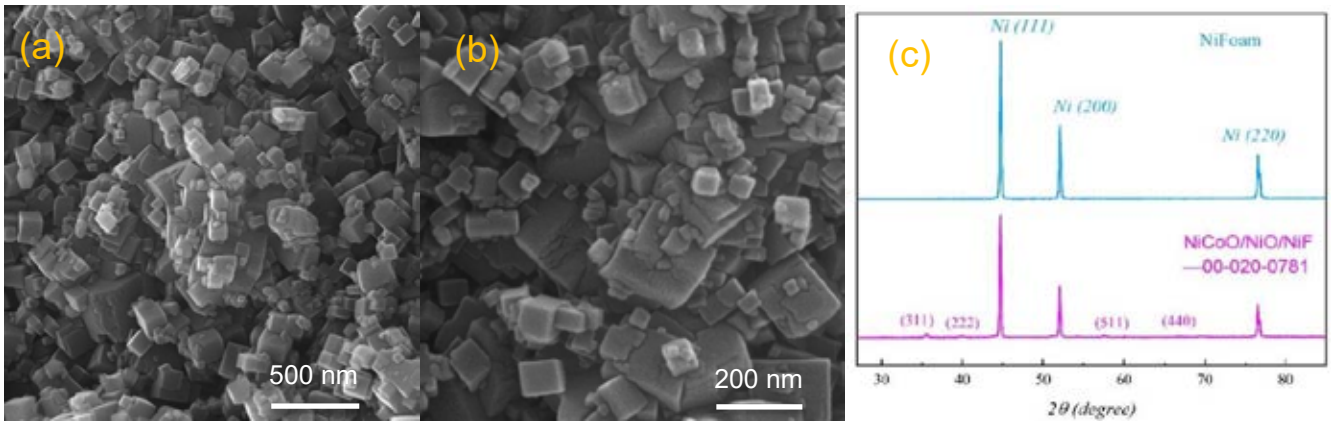


Fig. 1. (a, b) FE-SEM images of $NiCo_2O_4$/NF and (c) XRD patterns of $NiCo_2O_4$/NF and Ni Foam

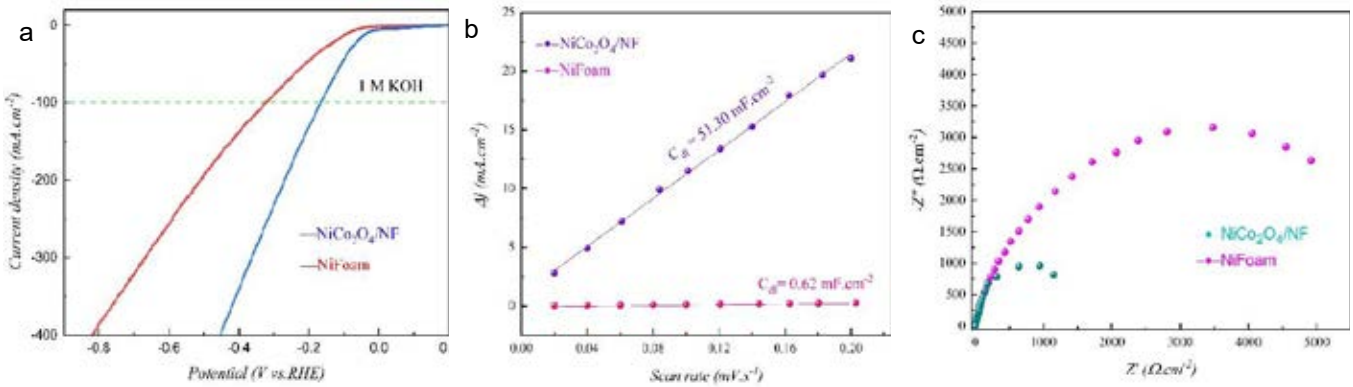


Fig. 2. (a) HER polarization curves in 1 M KOH, (b) ECSA value and (c) EIS Nyquist plots of $NiCo_2O_4$/NF and Ni Foam.

CONCLUSION

In summary, we have demonstrated a significant electrocatalytic HER activity of $NiCo_2O_4$/NF (overpotential of 38 mV to deliver current density 10 $mA.cm^{-2}$) could be ascribed to the 3D nanocubes unique structure. Nanocubes presence significantly reduces the interfacial resistance to accelerate the charge-transfer kinetics of H_2 evolution.

REFERENCES

1. F. Sun, J. Qin, Z. Wang, M. Yu, X. Wu, X. Sun, J. Qiu, Nature communications, 12 (2021) 1-11.
2. R. Saibi, R.P. Meethal, R. Srinivasan, in: ECS Meeting Abstracts, IOP Publishing, 2021, pp. 69.
3. F. Song, W. Li, J. Yang, G. Han, P. Liao, Y. Sun, Nature communications, 9 (2018) 1-10.
4. M. Bajdich, M. García-Mota, A. Vojvodic, J.K. Nørskov, A.T. Bell, Journal of the American chemical Society, 135 (2013) 13521-13530.
5. N. Cheng, S. Stambula, D. Wang, M.N. Banis, J. Liu, A. Riese, B. Xiao, R. Li, T.-K. Sham, L.-M. Liu, Nature communications, 7 (2016) 1-9.
6. I. Roger, M.A. Shipman, M.D. Symes, Nature Reviews Chemistry, 1 (2017) 1-13.
7. B. Chen, Z. Yang, Q. Niu, H. Chang, G. Ma, Y. Zhu, Y. Xia, Electrochemistry Communications, 93 (2018) 191-196.
8. Y. Feng, X.-Y. Yu, U. Paik, Chemical Communications, 52 (2016) 1633-1636.

WHEC-2022
23rd World Hydrogen Energy Conference
June 26-30, 2022 - Istanbul

#70

MODELING OF H_2O AND CO_2 ELECTROLYSIS IN A MOLTEN CARBONATE ELECTROLYZER

[1]Dayan Monzer, [1] Chakib Bouallou*
(MINES ParisTech, PSL - Research University, CES - Centre d'Efficacité Energétique des Systèmes), 60 Boulevard Saint Michel, 75006 Paris, France

*Corresponding author e-mail : chakib.bouallou@mines-paristech.fr

ABSTRACT

The reversible operation as an electrolyzer of a commercialized molten carbonate fuel cell for the generation of syngas (H_2 & CO) has recently provoked the interest of researchers. In general, Electrolyzers have the benefit of storing the surplus of renewable energy. This type of electrolyzer can additionally transform CO_2 into valuable fuel due to its unique properties at dissolving and reducing carbon dioxide in its molten carbonate electrolyte. The capability of such electrolyzer represents a conceptual revolution in the energy sector with a wide range of applications. This work presents the co-electrolysis of CO_2 and H_2O model of the Molten carbonate electrolyzer (MCEC). The one-dimensional steady-state model was created by making some changes to previously published work to introduce CO_2 electrolysis. To some extent, the model findings matched the previous model, which only took H_2O electrolysis into account. The discrepancies are driven by the chemical extent of the CO_2 electrolysis reaction in conjunction with the chemical reverse water gas shift reaction. These discrepancies highlighted the necessity of considering CO_2 electrolysis as the obtained cell voltage and temperature exhibited a higher value at the limiting current density by about 65% and 40%, respectively, than when CO_2 electrolysis is ignored.

Keywords: Molten carbonate Electrolysis cell, numerical modeling, co-electrolysis, Syngas production

INTRODUCTION

The molten carbonate electrolysis cell (MCEC) is a technology that may be utilized in power-to-gas systems. Its electrolyte's ability to trap large amounts of CO_2 offers an interest in reducing carbon dioxide within it to generate syngas (H_2 & CO) via a co-electrolysis process. The co-electrolysis of CO_2 and H_2O in molten carbonate electrolysis cells is being investigated to demonstrate the molten carbonates' capacity to electrolyze CO_2 into CO. Some studies were performed to examine the electrochemical conversion of CO_2 into CO in the MCEC. Peelen et al., 1998 [1] studied the electrochemical reduction of CO_2 into CO on a gold flag electrode in 62/38 mol % Li/K carbonate mixture in the temperature range 575–700 °C. Also, Kaplan et al., (2010,2012) [2], [3] reported the conversion of CO_2 to CO by using a cell with a molten electrolyte mixture of lithium carbonate and lithium oxide at 850-900 °C. The electrodes were graphite (anode) and titanium (cathode) and not conventional MCFC electrodes (Ni-based materials), and the working temperature was much higher than that of the MCFC system. All these studies proved the electrochemical conversion of CO_2 using flag electrodes instead of the conventional MCFC electrodes (Ni-based materials). Recently, Meskine et al., 2020 [4] have verified the electrochemical production of CO through CO_2 electrolysis with a limited maximum cell potential of 1.3 V to avoid the production of C instead of CO in the cell. Despite all of the research that has confirmed the CO_2 electrolysis inside the MCEC, no MCEC model study has considered CO_2 electrolysis. To date, all models assumed that CO is only generated chemically via the reverse water gas shift process. In this work, a developed model that considers only H_2O electrolysis, presented in [5], is adjusted to cover both H_2O and CO_2 electrolysis in the MCEC.

MODEL

In this model study, both H_2O and CO_2 electrolysis are considered assuming that the total current is divided between the two electrolysis according to the following equation Eq. (1) and Eq.(2).

$$I_{H2O} = \beta . I \quad (1)$$

$$I_{CO2} = (1 - \beta) I \quad (2)$$

The parameter β refers to the repartition of the electrode active sites between both electrochemical reactions [6]. It can be expressed by the relative percentage of inlet H_2O (Y^{in}_{H2O}) and CO_2 (Y^{in}_{CO2}) at the electrode interface (Eq. (3)).

$$\beta = \frac{Y^{in}_{H2O}}{Y^{in}_{H2O} . Y^{in}_{CO2}} \quad (3)$$

Based on this assumption, the developed model in [5] consisted of a material balance, energy balance, and electrochemical model is modified accordingly. The material balance involves both the electrochemical reactions (CO_2 and H_2O electrolysis) taking into account the current density split for determining the amount of H_2O and CO_2 reacted electrochemically, and the chemical reaction (the reverse water gas shift (RWGS) reactions), stated in [5]. The energy balance in [5] is generally unchanged; however, the heat of the reaction includes an additional term referring to the heat generated or consumed by the CO_2 electrolysis. As for the electrochemical model, the cell potential equation remains unchanged whereas the Nernst voltage (V_{nernst}) and reversible voltage (V_{rev}) are modified to consider the CO_2 electrolysis, as presented in Eq. (4) and Eq. (5), respectively.

$$V_{nernst} = V_{rev} - \frac{RT}{n_e F}\ln\left(\frac{P_{H2O}}{P_{H_2}.P_{CO}.P_{O2}}.\frac{P^3_{CO2,fe}}{P^2_{CO2,oe}}\right) \quad (4)$$

$$V_{rev} = \frac{\Delta G^0_{H2O\ electrolysis} + \Delta G^0_{CO2\ electrolysis}}{4F} \quad (5)$$

RESULTS AND DISCUSSION

The model results demonstrate the impact of the current density on the cell potential, the outlet composition of the cell, and the stream outlet temperature of the cell. In Fig. 1, the outlet composition of the H_2O, CO_2, H_2, and CO gases with the change in current density is depicted. The graph showed that the outlet H_2 gas composition (grey dotted line) increases in line with the decrease in the outlet H_2O gas composition (yellow dotted line), supporting the involvement of water in hydrogen production. However, the outlet CO gas composition (orange-solid line) drops with the increase in current density until reaching a specific current density (-0.2 A/cm^2), then suddenly increases. In parallel, the outlet CO_2 gas composition (blue-solid line) gradually decreases before falling rapidly to zero after a current density of -0.2 A/cm^2.

This discrepancy in the CO and CO_2 curves is better understood in Fig. 2, which explains the relationship of the outlet CO composition trend with the evolution of the CO_2 electrolysis and RWGS reactions. From this curve, two different sources can be extracted that define the cause of the deviation. The first source is the state where the RWGS equilibrium is not reached, which indicates that the RWGS reaction is not occurring in the cell, and CO is only

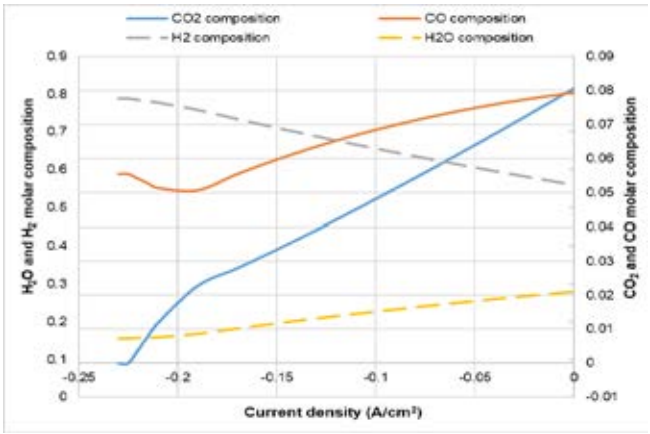


Fig. 1 : Gas Outlet Composition change with the current density (A/cm^2)

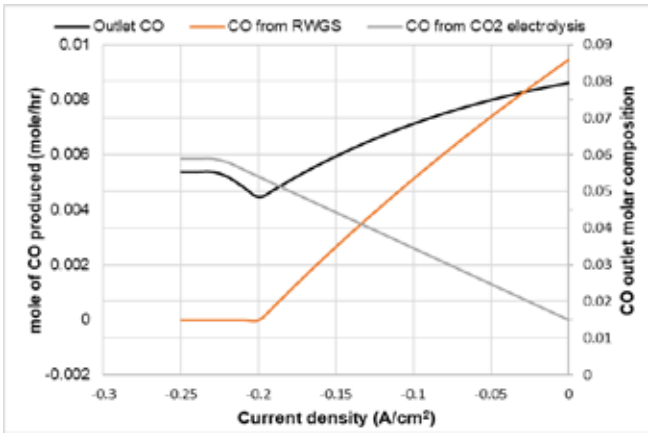


Fig. 2 : Outlet CO composition change and the mole of CO produced (mole/hr) from CO_2 electrolysis and RWGS versus current density (mA/cm^2)

produced by electrolysis process. From Fig. 2, it can be observed that at a current density -0.2 A/cm^2, the mole of CO produced by RWGS is zero, which means that the RWGS is not occurring. This state causes a deviated increase in the outlet CO trend, following the increasing trend of the CO produced by CO_2 electrolysis. The second source is the state where the limiting current density is reached by which CO_2 is totally consumed. It can be noticed in the CO_2 composition curve in Fig. 1 that after a certain current density (-0.23 A/cm^2), the outlet CO_2 composition reaches zero, which implies that the CO_2 is totally consumed. At this stage, the cell operation is at the limiting current density of -0.23 A/cm^2, and it can't function at a current density above this limiting one. This situation is also represented by a sudden increase in cell potential (Fig. 3) when approaching the limiting current density due to higher concentration losses created by the low CO_2 reacting agent. Besides, the outlet gas temperature sharply increases from 850°C (-0.225 A/cm^2) to 1060 °C (-0.23 A/cm^2) as the cell potential when reaching the limiting current density, as illustrated in Fig. 4. These outcomes of the cell potential and cell temperature in the case of limiting current density were corroborated by A. Szczęśniak et al., 2020 [7] when they investigated the impact of different malfunctions on the

molten carbonate fuel cell's operation. Low feed gas flow was one of these malfunctions that led to a drop in cell voltage during fuel cell operation and a significant increase in cell temperature. In the reverse mode, this malfunction reflects the sharp increase in cell voltage and temperature.

In comparison with the results of the previous model in [5], both models are comparable before reaching the state of deviation in the co-electrolysis case. This similarity can be explained by two factors. The first one is that the total current density applied to the cell is the same for both models, where this current is only employed for H_2O electrolysis in the previous model while it is split between H_2O and CO_2 electrolysis in the current model. The second one is the equilibrium balance of the reverse water gas shift reaction with the CO_2 electrolysis reaction, which results in a similar gas composition between the two models.

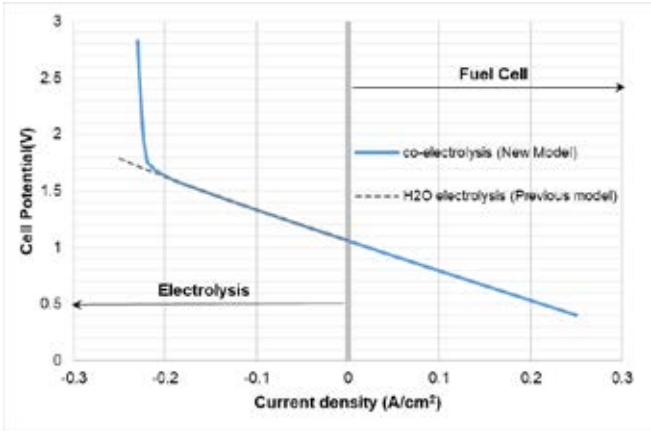


Fig. 3 : Cell potential versus the current density (A/cm^2) during electrolysis operation and fuel cell operation

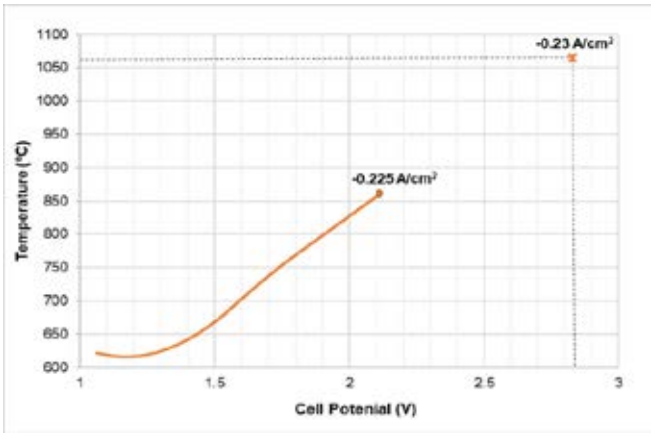


Fig. 4 : Gas outlet Temperature as a function of the cell potential (V)

CONCLUSION

The co-electrolysis model provides a helpful foresight on the operating conditions of the cell. The occurrence of the CO_2 electrolysis limits the current density for a safe cell operation. If the limiting current density is reached when considering CO_2 electrolysis, the cell voltage and temperature will be higher than the values obtained when neglecting CO_2 electrolysis ([5]) by around 65% and 40%, respectively. This state can be problematic for the safety of the cell operation as high cell voltages and temperatures can cause cell degradation.

NOMENCLATURE

P_i	Partial Pressure of the gas(i), kPa
n_e	Number of exchanged electrons
F	Faraday's constant, 96485 C/mol
R	Gas constant, J/mol.K
ΔG^0	Standards Gibbs Free energy change of the reaction, kJ/mol

Subscripts

fe	Fuel electrode
oe	Oxygen electrode

REFERENCES

1. W. Peelen., K. Hemmes, and J. de Wit., "CO_2 reduction in molten 62/38 mole% Li/K carbonate mixture," *Electrochim. Acta*, vol. 43, no. 7, pp. 763–769, 1998, doi: 10.1016/S0013-4686(97)00141-2.
2. V. Kaplan, E. Wachtel, K. Gartsman, Y. Feldman, and I. Lubomirsky, "Conversion of CO_2 to CO by Electrolysis of Molten Lithium Carbonate," *J. Electrochem. Soc.*, vol. 157, no. 4, p. B552, 2010, doi: 10.1149/1.3308596.
3. V. Kaplan, E. Wachtel, and I. Lubomirsky, "Titanium Carbide Coating of Titanium by Cathodic Deposition from a Carbonate Melt," *J. Electrochem. Soc.*, vol. 159, no. 11, pp. E159–E161, 2012, doi: 10.1149/2.016211jes.
4. H. Meskine *et al.*, "CO_2 electrolysis in a reversible molten carbonate fuel cell: Online chromatographic detection of CO," *Int. J. Hydrogen Energy*, vol. 46, no. 28, pp. 14913–14921, Apr. 2020, doi: 10.1016/J.IJHYDENE.2020.08.028.
5. D. Monzer, R. Rivera-Tinoco, and C. Bouallou, "Investigation of the Techno-Economical Feasibility of the Power-to-Methane Process Based on Molten Carbonate Electrolyzer," *Front. Energy Res.* | *www.frontiersin.org*, vol. 1, p. 650303, 2021, doi: 10.3389/fenrg.2021.650303.
6. J. Aicart, J. Laurencin, M. Petitjean, and L. Dessemond, "Experimental validation of two-dimensional H_2O and CO_2 Co-electrolysis modeling," *Fuel Cells*, vol. 14, no. 3, pp. 430–447, 2014, doi: 10.1002/fuce.201300214.
7. A. Szczęśniak, J. Milewski, Ł. Szabłowski, W. Bujalski, and O. Dybiński, "Dynamic model of a molten carbonate fuel cell 1 kW stack," *Energy*, vol. 200, 2020, doi: 10.1016/j.energy.2020.117442.

WHEC-2022
23rd World Hydrogen Energy Conference
June 26-30, 2022 - Istanbul

#72

INVESTIGATION OF ELECTRICITY, HYDROGEN AND CLEAN WATER PRODUCTION WITH RENEWABLE ENERGY SYSTEM INTEGRATED ONTO A SHIP: MOBILE ENERGY PRODUCTION ON A SHIP

[1]Mustafa Erden, [2]Ayhan Atiz, [3]Hatice Karakilcik, [1]Mehmet Karakilcik*
[1]Cukurova University, Faculty of Sciences and Letters, Department of Physics, 01330 Adana, Turkey
[2]Alanya Alaaddin Keykubat University, Faculty of Education, Department of Mathematics and Science Education Alanya 07400, Antalya, Turkey
[3]Cukurova University, Faculty of Engineering, Department of Geology Engineering, 01330 Adana, Turkey

*Corresponding author e-mail: kkilcik@cu.edu.tr

ABSTRACT

In this study, sustainable portable renewable energy generation system with hydrogen production and desalination of sea water is proposed. For this purpose, a wind turbine, photovoltaic panels (PVs), parabolic through solar collectors (PTSCs), flash turbine, organic Rankine cycle (ORC), water electrolysis system, reverse osmosis unit (RO) and storage tanks are constructed on a ship. This system is suitable for coastal settlements with high solar and wind potentials which are short of drinking water and electrical energy. It is an advantageous system in that going to a place where it is needed and meet the demand there. This integrated system is conceptually modeled and simulated using Engineering Equation Solver (EES) software. Thus, the system produces 5947.20 MJ electric energy and 468.56 g of hydrogen with 38.06% and 38.87% maximum energy and exergy efficiencies, respectively.

Keywords: Wind Turbine, Photovoltaic Panels, Parabolic Collectors, Hydrogen Production, Desalination.

INTRODUCTION

In recent years, the cost of electricity generation has been reduced by the use of wind turbines. The wind turbines have high efficiency and they can play an active role to meet the world's energy need. [1]. So, using wind turbines reduce the energy cost for desalination of sea water for the coastal settlements. The minimum energy needed for ideal desalination is the Gibbs free energies difference of the seawater and freshwater. The results show that the minimum energy consumption for the ideal desalination process increases with increase of the salinity of seawater and operation temperature [2]. The specific purpose of this study is to assist the studies that can be carried out in order to provide quick service to coastal settlements experiencing freshwater and electricity problems in certain time intervals.

MATERIALS AND METHODS

The proposed integrated system consists of a wind turbine which has a 34 m blade radius, PVs which has an area of 128 m^2, PTSCs which has an area of 200 m^2, a flash turbine, an ORC, a water electrolysis unit, a RO system and storage tanks. Fig.1 illustrates the overall system schematic. The integrated system is built on a ship for taking it to the other coastal places with high solar and wind potentials. It is aimed to meet the energy and potable water needs of people elsewhere. The output powers of the wind turbine and the PVs are integrated via wind-solar hybrid charge controller and connected to a power controller unit to deliver the city grid. In addition, the generated power by the flash turbine is also connected to the power controller unit. On the other hand, produced potable water and hydrogen are stored in suitable tanks.

Analyses of the system

This hybrid system generates electricity through wind turbine, PVs and PTSCs. The efficiency of the system is highly dependent on the generated electricity. Finding the performance of the hybrid system is extremely important for evaluating the system as thermodynamically. The energy and exergy efficiencies of the hybrid system are found as follows, respectively:

$$\eta_{sys} = \frac{\dot{E}_{U,sys}}{\dot{E}_{in,sys}} \quad (1)$$

$$\psi_{sys} = \frac{\dot{E}x_{U,sys}}{\dot{E}x_{in,sys}} \quad (2)$$

The net power is obtained for Fig.1 as follows:

$$\dot{W}_{net} = \dot{W}_{wind} + \dot{E}_{PV} + \dot{W}_{turbines} - \left(\dot{W}_{pump1} + \dot{W}_{pump2} + \dot{W}_{pump3} + \dot{W}_{pump4} + \dot{W}_{pump5}\right) \quad (3)$$

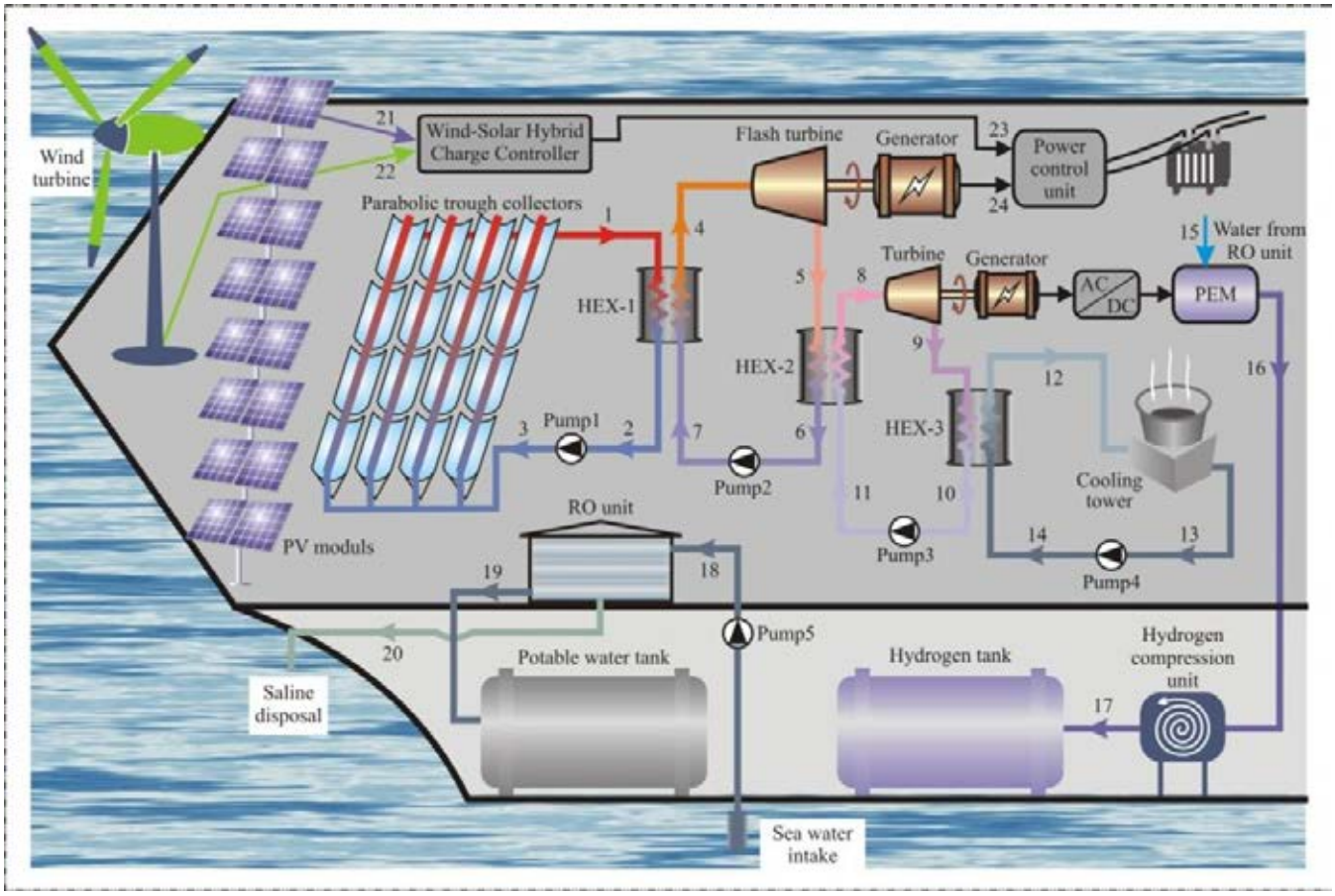


Fig. 1. Schematic of the proposed system harvesting wind and solar energy.

RESULTS AND DISCUSSION

The performance of the hybrid system was investigated under daily solar radiation and average wind speed for selected day in August. Fig. 2 shows the average energy on the wind turbine, PVs and PTSCs between 8:00 a.m. and 5:00 p.m. The maximum solar radiation on the PVs was found as 125.13 kW between 11:00 a.m. and 13:00 p.m. for the selected day in August. The minimum solar radiation on the PVs was found as 60.67 kW between 16:00 p.m. and 17:00 p.m. The maximum direct solar radiation on the PTSCs was found as 162.36 kW between 11:00 a.m. and 13:00 a.m. for the selected day in August. The minimum solar radiation on the PTSCs was found as 78.02 kW between 16:00 p.m. and 17:00 p.m. Wind speed was taken as constant at 5.3 m/s and the wind turbine generates 329.64 kW of energy for a day. Fig. 3 shows energy and exergy efficiencies of the overall system. The maximum and minimum energy efficiencies of the overall system were found as 38.06% and 29.94%, respectively. The maximum and minimum exergy efficiencies of the overall were found as 38.87% and 30.95%, respectively.

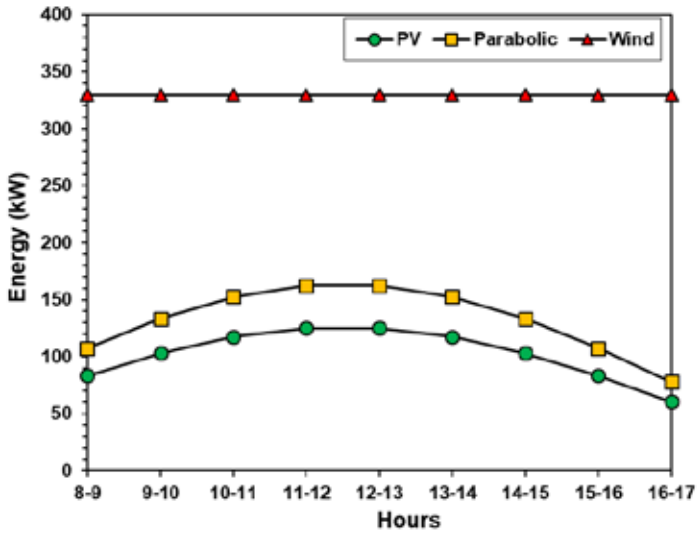


Fig. 2. Average energy on the wind turbine, PV and parabolic solar collectors

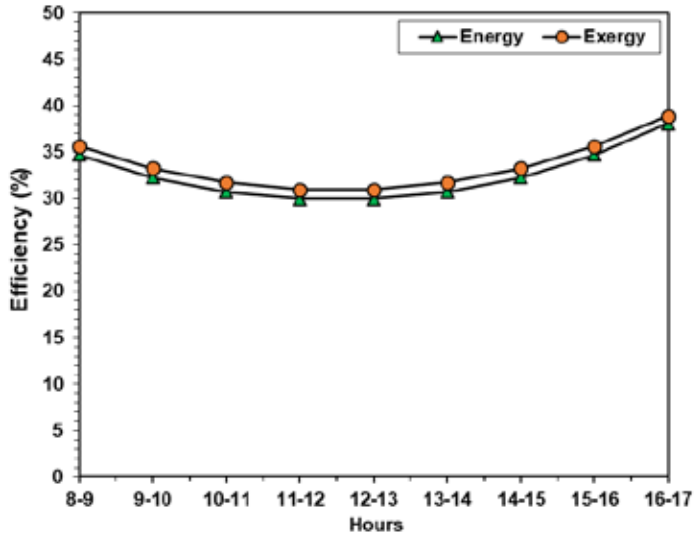


Fig. 3. Energy and exergy efficiencies of the overall system.

CONCLUSIONS

In this study, energy and exergy analyses and electricity and hydrogen production of the hybrid system were investigated. So, a total of 5947.20 MJ electric energy and 468.56 g of hydrogen were produced by hybrid system for a daylight selected in August.

ACKNOWLEDGEMENT

The authors acknowledge the support provided by University of Cukurova in Turkey (Grant Nos: FEF2013YL42, FYD-2017-6261 and FBA-2019-12023).

REFERENCES

1. Ehyaei, MA., Ahmadi, A., Rosen, MR. 2019. Energy, exergy, economic and advanced and extended exergy analyses of a wind turbine. Energy Conversion and Management 183: 369-381.
2. Zhao, D., Deng, S., Shao, Y., Zhao, L., Lu, P., Su, W. 2019. A new energy analysis model of seawater desalination based on thermodynamics. Energy Procedia 158: 5472–5478.

WHEC-2022
23rd World Hydrogen Energy Conference
June 26-30, 2022 - Istanbul

#74

PARABOLIC TROUGH SOLAR COLLECTOR INTEGRATED WITH SOLAR POND FOR ELECTRICITY AND HYDROGEN PRODUCTION BASED ON SOLAR ENERGY

[1]*Serdal Damarseckin*, [2]*Ayhan Atiz*, [2*]*Mehmet Karakilcik*
[1]Sırnak University, Faculty of Engineering, Department of Energy Systems Engineering, 73000 Sırnak, Turkey
[2]Cukurova University, Faculty of Sciences and Letters, Department of Physics, 01330 Adana, Turkey

*Corresponding author e-mail: aatiz@cu.edu.tr

ABSTRACT

In this work, electricity, hydrogen production performance of parabolic trough solar collectors (PTSCs) integrated with a solar pond is researched. The system consists of the PTSCs with the surface area of 100 m^2, a solar pond with the surface area of 100 m^2, an Organic Rankine Cycle (ORC) which is operated with n-butane for electricity production, and a proton exchange membrane (PEM). In order to improve the overall system performance, n-butane is selected as working fluid in the ORC and the waste heat of the ORC is used in the mushroom production unit. In addition, the low-temperature water coming from the solar pond was circulated to the PTSCs via a pump and the temperature of the water was increased by the PTSCs. Thus, the temperature of this preheated water is upgraded by the PTSCs, and it increase the electricity performance of the ORC. The electricity is used to produce hydrogen by PEM. The analyses of the integrated system are determined with Engineering Equation Solver (EES) for a daily solar energy in July. So, an integrated energy generation system is simulated and it is occurred entirely of renewable energy systems. As a result, it has been found that if the integrated system components are improved, the heat, electricity and hydrogen production can be increased considerably.

Keywords: Solar pond, Parabolic trough solar collectors, Organic Rankine Cycle, Hydrogen production, Exergy

INTRODUCTION

One of the most important renewable sources is solar energy. It uses for producing heat, electricity and hydrogen by solar energy technologies. One of the important solar technologies is solar pond. It is converted to solar energy to store as heat in the storage zone (HSZ) [1]. The stored thermal energy can be transferred to another technology to increase the heat performance in the integrated systems [2]. One of the systems producing thermal energy by using solar energy is parabolic trough solar collectors (PTSCs) that is known one of the most solar technologies to harvest solar energy [3]. High-grade thermal energy sources are already used for generating electricity. However, to generate electricity from low-temperature energy sources is also essentially important. ORC is one of the most important systems that produce electricity from low-grade sources. If the ORC is integrated with the solar energy technologies, electricity production of the ORC can be improved [4].

In this study, an integrated solar energy system for multiple energy generation based on solar energy was simulated by using the engineering program to solve with EES and the daily energy production performance of the system was tried to be improved. The inlet water of the parabolic solar collector was preheated through the solar pond and maximum outlet water was obtained in a sunny day in July. The maximum output of ORC with daily hot water is increased. At the same time, PEM was operated with this electricity and hydrogen was produced from water in it. In addition, the waste heat from the ORC was used in a mushroom production facility. Thus, this new integrated system was operated from 9 am to 3 pm for a sunny day in July to determine heat, electricity and hydrogen production performance of the system.

MATERIALS AND METHODS

The Fig.1 shows that the integrated energy system which occurs of solar pond, PTSCs, an ORC and electrolysis system. The purpose of the system is to generate high amounts of electricity and hydrogen and also to heat a mushroom production unit with waste heat. The role of the PTSCs is to provide the hot water for pumping the ORC. The temperature of the water coming from solar pond is upgraded by the PTSCs. Thus, the hot water is pumped the ORC to produce significant amount of electricity for hydrogen production as a final output. In Fig. 1 initially, the water transferred by a pump1 from the solar pond, it enters in the PTSCs from point 2. In a short time, the temperature of the water can reach up to higher than heat storage temperature of the solar pond and it enters the evaporator from point 3. A lot of the energy of water transfers to the evaporator to increase the temperature of working fluid (n-butane) in the ORC. Thus, n butane exits the evaporator from point 6 and it expands throughout the turbine to produce electricity. The electricity is transferred from point 12 to the PEM for hydrogen production. At the end of the process,

hydrogen is generated by electrolysis system from point 13 for storing in a tank. And also, n-butane come out of the turbine to enter the condenser from point 7 where it is condensed and the waste heat in the condenser is transferred for heating a mushroom production unit. Thus, the energy and exergy efficiencies of the overall system can be significantly increased.

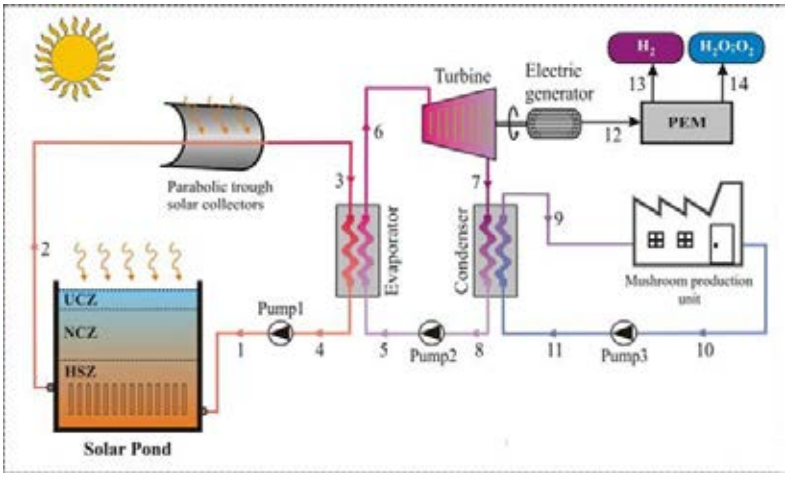


Fig. 1. Parabolic trough solar collectors integrated with solar pond for hydrogen production based on solar energy

Analyses of the integrated system.

Solar pond stores solar energy as thermal energy in the storage zone of it. Finding the performance of HSZ is extremely important for the solar pond. The energy efficiency of the HSZ is obtained as follows:

$$\eta_{HSZ} = \frac{\dot{E}_{HSZ}}{\dot{E}_{in,solar\ pond}} \quad (1)$$

Besides, another one of the solar energy technologies is the PTSC that converts solar energy into thermal energy. PTSC upgrades temperature of the inlet fluid from low-grade to high-grade to exit it. Energy efficiency of the PTSC is found as follows:

$$\eta_{PTSC} = \frac{\dot{E}_U}{\dot{E}_{PTSC}} \quad (2)$$

Thus, hot water is circulated to the ORC by a pump for producing electricity. The ORC operates the thermal energy that is transferred from low-middle grade sources for electricity production at. The net power is obtained for Fig.1 as follows:

$$\dot{W}_{net} = \dot{W}_G - \left(\dot{W}_{pump1} + \dot{W}_{pump2} + \dot{W}_{pump3}\right) \quad (3)$$

RESULTS AND DISCUSSION

In this study, performance of the integrated system was investigated under daily solar radiation for selected a day in July.

The integrated system produced a lot of electricity and hydrogen from solar energy. Fig. 2 shows the average solar radiation on the solar pond and parabolic solar collectors from 9 a.m. and 3 p.m. The maximum solar radiation on the solar pond was found as 890.6 W/m^2 and 890.6 W/m^2 between 11-12 hrs and 12-13 hrs for the selected day in July, respectively. The minimum solar radiation on the solar pond was found as 756.2 W/m^2 between 9-10 hrs and 14-15 hrs.

PTSC is geometrically different from the solar pond. Therefore, the solar radiation reaching on the surface of the PTSCs could be found different. The maximum solar radiation on the PTSCs was found as 795.4 W/m^2 and 795.4 W/m^2 between 11-12 hrs and 12-13 hrs for the selected day in July, respectively. The minimum solar radiation on the PTSCs was found as 663.8 W/m^2 between 9-10 hrs and 14-15 hrs. Fig. 3 shows that the hourly electricity and hydrogen production of the ORC and electrolysis system. The maximum hourly electricity production of the ORC was found as 10.16 MJ between 12-13 hrs for the selected day in July, respectively. The minimum hourly electricity production of the ORC was found as 7.63 MJ between 9-10 hrs. ORC produced total electricity via hot water that is produced in the integrated system. One of the best ways to store electricity in the system is to convert it to hydrogen. Therefore, the electricity produced by ORC is transferred to the electrolysis system. The electrolysis system was

operated in 80% efficiency. The maximum hourly hydrogen production of the electrolysis system was found as 54.02 g between 12-13 hrs for the selected day in July, respectively. The minimum hourly hydrogen production of the electrolysis system was found as 40.57 g between 9-10 for the selected day in July, respectively.

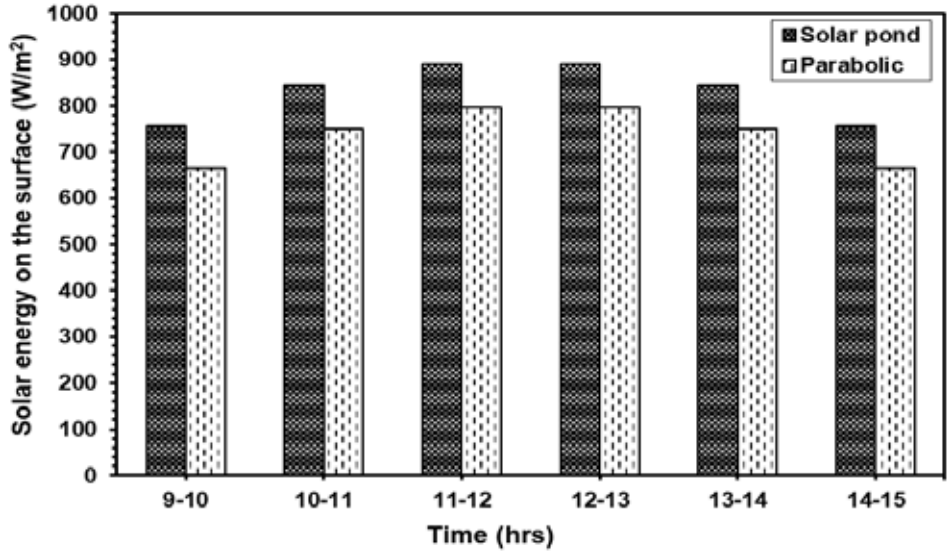


Fig. 2. Average solar radiation on the solar pond and parabolic trough solar collector

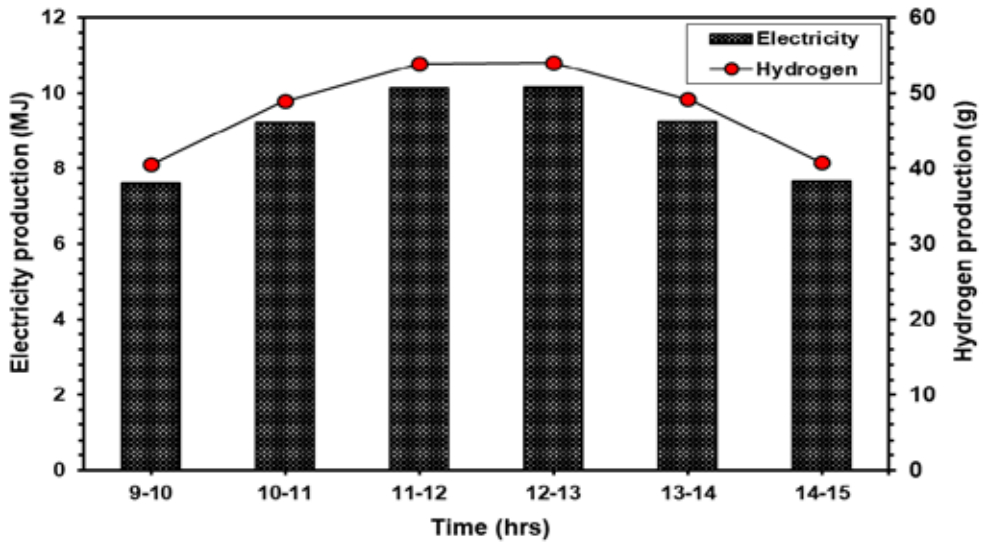


Fig.3. Hourly electricity and hydrogen production of the ORC and electrolysis systems

CONCLUSIONS

In this study, heat, electricity and hydrogen production of the integrated system were examined. The low temperature heat stored in the HSZ of the solar pond was increased to high temperature by means of PTSCs and then in the ORC was converted at high power electricity. Finally, the generated electricity by the ORC was used hydrogen production by the electrolysis system. As a result, 54.083 MJ of electricity and 287.56 g of hydrogen were produced for a selected day in July.

ACKNOWLEDGEMENT

The authors acknowledge the support provided by University of Cukurova in Turkey (Grant Nos: FEF2013YL42, FYD-2017-6261 and FBA-2019-12023).

REFERENCES

1. Karakilcik M, Kıymaç M, Dincer I. 2006. Experimental and theoretical temperature distributions in a solar pond. International Journal of Heat and Mass Transfer 49: 825-835.

2. Kalogirou SA., Karellas S, Badescu V, Braimakis K, 2016. Exergy analysis on solar thermal systems: a better understanding of their sustainability. Renew. Energy 85: 1328–1333.
3. Atiz A, Karakilcik H, Erden M, Karakilcik M. 2019. Assessment of electricity and hydrogen production performance of evacuated tube solar collectors. International Journal of Hydrogen Energy 44 (27):14137-14144.
4. Hung TC, Wang SK, Kuo CH, Pei BS, Tsai KF. 2010. A study of organic working fluids on system efficiency of an ORC using low-grade energy sources. Energy 35: 1403-1411.

WHEC-2022
23rd World Hydrogen Energy Conference
June 26-30, 2022 - Istanbul

#78

HYDROGEN PRODUCTION FLAT PLATE SOLAR COLLECTOR INTEGRATED WITH PV-T

[1*]Ayhan Atiz, [1]Mustafa Erden, [1]Mehmet Karakilcik
[1]Cukurova University, Faculty of Sciences and Letters, Department of Physics, 01330 Adana, Turkey

*Corresponding author e-mail: aatiz@cu.edu.tr

ABSTRACT

In this work, the electricity and hydrogen production performance of an integrated system is investigated. The system includes a flat plate solar collector (FPSC), a photovoltaic thermal (PV-T) panel, an Organic Rankine Cycle (ORC), a proton exchange membrane (PEM) and a building for fungus production. In order to improve electric production performance of the ORC is worked with n-butane. The FPSC and PV-T has 6.48 m^2 and 2.16 m^2 area for capturing efficiently solar energy. The analyses of the integrated system are found by employing Engineering Equation Solver (EES) under daily solar energy in July. So, the low-temperature water coming from the PV-T to FPSC via a pump is upgraded to higher degree. The heated water is transferred to ORC for generating electricity. Besides, electricity is produced by the PV-T. Thus, a lot of electricity is produced in the overall system, efficiently. Moreover, overall performance of the system is found for under daily solar radiation. As a result, it was found that integrated system generated much more thermal energy, electricity and hydrogen.

Keywords: Photovoltaic thermal panel, Flat-plate solar collectors, Organic Rankine Cycle, Hydrogen production, Energy and exergy analyses

INTRODUCTION

Solar energy is one of the most important clean and renewable sources that can be used instead of fossil sources. Technologies that generate electricity or thermal energy by using solar energy are solar collectors. One of the solar technologies is photovoltaic solar cell (PV) which directly generates electricity through solar energy [1]. Thus, PV can produce electrical and thermal energy through solar energy in a system that is known as photovoltaic thermal (PV-T). The waste thermal energy is transformed into beneficial shape by employing the heat exchanger through air or water [2]. One of the systems producing thermal energy by using solar energy is flat-plate solar collector (FPSC) [3]. One of the systems that produce electricity by utilizing the obtained thermal energy is ORC [4]. There has not been a study on the electricity and hydrogen production of FPSC integrated with PV-T for under daily solar energy. This work aim to analyze electricity and hydrogen production of new integrated system. For this purpose, a sunny day is selected in July. Thus, the system is investigated for electricity and hydrogen production in one of the warmest month of the year. System is operated under daily solar energy from 8 a.m. to 4 p.m. This case study is operated for Adana that one of the cities of Turkey.

MATERIALS AND METHODS

The system is seen Fig. 1 that consists of a PV-T, a FPSC, greenhouse and an ORC contains n-butane as an operating fluid for producing electricity, building for fungus production and a hot water storage tank. The system works as follows. Initially, fresh water is pumped to the PV-T by pump1 from point 1 to reach high-grade temperature by using waste heat energy in the PV-T via exchanger. The hot water is transferred from the PV-T to FPSC from point 2 to reach a higher degree than point 2. In a short time, the temperature of the water is increased to high-grade by the FPSC for pumping to the evaporator from point 3 and then water exits the evaporator from point 4 to enter the insulated hot water tank. While PV-T produces electricity, PV cells generate waste thermal energy which is extracted by water via exchanger to pump the FPSC. Also, the hot n-butane is pumped to the turbine by pump2 from point 5 for electricity production by using hot water in the system. Also, n-butane leaving the turbine from point 6 is condensed in the condenser and exits from point 7. Also, water is transferred from the fungus production building to the condenser by pump 3 from point 11, and the water enters from point 9 to the greenhouse for cooling and then it exits from point 10. Finally, the electricity is transferred from point 12 to the PEM for hydrogen production. At the end of the process, hydrogen is generated by the PEM electrolysis system from point 15 for storing in a tank.

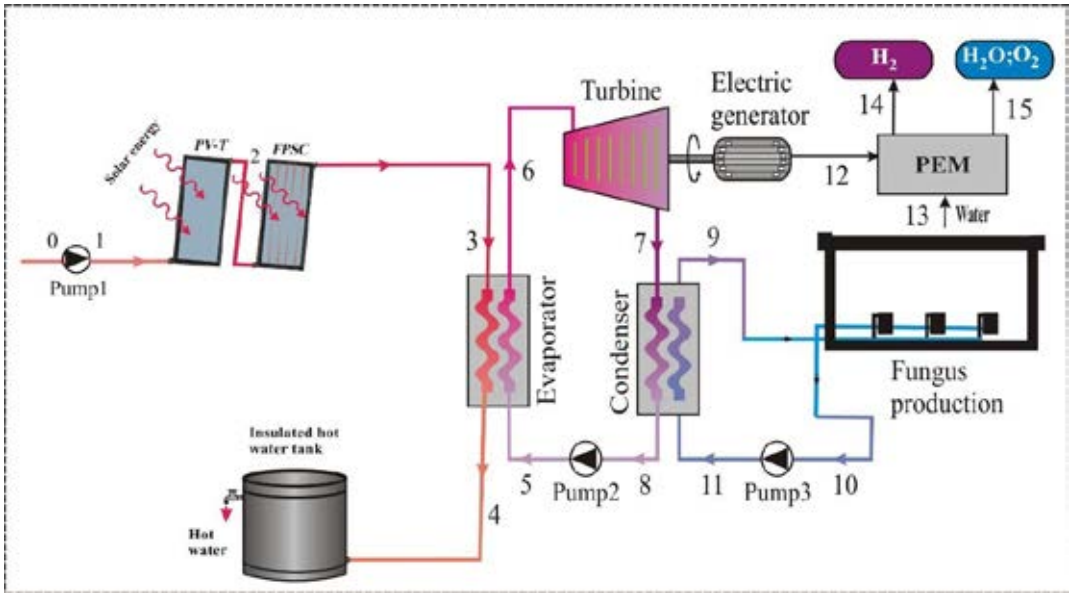


Fig. 1. A PV-T panel integrated with a FPSC for hydrogen production based on solar energy.

Energy analyses and electricity and hydrogen production off the system.

PV-T solar technology produces electrical and thermal energy by harvesting solar energy. While PV-T is converting solar energy into electricity, it also produces waste thermal energy. Electricity efficiency of the PV-T depends on the temperature of the PV which is given as follows [5]:

$$\eta_{el} = \eta_0[1 - \beta_{PV}(T_{PV} - T_0)] \quad (1)$$

One of the solar energy technologies is the FPSC that converts solar energy into thermal energy. FPSC upgrades temperature of the inlet water from low-grade to high-grade. Energy efficiency of the FPSC is found as follows:

$$\eta_{FPSC} = \frac{\dot{E}_U}{\dot{E}_{FPSC}} \quad (2)$$

The ORC operates the thermal energy that is transferred from the integrated system for electricity production at low-middle-high grade. The net power is obtained for Fig.1 as follows:

$$\dot{W}_{net} = \dot{W}_G - (\dot{W}_{pump1} + \dot{W}_{pump2} + \dot{W}_{pump3}) \quad (3)$$

RESULTS AND DISCUSSION

In this study, performance of the integrated system was investigated under daily solar radiation for selected a day in July. This integrated system produced a lot of electricity and hydrogen. Fig. 2 shows hourly electricity production of the PV-T and ORC from 8 a.m. and 4 p.m. for a day selected in July. The maximum hourly electricity production of the PV-T was found as 0.8997 MJ between 11-13 h for the selected day in July, respectively. The minimum hourly electricity production of the PV-T was found as 0.6551 MJ between 8-9 h and 15-16 h. ORC generates electricity with the help of hot water that is produced in the system from PV-T and FPSC. The maximum hourly electricity production of the ORC was found as 0.7075 MJ between 12-13 h for the selected day in July, respectively. The minimum hourly electricity production of the ORC was found as 0.4028 MJ between 8-9 h. One of the best ways to store electricity generated in the system is to convert it to hydrogen. Fig. 3 shows hourly hydrogen production of the electrolysis that is used electricity which was transferred from ORC and PV-T in the integrated system. The maximum hourly hydrogen production of the electrolysis (electricity was transferred from the PV-T) was found as 5.036 g and 5.036 g between 11-12 h and 12-13 h for the selected and the minimum hourly hydrogen production of the electrolysis was found as 3.667 g between 8-9 h and 15-16 h. The maximum hourly hydrogen production of the electrolysis (electricity was transferred from the ORC) was found as 3.762 g between 12-13 h for the selected and the minimum hourly hydrogen production of the electrolysis was found as 2.142 g between 8-9 h. The maximum hourly hydrogen production of the integrated system was found as 8.798 g between 12-13 h for the selected day in July, respectively. The minimum hourly hydrogen production of the system was found as 5.809 g between 8-9 h.

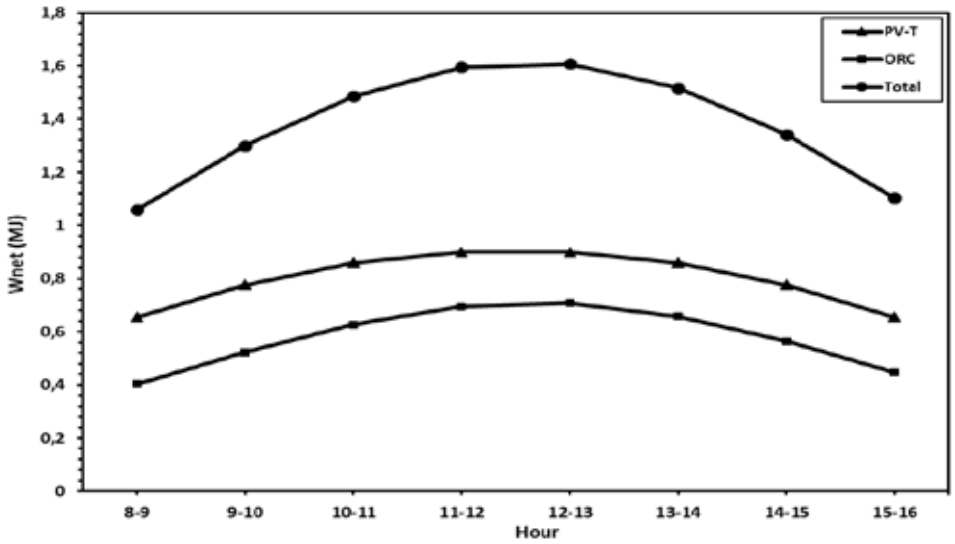


Fig.2 Hourly electricity production of the PV-T and ORC for a day selected in July.

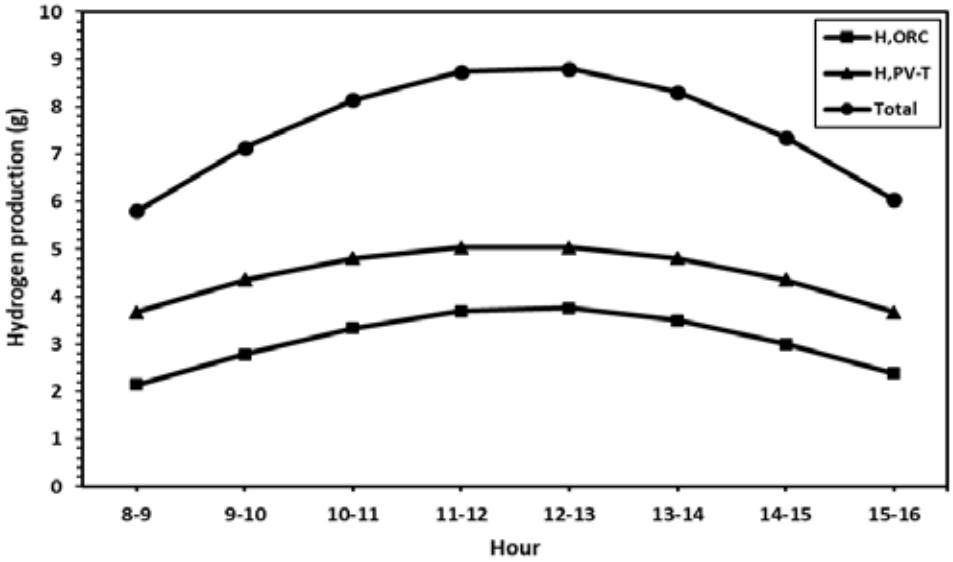


Fig.3 Hourly hydrogen production of the ORC, PV-T and integrated systems

CONCLUSIONS

In this study, electricity and hydrogen production of the integrated system were investigated. In this system, PV-T produced thermal and electrical energy under daily solar energy. If waste thermal energy of the PV-T is extracted by cold water, performance of the PV-T is increased. The waste thermal energy was transferred to the FPSC by means of cold water. Thus, the hot water coming from the PV-T was pumped to the FPSC and the temperature of the water in n the FPSC was upgraded from low-grade to high-grade via solar energy for pumping to the ORC to produce electricity. Finally, produced electricity in the ORC was transferred to electrolysis system for generating hydrogen to store a tank. A total of 11.0063 MJ and 60.314 g of electricity and hydrogen were produced by integrating for a day selected in July.

REFERENCES

1. Yavuz A, Başol D, Ertay MM, Yücedag I. 2013. An educatıon set for solar cell models. Journal of Advanced Technology Sciences 2:14-21.
2. Cilogullari M, Erden M, Karakilcik M, Dincer I. 2017. Investigation of hydrogen production performance of a photovoltaic and thermal system. International Journal of Hydrogen Energy 42: 2547-2552.
3. Yijie Tong, Hoseong Lee, Woobin Kang, Honghyun Cho. 2019. Energy and exergy comparison of a flat-plate solar collector using water, Al2O3 nanofluid, and CuO nanofluid. Applied Thermal Engineering 159: Article: 113959
4. Saleh B, Koglbauer G, Wendland M, Fischer J. 2007. Working fluids for low-temperature organic Rankine cycles. Energy 32: 1210–1221.
5. Zondag HA, de Vries DW, van Helden WGJ, van Zolingen RJC, van Steenhoven AA. 2003. The yield of different combined PV-thermal collector designs. Solar Energy 74(3): 253-269.

WHEC-2022
23rd World Hydrogen Energy Conference
June 26-30, 2022 - Istanbul

#94

CRITICAL ASSESSMENT OF THE PRODUCTION SCALE REQUIRED FOR FOSSIL PARITY OF GREEN ELECTROLYTIC HYDROGEN

*Joris Proost
Université catholique de Louvain, Division of Materials and Process Engineering, 1348 Louvain-la-Neuve, Belgium

*Corresponding author e-mail: joris.proost@uclouvain.be

ABSTRACT

Hydrogen produced from renewable electricity through Power-to-Hydrogen can facilitate the integration of high levels of variable renewable electricity into the energy system. An electrolyser is a device that splits water into hydrogen and oxygen using electricity. When electricity is produced from renewable energy sources, electrolytic hydrogen can be considered to be green. Key green hydrogen production technologies, mostly PEM and alkaline electrolysers, are still further maturing, both in technical (efficiency), economical (CAPEX) and durability (lifetime) performance. Nonetheless, we will show in this contribution how fossil parity for green hydrogen, i.e. a Total Cost of Ownership (TCO) similar to grey H_2 coming from CO_2 intensive SMR processes, can already be achieved today. Moreover, this can be realised at a scale which corresponds to the basic units of renewable electricity generation, i.e. a few MW.

Keywords: power-to-hydrogen, electrolyser, renewable electricity, fossil parity

INTRODUCTION

Although water electrolysis as such is already a well-established H_2 production technology for almost a century, its large-scale implementation for the production of green H_2 has been hampered mainly by cost issues. In this respect, the current price of fossil SMR-based H_2 provides a very challenging benchmark. According to [1], the global hydrogen feedstock market represented in 2015 a total estimated value of 115 billion $, corresponding to a hydrogen demand of about 56 Mton/yr. From these numbers, the average market price for fossil H_2 can be estimated as 2.0 $/kg. In the current paper, we aim at critically assessing the production scale required to reach such fossil parity for electrolytic hydrogen.

RESULTS

Hydrogen production today

As of today, hydrogen is mainly being used as a specialty chemical in a number of applications. These are generally classified into 4 main categories : (1) the chemical industry, where H_2 is a basic building block for the synthesis of ammonia, methanol and a number of technical polymers; (2) a number of downstream refining processes, like hydro-cracking and hydro-treating; (3) iron, steel and glass manufacturing, where H_2 is the preferred reducing gas during annealing, blanketing and forming processes ; (4) other specialty applications, like the semiconductor industry, the use as a propellant fuel or the cooling of generators. As of today, the great majority of all of the above H_2 is being delivered by a centralised, off-site hydrogen production, dominated by 2 large-scale chemical processes: steam methane reforming (SMR) and coal gasification. Unfortunately, both of these processes are heavily CO_2 intensive, SMR emitting upto 8 tons of CO_2 per ton of H_2 produced. Therefore, with the objective of reaching the CO_2 emission targets also in todays fossil-based H_2 production, the part of green electrolytic hydrogen production from renewable electricity (which represents less than 4% today) can be expected to significantly increase over the coming years. However, in order to meet the current global H_2 demand of around 70 Mton/year, a total of 300 GW installed electrolyser capacity would be needed. As this represents already about 20% of the total installed renewable power capacity today, such massive electrolyser deployment is currently not very realistic. As a result, a selection of technologically feasible market penetrations for electrolytic H_2 needs to be made. Such selection then also implies that todays local H_2 consumers, besides becoming local (on-site) producers of renewable electricity, also need to become local (on-site) producers of electrolytic H_2, at a production scale which still allows to meet the stringent requirement of fossil parity at about 2.0 $/kg.

Green hydrogen production scale-up

Contrary to the intrinsically large-scale SMR, water electrolysis is intrinsically small-scale. Both the geometrical area of the electrodes (a few m^2 at most) and the number of electrodes that can be compiled in series in a single stack is relatively limited. As a result, the unit size of water electrolysers has long been limited to the kW-range, a typical on-site containerized production unit being a few 100 kW at most. However, in order to be able to realize the mandatory coupling to renewables, mainly wind and solar, the power scale of water electrolysers needs to become of the same order of magnitude as the renewable electricity source itself. This requires a major scale-up from the kW-scale, typical for state-of-the art electrolysers about a decade ago, towards the multi-MW scale typical for state-of-the art on-shore

wind turbines. Such an electrolyser scale-up is typically being realised by increasing the number of cells per stack. However, from the state-of-the-art data that we recently collected from a number of electrolyser manufacturers [2], such a "keep-on-stacking" approach seems to have an intrinsic limit at around 100 cells/stack. Beyond that number, other balance-of-plant issues come into play, including the risk of electrical shorts and the technological complexity of a safe large-scale gas collection. Therefore, for multi-MW applications, multi-stack electrolyser systems are typically being used.

DISCUSSION

The cost of electrolytic hydrogen

While it is technically feasible to produce green electrolytic hydrogen with such multi-stack systems at the multi-MW scale (even > 100MW), the critical question still remains at what price/cost. In this respect, the 3 major parameters affecting the electrolytic H_2 production cost are the operational time of the electrolyser, the cost of renewable electricity, and the electrolyser CAPEX [3]. Hence, before becoming a realistic alternative production technology, there is a need for cheap(er) renewable electricity (well below 70 Euro/MWh), the investment cost of electrolysers needs to be brought down (well below 1000 Euro/kWh), and there should also be a clear industrial commitment to CO_2 reduction. Luckily, with respect to these parameters, significant progress has been made over the past years. First of all, a significant price reduction for renewable electricity has already been realised for both solar PV and on-shore wind, with prices on the order of 30-40 $/MWh becoming realistic by 2025. Moreover, for alkaline systems, a CAPEX of 750 Euro/kW is already realistic today for a single stack 2 MW system. Moreover, as seen in Fig. 1, a significant further reduction in CAPEX as low as 450 Euro/kW is currently being projected for multi-stack systems when scaling up to 50-100 MW. Also note from Fig. 1 that single stack electrolysers are much more susceptible to CAPEX reduction than multi-stack systems.

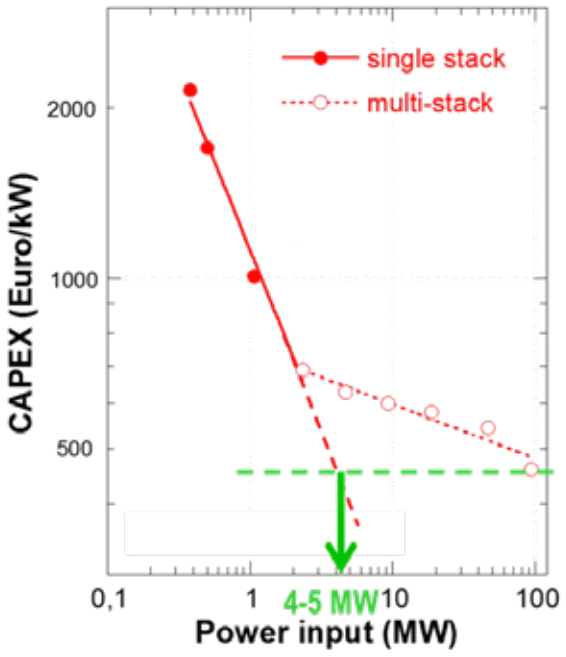


Fig. 1. State-of-the-art CAPEX data for alkaline electrolysers as a function of power input. The change in slope for alkaline electrolysers corresponds to the use of multi-stack systems.

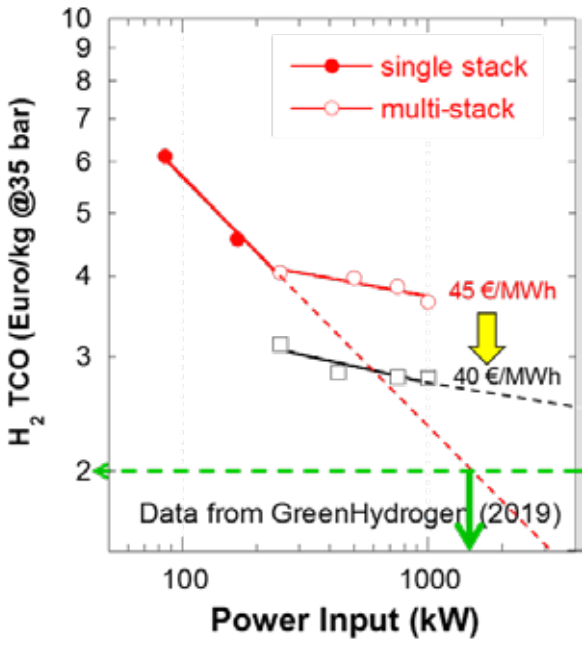


Fig. 2. Total Cost of Ownership (TCO) of electrolytic H_2, delivered at 35 bar, as a function of power input. OPEX includes the use of electricity, water and nitrogen (for purge), assuming a renewable electricity price of 40 and 45 €/MWh, respectively.

Based on the above updated numbers, a recent study from the International Energy Agency [4], allows to anticipate a significant reduction in the electrolytic H_2 production cost as a function of the available renewable electricity price, assuming the most favorable (but still realistic) CAPEX value of 450 Euro/kW. It shows that for a combination of high load factors and a non-zero but relatively low electricity cost, on the order of 30 $/MWh, the electrolytic H_2 production costs can be competitive with SMR.

The scale of fossil parity for green hydrogen

A final issue then relates to the production scale required for obtaining such fossil parity with electrolytic H_2. Indeed, from Fig. 1, one could wrongly conclude that reaching the required reduction in electrolyser CAPEX down to 450

Euro/kW would require very large-scale electrolytic H_2 production units, on the order of 50-100 MW. However, Figure 1 also suggests that there might still be a much smaller production scale for reaching such low CAPEX values. Indeed, based on an extrapolation of the currently available CAPEX data for single-stack alkaline electrolysers in Fig. 1, the level of 450 Euro/kW (dashed horizontal green line) can already be reached around 4-5 MW. Such a significant reduction in the scale required for fossil parity is directly related to the much steeper reduction in CAPEX that can be realised for single-stack as compared to multi-stack electrolyser systems.

Even more direct corroborating evidence for this relatively small scale fossil parity for green electrolytic H_2 is given in Figure 2. The latter represents state-of-the-art industrial data for the Total Cost of Ownership (TCO) of electrolytic H_2 as a function of power input. Values are based on a 10 years operation, including a 10 years' service & maintenance agreement, for a complete turnkey, containerized alkaline electrolyzer unit (including inverter and water treatment), delivered and installed in Europe. The electrolyser efficiency is guaranteed at 46.7 kW/kg at 100% load, and delivers H_2 at 35 bar. Until now, it was commonly agreed that the only option to decrease the electrolytic H_2 production cost towards fossil parity was to increase the capacity of the (multi-stack) system upto 50-100 MW, as already discussed in Fig. 1. However, as suggested by the dashed red line in Fig. 2 through the TCO data for single stack systems, there is yet another technological alternative. It consists in extending the power input that can be taken up by a single-stack electrolyser upto a few MW (2-4 MW, the exact number depending on the electrolyser technical characteristics like electrode size). This then also corresponds to the scale of the basic units of renewable electricity generation. The (only) remaining technological challenge on the electrolyser level would then be to try to increase the number of cells/stack for such a single stack system, or to increase the specific area of each individual electrode (e.g. by replacing classical 2-D plates by 3-D electrodes [5]).

CONCLUSIONS

In this paper, we have addressed the question what would be an economically viable (minimum) production scale for green hydrogen, produced from water electrolysis using renewable electricity. A realistic benchmark to do so is to take the current price of grey hydrogen (the so-called fossil parity), currently estimated at 2.0 $/kg and produced by fossil-based and thus CO_2 intensive processes. Using the most recent TCO values for electrolytic hydrogen, it was concluded that fossil parity could already be reached at a production scale on the order of a few MW. Although this might still require a further intensification of the water electrolysis process, e.g. by extending the power range of a single-stack electrolyser, such small-scale fossil parity provides an important paradigm shift. Indeed, with respect to the current, large-scale unit size fossil fuels (SMR) based centralised hydrogen production, it has the important advantage of allowing a decentralised local H_2 production. Renewables can then be harvested anywhere, and used directly for the local production and consumption of green electrolytic hydrogen, fully in line with the small-scale local H_2 demand.

ACKNOWLEDGEMENTS

We cordially thank Eric Dabe from NEL and Henrik Steen Pedersen from GreenHydrogen for providing their state-of-the-art CAPEX and TCO data on electrolytic hydrogen. This paper also benefited from a number of insightful discussions at the International Energy Agency with Uwe Remme and Cédric Philibert, respectively at the IEA's Energy Technology Policy Division and the Renewable Energy Division. Finally, financial support from the Public Service of Wallonia – Dept. of Energy and Sustainable Building is gratefully acknowledged as well for allowing these fruitful interactions with the IEA.

REFERENCES

1. IRENA report 2018 : *Hydrogen from Renewable Power : Technology Outlook for the Energy Transition*
2. J. Proost, International Journal of Hydrogen Energy, 44, 4406-4413 (2019)
3. J. Proost, International Journal of Hydrogen Energy, 45, 17067-17075 (2020)
4. C. Philibert, *Renewable Energy for Industry : from green energy to green materials and fuels*, IEA Insight Series 2017, p. 28
5. Q. de Radiguès, G. Thunis and J. Proost, International Journal of Hydrogen Energy 44, 29432-29440 (2019)

WHEC-2022
23rd World Hydrogen Energy Conference
June 26-30, 2022 - Istanbul

#109

ANALYSIS OF EXPERIMENTAL APPLICATION OF PERMANENT NEODYMIUM MAGNETS IN ALKALINE ELECTROLYZER FOR GREEN HYDROGEN PRODUCTION

[1*] *Matej Paranos,* [1] *Ankica Kovač*
[1] University of Zagreb, Faculty of Mechanical Engineering and Naval Architecture, Zagreb Croatia

*Corresponding author e-mail: matej.paranos@fsb.hr

ABSTRACT

This paper deals with the influence of magnetic filed on water electrolysis for green hydrogen production. Experimental setup was design and experimental research conducted. Results of influence of magnetic filed on the energy efficiency of the alkaline electrolyzer is analysed. Average energy efficiency for three cases is calculated and compared. In the first case, water electrolysis was conducted without application of the magnetic field. In the second case, magnetic filed is created with one pair of permanent neodymium magnets and applied on the electrolyzer, while in the third case the same experiment is repeated, but with stronger magnetic filed created by two pairs of neodymium magnets. Each type of the experiment is repeated several times and average values are calculated. Results indicated that magnetic filed is having positive impact on the energy efficiency of the process, and that with application of stronger magnetic field, the increase of energy efficiency is higher.

Keywords: green hydrogen, water electrolysis, alkaline electrolyzer, magnetic filed, permanent neodymium magnets

INTRODUCTION

In a world that is steaming towards a carbon-neutral society, hydrogen technologies are recognized as an essential part of the global energy transition. In the combination with renewable energy sources (RES), hydrogen can serve as a long-term energy storage solution with zero carbon dioxide (CO2) emissions. Hydrogen produced with the utilization of RES is generally known as green hydrogen, while grey and blue hydrogen are produced from fossil fuels [1]. Although the advantages of green hydrogen are well known, its ecological potential is not yet completely utilized, mainly due to economic reasons. The production of the components and equipment used in hydrogen production, storage, and utilization of hydrogen in fuel cells is still not large enough, so the production costs are too high. To reduce the costs, and make the technology economically viable, the production must scale up. This process is already happening by itself since the demand for hydrogen grows every day [2].

To speed up the process, ongoing research that are in progress in the world, must result in improvement of quality of the product. One way to do so is to increase the efficiency of the processes that occur in the application of hydrogen technologies, such as the process of hydrogen production, i.e., water electrolysis. One of the interesting solutions that can have positive effects on the process is the application of the magnetic field. The magnetic field is set in the inter-electrode space between two electrodes which results in the creation of the Lorentz force that accelerates the process of separation of bubbles of hydrogen from the electrodes [3]. Experiments were conducted with both smooth solid electrodes and porose electrodes, resulting in positive effects on the process [4]. Research shows that the application of foam electrodes combined with the influence of a uniform magnetic field results in energy consumption reduction by about 3.4% [5]. The next step for further research is a combination of both numerical and experimental approaches [6].

EXPERIMENTAL SETUP

The alkaline electrolyzer is the main part of the experimental setup (Figure 1.). Its construction is divided into two main parts: the upper tank where electrodes are placed, and the lower tank which is open to the atmosphere. Tanks are connected with the thin tube, ensuring that electrolyte can be transported from one tank to another. The upper tank is closed to the atmosphere because previous experimental research showed that bubbles of oxygen and hydrogen upon reaching the surface of the electrolyte splash the drops of the electrolyte out of the electrolyzer, that way disabling accurate measurement of the produced hydrogen. The housing of the electrolyzer is made of polymethyl methacrylate, commercially known as plexiglass. Sides of the upper tank are connected with epoxy adhesive resistant to alkaline solutions since 25% potassium hydroxide (KOH) water solution is used as the electrolyte in the experiments. Before the start of the experiment, the upper tank is filled with the electrolyte. The lower tank is filled as well, to the level above the end of the tube that is connecting both tanks. When the electrical circuit is closed, the process of water electrolysis begins, and bubbles of oxygen and hydrogen are starting to generate on electrodes. Produced gas is then accumulating

at the top of the upper tank as bubbles go up and the electrolyte is pushed down, raising the level of the electrolyte in the lower tank.

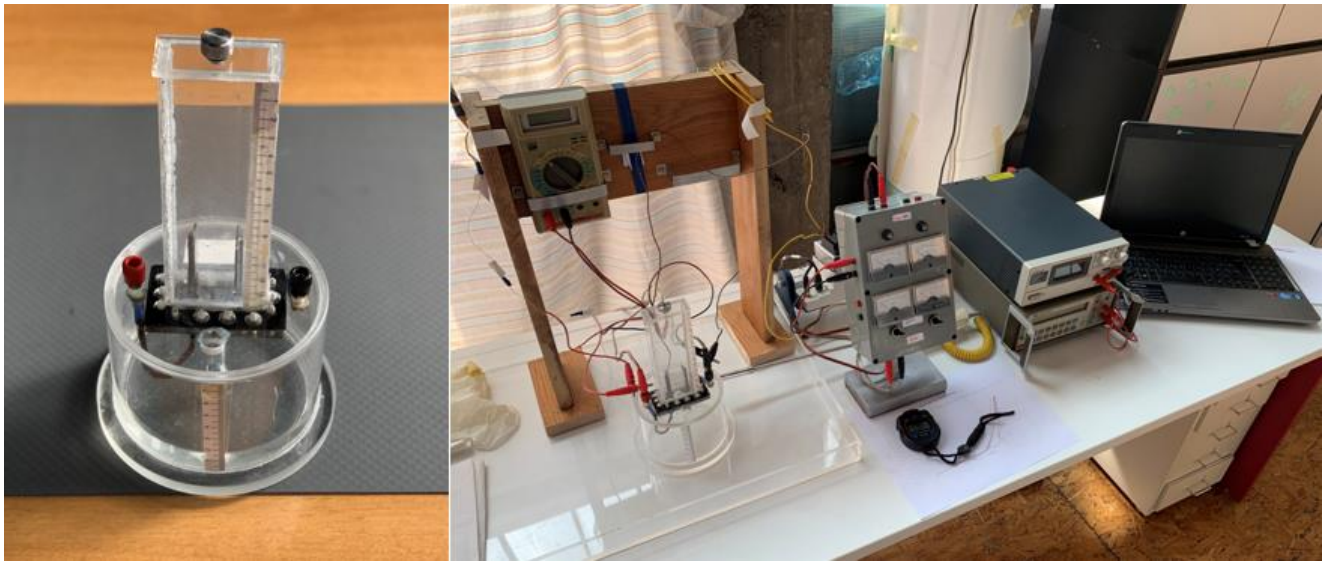


Fig.1. Alkaline electrolyzer (left) and complete experimental setup (right)

For the research, permanent neodymium magnets were used. Magnets are cubes, dimensions 25x25x25 mm. In the first case with magnets, magnetic field is created by a couples of magnets. They are placed on the magnet-holding device into positions where opposite poles are facing each other. That way, a stabile inhomogeneous magnetic field is created between magnets. In second case, another pair of magnets is added to the existing pair, therefore increasing the magnetic flux density in the filed. They are set in the same position. Magnets in both cases are presented in Figure 2. Distance between magnets can be manually adjusted. In this research the distance between magnets was 25 mm for both cases.

Since the magnetic filed in presented case depends on the distance between surfaces of two opposing magnets, the magnetic flux density was measured and mapped with the Hall sensor in both cases. The magnetic flux density at the surface of the magnets for the first case with one pair of magnets was approximately 610 mT at, at the middle of the side where the magnetic flux density is highest. Further away from the surface of the magnet, towards the middle of the field, the value of the magnetic flux density is dropping towards the minimum of approximately 350 mT. In the second case with two pairs of magnets, the magnetic flux density was approximately 630 mT at the surface of the magnets, with values dropping towards the minimum of approximately 380 mT in the middle of the field. Overall, for the same distance of 25 mm between surfaces of the opposing magnets, with addition of one extra pair of the magnets, the magnetic flux density of the field increased between 3% and 7%. The increase in magnetic flux density was not equal or proportional in all parts of the filed. Therefore, the middle of the filed and the middle of the surface were taken as the referent points.

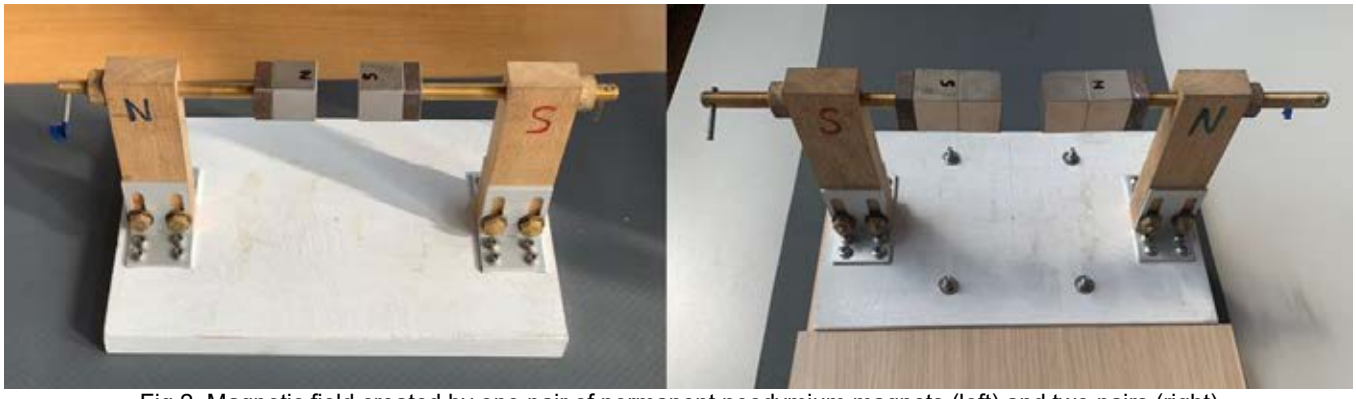


Fig.2. Magnetic field created by one pair of permanent neodymium magnets (left) and two pairs (right)

RESULTS AND DISCUSSION

The energy efficiency calculated for the experimental research was ratio of output energy in form of chemical energy stored in the hydrogen and input energy in form of the electrical energy used for the creation of the hydrogen. It was calculated for each and every experiment in the research. Since all experiments vary among themselves in the calculated energy efficiency due to any number of reasons, experiments are divided in three types, and average energy efficiency for each type is calculated. Three types of experiments, whit average energy efficiencies calculated are presented in Table 1.

Table 1. Comparison of the efficiencies of the processes in the dependence of the magnetic field

Magnetic field	Magnetic flux density on the surface of the magnets	Average efficiency of the process	Increase of efficiency compered to case without magnetic field
Without magnetic field	0 mT	65,95 %	0,00 %
One pair of magnets	610 mT	67,26 %	+ 1,98 %
Two pairs of magnets	630 mT	67,57 %	+ 2,46 %

The results of the experiment conclude that the application of one pair of magnets increased energy efficiency by 1,98% compered to the case without application of the magnetic field. With stronger magnetic filed of two pairs of magnets the energy efficiency increased for the 2,46% compared with the case without application of magnetic filed. Furthermore, Results show that the average energy efficiency of stronger magnetic filed yields in 0,46% increase of energy efficiency compered with the weaker magnetic filed.

CONCLUSIONS

Results of the research point out the increase of energy efficiency of the process when magnetic filed is applied. They also indicate that with the stronger magnetic filed that effect is stronger. In the experimental research, stronger magnetic filed was created by addition of extra pair of permanent neodymium magnets. This resulted with only slight increase of magnetic flux density for the same distance between magnets. This would indicate that with further addition of magnets the magnetic filed wouldn't get significantly stronger, which means that for further research different kind of experimental setup and magnets are needed.

ACKNOWLEDGEMENT

The authors thank the Croatian Science Foundation, which finances the project UIP-2020-02-7332 Advanced methods of green hydrogen production and its transportation, within which research was conducted, and the results of which are presented in this work.

REFERENCES

1. Joris Proost, Critical assessment of the production scale required for fossil parity of green electrolytic hydrogen, International Journal of Hydrogen Energy 45 (2020) 17067-17075, https://doi.org/10.1016/j.ijhydene.2020.04.259
2. Ankica Kovač, Matej Paranos, Doria Marciuš, Hydrogen in energy transition: A review, International Journal of Hydrogen Energy 46 (2021) 10016-10035, https://doi.org/10.1016/j.ijhydene.2020.11.256
3. Noriah Bidin, Siti Radhiana Azni, Shumaila Islam, Mundzir Abdullah, M. Fakaruddin Sidi Ahmad, Ganesan Krishnan, A. Rahman Johari, M. Aizat A. Bakar, Nur Syahirah Sahidan, NurFatin Musa, M. Farizuddin Salebi, Naqiuddin Razali, Mohd Marsin Sanagi, The effect of magnetic and optic field in water electrolysis, International Journal of Hydrogen Energy 42 (2017) 16325-16332, https://doi.org/10.1016/j.ijhydene.2017.05.169
4. Hong-bo Liu, Haotian Xu, Liang-ming Pan, Ding-han Zhong, Yang Liu, Porous electrode improving energy efficiency under electrode-normal magnetic field in water electrolysis, International Journal of Hydrogen Energy 44 (2019) 22780-22786, https://doi.org/10.1016/j.ijhydene.2019.07.024
5. Yang Liu, Liang-ming Pan, Hongbo Liu, Tianming Chen, Siyou Yin, Mengmeng Liu, Effects of magnetic field on water electrolysis using foam electrodes, International Journal of Hydrogen Energy 44 (2019) 1352-1358, https://doi.org/10.1016/j.ijhydene.2018.11.103
6. Hong-bo Liu, Liang-ming Pan, Qi-jun Qin, Peng-fei Li, Experimental and numerical investigation of gas–liquid flow in water electrolysis under magnetic field, Journal of Electroanalytical Chemistry 44 (2019) 29432-29440, https://doi.org/10.1016/j.ijhydene.2019.06.156

WHEC-2022
23rd World Hydrogen Energy Conference
June 26-30, 2022 - Istanbul

#127

AISI 442 AND 446 FERRITIC STAINLESS STEELS AS A SUPPORT FOR BIPOLAR PLATES IN PROTON EXCHANGE MEMBRANE WATER ELECTROLYZERS

[1] *Corneliu M. Crăciunescu,* [2] *A. Sigrid Lædre,* [1] *Nicolae Vaszilcsin,* [2] *Thulile Khoza*, [1] *Mircea L. Dan,* [1] *Andrea Kellenberger,* [1] *Delia Duca,* [1] *Aurel Ercuţa,* [1] *Ion Mitelea*
[1] Politehnica University Timişoara, 300006 Piata Victoriei, Timişoara, Romania
[2] SINTEF Industry, 7465 Trondheim, Norway

*Corresponding author e-mail: andrea.kellenberger@upt.ro

ABSTRACT

This paper presents the results obtained in the study of corrosion resistance of ferritic steels AISI 442 and AISI 446 with the objective of using them as substrate material for bipolar plates (BPPs) in proton exchange membrane water electrolyzers (PEMWEs). The overall objective is to reduce the cost by replacing titanium BPPs with cheaper steel alloys. Corrosion current and corrosion potential of AISI 442 and 446 steels have been determined by potentiodynamic polarization in solutions having a similar composition to the fluid from the anodic side of PEMWEs. Furthermore, to evaluate the corrosion resistance at anodic potentials, AISI 442 and 446 were subjected to a voltage stress test (VST) where the current is monitored while the samples are maintained at constant potentials of 1.5, 1.75 and 2.0 V for 8 hours. Both samples showed good corrosion resistance at 1.5 V, as indicated by the low current densities, but the current densities increased significantly at 1.75 and 2.0 V. This shows that the surface of the ferritic steels must be protected with a corrosion-resistant coating, which should also have high conductivity. After the VST the samples have also been investigated by electrochemical impedance spectroscopy (EIS) and scanning electron microscopy (SEM).

Keywords: Proton exchange membrane, Water electrolyzer, Bipolar plate, Voltage stress test, Tafel plots.

INTRODUCTION

In order to make the production of electrolytic hydrogen profitable, research has focused on the PEMWEs, which have several advantages over alkaline water electrolyzers: high energy efficiency, high current densities, as well as pressures more than 100 bar. Moreover, PEMWEs can operate at variable current densities, making them suitable for connection to wind and solar renewable energy sources [1-2].

One of the most important components of PEMWE stacks is the Bipolar Plate. In addition to separating single cells in a stack, the BPP also conduct electricity and heat away from active areas. The use of cheap metallic materials for BPPs is limited by the aggressiveness of the environment. In addition to a good mechanical strength, BPPs have to be corrosion resistant and electronic conductors. Moreover, the interfacial contact resistance needs to be low [3]. The costs of BPPs are very high, accounting for about 50% of the total costs of a PEMWE stack. The causes that lead to such high costs are the use of high purity Ti, difficult processing of the Ti plates, the need to plate Ti with noble metals to prevent surface anodizing, which would lead to an increased interfacial contact resistance [4]. Research have thus been focused on the use of austenitic stainless steels protected with highly conductive and corrosion resistant coatings. However, austenitic steels are expensive due to their high nickel content, and our research approaches the use of high chromium ferritic stainless steels as a support for BPPs.

MATERIALS AND METHODS

The anticorrosive properties of the AISI 442 and 446 were determined in 0.1 mol L^{-1} Na_2SO_4 solution, acidified with H_2SO_4 up to *pH* = 5. In order to simulate the working environment, KF was added to the solution so that F^- concentration reached 0.1 ppm. The solution was saturated with O_2 (3.5 degree - 99.5%) and the samples tested were made of AISI 442 and 446 sheets, having 1 cm^2 active area. The composition of the AISI 442 and 446 is given in Table 1.

Table 1. Elemental composition of the ferritic stainless-steel samples.

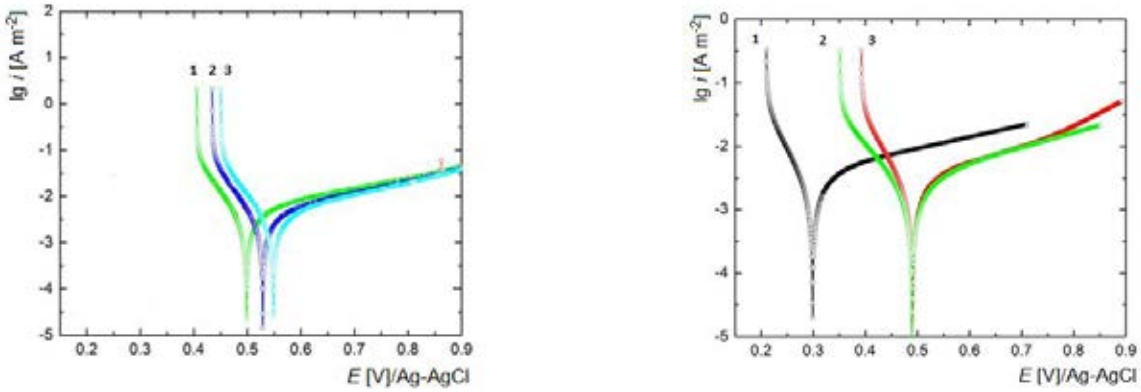
Element		C	Cr	Mn	Si	Al	Mo	P	S	N	Fe
Concentration % mass	AISI 442	0.12	22.1	0.79	0.82	0.72	0.18	0.031	0.028	-	rest
	AISI 446	0.14	24.90	1.08	0.72	-	-	0.032	0.026	0.18	rest

To investigate the anticorrosive characteristics of AISI 442 and 446 samples, potentiodynamic polarization method was used and the corrosion parameters (corrosion current density i_{corr} and corrosion potential E_{corr}) were determined from the Tafel plots. The polarization resistance R_p was calculated using the Stern-Geary relation [5]. The steel samples were subjected to VSTs at 1.5; 1.75 and 2.0 V/NHE for 8 h. Furthermore, the EIS spectra were plotted, in

the frequency range of 100 kHz - 10 mHz, using a sinusoidal signal of 5 mV amplitude. In all experiments, the temperature was 25°C.

RESULTS AND DISCUSSION

Figure 1a and b shows the polarization curves obtained on the AISI 442 and 446 ferritic stainless steel in the test solution. To verify the reproducibility of the results, three measurements were performed under the same conditions.



(a) (b)

Fig. 1. Linear polarization curves on AISI 442 (a) and AISI 446 (b).

Based on the linear polarization curves, parameters that characterize the corrosion process in the given environment have been calculated: corrosion current density i_{corr}, corrosion potential E_{corr}, cathodic- and anodic Tafel slopes (b_c, respectively b_a), as well as polarization resistance R_p. The results obtained are shown in Table 2.

Table 2. Corrosion parameters for AISI 442 and AISI 446 in 0.1 M Na_2SO_4 (pH = 5; 0.1 ppm F^{-1}).

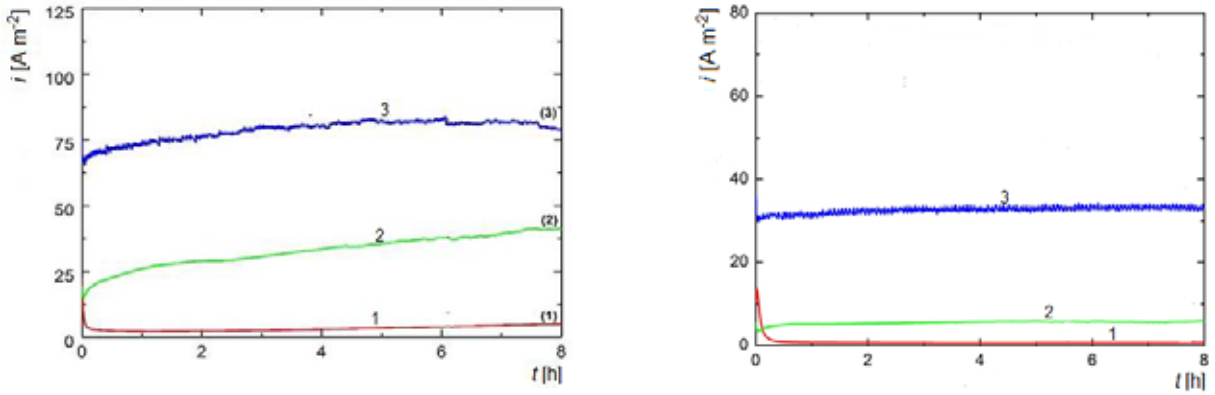
Sample	Experiment no.	i_{corr} [μA cm^{-2}]	E_{corr} [mV/Ag/AgCl]	$-b_c$ [mV dec^{-1}]	b_a [mV dec^{-1}]	R_p [kΩ cm^2]
AISI 442	1	0.190	468	119	58.7	90
	2	0.179	528	124	60.7	99
	3	0.178	548	127	61.0	101
AISI 446	1	0.145	294	56.1	150	122
	2	0.136	486	64.6	159	147
	3	0.134	489	97.5	173	202

Corrosion current density i_{corr} values show that both AISI 442 and 446 have a good corrosion resistance in the test solution. There are no official targets imposed for the corrosion current of BPPs in PEMWE, but it is meaningful to compare this value to the target imposed by the U.S. Department of Energy for BPPs in proton exchange membrane fuel cells (< 1 μA cm^{-2}). Corrosion currents decrease over time as the surface of the metal changes by thickening the oxides layer. In fact, due to the passivation, the polarization resistance R_p changes with the increase of the oxide layer thickness. Both i_{corr} and R_p values show that AISI 446 is more corrosion resistant than 442.

Voltage stress tests were performed at different values of potential, for several hours, to monitor the current density through the interface between stainless steel and the electrolyte. Figure 2 shows the evolution of the current versus time on AISI 442, respectively AISI 446, at different constant values of the potential: 1.5 V (1), 1.75 V (2) and 2.0 V (3).

From Figure 2a and 2b it can be seen that if the studied steels are polarized at 1.5 V, the current density shows an exponential decay in time and stabilizes at a low value, corresponding to the formation of a passive oxide layer. If the potentials are increased to 1.75 and 2 V, the current density increases significantly, due to both the oxygen evolution reaction and the corrosion process. Unlike AISI 442, on AISI 446 the current densities are stabilized at significantly lower values, effect caused by the higher stability of the protective oxides layer.

Electrochemical impedance spectroscopy measurements were performed after the VST and the results obtained by fitting the impedance data are summarized in Table 3. The Rp values obtained by EIS are higher than those obtained by potentiodynamic polarization, as they are measured after VSTs, when the surface is covered with an appreciable layer of oxides.



(a) (b)

Fig. 2. Current transients of AISI 442 (a) and AISI 446 (b) during polarization at constant potentials (1.5; 1.75 and 2.0 V) at 25°C.

Table 3. Calculated data of the circuit elements and experimental errors (between brackets) for AISI 442 and AISI 446.

Sample conditioning	R_s [Ω cm^2]		R_p [kΩ cm^2]		$C_{dl} \cdot 10^5$ [μF cm^{-2}]	
	AISI 442	AISI 446	AISI 442	AISI 446	AISI 442	AISI 446
After 8 h VST at E_1 = +1.5 V	32.9 (1.91%)	33.2 (1.73%)	1410 (1.63%)	980 (1.63%)	2.58	1.48
After 8 h VST at E_2 = +1.75 V	34.1 (1.08%)	39.7 (1.29%)	760 (2.76%)	775 (1.73%)	6.33	6.82
After 8 h VST at E_3 = +2.0 V	38.1 (0.99%)	41.6 (0.71%)	410 (1.91%)	395 (1.49%)	8.87	18.2

As expected, the polarization resistance decreases as the potential in VSTs increases as the alloy surface changes. In fact, the significant increase in the capacity of the double layer at the metal-solution interface indicates that over time, at extreme potentials, the actual surface area of the metal increases.

CONCLUSIONS

The obtained results show that the corrosion resistance of AISI 442 and 446 ferritic steels is high enough to be used as a support for BPPs in PEMWEs. As the corrosion resistance at higher potentials is not good enough, it is necessary to plate the surface of the steels with a thin layer of metal or alloy which additionally ensures a low interfacial resistance. Due to its higher chromium content, AISI 446 is more resistant to corrosion than AISI 442, as evidenced by SEM images (here not shown), which is why it is preferable as a support for BPPs in PEMWEs.

ACKNOWLEDGEMENT

The research leading to these results has received funding from the EEA Grants 2014-2021, under Project 338 no. 2/2019 CoDe-PEM (EEA RO-NO-2018-0502).

REFERENCES

1. Millet P, Ngameni R, Grigoriev SA, Mbemba N, Brisset F, Ranjbari A and Etievant C 2010. PEM water electrolyzers: From electrocatalysis to stack development. International Journal of Hydrogen Energy 35:5043-5052.
2. Chunbao Xu, Lirong Ma, Jinlai Li, Wei Zhao and Zhongxue Gan. 2012. Synthesis and characterization of novel high-performance composite electrocatalysts for the oxygen evolution in solid polymer electrolyte (SPE) water electrolysis. International Journal of Hydrogen Energy 37:2985-2992.
3. Lædre AS, Kongstein OE, Oedegaard A, Karoliussen H and Seland F. 2017. Materials for Proton Exchange Membrane water electrolyzer bipolar plates. International Journal of Hydrogen Energy 42:2713-23.
4. Gago AS, Ansar SA, Saruhan B, Schulz U, Lettenmeier P, Canas NA, Gazdzicki P, Morawietz T, Hiesgen R, Arnold J and Friedrich KA. 2016. Protective coatings on stainless steel bipolar plates for proton exchange membrane (PEM) electrolyzers. Journal of Power Sources 307: 815-825.
5. Roberge PR. 2008. Corrosion Engineering. New York, McGraw Hill.

WHEC-2022
23rd World Hydrogen Energy Conference
June 26-30, 2022 - Istanbul

#128
CHEMICALLY STABILISED SHORT SIDE CHAIN AQUIVION® MEMBRANES FOR OPERATION IN WATER ELECTROLYSIS

[1] Stefania Siracusano, [2]Claudio Oldani, [1]Nicola Briguglio, [1]Antonino S. Aricò*
[1]CNR-ITAE Institute of Advanced Energy Technologies, National Research Council, Via Salita S. Lucia Sopra Contesse 5, 98126 Messina, Italy
[2] Solvay Specialty Polymers Italy S.p.A., Viale Lombardia 20, 20021 Bollate Mi, Italy

*Corresponding author e-mail: siracusano@itae.cnr.it

ABSTRACT

Membrane-electrode assemblies based on chemically stabilised short-side-chain proton exchange Aquivion® membranes, prepared by extrusion or recast methods, have been investigated for operation at high current density (3 - 4 A cm^{-2}) in water electrolysis cells. A thickness of 90 µm was selected for these perfluorosulfonic acid membranes in order to provide proper resilience to hydrogen crossover under differential pressure operation while allowing operation at high currents. The membranes showed proper mechanical strength for high pressure operation and suitable conductivity to reduce ohmic losses at high current densities. Both membranes showed excellent performance in electrolysis cells by achieving a voltage efficiency better than 85% and 80% (1.85 V) at 3 and 4 A cm^{-2}, respectively, in polarisation curves at 90 °C.

Keywords: Electrolysis, Polymer electrolyte membrane, Hydrogen, Extruded membrane, Recast membrane

INTRODUCTION

One of the most advanced processes to produce highly pure “green” hydrogen from renewable energy is based on the polymer electrolyte membrane (PEM) water electrolysis [1]. PEM water electrolysers operate at high pressure to reduce down-stream gas compression thus allowing efficient hydrogen storage. A key aspect of this technology is its excellent dynamic behaviour for proper interfacing with intermittent renewable power sources and its suitable application in grid-balancing service [1]. However, the cost of the hydrogen produced from PEM electrolysis is still high compared to competitive technologies like central steam reforming of natural gas [1].

To allow for a widespread utilisation of the PEM electrolysis technology, a significant reduction of the capital costs is strongly necessary [1]. This will make the hydrogen produced from electrolysis competitive with respect to the currently used organic fuels thus favouring the diffusion of fuel cell vehicles. To achieve such objective, precious metal catalysts used in the electrolysis systems should be minimised and titanium bipolar plates possibly replaced by stainless steel treated with cheap coatings. These strategies are currently addressed, but probably they may not be sufficient because it is still needed to take into consideration the cost of the balance of plant of the PEM electrolyser. This cost is strongly influenced by the hydrogen production rate [1].

On the other hand, it is widely recognised that the most relevant effect on decreasing the cost of PEM electrolysers will be played in the future by the increase of the operating current density while keeping the system efficiency at suitable levels [2-3]. When an electrolyser is operated in a high current density regime, the efficiency losses associated to the ohmic drop play a relevant role. In this regard, the proton transport in the polymer electrolyte membrane is producing a major contribution to the ohmic losses at high current density. Electronic percolation in the catalytic layers, diffusion media and bipolar plates contributes to ohmic losses in a lower extent [4].

Beside a high proton conductivity, proper mechanical strength and low gas-cross over under differential pressure operation are important characteristics that govern the reliability of the membrane separator between the anode and cathode compartments in PEM cells [1].

MATERIALS AND METHODS

In this work, we have investigated Aquivion® membranes with equivalent weight of 980 g eq^{-1} and thickness of 90 µm, produced by extrusion or casting methods, with regard to their electrochemical performance and gas crossover characteristics in electrolysis cells. These membrane-electrode assemblies contained low precious metal loadings in accordance with the trend of decreasing the impact of critical raw materials on the overall cost of the PEM electrolysis system [3]. Interestingly, it was observed that the membrane fabrication method influences significantly the interfacial properties with the electrodes affecting the polarisation resistance and degradation rate in durability studies.

Electrolysis cells have been compared for operation at high current density (3-4 A cm^{-2}) as required to decrease significantly the capital costs of the electrolysis systems [2-3] while gas crossover was investigated during high differential pressure operation to examine the impact of the membrane fabrication method on the system safety

RESULTS AND DISCUSSION

In-plane conductivity has been measured at 80°C and in the relative humidity range from 20% to 120% R.H. (Fig. 1). Both membranes, having the same equivalent weight (980 g/mol.), show a similar trend. As expected, proton conductivity increases by increasing relative humidity. Both membranes reach the same value of 130 -140 mS cm^{-1} under full humidification. This result clearly show that the manufacturing process does not affect the ion conduction properties of Aquivion ® membranes under full humidification which are determined by the amount of $–SO_3H$ functional groups and their dissociation. At low R.H. values (20%) the extruded membrane shows larger conductivity.

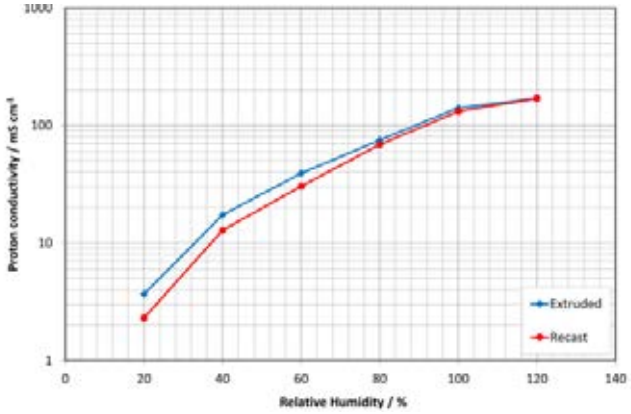


Fig. 1. In-plane proton conductivity at 80°C vs. relative humidity of extruded (E98-09S) and recast (C98-09S) membranes.

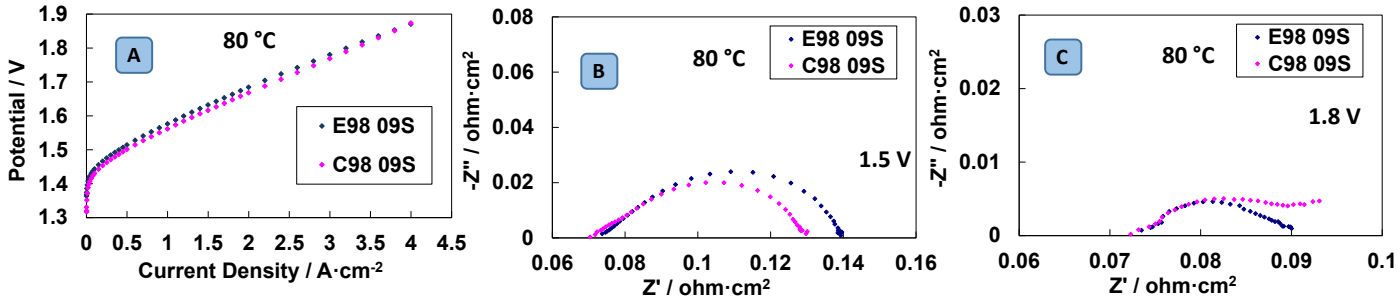


Fig. 2. Polarisation curves (a) and ac-impedance spectra at 1.5 V (b) and 1.8 V (c) at 80 °C of the MEAs with extruded and casted membranes.

A comparison of the polarisation curves at 80 °C for the two MEAs (Fig. 2a) shows a small but evident activation enhancement in the case of the recast membrane resulting from a lower polarisation resistance at 1.5 V (Fig. 2b). A very good reproducibility was observed for these initial polarisation curves by investigating different sets of the same MEAs. This indicates that the observed differences are specifically related to the membrane used in the MEA. The series resistance is just slightly lower for the recast membrane according to the fact that both membranes are based on the ionomer and have the same thickness. At 1.8 V (Fig. 2c), it seems that some small additional low frequency contribution is present in the case of the recast membrane as envisaged from the presence of the onset of a low frequency semicircle or possibly a Warburg-like diffusion-related contribution. As consequence of the different differential resistances, the extruded membrane recovers the performance gap with the recast membrane at 4 A cm^{-2} showing the same voltage efficiency.

CONCLUSIONS

Extruded and recast short-side chain proton exchange Aquivion® membranes have been assessed in membrane-electrode assemblies with regard to their operation at high current density in water electrolysis cells. The membranes were characterised by proper mechanical strength for high-pressure operation and good conductivity to minimise ohmic

losses at high current densities. Both membranes have shown a similar voltage efficiency (> 80%) at temperatures of 80–90°C and high current density (3-4 A cm^{-2}); whereas the recast membrane was slightly better performing in the activation region of the polarisation curves.

ACKNOWLEDGEMENT

The financial support from the NEPTUNE EU FCH JU project is acknowledged. This project has received funding from Fuel Cells and Hydrogen 2 Joint Undertaking under grant agreement No 779540. This Joint Undertaking receives support from the European Union's Horizon 2020 research and innovation programme and Hydrogen Europe and Hydrogen Europe Research.

REFERENCES

1. A.S. Aricò, S. Siracusano, N. Briguglio, V. Baglio, A. Di Blasi, V. Antonucci, Polymer electrolyte membrane water electrolysis: status of technologies and potential applications in combination with renewable power sources, J. Appl. Electrochem. 43 (2013) 107–118
2. S. Siracusano, V. Baglio, N. Van Dijk, L. Merlo, A.S. Aricò, Enhanced performance and durability of low catalyst loading PEM water electrolyser based on a short-side chain perfluorosulfonic ionomer, Appl. Energy 192 (2017) 477–489.
3. S. Siracusano, N. Hodnik, P. Jovanovic, F. Ruiz-Zepeda, M. Šala, V. Baglio, A.S. Aricò, New insights into the stability of a high performance nanostructured catalyst for sustainable water electrolysis, Nano Energy 40 (2017) 618–632.
4. S. Siracusano, S. Trocino, N. Briguglio, V. Baglio and A. S. Aricò, Electrochemical impedance spectroscopy as a diagnostic tool in polymer electrolyte membrane electrolysis, Materials, 11 (8) 1368.

WHEC-2022
23rd World Hydrogen Energy Conference
June 26-30, 2022 - Istanbul

#150

H_2BASQUE – TECHNOLOGIES FOR BOOSTING THE HYDROGEN ECONOMY IN THE BASQUE COUNTRY: GREEN HYDROGEN PRODUCTION

[1*] *Ekain Fernandez,* [2] *Beatriz Calleja Sanchez,* [3] *Francisco Alcaide,* [4] *Stefania Doppiu,* [5] *Mikel Oregui-Bengoechea,* [6] *Eva G-Berasategui,* [7] *Elias Unzueta,* [8] *Jone Irigoyen*

[1]TECNALIA, Basque Research and Technology Alliance (BRTA), Mikeletegi Pasealekua 2, 20009 Donostia-San Sebastián, Spain.

[2]TUBACEX INNOVACION AIE, Parque Científico y Tecnológico de Bizkaia, edificio nº 612, Astondo Bidea, 48160, Derio, Spain.

[3]CIDETEC, Basque Research and Technology Alliance (BRTA), Po. Miramón 196, 20014 Donostia-San Sebastián, Spain

[4]CIC energiGUNE, Basque Research and Technology Alliance (BRTA), C/Albert Einstein 48, 01510 Vitoria-Gasteiz, (Álava) Spain

[5]UPV/EHU, Plaza Ingeniero Torres Quevedo 1, 48013 Bilbao, Spain.

[6]Department of Physics of Surfaces and Materials, TEKNIKER, Basque Research and Technology Alliance (BRTA), Iñaki Goenaga 5, 20600 EIBAR, Spain.

[7]PETRONOR INNOVACIÓN, San Martín, Nº-5, 48550 Muskiz (Bizkaia) Spain.

[8]BASQUE ENERGY CLUSTER, C/ S. Vicente 8, II-4º Dcha., 48001 Bilbao, Spain.

*Corresponding author e-mail: ekain.fernandez@tecnalia.com

ABSTRACT

H2BASQUE is a strategic project funded by the Basque Government for developing innovative technologies (and their key components) for cost-competitive green hydrogen production. The green production technologies that will be developed in H2BASQUE are AEM electrolysis, PEM electrolysis and thermochemical cycles. In addition, this project at improving the scientific-technological and commercial positioning of the Basque Network of Science, Technology and Innovation and Basque companies in the hydrogen sector and in particular in green hydrogen generation technologies.

Keywords: Green Hydrogen production, Electrolysis, Thermochemical cycles

INTRODUCTION

Hydrogen will play a crucial role in the energy transition due to its high potential to contribute to the decarbonization of the economy. Green hydrogen, produced using energy from renewable sources, will serve as a raw material for the chemical industry, particularly in carbon dioxide-emitting industrial sectors (steel plants, refineries, cement plants), for mobility applications, for the residential and tertiary sectors, and for massive energy transportation or long-time energy storage. This last point is especially important since energy generation, in the case of renewables, does not always match in time with its demand.

Due to its characteristics, hydrogen is expected to be a fundamental energy vector in the energy transition, especially in sectors or processes that are difficult to electrify.

PROJECT DESCRIPTION

Hydrogen will play a crucial role in the energy transition due to its high potential to contribute to the decarbonization of the economy. Green hydrogen, produced using energy from renewable sources, will serve as a raw material for the chemical industry, particularly in carbon dioxide-emitting industrial sectors (steel plants, refineries, cement plants), for mobility applications, for the residential and tertiary sectors, and for massive energy transportation or long-time energy storage. This last point is especially important since energy generation, in the case of renewables, does not always match in time with its demand.

Due to its characteristics, hydrogen is expected to be a fundamental energy vector in the energy transition, especially in sectors or processes that are difficult to electrify.

A major challenge of the deployment of this promising energy vector is the generation of low-carbon or carbon-free hydrogen on a large scale and at a competitive cost. The H2BASQUE project will focus on the development of three innovative technologies for this purpose:

- Green hydrogen production by anion exchange membrane electrolysis (AEM)
- Green hydrogen production by proton exchange membrane electrolysis (PEM).
- Green Hydrogen production through thermochemical cycles.

Although the electrolysis process for green hydrogen generation is a known process, it is necessary to advance technologically to make it more efficient and reduce hydrogen generation costs. H2BASQUE contemplates the development of innovative components (membranes, catalysts, MEA ...) that reduce costs, decrease the use of critical materials and improve the performance of the hydrogen production process with respect to the state-of-the-art.

In addition, the project aims at developing three thermochemical cycles; the study of these cycles in custom-designed reactors and the conceptual process design for scaling them up to industrial scale.

Furthermore, the project will investigate the integration in industrial processes of the different green hydrogen generation technologies that will be developed in the project, and it will define the most suitable industrial uses for the implementation of each of them.

The project aims at improving the scientific-technological and commercial positioning of the Basque Network of Science, Technology and Innovation and Basque companies in the H2 sector and in particular in green H2 generation technologies.

H2BASQUE project is coordinated by TECNALIA and also has the participation of TUBACEX INNOVACIÓN, CIDETEC, CIC ENERGIGUNE, UPV / EHU, TEKNIKER, PETRONOR INNOVACIÓN and BASQUE ENERGY CLUSTER.

In this work, the progress made in the different activities of the project will be presented.

ACKNOWLEDGEMENT

This Project is funded by the Department of Economic Development, Sustainability and Environment of the Basque Government (ELKARTEK 2021 Program).

WHEC-2022
23rd World Hydrogen Energy Conference
June 26-30, 2022 - Istanbul

#156

ACTIVITY OF BINARY NON-PRECIOUS METAL OXIDE-BASED ELECTRODE FOR OXYGEN EVOLUTION REACTION IN ACID

[1*] *Koichi Matsuzawa,* [2] *Soma Hirayama,* [2] *Yuma Kohara,* [3] *Akimitsu Ishihara*
[1] Yokohama National University, Graduate School of Engineering, 79-5, Tokiwadai, Hodogaya-ku, Yokohama, Japan
[2] Yokohama National University, Graduate School of Engineering Science, 79-5, Tokiwadai, Hodogaya-ku, Yokohama, Japan
[3] Yokohama National University, Institute of Advanced Sciences, 79-5, Tokiwadai, Hodogaya-ku, Yokohama, Japan

*Corresponding author e-mail: matsuzawa-koichi-zs@ynu.ac.jp

ABSTRACT

In order to develop non-platinum group metals anode electrocatalyst for the proton exchange membrane water electrolysis, the catalytic activity of Ta and Mo oxide-based electrocatalyst with Mn addition for the oxygen evolution reaction (OER) have been investigated. The Ta and Mo oxide-based electrocatalyst with Mn addition (Mn-TaO_x and Mn-MoO_x) has increased current density than that Ta oxide-based electrocatalyst with Mn addition in our previous study (Mn-TaO_x(Pre)). From the slow scan voltammogram of Mn-TaO_x and Mn-MoO_x, the redox peak of Mn species was detected in both samples. Though the electric charge of redox peak and the OER current density was independent relation in Mn-TaO_x and Mn-MoO_x, the Mn content is affected on the enhancement of electrical conductivity in Mn-TaO_x and Mn-MoO_x compared to Mn-TaO_x(Pre).

Keywords: Oxide-Based Electrode, Oxygen Evolution Reaction, PEM Electrolyzers, Green Hydrogen

INTRODUCTION

It is not enough to install the hydrogen all over the world and the CO_2-free–hydrogen society, especially “Green Hydrogen[1]” society should be required for sustainable future. As is well known, water electrolysis is essential technology to produce “Green Hydrogen” from renewable energies. Proton exchange membrane water electrolysis (PEMWE) is one of promising water electrolysis to expand production and installation. In Japan, the High-purity Hydrogen Oxygen Generator(HHOG) and hydrogen-based autonomous energy supply system whose nick name is “H_2One^{TM}” have released from Kobelco Eco-Solutions and Toshiba Corp., and both system uses for distributed power supply. The PEMWE is used for the essential device installed in above systems. However, the conventional electrocatalysts for PEMWE are precious metal materials, and especially, the iridium oxide (IrO_2) uses as anode. As the iridium is by-product of platinum, its resources is very poor, and it is afraid that the cost will be higher with installation PEMWE system. Moreover, it is reported that the IrO_2 is easy to cause the degradation under dynamic operation condition which is simulated variable renewable energy (VRE) and the catalytic activity of oxygen evolution reaction (OER) became lower by dynamic operation[2-3]. Therefore, the non-platinum group metals (PGM) oxide anode should be required for Green Hydrogen production. We focused on group 5 and 6 metal oxide, such as tantalum (Ta) and molybdenum (Mo) oxide. In our previous results, Ta oxide-based electrocatlyst with Mn addition has OER activity in sulfuric acid. However, it does not have significant activity for the OER[4]. In this study, we have prepared not Ta oxide-based electrocatalyst with Mn addition but also Ta oxide-based electrocatalyst with Mn addition, and investigated its catalytic activities for the OER in acidic solution.

EXPERIMENTAL

Ta or Mo compound films were formed on Ti rods as a base material, using the R.F. magnetron sputtering. Target was Mn, Ta or Mo disks. Gas atmosphere in the chamber was a mixture of Ar and O_2 gas. After polishing and washing, the Ti rods were heated from 300 °C (TaO_x) or 400 °C (MoO_x). The flow rates of Ar and O_2 during the sputtering were kept at constant. Ta- or Mo-based thin film catalysts prepared by Mn target with Ta or Mo piece of plate are expressed as TaO_x or Mn-TaO_x, respectively. In the case of formation of binary electrode such as Mn-TaO_x, it is considered the difference of sputtering rate between Mn and Ta. Mn addition was varied from 0 to 80 at%. Partial pressures of Ar (p_{Ar}) and O_2 (p_{O2}) were calculated by multiplying the ratio of the flow rate of each gas by the total pressure in the chamber. Sputtering power and sputtering time were fixed at 150 W and 20 min, respectively. To compare with another oxide-based electrocatalyst, we also prepared Ti compound films with Mo addition of 10 at% formed on Ti rods (Mo-TiO_x) by the sputtering under at 0.23 Pa of p_{Ar} and p_{O2} at 100 °C of substrate heating temperature for 20 min of formation time.

All electrochemical measurements were carried out using a three-electrode cell at 30 °C in 1 M H_2SO_4. A reversible hydrogen electrode (RHE) and a carbon plate were used as a reference and a counter electrode, respectively. Ta compound films with and without addition formed on Ti rod used as working electrode. In order to evaluate the catalytic activity for the OER, slow scan voltammetry (SSV) was performed under N_2 atmosphere. Current density

was based on the geometric surface area of the working electrode. The resistance of the film (R_{film}) and charge transfer (R_{ct}) was evaluated by AC impedance spectroscopic measurements in the frequency range from 10^5 to 10^{-1} Hz.

RESULTS AND DISCUSSION

Fig. 1 shows the Tafel plots of Ta and Mo oxide-based electrocatalyst with Mn addition. The horizontal axis is based on geometric current density (i_{geo}). For the comparison, the results of IrO_2 film on Ti rod (IrO_2) which was fabricated thermal decomposition from iridium chloride and Mn-TaO_x which was prepared in our previous study (Mn-TaO_x(Pre))[4] are also shown in Fig. 1. Both Mn-TaO_x and Mn-MoO_x have higher OER activity than Mn-TaO_x(Pre). The Tafel slope of Mn-TaO_x and Mn-MoO_x are 76 and 73 mV dec^{-1}, respectively. Since the Tafel slope of Mn-TaO_x(Pre) was 105 mV dec^{-1}, the OER of both sample have improved compared to that of Mn-TaO_x(Pre). However, the OER activity of both Mn-TaO_x and Mn-MoO_x has lower than that of IrO_2.

From EIS results, both R_{ct} of Mn-TaO_x and Mn-MoO_x was drastically decreased than that of Mn-TaO_x(Pre). In addition, both R_{film} of Mn-TaO_x and Mn-MoO_x was also decreased than that of Mn-TaO_x(Pre). Therefore, the reason why the i_{geo} of Mn-TaO_x and Mn-MoO_x was much larger than that of Mn-TaO_x(Pre) is that both improvements for the catalytic activity for the OER and the electrical conductivity then that of Mn-TaO_x(Pre).

According to Fig. 1, both polarization curves of Mn-TaO_x and Mn-MoO_x have redox peak of Mn(III)/Mn(IV)[5] over 1.4 V as same as Mn-TaO_x(Pre). In the case of Mn-TaO_x(Pre), there was linear relation between the i_{geo} for the OER and the electric charge (Q) of redox peak of Mn species, but it does not show any relationship between i_{geo} for the OER and Q in the case of Mn-TaO_x and Mn-MoO_x. It means that Mn species including in Mn-TaO_x and Mn-MoO_x does not contribute on the OER activity.

From XPS analysis, the certain amount of Mn species has still remained in Mn-TaO_x after electrochemical measurement. It was greatly different from result of Mn-TaO_x(Pre) that the peak which was identified Mn oxides was completely disappeared. Thus, it is suggested that Mn species including in Mn-TaO_x and Mn-MoO_x enhances the electrical conductivity compared to Mn-TaO_x(Pre) from EIS and XPS results.
The chronopotentiometry of Mn-TaO_x for 1 mA cm^{-2} was also evaluated for 120 h. Though the Mn-TaO_x became higher potential in 10 h, the potential was keep constant after 10 h. Compared to the result of IrO_2, it was found that the Mn-TaO_x has relatively high stability in this condition.

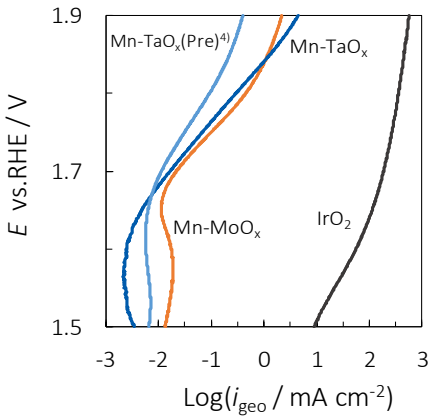


Fig. 1 Tafel plots of Ta and Mo oxide-based electrocatalyst with Mn addition in 1 M H_2SO_4 at 303 K.

CONCLUSIONS

In order to develop non-PGM anode electrocatalyst for proton exchange membrane water electrolysis, the catalytic activity of Ta and Mo oxide-based electrocatalyst with Mn addition for the oxygen evolution reaction (OER) have been investigated. According to results from electrochemical measurement, Ta oxide-based electrocatalyst film with Mn addition (Mn-TaO_x) and Mo oxide-based electrocatalyst film with Mn addition (Mn-MoO_x) have larger geometric current density (i_{geo}) than Ta oxide-based electrocatalyst film with Mn addition in our previous study (Mn-TaO_x(Pre)). According to EIS results, the reason why the i_{geo} of Mn-TaO_x and Mn-MoO_x was much larger than that of Mn-TaO_x(Pre) is that both improvements for the catalytic activity for the OER and the electrical conductivity then that of Mn-TaO_x(Pre). In addition, both polarization curves of Mn-TaO_x and Mn-MoO_x have redox peak of Mn(III)/Mn(IV) as same as Mn-TaO_x(Pre). It does not show any relationship between i_{geo} for the OER and Q in the case of Mn-TaO_x and Mn-MoO_x. It is suggested that Mn species including in Mn-TaO_x and Mn-MoO_x enhances the electrical conductivity compared to Mn-TaO_x(Pre).

ACKNOWLEDGEMENT

This work was partly supported by ENEOS Tonen General Research / Development Encouragement & Scholarship Foundation and Suzuki Foundation.

REFERENCES

1. Ota K, Ishihara A, Matsuzawa K, and Mitsushima S, 2010. Hydrogen energy system and environmental impact factor. Electrochemistry 78: 970-975

2. Alia S M, and Anderson G C, 2019. Iridium oxygen evolution activity and durability baselines in rotating disk electrode half-cells. *J Electrochem Soc*, 166: F282-F294
3. Papakonstantinou G, Algara-Siller G, Teschner D, Vidaković-Koch T, Schlőgl R, and Sundmacher K, 2020. Degradation study of a proton exchange membrane water electrolyzer under dynamic operation conditions. *Appl Ener*, 280: 115911-115921
4. Matsuzawa K, Hirayama S, Kohara Y, and Ishihara A, 2020. The impact of Mn addition on Ta oxide-based electrocatalysts for oxygen evolution reaction in acid. ECS Trans, 104(8): 431-436
5. Moria M, Iwakura C, and Tamura H, 1979. The anodic characteristics of massive manganese oxide electrode. *Electrochim Acta*, 24: 357-362

WHEC-2022
23rd World Hydrogen Energy Conference
June 26-30, 2022 - Istanbul

#157

SOEC AS ENABLER OF HIGHLY EFFICIENT HYDROGEN & E-FUEL PRODUCTION

[1*] *Juergen Rechberger,* [1] *Josef Macherhammer,* [1] *Martin Rothbart,* [1] *Rittmar von Helmolt,* [1] *Martin Hauth*
[1]AVL List GmbH, Hans List Platz 1, Graz, Austria

*Corresponding author e-mail: juergen.rechberger@avl.com

ABSTRACT

Production of green hydrogen from renewable sources shows a promising pathway for the long-term de-fossilization, now adopted by many countries in their national strategic vision. The business case hinges on widespread application in transport, stationary and industrial sectors. Cross-sectoral approach is critical, interconnection user profiles to guarantee energy security, despite intermittency. Energy efficiency of the hydrogen production process is of utmost importance to achieve hydrogen cost which are required for industry and energy applications. SOEC represents a particularly interesting technology to improve the production efficiency of hydrogen and e-fuels. This paper will discuss the technology advantages and potentials for improvement.

Keywords: SOEC, hydrogen, e-fuel, production

HYDROGEN PRODUCTION VIA ELECTROLYSIS FROM RENEWABLES

Green hydrogen production via electrolysis shows the lowest carbon footprint among the H2 production pathways. Several Electrolyzer technologies are available, which differ in technical parameter and maturity.

In the time range of 2030 SOEC H_2 production cost estimated to be 15-25% lower compared to PEM electrolysis. Approximately 70% of cost are OPEX and 30% are CAPEX. In the future SOEC has the potential to reach lower CAPEX than PEM electrolysis.

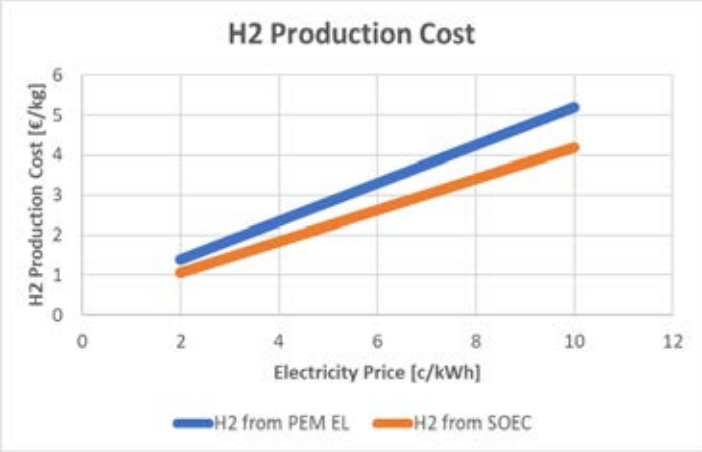


Fig. 1. Hydrogen production cost with PEM EL and SOEC – 2030 Technology scenario

SOEC is still in R&D phase with some pilot plants in the 100kW range in operation. With its working temperature between 600 and 800°C, SOEC has the potential to reach highest efficiencies due to thermodynamic characteristics with lower electricity demand at elevated temperatures for the splitting process of molecules like water into hydrogen and oxygen. Further advantages of this technology include the usage of non-precious catalysts at higher temperatures, the ability to operate the stacks reversibly and the possibility to convert carbonaceous feed gases directly and in combination with water.

AVL is at the moment with various partners developing industrial scale 1MW SOEC modules where the first systems will be deployed already in 2022. A design study of such a modular 1MW system is shown in Fig.2. The overall 1MW system contains of smaller Electrolyzer modules which are connected in series. Each module includes the required number of individual SOEC stacks and all hot balance of plant components. The overall plant will reach about 80% efficiency of hydrogen production based on liquid water input and up to 88% based on steam input.

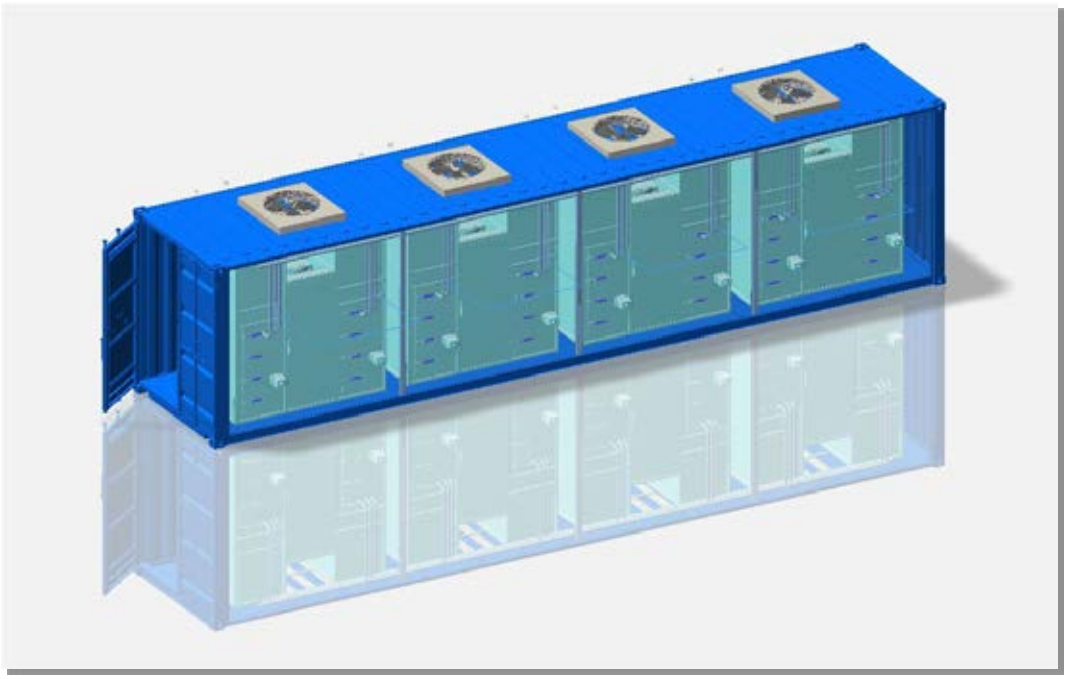


Fig. 2. AVL 1MW SOEC system design concept

E-FUEL PRODUCTION BASED ON THE SOEC PROCESS

As discussed above, SOEC has the ability to convert also carbonaceous feed gases. The conversion of water together with CO_2 is called “co-electrolysis”. Thereby, syngas consisting of hydrogen and carbon monoxide can be produced directly, which can, in addition, serve as a feedstock for various synthesis processes.

Existing PtG plants [1] that combine electrolysis and downstream synthesis like methanation, or Fischer-Tropsch, operate in two separated process steps using solely CO_2 methanation. These concepts still face challenging issues with respect to load flexibility, material degradation and high costs. However, the concept of co-electrolysis of steam and CO_2 in the Co-SOEC stack offers significant benefits. The overall system as well as the round-trip efficiencies for a closed circle system can be significantly improved. The reason for this is that the synthesis process is a stronger exothermal reaction, which positively affects the possibilities of heat recirculation and overall heat management in the system. Moreover, the chemical conversion of CO_2 to CO in the Co-SOEC stack is far more efficient due to the higher temperatures and the associated decrease in the Gibbs free energy of the electrolysis reactions. Furthermore, compared to conventional methods, enhanced conversion rates and reaction kinetics reduce the need for gas upgrading downstream after the methanation and increase power densities. This consequently reduces space and material requirements, which also have the potential to reduce the system costs. Improvements are under development for SOEs to overcome challenges like low dynamic responsiveness and to increase cell lifetime.

AVL has developed a complete Power-to-Liquid plant concept, where the SOEC process is thermally coupled to the Fischer-Tropsch process. Via this thermal coupling the production efficiency can be increased by roughly 30% compared to route via PEM or AL electrolysis. At the moment, AVL and IWO are building up the “IFE – Innovation flüssige Energie” demonstration plant in Austria based on this technology to proof the feasibility and efficiency of this process. The demonstration plant is planned to start operation in early 2023.

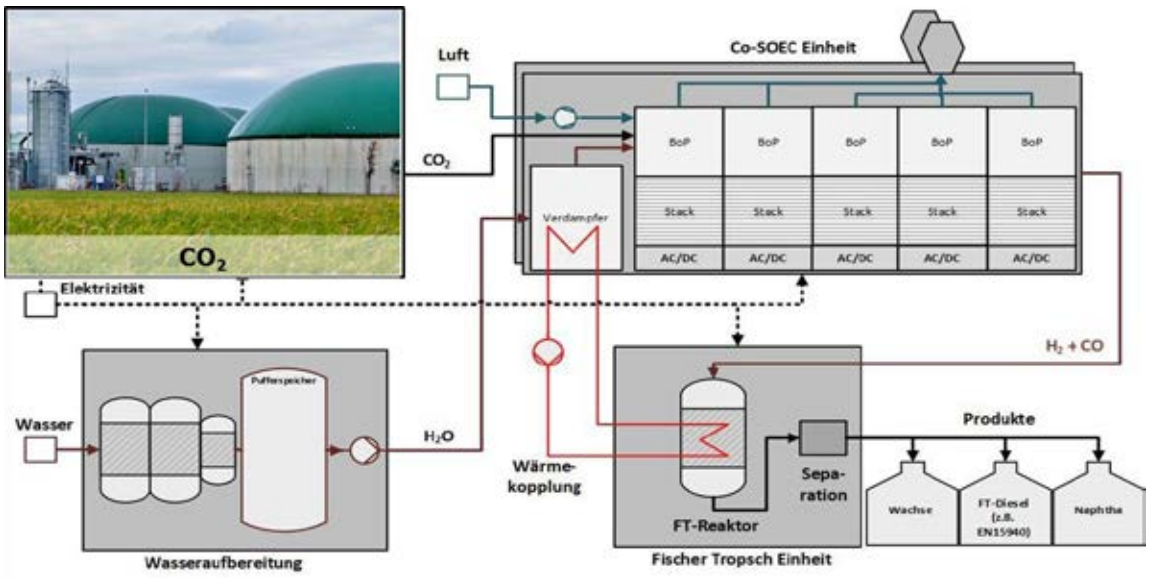


Fig. 3. AVL IWO PtL demonstration plant process

CONCLUSIONS

Optimizing hydrogen production efficiency is key to lower down the price of green hydrogen and to deal with mid-term scarce renewable electricity. AVL is developing hydrogen and e-fuel production technology based on an innovative SOEC process which enables an efficiency improvement by 15-30% compared to PEM and AL electrolyses. For both approaches - hydrogen & e-fuel production - industrial relevant technology demonstrators will be deployed in the timeframe 2022/23.

NOMENCLATURE

SOEC Solid Oxide Electrolyzer Cell
PEM EL Polymer Electrolyte Membrane Electrolysis
AL EL Alkaline Electrolysis

REFERENCES

1. Audi opens power-to-gas facility in Werlte/Emsland; e-gas from water, green electricity and CO2, 25/06/2013, https://www.greencarcongress.com/2013/06/audi-20130625.html
2. The Hydrogen Value Chain - Production and Use; Martin ROTHBART, Gernot HACKER, Martin HAUTH, Jürgen RECHBERGER, Christian SAVORA, Rittmar von HELMOLT; 2021 JSAE Annual Congress
3. E-Fuel production via renewables and their impact on WtW Fleet CO2 performance; M. Rothbart, B. Enzi; SIA Congress 2020

WHEC-2022
23rd World Hydrogen Energy Conference
June 26-30, 2022 - Istanbul

#167

A NOVEL HYDROGEN ECONOMY BASED ON ELECTROCHEMICAL CELLS INTEGRATED WITH FOSSIL FUEL ASSETS AND WASTEWATER RESOURCES

[1*] *Lateef A Jolaoso,* [1] *Javad Asadi,* [1] *Pejman Kazempoor*
[1] School of Aerospace and Mechanical Engineering, University of Oklahoma, Norman, OK, USA

*Corresponding author e-mail: pkazempoor@ou.edu

ABSTRACT

The availability of water for hydrogen production is a fundamental challenge threatening water security and its economic sustainability. This work addresses this by focusing on the design, performance and economic estimation of a novel, highly efficient and environmentally benign hydrogen production process which can be integrated with several power production units, including coal, natural gas-fired power plants and renewable energy sources. The system uses flue gas from coal power plants and various wastewater sources as the process's feedstock to generate steam for the SOEC unit. The SOEC and the balance of plant components are designed, simulated, and integrated using Aspen Hysys Software. The SOEC model is experimentally and numerically validated, and a piece-wise performance evaluation of the system is carried out. The result of this innovative system shows high system efficiencies, which can be improved depending on the energy source and by full energy Integration. The techno-economic analysis of the system gives a Levelized hydrogen cost of $2.99/kg, which can be improved to meet the U.S. Department of Energy (DOE) targets. The study offers insights into water-energy nexus for the researchers and policymakers for decision making and technology development.

Keywords: Solid Oxide Electrolytic Cell (SOEC), Hydrogen Production, Flue Gas, Water-Energy Nexus, Techno-Economic Analysis (TEA)

INTRODUCTION

The production of hydrogen from renewable and sustainable sources is a key to the green hydrogen economy. Water electrolysis has gained attention and looks promising as the process is greenhouse gas-free and yield 100% pure hydrogen. Even though water is abundant, its accessibility is a great challenge, and its use for this process will undermine water security for domestic and agricultural use. One of the major crises faced in this generation due to its increasing population is the availability of clean drinking water, particularly in developing countries. Even the developed ones can only access 2% of the available water[1]. China, most especially its coal-rich region, is faced with water scarcity[2] and projected to be severe in 2050 and the arid and semi-regions like the Middle East and the western U.S. [3].

There are three major commercialized and conceptualized water electrolytic cells for the generation of hydrogen in recent times [4] which include alkaline electrolytic cell (AEC), the most matured technology [5], polymer electrolyte membrane (PEM) electrolytic cell (PEMEC) and solid oxide electrolytic cell (SOEC). The AEC challenges range from low current density to low operational pressure, which aimed to be solved with the advent of PEMEC[6]. Likewise, the PEMEC suffers from high capital cost, pure water requirement, and increased system complexity, stemming from its operational pressure [6, 7]. However, the SOEC is an evolving and promising technology that is anticipated to overcome the setbacks plaguing these two electrolyzers [8, 9]. Solid ion-conducting ceramics are used as electrolytes in the SOECs, which operate at high temperatures ranging from 650-1000 ℃ [9]. Several works have been done on this technology both in the laboratories [8] and industries to commercialize it [9]. Kazempoor and Braun[10] modeled and evaluated a SOEC system to serve as a primary system-level performance prediction tool. Several contemporary studies on SOEC focused on hydrogen production directly from water and steam [11-13]. For better system optimization high round-trip efficiency, SOEC has been designed and studied alongside its reverse counterpart, solid oxide fuel cell (SOFC), to form regenerative solid oxide cell (rSOC) [14-16]. To eliminate the uncertainty concerning future cost and high capital cost of this technology, recent literature evaluates its techno-economic viability to encourage investments[17-19].

This work is distinctive in its water electrolysis in that it explores the flue gas from power plant and wastewater as a feedstock into the hydrogen production unit integrated with a different energy source. The net energy and techno-economic analyses are carried out on the entire system for performance evaluation and sensitivity analysis on the system's critical parameters.

SYSTEM AND MODEL DESCRIPTION

The proposed system is shown in fig. 1. It comprises two sections, namely the upper steam generating section and the high-temperature SOEC unit- hydrogen production unit.

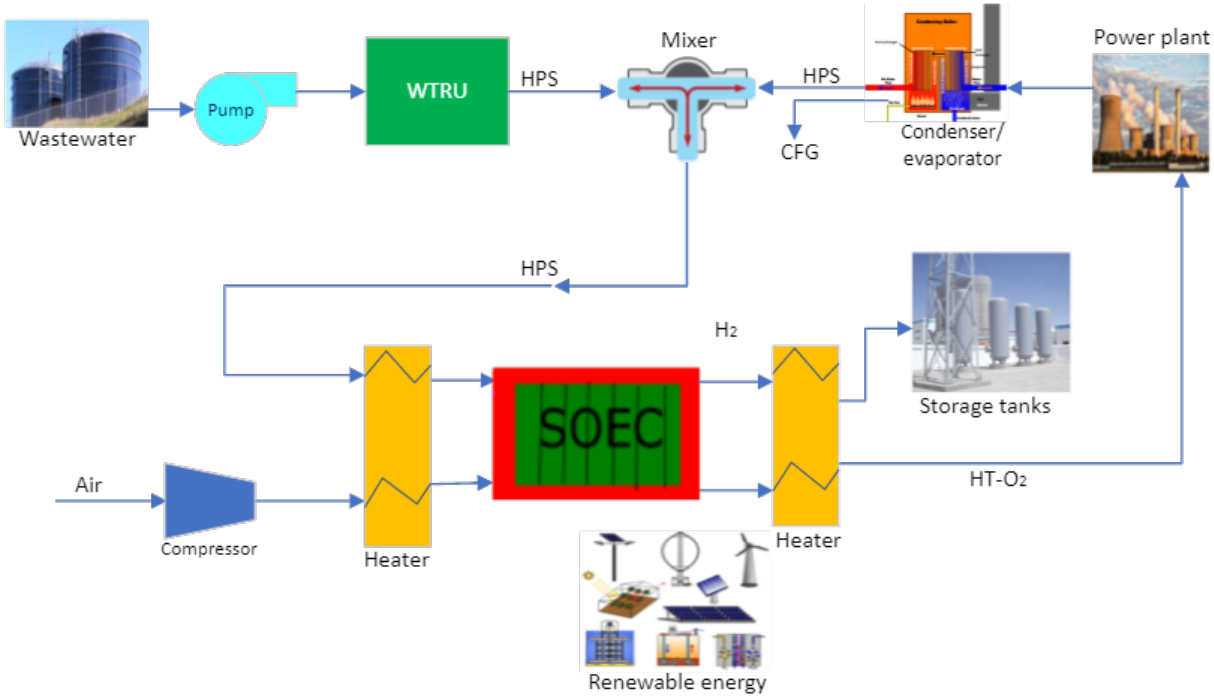


Fig 1: Water-energy integrated system for hydrogen production

In the upper section, high pressurized steam is generated from the wastewater reservoir after it is pumped to the water treatment and recovery unit (WTRU) where it is evaporated at atmospheric pressure and 101 ℃. This is mixed with the steam, which is concurrently generated from the power plant flue gas. The flue gas is cooled to 25℃ in the condenser for moisture recovery, and the heat regained is used in the WTRU. The recovered water is immediately evaporated and combined with the steam from the WTRU. The mixed stream is sent to the pre-heater to elevate its temperature to 750-850℃ before being fed into the SOEC to lower the required entropic heat for decomposition. Air from the ambient environment is compressed, preheated, and supplied to the system to flush out the produced oxygen from the electrolysis reactions in the SOEC. The exiting hydrogen product is stored in a compressed hydrogen tank.

The water decomposition reaction taking place in the SOEC is represented by the anodic oxidation and cathodic reduction reaction below

$$Anode: O^{2-} \rightarrow \frac{1}{2}O_2 + 2e^-$$

$$Cathode: H_2O \rightarrow H_2 + O^{2-}$$

$$Overall: H_2O \rightarrow H_2 + \frac{1}{2}O_2$$

Planar model configuration was used in the SOEC design with the system comprising of the balance of plant (BoP) such as condenser, heater, compressor, mixer, evaporator, separator, pump, heat exchanger to finally actualize a working model which are thermodynamically model using hysys. All other model assumptions are similar to that of Kazempoor and Braun[10].

RESULTS AND DISCUSSION

This section summarizes some of the important results of this work. The SOEC is in the developing stage, and this novel work is evaluated and validated. The system generated 242400 kg/day of hydrogen from the flue gas from a power plant with a capacity 333.7 MW. The voltage efficiency of the SOEC system is 92.9% at 850 ℃, and the overall thermal efficiency of the designed plant is 61.97%, which seems to be very prosperous compared to other plants of the same size. Even though it is shown from hysys that is potential to save over 25% of the utilized energy in the

system which reduces cost of production and optimize productivity. To live up to the progressive development in different sources of energy, the model is designed to be integrated with several energy sources. The Levelized cost of hydrogen (LCOH) production with some of these energy sources is evaluated and has shown in fig. 2. The LCOH ranges from $2.99-5.96/ kg hydrogen with the solar photovoltaic (P.V.) given the cheapest cost assuming the U.S. Department of Energy (DOE) target of 3 cent/kWh by 2020 and beyond. As such, the life cycle analysis (LCA) from cradle to gate for the plant is performed in SimaPro using the solar P.V. and the coal power plant to measure the severity of the environmental impact. Obviously, the COx emission with the coal power plant is higher. However, SimaPro revealed the higher effects of some other critical parameter factors like the human health, ecosystem and particulate matter formation associated with it. This puts solar P.V. and other renewable energy sources in the limelight.

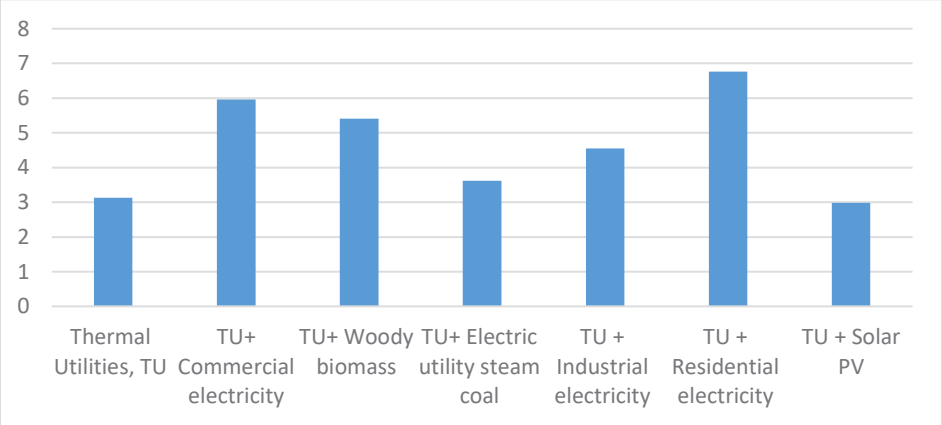


Fig. 2: Levelized cost of hydrogen with different feedstocks

CONCLUSIONS

The novel model designed in this work shows the possibilities of different energy integrations for hydrogen production and redefined a new approach to water-energy nexus. The LCOH of hydrogen can be as low as $2.99 per kg hydrogen, and this is a close route to meeting the DOE target for the cost of hydrogen for distribution and as potential energy storage. Further work needs to be embarked on to establish the exact environmental impact of large-scale hydrogen production to meet up the global requirement for sustainability and a green economy.

ACKNOWLEDGEMENT

This material is based upon work supported by the U.S. Department of Energy, under Award Number DE-FE0032005.

REFERENCES

1. K. Sutherland, "Drinking and pure water: Filtration improvements progress global clean water provision," *Filtration + Separation,* vol. 49, no. 2, pp. 12-16, 2012/03/01/ 2012, doi: https://doi.org/10.1016/S0015-1882(12)70098-8.
2. Y. Zhu *et al.*, "Life cycle water consumption for oxyfuel combustion power generation with carbon capture and storage," *Journal of Cleaner Production,* vol. 281, p. 124419, 2021/01/25/ 2021, doi: https://doi.org/10.1016/j.jclepro.2020.124419.
3. Z. Huang, X. Liu, S. Sun, Y. Tang, X. Yuan, and Q. Tang, "Global assessment of future sectoral water scarcity under adaptive inner-basin water allocation measures," *Science of The Total Environment,* vol. 783, p. 146973, 2021/08/20/ 2021, doi: https://doi.org/10.1016/j.scitotenv.2021.146973.
4. C. Wulf, J. Linssen, and P. Zapp, "Chapter 9-Power-to-Gas—Concepts, Demonstration, and Prospects, Editor (s): Catherine Azzaro-Pantel, Hydrogen Supply Chains," ed: Academic Press, 2018.
5. R. Navarro, R. Guil, and J. Fierro, "Introduction to hydrogen production," in *Compendium of Hydrogen Energy*: Elsevier, 2015, pp. 21-61.
6. M. Carmo, D. L. Fritz, J. Mergel, and D. Stolten, "A comprehensive review on PEM water electrolysis," *International Journal of Hydrogen Energy,* vol. 38, no. 12, pp. 4901-4934, 2013/04/22/ 2013, doi: https://doi.org/10.1016/j.ijhydene.2013.01.151.
7. M. Lehner, R. Tichler, H. Steinmüller, and M. Koppe, *Power-to-gas: technology and business models*. Springer, 2014.
8. X. Zhang *et al.*, "Towards a smart energy network: The roles of fuel/electrolysis cells and technological perspectives," *International Journal of Hydrogen Energy,* vol. 40, no. 21, pp. 6866-6919, 2015/06/08/ 2015, doi: https://doi.org/10.1016/j.ijhydene.2015.03.133.
9. O. Schmidt, A. Gambhir, I. Staffell, A. Hawkes, J. Nelson, and S. Few, "Future cost and performance of water electrolysis: An expert elicitation study," *International Journal of Hydrogen Energy,* vol. 42, no. 52, pp. 30470-30492, 2017/12/28/ 2017, doi: https://doi.org/10.1016/j.ijhydene.2017.10.045.
10. P. Kazempoor and R. J. Braun, "Model validation and performance analysis of regenerative solid oxide cells: Electrolytic operation," *International Journal of Hydrogen Energy,* vol. 39, no. 6, pp. 2669-2684, 2014/02/14/ 2014, doi: https://doi.org/10.1016/j.ijhydene.2013.12.010.

11. J. Nieminen, I. Dincer, and G. Naterer, "Comparative performance analysis of PEM and solid oxide steam electrolysers," *International Journal of Hydrogen Energy,* vol. 35, no. 20, pp. 10842-10850, 2010.
12. J. Laurencin, D. Kane, G. Delette, J. Deseure, and F. Lefebvre-Joud, "Modelling of solid oxide steam electrolyser: Impact of the operating conditions on hydrogen production," *Journal of Power Sources,* vol. 196, no. 4, pp. 2080-2093, 2011.
13. M. I. Aydin, A. E. Karaca, A. M. M. I. Qureshy, and I. Dincer, "A comparative review on clean hydrogen production from wastewaters," *Journal of Environmental Management,* vol. 279, p. 111793, 2021/02/01/ 2021, doi: https://doi.org/10.1016/j.jenvman.2020.111793.
14. C. H. Wendel, P. Kazempoor, and R. J. Braun, "A thermodynamic approach for selecting operating conditions in the design of reversible solid oxide cell energy systems," *Journal of Power Sources,* vol. 301, pp. 93-104, 2016/01/01/ 2016, doi: https://doi.org/10.1016/j.jpowsour.2015.09.093.
15. X. Jin and X. Xue, "Mathematical modeling analysis of regenerative solid oxide fuel cells in switching mode conditions," *Journal of Power Sources,* vol. 195, no. 19, pp. 6652-6658, 2010.
16. P. Kazempoor and R. Braun, "Model validation and performance analysis of regenerative solid oxide cells for energy storage applications: Reversible operation," *international journal of hydrogen energy,* vol. 39, no. 11, pp. 5955-5971, 2014.
17. K. Frick, D. Wendt, P. Talbot, C. Rabiti, and R. Boardman, "Technoeconomic assessment of hydrogen cogeneration via high temperature steam electrolysis with a light-water reactor," *Applied Energy,* vol. 306, p. 118044, 2022/01/15/ 2022, doi: https://doi.org/10.1016/j.apenergy.2021.118044.
18. K. Motazedi, Y. K. Salkuyeh, I. J. Laurenzi, H. L. MacLean, and J. A. Bergerson, "Economic and environmental competitiveness of high temperature electrolysis for hydrogen production," *International Journal of Hydrogen Energy,* vol. 46, no. 41, pp. 21274-21288, 2021/06/15/ 2021, doi: https://doi.org/10.1016/j.ijhydene.2021.03.226.
19. A. Mohammadi and M. Mehrpooya, "Techno-economic analysis of hydrogen production by solid oxide electrolyzer coupled with dish collector," *Energy Conversion and Management,* vol. 173, pp. 167-178, 2018/10/01/ 2018, doi: https://doi.org/10.1016/j.enconman.2018.07.073.

WHEC-2022
23rd World Hydrogen Energy Conference
June 26-30, 2022 - Istanbul

#180

PREPARATION AND ANALYSIS OF MEMBRANE ELECTRODE ASSEMBLIES FOR PEM WATER ELECTROLYSERS BASED ON LASER-GENERATED IRIDIUMOXIDE NANOPARTICLES AS ELECTROCATALYSTS FOR THE OXYGEN EVOLUTION REACTION

[1*] *Norbert Kazamer*, [2] *Sven Reichenberger*, [3] *Mathias Spree*, [1,4] *Ulrich Rost*, [2] *Meike Tack*, [5] *Tejas Bopardikar*, [1] *Florian Wirkert*, [1] *Haujin Salih*, [1] *Leonard Böhm*, [1] *Maximilian Cieluch*, [1,4] *Jeffrey Roth*, [5] *Tom Zoz*, [3] *Tim Hülser*, [2] *Stephan Barcikowski*, [1] *Michael Brodmann*

[1] Westphalian University of Applied Sciences Gelsenkirchen Bocholt Recklinghausen, Westphalian Energy Institute, Neidenburger Str. 43, 45897 Gelsenkirchen, Germany
[2] University Duisburg-Essen, Technical Chemistry I, Universitätsstr. 5, 45141, Essen, Germany
[3] Institut für Energie- und Umwelttechnik e.V. (IUTA), Bliersheimer Str. 58-60, 47229, Duisburg, Germany
[4] ProPuls GmbH, Neidenburgerstr. 10, 45897, Gelsenkichen, Germany
[5] ZOZ GmbH, Raiffeisenstr. 17, 57462, Olpe, Germany

*Corresponding author e-mail: norbert.kazamer@w-hs.de

ABSTRACT

One of the promising ways for green hydrogen production is polymer exchange membrane water electrolysis (PEMWE). To this day, precious metal electrocatalysts are necessary for high production rates in PEMWEs. Catalysts such as Ir/IrO_2 have been extensively studied for the oxygen evolution reaction, but their high costs and the scarcity of resources hinder their use on a large scale. In this work, we focussed on IrO_x nanoparticles produced by pulsed laser ablation as an electrocatalytic material with the potential of a low-cost production in large scale. Furthermore, we studied B-doped Si structures as promising support material for the IrO_x particles to enhance the precious metal utilisation. The laser-generated IrO_x and B-doped Si nanostructures were ultrasonically sprayed to achieve a homogeneous coating, that builds up the anode catalyst layer, showing a high catalytic activity and promising kinetic parameters. In-situ analysis performed in a self-developed PEMWE are planned to validate the electrochemical results.

Keywords: polymer exchange membrane, electrolysis, synthesis, IrO_x, Si:B

INTRODUCTION

Electrocatalysts will play an important role in energy conversion processes as they increase the efficiency, production rate and selectivity of the involved transformation [1]. Electrocatalytic water splitting through oxygen evolution reaction (OER) and hydrogen evolution reaction are a promising technique to trigger the penetration of green technologies into the everyday life. Catalysts based on precious metals like Ir or its alloys are needed for the acidic environment and high anodic potentials have been extensively studied for the OER in PEMWEs [2]. The state-of-the-art Ir loadings in the range of 1-3 mg cm^{-2} need to be reduced due to the high costs and the limited availability of these materials.

Chemical reduction techniques are a common way to produce Ir nanoparticles for the later application as catalysts in PEMWE. Such materials are commercially available and being used for both the preparation of anodic catalyst layers (ACLs) and the membrane electrode assemblies (MEAs). In order to reduce costs by reducing noble metal loadings in PEMWE, recent studies report on e.g. increasing the utilisation of Ir due to advanced ACL architectures. Much like the carbon supported platinum catalysts which are state-of-the art in PEM fuel cells, one promising way to design elaborated ACLs is to favor Ir nanoparticles on support structures like e.g., SnO_2-Sb that were reported to be stable in PEMWE anodes [3]. By this, it is possible to enlarge the mass specific electrochemical active surface area and, thus, enable more active sites for the OER compared to unsupported catalyst nanoparticles. Nevertheless, as tin oxide is an n-type semiconductor, it as a low conductivity at room temperature and a relatively low anodic stability.

In this work, we report ACL for PEMWE based on laser generated Ir nanoparticles supported on boron-doped Si nanoparticles synthesized in a hot-wall reactor. Additionally, MEAs are prepared utilising the laser-generated Ir nanoparticles and in-situ characterised in a PEMWE test cell. Hence, in this work we focus on a novel Si nanostructure for the use as Ir support material. To induce an electrical conductivity of the support, Si was doped with boron before getting decorated with Ir nanoparticles. The analyses of Ir/Si:B catalysts are also given and compared with the results of unsupported Ir.

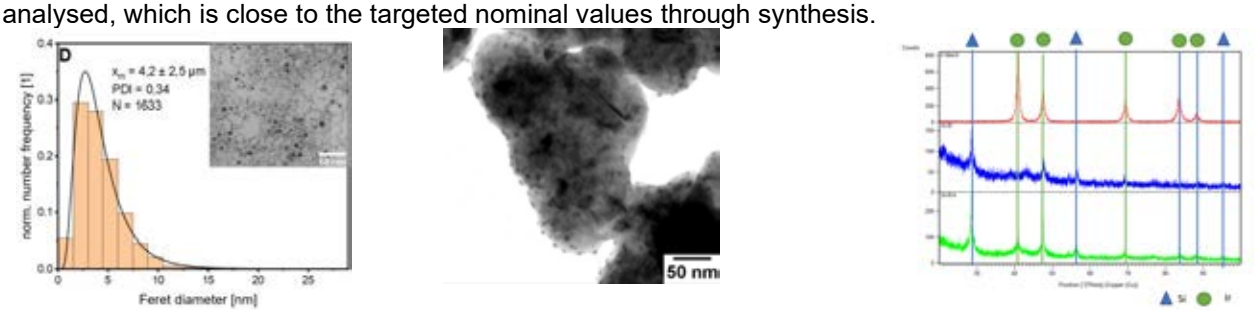
MATERIALS AND METHODS

A porous titanium transport layer (PTL) containing a diffusion bonded microporous Ti sintered powder plate was used as electrode substrate [4]. The design offers a large specific surface area and improved gas and water transport within the structure of the electrode.

For the catalyst preparation, surfactant-free iridium nanoparticles shown in Fig. 1(a) were synthesized by of colloidal nanoparticles in water. Parameters like the zeta potential, particle size, crystal structure and oxidation were determined [5]. On the other hand, doped silicon nanopowder has been synthesized by thermal decomposition of the gaseous precursors monosilane (SiH_4) and 6 at. %-diborane (B_2H_6) in argon, respectively. The incorporation of the p-type dopant boron, with an atom concentration of about 3 at.% is assumed to form a degenerated semiconductor. After the synthesis, Si:B material was loaded with 10 wt. % Ir nanoparticles, as displayed in Fig. 1(b), by a colloidal adsoption at pre-adjusted pH-value following an established colloidal procedure [5].
The obtained IrO_x and Ir-decorated Si:B 6 at. % nanoparticles were dispersed in a water based ink and sprayed on the substrate via an ultrasonic spray head in an Ar atmosphere, as schematically shown in Fig. 2(a) and Fig. 2(b). Physical characterisation was performed via scanning electron microscopy (SEM) and x-ray diffractometry (XRD). Linear sweep voltammetry methods in a three-electrode electrochemical cell were performed to determine the kinetics of the OER. Through-plane measurements were performed at 80°C and different pressures to investigate the electrical conductivity of the prepared electrode in an environment close to the one of a PEMWE. Finally, in-situ tests were performed in a self-developed single cell PEMWE based on hydraulic cell compression, facilitating an ideal contact between the materials.

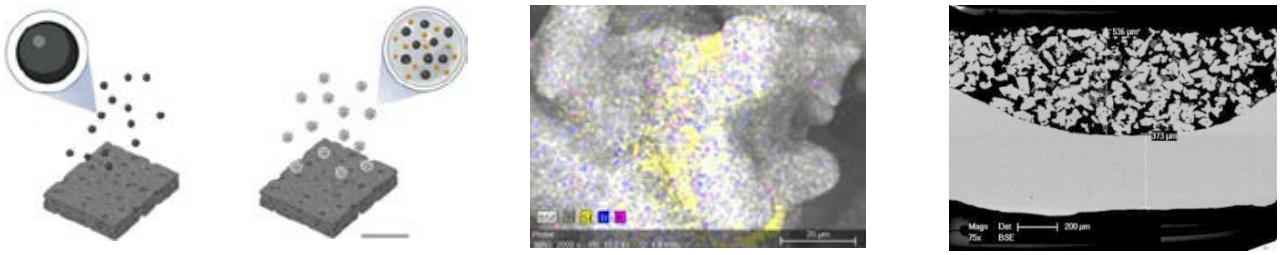
RESULTS AND DISCUSSION

A succesful synthesis of colloidal 4 nm nanoparticles was obtained (Figure 1(a)). Exemplifying TEMs from Fig. 1(a) and Fig. 1(b) confirm the nanostructure of the iridium and thereof gained Si:B-Ir catalysts, respectively. The XRD measurements reveal the structure of silicon and. Boron is not observed since it is incorporated into the Si lattice. A possible shift of the Si diffraction peaks, due to B incorporation cannot be resoluted due to the widening of the peaks caused by nanostructured Si crystals. The XRD measuremets validate a succesful Si synthesis and the nanoparticle decoration, without the formation of an alloyed phase. Plasma atomic emission spectroscopy tests confirmed the chemical composition of the Si:B-Ir nanopowders, an average of 86 wt. % Si, 4.6 wt. % B and 8.5 wt. % Ir being analysed, which is close to the targeted nominal values through synthesis.



(a) (b) (c)

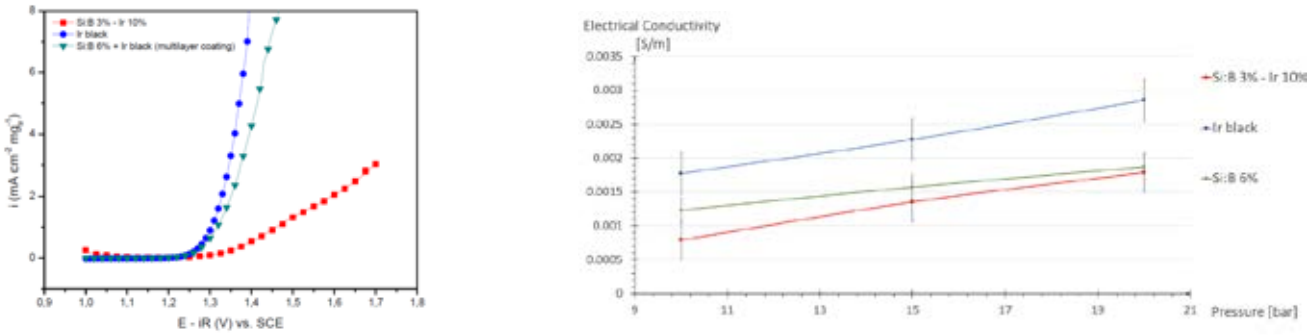
Fig. 1 Micrographs of the (a) laser-generated IrO_x nanoparticles, the (b) thereof synthetized Si:B-Ir electrocatalysts and (c) XRD measurements of the developed powders in comparison with a reference pure metallic Ir material



(a) (b) (c) (d)

Fig. 2 Idealistic view of the (a) IrO_x and (b) Si:B-Ir nanoparticles deposition on the substrate and the nanoparticle coated Ti PTL in (c) top and (d) cross-section view

The SEM from Fig. 2(b) show the distribution of the Ir nanocatalyst on the Ti PTL (cross-section view in Fig. 2(d)) indicating a high-quality catalytic layer. The tendency of formation of Si:B agglomerates was as well observed. It is imperatively that the interconnection of Si based agglomerates allow for an electrically conductive path through the electrode. Electrochemical measurements of the nanoparticles sprayed on the Ti-PTL (Fig. 3(a)) showed a promising electrocatalytic activity towards OER. Moreover, through-plane electrical conductivity measurements (Fig. 3(b)) of the sprayed electrodes show similar values to the ones of the reference Ir black material, being a good sign for in-situ measurements.



(a) (b)

Fig. 3 (a) Linear sweep voltamograms of 1 cm^2 Ti PTL samples performed at room temperature in 0.5M H_2SO_4 (pH ≈ 0.3), E_{step} 5 mV s^{-1}, scanrate 5 mV s^{-1} and (b) through plane electrical conductivity measurements performed on 2 cm^{-2} samples at 80°C

The ongoing research covers a complete and innovative chain of electrode preparation to be used in PEM electrolysis technology from powder production, deposition using a novel method and comprehensive characterization.

CONCLUSIONS

The whole process chain is a very promising approach to qualify electrocatalysts for environmentally friendly and cost-effective energy conversion as the minimal use of the high-priced novel catalyst revealed encouraging performances. Further work is being carried out to complete the measurements with the above-described methods for both approaches and to validate the performance of the synthesised nanoparticles through in-situ tests in self-built PEMWE

ACKNOWLEDGEMENT

The project LIKELY is funded under the framework of “Leitmarkt NeueWerkstoffe.NRW” by the European Regional Development Fund (EFRE.NRW) (contract EFRE-0801480) and the state government of North Rhine-Westphalia. Furthermore, we thank Prof. Dr. Deniz Kurumlu, Prof. Dr. Michael Schlüter and Mr. Christian Stromberg for using the infrastructure of their laboratories to conduct a part of the experimental work for the present research.

REFERENCES

1. U.P.M. Ashik, A. Viswan, S. Kudo, J. Hayashi, Chapter 3 - Nanomaterials as Catalysts, in: S. Mohan Bhagyaraj, O.S. Oluwafemi, N. Kalarikkal, S. Thomas (Eds.), Applications of Nanomaterials, Woodhead Publishing, 2018: pp. 45–82. https://doi.org/10.1016/B978-0-08-101971-9.00003-X.
2. M. Carmo, D.L. Fritz, J. Mergel, D. Stolten, A comprehensive review on PEM water electrolysis, International Journal of Hydrogen Energy. 38 (2013) 4901–4934. https://doi.org/10.1016/j.ijhydene.2013.01.151.
3. P. Bhanja, B. Mohanty, A.K. Patra, S. Ghosh, B.K. Jena, A. Bhaumik, IrO2 and Pt Doped Mesoporous SnO2 Nanospheres as Efficient Electrocatalysts for the Facile OER and HER, ChemCatChem. 11 (2019) 583–592. https://doi.org/10.1002/cctc.201801312.
4. S. Stiber, H. Balzer, A. Wierhake, F.J. Wirkert, J. Roth, U. Rost, M. Brodmann, J.K. Lee, A. Bazylak, W. Waiblinger, A.S. Gago, K.A. Friedrich, Porous Transport Layers for Proton Exchange Membrane Electrolysis Under Extreme Conditions of Current Density, Temperature, and Pressure, Advanced Energy Materials. 11 (2021) 2100630. https://doi.org/10.1002/aenm.202100630.
5. V. Amendola, D. Amans, Y. Ishikawa, N. Koshizaki, S. Scirè, G. Compagnini, S. Reichenberger, S. Barcikowski, Room-Temperature Laser Synthesis in Liquid of Oxide, Metal-Oxide Core-Shells, and Doped Oxide Nanoparticles, Chemistry – A European Journal. 26 (2020) 9206–9242. https://doi.org/10.1002/chem.202000686.

WHEC-2022
23rd World Hydrogen Energy Conference
June 26-30, 2022 - Istanbul

#183

ELECTRODEPOSITION OF A Ni-Mo ALLOY CATALYST WITH OPTIMIZED Mo-CONTENT FOR HYDROGEN EVOLUTION REACTION IN AEM-ELECTROLYSIS

[1] Leonard Böhm, [1] Klaus Thielker, [1] Norbert Kazamer, [1] Florian Wirkert, [1] , Ulrich Rost[1], Gabriela Marginean[2], Ulf-Peter Apfel[3,4], Michael Brodmann[1]*

[1]Westphalian University of Applied Sciences Gelsenkirchen Bocholt Recklinghausen, Westphalian Energy Institute, Neidenburger Str. 43, 45897 Gelsenkirchen, Germany

[2]Westphalian University of Applied Sciences Gelsenkirchen Bocholt Recklinghausen, Department of Materials Science and Testing, Neidenburger Str. 43, 45897 Gelsenkirchen, Germany

[3]Ruhr University Bochum, Inorganic Chemistry 1, Universitätsstraße 150, 44801 Bochum, Germany

[4]Fraunhofer UMSICHT, Osterfelder Str. 3, 46047 Oberhausen

*Corresponding author e-mail: leonard.boehm@w-hs.de

ABSTRACT

Various aqueous citrate electrolyte compositions for the Ni-Mo electrodeposition are explored in order to deposit Ni-Mo alloys with Mo-content ranging from 40 wt% to 65 wt% to find an alloy composition with superior catalytic activity towards the hydrogen evolution reaction (HER). The depositions were performed on copper substrates mounted onto a rotating disc electrode (RDE) and were investigated via scanning electron microscopy (SEM), X-ray fluorescence (XRF) and X-ray diffraction (XRD) methods as well as linear sweep voltammetry (LSV) and impedance spectroscopy. Kinetic parameters were calculated via Tafel analysis. Partial deposition current densities and current efficiencies were determined by correlating XRF measurements with gravimetric results. The variation of the electrolyte composition and deposition parameters enabled the deposition of alloys with Mo-content over the range of 40-65 wt%. An increase in Mo-content in deposited alloys was recorded with an increase in rotation speed of the RDE. Current efficiency of the deposition was in the magnitude of <1%, which is characteristic for the deposition of alloys with high Mo-content. The calculated kinetic parameters were used to determine the Mo-content with the highest catalytic activity for use in the HER.

Keywords: Anion Exchange Membrane Electrolysis, Nickel, Molybdenum, Electrodeposition, Hydrogen Evolution Reaction

INTRODUCTION

Hydrogen production via proton exchange membrane electrolysis (PEM) is a well established and commercially available technology, although still at a smaller scale than alkaline electrolysis. In an attempt to combine the benefits of both technologies, anion exchange membrane electrolysis (AEM) was created enabling high current densities like PEM-electrolyzers without the reliance on noble metal catalysts or highly concentrated and corrosive electrolytes, thus reducing the cost of the technology. [1]

Avoiding noble metal catalysts would also allow to replace platinum on the cathode side with cheaper materials, e.g. transition metal catalysts. Especially, Ni-Mo alloys showed superior activity for use in alkaline media for HER. For example, Xiao et al. reported one of the first AEM-cells with a pure water feed using Ni-Mo cathodes [2].

One technique to apply the catalyst material to the electrode that has already been used in PEM-electrolysis [3] is electrodeposition. This technique ensures that all catalyst particles are electrically connected to the substrate, thus, increasing catalyst utilization in the cell. Electrodeposition for Ni-Mo alloys is being researched for corrosion protection and HER catalysts. It follows the mechanism of induced co-deposition. Mo can only be deposited in the presence of transition metals like Ni and typically alkaline citrate baths are used [4].

An increase in the catalytic activity of electrodeposited NiMo alloys towards the HER has been reported with an increase in Mo-content from 10-40 wt% [5]. Decreasing activity has been reported with increasing Mo-content from 65-82 wt% [6]. For non-electrodeposited alloys an optimum was found at 50 wt% Mo-content [7]. Herein we showcase the creation and performance of electrodes with a Mo-content of 40-65 wt%, determined via physical and electrochemical characterization of the obtained electrodes.

EXPERIMENTAL

Manufacturing

An aqueous citrate bath with sodium hydroxide adapted from the work of Sun and Podlaha [6] was used as a base electrolyte. It contained 0.02 M nickel sulfate hexahydrate ($NiSO_4$ * 6 H_2O), 0.04 M sodium molydbate dihydrate (Na_2MoO_4 * $2H_2O$), 0.25 M tri-sodium citrate dihydrate ($C_6H_5Na_3O_7$ * 2 H_2O). The pH was adjusted via sodium hydroxide (NaOH) in the range of 8-10. Concentrations from the base electrolyte were varied in order to examine their effect on the alloy deposition and create different alloy compositions. Copper substrate discs with an exposed area of 1,3 cm² were used as the working electrodes for the deposition. A rotating disc electrode (RDE) serving as working electrode enabled defined hydrodynamics and better mass transport for the deposition, via variation of the rotation speed. A platinum wire served as the counter electrode. The deposits were created galvanostatically with an Ivium Vertex potentiostat with varied current densities. The substrates were polished and degreased before deposition.

Analysis

For the physical characterization of the samples, scanning electron microscopy (SEM), X-ray fluorescence spectroscopy (XRF) and X-ray diffractometry (XRD) measurements were conducted. Energy dispersive X-ray spectroscopy (EDS) mappings were conducted, to observe the distribution of the alloy components. XRF measurements were used to determine the composition of the deposited layers on a larger surface area. Based on these results and the loading of the samples, the current efficiency and partial deposition current densities of the metals and side reactions were calculated. Crystallographic information was obtained via XRD measurements.
For electrochemical characterization linear sweep voltammetry (LSV) measurements were conducted in an alkaline environment (1 M KOH) at AEM operating temperature (80°C). From these voltammograms Tafel plots were derived, to determine the kinetic parameters Tafel slope b, charge transfer coefficient α and exchange current density i_0. Moreover, impedance spectroscopy was performed in order to characterise the electrode-electrolyte interface.

RESULTS AND DISCUSSION

Effect of deposition parameters

The variation of different deposition parameters was analyzed in order to find effects of the parameters on the deposition and interactions between them. To achieve this, a response surface methodology design of experiments technique was used to create the experimental design for this study. The effect of the rotation speed on Mo- and Ni-content from preliminary experiments with lower Mo-content can be seen in Table 1. Increasing the mass transport of Molybdenum to the electrode surface via RDE increased the Mo-content in the alloys, analogous to reports on a rotating cylinder electrode [4].

Table 1. Effect of rotation speed on Mo- and Ni-Content in the alloy, determined by XRF

Rotation speed [1 min^{-1}]	Mo-Content [wt%]	Ni-Content [wt%]
0	10,3	89,7
2000	21,9	78,1
3000	24,0	76,0

Physical characterization

The physical characterization revealed the morphology of the samples and gave further information about the effects of the deposition parameters on the deposited alloy. Preliminary experiments with a slightly lower Mo-alloy content showed a homogeneous distribution of the components in the deposited alloy, presented in Fig. 1.

Electrochemical characterization

For the deposited alloys LSV was performed to evaluate their catalytic activity and find an optimum alloy composition with superior activity towards the HER. The cathodic sweeps were performed at AEM operating temperature to determine the overpotential of the HER on the prepared electrodes at defined current densities under operating conditions. To further examine the catalytic properties of the electrodes, Tafel plots were derived. The kinetic parameters charge transfer coefficient α and the Tafel slope b elucidate the reaction mechanism and allow for the determination of the rate determining step of the reaction. Additionally, the exchange current density i_0 in combination with the Tafel slope b describe the kinetic behaviour of the electrode, thus enabling comparisons between electrodes and reference samples to find optimal catalytic activity.

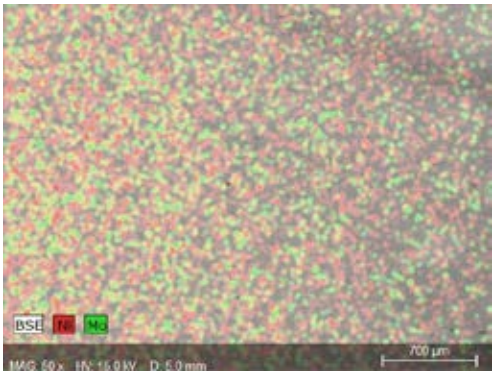


Fig. 1. EDS mapping revealing Ni- and Mo-distribution

CONCLUSIONS

The deposited NiMo alloys with Mo-contents in the range of 40-65 wt% showed promising physical and electrochemical properties for HER. The EDS-mapping revealed a quasi-homogeneous distribution of the alloy components. Additionally, the mass transport of the deposition was improved via RDE, resulting in increased transport of Mo-species to the electrode and thus increasing the Mo-content of the alloy.

ACKNOWLEDGMENT

The present work has been carried out under the project “Alkalische Membranelektrolyseure mit hydraulischer Verpressung (AEMruhr)”, being financially supported by the German Federal Ministry of Education and Research (contract number: 13FH06I62IA). Furthermore, we thank Prof. Dr. Deniz Kurumlu, Prof. Dr. Michael Schlüter and Mr. Christian Stromberg for using the infrastructure of their laboratories to conduct a part of the experimental work for the present research.

REFERENCES

1. Vincent I, Bessarabov D. Low cost hydrogen production by anion exchange membrane electrolysis: A review. Renewable and Sustainable Energy Reviews. 2018 Jan 1;81:1690–704.
2. Xiao L, Zhang S, Pan J, Yang C, He M, Zhuang L, et al. First implementation of alkaline polymer electrolyte water electrolysis working only with pure water. Energy Environ Sci. 2012 Jun 20;5(7):7869–71.
3. Park H, Choe S, Kim H, Kim D-K, Cho G, Park Y, et al. Direct fabrication of gas diffusion cathode by pulse electrodeposition for proton exchange membrane water electrolysis. Applied Surface Science. 2018 Jun 30;444:303–11.
4. Podlaha EJ, Landolt D. Induced Codeposition: I. An Experimental Investigation of Ni-Mo Alloys. J Electrochem Soc. 1996 Mar 1;143(3):885.
5. Manazoğlu M, Hapçı G, Orhan G. Effect of electrolysis parameters of Ni–Mo alloy on the electrocatalytic activity for hydrogen evaluation and their stability in alkali medium. J Appl Electrochem. 2016 Feb 1;46(2):191–204.
6. Sun S, Podlaha EJ. Electrodeposition of Mo-Rich, MoNi Alloys from an Aqueous Electrolyte. J Electrochem Soc. 2011 Dec 20;159(2):D97.
7. Jakšić JM, Vojnović MV, Krstajić NV. Kinetic analysis of hydrogen evolution at Ni–Mo alloy electrodes. Electrochimica Acta. 2000 Aug 31;45(25):4151–8.

WHEC-2022
23rd World Hydrogen Energy Conference
June 26-30, 2022 - Istanbul

#187

UPSCALING HIGH PERFORMANCE 3-D ELECTRODES FOR ALKALINE WATER ELECTROLYSIS TOWARDS NEAR-INDUSTRIAL CONDITIONS

[1*] *Renaud Delmelle,* [1] *Fernando Rocha,* [1] *Christos Georgiadis,* [2] *Jonathan Lambrechts and* [1] *Joris Proost*
[1]Université catholique de Louvain (UCLouvain), Institute of Mechanics, Materials and Civil Engineering, Division of Materials and Process Engineering, Place Sainte-Barbe, 2, 1348 Louvain-la-Neuve, Belgium
[2]Université catholique de Louvain (UCLouvain), Institute of Mechanics, Materials and Civil Engineering, Division of Applied Mechanics and Mathematics, Avenue Georges Lemaître, 4-6, 1348 Louvain-la-Neuve, Belgium

*Corresponding author e-mail: renaud.delmelle@uclouvain.be

ABSTRACT

Initial laboratory results using 3-D electrodes with forced electrolyte flow indicate a significant process intensification potential. This work aims to validate this process intensification on a larger scale, using a pilot-scale alkaline water electrolyser with a 6 kW cell stack working in the ranges 5-10 bar, 20-70°C and with 30% KOH. This pilot plant is also representative of industrial electrolysers in terms of gas collection, cell stacking and current distribution. In addition, it has been modified to allow for forced electrolyte flow using KOH compatible pumps.

The pilot system was first validated using standard 2-D electrodes and showed state-of-the-art results. Various cell stacks with 3-D electrodes were then tested under conditions of forced flow, showing interesting intensification potential. However, obstacles in terms of stack design still limit the flow effect. The latter are currently being tackled using CFD simulation tools.

Keywords: 3-D Electrodes, Alkaline Water Electrolysis, Pilot Demonstration, Process Intensification.

INTRODUCTION

Alkaline water electrolysis is a technology that is well proven, rather simple, mature and reliable. But the power density remains critically low. Previous work done in our group highlighted the synergetic effect of simultaneously using 3-D electrodes and forced electrolyte flow, leading to significant process intensification [1].

3-D electrodes, whose active surface is at least an order of magnitude larger than 2-D electrodes for the same projected surface, reduce the overpotential of the electrochemical reaction. But under natural convection, gas bubbles remain trapped inside these 3-D macroporous structures, which counterbalances their intrinsic advantage. Implementation of a forced electrolyte flow through the electrodes is therefore necessary in order to take full advantage of their increased surface area.

The present work describes the modifications done on a near industrial-scale electrolyser to allow the use of 3-D electrodes and forced electrolyte flow. State-of-the-art results were obtained using standard commercial 2-D electrodes, notably with no significant influence of the forced flow, as expected. Cell stacks with 3-D electrodes were then mounted and tested under varying conditions of forced flow. The flow effect is clearly present, but it is significantly weaker than what was previously obtained at the lab scale. The reason behind this performance gap clearly lies in the stack design, which is currently being improved through computational modeling. Furthermore, the effect of the 3-D stack configuration – i.e. pore size of both porous transport layers and catalyst layers – will also be reported.

MATERIALS AND METHODS

Fig. 1a shows a picture of the alkaline water electrolysis pilot system installed in our lab. It was initially a HyStat electrolyser from Hydrogenics. It has a flexible cell stack (up to 24 units) with a projected surface area of 314 cm². The standard 2-D electrodes are state-of-the-art catalyst-coated expanded nickel electrodes with a nickel mesh as pre-electrodes. The membranes are Zirfon Perl commercialized by Agfa. Without the use of pumps, the produced gas bubbles rise gravitationally to the liquid-gas separator, dragging some electrolyte with them. Fig. 1b shows the MagnoChem pumps with PumpDrive R variators, commercialized by KSB, that were added to allow forcing the electrolyte flow. The electrolyte flows back to the cell stack after the liquid-gas separator. The applied electrical field is perpendicular to the electrolyte flow (flow-by configuration).

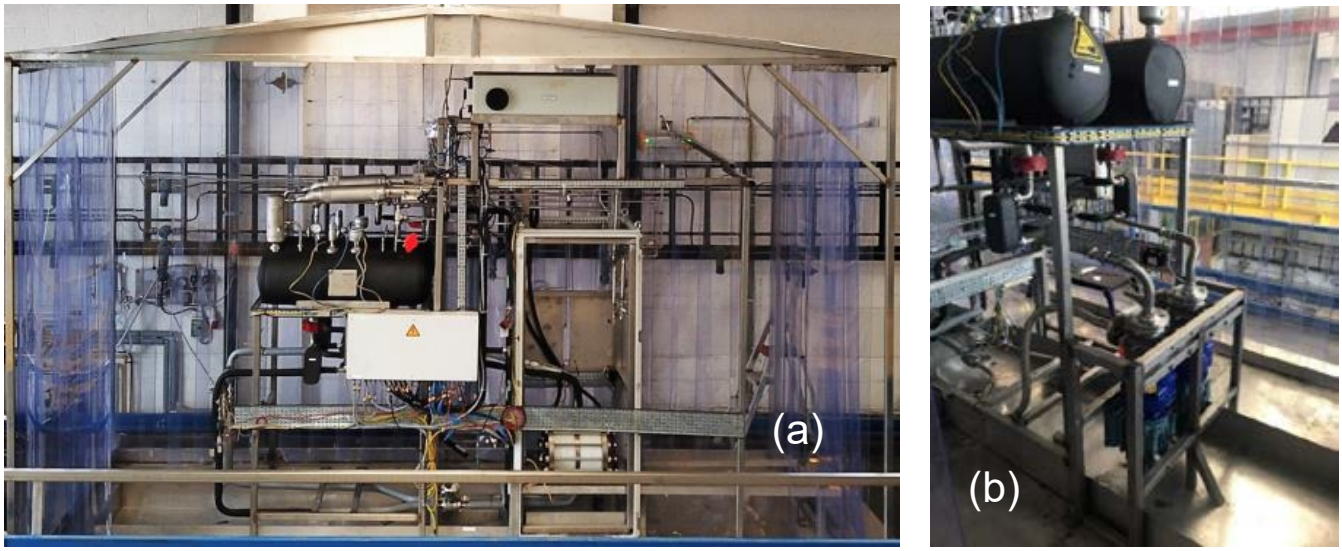


Fig. 1. (a) Picture of the pilot plant alkaline water electrolysis system and (b) added pumps used for forcing electrolyte flow.

The pilot allows applying a fixed current (DC), between 70 A and 140 A. The resulting cell stack voltage is obtained by measuring the voltage between the center of the stack and each end of the cell stack. For each applied current, one obtains the evolution of two voltages, one for each half stack, as shown in Fig. 2a. By dividing the applied current by the projected surface area, one obtains the applied projected current density. The average cell voltage for each half stack is in turn obtained by dividing the measured half-cell stack voltages by the number of cells in the half stack (12), as shown in Fig. 2b.

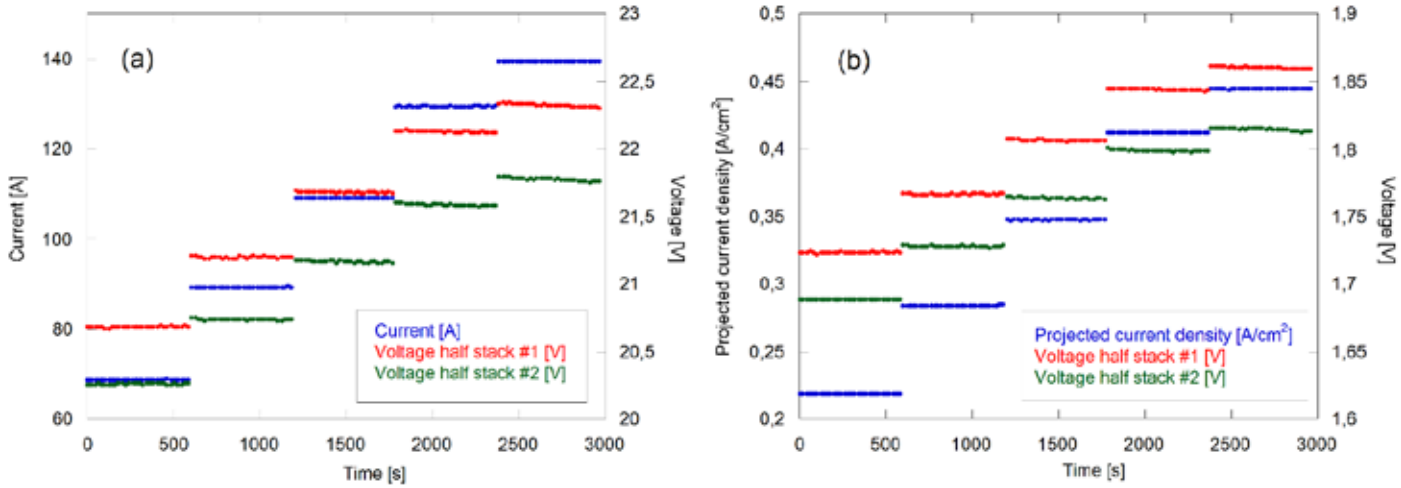


Fig. 2. (a) Applied current and resulting voltage on each half stack with standard 2-D electrodes at 6 bar and 40°C and (b) corresponding projected current density and cell voltage per stack. No forced flow.

RESULTS AND DISCUSSION

Fig. 3 shows the cell voltage of a custom 8-cell stack in benchmark conditions, where the standard 2-D electrodes have been replaced by 3-D nickel foams with 450 µm and 580 µm pore size. Each point in this figure is the average output voltage of a galvanostatic step, the latter being performed in the range 40-200 A. Unlike the projected current density in Fig. 2, Fig. 3 displays the cell voltage as a function of the so-called electrochemical current density j_{ECSA}, i.e. taking into account the entire electrochemical surface area (ECSA) of the 3-D catalyst layer.

The effect of pore size is clearly visible in Fig. 3, and confirms what we previously observed at the lab scale: big pore sizes allow for a more effective evacuation of gas bubbles, in turn exhibiting more surface area than small pore sizes. This observation can be extended to the porous transport layer (PTL), since, when the classic nickel mesh is replaced by a 580 µm pore size nickel foam, the cell voltage increases as bubble removal is less effective.

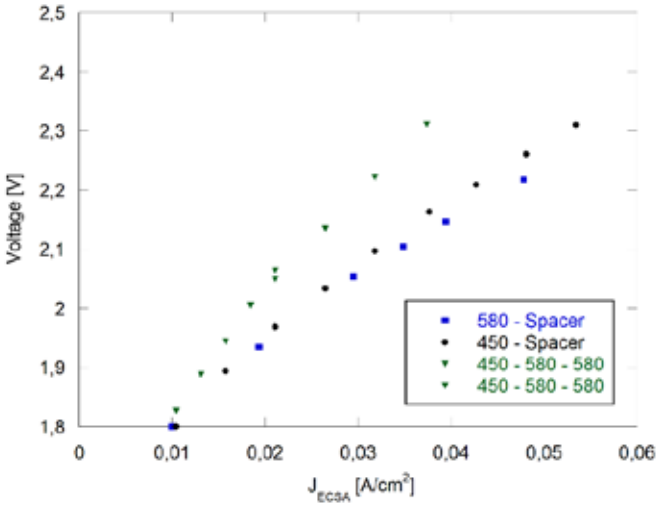


Fig. 3. Cell voltage as a function of j_{ECSA} at 6 bar and 70°C for three different nickel foam electrode configurations: 580 µm pore size as catalyst layer and nickel mesh (spacer) as PTL (blue), 450 µm pore size as catalyst layer and nickel mesh as PTL (black) and 450 µm pore size as catalyst layer and 580 µm pore size as PTL (green, two different data series). Forced flow: 560 L/h.

However, as explained above, the effect of forced flow on the cell voltage is much weaker than expected at the pilot plant. Limitations of the current cell design clearly appear when looking at the CFD simulations of the flow velocity in Fig. 4: the flow is turbulent when considering no friction on the walls, and inhomogeneous with friction. Bubble removal is clearly not optimal in such cases. Alternative stack designs are currently being considered.

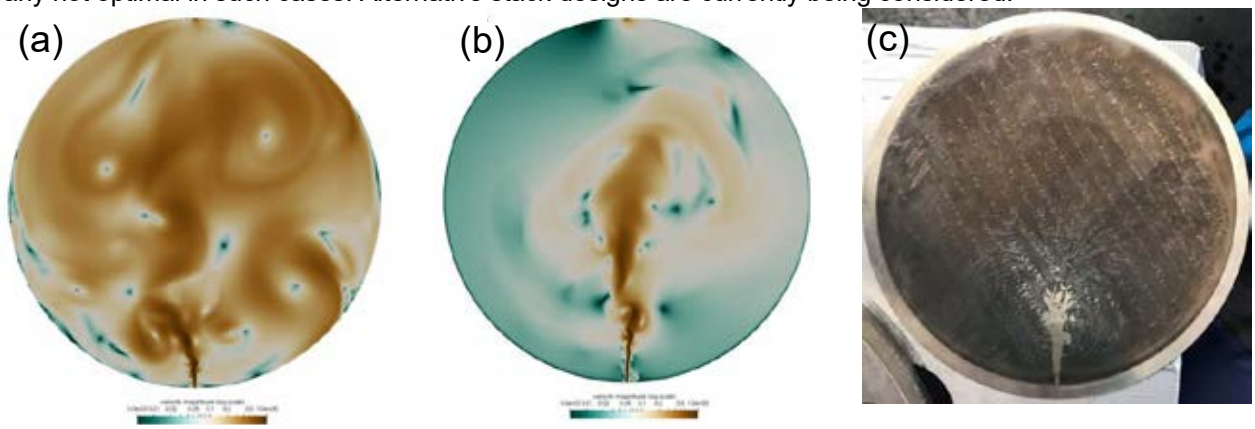


Fig. 4. Velocity Field [m/s] simulated by CFD for an empty cell (10 mm radius, 6 mm thickness) (a) without and (b) with friction on the cell walls. Picture (c) shows the pattern left by the electrolyte on a bipolar plate after experiments at the pilot plant.

CONCLUSIONS

An alkaline water electrolysis pilot plant was successfully adapted to forced electrolyte flow and 3-D electrode systems. The results not only confirm state-of-the-art data for industrial applications using 2-D electrodes, but also reliably reproduce results obtained at the laboratory scale on 3-D electrodes, notably highlighting the importance of PTL and catalyst layer design for effective bubble removal. Further design changes are necessary to unravel the full potential of forced flow.

ACKNOWLEDGEMENT

The authors acknowledge financial support of the European Commission Horizon 2020 programme – topic LC-NMBP-29-2019: Materials for non-battery based energy storage – through the NEXTAEC project.

REFERENCES

1. de Radiguès Q, Thunis G and Proost J. 2019. On the use of 3-D electrodes and pulsed voltage for the process intensification of alkaline water electrolysis. International Journal of Hydrogen Energy 44:29432-29440.

WHEC-2022
23rd World Hydrogen Energy Conference
June 26-30, 2022 - Istanbul

#205
ACTIVITY OF ELECTRODEPOSITED RHODIUM IN ACIDIC AND BASIC WATER ELECTROLYSIS

[1*] *Ryan Bonifacio,* [2] *Manolo Mena,*
[1,2] Department of Mining, Metallurgical and Materials Engineering, College of Engineering,
University of the Philippines Diliman, Quezon City, Philippines

*Corresponding author e-mail: ryan.bonifacio@up.edu.ph

ABSTRACT

Hydrogen is increasingly seen as a future fuel and a potential alternative to fossil fuels, as it is the cleanest and ideal energy carrier. Water electrolysis is one of the easiest methods to produce hydrogen, offering the advantage of simplicity. Rhodium is considered one of the best electrocatalysts for water electrolysis. This research was conducted to investigate the activity of electrodeposited Rh for its potential electrocatalytic application in acidic and basic water electrolysis. The electrode was fabricated from a 5g/L solution of $Rh_2(SO_4)_3$ electrodeposited at 3.00V for 3mins in a 92.5% Ag alloy substrate. Electrochemical characterizations were performed using cyclic voltammetry in a three-electrode set-up. The acidic electrolyte was a H_2SO_4 solution while the basic electrolyte was a NaOH solution. Results showed onset potentials of 1.4V and -0.2V for acidic OER and HER, respectively, while 0.6V and -0.9V for basic OER and HER, respectively. Consistent absolute value of limiting current, 8.00 x 10^{-3}A was observed for both reactions of the two electrolytes.

Keywords: Water Electrolysis, Cyclic Voltammetry, OER, HER

INTRODUCTION

Growing interest in renewable energy sources is an action to solve global energy crisis. As the development progresses, the need for energy storage system also increases. Hydrogen is a promising method to store energy. It can be produced through water electrolysis, a well-established conventional technology. The process requires a suitable electrocatalyst that provides the minimum possible overpotential to overcome various activation barriers. Inert metals like Rhodium are considered to be the best electrocatalysts. This study aimed to investigate the activity of Rhodium in an electrodeposit form when used as electrocatalyst in acidic and basic water electrolysis.

MATERIALS AND METHODS

The electrode is prepared by electrodepositing a thin coating of Rh in a 92.5% Ag alloy using a 5g/L solution of $Rh_2(SO_4)_3$. The electrodeposition was carried out in a two-electrode set-up, utilizing a Pt foil as non-consumable anode. The temperature during the process was maintained at 50°C. Optimal deposition parameter was identified to be 3V (0.587A) for 3mins deposition time.

The behavior of electrodeposited Rh has been investigated using cyclic voltammetry. A three-electrode electrochemical cell set-up with Ag/AgCl in KCl solution as reference electrode, Pt foil as counter electrode, and electrodeposited Rh as working electrode was employed. Voltammetric cycles were done at room temperature with scan rate of 25mV/s. Scans were started and ended at 0V potential. Measurement for acidic water electrolysis was done using 0.5M H_2SO_4 solution, with upper and lower vertex potentials of 2.0V and -1.0V, respectively. For basic water electrolysis, electrolyte was a 0.5M NaOH solution, upper vertex potential was 1.0V, and lower vertex potential was -1.5V. Short CV scans at the identified hydrogen and oxygen evolution regions were performed to assess stability of the electrode.

RESULTS AND DISCUSSION

Using Nernst equation, the operating voltage needed for a successful electrodeposition of Rh was identified to be greater than 1.861V to include the sum of overpotentials. Different combinations of deposition time and operating voltage were conducted. Results of experiment for Rh electrodeposition revealed the optimal parameter of 3V (0.587A) for 3mins deposition time, with an approximated deposit thickness of 1.88µm. Similar optimal deposition time and voltage has been defined by Rudolf, et.al. [1]. Excellent adhesion of Rh on Ag alloy was observed through adhesion test as per ASTM D3359-97 [2], and may be attributed to their properties satisfying the Hume-Rothery Rules for substitutional solid solution formation.
The activity of electrodeposited Rh in acidic and basic electrolytes has been investigated using cyclic voltammetry (CV). The set potential for CV was defined by calculating the corresponding reversible potentials for the anodic and

cathodic reactions using Nernst equation. The following conditions were used during CV scans: temperature, T = 25ºC; acid concentration, $[H^+]$ = 0.5M; basic concentration, $[OH^-]$ = 0.5M, oxygen gas pressure, P_{O2} = 0.21atm; hydrogen gas pressure, P_{H2} = 5 x 10^{-5}atm. Incorporating the given conditions to the Nernst equation, the following reversible potentials were calculated: $E_{anode(acidic)}$ = -1.202V; $E_{cathode(acidic)}$ = 0.109V; $E_{anode(basic)}$ = -0.408V; $E_{cathode(basic)}$ = -0.685V. Based on the calculated reversible potentials and adding the contribution of overpotentials, CV scans were done at 2.0V upper vertex potential and -1.0V lower vertex potential for acidic electrolyte, and 1.0V upper vertex potential and -1.5V lower vertex potential for basic electrolyte. Scans were started at 0V, varied linearly with time up to the upper vertex potential, scanned back with the same scan rate down to lower vertex potential, and finally scanned to reach back the 0V.

Figure 1A illustrates the full CV scan for acidic electrolyte and shows an abrupt increase in current at approximately 1.4V indicating an onset potential of OER, and an abrupt decline in current at approximately -0.2V indicating an onset of HER. Both reactions approached the same absolute value current of approximately 8.00 x 10^{-3}A, as shown in the plateau regions in Fig. 1Ac & i, providing the value of limiting current. In these regions, the change in current with increasing applied potential is minimal.

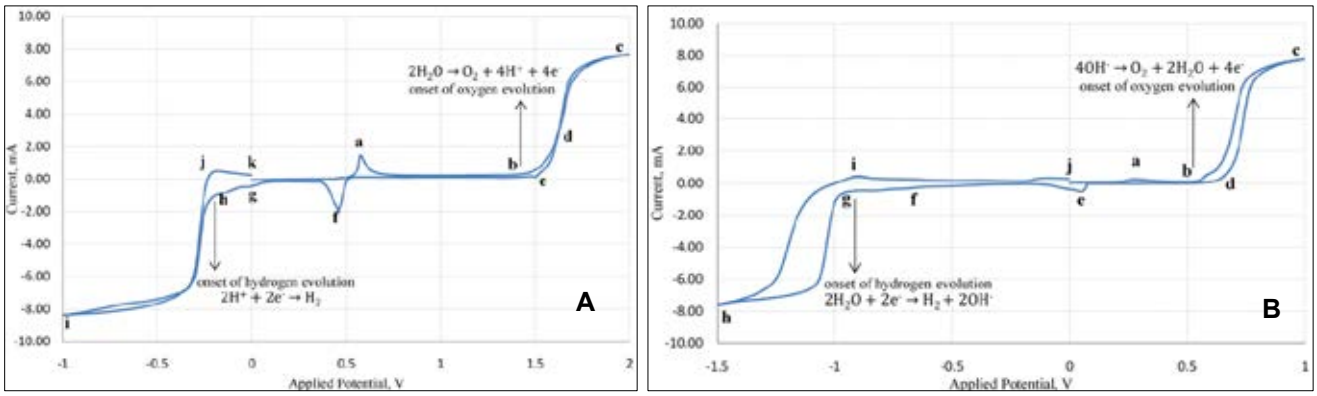


Fig. 1. Full CV scan of electrodeposited Rh in A) 0.5M H_2SO_4 and B) 0.5M NaOH taken at 25mV/s

$H_2O + Rh \rightarrow RhOH + H^+ + e^-$ (1)
$RhOH \rightarrow RhO + H^+ + e^-$ (2)
$RhO \rightarrow (1/2)O_2 + Rh$ (3)
$H^+ + e^- \rightarrow H_{ad}$ (4)
$2H_{ad} \rightarrow H_{2\,ad}$ (5)
$H_{2\,ad} \rightarrow H_2$ (6)
$OH^- + Rh \rightarrow RhOH + e^-$ (7)
$RhOH + OH^- \rightarrow RhO + H_2O + e^-$ (8)
$H_2O + e^- \rightarrow H_{ad} + OH^-$ (9)

The peaks observed at Fig. 1Aa (~0.6A) & f (~0.4A) correspond to oxygen adsorption and desorption, respectively on the electrode surface. Related studies proposed that the OER in acidic solution using a noble metal catalyst such as Rh follows the forward direction of reaction mechanisms given in Eqs. 1-3 [3, 4]. The first peak (Fig. 1Aa) corresponds to the dissociation of water to form the RhOH (Eq. 1) which immediately followed by oxidation to RhO (Eq. 2). Increasing the potential to 1.4V gives the onset for oxygen evolution (Fig. 1Ab, Eq. 3). From this point, the current rapidly increases with constant rate of potential until reaching a maximum value in Fig. 1Ac. On the reverse scan, a crossover potential (Fig. 1Ad) was observed at approximately 1.6V, indicating a nuclei formation. During the reverse scan, the system experienced an oxygen reduction reaction following the reverse directions of Eq. 1 to Eq. 3. The reduction peak in Fig. 1Ae corresponds to the reduction of O_2 into RhO immediately followed by the reduction to RhOH. The peak at Fig. 1Af corresponds to oxygen desorption. Upon reaching the starting point of CV which is at 0V, a downward peak started to form as an indication of HER. Based on a literature review by Hui Li, et.al, and a study by Jaksic, et.al, the HER in acidic medium using a noble metal catalyst may occur by the mechanisms described by Eqs. 4-6 [3, 4]. Figure 1Ag corresponds to hydrogen adsorption in which the H+ from the electrolyte upon meeting an e- diffuse and adsorbs on the electrode surface (Eq. 4). The onset for HER is displayed in Fig. 1Ah at ~-0.2V. The current rapidly decreased with constant rate of potential until it reached the value of limiting current in Fig. 1Ai. The scan from -1.0V to 0V shows a peak in Fig. 1Aj which corresponds to hydrogen desorption (reverse direction of Eq. 6 to Eq. 4). Fig. 1Ak may be attributed to void formation on the electrode surface due to hydrogen diffusion.

As with acidic electrolyte, CV scan in the basic medium revealed similar mechanisms for the HER and OER, but at different potential values. OER in basic solution using a noble metal catalyst follows the forward direction of reaction mechanisms given in Eqs. 7-8 then Eq. 3. [3, 4]. The first peak (Fig. 1Ba) corresponds to the adsorption of available hydroxide ion to form the RhOH (Eq. 7) which immediately followed by oxidation to RhO (Eq. 8). Increasing the potential to 0.6V gives the onset for OER (Fig. 1Bb, Eq. 3). Current then rapidly increases with constant rate of potential until limiting current value, Fig. 1Bc. The system experienced oxygen reduction during the reverse scan following the reverse directions of Eq. 3 and Eqs. 8 & 7. The reduction peak in Fig. 1Bd corresponds to the reduction of O_2 into RhO immediately followed by the reduction to RhOH. Fig. 1Be corresponds to oxygen desorption. HER for basic medium followed the mechanisms in Eq. 9 then Eq. 5-6 [3, 4]. Fig. 1Bf corresponds to hydrogen adsorption on the electrode surface (Eq. 9). The onset for HER is displayed in Fig. 1Bg at ~-0.9V. The current rapidly decreased until it reached the limiting current in Fig. 1Bh. A hysteretic portion observed on the HER region corresponds to hydrogen absorption [3]. Peak in Fig. 1Bi corresponds to hydrogen desorption (reverse direction of Eq. 9 then Eq. 6 & Eq. 5). Fig. 1Bj would be the effect of hydrogen diffusion forming voids on the surface of Rh electrode.

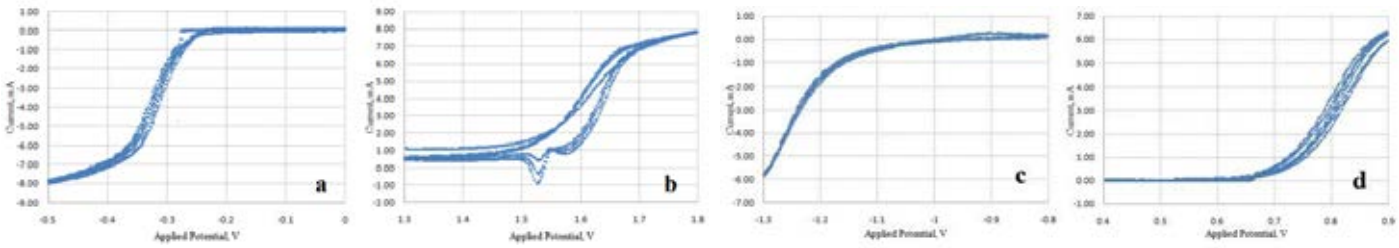


Fig. 2. Three-cycle CV scan of electrodeposited Rh taken at 25mV/s in a) 0.5M H_2SO_4 for HER; b) 0.5M H_2SO_4 for OER; c) 0.5M NaOH for HER; d) 0.5M NaOH for OER

The short CV scans of electrodeposited Rh in the HER and OER regions for both acidic and basic media are shown in Fig. 2. The figure indicates high stability of electrodeposited Rh; therefore, it can be used as both an anode and a cathode in acidic and basic water electrolysis. Further study was performed to confirm the stability of electrodeposited Rh during an extreme and long duration water electrolysis. The discussions were presented in the other paper of Bonifacio, et al [5].

CONCLUSIONS

Fabrication and characterization of electrodeposited Rh on Ag alloy for electrocatalytic applications in water electrolysis provided successful foundation of this study. From the identified optimal parameters, Ag alloy substrates were electrodeposited with thin coating of Rh. Cyclic voltammetry results showed the potential regions for HER and OER in both media and revealed the excellent activity of electrodeposited Rh in acidic and basic water electrolysis.

REFERENCES

1. Rudolf R et.al. 2013. Rhodium platings-experimental study. METABK 52(3):337-340.
2. Standard Test Methods for Measuring Adhesion by Tape Test. ASTM D3359-97.
3. Jaksic MM et.al. 1994. Electrochemical behavior of rhodium in alkaline and acidic solutions of heavy and regular water. International Journal for Hydrogen Energy 19: 35-51.
4. Zhang J. 2008. PEM Fuel Cell Electrocatalysts and Catalyst Layers. Springer.
5. Bonifacio R et al. 2016. Stability of electrodeposited rhodium on silver alloy in acidic and basic water electrolysis. 21st World Hydrogen Energy Conference.

WHEC-2022
23rd World Hydrogen Energy Conference
June 26-30, 2022 - Istanbul

#209

MEMBRANE ELECTRODE ASSEMBLIES FOR PEMWE BASED ON GLASS FIBRE REINFORCED PFSA/SSPS COMPOSITE MEMBRANES

[1*] *Maximilian Cieluch*, [2] *Dennis Düerkop*, [1] *Norbert Kazamer*, [1] *Florian Wirkert*, [3] *Ulrich Rost*, [1] *Michael Brodmann*, [2] *Achim Schmiemann*

[1] Westphalian University of Applied Sciences Gelsenkirchen, Westphalian Energy Institute, Neidenburgerstr. 43, 45897 Gelsenkirchen, Germany

[2] Ostfalia University of Applied Sciences, Institute of Recycling, Robert-Koch-Platz 8A, 38440 Wolfsburg, Germany

[3] ProPuls GmbH, Neidenburgerstr. 10, 45897 Gelsenkirchen, Germany

*Corresponding author e-mail: maximilian.cieluch@w-hs.de

ABSTRACT

Applied research is focussing on reducing costs for membrane electrode assemblies (MEA) and improving the performance by reducing polarization losses. The present research is investigating MEAs for proton exchange membrane water electrolysis (PEMWE) based on glass fibre reinforced composite membranes assembled with gas diffusion electrodes or processed as catalyst coated membranes. Membranes were prepared by casting a polymer suspension onto both sides of a glass fibre fabric. Subsequently, the reinforced composite membranes were ex-situ investigated showing promising proton conductivity and comparable thermo-oxidative stability compared to commercial Nafion115 membrane. In-situ tests were performed by assembling the composite membrane into an MEA either with gas diffusion electrodes prepared via electrochemical catalyst deposition or ultrasonic spray coating, or catalyst coating of the membrane by ultrasonic spay coating. Ir was used as anode catalyst, Pt as cathode catalyst, respectively. The polarization curves were recorded using a single cell, hydraulic compressed test system. Preliminary results with a slightly thicker ssPS(CL)-PPSU membrane than the used reference material, showed that the synthesized, composite membrane with the self-prepared catalyst coating reached a cell voltage of 2.4 V at a current density of 2 A*cm^{-2}, making it competitive to the reference Nafion115 sample prepared and tested the same way.

Keywords: MEA, water electrolysis, composite PFSA/SSPS membranes, glass fibre reinforcement, in-situ.

INTRODUCTION

Recently, the 26th UN Climate Conference underlined the importance of limiting global warming to 1.5°C in this decade [1]. Hence, implementing an energy supply based on fluctuating, renewable sources and using hydrogen as reliable energy carrier is discussed [2,3]. Electrochemical water splitting technologies like PEMWE can represent a sustainable solution for hydrogen-based energy systems, due to their high energy efficiency, flexible dynamic operation, and the capability to produce compressed and pure hydrogen. Moreover, PEMWE based hydrogen production offers the opportunity to reduce greenhouse gas emissions up to 75 % compared to hydrogen production based on steam methane reforming [4].

One of the key components in PEMWEs is the MEA, consisting of proton exchange membrane (PEM) and the electrodes, being responsible for the electrochemical reactions. State-of-the-Art PEMWE use catalyst coated membranes (CCMs) based on perfluorosulfonic acid as hydrogen proton carrier due to their sufficient mechanical and thermal stability and chemical inertness. Scaling up the production and thus system size of PEMWE leads to a sharp increase in the partial costs of the MEA, due to the increased quantity of noble metal catalysts and fluorinated membranes [5,6]. Reducing membrane thickness and using a different polymer can help to reduce raw material costs and increase the PEMWE efficiency by lowering the polarisation losses caused by ohmic membrane resistance or increasing the operation temperature by improving mechanical and thermal stability of the PEM. Further, the MEA performance can be adjusted by applying different preparation methods depending on the electrodes used. Gas diffusion electrodes (GDEs) prepared by electrochemical catalyst deposition offer the possibility to increase catalyst utilization and therefore reduce MEA costs, where else CCM preparation is state-of-the-art for PEMWE.

In the present work, composite membranes are synthesized consisting of proton conductor, cross-linked ssPS particles embedded into a PFSA polymer matrix and reinforced by glass fibre fabric. The synthesized membranes are ex-situ investigated regarding thermogravimetry, ion exchange capacity, electrical resistance, and proton conductivity. Further, the membranes were used for MEA preparation by GDE or CCM approach using Ir as catalyst and Ti as porous current collector for the anode, Pt and a carbon-based gas diffusion layer as cathode current collector, respectively. MEA characterisation was done by in-situ investigations in a self developed, single cell PEMWE test system based in the principle of hydraulic compression.

EXPERIMENTAL

Membrane Synthesis and Characterisation

The membranes were prepared by dispersing PFSA polymer (Aquivion) and cross-linked ssPS particles in N,N-dimethylacetamide at 140°C. In a second step, the dispersion is coated onto a glass plate. Immediately, a glass fibre fabric (25 g*m^{-2}) is placed as a second layer on the top of the coating followed by coating the glass fibre fabric with the polymer dispersion (3rd layer) after 30 minutes. After evaporating the solvent at 80°C and 120°C the membranes are protonated with 1M hydrochloric acid and rinsed with deionized water.

For ion exchange capacity (IEC) measurements the synthesized membranes were soaked in saturated sodium chloride solution for 24h and subsequently titrated with 0.1 M sodium hydroxide solution. Electrical resistance measurement was performed in deionized water using a through plane cell made of stainless steel with an electrode diameter of 11 mm connected to a Methrom Autolab potentiostat. Thermal-oxidative stability was investigated using thermal gravimetric analysis (TGA, Netzsch) in oxygen atmosphere.

Membrane-electrode-assembly preparation

For the MEA preparation, Ir was used as anode and Pt as cathode catalyst material, respectively. CCMs were prepared via ultrasonic spray coating using an USI Ultrasonic System, Inc. apparatus, equipped with a heated vacuum table. Therefore, catalyst inks were prepared consisting of catalyst powder, 5 wt.% ionomer-dispersion, isopropanol, and deionized water.
GDEs were prepared via electrochemical catalyst deposition or catalyst coating of the electrode substrate. Titanium was used as anode, commercial carbon-based gas diffusion layer as cathode substrate, respectively. Electrochemical catalyst deposition was performed using a two-electrode configuration and precious metal electrolytes. Catalyst coated substrates (CCSs) were prepared using ultrasonic spray coating and catalyst inks reported for CCM preparation.

In-situ testing

Polarisation curves were recorded following the “EU harmonised polarisation curve test method for low-temperature water electrolysis” [7]. The used test system consisted of a single cell PEMWE with a maximum geometrical active area of 25 cm². The polarisation curves were recorded, applying 8 bar hydraulic pressure on the MEA in several cell temperature steps up to 90°C. An MaterialsM Instruments potentiostat was connected to the test system to apply current density and record cell voltage.

RESULTS AND DISCUSSION

Membrane characterisation

The thickness of the prepared PFSA/ssPS membranes is about 50 – 70 µm. Electrical resistance measurement results show lower electrical resistance of the synthesized PFSA/ssPS membrane compared to the Nafion115 reference membrane.
Figure 1 shows the thermo-oxidative stability of Nafion115 and PSFA/ssPS membrane.
The weight-loss up to 200°C is caused by water evaporation followed by desulfonation starting between 250°C and 300°C. The desulfonation temperature of the PFSA/ssPS membrane is as high as the desulfonation temperature of the Nafion115 membrane, indicating similar thermal-oxidative stability.

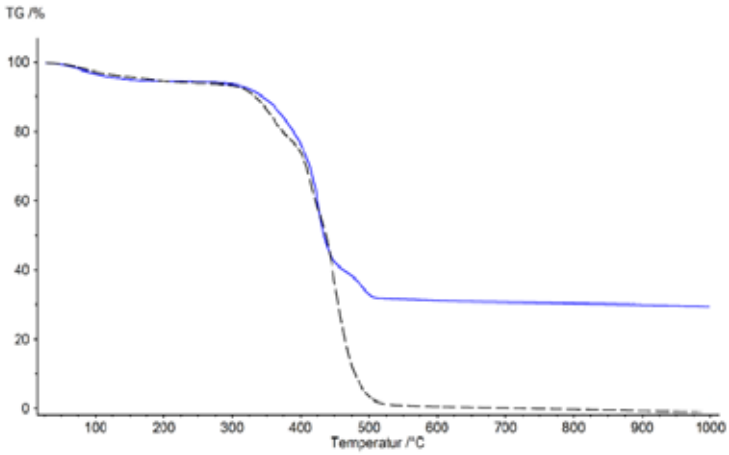


Figure 1: Thermo-oxidative stability of PFSA/ssPS, glass fibre reinforced composite membrane (blue) and Nafion115 (black).

Polarisation curves

Figure 2 shows the recorded in-situ polarisation curves at 80°C for the ssPS(CL)-PPSU membrane and the reference Nafion115 commercial membrane, both processed as CCMs via ultrasonic spray coating. The ssPS(CL)-PPSU membrane reached a cell voltage of 2.4 V @ 2 A*cm^{-2}, whereas the reference reached approximately 2 V @ 2 A*cm^{-2}, respectively.

In the region of low current densities, the polarisations curves superimpose, showing alike activation losses. In the linear region of the obtained polarisation curves the ssPS(CL)-PPSU membrane shows a higher slope and therefore

higher ohmic resistance compared to the reference membrane, leading to increased cell voltage at a current density of 2 A*cm^{-2}. These ohmic losses can be attributed to the increased membrane thickness of approximately 134 µm and therefore higher ohmic resistance, compared to the reference Nafion115 membrane (125 µm thickness). Additionally, the tested ssPS(CL)-PPSU membrane shows lower proton conductivity in the ex-situ characterizations, leading to a slightly poorer in-situ performance. Nevertheless, the composite ssPS-membrane shows promising performance for PEMWE that could be improved by further material improvements, e.g., changing the polymer matrix and adding a glass fibre reinforcement.

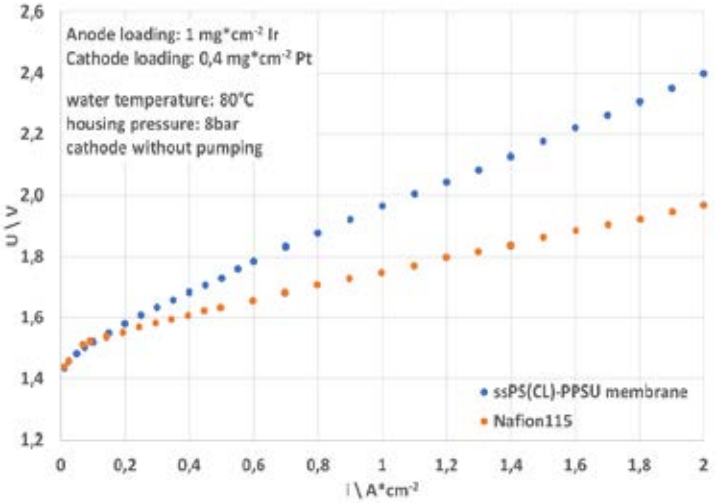


Figure 2: PEMWE polarisation curves recorded at 80°C working temperature, showing Nafion115 membrane (orange) and ssPS(CL)-PPSU membrane (blue).

CONCLUSIONS

The synthesized composite membrane indicates promising results for PEMWE. Additionally, a linear ionomer shall be developed and characterised. Therefore, in-situ tests with different MEA configurations are planned to be performed in the single cell, hydraulic compressed test system. Approaches containing GDEs with electrochemical deposited catalysts as well as CCS or CCMs prepared via ultrasonic spray coating will be used for MEA preparation. Moreover, the influence of the ionomer used for MEA preparation shall be investigated. Also, the operation temperature of the PEMWE will be varied to determine the thermal stability of the membrane.

ACKNOWLEDGEMENT

The present work has been carried out within the project “Entwicklung von kostengünstigen, langzeitstabilen und leistungsverbesserten Membran-Elektroden-Einheiten für PEM-Brennstoffzellen und PEM - Hochdruckwasserelektrolyseure vorzugsweise eingesetzt in Systemen mit hydraulischer Verpressung (HyPresMEA)“, part of the funding program “Forschung an Fachhochschulen”, being financially supported by the German Federal Ministry of Education and Research (contract number: 13FH257PA6). Furthermore, we thank GKN Sinter Metals Filters GmbH, Germany, for manufacturing the Ti-based current collectors and ProPuls GmbH, Germany, for supporting the in-situ investigations.

REFERENCES

1. United Nations. 2021. COP26: The Glasgow climate pact.
2. Sterner M, Stadler I (eds.). 2017. Energiespeicher - Bedarf, Technologien, Integration. 2nd ed. Berlin: Springer Vieweg.
3. Hydrogen Europe. 2020. A Historic Day for the Hydrogen Sector and the Beginning of a New Industrial Era. Brüssel.
4. Bareiß K, La Rua C de, Möckl M, Hamacher T. 2019. Life cycle assessment of hydrogen from proton exchange membrane water electrolysis in future energy systems. Applied Energy;237:862–72. https://doi.org/10.1016/j.apenergy.2019.01.001.
5. Schmidt O, Gambhir A, Staffell I, Hawkes A, Nelson J, Few S. 2017. Future cost and performance of water electrolysis: An expert elicitation study. International Journal of Hydrogen Energy;42(52):30470–92. https://doi.org/10.1016/j.ijhydene.2017.10.045.
6. Lagadec MF, Grimaud A. 2020. Water electrolysers with closed and open electrochemical systems. Nat Mater;19(11):1140–50. https://doi.org/10.1038/s41563-020-0788-3.
7. Malkow T. 2018. EU harmonised polarisation curve test method for low-temperature water electrolysis. Luxembourg: Publications Office of the European Union.

WHEC-2022
23rd World Hydrogen Energy Conference
June 26-30, 2022 - Istanbul

#218

ELECTROCHEMICAL PERFORMANCE OF 3-D PRINTED ELECTRODE GEOMETRIES IN VIEW OF ENHANCED GAS EVACUATION DURING ALKALINE WATER ELECTROLYSIS

[1*] *Fernando Rocha,* [1] *Nathan Wauthy,* [1] *Renaud Delmelle,* [1] *Christos Georgiadis,* [1] *Joris Proost*
[1] Université catholique de Louvain (UCLouvain), Div. of Materials and Process Engineering, Louvain-la-Neuve, Belgium

*Corresponding author e-mail: fernando.rocha@uclouvain.be

ABSTRACT

Water electrolysis plays a key role in the energy transition as it can be used to store energy by the conversion of electrical energy from renewable and intermittent sources to chemical energy in the form of hydrogen gas. Currently, the most mature technology is alkaline water electrolysis. The benchmark electrolyzer configuration is a zero-gap cell with porous electrodes. Gas evacuation is a challenge when using this kind of electrode, as bubbles can get trapped within the 3-D structure. This work aims to identify parameters that can help the construction of enhanced gas evacuation periodic electrodes. It was found that electrodes that direct the flow and present a lower pressure drop are better in terms of gas removal.

Keywords: Alkaline Water Electrolysis, Bubble Removal, Forced Electrolytic Flow, 3-D Printed Electrodes

INTRODUCTION

The state-of-the-art electrolysis cell configuration is a zero-gap assembly. In this configuration, the electrodes – often 2-D electrodes such as perforated plates, expanded metals, or meshes – are pressed against a separator with a thickness on the order of hundreds of micrometers [1]. Recently, 3-D electrode geometries such as foams and felts have been used with promising results [2]. Due to the stochastic nature of these geometries, the gas removal may not be optimal. As an example, Kou *et al.* (2020) observed an enhancement in gas evacuation when replacing foams by periodic 3-D structures [3]. An important method to build 3-D periodic metallic structures is additive manufacturing by means of laser beam melting. With the almost unlimited possible geometries that it allows to fabricate, it is important to find generic guidelines as to what kind of structure presents the best electrolytic performance. The study presented here analyzed two periodic geometries and found some trends in what kind of structures should the efforts be concentrated on to result in a more efficient gas removal. Computational fluid dynamics (CFD) simulations were used as well to quickly explore the potential of new geometries.

MATERIALS AND METHODS

The electrolytic solution used was 1 M potassium hydroxide (KOH), prepared by mixing KOH pellets (KOH > 85%, VWR chemicals) with deionized water (18.2 MΩ.cm, Sartorius Arium 611). The temperature was set at 70°C with the help of stirrer hotplates (C-MAG HS 7, from IKA). The cell contains the following parts: two end-plates with fittings for inlet and outlet of electrolyte; two nickel (> 99.5%, Alfa Aesar) current distributors to ensure removal/supply of electrical charge; two PTFE electrode housings to accommodate the electrodes and promote sealing; a Zirfon Perl UTP 500 diaphragm (500 ± 50 µm of thickness). Between each one of these parts, there is an ethylene propylene diene monomer (EPDM) layer to ensure sealing and to prevent mechanical wear. The electrode housing had a dimension of 2x2x0.8 cm. The electrolytic flow was controlled by gear pumps (GJ-N25.FF3S.A, Micropump) and measured by flow transmitters (Honsberg, model LABO-MID1-I/U/F/C). The electrolytic reservoirs were made of 316l stainless steel. To ensure sealing, the cell was pressed using 6 screws with a torque of 3 Nm each.

Current scans from 0-2 $A.cm^{-2}$ were performed with a scan rate of 0.025 $A.cm^{-2}.s^{-1}$. 5 minutes galvanostatic experiments were also realized with the help of a Solartron Modulab XM potentiostat equipped with a Booster 20 A. Computational fluid dynamic simulations were performed with the open-source MigFlow software [4]. The electrodes were built using laser beam melting and were composed, in view of ease of fabrication, of Inconel 625 alloy (Ni~60%, Cr~22%, Mo~9%, Fe~4%, Nb~3%) [5]. The shape of the electrodes was based on mathematical equations. The first one was a doubly-periodical minimum surface called Schwarz CLP, defined geometrically by:

$$t = \sin\left(\frac{2\cdot\pi\cdot z}{L}\right)\cdot\sin\left(\frac{2\cdot\pi\cdot x}{L}\right) - 0.4\cdot\sin\left(\frac{2.4\cdot\pi\cdot y}{L}\right)\cdot\cos\left(\frac{2\cdot\pi\cdot z}{L}\right)\cdot\cos\left(\frac{2\cdot\pi\cdot x}{L}\right) \quad (1)$$

and the second was a triply-periodical minimum surface called Gyroid, defined by:

$$t = \cos\left(\frac{2\cdot\pi\cdot x}{L}\right)\cdot\sin\left(\frac{2\cdot\pi\cdot y}{L}\right) + \cos\left(\frac{2\cdot\pi\cdot y}{L}\right)\cdot\sin\left(\frac{2\cdot\pi\cdot z}{L}\right) + \cos\left(\frac{2\cdot\pi\cdot z}{L}\right)\cdot\sin\left(\frac{2\cdot\pi\cdot x}{L}\right) \quad (2)$$

with *L* giving the periodicity and *t* being related to the void fraction. A value of *L* equal to 4 mm means that the structure repeats itself at each 4 mm. The lower the *L*, the higher the surface area. Notice that while Gyroids have the same symmetry in all directions, Schwarzs have a different symmetry for y-axis. In this study, all the Gyroidal structures had a *t* value equal to zero (50% void fraction), while the Schwarz CLP had a *t* value of 0.18 (61% void fraction). The electrochemical active surface area (ECSA) of each electrode was measured using the capacitance method: cyclic voltammetries (CVs) with different scan rates (50, 100, 150, 200, 250, 300, 350, 400 $mV.s^{-1}$) were applied in a range of 50 mV around open circuit potential (OCP) are used to estimate the capacitive current. This current is measured by taking half of the difference between the anodic current and the cathodic one. The slope of the plot of capacitive current against the CV scan rate gives out capacitance. To find the ECSA, the capacitance was divided by a specific capacitance of 20 $\mu F.cm^2$, as this value was reported recently in the literature [6]. This measurement was made at room temperature, 1 M KOH, Pt counter electrode, and Ag|AgCl *sat.* reference electrode. More details about the capacitance method can be found in ref. [7].

RESULTS AND DISCUSSION

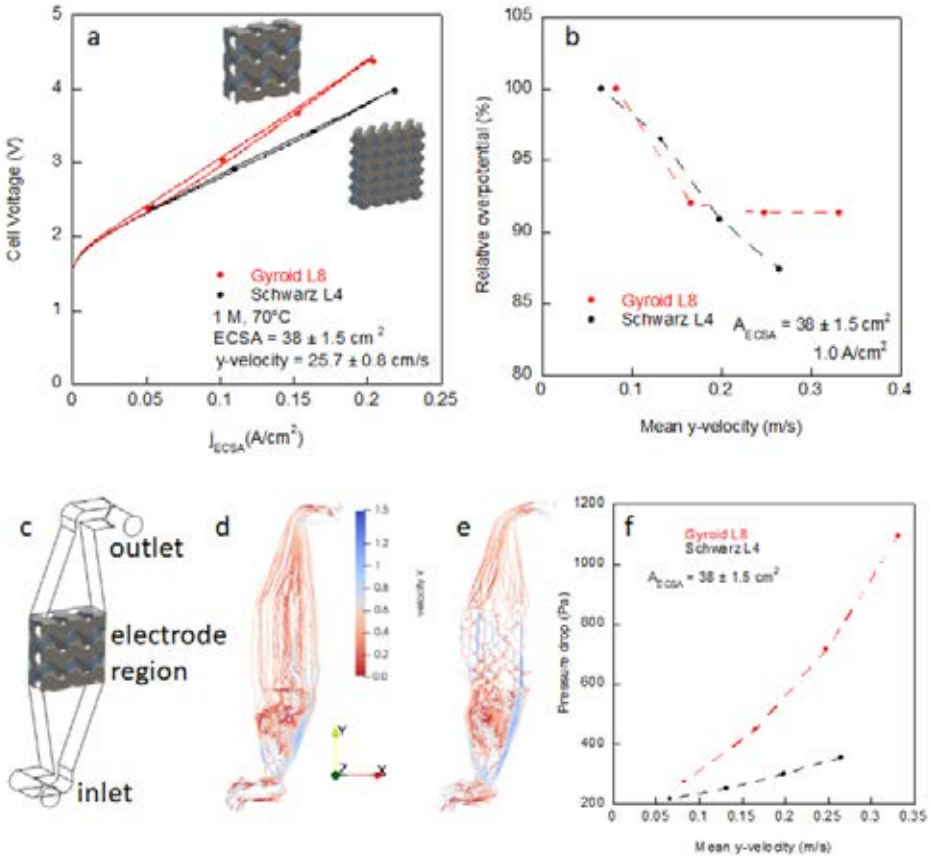


Fig. 1. a) Polarization curves for electrodes in the shape of a Gyroid with a lattice size of 8 mm and a Schwarz with a lattice size of 4 mm. ECSA for both electrodes was close to 38 cm^2 and the mean y-velocity close to 25.7 cm/s. Dots represent a current scan and circles the galvanostatic experiment b) Relative overpotential versus mean y-velocity for Gyroidal-shaped and Schwarz-shaped electrode at a current density of 1.0 A/cm^2 c) Geometry of a half-cell (could be the cathode or the anode). Streamlines colored by the y-velocity for a half-cell for d) Schwarz L8 e) Gyroid L4 f) Pressure drop caused by the electrode as a function of mean y-velocity for Gyroid L8 and Schwarz L4.

Comparing the two structures, it can be seen that for the same surface area and y-velocity, Schwarz CLP-shaped electrodes presented the best electrochemical performance, as shown in Fig. 1.a. The same trend was observed for all the y-velocities. Fig. 1.a compares a Gyroidal-structure with an *L*=8 mm with a Schwarz with an *L*=4 mm – both with approximately 38 cm^2. Decreasing further the *L* to 2 mm for all these structures, one reaches 81.6 ± 7.4 cm^2 of ECSA and, again, Schwarz presents the best performance. Since the electrodes are made of the same material, dismissing the presence of bubbles, one would expect the same polarization curves. The reason for the poorer performance for the Gyroidal-shaped electrode is the higher presence of trapped gas bubbles, covering part of the electrode area and thus reducing the electrochemical active surface area. To deepen the understanding of this process, one can look at the flow effect, shown in Fig. 1.b. It is shown that the increase in the flow causes a voltage reduction in all the structures. The higher percentual decrease in the overpotential indicates a more effective bubble removal caused by electrolytic flow in Schwarz-shaped electrodes. To explain the flow effect, computational fluid

dynamics simulations were performed. Fig. 1.c shows the geometry of a half-cell with electrode a Gyroidal electrode. Fig. 1.d show a half-cell with a Schwarz-shaped electrode (L=4) and Fig. 1.e shows a gyroidal-shaped electrode with an L=8. It is shown that while for Schwarz the flow is directed to y-direction (upwards) and almost no mixing was observed, Gyroidal structures deviate the flow, causing an increase in vorticity and dissipating more energy. From a quantitative point of view, we can look at the pressure drop caused by each electrode structure as a function of mean y-velocity. As shown in Fig. 1.f, for the same surface area, Gyroidal-shaped electrodes cause a higher pressure drop, meaning that more energy is needed to impose the same y-velocity. As a consequence, the removal of gases is less effective.

When comparing the couple of structures with an ECSA close to 38 cm^2 (Gyroid L = 8 mm and Schwarz L = 4 mm) with the couple with an ECSA of 81.6 cm^2 (Gyroid L = 2 mm and Schwarz L = 2 mm), it was observed that the Schwarz $L2$ presented a better performance than Schwarz $L4$. This can be attributed to the enhanced gas removal, allowing the increase in the active surface area, without a significant bubble entrapment. On the other hand, Gyroid L2 presented a poorer performance. Since the flow is not effective in this structure, the decrease in the periodicity (L) caused an important bubble entrapment, decreasing the active surface area to a value lower than the one obtained when L was equal to 8 mm.

CONCLUSIONS

After a careful comparison of two periodic 3-D electrode geometries, it was found that for the same ECSA and y-velocity, structures that present lower pressure drop allowed an efficient gas evacuation, increasing the electrochemical performance. It was observed that the deviation of the flow was the main responsible for the increase in the pressure drop. As a consequence, structures which direct the flow in only one direction should be privileged in the construction of new electrodes. Furthermore, an enhanced gas evacuation electrode allows the increase in the active surface area by the decrease in the “L” parameter, since the effect of gas coverage is highly reduced.

ACKNOWLEDGEMENT

We gratefully acknowledge financial support from the European Commission through the H2020 Project "NexTAEC" (Materials for Next Generation Alkaline Electrolyzers), under contract n° 862509.

REFERENCES

1. Koj M, Qian J, and Turek T. 2019. Novel alkaline water electrolysis with nickel-iron gas diffusion electrode for oxygen evolution. International Journal of Hydrogen Energy 44:29862–29875.
2. Yang F, Kim MJ, Brown M, and Wiley BJ. 2020. Alkaline Water Electrolysis at 25 A cm2 with a Microfibrous Flow-through Electrode. Advanced Energy Materials 10:2001174.
3. Kou T, Wang S, Shi R, Zhang T, Chiovoloni S, Lu JQ, Chen W, Worsley MA, Wood BC, Baker SE, Duoss EB, Wu R, Zhu C, Li Y. 2020. Periodic Porous 3D Electrodes Mitigate Gas Bubble Traffic during Alkaline Water Electrolysis at High Current Densities. Advanced Energy Materials 10:2002955.
4. Constant M, Dubois F, Lambrechts J, and Legat V. 2019. Implementation of an unresolved stabilised FEM–DEM model to solve immersed granular flows. Computational Particle Mechanics 6:213–226.
5. Ramenatte N, Vernouillet A, Mathieu S, Vande Put A, Vilasi M, and Monceau D. 2020. A comparison of the high-temperature oxidation behaviour of conventional wrought and laser beam melted Inconel 625. Corrosions Science 164:108347.
6. Zankowski SP and Vereecken PM. 2019. Electrochemical Determination of Porosity and Surface Area of Thin Films of Interconnected Nickel Nanowires. Journal of Electrochemistry Society 166:D227–D235.
7. Cossar E, Houache MSE, Zhang Z, and Baranova EA. 2020. Comparison of electrochemical active surface area methods for various nickel nanostructures. Journal of Electroanalytical Chemistry 870:114246.

WHEC-2022
23rd World Hydrogen Energy Conference
June 26-30, 2022 - Istanbul

#224

EXPERIMENTAL RESEARCH ON 100-BAR HIGH PRESSURE DIFFERENTIAL PROTON EXCHANGE MEMBRANE ELECTROLYZER

[1] Jian Dang, [2] Fuyuan Yang, [3] Yayang Jiang*
[1] Tsinghua University, School of Vehicle and Mobility, Tsinghua University Street, Haidian District, Beijing, China
[2] Tsinghua University, School of Vehicle and Mobility, Tsinghua University Street, Haidian District, Beijing, China
[3] Tsinghua University, School of Vehicle and Mobility, Tsinghua University Street, Haidian District, Beijing, China

*Corresponding author e-mail: dangj18@mails.tsinghua.edu.cn

ABSTRACT

A proton exchange membrane (PEM) electrolysis system including electrolyzers and accessory systems has been developed to allow direct electrolysis to produce hydrogen under high pressure difference. Based on the system, the performance of the high-pressure hydrogen production electrolyzer under high pressure has been analyzed. The influence of operating parameters including current, circulating water velocity, circulating water temperature and compression force on the performance of the electrolyzer was analyzed by means of polarization curve and electrochemical impedance spectrum (EIS). The experimental results show that the temperature has the greatest effect on the electrolysis performance in the form of ohmic loss, activation loss and mass transfer loss simultaneously. The circulating water flow and the compression force have no obvious influence on the performance of the electrolyzer within the range selected in this study. The current density mainly acts on the ohmic impedance of the electrolyzer. It is worth noting that no significant change in voltage efficiency was found by gradually increasing the cathode pressure to 90 bar while the anode was kept at atmospheric pressure.

Keywords: PEM Water Electrolysis, High-Pressure Difference, Efficiency, EIS

INTRODUCTION

As a very promising method for green hydrogen production, hydrogen production from water electrolysis has good adaptability with renewable energy resources. Producing high pressure green hydrogen directly can eliminate the compression process after hydrogen production and save the cost of compression energy consumption and fixed investment at the same time. And proton exchange membrane electrolysis of water to generate hydrogen is the only way with this ability among several hydrogen production methods by electrolysis of water. Only Japan's Honda [1] company had developed a 70Mpa differential pressure PEM electrolyzer so far around the world, and they pointed out the advantages of this method in energy saving. However, it is not clear how this technology can be realized. Besides them, there are relatively few studies on electrolysis of operating pressure exceeding 70bar. Trinkle et al. [2] also studied the problem of hydrogen permeation in differential pressure electrolysis (below 3MPa). Generally speaking, there are few studies on the influence of higher pressure (above 7MPa) on the performance of electrolyzer. This paper discussed the influence of several operating parameters on the performance of electrolyzer designed for high pressure.

EXPERIMENT

The direct high-pressure hydrogen production system investigated has been developed by Tsinghua University. Platinum-plated sintered titanium fiber blanket was used as porous diffusion layer for both anode and anode. A unique frame structure was adopted in the cause of the good working state of the membrane, moreover, the sealing ring instead of sealing gasket was used to meet the sealing requirements between anode and cathode as well as between the electrolyzer and the outside environment. Finally, the electrolyzer was compressed by hydraulic equipment. The physical photo of the system is shown in Fig. 1. The other main operating parameters of the system and electrolyzer have been listed in Table. 1.

Table 1. Main operating parameters of the system and electrolyzer

Parameters (Unit)	**Value**	**Parameters (Unit)**	**Value**
Power consumption rate (W)	500	Cathode pressure (bar)	1-100
Number of cells	1	Anode pressure (bar)	1
Active area (cm^2)	170	Flow rate of circulating water (L/h)	50-500
Flow rate of hydrogen (L/h)	100	Operating temperature (K)	293-353

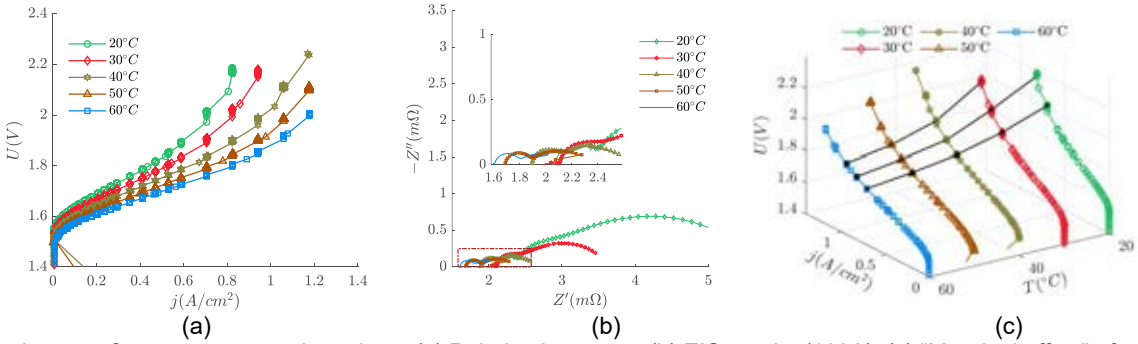


Fig. 1. The physical photo of the system

The circulating water temperature, circulating water flow, hydraulic equipment pressure and cathode hydrogen pressure were set as control variables respectively, and the standard measurement condition was stipulated as the temperature maintained at 333K, water flow at 150L/h, hydraulic pressure at 16MPa and hydrogen pressure at 1bar. When changing one of the parameters, keep the other parameters the same as the standard measurement condition. Among them, the test range of temperature was 293-333K, with 10K as the interval; the test range of water flow was 50-150L/h, with 25L/h as the interval; the test range of hydraulic pressure was 4-20MPa, with 4MPa as the interval; the test range of hydrogen pressure is 1-90bar, with 10bar as the interval. The polarization curve and EIS were tested at the same time after each change of working condition, and the current of EIS test was selected from 50-200A.

RESULTS AND DISCUSSION

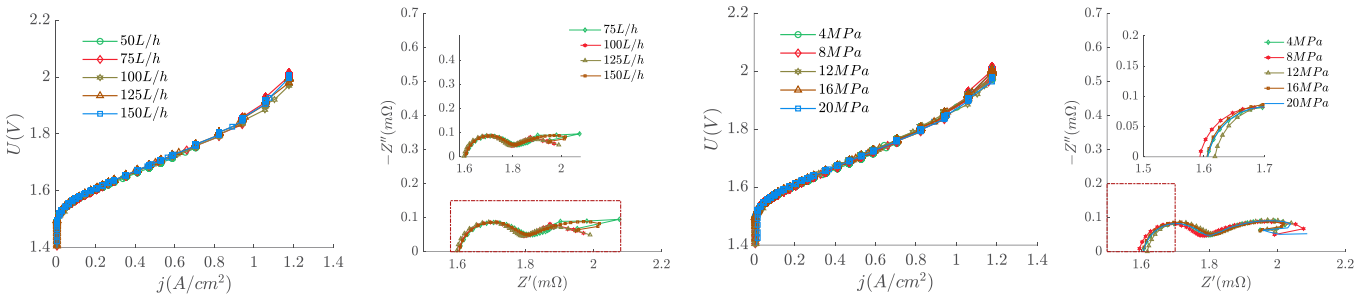
Fig. 2(a) shows the effect of temperature on the performance of electrolyzer. Obviously, the higher the cell temperature is, the more favorable it is to the performance of electrolysis cell (such as energy consumption et al.). On the other hand, this phenomenon can be explained from the results of impedance spectroscopy (Fig. 2(b)). When the temperature is lower, the ohmic impedance increases significantly, which can be explained by the conductivity of the membrane (Eq. (1)). Secondly, it is easy to find that the activation loss increases significantly at lower temperature, which can be explained by the composition of the activation overpotential (Eq. (2)). Finally, lower temperature will also lead to an increase in less obvious mass transfer loss. There is still no confirmed explanation for this part, which may be caused by the limiting current density. However, despite the positive impact of temperature increase on energy consumption, many literatures have reported the negative impact of high temperature (over 333K) on the durability of membrane. Meanwhile, there is a significant marginal effect of the benefits of temperature increase, which means that it is not a wise choice to simply increase temperature according to the black line in Fig. 2(c).



(a) (b) (c)

Fig. 2. The impact of temperature on electrolyzer (a) Polarization curve. (b) EIS results (100A). (c) “Marginal effect” of temperature

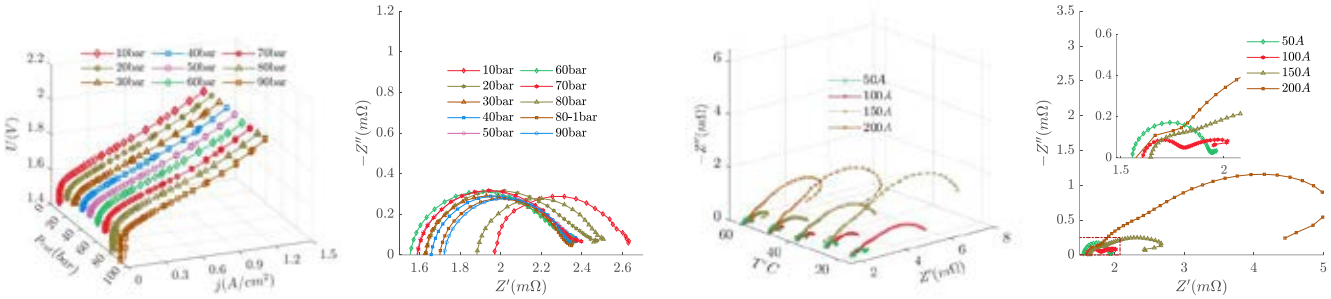
For circulating water flow and hydraulic pressure, the polarization curve results show that they have no significant effect on electrolysis performance, as shown in Fig. 3. An increase in water flow allows faster removal of the reactant oxygen, thus allowing the reaction rate to be unlimited. On the other hand, it has been reported that the increase of water flow will reduce the temperature on the membrane and thus reduce the efficiency. In this study, the heat produced by the cell is almost negligible, so the performance deteriorates with the increase of flow rate is not found. The reason why the compression force does not affect the sealing structure is related to the use of sealing ring and will not cause excessive compression of the reaction area in the middle.



(a) (b) (c) (d)

Fig. 3. The impact of flow rate and compression force (a)(c) Polarization curve. (b)(d) EIS results (100A).

The influence results of cathode pressure are shown in Fig. 4(a)(b). It is obvious that the increase of cathode pressure does not affect voltage efficiency (the polarization curve hardly changes), while the current efficiency will be seriously affected. The influence of current density can be shown by EIS results of different currents (Fig. 4(c)(d)). Obviously, the performance of electrolysis gradually deteriorates with the increase of current density, and all related polarization losses also increase, especially mass transfer losses.



(a) (b) (c) (d)

Fig. 4. The impact of H_2 pressure and current density (a) Polarization curve. (b) EIS (100A). (c) EIS versus temperature. (d) EIS (333K).

CONCLUSIONS

In this paper, the effect of different operating parameters on the performance of the electrolyzer was explored based on the self-developed high-pressure hydrogen production system. The main conclusions are as follows:

- Although temperature has a great influence on the performance of electrolyzer, this "positive effect" will gradually decrease as the temperature increases. In order to balance durability and energy consumption, it is necessary to reasonably optimize the operating temperature.
- The effect of flow rate and compression force has different conclusions in different electrolyzers (power, sealing structure, etc.), in general, the flow rate can be considered to have little effect for commercial electrolyzers.
- The cathode pressure does not significantly affect the voltage efficiency but the current efficiency.
- Increased current density is beneficial for hydrogen production rate, but at the same time increases system energy consumption and in addition has a negative impact on mass transfer losses.

REFERENCES

1. H. Ishikawa, E. Haryu, N. Kawasaki, H. Daimon, Development of 70 mpa differential-pressure water electrolysis stack, Honda, Research and Development Technical Review (2016).
2. P. Trinke, P. Haug, J. Brauns, B. Bensmann, R. Hanke-Rauschenbach, T. Turek, Hydrogen crossover in PEM and alkaline water
electrolysis: mechanisms, direct comparison and mitigation strategies, Journal of The Electrochemical Society 165 (2018) F502.

WHEC-2022
23rd World Hydrogen Energy Conference
June 26-30, 2022 - Istanbul

#231

ELECTROCATALYTIC AMMONIA OXIDATION COUPLED WITH HYDROGEN PRODUCTION - MOVING TOWARDS A CARBON-NEUTRAL WATER TREATMENT CYCLE

[1*] *Egle Latvyte*, [1] *Liang Wu*, [1] *Ming Zhu*, [2] *Peter Vale*, [1] *John Graves*
[1] Institute for Clean Growth and Future Mobility, Coventry University, Priory Street, Coventry, United Kingdom
[2] Severn Trent Water Ltd., St. John's Street, Coventry, United Kingdom

*Corresponding author e-mail: latvytee@coventry.ac.uk

ABSTRACT

This study presents a non-noble metal nickel-copper catalyst, as a durable anode for alkaline ammonia electrolysis. We report that a nickel-copper catalyst can electrochemically oxidise ammonia to nitrogen at room temperature and atmospheric pressure. Cyclic voltammetry experiments in a three-electrode cell confirmed the nickel-copper anode had a lower overpotential for ammonia electrolysis when compared with other precious metal catalysts. Electrodes were prepared at a larger scale and evaluated in a membrane flow cell. Gas chromatography of the off gases confirmed that both, nitrogen at the anode and hydrogen at the cathode, were generated with relatively high faradaic efficiencies. Anode morphology and structure before and after electrolysis were investigated by X-ray diffraction (XRD), X-ray fluorescence (XRF), X-ray Photoelectron Spectroscopy (XPS) and scanning electron microscopy (SEM-EDS). Overall, the electrode showed good stability after continuous electrolysis in an alkaline ammonia electrolyte and the nickel-copper system is a potential electrocatalyst for efficient ammonia oxidation. Morever, hydrogen can be generated as a useful by-product at the cathode. The ammonia is effectively cracked into nitrogen and hydrogen without the consumption of water. The hydrogen produced can be used to power fuel cells, can be burnt in combustion engines or has the possibility to be injected into the gas grid and blended with methane.

Keywords: Ammonia, Hydrogen, Electrolysis, Electrolyser, Nickel-copper, Wastewater

INTRODUCTION

Ammonia is a common pollutant, present in municipal wastewater streams and is also a carbon-free energy carrier. Recently, technological solutions have been introduced to strip ammonia from wastewater [1]. The recovered ammonia can be electrochemically oxidised to benign nitrogen in an electrolyser, which can offer a cost-efficient technology to couple wastewater remediation at an anode with a production of a valuable hydrogen by-product at the cathode. Currently, the commercialisation of ammonia electrolyser technology is hindered by slow reactions at the anode and the cathode as well as the deactivation or degradation of the catalysts over time [2,3]. Consequently, the development of an inexpensive, efficient anode material is imperative to reduce costs associated with ammonia destruction and electrochemical hydrogen production.

Activity-wise, considering only thermochemical properties, Pt was shown as the most active monometallic catalyst followed by Ir and Cu for ammonia oxidation (AO) [4]. However, platinum group metals are rare and expensive and can be poisoned by adsorbed nitrogen intermediates produced during ammonia oxidation [5]. While inexpensive transition metals such as nickel are inactive towards AO due to rapid corrosion in alkaline media, electrooxidation is possible at $Ni(OH)_2$/NiOOH electrodes [6]. Still, the electrodes can be corroded and deactivated over time [7]. Bimetallic nickel-copper catalysts have been reported to have high activity for ammonia oxidation and have shown improved stability [8,9].

In this work, a bimetallic NiCu catalyst has been used as an anode for ammonia electrolysis in a divided electrolyser cell to couple the destruction of ammonia with the generation of hydrogen.

MATERIALS AND METHODS

Bimetallic nickel-copper electrodes were prepared by electro co-deposition as shown in Figure 1a. Electrochemical characterisation of ammonia oxidation was performed in a three-electrode cell, Figure 1b, where the NiCu electrode was the working electrode, Pt mesh was the counter electrode and Hg/HgO (1M NaOH) was the reference electrode.

For ammonia electrolysis, a commercial electrolyser was used (Dioxide Materials, USA). The schematic of the electrolyser assembly is pictured in Figure 1c. Two half-cells were separated by an anion exchange membrane. The anode used was the prepared NiCu electrode and the cathode was a commercial-grade cathode (Dioxide Materials, USA). The electrolyser system was connected to either a potentiostat/galvanostat for electrochemical analysis or a 10V/10A rectifier as a DC power supply for electrolysis experiments. The gases produced were analysed by a Gas Chromatography equipped with a Thermal Conductivity Detector (GC-TCD, Perkin-Elmer, United Kingdom).

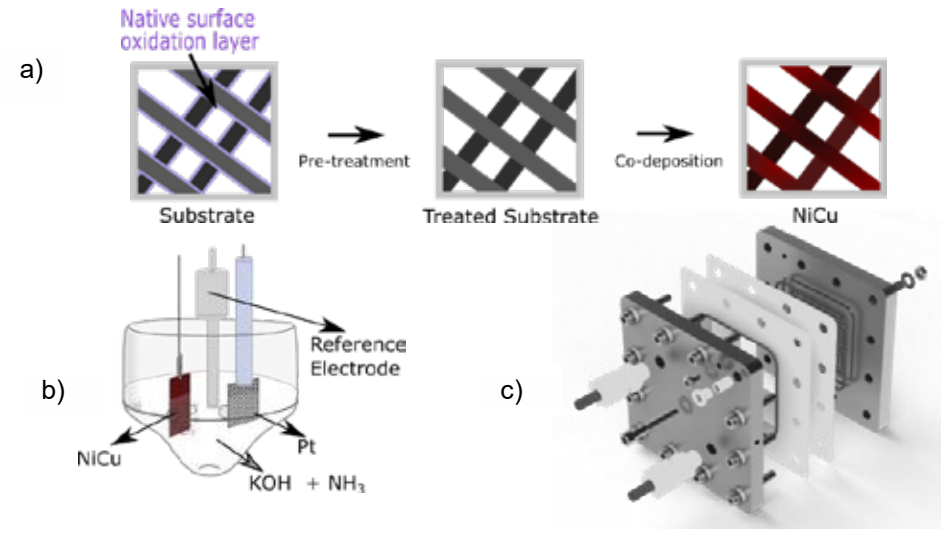


Fig. 1. a) NiCu electrode preparation b) Schematic of three-electrode cell c) Diagram of ammonia electrolyser (adapted from [10])

RESULTS AND DISCUSSION

To characterise the NiCu electrode, cyclic voltammetry experiments were performed, Figure 2a. Compared to 1M KOH, a sharp increase of anodic current density was observed when ammonia was introduced to the electrolyte, reaching 120 mA cm^{-2} at 0.7 V vs Hg/HgO. The overpotential at which the electrode reached 100 mA cm^{-2} was significantly lower (0.65V vs Hg/HgO), compared to an iridium oxide electrode (1.05 V vs Hg/HgO), pictured in Figure 2b.

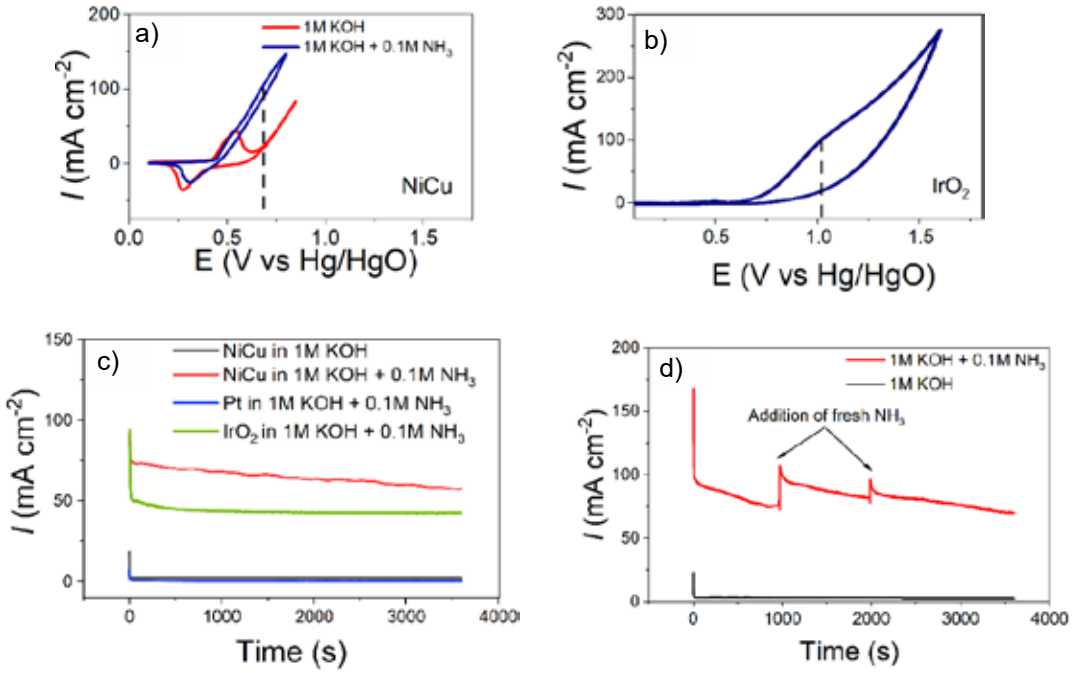


Fig. 2. a) NiCu electrode in 1M KOH and 1M KOH + 0.1M NH_3 (aq), recorded at 25 mV/s b) IrO_2 electrode in 1M KOH + 0.1M NH_3 (aq), recorded at 100 mV s^{-1} c), d) chronoamperograms of various electrode materials in 1M KOH and 1M KOH + 0.1M NH_3 recorded at potentials of ammonia electrochemical oxidation

To determine the stability of the NiCu electrode in ammonia, chronoamperometric experiments were performed, Figure 2c. NiCu electrode was able to maintain the highest current density of the electrodes tested (NiCu, IrO_2 and Pt). Furthermore, during chronoamperometry currents decreased with reducing NH_3 concentration but went up with an addition of fresh ammonia, showing high sensitivity and activity towards ammonia, Figure 2d.

In the electrolyser, the NiCu electrode exhibited lower cell potential when ammonia was added to the system, Figure 3. The GC-TCD data has confirmed nitrogen was generated at the anode while hydrogen was generated at a cathode.

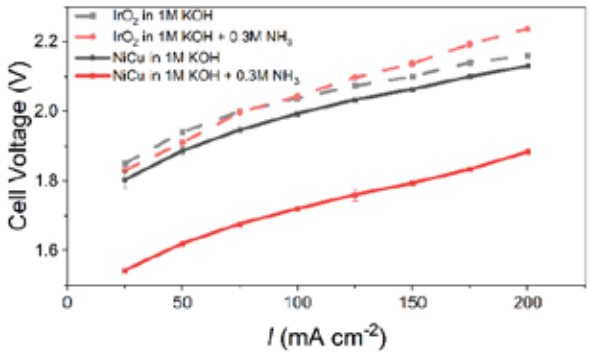


Fig. 3. Comparison of cell voltages recorded in an electrolyser using NiCu and IrO_2 anodes. Recorded at room temperature and ambient pressure, using an anion exchange membrane

CONCLUSIONS

The work has shown NiCu bimetallic catalyst as a suitable anode for electrochemical ammonia oxidation. Due to the electrode's high activity, stability and low cost, NiCu has the potential to be a good catalyst for ammonia oxidation which can be combined with hydrogen generation in large-scale commercial electrolysers.

REFERENCES

1. Kinidi L, Tan IAW, Abdul Wahab NB, Tamrin KFB, Hipolito CN and Salleh SF. 2018. Recent Development in Ammonia Stripping Process for Industrial Wastewater Treatment. International Journal of Chemical Engineering. 2018: 1–14.
2. Zhou B, Zhang N, Wu Y, Yang W, Lu Y, Wang Y and Wang S. 2021. An option for green and sustainable future: Electrochemical conversion of ammonia into nitrogen. Journal of Energy Chemistry. 60: 384–402.
3. Adli NM, Zhang H, Mukherjee S and Wu G. 2018. Review—Ammonia Oxidation Electrocatalysis for Hydrogen Generation and Fuel Cells. Journal of The Electrochemical Society. 165(15): J3130–J3147.
4. Herron JA, Ferrin P and Mavrikakis M. 2015. Electrocatalytic Oxidation of Ammonia on Transition-Metal Surfaces: A First-Principles Study. The Journal of Physical Chemistry C. 119(26): 14692–14701.
5. Vidal-Iglesias FJ, Solla-Gullón J, Rodríguez P, Herrero E, Montiel V, Feliu JM and Aldaz A. 2004. Shape-dependent electrocatalysis: ammonia oxidation on platinum nanoparticles with preferential (100) surfaces. Electrochemistry Communications. 6(10): 1080–1084.
6. Kapałka A, Cally A, Neodo S, Comninellis C, Wächter M and Udert KM. 2010. Electrochemical behavior of ammonia at Ni/Ni(OH)2 electrode. Electrochemistry Communications. 12(1): 18–21.
7. Yao K and Cheng YF. 2008. Investigation of the electrocatalytic activity of nickel for ammonia oxidation. Materials Chemistry and Physics. 108(2–3): 247–250.
8. Xu W, Du D, Lan R, Humphreys J, Miller DN, Walker M, Wu Z, Irvine JTS and Tao S. 2018. Electrodeposited NiCu bimetal on carbon paper as stable non-noble anode for efficient electrooxidation of ammonia. Applied Catalysis B: Environmental. 237: 1101–1109.
9. Zhang H, Wang Y, Wu Z and Leung DYC. 2017. An ammonia electrolytic cell with NiCu/C as anode catalyst for hydrogen production. Energy Procedia. 142: 1539–1544.
10. Dioxide Materials. https://dioxidematerials.com/product/complete-25-cm2-aem-water-electrolyzer/. Accessed December 8, 2021.
11. Gwak J, Choun M and Lee J. 2016. Alkaline Ammonia Electrolysis on Electrodeposited Platinum for Controllable Hydrogen Production. ChemSusChem. 9(4): 403–408.
12. Li Y, Li X, Pillai HS, Lattimer J, Mohd Adli N, Karakalos S, Chen M, Guo L, Xu H, Yang J, Su D, Xin H and Wu G. 2020. Ternary PtIrNi Catalysts for Efficient Electrochemical Ammonia Oxidation. ACS Catalysis. 10(7): 3945–3957.
13. Allagui A, Sarfraz S and Baranova EA. 2013. NixPd1−x (x=0.98, 0.93, and 0.58) nanostructured catalysts for ammonia electrooxidation in alkaline media. Electrochimica Acta. 110: 253–259.
14. Zöllig H, Morgenroth E and Udert KM. 2015. Inhibition of Direct Electrolytic Ammonia Oxidation Due to a Change in Local pH. Electrochimica Acta. 165: 348–355.

WHEC-2022
23rd World Hydrogen Energy Conference
June 26-30, 2022 - Istanbul

#250

POWDER METALLURGY: AN EFFICIENT AND SCALABLE PRODUCTION PROCESS OF ELECTRODES FOR THE GIGAWATT ELECTROLYSIS INDUSTRY

[1;*], Thomas Rauscher, [1]Christian Bernäcker, [1]Justin Albers, [1] Martin Anders, [1]Tilo Büttner, [1]Stefan Loos, [1]Thomas Weißgärber, [1] Lars Röntzsch
[1] Fraunhofer Institute for Manufacturing Technology and Advanced Materials IFAM, Winterbergstraße 28, Dresden Germany

*Corresponding author e-mail: Thomas.Rauscher@ifam-dd.fraunhofer.de

ABSTRACT

In this contribution a powder metallurgical (PM) production process is outlined to produce highly active electrodes for the alkaline water electrolysis. Different catalytic coatings were produced on porous substrates, including foams. The electrochemical activity of the electrodes towards the hydrogen (HER) and oxygen evolution reaction (OER) were analyzed considering technical conditions. It can be shown that the performance of the catalysts can significantly be improved by adjusting the chemical composition and the catalytic loading. Furthermore, the catalytic coating obtained by the PM production route exhibits an excellent mechanical stability on different substrates.

Keywords: Alkaline Electrolysis, Cathode, Anode, Production Process

INTRODUCTION

For a future GW-industry of alkaline electrolysers, a large number of efficient and inexpensive electrodes has to be produced. According to the state of the art, mainly batch-based production processes are used, e.g. electrodeposition (e.g. De Nora [1], MTV GmbH [2]). For the development of a production process with a very high throughput of electrodes, two issues have to be considered: First, the produced electrodes have to be very active for the hydrogen (HER) as well as the oxygen evolution reaction (OER) and, second, the process has to be scalable. In this contribution, a powder metallurgical (PM) production process is outlined [3] to manufacture highly active electrodes. In particular, PM technologies are suitable to produce advanced materials for water electrolysis [3, 4]. The manufacturing technology can be applied to flat as well as porous metal structures. Especially, porous 3D electrode structures with a high surface area, a well-defined porosity for gas transport, a mechanically stable structure and a good electrical conductivity can fulfill the requirements for highly active, long-term stable and cheap electrodes. Accordingly, porous substrate based on metallic foam and fibre fleeces structures are chosen as electrode template. In this study, different examples of porous electrodes with a catalytic coating produced by PM production process are discussed with respect to the electrochemical activity for the HER and OER.

MATERIALS AND METHODS

A PM production process is employed to produce highly active electrodes for the HER and the OER. The approach comprises the deposition of powdery precursor onto a metallic substrate and subsequently a heat treatment to form a mechanically stable and electrocatalytically active catalyst on the surface (schematically shown in Fig. 1). By varying the powder to mesh mass ratio (PMR) different catalyst loadings can be achieved. The electrodes are evaluated in a 3-electrode setup at ambient pressure, at 353 K and in a 30 wt.-% KOH solution.

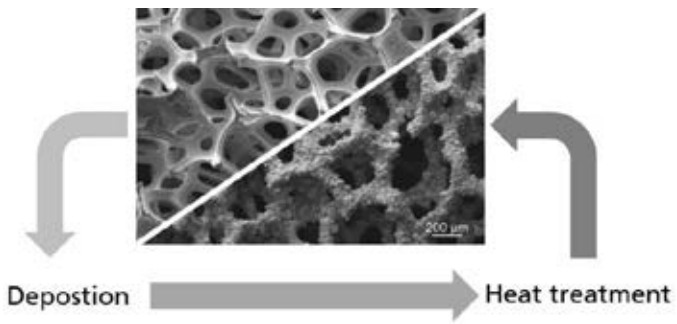


Fig. 1: Schematically description of the PM production process of electrodes.

RESULTS AND DISCUSSION

For the HER, Al was deposited onto different porous Ni materials (e.g. expanded metal, foam) in order to form a Raney-Ni layer on top of the substrate after heat treatment and a subsequent leaching step. The approach is

schematically given in Fig. 2. Due to the diffusion process during the thermal treatment, different Ni-Al phases are formed and a very homogeneous interface between the coating and the Ni core is formed. After the leaching step a lot of channels perpendicularly oriented to the bare Ni core can be seen, facilitating the easy detachment of gas bubbles. For the most active sample, the overpotential value for the HER was 50 mV at a current density of -0.3 A/cm². By using a higher PMR value, the stability of the Raney-Ni coating could be significantly enhanced, and the activity was strongly improved. For the best material, the HER caused no delamination of the catalyst layer, showing the high stability of the electrode. A plot of the HER overpotential versus the double layer capacitance C_{dl} (determined by cyclic voltammetry) suggests that the HER-activity is directly linked with the C_{dl}. Since the C_{dl} reflects the electrochemically active surface area, it is evident that the HER-activity also correlated with the surface area. These results demonstrate the high activity of Raney-Ni electrodes on the one hand and also the feasibility of a powder metallurgical approach to produce those electrodes. By applying a continuous heat treatment process, a high output of electrodes along with a strongly reduced CAPEX for the alkaline water electrolysis can be enabled.

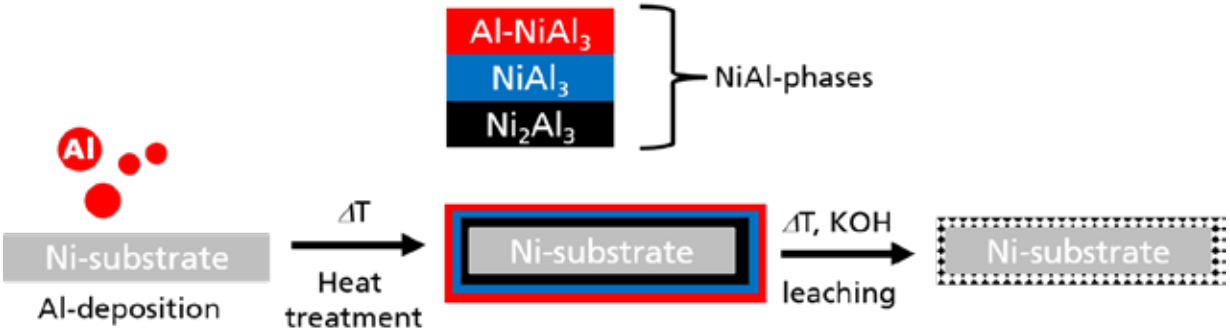


Fig. 2: Schematics of the powder metallurgical route to produce Raney-Ni electrodes.

For the OER a Ni-Mn coating was selected. Ni-Mn alloys have been described in the literature as supercapacitor materials [5], due to the high double layer capacitance. The approach was to coat the inner pores of a Ni foam with Ni-Mn to produce an active OER material. Therefore, Ni-Mn (70 at.-% Mn) powder was deposited onto the foam and after the heat treatment a mechanically stable electrode was formed. The cross section revealed the existence of two different Ni-Mn phases. As can be seen from Fig. 3 left, the post processing induces the leaching of the Ni-Mn phase with the highest content of Mn. This results in a hierarchical porosity: large pores of the substrate (> 200 µm) and small pores from the leached Ni-Mn coating (< 1 µm). The Ni-Mn modified substrate has a much lower OER overpotential in comparison to the bare substrate (see Fig. 3 right). The overpotential value was below 250 mV at 0.3 A/cm², reflecting the high OER activity. The excellent activity of the prepared anode is also underlined in the contribution with a benchmarking of literature known values. In contrast to the cathode, the surface area of the anode material has no major impact on the OER activity. However, the intrinsic activity appears to be the main parameter influencing the activity.

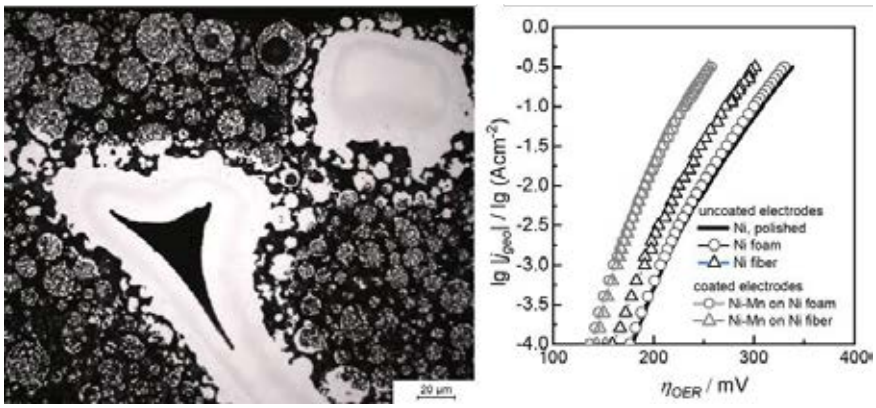


Fig. 3: left) SEM image of the catalyst attached to the substrate after a heat treatment and right) representative OER Tafel plots.

CONCLUSION

In summary, a powder metallurgical production process is outlined to produce highly active electrodes for the HER and OER in alkaline media. By using a continuous furnace for the heat treatment in future a high output can be realized.

With respect to the different alkaline electrolyzer technologies (gap or zero-gap design), the process is also applicable to flat (e.g. perforated metal sheets) as well as to porous (e.g. foams, fibre fleeces, meshes) substrate materials.

ACKNOWLEDGEMENT

This work has been carried out within the ELYntegration (funded by the EU, No. 671458) project and the AEL3D project (funded by the German federal ministry of education and research, 03ET6063A)

REFERENCES

1. Krstajic, JV, Antozzi AL. Electrode suitable as hydrogen-evolving cathode (EP2361324 B1); 2009.
2. Barisic M, Wilbuer KL Electrode for the alkaline electrolysis of water (EP3159433 A1); 2015.
3. Bernäcker CI, Rauscher T., Büttner T, Kieback B, Röntzsch L. 2019. A Powder Metallurgy Route to Produce Raney-Nickel Electrodes for Alkaline Water Electrolysis. J. Electrochem. Soc. 166:F357-F363.
4. Rauscher T., Bernäcker CI; Loos S., Vogt M., Kieback B., Röntzsch L. 2019. Spark-plasma-sintered porous electrodes for efficient oxygen evolution in alkaline water electrolysis, Electrochim Acta, 317. 128.
5. Fujita T, Kanoko Y, Ito Y, Chen L, Hirata A, Kashani H, Iwatsu O, Chen M. 2015. Nanoporous Metal Papers for Scalable Hierarchical Electrode. Adv. Sci. 2:1500086.

WHEC-2022
23rd World Hydrogen Energy Conference
June 26-30, 2022 - Istanbul

#251

INVESTIGATION OF ELECTROLYTE FORCED FLOW FOR ALKALINE WATER ELECTROLYSIS USING COMPUTATIONAL FLUID DYNAMICS

[1*] *Christos Georgiadis,* [1] *Fernando Rocha,* [2] *Jonathan Lambrechts and* [1] *Joris Proost*
[1]Université catholique de Louvain (UCLouvain), Institute of Mechanics, Materials and Civil Engineering, Division of Materials and Process Engineering, Place Sainte-Barbe, 2, 1348 Louvain-la-Neuve, Belgium
[2]*Université catholique de Louvain (UCLouvain), Institute of Mechanics, Materials and Civil Engineering, Division of Applied Mechanics and Mathematics, Avenue Georges Lemaître, 4-6, 1348 Louvain-la-Neuve, Belgium*

*Corresponding author e-mail: christos.georgiadis@uclouvain.be

ABSTRACT

Green hydrogen production by water electrolysis constitutes a fundamental process for the transition to the hydrogen economy. While alkaline water electrolysis is considered a mature technology to this end, recent work has shown that we can achieve further process intensification with forced electrolyte flow through macro-porous 3D electrodes. The objective of this work is to simulate and analyze electrolyte flow through an industrial-scale pilot and through lab-scale 3D printed electrodes using Computational Fluid Dynamics (CFD). Initial results show that our current pilot cell design is inadequate for forced flow and offer insights in order to design a cell structure that is more suited for gas removal.

Keywords: Computational Fluid Dynamics, Alkaline water electrolysis, Forced Flow

INTRODUCTION

Recent experimental results show that forced electrolyte flow through foams or 3D printed electrodes can offer a significant increase in performance [1,2]. Increased surface area offered by these structures leads to a higher hydrogen production rate while forced flow permits efficient bubble removal. The aim of this work is to complement experimental work with CFD simulations in order to obtain a better understanding of the full field flow characteristics inside the electrode. Reviewing the relevant literature, we observe this kind of analysis has rarely been addressed [3].

Our lab-scale experiments on 3D printed structures show the benefits in terms of performance. Unfortunately, we do not observe the same behaviour in an industrial-scale pilot that is modified for electrolyte flow. We perform here simulations of single-phase flow of electrolyte to assess the hydrodynamic behaviour of the cell for both cases: the industrial-scale pilot and the lab-scale 3D printed electrodes. Our objective is to associate electrochemical performance with flow characteristics in order to design an appropriate geometry for industrial-scale electrolyzers.

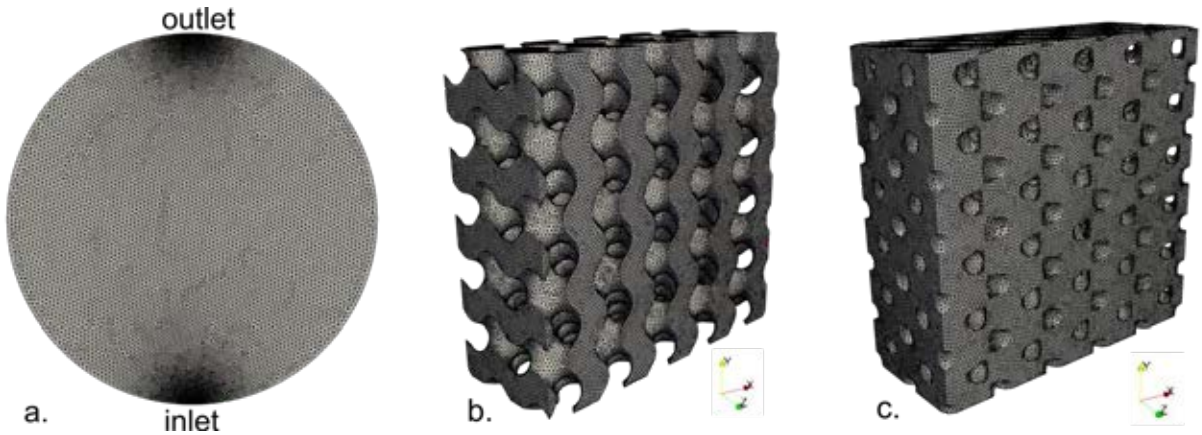


Fig. 1. Computational meshes. a) 2D pilot. b) Gyroid structure. c) Schwarz structure.

MODELING

The geometry of the pilot-scale electrolyzer is circular with a radius of 195 mm and a width between the front and the back plate of 6mm. The inlet at the bottom has a diameter of 2mm and the extractor outlet has a diameter of 4mm. The model geometry of the cell was created and meshed using Gmsh [4] with an interior mesh size of 0.025 m and reduced mesh size of 0.0125 m near the inlet and the outlet (Fig. 1.a.). For the 3D printed electrodes, we use the equations of [5] and create models for a Gyroid and a Schwarz structure. We generate the geometry on a 20x20x8 mm rectangular region and we mesh with an element size of 0.005 m (Gyroid on Fig. 1.b. and Schwarz on Fig. 1.c.). Mesh element sizes were chosen to resolve the flow scales of interest, for which the explicitly described geometries of the 3D printed electrodes require a smaller mesh size.

The incompressible Navier-Stokes equations for a single-phase flow were solved using the Finite Element Method (FEM) implemented in MigFlow software [6]. The electrolyte is water with density ρ = 1000 kg/m^3 and kinematic viscosity v = 0.003 Pa s. For the case of the pilot cell we make the assumption of a 2D flow since the width is small compared to the diameter. To account for the drag of the front and the back walls of the cell we make the hypothesis of a Poiseuille flow in the direction of the flow. For the electrode structures we run 3D simulations since we want to observe the associated flow phenomena such as the vorticity intensity. The boundary conditions for the simulation are the inlet velocity of the electrolyte and zero pressure at the outlet.

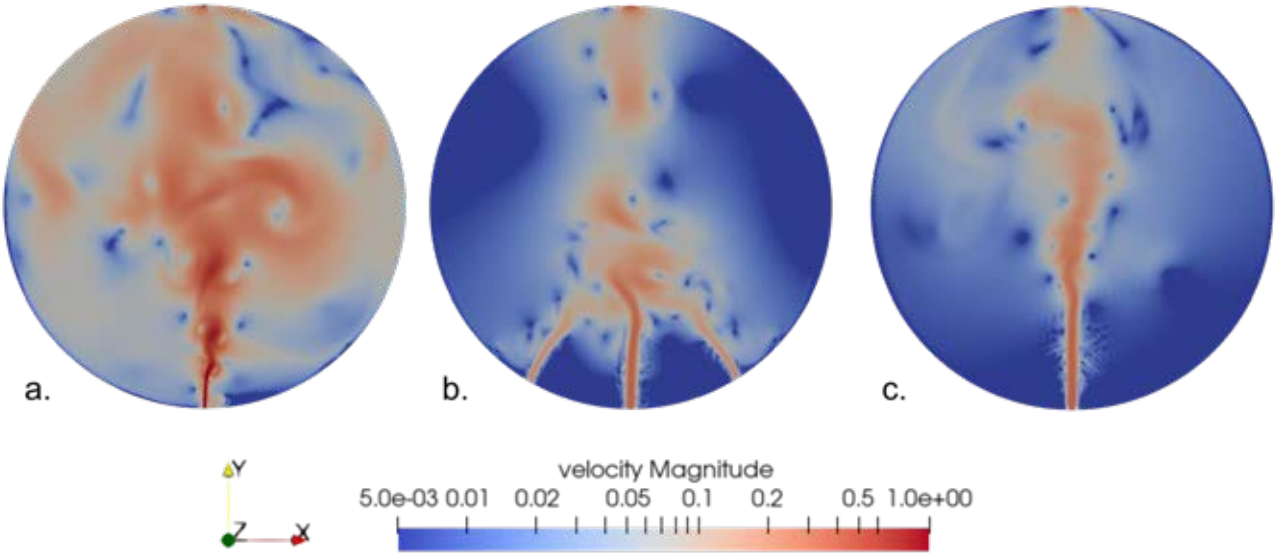


Fig. 2. Velocity profiles for three pilot inlet configurations. a) Current experimental setup. b) Three inlets. c) Inlet of bigger size.

RESULTS AND DISCUSSION

The flow rate chosen for the pilot simulations is 62.5 L/h. This value is a bit higher than the experimentally measured flow rate for the operation of the pilot cell with natural convection. It is therefore the lower limit for which we should consider forced flow. The inlet velocity of the fluid is then calculated at 1.45 m/s for an inlet area of 0.002 m x 0.006 m = 0.000012 m^2. High inlet velocity through the small opening produces a jet stream flow, which quickly evolves to a shear layer and leads to flow instabilities. Vortical structures are generated and convected throughout the domain, as visualized in Figure 2.a. This kind of flow would lead to concentration of gases that circulate or even remain stagnant in certain regions of the cell.

We investigated the possibility of modifying the inlet conditions in order to obtain smoother velocity profiles throughout the cell. At first, we use two supplementary inlets on symmetrical positions. The situation in this case gets more perplexed, as we would also have a mixing of the three jets in the middle of the cell (Fig. 2.b.). As another option, and since we identify as the cause of instability the high electrolyte velocity on the input, we also examined the possibility of a larger input area and thus lower velocity for the same flow rate. This choice only delays the onset of instabilities forming even though it leads to a less turbulent flow (Fig. 2.c.). In the general case though, we are aiming for flow rates up to 600 L/h where an enlarged inlet would not mitigate turbulent effects.

In the case of 3D printed structures the impact of forced flow is significant, and in particular we observe better performance on Schwarz structures compared to Gyroid ones. By performing 3D flow simulations on a Gyroid and a Schwarz structure of similar surface area, we can identify some qualitative characteristics that promote electrochemical efficiency. For average velocities of 1 m/s flow through the electrode, we can see that for Schwarz the flow is more laminar and thus could offer better gas removal (Fig. 3.b.). The structure of the Gyroid on the other hand leads to higher vorticity and mixing in the x-z directions, therefore there exist regions where gas evacuation may be hindered (Fig. 3.a.).

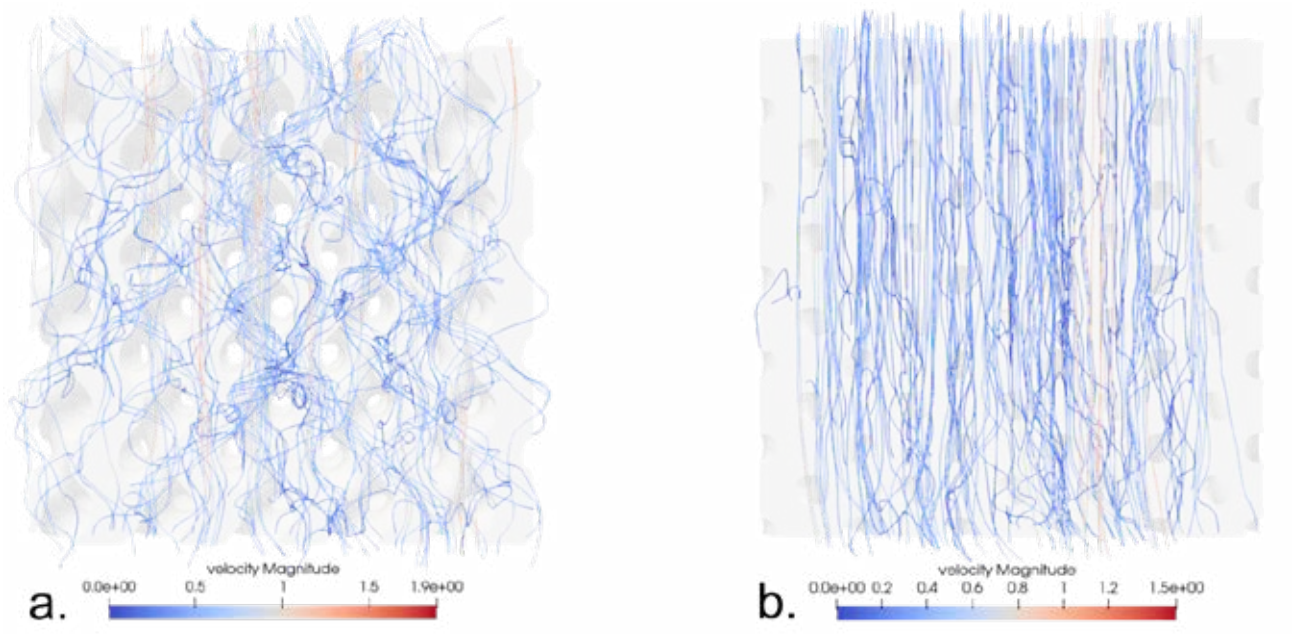


Fig. 3. Velocity streamlines on a) Gyroid and b) Schwarz 3D printed structures.

CONCLUSIONS

We performed computational fluid dynamics simulations to obtain insights about the performance of electrolysis with forced flow. Flow characteristics on the pilot show that the current setup is inadequate to enhance performance with forced flow. For 3D printed structures, we conclude that it is important to have geometries which on the one hand offer high surface area and on the other hand can accommodate a smooth flow evolution. The next step of our developments is to incorporate such a 'flow-guiding' structure in the pilot cell. This work is the initial step towards the modeling of the whole process that will simulate the two-phase flow of the electrolyte and the hydrogen gases.

ACKNOWLEDGEMENT

We gratefully acknowledge financial support from the European Commission through the H2020 Project "NexTAEC" (Materials for Next Generation Alkaline Electrolyzers), under contract n° 862509.

REFERENCES

1. Kou, T., Wang, S., Shi, R., Zhang, T., Chiovoloni, S., Lu, J. Q., Chen, W., Worsley, M. A., Wood, B. C., Baker, S. E., Duoss, E. B., Wu, R., Zhu, C., Li, Y., Periodic Porous 3D Electrodes Mitigate Gas Bubble Traffic during Alkaline Water Electrolysis at High Current Densities. Adv. Energy Mater. 2020, 10, 2002955. https://doi.org/10.1002/aenm.202002955
2. de Radiguès Q, Thunis G and Proost J. 2019. On the use of 3-D electrodes and pulsed voltage for the process intensification of alkaline water electrolysis. International Journal of Hydrogen Energy 44:29432-29440.
3. Rodríguez, Jesús & Amores, Ernesto. (2020). CFD Modeling and Experimental Validation of an Alkaline Water Electrolysis Cell for Hydrogen Production. Processes. 8. 1634. 10.3390/pr8121634.
4. C. Geuzaine and J.-F. Remacle. Gmsh: a three-dimensional finite element mesh generator with built-in pre- and post-processing facilities. International Journal for Numerical Methods in Engineering 79(11), pp. 1309-1331, 2009.
5. Nurshaun Sreedhar, Navya Thomas, Oraib Al-Ketan, Reza Rowshan, Hector Hernandez, Rashid K. Abu Al-Rub, Hassan A. Arafat, 3D printed feed spacers based on triply periodic minimal surfaces for flux enhancement and biofouling mitigation in RO and UF, Desalination, Volume 425, 2018, Pages 12-21, ISSN 0011-9164, https://doi.org/10.1016/j.desal.2017.10.010.
6. Constant M., Dubois F., Lambrechts J. and Legat V.Implementation of an unresolved stabilised FEM–DEM model to solve immersed granular flowsin Computational Particle Mechanics (2018). https://doi.org/10.1007/s40571-018-0209-4

WHEC-2022
23rd World Hydrogen Energy Conference
June 26-30, 2022 - Istanbul

#307

A NUMERICAL ENERGY AND EXERGY ANALYSIS OF THE EFFECT OF PHASE CHANGE MATERIALS ON A PHOTOVOLTAIC THERMAL COLLECTOR FOR HYDROGEN PRODUCTION IN NORTH CYPRUS

[1*] *Ahmad Sultan,* [2] *Muhammad Abid,* [1*] *Mustafa Dagbasi*
[1]Cyprus International University, Energy Systems Engineering, Nicosia, TRNC
[2] Universiti Brunei Darussalam, Integrated Technologies, Energy Systems Engineering, Brunei Darussalam

ABSTRACT

Thermal energy storage has been accompanying energy systems the moment their full potential was realized, from these, the phase change material is a key element in increasing the efficiency of the photovoltaic thermal system, through research it was shown that phase change materials increase the efficiency by lowering the temperature of the panel which leads to a higher efficiency. In the paper, the effects of several phase change materials will be observed in Cyprus and analyzed to assess the best PCM to optimize hydrogen production. A MATLAB model that was validated will be used to assess the performance of several PCMs in the production of hydrogen in north Cyprus. The study shows that the pcm causes an increase in efficiency and the power output of the total system, in addition to that the one that shows the most significance phase change material that will cause the optimal hydrogen production as well as the range of which t chose the PCM for better hydrogen production.

Keywords: Photovoltaic Thermal System, Phase Change Materials, Hydrogen Production

INTRODUCTION

The stepping stone that turned the events and raised awareness amongst nations was the aftermath of the industrial revolution that was the cause of several disasters inflicted on our environment. Olabi et al. [3] indicated in his review that the repercussions of this event created a mass increase in the C02 emissions and led to global warming. In the midst of this crisis, the early industrialized countries came together to prevent further damages. After the 1973 oil crisis adding to the problem, the countries came together in order to try to solve the problem at hand. They discussed the issue but it wasn't until the Kyoto protocol of 1997 which was an international treaty following the 1992 United Nations Framework Convention on Climate Change that a solution started to take place. After 21 years of negotiations the countries seemed to reached a global agreement to lower their emissions. Kannah [4] added that in Paris 2015 during the Conference of Parties meeting with the presence of almost 200 countries produced a legally binding agreement to ensure that the global warming is kept below 2°C which is a compulsive end that modulates and tells the economies around the globe to decarbonize spacious parts of the world's power system. From this history we can notice the importance of hydrogen and therefore further research towards improving and optimizing the use and production of this gas is the key to a greener future. Therefore, a system that produces hydrogen is needed and to be able to have a higher efficiency of that system we can use phase change materials to increase the efficiency pf the PVT system. Christopher et al. [2] explained in his research, the PCMs and their used in solar thermal application, in addition to that the researchers assessed the energy storage systems with cascaded configurations using phase change materials.

METHODOLOGY

In this study, the system observed in Fig. 1 part a is considered using the proposed photovoltaic thermal panel which is integrated with phase change material for the purpose of electricity, heat and hydrogen generation for a off grid setting. The design parameters were gathered and then the temperatures calculating based on the energy balance equations of the system which were then solved using a developed code using MATLAB. The energy and exergy analysis of the system has been calculated and shall be presented.

Equations

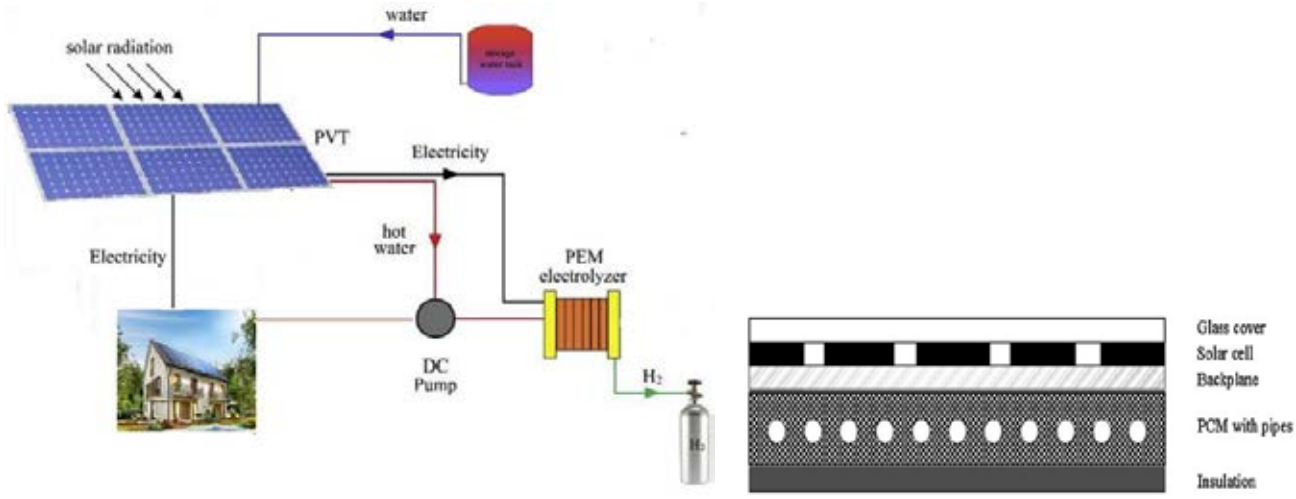
Some of the Energy balance equation as gotten from Brown et.al. [5] and Babayan et. Al [6] that have been used in the research are as follows:

$$\partial Qpcm = W \times L \times [Ubp \times (T_pm - T_pv))) - (hw \times (T_pm - T_fm)) - (U_bar_L \times (T_pm - T_in))]\partial t \quad (1)$$

$$if\ Qpcm < Qsol$$
$$Tp = Tmp - ((Qsol - Qpcm)/Cpcms), \lambda p = \lambda pcms$$

$$if\ Qsol\ < Qpcm < Qliq$$
$$Tp = Tmp, \lambda p = \lambda pcms \times ((Qliq - Qpcm)/(Qliq - Qsol)) + \lambda pcml \times ((Qpcm - Qsol)/(Qliq - Qsol))$$
$$if\ Qliq\ < Qpcm$$
$$Tp = Tmp - ((Qpcm - Qliq)/Cpcml),\ \lambda p = \lambda pcml$$

$$H_2O \Rightarrow H_2 + \frac{1}{2} O_2 \quad (2)$$



(a) (b)

Fig. 1. a) Proposed System Schematics b) PVT-PCM Proposed Panel

RESULTS AND DISCUSSION

As can be seen in Fig. 2, the simulation based on the MATLAB code personally designed is almost identical to the simulation done by Brown et. al [5] using the parameters indicated in the research, then the system was introduced as proposed in figure 1. The results of the temperature variation can be seen in Fig. 3 with shows an identical slope and behavior as seen in Babayan et. al [6] meaning the results gotten for the MATLAB code are reliable hence the research will try to assess the energy and exergy analysis of the system as well as the hydrogen production rate.

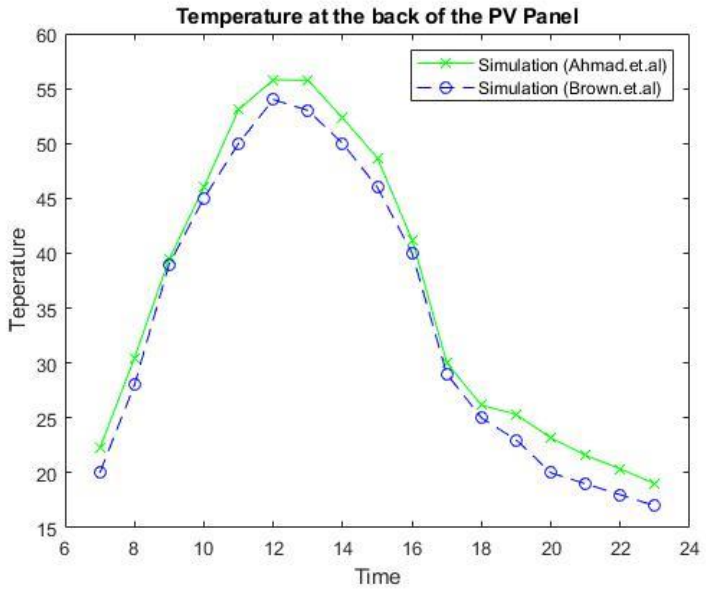


Fig. 2. Comparison between Simulated results

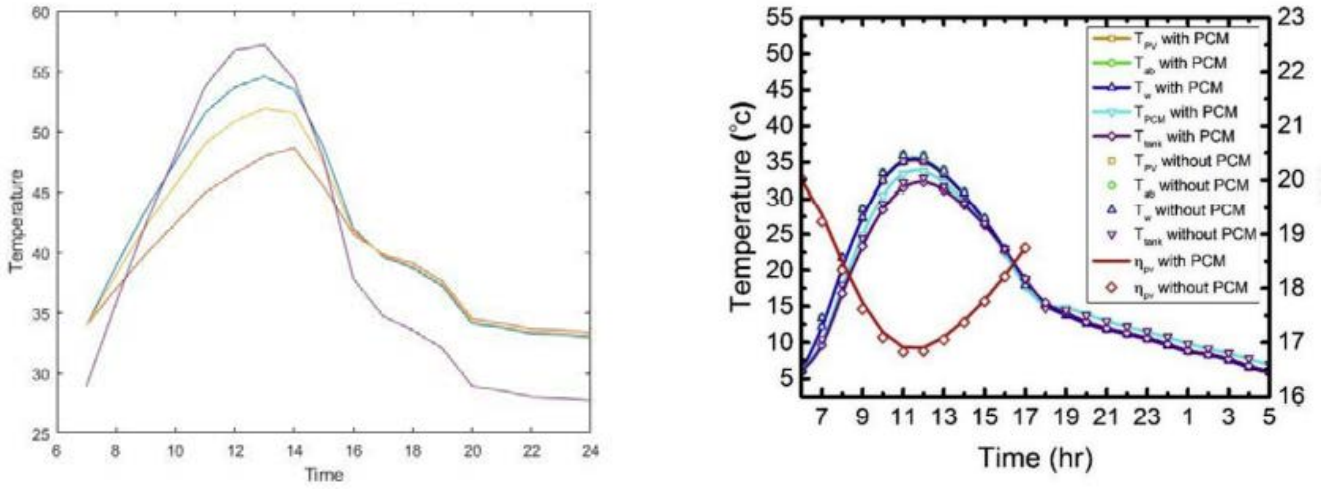


Fig. 3. Comparison of the variation of PV, water, absorber, PCM temperatures with respect to time

CONCLUSIONS

This study hopes to achieve

- The PVT temperature should decrease due to the phase change material which leads to a higher system efficiency
- The residue electricity for the panel is enough to initialize the proton exchange membrane which will start the production of hydrogen
- Hydrogen is stored in a tank which can be later connected to a fuel cell for further use in the energy production at night

REFERENCES

1. Shahid, UB, & Abdala, A. (2020). A critical review of phase change material composite performance through Figure-of-Merit analysis: Graphene vs Boron Nitride. Energy Storage Materials.
2. Christopher, S., Parham, K., Mosaffa, AH, Farid, MM, Ma, Z., Thakur, AK, & Saidur, R. (2020). A critical review on phase change material energy storage systems with cascaded configurations. Journal of Cleaner Production, 124653.
3. Olabi, A. G., Abdelghafar, A. A., Baroutaji, A., Sayed, E. T., Alami, A. H., Rezk, H., & Abdelkareem, M. A. (2021). Large-vscale hydrogen production and storage technologies: Current status and future directions. International Journal of Hydrogen Energy, 46(45), 23498-23528.
4. Kannah, R. Y., Kavitha, S., Karthikeyan, O. P., Kumar, G., Dai-Viet, N. V., & Banu, J. R. (2021). Techno-economic assessment of various hydrogen production methods–A review. Bioresource Technology, 319, 124175.
5. Brown, D., Jia, Y., Lin, Y., & Fang, G. (2017). Maximizing the energy output of a photovoltaic–thermal solar collector incorporating phase change materials. Energy and Buildings, 153, 382-391.
6. Babayan, M., Mazraeh, A. E., Yari, M., Niazi, N. A., & Saha, S. C. (2019). Hydrogen production with a photovoltaic thermal system enhanced by phase change materials, Shiraz, Iran case study. Journal of Cleaner Production, 215, 1262-1278.

WHEC-2022
23rd World Hydrogen Energy Conference
June 26-30, 2022 - Istanbul

#308

Ir-DECORATED Pt NANOPARTICLES AS A BIFUNCTIONAL CATALYST FOR OXYGEN EVOLUTION AND REDUCTION REACTIONS

[1]Lucinda Blanco Redondo, [1]Vladimír Matolín, [1]Yevheniia Lobko*
[1]Charles University, Faculty of Mathematics and Physics, Department of Surface and Plasma Science.
V Holesovickach 2, 180 00, Prague 8, Czech Republic

*Corresponding author e-mail: lublare93@gmail.com

ABSTRACT

The challenge of meeting the growing worldwide energy demand requires progress in using renewable energy sources and hydrogen technology. Regenerative fuel cells (URFCs) are expected to be part of this energy system shift. URFC is an electrochemical device that can operate alternately as a fuel cell (to produce electricity) or water electrolyser (to produce hydrogen). Merging of WE and FC in a unique device would decrease costs due to the reduced use of precious catalysts. However, the way to develop an efficient device is still opened. Oxygen electrode in URFC is a limiting component because of the sluggish kinetics of the oxygen reduction and oxygen evolution reaction (ORR and OER). Moreover, there is not a common material that catalyses both reactions: the most suitable materials for ORR and OER are platinum and iridium, respectively. Consequently, it is necessary to reach a compromise in the composition of a bifunctional oxygen catalyst (BOC) based on Pt and Ir to improve, or at least sustain, the activity and stability with the lowest noble metal loading possible. The present work reports the polyol synthesis of Ir-decorated Pt nanoparticles with different compositions (Ir10/Pt90, Ir20/Pt80, and Ir40/Pt60). For a good understanding of the electrochemical properties, morphological and chemical surface composition of the nanoparticles have been studied by means of XRD, EDS, TEM, XPS, and RDE techniques. The results showed that the nanoparticles with an Ir:Pt ratio 20:80 display the best results.

Keywords: PEM Unitized Regenerative Fuel Cell, Catalyst, Polyol Method, Iridium, Platinum.

INTRODUCTION

Nowadays, the world faces a great energy challenge that involves two main aspects: meeting the rise of the global energy demand and reducing of carbon emissions to the atmosphere. The efforts to reach these targets go through the electrification of end-use sectors and the energy transition from fossil fuels to renewable energy. Fuel cells (FCs) and water electrolysers (WEs) are green technologies for electricity and hydrogen production, respectively [1]. Merging of these devices in a Unitized Regenerative Fuel Cells (URFC) would represent substantial decrease of costs due to the reduced use of precious catalysts. However, the way of developing an efficient and durable unit is still opened.

Proton exchange membrane water electrolysers (PEM-WEs) and proton exchange membrane fuel cells (PEM-FCs) have similar configuration and both technologies work with a solid polysulfonated membrane. Nevertheless, the oxygen electrode has different requirements depending on the operation mode. There is not a common material that catalyses the Oxygen Reduction Reaction (ORR, for FC mode) and the Oxygen Evolution Reaction (OER, for WE mode). The most suitable material that catalyses the ORR is the platinum, whereas OER can be catalysed by iridium, but not Pt [2]. As a consequence, it is necessary to focus the attention on the development of a metal combination that works as bifunctional oxygen catalyst (BOC). In this regard, BOCs based on Pt and Ir have been investigated in the past years and most of those catalysts were obtained by mechanical mixing of powders [3]. Consequently, the bad dispersion of the components led to a low bifunctional performance. Herein, we present an efficient route for the preparation of Ir-decorated Pt nanoparticles in a two-steps one-flask synthesis by the polyol method containing polyvinyl pyrrolidone (PVP) as a capping agent. The use of PVP permits the Pt nanoparticles to stabilize during the synthesis and prevents from agglomeration enlarging their surface area [4]. Thus, Ir nanoparticles are highly dispersed on the Pt surface which is a great strategy for maximizing the utilization of precious metals. This work systematically studies the effect of catalyst composition ($Ir_{100-x\%}/Pt_{x\%}$) through a three-electrode system with the purpose of finding the best Pt-Ir mass ratio that optimizes the ORR and OER performance without compromising their stability.

EXPERIMENTAL

Materials

The metal precursors chloroplatinic acid hexahydrate ($H_2PtCl_6 \cdot 6H_2O$, 99.99%) and dihydrogen hexachloroiridate (IV) hydrate (($H_2IrCl_6 \cdot xH_2O$ 99.99%), polyvinylpyrrolidone (PVP) 10,000 MW, and ethylene glycol (99%) were acquired from Alfa Aesar. Sulfuric acid (H_2SO_4, 95.0-97.0%) was acquired from Honeywell Fluka. Hydrogen peroxide (H_2O_2, 30%) was acquired from Emsure. Isopropanol (p.a) was acquired from Penta, and commercial Pt black and Ir black were acquired from Fuel Cell Store. The water used in all tests was ultrapure (Millipore, 18.2 MΩ cm).

Synthesis of Ir-decorated Pt nanoparticles

The Ir-decorated Pt nanoparticles (NPs) were prepared by deposition of Ir NPs on the surface of Pt NPs through the polyol method. This method uses a polyol, ethylene glycol in this work, acting simultaneously as solvent and reducing agent. Prior of the synthesis, the metal precursor solutions were prepared by combining the metal precursor powder and ethylene glycol in a concentration of 0.04 M. Furthermore, PVP was added to each precursor solution and dispersed under sonication for 30 minutes. In a typical Pt NPs synthesis, the Pt precursor solution with PVP was contained in a round bottom flask submerged in an oil bath and heated under reflux and vigorous stirring at a temperature of 160º for one hour. Subsequently, the Ir precursor solution with PVP was introduced in the synthesis flask with the aim of reducing the Ir precursor directly on the surface of the already existing Pt NPs. The Ir synthesis parameters were kept the same as the Pt synthesis, 160ºC of temperature and 1 hour of reaction time. To remove the PVP from the nanoparticles surface, the methodology reported by Monzó et al. was followed. Briefly, the suspension of nanoparticles was mixed with a H_2O_2/H_2SO_4 solution, centrifugated and rinsed with ultrapure water.

Physicochemical and electrochemical analysis

The microscopy and spectroscopy techniques used are listed below. X-ray diffraction (XRD) patterns were recorded using a Rigaku SmartLab diffractometer with a Cu Kα-source (λ = 1.54059 Å) operating at 9 kW and completed in the angle range from 20º to 140º. The elemental chemical composition was evaluated by energy dispersive X-ray (EDX). The analysis was carried out at accelerating voltages of 20 kV in a Tescan MIRA 3 apparatus equipped with a Bruker Quantax detector XFlash 6|10 spectrometer. The surface chemical composition of the nanoparticles was measured through X-ray photoelectron spectroscopy (XPS). The analysis was performed in ultra-high vacuum chamber equipped with a SPECS Phoibos 150 hemispherical analyser and Mg (Kα) X-ray source. The morphology and structure of the catalysts were characterized by means of high-resolution transmission electron microscopy (HR-TEM), including scanning mode (STEM), supported by electron diffraction (ED) in a JEOL NEOARM 200 microscope at accelerating voltage of 200 kV. The electrochemical characterization of the nanoparticles was investigated by rotating disk electrode (RDE) technique in a three-electrode setup from Pine Research Instrumentation. The electrodes used were a Pt counter electrode (AFCTR5), a standard $Hg/HgSO_4$ reference electrode, and a glassy carbon disk as working electrode. All the experiments were conducted on an aqueous H_2SO_4 solution (0.5 M) electrolyte at room temperature and using a Bio-Logic SP-50 potentiostat.

RESULTS AND DISCUSSION

The physicochemical characterization confirms the raspberry-like morphology of the nanoparticles where Ir nanoparticles with a smaller size of about 2 nm decorate Pt nanoparticles of about 8 nm. Fig. 1 left shows the HR-TEM images of the catalyst. In addition, XPS spectra (Fig. 1 right) shows how Ir composition on the surface is enlarged in comparison with the EDS composition (bulk composition). This circumstance influenced the electrochemical behaviour of the catalysts compared to the pure commercial Ir and Pt nanoparticles (see Fig. 2). Activity towards ORR was slightly reduced due to the Ir coverage that reduced the number of Pt active sites accessible, while OER activity was improved in comparison with the commercial reference Ir black. The reason of the increased activity of the as-synthesized nanoparticles is linked to the non-reversible oxidation process occurred at the high potentials at which OER happens. In addition, it was discovered not only a complete oxidation of the Ir nanoparticles but their change into the highly active species (Ir hydroxides) directly related to the improvement of the OER rate [5]. The formation of these oxides was observed in the presence of the Ir3+ state at the XPS spectra obtained from the samples after an electrochemical activation by RDE technique. The origin and cause of the production of these species is still under development.

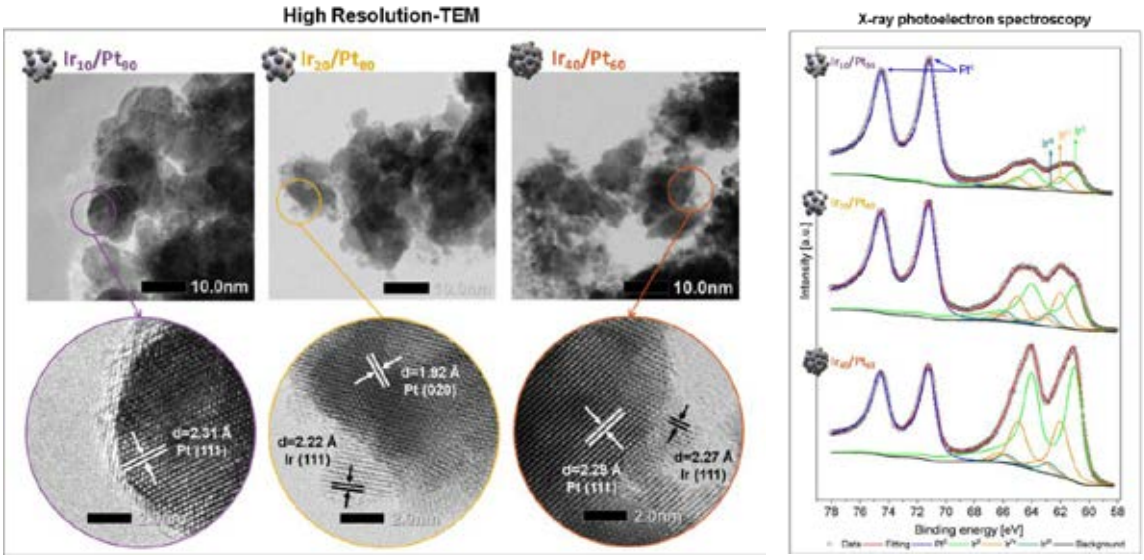


Fig. 1. HR-TEM images of the catalysts (left) and XPS spectra of the catalysts (right).

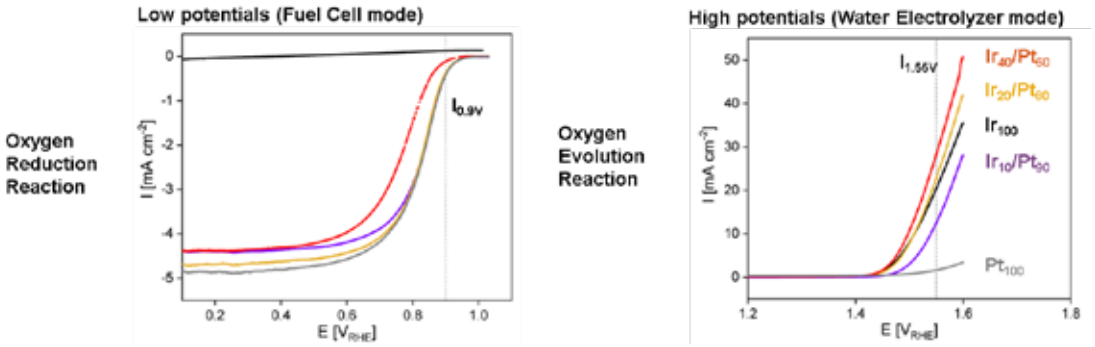


Fig. 2. Linear sweep voltammetry of the catalysts at low and high potentials.

CONCLUSIONS

Ir-decorated Pt nanoparticles with a raspberry-like structure was synthesized through polyol method. All the bimetallic samples displayed higher Ir mass activity than that of commercial Ir due to an improved utilization of the Ir nanoparticles and their complete oxidation to a highly active Ir3+ state. Finally, IrPt-based catalysts showed smaller Pt mass activity than that of commercial Pt due to the Ir coverage that reduces the availability of Pt active sites. Nevertheless, Ir10/Pt90, Ir20/Pt80 had a comparable activity. Also, $Ir_{20}Pt_{80}$ exhibited remarkable stability in both durability test modes. Thus, it is a promising candidate for the oxygen catalyst in PEM unitized regenerative fuel cells.

REFERENCES

1. Paul B. 2017. PEM unitised reversible/regenerative hydrogen fuel cell systems: State of the art and technical challenges. Renew. Sustain. Energy Rev., vol. 79, pp. 585–599.
2. Antolini E. 2014. Iridium as catalyst and cocatalyst for Oxygen Evolution/Reduction in Acidic Polymer Electrolyte Membrane Electrolyzers and Fuel Cells. ACS Catalyst, vol. 4, pp. 1426-1440.
3. Jung H. Y. 2009. Electrochemical studies of an unsupported PtIr electrocatalyst as a bifunctional oxygen electrode in a unitized regenerative fuel cell. J. Power Sources, vol. 191, no. 2, pp. 357–361.
4. Goel A. 2012. Effect of PVP, PVA and POLE surfactants on the size of iridium nanoparticles. Open Journal of Inorganic Chemistry, vol. 2, no. 3, pp. 67–73, 2012.
5. Freakley S. J. 2017. The X-ray photoelectron spectra of Ir , IrO2 and IrCl 3 revisited. Surface and Interface Analysis, vol. 49, no. 8, pp. 794-799.

WHEC-2022
23rd World Hydrogen Energy Conference
June 26-30, 2022 - Istanbul

#344

GREEN HYDROGEN FOR AMMONIA PRODUCTION – A CASE FOR THE NETHERLANDS

*Gianni Pagani, Canan Acar, Yashar Hajimolana
University of Twente, Faculty of Engineering Technology, 7500 AE Enschede, The Netherlands

*Corresponding author e-mail: g.l.paganiserrano@student.utwente.nl

ABSTRACT

An integrated system is studied to supply green hydrogen feedstock for ammonia production in the Netherlands. The system compares wind and solar resources when coupled to alkaline and PEM electrolysis with a compressed hydrogen storage system. The nominal installed capacity of the electrolysis plant is around 2.3 GW, the most suitable energy source is offshore wind, and the preferred storing technology is pressurized tubes. The levelized costs of hydrogen (LCOH) are 5.30 €/kgH_2 and 6.03 €/kgH_2, and the levelized costs of ammonia (LCOA) are 1.22 €/kgNH_3 and 1.34 €/kgNH_3 for alkaline and PEM technologies, respectively.

Keywords: Green Hydrogen, Green Ammonia, Levelized Cost, Renewable Energies

INTRODUCTION

Ammonia is the material with the highest emission intensity per ton of product in the industry sector, accounting for more than 1% of global emissions as 95% of the hydrogen feedstock is derived from fossil fuels [1]. One possible way to decarbonize ammonia and hydrogen production is combining industrial electrolysis and electricity generated by renewable sources, known as green hydrogen (GH). When GH is used as feedstock, the ammonia produced is called Green Ammonia (GA). Different initiatives and studies have been announced for GH and GA in the industry and in the academy. On one hand, the industry presents the information without revealing the methodology of the studies such as in [2]. On the other hand, the studies found in the academic literature develop methodologies for GH and GA production without linking the demand to the industry's requirements as in [4]. For this reason, this work is intended to bridge the gap between the development of a methodology with the needs of the industry sector for GH and GA production systems at a large scale.

MODEL DEVELOPMENT

The main components of the Green Hydrogen Integrated System (GHIS) are the variable energy resources (VRES), the Electrolysis Plant, and the Hydrogen Storage System, as shown in Fig. 1. The VRES are wind and solar. The technologies selected for the electrolysis plant are alkaline (AEL) and PEM (PEMEL). The storage system uses Compressed Hydrogen Technologies, and the Ammonia plant is considered to find the demand for hydrogen. The analysis is limited to the main components inside the red dashed line.

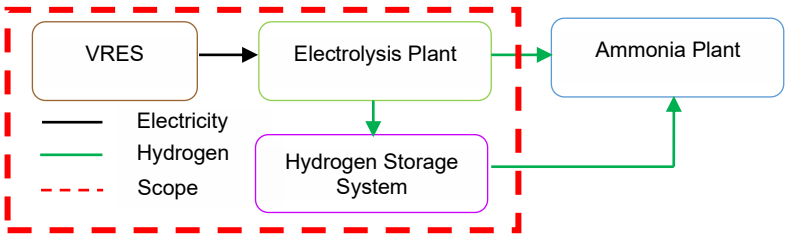


Fig. 1. General representation of the GHIS.

Hydrogen Demand

The nominal hydrogen demand is based on the production requirements of the largest fertilizer plant in the Netherlands, and it is assumed to be the addition of the stoichiometric plus the storage requirements of the ammonia synthesis process. The former is defined using Eq.(1), and the latter is defined as 25% of the stoichiometric demand that corresponds to the flexibility of the ammonia production process [6].

$$NH_3\ \ Synthesis: N_2 + 3H_2 \rightarrow 2NH_3 \quad (1)$$

Electrolysis Plant

The nominal installed capacity of the electrolysis plant is found using Eq.(2). The values for the E_s for AEL and PEMEL technologies are based on typical values for commercial electrolyzes here considered as 52 kWh/kg at 64% efficiency and 50 kWh/kg at 67% efficiency with flexible operation between 20-100% and 10-100% [7], respectively.

$$P_{plant} = E_s / \dot{V}_{H_{2-nom}} \quad (2)$$

Variable Renewable Energy Sources Characterization

The VRES are fully dedicated to power the electrolysis plant. The wind resource is assessed using a typical wind profile with hourly resolution of the Dutch part of the North Sea to find the Average Power Density in W/m^2 of the wind resource [8]. For the solar energy resource, the data for the global horizontal irradiation is retrieved from the Photovoltaic Geographical Information System (PVGIS) of the European Commission [9]. Both resources are compared using the C_F defined in Eq.(3).

$$C_F = AEP_{act}/AEP_{theo} \tag{3}$$

Green Hydrogen Production and Storage

First, the hourly power output of the VRES is compared with the flexible operation range of the electrolyzers. Then, each value of the VRES energy output above the minimum partial load threshold is divided by the specific energy consumption using Eq.(4) to find the actual hydrogen yield. When the energy output is below the minimum partial load, the electrolyzers cannot operate due to safety reasons. Above this threshold, the electrolyzer produces hydrogen. For example, at nominal capacity, the difference between the nominal demand and the stoichiometric demand fulfills the storage requirements.

$$\dot{V}_{H_2-act} = P_{VRES}/E_s \tag{4}$$

Economic Assessment

The production costs for hydrogen and ammonia are assessed with the LCOH and LCOA respectively.

RESULTS AND DISCUSSION

Applying Eq.(4), the actual production of hydrogen is 45% and 46% of the nominal demand and applying Eq.(1), it is possible to cover 56% or 58% of the total annual demand of ammonia using AEL and PEMEL, respectively. The effects of the ranges for flexible operation make PEM technologies operate more hours throughout the year, and the energy curtailed could power auxiliary systems and compressors. Oxygen and heat are valuable subproducts of the electrolysis process and can be further utilized in different industrial applications such as steel plants and low-temperature district heating respectively. The water requirements given the actual hydrogen production are equivalent to 650 Olympic swimming pools per year.

The nominal installed capacity of the electrolysis plant applying Eq.(2) corresponds to 2.38 GW and 2.29 GW for AEL and PEMEL technologies, respectively. The VRES have the same nominal installed capacity, assuming they are fully dedicated to powering the electrolysis plant. Applying Eq.(3), the C_F of the wind and the solar resources are 47% and 13% respectively. Due to the higher C_F of wind compared to solar, the analysis is narrowed down to the electrolysis plant coupled to offshore wind. The storage system capacity is 3.94 ktonH_2 and equals the entire storage product of the month with the highest yield, which is January. The storage technologies considered are geological storage pressurized tubes cylindrical and spherical vessels. The comparison is made considering the geographical location, storing pressure, and capacity of each technology. Based on this, the most suitable technology is pressurized tubes as geological caverns are in the north of the country, making this solution non-realistic due to the location of the ammonia plant in the south. The LCOHs are 5.30€/kgH_2 and 6.03€/kgH_2 and the LCOAs are 1.22 €/kgNH_3 and 1.34 €/kgNH_3 for AEL and PEMEL, respectively. The results are summarized in Fig. 2. and compared with the costs of producing hydrogen and ammonia with the steam methane reforming process (SMR) and using electricity from the grid to cover 100% of the hydrogen demand. The price of electricity makes up a considerable part of the total costs



Fig. 2. Comparison of the results for the LCOH and LCOA for the GHIS.

The current annual emissions of the ammonia plant are 3.2 $MtCO_2$ [10], or 12% of the total emissions of the industry sector in the country, which are 26$MtCO_2$ [11]. Using the GHIS would be possible to avoid approximately 1700ktCO2, the equivalent to reduce more than 50% the current total emissions of the plant or 6% of the emissions of the sector.

CONCLUSIONS

The GHIS consists of an electrolysis plant power by fully dedicated VRES. Due to geographical conditions, offshore wind energy is the most suitable source with the highest C_F compared to solar energy. To cope with seasonal fluctuation, pressurized tubes are the preferred storing technology. The LCOHs and LCOAs of the GHIS are higher than the production costs using SMR. Finally, with the GHIS, it would be possible to reduce the current total emissions of the industry sector in the Netherlands up to 50% compared to the current values.

NOMENCLATURE

P_{plant}	Electrolysis plant nominal power installed capacity, W
E_s	Electrolyzer specific energy consumption, kWh/Nm^3
$\dot{V}_{H_{2-nom}}$	Nominal hydrogen demand, Nm^3/h
C_F	Capacity factor
AEP_{theo}	Theoretical annual energy production, Wh
AEP_{act}	Actual annual energy production, Wh
$\dot{V}_{H_{2-act}}$	Actual hydrogen production, Nm^3/h
P_{VRES}	Power output from VRES, W

REFERENCES

1. IEA. 2021. Ammonia Technology Roadmap: towards more sustainable nitrogen fertilizer production. International Energy Agency.
2. https://www.yara.com/corporate-releases/orsted-and-yara-seek-to-develop-groundbreaking-green-ammonia-project-in-the-netherlands/. Accessed on February 8, 2021.
4. Armijo J and Philibert Cédric. 2020. Flexible production of green hydrogen and ammonia from variable solar and wind energy: case study of Chile and Argentina. International Journal of Hydrogen Energy, vol. 45, no. 3, pp. 1541-1558.
6. ISPT. 2017. Power to Ammonia: feasibility study for the value chains and business cases to produce CO_2-free ammonia suitable for various market applications. Institute for Sustainable Process Technologies.
7. Buttler A, Spliethoff H. 2018. Current status of water electrolysis for energy storage, grid balancing and sector coupling via power-to-gas and power-to-liquids: a review. Renewable and Sustainable Energy Reviews, Vols. 82, Part3, pp. 2440-2454.
8. Manwell JF, McGowan JG, AL Rogers. 2009. Wind Energy Explained. Theory, design and application. Second Edition. Chichester, John Wiley & Sons.
9. https://ec.europa.eu/jrc/en/pvgis. Accessed February 8, 2021.
10. Batool M, Wetzels W. 2019. Decarbonization options for the Dutch fertilizer industry. Netherlands Environmental Assessment Agency.
11. https://www.iea.org. Accessed February 8, 2021

WHEC-2022
23rd World Hydrogen Energy Conference
June 26-30, 2022 - Istanbul

#382
HIGH-PRESSURE PEM WATER ELECTROLYSIS BASED ON HYDRAULIC SINGLE CELL COMPRESSION

[1*] *Florian J. Wirkert,* [1] *Ulrich W. Rost,* [1] *Jeffrey Y. Roth,* [1] *Michael Brodmann*
[1]Westfälische Hochschule University of Applied Sciences, Neidenburger Str. 43, 45897 Gelsenkirchen, Germany

*Corresponding author e-mail: florian.wirkert@w-hs.de

ABSTRACT

Hydrogen needs to be compressed, such as up to above 100 bars for seasonal storage or even 700 bars to meet pressure levels for mobile applications. Up to now, high pressure hydrogen production in combination with high operation dynamics can only be handled by proton exchange membrane water electrolysis (PEMWE). However, not only but also due to still limited outlet pressures of about 40 bars, which requires additional compressors to meet storage pressure levels, PEMWE is still subject of intensive research. In this work a novel high-pressure electrolyzer system is described that was engineered with respect to hydraulic single cell compression to meet this task. Homogeneous pressure distribution throughout the entire active area is achieved via a hydraulic medium entirely surrounding the active cell components, also providing waste heat management independent of the electrochemical operation conditions. Construction details of a near industrial scale PEMWE system for an operation at a balanced 100 bar outlet pressure level are given. Further, findings related to cell performance indicated by polarization curves that were obtained up to 6 A cm^{-2} during 100 bar operation are described. Finally, a 600-hour long-term run at 2 A cm^{-2} is presented, revealing performance degradation to be in µV h^{-1} range and hydrogen crossover to be below 50 % of the lower explosion limit on the anode side.

Keywords: PEM Water Electrolysis, High-pressure, Hydraulic cell compression, Modular Stack Design

INTRODUCTION

Producing hydrogen at high pressures via polymer electrolyte membrane electrolysis (PEMEL) utilizes the mechanism of electrochemical gas compression along with the electrolysis process itself. This kind of compression provides a higher efficiency compared to mechanical gas compression. In addition to that, an additional device comprising moving parts can be omitted, saving further space and investment as well as maintenance costs. To make use of these potential advantages, it is necessary to create high-pressure PEMEL stacks with at least the efficiency and lifetime as stacks using conventional PEMEL technology. The concept based on the principle of hydraulic single cell compression described in this work is meant to address this issue. The applicability of this approach for high-pressure hydrogen production was already demonstrated on lab-scale [1], while in a later experiment, also, the performance preserving scalability to an industrial level was validated [2]. For a possible large-scale manufacturing and operation major design changes were implemented and a novel modular approach was created providing scalability both in stack size and size of the active cell area [3]. Now, to investigate the capability of the new development for high-pressure production and long-term stable operation, an experimental test run was conducted using a PEMEL stack consisting of three single cells with an active cell area of 210 cm^2 each.

SCIENTIFIC APPROACH

The principle of hydraulic cell compression is based on the approach of inserting a single PEMEL cell in flexible pockets as shown in figure 1. The force to compress the active cell components is provided via a hydraulic medium completely surrounding the flexible pocket. Once this hydraulic medium is pressurized, the pressure is homogeneously distributed over the active cell area. As this pressure is responsible for electrically connecting the single components of a cell (pole plates, porous current distributors (PCD), gas diffusion layers (GDL), and catalyst coated membrane (CCM)), the current distribution follows the pressure distribution and is, hence, also homogeneously distributed. This is profitable for an increased lifetime, as the formation of local hot spots is prevented. In addition, the compression level may easily be adapted to an optimum depending on the components used, especially the GDL and

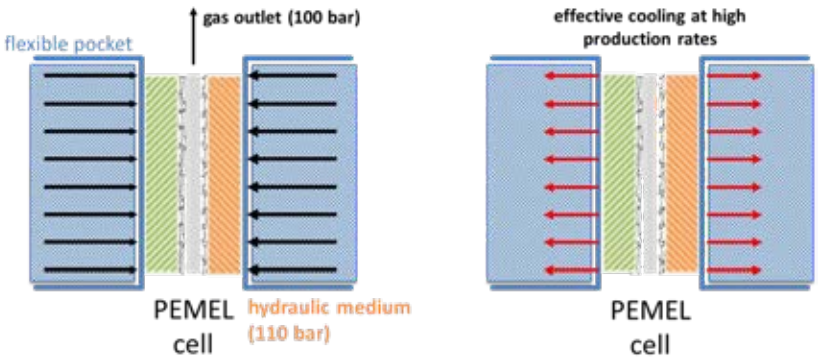


Figure 1: Schematic drawing of a PEMEL cell integrated in a flexible pocket.

the PCD. For the setup used here, previous findings show a minimum applicable pressure level of 6 bar, while during standard operation the hydraulic pressure is set to 10 bar. The pressure of the hydraulic medium may not just be adapted to the optimum compression level, but also kept constant as the overall pressure level is increased. With increasing gas pressure (oxygen and hydrogen) inside the cell, the pressure of the surrounding hydraulic medium is increased accordingly. In the example shown in figure 1, the optimum level of 10 bar cell compression is maintained at a gas outlet pressure of 100 bar by increasing the pressure of the hydraulic medium to 110 bar. Additionally, creating a circulation of the hydraulic medium, it may be used to control the temperature of the inserted PEMEL cell. Thus, temperature management is possible independent of the process media circulations providing an effective cell cooling without affecting the actual electrochemical process. Temperature management and hydrogen production may, therefore, be optimized independent from each other, providing possible advantages especially at elevated current densities and highly dynamic operation scenarios. Mentioned operational environments are equal for each single cell of a stack, as each cell is individually surrounded by the same hydraulic medium. For a future large-scale production and operation with an increased active cell area, a new approach was developed with the flexible pocket being part of the cell itself. In this approach, two half-cells comprising a plastic cell frame and a monopolar plate each form an empty space between those pole plates, in which the active cell components may be integrated, as shown on the left-hand side of figure 2. The channels for media conduction are integrated in the call frames, providing a parallel media supply of all cells once the cells are stacked together (right-hand side of figure 2). As the hydraulic medium is able to penetrate the space between the pole plates via respective channels, the active area of each single cell is still surrounded by the hydraulic medium guaranteeing the same operational environment as described above.

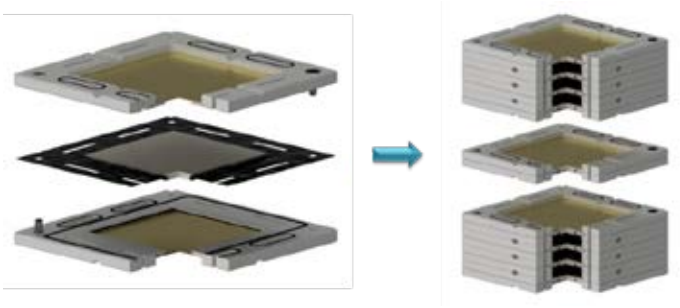


Figure 2: Schematic drawing of the presented modular stack design comprising single cells forming flexible pockets for active cell components.

MATERIALS AND METHODS

In order to investigate the capability for large-scale operation, a stack consisting of seven single cells has been manufactured with an active cell area of 210 cm^2, as shown in figure 3. For the experiments carried out for this work, the stack was operated with three single cells. The test run was performed with the stack being integrated in a containerized test system being capable of a 100 bar operation. For this purpose, it comprises an integrated pressure vessel, in which different stacks may be integrated for investigation. Pictures of the utilized test environment are also shown in figure 3. After stack installation followed by an initial break-in procedure (slowly increasing the current density to 1 A/cm^2 and maintaining this current density for 1 h), the experimental test run was started by increasing the hydrogen production pressure to 95 bar at a constant current density of 2 A/cm^2. Once high-pressure operation was established, a polarization curve was recorded up to a current density of 6 A/cm^2 at an operational temperature of 52°C, in order to investigate the capability of this design approach for high power density operation. Subsequently, the current density was set to 2 A/cm^2 and maintained for 600 h, to investigate the long-term behavior of the stack. The temperature of the stack was established at about 65 °C during this long-term test. Cell voltage of the cell placed in the middle of the stack was recorded the entire time representing the behavior of cells in the environment of a larger stack. [4]



Figure 3: Photograph of the PEMEL stack used for high-pressure operation (for this work it was operated with three single cells) and of the utilized test environment taken both from the inside and the outside.

RESULTS AND DISCUSSION

The polarization curve recorded initially at the beginning of the test run is depicted in figure 5. As our focus lay on the cell and stack design, the important result was, that there was no limitation due to insufficient media transport at high current densities.
However, this result may be addressed not just to the stack and cell design, but in particular also to the advanced inner cell components provided by the partners being described in detail in the collective publication [4]. The not entirely linear behavior of the cell voltage with increasing current may originate from an increasing temperature at elevated current densities.
Results obtained from the subsequently conducted long-term test are shown in figure 6. Fluctuations in the recorded curves are visible, as the system was sensitive to environmental temperature changes. The drop visible after around 500 h of operation was caused by an externally induced safety shutdown of the whole system. The average degradation recorded during 600 h of operation was 4.43 µV/h. [4]

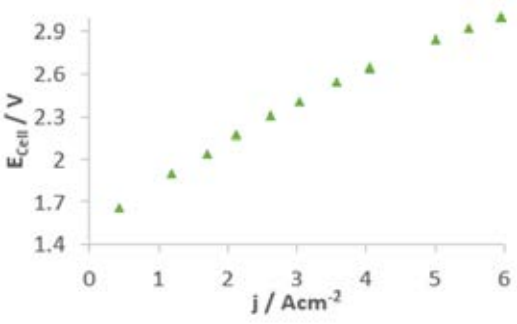


Figure 4: Polarization curve recorded at 52°C and ambient hydrogen output pressure.

CONCLUSIONS

It can be concluded that the investigated cell and with that the entire stack showed a polarization behavior and degradation rate similar to state-of-the-art PEMEL systems validating the capability for large-scale high-pressure hydrogen production. Nevertheless, further investigations are necessary to fully understand the influence of high-pressure operation, especially when high-pressure operation is maintained over a longer time.

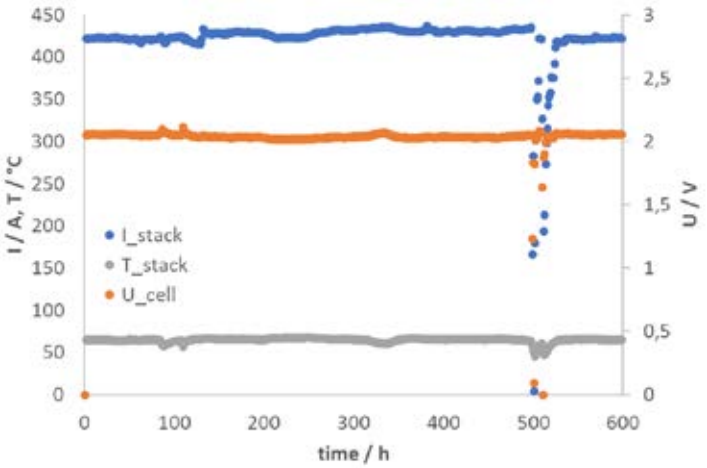


Figure 5: Cell voltage, overall current, and stack temperature recorded over 600 h of operation.

ACKNOWLEDGEMENT

Acknowledgement comes here. The research leading to these results has received funding from European Union's Horizon 2020 research and innovation program under grant agreement No. 779478 (PRETZEL project) supported by Fuel Cell and Hydrogen Joint Undertaking.

REFERENCES

1. Wirkert FJ, Roth J, Rost U and Brodmann M. 2017. A novel PEM Electrolysis System with Dynamic Hydraulic Compression for an Optimized High-pressure Operation. In NEIS Conference 2016. Edited by Schulz D. Wiesbaden, Germany: Springer Vieweg.
2. Wirkert FJ, Roth J, Rost UW and Brodmann M. 2017. Hydraulic cell compression for performance preserving upscaling of PEM electrolyzers. International Journal of Smart Grid and Clean Energy, vol. 6, no. 3.
3. Wirkert FJ, Roth J, Jagalski S, Neuhaus P, Rost U and Brodmann M. 2020. A modular design approach for PEM electrolyser systems with homogeneous operation conditions and highly efficient heat management. International Journal of Hydrogen Energy, Volume 45, Issue 2, 6 January 2020.
3. Stiber S, Balzer H, Wierhake A, Wirkert FJ, Roth J, Rost U, Brodmann M, Lee JK, Bazylak A, Waiblinger W, Gago AS and Friedrich KA. 2021. Porous Transport Layers for Proton Exchange Membrane Electrolysis under Extreme Conditions of Current Density, Temperature and Pressure. Advanced Energy Materials, Vol. 11, No. 33.

WHEC-2022
23rd World Hydrogen Energy Conference
June 26-30, 2022 - Istanbul

#391

EXTERNAL EFFECTS ON THE HIGH FREQUENCY EIS RESPONSE OF A PEM ELECTROLYSIS CELL

[1*] *Irene Franzetti,* [1] *Ai-Lin Chan,* [2] *Artem Pushkarev,* [1] *Sebastian Metz*
[1] Fraunhofer Institute for Solar Energy System ISE, Heidenhofstrasse 2, D-79110, Freiburg, Germany
[2] National Research University "Moscow Power Engineering Institute", Moscow, Russia

*Corresponding author e-mail: irene.franzetti@ise.fraunhofer.de

ABSTRACT

Electrochemical impedance spectroscopy (EIS) is a very useful tool to characterize and distinguish the electrochemical processes in an electrolysis cell. However, to exclude external influences on the results, a method to pre-evaluate them is suggested and its usefulness is demonstrated by a faster and better fitting of the equivalent circuit model (ECM). In fact, if not considered in the ECM, the inductance artificially increases the ohmic resistance obtained at high frequencies (HFR). This effect increases at higher current densities.

Keywords: Inductance, EIS, ECM, PEM electrolysis, HFR

INTRODUCTION

Electrochemical impedance spectroscopy (EIS) is an important method to monitor the state of health of an electrolysis cell. With this characterization method is possible to distinguish electrochemical processes in the cell, based on their frequency responses. However, in reality, the response of a cell does not only depend on the cell components and materials, but it is often also influenced by external noises, coming from cables and connectors. Especially for higher current densities, these effects can become so significant that they need to be taken into account in the equivalent circuit model (ECM) in order not to interpret the obtained EIS results incorrectly [1]. For instance, the PEM electrolyser response with positive imaginary part of the impedance is usually ignored [2], however this might lead to significant overestimation of the high frequency resistance of the cell [3]. While this has already occasionally been done in other studies on PEM electrolysers [4, 5], a stringent methodology to assess these external influences and to quantify their effects on the real response of a PEM water electrolysis cell is lacking.

EXPERIMENTAL

Electrochemical Impedance Spectroscopy (EIS)

EIS measurements are performed for reference and in-situ measurements at the following current densities 0.3, 1, 2, and 3 A/cm^2 and at 80°C, a water flow rate of 0.2 l/min and at ambient pressure for in-situ measurements. The spectra are recorded in a frequency range between 0.1 Hz and 10 kHz and with a stabilization time of 3 minutes.

Reference Measurements

The measurement type used for assessing the external influence is going to be referred from now on as reference measurement. The setup used in this test is sketched in Figure 1 and it is composed by current and sense cables that connect the potentiostat to the current collectors of a cell. The latter is a typical electrolysis cell, but with a gold coated titanium plate, instead of the catalyst coated membrane (CCM).

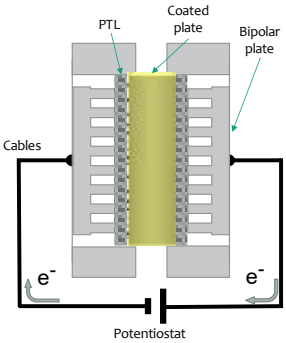


Figure 1. Schematic setup of reference measurement.

The response of this setup under different current densities is characterized via EIS, as explained in the subsection EIS. With this setup, the contribution of the hardware used for in-situ measurements except from those originating from the CCM can be obtained.

In-situ Measurements

The in-situ measurements are performed with the same cell (bipolar plates and porous transport layers), potentiostat, cables and their position as in the reference measurement, but a CCM is assembled instead of the gold coated plate. The cell is activated via two galvanostatic steps at 0.2 and 1 A/cm^2 for half an hour each, followed by a potentiostatic step at 2.2V held for 6 hours. After this, a characterization of the cell performance is carried out through polarization curve and EIS. In this report we will focus just on the results of EIS.

Fitting Model

Before applying any fitting to the collected data, the linearity, causality and time dependence of the data have to be evaluated and the non-conforming data would be filtered [4]. After this point, the evaluation of the Bode and Nyquist plot gives an indication of the elements composing the equivalent circuit model (ECM), which is going to be used to fit the behavior of the setup or cell under the different conditions. For the reference measurement, an ECM composed by an ohmic resistance (R_{ohm}) and a modified inductance (L_{alpha}) in series is used [6], while for the in-situ measurements, a modified inductance (L_{alpha}), an ohmic resistance (R_{ohm}), and two resistance-capacitance (R-C) elements are used. The analysis of the model is run using a specific package in python [7]. The recursive iteration to reach the best fit needs as input parameters the ECM, initial values for each element, and the domain of the fitting values.

RESULTS AND DISCUSSION

ECM of Reference Measurements

In the common approach, the setup used for the reference measurements with electrically conductive components and the interface between them, would be characterised as a resistor. However, already at frequencies higher than 70Hz, a change of behaviour towards a higher positive imaginary part is evident in the Niquist plot, as well as an increasing phase angle in the Bode plot, as per Figure 2. This evidence denotes an additional inductive effect to the supposed resistive behaviour of the setup. These results are therefore fitted by an ECM model that includes a modified inductance and a resistance. As the values of L_{alpha} acquired with the mentioned fitting model prove to be significant, a modified inductance is included in the ECM of the in-situ measurements (see below) and the values obtained in the reference measurements are used as initial parameters of the fitting.

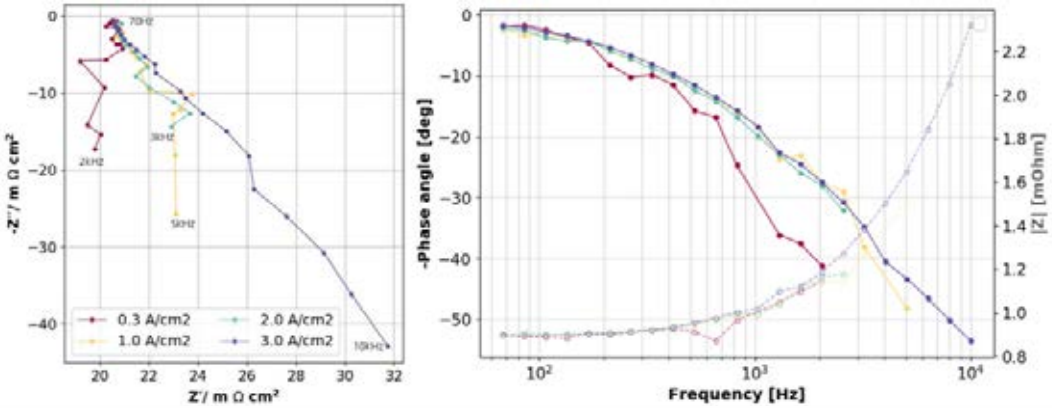


Figure 2. Niquist and Bode plot of reference measurement at different current densities.

ECM of In-situ Measurements

The EIS measured during in-situ measurements show at frequencies above 60 Hz an inductive behaviour under all current densities. After their initial evaluation, the ECM calculation is performed, and the values of each element of the ECM are obtained faster and result in a better fitting, when the initial values are defined by the L_{alpha} from the reference measurement.

The results of the fitting also present a discrepancy between the HFR, as intercept to the x-axis in Nyquist plot, and R_{ohm} calculated by the ECM model shows that the real R_{ohm} has a lower value than that obtained from the uncorrected HFR for all current densities. This shift to higher values of HFR can be assigned to the external influences as quantified via reference measurement. The interplay of HFR and inductance has also been quantified and modelled by Shin and Cruz-Manzo [1, 3]. As visible from Figure 3, this effect increases with increasing current density.

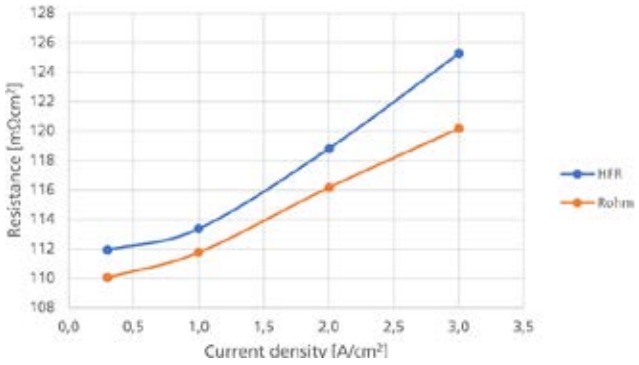


Figure 3. HFR from EIS and Rohm from ECM at different current densities for in-situ measurements.

CONCLUSIONS

A reference measurement procedure was used to quantify the influence of external components as demonstrated by fitting against an ECM including a modified inductance. The latter was therefore included in the ECM for in-situ measurements and the influence onto the HFR was quantified. The obtained results can then reduce the computing time of ECM, give a more correct evaluation of the ohmic resistance of the cell and also on other processes that are masked by the inductive effects deriving from external influences. While the external influences will depend on the used hardware, they in any case need to be checked in order to obtain accurate and reliable results.

REFERENCES

1. Cruz-Manzo S, Chen R, and Rama P. “Inductive Effect on the Fuel Cell Cathode Impedance Spectrum at High Frequencies” Journal of Fuel Cell Science and Technology, 2012.
2. Suermann M, Pătru A, Schmidt TJ, Büchi FN. “High pressure polymer electrolyte water electrolysis: Test bench development and electrochemical analysis” International Journal of Hydrogen Energy, 2017: 12076-12086.
3. Eui-Chol S, Pyung-An A, Hyun-Ho S, Jung-Mo J, Sun-Dong K, Sang-Kuk W, Ji H Y, Junichiro M, and Jong-Sook L. “Polarization mechanism of high temperature electrolysis in a Ni–YSZ/YSZ/LSM solid” Solid State Ionics, 2013: 80-96.
4. Van der Merwe, J H P. Characterisation of a proton exchange membrane electrolyser using electrochemical impedance spectroscopy. Doctoral Dissertation, North-West University, 2012.
5. Frensch SF, Olesen AC, Araya SS, Kær SK. “Model-supported characterization of a PEM water electrolysis cell for the effect of compression”. Electrochimica Acta, 2018: 228-236.
6. Murbach M, Gerwe B, Dawson-Elli N, and Tsui L. “Impedance.py: A Python package for electrochemical impedance analysis.” (Journal of Open Source Software) 5(52), 2349 (2020).
7. Murer N. “The modified inductance element La.” www.biologic.net. 08 2012.

WHEC-2022
23rd World Hydrogen Energy Conference
June 26-30, 2022 - Istanbul

#393

EFFICIENCY OF THE PRODUCTION PROCESS AND MANAGEMENT OF GREEN HYDROGEN THROUGH SIMULATION AND BALANCE OF PLANTS (BOF)

[1]C. Castañeda-Castañeda, [2] J.J. Ramos-Valencia, [3] M.T. Cadenas-González & G. Leo Avelino.*
[1]Plant engineering management. Centro de Tecnología Avanzada (CIATEQ, A.C.). Av. del Retablo 150. Col. Constituyentes FOVISSSTE. Querétaro, Qro., Mexico.
[2]Process engineering management. Centro de Tecnología Avanzada (CIATEQ, A.C.). Av. del Retablo 150. Col. Constituyentes FOVISSSTE. Querétaro, Qro., Mexico.
[3]Process engineering management. Centro de Tecnología Avanzada (CIATEQ, A.C.). 23 de agosto 213. Col. Jesús García. Villahermosa, Tabasco, Mexico.

*Corresponding author e-mail: carlos.castaneda@ciateq.mx

ABSTRACT

The research carried out presents an integrated analysis of the green hydrogen production process from water hydrolysis; and of the transformation stages from water treatment, electrolytic production, separation, drying, compression, cooling and conditioning operations to reach hydroduct injection specifications, through simulation and plant balance (BoF); considering effluent recovery; using a calculation model to determine the different energy consumptions and used; the renewable energy efficiency factor to quantify the energy demand required by the process for the target control flow, this allowed the determination of the production indices, which correspond to scaling and mass production parameters such as the overall process efficiency , hydrogen flow index and the generated power index, to achieve the operational specifications of hydrogen product delivery, these and aim to have a quick guide for the determination of capacities in scale systems.

Keywords: *Green Hydrogen; Energy efficiency; Balance of Plant (BoF).*

INTRODUCTION

The world production of H2 is around 40 million tons per year, according to data from the International Energy Agency (EIA). Currently, practically 96% of the world's hydrogen is produced from fossil fuels, mainly by reforming natural gas with water vapor, and is consumed as a component of conventional processes (chemical and petrochemical industry) (González, 2018).
On the other hand, hydrogen transport technologies are mature, but not widespread, this leads to the search for opportunities in the transmission of low-pressure pipelines (HBP) from 20 to 80 bar_g and high-pressure pipelines (HAP) from 350 at 700 bar_g (Zabrzeski, 2019).
The physical nature of hydrogen will provide capacitance restricting the cycles, reducing management costs and distribution of green energies, Figure 1 represents the management diagram; There are many demonstration projects of production systems that have been studied in isolation, but in the scaling-up processes they reveal the need to improve the efficiency, durability and reliability of the systems in order to work with renewable energies.

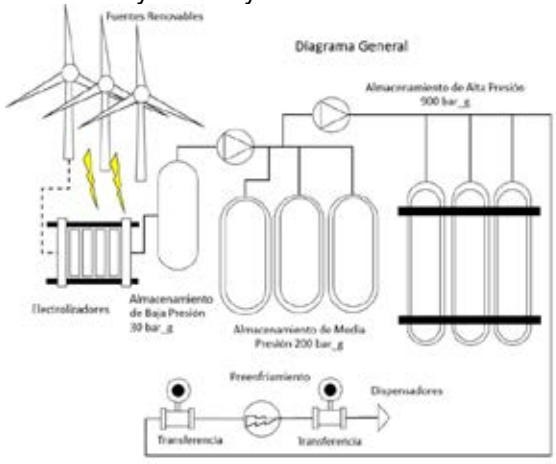


Fig. 1. H_2 handling overview diagram.

Based on the points mentioned; The present work seeks to establish a set of referential parameters and indicators, which facilitate the estimation in the rapid scaling analysis of hydrogen production units; that allow inferring the global energy demand of the system and the expected yields. These are indices of interest in the estimation processes and in

the quantification of the intensity of associated investment in renewable energies, likewise these indices and configurations encourage the development of future analyzes aimed at obtaining other parameters of interest that allow to serve as a reference to the development of hydrogen as an energy development agent.

MATERIALS AND METHODS

System configuration

It was developed based on the sequence of operations and unit processes for the determination of production and performance indices, starting from the general approach and from there to the discrete or elements following a process of increasing functional complexity.

The configuration process followed the following steps:

A. Synthesis: Allows the configuration of the topology of the production system (Figure 2), allowing the conceptual process to be developed and integrates the energy sources in their different forms such as electricity, heat and refrigeration. B.
B. Sequencing: Preparation of inputs and conditioning of materials: Integrates the activities to perform the removal of encrusting ions and impurities in the raw water up to the entrance to the electrolyzer.
C. Configuration: In this stage, a more detailed breakdown of operations is carried out prior to the configuration of the process flow diagram where particular elements will be represented in detail, each of these operations can be evaluated as a subsystem and its performance can be analyzed and analyzed. characterized.
D. Plant Balance: From the flowchart, the material and energy balance of the plant is developed for the target production volume; through the modeling of the system and serves as the basis for the approach of the process flow diagram in the CAPE OPEN type simulation software.

The Figure 2 presents the flowchart of matter and energy with the various operations and processes involved in the production of green hydrogen.

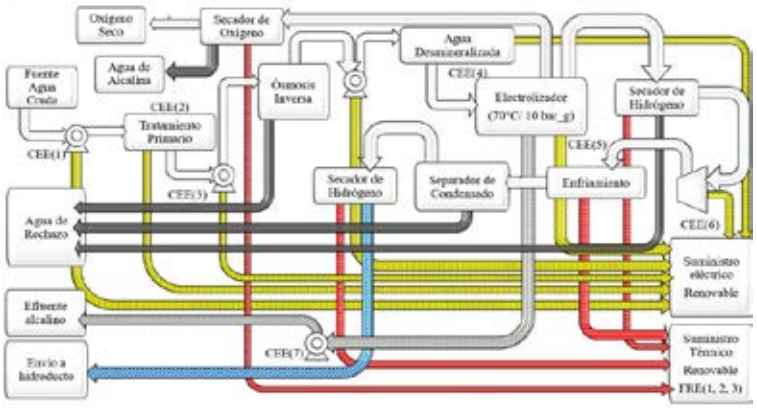


Fig. 2. Process flowchart.

System modeling

The modeling and simulation allowed to recreate in a virtual way the selected processes to be able to study their behavior, in order to analyze the consequences and effects of the different conditions and makes it possible to compare the design alternatives that may arise, without having to bring them to reality. Expensive scale models to carry out evaluations of the final performance of the systems from the unit balances.

This approach makes it the ideal tool for determining scaling parameters; and I imply the selection of the different components related to the process, as well as the thermodynamic packages, equations and methods to solve the general system once the various recirculation's and cycles have been defined; the material balance for each unit is defined as:

$$\sum_{1}^{j}(EM_j) = \sum_{1}^{i}(SM_i) \quad + ACM \tag{1}$$

For the energy balance we have:

$$\sum_{1}^{n}(EE_n) = \sum_{1}^{m}(SE_m) \ + ACE \tag{2}$$

With the simulation model in numerical convergence for the currents of matter and energy. The Balance of Plant BOF is carried out from operation “a” to “m”; the net energy balance expression is as follows:

$$BNE = \sum_{1}^{k}(FRE_i) - \sum_{1}^{g}\frac{(CEI_j)}{\varepsilon_j} \tag{3}$$

The global efficiency of the system is determined from the relationship established in equation 4.

$$\sum_{1}^{g}\frac{(CEI_g)}{\varepsilon_g} \rightarrow \frac{\dot{m}_{H_2}}{PM_{H_2}} \Delta H_{f H_2O}) \tag{4}$$

RESULTS AND DISCUSSION

Below are the results of the evaluation of the behavior of the production model for a control volumetric flow of 3,216 Nm3/day of H2, for this condition the energy consumption and the heat removal requirements for handling conditions for low pressure pipelines (HBP) and high-pressure pipelines (HAP). The main difference between HBP and HAP lies in the requirement of hypercompression and subsequent cooling.

This is an important factor due to the discharge pressure required by the second case, greater than 700 bar_g. The table 1 present the results generated by the model and are used as input data for the determination of the 3 plant scaling parameters IFH, IPG and IRQ.

Table 1. Summary of WHEC-2022 formatting details

Description	HBP kW	HAP kW
1) Primary Treatment	- 1.00	- 1.00
2) Secondary Treatment	- 2.90	- 2.90
3) Polished. and decarbonized	- 1.00	- 1.00
4) Alkalinizer	- 0.25	- 0.25
5) Electrolyzer	- 750.00	- 750.00
6) Dealkalizer	- 150.00	- 150.00
7) O_2 drying	- 1.00	- 1.00
8) Primary Drying H2	- 1.00	- 1.00
9) H_2 compression	- 11.50	- 11.50
10) Secondary Drying H_2	- 2.00	- 2.00
11) Hypercompression H_2	- ---	- 47.40
12) Cooling	- ---	- 39.50
- ***Consume Global***	- ***920.7***	- ***1007.6***

CONCLUSIONS

The production indices determined with this work are a valuable tool for sizing and scaling hydrogen production units and allow a rapid evaluation of elements such as energy consumption, production, heat removal requirements and generated energy capacity, it should be noted Given the structure and configuration of the model, these parameters are linear with respect to their dimensional analysis for the discharge operating scenarios evaluated for low and high pressure. Among the most relevant data of the present, the efficiency of the process in the case of HBP is 49% and HAP is 44%, this means that it discharges at 700 bar_g and implies a 5% reduction in efficiency due to the additional requirements of compression, meanwhile the hydrogen flow rate is reduced by 8.6% due to the increase in pressure between these scenarios.

REFERENCES

1. González García-Conde, A. 2018. Hidrógeno y pilas de combustible en la transición energética. http://www.ptehpc.org/
2. Zabrzeski, Ł. P. Janusz, K. Liszka, M. Łaciak, A. Szurlej. 2019. Hydrogen-Natural Gas mixture compression in case of transporting through high-pressure gas pipelines. 2nd International Conference on the Sustainable Energy and Environmental Development, 214, 1-12.

WHEC-2022
23rd World Hydrogen Energy Conference
June 26-30, 2022 - Istanbul

#434

PARAMETRIC ANALYSIS OF BIOMETHANOL PRODUCTION UNIT USING BIOMASS GASIFIER AND HIGH-TEMPERATURE ELECTROLYZER

[1*] *Hamed Ghiasirad*, [2] *Anna Skorek-Osikowska*
[1] Silesian University of Technology, Faculty of Energy and Environmental Engineering, 44-100 Gliwice, Poland
[2] Silesian University of Technology, Faculty of Energy and Environmental Engineering, 44-100 Gliwice, Poland
*Corresponding author e-mail: hamed.ghiasirad@polsl.pl

ABSTRACT

The so-called hydrogen economy has become particularly important in global and national energy policies. In this paper, a methanol generation system is proposed that uses a high temperature electrolysis process and biomass gasification unit to follow this trend. Biomass is subjected to gasification in the oxygen and steam atmosphere. Hydrogen is produced in solid-oxide electrolysis, to which heat is supplied from the reactor's cooling. As a result of gasification, synthesis gas is obtained, consisting mainly of CO_2, CO, H_2. The gas is cooled and cleaned, and the separated tars can be used for biofuels production. The heat from gas cooling is used in the electrolysis process, too. The purified gas is used for the production of methanol. The analysis aims to calculate the efficiencies of the proposed system and indicate the potential for optimization of the processes by pointing out strengths and bottlenecks. As a result, the proposed cycle consumes 14.2 kg/h biomass in the gasifier and 52.12 kW power in SOEC, contributing to 61.4 kg/h methanol generation. Accordingly, the total energy efficiency is found to be 42.16%. In addition, sensitivity analysis showed that higher target purity of methanol and lower syngas temperature could lead to more methanol production.

Keywords: Gasification, SOEC, Methanol production, Hydrogen production, Thermodynamic modelling.

INTRODUCTION

The Energy Union (EU) strategy adopted by the European Commission aims to reach net-zero greenhouse gas emissions by 2050 [1]. To do so, renewable energy sources (RES) are increasingly used, among which wind and solar are the most common. The specificity of their operation is that they deliver energy in a fluctuating manner, with a strong dependency on weather and daylight period. One of the options for wider use of RES and stable production of energy is energy storage in the form of fuels, such as hydrogen produced in the electrolysis process and potentially further converted to synthetic natural gas (SNG), methanol and others [2]. In this paper a system for production of methanol is proposed that is using high-temperature electrolysis and biomass gasification processes.

Several research has been done in this area, the most significant of which is Alzahrani and Dincer [3] in 2018. They optimized a 1 MW solid oxide electrolysis (SOE) unit from energy and exergy viewpoints to produce hydrogen. Compared to low-temperature electrolyzers, high-temperature ones have higher conversion efficiency. On the other hand, there are some disadvantages to using this kind of electrolyzer, the most significant of which is providing high-temperature steam. This novel configuration exploits an electric heater for steam generation so that several renewable energy sources can provide input electricity. Finally, they found that the highest second law efficiency would be 87.12% if stack temperature, pressure, and current density could be 1168 K, 8 MPa, and 5000 A/m^2 respectively. Daneshpour and Mehrpooya [4] integrated photovoltaic thermal (PVT) solar collector and planar cathode-supported solid oxide electrolysis cell (SOEC) for cogeneration of power and hydrogen. They validated their system by an exothermic mode which does not need an additional heater, and its efficiency reached 54% with 7458 kg/h hydrogen generation. Habibollahzade et al. [5] optimized and compared a biomass-based solid oxide fuel cell (SOFC), SOEC, and gas turbine (GT) using four gasification agents to produce power and hydrogen simultaneously. In their proposed system, the waste heat of SOFC is recovered in a GT which provides electricity for SOEC. They found that O_2 is by far the best gasification agent from both efficiency and cost perspectives. Having said that lowest emission and highest hydrogen production can be reached by using CO_2 as a gasification agent. Their optimization result showed that exergy efficiency and unit cost would be 45.25% and 16.21 $/GJ, respectively. Additionally, their proposed system's levelized emission and hydrogen generation were found to be 7.745 t/MWh and 8.561 kg/h, in turn.

According to the previous works, the integrated system proposed here has not been modelled yet. Some of its innovations can be written as follows: SOEC improvement by integration with energy & fuels production, Oxygen utilization improves SOEC, eliminating the necessity of an air separation unit (ASU), and Thermodynamic analysis of a negative carbon emission system.

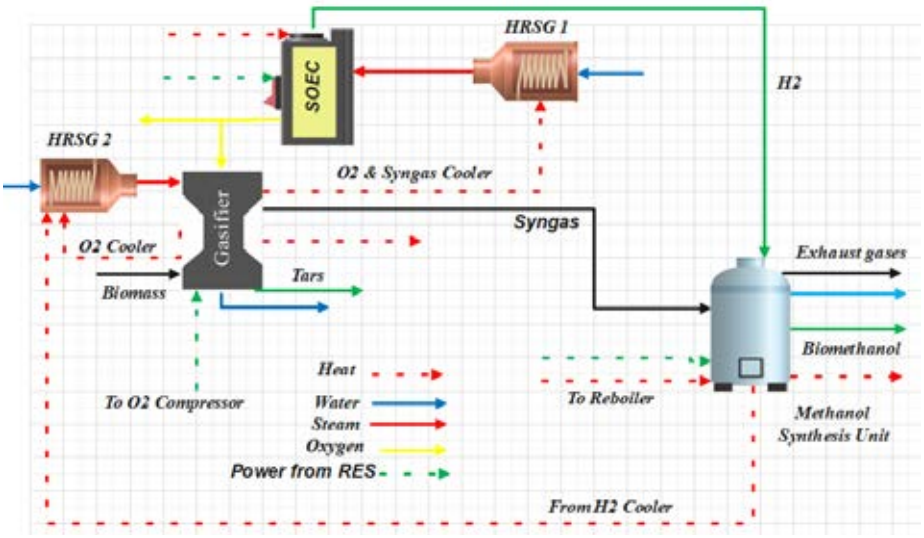


Fig. 1. Schematic diagram of the proposed system for biomethanol production.

MATERIALS AND METHODS

In the proposed system, biomass and input electricity are the prime movers aiming to generate biofuel. Specifically, oxygen from electrolyser and steam are the gasification agents allowing to produce syngas. Then, hydrogen generated in solid oxide electrolyser and syngas enter the methanol synthesis (MSU) unit to produce methanol. As shown in Fig. 1, the heat recovered from gasifier cooling is provided to SOEC. It is noteworthy that the high-temperature electrolyser is endothermic in this study, so additional heat is needed. In addition, the hydrogen and oxygen cooler provide thermal energy for heat recovery steam generator 2 (HRSG 2). All of the pinch point temperature differences are considered in these heat integrations. As the first stage of the modelling, the energy conservation or the first law of thermodynamics is considered. This rule 1st law and the mass balance of the equipment are commonly defined as follows [6]:

$$\dot{Q} - \dot{W} + \sum_{\mathrm{i}} \dot{m}_{\mathrm{i}} \left(h_{\mathrm{i}} + \frac{V_{\mathrm{i}}^2}{2} + g z_{\mathrm{i}} \right) - \sum_{\mathrm{e}} \dot{m}_{\mathrm{e}} \left(h_{\mathrm{e}} + \frac{V_{\mathrm{e}}^2}{2} + g z_{\mathrm{e}} \right) = \frac{\mathrm{dE}}{\mathrm{dt}} \quad (1)$$

$$\sum_{\mathrm{i}} \dot{m}_{\mathrm{i}} = \sum_{\mathrm{i}} \dot{m}_{\mathrm{e}} \quad (2)$$

Consequently, all the components are separately evaluated by the energy and the mass balance equations, which has been done using Aspen Plus and MATLAB software.

In order to calculate the total energy efficiency, the useful products should be divided by input energies, as shown below:

$$\eta_{\mathrm{En,tot}} = (\dot{m} \cdot LHV)_{\mathrm{Biomethanol}} \Big/ \left[(\dot{m} \cdot LHV)_{\mathrm{wood}} + \dot{W}_{\mathrm{SOEC}} + \dot{W}_{\mathrm{MSU}} + \dot{W}_{\mathrm{O2,Comp}} + \dot{Q}_{\mathrm{SOEC}} + \dot{Q}_{\mathrm{REB}} \right] \quad (3)$$

in which $\dot{m}$ and LHV refer to mass flow rate and lower heating value, in turn. Additionally, $\dot{W}_{\mathrm{O2,Comp}}$ refers to electricity consumption of oxygen compressors in the gasification unit, and $\dot{Q}_{\mathrm{REB}}$ indicates reboiler duty in the distillation column.

RESULTS AND DISCUSSION

Table 1 presents the essential properties of the designed system for methanol generation. As shown, the gasifier consumes 14.2 kg/h biomass. On the other hand, a high-temperature electrolyser uses 52.12 kW electricity and 64.99 kW thermal energy. Finally, the methanol synthesis unit consumes 3.81 kW of power, which is able to generate 61.4 kg/h methanol. In addition, there are two oxygen compressors in the gasification unit, which use 1.55 kW of electricity, and reboiler of the distillation column needs 28.08 kW of heat. As a result, the overall thermal efficiency of the cycle found to be 42.16%.

Table 1. Main specifications of the proposed cycle for methanol production.

Parameter	Unit	Result	Parameter	Unit	Result
Methanol production rate	kg/h	61.40	**Power consumption of MSU**	kW	3.81
LHV of biomethanol	kJ/kg	21011.1	**Power consumption of oxygen compressors**	kW	1.55
Biomass consumption of gasifier	kg/h	14.2	**Heat demand of SOEC**	kW	64.99
LHV of wood waste	kJ/kg	15830	**Reboiler duty**	kW	28.08
Power consumption of SOEC	kW	52.12	**Total energy efficiency**	%	42.16

Fig. 2 shows the impact of gasifier temperature on produced methanol in various target purities. This figure shows that the methanol production rate enhances by increasing the target purity of methanol. As can be seen in Fig. 2, the higher the gasifier temperature, the less methanol is generated. The reason behind that is that heat demand of the gasifier increases by enhancing its outlet temperature, so more vapour is produced in the outlet stream, which means less syngas and methanol can be generated.

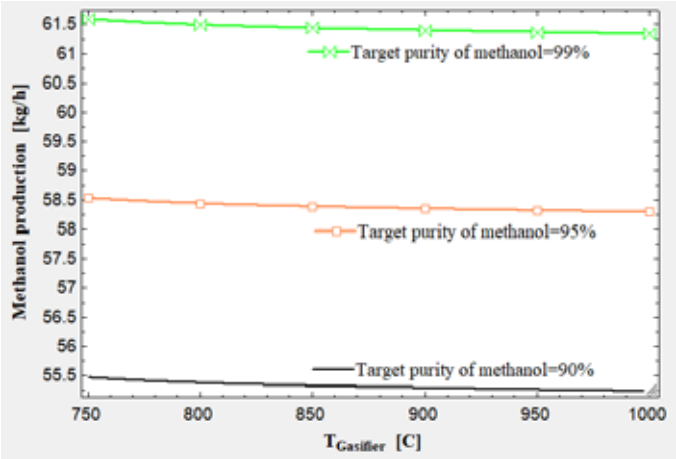


Fig. 2. The effect of gasifier temperature on methanol production rate in different target purities.

CONCLUSIONS

In the present study, a methanol synthesis unit that benefits from high temperature electrolyzer and biomass gasifier is modelled. Accordingly, it is found that the proposed cycle uses 14.2 kg/h biomass and 330 kW electricity in SOEC, leading to 61.4 kg/h methanol production. Additionally, a parametric study showed that a higher target concentration of methanol and lower gasifier temperature could cause more methanol production.

Acknowledgement

The scientific work was funded by the National Science Centre within the framework of the research project no. 2021/41/B/ST8/02846.

REFERENCES

1. https://www.h2greentech.eu/a-hydrogen-strategy-for-a-climate-neutral-europe/. Accessed on January 8, 2021.
2. European Commission. 2018. A Clean Planet for all. A European long-term strategic vision for a prosperous, modern, competitive and climate neutral economy. Depth analysis in support of the commission; Communication COM, 773.
3. AlZahrani, A. A. and Dincer, I. 2018. Modeling and performance optimization of a solid oxide electrolysis system for hydrogen production. Applied Energy, 225, 471-485.
4. Daneshpour, R. and Mehrpooya, M. 2018. Design and optimization of a combined solar thermophotovoltaic power generation and solid oxide electrolyser for hydrogen production. Energy Conversion and Management, 176, 274-286.
5. Habibollahzade, A., Gholamian, E. and Behzadi, A. 2019. Multi-objective optimization and comparative performance analysis of hybrid biomass-based solid oxide fuel cell/solid oxide electrolyzer cell/gas turbine using different gasification agents. Applied Energy, 233, 985-1002.
6. Kalan, A. S., Ghiasirad, H., Saray, R. K. and Mirmasoumi, S. 2021. Thermo-economic evaluation and multi-objective optimization of a waste heat driven combined cooling and power system based on a modified Kalina cycle. Energy Conversion and Management, 247, 114723.

WHEC-2022
23rd World Hydrogen Energy Conference
June 26-30, 2022 - Istanbul

#1449

A HIGH-PERFORMANCE ELECTROLYSIS CELL PROMISES MORE COST-COMPETITIVE RENEWABLE HYDROGEN

[1]Aaron Hodges, [1]Anh Linh Hoang, [1]George Tsekouras, [1,2]Klaudia Wagner, [1,2]Chong-Yong Lee, [1]Prerna Tiwari, [1,2,*]Gerhard F. Swiegers, [1,2]Gordon G. Wallace[1,2]

[1]Intelligent Polymer Research Institute, University of Wollongong, Wollongong, NSW 2522, Australia

[2] Australian Research Council Centre of Excellence for Electromaterials Research, University of Wollongong, Wollongong, NSW 2522, Australia

*Corresponding author e-mail: swiegers@uow.edu.au

ABSTRACT

We describe a new concept in water electrolysis – a '*capillary-fed electrolysis*' (CFE) cell. In such a cell, water is supplied to the hydrogen- and oxygen-evolving electrodes by capillary-induced transport along a porous inter-electrode separator, leading to inherently *bubble-free* operation at the electrodes. An alkaline CFE cell of this type is shown to outperform commercial alkaline and PEM electrolysis cells under normal operating conditions. The CFE cell required a cell voltage of only 1.51 V, equating to 98% energy efficiency (vs the Higher Heating Value, HHV, of hydrogen), at 0.5 A cm^{-2} and 85 °C, with an energy consumption of 40.4 kWh/kg hydrogen (vs. ~47.5 kWh/kg in commercial electrolysis cells). This surpasses the target set by the *International Renewable Energy Agency* (IRENA) for 2050 to decrease the energy consumption of water electrolysis cells to <42 kWh/kg. The high energy efficiency significantly decreases the *levelized cost of the hydrogen (LCOH)* produced.

Keywords: Hydrogen, Green Hydrogen, Electrolysis

INTRODUCTION

Many nations are seeking to move towards a greener economy in which hydrogen energy storage plays a pivotal role. However, uptake is limited by the uneconomical cost of producing renewable (*'green')* hydrogen. Low-cost green hydrogen, made from water using renewable energy, will be vital to achieve *'net zero'* emissions in the global energy system. Green hydrogen is needed to decarbonise sectors that cannot use renewable electricity directly, like heavy transport, chemicals, and steel.[1] It is estimated that 15-25% of energy in a net zero global economy, worth >$1 trillion p.a., will be provided by green hydrogen by 2050.

Inspired by the historic evolution of water electrolysis cells, which recently culminated in *polymer electrolyte membrane* (PEM) cells that directly produce one of the gases in a gas collection chamber rather than bubbling through the liquid electrolyte, a *capillary-fed electrolysis* (CFE) cell concept was developed in which both gases are produced directly (Fig. 1).[1] In such a cell, the aqueous electrolyte is constantly supplied to the electrodes by a spontaneous capillary action via the porous, hydrophilic, inter-electrode separator from a reservoir at the bottom of the cell.

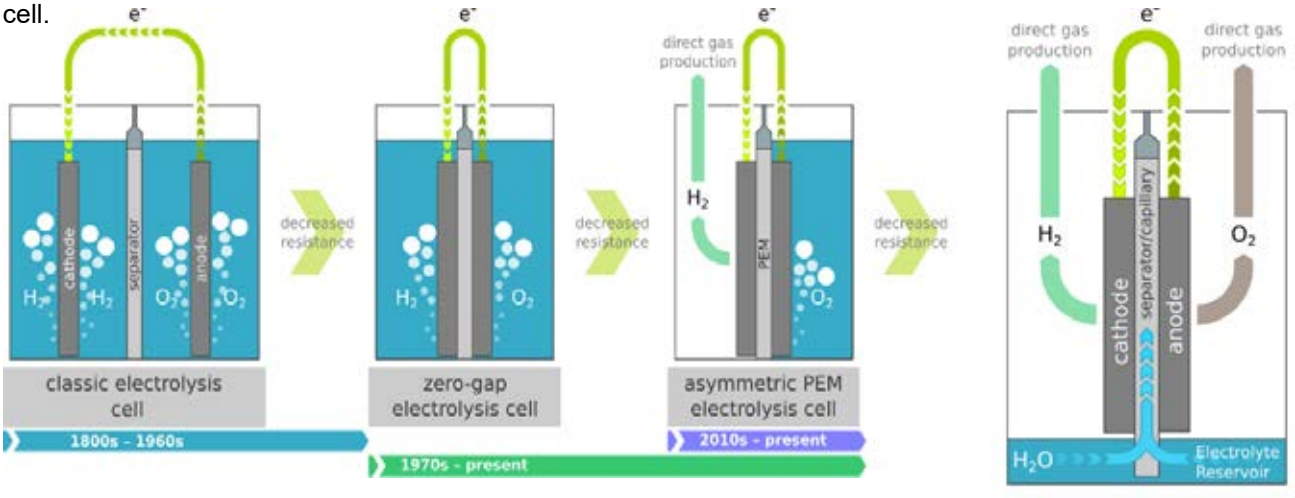


Fig. 1. Historic evolution of water electrolysis cells leading to the capillary-fed electrolysis (CFE) cell on the far right.

Porous gas diffusion electrodes are compressed against opposite sides of the separator. The electrodes draw in liquid laterally from the separator and are covered with only a thin layer of the liquid electrolyte. When a suitable voltage is applied to the electrodes, the generated H_2 and O_2 gases migrate through the thin layer of liquid on their respective electrodes, producing *bubble-free* electrolysis in which water is converted directly to the bulk gases without forming gas bubbles.

In avoiding gas bubbles 'masking' the electrodes, the liquid electrolyte maintains full access to the catalytic sites on the electrode, including the most active crevice, cleft and defect sites that are the first to be blocked by bubble formation, sometimes permanently so. The flow of water reactant to an electrode also does not counteract the flow of the gas products away from the electrode, thereby avoiding the counter multiphase flows and their associated mass transport limitations, found in conventional water electrolysers.

RESULTS AND DISCUSSION

A capillary-fed electrolysis cell with a rapidly wicking SUPOR microfiltration membrane as the separator, and employing existing, well-known NiFeOOH oxygen evolution and Pt/C (0.5 mg Pt/cm^2) hydrogen evolution electrocatalysts on fine Ni meshes, with 27% KOH electrolyte, yielded water electrolysis performance that exceeded conventional, bubbled control cells, and commercial alkaline and PEM cells (Fig. 2).[1] Faradaic efficiencies were shown to approach 100%, with low gas crossover (<0.14 vol% H_2 in the O_2 stream; 0 vol% O_2 in the H_2 stream).[1] The cell also required a less complex and less energy hungry balance-of-plant than conventional, bubbled alkaline and PEM electrolysis cells.[1]

Table 1 shows the performance of the capillary-fed cell at 85 °C.[1] At a current density of 0.5 A cm^{-2} that is commonly used by commercial alkaline electrolysis cells in operation, a cell voltage of only 1.506 V was needed to produce hydrogen (vs. ~1.77-1.79 V by commercial alkaline and PEM cells in normal operation, respectively). This represents 98% cell energy efficiency (HHV), with consumption of 40.4 kWh per kg of hydrogen produced, which is within the IRENA target for the year 2050.[1] The capillary-fed cell demonstrated sustained high and stable performance over extended periods from 1 day to 30 days continuously at 85°C and 20°C respectively, when held at a fixed voltage.[1]

Table 1. Performance at 85°C of the capillary-fed electrolysis cell with PTFE at the anode

Current density (A cm^{-2})	Cell voltage (V)	Energy efficiency (HHV) (%)	Energy consumption (kWh kg^{-1} H_2)	(kWh Nm^{-3} H_2)
0.294	1.470	100	39.4	3.55
0.500	1.506	98	40.4	3.64
0.800	1.551	95	41.6	3.75
1.000	1.575	93	42.2	3.80

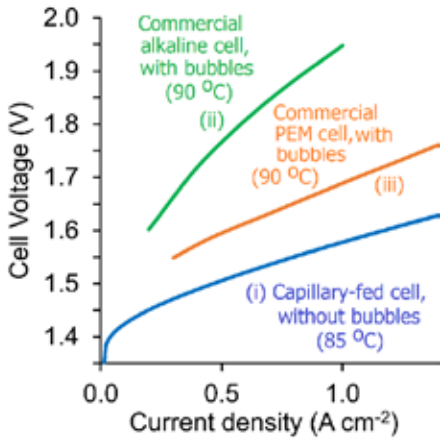


Fig. 2. V-I plots for water electrolysis by: (i) the capillary-fed cell, and a representative state-of-the-art commercial: (ii) alkaline cell, and (iii) PEM cell.[1]

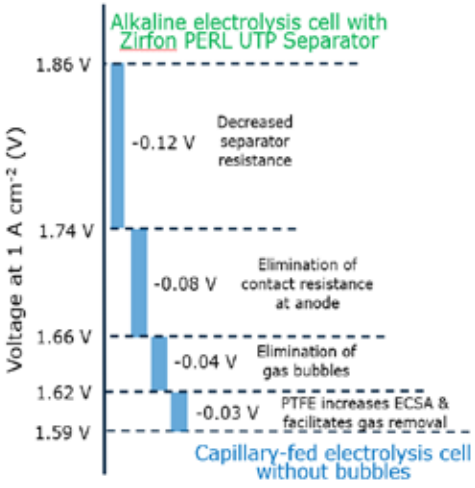


Fig. 3. Sources of the voltage decline at 1 A/cm^2 and 80 °C by the capillary-fed cell vs. a control, conventional, bubbled alkaline electrolysis cell with a Zirfon PERL UTP 500 separator and having identical electrodes and electrocatalysts. ECSA = electrochemically active surface area of the anode.[1]

Analysis of the capillary-fed cell relative to a control, conventional cell at 80 °C demonstrated that the improvement in energy efficiency did not have a single origin. Rather, there were several smaller contributions that, cumulatively, led to the observed 270 mΩ cm^2 reduction in cell resistance at 1 A cm^{-2} (with an accompanying 0.270 V decline in the voltage).

Fig. 3 schematically depicts the main contributions at 1 A cm^{-2} compared to a control, conventional alkaline cell with a standard commercial Zirfon PERL UTP 500 separator and having the same electrodes, with the same NiFeOOH and Pt/C electrocatalysts. As can be seen, the separator used in the capillary-fed cell had a 120 mΩ cm^2 lower resistance than the commercial Zirfon PERL separator, yielding a 0.120 V decline. It was also less resistive than the Nafion separators used in commercial PEM electrolysis cells, being 174 mΩ cm^2 less resistive than Nafion™ 117 and 96 mΩ cm^2 less than Nafion™ 115. Welding of the anode of the capillary-fed cell to its bipolar plate eliminated a contact resistance of 80 mΩ cm^2 (0.08 V) deriving from a poorly conductive Ni oxide layer on the Ni surfaces. Avoiding gas bubbles reduced the resistance by another 40 mΩ cm^2 (0.04 V), while incorporation of poly(tetrafluoroethyelene) (PTFE) in the anode increased its *electrochemically active surface area (ECSA)* by ~12-fold, to, potentially, ~241 cm^2 per 1 cm^2 geometric area, producing a further 40 mΩ cm^2 (0.04 V) decline.

CONCLUSIONS

This work introduced the concept of a capillary-fed electrolysis (CFE) cell and demonstrated that, using known catalysts, it significantly improved the energy efficiency of producing hydrogen from water. At an operating current density employed in commercial alkaline electrolysis cells of 0.5 A cm^{-2}, a cell voltage of only 1.506 V was needed to produce hydrogen at 85 °C. This represented a cell energy efficiency of 98% (HHV), with consumption of 40.4 kWh kg^{-1} H_2, or 3.64 kWh Nm^{-3} H_2. This result surpasses commercial electrolysis cells, which consume ~47.5 kWh kg^{-1} H_2, and exceeds the 2050 IRENA target of <42 kWh kg^{-1}.

REFERENCES

1. Hodges A, Hoang AL, Tsekouras G, Wagner K, Lee CY, Swiegers GF, and Wallace GG. A high-performance capillary-fed electrolysis cell promises more cost-competitive renewable hydrogen. Nature Communication 2022, DOI 10.1038/s41467-022-28953-x.

WHEC-2022
23rd World Hydrogen Energy Conference
June 26-30, 2022 - Istanbul

#1469

ENHANCING THE ELECTROCATALYTIC HYDROGEN EVOLUTION ACTIVITY OF BARE COPPER ELECTRODES THROUGH ULTRAFAST FEMTOSECOND LASER NANOSTRUCTURING

[1,2*] *Shahbaz Ahmad,* [1,2] *Mehmet Egilmez,* [1, 3] *Mehmet F. Orhan, and* [1,2] *Ali S. Alnaser*
[1]Material Science and Engineering Program, American University of Sharjah, Sharjah, United Arab Emirates
[2] Department of Physics, American University of Sharjah, Sharjah, United Arab Emirates
[3] Department of Mechanical Engineering, American University of Sharjah, Sharjah, United Arab Emirates

*Corresponding author e-mail: sahmad19@asu.edu

ABSTRACT

In this study, we report on enhancing the surface area of bare copper electrodes via femtosecond laser processing for its application in alkaline water electrolysis. It is shown that the laser nanostructuring process creates unique and hierarchal nanostructures superimposed over spiky microstructures. Analysing the effect of various laser parameters indicate that scanning speed greatly effects the microstructures by decreasing its dimensions and increasing porosity. The results also shows that laser processing has significantly enhanced the surface area with spiky and superhydrophilic structures. Furthermore, this process is expected to improve the hydrogen evolution reaction (HER) kinetics by allowing more electrode to electrolyte interface, which can favor the enrichment and formation of protons on structured Cu cathode.

Keywords: Femtosecond Laser; Hydrogen Evolution Reaction; Electrode; Nanostructuring

INTRODUCTION

The electrochemical water splitting for efficient renewable hydrogen production has been considered a critical step in hydrogen economy [1]. In commercialization of low temperature electrolyzers (PEM and AEM), the primary need is to develop a highly porous electrode materials as catalyst which is economical, durable and highly active [2]. To accelerate the sluggish oxygen evolution reaction (OER) and hydrogen evolution reaction (HER) in water electrolysis, different types of noble Platinum (Pt) alloys have been used as electrocatalyst materials which are costly and has adversely affected the electrochemical performance of electrolyzers due to its high loading effects and poor durability [3]. Under these circumstances extensive studies has been carried out to explore and develop non noble Pt less materials as an alternative option [4].

H_2 production from alkaline electrolysis is one the most efficient (I.e., conversion efficiency ≈ 80%) processes which can replace the conventional fossil fuel-based H_2 production techniques [5]. However, it comes with the highest production cost (~$4 - $6/kg H_2) which mainly comes from the use of noble metal as an electrode catalyst [6]. Nonnoble transition metal based electrodes (e.g., Ni, Ti, Cu, Co Mn, etc.) possess higher overpotentials for H_2 generation which make it inefficient (high electricity input required) [7]. Scientists have made a tremendous effort to reduce the overpotential of nonnoble metals by the formation of metal oxides (MOx), nitrides, and carbides using wet chemistry methods such as CVD, hydrothermal, and other electrochemical tuning techniques but the problem with these techniques is that they are limited to laboratory scale and comes with a lot of challenges [8].

Recently Ultrafast laser processing technology has been proved a viable technique in improving functions of solid surfaces through the creation of various microstructures through melting and ablation techniques [9]. It has been proved a useful tool in altering the optical, mechanical, and electrical properties of metals for a wide range of fields such as photonics, plasmonic [10], and energy fields [11]. Compared to etching, plasma ablation, and other surface treatments process, femtosecond laser (FS) surface processing is prompt and has higher accuracy, efficiency, controllability, and repeatability which can introduce favorable microstructures with higher physical stability and surface area. (surface area > tens fold compared to pristine) [12]. The higher surface area means more electrode to electrolyte interface and thus higher H_2 conversion output.

MATERIALS AND METHODS

Pristine Cu plates with dimensions 20×20mm area and 2mm thickness were used as cathode material for laser processing and electrochemical HER reaction in for alkaline electrolysis in1M KOH solution. All plates were washed with acetone and DI water multiple times and were dried in convection over at 80℃ overnight. An amplified high power-based laser system (model AFS-UFFL-300-2000-1030-300 from Active Fiber Systems GmbH, Jena, Germany) for surface nanostructuring (Fig. 1). The laser source delivers femtosecond laser pulses centered at 1030 nm, with 40 femtosecond duration and 50 kHz repetition rate. The laser power was controlled using a combination of a half-wave

plate (HWP) and a thin-film polarizer (TFP) to deliver single pulse energy of 200 µJ. Finally, the attenuated laser beam was focused on the Cu substrate through an F-Theta lens and a raster scanner using the scan head (FARO tech. Xtreme-20, Faro Technologies, Inc., Lake Mary, FL, USA). The focal spot diameter on the substrate was ~ 70 µm with a laser fluence of 4 J/cm^2. We selected a series of decreasing scanning speeds starting with 50, 20, 10 and 5 mm/s with a spacing width of 80 µm between two adjacent microgrooves (step size). The surface morphologies were investigated with scanning electron microscopy (SEM-EDX) (TESCAN VEGA3) SEM equipped with an EDX spectrometer (Tescan, Brno, Czechia). Water contact angle (WCA) measurement was conducted using Drop Shape Analyzer (DSA-100, KRUSS, Matthews, NC, USA). We will be performing electrochemical measurements with CHI 660 potentiostat (CH Instruments USA) in three electrodes cell setup in which Cu plates will be used as working electrode, Pt wires as counter electrode while Ag/AgCl as reference electrode.

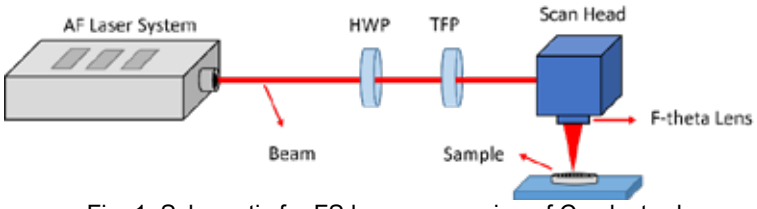


Fig. 1. Schematic for FS laser processing of Cu electrodes

RESULTS

Fig. 2 (A-D) shows the SEM micrographs of laser structured Cu electrodes with at scanning speed of 50, 20, 10 and 5 mm/s respectively. The analysis depicts that with decreasing scanning speed the morphology is significantly changing, and the microstructures are transforming from dorm shape structures towards Fig 2. (A & B) to spiky needle structures which much high surface area and porosity. There is an appearance of nanostructures superimposing over larger microstructures at low scanning speeds (Fig. 2D) along with nanoparticles which are due to the melting of Cu and rapid cooling in air. SEM analysis shows very hierarchical and reproducible structures which can be very promising in HER.

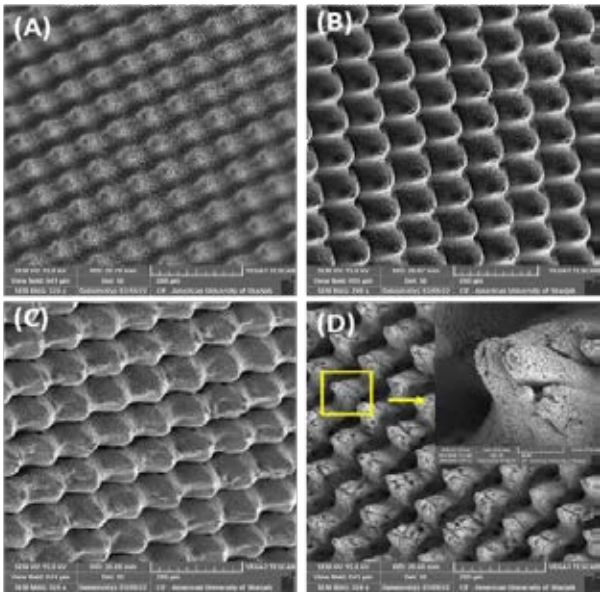


Fig. 2. SEM analysis of laser processed Cu plates with hierarchical microstructures

In order to determine the wettability of laser processed Cu electrodes (LS-Cu) we performed WCA analysis. As shown in Fig.3. the laser structured Cu electrodes surface possess superhydrophilic nature on which water drops expands immediately within fraction of second. The superhydrophilic nature along with high surface area allows more electrode to electrolyte interface thus increasing water splitting efficiency.

We are further characterizing and testing the electrochemical activity of LS-Cu electrodes for overall water splitting process in electrolysis cell which we cannot explain here due to max 3 pages limits. In case of short paper acceptance further data will be presented in conference in detail.

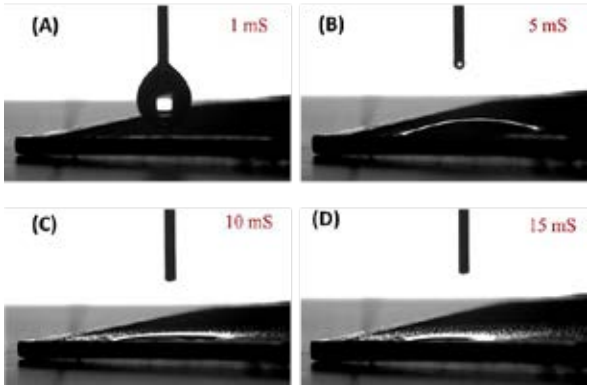


Fig. 3. WCA analysis of LS -Cu 0.5 mm/s electrode surface showing splitting of water in milliseconds (mS)

CONCLUSION

Femtosecond (FS) laser processing of nonnoble electrodes with unique surface micro/nano structures exhibits high surface area and superhydrophilicity compared to pristine plates. The nanoparticles on the top of needle shape microstructures can produces strong electric fields under negative polarization which in addition with former two surface properties favor the formation of protons and recombination of adsorbed hydrogen atoms in water splitting leading to an accelerated HER kinetics in alkaline water electrolysis.

REFERENCES

[1] Joya KS, Joya YF, Ocakoglu K, van de Krol R. Water-Splitting Catalysis and Solar Fuel Devices: Artificial Leaves on the Move. Angew Chemie Int Ed 2013;52:10426–37. doi:10.1002/anie.201300136.
[2] Jaouen F, Proietti E, Lefèvre M, Chenitz R, Dodelet JP, Wu G, et al. Recent advances in non-precious metal catalysis for oxygen-reduction reaction in polymer electrolyte fuel cells. Energy Environ Sci 2011;4:114–30. doi:10.1039/c0ee00011f.
[3] Pavel CC, Cecconi F, Emiliani C, Santiccioli S, Scaffidi A, Catanorchi S, et al. Highly Efficient Platinum Group Metal Free Based Membrane-Electrode Assembly for Anion Exchange Membrane Water Electrolysis. Angew Chemie Int Ed 2014;53:1378–81. doi:10.1002/anie.201308099.
[4] Millet P, Ngameni R, Grigoriev SA, Mbemba N, Brisset F, Ranjbari A, et al. PEM water electrolyzers: From electrocatalysis to stack development. Int J Hydrogen Energy 2010;35:5043–52. doi:10.1016/j.ijhydene.2009.09.015.
[5] Bodner M, Hofer A, Hacker V. H2 generation from alkaline electrolyzer. Wiley Interdiscip Rev Energy Environ 2015;4:365–81. doi:10.1002/WENE.150.
[6] Vickers J, Peterson D, Randolph K, Irwin L, Desantis D, Hamdan M, et al. DOE Hydrogen and Fuel Cells Program Record Title: Cost of Electrolytic Hydrogen Production with Existing Technology. 2000.
[7] Li C, Baek JB. Recent Advances in Noble Metal (Pt, Ru, and Ir)-Based Electrocatalysts for Efficient Hydrogen Evolution Reaction. ACS Omega 2020;5:31–40. doi:10.1021/ACSOMEGA.9B03550/ASSET/IMAGES/ACSOMEGA.9B03550.SOCIAL.JPEG_V03.
[8] Yuan N, Jiang Q, Li J, Tang J. A review on non-noble metal based electrocatalysis for the oxygen evolution reaction. Arab J Chem 2020;13:4294–309. doi:10.1016/J.ARABJC.2019.08.006.
[9] Stratakis E. Nanomaterials by ultrafast laser processing of surfaces. Sci Adv Mater 2012;4:407–31. doi:10.1166/SAM.2012.1297.
[10] Temnov V V. Ultrafast acousto-magneto-plasmonics. Nat Photonics 2012 611 2012;6:728–36. doi:10.1038/nphoton.2012.220.
[11] Sugioka K, Cheng Y. Ultrafast lasers—reliable tools for advanced materials processing. Light Sci Appl 2014 34 2014;3:e149–e149. doi:10.1038/lsa.2014.30.
[12] Vorobyev AY, Guo C. Direct femtosecond laser surface nano/microstructuring and its applications. Laser Photon Rev 2013;7:385–407. doi:10.1002/LPOR.201200017.

WHEC-2022
23rd World Hydrogen Energy Conference
June 26-30, 2022 - Istanbul

#1481

THIN FILM COATING OF PLATINUM ON 3D PRINTED POLYMERIC ANODE ELECTRODES FOR PEMWE

[1,2]Bulut Hüner,[1,2*] Nesrin Demir, [1,2]Mehmet Fatih Kaya
[1]Erciyes University, Engineering Faculty, Energy Systems Engineering Department, Heat Engineering Division, 38039, Kayseri, Turkey
[2]Erciyes University H2FC Hydrogen Energy Research Group, 38039, Kayseri, Turkey

*Corresponding author e-mail: nkayatas@erciyes.edu.tr

ABSTRACT

Three-dimensional (3D) printing technology presents a higher flexible technique to produce different complex geometric shapes compared to conventional manufacturing. This technology is known as additive manufacturing (AM) may be also suitable for industrial production. AM method is widely used in different areas, including construction, medicine, energy, and electrochemistry, recently. Polymeric materials such as polylactic acid (PLA) and acrylonitrile butadiene styrene (ABS) filaments are used in the 3D printing process. In this study, the conductive polymeric anode electrodes are prepared using 3D printing method. Then, these electrodes are coated with Pt in different thicknesses (0.5, 1, 1.5, and 2µm) by the electron beam evaporation (EBM) method. A thin Cr adhesion layer (20nm) is used to improve the adhesion of the Pt coating on the sample surface. After the completion of the coating process, the polymeric electrodes are named as Pt-0.5, Pt-1, Pt-1.5, and Pt-2. Pt coated 3D printed polymeric electrodes have been physically characterized by using Field Emission Scanning Electron Microscopy (FE-SEM), FE-SEM/Energy Dispersive X-Ray Spectroscopy (FE-SEM/EDX), FE-SEM mapping, and X-Ray Powder Diffraction (XRD) techniques. Cycling Voltammetry (CV), Linear Sweep Voltammetry (LSV), Electrochemical Impedance Spectroscopy (EIS), and Chronoamperometry (CA) analysis of the Pt coated electrodes have been conducted to evaluate their electrochemical performance.

Keywords: Additive Manufacturing, 3D Printed Polymeric Electrode, Thin Film

INTRODUCTION

Today, global energy consumption and energy needs have increased due to the increasing population and lifestyle. As a secondary energy source, hydrogen is considered as one of the most promising potential solutions and energy carriers to meet the growing energy demand [1]. Electrolysis of water is one of the easy methods to produce hydrogen, and it does not emit any by-product or carbon emissions other than oxygen and hydrogen. Proton Exchange Membrane Water Electrolysis (PEMWEs), which is another promising method among water electrolysis methods, has many advantages such as high efficiency, high current density, and operation at lower temperatures [2]. PEMWEs represent a concept in a solid electrolyte. PEMWE is known as an alternative to alkaline water electrolyser, and it can be operated under high current densities. PEMWE present a sustainable solution for the generation of hydrogen and oxygen, and they can be integrated with renewable or alternative energy sources like solar and wind. The membrane electrode assembly (MEA), bipolar layers (BPs) with flow channels, gas diffusion layer (GDL), or gas diffusion electrode (GDE) are essential components of PEMWEs. Among these components, GDEs have an important place for the distribution of flow. However, adherence to desired geometries and coating thicknesses of GDEs provide a significant cost disadvantage for researchers. To eliminate or minimize the effects of this disadvantage, the development of rapid production methods in PEMWEs has an important place. AM method, also known as 3D printing among rapid production methods, has recently paved the way for rapid prototyping (faster times to market) for industrial applications. With the use of the 3D printing method, complex designs can be turned into products or material quickly and cost-effectively [3, 4]. AM technology enables to be produced lighter, cost-effective, and faster for components of PEMWEs. Interest in AM technology has greatly increased since 2014, and it has become more common for using PLA and ABS filaments in the 3D printing process [5]. To increase the electrical conductivity and corrosion resistance of 3D printed materials (such as electrodes or supercapacitors), the process of coating is one of the most promising ways [6].

In this study, 3D printed graphene-based conductive electrodes are produced from conductive PLA filament (Volume Resistivity: 0.6 ohm-cm), and samples are coated with Pt by using a EBM thin film coating method. Electrochemical properties of polymeric electrode samples for OER in acidic media have been investigated by CV, LSV, EIS, Tafel curves, and CA techniques. The surface morphology, crystallinity, and elemental composition of polymeric electrodes have been examined with FE-SEM, FE-SEM/EDX, and XRD analysis.

MATERIALS AND METHODS

Preparation of Polymeric Electrodes by 3D Printing Method

Polymeric based electrodes were designed using SolidWorks drawing software with 22.40mmx22.40mmx1.5mm (length/width/thickness) dimensions, and electrodes were prepared by the 3D printing method. An 3D printer (Ultimaker 2^{++}) (with a 0.4mm diameter extrusion nozzle) and Black Magic conductive PLA filament (available from 3D compare) were used for 3D printing the anode electrode samples. The Standard Triangle Language (*STL) file format of the electrode designs was converted into Cura 2.0 3D printing slicer program software and saved as a GCode file to start printing the designed samples. For the printing process of polymeric electrodes, the printing speed was set at the rate of 30 mm/s, and the nozzle and bed temperature were adjusted to 60 and 200°C, respectively [7]. All polymeric electrodes were printed at 100% infill and 0.1mm layer thickness. The dimensions of the designed polymeric electrodes for electrochemical measurements can be seen in Fig.1.

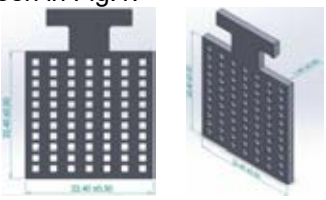


Fig. 1. Dimensions of the designed electrodes for electrochemical measurements a) front view and b) side view

Thin Film Coating of Polymeric Electrodes

Before starting the thin film coating of the electrodes, series of cleaning procedures were conducted to the electrodes. To ensure the surface of the electrode was clean, the samples were firstly immersed in ethanol for 5 minutes in an ultrasonic bath. Then, electrodes were carefully cleaned with deionized (DI) water and dried in a nitrogen (N_2) atmosphere. After the completion of the cleaning process of the polymeric electrodes, the samples were coated with different thicknesses (0.5, 1, 1.5, and 2µm) of Pt using the electron beam evaporation method [8, 9]. A thin Cr adhesion layer (20nm) is used for better adhesion of Pt film coating. Thin films prepared via the electron beam evaporation technique at different film thicknesses were denoted as Pt-0.5, Pt-1, Pt-1.5, and Pt-2. The schematic view of the thin film coating of the electrodes is given in Fig. 2.

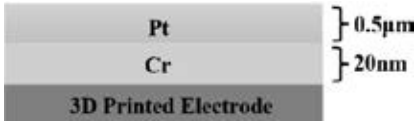


Fig. 2. Thin film coating process of polymeric electrodes

Determination of Electrochemical and Surface Properties of Polymeric Electrodes

The surface morphologies and elemental analysis of the polymeric electrodes were analyzed by using FE-SEM and FE-SEM/EDX techniques, respectively. The crystalline and phase structure of samples was investigated by using XRD analysis. Electrochemical properties of polymeric electrodes were investigated using CV, LSV, EIS, and CA analysis. All the electrochemical measurements were carried out in 0.5M H_2SO_4 solution using Pt wire as the counter electrode, Ag/AgCl (3M KCl saturated) was used as a reference electrode and polymeric electrode was used as the working electrode [10]. Fig. 3. shows three-electrode electrochemical cell configurations for electrochemical analysis.

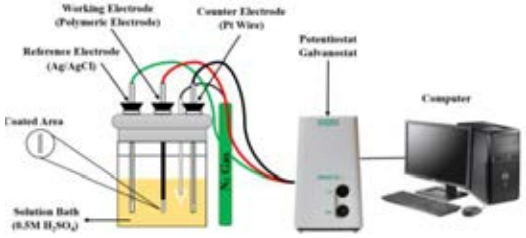


Fig. 3. The three-electrode electrochemical cell configuration

CONCLUSIONS

In this study, polymeric electrodes are prepared by the 3D printing method, and then the electrodes are coated with a thin film method. According to the electrochemical analysis measurements, an increase in the corrosion resistance of the polymeric electrodes is expected with the increase of the coating thickness in thin film coatings. Thanks to Cr

interlayer, adhesion performance of the Pt is enhanced. In addition, due to high conductivity of the Pt metal, contact resistance of the electrodes are improved.

ACKNOWLEDGEMENT

This study is supported by the Scientific and Technological Research Council of Turkey (TUBITAK) 1001 Research Projects Funding Program under the project number:120M234. The authors would like to thank the Scientific Research Projects Unit of Erciyes University for funding and supporting the project under the contract numbers: FDK-2020-10548 and FBA-2021-11073. Author Bulut HÜNER thanks the Turkish Republic Higher Education Institution 100/2000 Ph.D. Scholarship Program and the Scientific and Technological Research Council of Turkey (TUBITAK) for their scholarships under the “2211-C Priority Areas Ph.D. Scholarship Program (grant number 1649B032000098).

REFERENCES

1. Lædre, S., Kongstein, O. E., Oedegaard, A., Karoliussen, H., Seland, F. 2017. "Materials for Proton Exchange Membrane Water Electrolyzer Bipolar Plates", International Journal of Hydrogen Energy, 42(5), 2713-2723.
2. Ju, H., Badwal, S., Giddey, S. 2018. "A Comprehensive Review of Carbon and Hydrocarbon Assisted Water Electrolysis for Hydrogen Production", Applied energy, 231, 502-533.
3. Rohaizad, N., Mayorga-Martinez, C. C., Novotný, F., Webster, R. D., Pumera, M. 2019. "3d-Printed Ag/Agcl Pseudo-Reference Electrodes", Electrochemistry Communications, 103, 104-108.
4. Manzanares Palenzuela, C. L., Novotný, F., Krupička, P., Sofer, Z. k., Pumera, M. 2018. "3d-Printed Graphene/Polylactic Acid Electrodes Promise High Sensitivity in Electroanalysis", Analytical Chemistry, 90(9), 5753-5757.
5. Rossi, S., Puglisi, A., Benaglia, M. 2018. "Additive Manufacturing Technologies: 3d Printing in Organic Synthesis", ChemCatChem, 10(7), 1512-1525.
6. Kim, M. J., Cruz, M. A., Ye, S., Gray, A. L., Smith, G. L., Lazarus, N., Walker, C. J., Sigmarsson, H. H., Wiley, B. J. 2019. "One-Step Electrodeposition of Copper on Conductive 3d Printed Objects", Additive Manufacturing, 27, 318-326.
7. Ghosh, K., Ng, S., Iffelsberger, C., Pumera, M. 2020. "Inherent Impurities in Graphene/Polylactic Acid Filament Strongly Influence on the Capacitive Performance of 3d-Printed Electrode", Chemistry–A European Journal.
8. Dur, E., Cora, Ö. N., Koç, M. 2014. "Effect of Manufacturing Process Sequence on the Corrosion Resistance Characteristics of Coated Metallic Bipolar Plates", Journal of Power Sources, 246, 788-799.
9. Sripumkhai, W., Porntheeraphat, S., Saekow, B., Bunjongpru, W., Rahong, S., Nukeaw, J. 2010. "Effect of Annealing Temperature on Platinum Thin Films Prepared by Electron Beam Evaporation", Journal of the Microscopy Society of Thailand, 24(1), 51-54.
10. Gago, A. S., Ansar, A. S., Gazdzicki, P., Wagner, N., Arnold, J., Friedrich, K. A. 2014. "Low Cost Bipolar Plates for Large Scale Pem Electrolyzers", ECS Transactions, 64(3), 1039.

WHEC-2022
23rd World Hydrogen Energy Conference
June 26-30, 2022 - Istanbul

#1487

IMPROVING HYDROGEN EVOLUTION CATALYTIC ACTIVITY OF 2D CARBON ALLOTROPE BIPHENYLENE WITH B, N, P DOPING: DENSITY FUNCTIONAL THEORY INVESTIGATIONS

Mukesh Singh[a], Alok Shukla[a], Brahmananda Charkroborty[b,c,**]*
[a]Department of Physics, Indian Institute of Technology Bombay, Powai, Mumbai 400076, India
[b]High Pressure and Synchrotron Radiation Physics Division, Bhabha Atomic Research Centre, Trombay, Mumbai, India
[c]Homi Bhabha National Institute, Mumbai, India

*Corresponding authors: Mr. Mukesh Singh E-mail address: gkpmukeshsingh@gmail.com
**Dr. Brahmananda Chakraborty E-mail address: brahma@barc.gov.in

ABSTRACT
Using the first principle calculations, we studied the hydrogen evolution reaction (HER) activity of pristine Biphenylene (BPh) and B, N, P decorated BPh sheet. HER activity of BPh sheet is not encouraging, it is similar to pristine graphene. However, doping of P on top of one carbon atom of the BPh sheet improves its activity better than Pt-catalysts. We analyzed the adsorption mechanism of dopants (B, N, P) and hydrogen adsorption with Bader charge analysis and density of states (DOS) analysis. We have compared all our best HER activity results in the reaction coordinate and volcano plots of pristine, B, N, P-doped BPh sheets, and they indicate that P doped BPh is a powerful catalyst for HER activities.
Keywords: Hydrogen production, HER, Biphenylene, first principle calculation

INTRODUCTION
To fulfill the energy demands while keeping a pollution-free environment requires alternative resources, independent of fossils fuels. A high energy density of 143MJ/kg [1], abundant in composite form, and pollution-free utilization make hydrogen energy a promising fuel. However, ~ 96% of total produced H_2 is produced using fossil fuels through the steam reforming process [2]. Expensive Pt groups metal (Pt, Pd, Ru, Ir, and Rh) are employed in electrolysis to produce the remaining ~ 4% hydrogen. Hence, searching for cost-effective and pollution-free catalysts is of utmost importance. A new allotrope of carbon, 2D Biphenylene (BPh), is synthesized [3] recently and found to be mechanically robust and stable up to 4500K [4]. In this work, we have studied the HER activity of pristine BPh, and B, N, P-decoration on it in many different configurations. We found that Gibbs free energy ΔG^{H^*} of P-decorated Biphenyle 0.02 eV surpassed Pt-catalyst (ΔG^{H^*}=0.09) and analyzed the DOS and Bader's charge transfer for binding mechanism. All our results are compared with each other in the reaction coordinate and volcano plots.

COMPUTATIONAL METHODS
All the simulations are performed using plane wave density functional theory code VASP [5,6] with Perdew-Burke-Ernzerhof pseudopotential. Electronic configuration of $2s^22p^2$, 1s, $2s^22p^1$, $2s^22p^3$, $3s^23p^3$ were considered for C, H, B, N, P respectively. The kinetic energy cutoff and kpoints are selected in well converged ranges, which are 500eV and 7x7x1, respectively. Monkhrost special points were employed to integrate on Brillouin zone. The 2x2x1 supercell of Biphenylene sheet has been utilized with lattice constants a=9.03Å, b=7.51Å, and vacuum 10.5Å in the perpendicular direction to the sheet. For self-consistent DFT iterations and structural relaxation, energy convergence and Feymann-Hellman forces' convergence criteria are 10^{-5}eV and 10^{-2} eV/A, respectively.

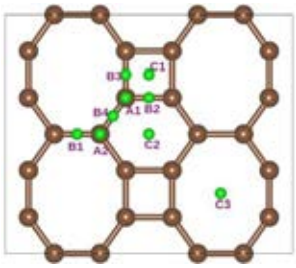
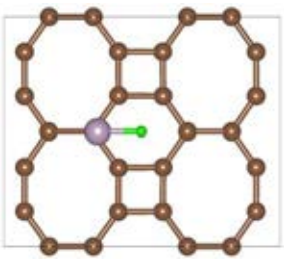


Fig. 1 (a) Different possible doping positions on BPh sheet


Fig. 1 (b): optimized structure of Bph+P+H(@A2)

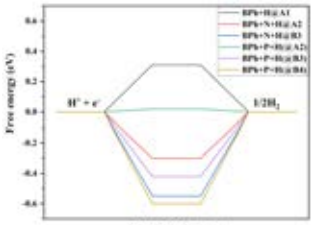


Fig. 1(c): HER reaction coordinates

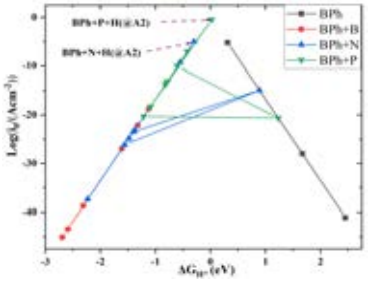


Fig. 1 (d): exchange current density i_0 and ΔG_{H^*} plots

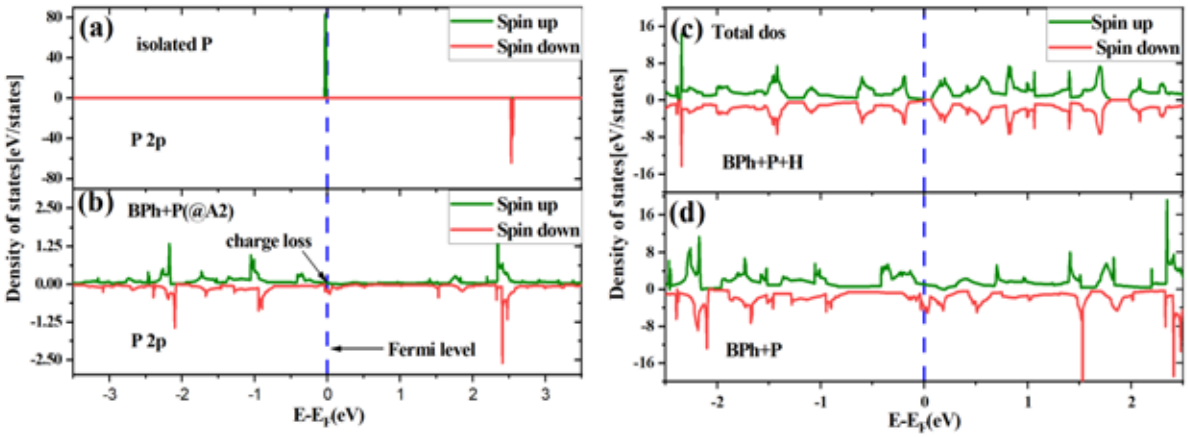


Fig. 2: Partial DOS of (a) isolated P-atom and (b) BPh+P(@A2); Total DOS of (c) BPh+P+H and (d) BPh+P for position A2. P-atom has lost some charges (a and b), and combined system become magnetic (d). After adsorbing H, it again becomes non-magnetic (c).

Table 1. Binding energy table for B+BPh, N+BPh, P+BPh along with their optimized distances:

System		@A1	@A2	@B1	@B2	@B3	@B4	@C1	@C2	@C3
BPh+B	B.E(eV)	-2.46	-2.22	-1.60	-2.46	-2.37	-2.46	-2.75	-1.67	-0.94
BPh+N	B.E(eV)	-1.51	-1.99	-0.04	-2.26	-3.83	-1.98	-1.64	-0.03	-0.06
BPh+P	B.E(eV)	-1.51	-1.26	-0.15	-1.55	-1.55	-1.26	-1.55	0.38	-0.04

Table 2. HER properties of optimized pristine, B, N, P decorated BPh sheet.

System	Properties	@A1	@A2	@B1	@B2	@B3	@B4	@C1	@C2	@C3
BPh+H	**ΔG**	0.31	2.45	2.45	2.45	1.67	0.31	2.45	2.45	2.45
BPh+N+H	**ΔG**	-2.23	-0.30	-1.40	-1.48	-0.55	-1.56	0.89	-1.40	-1.38
BPh+P+H	**ΔG**	-0.82	0.02	-1.09	-0.78	-0.42	-0.60	1.23	-1.21	-0.79

Table 3. Bader charge analysis on adsorption of H on BPh+P

	@A1	@A2	@B1	@B2	@B3	@B4	@C1	@C2	@C3
Charge gained by P	-0.37	-0.06	-0.24	-0.37	-0.31	-0.30	0.18	0.41	-0.38
Charge gained by H	0.36	0.36	0.35	0.41	0.41	0.37	0.44	0.40	0.36

RESULT AND DISCUSSION

We start with optimizing the structure of BPh and comparing their structural parameters like lattice parameter, bond-length, bond-angle, etc., with the previous literature [5,6]. We doped hydrogen atoms at several possible positions at 2Å away from the BPh sheet in different configurations, as shown in Fig. 1(a). After optimization, pristine BPh shows HER properties similar to graphene, except A1 and B4 positions. The adsorption energy, Gibbs free, the distance between H to the nearest C atom, are presented in table 1. The following equation is used to compute Gibbs free energy [7],

$$\Delta G^{H^*} = E_{ad} + 0.24 \quad (1)$$

where E_{ad} = E(H+system)–E(system)–0.5*E(H_2). Using eq^n (1), exchange current density can be calculated [7] by

$$I_0 = -ek_0(1+\exp(|\Delta G^{H^*}|/k_B T))^{-1} \quad (2)$$

Where k_0=1 (theoretical values) and T=300K.

From Table 1, we can see that BPh+H@A1 and BPH+H@B4 have small Gibbs free energy 0.31 eV. To improve HER activity, we consider doping external adatom D (where D=B, N, P) on BPh. The binding strength of dopant D and their distance to the nearest carbon atom are presented in table 2. B, N, P are bonded with the BPh sheet

more strongly through charge transfer. From Bader charge analysis, for BPh+P(@A2), P donate 0.5e to the BPh sheet. The same can be concluded from the partial density of states in Fig. 2(a), which shows that after decoration of P atom on BPh sheet, the states near Fermi level reduce significantly. BPh is non-magnetic (not shown here). However, on doping P atom, the density of stated becomes unsymmetric as in Fig. 2(c) because of 0.5e charge gain from P atom. After finding that adatom D binds strongly with the BPh sheet, we proceed with the adsorption of the H atom. After optimization, the results are presented in Table 3. The optimized structure of BPh+P+H(@A2) is plotted in Fig. 1(b). From the Gibbs energy analysis, we find that B doping is worsening the result. N doping barely improves the results, and P doping drastically improves HER activity which surpasses ΔG^{H^*} = 0.02 eV Pt catalyst (0.09 eV). From Bader charge analysis, we found that in optimized BPh+P+H(@A2), P and H gain -0.06e and 0.36e amount of charges. Table 4 shows that except BPh+P+H@A2, in all other configurations, the amount of lost/gained charge is more, resulting in strong bonding between P-H and hence higher ΔG^{H^*}. The same is verified using the partial density of states (Not plotted here). Also, from the total density of states profile, we observed that adsorption of H atom makes the whole system BPh+P+H non-magnetic. The small amount of charge transfer from P in the adsorption process of H might be leading to good values of binding energy, i.e., neither strong nor weak. All our best results are plotted in the reaction coordinate Fig 1. (c) and found exchange currents computing using eq^n (2) and the relation between ΔG^{H^*} and i_0 are shown in volcano plots Fig 1(d).

CONCLUSION

Using DFT calculation, we predicted that HER activities of biphenylene are mostly inactive, but its decoration with the P atom improves the result (ΔG^{H^*}=0.02eV) significantly, surpassing Pt-catalyst (ΔG^{H^*}=0.09 eV). From the reaction coordinate plots and volcano plots, we conclude that P-doped BPh is a promising catalyst for HER activity.

ACKNOWLEDGMENT

Mukesh Singh would like to express his special thanks to CSIR for funding his Ph.D. research projects and Spacetime High-Performance computing at IITB for resources.

REFERENCES

1. Mazloomi K, Gomes C. Hydrogen as an energy carrier: Prospects and challenges. Renewable and Sustainable Energy Reviews 2012; 16:3024–33.
2. Hydrogen from renewable power: Technology outlook for the energy transition. /Publications/2018/Sep/Hydrogen-from-Renewable-Power n.d.
3. Fan Q, Yan L, Tripp MW, Kachel SR, Chen M, Foster AS, et al. Biphenylene network: A nonbenzenoid carbon allotrope 2021:6.
4. Luo Y, Ren C, Xu Y, Yu J, Wang S, Sun M. A first principles investigation on the structural, mechanical, electronic, and catalytic properties of biphenylene. Sci Rep 2021;11:19008.
5. Kresse G, Furthmüller J. Efficiency of ab-initio total energy calculations for metals and semiconductors using a plane-wave basis set. Computational Materials Science 1996;6:15–50.
6. Kresse G, Furthmüller J. Efficient iterative schemes for *ab initio* total-energy calculations using a plane-wave basis set. Phys Rev B 1996;54:11169–86.
7. Nørskov JK, Bligaard T, Logadottir A, Kitchin JR, Chen JG, Pandelov S, et al. Trends in the Exchange Current for Hydrogen Evolution. J Electrochem Soc 2005;152:J23.

WHEC-2022
23rd World Hydrogen Energy Conference
June 26-30, 2022 - Istanbul

#1517

IRIDIUM-RUTHENIUM CATALYST ON SPUTTER-ETCHED MEMBRANE FOR PROTON EXCHANGE MEMBRANE WATER ELECTROLYZERS

[1] Tomáš Hrbek, [1]Peter Kúš, [1]Vladimír Matolín, [1]Iva Matolínová*
[1]Charles University, Faculty of Mathematics and Physics, Department of Surface and Plasma Science, v Holešovičkách 2, 180 00 Prague 8, Czech Republic

*Corresponding author e-mail: tomas.hrbek@mff.cuni.cz

ABSTRACT

We present an iridium-ruthenium-based catalyst (25 % Ir, 75 % Ru) for Proton Exchange Water Electrolyzers (PEM-WE) with low iridium loading (158 μg cm^{-2}), prepared by magnetron sputtering. We use no additional support for the PEM-WE's anode. The sputter-etching of the PEM replaces them – its simultaneous plasma and deposition of a cerium oxide layer during reactive magnetron sputtering leads to a pronounced fiber-like structure on its surface. The prepared catalyst is tested for 1272 hours in a single-cell PEM-WE, demonstrating excellent activity and stability. We focus on stability, which is the crux of a low-iridium-loading catalyst. We search for its origin through several electrochemical and surface analysis methods – Potential Electrochemical Impedance Spectroscopy, Energy X-Ray spectroscopy, X-ray Photoelectron Spectroscopy, and Scanning Electron Microscopy.

Keywords: magnetron sputtering, PEM-WE, lateral conductivity, iridium-ruthenium

INTRODUCTION

The ever-increasing energy demands of modern society and the nearly unanimous commitment to limiting global warming by lowering greenhouse gas emissions through renewable energy sources lead to a significant transformation of the worldwide energy and transportation sector [1]. Hydrogen Economy is built around the electrochemical "power-to-gas" conversion of electricity into H_2 through the process of electrolysis in times of energy overproduction and subsequent use of generated hydrogen in various ways. The key technology of the Hydrogen Economy is Proton Exchange Membrane Water Electrolyzer (PEM-WE) – a device that uses electrical power to drive electrochemical water splitting into hydrogen and oxygen utilizing a proton conductive membrane [2]. Nonetheless, the principal drawback of PEM-WEs that is becoming increasingly problematic as more significant numbers of units and installations appear worldwide is their dependence on noble metals essential for catalyzing the individual redox reactions in the cells. Specifically, it is platinum (1000 USD/oz) on the cathode of PEM-WE and iridium (5100 USD/oz) on the anode of PEM-WE [3], where iridium presents the problematic part due to the sluggish anodic Oxygen Evolution Reaction. Massive research is being conducted on the problematics of low- or zero- iridium catalysts for the anode [4–7], using several different approaches. This work presents a magnetron-sputtered, iridium-ruthenium-based catalyst for PEM-WE, which utilizes our two previous works: An iridium-ruthenium-based catalyst (25 % of iridium and 75 % of ruthenium), and a sputter-etching modification of PEM [6], which allows increasing the active surface area significantly. We present a study of this catalyst's activity and stability and explain why this PEM-WE is so stable compared to a similar PEM-WE with the same amount of Ir and without Ru.

EXPERIMENTAL

Sputter-etched structures were created on a Nafion PEM membrane (50.8 μm thick, Chemours) via a sputter-etching procedure as described in [6]. The modified membrane was covered by the investigated catalytical layers – pure iridium (70 nm) and mixed iridium-ruthenium (280 nm, 25 % of Ir). The layers were used for the assembly of PEM-WEs, the former called MEA Ir 100, the latter MEA Ir-Ru 25:75. As a liquid gas diffusion layer (LGDL) for the anode, a micro-grained sintered porous Ti (Mott) with a 50 nm protection layer of platinum was used. The commercial platinum catalyst supported by carbon (Pt 0.5 mg cm^{-2}, FuelCellStore) was used as a cathode gas diffusion electrode (GDE). Prepared MEAs were then pressed between an anodic current collector (made of Ti) and a cathodic current collector (made of carbon). Titanium was chosen as a material for the anode side due to its corrosion resistance. The PEM-WE performance was tested by the BioLogic SP-150 Potentiostat. The single cell operating temperature was 80 °C. For all measured samples, surface morphology was routinely checked by a Tescan MIRA III Scanning Electron Microscope (SEM) before and after the electrochemical procedure to follow possible morphological changes. A Quantax EDX detector (Bruker), installed within the MIRA III SEM, was used to estimate the bulk composition of the measured samples. XPS setup (K_α Mg X-ray source, 1253.6 eV) was used to unravel the surface chemical composition. A SPECS Phoibos 150 hemispherical analyzer made spectra acquisition in FAT (Fixed Analyzer Transmission) mode. The number of scans was individually set for each measured element to attenuate the noise. The charging effect was determined by the detailed measurements of the Fermi edge and compensated accordingly. Fitting of the obtained spectra was done by KolXPD software.

RESULTS AND DISCUSSION

The samples (MEA Ir-Ru 25:75 and MEA Ir 100) were investigated in long-term stability in a PEM-WE. The results can be seen in Figure 1. Immediately, it stands out that MEA Ir-Ru 25:75 shows a better performance than MEA Ir 100. The better activity can be easily explained by the improved activity of the iridium-ruthenium catalyst, which is known [8–10]. However, also much better stability is observed. That contradicts the standard belief that an iridium-ruthenium-based catalyst is always less stable than the iridium one. By various surface and electrochemical analytical techniques, we concluded that the origin of the instability of MEA Ir 100 is its insufficient layer thickness which leads to a decreased lateral conductivity with time.

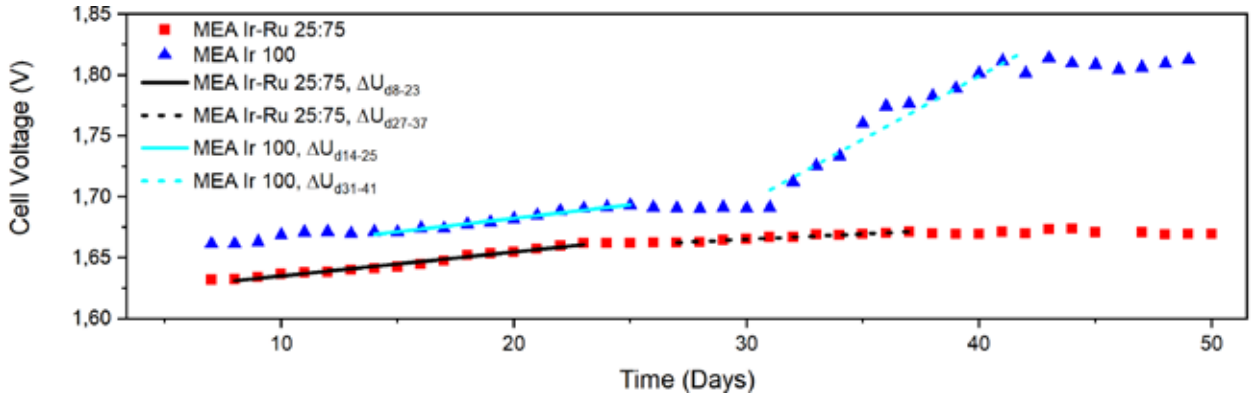


Figure 1. The long stability of MEA Ir 100 and MEA Ir-Ru 25:75. Linear regression fits the linear parts of the degradation curve.

CONCLUSIONS

Magnetron sputtering can be utilized for the preparation of a low-iridium-loading PEM-WE with good activity and stability without any additional supports. We concluded that the biggest issue of the catalysts with extremely low iridium loading is the lateral conductivity which decreases as the operation of the PEM-WE proceeds. A possible solution is to utilize magnetron sputtering of an iridium-ruthenium mixed catalyst. This approach has advantages: magnetron sputtering allows us to create a homogeneous and interconnected thin film. Secondly, the cheaper ruthenium enhances the catalysts activity and the thickness of the layer, which leads to better electrochemical performance.

REFERENCES

1. Abe JO, Popoola API, Ajenifuja E, Popoola OM. Hydrogen energy, economy and storage: Review and recommendation. Int J Hydrogen Energy. 44(29):15072–86.
2. Carmo M, Fritz DL, Mergel J, Stolten D. A comprehensive review on PEM water electrolysis. Int J Hydrogen Energy. 38(12):4901–34.
3. Bernt M, Hartig-Weiß A, Tovini MF, El-Sayed HA, Schramm C, Schröter J, et al. Current Challenges in Catalyst Development for PEM Water Electrolyzers. Chemie-Ingenieur-Technik. 92(1–2):31–9.
4. Kwen J, Doo G, Choi S, Guim H, Yuk S, Lee DH, et al. Identification of the electrical connection in the catalyst layer of the polymer electrolyte membrane water electrolyzer. Int J Hydrogen Energy. (xxxx).
5. Kúš P, Ostroverkh A, Ševčíková K, Khalakhan I, Fiala R, Skála T, et al. Magnetron sputtered Ir thin film on TiC-based support sublayer as low-loading anode catalyst for proton exchange membrane water electrolysis. Int J Hydrogen Energy. 41(34):15124–32.
6. Hrbek T, Kúš P, Yakovlev Y, Nováková J, Lobko Y, Khalakhan I, et al. Sputter-etching treatment of proton-exchange membranes: Completely dry thin-film approach to low-loading catalyst-coated membranes for water electrolysis. Int J Hydrogen Energy. 45(41):20776–86.
7. Hegge F, Lombeck F, Cruz Ortiz E, Bohn L, Von Holst M, Kroschel M, et al. Efficient and Stable Low Iridium Loaded Anodes for PEM Water Electrolysis Made Possible by Nanofiber Interlayers. ACS Appl Energy Mater. 3(9):8276–84.
8. Siracusano S, Van Dijk N, Payne-Johnson E, Baglio V, Aricò AS. Nanosized IrOx and IrRuOx electrocatalysts for the O2 evolution reaction in PEM water electrolysers. Appl Catal B Environ. 164:488–95.
9. Saveleva V. Investigation of the anodes of PEM water electrolyzers by operando synchrotron-based photoemission spectroscopy. :296.
10. Siracusano S, Baglio V, Van Dijk N, Merlo L, Aricò AS. Enhanced performance and durability of low catalyst loading PEM water electrolyser based on a short-side chain perfluorosulfonic ionomer. Appl Energy. 192:477–89.

WHEC-2022
23rd World Hydrogen Energy Conference
June 26-30, 2022 - Istanbul

#1538

EXERGETIC ANALYSIS OF A SOLAR ENERGY-BASED HYDROGEN PRODUCTION SYSTEM

[1*] *Hilal Akci,* [2] *Huseyin Gunerhan,* [3] *Arif Hepbasli*
[1] Ege University, Graduate School of Natural and Applied Science, Mechanical Engineering Program, 35100 Bornova, Izmir, Turkey
[2] Ege University, Faculty of Engineering, Department of Mechanical Engineering, 35100 Bornova, Izmir, Turkey
[3] Yasar University, Faculty of Engineering, Department of Energy Systems Engineering, 35100 Bornova, Izmir, Turkey

*Corresponding author e-mail: hilalakci@gmail.com

ABSTRACT

In this study, energy, exergy and sustainability analyses are performed for a solar energy-based hydrogen production system, which is modeled with TRNSYS and Engineering Equation Solver (EES) software packages. This system consists of solar photovoltaic panels (PVs), a controller, an electrolyzer, a metal hydride hydrogen tank used for hydrogen production and storage, and Proton Exchange Membrane Fuel Cell (PEMFC) for electricity storage. Dead state temperature is taken as 0 ºC. The results revealed that the PEMFC had the highest energy efficiency of 53.28%. Exergy efficiencies of the solar PV panel, the electrolyzer and the PEMFC were determined to be 9.66%, 60% and 29.39%, respectively. The exergetic sustainability index of the electrolyzer had the maximum value of 2.501.

Keywords: Exergy, Hydrogen Production, Electrolyzer, Efficiency, Solar Energy

INTRODUCTION

Hydrogen is considered to be the clean energy fuel of the future. Many attempts have been made for producing hydrogen in recent years using various technologies. Among the hydrogen production methods adopted in the world, 95% of hydrogen production belongs to stream reforming. Hydrogen production from fossil fuels causes increasing greenhouse gas emissions. For this reason, it is very essential for finding economic and environmentally friendly hydrogen production processes [1]. Solar energy based-hydrogen production techniques seem to be simpler and more convenient than other methods due to the sustainability and availability of the solar energy [2]. As far as some studies on solar-based multigeneration systems are concerned, Ozturk and Dincer [3] proposed a solar-based multi-generation system consisting of four main sub-systems, namely (i) Rankine cycle, (ii) organic Rankine cycle, (iii) absorption cooling and heating, and (iv) hydrogen production and utilization. The outputs were power, heating, cooling, hot water, hydrogen and oxygen. The energy and exergy efficiency values of the system were calculated to be 52.71% and 57.35%, respectively. Almahdi et al [4] proposed a novel solar thermal energy based multigeneration system and assessed its performance through energy and exergy analysis methods. They reported that the overall energy and exergy efficiencies were 20.7% and 13.7%, respectively. Tukenmez et al [5] proposed and analyzed both energetically and exergetically a solar energy supported plant with outputs of hydrogen, electricity, heating, cooling and hot water. Energetic and exergetic efficiencies of the solar power based combined cycle were reported to be 56.48% and 54.06%, respectively. The main objective of this study is to assess the performance of a solar energy-based hydrogen production system using energy and exergy analysis methods.

MODELING AND ANALYSIS

The considered system is modeled with TRNSYS, as shown in Fig. 1. Main power supply of the system is the solar photovoltaic panel (PV). In order to arrange voltage and current, a controller was used for the system. Electrolyzer and fuel cell are chosen for the continuity and storage of hydrogen production. For evaluating the performance of the system, energy and exergy analysis were performed while sustainable index calculations were also made to provide estimates on how to increase the benefits of the system.

The energy, exergy and sustainability analysis relations are given below [6-8]:

Energy Analysis

The energy balance of the solar PV is given as follows [6].

$$\bar{S}A_S = V_S I_S + \dot{E}n_{S,loss} \quad (1)$$

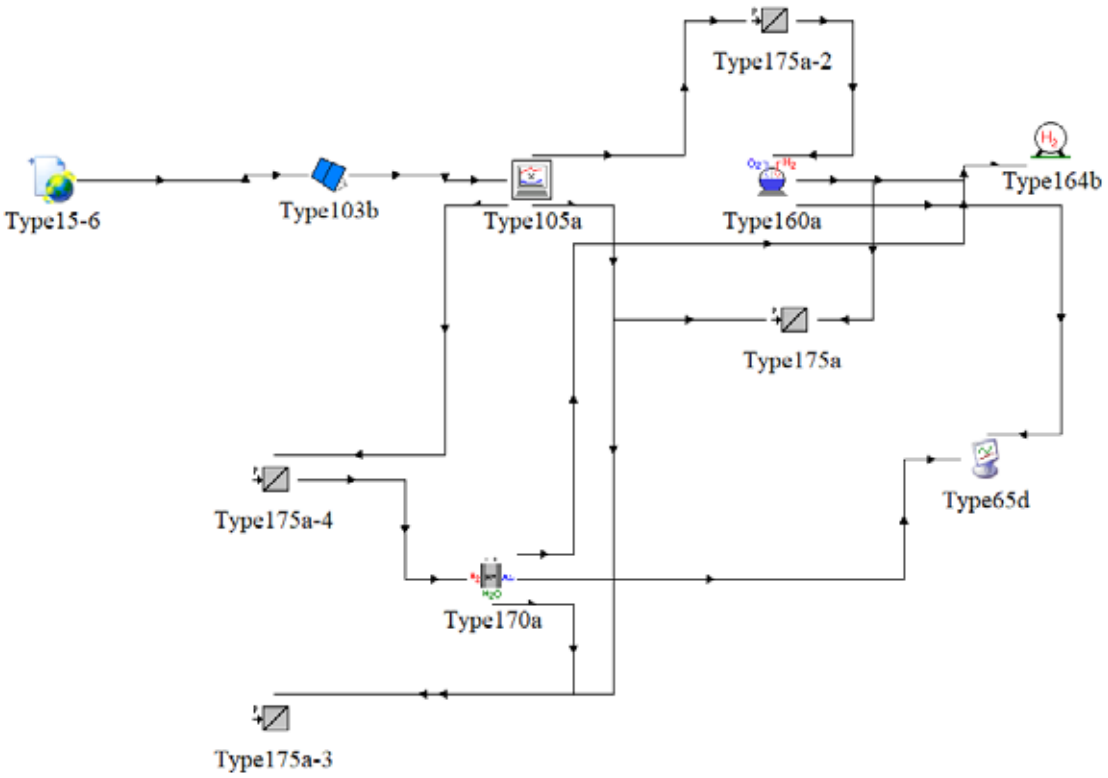


Fig. 1. TRNSYS scheme of the system

The energy balance of the electrolyzer is given by [7]

$$V_{El}I_{El} = \dot{m}_{El,H_2}(LHV)_{H_2} + \dot{E}n_{El,loss} \quad (2)$$

The energy balance of the PEMFC is written as [7]

$$\dot{m}_{FC,H_2}(LHV)_{H_2} = V_{FC}I_{FC} + \dot{E}n_{FC,loss} \quad (3)$$

Exergy Analysis

The exergy balance of the solar PV panel is as follows [6]

$$\bar{S}A_S\left[1 - \frac{4}{3}\left(\frac{T_0}{T_{sun}}\right) + \frac{1}{3}\left(\frac{T_0}{T_{sun}}\right)^4\right] = V_{S,m}I_{S,m} + \dot{Q}_{S,loss,HT}\left(1 - \frac{T_0}{T_{s,panel}}\right) \quad (4)$$

The exergy balance of the electrolyzer is given below [7]

$$V_{El}I_{El} = \dot{m}_{El,H_2}(ex_{ph} + ex_{ch})_{H_2,el} + \dot{E}x_{El,dest} \quad (5)$$

The exergy balance of the PEMFC is obtained from [6]

$$\dot{m}_{FC,H_2}(ex_{ph} + ex_{ch})_{H_2,FC} = V_{FC}I_{FC} + \dot{E}x_{FC,dest} \quad (6)$$

Sustainability Analysis

ψ is the exergetic efficiency. Thus, the sustainability index (SI) is given by [8]

$$SI = \frac{1}{1-\psi} \quad (7)$$

Relative Irreversibility (RI) is directly related to the exergy destruction of the components of the system, as indicated below [8]:

$$RI = \frac{\dot{E}x_{dest,in}}{\dot{E}x_{dest,all}} \quad (8)$$

RESULTS AND DISCUSSION

The energy and exergy analyses of the system along with its components, such as solar PV panel, electrolyzer and PEMFC, were done. Fig. 2 illustrates the energy and exergy efficiency comparison. As seen from the figure, exergy efficiency of the electrolyzer has the maximum value with 60%. The energy efficiency of the PEMFC appears to be higher than the exergy efficiency while the exergy efficiency of the electrolyzer is higher than the energy efficiency. Due to the low energy and exergy efficiencies of the solar PV and the highest exergy destruction rate of 101.688 W, the overall efficiency of the system was also low. Overall exergy destruction rate was calculated as 153.481 W. The SI rates of the components of the system are nearly same in the considered dead state temperature.

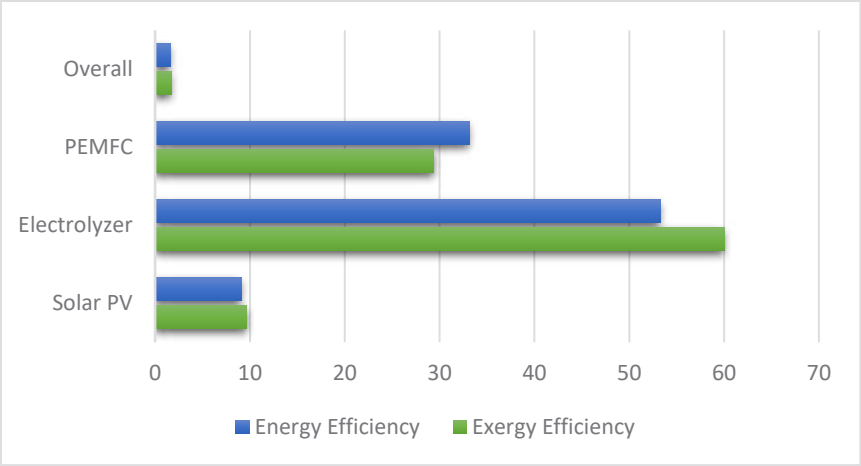


Fig. 2. Efficiency comparison

CONCLUSIONS

Since only solar PVs were chosen as the energy source for the system, the overall energy and exergy efficiencies of the system were determined to be close to each other. Although solar PV is a clean renewable energy source, its exergy destruction value is very high while its exergy efficiency is low. The solar PVs had the highest RI value with 0.66 at the dead state temperature considered.

REFERENCES

1. Preethi V. 2022. Solar hydrogen production in India. *Environ Dev Sustain*. https://doi.org/10.1007/s10668-022-02157-1.
2. Bozoglan E, Midilli A and Hepbasli A. 2012. Sustainable assessment of solar hydrogen production techniques. Energy 46:85-93
3. Ozturk M and Dincer I. 2013. Thermodynamic analysis of a solar-based multi-generation system with hydrogen production. Applied Thermal Engineering 51:1235-1244.
4. Almahdi M, Dincer I and Rosen MA. 2016. A new solar based multigeneration system with hot and cold thermal storages and hydrogen production. Renewable Energy 91:302-314.
5. Tukenmez N, Yilmaz F and Ozturk M. 2022. Parametric analysis of a solar energy based multigeneration plant with SOFC for hydrogen generation. International Journal of Hydrogen Energy 47:3266-3283.
6. Caliskan H, Dincer I and Hepbasli A. 2013. Exergoeconomic and environmental impact analyses of a renewable energy based hydrogen production system. International Journal of Hydrogen Energy 38(14):6104–6111.
7. Caliskan H, Dincer I and Hepbasli A. 2013. Energy, exergy and sustainability analyses of hybrid renewable energy based hydrogen and electricity production and storage systems: Modeling and case study. Applied Thermal Engineering 61(2):784–798.
8. Erzen S, Ünal C, Açıkkalp E and Hepbasli A. 2021. Sustainability analysis of a solar driven hydrogen production system using exergy, extended exergy, and thermo-ecological methods: Proposing and comparing of new indices. Energy Conversion and Management 23:114085.

WHEC-2022
23rd World Hydrogen Energy Conference
June 26-30, 2022 - Istanbul

#1543

UNDERSTANDING RESEARCH EVOLUTION IN HYDROGEN PRODUCTION FROM WATER ELECTROLYSIS: A BIBLIOGRAPHIC STUDY

[1] *Ibrar Ullah,* [2,3] *Muhammad Nihal Naseer,* [4] *Joongbae Kim,* [4] *Jae-Bum Pyo,* [1,4,*] *Bumjoo Kim*
[1] Department of Future Convergence Engineering, Kongju National University, Cheonan 1223-24, Korea
[2] National University of Sciences and Technology (NUST), 44000-Islamabad, Pakistan
[3] Department of Mechanical Engineering, College of Engineering, Seoul National University, Seoul 08826, Republic of Korea
[4] Department of Mechanical Engineering and Automotive Engineering, Kongju National University, Cheonan 1223-24, Korea

*Corresponding author e-mail: bumjoo@kongju.ac.kr

ABSTRACT

Hydrogen production from water electrolysis has been a topic of keen interest for the research community. Although an exponential growth in water electrolysis was observed, conducting quantitative analysis of literature is still a novelty. Therefore, authors took an initiative to use bibliographic and content analysis techniques to quantitatively analyze literature published on this topic during last 50 years indexed in Web of Science (WoS). A total of 9,277 published articles were extracted from WoS and were analyzed. Further, research evolution and recent hot topics of this field were also highlighted using the content analysis technique. Results shows that more than half of the literature on this topic was published during last fiver years (2017-2021). China followed by USA and Germany are the main research hubs of this field. Furthermore, performance enhancement of hydrogen production from electrolysis by using nanoparticles, nanosheets and nanoarrays are the hot topics of the filed. To pave path of electrolysis to industrial sector, techno-economic analysis is becoming a pivot to research community.

Keywords: Hydrogen, Electrolysis, Research trends, Bibliometric

INTRODUCTION

Due to enormous consumption of energy, which usually stem from non-renewable fossil fuels, world's natural energy resources are depleting [1]. Further, use of these fossil fuels is also a sign of ecological issues such as climate change, emission of pollutant gases, and waste production [2]. Despite these detrimental impacts, around 80% of the world's energy demand is fulfilled by non-renewable energy such as coal, natural gas and oil [3]. Therefore, sustainable, safe, salient and effective approaches needs be to use to meet world's energy demands and avoid exhaustion of non-renewable energy resources and climate change. In this regards, renewable energy resources have got much attention as a clean and green source of energy that can be integrated with existing systems to meet growing energy demands. Intermittent nature of renewable energy resources give rise to a lot of challenges [4]. An electric system powered by renewable energy resources lead to new challenges regarding consumption and storage of extra energy, operation of system, proper management of distributed generation, and incorporation of such energy with automotive sector which are based on electric vehicles. To meet these challenges hydrogen technologies can used which can contribute to the development of clean energy systems [5]. Hydrogen has unique characteristics like light weight, broad inflammability range and higher heating value [5]. Many hydrogen production technologies can be utilized to produce hydrogen, such technologies are thermal, electrolytic and photolytic; the later one uses sunlight to split water via electrochemical and biological materials; while, renewable liquid, coal gasification, and natural gas reforming comes in thermal process technology. Electrolysis of water can also be used to produced pure hydrogen. Using electrolysis technique, many resources can be used to produce hydrogen such natural gas, biomass, nuclear, coal, solar, hydroelectric, wind or geothermal energy.

In the recent years, a steady growth in the hydrogen literature has been observed due to unique characteristics of hydrogen. Hydrogen is being considered a potential fuel of future that has potential to revolutionize the energy sector. Despite this growth in the field, to the best of the authors knowledge, there is no study in the literature that quantitatively evaluates water electrolysis-based hydrogen production. Conducting quantitative analysis has been widely used in other fields of research such as medicine [6], climate change[7], food security [8] and many more. However, there is a gap in the literature to conducting a quantitative literature analysis of hydrogen production from water electrolysis. Authors have attempted to fill this gap by employing two techniques of quantitative literature analysis (bibliographic and content analysis) to map the field of hydrogen production from water electrolysis.

MATERIALS AND METHODS

One of the most authentic and reliable journal databases for searching relevant literature is Web of Sciences. It publishes an excellent quality novel and well-organized research from various disciplines. For this study, relevant keywords, titles, and abstracts were used to extract data from WoS. Data accumulated in the form of research articles,

review articles, letters, books, and book chapters, counted to 10,119 records. The staked data were further refined to make sure the correctness of the bibliometric analysis by excluding records lacking critical info such publication year, author keywords etc. Moreover, articles which were far from the scope of the relevant topic were also excluded manually by observing titles, keywords, abstracts. At the end, 9277 number of to the point or articles which covered the scope of the topic were recognized and exploited for bibliographic analysis. To analysis bibliometric analysis in this study, VOSViewer, Biblioshiny and HistCite software were used.

RESULTS AND DISCUSSION

Publication record

An increasing attention of research towards this topic was observed as represented by increasing number of publications each year. Last five years has been a golden time for the development of this topic as about 59% of total entities were published in last five years. Overall, an exponential growth was observed and it is forested that by 2030 cumulative publication count may reach 23,380 if literature keeps growing at the same rate. Last five decades of this field can be divided into two eras: the introductory era and the development era. In this case, 1972-90 can be referred as introductory era of this field. The very first articles introducing this concept of hydrogen generation by electrolysis were spotted in 1972 [9] and 1973 [10]. Surprisingly, the very first patent was filed in 1982 in USA by POMPEO GARUTI OF ITALY [10]. After this, on average, two articles were published each year until 1990. The major concepts introduced in this era were hydrogen production by solid polymer electrolyte fuel-cell, fusion reactor, alkaline water electrolysis, photovoltaic electrolysis and static feed water electrolysis. Further, hydrogen energy storage, temperature-dependent electrolysis behavior and hydrogen absorption were also introduced in the same era. In development era (1991-2021), the field got matured and an exponential growth was observed in the literature. Various topics were emerged as detailed in section Major research themes.

Major research themes

To find out major research themes in electrolysis research for hydrogen production, keywords analysis was performed. In this analysis, title and abstract of the articles are scanned and most frequent keywords are collected for analysis. In present case, a total of 13, 673 keywords were found out of which only 1.68% appeared more than 15 times and were selected for analysis, see Fig. 1. In Fig. 1, the size of the circle depicts frequency of the keyword and the thickness of the line joining two keywords shows their cooccurrence. Therefore, a bigger circle means higher frequency of apparency of a keyword and thicker line means higher cooccurrence frequency. There are eight different colors in Fig. 1, each depicting a different cluster. Cluster 1 corelates hydrogen production with renewable energy sources and thermodynamic modeling. It was observed that researchers have been active to find environmentally friendly methods of hydrogen production and ensure there is minimum carbon foot print of these technologies. Therefore, using renewable resources as a source of clean energy appeared among top frequent keywords of this field. Among different renewable energy sources, solar energy appears to be widely discussed in conjunction with hydrogen production from electrolysis followed by biomass, wind and geothermal energy. To bring renewable energy-based water electrolysis system to the industrial sector, economic perspective has been a topic of keen interest. To improve economy, researchers have made attempts to optimize system by adopting thermodynamic modeling, life cycle assessment and exergo-economic analysis. Cluster 2 and Clsuter4 sheds light on hydrogen evolution reaction and mainly highlights the significance of catalysts in this process. Although there are two routes of such electrolysis i.e., acidic and alkaline, latter is widely discussed by research community. Developing catalysts for hydrogen evolution reaction has been talk of the town and researchers tested many catalysts for this process. Use of metal organic frame works, nickel phosphide, cobalt, cobalt oxide, Ni foam, graphene, cobalt phosphide, nanoparticles, nanosheets, and nanowires appears among some famous catalysts used by researchers. Cluster 3 provides information about different bio-electrochemical systems used for hydrogen production from water electrolysis. Microbial electrolysis cell and Microbial fuel cell are the examples of such systems that have got enormous attention from research community. In such systems, microbes are used to produce electricity and then this green electricity is used for electrolysis process. This process benefits over others as wastewater is also treated simultaneously making bio-electrochemical process a promising future technology. However, this topic is still in development phase and some challenges spotted are low current density, costly electrode materials and membranes. Cluster 5 and Cluster 6 is all about different membranes used in electrolysis process. Two most widely discussed fuel cells for hydrogen production from water electrolysis are Proton Exchange Membrane Fuel Cell and Solid Oxide Fuel Cell. Membrane development to reduce cost of these fuel cells is a hot topic of last decade. Mass transfer enhancement, material stability and optimal membrane-electrode assembly some widely discussed challenged of this field. Cluster 7 sheds light on photocatalytic electrolysis and solar fuels development. This is one of the cleanest processes to produce hydrogen as it demands only three components water, photoenergy and a catalyst. Although it is a much promising technology, commercialization is still a challenge. In Cluster 8, seawater electrolysis is discussed which has got enormous attention in last century. Using seawater through various means such as desalination for drinking,

agricultural and industrial purposes has been a focal point for years, nevertheless, utilizing sea water for hydrogen production is a much promising technology that has potential to revolutionize future.

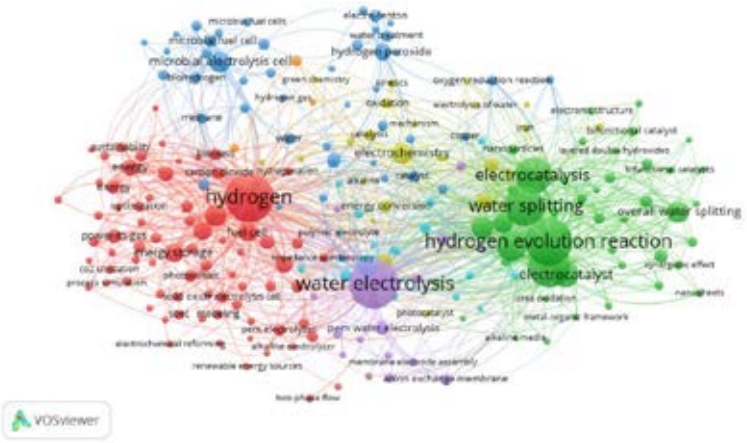


Fig. 1: Major research themes in hydrogen production from water electrolysis

CONCLUSIONS

A quantitative literature analysis of hydrogen production by water electrolysis was performed using Web of Science database. About 9,277 articles published during last five decades were analyzed using bibliographic analysis and content analysis. The analysis reveals that in the early twenty years (1970-90), on an average two articles per year were published whereas in the later years exponential growth was observed. During last five years about 60% of the total literature was published. Using content analysis, eight clusters of most frequent keywords were analyzed. The analysis reveals that electrocatalyst has been a topic of keen interest throughout 50 years of this topic followed by electrodeposition and integration with renewable energy sources. Further, it is reveled that performance enhancement of hydrogen production is a key challenge to the field. To cope with it, researchers have been recently using nanoparticles, nanosheets and nano arrays. The quest of developing an efficient and stable electrocatalysts is still a hot topic. Attempts to commercialise hydrogen production from water electrolyses is also talk of the town and researcher are using techno-economic analysis as a tool to study commercialisation feasibility.

REFERENCES

1. H. Wang *et al.*, "Scarcity-weighted fossil fuel footprint of China at the provincial level," *ApEn,* vol. 258, p. 114081, 2020.
2. F. Martins, C. Felgueiras, M. Smitkova, and N. Caetano, "Analysis of fossil fuel energy consumption and environmental impacts in European countries," *Energies,* vol. 12, no. 6, p. 964, 2019.
3. F. ezzahra Chakik, M. Kaddami, and M. Mikou, "Effect of operating parameters on hydrogen production by electrolysis of water," *international journal of hydrogen energy,* vol. 42, no. 40, pp. 25550-25557, 2017.
4. A. Kalair, N. Abas, M. S. Saleem, A. R. Kalair, and N. Khan, "Role of energy storage systems in energy transition from fossil fuels to renewables," *Energy Storage,* vol. 3, no. 1, p. e135, 2021.
5. A. Ursua, L. M. Gandia, and P. Sanchis, "Hydrogen production from water electrolysis: current status and future trends," *Proceedings of the IEEE,* vol. 100, no. 2, pp. 410-426, 2011.
6. P. Kokol, H. Blažun Vošner, and J. Završnik, "Application of bibliometrics in medicine: a historical bibliometrics analysis," *Health Information & Libraries Journal,* vol. 38, no. 2, pp. 125-138, 2021.
7. I. A. Rana, "Disaster and climate change resilience: A bibliometric analysis," *International Journal of Disaster Risk Reduction,* vol. 50, p. 101839, 2020.
8. W. M. Sweileh, "Bibliometric analysis of peer-reviewed literature on food security in the context of climate change from 1980 to 2019," *Agriculture & Food Security,* vol. 9, no. 1, pp. 1-15, 2020.
9. J. Huddleston and F. Greenwood, *Integrated Water Vapor Electrolysis Oxygen Generator and Hydrogen Depolarized Carbon Dioxide Concentrator Development*. American Society of Mechanical Engineers, 1972.
10. L. Nuttall, A. Fickett, and W. Titterington, "Hydrogen generation by solid polymer electrolyte water electrolysis," in *Hydrogen energy*: Springer, 1975, pp. 441-455.

WHEC-2022
23rd World Hydrogen Energy Conference
June 26-30, 2022 - Istanbul

#1573

DEVELOPMENT OF Pt-Cr COATED SS316L ELECTRODES FOR PEM ELECTROLYZERS BY SELECTIVE LASER MELTING METHOD

Murat KISTI[1,2], Emre ÖZDOĞAN[1,2,3], Süleyman UYSAL[1,2,3], Mehmet Fatih KAYA[1,2,3]*
[1]Erciyes University, Engineering Faculty, Energy Systems Engineering Department, Heat Engineering Division, 38039, Kayseri, Turkey
[2]Erciyes University H2FC Hydrogen Energy Research Group, 38039, Kayseri, Turkey
[3]BATARYASAN Enerji ve San.Tic. Ltd.Şti, Yıldırım Beyazıt Mah., Aşık Veysel Bul., ERÜ TGB İdare ve Kuluçka 4, No: 67/3/11, Melikgazi, Kayseri, Turkey

* Corresponding author. Tel.: +903522076666-32331.
E-mail address: kayamehmetfatih@erciyes.edu.tr

ABSTRACT

Proton exchange membrane (PEM) water electrolyzer (PEMWE) is used to obtain a high amount of hydrogen cleanly from water. However, to make PEMWE common in everyday life, their cost must be reduced, and the performance of these systems must be increased. Thus, alternative materials should be developed to obtain low-cost PEMWE systems. In this study, stainless steel 316L (SS316L) is used as gas diffusion electrode (GDE) materials. The selective laser melting (SLM) method is selected to produce the SS316L electrode. To enhance to SS316L electrodes' corrosion resistance and kinetic activity, SS316L electrodes are coated with Pt different thickness values using electron beam evaporation method (EBM) with a Cr interlayer film. Electrochemical properties of SS316L electrodes have been investigated by cyclic voltammetry (CV), linear sweep voltammetry (LSV), and electrochemical impedance spectroscopy (EIS) techniques. Durability of SS316L electrodes have been conducted by Tafel and chronoamperometry (CA) techniques. The surface morphologies of SS316L electrodes have been characterized by field emission scanning electron microscopy (FE-SEM), energy dispersive X-ray analysis (EDX), X-ray diffractometers (XRD), and X-ray fluorescence (XRF) analysis. As a result, electrochemical performance, kinetic activity, and corrosion resistance of the electrodes are enhanced significantly with Pt-Cr material by EBM coating.

Keywords: Proton Exchange Membrane Electrolyzers, Gas Diffusion Electrode, Selective Laser Melting, Electron Beam Evaporation, SS316L

INTRODUCTION

PEMWEs have an important place in electrochemical hydrogen production systems thanks to their high current density values, fast start up, their ability to operate relatively low temperatures, and achieve higher efficiency values even at low temperatures [1, 2]. In PEMWEs, the anode GDE layers distribute water in the entire active surface area. Performance in PEMWE systems is directly proportional to the amount of water delivered to the catalyst layer [3]. The anode side of the PEMWE has a corrosive environment. Thus, reducing corrosion effects cause higher cell performance due to lower contact resistance, ohmic and activation overpotentials in PEMWEs [4]. Thus, this component of the cell should have high corrosion resistant coating and materials. Generally, Pt-coated Ti mesh structures are preferred as a GDE on the anode side of PEMWEs [5]. When PEMWE costs are compared, 24% of the cell cost is due to membran electrode assembly (MEA) and 48% of these costs are due to GDE and bipolar plates [6]. Corrosion resistant alternatives to Pt coated Ti mesh materials are very crucial to wide spread of these systems. Amon the cheaper options, stainless steel materials are seen as one of the most suitable materials for PEMWE systems due to their accessibility, cheapness , and easy to form [7, 8]. Even they have low corrosion resistance and stability problems it is possible to improve it by a noble or non-noble metal coating [9, 10]. There are several coating methods for anode GDEs like thin film, electrochemical, spin coating, dip coating and electroless methods. Amon them thin film coating provides homogeneous layers on the GDE surfaces. Thus, they are very promising to obtain low cost GDEs. In the literature there are several thin film coating methods. Especially e-beam evaporation methods have some advantageous due to higher temperature evaporation conditions. Thanks to higher temperatures, time effective coatings are possible on the surface of the samples. For example, Park et all. [11] coated the carbon paper with the electron beam evaporation method to reduce Pt loading in the microbial fuel cells (MFC). They are observed that after 45 h of microbial fuel cell (MFC) testing conditions, e-beam coated carbon paper has increased the current density by changing peak intensity in the performance tests. They stated that the potential of e-beam coated Pt electrodes in improving efficiency with the minimal loading of Pt. Raso et all. [12] studied different Pt accumulation methods to reduce metal loading while maintaining their electroactivity. In this study, the behaviour of e-beam Pt coated electrodes for fuel cells were examined and they concluded that MEAs prepared with e-beam evaporated cathodes had clearly higher power density per Pt loading mass. As seen in the literature, electrodes coated with e-

beam evaporation method have been tested in different types of fuel cells for the lower loading of the catalysts. However, according to author's knowledge, SS316L mesh structures are not tested with thin film coating by Pt noble metals. Thus, in this study, SS316L electrodes are produced by SLM method, and these electrodes are coated with different thicknesses of Pt on by the help of a Cr interlayer. Electrode samples are tested in PEMWE simulated acidic environment to observe their electrochemical performance and the stabilization.

MATERIALS AND METHODS

In the experiments, firstly, the best geometry was determined before the coating process. GDE structures with circle, equilateral triangle, square, and rhombus holes were studied in the pressure drop experiments. To measure pressure drop of the GDE samples, 3D printed geometries were placed pressure drop test cell. GDEs with different geometric patterns can be seen in Fig. 1.



(a) (b) (c) (d)

Fig. 1. a) Circle, b) Equilateral triangle, c) Square, d) Rhombus GDE geometries.

100 ml/min water flow was supplied to the pressure drop cell by the help of a water peristaltic pump [13]. For each GDE samples, inlet and outlet pressure was measured. The amount of pressure change (ΔP) and the decrease were calculated proportionally according to the input and output pressure. The inlet pressure of the square geometry GDE was read as 3.866 kPa and the outlet pressure as 2.36 kPa. It exhibited the lowest change at 1.506 kPa ΔP[14]. The low pressure drop means that the PEMWE will better distribute the water sent into it. Thus, since GDE with square geometry will distribute water better than other geometries, square structures are preferred in electrodes designed for coatings.

Electrode samples were designed using SolidWorks software. Pore volume of the electrodes were arranged as 25%. The designed geometries can be seen in Fig. 2.



a) b)

Fig. 2. Electrode sample designs for a) in-situ electrochemical tests and b) corrosion tests

The designed geometries were produced with the SLM method using SS316L material. A cleaning procedure before the coating process were carried out. SS316L samples were kept in an ultrasonic bath for 10 minutes in distilled water, ethanol, acetone, and isopropanol, respectively. After the cleaning procedure, SS316L samples were dried with nitrogen. The samples were coated with 0.5 µm, 1.0 µm, 1.5 µm, and 2.0 µm thick Pt with and without Cr interlayer using electron beam evaporating methods. The coated SS316L electrodes were prepared for electrochemical measurements. The active surface area of the SS316L electrodes was determined to be 25 mm^2 (5 mm x 5 mm). The electrochemical characterization measurements were carried out using Potentiostat-galvanostat (PGSTAT204) with a three-electrode configuration. SS316L electrode was used as the working electrode. Pt wire and Ag/AgCl (3M Saturated) were used as counter electrodes and reference electrodes, respectively. CV, LSV, EIS, Tafel, and CA measurements were analyzed in a 0.5M H_2SO_4 solution. CV measurements were performed at a 50 mV/s scan rate and LSV measurements were conducted at a 10 mV/s scan rate. The EIS measurements were analyzed in a frequency range between 10 kHz to 0.1 Hz at 5mV amplitude. The stability tests of the SS316L electrodes were performed using the Tafel and CA method. Tafel and CA measurements were made using a corrosion test cell. The corrosion cell tests were carried out by keeping the temperature constant at 80°C using a circulator to simulate PEMWE conditions. Surface characterizations of SS316L electrodes were determined by FE-SEM, EDX, EDX Colour Mapping, XRD, and XRF methods.

CONCLUSIONS

In this study, SS316L was coated with Pt as an anode GDE for PEMWEs. By the help of electro beam evaporation method, Pt was coated with 0.5 µm, 1.0 µm, 1.5 µm, and 2.0 µm thickness with Cr interlayer. As a result of surface characterization and electrochemical analyses, the 2.0 µm Pt coated electrode performed as the best electrochemical performance due to higher catalyst content and higher electrochemical surface area. The importance of coating thickness for corrosion resistance has once again been demonstrated.

ACKNOWLEDGEMENT

The authors would like to thank the financial support from the Scientific and Technological Research Council of Turkey (TUBITAK) 1001 Research Projects Funding Program with project number 120M234. The authors would also like to thank the Scientific Research Projects Unit of Erciyes University for funding and supporting the project under the contract numbers: FYL-2020-10547. S.U. thanks for the Scientific and Technological Research Council of Turkey (TUBITAK) for their scholarship under the “2210-C National Priority Areas M.S.c Scholarships Program (grant number 1649B022006356)”. M.K. also thank the Turkish Higher Education Institution YÖK 100/2000 Ph.D. for their Scholarship Program.

REFERENCES

1. Nikolaidis, P., Poullikkas, A. 2017. "A Comparative Overview of Hydrogen Production Processes", Renewable and sustainable energy reviews, 67, 597-611.
2. Bessarabov, D., Wang, H., Li, H., Zhao, N. 2016. Pem Electrolysis for Hydrogen Production: Principles and Applications CRC press.
3. Lafmejani, S. S., Olesen, A. C., Kær, S. K. 2016. "Analysing Gas-Liquid Flow in Pem Electrolyser Micro-Channels", ECS Transactions, 75(14), 1121.
4. Mo, J., Steen III, S. M., Zhang, F.-Y., Toops, T. J., Brady, M. P., Green Jr, J. B. 2015. "Electrochemical Investigation of Stainless Steel Corrosion in a Proton Exchange Membrane Electrolyzer Cell", International Journal of Hydrogen Energy, 40(36), 12506-12511.
5. Kaya, M. 2018. "Investigation the Pem Water Electrolyzer Performance under Magnetic Field and Development of Electrocatalyst (Pem Elektrolizörlerin Manyetik Alan Altındaki Çalışma Performansının İncelenmesi Ve Katalizör Geliştirilmesi)[Doctoral Thesis]", Kayseri, Turkey: Erciyes University.
6. Ayers, K. E., Anderson, E. B., Capuano, C., Carter, B., Dalton, L., Hanlon, G., Manco, J., Niedzwiecki, M. 2010. "Research Advances Towards Low Cost, High Efficiency Pem Electrolysis", ECS transactions, 33(1), 3.
7. Shirvanian, P., van Berkel, F. 2020. "Novel Components in Proton Exchange Membrane (Pem) Water Electrolyzers (Pemwe): Status, Challenges and Future Needs. A Mini Review", Electrochemistry Communications, 114, 106704.
8. Hou, K., Yi, P., Peng, L., Lai, X. 2019. "Niobium Doped Amorphous Carbon Film on Metallic Bipolar Plates for Pemfcs: First Principle Calculation, Microstructure and Performance", International Journal of Hydrogen Energy, 44(5), 3144-3156.
9. Huang, N., Yu, H., Xu, L., Zhan, S., Sun, M., Kirk, D. W. 2016. "Corrosion Kinetics of 316l Stainless Steel Bipolar Plate with Chromiumcarbide Coating in Simulated Pemfc Cathodic Environment", Results in physics, 6, 730-736.
10. Gago, A., Ansar, S., Saruhan, B., Schulz, U., Lettenmeier, P., Cañas, N. A., Gazdzicki, P., Morawietz, T., Hiesgen, R., Arnold, J. 2016. "Protective Coatings on Stainless Steel Bipolar Plates for Proton Exchange Membrane (Pem) Electrolysers", Journal of Power Sources, 307, 815-825.
11. Park, H. I., Mushtaq, U., Perello, D., Lee, I., Cho, S. K., Star, A., Yun, M. 2007. "Effective and Low-Cost Platinum Electrodes for Microbial Fuel Cells Deposited by Electron Beam Evaporation", Energy & fuels, 21(5), 2984-2990.
12. Raso, M., Carrillo, I., Mora, E., Navarro, E., Garcia, M., Leo, T. 2014. "Electrochemical Study of Platinum Deposited by Electron Beam Evaporation for Application as Fuel Cell Electrodes", International journal of hydrogen energy, 39(10), 5301-5308.
13. Nie, J., Chen, Y. 2010. "Numerical Modeling of Three-Dimensional Two-Phase Gas–Liquid Flow in the Flow Field Plate of a Pem Electrolysis Cell", international journal of hydrogen energy, 35(8), 3183-3197.
14. Kıstı, M., Uysal, S., Kaya, M. F., Development of Cost-Effective Anode Gas Diffusion Layers for Pem Water Electrolyzers, The 5th International Conference on Alternative Fuels , Energy and Environment : Futures and Challenges (ICAFEE 2021). Kayseri, Türkiye, 2021.

WHEC-2022
23rd World Hydrogen Energy Conference
June 26-30, 2022 - Istanbul

#1576

A NEW EXPERIMENTAL INVESTIGATION ON HYDROGEN PRODUCTION OF NaCl, KCl AND $CaCl_2$ SOLUTIONS THROUGH CHLORALKALI REACTOR

[1*] *Mustafa Erden,* [2] *Mehmet Karakilcik*
[1]Cukuroca University, Faculty of Sciences and Letters, Department of Physics, 01330 Adana, Turkey

*Corresponding author e-mail: mustafaerden01@hotmail.com

ABSTRACT

In this experimental study, hydrogen production performance of NaCl, KCl and $CaCl_2$ solutions via electrochemical method through a small scale chloralkali reactor are investigated. A cation exchange membrane is placed in between the anode and cathode chamber to separate the anolyte and catholyte solutions. 316 stainless steel electrodes are used in the experiment due to its economic efficiency. While the anode compartment of the reactor is fed with NaCl, KCl and $CaCl_2$ solutions one by one, the cathode compartment is fed with a low-density NaOH, KOH and $Ca(OH)_2$ base solution depending on the type of salt used in the experiment. Experiments are carried out at cell voltage range of 3 to 5 volts according to three different brine densities (30 g/L, 60 g/L and 90 g/L), three different electrolyte flow rates (0.4 g/s, 0.6 g/s and 0.8 g/s) and three different electrolyte temperatures (30 °C, 50 °C and 70 °C). While a significant amount of hydrogen gas output was observed from the cathode compartment of the reactor, the expected chlorine gas output from the anode compartment was not observed. Since the chlorine gas is very active it reacts with many metals easily. Therefore, chlorine gas produced in the anode chamber caused serious corrosion and contamination on the electrode in this chamber.

Keywords: Hydrogen production, Electrochemical process, Chloralkali reactor, NaCl, KCl, $CaCl_2$.

INTRODUCTION

Due to the harmful effects of non-renewable energy usage on the environment, it has become necessary to meet the world's energy needs from clean energy sources. Hydrogen-based technologies are becoming increasingly important, as hydrogen can be produced and stored with excess electricity produced from renewable sources. When it is necessary, the need for energy can be easily met with stored hydrogen.

Jalali et al. (2009) were studied the effects of various operating parameters on the cell voltage and current efficiency of a laboratory-scale chloralkali cell were at low caustic concentrations (5–22 g/L). These operating parameters are anolyte pH (2–5), cell temperature (25–90 °C), electrolyte velocity (2.2–8.4 cm/s), brine concentration (200–300 g/L) and current density (1–4 kA/m2). Current density and cell temperature were found to be the most striking parameters on the cell voltage.

Rabbani et al. (2014) is discussed the electrochemical model for a newly designed photo electrochemical hydrogen production reactor. According to the results, a minimum voltage is required when the distance between the electrodes becomes a minimum. On the other hand, brine and electrolyte concentrations do not have significant effect on cell voltage.

Main aim of this study is to contribute the process of hydrogen production of salts.

MATERIALS AND METHODS

Fig.1 shows the schematic of the experimental system. Main components of the system are a laboratory scale chloralkali reactor, two peristaltic pumps to adjust the electrolyte flow rate, four containers for electrolyte feeding and dump collection, a graduated cylinder and a power supply. The cathode and anode compartments of the reactor, modeled with the appropriate computer program, are made of Kestamid in CNC machine due to its durability. The cation exchange membrane placed between the anode and cathode compartments of the reactor not only prevents the mixing of electrolytes in the anode and cathode compartments, but also allows positive ions to pass through. Chloralkali process is the electrolysis of NaCl solution producing hydrogen, chlorine and sodium hydroxide. NaCl is usually used in this process. However, salts such as KCl and $CaCl_2$ can also be used. In this case, the Na element leaves its place to the K or Ca element. The first pump sends the prepared salt solution to the anode compartment of the reactor, while the second pump sends the diluted base solution to the cathode compartment. In case of using appropriate electrodes, hydrogen gas is produced in the cathode compartment and chlorine gas is obtained in the anode compartment. Since chlorine gas can react with many metals, the electrode in the anode compartment must be corrosion resistant like platinum metal. However, due to its economy, stainless steel electrodes were used in this experiment. Therefore, no chlorine gas output was observed in the anode

compartment, but serious corrosion effects and contamination were observed on the electrode. On the other hand, an effective hydrogen gas output from the cathode compartment was observed and measurements were made on it.

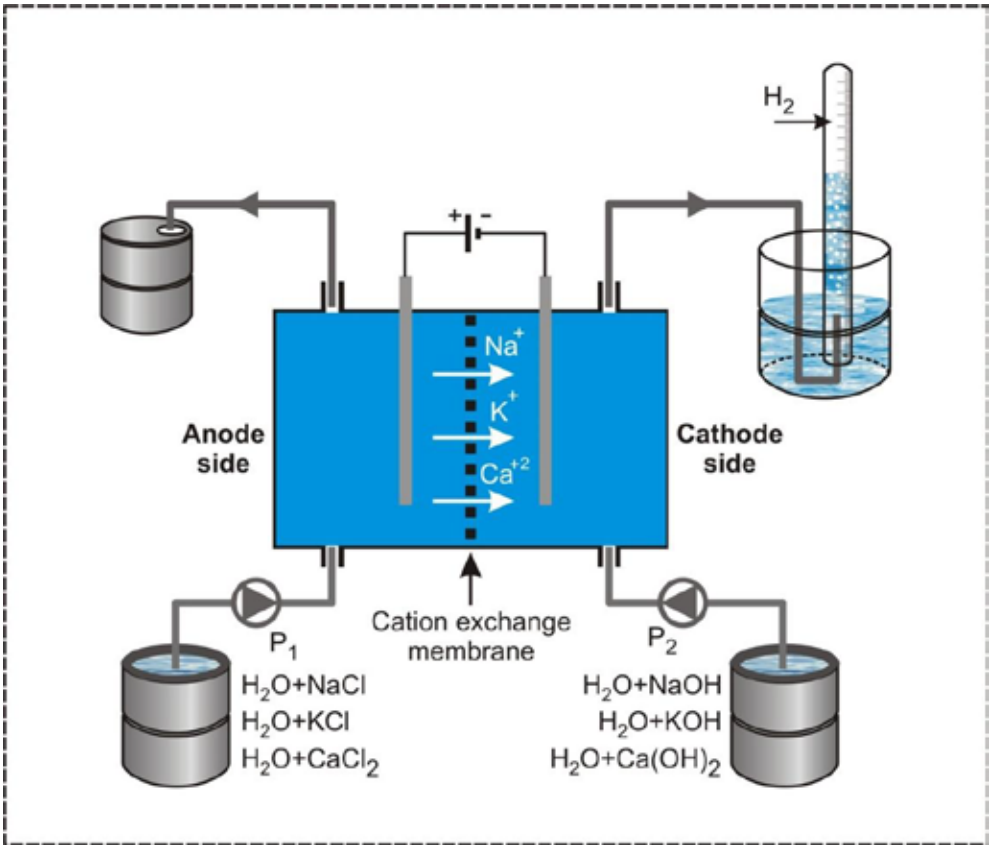


Fig. 1. Schematic of the experimental system.

To assess the system thermodynamically, balance equations should be written.

$$\sum \dot{m}_i = \sum \dot{m}_o \quad (1)$$

$$\dot{Q}_i + \dot{W}_i + \sum \dot{m}_i h = \dot{Q}_o + \dot{W}_o + \sum \dot{m}_o h \quad (2)$$

$$\sum \frac{\dot{Q}}{T_0} + \sum \dot{m}_i s_i + \dot{S}_g = \sum \dot{m}_o s_{\varsigma o} \quad (3)$$

$$\sum \dot{E}x_{Qi} + \sum \dot{E}x_{Wi} + \sum \dot{m}_i ex_i = \sum \dot{E}x_{Qo} + \sum \dot{E}x_{Wo} + \sum \dot{m}_o ex_o + \dot{E}x_{dest} \quad (4)$$

RESULTS AND DISCUSSION

Chlorine production is difficult because it easily reacts with many metals. Since 316 stainless steel electrodes were used in this experiment, corrosion occurred and no free chlorine gas output was observed. No difficulties were encountered in the production of hydrogen and the measurements were made on hydrogen. Experiments were repeated out for three different salt concentrations, three different temperatures and three different flow conditions for each salt.

Fig. 2 shows the hydrogen production rate of NaCl salt at 30, 50 and 70°C. It is clearly seen that the hydrogen production increases with increasing temperature.

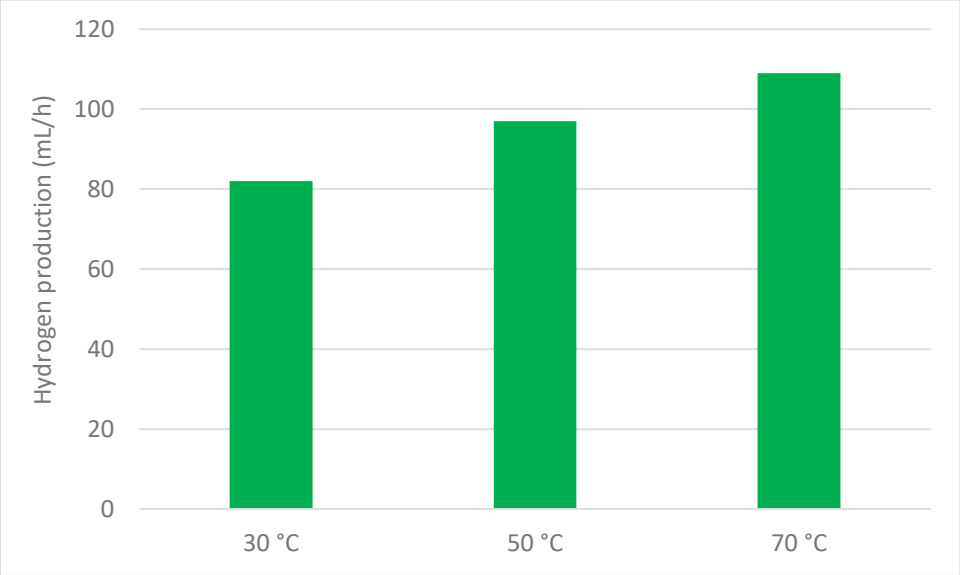


Fig. 2. Hydrogen production at different temperatures.

CONCLUSIONS

In this study, hydrogen production performances of NaCl, KCl and $CaCl_2$ electrolytes via chloralkali reactor are investigated experimentally. For this purpose, a laboratory scale chloralkali reactor is constructed. Experiments were conducted for hydrogen production according to different temperature, salt density and electrolyte flow rate parameters. There was no satisfactory chlorine gas output since the appropriate electrode could not be used. But an effective hydrogen gas output was observed.

ACKNOWLEDGEMENT

The authors acknowledge the support provided by University of Cukurova in Turkey (Grant Nos: FEF2013YL42, FYD-2017-6261 and FBA-2019-12023).

REFERENCES

1. Jalali, A.A., Mohammadi, F., Ashrafizadeh, S.N. 2009. Effects of process conditions on cell voltage, current efficiency and voltage balance of a chlor-alkali membrane cell. Desalination 237:126-139.
2. Rabbani, M., Dincer, I., Naterer, G.F. 2014. Electrochemical analysis of a photoelectrochemical chloralkali reactor. Chemical Engineering and Processing 82:42-53.

WHEC-2022
23rd World Hydrogen Energy Conference
June 26-30, 2022 - Istanbul

#1578

FLOW CHANNEL EFFECT ON PERFORMANCE OF PEM WATER ELECTROLYSIS

[1] *Seong Keun Kim*, [1*] *Sung Yong Jung*
[1]Chosun University, Department of Mechanical Engineering, 309 Pilmun-daero, Dong-gu Gwangju, Republic of korea

*Corresponding author e-mail: syjung@chosun.ac.kr

ABSTRACT

PEMWE (proton exchange membrane water electrolyzer) can operate at a high current density with a small size to obtain a large mount of hydrogen. However, when PEMWE operate under high current density conditions, lots of air bubbles are generated which causes the reduction of water electrolysis efficiency due to the increase of mass transport loss. In this study, three types of flow channels (single serpentine, double serpentine, and parallel) were designed to reduce mass transport loss and PEMWE performances were compared. Performance was measured with a current density ranging from 0 to 2.0 A/cm^2, and water at 50 and 70 °C was supplied to the anode at 1.5 to 14.1 ml/min, and to the cathode at 1.5 ml/min. Two-phase flow patterns were analyzed using an optical high-speed imaging to understand relationship between flow channel design and cell performance. Among tested channels, the parallel channel had the worst performance because slug flows with Tayler bubbles, that could disturb the water supply, were mainly occurred. Whereas, the single serpentine channel had the best performance because annular flows with a thin liquid film could reduce mass transport loss were dominant.

Keywords: Electrolyzer, Proton exchange membrane water electrolyzer, Flow channel design

INTRODUCTION

The increase in energy consumption with the development of technology leads to the climate change problem due to the greenhouse gas emissions, because most of the energy is commonly obtained from fossil fuels. Hydrogen energy has been received large attention as alternative energy to solve the gas emission problem since it does not emit environmental pollutants and has a high energy density. Although no gas emission occurs in the use of hydrogen energy, greenhouse gases such as CO and CO_2 are also emitted during hydrogen production by the generally employed natural gas reforming method [1,2]. Water electrolysis is a method to obtain hydrogen from water without any emissions of greenhouse gases. Among various methods for water electrolysis, PEMWE (proton exchange membrane water electrolyzer) can generate a relatively large amount of hydrogen with a small size because it can operate under a high current density condition. However, for practical applications of PEMWE at a high current density, the mass transport loss should be reduced. Therefore, in order to improve the performance of PEMWE, it is important to understand two-phase flows related with the water supply and produced gas removal in flow channels and porous transport layer.

Dedigam et al. investigated the relationship between flow and electrochemical performance and they showed that the mass transfer loss decreased by maintaining the slug flow as the flow rate increased [3]. Majasan et al. visualized two-phase flows in channels, and they found that the single serpentine channel had a worse performance than the parallel channel because longer gas slugs were formed [4]. Ito et al evaluated the flow characteristics as flow regime, frictional pressure drop, and flow rate with three kinds of channels (single serpentine, double serpentine, and parallel) [5], and it was confirmed that the mass transport of water can be improved by the parallel channel where bubbly flows with a lower pressure drop were dominated. Although previous studies investigated the relationship between cell performance and two-phase flow behavior during electrolysis, those studies were conducted only with qualitative analysis about the flow characteristics. In this study, flow channels were designed to reduce the mass transport loss of PEMWE, and the relationships between flow characteristics and water electrolysis performance were investigated through quantitative analysis of flows using a optical high-speed imaging.

EXPERIMENTAL

Fig. 1(a) shows the schematic diagram of the experimental set-up used in this study. The transparent window made of a quartz was placed as an endplate to observe the internal flow. As shown in Fig. 1(b), performances of three kinds of flow channels (single serpentine, double serpentine, and parallel) with 3 mm channel width and 2.2 mm rib were compared. Ti mesh with 0.27 mm thickness and 0.1 mm diameter pore size was used as PTL, and Nafion 115 with 25 cm^2 reaction area was employed as MEA. Cell performances were measured by changing the current density from 0 to 2.0 A/cm^2 in intervals of 0.04 A/cm^2 under the cell temperature of 50 and 70 °C. Two-phase flows inside flow channels during PEMWE operations were visualized using a high-speed camera, and images were captured at 125 during 30 s at each operating condition. The length and width of the bubble were obtained after applying image processing technique with Image J and MATLAB software. If water is not sufficiently supplied to the inside of the cell

during the electrochemical reaction, the MEA can dry and shrink, resulting in damage and overvoltage of the MEA [6]. Therefore, water was supplied to the anode at the electro-stoichiometric ratio of 50 corresponding flow rate of 1.5 to 14.1 ml/min. Water was also supplied to the cathode at a fixed flow rate of 1.5 ml/min to prevent drying of the MEA.

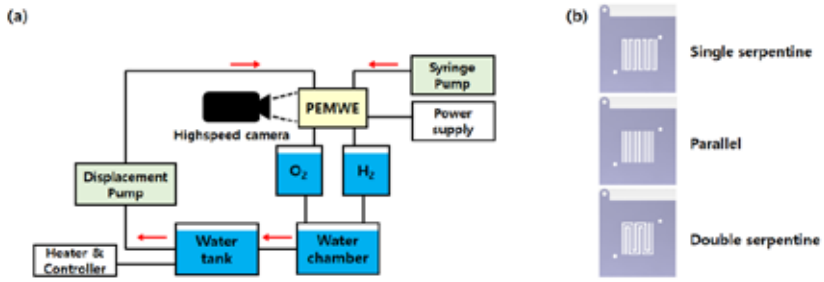


Fig. 1. (a) Schematic diagram of experimental set-up, and (b) designs of flow channels.

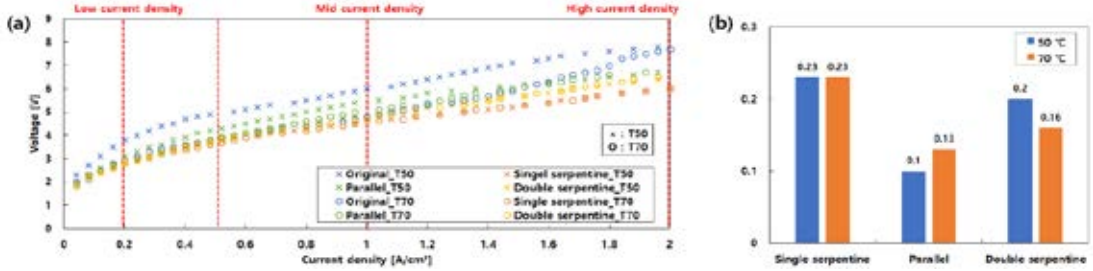


Fig. 2. Comparisons of (a) IV polarization curves, and (b) ratios of voltage drop to that of chamber type at 2.0 A/cm^2.

RESULTS AND DISCUSSION

Fig. 2(a) shows the IV polarization curve. Compared to the performance at 50 °C, the performances in all cases were higher at 70 °C. The voltages at 70 °C and 2.0 A/cm^2 where mass transport loss was dominant were 6 V for single serpentine, 6.5 V for double serpentine, and 6.7 V for parallel, which was 23%, 16%, and 13% lower than that of chamber type having 7.7 V, respectively, as shown in Fig. 2(b). Fig. 3(a) shows the procedure of image processing. Field flat correction was firstly applied with the background image obtained before operations where channels were fully filled with water. Thereafter, threshold correction and noise reduction were employed to classify water and gas regions. Two-phase flow information was analysed only at the straight part of channels marked in the blue box in Fig. 3(a) since it is difficult to distinguish the length and width of gases in regions where the channel direction is switched. Figs. 3(b) and (c) represent the probability density function of the normalized gas length and width, respectively. The length probabilities in Fig. 3(b) show that single and double serpentines have longer gases, and gas streams having same length with channels are generated. In contrast, parallel has a relatively short gases, and most gases have a length of 0.2 times or less of the channel length. The width distributions in Fig. 3(b) have an opposite tendency to the length. The width of most gases in the parallel channel is same with the channel width. While, the single and double serpentines have smaller gas width than the channel width, and highest probabilities for single and double serpentines are observed at the normalized width of about 0.6 and 0.9, respectively. From the width and length, it is known that dominant flows are slug flows with Taylor bubble similar to the channel width for parallel channel and annular flows with thin liquid films on surfaces single serpentine channels, respectively. Double serpentine channel has a mixed flow pattern with slug flows having Taylor bubbles and annular flow. Gas occupies the entire channel width when Taylor bubble flows occur. Therefore, it is difficult to supply enough water to the chemical reaction location through bubble generated regions when gases produced by electric-chemical reactions are discharged to flow channels and Taylor bubbles are emerged. If water is supplied in excess of the flow rate required for the electrochemical reaction of the PEMWE, the small diameter bubbles are discharged without sufficient growth due to the high flow rate. In this study, the water required for the controlled current density was appropriately supplied at constant rate. As a result, Taylor bubbles were generated in parallel channel with relatively low flow rate, disturbing the water supply, and different in previous studies, it had lower performance than other channels. On the other hand, in the annular flow, a gas column is continuously discharged in the middle of the channel, and it is possible to supply water through the edge of the channel. Therefore, gas discharge and water supply can simultaneously occur in the same area for annular flows. This leads to a smooth water supply providing higher cell performance by reducing the mass transport loss as shown in Fig. 2.

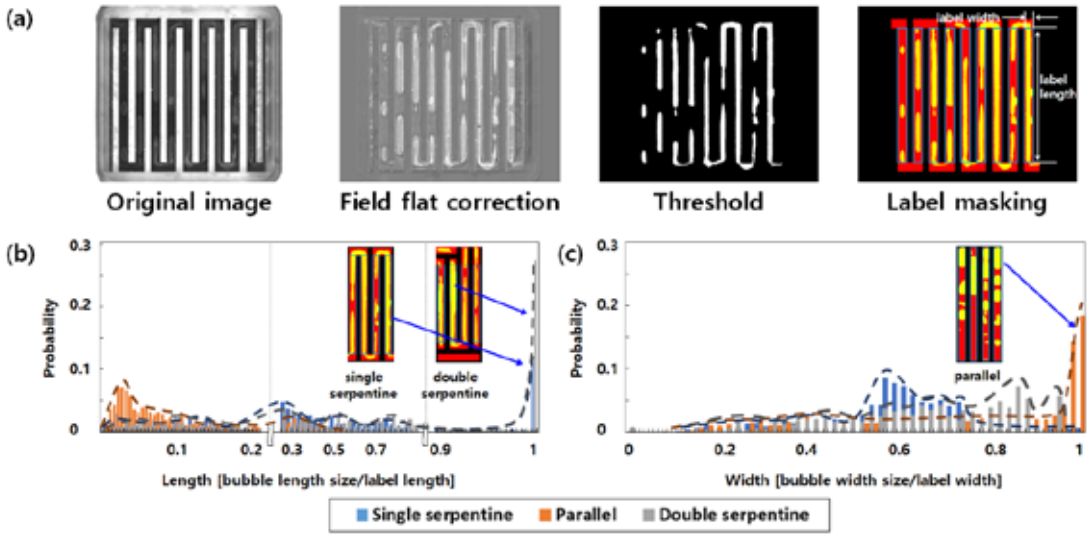


Fig. 3. (a) Image process, (b) probability of length per channel at 2.0 A/cm^2, and (c) probability of width per channel at 2.0 A/cm^2.

CONCLUSIONS

In this study, three kinds of channels were designed for PEMWE, and performances and two-phase flows inside flow channels were compared. Compared to the chamber type, flow channels can improve PEMWE performances, and single serpentine and parallel channels had the best and worst performance among tested channels, respectively. Taylor bubbles which can disturb water supply were dominant in the parallel channel. In contrast, annular flow with thin liquid films, which can reduce the mass transport loss because gas discharge and water supply are smoothly performed, mainly occurred in the single serpentine channel. It is expected that this study would contribute to the design of the flow channel to improve the performance of PEM water electrolysis.

ACKNOWLEDGEMENT

This study was supported the Technology Innovation Program (20011633) funded by the Ministry of Trade, Industry & Energy (MOTIE, Korea).

REFERENCES

1. Kumar SS and Himabindu V. 2019. Hydrogen production by PEM water electrolysis–A review. Materials Science for Energy Technologies 2.3:442-454.
2. Nikolaidis P and Andreas P. 2017. A comparative overview of hydrogen production processes. Renewable and sustainable energy reviews 67:597-611.
3. Dedigama I, Angeli P, Ayers K, Robinson JB, Shearing PR, Tsaoulidis D and Grett DJL. 2014. In situ diagnostic techniques for characterisation of polymer electrolyte membrane water electrolysers–Flow visualisation and electrochemical impedance spectroscopy. International Journal of Hydrogen Energy 39.9:4468-4482.
4. Majasan JO, Cho JIS, Dedigama I, Taoulidis D, Shearing P and Brett DJL. 2018. Two-phase flow behaviour and performance of polymer electrolyte membrane electrolysers: Electrochemical and optical characterisation. international journal of hydrogen energy 43.33:15659-15672.
5. Ito H, Maeda T, Nakano A, Hasegawa Y, Yokoi N, Hwang CM, Ishida M, Kato A and Yoshida T. 2010. Effect of flow regime of circulating water on a proton exchange membrane electrolyzer." International journal of hydrogen energy 35.18:9550-9560.
6. Olha P, Elena B, Walter Z, Franz JH, Martin B, Nikolay K, Tobias A, Ingo M, Martin M, Detlef S and Werner L. 2018. In-situ two-phase flow investigation of different porous transport layer for a polymer electrolyte membrane (PEM) electrolyzer with neutron spectroscopy. Journal of Power Sources 390:108-115.

WHEC-2022
23rd World Hydrogen Energy Conference
June 26-30, 2022 - Istanbul

#1594

EFFECT OF MOLYBDENUM OXIDE ADDITION TO METAL-SUPPORTED ZEOLITE CATALYST FOR REVERSE WATER GAS SHIFT REACTION

[1 *, 2] *Makoto Ryo Harada*, [2] *Atsushi Okemoto*, [2] *Norihito Hiyoshi*, [2] *Yasuhisa Hasegawa*, [2] *Koichi Sato*
[1] Tokai University, Department of Human Development, Course of Environment and Resources, 4-1-1 Kitakaname, Hiratsuka-shi, Kanagawa 259-1292, Japan
[2] National Institute of Advanced Industrial Science and Technology (AIST), 4-2-1, Nigatake, Miyagino-ku, Sendai 983-8551, Japan

*Corresponding author e-mail: MRHARADA@tsc.u-tokai.ac.jp

ABSTRACT

In this study, the effect of molybdenum oxide addition on metal catalysts in the reverse water gas shift reaction was investigated. By adding molybdenum to the copper, iron and cobalt supported catalysts, CO_2 conversion rate was improved while maintaining a high CO selectivity. In addition, it was made clear that the addition of molybdenum to ruthenium and nickel supported catalysts containing methane as the main product suppresses the production of methane and improves the selectivity for the reverse water gas shift reaction. The addition of molybdenum oxide from being presumed to suppress complete reduction of CO_2, proceeds highly selectively reverse water gas shift reaction. The addition of molybdenum oxide as a reverse shift reaction catalyst can be expected to be a useful method.

Keywords: Reverse shift reaction, Molybdenum oxide, Zeolite support, Carbon dioxide, Selectivity

INTRODUCTION

The increase in CO_2 in recent years has caused serious climate change and is a problem that greatly affects human society and the global environment. Reducing CO_2 emissions in industrial fields, which accounts for the majority of CO_2 emission sources, has become a major issue [1]. Effective use of CO_2 by converting it into chemical products by catalytic reaction is being promoted. Currently, as a technology to convert CO_2 into chemicals and liquid fuels using H_2, a gas phase catalytic reaction using a solid catalyst is considered. Multiple reaction occur from H_2 and CO_2, the selectivity of the reaction is important to develop a catalyst. As catalysts for RWS reactions, transition metal catalysts such as Cu, Fe and Co and noble metal catalysts such as Ru have been investigated [2].In this study, molybdenum oxide was added to metal catalysts such as Cu, Fe, Co, and Ru, which have a catalytic action on the hydrogenation reaction of CO_2, and the catalytic performance was studied [3]. Catalysts were prepared by co-impregnating these metals and molybdenum oxides and examined for activity using a flow-through integral reactor [4]. In this examination, the effects of H_2 and CO_2 partial pressure on the activity were measured, and the influence of the addition effect of molybdenum oxide was clarified.

MATERIALS AND METHODS

Materials

All materials of catalysts were used as received without further purification. The faujasite-type zeolite (FAU, HSZ-330HUA) was adopted from Tosoh Corporation. Hexaammonium heptamolybdate tetrahydrate $(NH_4)_6Mo_7O_{24}\cdot 4H_2O$ (GR), copper chloride (II) ($CuCl_2$, GR), hexa-ammine cobalt (III) ($[Co(NH_3)_6]Cl_3$, GR), nickel chloride (II) hexahydrate ($NiCl_2(II)\cdot 6H_2O$, GR), ruthenium chloride hydrate ($RuCl_3$, GR), and hydrochloric acid (HCl, GR) were made use of Wako Pure Chemical Corporation. Anhydrous iron chloride (III) ($FeCl_3$, Trace Metal Basis) was obtained from Sigma Aldrich.

Catalyst preparation

Metal oxide supported catalysts were prepared by incipient wetness impregnation method by using FAU as a support. The metal loading was fixed at 1.0 mmol/g-cat for each catalyst. Prior to impregnation, 1.0 g of FAU was placed in a side-arm flask under vacuum for 30 min at room temperature to remove adsorbed water molecules from the surface. As the impregnation solution, $CuCl_2$ (0.144 g), $FeCl_3$ (0.172 g), $[Co(NH_3)_6]Cl_3$ (0.284 g), $NiCl_2(II)\cdot 6H_2O$ (0.253 g), $RuCl_3$ hydrate (0.231 g) or $(NH_4)6Mo_7O_{24}\cdot 4H_2O$ (0.1953 g) was dissolved into 10 mL of HCl solution (0.01 mol/L). The solution was put into the flask with the FAU and left for 30 min at room temperature. The catalyst was evaporated in a 300 mL round-bottom flask for 1 h, followed by drying overnight in an electric oven at 328 K. Then, the sample was calcined in air at 773 K for 10 h. The obtained catalysts were named M(1)/FAU.M and x refer to element and its content mmol per gram of the catalyst.

Characterization

X-ray diffraction patterns were recorded using a SmartLab diffractometer (Rigaku) equipped with monochromatic Cu Kα radiation at room temperature. The 2θ range from 25° to 75° was scanned using a step size of 0.04° and a counting time of 4 s per step.

Catalytic activity examination for the reverse water gas shift reaction

The reverse water gas shift reaction was carried out in a fixed-bed flow type reactor. α-alumina tube (6 mm inner diameter) was used as the reaction tube. Catalyst (200 mg) diluted with 1.0 g of inert quartz sand were placed in the tube. The catalyst was sandwiched by 1.0 g of pure quartz sand layers. The catalyst was pretreated with a 55% H_2:N_2 mixture at a flow rate of 22.5 mL/min at 873 K for 1 h before the reaction. After pretreatment, the catalyst was set at the reaction temperature in N_2 gas, and the reaction gas (H_2:CO_2:N_2 = 12.5:12.5:10 mL/min, total flow: 35 mL/min) was fed into the reactor with a space velocity of 7000 $mL \cdot h^{-1} \cdot g^{-1}$. The gas lines from the reaction tube to the sampling valves were heated by electric heaters to avoid condensation of products. The products of the reaction were analyzed by two separate on-line GC systems equipped with a thermal conductivity detector (TCD) and a flame ionization detector (FID), respectively. The reaction products were measured as following column and detector: H_2, CO, and CH_4 were measured by GC-TCD with a Molecular Sieve 13X column; CO_2 and H_2O were measured by GC-TCD with a Gaskuropack 54 column (GL Science); and CH_3OH was measured by GC-FID with a Molecular Sieve 13X column. The conversion, yield, and selectivity for each product were calculated using the following equations:

$$\text{CO yield (\%)} = (\text{CO outlet (mol)}) / (\text{CO}_2 \text{ inlet (mol)}) \times 100$$
$$\text{CH}_4 \text{ yield (\%)} = (\text{CH}_4 \text{ outlet (mol)}) / (\text{CO}_2 \text{ inlet (mol)}) \times 100$$
$$\text{CO selectivity (\%)} = (\text{CO outlet (mol)}) / (\text{CO}_2 \text{ inlet-CO}_2 \text{ outlet (mol)}) \times 100$$

RESULTS AND DISCUSSION

Catalytic activity

Fig. 1 shows Cu(1)/FAU, Ru(1)/FAU, Mo(0.8)Cu(0.2)/FAU, Mo(0.8)Ru(0.2)/FAU and Mo(1)/FAU catalysts. The dependence of the reaction rate on the hydrogen partial pressure in the reverse water gas shift reaction was shown. The horizontal axis is the logarithm of the hydrogen partial pressure in the reaction gas, and the vertical axis is the logarithm of the CO_2 conversion rate at the reaction time of 3 hour. The reaction rate at each hydrogen partial pressure was measured, and the logarithm was plotted. In Cu (1)/FAU and Ru(1)/FAU, the slopes of the plots are 0.65 and 0.70. 0.8) Ru(0.2)/FAU were 0.70 and 0.72, respectively. The slope of the plot shows the dependence on the hydrogen partial pressure [5], and the larger the slope value, the stronger the contribution of the hydrogen partial pressure to the reaction rate. By co-supporting with Mo, the value of the slope increased, indicating that the degree to which the hydrogen partial pressure contributes to the reaction rate increased, that is, the ability to activate hydrogen was suppressed. From the XRD measurement results, it is considered that copper and ruthenium exist as metals and molybdenum exists as oxides in the catalyst. It is known that hydrogen is dissociatively adsorbed relatively easily on metal copper or metal ruthenium, and hydrogen atoms exist on the metal. On the other hand, it has been reported that the surface electrostatic field causes a heterogeneous dissociation reaction of hydrogen molecules on oxides such as MoO_2 due to charge separation. From the difference in the dissociation reaction of hydrogen molecules, it is considered that the hydrogen activity on the molybdenum oxide surface is lower than that of metallic copper or metallic ruthenium, and the contribution of hydrogen partial pressure to the reaction rate is increased.

Conversion and Selectivity

Fig. 2 shows the CO_2 conversion and CO selectivity of the series of the catalysts in the reverse water gas shift reaction. Among single metal supported catalysts, Mo(1)/FAU, Cu(1)/FAU, Fe(1)/FAU, Co(1) /FAU have very high CO selectivity in carbon dioxide hydrogenation reaction. The CO selectivity was over 90% for each catalyst. Ru(1)/FAU and Ni(1)/FAU had low CO selectivity of 50% or less in the carbon dioxide hydrogenation reaction, and the main product was CH4. Ru, in particular, has a high hydrogen activity and is known as a catalyst for methanation reactions that reduce CO_2 to CH_4 [6]. Mo(0.8)Cu(0.2)/FAU, Mo(0.8)Fe(0.2)/FAU, Mo(0.8)Co(0.2)/FAU maintain high CO selectivity, CO_2 conversion rate improved. Mo alone showed a high CO_2 conversion rate and was found to work as a selective CO production active site in the CO2 hydrogenation reaction. In particular, CO_2 conversion was improved by co-loading Mo and Cu. It was found that by co-loading with Mo, Mo(0.8)Ru(0.2)FAU and Mo(0.8)Ni(0.2)/FAU decreased in CO_2 conversion but improved in CO selectivity. CO_2 is completely reduced to CH_4 on Ru or Ni which have strong hydrogen activity. And, it is thought that the CO selectivity was improved by co-loading with Mo because the hydrogen activity is suppressed by Mo.

CONCLUSIONS

A reverse shift reaction catalyst with a high CO2 addition rate was developed while maintaining high CO selectivity. While maintaining high CO selectivity, Cu, Fe, the addition of Mo to Co supported catalyst, has succeeded in CO2

conversion rate is improved. The addition of Mo oxide suppresses the activation of hydrogen and promotes the reaction of carbon monoxide generation.

REFERENCES

1. Wenlei Zhu, Ronald Michalsky, Önder Metin, Haifeng Lv, Shaojun Guo, Christopher J. Wright, Xiaolian Sun, Andrew A. Peterson, Shouheng Sun, Am. Chem. Soc., 135, 45 (2013) 16833−16836.
2. Yixiong Yang, Jaime Evans, Jose A. Rodriguez, Michael G. Whiteac, Ping Liu, Phys. Chem. Chem. Phys., 12 (2010) 9909–9917.
3. Dae Han Kim, Sang Wook Han, Hye Soo Yoon, Young Dok Kim, Journal of Industrial and Engineering Chemistry, 23, 25, 67–71.
4. Yolanda A. Daza, Ryan A. Kent, Matthew M. Yung, John N. Kuhn, Ind. Eng. Chem. Res., 53, 14 (2014) 5828–5837.
5. Christos M. Kalamaras, Paraskevi Panagiotopoulou, Dimitris I. Kondarides, Angelos M. Efstathiou, Journal of Catalysis 264, 2, 2009, 117-129.
6. Frigyes Solymosi, András Erdöhelyi, Mária Kocsis, J. Chem. Soc., Faraday Trans. 1, 1981,77, 1003-1012.

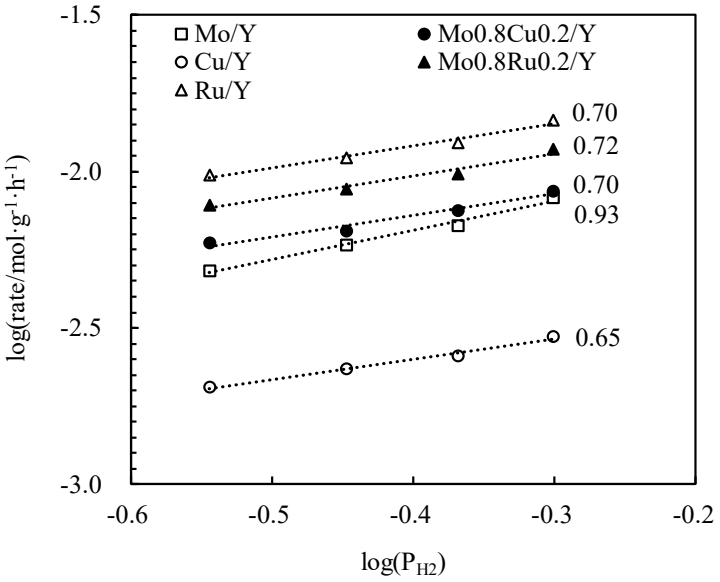


Fig. 1 Hydrogen partial pressure dependence of the overall conversion rate of CO_2 on Cu(1)/FAU,Ru(1)/FAU,Co(0.8)Cu(0.2)/FAU, Mo(0.8)Ru(0.2)/FAU and Mo(1)/FAU catalysts.

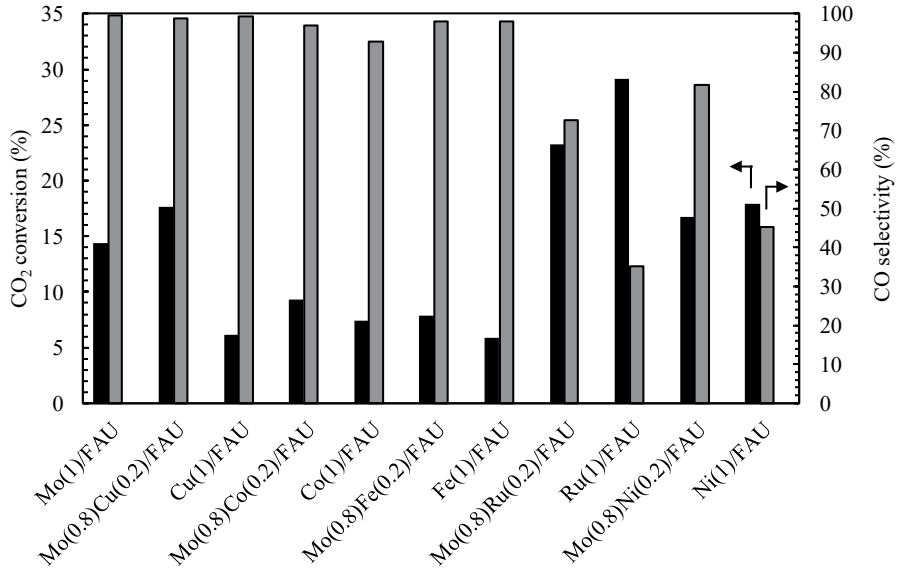


Fig. 2 Catalytic activity of metal and molybdenum co-supported FAU catalysts for reverse water gas shift reaction.

WHEC-2022
23rd World Hydrogen Energy Conference
June 26-30, 2022 - Istanbul

#1598

ON THE POTENTIAL OF COUPLING SOLAR CHIMNEY AND WIND ENERGY TO PRODUCE HYDROGEN AS GREEN-TO-GREEN SYSTEM

[1,2] *Mohamad Ramadan,* [2] *Ahmad Haddad,* [3] *Mohammad Alkhedher*
[1] International University of Beirut, PO Box 146404 Beirut, Lebanon
[2] Lebanese International University, Beirut, Lebanon
[3] Mechanical Engineering Department, Abu Dhabi University, United Arab Emirates

*Corresponding author e-mail: mohamad.ramadan@liu.edu.lb

ABSTRACT

The energy crisis, we are facing nowadays requires fast and efficient actions. Indeed, renewable sources are a main pillar, however storage systems are also principal pillars to overcome the intermittent nature of renewable sources. However, and to maintain a fully green system the storage should also be green and eco-friendly. Green to Green ($G2G$) are systems that gathers green sources and green storage. A typical solution is to couple renewable source to fuel cell. In this frame the present paper aims at studying the coupling of two renewable energy systems that are wind turbine and solar chimney to Fuel cell. A case study on the region of Rayak (Lebanon) is performed. Results show that in the first half of the year wind turbine-fuel cell coupling provides higher power supply whereas from June till November, solar chimney-fuel cell coupling is better.
Keywords: Green to Green, G2G, hydrogen, Fuel cell, wind turbine, solar chimney, renewable energy.

INTRODUCTION

Green to Green energy system (*G2G*) [1] is an optimal solution that can be adopted as a long run energy strategy. It allows to gather a green source of energy to a green storage system. On one hand, renewable energy is an efficient solution to reduce the negative impact of the technological development especially on the environmental level. Moreover, renewable energy systems cover wide range of natural sources of energies such as wind energy, solar energy, and geothermal energy. On the other hand, the main disadvantage of renewable energy sources is that they are intermittent and as a matter of fact they induce an oscillation in power supply if they are adopted alone without energy storage system such as super capacitors, batteries and compressed air storage. However, from an environmental point of view, not all storage system can be considered as green. From her is born the concept of (*G2G*) energy systems that could be constructed by coupling a renewable source to a green storage system such as fuel cell in order to obtain a pollution free system including both the source and the storage systems [2]. With this in mind, many works have been devoted to investigate different form of *G2G* energy systems [3]. Ramadan et al [4], suggest a system combining fuel cell and solar thermal system. The solar system is utilized to supply an electrolyser that supplies the fuel cell by hydrogen. Coupling geothermal energy and hydrogen has been also investigated [5]. Hybrid *G2G* energy systems have also been investigated [6]. In the frame of this paper a hybrid system coupling solar chimney, wind turbine and fuel cell is investigated.

MODELING

Green to Green (G2G)

The concept of green to green energy system (*G2G*), represents the simultaneous coupling of a green source to a green storage system. That said, and from an energetic stand point, any system combining a green source to a green storage could be labeled as *G2G*. Indeed, each *G2G* system includes, a green energy source such as wind energy, geothermal energy, solar energy, wave energy and hydropower. Concerning, green storage systems, many technologies can be labeled as green storage such as hydrogen, flywheel, pumped hydro and compressed air.

Coupling

The main contribution of this work is the coupling proposed between Fuel Cell (FC) and SC/WT systems through Hydrogen/Oxygen storage. The concept of coupling consists on using an Electrolyzer to produce Hydrogen and Oxygen from the power generated by SC system and/or WF system as shown in Fig. 1. During sunlight the SC is used to convert thermal energy to electrical power. In presence of wind extra power is produced by the WF. The total power generated by both systems is used to feed the load. The extra energy, if available, is used in the electrolysis process to produce hydrogen and oxygen. When solar radiations and wind speed are insufficient, hydrogen and oxygen are pumped to the FC to supply the load demand.

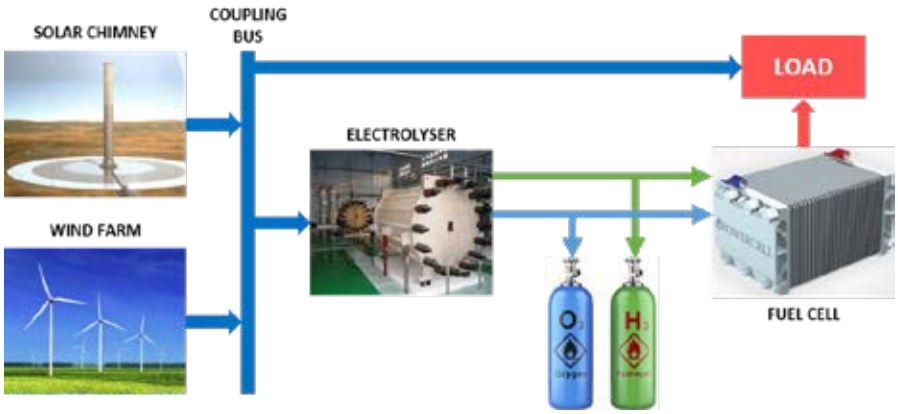


Fig. 1. Coupling Fuel Cell with Solar Chimney and Wind Farm systems.

RESULTS

Hence, coupling WT with SC results in better yearly power that can meet a higher load demand. However, during periods of low load demand with high solar radiations and wind speed there will be exceeds of energy that may be lost if not stored. This work proposes to store the extra energy in form of hydrogen using the electrolyzer. For this end, the AC power produced by the hybrid WT-SC system is converted to DC one using a rectifier before connection to the electrolyzer. Fig. 2 presents the hydrogen production rates of DC powers resulting from WT and SC in the region of Rayak.

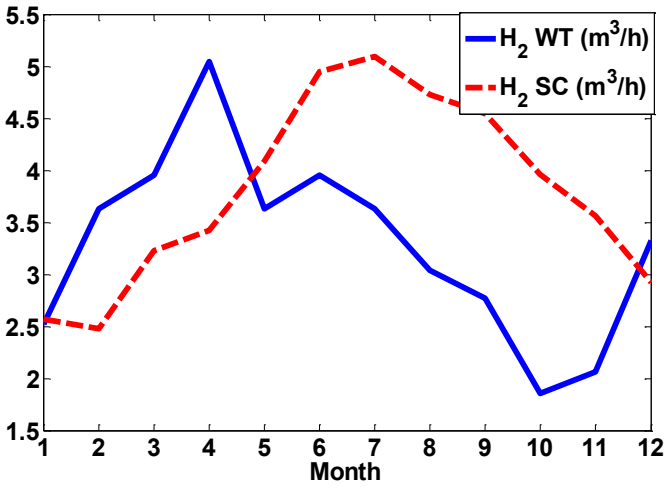


Fig. 2. Hydrogen production rates for WT and SC in Rayak Bekaa

CONCLUSION

Green to Green (*G2G*) energy systems, is the energy solution toward a pollution free environment. Coupling renewable sources to hydrogen is typical application of (*G2G*) systems. In this paper, the potential of coupling solar chimney, wind turbine and hydrogen is investigated. The potential of this coupling is studied in the region of Rayak. Results show that the hydrogen output and thus the output power depends on the period for instance in the first 5 months of the year wind turbine-hydrogen coupling provides higher amount of power whereas, in the second half of the yard solar chimney – hydrogen coupling provides higher amount of power.

REFERENCES

1. Ramadan M, A review on coupling green sources to green storage (G2G): Case study on solar-hydrogen coupling, International Journal of Hydrogen Energy, (2021), https://doi.org/10.1016/j.ijhydene.2020.12.165.
2. Kubilay Karayel G, Javani N, Dincer I, Green hydrogen production potential for Turkey with solar energy, International Journal of Hydrogen Energy, 2021, https://doi.org/10.1016/j.ijhydene.2021.10.240.
3. Karapekmez A, Dincer I, Thermodynamic analysis of a novel solar and geothermal based combined energy system for hydrogen production, International Journal of Hydrogen Energy, Volume 45, Issue 9, 2020, Pages 5608-5628, https://doi.org/10.1016/j.ijhydene.2018.12.046.
4. Mahmoud M, Ramadan M, Naher S, Pullen K, Abdelkareem M. A. and Olabi A.-G, A review of geothermal energy-driven hydrogen production systems, Thermal Science and Engineering Progress, 22 (2021) 100854, ISSN 2451-9049.

5. Ramadan M, Khaled M, Ramadan H S, Becherif M, Modeling and sizing of combined fuel cell-thermal solar system for energy generation, International Journal of Hydrogen Energy, Volume 41, Issue 44, 26 November 2016, Pages 19929-19935, ISSN 0360-3199, https://doi.org/10.1016/j.ijhydene.2016.08.222.
6. Haddad A, Ramadan M, Khaled M, Ramadan H S, Becherif M, Triple hybrid system coupling fuel cell with wind turbine and thermal solar system, International Journal of Hydrogen Energy, Volume 45, Issue 20, 2020, Pages 11484-11491, https://doi.org/10.1016/j.ijhydene.2019.05.143.

WHEC-2022
23rd World Hydrogen Energy Conference
June 26-30, 2022 - Istanbul

#1627

ENERGY PERSPECTIVE AND ANALYSES OF SEAWATER ELECTROLYZER FOR SEA VEHICLE

[1]Meryem Gizem Sürer, [2*] Hüseyin Turan Arat
[1]Iskenderun Technical University, Faculty of Engineering and Natural Sciences, Mechanical Engineering, Central Campus, Hatay, 31200, Turkey
[2]Sinop University, Faculty of Engineering and Architecture, Mechanical Engineering, Sinop, 57000, Turkey

* E-mail: htarat@sinop.edu.tr

ABSTRACT

In this study, a prototype marine vehicle is designed to produce hydrogen from sea water and convert it into electricity and use it as an auxiliary power in the main propulsion, and it is provided to look at this design from an energy perspective. In the designed marine vehicle, the main propulsion power was provided by a diesel generator. In this study, first of all, the requirements were determined, a conceptual design was made, and necessary evaluations were made from the energy perspective. In this study, high-weight hydrogen storage difficulties will be avoided by providing hydrogen production at any time, and costs will decrease in the long run. In addition, it will make great contributions to zero carbon dioxide studies.

Keywords: Hydrogen, Sea Vehicle, Purification, Energy Analyses, Electrolysis

INTRODUCTION

The important percent of hydrogen production handled with water electrolysis. Although it is not easy way to produce directly to hydrogen and it is not widely usage to produce hydrogen from seawater; is a crucial option to produce it. When looked up to the literature, the only work that has become a prototype that produces hydrogen from sea water and uses it for propulsion is the Energy Observer. The Energy Observer is the world's first hydrogen-generating and hydrogen-powered ship. The Energy Observer has a built-in PEM water electrolyzer (PEMWE) powered by a solar panel and wind turbine to produce hydrogen. The PEM water electrolyzer uses purified seawater and converts it to hydrogen. The hydrogen is then compressed and stored and used to power the ship via a Toyota fuel cell stack [1]. A schematic of the Energy Observer ship system is shown in Fig. 1 [1].

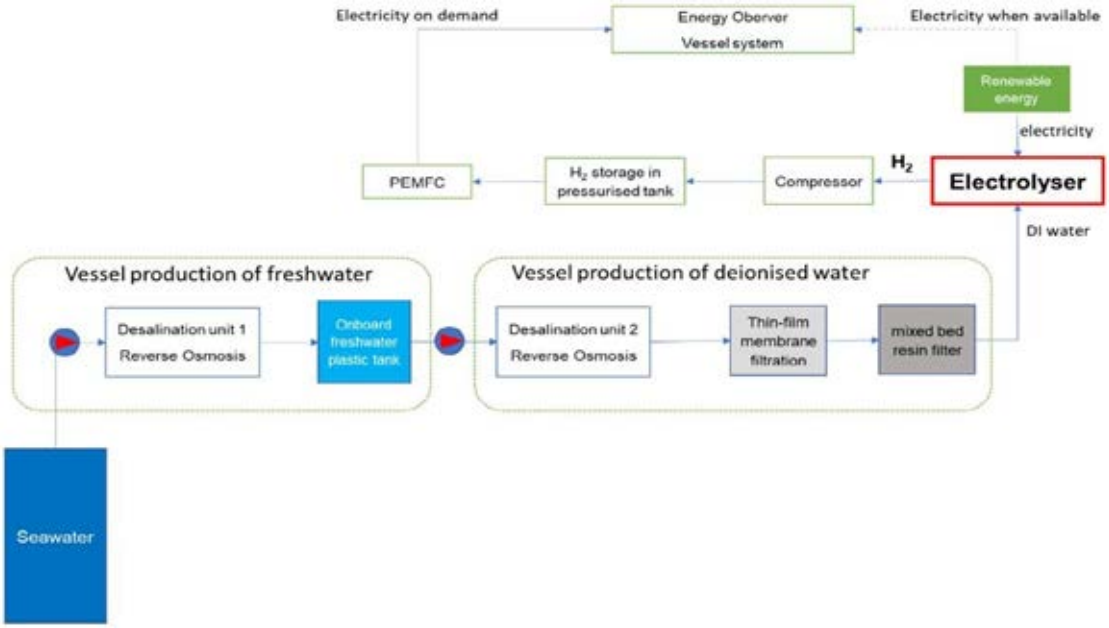


Fig. 1. A schematic of the Energy Observer ship system [1]

Unlike the literature, the hydrogen produced in this study will be used as auxiliary power in the main propulsion. Main power will be provided from diesel generator. In this way, the use of this system will be increased in heavier cargo ships and long-range ships for cargo, etc. purposes. It will also contribute to the literature on the production of hydrogen from sea water and its use in the propulsion system, and the increase of studies will be encouraged.

MATERIALS AND METHODS

In this study, hydrogen production from sea water is planned by purifying sea water, removing all dissolved salts, and giving it to the electrolysis cell. For this, reverse osmosis method, which is the most widely used method commercially, will be used. The conductivity of water, which is the inverse of the resistance with respect to the multiplication and is a measure of the fluid's ability to transmit electric current (the amount of ions in the water), is expressed in microSiemens/centimeter (µS / cm). In addition, an idea about the salinity of the water can be obtained by multiplying the conductivity value by 0.55-0.70. The resistance of the water is expressed as Mega-Ohm per centimeter (MΩ-cm) at 25°C [2]. Sea water is in the range of 40,000 to 100,000 microsiemens [3]. The water to be separated during electrolysis must meet many compositional requirements. These are standardized by the American Society for Testing and Materials (ASTM) Type II deionized (DI) water (resistance 41 MΩ cm), while ASTM Type I DI water (410 MΩ cm) is preferred [4]. The comparative feature is given in Table 1 [5].

Table 1. ASTM Standards (ASTM D1193-91 [5].

Measurement (unit)	Type I	Type II	Type III	Type IV
Resistivity (MΩ-cm)	> 18	> 1	> 4	> 0.2 (200KΩ)
Conductivity (µS/cm)	< 0.056	< 1	< 0.25	< 5.0
pH at 25°C	N/A	N/A	N/A	5.0 – 8.0
Total Organic Carbon (TOC) ppb or µg/L	<50	<50	<200	N/A
Sodium (ppb or µg/L)	< 1	< 5	< 10	< 50
Chloride (ppb or µg/L)	< 1	< 5	< 10	< 50
Silica (ppb or µg/L)	< 3	< 3	< 500	N/A

The designed treatment system and the complete marine propulsion system are given in Figures 2 and 3.

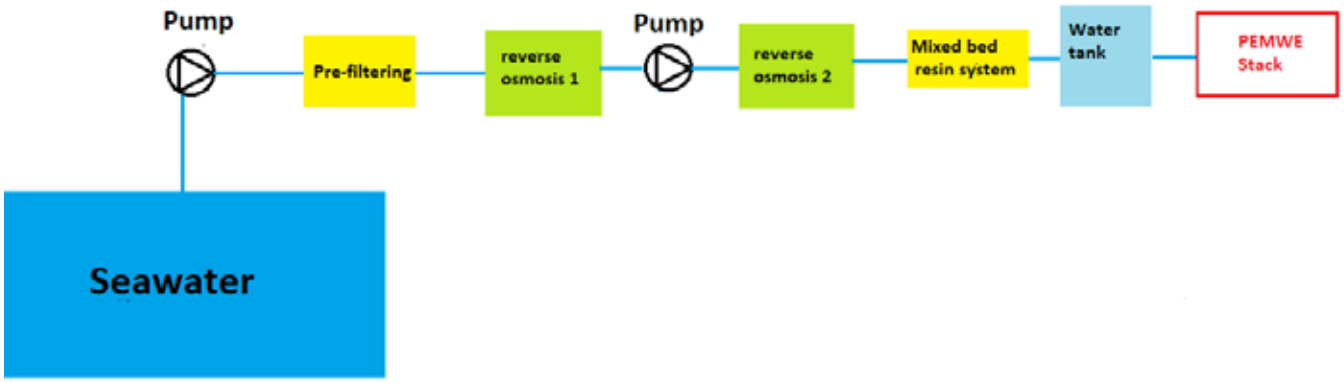


Fig 2. Designed treatment system

First, a pre-filtration is performed to remove very large particles in the seawater and to prevent any damage to the membrane and to prolong its life. In this filtration method, particles are captured using the physical sieving method. Here it is planned to use a sediment filter that captures particles up to 5 µm. Then the desalination of sea water will be carried out using two separate desalination units; both units will remove impurities by reverse osmosis (RO) to remove ions. The reverse osmosis semipermeable membrane (Ex. SW30, Dow Filtec membrane) acts as a barrier for all dissolved salts and inorganic molecules as well as organic molecules with a molecular mass greater than about 100 Daltons. RO units effectively achieve a high salt rejection of 99.2% to 99.5%. After two steps of reverse osmosis, the conductivity of water is expected to be about 3 µs/cm. RO filtrates may not be of the desired quality in single-stage purification. Therefore, two-stage reverse osmosis will be used. After desalination, additional step will be added to further remove impurities (thin film composite membrane).

The sea water treated in the design will be converted to hydrogen by electrolysis and stored in the hydrogen tank. From here, it will be converted into electricity in the fuel cell and feed the electric motor in the propulsion system. This system will be used as auxiliary power. There will be a separate propulsion system powered by a diesel generator as indicated in Figure 3, feeding a separate propeller as the main power. While the electricity produced here rotates the main propeller, a line will be drawn from the electricity produced to meet the electricity needs such as pump, electrolysis etc. Here, it is aimed to reduce the use of fossil fuels by making maximum usage of the fuel cell.

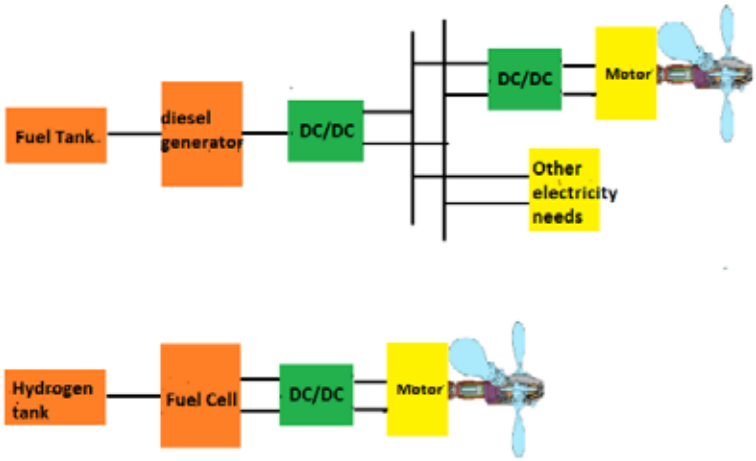


Fig 3. Propulsion system of sea vehicle

After the propulsion elements and the sea water treatment method were determined, the conceptual design stage was started. The paths followed in the conceptual design are as follows. Related formulas are taken from [6]. And the following steps have been followed.

a. Concept design—Feasibility study

At this stage, the mission and requirements were determined, and a feasibility study was carried out. L length, B beam, D side depth, T draft, CB block coefficient, PB powering etc. preliminary estimates of the basic ship dimensions were made. Alternative design solutions were explored.

b. Preliminary design

At this stage, the ship design determined in the first stage was detailed. The main characteristics of the ship, namely length L, beam B, sideboard depth D, draft T, block coefficient CB, and boost PB have been accurately determined. After the ship dimensions were determined, the power of the design materials etc. were determined. The combination of stages a and b is also known as basic design.

CONCLUSION

In this study, high-weight hydrogen storage difficulties were avoided by enabling hydrogen production at any time. Additionality, it will make great contributions to zero carbon dioxide studies. Unlike the literature, the hydrogen produced in this study was used as auxiliary power in the main propulsion. The main power was provided from a diesel generator. In this way, the use of this system will be increased in heavier cargo ships and long-range ships for cargo, etc. purposes. It will also contribute to the literature on the production of hydrogen from sea water and its use in the propulsion system, and the increase of studies will be encouraged.

REFERENCES

1. Bacquart, T., Moore, N., Wilmot, R., Bartlett, S., Morris, A. S. O., Olden, J., ... & Mattelaer, V. (2021). Hydrogen for maritime application—Quality of hydrogen generated onboard ship by electrolysis of purified seawater. *Processes*, *9*(7), 1252.
2. .pH, İLETKENLİK, ÇÖZÜNMÜŞ OKSİJEN, SICAKLIK, TDS ve BULANIKLIK TAYİNİ, https://cevre.erciyes.edu.tr/upload/5V2OV8N1-fiziksel-Olcum-yontemleri.pdf [Last Access Date:17.01.2022]
3. https://www.alarko-carrier.com.tr/Upload/Article/1c116da3-3242-448d-9321-e3e2cf57ba33.pdf [Last Access Date:17.05.2022]
4. Cavaliere, P. D., Perrone, A., & Silvello, A. (2021). Water electrolysis for the production of hydrogen to be employed in the ironmaking and steelmaking industry. *Metals*, *11*(11), 1816.
5. Water Quality Standards, https://puretecwater.com/downloads/water-quality-standards.pdf [Last Access Date:17.05.2022]
6. Papanikolaou, A. (2014). *Ship design: methodologies of preliminary design*. Springer.

WHEC-2022
23rd World Hydrogen Energy Conference
June 26-30, 2022 - Istanbul

#1629

THE EXPERIMENTAL STUDIES ON ELECTROLYSER MODE OPERATION OF UNITIZED REGENERATIVE PEM FUEL CELL

[1*] Nebi Yelegen, [1,2] Enis Selçuk Altuntop, [1] Gamze Atalmis, [1,2] Yüksel Kaplan
1 Nigde Omer Halisdemir University Prof. Dr. T. Nejat Veziroglu Clean Energy Research Center, 51245, Nigde, Turkey
2 Nigde Omer Halisdemir University, Mechanical Engineering Department, 51245, Nigde, Turkey

*Corresponding author e-mail: nebiyelegen@gmail.com

ABSTRACT

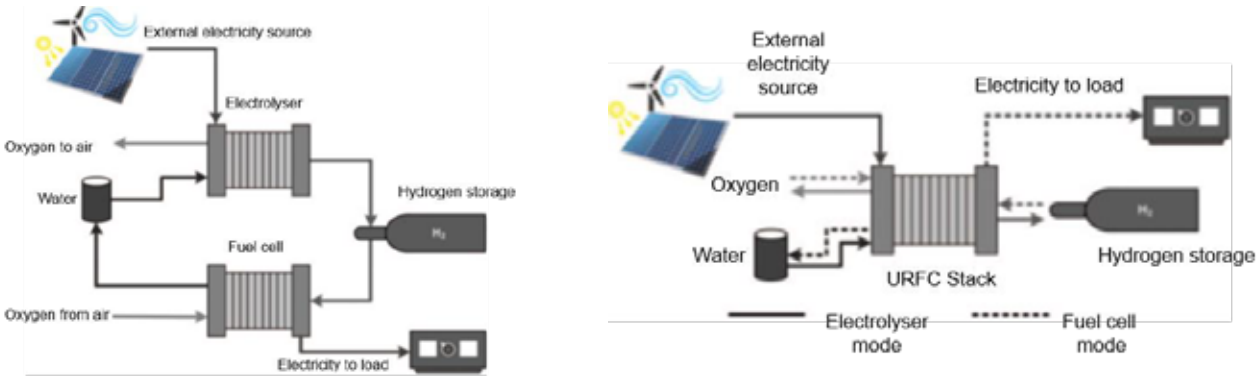
A unitized regenerative proton exchange membrane fuel cell (UR-PEMFC) is an electrochemical component that is capable of operating both as electrolyser and fuel cell mode. While UR-PEMFC produces hydrogen and oxygen by decomposing water in the electrolyser mode, it can also produce electricity and heat by using hydrogen as fuel in the fuel cell mode. A reversible system possesses several distinctive advantages for instance, high specific energy, pollution free, and most importantly, the decoupled energy storage capacity with rated power [1]. In this study, the performance of a unitized regenerative fuel cell and stack in electrolyser mode was investigated. The active areas of URFC are 100 cm^2, and the stack has three cell, which has a 100 cm^2 active area. The clamping pressure is optimized for cell and stack by using pressure film. Thus, the contact resistance was minimized, and optimum contact was achieved.

Keywords: Unitized regenerative fuel cell, PEM electrolyser stack, Experimental study

INTRODUCTION

Exhaust emissions from internal combustion engines are the primary source of pollution and are responsible for over 65 percent of global emissions worldwide [2]. As global energy demand is expected to increase continuously in the future, fundamental measures need to meet the growth of energy demand. The UN Framework Convention on Climate Change was adopted by the United Nations Conference on Environment and Development in 1992 to prevent global warming. Since the Kyoto Protocol has concrete action plans, it enforced the international environmental regulations to redeem greenhouse gas emissions [3]. This context supports increasing the interest and needs for renewable energy sources.

Hydrogen is not a primary energy source, but it is clean, efficient, and flexible energy carrier and easily convertible to electricity. Several types of electrolysers, such as, alkaline electrolyser (AEL), polymer electrolyte membrane electrolyser (PEMEL), and high temperature electrolysers (HTEL) are available for hydrogen generation. PEM electrolyser technology is becoming more competitive due to new improvements coming from increased research, developments, and the lower energy demand of the system. The combination of PEMEL and PEMFC into a regenerative fuel cell (RFC) system is an attractive energy storage method. Furthermore, the combination of PEMEL and PEMFC in one unit, the unitized regenerative fuel cell (URFC), provides advantages in system simplicity while compromising efficiency [4].



(a) (b)

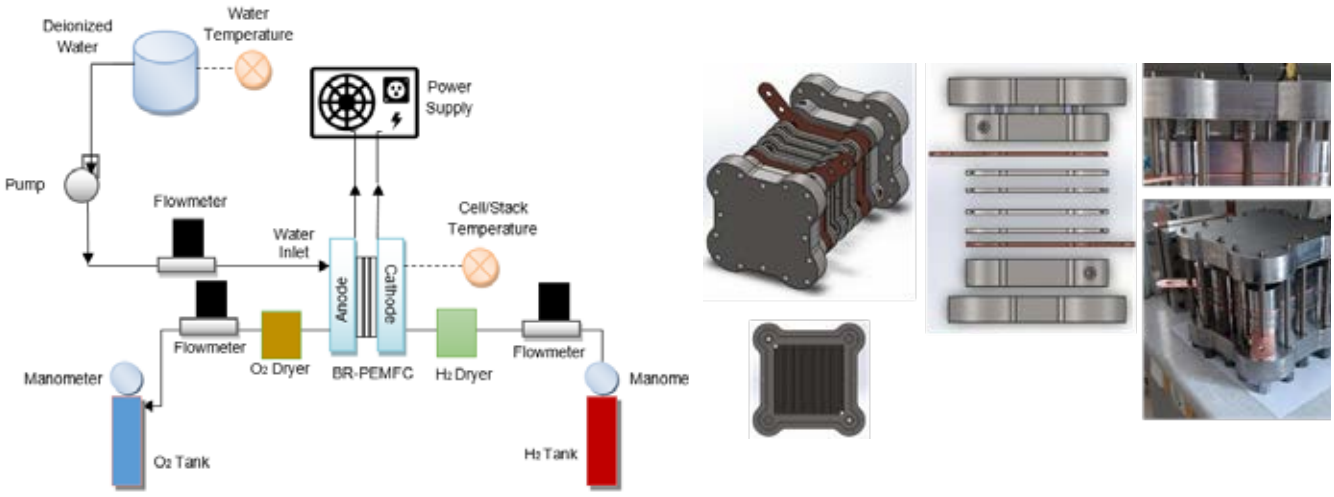
Fig. 1. Schematic diagram of a discrete reversible fuel cell (a), and unitized reversible fuel cell system (b) [5]

There are two basic types of RFC which are discrete regenerative fuel cells (DRFC) and unitised regenerative fuel cells (URFC). DRFC has separate units to perform the electrolyser and fuel cell, but these two devices are both integrated into a single system, as shown in Figure 1(a). The overall design of a DRFC system consists of a water management system, a control system, and a gas storage system to function as a standalone energy storage unit

[5]. To make a more compact system, the fuel cell and the electrolyser can be unitized into a single electrochemical cell. The URFC system, which can be seen in Figure 1(b), has several advantages against conventional discrete RFC, such as lower capital cost, simpler structure, higher specific energy, and no need for auxiliary heating [1].

EXPERIMENTAL SETUP

Within the scope of this experimental study, two different URFC were considered for different temperatures. One of the URFC has a 100 cm^2 active area, and the other one has three cell which has 100 cm^2 active areas. The experimental setup for the regenerative PEM fuel cell is shown in Fig. 2(a). Also, the bipolar plate flow channel of URFC and stack design can be seen in Fig. 2(b). DC power supply, air conditioning cabinet, ultra pure water, flowmeter, multimeter, and dryer were used to performed electrolyser mode tests. The electrolyser mode of URFC operated 20-60 ℃ to observe the effect of temperature.

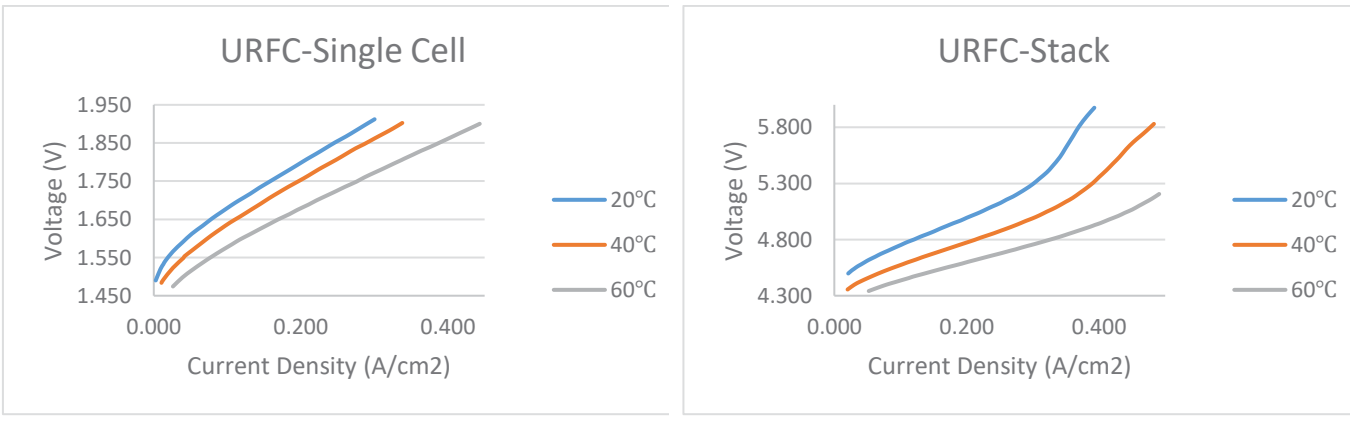


(a) (b)

Fig. 2. The experimental setup for URFC

RESULTS AND DISCUSSION

The experimental URFC's electrolyser mode performance data is given in Fig. 3. 10.38 liters of hydrogen gas is produced per hour from a single cell at 60 ℃ and 1,72 V, while 61.65 liters are produced in the stack at the same temperature and 5,2 V. The number of cells in the URFC stack is increased according to the required hydrogen flow and serially to each other. Thus, the hydrogen flow rate obtained from URFC is increased.



(a) (b)

Fig. 3. The URFC cell and stack experimental results

CONCLUSIONS

Storing energy such as hydrogen is becoming very popular. PEM electrolysers have become the favorite way to produce hydrogen, due to their higher operating current densities, high-pressure output, and ability to respond to dynamic demands. UR-PEMFCs provide direct conversion between hydrogen and electricity, and they are sizable systems to

meet the power and energy specifications of a variety of applications. Further research and development are necessary for UR-PEMFCs to become competitive with discrete PEM electrolysers.

ACKNOWLEDGEMENT

The authors would like to thank the Niğde Ömer Halisdemir University Scientific Research Projects Coordination for the financial support under contract number MMT 2021/7-LÜTEP. The first author, Nebi Yelegen, would like to thank the International Association for Hydrogen Energy for sponsoring the conference fee. The third author, Gamze Atalmis, would like to thank YÖK (100/2000 Phd. Scholarship Program).

REFERENCES

1. Wang, Y., Leung, D. Y. C., Xuan, J., & Wang, H. (2016). A review on unitized regenerative fuel cell technologies, part-A: Unitized regenerative proton exchange membrane fuel cells. Renewable and Sustainable Energy Reviews, 65, 961–977.
2. Lee, J., Kim, H.-M., Kim, T., Duy, V. N., Ahn, J., Park, S., & Kim, K. (2015). Dynamic simulations of under-rib convection-driven flow-field configurations and comparison with experiment in polymer electrolyte membrane fuel cells. Journal of Power Sources, 293, 447–457.
3. Park, K., Kim, H. M., & Choi, K. S. (2013). Numerical and experimental verification of the polymer electrolyte fuel cell performances enhanced by under-rib convection. Fuel Cells, 13(5), 927–934.
4. Mittelsteadt, C., Norman, T., Rich, M., & Willey, J. (2015). PEM Electrolyzers and PEM Regenerative Fuel Cells Industrial View. In Electrochemical Energy Storage for Renewable Sources and Grid Balancing. Elsevier B.V.
5. Shabani, B., Omrani, R., Seif Mohammadi, S., Paul, B., & Andrews, J. (2020). Chapter 9: Unitised Regenerative Fuel Cells. In RSC Energy and Environment Series (Vols. 2020-Janua, Issue 25).

WHEC-2022
23rd World Hydrogen Energy Conference
June 26-30, 2022 - Istanbul

#1637

TAKE YOUR ENERGY USING SERVİ DUT PEKMEZİ (MULBERRY MOLASSES): A NOVEL ELECTROACTIVE FILM FOR WATER ELECTROLYSIS

[1] *Yeşim Aydın DURSUN,* [2,*] *Ramazan SOLMAZ*
[1] Bingöl University, Science and Letters Faculty, Chemistry Department Bingöl, Türkiye
[2] Bingöl University, Health Sciences Faculty, Occupational Health and Safety Department, Bingöl 12000, Türkiye

*Corresponding author e-mail: rsolmaz01@gmail.com

ABSTRACT

A thin self-assembly monolayer (SAM) film of Servi Dut Pekmezi (mulberry molasses, Servi MM) was fabricated over a copper electrode (Cu/Servi MM-SAM) in ethanol as solvent. The prepared Cu/Servi MM-SAM electrode was used as cathode in 6 M KOH solution for electrochemical hydrogen gas production. The traditional Servi MM was obtained from Servi village of Bingöl province, Türkiye. In this way, the dissolution and corrosion rate of copper could be reduced as well as electroactive centers coming from the chemical structures of the components of the MM could be supplied for further enhancing the activity of the electrode. It was observed that, the Servi MM-SAM film was not soluble in 6 M KOH solution and the film was very adherent to the metal surface and stable. Modifying the surface improve water splitting activity of the electrode and facilitates the rate of hydrogen gas production.

Keywords: Water Electrolysis, Hydrogen Production, Servi Dut Pekmezi (Mulberry Molasses), Self-Assembly Monolayer Film

INTRODUCTION

Electrolysis of water is one of the most efficient and easy way to produce clean and sustainable hydrogen gas [1,2]. However, cost production must be reduced and the yield of the method should be improved. For this aim, the researchers have been searching for novel electrode materials to be used in electrolysers. Alkaline solutions are generally chosen for this aim since more metals could be used in this medium. On the other hand, many cheaper transition metals, such as copper, cannot be used as electrode materials or electrocatalysts in alkaline solutions since they can easily corrodes. Therefore, enhancing corrosion protection ability and reduce dissolution rate of these metals is essential to use these metals in alkaline or acidic solutions.

Covering metal surface with an organic film may solve this problem. But, the film should also be electroactive. Common conductive polymers could not be used for this aim since they remove from the metal surface during the excess gas evolution in the electrolysis system. Recently, we suggested a new type of organic film called SAM for this aim [3,4] and reported that such organic films could enhance the hydrogen evolution activity of the electrode by facilitating the charge transfer between the metal/solution interface.

In this study, we are reporting a novel SAM film of a natural product, Servi Dut Pekmesi, which is a very healthy and natural product. The most famous mulberry molasses in Turkey is produced completely naturally in Servi village, Bingöl, Türkiye. Servi Dut Pekmezi received a Geographical Indication Certificate by the Turkish Patent and Trademark Office in 2021 and organized by Bingöl Directorate of Provincial Agriculture and Forestry. “Mulberry molasses, which has a high energy-giving feature, is good for fatigue, fatigue and anemia. It has a strengthening effect on the liver and kidneys and is good for hemorrhoids, sciatica and stomach diseases. Its antioxidant compound content supports the body to stay alive and young at all times. It strengthens the body's immune system by removing toxins accumulated in the body. It is edematous and cleans the liver. Mulberry molasses, which is good for arteriosclerosis, ensures the regulation of blood circulation. It regulates the heartbeat and is good for high blood pressure. It has very beneficial effects on smokers due to its cleansing properties of the lungs. This natural product plays an active role against cough” [5].

The Servi Dut Pekmezi modified Cu/Servi MM-SAM electrode was tested as cathode for hydrogen production in 6 M KOH solution. The surface film was characterized by some surface characterization techniques. Its water splitting activity was studied using cathodic polarization and electrochemical impedance spectroscopy (EIS) measurements.

MATERIALS AND METHODS

The Servi MM-SAM films were prepared on a copper specimen in ethanol as solvent. 1000 ppm Servi MM solution in ethanol was used for this aim. 1000 ppm KI was added to the solution in order to facilitated the assembly by synergism.The temperature of the film formation solution was kept at room temperature. The exposure time for the

film formation was 24 hours. The preparation of copper electrode before the measurements was the same as described before in detail [6]. After film formation, the electrode was removed from the solution, cleaned with the same solvent and dried under nitrogen atmosphere.

The structure of the film modified surface was examined with SEM and EDX. Further surface characterizations are ongoing and will be reported in future papers.

Electrochemical activity of the modified electrode for water splitting to produce hydrogen gas was studied in 6 M KOH at 398 K with the help of cathodic current potential curves and EIS. The experiments were performed with a computer controlled CHI instrument. In the polarization studies, the potential of the electrode was scanned between the open circuit potential and hydrogen evolution potential. The EIS data were obtained from 100 kHz to 0.1-0.01 Hz frequency range (based on the over potential). A Pt sheet with dimension of 10mmx10mmx1mm and Ag/Ag/AgCl were used as counter and reference electrodes, respectively.

RESULTS AND DISCUSSION

The Servi-MM-SAM film formed on the metal surface was characterized using SEM and EDX. On Fig. 1, SEM, EDX spectrum and the distribution of C element, which is completely coming from the Servi MM-Sam film are shown. From Fig. 1, it is clearly seen that the Servi MM-SAM film covers the surface completely and adheres very well to the Cu surface. Cu electrode used in this study has not C element content. Therefore, C element is coming from only the composition of the film. Therefore, the distribution of the film was examined by obtaining the distribution of the C element over the metal surface by EDX-mapping. Apparently, the C element, namely the Servi MM-SAM film is distributes over the metal surface perfectly. This is very important for the electrocatalysis studies since water splitting over the electrode is a surface process.

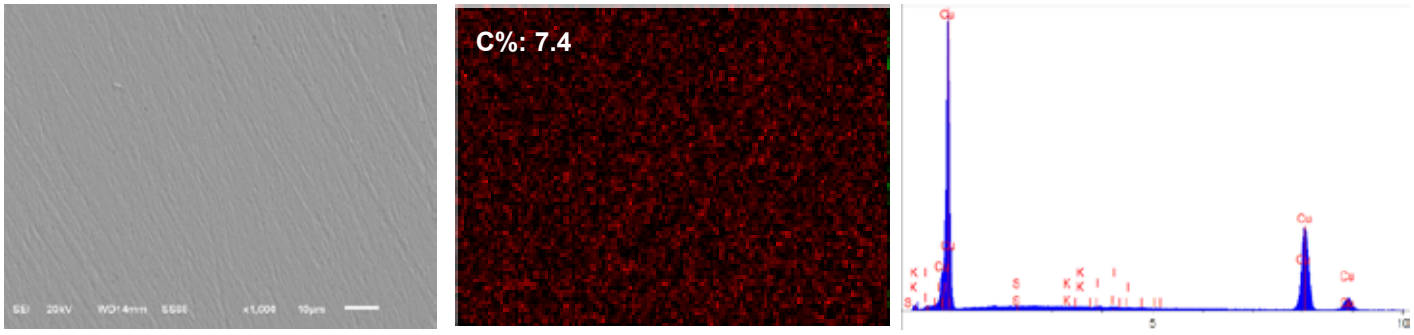


Fig 1. SEM, EDX mapping and EDX spectrum of the Cu/Servi MM-SAM surface

Water splitting activity of the Servi MM-SAM modified electrode was tested in 6 M KOH solution at 298 K. For this aim current-potential and EIS measurements were carried out. The data obtained are shown on Fig. 2 graphically. As it is seen form Fig. 2a, hydrogen gas evolution starts at lower overpotentials at the film modified electrode with respect to the bare Cu. Higher current density, which is directly related to the rate of hydrogen gas evolution reaction, at a specific potential is appeared at the Cu/Servi MM-SAM electrode. Therefore, we can conclude that modifying the copper surface with this natural film enhances its electrocatalytic activity and facilitates water splitting, which results with lower electricity consumption and make the electrolysis cheaper. The enhanced activity of the film can be assigned to the easier charge transfer ability of surface polymeric film.

Of course, the aim of this study is improving a protective as well as electroactive film over the copper metal, improving the stability of the copper and reduce corrosion rate of this metal in alkaline solution. In future studies, the corrosion performance of the electrode will also be reported. We also found that the surface SAM film is stable after the long–time electrolysis. Bu, we could not report these data here due to the limitation of short paper.

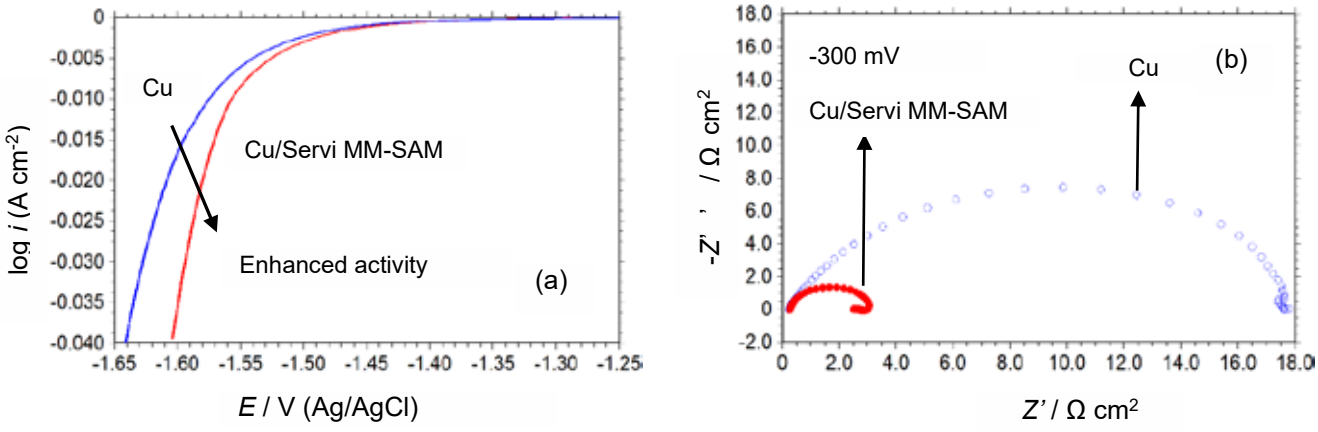


Fig. 3. Cathodic current-potential curves (a) and Nyquist plots of Cu and Cu/Servi MM-SAM electrodes obtained in 6 M KOH solution at 298 K

CONCLUSIONS

A thin Servi MM-SAM film was fabricated over a copper electrode in ethanol as solvent. KI was added to the film formation solution to facilitate the film formation and obtaining better quality film. The prepared Cu/Servi MM-SAM electrode was characterized for 6 M KOH electrolysis to produce hydrogen gas. Following major points were concluded:

- Homogenous and very adherent Servi MM-SAM film was prepared on the copper surface.
- The film has good appearance and nice color which also can be used for decorative aims.
- The film is physically and electrochemically stable.
- The film is promising organic subtract for further modifications and fabricating metal modified electrocatalysts.
- The Cu/Servi MM-SAM electrode has better water splitting activity with respect to the bare copper electrode.
- Further studies are continuing and will be reported later.

ACKNOWLEDGEMENT

The authors are greatly thankful to Bingöl University, Health Sciences Faculty, Occupational Health and Safety Department for experiments and Bingöl University Central Laboratory for characterization measurements.

REFERENCES

1. Veziroğlu TN and Şahin S. 2008. 21st century's energy hydrogen energy system. Energy Conversion and Management 49:1820 – 1831.
2. Veziroğlu TN and Barbir F. 1992. Hydrogen: the wonder fuel. International Journal of Hydrogen Energy 17:391 – 404.
3. Salcı A, and Solmaz R. 2019. Hydrogen Evolution Reaction Activity of Rhodanine Self Assembled Monolayer Films. 4th International Hydrogen Technologies Congress, Proceedings Book, 192-195 pp., Edirne, Türkiye.
4. Solmaz R and Öztürk D. 2022. The use of polyrhodanine-modified copper substrate for electrochemical hydrogen production. 6th International Hydrogen Technologies Congress (IHTEC-2022), Proceedings Book, 385-387 pp., Canakkale, Türkiye.
5. http://www.nefisyemektarifleri.com. Accessed on May 26, 2022
6. Salcı A, Altunbaş EA, Solmaz R. 2019. Methanol electrooxidation at nickel-modified rhodanine self-assembled monolayer films: A new class of multilayer electrocatalyst, International Journal of Hydrogen Energy 44:14228-34 – 404.

WHEC-2022

23rd World Hydrogen Energy Conference

TRACK 3. HYDROGEN PRODUCTION: BIOLOGICAL METHODS AND BIOHYDROGEN

TRACK 3. HYDROGEN PRODUCTION: BIOLOGICAL METHODS AND BIOHYDROGEN

#6 CARBON FOOTPRINT OF HYDROGEN PRODUCED FROM SPENT COFFEE GROUNDS	301
#23 THE POTENTIAL OF USING MICROALGAE IN PHOTOBIOREACTORS FOR H_2 PRODUCTION	304
#24 A NOVEL THREE-STAGE INTEGRATED SYSTEM (DARK FERMENTATION, METHANOGENESIS AND PHOTOFERMENTATION): DIFFERENT COMBINATIONS TO MAXIMIZE H_2 AND CH_4 PRODUCTION	307
#26 INVESTIGATION OF H_2 AND CH_4 PRODUCTION FROM YARD WASTES VIA TWO-STAGE ANAEROBIC DIGESTION AT DIFFERENT PRE-TREATMENT OPTIONS AND SOLIDS CONCENTRATIONS	310
#52 A THERMOSIPHON BASED PHOTOBIOREACTOR FOR PHOTOFERMENTATIVE HYDROGEN PRODUCTION	313
#114 GREEN HYDROGEN PRODUCTION FROM THE NON-CENTRIFUGAL SUGAR INDUSTRY	316
#136 A PRELIMINARY TECHNO-ECONOMIC ANALYSIS OF PHOTOBIOLOGICAL HYDROGEN PRODUCTION	319
#154 COMPARISON OF WILD TYPE AND UPTAKE HYDROGENASE DEFICIENT MUTANT STRAINS OF *RHODOBACTER CAPSULATUS* FOR HYDROGEN AND PHB PRODUCTION	322
#254 FOCUSING ON A NEW BIOHYDROGEN PRODUCTION STRATEGY USING *CHLAMYDOMONAS REINHARDTII* MUTANTS	325
#264 OPTIMIZATION OF BIOHYDROGEN PRODUCTION YIELDS WITH LOCALLY ISOLATED THERMOPHILIC BACTERIA FROM HOT SPRINGS	328
#358 VALORIZATION OF GREEN MARKET WASTE FOR BIOHYDROGEN PRODUCTION	331
#374 ASSESSMENT OF BIOHYDROGEN PRODUCTION ROUTES FROM ORGANIC SOLID WASTE: THE CASE OF CARTAGENA, COLOMBIA	335
#410 ADAPTATION OF *CALDICELLULOSIRUPTOR BESCII* TO UNPRETREATED CATTLE MANURE: A NOVEL APPROACH FOR HYPERTHERMOPHILIC BIOHYDROGEN PRODUCTION	338
#437 BIOELECTROCHEMICAL HYDROGEN PRODUCTION FROM DARK FERMENTATION EFFLUENTS IN HYPERTHERMOPHILIC MICROBIAL ELECTROLYSIS CELLS	342
#1529 BATCH DARK FERMENTATIVE BIOHYDROGEN PRODUCTION FROM FIG FRUIT: THE EFFECT OF C/N RATIO	346

WHEC-2022
23rd World Hydrogen Energy Conference
June 26-30, 2022 - Istanbul

#6

CARBON FOOTPRINT OF HYDROGEN PRODUCED FROM SPENT COFFEE GROUNDS

[1] Fehmi Gorkem Uctug, [2] Hakan Cay, [2] Gozde Duman, [2] Jale Yanik*
[1]Izmir University of Economics, Department of Mechanical Engineering, Sakarya Caddesi No: 156 35530 Balçova, Izmir - Turkey
[2]Ege University, Department of Chemistry, Erzene Mahallesi 35040 Bornova, Izmir - Turkey

*Corresponding author e-mail: gorkem.uctug@ieu.edu.tr

ABSTRACT

Life cycle carbon footprint of producing hydrogen from spent coffee grounds was calculated. The following scenarios were compared: direct gasification; gasification of biochar produced by carbonization at 300°C and at 500°C; and gasification of hydrochar produced by hydrothermal carbonization. In each scenario, two sub-scenarios for one-step and two-step gasification were also studied, respectively. CCaLC2 software was used with CML2001 methodology, and the functional unit was defined as 1 kg of hydrogen gas produced. Material inputs and emissions were obtained based on experimental data whereas energy consumption of the process was partially adopted from the literature. Hydrogen produced via the two-step gasification of hydrochar obtained as a result of hydrothermal carbonization was found to have the lowest carbon footprint (33.0 kg CO_2eq. per kg H_2) whereas hydrogen produced via direct one-step gasification of spent coffee grounds was found to have the highest carbon footprint (87.0 kg CO_2eq. per kg H_2). The results in general were observed to be in reasonable consistency with the values reported for the carbon footprint of other hydrogen production methods. The main conclusions of the study were the necessity of adding a carbonization step prior to the gasification process, and preferring two-step gasification instead of one-step so that the carbon footprint can be reduced.

Keywords: Hydrogen Production, Carbon Footprint, Spent Coffee Grounds, Carbonization, Gasification

INTRODUCTION

Hydrogen can be produced by several different methods. Conventional methods generally rely on chemical processing of fossil fuels to produce hydrogen. Recently, utilizing biomass to produce hydrogen has become a promising alternative. Hydrogen can be produced from biomass by thermochemical and biochemical processes. Thermochemical processes have technical advantages over the biological processes such as short process time with a relatively high efficiency and high availability for all types of biomass [1]. Different biomass types such as rice straw, palm kernel shell, pine kernel, miscanthus, switchgrass, coffee, grape waste, sawdust and chips, sewage sludge, apricot stones, algae, safflower seed cake have been tested for hydrogen production via gasification. Amongst these options, spent coffee grounds (SCG), which is the solid residue obtained after the roasted coffee brewing process, is especially interesting thanks to its high organic content as well as its widespread availability, as coffee is consumed extensively on a global scale. Furthermore, SCG is normally incinerated or disposed of in landfills, a practice that is considered unsustainable and potentially dangerous for both humans and the ecosystem, due to the fact that SCGs contain significant amounts of compounds with established toxicity [2]. Hence, utilizing SCGs to produce hydrogen appears to be a not only economically but also environmentally beneficial process.

In this study, we calculated the life cycle carbon footprint of utilizing SCGs to produce hydrogen via steam gasification. Details regarding different scenarios that were considered, system boundaries and assumptions can be found in the following sections.

ANALYSIS

Life cycle assessment (LCA) is an effective tool for evaluating a product's environmental burden by quantifying the impacts of all inputs and outputs associated with corresponding production processes. The methodological guidelines of LCA are laid out in the ISO 14040 and ISO 14044 standards. In this study, CCaLC2 LCA software was used to model the system and estimate its carbon footprint (CF) according to the CML 2001 methodology.
Technical details of producing hydrogen from SCG can be found elsewhere [1,3-7]. By using experimental data regarding the mass inputs and outputs and referring to the literature regarding the energy requirements of the process, a life cycle inventory table was prepared. Table 1 below shows the life cycle inventory for the hydrothermal carbonization followed by two-step steam gasification scenario. It must be noted at this stage that while similar tables were prepared for every single scenario, only one sample table was included in the manuscript so as to adhere to the rule on page limitation.

Table 1. Life cycle inventory of hydrogen production via two-step steam gasification of hydrochar obtained by hydrothermal carbonization

Step	Inputs	Outputs / Emissions	Amount	Ecoinvent dataset (as available in CCaLC library)
Hydrothermal carbonization	Water		0.006 kg	Water, ultrapure, at plant
	Electricity		0.216 MJ	Turkish electricity (manually adopted from [8])
	SCG		0.1 kg	-
		CO_2	0.005 kg	Carbon dioxide
		CO	0.001 kg	Carbon monoxide
		Hydrochar	0.1 kg	-
Drying	Hydrochar		0.1 kg	
	Thermal energy		0.15 MJ	Heat, at hard coal industrial furnace 1-10 MW
		Dried hydrochar	0.04 kg	-
Two-step steam gasification	Dried hydrochar		0.04 kg	-
	Nitrogen		0.0047 kg	Nitrogen
	Water		0.000012 kg	Water, ultrapure, at plant
	Thermal energy		0.670 MJ	Heat, at hard coal industrial furnace 1-10 MW
	Electricity		0.00003 MJ	Turkish electricity (manually adopted from [8])
		Hydrogen	0.00436 kg	-
		CO_2	0.047 kg	Carbon dioxide
		CO	0.00239 kg	Carbon monoxide
		Tar	0.0006 kg	Disposal, asphalt, 0.1% water, to sanitary landfill

RESULTS AND DISCUSSION

The results of our analysis can be found in Fig. 1 below.

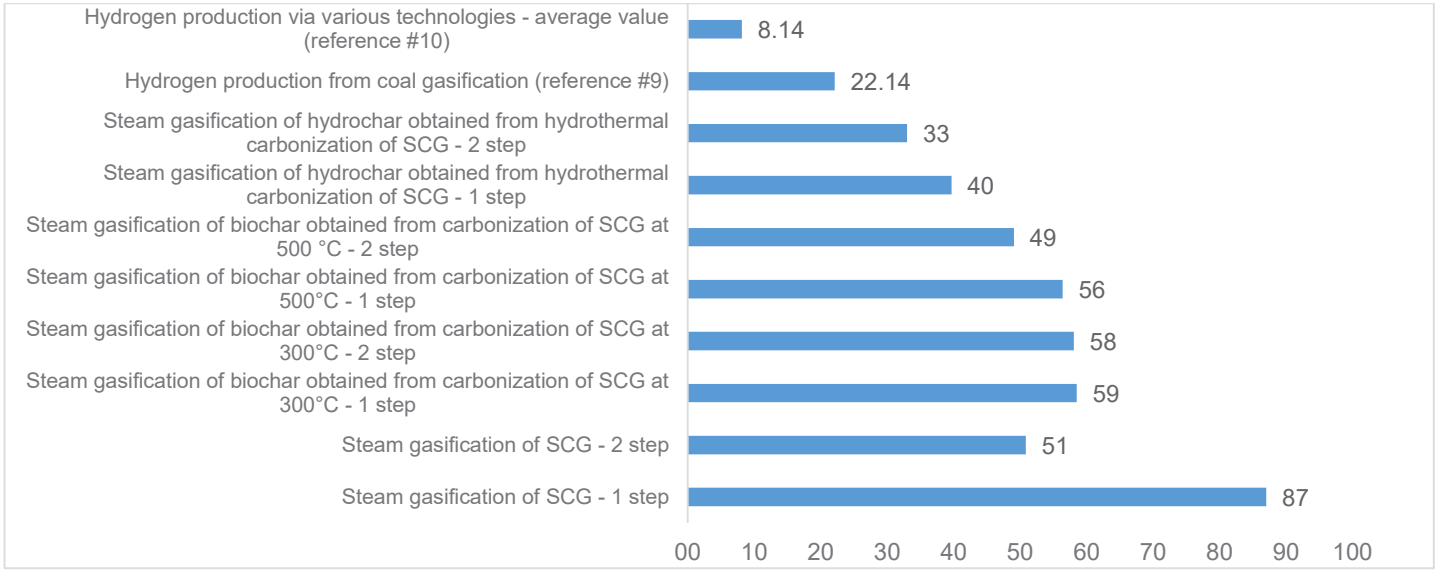


Fig. 1. CF of different hydrogen production from SCG scenarios and comparison with the literature

CF values presented in Fig. 1 were obtained by modelling the life cycle inventory of every single scenario in CCaLC and obtaining the respective CF values, and then calculating the CF value of not utilizing the SCG, i.e. landfilling it as biodegradable waste, and finally taking the difference of the CF value of hydrogen production and the CF value of SCG landfilling. In other words, we also considered the avoided CF as a result of not disposing the SCG.
As shown in the figure, the most environmentally friendly way of producing hydrogen from SCG is the two-step steam gasification of hydrochar obtained from hydrothermal carbonization whereas direct one-step gasification of SCG turned out to be the alternative with the highest carbon footprint. In general, two-step gasification was found to have

a lower carbon footprint compared to one-step gasification for a given process. Interestingly, this is not because of the reduced CO_2 emissions of the two-step gasification process, actually for the same amount of SCG input, the carbon footprint associated with the two-step gasification is on average 5.5% higher than that of one-step gasification. However, hydrogen yield of two-step gasification is significantly higher than that of one-yield gasification due to the improved degradation of the tar [1], with an average increase of 36.2%. Therefore, carbon footprint of producing unit amount of hydrogen turned out to be lower in the case of two-step gasification. Compared to the literature, the carbon footprint of hydrogen production from SCG is generally higher. This can be attributed to the fact that most of the data in this work is experimental and scaling up the process into industrial scale would reduce the energy consumption per unit of mass input, leading to results that would be more consistent with those reported in the literature.

CONCLUSIONS

It was concluded that having a carbonization stage prior to gasification is essential if carbon footprint is to be reduced. Obtaining hydrogen from hydrochar rather than biochar was found to be a more environmentally-friendly option. Two-step gasification was found to have a much lower carbon footprint compared to one-step gasification.

Future work concerning the environmental analysis of hydrogen production from SCG should focus on scaling up the process in order to be able to get more accurate results. Also, a more comprehensive LCA study that covers additional impacts such as acidification, eutrophication, and human toxicity potential can give a clearer idea about the environmental of footprint of utilizing SCG.

REFERENCES

1. Cay H, Duman G and Yanik J. 2019. Two-step gasification of biochar for hydrogen-rich gas production: effect of the biochar type and catalyst. Energy & Fuels 33:7398-7405.
2. Kookos IK. 2018. Technoeconomic and environmental assessment of a process for biodiesel production from spent coffee grounds (SCGs). Resources, Conservation & Recycling 134:156–164
3. Lucian M and Fiori L. 2017. Hydrothermal carbonization of waste biomass: process design, modeling, energy efficiency and cost analysis. Energies 10:211-228.
4. Berge ND, Li L, Flora JRV and Ro KS. 2015. Assessing the environmental impact of energy production from hydrochar generated via hydrothermal carbonization of food wastes. Waste Management 43:203-217.
5. Koroneos C, Dompros A and Roumbas G. 2008.Hydrogen production via biomass gasification—A life cycle assessment approach. Chemical Engineering and Processing 47:1261–1268.
6. Martinez-Merino V, Gil MJ and Cornejo A. 2017. Biomass Sources for Hydrogen Production. In Biohydrogen Production: Sustainability of Current Technology and Future Perspective. Edited by Singh A and Rathore D. India: Springer.
7. Valente A, Iribaren D and Dufour J. 2019. Life cycle sustainability assessment of hydrogen from biomass gasification: A comparison with conventional hydrogen. International Journal of Hydrogen Energy 44:21193-21203.
8. Atilgan B and Azapagic A. 2016. An integrated life cycle sustainability assessment of electricity generation in Turkey. Energy Policy 93:168-186.
9. Burmistrz P, Chmielniak T, Czepirski L and Gazda-Grzywacz M. 2016.Carbon footprint of the hydrogen production process utilizing subbituminous coal and lignite gasification. Journal of Cleaner Production 139:858-865.
10. Mehmeti A, Angelis-Dimakis A, Arampatzis G, McPhail SJ and Ulgiati S. 2018. Life Cycle Assessment and water footprint of hydrogen production methods: from conventional to emerging technologies. Environments 5:24-42.

WHEC-2022
23rd World Hydrogen Energy Conference
June 26-30, 2022 - Istanbul

#23
THE POTENTIAL OF USING MICROALGAE IN PHOTOBIOREACTORS FOR H_2 PRODUCTION

[1*]*Sergei Markov*
[1]Austin Peay State University, Biology Department, 601 College Street, Clarksville, TN, USA

[*]Corresponding author e-mail: markovs@apsu.edu

ABSTRACT

Many species of microalgae produce molecular hydrogen (H_2) in reactions catalyzed by the enzymes hydrogenase or nitrogenase. This H_2 production is coupled with photosynthesis. Thus, it is possible to design photobioreactors in which solar energy can be used for the production of H_2. Our research and development efforts were concentrated on designing hollow-fiber photobioreactors incorporating green algae and cyanobacteria. We have continuously for six months operated hollow-fiber photobioreactors for the photoproduction of H_2 from water using two metabolically different species of microalgae. One photobioreactor employed green alga *Chlamydomonas reinhardtii*. Hydrogen production was measured under partial vacuum at the average rate of 6.0 ml • g cell dry weight $^{-1}$ • h^{-1}. Another photobioreactor utilized cyanobacterium *Anabaena variabilis* with average H_2 photoproduction rate of 20 ml • g cell dry weight $^{-1}$ • h^{-1}. In both photobioreactors the duration of H_2 photoproduction was 6 months long.

Keywords: Biohydrogen, Photobioreactors, Hollow-fibers, Microalgae, Cyanobacteria

INTRODUCTION

Some photosynthetic microalgae, including cyanobacteria, can produce molecular hydrogen (H_2) from water using light as an energy source. Biological H_2-production based on photosynthetic water splitting is potentially attractive for industrial applications, because we have plenty of sunlight and water around. The industrial potential of microalgae for H_2 production will eventually be determined by their cultivation techniques [1]. Current production of microalgae for practical purposes is achieved in open “raceway” ponds of some thousand square meters in size [2]. These systems are not suitable for direct H_2 production by microalgae mainly due to H_2 collection. The demand to overcome this limiting factor has led to the development of H_2 production photobioreactors [3]. Photobioreactors are types of closed culture vessels used to grow photosynthetic organisms under controlled conditions with light as the energy source. Many types of photobioreactors are available for algal cultivation, but only few of them are suitable for H_2 production. Some important considerations for designing H_2-producing photobioreactors are the following: they should be simple and energy efficient, they should allow effective gas exchange and be gas tight to avoid the loss of H_2 and efficiently utilize solar energy. A hollow-fiber photobioreactor, specific only for H_2 production by microalgal species, was developed in our laboratory and it is the main subject of current paper. Hollow-fiber bioreactors contain hundreds of hollow fibers with cells attached to them [4]. Hollow fibers are made of semipermeable polymeric membranes, and salts and gases can diffuse freely through them. Microalgal cells, due to their larger size, cannot pass through the membrane, but rather grow on the hollow fiber surfaces as immobilized cells. The large surface-to-volume ratio of the hollow fibers also allows the algal cells to grow to high densities in this type of photobioreactor. Another advantage of photobiorectors containing algal cells immobilized on hollow-fibers is that they can be operated continuously for long periods of time [5].
Two types of metabolically distinct forms of microalgae were used in our photobioreactor: green alga *Chlamydomonas reinhardtii* and cyanobacterium *Anabaena variabilis*.

MATERIALS AND METHODS

Microalgal cultures. Cyanobacterium *A. variabilis* was cultivated in the medium of Allen and Arnon [6] without combined nitrogen. The *Chlamydomonas* CC-503 cw92 (mt+) cell wall-less strain was grown in a Tris-acetate-phosphate medium, pH 7.0 [8]. Both microalgae were cultivated in 250-mL Erlenmeyer flasks with a cell suspension volume of 100 mL. Continuous light was provided by cool white fluorescent lamps (15 µmol · m^{-2} · s^{-1} irradiance at the surface of the culture).
Photobioreactor. Sixty hollow fibers from an AM-40M-5D cartridge (Asahi Kasei Medical CO Ltd, Japan) were sterilized in 20 ppm hypochlorite solution with subsequent rinsing using sterile distilled water, cut into 110 mm lengths, and sealed together at one end with silicone rubber sealant (Aquaria, Dow Corning). To allow light penetration, the hollow fibers were packed into a transparent water-jacketed glass vessel (length, 110 mm; volume, 15 mL). The total surface area of the hollow fibers was 0.002 m^2. Algal cells (9-days old) were also added to the photobioreactor column under sterile conditions as described above. The photobioreactor (Figure 1) was designed in a way that the growth medium was added using a peristaltic pump (LKB 2232 MicroPerpex, Pharmacia LKB Biotechnology, Sweden) from the outside of the fibers within the column. Microalgal cells readily adsorbed to the outer surface of the hollow fibers. The used

growth medium went into the hollow fiber lumens and was pumped back (without being replaced with fresh medium) to the photobioreactor medium
reservoir, in order to create a closed system in which it was possible to measure H_2 production by the cells. Three percent (3%) CO_2 was added periodically to the gas phase (atmospheric levels of O_2 initially) of the photobioreactor reservoir under sterile conditions and maintained at the same level. The photobioreactor was illuminated continuously with cool white fluorescent lamps (45 µmol • m^{-2} • s^{-1} at the top surface of the photobioreactor column). It was operated under room temperature, and the water jacket around the photobioreactor column protected the microalgae from overheating.

Hydrogen production. The photobioreactor column and medium reservoir were vacuum degassed (up to 300 torr) to stimulate H_2 production. Hydrogen production was measured using a Gow-Mac gas chromatograph (Bethlehem, PA) equipped with a molecular sieve 5A column and a thermal conductivity detector. Nitrogen was used as a carrier gas.

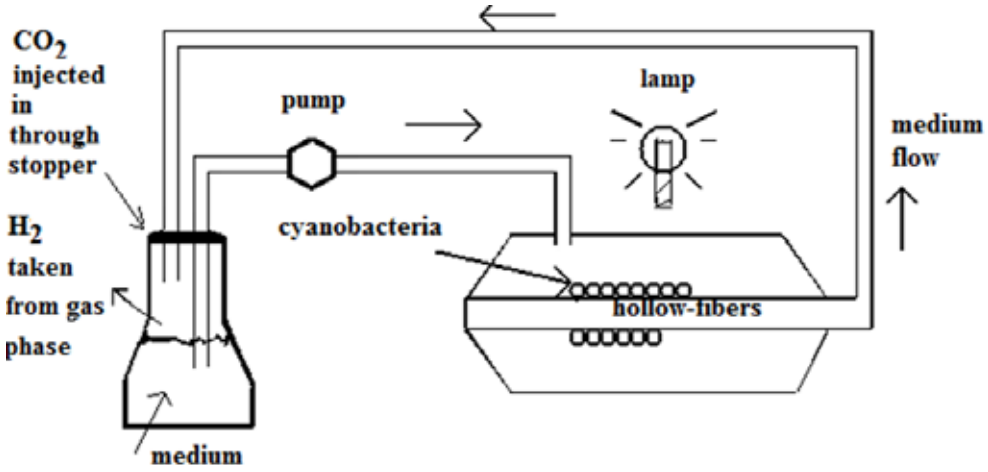


Fig. 1. Schematic representation of a hollow-fiber photobioreactor used for continuous production of H_2 by microalgae.

RESULTS AND DISCUSSION

Photobioreactors H_2 production by green algae

Green algae can produce H_2 from water in reactions catalyzed by the enzyme hydrogenase, but only under anaerobic conditions, because the enzyme is very sensitive to O_2. It very challenging to design photobioreactors for H_2 production by microalgae due to O_2 sensitivity of hydrogenase. Anything that can inhibit photosynthetic O_2 evolution can be useful to stimulate H_2 production by green algae in photobioreactors. One possible solution is to operate photobioreactors under partial vacuum. We produced H_2 in a photobioreactor at rate of 6.0 ml • g cdw^{-1} • h^{-1} continuously for 6 months using immobilized on hollow fibers cells of a green alga *C. reinhardtii* under partial vacuum. Another solution is to stimulate H_2 production in photobioreactors by green algae such as *C. reinhardtii* by photoinhibiting the photosynthetic oxygen-evolving system under high intensity illumination [8]. This high intensity light (more than 2000 µmol • s^{-1} • m^{-2}) is very common in summer in midday in warm climates such US Southern States.

Photobioreactors for H_2 production by cyanobacteria

Cyanobacteria in evolutionary terms are bacteria. They called also blue-green algae because their oxygen evolving photosynthesis is similar to those of algae. In many cyanobacteria specialized cells, heterocysts, are the site of H_2 production. Nitrogenase is the enzyme which catalyzed H_2 production in those cyanobacteria. This enzyme is also very sensitive to O_2. Heterocysts have a number of morphological and biochemical modifications designed to protect the nitrogenase from O_2 inactivation. Thus, compared to green algae, cyanobacteria are unique in their ability to produce H_2 in the presence of O_2. The main function of nitrogenase in cyanobacteria, and other N_2-fixing microorganisms, is to reduce N_2 to NH_3. Simultaneous evolution of H_2 along with N_2 fixation is an inherent property of the enzyme. Under normal conditions the volume of H_2 evolved is only a fourth that of the ammonia synthesized. This low rate of H_2 production is one of the problems of cyanobacterial H_2 production that all applied researchers in this area face. To solve this problem, we operated our photobioreactor under partial vacuum thus reduced the N_2 content (not to lower O_2 concentration as in case of green algae above). The average cyanobacterial H_2 production rate in our photobioreactor was 20 mL • g cdw^{-1} • h^{-1}. The photobioreactor was also operated for 6 months.

CONCLUSIONS

The main advantages of making H_2 by microalgae in our photobioreactors is that this H_2 is coming from water and it is light driven. Although, algal production of H_2 from water is attractive for practical applications, it is very difficult to achieve on a large scale. Rates of H_2 production by algae are much lower compared to bacterial H_2 production (Table 1).

Table 1. Comparative rates of H_2 production by microalgae and bacteria.

Organism	Hydrogen Production Rate in mL H_2 per g of dry weigh per hour	Reference
Microalga Chlamydomonas reinhardtii	up to 6.0	This paper
Cyanobacterium Anabaena variabilis	up to 20	9
Bacterium Enterobacter aerogenes	up to 400	10
Bacterium Rubrivivax gelatinosus	up to 700	11

Our current results demonstrate that it is possible to achieve long-term photobioreactor operation with microalgae immobilized on hollow-fibers. Hollow-fiber bioreactors may have the potential for leading to practical microbial H_2-producing systems in the future. One of the advantages of hollow-fiber photobioreactors is the ability to produce high cell densities, as mentioned above. However, hollow-fiber photobioreactors for H_2 production by microalgae are in their early developments, and are not as yet ready for practical microalgal systems. The price of hollow-fiber photobioreactor construction and operation is crucial factor for further development of these photobioreactors. In general, to improve the economics of H_2 production by microalgae in photobioreactors, H_2 production will have to be combined with synthesis of other useful products, such as single cell protein, specialty chemicals, and other commodities.

ACKNOWLEDGEMENT

The author thanks Asahi Kasei Medical CO Ltd (Japan) for supplying the hollow fiber cartridges.

REFERENCES

1. Lee Y-K, Ding S-Y, Low C-S, Chang Y-C, Forday WL, Chew P-C. 1995. Design and performance of an α-type tubular photobioreactor for mass cultivation of microalgae. J. Applied Phycology 7: 47-51.
2. Chisti Y. 2007. Biodiesel from microalgae. Biotechnol. Adv 25: 294–306.
3. Benemann JR. 1996. Hydrogen biotechnology: progress and prospects. Nature Biotechnology 14: 1101-1103.
4. Bunch AW. 1988. The uses and future potential of microbial hollow-fibre bioreactors. J. Microbiol. Methods 8: 103-119.
5. Markov SA, Weaver P, Seibert M. 1996. Hydrogen production using microorganisms in hollow-fiber bioreactors. In Hydrogen Energy Progress XI, Vol. 3. Edited by Veziroğlu TN, Winter C-J, Baselt JP, Kreysa G. Frankfurt: Schön & Wetzel GmbH.
6. Allen MB and Arnon DI. 1955. Studies on nitrogen fixing blue-green algae. I. Growth and nitrogen fixation by *Anabaena cylindrical* Lemn. Plant Physiol 30: 1366-1372.
7. Harris E. 1989. The *Chlamydomonas* Sourcebook: A comprehensive guide to biology and laboratory use. San Diego, Academic Press.
8. Markov SA, Eivazova ER and Greenwood J. 2006. Photostimulation of H_2 production in the green alga *Chlamydomonas reinhardtii* upon photoinhibition of its O_2-evolving system. Int. J. Hydrogen Energy 31: 1314-1317.
9. Markov SA, Bazin MJ. and Hall DO. 1995. Hydrogen photoproduction and carbon dioxide uptake by immobilized *Anabaena variabilis* in a hollow-fiber photobioreactor Enzyme and Microbial Technology 17: 306-309.
10. Markov S.A, Averitt J. and Waldron B. 2011. Bioreactor for glycerol conversion into H_2 by bacterium *Enterobacter aerogenes* Int. J. Hydrogen Energy 36: 262-266.
11. Markov SA and Weaver PF. 2008. Bioreactors for H_2 production by purple nonsulfur bacteria. Appl. Biochem. Biotechnol 145:79-86.

WHEC-2022
23rd World Hydrogen Energy Conference
June 26-30, 2022 - Istanbul

#24

A NOVEL THREE-STAGE INTEGRATED SYSTEM (DARK FERMENTATION, METHANOGENESIS AND PHOTOFERMENTATION): DIFFERENT COMBINATIONS TO MAXIMIZE H_2 AND CH_4 PRODUCTION

[1*] *Tuba Hande Erguder,* [1] *Melih Can Akman,* [1] *Engin Koç,* [1] *Ekin Güneş Tunçay,* [2] *Ufuk Gündüz,* [3] *İnci Eroğlu*
[1] Middle East Technical University, Department of Environmental Engineering, 06800, Ankara, Turkey
[2] Middle East Technical University, Department of Biology, 06800, Ankara, Turkey
[3] Middle East Technical University, Department of Chemical Engineering, 06800, Ankara, Turkey

* Corresponding author e-mail: etubahan@metu.edu.tr

ABSTRACT

A unique three-stage integrated system composed of dark fermentation (DF), methanogenesis (M) and photofermentation (PF) in series was developed to maximize the total energy production from unit organic matter (sucrose). The three-stage system aims to minimize the disadvantages of two-stage DF-PF systems and use the advantage of methanogenesis stage via CH_4 production. This study compares the total energy yields (kJ/g soluble chemical oxygen demand, sCOD) of six different reactor configurations, that is, both two-stage DF-M and DF-PF systems to three-stage DF-M-PF systems. Results revealed that three-stage configurations produced a maximum gross heat energy of 13.47-16.11 kJ/g $sCOD_{added}$ and maximum yield equivalence of 9.18-10.80 mol H_2/mol hexose. These values are 14-37% greater than 8 mol H_2/mol hexose, defined to be the economic threshold for application of two-stage DF-PF systems. A methanogenesis stage placed between DF and PF stages was the most significant stage in total energy production.

Keywords: Anaerobic Digestion, Energy, Hydrogen, Methane, Two-stage Systems

INTRODUCTION

Hydrogen is the cleanest energy among other energy sources. When it is produced from wastes via dark fermentation (DF) and photofermentation (PF), it becomes even more valuable because fossil fuels are not used in these processes and the sustainable environment and development approaches are realized. Yet there are some disadvantages of these processes to be economic in application [1]. The major problem in biohydrogen production is the low H_2 production yields and rates leading to the requirement of large volumes and long retention times [2]. The research topics such as development of reactor configurations, sludge immobilization, genetic modifications in microbial cultures, application of two-stage systems, pretreatment of raw materials have been studied to improve H_2 production [1]. The most suitable raw material types, pretreatment methods, operational conditions/modes, culture types and process configurations are still among the topics significant to be investigated. The most effective configuration type for DF-PF integration is still not certain [3].

Two-stage systems are composed of a first-stage DF, which is followed by either PF or a methanogenesis reactor as the second-stage. Anaerobic digestion, where methane is produced via the final methanogenesis (M) step, has been a well-known and widely applied technology all around the world. Yet, its integration into a DF-PF system has not been studied so far. The proposed novel three-stage DF-M-PF system, where the methanogenesis stage will be integrated between DF and PF stages, might have following advantages compared to a DF-PF system. 1) Methanogenesis has higher yields and rates, and is a much more stable process compared to DF; thus, its integration might improve the total energy yield per unit substrate. 2) Biohythane, which is more advantageous compared to sole H_2 and sole CH_4 [4], might be potential to produce in DF-M-PF system. 3) A variety of organics originated from DF stage would be removed in the following M stage. Thus, the effluent of M stage might have lower COD concentration than that of DF; in turn, be more suitable for PF, because PF stage would require less dilution and lower volumes compared to a DF-PF system.

Regarding these potential advantages, a novel three-stage system was developed in a project supported by TUBITAK (Project No: 112M252) [5]. This three-stage system, sequentially composed of DF, M and PF stages, were studied with six configurations differed in operational modes (either in batch, sequencing batch or semi-continuous modes). Two-stage DF-M and DF-PF systems were also operated. This paper, without getting into the details of the reactors' operations, aimed to compare the total energy produced from all two- and three-stage configurations per unit substrate (kJ/g $sCOD_{added}$). It was also aimed to investigate the effect of M stage and three-stage system on energy yield improvement and optimum configuration leading to the highest energy production per unit substrate (sucrose).

MATERIALS AND METHODS

Considering both two- and three-stage systems, six different configurations were compared in this study. Three-stage systems were composed of DF-M-PF in sequence. Two-stage systems were composed of DF-M and DF-PF systems. DF, the first-stage, was performed in sequencing batch reactors (SBRs) in all configurations, and operated at pH of 5.5 and with sucrose at 10 g/L chemical oxygen demand (COD). The effluent of DF was used as the influent of the following stage. In three-stage system, each stage's integration and optimization were gradually applied. This gradual integration involved the conversion of the reactor mode from batch to SBR, which was applied first for M stage and then for PF stage.

Two example configurations are shown in Fig.1a for ***SBR-DF + Batch-M + Batch-PF*** three-stage system and in Fig.1b for ***SBR-DF + SBR-M + SCR-PF*** three-stage system. The operational conditions of each stage shown in Fig.1 are the conditions leading to the maximum energy production from the integrated system. In other words, each stage's operational conditions were previously optimized to achieve the highest energy out of three-stage system. To explain this approach, ***SBR-DF + Batch-M + Batch-PF*** system is selected as an example. In this configuration, for SBR-DF stage, five different operational conditions were investigated [5]. The effluent of each SBR-DF operational condition was collected, stored and then fed to the following triplicate batch M reactors. When the incubation was over, the effluent of each M batch set (run with different DF effluents) was applied as the influent of the following batch PF reactors. In conclusion, SBR-DF + Batch-M + Batch-PF configuration was operated five times for each different DF conditions (five DF effluents). Total energy yields of the three-stage system were calculated for each of the five different DF effluents. The conditions leading to the highest total energy yield from three-stage system were selected as the optimum conditions for DF stage. After setting the optimum DF conditions, the optimization of SBR-M stage was further done in another configuration, where the DF effluent obtained under optimum conditions were applied to the SBR-M. The optimization of PF stage and its conversion from batch PF to semi-continuous reactor PF (SCR-PF) was also performed in another configuration (Fig 1b), following the same approach. All six different configurations studied are shown in Table 1, in Results and Discussion Section. The same reactor codes (such as SBR-DF) indicate that the same operational conditions are valid for that specific reactor type in all configurations (Fig 1).

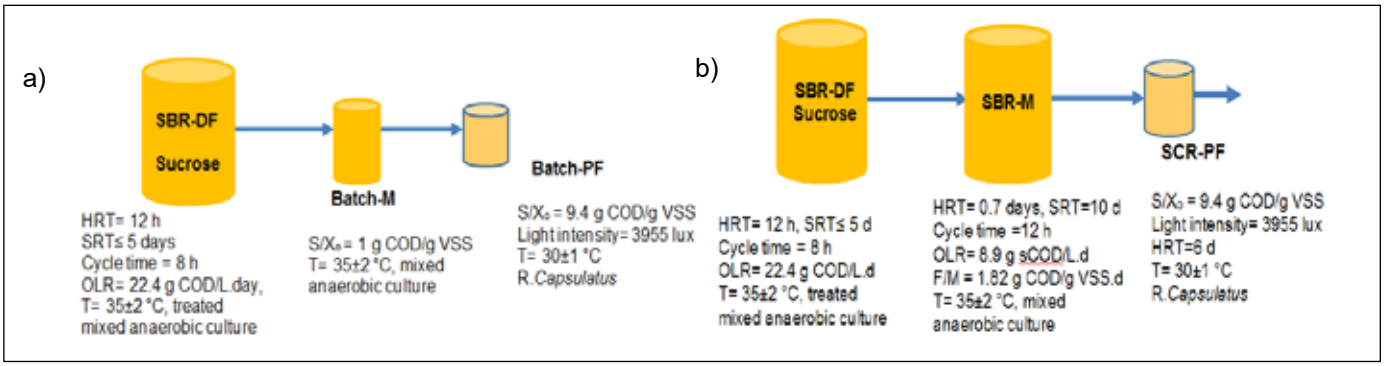


Fig 1. Examples configurations, a) SBR-DF + Batch-M + Batch-PF system, b) SBR-DF + SBR-M + SCR-PF system

In three-stage DF-M-PF system, the incubation period of M stage was shortened in order to remain substrate for the following PF stage; while in two-stage DF-M systems, the incubation period of M stage lasted till the cease of the gas production. In order to compare the total energy yields of each configuration, the yield of each stage was converted to the same unit; that is, g H_2 or g CH_4 produced per g soluble COD (g sCOD) and then the total energy was calculated on the basis of kJ/g sCOD.

RESULTS AND DISCUSSION

The energy yields and its corresponding H_2 yield equivalences obtained from all six configurations are given in Table 1. It is seen that the maximum total(gross) heat energy range of 13.47-16.11 kJ/g $sCOD_{added}$ and maximum yield of 9.18-10.80 mol H_2/mol hexose were obtained via the three-stage configurations (batch, SBR or SCR integrations). These yields are 27-50% greater than the maximum value of 7.2 mol H_2/mol hexose (10.60 kJ/g sCOD) practically obtained so far from two-stage DF-PF systems, and 14-37% greater than 8 mol H_2/mol hexose (11.78 kJ/g sCOD) defined as the economic threshold for application of two-stage DF-PF systems [6].

Among six three-stage configurations, the maximum energy and yield values (16.11 kJ/g sCOD and 10.80 mol H_2/mol hexose) were obtained in SBR-DF + SBR-M + Batch-PF system. This system even produced 7% higher energy yield than that of the theoretical yield (15.12 kJ/g $sCOD_{glucose}$) of a DF-M system. Other three-stage configurations are also of significance for reaching to 89-96% of the energy yield theoretically obtained from a two-stage DF-M system. Considering the energy yields obtained in two-stage DF-M systems (14.64-14.86 kJ/g sCOD),

three-stage systems produced similar energy yields. On the other hand, majority of the three-stage systems had greater energy yields than that of a single-stage anaerobic digestion system where the energy yield would be 13.85 kJ/g $sCOD_{glucose}$. The results also revealed that two-stage DF-M systems are much more advantageous than DF-PF systems.

Table 1. The maximum energy and H_2 equivalence yields obtained from two-stage and three-stage integrated systems

Stage type	Integrated reactors' configurations	Total gross energy of integrated systems [a] (kJ/g $sCOD_{added}$)		Yield Equivalences (Unit H_2/ unit C source) [a]	
		Gross	Net	g H_2/g sCOD	mol H_2/mol hexose
Three-stage systems	SBR-DF + Batch-M + Batch-PF	13.47	11.58	0.095	9.18
	SBR-DF + SBR-M + Batch-PF	16.11	14.11	0.110	10.80
	SBR-DF + SBR-M + SCR-PF	14.55	12.80	0.103	9.90
Two-stage systems	SBR-DF + Batch-M	14.64	13.03	0.103	9.90
	SBR-DF + Batch-PF	9.50	8.00	0.067	6.48
	SBR-DF + SBR-M	14.86	13.23	0.105	10.08

[a] Gross heating values; H_2: 141.8 kJ/g, CH_4: 55.58 kJ/g, Net heating values; H_2:119.47 kJ/g, CH_4: 49.98 kJ/g [7]

CONCLUSIONS

This study revealed that a novel three-stage system, composed of DF-M-PF in sequence, increased the energy obtained from unit organic matter by 7% to 50% compared to the studied two-stage DF-M and DF-PF systems and also theoretical values. More importantly, a methanogenesis stage integrated between DF and PF stages in a two-stage DF-PF system significantly improves the total energy yield, by 27-50%. The main role in energy production was found as M stage in a DF-M-PF system. Therefore, if it is aimed to improve the bioenergy obtained from unit organic matter in a DF-PF system, one should involve the methanogenesis stage and concentrate on optimization of this stage.

Three-stage systems have similar energy yields as that of DF-M systems; thus, seem to be less economical when the additional (a third) reactor's capital and operational costs are considered. However, in-depth economic analysis should also involve the expenses for the treatment of DF-M effluent required to improve the effluent characteristics to the discharge criteria. Three-stage systems would have lower effluent concentrations which will decrease the total operational/management costs. Three-stage systems might be of significance especially for high-strength (> 10 g/L COD) waste's operation, because the effluent of M stage would have higher carbon sources for the subsequent PF stage, which will have in turn higher H_2 yields and more significant role in total energy production.

ACKNOWLEDGEMENT

This study was funded by The Scientific and Technological Research Council of Turkey (TUBITAK), Project No: 112M252.

REFERENCES

1. Argun H and Kargi F. 2011. Bio-hydrogen production by different operational modes of dark and photo-fermentation: An overview. International Journal of Hydrogen Energy 36:7443-7459.
2. Das D and Veziroglu TN. 2008. Advances in biological hydrogen production processes. International Journal of Hydrogen Energy 33:6046-6057.
3. Guwy AJ, Dinsdale RM, Kim JR, Massanet-Nicolau J and Premier G. 2011. Fermentative biohydrogen production systems integration. Bioresource Technology 102:8534-8542.
4. Liu Z, Zhang C, Lu Y, Wu X, Wang L, Wang L and Han B. 2013. States and challenges for high-value biohythane production from waste biomass by dark fermentation technology, Bioresource Technology 135:292-303.
5. Erguder TH et al. 2015. The final report of the Project No. 112M252. The Scientific and Technological Research Council of Turkey (TUBİTAK), Ankara, Turkey.
6. Yokoi H, Maki R, Hirose J and Hayashi S. 2002. Microbial production of hydrogen from starch manufacturing wastes, Biomass and Bioenergy 22:389-395.
7. Lewandowski AD. 1999. Design of thermal oxidation systems for volatile organic compounds. Florida, CRC Press.

WHEC-2022
23rd World Hydrogen Energy Conference
June 26-30, 2022 - Istanbul

#26

INVESTIGATION OF H_2 AND CH_4 PRODUCTION FROM YARD WASTES VIA TWO-STAGE ANAEROBIC DIGESTION AT DIFFERENT PRE-TREATMENT OPTIONS AND SOLIDS CONCENTRATIONS

[1]*Nihan Nur Kalaycıoğlu*, [1]**Tuba Hande Ergüder*
[1]Middle East Technical University, Department of Environmental Engineering, 06800, Çankaya, Ankara

* Corresponding author e-mail: etubahan@metu.edu.tr

ABSTRACT

Yard waste, an abundant lignocellulosic biomass, was used as the substrate in a two-stage anaerobic digestion system (TSAD) conducted for hydrogen and methane production. The effect of initial solids concentration (2%, 5% and 8% Total Solids, TS) and pre-treatment options (alkaline, thermal and ultrasound) on H_2 or CH_4 production yield in TSAD were investigated. Batch experiments showed that the highest hydrogen production (30.5 mL H_2/g VS) was observed in alkaline pre-treated (AP) yard waste with 2% TS in the first-stage of TSAD. Alkaline pre-treatment was the best alternative for all three initial TS contents studied in terms of H_2 yields. The highest methane yield (around 40 mL CH_4/g VS), on the other hand, was obtained with thermal pre-treated (TP) yard waste with 2% TS in the second-stage of TSAD. Thermal pre-treatment improved the methane yield for all three TS contents. Overall, this study revealed that, despite the low yield levels, alkaline pre-treatment and 2% initial TS application provided the highest total energy gain from yard wastes in TSAD (2 MJ/kg VS_{addded}) followed by thermal pre-treatment. Independent of the pre-treatment type, the increase in TS contents decreases the yield and the energy production potential from yard wastes.

Keywords: Two-stage Anaerobic Digestion, Dark Fermentation, Biohythane, Yard Waste

INTRODUCTION

In the last two decades, global programs, working on alternative energy, are interested in new and sustainable energy sources since global economy cannot depend on fossil fuels anymore [1]. Biomass is one of the most important renewable energy sources. Yard waste is known as a high potential biomass source. It mainly consists of grass clippings, leaves, cut flowers, potted plants, weeds, bushes, branches and twigs [2]. In recent years, using yard wastes as biomass resource has been supported not only for its abundance but also its contribution to reduce greenhouse gas emissions, encourage regional economies, providing reliable biomass energy sources and limit the competition with food sources [3]. Yet, due to its lignocellulosic nature, pre-treatment or two-stage anaerobic digestion (TSAD) applications might be required for yard wastes to address their solubilization / biodegradability problem.

Hydrogen, has high energy content (141.8 kJ/g), which is 2.75 times higher than other hydrocarbons. For being a clean carbon-free fuel and generating only water after combustion, it is an effective option in researches to address global warming and increasing pollution problems [4]. In conventional anaerobic digestion, i.e. one-stage anaerobic digestion (OSAD), hydrogen can't be observed since it is degraded immediately to produce CO_2 and CH_4 [5]. However, H_2 can be generated individually by maintaining the proper engineering conditions. Lately, H_2 production through dark fermentation (DF) gained interest. The primary drawback is low energy recovery; because it does not reduce organic substrate totally and organic removal is below 20% which gives a low yield value of 10-20% [6]. To destruct all organic acids generated during DF and increase overall energy recovery, TSAD process, involving H_2 production by DF followed by CH_4 by methanogenesis is suggested [5;7]. TSAD is a relatively low-cost alternative to produce a mixture of H_2 (5-20%) and CH_4 (80-95%) labeled as "hythane", and in turn "biohythane" for being generated via biological means [8]. As an energy source, burning hythane is safer and cleaner than methane alone [9].

In this study, TSAD of yard waste (50% grass and 50%-yard trimmings, w/w) was investigated in terms of H_2 and CH_4 production yields. Three different pre-treatment options (alkaline, thermal and ultrasound) and initial total solids concentration (2%, 5% and 8% TS) were also integrated, in order to define optimum conditions leading to the highest energy production per unit solids.

MATERIALS AND METHODS

Inoculum and Substrate: Seed sludge (inoculum) used in all experiments was obtained from Greater Municipality of Ankara Wastewater Treatment Plant's anaerobic digestors. TS amount of inoculum is 6583±27 mg/L, VS is 51±1%. Yard wastes as the substrate, were gathered from METU Campus and sundried within the duties of METU Directorate of Construction and Technical Works. Foreign objects like plastic, branch and metal were sorted. Then,

grass and yard trimming wastes were dried at 40°C for 24 hours, in order to reduce moisture content less than 10% [10]. Size of wastes were reduced with food blender, ground in hammer mill and then screened from 20 mesh screen sieve. Grass and yard trimming wastes were then mixed with 1:1 ratio, sealed in plastic bags and stored at -20°C in order to prevent biological activity prior to use in all experiments. This dried and sieved waste mixture is defined as yard waste in the following text.

Pre-treatments: For alkaline pre-treatment (AP), 1 g yard waste was treated with 20 mL, 2% (w/v) NaOH solution. 5% (w/v) solids loading was achieved and pH was fixed at 12. This mixture was heated at 45°C for 30 minutes on a heater [11]. For thermal pre-treatment (TP), 1 g of yard waste is solubilized in 10 mL distilled water and heated at 120°C and 1.5 atm pressure in an autoclave for 30 minutes [12]. Ultrasound pre-treatment (UP) was done with an ultrasound bath (Sartorius Labsonic-P). The maximum power input of the sonicator was 400 W and sonication frequency was 24 kHz. For each TS% value, 1 g yard waste mixture was mixed with 40 mL distilled water. Without any temperature arrangement, sonication was experienced for 15 minutes.

TSAD experiments: In the first-stage of TSAD experiments, batch reactors with total volume of 110 mL and effective volume of 60 mL were used. Experiments were performed with four different batch set-ups, including blank, control and test reactors of raw and pretreated yard waste mixtures, individually. All reactors were composed of specified basal medium (BM) [13], pretreated or not-pre-treated yard waste with certain TS% amounts (2%, 5% and 8%) and inoculum. Inoculum was heat pre-treated for 1 hour at 105°C. Substrate/Inoculum ratio (S/I) was set as 4. Initial pH values were adjusted to 7. In the second-stage of TSAD (i.e. methanogenesis step), DF reactors were filtered and, these filtrates were used as substrate of methanogenesis stage. Batch reactors with 50 mL total volume and 30 mL effective volume were used. Proper amount of inoculum seed, basal medium and water were added in order to arrange S/I as 1 in the reactors. Initial pH values were set to 7. For both stages, after sealing with rubber stoppers, reactors were flushed with 100% N_2 gas for 5 minutes, placed on a shaker at 175 rpm in a hot room at 35±2°C. Daily biogas production and gas composition analyses were performed in order to determine the hydrogen and methane production potential of the reactors.

RESULTS AND DISCUSSION

- According to the results shown in Table 1, the highest H_2 yield was obtained with AP 2% test reactor as 30.5 mL H_2/g VS in the first-stage of TSAD. As solids percentage increases, H_2 yields generally decrease. AP was found as the best alternative in producing high H_2 yields from yard wastes for all solid contents studied.
- Maximum H_2 yield increases were obtained for 2% TS in all pre-treatment options. Compared to no pre-treatment (NP) case, AP increased H_2 yields for 2%, 5% and 8% TS by 73%, 48% and 85.5%, respectively.
- CH_4 production was also observed during DF in all test reactors, indicating the ineffective heat pre-treatment of inoculum and also intrinsic microorganisms potential to exist in the yard waste mix and contributing to CH_4 generation. Hydrogenotrophic methanogenesis as well as homoacetogenesis might have led to lower H_2 yields.
- For all three solid concentrations, the highest methane yield (~ 40 mL CH_4/g VS) was obtained with TP 2% test reactor in the second-stage. TP was found as the best alternative among others in terms of CH_4 yields. However, obtained CH_4 yield results are very low, compared to the theoretical methane yield (395 mL CH_4/g VS). This was attributed to the potential inhibitory by-products of DF and pretreatment methods, which remains to be researched.
- Overall, cumulative yield data shows that AP 2% reactor provides the optimum total energy gain in TSAD with yard waste, since there was additional methane production coming from the first-stage of TSAD, originated from intrinsic microorganisms which has not been exposed to heat pre-treatment.

CONCLUSIONS

This study revealed that alkaline pre-treatment is the optimum option leading to the highest H_2 production yields compared to thermal and ultrasound pre-treatment options. Alkaline pre-treatment improved the H_2 yields by 48-85% compared to the no pre-treatment case. The filtered effluent of the first-stage of TSAD, i.e. DF step, was used as the substrate of the second-stage (i.e. methanogenesis). In second-stage, thermal pre-treatment was found as the option leading to the highest CH_4 production for all three TS concentrations studied. Yet, it should be noted that the total CH_4 production from alkaline pre-treated waste was even greater than that of thermal pre-treated waste, because methane was also observed during DF step. Nevertheless, the total energy obtained from two-stage anaerobic digestion of yard waste achieved 0.3-2.00 MJ/kg VS_{added} of energy production. The highest total energy production per unit solids was obtained in alkaline pre-treated yard waste with 2% TS content. This study also revealed that lower initial solids concentrations (2% TS) enable to apply all pre-treatment options efficiently; but at higher TS%, gaining feasible yields and, in turn, energy productions become harder.

Table 1. Cumulative hydrogen and methane yields and related energy productions in each reactor type

Pre-treated yard waste [a]	TS, %	Yields (mL H_2 or CH_4 /g VS)			Energy (MJ/kg VS $_{added}$) [b]		
		1st stage, H_2	1st stage, CH_4	2nd stage, CH_4	from H_2	from CH_4	Total
NP	2	8.3	38.1	3.0	0.1	1.4	1.5
	5	5.1	2.4	2.9	0.1	0.2	0.3
	8	1.6	1.3	0.7	0.1	0.2	0.3
AP	2	30.5	37.3	11.4	0.3	1.7	2.0
	5	9.9	14.2	9.7	0.1	0.8	0.9
	8	11.4	6.3	8.5	0.1	0.5	0.6
TP	2	10.2	1.6	39.9	0.1	1.5	1.6
	5	5.2	2.3	33.1	0.1	1.3	1.4
	8	2.9	2.0	29.9	0.1	1.1	1.2
UP	2	12.6	4.9	19.5	0.2	0.7	0.9
	5	4.5	4.4	12.5	0.2	0.6	0.8
	8	6.9	1.1	13.05	0.1	0.5	0.6

[a] NP: Not pre-treated, AP: alkaline pre-treated, TP: Thermal pre-treated, UP: Ultrasound pre-treated yard wastes.
[b] Gross heating values of H_2 and CH_4 are 141.8 kJ/g and 55.58 kJ/g, respectively [5].

ACKNOWLEDGEMENT

This study is supported by the Scientific and Technological Research Council of Turkey (TUBİTAK) (Project No: 118Y359).

REFERENCES

1. Bhowmick GD, Sarmah A and Sen R. 2018. Lignocellulosic biorefinery as a model for sustainable development of biofuels and value added products, Bioresource Technology, 247:1144–1154.
2. Environment Bureau. 2014-2022. A Food Waste & Yard Waste Plan for Hong Kong.
3. Coyle WT. 2011.Next-generation biofuels: Near-term challenges and implications for agriculture. USDA, 41–74.
4. Ghimire A, Frunzo L, Pirozzi F, Trably E, Escudie R, Lens PNL and Esposito G. 2015. A review on dark fermentative biohydrogen production from organic biomass: Process parameters and use of by-products. Applied Energy, 144:73–95.
5. Lewandowski AD. 1999. Design of Thermal Oxidation Systems for Volatile Organic Compounds. CRC Press, Florida, 58-59.
6. Li Q., Li Y., 2019. Coproduction of hydrogen and methane in a CSTR-IC two-stage anaerobic digestion system from molasses wastewater. Water Science and Technology, 79(2):270–277.
7. Das D., Veziroğlu T.N., 2001. Hydrogen production by biological processes: a survey of literature. International Journal of Hydrogen Energy, 26(1):13–28.
8. Pakarinen O, Lehtomäki A and Rintala J. 2008. Batch dark fermentative hydrogen production from grass silage: The effect of inoculum, pH, temperature and VS ratio. International Journal of Hydrogen Energy, 33(2):594–601.
9. Liu Z, Zhang C, Lu Y, Wub X, Wangb L, Wang L, Han B and Xing X. 2013. States and challenges for high-value biohythane production from waste biomass by dark fermentation technology. Bioresource Technology. 135:292–303
10. Ueno Y, Tatara M, Fukui H, Makiuchi T, Goto M and Sode K. 2007. Production of hydrogen and methane from organic solid wastes by phase-separation of anaerobic process. Bioresource Technology 98:1861–1865.
11. Lin L, Yang L, Xu F, Michael Jr and Li Y. 2014.Comparison of solid-state anaerobic digestion and composting of yard trimmings with effluent from liquid anaerobic digestion. Bioresource technology. 169:439-446.
12. Ozkan L, Erguder TH and Demirer GN. 2011. Effects of pretreatment methods on solubilisation of beet-pulp and bio-hydrogen production yield, International Journal of Hydrogen Energy, 36, 382-389.
13.Tunçay EG. 2015. Investigating the operational conditions for enhancement of dark fermentative hydrogen production in batch and sequencing batch reactors. MSc Thesis, Middle East Technical University, June 2015.

WHEC-2022
23rd World Hydrogen Energy Conference
June 26-30, 2022 - Istanbul

#52

A THERMOSIPHON BASED PHOTOBIOREACTOR FOR PHOTOFERMENTATIVE HYDROGEN PRODUCTION

[1] Bovinille Anye Cho, [1] Calizé Bosman, [1]Steven Bradshaw [1] Robert W. M. Pott*
[1]Department of Process Engineering, Stellenbosch University, South Africa

*Corresponding author e-mail: rpott@sun.ac.za

ABSTRACT

Photofermentation is a process driven by, primarily, anaerobic photosynthetic bacteria. Significant advances have been made in the field with regards hydrogen productivity using these organisms, however, comparatively little work has been to develop reactors optimised for photofermentation. This paper presents a novel photobioreactor, designed with anaerobic photosynthetic organisms in mind: the thermosiphon photobioreactor (TPBR). This reactor utilises absorbed light to drive passive circulation, potentially reducing operating costs, and allowing for continuous hydrogen production. The prototype reactor's thermal and hydrodynamic performance was investigated using Computational Fluid Dynamics (CFD) and validated with experimentation. Using *Rhodopsueduomonas palustris* as an exemplary photofermentative organism, the TPBR operation was demonstrated at laboratory scale. Hydrogen production and bacterial growth were shown to be in line with that seen in test bioreactors. The CFD results demonstrated good agreement with experimental data, indicating that the model has functionality in predicting fluid operation in this reactor. Further, the TPBR demonstrated excellent liquid circulation with up to 88% of the microbial cells kept in free suspension, using only passive circulation. The TPBR is demonstrated as an anaerobic photobioreactor system entirely agitated using passive circulation, which has the potential to be used as a low energy-input reactor for photosynthetic organism cultivation.

Keywords: Thermosiphon Photobioreactor (TPBR), Photosynthetic Bacteria, Biohydrogen, Photofermentation

INTRODUCTION

The photosynthetic bacterium *Rhodopseudomonas palustris* demonstrates an exceptional metabolic diversity, consuming many compounds which other organisms find toxic [1]. Its metabolism makes it useful for the degradation of recalcitrant organic wastes, and the purification of industrial waste waters. Furthermore, it is robust and is therefore an attractive organism for use in industrial bioprocesses. *R. palustris* combines its metabolic diversity with the ability to produce high purity hydrogen, through the action of the enzyme nitrogenase. This biohydrogen can then be used in fuel cell for the production of electricity, or other hydrogen reliant processes [2,3].

Hydrogen is regarded as a clean, high energy fuel and is particularly useful in fuel cells owing to very high conversion efficiencies. Currently most hydrogen is produced by steam reforming of natural gas, which, rather than reducing the use of fossil fuels and carbon emissions, merely shifts them to an earlier production step[4]. Therefore methods for producing hydrogen which are not dependent on fossil feed-stocks are needed, such as the reforming of biomass, the electrolysis of water and biological hydrogen production [5].The biological production of hydrogen has a number of advantages over the biological production of other fuels and chemicals. For example, it circumvents the problem of producing a dilute aqueous product stream, which then requires significant purification, likely to be needed if the substrate were converted to liquid-phase products in a biological process, such as ethanol, or butanol. Hydrogen is relatively insoluble in water and so partitions almost entirely into the gas phase, significantly reducing purification costs compared with the production of a soluble biochemical [6,7].

Since its photometabolism is significantly different to that of microalgae (for which most photobioreactors (PBRs) are designed), a novel PBR can be designed to optimize hydrogen production and waste organics degradation. Because the metabolism of *R. palustris* requires incident light to drive the reformation of organic compounds to hydrogen, we can use this absorption as a driver for fluid mixing, utilising the thermosiphon effect, which is the physical effect of fluid flowing because of density differences due to temperature effects. The design of a PBR on the thermosiphon effect has not been described in the literature previously, although thermosiphons are commonly utilised in solar water heating systems [8,9].

This paper aims to demonstrate the utility of a novel photobioreactor, which utilises the thermosiphon effect to drive passive circulation, for the cultivation of anaerobic photosynthetic bacteria. A CFD tool is developed to understand the fluid flows, velocities and temperatures in the reactor, and experiments are conducted to examine the hydrogen production and cell circulation developed in the reactor.

MATERIALS AND METHODS

Bacteria and culture methods

Rhodopseudomonas palustris strain NCIB 11774 was obtained from ATCC (ATCC® 17007™) and grown in modified *Rhodospirillacea* minimal medium consisting of (/L): 0.57g KH2PO4, 1.86g K2HPO4, 0.4g NaCl, 0.2g yeast extract, 0.25g Na2S2O3.5H2O, 0.2g MgSO4.7H2O, 0.05g CaCl2.2H2O, 0.005g Ferric citrate, 0.002g para-aminobenzoic acid. Growth medium was adjusted to pH 7.2 before autoclaving, with subsequent addition of sterile glycerol and glutamate and 1ml per litre trace element solution as per [7].

Test Photobioreactor setup

Cultures were grown in 500 ml bioreactors comprised of borosilicate reagent bottles and lids fitted with gastight stainless-steel liquid and gas sampling tubes; sterilised by autoclave. Anaerobic conditions were induced by sparging cultures with argon through a 0.2 µm PTFE filter for 10 min. Agitation was provided by magnetic stirring at ±200 RPM with 50mm PTFE coated stirrer bars and illumination by 100W tungsten-filament incandescent lightbulbs. Irradiance intensity was calibrated to 200 W/m2 (± 20) in the wavelengths between 500 – 1100 nm, corresponding to the range utilised by *R. palustris*, using a compact spectrometer with cosine correcting probe (RGB photonics Qmini VIS-NIR). Temperature was controlled by immersion of bioreactors in a water-filled glass tank fitted with heating circulator and cooling as required to maintain temperature at 35°C ± 0.2°C. Gas produced was collected by displacement of water in inverted 1L measuring cylinders connected to each gas sampling port with low hydrogen-permeability tubing (Tygon E-3603, Saint-Gobain) and one-way check valves.

TPBR prototype setup and operation

A 1-L working volume laboratory scaleTPBR was designed and fabricated from glass (denoted in Figure 1), adapted from thermosiphon designed for solar water heating, and that published by [8]. Specifically the reactor was modified to meet the purpose of photosynthetic microorganism cultivation. For significantly more detail see: [10].

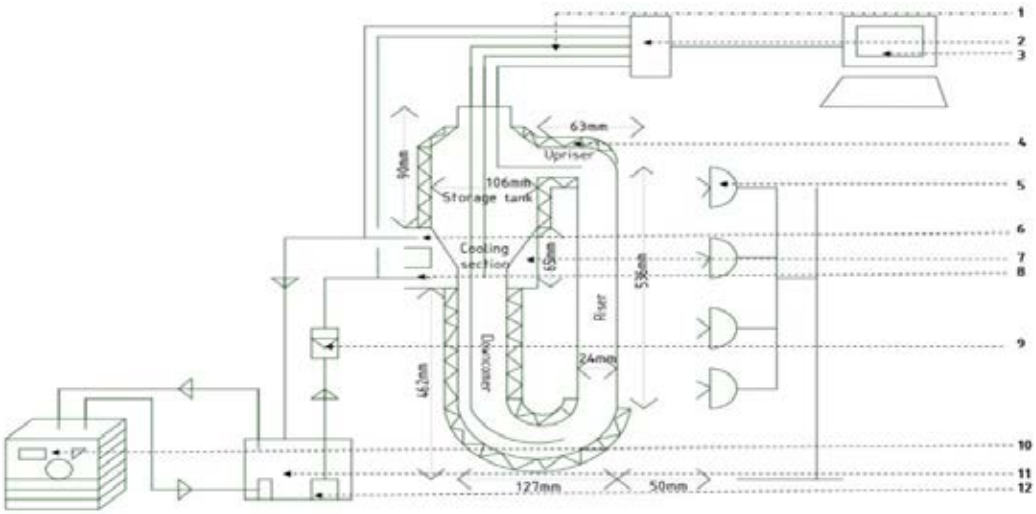


Figure 1: Schematic diagram of the experimental setup: (1) Thermocouples, (2) Data acquisition unit, (3) Computer, (4) Thermal insulation (5) Halogen lamps, (6) Cooling water outlet, (7) Cooling water inlet, (8) cooling section (9) Rotameter, (10) water Chiller, (11) Reservoir, and (12). Submersible water pump.

Circulation experiments were conducted with water, and heat treated bacterial cells, to determine temperature and velocity gradients within the TPBR. Additionally, growth and hydrogen production experiments were conducted with living *R. palustris*, at an initial loading rate of Kg/m^3. Illumination was provided by four halogen lamps (150 watt each, EUROLUX FS13B), to simulate sunlight. These lights illuminated the riser. Cooling was provided by a cooling jacket with circulating cooled water at 0.5L/min, 17°C. The thermocouples (RTD, PT100, Simplex, and Class A) within the reactor were connected to a 4 channel data-acquisition unit (WIKA Instruments REB(TR40)) with data recorded at intervals of 60s. Gas production was monitored via an inverted measuring cylinder in water, and the gas composition determined using gas chromatography. The biomass concentration was determined using optical density measurements at 660nm, tracked against a cell dry weight-OD calibration curve.

RESULTS AND DISCUSSION

The results of the CFD simulations adequately represented the physical thermosiphon experimentation.
shows the flow profile within the TPBR, with the greatest

velocity achieved at the light-side wall – unsurprisingly, as this is the area where most light energy is converted into heat, giving rise to the thermosiphon buoyancy effect. The simulation indicates that the circulation velocity is sufficient for biomass circulation; a finding which is strengthened by experiments in the laboratory scale thermosiphon showing good cell circulation. Nonetheless, there are potential limitations; for instance, if the thermosiphon operates on sunlight, then during the night the thermosiphon effect will dissipate, fluid will no longer circulate, and the cells will settle.

In this work, CFD modeling and experiments have been used to support the development of a thermosiphon photobioreactor (TBPR), where fluid circulation is achieved by temperature difference arising from light absorption.

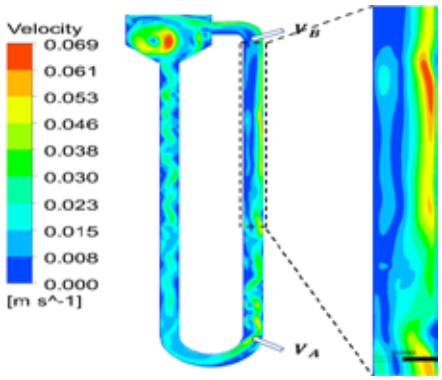


Figure 2: Velocity contours of the CFD simulations showing the two velocity notation points and the riser's flow profile.

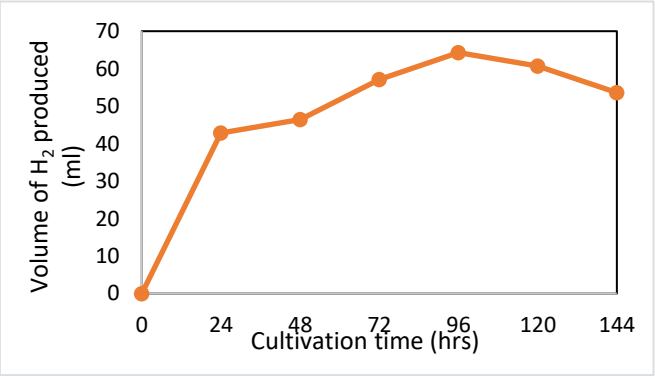


Figure 3: hydrogen production within the TPBR by *R. palustris* cultivated on 50mM glycerol

The hydrogen production of *R. palustris* in the TPBR compares well with that in normal test photobioreactors, with specific hydrogen production rates of around 5 $ml.g_{DCW}^{-1}.h^{-1}$. Indeed the hydrogen production appeared to improve cell circulation, by hydrogen bubbles coming out of solution in the riser, and adding to the heat-aided buoyancy effect. A larger scale TPBR has been fabricated, and is currently under assessment for its passive circulation with and without photofermentative bacteria present – instead of a cooling loop, in this larger reactors' case a set of metal cooling fins has been used (a more water-wise solution to cooling); similar velocities have been achieved in this reactor.

CONCLUSIONS

This paper has outlined the development, fabrication, experimentation and modeling of a novel photobioreactor, designed for use with photofermentative bacteria: the thermosiphon photobioreactor. The reactor was successfully fabricated, tested, and modelled using CFD, with good agreement between modelled and experimental validation. Sufficient flow velocities are achieved, within the temperature limits of the organism, and using simulated sunlight, for cell suspension. Hydrogen production experiments have shown the organisms continue to produce hydrogen at a comparable rate in these reactors, as opposed to normal test photobioreactors. Larger scale experiments indicate good cell circulation when using heating fins instead of cooling water, and these larger TPBRs have shown good hydrogen production under environmental conditions.

REFERENCES

1. Pott RWM, Howe CJ, Dennis JS. Photofermentation of crude glycerol from biodiesel using Rhodopseudomonas palustris: Comparison with organic acids and the identification of inhibitory compounds. Bioresour Technol 2013;130:725–30.
2. Keskin T, Abo-hashesh M, Hallenbeck PC. Bioresource Technology Photofermentative hydrogen production from wastes. Bioresour Technol 2011;102:8557–68.
3. Hallenbeck PC, Ghosh D. Advances in fermentative biohydrogen production: the way forward? Trends Biotechnol 2009;27:287–97.
4. Dincer I, Acar C. Review and evaluation of hydrogen production methods for better sustainability. Int J Hydrogen Energy 2015;40:11094–111.
5. Crabtree GW, Dresselhaus MS, Buchanan M V. The hydrogen economy. Phys Today 2004:39–44.
6. Ghosh D, Tourigny A, Hallenbeck PC. Near stoichiometric reforming of biodiesel derived crude glycerol to hydrogen by photofermentation. Int J Hydrogen Energy 2011:2–6.
7. Pott RWM, Howe CJ, Dennis JS. Photofermentation of crude glycerol from biodiesel using Rhodopseudomonas palustris: Comparison with organic acids and the identification of inhibitory compounds. Bioresour Technol 2013;130.
8. Close DJ. The performance of solar water heaters with natural circulation. Sol Energy 1962;6:33–40.
9. Ozgener O, Hepbasli A. A review on the energy and exergy analysis of solar assisted heat pump systems. Renew Sustain Energy Rev 2007;11:482–96.
10. Cho BA, Pott RWM. The development of a thermosiphon photobioreactor and analysis using Computational Fluid Dynamics (CFD). Chem Eng J 2019;363:141–54.

WHEC-2022
23rd World Hydrogen Energy Conference
June 26-30, 2022 - Istanbul

#114

GREEN HYDROGEN PRODUCTION FROM THE NON-CENTRIFUGAL SUGAR INDUSTRY

[1] Nestor Sanchez, [1] David Rodríguez-Fontalvo, [1] Nelly M. Cantillo, [2] Ruth Y. Ruiz-Pardo, [1] Martha Cobo*
[1]Group of Energy, Materials, and Environment. Universidad de La Sabana, Faculty of Engineering, Department of Chemical and Biochemical Processes. km 7 Autopista Norte Bogotá-Chía, Campus Universitario Puente del Común. Chia, Colombia
[2] Group of Agro-industrial Processes, Faculty of Engineering, Department of Chemical and Biochemical Processes. km 7 Autopista Norte Bogotá-Chía, Campus Universitario Puente del Común. Chia, Colombia

*Corresponding author e-mail: nestor.sanchez1@unisabana.edu.co

ABSTRACT

Decarbonizing the economy has become one of the main concerns in Colombia, where hydrogen (H_2) plays an outstanding role. H_2 is obtained through different pathways, including water electrolysis or by thermochemical pathways such as the ethanol steam reforming (ESR). The latter process is an interesting alternative for those areas where residual biomass is highly available. The non-centrifugal sugar agroindustry has an important role in the Colombian economy and produces different residual biomass that can be employed to produce H_2 by coupling alcoholic fermentation and ESR. Herein, the technical and environmental assessment of the conversion of sugarcane press-mud, a residual biomass of this sector, into H_2 was performed. Technical analysis revealed that sugarcane press-mud should be pretreated under hydrothermal conditions and fermented with a pH of 4.5 to decrease fusel alcohol which have a negative impact during ESR. In terms of environmental impact, H_2 could be used as energy vector to produce heat and replace sugarcane bagasse to mitigate greenhouse gases emissions. Therefore, the upgrading of sugarcane press-mud into H_2 will have a positive impact on climate change and this technology could be employed to decarbonize the Colombian economy.

Keywords: Bioethanol, HT-PEMFC, Life Cycle Assessment, Power, Steam Reforming.

INTRODUCTION

Overcoming the issues associated with climate change is aligned with the United Nations agenda and Sustainable Development Goals (SDG). Indeed, SDG 7 seeks to ensure access to affordable, reliable, sustainable, and modern energy for all. In addition, one of the main targets of SDG 7 is: *"By 2030, expand infrastructure and upgrade technology for supplying modern and sustainable energy services for all in developing countries".* Recently, Colombia stablished the Energy National Plan 2020-2050 that aims to move towards into a clean energy system where hydrogen (H_2) has become the main actor in the energy transition [1]. H_2 is an energy vector that could be employed to produce either heat or power without direct emissions of greenhouse gases by using fuel cells. These devices are affordable for rural areas where power grid is unavailable [2]. H_2 could be produced by water electrolysis boosted by solar and wind power. However, in areas where solar and wind are scarce, the use of other sources could be employed. Colombia, as an agricultural country, produces larger amount of residual biomass that could be upgraded into H_2. Among agro-industrial sectors, non-centrifugal sugar plays an outstanding role within the social and economic development of Colombia. During non-centrifugal sugar production, different residual biomass is yielded, including leaves, buds, bagasse, and sugarcane press-mud. The latter has been used for producing H_2 by coupling alcoholic fermentation and ethanol steam reforming (ESR), where the yields ranged between 4.0 to 6.0 g H_2/kg sugarcane press-mud [3]. One of the main issues associated with the conversion of biomass to H_2 by ESR is the presence of impurities (e.g., fusel alcohol and acetic acid) that limit the conversion of ethanol [4]. Hence, it is key to develop alternatives to mitigate those compounds to enhance H_2 by ESR. Recently, we assessed the effect of both pre-treatment and fermentation conditions on the production of bioethanol for its further conversion into H_2. According to those preliminary results, addition of nitric acid had a strong influence on the production of impurities during sugarcane press-mud fermentation [3]. Besides, the pH during fermentation also had an effect on the formation of impurities [4]. Based on the above, the next step is to design the complete process to produce H_2 from sugarcane press-mud with aim to be used in a non-centrifugal sugar facility. Therefore, the aim of this study was to determine the environmental benefits on the use of H_2 within a non-centrifugal sugar facility.

MATERIALS AND METHODS

Bioethanol production

Bioethanol was obtained through the pretreatment, fermentation, and distillation of sugarcane press-mud by using a stainless-steel Alembic of 24 L. The alembic was coupled with a stirrer. Two factors were assessed: type of pretreatment (i.e., hydrothermal and acid hydrolysis) and pH of fermentation (i.e., 4.5 and 5.5). Pretreatment of sugarcane press-mud was carried out at 70 °C for 2 h. Afterwards, alembic was cooled down, and supplemented with nutrients, as reported elsewhere [3]. Fermentation was performed using a *S. cerevisiae* yeast strain, previously propagated and activated in

YPD (yeast extract 10 g/L, peptone 20 g/L, and glucose 20 g/L), at room temperature and 200 rpm for 42 h. After fermentation, bioethanol was distilled until the steam-to-ethanol ratio was 4.2:1.0. Ethanol concentration was monitored using a digital refractometer (Anton Paar, Graz, Austria). Fusel alcohol was quantified by gas chromatography (GC) [4].

Syngas production and environmental analysis

Syngas production was carried out in a pilot plan scale which is formed by two reactors in series. The former reactor converts the bioethanol into syngas at 750 °C over a washcoated monolith of $RhPt/CeO_2$-SiO_2. The second reactor removes the carbon monoxide at 260 °C over a washcoated monolith of $AuCu/CeO_2$. Syngas was quantified by GC [5]. Environmental analysis was carried out through the Life Cycle Assessment (LCA) and following the ISO 14040/14044 guidelines [6]. The aim of the LCA is to determine the environmental benefits on the use of H_2 for the non-centrifugal sugar agro industry. Hence, the functional unit was set to 1 ton of non-centrifugal sugar. Life cycle inventory was gathered from interviews in a non-centrifugal sugar facility and experimental data obtained at pilot plant scale level. Impacts were calculated in terms of carbon footprint by using the ILCD midpoint methodology impact assessment.

RESULTS

Bioethanol production

Table 1 shows the ethanol profile after the pretreatment, fermentation, and distillation of sugarcane press-mud. According to Table 1, sample S3, which was pretreated under acid hydrolysis conditions and fermented with a pH of 4.5, delivered both the lowest ethanol (6.05 wt.%) and fusel alcohol concentration (631.8 ppm). While sample S2 yielded the highest ethanol concentration with low fusel alcohol concentration in comparison with the other samples. Sample S2 was pretreated under hydrothermal conditions and fermented at a pH of 4.5. Under acid hydrolysis conditions, H^+ boosts the decomposition of sucrose into glucose. Besides, the formation of organic acids, such as acetic acid, uronic acid, and formic acid, are also yielded. Those acids affect the central metabolism of yeast, and consequently reduce the ethanol concentration [4], [7]. Concerning the formation of fusel alcohol, at low pH values, fusel alcohol formation is inhibited since the key enzymes involved in the Ehrlich metabolic pathway are strongly affect under acidic conditions [8]. Therefore, sugarcane press-mud should be pretreated under hydrothermal conditions and fermented at a pH of 4.5 to produce a bioethanol stream with high ethanol content and less fusel alcohol concentration.

Table 1. Bioethanol profile after distillation

Sample	**S1**	**S2**	**S3**	**S4**
Pretreatment	Hydrothermal	Hydrothermal	Acid hydrolysis	Acid hydrolysis
Fermentation pH	5.5	4.5	4.5	5.5
Ethanol (wt.%)	6.86	7.20	6.05	6.78
Fusel alcohol (ppm)	810.5	793.8	631.8	807.1

Syngas production and environmental analysis

Syngas was obtained through ESR in a pilot plant scale. The H_2 yield was 3.2 mol H_2/mol ethanol whose composition at 750 °C was 29.5 mol.% H_2, 8.4 mol.% CO, 11.6 mol.%, CH_4, 0.1 mol.% CO_2, and 50.4 mol.% N_2. Afterwards, CO was removed at 260 °C, and the clean syngas composition was 25 mol.% H_2, 13 mol.% CH_4, 17 mol.% CO_2, and 45 mol.% N_2. This clean syngas could be fed into a HT-PEMFC to produce power that could substitute the fossil energy used during sugarcane milling or to be used as heat source to avoid the use of sugarcane bagasse. Environmental analysis is shown in Figure 1. Accordingly, non-centrifugal sugar industry has a carbon footprint of -2.57 kg CO_2-eq/kg non-centrifugal sugar. The negative value indicates environmental savings due to the carbon capture during sugarcane growth in the harvest stage. However, the upgrading of sugarcane press-mud into H_2, for its further use as energy source to avoid the use of diesel, will result in a higher carbon footprint. Furthermore, Figure 1 also shows that using H_2 as heat source to avoid the use of sugarcane bagasse will result in 5% environmental savings, since greenhouse gases are not directly emitted to the atmosphere. Hence, the upgrading of sugarcane press-mud into H_2 will have environmental benefits in the non-centrifugal sugar facility.

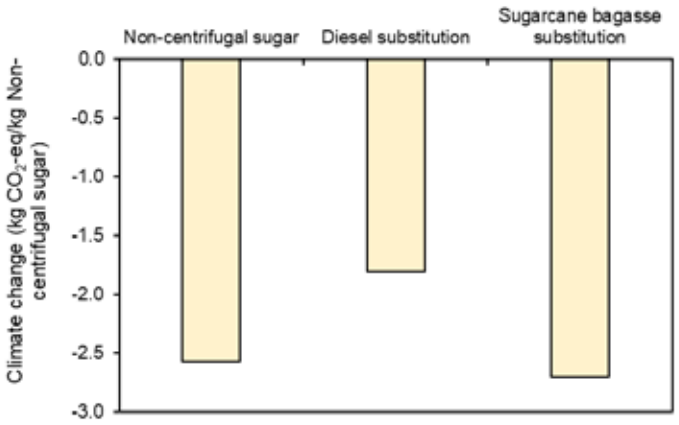


Figure 1. Climate change on the use of H_2 in a on-centrifugal sugar facility

CONCLUSIONS

Conversion of sugarcane press-mud into H_2 by coupling alcoholic fermentation and ethanol steam reforming would have a positive environmental impact if H_2 is directly employed as thermal source. Further studies must seek to design a complete non-centrifugal sugar facility where H_2 is integrated as energy vector. Besides, alternatives on the valorization of other residual biomass would be determined in order to move towards a low-carbon economy.

ACKNOWLEDGEMENT

The authors are grateful to Panelas Don Pedro for supplying the sugarcane press-mud samples. This research was funded by Minciencias and Universidad de La Sabana, project number ING 221 (Minciencias contract 548-2019). The doctoral scholarship granted to Nestor Sanchez was funded by Minciencias, grant number 727-2015.

REFERENCES

1. Unidad de Planeación Minero-Energética Nacional, “Plan Energético Nacional 2020 - 2050,” 2019.
2. S. Mekhilef, R. Saidur, and a. Safari, “Comparative study of different fuel cell technologies,” *Renew. Sustain. Energy Rev.*, vol. 16, no. 1, pp. 981–989, 2012, doi: 10.1016/j.rser.2011.09.020.
3. N. Sanchez, R. Ruiz, A. Plazas, J. Vasquez, and M. cobo, “Effect of pretreatment on the ethanol and fusel alcohol production during fermentation of sugarcane press-mud,” *Biochem. Eng. J.*, p. 107668, 2020, doi: https://doi.org/10.1016/j.bej.2020.107668.
4. N. Sanchez, M. Cobo, D. Rodriguez-fontalvo, M. Á. Uribe-laverde, and R. Y. Ruiz-pardo, “Bioethanol Production from Sugarcane Press-Mud : Assessment of the Fermentation Conditions to Reduce Fusel Alcohol,” *Fermentation*, vol. 7, pp. 194–215, 2021.
5. B. Cifuentes, F. Bustamante, D. G. Araiza, G. Diaz, and M. Cobo, “Hydrogen purification of actual syngas streams for energy applications: Au-Cu supported over nano-shaped CeO2 as stable catalysts for the carbon monoxide removal,” *"Applied Catal. A, Gen.*, vol. 598, no. April 2020, p. 117568, 2020, doi: 10.1016/j.apcata.2020.117568.
6. A. Roedl, “Production and energetic utilization of wood from short rotation coppice-a life cycle assessment,” *Int. J. Life Cycle Assess.*, vol. 15, no. 6, pp. 567–578, 2010, doi: 10.1007/s11367-010-0195-0.
7. L. J. Jönsson and C. Martín, “Pretreatment of lignocellulose : Formation of inhibitory by-products and strategies for minimizing their effects,” *Bioresour. Technol.*, vol. 199, pp. 103–112, 2016, doi: 10.1016/j.biortech.2015.10.009.
8. K. Pielech-Przybylska, M. Balcerek, U. Dziekońska-Kubczak, P. Patelski, and M. Różański, “Effect of starch liberation method and initial pH of sweet mashes on higher alcohols content in distillates obtained from different starchy raw materials,” *Process Biochem.*, vol. 73, no. August, pp. 29–37, 2018, doi: 10.1016/j.procbio.2018.08.014.

WHEC-2022
23rd World Hydrogen Energy Conference
June 26-30, 2022 - Istanbul

#136
A PRELIMINARY TECHNO-ECONOMIC ANALYSIS OF PHOTOBIOLOGICAL HYDROGEN PRODUCTION

[1] Şehnaz Genç, [2] Harun Koku*
[1]Eskişehir Technical University, Department of Chemical Engineering, İki Eylül Kampüsü, Tepebaşı, 26555 Eskişehir, Turkey
[2] Middle East Technical University, Department of Chemical Engineering, Dumlupınar Bulv. No. 1, 06800 Ankara, Turkey

*Corresponding author e-mail: harunk@metu.edu.tr

ABSTRACT

Photofermentation of cheap feedstock using sunlight is a promising route for sustainable hydrogen production. While successful laboratory and pilot-scale hydrogen production examples have been demonstrated, the economic feasibility remains to be improved. In this study, a preliminary techno-economic analysis of photobiological hydrogen production was performed, taking into consideration current production technologies.

First, several hydrogen production technologies were investigated and their costs were compiled from literature. The results show that conventional steam reforming of natural gas still offers the least cost. Future trajectories and prices for natural gas were investigated worldwide and for Turkey. In view of the fact that natural gas is a fossil-fuel, predictions show a continuously increasing unit price.

The cost of photobiological hydrogen production was based on an existing outdoor, pilot-scale photobioreactor design. The annual capital cost and operating costs of the plant were calculated as 195 USD/year and 33 USD/year, respectively. Overall, the specific hydrogen production cost was found as 3.8 USD/mol (1890 USD/kg H_2). While this cost is currently unfeasible, it can be decreased via the use of more productive strains combined with valorization of side-products and concurrent treatment of waste.

Keywords: Photofermentation, Biohydrogen, Economic Analysis

INTRODUCTION

Hydrogen is a clean and efficient energy carrier. The energy stored in the hydrogen can be extracted via several devices such as boilers, turbines, internal combustion engines or fuel cells. However for a viable and sustainable hydrogen economy, hydrogen has to be produced using renewable resources. Hydrogen can be produced biologically and renewably using several different types of microorganisms. Photofermentative production using purple non-sulfur bacteria (PNSB) is favorable because of its high theoretical conversion yield, high purity of produced hydrogen, the capability of PNSB to use a wide portion of the light spectrum and their ability to utilize wastes. Pilot-scale photobiological hydrogen production has been demonstrated using both suspension [1] and immobilized [2] cultures. However, to obtain better insight on the prospects of this method, an economic analysis is also necessary. This study highlights the results of a preliminary cost analysis for this purpose.

METHODS

Cost Estimation Methodology

The method utilized by Urbaniec and Grabarczyk [3] was adopted for this study. The fixed and capital costs are evaluated to estimate the price per unit of product, which in this case is hydrogen. The fixed component of the costs includes land and equipment, whereas the operating cost includes maintenance, power and raw materials.

Case Study

An existing 20 L pilot-scale photobioreactor system was selected as the model. The glass reactor has a stacked U-tube geometry, and is combined with a circulation pump, a cooler and a gas collector to constitute a compact, integrated system that can operate outdoors. The bacterial species is R. capsulatus, and the carbon source for hydrogen production is molasses, which is a sugar-rich carbon source that also includes essential nutrients such as amino acids and iron. The molasses is diluted to a concentration of 5 mM sucrose, based on previous studies [1].

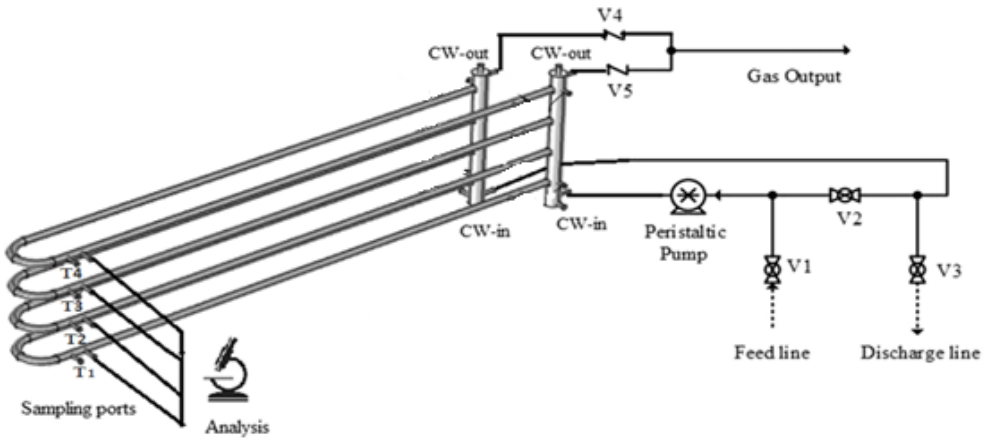


Fig. 1. The Photobioreactor Setup

Assumptions and Data

The reactor setup is assumed to occupy 200 m^2 on non-arable land. All cost data were based on market prices for Turkey. For the photobioreactor system components, the costs were based on the existing custom-manufactured pilot-scale glass photobioreactor, and off-the-shelf prices for the pump and chiller unit. The operating costs are for the electricity used to operate the chiller and the pump, and the water cost to dilute the molasses. The cooling duty of the chiller was based on the incident solar radiation during summer months and a coefficient of performance based on the Carnot efficiency. A life of 15 years was assumed for the plant. The total plant cost was estimated as the sum of the land and equipment costs, i.e. the Lang factor was assumed to be 1.0.

RESULTS AND DISCUSSION

The results of the analysis are summarized in the Table 1 below. Annual capital cost was calculated from the land price and total equipment price as 800 USD/year, whereas the operating cost, composed of maintenance, water, power, chemicals and molasses feedstock was 34 USD/year. Based on our prior studies, a hydrogen production rate of 0.17 mol/day can be achieved in a 20 L reactor operating under natural sunlight. As a result, specific hydrogen production cost was found as 3.8 USD/mol or 1890 USD/kg H_2.

Table 1. Summary of Cost Estimation

Specific Hydrogen Cost	Fixed Capital Cost (195 USD/year)	Total Equipment Cost (2900 USD)
		Land Price (34 USD)
(1890 USD/kg H_2)	Operating Cost (34 USD/year)	Maintenance Cost (16 USD/year)
		Power Cost (2.6 USD/year)
		Chemical Cost (11 USD/year)
		Molasses (4 USD/year)
		Water (0.15 USD/year)

CONCLUSIONS

Compared with current technologies, it is obvious that if photofermentative hydrogen production is to become an economically viable path, the unit cost needs to be decreased considerably, even for improved economies for larger scales. This can be achieved via the reduction of equipment cost e.g. by using passive cooling systems, the use of more productive strains combined with valorization of side-products and treatment of waste material favorable for hydrogen production.

REFERENCES

1. Savasturk D, Kayahan E, Koku H (2018) Photofermentative hydrogen production from molasses: Scale-up and outdoor operation at low carbon-to-nitrogen ratio. Int J Hydrogen Energy 43:11676–11687.
2. Sagir E, Ozgur E, Gunduz U, et al (2017) Single-stage photofermentative biohydrogen production from sugar beet molasses by different purple non-sulfur bacteria. Bioprocess Biosyst Eng 40:1589–1601.
3. Urbaniec, K., & Grabarczyk, R. (2014). Hydrogen production from sugar beet molasses – a techno-economic study. Journal of Cleaner Production, 65, 324–329.

WHEC-2022
23rd World Hydrogen Energy Conference
June 26-30, 2022 - Istanbul

#154

COMPARISON OF WILD TYPE AND UPTAKE HYDROGENASE DEFICIENT MUTANT STRAINS OF *RHODOBACTER CAPSULATUS* FOR HYDROGEN AND PHB PRODUCTION

[1] *Etkin Tarlan,* [2] *Ertan Hoşafcı,* [2] *Tuba Hande Ergüder,* [1*] *Harun Koku*
[1] Middle East Technical University, Department of Chemical Engineering, 06800 Ankara, Turkey
[2] Middle East Technical University, Department of Environmental Engineering, 06800 Ankara, Turkey

*Corresponding author e-mail: harunk@metu.edu.tr

ABSTRACT

In this study two strains of *Rhodobacter capsulatus* were compared in terms of efficiency of hydrogen (H_2) and poly-β-hydroxybutyrate (PHB) synthesis. One strain of *R. capsulatus* (YO3 (*hup*$^-$)) lacked the uptake hydrogenase enzyme, while the other was its wild type (WT). Both strains were grown in a medium with high carbon and minimal nitrogen. The H_2 and PHB contents of the reactors were all measured at the end of the experiment. The cell concentration measurements show that the growth trends were similar in both strains. The maximum H_2 productivities of the YO3 (*hup*$^-$) strain and WT strain were found as 0.534 mmol/(L.h) and 0.323 mmol/(L.h), respectively. While the PHB amount of the YO3 (*hup*$^-$) strain was 11.7%, the PHB amount of the WT strain was 10.1%. More studies will be conducted to further optimize the H_2 and PHB production, and to understand the partition of resources towards H_2 and PHB.

Keywords: Hydrogen, Poly-β-hydroxybutyrate (PHB), *Rhodobacter Capsulatus*, Acetate

INTRODUCTION

Due to the limited reserves and adverse environmental effects of fossil fuels, alternative energy sources have been intensively researched and among various renewable energy sources, hydrogen (H_2) receives attention for being a clean and efficient fuel. There are a variety of ways to produce hydrogen, and photobiological H_2 production is known as an environmentally harmless method [1]. Among various microorganisms, purple non-sulphur bacteria (PNSB), a subclass of photosynthetic bacteria, are suitable for large-scale production. Also, these species can utilize a wide variety of substrates and their substrate conversion efficiencies are high [2].

During biohydrogen production, one of the major by-products is poly-β-hydroxybutyrate (PHB). PHB is a biodegradable and biocompatible polymer that is used as a storage material by the bacteria and is a commercially valuable bioplastic. Like hydrogen, PHB is produced effectively at a high carbon to nitrogen ratio (C/N). The enzymes nitrogenase and hydrogenase are primarily involved in hydrogen production and consumption pathways. It is of interest to investigate the differences between H_2 and PHB production in the presence and absence of these enzymes in host species.

Several studies have investigated the co-production of PHB and H_2 in PNSB [3-5]. Various species, carbon sources and concentrations have been investigated for PHB production [6-8]. In the present study, the relationship between H_2 and PHB production was investigated in wild type (WT) and mutant (YO3 (*hup*-)) strains of *R. capsulatus*. The major difference between these strains is that the uptake hydrogenase gene of the YO3 strain was deleted [9]. Thus, this study indirectly reveals the effects of the uptake hydrogenase enzyme on both H_2 and PHB production.

MATERIALS AND METHODS

Bacteria, growth, and PHB production media

R. capsulatus YO3 (*hup*$^-$) and R. *capsulatus* WT were grown in the Biebl and Pfenning (BP) defined medium [10]. In this growth medium, 20 mM acetate and 10 mM glutamate were used as carbon and nitrogen sources, respectively. For PHB and H_2 production medium, 65 mM acetate and 2 mM glutamate were used. Vitamins, Fe-citrate and trace elements were added to the medium and pH was adjusted to 6.4 [5].

Bioreactor Start-up and Analytical Methods

Bacteria were inoculated (10% v/v) into 50 mL reactors, and four replicates were set up for each bacterial strain. Reactors were flushed with Argon for 3 minutes to provide anaerobic conditions. Temperature was kept constant at 30 ^oC and the light intensity was set to 2500-2600 lux. The batch operation of the reactors lasted 11 days.

Gas amount and composition, pH, and optical density (OD) measurements were performed daily. For these measurements, a gas chromatograph (GC, Agilent Technologies 6890N) equipped with a Supelco 1010 column, a pH

meter (Ezdo MP-103), and a UV spectrophotometer (Shimadzu UV-1800) were used. To control the light intensity, a lux meter (Lutron LX-105 Light Meter) was used regularly.

The protocol of PHB analysis was taken from Özsoy et al. [5]. At end of the experiment, to obtain the cell pellets, each reactor content was centrifuged at 13,000 rpm for 20 minutes. The supernatant was removed, and the cell pellets were placed into a freeze drier (Christ alpha 1-4 LD plus) for 24 hours. After freeze drying, weights of the pellets were recorded and added into 2 mL chloroform, then mixed with 2mL of acidic methanol solution (15% of H_2SO_4). The mixture was heated at 100°C for 4 hours. The reaction time was adapted from Braunegg [11]. Following the heating, 1 mL of distilled water was added into each mixture and vortexed for 10 minutes to separate phases. The lower phase, which contained methyl ester of 3-hydroxybutyrate, was filtered with a PTFE filter (22 µm, 13 mm Millipore). Concentration of PHB was determined via GC analysis [5].

RESULTS AND DISCUSSION

The biomass concentrations and cumulative H_2 productions of both strains are displayed in Figures 1 and 2, respectively. The growth trends were observed to be quite similar for both strains (Fig.1). The maximum biomass concentration for the WT was 0.849 g dcw/L, while the maximum biomass value was 0.850 g dcw/L for the YO3 type. A similar biomass concentration was observed for the YO3 type in the study of Oflaz et al. [12]. On the other hand, there is a difference in biomass concentration trend compared to another study by Özsoy et al. that used both acetate and the *R. capsulatus* WT, where the maximum biomass concentration was obtained as 0.85 g dcw/Lc [5]. However, the maximum biomass concentration in the present study was reached in 3 days, whereas study of Özsoy et al. did not attain maximum biomass concentration until day 6. By considering the H_2 (Fig. 2) and PHB (Fig.3) production results, it can be speculated that in the present study, bacterial metabolism might have shifted early on towards cell growth.

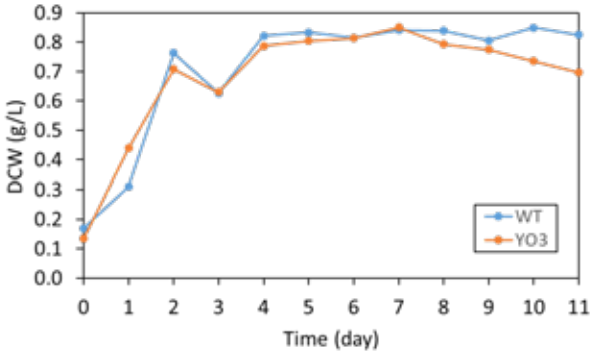


Fig.1. Biomass concentration

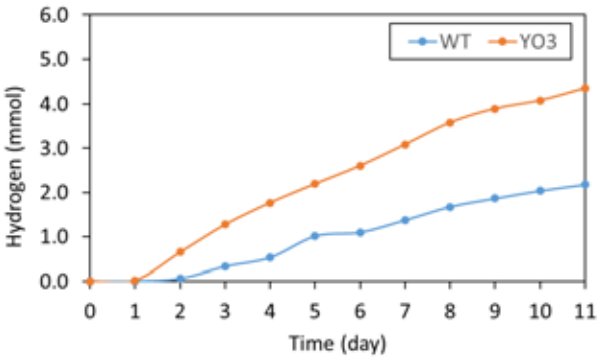


Fig.2. Cumulative hydrogen production

The cumulative H_2 production of the YO3 strain is twice that of produced H_2 by WT strain (Fig.2). This result was expected since YO3 strain is an uptake hydrogenase gene deleted mutant strain of *R. capsulatus* [9]; thus, the produced hydrogen cannot be recycled. The maximum molar H_2 productivities of YO3 and WT strains were found as 0.534 mmol/(L.h) and 0.323 (mmol/L.h), respectively. For the WT strain, Özsoy et al. [5] reported the molar productivity and cumulative molar H_2 production as 0.350 mmol/(L.h) and 11.4 mmol for 65 mM acetate and 120 mL reactor volume.

The final PHB content of the cells were determined at the end of the experiment. While the average PHB amount of the WT strain was 10.1±1% (as percentage of cell dry weight), the average PHB amount of the YO3 strain was 11.7±2.6% (Fig.3). It can be suggested that the presence of the uptake hydrogenase enzyme has a significant impact on H_2 production but its effect is relatively low for PHB production under the conditions studied. In particular, it is probable that the PHB produced could have been consumed in the later stages of the batch operation. In the literature, mixed results have been found regarding the relation of PHB to H_2 production based on differences in strains and operational conditions [13] and more investigation is necessary to determine and optimize the relation for our strains as well.

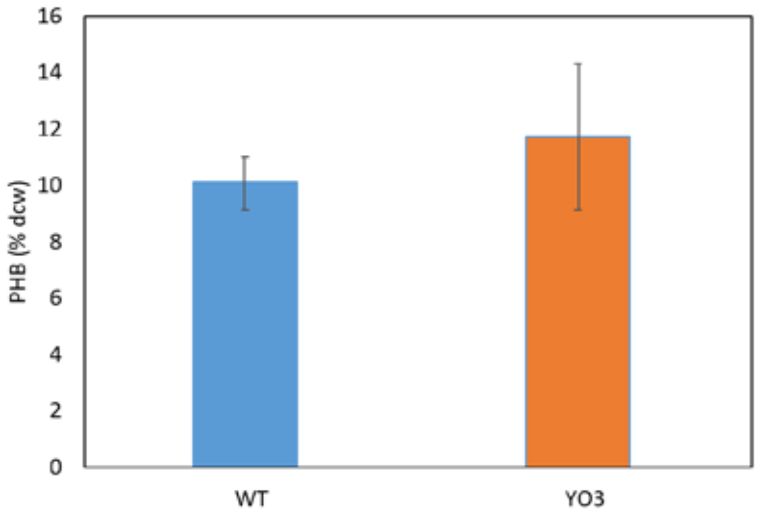


Fig.3. Final PHB content of cells (as percent dry cell weight) in the two strains

CONCLUSIONS

PHB and H_2 production in *R. capsulatus* YO3 and *R. capsulatus* WT under a nitrogen-limited environment was investigated. For both bacterial strains, the variation of pH and dry cell weights were similar. For the YO3 strain, the highest molar H_2 productivity was found as 0.534 mmol/(L.h) and this value was 1.65 times of the productivity of the wild strain. Since YO3 has no uptake hydrogenase enzyme, which consumes hydrogen, the increased H_2 production in this strain was an expected outcome. PHB accumulation in the YO3 strain was slightly higher than the wild strain. Further investigation is necessary to elucidate the details of the relation between H_2 and PHB production in these strains.

REFERENCES

1. Koku H, Eroğlu U, Gündüz MY and Türker L. 2003. Kinetics of biological hydrogen production by the photsynthetic bacterium *Rhodobacter sphaeroides* O.U.001. International Journal of Hydrogen Energy 28:381-388.
2. Koku H, Eroğlu U, Gündüz MY and Türker L. 2002. Aspects of the metabolism of hydrogen production by Rhodobacter sphaeroides. International Journal of Hydrogen Energy. 27:1315-1329.
3. Kemavongse K, Prasertsan P, Upaichit A and Methacanon P. 2008. Poly-β-hydroxyalkanoate production by halotolerant *Rhodobacter sphaeroides U.* World J. Microbiol. Biotechnol. 24:2073-2085.
4. Khatipov E, Miyake M, Miyake J and Asada Y. 1998. Accumulation of poly-β-hydroxybutyrate by Rhodobacter sphaeroides on various carbon and nitrogen substrates. FEMS Microbiology Letters 162:39-45.
5.Özsoy Demiriz B, Kars G, Yücel M, Eroğlu İ and Gündüz U. 2019. Hydrogen and poly-B-hydroxybutyric acid production at various acetate concentrations using Rhodobacter capsulatus DSM 1710. International Journal of Hydrogen Energy 44:17269–17277
6. McAdam B, Fournet MB, McDonald P and Mojicevic M. 2020. Production of polyhydroxybutyrate (PHB) and factors impacting its chemical and mechanical characteristics. Polymers 12:1-20.
7. Dalsasso RR, Pavan FA, Bordignon SE, de Aragão GMF and Poletto P. 2019. Polyhydroxybutyrate (PHB) production by Cupriavidus necator from sugarcane vinasse and molasses as mixed substrate. Process Biochemistry 85:12-18.
8. Gouda MK, Swellam AE and Omar SH. 2001. Production of PHB by a Bacillus megaterium strain using sugarcane molasses and corn steep liquor as sole carbon and nitrogen sources. Microbiol Research 156:201-207.
9. Öztürk Y, Yücel M, Daldal F, Mandacı S, Gündüz U, Türker L. 2006. Hydrogen production by using *Rhodobacter capsulatus* mutants with genetically modified electron transfer chains. International Association for Hydrogen Energy. 31:1545-1552.
10. Biebl H, Pfennig N. 1981. Isolation of members of the family Rhodospirillaceae. New York, Springer.
11. Braunegg G, Sonnleitner B and Lafferty RM. 1978. A Rapid Gas Chromatographic Method for the Determination of Poly-b-hydroxybutyric Acid in Microbial Biomass. European journal of applied microbiology and biotechnology 6:29-37.
12. Oflaz FB and Koku H. 2021. Pilot-scale outdoor photofermentative hydrogen production from molasses using pH control. Int. J. Hydrogen Energy. 46:29160-29172.
13. Hustede E, Steinbüchel A and Schlegel HG. 1993. Relationship between the photoproduction of hydrogen and the accumulation of PHB in non-sulphur purple bacteria. 39:87-93.

WHEC-2022
23rd World Hydrogen Energy Conference
June 26-30, 2022 - Istanbul

#254

FOCUSING ON A NEW BIOHYDROGEN PRODUCTION STRATEGY USING *CHLAMYDOMONAS REINHARDTII* MUTANTS

*Çağla Yarkent[1], İzel Oral[1], Deniz Şenyay Öncel[2], Suphi S. Oncel[1]**
University of Ege, Faculty of Engineering, Department of Bioengineering, 35100, Bornova, İzmir, Turkiye
Dokuz Eylul University, Dpt. of Biomechanics, Balçova, İzmir, Turkiye

*Corresponding author e-mail: suphi.oncel@ege.edu.tr

ABSTRACT

Microalgae have been drawn great attention due to their biohydrogen production potentials. In this study, we investigated biohydrogen production potentials of *Chlamydomonas reinhardtii* strains as D1 protein mutant strain D240-41, PGRL1 single mutant PGRL1 mt (+), PGRL1 double mutant PGRL1xΔnd4 Véro. Biohydrogen productions were carried out according to HS-HS strategy. This new strategy is based on performing hydrogen production by completing two successive phases, aerobic and anaerobic. In the first phase, the cultures were cultivated in HS medium under aerobic condition, then in the second phase they were transferred to anaerobic photobioreactors containing fresh HS medium. As result, we observed that all strains were able to produce hydrogen during this new HS-HS strategy.

Keywords: Biohydrogen*, Chlamydomonas Reinhardtii*, *C. Reinhardtii* Mutants, Photobioreactor, HS

INTRODUCTION

The concerns on energy demand are increasing rapidly. At this point, hydrogen is seen as our new energy source thanks to its high gravimetric energy density and ability to provides energy conversion without producing carbon-based emissions [1]. The researches have been proved that hydrogen can be obtained through biologically process. In these processes, microorganisms are considered as a bioconverters which use light energy and water to convert them to hydrogen via hydrogenase and nitrogenase enzymes [2]. In this respect, microalgae are more advantageous than plants due to their ability to be easily grown in closed systems in a wide variety of climatic conditions on lands that are not suitable for agriculture [3,4] Additionally, they can exhibit high hydrogen yields in a specially designed photobioreactor that can allow hydrogen retention [5].

Microalgal hydrogen production can be evaluated from two aspects, process development and genetic applications. In process development studies, the researchers have been focused on both producing high amount of starch and avoiding the hydrogenase enzyme inactivation caused by oxygen. For this purpose, a two-stage strategy has been developed, which includes microalgal cultivation in sulfur containing Tris-Acetate-Phosphate (TAP) medium under aerobic condition and biohydrogen production in sulfur-free TAP-S medium under anaerobic condition [6,7]. However, there is always a risk that photosynthetic mechanism disruptions will be occurred irreversibly. For this reason, new strategies are being developed for microalgal photoautotrophic hydrogen production without exposing the cultures to sulfur starvation [8–11]. From a genetic application perspective, the aim of the studies was to obtain microalgae species with increased biohydrogen production potential. According to this view, mutations have been carried out on chloroplast and mitochondria, since both organelles respond in continue communication to many different stimuli originating from the environment.

In our previous study, we investigated biohydrogen production potentials of *C. reinhardtii* strains as CC124, D1 protein mutants (D240, D239-40, D240-41), PGRL1 single mutants PGRL1 mt (-), PGRL1 mt (+), PGRL1 double mutants PGRL1xΔnd4 Véro, PGRL1xΔnd4 1130, mitochondrial mutant AOX, and control strains as WT and T-1. Biohydrogen productions were carried out based on TAP-TAP(-S) strategy in 1 L magnetically-mixed Roux-type Photo-bioreactors (PBRs). D240-41, PGRL1xΔnd4 Véro and PGRL1 mt (+) were selected as the most hydrogen productive strains, which attained the total biohydrogen amount of 152.05 mL/L, 170 mL/L and 143.04 mL/L, respectively. Then, biohydrogen productions were performed in 2.5 L continuous stirred-tank photobioreactors (CSTR) with these opted strains. It was observed that, D240-41, PGRL1xΔnd4 Véro and PGRL1 mt (+) produced 409.5 mL/L, 309.2 mL/L and 259.8 mL/L hydrogen, respectively. Also, a new strategy named as HS-HS strategy that came from the name of Sueoka's High Salt (HS) medium was developed. In this strategy, the cultures were first cultivated in HS medium under aerobic condition, then they were transferred to fresh HS medium and biohydrogen productions were performed under anaerobic condition. Most importantly, it was observed that all strains have ability to produce hydrogen in capped vials (50 mL) based on this strategy.

In this study, D1 protein mutant strain D240-41, PGRL1 single mutant PGRL1 mt (+), PGRL1 double mutant PGRL1xΔnd4 Véro, which was selected as the most effective hydrogen producers according to our above-mentioned study, was used. Now, their biohydrogen production potentials of them is being investigated in photobioreactor.

MATERIALS AND METHODS

C. reinhardtii strains cultivation

Among *C. reinhardtii* mutant strains D240 had single deletion at amino acid residue 240, PGRL1 mt (+) had single mutation at PGRL1 protein and PGRL1xΔnd4 Véro have also mutated in mitochondrial complex I gene Δnd4 in addition to this mutation. The strains were incubated in 250 mL erlenmeyer flasks containing HS medium [9]. Cultivations were started at pH 7.2 ± 0.2 and performed at 21±2℃, 100 rpm with continuous illuminating on top sides 40-45 $\mu E*m^{-2}*s^{-1}$ for 10 days.

Microalgal Biohydrogen Production

Biohydrogen production will be performed based on HS-HS strategy. In the first stage, once the culture reached its logarithmic phase in erlenmeyer scale will be transferred into the photobioreactor containing HS medium. The inoculation volume will be determined according to the initial chlorophyll concentration of 4±1 mg chlorophyll/L [12]. The culture will be aerated with gas mixture includes air-CO2 (v/v; 97/3). The microalgal biomass production will be performed under aerobic condition. Then, the culture in logarithmic phase will be inoculated to the photobioreactor which capped with plug. The inoculant amount will be arranged based on to reach 12 mg/L as the initial chlorophyll content in fresh HS medium [13]. The biohydrogen production will be started after flushing the culture with N_2 and incubated it in dark for 4 hours.

Both biomass and biohydrogen productions will be started at pH 7.8±0.2 and performed at 21±2℃, 40-45 $\mu E*m^{-2}*s^{-1}$ (on two sides) [14]. All productions will be monitored for 8 days.

Analytical methods

The microalgal growth phases were followed by according to daily taken samples. pH value detection, cell counting, dry weight measurement and optical density determination (at 560 nm and 750 nm) were performed. Photosynthetic activity will be detected by photosynthetic activity device. The chlorophyll-a determination will be performed according to our previous studies [15,16].

Biohydrogen production will be monitored via gas chromatography (GC). In addition, the hydrogen production will be also followed through utilizing a Proton-Exchange Membrane (PEM) fuel cell as described in our previous study [14].

RESULTS AND DISCUSSION

Microalgal cultivation

Microalgae strains reached their stationary phase in very close times to each other (Fig. 1). It has been known that high salt concentration can increase the photo-inhibition mechanisms [17]. As a result, decreased direct electron transfer from photosystem (PS) II to PS I can be observed [18]. Also, it was mentioned as decreased PSII activity causes more work falls on the PSI, and thus on the PGRL1 molecule [19]. This may explain that D240 strain, which has mutation only in the D1 protein complex of PS II, produced highest amount of biomass.

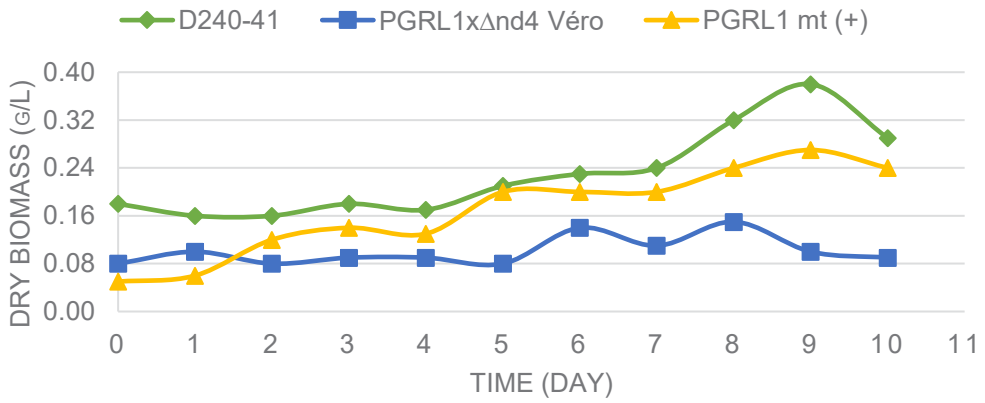


Figure 1. Microalgal growth of microalgae strains.

In addition, it is known that chloroplast and mitochondria are in constant communication to respond to many different stimuli from the environment [13]. Therefore, in considering the PGRL1 mutants, single point mutant PGRL1 mt (+) produced higher amount of biomass than PGRL1xΔnd4 Véro mutant strain. This can be explained as PGRL1xΔnd4 Véro, which has mutations in both chloroplast and mitochondrial organelles, was more affected by this stress condition.

CONCLUSIONS

In this study, it was proven that hydrogen producer PGRL1xΔnd4 Véro, D240-41 and PGRL1 mt (+) mutant strains can be cultivated in HS medium. Briefly, HS-HS strategy offers advantages such as (1) no need for washing the culture with the medium which used in anaerobic condition while transferring the culture from aerobic condition to anaerobic condition, (2) low risk of contamination as no organic carbon source (acetate) is used and (3) allows the cultures to still be photosynthetically active.

REFERENCES

1. Dincer I. 2012. Green methods for hydrogen production. International Journal of Hydrogen Energy. 37:1954–71.
2. Das D, Veziroglu TN. 2008. Advances in biological hydrogen production processes. International Journal of Hydrogen Energy. 33:6046–6057.
3. Khatoon N, Pal R. 2015. Microalgae in Biotechnological Application: A Commercial Approach. Plant Biology and Biotechnology Vol II Plant Genomics and Biotechnology. II:1–768.
4. Sharma N, Sharma P. 2017. Industrial and Biotechnological Applications of Algae: A Review. Journal of Advanced Plant Biology. 1:1-5.
5. Oncel S, Kose A. 2014. Comparison of tubular and panel type photobioreactors for biohydrogen production utilizing Chlamydomonas reinhardtii considering mixing time and light intensity. Bioresource Technology. 151:265–270.
6. Melis A. 2007. Photosynthetic H2 metabolism in Chlamydomonas reinhardtii (unicellular green algae). Planta. 226:1075–1086.
7. Melis A, Zhang L, Forestier M, Ghirardi ML, Seibert M. 2000. Sustained photobiological hydrogen gas production upon reversible inactivation of oxygen evolution in the green alga Chlamydomonas reinhardtii. Plant Physiology. 122:127–135.
8. Batyrova K, Gavrisheva A, Ivanova E, Liu J, Tsygankov A. 2015. Sustainable Hydrogen Photoproduction by Phosphorus-Deprived Marine Green Microalgae Chlorella sp. International Journal of Molecular Science. 16:2705–2716.
9. Nagy V, Podmaniczki A, Vidal-Meireles A, Tengölics R, Kovács L, Rákhely G, Scoma A, Tóth SZ..2018. Water-splitting-based, sustainable and efficient H2 production in green algae as achieved by substrate limitation of the Calvin-Benson-Bassham cycle. Biotechnology for Biofuels. 11:1–16.
10. Salakkam A, Sittijunda S, Mamimin C, Phanduang O, Reungsang A. 2021. Valorization of microalgal biomass for biohydrogen generation : A review. Bioresource Technology. 322:1–14.
11. Volgusheva A, Kukarskikh G, Krendeleva T, Rubin A, Mamedov F. 2015. Hydrogen photoproduction in green algae Chlamydomonas reinhardtii under magnesium deprivation. Royal Society of Chemistry Advances. 5:5633–5637.
12. Oncel SS, Kose A, Faraloni C, Imamoglu E, Elibol M, Torzillo G, Vardar-Sukan F. 2015. Biohydrogen production from model microalgae Chlamydomonas reinhardtii: A simulation of environmental conditions for outdoor experiments. International Journal of Hydrogen Energy. 40:7502–7510.
13. Oncel SS, Kose A, Faraloni C, Imamoglu E, Elibol M, Torzillo G, Vardar-Sukan F. 2014. Biohydrogen production using mutant strains of Chlamydomonas reinhardtii: The effects of light intensity and illumination patterns. Biochemical Engineering Journal. 92:47–52.
14. Oncel S, Vardar-Sukan F. 2011. Application of proton exchange membrane fuel cells for the monitoring and direct usage of biohydrogen produced by Chlamydomonas reinhardtii. Journal of Power Sources. 196:46–53.
15. Oncel S, Vardar-Sukan F. 2011. Effect of light intensity and the light: Dark cycles on the long term hydrogen production of Chlamydomonas reinhardtii by batch cultures. Biomass and Bioenergy. 35:1066–1074.
16. Oncel S, Vardar-Sukan F. 2009. Photo-bioproduction of hydrogen by Chlamydomonas reinhardtii using a semi-continuous process regime. International Journal of Hydrogen Energy. 34:7592–7602.
17. Morgan-Kiss RM, Priscu JC, Pocock T, Gudynaite-Savitch L, Huner NPA. 2006. Adaptation and Acclimation of Photosynthetic Microorganisms to Permanently Cold Environments. Microbiology and Molecular Biology Reviews. 70:222–252.
18. Skjånes K, Rebours C, Lindblad P. 2013. Potential for green microalgae to produce hydrogen, pharmaceuticals and other high value products in a combined process. Critical Reviews in Biotechnology. 33:172–215.
19. Hemschemeier A, Fouchard S, Cournac L, Peltier G, Happe T. 2008. Hydrogen production by Chlamydomonas reinhardtii: An elaborate interplay of electron sources and sinks. Planta. 227:397–407.

WHEC-2022
23rd World Hydrogen Energy Conference
June 26-30, 2022 - Istanbul

#264

OPTIMIZATION OF BIOHYDROGEN PRODUCTION YIELDS WITH LOCALLY ISOLATED THERMOPHILIC BACTERIA FROM HOT SPRINGS

[1]*İlayda Akaçin,*[1]*Şeymanur Ersoy,* [2]*Tuğba Keskin Gündoğdu,*[1]**Mine Güngörmüşler*
[1]Division of Bioengineering, Graduate School, Izmir University of Economics, Sakarya Caddesi No: 156, Izmir, 35330 Turkey
[2]Department of Environmental Protection Technologies, Izmir Democracy University, 35140, Izmir, Turkey

*Corresponding author e-mail: mine.gungormusler@ieu.edu.tr

ABSTRACT

Hydrogen, a carbon-free clean fuel and a strong alternative to conventional fossil energy sources, has many production strategies including biological routes, acknowledged as sustainable and environmentally friendly. The hydrogen yields acquired by those routes with either pure or mixed cultures are predominantly dependent on the environmental factors. Accordingly, in the literature, statistical experimental designs were proven to be useful to understand the effects of independent parameters including macro and micro nutrients, organic or inorganic substrates, pH and temperature. Within this scope, the aim of this study was to optimize the bio-H_2 yields using the Box-Behnken design (BBD) with 3 different independent parameters (temperature(^oC), pH and inorganic substrate (CO volume (mL)) with a comparative approach using both mixed and pure thermophilic cultures isolated from Izmir hot springs. The maximum H_2 yields were reported as 0.13 mmol H_2/mmol CO for mixed cultures at pH 7, 60^oC and 15 mL CO addition whereas the pure culture reached 2.5 fold higher yields by 0.46 mmol H_2/mmol CO. The results demonstrated the effectiveness of the utilization of the statistical design of experiments to improve the bioproduction yields via local thermophilic isolates.

Keywords: Biohydrogen, Box-Behnken Design, Water-Gas Shift reaction

INTRODUCTION

Carbon-based energy sources, fossil fuels, and accumulation of greenhouse gasses via consumption of fossil fuels in the industrialized world is imprinting unwanted and inevitable traces on the environment day by day. Worldwide CO_2 emissions are expected to increase over 33 billion tonnes by 2022 [1]. In the time of the emerging environmental crisis, the search for clean, renewable, and carbon-free energy sources that can reduce the energy burden of the industry is deemed to be crucial and the production of carbon-free energy sources such as hydrogen gas using sustainable and green routes, in particular, biotechnological routes, are vital. Hydrogen production using biological sources is divided into five categories; direct and indirect photolysis, photo-fermentation, anaerobic fermentation and water gas shift [2]. Water-gas shift (WGS) reaction is regulated by the metabolisms of carboxydotrophic hydrogenogenic microorganisms that can use CO gas as a carbon and electron source, and in the presence of H_2O converting it into molecular hydrogen (H_2)[3].

Mixed or pure cultures of microorganisms able to perform WGS can be used for the production of biohydrogen, both having their own advantages and disadvantages. Mixed cultures are reported to be more economically viable as sterilization requirements in pure culture processes are eliminated [4] however, the dynamics of the microbial consortia must be taken into consideration, such as the presence of H_2 consuming bacteria is known to decrease the H_2 production yields and the necessity of pre-treatment to eliminate these microorganisms should be taken into consideration [5].

This is the first report in the literature with local isolates collected from Izmir hot springs to demonstrate the optimization of H_2 yields employing Box-Behnken Design with a comparative approach using mixed and pure cultures.

MATERIALS AND METHODS

Microbial Cultures

Local isolates were collected from Doğanbey geothermal hot springs in Seferihisar, Izmir (38°07'32.8"N 26°54'35.8"E). The hot spring possesses a thermophilic (77.3^oC) environment with a pH of 6.42 and an oxidation reduction potential (ORP) of 43,8 mV. These parameters were recorded by a portable multiparameter meter (Milwaukee, USA). The samples were taken into sterile flasks aseptically and transported in thermal bags to the laboratory. The samples were cultivated under anaerobic conditions at incrementing temperatures (55, 60 and 65^oC) with a previously defined basal media [6-7]. All experiments were conducted in 50 mL serum bottles. Each bottle was filled with 27 mL anaerobic medium and flushed with pure N_2 gas for 30 seconds to provide anaerobic conditions.

The bottles were sealed with rubber septa and aluminum crimp caps then autoclaved at 121 °C for 15 min. Following sterilization, 3 mL of inoculum was added to each bottle. Stock cultures from previous studies were used as inoculum for all experiments. After inoculation, CO gas was added to the serum bottles using a gas-tight syringe with 3 different volumes as shown in Table 1.

Box-Behnken Design

Box–Behnken design ensures modeling of the response surface that was commonly used for fermentative hydrogen production processes [8-10]. The design was used to ensure maximizing hydrogen production yields to that end, three factors, namely temperature, pH and the CO addition were selected and three levels of each factor, which corresponds to low, middle and high for the variables (Table 1) were employed (Design Expert v13, USA). These factors and levels were selected according to literature [11-12] and results from previously conducted experiments. A set of 17 experiments were performed to comparatively analyze the effects of variables on hydrogen production yields. The values of each experiment that results in the maximum value of response (hydrogen production yield) was selected as optimal conditions. 5 validation experiments were carried out for each culture condition.

Table1. Factors and levels selected for the Box-Behnken Design (Design Expert v13, USA).

Factors and levels selected for the Box-Behnken Design			
Factors	Levels		
	1 (Low)	2 (Medium)	3 (High)
1 Temperature (°C)	55	60	65
2 pH	5.0	7.0	9.0
3 CO feed (mL)	5	10	15

Gas Analysis

In order to measure the quantity of H_2 produced and CO consumed, 1000 µL of samples were taken from the headspace of the bottles with a gas tight syringe (Hamilton, Nevada) at 0-3rd-7th-10th days of the experiments and analyzed with Gas Chromatography (Shimadzu, Nexis GC-2030, Japan). The device is equipped with a Restek ShinCarbon ST 100/120 packed column and TCD (Thermal Conductivity Detector). The temperature of the injector, column and detector were 150, 60 and 150°C, respectively. N_2 was used as a carrier gas. The hydrogen yield was expressed as a percentage of the H_2 gas produced per CO gas consumed (mol/mol).

RESULTS AND DISCUSSION

As reported in Figures 1 and 2, the significant results obtained with a fit to a quadratic model ($p<0,05$) in this study, reported maximum hydrogen yields of 0.46 mmol H_2/mmol CO (%) (8.02% H_2) using pure cultures and 0.13 mmol H_2/mmol CO (2.16% H_2) for mixed cultures with following conditions: pH 9, 60°C and 15 mL CO addition. The hydrogen production in the headspace was successfully improved compared to the authors' previously reported studies [13]. Biohydrogen production yields with the use of an organic substrate (e.g. glucose) were reported as 2.3 mol H_2/mol glucose for mixed cultures [14] and 1.35 mol H_2/mol glucose [15] for pure cultures. In the case of using an inorganic substrate, such as CO gas with application of the WGS pathway, biohydrogen production yields were reported to range between 0.606-0.808 mmol H_2/mmol CO [16]. As observed, the hydrogen production potential could remarkably be increased by altering operational conditions.

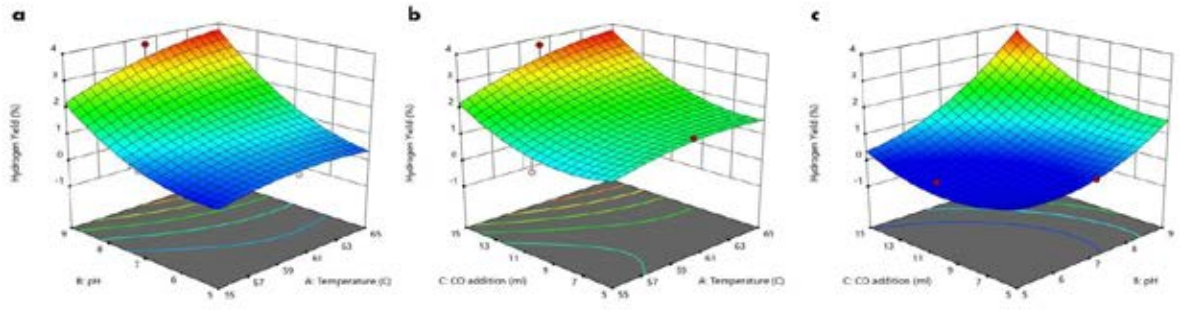


Figure 1. Effects of different parameters on the hydrogen yield for pure culture. (a) temperature (y-axis) and pH (x-axis) (b) CO addition (y-axis) and temperature(x-axis) (c) CO addition (y-axis) and pH(x-axis).

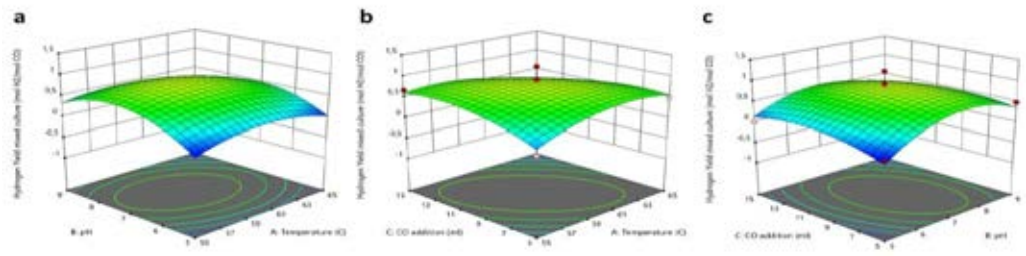


Figure 2. Effects of different parameters on the hydrogen yield for mixed culture (a) temperature (y-axis) and pH (x-axis) (b) CO addition (y-axis) and temperature (x-axis) (c) CO addition (y-axis) and pH(x-axis).

CONCLUSIONS

The results of the current study proved the effective optimization of the isolated cultures with the BBD tool reaching a 4 fold higher H_2 production in the headspace gas than the preliminary values obtained prior to optimization. The biohydrogen production yield from CO with the pure culture was significantly higher compared to the mixed culture. This can be explained by the microbial dynamics within the mixed culture, as both H_2 producing and H_2 consuming strains could be present at the same time. Overall, the CO fermentation of the local isolates in this study represent a promising alternative to the conventional fermentation processes.

ACKNOWLEDGEMENT

This research was financially supported by The Scientific and Technological Research Council of Turkey (TUBITAK-CAYDAG) with project number 120Y069.

REFERENCES

1. https://www.iea.org/reports/global-energy-review-2021/co2-emissions. Accessed on December 11,.2021
2. Das D and Veziroğlu TN. 2001. Hydrogen production by biological processes: a survey of literature. International journal of hydrogen energy, 26(1), 13-28.
3. Henstra, A. M., Sipma, J., Rinzema, A., and Stams, A. J. 2007. Microbiology of synthesis gas fermentation for biofuel production. Current Opinion in Biotechnology, 18(3), 200-206.
4. Argun, H., Kargi, F., and Kapdan, I. K. 2009. Microbial culture selection for bio-hydrogen production from waste ground wheat by dark fermentation. International journal of hydrogen energy, 34(5), 2195-2200.
5. Wang, J., and Yin, Y. 2021. Clostridium species for fermentative hydrogen production: An overview. International Journal of Hydrogen Energy. Wang, 46(70), 34599–34625.
6. Kevbrin VV and Zavarzin GA. 1992. The influence of sulfur compounds on the growth of halophilic homoacetic bacterium Aceto- halobium arabaticum. Microbiology (English translation of Mikro-biologiya) 61:812–817.
7. Wolin, EA, Wolin MJ. and Wolfe RS. 1963. Formation of methane by bacterial extracts. J Biol Chem 238: 2882–2886.
8. Lay, J. J. 2000. Modeling and optimization of anaerobic digested sludge converting starch to hydrogen. Biotechnology and bioengineering, 68(3), 269-278.
9. Levin, D. B., Pitt, L., and Love, M. 2004. Biohydrogen production: prospects and limitations to practical application. International journal of hydrogen energy, 29(2), 173-185.
10. Mu, Y., Wang, G., and Yu, H. Q. 2006. Response surface methodological analysis on biohydrogen production by enriched anaerobic cultures. Enzyme and Microbial Technology, 38(7), 905-913.
11. Pugazhendhi, A., Anburajan, P., Park, J. H., Kumar, G., Sivagurunathan, P., and Kim, S. H. 2017. Process performance of biohydrogen production using glucose at various HRTs and assessment of microbial dynamics variation via q-PCR. International Journal of Hydrogen Energy, 42(45), 27550-27557.
12. Mohr, T., Aliyu, H., Biebinger, L., Gödert, R., Hornberger, A., Cowan, D., and Neumann, A. 2019. Effects of different operating parameters on hydrogen production by Parageobacillus thermoglucosidasius DSM 6285. AMB express, 9(1),1-10.
13. Ersoy, Ş., Akaçin, İ., and Güngörmüşler, M. 2022. Comparative evaluation of the biohydrogen production potential of thermophilic microorganisms isolated from hot springs located in Izmir region. (Oral) The Sixth International Hydrogen Technologies Congress (IHTEC-2022). 23-26 January 2022. Çanakkale Onsekiz Mart University, Çanakkale, Turkey.
14. Lin, C. Y., and Lay, C. H. 2004. Effects of carbonate and phosphate concentrations on hydrogen production using anaerobic sewage sludge microflora. International Journal of Hydrogen Energy, 29(3), 275-281.
15. Pan, C. M., Fan, Y. T., Xing, Y., Hou, H. W., and Zhang, M. L. 2008. Statistical optimization of process parameters on biohydrogen production from glucose by Clostridium sp. Fanp2. Bioresource technology, 99(8), 3146-3154.
16. van Ginkel S, Sung S, Lay JJ. 2001. Biohydrogen production as a function of pH and substrate concentration. Enzyme Microb Technol 2001,35:4726–30.

WHEC-2022
23rd World Hydrogen Energy Conference
June 26-30, 2022 - Istanbul

#358

VALORIZATION OF GREEN MARKET WASTE FOR BIOHYDROGEN PRODUCTION

[1] İlknur Hacıoğlu, [1,2] Serpil Özmıhçı, [1,2]İlgi Karapınar, [3]Meltem Küs, [3]Ali Keleş, [3]İlhami Kargül*
[1] Dokuz Eylul University, Natural and Applied Sciences, Biotechnology Department, 35390, İzmir, Turkey
[2] Dokuz Eylul University, Engineering Faculty, Environmental Engineering Department, 35390, İzmir, Turkey
[3] GKE Energy R&D Center, 48200, Muğla, Turkey

*Corresponding author e-mail: serpil.ozmihci@deu.edu.tr

ABSTRACT

Hydrogen as a clean environmental friendly fuel has the potential to meet energy demand of the world. High organic carbon wastes can be used for biohydrogen production reducing raw material cost. In the energy sector the utilization of green market wastes (GMW) offers certain advantages to produce high value-added products with low cost. An important factor affecting biohydrogen production is temperature. In this study, the GWM (a mixture of lettuce, parsley, spring onion and dill) was used for biohydrogen production by dark fermentation using pretreated anaerobic sludge. Hydrogen production potential at mesophilic conditions (37°C, initial pH 7.2) at different initial substrate concentrations varying between 1000-5000 g wb was utilized. After mesophilic experiments, 5000 g wb was conducted to thermophilic conditions to compare the effect of temperature.

The highest CHF (8.9 L) and the highest yield (0.012 mol H_2/ g TOC) was obtained with 5000 g wet weight in mesophilic conditions. Thermophilic conditions gave higher CHF (14.2 L) when compared with mesophilic one. Thermophilic conditions gave 1.6 times higher yield than mesophilic conditions; demonstrating suitability for organic substrates having high density.

Keywords: Biohydrogen Production, Green Waste, Thermophilic, Mesophilic, Dark Fermentation

INTRODUCTION

Hydrogen, which is a clean and environmental friendly fuel, draws attention as the biggest alternative to fossil fuels in meeting the energy demand in the world [1]. A wide variety of substrates such as algae biomass, cellulose-based biomass, food waste, fruit and vegetable waste, organic waste and wastewater are used to produce biohydrogen by dark fermentation [2]. Market waste is an ideal substrate for biohydrogen production due to its high organic carbon concentrations and its readily degradable in nature [3]. Moreover, the use of waste substrates in energy production reduces the cost of raw materials [1].

The pretreatment method applied to the substrate is effective in increasing the hydrogen yield. Physical, chemical, enzymatic pretreatments are the most common ones but it increases the overall operation cost of production [2]. Therefore partial hydrolysis of the substrate or consolidated fermentation could be a solution to this problem [4,5]. One of the important factors affecting biohydrogen production in dark fermentation is the process temperature. Thermophilic conditions (42–75°C) offer advantages over mesophilic one, such as elimination of hydrogen-consuming bacteria [6], efficient conversion of simple sugars to hydrogen. Hence the biohydrogen production yield and productivity is found higher in thermophilic conditions [7]. For instance, Toledo-Cervantes et al. (2020), reported 1.7 times higher hydrogen production under thermophilic conditions when compared with mesophilic conditions [8].

The utilization of green market wastes in the energy sector offers certain advantages to produce high value-added products with low cost such as biohydrogen. By considering this fact, the aim of this study is to valorize the green waste for biohydrogen production by dark fermentation using mixed culture. For this purpose hydrogen production potential at mesophilic conditions (37°C) at different initial substrate concentrations varying between 1000-5000 g wet matter was evaluated. After mesophilic experiments, the substrate concentration giving the highest hydrogen production potential was conducted to thermophilic conditions to compare the effect of temperature.

MATERIALS AND METHODS

Substrate preparation

The green wastes made up of lettuce, parsley, spring onion and dill were collected from city markets in İzmir/Turkey. They were first chopped then mixed and finally blended. Partial hydrolysis of the substrate was conducted by applying heat (T>100°C) in a pressurized vessel for 30 minutes. The mixture had a characteristic of 94% moisture content, 0.523 g TOC/g dry matter and 7.16 g TOC/L in the liquid fraction, 10.95 g/L total sugar concentration of hydrolyzed waste liquor, 2940 mg/L total nitrogen, 298.5 mg/L total phosphorus.

Experimental set up

Serum bottles were used for batch dark fermentation experiments. Silicone stoppers and caps were used to prevent gas leakage. The substrate concentration varying between 1000 to 5000 g wet basis were subjected to fermentation. Mesophilic and thermophilic dark fermentations were carried out with pretreated anaerobic sludge. The fermentation media contained 2.8 g L^{-1} K_2HPO_4, 3.9 g L^{-1} KH_2PO_4, 0.05 g L^{-1} $FeSO_4.7H_2O$ and 0.1 g L^{-1} L-cysteine. The initial pH of the fermentation media was adjusted to 7.2 and autoclaved at 121°C for 15 min. Anaerobic conditions were maintained by passing nitrogen gas from head space of the bottles. 10% (v/v) inoculation was applied. The bottles were placed in an incubator at 37°C for mesophilic experiments and 55°C for thermophilic experiments.

Organism

The anaerobic sludge was taken from anaerobic wastewater treatment plant's acidogenic phase from PAKMAYA, İzmir, Turkey. In order to select the spore forming hydrogen producing bacteria, the sludge was heated over 100°C for 1 hour at pH 5. The pretreated anaerobic sludge was inoculated (10% v/v) in a media containing 10 g L^{-1} glucose, 2.8 g L^{-1} K_2HPO_4, 3.9 g L^{-1} KH_2PO_4, 0.25 g L^{-1} $MgSO_4$, 10 g L^{-1} peptone, 0.6 g L^{-1} yeast extract and 0.1 g L^{-1} L-cysteine. Anaerobic conditions were achieved by passing nitrogen gas through the medium prior to cultivation. The organisms were incubated at 37°C and 55°C an initial pH of 7.2. The cultivated organisms were incubated for 2 days and used as inoculum.

Analytical Methods

Samples were taken daily and centrifuged at 8000 rpm. pH analysis, total sugar concentration, simple sugar composition and total volatile fatty acid (TVFA) concentration were performed in the clear supernatant. The Dubois method [9] was used to measure total sugar concentration. Simple sugars and TVFA concentrations were determined by using HPLC with RID and UV detectors, respectively [10]. TOC was analysed with initial and final dry mass substrates.

Hydrogen gas samples were taken daily from the head space of the bottles. Hydrogen concentration was measured by using a GC with TCD, and total gas volume by water displacement method [10]. Cumulative hydrogen formation (CHF), yield, volumetric hydrogen production rate were calculated according to the [11].

RESULTS AND DISCUSSION

Batch dark fermentation experiments were carried out to evaluate the effects of substrate concentration (1000 g to 5000 g wet basis) on biohydrogen production. Fig. 1 gives the final CHF and Fig. 2 gives the hydrogen production yields for different substrate concentrations at mesophilic conditions. CHF and the hydrogen yield (mol H_2/ g TOC) increased with substrate concentration. The highest CHF (8.9 L) and the highest yield (0.012 mol H_2/g TOC) was obtained with 5000 g wet weight.

Fig. 3 shows the time-dependent variation of thermophilic and mesophilic CHF and TS in the liquor with 5000 g substrate. At the end of the fermentation period CHF was 14.2 L and 8.9 L in thermophilic and mesophilic conditions, respectively. The initial total sugar concentrations in the liquor phase of the substrate was 26.5 g/L and 12.8 g/L due to partial hydrolysis via heat. The substrate was simultaneously converted into simple sugars during the fermentation period and consumed by bacteria. At the end of the fermentation period the TS in the liquid phase was under 2.5 g/L in both conditions. The main VFAs were acetic and butyric acid. The total VFA concentration was 15.8 g/L in mesophilic conditions while it was 39.8 g/L in thermophilic conditions. Thermophilic conditions helped bacteria to convert simple sugars into VFA's faster than mesophilic conditions effecting positively hydrogen production yields.

Table 1 shows the comparison of mesophilic and thermophilic biohydrogen production in terms of CHF, yields. Depending on the increase of temperature, the hydrogen yield per mole of glucose increased 3.3 times. This may be related to the fact that sugar degradation and hydrolysis take place more effectively as the temperature increases. In the light of all these results, it has been observed that the production and yield performance of biohydrogen production in thermophilic conditions is higher than in mesophilic conditions when high density of organic waste substrate is used with dark fermentation.

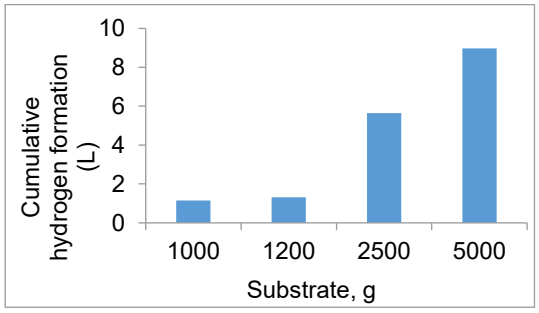


Fig. 1. Cumulative hydrogen formation at different amount of substrates

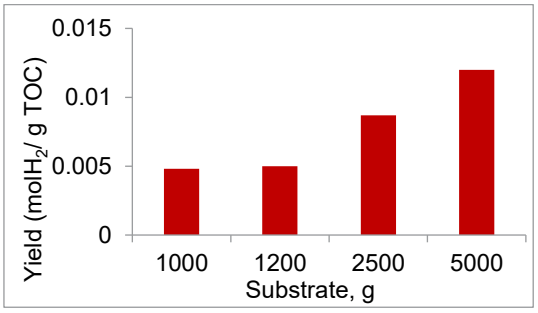


Fig. 2. Variation of hydrogen yield based on g TOC with different amount of substrates.

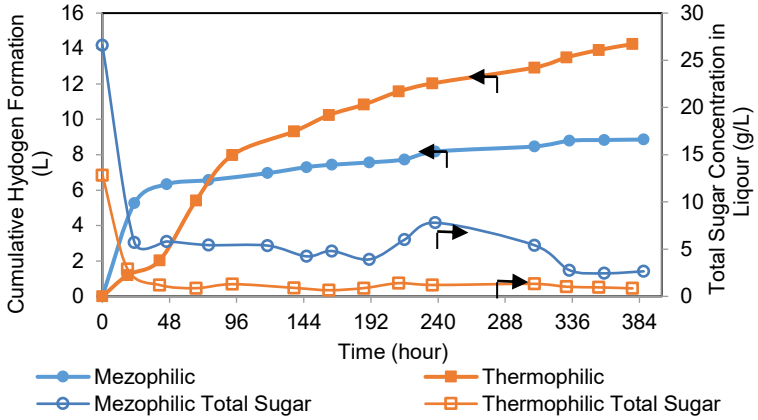


Fig. 3. Time dependent variation of CHF and total sugar (TS) concentrations in the liquor of mesophilic and thermophilic experiments with 5000 g wet basis substrate concentration.

Table 1. Comparison of mesophilic and thermophilic hydrogen production

	Mesophilic fermentation (5000 g)	**Thermophilic fermentation (5000 g)**
CHF (mmol H_2)	348	549
Yield (mol H_2/ mol total sugar)	0.43	1.42
Yield (mol H_2/ g TOC)	0.012	0.018
Yield (mL H_2/ g dry matter)	29.5	47.5

CONCLUSIONS

Batch dark fermentation experiments were carried out to evaluate the effects of substrate concentration (1000 g to 5000 g wb) on biohydrogen production. The substrate concentration that gave the highest biohydrogen production potential in mesophilic conditions was compared with thermophilic conditions to understand the effects of temperature on hydrogen production. The highest CHF (8.9 L) and the highest yield (0.012 mol H2/ g TOC) was obtained with 5000 g wet weight in mesophilic conditions. Thermophilic conditions gave higher CHF (14.2 L) when compared with mesophilic one. The main VFAs were acetic and butyric acid in both conditions. Thermophilic conditions helped bacteria to convert simple sugars into VFA's faster than mesophilic conditions effecting positively hydrogen production yields. In terms of hydrogen production yields per g dry matter thermophilic conditions gave 1.6 times higher yield than mesophilic conditions; demonstrating suitability for organic substrates having high density.

REFERENCES

1. Ramprakash B and Incharoensakdi A. 2022. Dark fermentative hydrogen production from pretreated garden wastes by *Escherichia coli*. Fuel 310:122217.
2. Wang J and Yin Y. 2017. Biohydrogen production from organic wastes. Singapore, Springer pp:123-195.
3. Mohanakrishna G, Goud RK, Mohan SV and Sarma PN. 2010. Enhancing biohydrogen production through sewage supplementation of composite vegetable based market waste. International Journal of Hydrogen Energy 35:533-541.

4. Morales-Martinez TK, Medina-Morales MA, Ortiz-Cruz AL, Rodriguez-De la Garza JA, Moreno-Davila M, Lopez-Badillo CM and Rios-Gonzalez L. 2020. Consolidated bioprocessing of hydrogen production from agave biomass by Clostridium acetobutylicum and bovine ruminal fluid. International Journal of Hydrogen Energy 45(26):13707-13716.
5. Bhatia SK, Jagtap SS, Bedekar AA, Bhatia RK, Rajendran K, Pugazhendhi A, Rao CV, Atabani AE, Kumar G and Yang YH. 2021. Renewable biohydrogen production from lignocellulosic biomass using fermentation and integration of systems with other energy generation technologies. Science of The Total Environment 765:144429.
6. Abubackar HN, Keskin T, Yazgın O, Gunay B, Arslan K and Azbar N. 2019. Biohydrogen production from autoclaved fruit and vegetable wastes by dry fermentation under thermophilic condition. International Journal of Hydrogen Energy 44(34):18776-18784.
7. Jaitalee L, Dararat S and Chavalparit O. 2010. Bio-hydrogen production potential from market waste. EnvironmentAsia 3(2):115-122.
8. Toledo-Cervantes A, Villafan-Carranza F, Arreola-Vargas J, Razo-Flores E and Mendez-Acosta O. 2020. Comparative evaluation of the mesophilic and thermophilic biohydrogen production at optimized conditions using tequila vinasses as substrate. International Journal of Hydrogen Energy 45(19):11000-11010.
9. Dubois M, Gilles KA, Hamilton JK, Rebers PAT and Smith F. 1956. Colorimetric method for determination of sugars and related substances. Analytical Chemistry 28:350-356.
10. Tosuner ZV, Taylan GG and Ozmihci S. 2019. Effects of rice husk particle size on biohydrogen production under solid state fermentation. International Journal of Hydrogen Energy 44:18785-18791.
11. Eker S and Erkul B. 2018. Biohydrogen production by extracted fermentation from sugar beet. International Journal of Hydrogen Energy 43:10645-10654.

WHEC-2022
23rd World Hydrogen Energy Conference
June 26-30, 2022 - Istanbul

#374

ASSESSMENT OF BIOHYDROGEN PRODUCTION ROUTES FROM ORGANIC SOLID WASTE: THE CASE OF CARTAGENA, COLOMBIA

[1]Carel Lizarazo, [1]William Hurtado, [1]Oscar Venegas, [1*]Oscar Pupo, [1]Lesme Corredor
[1]Universidad del Norte, Kilometer 5 Via Puerto Colombia, Barranquilla, Colombia

*Corresponding author e-mail: opupo@uninorte.edu.co

ABSTRACT

The growing demand for energy worldwide requires a transition towards clean and renewable energy sources in order to mitigate the negative effects of greenhouse gases. During the last decade, hydrogen has been included in multiple national energy roadmaps as a promising alternative to traditional fossil fuels due to its energy content and conversion efficiency. This study aims to assess different biohydrogen production routes from organic solid waste in order to select the best cost-effective alternative for the city of Cartagena, Colombia. Therefore, six different criteria were defined using the Analytical Hierarchy Process (AHP). Subsequently, these criteria were used in order to compare seven biohydrogen production routes. The results obtained in this study suggest that the production of hydrogen through the biogas steam reforming process could be an attractive technology compared to other methods.

Keywords: Biohydrogen, Biogas Steam Reforming, Anaerobic Digestion, Colombia, Analytical Hierarchy Process (AHP).

INTRODUCTION

Hydrogen is an element widely used at industrial level with around 60 million tons produced every year that are mainly used in oil refining and ammonia production [1]. However, the production of hydrogen is limited since this element does not exist by itself in nature and requires complex processes to obtain it [1], [2]. Most of the current hydrogen production worldwide is based on fossil fuels [3]. However, there is a growing interest in producing hydrogen from renewable sources in order to avoid the generation of greenhouse gases during the process. Biohydrogen production from organic solid waste and wastewater is a promising alternative for the development of a sustainable hydrogen production chain [2]. Technologies that use waste generated by human production to generate energy are a great alternative. In this study, the following technologies were reviewed: thermo-chemical gasification, supercritical conversion, biogas steam reforming, direct bio-photolysis, indirect bio-photolysis, photo-fermentation and dark fermentation [4]. Although photosynthetic hydrogen production is a theoretically good technique for converting solar energy into hydrogen using photosynthetic bacteria, putting it into reality is problematic due to poor light utilization efficiency and complex hydrogen reactors development. Hydrogen production from agriculture residue is reported to be more cost-effective than the photosynthetic hydrogen production. Fermentative hydrogen production is more feasible and thus widely used. However, fermentative hydrogen and steam Reforming production have the advantage of rapid hydrogen production rate and a simpler operation [4]. This study aims to assess and compare the different biohydrogen production routes from organic solid waste in order to select the best cost-effective alternative for the city of Cartagena, Colombia. This city, located on the northwest of Colombia, produces approximately 0.57 kg/inhabitant of urban solid waste each day, i.e., 190,273 tons/year [5]. Therefore, the amount of biogas produce by urban solid waste in this area of the country evidences its potential use for energy applications.

METHODOLOGY

The selection of the best cost-effective biohydrogen production route was based on the Analytical Hierarchy Process (AHP). This is a decision-aiding method developed by Saaty [6] that aims to quantify relative priorities for a given set of alternatives on a ratio scale. Furthermore, the consistency of alternative comparisons in the decision-making process. The AHP method aligns well with decision-maker behaviour because a decision-maker relies on judgements on knowledge and experience before making decisions. This approach's strength is that it collects physical and intangible aspects in a systematic manner and gives a structured yet relatively straightforward solution to decision-making challenges [6]. Six different selection criteria were defined by the authors based on previous studies [4]: cost, process yield, environmental impact, complexity, sizing, and environmental and occupational risk.

Table 1. Alternative selection criteria

Criteria	Cost	Environmental impact	Complexity	Sizing	Yield	Environmental and occupational risk	Criteria value	Total
Cost	0.14	0.14	0.22	0.11	0.09	0.12	0.14	14%
Environmental impact	0.25	0.25	0.22	0.40	0.29	0.20	0.27	28%
Complexity	0.08	0.15	0.13	0.10	0.29	0.11	0.15	16%
Sizing	0.09	0.05	0.11	0.08	0.06	0.11	0.08	9%
Yield	0.16	0.10	0.05	0.14	0.11	0.20	0.13	13%
Environmental and occupational risk	0.25	0.28	0.25	0.15	0.12	0.22	0.21	21%

The alternatives considered in the selection analysis were thermo-chemical gasification, supercritical conversion, steam reforming, direct bio-photolysis, indirect bio-photolysis, photo-fermentation and dark fermentation.

Table 2. Biohydrogen production routes assessment

	Cost	Environmental impact	Complexity	Sizing	Yield	Environmental and occupational risk	Total
Thermo-chemical gasification	1.51	0.32	0.65	1.64	1.10	0.90	6.12
Supercritical conversion	1.35	0.33	0.68	1.84	1.24	0.92	6.36
Biogas steam reforming	**1.13**	**0.34**	**0.70**	**2.11**	**1.42**	**1.02**	**6.74**
Direct bio-photolysis	0.83	0.61	0.96	1.72	1.16	0.52	5.81
Indirect bio-photolysis	0.78	0.62	0.99	1.63	1.10	0.45	5.58
Photo-fermentation	0.76	0.65	1.09	1.41	0.95	0.46	5.32
Dark fermentation	0.70	0.74	1.23	1.37	0.93	0.46	5.42

RESULTS AND DISCUSSIONS

The biohydrogen production routes assessment is shown in table 2. It was obtained that the best cost-effective alternative was the biogas steam reforming process. The selected process was used to estimate the output production for the city of Cartagena based on energy balances. The energy balance (Eb) was calculated using the following equations [7]:

$$Eb = Eout - Ein \quad (1)$$

$$Eout = 2.752 \times 0.535 \times 0.96 \times 0.8 \times MBiogas \times LHVH2 \quad (2)$$

$$Ein = ERSU + EDigestion + EDigestion - sep + ELiquid.dig + ESolid.dig + Ebiomethane + EH2 \quad (3)$$

Applying the selected production process could result in a total biohydrogen production of approximately 1697 tons each year. The required energy input is nearly 554 TJ/year, and this is mainly because of the huge amount of biogas required in the process.

CONCLUSIONS

In this study, different existing technologies used to produce hydrogen from biogas were assessed applying the Analytical Hierarchy Process (AHP). The biogas steam reforming alternative was selected and seems to be the best cost-effective of all the alternatives evaluated. In a future review, it would be essential to incorporate additional aspects, such as social components in order to estimate the overall sustainability of biogas routes, especially considering that innovation in the transformation of biogas into hydrogen is still in a developing stage.

NOMENCLATURE

E	Energy, TJ
M	Biogas flow, m^3/year
LHV	Low heating value, MJ/m^3

Subscripts

b	Balance
out	Output
in	Input
H2	Hydrogen
RSU	Solid urban waste

Sep	Separation
Dig	Digestate

REFERENCES

1. Surendra KC, Takara D, Hashimoto AG and Khanal SK. 2014. Biogas as a sustainable energy source for developing countries: Opportunities and challenges. Renewable and Sustainable Energy Reviews, vol. 31, pp. 846–859.
2. Osman AI, Deka TJ, Baruah DC and Rooney DW. 2020. Critical challenges in biohydrogen production processes from the organic feedstocks. Biomass Conversion and Biorefinery. Northern Ireland, Springer.
3. Situmorang YA. 2020. A novel system of biomass-based hydrogen production by combining steam bio-oil reforming and chemical looping process. Applied Energy, vol. 268, p. 115122.
4. Pandu K and Joseph S. 2012. Comparisons and limitations of biohydrogen production processes: a review. International Journal of Advances in Engineering & Technology 2231-1963
5. Londón E, Szantó NM, Pacheco JF, Contreras E and Gálvez A. 2016. Guía general para la gestión de residuos sólidos domiciliarios, vol. 1. CEPAL.
6. Al-Subhi K. 2001. Application of the AHP in project management. International Journal of Project Management, vol. 19, no. 1, pp. 19–27.
7. Cvetković SM, Radoičić TK, Kijevčanin M and Novaković JG. 2021. Life Cycle Energy Assessment of biohydrogen production via biogas steam reforming: Case study of biogas plant on a farm in Serbia. International Journal of Hydrogen Energy, vol. 46, no. 27, pp. 14130–14137.

WHEC-2022
23rd World Hydrogen Energy Conference
June 26-30, 2022 - Istanbul

#410

ADAPTATION OF *CALDICELLULOSIRUPTOR BESCII* TO UNPRETREATED CATTLE MANURE: A NOVEL APPROACH FOR HYPERTHERMOPHILIC BIOHYDROGEN PRODUCTION

[1] *Berivan Tunca, Yasemin Dilsad Yilmazel
[1]Middle East Technical University, Department of Environmental Engineering, Ankara, Turkey

*Corresponding author e-mail: dilsad@metu.edu.tr

ABSTRACT

Animal manure is an abundant, renewable, and cost-effective resource that is rich in valuable organic matter. In this work, utilization of unpretreated cattle manure (UCM) at high loadings (15, 25 and 50 g VS/L) as the sole carbon source for biohydrogen production by hyperthermophilic *Caldicellulosiruptor bescii* was examined. To enhance biohydrogen production, *C. bescii* was adapted to lower concentrations of UCM, which showed a significant increase in biohydrogen production compared to non-adapted *C. bescii*. The highest H_2 yield achieved from adaptation operation using 15 g VS/L of UCM as 161.3 ± 1.6 mL H_2/g VS_{added}, followed by 25 g VS/L as 89.1 ± 2.6 mL H_2/g VS_{added}. The achieved yields are the highest dark fermentative H_2 yields reported in the literature when unpretreated animal manure has been used for dark fermentation. A striking enhancement has been achieved via laboratory culture adaptation of the cellulolytic hyperthermophilic bacterium. Biohydrogen production has been improved by 124% at 15g VS/L and by 142% at 25 g VS/L compared to non-adapted culture of *C. bescii*. Even though the impact of inhibition was lowered by adaptation, the yield was still low in comparison to other concentrations studied.

Keywords: Manure, Hyperthermophilic, Biohydrogen, Laboratory Culture Adaptation, *Caldicellulosiruptor Bescii*

INTRODUCTION

Overuse of fossil fuels has contributed to dramatic exhaustion of natural resources, resulting in environmental pollution and greenhouse gas emissions. The efforts for developing alternative energy resources have been increased with a specific focus on renewable, sustainable, and cost-effective resources. Hydrogen (H_2) is proposed as a superior and clean energy carrier since its combustion generates only water vapor, and it has a substantial energy yield (122 kJ/g) approximately 3 times higher than any hydrocarbon fuels [1,2]. Yet, about 95% of H_2 generation is currently dependent on fossil fuels, thus, there is an urgent need to develop sustainable renewable hydrogen production methods [3]. Dark fermentation (DF) is a promising method for biohydrogen production through biomass conversion in the absence of light and oxygen. H_2 production via DF provides several benefits as low energy requirements, easier reactor design thus cost-effectiveness, and the use of various organic wastes as carbon source. The efficiency of the process is highly dependent on the activity of microorganisms, and the feedstock [4]. Among different microorganisms, hyperthermophiles are exceptional candidates for biohydrogen production and hyperthermophilic processes offer advantages such as minimal risk of contamination and significantly boosted reaction kinetics [5]. *Caldicellulosiruptor bescii*, a member of hyperthermophilic cellulolytic bacterial genus of *Caldicellulosiruptor*, has been identified as an excellent candidate for biohydrogen production from a wide range of polysaccharides, as well as unpretreated plant biomass [6,7]. Further, *C. bescii* has a superior ability to metabolize multiple six carbon and five carbon sugars simultaneously, owing to the absence of carbon catabolite repression mechanism (CCR). This is a very important feature for processing of various substrates. Formerly, we demonstrated that *C. bescii* can use pretreated wastewater biosolids [8] and cattle manure and their combinations at low concentration as the sole carbon source to produce biohydrogen [9]. However, the cost of pretreatment contributes up to 20% of biofuel generation cost; hence, our current focus is on the development of an efficient biohydrogen production process that does not require any pretreatment [10].

Use of widely accessible waste materials without any pretreatment, as a sole carbon source, is the key point to make the biohydrogen production sustainable and cost-efficient. Animal manure has an important potential as a renewable feedstock due to its abundance and low cost. Recently it was estimated that in EU more than 1.2 billion tons of animal manure is generated annually and cattle manure accounts for more than half of this amount [11]. Moreover, it is estimated that energy potential of cattle manure when used for biohydrogen production is about 10.6% of domestic crude oil supply of Turkey per year [9]. To utilize the untapped potential of cattle manure, we investigated its utilization by *C. bescii* at high organic loadings and without any pretreatment. The experiments were designed to assess the impact of culture adaptation on biohydrogen production yield.

MATERIALS AND METHODS

Inoculum and feedstock

C. bescii (DSM 6725) as an active culture was purchased from Germany Collection of Microorganisms and Cell Cultures (DSMZ), Braunschweig, Germany. It was grown as described elsewhere using crystalline cellulose as the carbon source with little modification as 1.5 g/L of $Na_2S.9H_2O$ was replaced with 0.5 g/L of L-cysteine and titanium citrate was removed from the media [8]. Cattle manure samples were obtained from Polres biogas plant in Polatlı, Ankara, Turkey. The sample was blended for 15 min and stored at 4 ˚C. The chemical oxygen demand (COD) analysis for manure was resulted as 123.9 ± 9.9 g/L. Total solids (TS) and volatile solids (VS) concentrations were 112.60 ± 1.91 mg/g and 79.4% ± 0.1% of TS, respectively. The fiber content analysis resulted as 50% of total fiber composition including 19.11% of cellulose, 18.42% of hemicellulose, and 12.47% of lignin, indicating this is a suitable substrate for *C. bescii*.

Experimental design and reactor operation

In this study, there were two sets: batch (non-adapted) and adaptation reactors. In Set 1, all reactors were inoculated with *C. bescii that was* grown in 5 g/L of crystalline cellulose for 15-18 hours (repeated for three consecutive cycles). In Set 2, *C. bescii* was first grown in 5 g/L of crystalline cellulose; then, active inoculum was adapted to lower concentration of UCM. To achieve, adaptive laboratory evolution (ALE) process serial batch cultivations were applied [12]. In the second cycle of ALE, carbon source for growth was replaced with 5 g VS/L of UCM and serial batch cultivations in this media has been repeated for a total of three cycles. *C. bescii* adapted to UCM was put into Set 2 reactors as an inoculum.

In each set, four types of reactors were operated as (i) blank, (ii) pure substrate control, (iii) cattle manure reactors, and (v) negative control. In brief, the aim of blank (B) was to define the background metabolic products. Pure feedstock control (PC) feeding with 5 g/L of crystalline cellulose were operated to prove the activity of *C. bescii*. Target feedstock, *i.e.* unpretreated cattle manure, reactors were operated as test reactors, fed with different manure concentrations (15, 25 and 50 g VS/L). Negative controls (NC) were fed with corresponding cattle manure concentrations without any *C. bescii* inoculum to determine any metabolic product generation due to the presence of native microorganisms of UCM.

Batch reactors used in this study have a total volume of 60 mL (an effective volume of 30 mL). Triplicate reactors were incubated in a water bath at 75 ˚C for 44 days in Set 1 and for 32 days for Set 2. Hydrogen was measured periodically during incubation and other metabolic products such as acetic acid have been measured at the end of operation.

Analytical methods

Characterization of cattle manure was achieved by using standard methods for total solids (Method 2540B), volatile solids (Method 2540E) and total COD (Method 5220D). Manure fiber analysis was conducted at Nutrilab (Konya, Turkey) [13]. The total gas generation was measured by liquid displacement method in the serum bottles. The content of the produced gas and quantification of volatile fatty acids (VFA) were analyzed as described elsewhere [14]. H_2 production values were given at standard temperature and pressure (STP) (0 °C and 1 atm).

The modified Gompertz equation (Eq. (1)) was used to compare H_2 production performance of different reactors [15].

$$H(t) = P.exp\{-exp[\frac{R_m.e}{P}(\lambda - t) + 1]\} \quad (1)$$

H(t) = H_2 generation (mL); P = maximum H_2 generation (mL); R_m = H_2 generation rate (mL/day); e = 2.71828; λ = lag-phase time (d); t = time (d). Data analysis was performed using Excel for Windows 8.0 software (Microsoft, USA).

RESULTS AND DISCUSSION

Hydrogen production from all reactors were given as net H_2 production at STP by subtracting the production in blank reactors. In batch-pure control reactors, average net H_2 production was 7.0 ± 0.4 mL H_2 proving that inoculated *C. bescii* was active. In the first set, 32.5 ± 0.6 mL H_2 was produced in 15 g VS/L reactors and 27.6 ± 2.9 mL H_2 was produced in 25 g VS/L added reactors (Fig. 1A). In the reactors containing 50 g VS/L of cattle manure, there was no hydrogen production, which is a clear proof of inhibition effect of cattle manure at this high loading. The highest H_2 yield from UCM for batch reactors was 72.2 ± 1.3 mL H_2/g VS_{added} achieved from 15 g VS/L, which indicates that there is a moderate inhibition at higher loadings of UCM (Table 1).

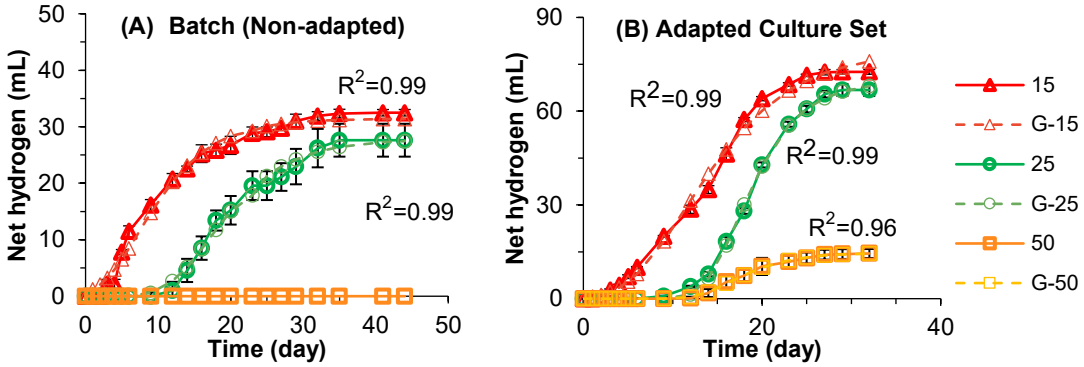


Figure 1. Average net hydrogen production (A) batch (non-adapted) reactors; (B) adapted reactors (15: 15 g VS/L of UCM; 25: 25 g VS/L of UCM, 50: 50 g VS/L of UCM; G: Gompertz model fitting)

Table 1. Hydrogen yields

	Batch (Non-adapted) Set			Adapted Culture Set		
Concentration (g VS/L)	15	25	50	15	25	50
Yield (mL H_2/g VS)	72.2 ± 1.3	36.8 ± 3.9	-	161.3 ± 1.6	89.1 ± 2.6	36.8 ± 3.9

Although biohydrogen production from UCM was significant with non-adapted culture, a considerable decrease on H_2 yield (~ 50%) was observed at higher loadings. To overcome this problem and produce H_2 more efficiently at industrially relevant concentrations of UCM, adaptation of *C. bescii* to UCM has been performed. Adapted inoculum showed a significant H_2 production in PC reactors (including 5 g/L of crystalline cellulose). The net average H_2 production of PC reactor was 14.2 ± 1.1 mL H_2, which is about 2 times higher than batch PC reactors (data not shown). This may be explained by the additional carbon source from growth reactors that is introduced to the reactor or adapted *C. bescii* can effectively degrade pure substrate. The adapted inoculum reactors containing 15, 25 and 50 g VS/L produced H_2 in the order of 72.6 ± 0.7 mL H_2, 66.8 ± 1.9 mL H_2 and 14.5 ± 1.5 mL H_2 (Fig. 1B). Adaptation of *C. bescii* enhanced H_2 generation from UCM significantly at which the enhancements for biohydrogen generation are 123.5% and 141.8% for 15 and 25 g VS/L compared to non-adapted culture of *C. bescii*. For adapted reactors, hydrogen yields were also increased to 161.3 ± 1.6 mL H_2/g VS_{added}, 89.1 ± 2.6 mL H_2/g VS_{added} and 36.8 ± 3.9 mL H_2/g VS_{added} for 15, 25 and 50 g VS/L. Yet, even with adaptation as the load was increased yield decreased. Nevertheless, here we report the highest dark fermentative yields obtained in the literature when unpretreated animal manure was used as a sole carbon source [16–19].

Modified-Gompertz model was run for data analysis to compare hydrogen production rate and lag-phase additional to the yield. The highest volumetric H_2 generation rate was 6.5 ± 0.3 mL H_2/day obtained from 25 g VS/L in adaptation operation. It is followed by adapted 15 g VS/L reactors with 4.4 ± 0.1 mL H_2/day. We have also checked the solubilization of UCM to assess the extent of biodegradation. The degree of solubilization was 73.1% for 15 gVS/L UCM and 57.1% for 25 g VS/L UCM with the adapted culture. These solubilization results are about 2 times higher than any other real feedstock solubilization that were used by *C. bescii* [20–22].

CONCLUSIONS

It is proved that hyperthermophilic bacterium *C. bescii* has an ability to degrade UCM at high loadings to produce biohydrogen. With the adaptation of *C. bescii* to UCM, biohydrogen production was significantly enhanced for all concentrations (15 - 25 g VS/L) about 2.2-2.4 times compared to non-adaptive operation. Even though there is an inhibition at 50 g VS/L of cattle manure loading, adaptation of inoculum has supported to decrease the negative effect, and enhanced biohydrogen generation. The results presented here indicate that *C. bescii* can be used as a microbial factory to process complex materials such as UCM for enhanced biohydrogen production and can be adapted to industrially relevant loads.

ACKNOWLEDGEMENTS

This work was supported by the Scientific and Technological Research Council of Turkey (TUBITAK) grant number 119C011 and the World Academy of Sciences (TWAS) grant number 18-302 RG/ REN/AS_C – FR3240305798.

REFERENCES

1. Gupta N, Pal M, Sachdeva M, Yadav M, Tiwari A. Thermophilic biohydrogen production for commercial application: the whole picture. Int J Energy Res 2016;40:127–45. https://doi.org/0.1002/er.3438.
2. Pawar SS, Van Niel EWJ. Thermophilic biohydrogen production: How far are we? Appl Microbiol Biotechnol 2013;97:7999–8009. https://doi.org/10.1007/s00253-013-5141-1.
3. Wang S, Zhang T, Bao M, Su H, Xu P. Microbial Production of Hydrogen by Mixed Culture Technologies: A Review. Biotechnol J 2020;15:1–8. https://doi.org/10.1002/biot.201900297.
4. Abreu AA, Tavares F, Alves MM, Cavaleiro AJ, Pereira MA. Garden and food waste co-fermentation for biohydrogen and biomethane production in a two-step hyperthermophilic-mesophilic process. Bioresour Technol 2019;278:180–6. https://doi.org/10.1016/j.biortech.2019.01.085.
5. Saidi R, Liebgott PP, Gannoun H, Ben Gaida L, Miladi B, Hamdi M, et al. Biohydrogen production from hyperthermophilic anaerobic digestion of fruit and vegetable wastes in seawater: Simplification of the culture medium of Thermotoga maritima. Waste Manag 2018;71:474–84. https://doi.org/10.1016/j.wasman.2017.09.042.
6. Yang SJ, Kataeva I, Hamilton-Brehm SD, Engle NL, Tschaplinski TJ, Doeppke C, et al. Efficient degradation of lignocellulosic plant biomass, without pretreatment, by the thermophilic anaerobe “Anaerocellum thermophilum” DSM 6725. Appl Environ Microbiol 2009;75:4762–9. https://doi.org/10.1128/AEM.00236-09.
7. Yang SJ, Kataeva I, Wiegel J, Yin Y, Dam P, Xu Y, et al. Classification of “Anaerocellum thermophilum” strain DSM 6725 as Caldicellulosiruptor bescii sp. nov. Int J Syst Evol Microbiol 2010;60:2011–5. https://doi.org/10.1099/ijs.0.017731-0.
8. Yilmazel YD, Johnston D, Duran M. Hyperthermophilic hydrogen production from wastewater biosolids by Caldicellulosiruptor bescii. Int J Hydrogen Energy 2015;40:12177–86. https://doi.org/10.1016/j.ijhydene.2015.06.140.
9. Yilmazel YD, Duran M. Biohydrogen production from cattle manure and its mixtures with renewable feedstock by hyperthermophilic Caldicellulosiruptor bescii. J Clean Prod 2021;292:125969. https://doi.org/10.1016/j.jclepro.2021.125969.
10. Mankar AR, Pandey A, Modak A, Pant KK. Pretreatment of lignocellulosic biomass: A review on recent advances. Bioresour Technol 2021;334:125235. https://doi.org/10.1016/j.biortech.2021.125235.
11. Li Y, Zhao J, Krooneman J, Jan G, Euverink W. Strategies to boost anaerobic digestion performance of cow manure : Laboratory achievements and their full-scale application potential. Sci Total Environ 2021;755. https://doi.org/10.1016/j.scitotenv.2020.142940.
12. Mavrommati M, Daskalaki A, Papanikolaou S, Aggelis G. Adaptive laboratory evolution principles and applications in industrial biotechnology. Biotechnol Adv 2022;54:107795. https://doi.org/10.1016/j.biotechadv.2021.107795.
13. APHA, AWWA, WPCF. Standard Methods for the Examination of Water and Wastewater. Am Public Heal Assoc Washingt 2005.
14. Kas A, Yilmazel YD. High current density via direct electron transfer by hyperthermophilic archaeon , Geoglobus acetivorans, in microbial electrolysis cells operated at 80 ° C. Bioelectrochemistry 2022; 145: 108072. https://doi.org/10.1016/j.bioelechem.2022.108072.
15. Zwietering MH, Jongenburger I, Rombouts FM, Van’t Riet K. Modeling of the Bacterial Growth Curve. Appl Environ Microbiol 1990;56:1875–81.
16. Yokoyama H, Yamashita T, Ogino A, Ishida M, Tanaka Y. Hydrogen fermentation of cow manure mixed with food waste. Japan Agric Res Q 2010;44:399–404. https://doi.org/10.6090/jarq.44.399.
17. Kotsopoulos TA, Fotidis IA, Tsolakis N, Martzopoulos GG. Biohydrogen production from pig slurry in a CSTR reactor system with mixed cultures under hyper-thermophilic temperature (70 °C). Biomass and Bioenergy 2009;33:1168–74. https://doi.org/10.1016/j.biombioe.2009.05.001.
18. Wang KS, Chen JH, Huang YH, Huang SL. Integrated Taguchi method and response surface methodology to confirm hydrogen production by anaerobic fermentation of cow manure. Int J Hydrogen Energy 2013;38:45–53. https://doi.org/10.1016/j.ijhydene.2012.03.155.
19. Xing Y, Li Z, Fan Y, Hou H. Biohydrogen production from dairy manures with acidification pretreatment by anaerobic fermentation. Environ Sci Pollut Res 2010;17:392–9. https://doi.org/10.1007/s11356-009-0187-4.
20. Zurawski J V., Conway JM, Lee LL, Simpson HJ, Izquierdo JA, Blumer-Schuette S, et al. Comparative analysis of extremely thermophilic Caldicellulosiruptor species reveals common and unique cellular strategies for plant biomass utilization. Appl Environ Microbiol 2015;81:7159–70. https://doi.org/10.1128/AEM.01622-15.
21. Straub CT, Khatibi PA, Otten JK, Adams MWW, Kelly RM. Lignocellulose solubilization and conversion by extremely thermophilic Caldicellulosiruptor bescii improves by maintaining metabolic activity. Biotechnol Bioeng 2019;116:1901–8. https://doi.org/10.1002/bit.26993.
22. Conway JM, McKinley BS, Seals NL, Hernandez D, Khatibi PA, Poudel S, et al. Functional Analysis of the Glucan Degradation Locus in Caldicellulosiruptor bescii Reveals Essential Roles of Component Glycoside Hydrolases in Plant Biomass Deconstruction 2017;83:1–22.

WHEC-2022
23rd World Hydrogen Energy Conference
June 26-30, 2022 - Istanbul

#437

BIOELECTROCHEMICAL HYDROGEN PRODUCTION FROM DARK FERMENTATION EFFLUENTS IN HYPERTHERMOPHILIC MICROBIAL ELECTROLYSIS CELLS

*Aykut Kas, Berivan Tunca, Yasemin Dilsad Yilmazel**
Middle East Technical University (METU), Department of Environmental Engineering, Ankara, Turkey

*Corresponding author e-mail: dilsad@metu.edu.tr

ABSTRACT

Biohydrogen production at extremely thermophilic conditions (>70°C) has a high potential as it provides increased reaction rates, enhanced feedstock solubilization, and lower risk of contamination. Hyperthermophilic cellulolytic bacteria *Caldicellulosiruptor bescii* is capable of utilizing cattle manure as the sole carbon source and produce hydrogen with a superior yield in comparison to other dark fermentation (DF) processes. Yet, acetic acid produced as an end product of DF remain unused in the system. Hyperthermophilic microbial electrolysis cells (MECs) offer a great potential to further process soluble DF products by employment of electro-active microorganisms with no need for chilling. In this study, *C. bescii* was used to produce hydrogen from untreated cattle manure and DF effluent was rich in acetate, thus sufficient for feeding to electro-active hyperthermophiles. Therefore, we designed experiments to process DF effluent of *C. bescii* based bioprocess in hyperthermophilic (80 – 85 °C) MECs to evaluate the potential of sequential operation of DF and MECs at hyperthermophilic conditions for the first time in the literature. To this purpose, experiments were conducted in single chamber MECs with an applied voltage of 0.7 V and inoculated with recently proven electro-active archaea, namely, *Geoglobus acetivorans* and *Ferroglobus placidus.* Hydrogen production rate of the sequential operation was around 0.11 ± 0.02 m^3 H_2/m^3/day, to which MECs contributed significantly as 0.08 ± 0.01 m^3 H_2/m^3/day. This study is the first report of sequential application of DF and MECs at hyperthermophilic conditions and presents a proof-of-concept.

Keywords: Dark Fermentation, Hydrogen, Microbial Electrolysis Cells, Electrohydrogenesis, Hyperthermophilic

INTRODUCTION

Microbial electrolysis cells (MECs) is a bioelectrochemical reactor used to produce hydrogen (H_2) from different feedstocks such as organic acids and complex substrates as dark fermentation effluents and wastewater [1–3]. The production of H_2 in MECs, known as electrohydrogenesis, depends on the anode biofilm possessing electro-active characteristics, which metabolize organic material and generate electrical current via transfer of electrons to the anode [4]. The electrons are then consumed at the cathode, where H_2 evolution reaction ($2H^+ + 2e^- \rightarrow H_2$) takes place upon application of an external voltage [4]. The external voltage is needed, because the reaction on the cathode is non-spontaneous. For example, bioelectrochemical acetate oxidation, a typical product generated during fermentation of organic materials, leads to a potential around -0.28 V, yet H_2 production requires a potential around -0.42 V [5]. Therefore, a minimum of 0.14 V is necessary to produce H_2 in MECs, yet in practice at least 0.5 V is applied, because of the electrode overpotentials and losses resulted from MEC materials [5]. Still, the required energy during electrohydrogenesis is significantly lower in comparison to what is needed (~1.8 V) water electrolysis process [6].

Dark fermentation (DF), on the other hand, is a widely used biohydrogen production process that offers a simple reactor operation and applicability to a variety of complex wastes [7]. Operation of bioreactors for processes such as DF and electrohydrogenesis at extremely thermophilic conditions (>70°C) has a higher application potential than mesophilic operations, specifically for industrial applications elevated temperature accelerates the rate of reactions, improves the degradation of insoluble substrates, minimize contamination risk and lowers the solubility of oxygen enabling easier maintenance of anaerobic conditions [8,9]. Recently, we have reported that *Caldicellulosiruptor bescii* can utilize various feedstocks such as wastewater biosolids and cattle manure with the highest fermentative yields of 86 mL H_2/g VS for biosolids and 106 mL H_2/g VS for cattle manure at 78 °C with pretreatment [10,11]. Biohydrogen production from cattle manure by *C. bescii* not only produce H_2, but also produce acetic acid in significant quantities and hence could potentially be used for further H_2 production in hyperthermophilic MECs operated at similar temperatures without the need for chilling [11]. So far there are only four hyperthermophilic species that are proven to be electro-active [12–15]. Among those, three of them namely *Ferroglobus placidus*, *Geoglobus ahangari* and *Geoglobus acetivorans* belongs to the family of Archaeoglobaceae and we have demonstrated that these iron reducing archaeal cultures possess electro-active properties and can produce electrical current in MECs, when fed with pure acetate at elevated temperatures ~ 80 ˚C [14,15]. The promising results of our proof-of-concept work with electro-active hyperthermophiles directed us to further examine the possibility of feeding DF effluent to hyperthermophilic MECs for further H_2 production. Therefore, in our current investigation experiments were designed

to assess the potential of sequential process of DF and MEC reactors at hyperthermophilic conditions and to determine the best fit culture for this process.

MATERIALS AND METHODS

Microorganisms and growth conditions

Active cultures of *C. bescii* (DSM 6725), *G. acetivorans* (DSM 21716) and *F. placidus* (DSM10642) were purchased from the German Resource Centre for Biological Material (DSMZ). *C. bescii* was grown in a media, where crystalline cellulose was used as carbon source at 75 °C as detailed elsewhere [11]. *G. acetivorans* and *F. placidus* were grown with acetate (10 mM) as electron donor and ferric citrate (56 mM) as electron acceptor at 80 °C and *at* 85 °C, respectively [14].

MEC configuration and reactor operation

MECs used in this study were constructed as single chamber with an active volume of 5 mL (total volume: 8 mL), called Mini MECs [14]. Anode was a graphite block (1 cm wide, 1.5 cm long and 0.3 cm deep). The stainless-steel mesh (1 cm wide and 1.5 cm long) was used as a cathode. All MECs were made oxygen free by purging with the mixture of N_2:CO_2 (80%:20%) gas and sterilization was completed by autoclaving before use. The hyperthermophilic medium without ferric citrate (electron acceptor) was filled into MECs inside an anaerobic chamber and the active culture of *G. acetivorans* (or *F. placidus*) were inoculated as 20% volume. The operation of all MECs were performed as fed-batch cycles and continuously a 0.7 V was applied to each MEC. Current generation was observed during the reactor operation, and the content of H_2 was analyzed at the end of each cycle. After the current drops by ~60% of its peak value, a new cycle was started by replacing MEC media including electron donor. A multimeter was used to record voltage measurements across 10 Ω resistor that is put in between the power supply and the anode, over the anode cable and measurements were taken at 10 min intervals [14]. Current was calculated using the data stored by applying Ohm's law. To find current density (A/m^2) current was normalized to total anode area. The impact of switching from pure acetate to acetate produced via DF process was tested using similar reactors (named as Midi MECs) constructed in larger size with a total volume of 25 mL (15 mL of active volume). A similar protocol was followed to produce Midi MECs, by inserting slightly larger electrodes (1 cm wide, 2 cm long and 0.3 cm deep anodes, 2 cm long and 1.0 cm wide cathodes) to larger size serum bottles.

Experimental design and calculations

DF reactors have been operated as batch reactors (60 mL of total volume and active volume of 30 mL) fed with 15 g VS/L of unpretreated cattle manure. Triplicate reactors were operated for 44 days, and H_2 production was analyzed periodically during incubation, and liquid metabolic products *e.g.* acetic acid was measured at the end of operation. There were two sets of experiments with MECs in this study. In the first set, Midi MECs were used only by *G. acetivorans* inoculation. Midi MECs were operated for 90 days reactors with a feed of pure acetate in concentrations ranging between 10 mM and 20 mM, and biofilm formation was monitored via cyclic voltammetry along with current generation. After this initial biofilm growth with pure acetate, feed was switched to filtered DF effluent as a carbon source, where the other medium components e.g. vitamin, trace element kept the same as in the original hyperthermophilic medium. DF effluent has been diluted to provide acetate concentrations of 10 mM and 20 mM acetate, and H_2 production has been monitored for four cycles, presented as cycle 1 – 4 in Midi MECs. The second set was conducted in Mini MECs with pure culture of *G. acetivorans*, pure culture of *F. placidus* and their co-culture. This time Mini MECs have been started directly by feeding DF effluent containing medium at a concentration of 10 mM acetate to assess whether there is an impact of DF on the initial biofilm growth and to assess hydrogen production rate (HPR) for three cycles. All MECs were operated in duplicate.

Coulombic efficiency, C_E, is calculated by Eq. 1 by dividing total coulombs (nC_E) and to the total Coulombs found from acetate consumption (n_{th}) by considering eight electrons per acetate. The calculation of cathodic recovery, r_{cat} (%), was achieved by Eq. 2, which gives relative the moles of H_2 recovered (n_R) (mole H_2) to that possible from the measured current (n_E). Eq. 3 was used to calculate the HPR, where J_V (A/m^3) is volumetric current density averaged over 6 hours, c_g (mol/L) is the concentration of gas at reactor T and P, F is the Faraday' constant (96,485 C/mol.e^-), and 43.2 is for unit conversion factor. The multiplication of C_E and r_{cat} provides the overall hydrogen recovery (R_{H2}) [5].

$$C_E\,(\%) = \frac{n_{C_E}}{n_{th}} = 100 \times \frac{\int_{t=0}^{t} I\,dt}{n_{th}} \quad (1)$$

$$r_{cat}\,(\%) = 100 \times \frac{n_R}{n_E} = 100 \times \frac{n_R}{\frac{\int_{t=0}^{t} I\,dt}{2F}} \quad (2)$$

$$HPR\left(\frac{m^3 H_2}{m^3\ active\ volume.day}\right) = \frac{43.2\ J_V\ r_{cat}}{F\ c_g(T)} \quad (3)$$

RESULTS AND DISCUSSION

H_2 production in DF reactors fed with 15 g VS/L of untreated cattle manure produced 32.5 ± 0.6 mL of H_2 with a yield of 72.2 mL H_2/g VS and a HPR of 0.03 $m^3/m^3/d$. The other major end product of *C. bescii* fermentation of cattle manure was acetic acid and produced as 54.4 ± 1.6 mM. There was also lower amounts of lactic acid, butyric acid and propionic acid at concentrations of 6.4 ± 0.5 mM, 7.5 ± 0.1, and 3.0 ± 0.2, respectively. No other volatile fatty acids were observed at the end of operation. The yield obtained here is considerably higher (about 3 times) than the studies using unpretreated animal manure as a sole carbon source [16–18]. Similar to our studies with pretreatment [10,11], the yield obtained here is the maximum dark fermentative H_2 yield when solely unpretreated animal manure is used for H_2 production.

DF effluent was first fed for four cycles to Midi MECs, in which biofilm formation was completed by pure acetate. In the first cycle, current density peaked around 0.32 ± 0.02 A/m^2 corresponding to > 65% of peak current density recorded by pure acetate (data not shown). It was decreased to 0.23 ± 0.03 A/m^2 in two subsequent cycles when the dosage was doubled, which may be due to the need of adaptation of biofilm to DF effluent as it contains other constituents, for instance, lactic acid present in DF effluent is not degradable by *G. acetivorans* [15]. When DF effluent was fed at a 10 mM acetate concentration, ~ 80% of acetate has been consumed and in cycles with 20 mM initial acetate concentration ~ 55% consumption has been recorded (Figure 1). Over four cycles of operation HPR did not change significantly, with average of 0.08 ± 0.01 m^3 H_2/m^3/day. C_E decreased from 150% to ~ 77% indicating that utilization of hydrogen by *G. acetivorans* in membraneless MECs was reduced over multiple DF cycles. Regardless, average R_{H2} in MECs was 65%.

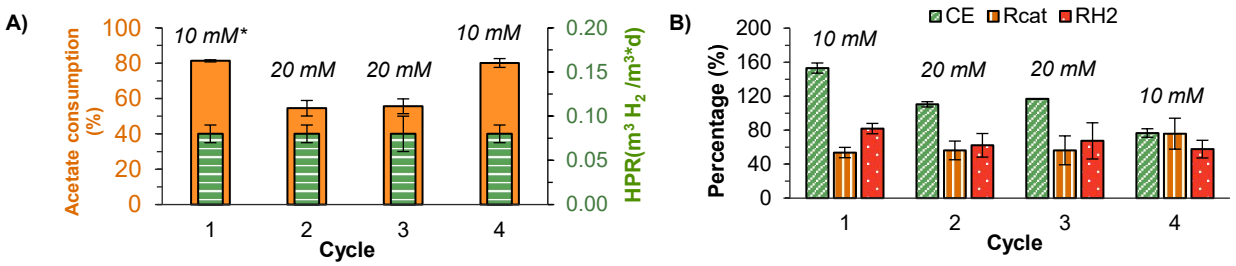


Figure 1. A) HPR and acetate consumption B) C_E, r_{cat}, and RH_2 in Midi MECs fed with DF effluent (*initial acetate concentration)

Further, DF effluent was directly used in Mini MECs inoculated by *G. acetivorans*, *F. placidus* and their co-culture and HPR recorded with these cultures is presented in Figure 2. By the third cycle of operation all MECs produced hydrogen with similar rates around 0.09 m^3 H_2/m^3/day.

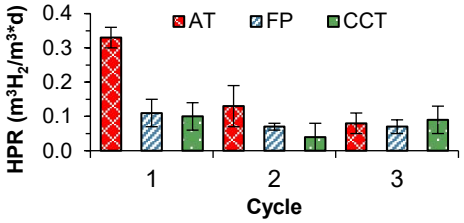


Figure 2. HPR in Mini MECs of directly fed with DF effluent *G. acetivorans* (AT), *F. placidus* (FP) and co-culture (CCT)

CONCLUSIONS

For the first time in the literature, it is proven that H_2 production could be enhanced by sequential operation of a hyperthermophilic DF process followed by hyperthermophilic MECs that were fed with DF effluent. HPR of series application of DF and electrohydrogenesis was 0.11 ± 0.02 m^3 H_2/m^3/day, which is 325% higher than DF process alone. Similar HPRs around 0.08 ± 0.01 m^3 H_2/m^3/day was achieved independent of hyperthermophilic culture used and overall H_2 yield is now further increased to 104.2 mL H_2/g VS. Yet, HPR is still small and optimization of MEC conditions is required to increase rate and the overall yield of H_2 from unpretreated cattle manure.

ACKNOWLEDGEMENTS
Authors thank the Scientific and Technological Research Council of Turkey (TUBITAK) grant no. 119C011, METU Office of Sponsored Research (grant IDs 10273 and10905), and COMSTECH (18-302 RG/ REN/AS_C – FR3240305798) grant from the World Academy of Sciences (TWAS).

REFERENCES

1. Dhar BR, Elbeshbishy E, Hafez H, Lee HS. Hydrogen production from sugar beet juice using an integrated biohydrogen process of dark fermentation and microbial electrolysis cell. Bioresour Technol 2015; 198:223–30. https://doi.org/10.1016/j.biortech.2015.08.048.
2. Lalaurette E, Thammannagowda S, Mohagheghi A, Maness PC, Logan BE. Hydrogen production from cellulose in a two-stage process combining fermentation and electrohydrogenesis. Int J Hydrogen Energy 2009; 34:6201–10. https://doi.org/10.1016/j.ijhydene.2009.05.112.
3. Wagner RC, Regan JM, Oh SE, Zuo Y, Logan BE. Hydrogen and methane production from swine wastewater using microbial electrolysis cells. Water Res 2009. https://doi.org/10.1016/j.watres.2008.12.037.
4. Rozendal RA, Hamelers HVM, Euverink GJW, Metz SJ, Buisman CJN. Principle and perspectives of hydrogen production through biocatalyzed electrolysis. Int J Hydrogen Energy 2006; 31:1632–40. https://doi.org/10.1016/j.ijhydene.2005.12.006.
5. Logan BE, Call D, Cheng S, Hamelers HVM, Sleutels THJA, Jeremiasse AW, et al. Microbial electrolysis cells for high yield hydrogen gas production from organic matter. Environ Sci Technol 2008; 42:8630–40. https://doi.org/10.1021/es801553z.
6. Li X, Zhao L, Yu J, Liu X, Zhang X, Liu H, et al. Water Splitting: From Electrode to Green Energy System. Nano-Micro Lett 2020; 12:1–29. https://doi.org/10.1007/s40820-020-00469-3.
7. Łukajtis R, Hołowacz I, Kucharska K, Glinka M, Rybarczyk P, Przyjazny A, et al. Hydrogen production from biomass using dark fermentation. Renew Sustain Energy Rev 2018; 91:665–94. https://doi.org/10.1016/j.rser.2018.04.043.
8. Pawar SS, Van Niel EWJ. Thermophilic biohydrogen production: How far are we? Appl Microbiol Biotechnol 2013; 97:7999–8009. https://doi.org/10.1007/s00253-013-5141-1.
9. Rathinam NK, Bibra M, Salem DR, Sani RK. Thermophiles for biohydrogen production in microbial electrolytic cells. Bioresour Technol 2019; 277:171–8. https://doi.org/10.1016/j.biortech.2019.01.020.
10. Yilmazel YD, Johnston D, Duran M. Hyperthermophilic hydrogen production from wastewater biosolids by *Caldicellulosiruptor bescii.* Int J Hydrogen Energy 2015; 40:12177–86. https://doi.org/10.1016/j.ijhydene.2015.06.140.
11. Yilmazel YD, Duran M. Biohydrogen production from cattle manure and its mixtures with renewable feedstock by hyperthermophilic *Caldicellulosiruptor bescii.* J Clean Prod 2021; 292:125969. https://doi.org/10.1016/j.jclepro.2021.125969.
12. Sekar N, Wu CH, Adams MWW, Ramasamy RP. Electricity generation by *Pyrococcus furiosus* in microbial fuel cells operated at 90°C. Biotechnol Bioeng 2017; 114:1419–27. https://doi.org/10.1002/bit.26271.
13. Pillot G, Frouin E, Pasero E, Godfroy A, Combet-Blanc Y, Davidson S, et al. Specific enrichment of hyperthermophilic electroactive Archaea from deep-sea hydrothermal vent on electrically conductive support. Bioresour Technol 2018; 259:304–11. https://doi.org/10.1016/j.biortech.2018.03.053.
14. Yilmazel YD, Zhu X, Kim KY, Holmes DE, Logan BE. Electrical current generation in microbial electrolysis cells by hyperthermophilic archaea *Ferroglobus placidus* and *Geoglobus ahangari*. Bioelectrochemistry 2018; 119:142–9. https://doi.org/10.1016/j.bioelechem.2017.09.012.
15. Kas A, Yilmazel YD. High current density via direct electron transfer by hyperthermophilic archaeon, *Geoglobus acetivorans*, in microbial electrolysis cells operated at 80 ° C. Bioelectrochemistry 2022;145:108072. https://doi.org/10.1016/j.bioelechem.2022.108072.
16. Aguilar-Aguilar FA, Longoria A, U. JA, S. SA, A. PL, Sebastian PJ. Optimization of Hydrogen Yield from the Anaerobic Digestion of Crude Glycerol and Swine Manure. Catalysts 2019. https://doi.org/10.3390/catal9040316.
17. Chen H, Wu J, Wang H, Zhou Y, Xiao B, Zhou L, et al. Dark co-fermentation of rice straw and pig manure for biohydrogen production: effects of different inoculum pretreatments and substrate mixing ratio. Environ Technol (United Kingdom) 2021; 42: 28, 4539-4549. https://doi.org/10.1080/09593330.2020.1770340.
18. Wang KS, Chen JH, Huang YH, Huang SL. Integrated Taguchi method and response surface methodology to confirm hydrogen production by anaerobic fermentation of cow manure. Int J Hydrogen Energy 2013; 38:45–53. https://doi.org/10.1016/j.ijhydene.2012.03.155.

WHEC-2022
23rd World Hydrogen Energy Conference
June 26-30, 2022 - Istanbul

#1529

BATCH DARK FERMENTATIVE BIOHYDROGEN PRODUCTION FROM FIG FRUIT: THE EFFECT OF C/N RATIO

[1]*Wasiu Abibu,* [2]*Musa Kaya,* [2]*Yağmur Karadas,* [1,2]*İlgi Karapınar*
[1] Dokuz Eylul University, Natural and Applied Sciences, Biotechnology Department, 35390, İzmir, Turkey
[2] Dokuz Eylul University, Engineering Faculty, Environmental Engineering Department, 35390, İzmir, Turkey

*Corresponding author e-mail: ilgi.karapinar@deu.edu.tr

ABSTRACT

In this study, mesophilic batch fermentation experiments were conducted to investigate the effects of varying C/N ratios on biohydrogen production. The fermentable sugar was obtained from microwave hydrolyzed waste Fig (*Ficus carica*) which is a Mediterranean fruit rich in sugar. The initial total sugar (TS) was kept constant at 40 g/L and nitrogen concentration was varied to adjust the C/N between 25 -150. A control experiment without external nitrogen addition was also conducted to evaluate if the nitrogen content of hydrolyzed fig sustains biohydrogen production. The highest cumulative hydrogen volume of CHV = 861 ml and volumetric production of 4.3 $L/L_{reactor}$ were obtained at C/N=50. The yield varied between 0.9 and 1.1 mol H_2/ mol TS $_{consumed}$ for C/N= 25-100. The highest production rates achieved were 11.5 ml/h and 57.5 ml/L h at C/N=50. Thus, the best ratio in terms of substrate conversion to hydrogen is C/N=50 which can be evaluated as the nitrogen-limited condition. The nitrogen content of the hydrolyzed waste fig is not sufficient for efficient biohydrogen production and external nitrogen addition is required to obtain a higher production rate.

Keywords: Fig, Biohydrogen, Microwave, Hydrolysis, Total Sugar Production.

INTRODUCTION

Biohydrogen research stemmed from the rising interest in renewable energy. It is a fermentation-based, microbial mediated value-added product and it forms an integral part of the production, promotion, and sustainability of green energy technologies. Researchers like Veeramalini and co-authors classified biohydrogen production technologies into "photo-fermentation, bio-pyrolysis, microbial electrolysis cell, microbial fuel cell, and dark fermentation" [1]. Enterobacter, Escherichia, and Clostridium are important microbial genera with high biohydrogen production potential [2]. Biohydrogen fermentation substrates pre-treatment is highly necessary. Pre-treatment makes fermentable sugar readily available for microbial utilization, thereby enhancing fermentation for biohydrogen production. Pre-treatment may be physical, chemical, or biological. Microwave is a physical pre-treatment type achieving lignocellulose substrate delignification within a short time via complete thermal penetration of biomass [3].

Lignocellulose materials are well documented in biofuel generation. Fig (*Ficus carica*) is an edible Mediterranean fruit widely cultivated in Turkiye with yearly export of approximately 200,000 tones [4]. It is a rich source of sugar, organic acids, and protein [5]. Aflatoxin contaminated figs are disposed of by incineration. However, the high sugar content of fig can act as a biohydrogen fermentation substrate.

Carbon and Nitrogen are vital elements needed by all life forms for energy, growth, and genetic build-up. “Carbon to Nitrogen ratio (C/N) translates into nutrient balance availability for microbial utilization in fermentation medium [6]. Anaerobic organisms are highly affected by nitrogen content. Argun et al. (2008) investigated the effects of C/N and C/P ratio on biohydrogen yield and specific production rate from waste wheat powder solution by external addition of N since the wheat powder was nutrient deficient [7]. C/N ratio was varied between 20 and 200, the maximum production yield was obtained at C/N=200 which is defined as a nitrogen-limited condition. Öztekin et al. used acid hydrolyzed waste wheat and the optimal C/N ratio maximizing the yield of formation was determined as C/N=50 [8]. Hydrogen production from microwave hydrolyzed peach pulp showed that nitrogen-limited conditions such as C/N=100-250 are more suitable to enhance hydrogen production. But nitrogen-rich condition as C/N=50 adversely affected hydrogen production [9]. Similarly, Argun et al. reported that C/N=45.7 is optimal for maximum hydrogen production from peach pulp [10].

MATERIALS AND METHODS

Substrate preparation

Waste figs were obtained from the Aegean Exporter Association, Izmir, Turkiye. The figs were cut into small sizes (≤ 5cm) with a handheld knife. This was followed by oven-drying at 72°C for 72 hours. Upon drying, fig wastes were blended using a laboratory-sized blender and sieved with the aid of a mechanized sieving machine to obtain

particle diameter sizes of 150 µm, 212 µm, 250 µm, and 300 µm. Our past microwave study with fig fruit resulted in a total sugar concentration of TS≥ 80 g/L which was achieved with fig pretreatment conditions of substrate concentration 100g/L, particle diameter 370.72 µm, pH 4.96, microwave power 253.67 W, and time 50 mins. These pre-treatment conditions were employed in this study with a total sugar concentration of 82 g/L obtained.

Experimental setup

Mesophilic batch fermentation experiments were conducted in 310 ml capacity serum bottles and capped with an air-tight stopper. The fermentation total working volume was 200 ml, initial TS concentration was kept constant at 40 g/L and nitrogen concentration was varied to obtain C/N= 25, 50, 100, and 150. Urea was used as the nitrogen source, and it was externally added to the fermentation media. A control experiment without nitrogen addition was conducted and named C/N=0. The Total Kjeldahl Nitrogen (TKN) and NH_4-N concentration in the 100 g/L microwave fig hydrolysate were 98 mg/L and 0.24 mg/L.

The fermentation media contained 3.9 g/L KH_2PO_4, 0.05 g/L $FeSO_4.7H_2O$, 0.1 g/L L-cysteine and 0.25 g/L $MgSO_4$ at pH 7.0. Media sterilization was done in an autoclave at 121°C for 15 min. The anaerobic condition in all experimental setups was ensured by passing nitrogen gas from the headspace of the bottles. Serum bottles were placed in a shaker incubator at 37°C.

Organism

C.pasteuranium DSM 525 obtained from DSMZ was used in our study. The organism was inoculated (10% v/v) in an inoculation media containing 40 g L^{-1} glucose, 20 g L^{-1} $CaCO_3$, 10 g L^{-1} yeast extract, and 0.1 g L^{-1} L-cysteine. The contribution of L-cystine to nitrogen content was negligible. Anaerobic conditions were achieved by passing nitrogen gas through the medium before cultivation. The organisms were incubated at 37°C with pH 7.0 for 48 hrs before being used as inoculum.

Analytical Methods

Daily hydrogen production from the five (5) experimental setups was carefully monitored by taking gas samples through the headspace of the bottles and also determining the total gas volume by the water displacement method [11]. Hydrogen concentration was measured using a Gas Chromatograph with TCD. Cumulative hydrogen formation (CHF), hydrogen formation yield, and volumetric hydrogen production rate were calculated [10].

pH range 6.5-7 was ensured throughout the study. Daily samples were carefully centrifuged at 8000 rpm before subjecting clear supernatants to total sugar concentration analysis with a UV-Vis spectrophotometer using the Dubois method [12]. Simple sugars and Total Volatile Fatty Acids (TVFA) concentrations were determined using HPLC [10].

RESULTS AND DISCUSSION

The effect of the C/N ratio (0, 25, 50, 100, and 150) on biohydrogen production was studied via batch fermentation under mesophilic conditions. The cumulative hydrogen production (ml) and hydrogen production yield (mol/mol $TS_{consumed}$) at different C/N ratios are found in Figures 1 and 2, respectively. The cumulative hydrogen volume increased with C/N ratio up to C/N=50 with maximum results CHV=of 861 ml and then decreased for the C/N>50. However, the yield was almost constant at around 1.1 mol H_2/ mol $TS_{consumed}$ for the C/N ratios between 25 and 100. The yield of hydrogen formation in the control experiment without nitrogen source addition was around 0.9 mol H_2/mol $TS_{consumed}$ which is not substantially different than the ones with nitrogen added. The sugar content of the hydrolyzed waste fig was effectively (80%) consumed for all C/N ratios studied. The main organic acids produced were acetic acid (Figure 3) and butyric acid (Figure 4), no lactic acid and propionic acids formed. The nitrogen concentration did not affect the organic acid types and their concentrations. The maximum rate of production was 11.5 ml/h and 57 ml /L h attained at C/N=50. The hydrogen purity in the total gas was 54% at the beginning of fermentation and then decreased to 17% at this ratio.

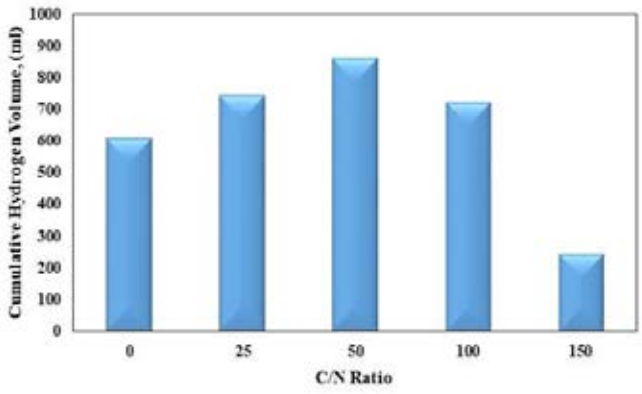


Fig 1. Cumulative hydrogen volumes at different C/N ratios.

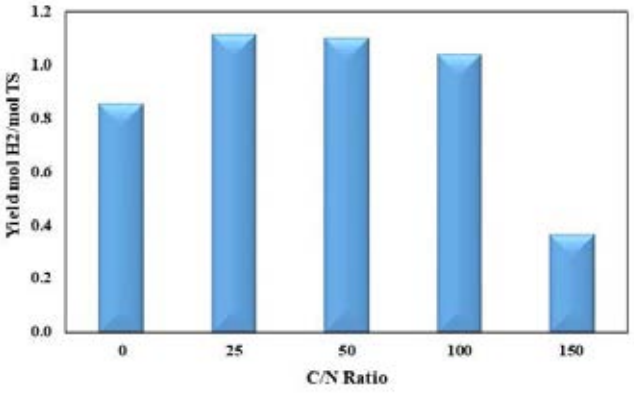


Fig. 2. Hydrogen production yields at different C/N ratios.

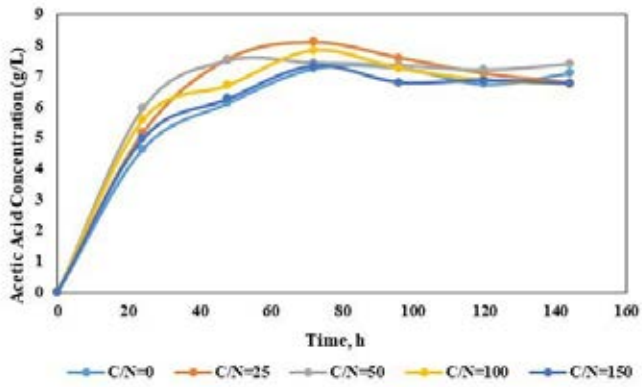


Fig. 3. Variation of acetic acid concentration with time at different C/N ratios.

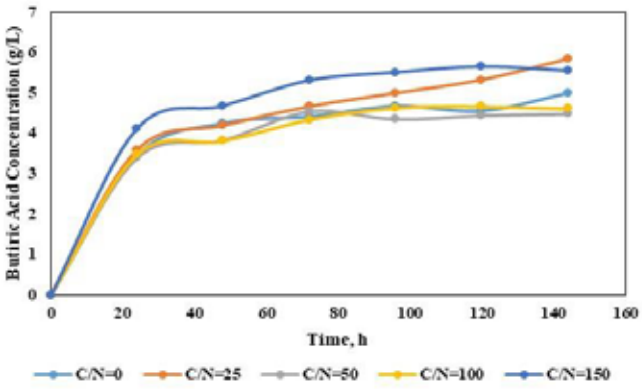


Fig. 4. Variation of butyric acid concentration with time at different C/N ratios.

CONCLUSIONS

The ever-increasing human population translates into an increasing need for energy which is mostly derived from fossil fuels. The environmental effect of fossil fuels shifted attention toward environmentally friendly renewable energy. Biohydrogen, a form of biofuel is renewable energy and capable of contributing its quota to reducing dependency on fossil fuels. Fig (*Ficus carica*) is a Mediterranean fruit rich in sugar. Pretreated waste figs can be subjected to anaerobic fermentation to yield value-added products like biohydrogen. Carbon and nitrogen are macronutrients needed by all life forms for existence. Batch dark fermentation of microwave hydrolyzed waste fig for biohydrogen production showed that waste fig has a high potential for hydrogen generation. Nitrogen content up to C/N=100 in the fermentation media does not substantially affect the yield of hydrogen formation. No external nitrogen addition is required for the yield around 1 mol H_2/mol $TS_{consumed}$. However, the hydrogen formation rate is affected by the nitrogen concentration and the maximum rate was obtained at C/N=50. The lower nitrogen content (C/N=150) limits hydrogen generation. Thus, a C/N ratio of 50 is highly recommended in terms of hydrogen formation rate.

REFERENCES

1. Veeramalini JB, Kumar P, Selvakumari I and Sreejith R. 2022. Process amelioration for production of biohydrogen using mutated Rhodobacter M 19 and Enterobacter aerogenesco-culture: Influence of nanoparticles. Fuel 317: 123558. 10.1016/j.fuel.2022.123558.
2. Goyal Y, Kumar M and Gayen K. 2013. Metabolic engineering for enhanced hydrogen production: a review. Canadian Journal of Microbiology 59(2):59–78.
3. Brasoveanu M and Nemtanu MR. 2014. The behavior of starch exposed to microwave radiation treatment. Starch Staerke 66 (1–2): 3–14. https://doi.org/10.1002/ star.201200191.
4. Ercisli S, Tosun M, Karlidag H, Dzubur A, Hadziabulic S and Aliman Y. 2012. Plant Food and Human Nutrition 67: 271.
5. Slatnar A, Klancar U, Stampar F and Veberic R. 2011. Journal of Agriculture and Food Chemistry 59: 11696.
6. Li R, Zhi Z and Wang H. 2014. Influence of carbon/nitrogen ratio on the anaerobic fermentative hydrogen production with cow dung compost. Journal of Renewable and Sustainable Energy 6: 033139. 10.1063/1.4885615.
7. Argun H, Kargi F, Kapdan I.K. and Oztekin R. 2008. Biohydrogen production by dark fermentation of wheat powder solution : Effects of C/N and C/P ratio on hydrogen yield and formation rate. International Journal of Hydrogen Energy 33:1813.

8. Oztekin R, Kapdan IK, Kargi F and Argun H. 2008. Optimization of media composition for hydrogen gas production from hydrolyzed wheat starch by dark fermentation. International Journal of Hydrogen Energy 33: 4083.
9. Dalak M, Karapınar I. 2022 The effect of C/N ratio on simultaneous biosolvent and biohydrogen production by dark fermentation 4th International Eurasian Conference on Biological And Chemical Sciences, Ankara, Turkey, 24 - 26 November 2021, pp.667-673
10. Argun H and Dao S. 2016. Hydrogen gas production from waste peach pulp by dark fermentation and electrohydrolysis, International Journal of Hydrogen Energy 41: 11568.
11. Dubois M, Gilles KA, Hamilton JK, Rebers PAT and Smith F. 1956. Colorimetric method for determination of sugars and related substances. Analytical Chemistry 28:350.

WHEC-2022

23rd World Hydrogen Energy Conference

TRACK 4. HYDROGEN PRODUCTION: NUCLEAR

TRACK 4. HYDROGEN PRODUCTION: NUCLEAR

#131 STUDY ON THE CATALYTIC PERFORMANCE OF SULFURIC ACID DECOMPOSITION IN IODINE-SULFUR CYCLE HYDROGEN PRODUCTION	352
#164 BUILDING THE BUSINESS CASE FOR HYDROGEN PRODUCTION WITH OPERATING NUCLEAR POWER PLANTS	355
#1484 A HYBRIDIZED SOLAR-NUCLEAR ENERGY SYSTEM FOR GENERATING MULTIPLE USEFUL OUTPUTS WITH HYDROGEN	359
#1526 MULTIOBJECTIVE OPTIMIZATION OF A PWR NUCLEAR COGENERATION PLANT FOR HYDROGEN PRODUCTION	362
#1592 NUCLEAR HYDROGEN PERSPECTIVES IN ROMANIA	365
#1593 NUCLEAR HYDROGEN PROJECTS TO SUPPORT CLEAN ENERGY TRANSITION	367

WHEC-2022
23rd World Hydrogen Energy Conference
June 26-30, 2022 - Istanbul

#131

STUDY ON THE CATALYTIC PERFORMANCE OF SULFURIC ACID DECOMPOSITION IN IODINE-SULFUR CYCLE HYDROGEN PRODUCTION

[1]Qunxiang Gao, [1,2]Ping Zhang, [1,2,*]Wei Peng, [1,2]Gang Zhao
[1]Institute of Nuclear and New Energy Technology, Advanced Nuclear Energy Technology Cooperation Innovation Center, Key Laboratory of Advanced Nuclear Engineering and Safety, Ministry of Education, Tsinghua University, Beijing 100084, China;
[2]Tsinghua University-Zhang Jiagang Joint Institute for Hydrogen Energy and Lithium-Ion Battery Technology, Tsinghua University, Beijing 100084, China

*Corresponding author e-mail: pengwei@tsinghua.edu.cn

ABSTRACT

The present study uses surface reaction and porous media models to calculate the decomposition performance of bayonet heat exchangers with different catalyst sizes. The results show that the first step of sulfuric acid decomposition reaction is relatively thorough, and the second step of sulfuric acid decomposition reaction is more efficient in the first two-thirds of the catalytic zone. At the same time, the smaller the porosity or particle size of the catalytic zone, the higher the system pressure drop and decomposition rate. The maximum decomposition rate and pressure drop under the current design conditions are 79% and 193Pa, respectively.

Keywords: Sulfuric Acid Decomposition, Surface Reaction, Porosity, Particle Size

INTRODUCTION

As the fourth-generation nuclear power technology, the high-temperature gas-cooled reactor has a higher outlet temperature, which can be used in a variety of process heat utilization methods. Hydrogen production by nuclear energy is one of the important applications. It is usually driven by nuclear heat and adopts a thermochemical iodine-sulfur cycle method to produce hydrogen. In the iodine-sulfur cycle process, it is mainly composed of three chemical reactions, namely Bunsen reaction, decomposition of sulfuric acid and decomposition of hydroiodic acid. The sulfuric acid decomposition reaction requires a high temperature, and the decomposition rate also has a greater impact on the hydrogen production efficiency, so this part is of great significance to the entire process.
Many scholars have carried out research on the decomposition of sulfuric acid through experiments and simulations. Giaconia et al. [1] used siliconised silicon carbide honeycombs coated with iron (III) oxide to conduct a 100-hour sulfur trioxide decomposition experiment, and the catalyst showed good activity and stability. Hong et al. [2] coupled components of multiple materials together, built a sulfuric acid decomposition circuit, and conducted corrosion experiments. Choi et al. [3] designed the unit reactor of the pressurized sulfuric acid decomposition (PSAD) reaction system to evaluate hydrogen production performance. Gao et al. [4] conducted a segmented simulation of the decomposition of sulfuric acid and compared the decomposition performance of the two catalyst forms. Sun et al. [5] developed a model for calculating the phase transition and decomposition of sulfuric acid at the same time and analyzed the influence of flow rate and temperature on decomposition. Shin et al. [6] conducted CFD analysis on the overall structure of the sulfuric acid decomposer and predicted that the decomposition rate of sulfuric acid could reach 60.4%.
At present, there are few simulation studies on the catalysts used for the decomposition of sulfuric acid. This study mainly focuses on the influence of the porosity and particle size of the catalyst bed on the decomposition rate of sulfuric acid and the pressure drop of the system. The catalysts with different particle diameters are arranged in sections to balance the pressure drop and decomposition rate, thereby achieving a higher cost performance.

MODELING AND METHODS

In this study, a two-dimensional axisymmetric model of the sulfuric acid decomposer unit is established for simulation calculation, which mainly includes the helium side and the sulfuric acid side. On the helium side, a heating tube bundle is assumed to provide heat for sulfuric acid. The helium side tube bundle has a radius of 35mm and a length of 1100mm. The radius of the inner tube and the outer tube on the sulfuric acid side are 7mm and 17mm, respectively, and the length is 1350mm. Sulfuric acid exchanges heat with helium in the outer tube, the temperature gradually increases, and then sulfur dioxide is generated in the catalyst area at the bottom of the outer tube, and finally flows out of the decomposer from the inner tube, as shown in Figure 1.

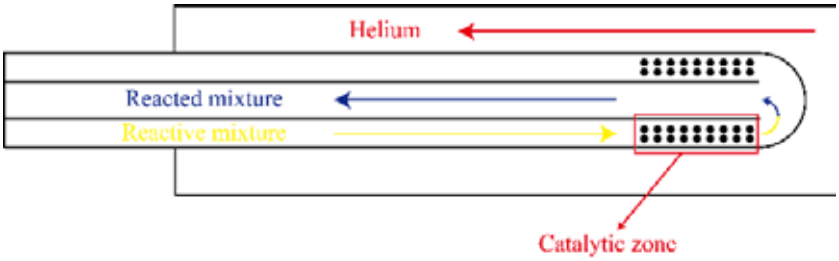


Fig. 1. Schematic diagram of sulfuric acid decomposer unit

The decomposition of sulfuric acid requires regular flow and heat transfer calculations, including continuity equations, momentum equations, and energy equations. In addition, the two-step decomposition reaction of sulfuric acid needs to be calculated using a component transportation model, as follows:

$$\nabla\cdot\left(\rho\mathbf{U}R_i\right)=-\nabla\cdot\vec{M}_i+S_i \quad (1)$$

where where ρ is the density of various fluids, **U** is the fluid velocity, R_i is the mass fraction of substance *i* at a certain local location, M_i is the diffusion flux of substance *i* and S_i is the net rate of reaction to obtain substance *i.*

The chemical reaction rate constant ($k_{f,r}$) has an important influence on the generation or disappearance of a certain substance, as follows:

$$k_{f,r}=A_r e^{-E_r/RT} \quad (2)$$

where A_r is the pre-index factor, T is the temperature, E_r is the reaction activation energy, R is the ideal gas constant. The boundary conditions of this study are shown in Table 1.

Table 1. Calculation condition

Parameter	Value
Mass flow rate of sulfuric acid(kg/s)	0.000175
Inlet velocity of helium(m/s)	0.1
Inlet temperature of sulfuric acid(K)	300
Inlet temperature of helium(K)	1123
Porosity of the catalytic zone	0.3、0.4、0.5
Catalyst particle size(mm)	5、6、7、8、9、10

RESULTS AND DISCUSSION

The particle arrangement of the catalyst bed affects the heat transfer of the flow of sulfuric acid and also affects the pressure drop of the system. This study assumes that the catalyst particles are regular spherical, evenly scattered in the 300mm long catalytic zone. Figure 2 shows the distribution of the proportions of sulfur trioxide and sulfur dioxide with a particle diameter of 5 mm. It can be seen that along the flow direction, sulfuric acid gradually decomposes in the first step to generate sulfur trioxide, and the first step decomposition reaction is basically completed in the middle section of the reactor. After sulfur trioxide enters the catalytic zone, it continues to decompose to produce sulfur dioxide. The first two-thirds of the catalytic zone has a high sulfur dioxide generation efficiency, and sulfur dioxide is mainly generated in this part.

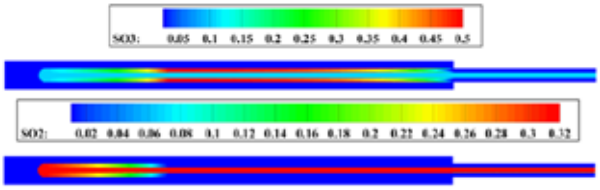


Fig. 2. Distribution of sulfur trioxide and sulfur dioxide

Figure 3 shows the effect of different particle sizes on the decomposition rate and pressure drop. When the porosity is constant, large particles are used to reduce the pressure loss of the system, but also significantly reduce the sulfuric acid decomposition rate. When the particle size is constant, the more compact the catalyst is packed, that is, the smaller the porosity, the greater the pressure loss of the fluid, but the close packing has a larger specific surface area, which also increases the decomposition rate. With the same porosity setting, the particles continue to decrease, the decomposition rate presents a similar linear increase trend, and the pressure drop presents an exponential

increase trend, indicating that the sensitivity between particle size and pressure drop is very high. With the same particle size setting, the porosity decreases by 0.1, the decomposition rate will increase by about 10%, and the pressure drop will increase exponentially. The setting of small particles will increase the pressure drop by about 6 times.The arrangement with porosity of 0.3 and particle size of 5mm has the largest decomposition rate and pressure drop, which are 79% and 193Pa, respectively.

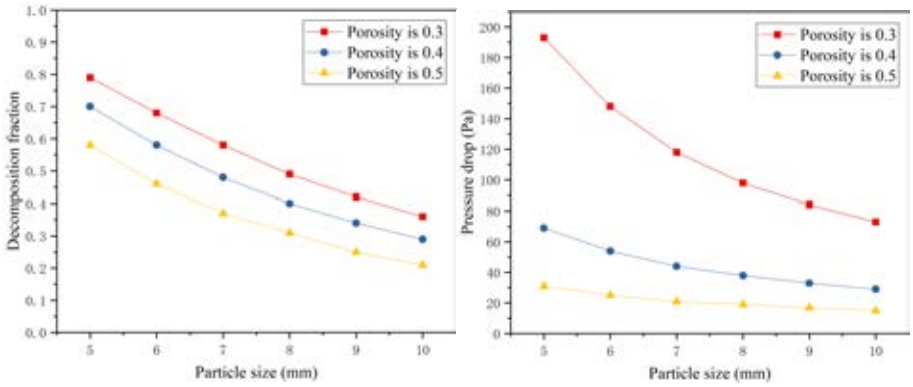


Fig. 3. The effect of catalyst bed layout on decomposition rate and pressure drop

CONCLUSIONS

The decomposition process of sulfuric acid was calculated based on the porous media and the surface reaction model, and the influence of the catalyst layout was studied. The calculation results show that:

- The first step of decomposition is basically completed in the middle of the reactor, and the second step of decomposition is the most efficient in the first two thirds of the catalytic zone. Arranging fine particles in this part is expected to further increase the decomposition rate.
- The particle size continues to decrease, the decomposition rate shows an almost linear increase trend, and the pressure drop shows a geometric increase. The average porosity decreases by 0.1, the decomposition rate increases by about 10%, and the pressure drop can increase by about 6 times at most.
- Under the current layout conditions, the maximum decomposition rate and pressure drop of the sulfuric acid decomposer unit can reach 79% and 193Pa.

ACKNOWLEDGEMENT

This project was supported by the National Key R&D Program of China (Grant No. 2020YFB1901604) and the National S&T Major Project (Grant No. ZX069).

REFERENCES

1. Giaconia A, Sau S, Felici C, Tarquini P, Karagiannakis G, Pagkoura C, et al. 2011. Hydrogen production via sulfur-based thermochemical cycles: Part 2: Performance evaluation of Fe2O3-based catalysts for the sulfuric acid decomposition step. International Journal of Hydrogen Energy. 36:6496-509.
2. Hong S-D, Kim C-S, Kim Y-W, Seo D-U, Park G-C. 2012. Design and analysis of a high pressure and high temperature sulfuric acid experimental system. Nuclear engineering and design. 251:157-63.
3. Choi J-S, Choi J-H. 2015. Experiment and numerical analysis for sulfuric acid decomposition reaction for applying hydrogen by nuclear. International Journal of Hydrogen Energy. 40:7932-42.
4. Gao Q, Sun Q, Zhang P, Peng W, Chen S. 2020. Sulfuric acid decomposition in the iodine–Sulfur cycle using heat from a very high temperature gas-cooled reactor. International Journal of Hydrogen Energy. 46(57): 28969-28979
5. Sun Q, Gao Q, Zhang P, Peng W, Chen S. 2020. Modeling sulfuric acid decomposition in a bayonet heat exchanger in the iodine-sulfur cycle for hydrogen production. Applied Energy. 277:115611.
6. Shin Y, Lim J, Lee T, Lee K, Jo C, Kim M. 2017. Designs and CFD analyses of H2SO4 and HI thermal decomposers for a semi-pilot scale SI hydrogen production test facility. Applied Energy. 204:390-402.

WHEC-2022
23rd World Hydrogen Energy Conference
June 26-30, 2022 - Istanbul

#164

BUILDING THE BUSINESS CASE FOR HYDROGEN PRODUCTION WITH OPERATING NUCLEAR POWER PLANTS

[1*] *Aliki van Heek,* [1] *Yuichiro Yuasa,* [1] *Brianna Lazerwitz*
[1]Planning and Economic Studies Section, International Atomic Energy Agency, Wagramer Str. 5, 1220 Vienna, Austria

*Corresponding author e-mail: A.vanHeek@iaea.org

ABSTRACT

Efforts to deploy hydrogen widely in the industrial, transportation and electric power sectors will support the creation of a decarbonized future. Nuclear power can provide 24/7 availability of both electricity and heat to support the efficient production of hydrogen through different processes. Hydrogen production from nuclear power can provide a strong opportunity for operating nuclear power plants to avoid curtailment and pair with renewable energy generation to create a decarbonized and flexible energy system. Regional and national nuances will indicate the best use for hydrogen in each country, and a combination of hydrogen applications in each sector will contribute to global decarbonization goals. The option of using currently operating nuclear power plants for hydrogen production, including when and how hydrogen production makes sense economically, is being explored at the International Atomic Energy Agency, by bringing together utilities with various hydrogen production projects. The study includes case studies of existing nuclear hydrogen demonstration projects to gauge project similarities and differences.

Keywords: Hydrogen, Nuclear, Electrolyser

INTRODUCTION

To significantly reduce global greenhouse gas emissions, two major undertakings must take place in tandem: all sectors must be electrified wherever possible, and the electricity sector must be decarbonized. In an increasingly electrified world, power sources will need to shift from fossil fuel to low-carbon generation sources, such as nuclear and renewable energy, to achieve climate goals.

As some heavy-emitting sectors are difficult to electrify, low-carbon hydrogen can be deployed across global industrial, transportation and electric power sectors will support the creation of a decarbonized future. While much of the world's low-carbon hydrogen is expected to come from renewables, nuclear power offers 24/7 availability which can help to lower the cost of hydrogen production. Nuclear hydrogen production has been technically feasible for some time but was previously too expensive in comparison to fossil fuel-produced hydrogen. As climate change mitigation sidelines fossil fuels, new opportunities arise for nuclear power. By 2050, the International Energy Agency (IEA) estimates that more than 60% of global hydrogen production will come from low-carbon sources [1]. In power systems with increasing shares of renewable generation, nuclear hydrogen production could provide a valuable alternative revenue stream for nuclear power plants, allowing for low carbon emitting power sources to remain economic.

Recent hydrogen policy developments

National interest in hydrogen has grown rapidly in recent years. Despite approximately 20 countries adopting or announcing the intention to create national hydrogen development strategies, only five have projects on nuclear hydrogen production with existing nuclear plants: Canada, Sweden, the Russian Federation, United Kingdom and United States. Even these are in nascent stages [2].

Canada [3], the Czech Republic [4], and the United Kingdom [5] mention hydrogen production from existing nuclear reactors in addition to advanced nuclear developments such as Small Modular Reactors, and the more specific, High Temperature Gas-cooled Reactor (HTGR), in their national hydrogen strategies. Both China and Japan are conducting demonstration projects with HTGR, a reactor type that is suitable for hydrogen production with energy efficient processes [6]. Beyond 2030, the Japan Atomic Energy Agency plans to develop hydrogen production facilities using a nuclear heat source [7].

HYDROGEN PRODUCTION METHODS

Unlike natural gas, hydrogen is produced in a chemical process powered by energy in the form of heat and/or electricity. Three main production methods for producing hydrogen are steam reformation, electrolysis, and thermochemical water splitting. The former typically uses energy from fossil fuels and heat; the latter two use water and electricity and/or heat from a variety of sources. Most of the hydrogen today is produced using steam methane reforming, a process which uses natural gas, or by coal gasification. Since both processes produce relatively high carbon emissions, the use of carbon capture and storage technologies may be deployed to reduce emissions before they enter the atmosphere.

Today's main electrolyser technologies can be divided into two types: low temperature electrolysers (LTE) and high temperature electrolysers (HTE). Electrolysers deploy either of these technologies to allow low-carbon hydrogen production using electricity from renewable energy or nuclear power [8,9]. LTE is an established technology and has already been deployed on a commercial scale. LTEs can be further divided into alkaline electrolysers and proton exchange membrane (PEM) electrolysers. Alkaline electrolysers are a mature and commercial-scaled technology that is easier to make in large scale compared to PEM electrolysers. HTEs use heat and electricity to produce hydrogen and are deployed using solid oxide electrolyser cells [10].

Thermochemical water splitting is a method by which water molecules are split into hydrogen and oxygen using heat. Examples include the Copper-Chloride cycle and the Sulfur-Iodine cycle; the latter is incorporated in the Japanese hydrogen project with HTGR [11].

THE BUSINESS CASE FOR NUCLEAR HYDROGEN

For hydrogen to fulfil its potential as an energy source for a decarbonized economy, it needs to be low-carbon, produced in large quantities, and cost-competitive with other hydrogen production methods. Three main parameters are crucial to optimize for the profitability of low-carbon hydrogen production: 1) the capital investment in the electrolyser, 2) the cost of electricity used in the production process, and 3) the capacity factor of the electrolyser.

Capital investments in the electrolyser may be reduced by economies of scale as module size increases, depending on electrolyser technology. The cost of electricity used in electrolysis may be reduced using low marginal cost nuclear or renewable energy compared to fossil fuel generators. Additionally, the relatively high capacity factor of nuclear plants compared to other generation sources allows for the electrolyser to operate over an increased time interval. The longer an electrolyser runs, the greater the impact of the cost of electricity and the lesser the impact of capital expenditures on the levelized cost of hydrogen. Therefore, it is essential to minimize the cost of hydrogen production by achieving an optional annual level of operating hours to balance this trade-off. According to the IEA, hydrogen production costs are minimized when an electrolyser operates with a capacity factor of 34-68% [12].

Demand and market conditions

At present, hydrogen demand is limited to the refining and chemical industrial sectors but is expected to grow significantly by 2050 [13]. "Clusters" are being developed as a tool to simultaneously develop integrated hydrogen production, storage, and transportation with various localized use cases. Cluster-based development can provide hydrogen producers with greater certainty on local hydrogen demand and de-risk their business case by ensuring off-takers. Additionally, clusters can support the development of several different end use applications in tandem, rapidly achieving economies of scale with the added benefit of focusing public support on developments which will benefit various companies and sectors [14].

UTILITY DEMONSTRATION PROJECTS

Four utilities in the US, three in Europe and one in Canada have started or are preparing to start nuclear hydrogen demonstration projects, but little progress has yet been made in Asia. The following are nuclear-powered hydrogen demonstration projects around the world, in order from most advanced to those in early stages of research or conception.

Energy Harbor, an American utility company, is planning a two-year demonstration project at the Davis-Besse nuclear power plant in Ohio, where the company plans to produce hydrogen beginning in 2023. The LTE used in the pilot project is a PEM electrolyser, which consumes 2 MW of electricity from the nuclear power plant and produces 800 to 1,000 kg of hydrogen per day. Energy Harbor's objective is to explore the economic viability of hydrogen production in nuclear power plants and to demonstrate the compatibility and synergy of the two technologies [15].

Xcel Energy plans to complete a hydrogen production demonstration project using high temperature steam electrolysis at the Prairie Island nuclear power plant in Minnesota, USA. Xcel intends to constantly produce hydrogen in the small-scale demonstration project but in the future will produce hydrogen when electricity prices are low due to high wind power output. The electrolyser is planned to produce about 90 kg of hydrogen per day [16].

Arizona Public Service Company in the US conducted a techno-economic assessment of using hydrogen produced from its Palo Verde nuclear generating station to co-fire in Unit 3 of the Saguaro natural gas fired turbine. The assessment concluded that the cost of capacity from co-firing hydrogen was competitive with battery storage for durations longer than four hours. A 17 MW electrolyser with a hydrogen compression and storage system project will start from 2022 [17].

Exelon plans to install a 1.25 MW PEM electrolyser at the Nine Mile Point nuclear plant in the US State of New York. The company also plans to explore dynamic operation of the electrolyser [18].

EDF UK completed a feasibility study for hydrogen production at the Heysham nuclear power station [19]. EDF identified potential off takers, but none were interested at the price point anticipated by EDF. The company is now exploring hydrogen production at the site of the Sizewell B nuclear power plant, where it plans to begin installation of a 2 MW electrolyser in 2022 and production of up to 800 kg of hydrogen per day. The planned nuclear plant Sizewell C is expected to eventually produce hydrogen as part of an energy hub to support global trade [20]. The plan is for Sizewell C to include a 1 GW electrolyser by 2030 to produce 145,000 tons of hydrogen annually [21].

Rosatom plans to build a hydrogen production and conversion test facility at the Kola nuclear power plant in Russia. The hydrogen complex is expected to be operational in 2024 and will be equipped with a 1 MW alkaline electrolyser which could be expanded to 10 MW later [22].

Vattenfall, a Swedish energy utility, has been producing hydrogen using the Ringhals nuclear power plant since 1997. The 0.8 MW electrolyser produces between 60 and 110 m^3 of hydrogen per hour. The hydrogen produced is used to cool the nuclear generators and is injected into the feed water to prevent corrosion. Vattenfall, having several non-nuclear hydrogen projects, does not currently plan to expand or develop hydrogen production at its nuclear power plants [23].

In 2021, Bruce Power of Ontario, Canada, examined the technical feasibility and business case for a pilot project to produce hydrogen using electricity from the Bruce nuclear power plant. The project will study the benefits of hydrogen production, including export opportunities, local interest, and jobs created [24].

For each of these utilities, the anticipated use of hydrogen differs by region and demonstration project (Table 1).

Table 1. Comparison of Intended Nuclear Hydrogen Applications Among Utilities with Demonstration Projects

	Utility name						
	Energy Harbor	**Xcel Energy**	**Arizona Public Service**	**Exelon Corporation**	**EDF UK**	**Rosatom**	**Bruce Power**
Technology and size of demonstration project	LTE PEM, 2 MW	HTE, 150 kW	LTE, 17 MW	LTE PEM, 1.25 MW	Sizewell B (LTE, 2 MW) Sizewell C (HTE)	LTE, 1 MW	LTE, 5 MW
Use for demonstration project's nuclear hydrogen	Manufacturing and transportation	Company's NPP	Company's natural gas-fired power plant	Company's NPP	Transportation and equipment for new NPP construction	Energy storage in remote and isolated areas	To be determined
Potential uses for nuclear hydrogen in the future	Manufacturing (oil refining and steel production), transportation	Oil, gas, and ammonia production, transportation , power generation	As an energy storage tool to balance the output of variable solar power	Injection into gas pipelines, co-firing of gas plants, ethanol production, petroleum refining	Cargo, public transportation, ships, aviation, industrial processes, district heating	Energy storage in remote and isolated areas	Fertilizer production, power and heat for heavy industry, transportation

CONCLUSIONS

To further deploy hydrogen production from nuclear power, it is important to understand demonstration projects based on their similarities and differences. Shared attributes of each of the projects are likely to be continued in the deployment of new projects. Conversely, unique aspects from each project should be carefully considered to determine whether they are due to the project's unique goals and regional considerations or matters for which a consensus must still be found. Additionally, technology improvements compared to what is available today such as advanced nuclear reactors with more efficient thermo-chemical splitting methods have the potential to redefine the future of hydrogen production.

Almost all nuclear hydrogen projects are still in an early demonstration stage, and most projects are expected to be completed in two to three years. It will be necessary to continue to follow these projects to identify successes and challenges in the deployment of hydrogen production from nuclear energy. As nuclear hydrogen production is scaled to commercial size, it is important to identify how to resolve challenges from scaling-up the electrolyser, meeting regulatory requirements, transporting and storing hydrogen, and further development of hydrogen demand.

REFERENCES

1. International Energy Agency. July 2021. Net Zero by 2050: A Roadmap for the Global Energy Sector.
2. http://bloomberg.com/netzeropathfinders. Low-Carbon Hydrogen Policies. Accessed October 25, 2021.

3. The Government of Canada. 2020. Hydrogen Strategy for Canada.
4. The Government of the Czech Republic. 2021. The Czech Republic's Hydrogen Strategy.
5. The UK Government. 2021. UK Hydrogen Strategy.
6. http://world-nuclear-news.org. China's HTR-PM reactor achieves first criticality. Accessed October 25, 2021.
7. Japan Atomic Energy Agency. 2021. IAEA Consulting Meeting.
8. International Energy Agency. 2019. The Future of Hydrogen.
9. http://iaea.org/data-and-statistics/data-product/hydrogen-projects-database. Accessed October 25, 2021.
10. Nuclear Industry Association. 2021. Hydrogen Roadmap.
11. Japan Atomic Energy Agency. 2021. IAEA Consulting Meeting.
12. International Energy Agency. 2019. The Future of Hydrogen.
13. International Energy Agency. 2021. Global Hydrogen Review.
14. Energy Transitions Commission. 2021. Making the Hydrogen Economy Possible.
15. GAIN. April 16, 2020. Clean Nuclear Energy for Industry webinar.
16. Idaho National Laboratory. 2020. Private-Public Partnership will use Nuclear Energy for Clean Hydrogen Production.
17. http://energy.gov/articles. DOE Announces $20 Million to Produce Clean Hydrogen From Nuclear Power. Accessed October 25, 2021.
18. http://exeloncorp.com/newsroom. Exelon Generation Receives DOES Grant to Support Hydrogen Production Project at Nine Mile Point Nuclear Station. Accessed October 25, 2021.
19. EDF Energy R&D UK Centre. October 2019. H2H – Hydrogen to Heysham Feasibility Report.
20. http://freeporteast.com/hydrogen. Accessed October 25, 2021.
21. HM Government. November 2020. The Ten Point Plan for a Green Industrial Revolution.
22. http://rosatom-asia.com/press-centre. Rosatom to launch hydrogen production at Kola NPP by 2023, construction of new units by 2028. Accessed October 25, 2021.
23. http://group.vattenfall.com/press-and-media. Ringhals' lesser-known hydrogen gas factory contributes to tomorrow's biofuel. Accessed October 25, 2021.
24. http://nuclearinnovationinstitute.ca. Canada's first-ever feasibility study on the case for nuclear hydrogen production now underway. Accessed October 25, 2021.

WHEC-2022
23rd World Hydrogen Energy Conference
June 26-30, 2022 - Istanbul

#1484

A HYBRIDIZED SOLAR-NUCLEAR ENERGY SYSTEM FOR GENERATING MULTIPLE USEFUL OUTPUTS WITH HYDROGEN

[1*] *Mert Temiz,* [1] *Ibrahim Dincer*
[1]Clean Energy Research Laboratory (CERL), Faculty of Engineering and Applied Science, Ontario Tech. University, 2000 Simcoe Street North, Oshawa, Ontario L1H 7K4, Canada

*Corresponding author e-mail: Mert.Temiz@uoit.ca

ABSTRACT

A unique, solar, and nuclear based hybrid system is developed to generate hydrogen, ammonia, heat, food, power and fresh water in an integrated and sustainable fashion. The integrated system is analyzed according to the first and second laws of thermodynamics, extensively, for five different cities in a time-dependent manner. The floating and bifacial PV options are considered and analyzed as two different options for the cities. In the average year in Istanbul, 2 × 250 MW_{th} high temperature gas cooled reactors with 120 MW_p PV plants in the integrated system met 738.7 GWh annual electrical load, generated 20828 tons of hydrogen in the floating PV option and 22360 tons of hydrogen in the bifacial PV option. The overall energy and exergy efficiencies are found to be 52.34% and 57.61% for the floating PV option 54.13% and 59.54% for the bifacial PV option in Istanbul.

Keywords: Floating Photovoltaic, Bifacial, Hydrogen Energy, Ammonia, Exergy

1. INTRODUCTION

In order to combat climate change, governments around the world take measures and target to reduce CO_2 emissions. Phasing out from fossil-based fuels as well as conflicts between countries lead to fuel shortages as well as indirect shortages such as fertilizer, food, water. In order to secure the emission targets to reach net zero emission by 2050 and 2060, renewable and sustainable energy systems needs to be developed in a smart fashion [1].

Renewable-nuclear hybrid energy systems has synergetic advantages to overcome challenges that can be faced if renewable or nuclear systems used alone. The intermittency is one of the major challenges of renewables that can be mitigated with the nuclear option. On the other hand, the high levelized cost of electricity of nuclear power can be reduced with low levelized costs of electricity from renewables [2,3].

The proposed system uses a hybridized nuclear solar system to generate ammonia, hydrogen, heat, electrical power, fresh water and food in a novel integration.

2. SYSTEM DESCRIPTION AND ANALYSIS

A high-temperature gas cooled small modular nuclear reactor design is used as Chinese high-temperature gas-cooled pebble bed module (HTR-PM), where each module has 250 MW_{th} capacity. Two reactors are used in the proposed system, which can generate up to 200 MW_e. On the other hand, two different photovoltaic (PV) plant options are used in the system. The first PV option is a bifacial PV plant where a land-based tracker system is used with bifacial PV modules. The other one is a floating PV plant where monofacial PV modules are used on floating platforms. Solid oxide electrolyzer, pressure swing adsorption air separator, ammonia reactor are among the other components of the integrated system. Fig. 1 shows the proposed system layout.

The proposed system is analyzed for five different cities around the globe, namely, Barcelona, Spain; Istanbul, Turkey; Los Angeles, United States; Toronto, Canada; Tokyo, Japan for both bifacial PV and floating PV options. Floating PV plants are considered especially for the cities with land shortages, such as Tokyo and Istanbul.

The nuclear plant and multi-effect distillation desalination system are simulated by using the DE-TOP software package. Both of the PV options are simulated by using PVSyst software package. The results are imported to analyze these systems with first and second laws of thermodynamics by using the mass, energy, entropy and exergy balance equations.

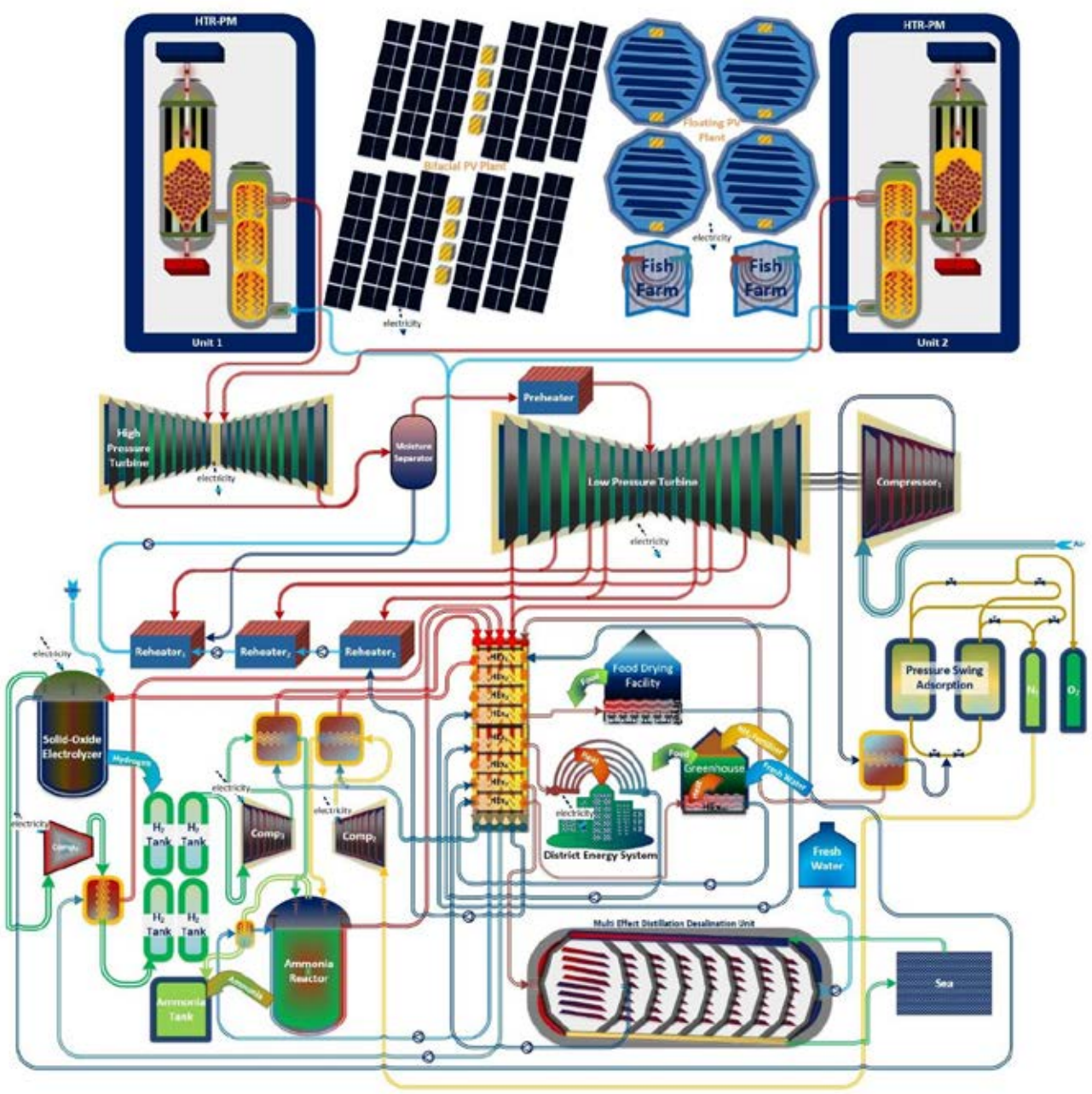


Fig. 1. A layout of the developed system

3. RESULTS AND DISCUSSION

The proposed system is simulated and analyzed with a thermodynamic based approach. The proposed system is considered to be connected with a virtual grid. The excess electricity is used to generate hydrogen and ammonia; the excess heat is used to generate hydrogen in the solid-oxide electrolyzer, fresh water with the desalination unit as well as to heat district energy system and agricultural facilities. The produced ammonia can be used in agricultural activities as a fertilizer, as well as it can be used as a fuel or feedstock in related sectors. In the average year in Istanbul, the proposed system met 738.7 GWh annual electrical load, generated 20828 tons of hydrogen in the floating PV option and 22360 tons of hydrogen in the bifacial PV option. The overall energy and exergy efficiencies are found to be 52.34% and 57.61% for the floating PV option 54.13% and 59.54% for the bifacial PV option in Istanbul. Fig. 2 shows the obtained results of the proposed systems' analysis for five different cities around the globe.

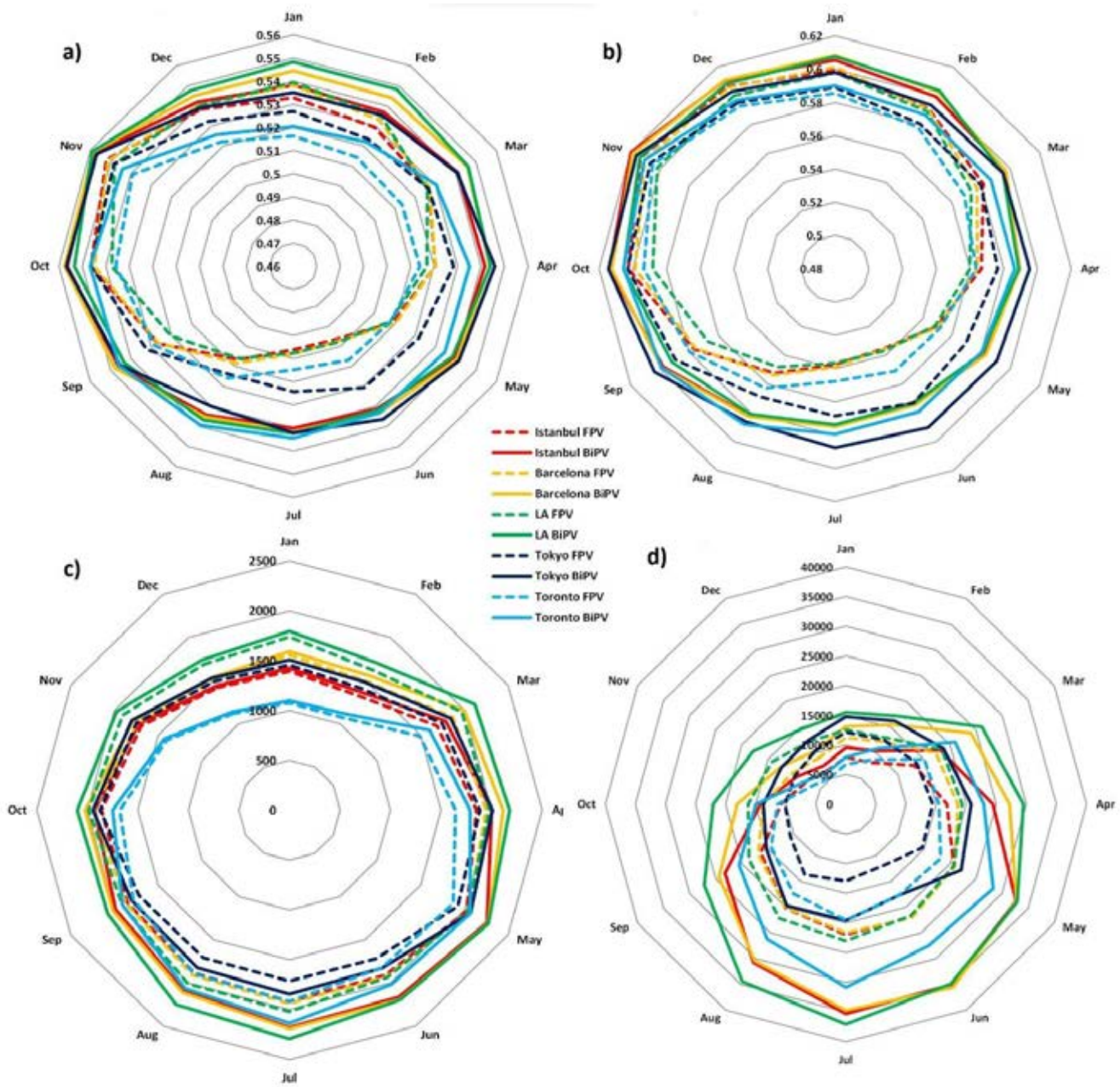


Fig. 2. For the overall systems: a) energy efficiency, b) exergy efficiency, c) hydrogen generation (tons/month), d) PV electricity generation (MWh/month)

4. CONCLUSIONS

The hybridization of nuclear and solar systems has achieved unique advantages by (i) preventing intermittencies in compared to the renewable-alone systems, (ii) reducing carbon emissions in compared to fossil-based systems, (iii) lowering the levelized cost of energy compared to the nuclear-alone systems. The bifacial option has increased both energy and exergy efficiencies and significantly increased the PV electricity production.

REFERENCES

1. Dincer I and Acar C. 2018. Smart energy solutions with hydrogen options. International Journal of Hydrogen Energy 43(18) pp.8579-8599.
2. Ruth M, Cutler D, Flores-Espino F, and Stark G. 2017. The economic potential of nuclear-renewable hybrid energy systems producing hydrogen (No. NREL/TP-6A50-66764). National Renewable Energy Lab.(NREL), Golden, CO (United States).
3. Temiz M and Dincer I. 2021. Design and analysis of a new renewable-nuclear hybrid energy system for production of hydrogen, fresh water and power. e-Prime-Advances in Electrical Engineering, Electronics and Energy 1 p.100021.

WHEC-2022
23rd World Hydrogen Energy Conference
June 26-30, 2022 - Istanbul

#1526

MULTIOBJECTIVE OPTIMIZATION OF A PWR NUCLEAR COGENERATION PLANT FOR HYDROGEN PRODUCTION

[1] Tayfun Tanbay, [2] Ahmet Durmayaz*
[1]Bursa Technical University, Faculty of Engineering and Natural Sciences, Department of Mechanical Engineering, Bursa, Türkiye
[2] Istanbul Technical University, Energy Institute, Maslak, Istanbul, Türkiye

*Corresponding author e-mail: tayfun.tanbay@btu.edu.tr

ABSTRACT

In this paper, the multiobjective optimization of a nuclear cogeneration plant for hydrogen production is carried out. The analysis focuses on the secondary cycle of a pressurized water reactor nuclear cogeneration plant providing process heat and electrical energy to a high-temperature steam electrolysis facility. The utopia point method is used to determine the values of heat/electricity energy ratio, hydrogen production capacity, live steam temperature and steam extraction node that yield a compromise optimum solution between thermal efficiency, thermal-to-hydrogen production efficiency, exergy efficiency and utilization factor. For a hydrogen production capacity of 7 kg/s, an energy ratio of 0.0561 results with the best overall performance, while an energy ratio of 0.10 gives the best performance for a capacity of 0.1 kg/s.

Keywords: Hydrogen Production, Nuclear, Multiobjective Optimization, PWR, High-Temperature Steam Electrolysis

INTRODUCTION

The rapid increase in global warming necessitates a fast transformation in energy infrastructure and transportation sector. Hydrogen is a promising candidate for the mitigation of greenhouse gas emissions. However, steam methane reforming is the most widely utilized process for hydrogen production, which caused an emission of 900 Mt of CO_2 in 2021 [1] corresponding to approximately 2.8% of the global annual emissions. Therefore, alternative production methods should be utilized in order to fully reveal the potential positive effect of hydrogen use on climate change. In this respect, nuclear energy is an advantageous option to produce hydrogen in an environmentally friendly manner.

Among the alternative hydrogen production methods, the high-temperature steam electrolysis (HTSE), which requires energy in both electrical and heat forms, is energetically more efficient than its counterparts [2]. Moreover, HTSE is also preferable to other alternatives in terms of its cradle-to-grave environmental impact [3,4]. Although, studies [5,6] focus on coupling the HTSE facility to high-temperature reactors, utilization of existing light water reactors (LWR) will accelerate the transformation of infrastructure intended for sustainable hydrogen production. In fact, techno-economic analysis of an HTSE facility coupled to an LWR showed that the nuclear facility would benefit from hydrogen production [7].

In this study, a multiobjective optimization (MOO) of a pressurized water reactor (PWR) based nuclear cogeneration plant for hydrogen production through HTSE process is carried out. A comprehensive thermodynamic parametric cycle analysis for the secondary cycle of the PWR plant is performed in order to investigate the impacts of the decision variables of heat/electricity energy ratio, hydrogen production capacity, live steam temperature and steam extraction node on the objective functions of thermal efficiency, thermal-to-hydrogen efficiency, utilization factor and exergy efficiency. Then, MOO of the plant is done with the utopia point method to determine the optimum compromise solutions for the decision variables.

THERMODYNAMIC ANALYSIS AND MOO OF THE NUCLEAR COGENERATION PLANT

The secondary cycle of the PWR nuclear cogeneration plant is illustrated in Fig 1. Thermal energy extracted from the reactor core via the primary cycle is transferred to the secondary cycle via the steam generator. The high- and low-pressure turbines produce electrical energy through the generator while the condenser cools the working fluid through a tertiary loop. Feedwater heaters (FWH) increase the thermal efficiency of the plant and provide operational flexibility for cogeneration. Green and yellow lines in Fig 1 represent the steam extraction and condensate return routes, respectively.

The thermodynamic model is constructed by applying the steady-state mass and energy conservation and entropy balance equations to all components of the cycle to determine the mass flow rate and thermodynamic properties of all states. Then, the thermal, thermal-to-hydrogen, exergy efficiencies and utilization factor of the cogeneration plant are calculated by

$$\eta_{th}=\frac{\dot{W}_{net}}{\dot{Q}_{SG}},\ \eta_{H_2}=\frac{\dot{m}_{H_2}\Delta H_{H_2}}{\dot{Q}_{process}+\dot{W}_{H_2}/\eta_{th}},\ \eta_{ex}=\frac{\dot{X}_{out,\dot{W}_{net}}+\dot{X}_{out,\dot{Q}_{process}}}{\dot{X}_{in,\dot{Q}_{SG}}},\ \varepsilon_u=\frac{\dot{W}_{net}+\dot{Q}_{process}}{\dot{Q}_{SG}} \quad (1)$$

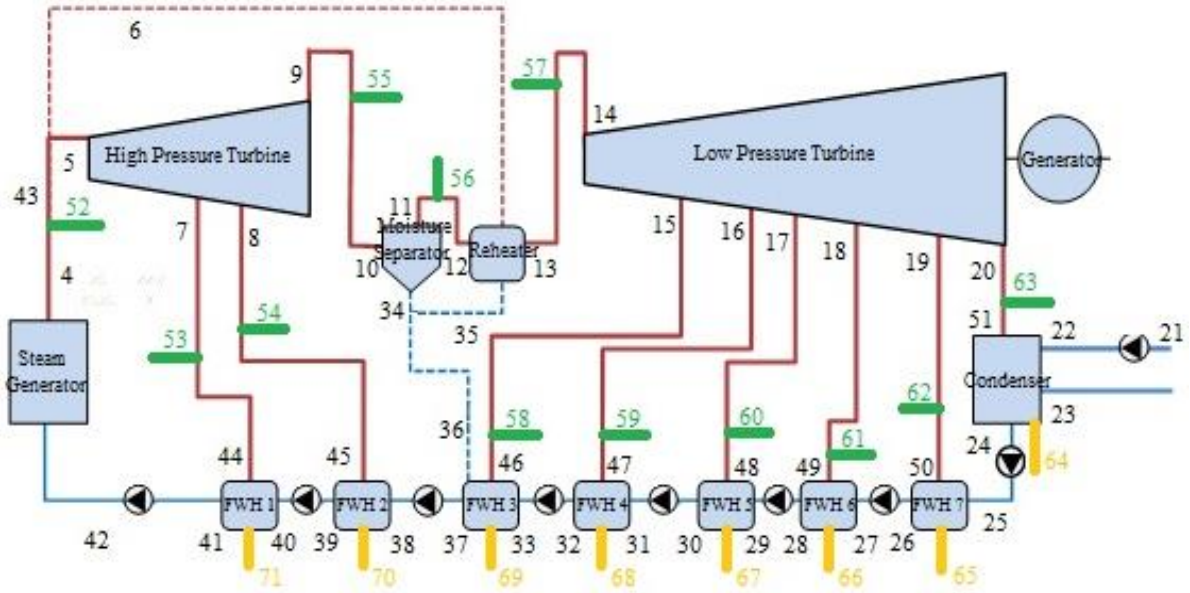


Fig. 1. Secondary cycle of the pressurized water reactor cogeneration plant.

respectively. In Eq. (1), $\dot{W}_{net}$ is the net electrical power, $\dot{Q}_{SG}$ is the heat transfer rate through the steam generator, $\dot{m}_{H_2}$ is the hydrogen production rate, ΔH_{H_2} is the formation enthalpy of hydrogen, $\dot{Q}_{process}$ is the rate of heat transferred from the secondary cycle to the HTSE facility, $\dot{W}_{H_2}$ is the rate of energy transfer to the HTSE facility in the form of electricity, $\dot{X}_{out,\dot{W}_{net}}$ and $\dot{X}_{out,\dot{Q}_{process}}$ are the rates of exergy output of the secondary cycle in form of electricity and heat, respectively, and $\dot{X}_{in,\dot{Q}_{SG}}$ is the exergy expended in the cycle. MOO of nuclear cogeneration plant's secondary cycle with the utopia point is carried out by minimizing a composite function that is formed through the objective functions:

$$\text{Minimize}\left\{\sum_{i=1}^{k}w_i^p\left[\frac{f_i(\boldsymbol{x})-f_i^u}{f_i^{max}}\right]^p\right\}^{1/p}\quad \text{subject to } a_j\le x_j\le b_j,\ j=1,2,...,m \quad (2)$$

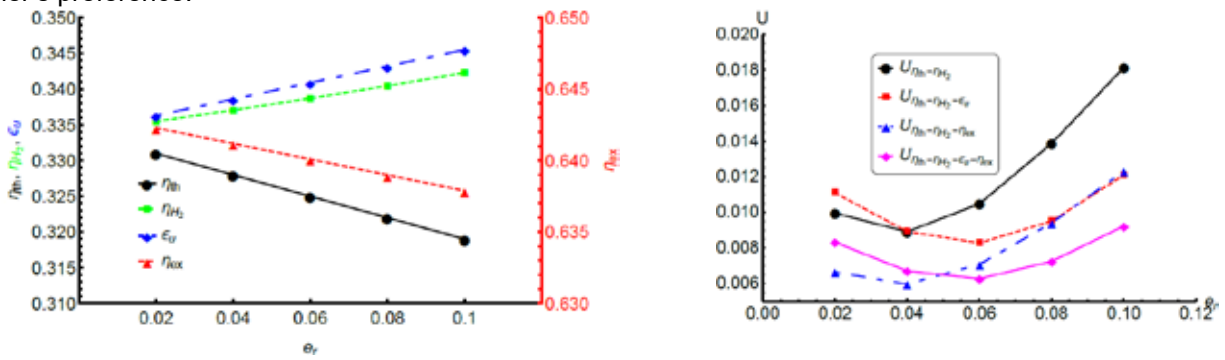
In Eq. (2), f_i and w_i are the objective functions and the corresponding weights, respectively, x is the set of decision variables, f_i^u and f_i^{max} are the utopia and maximum values of the objective functions, respectively, and a_j and b_j are the constraints of the decision variables.

RESULTS AND DISCUSSION

This work deals with the multiobjective optimization of a nuclear cogeneration plant for hydrogen production. Energy is transferred from the secondary cycle of the cogeneration plant to a HTSE facility in the form of process heat and electrical energy. Thermal, thermal-to-hydrogen, exergy efficiencies and utilization factor of the cogeneration plant are considered as the objective functions while energy ratio ($e_r=\dot{Q}_{process}/\dot{m}_{H_2}\Delta H_{H_2}$), hydrogen production capacity, live steam temperature and steam extraction nodes are the decision variables.

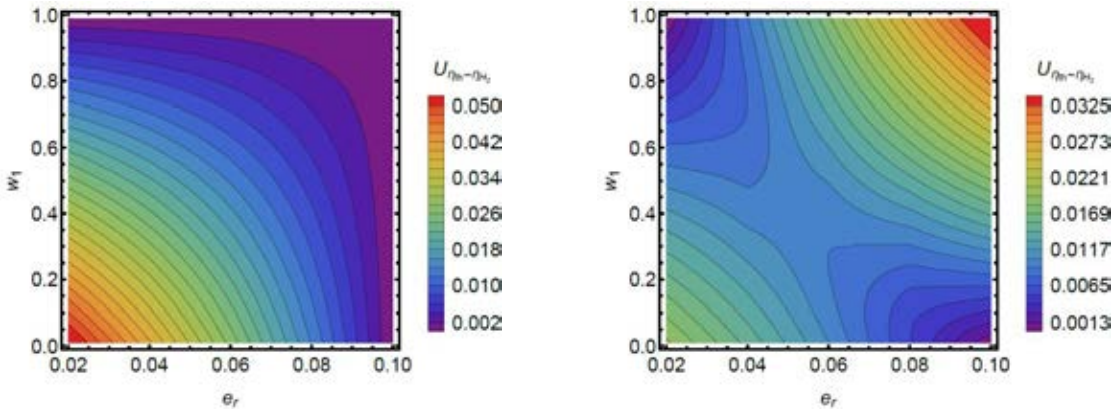
Fig. 2a illustrates the variation of the objective functions with the energy ratio for a hydrogen production rate of 7 kg/s where steam is extracted from node 52, the condensate returns at node 64 and steam temperature at the outlet of the steam generator is 277°C. It is observed that the thermal and exergy efficiencies decrease with an increase in energy ratio, while the thermal-to-hydrogen efficiency and utilization factor have an opposite behavior. These results propound the need for MOO, and Fig. 2b represents the impact of energy ratio on different composite functions where equal weights are used for all cases. The optimum value of energy ratio depends on designers preferences. $U_{\eta_{th}-\eta_{H_2}}$, $U_{\eta_{th}-\eta_{H_2}-\eta_{ex}}$, $U_{\eta_{th}-\eta_{H_2}-\varepsilon_u}$, $U_{\eta_{th}-\eta_{H_2}-\eta_{ex}-\varepsilon_u}$ are minimized at e_r values of 0.0380, 0.0375, 0.0569 and 0.0561, respectively.

The hydrogen production capacity has a significant impact on the MOO of the nuclear cogeneration plant. The contour plots in Figs. 3a and 3b show the Pareto set of $U_{\eta_{th}-\eta_{H_2}}$ with respect to energy ratio for hydrogen production capacities of 0.1 kg/s and 7 kg/s, respectively. When the hydrogen production rate is 0.1 kg/s, the optimum value of the energy ratio is 0.10 for all choices of weight functions, whereas for the production rate of 7 kg/s, it depends on designer's preference.



(a) (b)

Fig. 2. Variation of (a) objective functions and (b) MOO composite functions with the energy ratio.



(a) (b)

Fig. 3. Pareto set of $U_{\eta_{th}-\eta_{H_2}}$ for hydrogen production rates of (a) $0.1 kg/s$ and (b) $7 kg/s$.

CONCLUSIONS

The multiobjective optimization of a nuclear cogeneration plant aimed to produce hydrogen with high-temperature steam electrolysis is performed with the utopia point method. Thermal, thermal-to-hydrogen, exergy efficiencies and utilization factor of the cogeneration plant are chosen as the objective function, and energy ratio, hydrogen production capacity, live steam temperature, steam extraction nodes and ambient conditions are considered as the decision variables. The effects of energy ratio and hydrogen production rate are presented. Results show that, depending on the choice of composite function the optimum value of energy ratio lies in the range of 0.037-0.057 for a hydrogen production rate of 7 kg/s, and it is 0.10 for a production rate of 0.1 kg/s.

REFERENCES

1. IEA. 2021. Hydrogen, IEA, Paris https://www.iea.org/reports/hydrogen. Accessed on March 9, 2022.
2. Pinsky R, Sabharwall P, Hartvigsen J and O'Brien J. 2020. Comparative review of hydrogen production technologies for nuclear hybrid energy systems, Progress in Nuclear Energy, 123:103317.
3. Karaca AE, Dincer I and Gu J. 2020. Life cycle assessment study on nuclear based sustainable hydrogen production options. International Journal of Hydrogen Energy, 45, 22148-22159.
4. Utgikar V and Thiesen T. 2006. Life cycle assessment of high temperature electrolysis for hydrogen production via nuclear energy. International Journal of Hydrogen Energy, 31:939-944.
5. Kowalczyk T, Badur J and Bryk M. 2019. Energy and exergy analysis of hydrogen production combined with electric energy generation in a nuclear cogeneration cycle. Energy Conversion and Management, 198:111805.
6. Ni M, Leung MKH and Leung DYC. 2007. Energy and exergy analysis of hydrogen production by solid oxide steam electrolyzer plant. International Journal of Hydrogen Energy, 32:4648-4660.
7. Frick K, Talbot P, Wendt D, Boardman R, Rabiti C, Bragg-Sitton SM, Levie D, Frew B, Ruth M, Elgowainy A and Hawkins T. 2019. Evaluation of hydrogen production feasibility for a light water reactor in the Midwest, Idaho National Laboratory.

WHEC-2022
23rd World Hydrogen Energy Conference
June 26-30, 2022 - Istanbul

#1592
NUCLEAR HYDROGEN PERSPECTIVES IN ROMANIA

[1] Ioan Iordache, [2] Mihai Varlam, [2] Elena Carcadea, [2] Mihaela Iordache*
[1] National Institute for Research, Development and Testing in Electrical Engineering – ICMET, Decebal Str., Craiova, Romania
[2] National Research and Development Institute for Cryogenics and Isotopic Technologies -ICSI, Uzinei Str., Rm. Vâlcea, Romania

*Corresponding author e-mail: iordache.ioan@icsi.ro

ABSTRACT

This work presents the latest advances of nuclear hydrogen perspectives in Romania. The topic is really new and nuclear hydrogen is considered a new perspective through its low carbon or zero carbon production. The role of nuclear hydrogen production in a low-carbon economy is analysed now by many scientist and many stakeholders, especially national or local authorities, consider that as a new perspective for nuclear energy sector.

Keywords: Romania, Nuclear Hydrogen

INTRODUCTION

Romania is a country that traditionally produces hydrogen [1]. Romania's energy security must take in consideration all global perspective and the newest trends in nuclear energy. In this work authors show an accurate picture about national specific situations in the field of the nuclear hydrogen perspectives in Romania.

Romania recognise the opportunity to use the nuclear energy sector in order to produce hydrogen, of course others also understood this: Argentina, Canada, Germany, Hungary, Indonesia, Italy, Libya, Pakistan, Russia, the UK or the USA. Many form above list have very active progressing research and development initiatives.

The authors consider that nuclear hydrogen is an opportunity to decarbonise significant sectors not only the ability to produce clean hydrogen economically and sustainably in large scale; and are agree that the uncertainties related to nuclear hydrogen technologies and economics can be a barrier to their development. The potential for nuclear power plants can be valorised mere because there can be produced hydrogen using both, power and heat. Referring to the higher temperatures, today's commercial plants output is less 350°C. The nuclear community must focus his attention to the advanced high-temperature reactors for hydrogen production. The high temperature reactors will be the leading technology for future nuclear hydrogen production and nuclear-renewable hybrid energy systems must be considered [2-4].

The hydrogen market need to be developed concomitantly in all directions: the full supply/value chain, including supply, storage, transport, distribution and end use applications.

The most thermochemical cycles require temperatures that exceed 800 °C. The "coldest" cycle is copper-chlorine where the required maximum temperature does not exceed 550 °C. This advantage makes the connection between the Cu-Cl cycle and CANDU nuclear reactors. University of Ontario Institute of Technology (UOIT) and Atomic Energy of Canada Limited (AECL), both of Canada, together with other collaborators, have made a partnership to study, research and develop of this thermochemical cycle. The most studied cycle is the sulphur-iodine S-I or SI, with the next institutes or agencies conducting tests on pilot installations: Japan Atomic Energy Agency (JAEA), General Atomics (GA), Commissariat of Energy Atomic (CEA, France), etc.

NUCLEAR HYDROGEN ASPECTS IN ROMANIA

Romania, the National Hydrogen and Fuel Cell Centre (Fig. 1), is collaborating with Canada on nuclear hydrogen production with the thermochemical Cu-Cl cycle. The group of authors currently performs theoretical and experimental research in integrating renewable energy and low-carbon hydrogen production, catalytic membrane reformer design, thermo-chemical water splitting. The potential of low temperature thermo-chemical cycle as Copper-Chlorine (Cu-Cl) for large-scale hydrogen production using nuclear energy is under investigation to perform integrated lab-scale experiments. The Center was a part of an international project named "Clean Hydrogen Production with Water Splitting Technologies", with Ontario Tech University as the leader of the project. The Center has participated in projects involving the assessment of the potential and relevant business cases for large scale and seasonal storage of renewable electricity by hydrogen underground storage in Europe, HyUnder consortium. The scope of Romanian participation was to identify the most promising site for hydrogen underground storage. For large scale underground storage, hydrogen can be produced by both, renewable and nuclear. Above research and development projects have the mission to

implement, develop and disseminate nuclear hydrogen in Romania, as well as to support national priority policies in the field of energy.

The Romanian authorities need to understand that concerns about nuclear hydrogen are important to the international community and that it is time to take concrete action. Even if the scientific community has a limited number of initiatives, it can support national needs to integrate and participate in international initiatives in this field.



Fig. 1. National Center for Hydrogen and Fuel Cell

CONCLUSIONS

The hydrogen scientific community from Romania is conscious by the perspective and the role of nuclear hydrogen production as part of the whole hydrogen supply chain/lifecycle developed, including demand, production, storage and distribution. The decision to support it by national authorities must be in line with the projects' participation of scientific community. There are several ongoing initiatives in many countries which indicates to the Romanian authorities that the concerns are important at the level of the international community and that it is time to take concrete actions.

REFERENCES

1. Ionescu C. 2005. Study on the implementation of fuel cell in Romania (in Romanian), in Ministry of Education and Research, Fuel Cell. Bucharest, Universul Energiei.
2. Rami S. El-Emam, Hasan Özcan, Comprehensive Review on the Techno-Economics of Sustainable Large-Scale Clean Hydrogen Production, Journal of Cleaner Production, vol. 220, pp. 593-609, (2019).
3. Ruth M. F., O. R. Zinaman, M. Antkowiak, R. D. Boardman, R. S. Cherry, And M. D. Bazilian, Nuclear-renewable hybrid energy systems: Opportunities, interconnections, and needs, Energy Convers. Manag., vol. 78, pp. 684–694 (2014).
4. Ruth M., D. Cutler, F. Flores-Espino, G. Stark, T. Jenkin, T. Simpkins, J. Macknick, The Economic Potential of Two Nuclear-Renewable Hybrid Energy Systems, National Renewable Energy Laboratory, (2016).

WHEC-2022
23rd World Hydrogen Energy Conference
June 26-30, 2022 - Istanbul

#1593

NUCLEAR HYDROGEN PROJECTS TO SUPPORT CLEAN ENERGY TRANSITION

[1*]*Alina Constantin*
[1]International Atomic Energy Agency, Vienna, Austria

*Corresponding author e-mail: a.constantin@iaea.org

ABSTRACT

Hydrogen is expected to be a game changer in the fight against climate change, being able to support the clean energy transition through a variety of roles: decarbonizing different hard-to-abate industrial sectors (such as steel, cement production) and transport (in long haul vehicles, ships and aviation), direct use as a fuel, chemical feedstock or in the form of synthetic fuels, and providing the ability to integrate with hybrid energy systems and renewables, enhancing energy storage and tapping full potential of renewable energy sources. As a consequence, significant increase in hydrogen production is foreseen by 2050, with all the generation coming from zero-carbon processes (electrolysis/thermochemical cycles using clean electricity and heat) or from a low carbon process using steam methane reforming with carbon capture and storage. Nuclear energy can be capitalized on both electricity and heat to provide a clean and reliable source of hydrogen through various processes. There are currently various demonstration projects undergoing in several countries to showcase use of nuclear energy to produce clean hydrogen, considering both the current reactor fleet and advanced reactors. This paper provides an overview of these projects.

Keywords: Nuclear Power; Hydrogen; Decarbonization; Clean Energy

INTRODUCTION

Hydrogen is a commodity chemical species playing a vital role in many industries. As of today, industries such as petrochemical refining, ammonia and methanol production, as well as steel manufacturing, require the largest hydrogen amounts totalling around 70 Mt annually [1]. The hydrogen is produced almost entirely from fossil fuels (natural gas: 48%; off-gases: 30%; coal: 18%; water electrolysis: 4% [2]), leading to CO2 emission of around 830 million tonnes per year [1, 3]. About 6% of global natural gas and 2% of global coal feed the production of the necessary hydrogen [1]. As a fuel, hydrogen has the highest energy content by weight (3 times higher than gasoline) and its use does not release any carbon dioxide on combustion. However, it can have high upstream carbon intensity depending on the energy source and feedstock used to generate it. Hydrogen is a critical feedstock for the entire chemicals industry, including liquid fuels. The Energy Transitions Commission estimates a 5-7-fold increase of hydrogen utilization from today's level by 2050 [4]. The challenge the policy makers need to address consists in finding effective mechanisms to stimulate the production of "clean" hydrogen without generating greenhouse gas emissions as most of the hydrogen comes today from fossil fuel. Fossil fuels have still the biggest share in hydrogen production as the energy consumption in the process is lower than required by electrolysis of water [5] and the production cost is also lower. The most widespread technology to generate hydrogen (accounting for ~76% of the produced hydrogen [3]) is steam methane reforming (SMR). Hydrogen can be also produced by coal gasification method and this option is well represented in China where more than 80% of the world's coal gasification plants are located. This method has the lowest cost for hydrogen production [3]. The SMR technology results in emission of 10 tonnes of CO2/ 1 tonne of H2 while coal gasification produces 19 tonnes of dioxide CO2/ 1 tonne of H2

HYDROGEN PRODUCTION USING CURRENT NUCLEAR FLEET

The existing initiatives for demonstration nuclear hydrogen projects using the operating fleet of reactors focus first on considering electrolysis and introducing that as an additional means to capitalize the clean electricity produced by the nuclear plant. These projects imply a close coordination among industry partners and various stakeholders to evaluate the technical and the economic feasibility and to facilitate implementation. The successful deployment of the demonstration projects is expected to pave the way for large scale projects as they prove the technology and viability of such endeavours, while also supporting the creation of a market for these technologies and attracting more investment into the sector.

Canada. The Nuclear Innovation Institute (NII) has been conducting a study to evaluate the technical feasibility and business case for hydrogen production from nuclear power, also investigating the opportunity for a pilot project at the Bruce Nuclear Generating Station. The Hydrogen Strategy for Canada [6] outlines a role for nuclear electricity to produce hydrogen at off-peak times using nuclear reactors in Ontario, where three of the four nuclear generation stations are located, and in New Brunswick [6].

Europe. In July 2020, the European Commission published the Hydrogen Strategy for a Climate-Neutral Europe [7] to guide the steps towards achieving a hydrogen economy, containing targets, investment goals and regulatory mechanisms to support. Several EU countries (France, Germany, Netherlands, Portugal and Norway, as of September 2020) have already established national hydrogen strategies [3] with different approaches (e.g. France is supportive of nuclear-produced hydrogen while Germany relies on hydrogen imports). However, the European Hydrogen Strategy excludes nuclear power from making a contribution to hydrogen economy over a long-term, envisioning it entirely based on hydrogen produced using renewables sources [3], diminishing the commercial incentive for low carbon energy producers (nuclear, hydropower) to invest in hydrogen generating technologies and hydrogen network infrastructure [3].

United Kingdom. EDF is currently assessing hydrogen production using its fleet of UK nuclear reactors (including Hinkley Point C (under construction) and Sizewell C (proposed to be constructed)). A feasibility study on hydrogen production using electrolysis at Heysham Nuclear Power Station was conducted in 2019 [8], under the Hydrogen to Heysham (H2H) project, to investigate the possibility of replication and scaling up at other nuclear sites across the UK. The study included an assessment of the hydrogen market, engineering design at the Heysham Nuclear Power Station, process risk assessment and implementation steps, and confirmed that the H2H project is technically feasible and further development of this hydrogen supply solution could contribute to the UK's commitment to net zero carbon emissions by 2050. The H2H project was assessed to have a carbon footprint of 24 gCO2/kWh H2 compared to 509 gCO2/kWh H2 for an equivalent grid-connected project [8] and produce at maximum capacity 800 kg hydrogen per day, considering a 2MW electrolyser system (1 x 1MW Alkaline and 1 x 1MW PEM electrolysers). Assuming a wholesale electricity price of £63/MWh, over a 20-year lifetime of the H2H project, the levelized cost of hydrogen (LCOH) calculated was £6.73 – £8.60/kg [8]. The study also estimates that a future electrolyser capacity of about 550MW across UK's nuclear fleet could produce about 220000 kg of hydrogen per day by 2035, with a levelised cost of hydrogen as low as £ 1.89/kg ($ 2.44/kg) [4]. Due to the challenges in developing a successful business model arisen from the lack of support or incentives for end users to consume the hydrogen produced, the project was not able to progress to the demonstration phase [9]. The Nuclear Industry Association's (NIA) Hydrogen Roadmap, endorsed by the Nuclear Industry Council, and the cross-sector Action Plan prepared by the National Nuclear Laboratory (NNL) outline how nuclear power could contribute in producing massive quantities of zero carbon hydrogen to the emerging hydrogen economy [10]. In November 2020, Sizewell C announced its interest to develop a hydrogen demonstrator project. Current steps also include an Innovate UK funded study on transitioning from a diesel to a hydrogen fleet of vehicles at Sizewell [9]. A new nuclear project in Suffolk is looking to develop a demonstration electrolyser at around 2MW to produce up to 800 kg of hydrogen per day that can be used in bus transport for construction workers to and from Sizewell C site [9].

United States: U.S. Department of Energy (DOE) established the H2@Scale initiative bringing together various stakeholders to advanced clean and affordable hydrogen production, transport, storage and utilization. The DOE's H2@Scale Consortium facilitates R&D projects that leverage the world-class capabilities of the national laboratories in partnership with industry and academia. One of the free-to-access resources to inform hydrogen technology development that was prepared under H2@Scale initiative is a techno-economic analysis on the viability of retrofitting existing pressurized water reactors (PWRs) to produce hydrogen via high temperature steam electrolysis [11]. Partly funded by the H2@Scale, Exelon started developing a multi-year nuclear hydrogen demonstration project in August 2019 to install a 1 MW PEM electrolyser at one of its boiling water reactors (BWR) [12]. DOE is funding also 3 additional projects to demonstrate hydrogen production at 3 nuclear power plants: the Energy Harbor's Davis-Besse NPP in Ohio (using a 2 MW PEM electrolyser), the Arizona Public Service (APS) Palo Verde NPP in Arizona (to study the potential of a reversible PEM electrolyser, with the reactor producing electricity at peak demand and hydrogen during low peak demand) and an Xcel Energy NPP in Minnesota (using HTSE technology for hydrogen generation [13]), expecting to showcase significant advances for improving the long term economic competitiveness of LWRs. Hydrogen produced through these projects will have various applications: for example, the hydrogen from Davis-Besse may initially be used to supply public transportation fleets in Ohio or in new direct iron reduction plants being constructed to produce steel [13].

SUMMARY AND CONCLUSION

Nuclear hydrogen production has the potential to enable nations to achieve their Net Zero targets by supporting energy system and industrial decarbonization. There are still barriers and challenges that remain to be addressed for an accelerated deployment of nuclear hydrogen but also opportunities that comes from the benefits that nuclear energy can provide to support massive production of hydrogen, using various reactor technologies: either the current fleet, operating in cogeneration mode and producing hydrogen through electrolysis process, the advanced high temperature reactors coupled with thermochemical cycles, or the innovative small modular reactors that comes with an enhanced operational flexibility and can be at the heart of the growing hydrogen market. The nuclear industry's

entry into the hydrogen sector enables diversification of its role beyond supply of clean electricity and allows it to contribute to sustainable decarbonization of several other sectors, particularly the difficult to decarbonize industries. This strengthens its role and ensures its long term relevance in the national energy systems and economies.

Through its main pillars of work – nuclear safeguards, nuclear safety and security and the peaceful uses of nuclear technology, the International Atomic Energy Agency supports various activities on nuclear hydrogen production, aiming to provide technical expertise, dedicated mechanisms and tools for Member States considering nuclear hydrogen production in their national strategies for decarbonization of energy.

ACKNOWLEDGEMENT

The author acknowledges the valuable insights and review of this paper provided by Ms Rupsha Bhattacharyya, Bhabba Atomic Research Center, Department of Atomic Energy, India.

REFERENCES

1. International Energy Agency. 2019. The Future of Hydrogen.
2. Muradov, N. 2017. Low to near-zero CO2 production of hydrogen from fossil fuels: Status and perspectives, International Journal of Hydrogen Energy 42 20 14058-14088.
3. New Nuclear Watch Institute (NNWI). 2020. On the Role of Nuclear Power in the Development of a European Hydrogen Economy.
4. Energy Transition Commission. 2021. Making the Hydrogen Economy Possible: Accelerating Clean Hydrogen in an Electrified Economy.
5. Balta, M. 2008. Potential importance of hydrogen as a future solution to environmental and transportation problems, International Journal of Hydrogen Energy 33 15 4013-4029.
6. Hydrogen Strategy for Canada. 2020. https://www.nrcan.gc.ca/sites/www.nrcan.gc.ca/files/environment/hydrogen/NRCan_Hydrogen-Strategy-Canada-na-en-v3.pdf
7. Euopian Commission. 2020. Communication from the Commission to the European Parliament, the Council, the European Economic and Social Committee and the Committee of the Regions: A hydrogen strategy for a climate-neutral Europe, https://ec.europa.eu/energy/sites/ener/files/hydrogen_strategy.pdf
8. EDF Energy. 2019. H2H – Hydrogen to Heysham Feasibility Report, https://assets.publishing.service.gov.uk/government/uploads/system/uploads/attachment_data/file/866374/Phase_1_-_EDF_-_Hydrogen_to_Heysham.pdf.
9. Nuclear Industry Association. 2021. Hydrogen Roadmap, https://www.niauk.org/wp-content/uploads/2021/02/ Nuclear-Sector-Hydrogen-Roadmap-February-2021.pdf
10. National Nuclear Laboratories. 2021. Unlocking the UK's Nuclear Hydrogen Economy to Support Net Zero: A Cross-Sector Action Plan for Consideration by the Nuclear Industry Council, https://www.nnl.co.uk/wp-content/uploads/2021/07/Hydrogen-Round-Table-FINAL-v2.pdf
11. Frick, K.L. et al. 2019. Evaluation of Hydrogen Production Feasibility for a Light Water Reactor in the Midwest. United States, https://www.osti.gov/biblio/1569271/
12. https://www.powermag.com/hydrogen-may-be-a-lifeline-for-nuclear-but-it-wont-be-easy/
13. https://inl.gov/article/xcel-energy-inl-hydrogen-production/
14. https://www.powermag.com/three-more-nuclear-plant-owners-will-demonstrate-hydrogen-production/

WHEC-2022

23rd World Hydrogen Energy Conference

TRACK 5. HYDROGEN SEPARATION AND PURIFICATION

TRACK 5. HYDROGEN SEPARATION AND PURIFICATION

#34 NEW ASPECTS CONCERNING THE IMPROVING OF HYDROGEN ISOTOPES SEPARATION BY HYDROGEN-WATER ISOTOPIC EXCHANGE	372
#50 SIMULATION MODELING OF HYDROGEN PERMEATION ACROSS PURE PALLADIUM MEMBRANES	375
#140 CORROSION PHENOMENON IN DENSE MEMBRANE MADE OF PALLADIUM BASED ALLOY	378
#161 H_2/CO_2 SEPARATION WITH NEW IONIC LIQUID-BASED MEMBRANES	381
#170 GAS SEPARATION PROPERTIES OF MIXED MATRIX MEMBRANES PREPARED WITH GRAPHENE OXIDE	384
#184 H_2 SEPARATION FROM CO_2 AND CH_4 MIXTURES USING A SAPO-34 MEMBRANE	388
#236 MIXED MATRIX MEMBRANES FOR HYDROGEN RECOVERY FROM INDUSTRIAL WASTE STREAMS	391
#246 PSEUDO-DYNAMIC MODELING AND OPTIMIZATION OF HEAVY PARAFFIN DEHYDROGENATION PROCESS FOR SELECTIVE OLEFIN AND HYDROGEN PRODUCTION USING MEMBRANE REACTORS	394
#259 DEVELOPMENT AND INVESTIGATION OF A NOVEL ELECTROCHEMICAL HYDROGEN COMPRESSOR CELL DESIGN BASED ON HYDRAULIC CLAMPING	397
#268 TOWARDS A BETTER SUSTAINABILITY OF ELECTROLESS PORE-PLATED MEMBRANES: LIFE CYCLE ASSESSMENTS ON FABRICATION STRATEGIES	400
#312 ELECTROCHEMICAL HYDROGEN SEPARATION FROM REFORMATE USING POLYBENZIMIDAZOLE/MOF COMPOSITE MEMBRANES	403
#333 DEVELOPMENT OF BIMETALLIC ELECTROCATALYSTS FOR HIGH-TEMPERATURE ELECTROCHEMICAL HYDROGEN PURIFICATION	406
#426 DEVELOPMENT OF Pd-BASED DENSE METALLIC MEMBRANE WITH SULFUR RESISTANT MOF COATED FOR HYDROGEN SEPARATION	409
#1502 DEVELOPMENT OF HYDROGEN PURIFICATION MEMBRANE BASED ON Pd-Mn-Ag TERNARY SYSTEM	412
#1505 ENERGY ANALYSIS OF A MEMBRANE REACTOR-BASED HYDROGEN PRODUCTION SYSTEM	415
#1559 PARAMETRIC INVESTIGATION ON THE PURIFICATION CHARACTERISTICS OF $La_{0.9}Ce_{0.1}Ni_5$ UNDER VARIOUS ABSORPTION/DESORPTION CONDITIONS	418
#1566 INVESTIGATION OF LOW-TEMPERATURE POLYMER ELECTROLYTE MEMBRANE FOR ELECTROCHEMICAL HYDROGEN COMPRESSOR	421
#1580 EVALUATION OF THE EFFECT OF TEMPERATURE, AIR EXPOSURE AND GAS MIXTURE ON Pd_{82}-Ag_{15}-Y_3 FOR HYDROGEN SEPARATION	424
#1583 OVERVIEW OF ELECTROCHEMICAL HYDROGEN PURIFIER PERFORMANCE DIAGNOSTICS	427
#1612 PARAMETER OPTIMIZATION OF A PBI MEMBRANE-BASED HIGH TEMPERATURE-ELECTROCHEMICAL HYDROGEN COMPRESSOR FED WITH H_2 AND CO MIXTURE	430
#1635 SYNTHESIS AND CHARACTERIZATION OF A NOVEL NICKEL-RUTHENIUM BASED CATALYST FOR BIOGAS STEAM REFORMING TO GENERATE HYDROGEN IN CONVENTIONAL AND MEMBRANE REFORMERS	433

WHEC-2022
23rd World Hydrogen Energy Conference
June 26-30, 2022 - Istanbul

#34

NEW ASPECTS CONCERNING THE IMPROVING OF HYDROGEN ISOTOPES SEPARATION BY HYDROGEN - WATER ISOTOPIC EXCHANGE

Gheorghe Ionita, Ciprian Bucur and Ionut Spiridon*
National Research Institute for Cryogenics and Isotopic Technologies - ICSI Rm.Valcea,
ICSI Nuclear Department,Uzinei Street; No. 4; PO Box 7, Raureni, 240050 - Rm Valcea,Romania

*Corresponding author e-mail: gheorghe.ionita@icsi.ro

ABSTRACT

The isotopic exchange between hydrogen and liquid water (LPCE) is one of the most efficient process for hydrogen isotopes separation in order to remove tritium from nuclear effluents, produced in fission and fusion reactors. In order to increase the efficiency of isotopic exchange process, the chemical exchange (promoted by hydrophobic catalyst) is usually associated with conventional distillation process (promoted by hydrophilic packing), the both processes being promoted by using so called “mixed catalytic packing”. A new catalytic support (modified organic copolymer) and two new procedures (A and B), based on chemical and thermal treatments of hydrophilic packing has been proposed and tested. The main characteristics of the catalyst and hydrophilic packing have been evaluated and discussed in deep correlation with hydrogen isotopes separation performances. The experimental results showed as the new catalytic support and the treatment based on solution B, at increased temperature are a promising idea and can be applied to manufacture a new improved mixed catalytic packing. This type of mixed catalytic packing is under testing to be proposed to equip the isotopic exchange columns of the future Tritium Removal Facility for heavy water detritiation.

Keywords: Hydrogen isotopes, Hydrophobic catalysts, Hydrogen -water isotopic exchange, Mixed catalytic packing

INTRODUCTION

The separation of hydrogen isotopes (deuterium and tritium) is very important, especially in nuclear energy field but and others domains, too. During operation of CANDU fusion reactors, the tritium content in the heavy water increases and it has to be removed to protect the staff and to reduce potential contamination of the environment. On the same time, recovered tritium is a valuable material for various applications but especially as fuel for future fusion reactors-International Thermonuclear Experimental Reactor-ITER project [1]. ITER reactor is planned to begin its operation in 2027 and requires a total of 18 kg of tritium over its planned 20-years and will depend entirely on an external tritium source. The cryogenic distillation (CD) combined with catalysed isotopic exchange between hydrogen and liquid tritiated water (LPCE), it’s one of the most suitable technologies (CD-CE) for hydrogen isotopes separation. In LPCE process, the tritium from tritiated water is transferred to the hydrogen gas through the following consecutive steps [2]:

$$HTO_{(V)} + H_{2(G)} \leftrightarrow HT_{(G)} + H_2O_{(V)} \quad (1)$$

$$HTO_{(L)} + H_2O_{(V)} \leftrightarrow HTO_{(V)} + H_2O_{(L)} \quad (2)$$

$$HTO_{(L)} + H_{2(G)} \leftrightarrow HT_{(G)} + H_2O_{(L)} \quad (3)$$

Reaction (1) becomes effective only in presence of a *hydrophobic catalyst* which has to repel the liquid water but to allow to water vapour and hydrogen gas to reach the active catalytic centres and to accelerate the isotopic transfer process. On the other hand, the process (2) it’s a conventional water distillation process and need an efficient contact element (hydrophilic packing) in order to increase the contact area between water vapour and liquid water. The mixture consisting of hydrophobic catalyst and hydrophilic packing in various ratio it is called “mixed catalytic packing”.

This work presents the last proposals of the authors concerning the improvement of separation performances and stability of the mixed catalytic packing by increasing of wettability of hydrophilic component and a new catalytic support.

EXPERIMENTAL

The Hydrophobic Catalyst

The key element in increasing the hydrogen isotopes separation performances and in minimizing the LPCE column sizes is *the hydrophobic catalyst* which promotes tritium transfer from tritiated water vapor to deuterium, as in reaction (2). Over 100 metal/support catalyst types were prepared and tested at laboratory scale [3]. The main differences between them consists of support nature, active metal deposition method and wet-proofing method.

By authors work in Romania, a few catalyst types, based on platinum on carbon and polytetrafluoroethylene styrenedivinyl-benzene and have been prepared, characterized and tested in LPCE process. Though the both type of catalyst proved similar tritium separation performances, the stability of Pt/SDBC, quickly decreased and finally the Pt/C/PTFE has been selected for LPCE process [1, 4]. Therefore in this work, a new catalytic support based on modified organic copolymer is proposed and tested. The research efforts have been focused to optimize, preparation conditions, increasing of hydrophobicity and to get compatible characteristics for using in mixed catalytic packing.

Table 1. Composition and main caractheristics of St-DVB catalytic suport

Code	DVB, wt.%	ESt,[a] wt.%	St, wt%	Dilution Ration (mL/mL)	Q_T, g/g	Q_w, g/g	Surface Area m^2/g	Volum Pores cm3/g	Radius pores Å
St-DVB	50	25	25	0.5	1.128	0.082	328.8	0.523	45.02

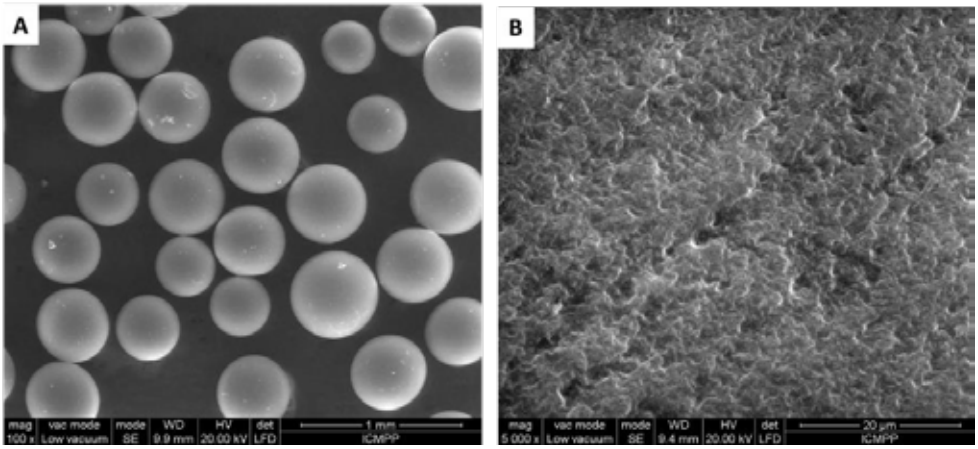


Fig. 1. SEM image (A) and in section (B) of SDB catalytic support

In order to increase the hydrophobicity of SDB, various amounts of silicone agent (CTMV-1) has been added in various ratios and simultaneously impregnated with a salt of metal active precursor by a new method, subject to be patented.

Hydrophilic packing and mixed catalytic packing

Usually in LPCE process are used structured Sulzer packing (made of metallic net) and their efficiency in water distillation process strongly depends on its wettability, therefore our research efforts have been focused on increasing the wettability packing by two new specific treatments:

a) chemical treatment to increase the roughness of metallic wire and specific area;

b) thermal treatment in controlled atmosphere to produce a thin layer of hydrophilic metallic oxides at wire surface

To increase the external surface (roughness) of metallic wire of metallic gauze , three solutions (A , B and C) of various composition at different duration and temperatures have been applied;

The increasing of the roughness of metallic wire after chemical treatment has been proved by SEM analyse and in is shown Fig. 2 [5]. The chemical treatment with B solution has increased the wettability with 20%, average.

Thermal treatment consists of in heating of hydrophilic packing in controlled atmosphere at various temperatures and contributes at creation of thin layer (3-7 μm) of metal oxides and to an average increasing of wettability with 15%;

By applying of the both treatments, firstly chemical and then thermal, the increasing of wettability has been around 28%, like as in Table 2 is shown.

Future investigations are still necessary concerning composition, the adherence of metal oxides layer and packing behavior under LPCE process conditions.

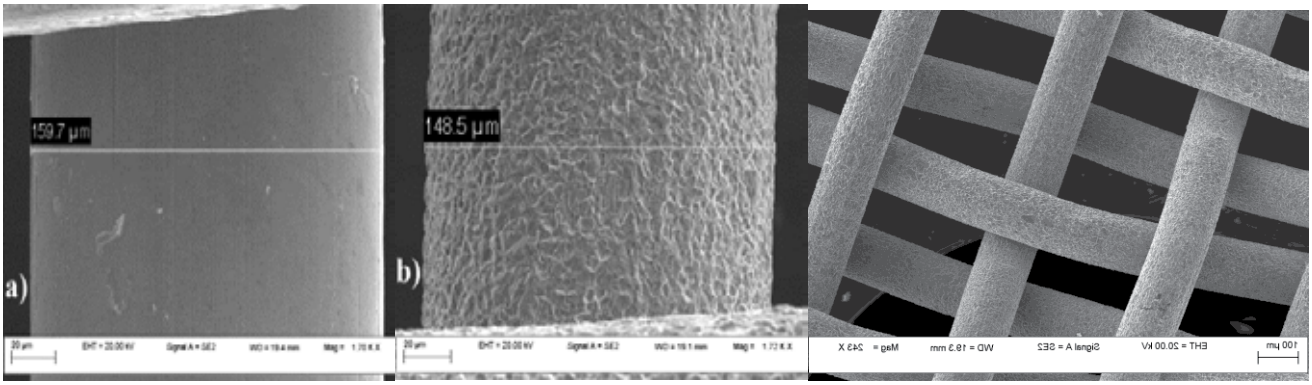


Fig. 2. SEM image of stainless-steel wire for untreated (a) and treated packing (b)

Table 2. The increasing of hydrophilic packing wettability after chemical and thermal treatments at various temperatures

Type of material	(T_1)ºC	(T_1 + 50)ºC	(T_1 + 150)ºC	(T_1 + 200)ºC	(T_1 + 300)ºC	(T_1 + 350)ºC
Bronze Phosphorous	9 %	12 %	17.5 %	19 %	26 %	29 %
Stainless steel	6 %	10.5 %	15.5 %	20.5 %	25.5 %	27 %

CONCLUSIONS

To increase the hydrogen isotopes separation performances by hydrogen-water isotopic exchange, a new catalytic support based on modified organic copolymer and two new procedures for improvement of hydrophilic packing wettability has been proposed and investigated, the new catalytic support shown physico-chemical characteristics and high hidrophobicity and could be a potential candidate for the future improved catalyst.

The both new treatments of hydrophilic packing for increasing of roughness and for covering the external surface with thin layer of hydrophilic metallic oxides have contributed to the significant increasing of the wettability of mixed catalytic packing.

Future investigations are still necessary concerning composition, the adherence of metal oxides layer and packing behavior under LPCE process conditions.

ACKNOWLEDGEMENT

This work was supported by Ministry of Research and Innovation (Romania), within PN projects no: 19 11 01 03/2019 and 18 12 02 01/2018

REFERENCES

1. Pearson R, Antoniazzi A and Nuttall W.J 2018. Tritium supply and use: a key issue for the development of nuclear fusion energy, Fusion Engineering and Design, https://doi.org/101016/j.fusengdes
2. Ionita Gh. and Stefanescu I. 1995. The Separation of Deuterium and Tritium on Pt/SDB/PS and Pt/C/PTFE Hydrophobic Catalysts", Fusion Technology, 28, *3*, 642.
3. Ionita Gh. et al, 2015. An Assessment on Hydrogen Isotopes Separation by Liquid Phase Catalytic Exchange Process, Journal Radioanalytical and Nuclear Chemistry, 305, *1*, 117.
4. Popescu I., Gh. Ionita 2008 Improved charactheristics of hydrophobic polytetrafluor etilene -platinum catalysts for titium recovery from tritiated water - Fusion Engineering and Design 83, pp. 1392 – 1394.
5. Gh. Ionita et.al. 2018. Hydrodynamic Characteristics of Mixed Catalytic Packing for Heavy Water Detritiation. Fusion Engineering and Design' 10.1016/j.fusgendes.2019.03.196

WHEC-2022
23rd World Hydrogen Energy Conference
June 26-30, 2022 - Istanbul

#50

SIMULATION MODELING OF HYDROGEN PERMEATION ACROSS PURE PALLADIUM MEMBRANES

[1*]*Mostafa El-Shafie*
[1]Gifu University, Environmental and Renewable Energy Systems Division, Graduate School of Engineering, 1-1 Yanagido, Gifu, 501-1193, Japan

*Corresponding author e-mail: mostafaelshafie81@gmail.com

ABSTRACT

Further advances in the hydrogen separation membranes field require investigating materials with high H_2 permeation and selectivity by predicting the performance from simulation modeling. In this study, a two-dimensional CFD simulation model is developed for investigating the hydrogen separation process across the pure palladium membrane type. The influences of feeding pressure, H_2 feeding flow rate, and membrane thickness on the hydrogen permeation process were investigated. Two Pd-membrane thicknesses of 15μm and 20μm were investigated to understand the hydrogen embrittlement and diffusion through pure Pd-membrane. The velocity, concentration, and diffusion mass transfer flux distribution were numerically achieved by the model. The results showed that the higher feeding pressure can promote the concentration and hydrogen flux distributions that lead to more separated hydrogen. The feeding pressure plays an important factor in membrane separation processes. The simulation analysis showed that the hydrogen velocity distribution increased with the feeding gas flow rate. Furthermore, the diffusion flux was enhanced with the permeation time and the feeding flow rate increased. It can be concluded that the hydrogen concentration and diffusion mass transfer flux through thick membranes was low compared with lower membrane thickness. However, high membrane cost has limited development that requires thin membranes because the best membrane separation materials are precious metals. It can be expected that the CFD simulation model will aid in the membrane separation design, selection, and development.

Keywords: Numerical simulation, Palladium membrane (Pd), Hydrogen separation, Hydrogen flux.

INTRODUCTION

Hydrogen production from different feed stocks is expected to enhance in the future and moves toward using hydrogen as a new energy carrier. Hydrogen can be generated by various industrial processes such as water electrolysis, steam reforming, and coal gasification, which it can be used for the hydrogen production from traditional energy sources [1, 2]. Hydrogen production from fossil fuels acts over 90% of total generated hydrogen (mainly natural gas steam reforming). Most of the produced hydrogen is utilized in a large-scale industrial application processes such as textile industries, chemical, petrochemical, metallurgical, and raw materials like ammonia, hydrogen peroxide, and methane [3]. The hydrogen permeation modeling becomes an important method for describing and identifying the permeation process through Pd-based membranes. Many efforts for H_2 permeation modeling have been investigated to predict the hydrogen diffusion and selectivity [4]. The hydrogen permeation through Pd-Cu40% membrane has been experimentally investigated under gas driven permeation and plasma driven permeation [5]. It has been investigated that the abatement of concentration polarization in the membrane separation process is a considerable issue because of its impact on decreasing efficiency of hydrogen separation and the operation cost increased [6]. Also, the literature survey elucidated the membrane design configuration importance in enhancing the membrane performance and mass transfer process across the membrane surface.

In this study, two-dimensional CFD simulation modeling is developed to investigate the hydrogen permeation process through Pd-membrane. The effects of hydrogen feeding flow rate, feeding pressure, and Pd-membrane layer thickness on the hydrogen permeation process through pure Pd-membrane are investigated. The velocity profile, concentration, and hydrogen diffusion flux distributions are evaluated at different permeation axial positions. The hydrogen separation through two different Pd-membrane thicknesses is evaluated to understand the hydrogen dissociation process across the pure palladium membrane.

NUMERICAL MODEL GOVERNING EQUATIONS AND BOUNDARY CONDITIONS

The numerical simulation and modeling give the ability to investigate the effect of different parameters on the membrane reactor performances. The numerical modeling governing equations include the transport species, continuity, and momentum equations. In this simulation, two-dimensional mathematical model, 2D-axisymmetric, isothermal, and laminar flow are considered as the model assumption. Figure (1) shows the designed reactor 2D geometry and the applied meshing to the membrane reactor domain.

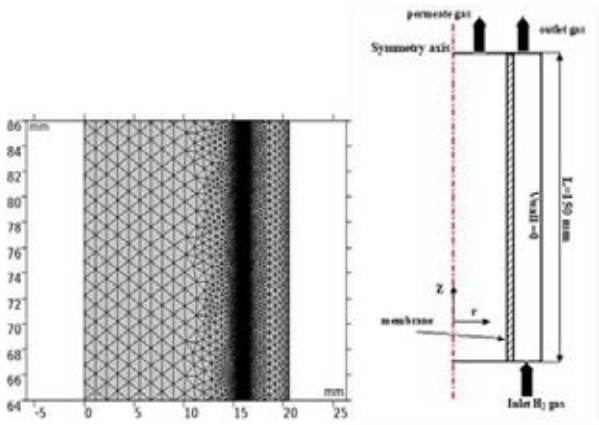


Fig. 1. Schematic diagram of 2D geometry and meshing domain.

The numerical model governing equations will be given in this section. The continuity governing equation of hydrogen species transport in general form of the Pd-membrane separation system is given as follows [7]:

$$\frac{\partial C_i}{\partial t} = -(\nabla . C_i V) - (\nabla . J_i) + R_i \quad (1)$$

Where V and t are velocity and time, respectively. The hydrogen separation process occurs in the cylindrical vertical z-direction coordinates and radius r. Navier-Stokes equation in cylindrical coordinates is used to determine fluid flow properties according to the following equation [8],

$$-\nabla . \mu(\nabla u + (\nabla u)^T) + \nabla P + \rho \frac{\partial u}{\partial t} + \rho(u . \nabla)u = F, \nabla . u = 0 \quad (2)$$

Where the fluid dynamic viscosity is μ (kg/m.s), u (m/s) denotes velocity, density of the fluid is ρ (kg/m^3), pressure is P (atm), and the body force is F (N/m^3).

The numerical model boundary conditions can be defined as follows, Initial concentration value is zero, no slip velocity, symmetry boundary, inlet velocity is V_0 at z=0, and the feed side inlet and outlet pressure is atmospheric pressure.

RESULTS AND DISCUSSION

Influence of feeding pressure on the permeation process

The hydrogen concentration at different feeding pressures is demonstrated in Figure (2). The hydrogen concentration results of all feeding pressures are increased with the reaction time. Moreover, it is noted that the hydrogen concentration of feeding pressure of 200 kPa is slight lower than other tested feeding pressures. However, the highest H_2 concentration is almost obtained at feeding pressure of 400 kPa. The H_2 concentration is varied at the beginning of permeation process then increased with time. The concentrations of hydrogen is slightly enhanced with the increase of feeding pressure, because of the main driving force of the permeation process is the partial pressure difference between retentate and permeate side.

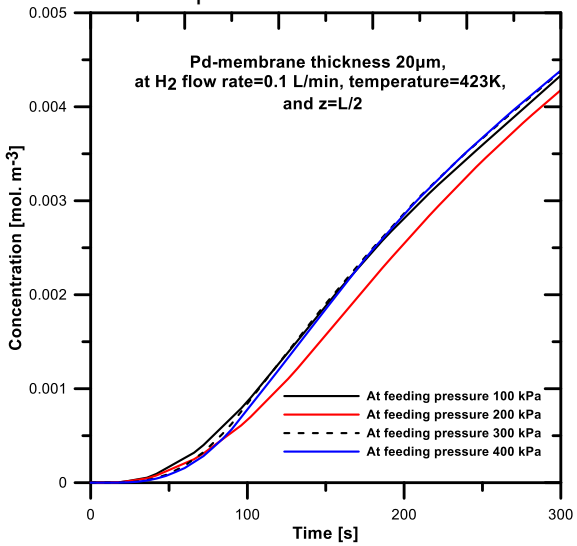


Fig. 6. Hydrogen concentration at different feeding pressures.

Influence of hydrogen feeding flow rate on hydrogen separation

The hydrogen concentration was evaluated at different permeation side positions. Figure (3) represents the hydrogen concentration results of H_2 flow rates of 0.5, 1 L/min at different z-direction positions. It was observed that the hydrogen concentration at zero position is greater than that obtained at the center and outlet of permeation side.

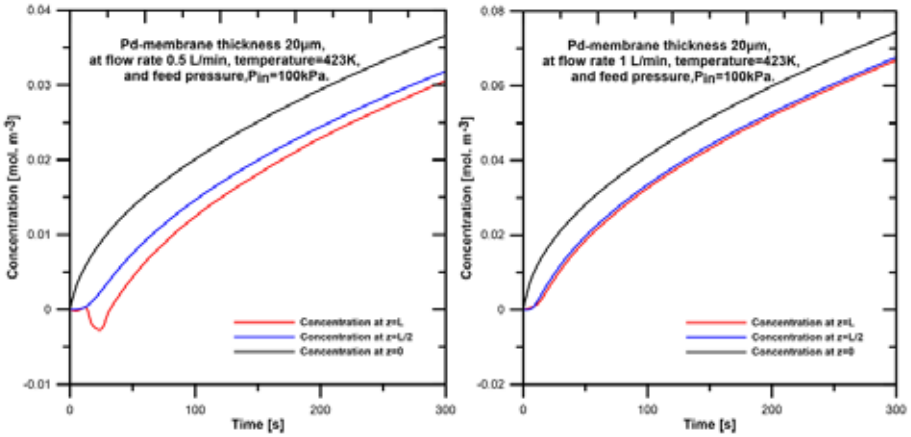


Fig. 3. Comparisons of H_2 concentrations at different positions.

CONCLUSIONS

The current study presented the two-dimensional CFD simulation model for two parameters influencing the hydrogen separation process across the Pd-membrane type. The effect of feeding pressure, reactor gap distance, hydrogen concentration, and heating temperature on the permeation process are investigated for both membrane types. Moreover, the simulation analysis results of pure Pd-membrane are investigated at different operating conditions. The results showed that the higher feeding pressure can promote the hydrogen flux and leads to more separated hydrogen. Also, the feeding pressure plays an important factor in membrane separation processes. The effect of H_2 feeding flow rate and membrane thickness on the hydrogen permeation process was investigated. The simulation analysis was carried out at a reactor temperature of 150ºC and feed pressure of 100 kPa. Pure hydrogen with a concentration of 100% was considered in this simulation analysis. The velocity, concentration, and diffusion mass transfer flux distribution were numerically reported by the model. The simulation results showed that the hydrogen velocity distribution increased with the feeding gas, while the velocity decreased and reach zero at the membrane wall. Furthermore, the diffusion flux increased with permeation time and the feeding flow rate increased. Also, the hydrogen concentration was influenced by the feeding hydrogen flow rate. It was clear that the hydrogen concentration gradient of feeding flow rate 1 L/min was greater than 0.1 and 0.5 L/min because of larger H_2 flow rate will lead to more H-atoms adsorbed by the Pd-membrane surface. Two Pd-membrane thicknesses were investigated by the current model. It can be concluded that the hydrogen concentration and diffusion mass transfer flux through thick membranes was low compared with small membrane thickness values. It can be expected that the CFD simulation model will be helpful in the membrane separation design and development.

REFERENCES

1. El-Shafie M, Kambara S, Hayakawa Y. Hydrogen production technologies overview. J Power Energy Eng 2019; 7:107-54.
2. Holladay JD, Hu J, King DL, Wang Y. An overview of hydrogen production technologies. Catal Today, 2009; 139:244-60.
3. Ogden, J. Lecture (Oct 2004); available electronically at http:// www.its.ucdavis.edu/education/classes/pathwaysclass/7-StationaryH2- (Ogden).pdf.
4. Kamakoti, P.; Morreale, B. D.; Ciocco, M. V.; Howard, B. H.; Killmeyer, R. P.; Cugini, A. V.; Sholl, D. S. Science 2005, 307, 569.
5. K. Zhang, J.D. Way. Palladium-copper membranes for hydrogen separation. Sep. Purif. Technol. 2017, 186, 39–44.
6. G. He, Y. Mi, P. Lock Yue, G. Chen, Theoretical study on concentration polarization in gas separation membrane processes, J. Membr. Sci. 153 (1999) 243-258.
7. Farjami M, Moghadassi A, Vatanpour V. Modeling and simulation of CO2 removal in a polyvinylidene fluoride hollow fiber membrane contactor with computational fluid dynamics. Chem Eng Process Process Intensif. 2015; 98:41-51.
8. Oxarango L, Schmitz P, Quintard M. Laminar flow in channels with wall suction or injection: a new model to study multi-channel filtration systems. Chem Eng Sci. 2004; 59(5):1039-1051.

WHEC-2022
23rd World Hydrogen Energy Conference
June 26-30, 2022 - Istanbul

#140
CORROSION PHENOMENON IN DENSE MEMBRANE MADE OF PALLADIUM BASED ALLOY

[1,2]Hatem Alsyouri, [3*]Farqad Al-Hadeethi, [3]Sohaib Dwairi
[1]Department of Chemical Engineering, School of Engineering, The University of Jordan, Amman, Jordan
[2]Department of Chemical Engineering, College of Engineering and Technology, American University of the Middle East, Egaila, Kuwait
[3] Independent Researchers, Amman, Jordan

*Corresponding Author: farqadfms@yahoo.com

ABSTRACT

Hydrogen is considered the energy of the future. In order to achieve this goal several technological obstacles and gaps related to the ultra-purification of hydrogen must be solved and improved. One of the adopted means used to purify Hydrogen is related to the usage of dense membranes made of Pd based alloys (i.e. Pd/Cu) due to its perfect permeability and selectivity towards hydrogen. Therefore, the current work was focused on showing the negative impact generated due to corrosion of Pd, Cu and Pd/Cu in accelerated corrosive acidic media (0.25 M HCl) at various operating conditions [temperatures (30 and 50ºC) and speeds of agitation (0, 300, 600, and 900 RPM)] to simulate the actual corrosion reaction resulted from hydrogen gas in real applications. The results reveled that copper will dissolute in a greater way if combined with palladium in an alloy to fabricate dense membranes to purify hydrogen.

Keywords: Corrosion, Hydrogen purifiers, Pd, Cu

INTRODUCTION

The fossil fuel-based economy caused several global crises during the elapsed 30 years such as greenhouse gases (GHG). Therefore, huge efforts were focused on developing renewable, sustainable and environmentally friendly technologies to utilize hydrogen in order to reduce the dependence on fossil fuels. One of these technologies are dense membranes made of Pd alloys used to produce ultra-pure hydrogen using single purification step based on solution-diffusion mechanism. Copper is used as an alloying element with palladium to form Pd/Cu to be used in these membranes due to the low price of copper as well as its great resistance to sulfur poisoning. In these kind of membranes, high-pressure feed gas mixture is applied to one end of the membrane whilst maintaining a relatively low pressure on the opposite side. Large hydrogen partial pressures will initiate a mechanism known as mass transport. Hydrogen will migrate across the membrane to form the permeate leaving behind the impurity gases as retentate [1,2,3]. Membrane performance is generally described by its permeability, selectivity and thermal stability. Permeability measures the capacity of a membrane to process the permeate gases and denotes the flux through a membrane per unit of area and time at a given pressure gradient. Selectivity measures the ability of separating the desired component from the other components of the gas mixture and is usually determined by the permeation rate of pure hydrogen and other pure gases such as nitrogen and helium [4]. Any change in the material of the dense membrane will be reflected on its permeability and selectivity to hydrogen, therefore the current work was focused on investigating the corrosion behavior of Pd and Cu using acidic medium (0.25 N HCl) at various operating temperatures (30 and 50ºC) and speeds of agitation (0, 300, 600, and 900 RPM) in order to accelerate and simulate the actual corrosion reaction occurred in dense membranes made of Pd/Cu.

EXPERIMENTAL WORK

Potentiodynamic corrosion tests were performed for single metallic specimens made of Pd or Cu in corrosive acidic media (0.25 M HCl) at various operating conditions [temperatures (30 and 50ºC) and speeds of agitation (0, 300, 600, and 900 RPM)]. Galvanic corrosion currents and coupling potential were measured for Pd/Cu at the given operating conditions using Zero Resistance Ammeter (ZRA). Taking into considerations that Open Circuit Potential (OCP) of copper and palladium were also measured before each run.

RESULTS AND DISCUSSION

Corrosion of Copper

The results revealed that increasing the speed of agitation from (0 to 900 RPM) at the given temperatures resulted an increase in the corrosion rate of copper, except at 50ºC and 600 RPM, where the rate was shifted to lower value (i.e. 0.288 mm/y) . The reason behind the decrease in the corrosion rate is due to the formation of a protective film made of the corrosion products on the copper surface, which slowed down the rate of mass transfer of hydrogen and oxygen ions to the copper surface, while increasing the speed from (0 – 900 RPM) caused a removal of the mentioned

protective film and as a result it increased the diffusion or migration of hydrogen and oxygen ions to copper surface. This trend is in agreement with Stupnis˘ek-Lisac et al. [5], Saeed et al. [6], Modestov et al. [7], Smyrl et al. [8], Habbache et al. [9], and Nielsen et al. [10].

Corrosion of Palladium

The results showed that corrosion rates of palladium were decreased with increasing temperature due its passive behavior, except at 600 RPM, where it was increased with increasing temperature. Basically, the corrosion rate of palladium at 30ºC was increasing with increasing speed of agitation from (0 – 300) RPM, then decreasing at (300 – 600 RPM), followed by an increase at (600 – 900 RPM). Whereas, at 50ºC corrosion rate of palladium was continuously increasing at (0 – 600 RPM) followed by a decrease at (600 -900 RPM). In other words, this condition caused palladium to lose its passivity as a result of the interactions among the operating conditions (i.e., temperature and speed of agitation) which is in agreement with the opinion given by Craig et al. [11] where they have mentioned that palladium corrodes anodically in hydrochloric acid at certain operating conditions. Maximum corrosion rate was observed at 30ºC and 300 RPM with 0.107 mm/y, while the minimum rate was observed at 50 ºC and 0 RPM with 0.018 mm/y. It is important to report that corrosion rates of palladium were significantly lower than that of copper under all studied operating conditions.

Galvanic Corrosion of Palladium/Copper Alloy

The results indicated that Cu was aggressively corroded in order to protect Pd in the galvanic couple of Pd/Cu because the location of coupling potentials were below the polarization curves of Pd at the mentioned operating conditions as well as the polarization curve of Cu indicated higher corrosion current densities than Pd based on the intersection value of the cathodic portion with the anodic portion of Tafel region within each polarization curve without forgetting the effect of increasing the speed of agitation (0, 300, 600 and 900 RPM) which played a vital role in changing the corrosion rates in both Cu and Pd. On the other hand, the results of the average galvanic currents (Ig, av) of Cu which represents the rate of galvanic corrosion of the active part in the Pd/Cu couple obtained by calculating the area under the curve using trapezoidal rule revealed that the average galvanic currents (Ig, av) of Cu were increasing with the increase in the speed of agitation from 0 to 900 RPM at both temperatures (30 and 50ºC). The extracted results were in agreement with Schweitzer [12], Revie et al. [13], and Katarzyna et.al [14].

CONCLUSIONS

The results revealed that increasing temperature and/or speed of agitation will affect the corrosion rate of Pd, Cu and Pd/Cu couple. In fact, copper showed a special behavior at 50ºC and 600 RPM, where the rate was shifted to lower value (i.e., 0.288 mm/y). The reason behind the decrease in the corrosion rate is due to the formation of a protective film made of the corrosion products on the copper surface, which slowed down the rate of mass transfer of hydrogen and oxygen ions to the copper surface. While, increasing the speed from (0 – 900 RPM) caused a removal of the mentioned protective film and as a result it increased the diffusion or migration of hydrogen and oxygen ions to copper surface. On the other hand, the results showed that corrosion rates of palladium were significantly lower than that of copper under all studied operating conditions. It is worth to mention that the results indicated that Cu was aggressively corroded in order to protect Pd in the Pd/Cu couple. As a result, it is obvious that coupling of Pd and Cu to form Pd/Cu alloy will have a negative impact on the performance when used as a dense membrane for hydrogen purification.

REFERENCES

1. Al-Mufachi N.A., Rees N.V., Steinberger-Wilkens R. 2015. Hydrogen selective membranes: A review of palladium -based dense metal membranes". Renewable and Sustainable Energy Reviews. 47:540-551.
2. Rahimpour M.R., Samimi F., Babapoor A., Tohidian T., Mohebi S. 2017. Palladium membranes applications in reaction systems for hydrogen separation and purification: A review. Chemical Engineering and Processing Journal.121:24-49.
3. Julio J., Marta M., José M. 2017.Pd-Based Membranes for Hydrogen Separation: Review of Alloying Elements and Their Influence on Membrane Properties", Separation and Purification Reviews. 46:152-177.
4. Yoshinori S., Tatsuya T, Tsutomu S., Isamu Y., Takafumi S., Naotsugu I. 2018. Improvement in Hydrogen Permeability of Palladium Membrane by Alloying with Transition Metals. Journal of Chemical Engineering of Japan. 5:123–125.
5. Stupnis˘ek-Lisac E., Gali´c N., and Ga˘sparac R. 2000. Corrosion Inhibition of Copper in Hydrochloric Acid Under Flow Conditions. Corrosion Journal, 56:1105-1111.
6. Saeed F, Abdelhadi A, Abbasi G. 2011. Managing galvanic corrosion in industry. Germany, LAP.
7. Modestov, A. D.; Zhou, G. D.; Ge, H. H; Loo, B. H. 1995. A study by voltammetry and the photocurrent response method of copper electrode behavior in acidic and alkaline solutions containing chloride ions. Journal of Electroanalytical Chemistry. 380: 63-68.
8. Smyrl, W. H.; Stephenson, L. L. 1985. Digital Impedance for Faradaic Analysis: III. Copper corrosion in oxygenated 0.1N HCl. Journal of. Electrochemical Society. 1563-1567.
9. Habbache N., Alane N., Djerad S., Tifouti L., Leaching of copper oxide with different acid solutions, Chemical Engineering Journal, 152:503-508.

10. Nielsen B., Dogan O., Howard B. 2015. Effect of temperature on the corrosion of Cu-Pd hydrogen separation membrane alloy in simulated syngas containing H2S, International Journal of Corrosion Science. 96: 74–86.
11. Craig, B. D.; Anderson, D. S. 2002. Handbook of Corrosion Data. USA, ASM International.
12. Schweitzer PA. 2010. Fundamentals of corrosion. New York, CRC Press.
13. Revie RW, Uhlig HH.; 2008. Corrosion and Corrosion Control. New York, John Wiley and Sons.
14. Katarzyna H., Julian K., Małgorzata P., Boz˙ena Ł., Andrzej C. 2021. Effect of the Alloying Metal on the Corrosion Resistance of Pd-Rich Binary Alloys with Pt, Rh, and Ru in Sulfuric Acid. Materials Journal. 14: 1-13.

WHEC-2022
23rd World Hydrogen Energy Conference
June 26-30, 2022 - Istanbul

#161
H_2/CO_2 SEPARATION WITH NEW IONIC LIQUID-BASED MEMBRANES

[1]Adele Brunetti, [1]Francesco Galiano, [2]Raffaella Mancuso, [3]Lorenzo Guazzelli, [4]Michele Mauri, [3]Cinzia Chiappe, [4]Roberto Simonutti, [3]Christian S. Pomelli, [1]Giuseppe Barbieri,[1,2]Bartolo Gabriele, [1]Alberto Figoli

[1] Institute on Membrane Technology, National Research Council (CNR-ITM), via P. Bucci 17/C, Rende (CS), 87036, Italy
[2] Laboratory of Industrial and Synthetic Organic Chemistry (LISOC), Department of Chemistry and Chemical Technologies, University of Calabria, Via Pietro Bucci 12/C, 87036Arcavacata di Rende (CS) Italy
[3] Department of Pharmacy, University of Pisa, Via Bonanno 33, 56126, Pisa, Italy
[4] Department of Materials Science, University of Milano-Bicocca, 2012 Milan, Italy

*Corresponding author e-mail: a.brunetti@itm.cnr.it

ABSTRACT

In this work, we report the synthesis and application of novel polymeric membranes, based on polymerized ionic liquids (PILs), to be used for the separation of hydrogen from gas mixtures with CO_2.
Dense membranes have been developed by using phosphonium-based PILs copolymerised within an original acrylate formulation that allowed to overcome some of the main limitations related to ionic liquid membranes. The membranes showed remarkable separation properties exceeding the Robeson upper bound for the CO_2/H_2 gas pair.

Keywords: Polymerizable ionic liquids, Ionic liquid membranes, CO_2 separation, Hydrogen

INTRODUCTION

The production of hydrogen from fossil but also renewable fuels in most of cases relies on reforming reactions which lead also to the formation of CO_2 as product. Therefore, the possibility to separate H_2 and capture CO_2 from these gas mixtures is of tremendous interest. Membrane technology is highly appreciated in this field thank to its simplicity in concept and operation, easy scalability, high selectivity and relatively low energy consumption [1]. In recent years, Ionic liquids (ILs) have gained a high interest from the scientific community owing to their low toxicity, high thermal stability, low volatility, and high tunability, which makes the ILs very versatile and useful for different applications. The combination of ILs with membrane technology is an approach that has been implemented during the last 20 years, particularly exploiting the higher solubility of CO_2 (with respect to CH_4 and N_2) in many available ILs.

In this work, we have developed a novel PIL-based membrane by copolymerization of a polymerizable phosphonium IL with acrylic monomers, which has shown interesting performances in CO_2/H_2 separation by membrane technology.

MATERIALS AND METHODS

Dense transparent membranes were prepared by mixing HEMA (52 wt%), water (8 wt%), DTAB (13 wt%) and the polymerizable IL (27 wt%). EGDMA (3 wt% on the weight of HEMA+PIL) and DMPA (0.6 wt%) were then added to the mixture to obtain a homogenous solution. Then, the mixture was cast between two glass plates and photo-polymerized for 3 minutes under UV light (lamp emission from 180 nm to visible light, 500 W, Purchased from Helios Italquarz s.r.l.). Polymerized membranes were then removed from the glass plates in water, then washed and stored in water until their use. Various membranes were prepared varying the length of the alkyl chain and the anion of the ionic liquid. All details on preparation and characterization can be found in [2, 3].
The separation properties of the membranes were investigated at 25 and 50 °C, with single gases (CO_2, N_2, CH_4, H_2) in saturated conditions under a feed pressure up to 10 bar, to measure the permeating flux and evaluate permeance and ideal selectivity. The flat sheet membranes were placed in a stainless-steel module located inside a furnace and the gases were fed by means of mass flow controllers opportunely calibrated. A back-pressure regulator on the retentate line controlled the pressure on feed/retentate and the streams flow rate were measured by means of two bubble soap flow meters. The pressure on permeate side was maintained atmospheric. The gas saturation was made by means of a humidifier allocated inside the furnace before the module inlet, so to have the same temperature and pressure and the level of humidity was measured by means of two sensors placed on feed and permeate lines.

RESULTS AND DISCUSSION

The mass transport properties of the various prepared membranes were assessed by feeding single gases, to determine the suitability of these materials for separating H_2 from other gases such as CO_2, CH_4, N_2. Both the length of n-alkyl chain and the different type of anion influenced the separation ability of the membranes (Fig. 1).

All membranes resulted selective toward CO_2 permeation, and this can be mainly attributed to the presence of PILs, which promote the solubility of CO_2, preferentially favoring its permeability, with respect to the other gases for which the transport is mainly influenced by diffusion. The permeability of all the investigated gases decreased with the length of the PIL alkyl chain. Therefore, membrane selectivity toward CO_2 permeation increased as the PIL chain length became longer, and the poly[P_{888}VB][BF_4]+acrylates showed the highest selectivity with respect to the other membranes prepared with a shorter n-alkyl chain length.

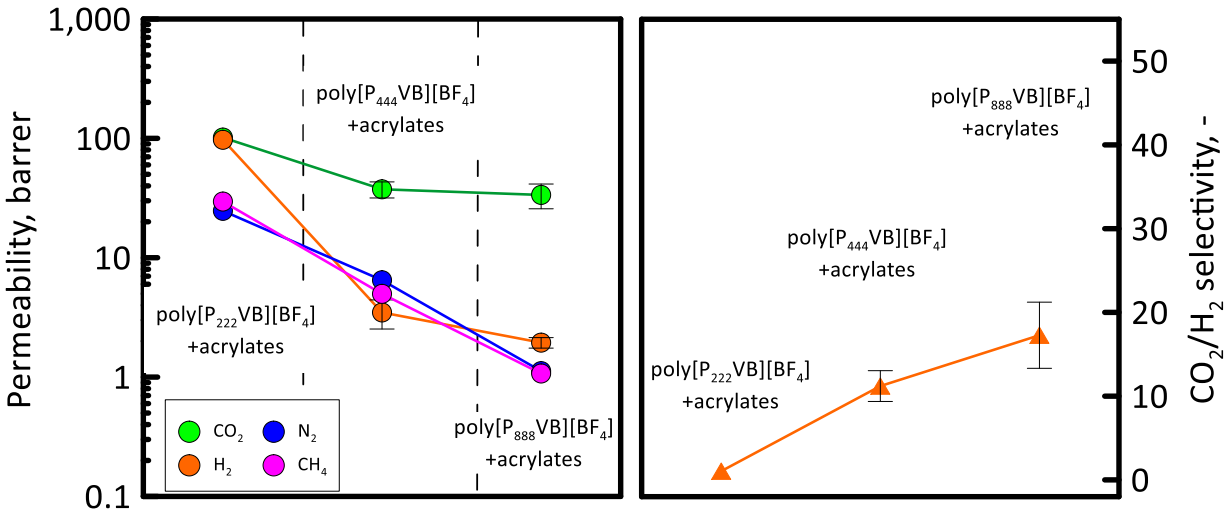


Fig.1 Single gases permeability and CO_2/H_2 selectivity as a function of PIL alkyl chain length. Temperature=25°C

The nature of the counteranion can also influence the mass transport properties. The poly[P_{888}VB][TF_2N]+acrylates membrane showed a higher permeability of all gases with respect to the one prepared using $BF4^-$ and also to both blank membranes. This is reflected in overall lower CO_2/H_2 selectivity, which was 4.6 against 17.3 of the poly[P_{888}VB][BF_4]+acrylates.

When reported in the Robeson trade-off diagram, poly[P_{444}VB][BF_4]+acrylates and poly[P_{888}VB][BF_4]+acrylates membranes exceeded the upper bound for CO_2/H_2 gas pair. Overall, it can be clearly seen the advantage, particularly in terms of selectivity offered by the addition of PILs with respect to the performance of the blank membrane (Fig. 2).

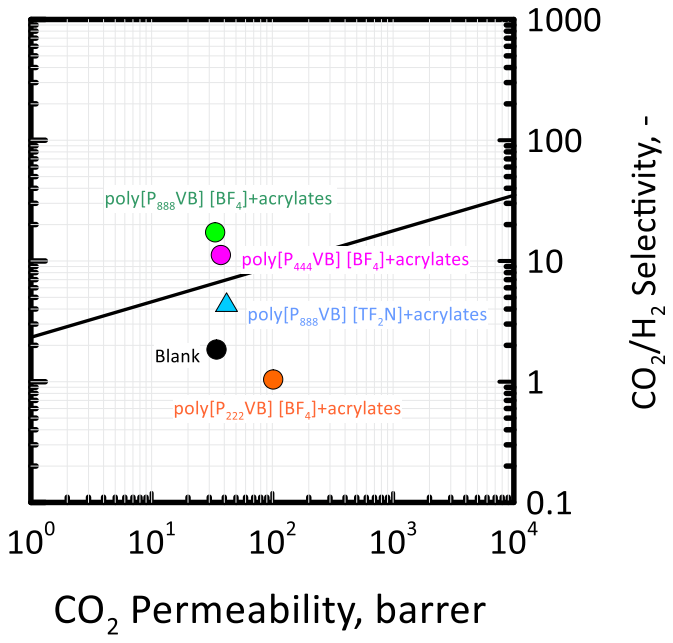


Fig. 2 Robeson plots for CO_2/H_2 gas pairs at 25°C, for different membranes

CONCLUSIONS

In this work, we developed a new copolymer-membranes containing polymerized ILs for hydrogen separation from carbon dioxide by employing a completely new formulation based on different acrylate compounds, including a polymerizable IL. The membranes with BF_4^- as the anion showed the best permeation properties and, among them, the poly[P_{888}VB][BF_4]+acrylates exceeded the Robeson upper bound for CO_2/H_2 gas pair, thanks to the favorable combination between a low water uptake and suitable dimensions of the free volumes in the polymeric network, as confirmed by advanced NMR investigations. The new developed membranes showed good potentialities to efficiently separate hydrogen from other gases in wet state, which simulates the conditions typically found in many H_2-CO_2-containing streams, where the high moisture content tends to negatively affect gas treatment.

ACKNOWLEDGEMENT

The program “MISSION INNOVATION”, Scientific Agreement (21A03302) (GU Serie Generale n. 133 del 05-06-2021) Italian Ministry of the Economic Development & the Italian National Agency for New Technologies Energy and Sustainable Economic Development and the project BIOVALUE “Advanced Membranes for biogas upgrading and high added value compounds recovery”, co-funded by Regione Calabria in the framework of M-Era.Net 2018 are gratefully acknowledged for co-funding this work. M.M thanks the support from the Italian Ministry of University and Research (MIUR) through the Dipartimenti di Eccellenza – 2019 grant.

REFERENCES

1. Brunetti A, Scura F, Barbieri G, Drioli E. 2010. Membrane technologies for CO_2 separation, Journal of Membrane Science 359: 115-125. DOI: 10.1016/j.memsci.2009.11.040.
2. Galiano F, Mancuso R, Guazzelli L, Mauri M, Chiappe C, Simonutti R, Brunetti A, Pomelli C.S, Barbieri G, Gabriele B, Figoli A. 2021, Phosphonium ionic liquid-polyacrylate copolymer membranes for improved CO2 separations” , Journal of Membrane Science 635: 119479. DOI: 10.1016/j.memsci.2021.119479
3. Figoli A, Galiano F, Barbieri G, Brunetti A, Giorno L, Pomelli C. S., Chiappe C, Gabriele B., Mancuso R, Itami Y, Membranes containing polymerised ionic liquid for use in gas separation, patent US16979030; 2021/2/25

WHEC-2022
23rd World Hydrogen Energy Conference
June 26-30, 2022 - Istanbul

#170

GAS SEPARATION PROPERTIES OF MIXED MATRIX MEMBRANES PREPARED WITH GRAPHENE OXIDE

[1*] *Sevgi Çança,* [1] *Sennur Deniz*
[1] Yıldız Technical University, Faculty of Chemical and Metallurgical Engineering, Chemical Engineering Department, 34220, Esenler, Istanbul, Turkey

* e-mail: f2020058@std.yildiz.edu.tr; deniz@yildiz.edu.tr

ABSTRACT

Hydrogen is a potential alternative for fossil fuels. Membrane technology has been a prominent separation approach for H2 purification. The recently discovered new membranes based on GO and rGO show superior properties such as high hydrophilicity, good dispersion in water, nanopores and good mechanical behavior. The main objective of this project is to develop mixed matrix membrane with different polymeric bases of PEBA and PI with graphene oxide (GO) incorporation as inorganic filler. Gas permeability and selectivity of polymer membranes prepared by solution casting method were tested. Gas separation tests of the membranes were carried out at 35°C and 3 bar feed pressure. Gas permeability and selectivity results indicated that PEBA/rGO membrane with 0.3 wt% of GO has the highest H_2 and CO_2 permeability at 10.3247 and 54.8786, respectively, H_2/N_2 selectivity of 7.9828 and CO_2/CH_4 selectivity of 21.0590. PI/rGO membrane with 0.3 wt% of GO has the highest H_2 and CO_2 permeability at 7.3533 and 0.9026 barrer at 3 bar, respectively, H_2/N_2 selectivity of 50.2650 Barrer and H_2/CH_4 selectivity of 287.6653. Work continues with the addition of copper-based MOF structures.
Keywords: *Gas separation, Mixed matrix membranes, Poly(ether-b-amide), Polyimide, Graphene oxide,* Reduced graphene oxide

INTRODUCTION

Membrane technology is a separation process which allows certain species to pass through the membrane while restricting the others depending on the properties of the membrane material [1]. Membrane technology is widely used in industrial applications such as air separation, ammonia production, carbon dioxide separation, nitrogen production and hydrogen recovery. The advantages of this technology over traditional separation processes include lower capital and operating costs, better efficiency, and lower risk. Hydrogen is seen as the energy carrier of the future with its high energy density and environmentally friendly features. Hydrogen, which is not found in pure form in nature, is separated from the gas mixture by various techniques. Gas mixtures are separated in industrial systems using cryogenic distillation, adsorption and polymeric membranes. While examining the efficiency of membrane systems, the most important parameters emphasized are selectivity and permeability. Permeability reflects the rates at which components (penetrants) are transported across a membrane, and selectivity is the ratio of the permeability of the more permeable component to the less permeable one. Permeability and selectivity are the two most important parameters for evaluating the separation performance of a membrane. High selectivity and high permeability are expected for an effective gas separation system [2].In recent years, research directions have been focused on both inorganic and organic materials to develop membranes with desirable hydrogen separation properties. Today the application of polymeric membranes for the H_2 recovery is limited due to the well-known trade off relationship between the permeability and the selectivity and therefore alternatives such as inorganic and mixed matrix membranes (MMMs) are proposed in many studies [3]. A new approach, mixed matrix membranes (MMMs), are mixed matrix materials consisting of homogeneously intertwined polymeric and inorganic particle matrices. Various types of Metal-organic frameworks (MOFs) can be synthesized by varying the combination of different organic binders and metal ions. This adaptability makes MOFs promising candidates for separation applications compared to zeolites and other inorganic fillers. The selection of suitable MOF/polymer pairs is crucial for experimental efforts to improve the performance of MMMs. GO nanosheets can assemble a graphene laminate membrane and GO can be used as the filler embedded in a polymer matrix to obtain MMMs. GO-based membranes are predicted to be highly selective owing to their inherent 2D channels[4]. In addition, the rGO would partially aggregate with in the polymer matrix, forming a stacked laminated structure with high efficient molecular sieving galleries between neighbouring nanosheets, while the planar pores on the graphene oxide ensured much shorter gas permeation pathways through the laminated rGO structure compared with nonporous GO[5]. Matrimid 5218®, was chosen for the manufacturing of the membranes. Matrimid® 5218 is a commercially available thermoplastic polyimide (PI). We decided to choose this glassy polymer because it presents a good trade off between H_2 permeability and both H_2/N_2 and H_2/CO_2 selectivities. Also, this polyimide is frequently used in the manufacture of MMMs and has attracted a lot of attention for gas separation membranes due to the combination of relatively high gas permeability coefficients and separation factors coupled with excellent mechanical properties, solubility in non-hazard organic solvents and commercial availability

[6]. And Pebax®1657 is a good candidate for separation of CO_2 from other gases. Pebax shows great flexibility and process ability; however, its separation performance has been constrained due to the trade-offbetween permeability and selectivity. Therefore, numerous studies have been performed to achieve the better permeability and selectivity for Pebax membranes. Among the available techniques, blending is aunique alternative and it is preferred due to its simplicity, commercial character, reproducibility and cost-effectiveness for tuning membranes properties[7]. In the current study, membranes are being developed for hydrogen separation with two different polymers, PEBA and PI, based on GO-rGO. In this way, it was possible to compare both fillers in both membranes. Cu-MOF, Cu-MOF@GO and Cu-MOF@rGO were prepared for the continuation of the study. In this way, the overall aim of the present work was extended to examine the effect of functionalization of MOFs on the performance of MMMs and to compare membranes obtained with MMMs made with the same polyimide matrix.

MATERIALS AND METHODS

Materials

Matrimid® 5218 (PI, polyimide of 3,3',4,4'-benzophenone tetracarboxylic dianhydride and diaminophenylidane)) polymer was kindly provided by Huntsman Advanced Polymers in powder form. The solvent for polyimide was N-methyl-2-pyrrolidone (NMP, 99% VWR Chemicals). Graphene oxide (GO) was supplied by AEROFEN (TR). Poly(ether-b-amide); PEBAX® 1657, Ethanol (C_2H_5OH), Copper (II) acetate monohydrate $Cu(AC)_2.H_2O$ was purchased from Acros Organics. Dimethylformamide (DMF), ($(CH_3)_2NCOH$) and 1,3,5-benzenetricarboxylic acid (BTC). All gases were purchased from Habas Co. (Turkey) with a purity of at least 99.95%.

Preparation of Membranes

The PEBA/GO MMMs were fabricated by a solution casting method. PEBA were dispersed in a solvent mixture of 70 wt % ethanol and 30 wt % water and GO powders were dispersed in a solvent mixture of 70 wt % ethanol and 30 wt % water and then treated by ultrasonication for 1 h. After that a homogeneous solution was obtained by mixing these two solutions. The suspension was poured into a clean Petri dish with a diameter of 11 cm and covered a glass plate to control the evaporation rate. After solvent evaporation at room temperature, the petri dish was placed in a vacuum 200 mbar. PEBA/rGO membranes were prepared by the same method. After drying of PI polymer powder at 120ºC for 12 h, polymeric solutions (7 wt.%) were prepared by using NMP as solvent. Thin films with a thickness ranging from 80 to 100 µm were prepared by solution casting on a glass petri dishes. For the preparation of the dope solution (7 wt% of solid), first of all, the desired amount of GO (to obtain 0.1, 0.2 and 0.3 wt% of GO in MMM) was dispersed into NMP and the mixture was stirred at room temperature and sonicated. Then, the polymer was added into the GO solution. A petri dish with a diameter of 11 cm was used for solution casting. After solvent evaporation at room temperature, the petri dish was placed in a vacuum. PI/rGO membranes were prepared by the same method. The PI MMMs were dried at room temperature for 24 h and were further dried in a vacuum oven (Binder ED23) at 120ºC for 24 h and 200 mbar.The membrane thickness was measured using a digital micrometer Mitutoyo Digmatic Series 369 (accuracy ± 0.001 mm). This micrometer is equipped with two plates of 2 mm diameter specially designed to measure thin films. The resulted values of thickness represent an average of five measurements, one in the center of the membrane and four in the borders. Thickness deviations from the average did not exceed 2 µm in any of the membranes used.

Gas Permeability Measurements

Fig. 1 shows the experimental set-up. The design of the feed part of the set-up confers the possibility of performing pure gas permeation experiments.

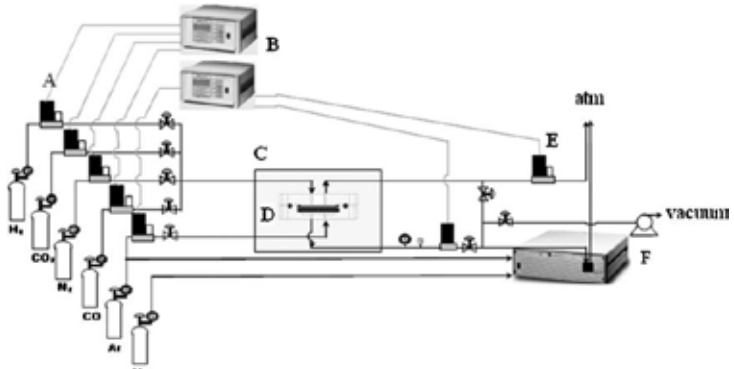


Fig. 1. The experimental permeation set-up: (A) mass flow controller, (b) control box, (c) heating oven, (d) membrane test cell, (e) backpressure regulator, (f) gas chromatograph.

RESULTS AND DISCUSSION

Gas permeability coefficients of membranes were calculated by using a constant volume-variable pressure gas permeability device. Permeability measurements were performed according to the steady-state method at 35 °C. In this study, single gases (H_2, N_2, CO_2, and CH_4) were used to measure gas separation performances of membranes. The circularly cut test specimens used in permeability tests were masked with a self-adhesive aluminum foil. And the vacuum pump were used. The membrane was sealed and tightened. The gas pressure fed to the system was kept constant at 3 ± 0.2 bar. Gas was fed to the system by a valve in the upper part of the cell and the pressure change in the lower part was recorded with the data recording program. The gas permeation of polymeric membranes is described by the solution–diffusion model [9]. The gas transport occurs when the gas molecules are dissolved in the membrane surface, and molecules diffuse across the membrane by way of the cavities present in the polymer. The permeability results from the contribution of these two mechanisms, and can be described by Equation (1):

$$P = D \times S \quad (1)$$

where *P* is the permeability of membrane in Barrer (1Barrer = 1×10^{-10} cm^3 (STP)-cm/cm^2 s cmHg), D is the diffusion coefficient, and S is the sorption coefficient. Typically, the selectivity (α) is defined as the relation of the permeability for the components A and B. Ideal selectivity, $\alpha_{A/B}$, is the ratio of individual permeability coefficients for the gas pairs. The general selectivity of a material defined in Equation (2) is a function of diffusivity (D_A/D_B) and selectivity ratios (S_A/S_B).

$$\alpha_{A/B} = \frac{P_A}{P_B} = \frac{D_A}{D_B} \times \frac{S_A}{S_B} \quad (2)$$

Table 1. Membranes Results of Gas Permeability and Selectivity

Membranes	Permeability, P (Barrer*)				Ideal Selectvity, α			
	N_2	H_2	CH_4	CO_2	H_2/N_2	H_2/CH_4	CO_2/N_2	CO_2/CH_4
PEBA	1.7342	10.1309	4.7985	39.9229	5.8420	2.1113	23.0214	8.3198
PEBA/GO-0.1	1.2387	11.3704	3.5398	38.0817	9.1795	3.2122	30.7439	10.7582
PEBA/GO-0.2	0.8875	10.7181	2.6357	37.6220	12.0765	4.0665	42.3901	14.2739
PEBA/GO-0.3	0.5799	9.7909	2.4915	35.6243	16.8841	3.9297	61.4330	14.2983
PEBA/rGO-0.1	1.7002	7.6548	3.6822	49.5442	4.5023	2.0789	29.1461	13.4551
PEBA/rGO-0.2	1.4117	9.3404	3.6232	49.7519	6.6162	2.5779	35.2417	13.7315
PEBA/rGO-0.3	1.2934	10.3247	2.6059	54.8786	7.9828	3.9620	42.4309	21.0590
PI	0.1492	12.9041	0.1942	1.0954	86.4747	66.4490	7.3405	5.6406
PI/GO-%0.1	0.1918	9.0023	0.1329	1.2278	46.9407	67.7473	6.4020	9.2396
PI/GO-%0.2	0.1915	9.2772	0.1647	1.2296	48.4433	56.3130	6.4207	7.4637
PI/GO-%0.3	0.1227	10.7152	0.1123	1.6477	87.3108	95.4184	13.4260	14.6728
PI/RGO-%0.1	0.1793	13.2468	0.1463	1.3624	73.8777	90.5442	7.5983	9.3125
PI/RGO-%0.2	0.1562	8.3845	0.0843	1.3429	53.6715	99.4185	8.5964	15.9236
PI/RGO-%0.3	0.1463	7.3533	0.0256	0.9026	50.2650	287.6653	6.1697	35.3093

CONCLUSIONS

PEBA/GO, PEBA/rGO and PI/GO, PI/rGO mixed matrix membranes were prepared by the adding 0.1; 0.2 and 0.3 wt.% of graphene oxide (GO) in PEBA and PI polymer matrix with solution-casting method. All membranes were prepared with good stability for gas permeation tests. The gas permeability measurements of MMMs were performed at 35 °C and 3 bar feed pressure for H_2, N_2, CH_4, and CO_2 gases. H_2/N_2 and CO_2/N_2 selectivities of membranes was determined by time-lag method. For PEBA/GO and PEBA/rGO membranes, it was found that CO_2 permeability increased and CO_2/N_2 and CO_2/CH_4 selectivity values increased as GO and rGO concentrations increased. For the PI/GO-0.3 and PI/rGO-0.3 membranes, it was found that the higher selectivity values were measured. In the continuation of this study, Cu-MOF based MOFs will be prepared and performed the gas permeability measurements for the enhancing of selectivity values.

REFERENCES

1. Lyu J and Wen X and Kumar U and You Y and Chen V and Joshi R. K. 2018. Separation and purification using GO and r-GO membranes. RSC Adv 8:41:23130-23151
2. PS Goh A.F Ismail SM Sanip B. Ng M Aziz. 2011. Recent advances of inorganic fillers in mixed matrix membrane for gas separation. Separation and Purification Technology. 81:243-264.
3. Seyed Saeid Hosseini May May Teoh Tai Shung Chung. 2008. Hydrogen separation and purification in membranes of miscible polymer blends with interpenetration networks. Polymern Pages 1594-1603.

4. Huang Dandan and Qingping Xin and Ni Yazhou and Shuai Yingqian and Shaofei Wang and Yifan Li and Hui Ye and Ligang Lin and Xiaoli Ding and Yuzhong Zhang. 2008. Synergistic effects of zeolite imidazole framework@graphene oxide composites in humidified mixed matrix membranes on CO_2 separation, RSC Advances. 8:6099-6109.
5. Guanying Dong Jingwei Hou Jing Wang Yatao Zhang Vicki Chen Jindun Liu Enhanced. 2016. CO_2/N_2 separation by porous reduced graphene oxide/Pebax mixed matrix membranes, of Membrane Science.860-868: 0376-7388
6. Oana Cristina David Daniel Gorri Ana Urtiaga Inmaculada Ortiz. 2011. Mixed gas separation study for the hydrogen recovery from $H_2/CO/N_2/CO_2$ post combustion mixtures using a Matrimid membrane. Journal of Membrane Science. 359-368
7. Mina Kheirtalab and Reza Abedini and Mohsen Ghorbani. 2020. A novel ternary mixed matrix membrane comprising polyvinyl alcohol (PVA)-modified poly (ether-block-amide)(Pebax{\textregistered}1657/graphene oxide nanoparticles for CO_2 separation. Process Safety and Environmental Protection. 144:208-224
8. Castro-Muñoz Roberto and Fíla Vlastimil.2018. Progress on Incorporating Zeolites in Matrimid®5218 Mixed Matrix Membranes towards Gas Separation. Membranes. 8:2077-0375

WHEC-2022
23rd World Hydrogen Energy Conference
June 26-30, 2022 - Istanbul

#184

H_2 SEPARATION FROM CO_2 AND CH_4 MIXTURES USING A SAPO-34 MEMBRANE

[1]Pasquale Francesco Zito, [1]Adele Brunetti, [1]Alessio Caravella, [1]Giuseppe Barbieri*
[1]Institute on Membrane Technology, National Research Council (ITM-CNR), via P. Bucci, Cubo 17C, 87036 Rende, Cosenza, Italy

*Corresponding author e-mail: a.brunetti@itm.cnr.it

ABSTRACT

The performance of a SAPO-34 membrane for separation of H_2 from CO_2 and CH_4 was investigated in this work. In particular, a mass transport model that takes into account the competition between surface and gas translation diffusion was proposed for describing the mixture permeation [1]. It was found that the presence of CO_2 and CH_4 drastically reduce the hydrogen permeation in mixture compared to its behavior as pure gas. In fact, although hydrogen presents a higher diffusivity than carbon dioxide and methane, the much stronger CO_2 and CH_4 adsorption is prevalent, exerting a hindering effect on H_2. In addition, permeation of CO_2 and CH_4 was improved by the presence of faster hydrogen. These two effects caused a significant difference in membrane behavior from single gas to mixture. In fact, CO_2/H_2 selectivity was increased, whereas H_2/CH_4 was decreased.

Keywords: Membrane selectivity, Gas separation, Surface diffusion

INTRODUCTION

Hydrogen represents a green alternative to the traditional fossil fuels, which have a bigger impact on environment since a large amount of CO_2 is produced by their combustion. In addition, H_2 is the most present element on earth, even if it is often stored in components as hydrocarbons, from which it can be obtained from by means of steam reforming (followed by water gas shift reaction), dehydrogenation and partial oxidation. All these processes provide H_2 mixed with other species, especially CO_2 and CH_4; therefore, a purification stage is necessary. A possible solution for H_2 separation from gas mixtures is represented by zeolite membranes, as showed in several works reported in the literature [2-3]. This work analyzed the potentiality of a SAPO-34 membrane to separate H_2 from carbon dioxide and methane, focusing on the reciprocal interaction between the permeating species in binary mixture.

MODELING

An already validated model was used for mass transport [1]. This model pairs surface and gas translation diffusion, which are considered to be dependent on each other. Eq.1 provides the overall molar flux, which is expressed as the sum of the two contributions, considering a dependence of porosity and tortuosity on the adsorption coverage [4].

$$N_{Overall} = -\left(\rho C_{\mu s} D_{SD}^{0} e^{-\frac{E_{SD}}{RT}} \Gamma \frac{d\theta}{dz} + \frac{\varepsilon(C_\mu)}{\tau(C_\mu)} \frac{1}{\zeta} I \frac{1}{RT} \sqrt{\frac{8RT}{\pi M}} e^{-\frac{E_{GT}}{RT}} \frac{dP}{dz}\right) \quad (1)$$

In a mixture consisting of species *i* and *j*, surface diffusion contribution can be obtained by the Maxwell-Stefan equation [5]

$$-\rho\theta_i \frac{\nabla\mu_i}{RT} = \sum_{j=1}^{n_{species}} \frac{C_{\mu,j}N_{SD,i} - C_{\mu,i}N_{SD,j}}{C_{\mu s,j}C_{\mu s,i}D_{ij,SD}} + \frac{N_{SD,i}}{C_{\mu s,i}D_{i,SD}} = -\rho \sum_{j=1}^{n_{species}} \Gamma_{ij} \nabla\theta_j \quad (2)$$

Table 1. Surface and gas translation properties of each species [1]

	Surface diffusion	Gas translation diffusion
H_2	E_{SD} = 7197 J mol^{-1} D^0_{SD} = 2.32E-8 m^2 s^{-1}	E_{GTD} = 10981 J mol^{-1}
CO_2	E_{SD} = 7818 J mol^{-1} D^0_{SD} = 2.89E-9 m^2 s^{-1}	E_{GTD} = 20432 J mol^{-1}
CH_4	E_{SD} = 6459 J mol^{-1} D^0_{SD} = 2.74E-10 m^2 s^{-1}	E_{GTD} = 15800 J mol^{-1}

RESULTS AND DISCUSSION

Fig.1 shows the results in terms of H_2, CO_2 and CH_4 permeability as a function of temperature for two different equimolar binary mixtures (i.e., H_2:CO_2 and H_2:CH_4). It can be observed that hydrogen permeability is drastically reduced in the whole temperature range investigated by the remaining component, which is more strongly adsorbed and, therefore, hinders H_2 surface diffusion contribution in terms of lower coverage. Moreover, also H_2 gas translation contribution is reduced by a reduction of the effective porosity and a higher effective tortuosity. At 303 K, hydrogen permeability diminished of 76 and 71% in presence of CO_2 and CH_4, respectively (from about 2160 to 520 and 620 Barrer). The higher H_2 permeability drop in mixture with CO_2 is due to its stronger adsorption compared to methane. On the other hand, permeation of both CO_2 and CH_4 is favored by the presence of faster H_2. This can be attributed to the very high value of hydrogen diffusivity that promotes the permeation by surface diffusion of the other components. These two combined effects causes a significant increment of CO_2/H_2 selectivity and, at the same time, a drastically reduction of H_2/CH_4 selectivity with respect to the ideal values. In particular, CO_2/H_2 selectivity passes from about 1.4 to 9, whereas H_2/CH_4 from to 13.4 to 2.6 at 303 K and 10^6 Pa of feed pressure.

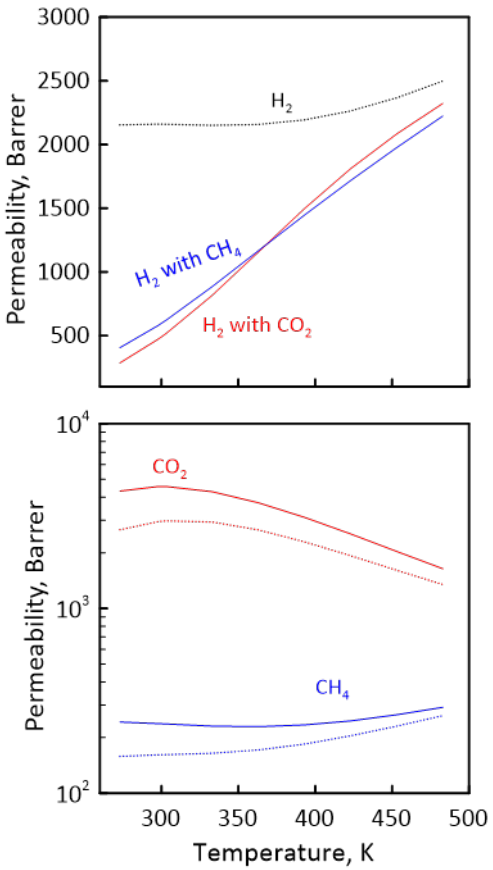


Fig. 1. H_2, CO_2 and CH_4 permeability as a function of temperature as pure gases (dotted lines) and in equimolar binary mixture (solid lines) at 10^6 Pa of feed pressure.

CONCLUSIONS

Permeation of hydrogen in mixture with carbon dioxide and methane is strongly affected, being significantly diminished if compared to what happen as single gas. In particular, the adsorbed carbon dioxide and methane reduce H_2 permeation of more than 70% at 303 K. At the same time, CO_2 and CH_4 are advantaged by the presence of the faster H_2 that promotes their permeation. Selectivity is significantly changed in mixture (e.g., CO_2/H_2 passes from 1.4 to 9 at 303 K and 10^6 Pa), making this material suitable for hydrogen upgrading.

ACKNOWLEDGEMENT

The program “MISSION INNOVATION”, Scientific Agreement (21A03302) (GU Serie Generale n. 133 del 05-06-2021) Italian Ministry of the Economic Development & the Italian National Agency for New Technologies Energy and Sustainable Economic Development and the project BIOVALUE “Advanced Membranes for biogas upgrading and high added value compounds recovery”, co-funded by Regione Calabria in the framework of M-Era.Net 2018 are gratefully acknowledged for co-funding this work

NOMENCLATURE

C_μ	Molecular loading, mol kg^{-1}
$C_{\mu S}$	Saturation loading, mol kg^{-1}
D_{SD}^0	Pre-exponential factor for surface diffusivity, m^2 s^{-1}
D_{SD}	Surface self-diffusivity, m^2 s^{-1}
$D_{SD,ij}$	Surface binary diffusion coefficient, m^2 s^{-1}
E_{GT}	Activation energy for gas translation diffusion, J mol^{-1}
E_{SD}	Activation energy for surface diffusion, J mol^{-1}
l	Diffusional length, m
M	Molar mass, kg mol^{-1}
N	Molar flux, mol s^{-1} mol^{-1}
P	Pressure, mol s^{-1} mol^{-1}
R	Gas constant, 8.314 J mol^{-1} K^{-1}
T	Temperature, K
z	Membrane space coordinate, m

Greek Letters

Γ	Thermodynamic factor, -
ε	Effective porosity, -
ζ	Coordination number, -
θ	Loading degree, -
μ	Chemical potential, J mol^{-1}
ρ	Zeolite density, kg/m^3
τ	Effective tortuosity, -

REFERENCES

1. Zito PF, Brunetti A, Caravella A, Drioli E, Barbieri G. 2020. Mutual influence in permeation of CO_2-containing mixtures through a SAPO-34 membrane, Journal of Membrane Science 595: 117534.
2. Hong M, Li S, Falconer JL, Noble RD. 2008. Hydrogen purification using a SAPO-34 membrane, Journal of Membrane Science 307: 277-283.
3. Mei W, Du Y, Wu T, Gao F, Wang B, Duan J, Zhou J, Zhou R. 2018. High-flux CHA zeolite membranes for H_2 separations, Journal Membrane Science 565: 358-369.
4. Caravella A, Zito PF, Brunetti A, Drioli E, Barbieri G. 2016. A novel modelling approach to surface and Knudsen multicomponent diffusion through NaY zeolite membranes, Microporous Mesoporous Materials, 235: 87-99.
5 Kaptejin F, Moulijn JA, Krishna R. 2000. The generalized Maxwell-Stefan model for diffusion in zeolites: sorbate molecules with different saturation loadings, Chemical Engineering Science 55: 2923-2930.

WHEC-2022
23rd World Hydrogen Energy Conference
June 26-30, 2022 - Istanbul

#236

MIXED MATRIX MEMBRANES FOR HYDROGEN RECOVERY FROM INDUSTRIAL WASTE STREAMS

[1] Gonzalo Moral, [1*] Alfredo Ortiz, Daniel Gorri, [1] Inmaculada Ortiz
[1]Chemical and Biomolecular Engineering Department, University of Cantabria, Av. Los Castros 46, 39005, Santander, Spain

*Corresponding author e-mail: ortizal@unican.es

ABSTRACT

The increase of the energy efficiency is one of the main challenges which is facing the manufacturing sector since the rising price of fossil fuels and political framework of the decarbonization roadmap. In this sense, the recovery of hydrogen from industrial waste streams is presented as a great niche of opportunities due to the wide range of applications of hydrogen as energy vector. Among hydrogen-containing off-gases, coke oven gas (COG), ammonia purge gas (APG) and methanol purge gas (MPG) stands out since the high hydrogen concentration (>50 vol.% H_2). Nevertheless, the recovery of hydrogen requires a purification system. In this study, the synthesis and characterization of mixed matrix membranes (MMMs) are analyzed as an alternative to improve the separation performance of pristine polymer membranes. ZIF-8 and ZIF-90 were selected as fillers with potential to improve H_2-selectivity and Matrimid® 5218 as high-performance polyimide. The permeability and selectivity of the membranes were evaluated by continuous permeation experiments with multicomponent gas mixtures whose composition correspond to the industrial waste streams. Furthermore, the influence of the temperature on transport parameters in gas permeation was studied.

Keywords: Hydrogen recovery, Mixed matrix membranes, Coke oven gas, Methanol purge gas, Ammonia purge gas

INTRODUCTION

The search for new renewable energy sources and sustainable use of fossil fuels are the main challenges in the energy transition to low carbon economy [1]. In this sense, the industry is an energy intensive sector which accounts 29.4% of global greenhouse gas emissions [2]. To overcome this problem, attention has been paid to hydrogen as energy vector with different purposes such as: a) the production of clean energy using fuel cells (power-to-power), b) to be blended in the natural gas grid or synthetic natural gas production (power-to-gas), c) in transport sector (power-to-fuel) and d) as feedstock in the manufacturing sector (power-to-feedstock) [3-4]. Thus, the recovery of hydrogen from industrial waste streams (COG, APG and MPG) by means of low cost and low energy consumption membrane technology has been widely studied [5]. The composition and properties of the waste streams are found in Table 1 [6].

Table 1. Composition of industrial waste streams.

	Gas composition (vol.%)						
Stream	**H_2**	**N_2**	**CO_2**	**CO**	**CH_4**	**T (ºC)**	**P (bar)**
APG	58.6	25.7	-	-	15.7	15-30	>100
COG	60.2	4.7	2.1	6.8	26.2	15-30	5-20
MPG	63.1	11.3	11.1	3.4	11.2	15-45	70

However, the membrane separation performance of commercial alternatives is not able to meet fuel cell purity specifications. Thus, research has focused on developing tailor-made membranes with higher performance. Inorganic fillers such as zeolitic imidazole framework (ZIF) have been proposed to increase the H_2-selectivity due to their small pore size [7].

This work provides the comparison of pristine polymer and mixed matrix membranes as hydrogen recovery technology. The membranes were characterized by the calculation of the permeability and selectivity by the analysis of the gas permeation experiments.

MATERIALS AND METHODS

The membranes were prepared by the well-known solvent-casting method. The polymer and ZIF-8, ZIF-90 (15 wt.% of ZIF) were weighted and dissolved separately in dichloromethane. In addition, the solution of ZIF was sonicated to prevent the agglomeration of the particles which could lead to the formation of defects in the mixed matrix membranes. Then, the polymer solution was added to the ZIF solution and sonicated to obtain a homogeneous mixture. Finally, the Matrimid®-ZIF solution was poured in the Petri dish and left-over night at room temperature to evaporate the solvent.

The membranes were placed in the membrane modules inside the thermostated chamber to ensure isothermal operation. The feed and sweep gas flowrates were controlled using mass flow controllers while needle valves together with pressure transducers allow to set the permeate and feed pressures. Then, once the steady state has been reached, the composition of the permeate and retentate streams were measured by using a gas chromatograph (GC-BID) which consists of two separation columns and a barrier ionization discharge detector of ppb quantity level. The schematic representation of the experimental setup is shown un Figure 1.

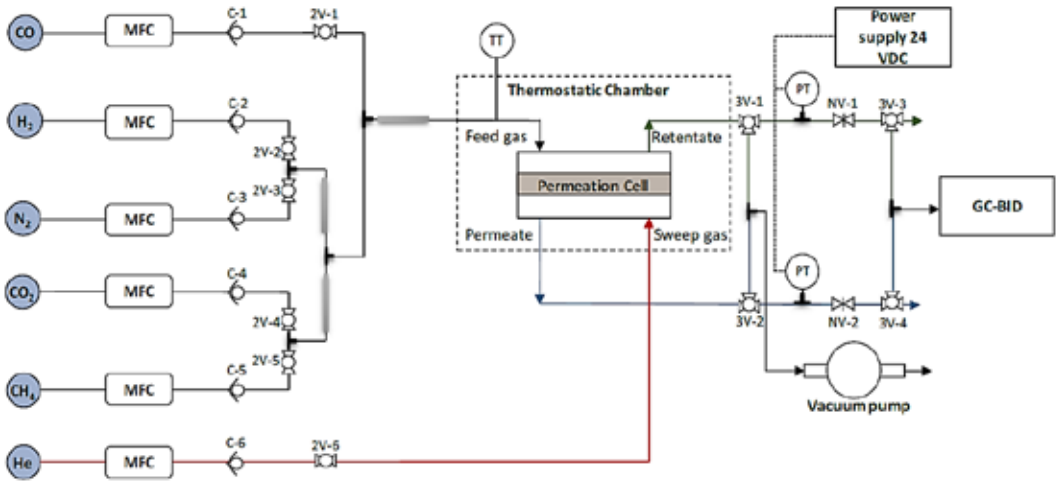


Fig. 1. Experimental set-up. MFC, mass flow controller; C, check valve; 2V, 2-way valve; 3V, 3-way valve; TT, thermocouple; PT, pressure transducer; NV, needle valve; GC-BID, gas chromatograph. Feed (black), sweep gas (red); permeate (blue); retentate (green).

RESULTS AND DISCUSSION

Results confirmed that the addition of ZIF-8 and ZIF-90 to Matrimid® increases the gas separation grade of pristine polymer membrane. On the one hand, the increase in permeability (≈50% compared to pristine polymer) is related to the increase in the free volume of the polymer, while the increase in selectivity (≈20% for H_2/CO_2 and 40-80% for H_2/N_2, H_2/CH_4 and H_2/CO compared to pristine polymer) is related to the formation of hydrogen-selective micro channels in the mixed polymer-ZIF matrix. Therefore, solution-diffusion transport mechanism is improved by molecular sieving enhancing the permeation of hydrogen compared to bulk compounds (N_2, CH_4, CO). Since ZIF-8 and ZIF-90 have close pore openings, 3.4 and 3.5 Å respectively, the contribution of the molecular sieve to the transport mechanism of both fillers is similar. However, ZIF-90 is able to offer greater resistance to the mass transport of carbon dioxide, increasing selectivity. This is attributed to the strong interaction of the carbon dioxide molecule with the aldehyde group of the 2-carboxyaldehyde imidazole bonds of the ZIF-90, which hinders its diffusion through the membrane [8]. Figure 2 shows an illustration of transport mechanisms in mixed matrix membranes.

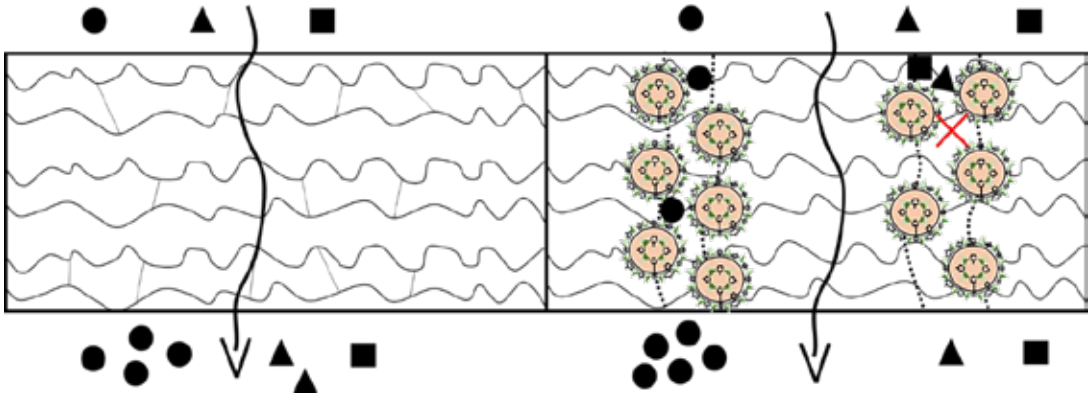


Fig. 2. Illustration of solution-diffusion (left side) and molecular sieve (right side) transport mechanisms. Circle: H_2; Triangle; CO_2; Square: N_2, CH_4, CO.

CONCLUSIONS

The addition of ZIFs as fillers to the polymer matrix is a novel alternative to surpass the separation performance of the polymeric membranes. In this sense, Matrimid®-ZIF MMMs deliver higher H_2 permeabilities and selectivity. Nevertheless, MMMs must cope with some challenges before industrial scale-up. The selection of the optimum ZIF wt.% ratio is a key point since higher loadings could lead to a significant decrease in selectivity and manufacturing issues. Moreover, further investigation on the synthesis of mixed matrix hollow fiber membranes and the design of the membrane configuration system is required. Therefore, this study aims to increase the knowledge on the synthesis and the separation performance of high performance mixed matrix membranes for hydrogen purification.

ACKNOWLEDGEMENT

This research is being supported by the Projects “SUDOE ENERGY PUSH SOE3/P3/EO865” and “HYLANTIC”-EAPA_204/2016 and, which are co-financed by the European Regional Development Fund in the framework of the Interreg Sudoe and Atlantic programs and the Spanish Ministry of Science, Innovation, and Universities (Projects: RTI2018-093310-B-I00, PID2019-104369RB-I00 and PLEC2021- 007718).

REFERENCES

1. https://www.iea.org/reports/net-zero-by-2050. Accessed on October. 13, 2021.
2. https://ourworldindata.org/emissions-by-sector. Accessed on December. 13, 2021.
3. M. Yáñez, A. Ortiz, B. Brunaud, I. E. Grossmann, and I. Ortiz, “Contribution of upcycling surplus hydrogen to design a sustainable supply chain: The case study of Northern Spain,” *Appl. Energy*, vol. 231, pp. 777–787, 2018, doi: 10.1016/j.apenergy.2018.09.047.
4. Fuel Cells and Hydrogen Joint Undertaking (FCH), *Hydrogen Roadmap Europe*. 2019.
5. M. Yáñez, A. Ortiz, D. Gorri, and I. Ortiz, “Comparative performance of commercial polymeric membranes in the recovery of industrial hydrogen waste gas streams,” *Int. J. Hydrogen Energy*, vol. 46, no. 33, pp. 17507–17521, 2021, doi: 10.1016/j.ijhydene.2020.04.026.
6. M. Yáñez, “Hydrogen recovery from industrial waste gas streams for fuel cell application,” Doctoral Thesis, University of Cantabria, 2019.
7. P. Fernández-Castro, A. Ortiz, and D. Gorri, “Exploring the potential application of matrimid® and ZIFs-based membranes for hydrogen recovery: A review,” *Polymers (Basel).*, vol. 13, no. 8, article 1292, 2021, doi: 10.3390/polym13081292.
8. L. Diestel, N. Wang, A. Schulz, F. Steinbach, and J. Caro, “Matrimid-based mixed matrix membranes: Interpretation and correlation of experimental findings for zeolitic imidazolate frameworks as fillers in H2/CO2 separation,” *Ind. Eng. Chem. Res.*, vol. 54, no. 3, pp. 1103–1112, 2015, doi: 10.1021/ie504096j.

WHEC-2022
23rd World Hydrogen Energy Conference
June 26-30, 2022 - Istanbul

#246

PSEUDO-DYNAMIC MODELING AND OPTIMIZATION OF HEAVY PARAFFIN DEHYDROGENATION PROCESS FOR SELECTIVE OLEFIN AND HYDROGEN PRODUCTION USING MEMBRANE REACTORS

[1]M. Dehdashti, [2]*M. Binazadeh, [3]M. Farsi
[a] Department of Chemical Engineering, School of chemical and Petroleum Engineering, Shiraz University, Shiraz 71345, Iran

*Corresponding author e-mail: binazadeh@shirazu.ac.ir

ABSTRACT

Linear alkyl benzenes (LABs) are used in alkyl sulfonates production, which are utilized in biodegradable detergents and emulsifiers. Catalytic dehydrogenation of heavy paraffin molecules ($C_{10} - C_{14}$) is the most well-known path of LAB production. In this study, a radial flow Pd/Ag membrane reactor (RF-MR) is pseudo-dynamically modeled and its outputs are compared with an industrial conventional reactor to prove RF-MR efficacy in the enhancement of olefins and hydrogen yields. Steady-state and pseudo-dynamic RF-MR simulations. It is shown that olefin production increases in RF-MR compared to that of RF-TR mainly due to hydrogen permeation through the Pd/Ag membrane. Finally, the optimal RF-MR operating conditions were obtained *via* a multi-objective genetic algorithm optimization.

Keywords: Heavy paraffin dehydrogenation, Radial flow membrane reactor, Pseudo-dynamic model, Pd/Ag membrane, Genetic algorithm

INTRODUCTION

Linear alkyl benzenes (LABs) are routinely used in the production of biodegradable detergents and emulsifiers. Catalytic dehydrogenation of heavy paraffin molecules ($C_{10} - C_{14}$) is widely used in LAB production. In chemical industries, dehydrogenation of heavy paraffin typically occurs in gas phase axial or radial plug flow adiabatic reactors in the presence of hydrogen [1].

Membrane dictates selective mass transfer under pressure, temperature, or electric potential driving force. Membrane reactor is a unit that allows simultaneous catalytic reaction and permeation processes. Nowadays, membrane reactors are extensively used in chemical and biochemical industries including hydrogen production from hydrocarbons [2, 3]. Limited studies are conducted on modeling and optimization of heavy paraffin dehydrogenation process in membrane reactors. Bayat *et al.* proposed a RF-MR with sweep gas to produce ultra-pure hydrogen and statically modeled the RF-MR and optimized it using NSGA-II method [4]. Later, Bayat *et al.* also dynamically modeled the same reactor [5].

In this paper, a radial flow Pd/Ag membrane reactor is pseudo-dynamically modeled and its process outputs are compared with those of an industrial conventional reactor. Finally, the model is optimized using genetic algorithm to obtain the optimal operating conditions for olefins and hydrogen production.

MODEL DESCRIPTION

A pseudo-dynamic mathematical model of a radial flow fixed bed Pd/Ag membrane reactor is developed. Kinetics of heavy paraffin dehydrogenation and catalyst deactivation equation were reported elsewhere [6, 7]. Axillary equations are listed in Table 1. The radial differential element of the membrane reactor is shown in Figure 1(a) and dominant reactions of the overall dehydrogenation of heavy paraffin process is represented in Figure 1(b). Important assumptions of the model are: (a) gas phase are ideal, (b) external reactor shell wall is insulated, (c) gas phase moves radially, (d) no mass and heat transfer occurs between catalyst particles, (e) molecular diffusion is negligible compared to bulk flow, (f) only hydrogen permeates through the membrane, (g) no pressure drop occurs in permeation side. Mass, energy, and Ergun momentum balance, kinetics and catalyst deactivation were simultaneously solved *via* backward Euler method.

Table 1. Governing equations

Reaction side equations		
Component mass balance	$(N)_i = (N)_{i+1} + (a \times \rho_b \times -r_j \times A_{c_1} - P_{per} \times \begin{cases} 0, & J \neq H_2 \\ J_{H_2}, & J = H_2 \end{cases} \quad j = 1,2,\dots,n) \times \Delta r$	(1)
Energy balance	$(T_g)_i = [(T_g)_{i+1} + (a\rho_B \sum_{i=1}^{m}(-\Delta H_i \times r_i) - \frac{P_{per}}{A_{c_1}} \times U_{Sh} \times (T^s - T) - \frac{P_{per}}{A_{c_1}} C_{P_{H^2}}(T^s - T) \times \begin{cases} 0, & J \neq H_2 \\ J_{H_2}, & J = H_2 \end{cases}) \times \Delta r]/F_t C_{Pg}$	(2)
Ergun Equation	$(\mathrm{P})_i = (\mathrm{P})_{i+1} + ((150\frac{(1-\varepsilon)^2\mu}{\varepsilon^3 d_p^2}.\frac{Q}{2\pi L}.\frac{\theta_1+\theta_2}{\theta_1})\frac{1}{r} + (1.75\frac{(1-\varepsilon)\rho}{\varepsilon^3 d_p}.(\frac{Q}{2\pi L}.\frac{\theta_1+\theta_2}{\theta_1})^2)\frac{1}{r^2}) \times \Delta r$	(3)
Catalyst Deactivation	$t = [1 - a_c^{(1-n-E_d/E_A)}] \div [k_{d0}(1 - n + E_d/E_A)]$	(4)
Permeating side equations		
Nitrogen mass balance	$(N_p)_i = (N_p)_{i+1}$	(5)
Hydrogen mass balance	$(N_p)_i = (N_p)_{i+1} + (P_{per} \times J_{H_2}) \times \Delta r$	(6)
Energy balance	$(T_{gp})_i = [(T_{gp})_{i+1} + ((P_{per} \times U_{Sh} \times (T^s - T) + P_{per} \times C_{P_{H^2}}(T^s - T) \times \begin{cases} 0, & J \neq H_2 \\ J_{H_2}, & J = H_2 \end{cases}) \times \Delta r)]/F_{tp} C_{Pg}$	(7)
Hydrogen permeation rate	$J_{H_2} = \frac{Q_0 . \exp(-\frac{E_{H_2}}{RT})}{\delta_{H_2}} (\sqrt{P_{H_2}^{Tube}} - \sqrt{P_{H_2}^{Shell}})$	(8)
Additional correlations	$A_{c_1} = \theta_1 \times NOS \times r \times L$	(10)
	$A_{c_2} = \theta_2 \times NOS \times r \times L$	(11)
	$P_{per} = 2 \times NOS \times L$	(12)

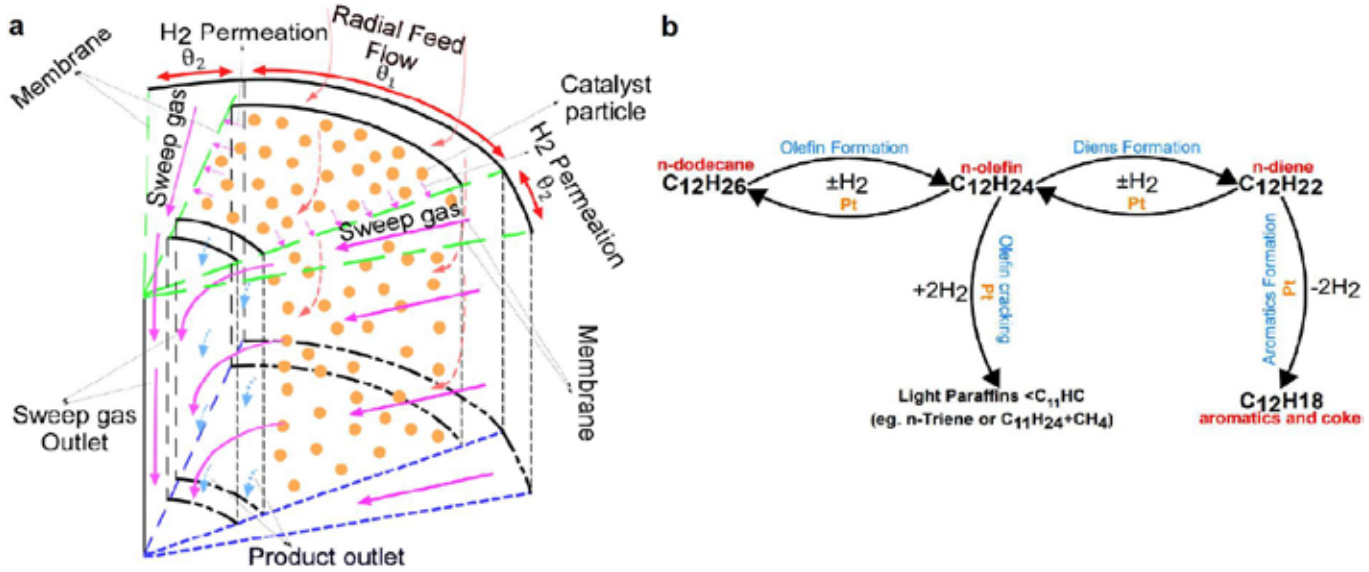


Figure 1. (a) A differential element of membrane reactor and (b) Overall paraffin dehydrogenation process reactions

RESULTS AND DISCUSSION

Steady-state and pseudo-dynamic simulations were performed on RF-MR model and tube side (reaction side) and shell side (permeation side) output parameters were obtained. Figure 2(a) compares paraffin and olefin molar flow

rate *vs.* mass of catalyst for RF-TR and RF-MR. Clearly, hydrogen permeation through the Pd/Ag membrane and its subsequent reaction rate enhancement increases olefin production in RF-MR compared to that of RF-TR.

Figure 2(b) demonstrates radial hydrogen permeation flux and hydrogen partial pressure in both reaction and permeation sides. Hydrogen partial pressure in reaction side decreases due to selective removal of hydrogen from reaction side while hydrogen partial pressure in permeation side increases due to selective addition of hydrogen. Driving force for Hydrogen permeation decreases radially resulting in hydrogen permeation flux decline.

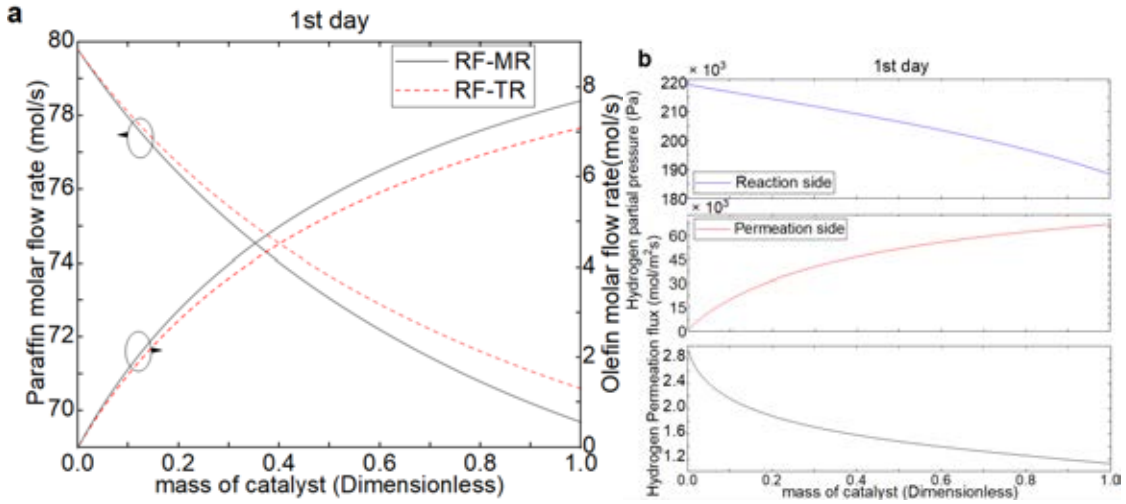


Figure 2. (a) Paraffin and olefin molar flow rate profiles in RF-MR and RF-TR and (b) Hydrogen partial pressure and hydrogen permeation flux according to mass of catalyst

CONCLUSIONS

Steady-state and pseudo-dynamic simulations and validation of RF-MR were performed. Membrane integration in the reactor resulted in 8.46 and 0.07% increase of olefin and hydrogen production compared to those at RF-TR, respectively. Finally, multi-objective RF-MR optimization using genetic algorithm method revealed 22.9 and 0.55% olefin and hydrogen production compared to those at RF-TR, respectively

REFERENCES

1. Lira, A. and R.G. Tailleur, Dehydrogenation of C12–C14 paraffins on PtCu/meso-structured Al2O3 catalyst for LAB production: Process simulation. Fuel, 2012. **97**: p. 49-60.
2. Koros, W., Y. Ma, and T. Shimidzu, Terminology for membranes and membrane processes (IUPAC Recommendations 1996). Pure and Applied Chemistry, 1996. **68**(7): p. 1479-1489.
3. McLeary, E., J. Jansen, and F. Kapteijn, Zeolite based films, membranes and membrane reactors: Progress and prospects. Microporous and mesoporous materials, 2006. **90**(1-3): p. 198-220.
4. Bayat, M. and M.R. Rahimpour, Enhanced olefin production via a novel radial-flow membrane reactor of heavy paraffin dehydrogenation in LAB plant. Journal of the Taiwan Institute of Chemical Engineers, 2014. **45**(6): p. 2906-2919.
5. Bayat, M., Z. Dehghani, and M.R. Rahimpour, Ultrapure Hydrogen Production via Dehydrogenation of Heavy Paraffin in a Linear Alkyl Benzenes Plant: Dynamic Modeling Study. Energy & Fuels, 2014. **28**(11): p. 7097-7108.
6. Zahedi, G., H. Yaqubi, and M. Ba-Shammakh, Dynamic modeling and simulation of heavy paraffin dehydrogenation reactor for selective olefin production in linear alkyl benzene production plant. Applied Catalysis A: General, 2009. **358**(1): p. 1-6.
7. Vafajoo, L., et al., Kinetic Parameters Optimization and Modeling of Catalytic Dehydrogenation of Heavy Paraffins to Olefins. Petroleum Science and Technology, 2014. **32**(7): p. 813-820.

WHEC-2022
23rd World Hydrogen Energy Conference
June 26-30, 2022 - Istanbul

#259

DEVELOPMENT AND INVESTIGATION OF A NOVEL ELECTROCHEMICAL HYDROGEN COMPRESSOR CELL DESIGN BASED ON HYDRAULIC CLAMPING

[1]Ulrich W. Rost, [2]Lester Engelhardt, [2]Florian J. Wirkert, [2]Michael Brodmann*
[1]ProPuls GmbH, Neidenburger Straße 10, D-45897 Gelsenkirchen, Germany
[2] Westfälische Hochschule University of Applied Sciences, Westfälisches Energieinstitut, Neidenburger Straße 43, D-45897 Gelsenkirchen, Germany

*Corresponding author e-mail: ulrich.rost@propuls.de

ABSTRACT

Due to low outlet pressure level of hydrogen production facilities, high-pressure hydrogen storage systems today still require an additional gas compression unit. However, typical mechanical compressors decrease the overall system efficiency, emit noise, and increase investment costs as well as operational expenditures due to regular maintenance. In this work a novel electrochemical hydrogen compressor based on hydraulic cell clamping is presented. In comparison to the state-of-the-art mechanical cell clamping, according to this design variant, a hydraulic medium whose pressure level is e.g., 15 bar above the hydrogen outlet pressure level, surrounds the single cells of a stack entirely and compresses the cells to ensure the contact of the active components. A laboratory device was realised with a single cell offering a 25 cm^2 active area that showed a pressure increase from 0 bar at the anode to 10 bar at the cathode. Due to homogeneous operation condition related to pressure, current density, and temperature distribution over the active cell area, the novel design seems promising for future devices, especially in large scale.

Keywords: Electrochemical hydrogen compressor, Stack design, Hydraulic clamping

INTRODUCTION

In the framework of the transition of the world's energy economy towards a wide use of renewable and sustainable energy systems, the importance of hydrogen as an energy carrier that can be stored in large scale, increases tremendously. Even if more renewable energy systems (RES) will be installed in the grids and peak power will quickly increase in the near future, it is most likely to experience times when the actual renewable power is too low to cover the demand. To overcome periods in which just little power can be supplied by RES, especially, wind and water turbines as well as photovoltaics that are highly dependent on current weather situations, hydrogen can be used to cover the energy demand. E.g., electrical energy generation can be facilitated by hydrogen driven fuel cells, turbines, or other energy systems. Further, hydrogen can also be used e.g., as a feed stock for the industry, as a fuel for the transport sector, or to generate heat for industrial applications or private households. If the hydrogen was produced from renewable sources, such as from RES driven water electrolysis, the entire conversion chain can be carbon neutral.

However, to store the so-called green hydrogen, it needs to be compressed, e.g., up to 1,000 bar in hydrogen refilling stations for fuel cell driven passenger cars. For this purpose, the use of mechanical compressors is state-of-the-art. However, the mechanical hydrogen compression is achieved as simultaneously also the temperature of the gas increases. If heat recuperation is not applied the hydrogen compression leads, therefore, to significant losses on system level. Further, due to e.g., friction, losses as high as up to 12% of the stored chemical energy were reported as losses for hydrogen compression [1]. Furthermore, vibrations arising from rotating pistons or turbine blades etc. lead to relevant noise emissions. Beside the mentioned losses, the moving parts in mechanical compressors as well as the high-pressure gaskets underlie continuous wearing and degradation. To ensure safety and full operability of a mechanical hydrogen compressor, regular maintenance is necessary which also increases operational costs for such devices.

In this work, a new concept for an electrochemical compressor for hydrogen utilising polymer electrolyte membrane (PEMEC) is presented as a promising alternative for mechanical compression. The principal design of PEMECs is similar to PEM fuel cells (compare to Fig. 1). At the anode of PEMEC hydrogen is fed and hydrogen oxidation reaction (HOR) happens at the surface of platinum based electrocatalysts. During HOR, hydrogen molecules are split into protons and electrons. Protons will then be transported through the gas-tight and electrical insulating PEM. A voltage source drives electrons over an external circuit. The back reaction, respectively, the hydrogen evolution reaction (HER) during which the protons and the electrons form hydrogen molecules again, happens also on platinum based electrocatalysts at the cathode of PEMEC. By supplying sufficient voltage to a PEMEC, it becomes possible to increase the pressure level in the cathodic compartment. The electrochemical process happens at low temperatures like e.g., 80 °C and is entirely quiet. By using highly stable materials like CNF based Pt or Pt alloy catalysts degradation is limited, and a long-term operation can be ensured [2]. A high compression efficiency above 50% has

already been reported [3]. Although first companies provide hydrogen compressors based on PEMEC to the market, this technology is not yet widely used, especially, due to a high need of further developments and high costs. In this work we present a novel design approach for PEMEC based on hydraulic cell clamping, which is modular, scalable and has the potential to lead to significant cost reductions for future hydrogen storage devices.

MATERIALS AND METHODS

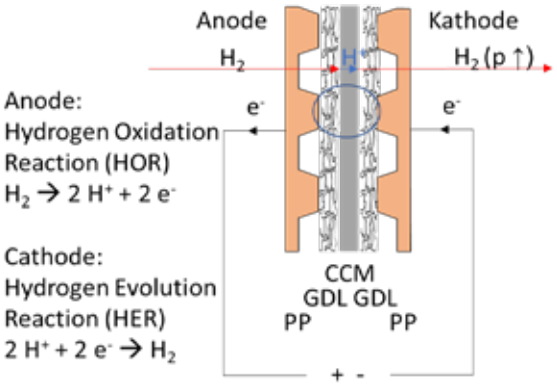


Fig. 1 Schematic design and principal of a PEMEC cell

Like typical PEM fuel cells, the reported PEMEC consists of layered electrode structure comprising a pole plate (PP), a gas diffusion layer (GDL), and a catalyst layer. However, to ensure contact of the catalyst layer to the electrolyte, typically the catalyst layer is directly attached to the PEM forming a catalyst coated membrane (CCM). Several PEMEC cells can be connected to each other as a stack. To contact the different layers in PEMEC, massive pressure plates at each end of a stack are mechanically clamped by tie bolts.

This study is about a novel PEMEC design based on hydraulic cell clamping instead of mechanical clamping. The concept was earlier reported for PEM fuel cells and PEM electrolysers and was now adapted as an alternative for modular and large-scale PEMEC stacks [4, 5]. Here, the clamping is achieved by a hydraulic medium that entirely surrounds each PEMEC single cell of a stack. The pressure level of the hydraulic medium is controlled to be always 4-15 bar above the cathode pressure level in order to induce compression forces to the active cell components. Such a stack is encapsuled in a pressure housing to keep the pressure of the hydraulic medium. A laboratory scale single cell device was worked out like shown in Fig. 2. In this PEMEC a 25 cm^2 square design was achieved. The used materials comprise gold coated copper pole plates, GDLs type 1500 by Caplinq, and a Nafion™ 212 based CCM with a loading of 0.25 mg cm^{-2} platinum for each side.

Prior to in-situ investigations, the laboratory cell was analysed according to the pressure distribution at different pressure levels of the hydraulic medium. To determine pressure distribution sensitive film Prescale LLLW by Fuji was utilised. For our analyses the investigated PEMEC cell was assembled with pressure sensitive film instead of a CCM. Like the CCM the film overlaps the gasket system that is arranged around the active area of the PEMEC cell.

The presented PEMEC was further investigated and characterised according to voltage-current characteristic in different load points and under different operation conditions related to temperature and outlet pressure. The necessary hydrogen for these experiments was provided by a former fuel cell test bench that delivers dry gas with a 5.0 quality at room temperature. Hydrogen flux to the cell's anode is controlled by a mass flow controller type LMD 500-03 by GCE. The pressure level of the hydrogen stream is 200 mbar at the inlet of the investigated cell. The hydrogen was fed to the PEMEC cell without circulation (dead-end operation). The outlet pressure was adjusted by an overflow valve. Cell and gas temperature can be assumed to be at room temperature as the utilised test bench does not provide the possibility to heat up the gases or the cell at this moment. Polarisation curves were determined using a potentiostat/galvanostat type Ivium Vertex 5A connected to an additional booster type Ivium Boost 10012. The measured data of the potentiostat/galvanostat was used to determine the polarisation curves.

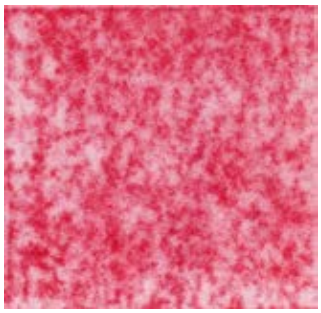


Fig. 2 Exemplary scan of pressure sensitive film applied to a 25-cm^2 PEMEC single cell based on hydraulic clamping with a pressure level of 4 bar

RESULTS AND DISCUSSION

Fig. 2 shows exemplarily the results gathered with pressure sensitive film type Prescale LLLW for a cell clamping with the hydraulic medium being at a pressure level of 4 bar, while the anode and the cathode is at ambient pressure. It can be seen that the cell compression is even over the active cell area. Like in our earlier studies on PEM fuel cells it can be expected that current density and temperature distribution is also homogeneous over the active area for out PEMEC test cell.

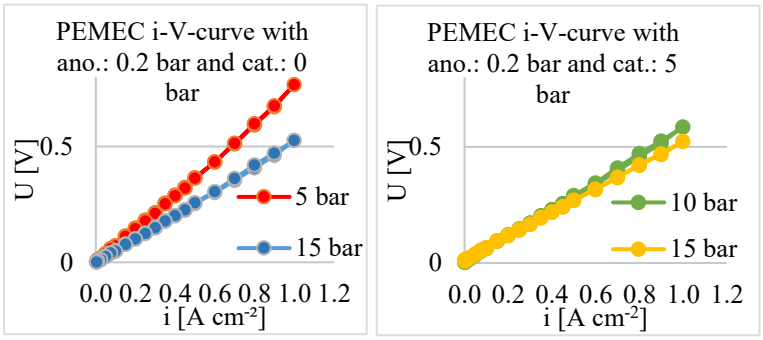


Fig. 3 Exemplary polarisation curves of the novel PEMEC single cell up to 1 A cm^{-2} dependent on hydraulic clamping pressure level as well as hydrogen outlet pressure

After the tightness of the cell's gasket system was checked up to 20 bar for the hydraulic medium and up to 10 bar for the cathode compartment, when at the same time the anode compartment was at atmospheric pressure level, in-situ measurements were performed. Polarisation curves were determined at hydrogen outlet pressures of 0 bar and 5 bar, respectively. Fig. 3 shows exemplarily polarisation curves dependent on different hydraulic media pressure level. As can be seen from Fig. 3 the increase of the hydraulic pressure level leads to a decrease in Ohmic over potential and, therefore, to more efficient PEMEC operation. For a pressure increase from 0 bar to 5 bar no significant cell voltage increase was analysed, due to predominate Ohmic losses.

CONCLUSIONS AND OUTLOOK

In experiments it was shown that our prototype based on the new way of PEMEC clamping realised a hydrogen compression from 0 to 5 bar. The use of our novel system design based on hydraulic clamping for PEMEC leads to advantageous operation conditions like homogenous cell compression distribution. From this an even current density as well as even temperature distribution over the active cell area can be expected. For prospective prototypes with higher hydrogen outlet pressure level, larger cell area and more than one cell, this could be beneficial. However, such studies will be performed in a later step after our small-scale device is fully understood.

Further, the performance indicated by the polarisation curves was appropriate for ambient and dead-end operation conditions as well as for the use of dry hydrogen feed gas. However, in comparison to earlier work in the field of PEMEC based on state-of-the-art cell types and due to low temperature level, the cell voltage of our device seems higher. Therefore, a revised experimental setup is being established soon, in order to also determine polarisation curves at higher cell and gas temperature as well as to analyse the effect of feed gas humidification.

ACKNOWLEDGEMENT

The research leading to the presented results has received funding from the Ministry for Environment, Agriculture, Conservation and Consumer Protection of the State of North Rhine-Westphalia under the framework of the "Sonderprogramm Umweltwirtschaft im Rahmen der Corona-Hilfe" (funding number UW-01-027A for ProPuls and UW-01-027D for Westfälische Hochschule University of Applied Sciences).

REFERENCES

1. Kurzweil P, Dietlmeier OK. 2018. Elektrochemische Speicher. Chapter 8.2 Wasserstoffspeicherung. Wiesbaden. Springer Fachmedien.
2. Muntean R, Pascal DT, Rost U, Marginean G, Brodmann M, Vaszilcsin N, 2020. Synthesis and Characterization of Platinum-Cobalt-Manganese Ternary Alloy Catalysts Supported on Carbon Nano Fibers: An Alternative Catalyst for Hydrogen Evolution Reaction, International Journal of Hydrogen Energy, 45,49:26217-26225.
3. Catalano J et al. 2015. Efficiency of electrochemical gas compression, pumping and power generation in membranes. Journal of Membrane Science 478:37-48.
4. Wirkert FJ, Roth J, Jagalski S, Neuhaus P, Rost U, Brodmann M. 2020. A modular design approach for PEM electrolyser systems with homogeneous operation conditions and highly efficient heat management, International Journal of Hydrogen Energy. 45,2:1226-1235.
5. Rost U, Mutascu C, Roth J, Sagewka C, Brodmann M. 2015. Proof of concept of a novel PEM fuel cell stack design with hydraulic compression, Journal of Energy Power Engineering. 9:775-783.

WHEC-2022
23rd World Hydrogen Energy Conference
June 26-30, 2022 - Istanbul

#268

TOWARDS A BETTER SUSTAINABILITY OF ELECTROLESS PORE-PLATED MEMBRANES: LIFE CYCLE ASSESSMENTS ON FABRICATION STRATEGIES

[1]David Alique, [2]Pedro Leo, [3]David Martinez-Diaz, [2]Raúl Sanz, [1]José Antonio Calles*
[1] Department of Energy, chemical and Mechanical Engineering, Rey Juan Carlos University, c/ Tulipan s/n 28933 Móstoles, Spain
[2] Department of Chemical and Environmental Engineering, Rey Juan Carlos University, c/ Tulipan s/n 28933 Móstoles, Spain
[3] Department of Applied Mathematics, Material Science and Engineering and Electronic Technology, Rey Juan Carlos University,
c/ Tulipan s/n 28933 Móstoles, Spain

*Corresponding author e-mail: david.alique@urjc.es

ABSTRACT

Pd-based membranes attract great attention to be used as independent separators or combined with catalysts in a membrane reactor for H_2-production. The membrane fabrication was improved for years, reaching ultra-thin Pd-films with high permeability and selectivity. However, commercialization at industrial level is still scarce due to the limited knowledge about their economy, lifespan and environmental concerns. In this context, the current study expands the unique life cycle assessment focused on the preparation of Pd-based composite-membranes by Electroless Pore-Plating (ELP-PP) in literature. Based on this, the current research go into deep when the membrane incorporates Pd-CeO_2 as intermediate layer and the total length of the membrane is increased up to 100 cm. The associated environmental impacts were estimated through ReCiPe methodology by using Simapro 8.5. Climate change, human toxicity, acidification, freshwater ecotoxicity, metal depletion and fossil fuel resources depletion were the most relevant impacts generated during the membrane manufacturing, although they were reduced up to 50% respect to membranes without ceramic intermediate barriers. Moreover, CeO_2 doping reduces the number of ELP-PP recurrences, hence further improving the environmental sustainability. Finally, an additional reduction of the environmental impacts was also achieved by scaling-up the process for the preparation of longer membranes.

Keywords: Membrane fabrication, Palladium, Electroless plating, Life cycle assessment, Scale-up

INTRODUCTION

As a clean energy vector, hydrogen is one of the most promising alternatives to facilitate the above-mentioned progressive transition towards a net-zero carbon emissions system. Among other multiple reasons, the possibility to be produced from a wide variety of feedstock by diverse technologies, some of them very mature, could definitively promote its penetration in the industry with assumable risks. In fact, most of the current hydrogen is produced by methane steam reforming, although many other hydrocarbons can also be considered with similar technologies. The use of biomass-derivate compounds and wastes to generate hydrogen could be especially attractive for a circular economy. However, in all these processes involving traditional thermochemical routes, hydrogen is not directly obtained in its pure form but accompanied by other sub-products such as carbon monoxide, carbon dioxide, methane, or steam water, among others. Therefore, down-stream additional purification steps are always required to adjust the hydrogen purity for each particular final application [1]. In this context, Pd-based membranes provides the possibility to reach an ultra-high purity in a wide variety of operating conditions, including the combination of both production and separation steps in a unique device so-called membrane reactor. The continuous separation of hydrogen throughout the membrane from the bulk reaction promotes its generation by an equilibrium displacement towards the products. This technology simultaneously aims to facilitate the process intensification and increase their overall efficiency. Great efforts are being carried out during last years to reduce as much as possible the metal thickness of these membranes by using different ceramic particles as intermediate layer [2], among other alternatives, although environmental implications of diverse fabrication strategies are certainly scarce in literature. Only a pioneer work addressing a systematic environmental analysis throughout LCA to fabricate Pd-based membranes by Electroless Pore-Plating can be found [3]. This study completes the preliminary study by analyzing the influence of diverse CeO_2 particles and membrane scale-up on the main environmental impacts.

MATERIALS AND METHODS

Different composite Pd-based membrane containing CeO_2 intermediate layer onto PSS tubular supports were prepared by ELP-PP and fully characterized in terms of morphology and permeation capacity. Raw CeO_2 particles and doped ones with Pd nuclei before their incorporation on the membrane by vacuum-assisted dip-coating (VA-DC) were considered for the preparation of the intermediate layer. Moreover, diverse membrane lengths up to 100 cm

were also considered by scaling-up the fabrication process. Taking into account all the raw materials and energy requirements, as well as the residues generated during the fabrication, LCA analyses were performed according to standards ISO-14040 and ISO-14044 to determine the effects of each material and energy input/output used in the previously described membranes manufacturing process on both human health and the environment.

RESULTS AND DISCUSSION

First, a complete characterization of the membranes are analyzed. As it can be seen, the use of doped Pd-CeO_2 particles as intermediate layer significantly improve the membrane characteristics by reducing the final thickness of the Pd film reached by subsequent ELP-PP, while simultaneously increase the H_2-permeance, always maintaining a complete selectivity to hydrogen. A Summary of the main properties evaluated for the membranes are presented in Figure 1.

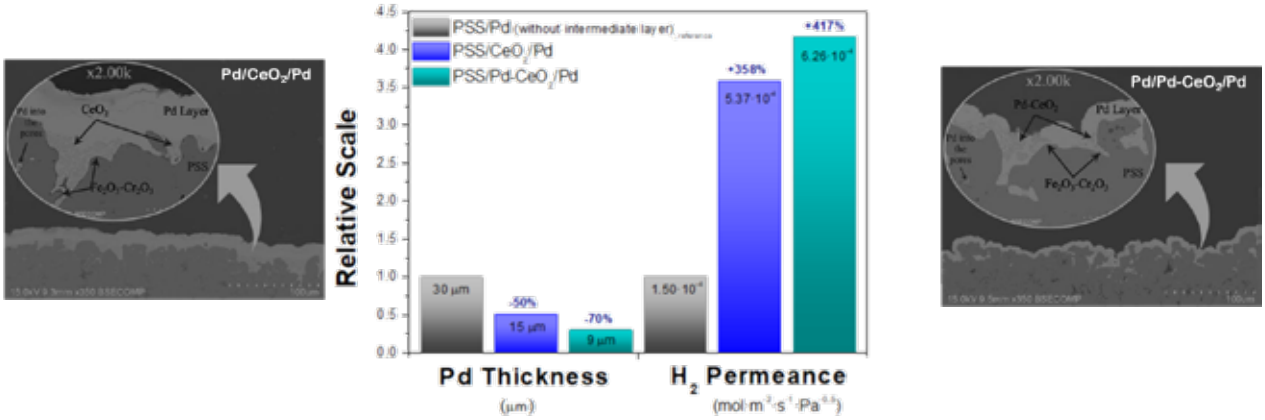


Figure 1. Summary of most relevant properties of Pd-membranes analyzed in this work.

For these membranes, the positive effect of doping the CeO_2 particles on both Pd-thickness and H_2-permeance was also relevant in case of analyzing the main environmental impacts generated during the membranes' fabrication. As it can be seen in Figure 2, all the considered impacts were reduced in a relevant amount.

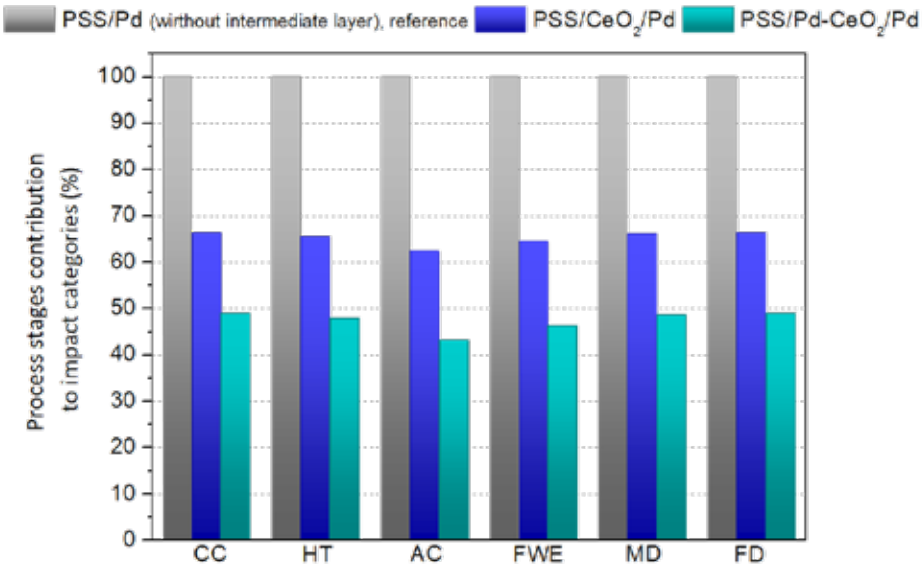


Figure 2. Main environmental impacts extracted from LCA on the membrane fabrication strategies.

Finally, the influence of scaling-up the selected fabrication strategy, Pd incorporation by ELP-PP onto PSS supports containing Pd-CeO_2 intermediate layers, was also performed and evaluated by LCA. First, it should be highlighted that similar properties in terms of morphology, homogeneity of layers in axial direction and permeation capacity per membrane length, were reached for all the prepared membranes, independently of their total length. However, further improvements in their sustainability were observed for longer membranes. Greater improvements were reached while increasing the membrane length from 3 to 25 cm, while minor effects were obtained for longer membranes, despite the main environmental impacts further decrease up to 100 cm (Figure 3).

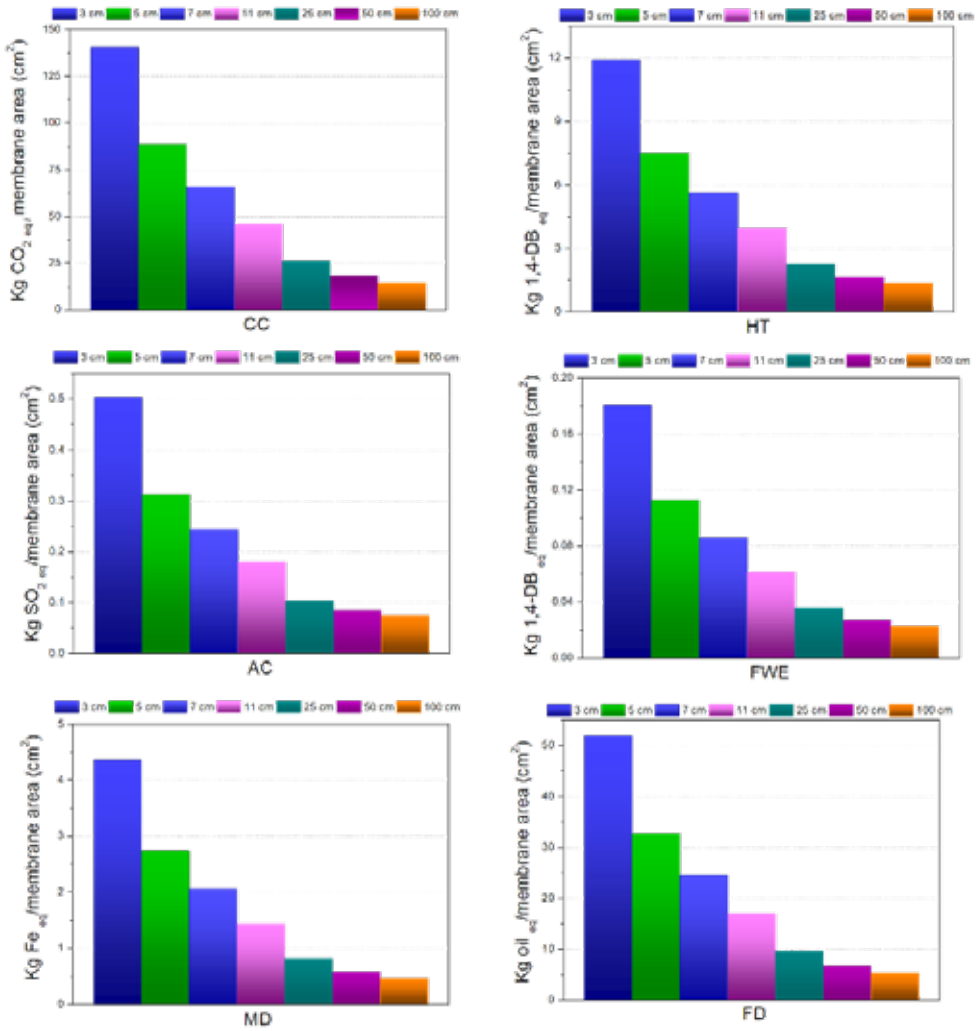


Figure 2. Evolution of environmental impacts during scaling-up the membrane length.

CONCLUSIONS

The main conclusions extracted from the current research can be summarized in:

- The use of CeO_2-based intermediate layers allows reducing the required palladium amount to reach a fully dense membrane (up to -70%) while increasing the H_2-permeance (up to +417%) without losing selectivity.
- This strategy also allows limiting the most relevant environmental impacts below 50% related to the referred value (ELP-PP membranes with absence of any intermediate layer) due to the minor number of ELP-PP recurrences and associated drying steps (with noticeable energy demand).
- A further drastic reduction of the most relevant environmental impacts can be reached during the membrane fabrication scale-up from 3 to 25 cm total length, while only slight improvements are predicted for longer dimensions up to 100 cm.

ACKNOWLEDGEMENT

The authors thanks the financial supports received from the Spanish Government through the competitive projects ENE2017-83696-R and PID2020-117273RB-I00. Moreover, David Alique wants to exress his gratitude for funds received from Young Researchers R&D proyect ref. M2182-MEMRESPIP, financed by the Community of Madrid and Rey Juan Carlos University.

REFERENCES

1. Martinez-Diaz D., Sanz R., Calles J.A. and Alique D. 2019. H_2 permeation increase of electroless pore-plated Pd/PSS membranes with CeO_2 intermediate layers. Separation and Purification Technology 216: 16-24.
2. Martinez-Diaz D., Alique D., Calles J.A. and Sanz R. 2020. Pd-thickness reduction in electroless pore-plated membranes by using doped-ceria as interlayer. International Journal of Hydrogen Energy 45: 7278-7289.
3. Martinez-Diaz D., Leo P., Sanz R., Carrero A., Calles J.A. and Alique D. 2021. Life cycle assessment of H_2-selective Pd membranes fabricated by electroless pore-plating. Journal of Cleaner Production 316: 128229.

WHEC-2022
23rd World Hydrogen Energy Conference
June 26-30, 2022 - Istanbul

#312

ELECTROCHEMICAL HYDROGEN SEPARATION FROM REFORMATE USING POLYBENZIMIDAZOLE/MOF COMPOSITE MEMBRANES

[1, 2] Gizem Nur Bulanık Durmuş, [3] Enis Oğuzhan Eren, [1 *] Yılser Devrim, [4] C. Ozgur Colpan, [5] Necati Özkan

[1]Atılım University, Department of Energy Systems Engineering, Incek Golbasi Ankara, 06830, Turkey
[2]Atılım University, Graduate School of Natural and Applied Sciences, Department of Mechanical Engineering, Incek Golbasi Ankara, 06830, Turkey
[3]Max Planck Institute of Colloids and Interfaces, Potsdam, 14476, Germany
[4]Department of Mechanical Engineering, Dokuz Eylul University, Buca, Izmir, Turkey
[5]Middle East Technical University, Polymer Science & Technology, Ankara, 06800, Turkey

*Corresponding author e-mail: yilser.devrim@atilim.edu.tr

ABSTRACT

This study introduces the experimental results of a high-temperature electrochemical hydrogen purification (ECHP) cell through poly 2.2-m-phenylene-5.5-bibenzimidazole/metal organic framework (PBI/MOF) composite membranes in the temperature range of 140°C-180°C. Synthesis of ZIF-8 and UiO-66 MOFs was conducted through a typical solvothermal method, and composite membranes containing 2.5 wt. %. MOF was fabricated. Experiments were conducted with pure hydrogen (H_2) and reformate gas mixtures containing H_2, carbon monoxide (CO), and carbon dioxide (CO_2). A gas chromatography device (GC) was used to analyze the gas composition at the exit of the ECHP cell. The final output H_2 purity was found to be >99.9 % for the H_2/CO_2/CO mixed-phase and >99.7% for the H_2/CO mixed phase.

Keywords: Electrochemical hydrogen separation, Metal-organic framework, ZIF-8, UIO-66

INTRODUCTION

Removing the carbon footprint in terms of using clean and renewable resources and reducing the usage of fossil fuels is an emerging trend in energy applications. H_2 stands out among the innovative energy sources. However, due to the widespread conventional production of H_2, the produced H_2 must be separated from other impurities. To obtain efficient results from fuel cell applications, high purity H_2 needs to be used, and for easy transportation, H_2 must be compressed. The electrochemical H_2 purification (ECHP) system is a remarkable and efficient technology that can separate H_2 from a reformate gas mixture and compress it in one step [1]. The ECHP systems are relatively portable and have no moving parts, and they can operate without notable noises regarding vibration. The ECHP cell can separate H_2 from a gas mixture by H_2 oxidation reaction (Eq. 1) and H_2 evolution reaction (Eq. 2) occurring at the cathode side. Impurities leave the cell from the anode exit. Only protons pass through the proton-conducting membrane towards the cathode and recombine with electrons from the external circuit to form H_2. The overall reaction of the cell is shown in Eq 3.

Anode side: $H_2(LP) \rightarrow 2H^+ + 2e^-$ (1)

Cathode side: $2H^+ + 2e^- \rightarrow H_2$ (HP) (2)

Overall cell reaction: H_2 (LP) $\rightarrow H_2$ (HP) (3)

Various studies have been conducted in recent years to investigate H_2 purification at higher temperatures, as proton conductivity at low operating temperatures is achieved with humidified Nafion® membranes. At high temperatures, the tolerance to CO and the reaction rate increases significantly. Proton conduction is often accomplished through phosphoric acid-doped polybenzimidazole (PBI) membranes. High-temperature PBI-based systems have an advantage over Nafion-based systems in their ability to operate in the presence of higher levels of contaminants, especially CO. For the improvement of proton conduction, one of the well-known approaches is the doping of metal-organic frameworks (MOF) within the membrane [2]. In this study, the PBI membrane was doped with ZIF-8 and UIO-66 to enhance the proton conductivity of PBI [3]. The performance of ECHP and the purification rate of H_2 using a gas chromatography device were performed with the experiments carried out in the temperature range of 140-180°C. The effects of H_2 concentration and operating temperature on the ECHP performance were studied to prove the feasibility of the high-temperature ECHP system.

EXPERIMENTAL SET-UP AND PROCEDURE

ZIF-8 and UIO-66 types of MOFs were synthesized through the solvothermal method [4]. The PBI polymer was dissolved in DMAc under a magnetic stirrer at 75°C. Then, UIO-66 and ZIF-8 powders (2.5 wt. %) were added to the PBI solution and mixed for 15 min. The prepared suspension was ultrasonicated for about 30 min to provide a uniform dispersion of MOF powders and then it was cast to the petri dish. Membranes were dried overnight at 100°C. Before

conducting the ECHP cell performance tests, the membranes were immersed in H_3PO_4 for ten days. MEAs were prepared using the ultrasonic coating method [5]. High-temperature H_2 purification tests were executed using the HT-ECHP test station. The performance tests were obtained at 140, 150, 160, 170 and 180°C with various gas streams, including, reformate gases RG-1 (H_2:CO_2:CO-75:25:0), RG-2 (H_2:CO_2:CO-72:26:2) and RG-3 (H_2:CO_2:CO-95:0:5). H_2 purity level was determined by a gas chromatograph with a TCD detector (Ar as carrier gases) located at the cathode exit of the ECHP cell.

RESULTS AND DISCUSSION

Proton conductivity is an important parameter influencing the performance of the ECHP system. The proton conductivities of the PBI-ZIF8 and PBI-UiO66 membranes were determined as 0.311 and 0.316 $S \cdot cm^{-1}$ at 160°C, respectively. Figure 1 illustrates the H_2 purity results of the PBI/MOF composite membranes at different temperatures. The highest H_2 purities of 99.999 % were achieved with PBI/UIO-66 membranes for RG-1 gas.

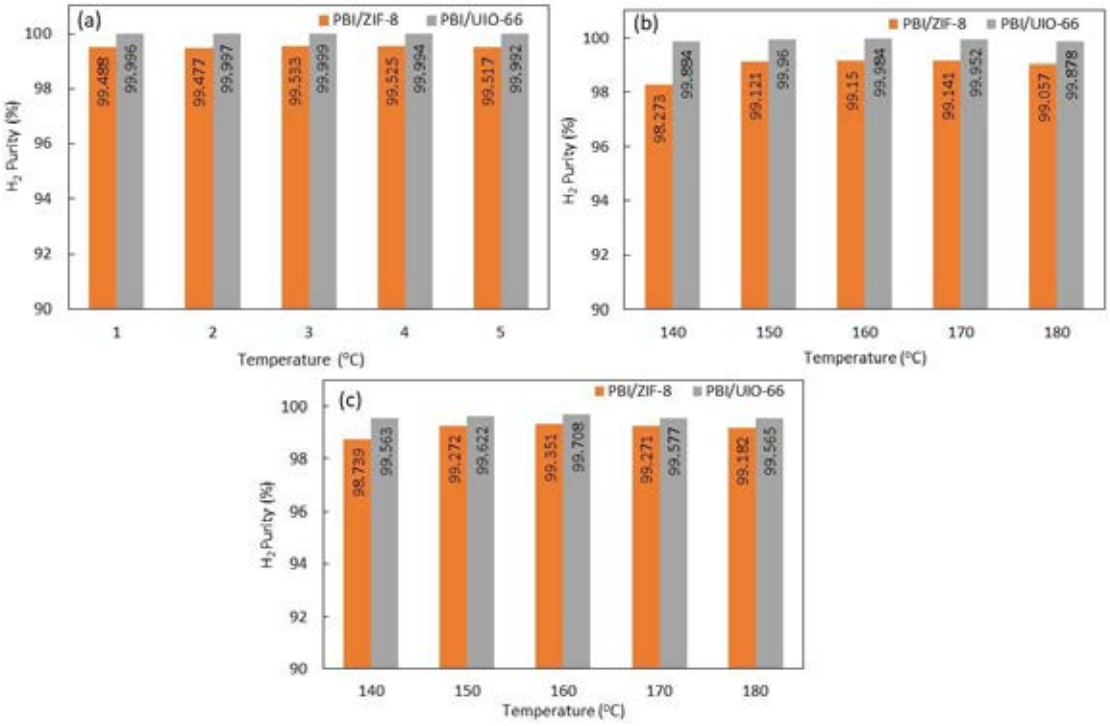


Fig. 1: H_2 purity results of the ECHP system with reformate gases a) H_2:CO_2:CO (75:25:0), b) H_2:CO_2:CO (72:26:2) and c) H_2:CO_2:CO (95:0:5)

The highest degree of purification was obtained as 99.999% (RG-1 @160°C) and 99.533 % (RG-1@160°C) for PBI/UiO-66 and PBI/ZIF-8 membranes, respectively. With the increase in temperature, a slight decrease in H_2 purification degrees was observed. The performance loss at high temperatures can be related to the conversion of CO_2 to CO by the reverse water-gas shift (RWGS) reaction because of the high operating temperature. It has been determined that the increase in the amount of CO in the gas stream causes a decrease in the degree of H_2 purification. Because of its low heat of adsorption, CO is more easily adsorbed on the Pt surface than H_2. As more CO is adsorbed on the catalyst surface, less active sites may be available for H_2 oxidation. Therefore, a decrease in ECHP cell performance occurs. However, the harmful effect of CO on the H_2 purification was less pronounced for the PBI/UiO-66 and PBI/ZIF-8 membranes [6].

CONCLUSIONS

In this study, PBI/ZIF-8 and PBI/UIO-66 composite membranes were successfully prepared for ECHP application. It has been proved that the proton conductivity of the PBI membrane can be improved through the MOF fillers. The performances of the prepared ECHP cell were determined using pure H_2 and different reformate gas mixtures in the temperature range of 140-180°C. The results show that the ECHP system, which can operate at high temperatures without the need for humidification, has great potential for the recycling and purification of H_2 in the future.

ACKNOWLEDGMENT

This study was supported by The Scientific and Technological Research Council of Turkey (TUBITAK) under grant no 219M333.

REFERENCES

1. Gardner CL, Ternan M. 2007. Electrochemical Separation of Hydrogen from Reformate Using Pem Fuel Cell Technology. Journal of Power Sources 171(2):835-841.
2. Liang X, Zhang F, Feng W, Zou X, Zhao C, Na H, Liu C, Sun F, Zhu G. 2013. From metal-organic framework (MOF) to MOF-polymer composite membrane: Enhancement of low-humidity proton conductivity. Chemical Science 2013;4:983–92.
3. Escorihuela J, Olvera-Mancilla J, Alexandrova L, del Castillo LF, Compañ V. 2020. Recent progress in the development of composite membranes based on polybenzimidazole for high temperature proton exchange membrane (PEM) fuel cell applications. Polymers 12(9),1861.
4. Eren EO, Özkan N, Devrim Y. 2021. Preparation of polybenzimidazole/ZIF-8 and polybenzimidazole/UiO-66 composite membranes with enhanced proton conductivity. International Journal of Hydrogen Energy 2021.11.045.
5. Devrim Y, Erkan S, Baç N, Eroglu I. 2012. Improvement of PEMFC performance with Nafion/inorganic nanocomposite membrane electrode assembly prepared by ultrasonic coating technique. International Journal of Hydrogen Energy 37:16748–58.
6. Molochas C and Tsiakaras P. 2021. Carbon Monoxide Tolerant Pt-Based Electrocatalysts for H2-PEMFC Applications: Current Progress and Challenges. Catalysts 11(9), 1127.

WHEC-2022
23rd World Hydrogen Energy Conference
June 26-30, 2022 - Istanbul

#333

DEVELOPMENT OF BIMETALLIC ELECTROCATALYSTS FOR HIGH-TEMPERATURE ELECTROCHEMICAL HYDROGEN PURIFICATION

[1]İlay Bilge Bal, [1,2]Gizem Nur Bulanık Durmuş, [2]Yılser Devrim*
[1]Atılım University, Graduate School of Natural and Applied Sciences, Department of Mechanical Engineering, Ankara, Turkey
[2]Atılım University, Department of Energy Systems Engineering, Ankara, Turkey

*Corresponding author e-mail: yilser.devrim@atilim.edu.tr

ABSTRACT

In this study, PtRu/GNP, PtIr/GNP, and RuIr/GNP bimetallic catalysts were synthesized by microwave-assisted synthesis method, and their performances on the high-temperature electrochemical hydrogen purification (HT-ECHP) were compared. The structural and electrochemical characteristics of the bimetallic catalysts were examined by the TGA, XRD, XPS, and CV techniques. ECHP Tests were performed with reformate gas mixtures containing hydrogen (H_2), carbon monoxide (CO), and carbon dioxide (CO_2) at temperatures between 140-180°C. The gas at the exit of the ECHP cell was analyzed with the gas chromatography device (GC), and high H_2 purity was achieved.

Keywords: Electrochemical hydrogen purification, Bimetallic catalyst, Graphene nanoplatelet, High temperature

INTRODUCTION

In order for hydrogen (H_2) to be used efficiently in innovative and promising applications such as fuel cells, it must be supplied in high purity and H_2 needs to be pressurized for easy storage and transport. In this context, electrochemical hydrogen purification (ECHP) is considered a promising technology to meet the global demand for H_2 and become a widely used resource, as it provides both purification and compression in one step. The ECHP has almost the same configuration as the proton exchange membrane fuel cell (PEMFC), and the catalyst layer plays a critical role in achieving the desired operating conditions. Since H_2 containing gas mixture is fed to the ECHP by the anode, specifically the anode side catalyst contacts with the impurity containing reformate gas, it must have a high tolerance to impurities and be low cost to facilitate commercialization [1]. Alloying Pt metal with another transition metal such as Ruthenium (Ru), Iridium (Ir), etc. is an attention-grabbing approach since it provides decreasing cost by reducing the Pt-loading as well as the enhanced catalyst stability [2]. In a recent study [3], the performances of Pd/C, Pt/C, and PtPd/C catalysts for ECHP application were compared and because of the electrochemical characterization analyses, it was stated that the bimetallic PtPd/C catalyst exhibited higher catalytic activity. Furthermore, it is a well-known fact that high operating temperatures yield improved catalyst tolerance to impurities inside the reformate gas and accelerated reaction kinetics for both H_2 oxidation (HOR) and H_2 evolution reactions (HER) [4]. In the present study, the influences of the graphene nanoplatelet (GNP) supported bimetallic PtRu, PtIr, RuIr catalysts on the HT-ECHP performance were compared. To examine the performances of the prepared catalysts on ECHP, the membrane electrode assembly (MEA) prepared using the synthesized catalysts was integrated into the ECHP test cell and performance tests were conducted with H_2:CO_2:CO (75:22:3) containing reformate gas mixture at the temperatures between 140-180°C.

EXPERIMENTAL SET-UP AND PROCEDURES

The bimetallic PtRu/GNP, PtIr/GNP, RuIr/GNP catalysts were prepared by microwave-assisted synthesis method since it provides a more uniform distribution of the metal nanoparticles on the support material, uniform heat distribution and rapid synthesis [5]. Firstly, 100 mg GNP support material was dispersed in the 48 ml EG and 12 ml IPA mixture with ultrasonic mixing for 1 h. Then, an adequate amount of $H_2PtCl_6.6H_2O$, $RuCl_3.xH_2O$, and $IrCl_3.xH_2O$ metal salts were added into the solution to obtain 30% metal content and mixed ultrasonically for 10 min. The final solution was washed with acetone and DI water to remove impurities and then left to dry in an oven at 100 ℃ overnight.

The structural characterization of the catalysts was performed by the Thermogravimetric Analysis (TGA), X-ray Diffraction (XRD), X-ray Photoelectron Spectroscopy (XPS) methods while the electrochemical characterization was conducted by Cyclic Voltammetry (CV). TGA method was performed to examine the thermal stability of the prepared catalysts and to determine the metal loading on the GNP support material, while the crystalline structure of the catalysts was investigated by XRD analysis. CV was conducted to examine the electrochemical stability and to calculate the electrochemical active surface area (ECSA) of the synthesized catalysts.

Ink solutions containing synthesized catalysts, PTFE binder, IPA and DI water were added to the beaker and mixed ultrasonically for 30 minutes. Prepared ink was coated on the commercial carbon paper by the ultrasonic coating method, which provides homogeneous distribution and minimizes the catalyst loss. Gas diffusion electrodes (GDEs) were attached on both sides of phosphoric acid doped PBI membranes by hot pressing method at 150°C and 172 N/cm^2 for 15 minutes. The obtained MEAs were integrated into the HT-ECHP cell and were tested in the ECHP test system with H_2:CO_2:CO-75:22:3 reformate gas at the temperatures between 140-180°C. The reformate gas was fed to the cell from the anode side, and the gas from the cathode outlet was sent to the gas chromatography device to observe the purification rate. Besides, the polarization curves were obtained by keeping the limiting voltage of the DC power supply at 1.4 V.

RESULTS AND DISCUSSION

The thermal behavior of the PtRu/GNP, PtIr/GNP, and RuIr/GNP is illustrated in Fig. 1a. According to TGA results, the metal loading on the support material was obtained as 17.11%, 17.10%, and 22.63% for the PtRu/GNP, PtIr/GNP, RuIr/GNP catalysts, respectively. The difference between the obtained metal amount and the targeted 30% metal amount can be explained by the incomplete reduction of the metal salts that are used as precursors to the metals.

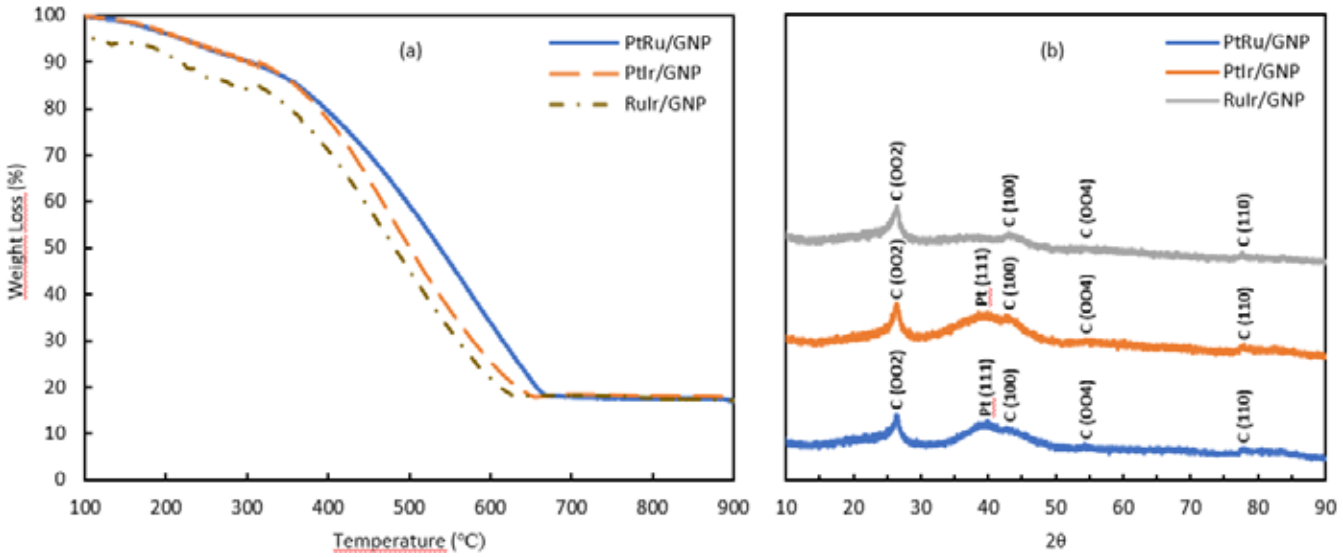


Fig. 1. a) Thermal analysis and b) XRD analysis of the PtRu/GNP, PtIr/GNP, and RuIr/GNP bimetallic catalysts

Fig. 1b illustrates the XRD pattern of the prepared catalysts and the corresponding planes to the 2θ diffraction peaks [6]–[8]. Some plane-associated peaks did not appear in the XRD graph, this may be caused by the amorphous nature of the catalysts or the broadening of the peaks due to the very small size of the catalyst nanoparticles [6]. XPS was performed to examine the chemical composition of the PtRu/GNP, PtIr/GNP, and RuIr/GNP catalysts. XPS results demonstrate that bimetallic catalysts were successfully synthesized. The CV analysis was performed with a potentiostat by three-electrode system which uses glassy carbon (GC) disk electrode (0.0707 cm^2) as working electrode (WE), Ag/AgCl filled with saturated KCl solution as the reference electrode (RE), and Pt coil as the counter electrode (CE). The CV measurements were conducted between 1.2 V to -0.25 V with a scan rate of 100 mV/s at 25 °C in 0.1 M $HClO_4$ electrolyte solution for 1000 cycles. Fig.2. shows the CV result of each catalyst. After 1000th cycles, the ECSA loss of the bimetallic catalysts was calculated as 74.55%, 46.60%, and 77.39% for PtRu/GNP, PtIr/GNP, and RuIr/GNP, respectively.

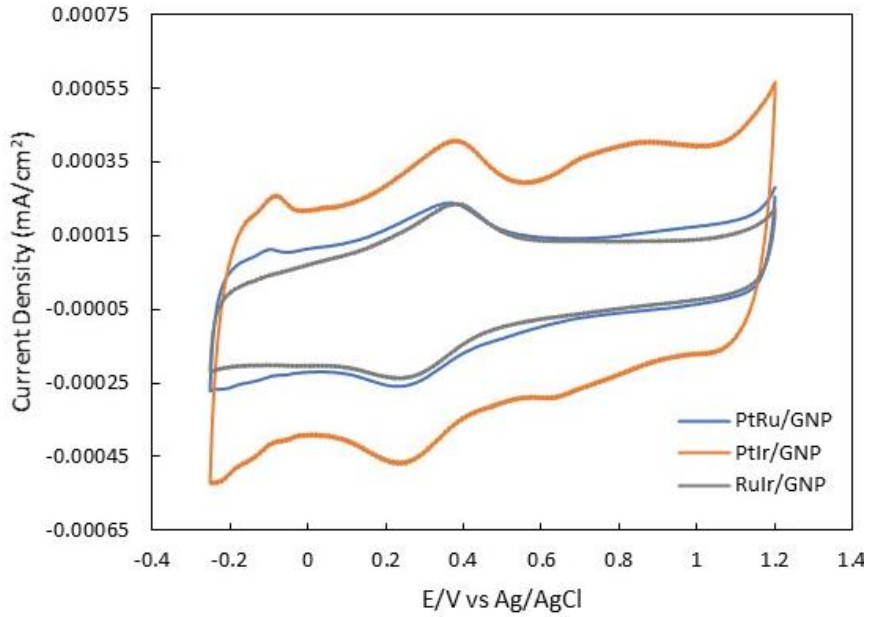


Fig. 2. CV analysis of the PtRu/GNP, PtIr/GNP, and RuIr/GNP bimetallic catalysts

CONCLUSIONS

In present study, bimetallic catalysts were prepared for the ECHP system. Catalysts were synthesized by reducing Pt, Ru and Ir nanoparticles on GNP support by microwave heating method. Successfully synthesized PtRu/GNP, PtIr/GNP, and RuIr/GNP catalysts were characterized using electrochemical and physical analysis methods. In accordance with the obtained results, it was indicated that the prepared bimetallic PtRu/GNP, PtIr/GNP, and RuIr/GNP catalysts perform better electrocatalytic activity in the ECHP system. The gas at the exit of the ECHP cell was analyzed with the gas chromatography device (GC), and high H_2 purity was achieved.

ACKNOWLEDGMENT

This study was supported by The Scientific and Technological Research Council of Turkey (TUBITAK) under grant number 219M333.

REFERENCES

1. Trégaro M, Rhandi M, Druart F, Deseure J and Chatenet M. 2020. Electrochemical hydrogen compression and purification versus competing technologies: Part II. Challenges in electrocatalysis. Chinese Journal of Catalysis 41:770-782.
2. Zou J, Han N, Yan J, Feng Q, Wang Y, Zhao Z, Fan J, Zeng L, Li H and Wang H. 2020. Electrochemical Compression Technologies for High-Pressure Hydrogen: Current Status, Challenges and Perspective. Electrochemical Energy Reviews 3:690-729.
3. Aykut Y and Bayrakçeken Yurtcan A. 2022. Catalyst development for viability of electrochemical hydrogen purifier and compressor (EHPC) technology. International Journal of Hydrogen Energy in press.
4. Huang F, Pingitore AT and Benicewicz BC. 2020. Electrochemical Hydrogen Separation from Reformate Using High-Temperature Polybenzimidazole (PBI) Membranes: The Role of Chemistry. ACS Sustainable Chemistry & Engineering 8:6234-6242.
5. Al-Tememy MGH and Devrim Y. 2021. Development of effective bimetallic catalyst for high-temperature PEM fuel cell to improve CO tolerance. International Journal of Energy Research 45:3343-3357.
6. Wang H, Da H, Wang R and Ji S. 2014. Beef-derived Mesoporous Carbon as Highly Efficient Support for PtRuIr Electrocatalysts and their High Activity for CO and Methanol Oxidation. South African Journal of Chemistry 67:33-39.
7. Li W, Wang X, Chen Z, Waje M and Yan Y. 2006. Pt-Ru Supported on Double-Walled Carbon Nanotubes as High-Performance Anode Catalysts for Direct Methanol Fuel Cells. Journal of Physical Chemistry B 110:15353-15358.
8. Eguiluz KIB, Salazar-Banda GR, Miwa D, Machado SAS and Avaca LA. 2007. Effect of the catalyst composition in the Ptx(Ru-Ir)1-x/C system on the electro-oxidation of methanol in acid media. Journal of Power Sources 179:42-49.

WHEC-2022
23rd World Hydrogen Energy Conference
June 26-30, 2022 - Istanbul

#426
DEVELOPMENT OF Pd-BASED DENSE METALLIC MEMBRANE WITH SULFUR RESISTANT MOF COATED FOR HYDROGEN SEPARATION

[1]Sevgi Kalkan, [2*]Gamze Gümüşlü Gür
[1] Istanbul Technical University, Chemical Engineering Department, Istanbul, Turkey
[2] Istanbul Technical University, Chemical Engineering Department, Istanbul, Turkey

*Corresponding author e-mail: gamgur@itu.edu.tr

ABSTRACT

Hydrogen plays a key role in both the chemical and energy industries. However, it is essential for H_2 to be in high purity in order to be used. In countries with large coal reserves, H_2 is separated from the syngas ($CO+H_2$) obtained from coal gasification. The separation process includes units that adjust the required operational temperature and pressure with high energy needs and costs. The use of Pd-based dense metallic membranes allows the production of ultra-high purity H_2 without significant changes in temperature and pressure. However, sulfur compounds in coal-derived syngas limit the use of these membranes. Sulfur sticks to Pd atoms disrupt the membrane structure and prevent the dissociation of hydrogen on the membrane surface. Therefore, developing a thin Pd film, coated on low-cost support with an additional layer that will protect this film from sulfide compounds will make an important contribution to the literature and improve the applications of these membranes. In this study, a new membrane structure was developed by coating a thin layer of Pd film on low-cost α-Al_2O_3 tablets and growing a secondary UiO-66 layer on Pd. The experimental data proved the effect of the UiO-66 layer in preventing the Pd layer from sulfur compounds.

Keywords: Dense metallic membranes, Pd, Metal-organic frameworks, Hydrogen

INTRODUCTION

Although the focus is on clean and renewable energy sources, fossil fuels are still used in large quantities all around the world. Especially in countries with large coal reserves, energy production will continue to be obtained by burning coal until clean energies are adapted to industry. Rather than burning coal as a direct energy source, it is a more preferred method to use it with gasification [1]. The gasification process transforms the coal into syngas (mainly CO and H_2) that can be used in the energy or chemical industries , a gas mixture rich in H_2 is obtained in the presence of water-gas shift reaction [2]. In order for these gases to be evaluated in the following processes, they must be obtained as pure as possible at the end of this process or prepared in such a way as to achieve certain ratios. It is possible to reduce the H_2:CO ratio to the required levels by separating a certain amount of H_2 in the syngas. In addition, the synthesis gas released as a result of gasification contains sulfurous compounds that cause pollution, especially H_2S, in nonignorable amounts.

Commercial methods such as pressure swing adsorption (PSA), which are used to separate hydrogen from the gas mixture it is in, require huge capital and energy. For these reasons, dense metallic membranes, which can separate the desired gases in high purity under pressure and temperature conditions of the gas mixture, without requiring an additional energy input or high budgets, have started to attract attention. Especially Pd (Palladium) membranes have come to the fore with their high hydrogen permeability and high activity against hydrogen [3]. Pd is an important transition metal with a hydrogen absorption capacity of 900 times its volume. However, the H_2S existing in the gas mixture where the hydrogen is desired to be decomposed causes the Pd membrane to become unusable [4]. In this study, MOF (metal-organic framework) was used to overcome this problem.

MOFs are a type of lattice-structured materials. Lattice-structured materials are crystalline and porous solid materials constructed from organic "struts" whose chemical structures are interconnected by "joints" (organic or metal oxide-based). MOFs are highly efficient in retaining sulfide compounds, thanks to their extraordinarily large surface areas and metal knots [5,6].In addition, since their pore diameters are much larger than the lattice spaces in metal membranes, the resistance to diffusion is much lower than the use of metal membranes. In the literature, it can be seen that some of the MOFs that show high H_2S holding capacity without any defect in their structures are as follows: MIL-47, MIL-53, MIL-68, MIL-100, MIL-101, MOF-5, UiO-66 [7–10]. In studies with these MOFs, especially on CH_4/H_2S mixtures, it has been reported that almost all of the H_2S is retained and the MOFs preserve their structure. In addition, it has been observed that due to their high surface area, they can work for a long time and their regeneration is easily performed. In line with these results, it has been stated that MOFs can be used for natural gas purification [7,11]. Among

the mentioned MOFs with H_2S holding capacity, UiO-66 could be synthesized in 12 hours without the need for high temperatures and autoclaving. UiO-66 has now become the MOF of the first choice in many applications mostly because it is more resistant to temperature and pressure increase compared to other MOFs [12]. For the reasons mentioned, it was preferred to use UiO-66 as the Pd protective layer in the study.

In this study, the development of a sulfur-resistant double-layer Palladium-based dense metallic membrane for the separation of hydrogen from the sulfide-containing syngas is discussed. Pd is not resistant to sulfur, so the presence of sulfur causes defects in its structure and prevents the membrane from working. To solve this problem, a double-layered structure is used. The first layer is Pd-based metal, while the second layer consists of a thin MOF structure. The aim is to keep the sulfur impurity in the syngas in the MOF structure and prevent it from reaching the membrane surface and thus destructing the structure. With this study, Pd membrane structure with MOF protection layer was introduced in the literature.

MATERIALS AND METHODS

Al_2O_3 was preferred as the membrane support material. Powder α-Al_2O_3 (Alfa Aesar, activated, neutral, Brockmann Grade II) was pressurized to form a tablet shape, sintered at 600℃, and made ready for use. After that, tablets were cleaned with acetone to get rid of the oil and dirt that may be on the surface and dried. Pd film, which will act as a membrane, was coated on the prepared tablets by the electroless plating (ELP) method. The coating process on the dried tablets was carried out in two stages as seeding and plating by a method similar to Gade et al [13]. Seeding was carried out by keeping the support material in the prepared Pd-acetate solution for a short time. The tablet, which was removed from the acetate solution, was thrown into the H_2O_2 solution to get rid of the acetates, and then kept in the reducing solution. Then after being kept in an oven for 24 hours, the dried tablet was placed in the plating solution. Finally, they were left to dry at 120°C overnight.

The second layer, sulfur resistant MOF, was prepared after the hydrogen-selective Pd dense membrane layer developed. After surface conditioning with Pd acetate, the Pd coated samples were kept in the UiO-66 solution at 120°C for 12 hours. After washing with acetone to get rid of DMF residues, the UiO-66 coated Pd dense membrane became ready to use.

RESULTS AND DISCUSSION

Palladium dense metallic membranes synthesized by the electroless plating method. 3 separate plating bath was used for more than 1-hour cycle to increase the stability of the membranes. SEM analysis which is given in Figure 1. indicates that produced Pd films are very dense and have little porosity. After the application of the MOF layer onto the Pd dense metallic surface as described before, the whiteness of UiO-66 particles was observed on the sample surface. The SEM result of the study is given in Figure 2. indicates that the second layer has been successfully created. The UiO-66 MOF layer showed a nearly homogeneous distribution. With the continuation of the experimental studies, homogeneity will be tried to be achieved perfectly.

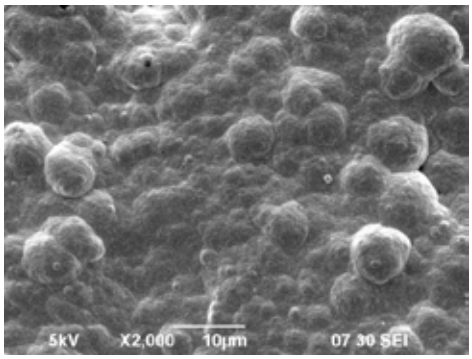


Figure 1. Pd coating morphology

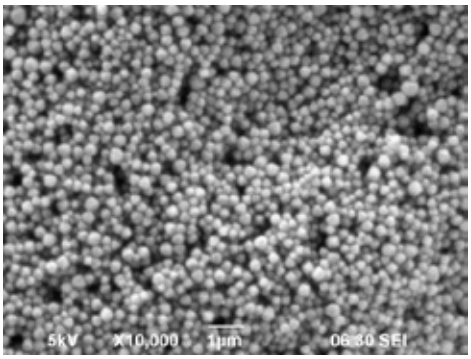


Figure 2. UiO-66 coated membrane

The study aims to form a UiO-66 layer on the Pd surface, thereby reducing the interaction of Pd with sulfur. In this context, the surface was exposed to a sulfur compound to test the function of the UiO-66 layer formed on the surface. The XRD result for the changes in the surface as a result of this process is given in Figure 3. As a result of the interaction of the Pd surface with SO_2, there are peaks compatible with PdS, Pd_4S, and $Pd_{16}S_{17}$ on the surface. The presence of these peaks was not observed in the UiO-66 coated sample, which was exposed to SO_2 under the same conditions as the Pd surface. This situation proves the conclusion of the study's hypothesis that the UiO-66 structure will protect the Pd surface.

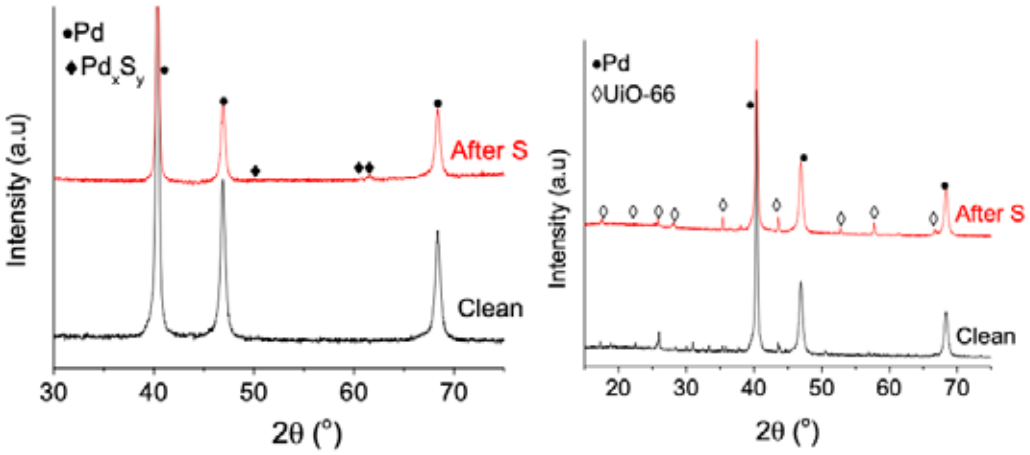


Figure 3. XRD profiles of Pd surface (left) and Pd-UiO-66 surface (right) clean and after sulfur exposure

CONCLUSIONS

Highly selective hydrogen-permeable palladium membranes are cost and energy-effective for industrial applications. However, their weakness towards sulfur compounds makes them an undesired and not preferred option. To overcome this problem, and relatively easy synthesized, resistant to temperature and pressure changes MOF type, UiO-66 was used. Thanks to the developed double-layered structure, the UiO-66 lattices in the upper layer retain the sulfide compounds while protecting the Pd metal in the lower layer from damage. Thus, H atoms that can pass through the Pd metal cavities are separated from the gas mixture, allowing ultra-pure H_2 to be obtained.

REFERENCES

1. Olah GA. 2005. Beyond Oil and Gas: The Methanol Economy. Angewandte Chemie International Edition 44:2636-2639.
2. Liu SQ, Wang YY, Zhao K and Yang N. 2009. Enhanced-hydrogen gas production through underground gasification of lignite. Mining Science and Technology (China) 19:389-394.
3. O'Brien CP, Howard BH, Miller JB, Morreale BD and Gellman AJ. 2010. Inhibition of hydrogen transport through Pd and Pd47Cu53 membranes by H2S at 350 °C. Journal of Membrane Science 349:380-384.
4. Roa F, Douglas Way J, McCormick RL and Paglieri SN. 2003. Preparation and characterization of Pd–Cu composite membranes for hydrogen separation. Chemical Engineering Journal 93:11-22.
5. Britt D, Tranchemontagne D and Yaghi OM. 2008. Metal-organic frameworks with high capacity and selectivity for harmful gases. Proceedings of the National Academy of Sciences 105:11623-11627.
6. Khan NA, Hasan Z and Jhung SH. 2013. Adsorptive removal of hazardous materials using metal-organic frameworks (MOFs): A review. Journal of Hazardous Materials 244-245, 444-456.
7. Hamon L et al. 2009. Comparative study of hydrogen sulfide adsorption in the MIL-53(Al, Cr, Fe), MIL-47(V), MIL-100(Cr), and MIL-101(Cr) metal-organic frameworks at room temperature. Journal of the American Chemical Society 131:8775-8777.
8. Hamon L et al. 2011. Molecular insight into the adsorption of H2S in the flexible MIL-53(Cr) and rigid MIL-47(V) MOFs: Infrared spectroscopy combined to molecular simulations. Journal of Physical Chemistry C 115:2047-2056.
9. Barea E, Montoro C and Navarro JAR. 2014. Toxic gas removal – metal–organic frameworks for the capture and degradation of toxic gases and vapours. Chemical Society Reviews 43:5419-5430.
10. Li Z et al. 2016. Capture of H2S and SO2 from trace sulfur containing gas mixture by functionalized UiO-66(Zr) materials: A molecular simulation study. Fluid Phase Equilibria 427:259-267.
11. Li JR, Sculley J and Zhou HC. 2012. Metal-organic frameworks for separations. Chemical Reviews 112:869-932.
12. Winarta J et al. 2019. A Decade of UiO-66 Research: A Historic Review of Dynamic Structure, Synthesis Mechanisms, and Characterization Techniques of an Archetypal Metal–Organic Framework. Crystal Growth & Design 20, 1347–1362.
13. Gade SK, Thoen PM and Way JD. 2008. Unsupported palladium alloy foil membranes fabricated by electroless plating. Journal of Membrane Science 316:112-118.

WHEC-2022
23rd World Hydrogen Energy Conference
June 26-30, 2022 - Istanbul

#1502

DEVELOPMENT OF HYDROGEN PURIFICATION MEMBRANE BASED ON Pd-Mn-Ag TERNARY SYSTEM

[1,2*]*Mehmet Mert Köse,* [2,3]*Fatih Piskin,* [1,2]*Tayfur Öztürk*
[1] Dept. of Metallurgical and Materials Engineering, Middle East Technical University, Ankara, Turkey
[2] ENDAM, Center for Energy Storage Materials and Devices, Middle East Technical University, Ankara, Turkey
[3] Dept. of Metallurgical and Materials Engineering, Muğla Sıtkı Koçman University, Muğla, Turkey

*Corresponding author e-mail: mehmetmertkose@gmail.com

ABSTRACT

In this paper, we investigate Pd-Mn-Ag ternary system for potential alloys as separation membranes. For this purpose, thin film membranes of varying compositions were produced via magnetron sputtering. These were evaluated via four probe resistivity measurements up to temperature of 450°C. A reactivity index ρ_{H2}/ρ_{Ar} was used as a measure of the suitability of the thin film as separation membrane. Here ρ_{H2} and ρ_{Ar} are the resistivity of the film under hydrogen and argon respectively. The temperature at which this index was maximum was taken as potential operating temperature of the membrane. The preliminary results show that alloys with compositions confined to a triangle where Pd >=38 are candidates for possible hydrogen separation membrane
Keywords: Hydrogen separation, Dense metallic membranes, Palladium alloys

INTRODUCTION

Hydrogen can be produced by a variety of methods; steam reforming of methane, biomass gasification etc [1]. The resulting mixtures can contain hydrogen which would vary depending on the case. In biomass gasification, hydrogen content is not more than 40% [2]. In steam reforming of methane or coal, hydrogen is typically 75 % [3]. More recently hydrogen generated via water electrolysis from renewable sources are injected into natural gas pipelines where, the fraction in the pipeline can vary from 5 to 20%H_2 [4].

To separate hydrogen from these sources in a purity level suitable for PEM fuel cells, it is necessary to use separation membranes adapted to the process. So, for steam reforming of natural gas we need separation membranes with typical operation temperature of 350-550 oC [5]. This temperature in the case of hydrogen injected in gas pipelines are close to ambient temperatures.

PEM fuel cell requires hydrogen which should be at least 99.97% pure, free from CO (< 25 ppm) and sulfur (< 2.5 ppm) [6]. Dense separation membrane already satisfies these requirements as it would separate hydrogen which is extremely pure. Currently separation membranes in use are Pd-Ag alloys, where Pd content is more than 75%.

The current work was undertaken to investigate in Pd-Mn-Ag system so as to identify possible compositions suitable for separation purposes. Following the previous studies [7-9], the current work involves fabrication of thin film membranes via sputter deposition and fast screening of membranes via resistivity measurement.

EXPERIMENTAL

Targets used for sputter deposition were palladium, silver and manganese each in 2-inch diameter. Sputter targets were 300 mm forming an equilateral triangle, the head inclined 45°. Above the targets there were 21 glass substrates 18 mm in diameter placed in substrate magazine in triangular form mimicking the targets underneath. This would allow the deposition of thin film membranes each with a different composition. Sputtering was carried out in with an argon flow maintained at 5mTorr pressure (the base pressure was $5x10^{-8}$ Torr).

Thin film membranes are first subjected to stabilization treatment. This was carried out under argon (1 bar) by heating the membranes 2.5 °K/min to 450 °C, then holding it at that temperature for 9 hours followed by cooling with 1.6 K/min to room temperature.

Thin films were then screened via resistivity measurement. Measurements were taken with 4 probe technique using Keithley 2700 data acquisition system. The measurements are first taken under argon while heating the thin film to 450 °C (heating rate: 3K/min) and cooling it down to room temperature (1.6 K/min). At the end of experiment, argon was discharged, and hydrogen (again 1 bar) was loaded into the reactor. The measurements were then repeated with hydrogen under exactly the same heating and cooling conditions. Results were expressed in terms of

a reactivity index, i.e., ρH2/ρAr, where ρH2 and ρAr are resistance values measured under hydrogen and argon atmospheres at a given temperature.

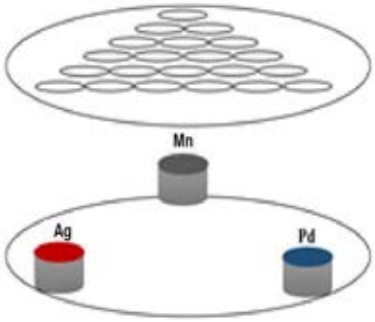
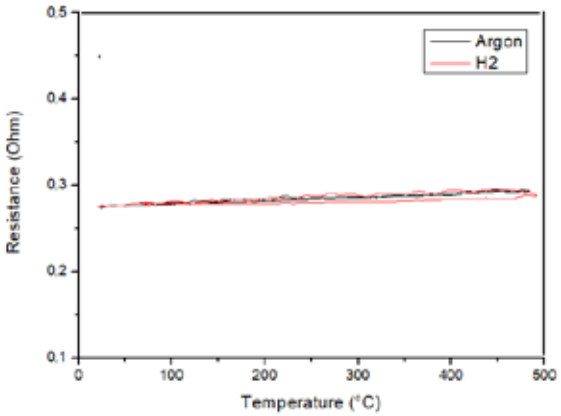


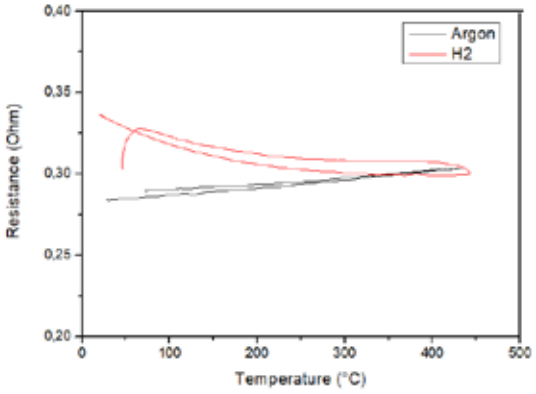
Figure 1 Schematic representation of sputter deposition of thin film membranes in combinatorial geometry

RESULTS AND DISCUSSION

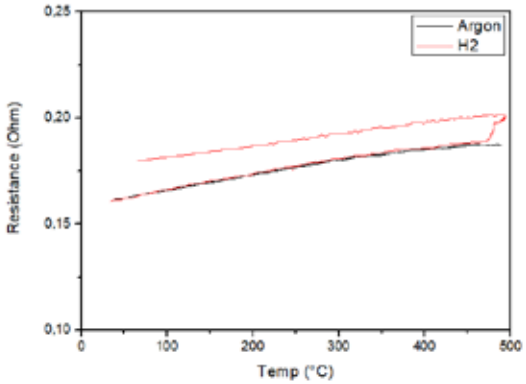
Typical examples of the resistivity curves under argon and hydrogen are given in Fig.2. Here three examples are given. Fig. 2(a) refers to Pd23Mn34Ag43 where the resistivity under argon and hydrogen traces the same curve implying that the values are the same at all temperatures. Therefore ρH2/ρAr=1 implying that the thin film does not react with hydrogen. Fig. 2(b) refers to Pd38Mn21Ag41 where resistivity under argon traces a similar curve. However, under hydrogen there is a fast rise of resistivity reaching a maximum at approx. 80oC. The resistivity then gradually decreases reaching almost the same value as that under argon at 450°C. Upon cooling the curve traces back almost the same curve and therefore continues to rise and reaches its highest value at room temperature. Fig. 2(c) is altogether a different example. This curve refers to Pd14Mn49Ag37. The curve under argon and hydrogen are almost the same up to 430°C. But the resisvity makes a jump at this temperature and continues to rise upto 450oC. Upon cooling the resistivity decreases at some distance above the argon line.



(a) Pd23Mn34Ag43



(b)Pd38Mn21Ag41



(c) Pd14Mn49Ag37

Figure 2. Resistivity curve under argon(black) and hydrogen (red) in selected thin film membranes;

a) Pd23Mn34Ag43 where ρH2/ρAr=1 at all temperatures.
b) Pd38Mn21Ag41 where ρH2/ρAr>1 reaching a maximum at T =80oC.
c) Pd14Mn49Ag37 where ρH2/ρAr>1 at T>= 430oC

A map of reactivity index is given in Fig. 3 which refers to the temperature of 300°C. The area mapped here implies that a triangle defined with Pd >=38, i.e., a triangular region close to Pd corner is the most active region in this ternary diagram. Here ρH2/ρAr> 1. The value is even higher close to Mn-Pd line.

It should be noted that Pd content of 38 at % is quite low as compared to the commercial alloy Pd77Ag23. However, these are just candidate compositions and further work is needed to see if they have acceptable hydrogenpermeability.

In this respect membranes lean in Pd content is of particular interest and provided that they have permeability values comparable to that of Pd77Ag23, they would provide a considerable saving in the cost of separation membranes.

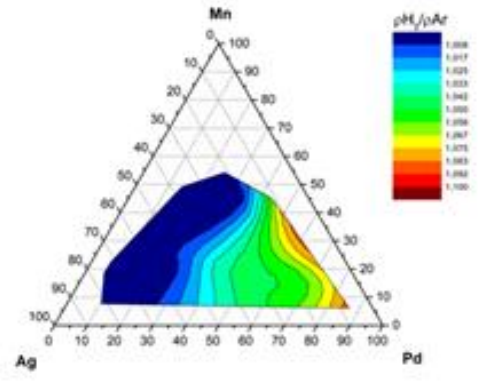


Figure 3 A map of reactivity index, ρH2/ρAr in Ag-Mn-Pd ternary system

ACKNOWLEDGEMENT

This work is supported by TUBITAK with project number 117M265, which authors gratefully acknowledge.

REFERENCES

1. Lang, Y., (2011). A Review on Hydrogen Production: Methods, Materials and Nanotechnology. Journal of Nanoscience and Nanotechnology, 11(5), 3719–3739.
2. Neubauer, Y. (2013). Biomass gasification. Biomass Combustion Science, Technology and Engineering, 106–129.
3. Neiva, L. (2010). A Study on The Characteristics Of The Reforming Of Methane: A Review. Brazilian Journal of Petroleum and Gas, 4, 119-127.
4. Melania, M. (2013). Blending Hydrogen into Natural Gas Pipeline Networks: A Review of Key Issues (Tech. No. HT12.2010). Denver, CO: NREL.
5. Iulianelli, A., (2016). Advances on methane steam reforming to produce hydrogen through membrane reactors technology: A review. Catalysis Reviews, 58(1), 1–35.
6. Engström, A. (2014). Determination of acceptable contaminant levels for PEM fuel cell stacks and poisoning mitigation strategies (Unpublished master's thesis). Sweden/ Chalmers University of Technology. Retrieved July 27, 2019.
7. Pişkin F. Akyıldız H and Öztürk T. Ti modified Pd-Ag membranes for hydrogen separation, International Journal of Hydrogen Energy, 40(2015), 7553-7558
8. Pişkin F, Öztürk T Combinatorial screening of Pd-Ag-Ni membranes for hydrogen separation, Journal of Membrane Science 524 (2017) 631–636
9. Pişkin F and Öztürk T, Nb-Pd-Ti BCC thin films for hydrogen separation, Journal of Alloys and Compounds 775 (2019) 411-418

WHEC-2022
23rd World Hydrogen Energy Conference
June 26-30, 2022 - Istanbul

#1505

ENERGY ANALYSIS OF A MEMBRANE REACTOR-BASED HYDROGEN PRODUCTION SYSTEM

[1*]*Yagmur Nalbant Atak,* [2]*C. Ozgur Colpan,* [3]*Adolfo Iulianelli*
[1] Dokuz Eylul University, School of Natural and Applied Sciences, Mechanical Engineering Department, Buca, Izmir/Turkey
[2] Dokuz Eylul University, Faculty of Engineering, Mechanical Engineering Department, Buca, Izmir/Turkey
[3] Institute on Membrane Technology of the National Research Council of Italy (CNR-ITM), at University of Calabria, Rende, Italy

*Corresponding author e-mail: yagmurnalbant.yn@gmail.com

ABSTRACT

In the present time, hydrogen is generally produced from natural gas using the conventional reactors that have some disadvantages such as thermodynamic equilibrium equation, high temperature, and carbon deposition. To overcome these disadvantages, the interest in the membrane reactors that provides both hydrogen production and hydrogen separation in the same unit is increasing, therefore the produced hydrogen is permeated from the reaction side to the permeation side continuously, and thus this decreases the thermodynamic equilibrium limitation. In this study, a mathematical model of a membrane reactor was coupled with the models of the balance of plant components (compressor, boiler, burner, pump, blower, and two mixers), and a system-level energy analysis was conducted. Molar flow rates, temperatures, and pressures for all states in the system were found. In addition, the effects of reaction temperature on H_2 production, CO_2 production, H_2 yield, and system efficiency were investigated. When the membrane reactor operating temperature increases from 673 K to 773K, the H_2 production, collected CO_2, H_2 yield, and system efficiency are increased by 9.88%, 1.48%, 9.94%, and 9.86%, respectively.

Keywords: Membrane reactor, Hydrogen production, Energy analysis

INTRODUCTION

Hydrogen can be produced by different methods (thermochemical, electrolytic, photonic, and biological processes) [1]. The mostly used method in industrial applications is the steam reforming process from natural gas. This method generally includes the use of a steam reformer, two-stage water-gas shift reactors, and a purification unit [1, 2]. In recent years, membrane reactors have attracted attention due to enabling production and separation of hydrogen in the same reactor in addition to overcoming the disadvantages of the conventional reactors such as being limited to thermodynamic equilibrium and carbon deposition problem [1, 3]. Membrane reactors can be combined with different technologies such as fuel cells or carbon dioxide capture systems. In the literature, some studies related to integration of membrane reactors with fuel cell systems can be found. However, few studies related to membrane reactor integrated with the CO_2 capture system are found. For example, Parvasi et al. [4] developed a 1-D model of a membrane reactor system that provides hydrogen production and separation for fuel cell vehicles. The results demonstrated that this system produces 5 kg/day of pure hydrogen for a 500 km range. To produce 1 kg of pure hydrogen, the total requirement amounts of methane and water were calculated as 50 kg and 70 kg, respectively. Shirasaki et al. [5] investigated a case study related to hydrogen production and CO_2 capture in Tokyo Gas Company. This company developed a large-scale membrane reactor system that has 40 Nm^3/h nominal hydrogen production capacity. The off-gas including high CO_2 concentration (90%) can easily be liquefied and captured. Therefore, this company designed and assembled CO_2 capture apparatus that includes a gas compressor, gas-liquid separator, chiller, and tank. This system was integrated with the large-scale membrane reactor system. The results showed that total CO_2 emissions for hydrogen production were reduced by 50% with only 3% energy loss. In this study, a model of a membrane reactor was integrated with the balance of plant components (compressor, boiler, burner, pump, blower, and two mixers). Energy analysis of this system was conducted and parametric analysis was doneto study the effects of membrane reactor operating temperature on the H_2 production, collected CO_2, H_2 yield, and system efficiency.

SYSTEM LEVEL MODELING

Fig. 1 shows the schematic of the membrane reactor system modeled in this study. This system includes a membrane reactor, a pump, a boiler, a compressor, mixers, and a burner. In this study, firstly, the 1-D membrane reactor model was developed and validated for 773 K using the data of the reference study [6]. After that, this membrane reactor

model was used in the system- level model. In the boiler and burner, methane and air are burned with complete combustion, and the hot product gases are used to heat the water and methane. Heated feed gas is fed to the membrane reactor and hydrogen is produced. The other gases (retentate gas) that do not pass through the membrane and enters the Mixer-2. Finally, three exhaust gases (outlet gas of boiler, outlet flue gas of burner, and the retentate gas) are mixed in the Mixer-2.

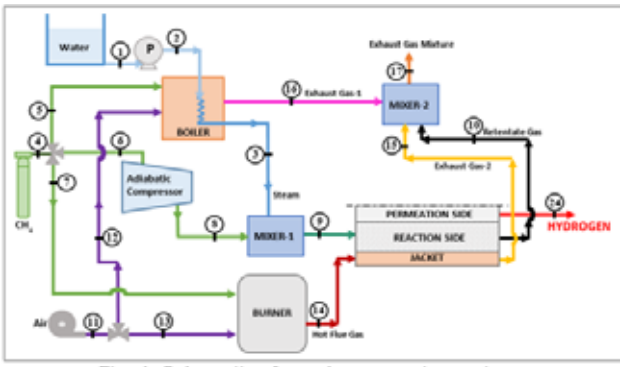


Fig. 1. Schematic of membrane reactor system

Reaction Kinetics and Hydrogen Permeation in Membrane Reactor

The membrane reactor consists of the reaction and permeation sides. On the reaction side, the feed gas enters the catalyst filled reactor after passing the Mixer-1, and three steam reforming reactions occur here. These chemical reactions are steam-methane reforming, water-gas shift, and direct steam-methane reforming reactions. Their reaction kinetic equations are given as follows:

$$R_1 = k_{0,1} exp\left(\frac{-E_1}{RT}\right)\left[P_{CH_4}P_{H_2O} - \frac{P_{H_2}^3 P_{CO}}{K_{eq,1}}\right]/\left(P_{H_2}^{2.5}\cdot DEN^2\right) \quad (1)$$

$$R_2 = k_{0,2} exp\left(\frac{-E_2}{RT}\right)\left[P_{CO}P_{H_2O} - \frac{P_{H_2}P_{CO_2}}{K_{eq,2}}\right]/\left(P_{H_2}\cdot DEN^2\right) \quad (2)$$

$$R_3 = k_{0,3} exp\left(\frac{-E_3}{RT}\right)\left[P_{CH_4}P_{H_2O}^2 - \frac{P_{H_2}^4 P_{CO_2}}{K_{eq,3}}\right]/\left(P_{H_2}^{3.5}\cdot DEN^2\right) \quad (3)$$

All coefficients used here are taken from the study of Xu and Froment [7]. Some portion of the produced H_2 in the reaction side passes through the H_2 selective membrane to the permeation side, whereas the retentate gas that does not pass through the membrane and leaves from the outlet of the reaction side. The hydrogen flux passing through the membrane is calculated by using the Sieverts-Fick Law.

$$J_{H_2} = \frac{B_{H_2}}{\delta}\left(P_{H_2,ret}^{0.5} - P_{H_2,perm}^{0.5}\right) \quad (4)$$

Mass and Energy Balance Equations for All Components

Mass and energy balance equations for steady-state conditions are given in Eqs (5) and (6). These equations are applied for all components used in this model.

$$\sum \dot{m}_i - \sum \dot{m}_e = 0 \quad (5)$$

$$\sum \dot{m}_i \cdot \left(h_i + \frac{V_i^2}{2} + gz_i\right) - \sum \dot{m}_e \cdot \left(h_e + \frac{V_e^2}{2} + gz_e\right) + \dot{Q}_{cv} - \dot{W}_{cv} = 0 \quad (6)$$

where $\dot{n}$ and MW are defined as mole flow rate (mol/s) and molecular weight (g/mole). $\bar{h}$, Q, and W are defined as specific enthalpy (J/mole), rate of heat transfer (J/s), and rate of work transfer (J/s), respectively.

RESULTS AND DISCUSSION

In this study, a system level model for a membrane reactor-based hydrogen production system was developed and the energy analysis was applied to all components. In our previous study, a 1-D model of the membrane reactor was developed and validated using the study of Alavi et al. [6], and the input parameters for the membrane reactor used in this system model were taken from this study. Then, the design and operation parameters were defined according to the membrane reactor conditions. Table 1 shows the molar flow rates, temperatures, and pressures of all states.

Table 1. Molar flow rates, temperatures, and pressures for all states at the reaction temperature of 773

State No.	Molar Flow Rate (mol/s)	Temperature (K)	Pressure (bar)	State No.	Molar Flow Rate (mol/s)	Temperature (K)	Pressure (bar)
1	444.86	400	3	10	552.45	820	10.10
2	444.86	400.32	29.29	11	7440.50	865.88	10.10
3	444.86	930.25	29.29	12	2232.10	865.88	10.10
4	347.22	400	10.10	13	5208.30	865.88	10.10
5	104.17	400	10.10	14	4427.10	950	10.10
6	138.89	400	10.10	15	4427.10	951.88	10.10
7	104.17	400	10.10	16	2075.90	1168.50	10.10
8	138.89	503.97	29.29	17	7055.40	1002.90	10.10
9	612.93	773	29.29				

Effect of Reaction Temperature

Table 2 shows the effect of reaction temperature on the molar flow rate of produced H_2 and collected CO_2, H_2 yield, and system efficiency. When the temperature increases, the molar flow rates of produced H_2 and collected CO_2 increase. The reason for the increase in H_2 production is that the higher hydrogen permeating flux occurs with the increasing temperature. Moreover, temperature affects the reaction rates of the reforming reactions. When the temperature increases, the reaction kinetics increase, and thus the amount of CO_2 in the retentate gas increases. Consequently, temperature has a positive effect on the system efficiency and hydrogen yield.

Table 2. Calculated values of some variable according to the changing reaction temperature at 29.29 bar reaction pressure

Variable	Calculated Values		
	T=673 K	T=723 K	T=773 K
Molar Flow Rate of Produced H_2 at State 24 (mol/s)	150.80	158.08	165.71
Molar Flow Rate of Collected CO_2 at State 17 (mol/s)	262.52	264.43	266.41
Hydrogen Yield, η_{H_2}, (%)	43.43	45.53	47.75
System Efficiency, η_{system}, (%)	13.07	13.70	14.36

CONCLUSIONS

In this study, the energy analysis of this system was conducted and parametric analysis was done to study the effects of membrane reactor operating temperature on the H_2 production, collected CO_2, H_2 yield, and system efficiency. The results showed that when the temperature increases, the rates of produced H_2 and collected CO_2, H_2 yield, and system efficiency increase. When the membrane reactor operating temperature increases from 673 K to 773 K, the H_2 production, collected CO_2, H_2 yield, and system efficiency are increased by 9.88%, 1.48%, 9.94%, and 9.86%, respectively. The best molar flow rates of produced H_2 and collected CO_2 were found as 165.71 mol/s and 266.41 mol/s, respectively, at 773 K and 29.29 bar. In a future study, this system can be integrated with a HT-PEMFC system and its energy and exergy analyses can be conducted.

ACKNOWLEDGEMENT

This work has been supported by Dokuz Eylul University's Scientific Research Projects with the project number 2019.KB.FEN.022.

REFERENCES

1. Nalbant Atak, Y., Colpan, C. O., & Iulianelli, A. 2021. A review on mathematical modeling of packed bed membrane reactors for hydrogen production from methane, International Journal of Energy Research, 45(15): 20601-20633.
2. Adolf, J., Balzer, C. H., Louis, J., Schabla, U., Fischedick, M., Arnold, K., ... & Schüwer, D. 2017. Energy of the future: Sustainable mobility through fuel cells and H2; Shell hydrogen study.
3. Lu, N., & Xie, D. 2016. Novel membrane reactor concepts for hydrogen production from hydrocarbons: a review, International Journal of Chemical Reactor Engineering, 14:1-31.
4. Parvasi, P., Mohammad Jokar, S., Basile, A., & Iulianelli, A. 2020. An on-board pure H2 supply system based on a membrane reactor for a fuel cell vehicle: A theoretical study. Membranes, 10(7), 159.
5. Shirasaki, Y., & Yasuda, I. 2013. Membrane reactor for hydrogen production from natural gas at the Tokyo Gas Company: A case study. In Handbook of membrane reactors, 487-507, Woodhead Publishing.
6. Alavi, M., Eslamloueyan, R., & Rahimpour, M. R. 2018. Multi objective optimization of a methane steam reforming reaction in a membrane reactor: considering the potential catalyst deactivation due to the hydrogen removal. International Journal of Chemical Reactor Engineering, 16(2).

WHEC-2022
23rd World Hydrogen Energy Conference
June 26-30, 2022 - Istanbul

#1559

PARAMETRIC INVESTIGATION ON THE PURIFICATION CHARACTERISTICS OF $La_{0.9}Ce_{0.1}Ni_5$ UNDER VARIOUS ABSORPTION/DESORPTION CONDITIONS

[1] *Alok Kumar*, [2*] *P Muthukumar*
[1]School of Energy Science and Engineering, Indian Institute of Technology Guwahati, Guwahati, Assam 781039, India
[2]Department of Mechanical Engineering, Indian Institute of Technology Guwahati, Guwahati, Assam 781039, India

[*]Corresponding author e-mail: pmkumar@iitg.ac.in

ABSTRACT

Metal hydride-hydrogen system can provide efficient solution for hydrogen separation from the impure gas mixtures. The present study reports the effect of various absorption/desorption conditions on the hydrogen separation and alloy poisoning characteristics of $La_{0.9}Ce_{0.1}Ni_5$. The experiments is being conducted by varying absorption pressure in the range of 5-20 bar, absorption temperature between 20-30 °C and desorption temperature between 60-90 °C. According to the experimental outcomes, absorption kinetics improves with increase in the absorption pressure and decrease in the absorption temperature. For 20 bar and 20 °C, 12.8232 g of hydrogen get absorbed for 10% impure gas mixture. The desorption temperature played a significant effect on the bed poisoning characteristics of the reactor bed. Desorption kinetics improves with increase in the bed temperature, and is significant for 80-90 °C. For lower range of desorption temperature (60-70 °C), the bed poisoning was significant. Even for 10% impurity, the reaction kinetics of alloy decreases significantly after 4-5 purification cycle. However, for higher desorption temperature (90 °C), the alloy regenerated itself and the bed poisoning is delayed. The system is capable of delivering 99.9995% pure hydrogen for an impurity range from 5-15% for gaseous impurities like CO_2, CH_4, N_2, Ar etc.

Keywords: Metal hydride, Hydrogen storage, Hydrogen purification, Alloy poisoning, Alloy regeneration

INTRODUCTION

In order to restrict the global rise in the temperature within 1.5 °C, the world is shifting their energy dependency to renewables like, wind, solar, hydro, hydrogen etc. Hydrogen is available in plenty in the form of hydrocarbons and chemical compounds; however, it has to be extracted through certain processes for the end user application. However, in most of the extraction processes, the hydrogen delivery is not 100% pure [1]. Hence, it becomes essential to purify hydrogen for end user application. There are several well established hydrogen purification techniques such as membrane diffusion, pressure swing adsorption, cryogenic separation, catalytic purification, metal hydride based purification, etc. available for hydrogen purification from gas mixture (hydrogen & other gases) of different impurities level, [1-4]. In comparison to different purification techniques, metal hydride (MH) based hydrogen purification technique is the simplest one to purify/separate hydrogen through thermally driven procedure, wherein the purification process is accomplished in three simple steps, i.e. absorption, flushing and desorption [5].

Schweppe et al. [6] reported the poisoning effect of O_2, CO_2, H_2S, CO or N_2 gases on $LaNi_5$ alloy used for hydrogen storage application. They used Sieverts apparatus, which was attached with a diffusion pump, to perform experimental studies related to reactor activation, absorption and alloy poisoning. It was observed that the presence of N_2 in the void space of the reactor, did not affect the rate of hydrogen absorption at all, while for the other prefilled gases, the initial rate of reaction got reduced by a range of 2 times to 10 times. However, O_2 critically damaged the absorption characteristics of the alloy by forming an oxide layer on the surface of $LaNi_5$ alloy. Similarly, Oztek [7] tested Mg_2Ni, VTiNi and $LaNi_5$, as a separation platform to purify hydrogen from a mixture of hydrogen and helium. Considering the reversible characteristics of $LaNi_5$ on interaction with the mixture, it was considered as suitable alloy for hydrogen separation. Further, Lin et al. [8] explored $LmNi_{4.8}Al_{0.2}$ alloy from AB_5 group of alloys, and studied its anti-poisoning characteristics for hydrogen storage application. The alloy was activated in the presence of pure hydrogen, and then they were exposed to CO and H_2S, each 1000 ppm as impurity with pure hydrogen. The poisoning effect of CO was more dominating as compared to H_2S.

Several studies have been reported on bed poisoning and hydrogen separation through metal hydride systems. However, the studies related to optimizing the operating parameters for a particular metal hydride and alloy regeneration are lagging in the literature. This motivates for the present study, wherein the hydrogen purification parameters and alloy regeneration has been discussed for $La_{0.9}Ce_{0.1}Ni_5$.

EXPERIMENTAL SETUP

The experimental setup was developed to carry out detailed purification study on the $La_{0.9}Ce_{0.1}Ni_5$ based MHHPS, wherein the impure sample preparation, absorption of impure mixture, flushing, desorption and sample collection for gas chromatography were carried out using a single gas circuit of specific configuration, as depicted in Fig. 1. The experimental setup mainly comprised of a MH reactor of embedded cooling tube (ECT) design with 6 ECT, Coriolis mass flowmeter to record amount of gas transferred, high & low temperature recirculating baths, vacuum pump, valves & fittings for gas and HTF circuit, gas cylinders, gas regulators, gas chromatograph and data acquisition system.

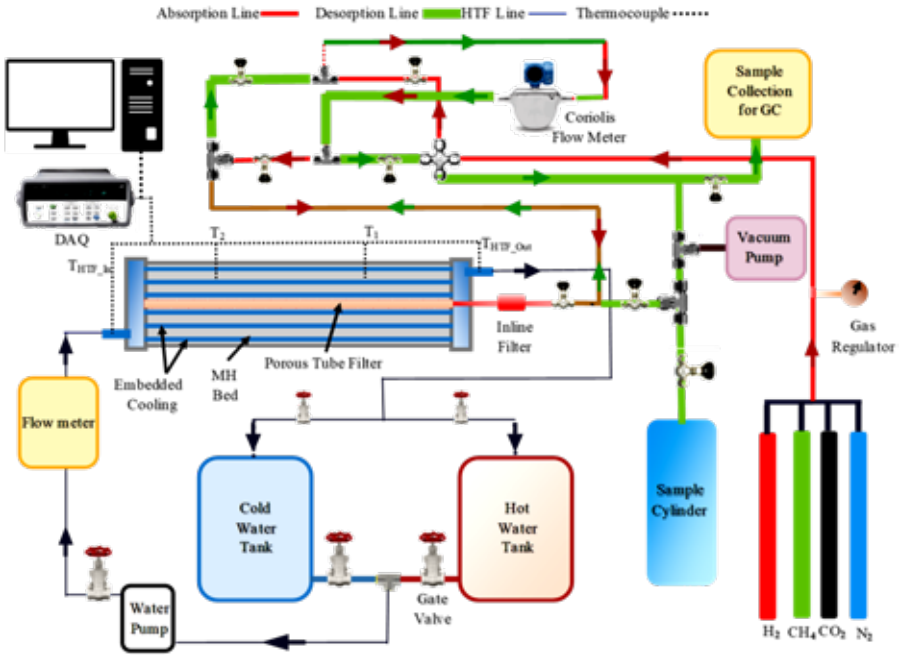


Fig. 1. Schematic of experimental test setup

REACTOR ACTIVATION AND EXPERIMENTAL PARAMETERS

Table 1. Experimental Parameters

Type of Study	Half Cycle	Operating parameters	Value
Parametric Study with Impure Hydrogen	Absorption	Supply pressure (P_s)	5, 10, 15 and 20 bar
		Absorption temperature (T_a)	20, 25 and 30 °C
		HTF flow rate	4 lpm
		Impurity level	5%, 10%, 15%
	Desorption	Desorption temperature (T_d)	60, 70, 80 and 90 °C
		HTF flow rate	4 lpm
	Purification Cycle	No. of Cycle	25 Cycle

Parametric studies with impure hydrogen was performed to obtain optimum absorption, desorption and flushing temperatures. The experimental parameter is summarised in Table 1. Before activation, the reactor was tested with argon gas at 80 bar to ensure leak proof system. Further, it was heated up to 90 °C, and evacuated up to 0.02 mbar to ensure no moisture was present in the alloy bed. The reactor activation was performed at hydrogen supply pressure (P_s) of 30 bar and 25 °C absorption temperature (T_a). In the first activation cycle, 14.4501 g hydrogen was absorbed in 527 s, while the peak bed temperature recorded was around 44 °C. Considering slow reaction kinetics, reactor was again evacuated keeping the bed at 90 °C. Further, the activation cycle was repeated 3 times to ensure the complete activation of the MH bed, where in amount of hydrogen absorbed was recorded as 15.4484 g, 15.8293 g & 15.5207 g, respectively in 2nd, 3rd and 4th activation cycle, with absorption time of 190 to 200 s. The repeatability in the amount of hydrogen absorbed and bed temperature variation during 2nd, 3rd and 4th activation cycle presented in Fig. 2, depicts the successful activation of the MH reactor with 1.2 kg of $La_{0.9}Ce_{0.1}Ni_5$, having storage capacity of 1.32 wt.%. The uncertainties in the experimental measurements were estimated using the method adopted by Moffat J Robert [8]. The uncertainties in measuring HTF flow rate and H_2 supply pressure were ± 1.67% and ± 3.0%, respectively, while the uncertainty in assessment of H_2 storage capacity was ± 2.5%. The error in the thermocouple reading was recorded ± 0.5 °C.

The detailed study and experimental outcomes will be reported in the full manuscript.

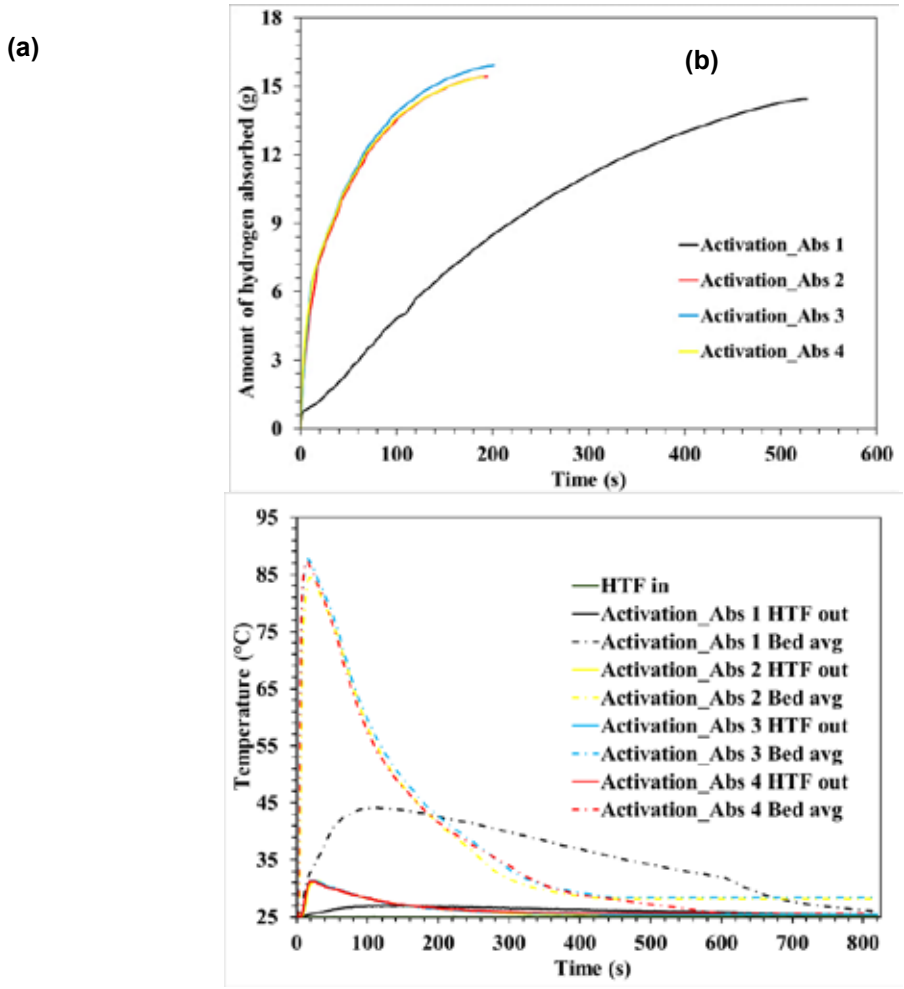


Fig 2. (a) Amount of hydrogen absorbed during each activation cycle, and (b) the average bed and HTF temperature variation for respective activation cycle.

ACKNOWLEDGEMENT

The authors acknowledges DST-Government of India, for their financial support through project no. DST/TMD/MECSP/2k17/14(C).

REFERENCES

1. Grashoff GJ, C.E. Pilkington CE and Corti CW. 1983. Purification of Hydrogen. *Platin. Met. Rev.* 27: 157–169.
2. Chenv XY, Wei LX, Deng L, Yang FS and Zhang ZX. 2014. A review on the metal hydride based hydrogen purification and separation technology. *Appl. Mech. Mater.* 448–453: 3027–3036.
3. Bhuiya MMH, Kumar A and Kim KJ. 2015. Metal hydrides in engineering systems, processes, and devices: A review of non-storage applications. *Int. J. Hydrogen Energy*. 40: 2231–2247.
4. Ngene P, Longo A, Mooij L, Bras W and Dam B. 2017. Metal-hydrogen systems with an exceptionally large and tunable thermodynamic destabilization. *Nat. Commun*. 8.
5. Muthukumar P, Kumar A, Raju NN, Malleswararao K and Rahman MM. 2018. A critical review on design aspects and developmental status of metal hydride based thermal machines. *Int. J. Hydrogen Energy*. 43: 17753–17779.
6. Schweppe F, Martin M and Fromm E. 1997. Hydrogen absorption of $LaNi_5$ powders precovered with O_2, CO, H_2S, CO_2 or N_2. *J. Alloys Compd.* 253–254: 511–514.
7. Oztek MT. 2005. Recovery of hydrogen and helium from their mixtures using metal hydrides. *Thesis, Master Sci. Univ. Cent. Florida Orlando*, Florida.
8. Moffat RJ. 1988. Describing the Uncertainties in Experimental Results. *Exp. Therm. Fluid Sci*. 1: 3–17.

WHEC-2022
23rd World Hydrogen Energy Conference
June 26-30, 2022 - Istanbul

#1566

INVESTIGATION OF LOW-TEMPERATURE POLYMER ELECTROLYTE MEMBRANE FOR ELECTROCHEMICAL HYDROGEN COMPRESSOR

[1,2]*Anil Can Turkmen, [3]Ceyda Elif Meydan, [3]Kubranur Agtoprak, [4]Hilal Acidereli [3]Ramiz Gultekin Akay , [3]Murat Efgan Kibar, [1]Cenk Celik

[1]Kocaeli University Faculty of Engineering, Department of Chemical Engineering, Kocaeli 41380, Turkey
[2]ACT Scientific Ltd., Budotek Teknopark, Istanbul, 41380, Turkey

[3]Kocaeli University Faculty of Engineering, Department of Mechanical Engineering, Kocaeli 41380, Turkey
[4]Dumlupınar University, Faculty of Arts & Sciences, Department of Chemistry, Kütahya, 43266, Turkey

*Corresponding author e-mail: anilcan.turkmen@hotmail.com

ABSTRACT

In recent years, one of the most important sources used as fuel for energy production is hydrogen. Especially, research in hydrogen technologies has gained importance with the increase in commercialization applications of fuel cells. When it comes to the development of hydrogen technologies, it is of great importance to carry out studies in the field of purification and storage of hydrogen as well as production methods. Considering the disadvantages of conventional compressors, which are widely used in the world, electrochemical hydrogen compressor technology that can pressurize hydrogen with an electrochemical method is the best alternative. In this study, the development of low-cost, long-life materials and compressor systems for the compression of hydrogen were investigated. In this study, Nafion 117 membrane and commercial Pt/C electrocatalyst were tested in the EHC system.

Keywords: Hydrogen, Polymer electrolyte membrane, Electrocatalyst, Pressurization, EHC, Compression

INTRODUCTION

Considering the increase in energy need and the problems experienced with the consumption of fossil fuels, the alternative energy source to be used should be both environmentally friendly and sustainable. Researches conducted for this purpose have highlighted hydrogen technologies as the most important candidate for energy production. Nowadays, for the sustainability of hydrogen technologies, medium and long-term policies based on hydrogen are prepared in many countries as well as the most developed countries, and detailed studies are carried out for their implementation. Within the scope of these studies, the evaluation of the existing methods used in all stages from the production of hydrogen to its purification and storage, elimination of deficiencies, and the development of new methods are important for ensuring integrity in this field.

Lee et al. tested the Nafion 115 membrane in the EHC system to purify H_2 from the reformate mixture. They operated the system between 30-70 ^oC and 1-3 atm supply pressure. They found that hydrogen purity increased with applied current and temperature [1].

Rohland et al. investigated an electrochemical compressor to increase the cathode pressure to 43 bar in a study. In their research, the surface area of the electrode is 100 cm2 and they used Nafion 117 as the membrane. They measured the cathode pressure at current densities of 100 to 150 mA cm−2. The results showed that increasing current density leads to a higher hydrogen flow rate at the cathode side [2].

MATERIALS AND METHODS

MATERIALS

Commercial Nafion 117, Sulfuric acid (Sigma, 97%), Hydrogen peroxide (Sigma, 35%), Nafion solution (Alfa Aesar, 5 wt. %), Commercial Pt/C (Fuel cell store, 20% wt.), Isopropyl alcohol (Merck,99.8%).

METHODS

Membrane conditioning procedure; Nafion 117 membrane was kept in 3% H_2O_2 boiling at 80 °C for 1 hour. It was then rinsed with water and kept in boiling water for 2 hours. Then it was kept in 0.5 M H_2SO_4 for 1 hour. Finally, it was rinsed in deionized water boiling between 80-90 °C.

Preparation of catalyst ink; the water was added to the commercial Pt/C catalyst and mixed ultrasonically, and then Nafion ionomer was added and subjected to ultrasonic treatment again. 2-propanol was added as the solvent and mixed ultrasonically. A homogeneous ink solution was obtained.

20% Pt/C catalyst was used as both anode and anode catalyst. The amount of anode and cathode catalyst coating is equal and is 0.4 mg/cm^2. The anode side hydrogen feed is 0.2 ml/min and 1 bar. Cell operating temperature is 30°C. Hydrogen was fed with 100% moisture.

The electrochemical hydrogen pump test system and cell are given in Figure 1. The anode side output is open to the environment. At the cathode side output, pressure measurement is made with both a manometer and a pressure sensor. The cathode outlet pressurization is set by the backpressure regulator and at the same time, the outlet flow is measured with a flow meter.



Fig. 1. Electrochemical hydrogen pump test system and cell

RESULTS AND DISCUSSION

The polarization curve of the test results is given in Figure 2. In Figure W, the pressure-flow rate performance of the system is given. As can be seen from the curves, hydrogen at a value of 0.17 A/cm^2@0.75V began to pass from the anode to the cathode. In the meantime, since the set value of the backpressure regulator was 0, the hydrogen was ejected freely and the cathode side was not pressurized.

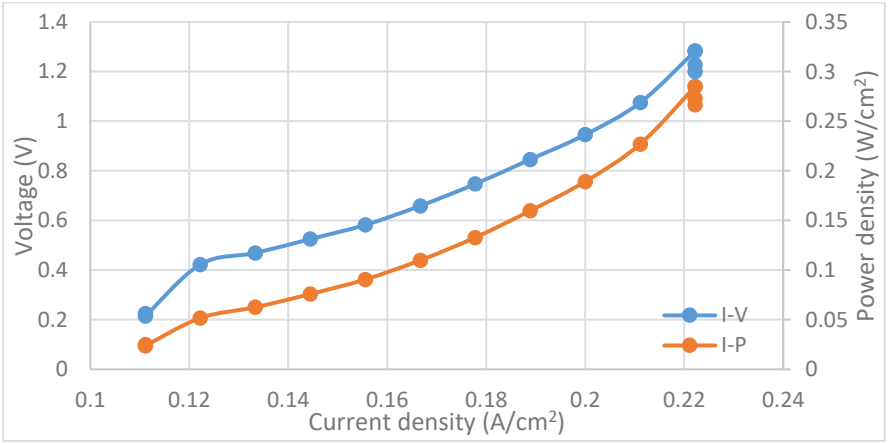


Fig. 2. Polarization curve

When the backpressure regulator value is set to 2 bar, the output flow rate is reduced to 0 and the cathode is pressurized. While the current value was 0.22 A/cm^2, the cathode pressure value reached 1.38 bar.

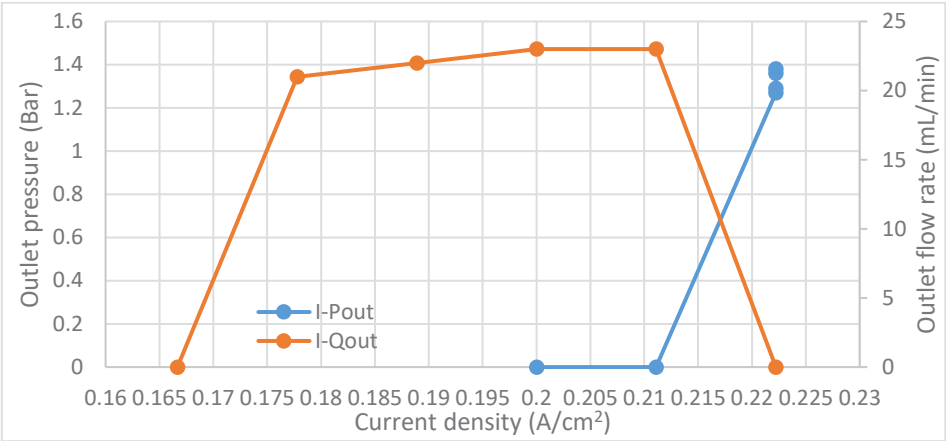


Fig. 3. Pressure-flow rate curve

CONCLUSIONS

In the study, electrochemical hydrogen pump tests were carried out using commercial Nafion 117 membrane and 20% Pt/C catalyst. In these tests carried out at room temperature, the cathode pressure value was increased by 1.38 times compared to the inlet pressure, despite the use of a catalyst with a low metal percentage. Unlike the tests generally done in the literature, the open cathode was used and both the output flow rate and the pressure value were measured simultaneously. 11.5% of the inlet flow could be transferred to the cathode side. It is predicted that when the temperature value is increased, both the output pressure and the output flow performance will increase. However, the long line at the cathode outlet reduces the rate of increase in pressure.

ACKNOWLEDGEMENT

This project is supported by Tübitak with the project code 218M806.

REFERENCES

1. Lee, H.K, Choi, H.Y., Choi, K.H., Park, J.H., Lee, T.H. 2004. “Hydrogen separation using electrochemical method”, Journal of Power Sources, 132, 92-98.
2. Rohland, B., Eberle, K., Ströbel, R., Scholta, J., & Garche, J. (1998). Electrochemical hydrogen compressor. Electrochimica acta, 43(24), 3841-3846.

WHEC-2022
23rd World Hydrogen Energy Conference
June 26-30, 2022 - Istanbul

#1580

EVALUATION OF THE EFFECT OF TEMPERATURE, AIR EXPOSURE AND GAS MIXTURE ON Pd_{82}-Ag_{15}-Y_3 FOR HYDORGEN SEPARATION

[1]Omid Jazani, [1]Moses Adejumo, [1] Simona Liguori*
[1]Chemical and Biomolecular Engineering Dept, Clarkson University, Potsdam, NY, USA

*Corresponding author e-mail: sliguori@clarkson.edu

ABSTRACT

Hydrogen permeation and separation properties of a ternary Pd-alloy are evaluated at temperature and pressure range of 300 °C and 600 °C and 2 – 5 bar (abs), respectively. The membrane Pd_{82}-Ag_{15}-Y_3 is unsupported, prepared by cold rolling and it is characterized by ~ 35 µm of thickness. The membrane shows good thermal and chemical stability when exposed to air and at different temperature. In particular, its surface area increases by 2.5x from room temperature to 600 °C indicating a potential improvement of hydrogen permeation. The permeation characteristics of the membrane and the effects of the other gases on hydrogen permeation will be investigated by varying temperature and pressure evaluating the effects of dilution, depletion, concentration polarization, and competitive adsorption on the H_2 permeating flux.

Keywords: Ternary alloy membrane, Pd-based, Hydrogen separation

INTRODUCTION

In the view of a significant reduction of greenhouse gases emissions amidst fossil fuel exploitation, the use of sustainable energy sources is a mandatory option as well as the use of alternative fuels for the transportation sector. In this context a strong interest has been addressed towards the possible development of a global 'hydrogen economy', by considering hydrogen as the energy carrier of the future and as reliable fuel source for transportation. Currently, hydrogen is mainly produced by the methane steam reforming, which is an energy-intensive process emitting approximately 9 $kgCO_2/kg_{H2\text{-}produced}$ [1]. Alternatively, highly pure hydrogen can be produced in a membrane reactor (MR), which can be implemented at lower operating conditions than conventional reactors. The MR has the co-benefits to produce a stream mainly composed by CO_2, which can be easily captured, thus generating blue hydrogen [2-3]. In this contest, the membrane plays the main role. Dense metal membranes are commonly used for high purity hydrogen separation due to their unique characteristic of being completely selective toward hydrogen permeation and the most metal used for this approach is palladium. Pure Pd membranes have shown great potential for their application to H_2 separation at high temperature. However, they are affected by problems such as the embrittlement, deposition of carbonaceous impurities, and poisoning by CO and H_2S, which often result in a mechanical failure of the membrane and in low chemical stability [4]. It has been reported that the use of Pd-alloy membranes (mainly Pd-Ag, Pd-Cu and Pd-Au) decrease these issues and even increase the permeability of H_2 compared to pure Pd [5-7]. The Pd-Ag alloy system is the most widely studied. It is a stable alloy with face centered cubic (FCC) structure, which reduces the temperature for metallic hydride formation, which causes hydrogen embrittlement and affecting membrane permeability. However, although considerably better than pure palladium, Pd-Ag still has relatively low strength and expands significantly on hydrogen absorption [5]. So, the development of Pd-Ag-based ternary alloys aims to improve these challenges. In this study, a self-supported Pd_{82}-Ag_{15}-Y_3 membrane has been considered, where yttrium was added to improve the permeability characteristics of the membrane and increase its strength.

In this work, the effects of temperature, air exposure, and several gases on the H_2 permeation flux are studied in detail. In particular, the negative effects (concentration polarization, dilution, depletion, and competitive adsorption on the Pd surface) through which each gas can reduce the H_2 permeating flux are analyzed by performing permeation tests of binary mixtures of H_2 with He, Ar, N_2, CH_4, CO, CO_2, and H_2O. Next, the study is extended to ternary and quaternary mixtures to explore the cumulative gases effects on the H_2 permeating flux. Scanning electron microscopy (SEM), energy dispersive system (EDS) and atomic force microscopy (AFM) were performed on the pristine and used membrane to characterize the membrane.

MATERIALS AND METHODS

Disc foils of Pd_{82}-Ag_{15}-Y_3 with a diameter of 25.4 mm were used for this work. The thickness of the membrane was approximately 35 µm. The membrane was self-supported and prepared by cold-rolled technique. The total active area corresponds to approximately 1.79×10^{-4} m^2. Figure 1 shows the details of the membrane module. A porous disc made of Hastelloy-X with a pore size of 0.2 µm is placed on the hole of the membrane module to mechanically support the

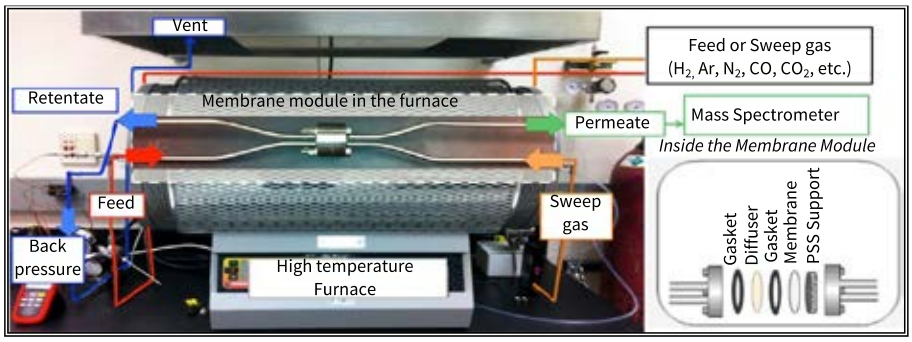


Figure 1. System for testing metallic membranes

membrane foil and it is placed in a custom-made membrane module. The membrane module is sealed with two graphite gaskets, between which a diffuser (alumina fiber, APA-3, Zircar Ceramics) is placed to evenly distribute the gas flow onto the membrane. The membrane module was heated using a Carbolite oven and the temperature was monitored via a K-type thermocouple (Omega Engineering) housed on the retentate side of the membrane system.

The operating temperature are varied between 300 °C and 600 °C, while retentate pressures are changed between 2 bar (abs) and 5 bar (abs). The permeate pressure is kept constant at 1 bar (abs). The gases such as H_2, He, Ar, N_2, CH_4, CO, CO_2, are regulated and supplied to the system via Aalborg GFC17 thermal mass flow controllers, while H_2O is supplied by a peristaltic pump. A HP 7890 GC is utilized for analyzing the permeate stream. Before beginning the testing, the GC is calibrated using the standard addition method [8] in order to obtain accurate molar compositions for the permeate stream.

The permeating characteristics of the membrane are evaluated by the hydrogen permeating flux through the membrane – when pure hydrogen and mixtures are fed. The ideal selectivity is also analyzed to measure the extent of membrane selectivity toward hydrogen.

RESULTS AND DISCUSSION

The effect of temperature and air treatment on the Pd_{82}-Ag_{15}-Y_3 membrane are investigated to evaluate the stability of the membrane. In particular, temperature was varied from 300 °C and 600 °C while exposing the membrane to the air.

Figure 2 shows the SEM images of the Pd_{82}-Ag_{15}-Y_3 membrane at different temperatures. Cracks and polishing lines are present on the surface of the membrane and the cracks increased by increasing the temperature. These surfaces defects are due to the production method, and they are emphasized during the temperature increase. The EDS analysis indicates that the membrane surface was affected by oxygen and the amount of oxygen increased with the increasing of the temperature. However, as reported by literature the formation of some oxides can increase the hydrogen permeation flux [9] due to the membrane morphology change (AFM).

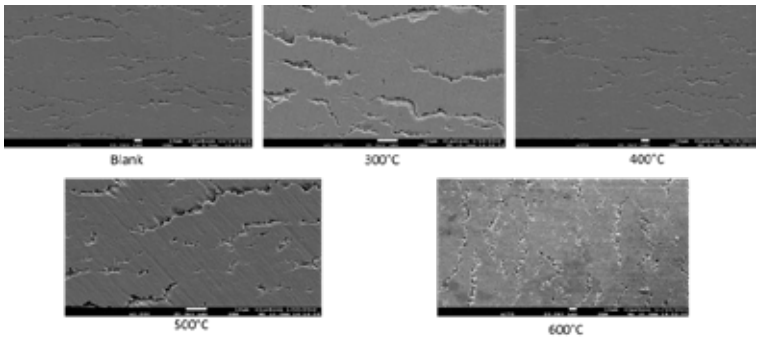


Figure 2. SEM analysis of Pd_{82}-Ag_{15}-Y_3 membrane at different temperature.

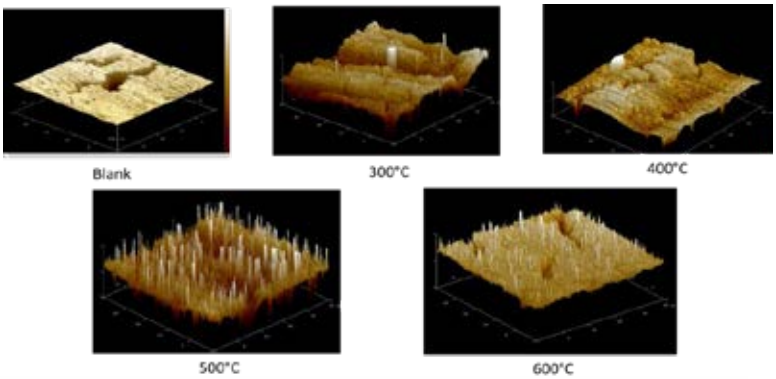


Figure 3. 3D AFM images of Pd_{82}-Ag_{15}-Y_3 membrane at different temperature.

The surface and morphology of the Pd_{82}-Ag_{15}-Y_3 membrane were evaluated by the AFM. In figure 3, the 3D AFM images of the membrane is shown. It is possible to note that the roughness of the membrane as well as the surface area increase with the increasing of the temperature. In particular, the surface area improved from 271 μm^2 at 300 °C to 625 μm^2 at 600 °C. It is worth mentioning that the cracks participated in calculating the roughness. It is postulated that more peaks and active areas enhances the hydrogen permeation. So, it can be concluded that if the membrane will show a decline in performance, an air treatment at high temperature can be performed to restore the initial permeation characteristics of the membrane.

The next step will be the evaluation of the permeation characteristics of a ternary Pd-alloy membrane at different temperatures and pressures, such as 300 – 600 °C and 2 – 5 bar, respectively. Additionally, the effect of concentration polarization, dilution, and competitive adsorption on hydrogen permeation is analyzed in the presence of other gases. Finally, the membrane will be characterized by SEM, EDS, AFM and X-ray diffraction (XRD) analysis.

CONCLUSIONS

A self-supported ternary Pd-alloy membrane, i.e. Pd_{82}-Ag_{15}-Y_3, was used in this work to analyze the effect of temperature, air exposure and mixture gases on H_2 permeation. Initial testing was performed to investigate the stability of the membrane in presence of air at different temperature. The SEM shows that the membrane is affected by superficial cracks, which increase with the temperature increasing, while the EDS shows the formation of some oxides on the surface. However, the formation of oxides and the presence of cracks on the surface can paradoxically increase the hydrogen permeation flux due to the membrane morphology change. Indeed, AFM analysis shows an increase of surface area by 2.5x, which indicates a potential increase of the hydrogen permeation.
The effect of the gas mixture on hydrogen permeation through the ternary membrane will be studied in detail at different temperature and pressure. If the membrane will show a decline in performance, an air treatment at high temperature will be performed to restore the initial permeation characteristics of the membrane.

REFERENCES

1. Sun, Pingping, and Amgad Elgowainy. "Updates of hydrogen production from SMR process in GREET® 2019." Argonne National Laboratory (2019).
2. Iulianelli, A., Liguori, S., Wilcox, J., & Basile, A. (2016). Advances on methane steam reforming to produce hydrogen through membrane reactors technology: A review. Catalysis Reviews, 58(1), 1-35.
3. Kian, K., Woodall, C. M., Wilcox, J., & Liguori, S. (2018). Performance of Pd-based membranes and effects of various gas mixtures on H2 permeation. Environments, 5(12), 128.
4. Mendes, D.; Mendes, A.; Madeira, L. M.; Iulianelli, A.; Sousa, J. M.; Basile, (2010) A. The Water-Gas Shift Reaction: From Conventional Catalytic Systems to Pd-Based Membrane Reactors- A Review. Asia-Pacific J. of Chemical Eng., 5 (1), 111–137.
5. Paglieri, S. N.; Way, J. D. INNOVATIONS IN PALLADIUM MEMBRANE RESEARCH. Separation and Purification Methods 2002, 31 (1), 1–169.
6. Howard, B. H.; Killmeyer, R. P.; Rothenberger, K. S.; Cugini, A. v.; Morreale, B. D.; Enick, R. M.; Bustamante, F. (2004) Hydrogen Permeance of Palladium-Copper Alloy Membranes over a Wide Range of Temperatures and Pressures. Journal of Membrane Science, 241 (2), 207–218.
7. Gade, S. K.; DeVoss, S. J.; Coulter, K. E.; Paglieri, S. N.; Alptekin, G. O.; Way, J. D. (2011) Palladium–Gold Membranes in Mixed Gas Streams with Hydrogen Sulfide: Effect of Alloy Content and Fabrication Technique. Journal of Membrane Science, 378 (1–2), 35–41.
8. Saxberg B.E., Kowalski B.R., (1979) Generalized standard addition method, Anal. Chem. 51, 1031–1038.
9. Zhang, Ke, Sabina K. Gade, and J. Douglas Way. (2012). Effects of heat treatment in air on hydrogen sorption over Pd–Ag and Pd–Au membrane surfaces. Journal of membrane science, 403, 78-83.

WHEC-2022
23rd World Hydrogen Energy Conference
June 26-30, 2022 - Istanbul

#1583

OVERVIEW OF ELECTROCHEMICAL HYDROGEN PURIFIER PERFORMANCE DIAGNOSTICS

[1,2,3*] *Anamarija Stoilova Pavasovic,* [1,2] *Ivan Pivac,* [1,2] *Frano Barbir*
[1] Center of Excellence STIM, R. Boskovica 31, Split, Croatia
[2] University of Split, FESB, R. Boskovica 32, Split, Croatia
[3] University of Split, KTF, R. Boskovica 35, Split, Croatia

*Corresponding author e-mail: astoilov@fesb.hr

ABSTRACT

The energy world is moving beyond fossil fuels and should power our entire society with clean energy in the future. For hydrogen to become a widespread energy carrier that can provide an emissions-free transportation fuel, it must be produced from the clean energy sources. Therefore, clean hydrogen production and storage is currently undergoing extensive research. However, none of the present widely-use hydrogen production processes, besides electrolysis, are sufficiently pure to enable immediate use of hydrogen as an energy carrier in fuel cells or in storage. Therefore, purification of hydrogen is mandatory, especially on a large scale. This paper gives a brief literature overview of the current state-of-the-art electrochemical hydrogen purifiers (EHPs), with emphasis on their performance diagnostics, including current technology issues, challenges, and different approaches with suggestions for potential solutions and improvements in future.

Keywords: electrochemical hydrogen purifier, performance diagnostics, polarization curve, electrochemical impedance spectroscopy, gas chromatography

INTRODUCTION

The most likely application of electrochemical hydrogen purifier (EHP) is the purification of hydrogen gas commonly produced by reforming gas streams, coal gasification, and other large-scale hydrogen productions from oil and biomass sources. Most industrial techniques of hydrogen post-treatment upon production use different purification steps, such as condensation of impurities (cryogenic processes), adsorption of impurities (pressure-swing adsorption), or using a perm-selective membrane (a membrane separation process) to remove hydrocarbon residues from hydrogen mixture fuels [1]. However, EHP enables hydrogen purification in only one step, with the theoretical possibility of simultaneous compression as well. Furthermore, besides their silent work due to lack of moving parts, EHP offers numerous advantages, such as its scalability, instant remote control-ability, high-purity hydrogen in only one step operation at low cell voltages (up to 0.5 V) with a high separation efficiency compared with classical technologies currently used in industrial scale [2,3]. The most common pollutants of hydrogen can be as follows: a small percentage of inert gases, such as nitrogen (N_2) or argon (Ar), methane (CH_4), carbon dioxide (CO_2) and monoxide (CO), ammonia (NH_3), and sulphur impurities. For instance, inert gases influence hydrogen dilution, deplete the hydrogen content on the anode side and have detrimental effect on cell lifetime. On the other hand, CO_2 presents the main impurity in hydrogen reformate. It reacts with hydrogen in gaseous phase through reverse water gas shift reaction (RWGS) so the formation process of CO is unavoidable. Additionally, RWGS reaction can be further accelerated in the presence of a catalyst. However, formed CO molecules easily poison catalyst surface by blocking their sites for main reaction implementation [1]. In this paper, an overview of the experimental investigations' findings of hydrogen purification from various mixtures under different operating conditions is provided, right after EHP working principle briefly given in the next section.

PRINCIPLE OF ELECTROCHEMICAL HYDROGEN PURIFICATION

In general, the gas mixture is being fed to the anode side of the EHP at a pressure slightly above atmospheric pressure, where hydrogen oxidation reaction (HOR) occurs on platinum catalyst sites and splits hydrogen molecules into protons and electrons. Hydrogen protons are selectively transported across the membrane, while electrons are transferred through an external circuit to the cathode side of the cell. Since proton conduction of membrane is a function of water content, the membrane chain must be moistened so protons can be transported from the anode to the cathode side through the network of hydrogen bonds. On the cathode side, protons and electrons combine together in a hydrogen evolution reaction (HER) to evolve high-purity hydrogen gas, Fig. 1. A net electrochemical reaction is energy neutral since it does not bring out any new products. As the process does not occur spontaneously, an external power source is required to drive the electrochemical reactions, and the process continues as long as the driving force, i.e. electrical energy supplied to the EHP exceeds the internal energy of the system itself. It has to be emphasized that pure hydrogen can be separated with or without

pressurization. The simplest way to supply hydrogen to the EHP is in dead-end mode to assure long-term operation.

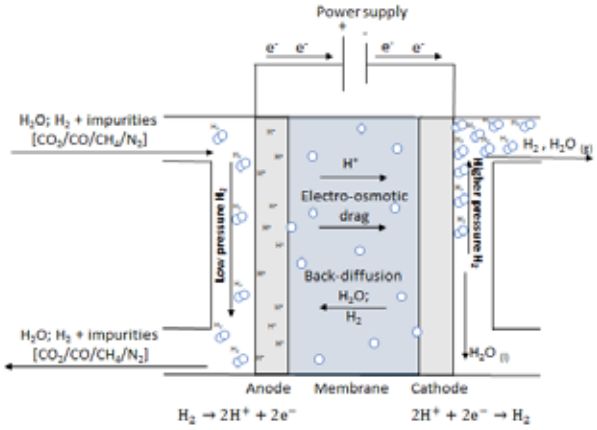


Fig. 1. Schematic representation of electrochemical hydrogen purification

EHP PERFORMANCE DIAGNOSTICS

In general, real-time characterization of the EHP membrane at constant current/voltage is used to better understand the processes within the cell and impact of various operating conditions on the cell performance, while the outlet gas composition in real-time operation is mostly examined by a gas chromatography. Researchers mainly combine different diagnostic methods, primarily polarization (*I-V*) curve measurements to get insight into the EHP overall voltage, and/or electrochemical impedance spectroscopy (EIS) measurements to distinguish and evaluate individual voltage losses. As non-optimal values of various operating parameters (pressure, temperature and humidification) can have deterioration impact on long-term performance decay and potential membrane failure [2], their optimization to obtain effective operation with high hydrogen purity is the main goal of the most studies. In 1980, Sedlak et al. [4] presented the hydrogen compression and purification pioneer study, which theoretically and experimentally observes energy efficiency of hydrogen separation from H_2/N_2 mixture. Their experiments were conducted at room temperature under cell pressure difference of 11.7 bar. With the fact that high-pressured pure H_2 stream abstraction was obtained from a low-pressure feed stream, they proved for the first time that solid polymer electrolyte cell functions as a single-stage purifier/compressor as long as it has proper membrane support structure. Due to its negligible effect on performance, they concluded that CH_4, N_2, and CO_2 simply act as diluents, while hydrogen sulfide (H_2S) is the only hazardous pollutant that must be removed before the gas stream enters the cell. Guided by Sedlak work, Lee et al. [5] based their work on hydrogen separation from $H_2/N_2/CO_2$ mixture via electrochemical method that also uses proton exchange membrane (PEM), while the compression process was left out in their investigation. Polarization curve results were used for characterization of purification process under various temperatures (30-70°C) and feed pressures (1-3 bar). Under the same conditions, they also evaluated N_2 and CO_2 permeation, as a major factor that degrades hydrogen purity, using the time-lag method. However, despite the fact that RWGS is unavoidable in the CO_2 presence, they did not report any information regarding CO. Ibeh et al. [6] conducted hydrogen separation from H_2/CH_4 mixtures at negligible compression difference between anode and cathode of PEM fuel cell, using two different membrane electrode assembly (MEA) setups with different catalyst loadings to investigate methane adsorption and blockage of the active sites. They compared polarization curves at three different temperatures obtained with H_2/CH_4 and H_2/Ar mixtures at the same conditions and proved that methane acts as inert gas without causing any catalyst degradation. Doucet et al. [7] based their study on feasibility of hydrogen separation from H_2/C_2H_4 mixtures also with PEM fuel cell. Their results showed that the bulk of hydrogen reacts with ethylene (C_2H_4) to form ethane (C_2H_6) so the authors suggest the usage of different catalyst materials which have a lower rate of hydrogenation or different selectivity for hydrogen to improve the separation process. Grigoriev et al. [8], thirty years after Sedlak work [4], reported experimental work of hydrogen compression and separation from H_2/N_2 mixture using EHP based on solid polymer electrolyte technology. Because they have conducted their research up to 130 bar, they suggested catalyst impregnation with zirconium particles to obtain larger membrane resistance. Using current-voltage characteristics, they reported a deterioration of compression efficiency as a function of small hydrogen concentration in the mixture which affects the creation of mass transport limitation. Kim et al. [9] in their study used EHP at high operating temperatures (160 °C) to provide improved hydrogen separation from the H_2/CO_2 mixture. Therefore, instead of perfluorosulfonic-acid (Nafion) membrane, they used polybenzimidazole (PBI) membrane. By polarization and EIS measurements, they compared EHP performance of Nafion membrane at different levels of humidification with non-humidified PBI membrane to prove that humidification is not required for PBI, while the catalyst tolerance of PBI membrane on CO is also much higher. Nordio et al. [10] reported an experimental study on hydrogen separation from H_2/CH_4 and H_2/inerts

mixtures. They confirmed Ibeh's finding regarding the fact that methane acts inert and has no impact on catalyst inhibition. Furthermore, using polarization curve and EIS analysis, they confirmed the obtaining of 100% pure hydrogen during EHP operation. Also, they investigated the elevated temperature effect on EHP performance. In their following paper [11], they focused on the negative effect on EHP performances closely related to CO formation responsible for catalyst inhibition in case when the system works with H_2/CO_2 mixtures under the different operating conditions. Authors confirmed that higher voltage and operating temperature have negative impact on catalyst, as well as higher concentration of impurities.

CONCLUDING REMARKS AND PERSPECTIVES

Considering all of these literature findings, there is still a knowledge gap regarding the optimal operating conditions and their unclear impact on EHP efficiency, especially when compression and purification occur simultaneously, as high-pressure environment in combination with purification process can contribute to unavoidable deterioration of catalyst layer and increase of mass transport losses. Therefore, further real-time characterization under various operating conditions definitely should be extended, not only on measuring the output at constant current/voltage and analyzing the polarization curves, but also on more often usage of EIS analysis to effectively distinguish and evaluate individual voltage losses (the ohmic resistance, charge transfer and mass transfer resistances). It could be done through the coupled equivalent circuit model application, novel or at least modified version of some already common model in literature. In order to evaluate the gas permeability of the membrane in EHPs, the linear scanning/sweep voltammetry (LSV), as the established diagnostic method for the measuring the fuel cells hydrogen crossover (back to the anode from the cathode in EHPs) during the fed with nitrogen (at anode in EHPs), is imposed also as a candidate for the testing in further EHP diagnostic studies. Foregoing, it is necessary to improve catalyst microstructure and to maximize catalyst active surface at the same time to obtain higher utilization and consequently higher EHP efficiency. Furthermore, to alleviate the effect of possible CO catalyst contamination, further evaluation of various existing recovery strategies in literature, like alloying of Pt with other transition/noble metals, formation of core-shell structures, modification of catalyst support materials, and “air/O_2 bleeding” to oxidize CO, is needed to improve assessment of catalyst recovery rate.

REFERENCES

1. Durmus GNB, Colpan CO and Devrim Y. 2021. A review on the development of the electrochemical hydrogen compressors. Journal of Power Sources 494:229743.
2. Zou J, Han N, Yan J, et al. 2020. Electrochemical Compression Technologies for High-Pressure Hydrogen: Current Status, Challenges and Perspective. Electrochemical Energy Reiews 3:690-729.
3. Sdanghi G, Maranzana G, Celzard A and Fierro V. 2019. Review of the current technologies and performances of hydrogen compression for stationary and automotive applications. Renewable & Sustainable Energy Reviews 102:150-170.
4. Sedlak J, Austin J and LaConti A. 1981. Hydrogen recovery and purification using the solid polymer electrolyte electrolysis cell. Internation Journal of Hydrogen Energy 6:45-51.
5. Lee HK, Choi HY, Choi KH, Park JH and LeeTH. 2004. Hydrogen separation using electrochemical method. Journal of Power Sources 132:92-98.
6. Ibeh B, Gardner C and Ternan M. 2007.Separation of hydrogen from a hydrogen/methane mixture using a PEM fuel cell. Internation Journal of Hydrogen Energy 32:908-914.
7. Doucet R, Gardner CL and Ternan M. 2009. Separation of hydrogen from hydrogen/ethylene mixtures using PEM fuel cell technology. International Journal of Hydrogen Energy 34:998-1007.
8. Grigoriev SA, Shtatniy IG, Millet P, Porembsky VI and Fateev VN. 2011. Description and characterization of an electrochemical hydrogen compressor/concentrator based on solid polymer electrolyte technology. International Journal of Hydrogen Energy 36:4148-4155.
9. Kim SJ, Lee BS, Ahn SH, et al. 2013. Characterizations of polybenzimidazole based electrochemical hydrogen pumps with various Pt loadings for H2/CO2 gas separation. International Journal of Hydrogen Energy. 38:14816-14823.
10. Nordio M, Rizzi F, Manzolini G, et al. 2019. Experimental and modelling study of an electrochemical hydrogen compressor. Chemical Engineering Journal 369:432-442.
11. Nordio M, Eguaras Barain M, Raymakers L, Van Sint Annaland M, Mulder M and Gallucci F. 2020. Effect of CO2 on the performance of an electrochemical hydrogen compressor. Chememical Engineering Journal 392:123647.

WHEC-2022
23rd World Hydrogen Energy Conference
June 26-30, 2022 - Istanbul

#1612

PARAMETER OPTIMIZATION OF A PBI MEMBRANE-BASED HIGH TEMPERATURE-ELECTROCHEMICAL HYDROGEN COMPRESSOR FED WITH H_2 AND CO MIXTURE

[1]Cemil Kuzu, [2]C. Ozgur Colpan, [3,4]Gizem Nur Bulanık Durmuş, [3]Yilser Devrim,*
[1] Dokuz Eylul University, Graduate School of Natural and Applied Sciences, Tinaztepe Campus, Izmir, 35397, Turkey
[2] Dokuz Eylul University, Faculty of Engineering, Mechanical Engineering Department, Tinaztepe Campus, Izmir, 35397, Turkey
[3]Atılım University, Graduate School of Natural and Applied Sciences, Department of Mechanical Engineering, Incek Golbasi Ankara, 06830, Turkey
[4] Atılım University, Department of Energy System Engineering, Ankara, 06836 Incek, Turkey

* Corresponding author e-mail: kuzucemil@gmail.com

ABSTRACT

In today's world, the increase in the amount of energy needed with the increase in the human population and the depletion of fossil fuels has pushed researchers to search for alternative fuels. Hydrogen is expected to take an important share among the alternative fuels in the future. However, it has some challenges in terms of its storage and pressurization. In this study, the effect of back diffusion on the performance of a PBI membrane-based electrochemical hydrogen compressor operating at 160 °C. Pressure values are calculated and validated with experimental results; and the change of flux, voltage and cell efficiency with time are presented.

Keywords: Electrochemical hydrogen compressor, modeling, compression, back diffusion polarization curve, reformate gas, PBI membrane

INTRODUCTION

Green energy resources and technologies are crucial since the number of available fossil fuels will be insufficient to meet the energy demands of the growing global population in the coming years. Many studies on green hydrogen production systems have been published in the literature [1]. The produced hydrogen needs to be compressed if hydrogen is to be stored in a pressurized tank. In this regard, the electrochemical hydrogen compressor (ECHC) emerges as a technology that can be used both in hydrogen refueling systems for vehicles and for pressurizing hydrogen in containers [2]. In addition to pressurization, the fact that it can purify hydrogen in the situation of reformate gas feeding makes this technology more advantageous. PBI membrane is known to be used in high-temperature fuel cells due to the high mechanical and thermal resistance it provides [3], therefore the use of PBI membrane in the electrochemical hydrogen compressor also has the benefits of the aforementioned advantages.

There are several studies on the modeling of ECHCs. With a highly efficient PEM-based electrochemical hydrogen compressor, compressing to 54 bar is conceivable, and with an upgraded sealing structure and cell design, this value can be increased to above 100 bar [4]. Chouhan et al. [2] showed that with a Nafion 115 membrane type-based ECHC operating at room temperature, the values exceeding 150 bar may be obtained at a low operating voltage of 0.1 V. Back diffusion, which is one of the most critical factors determining ECHC performance, was also highlighted in their study, and its impact on performance was investigated. Because working at lower voltages reduces the relevant compression ratio, the value of back diffusion decreases, resulting in better ECHC efficiency. Rohland et al. [5] achieved compression up to 43 bar in a low-temperature ECHC having Nafion 117 as the membrane.

The aim of this study is to observe the pressure change with time for a given temperature and cell voltage, and to examine the change of voltage, flux and cell efficiency with time considering the effect of back diffusion.

EXPERIMENTAL SETUP

All pressurization experiments were carried out with a single cell of 100 cm^2 active area at 160 °C and hydrogen with a high purity (99.999% purity) was fed to cell. Firstly, current and voltage data were recorded at pressure values between 0-38 bar. For each pressure value, the experiments were repeated three times. In the second part of the experiment, the voltage fed to the cell was kept constant and the pressure and current values were recorded against time. The maximum pressure values that can be reached at 0.1 V, 0.2 V, 0.4 V, 0.6 V, 0.8 V and 1 V constant voltage were recorded as 10 bar, 14 bar, 22 bar, 30 bar, 36 bar and 38 bar, respectively.

MATHEMATICAL MODELING COMPRESSION OF ECHC

To calculate the net molar flow rate of hydrogen, the forward molar flow rate, which expresses the amount of hydrogen

passing from the anode part to the cathode part, must be calculated. This value is calculated using Faraday's law as shown in the Eq. (1) [2].

$$\dot{n}_f = \frac{I(t)}{z \cdot F} \tag{1}$$

where $\dot{n}_f$ is the hydrogen generated with unit of mol/s, I is the current in unit of Amperes, F is Faraday's constant and it is equal to 96485 C/mol, .

Eq. (2), a combination of Fick's and Henry's laws, is used to calculate the backward flux. As can be seen in Eq. (2), while back diffusion is directly proportional to the cell active area, pressure difference and the permeability coefficient of the membrane, it is inversely proportional to the membrane thickness.

$$\dot{n}_b = \frac{D_H \cdot A \cdot (P_c(t) - P_a)}{d} \tag{2}$$

where $\dot{n}_b$ is the backward hydrogen flux in unit of mol/s, D_H is the permeability constant, P_c *and* P_a are the pressure of cathode and anode, respectively, *A* is the active area, and *d is* the thickness of the membrane.

As shown in Eq. (3), the net molar flow rate of hydrogen is obtained by subtracting the backward flux from the forward flux. Using the ideal gas law, the expression for the pressure change over time is obtained as shown in Eq. (4).

$$\dot{n}_n = \dot{n}_f - \dot{n}_b = \frac{I(t)}{2 \cdot F} - \frac{D_H \cdot A \cdot (P_c(t) - P_a)}{d} \tag{3}$$

$$P_c(t+1) = \left(\frac{R \cdot T \cdot I(t)}{2 \cdot F \cdot V_c} - \frac{R \cdot T}{V_c} \cdot \frac{D_H \cdot A}{d} \cdot P_c(t) + \frac{R \cdot T}{V_c} \cdot \frac{D_H \cdot A}{d} \cdot P_a \right) \cdot \Delta t + P_c(t) \tag{4}$$

where R is the universal gas constant (8.3144 J/mol·K), T is the operating temperature (K), V_c is the cathode volume (m^3), $\cdot \Delta t$ is the time difference (s). Two essential performance assessment factors for ECHC are voltage Eq. (5), flux Eq. (6) and cell Eq. (7) efficiency [2].

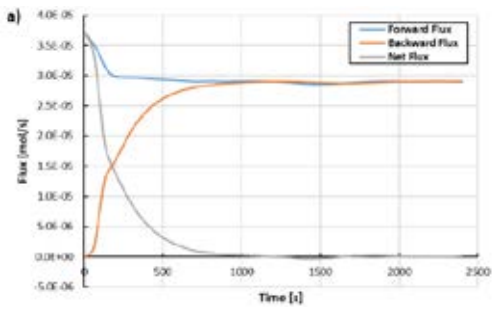
$$\eta_{voltage} = \frac{E_{Nersnt}}{E_{cell}} = \frac{\frac{RT}{zF} \ln\left(\frac{P_c}{P_a}\right)}{E_{cell}} \tag{5}$$

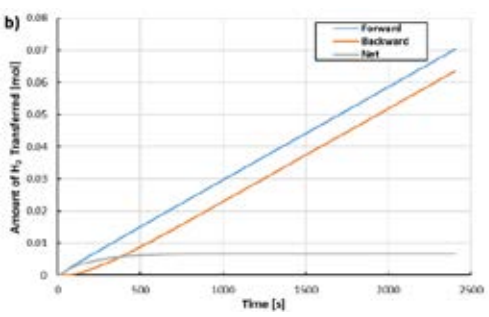
$$\eta_{flux} = \frac{\dot{n}_n}{\dot{n}_f} = \frac{\dot{n}_f - \dot{n}_b}{\dot{n}_f} \tag{6}$$

$$\eta_{ECHC,cell} = \eta_{voltage} \cdot \eta_{flux} \tag{7}$$

RESULTS AND DISCUSSION

The forward and backward flux, the amount of accumulated hydrogen, the pressure value reached and finally the time-dependent flux, voltage and cell efficiency with a constant cell voltage of 0.1 are shown in Fig. 1. The pressure value reached in the modeling is 11.26x10^5 Pa (absolute pressure), and the obtained values have been validated with experimental results. It is thought that the minor differences between the test and modeling results are due to the voltage losses experienced in the cables during the experiment. It is found that when the voltage increased, the membrane's gas permeability constant increased as well. This situation was evaluated for 6 different cell voltages.





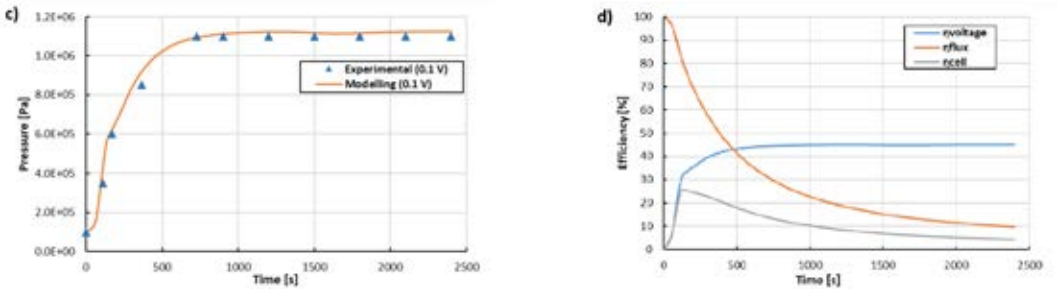


Fig. 1. a) Forward and backward flux in mol/s, b) amount of H_2 transferred in mol, c) time dependent pressure curve, d) current, voltage and cell efficiency at 0.1 V.

CONCLUSIONS

The pressure value and the membrane gas permeability coefficient increased with the increase of the cell voltage. At constant 1 V cell voltage, the highest value of 38 bar pressure has been reached. In a future study, a current-voltage curve will be created by developing a mathematical model of electrochemical hydrogen compressor with the obtained values.

ACKNOWLEDGEMENTS

This study was supported by The Scientific and Technological Research Council of Turkey (TUBITAK) 1001 (Grant number: 219M333) Project.

REFERENCES

1. Dincer I, Acar C. Smart energy solutions with hydrogen options. Int J Hydrogen Energy 2018;43:8579–99. https://doi.org/10.1016/j.ijhydene.2018.03.120.
2. Chouhan A, Bahar B, Prasad AK. Effect of back-diffusion on the performance of an electrochemical hydrogen compressor. Int J Hydrogen Energy 2020;45:10991–9. https://doi.org/10.1016/j.ijhydene.2020.02.048.
3. Chandan A, Hattenberger M, El-Kharouf A, Du S, Dhir A, Self V, et al. High temperature (HT) polymer electrolyte membrane fuel cells (PEMFC)-A review. J Power Sources 2013;231:264–78. https://doi.org/10.1016/j.jpowsour.2012.11.126.
4. Èbel RS, Oszcipok M, Fasil M, Rohland B, Èrissen LJ, Garche J. The compression of hydrogen in an electrochemical cell based on a PE fuel cell design. n.d.
5. Rohland B, Eberle K, Stroè R, Scholta J, Garche J. Electrochemical hydrogen compressor. n.d.

WHEC-2022
23rd World Hydrogen Energy Conference
June 26-30, 2022 - Istanbul

#1635

SYNTHESIS AND CHARACTERIZATION OF A NOVEL NICKEL-RUTHENIUM BASED CATALYST FOR BIOGAS STEAM REFORMING TO GENERATE HYDROGEN IN CONVENTIONAL AND MEMBRANE REFORMERS

[1*]*Adolfo Iulianelli*, [2]*Cristina Italiano*, [1]*Adele Brunetti*, [2]*Antonio Vita*
[1] Institute on Membrane Technology of the Italian National Research Council, Via P. Bucci 17C, Rende (CS), 87036, Italy
[2] The Advanced Energy Technology Institute of the National Research Council of Italy (CNR-ITAE), Salita Santa Lucia Sopra Contesse 5, 98126, Messina (ME), Italy

*Corresponding author e-mail: a.iulianelli@itm.cnr.it

ABSTRACT

Nowadays, the application of the principles of Process Intensification Strategy is gradually leading to a revolution of the conventional H_2 energy production processes and, among a number of alternative technologies, membrane engineering is playing a crucial role in the substitution of traditional devices used in the process engineering with membrane-based units. According to the requests of the Circular Economy and in the framework of the so-called H_2 Economy, H_2 generation coming from derived of biomass as renewable sources may play an interesting role as a valid option to the fossil fuels exploitation. In this work, the production of blue H_2 via reforming reactions of a synthetic biogas mixture was performed in a Pd-Ag membrane reformer packed with a novel Ni-Ru/La-Y-ZrO_x catalyst at 673 K and between 150 and 250 kPa of reaction pressure. As best result, 99% of CH_4 conversion was reached at 673 K, 250 kPa and S/C = 2/1, recovering 40% of H_2 with a purity > 99.9999%, meanwhile collecting a CO_2 reach stream in the unpermeated stream, to be further captured.

Keywords: Hydrogen, Biogas steam reforming, Membrane reactor technology, Pd-based membranes

INTRODUCTION

In light of the growing interest toward the so-called H_2 Economy [1], the production of H_2 – generally seen as the energy carrier of the future – from renewable sources may represent a viable option to the fossil fuels dependence, meanwhile contributing to allowing the process decarbonisation in various areas [2]. In the last decades, H_2 production and purification technologies are attracting considerable interest and, among them, membrane reformers (MRs) technology received a growing attention, because able to combine the exploitation of renewable sources with the simultaneous production and purification of H_2 via reforming reactions [3]. In a MR, the presence of a H_2 perm-selective membrane allows its selective removal from the reaction toward the permeate side, involving the so-called “shift-effect” on the reaction system, responsible for higher reaction products formation and further feed product conversion than an equivalent conventional reformer (CR) (for thermodynamically equilibrium limited reactions). To date, most of the production of H_2 at larger scale comes from natural gas steam reforming reaction, which involves the exploitation of fossil fuels and the consequent formation of greenhouse gases. On the other hand, biogas as a renewable source could represent an alternative to natural gas utilization in reforming processes for H_2 generation. The composition of biogas may vary largely, depending on the nature of the residual biomass (sewage treatment plants, animal waste etc.) used during the anaerobic digestion process, even though it is mostly constituted of CH_4 and CO_2, besides N_2, H_2, volatile organic compounds, H_2S etc. The combination of biogas fuel processing with MRs technology was not largely studied in literature, particularly because of the presence of H_2S as main responsible for the membrane and catalyst poisoning and consequent performance loss. However, in the last years a growing attention toward the development of high-performance reforming catalysts (showing high catalytic activity, high carbon deposition resistance etc.) was noticed. Metal catalysts such as Rh, Pd or Ru, Pt and Ni show a high activity and selectivity for H_2 generation via steam reforming of biogas (SRB) [4]. Most of the scientific literature about SRB reaction in CRs is based on Ni catalysts utilization because cheaper solution than Pt, Rh or Pd adoption. However, Ni is susceptible to a strong deactivation caused by coke formation as a consequence of the conventional high temperature operations, whereas Pt and Pd catalysts result to be more catalytically stable and Rh presents a greater catalytic activity than Ni associated to a lower coke formation tendency [5].

On the other hand, only a few studies deal with the utilization of Pd-based MRs to carry out SRB reaction. The aim of this experimental work is to perform the steam reforming of a synthetic biogas mixture containing in a self-supported Pd-Ag MR, packed with a novel, not commercial Ni-Ru based catalyst, in order to produce blue H_2 and avoid that CO_x may be released in the ambient. In particular, the catalytic performance in terms of methane conversion, and H_2 recovery, yield and purity, are analysed in the Pd-Ag MR and compared to an equivalent CR.

EXPERIMENTAL

The bench-scale membrane reformer is constituted of a stainless-steel module, housing a self-supported Pd-Ag membrane tube (Johnson Matthey, UK), with an active length equal to 10 cm and outer diameter of 10 mm, Fig. 1. 3 g of Ni-Ru/La-Y-ZrO_x catalyst are packed in the membrane lumen. The feed stream is supplied directly inside the membrane core; on the other hand, the generated H_2 permeating through the membrane is recovered in the "permeate" stream, supplying N_2 as a sweep-gas, while the unpermeated products are collected in the "retentate" stream.



Fig. 1. Unsupported Pd-Ag membrane provided by Johnson Matthey (London, UK).

The experimental campaign consisted of single gas (H_2, N_2, CO_2, CH_4) permeation tests to evaluate the perm-selectivity characteristics of the membrane by varying the temperature between 573 and 673 K, and the pressure between 150 and 250 kPa (abs.). Afterwards, the SRB reaction was carried out in the MRs at 673 K. The composition of the synthetic biogas feed stream was CH_4:CO_2:N_2 = 60:35:5, whereas the S/C feed molar ratio ranged between 1.5:1 and 2:1, and the weight hourly space velocity (WHSV) from 0.2 to 0.6 h^{-1}. All the outlet streams were analysed by a temperature programmed HP 6890 gas-chromatograph (GC). Both gas permeation and catalytic performances were evaluated in terms of H_2 permeating flux and ideal perm-selectivity, CH_4 conversion, H_2 yield and recovery, and H_2 permeate purity.

RESULTS AND DISCUSSION

Before the reaction measurements, the permeation characteristics of the fresh self-supported Pd-Ag membrane were investigated between 573 and 673 K, varying the transmembrane pressure between 0 and 250 kPa, Fig. 2.

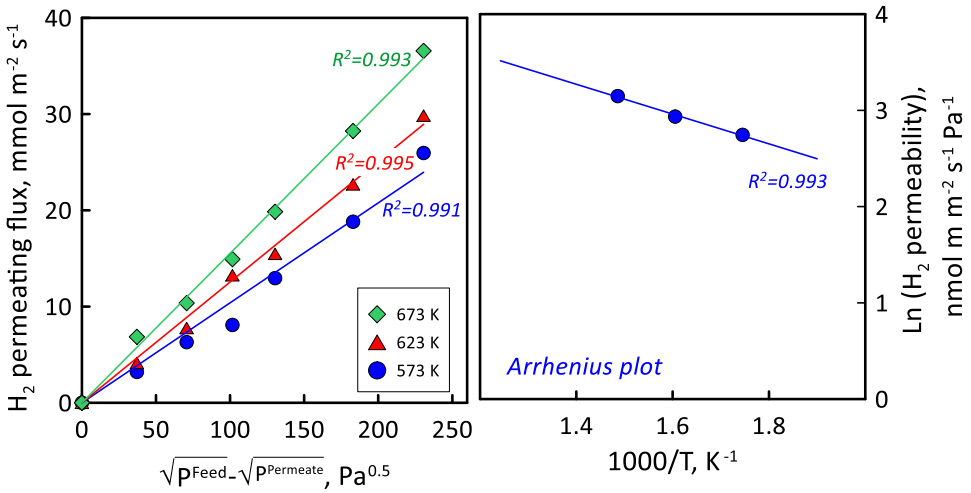


Fig. 2. Flux of hydrogen permeating through the Pd-Ag membrane as a function of transmembrane pressure at different operating temperatures; in the smaller plot: hydrogen permeability vs 1/T at 50 kPa of transmembrane pressure.

Single gas permeation measurements demonstrated that, apart from H_2, the other gases may not pass through Pd-Ag membrane, confirming that the former is fully H_2 perm-selective. This evidenced that the H_2 permeation depends on the diffusion through the Pd-Ag membrane bulk, and the Sieverts-Fick mechanism regulates the H_2 permeating flux.

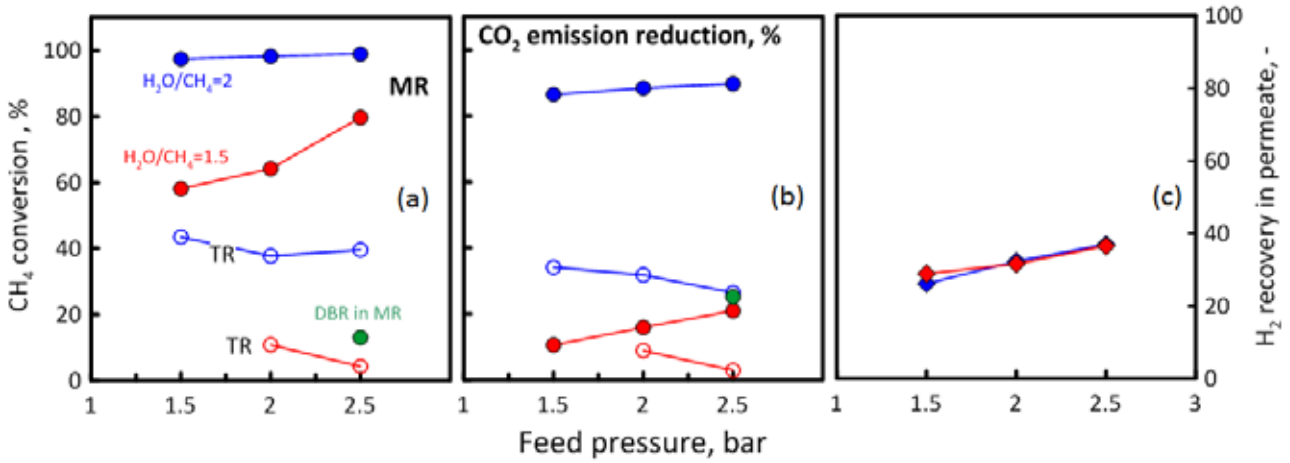


Fig. 3. SRB reaction at 673 K and as a function of feed pressure and different H_2O/CH_4 feed molar ratio: (a) CH_4 conversion in MR and CR; (b) CO_2 emission reduction in MR and CR; (c) H_2 recovery in the MR.

Fig. 3(a) points out how an increase of pressure acts differently in the traditional and membrane reformers. Increasing the feed pressure in the membrane reformer, CH_4 conversion was progressively enhanced, demonstrating that the shift effect overcame the thermodynamic one due to the removal of H_2 for permeation through the membrane. This allowed better performance in the MR with respect to the CR. In this regard, under defect of steam, methane conversion was improved from 60 to ~ 80%, whereas at stoichiometric feed molar ratio from 97 to 99%. In the meanwhile, 40% of high grade H_2 was recovered over the total produced, with a maximum CO_2 reduction equal to 85%.

CONCLUSIONS

In this study, a Pd-Ag MR was packed with a novel Ni-Ru based catalyst in order to perform the SRB reaction for blue H_2 generation. The best performance was reached at 673K, WHSV = 0.2 h^{-1} and 2.5 bar with a CH_4 conversion of 99% and 40% of CO_x-free H_2 recovery with a H_2 purity > 99.9999%, meanwhile reducing the CO_2 emission around 85%.

ABBREVIATIONS

CR	Conventional reactor
GHG	Greenhouse gases
MR	Membrane reactor
SRB	Steam reforming of biogas
WHSV	Weight hourly space velocity

ACKNOWLEDGEMENT

This research was funded by the “Process for Low-carbon blue & green hydrogen Generation via Intensified electrified reforming of Natural gas/biogas (PLUG-IN)” project, under the Italian research program of Projects of Relevant National Interest (PRIN) - Prot. 2020N38E75 – Bando MUR 2020, D.D. 2436 del 20/10/2021.

REFERENCES

1. Biegler T. 2005. The hydrogen economy, The Skeptic, 25:1-29.
2. Handayani K, Krozer Y and Filatova T. 2019. From fossil fuels to renewables: An analysis of long-term scenarios considering technological learning, Energy Policy, 127:134-146.
3. Amiri TY, Ghasemzadeh K, Iulianelli A. 2020. Membrane reactors for sustainable hydrogen production through steam reforming of hydrocarbons, Chemical Engineering and Processing: Process Intensification, 157:108148.
4. Luneau M, Gianotti E, Meunier FC, Mirodatos C, Puzenat E, Schuurman Y and Guilhaume N. 2017. Deactivation mechanism of Ni supported on Mg-Al spinel during autothermal reforming of model biogas, Applied Catalysis B Environmental, 203:289-299.
5. Iulianelli A, Liguori S, Wilcox J, Basile A. 2016. Advances on methane steam reforming to produce hydrogen through membrane reactors technology: a review, Catalysis Reviews Science and Engineering, 58: 1-35.

WHEC-2022

23rd World Hydrogen Energy Conference

TRACK 6.
HYDROGEN STORAGE

TRACK 6. HYDROGEN STORAGE

#28 LABVIEW MODELING AND SIMULATION OF A STAND ALONE PHOTOVOLTAIC/WIND SYSTEM WITH HYBRID STORAGE H_2-BATTERY	440
#77 TECHNO-ECONOMIC REQUIREMENTS FOR UNDERGROUND RENEWABLE HYDROGEN STORAGE IN POROUS MEDIA	443
#90 FROM BATCH REACTOR TO CONTINUOUS FLOW MICROCHANNEL REACTOR FOR DEHYDROGENATION OF PERHYDRO-DIBENZYLTOLUENE: A PRELIMINARY STUDY	446
#119 DIGITAL DEVELOPMENT OF AN OPTIMIZED HEAT MANAGEMENT DESIGN FOR AN INTEGRATED SOLID-STATE H_2-STORAGE RESERVOIR	449
#120 MODELING AND PROCESS SIMULATION OF A METAL HYDRIDE TANK COUPLED WITH A PEM ELECTROLYZER	452
#122 HIGH H_2 UPTAKE ON Co(II)- AND Ni(II)- EXCHANGED ZSM-5 AND US-Y HAVING OPTIMAL HEAT OF ADSORPTION VALUES	455
#126 HYDROGEN ABSORPTION/DESORPTION OF THE $(TiVNb)_{85}Cr_{15}$ MULTICOMPONENT ALLOY	458
#133 EASY UP-SCALEABLE APPROACH TO IMPROVE THE PROPERTIES OF METAL-ALLOYS FOR HYDROGEN STORAGE	462
#134 HYDROGEN - HEAT STORAGE SYSTEM BASED ON METAL HYDRIDE AND PHASE CHANGE MATERIAL	465
#139 MODELING AND PARAMETERIZATION OF A PEM FUEL CELL STACK FOR A SYSTEM INTEGRATION INTO A METAL HYDRIDE BASED HYDROGEN STORAGE SYSTEM	468
#142 SIZE OPTIMIZATION OF A HYBRID WIND/PHOTOVOLTAIC/FUEL CELL GRID-CONNECTED SYSTEM WITH HYDROGEN STORAGE	471
#145 INVESTIGATION OF TEMPERATURE AND PRESSURE EFFECT ON THE HYDROGEN SORPTION KINETICS IN THE INTERFACE OF Mg/MgH_2 BY MOLECULAR DYNAMICS	475
#149 EFFECTS OF INITIAL AND BOUNDARY CONDITIONS ON HYDROGEN REFUELING PERFORMANCES	478
#155 MODELING THE KINETIC BEHAVIOR OF THE Li-RHC SYSTEM FOR HYDROGEN STORAGE UNDER DESORPTION CONDITIONS	482
#171 HYDROGEN PRODUCTION FROM THE CATALYTIC DEHYDROGENATION OF HYDRAZINE BORANE OVER Pd-Ni-B CATALYST	485
#181 EFFICIENT HYDROLYTIC DEHYDROGENATION OF ETHYLENE DIAMINE BISBORANE OVER Pd-Ni-Zr-B CATALYST IN THE ETHYLENE DIAMINE MEDIA	488
#192 DEVELOPMENT OF NOVEL POLYMERIC MATERIAL GRADES AND EXPERIMENTAL METHODS TO BE USED IN HIGH-PRESSURE H_2 GAS ATMOSPHERES	491
#196 DIFFERENT WAYS TO STORE MASSIVE QUANTITIES OF HYDROGEN	494
#203 EVALUATION OF THE BIMETALLIC Pt-Ni AND Pt-Co CATALYSTS ON THE LOHC DEHYDROGENATION	497
#221 HIGH SURFACE AREA ZEOLITIC IMIDAZOLATE FRAMEWORKS FOR HYDROGEN STORAGE AT ROOM TEMPERATURE	500
#234 ELASTIC BRITTLE BEHAVIOR OF AN IRON – TITANIUM ALLOY DEDICATED TO HYDROGEN STORAGE	504
#247 MATHEMATICAL MODELLING OF ELECTROCHEMICAL HYDROGEN COMPRESSOR: TEMPERATURE INFLUENCE SIMULATION ANALYSIS	508
#263 EXPERIMENTAL PROOF OF CONCEPT OF A NOVEL HIGH DENSITY, LOW PRESSURE HYDROGEN STORAGE SYSTEM UTILIZING THERMOCHEMICAL HEAT STORAGE	511
#269 CONTRIBUTION TO MODELING HYDROGEN PERMEATION AND BARRIER LAYER OPTIMIZATION IN BLOW MOLDED PLASTIC LINERS FOR AN ON-BOARD COMPRESSED HYDROGEN TANKS	514
#271 A MULTICRITERIA ANALYSIS DECISION FOR PRIORIZATION OF LIQUID ORGANIC HYDROGEN CARRIERS	517

#279 SYNTHESIS AND STABILIZATION OF ENERGY FUEL MATERIAL ALUMINUM HYDRIDE: A REVIEW	520
#282 NUMERICAL SIMULATION AND PARAMETRIC ANALYSIS OF THE WALL STRAIN DISTRIBUTION OF VERTICALLY PLACED METAL HYDRIDE BASED HYDROGEN STORAGE CONTAINER	523
#290 STUDIES ON HYDROGEN STORAGE PERFORMANCE OF CATALYZED MgH_2	526
#300 PERMEABILITY OF A DEFORMABLE METAL HYDRIDE BED DURING HYDROGEN ABSORPTION	529
#301 APPLICATION OF MISCHMETAL BASED LOW PRESSURE METAL HYDRIDES FOR SOLAR ENERGY STORAGE	532
#303 STUDY OF THE EFFECT OF Zr_3Fe ADDITION ON HYDROGEN STORAGE BEHAVIOR OF Ti_2CrV ALLOYS	535
#317 HYSTORIES PROJECT: TECHNICAL DEVELOPMENTS AND DEPLOYMENT OUTLOOKS FOR PURE HYDROGEN STORAGE IN DEPLETED FIELDS AND AQUIFERS	539
#332 THE EFFECT OF FIBER BANDWIDTH ON STRESS DISTRIBUTION AND LAYER THICKNESS CHANGE AT THE DOME PART OF HYDROGEN STORAGE VESSEL	542
#345 EXPERIMENTAL STUDIES OF WELL INTEGRITY ISSUES RELATED TO CEMENT DURING UNDERGROUND HYDROGEN STORAGE	545
#347 EFFECTS OF HYDROGEN-METHANE GAS BLEND ON WELLBORE INTEGRITY IN UNDERGROUND HYDROGEN STORAGE: AN EXPERIMENTAL INVESTIGATION OF ELASTOMER PERFORMANCE	547
#361 THERMODYNAMIC ANALYSIS OF A METAL HYDRIDE BASED HYDROGEN COMPRESSOR USING $La_{1-x}Ce_xNi_5$ HYDRIDES	550
#364 THE EFFECT OF DIFFERENT ORGANIC ACIDS ON THE HYDROLYSIS OF MAGNESIUM HYDRIDE	553
#369 DEVELOPMENT AND IMPLEMENTATION OF METAL HYDRIDE MATERIALS AND TECHNOLOGIES IN SOUTH AFRICA	556
#376 EFFECT OF STARTING RAW MATERIAL IN MECHANICAL ALLOYING OF TiFe HYDROGEN STORAGE ALLOY	559
#378 INTRODUCTION OF SPERA HYDROGEN SYSTEM™ FOR MASSIVE HYDROGEN STORAGE AND TRANSPORTATION	561
#390 PERFORMANCE OF BENZYLTOLUENE AS PURE HYDROCARBON LIQUID ORGANIC HYDROGEN CARRIER (LOHC) IN STORAGE CYCLES	563
#399 PERFORMANCE ANALYSIS OF A SOLAR TOWER POWER PLANT INTEGRATED WITH HYDROGEN ENERGY STORAGE SYSTEM	567
#413 3D COFs FOR PHOTOCATALYTIC N_2 FIXATION: A COMPUTATIONAL STUDY	571
#416 COMPATIBILITY OF POLYMERS AND COMPOSITES WITH HYDROGEN IN TRANSPORT AND STORAGE EQUIPMENT	574
#441 NUMERICAL AND EXPERIMENTAL EVIDENCE OF DEFECTS CREATION IN EPDM AFTER HYDROGEN DECOMPRESSION	577
#1446 EFFECTIVE HYDROLYSIS OF ALKALINE SODIUM BOROHYDRIDE: CoB-TRITON CATALYST	580
#1453 ANALYSIS OF THE FIRST STEP OF HYDROGEN RELEASE OF AMMONIA BORANE FOR PCA WITH DIFFERENT HEATING RATES	583
#1459 NUMERICAL SIMULATION ON PRESSURE REDUCTION PHENOMENON WITH LARGE-SCALE LIQUEFIED HYDROGEN TANK	587
#1460 MACHINE LEARNING AS A TOOL FOR INTERPRETING VARIABLES IN HYDROGEN SORPTION DATA	590
#1465 CFD-ASSISTED HYDRODYNAMIC CHARACTERIZATION OF A CENTRIFUGAL LIQUID ORGANIC HYDROGEN CARRIER DEHYDROGENATION UNIT	593
#1466 METAL HYDRIDE COMPOSITE MATERIALS FOR THERMO-CHEMICAL HYDROGEN COMPRESSION	596
#1488 REACTION PROCESS OF AMMONIA PRODUCTION FROM IRON NITRIDE AND CARBONATED WATER	598

#1491 EFFECT OF IRON PARTICLE SHAPE AND ALLOY COMPOSITION ON HYDROGEN PRODUCTION EFFICIENCY IN THE WATER-IRON REACTION	601
#1506 MODELING OF A HYDROGEN STORAGE SYSTEM BASED ON METAL HYDRIDE AND PHASE CHANGE MATERIAL	604
#1508 BORON-HYDROGEN MATERIALS TOWARDS DECARBONISATION	607
#1518 INFLUENCE OF DIFFERENT ADDITIVES IN THE HYDROLYSIS OF SODIUM BOROHYDRIDE	610
#1528 SYNTHESIS OF CALCIUM BOROHYDRIDE WITH BORON-FLORIDE EXCHANGE AT HIGH PRESSURES	613
#1532 STRUCTURAL EVOLUTION OF A Mg-C COMPOSITE OVER 1000 H_2 STORAGE CYCLES	616
#1533 DEVELOPMENT OF THE NEC/12H-NEC LOHC SYSTEM AT CANADIAN NUCLEAR LABORATORIES	619
#1539 EVALUATION OF BASIC PHYSICAL PROPERTIES OF AMMONIA BORANE STORED IN LIQUID AMMONIA	622
#1557 A SIMPLE DYNAMIC MODEL FOR PREDICTING THE ABSORPTION AND DESORPTION BEHAVIOUR OF METAL HYDRIDE SYSTEMS	624
#1565 NUMERICAL OPTIMIZATION OF MULTISTAGE MAGNETIC REFRIGERATION SYSTEM IN THE TEMPERATURE RANGE OF LIQUID HYDROGEN	627
#1602 COMPARATIVE STUDY ON ACTIVE AND PASSIVE THERMAL MANAGEMENT OPTIONS OF A METAL HYDRIDE HYDROGEN STORAGE TANK	630
#1603 OPTIMIZATION OF DESIGN PARAMETERS FOR A PHASE CHANGE MATERIAL INTEGRATED METAL HYDRIDE HYDROGEN STORAGE TANK	634
#1614 INVESTIGATION OF INFRASTRUCTURE STUDY AND OPERATION PLANNING OF UNDERGROUND HYDROGEN STORAGE AREA	638
#1619 INVESTIGATION OF HYDROGEN KINETICS OF COPPER PELLETS WITH ENG ADDITIVES	641
#1636 NUMERICAL AND EXPERIMENTAL ASSESSMENT OF A THERMAL MANAGEMENT SYSTEM FOR METAL HYDRIDE HYDROGEN TANK	644

WHEC-2022
23rd World Hydrogen Energy Conference
June 26-30, 2022 - Istanbul

#28

LABVIEW MODELING AND SIMULATION OF A STAND ALONE PHOTOVOLTAIC/WIND SYSTEM WITH HYBRID STORAGE H_2-BATTERY

[1*] *Hakim Azoug,* [2] *Hocine Belmili*
[1]University of Science and Technology Houari-Boumédiène USTHB, Department of Electrical Engineering, Bab Ezzouar, Algeria
[2]Unité de Développement des Equipements Solaires, UDES, Centre de Développement des Energies Renouvelables, CDER, Tipaza, Algeria

*Corresponding author e-mail: hm.azoug@gmail.com

ABSTRACT

This paper investigates in the modeling and simulation under LabVIEW Software of stand-alone photovoltaic/wind power system using hybrid storage hydrogen and lead-acid battery. The proposed graphical programming environment has proven to be a versatile platform for the design, sizing, data acquisition, analysis and parameter identification of each compound of these systems, including PV generator, wind generator, storage systems, power converter, electrolyzer, fuel cell, gas compressor and tank for pressurized hydrogen storage. Combining solar and wind energy is a very important issue, but it depends on geographical position. The proposed system can be very useful for Engineers and experts who require a simple, fast, and accurate PV/ wind storage simulator to design their systems.

Keywords: PV/WIND-H_2-Battery System, Hybrid Storage, Hydrogen, Fuel Cell, Lead-Acid Battery.

INTRODUCTION

Along with the crisis of the exhaustion of the traditional energy resources, and with environmental damage caused by increased carbon dioxide emissions, the use of renewable energy has become the goal for energy development. Hybrid energy system (HES) describes a stand-alone energy system, which combines renewable and conventional energy sources with lead-acid batteries for chemical storage [1] and hydrogen storage which will be converted to electrical energy via fuel cells (FCs). This type of energy storage offers significant advantages over conventional batteries in terms of energy density and long-term storage. The conversion of hydrogen allows the storage of a large amount of power as well as its transport.[2].

This work presents the modeling and simulation of a hybrid photovoltaic/ wind power system with hybrid storage H_2-Battery by using the LabVIEW software which is ordinarily taken as a tool of virtual instrumentation and automation, it can also be used in the fields of simulation because it has provided a unique way of modeling and simulating with a high-level graphic programming language and can be executed much faster than in other languages [3].

A typical hybrid energy generation system is considered and shown in Fig.1, which the wind and the PV generators are connected to the load via converters (The AC/DC converter for wind generator and the DC/DC converter for PV generator). The Power will be generated by wind generator and PV system to feed load demand and the excess power will be eventually stored in both battery and H_2 tank.

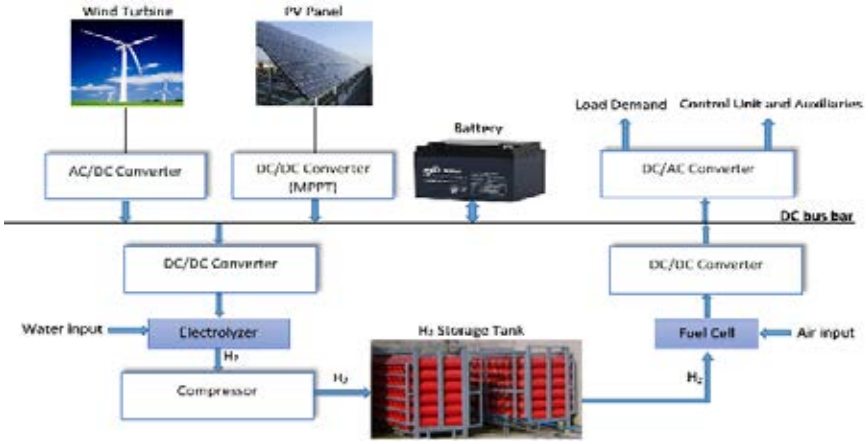


Fig. 1. Configuration of the stand-alone PV-Wind System with hybrid storage under study.

HYBRID SYSTEM MODELING USING LABVIEW SOFTWARE

The used model in photovoltaic system is one-diode model, the relationship between current and voltage [4],the power output of wind turbine P_t(W) [5], the charging V_c(V) of the battery (Lead-acid battery type Tudor STTH-180),the normalized inverter input power $P_{in,inv}$(W) [6], the output voltage of a single cell V_{FC}(V) [7], the compressor power P_c and the basic equations (Van der Waals law) that describes the pressure inside the storage tanks P_{ht} are as follows [8]:

$$I = I_L - I_D = I_L - I_0\left(\exp\left(\frac{q(V+R_S I)}{\gamma k T_C}\right)-1\right) \quad (1)$$

$$P_t = \frac{1}{2}\rho\pi R^2 C_P(\lambda,\beta)V_V^3 \quad (2)$$

$$V_c = (2+0{,}160SOC_{bt}(1-DOD)) - \frac{I_b}{C_{10}}\left(\frac{6}{1+I_b^{0.6}} + \frac{0{,}480}{(1-SOC_{bt})^{1.2}} + 0{,}036\right)(1-0{,}025\Delta T) \quad (3)$$

$$P_{in,inv} = \frac{P_{in}}{P_{nom}} \quad (4)$$

$$V_{FC} = E_{Nernst} - V_{act} - V_{ohm} - V_{conc} \quad (5)$$

$$P_C = C_P T_{cp,in}\left(\left(\frac{P_{cp,out}}{P_{cp,in}}\right)^{\frac{\gamma-1}{\gamma}} - 1\right) / \left(\frac{U_c^2}{2}\right) \quad (6)$$

$$P_{ht} = \frac{nRT_{ht}}{V_{ht} - (n.b)} - a\frac{n^2}{V_{ht}^2} \quad (7)$$

RESULTS AND DISCUSSION

The modeling and simulation of the stand-alone Photovoltaic/Wind system with hybrid storage H_2-Battery and the different from panel control under LabVIEW is presented in Fig.2 (the Simulate Button will show a simulation of the system, Next and Previous button to Navigate through the front panel). The instantaneous values of system variables are dynamically changing according to input variables (solar radiation, wind speeds and temperature). The detailed power production of each source, the state of charge (SOC) level of the accumulator and storage tank are also illustrated.

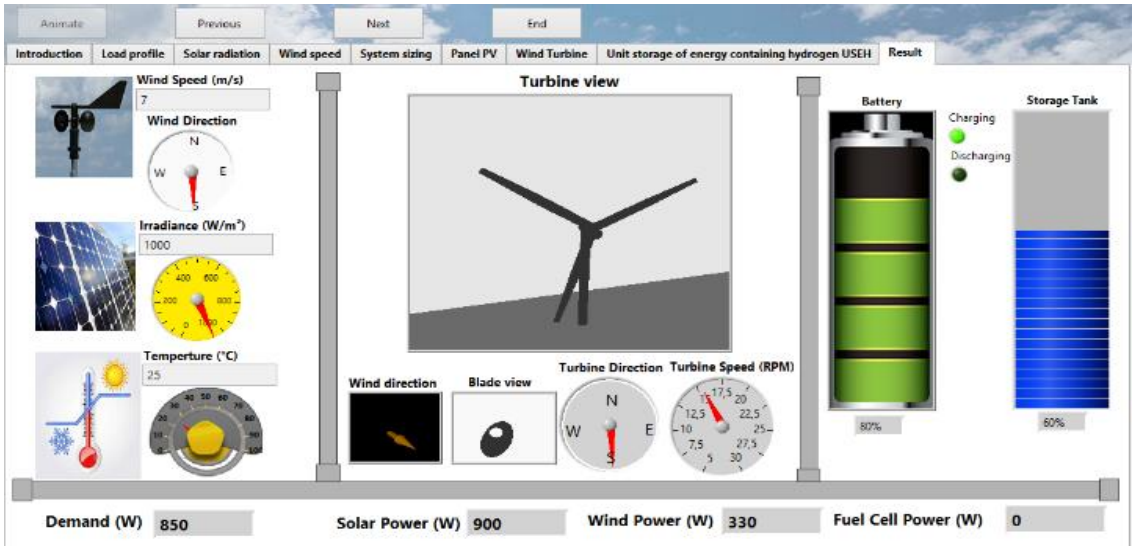


Fig. 2. LabVIEW Platform of Hybrid photovoltaic/wind system with hybrid storage (H_2-Battery)

As regards, Fig.3 shows the simulation result of our system where Fig.3.a, Fig.3.b, Fig.3.c, Fig.3.d, Fig.3.e, Fig.3.f, Fig.3.g and Fig.3.f are respectively: P(V) and I(V) curves for modules Shell SP75, wind turbine Power-Wind speed

curve of WFD500W, voltage versus time in charge and discharge at I_{10}=18 A and 25°C, efficiency η_{inv} vs normalized input power $P_{in,\ inv}$, ballard PEMFC cell voltage and power curves, electrolyzer cell voltage at 70°C , compressor output power as a function of the hydrogen flowrate for two pressure ratios and tank pressure versus stored hydrogen for various total tank volumes

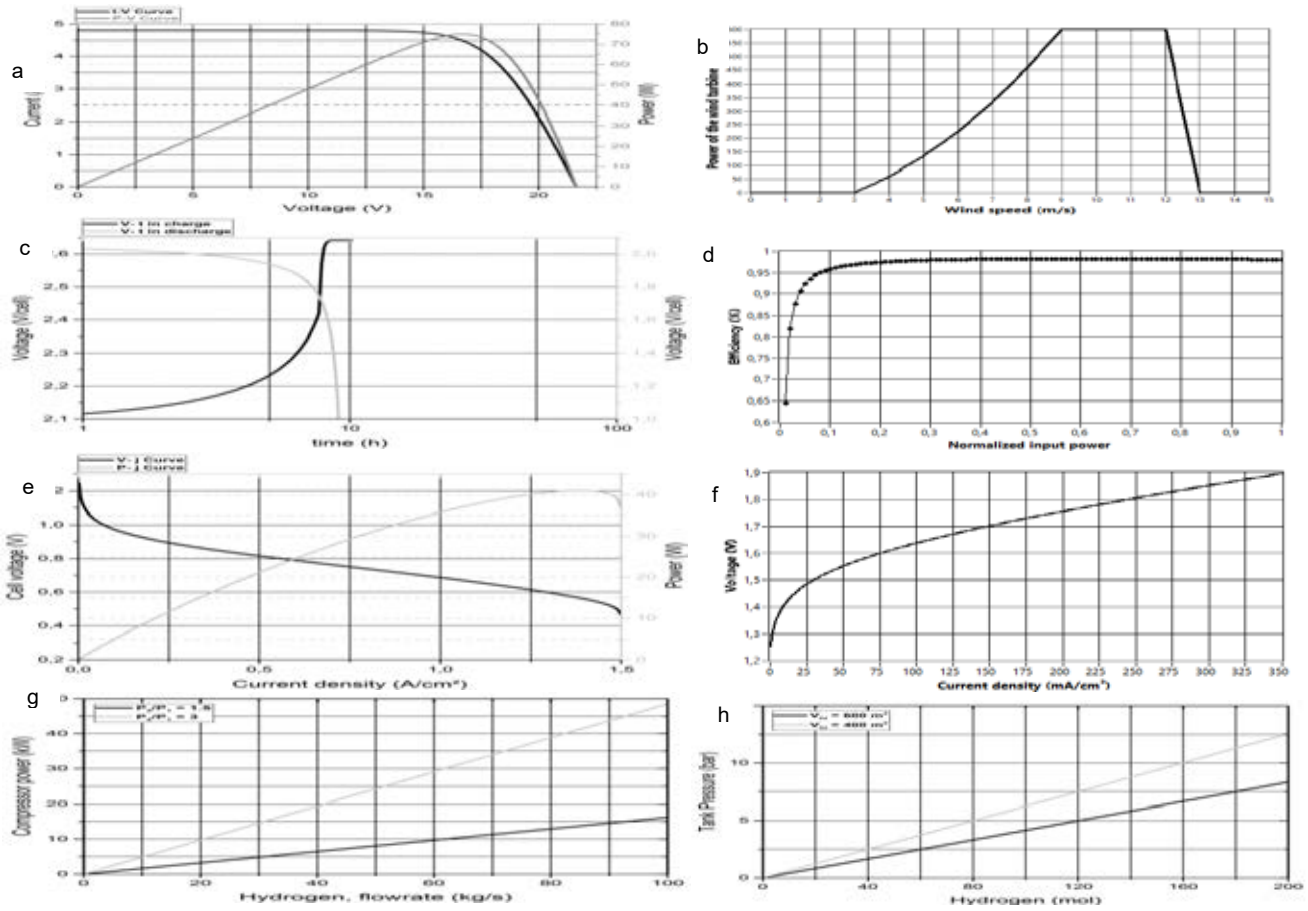


Fig. 3. Simulation result of the stand-alone Photovoltaic/Wind system with hybrid storage H_2-Battery under LabVIEW

CONCLUSIONS

This paper describes the developed platform to study the behavior of photovoltaic/wind power system with hybrid H_2-Battery storage, by using LabVIEW software. This platform permits simulation, parameters identification of different compounds of the system. Using LabVIEW is very suitable for the graphical modeling. It can help us to understand the functioning of all parts of the studied system. This platform can be easily connected with Compact Rio hardware for the date acquisition and analysis of the signals issues from the operating system.

REFERENCES

1. Belmili H, Haddadi M, Bacha S, Almi MF and Bendib B. 2014. Sizing stand-alone photovoltaic–wind hybrid system: Techno-economic analysis and optimization. Renewable and Sustainable Energy, Reviews 30: 821-832.
2. Onar O.C, Uzunoglu M. and Alam M.S. 2006. Dynamic modeling, design, and simulation of a wind/fuel cell/ultra-capacitor-based hybrid power generation system. Department of Electrical and Computer Engineering, South Alabama Univ, USA.
3. Yang G and Chen M. 2009. LabVIEW based simulation system for the output characteristics of PV cells and the influence of internal resistance on it. Conference on Information Engineering.
4. Amrouche F, Mahmah B, Belhamel M and Benmoussa H. 2005. Modélisation d'une Pile à Combustible PEMFC alimentée directement en Hydrogène-Oxygène et validation expérimentale. Revue des Energies Renouvelables, vol. 8, N°2, 109: 120.
5. Belmili H, Almi MF, Bendib B and Bolouma S. 2013. A Computer program development for sizing stand-alone photovoltaic-wind hybrid systems. Energy Procedia. Reviews 36: 546-557.
6. Peippo LK. and Lund P.D. 1994. Optimal sizing of solar array and inverter in grid-connected photovoltaic systems. Solar Energy Materials and Solar Cells. Reviews 32: 95-114. Finland.
7. Pukrushpan Jay T, Stefanopoulou Anna G and Huei Peng. 2004. Control of fuel cell power systems. First edition.
8. Voutetakis S and Seferlis P. Design-optimization and control of stand-alone power systems using renewable energy and hydrogen production., PhD. Neo Olivio, Greece.

WHEC-2022
23rd World Hydrogen Energy Conference
June 26-30, 2022 - Istanbul

#77

TECHNO-ECONOMIC REQUIREMENTS FOR UNDERGROUND RENEWABLE HYDROGEN STORAGE IN POROUS MEDIA

*Jan Michalski**
Ludwig-Bölkow-Systemtechnik GmbH (LBST), Daimlerstr. 15, 85521 Ottobrunn, Germany

*Corresponding author e-mail: jan.michalski@lbst.de

ABSTRACT

This paper provides first results from the FCH JU funded HyStorIES project (**Hy**drogen **Stor**age **I**n **E**uropean **S**ubsurface) addressing the main technical feasibility questions and assessing the techno-economical potential of underground large-scale storage of renewable hydrogen in porous media by 2050. Within the project Work Package 5 (WP5) conducts an in-depth techno-economic assessment of the future scenarios for a widespread deployment of underground renewable hydrogen storage in the EU across the period 2025-2050. In this context, it models and analyses optimal design and operation of different elements of the future energy system including renewable electricity supply, production of renewable hydrogen, associated gas compression and hydrogen pipeline networks to transfer hydrogen to/from the underground storage. The preliminary analysis of expected techno-economic requirements for underground renewable hydrogen storage reveals significant energy storage needs across Europe between 40 to 700 TWh_{H2} in the long-term. In particular, the six big economies with the largest energy demand in Europe including Germany, France, Italy, the UK, Spain and Poland would account for 75% of the overall storage capacities in Europe. Based on the long-term assumption of climate neutrality in Europe the underground renewable hydrogen storage would be operated on a seasonal basis with 1-9 full cycle equivalents regardless of hydrogen demand and storage capacity in all countries.

Keywords: Underground H_2 Storage, Aquifers, Storage Needs, Energy System Modelling

INTRODUCTION

Hydrogen technologies could be one of the pillars of future European energy and transport systems, making a valued contribution to the European Union (EU) transformation to a low carbon economy by 2050. Renewable hydrogen, when combined with large scale underground storage in aquifers, depleted fields (porous media) or salt caverns, enables transportation of energy through time balancing out the impacts of variable energy production from renewable energy sources. While storing pure hydrogen in salt caverns has been practiced since the ‘70s in Europe, hydrogen storage has not yet been carried out anywhere in depleted fields or aquifers. Although many aspects will be similar to the existing industry of natural gas underground storage, technical developments are still needed to validate this solution, particularly in terms of bio- and geo-chemical impacts of storage on the subsurface and in terms of the quality of hydrogen subsequently extracted from the store. This paper presents first results from WP5 of the ongoing HyStorIES project in respect to expected underground H_2 storage needs in future European energy system based on a detailed modelling exercise of the European energy system.

MATERIALS AND METHODS

The modelling of the European energy system in WP5 is based on a simulation platform developed by LBST to perform detailed techno-economic system analyses with a flexible technology focus and geographical scope at various scales. The LENS model (**L**BST **EN**ergy **S**ystem model) optimizes the size and operation of different elements of a predefined system in a given location and for a given time frame. It is formulated as linear programming (LP) problem for the purposes of this study with the objective to minimize the overall system costs subject to a number of techno-economic constraints in each of the modelling steps. The initial model formulation is related to the analyses on the role of energy storage from the microeconomic perspective and can be traced back to the work provided in [1]. More recent studies employed an extended model version with a larger scope but in smaller technological detail in order to analyze whole supply infrastructures, e.g., for hydrogen refueling stations [2], or integrated energy system at national [3] and pan-European level [4].

The analysis is mainly based on data from the study provided in [4]. In cases with low H_2 demand level almost 90% of the concerned final energy consumption is based on electricity (ca. 4,500 TWh/a) whereas hydrogen has a small share of only 10% (ca. 550 TWh/a). In cases with high H_2 demand level power demand is still significant (ca. 65% or 3,800 TWh/a), but hydrogen-based end-user applications play a much larger role (ca. 35% or more than 2,000 TWh/a). The

overall potential for renewable electricity generation in EU-27 and the UK of ca. 11,000 TWh/a is much larger than the expected power and hydrogen demand.

The major factors influencing the storage needs taken into account in this study are (see Fig. 1):

- general H_2 demand levels in end-user sectors including transport, heating and industry (low in Cases 1, 3, 5 and 7 and high in Cass 2, 4, 6 and 8),
- demand in the power sector from H_2 re-electrification in dedicated gas turbines and fuel cells (Cases 5-8) and
- supply pathways, i.e. variable H_2 production from domestic intermittent sources (Cases 1, 2, 5 and 6) vs. constant supply from conventional H_2 production or imports (Cases 3, 4, 7 and 8).

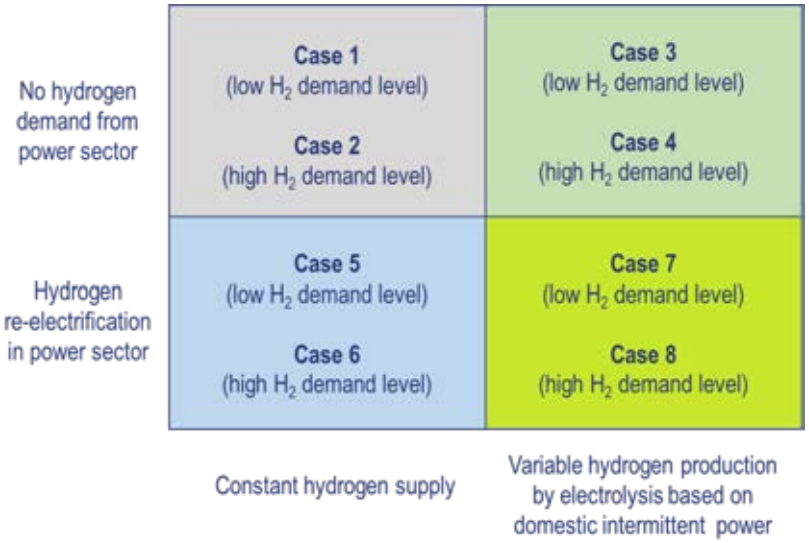


Fig. 1. Cases for analysis in respect to major impact criteria

RESULTS AND DISCUSSION

Generally, the larger the energy demand in a country the greater both the storage capacity and the range between the analysed cases (Fig. 2). In this context, the “big six” (i.e. Germany, France, Italy, the UK, Spain and Poland) account for ca. 75% of the overall required storage capacities in Europe. All other countries have a required storage capacity of less than 25 TWh_{H2} each in all cases. As expected, the largest requirements occur in Case 8 including the power sector and high variable hydrogen supply whereas the lowest required capacities can be observed in Case 1 with low constant H_2 supply and without need for H_2 re-electrification in the power sector. The largest capacity-to-input ratio occurs for Case 1 (constant H_2 supply and lower H_2 demand) with more than 4,100 h (170 days) for most countries. This means that in this case the input capacity is very small and it would take at least 4,100 h to fully fill the storage at constant input capacity. The lowest ratio ranges between 170-670 h and strongly depends on the relationship between hydrogen production profiles and thus renewable feed-in and electricity consumption patterns (or power residual load). In respect to required capacity-to-output ratio the spread between the highest and lowest case and the differences between the countries are much smaller than for storage input. Typically, output capacity correlates directly with hydrogen demand. Hence, the lowest capacities and highest capacity-to-input ratio of more than 1,200-1,600 h occur in Case 1 or Case 2 without the power sector for most countries whereas the highest capacities and lowest ratio can be observed for cases with explicit hydrogen re-electrification needs in the power sector in Case 5 to 8 (140-730 h).

The storage is operated on a seasonal basis in a similar way in all cases and in all countries. The highest number of full cycle equivalents can be observed in cases with high hydrogen demand and variable supply (Cases 5 to 8) of up to 8.5 cycles (or 43 days). In contrast, in Cases 1 to 4 the underground storage operation is characterized by ca. one cycle per year regardless of hydrogen demand and storage capacity. This means that low hydrogen demand excluding the power sector and constant hydrogen supply reduce the fluctuation of storage filling level significantly. The corresponding European electrolysis capacity for variable hydrogen production ranges between ca. 200-2,220 GW_{el}.

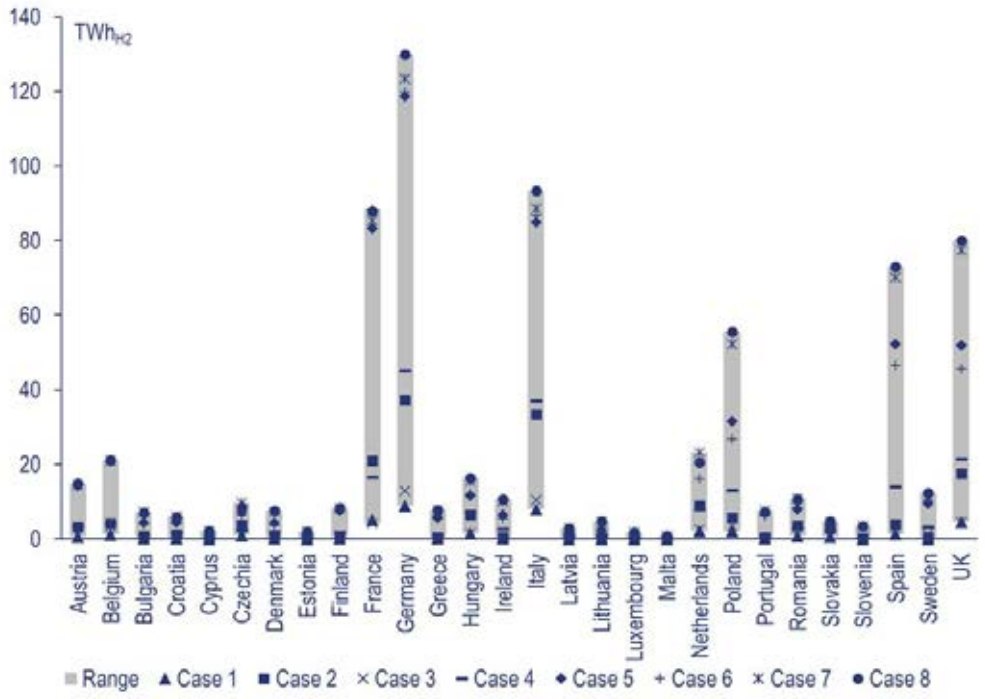


Fig. 2. Required capacity for underground hydrogen storage in selected cases.

CONCLUSIONS

The results of our analysis underline the need for large-scale underground hydrogen storage in the context of climate neutrality across Europe. According to study outcomes in Cases 5, 6, 7 and 8 ca. 1,600-2,200 TWh_{H2}/a need to be stored in European underground facilities corresponding to ca. 34%-60% of the overall annual hydrogen demand (including re-electrification in the power sector) in Europe. Since salt caverns are limited to selected countries in Europe due geological conditions aquifers and depleted gas fields might be an attractive alternative for such underground hydrogen storage. However, further analyses in the HyStorIES project will be conducted to better understand the role of hydrogen storage in porous media by taking additional constraints such as gird constraints and technology developments int account.

ACKNOWLEDGEMENT

This project has received funding from the Fuel Cells and Hydrogen 2 Joint Undertaking under grant agreement No 101007176. This Joint Undertaking receives support from the European Union's Horizon 2020 research and innovation programme and Hydrogen Europe and Hydrogen Europe Research

REFERENCES

1. Michalski J. 2016. The Role of Energy Storage Technologies for the Integration of Renewable Electricity into the German Energy System. Dissertation, Technische Universität München.
2. Bünger, U, Michalski J, Crotogino F and Kruck O. 2016. Large-scale underground storage of hydrogen for the grid integration of renewable energy and other applications. In: Compendium of Hydrogen Energy Volume 4: Hydrogen Use, Safety and the Hydrogen Economy. Edited by Ball M, Basile A and Veziroglu TN. Cambridge, Woodhead Publishing.
3. Michalski J, Poltrum, M and Bünger U. 2019. The role of renewable fuel supply in the transport sector in a future decarbonized energy system. International Journal of Hydrogen Energy 44: 12554-12565.
4. Trinomics/LBST/E3M. Impact of the use of the biomethane and hydrogen potential on trans-European infrastructure. Report for European Commission DG Energy. Brussels, September 2019.

WHEC-2022
23rd World Hydrogen Energy Conference
June 26-30, 2022 - Istanbul

#90

FROM BATCH REACTOR TO CONTINUOUS FLOW MICROCHANNEL REACTOR FOR DEHYDROGENATION OF PERHYDRO-DIBENZYLTOLUENE: A PRELIMINARY STUDY

[1,2] Ahsan Ali, [1] Ajith Krishnan R, [1] Hee Joon Lee*
[1] School of Mechanical Engineering, Kookmin University, Seoul, Republic of Korea
[2] Department of Mechanical Engineering, Gachon University, Seongnam, Republic of Korea

*Corresponding author e-mail: joellee@kookmin.ac.kr

ABSTRACT

Hydrogen stored in liquid organic hydrogen carriers (LOHCs) like dibenzyltoluene makes it a simple and safe technology along with long term storage. In this study, a preliminary study regarding the dehydrogenation of perhydro-dibenzyltoluene with switching from a stirred batch reactor to a continuous flow microchannel reactor is presented. The performance of the reactors was investigated with a 2% Pt/Al_2O_3 catalyst. The hydrogen production percentage in the case of a continuous flow microchannel reactor was found higher (58% hydrogen production) when compared to that of a stirrer type reactor (only 12% hydrogen production) in 12 hours of operation. Moreover, the effect of microchannel bottom plate temperature on the hydrogen production was also investigated. The hydrogen production was increased from 64.15% to 82.20% with the increase in bottom plate temperature from 260 to 320°C for 0.01 mL/min flow rate of H18-DBT and 20 hours experiment. With the increase in the operating time, the hydrogen production found to increase slowly. A maximum of 88% of hydrogen was generated for a 40 hours' operation, at a bottom wall temperature of 290°C. The results revealed that a continuous microchannel reactor can be an appropriate technology for the dehydrogenation of H18-DBT.

Keywords: Dehydrogenation, Liquid Organic Hydrogen Carrier, Microchannel Reactor, Dibenzyltoluene

INTRODUCTION

Sustainable techniques for power generation and renewable energy sources will play a vital role in maintaining a healthy climate for future generations. In particular, hydrogen is attracting attention as an efficient energy source that can be produced and stored without the emission of greenhouse gases. The uses of hydrogen as a fuel are well known and hydrogen has applications as fuel in the transport sector. For use as a fuel, LOHCs store and release hydrogen through controlled hydrogenation and dehydrogenation processes. LOHCs are efficient choice for long term energy storage without any loss, safe transport, hydrogen production and generation of electric power via fuel cells in applications such as automobiles. Considered herein, dibenzyltoluene (DBT) belongs to the family of cycloalkanes and is widely used as an industrial heat transfer oil. DBT was first proposed as an LOHC in 2014 by Brucker et al [1]. Dehydrogenation of LOHCs in liquid form is typically studied in batch type reactors. However, continuous flow reactors have many advantages over batch reactors. Batch reactors has inefficient heat mass transfer and slow temperature control. The continuous flow reactors allow instantaneous heating and cooling along with very fast mixing. Continuous flow microchannel reactors (MCHRs) are primarily closely packed reactors with channel dimensions in the range of millimeters (Hydraulic diameter (D_h) < 1mm). They have high surface to volume ratios, uniform heat transfer catalyst zones and compact sizes.

However, there is no study to use microchannel reactor for LOHC (in liquid form) dehydrogenation based on the literature review. The novelty of this work lies in the implementation of a MCHRs for the dehydrogenation of perhydro-dibenzyltoluene instead of the existing studies using a stirrer type reactor. The aim of the study was to introduce the microreactor to investigate the dehydrogenation of H18-DBT (liquid form). To do that, we consider two different reactor types for the dehydrogenation of H18-DBT: a batch reactor and a continuous flow MCHR. The performances of both reactors are evaluated for hydrogen generation from H18-DBT with a 2 wt.% Pt/Al_2O_3 catalyst.

EXPERIMENTAL APPARATUS

The batch reactor (HR-8300, 10 bar operating pressure, attached mechanical stirrer) was the same as that in [2]. The continuous flow reactor was a microchannel reactor. Both a schematic of the experimental apparatus with the microchannel reactor for the dehydrogenation study and a photograph of the experimental setup are provided in Fig. 1.

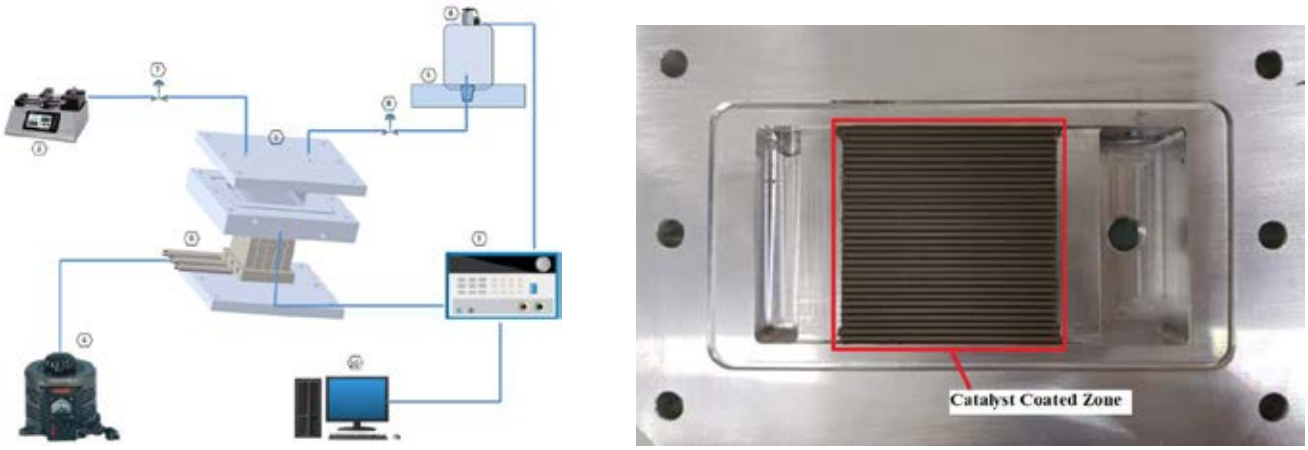


Fig. 1. Schematic of the experimental apparatus. 1 – Microchannel reactor; 2 – Syringe pump; 3 – Data logger; 4 – Power supply; 5 – Water bottle; 6 – Ultrasonic level transmitter; 7 – Check valve; 8 – Drain valve; 9 – Cartridge heaters; 10 – Computer, Photograph of the catalyst coated microchannel substrate

The experimental facility consisted of a microchannel reactor, thermocouples (TCs), valve, syringe pump, pressure transducers (PTs), data acquisition system, power supply, cartridge heaters, and a water displacement apparatus for measuring the generated hydrogen. A MCHR was designed and fabricated to carry out the dehydrogenation experiments. The material used for the MCHR was aluminum. Parallel microchannels (depth 900 μm, width 400 μm, length 50 mm) were fabricated on the aluminum plate by an electrode discharge machining process. The 2% Pt/Al_2O_3 catalyst was coated on the microchannel walls using the wash coating method [3].

RESULT AND DISCUSSION

The dehydrogenation of H18-DBT was carried out in the microchannel reactor within a temperature range of 260 to 320°C as reported previously [4]. The hydrogen production as a function of reaction zone temperature is shown in Fig. 2. The hydrogen production increased from 64.15% at 260°C to 82.20% at 320°C.

To prove the repeatability of the dehydrogenation experiments in the microchannel reactor another trial was conducted with a reaction zone temperature of 290°C. A duration of 40 h was chosen for the experiment to understand the effect of dehydrogenation reaction duration on the hydrogen production in the microchannel reactor. The supply of DBT in microchannel was stopped after a period of 20 h and the remaining DBT adsorbed to the walls of the microchannels channel reacted to produce hydrogen. The hydrogen production for the two runs match closely during the initial 20 h. Increasing the duration of the reaction to 40 h increased the hydrogen production from 78 to 88%.

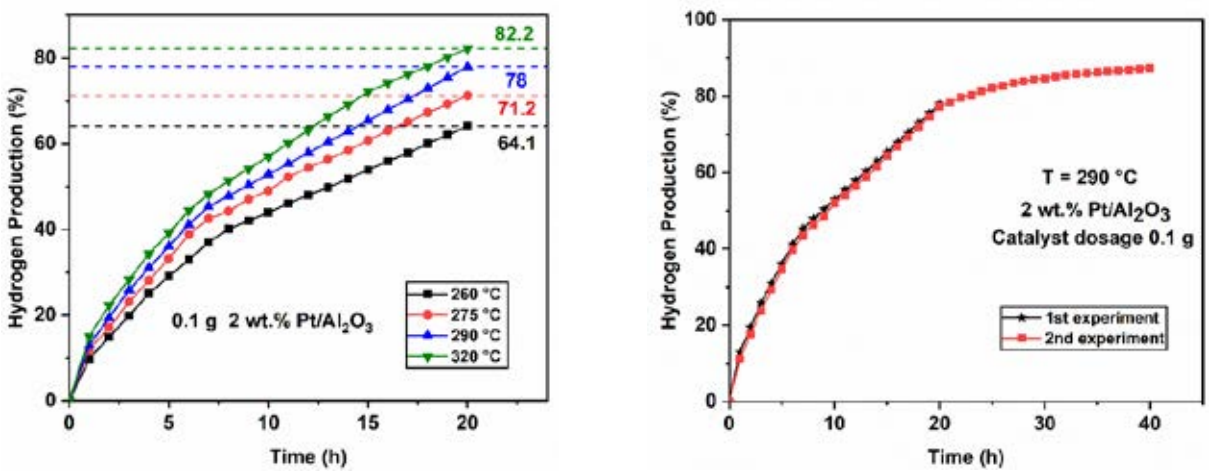


Fig. 2. Hydrogen production% from H18-DBT at different temperatures and Dehydrogenation of H18-DBT in the microchannel reactor with 20 h and 40 h of duration

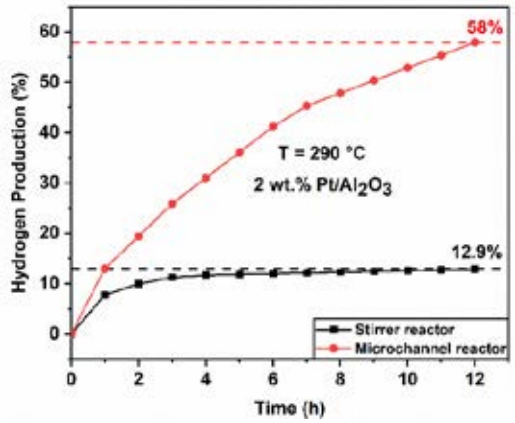


Fig. 3. Comparison of stirrer and microchannel reactor

The continuous flow microchannel reactor was introduced as an alternative to the batch type reactors. However, an exact comparison between the two reactors is not possible, as in a batch type reactor, the reactants are all added before the reaction begins and the products are discharged after reaction is completed, whereas the reactants and the products are added and discharged throughout the reaction process in flow reactors.

A comparison of the hydrogen production in the two reactors is shown in Fig. 3. For microchannel reactor, only part of the catalyst mass coated on the channel wall will actively participate in the dehydrogenation reaction. To account for this, the amount of catalyst was doubled in the case of microchannel reactor (estimated mass of 0.1 g). The hydrogen production percentage was higher for the case of microchannel reactor than the stirrer batch reactor. The initial hydrogen production after 2 h of reaction time was very high for the batch stirrer but progresses little with increased time beyond that point. The microchannel reactor almost has a linear hydrogen production trend with time. Hence, the performance of MCHR was better than the batch reactor.

CONCLUSIONS

The dehydrogenation of H18-DBT was conducted in the microchannel within a temperature range of 260 to 320°C over 2 wt.% Pt/Al_2O_3 catalyst. The reaction was compared to that in a conventional batch reactor. The reaction rate was increased with the increasing temperature and the maximum hydrogen production (82.20%) was obtained at 320°C after 20 h reaction time. The 88 % of the stored hydrogen was produced after 40 h in the microchannel reactor.

The hydrogen production of 58% in microchannel reactor at 290°C after 20 h was greater than that in the stirrer batch reactor (12%) under similar conditions. Moreover, the microchannel reactor also has the advantage of utilizing a lower amount of the catalyst.

ACKNOWLEDGEMENT

This work was supported by the National Research Foundation of Korea (NRF) grant funded by the Korean government (MSIT) (NRF-2018R1A2B6006160). This work was supported by the Brain Pool Program through the National Research Foundation of Korea (NRF) funded by the Ministry of Science and ICT (KRF grant No. 2019H1D3A1A01102855).

REFERENCES

1. Brückner N, Obesser K, Bösmann A, Teichmann D, Arlt W, Dungs J and Wasserscheid P. 2014. Evaluation of industrially applied heat-transfer fluids as liquid organic hydrogen carrier systems. ChemSusChem 7:229-235.
2. Ali A, Kumar UG and Lee HJ. 2020. Parametric study of the hydrogenation of dibenzyltoluene and its dehydrogenation performance as a liquid organic hydrogen carrier. ChemSusChem 7:229-235.
3. Zapf R, Kolb G, Pennemann H and Hessel V. 2006. Basic study of adhesion of several alumina-based washcoats deposited on stainless steel microchannels. Chemical Engineering and Technology 29:1509-1512.
4. Modisha PM, Ouma CNM, Garidzirai R, Wasserscheid P and Bessarabov D. 2019. The prospect of hydrogen storage using liquid organic hydrogen carriers. Energy and Fuels 33:2778-2796.

WHEC-2022
23rd World Hydrogen Energy Conference
June 26-30, 2022 - Istanbul

#119

DIGITAL DEVELOPMENT OF AN OPTIMIZED HEAT MANAGEMENT DESIGN FOR AN INTEGRATED SOLID-STATE H_2-STORAGE RESERVOIR

[1,2*] *Phillip S. Krause,* [1,2] *Jan Warfsmann,* [1,2] *Eike Wienken,* [1,2] *Julian Jepsen,* [1,2] *Thomas Klassen,*[1,2] *Julián Puszkiel*
[1] Institute of Materials Research, Helmholtz-Zentrum HEREON, Max-Planck-Straße 1, 21502 Geesthacht,Germany;
[2] Faculty of Mechanical Engineering, Institute of Materials, Helmut Schmidt University, Holstenhofweg 85, 22043,Hamburg,Germany

*Corresponding author e-mail: Phillip.Krause@hereon.de

ABSTRACT

The main drawback of large-scale metal hydride storage systems is the low thermal conductivity of most metal hydrides and the corresponding difficulties for the heat management system. In this work, the optimization of the internal heat management of a hydrogen storage tank is investigated by finite element simulations. Different design parameters of internal fins are analyzed, such as number, thickness, and length of the fins. It is found that a specific configuration of fins results in a notable improvement of heat transfer and corresponding improvement in desorption kinetics.

Keywords: Hydrogen Storage, Room Temperature Metal Hydride, Heat Transfer Management, Tank Design, AB2-Alloy

INTRODUCTION

In the last decades, hydrogen has gained more interest in the scientific and industrial community as an energy carrier due to its high gravimetric energy density. One of the main bottlenecks for hydrogen introduction in society is finding an efficient and safe hydrogen storage system. As a storage method, the solid-state storage in room temperature metal hydrides has beneficial properties such as low operating pressures and moderate working temperatures [1].

One significant drawback of metal hydrides for commercial application is that most metal hydride materials present a low thermal conductivity [2]. Therefore, most metal hydride systems have inefficient hydrogen absorption and desorption performances in scaled-up systems. Several methods to improve the thermal conductivity of the metal hydride have been investigated. Those methods integrate materials with higher thermal conductivity like aluminum or copper in foam or as a net structure, a mixture of expanded graphite and metal hydride, or an internal heat exchanger [3-7]. A different method is the integration of fins made of copper or aluminium to improve the heat exchanger [8,9].

This work investigates the optimal internal heat management design of a cylindrical metal hydride storage tank with an external heat exchanger using finite element modeling. The aim of developing such a storage system is to couple it with a 10 kW PEM fuel cell that consumes 670 g/h of hydrogen at full load. The addition of internal aluminium fins is studied, and parameters such as the number, thickness, and length of fins are evaluated and optimized to provide the required hydrogen flow to the fuel cell.

MODELING DESCRIPTION

The metal hydride storage tank was modeled in a 2D geometry with COMSOL Multiphysics 5.6. The cylindrical tank was calculated with a capacity of 0.5 kg H_2, thus containing 62.5 kg of the commercial room temperature AB2-alloy, Hydralloy C5® with a maximum experimental capacity of 1.1 wt.% H_2. This simulation implemented the hydrogen absorption and desorption kinetic behavior using the separated variables approach with the van't Hoff equation for the equilibrium pressure. Table 1 describes the essential parameters for the simulation.

Table 1. Important parameters for 2D model

Variable	Value	Name
A1	14.96 [1/s]	Frequency factor
Ea1	15.00 [kJ/mol H_2]	Dehydrogenation activation energy
R_g	8.314 [J/mol H_2]	Gas universal constant
DeltaH1	28.4 [kJ/mol H_2] [10,11]	Dehydrogenation enthalpy
DeltaS1	112.0 [J/mol H2] [10,11]	Dehydrogenation entropy
rho_bulk	3540.0 [kg/m^3]	Initial bulk density of the alloy
k_alloy	1.0 [W/m*K]	Effective thermal conductivity of the hydride bed
k_fin	117.0 [W/m*K]	Thermal conductivity of the aluminium for the fins

The objective of this study is to research the possibility of improving the desorption performance of the tank by changing the internal geometric shape of aluminium fins. Significant boundary conditions are that the external cooling

fluid is water with a temperature of 55°C and is modeled as natural convection. In addition, some assumptions are considered for the simulation. The most important assumptions are that all the hydrogen released is taken from the system and that there is a local thermal equilibrium between the hydrogen gas and the hydride bed. The expansion of the metal hydride is also not taken into account and the hydride bed is assumed to be isotropic.

As design variables for the optimization, three different options were considered. The calculated number of fins were 4, 8, 12, and 16. The thickness of the fins was changed between 1.5 mm and 4 mm. The length of the fins was evaluated between 45 mm and 65 mm. The outer diameter remained the same as did the wall thickness of the tank shell. In addition, the length of the vessel was adjusted accordingly to the change of the internal geometry, in order to keep the amount of alloy inside of the tank constant.

RESULTS AND DISCUSSION

Figure 1 shows 2D geometry sketches of the temperature profiles at different concentrations and desorption kinetic curves for different lengths of fins with a thickness of 2 mm and a total number of 12 fins. The dehydrogenation kinetic curves show the hydrogen weight percent (wt.%) over the simulation time (wt.%: mass of hydrogen released upon desorption over the maximum mass of hydrogen released).

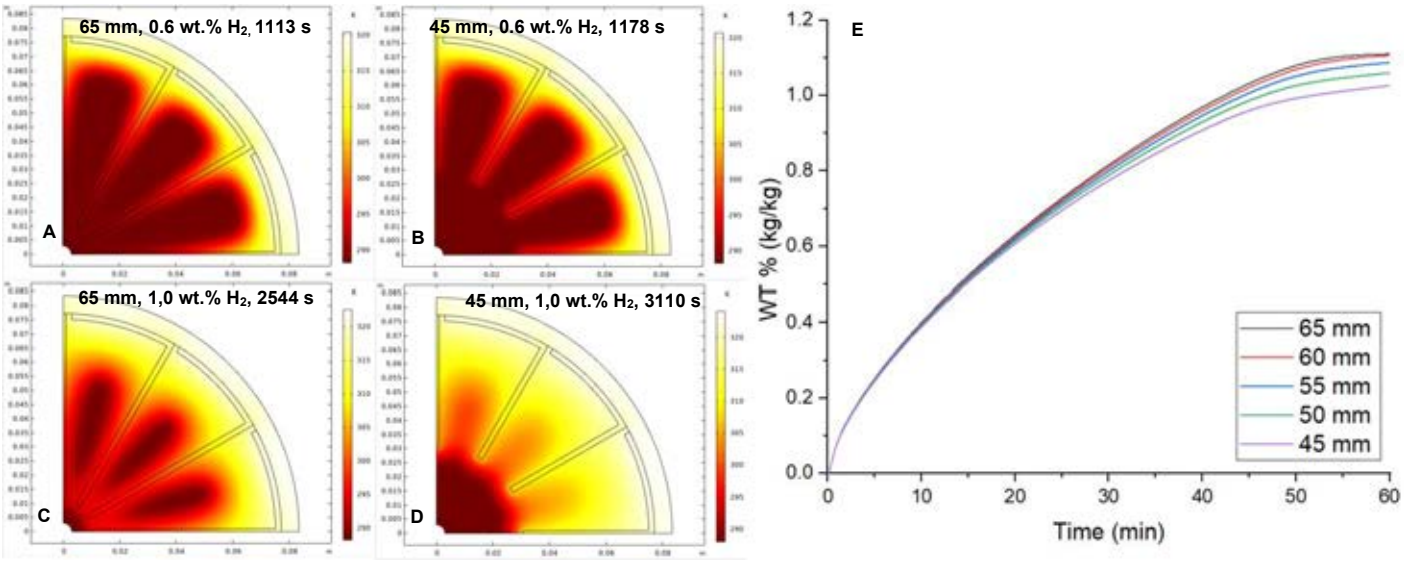


Figure 1: Example of the temperature evolution in a 2D tank geometry for 45 and 65 mm fins at 0.6 wt.% and 1.0 wt.% of the hydrogen capacity released (left) and example of the desorption kinetics for the released hydrogen (right).

In Figure 1, it can be seen that longer fins lead to slightly faster desorption kinetics. Lengths between 65 and 55 mm show almost no difference in terms of kinetic behavior. For lengths shorter than 55 mm, the kinetic behavior slows down more notably. Considering that the tank is heated up on the external shell, the dehydrogenation process starts from the hydride bed in contact with the internal part of the shell and fins. Up to about 0.6 wt.% H_2, the curves do not show almost any difference because all the fins' lengths cover the radial hydride bed portion. This fact is clearly seen by the temperature distribution at 0.6 wt.% H_2 by comparing 65 and 45 mm lengths of the fins (Figure 1A and B). As the fins' lengths are short, the heat transfer to the center of the tank becomes less efficient. Therefore, the differences are more notable for lengths shorter than 55 mm and after a dehydrogenation stage of about 0.6 wt.% H_2. In Figure 1C and 1D, the temperature profile between 45 and 65 mm fin's length at 1.0 wt.% H_2 is quite different. The reaction proceeds more slowly and, in the case of the 45 mm long fins, is practically terminated at 1.0 wt% H2, while in the case of the 65 mm long fins it proceeds more rapidly until about 1.1 wt%.

Figure 2 presents the hydrogen release rate and hydrogen supply time for different configurations. It is important to mention that the design is developed to provide 670 g/h. This rate is calculated with the amount of alloy in one tank (62.5 kg of Hydralloy C5®; wt.% max: 1.1). Figure 2A shows the hydrogen flow provided by tanks with 12 fins and with different thicknesses as a function of time. As seen, a thicker fin leads to the faster release of hydrogen. This behavior results in a faster response, though it does not provide hydrogen to the fuel cell for a long time. In Figures 2B and 2C, it is possible to observe that thicker or longer fins usually lead to better system performance. This is due to the better distribution of heat inside of the tank due to the enhanced thermal conductivity of the hydride bed due to the fins.

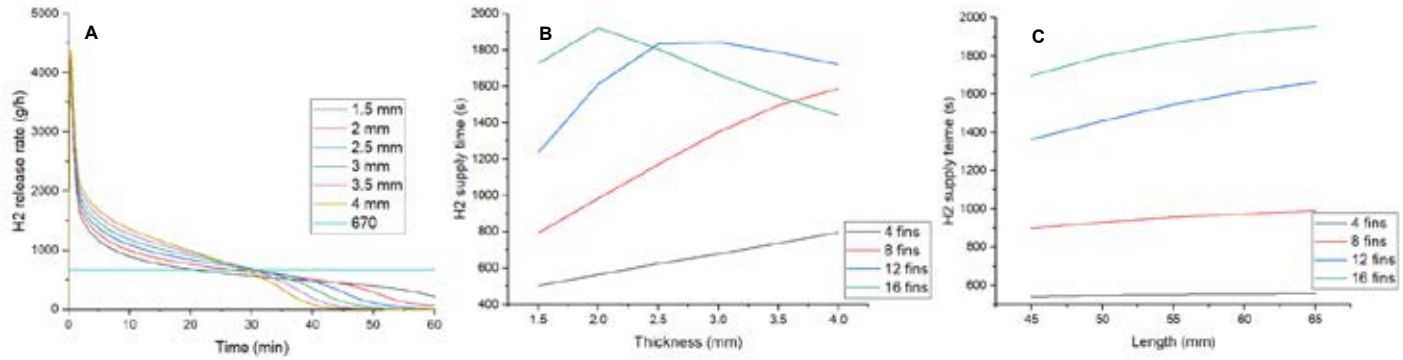


Figure 2: hydrogen release rate for different fin thicknesses (left), time until the tank cannot supply 670 g/h of hydrogen as a function of the thickness (middle) and the length (right) of the fins.

CONCLUSIONS

The limiting factor for metal hydride tanks is the heat transfer inside the pressure vessel in a scaled-up system. An efficient approach to improving the internal heat management of a scale-up metal hydride-based hydrogen storage reservoir is the addition of an internal structure that can provide a better heat distribution and enhanced heat conduction. This study shows that the system can be efficiently improved by adding fins inside of the tank. An optimal tank design configuration is found. A metal hydride-based tank with 16 aluminium inner fins of 2 mm thickness and 65 mm length is the most efficiant configuration, as it can provide the 670 g/h of hydrogen for more than 1900 seconds.

ACKNOWLEDGEMENT

The authors acknowledge the funding provided by dtec.bw® - Zentrum für Digitalisierungs- und Technologieforschung der Bundeswehr in the frame of the project “HyReflexS” and the associated project partners Helmut Schmidt University and Helmholtz-Zentrum Hereon.

REFERENCES

1. Bellosta von Colbe J., et. al. 2019. Application of Hydrides in Hydrogen Storage and Compression. International Journal of Hydrogen Energy 44:7780-7808.
2. Shafiee S., McCay M. H. 2016. Different reactor and heat exchanger configurations for metal hydride hydrogen storage systems. International Journal of Hydrogen Energy 41:9462-9470.
3. Chen Y., Sequeira CAC., Chen C., Wang X., Wang Q. 2003. Metal hydride beds and hydrogen supply tanks as minityp PEMFC hydrogen sources. International Journal of Hydrogen Energy 28:329-333.
4. Lèvesque S., Ciureanu M., Roberge R., Motyka T. 2000. Hydrogen storage for fuel cell systems with stationary applications. International Journal of Hydrogen Energy. 25:1095-1105.
5. Nagel M., Komazaki Y., Suda S. 1986. Effective thermal conductivity of a metal hydride bed augmented with a copper wire matrix. Journal of Less Common Metals. 120: 35-43.
6. Klein HP., Groll M. 2004. Heat transfer characteristics of expanded graphite matrices in metal hydride beds. International Hournal of Hydrogen Energy n29:1503-1511.
7. Oi T., Maki K., Sakaki Y. 2004. Heat transfer characteristics of the metal hydride vessel based on the plate-fin type heat exchanger. Journal of Power Sources. 125:52-61
8. Krishan KV., Manelil NP., Maiya MP. 2021. Geometrical optimization of longitudinal cooling fins for metal hydride based hydrogen storage reactors. ICCIKE
9. Kukkapalli VK., Kim S. 2016. Optimization of internal cooling fins for metal hydride reactors. Energies 447:9-15.
10. Weckerle C., Bürger I., Linder M. 2017. Novel reactor design for metal hydride cooling systems. International Journal of Hydrogen Energy. 42:8063-8074.
11. Capurso G., et. al. 2016. Development of a modular room-temperature hydride storage system for vehicular applications. Appl. Phys. A. 122:236-247.

WHEC-2022
23rd World Hydrogen Energy Conference
June 26-30, 2022 - Istanbul

#120

MODELING AND PROCESS SIMULATION OF A METAL HYDRIDE TANK COUPLED WITH A PEM ELECTROLYZER

[1,2]* Eike S. Wienken, [1,2] Phillip S. Krause, [1,2] Jan Warfsmann, [1] José Bellosta von Colbe, [1,2] Julian Jepsen, [1,2] Thomas Klassen, [1,2] Julián A. Puszkiel

[1] Helmholtz-Zentrum Hereon, Institute of Hydrogen Technology, Max-Planck-Straße 1, 21502 Geesthacht, Germany
[2] Helmut Schmidt University, Faculty of Mechanical Engineering, Institute of Materials, Holstenhofweg 85, 22043, Hamburg, Germany

*Corresponding author e-mail: eike.wienken@hereon.de

ABSTRACT

To cope with the tight timeframe of the global transformation from fossil to renewable energy sources, efficient methods and tools such as process and system simulation are essential for rapid development, cost-efficient design and scale-up validation of new energy systems. This numerical analysis investigates the coupling of a stationary metal hydride (MH) hydrogen storage system with a low-temperature 10 kW proton exchange membrane (PEM) electrolyzer as a fast-responding and well-controllable hydrogen source. The heat management of the solid-state storage tank is improved through additional aluminium fins and an external cooling jacket. For modeling and process simulation, Aspen Custom Modeler® is used to study the mass and heat transfer phenomena in the hydrogen storage tank, as well as the interaction with the electrolyzer. The hydrogen tank is designed to store a total capacity of 700 g of H_2 using 62.5 kg commercial room temperature AB_2-alloy, Hydralloy C5®. The operating pressure varies from 5 to 38 bar H_2, while the coolant temperature varies from 20 to 60°C depending on the exothermic absorption or endothermic desorption processes.

Keywords: Simulation, Hydrogen Storage, Room Temperature Hydrides, PEM Electrolyzer, Emergency Power Supply

INTRODUCTION

The efficient storage and transport of hydrogen in stationary and mobile applications is considered the central technological challenge of the global energy transition [1–4]. Due to hydrogen's low volumetric energy density at ambient temperature and pressure, it is necessary to develop improved storage methods and strategies to store hydrogen economically, practicably and safely [1,5]. While physically-based hydrogen storage systems such as compressed gas, cold/cryo-compressions and liquid hydrogen technologies are already utilized in many industrial applications, the group of material-based hydrogen storage systems such as adsorbents, liquid organic, interstitial and complex hydrides as well as chemical hydrides are still under development or used in niche applications, respectively [1,4]. However, since the low gravimetric energy density of MH-based hydrogen storage systems usually limits the mobile application, MH provides more promising properties for stationary storage solutions due to their relatively high volumetric storage capacity, intrinsic safety and long-term stability with low requirements in terms of operating pressure and temperature [4–6]. Since the use of renewable energies such as wind turbines and photovoltaics naturally leads to an unsteady power supply, a particular focus remains on the investigation of suitable stationary energy storage systems based on MH in combination with electrolyzers and fuel cells for demand-side management to balance the power grid and emergency power supply [7–9]. By developing process simulation models, the performance of a stationary MH storage system in interaction with a PEM electrolyzer and its performance for supplying hydrogen to a PEM fuel cell is investigated here.

MODELING AND SIMULATION

In the first approach, the MH tank was modelled with Aspen Custom Modeler® V11 as a dynamic 0D simulation that considered the equations for mass and energy conservation, the chemical reaction kinetics, and the thermodynamic properties - hydrogen pressure and temperature. The van't Hoff law: $ln\left(\frac{p_{eq}}{p_0}\right) = \frac{\triangle H}{RT} + \frac{\triangle S}{R}$ Eq. (1) was used to describe the equilibrium pressure of the AB_2-alloy as a function of the temperature of the MH bed [5]. As Hydralloy C5® is a commercial and well-characterized MH forming alloy, the material properties for the reaction kinetics were taken from the literature [10,11]. The modeling of the MH intrinsic reaction kinetic was expressed according to the equation (2): $d\alpha/dt = k(T)f(p_{op}, p_{eq})g(\alpha)$ Eq. (2) with $d\alpha/dt$ as the hydrogenation reaction rate, $k(T)$ for the Arrhenius rate term as a function of T, $f(p_{op}, p_{eq})$ as a function of the tank operating and equilibrium pressures and $g(\alpha)$ as a function of the reacted hydrogenation fraction to describe the intrinsic gas-solid reaction behavior [10,12]. The tank was designed with inner fins to enhance the effective thermal conductivity of the hydride bed. Thus, the effective thermal conductivity of the inner part of the tank, including the MH, the hydrogen gas phase and the aluminium fins was calculated as a weighted value considering the mass of hydride forming alloy and the mass of aluminium. In this

regard, the thermal conductivity of the hydride phase was taken as κ_{Alloy} = 1 W/m*K [13] and the aluminium alloy as κ_{Al} = 215 W/m*K [14]. Forced convection was considered on the outer wall of the tank with a convective heat coefficient of h_{wall} = 500 W/m²*K and a coolant reservoir of 1 m³ with an initial temperature of 20 °C. For the first simulation step, the model of the 10 kW PEM electrolyzer was simplified to an independent hydrogen source with a constant mass flow of 170 g H_2/h and without connection to the energy balances of the hydrogen tank. The filling of the MH tank was simulated at a constant inlet pressure of 38 bar H_2 and a relatively low coolant flow of 10 NL/min (pure water) at an inlet temperature of 20 °C. The dehydrogenation, in turn, took place with a constant hydrogen discharge of 670 g H_2/h at 5 bar and a coolant flow of 60 NL/min at 60 °C. Radiation heat losses and pressure losses due to friction were neglected. In addition, uniform distribution and temperature of the hydrogen gas phase, AB_2-alloy, and MH, respectively, was assumed. The simulation was done as a closed loop of charging and discharging the tank. Therefore, the final values of the hydrogenation process were defined as the initial values of dehydrogenation and vice versa in terms of masses and the internal tank pressure.

RESULTS AND DISCUSSION

The left side in Fig. 1 shows the cumulative masses of AB_2-alloy, hydride, and absorbed H_2 (Fig. 1a), and the center shows the inner tank plus coolant inlet and outlet temperatures (Fig. 1b) as a plot against absorption time. In addition, the right side shows the tank operating, the van't Hoff equilibrium and the PEM electrolyzer H_2 feed pressures (Fig. 1c).

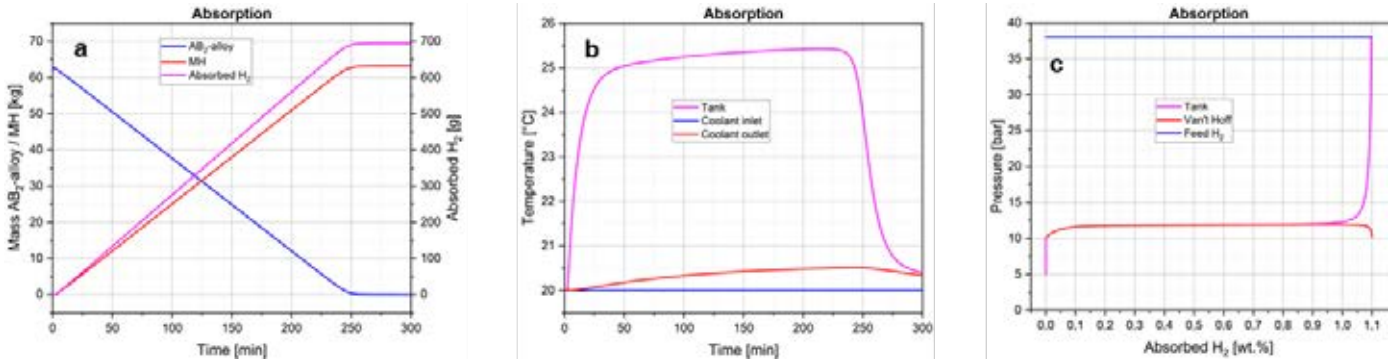


Figure 1: Masses vs. time (1a), temperature vs. time (1b) and pressure vs. wt.% of H_2 (1c) during the absorption.

The hydrogenation process is exothermic, and it results in the release of thermal energy to the environment. For this reason, the internal temperature profile of the tank (Fig. 1b) increases as soon as the hydrogenation reaction starts and reaches a maximum temperature of about 25.5 °C after 220 min. In contrast, the coolant temperature does not change significantly due to the forced convection conditions for the heat exchanger. The initial internal tank pressure is given as 5 bar, since it is the required minimum operating pressure for the PEM fuel cell virtually connected to the hydrogen tank. In Fig. 1c, it is possible to notice that the hydrogenation process does not start immediately, but only after approx. 2.5 min, because the initial internal tank pressure is lower than the equilibrium pressure of the AB_2-alloy-MH hydride system of about 10 bar at the initial operating temperature of 20 ºC. While the mass rates of hydride and hydrogen absorption increase due to the provided feed rate of 170 g H_2/h, the mass rate of AB_2-alloy decreases since it is consumed (Fig. 1a). As seen in Fig. 1a, the charging rate is relatively slow, and the entire hydrogenation process takes about 250 min to reach the total storage capacity of the tank. Under this low flow condition and proper heat release, the pressure evolution of the tank follows the equilibrium pressure of the solid phase between 20 and 25.5 ºC as shown in Fig. 1b. After about 1 wt.% of hydrogen is absorbed, the reaction rate slows down to zero and the tank pressure eventually rises to the hydrogen inlet pressure of the PEM electrolyzer of 38 bar (Fig. 1c).

The desorption characteristics in terms of mass balances and temperatures as a function of time, as well as the pressures vs. wt.% of hydrogen, are shown in Fig. 2. Taking into consideration that, at the beginning of the dehydrogenation process, the tank is in the hydrogenated state under 38 bar, the desorption from the solid phase does not start until reaching an operating pressure below the equilibrium pressure of about 6 bar at 20 °C (Fig. 2a and c). For nearby 3 min hydrogen is released from the gas phase with a mass flow rate of 670 g H_2/h, and then the MH starts to release hydrogen (Fig. 2c). In contrast to the absorption, the desorption of hydrogen from hydrides is an endothermic process that requires energy and results in cooling of the inner tank bed. The tank temperature initially decreases with the onset of dehydrogenation and reaches a minimal temperature of about 15.5 °C. Then, due to the heat provided by the coolant and the slower reaction rate as the residual amount of hydride decreases, temperature increases again (Fig. 2b). After about 60 min, most of the hydrogen bond in the hydride is desorbed, leading to a stagnation of the mass rates of desorbed hydrogen and formation of the AB2-alloy (Fig. 2a). In addition, the temperature curve's slope of the tank increases and the operating tank pressure drops to the given PEM fuel cell

operating pressure of 5 bar. The tank and thermal management configuration shows that the MH storage system is capable of providing 670 g H_2/h for about 1 h, which is approx. equivalent to providing 10 kW of power for 1 h.

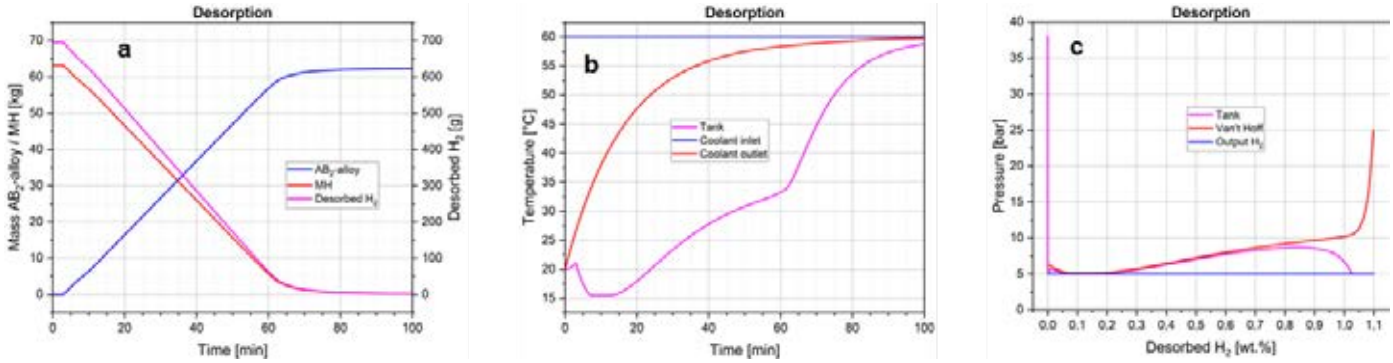


Figure 2: Masses vs. time (2a) and temperature vs. time (2b) and pressure vs. wt.% of H_2 (2c) during the desorption.

CONCLUSIONS

This research work deals with the process simulation of a hydrogen storage system based on a room temperature hydride coupled with a PEM electrolyzer. The developed MH storage-fuel cell-electrolyzer system is able to store about 700 g of hydrogen in approx. 250 min and provide about 10 kW of electrical energy for 1 h considering the hydrogen mass flow of 670 g/h. Aspen Custom Modeler® is used to create and investigate a numerical model of the hydrogen storage tank, taking into account mass and energy conservation, chemical reaction kinetics, pressures and temperatures. A model is presented that enables the simulation of MH hydrogen storage systems as a basis for further investigations on charging and discharging strategies of storage systems connected in parallel and series, respectively. Furthermore, in terms of system simulation and evaluation, this model also allows the coupling of heat exchangers, electrolyzers and fuel cells.

ACKNOWLEDGEMENT

The authors acknowledge the funding provided by dtec.bw® - Zentrum für Digitalisierungs- und Technologieforschung der Bundeswehr in the frame of the project “HyReflexS” and the associated project partners.

REFERENCES

1. https://www.energy.gov/eere/fuelcells/hydrogen-storage. Accessed on November 20, 2021.
2. Hassan IA, Ramadan HS, Saleh MA et al. 2021. Hydrogen storage technologies for stationary and mobile applications: Review, analysis and perspectives. Renewable and Sustainable Energy Reviews 149:111311.
3. https://www.fch.europa.eu/sites/default/files/documents/hfp_ds_report_aug2005.pdf. Accessed on November 21, 2021.
4. Bellosta von Colbe J, Ares JR, Barale J et al. 2019. Application of hydrides in hydrogen storage and compression: Achievements, outlook and perspectives. International Journal of Hydrogen Energy 44:7780-7808.
5. Gambini M, Manno M and Vellini M. 2008. Numerical analysis and performance assessment of metal hydride-based hydrogen storage systems. International Journal of Hydrogen Energy 33:6178-6187.
6. Rizzi P, Pinatel E, Luetto C et al. 2015. Integration of a PEM fuel cell with a metal hydride tank for stationary applications. Journal of Alloys and Compounds 645:338-342.
7. Stark M, Krost G, Lemken D et al. 2011. Neural network based modeling of metal-hydride bed storages for small self-sustaining energy supply systems. IEEE Xplore 1-7.
8. Valverde L, Rosa F, Del Real AJ et al. 2013. Modeling, simulation and experimental set-up of a renewable hydrogen-based domestic microgrid. International Journal of Hydrogen Energy 38:11672-11684.
9. Zhang Z, Sato K, Nagasaki Y et al. 2019. Continuous operation in an electric and hydrogen hybrid energy storage system for renewable power generation and autonomous emergency power supply. International Journal of Hydrogen Energy 44:23384-23395.
10. Skripnyuk V and Ron M. 1999. Evaluation of kinetics by utilizing the normalized pressure dependence method for the alloy $Ti_{0.95}Zr_{0.05}Mn_{1.48}V_{0.43}Fe_{0.08}Al_{0.01}$. Journal of Alloys and Compounds 293-295:385-390.
11. Capurso G, Schiavo B, Jepsen J et al. 2016. Development of a modular room-temperature hydride storage system for vehicular applications. Applied Physics A 122:1-11.
12. Hariyadi A, Suwarno S, Denys RV et al. 2021. Modeling of the hydrogen sorption kinetics in an AB_2 laves type metal hydride alloy. Journal of Alloys and Compounds 893:162135.
13. Hahne E. 1998. Thermal conductivity of metal hydride materials for storage of hydrogen: Experimental investigation. International Journal of Hydrogen Energy 23:107–114.
14. Hesse W. 2016. Aluminium Material Data Sheets. Berlin, Beuth Verlag.

WHEC-2022
23rd World Hydrogen Energy Conference
June 26-30, 2022 - Istanbul

#122

HIGH H_2 UPTAKE ON Co(II)- AND Ni(II)- EXCHANGED ZSM-5 and US-Y HAVING OPTIMAL HEAT OF ADSORPTION VALUES

[1] Nurkan Sarohan, [2] M. Olus Ozbek, [1] Yasemin Kaya, [1*] Bahar Ipek
[1]Middle East Technical University, Faculty of Engineering, Department of Chemical Engineering, 06800, Ankara, Turkey
[2] Gebze Technical University, Faculty of Engineering, Department of Chemical Engineering, 41400, Gebze, Kocaeli, Turkey

*Corresponding author e-mail: bipek@metu.edu.tr

ABSTRACT

Hydrogen adsorption capacity of Ni(II) and Co(II)- exchanged ZSM-5 and US-Y were investigated at 298 K and 10 bar. Mesopore added zeolites that have a total pore volume value reaching 0.5 cm^3/g, showed a gravimetric H_2 storage capacity of 0.14wt.% and a volumetric storage capacity of 4.2 g/L at 298 K and 10 bar. The calculated isosteric heat of H_2 adsorption values ranged from 16 and 32 kJ/mol with the highest values observed on Ni(II)-ZSM-5. Theoretical heat of H_2 adsorption values were also calculated using density functional theory utilizing both cluster and periodic models for Co(II)- or Ni(II)- exchanged ZSM-5. The theoretical heat of adsorption values were calculated between 11 and 38 kJ/mol, in consistence with the experimental values.

Keywords: Cobalt, Nickel, Zeolite, Isosteric Heat of Adsorption, Density Functional Theory

INTRODUCTION

Fuel cell electrical vehicles (FCEVs) that use hydrogen as an energy carrier, are one of the fastest growing transportation areas. However, lack of a safe and efficient H_2 storage system is still an essential concern in the practical usage of hydrogen. Operating targets for the year of 2025 for a storage system set by US DOE (Department of Energy) are a gravimetric capacity of 5.5 wt % and volumetric capacity of 40 g/L that operates within the temperature range of 233 K and 333 K under a maximum storage pressure of 100 bar. Among the various H_2 storage systems, physisorption using porous materials (carbon-based materials, metal organic frameworks (MOF), covalent organic framework (COF), and zeolites) is a candidate application considering fully reversible and fast hydrogen uptake due to weak Van der Waals forces. Among the MOFs, the reported highest storage capacity in ambient conditions belongs to Ni_2(m-dobdc) and Co_2(m-dobdc) MOFs 11 g/L or 0.9 wt.% at 298 K and 100 bar [1] with reported heat of H_2 adsorption value of ~12 kJ/mole [2]. According to theoretical studies, adsorption enthalpy of porous materials at ambient temperature should be between 15–25 kJ/mole to ensure maximum adsorption capacity as well as reversibility [3]. H_2 storage capacity values of zeolites containing protons or alkali metal cations are reported to be between 1 and 2 percent by weight (77 K at 1 atm) [4]. In addition to the low heat of H_2 adsorption values on alkali metal exchanged zeolites, low micropore volumes (maximum 0.33 cm^3/g) cause limited H_2 uptake amounts (maximum 2.86 wt.% on FAU framework [5]). Although some of transition metal cations were investigated on zeolites (such as Cu(I)), there is only one study associated with Ni(II) cations [6]. One density functional theory study for Ni(I)-ZSM-5 reported the heat of adsorption as 67 kJ/mole when one hydrogen molecule binds to cation [7]. In current study, hydrogen adsorption capacities of Ni(II) or Co(II)-exchanged ZSM-5 and US-Y were investigated up to 10 bar at 298 K. To overcome micropore volume restriction, mesopore addition was performed using desilication (top-down method) to ZSM-5. Hydrogen binding energy on Ni(II)- and Co(II)-ZSM-5 was also studied theoretically.

MATERIALS AND METHODS

NH_4^+-USY (US-Y,ultra-stable Y is steam treated form of zeolite Y, Alpha Aesar, Si/Al=6, CAS:1318-02-0.1) was obtained commercially. ZSM-5 having Si/Al ratios of 33 and 20 were prepared hydrothermally at 423 K for 72 h following the procedure reported by Schmith et al. [8] using molar gel formulas of $1SiO_2{:}0.01Al_2O_3{:}0.125Na_2O{:}0.051TPABr{:}36H_2O$. and $1SiO_2{:}0.02Al_2O_3{:}0.125Na_2O{:}0.051TPABr{:}36H_2O$, respectively. Desilication at 0.2 M NaOH (Merck, >%99) solution at 358 K was performed on Na-ZSM-5 as reported by Groen et al. [9] to create mesopores. Ion-exchange of ZSM-5 and mesoporous ZSM-5 (Meso-ZSM-5) were performed using 0.2 M cobalt-(II)nitrate hexahydrate (Merck, 98%) or nickel-(II)nitrate hexahydrate (Merck, 98%) solutions for 24 h at 333 K two or three times. 1g NH_4^+-US-Y (Si/Al=6) was also ion-exchanged twice using 75 ml of 0.5 M cobalt-(II)nitrate hexahydrate (Merck, 98%) or nickel-(II)nitrate hexahydrate (Merck, 98%) for 24 h at 298 K.

The crystallinity of prepared zeolites were tested in METU Central Laboratory using Rigaku Ultima-IV X-Ray Diffraction Device (Cu Kα source, λ = 1.54 Å). Scanning electron microscope pictures of zeolites were obtained with QUANTA 400F Field Emission electron microscope. The elementary analysis was performed using inductively coupled plasma-optical emission spectrometer (Perkin Elmer Optime 4300DV). Surface area and pore volumes of zeolites were calculated using N_2 adsorption experiments conducted at 77 K by Micromeritics Tristar II 3020.

The periodic DFT simulations were performed using the Quantum Espresso package [10]. PBE functional was used along with PAW basis sets The Brillouin zone sampling was done using a single K-point (gamma point) The cut-off energies used for the wavefunctions and the charge densities were 76 Ry and 476 Ry, respectively. All the results presented were obtained by relaxing the whole structures until the net force acting on the ions was Fnet < 0.001 Ry/Bohr. Cluster model optimizations were performed using Gaussian09 [11] package with B3LYP functional and 6-31G(d,p) basis set.

H_2 Adsorption Measurements

Hydrogen adsorption isotherms for pressures in the range 0–10 bar were determined with volumetric method using a home-made high pressure volumetric adsorption system. Primarily, 0.3–0.5 grams of prepared zeolites were degassed under vacuum for 1 hour at 653 K using a scroll vacuum pump (Agilent Technologies, Model IDP3) for dehydration and pore cleaning processes. Afterwards, free space was determined using volumetric calculations with He (Hatgaz, %99.999), then the sample was degassed at 653 K for one more hour. H_2 adsorption experiments were carried out at room temperature using incremental doses of hydrogen gas (Hatgaz, 99.999%) up to 10 bar (0.5 bar increments). Hydrogen adsorption experiments were performed at three different temperatures to implement Clasius-Clapeyron equation (Equation.1) for isosteric heat determination.

$$\ln\left(\frac{P_2}{P_1}\right) = -\frac{Q_{st}}{R}\left(\frac{1}{T_2}-\frac{1}{T_1}\right) \quad (1)$$

RESULTS AND DISCUSSION

Hydrogen adsorption experiments were performed at 298 K up to 10 bar. The highest storage capacity belongs to Meso-Ni(II)-ZSM-5 with 0.14 wt% gravimetric capacity (3 g/L volumetric capacity at 298 K and 10 bar, see Figure 1.a) that is higher than Ni_2(m-dobdc) which shows 0.13 wt.% at 10 bar [1]. The volumetric capacity reaches 4.2 g/L on Ni(II)-ZSM-5 at 298 K and 10 bar, which is nearly double of the value observed for Ni_2(m-dobdc) [1]. The dominant parameter controlling the adsorption capacity is suggested to be the heat of H_2 adsorption at room temperature adsorption experiments. Calculated H_2/Metal ratios lower than 2 (see Figure 1.b) indicate adsorption of H_2 molecules on metal cation sites at room temperature at pressures lower than 10 bar. Similar H_2/Metal ratios observed on Meso-ZSM-5 and ZSM-5 samples, indicating that existence of mesopores is not changing the adsorption capacity under 10 bar pressure. Also, the order of zeolites from higher to lower H_2/Metal ratios (Meso-Ni(II)-ZSM-5~Ni(II)-ZSM-5>Meso-Co(II)-ZSM-5~Co(II)-ZSM-5~Ni(II)-USY>Co(II)-USY) is consistent with the order of the zeolites having higher heat of H_2 adsorption values (see Figure 1.c). The highest isosteric heat is achieved on Meso-Ni(II)-ZSM-5 with 32 kJ/mole. Heat of adsorption results of all zeolites are in the optimum range (15–25 kJ/mole). Ni(II)-US-Y and Co(II)-USY showed lower gravimetric H_2 adsorption capacity values when compared to Ni(II)-ZSM-5 (0.22 mmol Ni/g) even though they have a higher metal content (0.35 mmol Ni/g and 0.42 mmol Co/g). This is due to the lower heat of adsorption values observed on these zeolites as well as potential distribution of the cation sites in FAU, where the majority of the cations could be at the window of the 6MRs that are not accessible to H_2 molecules.

Theoretical calculations predicted heat of H_2 adsorption values between 11 and 38 kJ/mol, which is close to the experimentally calculated isosteric heat of adsorption values. Both techniques predicted higher heat of adsorption values for Co(II)- and Ni(II)- cations located at the α-sites.

Table.1 Heat of H_2 adsorption results calculated experimentally, cluster and periodic of DFT computations.

Zeolite	Experimental ($-Q_{st}$ kJ/mole)	DFT Gaussian ($-E_{ads}$ kJ/mole)	DFT ab-initio ($-E_{ads}$ kJ/mole)
Ni(II)-ZSM-5(α)	22–32	17–37	25–33
Ni(II)-ZSM-5(γ)		25–32	12–27
Co(II)-ZSM-5(α)	13–20	11–30	18–38
Co(II)-ZSM-5(γ)		4–16	1–34

CONCLUSION

Hydrogen adsorption capacity of Ni(II) and Co(II)- exchanged ZSM-5 and US-Y are investigated at 298 K and 10 bar. Mesopore added zeolites showed a maximum volumetric storage capacity of 4.2 g/L at 298 K and 10 bar. Ni(II)-exchanged zeolites show higher storage capacity than Co(II)-exchanged ones up to 10 bar, due to the high binding energy between nickel cation and hydrogen molecule. The calculated isosteric heat of H_2 adsorption values ranged from 16 and 32 kJ/mol with the highest values observed on Ni(II)-ZSM-5. Heat of adsorption results of all zeolites are in the optimum range (15–25 kJ/mole). According to theoretical calculations, the alpha site is preferable for both cations.

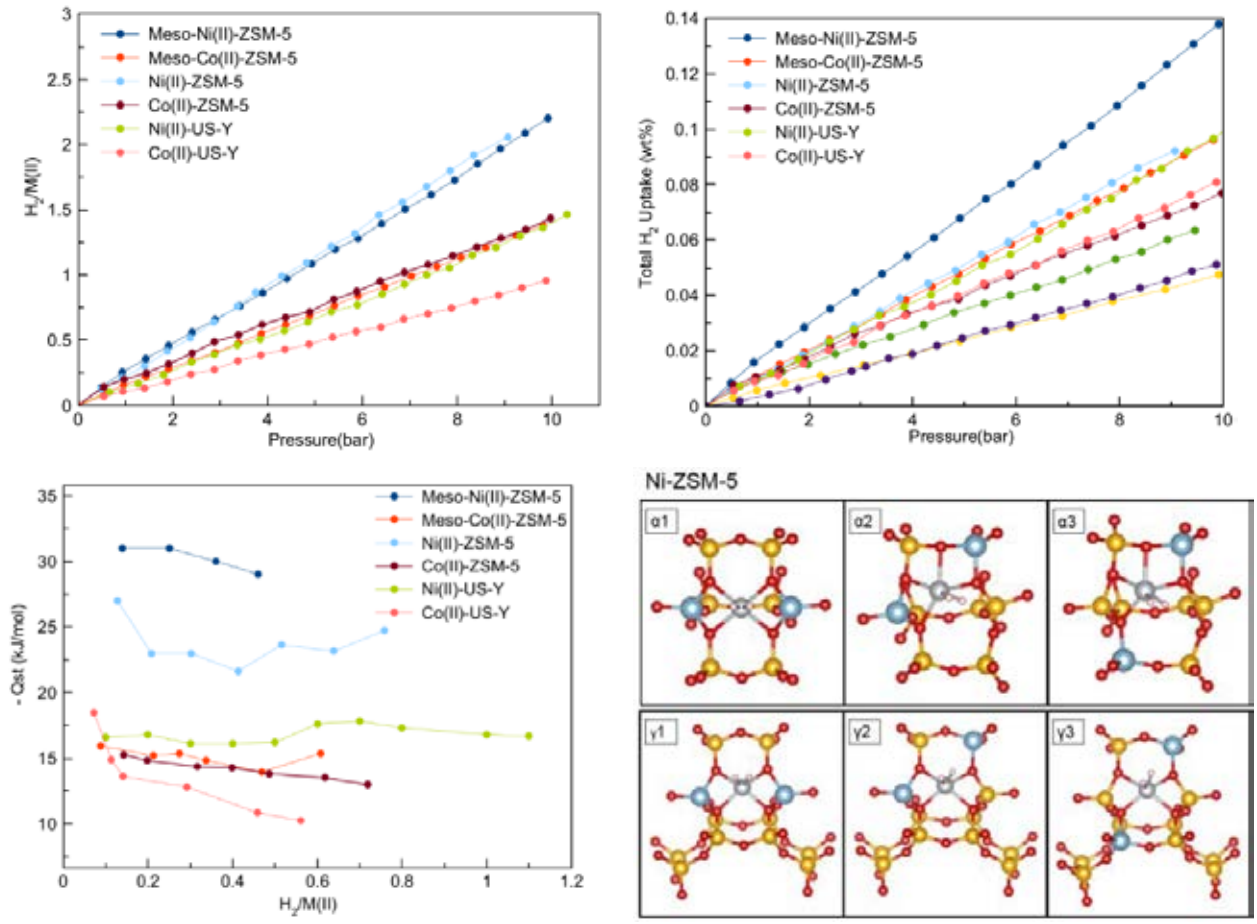


Fig.1 (a) Gravimetric H_2 storage of Ni(II)-and Co(II)-exchanged zeolites, (b) H_2/Metal molar ratios calculated for (a), (c) Isosteric heat of H_2 adsorption values, (d) Optimized geometries of H_2 adsorption on alpha and gamma sites of Ni(II)-ZSM-5 calculated by DFT

REFERENCES

[1] Kapelewski MT, Runčevski T, Tarver JD, Jiang HZH, Hurst KE, Parilla PA, et al. 2018. Record High Hydrogen Storage Capacity in the Metal-Organic Framework Ni_2(m-dobdc) at Near-Ambient Temperatures. Chem Mater 30:8179–89.
[2] Kapelewski MT, Geier SJ, Hudson MR, Stück D, Mason JA, Nelson JN, et al. 2014. M_2(m-dobdc) (M = Mg, Mn, Fe, Co, Ni) metal-organic frameworks exhibiting increased charge density and enhanced H2 binding at the open metal sites. J Am Chem Soc 136:12119–29.
[3] Bae YS and Snurr RQ. 2010. Optimal isosteric heat of adsorption for hydrogen storage and delivery using metal-organic frameworks. Microporous Mesoporous Mater 132:300–3.
[4] Langmi HW, Book D, Walton A, Johnson SR, Al-Mamouri MM, Speight JD, et al. 2005. Hydrogen storage in ion-exchanged zeolites. J Alloys Compd 404–406:637–42.
[5] Vitillo JG, Ricchiardi G, Spoto G, Zecchina A. 2005. Theoretical maximal storage of hydrogen in zeolitic frameworks. Phys Chem Chem Phys 7:3948–54.
[6] Raj MC, Prasanth KP, Dangi GP, Bajaj HC. 2012. Hydrogen sorption in transition metal exchanged zeolite Y: Volumetric measurements and simulation study. J Porous Mater 19:657–66.
[7] Georgiev PA and Albinati A. 2012. Nonclassical hydrides of Ni+ in ZSM-5 zeolite structures: A hybrid DFT study. Chem Phys Lett 545:66–70.
[8] Schmidt F, Lohe MR, Büchner B, Giordanino F, Bonino F, Kaskel S. 2013. Improved catalytic performance of hierarchical ZSM-5 synthesized by desilication with surfactants. Microporous Mesoporous Mater 165:148–57.
[9] Groen JC, Jansen JC, Moulijn JA, Pérez-Ramírez J. 2004. Optimal aluminum-assisted mesoporosity development in MFI zeolites by desilication. J Phys Chem B 108:13062–5.
[10] Giannozzi P, Baroni S, Bonini N, Calandra M, Car R, Cavazzoni C, et al. 2009. QUANTUM ESPRESSO: a modular and open-source software project for quantum simulations of materials. J Phys Condens Matter 21:395502.
[11] Frisch, M.F., et al. 2009. Gaussian 09. Gaussian Inc.: Wallingford, CT

WHEC-2022
23rd World Hydrogen Energy Conference
June 26-30, 2022 - Istanbul

#126
HYDROGEN ABSORPTION/DESORPTION OF THE $(TiVNb)_{85}Cr_{15}$ MULTICOMPONENT ALLOY

[1] Bruno Hessel Silva, [2] Claudia Zlotea, [1,4] Walter José Botta, [4] Yannick Champion, [1,4] Guilherme Zepon*
[1]Federal University of São Carlos, Graduate Program in Materials Science and Engineering (PPGCEM/UFSCar), Rodovia Washington Luiz – km 235, São Carlos, São Paulo, Brasil
[2] Univ Paris Est Créteil, CNRS, ICMPE, UMR 7182, 2 Rue Henri Dunant, 94320, Thiais, France
[3] Univ Grenoble Alpes, CNRS, G-INP, SIMap, 38000 Grenoble, France
[4] Federal University of São Carlos, Department of Materials Engineering (DEMa/UFSCar), Rodovia Washington Luiz – km 235, São Carlos, São Paulo, Brasil

*Corresponding author e-mail: brunohesselpgb@gmail.com

ABSTRACT

Ti-V-Nb-Cr multicomponent alloys are promising materials for hydrogen storage. In this work, we investigated in detail the hydrogen absorption/desorption reactions of the $(TiVNb)_{85}Cr_{15}$ alloy. The alloy was produced via electric arc melting and characterized by X-ray diffraction (XRD), Scanning Electron Microscopy (SEM) and Energy Dispersive X-ray Spectroscopy (EDS) analyses. The alloy presented single-phase BCC structure and dendritic morphology with small segregation of Ti and Cr to the interdendritic regions. Samples of the alloy were hydrogenated at different H/M (number of hydrogen atoms per metal atoms) ratio. XRD and Thermo Desorption Spectroscopy (TDS) analyses showed multi-step processes of hydrogenation/dehydrogenation. XRD analyses suggest that the alloy initially absorbs hydrogen via solid solution and subsequently forms an intermediate BCC hydride up to low levels of H/M absorbed (0.83 H/M). Afterwards, the intermediate hydride also absorbs hydrogen via solid solution leading to the formation of a FCC hydride, which absorbs hydrogen up to 2 H/M. TDS results showed multi-step desorption reactions which were associated to the desorption of the FCC and BCC hydrides. Moreover, Pressure Composition Isotherms (PCI) measurements indicated the existence of two plateaus of absorption and desorption, which also were associated to the BCC and FCC hydrides.

Keywords: Hydrogen storage, Multicomponent alloy, BCC alloy, Metal hydrides

1. INTRODUCTION

Metal hydrides are considered as an option to store hydrogen in a relatively safer and compact way in comparison to high pressure vessels [1,2]. However, most conventional metal hydrides present limitations such as poor cyclability, slow kinetics of hydrogen absorption/desorption, low gravimetric storage and/or undesirable thermodynamic properties [3,4]. Therefore, there is a demand for new materials that can potentially avoid these issues. Recently, a new group of alloys generically known as multicomponent alloys have been investigated for hydrogen storage applications [5–9]. These alloys present at least 3 elements in their chemical composition with substantial atom fractions and often form complex solid solution phases [10]. The versatility of combining elements with different characteristics in the complex solid solution phases might be the key factor to optimize hydrogen storage properties in multicomponent alloys. For example, a few works have been attempting to improve the thermodynamic behavior of hydrides from multicomponent alloys by combining elements with different hydrogen affinity such as Ti, V, Co, Ni, Cr, etc [6,8,9,11]. In this context, Ti-V-Nb-Cr alloys have been showing promising properties for hydrogen storage applications [6,8,11]. Strozi et al.[11] showed that changing the Cr content from 15 to 35 at.% on $(TiVNb)_{100-x}Cr_x$ alloys resulted in a change of the hydrogen equilibrium pressures at room temperature from 0.01 bar to 1-1.5 bar. However, the understanding of the hydrogenation reactions in multicomponent alloys is still in the early stages. Hydride structures of multicomponent alloys have been investigated and several differences are already reported. For example, a few alloys are reported to present single-step absorption reaction forming FCC/BCT hydrides [5,12], whereas other alloys present multi-step reactions forming intermediate hydrides [13–15]. Ti-V-Nb-Cr alloys have been suggested to form intermediate hydrides [6,8,11,14]. However, the complete hydrogenation reactions of these alloys are still unclear. In the present work we investigate in detail the absorption/desorption reactions of the $(TiVNb)_{85}Cr_{15}$ multicomponent alloy.

2. MATERIALS AND METHODS

2.1. Alloy synthesis and hydrogen storage measurements

The alloy was synthesized in an electric arc melting furnace under argon atmosphere using Ti, V, Nb and Cr pieces with purity level higher than 99.5%. A Ti getter piece was melted prior to the alloy synthesis to minimize the oxygen content in the sample. The alloy was remelted five times to improve chemical homogenization. Small pieces of the alloy were loaded into Sieverts-type apparatus and subjected to an activation procedure to facilitate hydrogen

absorption (heat treatment at 390 ºC under dynamic vacuum for 12 hours). PCI measurements were performed at room temperature and three other temperatures between 100 ºC and 200 ºC. Partially hydrogenated samples were produced at different levels of H/M absorbed to investigate the absorption reactions. Before hydrogenating the samples with the desired amount of hydrogen, the samples were subjected to a complete cycle of hydrogen absorption/desorption to ensure complete pulverization. This procedure was paramount for structural characterization.

2.2. Structural characterization and desorption analyses

Structure characterization analyses were performed using XRD, SEM and EDS techniques. XRD analyses were carried out in a D8 Advance Brucker diffractometer using Cu-Kα radiation ($\lambda_{K\alpha1}$ = 1.5406 Å, $\lambda_{K\alpha2}$ = 1.5444 Å). Phase structure identification and Rietveld refinement analyses were performed in the software General Structure Analysis System II (GSAS-II) [16]. SEM and EDS analyses were done in a Zeiss Merlin microscope. Desorption behavior was analyzed via TDS curves, which were obtained in a homemade apparatus with a Quadrupole Mass Spectrometer (QMS) detector. The apparatus measured hydrogen partial pressures from samples that were heated up to 450 ºC (heating rate of 5 ºC/min). The equipment was attached to a vacuum pump that provided pressures of 10^{-6} mbar. Moreover, temperatures were recorded via a K-type thermocouple in direct contact with the samples analyzed.

3. RESULTS AND DISCUSSION

Figure 1 (a) and (b) shows that the alloy presented a dendritic microstructure morphology with interdendritic regions richer in Ti and Cr. EDS assessments of the overall, dendritic and interdendritic regions are displayed in Table 1. The overall chemical composition was similar to the nominal composition. The measurements in the interdendritic region confirmed the segregation of Ti and Cr. XRD analyses of the as-cast sample in Figure 1 (c) shows the alloy formed a single-phase BCC structure. Upon hydrogenation, the alloy showed several structural changes as presented in the XRD patterns of the partially and fully hydrogenated samples (Figure 1(c)). It seems that for low levels of hydrogen absorption (0.5 H/M) there is a miscibility gap for the formation of an intermediate hydride which resulted in the co-existence of two BCC phases at this condition. Figure 1 (d) shows the (220) diffraction reflection exhibiting the splitting of this peak and the deconvolution of the two BCC phases. A similar miscibility gap has already been reported in Ti-Cr-V BCC alloys [17]. The sample with 0.83 H/M presented only one BCC phase with larger lattice parameters than the BCC phases of the previous samples. We believe this pattern is associated only to the intermediate hydride, which increased its lattice parameters due to further absorption via solid solution. In higher levels of hydrogen absorption (1.6 H/M) the alloy presented the co-existence of the BCC hydride and an FCC hydride. It is important to notice that the lattice parameters of the BCC hydride are very similar in the samples with 0.83 and 1.6 H/M. This indicates that the intermediate hydride attained its hydrogen solubility limit around 0.83 H/M. Lastly, the fully hydrogenated sample (2 H/M) showed the presence of the FCC hydride solely indicating that the absorption process was completed. The formation of FCC hydrides are often reported in TiVNbCr alloys and other multicomponent alloys [6–8,18]. Figure 1 (d) shows the TDS measurements of the partially and fully hydrogenated samples. One can see that the desorption profiles of the samples with 0.5 and 0.83 H/M were very similar. Single desorption peaks at high temperature conditions were observed for both samples. This desorption event can be related to the intermediate hydride desorption. The deviations on the onset temperatures were probably caused due to different fractions of BCC hydrides in the samples. Multi-step reactions of hydrogen desorption were observed in the samples with 1.6 and 2 H/M. Both samples presented two main desorption peaks that might be associated to the desorption reactions of the BCC and FCC hydrides. However, it is unclear the reasons for the different desorption profile and onset temperatures observed. Lastly, Figure 1 (e) shows the PCI measurements in absorption and desorption of the $(TiVNb)_{85}Cr_{15}$. The PCI curves suggest the existence of two plateaus, the first plateau presents low equilibrium pressures up to 0.8 H/M even at 200 ºC, whereas the second plateau present high equilibrium pressures that could be reasonable measured even at room temperature. The existence of these two plateaus is also consistent to the proposed reactions of BCC and FCC hydride formation. Therefore, we propose the following sequence of hydrogenation/dehydrogenation in the $(TiVNb)_{85}Cr_{15}$ alloy: BCC alloy ↔ solid solution absorption in the BCC alloy ↔ BCC hydride ↔ increase/decrease of H content in the BCC hydride ↔ FCC hydride. Summarizing, in this work we showed a detailed investigation of the hydrogen absorption/desorption reactions of the $(TiVNb)_{85}Cr_{15}$ alloy.

4. CONCLUSIONS

The $(TiVNb)_{85}Cr_{15}$ was successfully produced by arc melting and presented single-phase BCC structure with dendritic morphology. Segregation levels of Ti and Cr at the interdendritic regions were found. By means of several analyses, the absorption and desorption reactions of $(TiVNb)_{85}Cr_{15}$ alloy were proposed as follows: BCC alloy ↔ solid solution absorption in the BCC alloy ↔ BCC hydride ↔ increase/decrease of H content in the BCC hydride ↔ FCC hydride.

Table 1: Chemical composition of the overall, dendritic and interdendritic regions of the $(TiVNb)_{85}Cr_{15}$ alloy measured by EDS.

Region	Area	Ti (at.%)	V (at.%)	Nb (at.%)	Cr (at.%)
Overall	1	28.7	28.4	28.2	14.7
	2	28.6	28.4	28.3	14.7
	3	28.6	28.5	28.3	14.7
Dendritic	1	26.4	27.5	33.4	12.8
	2	25.9	27.0	35.8	11.3
	3	27.0	27.8	32.4	12.7
Interdendritic	1	32.9	28.1	20.8	18.2
	2	31.5	28.5	23.1	16.8
	3	31.7	28.5	22.8	17.0

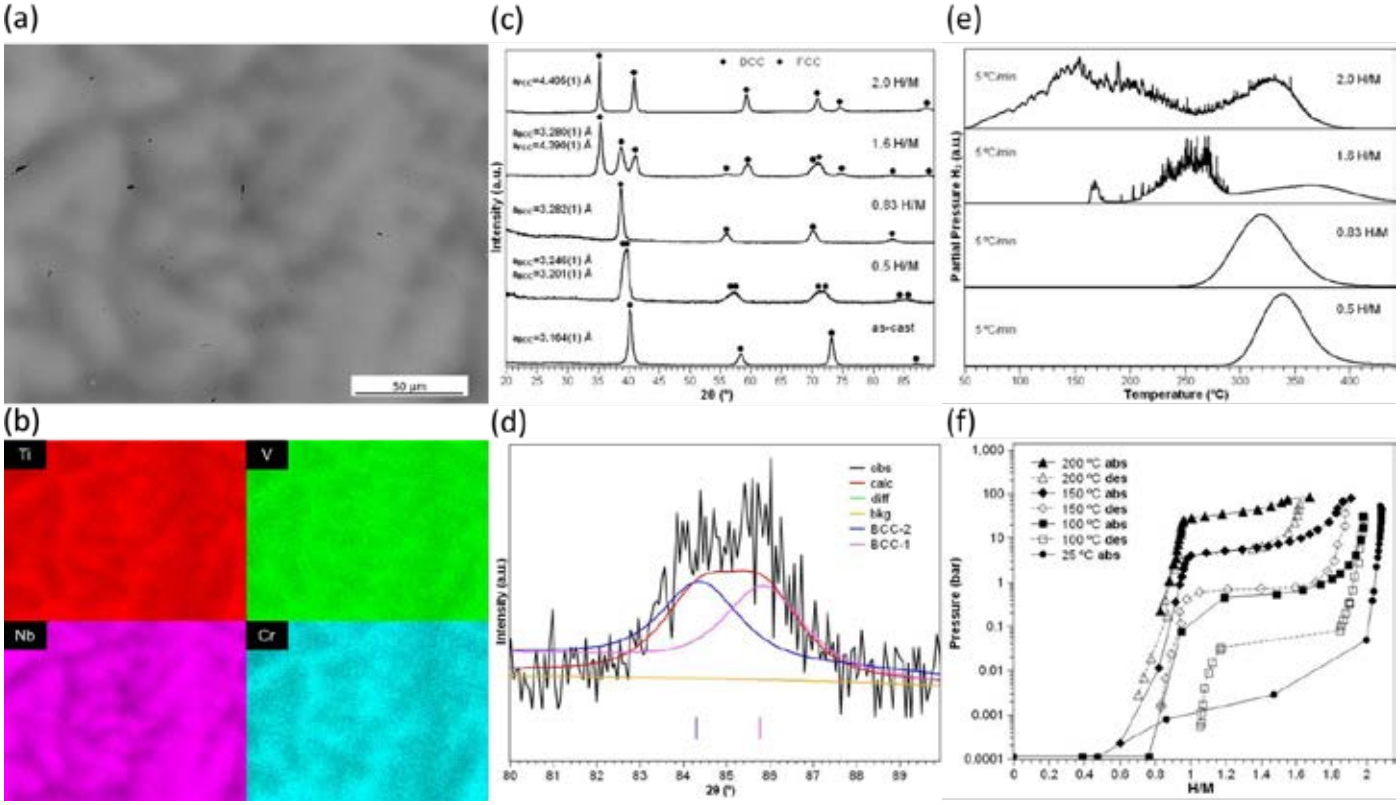


Figure 1: (a) Microstructure of the as-cast $(TiVNb)_{85}Cr_{15}$ alloy, (b) EDS mapping of the as-cast microstructure (c) XRD patterns showing the phases evolutions upon hydrogenation (d) deconvolution of the (220) reflection diffraction peak of the sample with 0.5 H/M) (e) TDS profiles of the partially hydrogenated samples (f) PCT diagram of the $(TiVNb)_{85}Cr_{15}$ alloy.

ACKNOWLEDGEMENTS

This work was financed in part by the Serrapilheira Institute (grant number Serra-1709-17362), in part by the Conselho Nacional de Desenvolvimento Científico e Tecnológico - CNPq (Project number: 142446/2019-0), in part by the CAPES-COFECUB cooperation program process number 88887.387430/2019-00, project number 88887.191910/2018-00 and in part by the grant 2020/07707-6, São Paulo Research Foundation (FAPESP).This study was financed in part by the Coordenação de Aperfeiçoamento de Pessoal de Nível Superior - Brasil (CAPES) - Finance Code 001.

REFERENCES

[1] Davids MW, Lototskyy M, Malinowski M, Schalkwyk DV, Parsons A, Pasupathi S, Swanepoel D and Niekerk TV. 2019. Metal hydride hydrogen storage tank for light fuel cell vehicle. International Journal of Hydrogen Energy. 44:29263–29272.
[2] Wyckaert P, Nadeau S and Bouzid H. 2017. Analysis of Risks of Pressure Vessels. Kongress Der Gesellschaft Für Arbeitswiss. 1-6
[3] Dornheim M. 2011. Thermodynamics of Metal Hydrides: Tailoring Reaction Enthalpies of Hydrogen Storage Materials, Thermodynamics - Interaction Studies - Solids, Liquids and Gases. Germany, Intech.

[4] Sandrock G. 1999. Panoramic overview of hydrogen storage alloys from a gas reaction point of view. Journal of Alloys and Compounds. 293:877–888.
[5] Sahlberg M, Karlsson D, Zlotea C and Jansson U. 2016. Superior hydrogen storage in high entropy alloys. Scientific Reports. 6:1–6.
[6] Nygård MM, Ek G, Karlsson D, Sørby MH, Sahlberg M and Hauback BC. 2019. Counting electrons - A new approach to tailor the hydrogen sorption properties of high-entropy alloys. Acta Materialia. 175:121–129.
[7] Marques F, Balcerzak M, Winkelmann F, Zepon G and Felderhoff M. 2021. Review and outlook on high-entropy alloys for hydrogen storage. Energy Environmental Science. 14:5191-5227.
[8] Silva BH, Zlotea C, Champion Y, Botta WJ and Zepon G. 2021. Design of TiVNb-(Cr, Ni or Co) multicomponent alloys with the same valence electron concentration for hydrogen storage. Journal of Alloys Compounds. 865:158767.
[9] Zepon G, Silva BH, Zlotea C, Botta WJ and Champion Y. 2021. Thermodynamic modelling of hydrogen-multicomponent alloy systems: Calculating pressure-composition-temperature diagrams. Acta Materialia. 215:117070.
[10] Miracle DB and Senkov ON. 2017. A critical review of high entropy alloys and related concepts. Acta Materialia. 122:448–511.
[11] Strozi RB, Leiva DR, Zepon G, Botta WJ and Huot J. 2021. Effects of the chromium content in (TiVNb)100−xCrx body-centered cubic high entropy alloys designed for hydrogen storage applications. Energies. 14:3068
[12] Montero J, Zlotea C, Ek G, Crivello J, Laversenne L and Sahlberg M. 2019. TiVZrNb Multi-Principal-Element Alloy : Sorption Properties. Molecules. 24:1–14.
[13] Sakaki K, Kim H, Asano K and Nakamura Y. 2020. Hydrogen storage properties of Nb-based solid solution alloys with a BCC structure. Jounal of Alloys and Compounds. 820:153399.
[14] Nygård MM, Fjellvåg ØS, Sørby MH, Sakaki K, Ikeda K, Armstrong J, Vajeeston P, Sławiński WA, Kim H, Machida A, Nakamura Y and Hauback BC. 2021. The average and local structure of TiVCrNbDx (x=0,2.2,8) from total scattering and neutron spectroscopy. Acta Materialia. 205:116496.
[15] Zlotea C, Sow MA, Ek G, Couzinié JP, Perrière L, Guillot I, Bourgon J, Møller KT, Jensen TR, Akiba E and Sahlberg M. 2019. Hydrogen sorption in TiZrNbHfTa high entropy alloy. Journal of Alloys and Compounds. 775:667–674.
[16] Toby BH and Von Dreele RB. 2013. GSAS-II: the genesis of a modern open-source all purpose crystallography software package. Journal of Applied Crystallography. 46:544–549.
[17] Tamura T, Kamegawa A, Takamura H and Okada M. 2001. Protium absorption properties of Ti-Cr-V alloys in low hydrogen pressure regions. Materials Transactions 42:1862–1865.
[18] Nygård MM, Ek G, Karlsson D, Sahlberg M, Sørby MH and Hauback BC. 2019. Hydrogen storage in high-entropy alloys with varying degree of local lattice strain. International Journal of Hydrogen Energy. 44:29140–29149.

WHEC-2022
23rd World Hydrogen Energy Conference
June 26-30, 2022 - Istanbul

#133

EASY UP-SCALEABLE APPROACH TO IMPROVE THE PROPERTIES OF METAL-ALLOYS FOR HYDROGEN STORAGE

[1,2*] Jan Warfsmann, [1]Maximilian Passing, [1,2] Phillip S. Krause, [1,2] Eike Wienken, [1,2] Julian Jepsen, [1,2]Thomas Klassen, [1,2] Julián Atilio Puszkiel
[1]Helmholtz-Zentrum Hereon, Institute of Hydrogen Technology, Max-Planck-Straße 1, 21502 Geesthacht, Germany
[2] Helmut Schmidt Universität – University of the Federal Armed Forces Hamburg, Holstenhofweg 85, 22043 Hamburg, Germany

*Corresponding author e-mail: jan.warfsmann@hereon.de

ABSTRACT

Methods to increase the heat conductivity and reduce the expansion stress of metal alloys during hydrogen absorption are investigated. The applied approach focuses on strategies, which are time-efficient and can be up-scaled for larger batches of metal alloy. The properties of the commercial available room-temperature metal alloy HydralloyC5 ($Ti_{0.95}Zr_{0.05}Mn_{1.46}V_{0.45}Fe_{0.09}$) are successfully improved by applying wash-coating techniques. By adding 10 wt.% ENG (expanded natural graphite) or aluminium-powder onto the metal surface prior to hydrogen absorption, the heat conductivity of the samples is improved. Furthermore, the overall expansion stress of the metal alloy during hydrogen absorption is reduced by 20% by adding only small amounts of Aerosil as a glidant agent (0.2 wt.%) to the coating mixture.

Keywords: hydrides, hydrogen storage, swelling, heat transfer, wash coating

INTRODUCTION

In a time of increasing global temperatures and the still significant dependency on fossil fuels, there is a more and more pressing demand for a sustainable alternative. Green hydrogen is one of the most promising candidates because its use does not release any CO_2 and has further the advantage of acting as a universal energy carrier. The most common hydrogen storage systems are high-pressure vessels (up to 700 bar) or the storage as liquid hydrogen. The high-pressure storage has the disadvantage of low volumetric capacity and expensive tank design, while the liquid hydrogen storage is problematic due to the high-energy penalty to condense the hydrogen and boil-off effects. The storage as hydride in the solid-state (e.g. in various metal alloys) is a promising alternative, but comes with its own challenges.

One of the challenges is to reduce the inevitable stress caused by swelling of the material during the hydrogen absorption (up to 20% [1]). This phenomenon occurs due to the larger lattice parameters of the hydride phase in comparison to the hydride forming alloy and the precipitation caused by the hydrogen cycling process. In order to maintain the mechanical stability of the tank, the stress caused by the swelling of the metal hydrides must be considered during the design of a solid-state hydrogen storage vessel. Free space is left in the storage tanks, which reduces the overall stress, but also the volumetric capacity. However, some reports show that adding a glidant material such as Aerosil might be a possibility to reduce this expansion stress [1].

Another challenge is the improvement of the low thermal conductivity of the hydride, which results in a challenging heat management. Regardless of the initial particle size, the metal alloy disintegrates into powders in the size range of microns after several hydrogen absorption and desorption cycles, which leads to a very low thermal conductivity (~1 $Wm^{-1}K^{-1}$). As a result of the exothermic hydrogen uptake, heat is accumulated in the metal alloy bed during hydrogen absorption, leading to hot-spots with decreasing kinetic performance. The heat transfer becomes the predominant effect within larger storage systems and represents the bottle-neck for its practical application [2].

Different methods to increase this heat conductivity have been investigated. While some methods try to improve the tank systems, e.g., adding aluminium fins [3] to have a large surface with high conductivity, it is also possible to directly improve the properties of the metal alloy, e.g. by coating with materials of high thermal conductivity [4]. Aluminium powder, which has high thermal conductivity and is inert in hydrogen atmosphere [5], and expanded natural graphite (ENG), a graphite modification with increased thermal conductivity, are some of the most commonly used compounds. These materials are added by simply mixing in a protective atmosphere (to prevent oxidation of the metal alloy) or compressed with the metal alloy to form pellets [6].

In our research, we have focused on using “room-temperature” metal hydrides, which have several advantages, such as fast kinetics and moderate working pressure and temperature conditions. Further, they can be handled without a protective atmosphere before the cycling, which makes loading of tanks and modifying the material much more

effortless. Room temperature hydrides have a low gravimetric capacity ranging ~2 wt.% of hydrogen, but a proper volumetric capacity of about 100 kg of H_2/m^3. In the case of stationary applications, room temperature metal hydrides are quite suitable. In such systems, the gravimetric capacity is a less critical parameter, and the lower operating temperatures make thermal management system much more simple to design. However, for larger systems, several hundreds of kg or even tons of material are needed, and the methods, as mentioned above, to improve the material's properties are expensive or not practical.

Therefore, we have investigated methods to add conductive material and glidant agent to the metal alloy surface, which are both time-efficient and can be scaled-up with relative ease.

MATERIALS AND METHODS

The metal alloy HydralloyC5 (AB_2-metal alloy; $Ti_{0.95}Zr_{0.05}Mn_{1.46}V_{0.45}Fe_{0.09}$) was brought from GfE (Gesellschaft für Elektrometallurgie) and the size was reduced to ~3 mm in a jaw crusher before use. ENG (particle size 5 µm; SGL-Carbon), polyvinylacetate (PVAct) (Arcos Organics), aluminium powder (particle size 11 µm, Alfa Aesar), Aerosil R805 (Evonik Operations) and acetone (Merck) were used as received. In a typical experiment, 10 g of HydralloyC5 was coated with a dispersion of PVAct as binder (0.5 g; 5 wt.%), ENG or Al-powder (1 g, 10 wt.%), and optionally Aerosil R805 (0.02 g; 0.2 wt.%) in acetone as solvent (80 ml). The solvent was evaporated during movement (60 RPM) in a rotation evaporator. The water bath was set to 60 °C and the pressure kept at ambient conditions. To remove excess binder after coating, the sample was heated in a furnace at 400 °C for 4 h. SEM images were done with a FEI Quanta 650. The hydrogen absorption-desorption behaviour was measured with an in-house produced Sieverts apparatus. The temperature and strain was measured in-situ, where a strain gauge and a thermocouple were attached directly onto the sample holder.

RESULTS AND DISCUSSION

The SEM images of the samples (Fig.1 a-d) show that for a good distribution of conductive material in the hydride bed during cycling, good coverage on the metal alloy particles before the disintegration to powder was necessary.

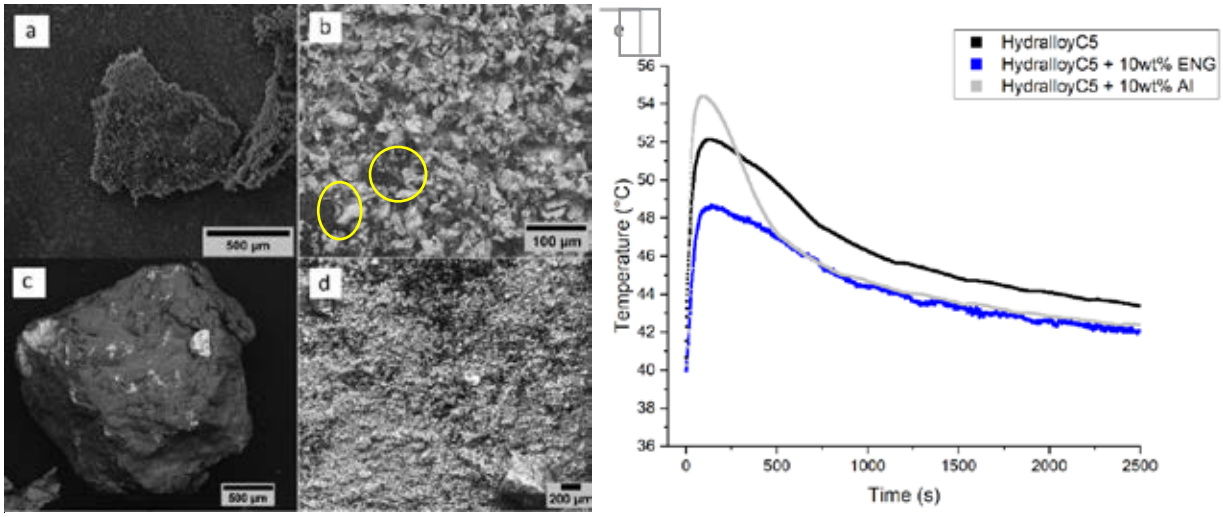


Fig. 1: (a) SEM-images of HydralloyC5 coated with ENG before and (b) after cycling in hydrogen atmosphere; (c) SEM-images of HydralloyC5 coated with Al-powder before and (d) after cycling in hydrogen atmosphere; (e) Measured temperature during hydrogen absorption of the pristine HydralloyC5 (black), ENG-coated sample (blue) and the aluminium-coated sample (grey)

With a modified version of the wash-coating process, the HydralloyC5 could be successfully coated with a layer of ENG (Fig.1a). For aluminium, the image shows also good coverage with a mostly closed coated surface (Fig.1c). After the hydrogen cycling, the particle size of the HydralloyC5 is reduced to ~20 µm, and small clusters of ENG are distributed between the particles (Fig.1b, yellow circles). In the case of aluminium powder, it has agglomerated to larger particles between the disintegrated HydralloyC5 (Fig.1d). However, in both cases, heat management is improved. Fig.1e shows a comparison of the measured temperature profiles during hydrogen absorption (at 40 °C and 40 bar H_2-pressure). For the ENG-coated sample, the peak temperature is reduced to 48.6 °C (blue line) compared to 52.2 °C (black line) in the uncoated sample. In contrast, it shows for the aluminium-coated sample a higher peak temperature (54.1 °C; grey line), but the heat is dispersed much faster.

The results of Fig. 2 show the strain measurement for pristine HydralloyC5 and a sample with added small amounts (0.2 wt.%) of Aerosil as glidant agent. According to Fig.2, during 12 hydrogen absorption-desorption cycles, the strain

to the sample holder increses with every cycle. The same trend is also noted when Aerosil is added. However, the maximum strain was reduced by 20% over the same number of cycles.

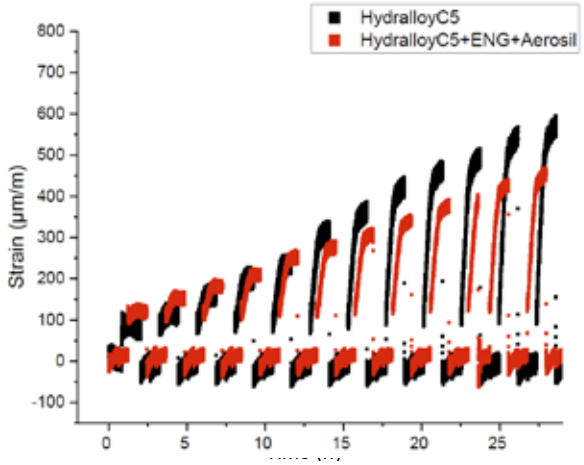


Fig. 2: Strain measurement on a completely filled sample holder was tested for 12 cycles of hydrogen absorption and desorption. Even with low concentrations of 0.2 wt.% of the Aerosil (red), a reduction of the expansion stress was observed in comparison with the unmodified metal alloy (black).

CONCLUSIONS

To the best of our knowledge, this is the first time where a straightforward method is applied for the coating of hydrogen storage material with 10 wt.% of a conductive material (aluminium powder and ENG). In both cases, the heat management could be improved compared to the unmodified metal alloy. For ENG, the temperature peak during hydrogen absorption was reduced, while the heat could be faster dispersed for aluminium powder. It could be further shown that by adding even a tiny amount of glidant material to the coating mixture, the expansion stress during hydrogen absorption could be significantly reduced.

ACKNOWLEDGEMENT

The authors acknowledge the Zentrum für Digitalisierungs- und Technologieforschung der Bundeswehr (dtec.bw) for the partial funding of this work in the frame of the HyReflexS project.

REFERENCES

1. Cuscueta D.J., Silin N., Melnichuk M., 2020, Stress reduction in a hydride container by the addition of a glidant agent, International Journal of Hydrogen Energy, 45: 27452-27456.
2. Lozano, G.A., Bellosta von Colbe, J. M., Klassen, T., Dornheim, M., 2014, Transport phenomena versus intrindic kinetics: Hydrogen sorption limitin gsubprocess in metal hydride beds, International Journal of Hydrogen Energy, 39, 18952-18957.
3. Garrison, S.L., Hardy, B.J., Gorbounov, M.B., Tamburello, D.A., Corgnale, C., van Hassel, B.A., Mosher., A.D., Anton, D.L., 2012, Optimizatinon of internal heat exchangers for hydrogen storage tanks utilizing metal hydrides, International Journal of Hydrogen Energy, 37, 2850-2861.
4. van Hassel, B.A., Mosher, D., Pasini, J.M., Gorbounov, M., Holowczak, J., Tang., X., Brown, R., Laube, B., Pryor., 2012, Engineering improvements of NaAlH4 system, International Journal of Hydrogen Energy, 37, 2756-2766.
5. Dieterich, M., Pohlmann, C., Bürger, I., Linder, M., Röntzsch, L., 2015, Long-term cycle stability of metal hydride-graphite composites, International Journal of Hydrogen Energy, 40, 16375-16382.
6. Puszkiel, J., Belosta von Colbe, J. M., Jepsen, J., Mitrokhin., S. V., Movlaev, E., Verbetsky, V., Klassen, T., 2020, Designing an AB2-Type Alloy (TiZe-CrMnMo) for the Hydrid Hydrogen Storage Concept, Energies, 13, 2751.

WHEC-2022
23rd World Hydrogen Energy Conference
June 26-30, 2022 - Istanbul

#134

HYDROGEN - HEAT STORAGE SYSTEM BASED ON METAL HYDRIDE AND PHASE CHANGE MATERIAL

[1]*Jussara Barale, [2]Giovanni Capurso, [3]Thorbjorn Stühff, [4]Federico Nastro, [5]Bettina Neumann, [2]José Bellosta von Colbe, [1]Paola Rizzi, [4]Carlo Luetto, [3]Holger Stühff and [1]Marcello Baricco

[1] Department of Chemistry and NIS - INSTM, University of Turin, Via Pietro Giuria 7, 10125 Torino, Italy
[2] Institute of Hydrogen Technology, Helmholtz-Zentrum Hereon, Max-Plank-Straße 1, 21502 Geesthacht, Germany
[3] Stühff Maschinen- und Anlagenbau GmbH, Mercatorstraße 53, 21502 Geesthacht, Germany
[4] Tecnodelta S.r.l., Via Francesco Parigi 5H, 10034 Chivasso (To), Italy
[5] GKN Sinter Metals Engineering GmbH, Krebsöge 10, D-42477 Radevormwald, Germany

*Corresponding author e-mail: jussara.barale@unito.it

ABSTRACT

The goal of the HyCARE project is to store renewable energy using hydrogen as energy carrier by means of a metal hydride (MH), coupling a phase change material (PCM) for the heat management. The feasibility of the concept has been investigated thanks to the realization of a prototype including a MH-tank and a PCM module storing about 0.5 kg of H_2. The innovation of the use of PCM in the heat management of MH system is linked to the reduction of external heat intake, and during the tests the optimal conditions of hydrogen flow, thermal fluid flow, starting temperature have been evaluated, in order to minimize the external power contribution. It was highlighted that, in the optimal conditions, the PCM was able to collect and supply the heat generated/required by the MH storage system, with the external power source contributing only to compensate the heat losses.

Keywords: Hydrogen storage, Heat storage, Metal hydride, Phase change material

INTRODUCTION

In the use of H_2 as widespread energy vector, its storage in the solid state with metal hydrides (MH) has the advantage of requiring low pressures and temperatures, when using intermetallic compounds (IMCs), reaching a high volumetric capacity. A MH storage system needs a suitable heat management to operate, so that a thermal fluid is usually used to remove/supply heat, since hydride formation implies the production of heat, while hydrogen release requires it. Generally, heat is released in the environment during charging, and therefore a quite low thermal efficiency is achieved, of the order of a few tens of percentage points. An interesting strategy, to increase the efficiency and thus to reduce the amount of requested external power for discharging hydrogen, is to store the heat generated during the exothermic absorption, to be reused during the endothermic desorption. In this regard, the use of phase change material (PCM) has been suggested to be an efficient solution [1] and the coupling of PCM- and MH-tanks is a novel concept, that could increase the efficiency above 70% [2–5]. The coupled system implies that, during MH absorption, the PCM consumes heat to melt, and then, in the desorption phase, the solidification of the PCM releases almost the same amount of energy.

In the framework of the EU-project HyCARE, a prototype of hydrogen and heat storage coupled system, based on MH and PCM, respectively, has been developed and tested [6]. The goal of the HyCARE project is to store renewables using H_2 as energy vector, developing an integrated system composed by an electrolyzer (EL), the mentioned hydrogen - heat storage system, and a Fuel Cell (FC), for the storage of energy for smart grid applications. The plant will be installed at ENGIE Crigen lab near Paris in 2022 and involves European industries, research institutes and universities. About 40 - 45 kg of H_2 will be stored directly form the EL at ~ 55°C, at a pressure between 25-30 bar, and it will be released at 1-2 bar to directly supply the FC. As MH, the IMC $TiFe_{0.85}Mn_{0.05}$ has been selected [7] and it has been produced at industrial scale, showing suitable properties for hydrogen storage in the plant conditions [8]. Whereas, for the heat storage a sustainably sourced and bio-based material has been selected as PCM. The feasibility of the HyCARE concept was proven through a prototype composed by a PCM module and MH-tank. This work reports the results of the tests performed to understand how the two modules can operate together in the best operative conditions, reducing the amount of external heat supplied.

MATERIALS AND METHODS

The set-up of the MH-PCM system is depicted in Fig. 1. An external power source (EPS) is used to circulate the thermal vector fluid (TVF), controlling its temperature, with both heating and cooling contributions. The TVF flows from the EPS to the MH-tank, to the PCM-module to finally return to the EPS. The flow is controlled by setting the pressure level in

the EPS, resulting in different flowrates, depending on the pressure drop of the circuit, and it is measured by a liquid flowmeter placed between the EPS and the MH unit. Thermocouples are located inside the MH-bed, the PCM-volume and at the inlet and outlet of the thermal fluid of each system. Also, hydrogen pressure and flow are monitored thanks to suitable sensors. The prototype has about 1/5 of the size of a final module; in the final HyCARE demonstrator 12 modules each for PCM and MH are planned. The MH prototype tank consists of a tube of 6 inch of diameter and about 1 m long, capable of storing ~ 0.5 kg of H_2.

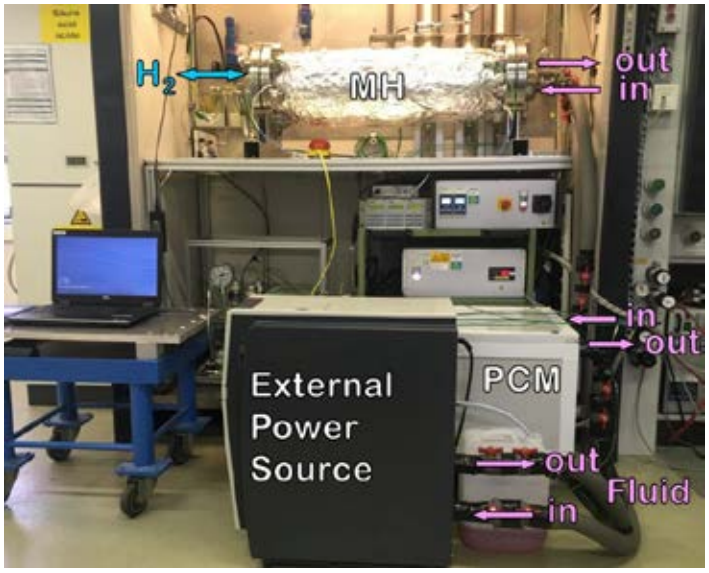


Fig. 1. Set-up of the coupled PCM-MH system with the EPS

RESULTS AND DISCUSSION

In order to find the best operative conditions, to minimize the amount of external power required, different parameters were evaluated during the tests, *i.e.,* external power contribution, started working temperature, as well as H_2 and thermal fluid flowrates. In all experiments, the hydrogen loading (absorption) occurs up to 30 bar, while the hydrogen unloading (desorption) takes place at about 2 bar, according to the plant operative conditions, defined for the selected alloy [8], that represent the integration of the system with an electrolyser upstream and a fuel cell downstream. Different H_2 flowrates have been considered:

- 160 Nl/min, *i.e.* the maximum available flow from the electrolyzer in the final HyCARE demonstrator,
- 80 Nl/min, corresponding to half of the maximum flow,
- 32 Nl/min, that is 1/5 of the maximum flow, since the prototype size is about 1/5 of the final module.

According to the selected H_2 flowrate, the flow of the thermal fluid is calculated and adjusted to manage properly the maximum power developed/required, in order to keep a temperature difference of approximately 7 °C between MH and PCM tanks. These boundary conditions imply that, for an H_2 flow of 160 Nl/min, a TVF flow of about 6 l/min is necessary; similarly, for an H_2 flow of 80 Nl/min, about 3 l/min of TVF flow are needed, while for an H_2 flow of 32 Nl/min, the TVF flow must be about 1 l/min. The influence of the EPS on the thermal management of the coupled system has been evaluated, considering the effect of its energy intake with heating/cooling both active, or completely deactivated, or only providing heat. The latter setup represents the scenario most similar to the contribution of solar panels in the final demonstrator. Different starting temperatures were also considered, to maximize the PCM contributions in the heat management of the coupled system, starting the absorption with the PCM totally solid, or partially liquid.

Finally, in some tests, the absorption occurred only when the pressure in the tank allowed a constant H_2 flowrate, resulting in an intermittent process. After several trials, the optimal working conditions were established. It was proven that the two modules are able to work nicely together, limiting contributions from the EPS, which mainly acted during the early stages of the reactions, just to overcome the heat losses. Then, in the final part of the reactions, its contribution increased again, because of the lower amount of H_2 absorbed/desorbed that implied a lower amount of heat exchanged between the two modules. Due to this reason, the best strategy includes the use of only constant hydrogen flow.

CONCLUSIONS

The feasibility of a coupled system for hydrogen-heat storage, based on metal hydride and phase change material, has been successfully proven through the realization and test of a prototype system that involves a $TiFe_{0.85}Mn_{0.05}$ as MH

and a bio-based materials as PCM. By varying the parameters, like the hydrogen and thermal fluid flowrates and the starting working temperature, it was possible to develop a strategy that allows a minimal contribution of an external power source. Indeed, the external power intake has been found to be necessary just to compensate the heat losses, while the PCM is able to successfully manage the heat for the MH processing. In particular for the final system, it has been evaluated to proceed starting the absorption with the PCM partially melted, *i.e.,* close to 53°C, performing reaction by applying only a constant hydrogen flow, in order to avoid that the external power source needs to contribute in the final part of reaction, because of the lower amount of hydrogen that can be processed.

ACKNOWLEDGEMENT

The project leading to this publication has received funding from the Fuel Cells and Hydrogen 2 Joint Undertaking (JU) under grant agreement No 826352, HyCARE project. The JU receives support from the European Union's Horizon 2020 research, Hydrogen Europe, Hydrogen Europe Research, innovation program and Italy, France, Germany, Norway, which are all thankfully acknowledged.

REFERENCES

1. Lototskyy M. V., Tolj I., Pickering L., Sita C., Barbir F., Yartys V., The use of metal hydrides in fuel cell applications, Prog. Nat. Sci. Mater. Int. 27 (2017) 3–20.
2. Garrier S., Delhomme B., De Rango P., Marty P., Fruchart D., Miraglia S., A new MgH_2 tank concept using a phase-change material to store the heat of reaction, Int. J. Hydrogen Energy. 38 (2013) 9766–9771.
3. Mellouli S., Ben Khedher N., Askri F., Jemni A., Ben Nasrallah S., Numerical analysis of metal hydride tank with phase change material, Appl. Therm. Eng. 90 (2015) 674–682.
4. Rabienataj Darzi A.A., Hassanzadeh Afrouzi H., Moshfegh A., Farhadi M., Absorption and desorption of hydrogen in long metal hydride tank equipped with phase change material jacket, Int. J. Hydrogen Energy. 41 (2016) 9595–9610.
5. Ben Mâad H., Askri F., Ben Nasrallah S., Heat and mass transfer in a metal hydrogen reactor equipped with a phase-change heat-exchanger, Int. J. Therm. Sci. 99 (2016) 271–278.
6. www.hycare-project.eu
7. Dematteis E.M., Dreistadt D.M., Capurso G., Jepsen J., Cuevas F., Latroche M., Fundamental hydrogen storage properties of TiFe-alloy with partial substitution of Fe by Ti and Mn, J. Alloys Compd. 874 (2021) 159925.
8. Barale J., Dematteis E.M., Capurso G., Neumann B., Deledda S., Cuevas F., Rizzi P., Latroche M., Baricco M., Industrial production and characterisation of $TiFe_{0.85}Mn_{0.05}$ alloy for a hydrogen storage plant, to be submitted.

WHEC-2022
23rd World Hydrogen Energy Conference
June 26-30, 2022 - Istanbul

#139

MODELING AND PARAMETERIZATION OF A PEM FUEL CELL STACK FOR A SYSTEM INTEGRATION INTO A METAL HYDRIDE BASED HYDROGEN STORAGE SYSTEM

[1,2]* Myriam Covarrubias Guarneros, [1,2] David Dreistadt, [1,2] José Bellosta von Colbe, [2] Giovanni Capurso, [3] Marion Siegers
[1,2]Julian Jepsen, [1,2] Julián Puszkiel, [1,2] Thomas Klassen
[1] Faculty of Mechanical Engineering, Institute of Materials, Helmut Schmidt University, Holstenhofweg 85, 22043, Hamburg, Germany
[2] Institute of Materials Research, Helmholtz-Zentrum HEREON, Max-Planck-Straße 1, 21502 Geesthacht,Germany;
[3] Environmental Engineering Department, Faculty of Life Science, Hamburg University of Applied Science, Ulmenliet 20, 21033, Hamburg, Germany

*Corresponding author e-mail: covarrum@hsu-hh.de

ABSTRACT

Power systems using renewable energy sources have emerged as a sustainable solution for decarbonizing the energy sector. Implementing such systems requires integrating them with an efficient storage medium to improve their reliability and flexibility. This work explores the modeling and parameterization of a fuel cell system, with the purpose of coupling it with a metal hydride-based hydrogen storage reservoir. An electrical and thermal 0D simulation model for a 1.6 kW air-cooled proton exchange fuel cell stack is developed to investigate its performance, heat transfer and temperature development. The model validation and simulation are done by testing it with four different steady-state power demand scenarios. Experimental results show an efficient thermal coupling between the fuel cell stack and the metal-hydride system. Simulations and experimental results show an excellent agreement. The developed modeling approach is also appliccable to the design of different gas-to-power configurations and sizes, for the design of fuel cell–metal hydride storage systems.

Keywords: PEM fuel cell, 0D-modelling, Matlab-Simulink-Simscape, system integration, gas-to-power

INTRODUCTION

In view of the increasing energy consumption of the world's population, the search for reliable and sustainable fuels and energy sources is becoming increasingly important to decarbonize the energy sector. Efficient and flexible energy storage systems are essential to compensate for insufficient energy generation periods and temporarily store excess energy production. One promising way of storing electrical energy from renewable sources is to use hydrogen as an energy carrier, due to its large gravimetric energy density of 142 MJ/kg [1]. Hydrogen production *via* electrolysis and its combination with different kinds of hydrogen storage systems has been increasingly investigated as a potential solution for large-scale applications to cover the rising energy demand [2]. Among the explored power-to-gas configurations, using a solid-state hydrogen storage system offers an efficient and safe solution for long-term storage. In this way, hydrogen can be provided to a fuel cell for electrical power generation as required [3-5].

This work presents the design of a simulation model for a 1.6 kW air-cooled proton exchange membrane fuel cell (PEMFC) developed using Matlab/Simulink/Simscape. In the frame of the MH2-Powerbank [6] and Digi-Hypro projects, the developed simulation model is validated *via* experiments carried out in an integrated backup fuel cell and a metal hydride storage system composed of TiFeMn hydride forming alloy.

MODEL CONCEPTUALIZATION AND EXPERIMENTAL SETUP

The working principle of a PEMFC is governed by a redox reaction where hydrogen and oxygen react to produce electrical power (P_{el}) as the main product, water, and heat (Q) as a by-product. In this way, the electrical power and heat generation are connected.

$$2H_2+O_2 \rightarrow 2H_2O+P_{el}+Q \quad (1)$$

Fig.1 a) shows a diagram of the entire PEMFC simulation model concept. For the determination of the electrical power (V_{fc}), the electrical model takes into consideration the thermodynamic output voltage (E) minus the activation and ohmic losses ($R_{ohm} \cdot i_{fc}$) from the fuel cell by applying equation (2):

$$V_{fc} = E - R_{ohm} \cdot i_{fc} \quad (2)$$

The thermal model calculates the temperature of the cooling air at the exhaust area of the fuel cell (T_{out}) and the fuel cell temperature (T_{fc}) using the generated heat from the fuel cell ($\dot{Q}_{gen}$) in the description of the total heat flow of the fuel cell stack as described by equation (3):

$$\Delta\dot{Q} = -\dot{Q}_{gen} - \dot{Q}_{diss} \quad (3)$$

where the heat losses are due to forced convection ($\dot{Q}_{conv}$) and conduction ($\dot{Q}_{cond}$)

$$\dot{Q}_{diss} = \dot{Q}_{conv} + \dot{Q}_{cond} \quad (4)$$

$$\dot{Q}_{conv} = h \cdot A_{stack} \cdot (T_{FC} - T_{amb}) \quad (5)$$

The heat transfer coefficient (h) calculation was done using three non-dimensional numbers, Prandtl, Reynolds and Nusselt, assuming for the case of Nusselt number a stream length surrounding a flat plate.

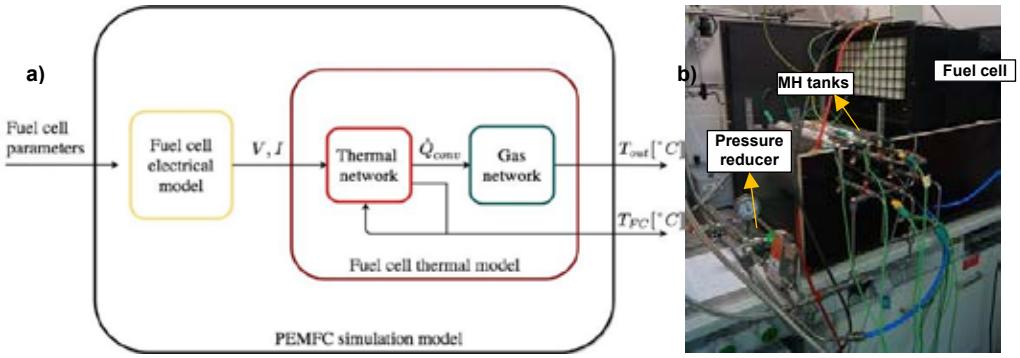


Fig 1. Diagram of the PEMFC simulation model (a) and the experimental setup used in MH2 Powerbank (b)

The general assumptions for the thermal model are that:

- The fuel cell stack is enclosed in a adiabatic casing.
- The fuel cell stack is a rectangular-shaped solid block uniformly heated and gets cooled by external flow of air.
- The radiation losses are neglected.

The experimental setup is shown in Fig. 1 b) and it was operated at standard temperature (25 °C). The fuel cell was tested with an external electrical load in a dynamic state and pressurized tanks to obtain the polarization curve. The operative pressure of the fuel cell is 1.4 bar and it was regulated with a pressure reducing valve. To test the thermal coupling of MH2 Powerbank (metal hydride tanks and fuel cell) the electric load was used for four different power scenarios (60.8 W, 121.4 W, 240.3 W, and 467.4 W) at a steady state for 1 hour. The experimental setup was equipped with an anemometer to measure the exhaust air velocity coming from the fuel cell to calculate the thermal behavior.

RESULTS AND DISCUSSION

Figure 2 shows the experimental and simulated results of the compensated polarization curves and the temperature profile of the exhaust air of the fuel cell (T_{out}) for 240.3 W as an example of all carried out experiments. As seen in Figure 2 a), the validation for the electrical model is done by comparing the compensated polarization curve and the simulated data in a range between 0 A and 34.24 A where the linear voltage drops from 49.5 V to 47.95 V. The voltage compensation installed in the FC (green line in Figure 2 a)) after 34.24 A does not work properly anymore. Thus, the voltage starts to fluctuate and then decreases until it reaches a value of 14.15 V. The simulated data (red line) defines the useful work range of the fuel cell. The results provided by the electrical model exhibit an excellent agreement with the experimental results with a correlation coefficient 0.9223.
The validation for the thermal model has been done under four different power demand scenarios by comparing the experimental data of the exhaust air temperature (T_{out}) of the fuel cell and the simulated data. Figure 2. b) shows an example of the results for a power demand of 240.3 W under steady-state. Measured data shows a significant drop in temperature of about 10 °C at 1.6 min. This drop is due to a misreading in the anemometer located at the exit of the fuel cell case. The model is in perfect agreement with the measured (correlation coefficient 0.9808). The simulated fuel cell temperature is also obtained (T_{fc}) and applied as a reference parameter for the accuracy of the thermal model.

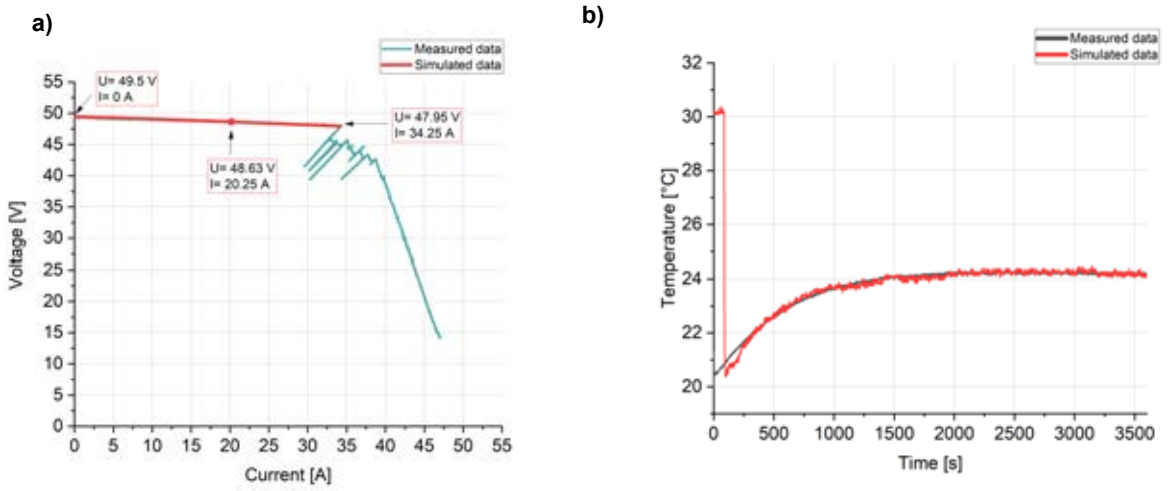


Fig 2. Simulation and experimental results for the electrical a) and the thermal b) behavior of the PEMFC for an experiment carried out at 240.3 W. The correlation coefficient for the electrical model validation is 0.9223 and for the thermal model 0.9808.

CONCLUSIONS

The integrated system (MH2 Powerbank) can provide constant electrical power from 60.8 W to 467.4 W at steady-state conditions. The experimental outcomes show that the output voltage of the fuel cell is compensated for delivering a constant voltage of about 48 V in the case of an emergency power supply. Despite this, the developed electrical and thermal system models allow defining an operative work range of the fuel cell and show an excellent agreement with the experimental results having correlation coefficients of 0.9223 and 0.9808, respectively. The developed fuel cell system model can be applied for system integration into a fuel cell-metal hydride storage system, to test it under dynamic power demand scenarios.

ACKNOWLEDGEMENT

The authors acknowledge the Fuel Cells and Hydrogen 2 Joint Undertaking (JU) under grant agreement No 826352, HyCARE project for the partial funding. Furthermore, the authors thank the Zentrum für Digitalisierungs- und Technologieforschung der Bundeswehr (dtec.bw) for the partial funding of this work in the frame of the Digi-Hypro project.

REFERENCES

[1] Rusman, N. A. A., & Dahari, M. (2016). A review on the current progress of metal hydrides material for solid-state hydrogen storage applications. *International Journal of Hydrogen Energy*, *41*(28), 12108-12126.
[2] Egeland-Eriksen, T., Hajizadeh, A., & Sartori, S. (2021). Hydrogen-based systems for integration of renewable energy in power systems: Achievements and perspectives. *international journal of hydrogen energy*.
[3] Ancona, M. A., Bianchi, M., Branchini, L., De Pascale, A., Melino, F., Peretto, A., ... & Scarponi, L. B. (2017). From solar to hydrogen: Preliminary experimental investigation on a small scale facility. *International Journal of Hydrogen Energy*, *42*(33), 20979-20993.
[4] Khayrullina, A. G., Blinov, D., & Borzenko, V. (2019). Novel kW scale hydrogen energy storage system utilizing fuel cell exhaust air for hydrogen desorption process from metal hydride reactor. *Energy*, *183*, 1244-1252..
[5] Zhang, Y., Sun, H., & Guo, Y. (2020). Integration Design and Operation Strategy of Multi-Energy Hybrid System Including Renewable Energies, Batteries and Hydrogen. *Energies*, *13*(20), 5463.
[6] Dreistadt, D.M., Puszkiel,J., Bellosta von Colbe, J.M., Capurso, G., Steinebach, G., Meilinger, S., Le,T.-T., Covarrubias Guarneros, M., Klassen, T., Jepsen, J. (2021). Novel emergency gas-to-power system based on efficient and long-lasting solid-state hydride storage system: Modeling and experimental validation. *Energies* (Preprint submitted).

WHEC-2022
23rd World Hydrogen Energy Conference
June 26-30, 2022 - Istanbul

#142

SIZE OPTIMIZATION OF A HYBRID WIND/PHOTOVOLTAIC/FUEL CELL GRID-CONNECTED SYSTEM WITH HYDROGEN STORAGE

[1] *Leila Abdolmaleki,* [1*] *Umberto Berardi*
[1] Department of Architectural Science, Ryerson University, 350 Victoria Street, Toronto, ON, M5B 2K3, Canada

*Corresponding author e-mail: uberardi@ryerson.ca

ABSTRACT

Sustainable resource and energy management are essential considerations in designing hybrid energy systems. Finding an optimal framework that combines the requirements for a reliable design and satisfaction of continuous operation at minimal costs in all operating conditions is essential to clients and investors. This study emphasizes the size optimization of grid-connected hybrid photovoltaic, wind, and hydrogen storage systems. In this regard, by adopting the Hybrid Optimization Model for Electric Renewable (HOMER) energy-balance methods, the optimal design architecture is established. Additionally, the system's technical and economic aspects were examined in this study. Analysis of hourly simulations was performed to decide the optimal size, cost, and performance of the hybrid system. The optimum design configuration consists of a 2 kW PV array, 1 wind turbine, 1.33 kW converter, 2 kW electrolyzer, 5 kg hydrogen tank, 2.5 kW fuel cell, and 100 kW grid. Levelized Cost of Energy (COE) and Net Present Cost (NPC) are 0.169 $/kWh and $ 25,879.11 respectively, for different renewable energy fraction (RF) values of 91.5%.

Keywords: Renewable energy, Optimum sizing, Solar energy, Wind energy, Hydrogen

INTRODUCTION

Population growth and rapid technological advancements have led to a significant rise in energy demand and energy consumption worldwide. Globally, fossil fuels are a prominent source of electricity which increasing utilizing of them, increases global warming and greenhouse effect risks [1]. An important and reliable alternative energy source is solar energy; however, its storage is essential to utilize this resource [2]. In addition to batteries, hydrogen increases interest in storing renewable energy sources such as solar energy and wind energy. Hydrogen is the lightest, simplest, and most abundant element of the universe and has the biggest energy content per unit mass of any other fuel [3]. In addition to being a fuel, hydrogen can also be an energy carrier that can store and transport energy [4]. Practical hydrogen storage is still a big challenge which implementing hydrogen in our daily life still has many problems [5]. Several studies are being carried out on hydrogen to store energy longer than batteries[6-8].

The water electrolyzer, fuel cell, and hydrogen tank are considered as alternative storage systems. In this system, the generated power through solar power covers the load demand, and the excess energy runs through the water electrolyzer to produce hydrogen. The hydrogen tank is considered for storing the hydrogen for later use.

Based on an analytical model, Yunez-Cano et al. [9] proposed a hybrid photovoltaic/hydrogen (PV/H_2) system consisting of electrolyzer, hydride metal alloy tanks, and polymeric fuel cells system as a safe, small, and reliable electricity backup system that can meet the electricity of an isolated mobile home in Mexico. In another study, D. Maclay et al. [10] developed and tested an experimental solar-hydrogen-powered residence simulator. The system consisted of an electrolyzer powered by a solar photovoltaic array that produced hydrogen to serve as a storage device for energy. Fuel cells generated electricity from hydrogen in parallel with batteries to meet the dynamic power demands of residential applications. In order to compete with conventional energy storage systems, such systems would need to be significantly less expensive. Taking into account the climatic conditions of Saudi Arabia, Rahman et al. [11] examined the energy storage systems to store electricity generated by renewable sources. As a result of their findings, they concluded that no one storage system could satisfy all the requirements for an ideal electrical energy storage system.

This paper aims to optimize the size of a hydrogen fuel cell/photovoltaic/wind grid-connected hybrid system using the Hybrid Optimization of Multiple Energy Resources (HOMER) algorithm. The hybrid system is expected to satisfy daily and yearly load requirements of a typical single house in Toronto, Canada, at a low energy cost and a high renewable energy contribution and reduce excess power and harmful emissions. Previous studies have made a few efforts to apply hybrid systems (wind and solar energy) in cold climate countries to evaluate an on-grid connected system.

MATERIALS AND METHODS

As part of a feasibility study, load profiles, climate data of solar radiation (average solar radiation intensity of 3.53 kWh/m^2/day), and wind speed (average wind speed of 6.88 m/s) at the selected area are collected. Then a computer-aided renewable energy simulation tool was used to estimate the optimum design configuration and the cost of implementing the solution. The system modeling includes photovoltaic panels, wind turbines, electrolyzer, fuel cell, hydrogen tank, and converter systems (Figure 1).

This study uses HOMER software to design, simulate, analyze, and determine the economic feasibility of the system. The total Net Present Cost is calculated for evaluating the life-cycle cost in HOMER. NPC comprises set-up, replacement, operations, maintenance, and mixing costs associated with emissions. In designing a system in HOMER, the cost of energy (COE) is another crucial factor to consider.

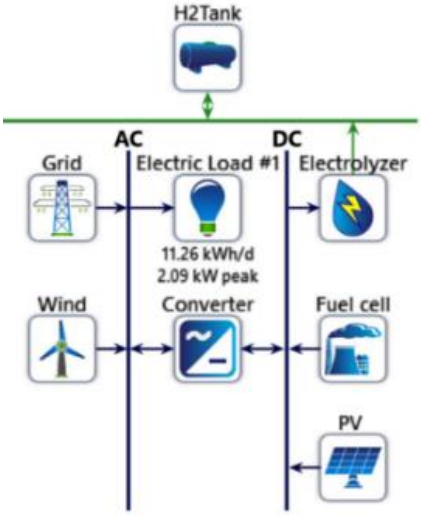


Figure 1. Schematic diagram of the system.

RESULTS AND DISCUSSION

According to the previous results, renewable energy systems with solar modules, wind turbines, and any storage system have the lowest cost of production due to the availability of resources [13,14]. It is impossible to generate solar power at night and wind power when the local wind speed at the hub height is less than the wind turbine's cut-in wind speed. In this study, the system integrates solar and wind energy to make up for the weaknesses of the other. As a result, the levelized and total energy costs would be decreased. The PV array and wind turbine provide load demand, while the stored hydrogen in the tank produces electrical energy through the fuel cell. The results showed that wind turbines have the crucial role in electrical energy production than fuel cell and photovoltaic panels.

During the simulations, many configurations are designed to find the optimum one. The size of the PV array varies from 1 to 5 kW; the number of the wind turbines varies from 1 to 3; the size of the electrolyzer varies from 1 to 10 kW; the size of the hydrogen tank varies from 1 to 20 kg. Table 1 shows the optimum size and cost of the system components. The optimum design configuration consists of a 2 kW PV array, 1 wind turbine, 1.33 kW converter, 2 kW electrolyzer, 5 kg hydrogen tank, 2.5 kW fuel cell, and 100 kW grid with COE of 0.169 $/kWh and NPC of $ 25,879.11. Figure 2 shows the cost summary for each of the components in the simulated system. By deducting the cost of the system, which includes the cost of purchase, repair, and replacement of equipment, the colored bars below the zero line represent the income of hybrid systems and as negative costs to calculate the total net cost of the hybrid system. The wind turbine has the highest capital cost ($22,831), followed by PV ($5,259).

This simulated hybrid power plant is connected to the grid, and simulations have been conducted using the grid. Table 2 provides information about the grid for the simulated hybrid power plant. As shown, 7,521 kWh of energy is sold compared to 987 kWh of it is purchased annually. Based on these results, a hybrid system consisting of both solar and wind power can meet the load demand all over the year with a minimum cost.

Table 1. Results of the economic analysis for the system based on HOMER.

Parameters	Value
Fuel cell (kW)	2.50
PV (kW)	2
Wind (each)	1
System Converter (kW)	1.33
Electrolyzer (kW)	2
Hydrogen Tank (kg)	5
Grid (kW)	100
COE ($/kWh)	0.169
Total NPC ($)	25,879.11

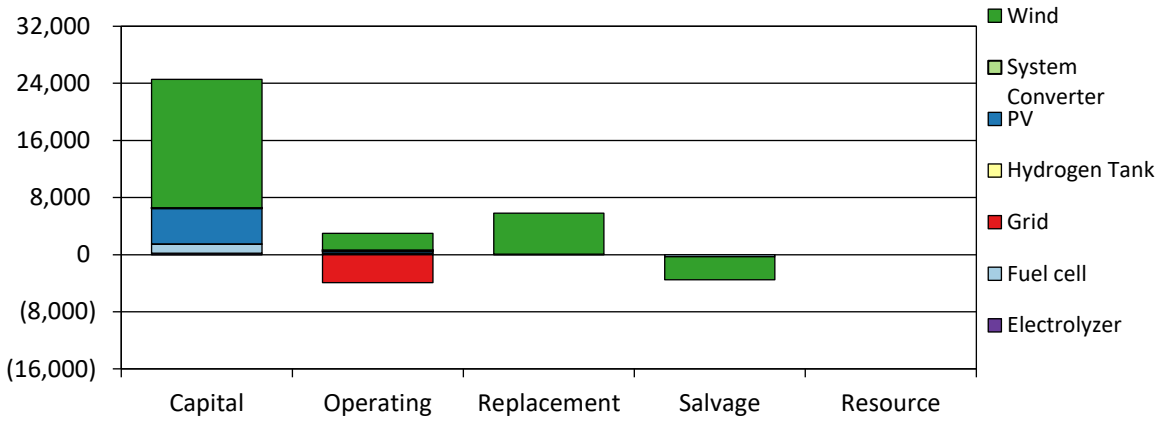


Figure 2. Cost summary of the system.

Table 2. Grid specifications for the power plant.

Month	Energy Purchased (kWh)	Energy Sold (kWh)	Net Energy Purchased (kWh)	Peak Demand (kW)	Energy Charge
January	67.4	429	-362	1.23	-$15.73
February	56.3	771	-715	1.22	-$33.76
March	72.5	815	-743	1.48	-$34.60
April	72.6	729	-656	1.41	-$30.27
May	83.3	599	-516	1.37	-$22.87
June	86.7	492	-405	1.38	-$17.23
July	101	468	-366	1.93	-$14.75
August	123	426	-303	1.73	-$10.83
September	100	535	-435	1.63	-$18.24
October	79.2	692	-613	1.52	-$27.86
November	81.3	756	-675	1.95	-$30.91
December	63.4	809	-746	1.47	-$35.08
Annual	987	7,521	-6,534	1.95	-$292.14

CONCLUSIONS

This paper develops and investigates a grid-connected renewable energy-based system in Toronto, Canada, consisting of a photovoltaic array, wind turbine, electrolyzer, hydrogen tank, and fuel cell. The system's solar and wind energy combination leads to 100% renewable energy contribution in around a year. For example, During the night where no solar radiation is available, wind energy supplies energy, and the storage system meets the load requirements if the wind speed is less than the wind turbine's cut-in wind speed. HOMER software is used to find the

optimum configuration with ideal components size and minimum COE and NPC. According to the results, the optimum design configuration consists of a 2 kW PV array, 1 wind turbine, 1.33 kW converter, 2 kW electrolyzer, 5 kg hydrogen tank, 2.5 kW fuel cell, and 100 kW grid which leads to a minimum COE of 0.169 $/kWh and NPC of $ 25,879.11. The production of hydrogen using renewable energy resources allows the use of an environmentally friendly fuel. Study results demonstrate that the proposed flexible design can meet the loads, support continuous operation, and reduce harmful environmental emissions.

REFERENCES

[1] M. Gökçek and C. Kale, "Techno-economical evaluation of a hydrogen refuelling station powered by Wind-PV hybrid power system: A case study for İzmir-çeşme," *Int. J. Hydrogen Energy*, vol. 43, no. 23, pp. 10615–10625, 2018, doi: 10.1016/j.ijhydene.2018.01.082.

[2] W. Zhou, H. Yang, and Z. Fang, "Battery behavior prediction and battery working states analysis of a hybrid solar–wind power generation system," *Renew. Energy*, vol. 33, no. 6, pp. 1413–1423, Jun. 2008, doi: 10.1016/J.RENENE.2007.08.004.

[3] Y. Hu *et al.*, "Rapid response hydrogen sensor based on nanoporous Pd thin films," *Int. J. Hydrogen Energy*, vol. 41, no. 25, 2016, doi: 10.1016/j.ijhydene.2016.04.101.

[4] Z. Abdin, C. J. Webb, and E. M. A. Gray, "Solar hydrogen hybrid energy systems for off-grid electricity supply: A critical review," *Renew. Sustain. Energy Rev.*, vol. 52, pp. 1791–1808, Dec. 2015, doi: 10.1016/J.RSER.2015.08.011.

[5] "The future of hydrogen – opportunities and challenges | Elsevier Enhanced Reader." https://reader.elsevier.com/reader/sd/pii/S0360319908015061?token=6158FA8EE0AB167DAF673871563CD1D65D37C6369202695BC036ED79D1F4BB8A4C5D838C5B6BF1F09507C993764E06DD&originRegion=us-east-1&originCreation=20211120165456 (accessed Nov. 20, 2021).

[6] D. Parra, G. S. Walker, and M. Gillott, "Modeling of PV generation, battery and hydrogen storage to investigate the benefits of energy storage for single dwelling," *Sustain. Cities Soc.*, vol. 10, no. March 2012, pp. 1–10, 2014, doi: 10.1016/j.scs.2013.04.006.

[7] E. Bocci, F. Zuccari, and A. Dell'Era, "Renewable and hydrogen energy integrated house," *Int. J. Hydrogen Energy*, vol. 36, no. 13, pp. 7963–7968, 2011, doi: 10.1016/j.ijhydene.2011.01.098.

[8] E. M. Stewart *et al.*, "Modeling, analysis and control system development for the Italian hydrogen house," *Int. J. Hydrogen Energy*, vol. 34, no. 4, pp. 1638–1646, 2009, doi: 10.1016/j.ijhydene.2008.12.008.

[9] A. Yunez-Cano, R. de G. González-Huerta, M. Tufiño-Velázquez, R. Barbosa, and B. Escobar, “Solar-hydrogen hybrid system integrated to a sustainable house in Mexico,” *Int. J. Hydrogen Energy*, vol. 41, no. 43, pp. 19539–19545, 2016, doi: 10.1016/j.ijhydene.2016.06.203.

[10] J. D. MacLay, J. Brouwer, and G. S. Samuelsen, "Experimental results for hybrid energy storage systems coupled to photovoltaic generation in residential applications," *Int. J. Hydrogen Energy*, vol. 36, no. 19, pp. 12130–12140, 2011, doi: 10.1016/j.ijhydene.2011.06.089.

[11] F. Rahman, S. Rehman, and M. A. Abdul-Majeed, "Overview of energy storage systems for storing electricity from renewable energy sources in Saudi Arabia," *Renew. Sustain. Energy Rev.*, vol. 16, no. 1, pp. 274–283, Jan. 2012, doi: 10.1016/J.RSER.2011.07.153.

[12] A. Al-Sharafi, A. Z. Sahin, T. Ayar, and B. S. Yilbas, "Techno-economic analysis and optimization of solar and wind energy systems for power generation and hydrogen production in Saudi Arabia," *Renew. Sustain. Energy Rev.*, vol. 69, no. October 2016, pp. 33–49, 2017, doi: 10.1016/j.rser.2016.11.157.

[13] M. Qolipour, A. Mostafaeipour, and O. M. Tousi, "Techno-economic feasibility of a photovoltaic-wind power plant construction for electric and hydrogen production: A case study," *Renew. Sustain. Energy Rev.*, vol. 78, pp. 113–123, 2017, doi: 10.1016/J.RSER.2017.04.088.

WHEC-2022
23rd World Hydrogen Energy Conference
June 26-30, 2022 - Istanbul

#145

INVESTIGATION OF TEMPERATURE AND PRESSURE EFFECT ON THE HYDROGEN SORPTION KINETICS IN THE INTERFACE OF Mg/MgH_2 BY MOLECULAR DYNAMICS

[1,2] Mehmet Fazıl Kapçı, [1] Zhen Wu, [2] Burak Bal*
[1]Xi'an Jiatong University, School of Chemical Engineering and Technology, 710049, Xi'an, PR China
[2] Abdullah Gul University, Department of Mechanical Engineering, 38080, Kayseri, Turkey

*Corresponding author e-mail: wuz2015@mail.xjtu.edu.cn

ABSTRACT

Molecular dynamics simulations were performed in order to analyze the hydrogen sorption kinetics between α-MgH_2 and hcp Mg structures under different temperatures and pressures. Results showed that hydrogen desorption from magnesium hydride and absorption by hcp magnesium increase at the higher temperatures. During the hydrogen desorption from magnesium hydride and absorption into hcp magnesium, crystallographic orientation change in the magnesium atoms was observed. At 400 °C, the pressure was found to have a negative impact during the hydrogen desorption from magnesium hydride due to the prevention of recrystallization.

Keywords: Magnesium hydride, Hcp magnesium, Molecular dynamics, Hydrogen sorption kinetics

INTRODUCTION

Increasing demand for alternative energy sources and the harmful effects of fossil fuel usage gradually draw attention to hydrogen energy [1,2]. However, in order to use hydrogen in practical applications, several obstacles still need to be overcome. One of the most important challenges in this regard is the storage of hydrogen [3,4]. Conventional storage techniques such as storing the hydrogen as a liquid at cryogenic temperatures or in the form of pressurized gas are quite inefficient way in terms of the small gravimetric and volumetric capacity and also for the high cost of operation [5]. However, new materials and methodologies are being developed in recent years for solid storage of hydrogen that has significant advantages compared to the conventional methods. Within these solid storage materials, magnesium hydride structures constitute a promising solution for the storage of hydrogen in high capacities [6,7]. Besides, for a better understanding of the hydrogen uptake and release kinetics and also for developing new Mg-based hydrogen storage structures, atomistic modelling of the hydrogen sorption mechanisms is crucial. In this study, hydrogen diffusion in the interface of Mg/MgH_2 was investigated under the effect of different temperatures and pressures by Molecular Dynamics (MD).

METHODOLOGY

Molecular dynamics simulations were performed by LAMMPS [8] (Large-scale Atomic/Molecular Massively Parallel Simulator) software. A bicrystal was constructed that is composed of alpha magnesium hydride and hcp magnesium where the two structures were merged along one direction (figure 1). Temperature and pressure equilibration was performed on the bicrystal by NPT ensemble at room temperature and 0 isobaric pressure for 0.25 ns. Simulations for the diffusion of hydrogen were performed under 3 different temperatures (200 °C, 300 °C, 400 °C) and 3 different isobaric pressures (0 GPa, 0.5 G, 1 GPa), i.e. 9 simulations were performed in total, by NPT ensemble for 1.5 ns. Periodic boundary conditions were utilized in all three directions. In order to evaluate the hydrogen absorption of the hcp magnesium and desorption from magnesium hydride, total diffused hydrogen number in the half bottom part of the simulation cell along y direction (N_d) was tracked during the NPT ensemble, and normalization was applied with respect to total hydrogen content in the simulation cell (N_t) where the normalized hydrogen content is:

$$N_n = \frac{2N_d}{N_t} \quad (1)$$

For the interatomic interactions, angular dependent potential (ADP) was utilized [9]. Visualization, common neighbor analysis (CNA), and determination of the atomic positions were performed by OVITO software [10].

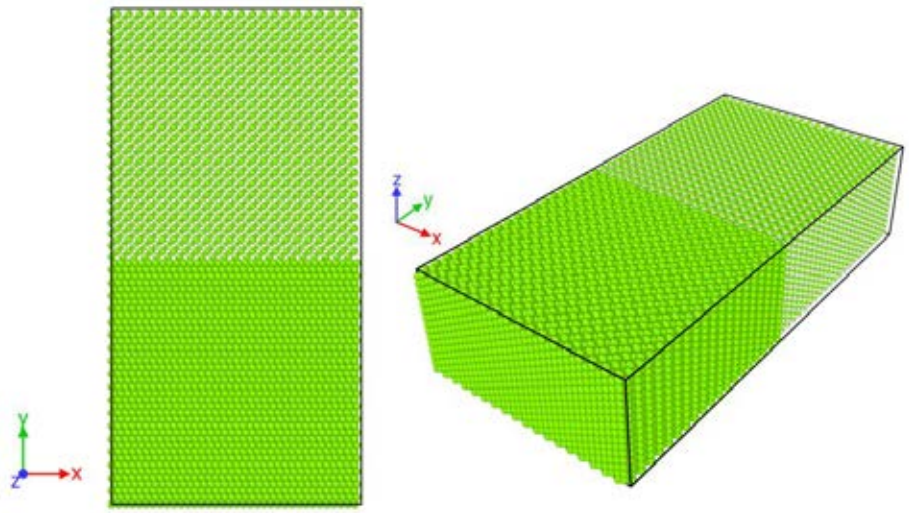


Fig. 1. Initial configuration of simulation cell; green balls represent the magnesium atoms and white balls represents the hydrogen atoms.

RESULTS AND DISCUSSION

Figure 2 shows the normalized diffused hydrogen content under different temperatures and pressures during the NPT ensemble. Results indicate that diffusion of the hydrogen increases when increasing the temperature. The most diffusion takes place under 400 °C for all pressure values. On the other hand, at both 200 °C and 300 °C, it was observed that normalized concentration does not exceed 0.1 and the concentration was equilibrated before 0.2 ns. Distinctive desorption of hydrogen from MgH_2 and absorption by the Mg was observed under 400 °C temperature and 0 isobaric pressure. Although the hydrogen uptake rate is equal under all pressures values at 400 °C until 1 ns, an earlier decrease in the rate was observed at pressurized simulations.

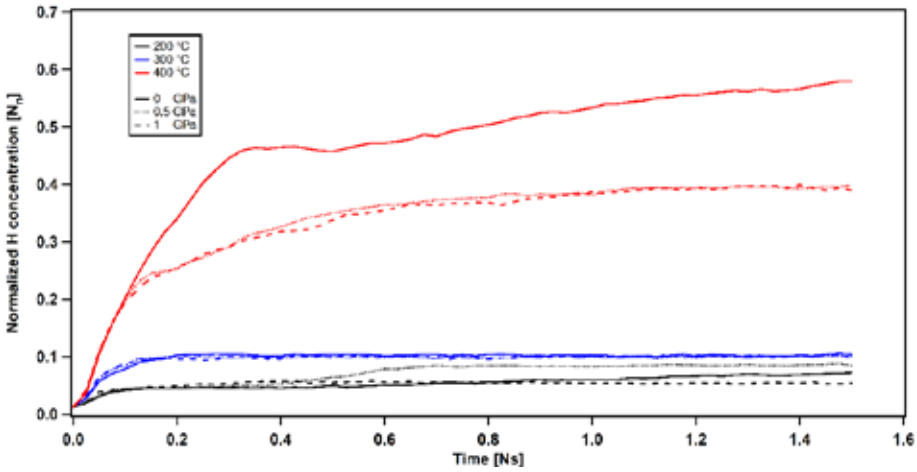


Fig. 2. Absorbed hydrogen content by initial hcp magnesium region (half bottom part along y axis) under different temperatures and pressures.

Crystallographic structure types according to common neighbour analysis (CNA) were shown in figure 3. In the initial case, evaluating the positions of only Mg atoms provides a crystal structure similar to BCC at the upper half part of the simulation cell (α-MgH_2) where the bottom part consists of hcp Mg (figure 3a). Similarly, figure 3b, 3c, 3d, and 3e show the structure types of the Mg atoms after the sorption of hydrogen. It was found that hydrogen desorption from α-MgH_2 and absorption by the hcp magnesium crystals lead to a transformation to fcc type structure during the temperature and pressure simulations starting from the Mg/MgH_2 interface. In both 200 °C and 300 °C, transformation from bcc to fcc and hcp to fcc structure takes place at the interface in a very limited region. However, at 400 °C for each pressure value, bcc type crystallographic structure of the Mg atoms in MgH_2 completely transforms to fcc type structure at the end of the simulations. Only in the 400 °C and 0 GPa (figure 3e), a different crystallographic orientation in the fcc structure was observed after recrystallization. On the other hand, in

pressurized simulation cells under the same temperature (figure 3d), the formation of the fcc structures is in the same orientation with the lower temperature simulations and no recrystallization was observed.

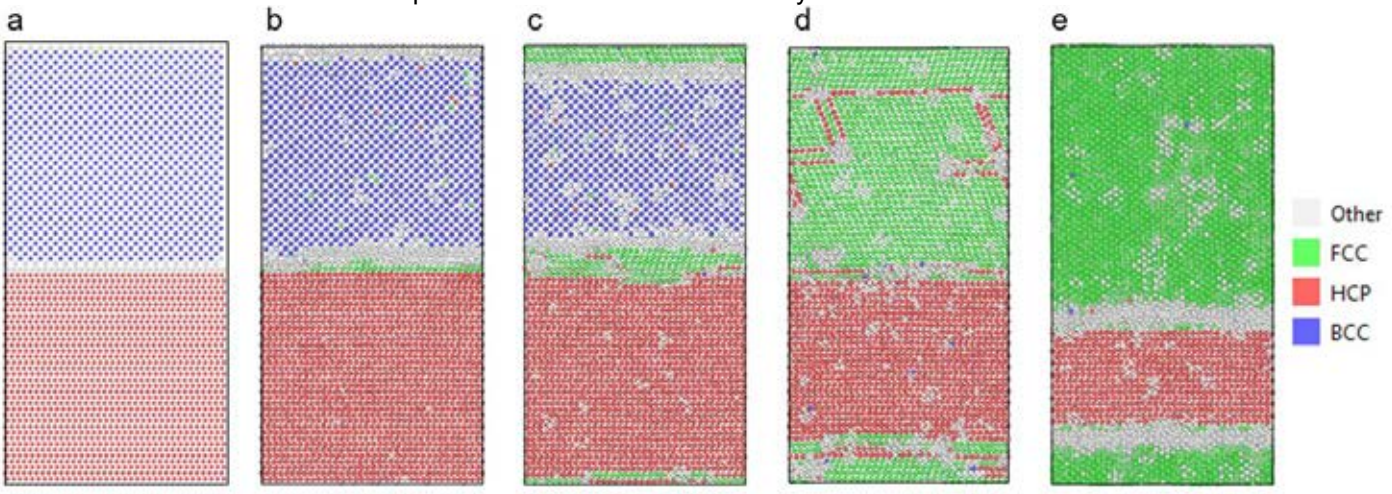


Fig. 3. Crystallographic structure types of only magnesium atoms for a) initial relaxed simulation cell and b), c), d), and, e) after the hydrogen diffusion simulations at 200 °C 0 GPa, 300 °C 0 GPa, 400 °C 1 GPa and, 400 °C 0 GPa respectively.

CONCLUSIONS

In conclusion, the effect of the temperature and pressure on the sorption of hydrogen in magnesium and magnesium hydride was investigated by molecular dynamics simulations. It was observed that higher temperatures lead to an increased uptake and release rate for all pressures values. Additionally, during the hydrogen desorption from magnesium hydride phase at elevated temperature, recrystallization of the magnesium atoms was observed under 0 GPa pressure which enhanced the hydrogen desorption.

REFERENCES

1. J.O. Abe, A.P.I. Popoola, E. Ajenifuja, O.M. Popoola, Hydrogen energy, economy and storage: Review and recommendation, Int. J. Hydrogen Energy. 44 (2019) 15072–15086. doi:10.1016/j.ijhydene.2019.04.068.
2. I. Dincer, Green methods for hydrogen production, Int. J. Hydrogen Energy. 37 (2012) 1954–1971. doi:10.1016/J.IJHYDENE.2011.03.173.
3. A.F. Dalebrook, W. Gan, M. Grasemann, S. Moret, G. Laurenczy, Hydrogen storage: Beyond conventional methods, Chem. Commun. 49 (2013) 8735–8751. doi:10.1039/c3cc43836h.
4. B. Sakintuna, F. Lamari-Darkrim, M. Hirscher, Metal hydride materials for solid hydrogen storage: A review, Int. J. Hydrogen Energy. 32 (2007) 1121–1140. doi:10.1016/j.ijhydene.2006.11.022.
5. J. Ren, N.M. Musyoka, H.W. Langmi, M. Mathe, S. Liao, Current research trends and perspectives on materials-based hydrogen storage solutions: A critical review, Int. J. Hydrogen Energy. 42 (2017) 289–311. doi:10.1016/j.ijhydene.2016.11.195.
6. C.N.C. Hitam, M.A.A. Aziz, A.H. Ruhaimi, M.R. Taib, Magnesium-based alloys for solid-state hydrogen storage applications: A review, Int. J. Hydrogen Energy. 46 (2021) 31067–31083. doi:10.1016/J.IJHYDENE.2021.03.153.
7. J. Zhang, S. Yan, H. Qu, Recent progress in magnesium hydride modified through catalysis and nanoconfinement, Int. J. Hydrogen Energy. 43 (2018) 1545–1565. doi:10.1016/j.ijhydene.2017.11.135.
8. S. Plimpton, Fast parallel algorithms for short-range molecular dynamics, J. Comput. Phys. 117 (1995) 1–19. doi:10.1006/jcph.1995.1039.
9. D.E. Smirnova, S. V. Starikov, A.M. Vlasova, New interatomic potential for simulation of pure magnesium and magnesium hydrides, Comput. Mater. Sci. 154 (2018) 295–302. doi:10.1016/j.commatsci.2018.07.051.
10. A. Stukowski, Visualization and analysis of atomistic simulation data with OVITO–the Open Visualization Tool, Model. Simul. Mater. Sci. Eng. 18 (2010) 015012. doi:10.1088/0965-0393/18/1/015012.

WHEC-2022
23rd World Hydrogen Energy Conference
June 26-30, 2022 - Istanbul

#149

EFFECTS OF FILLING STRATEGIES ON HYDROGEN REFUELING PERFORMANCES

[1,2] Hao Luo, [2] Richard Chahine, [2] Pierre Bénard, [1,2,*] Jinsheng Xiao
[1] Wuhan University of Technology, School of Automotive Engineering, Hubei 430070, China
[2] Université du Québec à Trois-Rivières, Hydrogen Research Institute, QC G8Z 4M3, Canada

*Corresponding author e-mail: Jinsheng.Xiao@uqtr.ca

ABSTRACT

To ensure the safety of hydrogen refueling systems and fuel cell vehicles under different conditions, the filling parameters are usually set very conservatively and lead to waste energy consumption and investment. The lumped parameter hydrogen gas model and one-dimension tank wall model of the hydrogen filling process previously proposed by our team are improved by considering the Joule Thomson effect and kinetic energy and using a more accurate model of the heat transfer coefficients between hydrogen gas and inner tank wall and between ambient and outer tank wall. Based on our validated model, the effects of constant and two-stage average pressure rise rate (APRR) and inlet temperature on refueling performance were investigated, respectively. Compared with the optimal filling strategies of the reference papers, the current strategies with two-stage APRRs and inlet temperatures can further reduce the cooling power by 23.8% and 16.3%, respectively, without increasing the cooling consumption. It is beneficial to reduce the equipment cost of the refrigeration system.

Keywords: Hydrogen refueling, Precooling, Average pressure rise rate, Filling strategies, Refueling performance

INTRODUCTION

SAE J2601 protocol stipulates that during the hydrogen refueling, the temperature inside the onboard tank should not exceed 85 ℃, the pressure should not exceed 125% of the nominal working pressure, and the refueling time required to be within 3-5 min. The look-up table method and the MC method meet the above requirements. However, to ensure the safety of the hydrogen refueling systems and fuel cell vehicles under different conditions, the filling parameters are usually set very conservatively. The filling parameters that affect the refueling performance should be studied and adjusted according to the specific situation to obtain a higher state of charge (SOC), less energy consumption and investment. The filling parameters such as ambient temperature, initial temperature and initial pressure in different regions or vehicles are not easily controlled manually, so this paper only studies the precooling/inlet temperature, filling rate (APRR) and filling time. Our team has built three lumped parameter models of hydrogen storage tanks: single-zone (hydrogen), dual-zone (hydrogen and tank wall) and triple-zone (hydrogen, tank wall liner and shell) models. These models are well-validated and used to predict filling time, final hydrogen temperature, and mass and inlet temperature based on experimental data and references. This paper further improves our previous model by considering the Joule Thomson effect and kinetic energy and using a more accurate model of the heat transfer coefficients between hydrogen gas and the inner tank wall and between the ambient and outer tank wall. Based on our validated model, the effects of constant and two-stage APRRs and inlet temperatures on refueling performance were investigated, respectively.

2 THERMODYNAMICS MODEL

Fig. 1 shows the thermodynamic model of a hydrogen refueling system, improved from our previous model [1]. The Joule Thomson effect and the kinetic energy are expressed in Eq. (1-2). The accurate formula for the heat transfer coefficients between hydrogen and the inner tank wall and between ambient outer tank wall and ambient are expressed in Eq. (3-4) [2].

$$\mu_{JT} = \left(\frac{\partial T}{\partial p}\right)_h \tag{1}$$

$$\dot{E}_k = \frac{\partial}{\partial t}\left[\int_{CV}\left(\frac{1}{2}v^2\right)\rho dV\right] = \frac{8\dot{m}^3}{\pi^2\rho^2 d_{\text{in}}^4} \tag{2}$$

$$\text{Nu}_{D_{\text{in}}} = \frac{a_{\text{in}} D_{\text{in}}}{\lambda_{\text{gas}}} = a\text{Ra}_{D_{\text{in}}}^{b} + c\,\text{Re}_{d_{\text{in}}}^{d}\ ,\ \ \text{Ra}_{D_{\text{in}}} = \frac{g\beta|T - T_w|c_p\rho^2 D_{\text{in}}^3}{\mu\lambda}\ ,\ \ \text{Re}_{d_{\text{in}}} = \frac{\rho v d_{\text{in}}}{\mu} = \frac{4\dot{m}}{\pi\mu d_{\text{in}}} \tag{3}$$

$$\text{Nu}_{D_{\text{out}}} = \frac{a_{\text{out}} D_{\text{out}}}{\lambda_{\text{air}}} = \left(0.4\text{Re}_{D_{\text{out}}}^{0.5} + 0.06\text{Re}_{D_{\text{out}}}^{2/3}\right)\text{Pr}_{\text{air}}^{0.4}\ ,\ \ \text{Re}_{D_{\text{out}}} = \frac{\rho_{\text{air}} v_{\text{air}} D_{\text{out}}}{\mu_{\text{air}}}\ ,\ \ \text{Pr}_{\text{air}} = \frac{\mu_{\text{air}} c_{p_{\text{air}}}}{\lambda_{\text{air}}} \tag{4}$$

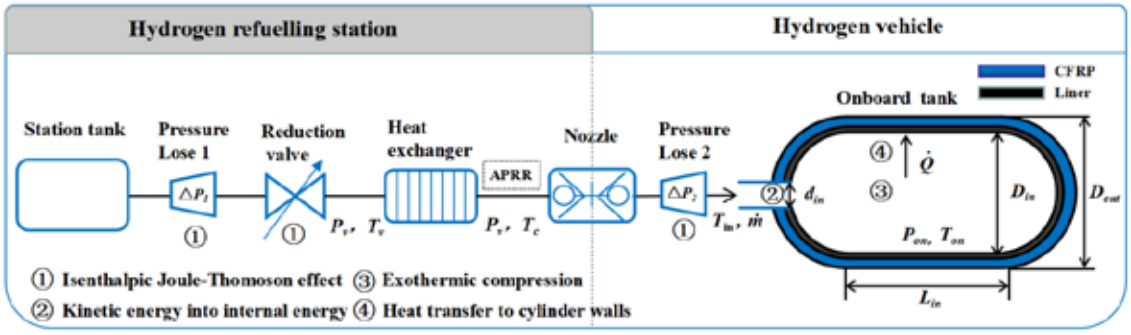


Fig. 1. Structure diagram of hydrogen refueling system.

3 MODEL IMPLEMENTATION, VALIDATION

3.1 Model implementation

The model is implemented on Matlab/Simulink platform. Table 1 shows the parameters of onboard tank in current study.

Table 1. Parameters of the onboard tank in the current study.

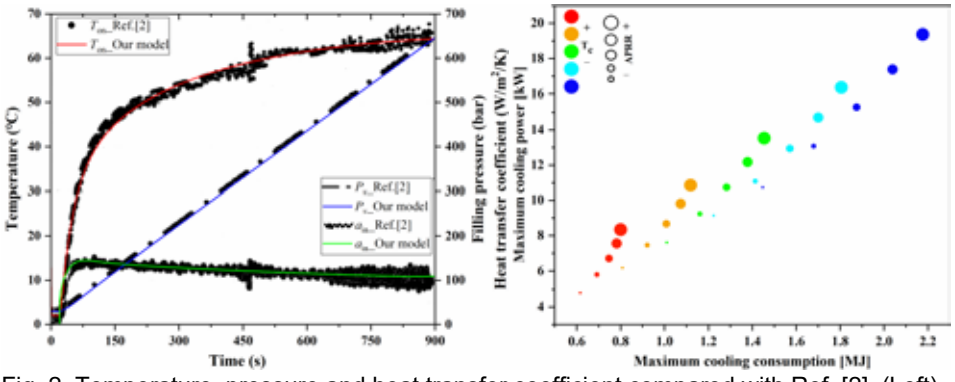
Tank geometry [2]		Tank characteristics [3]	
Volume of the tank, L	90.5	Thermal conductivity for Liner, W/(m·K)	0.4
Nominal working pressure, MPa	70	Specific heat capacity for Liner, J/(kg·K)	1917
Internal length, m	0.58	Density for Liner, kg/m³	954
Internal diameter, m	0.434	Thermal conductivity for CFRP, W/(m·K)	0.53
Outer diameter, m	0.484	Specific heat capacity for CFRP, J/(kg·K)	942
Diameter of the injector, m	0.006	Density for CFRP, kg/m³	1442

Table 2. Initial and boundary conditions for model validation [2].

Initial pressure, MPa	3
Initial temperature, ℃	1.9
Ambient temperature, ℃	1.9
Inlet temperature, ℃	7.9
APRR, MPa/s	0.07

3.2 Model validation

Table 2 shows initial and boundary conditions for model validation. Fig. 2 shows the model verification results. The simulation values are consistent with reference data [2].



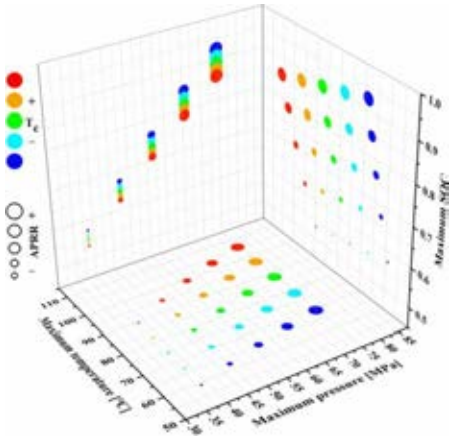


Fig. 2. Temperature, pressure and heat transfer coefficient compared with Ref. [2]. (Left)
Fig. 3. Effects of constant APRRs and inlet temperatures on maximum cooling consumption and power. (Middle)
Fig. 4. Effects of constant APRRs and inlet temperatures on maximum temperature, pressure and SOC in the onboard tank. (Right)

4 PARAMETRIC STUDY

4.1 Constant APRR and inlet temperature

We investigated the refueling performance of different constant APRRs and inlet temperatures. The parameters are shown in Table 3. There are 5 sets of parameters for APRR and inlet temperature, respectively, so there are 25 kinds of results. As shown in Fig. 3, maximum cooling consumption and power increase almost linearly when APRR increases or inlet temperature decreases. Fig. 4 shows the projection of the 25 results on three faces. The inlet temperature has little effect on the pressure, has a large effect on the SOC, and has the greatest effect on the temperature. The APRR has a small effect on the temperature and a large effect on the SOC and pressure.

Table 3. Value of parameters.

Time [s]	APRR [MPa/s]	Tc [℃]
180	0.2	−20
180	0.25	−10
180	0.3	0
180	0.35	10
180	0.4	20

Table 4- Maximum results of typical cases and relative rate of change.

Case		Temperature [℃]	SOC	Cooling consumption [MJ]	Cooling power [kW]
Inlet temperature = −20 ℃	**Case1**	**69.988**	**0.966**	**2.124**	**19.999**
	Case4	70.379 (+0.5%)	0.959 (−0.7%)	2.118 (−0.3%)	15.246 (−23.8%)
APRR = 0.428 MPa/s	Case1	79.987	0.947	1.697 (−1.7%)	14.846 (−11.3%)
	Case2	**79.983**	**0.947**	**1.727**	**16.730**
	Case4	80.001	0.947	1.687 (−2.3%)	16.199 (−3.2%)
	Case5	79.929	0.947	1.709 (−1.0%)	15.854 (−5.2%)
	Case6	79.937	0.947	1.693 (−2.0%)	13.999 (−16.3%)

4.2 Two-Stage APRR and inlet temperature

We investigated the refueling performance of different two-stage APRRs at inlet temperatures of -20, -10, 0, 10 and 20 °C. Since the pattern is similar at each inlet temperature, only the one at −20 °C is shown in Fig. 5. Cases 2, 3 and 5 are significantly worse in temperature, pressure and SOC, so we can compare only cases 1 and 4, as shown in Table 4. Case 4 is significantly better than case 1. We also investigated the refueling performance of different two-stage inlet temperatures at APRR of 0.428. Case 6 is significantly the best, as shown in Table 4.

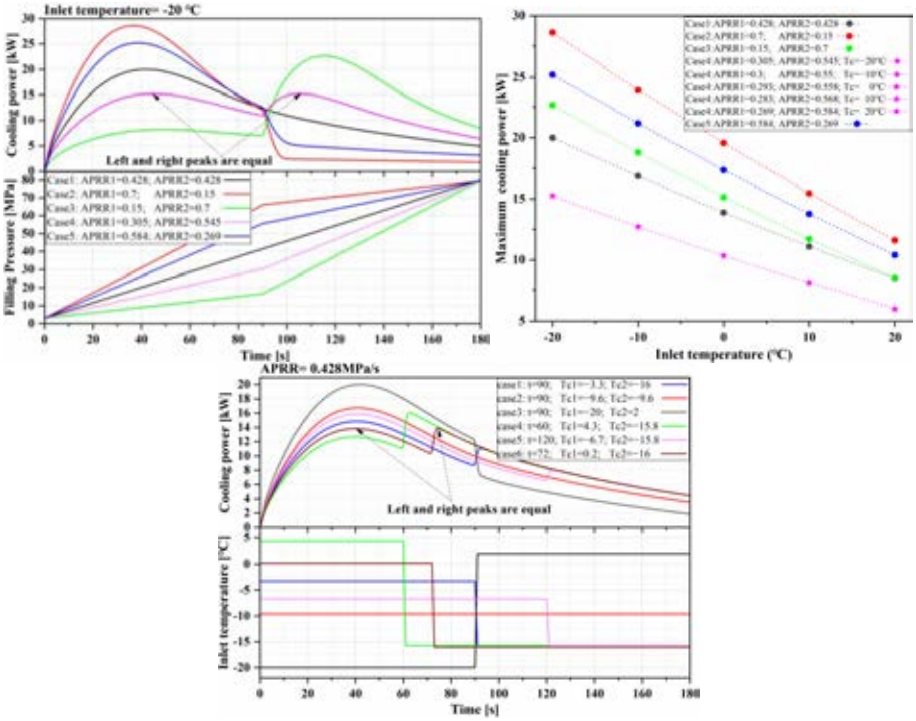


Fig. 5. Effect of different two-stage APRR strategies on cooling power at an inlet temperature of -20°C. (Left)
Fig. 6. Effect of different two-stage APRR strategies on maximum cooling power at different inlet temperatures. (Middle)
Fig. 7. Effect of different two-stage inlet temperature strategies on cooling power at APRR of 0.428. (Right)

5 CONCLUSIONS

We improved the lumped parameter hydrogen gas and one-dimension tank wall model of the hydrogen filling process previously proposed by our team, mainly including adding the Joule Thomson effect, the conversion of kinetic energy to internal energy, and the accurate modeling of the heat transfer coefficients between hydrogen and inner tank wall and between ambient and outer tank wall. The effects of constant and two-stage APRRs and inlet temperatures on hydrogen refueling performances are studied based on our validated model. The specific conclusions are as follows:

- Compared with the previous research results where the best filling strategy is linear APRR [4], we can always find two-stage APRR1 and APRR2 at different inlet temperatures, which can further reduce the cooling power by 23.8% without increasing the cooling consumption.
- Compared with the previous results obtained using a constant precooling/inlet temperature solved by the analytical solution, we can always find two-stage precooling/inlet temperatures Tc1 and Tc2 to further reduce the cooling power by 16.3% without increasing the cooling consumption.

REFERENCES

1. Luo H, Xiao J, Bénard P, Chahine R, Yang T. Multi-objective optimization of cascade storage system in hydrogen refuelling station for minimum cooling energy and maximum state of charge. International Journal of Hydrogen Energy 47(20):10963-75.
2. Bourgeois T, Ammouri F, Weber M, Knapik C. Evaluating the temperature inside a tank during a filling with highly pressurized gas. International Journal of Hydrogen Energy 40(35):11748-55.
3. Bourgeois T, Brachmann T, Barth F, Ammouri F, Baraldi D, Melideo D. Optimization of hydrogen vehicle refueling requirements. International Journal of Hydrogen Energy 42(19):13789-809.
4. Melideo D, Baraldi D. CFD analysis of fast filling strategies for hydrogen tanks and their effects on key-parameters. International Journal of Hydrogen Energy 40(1):735-45.

WHEC-2022
23rd World Hydrogen Energy Conference
June 26-30, 2022 - Istanbul

#155

MODELING THE KINETIC BEHAVIOR OF THE Li-RHC SYSTEM FOR HYDROGEN STORAGE UNDER DESORPTION CONDITIONS

[1,2*] *André Neves,* [1,2] *Julián Puszkiel,* [2] *José Maria Bellosta von Colbe,* [1,2] *Thomas Klassen,* [1,2] *Julian Jepsen*
[1]Helmut Schmidt University (HSU), University of the Federal Armed Forces, Department for Mechanical Engineering, Holstenhofweg 85, 22043, Hamburg, Germany
[2] Helmholtz-Zentrum Hereon, Institute for Hydrogen Technology, Design for Mobility, Max-Planck-Straße 1, 21502, Geesthacht, Germany

*Corresponding author e-mail: andre.neves@hereon.de

ABSTRACT

In the current work, we present an investigation about modeling the lithium reactive hydride composite (Li-RHC) under desorption conditions. Such modeling is fundamental to enable finite element simulations (FEM) to design optimized hydrogen storage systems. In order to obtain the kinetic data for the study, the dynamic behavior of ball-milled Li-RHC powder is characterized in a Sievert apparatus. Different combinations of pressure and temperature are assessed and the reaction mechanisms of both MgH_2 and $LiBH_4$ are individually identified. The MgH_2 decomposition follows a JMAEK with n = 1 reaction mechanism, while the Prout-Tompkins (PT) model describes the reaction mechanism of $LiBH_4$ very well. However, the PT model involves a new parameter, t_0, associated with the vertical translation of the fitted curve. In order to make the equation applicable for FEM simulations, a novel method is here developed to represent t_0 as a function of the system's parameters, namely, temperature and pressure. This study provides new capabilities of using the PT model to predict the behavior of the desorption of $LiBH_4$ within a wide range of temperature and pressure conditions.

Keywords: Hydrogen Storage, Kinetic Modeling, Reactive Hydride Composite, Desorption, Borohydrides

INTRODUCTION

The need for new energy storage systems has led to the development of different hydrogen storage systems. One of these systems, the Lithium Reactive Hydride Composite (Li-RHC), shows great promise for applications in which a high gravimetric capacity is critical for practical application. However, for the application of hydride systems, the tank's design plays a critical role in the overall performance and the technical and economic feasibility of the system. For this reason, simulation, such as finite element simulation (FEM), has been used to design optimized systems. For that, descriptions of the heat flow, mass transfer and reaction kinetics are necessary. While the absorption kinetics of the Li-RHC system has been described elsewhere in detail [1], the desorption kinetics of the Li-RHC has not been the subject of a comprehensive study.

The desorption of the Li-RHC system usually follows two steps, of which the desorption of the MgH_2 is the first one.

$$MgH_2 \rightarrow Mg + \frac{1}{2} H_2 \quad (1)$$

This reaction proceeds rapidly in the usual temperatures (T) for Li-RHC desorption.

For the T and pressure (P) ranges in which the material in this work is investigated, the reaction is expected to follow

$$2\ LiBH_4 + Mg \rightarrow 2\ LiH + MgB_2 + 3\ H_2 \quad (2)$$

While the complete kinetic description of the absorption has been previously done [1], the two-step desorption reaction is yet to be described comprehensively. In the work of Puszkiel et al. [2], the authors have used the Prout-Tompkins (PT) model to describe the $LiBH_4$ decomposition. However, this requires the use of a new variable, t_0. This variable can be determined empirically with relative ease, as this is a parameter for the non-linear fitting of the kinetic curve. However, up to this day, and to the best of our knowledge, there is no description of how to predict or model the value of t_0 as a function of the system's parameters. Such modeling is necessary in order to be able to use the integrated kinetic equation to perform simulations that account for changes in both T and P. In this work, we present the kinetic modeling of Li-RHC under desorption conditions, including a novel, empirical approach for the determination of t_0 as a function of the system's variables, developing a method that can be applied to different systems which depend on this variable for a complete description of the reaction kinetics.

EXPERIMENTAL PROCEDURE AND MODELING

In this work, a high-energy ball milling was used to prepare the Li-RHC powders. The experimental parameters were described elsewhere [1]. The prepared powders were put inside a sample holder to investigate the material's desorption

kinetics. All the experiments were carried out using ca. 150 mg of powder in a Sievert-type Apparatus (HERA, Canada, Canadian Patent). The material was cycled at least 7 times to ensure the reproducibility of the material's kinetic behavior. Then, a series of experiments under different T and P were carried out to investigate the kinetic behavior of the material under desorption conditions (green circles, in Fig. 1). All the absorption reactions were carried out with the same conditions (400 °C, 30 bar initial H_2-pressure). As seen, several conditions of P and T were investigated to increase the reliability and the range of applicability of the developed kinetic model.

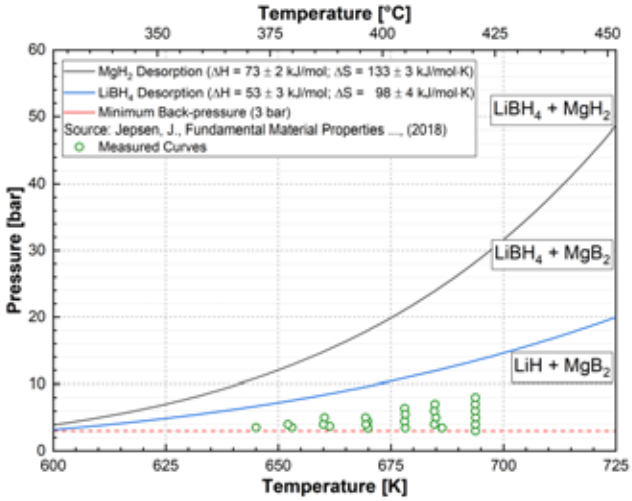


Fig. 1. Thermodynamic equilibrium lines and P-T pairs for the kinetic curves measured for the assessment. The red dotted line represents the minimum overpressure used.

MODELING APPROACH

For all the considered calculations, the variable reacted fraction α can be used to follow the progress of the desorption reaction. α varies from 0 to 1. The modeling approach is described by the separable variable method as described by equation (3):

$$\frac{d\alpha}{dt} = K(T) \cdot F(P) \cdot G(\alpha) \quad (3)$$

, in which α is the reacted fraction, t is time, K(T) is related to the temperature dependency (Arrhenius term), F(P) is related to the pressure dependency, and G(α) is related to the reaction mechanism. A detailed description of the equations, methods, and application of the method is out of the scope of this work and can be seen in ref. [1,3,4].

RESULTS AND DISCUSSION

The dehydrogenation process occurs in two series reaction: First, MgH_2 decomposition (Eq. 1) and then, the desorption reaction of $LiBH_4$ (Eq. 2). Therefore, a model should account for the different reaction mechanisms. The G(α) expression has been identified for each desorption reaction. The found reactions coincide with the ones found by Puszkiel et al. [2]. The best models have been found: for Eq. 1, the JMAEK with n = 1, and Eq. 2, the PT model. The integrated model is as shown in equation (4):

$$\alpha = A_1 \cdot (1 - exp[-(k_1 \cdot t)]) + A_2 \cdot \left(1 + \exp\left(-k_2 + (t - t_0)\right)\right)^{-1} + adj \quad (4)$$

, in which α is the reacted fraction, the indices 1 and 2 refer, respectively, to reactions shown in Eq. 1 and Eq. 2, k is the kinetic constant (in s^{-1}) and depends on the system's T and P, t_0 is a PT model variable (in seconds) and t is the time in seconds. The variables A_1 and A_2 approximately represent each reaction's contribution to the total system H_2-capacity and are nearly constant across different T and P ranges. For all the fitted curves, the mean values of 0.37 and 0.80 are used for, respectively, A_1 and A_2. An excess of 0.17 is observed, and it is a product of the mathematical expression that defines the PT model. This excess comes from the values of the PT model at t = 0 s. In this particular case, by assuming "adj" as -0.17, it is possible to compensate for this behavior. Finally, the t_0 variable can be understood as the vertical translation in the x-axis. This vertical translation can be interpreted graphically as an inflection point in the second desorption reaction (as shown in the blue arrow in Fig. 2.a)).

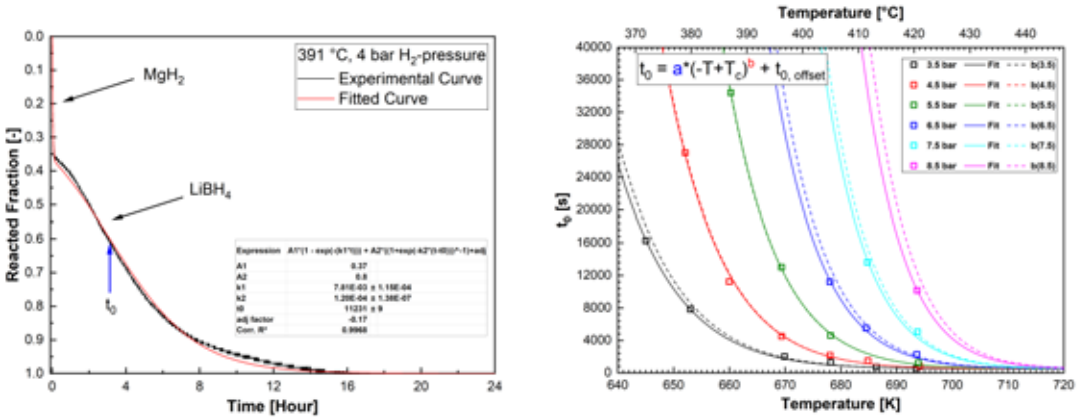


Fig. 2. – a) Experimental and fitted Desorption curves of the Li-RHC under 391 °C and 4 bar of initial H_2-pressure. b) Plot of the t_0 variable as a function of T for several pressures. The squares are the points obtained from the experiments as shown in Fig. 2 a), the full curves are the best fit obtained from the used expression and the dotted lines are the back-calculated values after performing a fit to obtain an expression b(P) (b as a function of P).

The plot of t_0 against T shows that by grouping the values in pressure ranges and using an appropriate equation, it is possible to find mathematical expressions that can successfully describe the variation of t_0 as a function of T and P. In this equation, a is a constant (concerning T and P), and b is a function of P.

CONCLUSIONS

In this work, the desorption kinetic behavior of the Li-RHC under a wide range of different combinations of pressure and temperature is investigated. A combined approach for the reaction kinetics is employed, and a novel method for modeling the t_0 parameter (from the Prout-Tompkins model) is proposed. The proposed equation accounts for the system conditions such as temperature and pressure. This novel approach allows performing simulations with systems that follow the Prout-Tompkins model despite the additional parameter being necessary for the complete description of the kinetic behavior.

ACKNOWLEDGEMENT

The authors would like to thankfully acknowledge the Karl-Vossloh-Stiftung for the financial support provided for this project (Project Number S047/10043/2017). Also, thanks to Carolin Fritsch for all the support with some of the experimental work.

REFERENCES

[1] Neves AM, Puszkiel J, Capurso G, Bellosta von Colbe JM, Milanese C, Dornheim M, et al. 2021. Modeling the kinetic behavior of the Li-RHC system for energy-hydrogen storage: (I) absorption. Int J Hydrogen Energy. Volume 46, Issue 63, pages 32110–25.

[2] Puszkiel JA, Castro Riglos M V., Ramallo-López JM, Mizrahi M, Karimi F, Santoru A, et al. 2017. A novel catalytic route for hydrogenation-dehydrogenation of 2LiH + MgB_2: Via in situ formed core-shell Li_xTiO_2 nanoparticles. J Mater Chem A. Volume 5, Issue 25, Pages 12922–33.

[3] Puszkiel JA. Tailoring the Kinetic Behavior of Hydride Forming Materials for Hydrogen Storage. 2016. Gold Nanoparticles - Reaching New Heights. Edited by Mohammed Muzibur Rahman and Abdullah Mohammed Asiri (Co-editor): IntechOpen.

[4] Khawam A, Flanagan DR. Solid-state kinetic models: Basics and mathematical fundamentals. J Phys Chem B. Volume 110, Issue 35, Pages 17315–28.

WHEC-2022
23rd World Hydrogen Energy Conference
June 26-30, 2022 - Istanbul

#171

HYDROGEN PRODUCTION FROM THE CATALYTIC DEHYDROGENATION OF HYDRAZINE BORANE OVER Pd-Ni-B CATALYST

[1] Merve Rabia Gürlük, [1] Göksel Özkan*
[1]Gazi University, Faculty of Engineering, Department of Chemical Engineering, Maltepe, Ankara, Turkey

*Corresponding author e-mail: gozkan@gazi.edu.tr

ABSTRACT

This study aimed to investigate the hydrogen generation from the hydrazine borane. Efficient and reversible hydrogen release can be achieved from the boron based materials such as M_xBH_4 (M: Li, Na, Ca, Mg), B-N-H (amine boranes) through catalytic and non-catalytic dehydrogenation. Particularly, hydrazine borane ($N_2H_4BH_3$) has been taken into account as a chemical hydrogen storage material due to its high hydrogen content (15.4%). Hydrogen production was carried out by catalytic dehydrogenation of as-synthesized hydrazine borane. Therefore, palladium-nickel (Pd-Ni) bimetallic catalyst supported on Ni-B-O (boride and oxide mixtures) was successfully prepared by co-precipitation method, and its catalytic properties and performance were assessed (SEM, XPS and XRD analyses) for catalytic dehydrogenation. The results showed that 3.58 moles of (H_2+N_2) gas were produced in the presence of Pd-Ni-B catalyst by the hydrolysis of hydrazine borane.

Keywords: Hydrogen, Hydrazine borane, Catalytic dehydrogenation

INTRODUCTION

Hydrogen is regarded as one of the best alternative energy carriers in the increasing demand for an efficient and clean energy source because of its abundance, high energy density and environmentally friendly [1, 2]. Recently, boranes and boron–nitrogen–hydrogen (BNH) compounds have been proposed as hydrogen storage materials in the last decade. Among these boron containing materials, hydrazine borane is an attractive hydrogen carrier owing to its theoretically high hydrogen storage capacity (15.4% by mass) and its stability at optimum conditions. Although hydrazine borane (HB) has a high hydrogen storage capacity with its protic ($4H^{\delta+}$) and hydridic hydrogens ($3\ H^{\delta-}$), it is difficult to release all the hydrogen in the borane complex [2, 3].

The first synthesis and thermal decomposition of hydrazine borane were described by Goubeau and Ricker in the beginning of 1960s. They demonstrated that the most efficient method to produce hydrazine borane was the reaction of sodium borohydride and hydrazine hemisulfate salt in 1,4-dioxane [4]. Generally, hydrogen stored in HB can be generated through hydrolysis in the presence of selective catalysts according to the following equation (Eq. (1)) [5, 6]:

$$N_2H_4BH_3\,(aq) + 3H_2O \rightarrow B(OH)_3 + 5H_2 + N_2 \quad (1)$$

The dehydrogenation mechanism of hydrazine borane depends on both the hydrolysis of BH_3 group and the decomposition of N_2H_4 moiety in the presence of metal catalysts. In the first step, 3 moles of H_2 are released with the hydrolysis of the BH_3 group, and in the second step, 6 moles of gas (5 moles of H_2 and 1 mole of N_2) are generated by the hydrolysis of both the N_2H_4 and BH_3 groups in the hydrazine borane. The catalysts studied for the dehydrogenation reaction are divided into 3 categories [2, 3]:

- Fe and Re-based catalysts, incomplete conversion in the hydrolysis of the BH_3 group (< 3 moles of H_2)

- Co, Ni, Pd, Pt and Au-based catalysts, active only in the hydrolysis of the BH_3 group (3 moles of H_2/1 mole of BH_3)

- Ru, Rh and Ir based catalysts, active in the hydrolysis of both the BH_3 and N_2H_4 group.

Different catalysts have been tested for hydrogen generation from the dehydrogenation of HB including reduced noble metal catalysts, bimetallic catalysts. Indeed, it has been discussed that monometallic catalysts (Fe, Re, Ni, Cu, Co, Pt) are effective in hydrolysis of BH_3 group, whereas Ru-, Rh-, and Ir-based catalysts are active in the decomposition of N_2H_4 moiety [6, 7]. Karahan et al. have proved that $RhCl_3$ catalyst was used to release approximately 3 equivalents of H_2 [6]. In addition, Yao et al. have found that NiPd nanoparticles modified with MoO_x catalyst was an active catalyst for the dehydrogenation of HB [8].

Gurluk and Ozkan studied the synthesis of the Zr-Ni-B supported Rh-based catalyst for the hydrogen generation from the hydrazine borane. Rh based ternary catalyst was prepared from simultaneous reduction of zirconium,

nickel and rhodium salts by using sodium borohydride as a reducing agent. They found that approximately 3 equivalents of H_2 was released from the dehydrogenation of hydrazine borane [9].

MATERIALS AND METHODS

The Synthesis of Pd-Ni-B Catalyst

Pd-Ni-B catalyst (containing 5% Pd by mass) was synthesized by co-precipitation method. Firstly, dilute solutions were prepared by weighing 3.85 g nickel chloride hexahydrate ($NiCl_2.6H_2O$) and 0.083 g $PdCl_2$. After that, the diluted solutions were taken into a beaker in an ice water bath and mixed in a magnetic stirrer. In order to reduce palladium and nickel, 0.2 M $NaBH_4$ solution was added slowly to the aqueous solutions. Later, the sample was washed 3-4 times with hot distilled water, and the resulting product was dried in a vacuum dryer.

The Catalytic Dehydrogenation Experiments

Experimental studies have been carried out for hydrogen production from as-synthesized hydrazine borane by catalytic hydrolysis. Firstly, the aqueous solution of the synthesized catalyst was added to the reactor. After that, 20 mL of HB solution (0.1% by mass) was placed in the feeding apparatus. The temperature of the water bath was kept in the working temperature. The gas burette system in the experimental setup was filled with water and checked for any leakage. When the temperature of the reactor reached the desired temperature, the fresh aqueous solution of HB was injected into the reactor and the chronometer was started with the reaction. The time corresponding to the volume change in the gas burette system was recorded and the experiments were completed in which the water level in the gas burette system stabilized.

RESULTS AND DISCUSSION

Hydrogen production by catalytic dehydrogenation from boron-based compounds was carried out using an aqueous solution in the presence of a catalyst. One of the main drawbacks in the hydrolysis of hydrazine borane is the slow reaction rate and the formation of unwanted by-products such as hydrazine [5, 6]. Therefore, different catalytic systems have been developed and used for the dehydrogenation of hydrazine borane.

After the synthesis of hydrazine borane, Pd based catalyst was synthesized and its catalytic performance in hydrogen release was investigated. According to the literature, it has been revealed that bimetallic/trimetallic catalysts with noble metals (especially Ru, Rh and Pt) showed high catalytic activity in the hydrolysis of hydrazine borane because adding a second element to the monometallic catalysts increased the catalytic activity [2, 5-7]. Consequently, Pd-Ni/B bimetallic catalyst was used for the catalytic hydrolysis of hydrazine borane. In the dehydrogenation of the hydrazine moiety, the presence of a second metal such as nickel made the catalyst more active and selective [5]. The prepared Pd-Ni-B catalyst was characterized by Scanning Electron Microscopy (SEM) with Energy Dispersive X-Ray Analysis (EDX), X-ray diffraction (XRD) and X-ray photoelectron spectroscopy (XPS).

The plots of mol (H_2+N_2)/mol $N_2H_4BH_3$ (n (H_2+N_2)/n HB) against time for the hydrolysis of HB aqueous solution by Pd-Ni-B catalyst at different temperatures (30-60°C) are shown in Figure 1. The hydrogen release started immediately and proceeded until the complete hydrolysis of HB. From the Fig. 1, the hydrogen production went up with the increase in the temperature. As a result, the maximum hydrogen generation was acquired as nearly 3.5 moles of (H_2+N_2) gas at 60°C.

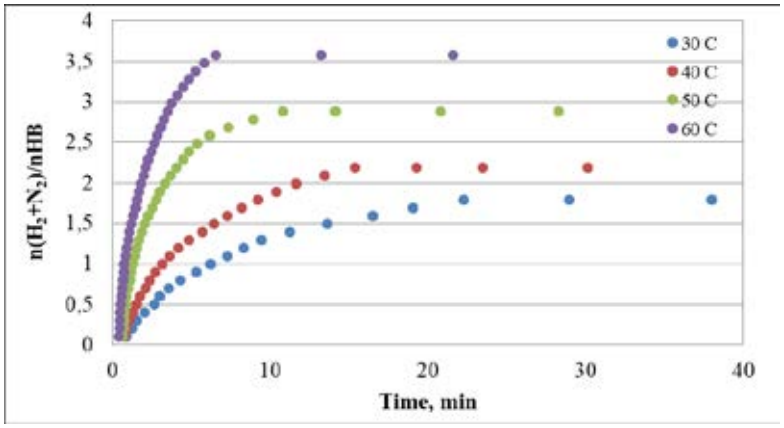


Fig. 1. The catalytic dehydrogenation of HB at different temperatures

CONCLUSIONS

In this study, Pd-Ni bimetallic catalyst supported on Ni-B-O (boride and oxide mixtures) was prepared by co-precipitation method for the catalytic hydrolysis of hydrazine borane. Furhermore, the catalyst was characterized by SEM-EDX, XRD and XPS. Pd-Ni-B catalyst exhibited good catalytic activity and stability for the dehydrogenation of hydrazine borane. Accordingly, 3.58 moles of (H_2+N_2) gas were generated in the presence of Pd-Ni-B catalyst

REFERENCES

1. Adamson A, Guillemin JC, Burk P. 2015. Proton transfer reactions of hydrazineboranes. Journal of Physical Organic Chemistry 28. 244-249.
2. Hannauer J, Akdim O, Demirci UB, Geantet C, Herrmann J, Miele P, Xu Q. 2011. High-extent dehydrogenation of hydrazine borane $N_2H_4BH_3$ by hydrolysis of BH_3 and decomposition of N_2H_4. Journal of Energy and Environmental Science.
3. Moury R, Demirci UB. 2015. Hydrazine borane and hydrazinidoboranes as chemical hydrogen storage materials. Energies 8. 3118-3141.
4. Goubeau VJ and Ricker E. 1961. Borinhydrazin and seine pyrolyseprodukte. Zeitschrift für anorganische und allgemeine Chemie 310. 123-142.
5. Aziza BW, Petit JF, Demirci UB, Xu Q, Miele P. 2014. Bimetallic nickel-based nanocatalysts for hydrogen generation from aqueous hydrazine borane: Investigation of iron, cobalt and palladium as the second metal. International Journal of Hydrogen Energy 39. 16919-16926.
6. Karahan S, Zahmakiran M, Özkar S. 2011. Catalytic hydrolysis of hydrazine borane for chemical hydrogen storage: highly efficient and fast hydrogen generation system at room temperature. International Journal of Hydrogen Energy 36. 4958-4966.
7. Lu ZH, Yao Q, Zhang Z, Yang Y, and Chen X. 2014. Nanocatalysts for hydrogen generation from ammonia borane and hydrazine borane. Journal of Nanomaterials Volume 11.
8. Yao Q, Yang, K, Nie W, Li Y, Lu Z. 2020. Highly efficient hydrogen generation from hydrazine borane via a MoOx-promoted NiPd nanocatalyst. Renewable Energy 147. 2024-2031.
9. Gurluk MR, Ozkan G, Ozkan G. 2020. Rh-based ternary catalyst for the catalytic dehydrogenation of hydrazine borane as a chemical hydrogen storage material. Journal of The Indian Chemical Society 97.

WHEC-2022
23rd World Hydrogen Energy Conference
June 26-30, 2022 - Istanbul

#181

EFFICIENT HYDROLYTIC DEHYDROGENATION OF ETHYLENE DIAMINE BISBORANE OVER Pd-Ni-Zr-B CATALYST IN THE ETHYLENE DIAMINE MEDIA

[1*] *Hatice Begüm Murathan,* [2] *Gülay Özkan,* [3] *Göksel Özkan*
[1, 3] Gazi University, Department of Chemical Engineering, Ankara, Turkey
[2] Ankara University, Department of Chemical Engineering, Ankara, Turkey

begummurathan@gazi.edu.tr, gozkan@eng.ankara.edu.tr, gozkan@gazi.edu.tr

ABSTRACT

This study focuses on the catalytic dehydrogenation of ethylene diamine bisborane (EDABB). For this goal, Pd-Ni-Zr-B catalyst was prepared in two steps by using co-precipitation method with $NaBH_4$ and impregnation method. The catalyst was characterized with XRD, XPS, SEM-EDX and multi-point BET analysis. The effect of temperature (90°C-120°C) was investigated on dehydrogenation of EDABB. The hydrogen production yield significantly increased at the temperature increases and also the reaction time reduced as well. Highest yield of equivalent hydrogen has reached 5.94 moles at 120°C. Reusability test of the catalyst was also carried out and average HGR result was obtained.

Keywords: Catalytic dehydrogenation, Ethylene diamine bisborane, Ethan 1, 2-diamine borane

INTRODUCTION

Reducing fossil-based fuels and environmental issues have led to rise of a number of alternative energy sources. Hydrogen that has a zero carbon emissions and high capacity of energy is well-known material and it can be used as energy storage material. Hydrogen can be played an important role for sustainable and eco-friendly solution. At this point, hydrogen storage is one of the key roles. A part of the hydrogen storage is using chemicals as a storage material. In this area borane based chemical material has significantly investigated in literature [1].

The most well known amine borane is ammonia borane used as hydrogen storage material because of being high hydrogen capacity (19.6% by mass) and non-toxicity material. It is important on fuel cell applications that the most amine borane groups like mono- and di-alkyl amine boranes release hydrogen as high purities at the mild conditions [2].

It has recently started to attract attention as a hydrogen storage material in the class of amine boranes in the literature. Ethylenediamine bisborane (EDABB, $C_2H_{14}B_2N_2$) also known as ethane 1,2-diamine borane is an alkyl diamine borane in amine borane derivatives, which makes EDABB interesting because it is faster in thermolysis than ammonia borane and does not contain gaseous impurities such as borazine as a by-product. During solvolysis, 3 moles of equivalent hydrogen can be taken from 1 mole ammonia borane, while 4-6 moles of equivalent hydrogen can be taken from 1 mole EDABB. It is a stable compound and containing 11.49% hydrogen as a mass [3].

In this work, EDABB dehydrogenation in ethylenediamine (EDA) media has been focused. For this purpose, EDABB was synthesized, and Pd-Ni-Zr-B catalyst was prepared. Catalytic reaction was carried out at different temperatures.

MATERIALS AND METHODS

Materials

Ethylenediamine dihydrochloride (Sigma-Aldrich), tetrahydrofuran (Sigma- Aldrich), nickel (II) chloride hexahydrate ($NiCl_2.6H_2O$, Aldrich), zirconium (IV) chloride ($ZrCl_4$, Merck-Schuchardt), palladium (II) chloride ($PdCl_2$, Merck), sodium borohydride ($NaBH_4$, Fluka) and deionized water were used.

EDABB Synthesis

EDABB was prepared according to literature with minor modifications [4]. For the synthesis, ethylenediamine dihydrochloride salt (11.39 mmol) and sodium borohydride (22.78 mmol) were added in THF. The reaction mixture was stirred at room temperature for 4 h under the reflux. After reaction, the mixture was filtered, and then the solvent was removed under vacuum evaporation. The solid washed with hexane and then filtrated. Filtrate cake was dried under vacuum at room temperature (White solid, 85% efficiency, 90% purity). Purity of EDABB was analyzed with hydrolysis reaction using with $RuCl_3$. Also, FTIR and ^{11}B NMR analysis was applied.

Catalyst preparation and characterization

Briefly, 0.059M nickel chloride hexahydrate and 0.065M zirconium chloride was mixed for 1 g of Ni-Zr-B catalyst. 0.18 M sodium borohydride was added drop wise to the mixture under intense stirring at 5°C. The precipitate was separated by centrifuge, washed 4 times using deionized hot water to separate from impurities and finally left to dry at 105ºC. 5% by mass of Pd active substance was added to the Ni-Zr-B sample by the impregnation method. PdCl2 solution (0.281mmol for 1 g sample) was added to the Ni-Zr-B catalyst sample and impregnated at 110°C by mixing until dryness in a stirred vessel. The sample was activated by using hydrogen and helium gas mixture for 1 hour. Catalyst was characterized with XRD, XPS, SEM-EDX and multi-point BET.

Dehydrogenation of EDABB

Dehydrogenetion of 0.5% by weight EDA solution of EDABB was performed at 90 ºC, 100 ºC 110 ºC and 120 ºC having with 0.02 g catalyst. The reaction system contains 50 ml volume 2 neck glass reactor, 50 ml volume pressure stabilizing liquid feeding apparatus and washing bottle having 0.1M H_2SO_4 solution. The produced hydrogen was measured as function of time in a gas burette system.

RESULTS AND DISCUSSION

Non-catalytic and catalytic dehydrogenation of 0.5% by mass of EDABB in the presence of ethylenediamine solvent were studied. In the experimental studies, ethylenediamine was chosen as the solvent and worked around 120°C, which is close to the boiling point of ethylenediamine (116 - 118°C). The non-catalytic dehydrogenation experiment was carried out only at 120 °C. Catalytic dehydrogenation experiment was carried out at 90°C, 100°C, 110°C and 120°C with 0.02 g Pd-Ni-Zr-B catalyst. In Fig. 1, nH_2/nEDABB versus the reaction time curves for both cases are given comparatively.

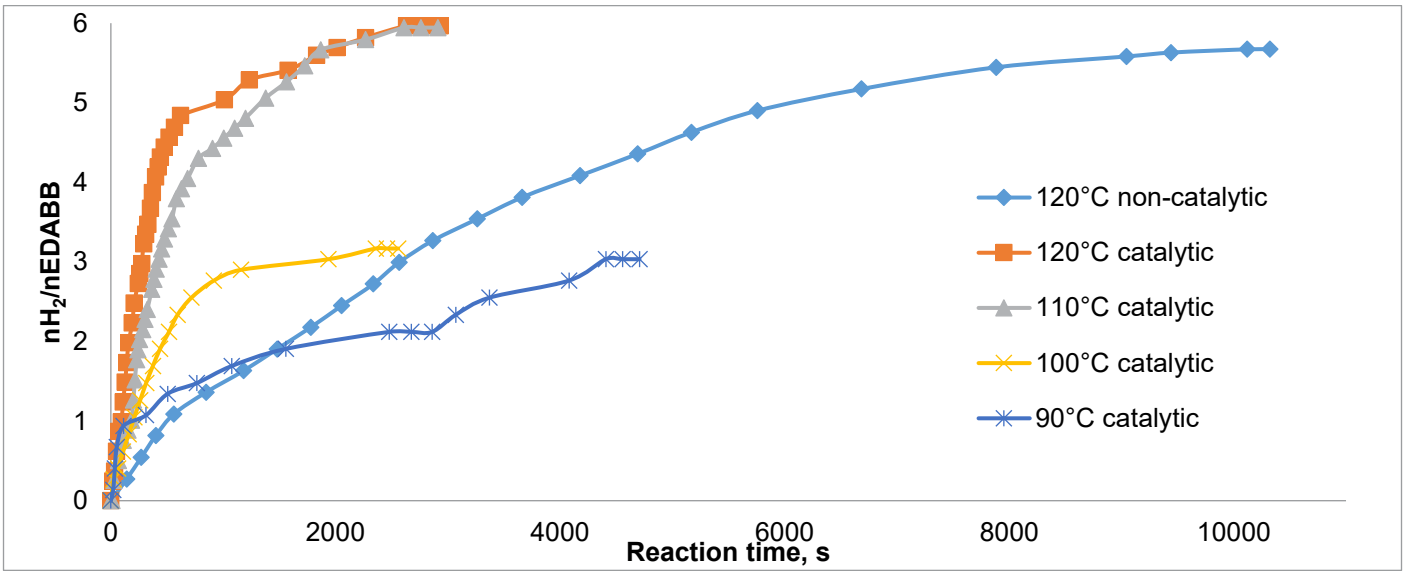


Fig. 1. Dehydrogenation of EDABB with EDA (0.02 g Pd-Ni-Zr-B)

In the non-catalytic dehydrogenation of EDABB at 120°C, 5.67 moles of hydrogen per mole of EDABB (94.5% molar production yield) were released in approximately 3 hours [5]. It has been shown that 6 moles of hydrogen can be produced per 1 mole of EDABB. When the results of dehydrogenation in the catalyst environment were examined, it was observed that 5.96 moles of hydrogen were released at 120°C in 2633 s, that is, in approximately 44 min. In addition, at temperatures of 90°C, 100°C and 110°C, it was determined that 3.03 mole of hydrogen was released in 4408 s, 3.16 mole in 2358 s and 5.94 mole in 2611 s, respectively. It has been determined that around 6 moles of hydrogen (99% molar hydrogen production efficiency) can be taken catalytically within 40-45 min at 110°C and 120°C temperatures. However, when the temperature drops to 100°C and below, it has been observed that the amount of hydrogen production decreases by about half. Although it can be operated at 120°C without catalysis, it has been understood that hydrogen can be released effectively by shortening the reaction time at 110°C and 120°C with catalyst. Reusability test was also carried out with 5th cycle as shown in Fig. 2 and the average HGR result of Pd-Ni-Zr-B was found 66.64 $ml.min^{-1}.g^{-1}$.

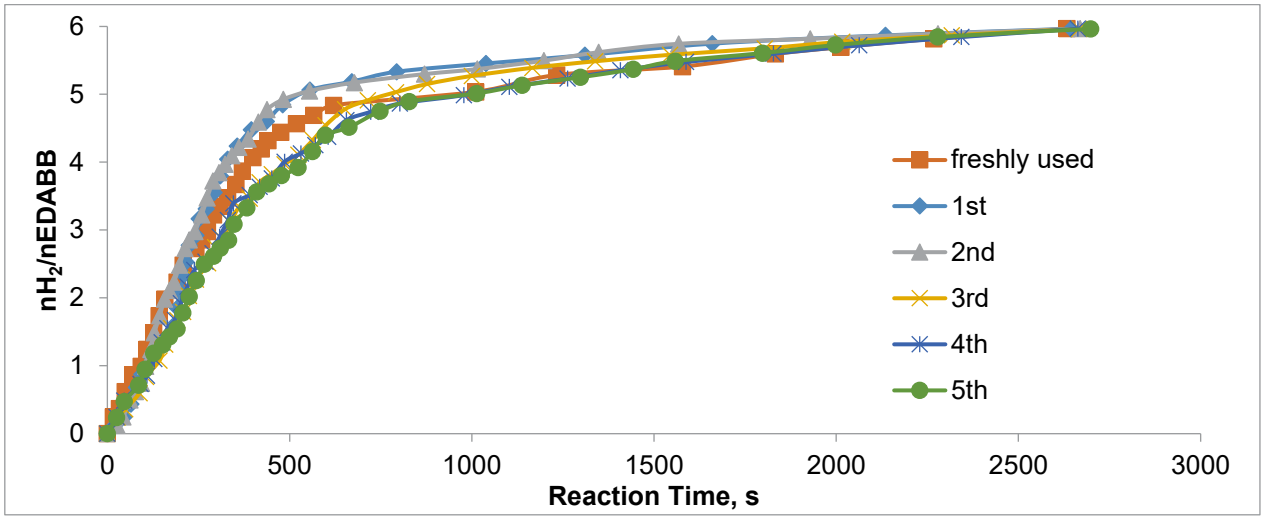


Fig. 2. Reusability of Pd-Ni-Zr-B

CONCLUSIONS

In this work, EDABB successfully synthesized at high yield and purity. After then catalytic dehydrogenation of EDABB was investigated at different temperature. For dehydrogenation reaction, Pd-Ni-Zr-B catalyst was prepared with reduction and impregnation methods respectively. The effect of temperature was examined. Hydrogen production yield was increased by increasing the temperature. Also, the reaction time was reduced. Nearly, 6 per equivalent mole of pure hydrogen were taken from 1 per equivalent mole of EDABB.

ACKNOWLEDGEMENT

The authors appreciate the financial support from the Gazi University Projects of Scientific Investigation (BAP) within the project “06/2018-08”.

REFERENCES

1. Züttel, A. (2004). Hydrogen storage methods. Naturwissenschaften, 91(4), 157-172.
2. Murathan, H. B., Özkan, G., Akkuş, M. S., Özgür, D. Ö., & Özkan, G. (2018). Hydrogen production from the methanolysis of ammonia borane by Pd-Co/Al_2O_3 coated monolithic catalyst. International Journal of Hydrogen Energy, 43(23), 10728-10733.
3. Onder, A., & Ozay, O. (2020). Fly ash as catalyst support material in the hydrolysis of ethylenediamine bisborane for hydrogen production: The use of coal-fired power plant waste. International Journal of Hydrogen Energy, 45(20), 11651-11661.
4. Kelly, H. C., & Edwards, J. O. (1963). Evidence for the open chain structure of ethane 1, 2-diamineborane. Inorganic Chemistry, 2(1), 226-227.
5. RamachandranPravin P.V., Gagare P. D.,Mistry H., and Biswas B. (2017). Procedures for the synthesis of ethylenediamine bisborane and ammonia borane. U.S. Patent No. 9,534,002. Washington, DC: U.S. Patent and Trademark Office.

WHEC-2022
23rd World Hydrogen Energy Conference
June 26-30, 2022 - Istanbul

#192

DEVELOPMENT OF NOVEL POLYMERIC MATERIAL GRADES AND EXPERIMENTAL METHODS TO BE USED IN HIGH-PRESSURE H_2 GAS ATMOSPHERES

[1*] *Winoj Balasooriya,* [1] *Clara Clute,* [2] *Karabi Halder,* [2] *Géraldine Theiler,* [1] *Andreas Hausberger,* [3] *Gerald Pinter*
[1] Polymer Competence Center Leoben GmbH, Roseggerstrasse 12, 8700, Leoben, Austria
[2] Bundesanstalt für Materialforschung und -prüfung (BAM), 12203, Berlin, Germany
[3] Chair of Materials Science and Testing of Polymers, Montanuniversität Leoben, Otto Glöckel-Strasse 2, 8700, Leoben, Austria

*Corresponding author e-mail: Winoj.balasooriya@pccl.at

ABSTRACT

Polymeric grades play a vital role with their unique properties in many components realizing the "Hydrogen Economy". The elastomeric grades in sealing applications are exposed to high-pressure hydrogen (H_2) gas and a wide range of temperatures, therefore, the development of novel materials is an ongoing process in order to fulfill the future requirements. This study focuses on the development of novel elastomeric grades, introducing novel filler strategies to improve the transport and mechanical properties, and subsequently minimizing possible degradation/damage. The proposed grades were initially tested for identifying the fulfillment of required properties, the resistance to rapid gas decompression (RGD), and deviations in high-pressure H_2 conditions. The used filler modification methods provided promising results on 2D filler functionalization and hydrogen exposure tests revealed dissolution of gas into the material and subsequent possible alterations of properties.

Keywords: Hydrogen gas storage, Sealing, Elastomers, Filler modification, Rapid gas decompression

INTRODUCTION

In a response to the climate crisis the world is facing, the European Union presented a Green Deal in 2019/20 to reduce the net emissions of greenhouse gases at least 55% by 2030 compared to 1990 levels, and to reach a climate-neutral continent by 2050 [1]. These ambitious targets encourage all the stakeholders to reach viable alternative resources. Therefore, hydrogen receives great attention as a clean energy carrier as well as a feasible and cost-effective renewable energy storage solution [2]. However, this emphasizes the importance of improvement of technologies and materials involved in these systems. Fig.1 shows an illustration of vital roles played by polymeric materials in a typical hydrogen gas system in the transportation sector. These systems demand materials to work up to ~100 MPa in gas storage tanks and wide temperature ranges (-40 to 85 °C) fulfilling the near future requirements [2,3].

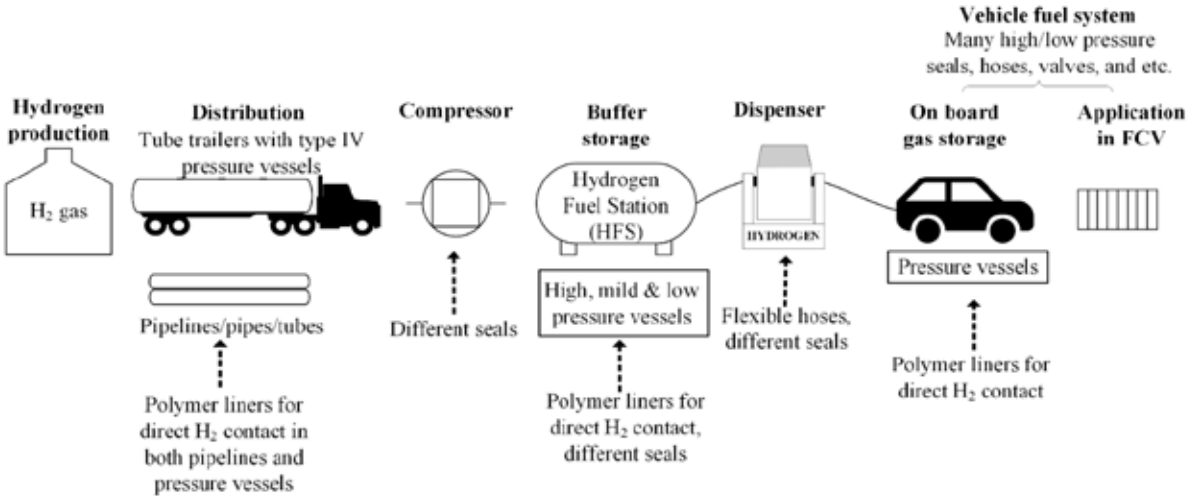


Fig. 1. Illustration of applications of polymeric grades as vital components in a typical hydrogen energy system [2]

Especially, leaking through sealings as a result of permeation and possible mechanical damage in prevailing harsh conditions is a major concern in economical and safety point of view. RGD is a well-known damage expected in sealing applications due to gas dissolution under exposure and subsequent sudden release in loading-unloading routines [4]. As a part of the Polymers4Hydrogen project, which is an Austrian Research Promotion Agency (FFG)-funded project to develop novel polymeric material grades, experimental methods, and simulation tools to facilitate the H_2 economy, this study presents an approach to develop elastomeric grades and novel filler strategies with intended properties, for

example, possibility to use in wide temperature range and transport properties which is an important parameter in terms of permeation and RGD. Further, literature mentions the possibility of adding two-dimensional (2D) fillers for improvement of barrier properties due to the possible tortuous path [5]. Therefore, this study intends to eliminate the possible drawbacks in 2D filler incorporation to elastomer by exfoliation and filler functionalization.

MATERIALS AND METHODS

Arlanxeo Deutschland GmbH, Dormagen, Germany, provided four cross-linked elastomer grades, which can be used as sealing materials, as shown in Table 1. The benchmark characterization of these grades was conducted identifying the material properties and relevance of different compositions. Therefore, mechanical, thermo-mechanical, hardness, and compression set measurements were conducted according to the respective standards. The RGD properties of the proposed grades were tested at the facility of SKF Sealing Solutions Austria GmbH, Judenburg, Austria, based on the NORSOK standard [6]. The hydrogen exposure tests were performed at the facility of "Bundesanstalt für Materialforschung und -prüfung" (BAM), Berlin, Germany, at different pressures (up to 100 MPa) at different temperatures (up to 120 °C) for a period of 7 and 21 days.

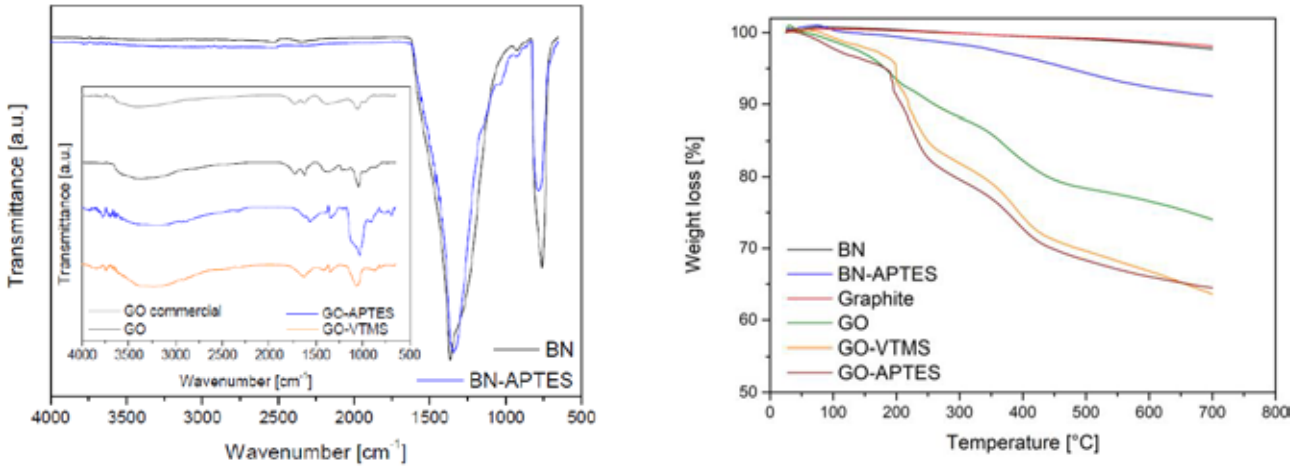
Table 1. Proposed elastomer grades and composition

Material	Composition
HNBR 1	Carbon black (CB) N 550: 75phr, Acrylonitrile (ACN) content: 21%
HNBR 2	CB N 550: 67phr, Polyamide (PA): 10phr, ACN content: 21%
NBR 1	CB N 550: 75phr, ACN content: 18%, Peroxide cured
NBR 2	CB N 550: 75phr, ACN content: 18%, Sulfur cured

The step of development of novel filler strategies considered two types of layered 2D fillers (hexagonal boron nitride (BN) and oxidized graphite flakes (GO)) for improvement of transport properties. The surface was activated prior to modification steps and silane coupling agents (SCA) with suitable functional groups, for example, aminopropyltriethoxysilane (APTES) and vinyltrimethoxysilane (VTMS), which could be useful for different matrix materials, were attached to the activated surface. The modified fillers were characterized using infrared spectroscopy (FT-IR), thermogravimetric analysis (TGA), X-ray photoelectron spectroscopy (XPS), and zeta potential measurements (ZP).

RESULTS AND DISCUSSION

The proposed elastomeric grades showed relatively higher hardness ~80 ShA, tensile strength in a range of ~25-30MPa, above 10 MPa of stress at 100% strain, and positive results on the resistance to rapid gas decompression based on NORSOK ranking. Based on mechanical properties, the addition of PA in HNBR2 and sulfur curing step in NBR2 provided improvements compared with their counterparts. Considering the low-temperature properties, which is important in these conditions, NBR grades (T_g ~ -45 °C) showed an edge over the HNBR grades (T_g ~ -30 °C). Exposure to high-pressure H_2 gas showed slight influence for the tests up to 20 MPa in visible dimensional changes, however, tests at 100 MPa exposure showed even visible blisters as a result of rapid gas release (< 5 sec) of pressure. After exposure, the weight and volume of the specimens were increased and density and hardness were decreased revealing the dissolution of gas. Tensile tests of these exposed specimens showed reduced mechanical properties indicating possible incurred micro damages inside the material.
FT-IR, TGA, XPS, and ZP results showed promising results of the 2D filler modification study and Fig. 2 summarizes the ATR-FT-IR spectra (Fig. 2a) and weight loss indications based on TGA measurements (Fig. 2b). According to Fig. 2a, BN indicates minor changes after the silanization process in the range of the Si-O stretching vibration at ~1000 cm^{-1}, however, GO reveals decreased intensities in C-O peaks as well as traces of the Si-O vibration and C-H vibrations at ~3000 cm^{-1}. As illustrated in Fig. 2b, the GO fillers show a better functionalization ability with significant weight loss in both VTMS and APTES, compared with BN-based methods.



(a) (b)

Fig. 2. FT-IR and TGA results of treated fillers [7]

CONCLUSIONS

The applicability of proposed elastomeric grades, novel filler strategies for improving intended properties, and possible degradation in high-pressure H_2 gas conditions were briefly discussed in this paper. The mechanical, thermo mechanical and RGD results showed the relevance of these grades in expected conditions. The 2D filler modification step provided good results on filler functionalization and possible incorporation in to relevant polymeric grades. Gas exposure tests revealed the dissolution of H_2 into the rubber grade and possible damage in subsequent sudden gas release. Therefore, the promising findings of this study provide a meaningful direction to reach the goals of intended material development.

ACKNOWLEDGEMENT

The research work was performed within the COMET-project “Polymers4Hydrogen“ (project-no.: 21647053) at the Polymer Competence Center Leoben GmbH (PCCL, Austria) within the framework of the COMET-program of the Federal Ministry for Climate, Action, Environment, Energy, Mobility, Innovation and Technology and the Federal Ministry for Digital and Economic Affairs with contributions by Montanuniversität Leoben (Department Polymer Engineering and Science, Chair of Chemistry of Polymeric Materials, Chair of Materials Science and Testing of Polymers), Politecnico di Milano, Technical University of Munich, Tampere University of Technology. Bundesanstalt für Materialforschung und -prüfung (BAM) and Arlanxeo Deutschland GmbH, ContiTech Rubber Industrial Kft., Peak Technology GmbH, SKF Sealing Solutions Austria GmbH, Faurecia.
The PCCL is funded by the Austrian Government and the State Governments of Styria, Lower Austria and Upper Austria.

REFERENCES

1. https://ec.europa.eu/info/strategy/priorities-2019-2024/european-green-deal/delivering-european-green-deal_en. Accessed on November 30, 2021.
2. Balasooriya W, Clute C, Schrittesser B and Pinter G. 2021. A review on applicability, limitations, and improvements of polymeric materials in high-pressure hydrogen gas atmospheres. Polymer Reviews. DOI: 10.1080/15583724.2021.1897997
3. Barth RR, Simmons KL and San Marchi CW. 2013. Polymers for hydrogen infrastructure and vehicle fuel systems: applications, properties, and gap analysis. Pacific North West National Laboratory (U.S.), Richland, WA and Sandia National Laboratories, Livermore, CA.
4. Ono H, Fujiwara H and Nishimura S. 2018. Penetrated hydrogen content and volume inflation in unfilled NBR exposed to high-pressure hydrogen–what are the characteristics of unfilled-NBR dominating them. Int. J. Hydrogen Energy 43:18392–18402.
5. Choudalakis G and Gotsis AD. 2009. Permeability of polymer/clay nanocomposites: A Review. Eur. Polym. J. 45:967–984.
6. NORSOK Standard M-710, Rev. 2. 2001. Norwegian Technology Centre, Qualification of non-metallic sealing materials and manufacturers.
7. Clute C, Balasooriya W, Schrittesser B and Schlögl S. 2021. Surface modification of fillers for materials in high-pressure hydrogen applications. Poster presentation, LKK Leoben.

WHEC-2022
23rd World Hydrogen Energy Conference
June 26-30, 2022 - Istanbul

#196
DIFFERENT WAYS TO STORE MASSIVE QUANTITIES OF HYDROGEN

[1*] *Louis Londe*, [1] *Arnaud Réveillère*
[1]Geostock SAS, 2 rue des Martinets, 92569 Rueil-Malmaison Cedex, France

*Corresponding author e-mail: louis.londe@geostock.fr

ABSTRACT

Hydrogen can be stored in underground caverns or geological structures in various ways. The easiest way to store hydrogen is in salt caverns. These are created by injecting water into a well down to a salt geological layer, with the extraction of salt-saturated brine. This type of storage is suitable for storing hydrogen at extremely high pressures.
The second way to store large quantities of hydrogen is to inject pure hydrogen or a hydrogen-methane mix into porous rock. The hydrogen content may vary from a few per cent to 100 per cent. Hydrogen can also be stored underground by converting it into a liquid carrier, such as ammonia, which can then be stored in a Lined Rock Cavern. A liner is often required to prevent contact between ammonia and water. Lastly, hydrogen can be stored underground by injecting it into a Lined Rock Cavern. This may take the form of compressed storage (gaseous hydrogen) or cryogenic storage (liquid hydrogen. A liner is required owing to extremely high pressures or extremely low temperatures. The present article exposes state of the art of all these techniques of hydrogen underground storage, outlines technical gaps and identifies main ongoing or required technology developments needed to bridge them.

Keywords: Underground, Storage, Salt, Cavern, Rock

INTRODUCTION

Underground storage is likely to be the best solution for fulfilling extensive storage needs (Jens, 2021 [1]) as it boasts numerous advantages in terms of environment protection, safety and, above all, CAPEX (for high storage capacity) and OPEX.

HYDROGEN STORAGE IN SALT CAVERNS

Salt caverns are a proven technology for storing hydrocarbons, including natural gas, liquid hydrocarbons such as crude oil or refined products, and liquefied hydrocarbons such as LPG. More than 1,900 salt caverns exist worldwide. Salt caverns are created by solution mining, i.e., by injecting fresh water or sea water into a deep well. Solution mining is also referred to as the “leaching” process. A large variety of sizes exist, ranging from 50,000 m3 to more than 1,000,000 m^3.

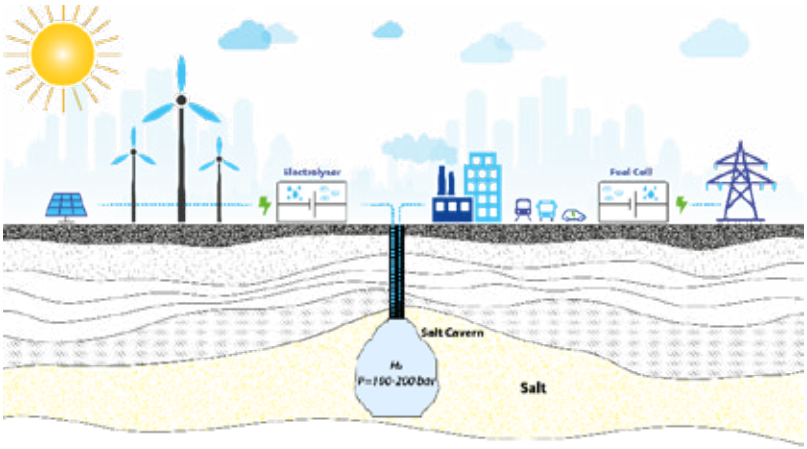


Figure 1: Hydrogen storage in salt cavern

Salt caverns were first used for hydrogen storage five decades ago in the UK, the first such cavern being commissioned near Teesside in 1972. Five decades later, only six salt caverns have been built for hydrogen storage. There is obviously no technical showstopper to create salt caverns for hydrogen. Nevertheless, a few specific items deserve attention and explain why some of the new ongoing projects are presented as demonstrators.

HYDROGEN STORAGE IN POROUS ROCK

Porous rocks, either in depleted fields or in aquifers, have been used for storing natural gas for over a century. Unlike salt caverns, porous rock storages use natural voids. Wells are drilled to inject and withdraw the gas. Pressures as high as 200 bar are common practice. Storing hydrogen into porous rock is considered today as a blending of natural gas (i.e., mainly methane) and hydrogen. The hydrogen-methane mix can be burnt as such to produce energy. Alternatively, hydrogen can be separated from methane at the well head, for example using pressure swing adsorption technology. Storing methane-hydrogen mix in porous rock has been done in the past. Town gas, often containing up to 50% hydrogen, has been stored in a dozen of European underground storage facilities, in depleted fields or aquifers (Marcogaz, 2017 [2]). The gas industry is currently launching research programs and pilot plants to provide scientific evidence that the town gas experience can be repeated as part of a controlled and documented approach. Various items are being investigated (Heinemann, 2021 [3]).

HYDROGEN STORAGE AFTER ITS TRANSFORMATION INTO A LIQUID CARRIER

It is likely that ships will be used for the intercontinental transportation of hydrogen. Hydrogen tankers could transport liquid hydrogen (LH2) at very low temperatures (-253°C). A promising alternative is to use molecules containing hydrogen, providing that the molecules are easy to liquefy. A popular hydrogen liquid carrier is ammonia (NH3). Ammonia is easy to liquefy for transport purposes. Underground storage of liquid hydrogen carriers is an option that could offer all the advantages of underground storage where salt is not available.
Ammonia could be stored in hard rock caverns in almost any kind of rock providing that it is strong enough to be excavated without heavy support.

However, the underground storage of ammonia is not straightforward, as ammonia has a high affinity with water. Consequently, ammonia often needs to be isolated from water with a steel liner.These “Lined Rock Caverns” (LRC) are feasible with a limited R&D effort. The LRC concept was demonstrated in 2004 in Sweden for natural gas with a pressure higher than 200 bar and for fast cycling conditions (Sydkraft AB, 2004). There should not be any significant difficulty for ammonia around a few tens of bars. Alternatives at lower pressure and lower temperature, say between 0°C and -40°C, are also feasible.

HYDROGEN STORAGE IN LINED ROCK CAVERNS

The fourth hydrogen storage technology is the Lined Rock Cavern, directly as hydrogen rather than as a transformed molecule such as ammonia. Two different options are to be considered:

- Option 1: For pipeline transport, hydrogen is to be stored as a gas.
- Option 2: For tanker transport, hydrogen is to be stored as a cryogenic liquid, at -253°C.

Options 1 and 2 generate different challenges. In both cases, these challenges are greater than for ammonia LRC, owing to high pressure (option 1) or very low temperature (option 2). But both options are advantageous in terms of environmental protection and safety, and may prove economically attractive for large capacities.

LPG and liquid hydrocarbons are stored around the world in unlined mined caverns. However, a pressure of 100 or 200 bar would require building an unlined rock cavern at a depth of 1,000 m to 2,000 m to fulfil the Hydrodynamic Containment Principle (Aberg, 1975 [4]; Van Hasselt, 2003 [5]). A shallower cavern with a liner is therefore highly recommended. The feasibility of such an LRC for pressurised hydrogen has been confirmed by the Skallen project, in which pressures of higher than 200 bar have been reached with success (Sydkraft AB, 2004 [6]).

Let us now consider a cryogenic cavern for LH2. A similar concept has been developed for liquefied natural gas (LNG) (Amantini, 2005 [7]). The principle of the cryogenic cavern combines two proven technologies: the rock cavern commonly used for LPG and liquid hydrocarbon storage, and the containment system used in LNG tankers and LNG tanks. Tightness is ensured by a steel membrane. Insulation layers are installed behind the steel membrane, protecting the rock mass against thermal shock. This insulation also reduces the initial boil-off rate. Adapting this LNG cryogenic cavern to hydrogen storage will require R&D studies as the temperature of LH2 (-253°C) is lower than that of LNG (-162°C).

CONCLUSION: UNDERGROUND HYDROGEN STORAGE IN THE COMING YEARS

Large-scale hydrogen storage is required to face future challenges in terms of energy and the environmental transition. Hydrogen will be used primarily for industrial decarbonisation, carbon-free mobility, and carbon-free power generation. It will be used initially to decarbonize industry and mobility, for which underground storage will be required within a couple of years. Underground pure hydrogen storage for power generation will also emerge, but large-scale

demand may come later, in all likelihood after 2040. Meanwhile, the gas and power generation industries will use a methane-hydrogen mix, well before 2040. The methane-hydrogen mix will gradually reach 20% hydrogen, and possibly more, and will be stored underground, mainly in porous rock reservoirs.

Salt caverns will probably account for the largest share of underground storage needs, followed by porous rock reservoirs, especially for methane-hydrogen mixes. When the technology is ready, mined caverns will find their place in the value chain for international trading (ammonia, liquid hydrogen) or where pure hydrogen is to be stored in places without salt.

R&D efforts vary for these various techniques. For pure hydrogen storage, salt caverns are ready for commercialisation, and porous media is nearly ready as well. Both are ready for storing blends of hydrogen and natural gas, which is actually authorized in many countries and can happen tomorrow, should the business model enable it. Current research is aiming aimed at furthering our knowledge and establishing standards.
Mined cavern techniques – for pressurised hydrogen, pressurised substitutes (such as ammonia) or liquefied hydrogen – will require a few years of technical developments. The corresponding caverns will be lined. Lined Rock Caverns (LRCs) for pressurised hydrogen or pressurised ammonia could be ready for commercialisation in the near future. LRCs for liquid hydrogen present greater challenges owing to the very low temperature involved (-253°C).
These mined cavern techniques will remain more expensive than salt caverns and porous rock reservoirs. However, owing to their geological adaptability, mined cavern solutions will be needed to complete the hydrogen storage portfolio.

ACKNOWLEDGMENTS

Part of the work described in this article has been funded in part by the Hystories project. This project has received funding from the Fuel Cells and Hydrogen 2 Joint Undertaking under grant agreement No. 101007176. This Joint Undertaking receives support from the European Union's Horizon 2020 research and innovation programme and Hydrogen Europe and Hydrogen Europe Research.

REFERENCES

1. Jens, J. et al., 2021, Extending the European Backbone - A European Hydrogen Infrastructure Vision Covering 21 Countries, Creos, DESFA, Elering, Enagás, Energinet, Eustream, FGSZ, Fluxys Belgium, Gasgrid Finland, Gasunie, GAZ-SYSTEM, GCA, GNI, GRTgaz, National Grid, NET4GAS, Nordion Energi, OGE, ONTRAS, Plinovodi, Snam, TAG, Teréga, https://gasforclimate2050.eu/wp-content/uploads/2021/06/European-Hydrogen-Backbone_April-2021_V3.pdf
2. Marcogaz, 2017, Guidance - Injection of Hydrogen/Natural Gas Admixtures in Underground Gas Storage (UGS), https://www.marcogaz.org/publications/injection-of-hydrogen-natural-gas-admixtures-in-underground-gas-storage-ugs/
3. Heinemann, N. et al., 2021, Enabling large-scale hydrogen storage in porous media – The scientific challenges, Energy & Environmental Science, https://pubs.rsc.org/en/content/articlepdf/2021/ee/d0ee03536j
4. Aberg, B., 1978, Prevention of gas leakage from unlined reservoirs in rock, Proc. Rockstore 77, Pergamon Press, Oxford.
5. Van Hasselt, B., Amantini, E., Cabon, F., Bodin, J.-L., 2003, Hydrogeological monitoring during construction and operation of underground LPG storage facilities in mined caverns, IAH Congress, Prague 2003.
6. Sydkraft AB & Gaz de France, 2004, Lined Rock Cavern Storage for Natural Gas – Final Technical Report, Thermie B – Project N° OG./270/97/SE/FR
7. Amantini, E., Chanfreau, E., Kim, H.-Y., The LNG Storage in Lined Rock Cavern - Pilot Cavern Project in Daejon (South Korea), Gastech 2005.

WHEC-2022
23rd World Hydrogen Energy Conference
June 26-30, 2022 - Istanbul

#203

EVALUATION OF THE BIMETALLIC Pt-Ni AND Pt-Co CATALYSTS ON THE LOHC DEHYDROGENATION

[1] K. Alconada,[1*] V.L. Barrio
[1]School of Engineering (University of the Basque Country UPV/EHU), Plaza Ingeniero Torres Quevedo 1, 48013 Bilbao (Spain)

*Corresponding author e-mail: laura.barrio@ehu.eus

ABSTRACT

Liquid organic hydrogen carrier systems (LOHC) are presented as an alternative for energy storage and transportation. Platinum group metals (PGM) have proven to be efficient in LOHC hydrogenation/dehydrogenation reactions for hydrogen storage cycles. However, their cost and the high Pt/LOHC ratio are their major drawbacks. In this work, the performance of low-PGM and/or PGM-free catalysts on LOHC dehydrogenation is studied. Bimetallic systems are good candidates to replace or to decrease the PGM content increasing also the dehydrogenation yield.

Keywords: Hydrogen storage, liquid-organic hydrogen carrier (LOHC), dehydrogenation, bimetallic catalyst.

INTRODUCTION

Liquid Organic Hydrogen Carrier (LOHC) systems have recently been considered as a promising candidate for hydrogen storage and transport. In this concept, aromatic compounds can be catalytically hydrogenated and dehydrogenated without changing their chemical properties (Figure 1). The LOHCs offer numerous advantages such as:

(i) moderate to high hydrogen storage capacities,
(ii) easily reversible hydrogenation/dehydrogenation reaction, and
(iii) no additional infrastructure is needed as the same distribution network of liquid fuels can be used [1].

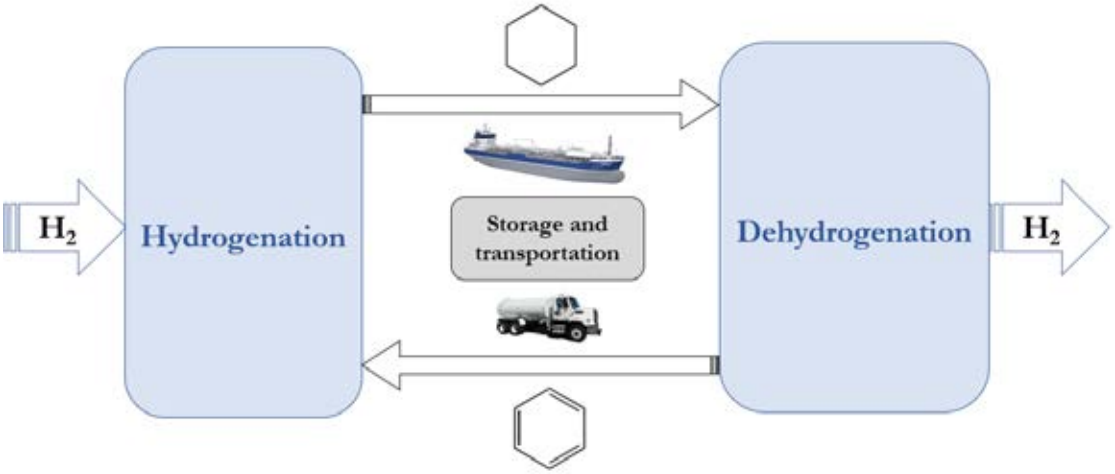


Figure 1. Schematic two-way LOHC cycle. Hydrogen lean benzene is hydrogenated into a hydrogen rich molecule cyclohexane.

The dehydrogenation process consists of an exothermic reaction thermodynamically favourable at low temperatures and pressures. In the dehydrogenation process, Pt-based catalysts have shown a high activity [2,3]. However, the performance of non-noble metal-based catalyst and their promoting effect on Pt has not yet been studied in detail. For these purpose, monometallic and bimetallic Pt-Ni and Pt-Co catalyst were prepared, characterized and tested.

MATERIALS AND METHODS

The dehydrogenation experiments were performed in a lab-scale reactor at 260ºC and atmospheric pressure with a molar ratio of 1/2000 (mol Pt/mol LOHC). The reactor outgoing gas phase was quantified using a flow indicator and monitored by a μ-GC. The reaction progress was evaluated analyzing liquid samples by GC-MS and H-NMR.

RESULTS AND DISCUSSION

Physicochemical characterization of catalytic samples by ICP, TPR, CO chemisorption, XPS and SEM showed differences in chemical state, metal-support interactions and average crystallite sizes, indicating the importance of the morphological and surface properties of metal phases in driving the dehydrogenation activity of the catalyst. The activity results revealed that the reaction takes place mainly in the first thirty minutes of the experiment. After that, the reaction rate slowed down due to the presence of partially hydrogenated compounds (Figure 2).

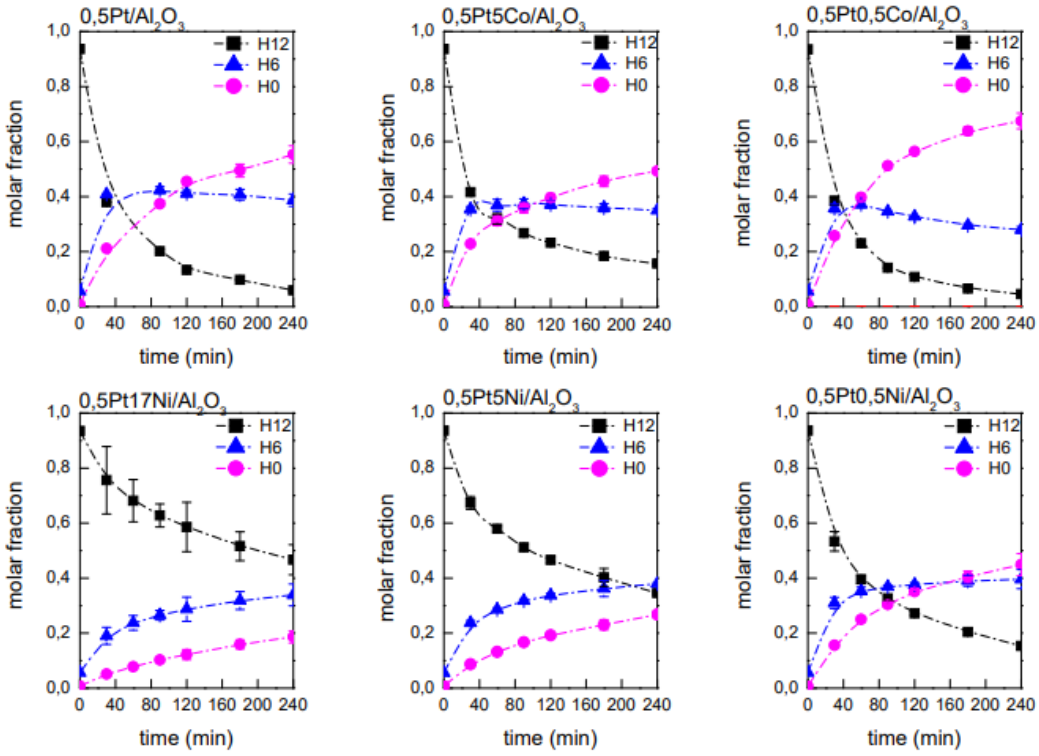


Figure 2. Composition profile for dehydrogenation experiments at lab scale reactor for Pt, Pt-Ni and Pt-Co catalysts (T=260 ºC; P=1 bar; n=1500 rpm; 1/2000 mol_{Pt}/mol_{LOHC}). H12 (full hydrogenated LOHC), H6 (partially hydrogenated LOHC) and H0 (full dehydrogenated LOHC).

The activity and selectivity of Pt-Ni bimetallic catalyst improved decreasing the Ni loading, however, they showed poorer performance than the monometallic Pt sample. On the opposite, the Pt-Co sample with the lower Co content enhanced high dehydrogenation activity and productivity with an increase of a 36% (Table 1). Regarding to the monometallic Ni and Co catalysts, they did not show significant conversion with a degree of dehydrogenation lower than a 3%.

Table 1. Productivity values in the LOHC dehydrogenation reaction.

Catalyst	Productivity, $g_{H2}/g_{Pt}/min$
$1Pt/Al_2O_3$	1,27
$0,5Pt/Al_2O_3$	1,80
$0,5Pt5Co/Al_2O_3$	1,98
$0,5Pt0,5Co/Al_2O_3$	2,45
$0,5Pt17Ni/Al_2O_3$	0,22
$0,5Pt5Ni/Al_2O_3$	0,60
$0,5Pt0,5Ni/Al_2O_3$	1,35

CONCLUSIONS

Bimetallic systems including a non-noble metal are a great alternative to reduce the Pt/LOHC ratio in the dehydrogenation reaction. It has been proved that small Co loadings improve the productivity compared to the bare sample with a higher platinum content. Thus, the overall catalytic performance is affected by the total number of active sites available and the metal-support interactions. Cobalt has demonstrated to act as a promoter, enhancing higher dehydrogenation conversion for hydrogen storage and transportation and decreasing the quantity of PGM used.

ACKNOWLEDGEMENT

This research was supported by the University of the Basque Country (UPV/EHU), Basque Government (Project: IT993-16), the Spanish Ministry of Economy, Industry and Competitiveness (PID2020-112889RB-I00) and the Fuel Cells and Hydrogen 2 Joint Undertaking (ID: 101007223).

REFERENCES

1. Paragian K, Li B, Massino M and Rangarajan S. 2020. A computational workflow to discover novel liquid organic hydrogen carriers and their dehydrogenation routes. Molecular Systems Design and Engineering 5(10):1658-1670.
2. Modisha P, Gqogqa P, Garidzirai R, Ouma CNM and Bessarabov D. 2019. Evaluation of catalyst activity for release of hydrogen from liquid organic hydrogen carriers. International Journal of Hydrogen Energy 44: 21926-21935.
3. Bulgarin A, Jorschick H, Preuster P, Bösmann A and Wasserscheid P. 2020. Purity of hydrogen released from Liquid Organic Hydrogen Carrier compound perhydro dibenzyltoluene by catalytic dehydrogenation. International Journal of Hydrogen Energy 45: 712-720.

WHEC-2022
23rd World Hydrogen Energy Conference
June 26-30, 2022 - Istanbul

#221

HIGH SURFACE AREA ZEOLITIC IMIDAZOLATE FRAMEWORKS FOR HYDROGEN STORAGE AT ROOM TEMPERATURE

[1,2]*Syedvali Pinjari,* [2]*Tapan Bera,* [2]*Rajesh M Badhe,* [1*]*Erik Kjeang*
[1]Fuel cell research laboratory, Simon Fraser University, 250-13450 102 Avenue, Surrey, BC V3T0A3, Canada
[2] Alternative Energy – 1, Indian Oil R&D Centre, Sector-13, Faridabad, Haryana 121002, India

*Corresponding author e-mail: ekjeang@sfu.ca

ABSTRACT

Cost-effective hydrogen storage at commercial scale is a limiting factor for the propagation of hydrogen energy. Physisorption enhanced hydrogen storage at low to moderate pressure may offer a possible solution. In this paper, we report the synthesis of zeolitic imidazolate frameworks (ZIF-8) and hybrid material of ZIF-8 and carboxylate functionalized carbon nanotubes (ZIF/*f*CNT) for hydrogen storage applications at room temperature and moderate pressures. Both materials were further characterized by various physicochemical characterization tools to investigate the morphology, crystallinity, thermal stability, and textural properties. ZIF-8 exhibits the highest specific surface area of 2023.6 m^2/g whereas 1576.9 m^2/g was obtained for the hybrid material. Both samples showed rhombic dodecahedron morphology with three-dimensional framework structures. Thermogravimetric analysis revealed that the hybrid material possesses higher thermal stability, of securing 53 wt. % of the structure, than pure ZIF-8 due to the addition of *f*CNT. The carboxylate functionalized carbon nanotubes stored 0.15 wt. % of hydrogen at room temperature and pressure up to 50 bar. The process was reversible at this temperature, indicating a physisorption based storage mechanism. The results of hydrogen storage measurements of ZIF-8 and ZIF/*f*CNT will also be presented and discussed.

Keywords: Zeolitic Imidazolate Frameworks, Hybrid material, Hydrogen storage

INTRODUCTION

Hydrogen is a clean fuel which has a long history in the energy sector since the 1800s. Given the rise of greenhouse gas emission originating from fossil fuels, it is noteworthy that abundant hydrogen could play a predominant role in developing alternative energy in the transportation sector and manufacturing industries [1,2]. Hydrogen can be stored through compressed gas method, and in liquid form, however, both methods are impeded by high cost due to high pressure and low cryogenic temperature, respectively [3,4]. Solid-state materials have emerged in the past decade as promising alternative materials for hydrogen storage [5–7] [8]. Particularly, physisorption based hydrogen storage materials show fast kinetics, reversibility, low dissociation temperature, moderate pressure, and acquired low enthalpy of adsorption which lessen the thermal management difficulties [8]. Generally, physisorption materials show high hydrogen uptake at 77 K, however, storage capacities must be improved at ambient conditions to meet the US Department of Energy (DOE) targets. A wide range of carbon-based materials, metal-organic frameworks (MOFs), and zeolites have been investigated as possible physisorption materials for hydrogen storage applications.

Among the MOFs, zeolitic imidazolate frameworks (ZIFs) possess favorable surface area, microporous structure, and thermal and chemical stabilities [10]. These advantages make ZIFs a promising material for H_2 storage applications. However, more research is needed on fundamental approaches to achieve higher hydrogen uptake and understand the nature of H_2 interaction to improve ZIF materials for commercial applications. On the other hand, carbon materials such as carbon nanotubes (CNTs) are one of the best options for hydrogen storage because of their unique properties – highly porous structure, better reversibility of hydrogen, and low mass density [11]. In the present work, we report the synthesis of ZIF-8 which was further added to carboxylate functionalized carbon nanotubes (ZIF/*f*CNT) as a hybrid material for hydrogen storage applications. It is to be noted that the synergistic effects arise from the mesopores and carboxylate groups of CNTs and highly microporous frameworks of ZIF which may create significant performance benefits for hydrogen adsorption. These nano-adsorbents were characterized by a range of physicochemical techniques and hydrogen storage measurements. The introduction of functionalized carbon nanotubes made the hybrid material a highly stable compound for the higher adsorption capacity of hydrogen.

MATERIALS AND METHODS

Chemicals: Zinc nitrate hexahydrate ($Zn(NO_3).6H_2O$, >99.0%), 2-methylimidazole ($C_4H_6N_2$ (HmIm), >98.0%), and Methanol (CH_3OH (MeOH), >99.5%) were obtained from Sigma Aldrich. Carboxylate functionalized carbon nanotubes (*f*CNT) were purchased from Nanostructured & Amorphous Materials, Inc. USA. All the chemicals were used directly without any further pre-treatments.

Synthesis methods of ZIF-8 and ZIF/*f*CNT: In a typical procedure, 2.971 g of $Zn(NO_3).6H_2O$ and 6.572 g of HmIm were dissolved, separately, in 20 ml MeOH and stirred for 10 minutes. Then HmIm solution was slowly poured into zinc

solution and continued stirring for 1 hr, at the speed of 250 rpm. The Zn^{2+}:HmIm:MeOH ratio were 1:8:100. After the reaction, the heterogeneous mixture was centrifuged at 4000 rpm speed for 30 minutes. After that the clear solution was decanted and 15 ml of MeOH was added to the solid product, for washing purpose, and centrifuged again at similar conditions. This washing step was repeated three times. Next, the product was dried in an air oven at 80 °C for 10 hr. Finally, the solid product was carefully grounded using mortar and pestle. The synthesis of ZIF/*f*CNT followed the same procedure except that the *f*CNTs were sonicated in 10 ml MeOH for 30 minutes before being added to the Zn and HmIm mixture.

RESULTS AND DISCUSSION

The morphological structures of ZIF-8 and ZIF/*f*CNT measured by scanning electron microscopy (SEM) are shown in Fig.1. ZIF-8 exhibited rhombic dodecahedron structures with 12 faces, with average particle size of 550 nm (Fig. 1a), similar to the reported literature [12]. Interestingly these structures did not collapse after adding *f*CNTs (Fig. 1b), which was attributed to the successful synthesis of hybrid material. The *f*CNTs were uniformly well dispersed among the ZIF-8 crystal particles. As shown in the images, no residual of zinc material was found which indicates that the zinc precursor was completely reacted with HmIm during the synthesis.

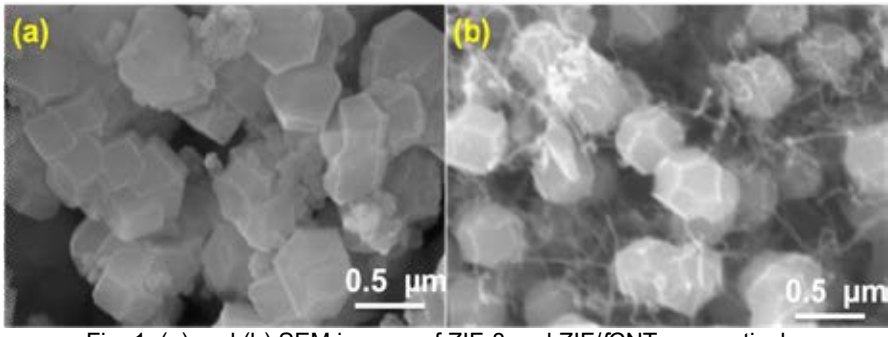


Fig. 1. (a) and (b) SEM images of ZIF-8 and ZIF/*f*CNT, respectively.

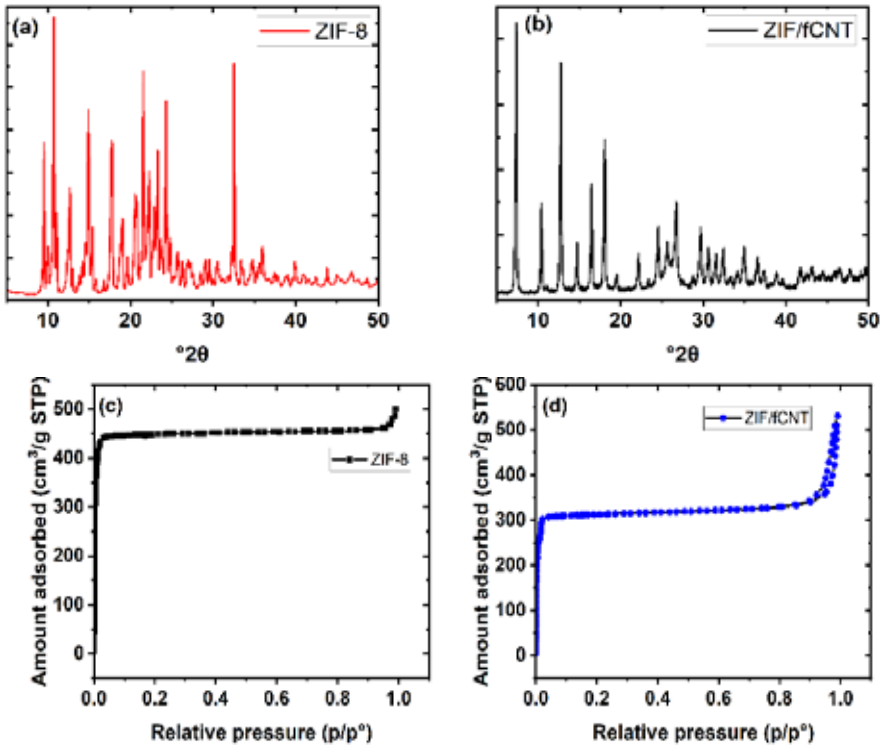


Fig. 2. (a-b) XRD profile of ZIF-8 and ZIF/*f*CNT; and (c-d) Nitrogen isotherms of ZIF-8 nanocrystals and ZIF/*f*CNT hybrid material.

The X-ray diffraction (XRD) profiles of the ZIF-8 base and hybrid materials are represented in Fig. 2a and b, respectively. The detection of strong peaks corresponds to the good crystallization of the ZIF-8 (Fig. 2a) sample and are in accordance with the published reports. Although the presence of CNTs makes broad peaks between 7° and

15° in Fig. 2b, the hybrid material obtained similar peaks as in the base material [13]. This shows that the incorporation of *f*CNTs did not have a detrimental effect on the growth and crystalline structure of ZIF-8.
Fig. 2c and d display the N_2 sorption analysis of ZIF-8 and ZIF/*f*CNT to determine the adsorption properties. The base material exhibited type-1 isotherm indicating that the material was microporous in nature. In contrast, the hybrid material showed type-4 isotherm along with hysteresis loop, which was attributed to the increase of mesopores, which could potentially aid the hydrogen transport and adsorption processes. The measured Brunauer–Emmett–Teller (BET) specific surface area of the two materials was high in both cases and of the same order of magnitude, being 2023.6 m^2/g for ZIF-8 and 1576.9 m^2/g for ZIF/*f*CNT. The reason behind the decrement in the latter sample could be surface coverage of ZIF by the *f*CNTs. The total pore volume increased from 0.77 cm^3/g for ZIF-8 to 0.81 cm^3/g obtained for ZIF/*f*CNT. The average pore size also increased when CNTs were added to ZIF-8 to 2.07 nm; whereas it was 1.52 nm for the base material. The increment in pore size corresponds to new pores created when carbon nanotubes were attached with ZIF-8 nanocrystals [14].

Thermal stability of as-synthesized samples was measured by thermogravimetric analysis (TGA), with obtained curves shown in Fig. 3a. As seen in the TG curves, both materials did not exhibit major change up to 400 °C; after that, the organic linkers in the ZIF-8 framework started decomposing where sudden weight loss was recorded, thus, the structure collapsed. Interestingly, the hybrid material curve shifted to higher temperature and secured 53.32 wt. % of the structure, whereas ZIF-8 holds back 46.7 wt.% of the sample. This quality indicates that the hybrid material has improved the thermal stability due to addition of more stable *f*CNTs. Moreover, *f*CNTs provide as nucleation sites for the growth of ZIF-8 structure [15]. Hydrogen storage measurements carried out on gravimetric apparatus at room temperature and pressure up to 50 bar. Outgassing was done 250 °C for 10 hours prior to the measurements. The H_2 storage results of *f*CNT reference sample are presented in Fig. 3b. Hydrogen uptake showed monotonous dependence on pressure meaning that the uptake increases proportionally to the pressure. As shown, *f*CNT achieved hydrogen storage capacity of 0.15 wt. % which is more than pristine CNTs reported elsewhere [16]. However, the sample desorbed merely 51% of stored hydrogen due to the kinetic changes, and functional groups that could impede hydrogen diffusion inside the cavities. The H_2 storage measurements of ZIF-8 and ZIF/*f*CNT will also be reported and discussed.

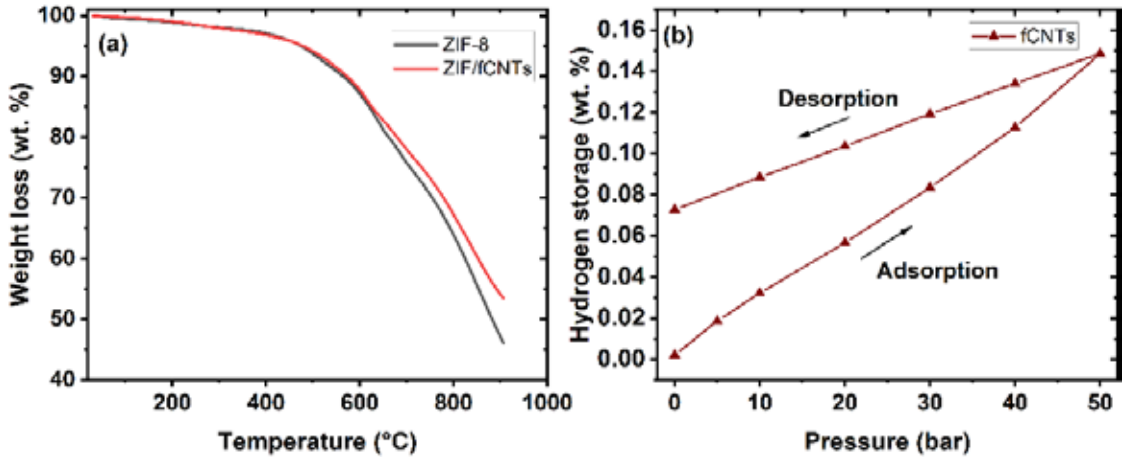


Fig. 3. (a) Thermogravimetric curves of ZIF-8 and ZIF/*f*CNT, and (b) Hydrogen adsorption/desorption isotherms of *f*CNTs.

CONCLUSIONS

Chemical synthesis of zeolitic imidazolate framework (ZIF-8) and hybrid material (ZIF/fCNT) was reported using methanol as solvent at room temperature and atmospheric conditions. A clear and complete crystalline structure of ZIFs are obtained from this method, and both materials showed rhombic dodecahedron morphology with three-dimensional frameworks. There was no detrimental effect seen on the ZIF-8 structure after adding the *f*CNTs. Further, the hybrid material sustained 53.32 wt. % of structure in thermal stability test due more stability of *f*CNT. However, ZIF-8 exhibited the highest surface area of 2023.6 m^2/g whereas 1576.9 m^2/g was obtained for ZIF-8/*f*CNT which is due to the surface coverage of nanotubes on the surface of ZIF-8. The carboxylate functionalized carbon nanotubes stored 0.15 wt. % of hydrogen at room temperature and pressure up to 50 bar which is higher than the pristine CNTs in the published literature.

REFERENCES

1. Tollefson J. 2010. Hydrogen vehicles: Fuel of the future? Nature 464:1262–4.
2. McKinsey. 2010. A portfolio of power-trains for Europe: a fact-based analysis - The role of Battery Electric Vehicles, Plug-in Hybrids and Fuel Cell Electric Vehicles. Fuel Cell 68.

3. O'Malley K, Ordaz G, Adams J, Randolph K, Ahn CC, Stetson NT. 2015. Applied hydrogen storage research and development: A perspective from the U.S. Department of Energy. Journal of Alloys and Compounds 645:S419–22.
4. Ahmed A, Al-Amin AQ, Ambrose AF, Saidur R. 2016. Hydrogen fuel and transport system: A sustainable and environmental future. International Journal of Hydrogen Energy 41:1369–80.
5. Salehabadi A, Umar MF, Ahmad A, Ahmad MI, Ismail N, Rafatullah M. 2020. Carbon-based nanocomposites in solid-state hydrogen storage technology: An overview. International Journal of Energy Research 44:11044–58.
6. Mohtadi R, Orimo S. 2017. The renaissance of hydrides as energy materials. Nature Reviews Materials 2:16091.
7. Pyle DS, Gray EMacA, Webb CJ. 2016. Hydrogen storage in carbon nanostructures via spillover. International Journal of Hydrogen Energy 41:19098–113.
8. Pei P, Whitwick MB, Kureshi S, Cannon M, Quan G, Kjeang E. 2020. Hydrogen storage mechanism in transition metal decorated graphene oxide: The symbiotic effect of oxygen groups and high layer spacing. International Journal of Hydrogen Energy 45:6713–26.
9. Niaz S, Manzoor T, Pandith AH. 2015. Hydrogen storage: Materials, methods and perspectives. Renewable and Sustainable Energy Reviews 50:457–69.
10. Jin C-X. 2021. Synthetic methods, properties and controlling roles of synthetic parameters of zeolite imidazole framework-8: A review. Journal of Solid State Chemistry 17.
11. Darkrim FL, Malbrunot P, Tartaglia GP. 2002. Review of hydrogen storage by adsorption in carbon nanotubes. International Journal of Hydrogen Energy 27:193–202.
12. Zhang Y, Jia Y, Li M, Hou L. 2018. Influence of the 2-methylimidazole/zinc nitrate hexahydrate molar ratio on the synthesis of zeolitic imidazolate framework-8 crystals at room temperature. Scientific Reports 8:9597.
13. Dumée L, He L, Hill M, Zhu B, Duke M, Schütz J. 2013. Seeded growth of ZIF-8 on the surface of carbon nanotubes towards self-supporting gas separation membranes. Journal of Material Chemistry A 1:9208.
14. daraee M, Saeedirad R, Ghasemy E, Rashidi A. 2021. N-CNT/ZIF-8 nano-adsorbent for adsorptive desulfurization of the liquid streams: Experimental and. Journal of Environmental Chemical Engineering 9:104806.
15. Ghasemy E, Motejadded HB, rashidi A, Hamzehlouyan T, Yousefian Z. 2018. N-doped CNT nanocatalyst prepared from camphor and urea for gas phase desulfurization: Experimental and DFT study. Journal of the Taiwan Institute of Chemical Engineers 85:121–31.
16. Sharma A. 2020. Investigation on platinum loaded multi-walled carbon nanotubes for hydrogen storage applications. International Journal of Hydrogen Energy 45:2967–74.

WHEC-2022
23rd World Hydrogen Energy Conference
June 26-30, 2022 - Istanbul

#234

ELASTIC BRITTLE BEHAVIOR OF AN IRON – TITANIUM ALLOY DEDICATED TO HYDROGEN STORAGE

[1,2] *Ludovic Bebon,* [1,2] *Anne Maynadier,* [1] *Yves Gaillard,* [1,2] *David Chapelle*
[1] Université Bourgogne Franche-Comté, Femto-ST Institute UMR 6174, Department of Applied Mechanics,
[2] Fuell Cell LAB - FCLAB/UAR2200, 90000 Belfort, France
24 rue de l'Epitaphe, 25000 Besançon, France

*Corresponding author e-mail: ludovic.bebon@univ-fcomte.fr

ABSTRACT

Hydrogen solid state storage technology uses absorption and desorption of di-hydrogen gas at low pressure in metal alloys. In the tank the powder swells, shrinks and decrepitates leading to stress over the wall. The present study first deals with the mechanical characterization by three different methods at different scales, of a storage TiFe alloy. Compression tests of macroscopic samples, ultrasonic elastic characterization, and microscopic scale nano indentation give respectively: 50, 153 and 24 1~305 GPa. This discrepancy is directly linked to the scale and microstructural heterogeneities. An optimization process is proposed to identify a set of numerical parameters able to simulate with DEM the elastic brittle behaviour of our hydride under compression. These data are a first step to model the decrepitating phenomenon and to help design of solid storage tank of hydrogen.

Keywords: hydrogen solid state storage, discrete element modeling, multiscale mechanical characterization

INTRODUCTION

Some metallic compounds react in presence of hydrogen in a reversible way. Hydridation, a true phase transformation is associated to strong volume growth (up to 30%) [1]. During the lifetime of a tank, the storage material, crushed into powder, undergoes repeated swelling and shrinking. It leads to fracture and segregation of particles within the tank and fatigue of the container walls [2]. To better understand and control this phenomenon, identifying the mechanical behavior of these intermetallic compounds is a key challenge.

Indeed, designing hydrogen storage tank require an efficient numerical tool taking into account the decrepitation phenomenon at different scales, from particle size to whole container. In the DEM framework, we aim at identifying the elastic modulus. Here, we propose three experimental methods to assess the elastic modulus of an industrially used TiFe alloy: macroscopic compression test, ultrasonic measurement, nano indentation test. In parallel, a DEM simulation of the compression test is optimized to validate the representation of both elastic and brittle response of the material.

EXPERIMENTAL METHODS

Material and sample preparation

The TiFe ingot is produced in an induction furnace by melting the pure components into a cupper mold. This material can store 1.6 wt.% of hydrogen at 22 °C, at 25 bar. Thus, TiFe is a good candidate to store hydrogen due to absence of rare earth compounds. Usually, the ingot is then crushed to fill the tank. Here after, to perform mechanical characterizations, we deal with the as cast material. Cylindrical samples with a radius $r = 5\,mm$ and a height $h = 15\,mm$ are withdrawn with Electrical Discharged Machine. We obtain 15 samples for compression and ultrasonic tests. In parallel, millimetric particles, from the same ingot, are coated and polished for nano indentation.

Compression tests

Compression tests are carried out over the 15 samples to assess the elastic modulus. We use a 100 kN electromechanical Instron testing machine with two compression plates. The tests are displacement controlled with a velocity of 0.02 mm/s. We acquire the displacement of the crosshead and the resulting force. To correct the device compliance, a compression of the mounting alone is carried out: the displacement on the upper face of the sample is inferred. To get rid of the first contact transitory perturbation while remaining in the elastic domain, the data are processed for forces between 10 kN and 15 kN (~130 to 170 MPa).

Ultrasonic elastic characterization

The elastic modulus can be identified thanks to the velocity of elastic waves in the material. The modulus is related to the velocity by: $E = \rho V^2 A$ with ρ the density, V the velocity of the waves and A a constant. Here the elastic waves are propagated along the longitudinal direction of the compression cylinders (~15 mm long). The wave velocity is inferred from the reflected wave time delay. A parameter is related to the Poisson ratio through $(1-2\nu)(1+\nu)/(1-\nu)$. An error of 4% over ν (± 0.015) induces a variation of 4.5% on E. Here after, the used Poisson ratio is 0.32 (between the raw titanium and raw iron Poisson ratio).

Nano indentation measurement

Measurements have been performed on the surface of one polished particle (~1mm^3) with a CSM ultranano indentor device with a berkovitch indentor (F<50 mN). Two matrices of 10x10 indents spaced 4.5 µm apart, over two different areas on the particle surface have been tested (Fig 1). Each indentation generates a typical displacement-force curve from which an apparent elastic modulus is computed. From the 200 measurements, a clustering analysis is carried out to assess the heterogeneity and an average elastic modulus.

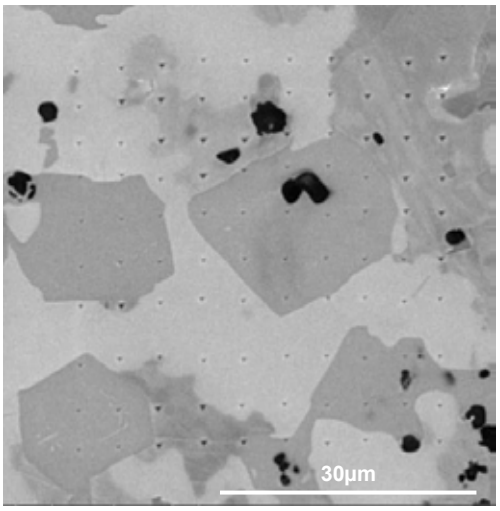


Fig 1. Backscattered SEM micrograph of one matrix of 100 nano indents

NUMERICAL METHODS

Discrete Element Modeling (DEM) data settings

Our final purpose (not discussed here) is to identify the optimal numerical parameters and simulate one hydriding particle response. The compression test is simulated in the framework of DEM, using YADE [3]. We aim to define a set of numerical parameters, at the element scale, which allows predicting the previously identified macroscopic elastic modulus and roughly the brittle fracture. The unknowns are the size of spherical elements, the numerical Young modulus E_N (stiffness between two elements), the admissible tensile strength between two elements σ_N and the cohesion factor C_N. The digital specimen is a cylinder discretized with spherical elements. Its aspect ratio is $r/h = 1/3$ as in experiments. Its volume is similar to one particle volume right after crushing in the tank. The numerical parameters are varied, each simulation return a macroscopic compression curve from which the elastic modulus and the ultimate compression strength are compared to target values.

Numerical parameters identification method

In the framework of DEM, the element size has a critical influence both on the calculus time and on the mechanical response (E_N does not directly correspond to macro rigidity, but only to inter-element interaction description). The trade-off between discretization and calculus time leads to 0.09 mm elements.

Once element size defined, the numerical parameters E_N, σ_N and C_N are varied to fit the macroscopic elastic modulus correlated to experimental compression test results. An optimization based only on the elastic modulus leads to unphysical ultimate compression strength. Thus, fracture limit must be considered in the parameters fitting process. A multi-parameter optimization with two objectives is introduced: E_{obj} (elastic modulus) and UCS_{obj}(ultimate compressive strength). For computation sake, a mono-objective formulation is obtained by defining the relative error average: $\varepsilon = \frac{1}{2}\left(\left|\frac{E_{mes}-E_{obj}}{E_{obj}}\right| + \left|\frac{UCS_{mes}-UCS_{obj}}{UCS_{obj}}\right|\right)$. For simplicity, optimization is based on a simplex method [4]. We perform the optimization method from several initial sets of parameters to analyse the impact of initial conditions on the convergence quality: occurrence of a global minimum or several local minima.

RESULTS AND DISCUSSION

Compression test

Most of the specimen collapse in a brittle way before a linear behaviour is settled down. Fig 2 shows the engineering stress-strain curves of the seven non-fractured samples. Elastic modulus is identified around 50 GPa with a standard deviation of 8 GPa. This value is surprisingly low, and we suspect an important effect of the casting defaults, mainly pre-existing cracks, inner shrinking and heterogeneity of the metallurgical microstructure. It appears that the macro scale is not well suited to characterize such a damaged material elasticity.

Ultrasonic elastic characterization

Three non-fractured samples are analysed. The wave velocity for all specimens is found at 5875 m/s. Consequently, the elastic modulus is assessed at 153 GPa $\pm$ 7 GPa, (4.5% on E). This value seems peculiarly satisfactory when considering elastic modulus of both Iron and Titanium. Nevertheless, the ultrasonic technic remains sensitive to damage, such as cracks, that might disturb wave propagation. Thus, additional characterization was needed to investigate the elastic property at a different scale.

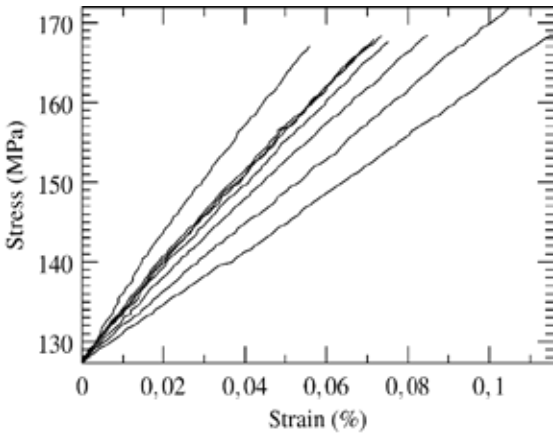


Fig 2. Stress-strain curves of the non-fractured samples

Nano indentation measurement

The SEM micrograph (Fig 1) shows one of the matrices of indents. The studied alloy exhibits strong heterogeneity at the microscale (domains radius ~15µm, numerous spheroidal inclusions…). A clustering analysis of the 200 concatenated measurements [5] reveals four co-existing populations, well correlated with microstructural domains, each characterized by one indentation elastic modulus (see Table 1). The hardest domain (area 4: E=350 ± 29 GPa) corresponding to precipitates. The rest of the sample is composed of similar metallurgical phases whose local elastic modulus is between 241 GPa and 305 GPa.

Table 1. Elastic modulus of the four populations measured by nano indentation

Area number	Indentation Elastic Modulus (GPa)	Corresponding color on SEM micrograph (Fig 3)
1	257 ± 14	Lightest grey
2	241 ± 7	Tabby grey
3	305 ± 12	Darkest grey
4	350 ± 29	Black dots

Even if the stiffness is revealed highly heterogeneous at micro scale, the different domains in the core material, with a typical size of 15 µm, are nested with each other. The use of a homogenized modulus at an upper scale seems relevant. It should also be noted that this very small-scale method tests the medium between structural defects (joints, cracks, shrinkage), so it is normal to obtain a rather high estimate of the stiffness.

Experimental summary

Table 2 summarises the identified elastic modulus. The values are significantly different from one method to another according to the working scale. Each technic is sensitive to specific heterogeneities or structural defects. Further numerical investigations deal with an intermediate scale: the millimetric particle. It stands on two scalar material parameters to give account rigidity and brittleness. We have arbitrary chosen E_{obj} = 200 GPa and UCS_{obj} = 400 MPa.

Table 2. Summary of the elastic modulus measurements

Nano Indentation	Compression Test	Ultrasonic method
241~300 GPa	50 GPa	150 GPa

Numerical parameters identification

Every optimisation converges in 5 hours on a desktop computer; results are summed up in Table 3 . Depending on the initialization, the simplex method converges toward a local minimum. In the DEM framework, a given macro behavior can potentially be simulated with several set of micro- numerical parameters. A suitable one set of parameter presents both small error (ε) and a good physical agreement. In our case, only one is suitable (bolted line on the Table 3).

Table 3. Results of the optimizations from different set of initial parameters

Initiation micro parameters			**Optimized micro parameters**			**Macroscopic elastic parameters**		
E_N	σ_N	C_N	E_N	σ_N	C_N	E (GPa)	UCS (MPa)	ε (%)
500	500	12	504	504	12.3	215	1100	1330%
430	670	13	417	703	13.2	176	14200	1730%
350	**102**	**3**	**451**	**736**	**2.16**	**191**	**449**	**5%**
100	200	15	100	203	15	0.43	4010	490%
800	200	3	945	843	2.67	241	288	24%

CONCLUSION

We paid attention on the mechanical behaviour of TiFe alloy to predict the breathing phenomenon during the lifetime of solid storage state tank. Experimental investigations using different methods permit to estimate the elastic modulus

at 50, 150 or 241~305 GPa: unfortunately, dependant on the considered scale of a highly heterogeneous and damaged material. A range of order (200 GPa) is nonetheless argued for simulation of millimetre particle. In parallel a DEM simulation of compression on a millimetric sample is optimized to link numerical inter-elements parameters to the macroscopic response. Several sets of optimum parameters regarding the elastic modulus and the ultimate compression strength are found. Among theses sets one is identified as suitable for further numerical investigation about the phenomenology of decrepitation or the design of storage tank

REFERENCES

1. S. Challet, M. Latroche, and F. Heurtaux. 2007. Hydrogenation properties and crystal structure of the single BCC (Ti0.355V0.645)100−xMx alloys with M=Mn, Fe, Co, Ni (x=7, 14 and 21). J. Alloys Compd. 10.1016/j.jallcom.2006.08.070.
2. F. Qin, L.H. Guo, J.P. Chen and Z.J. Chen. 2008. Pulverization, expansion of La0.6Y0.4Ni4.8Mn0.2 during hydrogen absorption–desorption cycles and their influences in thin-wall reactors. Int. J. Hydrog. Energy 10.1016/j.ijhydene.2007.10.029.
3. V. Šmilauer et al. (2015), Using and programming. In Yade Documentation 2nd ed. The Yade Project, DOI 10.5281/zenodo.34043 (http://yade-dem.org/doc/)
4. Nelder and Mead. 1965. A simplex method for function minimization. Comput. J.
5. F.-J. Ulm, M. Vandamme, C. Bobko, J. A. Ortega, K. Tai, and C. Ortiz. 2007. Statistical Indentation Techniques for Hydrated Nanocomposites:Concrete, Bone, and Shale. J. Am. Ceram. Soc. 0.1111/j.1551-2916.2007.02012.x.

WHEC-2022
23rd World Hydrogen Energy Conference
June 26-30, 2022 - Istanbul

#247

MATHEMATICAL MODELLING OF ELECTROCHEMICAL HYDROGEN COMPRESSOR: TEMPERATURE INFLUENCE SIMULATION ANALYSIS

[1] Doria Marciuš, [1] Dinko Brezak, [1*] Ankica Kovač*
[1]University of Zagreb, Faculty of Mechanical Engineering and Naval Architecture, Department of Energy, Power and Environmental Engineering, Zagreb, Croatia
* Corresponding author e-mail: doria.marcius@fsb.hr, ankica.kovac@fsb.hr

ABSTRACT

High-pressure hydrogen storage systems are indispensable for the widespread implementation of hydrogen technology, which is why there is a requirement for an efficient compressor. The most used method of hydrogen compression is via mechanical compressors, but lately, electrochemical hydrogen compressors (EHCs) are increasingly getting more attention due to their many advantages. However, in published articles, there is a limited number of mathematical models due to the intricate nature of the EHC operating mechanism. In this paper, a mathematical model of EHC made in MATLAB/Simulink Software is described through simple equations based on the fundamental physics laws and electrochemical relations, considering occurring overvoltages, including hydrogen back-diffusion. The results obtained as time functions are analysed for various operating temperatures to give more detailed insight on temperature influence on different parameters which affect EHC performance. The simulation indicates temperature effect on multiple inner processes, necessitating optimisation of parameters to balance adverse temperature impact according to required EHC features.

Keywords: Electrochemical hydrogen compressor, Proton exchange membrane, MATLAB/Simulink, Temperature

INTRODUCTION

To store gaseous hydrogen at higher pressures (350 bar or 700 bar, depending on the hydrogen storage type), a compressor is needed. Theoretically, compression could be possible in the process of hydrogen production with a proton exchange membrane (PEM) electrolyzer, if not for the hydrogen permeation to the oxygen side forming a potentially explosive mixture [1]. EHC has an analogous working principle, only without hydrogen back-diffusion presenting a critical safety issue but limiting the compressor's performance. Humidified hydrogen at low pressure is fed to the anode flow field plate and collected at the cathode flow field plate at higher pressure due to potential difference applied on the electrodes from the outside power source. The hydrogen molecule is divided into atoms and oxidized at anode catalyst layer into electron and proton, which transports through the selective PEM, reducing with electron to hydrogen molecule again at the cathode catalyst layer. Presently, the highest achieved EHC stack output pressure amounts to 1000 bar [2], while for the one EHC cell, the highest reached value is 168 bar [3]. The pressure limiting critical issues are membrane deformation and hydrogen back-diffusion due to significant pressure difference, both creating a requirement for further research to improve the EHC performance. Also, other limiting factors are present overvoltages, which are the reason why the total applied cell voltage must be increased. One of the enhancement approaches is the optimisation of EHC operation with parameter change, such as temperature, input pressure, or stoichiometric ratio, to increase the output pressure [4]. The easiest way to determine different parameters influence on the EHC performance can be achieved via mathematical modelling. Several authors have published their modelled results [5–8], but there is a literature gap for detailed models describing EHC dynamics, especially accounting for back-diffusion, as Durmus et al. [9] highlighted in review on the development of the EHCs.

MATHEMATICAL MODELLING OF ELECTROCHEMICAL HYDROGEN COMPRESSOR

Equations described in this chapter are implemented in the mathematical model of single-cell EHC made with MATLAB/Simulink, which was then validated with experimental results published by Chouchan et al. [10] at 275 K. The EHC operating temperature range analysed is stated according to optimal PEM temperature (295 – 355 K), i.e., Nafion – the most frequently used low-temperature membrane [11]. The maximum temperature is limited due to a decrease in membrane moisture level with high temperatures, which strongly reflects on the membrane proton conductivity [12]. Relevant input parameters for EHC mathematical model are listed in
Table 1.

The overall EHC efficiency (Eq. 1) is defined by voltage (Eq. 2) and current efficiency (Eq. 3), where voltage efficiency is the ratio of theoretical voltage and applied cell voltage and current efficiency as output and theoretical value of compressed hydrogen governed by Faraday's law.

$$\eta_{EHC} = \eta_{voltage} \times \eta_{current} \quad (1)$$

$$\eta_{voltage} = E_{Nernst} / E_{EHC} \quad (2)$$

$$\eta_{current} = q_{n,output} / q_{n,theoretical} \quad (3)$$

Table 1. Input parameters for EHC mathematical model

Input	Label	Amount	Unit	Reference
Membrane thickness	φ	0.0125	cm	Nafion 115 manufactured thickness
Temperature	*T*	295 – 355	K	Nafion temperature range
Active area	*A*	25	cm^2	Nafion 115 manufactured area
Anode pressure	p_{input}	101325	Pa	Constant atmosphere pressure
Total cell voltage	E_{EHC}	0.025 – 0.1	V	[10]
Membrane water content	λ	17	-	Hydrated Nafion membrane [13]
Charge transfer coefficient at anode and cathode	α	0.5	-	Equal to the symmetry factor for both electrodes
Permeability constant	*DH*	$8.61* 10^{-15}$	mol/(Pa*m*s)	Average value for Nafion 115 [10]
Cathode volume	V_c	24.14	cm^3	[10]

The voltage efficiency evaluates the irreversibility and resistance of EHC accounting for the activation overpotentials, ohmic overpotential, mass-transfer overpotential, and diffusion overpotential, as shown in Eq. 4, while the current efficiency describes EHC mechanical reliability and is affected by the possible leakage on the cathode side and hydrogen back-diffusion [10].

$$E_{EHC} = E_{Nernst} + \eta_{act} + \eta_{ohm} + \eta_{mass-transf} + \eta_{diff} \quad (4)$$

Nernst voltage is the theoretical minimum voltage that needs to be applied to achieve a relative pressure difference. The activation overpotentials describe the kinetics of electrochemical reactions occurring at anode and cathode, ohmic overpotential shows the resistance due to the EHC component's contact, as well as resistance to proton transfer through PEM, depending on membrane's dimensions, water content and the operating current. Mass-transfer overvoltage includes flow limitations that hydrogen encounters when approaching catalyst due to high current inserting faster pace. Diffusion overpotential accounts for the concentration difference due to hydrogen back-diffusion [14] and is calculated by reducing the total voltage by other overvoltages. All listed limitations are surmounted by increasing the applied potential difference (total cell voltage), which lowers the EHC efficiency as shown in Eq. 2.

RESULTS AND DISCUSSION

The polarization curve has been registered while changing the temperature from 295 K to 355 K and applied potential from 0.025 V to 0.1 V. The current density, as well as the hydrogen flux, increase with the temperature rise [7] at the start of a simulation due to the positive impact on the membrane proton conductivity. While reaching equilibrium (*i* = const., *p* = const., $q_{n,output}$ = 0), higher temperature EHCs current density drops faster, resulting in output pressure lower equilibrium values. Better hydrogen permeability through PEM also causes a decrease in ohmic resistance, which consequently heightens EHC voltage efficiency [4], hence, to pump the same amount of hydrogen (constant current density), at lower temperatures EHC requires more electric power than at higher temperatures [15]. However, the mass transfer and activation overpotentials are higher with temperature increase [16]. Furthermore, hydrogen back diffusion has higher rates [5], which lowers the EHC current efficiency. As can be seen in Fig. 1, by applying the higher potential difference, hydrogen is compressed to higher pressures with the consequence of lower efficiency. Also, for all simulated total voltages, with lower temperatures, higher output pressure can be achieved. However, for smaller pressure differences, increased temperature ensures improved EHC efficiency. Nonetheless, the energy needed for increasing the temperature should also be considered.

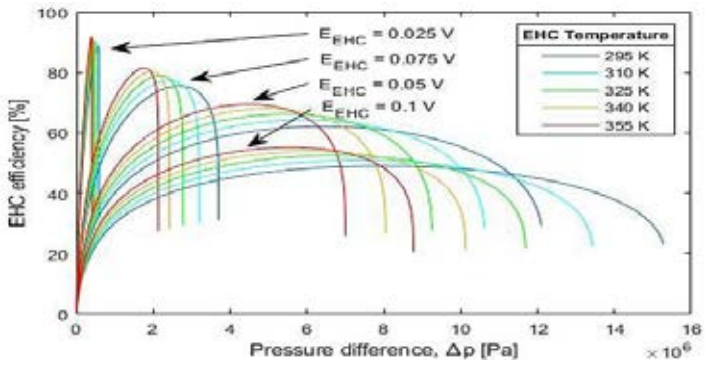


Fig. 1. Simulated temperature influence on EHC efficiency for different applied voltages regarding achieved output pressure

CONCLUSIONS

Simulation analysis has been conducted for the simplified mathematical model of EHC to better understand its performance, described with essential governing equations, under different operating temperatures. The model accounted for Nernst potential, activation overpotentials, ohmic overpotential, and hydrogen back-diffusion. Temperature change affects the EHC performance in multiple ways, principally, membrane proton conductivity, overvoltages, Nernst potential, and hydrogen back diffusion, all impacting the efficiency and output pressure. Taken all into account, the simulation indicates that the EHC should operate at the optimum operating temperature depending on the required output parameters. For further research, a comprising mathematical model accounting more detailed water management will be conducted with accompanying experiment validation.

ACKNOWLEDGEMENT

This research has been done within the project KK.05.1.1.02.0014 titled Securing electrical energy in the case of climate extremes and natural disasters funded from the European Fund for Regional Development. The authors thank the Ministry of Economy and Sustainable Development of Republic of Croatia and the Fund for Environmental Protection and Energy Efficiency of Republic of Croatia for selected this project for funding.

REFERENCES

1. Scheepers F et al. Improving the Efficiency of PEME through Membrane-Specific Pressure Optimization. *Energies* 2020;13:612.
2. Zou J et al. Electrochemical Compression Technologies for High-Pressure Hydrogen: Current Status, Challenges and Perspective. *Electrochem Energ Rev*. Epub ahead of print 7 August 2020
3. Bouwman P. Electrochemical Hydrogen Compression solutions for hydrogen infrastructure. *Fuel Cells Bull* 2014: 12–16.
4. Zou J et al. Insights into electrochemical hydrogen compressor operating parameters and membrane electrode assembly degradation mechanisms. *J Power Sources* 2020; 229249.
5. Rohland B et al. Electrochemical hydrogen compressor. *Electrochimica Acta* 1998; 43: 3841–3846.
6. Dale N et al. *Modeling and analysis of electrochemical hydrogen compression*. FG02-04-ER46115, North Dakota University
7. Nordio M et al. Experimental and modelling study of an electrochemical hydrogen compressor. *Chem Eng J* 2019;369: 432–442.
8. Bampaou M et al. An electrochemical hydrogen compression model. *Chemical Engineering Transactions* 2018; 70: 1213–1218.
9. Durmus GNB, Colpan CO, Devrim Y. A review on the development of the electrochemical hydrogen compressors. *J Power Sources* 2021; 494: 229743.
10. Chouhan A, Bahar B, Prasad AK. Effect of back-diffusion on the performance of an electrochemical hydrogen compressor. *Int J Hydrogen Energy* 2020; 45: 10991–10999.
11. Vermaak L, Neomagus HWJP, Bessarabov DG. Recent Advances in Membrane-Based Electrochemical Hydrogen Separation: A Review. *Membranes* 2021; 11: 127.
12. Bernardo G, Araújo T, da Silva Lopes T, et al. Recent advances in membrane technologies for hydrogen purification. *Int J Hydrogen Energy* 2020; 45: 7313–7338.
13. Weber AZ, Borup RL, Darling RM, et al. A Critical Review of Modeling Transport Phenomena in Polymer-Electrolyte Fuel Cells. *J Electrochem Soc* 2014; 161: F1254–F1299.
14. Marangio F, Santarelli M, Cali M. Theoretical model and experimental analysis of a high pressure PEM water electrolyser for hydrogen production. *Int J Hydrogen Energy* 2009; 34: 1143–1158.
15. Bouwman PJ. Advances in Electrochemical Hydrogen Compression and Purification. *ECS Trans* 2016; 75: 503–510.
16. Choi J, Shin M, Kim B, et al. High-performance ceramic composite electrodes for electrochemical hydrogen pump using protonic ceramics. *Int J Hydrogen Energy* 2017; 42: 13092–13098.

WHEC-2022
23rd World Hydrogen Energy Conference
June 26-30, 2022 - Istanbul

#263

EXPERIMENTAL PROOF OF CONCEPT OF A NOVEL HIGH DENSITY, LOW PRESSURE HYDROGEN STORAGE SYSTEM UTILIZING THERMOCHEMICAL HEAT STORAGE

[1*] *Michael Lutz,* [1] *Marc Linder,* [1] *Inga Bürger*
[1] Institute of Engineering Thermodynamics, (DLR), Pfaffenwaldring 38-40, D-70569 Stuttgart, Germany

*Corresponding author e-mail: inga.buerger@dlr.de

ABSTRACT

In the next decades the global energy system will shift towards renewable energy. Hydrogen technologies have the potential to play a major role in the future´s energy grid. With hydrogen becoming more and more important, safe and efficient hydrogen storage systems are required. Metal hydrides are able to chemically store hydrogen free of loss, at low pressures and potentially high storage densities. However, hydrides with exceptionally high storage densities, such as magnesium hydride, require high operation temperatures above 250 °C. Therefore, heat management is challenging, since heat at that temperature level has to be supplied and removed for hydrogen desorption and absorption, respectively. In this work, the experimental proof of concept of a novel hydrogen storage system using magnesium hydride and the thermochemical heat storage system $Mg(OH)_2$ / MgO is presented. Thereby, the heat of absorption is stored in the same reactor and – with the supply of water vapor - it is available for the hydrogen desorption again. Potentially, storage densities of 20.8 g_{H2} L^{-1} can be stored at a hydrogen pressure of 9 bar. A water vapor pressure of 9.75 bar is sufficient to reach 300 °C in the MgO compartment, which is sufficiently high to drive the H_2 desorption.

Keywords: Hydrogen storage, thermochemical heat storage, magnesium hydride, magnesium hydroxide

INTRODUCTION

With the shift of our global energy system from energy carriers based on fossil fuels towards renewable ones, new energy storage technologies have to be developed. One possibility to store excess electrical energy for later use is its conversion to chemically stored energy such as hydrogen. With hydrogen becoming more and more important, there is a need for safe and efficient hydrogen storage technologies. State of the art systems for that purpose are pressurized storage or liquefaction which have either low efficiency or their safety is questionable.

Metal hydrides represent one option to store hydrogen [1], reaching high volumetric storage densities at low pressures along with loss-free long-time storage. However, due to their chemical reaction, heat is being released and required during hydrogen absorption and desorption, respectively. This heat management is challenging, as e.g. for magnesium hydride showing an exceptionally high storage density of 7.7 w.t%, the temperature level is above 250 °C.

In this contribution we experimentally proof the concept of a novel stationary adiabatic hydrogen storage system, which utilizes magnesium hydride due to its high storage density at a pressure below 10 bar without requiring excessive external heat management. We incorporated a thermochemical heat storage system, namely the $Mg(OH)_2$ / MgO system, into the same reactor. The heat being released during the hydrogen absorption in the metal hydride is thermochemically stored via the dissociation of $Mg(OH)_2$ to MgO and water vapor. To reverse the reaction, water vapor is supplied to the MgO, the previously stored heat is released leading to the desired hydrogen release from the magnesium hydride. While this system has been investigated before analytically [2] and numerically [3] [4], this contribution provides the experimental proof of concept of the adiabatic storage system with high density at low pressure. Further results of this experimental proof have been published in [5].

EXPERIMENTAL

The adiabatic storage reactor was constructed and tested in laboratory scale. It was connected to a test bench which is able to provide hydrogen in the pressure range of 1 to 50 bar and water vapor in the pressure range of 50 mbar to 10 bar. Furthermore, constant pressure can be applied during the experiments. The reactor itself consists of a double walled tube with 234 g magnesium hydride in the inner tube and 400 g magnesium hydroxide in the outer tube, separated by a steel wall. Therefore, heat transfer between the materials is possible while mixing of the gases is prevented. An alloy of 90% magnesium and 10% nickel along with 10 wt.% expanded natural graphite was used as hydrogen storage material. These compounds were compressed to pellets with a diameter of 30 mm. For hydrogen supply and incorporation of thermocouples into a stack of pellets, a central hole was drilled. The pellets were manufactured at Fraunhofer Institute for Manufacturing Technology and Advanced Materials IFAM in Dresden,

Germany [6] The unmodified magnesium hydroxide was obtained from Sigma-Aldrich (Nr. 63081). Both materials and a section of the reactor are shown in Fig. 1.

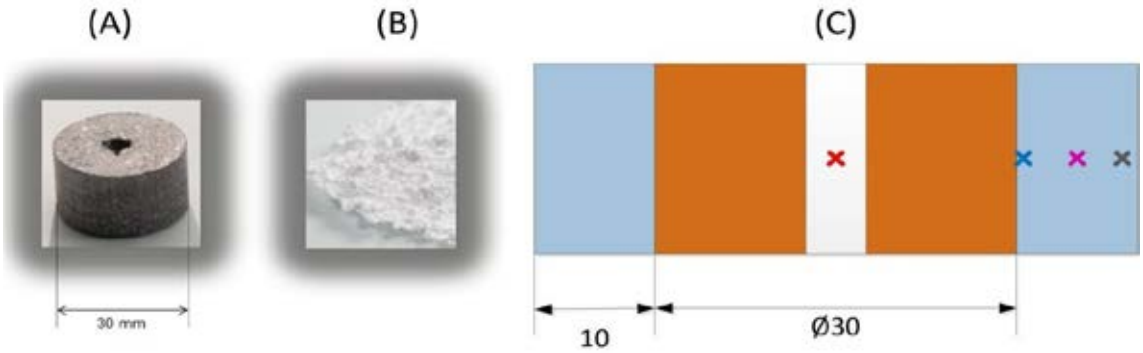


Fig. 1. (A) Mg90Ni10 Pellets; (B) Magnesium hydroxide powder; (C) Reactor system, magnesium hydride in the central tube, magnesium hydroxide in the outer tube. Positions of thermocouples are denoted with x

RESULTS AND DISCUSSION

In the reactor, two thermochemical gas-solid reactions take place. To proof that there is an enhancing effect of the thermochemical heat storage material on the hydrogen uptake and release, a reference experiment was conducted. Therefore, only the magnesium hydride was reacting, while the thermochemical heat storage material was in the MgO state (inert unless exposed to water vapor). This reference experiment is shown by the lines with the open markers in Fig. 2. Afterwards, the same experimental procedure was applied involving the dehydration and hydration, respectively. These experiments are visualized with the full markers in Fig. 2.

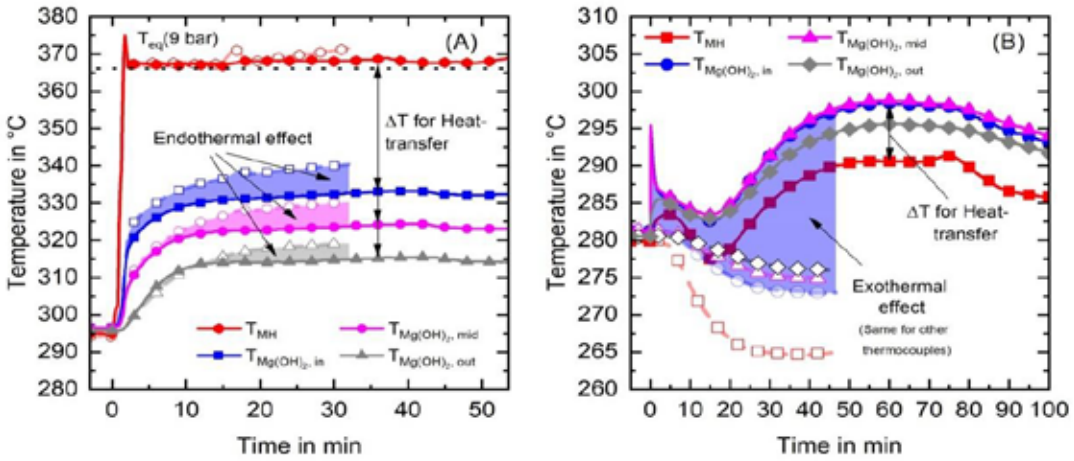


Fig. 2. Reactor temperatures during hydrogen storage (A) and release (B). p(H_2,storage)=9 bar, p(H_2O,storage)=60 mbar, p(H_2,release)=1 bar, p(H_2O, release)=9.75 bar; Open markers: Reference; Closed markers: Combined experiment

For the hydrogen absorption (Fig. 2 A), the reactor was preheated, before the pressure was increased to 9 bar. The temperature in the metal hydride rises sharply to its equilibrium temperature for both the reference and the combined experiment. Heat transfer to the MgO bed (reference) and $Mg(OH)_2$ bed (combined) takes place resulting in a slow heatup of the material. The part of the material close to the heat conducting steel wall heats up more quickly than the outer one. Hence, a temperature gradient in the bed can be observed, which is due to the poor thermal conductivity of the powdery material. The difference in the heat-up of the $Mg(OH)_2$ bed can be seen in the shaded areas in Fig. 2 (A). The temperature increase is less pronounced in the combined experiment. This is because the $Mg(OH)_2$ dissociates endothermally into MgO and water vapor creating a heat sink. After around 15 min the hydrogen supply was switched from constant pressure to contend inflow-rate of 4.3 g_{H2} h^{-1}. It can be seen that the metal hydride temperature (red) increases afterwards, which is attributed to a pressure increase which is now shown. This indicates that the overall hydrogen absorption rate is below 4.3 g_{H2} h^{-1}. In contrast, for the combined experiment, the temperature remains constant indicating that the overall hydrogen absorption rate is at

least 4.3 g_{H2} h^{-1}. Therefore, it can be concluded that the hydrogen absorption is faster in the combined experiment due to thermochemical cooling.

For the hydrogen release shown in Fig. 2 (B) the experimental procedure was similar. Hydrogen was supposed to be released at a constant pressure of 1 bar. In the reference experiment, the temperature in the metal hydride drops quickly. This behaviour is due to heat consumption of the dehydrogenation from the hot metal hydride itself. Since there is no additional heating, the temperature drops until the reaction rate becomes almost zero, since it is too cold. The combined experiment was initiated with the sudden increase of the water vapor pressure to 9.75 bar. Thereby, the previously stored thermal energy is released again. After an initial temperature spike, which is probably attributed to adsorption, and interim cooldown, the exothermal MgO hydration reaction accelerates. This causes the temperature increase to a maximum of 299 °C. A clear difference to the reference experiment can be observed. Since the metal hydride temperature was kept higher than in the reference experiment, more hydrogen can be released.

The experimental results of this first lab-scale reactor confirmed that hydrogen can be stored reversibly at 20.8 g_{H2} L^{-1} at a storage pressure of 9 bar. This value was calculated with the materials only, without the reactor vessel.

CONCLUSION

In this contribution experimental results of a novel hydrogen storage system are presented working at high capacity and low pressure. Magnesium hydride was coupled with magnesium hydroxide working as thermochemical heat storage material. Therefore, an exothermal and endothermal reaction are compensating for each other allowing the system to be operated with minimal external heat management. Thereby, the main disadvantage of magnesium hydride was overcome while maintaining its advantages, such as high capacity at a pressure below 10 bar. The storage capacity based on the volume of the two materials is 20.8 gH_2 L^{-1} at a pressure of 9 bar, which is greater than the 350 bar pressure tank (16.1 gH_2 L^{-1}) and approximately equal to 700 bar pressure [7]. However, the pressure of 9 bar is more feasible. Summing it all up, the adiabatic hydrogen storage system is a promising system to contribute to the future´s hydrogen infrastructure for stationary storage.

ACKNOWLEDGEMENT

The authors want to thank the Karl-Vossloh-Stiftung (Project No.: S047/10043/2017) for partially funding this work.

REFERENCES

[1] B. Sakintuna, F. Lamari-Darkrim and M. Hirscher, "Metal hydride materials for solid hydrogen storage: a review," *International journal of hydrogen energy,* vol. 32, no. 9, pp. 1121-1140, 2007.

[2] M. Bhouri, I. Bürger and M. Linder, "Feasibility analysis of a novel solid-state H2 storage reactor concept based on thermochemical heat storage: MgH2 and Mg (OH) 2 as reference materials," *International Journal of Hydrogen Energy,* vol. 41, no. 45, pp. 20549-20561, 2016.

[3] M. Bhouri and I. Bürger, "Numerical investigation of H2 absorption in an adiabatic high-temperature metal hydride reactor based on thermochemical heat storage: MgH2 and Mg (OH) 2 as reference materials," *International Journal of Hydrogen Energy,* vol. 42, no. 26, pp. 16632-16644, 2017.

[4] M. Lutz, M. Bhouri, M. Linder and I. Bürger, "Adiabatic magnesium hydride system for hydrogen storage based on thermochemical heat storage: Numerical analysis of the dehydrogenation," *Applied energy,* vol. 236, pp. 1034-1048, 2019.

[5] M. Lutz, M. Linder and I. Bürger, “High capacity, low pressure hydrogen storage based on magnesium hydride ad thermochemical heat storage: Experimental proof of concept," *Applied energy,* vol. 271, pp. 115226, 2020

[6] C. Pohlmann, L. Röntzsch, S. Kalinichenka, T. Hutsch, T. Weißgärber and B. Kieback, "Hydrogen storage properties of compacts of melt-spun Mg90Ni10 flakes and expanded natural graphite," *Journal of Alloys and Compounds,* vol. 509, pp. S625-S628, 2011.

[7] M. Hirscher and K. Hirose, Handbook of Hydrogen Storage: New Materials for Future Energy Storage, Weinheim: John Wiley & Sons, 2010, p. 13.

WHEC-2022
23rd World Hydrogen Energy Conference
June 26-30, 2022 - Istanbul

#269

CONTRIBUTION TO MODELING HYDROGEN PERMEATION AND BARRIER LAYER OPTIMIZATION IN BLOW MOLDED PLASTIC LINERS FOR AN ON-BOARD COMPRESSED HYDROGEN TANKS

Zohir Benrabah, Anna Bardetti, Florin Ilinca, Sylvain Bournival*
National Research Council Canada – Automotive and Surface Transportation
75 de Mortagne Blvd., Boucherville, QC J4B 6Y4, Canada

*Corresponding author e-mail: zohir.benrabah@cnrc-nrc.gc.ca

ABSTRACT

Blow Molded Plastic Liners (BMPL) for on-board type IV Compressed Gaseous Hydrogen (CGH2) storage tanks consist of a high-molecular-weight polymer wall that serves as a permeation layer for hydrogen gas. This paper presents the latest numerical model integrated in the BlowView[1] software for predicting the hydrogen permeation in a BMPL. The prediction model is based on Fick's solution-diffusion laws, with pressure and temperature dependent transport properties, for steady/unsteady state permeation regimes through a polymeric wall. An overview of key simulation results for an industrial BMPL for a CGH2 tank, as well as the adopted methodology addressing the challenge to maximize the enclosed volume, while optimizing the wall thickness for light weighting and permeability performance, are also presented.

Keywords: type IV hydrogen tank, hydrogen permeation, plastic liner, simulation, fuel cell electrical vehicle (FCEV).

INTRODUCTION

A key challenge to the widespread commercialization of FCEV, is to design compact and cost effective on-board CGH2 tanks which store sufficient quantities of H2 without sacrificing passenger and cargo space. The first generation of FCEVs use 700 bar Type IV pressure vessels to store hydrogen [1]. These vessels have a cylindrical BMPL, overwrapped by carbon-fiber composite material to maintain the internal pressure, which serves as a hydrogen gas permeation layer. However, due to its small molecular size, H2 permeates through the plastic liner wall. This represents a serious issue that should be addressed early in the design stage in order to minimize H2 emissions from the liner and conform to legal safety requirements and standards. Thereby, automotive OEMs and their suppliers are being challenged to design longer and thinner liners with very consistent wall thickness. One way to meet the hydrogen permeation rate requires a judicious choice of liner material. In the thermoplastic forming industry, it is still common practice to rely on trial and error to find the appropriate barrier layer configuration/thickness required to meet the permeation rate limit requirement. A tool offering a more efficient alternative, based on reliable predictive/virtual analysis of the H2 diffusion through the BMPL, could significantly shorten the design/development cycle by allowing product prototypes to be analyzed and tested virtually. A finite element-based model that could help a designer better understand barrier layer properties was integrated in the latest version of NRC's BlowView software [2, 3]. The mathematical diffusion model adopted is based on Fick's diffusion law to predict H2 diffusion through a polymeric wall. Promising results, in terms of H2 permeation rate on an industrial BMPL, were obtained using BlowView.

THE PERMEATION MECHANISM AND MATHEMATICAL MODEL

The permeation mechanism occurs in three main phases: The first phase is the absorption of the permeant (H2) into the polymer that occurs at the upstream side of the polymer wall. The second phase is the diffusion of the permeant from the surface to the core of the polymer due to the concentration gradient. Finally, the permeant desorbs on the downstream side of the membrane and is removed from the surface by convection to the surrounding air. Given the inherently low diffusivity of plastics and the special geometrical configuration of a BMPL, which is relatively thin compared to their surface area, one dimensional diffusion is usually assumed though the thickness. The permeant diffusion equation for a diffusivity, D, is given by the following expression of Fick's second law [4]:

$$\frac{\partial C}{\partial t} = -\frac{\partial}{\partial x}(J_{H2}) = -\frac{\partial}{\partial x}\left(D\frac{\partial C}{\partial x}\right) \quad (1)$$

[1]BlowView is an engineering simulation software developed at NRC and used to simulate and optimize several forming processes: conventional, twin sheet and 3D extrusion blow molding, thermoforming and injection stretch blow molding.

Where, C is the permeant concentration in the polymer matrix, t is the time, and x the distance through the thickness. However, since the measurement of concentrations is not always a simple task, we instead use Henry's law, Eq. (2), where S is Henry's solubility coefficient and p_{H2} is the H2 pressure:

$$C = S.p_{H2} \quad (2)$$

The new partial differential equation (PDE) is obtained by substituting Eq. (2) in Eq. (1) as follows:

$$\frac{\partial}{\partial t}(S.p_{H2}) = -\frac{\partial}{\partial x}\left(D\frac{\partial}{\partial x}(S.p_{H2})\right) \quad (3)$$

EFFECT OF TEMPERATURE AND PRESSURE ON TRANSPORT COEFFICIENTS

Many references exploring the influence of temperature on the gas solubility coefficient S, diffusion coefficient D, and permeability coefficient P, in polymers have proved that the variation of the coefficients obeys an Arrhenius-type relationship over a small temperature range as [4]:

$$S = S_\infty.\exp\left(-\frac{\Delta H_S}{R.T}\right); \qquad D = D_\infty.\exp\left(-\frac{E_D}{R.T}\right); \qquad P = P_\infty.\exp\left(-\frac{E_P}{R.T}\right) \quad (4)$$

Where, S_∞, D_∞ and P_∞ represent the limit values of various transportation coefficients when the temperature tends to infinity. ΔH_S, E_D and E_P represent the heat of dissolution required for the penetrant to dissolve in the polymer matrix, the activation energy diffusion process, and the apparent activation energy for permeation, respectively. It is obvious from the relationship $P = S \times D$ that $E_P = \Delta H_s + E_D$. For hydrogen, both ΔH_S and E_D are positive values [4]. R and T denote the universal gas constant and the absolute temperature (in Kelvin). In general, this temperature dependence, Eq.(4), is obeyed for polymer materials at low pressures as long as the microstructure of the material is not changing. On the other hand, high pressures will affect the microstructure, and therefore, the permeation depends on the imposed stresses and material characteristics. The polymer transport properties will be considered for ideal sorption where the effects of hydrostatic pressure on the polymeric structure can be idealized as arising from two opposing effects: (1) the compression of the polymer due to imposed hydrostatic pressure, which reduces diffusion (negative β_D); and (2) the swelling of the polymer due to hydrogen solubility, which enhances diffusion (positive β_s) [5].. These two effects are combined in a single parameter β as described in equation (5).

$$S = S_0.\exp(\beta_s.p_{H2}); \qquad D = D_0.\exp(\beta_D.p_{H2}); \qquad P = P_0.\exp((\beta_{s+}\beta_D).p_{H2}) \quad (5)$$

Where, S_0, D_0 and P_0 represent values of various transportation coefficients at atmospheric pressure and $\beta = \beta_{s+}\beta_D$. Therefore, the combined effect of the temperature and pressure on the transport coefficients can be obtained by substituting Eq.(4) in Eq.(5):

$$S = S_\infty.exp\left(\beta_s.p_{H2} - \frac{\Delta H_S}{R.T}\right); \qquad D = D_\infty.exp\left(\beta_D.p_{H2} - \frac{E_D}{R.T}\right); \qquad P = P_\infty.exp\left((\beta_{s+}\beta_D).p_{H2} + \frac{\Delta H_S + E_D}{R.T}\right) \quad (6)$$

NUMERICAL RESOLUTION

After substituting the solubility and diffusivity expression from Eq.(6) in Eq.(3) we obtain the following PDE:

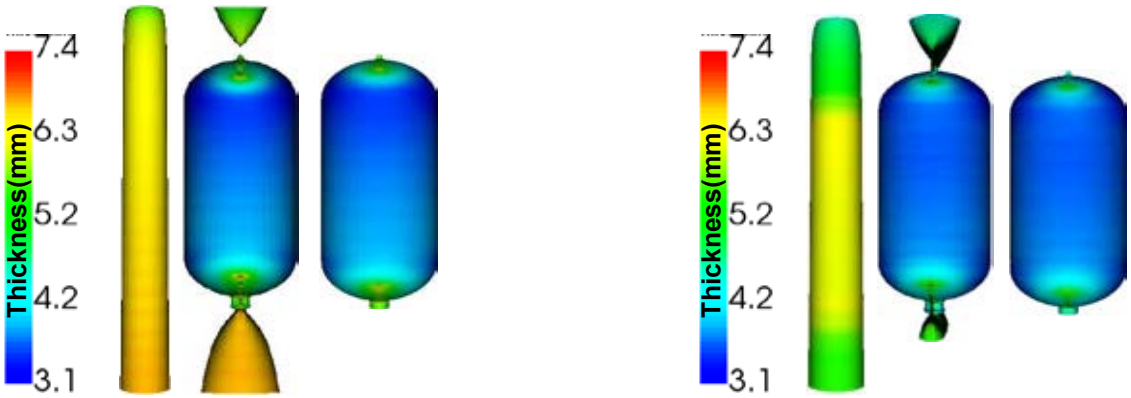
$$\frac{\partial}{\partial t}\left(S_\infty.\exp\left(\beta_s.p_{H2} - \frac{\Delta H_S}{R.T}\right).p_{H2}\right) + \frac{\partial}{\partial x}\left(D_\infty.\exp\left(\beta_D.p_{H2} - \frac{E_D}{R.T}\right)\frac{\partial}{\partial x}\left(S_\infty.\exp\left(\beta_s.p_{H2} - \frac{\Delta H_S}{R.T}\right).p_{H2}\right)\right) = 0 \quad (7)$$

An appropriate numerical method is used to solve the obtained transient nonlinear PDE with respect to the initial boundary conditions. The finite element method is used for space discretization and the Euler implicit scheme for time integration. Details regarding the mathematical formulation of the space discretization and the time integration are not provided here since they fall out of the scoop of this work.

PLASTIC LINER SIMULATION RESULTS

The H2 permeation rate for a typical BMPL was predicted using BlowView for different permeation scenarios and the results are presented below. The length and the diameter of the industrial liner are 365 and 720 mm, respectively. The corresponding enclosed volume capacity is 62.4L. Figures 1a and 1b show the predicted thickness distribution at the end of parison extrusion, inflation and finally after mapping, for the initial and optimized design. The liner weight was reduced from 10.6 kg to 10.3 kg after 19 optimization iterations by improving the thickness uniformity. It is important to note that the permeability analysis was performed on the optimized mapped part, with the H2 stored at a constant pressure of 70 MPa. The temperature and pressure dependent H2 solubility and diffusivity coefficients for three HDPE grades are reported in Table 1 [4, 5]. Figure 2 illustrates the predicted H2 flux over the monolayer liner shell for the different HDPE grades at 20°C. The overall H2 permeation is also reported and should be compared to the maximum allowable limit at 20°C and 45°C provided by [6]. From Figure 2.a, we notice that the H2 permeation of the HDPE-1 liner (i.e., 17.2 NmL/hr/L) exceeds the maximum allowable limit at 20°C (i.e., 8.0 NmL/hr/L). However,

as illustrated in Figures 2.b and 2.c, the permeation of the liners made from materials HDPE-2 and HDPE-3 are, respectively, 5.1 and 3.5 NmL/hr/L, both below the maximum allowable. From Figure 2.d, we also observe that the H2 permeation for HDPE-3 increases to 26.4 NmL/hr/L at 45°C, which represents +700% compared to 20°C. Unfortunately, we can't compare this result to the maximum allowable permeation rate at 45°C since this information is not available in the literature.

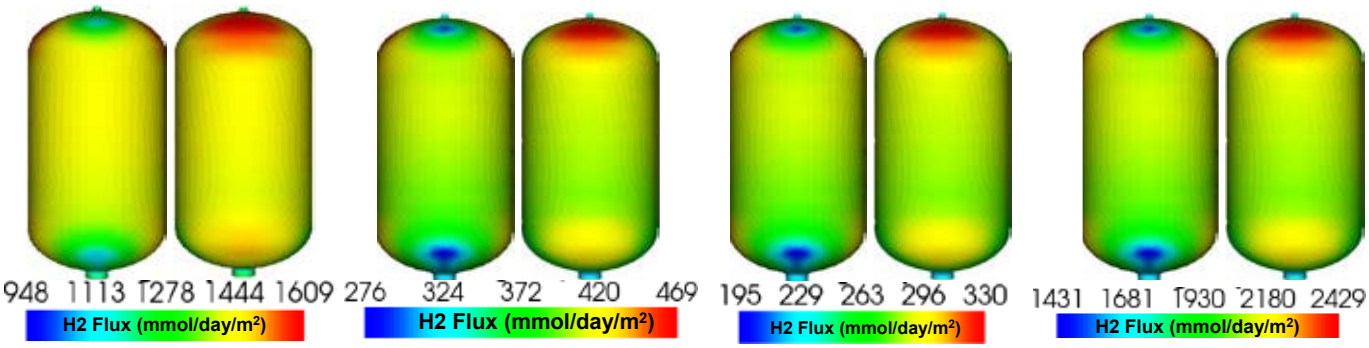


a: Initial design (6.6 kg) b: Optimized design (6.3 Kg)

Figure 1: BlowView predicted thickness distribution

Table 1: H2 solubility and diffusivity coefficients for 3 different HDPE grades

Diffusivity	D_∞(m^2/s)	$E_D(J/molH2)$	β_D(MPa-1)	**Solubility**	S_∞(mol H2/m^3/MPa)	$\Delta H_S(J/molH2)$	β_S(MPa-1)
HDPE-1	0.0970	48837.0	0.0	HDPE-1	0.097	48837.0	0.0
HDPE-2	0.0970	48837.0	-0.05	HDPE-2	0.097	48837.0	0.003
HDPE-3	0.0970	48837.0	-0.07	HDPE-3	0.097	48837.0	0.003



a: HDPE-1 (pressure independent) 17.2 NmL/hr/L at 20°C

b: HDPE-2 5.1 NmL/hr/L at 20°C

c: HDPE-3 3.5 NmL/hr/L at 20°C

d: HDPE-3 26.4 NmL/hr/L at 45°C

Figure 2: Hydrogen permeation and flux density for 3 different HDPE grades

CONCLUSIONS

A finite element based numerical simulation model for the prediction of H2 permeation through a BMPL for a CGH2 storage tank in steady and unsteady regimes, incorporating a novel method for the treatment of the diffusion in the pinch-off zone, was developed. This H2 permeation model was incorporated in BlowView to optimize the barrier layer to satisfy the daily permeation rate constraint. More results will be shared during the conference presentation.

REFERENCES

1. Johnson, K., Veenstra, M., Gotthold, D., Simmons, K. et al., SAE Int. J. Alt. Power. 6(2):2017.
2. Benrabah Z., Thibault P., DiRaddo R., SAE Transactions Journal of Fuel and Lubricants, V 115, 4, pp219-226, 2006.
3. Benrabah Z., Thibault P., DiRaddo R., SAE International Journal of Materials and Manufacturing, pp. 449-459, 2011.
4. Neogi, P., Transport Phenomena in Polymer Membranes, New York: Marcel Dekker, (1996).
5. Barth R. R., Simmons K. L., Marchi C. S., Polymers for Hydrogen Infrastructure and Vehicle Fuel Systems:Applications, Properties, and Gap Analysis, Sandia Report, SAND2013-8904, October 2013
6. Adams P., Bengaouer A., Cariteau B., Molkov V., Venetsanos A.G., Allowable hydrogen permeation rate from road vehicles, int. jour. of hydrogen energy 36 (2011) 2742-2749

WHEC-2022
23rd World Hydrogen Energy Conference
June 26-30, 2022 - Istanbul

#271

A MULTICRITERIA ANALYSIS DECISION FOR PRIORIZATION OF LIQUID ORGANIC HYDROGEN CARRIERS

[1*] *Monica Almansa-Ortegon,* [1] *Juan Carlos Osorio,* [1] *Diego F. Manotas-Duque*
[1]Universidad del Valle, Facultad de Ingeniería, Escuela de Ingeniería Industrial, Calle 13 No 100-00, Cali, Colombia

*Corresponding author e-mail: diego.manotas@correounivalle.edu.co

ABSTRACT
The use of Liquid Organic Hydrogen Carriers (LOHC) is widely studied as a promising material for long-term hydrogen transport and storage, these materials have different techno-economic characteristics that directly influence the operating conditions and cost of the hydrogenation and dehydrogenation process. The selection Three LOHC pairs were selected and prioritized through TOPSIS multicriteria methodology and CRITIC weighting, through the ten technical criteria.

Keywords: LOHC priorization, multicriteria decision, CRITIC methodology, hydrogen storage, TOPSIS.

INTRODUCTION
The increase in world energy consumption and dependence on fossil energy sources that result in the upgrown in greenhouse gases and with them global warming [1] In this way, the need to use other fuels that are sustainable and clean is generated to replace conventional fuels [2] hydrogen as an energy vector has an enormous potential for application in this way, it has been considered as an alternative to largely satisfy the demand for renewable energy expected by 2050 [3]. The energy density of hydrogen exceeds three times that of oil, and its combustion also has zero greenhouse gas emissions[4].

Liquid organic hydrogen carriers (LOHC) have been proposed for the storage and transport of hydrogen with the aim of its application in industries, power plants and as fuels. These are materials with a high storage and transport capacity without the risks and costs that consider liquefaction and compression of pure hydrogen gas [5].
Hydrogenation and dehydrogenation processes are used as key elements in the use of technology, since they take advantage of the advantages of working with liquids in industry [7].The most relevant aspects in the area are the development of dehydrogenation and hydrogenation equipment, synthesis and evaluation of the most suitable catalysts, design and selection of new organic materials with greater capacity for hydrogenation and dehydrogenation; greater ease of processing and lower associated [6], [8]. Decision-making in the energy sector and the need to process specific information under conditions of uncertainty has increased the importance of decision-making methods as a tool for problem solving [9]. Multi-criteria analysis decision analysis (MCDA) are widely used in decision-making and policy-making problems [10], AHP, ANP, ELECTRE and TOPSIS are commonly found; they are used due to their simplicity and in built-in models [11]. The selection of LOCH materials has been approached by evaluating their physicochemical properties by [5], [12], [13]; in none of these cases has MCDA been used. In this work, the chosen MCDA method is the Technique of Order Preference Similarity to the Ideal Solution (TOPSIS) is a multi-criteria decision-making analysis for choosing the best alternative with the shortest distance from ideal solution and the longest distance from negative ideal solution[12]. The advantage of using this methodology is that it allows evaluating qualitative and quantitative criteria, offering a reliable answer that is easy to apply.

The evaluation of this methodology requires establishing a weight for the evaluation of criteria or weighting of criteria, these weights are of great importance in the decision-making process, there are numerous subjective and objective approaches[9], due to the limited availability of experts in LOHC and to eliminate possible contradictions in the most common evaluations such as AHP and ANP.

The Criteria importance through intercriteria (CRITIC) is a method that proposes the determination of objective weights which is based on the quantification of two fundamental notions of MCDM: the contrast intensity and the conflicting character of the evaluation criteria [13]. This work proposes a prioritization of LOHC materials through technical criteria with the use of multicriteria analysis tools that have not been applied in this type of decisions and the application of the CRITIC method for objective decision making and eliminating the biases of the methods AHP and ANP.

MATERIALS AND METHODS

The selection of alternatives and criteria were carried out by means of a bibliographic search, all the LOHCs used for studies with feasibility of application were considered, the materials that are not fully available in hydrothermal markets and which did not have economic or logistic feasibility were discarded.

Criteria weighting CRITIC. In this method, the weights are determined based on the contrast intensity and conflict evaluation of the decision problem. Additionally, human intervention is not required for the evaluation process. Sahin shows in details the step of method used [9], the main structure of the method can be summarized as[9].

RESULTS AND DISCUSSION

The table 1 shows the main pairs of LOHC used, the selection is based on its importance for industrial applications, on the largest number of studies reported in the literature and the technological available information.

Table 1. The main properties of LOHC pairs [7][14]

No	Factor criteria	Dibenziltoluene–perhydro-dibenzyl toluene (DBT – H18-DBT)	N-ethyl-carbazole-dodecahydro-N-ethylcarbazole (NEC-H12-NEC)	Toluene-Methylcyclohexane (TOL-MCH)
1	**H_2 storage capacity**	6.2%	5.8%	6.2%
2	**Melting point (discharged) ºC**	-58	43	-127
3	**Boiling point (discharged) ºC**	350	281	101
4	**Melting point (charged) ºC**	39	69	-95
5	**Boiling point (loaded) ºC**	390	378	111
6	**Reaction enthalpy**	65.4	53.2	68.3
7	**P (bar) hydrogenation**	50	70	30
8	**T(ºC) hydrogenation**	150	170	110
9	**P(bar) dehydrogenation**	1,013	1,013	3
10	**T(ºC) dehydrogenation**	310	270	450

The Table 2 shows the weight for the ten criteria used, the factor with the lowest weight is the storage capacity because the method gives better weight to the criteria that have the highest standard deviation and the lowest correlation. With these weights the LOHC materials are evaluated according to the TOPSIS methodology. Each value of the matrix is normalized, then the matrix is weighted, then the positive ideal solution and the negative ideal solution are defined. Finally, the relative proximity index is calculated for each of the alternatives, and they are ordered from highest to lowest.

Table 2. LOHC selection criteria weights

Factor	1	2	3	4	5	6	7	8	9	10
Weight	6.56714 E-06	0.1415	0.1860	0.1269	0.2250	0.0145	0.0645	0.1012	0.0016	0.1383

Table 3 shows the rankings of the selected alternatives, the DBT-H18-DBT has the first place by CRITIC-TOPSIS methods, this result is according to the literature, this compound is one of the most used in this technology due to its chemical and processing properties. So, the CRITIC_TOPSIS methods can be used for a large list of LOHC pair. The main difficulty in applying the method is the quality and type of information required to establish the rankings. In the case of LOHC pairs, the information is scattered and there is no complete technical information on the possible pairs.

Table 3. Ranking for LOCH selection by MCDA methods

LOCH pairs	(DBT – H18-DBT)	(NEC-H12-NEC)	(TOL-MCH)
Ri	0.772305281	0.669781847	0.316478716

CONCLUSIONS

The criterion with the most weight is the loaded boiling point due to its high standard deviation. The one with the lowest weight is storage capacity since all materials have a similar load capacity. Dibenziltoluene is the material with the least proximity to the ideal negative solution, thus being the best qualified LOHC material through this method and with this it presents the availability for subsequent studies of catalysts and reactor design to generate a LOHC

system with the use of this material. The (TOL-MCH) is the lowest rated material due to the high temperature required for dehydrogenation.

REFERENCES

[1] "The Future of Hydrogen," *Futur. Hydrog.*, no. June, 2019.
[2] J. Loy-Benitez, U. Safder, H.-T. Nguyen, Q. Li, T. Woo, and C. Yoo, "Techno-economic assessment and smart management of an integrated fuel cell-based energy system with absorption chiller for power, hydrogen, heating, and cooling in an electrified railway network," *Energy*, vol. 233, 2021.
[3] X. Zhao, H. Chen, S. Liu, and X. Ye, "Economic & environmental effects of priority dispatch of renewable energy considering fluctuating power output of coal-fired units," *Renew. Energy*, vol. 157, pp. 695–707, 2020.
[4] S. Griffiths, B. K. Sovacool, J. Kim, M. Bazilian, and J. M. Uratani, "Industrial decarbonization via hydrogen: A critical and systematic review of developments, socio-technical systems and policy options," *Energy Res. Soc. Sci.*, vol. 80, no. June, p. 102208, 2021.
[5] P. M. Modisha, C. N. M. Ouma, R. Garidzirai, P. Wasserscheid, and D. Bessarabov, "The Prospect of Hydrogen Storage Using Liquid Organic Hydrogen Carriers," *Energy and Fuels*, vol. 33, no. 4, pp. 2778–2796, 2019.
[6] S. Dürr *et al.*, "Experimental determination of the hydrogenation/dehydrogenation - Equilibrium of the LOHC system H0/H18-dibenzyltoluene," *Int. J. Hydrogen Energy*, vol. 46, no. 64, pp. 32583–32594, 2021.
[7] M. Hurskainen and J. Ihonen, "Techno-economic feasibility of road transport of hydrogen using liquid organic hydrogen carriers," *Int. J. Hydrogen Energy*, vol. 45, no. 56, pp. 32098–32112, 2020.
[8] K. Müller, "Technologies for the Storage of Hydrogen Part 1: Hydrogen Storage in the Narrower Sense," *ChemBioEng Rev.*, vol. 6, no. 3, pp. 72–80, 2019.
[9] M. Şahin, "A comprehensive analysis of weighting and multicriteria methods in the context of sustainable energy," *Int. J. Environ. Sci. Technol.*, vol. 18, no. 6, pp. 1591–1616, 2021.
[10] M. Çolak and İ. Kaya, "Multi-criteria evaluation of energy storage technologies based on hesitant fuzzy information: A case study for Turkey," *J. Energy Storage*, vol. 28, no. July 2019, 2020.
[11] İ. Kaya, M. Çolak, and F. Terzi, "Use of MCDM techniques for energy policy and decision-making problems: A review," *Int. J. Energy Res.*, vol. 42, no. 7, pp. 2344–2372, 2018.
[12] J. V. M. Lopes, A. E. Bresciani, K. M. Carvalho, L. A. Kulay, and R. M. B. Alves, "Multi-criteria decision approach to select carbon dioxide and hydrogen sources as potential raw materials for the production of chemicals," *Renew. Sustain. Energy Rev.*, vol. 151, no. June, p. 111542, 2021.
[13] C. Kahraman, B. Öztayşi, and S. Ç. Onar, "Spherical Fuzzy CRITIC Method: Prioritizing Supplier Selection Criteria," *Lect. Notes Networks Syst.*, vol. 308, pp. 705–714, 2022.
[14] I. Dincer and C. Acar, "Review and evaluation of hydrogen production methods for better sustainability," *Int. J. Hydrogen Energy*, vol. 40, no. 34, pp. 11094–11111, 2014.

WHEC-2022
23rd World Hydrogen Energy Conference
June 26-30, 2022 - Istanbul

#279

SYNTHESIS AND STABILIZATION OF ENERGY FUEL MATERIAL ALUMINUM HYDRIDE: A REVIEW

[1] *Youhai Liu,* [2]*Yang Zhang,* [1*] *Fusheng Yang,*[2 *]*Fengqi Zhao* [1] *Zhen Wu,* [1] *Zaoxiao Zhang*
[1]Xi'An Jiaotong University, School of chemical Engineering and Technology, Xi'An, Shaanxi, China
[2] Xi'An Model Chemistry Research Institute, Xi'An, Shaanxi, China

[1*]Corresponding author e-mail: yang.fs@mail.xjtu.edu.cn
[2*] Corresponding author e-mail: zhaofqi@163.com

ABSTRACT

Aluminum hydride(AlH_3) has a high gravimetric hydrogen energy density of more than 10.0 wt.% and volumetric density (148 kgH_2/m^3). The material has drawn much attention because of its high hydrogen storage capacity and rapid dehydrogenation at low temperatures, and has been used in various areas, including catalysts, fuel cell, reducing agents and rocket fuel additive. AlH_3 can largely promote the specific impulse of propellants when used as energetic additive in solid propellant. In this article, we focus on the research development in the field of synthesis and stabilization of AlH_3 in recent decades. Particularly, the stability of AlH_3 is critical for its application in solid propellants. The most widely used strategies are also introduced and compared, based on which some suggestions for possible future research directions are provided.

Keywords: Aluminum hydride, energy material, stability, solid propellant

INTRODUCTION

Solid propellants play an important role in military and aerospace fields, and increasing the energy level has always been the core direction of its development. An effective way to improve the specific impulse of the propellants is to reduce the molecular weight of the combustion gas products. Therefore, it is a good choice to adopt energetic materials with high hydrogen content in the propellants [1-3]. In recent years, metal hydride has attracted great attention as energetic additive of propellants. As one of the most promising hydrogen storage materials, AlH_3 has high weight and bulk density. The theoretical estimate can reach 10.1 wt.% and 148 kgH_2/m^3, respectively, which is twice higher than that of liquid hydrogen [4-6]. When used as additive in propellant, it can reduce the adiabatic temperature while increasing the specific impulse. For example, by fully replacing 18% of Al in the traditional AP/HTPB-based rocket propellants with AlH_3[7], the theoretical specific impulse is increased by 10% and the flame temperature reduced by 5%, simultaneously. Studies show that the stability of AlH_3 is strongly related to the crystal structure. AlH_3 has seven crystal structures, α-、α'-、β-、γ-、δ-、ε-and ξ-AlH_3, among these the α crystal phase is the most stable structure theoretically and experimentally [8-10]. However, AlH_3 is still not stable enough to avoid decomposing at room temperature, besides it can also react with oxygen and water vapour at the ambient atmosphere. Moreover, the poor compatibility of AlH_3 with certain propellant components could also limit its application in solid propellants [11].

In recent years, numerous investigations have been published focus on the synthesis and stabilization of AlH_3 [12-18], for the purpose of generating more stable, higher quality and more cost effective AlH_3. In this review, we first introduce the common methods of synthesizing of AlH_3, followed by the technologies to improve the stability of AlH_3. Lastly the future research direction of AlH_3 is prospected.

SYNTHESIS OF ALH_3

The synthesis of AlH_3 has a long history, dating back to the 1940s. In general, there are several ways to synthesize AlH_3, include wet synthetic methods, dry synthesis and new synthesis methods that have merged in recent years.

AlH_3 can be attained through wet chemical reactions of hydrides or alkaline earth metals to form AlH_3-ether complexes [19,20]. However, the formation of $AlH_3 \cdot Et_2O$ requires a large amount of organic solvents which are toxic and unfriendly to the environment, such as ethers and amines. This method is also highly cost and difficult to control due to its sensitivity to temperature and time. Therefore, large-scale industrial production is therefore impractical.

In order to avoid the use of toxic and costly solvents, some dry synthesis methods without liquid solvents have been developed, for example direct reaction of aluminum with hydrogen under high pressure. In addition, AlH_3 can be prepared through cheaper metal hydrides, such as LiH, NaH, and CaH_2 rather than traditional high consumption

$LiAlH_4$. The process of synthesizing AlH_3 mixture through the pathway of mechanically activated reaction between MgH_2 and $AlCl_3$ is shown in Fig.1. This method is often named as mechanochemical method.

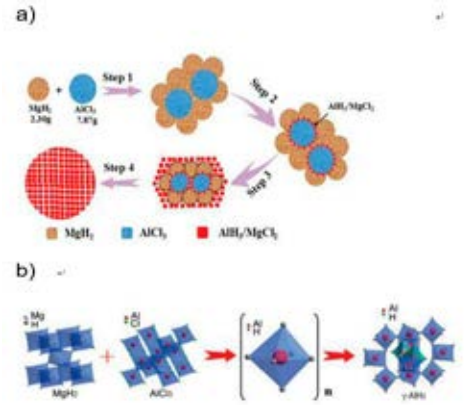


Fig.1 a) The pathway of the mechanically activated reaction between MgH_2 and $AlCl_3$ [21];
b) Mechanism of the solid-state synthesis of nano-sized γ-AlH_3

Recently, in order to synthesize AlH_3 without the usage of ether solvents, some novel technologies have been developed including preparation of AlH_3 by organoaluminum decomposition [22] and supercritical synthesis [23]. For the former method, AlH_3 can be generated through decomposing triethylaluminium under hydrogen pressure 10MPa. The path of decomposing Et_3Al are as follow: $Et_3Al \rightarrow Et_2AlH \rightarrow AlH_3 \rightarrow Al$, For the purpose of preventing further decomposition of AlH_3, tetraoctyl ammonium bromide (TOAB) and tetrabutylammonium bromide (TBAB) are used to stabilize Al/AlH_3 particles. However, this method also shows some disadvantages, some impurities can be generated during the process, such as surfactants and other catalysts. For the supercritical method, the dissolving and mixing ability of the supercritical fluid is utilized in the chemical reaction system to make the raw material undergo a certain catalytic reaction, so as to achieve promoted chemical reaction. AlH_3 can be obtained by the reaction of activated Al with H_2 in supercritical CO_2 liquid medium. Nevertheless, due to the limitation of the supercritical conditions, the reaction system cannot proceed at a higher temperature, which will affect the activity of the reactants. This synthesis method is still in the laboratory stage and has a long way to realize industrial scale production.

STABILITY OF ALH3

AlH_3 is sensitive to surrounding oxygen and moisture, making it unstable under ambient conditions, and therefore can be spontaneously decomposed into Al and H_2. The factors leading to the instability of α-AlH_3 can be divided into two categories: intrinsic and extrinsic causes. Essentially, α-AlH_3 is composed of two strongly reducing elements (Al and H) with an average enthalpy of formation at room temperature of (-11.4±0.8) kJ/mol and an absolute entropy of (30.0±0.4)kJ/(mol℃), and the Gibbs free energy is (45.4±1.0)kJ/mol. Therefore, from the thermodynamic point of view, AlH_3 can spontaneously decompose into metallic Al and H_2 in ambient atmosphere. Meanwhile there are also extrinsic reasons that affect the thermal stability of α-AlH_3, including the environment (humidity, light [24], chemical reactions, etc.), its own crystal structure and purity. For example, impurities (such as LiCl, $NaBH_4$, LiBH and $LiAlH_4$, etc.) will be generated during the synthesis of α-AlH_3, as well as other unstable crystal forms, which could affect its thermal stability and safety.
At present, the methods being applied to improve the thermal stability and compatibility of α-AlH_3, are dedicated not only to enhance the crystallinity and the purity of α-AlH_3 by optimizing the synthesis and preparation conditions, but also to modify the surface and interface of α-AlH_3. The main methods include: surface coating method, surface passivation method and doping method, etc.

CONCLUSIONS

AlH_3 is an attractive high-energy material. This review covers the published results on synthesis/stabilization methods of AlH_3. To date, the wet chemistry synthesis and mechanochemical method are commonly used as the approaches for synthesis of AlH_3, However, the current synthetic methods are still not cost-effective enough to be adopted for large scale industrial production, thus exploring more efficient and low-cost synthetic methods of AlH_3 for industrial-scale production is urgent. And the way to improve the stability of AlH_3 without compromising the overall energy performance is another problem to be addressed.

REFERENCES

1. G. Young, G.A. Risha, T.L. Connell, R.A. Yetter. 2019. Combustion of HTPB based solid fuels containing metals and metal hydrides with nitrous oxide. Propellants Explos. Pyrotech. 44:744–750
2. S.H. Chen, Y. Tang, H.S. Yu, L.R. Bao, W. Zhang, L.T. DeLuca, R.Q. Shen, Y.H. Ye. 2019. The rapid H_2 release from AlH_3 dehydrogenation forming porous layer in AlH_3/ hydroxyl-terminated polybutadiene (HTPB) fuels during combustion. J. Hazard. Mater. 371:53–61.
3. G. Young, R. Jacob, M.R. Zachariah. 2015. High pressure ignition and combustion of Aluminum hydride, Combust. Sci. Technol. 187:1335–1350.
4. Y. Zhao, F.Q. Zhao, S.Y. Xu, X.H. Ju. 2021. Thermal decomposition mechanism of nitroglycerin by nano-aluminum hydride (AlH3): ReaxFF-lg molecular dynamics simulation. Chem. Phys. Lett. 770:138443.
5. Y. Zhao, F.Q. Zhao, S.Y. Xu, X.H. Ju. 2021. Molecular dynamics insight into the evolution of AlH_3 nanoparticles in the thermal decomposition of insensitive energetic materials. J. Mater. Sci. 56:9209–9226.
6. X.S. Liu, H.Z. Liu, N. Qiu, Y.B. Zhang, G.Y. Zhao, L. Xu, Z.Q. Lan, J. Guo. 2020. Cycling hydrogen desorption properties and microstructures of MgH2–AlH3–NbF5 hydrogen storage materials. Rare Met. 40:1003–1007.
7. S.H. Chen, Y. Tang, H.S. Yu, L.R. Bao, W. Zhang, L.T. DeLuca, R.Q. Shen, Y.H. Ye. 2019. The rapid H2 release from AlH_3 dehydrogenation forming porous layer in AlH_3/ hydroxyl-terminated polybutadiene (HTPB) fuels during combustion. J. Hazard. Mater. 371:53–61.
8. H.P. Li, D.L. Liang, M.H. Yu, J.Z. Liu, Y. Wang, A.M. Pang, G. Tang, X.F. Huang.2020. Study on dehydrogenation and oxidation kinetics mechanisms of micron α-AlH_3 in an oxidative atmosphere. Int. J. Hydrogen Energy 45:24958–24967.
9. J. Graetz, Metastable metal hydrides for hydrogen storage.2012. ISRN Materials Science. 2012:1–18.
10. J. Graetz, J.J. Reilly, V.A. Yartys, J.P. Maehlen, B.M. Bulychev, V.E. Antonov, B. P. Tarasov, I.E. Gabis.2011. Aluminum hydride as a hydrogen and energy storage material: Past, present and future, J. Alloy. Compd. 509:517–528.
11. Z.F. Jiang, F.Q. Zhao, M. Zhang, H. Li, J.K. Zhang, Y.J. Yang, N. Li. 2020. Research progress in the stabilization of aluminum hydride. Chinese J. Explosives Propellants. 43:107–115.
12. M.N. Qin, Y. Zhang, W. Tang, Q. Shi, W. Wang, S.J. Qiu.2017. α-AlH_3 coated with stearic acid: preparation and its electrostatic sensitivity. Chinese J. Energetic Mater. 25:59–62.
13. J.H. Xing, Y. Xia, J.W. Wang.2018. A method for improving thermal stability of aluminum hydride, CN 109019507A[P].
14. X.W. Cai, J.H. Yang, J.L. Zhang, D.X. Ma, Y.P. Wang.2016. Liquid carbon dioxide as anti-solvent coating aluminum hydride. Propellants Explos. Pyrotech. 40:914–919.
15. M.A. Petrie, J.C. Bottaro, R.J. Schmitt, P.E. Penwell, D.C. Bomberger. 2001. Preparation of aluminum hydride polymorphs, particularly stabilized α-AlH3, US, 6228338 B1[P].
16. D. Schmidt. 1974Non-solvated particulate aluminum hydride coated with a cyanocoating compound useful in solid propellants, US 3850709[P].
17. C.B. Roberts, D.D. Toner. 1974. Stabilization of light metal hydride (U), US 3803082[P].
18. J. Flynn. 1974. Particulate aluminum hydride with nitrocellulose coating suitable for use in solid propellants, US 3855022[P].
19. C. Duan, Y. Cao, L. Hu, D. Fu, J. Ma, J. Youngblood. 2019. An efficient mechanochemical synthesis of alpha-aluminum hydride: Synergistic effect of TiF3 on the crystallization rate and selective formation of alpha-aluminum hydride polymorph. J. Hazard. Mater. 373:141–151.
20. C.W. Duan, Y.Z. Cao, L.X. Hu, Y.L. Zhang, D. Fu, J.L. Ma, J.H. Zhang. 2019. Mechanochemical synthesis of the α-AlH3/LiCl nano-composites by reaction of LiH and AlCl3: Kinetics modeling and reaction mechanism. Int. J. Hydrogen Energy 44:23716–23725.
21. Hlova, I.Z.; Gupta, S.; Goldston, J.F.; Kobayashi, T.; Pruski, M.; Pecharsky, V.K. 2014. Dry mechanochemical synthesis of alane from LiH and AlCl3. Faraday Discuss. 170:37–153.
22. L. Wang, A. Rawal, M.Z. Quadir, K.-F. Aguey-Zinsou. 2018. Formation of aluminium hydride (AlH3) via the decomposition of organoaluminium and hydrogen storage properties. Int. J. Hydrogen Energy 43:16749–16757.
23. Zidan, R.; Garcia-Diaz, B.L.; Fewox, C.S.; Stowe, A.C.; Gray, J.R.; Harter, A.G. 2009. Aluminium hydride: A reversible material for hydrogen storage. Chem. Commun. 2009:3717–3719.
24. GABIS I E, BARABAN A P, KUZNETSOV V G, et al. 2014. A mechanism of ultraviolet activation of the alpha-AlH3 decomposition. Int. J. Hydrogen Energy. 39: 15844-15850.

WHEC-2022
23rd World Hydrogen Energy Conference
June 26-30, 2022 - Istanbul

#282

NUMERICAL SIMULATION AND PARAMETRIC ANALYSIS OF THE WALL STRAIN DISTRIBUTION OF VERTICALLY PLACED METAL HYDRIDE BASED HYDROGEN STORAGE CONTAINER

[1] *Shuaijie Cao,* [2]*Xuwen Yin,* [1*] *Fusheng Yang,*[3] *Lijun Jiang*，[3] *Yuanfang Wu*，[1] *Zhen Wu,* [1] *Zaoxiao Zhang*
[1] Xi'an Jiaotong University, School of Chemical Engineering and Technology, Xi'an, Shaanxi, P. R. China
[2] Xinjiang University, School of Mechanical Engineering, Urumqi, Xinjiang Uygur Autonomous Regions, P.R. China
[3] General Research Institute for Nonferrous Metals (GRINM) Co. LTD，Beijing, P.R. China

*Corresponding author e-mail: yang.fs@mail.xjtu.edu.cn

ABSTRACT

Pulverization, settling and agglomeration, and the consequent densification may occur for metal hydride particles during the charge-discharge cycles, which will affect the wall strain of their container for hydrogen storage. In order to study the effects of different factors on the wall strain of metal hydride hydrogen storage vessel, a reaction-thermal-mechanical coupling model for $LaNi_5$ alloy was modified with regard to some relevant parameters, by which sensitivity analysis was conducted. Finally, the strain distribution along the height of reactor filling Mg_2Ni was predicted by the model and compared with experimental results reported in literature.

Keywords: Metal hydride, Volume expansion, Wall strain, Parametric analysis

INTRODUCTION

Hydrogen energy has attracted much attention in recent years because of its clean, renewable properties. However, the safety concern of the mainstream hydrogen storage technology via high pressure gas, seriously restricts the popularization of hydrogen energy. Solid hydrogen storage by metal hydrides, features high volumetric hydrogen storage density, as well as mild conditions of hydrogen absorption and release, hence largely overcoming such disadvantage. However, mechanistic strength is known to be a key issue for design of metal hydride hydrogen storage vessel [1]. When a metallic alloy absorbs hydrogen, its volume will expand by a ratio of 20~30% [2,3] when transformed from solid solution to saturated hydride. Such volume expansion can induce wall stress and deformation or even failure in the metal hydride storage vessel. Lekshmi and Mohan [4] presented a mathematical model to describe the formation of wall strain in the vessel packing $LaNi_5$ powders, which is modified here for improved accuracy. The influences of key factors on the wall strain are investigated, and the applicability of the modified model to other material systems is discussed.

MODELING

The original model coupling reaction, heat and mass transfer for packed bed of hydride powders is referred to Ref. [4], and an empirical relationship between bed porosity and height [5] was given as,

$$\phi = Ce^{kz} \tag{1}$$

The coefficients C and k depend on bed height h_b and the porosity at the top region of the bed, ϕ_1.

$$\phi_0 \cdot h_b = \int_0^{h_b} \phi \cdot dz \tag{2}$$

$$\phi_1 = C \cdot e^{kh_b} \tag{3}$$

ϕ_0 represents the average porosity.

As the hydride volume increases linearly with hydrogen concentration [6], an effective expansion coefficient which accounts for both thermal expansion and volume expansion of alloy particles during hydriding is formulated as,

$$\alpha_e = \alpha_t \left[1 + \alpha_t \Delta T + \frac{0.167}{3\alpha_t \Delta T}\left(1 - \left[\frac{\rho_{sat} - \rho_s}{\rho_{sat} - \rho_a}\right]\right)\right] \tag{4}$$

where α_t is the coefficient of thermal expansion of $LaNi_5$, ΔT is the temperature difference and ρ is the hydrogen concentration in the hydride bed.

Taking the porosity of hydride bed into account, the effective Young's modulus is calculated as [7]

$$\mathrm{Y_e} = \mathrm{Y_0}\left(1 - \frac{\phi}{\phi_{\mathrm{cr}}}\right)^{\mathrm{p}} \tag{5}$$

where Y_0 is the Young's Modulus of non-porous material, ϕ is the porosity, ϕ_{cr} is the critical porosity at which the Young's Modulus becomes zero and 'p' is a material specific exponent.

Please note in Eq. (5), the parameter p needs to be determined through experiments, and relevant data is absent for most material systems. In addition, the solution of critical porosity ϕ_{cr} is complicated yet inaccurate. Li et al. [8] proves that the formula (6) is more suitable for Young's modulus of porous materials, and is hence adopted as modification

$$Y_e = \frac{1-\phi}{1+a\phi} \cdot Y_0 \quad (6)$$

Parameter a is related to the Poisson's ratio and pore shape of the material, which is given as follows.

$$a = \frac{1+v_m}{2(1-2v_m)} \quad (7)$$

RESULTS AND DISCUSSION

Figure 1 presents the simulation results of original model, modified model and experimental data from [9]. It can be seen that the accuracy of original model is improved after modification and meets the requirements for analysis.

The sensitivity analysis of parameters used in the model was carried out. The results show that hydrogen pressure and cooling fluid temperature have little impact on the wall stress of hydrogen storage vessel, which confirms the conclusion in Ref. [4]. On the other hand, the influences of the packing density, as well as the cycling on the wall strain, are much more significant, see Fig. 2 and 3. With the increase of average porosity, the wall strain tends to decrease, while the length of the area with wall strain shows an obvious decreasing trend. The porosity at the top of the bed will increase with cycling, resulting in gradual increases of wall strain at different heights, which is consistent with experimental observation.

Further more, the model was attempted for use for the reactor packing Mg_2Ni alloy. Maximum error of <20% is determined from the comparison between the prediction and experimental results [10], and the applicability of the model is proved.

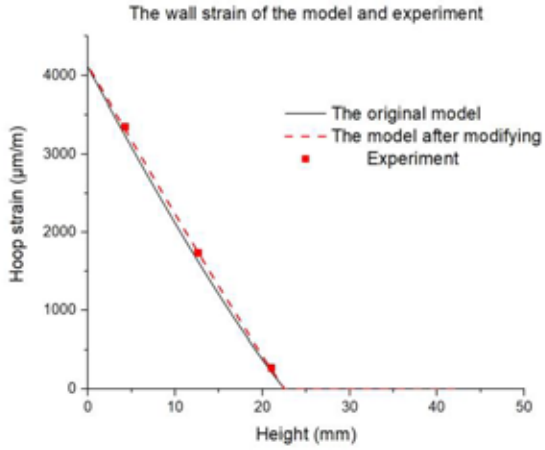


Fig. 1. The Comparison of wall stress of hydrogen storage vessel before and after modifying the formula (packing height:70%, mesh 100, average porosity:0.5, top porosity:0.75)

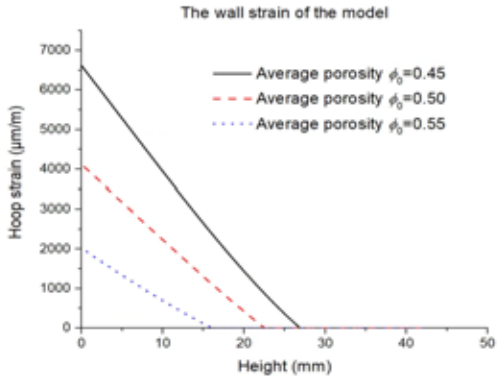


Fig. 2. The Comparison of wall stress of hydrogen under different average porosity conditions (packing height:70%, mesh 100, top porosity:0.75)

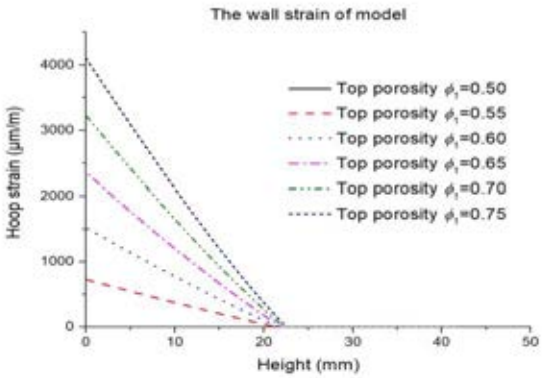


Fig. 3. The Comparison of wall stress of hydrogen storage vessel storage vessel under different top porosity conditions (packing height:70%, mesh 100, average porosity:0.50)

CONCLUSIONS

In this paper, the reaction-thermal-mechanical coupling model of a longitudinal reactor containing $LaNi_5$ hydride is improved and verified. In addition, the effects of key parameters of the model are analyzed, and the following conclusions can be drawn:

- The factors that affect the average porosity of the alloy, such as the initial filling method, have a significant effect on the wall stress of the hydrogen storage vessel.
- With the increase of cycles, the strain distribution on the wall of hydrogen storage container increases along the height of the container, and the length of the area with wall strain increases slightly.
- The modified model was successfully used to predict the strain distribution along the height of reactor filled with Mg_2Ni.

ACKNOWLEDGEMENT

Financial support from National Key Research and Development Program of China (No.2018YFE0202000) is greatly acknowledged.

REFERENCES

1. Yang FS, Wang GX, Zhang ZX, Meng XY, Rudolph V. Design of the metal hydride reactor a review on the key technical issues. Int J Hydrogen Energy 2010;35:3832-40
2. F. Qin, L.H. Guo, J.P. Chen, Z.J. Chen, Int. J. Hydrogen Energy 33 (2008) 709–717.
3. S. Enache, W. Lohstroh, R. Griessen, Phys. Rev. B 69 (2004), 115326-1–115326- 12.
4. D. Lekshmi, G. Mohan, Numerical simulation of the parametric influence on the wall strain distribution of vertically placed metal hydride based hydrogen storage container, Int. J. Hydrogen Energy 40 (2015) 5689-5700
5. Haque E. Void fraction as a function of depth and pressure drops of packed beds of porous media formed by granular material. Trans Am Soc Agric Biol 2011;54:2239-43.
6. Joubert JM, Cerny RC, Latroche M, Parcheron-Guegan A, Yvon K. Compressibility and thermal expansion of LaNi5 and its substitutional derivatives. Intermetallics 2005;13:227-31.
7. Phani KK, Niyogi SK. Young's modulus of porous brittle solids. J Mater Sci 1987;22:257-63.
8. Li Chun-guang, Wang Shui-lin, Zheng hong. Relationship between bulk modulus and porosity of poro medium. Rock and Soil Mechanics 2007;28:293-04
9. Lin CK, Chen YC. Effect of cyclic hydriding-dehydriding reactions of LaNi5 on the thin-wall deformation of metal hydride storage vessels with various configurations. Renew Energy 2012;48:404-10.
10. Askri F, Jemni A, Nasrallah SB. Study of two dimensional and dynamic heat and mass transfer in a metal-hydrogen reactor. Int J Hydrogen Energy 2003;28:537-57.

WHEC-2022
23rd World Hydrogen Energy Conference
June 26-30, 2022 - Istanbul

#290

STUDIES ON HYDROGEN STORAGE PERFORMANCE OF CATALYZED MgH_2

Satish Kumar Verma[*], *Mohammad Abu Shaz and Thakur Prasad Yadav*
Hydrogen Energy Centre, Department of Physics, Banaras Hindu University, Varanasi-221005, India.

*Corresponding author email: satish16kumar@gmail.com

ABSTRACT

MgH_2 is the widely investigated and one of the most prominent solid state hydrogen storage materials because of its high hydrogen storage capacity, low cost, and enormous elemental reserves in the earth crust and seawater. However, the high desorption temperature, sluggish kinetics and high thermal stability hinder its further onboard application. In present investigation, we have reported the enhanced kinetics and thermodynamics for MgH_2 catalyzed through different prominent catalysts/additives like graphene (Gr), VS_2, TiH_2@Gr, Ti@Gr, TiO_2@Gr, and high entropy alloy (HEA). Amongst these catalysts TiH_2@Gr is most suitable catalyst for empowering the kinetics and thermodynamics of MgH_2. The temperature programmed study reflects that MgH_2-TiH_2@Gr has lowest onset desorption temperature *i.e.,* ~231 ^{o}C with a storage capacity ~6.55 wt% which is ~190 ^{o}C lower than the desorption temperature of pristine MgH_2. The better catalytic behavior of MgH_2-HEA on TiH_2@Gr also persists during de/re-hydrogenation kinetics of MgH_2. Thus, MgH_2 catalyzed by HEA absorbs ~5.9 wt% of hydrogen at 300 ^{o}C under 15 atm pressures in 1.5 min. A remarkable result coming out of the present investigation is concerning cyclability (reversibility) of MgH_2-HEA, up to 25 cycles.

Keywords: Hydrogen Storage, Magnesium Hydride, Graphene templated Ti-based catalyst, 2-d materials, Reversibility.

INTRODUCTION

MgH_2 is a widely investigated solid-state hydrogen storage material due to its very high storage capacity (110 g/L volumetric and 7.6 wt% gravimetric) and large elemental abundance in nature. It's very high hydrogen desorption temperature (~400ºC), slow kinetics, and high thermodynamics makes an obstacle on the way to use MgH_2 as onboard applications. These obstacles can be vanished by opting the methods alloying, scaffolding, Nanoconfinement, and addition of catalyst. Different research groups have adopted different methods to use the MgH_2 as onboard applications[1–3]. The $TiVO_{3.5}$ catalyst for improving the kinetics of the MgH_2 was reported by Zhang et al. [4]. TiF_4 works as an effective catalyst for improving the re/de-hydrogenation kinetics of the MgH_2 [5]. Kwon et al. [6] synthesized MgH_2 catalyzed by Ni, Fe, Ti through the reactive milling method and reported that Ni, Fe, Ti works as an effective catalyst for improving the hydrogen storage properties of MgH_2. MgH_2-Graphene nanosheets have been synthesized by Liu et al.[7,8]. They have shown that graphene nanosheets provide a more diffusion path to hydrogen and restrict the agglomeration of MgH_2.

Keeping the above investigations in view, it is clear that metal (Ti-based) catalyst and 2D materials (like graphene) both separately work as catalyst for improving the kinetics and thermodynamics of MgH_2 but a synergistic effect of both (Ti-based compound and graphene) will be a worthy topic of study.

Given the above, we have synthesized graphene (Gr), VS_2, HEA, and graphene templated Ti-based compound (Ti@Gr, TiH_2@Gr, and TiO_2@Gr) for catalytic action on MgH_2. The catalytic action on MgH_2 of all such synthesized catalyst was examined through its structural, microstructural, spectroscopic, and hydrogen storage characterizations.

MATERIAL SYNTHESIS METHODS

All the materials have been synthesized by using high grade chemicals. Graphene Oxide (GO) was synthesized by improved Hummers method[9] and reduced it by using 5% H_2 balanced Ar gas at 850 ^{o}C for 5 h. This resulted in the formation of reduced graphene oxide (rGO), which is further used for work as graphene. Ammonium metavanadate (NH_4VO_3) (1.5 g), and thioacetamide (C_2H_5NS) (5.4 g) procured from Sigma Aldrich with a purity of 99% was used for synthesis of VS_2 via hydrothermal method. The $NaVO_3$ and C_2H_5NS dissolve into the 100 ml deionized water and put into a Teflon-lined stainless-steel autoclave and heated to 190°C in a hydrothermal oven for 24 hours. The residue obtained after filtration was first washed with deionized water (4 times) and then washed with ethanol (4 times) and dried at 60 ºC under vacuum for 20 hours. The dried sample so obtained was sonicated for 20 h before further investigations. The synthesis routes for Ti@Gr, TiH_2@Gr, and TiO_2@Gr have been given in previous

reported study[10]. The HEA was prepared by radio frequency (RF) melting with the appropriate ratio of constituent elements using an RF induction furnace (Inductotherm). The melted materials crushed in the form of powder. The powder thus obtained will be referred as-cast HEA alloy. As-cast HEA powder was leached with 2M of NaOH aqueous solution for 10 minutes followed by washing with deionized water and methanol for 30 minutes each and dried under vacuum. The resultant sample is termed as leached HEA (LHEA).

These as-prepared materials have been used as catalyst to catalyze the MgH_2. The MgH_2 catalyzed by 5 wt% of catalyst (Graphene, VS_2, TiH_2@Gr, Ti@Gr, TiO_2@Gr, and LHEA) have been synthesized through mechanical ball-milling using Retsch PM400 ball-miller at 180 rpm for 24 hours with the ball to powder ratio 50:1 (by weight). All the handlings of samples were done inside N_2 filled glove box (MBRAUM MB10 compact). These catalyzed samples are known as MgH_2 catalyzed by graphene (MgH_2-Gr), MgH_2 catalyzed by VS_2 (MgH_2-VS_2), MgH_2 catalyzed by graphene templated Ti (MgH_2-Ti@Gr), MgH_2 catalyzed by graphene templated TiH_2 (MgH_2-TiH_2@Gr), MgH_2 catalyzed by graphene templated TiO_2 (MgH_2-TiO_2@Gr), and MgH_2 catalyzed by leached HEA (MgH_2-LACFMCN).

STRUCTURAL CHARACTERIZATION

The structural characteristics of the as-prepared samples have been examined by XRD studies using PANalytical Empyrean x-ray diffractometer with CuKα radiation (λ = 1.5415 Å). The XRD patterns of as-synthesized materials have been shown in Fig.1. All the XRD patterns matches well with their corresponding phase structures.

HYDROGEN SORPTION ANALYSIS

The hydrogen sorption measurements were performed by using an automated two-channel volumetric sieverts type apparatus (Advanced Materials Corporation Pittsburgh, USA). The temperature programmed desorption (TPD) were carried out at a heating rate of 5ºC/min and shown in Fig. 2. The onset desorption temperatures of as-prepared materials MgH_2-Gr, MgH_2-VS_2, MgH_2-Ti@Gr, MgH_2-TiH_2@Gr, MgH_2-TiO_2@Gr, and MgH_2-LACFMCN are ~301 ^{o}C, ~290 ^{o}C, ~257 ^{o}C, ~231 ^{o}C, ~240 ^{o}C, ~340 ^{o}C, and it desorbs ~4.63 wt%, ~6.48 wt%, ~6.94 wt%, ~6.55 wt%, ~5.73 wt%, ~6.79 wt% respectively. The pristine MgH_2 releases 7.12 wt% of hydrogen at ~ 420 ^{o}C (Fig. 2(a)). This shows the onset desorption temperature of MgH_2-TiH_2@Gr more lower than MgH_2-LACFMCN and other catalyzed samples. To check the stability and reversibility of catalyzed and uncatalyzed MgH_2, the rehydrogenation kinetics was carried out at 300 ^{o}C under 15 atm hydrogen pressures as shown in Fig. 3. As can be seen, the MgH_2-LACFMCN has rapid rehydrogenation kinetics and sustains more storage capacity than other catalyzed samples. After that rehydrogenated samples were dehydrogenated at 300 ^{o}C under 1 atm hydrogen pressure. It can be seen clearly that MgH_2-LACFMCN has strong enough dehydrogenation kinetics than other catalyzed samples. MgH_2-LACFMCN also shows the lower activation energy than other catalyzed MgH_2.

CONCLUSIONS

The catalytic effect of graphene, VS_2, TiH_2@Gr, Ti@Gr, TiO_2@Gr, and leached HEA were evaluated and compared. Based on de/re-hydrogenation study leached HEA was found to be the optimum catalyst as leached HEA catalyzed MgH_2 has the onset dehydrogenation temperature of ~340 ^{o}C. The superior catalytic activity of leached HEA also persists in de/re-hydrogenation kinetics. Moreover, the change in enthalpy of MgH_2-TiH_2@Gr is ~2.12 kJ/mol lower than pristine MgH_2. There is slight decrease (0.1 wt%) in hydrogen storage capacity of MgH_2-LACFMCN up to 3 cycles and then capacity remains constant up to 25 cycles.

ACKNOWLEDGMENTS

This work is dedicated to Prof. Onkar Nath Srivastava who passed away on April 24, 2021. Financial support as CSIR-SRF (Award No. 09/013(0872)/2019-EMR-I) from Council of Scientific and Industrial Research (CSIR) New Delhi, India is thankfully acknowledged.

REFERENCES

1. Bhatnagar, A. *et al.* Fe3O4@graphene as a superior catalyst for hydrogen de/absorption from/in MgH2/Mg. *Journal of Materials Chemistry A* 4, 14761–14772 (2016).
2. Hao, S. & Sholl, D. S. Effect of TiH2–Induced Strain on Thermodynamics of Hydrogen Release from MgH2. *The Journal of Physical Chemistry C* 116, 2045–2050 (2012).
3. Huen, P., Paskevicius, M., Richter, B., Ravnsbæk, D. B. & Jensen, T. R. Hydrogen Storage Stability of Nanoconfined MgH2 upon Cycling. *Inorganics* 5, (2017).
4. Zhang, X. *et al.* A novel complex oxide TiVO3.5 as a highly active catalytic precursor for improving the hydrogen storage properties of MgH2. *International Journal of Hydrogen Energy* 43, 23327–23335 (2018).

5. Jangir, M. *et al.* Catalytic effect of TiF4 in improving hydrogen storage properties of MgH2. *International Journal of Hydrogen Energy* 41, 14178–14183 (2016).
6. Kwon, S. N., Baek, S. H., Mumm, D. R., Hong, S. H. & Song, M. Y. Enhancement of the hydrogen storage characteristics of Mg by reactive mechanical grinding with Ni, Fe and Ti. *International Journal of Hydrogen Energy* 33, 4586–4592 (2008).
7. Liu, G. *et al.* Excellent catalytic effects of highly crumpled graphene nanosheets on hydrogenation/dehydrogenation of magnesium hydride. *Nanoscale* 5, 1074–1081 (2013).
8. Liu, G., Wang, Y., Jiao, L. & Yuan, H. Understanding the role of few-layer graphene nanosheets in enhancing the hydrogen sorption kinetics of magnesium hydride. *ACS Applied Materials and Interfaces* 6, 11038–11046 (2014).
9. Marcano, D. C. *et al.* Improved Synthesis of Graphene Oxide. *ACS Nano* 4, 4806–4814 (2010).
10. Verma, S. K. *et al.* Multiple improvements of hydrogen sorption and their mechanism for MgH2 catalyzed through TiH2@Gr. *International Journal of Hydrogen Energy* 45, 19516–19530 (2020).

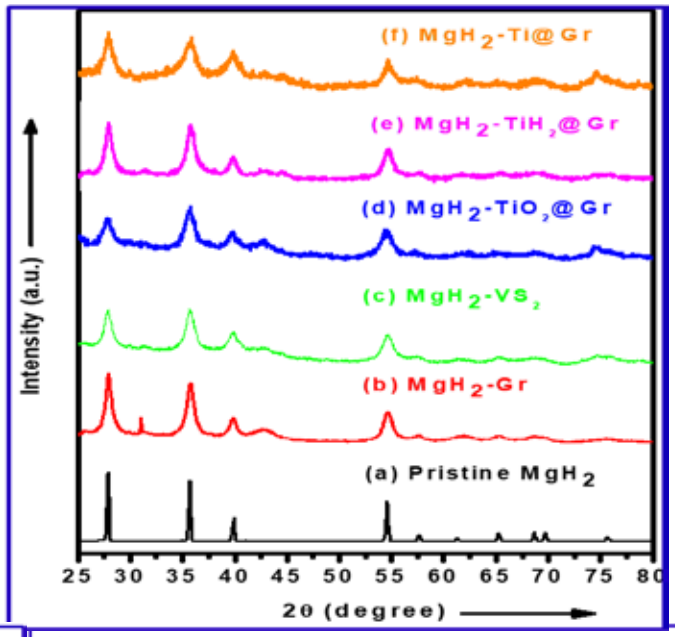


Fig.1: XRD patterns of (a) pristine MgH2, (b) MgH2-Gr, (c) MgH2-VS2, (d) MgH2-TiO2@Gr, (e) MgH2-TiH2@Gr, and (f) MgH2-Ti@Gr.

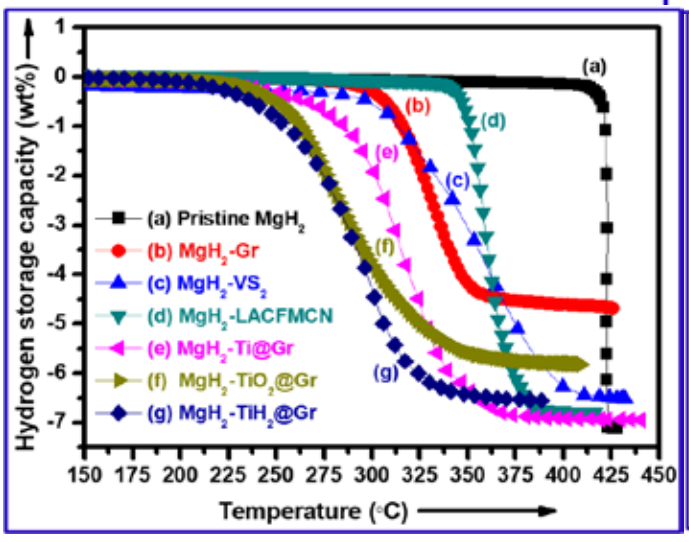


Fig. 2: TPD plots of catalyzed and uncatalyzed MgH_2.

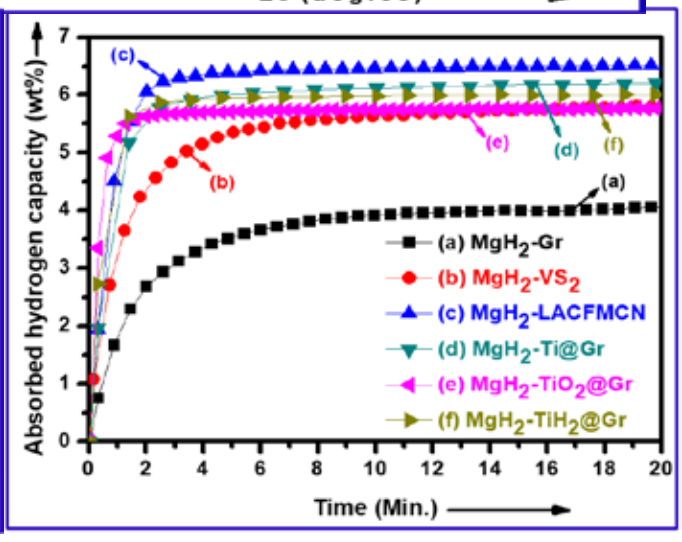


Fig. 3: Rehydrogenation kinetics of pristine and catalyzed MgH_2 measured at 300°C under 15 atm H_2 pressure.

WHEC-2022
23rd World Hydrogen Energy Conference
June 26-30, 2022 - Istanbul

#300

PERMEABILITY OF A DEFORMABLE METAL HYDRIDE BED DURING HYDROGEN ABSORPTION

[1,2*] *Dmitry Dunikov*, [1,2] *Dmitry Blinov*
[1]Joint Institute for High Temperatures of the Russian Academy of Sciences, Laboratory for Hydrogen Energy Technologies, 125412 Izhorskaya st. 13 bld. 2, Moscow, Russia
[2] National Research University "Moscow Power Engineering Institute", 111250 Krasnokazarmennaya 14, Moscow, Russia

*Corresponding author e-mail: ddo@mail.ru

ABSTRACT

Permeability of a metal hydride bed during hydrogen absorption is experimentally investigated by filtration of a H_2(10%)/CH_4 mixture through the bed (1 kg $LaNi_{4.8}Mn_{0.3}Fe_{0.1}$). Deformation of the bed due to swelling of the particles at absorption causes significant changes of the bed permeability, it decreases from 0.16 μm^2 at the start of the absorption to 0.031 μm^2 at C = 1.12%wt. The effect can be contributed to decrease of the bed porosity at absorption.

Keywords: metal hydride, AB_5, permeability, deformable bed

INTRODUCTION

Metal hydrides (MH) are used for safe and compact hydrogen storage, purification, compression, thermal storage and other applications. Successful results are mostly obtained at laboratory prototype scale levels and scale up issues should be resolved to introduce metal hydrides into commercial market [1]. At scale up, non-uniformities of MH beds and variability of their properties come to play. Due to absorption of hydrogen, a powder material swells and shrinks in a container, which is referred to as the hydride breathing, causing severe mechanical stresses [2] and change of the bed structure, e.g. a fill density could vary in 15% along the bed [3]. In addition, the bed porosity decreases with absorption and increases with desorption [4], and cycling also affects the porosity [4-6]. Generally, the bed breathing is not taken into account, Mellouli et al. have performed investigation of a deformable MH bed and found no significant effect of the volume variation on the heat and mass transfer [7]. By the Kozeny-Carman equation the bed permeability is the function of the mean particle size and porosity, thus deformation of the metal hydride bed should have an effect on the bed properties. The bed permeability is essential for flow-through (continuous) reactors used for hydrogen purification, since it directly affects the hydraulic resistance of the reactor and thus the efficiency. Thus, investigation of permeability of deformable metal hydride bed is essential for understanding of energy efficiency and predictability of operation of metal hydride reactors and economic viability of metal hydride technologies. In the present paper, we present results of permeability measurement during hydrogen extraction from a H_2/CH_4 mixture in a flow-through reactor.

EXPERIMENT

Flow-through type reactor RSP-8e [8] is used for experiments (Fig. 1). A 399 mm reaction chamber is made from 40x2 mm and 18x1 mm coaxial steel tubes and filled with 1 kg of $LaNi_{4.8}Mn_{0.3}Fe_{0.1}$ intermetallic alloy. The reactor is cooled by silicon oil CAS: 63148-62-9 from a Julabo FP45-HE thermostat. Gases are provided from cylinders (H_2, H_2/CH_4 mixture, N_2 and He for purge). Measurement and control: gas flows by Bronkhorst EL-FLOW Select mass flow meters/controllers (FR); outlet gas composition by AG-0012 thermal conductivity gas analyzer (GA); pressure by Aplisens pressure transmitters model PC28; temperature by thin film platinum sensors Heraeus M422, 1 kΩ. The test bench has connections to a vacuum system and an automatic control system using LabView software.

RESULTS AND DISCUSSION

A mixture of 10% H_2 and 90% CH_4 (90%) was filtered through the MH bed at inlet pressure 0.95 MPa. At absorption the thermostat temperature was set to 0°C. Hydrogen absorption was divided into two stages: at the start, the reactor was charged up to almost half of its hydrogen capacity, then the reaction was stopped, the reactor was heated to ambient temperature for 12 hours, and then again cooled and charged up to full capacity. The set point for outlet gas flow was 2 st.L/min, and the flow controller maintained it quite well during the first stage and gas flow was almost constant, while outlet pressure decreased from 0.80 to 0.45 MPa. The thermal relaxation by heating of the reactor to ambient temperature has made the bed less permeable to hydrogen. Outlet pressure immediately dropped from 0.45

to 0.39 MPa, and outlet flow controller could not maintain gas flow at 2 st.L/min no more. The absorption steadily slowed down and stopped at outlet pressure 0.27 MPa, when the gas analyzer indicated a hydrogen breakthrough.

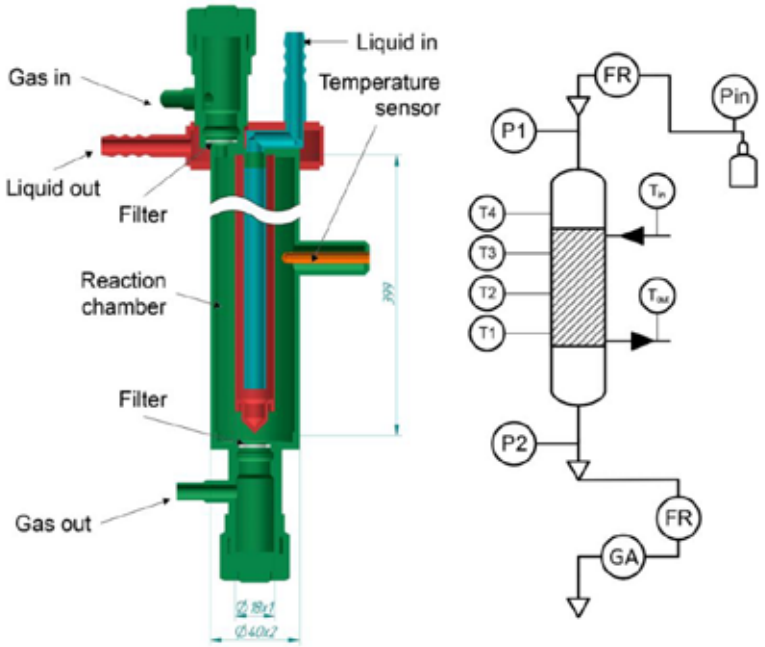


Fig. 1. Metal hydride reactor PSP-8e (left): gas part is green, liquid heat exchanger is blue (inlet) and red (outled), themperature sensor is orange, filters are white. Simplified scheme of experiments (right): *FR* – mass flow meters/controllers; *GA* - thermal conductivity gas analyzer; *P* – pressure gauges; *T* – temperature sensors

The permeability was estimated by standards procedure following the ASTM D6539 Standard:

$$k = 2\mu q \frac{p_{ST}}{(p_{in}^2 - p_{out}^2)} \frac{T}{T_{ST}} \frac{h}{A} \quad (1)$$

where μ is dynamic viscosity, h is the height and A is the cross-section of the metal hydride bed, p_{ST} and T_{ST} are standard pressure and temperature at which the flow meter is calibrated (1 bar and 0°C). We use an "effective" height L_{eff} = 36.4 cm calculated on the base of the average fill density of the MH bed of ρ_{MH} =3.6 g/cm^3 [3], the MH mass 1 kg and the cross-section of A = 7.63 cm^2. Gas properties were calculated using REFPROP. Viscosity of H_2/CH_4 mixture varies between 10.2 μPa·s (90% CH_4 at 1 bar and 0°C) and 10.7 μPa·s (100% CH_4 at 10 bar and 20°C), and we use 10.4 μPa·s in our calculation. The mixture mass flow is the average between q_{in} and q_{out}. Calculation uncertainties: for L_{eff} due to bed breathing is ca. 10%, for q is 10%, for μ is 3%, for A is 5%, and uncertainties for other variables are negligibly smaller. Thus, the overall uncertainty for k is within 15%.

Results for the permeability of the metal hydride bed during absorption of hydrogen are in Fig. 2. At the start of the absorption the bed permeability is 0.16 μm^2, and it drops down to 0.031 μm^2 at C= 1.12%wt. Possible change of L_{eff} due to expansion of the bed has a little influence on permeability: assuming the height enlargement of 10%, k is 0.033 μm^2 at the end of absorption. Thus, the fivefold change of permeability at hydrogenation cannot be contributed to any measurement uncertainty and is the result of the change of porosity and particle size at absorption.

Similar behavior is observed for the permeability of coal mass, which is influenced by stress, gas pressure, swelling deformation induced by methane adsorption, and shrinkage deformation caused by methane desorption [9]. When the amount of adsorption is high the permeability reduces exponentially with sorption-induced strain [10].

On the first glance, our results oppose [7], in which no significant influence of the bed deformation on heat and mass transfer was found. Nevertheless, there is no contradiction. By the van't Hoff equation the equilibrium pressure is exponentially connected with the inverse temperature, therefore a pressure variation has a little influence on the distribution of temperature over the MH bed and consequently on heat transfer. Variations of pressure over a thin MH bed only slightly affect a reactor kinetic performance. However, for a thick MH bed the pressure drop could be comparable with the inlet pressure, causing a significant impact on the performance, especially for flow-through reactors.

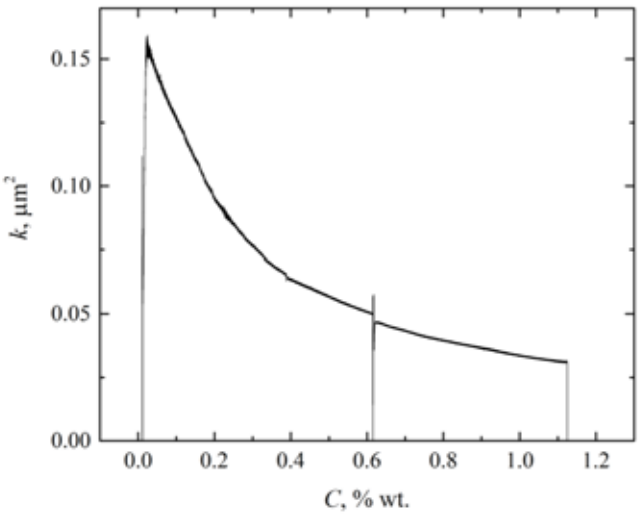


Fig. 2. Permeability of the MH bed

CONCLUSIONS

Deformation of the metal hydride bed due to swelling of the particles at absorption causes significant changes of the bed permeability. In the experiment on filtration of the H_2(10%)/CH_4 mixture through the MH bed of1 kg $LaNi_{4.8}Mn_{0.3}Fe_{0.1}$, the permeability has decreased from 0.16 μm² at the start of the absorption to 0.031 μm² at *C*= 1.12%wt. The effect can be contributed to decrease of the bed porosity at absorption.

REFERENCES

1. Muthukumar P, Kumar A, Raju NN, Malleswararao K and Rahman MM. 2018. A critical review on design aspects and developmental status of metal hydride based thermal machines. International Journal of Hydrogen Energy. 43: 17753-79
2. Salque B, Chaise A, Iosub V, Gillia O, Charlas B, Dupuis C and Guenoux L. 2015. Measure of the hydride breathing while cyclically absorbing and desorbing hydrogen. Journal of Alloys and Compounds. 645, Supplement 1: S353-S6
3. Borzenko VI, Romanov IA, Dunikov DO and Kazakov AN. 2019. Hydrogen sorption properties of metal hydride beds: Effect of internal stresses caused by reactor geometry. International Journal of Hydrogen Energy. 44: 6086-92
4. Charlas B, Gillia O, Doremus P and Imbault D. 2012. Experimental investigation of the swelling/shrinkage of a hydride bed in a cell during hydrogen absorption/desorption cycles. International Journal of Hydrogen Energy. 37: 16031-41
5. Matsushita M, Monde M and Mitsutake Y. 2013. Experimental formula for estimating porosity in a metal hydride packed bed. International Journal of Hydrogen Energy. 38: 7056-64
6. Matsushita M, Tajima I, Abe M and Tokuyama H. 2019. Experimental study of porosity and effective thermal conductivity in packed bed of nano-structured FeTi for usage in hydrogen storage tanks. International Journal of Hydrogen Energy. 44: 23239-48
7. Mellouli S, Askri F, Dhaou H, Jemni A and Ben Nasrallah S. 2016. A study of the thermal behavior of a deformable metal-hydride bed. International Journal of Hydrogen Energy. 41: 1711-24
8. Dunikov D, Borzenko V, Blinov D, Kazakov A, Lin CY, Wu SY and Chu CY. 2016. Biohydrogen purification using metal hydride technologies. International Journal of Hydrogen Energy. 41: 21787-94
9. Kong X, Wang E, Liu Q, Li Z, Li D, Cao Z and Niu Y. 2017. Dynamic permeability and porosity evolution of coal seam rich in CBM based on the flow-solid coupling theory. Journal of Natural Gas Science and Engineering. 40: 61-71
10. Lin W and Kovscek AR. 2014. Gas Sorption and the Consequent Volumetric and Permeability Change of Coal II: Numerical Modeling. Transport in Porous Media. 105: 23-42

WHEC-2022
23rd World Hydrogen Energy Conference
June 26-30, 2022 - Istanbul

#301

APPLICATION OF MISCHMETAL BASED LOW PRESSURE METAL HYDRIDES FOR SOLAR ENERGY STORAGE

* *K. Sarath Babu, E. Anil Kumar*
Department of Mechanical Engineering, Indian Institute of Technology Tirupati, 517506, Tirupati, India

*Corresponding author e-mail: me18d001@iittp.ac.in

ABSTRACT

Efficient utilization of solar energy reduces the carbon footprints in the atmosphere. The intermittent nature of solar energy requires efficient energy storage systems. Solar energy available at low temperature (<120°C) find application in many domestic devices. In the present study, mischmetal based metal hydrides are selected to store solar energy as these hydrides are operated at low temperature and low pressures. Pressure concentration isotherms (PCIs) of mischmetal based hydrides namely, $MmNi_{4.2}Al_{0.8}$, $MmNi_4Al$ and $MmNi_{3.9}Co_{0.5}Al_{0.6}$ are measured. The thermodynamic properties such as enthalpy and entropy are evaluated from van't Hoff plot. The suitability of these materials for developing an absorption thermal energy storage (ATES) system to store solar thermal energy is studied. The ATES system is thermodynamically analysed to evaluate the performance parameters such as COP and energy storage density (ESD).

Keywords: Solar energy, Energy storage, Mischmetal, Metal hydrides

INTRODUCTION

Thermal energy storage (TES) system is a key for efficient utilization of solar energy for low temperature applications. The unavailability of solar energy during nighttime and cloudy days urges the researchers to develop energy storage systems. Metal hydride based thermal energy storage systems have become promising option due to their reversible hydrogen absorption and long-term energy storage [1]. Besides lanthanum and zirconium-based hydrides, mischmetal based hydrides are very promising option for low temperature applications due to low operating pressure and availability at low price. Sharma et al studied performance of heat transformer that upgrades the heat energy from 140°C to 180°C by using lanthanum-based hydrides [2]. Recently, Sarath babu et al estimated the maximum possible energy storage efficiency of Mg-50wt% $LaNi_5$ that can store heat energy around 350°C [3]. The same group has studied the TES system based on Sn substituted lanthanum-based metal hydrides which stored energy at temperature above 100°C [4]. Malleswararao et al developed a 3D model to predict the performance of the coupled hydride beds for energy storage around 300°C [5]. It is noticed that studies on energy storage systems that stores solar energy around 100°C are very few. Also, the operating pressures of above TES systems are high which causes the more parasitic losses [6]. Therefore, low-pressure metal hydrides need to be chosen to efficiently store solar energy around 100°C. In the present study, mischmetal based metal hydrides are selected as energy storage hydrides. To study the performance of energy storage system, thermodynamic properties need to be evaluated by measuring PCIs during hydrogen absorption and desorption.

MEASUREMENT OF PRESSURE CONCENTRATION ISOTHEMS (PCIS)

PCI represents the relation between the amount of hydrogen absorbed and the equilibrium pressure at isothermal condition. The PCIs are measured by using seteram's PCT Pro which works on the sievert's principle. The PCI curves show the sloped plateau in the plateau region. The maximum hydrogen absorption capacity of $MmNi_{4.2}Al_{0.8}$, $MmNi_4Al$ and $MmNi_{3.9}Co_{0.5}Al_{0.6}$ is 1.31, 1.31 and 1.29wt%, respectively. The absorption and desorption PCIs compared at 20 and 80°C as shown in Figs. 1a and 1b, respectively. The shape of the PCI curve is similar for all selected metal hydrides representing α, α+β and β region. The absorption capacity is almost same for $MmNi_{4.2}Al_{0.8}$ and $MmNi_4Al$ at 20°C as well at 80°C. But the absorption capacity of $MmNi_{3.9}Co_{0.5}Al_{0.6}$ is slightly lower than that of other two hydrides at 20°C and slightly higher than that of other two hydrides at 80°C. The plateau pressure is higher for $MmNi_{4.2}Al_{0.8}$ than the that of other two hydrides. It is concluded that plateau pressure decreased with the increase in Al content in the hydride. The plateau pressure still reduced with multi element substitution.

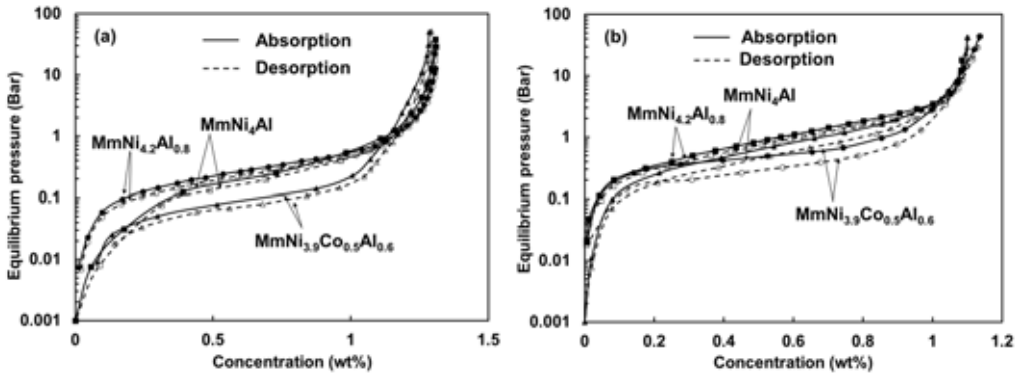


Fig. 1. Comparison of PCIs at (a) 20°C and (b) 80°C

Estimation of thermodynamic properties

Thermodynamic properties such as enthalpy and entropy during hydrogen absorption and desorption are evaluated by constructing van't Hoff plot. The van't Hoff plots of mischmetal based metal hydrides are given in Fig. 2. The slope of the linear line gives reaction enthalpy, and the intercept gives reaction entropy.

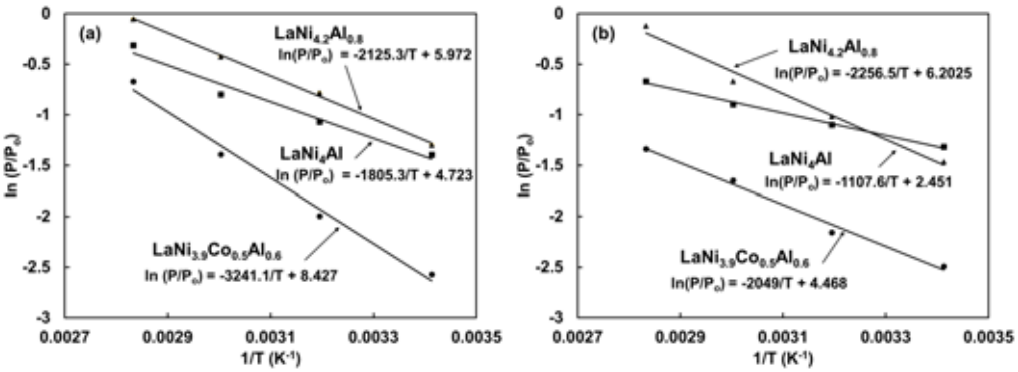


Fig. 2. Van't Hoff plot of mischmetal based hydrides during (a) hydrogen absorption and (b) hydrogen desorption

Absorption system for solar energy storage

An ATES device is proposed to store solar energy. A metal hydride reactor and an H_2 reservoir are included in the absorption system. The following is a description of the solar energy storage and recovery process. The metal hydride bed is powered by solar energy collected during the day or on sunny days. Due to the supply of solar energy, hydrogen gas is desorbed from the metal hydride bed. The gas that has been desorbed is stored in the H_2 reservoir. Whenever energy is needed during the night or on cloudy days, the H_2 reservoir's stored gas is delivered to a metal hydride reactor for hydrogen absorption. Thermal energy is released when hydrogen is absorbed in a metal hydride. The schematic of absorption system based on mischmetal based hydrides is shown in Fig. 3.

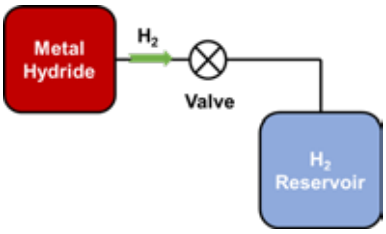


Fig.3. Schematic absorption thermal energy storage system

Thermodynamic analysis of absorption system

The proposed absorption system for solar energy storage is analysed thermodynamically. The temperature of energy storage is taken as 100°C. The temperature of energy recovery will be obtained by knowing the equilibrium pressure during hydrogen absorption in metal hydride bed. Therefore, the metal hydride bed is operated between energy storage temperature and recovery temperature. The quantities of energy stored and recovered is calculated using the formulae given in author's previous article [4]. The COP and ESD of the ATES system are estimated from the thermodynamic properties, and these values are given in Table 1.

RESULTS AND DISCUSSION

The ATES is generally operated in the plateau region. Therefore, the absorption capacity of metal hydride in the plateau region is taken as 70% of its maximum absorption capacity. The calculated values of performance parameters of ATES system are given in Table 1. It is noticed that the temperature of energy recovery is lower that of energy storage. This is because the absorption equilibrium pressure during energy recovery is lower than that of desorption equilibrium pressure during energy storage. The energy recovery temperature decreases with increase in Al content. The recovery temperature is even low for multi element substitution due lower absorption equilibrium pressure. COP of ATES system based on $MmNi_{4.2}Al_{0.8}$ is less than 1 whereas COP of ATES system based on other two hydrides is greater than 1. This is because the amount of energy recovered is less than the amount of energy stored for $MmNi_{4.2}Al_{0.8}$. In case of other two hydrides, the amount of energy recovered is higher than the amount of energy stored. The maximum and minimum ESD is observed for $MmNi_{3.9}Co_{0.5}Al_{0.6}$ and $MmNi_4Al$, respectively. Hence, a more compact ATES system can be developed using $MmNi_{3.9}Co_{0.5}Al_{0.6}$.

Table 1. Performance parameters of ATES

Metal Hydride	T_S (°C)	T_R (°C)	Q_S (kJ)	Q_R (kJ)	COP	ESD (kJ/kg)
$MmNi_{4.2}Al_{0.8}$	100	64	228.270	211.659	0.92	103.593
$MmNi_4Al$	100	40	159.835	208.343	1.30	72.572
$MmNi_{3.9}Co_{0.5}Al_{0.6}$	100	26	255.147	342.537	1.34	113.894

CONCLUSIONS

The use of low-pressure hydrides for solar energy storage is explored in the present study. PCIs of three different Al substituted mischmetal based hydrides are measured. The maximum absorption capacity of $MmNi_{4.2}Al_{0.8}$, $MnNi_4Al$ and $MmNi_{3.9}Co_{0.5}Al_{0.6}$ is 1.307, 1.307 and 1.285wt%, respectively. ATES system is proposed for solar energy storage at 100°C. Thermodynamic analysis shows that the highest COP and ESD of 1.34 and 113.894 kJ/kg, respectively is obtained by using $MmNi_{3.9}Co_{0.5}Al_{0.6}$.

ACKNOWLEDGEMENT

The authors thank Department of Science & Technology, Govt. of India for financial aid (DST/TMD/MES/2k16/50).

REFERENCES

1. Choudhary MS, Sharma VK and Paswan M. 2021. Metal hydrides for thermochemical energy storage applications. International Journal of Energy Research 45:14465-14492.
2. Sharma VK and Emadabathuni AK. 2018. Thermodynamic simulation of hydrogen based solid sorption heat transformer. International Journal of Thermal Sciences 125:74-80.
3. Kaki SB and Emadabathuni AK. 2021. Thermodynamic characterization of Mg-50wt% $LaNi_5$ composite hydride for thermochemical energy storage application. Energy Storage 3:1-16.
4. Kaki SB and Emadabathuni AK. 2022. Thermodynamic analysis of thermochemical energy storage system based on AB5 type hydride pairs. Materials Today: Proceedings 49:2042-2047.
5. Malleswararao K, Aswin N, Murthy SS and Dutta P. 2020. Performance prediction of a coupled metal hydride based thermal energy storage system. International Journal of Hydrogen Energy 45:16239-16253.
6. Sandrock G. 1999. A panoramic overview of hydrogen storage alloys from a gas reaction point of view. Journal of Alloys and Compounds 293-295:877-888.

WHEC-2022
23rd World Hydrogen Energy Conference
June 26-30, 2022 - Istanbul

#303

STUDY OF THE EFFECT OF Zr_3Fe ADDITION ON HYDROGEN STORAGE BEHAVIOR OF Ti_2CrV ALLOYS

[1,2*] *Daniela Bellon Monsalve,* [1] *Jacques Huot,* [2] *Alejandro David Martínez Amariz*
[1] Hydrogen Research Institute, Université Du Québec à Trois-Rivières, QC, G9A 5H7, Canada
[2] Universidad de Santander, Facultad de Ingenierías y Tecnologías, Instituto de Investigación Xerira, Bucaramanga, Colombia

*Corresponding author e-mail: daniela.bellon@irh.ca

ABSTRACT

The aim of this study was to improve the first hydrogenation behavior of Ti_2CrV alloy, with the Zr_3Fe addition. The Ti_2CrV + X% Zr_3Fe (X= 0, 2, 4, 6, 8, and 10) system were studied. The compositions were synthesized by arc-melting. The powder was characterized by scanning electron microscopy and x-ray diffraction. In the as-cast samples, microstructure reveals a single bcc structure for Ti_2CrV, and the presence of a Zr-rich area for the samples with Zr_3Fe addition. The hydride fcc phase for 6%, 8% and 10% addition of Zr_3Fe was confirmed by x-ray diffraction. We found that when at least 6% of Zr_3Fe is added to the alloy, the first hydrogenation is improved not only in terms of hydrogen storage capacity but also kinetics. The sample with 6% of Zr_3Fe absorbs its maximum capacity of 4.2 wt.% in approximately 8 minutes at room temperature without any heat treatment.

Keywords: Hydrogen Storage, TiCrV system, bcc alloy

INTRODUCTION

Hydrogen is an energy carrier; thus, it must be produced. Also, except for certain processes in the petrochemical industry where H_2 is used directly after its production, the hydrogen economy requires a storage medium after production before final use. This means that, in the transition from a fossil economy to a hydrogen economy, the challenges associated with hydrogen production and storage must be solved [1]. Various production methods have been developed and are very well established, such as natural gas reforming, electrolysis, biomass gasification, among others. Referring to storage, several methods have been studied for many decades to develop a safe, reliable, and compact storage system with an acceptable cost. Three well-known systems stand out: i) Compressed gas in high-pressure tanks, which is the method used in most applications. However, these are bulky due to hydrogen's low volumetric density; ii) Liquid hydrogen, where a temperature of approximately -252 °C is needed [2]; and, iii) Solid-state storage system, where metal hydrides, complex hydrides, high specific surface materials, microporous materials, among others, are being considered. In to the case of metal hydrides, these have been attractive materials for hydrogen storage, due to their high volumetric densities, safety, low cost, no toxicity emission, good absorption, and desorption capacities [1], [3], [4]. However, their applicability is limited by their low gravimetric hydrogen density, absorption kinetics, cycle life, non-reversibility, and activation procedures. It is important to mention that metal hydrides are not restricted to hydrogen storage only, their use are extended to heat storage, hydrogen generation, or as a negative electrode in the Ni-MH batteries [5].

Ti-Cr-V alloys have been investigated extensively due to their high hydrogen storage capacity at moderate working temperatures and under low hydrogen pressure [6], [7]. However, the reversible capacity is lower due to the low plateau pressure of the monohydride and shows a long incubation time during their first hydrogenation [8], [9]. In the present study, Ti_2CrV alloy is selected because of the high theoretical hydrogen absorption capacity. However, in order to get activated, this alloy needs to be heated till 400 °C. On the other hand, the Zr-rich compound is well known for its hydrogen absorption capability [10]. The effect of Zr_3Fe on hydrogen storage characteristics of hydrogen storage alloys has been studied by [10]–[14]. In the case of Zr_3Fe it has an absorption capacity of 2.0 wt.% at room temperature (RT) under low pressure and would be a candidate for stationary hydrogen [11]. Nevertheless, some issues need to be addressed to find a good composition that can meet the DOE's requirements for metal hydride applications.

The present research aims to investigate the effect on the crystal structure, microstructure and first hydrogenation behavior of adding Zr_3Fe on the Ti_2CrV alloy. In this work, the composition Ti_2CrV + X% Zr_3Fe (X=0, 2, 4, 6, 8 and 10) is investigated.

MATERIALS AND METHODS

The synthesis was done by arc-melting under argon atmosphere. All the elements Ti (99.95%), Cr (99%), V (99.7%), Zr (99.5%), and Fe (99.99%) were purchased from Alpha Aesar and used without further purification. During the melting process, each pellet was turned over and remelted four times to ensure homogeneity.

The material characterization was carried out using different techniques. To study the morphology of the samples, Scanning Electron Microscope (SEM) was performed. To probe the chemical composition of the alloys the Energy Dispersive Spectroscopy (EDS) was used. To study the crystal structure of the alloys, X-ray diffraction (XRD) measurement was carried out. The XRD patterns were analyzed by the Rietveld method using TOPAS software to determine the phase abundance, lattice parameter, microstrain, and crystallite size of the alloys.

In hydrogenation measurements, the synthesized alloys were hand crushed using a steel mortar in Ar atmosphere. Around 600 mg of the material was filled in a reactor cell to measure the hydrogen sorption properties using a homemade Sievert-type apparatus. The activation procedure of the sample Ti2CrV involved heating the alloy at 400 °C under vacuum, and a pressure of 2000 kPa. The first hydrogenation study of the other alloys was done at RT and a hydrogen pressure of 2000 kPa, without any heating treatment.

RESULTS AND DISCUSSION

From the backscattered electron images obtained by SEM of the as-cast samples, we see that Ti_2CrV alloy has a single-phase structure. For Ti_2CrV + 2% Zr_3Fe and Ti_2CrV + 4% Zr_3Fe alloys, we observed that the internal structure consists of a matrix (grey phase), and a bright spots region. As this region is too small, we can not claim for a second phase. This bright contrast in the image comes from the Zr in the samples. For the alloys with 6%, 8% and 10% of Zr_3Fe the secondary phase (bright phase) is clear, and those alloys present a two-phase structure.

Figure 1 shows the activation curves at RT and 2000 kPa of hydrogen pressure, for the different compositions from 0 to 10% of Zr_3Fe. After 24 hours, the alloys with composition Ti_2CrV, Ti_2CrV + 2% Zr_3Fe, Ti_2CrV + 4% Zr_3Fe, and Ti_2CrV + 6% Zr_3Fe did not activate. However, the Ti_2CrV + 8% Zr_3Fe composition showed an incubation time of approximately 158 minutes and a maximum hydrogen storage capacity of 3.7 wt.%. One curious fact arises from the curve shown for composition with 8% Zr3Fe. The curve appears to have two different kinetics. Faster kinetics until reaching approximately an absorption capacity of 1.3 wt.%. After that 1.3 wt.%, the kinetic until reaching the maximum absorption capacity is slower. This behavior leads us to the question of how the two phases are working together in the activation process. This question will also be addressed as future work, but one possible explanation is that the Zr-rich phase allows a faster diffusion of hydrogen, and also it could be absorbing hydrogen. Composition Ti_2CrV + 10% Zr_3Fe showed an incubation time of 10 minutes and a maximum hydrogen storage capacity of 3.8 wt.%. We see that the addition of the 10% Zr_3Fe in the alloy not only improves the activation, but also reduces the incubation time and increases the hydrogen absorption capacity.

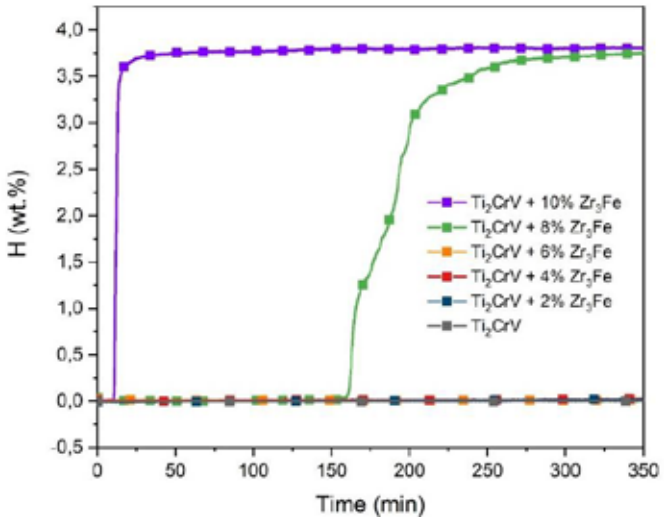
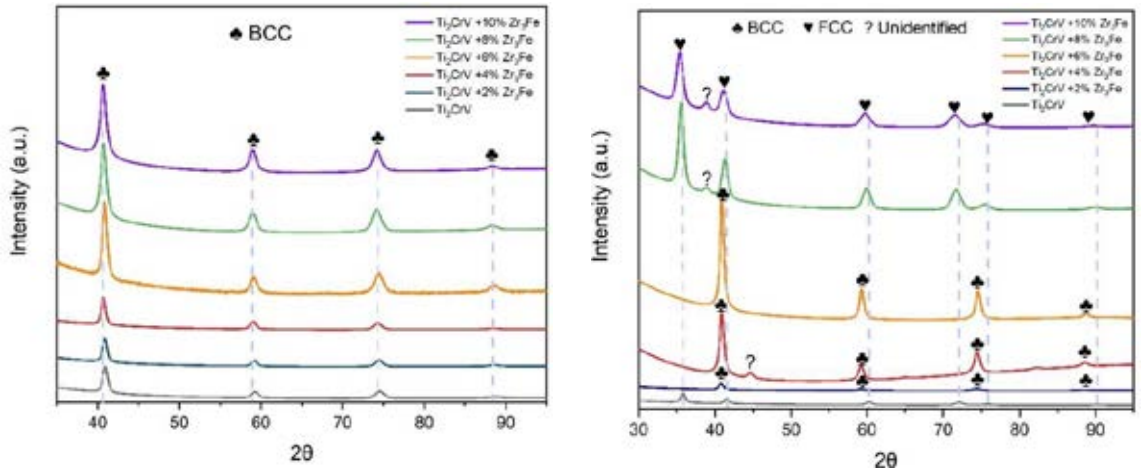


Fig. 1. First hydrogenation of Ti_2CrV +X% Zr_3Fe (X= 0, 2, 4, 6, 8, and 10) under 2000 kPa and at RT.

The XRD patterns of as-cast and first hydrogenation alloys are shown in Figure 2. From Figure 2(a) we observe that all the as-cast alloys present a BCC phase. By correlating the phases identified by SEM and EDS, it can be assumed that the matrix is BCC, however, the secondary phase (bright phase) was not identified in the pattern. One possible explanation as to why this secondary phase was not identified in the XRD, is that the phase could be present but buried in the background. However, for confirming the information, this specific phase will be synthesized and studied separately.

The XRD patterns of the activated samples are shown in Figure 2(b). The pattern of the Ti_2CrV alloy presented corresponds to its activation at 400 °C. The other alloys were activated at room temperature. From Figure 2(b) we

observe a full activation of the Ti_2CrV, Ti_2CrV +8% Zr_3Fe and Ti_2CrV +10% Zr_3Fe alloys. Those alloys changed their initial BCC structure to FCC structure. However, those alloys also showed a small peak that could not be identified. For the alloy with compositions of Ti_2CrV +4% Zr_3Fe and Ti_2CrV +6% Zr_3Fe that did not activate, they conserved the BCC crystal structure. Nevertheless, the Ti_2CrV +4% Zr_3Fe alloy showed a small unidentified peak.



(a) (b)

Fig. 2. X-ray diffraction patterns of Ti_2CrV + X% Zr_3Fe (X=0, 2, 4, 6, 8, 10) (a) as-cast alloys and (b) First hydrogenation alloys.

Table 1 presents the crystallographic parameters for the hydrogenated alloys. The alloys with 4% and 6% of Zr_3Fe did not activate, then, their lattice parameters are almost the same as the as-cast alloy. In reference to alloys with 8% and 10% of Zr_3Fe, the hydrogenation is complete, and we see an increase of the microstrain compared to the as-cast alloys.

Table 1. Crystallographic parameters of the activated alloys. The number in parenthesis is the uncertainty on the last significant digit.

Alloy	Rwp	Phase	a (Å)	V (Å^3)	Crystallite size (nm)	Microstrain (%)
Ti_2CrV	5.84	FCC	4.352 (1)	82.47 (7)	21.2 (1)	0.98 (5)
Ti_2CrV + 2% Zr_3Fe	7.81	BCC	3.1222 (1)	30.43 (4)	27.0 (3)	0.95 (7)
Ti_2CrV + 4% Zr_3Fe	1.52	BCC	3.1259 (6)	30.54 (1)	22.5 (5)	1.08 (2)
Ti_2CrV + 6% Zr_3Fe	3.54	BCC	3.1196 (4)	30.36 (1)	28.4 (8)	0.96 (2)
Ti_2CrV + 8% Zr_3Fe	2.85	FCC	4.3637 (6)	83.09 (3)	20.5 (5)	1.44 (2)
Ti_2CrV + 10% Zr_3Fe	3.39	FCC	4.364 (1)	83.11 (6)	17.4 (7)	1.77 (4)

CONCLUSIONS

The addition of 8% and 10% of Zr3Fe to the Ti2CrV alloy, seems to improve considerably the activation process, not only in terms of hydrogen storage capacity but also the kinetics. When the XRD patterns of as-cast alloys were analyzed and contrasted with the SEM results, the secondary phase (Zr-rich phase) was not identified in the patterns. For this reason, as future work this specific phase will be synthesized and studied separately. Finally, when the activation is analyzed deeper, a new question arises from the curve corresponding to the Ti2CrV + 8% Zr3Fe alloy. That is, how the two phases are working together in the activation process. This question will also be addressed in the final experiments as future work.

REFERENCES

[1] K. Benyelloul, L. Seddik, Y. Bouhadda, M. Bououdina, H. Aourag, and K. Khodja, “Effect of pressure on structural, elastic and mechanical properties of transition metal hydrides Mg7TMH16 (TM = Sc, Ti, V, Y, Zr and Nb): First-principles investigation,” *J. Phys. Chem. Solids*, vol. 111, no. May, pp. 229–237, 2017, doi: 10.1016/j.jpcs.2017.08.001.

[2] L. Schlapbach and a Züttel, “Hydrogen-storage materials for mobile applications.,” *Nature*, vol. 414, no. 6861, pp. 353–358, 2001, doi: 10.1038/35104634.

[3] M. M. Nygård, G. Ek, D. Karlsson, M. Sahlberg, M. H. Sørby, and B. C. Hauback, “Hydrogen storage in high-entropy alloys with varying degree of local lattice strain,” *Int. J. Hydrogen Energy*, vol. 44, no. 55, pp. 29140–29149, 2019, doi: 10.1016/j.ijhydene.2019.03.223.

[4] S. K. Chen, P. H. Lee, H. Lee, and H. T. Su, “Hydrogen storage of C14-CruFevMnwTixVyZrz alloys,” *Mater. Chem. Phys.*, vol. 210, pp. 336–347, 2018, doi: 10.1016/j.matchemphys.2017.08.008.

[5] P. Lv and J. Huot, “Hydrogenation improvement of TiFe by adding ZrMn2,” *Energy*, vol. 138, pp. 375–382, 2017, doi: 10.1016/j.energy.2017.07.072.
[6] V. Dixit and J. Huot, “Investigation of the microstructure, crystal structure and hydrogenation kinetics of Ti-V-Cr alloy with Zr addition,” *J. Alloys Compd.*, pp. 1115–1120, 2019, doi: 10.1016/j.jallcom.2019.01.292.
[7] A. Kamble, P. Sharma, and J. Huot, “Effect of addition of Zr, Ni, and Zr-Ni alloy on the hydrogen absorption of Body Centred Cubic 52Ti-12V-36Cr alloy,” *Int. J. Hydrogen Energy*, vol. 43, no. 15, pp. 7424–7429, 2018, doi: 10.1016/j.ijhydene.2018.02.106.
[8] H. C. Lin, K. M. Lin, K. C. Wu, H. H. Hsiung, and H. K. Tsai, “Cyclic hydrogen absorption-desorption characteristics of TiCrV and Ti0.8 Cr1.2 V alloys,” *Int. J. Hydrogen Energy*, vol. 32, no. 18, pp. 4966–4972, 2007, doi: 10.1016/j.ijhydene.2007.07.057.
[9] J. M. Abdul and L. H. Chown, “Influence of Fe on hydrogen storage properties of V-rich ternary alloys,” *Int. J. Hydrogen Energy*, vol. 41, no. 4, pp. 2781–2787, 2016, doi: 10.1016/j.ijhydene.2015.11.154.
[10] F. Stein, G. Sauthoff, and M. Palm, “Experimental determination of intermetallic phases, phase equilibria, and invariant reaction temperatures in the Fe-Zr system,” *J. Phase Equilibria*, vol. 23, no. 6, pp. 480–494, 2002, doi: 10.1361/105497102770331172.
[11] W. Liu, O. D. Feya, T. T. Debela, J. R. Hester, C. J. Webb, and E. M. A. Gray, “Experimental and computational modelling study of Ni substitution for Fe in Zr3Fe and its hydride,” *J. Alloys Compd.*, vol. 781, pp. 131–139, 2019, doi: 10.1016/j.jallcom.2018.12.054.
[12] B. O. Mukhamedov *et al.*, “Thermodynamic and physical properties of Zr 3 Fe and ZrFe 2 intermetallic compounds,” *Intermetallics*, vol. 109, no. July 2018, pp. 189–196, 2019, doi: 10.1016/j.intermet.2019.01.018.
[13] S. F. Matar, a. F. Al Alam, D. Gédéon, and N. Ouaini, “Changes in electronic, magnetic and bonding properties from Zr2FeH5 to Zr3FeH7 addressed from ab initio,” *Solid State Sci.*, vol. 25, pp. 55–62, 2013, doi: 10.1016/j.solidstatesciences.2013.08.002.
[14] I. Y. Zavaliy, R. V. Denys, R. Černý, I. V. KovaL’Chuck, G. Wiesinger, and G. Hilscher, “Hydrogen-induced changes in crystal structure and magnetic properties of the Zr3MOx (M = Fe, Co) phases,” *J. Alloys Compd.*, vol. 386, no. 1–2, pp. 26–34, 2005, doi: 10.1016/j.jallcom.2004.05.064.

WHEC-2022
23rd World Hydrogen Energy Conference
June 26-30, 2022 - Istanbul

#317

HYSTORIES PROJECT: TECHNICAL DEVELOPMENTS AND DEPLOYMENT OUTLOOKS FOR PURE HYDROGEN STORAGE IN DEPLETED FIELDS AND AQUIFERS

[1*] *Arnaud Réveillère, [2]Jan Michalski, [3]Bernd Löder, [4]Ceri Vincent, [5]Martin Wagner, [6]Jesús Simón, [7]Katarzyna Luboń*
[1]Geostock, 2, rue des Martinets 92500 Rueil-Malmaison, France
[2]Ludwig-Boelkow-Systemtechnik GmbH (LBST), Daimlerstr. 15, Ottobrunn 85521, Germany
[3]Montanuniversitaet Leoben, Franz Josef Strasse 18, Leoben 8700, Austria
[4]Co2geonet, 3 Av. Claude Guillemin, Orleans, France
[5]MicroPro GmbH, Magdeburger Str. 26b, Gommern 39245, Germany
[6]Foundation for the Development of New Hydrogen Technologies in Aragon (FHa), Parque Tecnológico Walqa
[7]MEERI PAS, Ul. Jozefa Wybickiego 7a, Krakow 31 261, Poland

*Corresponding author e-mail: arnaud.reveillere@geostock.fr

ABSTRACT

While storing pure hydrogen in salt caverns has been practiced since the 70s in Europe, pure hydrogen storage has not yet been carried out anywhere in depleted fields or aquifers. The Hystories project [1] is delivering technical developments applicable to a vast range of future aquifer or depleted field storage sites and is providing insights into underground hydrogen storage for decision makers in government and industry. It has started in January 2021, is gathering 24 European Companies, Universities or Research Institutes (as Partners or Third Parties), is supported by an advisory board composed of 13 large European companies and will have half of its results delivered by the time of the conference. Some results will be presented in detail during this WHEC. The present paper will complement them by giving an overall view on the technical gaps and improvements, and on the techno-economic insights for hydrogen subsurface storage.

Keywords: underground, storage, aquifer, depleted field

INTRODUCTION

Hystories project work is bringing subsurface technical developments for pure hydrogen storage in depleted fields or aquifers and is providing techno-economic insights on hydrogen underground storage deployment in the Europe-an energy system, as presented in Fig. 1 and detailed in the following sections.

Once these both parts will be finalized, major conclusion will be drawn.

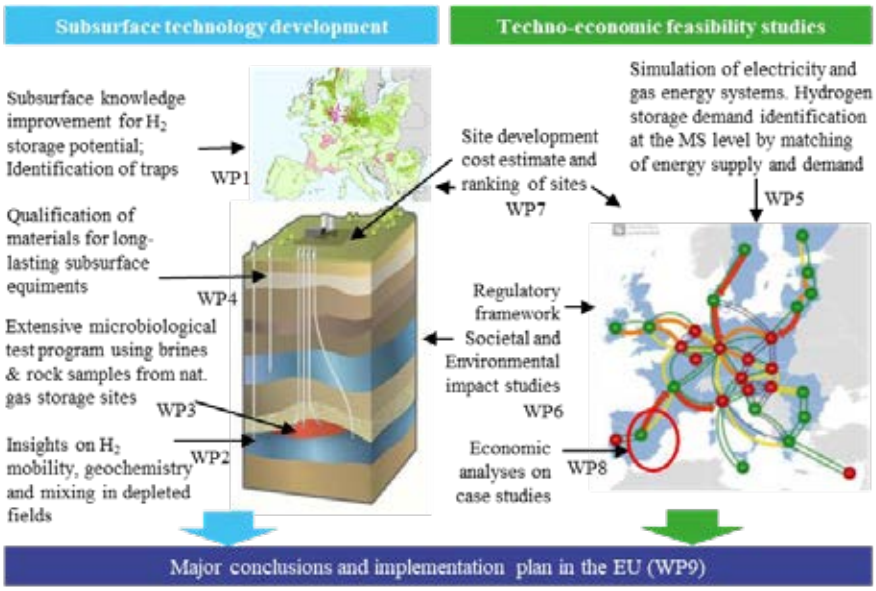


Figure 1. Overall workplan of the Hystories project

SUBSURFACE TECHNICAL FEASIBILITY STUDIES

Subsurface technical feasibility studies for a future hydrogen storage in depleted field or aquifer are site specific, as they are for natural gas and for other geological related activities. To provide the best possible insights to project developers of storage sites that are yet to be defined, different strategies have been applied for each of the technical challenges requiring development:

- Based on the experience in screening sites for developing new natural gas storages, scoring, and screening criteria have been proposed to support the selection of porous media storage site candidates for pure hydrogen storage [2]. 27 properties have been grouped into three categories: geological and reservoir engineering; geological context and surface environment. For each property, a criterion is proposed, and its importance is estimated regarding local impacts, the storage capacity (in Nm3) and the storage performance (in Nm3/h). This is used to advance a database of geological storage opportunities at the European scale by addition of data of specific relevance to geological storage of hydrogen.

Properties	Proposed criteria for H_2 Storage	Comments	Importance of the criteria for: N/A: not applicable 1: minor for scoring 2: major for scoring 3: exclusion criteria (screening)		
			Location	Capacity	Performance
Min depth to the top of the reservoir	500 m	Below typical grid pressure if above	N/A	2	1

Figure 2 One of the 27 proposed selection criteria from [2]

- To answer reservoir engineering questions such as effects of mixing, structural trapping for H_2, a high mobility gas, a workflow has been set to use results of the above-mentioned database and build synthetic models based on available properties. Estimates of the storage capacity and deliverability are made at a European scale.

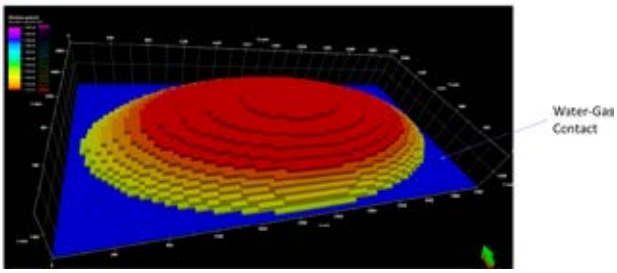


Figure 3 Synthetic dynamic model of a reservoir candidate used for hydrogen storage.

To determine expected microbial activity and impacts, seven different brines and rocks (cores or cuttings) from gas storage sites are being used in a large experimental microbiological investigation. The outcome of this extensive sampling and lab experimental program and data gathering from a wide range of relevant geological conditions is a rare opportunity to propose results across a large variety of possible conditions.

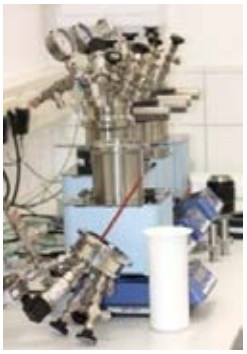


Figure 4 High pressure unit for microbial activity tests

- Determining what steel grade can be used for underground hydrogen storage is a question faced by technical developers of underground hydrogen storage today. Contrarily to hydrocarbons (not corrosive), hydrogen contact with steel creates risks of Hydrogen embrittlement. The project is investigating what material (steel grade) can be used for underground hydrogen storage under which conditions. To cover a diversity of reservoir conditions (temperature and pressure) and gas compositions, tests are done to investigate the mechanical response of several steel grades in reservoir conditions. Autoclave testing are done to observe possible cracking and corrosion attack on specimens, and the Hydrogen uptake in steel coupons is analysed by hot carrier gas extraction. Permeation tests are also conducted to test the effective Hydrogen diffusion in the steel.



Figure 5 Autoclave testing of the steel specimens. From [3]

TECHNO-ECONOMIC FEASIBILITY STUDIES

Techno-economic feasibility studies are providing insights to support a decision whether to proceed to pilot and large-scale demonstration projects. This work aims to inform decision makers in government and industry:

- Energy system modelling has been used to investigate the role of a widespread deployment of underground renewable hydrogen storage in EU-27 + UK in future scenarios across 2025-2050. The scenarios are based on several hypotheses on the hydrogen production (domestic vs. imports from non-

EU), storage technologies (salt caverns, porous media, aboveground technologies) and spatial distribution (centralized or distributed storage and production). Preliminary result show that the required long-term hydrogen storage capacities range between 40 to 700 TWhH2 in EU-27 and the UK, i.e., 1.2 to 25 MtH2. As an order of magnitude, assuming it is only done through salt caverns, and that 4000 tons of H2 can be stored per cavern, it is 300 to 6250 salt caverns. [4]

- An assessment of the regulatory framework for Hydrogen Underground Storage in Europe has been done, based on surveys throughout the industry and research institutes. Main barriers are identified, and a ranking of countries is proposed according to the status of underground hydrogen legislation [5].
- Depleted fields or aquifers, salt caverns and possibly other surface technologies will become competing solutions to meet a local storage demand. The cost of developing each of them requires finding the most competitive. Cost model of subsurface storage options have been developed to support these analyses [6].

CONCLUSIONS

Hystories has already brought technical developments to hydrogen storage in depleted fields or aquifers, notably by recommending criteria to select sites, by gathering the reservoir candidates in a GIS database and assessing their storage capacity, and by classifying the microbial activity in aquifers based on a large brine sampling and laboratory work. It has also brought insights to the decisionmakers by proposing a first storage demand estimation in each EU-27 member states, and by reviewing the legal framework throughout Europe. Last, it has built a cost model of the development of a new storage site to enable assessing whether underground storage can be competitive against other options.

ACKNOWLEDGEMENT

This work has been funded by the Hystories project. This project has received funding from the Fuel Cells and Hydrogen 2 Joint Undertaking under grant agreement No. 101007176. This Joint Undertaking receives support from the European Union's Horizon 2020 research and innovation programme and Hydrogen Europe and Hydrogen Europe Research.

REFERENCES

1. Grant Agreement nº 101007176. Project description and all public deliverables are available on www.hystories.eu
2. M. Bouteldja, T. Acosta, B. Carlier, A. Réveillère, H. Jannel, C. Fournier, Definition of Selection Criteria for a Hydrogen Storage Site in Depleted Fields or Aquifers. Hystories deliverable D1.1-0, 5 March 2021
3. B. Loder, Final protocol for material testing, Hystories deliverable D4.1, February 2021
4. J. Michalski, U. Bünger, J. Zerhusen, Expected techno-economic requirements for underground renewable hydrogen storage. Hystories D5.2-0, 31 March 2021
5. S. Martinez, J. Simón, 2021, Assessment of the Regulatory Framework, Hystories deliverable D6.1-1
6. B. Bourgeois, L. Duclercq, H. Jannel, A. Réveillère, Life Cycle Cost Assessment of an underground storage site. Hystories Hystories Deliverable D7.2-0, Jan. 2022 (expected)

WHEC-2022
23rd World Hydrogen Energy Conference
June 26-30, 2022 - Istanbul

#332

THE EFFECT OF FIBER BANDWIDTH ON STRESS DISTRIBUTION AND LAYER THICKNESS CHANGE AT THE DOME PART OF HYDROGEN STORAGE VESSEL

[1,2*] *İbrahim YILMAZ,* [1,2] *Ebubekir PINAR,* [2] *Osman Vedat AKGÜN*
[1] Uludag University, Engineering Faculty, Mechanical Engineering Department, 16059, Bursa, Turkey
[2] B Plas A.Ş., R&D Center, 16369, Bursa, Turkey,

*Corresponding author e-mail: ibrahimyylmz@gmail.com

ABSTRACT

In this study, dome thickness distribution and burst pressure determination were made for a type IV high-pressure hydrogen storage vessel. The netting theory and cubic spline function (CSF) method were used to design the cylindrical sections lay-up and accurately predict the dome thickness. The rowing numbers and bundle width were determined by considering burst pressure and fiber consumption, and finite element analysis models were created. In finite element analysis, these models were evaluated using Puck failure criteria to accurately predict the damage in composite layers.

Keywords: Type IV hydrogen vessel, Filament winding, Dome thickness

INTRODUCTION

In the last half-century, significant advances have been made in composite pressure vessels produced by the filament winding method. They are more commonly used to store gases such as LPG, CNG, and compressed hydrogen rather than liquids to achieve compressibility and high energy density [1]. The pressure level for the specified application areas ranges from 1 MPa to 70 MPa. Type IV vessels are preferred in hydrogen fuel storage systems for fixed or mobile applications due to their advantages, such as lightweight, high strength, fatigue, and corrosion resistance [2]

Type IV composite pressure vessels are manufactured with a fiber-reinforced composite structure wrapped around a high-density polymer liner (HDPE). The composite structure consists of glass, carbon, or aramid fiber reinforced epoxy resin according to the designed working pressures [3].

In this study, optimum fiber bandwidth and dome thickness were calculated by examining the effect of fiber bandwidth on thickness variation and burst pressure in composite vessel design. The effect of the bandwidth on the thickness change was calculated by the netting theory and CSF method. Modeling was created, and the strengths of the composite vessel were calculated with Ansys software. The resulting stress values were examined and compared according to Puck criteria.

GEOMETRY AND MATERIAL PROPERTIES

Type IV high-pressure hydrogen vessel examined in this study has a volume capacity of 26 L and a working pressure limit of 25 MPa [4]. The vessel comprises a liner and composite layer with a thickness of approximately 2.5 mm and 8 mm, respectively. The composite part is composed of carbon fiber and epoxy resin. The high-pressure vessel modeled is a type IV hydrogen storage, composed of a metal boss playing the role of connecting the vessel, an HDPE liner used to seal the vessel, and the composite layer whose role is to ensure the strength of the structure.

The material properties of the composite structure are shown in Table 1. The HDPE (high-density polyethylene) liner properties are shown in Table 2.

Table 1. Material Property of Carbon Fiber/Epoxy Composite

E_1	$E_2 = E_3$	$\nu_{12} = \nu_{13}$	ν_{23}	G_{12}	Xt	Xc	$S_{12} = S_{13}$	S_{23}
123.34 GPa	7.78 GPa	0.27	0.42	5 GPa	1632 MPa	704 MPa	80 MPa	55 MPa

Table 2. Mechanical Properties of HDPE

Flexural modulus of elasticity	Elongation at break	Tensile Strength at Yield	Tensile Strength at Break	Density
1400 MPa	800%	30 MPa	30 MPa	958 kg/m^3

The netting theory [5], as a well-suited and straightforward method for the design of filament-wound pressure vessels, assumes that the fibers support all the internal pressure and the failure of the structure occurs due to fiber breakage; therefore, the effect of the matrix is negligible. Based on the netting theory, the thickness of composite layers is shown as

$$t_{hoop} = \frac{RP_b}{2\sigma_f}\left(2 - \frac{tan^2\alpha}{k}\right) \quad (1)$$

$$t_{hel} = \frac{RP_b}{2\sigma_f k cos^2\alpha} \quad (2)$$

$$P_b = \frac{2kt\sigma_f}{(2k+1)R} \quad (3)$$

where t_{hel} and t_{hoop} are the thickness of helical layers and hoop layers, respectively; P_b is the burst pressure; R stands for the outside radius of the liner; σ_f is the developed fiber strength; α is the winding angle; k is the stress equilibrium factor, usually set as 0.6-0,8.
CSF is a method created to model the fiber thickness distribution at values close to the thickness distribution during production [6]. Compared with the netting theory, we can acquire dome thickness more accurately when fiber tows continue at the polar radius, as shown in Fig. 1. The geometric relationship of the thickness accumulation calculation with the composite vessel is shown by the formulas below:

$$t(r) = \frac{m_R n_R}{\pi}\arccos\left(\frac{r_0}{r}\right)t_p, \quad (r_0 \le r \le r_0 + b) \quad (4)$$

$$t(r) = \frac{m_R n_R}{\pi}\left\{\arccos\left(\frac{r_0}{r}\right) - arccos\left(\frac{r_0+b}{r}\right)\right\}t_p, \quad (r_0 + b \le r \le R) \quad (5)$$

Where m_R and n_R are fiber tows quantity to cover entirely in a ply and the number of the single plies; t_p the thickness of a fiber tow which is constant; r_0 the polar radius; b the width of a fiber tow; r arbitrary shell radius.

RESULTS AND DISCUSSION

Considering the netting theory and cubic spline method, a graph, as shown in Fig. 1, was obtained. The CSF method modeled a more realistic thickness distribution where different bandwidths reach the maximum thickness on the dome region. According to the finite element analysis results, as shown in Table 3, the burst pressure of the composite pressure vessel was determined as 50 MPa. Consequently, the maximum stress value was calculated as 1679 MPa, wherein cylindrical surface in the tolerance range of ±0.48%, and it was observed that the thickness change did not affect the burst pressure; nevertheless, stress values was shown change on the dome parts. While stress distribution was between 35 and 200 MPa on round polar opening of composite pressure vessel, which has 18 mm bandwidth, stress distribution was between 172 and 640 MPa on round polar opening of composite pressure vessel, which has 30 mm bandwidth.

Table 3. Design Parameters and Stress Values of FEA

Band Width	18 mm	20 mm	22 mm	24 mm	26 mm	28 mm	30 mm
Number of Coverage Cycle	54	48	44	40	37	35	32
Number of Roving	9	10	11	12	13	14	15
Max. Thickness	10 mm	9,7 mm	9,4 mm	9 mm	8,6 mm	8,2 mm	7,9 mm
Stress Distribution within one-band width	(35 - 200) MPa	(38 - 258) MPa	(50 - 320) MPa	(73 - 390) MPa	(100 - 465) MPa	(143 - 547) MPa	(172 - 640) MPa
Stress Value on Cylindrical Surface	1680 MPa	1680 MPa	1679 MPa	1679 MPa	1679 MPa	1679 MPa	1679 MPa

On the other hand, if we consider the number of coverage cycles and the number of roving, production time decreases because the bandwidth increases as the number of cycles required to completely cover the composite vessel decrease. However, the increment in bandwidth also increases the possibility of slippage of the fibers during the winding process, which is undesirable [7]. Considering all the parameters above and the possibility of slippage, the optimum bandwidth was chosen as 24 mm. The thickness accumulation that is unrealistic on dome parts was decreased using CSF.

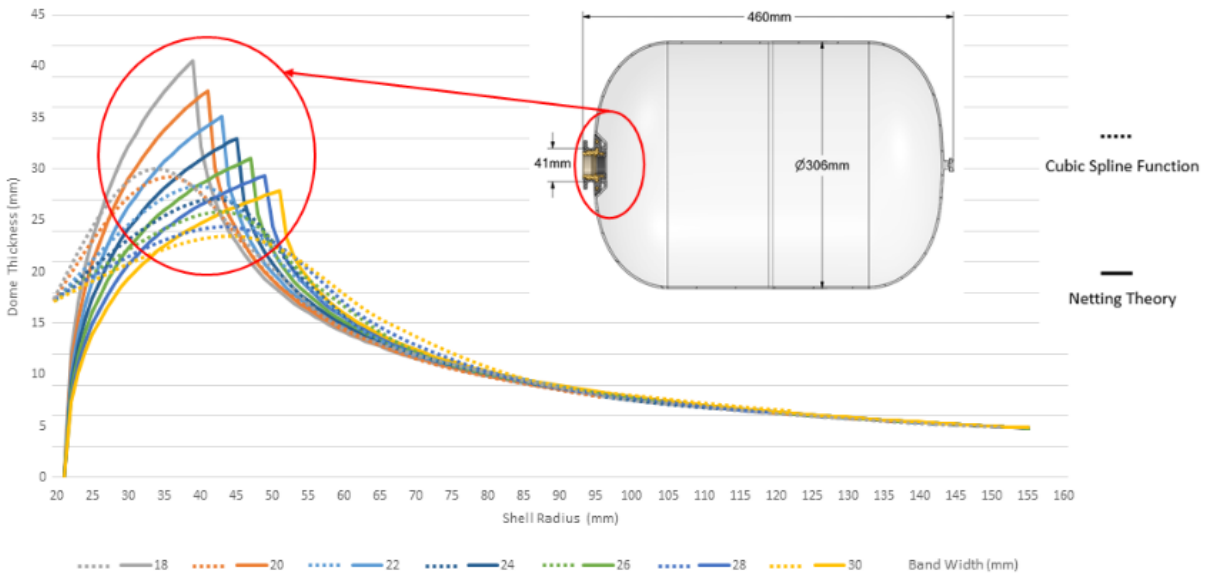


Fig. 1. Dome Thickness Distribution as a Function of Fiber Band Width

CONCLUSIONS

In this study, the effect of fiber bandwidths on dome thickness of type IV high-pressure hydrogen vessels was predicted based on Netting Theory and CSF. The burst pressure was calculated according to puck criteria. The following conclusions were made:

1. As the fiber bandwidth increases, the thickness of the composite layer reduces, and the stresses increase in the polar opening.
2. A fiber bandwidth does not affect the burst pressure since the burst occurs on the cylindrical surface of the composite pressure vessels.
3. The number of roving is a significant parameter for the covering layer during mass production. The number of roving increases as the number of coverage cycles decreases.

REFERENCES

[1] D.J. Durbin, C. Malardier-Jugroot, Review of hydrogen storage techniques for on board vehicle applications, International Journal of Hydrogen Energy, Volume 38, Issue 34, 2013, 14595-14617, 0360-3199.
[2] Zheng J, Liu X, Xu P, Liu P, Zhao Y, Yang J. Development of high-pressure gaseous hydrogen storage technologies. Int J Hydrogen Energy 2011; 37:1048e57
[3] Peters S.T. (Ed.). Composite filament winding. ASM International, Materials Park, OH, 2011.
[4] Gaseous hydrogen — Land vehicle fuel containers. ISO/FDIS 19881. Geneva, Switzerland: ISO
[5] De Jong Th. Theory of filament wound pressure vessels. Report LR-379. Structures and materials laboratory. Delft: Faculty of Aerospace Engineering, Delft University of Technology; 1983.
[6] Wang R, Jiao W, Liu W, et al. Dome thickness prediction of composite pressure vessels by a cubic spline function and finite element analysis. Polym Polym Compos 2011;19(2):227–34.
[7] Pranjali S, Parivesh C, Swati N, Study to methodize the design of a safe Type-4 CNG storage vessel using finite element analysis with experimental validation. International Journal of Pressure Vessels and Piping, Volume 192, 2021, 104425

WHEC-2022
23rd World Hydrogen Energy Conference
June 26-30, 2022 - Istanbul

#345

EXPERIMENTAL STUDIES OF WELL INTEGRITY ISSUES RELATED TO CEMENT DURING UNDERGROUND HYDROGEN STORAGE

[1*] *Esteban R. Ugarte,* [1]*Daniel Tetteh,* [1]*Saeed Salehi*
[1]The University of Oklahoma, 660 Parrington Oval, Norman, OK, US

*Corresponding author e-mail: esteban.r.ugarte-1@ou.edu

ABSTRACT

Underground Hydrogen Storage (UHS) in the subsurface is an alternative to overcome limitations associated with renewable energy sources. The excess energy produced from a fluctuating production can be converted to hydrogen and stored in porous media. Hydrogen is injected and produced from geological formations via wells. There are a number of concerns regarding the interactions of hydrogen with the different well components such as cement. This experimental study aims to investigate the interaction between hydrogen and cement Class H by comparing the results obtained. The methodology consists of studying physical and chemical properties and their interactions with fluid through multiple experiments. Samples exposed to hydrogen exhibited a greater compressive strength in both short and long terms. In terms of casing-cement bond strength, no change was observed. Porosity analyzed using neuron magnetic resonance exhibited minimal difference while permeability measured using a permeameter showed a considerable difference in samples aged in a hydrogenated environment. Finally, based on the scanning electron microscopy aided by Fourier transform infrared spectroscopy, a model has been propped to explain and compare the difference between the samples aged in water and in a hydrogenated water environment.

Keywords: underground hydrogen storage, alternative energy sources, petroleum wells-drilling/production/construction, well integrity

INTRODUCTION

Energy production from renewable resources is considered an alternative to replace fossil fuel energies deemed adverse for the environment. The interest in renewable energies is constantly increasing; in the same manner, newer technologies are continually being developed. One of the most significant limitations associated with renewable energies such as solar or wind is the dependency on uncontrollable factors such as the weather. The fluctuating production from renewable energies creates a gap between supply and demand, making these alternative energies unreliable as being unable to maintain a steady supply [1]. Energy storage is set to be a viable alternative to solve this issue by storing the produced energy during periods of surplus and producing it during periods of peak consumption.

Hydrogen is a clean energy source that can act as a carrier to be implemented in storage applications. This element can be generated through several physical processes and naturally produced by different sources. Hydrogen can be stored by several methods such as gas cylinders, cryogenic tanks, ammonia, absorbed on metals, or through oxidation of reactive metals [2]. These methods can be expensive and space-limited, meaning large investments would produce only small volumetric capacities. To overcome the volumetric needs, it is possible to use the subsurface to store hydrogen in porous media of different geological formations. Underground storage is the cheapest and most volumetric feasible method to store hydrogen. Yet, Underground hydrogen storage (UHS) is still in an early stage of development, with only a small number of projects worldwide compared to more developed analogous storage types [3].

Wells involved in this process are exposed to a number of injection/production phases and have to maintain successful long-term containment. The main concern is hydrogen interaction in the subsurface with different well components such as cement. This study provides a comparison of experimental tests to highlight any effects hydrogen might have in cement during aging conditions. Hydrogen interaction with cement is not well understood, as the behavior can be unpredictable if the cement barrier does provide containment. This study aims to understand the physical and chemical characteristics of cement exposed to a hydrogenated environment to provide insights into any potential integrity issues over short and long aging timeframes.

MATERIALS AND METHODS

In this study, Class H cement sheath was used to fabricate samples that were aged in two different environments consisting of distilled water and hydrogenated water (0.2-0.5 ppm). The concentration of hydrogen and pH was measured using a portable hydrometer. All Class H cement samples were prepared using a water-cement ratio of 0.38 in accordance with ASTM C 109 [4]. Samples had a cylindrical shape with a 1-inch diameter and 2-inch height for dimensions. Soon after preparing the cylindrical cement samples, these were immediately placed in a hot water bath to cure for 12 hours at temperatures of 130 ± 5 ^{o}C. After the desired hydration periods, the hardened samples were then

placed in the different environments to age for timeframes of 3 days, 1 week, 2 weeks, 1 month, 3 months, and 6 months. The aged samples were then characterized using different physical and chemical tools such UCS, SEM, FTIR, NMR, microscopy, and permeameter.

In order to evaluate the impact of hydrogen present in water during aging conditions, a systematic experimental program was designed. Unconfined Compressive Strength (UCS) was measured using a universal testing machine. In this experiment, the compressive strength of the cement samples was measured using a loading rate of 0.6 MPa/min in accordance with ASTM C 109 [4]. To statistically capture any variance, at least 5 specimens from each sample batch were used in this test. The analytical characterization of the samples cured in the different environments was compared using a Scanning Electron Microscopy (SEM) analyzer to observe any difference in the microstructure. Fourier transform infrared spectroscopy (FTIR) was performed to monitor the amount of hydrated product. Porosity was measured using two different methods. Nuclear Magnetic Resonance (NMR) was used to measure the porosity of the sample being fully saturated while the permeameter used samples fully dried. These samples were placed in an oven for 24 hours at temperatures around 100 ^{o}C prior to the experiment. However, it is known to have an adverse effect due to the removal of bound water of some hydrated products and decomposition. Finally, permeability was measured using the permeameter, with helium gas being the closet in molecular weight to hydrogen. The aforementioned experiments provided a complete methodology to quantify the impact of hydrogen present in water during aging conditions by comparing results to base samples aged in pure water.

RESULTS AND DISCUSSION

With the aim of evaluating the impact of hydrogen in cement, the petrophysical properties, including compressive strength, permeability, porosity, mineralogy, and microscopy, were analyzed to observe the behavior over time. The results in terms of mechanical tests showed a minor change in compressive strength for samples aged for short periods of 3, 5, and 7 days. Results exhibited a similar trend for mechanical tests of samples exposed for long time frames of 1, 3, and 6 months. In addition, mechanical tests for cement-casing bond strength showed no change. Dry porosity using the parameter exhibited moderate change after samples had been dried in the oven for 24 hours at temperatures of 100 ^{o}F following accepted procedures. Permeability showed higher values for samples exposed to hydrogen. A possible explanation for this is that hydrogen gas occupies some space within the cement pores, making it easier for any fluid or gas to displace, making the values higher. Mineralogy results showed a gradual increase over time in Ca for samples exposed to a hydrogenated environment. Similarly, the amount of Si was greater in samples exposed to hydrogenated water compared to samples exposed to no-hydrogen water. Microstructure analysis performed using SEM showed that samples exposed to a hydrogenated environment during aging conditions developed a greater amount of hydrated product (ettringite and $Ca(OH)_2$). This behavior increased with exposure time. Although in long-term samples, there was not much change appreciated.

CONCLUSIONS

In this study, the effect of hydrogen during the aging of cement has been investigated through a number of experimental procedures. Unconfined compressive strength shows minor changes in the short and long aging timeframes. Casing-Cement bond strength had no impact. Hydrogen presence in the water can accelerate the hydration process. Porosity and permeability showed a smaller increase in samples exposed to hydrogen. Mineralogy exhibited a gradual increase of Si and Ca over time, while SEM in hydrogenated samples showed the formation of more ettringite and $Ca(OH)_2$. It is assessed that hydrogen has a minor impact in subsurface conditions. Yet, there are some concerns regarding permeability due to hydrogen molecules size as it might permeate the cement body.

REFERENCES

1. Sharan P, Kitz K, Wendt D, McTigue J, and Zhu G. 2020, Using Concentrating Solar Power to Create a Geological Thermal Energy Reservoir for Seasonal Storage and Flexible Power Plant Operation. ASME Journal of Energy Resources Technology 143: 010906.
2. Reuß M, Grube T, Robinius M, Preuster P, Wasserscheid P, and Stolten D. 2017. Seasonal Storage and Alternative Carriers: A Flexible Hydrogen Supply Chain Model. Applied Energy 200: 290–302.
3. Ugarte ER, and Salehi S. 2021. A Review on Well Integrity Issues for Underground Hydrogen Storage. ASME Journal of Energy Resources Technology 144: 042001.
4. ASTM C 109/C 109M. 2004. Standard test method for compressive strength of hydraulic cement mortars. American Society for Testing and Materials. West Conshohocken, Pennsylvania.

WHEC-2022
23rd World Hydrogen Energy Conference
June 26-30, 2022 - Istanbul

#347

EFFECTS OF HYDROGEN-METHANE GAS BLEND ON WELLBORE INTEGRITY IN UNDERGROUND HYDROGEN STORAGE: AN EXPERIMENTAL INVESTIGATION OF ELASTOMER PERFORMANCE

[1*] *Daniel Tetteh,* [2] *Esteban Ugarte,* [3] *Saeed Salehi,*
[1]University of Oklahoma, Mewbourne College of Earth and Energy, MPGE, 100 Boyd St, Norman, United States of America

*Corresponding author e-mail: Daniel.A.Tetteh-1@ou.edu

ABSTRACT

Although depleted natural gas reservoirs are the most economical option for large-scale underground hydrogen storage, minimal knowledge exists on the effects of interactions between the downhole gases and materials, given the novelty of the process. In this study, three selected API grade elastomers; Ethylene propylene diene monomer (EPDM), Fluoroelastomer (FKM/Viton), and Nitrile Butadiene Rubber (NBR), were aged in an autoclave pressurized with different gas mixtures (i.e., hydrogen, methane, and carbon dioxide) to investigate their interactions. Aging parameters were varied to determine their influence on elastomer performance, and this was measured via hardness, volumetric swelling, compressive strain-stress, and Scanning Electron Microscopy (SEM) tests. Preliminary test results showed less than 3% reduction in hardness of all samples when aged in a 100% Hydrogen environment at 22°C and 3Mpa. However, aging samples in a hydrogen-methane gas blend environment at similar conditions caused more significant hydrogen damage. Samples experienced up to a 5% reduction in hardness, and Viton was the most affected. CO_2 was the most corrosive of all three gases and caused between 2% and 9% reduction in hardness of samples. Hydrogen and hydrogen-methane blend damage on elastomers due to elastomer chain rupture are more severe at higher temperatures.

Keywords: *Hydrogen, Autoclave, Elastomers, Well Integrity, Underground Storage.*

INTRODUCTION

In a hydrogen economy, large-scale hydrogen storage is vital in moderating variations in seasonal energy demands and ensuring continuity in energy supply [1]. Techniques for geological storage of hydrogen include storage in depleted hydrocarbon reservoirs, salt caverns, aquifers, and hard rock caverns, with depleted natural gas reservoirs being the most common. The integrity of wells is paramount in underground hydrogen storage as wells should withstand harsh conditions during their entire service life without corrosion and leakage problems [2]. Elastomers play a vital role in this by their use in seal assemblies to hold well pressures and withstand corrosive fluids. They are typically used in packers, O-rings, hydraulic seals, and other downhole equipment in underground hydrogen storage wells. At downhole pressure conditions, hydrogen can permeate or diffuse into elastomers and lead to internal blistering on decompression, thus failure of elastomers [3]. Elastomer failures can cause leakage via gas permeation through sealing or gaps due to inadequate contact between elastomeric materials and equipment [4].

Shi et al. investigated the impacts of hydrogen-methane blends on elastomeric materials used in large-scale underground hydrogen storage in depleted natural gas reservoirs. Elastomers were aged in pressurized incubators with an H_2-CH_4 gas ratio of 13:87 at 26.2Mpa and 353.15K. Their results showed that the diameter of an elastomer aged in H_2 containing gas mixture increased by about 14.3% compared to a 3.05% increase for elastomers aged in a pure methane environment [5]. Yamabe et al. exposed an EPDM elastomer grade to a high-pressure hydrogen environment to quantify the effects of temperature on elastomer damage. They observed more critical damage on the cross-section of the elastomer with higher temperatures [6]. Koga et al. exposed EPDM and vinyl methyl silicon (VMQ) elastomers to 10Mpa of high-pressure hydrogen for a rapid gas decompression (RGD) test. Their results showed that the chances of propagation of fractures in these elastomers are higher for a constant load [3]. However, a gap in research exists in investigating the combined effects of stress changes (i.e., pressure and temperature variation), hydrogen concentration, and hydrogen-methane gas mixtures ratios on the performance of elastomers.

This paper investigates the performance of elastomers in the presence of varied combinations of hydrogen, methane, and carbon dioxide mixtures at different pressures and temperatures. Although the focus was on hydrogen-methane gas blends, CO_2 was included to investigate the impacts of its presence as an associated gas in a typical underground hydrogen storage environment.

MATERIALS AND METHODS

Materials

Three different elastomers; Nitrile Butadiene Rubber (NBR), Ethylene Propylene Diene Monomer (EPDM), and Viton (FKM), were selected and studied based on their wide use in the oil and gas industry. Cylindrical samples with 0 0.0084m and 0.0254m (0.33 and 1-inch) thickness and 0.0191 (0.75-inch) diameter were cut from the three elastomers based on ASTM D575-91[7] specifications. 0.0084m thick elastomers were used for hardness and compressive strength tests, whereas 0.0254m was used volumetric swelling test.

Aging Experiments

All samples would be aged for 24 hours, 3 days, and 1 week in an autoclave reactor vessel. A preliminary test was run for all stipulated gas mixtures, where the samples were aged at 3MPa and 295.1K (22^{o}C) for twenty-four (24) hours. In subsequent experimental batches, aging parameters. i.e., time of exposure, pressure, temperature, and gas mixture ratios would be varied to ascertain their impacts on experimental results. The reactor vessel is pressurized with the gas mixtures based on their partial pressure ratios. Elastomers were stacked on sieve mesh inside the vessel to ensure uniform exposure to the gases.

Mechanical and Physical Property Measurements

The following tests were run on elastomer samples before and after aging to evaluate the influence of aging conditions on the material properties and performance.

Hardness and Compression

Elastomer hardness is an essential property in determining sealing efficiencies at high pressures. A shore A durometer was used to measure the hardness of elastomers in preliminary aging tests. The process would be repeated at different aging conditions for subsequent batches of experiments. The strain in elastomers for a given compressive stress load was determined with ALX-S spiral compression tester machine before and after aging, and the results were compared. The ASTM D575-91[7] "Test Method B-Compressive stress at specified force" was observed in compression tests for samples after preliminary aging experiments and would be repeated for different aging conditions in ensuing experiments. The aim of this test was to measure the extent of damage (change in strain for a given load) due to aging.

Volumetric Swelling

Change in elastomer volume due to chain growth or rupture is vital in failure assessments. Volumetric calculations would be used in measuring elastomer volume before aging, taking its diameter at a single point along its length. After aging, the diameter of elastomers would be taken at three different points along its length; at both ends and at the middle, where there is usually the maximum swelling. The average of these diameters would be taken and used to calculate the elastomers' volume after aging. The difference in volume, before and after aging, would be measured as volumetric swelling.

Material Characterization

Scanning Electron Microscopy (SEM) tests would be run on the elastomer samples for each experiment batch to identify degraded regions and their boundaries. In addition, Energy Dispersive X-Ray (EDX) analysis would be done as a supplementary test to determine the mineral compositions in these zones.

RESULTS AND DISCUSSION

The results obtained for preliminary hardness and compressive strength tests for elastomers are discussed in this section. Two batches of experiments were run for each gas combination, and the standard error in the measurements was calculated.

Hardness Test

No more than 3% reduction in hardness was seen in all samples aged in 100% hydrogen, with EPDM elastomer showing the highest reduction. However, a methane hydrogen mixture caused between 2 to 5% reduction in hardness with the highest seen in Viton elastomer (~4.86%). Aging in 100% CO2 showed the highest reduction in hardness with values between 2 and 9%. NBR was most affected by CO2. Reduction in hardness could be linked with rupturing of cross-linkage in elastomer chains. This implies that CO2 reacted more with elastomer chain structures compared to hydrogen. Also, the hydrogen-methane mixture caused more chemical damage to elastomers than each gas alone. Chemical damage by the hydrogen atom is suspected to be a direct cause of this outcome. However, further tests would be run to ascertain this proposition.

Compression Test

An increase in compressive strain for a given stress load due to a reduction in hardness was observed for all three elastomers after aging. Strain values increased from between 4% to 28%. Results showed that aging in a hydrogen-methane environment caused between a 4% and 9% increase in the strain of samples for a given load. The maximum deflection was seen in the NBR elastomer sample aged in a 100% CO_2 environment.

CONCLUSIONS

- Exposure of elastomers to hydrogen and hydrogen-methane gas mixture causes chemical degradation, which reduces the hardness of elastomers, as seen in this study.
- Aging in a methane-hydrogen mixture environment causes a considerably higher reduction in hardness than in a 100% hydrogen environment. A suspected cause of this is chemical damage by hydrogen atoms.
- Carbon dioxide caused a higher reduction in the hardness of samples compared to methane and hydrogen in this study.
- Further tests are needed to ascertain results from preliminary tests.

REFERENCES

1. Amid A, Mignard D and Wilkinson M. 2016. Seasonal storage of hydrogen in a depleted natural gas reservoir. International journal of hydrogen energy.
2. Zhao L, Yan Y, Wang P, and Yan X. 2019. A risk analysis model for underground gas storage well integrity failure. Journal of Loss Prevention in the Process Industries.
3. Koga A, Yamabe T, Sato H, Uchida K, Nakayama J, Yamabe J, and Nishimura S. 2013. A visualizing study of blister initiation behavior by gas decompression. Tribology online.
4. Balasooriya W, Clute C, Schrittesser B, and Pinter G. 2021. A review on applicability, limitations, and improvements of polymeric materials in high-pressure hydrogen gas atmospheres. Polymer Reviews.
5. Shi Z, Jessen K, and Tsotsis T. T. 2020. Impacts of the subsurface storage of natural gas and hydrogen mixtures. International Journal of Hydrogen Energy.
6. Yamabe J, and Nishimura S. 2009. Influence of fillers on hydrogen penetration properties and blister fracture of rubber composites for O-ring exposed to high-pressure hydrogen gas. International Journal of Hydrogen Energy.
7. ASTM D575-91, Standard Test Methods for Rubber Properties in Compression 2012. West 762 Conshohocken, PA: ASTM International.

WHEC-2022
23rd World Hydrogen Energy Conference
June 26-30, 2022 - Istanbul

#361

THERMODYNAMIC ANALYSIS OF A METAL HYDRIDE BASED HYDROGEN COMPRESSOR USING $La_{1-x}Ce_xNi_5$ HYDRIDES

[1*]*Dinesh Dashbabu,* [2]*E. Anil Kumar*
[1,2]Indian Institute of Technology, Tirupati, Tirupati, India

*Corresponding author e-mail: me19d503@iittp.ac.in

ABSTRACT

The theoretical performance of a metal hydride based hydrogen compressor is studied using the materials $La_{1-x}Ce_xNi_5$ (where x=0,0.1,0.2), and the effect of cerium substitution for La in $LaNi_5$ on its performance is discussed. Using these hydrides hydrogen can be compressed from 20 to 142 bar using thermal energy at 140˚C. A maximum isentropic efficiency of 0.23 and a pressure ratio of 7.1 can be achieved.

Keywords: Metal hydride compressor, Pressure Concentration Isotherm, Cerium Substitution

INTRODUCTION

The use of $LaNi_5$ in metal hydride based hydrogen compressor is pretty common because of the versatility and tunability of thermodynamic propreties with parial substitutions for both La and Ni. Researchers have studied the partial substitution of other rare earth materials like Mischmetal, Ce, Ca [1], etc. for Lanthanum. On the other hand, partial substitution of Cu, Fe, Mn, etc. [2] for Nickel resulted in alloys/intermetallics with a varied hydrogen absorption and desorption charcterstics. In this work, the effect of cerium substitution is studied from a performance viewpoint of a metal hydride hydrogen compressor. Performance analyses has already been done by other researchers who considered properties at a fixed operating parameter [3], while this work studies the effect of operating parameters over wide range while looking at the changes and trade-offs that could be made.

MATERIALS AND METHODS

The Pressure Concentration Isotherms (PCIs) of materials $La_{1-x}Ce_xNi_5$ (where x=0, 0.1, 0.2) are measured using a Sievert's instrument at various temperatures ranging from 20 to 140˚C for both hydrogen absorption and desorption. Before measuring the PCIs, the materials were activated by repeated absorption and desorption until there was a negligible difference in the amount of hydrogen absorbed for the two consecutive cycles. The measured PCIs were used to construct van't Hoff plots and thereby calculate Enthalpy of formation (ΔH) and Entropy of formation (ΔS).

The performance parameters like throughput, pressure ratio, and efficiency were calculated by varying the operating parameters like supply pressure (P_s) and absorption (T_c), and desorption (T_h) temperatures. The supply pressure was varied from 20 to 40 bar pressure, the absorption temperature was varied from 20 to 40˚C and desorption temperature was varied from 80 to 140˚C. For the analysis the mass of the material is taken as 1 kg. The equations used for the analysis is taken from the work of V. K. Sharma and E. Anil Kumar [3].

RESULTS AND DISCUSSION

Figure 1 shows the comparison of the absorption and desorption isotherms at 100°C for the three materials. The equilibrium absorption pressure of $LaNi_5$, $La_{0.9}Ce_{0.1}Ni_5$ and $La_{0.8}Ce_{0.2}Ni_5$ is 14.25, 48, 76.5 bar and the maximum weight percentage is 1.31, 1.37, 1.34 wt.%, respectively. There is a significant increase in equilibrium pressures for both absorption and desorption with the increase in cerium content. There is also a noticeable increase in plateau slope and hysteresis with the increase in the cerium content. A similar conclusion can be drawn from the van't Hoff plot (Fig.2), and the enthalpies are tabulated in Table 1. There is a decrease in ΔH as the cerium content increases because of the lattice shrinkage caused by the substitution of Cerium for Lanthanum [4].

Table 1. Thermodynamic properties of the materials

	ΔH absorption (kJ/mol)	ΔH desorption (kJ/mol)	ΔS absorption (kJ/mol K)	ΔS desorption (kJ/mol K)
$LaNi_5$	-25.504	25.102	0.090	0.087
$La_{4.9}Ce_{0.1}Ni_5$	-23.795	22.770	0.0964	0.091
$La_{4.8}Ce_{0.2}Ni_5$	-21.8483	21.364	0.0946	0.092

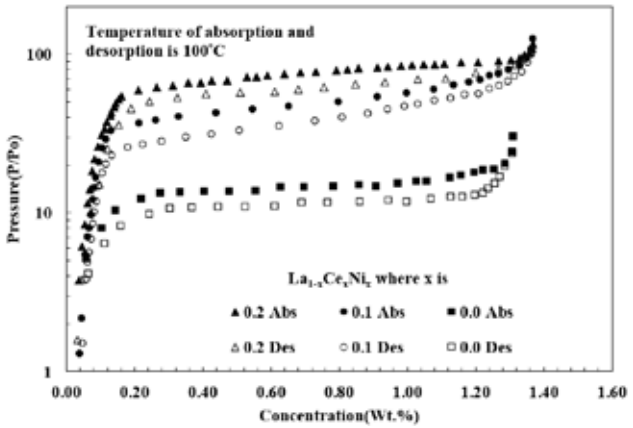


Figure 1 Comparison of PCIs at 100˚C

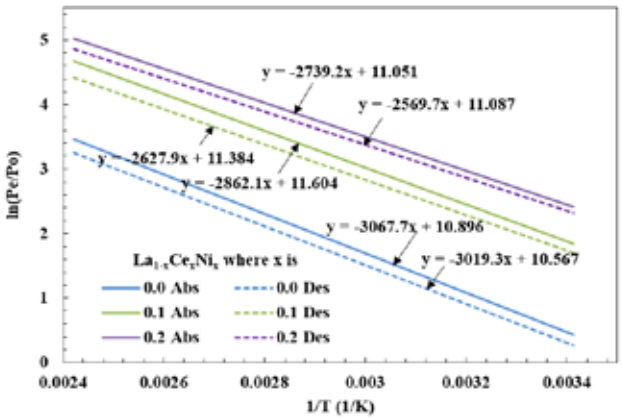


Figure 2 van't Hoff plots of the materials

The variation of throughput is shown in Fig. 3 for the three materials. It can be seen that $LaNi_5$ gives throughput only at 20 bar, whereas it is zero at rest of the pressures studied because it is a low-pressure hydride, i.e., the equilibrium pressure for the desorption falls below the supply pressure. The absorption capacity of the materials decreases with the increase in cerium content but throughput of $LaNi_5$ falls below the $La_{0.9}Ce_{0.1}Ni_5$ because of incomplete desorption. In the case of $La_{0.8}Ce_{0.2}Ni_5$ a slight increase in the throughput is noticed at higher supply pressure because of the increase in absorbed quantity. Fig. 4 describes the change of pressure ratio with desorption temperature. The steady increase in Pr is noticed with the increase of T_h due to the rise in equilibrium pressure, and higher Cerium content material has equilibrium pressure for any desorption temperature. 80˚C is the minimum temperature of desorption at which $La_{0.9}Ce_{0.1}Ni_5$ starts giving out hydrogen where $La_{0.8}Ce_{0.2}Ni_5$ gives proper pressure output even at 80˚C. $LaNi_5$ fails to work at high supply pressures at almost all desorption temperatures.

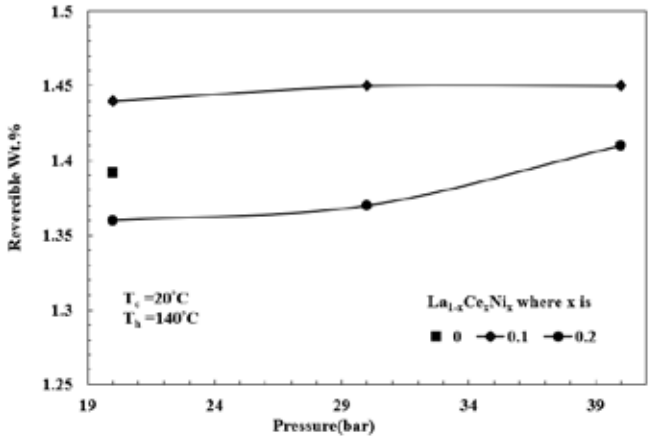


Figure 3 Comparison of Throughput at various P_s

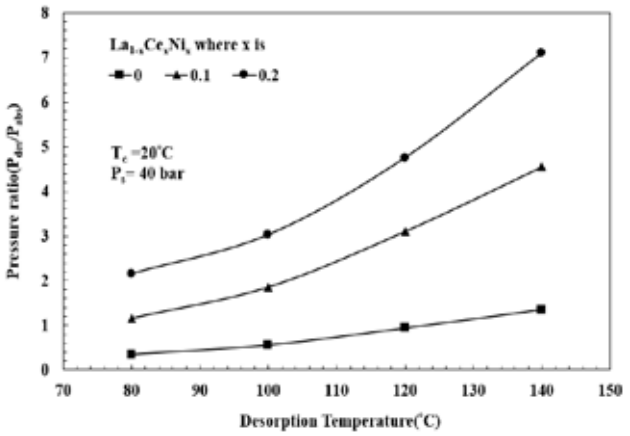


Figure 4 Variation of Pressure ratio with T_h

Fig. 5 explains the variation in isentropic efficiency with T_h for the three materials. The efficiency of $LaNi_5$ is almost zero at all the studied operating conditions because of the low throughput whereas, a steady increase in efficiency is noted in $La_{0.9}Ce_{0.1}Ni_5$, but a dip is noted for $La_{0.8}Ce_{0.2}Ni_5$ at higher absorption temperature because of the decrease of throughput for the material at higher temperature. A similar drop in performance can be noted in Fig. 6, which explains the isentropic work done at different desorption temperatures. Work done is directly proportional to the pressure ratio, which explains the increase in work done with T_h, but the rate of increase is low for $La_{0.8}Ce_{0.2}Ni_5$ because of the reduction of throughput at higher absorption temperatures.

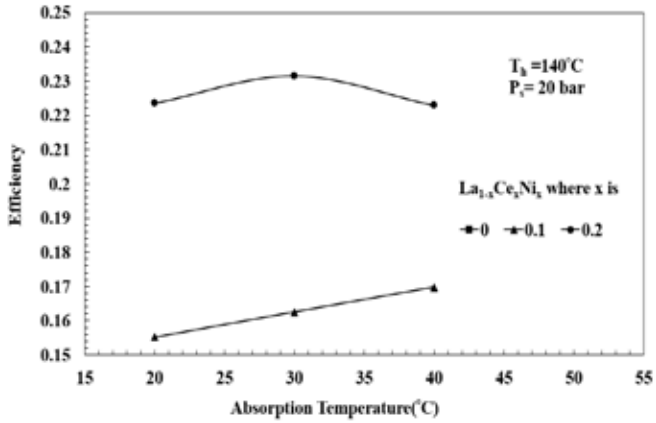


Figure 5 Isentropic efficiency achieved at various T_c

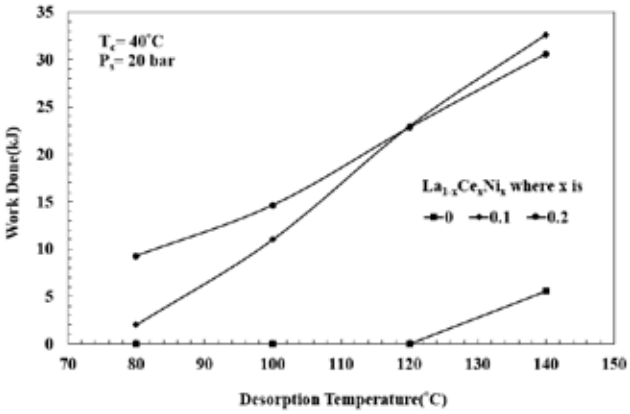


Figure 6 Variation of Isentropic work done with T_h

CONCLUSIONS

The performance of metal hydride based hydrogen compressor using $La_{1-x}Ce_xNi_5$ (where x=0, 0.1, 0.2) hydrides is estimated at various operating conditions. The alloys with cerium substitution allow the compressor operation at high supply pressures i.e., around 20 bar, while $LaNi_5$ can be used where the supply pressure is around 5 bar. $La_{0.9}Ce_{0.1}Ni_5$ hydride gives better throughput at low supply pressures. The maximum efficiency of 0.23 is achieved within the studied operating conditions for $La_{0.8}Ce_{0.2}Ni_5$ at 30˚C absorption temperature, 140˚C desorption temperature, and 20 bar supply pressure with a pressure ratio of 7.1.

ACKNOWLEDGEMENT

The authors acknowledge Department of Science Technology, Government of India, for funding this work vide Project No. DST/TMD/MECSP/2k17/14 (G).

REFERENCES

1. J. Shinar, D. Shaltiel, D. Davidov, and A. Grayevsky. 1978 . Hydrogen sorption properties of the $La_{1-x}Ca_xNi_5$ and $La(Ni_{1-x}Cu_x)_5$ systems. J. Less-Common Met., vol. 60, no. 2, pp. 209–219.
2. H. H. Van Mal, K. H. J. Buschow, and A. R. Miedema.1974. Hydrogen absorption in $LaNi_5$ and related compounds: Experimental observations and their explanation. J. Less-Common Met., vol. 35, no. 1, pp. 65–76.
3. V. K. Sharma and E. Anil Kumar. 2018. Thermodynamic Analysis of Two-Stage Metal Hydride Based Hydrogen Compressor. Materials Today: Proceedings, vol. 5, no. 11, pp. 23218–23223.
4. Pęska, M., Dworecka-Wójcik, J., Płociński, T. and Polański, M. 2020. The Influence of Cerium on the Hydrogen Storage Properties of $La_{1-x}Ce_xNi_5$ Alloys. *Energies*, *13*(6), p.1437.

WHEC-2022
23rd World Hydrogen Energy Conference
June 26-30, 2022 - Istanbul

#364

THE EFFECT OF DIFFERENT ORGANIC ACIDS ON THE HYDROLYSIS OF MAGNESIUM HYDRIDE

[1*] *Moegamat Wafeeq Davids,* [1] *Tshepo Kgokane Sekgobela,* [1] *Mykhaylo Lototskyy,*
[1]University of the Western Cape, South African Institute for Advanced Materials Chemistry (SAIAMC), Bellville, South Africa

*Corresponding author e-mail: mwdavids@uwc.ac.za

ABSTRACT

The influence of organic acids such as acetic acid, citric acid and oxalic acid and their concentration in aqueous solutions on the hydrolysis of magnesium hydride (MgH_2) has been investigated. The hydrolysis of MgH_2 was performed in a hydrogen generation reactor operated in a batch mode where the temperature and H_2 flow rate were logged. Different organic acid concentration of 1, 2, and 3 wt. % was used to study the effect on the hydrolysis of MgH_2. The hydrogen generation results indicate that the addition of organic acids to the aqueous solution increases the rate of H_2 generation as it limits the formation of the $Mg(OH)_2$ passivation layer. The increase in the concentration of the organic acid solutions leads to the increase in the rate and generation of H_2 via hydrolysis of MgH_2. The organic acid with the fastest hydrogen generation rate is oxalic acid, acetic acid and then citric acid. The pH before and after hydrolysis was recorded and showed that the addition of organic acids suppress the formation of $Mg(OH)_2$ passivation layer causing the aqueous solution to be more acidic which leads to less OH^- being formed during hydrolysis in the solution.
Keywords: Hydrolysis, Hydrogen generation, MgH_2, Organic acids

INTRODUCTION

Hydrogen as energy carrier is one of the most promising solutions to address the energy and environment issues and to meet future energy needs. Energy systems based on hydrogen fuel cells are characterised by high efficiency and power density and presently used in a number of stationary, portable and vehicle applications [1,2]. However, the main issue that hinders further implementation of hydrogen fuel cell technologies is compact, safe and efficient hydrogen storage. In recent years, special attention of researchers and engineers has focused on the on-board generation of hydrogen by the hydrolysis of various lightweight materials like ammonia borane, NH_3BH, sodium borohydride, $NaBH_4$, aluminium, Al, magnesium hydride, MgH_2, and so on. These materials can undergo hydrolysis at near-ambient conditions, in alkaline or acidic medium. Potentially, they can be used for efficient generation of hydrogen on-board thus mitigating the hydrogen storage challenge. Their practical implementation, however, requires solution of a number of problems including; (i) suppression of side reactions (particularly dangerous for the boron-containing compounds when a toxic diborane can appear), (ii) improvement of reaction kinetics and, at the same time, (iii) possibility to control H_2 release depending on the fuel cell need. Therefore, looking for a cheap and practical technology to generate hydrogen remains a keen focus of research all over the world.

Magnesium is an inexpensive and readily available metal, which is abundant in the earth's crust (2.4 %) and not harmful on the environment making it a suitable candidate for high-quality hydrogen generation material. Magnesium hydride readily oxidized when it comes in contact with water to form $Mg(OH)_2$ accompanied by H_2 gas evolution. Hydrogen is generated by hydrolysis of MgH_2 according to equation 1.

$$MgH_2 + 2H_2O \rightarrow Mg(OH)_2 + 2\,H_2 \qquad \Delta H^{\ominus}(298\ K) = -134.325\ kJ/mol.H_2 \quad (1)$$

Hydrolysis of MgH_2 has a high theoretical hydrogen yield, 15.2 wt.% and 6.4 wt.% without and with accounting the weight of water, respectively. This is almost double than the amount of H_2 generated by hydrolysis of individual Mg.

Though the hydrolysis of MgH_2 occurs immediately when in contact with water but it is interrupted because of the formation of a passive magnesium hydroxide layer, which prevents the diffusion of the water to the particle inside, therefore the hydrolysis reaction is quickly stagnates. To improve the hydrolysis efficiency and the reaction rate of MgH_2, the main methods employed were carrying out the process in acidic medium [6], alloying with other metals [7], addition of chlorides [8] or ammonium salts [9], ball milling [**Error! Reference source not found.**], addition of graphite [**Error! Reference source not found.**], as well as ultra-sonication [**Error! Reference source not found.**]. The above-mentioned methods are all actively investigated and have been shown to enhance hydrogen generation during the hydrolysis of MgH_2. The crucial issue relating to hydrolysis of MgH_2 remains the avoidance of the barrier of hydroxide layer formation during the hydrolysis process to realize complete hydrolysis. The present work is aimed at studying the effect of organic acids such as acetic, citric and oxalic acids, which potentially have a smaller

environmental impact than that of mineral acids on the hydrolysis of MgH_2 by limiting the $Mg(OH)_2$ passivation layer to enhance the hydrolysis rate and hydrogen generation yield.

MATERIALS AND METHODS

MgH_2 powder 99.8% purity (Rockwood Lithium Germany) with average particle size of 50 μm was used as the substrate for hydrogen storage media. Different organic acids, acetic acid 99.8 %, citric acid 99.5 % and oxalic acid 99.5% purity (Alfa Aesar), were used to increase the rate of hydrogen generation. The investigation of the influence of different concentrations of organic acids (1 wt. %, 2 wt. % and 3 wt. %) on the hydrolysis rate and hydrogen generation was performed.

The hydrogen generation set-up consists of a three-neck round bottom flask that serves as the reaction vessel, thermostatic regulated water bath, the moisture absorbent unit, the flow meter (Bronkhorst 1 NL/min) and the data logger. The hydrolysis reaction of MgH_2 (m=200 mg, theoretical H_2 generation after complete hydrolysis 0.34 NL) with different organic acids was carried out in a 250 ml round bottom flask with three openings, one for water/organic acid addition, one for hydrogen exhausting and one for inserting the thermocouple. The reaction flask was submerged in a thermostat. Hydrolysis reaction was initiated by quick pouring of the acid solution (50 mL) in the reaction flask. The generated hydrogen was passed through a moisture absorbent before entrance to the flow meter. The pH of the solutions before and after hydrolysis were recorded using a Metrohm 827 pH meter.

RESULTS AND DISCUSSION

Figure 1 shows the hydrolysis performance of MgH_2 with different organic acids such as acetic, citric and oxalic acid at different concentrations 1, 2 and 3 wt. %. It can be observed that hydrogen generation from MgH_2 in deionized water is extremely slow: only 0.048 NL H_2 released after 10 minutes, this was expected due to the formation of the $Mg(OH)_2$ passive layer on the surface of the unreacted MgH_2. In contrast, the addition of organic acids considerably improves the hydrogen generation of MgH_2. In all cases both the rate and degree of hydrogen generation increased with higher concentrations of organic acids shown in figure 1 (A), (B) and (C); for the acids concentration of 3 wt. %, 100% hydrogen yield is achieved in 3–5 minutes after reaction started. From figure 1 (D) it is shown that the organic acid with the fastest hydrogen generation rate is oxalic acid, followed by acetic acid and then citric acid.

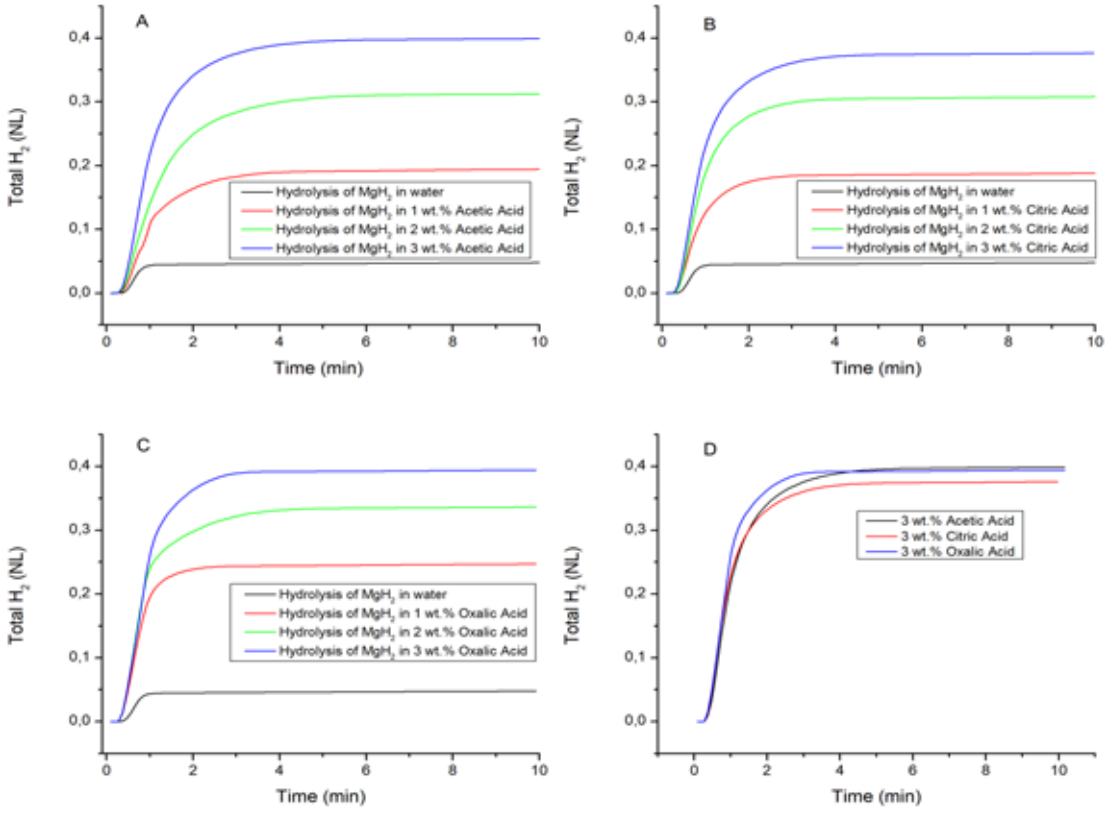


Figure 1. Hydrogen generation curves of MgH_2 at T=20 °C in different concentration of organic acids 1, 2 and 3 wt. %, (A) Acetic Acid, (B) Citric Acid, (C) Oxalic Acid, (D) Hydrogen generation of MgH_2 in 3 wt. % organic acid solutions.

The hydrolysis of MgH_2, leads to an increase in the pH of the reaction solution, this is due to the release of OH^- as a result causing the formation of the $Mg(OH)_2$ passive layer on the surface of MgH_2. This is a major problem with generating hydrogen by MgH_2 hydrolysis. From Table 1 it can be observed that the hydrolysis of MgH_2 in deionized water the pH increased drastically, which is expected due to the $Mg(OH)_2$ passive layer being formed. The addition of organic acids however suppress the formation of $Mg(OH)_2$ this was mainly due to the initial pH becoming acidic which causes less OH^- to be released into the solution. It can be seen that the samples with the lowest pH after hydrolysis have the fastest rate and amount of hydrogen generated, which was oxalic acid, acetic acid then citric acid the same as the hydrogen generation results

Table 1. pH of MgH_2 solution before and after hydrolysis

	Deionized Water	Acetic Acid			Citric Acid			Oxalic Acid		
Concentration		1 wt.%	2wt.%	3wt.%	1 wt.%	2 wt.%	3wt.%	1 wt. %	2 wt. %	3 wt. %
Initial pH	6.55	2.95	2.81	2.69	2.43	2.25	2.16	1.53	1.32	1.21
Final pH	11.04	5.54	5.28	4.28	5.32	4.98	4.53	4.84	3.32	2.11

CONCLUSIONS

The effect of organic acids such as acetic, citric and oxalic acid on the hydrolysis of MgH_2 at various concentration on hydrogen generation were evaluated experimentally. The main results are shown below.

- The hydrogen generation was considerably improved by using organic acid solution instead of only deionized water, this is due to the organic acid dissolving the $Mg(OH)_2$ passivation layer.
- By increase the concentration of the organic acid solutions, the rate of hydrogen generation and amount increased as well, the organic acid with the fastest hydrogen generation rate is oxalic acid, followed by acetic acid and then citric acid. For all the acids applied, at the acid concentration of 3 wt. %, 100% H_2 yield was observed after 3–5 minutes after starting the hydrolysis reaction.
- The addition of organic acids to the hydrolysis solution caused the solution to be acidic, therefore during hydrolysis of MgH_2 in the acidic solution causes less OH^- to be released into the solution and in-turn limiting the formation of the $Mg(OH)_2$ passivation layer.

ACKNOWLEDGEMENT

This work is funded by South African Department of Science and Innovation (DSI) within HySA program (projects KP6-S01 and KP6-S03). MWD and ML also acknowledge support of National Research Foundation (NRF) of South Africa, grant numbers 116278 (MWD) and 132454 (ML)

REFERENCES

1. Dell RM, Rand DAJ. 2001. Energy Storage a Key Technology for global energy sustainability, J. Power Sources 100: 2-17
2. Barbir F. 2013. Fuel cells: theory and practice. 2nd edition, Elsevier / Academic Press.
3. Gil-San-Millan R., Grau-Atienza A., Johnson D.T., Rico-Francés S., Serrano E., Linares N., García-Martínez J. 2018. Improving hydrogen production from the hydrolysis of ammonia borane by using multifunctional catalysts, Int. J. Hydrogen Energy 43: 17100-17111
4. Mostajeran M., Prévot V., Mal S.S., Mattiussi E, Davis B.R., Baker R.T. 2017. Base-metal catalysts based on porous layered double hydroxides for alkaline-free sodium borohydride hydrolysis, Int. J. Hydrogen Energy 42: 20092-20102
5. Liu H, Yang F, Yang B., Zhang Q, Chai Y, Wang N. 2018. Catalysis Today 318: 52–58
6. Kojima Y, Suzuki K-I, Kawai Y. 2004. Hydrogen generation by hydrolysis reaction of magnesium hydride, Journal of Material Science, 39:2227-2229
7. Grosjean, M.H.; Zidoune, M.; Roué, L.; Huot J.Y. 2006. Hydrogen production via hydrolysis reaction from ball-milled Mg-based materials. International Journal of Hydrogen Energy 31: 109–119.
8. Uan J.Y, Lin M.C, Cho C.Y, Liu K.T, Lin H.I. 2009. Producing hydrogen in an aqueous NaCl solution by the hydrolysis of metallic couples of low-grade magnesium scrap and noble metal net, International Journal of Hydrogen Energy 34:1677–1687.
9. Makhaev V.D, Petrova L.A, Tarasov B.P. 2008. Hydrolysis of Magnesium Hydride in the Presence of Ammonium Salts, Russian Journal of Inorganic Chemistry 53:858–860

WHEC-2022
23rd World Hydrogen Energy Conference
June 26-30, 2022 - Istanbul

#369

DEVELOPMENT AND IMPLEMENTATION OF METAL HYDRIDE MATERIALS AND TECHNOLOGIES IN SOUTH AFRICA

Mykhaylo Lototskyy, Vladimir Linkov, Sivakumar Pasupathi*
University of the Western Cape, South African Institute for Advanced Materials Chemistry, HySA Systems Centre of Competence, Robert Sobukwe Road, Private Bag X17, Bellville 7535, South Africa

*Corresponding author e-mail: mlototskyy@uwc.ac.za

ABSTRACT

Metal hydrides (MH) offer promising solutions in several niche applications related to hydrogen storage – the most challenging problem which hinders implementation of efficient and environment-friendly hydrogen energy technologies. Additional motivation for the development and implementation of the MH materials and technologies in South Africa is in the necessity to beneficiate vast mineral resources of the country which include all the components used as raw materials for the manufacturing of main kinds of practically important MH alloys, particularly, AB_2- and AB_5-type ones. This presentation overviews research, development and innovation (RDI) activities in South Africa in the field of MH materials and related technologies. Since the first decade of 2000s, these activities are mostly carried out by the South African Institute for Advanced Materials Chemistry (SAIAMC) at the University of the Western Cape (UWC). The MH-related activities are one of the key technologies developed within Hydrogen South Africa (HySA) RDI Strategy in hydrogen and fuel cell technologies (2008–2023) coordinated by the Department of Science and Innovation (DSI). This key technology is implemented by HySA Systems Centre of Competence hosted by SAIAMC / UWC.

Keywords: metal hydrides, South Africa, hydrogen storage, hydrogen separation and purification, hydrogen compression

INTRODUCTION

In 2008, the South African Government launched a long-term (15 years) National Strategy on the development and commercialisation of hydrogen and fuel cell technologies “Hydrogen South Africa” (HySA). The implementation of HySA Strategy is managed by the Department of Science and Innovation of South Africa and performed by three Centres of Competence established at the leading South African universities and research institutions, including the System Integration and Technology Validation Centre of Competence (HySA Systems) hosted by the South African Institute for Advanced Materials Chemistry (SAIAMC) at the University of the Western Cape (UWC). One of the HySA Systems activities is development and implementation of metal hydride (MH) materials and technologies. Main motivation for these works is in the beneficiation of vast mineral resources of the country. Apart from Platinum Group Metals (PGMs) whose beneficiation is a primary goal of the HySA Strategy, South Africa is in the top-ten countries which have the highest mineral reserves of all the components (Ti, Zr, V, Ni, Mn, etc.) used as raw materials for the manufacturing of main kinds of the practically important MH alloys, particularly, AB_2- and AB_5-type ones [1].

The most promising path towards beneficiation is through the applied chemistry and engineering solutions related to metal hydride technologies for hydrogen storage and related applications. Specifically, it relates to R&D on the use of South African minerals to produce metal hydrides for hydrogen storage, its separation and purification, and thermally driven compression. National industries, such as the petrochemical sector (PetroSA), production of synthetic fuels from coal (Sasol), metallurgy of PGMs and base metals (Anglo-American, Impala), – are currently consumers and/or producers of hydrogen. As the Hydrogen economy develops, these industries will shift into commercial producers and suppliers, and power generation companies (Eskom) may also become producers and/or consumers of hydrogen. Thus, within South Africa there will be a growing demand for the potential technological outputs, including hydrogen storage systems and thermal sorption technologies utilising metal hydrides.

This presentation overviews research, development, and innovation activities in South Africa in the field of MH materials and related technologies, mainly considering the works performed at the HySA Systems Centre of Competence hosted by SAIAMC / UWC.

BACKGROUND

Applications of metal hydrides (MH) utilise a reversible interaction of a hydride-forming metal/alloy, or intermetallic compound with hydrogen (either from gas phase or electrolyte). Due to unique combination of their properties, MH found numerous applications belonging to three main groups [2,3]:

- Gas phase applications (compact hydrogen storage; thermally-driven hydrogen compression and heat management; hydrogen separation and purification; catalysis; powder metallurgy; vacuum-plasma technologies).
- Electrochemical applications (NiMH batteries; air – MH batteries and fuel cells).
- Other applications (nuclear technologies; switchable mirrors; H_2 sensors).

MH technologies is a typical application-driven niche area able to provide very efficient solutions for hydrogen handling in a particular end-use application, by the tuning of a number of parameters, including component and phase composition of the parent MH material, system layout, operating conditions, etc. For every particular case, the success requires to pass whole way from material to system, including specification of target composition of the MH material, its manufacturing in the necessary amounts, development and further manufacturing of non-standard system components on the basis of MH materials, and, further, the system as a whole.

Most of the MH applications are very important for energy storage technologies including hydrogen and fuel cell ones. Metal hydrides can become an important link between components of such systems, allowing to combine realisation of processes of compact and safe hydrogen storage and its supply, along with the utilisation of waste heat released during operation of other system components [4].

Significant past activities on the MH research in South Africa took place in 1970's at CSIR. The research outputs were focused on the thermodynamics and kinetics of metal – hydrogen systems, including investigations on magnesium hydride [5,6]. Over the next two decades, the work carried out by South African researchers in the field of metal hydrides included theoretical investigations on electronic properties of metal hydrides including the palladium – hydrogen system [7,8]. More recent publications, from the year 2000 onwards, comprise of articles on the problems associated with hydrogen embrittlement of metals [9], theoretical studies on metal – hydrogen bonding [10], and the palladium hydrogen system [11].

Launching the HySA Strategy, where MH for hydrogen storage and related applications were recognised as a key technology allocated at HySA Systems, resulted in a significant increase of the South African contribution into R&D activities in this field. A brief overview of these activities is presented below.

METAL HYDRIDE RELATED ACTIVITIES AT SAIAMC AND HYSA SYSTEMS

The R&D on MH materials and technologies carried out at SAIAMC and HySA Systems since 2007 were focused on:

- Development of poisoning-tolerant MH materials and their use in systems for hydrogen extraction and purification [12,13].
- Ti-based MH alloys: development, preparation (up to 10 kg/load) and characterisation [14,15].
- Modelling of phase equilibria in the systems of H_2 gas with hydride-forming metals and alloys [16], as well as heat-and-mass transfer in the metal hydride reactors [17].
- New highly efficient hydrogen storage nanocomposites on the basis of magnesium hydride [18,19].
- Development of metal hydride systems for gas-phase applications including hydrogen storage tanks for utility vehicles [20] and industrial-scale hydrogen compressors [21].
- Development of the integrated hydrogen energy systems utilising MH [4] including a pilot prototype of hydrogen refuelling station with integrated MH compressor [22].

Presently, HySA Systems develops and implements specific products for the local and international markets, particularly, metal hydride-based technologies for hydrogen storage and compression (HySA Key Programme KP6). The Key Programme presently includes two projects: KP6-S01 "Metal hydride-based hydrogen storage systems" and KP6-S02 "Metal hydride hydrogen compressors and their integration in hydrogen refuelling stations". The focus is put on the MH-based technologies of hydrogen storage on-board heavy-duty utility vehicles (e.g., forklifts and underground mining vehicles), as well as development of MH hydrogen compressors and their integration in refuelling stations.

CONCLUSIONS

South Africa has a solid background in the R&D on metal hydride materials and technologies mainly motivated by a possibility to beneficiate the abundant local feedstock suitable for the manufacturing of the MH materials. The RDI

activities in the field have been intensified after launch of HySA Strategy in 2008 and are mainly carried out by HySA Systems CoC hosted by SAIAMC / UWC.

ACKNOWLEDGEMENT

The MH Related Activities at SAIAMC and HySA Systems were funded by the Department of Science and Innovation of South Africa, as well as by South African industry partners including Eskom Holdings Ltd and Impala Platinum Ltd. The international collaboration in the field was supported by the EU including FP7 ERAfrica and Horizon-2020 RISE programs.

REFERENCES

1. Pollet BG, Pasupathi S, Swart G, Lototskyy M, Williams M, Bujlo P, Ji S, Linkov V and Bladergroen BJ. Hydrogen and Fuel Cell Technologies at the Hydrogen South Africa (HySA) Systems Competence Centre. 2014. Platinum Metals Review 58: 68-81.
2. Hirscher M, Yartys VA, Baricco M, et al. 2020. Materials for hydrogen-based energy storage – past, recent progress and future outlook. Journal of Alloys and Compounds 827: 153548.
3. Bhuiya MMH, Kumar A and Kim KJ. 2015 Metal hydrides in engineering systems, processes, and devices: A review of non-storage applications. International Journal of Hydrogen Energy 40: 2231-2247.
4. Lototskyy MV, Tolj I, Pickering L, Sita C, Barbir F and Yartys V. 2017. The use of metal hydrides in fuel cell applications. Progress in Natural Science: Materials International 27: 3-20.
5. Stander CM. Kinetics of decomposition of magnesium hydride. 1977. Journal of Inorganic and Nuclear Chemistry 39: 221-223.
6. Stander CM. The stability of metal hydrides. 1977. Tydskrif vir Natuurwetenskappe 17: 42-52.
7. Lowther JE. Localized theory of the electronic properties of metal hydrides. 1982. Journal of Physics F: Metal Physics 12: 895-906.
8. McLachlan DS and Burger JP. An analysis of the electrical conductivity of the two phase palladium-hydride (PdHx) system. 1988. Solid State Communications 65: 159-161.
9. Carter TJ and Cornish LA. 2001. Hydrogen in metals. Engineering Failure Analysis, 8: 113-121.
10. Govender MG, Rootman SM and Ford TA. An ab initio study of the properties of some hydride dimers. 2003. Crystal Engineering 6: 263-286.
11. Jewell LL and Davis BH. Review of absorption and adsorption in the hydrogen–palladium system. 2006. Applied Catalysis A: General 310: 1-15.
12. Lototsky MV, Williams M, Yartys VA, Klochko YV and Linkov VM. Surface-modified advanced hydrogen storage alloys for hydrogen separation and purification. 2011. Journal of Alloys and Compounds 509: S555-S561.
13. Lototskyy M, Modibane KD, Williams M, Klochko Y, Linkov V and Pollet BG. Application of surface-modified metal hydrides for hydrogen separation from gas mixtures containing carbon dioxide and monoxide. 2013. Journal of Alloys and Compounds 580: S382-S385.
14. Davids MW, Lototskyy M and Pollet BG. Manufacturing of Hydride-Forming Alloys from Mixed Titanium – Iron Oxide. 2013. Advanced Materials Research 746: 14-22.
15. Pickering L, Lototskyy MV, Davids MW, Sita C and Linkov V. Induction melted AB_2-type metal hydrides for hydrogen storage and compression applications. 2018. Materials Today: Proceedings 5: 10470-10478.
16. Lototskyy MV. New model of phase equilibria in metal – hydrogen systems: Features and software. 2016. International Journal of Hydrogen Energy 41: 2739-2761.
17. Satya Sekhar B, Lototskyy M, Kolesnikov A, Moropeng ML, Tarasov BP and Pollet BG. Performance analysis of cylindrical metal hydride beds with various heat exchange options. 2015. Journal of Alloys and Compounds 645: S89-S95.
18. Lototskyy M, Sibanyoni JM, Denys RV, Williams M, Pollet BG and Yartys VA. 2013. Carbon 57: 146-160.
19. Lototskyy M, Denys R, Yartys VA, Eriksen J, Goh J, Nyallang Nyamsi S, Sita C and Cummings F. An outstanding effect of graphite in nano-MgH_2–TiH_2 on hydrogen storage performance. 2018. Journal of Materials Chemistry A 6: 10740-10754.
20. Lototskyy M., Tolj I, Klochko Y, Davids MW, Swanepoel D and Linkov V. 2020. Metal hydride hydrogen storage tank for fuel cell utility vehicles. International Journal of Hydrogen Energy 45: 7958-7967.
21. Lototskyy M., Klochko Y, Davids MW, Pickering L, Swanepoel D, Louw G, van der Westhuizen B, Chidziva S, Sita C, Bladergroen B and Linkov V. Industrial-scale metal hydride hydrogen compressors developed at the South African Institute for Advanced Materials Chemistry. 2018. Materials Today: Proceedings 5: 10514-10523.
22. Lototskyy M, Davids MW, Swanepoel D, Louw G, Klochko Y, Smith F, Haji F Tolj I, Chidziva S, Pasupathi S and Linkov V. Hydrogen refuelling station with integrated metal hydride compressor: Layout features and experience of three-year operation. 2020. International Journal of Hydrogen Energy 45: 5415-5429.

WHEC-2022
23rd World Hydrogen Energy Conference
June 26-30, 2022 - Istanbul

#376

EFFECT OF STARTING RAW MATERIAL IN MECHANICAL ALLOYING OF TiFe HYDROGEN STORAGE ALLOY

[1*] *Kanta Tsuchikawa,* [2*]*Saule Zholdayakova,* [3*]*Haru-Hisa Uchida,*
[1]Graduate School of Human Environment, [2]Graduate School of Science and Technology,
[3]Department of Human Development, Tokai University,
4-1-1 Kitakaname, Hiratsuka, Kanagawa, Japan

*Corresponding author e-mail: kanta.t.0611@gmail.com

ABSTRACT

With its relatively high hydrogen storage capacity (1.8 wt%), TiFe hydrogen storage alloy is expected to be a low-cost material compared to other storage alloys. However, TiFe requires an initial activation process under high temperature and pressure. In order to improve the initial activation properties, the mechanical alloying (MA) process has been proposed to give a disordered surface structure; the MA process can obtain alloys with less energy than the solidification process and is considered to be environmentally and economically suitable.

In this study, we have investigated how the difference between metallic Ti and Ti hydride (TiH_2), the starting material of the MA process, affects the alloy formation. Ti hydride is obtained during the refining process of metallic Ti and is easily pulverized. We also added a small amount of a third element, such as Mn, to TiFe to study its effect on alloying and absorption properties. The obtained sample powder was observed by scanning electron microscopy (SEM) and the structure of the sample was identified by powder X-ray diffractometer (XRD).

Keywords: Hydrogen storage alloy, crystallization, storage capacity

INTRODUCTION

Currently, Japan is being urged to shift from fossil resources to renewable energy sources in response to global warming issues and the international situation. However, renewable energy has the inherent characteristics of unstable supply and low energy density. Using hydrogen as an energy carrier to store and dense renewable energy is the most suitable means to overcome the negative characteristics of renewable energy.

However, the use of hydrogen is not sufficiently widespread at present because the infrastructure for its storage, transportation, and utilization is not well developed. Metal hydrides made of hydrogen storage materials have a higher hydrogen density than liquid hydrogen at normal temperature and pressure [1]. Low-cost, lightweight, and high-hydrogen-capacity hydrogen storage alloys may contribute to the realization and diffusion of future energy systems.

Among the many hydrogen storage materials proposed, TiFe is expected to be used because of its relatively low cost [2]. However, it requires high temperature and high pressure for the activation process, and research to improve the activation properties of TiFe has been continued and discussed [3-5]. As one of them, it is known that the activation of alloys prepared by the mechanical alloying (MA) process is easy, and the MA requires less energy input than the conventional melting method, which may reduce the environmental impact [6,7]. In this study, we examined to fabricate an alloy with a small amount of a third element such as Mn to facilitate the activation of TiFe, and to investigate the effect of the difference between metallic Ti and Ti hydride as the starting material for fabricating the alloy.

EXPERIMENTAL

We attempted to synthesize samples by the MA method from powdered metallic Ti, Ti hydride, and Fe (particle size less than 45 μm). The particle size of metallic Ti was adjusted to be the same as that of Ti hydride powder by ball milling for 50 hours before. In the grove box (GB), 20 stainless steel balls of 10 mm in diameter and the sample powder were sealed in a 60 ml stainless steel ball mill container. A planetary ball mill was used as the MA method, and ball milling (grinding) was carried out for 10 to 100 hr. The volume ratio of sample, stainless steel balls, and space was 1:20:100, and the rotation speed was 300 rpm. We also prepared a sample with a small amount of Mn as a third element to investigate the characteristics of the material obtained by the MA method. The shapes of the obtained samples were observed by scanning electron microscopy (SEM) and the structures of the samples were identified by powder X-ray diffractometer (XRD). In addition, 1 g of the sample containing Mn was sealed in a reaction tube in GB and hydrogenated in a high-pressure Sieverts' type apparatus to evaluate its hydrogen sorption properties.

RESULTS AND DISCUSSION

In the case of the alloy prepared using metallic Ti as the starting material, the XRD diffraction results showed that the samples milled for 10 and 20 hours were not alloyed. However, as the milling time increased to 50 and 100 hours, the alloying process was observed. However, it was also observed that the crystallinity became disordered as the milling time increased.

In the case of the sample prepared with Ti hydride as the starting material, the XRD diffraction results showed no alloying up to 50 hours, while the sample milled for 100 hours showed alloying. 50 hours of milling showed a clear difference, indicating that more time is required for alloying when using Ti hydride. A clear difference was observed at 50 hours of milling, indicating that more time is required for alloying when using Ti hydride. It was observed that the crystallinity of both Ti metal and Ti hydride was disordered.

Scanning electron microscopy showed that the shorter the milling time, the more angular the grains were, and the more the grains stuck to each other. However, as the milling time increased, the powder grains became more rounded and the grain size became 5 to 10 μm.

In both cases, the longer milling time disturbs the crystallinity of the material, and the amorphous like structure contains more grain boundaries and defects that can trap hydrogen, resulting in an increase in the alpha phase region of the phase diagram. At the same time, however, greater crystallinity disorder leads to a decrease in the number of hydrogen storage sites and thus a decrease in the maximum hydrogen storage capacity. Considering these effects, using metallic Ti as the starting material is more suitable for the fabrication of hydrogen storage alloys, as it can be alloyed in a shorter time.

CONCLUSIONS

It was found that the process of MA using metallic Ti as starting material enable faster alloying than that using Ti hydrides. Although Ti hydride is often regarded as a more suitable starting material for alloying than Ti metal because of its brittleness, ease of powdering, and reducing effect of hydrogen, Ti hydride requires extra energy to break the bond between hydrogen and titanium, thus needs a longer milling time.

REFERENCES

[1] AKIBA. Etsuo, The Method of High-Density Hydrogen Storage and Transportation, Journal of the Combustion Society of Japan, Vol.53 No.163 (2011), P.16~21.
[2] Yasuo Sasaki and Toshiya Hirata, Hydrogen Storage Materials, National Research Institute for Metals, Tokyo, (1983)
[3] S. M. Lee and T. P. Perng, Effect of the second phase on the initiation of hydrogenation of $TiFe_{1-x}M_x$(M=Cr,Mn) alloys, International Journal of hydrogen energy, Vol. 19 No. 3(1994), P.259~263.
[4] Muneyuki Amano, Yasuo Sasaki and Takayuki Yoshioka, Effect of Oxide Phase and βTi phased on Hydriding Characteristics of FeTi phase, J. Japan Inst. Metals. Vol. 45 No. 9(1981), p.967~964.
[5] M. Abe, T. Kuji, Hydrogen Absorption of TiFe alloy synthesized by ball milling and post-annealing, J. of Alloys and Compounds, volumes 446-447(2007), P.200~203.
[6] RITE Energy System Research Group Report, “Estimated Energy Intensity as of 2015 (Iron and Steel Sector - Converter Steel)”, Research Institute of Innovative Technology for the Earth (RITE), 2018
[7] Y. Ishikawa, Y. Iijima, K. Ohmura, Grindability-Index given as a Function of the Specific Surface, J. of The Society of Powder Technology, Vol. 15 No. 12 (1978), p.704~710.

WHEC-2022
23rd World Hydrogen Energy Conference
June 26-30, 2022 - Istanbul

#378

INTRODUCTION OF SPERA HYDROGEN SYSTEM™ FOR MASSIVE HYDROGEN STORAGE AND TRANSPORTATION

[1*] *Yoshimi Okada,* [2] *Kenichi Imagawa,* [3] *Hironori Kawai,* [3] *Tomoyuki Mikuriya* [2] *Fuyuki Yagi,* [4] *Naohiro Kaji*
[1]Chiyoda Croporation, Technology Development Department and Hydrogen Business Department,
4-6-2 Minatomirai Nishi-ku, 2208765 Yokohama, Japan
[2]Chiyoda Croporation, R&D Center, Technology Development Department,
3-13 Moriya-cho Kanagawa-ku, 2208765 Yokohama, Japan
[3]Chiyoda Croporation, Technology Development Department, 4-6-2 Minatomirai Nishi-ku, 2208765 Yokohama, Japan
[3]Chiyoda Croporation, Hydrogen Business Department, 4-6-2 Minatomirai Nishi-ku, 2208765 Yokohama, Japan

*Corresponding author e-mail: https://www.chiyodacorp.com/en/contact/index.php

ABSTRACT

Hydrogen energy carrier system is indispensable for decarbonisation through the expansion of renewable energy. The organic chemical hydride method for storing and transporting hydrogen under normal temperature and pressure conditions in the liquid state by incorporating hydrogen atoms into the molecular structure of liquid organic hydrogen carrier (LOHC) is safe and low risk method. Chiyoda started the development of a system employing the method since 2002, named the system “SPERA Hydrogen™” and system completed the international demonstration of massive hydrogen supply chain from Brunei Darussalam to Japan in 2020. It is the only system that has completed the international demonstration of the entire process and has moved to the commercialization stage. It is considered that the system is the most inexpensive except ammonia direct combustion with boiler at present and also has a high potential for cost reduction towards the future compared to other methods.

Keywords: Hydrogen, Storage, Transportation, SPERA Hydrogen

INTRODUCTION

Expanding the use of renewable energy is essential for the decarbonization, and the role of hydrogen energy, which can be used as a clean fuel converted from primary energy including renewable energy, is indispensable. In order to expand the use of hydrogen energy, technologies that can "store" and "transport" hydrogen on a large scale, as well as fossil fuels such as oil and natural gas are essential. The method for storing and transporting hydrogen under normal temperature and pressure conditions in the liquid state by incorporating hydrogen atoms into the molecular structure of liquid organic hydrogen carrier (LOHC) is safe and low risk method.

Chiyoda started the development of a system employing the method since 2002, named the system “SPERA Hydrogen™” and system completed the international demonstration of massive hydrogen supply chain from Brunei Darussalam to Japan in 2020. It is the only system that has completed the international demonstration of the entire process and has moved to the commercialization stage. In addition, the organic chemical hydride method, which uses LOHC as a hydrogen carrier, is a chemical method that allows for innovative technological improvements such as simplification of the process. It is considered that the system is the most inexpensive except ammonia direct combustion with boiler at present and also has a high potential for cost reduction towards the future compared to other methods. In this presentation, we will introduce the outline of the method, International Demonstration Project with “SPERA Hydrogen™” system, and prospect for the commercialization and innovative cost down scenario toward the future.

SPERA HYDROGEN SYSTEM

Hydrogen is reacted with toluene (TOL) to produce methylcyclohexane (MCH), which is converted to a liquid with hydrogen in its molecule enables that hydrogen to be "stored" and "transported" in a liquid state at normal temperature and pressure. Hydrogen can be generated at the place of use through dehydrogenation reaction. TOL is used repeatedly. Figure 1 shows scheme of SPERA Hydrogen System.

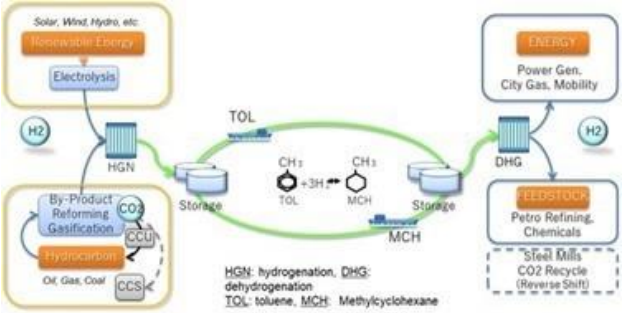


Fig. 1. Scheme of SPERA Hydrogen System

INTERNATIONAL DEMONSTRATION PROJECT

That project launched in 2015, was conducted by the Advanced Hydrogen Energy Supply Chain Association for technology Development (AHEAD) which was established by Chiyoda Corporation, Mitsubishi Corporation, Mitsui & Co., Ltd. and NYK Line. It was founded by New Energy and Industrial Technology Development Organization (NEDO). The demonstration was more than 100 tons of hydrogen transported from Brunei Darussalam to Japan over ten month and the project was successfully completed in Dec.2020[1,2].

The demonstration verified that the system is technically ready for commercial use and confirm SPERA Hydrogen's potential contribution to global carbon neutrality in 2050. Since the entire system for demonstrated in large-scale internationally was the first demonstration in the world, SPERA Hydrogen System is the only system for massive hydrogen storage and transportation in the commercialization phase. Fig.3 shows the photograph of the international demonstration.



Fig. 3. Photograph of the international demonstration

PROSPECT OF COMMERCIALIZATION AND INNOVATION FOR THE FUTURE

Chiyoda joined the "Hydrogen Utilization Study Group in Chubu, Japan" to commercialize the system in Japan[3] and signed a MOU on with Sembcorp industries (Singapore) to explore the feasibility and implementation of a commercial scale supply chain to deliver decarbonized hydrogen to Singapore[4]. The Ministry of Economy, Trade and Industry (METI) of Japan selected Chiyoda and Mitsubishi Corporation to conduct a "Feasibility Study on the Construction of a Hydrogen Supply Chain using SPERA Hydrogen", as part of their "Feasibility Study for the Overseas Development of High-quality Energy Infrastructure"[5].

The Japanese government's Basic Hydrogen Strategy targets a hydrogen supply cost of 30¥/Nm3 (3$/kg) by 2030 and 20¥/Nm3 (2$/kg) by 2050, and we aim to meet the 2030 target based on the current scheme demonstrated above. For the 2050 target, since innovative technologies such as direct production of MCH by photo-catalyst and direct MCH fuel cells etc. are required, we have already started basic research. We are also cooperating with ENEOS in the practical application of their Direct MCH electrolysis technology.

CONCLUSIONS

SPERA Hydrogen System has shift to commercialization phase. It is the only system that has completed the international demonstration of the entire process in Large-scale. It is considered the system is the most inexpensive method except ammonia direct combustion with Boiler, and the system also has a high potential for cost reduction towards the future compared to other methods since it is chemical method. Chiyoda would like to contribute the hydrogen business through the system licence, catalyst supply etc. to the player enterprise globally.

ACKNOWLEDGEMENT

The international hydrogen supply chain demonstration project was found by the New Energy and Industrial Technology Development Organization (NEDO). We express words of gratitude to NEDO.

REFERENCES

1. Chiyoda Corporation, HP, https://www.chiyodacorp.com/en/service/spera-hydrogen/, Accessed on January 14, 2022
2. Chiyoda Corporation, https://www.chiyodacorp.com/media/210202_e.pdf, Accessed on January 14, 2022
3. Chiyoda Corporation, https://www.chiyodacorp.com/media/210409_e.pdf, Accessed on January 14, 2022
4. Chiyoda Corporation, https://www.chiyodacorp.com/media/211004_e.pdf, Accessed on January 14, 2022
5. Chiyoda Corporation, https://www.chiyodacorp.com/media/211115_e_1.pdf, Accessed on January 14, 2022

WHEC-2022
23rd World Hydrogen Energy Conference
June 26-30, 2022 - Istanbul

#390

PERFORMANCE OF BENZYLTOLUENE AS PURE HYDROCARBON LIQUID ORGANIC HYDROGEN CARRIER (LOHC) IN STORAGE CYCLES

[1*] *Timo Ruede, [1]Patrick Preuster, [1]Moritz Wolf, [1]Peter Wasserscheid*
[1] FZ Jülich, Helmholtz-Institute Erlangen-Nuernberg for Renewable Energy (IEK 11), Egerlandstr. 3, Erlangen, Germany

*Corresponding author e-mail: t.ruede@fz-juelich.de

ABSTRACT

This study presents benzyltoluene/perhydro benzyltoluene (H0-BT/H12-BT) as favourable liquid organic hydrogen carrier (LOHC) system for potential technical applications. LOHCs can enable safe and efficient hydrogen logistics using the existent fuel infrastructure. Compared with the well-established LOHC systems toluene/methylcyclohexane and dibenzyltoluene/perhydro dibenzyltoluene (H0-DBT/H18-DBT), the H0-BT/H12-BT system combines a similarly high volumetric storage density and excellent robustness in hydrogenation/dehydrogenation cycles with low viscosity for easy handling in colder operation conditions. Herein, we report repeated hydrogenation and dehydrogenation cycles of technical grade LOHCs in semi continuous operation at 290 °C with a commercial platinum on alumina catalyst (Pt/Al_2O_3). Reaction rates for both, hydrogen uptake and release, are generally found to be higher for H0-BT/H12-BT when compared to the DBT-based LOHC system at identical reaction conditions. By-product formation is low during cycling of the H0-BT/H12-BT system and only small amounts of the dehydrocyclisation products, such as methylfluorene species, are formed that can themselves act as hydrogen carrier.

Keywords: Chemical Hydrogen Storage, Benzyltoluene, repeated storage cycles, reaction rate, by-product formation

INTRODUCTION

Transformation of the global energy system requires green hydrogen technologies since they enable energy storage in large quantities and over long periods of time as well as global energy distribution. For such large-scale hydrogen storage and transport, many different technology options have been discussed. The LOHC technology offers a unique selling point, as the hydrogen is reversibly chemically bound in a liquid hydrocarbon carrier by catalytic hydrogenation and dehydrogenation reactions. This enables the utilisation of existing infrastructure for liquid fuels for the hydrogen logistics [1, 2]. To date, two hydrocarbon-based heteroatom-free LOHC systems have been intensively studied in the literature, namely toluene/methylcyclohexane [3, 4] and dibenzyltoluene/perhydro dibenzyltoluene [5-7]. Despite the fact, that the benzyltoluene/perhydro benzyltoluene system was already mentioned in 2014 [8], this alternative system has been studied far less. Only recently, two studies examined the H0-BT/H12-BT LOHC system in greater detail [9, 10]. They concluded that H0-BT/ H12-BT is particularly interesting as it combines fast production of high purity hydrogen, which is typically associated to dibenzyltoluene-based LOHC systems, with the technically relevant low viscosity and fast pore diffusion characteristics during dehydrogenation, which is typically associated with methylcyclohexane. Motivated thereby, we conduct a more detailed study of the H0-BT/H12-BT LOHC system with analysis of the rate of hydrogen storage and hydrogen release and assessed the stability of this LOHC system in repeated storage cycles.

EXPERIMENTAL

Semi continuous experiments for studying the hydrogenation/dehydrogenation cycles were carried out in a stainless-steel high pressure/high temperature autoclave (Type 4575A, Parr Instruments). The general procedure for performing the cycles was adopted from a previous study focussing on catalyst testing and LOHC stability [5, 11]. Hydrogenation reactions were performed in a dead-end mode and a pressure of typically 30 bar_{abs} was maintained in the reactor by a pressure regulator. The dehydrogenation reactions were initiated by stopping hydrogen supply and opening the reactor to a back pressure regulator. For dehydrogenations, the overall pressure was set to ensure a hydrogen partial pressure of 1.6 bar_{H2}. The temperature was controlled by an electric heating mantle and an immersed cooling coil. The utilized LOHC of technical quality was applied without further preconditioning or purification and the finely ground EleMax-102D (Cl#102, 0.3 wt.-% Pt/Al_2O_3, Clariant) served as catalyst [12].

The degree of hydrogenation (DoH) and the by-product formation were determined by liquid sample analysis by means of gas chromatography (GC). The GC was equipped with mass-spectrometry (MS) and flame-ionisation (FID) detectors to identify and quantify the LOHC species. The DoH of the sample is calculated from GC peak areas (equation (1)):

$$DoH\ /\ \% = \frac{100\ \% \cdot Area_{H12BT} + 50\ \% \cdot Area_{H6BT}}{Area_{H12BT} + Area_{H6BT} + Area_{H0BT} + Area_{MeFl}} \quad (1)$$

RESULTS AND DISCUSSION

Hydrogenation/dehydrogenation reaction path analyses

Our experiments confirmed that hydrogenation of the toluene ring in H0-BT is slower than hydrogenation of the unsubstituted benzene ring [13]. In contrast, neither the methylcyclohexyl nor the cyclohexyl ring was preferentially formed during dehydrogenation. The applied commercial catalyst has been optimised to suppress by-products formed by cleavage of C-C bonds and condensation to heavy boilers [14]. Accordingly, the concentration of cracking products, such as benzene, methylcyclohexane, toluene or diphenylmethane (and their hydrogenated analogues), in the liquid samples after each hydrogenation/dehydrogenation reaction was consistently below 0.1%. Nevertheless, the GC-MS data of our Hx-BT storage cycle experiments revealed the formation of small amounts of methylfluorenes. Traces of anthracene can also be identified as oxidative cyclisation product of the ortho-BT regioisomer, but to substantially lower quantities than methylfluorenes. Figure 1 summarises the more comprehensive reaction scheme of the H0-BT/ H12-BT LOHC system developed from our detailed intermediate product and by-product analysis.

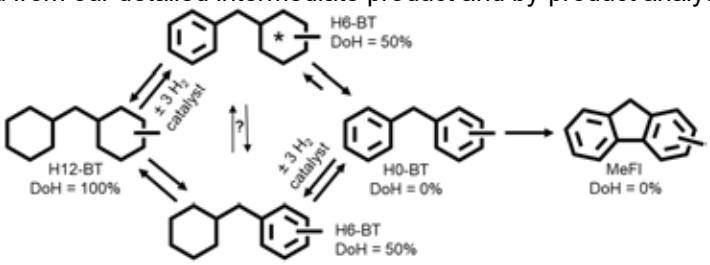


Figure 1. Reaction scheme of the H0-BT/H12-BT LOHC system showing the two different reaction pathways via H6-BT; the main by-products are methylfluorene regioisomers formed by oxidative cyclisation of H0-BT [11].

Hydrogenation of H0-BT and dehydrogenation of H12-BT in repeated cycles

Single hydrogenation/dehydrogenation reactions of the H0-BT/H12-BT LOHC system have been demonstrated in the literature [8, 13, 15-17]. Here, we demonstrate up to seven repeated storage cycles at 290 °C. Hydrogenation was completed after 4 h with a mean DoH of (99.6 ± 0.2)%. In the subsequent dehydrogenation sequences over , DoHs of 26.2% were reached as consequence of the relatively elevated hydrogen partial pressure. The prolonged 5th dehydrogenation resulted in a DoH of 17.9%, which represents the chemical equilibrium under the applied conditions [11]. In another experimental series, the H0-BT hydrogenations were repeatedly demonstrated to be 260% more productive than the H0-DBT hydrogenations. The H12-BT dehydrogenations were 30% more productive than H18-DBT dehydrogenations, with the latter showing a decreased hydrogen storage capacity over the cycles, whereas the H12-BT dehydrogenation sequences showed remarkably stable productivities up to a total operation time of 216 h [11].

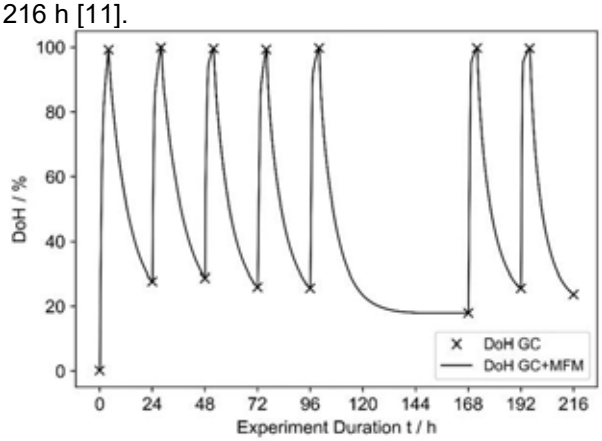




Figure 2. Left: Seven one-pot storage cycles with semi-batch hydrogenation of H0-BT and subsequent dehydrogenation of H12-BT – long-term 5th dehydrogenation over 70 h (270 g H0-BT; CI#102; 0.3wt.-% Pt/Al_2O_3 ground catalyst; n_{Pt}:$n_{H2,max}$ = 1:60000; 290 °C, $p_{H2,hy}$ = 30 bar_{H2}, $p_{H2,dehy}$ = 1.6 bar_{H2}). Right: 15 liquid samples taken at the start and after each hydrogenation/dehdrogenation [11].

Comparing these results from Figure 2 with literature reports on storage cycles with H0-DBT/H18-DBT under identical conditions is quite instructive. Jorschick et al. reported significant catalyst deactivation during long-term dehydrogenation [18]. In contrast, the herein reported storage cycles with H0-BT/H12-BT, the catalyst activity and LOHC stability appeared unaltered. Even the long-term 5th dehydrogenation over 70 h reaching equilibrium

conversion did not impair the catalyst, while yielding exactly the same DoH (25.6%) in the 6th as in the 4th dehydrogenation.

Monitoring of fluorene formation during extended storage cycles

Exposure of the hydrogenation/dehydrogenation catalyst to LOHC systems at low hydrogen partial pressures in combination with elevated temperatures may result in catalyst deactivation and high-boiling by-product formation [18]. In our experiments, four high-boiling regioisomeric methylfluorenes were the only significant by-products detected by means of GC-MS and GC-FID. Expectedly, their concentration increased with every storage cycle. However, fluorene derivatives themselves have been considered as promising LOHC compounds in the literature reflecting their ability to store/release six hydrogen molecules resulting in a comparable hydrogen storage capacity as the H0-BT/H12-BT LOHC system [19]. Unfortunately, fluorene derivatives can also trigger the formation of even larger condensation products and finally coke [20]. Therefore, we investigated the methylfluorene formation in four storage cycles at 290 °C and 1.0 bar_{H2} during dehydrogenations. By linear regression, an increase of fluorene derivatives with each dehydrogenation of about 0.32%-points can be estimated (Figure 3). The experiments indicate that BT could form less by-products than DBT [11]. Aside from this quantitative analysis, the liquid samples of BT experiments (such as those shown in Figure 2) hardly displayed any visible coloration with increasing operation time. This can be seen as strong indication for the formation of only trace amounts of heavy-boiling by-products, which are distinguishable by a yellow or brownish colouring [21].

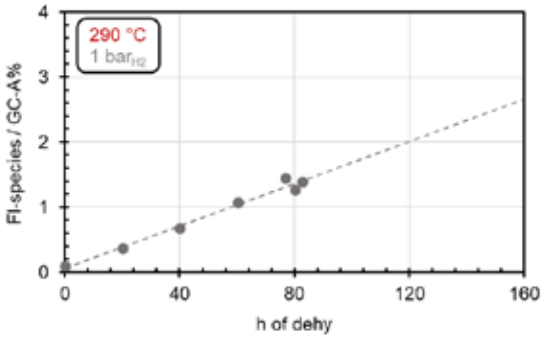


Figure 3. Fluorene-species accumulation during four dehydrogenation sequences for H18-DBT and H12-BT. Dashed lines indicate a linear trend. (270 g LOHC-; Cl#102; 0.3wt.-% Pt/Al_2O_3 ground catalyst; n_{Pt}:$n_{H2,max}$ = 1:30000; 290 °C, $p_{H2,dehy}$ = 1 bar_{H2}) [11].

CONCLUSIONS

Inspired by the low viscosity of H12-BT, when compared to H18-DBT, we have collected additional technically relevant data to assess the H0-BT/system for technical use in the frame of the LOHC technology. In detail, we have studied the stabilities of the LOHC compounds and the performance of a technical Pt-based hydrogenation/dehydrogenation catalyst over repeated storage cycles. We found that the hydrogen storage cycles under benign conditions (290 °C with 30 bar hydrogen pressure in loading and 1.0 – 1.6 bar_{H2} hydrogen pressure in release sequences) showed an excellent reproducibility. Seven storage cycles with one long-term dehydrogenation over several days neither showed signs for degradation of the catalyst nor of the LOHC compounds. We anticipate that the H0-BT/H12-BT LOHC system may represent the preferred hydrocarbon-based and heteroatom-free LOHC system for further technical application with clear advantages over the more traditional toluene/methylcyclohexane and H0-DBT/H18-DBT LOHC systems.

NOMENCLATURE

DoH	Degree of Hydrogenation, %
n	*Moles, mol*
p	Pressure, bar

Subscripts

H2	Hydrogen
H2,dehy	Hydrogen during dehydrogenation
H2,hy	Hydrogen during hydrogenation
Pt	Platinum

REFERENCES

1. Niermann, M, Drünert, S, Kaltschmitt, M, and Bonhoff, K. 2019. Liquid organic hydrogen carriers (LOHCs) – techno-economic analysis of LOHCs in a defined process chain. Energy & Environmental Science 12:290-307.
2. Niermann, M, Timmerberg, S, Drünert, S, and Kaltschmitt, M. 2021. Liquid Organic Hydrogen Carriers and alternatives for international transport of renewable hydrogen. Renewable and Sustainable Energy Reviews 135:110171.
3. Ichikawa, M. 2008. Organic liquid carriers for hydrogen storage. In Solid-State Hydrogen Storage, Vol. 1. Edited by Walker, G. Sawston, Cambridge: Woodhead Publishing.
4. Okada, Y and Shimura, M. 2013. Development of large-scale H2 storage and transportation technology with Liquid Organic Hydrogen Carrier (LOHC). In Technical paper at Joint GCC-JAPAN Environment Symposia. Japan.
5. Jorschick, H, Preuster, P, Dürr, S, Seidel, A, Müller, K, Bösmann, A, and Wasserscheid, P. 2017. Hydrogen storage using a hot pressure swing reactor. Energy & Environmental Science 10:1652-1659.
6. Modisha, P and Bessarabov, D. 2020. Stress tolerance assessment of dibenzyltoluene-based liquid organic hydrogen carriers. Sustainable Energy & Fuels 4:4662-4670.
7. Müller, K, Aslam, R, Fischer, A, Stark, K, Wasserscheid, P, and Arlt, W. 2016. Experimental assessment of the degree of hydrogen loading for the dibenzyl toluene based LOHC system. International Journal of Hydrogen Energy 41:22097-22103.
8. Brückner, N, Obesser, K, Bösmann, A, Teichmann, D, Arlt, W, Dungs, J, and Wasserscheid, P. 2014. Evaluation of Industrially applied heat-transfer fluids as liquid organic hydrogen carrier systems. ChemSusChem 7:229-235.
9. Jorschick, H, Geißelbrecht, M, Eßl, M, Preuster, P, Bösmann, A, and Wasserscheid, P. 2020. Benzyltoluene/dibenzyltoluene-based mixtures as suitable liquid organic hydrogen carrier systems for low temperature applications. International Journal of Hydrogen Energy 29:14897-14906.
10. Kwak, Y, Kirk, J, Moon, S, Ohm, T, Lee, Y-J, Jang, M, Park, L-H, Ahn, C-i, Jeong, H, Sohn, H, Nam, SW, Yoon, CW, Jo, YS, and Kim, Y. 2021. Hydrogen production from homocyclic liquid organic hydrogen carriers (LOHCs): Benchmarking studies and energy-economic analyses. Energy Conversion and Management 239:114124.
11. Rüde, T, Dürr, S, Preuster, P, Wolf, M, and Wasserscheid, P. 2022. Benzyltoluene/perhydro benzyltoluene – Pushing the performance limits of pure hydrocarbon liquid organic hydrogen carrier (LOHC) systems. Sustainable Energy & Fuels.
12. https://www.clariant.com/en/Solutions/Products/2019/05/21/15/19/EleMax-Series. Accessed on 2021-09-13
13. Leinweber, A and Müller, K. 2018. Hydrogenation of the liquid organic hydrogen carrier compound monobenzyl toluene: reaction pathway and kinetic effects. Energy Technology 6:513-520.
14. Auer, F, Blaumeiser, D, Bauer, T, Bösmann, A, Szesni, N, Libuda, J, and Wasserscheid, P. 2019. Boosting the Activity of Hydrogen Release from Liquid Organic Hydrogen Carrier Systems by Sulfur-Additives to Pt on Alumina Catalysts. Catalysis Science & Technology 9:3537-3547.
15. Lamneck, JH and Wise, PH. 1954. Dicyclic hydrocarbons. IX. Synthesis and physical properties of the monomethyldiphenylmethanes and monomethyldicyclohexylmethanes. Journal of the American Chemical Society 76:1104-1106.
16. Rader, CP and Smith, HA. 1962. Competitive Catalytic Hydrogenation of Benzene, Toluene and the Polymethylbenzenes on Platinum. Journal of the American Chemical Society 84:1443-1449.
17. Jorschick, H, *Ein-Reaktor-Konzept und Mischgashydrierung als Verfahrensvarianten zur Effizienzsteigerung in der LOHC-basierten Wasserstoffspeicherung*, in *Chemie- und Bioingenieurwesen*. 2019, Friedrich-Alexander-Universitaet: Erlangen.
18. Jorschick, H, Dürr, S, Preuster, P, Bösmann, A, and Wasserscheid, P. 2019. Operational Stability of a LOHC-Based Hot Pressure Swing Reactor for Hydrogen Storage. Energy Technology 7:146-152.
19. Sotoodeh, F, Huber, BJ, and Smith, KJ. 2012. The effect of the N atom on the dehydrogenation of heterocycles used for hydrogen storage. Applied Catalysis A: General 419:67-72.
20. Guisnet, M and Magnoux, P. 2001. Organic chemistry of coke formation. Applied Catalysis A: General 212:83-96.
21. Mullins, OC and Sheu, EY. 2013. Structures and dynamics of asphaltenes. Springer Science & Business Media.

WHEC-2022
23rd World Hydrogen Energy Conference
June 26-30, 2022 - Istanbul

#399

PERFORMANCE ANALYSIS OF A SOLAR TOWER POWER PLANT INTEGRATED WITH HYDROGEN ENERGY STORAGE SYSTEM

[1] *Mohammad Hashem Mirbagheri,* [1*] *Ehsan Baniasadi,* [2]*Hadi Genceli*
[1] University of Isfahan, Department of Mechanical Engineering, Faculty of Engineering, Hezar Jerib Ave., Isfahan, Iran
[2]Yildiz Technical University, Faculty of Mechanical Engineering, Mechanical Engineering Department, Besiktas, Istanbul, 34349, Turkey

*Corresponding author e-mail: e.baniasadi@eng.ui.ac.ir

ABSTRACT

In this paper, an exergy-economic model is developed to analyze the performance of a direct steam solar tower - steam turbine - organic Rankine cycle (ORC) power plant under different working conditions. The solar power plant is connected to a power grid, and it is integrated with a hydrogen storage system. The hydrogen storage system is composed of an electrolyser, fuel cell, steam turbine and organic Rankine cycle. When solar energy is not available, electrical power is generated by the fuel cell, steam turbine and ORC using the hydrogen produced by the electrolyzer. The analyses are made for the maximum solar irradiation that is available in the city of YAZD in Iran. The effects of the current density and operating temperature on the performance of the solid oxide electrolyzer cell (SOEC) and solid oxide fuel cell (SOFC) are investigated. The effect of solar irradiation on the energy and exergy efficiencies of the cycle is investigated. The results indicate that increase of the solar irradiation leads to an increase of the energy and exergy efficiencies of the cycle. The solar tower has the highest exergy destruction and capital investment cost.

Keywords: Direct steam solar power tower, Solid oxide electrolyzer cell, solid oxide fuel cell, Organic Rankine cycle

INTRODUCTION

Finding efficient power systems is of major concerns, especially with the depletion of fossil fuel sources with time. Energy demands are expected to keep increasing in the future. Thus, finding efficient systems is vital to reduce the unit of energy produced per the unit of fuel consumed. On the other hand, producing energy from fossil fuel causes some problem to the environment, such as global warming, air pollution, acid precipitation, ozone depletion, forest destruction and emission of radioactive substances [1].

The solar power tower is one of the most unique technologies for converting solar energy to electricity due to its high working temperature and thermodynamic efficiency [2]. Solar tower power system uses a central tower as a solar collector that is used to heat or evaporate the working fluid the thermal energy of the fluid force is utilized to generate electricity by a turbine.

To better harness renewable energy, hydrogen has been identified as a potential alternative fuel as well as an energy carrier for the future energy supply. Hydrogen is produced in different ways such as thermolysis, coal gasification, biomass conversion, electrolysis, etc. The benefits of water electrolysis include low pollution, reliability, large-scale applications, durable and inexpensive materials and capability of integration with renewable sources such as solar energy systems [3].

Solid oxide fuel cells (SOFC) are considered an emerging technology as characterized by their high efficiency and lowCO2 emissions. An SOFC operates at high temperature and thus has high waste energy that can be integrated efficiently with a bottoming cycle. One of the potential systems that can be integrated with SOFC is organic Rankine cycle (ORC). ORC is similar to steam Rankine cycle; however, it uses organic working fluid instead of steam and requires less input heat to operate compared with steam Rankine cycle. SOFC and ORC are potential subsystems that can be used in trigeneration plants [4].

SYSTEM DESCRIPTION

The schematic of investigated system in this current research paper is shown in Figure 1. The solar tower-hydrogen power plant consists of a direct steam solar tower, solid oxide electrolyzer (SOEC), solid oxide fuel cell (SOFC), steam turbine (ST), Organic Rankine cycle (ORC) and hydrogen and oxygen storage tanks. During charging cycle, solar radiation is reflected from the heliostats to the receiver above the solar tower where liquid water is converted into superheated steam. The thermal energy of the steam is then used in the steam turbine 1 (ST1) to generate electric power. A part of the generated power with the capacity of 70 MW is fed to the grid and the rest is supplied to the SOEC. In the SOEC, water is decomposed to hydrogen and oxygen gases. The produced gases are sent to the hydrogen and oxygen tanks for storage. The high-pressure hydrogen and oxygen stored in the tanks are first used in SOFC to generate electricity during the discharge mode. Outlet water steam used in the steam turbine 2 and then flow through

heat exchangers to transfer heat to the ORC fluid. The discharge cycle is performed when solar energy is not available. Based on the solar irradiation data of Yazd city, the operating hours of the charging and discharging cycle are considered as 11 hours and 7 hours, respectively. The Yazd city, with an area of 110 km^2 is at an altitude of 1216 m and in coordinates of 54.3569 °E, 31.8974 °N.

THERMODYNAMIC ANALYSIS

The thermodynamic analysis is performed to determine the system's energy losses and exergy destructions in detail.

The total exergy per unit mass is summation of physical and chemical exergies as follows:

$$Ex = Ex^{ph} + Ex^{ch} \quad (1)$$

$$Ex^{ph} = (h - h_0) - T_0(s - s_0) + \left[\frac{v^2 - v_0^2}{2}\right] + g(z - z_0) \quad (2)$$

$$Ex^{ch} = \sum x_n Ex_n^{ch} + RT_0 \sum x_n \ln x_n \quad (3)$$

first and second laws of thermodynamics for an open system at steady state condition is as follows:

$$\sum_k \dot{Q}_k + \sum_i^N (\dot{m}_i h_i)_k = \dot{W}_k + \sum_e^N (\dot{m}_e h_e)_k \quad (4)$$

$$\sum_k \left(1 - \frac{T_0}{T}\right) \dot{Q}_k + \sum_i^N \dot{E}x_{i,k} = \dot{E}x_{w,k} + \sum_e^N \dot{E}x_{e,k} + \dot{E}x_{D,k} \quad (5)$$

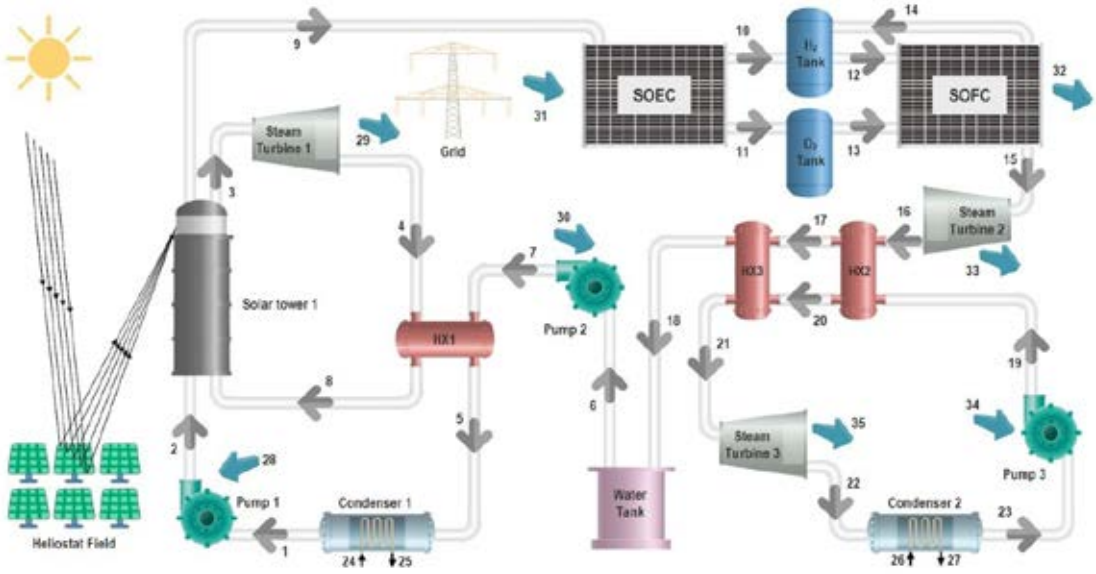


Figure 1. Diagram of the solar power tower, Hydrogen and ORC hybrid power plant

EXERGOECONOMIC ANALYSIS

Exergoeconomic analysis is performed to determine the exergy cost of the system's products. The analysis is based on the exergy- cost principle as suggested by Noaman et al. [5].

The cost balance for each component based on exergy of the fuel and products is as follows:

$$\sum_e^N \left(c_e \dot{E}x_e\right)_k + c_{w,k}\dot{W}_k = c_{q,k}\dot{W}_{q,k} + \sum_i^N \left(c_i \dot{E}x_i\right)_k + \dot{Z}_k \quad (6)$$

where c and $\dot{Z}_k$ denote the average cost per unit exergy and the capital investment, operation, and maintenance cost rate of k_{th} component, respectively. The term $\dot{Z}_k$ is calculated as follows:

$$\dot{Z}_k = \frac{Z_k CRF \varphi}{N} \quad (7)$$

The capital recovery factor (CRF) is calculated based on lifetime (n=20) and interest rate (ir=10%) as follows:

$$CRF = \frac{ir(1+ir)^n}{(1+ir)^n - 1} \quad (8)$$

The cost of exergy destruction in each component, the relative cost difference (r_k) and exergoeconomic factor (f_k) for each component are defined as follows:

$$\dot{C}_{D,k} = c_{F,k}\dot{E}_{D,k} \quad (9)$$

$$r_k = \frac{c_{P,k} - c_{F,k}}{c_{P,k}} \quad (10)$$

$$f_k = \frac{\dot{Z}_k}{\dot{C}_{D,k} + \dot{Z}_k} \quad (11)$$

RESULTS AND DISCUSSION

The performance of the direct steam solar power-hydrogen power plant is modeled based on the first and second laws of thermodynamics. Moreover, the exergy destruction of each component is also calculated. The exergy analysis and exergo-economic results are given in Table 1. The highest value of the exergy destruction rate is related to the solar tower system that; this is due to the conversion of a large amount of solar energy to thermal energy at a specific operating temperature and the high heat loss in the receiver of the solar tower. It is concluded that the highest value of the cost rate of the capital investment ($\dot{Z}$) is related to solar tower system. The exergoeconomic factor for the solar tower shows that the capital investment cost is the primary determinant in the exergy destruction cost.

Table 1.The results of exergies and efficiencies and exergy economic for all components of the entire cycle

Component	$\dot{E}X_{f,k}$[kW]	$\dot{E}X_{p,k}$[kW]	$\dot{E}X_{D,k}$ [kW]	η [%]	ψ [%]	$\dot{C}_{D,k}$ [$/h]	$\dot{Z}$ [$/h]	r_k [%]	f_k [%]
Solar Tower	528084	161508	161489	66.14	39.86	0	2265	100	100
Steam Turbine 1	92715	83161	9555	86.8	89.69	126.9	299.4	38.61	70.24
Condenser 1	68343	14336	80032	90	28.85	1063	4.138	378.9	0.3879
Pump 1	886	715.6	170.4	75	80.77	3.135	7.867	83.55	71.51
Pump 2	0.4807	0.3605	0.1202	75	74.99	0.002212	0.0378	602.9	94.47
Heat Exchanger 1	2647	18.96	2628	90	0.716	34.89	0.7184	14149	2.017
SOEC	15472	8083	7389	67.55	66.54	136	26.28	109.1	16.2
SOFC	13355	7722	5633	36.53	57.82	281.2	24.44	258.6	7.995
Steam Turbine 2	626.8	592.6	34.18	86.8	94.55	3.06	9.402	23.49	75.45
Heat Exchanger 2	296.9	99.19	197.7	90	33.41	17.7	0.7959	208.3	4.304
Heat Exchanger 3	104.7	56.81	47.91	90	54.25	4.288	0.934	102.7	17.88
Steam Turbine 3	132.7	117.5	15.22	86.8	88.53	3.901	3.044	23.06	43.83
Condenser 2	23.54	17.23	40.77	90	76.13	10.45	0.0691	43.55	0.6569
Pump 3	7.459	0.2698	7.189	75	3.617	2.267	0.0133	2680	0.5813

In Figure 2 and Figure 3 the exergy destruction rates related to charge and discharge cycle are shown. In charge cycle, the exergy destruction rate of the solar tower is 61.81% and it has the highest exergy destruction rate because of low solar irradiation absorbed by receiver in comparison with high solar radiation reflected to heliostats. The highest exergy destruction rate in discharge cycle occurs in the SOFC i.e., is 94.26%.

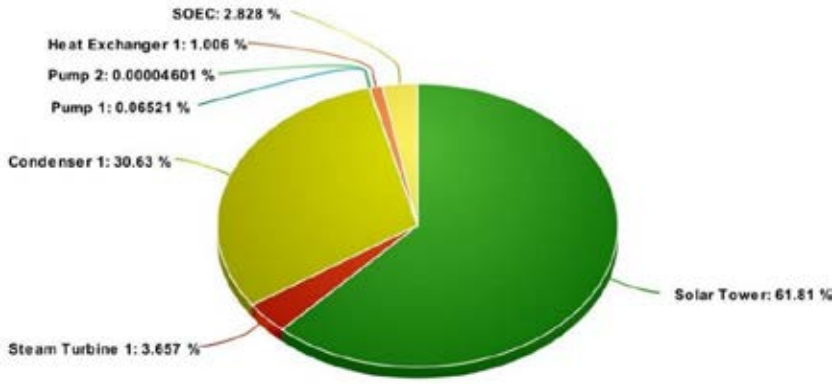


Figure 2. The rate of the exergy destruction of the components in charge cycle

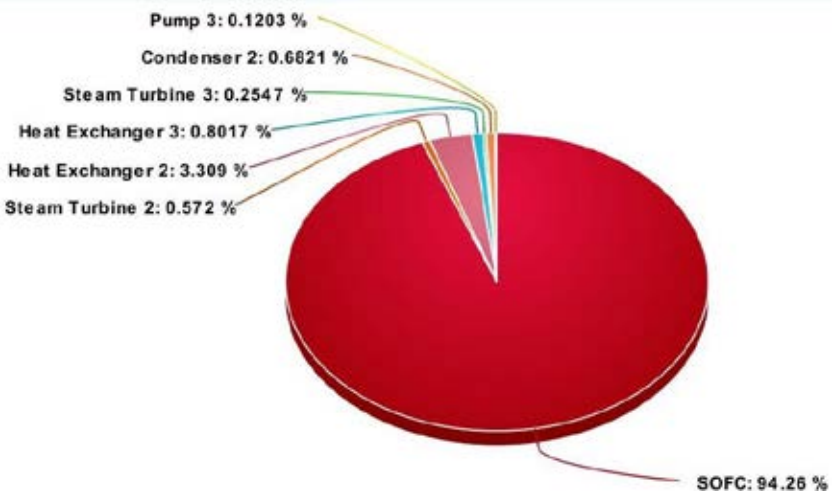


Figure 3. The rate of the exergy destruction of the components in discharge cycle

CONCLUSIONS

The following conclusions are made in summary:

- Inlet steam to the steam turbine has the highest rate of exergy destruction due to the conversion of large amounts of solar energy to lower quality energy at fluid operating temperatures. The ambient temperature affects the exergy destruction of the components.
- Exergy destruction of condenser 1 decreases with increasing ambient temperature due to the lower fluid temperature difference with ambient temperature in the phase change process.
- The exergo-economic factor for all components is calculated and it was found that solar tower, pump 1 and ST1 have the highest exergoeconomic factor which shows it is needed to be considered these components from the economic view. Condenser1, SOEC and SOFC have the highest cost of the exergy destructions.

REFERENCES

[1] Dincer I. 1999. Environmental impacts of energy. Energy Policy 27:845–854.
[2] Collado FJ and Guallar J. 2012. Campo: Generation of regular heliostat fields. Renewable Energy 46:49-59.
[3] Moradi Nafchi F, Afshari E, Baniasadi E, and Javani N. 2019. A parametric study of polymer membrane electrolyzer performance, energy and exergy analyses. International Journal of Hydrogen Energy 44:18662-18670.
[4] Al-Sulaiman FA, Dincer I, and Hamdullahpur F. 2010. Exergy analysis of an integrated solid oxide fuel cell and organic Rankine cycle for cooling, heating and power production. Journal of Power Sources 195: 2346–2354.
[5] Noaman M, Saade G, Morosuk T, and Tsatsaronis G. 2019. Exergoeconomic analysis applied to supercritical CO2 power systems. Energy, 183:756-765.

WHEC-2022
23rd World Hydrogen Energy Conference
June 26-30, 2022 - Istanbul

#413
3D COFs FOR PHOTOCATALYTIC N_2 FIXATION: A COMPUTATIONAL STUDY

[1] Amro M. O. Mohamed,[1] Yusuf Bicer*
[1] Division of Sustainable Development, College of Science and Engineering, Hamad Bin Khalifa University, Qatar Foundation, Doha, Qatar

*Corresponding author e-mail: ammohamed@hbku.edu.qa

ABSTRACT
As a result of permanent porosity, tunability, and structural stability, covalent-organic frameworks (COFs) have been introduced in various environmental-related applications. COFs have been studied for various gas separation-related applications, primarily CO2 capture from natural gas and flue gas. The performance of COFs towards gas separation can be investigated by computational techniques, including density functional theory (DFT) and molecular simulations based on force fields. In this work, several atomistic and molecular simulations techniques are used to identify COFs for the nitrogen conversion to ammonia photocatalytically. The experimental database is screened for desired conduction, valence band, and bandgap. A total of six structures are selected from the 3D structures. COF-300 has been shown to have desirable electronic properties (bandgap approximately 3.5 eV) and the highest N_2 adsorption among the six COFs.The simulations are performed using GCMC simulations to determine the nitrogen capacity of the COFs. Structures with one of the desired valence or conduction bands with desirable bandgaps are coupled in a COF/COF junction that potentially enhances charge separation and reduces charge carrier recombination rates. The study reports a 40 COF/COF heterojunction for the required application. Such high throughput screening typically involves databases (experimental based) and results in an essential structure-function relationship that accelerates materials discovery in several energy applications.

Keywords: Photofixation of nitrogen, Green ammonia, COFs, Computational screening

INTRODUCTION

Covalent organic frameworks (COFs) are orderly porous crystalline organic materials. They have several features that make them intriguing in various applications. COFs have low density and possess high thermal and chemical stabilities. COFs have been investigated as adsorbents, catalysts, sensors, energy storage applications, and membrane treatment [1]. Due to the growth of nanoporous materials, researchers developed frameworks and procedures to screen and select top-performing materials for different applications. Due to the development in computational power, computational modeling and simulation at the molecular level can provide essential information about the applications that a particular material can enhance [2]. Possible nanoporous structures are enormous due to tunability and variations in building blocks. Gas separation applications are by far the most screened for application, either through adsorption-based or membrane-based separations. Materials are compiled first in databases; these databases are either based on experimental synthesis or hypothetical structures.

Screening and properties evaluations of efficient and large-scale databases can result in an essential relationship between structural and topological properties and performance under particular applications' conditions. As a result of efficient databases and tools to differentiate between materials, we can learn more about what strongly governs the performance, leading to better understanding and, thus, the design of modern materials. Various metrics have been developed throughout research to rank materials depending on the type of application. For instance, for the adsorption-based separation, top-performing materials are expected to have high loading of the desired component, high selectivity, and regeneration effectiveness. These properties are essential, but the material should perform exceptionally under conditions near practical operations. Photofixation of N_2 to produce ammonia is considered the most environmentally benign process. Screening for porous 3D structures for photofixation of N_2 was accomplished from hypothetical metal-organic frameworks (hMOFs) database and experimental-based dataset [3,4]. In this work, we investigate the 3D structures of COFs for the photocatalytic activity towards ammonia production from N_2. The study includes electronic properties calculations besides adsorption and structural properties.

MATERIALS AND METHODS

The experimental COFs database is used in this work, comprised of 449 COFs [5]. This screening aims to find 3D structures suitable for the N_2 fixation process. COFs in the dataset are divided into 2D and 3D structures. The most important parameters used in the study are the bandgap and band edges of the structures. Density functional theory (DFT) is used to determine the highest occupied molecular orbital (HOMO) and lowest unoccupied molecular orbital (LUMO). Two different theories are used to compare and establish a potential correlation. Generalized gradient approximation (GGA) functional in PBE and hybrid functional HSE06 is used. The work uses the HSE06 as GGA functionals tend to underestimate the bandgap of semiconductors. The correlation between PBE and HSE06 bandgap could help reduce the required computational power to compute hybrid functional properties. In this work, the desired

band edges are conduction band higher than -1.26 eV and valence band lower than 1.23 eV vs. standard hydrogen electrode. Besides, adsorption properties are mainly calculated for the selected structure to assess and compare N_2 adsorption in these COFs. The higher the adsorption, the better since the process requires the adsorption of molecular N_2. It has to be mentioned that other photocatalytic properties such as charge separation and recombination could be of higher importance than molecular adsorption of reactant; however, this is still considered an indication of the process. N_2 is modeled using TraPPE force-field with tail correction 12.8 Å. Charges on the structures are calculated using the RASPA equilibration scheme.

RESULTS AND DISCUSSION

The screening is initiated by determining important structural properties for efficient structures. Two parameters are sought: the available surface area (ASA) and pore limiting diameter (PLD). A structure is selected if ASA>0 and PLD ensures the reactant and product can diffuse through the cages. Following that, the COFs are divided into 2D and 3D structures. In this work, initially, we focus on 3D COFs to be proposed for the photocatalysis application. A total of 44 COFs are porous 3D solids having the necessary PLD to facilitate the process. The number of 3D COFs is lower than 2D COFs due to difficulty finding organic units with multiple reactive sites. The 44 eligible structures have a wide range of surface area 280-8500 m^2/g and PLD between 4 and 25 Å.

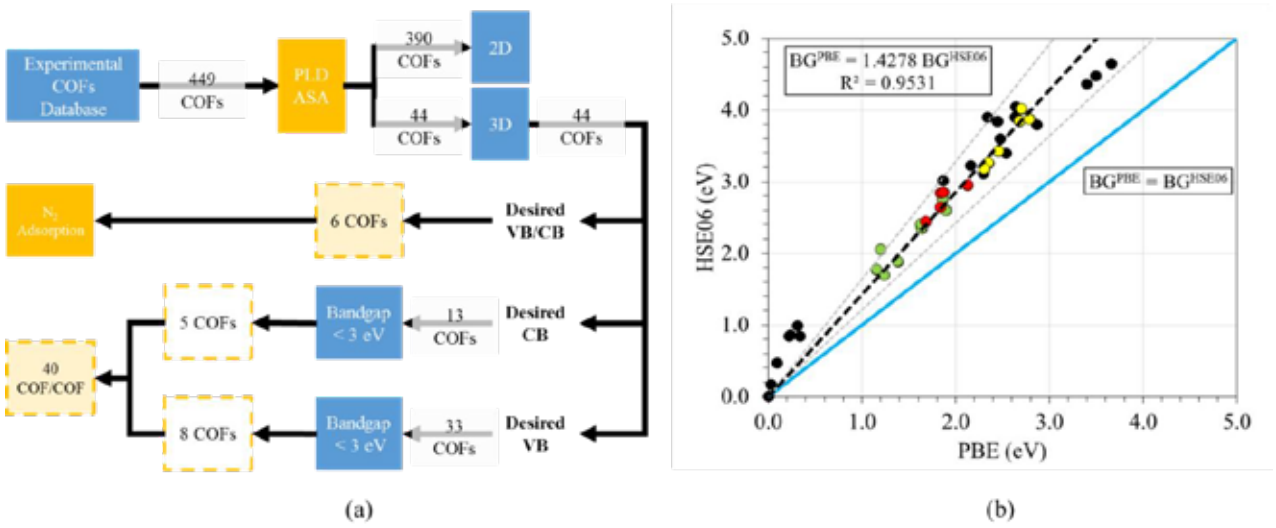


Figure 1. (a) Process flow used in this work starts from the database and ends with selecting desired COFs for photofixation of N_2 and COF/COF heterojunction. (b) Bandgaps of the studied list of COFs using PBE and HSE06 functionals. Yellow circles show the six structures selected for the sole photocatalytic process. Green and red circles are structures selected for heterojunction systems as semiconductors I and II, respectively.

Next, single-point DFT computations are performed on the 3D structures using PBE and HSE06 functionals. The results and comparison between the bandgaps are reported in Figure 2. The figure shows that the bandgaps obtained via the hybrid functional are higher than GGA based functional. A correlation is determined using a straight line with a coefficient of determination of 0.953. Out of the 44 COFs, only 6 had desirable conduction and valence bands (yellow circles in Figure 2). However, these 6 COFs have bandgaps between 3 and 4 eV. To investigate other COFs for the application, COF/COF heterojunctions are planned by combining COFs with desired conduction bands with COFs with a desirable valence band. Also, these COFs have to have a bandgap lower than 3 to increase light absorption in the visible light region. The results showed that 11 and 33 COFs had desired Condiction band and valence band, respectively. However, only 4 and 8 COFs have the set bandgap. This number of COFs makes it possible to manufacture a total of 32 different COF/COF junctions from a theoretical point of view. In order to differentiate between these combinations, a list of computations can be implemented. Additional computational work can follow, including charge separation and mobility, to assess the effectiveness of the junction.

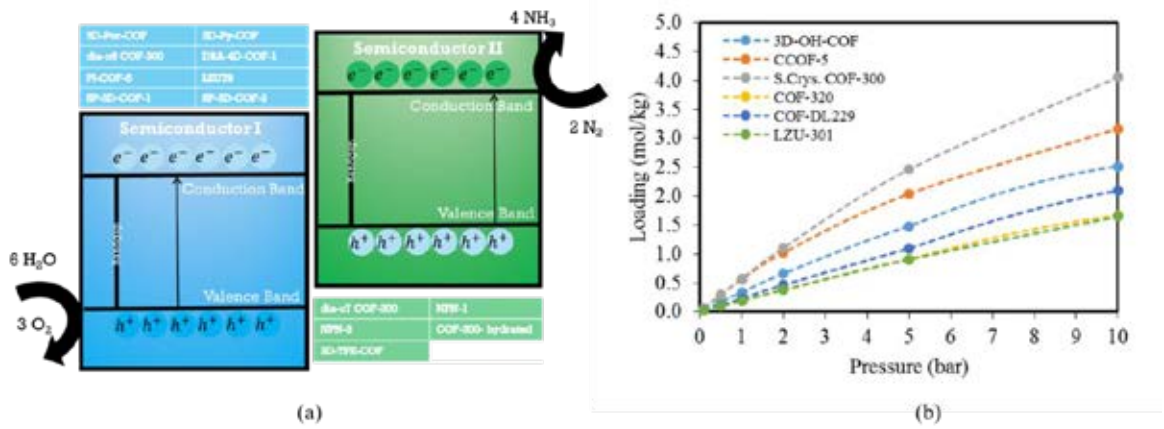


Figure 2. (a) COF/COF heterojunction towards ammonia production representation (b) N_2 adsorption isotherms for the six selected structures at 298K and pressure range of 0.1-10 bar. Dashed lines are used for visual aid.

In this work, following the DFT computations, we use GCMC simulation to compute the N_2 isotherms in the select 6 COFs. The adsorption isotherms are computed at several pressure points, 0.1, 0.5, 1, 2, 5, 10, and 50 bars, adsorption isotherms from 0.1-10 bars are shown in Figure 3. A comparison between the 6 COFs is made based on the N_2 loading at 1 bar. At a pressure of 1 bar and 298K, CCOF-5 and COF-300 have the highest adsorption of N_2 among the 6 COFs, with COF-300 having a slightly higher value. The adsorption at 50 bar is also reported to indicate N_2 saturation in the structure; COF-300 has the edge at the 50 bar pressure point. COF-300 has a higher surface area, three times the surface area of CCOF-5. Nevertheless, CCOF-5 has a lower bandgap (HSE06) than COF-300, which is desirable for the application ($BG^{COF\text{-}300}$=3.462 eV and $BG^{CCOF\text{-}5}$=3.183 eV).

CONCLUSION

COFs are materials with excellent properties desirable for various applications in gas separation, catalysis, and other functionalized applications. In this work, and for the first time, 3D COFs are screened for the efficient N_2 fixation process in a photocatalytic system. The screening uses several atomistic and molecular simulations techniques to determine the structural, adsorption, and electronic properties. Following some atomistic and molecular simulations steps, six different COFs are selected for the application using a pre-selected mechanism for N_2 fixation. These selected COFs were also tested for N_2 adsorption at a range of pressure points. Besides, a list of 3D COF/COF heterojunction materials was proposed that satisfies the required energy levels. At the same time, each has a bandgap of less than 3 to increase the light absorption ability of the composing structure. The work shed light on the possibility of screening COFs and other porous materials for catalytic applications. Also, the results showed an excellent correlation between bandgap obtained via relatively fast PBE functional and slower, more accurate functionals, which can be helpful to accelerate the determination of COFs for various electronic properties.

ACKNOWLEDGEMENT

This publication was made possible by an award from the Qatar National Research Fund (a member of Qatar Foundation) with scholarship number GSRA5-1-0513-18051. We are grateful to the High-Performance Computing Center of Texas A&M University at Qatar for its generous resource allocation.

REFERENCES

1. Niu L, Zhao X, Wu F, Tang Z, Lv H, Wang J, et al. 2021. Hotpots and trends of covalent organic frameworks (COFs) in the environmental and energy field: Bibliometric analysis. Science of the Total Environment 783:146838.
2. Ongari D, Talirz L, Smit B. 2020. Too Many Materials and Too Many Applications: An Experimental Problem Waiting for a Computational Solution. ACS Central Science 6:1890–900.
3. Mohamed AMO, Bicer Y. 2021. A comprehensive methodology to screen metal-organic frameworks towards sustainable photofixation of nitrogen. Computers & Chemical Engineering 144:107130.
4. Mohamed AMO, Bicer Y. 2022. The Search for Efficient and Stable Metal-Organic Frameworks for Photocatalysis: Atmospheric Fixation of Nitrogen. Applied Surface Science 583:152376.
5. Tong M, Lan Y, Yang Q, Zhong C. 2017. Exploring the structure-property relationships of covalent organic frameworks for noble gas separations. Chemical Engineering Science 168:456–64.

WHEC-2022
23rd World Hydrogen Energy Conference
June 26-30, 2022 - Istanbul

#416

COMPATIBILITY OF POLYMERS AND COMPOSITES WITH HYDROGEN IN TRANSPORT AND STORAGE EQUIPMENT

[1*] *Xavier Lefebvre,*[1] *Marie-Hélène Klopffer,* [1] *Camilo Castro Lopez*
[1] IFP Energies Nouvelles, Applied Physical Chemistry and Mechanics Division,
1&4 avenue de Bois-Préau, 92852 Rueil-Malmaison Cedex, France

*Corresponding author e-mail: xavier.lefebvre@ifpen.fr

ABSTRACT

With the growing place taken by hydrogen, some questions still remain about its delivery, transport and storage. In these domains, one of the key challenges to compete is the great permeability of hydrogen through polymer and composite infrastructures (pipes, connecting parts, pressure vessels, …) compared to other gases such as methane for instance. In this context, the compatibility of hydrogen with polymeric components must be carefully qualified regarding permeation properties, blistering and collapse resistance. Long-time behaviour may be assessed with specific modelling. Beyond qualification aspects, this approach can be useful to support standards elaboration.

Keywords: Polymer, Composite, Permeation, Blistering, Hydrogen

INTRODUCTION

In the challenging context of the oil and gas industry, many studies have been carried out at IFPEN to understand, describe and model the permeability and the blistering of thermoplastic polymers and composites [1-3]. This background is a big advantage to deal with hydrogen interactions with polymers, since experimental equipment and numerical tools are available and can be adapted to the specific case of hydrogen.

SEVERAL MECHANISMS INDUCED BY DIFFUSION

The permeability of a polymer to a gas is defined as its property to absorb and transport the species in a molecular state, according to the gradient of chemical potential. Therefore, the permeability coefficient is the product of the solubility coefficient, describing the solute concentration in the polymer at steady-state and the diffusion coefficient, representing the solute mass transport inside the polymer.
When service conditions consist in cyclic fillings and pressurization, one of the main issues regarding polymers is the risk of blistering that can be caused by rapid gas decompression. Linked to the above-described permeation mechanism, after a given service time, a polymer matrix contains a certain amount of dissolved gas. Then, considering a low depressurization rate of the system, this amount of gas could have the time to escape from the material without causing any damage. But, if the decompression rate is high, the dissolved gas can even lead to the formation of bubbles inside the polymer. Therefore, the occurrence of blistering depends on many parameters such as gas and polymer natures, gas-polymer interactions, temperatures and pressures profiles during service and depressurization steps (Fig. 1).

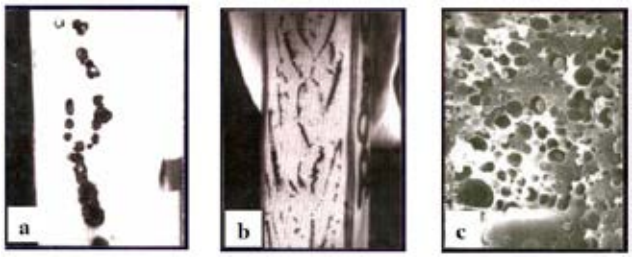


Fig. 1. Illustration of blistering obtained in various gas-polymer systems [4]
(a: PE/CH4 at low decompression rate – b: PE/CH4 at high decompression rate – c: PVDF/CO2 at high decompression rate).

In addition to blistering, another kind of damage due to gas diffusion might be observed in multi-layer systems, such as in type IV pressure vessels, in which a polymer liner is winded up with a fiber composite. During service, gas can be trapped at the interface between the liner and the composite layer. During high-rate decompression, the cumulated gas in the interface exposes the liner to a much larger external pressure in comparison with the internal pressure, thus causing the collapse of the liner.

EXPERIMENTAL APPROACH

For many years, IFPEN has developed specific devices to measure permeation coefficients and assess blistering resistance with the objective to represent, as closely as possible, the real operating conditions of polymers under various settings of pressure and temperature [1-5].
Several permeation devices make it possible to work with pure hydrogen or in mixture with methane. It has been used in previous projects when some preliminary solutions have been evaluated and assessed to cope with present problems for hydrogen gas distribution and to sustain higher pressures compared to classical high-density polyethylene pipe (Fig. 2).
For blistering consideration, we are currently working to make our devices compatible with high hydrogen pressure (typically 1000 bar).

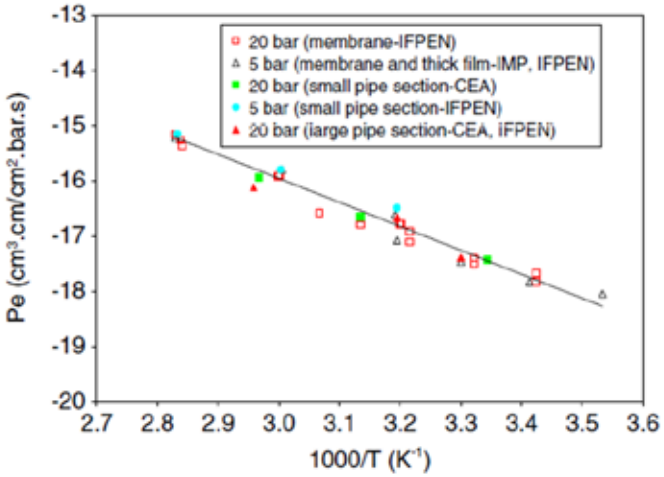


Fig. 2. Evolution of the permeability coefficient (Pe) with temperature (T) in an Arrhenius representation for pure H2 through HDPE at two different pressures, for various geometries and devices - polHYtube project [5]

NUMERICAL APPROACH

In parallel to experimental studies, IFPEN has also developed specific modelling for polymers and composites to simulate and predict long term behaviour. For instance, based on analytic laws [6,7], a specific finite elements model has been developed to evaluate the permeation properties of composites, based on the inner properties of the matrix and the fiber volume fraction. The repartition of the fibers fraction inside the composite and the presence of voids can also be considered as parameters that will impact the transport properties (Fig. 3.).
Dealing with blistering considerations, a coupling has been made between diffusion, mechanics and thermodynamics in order to describe as best as possible the behaviour of the species dissolved in the polymer, their interaction, and the impact on mechanical properties. For that purpose, a diffuso-elastoviscoplastic model for semicrystalline polymers has been developed using a porous media approach [8,9]. The material is represented by two phases: the crystalline phase (skeleton) and the mixture of dissolved gas and free amorphous (fluid). Damage is represented by plastic porosity (cavitation) within the amorphous phase due to a stress gradient induced by a gas concentration gradient during decompression (Fig. 4). The development of this kind of coupled model is still in progress and evolution.

CONCLUSION

IFPEN is in position to cope with the great challenge of the compatibility of polymers and composites with hydrogen. The oil & gas background in terms of permeation, blistering and collapse resistance are key advantages to be quickly relevant on these topics, both on experimental and numerical studies.

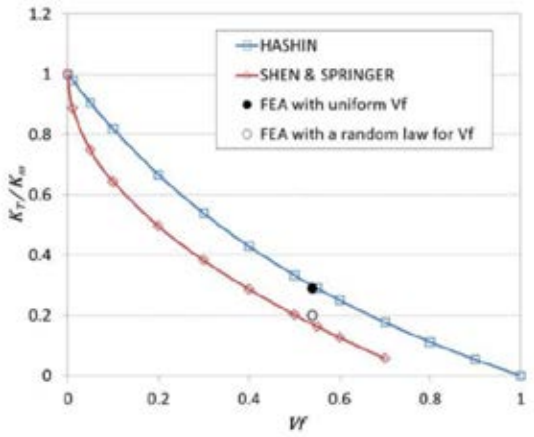


Fig. 3. Impact of the distribution of fibers Vf on the transverse permeability of the composite K_T. K_m is the permeability of the matrix

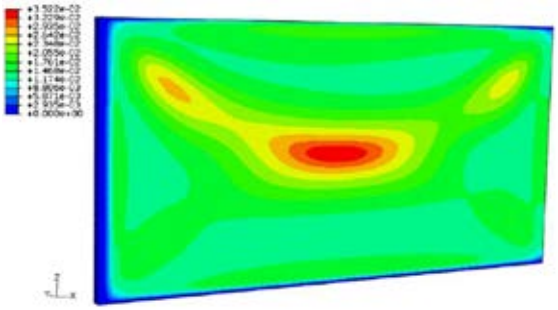


Fig. 4. Representation of cavitation in a section of a semicrystalline polymer membrane at the end of the gas decompression stage obtained with the diffuso-elastoviscoplastic-damage model [10]

REFERENCES

1. Flaconnèche B., Martin J., Klopffer M.H. (2001) Permeability, Diffusion and Solubility of Gases in Polyethylene, Polyamide 11 and Poly(vinylidene fluoride), OGST J., 56 (3) 261-278
2. Grandidier J.C., Baudet C., Boyer S., Klopffer M.H., Cangémi L. (2015) Diffuso-Kinetics and Diffuso-Mechanics of Carbon Dioxide / Polyvinylidene Fluoride System under Explosive Gas Decompression, OGST J., 70 (2) 251-266
3. Castro López C., Lefebvre X., Brusselle-Dupend N. et al. (2016) Effect of porosity and hydrostatic pressure on water absorption in a semicrystalline fluoropolymer. J Mater Sci 51, 3750–37612.
4. Cangémi L., Klopffer M-H., Martin J., Grandidier J-C., Une approche multiphysique de l'endommagement de polymères en milieu pétrolier : Exemple du blistering, L'actualité chimique, n° 289, 2005
5. Klopffer, M.H., Berne P., Espuche E. (2015) Development of Innovating Materials for Distributing Mixtures of Hydrogen and Natural Gas. Study of the Barrier Properties and Durability of Polymer Pipes - OGST J.,70 (2) 305–315.
6. Hashin Z. (1972) Theory of Fiber Reinforced Materials, NASA CR-1974.
7. Shen C.H., Springer G.S. (1976) Moisture Absorption and Desorption of Composite Materials. Journal of Composite Materials. vol. 10. n° 1. p. 2–20.
8. Cangémi L., Meimon Y. (2001) A Two-Phase Model for the Mechanical Behavior of Semicrystalline Polymers, OGST J., 56 (6) 555-580
9. Rambert G. Grandidier J.C., Cangémi L., Meimon Y. (2003) A Modelling of the Coupled Thermodiffuso-Elastic Linear Behaviour. Application to Explosive Decompression of Polymers, OGST J., 58 (5) 571-591
10. Baudet C. Grandidier J.C., Cangémi L. (2009). Damage model for the blistering of polyvinylidene fluoride subjected to carbon dioxide decompression. International Journal of Solids and Structures. 46. 1389–1401.

WHEC-2022
23rd World Hydrogen Energy Conference
June 26-30, 2022 - Istanbul

#441

NUMERICAL AND EXPERIMENTAL EVIDENCE OF DEFECTS CREATION IN EPDM AFTER HYDROGEN DECOMPRESSION

Quentin Gardavaud, Maximiliano Melnichuk, Frédéric Thiébaud, Dominique Perreux
Univ. Bourgogne Franche-Comté, FEMTO-ST Institute, UMR CNRS 6174, Department of Applied Mechanics,
24 rue de l'épitaphe, 25000 Besançon, FRANCE

*Corresponding author e-mail: quentin.gardavaud@femto-st.fr

ABSTRACT

Elastomers are main components in hydrogen systems. It was reported that these materials could be damaged when submitted to hydrogen high-pressure, especially in case of fast depressurisation. In order to predict this phenomenon, we define a prediction model, and assess it by depressurised elastomer samples.

Keywords: type IV tanks, EPDM, cavitation, fast depressurization, tomography.

INTRODUCTION

Elastomeric materials subjected to gases at high-pressure can have issues during decompression [1]. For instance, a sudden decompression can promote the formation of cavities inside the material [2]. This phenomenon is known as cavitation. There is a body of scientific articles treating different aspects of it, indicating for instance that the damage initiation depends on saturation pressure, depressurisation rate, and material thickness, among other parameters [2]. In the present paper, we use a previously developed general approach by non-dimensional parameters to estimate the risk of cavitation [3]. We subjected EPDM samples to saturation pressure up to 18.5 MPa, followed by a fast depressurisation. Defects formation was confirmed by tomography. Experimental results are in accordance with numerical predictions. Present results suggest that we can use the non-dimensional approach as a guideline for the design of systems involving elastomers under high pressure, such as O-rings in type IV hydrogen containers.

MATERIALS AND METHODS

We studied an elastomer material frequently used to produce O-rings: EPDM 70. Materiel properties were defined in our laboratory using a MTS device (Platform Ametiste, FEMTO-ST). Considering a Neo-Hookean behaviour, we obtained a shear modulus μ=2 MPa. We measured diffusion with hydrogen: D=1.6E^{-10} m²/s. Both values correspond with literature. We made disk samples, obtained from extruded boards with a thickness of 10 mm. In order to favour hydrogen entrance and exit of the sample perpendicular to the geometrical flat surface, we fixed a minimal five-time ratio of samples (Ø > 5 thickness). Under this geometrical condition, we assume that at the centre of the samples border effects are negligible.

Sample handling under hydrogen pressure was attained in a stainless-steel pressure chamber designed to work at 40 MPa. Because of safety reasons, hydrogen handling was performed in a safety pit, with no temperature control: ambient temperature was 10 ± 5°C. Saturation pressure was 18.5 ± 0.5 MPa. We calculated the evolution of hydrogen concentration [4], to conclude that 48 h time was enough to saturate the samples under study. Then, a fast depressurisation was performed. Depressurisation rate was maximized in order to boost cavitation phenomenon, reaching ≈100 MPa/min.

To determine the creation of cavities inside EPDM, tomography analysis was performed on as-received and depressurised samples, with an EasyTom Nano tomography system (RX Solutions/Platform Mifhysto, FEMTO-ST) with a voxel resolution of ≈8 μm^3.

RESULTS AND DISCUSSION

Defects appearance

We saw the formation of a macroscopic defect or blister in one of the samples (Figure 1a). This blister appeared some hours after the depressurisation, and grew during the following days until it reached its maximum size and disappeared. Figure 1b shows a tomography cut view of the blister near its bigger size, at 50h after depressurisation. Figure 1c shows tomography images of the sample as received and 167 h after depressurization, a time when we consider that transient effects are irrelevant. Three depths are presented: surface level, 1 mm depth and 2 mm depth.

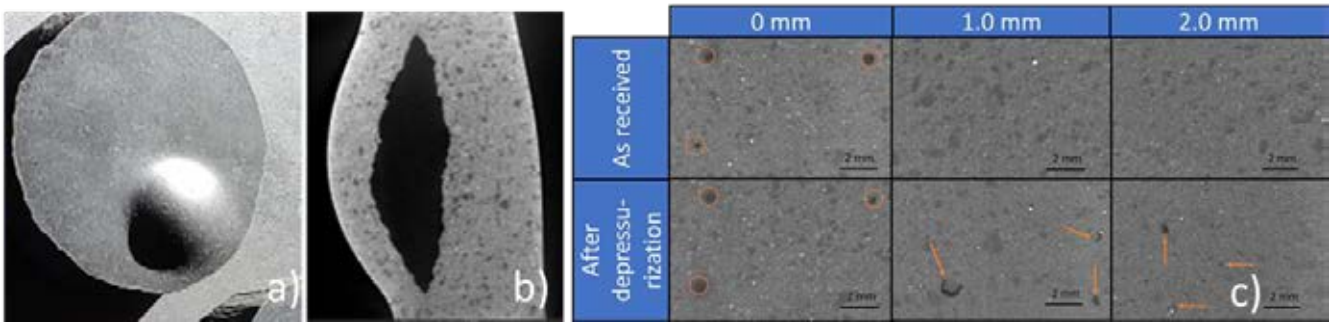


Figure 1: a) Blister appearance on the sample b) lateral tomography of blister c) tomography images before and after depressurisation.

The analysis of tomography images allows exploring the creation of defects inside EPDM samples. Particularly, in Figure 1c, it is possible to see cavities formation (orange arrows). These cavities appeared around higher density areas and charges, and seems to be more frequent as a function of depth. Blister and cavities appearance confirms material degradation through the creation of macroscopic and microscopic defects after exposure to hydrogen.

Degradation predictions model

We developed a numerical approach to address cavitation risk [3]. A spherical defect in which there is a pressure of P_{int}, is embedded in the material, submitted to an external pressure P_{ext}. We consider the sample fully saturated by hydrogen, and a geometry of plane sheet. Then a fast depressurization is applied on it, promoting cavitation as the pressure inside the defect will decrease slowly compared to external pressure. In order to analyse the influence of depressurization rate, Yersak et al. [5] defined a parameter called P_{pore}, which accounts the level of unbalance between P_{int} and P_{ext} ($P_{pore} = P_{int} - P_{ext}$). Comparison of P_{pore} and a defect propagation criterion, called P_y, allows to address cavitation risk.

The expression of internal pressure P_{pore}, depending on P_{ext}, x, t, and P_{int}. In case of a fully saturated sample, it is possible to derive equation (1), calculating P_{int}. Based on the work of Crank [4], this equation is valid for diffusion into a plane sheet of material and a depressurisation situation.

$$\frac{DP_{int}(t_{deso}-t_0)}{(P_{sat}-P_{min})l^2} = \frac{\mathrm{Dt}}{l^2} + \frac{1}{2}\left(\frac{x^2}{l^2} - 1\right) + \frac{16}{\pi^3}\sum_{n=0}^{\infty}\frac{(-1)^n}{(2n+1)^3} exp\left\{\frac{-D(2n+1)^2\pi^2 t}{4l^2}\right\} cos\frac{(2n+1)\pi x}{2l} \quad (1)$$

D is the diffusion coefficient, *l* half-thickness of plate, the term $(P_{sat} - P_{min})/(t_{deso} - t_0)$ accounts depressurisation rate, *x* the position in the plate and *t* the time.

From several works [1, 6, 7], maximal pressure inside an elastomer pore must not excess 5*μ*/2, with *μ* the share modulus of Neo-Hookean model (eq. (2)). Otherwise, external works acting on material will overpass internal energy required to ensure the wholeness of the elastomer [8]. Then, there is risk of plasticization or breakage, the latter being expected elastomer behavior. We assume two reasonable assumptions: there is no heat generation and surface tension are negligible.

$$P_y = \frac{5\mu}{2} \quad (2)$$

Knowing P_{pore} and P_y (eq. (1) and (2)), to simplify our analysis, we moved forward to a non-dimensional approach. This way, we defined a parameter called non-dimensional cavitation (NDCav, eq. (3)), and two complementary M_y and T_{deso} parameters to address if a polymer is likely to cavitate (Eqs. (4) and (5)).

$$NDCav = \frac{P_{pore}}{P_y} \quad (3)$$

$$M_y = \left(\frac{P_{sat}-P_{min}}{P_y}\right) = \frac{\Delta P}{P_y} \quad (4)$$

$$T_{deso} = \frac{Dt_{deso}}{l^2} \quad (5)$$

NDCav lower than 1 implies no cavitation risk. Contrary, the higher the P_{pore} to P_y rate, the higher the risk of cavitation, as the expected pressure inside the pore overpass the mechanical capacity of the material. For further details, refer to [3]. Eq. (3), (4), (5) are still valid in any material situation. Figure 2 shows the numerical results of T_{deso} vs. M_y, for

different NDCav curves. The graph indicates the zone where cavitation is unlikely (NDCav < 1), and on the other corner the zone where cavitation is highly probable.

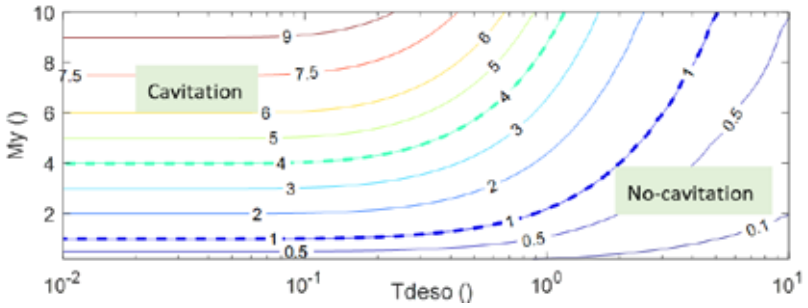


Figure 2: non-dimensional results for cavitation estimation, NDCav abacus.

Comparison between experiment and modelling

In order to compare experimental results with numerical prediction, we identified NDCav values corresponding to present experiments. Parameters retained are D=1.6E-10 m²/s; l=0.005 m; ΔP=185 bars; t_{deso}=10 s; μ=2 MPa. From eq. (4) et (5), we obtain: $M_y = 3.7$ and $T_{deso} = 6.4E-5$. From Fig. 2 we see that for present experimental configuration, $NDCav = 3.7 > 1$. As NDCav is higher than 1, degradations are likely to occur in our material.

Indeed, experiments have shown degradations of EPDM samples under fast depressurisation, increasing towards the centre of the sample. In terms of NDCav equations, the proximity of the surface can be interpreted as a lower l parameter, which implies a lesser cavitation risk. Full validation of NDCav abacus to elastomer materials requires further experimentation with other materials and experimental conditions, which is out of the scope of present work.

CONCLUSIONS

Degradations in elastomers exposed to high-pressure hydrogen is a relevant topic in hydrogen technologies, especially in the case of a fast depressurisation condition. We developed a model allowing to predict degradations due to hydrogen. This model was assessed by comparing its prediction with experimental results on EPDM samples after a sudden depressurisation. Cavities were highlighted with tomography technique, confirming model predictions by direct comparison of material before and after hydrogen exposure.

ACKNOWLEDGMENTS

The authors want thank support from EIPHI Graduate school (contract "ANR-17-EURE 0002"). Financial support has been provided by BPI and FEDER from Region Bourgogne Franche-Comté, France (Vhyctor project). Constant support from Mahytec SARL team with hydrogen handling is highly appreciated. The authors also thank sustenance from Mifhysto and Ametiste research platforms of FEMTO-ST Institute for materials characterisation (Besançon, France).

REFERENCES

1. Yamabé, J., A. Koga, et S. Nishimura. 2013. « Failure behaviour of rubber O-ring under cyclic explosure to high-pressure hydrogen gas. » *International Journal of Hydrogen Energy* 35: 193-205.
2. Jaravel, Julien, et al. 2011. « On key parameters influencing cavitation damage upon fast decompression in a hydrogen saturated elastomer ». *Polymer testing* 30: 811-18.
3. Melnichuk, Maximiliano, Frédéric Thiébaud, et Dominique Perreux. 2020. « Non-dimensional assessments to estimate decompression failure in polymers for hydrogen system ». *International Journal of Hydrogen Energy* 45: 6738-44.
4. Crank J. 1975. The Mathematics of Diffusion, Oxford University Press.
5. Yersak T. A., Baker D. R., Yanagisawa Y., Slavik S., Immel R., Mack-Gardner A., Herrmann M., Cai M. 2017. Predictive model for depressurization-induced blistering of type IV tank liners for hydrogen storage. International Journal of Hydrogen Energy 42:28910-28917.
6. Gent, A. N., et P. B. Lindley. 1958. « Internal rupture of bonded rubber cylinders in tension ». *Sir Eric Rideal, F. R. S.* 249: 195-205
7. Fond, Christophe. 2001. « Cavitation Criterion for Rubber Materials: A Review of Void-Growth Models ». *Journal of Polymer Science* 39: 2081-96.
8. Diani, Julie. 2001. « Irreversible growth of a spherical cavity in rubber-like material: a fracture mechanics description ». *International Journal of Fracture* 112: 151-61.

WHEC-2022
23rd World Hydrogen Energy Conference
June 26-30, 2022 - Istanbul

#1446

EFFECTIVE HYDROLYSIS OF ALKALINE SODIUM BOROHYDRIDE: CoB-TRITON CATALYST

[1*]Cenk Kaya, [2] Jülide Hazal Türkcan, [3]Hüseyin Elçiçek, [2]Oğuz Kaan Özdemir, [4]Görkem Kökkülünk, [4]Kaan Ünlügençoğlu
[1*]Istanbul Technical University, Marine Engineering, Istanbul, Turkey
[2]Yildiz Technical University, Metallurgical and Materials Engineering, Istanbul, Turkey
[3]Maritime Higher Vocational School, Sakarya University of Applied Sciences, Sakarya, Turkey
[4]Yildiz Technical University, Marine Engineering, Istanbul, Turkey

*Corresponding author e-mail: cenkkaya@itu.edu.tr

ABSTRACT

Chemical hydrides show promise in solving the storage challenge, which is one of the important problems in the widespread use of hydrogen. An important issue that needs to be developed regarding chemical hydride storage is the high speed of hydrogen release. For this reason, this study focuses on hydrogen release rates of alkaline sodium borohydride with different prepared catalysts. Different amounts of surfactant as Triton X-100 including CoB catalysts have been prepared and hydrogen release rates (HGR) have been compared. Results indicate that Triton addition has different effects, but optimum ratio improves catalyst performance. 150 µl Triton addition (CoB-T150) raises HGR from 12.61 $L_{H2}*g^{-1}_{cat}*min^{-1}$ to 17.69 $L_{H2}*g^{-1}_{cat}*min^{-1}$, as 40.2% increase compared to pure CoB catalyst. As a result, surfactants offer alternative to enhance catalyst performance and need further research.

Keywords: CoB catalyst, $NaBH_4$ hydrolysis, surfactant, Triton X-100, hydrogen storage.

INTRODUCTION

Cobalt is effective transition metal in regard of chemical hydride hydrolysis. Its abundancy, low cost [1] and relatively high hydrolysis performance [2] are significant advantageous but it still needs an improvement considering its tendency to agglomeration during exothermic hydrolysis reaction [3]. This agglomeration leads to a reduction of the area where the interaction takes place [4]. Various stabilizing agents are used in the literature for stabilization [5][6]. One of them is surfactant as “surface active agent”. It is effective on the crystal formation, determining shape of material [7] and thus it may be a solution in the research for a catalyst with high catalytic activity for the hydrolysis reaction. For this reason, this study investigates that different amount of Triton X-100 -as nonionic surfactant- usage during cobalt boride catalyst preparation and activation of prepared catalysts within NaOH stabilized sodium borohydride solution.

MATERIALS AND METHODS

In this section, details of catalyst preparation and hydrogen releasing processes have been summarized.

Catalyst Preparation

Pure CoB and surfactant as Triton X-100 added CoB-Triton catalysts have been prepared using chemical reduction method. First of all, cobalt(II) chloride hexahydrate (Merck) and ethanol were mixed in a volumetric flask and 0.02 mole solution was formed. Certain amounts of prepared solution and ethanol were mixed in a beaker. Triton X-100 was added by micropipette as microliter level. Last pH was regulated with benchtop pH meter (Orion Star A111) to 4 for all catalysts with HCl or NaOH addition. Then, pH regulated solutions were cooled down 6 ºC in the circulating water bath (Heidolph Rotachill) and reduction was carried out injecting sodium borohydride (Alfa Aesar)-distilled water solution with constant 5 ml/min flow ratio by syringe pump (Chemyx-Fusion 6000), during 500 rpm stirring conditions. Mud like black stack was separated and washed with one time ethanol and two-time distillated water to eliminate contamination. Afterthat, extracted catalyst particles were dried in oven (Nuve EV 018) at 110 ºC, under 75% vacuum at least 2 hours. The flocculated catalysts removed from the oven were crushed by pressing in a mortar. Table 1 represents abbreviations of catalysts, according to Triton amount.

Table 1. Abbreviations of prepared catalysts.

Amount of Triton X-100, µl	Abbreviation
0	CoB
25	CoB-T25
50	CoB-T50
100	CoB-T100
150	CoB-T150
200	CoB-T200
250	CoB-T250

Hydrogen Releasing Tests

Experimental studies of hydrogen releasing rate determination have been carried out in Yildiz Technical University, Faculty of Chemical and Metallurgical Engineering Laboratory. Figure 1 illustrates test stand. First of all, sodium borohydride (Alfa Aesar), sodium hydroxide pellets (Merck, 99-100%) and distilled water are mixed in a small beaker. Prepared fuel in beaker is placed in a water bath (JSRC-13C) adjusted to the 65 ºC temperature. 10 mg weighed catalyst with analytical balance (Radwag-AS 220.R2) and heated fuel is poured into volumetric flask and the flask is closed with flexible hose which connected to bubbler and gas burette. Released hydrogen gas from hydrolysis reaction passess from bubbler and replaces the water in the gas burette. During all reaction, circulating water bath keeps the temperature constant and magnetic stirrer ensures 500 rpm.

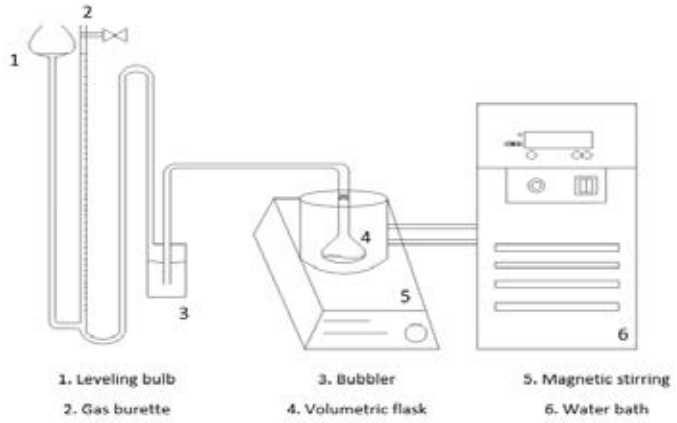


Fig. 1. Experimental setup of hydrogen release tests.

Total released hydrogen per gram catalyst and minute ($L*g^{-1}*min^{-1}$) is defined as hydrogen generation rate:

$$HGR = \frac{L_{H2}}{g_{cat}*min} \quad (1)$$

RESULTS AND DISCUSSION

In this section, performance of pure CoB and Triton added CoB catalysts were compared according to hydrogen release rates. Fig. 2 presents HGR results. It was observed that small amount (25 µl and 50 µl) of Triton addition reduces HGR and afterthat continuous increment raises HGR value until peak point as 150 µl. At this point, HGR rate is 17.69 $L_{H2}*g^{-1}_{cat}*min^{-1}$, 40.2% higher than pure CoB value. This may be attributed to anti-agglomeration effect of the surfactant [8]. Thus, raising surface area/mass ratio enhances catalytic activity. Moreover, decreased tension between fuel and catalyst may enhance wettability and result as higher interaction [9]. Also, Figure 3. represents emitted total hydrogen volume -against time- from 500 mg sodium borohydride, 500 mg NaOH and 10 ml distillated water solution, in the presence of 10 mg catalyst. It is clearly observed that Triton 150 releases maximum hydrogen volume in a short time, whereas Triton 50 releases less hydrogen with long time as parallel to HGR result. In addition to this, Triton 150 is obviously advantageous compared to pure CoB catalyst. Therefore, optimum amount of surfactant is 150 µl which indicates that further research like characterization and optimum conditions finding will be carried out with this catalyst.

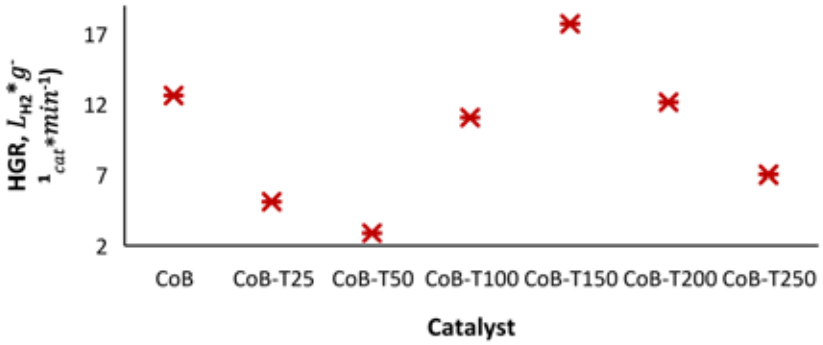


Fig. 2. HGR results of different catalysts.

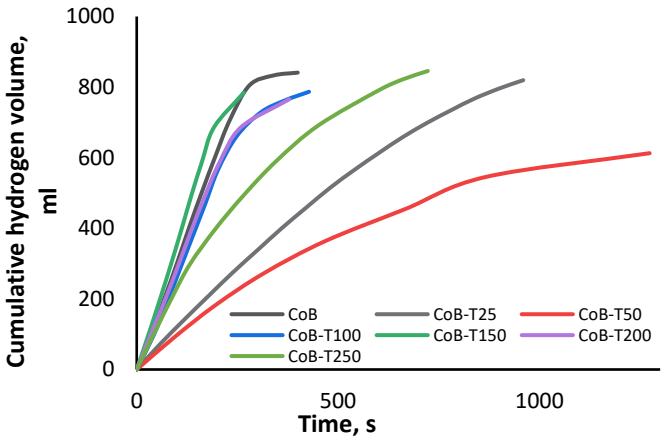


Figure 3. Released H_2 volume against time.

CONCLUSIONS

In this study, hydrolysis experiments of alkaline $NaBH_4$ in the presence of prepared CoB-Triton catalysts were carried out. According to HGR results, CoB-Triton 150 (150 µl Triton) is optimum catalyst that increases HGR as 40.2% compared to pure CoB. Our further research will be investigation of reaction temperature effect, optimum fuel concentration and SEM analysis.

REFERENCES

[1] S. Guan *et al.*, "Stabilized cobalt-based nanofilm catalyst prepared using an ionic liquid/water interfacial process for hydrogen generation from sodium borohydride," *Journal of Colloid and Interface Science*, vol. 608, pp. 3111–3120, Feb. 2022.

[2] S. U. Jeong *et al.*, "A study on hydrogen generation from NaBH4 solution using the high-performance Co-B catalyst," *Journal of Power Sources*, vol. 144, no. 1, pp. 129–134, Jun. 2005.

[3] F. O. Baydaroglu, E. Özdemir, and A. G. Gürek, "Polypyrrole supported Co–W–B nanoparticles as an efficient catalyst for improved hydrogen generation from hydrolysis of sodium borohydride," *International Journal of Hydrogen Energy*, vol. 47, no. 16, pp. 9643–9652, Feb. 2022.

[4] N. Patel, R. Fernandes, and A. Miotello, "Promoting effect of transition metal-doped Co–B alloy catalysts for hydrogen production by hydrolysis of alkaline NaBH4 solution," *Journal of Catalysis*, vol. 271, no. 2, pp. 315–324, May 2010.

[5] M. H. Loghmani and A. F. Shojaei, "Hydrogen production through hydrolysis of sodium borohydride: Oleic acid stabilized Co–La–Zr–B nanoparticle as a novel catalyst," *Energy*, vol. 68, pp. 152–159, Apr. 2014.

[6] O. Metin and S. Ozkar, "Hydrogen Generation from the Hydrolysis of Ammonia-borane and Sodium Borohydride Using Water-soluble Polymer-stabilized Cobalt(0) Nanoclusters Catalyst," *Energy&Fuels*, vol. 23, pp. 3517–3526, 2009.

[7] M. Singh Bakshi, "How Surfactants Control Crystal Growth of Nanomaterials," *Crystal Growth Design*, vol. 16, pp. 1104–1133, 2016.

[8] F. O. Baydaroglu, E. Özdemir, and A. G. Gürek, "Ruthenium nanoparticles immobilized on surfactant-directed polypyrrole as an effective and reusable catalyst for hydrogen generation," *Reaction Kinetics, Mechanisms and Catalysis 2017 122:1*, vol. 122, no. 1, pp. 575–591, Jul. 2017.

[9] H. Elçiçek, M. Erol, and O. K. Özdemir, "Preparation of highly efficient NiB catalyst via triton-stabilized for alkaline NaBH4 hydrolysis reaction," *International Journal of Energy Research*, 2021.

WHEC-2022
23rd World Hydrogen Energy Conference
June 26-30, 2022 - Istanbul

#1453

ANALYSIS OF THE FIRST STEP OF HYDROGEN RELEASE OF AMMONIA BORANE FOR PCA WITH DIFFERENT HEATING RATES

[1,2*] *Roberto Hinojosa-Nava,* [2] *E.V. Mejía-Uriarte,* [2] *R.Y. Sato-Berrú*
[1]Instituto de Ciencias Aplicadas y Tecnología, [2] Facultad de Ciencias,
Universidad Nacional Autónoma de México,
Circuito Exterior S/N, Ciudad Universitaria, 04510, México City, México

*Corresponding author e-mail: hinro36@ciencias.unam.mx

ABSTRACT

Ammonia borane is a material with high hydrogen content, so it receives a lot of attention. Its handling and operating conditions are of great importance for technological applications. For this reason, in this work a study was carried out using high resolution Raman spectroscopy on the behavior of ammonium borane with four different heating ramps, in the first step of hydrogen release. With the data obtained, a principal component analysis (PCA) was made, in which the stability of AB in the release process can be noted. Stability is important in the release process, as it can be related to the formation of by-products.

Keywords: ammonia borane, Raman spectroscopy, principal analysis component, heating rates

INTRODUCTION

Ammonia borane (NH_3BH_3, AB) is one of the materials with high hydrogen content (19.6 wt. %), it was synthesized in 1955 [1], to which multiple studies have been carried out in the release process. Three steps of hydrogen release from AB by thermolysis are known. The temperature ranges in which this release occurs depend on the experimental conditions applied: the heating rate, pressure, purity, etc. [2]. AB releases about 1mol of H_2 in each release step and loses approximately 6.5 wt.% [3]. The first release step takes place between 100 and 130°C; at this point, mainly hydrogen and a few gaseous residues are released such as diborane (B_2H_6), borazine ($B_3N_3H_6$), and NH_2BH_2 [4, 5]. The second release step occurs between 130 and 200°C, in which a little more than one equivalent of H_2 is released per mole of AB, the main residue in this step is borazine; complex solid residues of type $[BNH_x]_n$ (with $x < 2$) is also formed [6]. And above 500°C, the last release step is observed, which is characterized by the residual loss of hydrogen and the formation of hexagonal boron nitride [7]. Five vibrational regions of borane ammonium are reported and defined: (i) a low-frequency region (100−500 cm^{-1}), which contains the lattice modes; a medium-low spectral region (500−900 cm^{-1}), containing the B-N stretching modes; (ii) an intermediate region (900−1300 cm^{-1}), which contains the BH_3 deformations; (iii) a medium-high spectral region (1300−1700 cm^{-1}), where the NH_3 deformations are observed; (iv) a high-frequency region (2200−2500 cm^{-1}), containing the B−H stretching modes; and (v) a very high-frequency region (3100−3400 cm^{-1}), containing the N−H stretching modes [8, 9]. In this work Raman spectra were obtaining in four regions: R1 (from 40 to 937 cm^{-1}), (from 966 to 1670 cm^{-1}), R3 (from 2180 to 2770 cm^{-1}) and R4 (from 3100 to 3400 cm^{-1}). The PCA was used to discriminate the Raman signals and show their differences, being registered in the main components (PCs), to which a statistical weight was associated.

MATERIALS AND METHODS

Ammonia borane, 97%, was purchased from Sigma-Aldrich and stored in a vacuum chamber. To carry out the analysis, a pellet of AB (16 mg) was prepared, subsequently it was heated in a THMS600 cell (Linkam Scientific Instruments), at a controlled temperature and with a precision of 0.01°C, to obtain Raman spectra as a function of temperature. The heating rates used were of 1, 2, 10 and 30°C/min. Raman spectra were obtained with backscatter geometry using a micro-Raman TriVista 557 spectrometer (Princeton Instrument) in a mono view configuration (1200 lines / mm grating and 700 mm optical path). The excitation line was 532 nm, double frequency of a Nd:YVO_4 laser and the instrument resolution was 1.9 cm^{-1}. Data acquisition of 10 s with an average of 15 times was used in all measurements.

For data analysis, a developed program in the MATLAB platform, based on the principal component analysis (princomp) was used. In this work, the PCA program used the covariance matrix in the four spectral regions. The changes between the shapes of the Raman spectra were recorded in the PCs with the highest percentage weight and plotted for their analysis.

RESULTS AND DISCUSSION

The Raman shift of spectra for the four heating rates in four regions is shown in Fig. 1; the bands that indicate the formation of species with NH_2 and $(BHNH)_n$ are observed. The hydrogen release temperature in the first step, for each heating rate, occurred in the range of 95-100°C.

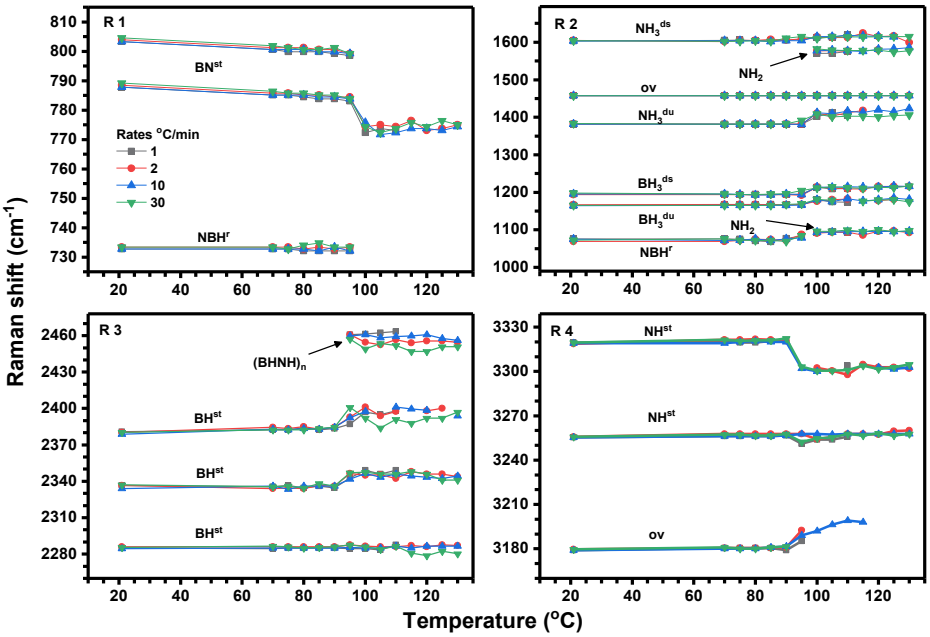


Figure 1. The shift of the AB bands, as a function of temperature, for the first release step, in the four AB spectral regions. The appearance of new bands for species with NH_2 and the formation of $(BHNH)_n$ are indicated with arrows.

In the spectra, a decrease in intensity is observed with increasing temperature; under these conditions, the material approaches the first step of hydrogen release. In region two, Fig 1, corresponding to the NH_3 modes, the appearance of two bands, located at 1576 and 1611 cm^{-1}, was observed after the first release step. With increasing temperature, the intensities of the bands changed; the intensity at 1611 cm^{-1} decreased and at 1576 cm^{-1} it increased.

The 1611 cm^{-1} band is the result of the 1604 cm^{-1} band shift. The 1604 cm^{-1} (NH_3ds) band is divided into two bands, 1576 cm^{-1} and 1090 cm^{-1} (which are also observed in the spectra for rates of 1, 2 and 10°C/min. These bands correspond to species with NH_2 and may correspond to polyaminoborane ((NH_2BH_2) PAB) formed at a temperature lower than 120°C [10, 11]. In region three, a new band also appeared after hydrogen release at 2460 cm^{-1}. This band is characteristic of stretching of the BH mode in polyiminoborane ((BHNH)n, PIB), formed at temperatures above 120ºC, which suggests the formation of this by-product [11]. These bands agree with what was observed by MJ Valero et al in Raman Spectra Obtained as a Function of Temperature [12].

According to the PCA analysis, PCA1 is related to intensities, which are associated with several molecules that provide the signal for each band. PCA2 is related to the position of bands (shift, disappearance, or appearance). In this sense, we can determine that in Fig 2 a dispersion of points (spectra) for a heating rate is associated with irregular intensity changes and shifting of the bands in a large interval of PCA 2. We can associate this with the instability of the AB when approaching the point of hydrogen release. According to Fig 2, when comparing the intervals of PCA 1 and 2, between the four heating rates, for the four regions, a large dispersion of points is observed for the rates 1, 2 and 10°C/min, and for the heating rate of 30°C/min, the points cover smaller intervals of PCA 1 and 2, for which it is considered that for this rate the release is under a more stable path and more directed to the release.

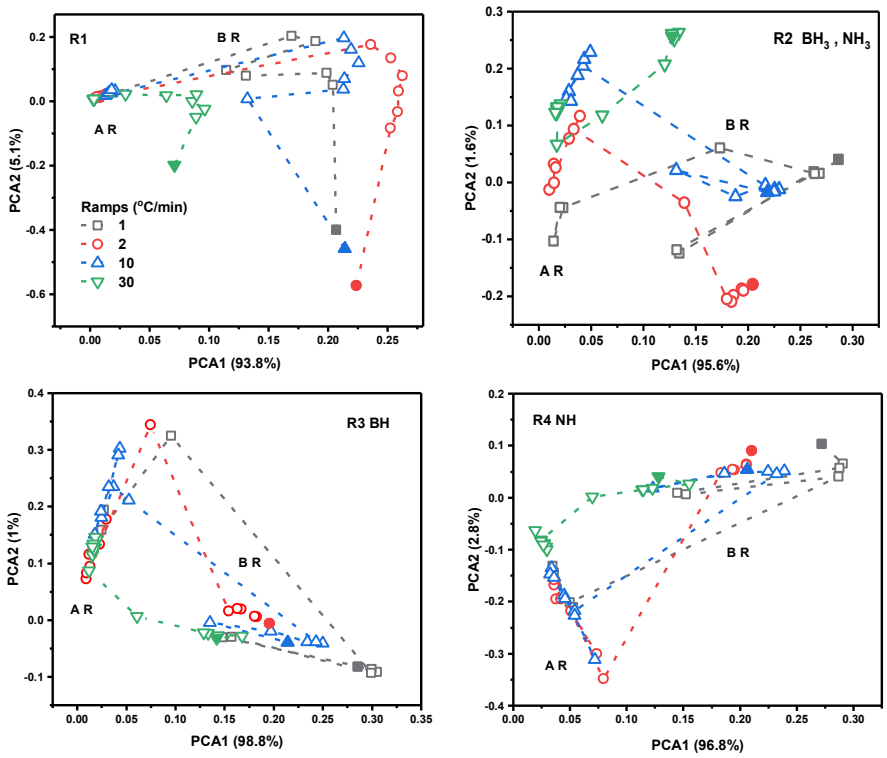


Figure 2. PCA analysis of different spectral regions of AB, in the first release step with different heating ramps. For each region, points within the dotted ellipse indicate spectra after release (AR) and the points outside (BR, before release) represent the Raman spectra obtained from room temperature (RT, full points) until the moment when the hydrogen release begins (95 °C).

CONCLUSIONS

The first release step took place between 95 and 100°C. It was observed that the formation of by-products was more evident in the spectra for the heating rates of 1, 2 and 10°C/min. PCA1 was associated with changes in intensity and PCA 2 with changes in bands. The release process for the heating rate of 30°C/min shows more stability. For this reason, a high heating rate was considered more convenient to improve the hydrogen release process.

ACKNOWLEDGEMENT

The authors acknowledge the support from PAPIIT projects IN108519, and PAPIME PE-107521 (UNAM); the *Programa de Maestría y Doctorado en Ingeniería-Eléctrica*-UNAM; to CONACYT for the grant awarded; to University Laboratory for Spectroscopy Characterization (LUCE-ICAT-UNAM); Acknowledgement comes here.

REFERENCES

1. Shore SG and Parry RW. 1955. The crystalline compound ammonia-borane, H_3NBH_3 J. Am. Chem. Soc. 6084–6085
2. 2013 Hydrogen Storage Technology, Materials and Applications. Edited by Lennie Klebanoff. CRC Press.
3. Petit JF, Miele P, Demirci UB.2016. Ammonia borane H_3N-BH_3 for solid-state chemical hydrogen storage: different samples with different thermal behaviors Int. J. Hydrog. Energy 41:15462–15470.
4. Hu MG, Geanangel RA and. Wendlandt WW. 1978. The thermal decomposition of ammonia borane Thermochim Acta 23:249-55.
5. Baitalow F, Baumann J, Wolf G, Jaenicke-Rössler K and Leitner G.2002. Thermal decomposition of B-N-H compounds investigated by using combined thermoanalytical methods, Thermochimica Acta 391:159-68.
6. Summerscales OT and Gordon JC. 2013. Regeneration of ammonia borane from spent fuel, Dalton Trans 42:10075-84.
7. Frueh S, Kellett R, Mallery C, Moller T, Willis WS, Kong'ondu C and Suib SL. 2011. Pyrolytic decomposition of ammonia borane to boron nitride, Inorg. Chem. 50:783-92.
8. Hess NJ, Bowden ME, Parvanov VM, Mundy C, Kathmann SM, Schenter GK and Autrey T. 2008. Spectroscopic studies of the phase transition in ammonia borane: Raman spectroscopy of single crystal NH_3BH_3 as a function of temperature from 88 to 330 K, J. Chem. Phys. 128: 034508.
9. Ziparo C, Colognesi D, Giannasi A and Zoppi M. 2012. Raman spectra of ammonia borane: low frequency lattice modes, J. Phys. Chem. A 116:8827–8832.
10. Dresser MJ, Taylor PA, Wallace RM, Choyke WJ and Yates JT. 1989. The adsorption and decomposition of NH_3 ON Si (100)—detection of the NH_2(a) species, Surf. Sci. 218:75-107.

11. Chellappa RS, Autrey T, Somayazulu M, Struzhkin VV and Hemley RJ.2010. High-Pressure Hydrogen Interactions with Polyaminoborane and Polyiminoborane, Chem. Phys. Chem. 11:93-96.
12. Valero-Pedraza MJ, Gascón V, Carreón MA, Leardini F, Ares JR, Martín Á, Sánchez-Sánchez M and Bañares MA. 2016. Operando Raman-mass spectrometry investigation of hydrogen release by thermolysis of ammonia borane confined in mesoporous materials, Microporous and Mesoporous Materials 226:454-465.

WHEC-2022
23rd World Hydrogen Energy Conference
June 26-30, 2022 - Istanbul

#1459

NUMERICAL SIMULATION ON PRESSURE REDUCTION PHENOMENON WITH LARGE-SCALE LIQUEFIED HYDROGEN TANK

[1*] Kazuma Tani, [1] Takehiro Himeno, [1] Toshinori Watanabe, [2] Hiroaki Kobayashi,
[3] Shuntaro Unno, [3] Shoji Kamiya, [3] Yasumasa Nakashima, [3] Osamu Muragishi, [3] Katsuhiro Kanbe
[1]The University of Tokyo, Department of Astronautics and Aeronautics, 7-3-1 Hongo, Bunkyo-ku, Tokyo, 113-8654, Japan
[2] Japan Aerospace Exploration Agency (JAXA), Institute of Space and Astronautical Science, 3-1-1 Yoshinodai, Chuo-ku, Sagamihara City, Kanagawa Prefecture, 252-5210, Japan
[3] Kawasaki Heavy Industries, Ltd., 1-1, Kawasaki-cho, Akashi City, 673-8666, Japan

*Corresponding author e-mail: tani@aero.t.u-tokyo.ac.jp

ABSTRACT

Kawasaki Heavy Industries, Ltd. has established the Hydrogen Energy Supply Chain (HESC) which aims to introduce a large amount of liquid hydrogen (LH2) to Japan. LH2 will be produced from brown coal in Australia and then shipped to Japan with LH2 Carrier. After a long transportation, LH2 inside the tanks of the Carrier will be pressurized and saturated by heat leakage from outside. Therefore, reducing the pressure to 1 atmosphere will be required for the safe tank operation. However, decreasing pressure will cause flashing, which will cause an excess of the venting capacity or liquid leakage because of an increase of vent mass. Hence, the purpose of this research is to reveal the pressure reduction rate and liquid behaviour through experimental and numerical approaches. Pressure reduction experiments were conducted by using 30 m^3 tank whose around 80% volume was filled with saturated LH2. The experiments showed that the pressure undershoot occurred at the beginning, and then the pressure decreased based on the Clausius-Clapeyron equation. From numerical analysis by VOF based in-house CFD code, it was found that the pressure undershoot was caused by the boiling delay, and the tank pressure followed the saturation pressure after the liquid fully stirred.

Keywords: HESC, Liquid hydrogen, Large-scale liquid hydrogen tank, Flashing, Pressure undershoot

INTRODUCTION

The Japanese government established the Basic Hydrogen Strategy which aimed to realize hydrogen-based society [1]. In this strategy, the Hydrogen Energy Supply Chain (HESC) was one of the main projects to develop international hydrogen supply chain. As Fig.1 showed, liquid hydrogen would be produced in Australia and delivered to Japanese users [2]. This is the world's first project to transport a large amount of liquid hydrogen over a long distance, thus our research focused on the issues of this transportation, especially related to pressure reduction phenomenon. Considering the situation unloading LH2 at a Japanese terminal, the liquid inside the tanks will be fully saturated under the high pressure and filled up to 98% liquid level because of heat input during a long transportation. Although the tank pressure had to be decreased to 1 atmosphere for the safe tank operation, flashing or flash evaporation would occur when saturated liquid undergoes pressure drop as Fig.2 showed. This would lead to exceeding the venting capacity or a liquid leakage because of a large amount of the boiling gas. The flashing phenomenon, particularly inside large-scale tank, was not examined sufficiently, thus the purpose of our research was to examine the pressure reduction phenomenon of saturated liquid in terms of pressure reduction rate and liquid behaviour. Our previous study pointed out that the pressure reduction rate in the case of low liquid level and saturated liquid followed the Clausius-equation during depressurizing from the thermodynamic analysis [4]. However, it was clear that the ullage gas volume had a great impact on the pressure reduction rate, thus the case of the high liquid level and saturated liquid also had to be considered. In this paper, this high filling level case would be discussed.



Fig. 1. Overview of the Hydrogen Energy Supply Chain

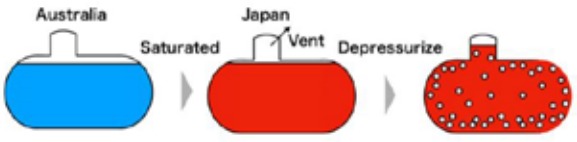


Fig. 2. Schematic of LH2 tanker operation

EXPERIMENT ON PRESSURE REDUCTION

The purpose of the experiment was to obtain the data of pressure reduction with high filling level and verify the results by using the thermodynamic model. 30 m^3 LH2 tank (Fig. 3) was used for this research. As Fig.4 showed, pressure gauge and 16 thermometers (named TIE-01~16 from top to bottom) were located inside LH2 tank, and LH2 pressurizing evaporator, thermometers, pressure gauges, and flowmeters were equipped on the vent line. To do the high liquid level and saturated liquid experiment by using only valve operation, the bubble vaporized by LH2 pressurizing evaporator was repeatedly introduced from the bottom of the tank by using the red line in Fig.4(a), and the large amount of liquid hydrogen was made saturated at 323 kPaG. After this procedure, GH2 vent valve was released, and tank pressure reduction started.

Results and discussion

The experimental results were shown in Fig. 5-7. As the time variation of pressure (Fig. 5) showed, the pressure under-shoot occurred around the beginning of the experiment, and then the pressure gradually decreased to 1 atmosphere. Figure 6 showed comparing the experimental result and the thermodynamic analysis we developed in previous research [4]. Since the both results matched well, it was found that the tank pressure obeyed the Clausius-Clapeyron equation during the pressure reduction experiment except pressure undershoot phase. Next, considering the pressure undershoot, this phenomenon was caused by the delay of the boiling. However, the question was that the thermometers' values inside liquid phase (TIE-05-16 in Fig. 7) always followed the fluctuation of the saturation temperature because of boiling. It was explained that many bubbles on the solid wall made easy to boil and the liquid around the wall boiled with decline of saturation temperature, on the other hand, the saturated bulk liquid was hard to boil and didn't boil with the pressure reduction. Consequently, this difference made the pressure undershoot. Moreover, the boiling difficulty of the bulk liquid led to the rise of the temperatures from 6 sec to 15 sec. After the pressure undershoot phase, it was clear that the whole liquid was uniformly stirred by the bubbles and boiled for keeping the thermal equilibrium state.

CFD ANALYSIS ON PRESSURE UNDERSHOOT

The CFD research with the VOF based in-house code (CIP based Level Set & MARS [5], [6]) was conducted for clarifying liquid behaviour during pressure undershoot. The CFD method employed TCUP (Temperature-based CIP-CUP) to solve hydrodynamic equations for free-surface flow and HLSM (Hybrid Level Set method and MARS) for the tracking of surface position on the fixed grid system. This numerical model could also deal with phase change phenomenon on sub-grid and grid scale [7].

Results and discussion

The time variation of pressure and the 2-D visualized results were shown in Fig.8. It was found that the pressure declined sharply, and the large amount of the boiling bubble emerged by overheating. After that, the pressure increased up to the saturation pressure and the liquid was stirred by the bubbles from the tank wall. Finally, the tank pressure declined following the Clausius-Clapeyron equation as we mentioned in the experimental analysis. The phenomenon was qualitatively understood, however, there remained problems with the quantitative analysis related to the boiling model.

CONCLUSIONS

1. The data of pressure reduction experiment in the case of high filling level with saturated liquid was obtained.
2. The pressure undershoots occurred at the beginning of the experiment, and then the tank pressure followed the Clausius-Clapeyron equation.
3. From CFD analysis, it was found that the pressure undershoot was caused by the delay of boiling. After the pressure undershoot, the tank pressure declined following the equilibrium state, because the boiled bubble stirred the liquid.

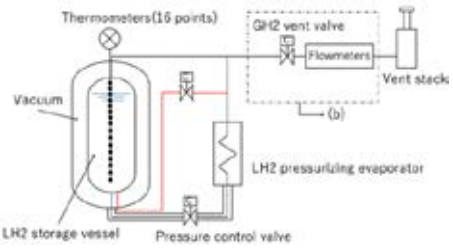
REFERENCES

1. https://www.meti.go.jp/english/press/2017/1226_003.html. Accessed on November 27, 2019
2. Kawasaki Heavy Industries, Ltd., 2016, CO2-Free Hydrogen Supply Chain, 2016 CSLF Technology Workshop, Japan.
3. Takaoka, Y., Saeed, A., Nishifuji, K., and Kanbe, K., 2019, Design and Operation of the First LH2 Carrier, Gastech 2019 Conference.

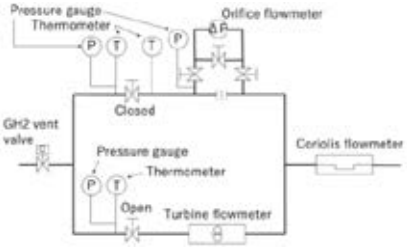
4. Tani, K., Himeno, T., Sakuma, Y., Watanabe, T., Kobayashi, H., Toge, T., Kagaya, H., Kamiya, S., and Muragishi, O., 2019, Prediction of Pressure Reduction Rate in 30m^3 Liquid Hydrogen Tank Based on Experimental and Numerical Analysis, International Conference on Hydrogen Safety 2019.
5. Himeno, T., Watanabe, T., and Konno, A., 1999, Numerical Analysis of Two-phase Flow Behaviour in a Liquid Propellant Tank, 35th Joint Propulsion Conference and Exhibit, Los Angeles, AIAA 99-2177.
6. Umemura, Y., Himeno, T., and Watanabe, T., 2012, Numerical Simulation of Bubble Growth and Departure on Heat Transfer Surface, J. Jpn. Soc. Microgravity Appl., Vol 29(1), 2-7.
7. Umemura, Y., Himeno, T., Kinefuchi, K., Tani, N., Negishi, H., Kobayashi, H., Ohira, K., and Fukasawa, O., 2015, Numerical Modelling of Boiling Flow in a Cryogenic Propulsion, 51st AIAA/SAE/ASEE Joint Propulsion Conference, Orland, FL, July 27-29.



Fig. 3. LH2 tank



(a) Overview of LH2 tank and vent line



(b) Arrangement of measuring equipments

Fig. 4. Schematic of LH2 tank and vent line

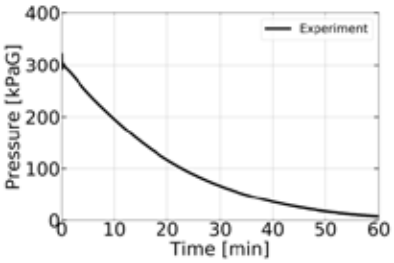


Fig. 5. The time variation of pressure

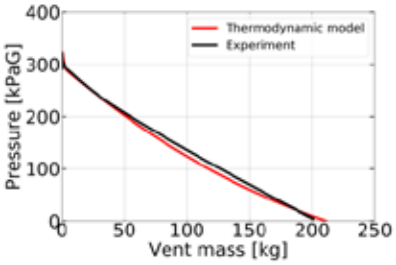


Fig. 6. Pressure vs sum of vent mass

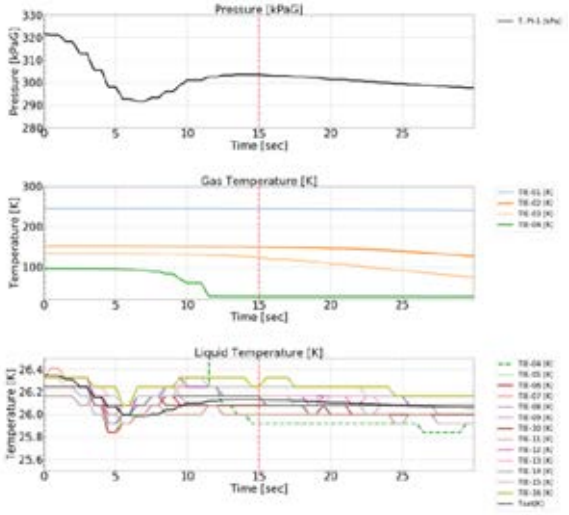


Fig. 7. The time variation of pressure, gas temperatures, and liquid temperatures around the beginning of the experiment

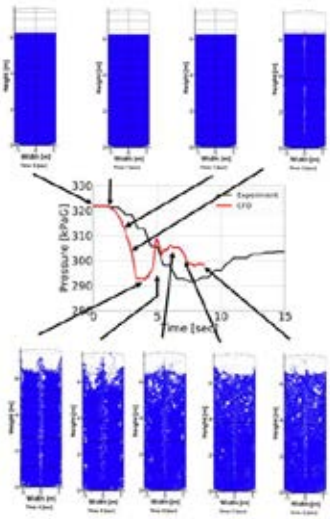


Fig. 8. The time variation of pressure and visualization (Blue color means liquid phase)

WHEC-2022
23rd World Hydrogen Energy Conference
June 26-30, 2022 - Istanbul

#1460

MACHINE LEARNING AS A TOOL FOR INTERPRETING VARIABLES IN HYDROGEN SORPTION DATA

[1] *Muhammad Irfan Maulana Kusdhany,*[1*] *Stephen Matthew Lyth*
[1] Department of Automotive Science, Kyushu University, 744 Motooka Nishi-ku, 8190374, Fukuoka, Japan

*Corresponding author e-mail: lyth@i2cner.kyushu-u.ac.jp

ABSTRACT

To realize the hydrogen economy, it is important to develop methods of storing hydrogen that are cost-effective, safe, and compact. One method of storing hydrogen which shows a lot of potential is through physisorption on high surface area carbon. However, the scientific literature offers conflicting information on which properties of the carbons are important to hydrogen storage and to what extent. This is chiefly because each experimental study on carbon materials only analyzes results on an incredibly small subset of carbon materials. To remedy this, we conducted an integrative data analysis wherein we collected experimental data from many studies in the literature to construct a large dataset. We then used this dataset to develop a machine learning model which can predict the hydrogen adsorption isotherm at 77K based on the porosity and chemical composition of the carbon. By analyzing this model using a post-hoc explanation method called Shapley Additive Explanations, we can analyze the structure-property relationships clearly.

Keywords: Hydrogen storage, porous carbon, machine learning

INTRODUCTION

Hydrogen shows great potential as an energy carrier due to its large gravimetric energy density, and efficient utilization in fuel cells. However, one issue with hydrogen is it has a low volumetric energy density, i.e., it takes up a lot of space. To counter this issue, hydrogen is usually compressed to high pressures of up to 70 MPa, but that comes with its own set of problems such as energy losses during compression and stringent materials requirements due to hydrogen embrittlement of storage tanks at higher pressures. One way to get around this problem is by storing hydrogen through physisorption on a material with large surface area, which allows more hydrogen to be stored at lower pressures. This is because the weak van der Waals interaction between the surface of the material and the hydrogen molecules result in hydrogen being stored at a higher density near the surface. For this application, many different materials have been suggested, such as zeolites, metal organic frameworks (MOFs), and porous carbon materials. Porous carbon materials have the advantages of being relatively cheaper and being already scalable as it is a mature technology. For example, in our recent work we synthesized a carbon foam material which is able to store >10 wt% in total at 9.5 MPa and 77K, as well as >2 wt% at 9.5 MPa and 298K, which is competitive with MOFs and zeolites but requiring only very simple synthesis steps and common precursors such as ethanol [1].

However, porous carbon materials are relatively unpopular in the scientific literature due to our limited understanding of how the properties of the carbons affect adsorption. This issue is largely a limitation of the experimental design that we use in materials science. In each experimental study of porous carbon materials, we typically study a small group (5-10 samples at most) of carbon materials which are made using incredibly similar precursors and synthesis method. Although using this data to analyze the synthesis-structure or synthesis-property relationships for that particular synthesis method is possible, anything beyond that would be difficult. First, since the data is only limited to that one synthesis method, the generalizability of those conclusions to other carbon materials made with other methods is questionable. In addition, since we are considering only a very small number of samples in each study, any quantitative conclusions we make will be highly biased.

To solve this issue, we conducted an integrative data analysis. We collected studies from the scientific literature to construct a dataset containing the porosity and chemical composition of various carbon materials and their hydrogen adsorption isotherm at 77K. Then, we fitted and evaluated several different machine learning models. The best model was then explained using a method called Shapley Additive Explanations (SHAP), which allows us to visualize the relationships as well as interaction effects in the form of dependence plots [2].

METHODS

Data Collection

We collected data from 14 experimental studies in the literature which fulfill our search criteria. Our criteria for inclusion are:

- The study includes chemical composition analysis

- The study conducted hydrogen adsorption experiments at 77K
- The study measured nitrogen sorption at 77K and/or CO_2 sorption at 273K and used them to calculate the pore size distribution using Non-Local Density Functional Theory (NLDFT) up to the ultramicropore range (pore diameter < 0.7 nm) in addition to the Brunauer-Emmett-Teller (BET) specific surface area and pore volume

A majority of the studies do not include their data in tabular format, in which case we convert them from the graphs using a software called Plot Digitizer.

Model Fitting and Evaluation

We fitted five different predictive models which use the porosity and chemical composition as inputs to predict the hydrogen adsorption isotherm at 77K. Those models are: (1) least squares linear regression (LR); (2) support vector regressor with linear kernel (SVR(L)); (3) SVR with radial basis function kernel (SVR (RBF)); (4) extreme gradient boosted trees (XGBT, implemented using the XGBoost library); and (5) random forest (RF).

To evaluate their performance, we conducted 5-fold group cross validation. Here, 1\5 of the dataset is used as a validation set while the others are used as training, and the process is repeated five times. We used group cross validation with the sample names as a group identifier instead of completely randomizing it to ensure that the models have to predict a new isotherm from a completely unseen material rather than just interpolating the isotherm between pressure points for known materials.

Finally, after choosing the model with the best predictive performance, the model is refit with the entire dataset. Then, we use an algorithm developed by Lundberg et al. [2] to calculate Shapley values for each prediction. Shapley values are the measure of a contribution of a feature to the predicted value. Simply, they are the difference between expected prediction when the feature is included in the predictor vs when the feature is missing averaged over different orderings of feature inclusion in the model. We calculate the Shapley values for each prediction, and then plot them over all the predictions to visualize the overall trends in a dependence plot.

RESULTS AND DISCUSSION

From the cross-validation, we found that RF has the best out-of-sample predictive performance with an R^2 of 0.910. We then fitted it to the full dataset and explained it with SHAP (Fig. 1A). From this, we found that BET surface area is the most important carbon property in determining hydrogen uptake, although the strength of this relationship is not as strong as is implied by the empirical Chahine's rule. This is due to the fact that this model includes both pore volume and surface area, resulting in the attribution being split between them. We found that there was a correlation between oxygen content and uptake, which supports some suggestions from early experimental data [3]. The pore size distribution of the carbons also has some effect on uptake, with ultramicropore volume (pore diameter < 0.7 nm) contributing significantly more than micropore volume (pore diameter < 2 nm) alone (Fig. 1B). Although, this relationship is not nearly as strong as the effect of surface area and total pore volume on uptake and the effect of an improved pore size distribution is diminished at larger pressures. We also conducted some sensitivity analyses and found that the conclusions are generally robust to model selection and dataset size.

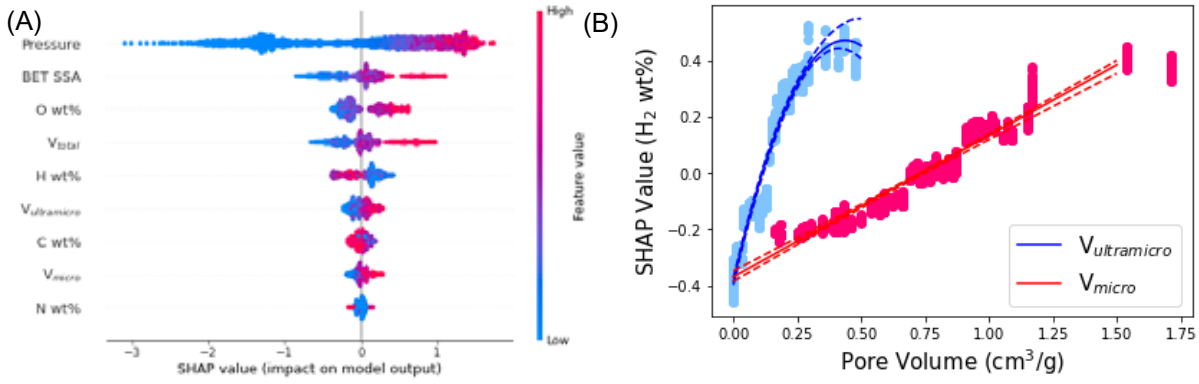


Fig. 1. (A) Plot showing relative importance of the different variables which predict hydrogen uptake and (B) plot showing that ultramicropore volume affects hydrogen uptake more strongly than micropore volume.

CONCLUSIONS

In summary, we have a developed a model which can predict the hydrogen sorption isotherm of various porous carbon materials based on their chemical composition and porosity parameters. We then used a post-hoc explanation method

to then understand and analyze the quantitative structure-property relationships governing hydrogen uptake on porous carbon materials, which led to some important insights on which variables are important to hydrogen uptake.

REFERENCES

1. Kusdhany MIM, Li H-W, Mufundirwa A, Sasaki K, Hayashi A, and Lyth SM. 2020. Hydrogen Storage on Nanoporous Carbon Foam for Electrochemical Applications. ECS Meeting Abstracts 7:1123.
2. Lundberg SM, Erion G, Chen H, DeGrave A, Prutkin JM, Nair B, Katz R, Himmelfarb J, Bansal N, and Lee S-I. 2020. From local explanations to global understanding with explainable AI for trees. Nature Machine Intelligence 2:56-67.
3. Blankenship LS, Balahmar N, and Mokaya R. Oxygen-rich microporous carbons with exceptional hydrogen storage capacity. 2017. Nature communications 8:1545.
4. Kusdhany MIM and Lyth SM. 2021. New insights into hydrogen uptake on porous carbon materials via explainable machine learning. Carbon 179:190-201.

WHEC-2022
23rd World Hydrogen Energy Conference
June 26-30, 2022 - Istanbul

#1465

CFD-ASSISTED HYDRODYNAMIC CHARACTERIZATION OF A CENTRIFUGAL LIQUID ORGANIC HYDROGEN CARRIER DEHYDROGENATION UNIT

[1] *Laurens Van Hoecke,* [2*] *Patrice Perreault*
[1] University of Antwerp, Faculty of Sciences, Department of Bioscience Engineering, Sustainable Energy Air and Water Technology (DuEL), Groenenborgerlaan 171 – 2020 Antwerpen, Antwerp, Belgium
[2] University of Antwerp, Faculty of Sciences/Blue App, Department of Bioscience Engineering, Instituut voor Milieu & Duurzame Ontwikkeling (IMDO), Groenenborgerlaan 171 – 2020 Antwerpen, Antwerp, Belgium
*Corresponding author e-mail: Patrice.Perreault@uantwerpen.be

ABSTRACT

Hydrogen release units from Liquid Organic Hydrogen Carriers suffer from two main drawback: high energy demand at high temperature, and inefficient H_2 release due to the viscosity of both the hydrogen gas produced and the liquid carrier. In this work, we present the CFD-assisted design of a centrifugal dehydrogenation reactor for the H_2 release from perhydro-dibenzyl toluene. Our proposed technology allows to negligibly affect the required residence required for the slow dehydrogenation of perhydro dibenzyl toluene, while allowing an extensive degassing of the LOHC by a combination of applied shear stress and radial pressure drop in the reactor. Reactive simulations are underway, in addition to experimental validation of the degassing rates.

Keywords: Liquid Organic Hydrogen Carriers (LOHC), Reactor design, Centrifugal fields

INTRODUCTION

H_2 is a crucial energy carrier and critical chemicals to the chemical industry, but its storage is one of the current bottleneck for the H_2 economy due to its low density. State-of-the-art in H_2 storage is highly energy intensive: Liquified H_2 (i.e. LH_2, at -253 °C) can require as much as 36-45% of the H_2 energy content in actual plants (between 12 and 15 kWh kg^{-1} H2) [1], while compressed gas H_2 (CGH_2) at 350-700 bar up to 10-20% [2-4]. Fortunately, it is possible to store H_2 at milder process conditions, making use of the Liquid Organic Hydrogen Carrier (LOHC) concept: H_2 is reversibly stored at 30-50 bars and 150-300 °C via a catalytic exothermic reaction by saturating the double bonds of organic molecules. H_2 is then released on-demand at atmospheric pressure in an endothermic catalytic reaction occurring at 250-300 °C. LOHC represents an interesting compromise between a high storage of energy (up to 2.05 kWh/l [5]) and required energy (8.9 kWh/kg H_2, i.e. representing 27% of the LHV of the H_2 stored [6]).

The main impediment to the commercial deployment of LOHC is the heat requirements at high temperature for H_2 release. The dehydrogenation of LOHC is typically performed in packed bed reactors that are optimized for optimal heat input and product gas removal [7, 8]. To avoid perturbing the fluid flow and the required long residence time for dehydrogenation, a degassing volume is planned. However, due to the high viscosity of some LOHCs (e.g., ranging from 0.04 to 0.22 Pa*s for dibenzyl toluene (H0-DBT) and perhydro-dibenzyl toluene (H18-DBT), respectively), the H_2 bubbles produced during the dehydrogenation tend to stay in the bed in the interstices between the catalyst particles.

Considering the critical requirements for lower energy, we designed an electrified unit for the dehydrogenation of the H18-DBT (induction heating). In addition, in order to improve the removal of H_2 bubbles during dehydrogenation, we further intensified the unit by generating a swirling flow pattern of the LOHC via tangential injection. In this work, we present the results of the computational fluid dynamics (CFD) simulation that lead to the design of the continuous experimental setup including the 21 litres centrifugal reactor.

COMPUTATIONAL METHODS

Multiphase turbulent gas-liquid bubbly flows simulations were carried out following the Eulerian-Eulerian framework implemented in OpenFoam v8. Turbulence was accounted for using the k - Omega Shear Stress Transport model, i.e., a two equation model solving for the turbulence kinetic energy (k) and specific dissipation rate (ω), a blended model shifting to the well-known standard k – Epsilon model in free-stream regions. The reactor's geometry was drawn using Salome 9.7, and the CFD simulation domain was meshed with the OpenFOAM's native snappyHexMesh meshing tool. The reactor (now built and ready to be used to gather experimental data for validation) has two 25 mmID inlets positioned at the bottom of the reactor at a 10% angle with respect to the horizontal plane, a lower 0.150 mID diameter cylindrical section (0.150 m high), followed by an expansion zone, and a 0.300 mID diameter larger section (0.200 m high) where two outlets are positioned tangentially (Fig. 1 a).

As the development of the chemistry solver is still underway in our group for the heterogeneous catalytic reaction yielding H_2 and H_2-poor LOHC from a H_2-rich LOHC, we designed the current unit by generating 1 mm bubbles using a source term applied to the bottom part of the reactor. The thermophysical properties of perhydro dibenzyl toluene and hydrogen at 300 °C were used for the continuous and dispersed phase, respectively. Velocity fields and the residence time distribution were monitored using OpenFOAM native functions.

RESULTS AND DISCUSSION

The required long resistance time in packed bed dehydrogenation unit results in low LOHC superficial velocity, and a low flow axial pattern limiting the removal of the small H_2 bubbles generated at the surface of the catalyst particles. Our proposed configuration with tangential inlets creates a strong swirl and has the advantage of completely removing the bubbles from the bed without affecting the liquid residence time. We calculated the F-curve from a step change in tracer concentration using the scalar passive transport approach: the residence time for the liquid phase reduced only from 25 to 19 s (equivalent packed bed reactor volume and swirling unit, respectively). However, the striking difference with the conventional packed bed configuration is the combination of strong shear rates due to strong swirl of the liquid phase (Fig. 2 b) resulting in an annulus-type gas-phase distribution (Fig. 2 c).

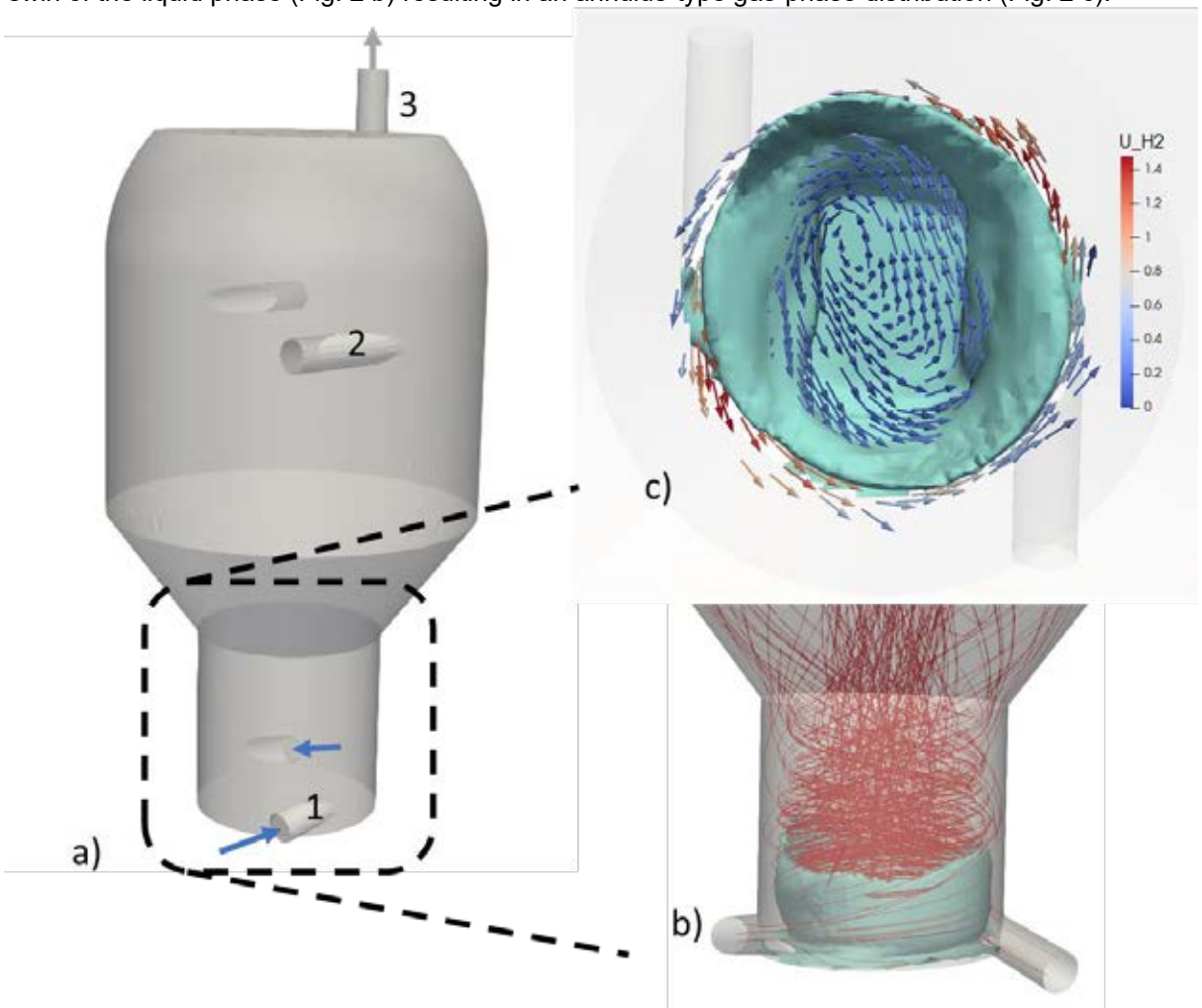


Fig. 1. Overview of the a) centrifugal 21 l dehydrogenation unit highlighting the (1) two LOHC inlets and (2) outlets, and (3) H_2 outlet; b) streamlines for the LOHC (red) and contour plot of the hydrogen generated during 0.5 s of reaction (light turquoise); and c) top view of the contour plot and vector field for the hydrogen generated.

Even though the liquid velocity can exceed 2.5 m/s in the vicinity of the circumferential wall near the bottom of the reactor, we expect the global conversion of perhydro dibenzyl toluene to be substantial due to the high number of turns that the liquid passes in the catalyst bed. Reactive simulations and experimental validations underway will allow to confirm this assumption. In addition, we can observe that most of the hydrogen produced in the packed bed is pushed towards the outer circumferential wall, thanks to the strong swirl and resulting shear stress enhancing degassing of the centre-part of the bed. The swirling motion of the LOHC also creates a 0.2 kPa pressure drop in the radial direction (lowest pressure in the centre of the bed), thus further contributing to the enhanced degassing of the

bed. Interestingly, as theoretically demonstrated by Tsori and Leibler [9], the sharp separation of miscible liquids is possible in a centrifuge as the rotation exceeds a critical threshold. If this is the case, our centrifugal unit would allow to circumvent another disadvantage of the state-of-the-art packed bed technology. Catalyst deactivation by the liquid products is a known issues in dehydrogenation of LOHC. The rotational flow could lead to perhydro dibenzyl toluene enriched regions towards the centre of the unit (the density of plain dibenzyl toluene being higher than that of perhydro dibenzyl toluene), in which case, by circumscribing the location of the catalyst towards the centre of the unit, our unit would allow selective contact between perhydro dibenzyl toluene and the catalyst.

CONCLUSIONS

The centrifugal dehydrogenation unit designed in our laboratory was numerically characterized for its hydrodynamic: we were able to show that despite a depreciable decrease in the required residence time for dehydrogenation reactions to take place, we are able to achieve a complete degassing of the bulk of the packed bed. Hydrogen bubbles generated during the dehydrogenation reaction are pushed towards the circumferential walls, thanks to the combination of strong shear stress and radial pressure drop contributing to enhanced degassing of the LOHC. This technology could circumvent thus both the degassing issues observed in state-of-the-art packed technology, as well as selective contact between the H2-rich LOHC and the catalyst particles. Experimental validation and reactive simulations underway will allow to confirm these observations.

ACKNOWLEDGEMENT

We thank the Industrial Research Fund (Industrieel Onderzoeksfonds, IOF) of the University of Antwerp, as well as the Port of Antwerp for the financial support for this project. We also sincerely thank Hydrogenious LOHC Technologies for supplying the dehydrogenation catalyst and perhydro-dibenzyl toluene which will be used for the experimental validation of the centrifugal dehydrogenation unit.

REFERENCES

1. Reuß, M., *et al.* 2017. Seasonal storage and alternative carriers: A flexible hydrogen supply chain model. Applied Energy. 200:290-302.
2. https://www.nrel.gov/docs/fy14osti/58564.pdf. Accessed on May 15, 2020.
3. Dagdougui, H., et al. 2018, Chapter 4 - Hydrogen Storage and Distribution: Implementation Scenarios, in Hydrogen Infrastructure for Energy Applications. Edited by Dagdougui, et al. London. Academic Press.
4. Di Profio, P., et al. 2009. Comparison of hydrogen hydrates with existing hydrogen storage technologies: Energetic and economic evaluations. International Journal of Hydrogen Energy.34(22): 9173-9180.
5. Brückner, N., et al. 2017. Evaluation of Industrially Applied Heat-Transfer Fluids as Liquid Organic Hydrogen Carrier Systems. ChemSusChem. 7(1): 229-235.
6. Sievi, G., et al. 2019. Towards an efficient liquid organic hydrogen carrier fuel cell concept. Energy & Environmental Science. 12(7): 2305-2314.
7. Rathke, J., et al. 2019. Reactor apparatus for dehydrogenating a carrier medium. Hydrogenious Technologies GMBH: Germany.
8. Bösmann, A., et al. 2016. Reactor device for the release of a gas from a starting material. Hydrogenious Lohc Technologies GmbH.
9. Tsori, Y., Leibler, L. 2007. Phase-separation of miscible liquids in a centrifuge. Comptes Rendus Physique. 8(7):955-960.

WHEC-2022
23rd World Hydrogen Energy Conference
June 26-30, 2022 - Istanbul

#1466
METAL HYDRIDE COMPOSITE MATERIALS FOR THERMO-CHEMICAL HYDROGEN COMPRESSION

[1]Marius Lau, [1,2] Oliver Ehrensberger, [1]Felix Heubner
[1] Fraunhofer Institute for Manufacturing Technology and Advanced Materials IFAM, Branch Lab Dresden, Winterbergstraße 28, 01277 Dresden, Germany;
[2] Mut Advanced Heating GmbH, Fritz-Winkler-Straße 1 - 2, 07749 Jena, Germany

*Corresponding author e-mail:
marius.lau@ifam-dd.fraunhofer.de felix.heubner@ifam-dd.fraunhofer.de ehrensberger@mut-jena.de

ABSTRACT

Low temperature waste heat (e.g., 100°C) can be utilized for hydrogen compression with hydride forming materials. In order to increase productivity and to decrease cycle time of a metal hydride-based hydrogen compressor, it is necessary to face heat transport limitations and to accelerate the overall rate of reaction. The compression cycle time can be significantly decreased by using metal hydride composite materials (MHC) with increased thermal conductivity. In this contribution, the use of composite materials is compared with conventional metal hydride (MH) materials with low thermal conductivity. A dual stage hydrogen compressor was built in laboratory scale and demonstrated with MH and innovative MHC. MHC increase the productivity of a MH compressor by up to 500%.

Keywords: *Hydrogen compression, Metal hydride, Metal hydride composite, thermo-chemical compression*

INTRODUCTION

Solid hydrogen carriers like metal hydrides can fulfill various applications for industrial hydrogen technologies such as storage, compression, purification, and isotope separation. Hydrides operate at moderate temperatures (25 °C to 300°C) and enable highest volumetric storage densities (100 g_{H2}/l) [1]. During exothermal hydrogen absorption, i.e., the formation of MH, heat of reaction is released. The technical reaction speed depends on the heat dissipation or heat supply for hydride decomposition. Rapid hydrogen absorption or release cannot be guaranteed in the event of heat accumulation. Thus, the low thermal conductivity of MH powders represents an obstacle to its applicability in fast-operating technical systems. However, the heat transport can be significantly increased by adding a second material with a high intrinsic thermal conductivity, such as graphite, aluminum, or copper, forming MHC [2,3].

MATERIALS AND METHODS

In this contribution, we report about a dual-stage MH compressor using MH or MHC to estimate the impact on productivity. For this purpose, a powdered AB_5 alloy (La-Ni based) and an AB_2 alloy (Ti-Mn-based, Hydralloy C5) were used with and without expanded natural graphite (ENG) and compacted between 50 and 300 MPa in inert gas atmosphere, respectively. The materials were filled into two double-walled pressure vessels and cycled between 20 and 100°C. The supply and release of hydrogen into the pressure vessels was realized using a lab-scale hydrogen compression test rig.

RESULTS AND DISCUSSION

For MH based compression systems hydrogen is absorbed at low temperature and released at higher temperature and thus higher pressure [4]. By using metal hydrides, low temperature waste heat (e.g. 100 °C) can be used to realize high purity hydrogen compression. In comparison to loose MH powder beds, the use of MHC with high thermal conductivity decreases the compression cycle time drastically. Thus, the productivity of the thermochemical compressor increases.
Figure 1 depicts manufactured MHC with high thermal conductivity (A), the double-walled pressure vessels for hydrogen compression (B) and the laboratory test rig for hydrogen compression (C). After integration of the materials into the pressure vessels and into test rig, the materials were activated and cycled individually (1.5 bar/20-40 bar, 20°C/50°C). The results were compared to pressure-composition-isotherms of the hydride forming materials to maximize the compression ratio. By using MHC with high thermal conductivity, the productivity of the individual stages of the compressor could be increased by up to 500 %. The two-stage compressor realized hydrogen compression

with simulated waste heat between 20°C and 100°C from 5 to 70 bar. In comparison to loose MH powder beds, the use of MHC with high thermal conductivity decreases the compression cycle time by up to a factor of 5.

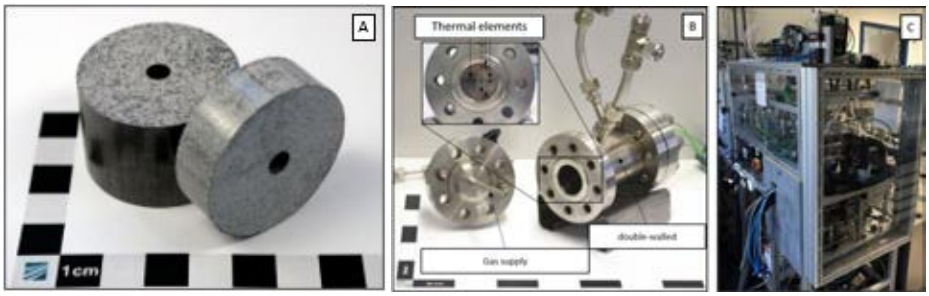


Figure 1: Metal hydride composites (MHC, A) were filled in a double-walled pressure vessel (B, [5]) to perform a thermo-chemical compression in a test rig (C).

CONCLUSION

Metal hydride forming materials can serve as innovative hydrogen compression materials. MHC have an increased thermal conductivity and can realize hydrogen absorption/desorption and temperature changes in a few minutes. By using MHC with highest thermal conductivity, the productivity of the two-stage compressor was increased by up to 500 % compared to loose MH powder beds.

REFERENCES

1. Heubner F., Röntzsch L. 2021. White paper solid hydrogen carriers
2. Pohlmann C., Röntzsch L., Heubner F., Weißgärber T., Kieback B. 2013. Journal of Power Sources 231:97-105
3. Heubner F., Hilger A., Kardjilov N., Manke I.. et. al 2018. Journal of Power Sources 397:262-270
4. Lototskyy M.V., Yartys V.A., Pollet B.G., Bowman Jr. R.C. 2014. International Journal of hydrogen Energy 39:5818-5851
5. Herbrig K., Röntzsch L., Pohlmann C., Weißgärber T., Kieback B. 2013. International Journal of hydrogen Energy 38:7026-7036

WHEC-2022
23rd World Hydrogen Energy Conference
June 26-30, 2022 - Istanbul

#1488

REACTION PROCESS OF AMMONIA PRODUCTION FROM IRON NITRIDE AND CARBONATED WATER

*Hiromi Eba, Tian Liu, Keiichi Fukami
Faculty and Graduate School of Science and Engineering, Tokyo City University, Tamazutsumi 1-28-1, Setagaya, Tokyo, Japan

*Corresponding author e-mail: heba@tcu.ac.jp

ABSTRACT

The interstitial compounds, Fe_3N and Fe_4N, reacted with water to generate NH_3 and H_2. The reaction proceeded under normal temperature and pressure when carbon dioxide was added to the reaction system. The product ratio, NH_3/H_2, was larger than the value calculated from the reaction formula when iron nitride had reacted completely. The NH_3 formation proceeded easily because the activation energy calculated from the Arrhenius plot of temperature vs. reaction rate was lower for NH_3 formation than for H_2. As the reaction progressed, the lattice constant of iron nitride decreased, suggesting that N diffused between the lattices and moved to the surface to produce ammonia. Fe_3N, which has a crystal structure in which N readily diffuses between lattices, had a higher ammonia production rate than Fe_4N. Adding carbonate to the system accelerated the reaction. The elementary reaction involving carbonic acid was the rate-determining step: the reduction of H^+ in carbonic acid by reacting with Fe or removing Fe^{2+} from the reaction system by forming a soluble Fe^{2+} carbonate complex was the slowest reaction step.

Keywords: Ammonia production, Carbon dioxide, Carbonic acid, Iron and steel, Iron nitride

INTRODUCTION

Ammonia (NH_3) is an essential raw material for nitrogen fertilizers used in agriculture, and has been identified as a potential hydrogen carrier in recent years. However, NH_3 is mainly synthesized through the Haber–Bosch process, requiring high temperature and pressure. To reduce this environmental burden, it is necessary to achieve NH_3 synthesis under milder conditions. We have investigated NH_3 generation from iron nitride (Fe_3N and Fe_4N) and carbonated water at ambient temperatures and pressures [1]. In this study, the activation energies and amounts of NH_3 and H_2 produced were determined and compared.

MATERIALS AND METHODS

Iron nitride (Fe_3N or Fe_4N) powders and a small amount of carbonated water were sealed in a bottle under 101.3 kPa CO_2. The bottle was stirred at a constant temperature between 298 and 328 K. The gas-phase H_2 and CO_2 and liquid-phase NH_3 were quantified by gas chromatography every 30 min. After the reaction, the bottle contents were dried, and qualitative and quantitative analyses were performed using X-ray diffraction (XRD). Additionally, an Na_2CO_3 aqueous solution was prepared and used instead of carbonated water, repeating the same measurements.

RESULTS AND DISCUSSION

NH_3 and H_2 generation

Fig. 1 shows the changes in the amounts of H_2 and NH_3 with time at each temperature. For both NH_3 and H_2, the production rate and final production amount increased as the reaction temperature increased. The ratio of NH_3 produced to H_2 was always higher than that of NH_3/H_2 described in Eq. (1). In Eq. (1), 1 mol of Fe_4N produces 1 mol of NH_3, and 4 mol of Fe in Fe_4N provides eight electrons. Hence, 5 mol of H was expected to be produced in addition to 1 mol of NH_3, i.e., 2.5 mol of H_2 would be produced. We presumed that N escaped from the lattice of Fe_4N, an interstitial compound, and reacted preferentially with H on the Fe_4N surface.

$$Fe_4N + 4H_2O + 4CO_2 \rightarrow 4FeCO_3 + NH_3 + 2.5H_2 \quad (1)$$

Confirming the reaction progress by XRD

The XRD measurements of the solid phase after the reaction revealed unreacted Fe_4N and $FeCO_3$ production. The amount of substance of each crystal phase was quantified from the XRD pattern by the powder pattern fitting method. Consequently, the amount of Fe_4N consumed and the amount of $FeCO_3$ produced were determined. Theoretically, consuming 1 mol of Fe corresponds to producing 2 mol of H ($Fe + 2H^+ \rightarrow Fe^{2+} + 2H$). The amount of Fe_4N consumed, as determined from XRD analysis, corresponded well with the amounts of NH_3 and H_2 produced. On the other hand,

regarding the amount of substance of N, the amount of NH_3 produced was higher than the amount of Fe_4N consumed. The higher amount NH_3 can be explained by assuming that N escaped from the lattice of Fe_4N by interstitial diffusion to generate NH_3, as described above. The lattice constant of Fe_4N decreased slightly as the reaction progressed, suggesting N escaped.

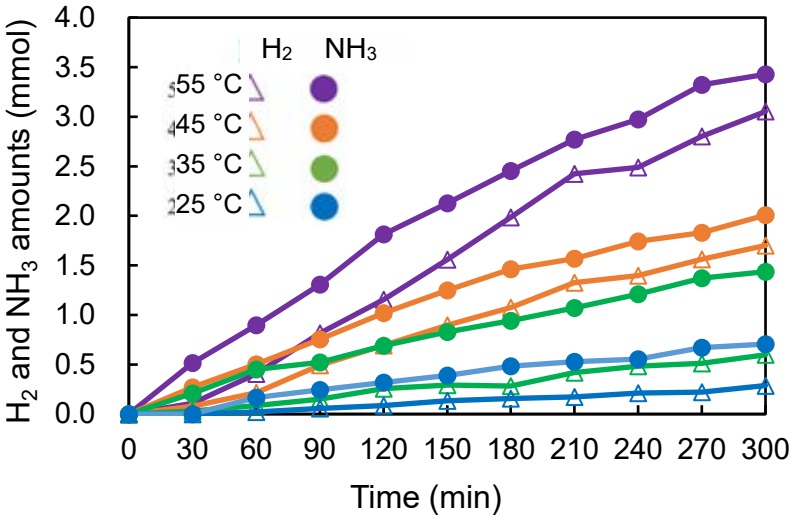


Fig. 1. Changes in the amounts of NH_3 and H_2 with time in the reaction between Fe_4N and carbonated water.

Activation energy estimation

The activation energies, ΔE_a, calculated using the Arrhenius plot of the reaction rate constants obtained at different temperatures were 27 and 50 kJ/mol for NH_3 and H_2 formation, respectively. A small ΔE_a value indicated that NH_3 production was advantageous.

Comparison of NH_3 production activity of Fe_3N and Fe_4N

Fe_3N showed a higher reaction rate for NH_3 production than Fe_4N did because of differences in their crystal structures. As shown in Fig. 2, Fe_3N is based on the hexagonal close-packed structure of ε-Fe, in which N regularly occupies one-third of its octahedral sites. In contrast, in Fe_4N, N regularly occupies a quarter of the octahedral sites of the face-centered cubic lattice (γ-Fe, austenite phase) of Fe. In this structure, Fe occupies both the Ca and O sites of the perovskite-type structure ($CaTiO_3$), and N occupies the Ti site. In Fe_4N, the Fe octahedra share edges; therefore, N must move via a small tetrahedral site. However, in Fe_3N, N can move between octahedral sites through faces and easily move and diffuse between lattices because Fe octahedra share faces.

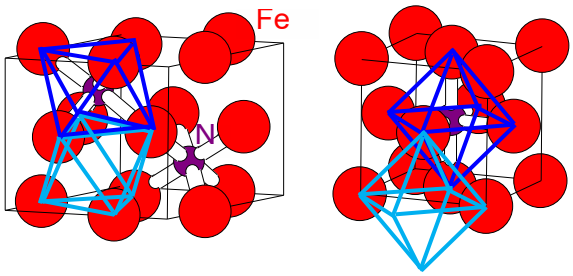


Fig. 2. The crystal structure of Fe_3N (left) and Fe_4N (right) and the connection of Fe octahedra.

Addition of water-soluble carbonate

Adding Na_2CO_3 increased the NH_3 formation rate and total NH_3 amount. Adding carbonate increased both the pH and HCO_3^- concentration, improving the rate of the redox reaction involving HCO_3^- and the formation of the Fe^{2+} carbonato complex. Therefore, one of these processes was expected to be the rate-determining step.

CONCLUSIONS

Experiments on generating NH_3 by reacting iron nitride and carbonated water were conducted, and the following results were obtained.

- The NH_3/H_2 ratio was higher than that produced when Fe_4N reacted completely. Because the lattice constant of Fe_4N in the solid phase decreased as the reaction proceeded, it was understood that N atoms diffused between the iron nitride lattices, moved to the surface, and combined with the H atoms. The activation energy of the formation reaction was smaller in NH_3 than in H_2, and the generation of NH_3 was more advantageous.
- Fe_3N was superior to Fe_4N in terms of the rate and amount of NH_3 produced. The crystal structure in which N diffuses easily is advantageous for NH_3 formation.
- Adding alkali metal carbonates to the reaction increased both the rate and amount of NH_3 produced. While N in iron nitride was ready to combine with H immediately, one of the elementary reactions involving carbonic acid was the rate-determining step. Carbonic acid was thought to be involved in decomposing water to provide H for N and removal of Fe ions from the iron nitride surface by carbonato complex ion formation after the reaction.

ACKNOWLEDGEMENT

This work was subsidized by JKA through its promotion funds from KEIRIN RACE, Japan.

REFERENCES

1. Eba H, Masuzoe Y, Sugihara T, Yagi Y, Liu T. 2021. Ammonia production using iron nitride and water as hydrogen source under mild temperature and pressure. International Journal of Hydrogen Energy 46:10642-10652.

WHEC-2022
23rd World Hydrogen Energy Conference
June 26-30, 2022 - Istanbul

#1491

EFFECT OF IRON PARTICLE SHAPE AND ALLOY COMPOSITION ON HYDROGEN PRODUCTION EFFICIENCY IN THE WATER-IRON REACTION

*Hayao Yagi, *Hiromi Eba*
Faculty and Graduate School of Science and Engineering, Tokyo City University, Tamazutsumi 1-28-1, Setagaya, Tokyo, Japan

*Corresponding author e-mail: heba@tcu.ac.jp

ABSTRACT

The relationship between the properties and reactivity of iron particles was investigated to develop a hydrogen production process from scrap iron using carbonated water. To evaluate the effect of alloy composition, Ni was selected from the range of alloy elements commonly present in steel that constitute scrap iron. A Ni salt was added to pure iron powder, stirred in an organic solvent, and dried. Subsequently, the redox reaction using the iron powder for hydrogen generation from water was analyzed. The final amount of hydrogen produced increased, which suggested that Ni may have penetrated the iron crystals. The hydrogen production efficiencies of pure iron powder and alloyed steel powders from the manufacturer were also compared. Ni partially alloyed steel powder (SIGMALOY2010) generated more hydrogen than pure iron powder of the same particle size. Moreover, a clear correlation between the particle size and hydrogen production was observed for SIGMALOY2010; the smaller the particle size, the higher the hydrogen production, which suggested that the reaction rate corresponds to the specific surface area. However, for other alloyed steel, no clear correlation exists with particle size. It was found that shape, porosity, and specific surface area also need to be analyzed and discussed.

Keywords: Hydrogen generation, Carbon dioxide, Iron and steel, Scrap iron, Ni alloyed steel

INTRODUCTION

The demand for clean and sustainable hydrogen energy is expected to increase in the near future as the utilization of fuel cells increases. Furthermore, because the amount of scrap iron generated is increasing in Japan, we focused on hydrogen gas (H_2) production through the reaction of Fe metal obtained from scrap iron with carbon dioxide (CO_2) in Eq. (1). Carbon dioxide is used to accelerate the reaction, and can simultaneously be immobilized in the form of a carbonate.

$$Fe + H_2O + CO_2 \rightarrow FeCO_3 + H_2,\ \Delta H(298K) = -69\ kJ/mol \quad (1)$$

In this study, Ni was selected from various alloy elements commonly present in steel that constitute scrap iron, and the effect of Ni addition to pure iron on hydrogen production was evaluated. The obtained results were compared with the effects of pure iron and alloy steel powders.

MATERIALS AND METHODS

Ni addition to pure iron powder

First, 0.9 g of $Ni(NO_3)_2{\cdot}6H_2O$ (99.9%) was dissolved in 15 mL of acetone (99%) in a bottle, to which 3.0 g of pure iron powder (99.9%, particle size 3–5 μm) was added. Subsequently, the mixture was stirred at room temperature at 2000 rpm (rotations per minutes) for 4 d using a constant-temperature shaker. The mixture was then placed into a vacuum dryer and dried at 80°C for 5 h. Excess $Ni(NO_3)_2$ was removed by adding 15 mL of acetone, and the resultant solid-liquid mixture was separated using a centrifuge at 5000 rpm for 15 min. The recovered solid phase was designated as Sample A. The Fe powder was recovered by stirring in acetone under the same conditions, without $Ni(NO_3)_2{\cdot}6H_2O$, and was designated as Sample B.

Evaluation of hydrogen production reaction

Reagent pure iron powder and samples A and B were used as reactants. Pure iron powders (KB-90, K-100T, 303A-60) and alloy steel powders (SIGMALOY2010, 4100V, 20CRV, 30CRV) manufactured by JFE Steel Corporation were also used as reactants. Table 1 lists the compositions of seven JFE steel samples. The JFE steel samples were screened using sieves to classify particles with sizes of <45 μm, 45–106 μm, and 106–180 μm. Each sample (2.0g) was sealed in a 295-mL bottle and filled with 101.3 kPa CO_2. Carbonated water (5mL), prepared by bubbling 101.3 kPa of CO_2 until equilibrium was reached, was added to the sample, and the mixture was stirred in a constant-temperature shaker at 50°C and 2000 rpm. The gas phase in the bottle was analyzed by gas chromatography at regular intervals after the reaction initiated, and changes in H_2 and CO_2 concentrations over time were analyzed.

Table 1 Composition of iron and steel manufacturing powders

Types	Designation	Chemical composition
Pure iron powder	KB-90	87.0% ≤ M.Fe
	K-100T	90.0% ≤ M.Fe
	303A-60	99.0% ≤ T.Fe
Alloyed steel powder	SIGMALOY2010	Fe – 2%Ni – 1%Mo
	4100V	Fe – 1%Cr – 0.8%Mn – 0.3%Mo
	20CRV	Fe – 2%Cr – 0.8%Mn– 0.2%Mo – 0.2%S
	30CRV	Fe – 3%Cr – 0.3%Mo – 0.3%V

RESULTS AND DISCUSSION

Evaluation of Ni-doped Samples

Fig.1 shows the time variation of H_2 concentration when pure iron powder and samples A and B were used as reactants. The H_2 concentration of the pure iron powder after 300 min was approximately 50%, whereas those of samples A and B were approximately 80% and 60%, respectively. Ni is known to be an austenite-forming element in stainless steel; hence, Ni addition probably altered the atomic arrangement of Fe and enhanced its reactivity. Meanwhile, NO_3^- anions may have remained in Sample A and coordinate with Fe^{2+} ions that are generated by the redox reaction with carbonated water to form soluble complex ions. When $FeCO_3$ generated by the reaction precipitates on the surface of raw iron particles, the reaction is inhibited; however, the precipitation can be suppressed by solubilizing Fe^{2+}, and the surface reaction of iron particles can continue.

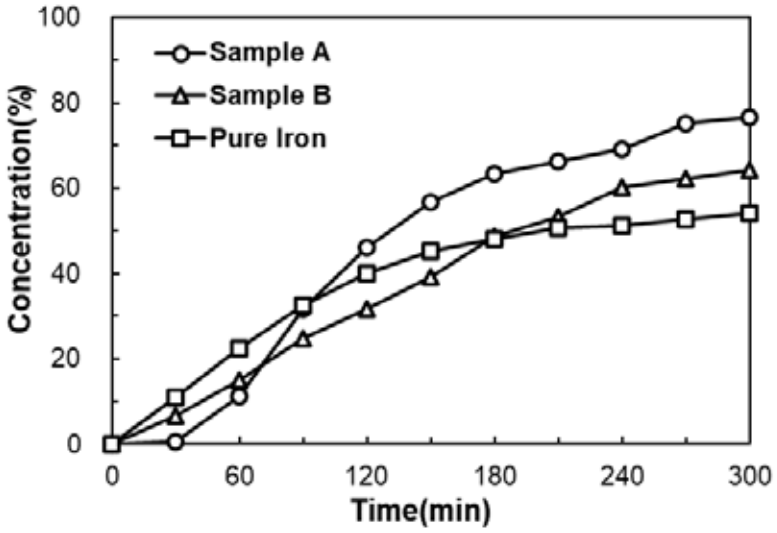


Fig.1 Time variation of H_2 concentration generated by Ni-doped iron

Evaluation of Hydrogen Production Reaction using JFE Steel Samples

Fig.2 shows the H_2 concentration of the JFE steel samples after 300 min of reaction. The H_2 concentrations of KB-90 and K-100T, which are reduced iron powders, were higher than those of 303A-60, which is an atomized iron powder. This is proposed to be because the former samples are porous, whereas the latter sample has spherical particle shape with a smaller specific surface area and relatively lower reaction rate. The H_2 concentration of the alloyed steel powders were higher than that of pure iron powder 303A-60, which is possibly owing to the change in particle shape during alloy treatment that may have increased the specific surface area. Generally, the smaller the particle size, the higher the reactivity and specific surface area. It is also possible that fine particles may become more reactive as they are dispersed during the reaction. The trend was particularly clear in SIGMALOY2010

containing Ni; however, the overall trend remains unclear. When particles aggregate into clusters and form larger particles, the specific surface area is large, even if the aggregated particle size is large, and the reactivity is high.

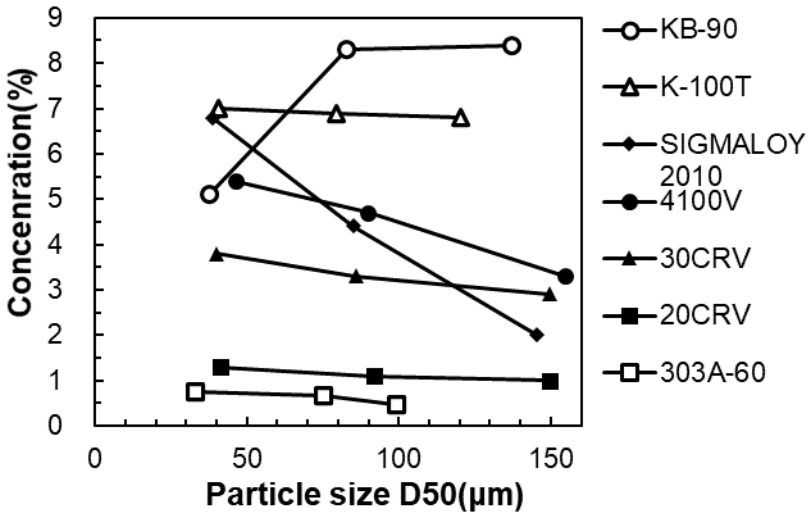


Fig.2 Concentrations of H_2 produced from iron and steel manufacturing powders after 300 min

CONCLUSIONS

The addition of $Ni(NO_3)_2$ to the pure iron powder resulted in higher hydrogen production. The Ni-containing steel powder SIGMALOY 2010 produced more hydrogen than pure iron powder, and a clear correlation between particle size and hydrogen production was observed. However, for other steel powders, it is necessary to confirm and discuss not only the particle size but also the shape, porosity, and specific surface area. In the future, the complex ion-forming ability of NO_3^- and the solubility of $FeCO_3$ will be evaluated to elucidate the effect of counterions. The conditions for improving the reactivity may be investigated by measuring the specific surface area and evaluating other properties.

ACKNOWLEDGEMENT

This work was subsidized by JKA through its promotion funds from KEIRIN RACE, Japan.

REFERENCES

1. Hiromi Eba, Masashi Takahashi, Kenji Sakurai. 2020. Progress of hydrogen gas generation by reaction between iron and steel powder and carbonate water in the temperature range near room temperature. International Journal of Hydrogen Energy 45:13832-13840. https://doi.org/10.1016/j.ijhydene.2020.03.087

WHEC-2022
23rd World Hydrogen Energy Conference
June 26-30, 2022 - Istanbul

#1506

MODELING OF A HYDROGEN STORAGE SYSTEM BASED ON METAL HYDRIDE AND PHASE CHANGE MATERIAL

*Walter H. Wiersma, Canan Acar
University of Twente, Drienerlolaan 5, Enschede, Netherlands
*Corresponding author e-mail: walter-wiersma@live.nl

ABSTRACT

This study analyzes the viability of a metal hydride–phase change material (MH-PCM) onboard storage system. Additionally, the effect of natural convection and thermal enhancements on the absorption time and gravimetric capacity are studied. To this study's knowledge, no studies have been performed on MH-PCM configurations while including natural convection. No significant attempts to include thermal enhancements were neither found in the literature. The results show that natural convection plays a significant role during the melting of PCM and absorption of hydrogen by the MH. The addition of natural convection causes a reduction of 68.9% in absorption time. Introducing thermal enhancements to the MH-PCM tank, the absorption is reduced by 92.4% while seeing a decrease of the gravimetric capacity of 30.42% compared to the case not including thermal enhancements. Performance indicators are gathered by having a defined car and the currently defined storage subjected to different driving cycles. From comparing these performance indicators with the targets set by the Department of Energy, it is concluded that an MH-PCM onboard storage system is not viable. The cause is contributed to the PCM mass required to store the released heat during absorption.

Keywords: Hydrogen storage, Metal hydride, Phase change material, Heat transfer, Thermal management

INTRODUCTION

New challenges are revealed as the energy sector must move towards sustainable energy. These challenges include transforming fossil-based fuels into green alternatives such as green electricity and hydrogen (H_2) for the automotive industry. Metal hydrides (MHs) are a potential storage medium of H_2 for automotive applications. During the absorption of H_2 by the metal, heat is released as this said reaction is exothermic. In an ideal case, the heat required for the desorption of H_2 is equal to that of the heat released during absorption. Therefore, multiple researchers have proposed to combine the MH with phase change material (PCM). The downside of an MH-PCM configuration is the poor heat transfer capability, thus resulting in high absorption times. Multiple studies have already discussed the application of an MH-PCM tank and numerically simulated such a system [1]. However, these papers did not include natural convection (NC) and applied barely any thermal enhancements (TE). Therefore, this study first focuses on numerically implementing these subjects into a numerical model describing the thermal behavior of an MH-PCM configuration to study the effect of NC and TE on the AT and GC. Second, this study performs a sensitivity analysis to determine the influence of a selected group of parameters on the AT and GC. Third, this study determines the viability of an MH-PCM configuration as an onboard storage system. Last, this study also answers whether simultaneously achieving an AT and GC of 5 minutes and 4.5 wt.% is possible.

METHODOLOGY

Different designs are formulated to determine the NC and TE effect on the AT and GC, and their thermal behavior is numerically solved in COMSOL Multiphysics. A few selected designs are mentioned. The first design is denoted as BD and is based on the findings of Alqahtani et al. [1]. The second design is proposed to manipulate the PCM flow beneficially to lower the AT. This design, denoted as 4C, sees the addition of fins within the PCM, extending outwards from the origin. The final two designs include a PCM-foam composite where the foam has a porosity of 85%. This design also includes fins. These designs are denoted by F-fins and F85, respectively. Schematics of these designs are displayed in Figure 1.

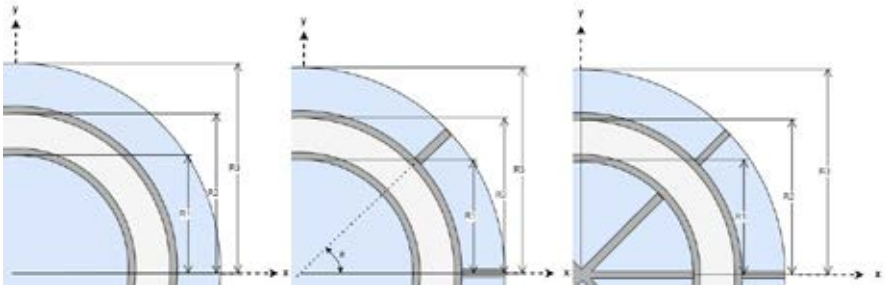


Figure 1. Schematic overview of the BD and F85 (left), 4C (middle) and F-fins (right). The PCM, MH-bed and wall or fins are represented by blue, white and grey respectively.

The following simplistic design is proposed to check the viability of an MH-PCM onboard storage system, as presented in Figure 2. The storage system in this design includes an MH-PCM tank, expansion valve, heat exchanger (HE), and heater. The decision is to rely on the pressure difference between the MH-PCM tank and fuel cell to deliver the required H_2 mass. Performance indicators are collected to check the current MH-PCM onboard storage system's viability. This is done by having a defined automobile go through selected driving cycles. This gives a required power profile from which a required H_2 can be obtained. This required H_2 profile is then applied to the storage system, from which then performance indicator values are collected. Comparing the obtained performance indicators with the targets set by the DOE and other hydrogen onboard storage systems, the viability of an MH-PCM onboard storage system is checked.

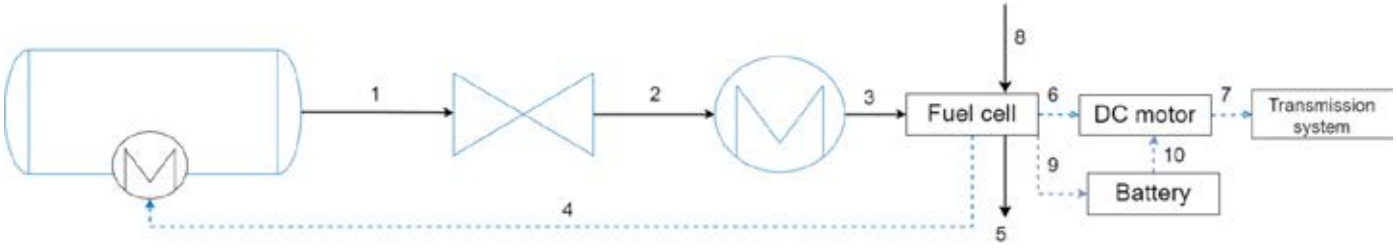


Figure 2. Schematic overview of a simplistic MH-PCM storage system.

MH selection

The MH that is selected for this study is based on $LaNi_5$. However, for this study, $LaNi_5$ is altered. The GC of this MH is increased to 10 wt.%, which makes this MH non-existent. A non-existing MH is selected to be still able to reach the set target of 4.5 wt.% by the DOE. Due to this alteration, the saturation density of the MH also changes to 7960 kg/m^3.

Validation of the numerical model

The developed numerical model is validated with experimental results. The equations governing the behavior of the MH-bed are validated with experimental results from Jemni et al. [2]. The equations describing the PCM are validated with experimental results from Jones et al. [3]. The governing equations regarding a PCM-foam application are validated with the experimental results from Zhao et al. [4]. All numerical results show a good agreement with the experimental data.

RESULTS AND DISCUSSION

This section presents the thermal behavior of the different proposed designs. This is followed by an analysis of the viability of MH-PCM configuration as an onboard storage system.

Designs and Sensitivity analysis

Figure 1 shows the temperature and velocity profile of the BD during the absorption process. Within the melted PCM, NC sets in. Hot fluidized PCM moves upwards, forming a thermal bottleneck that significantly slows down the absorption of H_2 in the upper section of the MH-bed. However, due to the transport of hot PCM away from the lower half of the cylinder, the absorption of H_2 is accelerated within that area. Table 1 shows the AT and GC of designs mentioned within this short paper. The lowest AT is obtained by conduction only in the BD (Cond) case and is significantly slower in case NC is included. This shows that NC is an important aspect when simulating MH-PCM configurations and can thus not be neglected. The 4C case shows a decrease in AT of 25% while seeing a decrease in the GC no higher than 2%. The fastest AT is observed by F-fins, which can be expected as the effective thermal conductivity of the PCM-foam composite is significantly increased. The results show that adding fins that block the flow of liquid PCM effectively decreases the AT while having a very low decrease in the GC.

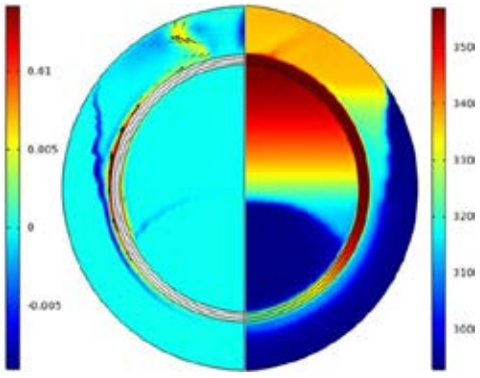


Figure 3. The temperature profile in Kelvin and velocity profile in m/s of the BD at 840 seconds after the start of the absorption process.

Sensitivity analysis

During the sensitivity analysis, the latent heat, pressure of the H_2, thermal conductivity, standard enthalpy of formation, and stored H_2 mass. To quickly summarize, the effects of these parameters diminish or grow stronger as the MH-PCM tank's size increases or decreases. An interesting result is an increase in AT when the latent heat increases. This is unsatisfactory as selecting a PCM with a higher latent heat would result in a higher AT and GC.

Table 1. Absorption times and gravimetric capacities of the mentioned designs.

	Absorption time (s)	**Gravimetric capacity (wt.%)**
Cond	12650	0.996
BD	3940	0.996
4C	2920	0.982
F85	460	0.705
F-fins	300	0.693

Storage system performances

The performances are compared in Table 2 with the targets set by the DOE. The term “opt” represents the case where all the H_2 is extracted, whereas the others represent cases where not all the H_2 can be extracted due to limitations of the system. The cases that end with an “S” represent constant velocity cases where the number in front dictates the velocity in km/h. The FUDC and WLTC represent cases developed by organizations and/or countries to determine, for example, emissions from the engine of a car. It can be seen that all values are significantly lower than the target values. Due to the highly required PCM mass, the currently defined MH-PCM configuration is not viable as an onboard storage system to store the exothermic heat. However, the ranges the car can travel do look promising. If the weight of the PCM could be reduced, the viability of an MH-PCM onboard storage system would increase.

CONCLUSIONS

The influence of natural convection (NC) and thermal enhancements (TE) on the absorption time (AT) and gravimetric capacity (GC) are studied. It can be concluded that NC has a significant and satisfactory impact on the AT of a metal hydride-phase change material (MH-PCM) configuration and should be considered when simulating such a case. TE reduces the AT even further, where the combination of separating the PCM into chambers and imbed them in foam showed the lowest AT among the different designs. The sensitivity analysis showed that if the latent heat increases, it decreases the GC but increases the AT for the range in which it was varied. A simplistic storage system is proposed from which performance indicators are gathered by applying different driving cycles to the defined vehicle. From the retrieved data, it can be concluded that an MH-PCM storage system is not a viable option for an onboard application. The main drawback of such a system is the weight of the required PCM, which is too high.

Table 2. Values of the targets set by the DOE and the values of the performance indicators retrieved after applying a certain driving cycle.

Parameter	DOE	Opt	120S	100S	80S	50S	FUDC	WLTC
kWh/kg	1.5	0.19	0.0419	0.0709	0.117	0.126	0.109	0.0719
kWh/m^3	1000	521	110.89	187.6	309	334.22	289	190.31
GC (wt.%)	4.5	0.58	0.13	0.21	0.35	0.38	0.33	0.22
Kg-H_2/m^3	30	15.64	3.33	5.63	9.28	10.04	8.68	5.71
Mass [kg]	-	960.8	960.8	960.8	960.8	960.8	960.8	960.8
Volume [m^3]	-	0.363	0.363	0.363	0.363	0.363	0.363	0.363
Range [km]	-	-	85.2	197.4	452.8	788.8	287.76	186

REFERENCES

1. Alqahtani T, Melloulu S. 2016. Thermal performance analysis of a metal hydride reactor encircled by a phase change material sandwich bed 5:23076–23092.
2. Jemni A, Ben Nasrallah S. 1999. Experimental and theoretical study of a metal-hydrogen reactor 24:631–644.
3. Jones B, Sun D. 2006. Experimental and numerical study of melting in a cylinder 49:2724-2738.
4. Zhao C.Y, Lu W, Tian Y. 2010. Heat transfer enhancement for thermal energy storage using metal foams embedded within phase change materials (PCMs) 84:1402-1412.

WHEC-2022
23rd World Hydrogen Energy Conference
June 26-30, 2022 - Istanbul

#1508

BORON-HYDROGEN MATERIALS TOWARDS DECARBONISATION

[1*] Sonnur Kurtuluş, [2]*Bilge Coşkuner Filiz,* [3]*Hülya Civelek Yörüklü,* [4]*Korkut Açıkalın,* [1]*Halit Eren Figen,* [6]*Umit Bilge Demirci,* [1]*Aysel Kantürk Figen*
[1] Department of Chemical Engineering, Yildiz Technical University, İstanbul, Turkey
[2] Department of Metallurgy and Materials Engineering, Yildiz Technical University, İstanbul, Turkey
[3] Department of Environmental Engineering, Yildiz Technical University, İstanbul, Turkey
[4] Department of Energy Systems Engineering, Yalova University, Yalova, Turkey
[6] Institut Europeen des Membranes, IEM – UMR 5635, Univ Montpellier, ENSCM, CNRS, Montpellier, France

*Corresponding author e-mail: kurtulussonnur@gmail.com

ABSTRACT

Boron-hydrogen (B-H) materials are used as hydrogen and heat sources, due to their reducing potential. It has been shown again with the COVID-19 pandemic that greenhouse gas activities are anthropogenic in origin. In particular, the conversion of carbon dioxide (CO_2) into valuable chemicals has an important place in the fight against the climate crisis. The conversion of anthropogenic CO_2 into valuable chemicals has important implications for a habitable world. In many studies in the literature, boron hydrides have been used to produce, hydrogen and convert carbon dioxide into valuable chemicals. Formic acid and methanol obtained by hydrogenation can be seen as the clean energy movement of the future with its value in hydrogen storage. The type of valuable chemicals that will be formed by the hydrogenation of CO_2 is directly related to the method to be followed. The type of catalyst used, or how much hydrogen molecule interacts with CO_2, determines the valuable chemical that will form. Disturbances in the thermodynamics of the hydrogenation of CO_2 have been tried to be eliminated by various types of catalysts and necessary condition optimizations. Many catalysts and methods developed for the hydrogenation of CO_2 were examined. This study discusses the use of B-H materials via catalytic conversion of CO_2 into valuable chemicals in terms of critical factors such as reaction conditions, selection of catalyst, and solvent.

Keywords: Hydrogenation, Decarbonization, Borane-Hydrogen Materials, Carbon dioxide reduction

INTRODUCTION

The existence of human beings on earth and their increasing demands appear as CO_2 and global warming in nature. One of the important steps taken for a clean and livable world is the European Union's goal of transitioning to a carbon-free economy by 2050, within the scope of the "Green Deal". To keep global warming below 2°C, which is also the target of the Paris Agreement, many sectors have become obligated to make investments to reduce environmental impact based on their product portfolio [1]. Despite the political measures taken by the countries, the inability to reduce the amount of CO_2 in industrial flue gases necessitated the implementation of carbon capture technologies. One of the most practical solutions in the face of increasing global warming data is to see CO_2 in nature as a source and to carry out studies for this purpose. The main goal is to see harmful and waste CO_2 as a production potential. It is a field of work that has important effects on many industrial organizations that have determined environmentally friendly, innovative, and sustainable working principles at home and abroad. This aim means that research in this area will create a direct supply on the industrial platforms.

CO_2 HYDROGENATION STRATEGIES

Chemical boron hydrides produce hydrogen by hydrolysis in the aqueous medium. Hydrogen is a high-energy substance that can be used as a reagent for the conversion of CO_2. As a result of the hydrogenation of CO_2, fuels such as methane (CH_4), hydrocarbons with high added value, and chemicals such as methanol (CH_3OH), formic acid (HCOOH), CH_4, and carboxylic acids (-COOH) are formed. The species that may occur after hydrogenation are shown in Fig.1 in the cycle. In the CBH cycle in the figure, the commercially important $MB(OR)_4$ product is obtained after hydrogenation. It is predicted that the approach of detecting the $MB(OR)_4$ structured product and converting the CO_2 retained in the structure into a valuable chemical as a result of its hydrolysis, can enable a single CO_2 source to turn into two different valuable chemicals.

There are many studies examining the production and structural properties of catalysts used to increase hydrogenation efficiency. Studies in which biomass is added to HCOOH by using hydrolysis, wet and catalytic oxidation, and CO_2 is reduced to COOH by various methods have been investigated in the literature. In addition, research has been carried out in which an artificial photosynthesis mechanism is considered with the photoelectrochemical conversion of CO_2 [2]. In studies examining the hydrogenation mechanism, it has been reported that the CO_2 hydrogenation efficiency is in the range of %40-50 [3].

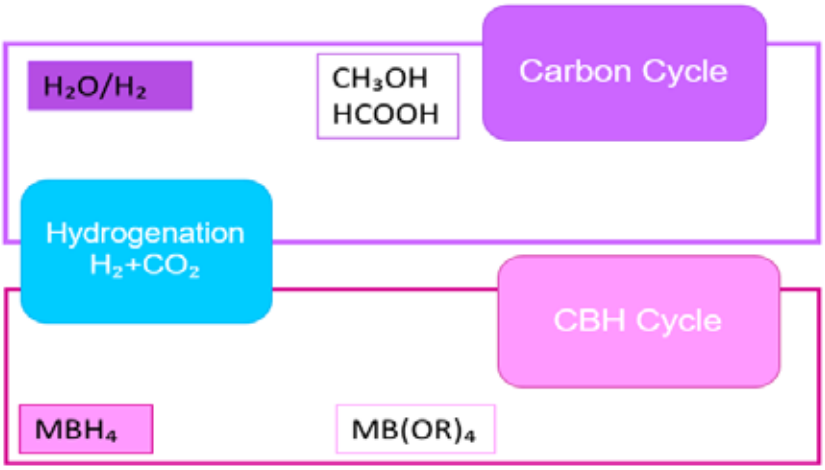


Figure 1 B-H compounds and carbon cycle

B-H materials have been investigated for the production of HCOOH and CH_3OH by the hydrogenation of CO_2 gas. Researches in this field aim to convert the pollution source CO_2 into valuable chemicals via CO_2 hydrogenation. In general, the interaction of sodium borohydride ($NaBH_4$) with CO_2 is directly dependent on the reaction conditions. Studies on the use of various B compounds for the hydrogenation of pure CO_2 have focused on B-containing metal hydrides and organic compounds [4, 5]. As a result of the reaction of B-H compounds with water, the molecular hydrogen (H_2) in its structure becomes free and the borate compound is formed as a by-product. With the presence of CO_2 in the reaction medium, H_2 released from the B-H compound during the reaction interacts with the CO_2, forming HCOOH, and CH_3OH according to the H/C stoichiometry. As seen in Figure 2, the CO_2 is reduced by H_2 to the released one from the B-H materials.

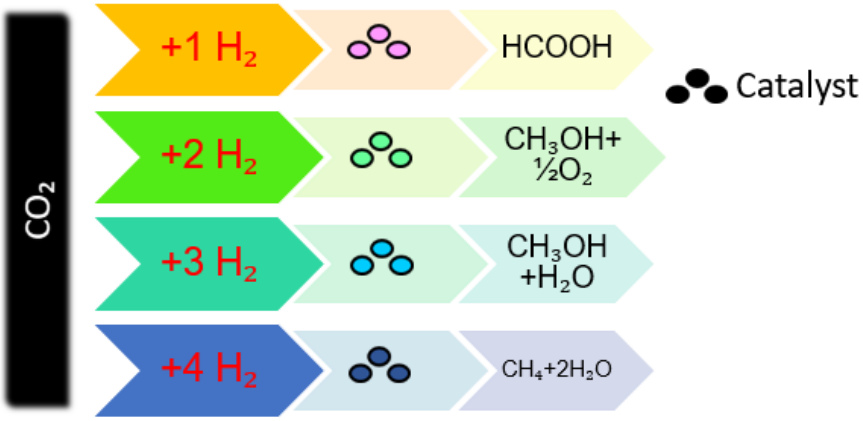


Figure 2 Synthesis of valuable products via catalytic CO_2 hydrogenation

CONCLUSION

In the literature, they investigated the reduction of the CO_2 they produced under in-situ conditions with $NaBH_4$ using $(NH_4)_2CO_3$ as a CO_2 source and determined that the compound formed as a result of the reaction carried out under microwave conditions was sodium formate [6]. In another study, $NaBH_4$ was used as a hydrogen source, and they determined that they produce formic acid when pure CO_2 and bicarbonate are used as a CO_2 source [7]. In studies on the use of $NaBH_4$, one of the B-H compounds, $Na[HB(OCHO)_3]$ and $Na[H_2B(OCHO)_2]$ were obtained as a result of the reaction of $NaBH_4$ with CO_2 in an acetonitrile environment [8].

In the studies in the literature, solvents such as water, ethanol (C_2H_5OH), and acetonitrile (CH_3CN) were used, as well as in solvent-free conditions. In a study on the conversion of CO_2 with a borohydride in solvent-free conditions, formate and alkoxide-like compounds are formed as a result of the rapid reaction between porous γ-$Mg(BH_4)_2$ and CO_2 under 30°C and 1 bar conditions [9]. In a study, HCOOH was obtained with a 24% yield as a result of the reaction of aqueous potassium borohydride (KBH_4) solution with CO_2 under ambient conditions [10]. In addition to this, in another research, potassium formylhydroborates $K[H_xB(OCHO)_{4-x}]$ (x =1-3) was synthesized as the main product as a result of the reaction between KBH_4 and CO_2 under mechanochemical and thermal conditions [11]. As a result, it

has been stated that the reaction conditions should be optimized and studies should be continued for this purpose to realize the conversion of CO_2 into valuable organic chemicals with the use of complex hydrides with high selectivity and sustainability.

ACKNOWLEDGEMENT

The authors gratefully acknowledge the financial support of TÜBİTAK for the following project; Grant no: 221M293

REFERENCES

1. Tcvetkov P. 2021. Climate policy imbalance in the energy sector: Time to focus on the value of CO_2 utilization. Energies, 14:2: 411:1-22
2. Chen X, Liu Y and Wu J. 2020. Sustainable production of formic acid from biomass and carbon dioxide. Molecular Catalysis, 483:110716.
3. Ménard G and Stephan DW. 2010. Room temperature reduction of CO_2 to methanol by Al-based frustrated Lewis pairs and ammonia borane. Journal of the American Chemical Society, 132:6:1796-1797.
4. Suna Y, Ertem MZ, Wang WH, Kambayashi H, Manaka Y, Muckerman JT, Fujita E and Himeda Y. 2014. Positional effects of hydroxy groups on catalytic activity of proton-responsive half-sandwich Cp*Iridium (III) complexes. Organometallics, 33:22:6519-6530.
5. Gunasekar GH, Park K, Jung KD and Yoon S. 2016. Recent developments in the catalytic hydrogenation of CO_2 to formic acid/formate using heterogeneous catalysts. Inorganic Chemistry Frontiers, 3:7:882-895.
6. Pulidindi IN, Kimchi BB and Gedanken A. 2014. Selective chemical reduction of carbon dioxide to formate using microwave irradiation. Journal of CO_2 utilization, 7:19-22.
7. Grice KA, Groenenboom MC, Manuel JDA, Sovereign MA and Keith JA. 2015. Examining the selectivity of borohydride for carbon dioxide and bicarbonate reduction in protic conditions. Fuel, 150:139-145.
8. Knopf I, and Cummins CC. 2015. Revisiting CO_2 reduction with $NaBH_4$ under aprotic conditions: synthesis and characterization of sodium triformatoborohydride. Organometallics, 34:9:1601-1603.
9. Vitillo JG, Groppo E, Bardají EG, Baricco M, and Bordiga S. 2014. Fast carbon dioxide recycling by reaction with γ-$Mg(BH_4)_2$. Physical Chemistry Chemical Physics, 16:41:22482-22486.
10. Fletcher C, Jiang Y and Amal R. 2015. Production of formic acid from CO_2 reduction by means of potassium borohydride at ambient conditions. Chemical Engineering Science, 137:301-307.
11. Picasso CV, Safin DA, Dovgaliuk I, Devred F, Debecker D, Li HW, Proost J and Filinchuk Y. 2016. Reduction of CO_2 with KBH_4 in solvent-free conditions. international journal of hydrogen energy, 41:32:14377-14386.

WHEC-2022
23rd World Hydrogen Energy Conference
June 26-30, 2022 - Istanbul

#1518

INFLUENCE OF DIFFERENT ADDITIVES IN THE HYDROLYSIS OF SODIUM BOROHYDRIDE

[1]Lucía Gómez-Coma, [2]Diogo Silva,[1*]Alfredo Ortiz, [2]Alexandra M.F.R. Pinto, [1]Inmaculada Ortiz
[1]Department of Chemical and Biomolecular Engineering. Universidad de Cantabria,
Av. Los Castros 46, 39005 Santander, Spain
[2]Transport Phenomena Research Center, Chemical Engineering Department, Faculty of Engineering, University of Porto
Rua Dr. Roberto Frías s/n, 4200-465 Porto, Portugal

*Corresponding author e-mail: ortizal@unican.es

ABSTRACT

Achieving net-zero emissions in the atmosphere is one of the most critical challenges faced by society. Thus, the research efforts should be intended to develop and implement new green sources to substitute the traditional fossil fuels avoiding carbon dioxide emissions. Among others, hydrogen energy is positioned as promising renewable energy but still requires overcoming the disadvantages of storage. In this context, ensuring a safe process employing reasonable volumes and pressures is one of the hotspots which are needed to address. Sodium borohydrides with significant advantages such as low vapor pressure, stability, or high hydrogen storage capacity have been largely studied in the last years. Catalysts and the different operating conditions are well known in this field. This work intends to demonstrate the benefits of the employment of additives to improve process control in terms of yield. Specifically, sodium carboxymethyl cellulose additive in 1 wt %, provides performance of 85 %, concluding that although further efforts are required, this approach could improve the hydrolysis of borohydrides for hydrogen storage.

Keywords: hydrogen storage, sodium borohydrides, additives, hydrogen generation rate.

INTRODUCTION

One of the key aspects that must be addressed to mitigate climate change is carrying out innovative renewable sources of energy which can compete with conventional sources based on fossil fuels. Nevertheless, the most currently developed green energies, solar and wind have major drawbacks such as low performance or their intermittent character. In this context, hydrogen-based energy presents itself as a promising alternative. However, this type of H_2 energy technologies still have some limitations that need to be approached, especially regarding storage for onboard applications [1]. At present, traditional systems are based on i) gaseous form, which, in addition to working at 273 K, requires the use of high pressures or ii) in liquid form, which, although works at ambient conditions of pressure, demands cryogenic temperatures, below 25 K [2]. The US Department of Energy (DOE) recommends searching for new systems capable of achieving high storage capacity targets, high regeneration capacities, and lower costs [3]. In this framework, hydrogen storage in solid materials could constitute a step forward in developing this energy source. Concretely, the chemical hydride sodium borohydride (NaBH4) has been widely studied in the last years due to its inherent advantages, i) stability under inert conditions and wide range of temperature, ii) low work pressures, iii) high purity, iv) high hydrogen storage capacity (10.8 wt. %), v) exothermic reaction (ΔH= -210 kJ·mol-1), vi) capacity of simultaneous generation and storage, vii) H_2 released can be directly fed to a PEM fuel cell to generate electric energy and viii) is a non-toxic compound [4–6]. Moreover, its main limitations, the hydrogen release rate and the stabilization of the kinetics, can be overcome by using enhanced catalysts and additives, respectively [7]. In this regard, additives are introduced to optimize the $NaBH_4$ hydrolysis because of, apart from the stabilization, the improvement on the hydrogen rates and, consequently, the higher yields and better performance of the process. Thus, this work aims to optimize the hydrolysis of sodium borohydride through the study of different additives to improve the hydrogen generation. Consequently, 4 different non-toxic and environmentally friendly additives, sodium carboxymethyl cellulose (CMC), polyacrylamide (PAM), sodium dodecyl sulfate (SDS), and β-cyclodextrin (BCD), were chosen to progress in the understanding of storage and release of hydrogen using $NaBH_4$.

MATERIALS AND METHODS

Hydrogen is released by the $NaBH_4$ hydrolysis at moderate temperature, according to the following equation (ec. 1.) Excess of water, x, is required to increase the H_2 yield due to by-product's water retention. In the case of this work, an x = 15 was considered.

$$NaBH_4 + (2 + x)\, H_2O \rightarrow NaBO_2 \bullet x H_2O + 4\, H_2 \qquad (1)$$

Four additives have been tested (1 wt. %) to study their influence on hydrogen release and kinetics stabilization. Sodium carboxymethyl cellulose (CMC, Sigma Aldrich, average Mw≈700,000), Polyacrylamide (PAM, Polysciences. Inc, Mw=18,000,000), sodium dodecyl sulfate (SDS, Sigma Aldrich, ≥98.5 %) and β-cyclodextrin (BCD, Sigma Aldrich, ≥97.0 %. CMC is a derivative of cellulose, non-toxic and generally non-allergenic which dissolves rapidly in cold water. Its viscosity drops during heating, which could promote the improvement of hydrogen release rate. PAM is often used as a viscosity modifier, and friction reducer and consequently could also help control the hydrogen release. However, its high molecular weight could impede the formation of a homogenous aqueous solution. In the case of SDS, this additive has widely used to improve the storage capacity and induction time of multiple compounds. Finally, BCD is a non-toxic, green, and cyclic oligosaccharide and has proven to be suitable support due to its potentiality to construct strong interaction between the metal, in this case the catalyst, and the solution, which is beneficial for the enhancement of performances.

The catalyst is composed of Ni-Ru based in powder form and was prepared from a mixture of precursors in the deionized water. The synthesis procedure is extensively described in previous works [8]. All the experiments were carried out in a stainless-steel batch reactor with a free internal volume of 229 cm3 [7], and the tests were performed at room temperature (26 ± 1 ºC), without stirring, and at least in duplicate under the same conditions to ensure the reproducibility of the system.

RESULTS AND DISCUSSION

One of the critical parameters in a process is the H_2 yield because it is intimately related to the overall performance of the process. Thus, this section discusses the different yields achieved in the hydrolysis of sodium borohydride using the CMC, PAM, SDS, and BCD additives.

Figure 1 illustrates the mean value reached employing each of the four additives and compared with the conventional process without additives, as well as the deviation standard for each case. It is important to remark that the yields were calculated considering the real and theoretical pressure of the system. In all cases, the additives were added to the aqueous solution in a proportion of 1 wt. %.

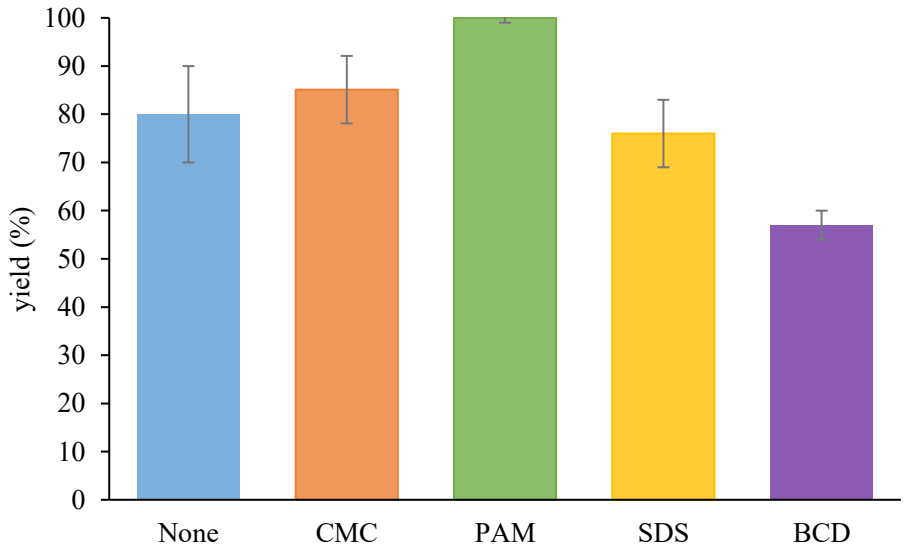


Figure 1: Hydrogen generation yield (%) achieved in a batch reactor using different additives.

Polyacrylamide additive (PAM) is presented as the most promising precursor since it allows H_2 yields close to 100 %, and the standard deviations are under 1.5 %. In contrast, the compound β-cyclodextrin (BCD) offers the worst outcomes. In this case, the performance is about 57 %, far from the desirable values for $NaBH_4$ hydrolysis. Moreover, BCD had even lower values than the system when no admixtures were added. However, the method without a precursor has the most variability, although the average yield is over 80 %, the standard deviation is about 10 %. Finally, CMC and SDS meet yields of 85 % and 80 %, respectively and standard deviations are in the range of 5-7 %, which could be considered admissible and therefore the use of these admixtures could stabilize the process. In addition, the Hydrogen generation rates (HGR) have been calculated, resulting in values as high as 1374±40 H_2 $mL \cdot min^{-1} \cdot gcat^{-1}$ for the CMC additive. However, only a generation rate of 788±120 $mL \cdot min^{-1} \cdot gcat^{-1}$ has been reached using the SDS precursor.

CONCLUSIONS

This manuscript contributes to giving a step forward employing precursors in low quantity, specifically 1 wt. %, identifying and describing the most variables that affect the process of the $NaBH_4$ hydrolysis in comparison with the conventional system where no additives are used. For this purpose, four additives based on different viscosities and nature have been evaluated, analyzing the yields obtained.

The results show that Polyacrylamide additive presents the most yields, close to 100 %. In the case of sodium carboxymethyl cellulose provides reasonable yield values (85 %). Finally, the other two additives studied, β-cyclodextrin and sodium dodecyl sulfate achieving lower values in terms of H_2 release or yield but, in both cases, offer higher replicability with respect to blank-case (without additive).

ACKNOWLEDGEMENT

This work has been conducted with financial support from the Spanish Ministry of Economy and Competitiveness (project RTI2018-093310-B-100). This research is also being supported by the Projects “HYLANTIC”-EAPA_204/2016” & ENERGY PUSH SOE3/P3/E0865, which are co-financed by the European Regional Development Fund in the framework of the Interreg Atlantic and Interreg Sudoe Programmes.

REFERENCES

1. Hydrogen Storage Challenges | Department of Energy, (n.d.). https://www.energy.gov/eere/fuelcells/hydrogen-storage-challenges (accessed September 9, 2021).
2. I.A. Hassan, H.S. Ramadan, M.A. Saleh, D. Hissel, Hydrogen storage technologies for stationary and mobile applications: Review, analysis and perspectives, Renewable and Sustainable Energy Reviews. 149 (2021) 111311. https://doi.org/10.1016/j.rser.2021.111311.
3. H.X. Nunes, D.L. Silva, C.M. Rangel, A.M.F.R. Pinto, H.X.; Nunes, D.L.; Silva, C.M.; Rangel, A.M.F.R. Pinto, Rehydrogenation of Sodium Borates to Close the NaBH 4-H 2 Cycle: A Review, Review. Energies. 14 (2021) 3567. https://doi.org/10.3390/en14123567.
4. J. Mao, D.H. Gregory, Recent advances in the use of sodium borohydride as a solid state hydrogen store, Energies. 8 (2015) 430–453. https://doi.org/10.3390/en8010430.
5. Q. Yao, Y. DIng, Z.-H. Lu, Noble-metal-free nanocatalysts for hydrogen generation from boron- And nitrogen-based hydrides, Inorganic Chemistry Frontiers. 7 (2020) 3837–3874. https://doi.org/10.1039/d0qi00766h.
6. U.B. Demirci, About the Technological Readiness of the H_2 Generation by Hydrolysis of B(−N)−H Compounds, Energy Technology. 6 (2018) 470–486. https://doi.org/10.1002/ente.201700486.
7. M.J.F. Ferreira, L. Gales, V.R. Fernandes, C.M. Rangel, A.M.F.R. Pinto, Alkali free hydrolysis of sodium borohydride for hydrogen generation under pressure, International Journal of Hydrogen Energy. 35 (2010) 9869–9878. https://doi.org/10.1016/j.ijhydene.2010.02.121.
8. A.M.F.R. Pinto, M.J.F. Ferreira, V.R. Fernandes, C.M. Rangel, Durability and reutilization capabilities of a Ni-Ru catalyst for the hydrolysis of sodium borohydride in batch reactors, Catalysis Today. 170 (2011) 40–49. https://doi.org/10.1016/j.cattod.2011.03.051.

WHEC-2022
23rd World Hydrogen Energy Conference
June 26-30, 2022 - Istanbul

#1528

SYNTHESIS OF CALCIUM BOROHYDRIDE WITH BORON-FLORIDE EXCHANGE AT HIGH PRESSURES

[1] Gökhan Gizer, [1] Fahim Karimi, [1] Claudio Pistidda, [1] Julián A. Puszkiel*
[1] Helmholtz-Zentrum Hereon, Institute of Hydrogen Technology, Max-Plank-Str. 1, 21502 Geesthacht, Germany

*Corresponding author e-mail: goekhan.gizer@hereon.de

ABSTRACT

In the present work, $Ca(BH_4)_2$ is synthesized by ball milling MgB_2 with CaF_2 and thereafter applying H_2 pressures of 1000 bar and temperatures of 350°C. Formation of α,β and γ-$Ca(BH_4)_2$ phases are confirmed, using in-situ synchrotron powder X-ray diffraction (SR-PXD). Volumetric measurements with a Sieverts' apparatus and mass spectrometry results indicate that 3.5 wt.% of H_2 can be stored reversibly. During hydrogenation, boron-fluoride exchange between MgB_2 and CaF_2 occurs. As a result, $Ca(BH_4)_2$ and MgF_2 are formed. During dehydrogenation, starting materials MgB_2 and CaF_2 are formed back, together with the H_2 release. Applying high pressures of H_2 can be helpful to investigate hydrogen storage systems that were reported to be partially reversible previously in the literature.

Keywords: High pressure, Hydrogen storage, Complex hydrides

INTRODUCTION

Light metal borohydrides ($Ca(BH_4)_2$, $Mg(BH_4)_2$, $LiBH_4$, etc.) are interesting hydrogen storage materials due to their high gravimetric capacities [1]. For example, $Ca(BH_4)_2$ has a theoretical H_2 storage capacity of 11.6 wt.% with a dehydrogenation enthalpy of 36 kJ/mol. Possible dehydrogenation reactions of $Ca(BH_4)_2$ are presented as in Eq. 1-3.

$$Ca(BH_4)_2 \rightarrow Ca + 2B + 4H_2 \ (11.6\,wt.\%) \quad (1)$$

$$Ca(BH_4)_2 \rightarrow 1/3CaB_6 + 2/3CaH_2 + 10/3H_2 \ (9.6\,wt.\%) \quad (2)$$

$$Ca(BH_4)_2 \rightarrow CaH_2 + 2B + 3H_2 \ (8.7\,wt.\%) \quad (3)$$

Significant hydrogen amount is released from reactions in Eq.1-3. However, poor rehydrogenation of the dehydrogenation products; CaB_6, amorphous boron or CaH_2 hinders the practical use of $Ca(BH_4)_2$. Rönnebro *et al*. reported that hydrogenation of CaB_6 and CaH_2 to produce $Ca(BH_4)_2$ was not successful even at high temperature and pressure conditions (T= 400-440°C and $p(H_2)$ = 700 bar) [2]. In the present work, an alternative path is proposed to synthesize $Ca(BH_4)_2$. MgB_2 - CaF_2 mixture was ball milled and high hydrogen pressure (1000 bar) and temperature (350°C) was applied. In-situ dehydrogenation with SR-PXD was carried out to identify the desorption products. Hydrogen capacity was determined via in-house made Sieverts apparatus.

MATERIALS AND METHODS

Appropriate amount (1/1 molar ratio) of starting materials MgB_2 and CaF_2 (purchased from Sigma Aldrich, ≥ 99% purity) were ball milled for 40 hours using Spex 8000M shaker mill under Ar atmosphere. In order to prevent contaminations, sample preparation and milling were carried out in a dedicated Ar-filled glovebox (O_2 and H_2O below 10 ppm).

Hydrogenation reactions were carried out at an in-house made Sieverts apparatus (rated to max. 2000 bar of H_2 pressure), using absolute pressure method. 1000 bar of H_2 was loaded into the sample reactor (sample amount ~ 400 mg) and data was collected starting from room temperature until 350°C. Total measurement volume is ~ 15 ml, which allows obtaining sufficient pressure difference due to hydrogen absorption. An in-house made Sieverts apparatus was utilized to determine the released hydrogen amount, using differential pressure method. 50 mg of sample was loaded into the sample holder. Desorption kinetic data was collected starting from room temperature until 400°C with 10°C/min heating rate, under 1 bar of H_2 backpressure. In-situ SR-PXD measurements were carried out at Desy P02.1-Powder diffraction and total scattering beamline (wavelength λ ~ 0.2 Å, sample to detector distance: 160 cm). Small amount of powder was loaded into the measuring cell, which is later connected to a stage in the beamline. Diffraction data was collected every 10 seconds, while the sample is heated from room temperature to 400°C with 10°C/min heating rate.

RESULTS AND DISCUSSION

Hydrogen absorption trial was carried out for the ball-milled MgB_2-CaF_2 mixture, as seen in Figure 1. 1000 bar of H_2 was loaded into the reactor with 400 mg of sample at room temperature. Following, sample temperature was raised

to 350°C. As temperature rises, hydrogen pressure is also rising as expected. At temperatures of ~300°C, hydrogen pressure is decreasing sharply, due to hydrogen absorption.

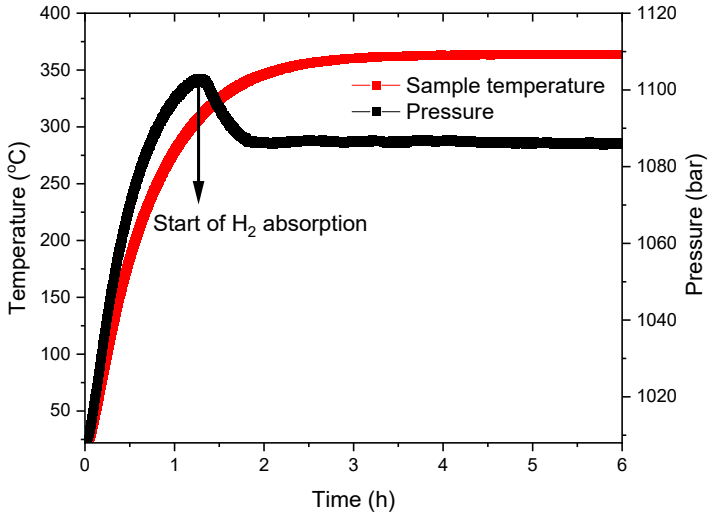


Figure 1: Hydrogen absorption of ball milled MgB_2-CaF_2 mixture. Corresponding data for sample temperature and pressure in red and black colour, respectively.

Structural characterization on the hydrogenated sample was carried out with in-situ SR-PXD, as seen in Figure 2. Hydrogenated sample at room temperature is composed of α, β and γ-$Ca(BH_4)_2$. Additionally starting materials MgB_2 and CaF_2 are identified, together with MgF_2. Presence of MgB_2 and CaF_2 indicate that sample is not fully hydrogenated, which means, ball milled composite doesn't have a homogenous mixture of starting materials. Boron-fluoride exchange between MgB_2 and CaF_2 during hydrogenation results with formation of MgF_2 in addition to $Ca(BH_4)_2$. At temperatures of ~ 120°C, diffraction peaks related to α and γ-$Ca(BH_4)_2$ disappear, β-$Ca(BH_4)_2$ becomes the main phase. Desorption of β-$Ca(BH_4)_2$ starts at 300°C, since diffraction intensity of $Ca(BH_4)_2$ decreases and intensity of CaF_2 increases. 3.5 wt.% of gas is released from its desorption, as seen in Figure 3. It is confirmed with mass-spectroscopy that desorbed gas is purely hydrogen.

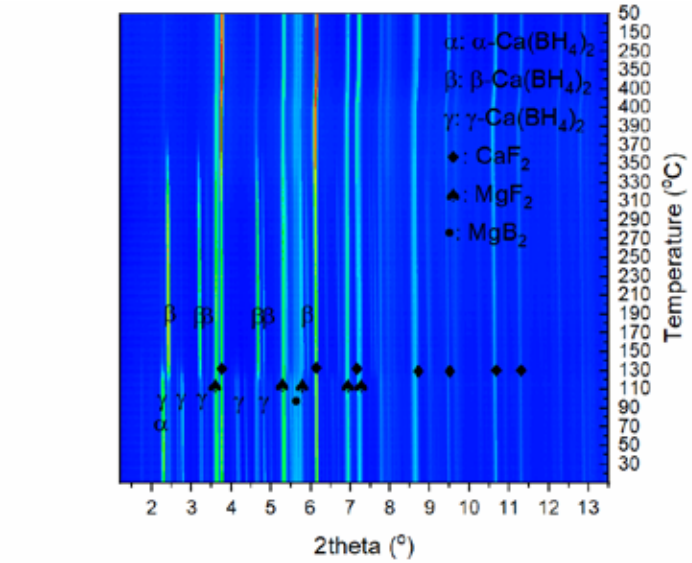


Figure 2: In-situ dehydrogenation of hydrogenated sample with SR-PXD, starting from room temperature until 400°C (10°C/min heating rate) under 1 bar of Ar pressure.

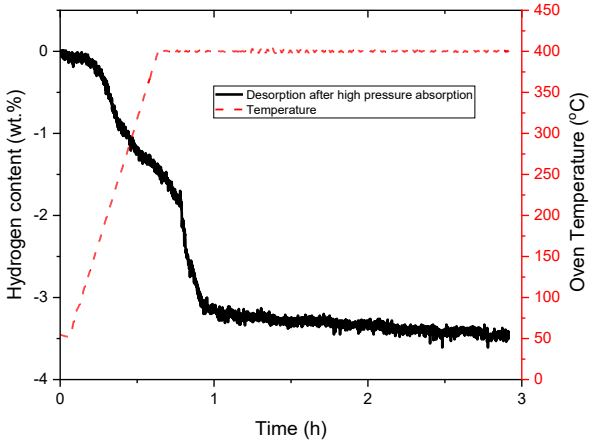


Figure 3: Dehydrogenation kinetics of hydrogenated MgB_2 - CaF_2 mixture. Sample was heated from room temperature to 400°C with 10°C/min heating rate.

CONCLUSIONS

Application of high pressure of hydrogen (1000 bar) on the MgB_2 - CaF_2 results in $Ca(BH_4)_2$ formation. During dehydrogenation, boron-flouride exchange between $Ca(BH_4)_2$ and MgF_2 results in formation of desorption products CaF_2 and MgB_2. Desorbed gas amount is calculated as 3.5 wt.%, and it is purely hydrogen according to the mass-spectroscopy result. Reactions are expected to be fully reversible, cycling experiments are still ongoing. Application of high-pressure hydrogen allows investigating H_2 storage systems that are reported to be partially reversible in the literature.

REFERENCES

[1] B. Bonnetot and L. Laversenne, “Hydrogen storage using borohydrides,” in *16th World Hydrogen Energy Conference 2006, WHEC 2006*, 2006, vol. 1, pp. 775–782.
[2] E. Rönnebro and E. H. Majzoub, “Calcium borohydride for hydrogen storage: Catalysis and reversibility,” *J. Phys. Chem. B*, vol. 111, no. 42, pp. 12045–12047, 2007, doi: 10.1021/jp0764541.

WHEC-2022
23rd World Hydrogen Energy Conference
June 26-30, 2022 - Istanbul

#1532

STRUCTURAL EVOLUTION OF A Mg-C COMPOSITE OVER 1000 H_2 STORAGE CYCLES

[1,2] *Robert Carson,* [1*] *Brian Ellis,* [2] *Suraj Persaud*
[1] Canadian Nuclear Laboratories, Hydrogen Technologies Branch, 286 Plant Rd., Chalk River, Ontario, Canada
[2] Queen's University, Dept. of Mechanical and Materials Engineering, 130 Stuart St., Kingston, Ontario, Canada

*Corresponding author e-mail: brian.ellis@cnl.ca

ABSTRACT

With its high capacity (7.6 wt%), magnesium is a promising material for high temperature hydrogen storage applications [1]. To date, few studies have systematically tracked the morphological evolution of a material over a large number of hydrogen (de)sorption cycles. A Mg-C composite was prepared and exposed to 1000 hydrogen (de)sorption cycles. The experiment was interrupted at several points during cycling to retrieve a small aliquot of powder in order to characterize the crystallographic and morphological changes that were taking place in the material. The material demonstrated good capacity retention until about 700 cycles had been completed, at which point the kinetics of hydrogen (de)sorption began to slow. This could be explained by grain growth and particle densification observed in the material on extended cycling.

Keywords: Magnesium, Magnesium Hydride, Hydrogen Storage, Long-term Cycling, Structural Evolution

INTRODUCTION

To realize a functional hydrogen economy, hydrogen storage applications are required which are suited to various scales and end uses. Mg/MgH_2 has been studied for decades owing to its low cost, high abundance, and high gravimetric hydrogen capacity [1]. Due to the thermodynamic stability of the Mg-H bond, Mg is limited in terms of its usefulness in low temperature applications, however, applications are being sought which either require frequent hydrogen (de)sorption or where a suitable waste heat stream is available to offset heat requirements.

This study aimed to elucidate the structural evolution of Mg-C on extended cycling and its effect on performance.

To that end, the results of a long-term hydrogen (de)sorption cycling study on a magnesium-carbon composite material are presented herein. The study started with two grams of material cycled in a custom rig at in the Hydrogen Laboratory Complex at Canadian Nuclear Laboratories (CNL). At predetermined intervals, aliquots of the material were removed to characterize the crystallographic and morphological changes in the material. The study concluded after 1000 cycles which demonstrates the cycling stability of this magnesium-carbon composite for solid-state hydrogen storage.

EXPERIMENTAL

A composite material, comprised of Mg and C powders was prepared by high energy ball milling. All material handling was performed in an ultra-high purity (UHP) argon atmosphere glovebox containing <0.1 ppm each of O_2 and H_2O. Mg powder (98%, Sigma Aldrich) and C powder (used as received from CNL) were sealed in WC milling tools with a ball-to-powder weight ratio of 19.4:1 under argon before being moved to a ball mill and milled to produce a powder. 2 g of the resulting material were placed in a borosilicate test tube and plugged with glass wool. Hydrogen (de)sorption cycling was performed in a custom-built Sievert's apparatus at CNL. All cycles in this work were carried out isothermally at 330 °C using UHP H_2.

Sampling of the powder material was performed at various stages of the experiment. Sampling was performed by cooling the reactor and returning it to the glovebox for material retrieval. A 50 mg aliquot of the material was removed from the reactor at each sampling point and the remainder was returned to the Sievert's apparatus to continue cycling. X-ray diffraction (XRD) was performed using a Bruker D2 Phaser at CNL. Scanning electron microscopy (SEM) was performed using an FEI Nova NanoSEM 450 at the Reactor Materials Testing Laboratory (RMTL) at Queen's University.

RESULTS AND DISCUSSION

The SEM images shown in Figure 1 show the progression of the morphology of the Mg-C material over the first 50 cycles. The morphology of the material changed drastically during activation. After one cycle, the material was observed growing in pristine, faceted hexagonal pillars. This results from growth of Mg at the surface of the bulk material on the phase transformation from magnesium hydride to magnesium metal during desorption. XRD data suggests that growth occurs preferentially in the 'c' crystallographic direction. As cycling continued, the pillars began to deform and quickly covered the entire surface of the particles. They continued to grow from the particle surface as the bulk material was slowly transformed entirely into a branching, ligamented structure we observed as the activated structure. Each cycle

results in a lattice expansion and contraction of about 30%, which imparts significant stress on the material; it is also known that the hydride phase (α-MgH_2) is brittle, and fractures easily [2]. Between cycles 10 and 50, the ligamented particles continued to grow in length, but did not appear to grow in diameter, which did not exceed 5 μm during this time. This is consistent with c-directional growth being preferred. As the particles break up and entangle, it was difficult to measure the particle lengths, but many appeared to be continuous in the tens of microns, and some exceeded 100 μm in length.

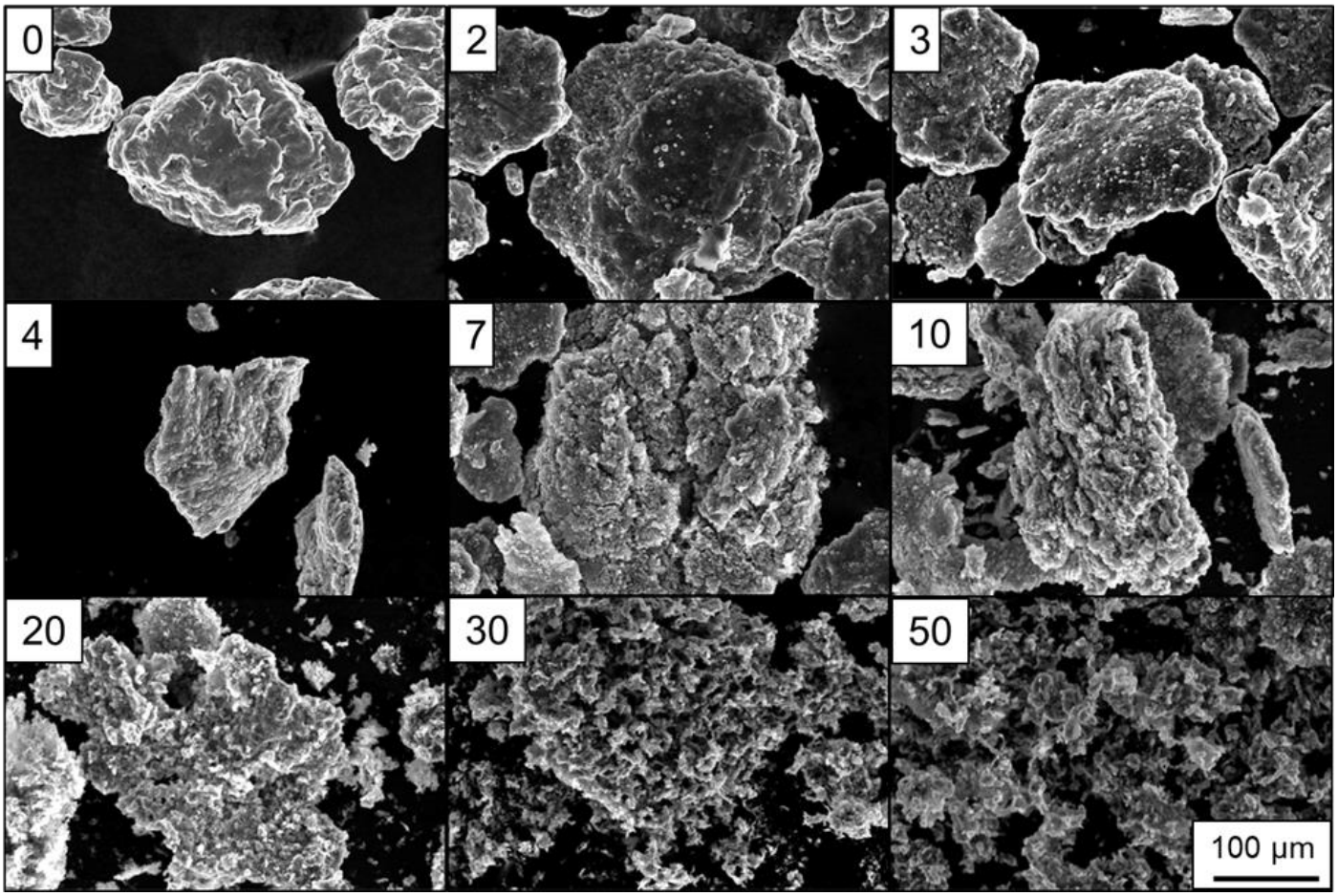


Fig. 1. SEM images showing the morphological evolution of the composite over the first 50 cycles. All images are shown at 500X magnification and the cycle count is shown in the top-left corner of each image.

Figure 2 shows the SEM images acquired after cycles 100, 200, and 300. These cycles show a slight increase in individual particle size. The individual branches of the ligamented structure had typical diameters between 2-5 μm by cycle 50. By cycle 100, these were typically between 2-10 μm. The samples obtained for cycles 200 and 300 had typical particle diameters ranging from 5-10 μm. All three of these samples had particle agglomerates comprised of sintered ligaments ranging from 50-1000 μm across; the agglomerates generally increased in size with increasing cycle count.

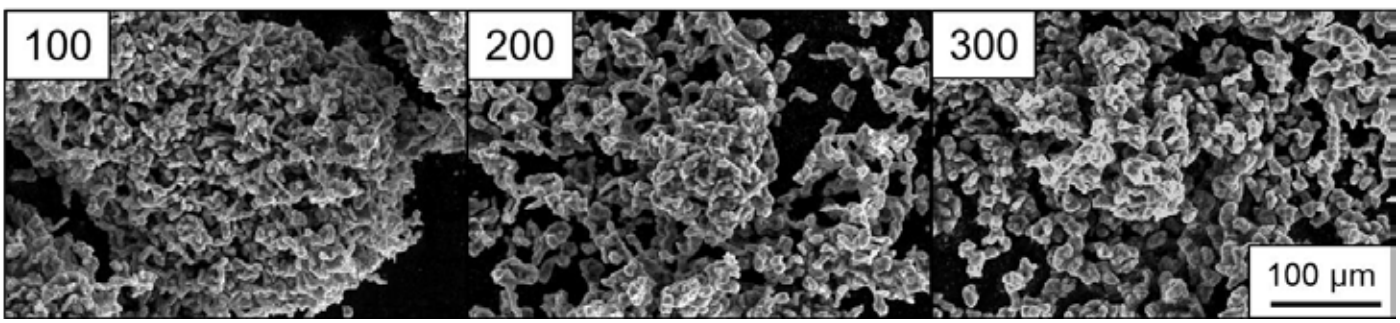


Fig. 2. SEM images showing the morphological evolution at cycles 100, 200, and 300. Images are shown at 500X magnification.

Figure 3 (Right) shows the amount of hydrogen desorbed during selected desorptions from cycles 301-1000. The hydrogen capacity experienced a slow decline from 6.3 wt% on cycle 330 to 4.7 wt% on cycle 917. Increasing the absorption time to 45 minutes (cycles 918+) increased the amount of hydrogen absorbed and, thus, the amount of

hydrogen that was desorbed (5.5 wt. %). The significant decline observed between cycles 725 and 917 was a result of the automated testing software which assigned a fixed time for hydrogen absorption of 30 minutes. As cycling progressed, the kinetics of hydrogen absorption decreased and, as a result, less hydrogen was absorbed during that fixed time. Thus, less hydrogen was available for desorption. This slowing of kinetics can be explained by the morphological evolution across the late cycles which showed the slow increase in both particle and agglomerate size. Figure 3 also shows SEM images of the material after cycles 500 and 1000. By cycle 500, typical ligament diameters fell between 10-20 µm, and by cycle 1000 it increased to 20-50 µm. Typical agglomerate sizes at cycle 500 fell between 50-1000 µm, and by cycle 1000 they were 100-1000 µm. We have also shown that the material had undergone significant densification by cycle 1000, which is typical of the late stage of the sintering processes. [3] The decrease in both high-diffusivity grain boundary area and surface area both contributed to the decline in (de)sorption kinetics as the required hydrogen diffusion depths increased and thicker hydrides were formed. This eventually led to the apparent loss of hydrogen capacity as the time required to form and decompose the hydride phase exceeded the cycle times allowed by the experiment.

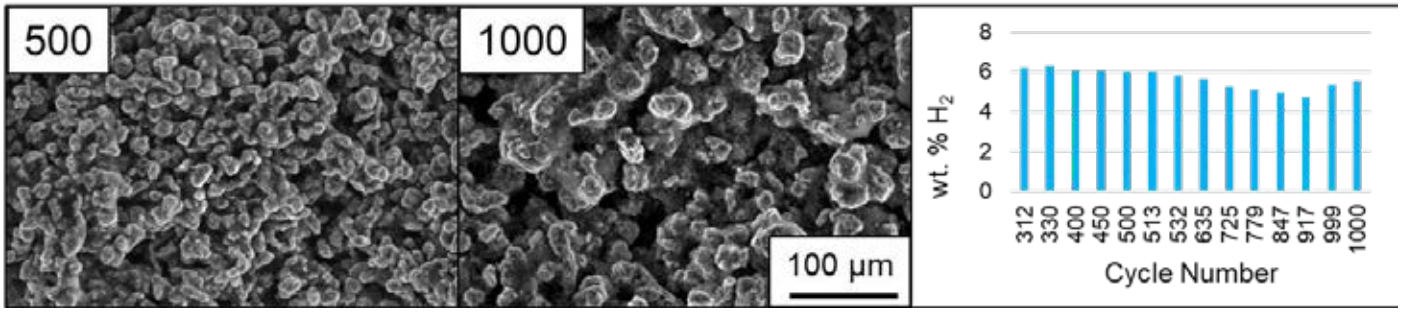


Fig. 3. (Left, center) SEM images showing the morphological evolution at cycles 500 and 1000. Images are shown at 500X magnification. (Right) Hydrogen desorbed at selected cycles between 300-1000.

CONCLUSIONS

In the early stage of structural evolution, magnesium undergoes significant morphological changes, this occurred over approximately the first 50 hydrogen storage cycles. Hydrogen absorption causes lattice expansion, atomic rearrangement and embrittlement of magnesium which comminuted into small particles on cycling. In the later stage of evolution (>cycle 50) the magnesium particles undergo a much slower process of sintering to form agglomerates and densification owing to the heat from their surroundings which reduces the kinetics of hydrogen (de)sorption. The agglomerate sizes generally increase with cycle count during this stage. At higher cycle counts (>cycle 200), particle growth becomes more apparent, and is accompanied by more severe kinetic limitations resulting from densification and associated diffusion limitations. [4]

REFERENCES

1. Crivello J.-C. et al. 2016, Review of magnesium hydride-based materials: development and optimisation. J. of Applies Physics A 122:97.
2. Jain P., Lang J., Skryabina N.Y., Fruchart D., Santos S.F., Binder K., Klassen T., and Huot J. 2013. MgH2 as dopant for improved activation of commercial Mg ingot. Journal of Alloys and Compounds 575:364-369
3. W.D. Callister Jr. and D.G. Rethwisch, Materials Science and Engineering: an Introduction, Eighth Edition (John Wiley & Sons, Inc., 2012), pp. 523-252
4. Borgschulte A., Bösenberg U., Barkhordarian G., Dornheim M., and Bormann R. 2007. Enhanced hydrogen sorption kinetics of magnesium by destabilizing $MgH_{2-\delta}$. Catalysis Today 120:262-269

WHEC-2022
23rd World Hydrogen Energy Conference
June 26-30, 2022 - Istanbul

#1533

DEVELOPMENT OF THE NEC/12H-NEC LOHC SYSTEM AT CANADIAN NUCLEAR LABORATORIES

[1*] *Lorne Stolberg,* [1] *Blessing Ibeh,* [1] *Hongqiang Li,* [1] *Donald Ryland,* [1] *Sam Suppiah*
[1]Canadian Nuclear Laboratories, 286 Plant Road, Chalk River, Ontario, Canada

*Corresponding author e-mail: lorne.stolberg@cnl.ca

ABSTRACT

Because of the evolving hydrogen economy, there is a growing interest in the development and commercialization of suitable hydrogen storage technologies like liquid organic hydrogen carriers (LOHCs). N-ethylcarbazole/dodecahydro –N-ethylcarbazole (NEC/12H-NEC) LOHC application, although not currently commercialized, requires relatively low temperatures for the dehydrogenation step when compared to other systems that have been commercialized. What is reported in this study are results from ongoing efforts to develop and scale-up the NEC/12H-NEC LOHC system at Canadian Nuclear Laboratories. Preliminary dehydrogenation results using an in-house catalyst show the achievement of a target hydrogen release rate of 1.4 x 10^{-5} m^3/s, clearing the way for further scale-up.

Keywords: Liquid organic hydrogen carrier, Catalysis, Dehydrogenation, N-ethylcarbazole, Hydrogenation

INTRODUCTION

Liquid organic hydrogen carriers (LOHCs) are liquids or low temperature melting solids that can be reversibly hydrogenated and dehydrogenated in the presence of a suitable catalyst and under appropriate conditions of temperature and pressure. On hydrogenation, these materials store a certain amount of hydrogen related to their structure and release the corresponding amount of hydrogen during the dehydrogenation step, making them an excellent choice for hydrogen storage and release. Such storage and release of hydrogen can be leveraged in situations where hydrogen production is variable (for example using renewable energy sources like wind and solar), or for the storage and subsequent release of hydrogen produced from nuclear energy. Fig. 1 shows a schematic of the NEC/12H-NEC LOHC.

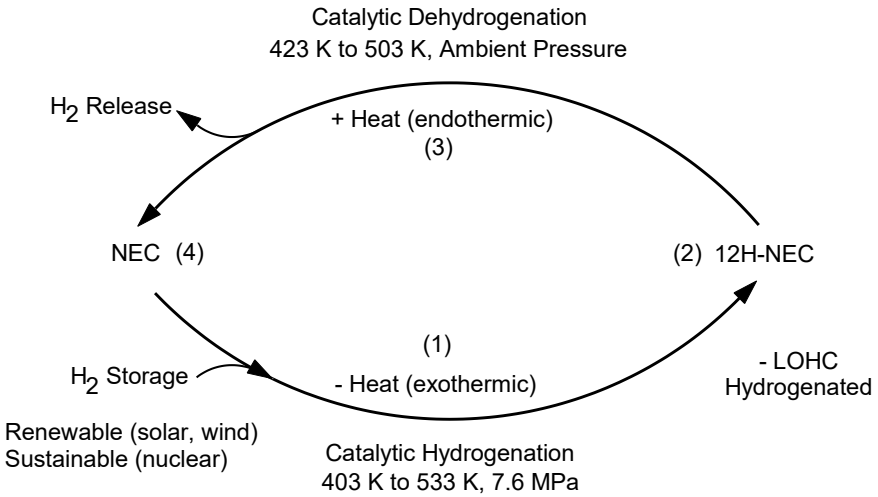


Fig. 1. Schematic of the NEC/12H-NEC LOHC system

Ongoing efforts have focused on the development of various LOHCs, mostly at laboratory scale [1-3]. However, there are a few systems that have been commercialized. For example, Hydrogenious has developed a commercially available LOHC based on dibenzyltoluene/perhydro-dibenzyltoluene (DBT/18H-DBT) [4]. Chiyoda has also successfully demonstrated a commercial scale LOHC based on toluene/methylcyclohexane (TOL/MCH) [5]. The dehydrogenation step of these two commercially available LOHCs require relatively high temperatures (563 to 623 K) compared to the N-ethylcarbazole/dodecahydro-N-ethylcarbazole (NEC/12H-NEC) which has low enthalpies of hydrogenation and dehydrogenation (50 - 54 kJ/mol) and dehydrogenation temperatures in the range of 453 K to 503 K only. To the best of the authors' knowledge, there is no commercially available LOHC system based on NEC/12H-NEC. Therefore, there is a need to develop and commercialize the NEC/12H-NEC LOHC system because it can operate at a lower temperature, and when compared to TOL/MCH system, is non-flammable and nontoxic.

Experimental investigations of the NEC/12H-NEC system as reported in the literature have focused on catalyst development [4], identification of intermediates [6], development of plausible mechanisms and kinetics [7-9], and operating conditions. With respect to catalyst development, efforts have been made to study different noble metals and supports [10-12]. The results of these studies indicate that the same noble metal can have a different activity towards 12H-NEC dehydrogenation when placed on a different support. Similarly, different noble metals can have different activities when placed on the same support. For example, Jiang et al. [10] investigated a series of noble metal catalysts using titanium dioxide (TiO_2) as the support and found that the activity of these catalysts decreased in the order Pt/TiO_2 > Pd/TiO_2 > Pd/Al_2O_3 > Rh/TiO_2 > Au/TiO_2 > Ru/TiO_2. While Feng et al. [11] studied the effect of Pd catalysts supported on different supports and found a sequence of decreasing activity as follows: Pd/C > Pd/Al_2O_3 > Pd/TiO_2 > Pd/SiO_2. The order observed for the Pd/Al_2O_3 and Pd/TiO_2 is reversed compared to the sequence given by Jiang et al. [12]. Incidentally, studies involving the use of zeolites as supports for the dehydrogenation of 12H-NEC are scarce. It is therefore important to investigate Pd on different supports (including zeolites) for the dehydrogenation of 12H-NEC. With respect to operating conditions, it has been reported that by reducing the pressure, the dehydrogenation reaction can be carried out at a temperature of 433 K with favourable kinetics [12].

For several decades, Canadian Nuclear Laboratories (CNL) has been developing noble metal based catalysts for nuclear applications. These catalysts were developed using a variety of supports including carbon and zeolites. Presently, CNL has an active hydrogen program for which hydrogen storage technologies is a component. The NEC/12HNEC LOHC system is one of the hydrogen storage technologies being developed at CNL for commercialization. Current efforts have led to the development and testing of a proprietary Pd based catalyst on a modified zeolite support for 12H-NEC dehydrogenation with comparable activity and selectivity as the commercially available Pd/Al_2O_3 catalyst. Scale up is in progress. Details of some of these experimental campaigns will be presented in this paper.

EXPERIMENTAL

Experimental work was carried out with the goal of demonstrating the LOHC system for 0.1 to 0.128 kg of NEC and 12H-NEC corresponding to hydrogen storage and release of at least 1.4 x 10^{-5} m^3/s of hydrogen during hydrogenation and dehydrogenation, respectively. For the chemicals used in this study, NEC (97 %) and 5 wt% Ru/Al_2O_3 (reduced) were purchased from Sigma Aldrich and were used as received without further purification. 12H-NEC, which is used as a starting material for all dehydrogenation reactions, was prepared by hydrogenating NEC. The commercial catalyst used in the present study for hydrogenation was the 5 wt% Ru/Al_2O_3 catalyst. A proprietary 5.5 wt% palladium/zeolite catalyst was prepared and used for the dehydrogenation reaction. The metal loading (wt% of metal) of this catalyst was determined using inductively coupled plasma - optical emission spectrometry (ICP-OES). All prepared catalysts were calcined in air and subsequently reduced in flowing hydrogen. Following reduction, the catalyst was purged with helium and subsequently kept in an inert (helium) atmosphere until use.

Experimental Setup

The reactor used for hydrogenation and dehydrogenation studies was a PARR Model 4561 Mini Bench-top reactor with a volume of 0.0003 m^3 equipped with a PARR Model 4848B Reactor Controller (PARR Instrument Company, Moline, IL). The NEC hydrogenation reaction was carried out at 423 K and 7.6 MPa. The 12H-NEC dehydrogenation reaction was carried out at 488 K and ambient pressure. For each hydrogenation reaction, 0.1 kg of NEC and 0.010 kg of 5 wt% Ru/Al_2O_3 corresponding to a 10:1 ratio was loaded into the PARR reactor. For dehydrogenation, a similar ratio was maintained, however, 0.128 kg of 12H-NEC and 0.0128 kg of catalyst were used. The hydrogen released during dehydrogenation was swept by nitrogen and measured on a volumetric basis. LabView (National Instruments) was used for data acquisition with ten seconds (10 s) set as the capture frequency (interval between two data points).

RESULTS AND DISCUSSION

Fig. 2 and Fig. 3 show the results from the hydrogenation of NEC (at 423 K) and dehydrogenation of 12H-NEC (at 488 K), respectively. Both experiments were carried out using a catalyst to reactant ratio of 1:10. From Fig.2, the two hydrogenation experiments performed show good reproducibility. Fig. 2 also indicates that more than 0.05 m^3 of hydrogen was stored in less than one hour. The results from the dehydrogenation experiment shown in Fig. 3 indicates that a hydrogen release rate of 1.88 x 10^{-5} m^3/s was achieved which is greater than the scaling-up target of 1.40 x 10^{-5} m^3/s.

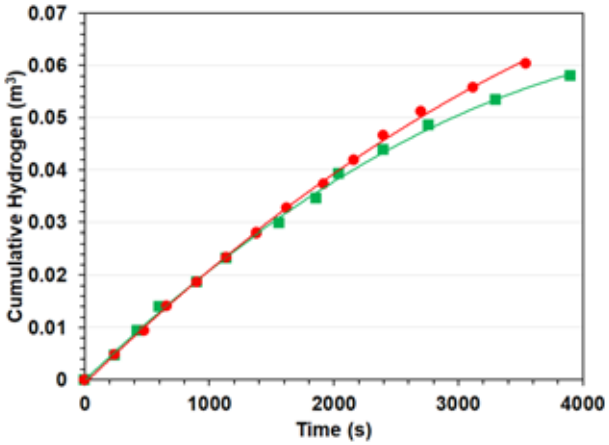


Fig. 2. Hydrogenation of NEC at 423 K

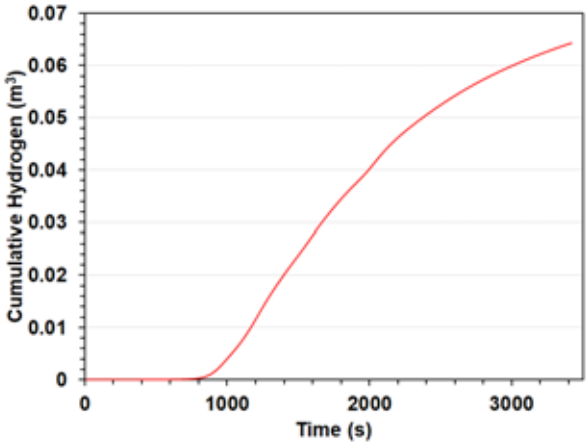


Fig. 3. Dehydrogenation of 12H-NEC at 488 K

CONCLUSIONS

The NEC/12H-NEC LOHC system is being developed at CNL for hydrogen storage and release. A proprietary Pd based catalyst has been developed for the dehydrogenation reaction. As part of our effort to scale-up the LOHC process, hydrogenation and dehydrogenation experiments were carried out with the goal of storing and releasing at least 1.4 x 10^{-5} m^3/s of hydrogen. The experimental data presented indicate that the initial target has been achieved with ongoing efforts focused on further scale-up as well as optimization of the catalyst performance.

REFERENCES

1. Tan KC, He T, Chua YS and Chen P. 2022. Recent Advances of Catalysis in the Hydrogenation and Dehydrogenation of N-Heterocycles for Hydrogen Storage. Journal of Physical Chemistry C 125:18553-18566.
2. Jiang Z, Gong X, Guo S, Bai Y and Fang T. 2021. Engineering PdCu and PdNi bimetallic catalysts with adjustable alloying degree for the dehydrogenation reaction of dodecahydro-N-ethylcarbazole. International Journal of Hydrogen Energy 46:2376-2389.
3. Sekine Y and Higo T. 2021. Recent trends on the dehydrogenation catalysis of liquid organic hydrogen carrier (LOHC): A review. Topics in Catalysis 64:470-480.
4. Hydrogenious-LOHC-technologies-product-brochure_short.pdf. Accessed on February 18, 2022.
5. Introduction of liquid organic hydrogen carrier....pdf. Accessed on February 18, 2022.
6. Yang M, Dong Y, Fei S, Ke H and Cheng H. 2014. A comparative study of catalytic dehydrogenation of perhydro-N-ethylcarbazole over noble metal catalysts. International Journal of Hydrogen Energy 39:18976-18983.
7. Mehranfar A, Izadyar M and Esmaeili AA. 2015. Hydrogen storage by N-ethylcarbazole as a new liquid organic hydrogen carrier: A DFT study on the mechanism.
8. Dong Y, Yang M, Mei P, Li C and Li L. 2016. Dehydrogenation kinetics study of perhydro-N-ethylcarbazole over a supported Pd catalyst for hydrogen storage application. International Journal of Hydrogen Energy 41:8498-8505.
9. Ye X, An Y and Xu G. 2011. Kinetics of 9-ethylcarbazole hydrogenation over Raney-Ni catalyst for hydrogen storage. Journal of Alloys and Compounds 509:152-156.
10. Jiang Z, Gong X, Wang B, Wu Z and Fang T. 2019. A experimental study on the dehydrogenation performance of dodecahydro-N-ethylcarbazole on M-TiO_2 catalysts. 2019. International Journal of Hydrogen Energy 44:2951-2959.
11. Feng Z, Chen X and Bai X. 2020. Catalytic dehydrogenation of liquid organic hydrogen carrier dodecahydro-N-ethylcarbazole over palladium catalysts supported on different supports. Environmental Science and Pollution Research 27:36172-36185.
12. Kiermaier S, Lehmann D, Bosmann A and Wasserscheid P. 2021. Dehydrogenation of perhydro-N-ethylcarbazole under reduced total pressure. International Journal of Hydrogen Energy 46:15660-15670.

WHEC-2022
23rd World Hydrogen Energy Conference
June 26-30, 2022 - Istanbul

#1539

EVALUATION OF BASIC PHYSICAL PROPERTIES OF AMMONIA BORANE STORED IN LIQUID AMMONIA

[1] Fangqin Guo*, [2] Yufeng Wang, [2]Tomoyuki Ichikawa, [3]Hiroki Miyaoka, [4]Yoshihiro Shimizu, [4]Shuji Takamine, [4]Tessui Nakagawa, [1]Takayuki Ichikawa.*
[1]Graduate School of Advanced Science and Engineering, Hiroshima University, 1-3-1 Kagamiyama, Higashi-Hiroshima 739-8530, Japan
[2] Hydrolabo Inc., 3-10-31, Kagamiyama, Higashi-Hiroshima, 739-0046, Japan
[3] Natural Science Centre for Basic Research & Development, Hiroshima University, 1-3-1 Kagamiyama, Higashi-Hiroshima 739-8530, Japan
[4] Faculty of Science, University of the Ryukyus, 1 Senbaru, Nishihara-cho, Okinawa 903-0213, Japan
*Corresponding author e-mail: fang-qin-guo@hiroshima-u.ac.jp

ABSTRACT

Ammonia borane (AB: NH_3BH_3), as a potential hydrogen storage material, has been considered to be stored in different mediums for long-distance and safe transportation for practical usage. Three possible ways to store ammonia borane were parallelly considered: in the solid-state, liquid state of AB-NH_3 (NH_3 adducts or solution), and aqueous solution of AB. Among them, the liquid AB-NH_3 method shows promising advantages over other methods, In further, the basic properties of the AB-NH_3 system were studied in detail, such as absorption amount/pressure, temperature dependency of the density of the AB-NH_3 liquid, viscosity change when solved in liquid NH_3, and the thermal stability (shelf-life). The thermodynamical parameters of the reaction between AB and NH_3 were estimated and the enthalpy and entropy values were calculated to be -19.87kJ/mol and 67.76 J/mol·K respectively. In this way, the above basic properties were clarified.

Keywords: ammonia borane, liquid ammonia, viscosity, thermodynamics, storage density.

INTRODUCTION

With the depletion of traditional fossil fuels and relevant air pollution problems, seeking a sustainable and clean energy source has been an important task in the current now for all the people on our earth. Hydrogen energy attracts worldwide attention because it is a feasible solution and clean way to the environmental problems that are caused by the combustion of fossil energy. Furthermore, it can be renewable through many possible methods. The utilization of hydrogen storage materials is considered a priority means of storing hydrogen. Ammonia borane (AB: NH_3BH_3), a potential hydrogen storage material, attracts a lot of attention because of its high hydrogen content (19.6 wt.%), nontoxicity, and high stability under ambient conditions, as well as high solubility in common solvents such as water[1-3]. Additionally, hydrogen production from AB has been studied a lot and hydrogen can be released easily by thermolysis or hydrolysis [4-6]. To make it commercial and applicable, safe, stable, and easy storage and transportation are the crucial aspects. However, there are few studies related to the evaluation of the influence of storage medium and durability of AB. Therefore, in this study, the physical properties of AB-NH_3 system were investigated for a deeper understanding of handling and storing ammonia borane in liquid NH_3.

MATERIALS AND METHODS

As purchased AB with a purity of 97% (Sigma-Aldrich Japan) was used as the starting materials. The samples were stored in the glove box (Miwa MFG, MP-P60W) filled with a high purity Ar (99.9999%) to avoid the impact of air and moisture. The thermodynamic properties of the AB stored in liquid NH_3 were checked by the pressure composition isothermal (PCI) measurements of absorption/desorption processes by using BELSORP instruments. The structural and phase identification of samples before and after PCI was characterized by X-Ray diffraction (XRD) measurements using Rigaku RINT-2500. The density evaluation was conducted in a hyper glass cylinder with a homemade ammonia filling system equipped with a pressure gauge at room temperature. For kinematic viscosity analysis, stainless cells with glass windows were used and a magnetic stirrer was put in the cells, which was attached to an ammeter to measure the current density. The viscosity was calculated by a calibrated curve that was obtained by using standard solutions with different viscosities. Nuclear magnetic resonance (NMR) spectroscopy was performed to check the stability of ammonia borane in liquid NH_3.

RESULTS AND DISCUSSION

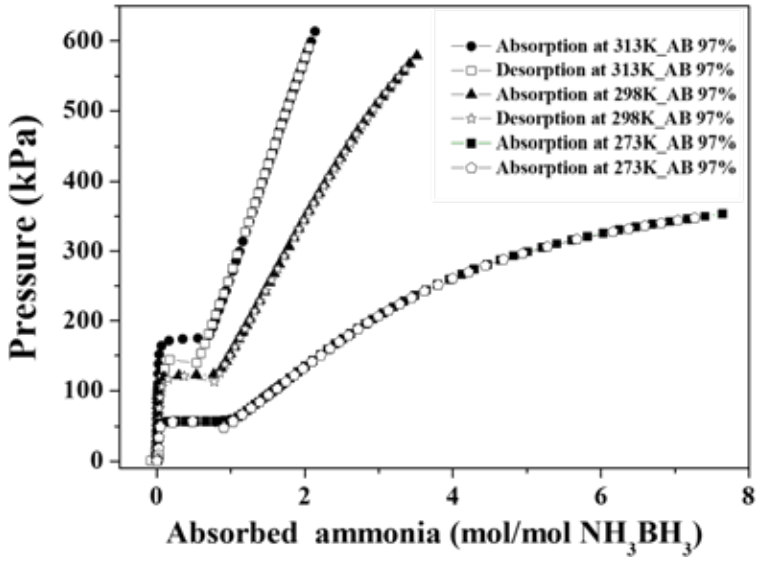


Fig.1 Pressure composition isotherm (PCI) measurements of ammonia borane for NH_3 absorption and desorption processes at different temperatures.

As the main thermodynamical properties of AB-NH_3 system, the pressure composition isotherm (PCI) measurements of ammonia borane for NH_3 absorption and desorption processes at three different temperatures of 273K, 298K as well as 313K were presented in Fig.1. At 273K, with the increase of NH_3 amount in the system, the pressure was increased to 53.78kPa, and a plateau region was observed. In this region, ammonia borane absorbed NH_3 and then formed a composite with the coexisting phase of solid and liquid. Totally 1 mol NH_3 was absorbed by AB at this temperature and then NH_3 was liquified continuously with the increasing NH_3 pressure. The plateau pressure of NH_3 absorption at different temperatures was measured and thus according to the Vant' hoff plot, the enthalpy and entropy values were calculated to be -19.87kJ/mol and 67.76 J/mol.K respectively. Other results such as density, viscosity, and shelf-life measurements will be discussed in detail in the online presentation.

CONCLUSIONS

The safe storage of AB was studied systematically in this work. NH_3 was used to store AB for the first time. The physical properties of ammonia borane stored in liquid ammonia were clarified. The thermodynamical parameters of the reaction between AB and NH_3 were estimated by measuring the pressure composition isotherm at different temperatures. the enthalpy and entropy values were calculated to be -19.87kJ/mol and 67.76 J/mol·K respectively. Other results like density and viscosity measurements as well as the durability test will be discussed in detail in the online presentation.

REFERENCES

1. Staubitz A, Robertson APM, Manners I. Ammonia-Borane and related compounds as dihydrogen sources. Chem Rev 2010;110:4079-124.
2. Serdar A, Saim O. Ammonia borane as hydrogen storage materials. International Journal of Hydrogen Energy 43:18592-18606
3. Feng X, Zhao Y, Liu D, Mo Y, Liu Y, Chen X, Yan W, Jin X, Chen B, Duan X, Chen D, Yang C. Int J Hydrogen Energy 2018;43:17112e20.
4. Sanyal U, Demirci UB, Jagirdar BR, Miele P. Hydrolysis of ammonia borane as a hydrogen source: fundamental issues and potential solutions towards implementation. ChemSusChem 2011;4:1731-9.
5. Chandra M, Xu Q. A high-performance hydrogen generation system: transition metal-catalyzed dissociation and hydrolysis of ammonia borane. J Power Sources 2006;156:190-4.
6. Ceren Y, Senem K, Colpan C. A review on the catalysts used for hydrogen production from ammonia borane. International Journal of Hydrogen Energy 45:3414-3434.

WHEC-2022
23rd World Hydrogen Energy Conference
June 26-30, 2022 - Istanbul

#1557

A SIMPLE DYNAMIC MODEL FOR PREDICTING THE ABSORPTION AND DESORPTION BEHAVIOUR OF METAL HYDRIDE SYSTEMS

*Abhishek Parida, Sunku Prasad Jenne, *Muthukumar Palanisamy*
Department of Mechanical Engineering, Indian Institute of Technology Guwahati, Assam, India-781039
*Corresponding author e-mail: pmkumar@iitg.ac.in; pmkumariitg@gmail.com

ABSTRACT

In this study, a dynamic model is developed for predicting the absorption and desorption characteristics of the MH systems. The accuracy of the developed dynamic model is compared with the actual model. Further, the effect of reactor size on the overall performances of the system is studied. The dynamic model predicted the average bed temperature during absorption with a maximum deviation of 3.0% for the considered operating conditions compared to the actual model. At the same time, a maximum deviation of 2.06% was observed during desorption. The dynamic model exactly predicted the reaction completion time during absorption and desorption processes. The dynamic model is 306 times faster than the actual model reported in the literature, which saves computational time and cost with appreciable accuracy. The dynamic model can also be used to compute coupled systems like heat pumps, energy storage systems, compressors, and heating and cooling systems, which will be presented in our future work.

Keywords: Metal hydride, dynamic model, absorption; desorption; $LaNi_5$

INTRODUCTION

Metal hydrides (MHs) find a wide range of applications, including hydrogen storage, hydrogen compression, thermal energy storage, heat pumps, and heat transformers [1]. The study of MH systems involves the selection of suitable alloys/ alloy pairs based on the application, design of an efficient reactor, selection of optimum process parameters, and energy-efficient operating strategy [2]. Thermodynamic studies have been performed to select the MH alloy pairs and evaluate the cycle performance of MH-based thermal machines [3]. However, the thermodynamic model doesn't consider the highly dynamic nature of the MH systems, which makes it not suitable for the accurate selection of metal hydride alloy pairs for several applications. On the other hand, complete thermal models solving for mass, momentum, and energy balances involve extremely high computational costs. In this perspective, researchers developed lumped/dynamic model for predicting the performance of the MH-based thermal machines [4]. The main advantage of the lumped model is its lower computational cost. However, the validity of such a model over a range of reactor sizes and operating conditions is seldomly presented.

The main objective of the present work is to develop a dynamic model (where the dependent variables are a function of time) for predicting the absorption and desorption characteristics of the MH systems. Also, the dynamic model results are compared with the actual model, where the dependent variables are functions of space and time. Further, the percentage deviation of the dynamic model from the actual model as a function of reactor size and supply hydrogen pressure is elucidated. Tubular reactors are selected for the analysis as they are simple, easy to construct, and involve comparatively lesser hydraulic losses among several reactor designs [5].

PHYSICAL SYSTEM AND NUMERICAL MODELING

Physical system

The present study is focused on predicting the absorption and desorption characteristics of MHs filled inside a tubular reactor using a dynamic model. In the case of tubular reactors, the MH alloy is filled inside the tube, and heat transfer fluid (HTF) flows over the tube [6]. The widely studied alloy, $LaNi_5$, is considered for the analysis, and the properties are obtained from the Sunku Prasad and Muthukumar [7]. Water is used as HTF for removing/ supplying the heat to the MH reactor. The primary purpose of the dynamic model is to quantify the performance (charging and discharging times, energy density, storage efficiency, etc.) of candidate MHs.

Governing equations and boundary conditions

The assumptions and governing equations for the dynamic and actual models are presented in Table 1. The numerical solution for the equations given in Table 1 has been obtained using the finite element-based simulation tool, COMSOL Multiphysics 5.3. The relative tolerance of 10^{-6} is used for both models.

RESULTS AND DISCUSSION

The comparison results of the dynamic model and the actual model for different sizes of the tubular reactors are shown in Fig. 1. The temperature variations show that the final absorption time predicted by the dynamic model is

almost the same as the actual model, despite marginal intermediate deviations. The maximum percentage of deviations for cases A and D are 1.06 % and 3%, respectively. The percentage deviations for cases B and C fall between 1.06 % and 3%, as shown in Fig. 1. It is observed that the percentage deviation increased with the reactor size. This is due to higher temperature gradients along the radial direction for larger reactors. During desorption (Figs. 3 and 4), it is seen that the reaction completion time and the minimum temperature predicted by the dynamic model are almost the same as the actual model. Like absorption, the percentage deviation between the models increased with the reactor size during desorption, and the maximum deviation for case D was found to be 2.06%.

Table 1. Description of dynamic and actual models

<table>
<tr><th>Dynamic model</th><th>Actual model</th></tr>
<tr><td colspan="2">Assumptions and governing equations:
The dynamic model considers all the assumptions that are valid for the actual model and in addition, it includes: dependent variables are invariant with space. The mass and energy balance equations for the dynamic model are given below.</td></tr>
<tr><td>Mass balance:
$(1-\varepsilon)\frac{\partial \rho_s}{\partial t}=(1-\varepsilon)\dot{m}_{a,d}$
Energy balance:
$\left(m_{MH}C_{pMH}+m_cC_{pc}\right)\frac{\partial T}{\partial t}=-V_{MH}(1-\varepsilon)\dot{m}_{a,d}\left(\frac{\Delta H}{M_{H_2}}\right)-UA_s\left(T-T_\infty\right)$
Reaction kinetics:
$m_a=C_a\exp\left(-\frac{E_a}{R_gT}\right)\ln\left(\frac{P_g}{P_{eq}}\right)(\rho_{ss}-\rho_s);m_d=C_d\exp\left(-\frac{E_d}{R_gT}\right)\left(\frac{P_g-P_{eq}}{P_{eq}}\right)(\rho_s-\rho_{emp})$</td><td>$T(t)$
$\rho_s(t)$</td><td>Hydrogen mass balance:
$\varepsilon\frac{\partial \rho_g}{\partial t}+\nabla\cdot\left(\rho_g\vec{u}_g\right)=-(1-\varepsilon)m_{a,d}$
Hydride mass balance:
$(1-\varepsilon)\frac{\partial \rho_s}{\partial t}=(1-\varepsilon)m_{a,d}$</td><td>$T(r,z.t)$
$\rho_s(r,s,t)$
Metal hydride
h, T_∞</td></tr>
<tr><td>Equilibrium pressure:
$P_{eq}=\exp\left\{\left[\frac{\Delta H}{RT}+\frac{\Delta S}{R}\right]+(\varphi_s\pm\varphi_0)\tan\left[\pi\left(\frac{c}{c_{sat}}-\frac{1}{2}\right)\right]\pm\frac{\beta}{2}\right\}\times10^5$
Overall heat transfer coefficient is defined based on the outer diameter of the tubular reactor, as follows.
$\frac{1}{U}=\frac{1}{h}+\frac{r_o\ln\left(\frac{r_o}{r_i}\right)}{k_c}+\frac{r_o\ln\left(\frac{r_i}{r_e}\right)}{k_{MH}};\ r_e=\frac{r_i}{2};r_e=equivalent\ radius$
The heat transfer coefficient is estimated using the Dittus-Boelter equation, as shown below.
$Nu=0.0238\,\mathrm{Re}^{0.8}\,\mathrm{Pr}^{0.33}$
$Hydraulic\ diameter\ =\ 6\ mm$
Velocity of HTF = 0.3 m/s</td><td colspan="2">Momentum equation:
Darcy's law describes the velocity of the hydrogen in porous metal hydride.
$\vec{u}_g=\frac{K}{\mu_g}\nabla P_g;\ \ P_g=\rho_gR_gT$
Energy equation:
$\left(\rho C_p\right)_e\frac{\partial T}{\partial t}+\rho_gC_{p_g}\vec{u_g}\cdot\nabla T=k_e\nabla^2T+(1-\varepsilon)m_{a,d}\left(\frac{\Delta H}{M_{H_2}}\right)$
Reaction kinetics:
$m_a=C_a\exp\left(-\frac{E_a}{R_gT}\right)\ln\left(\frac{P_g}{P_{eq}}\right)(\rho_{ss}-\rho_s);m_d=C_d\exp\left(-\frac{E_d}{R_gT}\right)\left(\frac{P_g-P_{eq}}{P_{eq}}\right)(\rho_s-\rho_{emp})$</td></tr>
<tr><td>Initial conditions
Absorption:
$T=T_{initial}=298.15K$
$\rho_s=\rho_{so}=8405.8kg/m^3$
$T_\infty=298.15K$

Desorption:
$T=T_{initial}=323.15K$
$\rho_s=\rho_{so}=8515.8kg/m^3$</td><td colspan="2">Initial conditions
Absorption:
$T=T_{initial}=298.15K$
$\rho_s=\rho_{so}=8405.8kg/m^3$
Desorption:
$T=T_{initial}=323.15K$
$\rho_s=\rho_{so}=8515.8kg/m^3$

Boundary conditions
$p=P_{supply}$
$-k_{MH}\nabla T\big\vert_{MH}=-k_{tube}\nabla T\big\vert_{tube}$
$\dot{n}\,k_{tube}\nabla T=h\left(T_f-T\right)$</td></tr>
</table>

From Figs 1-4, it is observed that the dynamic model predicts the transient absorption and desorption behavior with considerable accuracy. Further, the computational time for the developed dynamic model is 306 times lesser than the actual model. Hence, the dynamic model can be used to save the computational cost drastically without compromising accuracy.

CONCLUSIONS

In this study, a dynamic model is developed for predicting the absorption and desorption characteristics of the MH systems. The developed dynamic model predicts the absorption and desorption behavior with a maximum deviation of 3% for the considered operating conditions compared to the actual model. The developed model was over 300 times faster than the actual model. The developed model can be used to predict the transient absorption desorption behavior in single metal hydride and coupled MH reactor systems with reasonable accuracy which will be demonstrated in further studies.

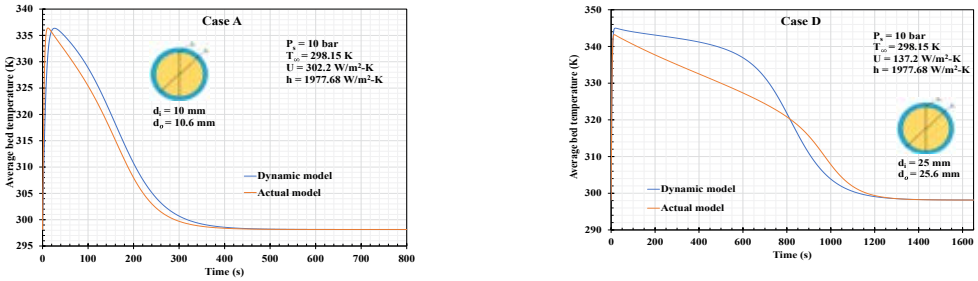


Fig. 1. Temperature variations for case A and case D during absorption

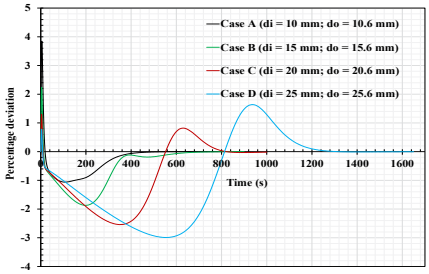


Fig. 2. Effect of reactor size on percentage deviation between both the models

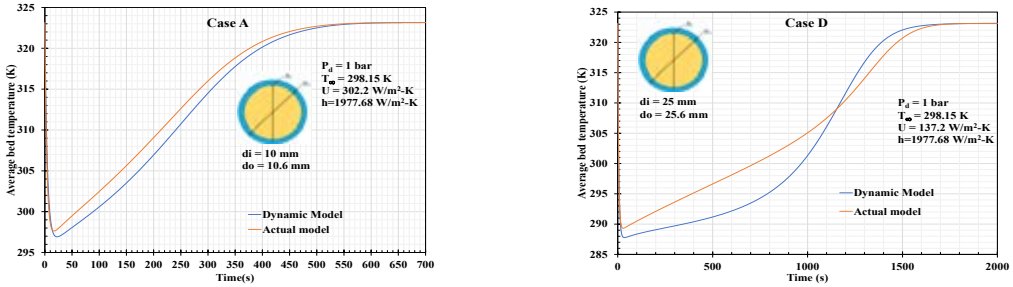


Fig. 3. Temperature variations for case A and case D during desorption

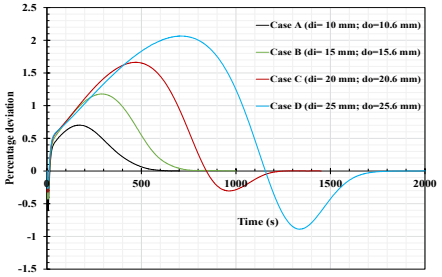


Fig. 4. Percentage deviation between both models for all the cases during desorption

REFERENCES

[1] Muthukumar P, Kumar A, Raju NN, Malleswararao K, Rahman MM. 2018. A critical review on design aspects and developmental status of metal hydride based thermal machines. Int J Hydrogen Energy 1–27.
[2] Mazzucco A, Dornheim M, Sloth M, Jensen TR, Jensen JO, Rokni M. 2014. Bed geometries, fueling strategies and optimization of heat exchanger designs in metal hydride storage systems for automotive applications: A review. Int J Hydrogen Energy 39:17054–74.
[3] Sarath Babu K, Anil Kumar E. 2022. Thermodynamic analysis of thermochemical energy storage system based on AB5 type hydride pairs. Mater Today Proc. 49:2042–7.
[4] Gambini M, Stilo T, Vellini M. 2020. Selection of metal hydrides for a thermal energy storage device to support low-temperature concentrating solar power plants. Int J Hydrogen Energy 2020;45:28404–25.
[5] Yang FS, Wang GX, Zhang ZX, Meng XY, Rudolph V. Design of the metal hydride reactors – A review on the key technical issues. Int J Hydrogen Energy 2010;35:3832–40.
[6] Jana S, Muthukumar P. 2021. Design and Performance Prediction of a Compact MmNi4.6Al0.4 based Hydrogen Storage System. J Energy Storage 39:102612.
[7] Sunku Prasad J, Muthukumar P. 2021. Design and performance analysis of an annular metal hydride reactor for large-scale hydrogen storage applications. Renew Energy. 181:1155–66.

WHEC-2022
23rd World Hydrogen Energy Conference
June 26-30, 2022 - Istanbul

#1565

NUMERICAL OPTIMIZATION OF MULTISTAGE MAGNETIC REFRIGERATION SYSTEM IN THE TEMPERATURE RANGE OF LIQUID HYDROGEN

[1,2] *Wenshuai Zheng,* [1,2*] *Jun Shen* [1,2,3*] *Zhenxing Li,* [1,2,3] *Ke Li,* [1,2] *Wei Dai,* [3] *Peng Hai,* [1,2] *Hongmei Huang,*
[1] Key Laboratory of Cryogenics, Technical Institute of Physics and Chemistry, Chinese Academy of Sciences, Beijing, China
[2] University of Chinese Academy of Sciences, Beijing, China
[3] Ganjiang Innovation Academy, Chinese Academy of Sciences, Ganzhou, Jiangxi, China

*Corresponding author e-mail: jshen@mail.ipc.ac.cn; zxli@mail.ipc.ac.cn

ABSTRACT

Based on a multi-stage regenerator design of magnetic refrigeration hydrogen liquefaction device, a two-dimensional transient numerical magnetic refrigeration model in the temperature range of liquid hydrogen was constructed. Some various factors on the cooling performance of the high temperature active magnetic regenerator (60 K - 80 K) were focused on, including operating frequency, fluid flow time ratio and filling mass of the magnetocaloric material. The simulation results showed that, as the operating frequency increases from 0.25 Hz to 4.00 Hz, the active magnetic regenerator can obtain is larger cooling power. Especially, under the condition of higher frequency and lower utilization factor, the larger cooling power and COP could be obtained. For fluid flow time ratio, the cooling power and efficiency increases with the increase of fluid flow time ratio from 40% to 80%. There is an increasing trend of corresponding utilization factor of the maximum cooling power, as the fluid flow time ratio increase. For the filling mass, the maximum cooling power has a linear relationship with the filling mass of the magnetocaloric material.

Keywords: hydrogen Liquefaction, Multistage magnetic refrigeration, Active magnetic regenerator, Numerical simulation

INTRODUCTION

Since Ohira et al. [1] first proposed the use of magnetic refrigeration technology for hydrogen liquefaction in 1997, some magnetic refrigerators [2] in the temperature range of liquid hydrogen (TRLH) have been developed and tested recently. In 2017, Park et al. [3] successfully developed a two-stage magnetic refrigeration equipment based on liquid nitrogen pre-cooling, which reached a minimum no-load temperature of 25.4 K. At the same time, the numerical simulation research[4] have been done. In 2014, Numazawa [5] constructed a magnetic refrigeration hydrogen liquefaction process based on simulation calculations, which was composed of a multi-stage active magnetic refrigeration cycle for precooling and a magnetic Carnot cycle for condensation. By numerical optimization, the theoretical liquefaction efficiency of this process could reach 46.9%. In 2020, Feng et al. [6] developed a one-dimensional magnetic refrigeration model in the TRLH, using liquid nitrogen pre-cooling. The liquefaction efficiency of a 12-stage magnetic refrigeration liquefaction device could reach 76.9% of the Carnot efficiency.

In a word, the abovementioned research focus on the system performance, and there are few studies on performance impact factors in each active magnetic regenerator (AMR) in the multi-stage magnetic refrigeration system. In this paper, based on COMSOL Multiphysics, a two-dimensional transient AMR model was constructed. Helium was used as the heat transfer fluid. The effects of various factors on the cooling performance of AMR were investigated. It provided theoretical guidance for the overall optimization design and experimental research of the multi-stage magnetic refrigeration system.

SIMULATION METHOD

In the multi-stage regenerator design, taking high-temperature stage AMR (temperature range 60 K - 80 K) as an example, a two-dimensional axisymmetric model was developed, as shown in Fig. 1. The geometry and operating parameters of the AMR model were shown in Table 1.

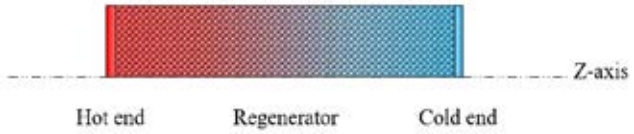


Fig. 1. Geometric model diagram of two-dimensional axisymmetric AMR

Table 1. Geometrical and operational parameters of AMR

Parameter	Value	Parameter	Value
Length of regenerator (*L*)	100 mm	Utilization factor (*U*)	0.0005 - 0.7
Diameter of regenerator (*D*)	20 mm	Frequency (*f*)	0.25 Hz - 4 Hz
Particle diameter of MCE material (*d*)	0.4 mm	Fluid flow time ratio (φ)	0.4 - 0.8
Porosity (ε)	0.36	Cold end temperature (T_C)	60 K
Magnetic induction intensity ($\mu_0 H$)	0.05 T – 1 T	Hot end temperature (T_H)	80 K

The governing conservation equations of the heat exchange fluid and the magnetocaloric material in AMR were established. For helium, the continuity equation, momentum equation and energy equation are as follows:

$$\frac{\partial \rho_f(T_f,p)}{\partial t}+\nabla\cdot\left(\rho_f(T_f,p)\mathbf{u}\right)=0 \tag{1}$$

$$\rho_f(T_f,p)\frac{\partial \mathbf{u}}{\partial t}+\rho_f(T_f,p)\mathbf{u}\cdot\nabla\mathbf{u}+\nabla p-\nabla^2\left(\mu_f(T_f,p)\mathbf{u}\right)=0 \tag{2}$$

$$\rho_f(T_f,p)c_{p,f}(T_f,p)\left(\frac{\partial T_f}{\partial t}+\mathbf{u}\cdot\nabla T_f\right)=\alpha_p T_f\left(\frac{\partial p}{\partial t}+\mathbf{u}\cdot\nabla p\right)+\nabla\cdot\left(k_f(T_f,p)\nabla T_f\right)+\frac{q_{sf}}{\varepsilon}(T_s-T_f) \tag{3}$$

The energy equation for magnetocaloric materials is as follows：

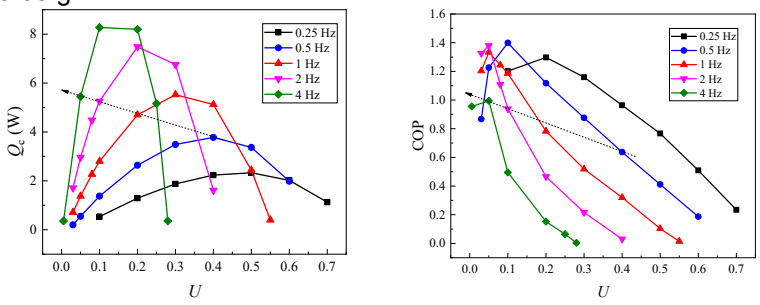
$$\rho_s c_{p,s}(T_s,\mu_0 H)\frac{\partial T_s}{\partial t}=\nabla\cdot\left(k_s(T_s)\nabla T_s\right)+\frac{q_{sf}}{1-\varepsilon}(T_f-T_s)+Q_{MCE} \tag{4}$$

The initial pressure of the magnetic refrigeration system was 1.6 MPa and the initial temperature was 80 K.

RESULTS AND DISCUSSION

Influence of operating frequency

Fig. 2 showed the variation of cooling power and COP of AMR with utilization factor under different operating frequencies *f* (0.25 Hz - 4 Hz). It could be seen that under the same frequency, the cooling power and COP of AMR first increase and then decrease with the increase of utilization factor. From Fig. 2 (a), it could be found that the cooling power has a significant improvement with the increase of frequency under the lower utilization factor. As the utilization factor was 0.1, the cooling power of the AMR increased from 0.54 W (0.25 Hz) to 8.28 W (4 Hz). This was because as the frequency increased, the mass flow rate of helium under the same utilization factor increased. Therefore, the convective heat transfer between the fluid and solid in the regenerator enhanced. Furthermore, the optimal utilization factor corresponding to the maximum cooling power of the AMR decreased as the frequency increased. For example, the optimal utilization factor was reduced from 0.5 (0.25 Hz) to 0.1 (4 Hz). At the same time, the dotted line in Fig. 2 showed that both the cooling power and COP of AMR increased with the increase of frequency at the helium flow rate of 5.65 g s^{-1}.

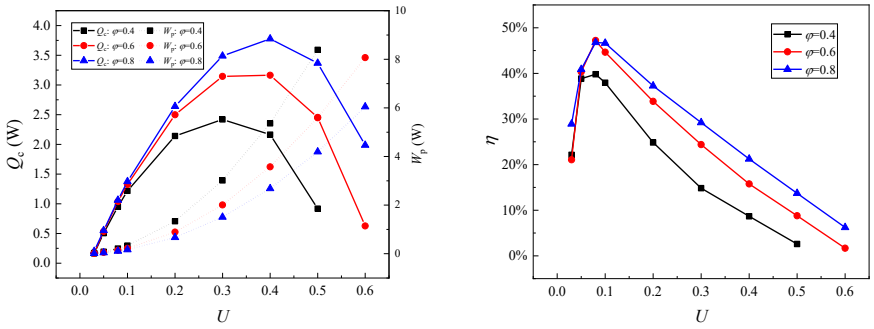


(a) cooling power (b) COP

Fig. 2. Cooling power (a) and COP (b) as a function of utilization factor at different frequencies (dotted line represents the same mass flow rate)

Influence of fluid flow time ratio

The flow time ratio φ of helium is defined as the ratio of the flow time of helium gas in the cycle, which is an important operating parameter. Fig. showed the cooling power, pump work and thermodynamic second efficiency of the AMR at 0.5 Hz when flow time ratio was 0.4, 0.6 and 0.8, respectively. It could be known that under the same utilization factor, with the increase of fluid flow time ratio, the AMR could have a longer heat exchange time per unit cycle. Meanwhile, it could be found that the maximum cooling power and the corresponding second thermodynamic efficiency of AMR both increased with the increase of the flow time ratio. For example, when the frequency was 0.5 Hz, the maximum cooling power of AMR increased from 2.42 W (φ=0.4, *U*=0.3) to 3.78 W (φ=0.8, *U*=0.4), and its corresponding thermodynamic second efficiency also increased from 14.83 % (φ=0.4, *U*=0.3) to 21.23% (φ=0.8, *U*=0.4).

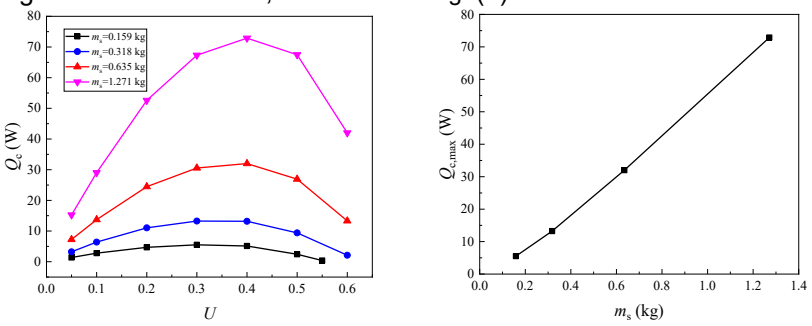


(a) cooling power and pump power (b) thermodynamic second efficiency

Fig. 3. Cooling power, pump power (a) and efficiency (b) as a function of utilization factor at different fluid flow time ratios

Influence of filling mass of magnetocaloric materials

When the frequency *f* was 1 Hz and the flow time ratio *φ* was 0.8, the cooling performance of AMRs with different filling mass m_s (0.159 kg, 0.318 kg, 0.635 kg and 1.271 kg) of magnetocaloric materials was investigated. Fig. (a) shows the cooling power and thermodynamic secondary efficiency of AMR as a function of utilization factor. It could be known that the more the filling mass of the magnetocaloric material, the more the cooling power of the AMR. With the increase of utilization factor, the cooling power of AMR firstly increased and then decreased. Meanwhile, the AMRs with different filling mass had different maximum cooling power $Q_{c,max}$. which increased roughly linearly with the filling mass of the magnetocaloric material, as shown in Fig. (b).



(a) cooling power (b) maximum cooling power

Fig. 4. Cooling power (a) and maximum cooling power (b) at different filling qualities of magnetocaloric materials

CONCLUSIONS

The influence of various factors on refrigeration performance of AMR was investigated, including the operating frequency, fluid flow time ratio and filling mass of magnetocaloric materials.

- The higher the operating frequency of the system, the greater the maximum cooling power that the AMR could obtain.
- At the same frequency, as the utilization factor increases, the COP of AMR first increases and then decreases.
- At the same utilization factor, with the increase of the flow time ratio, the cooling power of the AMR gradually increases and the pumping power gradually decreases.
- The maximum cooling power of AMR has a linear relationship with the filling mass of the magnetocaloric material, which has important guiding significance for the size design of the magnetic refrigeration hydrogen liquefaction device.

REFERENCES

1. Ohira K, Matsuo S and Furumoto H. 1997. The Characteristics of Magnetic Refrigeration Operating at the Temperature of 20 K. Proceedings of the Sixteenth International Cryogenic Engineering Conference/International Cryogenic Materials Conference 1: 403-406.
2. Kamiya K, Takahashi H and Numazawa T. 2007. Hydrogen Liquefaction by Magnetic Refrigeration. International Cryocooler Conference.
3. Park I and Jeong S. 2017. Development of the active magnetic regenerative refrigerator operating between 77 K and 20 K with the conduction cooled high temperature superconducting magnet. Cryogenics 88: 106-115.
4. Barclay J A and Brook T C. 2002. Apparatus and methods for cooling and liquefying a fluid using magnetic refrigeration. U.S.
5. Numazawa T, Kamiya K and Utaki T. 2014. Magnetic refrigerator for hydrogen liquefaction. Cryogenics 62: 185-192.
6. Feng T, Chen R and Ihnfeldt R V. 2020. Modeling of hydrogen liquefaction using magnetocaloric cycles with permanent magnets. International Journal of Refrigeration 119: 238-246.

WHEC-2022
23rd World Hydrogen Energy Conference
June 26-30, 2022 - Istanbul

#1602

COMPARATIVE STUDY ON ACTIVE AND PASSIVE THERMAL MANAGEMENT OPTIONS OF A METAL HYDRIDE HYDROGEN STORAGE TANK

[1*] *Tacettin Dişli,* [1] *Sera Ayten Çetinkaya,* [2] *Mehmet Akif Ezan,* [2] *C. Ozgur Colpan*
[1] The Graduate School of Natural and Applied Sciences, Dokuz Eylul University, Izmir, Turkey
[2] Department of Mechanical Engineering, Faculty of Engineering, Dokuz Eylul University, Izmir, Turkey

*Corresponding author e-mail: dislitacettin@gmail.com

ABSTRACT

With the increase in the importance of hydrogen energy, studies on storage for the use of hydrogen have also increased. Although metal hydride tanks have a higher hydrogen storage capacity in terms of volume, they are more inefficient in terms of weight and thermal management than the other storage systems. The bonding of hydrogen to the metal in MH tanks is exothermic during the absorption event, while the separation of hydrogen from the metal is endothermic during the desorption event. By incorporating phase change material (PCM) around the metal hydride tank, a 2D mathematical model is developed in this work. In terms of thermal management, this model is investigated both actively and passively.

Keywords: Metal-hydride hydrogen storage, PCM, Hydrogen energy, Hydrogen storage

INTRODUCTION

The use of fossil fuels is causing an increase in environmental challenges. As a result, governments have begun to contribute to the use of alternative energy sources like wind and wave, as well as energy carriers like hydrogen and batteries. Hydrogen has become more popular due to its high gravimetric energy density. However, in order to increase its volumetric density, research on hydrogen storage has increased. Metal hydrides have higher volumetric energy densities of any hydrogen storage technique, however, slow charging time is one of the main issues. Thermal management is another challenge as the metal hydride hydrogen storage tank heats up during absorption and cools down during desorption. A proper thermal management strategy should be selected to adjust the charging and discharging period of the metal-hydride tank.

Thermal management in metal hydride tanks can be accomplished in different ways. Askri et al. [3] investigated a cylindrical metal hydride tank with different cooling methods such as using external fins, and pumping cooling fluid through a 2D mathematical model. They validated their model experimentally, and examined the thermal interaction on the metal hydride tank surface and investigated the effect of different design on the duration of hydrogen hydration process. To understand how bed geometry affects the hydrogen absorption/desorption, Mellouli et al. [2] used PCM material as latent heat storage in a MgNi2-based metal hydride tank and performed heat and mass analyses in different bed designs (spherical shells, hexagonal tubes, and cylindrical tubes as phase change heat exchangers). Tong et al. [3] created a hydrogen storage system by integrating PCM and coiled tubes into an MH tank. To determine the acceptable hydrogen storage capacity and increase the heat and mass transfer performance, the design and production parameters of the hydrogen storage system were examined. They created a simple asymmetric model and compared the model with experimental data.

In this work, a 2D metal hydride hydrogen storage tank model with and without PCM was created, using a straight pipe integrated PCM. Pressure (5,8,12,20 and 30 bar) convection coefficient (5,10,20,100,500,1000 and 2000 W/m^{2}K), and temperature (278,283,288,298 and 313 K) for the case without PCM; whereas pressure (5,8,12,20 and 30 bar) and melting temperature (278,283,288,298,313 K) for the case with PCM were analyzed parametrically, and the cases, in which PCM becomes feasible according to the storage time and tank temperature, were examined.

MATHEMATICAL MODELING

In this section, the equations used for mathematical modeling of the metal hydride storage tank and PCM are given. Tank properties were listed in our previous study [4]. PCM specifications can be found in [3]. A schematic of the geometry of the model is given in Figure 1.

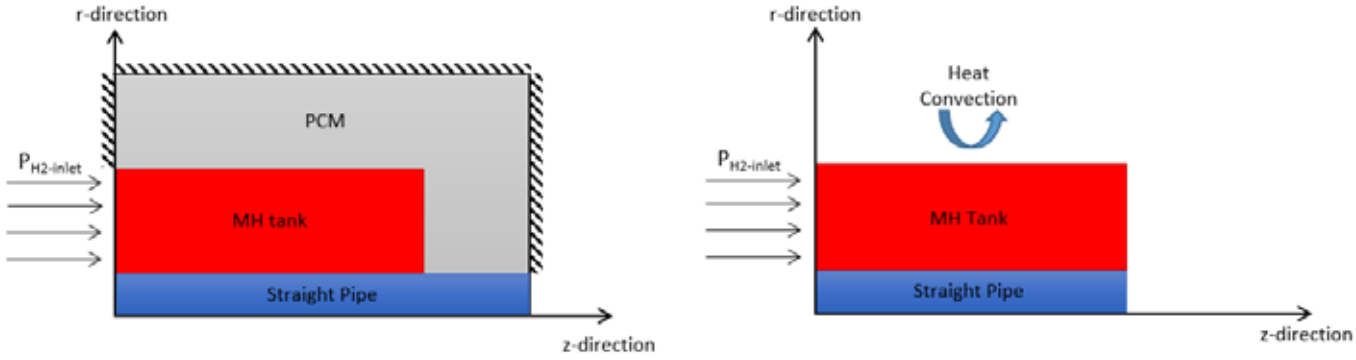


Fig 1. The geometry of MH tank (a) with PCM and (b) without PCM

Metal Hydride Hydrogen Storage Model

From the mass balance, $\dot{m}'''$ is the absorption reaction rate and can be calculated as follows,

$$\dot{m}''' = C_a \exp\left[-\frac{E_a}{R_g T}\right] \ln\left(\frac{P_g}{P_{eq}}\right) [\rho_{ss} - \rho_s] \tag{1}$$

where C_a is the heat capacity, E_a is the activation energy, R_g is the ideal gas constant, T is the hydride temperature, P_g is the gas pressure, ρ_{ss} is the hydride density at saturation state, and ρ_s is the gas pressure. P_{eq} is the equilibrium pressure and can be obtained from Van't Hoff equation [3]. The energy conservation of the metal hydride tank system can be calculated as follows,

$$\rho c_{eff} \frac{\partial T}{\partial t} = \frac{1}{r}\frac{\partial}{\partial r}\left[k_{eff} r \frac{\partial T}{\partial r}\right] + \frac{\partial}{\partial z}\left[k_{eff}\frac{\partial T}{\partial z}\right] + \dot{q}_{source} \tag{2}$$

where $(\rho c)_{eff}$ is the effective heat capacity, k_{eff} is the thermal conductivity, and $\dot{q}_{source}$ is the source term of the energy equation.

Phase Change Material Model

The temperature transform method was used and the equation for PCM can be obtained as follows,

$$\frac{\partial (C.T)}{\partial t} = \frac{1}{r}\frac{\partial}{\partial r}\left(k_{en} r \frac{\partial T}{\partial r}\right) + \frac{\partial}{\partial z}\left[k_{en}\frac{\partial T}{\partial z}\right] - \frac{\partial S}{\partial t} \tag{3}$$

where C is the volumetric heat capacity, k_{en} is the enhanced thermal conductivity, and S is the source term. C and S can be calculated with the equations shown below [5],

$$C = C(T) = \begin{cases} C_s & T < T_m - \delta T_m \quad Solid\ Phase \\ C_m + \delta \dfrac{h_{sf}}{2\delta T_m} & T_m - \delta T_m \le T \le T_m + \delta T_m \quad Mushy\ Phase \\ C_l & T > T_m + \delta T_m \quad Liquid\ Phase \end{cases} \tag{4}$$

$$S = S(T) = \begin{cases} C_s(\delta T_m - T_m) & T < T_m - \delta T_m \quad Solid\ Phase \\ \left(C_m + \delta \dfrac{h_{sf}}{2\delta T_m}\right)(\delta T_m - T_m) & T_m - \delta T_m \le T \le T_m + \delta T_m \quad Mushy\ Phase \\ C_l \delta T_m - C_l T_m + \delta h_{sf} & T > T_m + \delta T_m \quad Liquid\ Phase \end{cases} \tag{5}$$

where T_m is melting temperature, δT_m is mushy range. Natural convection correlations inside annular cylindrical gaps are used to assess the liquid PCM's improved thermal conductivity [6].

RESULTS AND DISCUSSION

In this section, different parameters (convection coefficient, pressure, ambient temperature) are examined for metal hydride tank without PCM in order to examine the weight fraction and metal hydride temperature. In the PCM integrated metal hydride tank, the same outputs were examined for different pressures and melting temperatures.

The percentage filling rate of the tank for the case with and without PCM is shown in Fig 2a for a pressure of 20 bar.This figure shows that PCM is more feasible when the convection coefficient is less than 500 W/m^{2}K. Results show that, when the convective heat transfer coefficient around the MH tank exceeds 500 W/m^{2}K, the thermal resistance reduces significantly and the generated heat inside the MH tank extracted by the surrounding air. In contrast, inside the PCM, due to the low thermal conductivity of paraffin, the thermal resistance slows down the heat transfer process and adversely affects the heat extraction. It looks like that the PCM usage becomes unfeasible when the convective heat transfer coefficient is beyond a critical value. As a result, it can be seen that there are some instances where PCM is feasible. For 20 bar,no difference was observed in terms of weight fraction at melting temperatures of 5 ºC and 20 ºC. In the low pressure in the absorption process, the influence of PCM melting temperature is more effective.

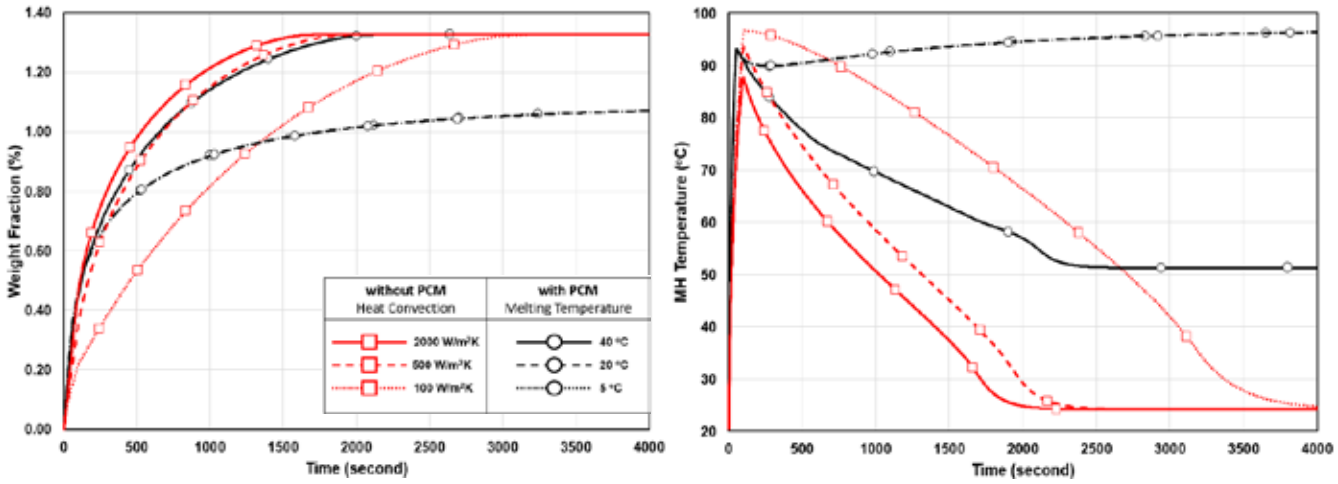


Fig. 2. Variations in (a) hydrogen weight fraction and (b) temperature under different heat convection coefficients and melting temperature at 20 bar

Fig 3a shows the metal hydride tank's percent hydrogen filling ratio. While the effect of melting temperature is studied in PCM analyses, the effect of convection coefficient is studied in non-PCM analyses. In comparison to other analyses, PCM-containing analyses have more efficient storage at a melting temperature of 20 ℃. This is because, PCM melts instantly at 5 ºC, but it can not change phase for the majority of the reaction time at 40 ℃. The influence of the convection coefficient on the percent hydrogen filling ratio is shown in Fig 3b. Since there is no increase in temperature during absorption, as the convection coefficient increases, the hydrogen filling rate of the tank increases.

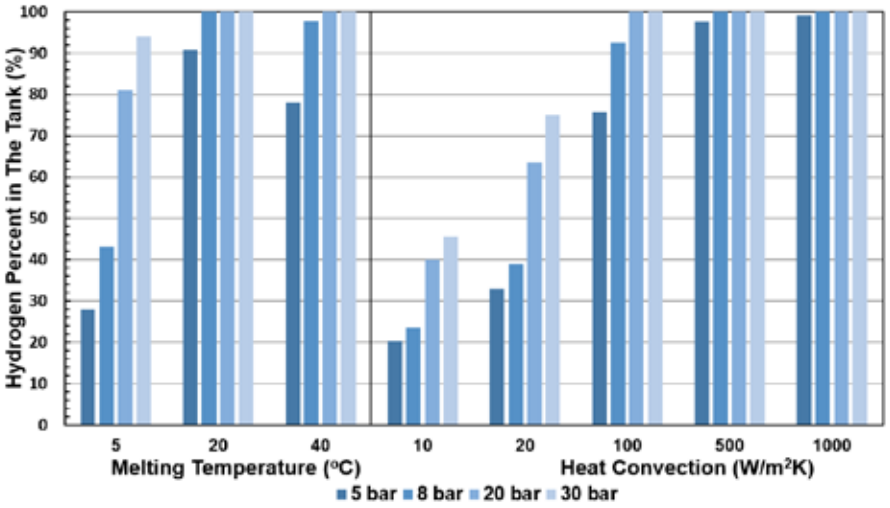


Fig. 3. Variations in hydrogen percent in the tank under different (a) melting temperature and (b) heat convection coefficient

CONCLUSIONS

In this study, 2D mathematical modeling of metal hydride hydrogen storage tank (with PCM and without PCM) was. It is observed that PCM is suitable for metal hydride hydrogen storage tanks with and without PCM by using different operating parameters. Weight fraction, tank temperature and major results were compared for two different models

in examining the effects of convection coefficient, pressure, melting temperature, and ambient temperature. The results of a tank with an active thermal management using the effect of the convection coefficient and a passive thermal management using PCM are shown. While the effect of PCM on weight fraction is higher at low convection coefficients used for active thermal management; It is not advantageous to use PCM in cases where the convection coefficient is high.

Acknowledgment

This research was supported by The Scientific and Technological Research Council of Turkey (TUBITAK) with project number 220N405.

REFERENCES

1. Askri, F., Salah, M. B., Jemni, A., & Nasrallah, S. B. (2009). Optimization of hydrogen storage in metal-hydride tanks. International journal of hydrogen Energy, 34(2), 897-905.
2. Mellouli, S., Abhilash, E., Askri, F., & Nasrallah, S. B. (2016). Integration of thermal energy storage unit in a metal hydride hydrogen storage tank. Applied Thermal Engineering, 102, 1185-1196.
3. Tong, L., Yuan, Y., Yang, T., Bénard, P., Yuan, C., & Xiao, J. (2021). Hydrogen release from a metal hydride tank with phase change material jacket and coiled-tube heat exchanger. International Journal of Hydrogen Energy, 46(63), 32135-32148.
4. Disli, T., Ezan, M. A., Çetinkaya, S. A., Colpan, C. O. (2022). 2D Mathematical Modeling of a Metal Hydride Hydrogen Storage Tank. 6th International Hydrogen Technologies Congress (IHTEC-2022), January 23-26, 2022, Canakkale, Türkiye.
5. Dincer, I., & Ezan, M. A. (2018). System Modeling and Analysis. In Heat Storage: A Unique Solution For Energy Systems (pp. 137-182). Springer, Cham.
6. Incropera, F. P., DeWitt, D. P., Bergman, T. L., & Lavine, A. S. (1996). Fundamentals of heat and mass transfer (Vol. 6, p. 116). New York: Wiley.

WHEC-2022
23rd World Hydrogen Energy Conference
June 26-30, 2022 - Istanbul

#1603

DESIGN PARAMETERS OPTIMIZATION OF PHASE CHANGE MATERIAL INTEGRATED METAL HYDRIDE HYDROGEN STORAGE TANK

[1*] *Sera Ayten Çetinkaya,* [1] *Tacettin Dişli,* [2] *Mehmet Akif Ezan,* [2] *C. Ozgur Colpan*
[1] The Graduate School of Natural and Applied Sciences, Dokuz Eylul University, Izmir, Turkey
[2] Department of Mechanical Engineering, Faculty of Engineering, Dokuz Eylul University, Izmir, Turkey

*Corresponding author e-mail: sera.cetinkaya@ogr.deu.edu.tr

ABSTRACT

Nowadays, with the development of technology and the increase in energy demand, hydrogen has become one of the important energy carriers. Hydrogen must be stored before it can be used in hydrogen-based applications. Among the various storage options, metal hydride (MH) tanks can store more hydrogen in volume than the other ways. However, to realize the charging and discharging of hydrogen in MH tanks, thermal management must be done properly. For thermal management in MH tanks, many applications such as phase change material (PCM), heat exchangers, or fins can be used. In this study, a 1D mathematical model of a metal hydride tank and PCM is developed. Hydrogen weight fraction and PCM liquid fraction values were calculated for different values of PCM thickness (1 cm to 5 cm) and PCM melting temperature (27 ^{o}C to 35 ^{o}C) under different cases where MH radius (2.5, 3, 4, and 5 cm) and inlet pressure (8, 10, 12 bar) change. PCM thickness and melting temperature values have been optimized for cases where the weight fraction and liquid fraction are maximum for all cases.

Keywords: Metal-hydride hydrogen storage, PCM, Hydrogen energy, Optimization

INTRODUCTION

Due to the chemical structure of metal hydride (MH), hydrogen absorption is exothermic and desorption is endothermic. To have the desired hydrogen flow rate and shorter durations of charging and discharging processes, proper thermal management of the tank should be done. The tank's thermal management could be handled in a variety of methods. One of these methods is to use phase change material (PCM) that covers the tank.

There are several studies in the literature about PCM integrated MH tanks. Darzi et al. (2016) covered the outside of the $LaNi_5$-based MH tank with PCM material and performed a parametric analysis with different pressure and porosity values to examine the absorption and desorption characteristics of hydrogen. El Mghari et al. (2019) developed a 2D mathematical model to investigate the effect of PCM material on the MH tank and compared their model with the other numerical and experimental studies in the literature. They examined the effect of PCM on hydrogen absorption, desorption, and melting kinetics by varying the thermal conductivity and latent heat. Algahtani et al. (2020) investigated the effects of different designs on hydrogen absorption and desorption using two distinct PCMs. The charging and discharging times of hydrogen were investigated by parametric analysis using different PCMs. Nyamsi et al. (2020) developed a 2D mathematical model to examine the performance of the thermal energy storage (TES) system to recover the waste heat extracted from the two MH tanks ($Mg_2Ni/LaNi_5$). They employed a multi-objective optimization algorithm to optimize the characteristics of the PCM in this system, which included integrating paraffin-based PCM material to store the heat of reaction in the high temperature (HT) portion.

In this study, a 1D model of a metal hydride hydrogen storage tank covered with PCM was developed and the modeling equations were solved in MATLAB using the finite volume method. PCM thickness and melting temperature were optimized to find the optimum values of liquid fraction and weight fraction. Parametric analysis was conducted to evaluate the effects of inlet pressure of hydrogen (8,10, and 12 bar) and MH radius (2.5 cm, 4 cm, and 5 cm) on the time-wise variations for optimum values of PCM thickness (1cm to 5 cm) and melting temperature (27 ^{o}C to 35 ^{o}C).

MATHEMATICAL MODELLING

In this section, the mathematical modeling and solver algorithm of the metal hydride tank were given. The schematic of the MH tank can be shown in Fig. 1.

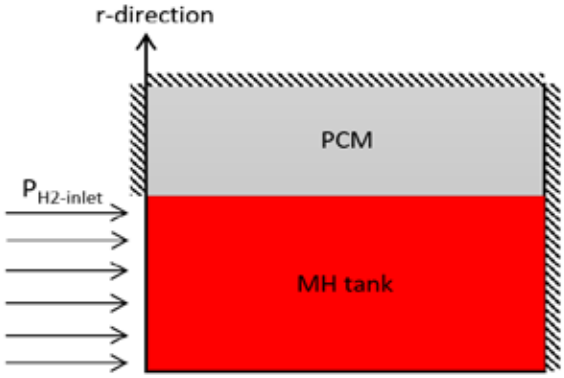


Fig. 1. The geometry of the MH tank

Metal Hydride Hydrogen Storage Model

The energy conservation of the MH tank system can be obtained as follows [5],

$$(\rho c)_{eff}\frac{\partial T}{\partial t}=\frac{1}{r}\frac{\partial}{\partial r}\left[k_{eff}r\frac{\partial T}{\partial r}\right]+\dot{q}_{source} \quad (1)$$

where $(\rho c)_{eff}$ is the effective heat capacity, k_{eff} is the thermal conductivity, and $\dot{q}_{source}$ is the heat generation within the MH tank due to the absorption reaction.

Phase Change Material Model

For PCM, the temperature transform method was used and the equation can be explained as follows [6],

$$\frac{\partial(CT)}{\partial t}=\frac{1}{r}\frac{\partial}{\partial r}\left(k_{en}r\frac{\partial T}{\partial r}\right)-\frac{\partial S}{\partial t} \quad (2)$$

where C is the volumetric heat capacity, k_{en} is the enhanced thermal conductivity, and S is the source term The C and S can be calculated using the equations given in [6]. The enhanced thermal conductivity of the liquid PCM is evaluated from the natural convection correlations inside the annular cylindrical gaps [7].

RESULTS AND DISCUSSION

The variation of weight fraction and liquid fraction for different PCM thickness (1 cm to 5 cm) and melting temperature (27 ºC to 35 ºC) values for cases where MH radius (2.5, 3, 4, and 5 cm) and inlet pressure (8, 10, 12 bar) change are examined in this section. PCM thickness and melting temperature values at maximum weight fraction and liquid fraction was determined by optimization. Optimizations were made using the Minitab program. For various MH radius and inlet pressure cases, Table 1 shows the ideal PCM thickness and melting temperature value for the maximum liquid fraction and weight fraction. It can be seen from this table that the melting temperature does not change in different cases and its optimum value is 27 ºC. Contrary to the melting temperature, it can be said that the PCM thickness takes different values in different situations, and it can be said that it is more effective than the melting temperature.

Table 1. Optimization results for different MH radius and inlet pressure values

MH Radius (cm)	Inlet Pressure (bar)	PCM thickness (cm)	Melting Temperature (ºC)	MH Radius (cm)	Inlet Pressure (bar)	PCM thickness (cm)	Melting Temperature (ºC)
2.5	8	3.22	27	4	8	3.38	27
	10	3.26	27		10	3.63	27
	12	3.43	27		12	3.90	27
3	8	3.26	27	5	8	3.47	27
	10	3.46	27		10	3.78	27
	12	3.58	27		12	3.99	27

In Table 2, MH temperature, PCM temperature, liquid fraction, and weight fraction values obtained using the values in Table 1 are given. It can be observed that in all cases, the liquid fraction achieves its maximum amount. When the

MH radius is 2.5 cm and the inlet pressure is 12 bar, the maximum weight fraction value can be obtained. According to this, the absorption rate of hydrogen is the highest in this case. In Fig. 2, the time-dependent changes in the weight and liquid fractions are shown for the PCM thickness and melting temperature calculated from the parameters obtained in Table 1. From this figure, it can be seen that a higher hydrogen absorption occurs when the MH radius is 2.5 cm and the inlet pressure is 12 bar. The change of MH radius and melting temperature does not cause any particular effect on the liquid fraction. In general, an increase in the pressure causes an increase in the liquid fraction and weight fraction, but increasing the MH radius causes these values to decrease.

Table 2. The results of the cases obtained as a result of optimization

MH radius (cm)	Inlet Pressure (bar)	MH Temperature (°C)	PCM Temperature (°C)	Liquid Fraction	Weight Fraction
2.5	8	57.75	45.36	1	1.061
	10	62.73	51.51	1	1.15
	12	63.64	51.60	1	1.22
3	8	61.005	49.18	1	0.89
	10	65.42	52.008	1	0.99
	12	68.96	54.75	1	1.06
4	8	63.23	51.51	1	0.68
	10	68.66	54.43	1	0.76
	12	72.26	54.64	1	0.84
5	8	64.06	52.23	1	0.55
	10	69.86	54.92	1	0.63
	12	74.75	57.21	1	0.69

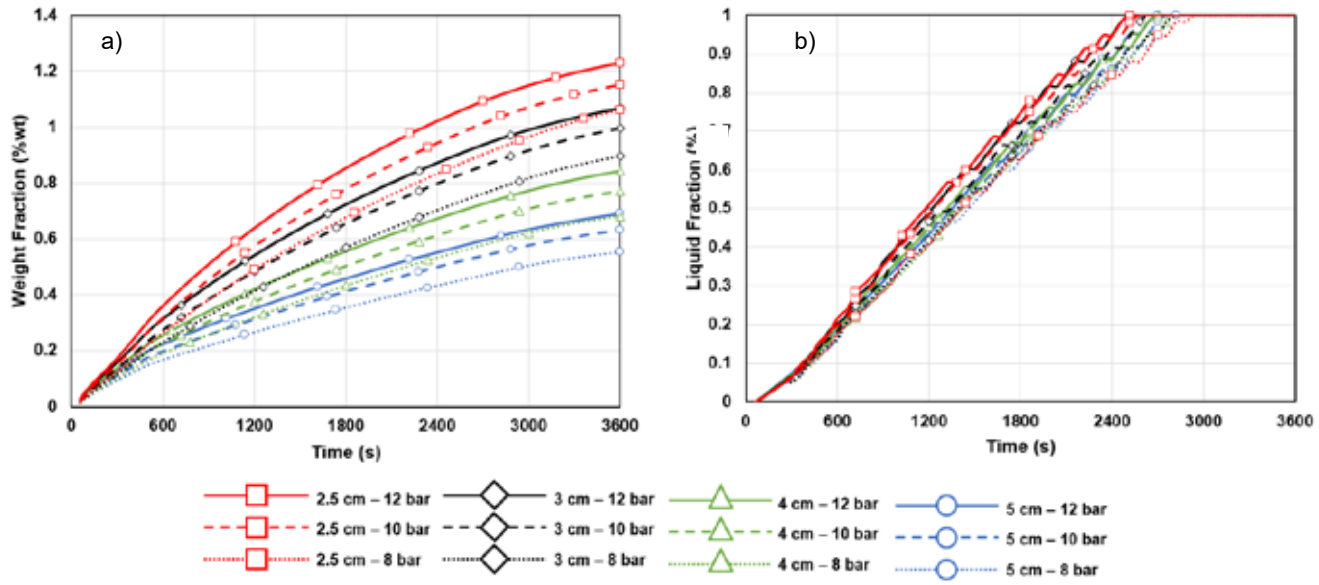


Fig. 2. Time-dependent change of (a) weight fraction and (b) liquid fraction for the best values of PCM thickness and melting temperature

For the maximum value of the weight fraction (2.5 cm MH radius and 12 bar inlet pressure), Fig. 3 shows the effect of inlet pressure on hydrogen percent in the tank at various PCM thicknesses. This figure shows that as the pressure increases, the weight fraction increases as well. In the case where the PCM thickness is 4 cm, the hydrogen percent is higher than that found for the other thicknesses. This is because PCM melts faster when it has 4 cm thickness compared to 5 cm thickness.

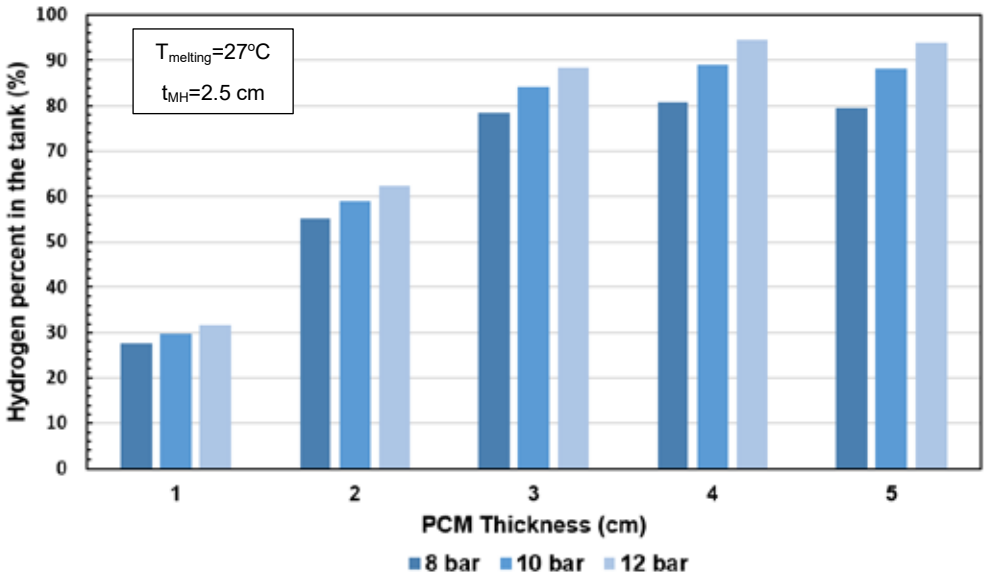


Fig. 3. Hydrogen percent in MH tank under different pressures

CONCLUSIONS

In this study, a 1D mathematical model of a PCM integrated metal hydride hydrogen storage tank is developed. For different MH tank diameter and inlet pressure values, the optimum PCM thickness and melting temperature values are obtained using the Minitab program when the weight fraction and liquid fraction are maximum. As a result, it is found that the weight fraction increases with the increase of the inlet pressure, on the contrary, the weight fraction decreases as the MH radius increases. Changing the inlet pressure and the MH radius does not have a specific effect on the liquid fraction.

Acknowledgments

This research was supported by The Scientific and Technological Research Council of Turkey (TUBITAK) with project number 220N405.

REFERENCES

1. Darzi, A. A. R., Afrouzi, H. H., Moshfegh, A., & Farhadi, M. (2016). Absorption and desorption of hydrogen in long metal hydride tank equipped with phase change material jacket. *international journal of hydrogen energy*, *41*(22), 9595-9610.
2. El Mghari, H., Huot, J., & Xiao, J. (2019). Analysis of hydrogen storage performance of metal hydride reactor with phase change materials. *International Journal of Hydrogen Energy*, *44*(54), 28893-28908.
3. Alqahtani, T., Bamasag, A., Mellouli, S., Askri, F., & Phelan, P. E. (2020). Cyclic behaviors of a novel design of a metal hydride reactor encircled by cascaded phase change materials. *International Journal of Hydrogen Energy*, *45*(56), 32285-32297.
4. Nyamsi, S. N., Lototskyy, M., & Tolj, I. (2020). Optimal design of combined two-tank latent and metal hydrides-based thermochemical heat storage systems for high-temperature waste heat recovery. *Energies*, *13*(16), 4216.
5. Tong, L., Yuan, Y., Yang, T., Bénard, P., Yuan, C., & Xiao, J. (2021). Hydrogen release from a metal hydride tank with phase change material jacket and coiled-tube heat exchanger. *International Journal of Hydrogen Energy*, *46*(63), 32135-32148.
6. Dincer, I., & Ezan, M. A. (2018). System Modeling and Analysis. In Heat Storage: A Unique Solution For Energy Systems (pp. 137-182). Springer, Cham.
7. Incropera, F. P., DeWitt, D. P., Bergman, T. L., & Lavine, A. S. (1996). *Fundamentals of heat and mass transfer* (Vol. 6, p. 116). New York: Wiley.

WHEC-2022
23rd World Hydrogen Energy Conference
June 26-30, 2022 - Istanbul

#1614

INVESTIGATION OF INFRASTRUCTURE STUDY AND OPERATION PLANNING OF UNDERGROUND HYDROGEN STORAGE AREA

[1*]*Hatice Karakilcik*
[1]Faculty of Engineering, Department of Geology Engineering, Cukurova University, 01250, Adana, Turkey

*Corresponding author e-mail: hkilcik@cu.edu.tr

ABSTRACT

In this study, infrastructure works and operation planning of underground hydrogen storage areas was examined. Important points to be considered in the feasibility study were determined in the creation of salt caverns to built in salt domes, which are an important underground storage area. As well as producing hydrogen with clean energy sources such as wind and sun, it is also very important to store it economically in very large volumes. It has been seen that infrastructure works and operational planning are of great importance for the hydrogen storage areas created in salt domes to be technically, economically and financially efficient and sustainable. It was determined that hydrogen could be stored efficiently and economically in well-planned salt caverns at low pressure and on a very large scale. For this purpose, it is found that the storage cost, which is one of the most important problems in front of the hydrogen economy in the future, can be reduced. At the same time, it is seen that very important effects on the development of hydrogen economy and technologies. As a result, it has been seen that operational planning plays a key role in the use of salt caverns for long-term safe and healthy hydrogen storage.

Keywords: Underground hydrogen storage, salt dome, salt cavern, hydrogen economy

INTRODUCTION

Nowadays, electricity and hydrogen fueled vehicles are the only solution to reduce the environmental effects caused by the transportation sector, both electricity generation and hydrogen production are provided from renewable energy sources. This will help to significantly reduce carbon dioxide emissions, especially for the transport sector. Various energy storage techniques seem to be a critical solution to overcome such challenges by increasing the availability of renewable resources or balancing energy supply demand and fluctuating processes in generation. Today, various energy storage methods are practically possible to integrate into engineering applications in various industries [1]. In particular, very large-scale safe and economical hydrogen storage methods should be developed. One of the most suitable methods for this purpose is to explore underground geological structures. Salt cavern is another underground storage medium that can be used as a high-pressure gas storage area in very large volumes under certain conditions and conditions [2-4].

It is one of the most suitable options for large-scale and long-term storage of hydrogen in underground (geological) salt caverns. With the increase in supply and demand for renewable energy sources, hydrogen storage, especially in underground salt caverns, will have even more strategic importance. In the future, hydrogen storage will be key, with hydrogen being used on massive scales as a fuel in cars and airplanes, as heating in buildings and residences, and as electrical power in industry and other fields. Therefore, In this study, it was tried to determine the prominent issues and methods in the operational planning and infrastructure studies of the underground salt caverns which have a key role in the economical storage of hydrogen produced with renewable energy sources. And also they have a key role maintain the supply-demand balance with a continuous supply flow and delivery to suppliers as liquid or gas. The fact that hydrogen, which is an important energy source of the future, can be stored in salt caverns in large volumes and economically at low pressures, and the insufficient lack of scientific studies in this field that has been an important source of my motivation.

MATERIALS AND METHODS

Underground storage caverns are used for large-scale production and distribution for Hydrogen Gas production and distribution business, and especially for the storage of surplus gas. Hydrogen is produced with the surplus of electricity produced on the basis of solar and wind energy. The gas is compressed by compressor units and transported to the storage facility by long-distance pipelines. The gas stored here is transported to hydrogen distribution stations by mobile tankers (Figure 1). The hydrogen produced flows through the pipelines to the storage facility.

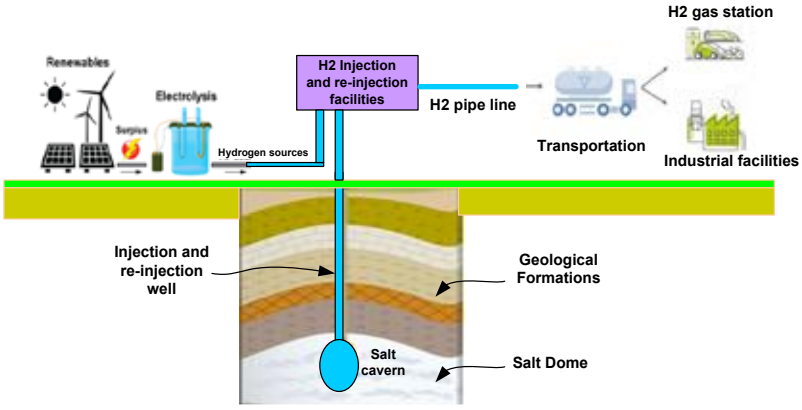


Figure 1. Hydrogen production and storage processes

There are important technical issues that should not be considered in underground hydrogen storage. Planning stages and well engineering studies are important in defining operations in underground projects. Here, it should be determined in which storage medium the hydrogen will be stored underground and the operation should be planned accordingly.

RESULTS AND DISCUSSION

Economic, technical and financial research of underground salt caverns should be carried out at the top of the issues to be considered in the feasibility study of underground hydrogen storage areas. In order to realize these, it is possible with the correct planning of infrastructure works and operational studies in the hydrogen storage area. Thus, it can be ensured that salt caverns are technically, economically and financially sustainable.

Infrastructure Works at the Hydrogen Storage Site:

- Inspection of the underground storage area, determination of existing or required new roads, legal permits to be obtained for all these and the cost of the investment are determined.
- Appropriate area is determined for the disposal of the salty water that comes out as a result of the construction of the caverns formed in the salt domes.
- The annual weather conditions of the underground storage area and the distance of the storage area to the residential areas are determined.
- In order to protect nature and the environment, necessary measures are taken to determine the negative effects of waste materials and to eliminate them.
- The operating mode of the facility built on the surface of the underground storage area is determined.
- The cost incurred in case of complete closure of the facility or temporary suspension of activities is calculated.
- For the safety of the facility, the presence of an emergency shutdown feature, taking the necessary precautions to prevent fire and explosions, and the establishment of a pressure relief system are taken into consideration.
- Materials used for hydrogen storage in underground salt domes and surface facilities must be of the best quality to avoid any problems.
- The technology and equipment to be used for underground cavern construction and for facilities located on the surface must be the latest, safest and most accepted by the authorities.
- Personnel to be employed in the underground storage facility should be experts, in-service training seminars should be given to the personnel at certain times, and maximum attention should be paid to the maintenance and repair needs of the facility over time.

Operational Planning in Underground Hydrogen Storage:

- Renewable energy resources of the region are determined.
- The geological and geophysical features of the region are examined.
- Suitable geological structures for underground storage are determined.
- The depth and dimensions of the salt domes are determined by geophysical methods.
- The physical and chemical properties of salt formation are analyzed.
- Architectural plans of the caverns planned to be built in salt domes are drawn up.
- The areas to be built in the salt domes and the size of the cavern to be built are determined.
- Well planning studies are created for the caverns where hydrogen will be stored.
- All risks that may occur in underground hydrogen storage are included in the technical well planning by providing the appropriate drilling site selection, and injection and re-injection well cost estimation is made.
- The hydrogen storage potential of the caverns is calculated.
- Optimum storage capacity and performance are determined.

- The ratio of working gas and pillow gas required for hydrogen storage in the cavern is determined.
- The flow and distribution of hydrogen injected and re-injected into salt caverns should be identified and evaluated.
- For long-term periods, the interaction of hydrogen with the salt cavern is evaluated.
- Possible underground risks for hydrogen operations are evaluated and risks are minimized.
- The interior structure and design of the cavern is constantly monitored by the underground ultrasonic imaging system.
- The maximum hydrogen storage and extraction capacity of each well is calculated.
- Presence, excess and transit time of hydrogen stored in salt caverns are determined.
- The mechanical effect of pressure changes caused by temporary or seasonal hydrogen storage in salt caverns is also evaluated.
- A management plan is created for the efficient operation of the cavern.

CONCLUSIONS

State Storage of hydrogen by compression in large volumes of high-pressure tubes or tanks increases the energy cost. In underground salt caverns, it can be stored in very large volumes with lower pressure. Hydrogen is produced with electricity produced in surplus from renewable sources such as solar and wind and stored in the salt cavern, providing a significant advantage in securing the energy supply chain for the next energy transition and in the hydrogen economy. It also has great potential to overcome the natural temporal fluctuations inherent in renewable energy generation. For this reason, it has been seen that structural planning is a necessity for the efficient storage and operation of hydrogen in salt caverns. By associating it with the feasibility of large-scale hydrogen storage, as well as operational planning and infrastructure studies, both structural uncertainties and the cost of the cavern can be reduced. Hydrogen production centers working with renewable energy systems and salt caverns can be safely and economically integrated. As a result, it has been seen that well-planned and safe underground salt caverns are a good alternative to ensure the continuity of the power supply, which is one of the most important parameters sought in renewable energy systems, and to store the excess power as hydrogen energy. An important part of the energy problem can be easily solved by storing hydrogen in caverns created in salt domes. Thus, it will be able to provide continuity in access to energy and the opportunity to have a clean and reliable energy source.

REFERENCES

1. Erdemir D and Dincer I. 2022. Development of solar-driven charging station integrated with hydrogen as an energy storage option. Energy Conversion and Management 257:115436.
2. Gabrielli P, Poluzzi A, Kramer GJ, Spiers C, Mazzotti M, Gazzani M. 2020. Seasonal energy storage for zero-emissions multi-energy systems via underground hydrogen storage. Renewable and Sustainable Energy Reviews 121:1096-29.
3. Hassanpouryouzband A, Joonaki E, Edlmann K and Haszeldine HS. 2021. Offshore Geological Storage of Hydrogen: Is This Our Best Option to Achieve Net-Zero? ACS Energy Letters 6(6): 2181-2186, DOI: 10.1021/acsenergylett.1c00845
4. Pudlo D, Ganzer L, Henkel S, Kühn M, Liebscher A, Lucia MD, Panfilov M, Pilz P, Reitenbach V, Albrecht D, Würdemann H, Gaupp R. 2013. The H2STORE Project: Hydrogen Underground Storage–A Feasible Way in Storing Electrical Power in Geological Media?, Springer Series in Geomechanics and Geoengineering, Edited by M.Z. Hou et al. (Eds.): Clean Energy Systems in the Subsurface: Production, Storage and Conversion, Springer-Verlag Berlin Heidelberg, 395–412. DOI: 10.1007/978-3-642-37849-2_31.

WHEC-2022
23rd World Hydrogen Energy Conference
June 26-30, 2022 - Istanbul

#1619

INVESTIGATION OF HYDROGEN KINETICS OF COPPER PELLETS WITH ENG ADDITIVES

[1,2*] *Gamze Atalmis,* [1,2] *Nebi Yelegen,* [3] *Mehmet Demiralp,* [1,2] *Yuksel Kaplan*
[1] Nigde Omer Halisdemir University, Mechanical Engineering Department, 51245, Nigde, Turkey
[2] Nigde Omer Halisdemir University Prof. Dr. T. Nejat Veziroglu Clean Energy Research Center, 51245, Nigde, Turkey
[3] Nigde Omer Halisdemir University, Nigde Vocational School of Technical Sciences, 51200, Nigde, Turkey

*Corresponding author e-mail: gamzee_umudum@hotmail.com

ABSTRACT

In this study, the hydrogen storage capabilities and thermal conductivity of the materials will be improved by applying both expanded natural graphite (ENG) addition and copper plating methods to the $LaNi_5$ alloy. The optimized $LaNi_5$-Cu alloy will be selected, ENG will be added at 1%, 5%, 10% and 20% ENG to this alloy and its application together with copper will be optimized. The obtained materials were characterized by XRD, SEM, BET and their thermal conductivity coefficients were measured with the Hot Disk Thermal Constants Analyzer device. In addition, the effect of storage materials with improved thermal conductivity on the hydrogen charging/discharging process in the metal hydride reactor will be experimentally investigated at the determined pressure.

Keywords: Hydrogen storage, Expanded natural graphite (ENG), Metal hydrides, Thermal conductivity

INTRODUCTION

Due to its high calorific value and being a clean fuel, hydrogen draws attention as the most studied energy carrier. However, the storage problems of hydrogen limit both its application areas and its commercialization. Recently, metal hydride reactors, which can store large amounts of hydrogen in small volumes and operate at high pressures, have attracted great interest. However, the biggest obstacle in the development of metal hydride reactors is the poor heat transfer properties of the alloys used [1]. As expected, this situation negatively affects the exothermic charge and endothermic discharge time and storage/release capacity. In this study, it is aimed to improve the heat transfer properties of hydrogen storage materials. One of the most effective methods for improving the thermal conductors of hydrogen storage materials is the method of coating the storage materials with copper. Recently, a lot of research has been done in this area. To improve the heat transfer of metal hydride reactors [2], they designed the reactor by using 10 kg of $LaNi_5$ alloy in their study and examined the system performance. With their work, they examined the effect of geometry and operational parameters and used them for reactor design and fabrication. They optimized the hydrogen charge and discharge at different pressures and flow rates. The results obtained from the experimental and numerical solutions show that the hydrogen storage rates of the reactors are significantly limited by the heat transfer between the metal alloy inside the reactors where the reactions take place and the external environment. Therefore, the improvement of heat transfer plays an important role in the design of reactors. In this context, researchers have proposed various designs to increase heat transfer in metal hydride reactors to reduce hydrogen charging time and increase stable discharge time. Pressing copper-coated metal alloy powders to increase the effective thermal conductivity of metal hydride reactors [3-5] are the process of producing metal hydride pellets by adding expanded natural graphite to metal alloy powders [6-7]. Lototskyy et al. [8] used C_{14} /$MgZn_2$ type AB_2 intermetallic metal hydride material and added 1% by mass of expanded natural graphite (ENG) to increase thermal conductivity during hydration. They reported that they reached a hydrogen storage capacity of 1.4% by mass when charged below 60 °C and above 50 bar pressure. The aim of this study; is to determine the main parameters to develop advanced hydrogen storage systems by improving the heat transfer coefficients and storage capacities of hydrogen storage materials with ENG and copper additives by forming metal hydride pellets to accelerate the hydrogen charge/discharge processes Fig. 1.

MATERIALS AND METHODS

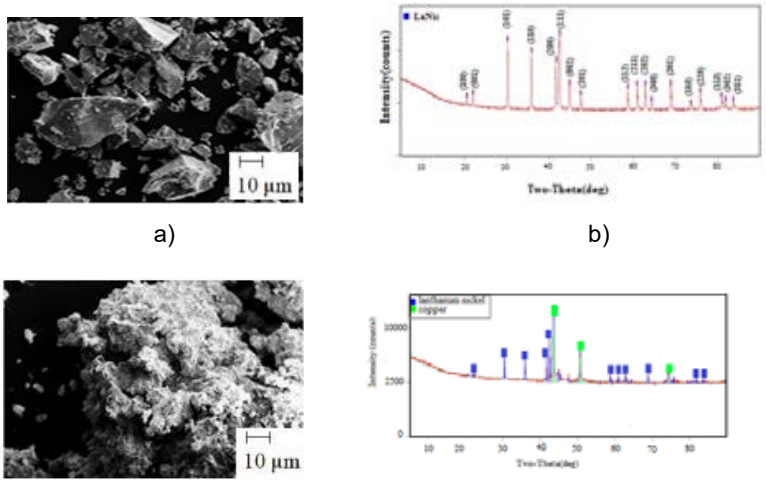
$LaNi_5$, the hydrogen storage material, is available in powder form. Metal hydride pellets are obtained by coating this powder material with copper using additional chemical materials and pressing it at high pressure. The copper plating process starts with a solution of copper sulfate ($CuSO_4$), water (H_2O), and sulfuric acid (H_2SO_4). This solution is thoroughly stirred at room temperature until the copper sulfate powders are completely dissolved. Then $LaNi_5$ is added and mixed for the specified time. The dried powders are then pelletized Fig. 1. The sample powders are weighed out to approximately 40 g, poured into a stainless-steel die, and then compacted by a manually operated hydraulic press at 15x104 N.



Fig. 1. $LaNi_5$ pellet coated with copper

RESULTS AND DISCUSSION

SEM and XRD analysis of $LaNi_5$ nanoparticles coated with copper $LaNi_5$ are shown in Fig.2. The coated image of $LaNi_5$ powder is shown in Fig.2c. by scanning electron microscopy. The copper coating can be distinguished by its lighter color. The result of BET analysis showed $LaNi_5$ 0.114019 m^2/g, $LaNi_5$-Cu 2.56732 m^2/g.



a) b)

c) d)

Fig. 2. a) Microstructure images b) XRD images of $LaNi_5$ c) Microstructure images copper–coated $LaNi_5$ powder d) XRD images of copper-coated $LaNi_5$

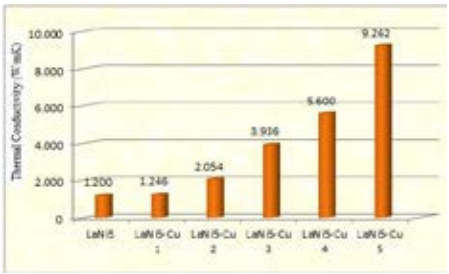


Fig. 3. Thermal conductivity analysis results of pellets optimized and prepared according to the amount of copper

The thermal conductivity of $LaNi_5$ powder was measured as 1.2 W/m-K (Fig.3). The thermal conductivity of the coating copper $LaNi_5$ metal hydride pellets were measured between 6 and 9 W/m-K. Within the scope of experimental studies, the thermal conductivity coefficients of $LaNi_5$ materials coated with copper have been increased by 500-750 %, and the copper coating ratios have been optimized.

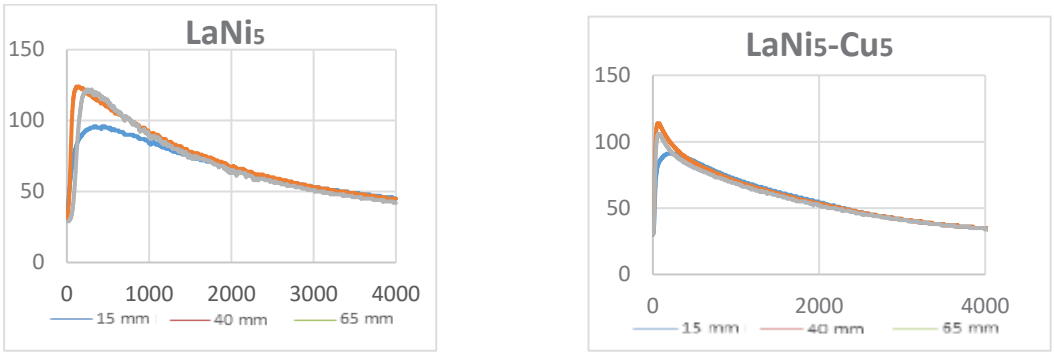


Fig. 4. Temperature development measured in the reactor at 10 bar a) $LaNi_5$ (standard) b) $LaNi_5$-Cu

To determine the effect of hydrogen charge pressure on storage kinetics in the study, experiments were carried out for 4000 s for a charge pressure of 10 bar. In these experiments, thermocouples were connected to 15 mm, 40mm and 65 mm points along the z-axis of the reactors, and time-dependent temperature change was measured.

CONCLUSIONS

To develop hydrogen storage materials, the main parameters were determined and the alloy was coated with copper. Thus, the heat transfer in metal hydride reactors is increased, the hydrogen charging time is reduced and the stable discharge time is increased. Coating the alloy with copper significantly increased the reaction kinetics and lowered the reactor temperature. As a result, hydrogen will be able to be stored in more reactors. The study determined the alloy with the most improved thermal conductivity. This alloy will be optimized with ENG and the results will be shared.

ACKNOWLEDGMENT

The authors would like to thank the Scientific and Technical Research Council of Turkey (TUBITAK) for the financial support under contract number 121M529. The first author, Gamze ATALMIŞ, would like to thank the Council of Higher Education (YÖK) for the 100/2000 Ph.D. Scholarship Program and International Association for Hydrogen Energy for sponsoring the conference fee.

REFERENCES

[1] Sun DW and Deng SJ. 1990. A theoretical model predicting the effective thermal conductivity in powdered metal hydride beds. International Journal of Hydrogen Energy 15:331-336.
[2] Karmakar A, Mallik A, Gupta N, Sharma P. 2021. Studies on 10 kg alloy mass metal hydride-based reactor for hydrogen storage. International Journal of Hydrogen Energy 46:5495 -5506.
[3] Kim KJ, Park IS, Kim KJ and Gawlik K. 2008. A hydrogen-compression system using porous metal hydride pellets of $LaNi_{5-x}Al_x$. International Journal of Hydrogen Energy 33:870-877.
[4] Kim S and Kim KJ. 2014. Hydrogen Storage with Annular $LaNi_5$ Metal Hydride Pellets. Advanced Materials Research Volumes 875-877:1671-1675.
[5] Lee M, Kima KJ, Hopkins RR and Gawl K. 2009. Thermal conductivity measurements of copper-coated metal hydrides ($LaNi_5$, $Ca_{0.6}Mm_{0.4}Ni_5$, and $LaNi_{4.75}Al_{0.25}$) for use in metal hydride hydrogen compression systems. International Journal of Hydrogen 34: 3185 – 3190.
[6] Chaise A. Rango PD, Marty P. Fruchart D. Miraglia S. Olive`s R and Garrier S. 2009. Enhancement of hydrogen sorption in magnesium hydride using expanded natural graphite. International Journal of Hydrogen Energy 34: 8589 – 8596.
[7] Palla S, Kaisare NS. 2020. "Evaluating the impact of pellet densification and graphite addition for design of on- board hydrogen storage in a fixed bed of MOF-5 pellets" International Journal of Hydrogen Energy 45: 25875-25889.
[8] Lototskyy MV, Davids MW, Tolj I, Klochko YV, Sekhar BS, Chidziva S and Pollet BG. 2015. Metal hydride systems for hydrogen storage and supply for stationary and automotive low temperature PEM fuel cell power modules. International Journal of Hydrogen Energy 40:11491–11497.

WHEC-2022
23rd World Hydrogen Energy Conference
June 26-30, 2022 - Istanbul

#1636

NUMERICAL AND EXPERIMENTAL ASSESSMENT OF A THERMAL MANAGEMENT SYSTEM FOR METAL HYDRIDE HYDROGEN TANK

*Asena Efekan, Bilalcan Yaşar, Erdem Karakahya, Işıl Dalgiç, Muhammed Hakan Demir, Musa Demir
Nadide Asuman Yaraş, Mehmet Akif Ezan, Can Ozgur Colpan
Department of Mechanical Engineering, Faculty of Engineering, Dokuz Eylul University, Izmir, Turkey

*E-mail: asenaefekann@gmail.com

ABSTRACT

One of the most promising ways to store and reuse hydrogen is the usage of metal hydride tanks. During the charging process, i.e., absorption, heat is generated inside the hydride tank due to the exothermic nature of the absorption reaction. In contrast, the discharging process is endothermic, and heat should be supplied to the hydride tank. Thermal management is critical in metal hydride tanks (MHT), as overheating the tank during charging or supercooling during discharge significantly reduces the reaction rate and limits the amount of hydrogen stored/released to/from the tank.

This study aims to design a water jacket for the thermal management of a metal hydride tank. For this purpose, preliminary parametric flow analyses were conducted for a 3D water jacket design to determine the suitable geometrical configurations that provide uniform convective currents around the tank with lower pressure drops. $LaNi_5$ tank material is then implemented into the model, and the charging process was examined by varying the major hydrogen supply pressure from 10 to 25 bar. The model is developed in ANSYS-FLUENT software. A dedicated UDF code is implemented into the software to incorporate the reaction kinetics equation, the hydride's mass balance, and the hydride's energy source term. The validity of the developed procedure is assured by reproducing a recent numerical work from the literature, and comparative results showed a satisfactory agreement. The parametric analyses showed that increasing the hydrogen supply pressure from 10 to 25 bar reduces the charging time from 12 minutes to 6 minutes. In addition to the numerical survey, experiments are conducted for an HYDROSTIK metal hydride tank in water and air ambients. Based on the numerical simulations, a novel 4-port cooling jacket was produced with a 3D printer and the experiments were conducted under various hydrogen supply pressure. Results showed that in comparison to the reference condition inside stagnant air ambient, the implementation of a water jacket reduces the charging time from 6 hours to 30 minutes.

Keywords: Hydrogen, Metal hydride tank, Thermal management, Water jacket, CFD

INTRODUCTION

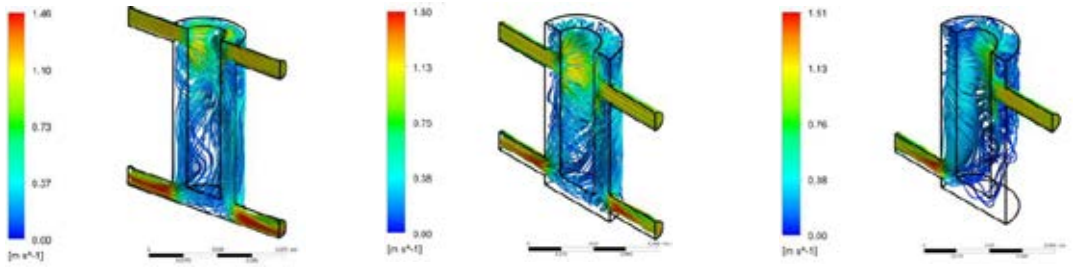
As a renewable energy source, hydrogen can be stored in metal hydride tanks. The aim of this paper to develop of thermal management system for this storage method. As a result of the literature review, Ben Nasrallah et al. examined a thermal management system with a water jacket. In this study, they used the two-port water jacket design and carried out numerical and experimental studies [1-2]. Souahlia et al. also examined a thermal management system with a water jacket and helical heat exchanger [3]. In this paper, as a difference of these studies, three different water jacket geometries were designed and the one with the most suitable flow distribution was selected from these water jackets. In addition, the effect of different inlet/outlet port combinations on flow distrubition were examined.

NUMERICAL ANALYSES

In this study, the charging process of a cylindrical MHT with time dependent heat generation was investigated using commercial software ANSYS-Fluent. The tank, which is thermally managed with a water jacket, is modeled in 3D and the charging process is examined. In the study to examine the flow distributions of the water jacket geometry, 3D flow analyses were made and the geometry was determined. The geometry and MHT determined as a result of flow analysis were modeled together, thermal analyses were made and the effects of different parameters on the charging process were examined.

THREE DIMENSIONAL ANALYSES

The flow distribution on the tank surface and the manufacturability of the design were taken into account in determining the appropriate water jacket design and inlet/outlet port combinations. Three different designs were created. At Fig.1 (b), it is seen that the flow distribution is mostly uniform compared to Fig.1 (a) and Fig.1 (c). Therefore, all analyses were performed according to Fig.1 (b) geometry.



(a) 4PD1 (b) 4PD2 (c) 2PD

Fig.1. Flow Distributions for different geometries

Looking at Fig.2, increasing mass flow rate at the same pressure reduces the charging time of the MHT. At a constant flow rate, increased pressure has a similar effect and decreases the charging time. Looking at Fig.3, increasing mass flow rate at a constant pressure reduces the MHT temperature. While the flow rate is constant, increasing pressure increases the MHT temperature. Looking at Fig.4, while the pressure is constant, the increasing mass flow reduces the water outlet temperature.

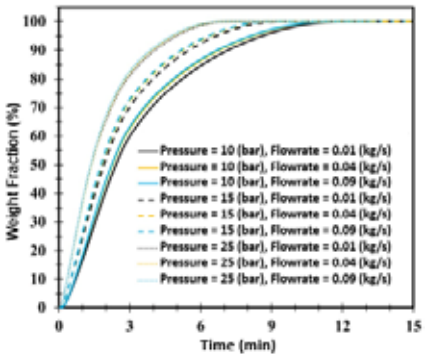


Fig.2. Weight fraction

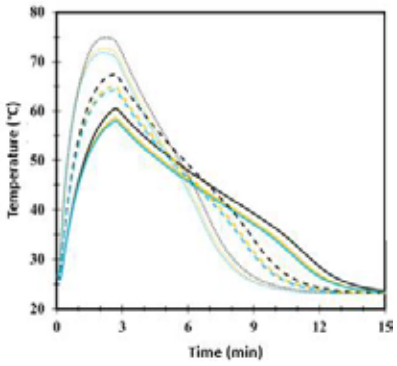


Fig.3. Average temperature of the tank

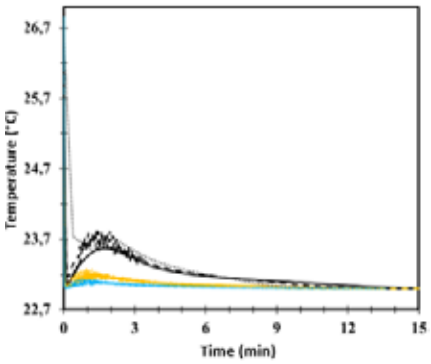


Fig.4. Outlet temperature of the water

EXPERIMENTAL STUDIES

Experiments were carried out to observe The effect of the water jacket on the discharge/charge processes. In Fig.5., it is seen that the charging and discharging processes of the MHT are carried out in a single experimental setup.

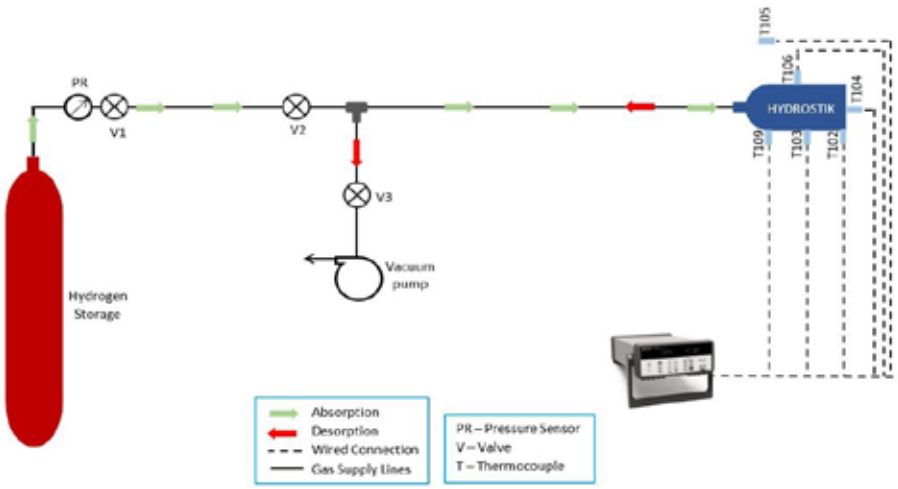


Fig.5. Experimental setup

Thermocouples numbered 102,103,104,106 and 109 were placed at different locations in order to measure the temperature changes on the surface of the MHT during the charging and discharging processes. In addition, thermocouples numbered 105,107, and 108 were used to measure ambient temperatures. In stagnant air ambient, the charging process took 6 hours and the discharging process took 3 hours, Fig.6.

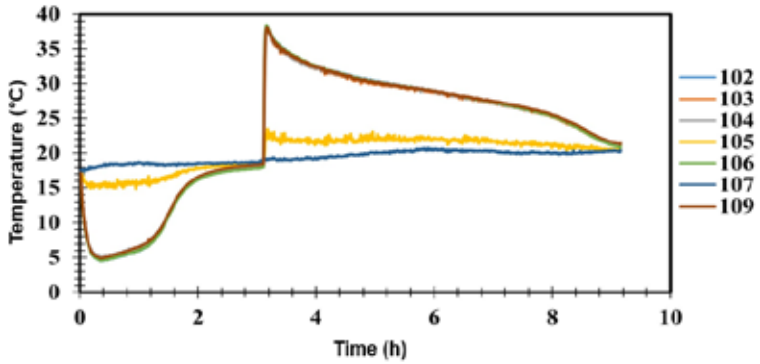


Fig.6. Charge and discharge process in stagnant air ambient

In experiments with the water jacket when water enters through the lower ports at Fig.7., the charging time took 30 minutes and the discharge time took 40 minutes, Fig.8. In the experiments using the water jacket, the total charging and discharging time was approximately 8 hours shorter than the stagnant air environment.

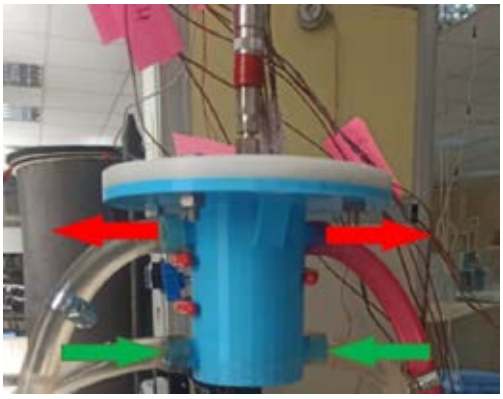


Fig.7. bottom-entry water jacket

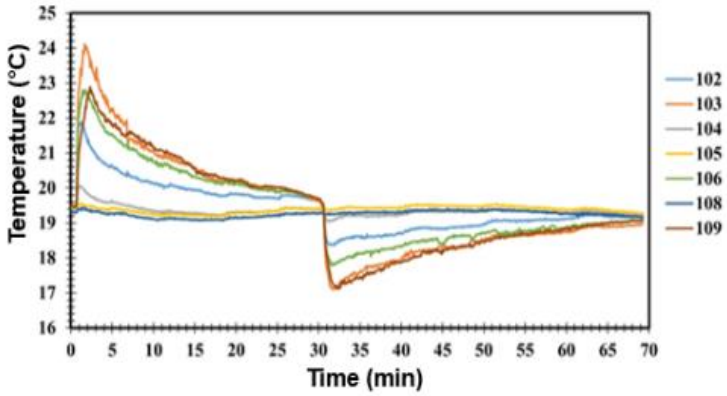


Fig.8. Charge and discharge process

CONCLUSIONS

As a result of flow analysis, it was decided to use 4PD2 which flow is uniformly distributed in the tank. It has been observed that hydrogen supply pressure is much more effective than mass flow rate in reducing the charging time. However, although the charging time decreases with the increase of hydrogen supply pressure, the maximum temperature in the MHT increases. In the experiments with the water jacket, it was observed that the charging and discharging times were shorter in the experiment with water inlet from the lower ports.

REFERENCES

[1] Mellouli, S., Dhaou, H., Askri, F., Jemni, A. and Nasrallah, S.B., 2009. Hydrogen storage in metal hydride tanks equipped with metal foam heat exchanger. International Journal of Hydrogen Energy, Cilt. 34, s. 9393-9401.
[2] Dhaou, H., Souahlia, A., Mellouli, S., Askri, F., Jemni, A., & Nasrallah, S. B. (2010). Experimental study of a metal hydride vessel based on a finned spiral heat exchanger. international journal of hydrogen energy, Cilt. 35, s. 1674-1680.
[3] Souahlia, A., Dhaou, H., Mellouli, S., Askri, F., Jemni, A. and Nasrallah, S.B., 2014. Experimental study of metal hydride-based hydrogen storage tank at constant supply pressure. international journal of hydrogen energy, Cilt. 39, s. 7365-7372.

WHEC-2022

23rd World Hydrogen Energy Conference

TRACK 7.
FUEL CELLS: PEMFC

TRACK 7. FUEL CELLS: PEMFC

#16 COMPACT FUEL CELL SYSTEM WITH DIESEL REFORMING	651
#20 ON THE ORIGIN OF FUEL-CELL CATALYST-LAYER LOCAL RESISTANCES	654
#27 THERMAL MANAGEMENT OF EDGE-COOLED 1 kW PORTABLE PROTON EXCHANGE MEMBRANE FUEL CELL STACK	657
#30 ELECTROSPUN HYBRID ELECTRODES WITH LOW PLATINUM LOADING FOR PEM FUEL CELLS	660
#44 SYNTHESIS AND INVESTIGATION OF THE Pt-DECORATED POLYPYROLLE NANOTUBES IN PEM FUEL CELLS	663
#45 PREPARATION OF ELECTROCONDUCTIVE THERMALLY EXPANDED GRAPHITE FOR PEM FUEL CELLS' COMPOSITE BIPOLAR PLATES	666
#54 MASS TRANSFER ANALYSIS OF MICROPOROUS LAYERS FOR POLYMER ELECTROLYTE FUEL CELLS USING PORE NETWORK MODEL	669
#65 DYNAMIC MODELING OF A RESIDENTIAL INTEGRATED PEMFC-BASED MICRO-CHP SYSTEM	672
#79 DESIGN AND INVESTIGATION OF A VARIABLE-NOZZLE EJECTOR FOR A 120 kW PEMFC STACK	675
#91 GIANTLEAP PROJECT: DEVELOPMENT OF A FUEL CELL RANGE EXTENDER FOR A BATTERY ELECTRIC BUS	678
#96 MULTI-OBJECTIVE OPTIMIZATION OF A TURBINE IMPELLER FOR FUEL CELL VEHICLES	681
#103 SYNTHESIS AND CHARACTERIZATION OF MWCNT-SUPPORTED PBI MEMBRANES FOR HT-PEM FUEL CELLS	684
#110 DEVELOPMENT AND TESTING OF A PROTON EXCHANGE MEMBRANE FUEL CELL STACK ENVISIONING UNMANNED AERIAL VEHICLE APPLICATIONS	687
#124 EXPERIMENTAL DYNAMIC LOAD CYCLING AND CURRENT DENSITY MEASUREMENTS OF A PARALLEL SERPENTINE PEMFC DESIGN	690
#143 OPTIMIZING FUEL CELL MEMBRANES THROUGH THICKNESS AND CATION DOPING	693
#147 MODELING OF AN ASSISTED COLD START OF A PEMFC COUPLED WITH A METAL HYDRIDE REACTOR	696
#163 COMBINED NUMERICAL AND EXPERIMENTAL ANALYSIS OF LIQUID WATER DISTRIBUTION INSIDE PEMFCs	699
#190 TOPOLOGY OPTIMIZATION OF RADIAL FLOW FIELD IN CIRCULAR PEM FUEL CELLS	702
#222 INVESTIGATION ON AIRFLOW PERFORMANCE OF OPEN CATHODE PROTON EXCHANGE MEMBRANE FUEL CELL	705
#230 EFFECT OF PLATINUM PARTICLE GRADIENT DISTRIBUTION IN LOW PLATINUM LOADING CATHODE CATALYST LAYER ON MEA PERFORMANCE	708
#262 SURFACE TOPOGRAPHY EVALUATION DURING LONG-RUN MICRO-STAMPING OF BPPs AND ITS EFFECT ON CORROSION AND CONTACT RESISTANCE CHARACTERISTICS	711
#276 HIGHLY EFFICIENT LOW METAL LOADING NANOSTRUCTURED ELECTROCATALYSTS	714
#288 EFFECTS OF CATALYST LOADING ON THE PERFORMANCE IMPROVEMENT OF PEMFCs APPLYING A MAGNETIC FIELD	717
#297 EFFECT OF CHITOSAN ON THE CORROSION INHIBITION FOR ALUMINIUM ALLOY IN H_2SO_4 MEDIUM	720
#305 DESIGN, INTEGRATION AND VALIDATION OF A TESTING SETUP FOR PEMFC STACK CHARACTERISATION AT HEAVY DUTY AND MARITIME LOAD PROFILES	723
#320 EXPERIMENTAL STUDY OF MODIFIED POLYBENZIMIDAZOLE/ PHOSPHONATED POLYVINYL ALCOHOL BLEND MEMBRANE FOR FUEL CELL OPERATIONS	726
#321 INTELLIGENT MONITORING OF HYDROGEN/VANADIUM REDOX FLOW BATTERY	729
#322 DEVELOPMENT OF MONITORING TOOL FOR HIGH VOLTAGE PROTON EXCHANGE MEMBRANE WATER ELECTROLYZE	731
#341 COMPARATIVE STUDY ON THE EFFECT OF SELECTED DISPERSION TECHNOLOGIES FOR FUEL CELL INK PREPARATION ON THE OVERALL PEMFC PROCESS CHAIN	733

#371 INFLUENCE OF OPERATING PARAMETERS ON THE COLD START OF POLYMER ELECTROLYTE FUEL CELL SYSTEMS FOR TRANSPORTATION AND AEROSPACE APPLICATIONS	736
#372 INVESTIGATIONS ON THE MICRO-SCALE SURFACE INTERACTIONS AND TRIBOLOGICAL SIZE EFFECT IN MICRO-STAMPING OF SS316L SHEETS	739
#385 SYNTHESIS AND CHARACTERIZATION OF CATIONIC MEMBRANES WITH POLY(INDENE) SULPHONATED POLYELECTROLYTE FOR FUEL CELL APPLICATION	742
#386 USE OF TWO-PHASE COOLING FOR THE FUEL CELL SYSTEM	745
#405 TWO-DIMENSIONAL SIMULATION OF COLD START PROCESS FOR PEMFC STACK WITH VARIOUS CURRENT LOADING MODES	748
#418 AIR SUPPLY MODULE FOR PRESSURIZING FUEL CELLS IN AIRBORNE APPLICATIONS	751
#423 THE OPTIMISATION OF GRAPHENE-BASED MICROPOROUS LAYERS FOR POLYMER ELECTROLYTE FUEL CELLS	754
#1454 A STUDY ON CORROSION DURABILITY IMPROVEMENT OF CrAl COATED METAL BIPOLAR PLATE FOR PEMFC BY 3D LASER CLADDING METHOD	758
#1455 INVESTIGATION OF WASTE HEAT RECOVERY FROM PROTON EXCHANGE MEMBRANE FUEL CELL USING ORGANIC RANKINE CYCLE WITH ZEOTROPIC	761
#1457 NUMERICAL INVESTIGATION ON THE EFFECTS OF INHOMOGENEOUS GAS DIFFUSION LAYER AND IMPACT OF INTERFACIAL CONTACT RESISTANCE ON PERFORMANCE OF POLYMER ELECTROLYTE FUEL CELLS	763
#1461 PERFORMANCE EVOLUTION OF PEM FUEL CELLS WITH STRAIGHT AND WAVY PARALLEL FLOW CHANNELS OF VARIOUS WAVELENGTHS USING CFD SIMULATION	766
#1464 SUPERHYDROPHOBIC FLUORINATED CARBON FOR IMPROVED MICROPOROUS LAYERS IN POLYMER ELECTROLYTE FUEL CELLS	769
#1489 INVESTIGATING THE WATER FLOODING EFFECTS ON THE PERFORMANCE OF LOW-TEMPERATURE PROTON EXCHANGE MEMBRANE FUEL CELLS	772
#1493 MICROWAVE-ASSISTED SYNTHESIS OF POROUS CARBON FROM PEANUT SHELLS	775
#1494 FACILE SYNTHESIS FOR POROUS CARBON FROM BIOMASS SUGARCANE BAGASSE	778
#1498 EVALUATION OF ETHANOL MICROFLUIDIC DEVICE AT LOW ELECTROCATALYSIS LOADING	781
#1507 GRAPHITE BASED-POLYMER COMPOSITE BIPOLAR PLATES FOR PEM FUEL CELLS	783
#1510 HIGHLY POROUS PT-CEO_2-C THIN FILM CATALYST PREPARED BY MAGNETRON CO-SPUTTERING FOR PROTON EXCHANGE MEMBRANE FUEL CELLS	786
#1530 EXPERIMENTAL VALIDATION OF A 2-D MULTI-LAYER MODEL FOR FUEL CELL DIAGNOSIS USING MAGNETO-TOMOGRAPHY	789
#1551 NUMERICAL ANALYSIS OF LIQUID WATER PERMEATION PROCESS THROUGH THE DEFORMED GAS DIFFUSION LAYER OF PEM FUEL CELL	793
#1558 THE IMPACT OF AMBIENT TEMPERATURE ON HIGH-TEMPERATURE PEM FUEL CELL	796
#1567 MODELING OF H_2/BR_2 REDOX FLOW BATTERY IN FUEL CELL MODE	799
#1569 DEVELOPMENT OF HYDROGEN RANGE EXTENDER FOR A SPECIALIZED MULTIPURPOSE VEHICLE	802
#1570 TRANSIENT CHARACTERISTICS OF IN-PLANE WATER TRANSPORT IN THE GAS DIFFUSION LAYER OF PEM FUEL CELLS	805
#1579 GDL DEGRADATION EFFECT ON FLOWS INSIDE FLOW CHANNEL ON POLYMER ELECTROLYTE MEMBRANE FUEL CELL	808
#1585 A SCALABLE ANALYTICAL MODEL FOR RAPID MULTIPHYSICAL ANALYSIS AND STRUCTURAL OPTIMIZATION OF PEM FUEL CELLS	811
#1590 STUDY OF CATALYST LOADING AND GDL POROSITY GRADIENT VARIATION EFFECT TO PEMFCs PERFORMANCE THROUGH RECURRENT NEURAL NETWORK (RNN) DATA-DRIVEN ASSISTED MODELLING	814
#1591 SULFONATED SILICA/NAFION® BASED COMPOSITE ELECTROSPUN MEMBRANES FOR PEM FUEL CELLS	816

#1596 PREPARATION OF KAOLIN AND BENTONITE ADDED NAFION COMPOSITE MEMBRANES	818
#1617 MODELING OXYGEN TRANSPORT IN CARBON SUPPORT MICROSTRUCTURE OF PROTON EXCHANGE MEMBRANE FUEL CELL ELECTRODES USING PORE NETWORKS	821
#1623 OPTIMIZATION OF CHARACTERIZATION ROUTINES FOR CARBON BLACKS USED IN ENERGY RELATED APPLICATIONS	824

WHEC-2022
23rd World Hydrogen Energy Conference
June 26-30, 2022 - Istanbul

#16
COMPACT FUEL CELL SYSTEM WITH DIESEL REFORMING

[1*] *Remzi Can Samsun,*[1] *Matthias Prawitz,* [1] *Andreas Tschauder,* [1] *Jan Meißner,* [1] *Joachim Pasel,* [1] *Ralf Peters*
[1] Forschungszentrum Jülich, Institute of Electrochemical Process Engineering (IEK-14), 52425, Jülich, Germany

*Corresponding author e-mail: r.c.samsun@fz-juelich.de

ABSTRACT

A compact auxiliary power unit in the 7.5 kW_e class was developed. The system is composed of two high-temperature PEFC stacks operated on reformate produced by a diesel fuel processor and the corresponding balance of plant components. In order to maximize the power density, each fuel processor component is designed as a multifunctional reactor. The stacks and the fuel processor are combined using manifolds applying additive manufacturing technology. Using the developed reactors, manifolds, as well as the selected fuel cell stacks and the balance of plant components, a compact system was designed and manufactured with a volume of 187.5 l. Preparatory experiments with the fuel processor focused on the validation of the system concept, aiming to maximize the fuel conversion while keeping the CO level in the fuel processor outlet below 1% for the ideal operation of the high-temperature PEFC. With various diesel and kerosene fuels, it was possible to identify the best operating parameters with each fuel at a very high fuel conversion of > 99.95% at full load of the fuel processor. In each experiment, the CO concentration remained stable and below the target value mentioned above.

Keywords: autothermal reforming, fuel cell system, fuel processor, HT-PEFC, jet fuel

INTRODUCTION

This study focuses on the development process of a compact fuel cell system using a combination of autothermal diesel reforming and high-temperature PEFC technologies. The motivation for such a system is to extend the availability of the fuel cell technology for areas in which it is hard to realize a hydrogen infrastructure. Today, the wide availability of diesel and jet fuels makes such a system concept attractive for mobile and distributed power supply. In the future, synthetic fuels from biomass or hydrogen produced from renewable electricity can be utilized. The proof-of-concept was already demonstrated in a first generation with an integrated 5 kW_e system [1]. The current development, however aims to achieve the power density and start-up time targets of U.S. DOE for diesel-based fuel cell auxiliary power units (APU). According to these targets, the complete fuel cell APU must show a minimum power density of 40 W_e/l and 30 min start time [2]. Despite the big progress in diesel reforming in the recent years [3-6], a fuel cell operated on diesel reformate brings a high level of challenges on the systems level [7, 8]. The main issues are start-up, load change, shutdown as well as stability and the overall complexity of the process. Here, we firstly present the system layout and its final design. In the second part, we report on results from preparatory experiments from the fuel processing system.

SYSTEM LAYOUT AND DESIGN

To achieve a compact fuel cell system, multifunctional fuel processing reactors were developed. According to this approach, several system functions are integrated in the reactors of the fuel processing system. In addition to its main function of producing a hydrogen rich reformate, the reformer also includes a superheater, a mixer for producing a saturated steam for further heat exchange and an electrical heating wire for the start. The shift reactor can on one side reduce the CO content of the reformate to ideally 1% in two stages placed under a single reactor shell before the stack inlet. On the other side the reactor includes components such as evaporation cooling between stages, an electrical heating wire and a heat exchanger to cool the reformate and heat the cathode air before the stack inlets. Finally, the catalytic burner has the function of combusting the remaining H_2, CO and CH_4 present in the anode off-gas during normal operation and system start. In addition to its main function, this reactor also includes several heat exchangers in order to pre-heat the reforming air, superheat a big share of reforming water and heat up the heat transfer fluid to heat the fuel cell during start-up. Additionally, a glow plug is integrated in this reactor for start-up. The system layout presented in Fig. 1 (left side) shows the above-explained system design approach together with the conceptual design of the reactors. On the right hand side, Fig. 1 shows the 3D design of the system including the fuel processing system, the fuel cell stacks and the balance of plant components. Two HT-PEFC fuel cell stacks are used in the system, which are originally designed for commercial methanol-fueled systems [9]. In order to combine both stacks effectively, manifold plates were developed and optimized with CFD simulations, and finally produced via laser-additive manufacturing. The balance of plant components include turbo-compressors, pressure sensors, a micro diesel pump, diaphragm pumps, flow meters, check valves, relief valves, filters, coolers, a peripheral pump, fluid reservoirs and further valves. Following

a tight packaging approach analogous to automotive architectures, the APU volume could be restricted to 187.5 l. Based on the previous experience with similar stack technology, a power output of 7.5 kW_e is expected. These figures result in the target power density of 40 W_e/l.

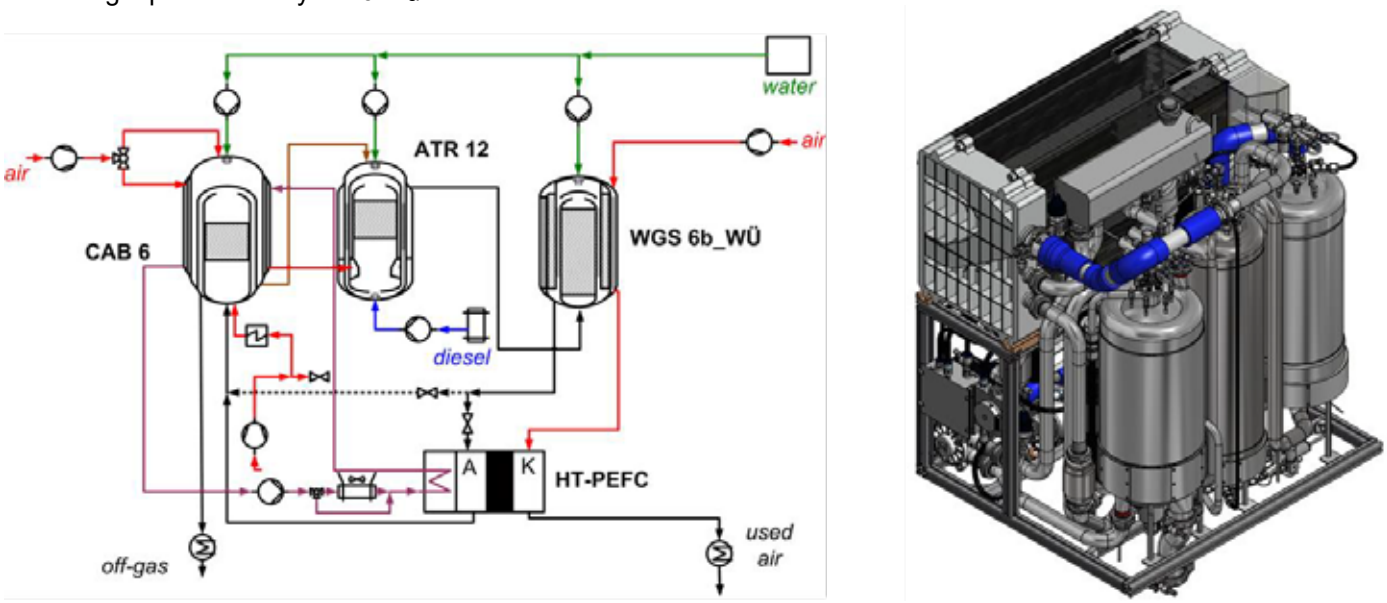
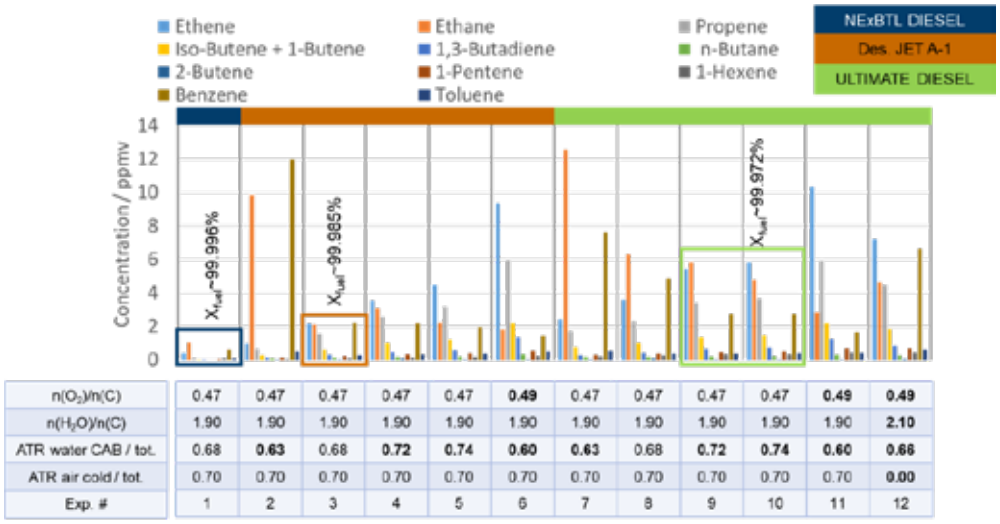


Fig. 1. System layout and CAD design of the HT-PEFC system in the 7.5 kW_e power class including the diesel fuel processor and the balance of plant components.

RESULTS AND DISCUSSION

In preparatory experiments, several system aspects were tested, validated and optimized. One challenge of the system was to identify the best operation parameters with various fuels to maximize the fuel conversion on one side and to keep the CO content at the target level of < 1% at the anode inlet on the other side. For this purpose, various fossil-based and non-fossil based diesel and kerosene fuels including desulphurized Jet A-1, NExBTL diesel and Aral Ultimate diesel were utilized. Fig. 2 shows the results from 12 experiments focusing on the undesired by-products at the reformer outlet using different fuels and operation parameters. In all of the experiments, the reformer was operated at 100% load with 2.7 kg h^{-1} fuel and the CO content could be kept below the target. Due to the high level of system integration, all reactors are thermally coupled with each other. The reformer can however be considered as the key component of the system since it defines the main control parameters, which are the molar O_2/C ratio and the H_2O/C ratio. In addition, two additional ratios must be tuned, which influence the reformer - catalytic burner coupling and the reformer - shift reactor coupling. The first one is the ratio of water superheated in the burner to the total amount of water used for reforming. Higher ratios increase the temperature level in the reformer, which can have a positive effect on the reforming processes, but simultaneously the inlet temperature of the shift reactor increases, which might be negative for achieving the target CO level in the shift steps. The second is the ratio of cold air feed to the reformer to the total amount of reforming air. Since the remaining part of air is pre-heated to the same temperature with steam in the reformer, higher ratios lead to the opposite effect compared to the first case. Using NExBTL diesel, it was possible to achieve a very high conversion level in the reformer with all by-products below 2 ppmv. A switch to desulphurized Jet A-1 showed a very slight increase in the by-products with the same operation parameters, where ethane, ethene and benzene concentrations reached the 2 ppmv level. Still, further experiments were performed to check, if even lower concentrations can be achieved. Operation with lower heat input to the ATR with a reduced share of superheated steam (exp. 2) led to a sharp increase in ethane and benzene concentrations. Higher heat input (exp. 4&5) led to lower concentrations, which were however not better than those with standard parameters (exp. 3). Operation with higher oxygen to carbon ratio (exp. 6) did not lead to a better performance. After switching to Ultimate diesel, the same parameters were applied in experiments 7 – 11 as in experiments 2 – 6. The overall trend being the same, Fig. 2 shows that the measured concentrations are higher than those with desulphurized Jet A-1. The lowest concentrations were observed in experiments 9 and 10. Therefore, it can be concluded that the higher heat input to ATR had a positive effect in this case. A stronger increase in terms of increasing the O_2/C ratio in exp. 11 or even increasing the H_2O/C ratio and pre-heating the complete reforming air in exp. 12 did not improve the conversion further. As a result, experiments 1 (NExBTL), 3 (Jet A-1) and 9 and 10 (Ultimate), resulted in the parameter combinations leading to maximum conversion with each fuel used.



$n(O_2)/n(C)$	0.47	0.47	0.47	0.47	0.47	**0.49**	0.47	0.47	0.47	0.47	**0.49**	**0.49**
$n(H_2O)/n(C)$	1.90	1.90	1.90	1.90	1.90	1.90	1.90	1.90	1.90	1.90	1.90	**2.10**
ATR water CAB / tot.	0.68	**0.63**	0.68	**0.72**	**0.74**	**0.60**	**0.63**	0.68	**0.72**	**0.74**	**0.60**	**0.66**
ATR air cold / tot.	0.70	0.70	0.70	0.70	0.70	0.70	0.70	0.70	0.70	0.70	0.70	**0.00**
Exp. #	1	2	3	4	5	6	7	8	9	10	11	12

Fig. 2. Analysis of the side products of autothermal reforming using NExBTL, des. Jet A-1 and Aral Ultimate for different combinations of operation parameters.

CONCLUSIONS

In this work, the design of a compact fuel processor based on diesel reforming and high-temperature polymer electrolyte fuel cells was presented. Furthermore, results from preparatory experiments with the fuel processing system were shown.

The focus of the system design was given to achieving the power density and start-up time targets defined by U.S. DOE. After a high-level engineering of the complete system components, it was possible to design and manufacture a 7.5 kW_e system including all balance of plant components at a volume of 187.5 l achieving the target power density. Parallel to system design, operation parameters were optimized using various fuels. It was possible to identify proper operating parameters, which led to a very high fuel conversion of > 99.95% at full load, at the same time keeping CO content at the shift outlet < 1% for stable operation of a HT-PEFC with reformate gas. As the next step, the developed fuel cell system was characterized. The results from the operation of the complete system using renewable diesel fuel will be presented in the conference talk, with a focus on achieved power density and start-up time compared with the DOE targets.

REFERENCES

1. Samsun RC, Pasel J, Janßen H, Lehnert W, Peters R, Stolten D. 2014. Design and test of a 5 kW_e high-temperature polymer electrolyte fuel cell system operated with diesel and kerosene. Applied Energy 114:238-49.
2. Spendelow JS, Papageorgopoulos DC. 2016. Application Requirements/Targets for Fuel Cell APUs. In: Fuel Cells : Data, Facts and Figures, Edited by Stolten D, Samsun RC, Garland N. Weinheim: Wiley-VCH; p. 197-201.
3. Xu X, Li P, Shen Y. 2013. Small-scale reforming of diesel and jet fuels to make hydrogen and syngas for fuel cells: A review. Applied Energy 108:202-17.
4. Meißner J, Pasel J, Peters R, Samsun RC, Thimm F, Stolten D. 2019. Quantitative analysis of sub-ppm traces of hydrocarbons in the product gas from diesel reforming. Int J Hydrogen Energ 44:4020-30.
5. Pasel J, Samsun RC, Tschauder A, Peters R, Stolten D. 2017. Advances in autothermal reformer design. Applied Energy 198:88-98.
6. Lee K, Han G, Cho S, Bae J. 2018. Pressurized diesel fuel processing using hydrogen peroxide for the fuel cell power unit in low-oxygen environments. J Power Sources 380:37-45.
7. Engelhardt P, Maximini M, Beckmann F, Brenner M, Moritz O. 2014. Coupled operation of a diesel steam reformer and an LT- and HT-PEFC. Int J Hydrogen Energ 39:18146-53.
8. Samsun RC, Prawitz M, Tschauder A, Pasel J, Peters R, Stolten D. 2019. An autothermal reforming system for diesel and jet fuel with quick start-up capability. Int J Hydrogen Energ 44:27749-64.
9. https://serenergy.com/wp-content/uploads/2019/10/H3-5000-Datasheet.pdf. Methanol Power System H3 5000. Accessed on 21.11.2019

WHEC-2022
23rd World Hydrogen Energy Conference
June 26-30, 2022 - Istanbul

#20
ON THE ORIGIN OF FUEL-CELL CATALYST-LAYER LOCAL RESISTANCES

*A. Chowdhury, S. A. Berlinger J. Petrovick, A. Kusoglu, C. J. Radke, and A. Z. Weber**
Lawrence Berkeley National Laboratory, Energy Technologies Area, 1 Cyclotron Rd, Berkeley, CA 94720, USA

*Corresponding author e-mail: azweber@lbl.gov

ABSTRACT

To achieve high mass activity at low platinum loading, the local transport resistance endemic to polymer-electrolyte fuel cells must be ameliorated. This transport resistance is intimately linked to interactions between and within the proton-conducting polymer (ionomer) and the metal electrocatalyst in the porous catalyst layers. In this talk, the origin and impact of this resistance will be discussed. Specifically, both *in-situ* measurements using limiting current and *ex-situ* ones using a novel microelectrode setup and other techniques will discussed. Such studies provide a holistic view of the resistance components including interfacial effects and transport phenomena. Finally, discussion on the origin of these resistances during catalyst-layer formation and ink processing will be detailed. Throughout, theory will compliment the experimental studies, and various mitigation pathways to decrease the local resistance will be suggested.

Keywords: Fuel cell, resistance, transport phenomena, ionomer, microelectrode

INTRODUCTION

To commercialize successfully polymer-electrolyte fuel cells (PEFCs), the cost must be reduced without sacrificing performance and lifetime. Such cost reductions come about through simplification of balance of plant, increasing cell and stack durability and lifetime, improving cell performance. Of particular importance reducing the amount of the relatively expensive platinum-group-metal (PGM) catalysts [1]. As discussed previously, it is thought that current architectures and materials reach a limit, below which unacceptable performance losses are realized as the PGM loading is decreased [2]. This limit is believed to be due to interactions at the local level where the thin-film proton-conducting polymer (i.e., ionomer) interacts and covers the electrocatalyst particles composed of nanoparticles of Pt on larger carbon particles. These interactions including restricted reactant gas permeation through the ionomer thin-film [3] as well as adsorption and poisoning of Pt sites by the sulfonic-acid moieties endemic in the ionomer.

To quantify the local catalyst-layer resistance and its constituents, there are various methods that have been used. These approaches include analyses on both catalyst layers as well as with model systems. For the former, limiting-current analysis using both hydrogen and oxygen have been implemented. For the latter, ionomer thin-film studies in terms of structure/function relationships have been conducted using planar substrates and microelectrodes. Microelectrodes are sub-milometer electrodes that allow well-defined electrochemical measurements to be performed in a non-liquid (that is, a humidified solid ionomer) electrolyte environment.

In this work, multiple techniques will be used to explore the impact and origin of the local transport resistances in standard fuel-cell electrodes. In addition, a novel microelectrode setup will be described that overcomes several existing limitations in the literature.

EXPERIMENTAL

For this study, Nafion or 3M ionomers were used at different equivalent weights (EWs) to investigate the effect of sidechain density and sidechain length. Vulcan XC72 Pt/C was used as the catalyst.

All electrochemical cell measurements (ECSA, CO displacement, polarization, etc.) were performed with an SP-150 potentiostat with a low current card (Bio-Logic, France). Gases were fed and humidified using a fuel-cell test stand, which also controlled temperature. CL transport resistance was estimated from limiting current measurements using the H_2-pump setup and test protocol as described in [4] using 2% or 1000 ppm H_2 or D_2 in Ar.

Model studies were conducted using analogs of the catalyst-layer interfaces including casting ionomer solutions onto planar platinum and silicon substrates to perform QCM-D, GISAXS, ellipsometry, and conductivity. In addition, solutions were analyzed for properties using isothermal titration calorimetry (ITC), DLS, and zeta potential. Finally, a microelectrode cell was designed and used for permeation experiments through the thin films using a 50-µm platinum microelectrode and small cell heated compartment.

RESULTS AND DISCUSSION

Figure 1 shows the catalyst-layer gas-transport resistance as a function of ionomer:carbon ratio measured from H_2 pump for different ionomer EWs. At low Pt loadings, as was maintained for the examined samples, CL gas transport resistance is mainly due to local transport resistance caused by the ionomer thin film. Thus, the linear increase in gas-transport resistance with ionomer content for the measured samples can be attributed to increased transport resistance through thicker ionomer thin-films that form due to the presence of more ionomer.

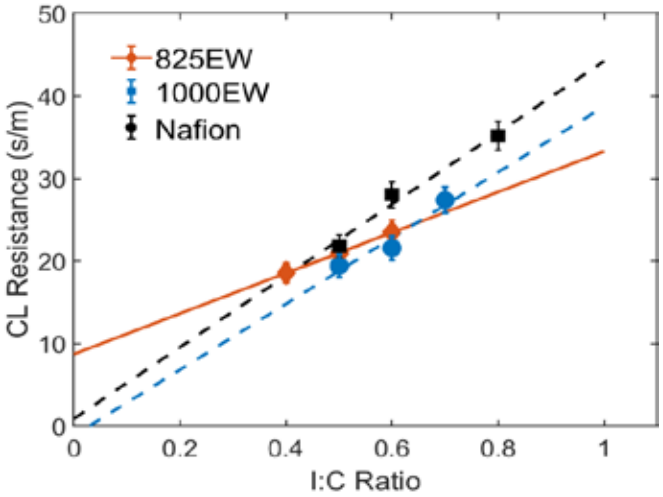


Figure 1. Catalyst layer resistance from limiting current experiments for three different equivalent weight ionomers as a function of ionomer:carbon ratio.

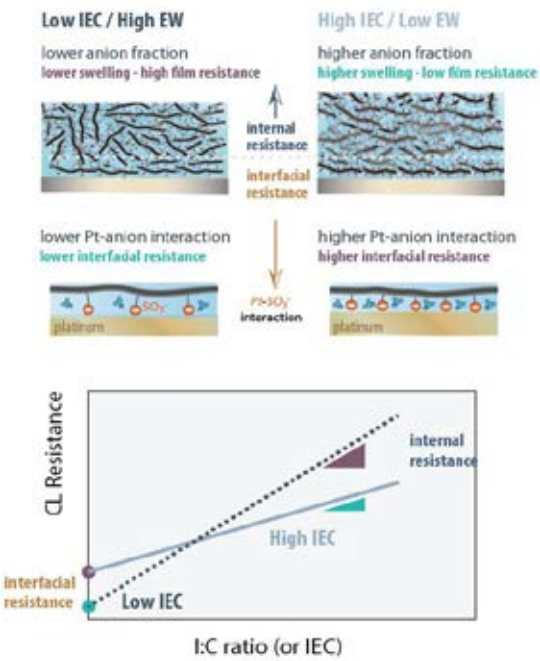


Figure 2. Schematic of resistance interpretation for different ionomer equivalent weights in terms of interfacial and bulk transport components.

Utilizing the analytical model developed by Schuler et al. [4], we divide the overall CL gas-transport resistance into transport and interfacial components. The transport component is due to gas transport through the ionomer thin-film, while the interfacial component is due to catalyst poisoning from sulfonate/Pt interactions. The interfacial resistance is proportional to the intercept and the slope is proportional to transport resistance (i.e, inversely proportional to permeability). Low EW ionomer samples demonstrate higher interfacial resistance and lower

transport resistance indicating more surface interactions and higher gas permeability, respectively. These results agree with model compound trends in that thinner films demonstrate a more structured morphology and lower permeabilities and lower water uptake as measured by the *ex-situ* studies. Similarly, the lower EW samples exhibited sharper morphology in GISAXS, again indicating more ordering and interactions that track with the higher interfacial resistance. Figure 2 shows schematically these trends and explains the experimental observation.

CONCLUSIONS

In this work, both ex-situ model studies of ionomer thin films and in-situ cell studies demonstrate that the local mass-transport resistances at low loadings depend on the ionomer chemistry and are comprised of both a transport dominated by gas permeation and an interfacial components dominated by interactions between the sulfonic-acid moieties and the platinum surface. It is shown that lower equivalent weights cause higher interfacial and lower transport constituents of the local resistance. Furthermore, these interactions are due to ionomer morphology that is a function of the original solvent environment during catalyst-layer formation.

ACKNOWLEDGEMENTS

This work was supported by the Million Mile Fuel Cell Truck Consortium (M2FCT) of Energy Efficiency and Renewable Energy, Hydrogen and Fuel Cell Technologies Program of the U.S. Department of Energy under Contract No. DE-AC02-05CH11231 and by CRADA agreement between Lawrence Berkeley National Laboratory and Toyota Motor Company.

REFERENCES

1. Fuel Cell Technologies Office Multi-Year Research, Development and Demonstration Plan, U.S. Department of Energy, 2018.
2. Weber AZ and Kusoglu A. 2014. Unexplained transport resistances for low-loaded fuel-cell catalyst layers, J. Materials Chemistry A 2:17207-17211.
3. Kusoglu A and Weber AZ. 2017. New Insights into Perfluorinated Sulfonic-Acid (PFSA) Ionomers. Chemical Reviews 117:987-1104.
4. Schuler T, Chowdhury A, Freiberg AT, Sneed B, Spingler FB, Tucker MC, More KL, Radke CJ, and Weber AZ. 2019. Fuel-Cell Catalyst-Layer Resistance via Hydrogen Limiting-Current Measurements. Journal of the Electrochemical Society 166:F3020-F3031.

WHEC-2022
23rd World Hydrogen Energy Conference
June 26-30, 2022 - Istanbul

#27

THERMAL MANAGEMENT OF EDGE-COOLED 1 kW PORTABLE PROTON EXCHANGE MEMBRANE FUEL CELL STACK

[1*] Ivan Tolj, [1] Željko Penga, [1] Frano Barbir
[1] Faculty of Electrical Engineering, Mechanical Engineering and Naval Architecture
University of Split, R. Boskovica 32, 21000 Split, Croatia

*Corresponding author e-mail: itolj@fesb.hr

ABSTRACT

In order to study thermal management influence on the performance od 1kW edge-cooled proton exchange membrane fuel cell stack without external humidification comprehensive numerical analyses are conducted. Two numerical approaches are considered and compared for a prescribed load profile: (i) lumped model and novel (ii) real-time transient computational fluid dynamics model incorporating realistic modeling of forced air convection on the edge-cooling of the stack. The developed computational fluid dynamics model is used to study the influence of (i) bipolar plate materials (ii) operating delta pressure along the flow field and (iii) different cooling fin configurations on the water and heat balance inside the stack. The results indicate that (i) maximal and average temperatures of the stack are almost linearly correlated to the thermal conductivity of bipolar plate materials and maximal temperatures can be significantly higher (ii) the operating delta pressure can be manipulated to increase the performance of the stack and (iii) the cooling fin redesign has major influence on the overall temperature uniformity across the stack. Additionally, the heat transfer between the stack and metal hydride tank is studied.

Keywords: PEM fuel cell, Portable stack, Water and heat management

INTRODUCTION

Air-cooled proton exchange membrane (PEM) fuel cell stacks are gaining momentum as power sources for portable applications such as electric bikes, unmanned aerial vehicles (UAVs), forklifts, etc. Usually the power of portable stacks (PS) is up to several kW [1,2]. Most of the heat generated during PS operation is dissipated into the surrounding atmosphere via forced air convection along the cooling channels or edge-cooling fins, while the higher power stacks require liquid cooling. The emphasis during the design phase of PS is primarily directed towards determining the most suitable material for bipolar plates and the accompanying thermal management. Some of the thermal management objectives are: (i) ensuring the appropriate heat transfer from the stack during startup, i.e. accurately determining the required convection flow rate, to achieve sufficiently high operating temperature from startup at ambient temperature, thus preventing flooding (occurring if the flow rate is high and temperature of the stack is low) or membrane dehydration (occurring if the flow rate is low and temperature inside the stack is high); (ii) ensuring sufficiently high heat removal rates via forced air convection during the operation characterized by stable temperature of the stack, i.e. loosely termed steady-state operation; (iii) ensuring as low as possible temperature difference between the inside and outside portions of the stack by choosing the materials with favorable thermal properties; (iv) properly design the stack and edge-cooling fins to ensure sufficiently high heat removal rates; (v) design the frame for the stack which will ensure that the cooling air is directed to uniformly flow along the edge-cooling fins. In previous studies [3,4] it was shown that the operating temperature inside PEM fuel cell is highly non-uniform and it is not accurate to represent the operating temperature with just one parameter, while at the same time if the temperature profile is controlled it can be exploited to result in high performance of the cell by manipulating the water vapor saturation profile, i.e. relative humidity profile inside the cell. The main contributions of this work to the research field are evident in outlining that the commonly used lumped models can be misleading for dynamic analysis of PEM fuel cell performance due to inability to accurately calculate the maximal temperature inside the stack and this work also outlines under which circumstances the lumped models can be used. This work also presents a novel transient CFD model for analysis of thermal management of PS which gives insight in mass and heat transfer both inside and outside of the cell (internal heat and mass transfer and forced air convection edge-cooling), while other works focus on only one aspect and simplify the other to a significant extent.

MATERIALS AND METHODS

The stack used in this study, Figure 1, was developed by Proton Energy Systems. The stack displays many innovative features including in-flow configuration, cooling and stack clamping. It consists of 60 cells, each with an active area of 65 cm^2. The design is rectangular with 10:1 aspect ratio to allow for efficient heat conduction of the edge of the cells, where fins are extended for cooling.

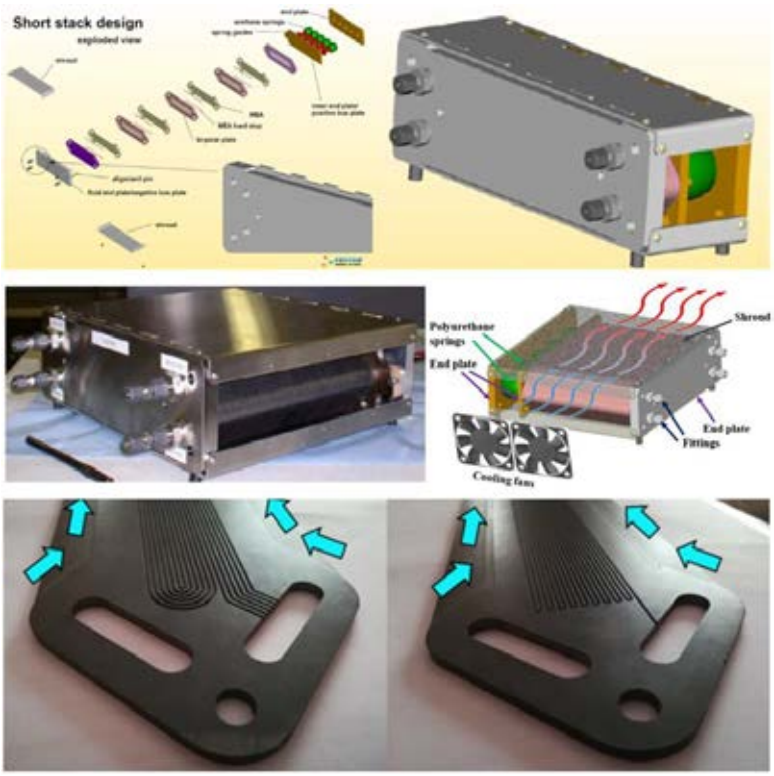


Figure 1. Above: Proton Energy System's short stack exploded view (left) with annotated parts and assembly (right); Middle: Proton Energy System's 1-kW fuel-cell stack (left) and transparent shroud assembly (right); Below: Cathode (left) and anode (right) flow fields with annotated air-coolant flow direction along the edge-cooling fins.

The bipolar plates including the fins are fabricated from a molded polymer/graphite mixture (made by SGL Carbon) with effective thermal conductivity of 20 W m^{-1} K^{-1}. The stack is cooled by air flow along the longer edge of the cells where the fins are located.

RESULTS AND DISCUSSION

The results of the lumped model and CFD analysis are shown in Figure [5]. The cell temperature increases from ambient to steady-state shows similar trends, although the lumped model predicts slightly lower steady-state temperature. The CFD data also indicates that the temperature fluctuations are always present due to the unsteady nature of the flow and modeling of the air as ideal gas, resulting in convective flow and vortex genesis in the wake region behind the stack. The temperature decrease after 5500 s reaches higher minimal value in the CFD model vs. lumped model, and after increasing the current the temperature oscillations of the CFD model are more severe and it can be noted that the steady-state predicted by the lumped model near ca. 10000 s is not yet steady-state when CFD model is observed. The highest difference between the lumped model vs. CFD model is evident after 10000 seconds by comparing the 3 cases. For case (i) the steady-state temperature of the cell in the CFD model is decreased at a slower rate when compared to the lumped model and converges to a significantly higher steady-state value (by ca. 10 °C), and similarly also in case (ii). In case (iii) the fan must be turned on and off approx. 6 times more frequent to keep the stack temperature between the 55 and 60 °C range. The differences are a result of directly calculating the heat transfer coefficient in the CFD analysis vs. fixing the value in the lumped model and a result of modeling the complex flow involving air as ideal gas in the CFD model. Regardless of the differences, it can be noted that the average temperatures predicted by the lumped model and time to reach steady-state are reasonably well predicted by the lumped model but the CFD model is more physically valid therefore it will be used in the following chapters for more detailed analysis.

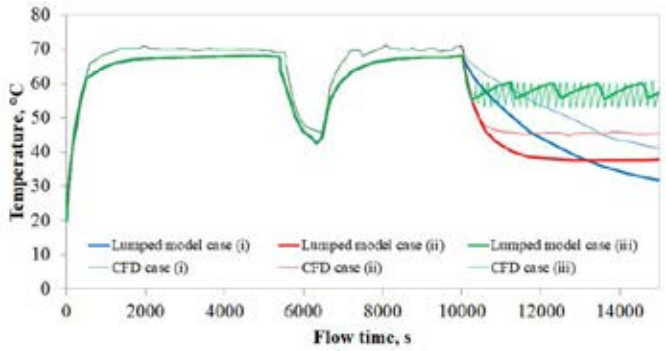


Figure 2. History of cell temperature: lumped model vs. CFD for cases (i), (ii) and (iii).

CONCLUSIONS

The following conclusions are drawn from this work:
(i) although commonly used, the lumped model is not accurate for predicting the temperature of the edge-cooled stacks due to the capability for only predicting the average temperature of the stack, while the maximal temperature can be several tens of degrees higher inside the stack when materials with low thermal conductivity are used, thus leading to severe dehydration of the membrane; (ii) by comparing the average and maximal temperature of the stack for different bipolar plate materials, it can be seen that the outside temperature of the stack is quite similar for graphite (thermal conductivity 20 W m^{-1} K^{-1}) and nickel (thermal conductivity 91.74 W m^{-1} K^{-1}), i.e. 57.53 °C vs 52.41 °C, respectively, during steady-state operation, while the internal maximal temperature of the stack is significantly different (77.36 °C vs. 58.29 °C, respectively), indicating the requirement for carefully determining the appropriate material to be used for production of bipolar plates for edge-cooled stacks; (iii) higher pressure drop along the flow field can be used as a supplementary method for achieving higher performance of the stack since the water vapor saturation profile is pressure-dependent, or the whole stack can be operated at elevated pressure to increase the performance;
(iv) the edge-cooling fin geometry has significant influence on the overall temperature distribution, by redesigning the edge-cooling fins the maximal temperature and average temperature of the stack was reduced from 77.60 °C and 57.53 °C to 63.55 °C and 46.57 °C, respectively, indicating the necessity for careful design of the flow distributors for edge-cooling portable stacks; (v) the developed CFD model can also be used to study the heat transfer between the stack and MH tank. Although the heat generated by the stack was not sufficient to release the required mass flow rate of hydrogen for stack operation at 1 kW power, which was also experimentally demonstrated using similar power air-cooled stack (Nexa 1.2 kW) where 3 MH tanks were used and in that case it was possible to release the required amount of hydrogen from the tanks.

ACKNOWLEDGMENT

The authors of this work would like to acknowledge the support received from the EU Horizon 2020/RISE project “Hydrogen fuelled utility vehicles and their support systems utilising metal hydrides—HYDRIDE4MOBILITY, Project Number: 778307.

REFERENCES

1. Barbir F. 2012. PEM Fuel Cells: Theory and Practice. Waltham, Elsevier.
2. Hoogers G. 2002. Fuel Cells Technology Handbook. Boca Raton, CRC Press LLC.
3. Tolj I, Bezmalinovic D, Barbir F. 2011. Maintaining desired level of relative humidity throughout a fuel cell with spatially variable heat removal rates. International Journal of Hydrogen Energy 20:13105-13113.
4. Penga Z, Tolj I, Barbir F. 2016. Computational fluid dynamics study of PEM fuel cell performance for isothermal and non-uniform temperature boundary conditions. International Journal of Hydrogen Energy 39:17585-17594.
5. Tolj I, Penga Z, Vukicevic D, Barbir F. 2020. Thermal management of edge-cooled 1 kW portable proton exchange membrane fuel cell stack. Applied Energy 257: 114038.

WHEC-2022
23rd World Hydrogen Energy Conference
June 26-30, 2022 - Istanbul

#30

ELECTROSPUN HYBRID ELECTRODES WITH LOW PLATINUM LOADING FOR PEM FUEL CELLS

[1*] Begüm Yarar Kaplan, [2] Bilal Sayyed Said Iskandarani,[2] Naeimeh Rajabalizadeh Mojarrad [1] Alp Yürüm, [1,2] Selmiye Alkan Gürsel

[1] Sabancı University, Faculty of Natural Science and Engineering, 34956, Istanbul, Turkey
[2] Sabancı University Nanotechnology Research and Application Center (SUNUM), 34956, Istanbul, Turkey

*Corresponding author e-mail: begumyarar@sabanciuniv.edu

ABSTRACT

In the present study, sulfonated silica (S-SiO_2) nanoparticles (NPs) which are cheap and stable at low humidity are synthesized and employed in electrode structure of PEM fuel cell. Here, electrospinning is utilized to prepare hybrid fiber PEM fuel cell electrodes containing commercial Pt/C catalyst and S-SiO_2 NPs with poly(vinylidene fluoride) (PVDF) and poly(vinylidene fluoride-*co*-trifluoroethylene) (PVDF-TrFE) binders (carrier polymers). The morphology of electrospun electrodes have been investigated by scanning electron microscopy (SEM) to determine optimum electrospinning conditions to achieve a uniform Pt/C and S-SiO_2 NPs distribution on carrier polymer and fiber thickness. Consequently, catalyst distribution along the nanofibers have also been investigated by transmission electron microscopy (TEM). Moreover, sprayed electrodes are prepared and morphology of electrospun and sprayed electrodes are compared. After obtaining fiber-based hybrid and sprayed electrodes, membrane electrode assemblies (MEA) are prepared and fuel cell tests are performed with using H_2/air at different humidity. In-situ cyclic voltammetry (CV) and impedance analysis have also been performed. These novel electrospun hybrid electrodes possess not only superior PEM fuel cell performance compared to sprayed electrodes but also better performance at low humidity.

Keywords: Electrospinning, Catalyst layer, Electrode, Sulfonated silica, PEM fuel cells

INTRODUCTION

Polymer electrolyte membrane (PEM) fuel cells draw great attention due to their clean operation, high power density and efficiency, compactness and fast start-up and response times [1]. Membrane electrode assembly (MEA) is the heart of the PEM fuel cells. Therefore, development of MEA design and materials is one of the most important research areas. The two main problems of MEA are: i) commonly used perfluorosulfonic acid based membrane/ionomer (commercial Nafion® membrane/ionomer)is very expensive, its ionic conductivity is strongly based on humidity of environment, degrades easily under low humidity conditions; ii) platinum (Pt) which is used as a catalyst in electrode structure is very expensive and its reserves are limited. For that reasons, there are barriers to commercialization of PEM fuel cells. Therefore, development of electrodes with low-Pt loading, non-Pt group metal (non-PGM) catalysts, and alternative hydrocarbon-based/inorganic ionomers has gained growing attention in the past few decades [2, 3]. Compared to other inorganic ionomers, sulfonated silica provides higher surface area, water retention and proton conductivity, even if used very little in the electrode structure [4].

In recent years, electrospinning is frequently used technique to produce nanomaterials especially in the field of energy (for examples; solar cells, fuel cells, lithium ion batteries, lithium sulfur batteries, supercapacitors) [5]. Electrospinning is also a promising technique for creating nanostructured fuel cell electrodes with superior catalyst utilization and long-term durability [6,7]. This technique provides enhancement of the triple phase interface where electrochemical reactions occurred at active catalyst site.

Herein, we report novel hybrid PEM fuel cell electrodes fabricated to provide better Pt utilization and improved water management via electrospinning and sulfonated silica ionomer. Our experiments focused on determining the effects of electrospinning ink composition, carrier polymer, and nanofiber diameter on catalytic activity and fuel cell power output.

MATERIALS AND METHODS

Materials

Johnson Matthey HiSpec 4000 (40% Pt on Vulcan carbon) catalyst was used for all electrodes. High molecular weight (Solef®, Mw = 380,000) polyvinylidene fluoride (PVDF) powder was purchased from Solvay. PVDF-TrFE with 70/30

mol composition powder purchased from PolyK Technologies, LLC. All solvents (Dimethylformamide, acetone, tetrahydrofuran, dimethylacetamide) were supplied from Sigma-Aldrich. Nafion® NR212 membrane and Sigracet 39BC GDL were obtained from FuelCellStore.

Methods

The electrospinning ink was prepared via a facile method in which the DMAc is first added to Pt/C catalyst followed by bath sonication. Afterwards, acetone and sulfonated silica were added to the ink followed by another bath sonication while stirring it intermittently to obtain a homogeneous ink. Finally, the previously prepared carrier polymer solution was added to the ink and the final ink solution was stirred overnight. Tab. 1 shows summary of ink and electrode composition. After preparation of ink, it was loaded into a 5 mL syringe and was electrospun onto the collecting drum collector. Fig.1 shows schematic of electrospinning setup used in experiments. The obtained fiber material was then pealed for further morphological and electrochemical analysis.

MEAs were fabricated using 5 cm^2 electrospun electrodes as a cathode, and sprayed electrodes as an anode (0.1 and 0.2 mg_{pt}/cm^2 loading). Commercial Nafion®212 membrane was located these two electrodes and hot pressed 5 min. hot pressed at 133 °C.

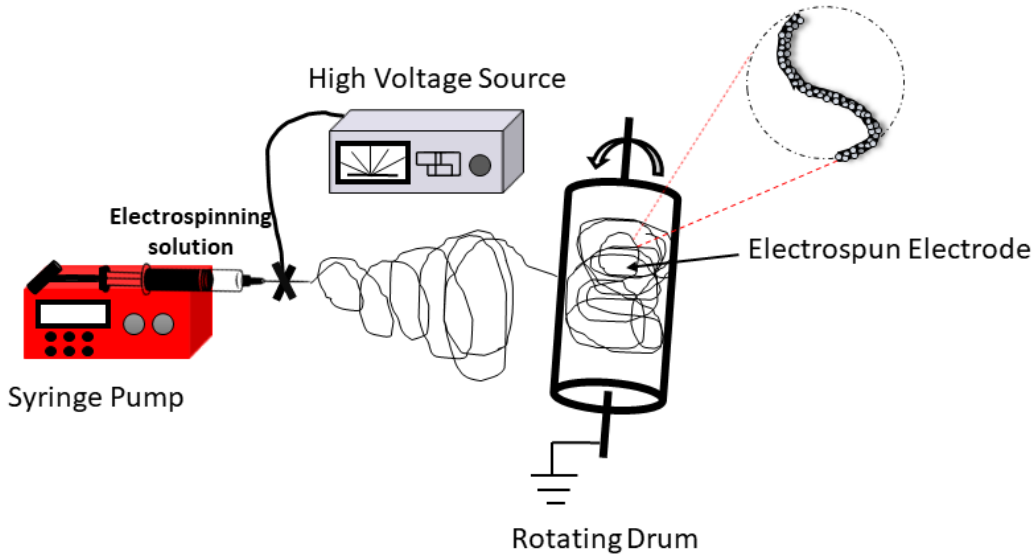


Fig. 1. Schematic diagram of electrospinning set-up and electrospun electrode preparation

Table 1. Summary of ink and electrospun electrode composition

INK	BINDER	Total Solid Ratio Wt. %	ELECTRODE COMPOSITION Wt. %
1	PVDF	12	65 Catalyst, 20 PVDF, 15 S-SiO_2
2	PVDF	13	65 Catalyst, 20 PVDF, 15 S-SiO_2
3	PVDF	15	65 Catalyst, 20 PVDF, 15 S-SiO_2
4	PVDF-TrFE	12	65 Catalyst, 20 PVDF-TrFE, 15 S-SiO_2
5	PVDF-TrFE	13	65 Catalyst, 20 PVDF-TrFE, 15 S-SiO_2
6	PVDF-TrFE	15	65 Catalyst, 20 PVDF-TrFE, 15 S-SiO_2

RESULTS AND DISCUSSION

Morphology of electrospun electrodes are investigated by SEM. Fig. 2.a shows the SEM image of 65Pt/C/20PVDF/15S-SiO_2 (Ink 2) electropun electrode and Fig. 2.b. 65Pt/C/20PVDF-TrFE/15S-SiO_2 (Ink 6). It can be depicted that Pt/C and S-SiO_2 NPs well distributed along the PVDF and PVDF-TrFE carrier. The average fiber diameter is 510 nm for PVDF and 520 nm for PVDF-TrFE carrier.

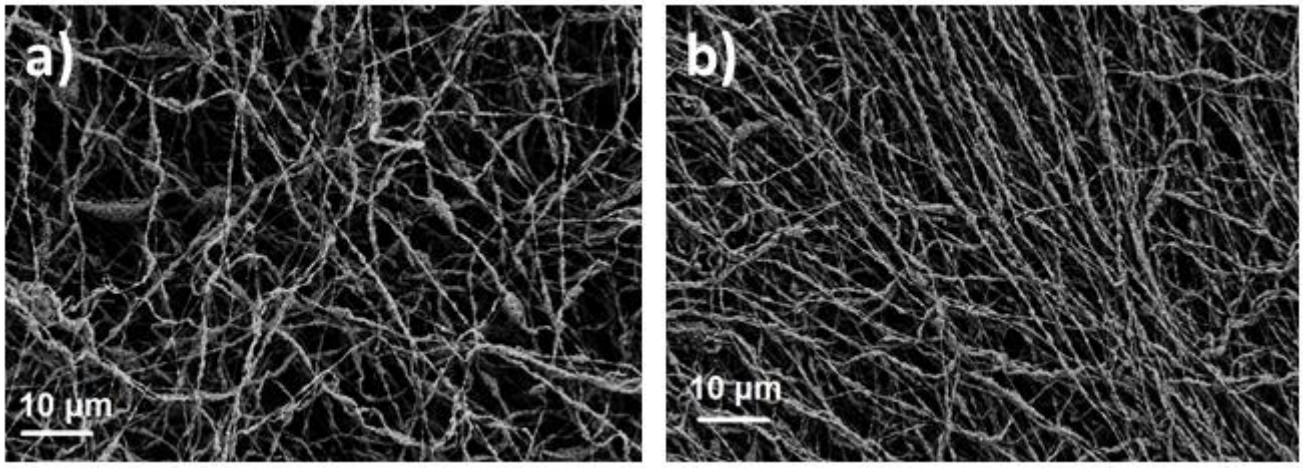


Fig. 2. SEM images of electrospun a) Pt/C/S-SiO_2/PVDF, and b) Pt/C/S-SiO_2/PVDF-TrFE electrodes

CONCLUSIONS

In conclusion, electrospun Pt/C/S-SiO_2/PVDF, and Pt/C/S-SiO_2/PVDF-TrFE electrodes were fabricated, characterized and tested in PEM fuel cell for the first time in literature. Electrospinning is a powerful, robust, and effective technique for fabricating high-performance PEM fuel cell electrode with Pt/C catalyst and S-SiO_2 particles. Optimization of electrospinning solution (solvent, polymer, ionomer (S-SiO_2) amount), and setup parameters (flow rate, voltage, humidity) are crucial to obtain porous and uniform catalyst layers. Carrier polymer type and amount in electrospinning solution are also very important to obtain uniform fiber network, and relatedly high-power output during PEM fuel cell operation. According to obtained result, electrospun Pt/C/S-SiO_2/PVDF and Pt/C/S-SiO_2/PVDF-TrFE show superior electrochemical activity and fuel cell performance compared to sprayed electrode. Moreover, utilization of S-SiO_2 as an ionomer, provides better performance at lower humidity during fuel cell testing. The outstanding performance of electrospun electrodes arise from uniform distribution of Pt/C catalyst, high catalytic activity, and better proton and reactant gas transport to the catalysts during fuel cell operation.

ACKNOWLEDGEMENT

The authors gratefully acknowledge the financial support of The Scientific and Technological Research Council of Turkey (TÜBİTAK) (Grant Number: 217M639)

REFERENCES

1. Sopian K and Wan Daud WR. 2006. Challenges and future developments in proton exchange membrane fuel cells. Renewable Energy 31:719-727.
2. Paddison SJ and Gasteiger HA. 2012. PEM Fuel Cells: Materials and Design Development Challenges. In: Lipman T., Weber A. (eds) Fuel Cells and Hydrogen Production. Encyclopedia of Sustainability Science and Technology Series. Springer, New York, NY
3. Easton EB, Acheampong R, Esfahani RAM, Cavallari VJ, Moghaddam RB, Fruehwald HM, Afsahi F. 2019. Recent Advances with Sulfonated Silica Ceramic Carbon Electrodes for Fuel Cells. ECS Transactions 92(8):559.
4. Eastcott JI and Easton EB. 2015. Investigation of transport mechanisms for sulfonated silica-based fuel cell electrode structures. Journal of The Electrochemical Society 162(7):764-771.
5. Santangelo S. 2019. Electrospun Nanomaterials for Energy Applications: Recent Advances. Applied Sciences 9(6): 1049.
6. Zhang W and Pintauro, P N. 2011. High-Performance Nanofiber Fuel Cell Electrodes. ChemSusChem 4(12):1753-1757.
7. Brodt M, Wycisk R, Dale N, Pintauro, P. 2016. Power output and durability of electrospun fuel cell fiber cathodes with PVDF and nafion/PVDF binders. Journal of The Electrochemical Society 163(5): 401-410.

WHEC-2022
23rd World Hydrogen Energy Conference
June 26-30, 2022 - Istanbul

#44

SYNTHESIS AND INVESTIGATION OF THE Pt-DECORATED POLYPYROLLE NANOTUBES IN PEM FUEL CELLS

[1]Yevheniia Lobko, [1]Yaroslava Novakova, [1]Yurii Yakovlev, [2]Dušan Kopecký, [3]Maryna Vorokhta, [1]Alina M. Darabut, [1]Lucinda Blanco Redondo, [1]Vladimir Matolin, [1]Iva Matolinova*

[1]Charles University, Faculty of Mathematics and Physics, Department of Surface and Plasma Science, V Holešovičkách 747/2, 180 00 Praha 8, Prague, Czech Republic

[2]University of Chemistry and Technology, Technická 5, 166 28 Praha 6, Prague, Czech Republic

[3]Czech Academy of Sciences, Institute of Rock Structure and Mechanics, Department of Geochemistry, V Holešovičkách 41, 180 00 Praha 8, Czech Republic

*e-mail: yevheniia.lobko@mff.cuni.cz

ABSTRACT

The catalysts for fuel cells, based on the platinum-decorated polypyrrolle nanotubes were synthesized. The structure, element contents, electrochemical surface areas of the catalysts' nanoparticles were investigated using TEM, EDX, XPS, RDE analysis. Using obtained catalysts, the catalyst-coated membranes were prepared by ultrasonic spraying techniques. The performance, electrochemical surface areas, high frequency resistance and durability of the CCMs were tested in proton exchange fuel cells.

Keywords: fuel cells, polypyrrolle nanotubes, platinum nanoparticles, performance, durability.

INTRODUCTION

The renewable and clean energy, including fuel cell (FCs) technologies, is very important and promising direction for nowadays [1]. One of the most crucial parts of the fuel cells is catalysts. In this field there are two main tendencies. One of them is decreasing of amount of platinum group metal catalysts [2]. Nevertheless, platinum or platinum-contained catalysts still are the most effective in electrochemical reaction in fuel cells. Other direction is finding durable and stable catalysts' supports. Now, the most popular support for catalysts is carbon, which is lightweight and cheap, but unstable under electrochemical potential. It is lead to low durability and limited working period of the catalysts [2, 3].

In our work we propose to use polypyrrole nanotubes (PPy NTs) as a supports for catalysts for proton exchange membrane FCs. The ordered structure, as well as the presence of nitrogen atoms in the PPy NTs could increase the durability of such type of the catalysts during the *in situ* test in real fuel cells. Moreover, it is also possible to increase the utilization of the platinum, which will lead to the decreasing of metal loading.

EXPERIMENTAL

PPy NTs were synthesized as described in [4]. Pt nanoparticles were deposited on PPy NTs by solvothermal method using ethylene glycol (EG) as the reducing agent. PPy NTs with calculated amount of H_2PtCl_6 precursor and polyvinylpyrrolidone (PVP) as capping agent were ultrasonicated in EG by ultrasound probe (Sonopuls HD 3100, Germany) for 10 min at 20 kHz to obtain the homogeneous dispersion. Than the mixture was added to the reactor and heated at 160 °C under continuous stirring during 1 h. After cooling to the room temperature the dispersion was centrifugated, cleaned with a plenty of water and dried at 60 °C.

RESULTS AND DISCUSSION

The structure of the platinum-decorated PPy NTs was investigated using TEM measurements. As you can see from fig. 1, the PPy NTs are decorated with Pt NPs homogeneously. The size of the precipitated Pt NPs is equal 3-6 nm.

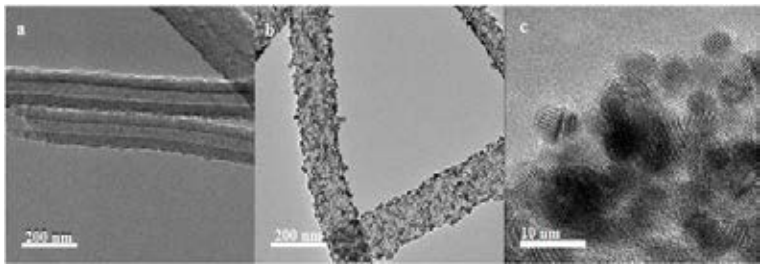


Fig. 1. TEM images of the PPy NTs (a) and Pt-decorated PPy NTs (b, c).

The amount of Pt on the PPy NTs-Pt NPs according EDX analysis is equal 24.4 $\%_{wt.}$

The porous structure and the specific surface areas of the NPs were measured using N_2 adsorption/desorption analysis (Table 1).

Table 1. Microporous and mesoporous structure of the PPy NTs and Pt-decorated PPy NTs according to the N_2 adsorption/desorption analysis.

Samples	BJH from desorption		Gurvich	BET		DR	
	S_{cumul}	D	V_{tot}	V_m	S_{BET}	V_m	V_{micro}
	m^2/g	nm	cm^3/g	cm^3/g	m^2/g	cm^3/g	cm^3/g
PPy NTs	43.91	4.03	0.1608	7.9391	34.6	8.7475	0.0135
PPy NTs-Pt	22.16	3.81	0.0598	1.4907	6.5	1.3625	0.0021

As you can see (Table 1), both PPy NTs and PPy NTs-Pt have both macro and mesopores. However, after decoration of PPy NTs with Pt nanoparticles all parameters, which characterized porous structure and surface of the materials significantly decrease. It is connected with possible precipitation of the Pt NPs on the surface's roughness, such as pores.

The electrochemical activity of the synthesized catalyst NPs was measured using rotating disk electrode (RDE) method. The current-voltage (C-V) curve of the Pt catalyst (fig. 2) demonstrates the intensive peak of H_2 desorption with the shape, characterised for polycrystalline Pt [5]. The electrochemical surface area is equal 284 cm^2/mg.

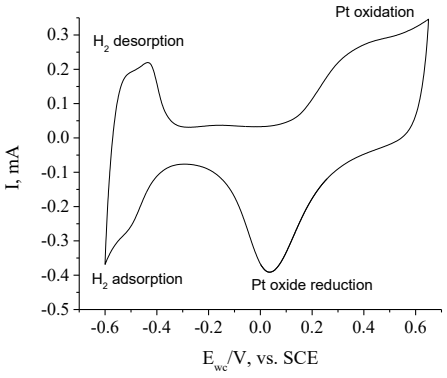


Fig. 2. C-V curve (RDE) of PPy NTs – Pt (speed 50 mV/s, 30 cycles, in N_2-purged 0.5 M H_2SO_4, 25 ^{0}C, range from -0.6 to 0.6 V).

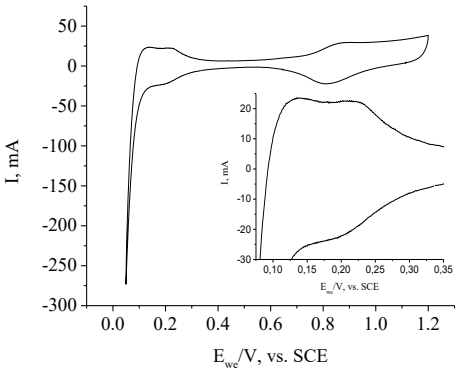


Fig. 3. C-V curve (*in situ* in fuel cell station) of PPy NTs – Pt (speed 50 mV/s, 30 cycles, 70 ^{0}C, 100% RH, N_2/H_2, no backpressure, range from 0 to 1.1 V).

Then the catalytic ink, based on synthesized catalyst, Nafion ionomer and solvents, was prepared. Catalyst-coated membrane (CCM) was prepared by ultrasonic spraying techniques using SonoTek ExactaCoat machine. Nafion® PFSA NR-212 (Chemours, USA) was used as polymer electrolyte membranes. The Pt loading of the cathode was 0.3 $mgPt/cm^2$. The sprayed catalytic layer was covered by GDL (Sigracet 25 BC). 0.3 mg/cm^2 Pt/C 40% on Sigracet 29 BC carbon paper was used as anode. The active area was 4 cm^2.

Prepared CCMs were tested in fuel cell using 3 kW FC testing station (MTM (LC), Czech Republic). Testing in fuel cells were carried out at 70 °c, 100 % relative humidity, 8 bar pressure cell, 0.5/0.5 bar O_2/H_2 or air/H_2 atmosphere, 2/1 or 3/2 stoichiometric value of O_2/H_2 or air/H_2, respectively.

C-V curve *in situ* was measured in fuel cell (fig. 3). The ECSA of the CCMs is 133 cm^2/mg. The power densities are 0.9 and 0.4 W/cm^2 in O_2/H_2 and air/H_2, respectively. It is also possible to improve the CCM performance by

optimization of Nafion ionomer content. Also due to the investigation of the PPy NTs influences on the catalyst's stability, the durability test of the CCM is continuing.

CONCLUSIONS

The Pt-decorated polypyrrole nanotubes were obtained. The catalyst powder demonstrates the high electrochemical activity in half-cell. Using synthesized catalyst, the catalyst-coated membrane was prepared using ultrasonic spraying techniques. The power density and electrochemical surface area of the CCM were measured in the fuel cell station. The performance of the prepared catalysts is equal 0.9 and 0.4 W/cm^2 in O_2/H_2 and air/H_2, respectively. The durability test of the catalysts support is continued.

ACKNOWLEDGEMENT

The authors acknowledge financial support from the grant CZ.02.1.01/0.0/0.0/16_025/0007414 OP VVV project PaC NG.

NOMENCLATURE

BJH	Barrett – Joyner - Halenda model for calculating mesopore size.
DR	Dubinin –Radushkevich model forcalculating micropore volume.
BET	Brunauer–Emmett–Teller theory for calculating specific surface area.
S_{cumul}	Cumulative mesopore area, m^2/g
D	Maximum mesopore diameter, nm
V_{tot}	Total pore volume at p/p_0=0.99, cm^3/g
V_m	Monolayer adsorption capacity, cm^3/g
S_{BET}	BET specific surface area, m^2/g
V_{micro}	Micropore volume. cm^3/g

REFERENCES

1. Garland NL, Papageorgopoulos DC and Stanford JM. 2012. Hydrogen and Fuel Cell Technology: Progress, Challenges, and Future Directions. Energy Procedia 28: 2–11.
2. https://www.energy.gov/eere/fuelcells/doe-technical-targets-polymer-electrolyte-membrane-fuel-cell-components.
3. Wang J, Yin G, Shao Y, Zhang S, Wan Z and Gao Y. Effect of carbon black support corrosion on the durability of Pt/C catalyst. 2007. Journal of Power Sources 171 (2): 331-339.
4. Galář P, Khun J, Kopecký D, Scholtz V, Trchová M, Fučíková A, Jirešová J. and Fišer L. 2017. Infuence of non-thermal plasma on structural and electrical properties of globular and nanostructured conductive polymer polypyrrole in water suspension. Scientific Reports 7: 1-10.
5. Zhan D, Velmurugan J and Mirkin MV. 2009. Adsorption/Desorption of Hydrogen on Pt Nanoelectrodes: Evidence of Surface Diffusion and Spillover. J. Aerican Chemical Society 131: 14756–14760.

WHEC-2022
23rd World Hydrogen Energy Conference
June 26-30, 2022 - Istanbul

#45

PREPARATION OF ELECTROCONDUCTIVE THERMALLY EXPANDED GRAPHITE FOR PEM FUEL CELLS' POLYMER COMPOSITE BIPOLAR PLATES

[1*] *Alina Madalina Darabut,* [1] *Yevheniia Lobko,* [1]*Yurii Yakovlev,* [1]*Miquel Gamon Rodriguez,* [1]*Kateřina Veltruska,*[1] *Peter Kuš,* [1]*Jaroslava Nováková,*[2]*Maryna Vorokhta,* [3]*Vladimír Kopecký,* [3]*Marek Procházka,* [4]*Milan Dopita,* [1]*Iva Matolínová* [1]*Vladimír Matolín*

[1]Charles University, Faculty of Mathematics and Physics, Department of Surface and Plasma Science, V Holešovičkách 747/2, 180 00 Prague 8, Prague, Czech Republic

[2] Czech Academy of Sciences, Institute of Rock Structure and Mechanics, Department of Geochemistry, V Holešovičkách 41, 180 00 Prague8, Czech Republic

[3]Charles University, Faculty of Mathematics and Physics, Institute of Physics, Division of Biomolecular Physics, Ke Karlovu 5, 12116 Prague 2, Czech Republic

[4]Charles University, Faculty of Mathematics and Physics, Department of Condensed Matter Physics, Ke Karlovu 5, 12116 Prague 2, Czech Republic

*Corresponding author e-mail: alinadarabut@gmail.com

ABSTRACT

The thermally expanded graphites (TEGs) as fillers for PEM bipolar plates were obtained. The influence of the air and nitrogen atmosphere, as well as the different temperatures on the structure and properties of TEGs were investigated. The morphology, porous structure, chemical composition of the TEGs were analysed using SEM, XRD, BET, EDX, and XPS. It was shown that the obtained TEGs have three times higher electrical conductivity, comparable with commercial graphites. The obtained TEG is used as filler in the preparation of the polymer composites bipolar plates with electrical conductivity reaching DOE targets.

Keywords: Thermally expanded graphite, Carbon fillers, Polymer composites, Bipolar plates, PEM fuel cells

INTRODUCTION

The EU climate challenges for 2030 are to reduce greenhouse gas emissions (basically CO_2) by 40% versus 1990 emissions, raise the share of renewable energy and energy efficiency by 27% [1]. Achieving the Paris Agreement's targets may be accomplished through application of renewable energies using innovative technologies such as fuel cells (FCs). Fuel cells have been developed as a candidate for zero emission and alternative power sources for both mobile and stationary applications. These devices convert chemical energy into electrical energy, water and heat, without any pollutant emission. Moreover, FCs, especially proton exchange membrane FCs (PEM FCs), have been proposed as a power source due to high energy efficiency, high power density, low operating temperature and other advantages [2].

The bipolar plates (BPs) are one of the most important components of fuel cells' technology. The BPs conduct heat and electricity between cells, provide a gas flow field, remove heat and are a physical barrier avoiding the mixing of the oxidant, fuel and coolant fluids [3]. According to *Tsuchiya et al* [4], the BPs account for about 80% of total weight and 45% of the cost of PEM FCs. Developing effective nonporous materials for BPs with high electrical and thermal conductivity, high mechanical and chemical resistivity, etc., is an actual challenge nowadays. In spite of the variants of BPs from different materials such as metal, graphite or composite [3]–[5], it still has many problems with achieving desired properties and reliable production.

The electrically conductive carbon-based polymer composites are promising materials for the creation of BPs for PEM FCs because of such advantages as high stability in acidic solution, high mechanical strength, lightweight, low cost and the chance to mold into different shapes and sizes. Nevertheless, high electrical and thermal conductivity and flexural strength are the main problem which are not completely solved yet. Owing to improve these parameters of BPs it is necessary to prepare high electrically conductive fillers, which will form the conductive channels in the bulk of the polymer matrix. In recent studies, electrically conductive polymer composite BPs have been obtained with such carbon fillers as natural graphite flakes [6], carbon black [7] or from the combination of various fillers such as graphene, carbon fibers and natural graphite [8], etc. But the filling factor for these composites is high and the electrical conductivity does not always reach the DOE targets [9].

In this study, the preparation of the thermally expanded graphites (TEGs) as the high electrically conductive fillers for PEM BPs is investigated. The TEGs' microstructure and the chemical structure are studied by different techniques. Additionally, the polymer composites bipolar plates are prepared using commercial graphite mixed with the obtained TEG.

MATERIALS AND METHODS

Production of the thermally expanded graphites

For TEGs preparation, the expandable graphite flakes (ES 350 F5) were put into the muffle oven either air or N_2 atmosphere for 1 minute. The temperature was varied from 400 to 800ºC (for air atmosphere, because of the oxygen degradation of the materials) or from 600 to 1200ºC (for N_2 atmosphere).

The morphology of the TEG was analyzed using Scanning Electron Microscopy (SEM). The crystalline structure was investigated by Transmission Electron Microscopy (TEM) and X-ray Diffraction (XRD). The chemical content of the elements was determined by energy dispersion X-ray Spectroscopy (EDX), X-ray photoelectron Spectroscopy (XPS) and Fourier-Transform Infrared Spectroscopy (FTIR). For the analysis of specific surface area and porous structure of the TEGs, the nitrogen adsorption was measured using the Brunauer-Emmett-Teller analysis (BET). The resistance (R) of the fillers was measured by impedance spectroscopy (four-point probe measurement arrangement).

Preparation of the polymer composite bipolar plates

The polymer composites are based on epoxy resin and carbon-based powders, as matrix and fillers, respectively. In order to obtain good interaction between the matrix and the fillers, increase the amount of latter, and, as a result, increase the electrical conductivity of the bipolar plates, a solvent is used. After the solvent's evaporation, the hot compression molding is used in order to obtain the polymer composites samples. The electrical conductivity of the polymer composites is analysed using the impedance spectroscopy.

RESULTS AND DISCUSSION

In this section, the influence of different preparation conditions (temperature, atmosphere) of the TEGs on the morphology, the chemical and physical structure and the electrically conductive properties of the fillers will be discussed. SEM images (Fig. 1a-d) show significant differences in the morphology of graphite before (Fig. 1a, b) and after (Fig.1c, d) the thermal treatment. It is possible to see flakes did not change the xy dimensions (0.5 -1 mm) but drastically increased the thickness (from 30-50 µm to more than 3mm).

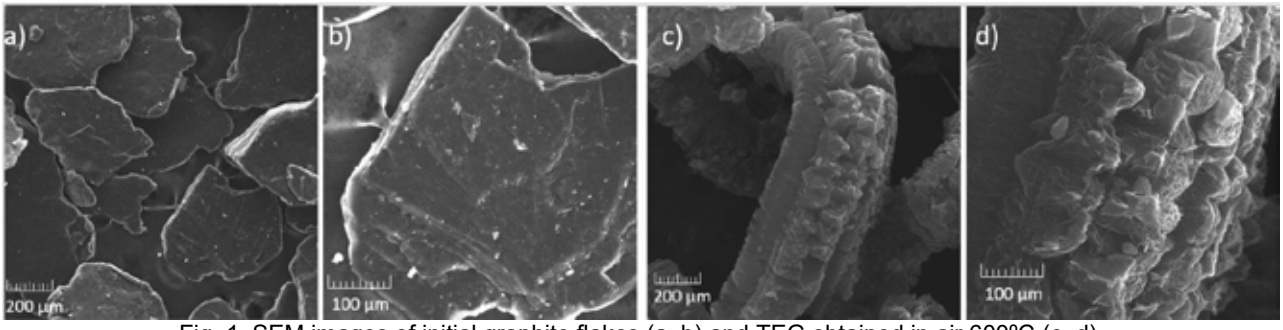


Fig. 1. SEM images of initial graphite flakes (a, b) and TEG obtained in air 600ºC (c, d).

Worth to notice, that the temperature and atmosphere of the TEGs' preparation do not influence on the sizes and shapes of the particles, but it can change their chemical composition.

EDX analyse demonstrate the elemental content in the TEGs, prepared in different conditions (Table 1). Table 1 shows that the amount of Carbon slightly increases but, Oxygen and Sulfur contents decrease for TEGs, comparable with initial graphite flakes. Also, the difference between the samples obtained at the same temperature but different atmosphere is negligible.

Table 1. Chemical composition of graphites before and after thermal treatment in both air and nitrogen atmosphere at different temperatures according EDX.

Samples	C [wt%]	O [wt%]	Na [wt%]	S [wt%]
Expandable graphite	92.29	6.23	0.06	1.43
TEG at 600ºC in air	97.42	1.73	0.34	0.51
TEG at 600ºC in N_2	97.66	1.25	0	0.33

The porosity and average surface area of TEGs were analysed. It was found that the conditions of preparation of TEGs do not influence critically on these parameters. The average surface area of TEGs is equal to 27 m^2/g and a mesopore diameter is around 4 nm.

In the same way as the different conditions of the TEGs' preparation have insignificant changes in the morphology, the electrical conductivity behave similar. The TEGs obtained in air and 600 ºC has 1670 S/cm, meanwhile for the TEG obtained in nitrogen but same temperature, the electrical conductivity is equal 1730 S/cm. For comparison, the electrical conductivity of the commercial graphites is 3 times lower (~500 S/cm) than the conductivity of TEGs.

The polymer composites bipolar plates with own design of flow fields are prepared using epoxy resin and the obtained TEG as filler. The electrical conductivity of prepared BPs reaches the DOE target. The performance of membrane electrode assemblies in prepared BPs is tested in-situ in the fuel cell station.

CONCLUSIONS

Thermally expanded graphites for BPs' preparation were obtained at different temperatures and atmospheres. It was shown that the conditions of TEGs' obtaining have not significant influences on the morphology, the chemical composition nor electrical conductivities of the fillers. The electrical conductivity of the obtained TEGs (1670S/cm) is three times higher than for the commercial graphites. Moreover, due to the high electrical conductivity of TEGs, the polymer composites bipolar plates reach the DOE target in terms of electrical conductivity.

ACKNOWLEDGMENTS

This study was financially supported by the grant CZ.02.1.01/0.0/0.0/16_025/0007414 OPVVV PaC NG.

REFERENCES

1. https://www.europarl.europa.eu/RegData/etudes/BRIE/2019/631047/IPOL_BRI(2019)631047_EN.pdf. Accessed on October, 2021.
2. Alo O, Otunniny I, Pienaar H and Iyuke S. 2017. Materials for Bipolar Plates in Polymer Electrolyte Membrane Fuel Cell: Performance Criteria and Current Benchmarks. Procedia Manufacturing 7:395-401.
3. Hermann A, Chaudhuria T and Spagnol P. 2005. Bipolar Plates for PEM Fuel Cell: A Review. International Journal of Hydrogen Energy 30:1297-1302.
4. Tsuchiya H and Kobayaski O. 2004. Mass production cost of PEM Fuel Cell by Learning Curve. Imtermational Journal of Hydrogen Energy 29:985-990.
5. Cunningham BD, Huang J and Baird DG. 2007. Review of Materials and Processing Methods Used in the Production of Bipolar Plates for Fuel Cells. International Materials Reviews 52:1-13.
6. Gautam RK and Kar KK. 2016. Synthesis and Properties of Highly Condcuting Natural Flake Graphite/Phenolic Resin Composite Bipolar Plates for PEM Fuel Cells. Advanced Composites Letters 25:87-97.
7. Del Rio C, Ojeda MC, Acosta JL, Escudero MJ, Hontañon E and Daza L. 2002. New Polymer Bipolar Plates for Polymer Electrolyte Membrane Fuel Cells: Symthesis and Characterization. Journal of Applied Polymer Science, 83:2817-2822.
8. Kakati BK, Ghosh A and Verma A. 2013. Efficient Composite Bipolar Plate Reinforced with Carbon Fiber and Graphene for Proton Exchange Membrane Fuel Cell. International Journal of Hydrogen Energy 38:9362-9369.
9. https://www.energy.gov/eere/fuelcells/doe-technical-targets-polymer-electrolyte-membrane-fuel-cell-components. Accessed on October, 2021.

WHEC-2022
23rd World Hydrogen Energy Conference
June 26-30, 2022 - Istanbul

#54

MASS TRANSFER ANALYSIS OF MICROPOROUS LAYERS FOR POLYMER ELECTROLYTE FUEL CELLS USING PORE NETWORK MODEL

[1*] *Hironori Nakajima,* [2] *Shintaro Iwasaki,* [1] *Tatsumi Kitahara*
[1] Department of Mechanical Engineering, Faculty of Engineering, Kyushu University, 744 Motooka, Nishi-ku, Fukuoka, Japan
[2] Department of Hydrogen Energy Systems, Graduate School of Engineering, Kyushu University, 744 Motooka, Nishi-ku, Fukuoka, Japan

*Corresponding author e-mail: nakajima@mech.kyushu-u.ac.jp

ABSTRACT

Liquid water accumulated in the catalyst layer and gas diffusion layer (GDL) of a polymer electrolyte fuel cell (PEFC, PEMFC) results in performance deterioration due to inhibition of transport of the reactant oxygen in the cathode (Flooding). To enhance the drainage in the GDL, the application of a microporous layer (MPL) is effective to the catalyst layer side of the GDL substrate. To elucidate the effects of two-phase flow on the oxygen transport in an MPL for its optimized designs, we model three-dimensional porous structures of in-house MPLs with pore network model (PNM) for convective air permeation and oxygen diffusion. Pore diameter distribution derived by a focused ion beam scanning electron microscope is employed in the PNM. Air permeation measurements combined with oxygen diffusion measurements with changing liquid saturation by using gas chromatography validate the model.

Keywords: Polymer electrolyte fuel cell, Gas diffusion layer, Microporous layer, Pore network model, Pore diameter distribution

INTRODUCTION

Polymer electrolyte fuel cells (PEFCs, PEMFCs) are promising as zero-emission power sources for future automobiles and houses. However, proper water management among the catalyst layer, gas diffusion layer (GDL), and flow channels of a PEFC is necessary to improve its performance. In particular, excess liquid water is generated in a high current density region. The liquid water may cause clogging in the catalyst layer and GDL, resulting in performance deterioration due to inhibition of transport of the reactant oxygen in the cathode (Flooding). To enhance the drainage in the GDL, the application of a microporous layer (MPL) composed of carbon black (acetylene black) and water repellent polytetrafluoroethylene (PTFE) is effective to the catalyst layer side of the GDL substrate[1][2]. In this research, we focus on mass transfer in the three-dimensional porous structure of MPLs. Pore diameter distributions of our in-house MPLs derived by a focused ion beam scanning electron microscope (FIB-SEM) have been employed in pore network models (PNMs)[3][4][5] with convective air permeation and oxygen diffusion. Gas permeation measurement for air permeabilities as well as gas chromatography for oxygen diffusivities was also carried out to validate the models. Oxygen diffusivities were evaluated for dry MPLs and those with a wetting liquid of different liquid saturations. The aim of this research is thereby to develop reliable and practical numerical models validated with experiments taking into account liquid saturation for the optimized design of the MPLs, elucidating the effects of two-phase flow and water clogging on oxygen transport in an MPL.

MATERIALS AND METHODS

MPL slurries (20wt% PTFE) were applied to GDL substrates (Toray TGP-H-030: 5wt% PTFE) with changing added water amount so that the MPLs have maximum pore diameters, d_{max}, of ca.2 μm, 5 μm, and 15 μm (referred to as Samples A, B, and C, respectively). The porosity of the MPLs was estimated with the Archimedes method by immersing the MPL-coated GDL substrates in a non-volatile wetting liquid (GALWICK, Porous Materials Inc., USA) having a sufficiently small surface tension. Three-dimensional structural analysis of these MPLs was performed using an FIB-SEM to determine pore diameter distribution. PNM models (Open PNM 1.2) constructed based on the porosities and pore diameter distributions gave air permeabilities and oxygen diffusion resistances. In addition, air permeability was measured with the equipment shown in Fig. 1. The air permeability (permeance) was obtained by dividing the air flow rate through a GDL by the air permeation area and the pressure difference (ΔP = 1.2 kPa). Fig. 2 shows an experimental set-up for ex-situ measuring oxygen diffusion resistance in a GDL. Differential pressure in a GDL was minimized by the flow rate of air and nitrogen with a mass flow controller and a pressure gauge during the measurement of oxygen diffusion resistance. Oxygen concentration in outlet gas of the lower channel in Fig. 2 was determined by gas chromatography (GC). Oxygen diffusion resistance in a GDL was obtained by dividing oxygen diffusion flux in a GDL

by the logarithmic mean concentration difference of oxygen between GDL surfaces, given the dimensions of the fixture. On the other hand, for measurement under wet conditions, a GDL fully impregnated with GALWICK was discharged by increasing differential air pressure in a GDL every 20 kPa to reduce liquid saturation from unity because ex-situ control of liquid saturation with GALWICK in hydrophobic pores is more reliable than that with water in terms of equilibrium of forces. Oxygen diffusion resistance was then similarly determined.

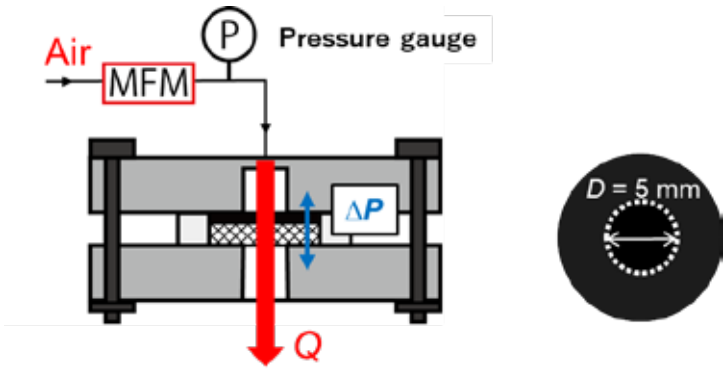


Fig. 1 Schematic of air permeability measurement

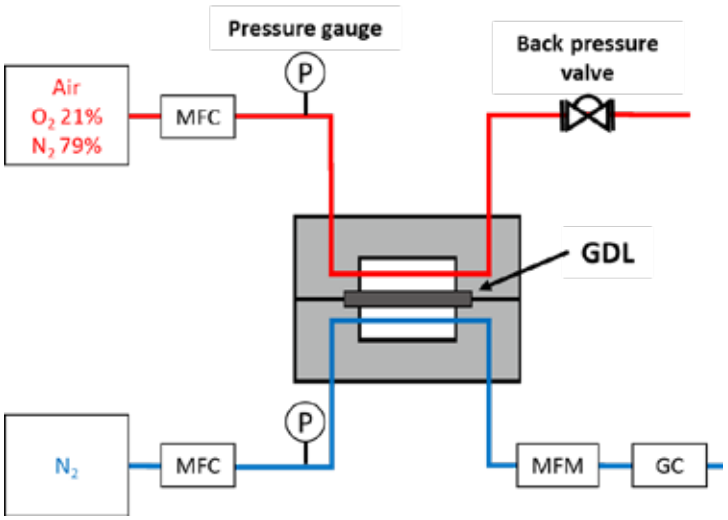


Fig. 2 Schematic of the oxygen diffusivity measurement

RESULTS AND DISCUSSION

Air permeability (permeance) (Fig. 3) and oxygen diffusion resistance of the GDLs under dry conditions derived with the PNM calculation were compared with measured values. PNM of the MPL with the larger maximum pore diameter showed higher air permeability and lower oxygen diffusion resistance, which were consistent with the experiment. On the other hand, in the MPLs impregnated with GALWICK, the oxygen diffusion resistance decreased when the liquid saturation decreased with the discharge of GALWICK. In addition, the pressure at which GALWICK begins to discharge and it is fully discharged (saturation ≈ 0) were both higher for the MPL with the smaller maximum pore diameter. Because these trends were consistent with the experiment, the change in oxygen diffusion resistance with the change in liquid saturation with GALWICK was successfully reproduced by PNM.

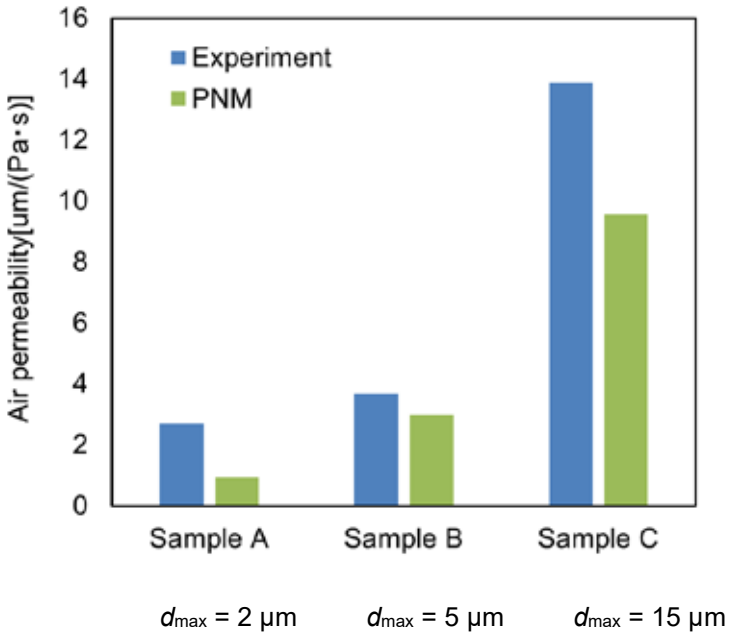


Fig. 3 Air permeability by the PNM calculations and experiments

CONCLUSIONS

Air permeabilities and oxygen diffusion resistances for dry and wet conditions of the MPLs having different pore diameter distributions agree in their trends between PNM and experiment. Thus PNM is validated and useful to model oxygen and water transports in MPLs with employing wettability (contact angle) of the pores. Numerical models with PNM for optimized designs of MPLs are feasible.

ACKNOWLEDGEMENT

The authors are indebted to graduate students, Messrs. Yuhang Liu, Kentaro Harano, Yuki Monde, and Dingfeng Chen for help in the modeling and experiment. Thanks are offered to Professor Kohei Ito of Kyushu University for valuable discussions. The authors acknowledge Ms. Chie Uryu of the International Research Center for Hydrogen Energy, Kyushu University for operating the FIB-SEM. SEM and X-ray CT observations were performed at the Center of Advanced Instrumental Analysis, Kyushu University with the help of Ms. Akiko Inada of the Center for Co-Evolutional Social Systems, Kyushu University.

REFERENCES

1. Nakajima H, Konomi T and Kitahara T. 2007. Direct water balance analysis on a polymer electrolyte fuel cell (PEFC): Effects of hydrophobic treatment and micro-porous layer addition to the gas diffusion layer of a PEFC on its performance during a simulated start-up operation. Journal of Power Sources 171:457-463.
2. Kitahara T, Konomi T and Nakajima H. 2010. Microporous layer coated gas diffusion layers for enhanced performance of polymer electrolyte fuel cells. Journal of Power Sources 195:2202-2211.
3. Gostick J, Aghighi M, Hinebaugh J, Tranter T, Hoeh MA, Day H, Spellacy B, Sharqawy MH, Bazylak A, Burns A, Lehnert W and Putz A. 2016. OpenPNM: A pore network modeling package. Computing in Science & Engineering 18: 60-74.
4. http://openpnm.org/. Accessed on October 15, 2021
5. Nakajima H, Iwasaki S and Kitahara T. 2021. Mass transfer in microporous layers for polymer electrolyte fuel cells analyzed with pore network modeling. ECS Transactions 104(8):129-135.

WHEC-2022
23rd World Hydrogen Energy Conference
June 26-30, 2022 - Istanbul

#65

DYNAMIC MODELING OF A RESIDENTIAL INTEGRATED PEMFC-BASED MICRO-CHP SYSTEM

[1*] *RafikElkhatib*, [2] *Hasna Louahlia*
[1]Caen university, LUSAC, 120 rue de l'exode, 5000, Saint Lo, France
[2] Caen university, LUSAC, 120 rue de l'exode, 5000, Saint Lo, France
*Corresponding author e-mail: rafik.elkhatib@unicaen.fr

ABSTRACT

Cogeneration is the parallel high-efficiency generation of thermal and electrical energy from a single main energy source. It allows the recuperation of lost heat during the generation of power, resulting in 20 to 30% more efficient than independent generation. Recently, among many candidates in micro-cogeneration systems, the PEMFC (proton-exchange membrane fuel cell) represents a promising technology, allowing the use of hydrogen (H2) as a fuel source in the building and outperforming by its higher flexibility and low investment cost. In this article, the behavior of a micro-cogeneration system based on a PEFMC for a 120 m2 inhabited house is studied. This system is used to meet the thermal (DHW and heating) and electrical needs of a family of 3 people which its annual electrical and thermal energy demands are 2607 kWh and 12705 kWh respectively. The system component are a PEMFC cell, a hydrogen boiler, a hydrogen supply circuit, an air supply circuit, water management system and a heat management and recovery system. The findings indicate that this technology is very promising. The total efficiency of the system exceeds 75% in most of the time and the effective coverage rate of annual thermal and electrical needs is achieved.

KEYWORDS: Micro-cogeneration, Fuel cells, Hydrogen

INTRODUCTION

In this period, mostly of researcher head to developing cogeneration system based on fuel cell (FC) for small-scale to its various advantages comparing with other listed systems. Jaouhar et al [1], investigated the performance of a micro-cogeneration system based on PEMFC by studying the effect of the different key parameters and system response to the simulated demands. Two system design (1-KW, 5-KW) and two operational strategies were used. The results show that the system has a primary energy consumption 30% less than the conventional system. After the rapid growing of research in this domain, the researcher head to find the optimal operation of PEMFC based micro-cogeneration system. As OH et al [2], where they determined the optimal operation of a micro-combined heat and power (CHP) system with a 1-KW PEMFC as prime mover. In this article, we seek to investigate the performance of a developed micro-CHP system composed of 750-W PEMFC, backup boiler, gas management unit, water and heat recovery control unit. The system goal is to respond to the electrical and thermal needs of a single-family house. Thus, an hourly dynamic simulation was applied in Caen, France (49.1811 N, -0.3712 E) for a 120m2 single-family house, where the FC performance was detail studied.

SYSTEM DESCRIPTION

The proposed micro-CHP system is composed of 750-W PEMFC (70°C) cooled with water circuit in order to absorb the waste heat. The PEMFC power is constant throughout operation. Therefore, a 1080-W of thermal power is extracted of the fuel cell to cover the domestic hot water (DHW) and space heating demands(SHD). The mathematical modeling of the fuel cell is described by the equations bellows [3,4]:

$$P_e = N_{cell}\, i\, A\, V_{cell} \quad (1)$$

where P_e is the electrical power produced by the fuel cell, N_{cell} is number of cells, i the current density, A the cell area and V_{cell} the cell voltage.

$$Q_{stack} = N_{cell}\, i\, A(1.48 - V_{cell}) \quad (2)$$

A backup condensing boiler with maximum thermal capacity of 12-kW, which use the hot fume to heat the boiler water return. This type of boiler has a high efficiency. The boiler interferes when a highly demand exist in order to meet the needs. The power given by the boiler is calculated by:

$$Q_b = n_{H2,b}\, \Delta H_{H2} \quad (3)$$

where Q_b is the boiler thermal power, $n_{H2,b}$ is the molar hydrogen fraction consumed by the boiler and ΔH_{H2} is enthalpy of combustion of H2.

Fig.1 represent the system scheme. Two tanks of 170L and 45L respectively were adopted in order to respond to the thermal demands. The large tank was responsible of the space heating demand where it was heated principally by the fuel cell in operation time and secondly by the boiler. The domestic hot water was delivered by the 45-L tank which is heated by the first tank and the boiler in case of large demand. The hydrogen and air supply circuits are equipped by the different management apparatus (filter, compressor, humidifier), measuring and controlling equipment (mass flow controller, pressure gauge, thermocouple…) in order to deliver the inlet gases to fuel cell as required. As well, a heat recovery unit composed of heat exchangers, pumps, valves..., was integrated to perform a good use of the extracted heat.

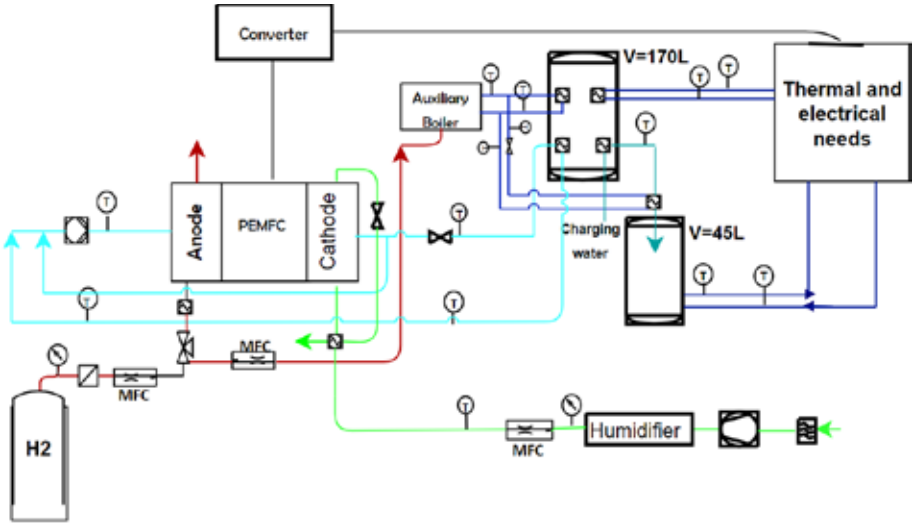
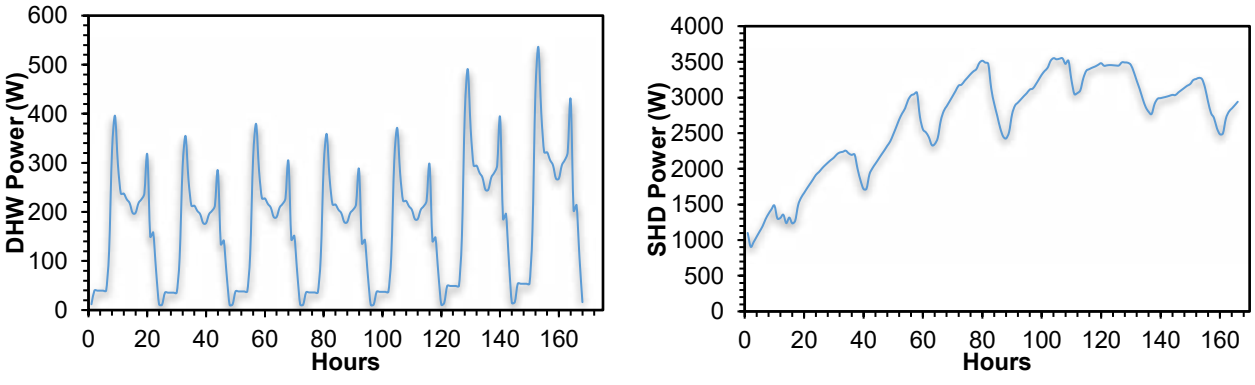


Fig. 1-System scheme

THERMAL AND ELECTRICAL DEMANDS

In order to evaluate the system feasibility, it's necessary that the system be examined with a thermal and electrical demands that represents the real case. Thus, the hourly electrical and thermal demands for the proposed scenario were simulated over a year based on statistical approach [5][6]. The SHD and DHW profile for one week is represented by Fig.2.



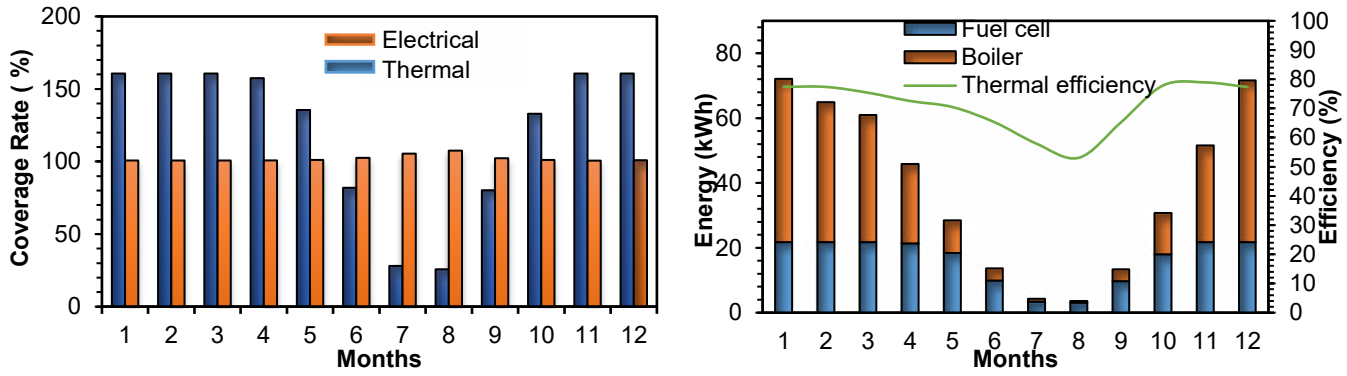
(a) (b)

Fig. 2- Weekly profile of : (a) space heat demand , (b) domestic hot water demand

RESULTS

In order to evaluate the system, a simulation was performed for one year, where the daily, monthly and yearly performance of the system was examined. Fig.3-a shows the system electrical and thermal response to the needs represented by the coverage rate (CR) which is the ratio between the produced and demanded energy. As it can be seen, the system response to the thermal needs was satisfying, which according to the strategy adopted, the system must cover all the thermal needs by priority. Thus, the effective thermal coverage rate of the system was 100% throughout the year. This results reflect the system stability in responding to the needs despite the varied weather from winter to summer. Even though the system priority was to feed the thermal demands, the system was capable to

feed the house electrical needs in most of the time with an effective electrical coverage rate of 120%. The low system production in summer months refer to the low space heating and domestic hot water demands in this period, where the fuel cell power produced (1080-W) can be enough to cover the needs. As declared before, in low heat demands the fuel cell stop working to prevent any damage.



(a) (b)

Figure 3- (a) Monthly system electrical and thermal coverage rate, (b) Monthly average system components thermal energy produced

As discussed earlier, the boiler role is to provide the needed power to feed the excess needs that fuel cell can't provide it alone. The condensing boiler with its high efficiency help the system to be stabilized all the operation time. Fig.3-b shows the monthly average energy produced by each of the heat source unit. It's remarkable that the boiler has produced much more than the fuel cell did in the winter period where the demand were really huge. The fuel cell must produce in normal operation 21-KWh of thermal energy per day (20 hours/day). The effective thermal energy produced by the fuel cell throughout the year was 16-KWh due to the low operation time of fuel cell in summer, while the boiler effective energy produced was 22-KWh with a maximum of 80-Kwh in December and minimum of 0.5-KWh in August. The thermal efficiency represented in Fig.3-b shows the effect of the fluctuated demands in summer on the system. While the system was standing with a thermal efficiency of 70-80%, it decreased to nearly 50% in July-August where the consumed energy was high with respect to the operation time.

CONCLUSION

In this study, we discussed the feasibility of an improved micro-CHP system based on low temperature PEMFC. The system was equipped by a condensing boiler, heat tank, and control and management units. All component were mathematically modeled and validated using experimental data. The system shows a good performance in responding to the estimated needs where the effective electrical and thermal coverage rate were 120% and 100% respectively

ACKNOWLEDGMENTS

This work is financed by the departmental council of the Manche. The authors would like thank them for the funding of this work.

REFERENCES

[1] Romdhane, Jaouher & Louahlia, Hasna & Marion, Michaël. (2018). Dynamic modeling of an eco-neighborhood integrated micro-CHP based on PEMFC: Performance and economic analyses. Energy and Buildings. 166. 10.1016/j.enbuild.2018.01.054.
[2] Oh, Si-Doek & Kim, Ki-Young & Oh, Shuk-Bum & Kwak, Ho-Young. (2012). Optimal operation of a 1kW PEMFC-based CHP system for residential applications. Applied Energy. 95. 10.1016/j.apenergy.2012.02.019.
[3] Omrani, R., Nguyen, H. Q., & Shabani, B. (2019). Open-cathode PEMFC heat utilisation to enhance hydrogen supply rate of metal hydride canisters. Energy Procedia, 160, 542-549.
[4] Larminie, J., Dicks, A., & McDonald, M. S. (2003). Fuel cell systems explained (Vol. 2, pp. 207-225). Chichester, UK: J. Wiley.
[5] Rocheron, C. (2012). Domestic hot water-an energy approach. Application of heat pumps for residential apartment buildings.
[6] Bianchi, M., De Pascale, A., & Spina, P. R. (2012). Guidelines for residential micro-CHP systems design. Applied Energy, 97, 673-685.

WHEC-2022
23rd World Hydrogen Energy Conference
June 26-30, 2022 - Istanbul

#79

DESIGN AND INVESTIGATION OF A VARIABLE-NOZZLE EJECTOR FOR A 120 kW PEMFC STACK

[1] Yikang Lu, [2] Xuhui Wang, [3*] Sichuan Xu
School of Automotive Studies, Tongji University, 201804, Shanghai, China

*Corresponding author e-mail: scxutj@163.com

ABSTRACT

Ejector is an ideal recirculation device which entrains anode exhaust from PEMFC stack via the entraining effect of supersonic low-pressure jet. Ejectors have advantages of tiny size, light weight, simple structure and no parasitic power consumption but achieves bad performance in off-design conditions, especially when stack load is relatively low. A variable-nozzle ejector applied for 120kW stack is designed based on a 1-D ejector model. The results show that through shrinking throat ejector's entraining performance can be improved effectively. When stack load is higher than 60kW, the performance with maximum throat can meet the requirements. With load decreasing to 8.9kW, the throat diameter should be gradually reduced to 0.4mm and the demand of primary pressure is raised to 1181kPa accordingly.

Keywords: PEMFC ejector, Variable-nozzle, Entrainment ratio

INTRODUCTION

In vehicle PEMFC (proton exchange membrane fuel cell) system, hydrogen recirculation is mostly adopted to achieve a high fuel utilization as well as a good water balance inside the stack. Ejectors are ideal recirculation devices. Under the entraining effect of supersonic jet, the anode exhaust is drawn into the ejector thus to perform recirculation. Due to the demand of recirculation rate in PEMFC water management, ejector's entraining effect is much more important than its compressing effect. Ejectors have advantages of tiny size, light weight, simple structure and no power consumption but achieve bad entraining performance in off-design conditions. When PEMFC stack output is low, ejectors couldn't produce sufficient hydrogen recirculation.

Through changing the internal structure, the working range of ejectors can be enlarged. Xue et al.[1] placed 4 nozzles in suction chamber and through the cooperation of different nozzles the ejector operates well within stack loads of 20-25kW and 35-100kW. Brunner et al.[2] proposed a variable-nozzle design and adjusts throat's opening dynamically through controlling the axial position of a taper needle in the nozzle. Their results show that shrinking throat is beneficial to entraining performance when hydrogen supply rate is low. Hosseinzadeh et al.[3] designed 2 ejectors according to current levels of 85A and 180A, by the parallel work of which the hydrogen recirculation system can achieve an entrainment ratio of over 2 within current range of 60A-180A. Brunner's variable-nozzle design was later compared in their work, the results show that a variable-nozzle ejector has nearly the same working range as 2 parallel ejectors.

In this work, a 1-D ejector model is built based on Soklov's theory[4] and validated with ejector's bench test applied for a 60kW PEMFC stack. Ejector's performance curves with different throat diameter were studied and a variable-nozzle ejector applied for a 120kW PEMFC stack was designed.

MODEL DEVELOPMENT

Model assumption

1. Primary and secondary fluid are regarded as single-phase ideal gas. Because in bench test there isn't a real stack, primary and secondary fluid are pure hydrogen with equal temperature.

2. The mixing of primary and secondary fluid starts at the entrance of mixing chamber and ends before the exit.

3. The velocity distribution at the cross section of mixing chamber's inlet can be divided into primary region and secondary region and in each region the velocity distributes uniformly.

4. Flow in ejectors is isentropic and no shock wave or vortex take place.

5. Gas at the inlet of primary and secondary fluid is in stagnation condition.

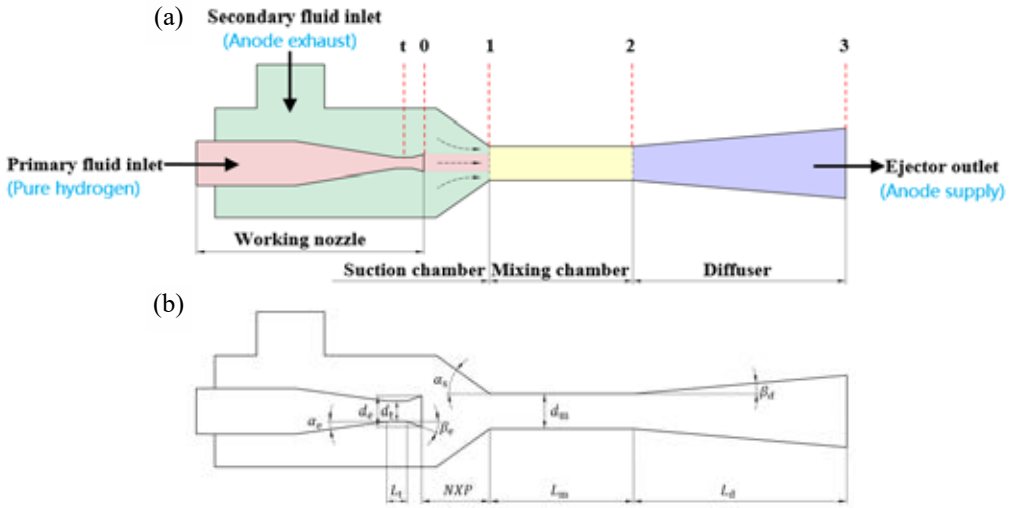


Fig.1 Structure of a PEMFC ejector: (a) internal flow field, (b) dimensions

Model functions

$$\dot{m}_p = \begin{cases} P_p A_e q_{p0} \sqrt{\frac{k}{R_g T_0}\left(\frac{2}{k+1}\right)^{\frac{k+1}{k-1}}} & \left(\frac{P(\lambda_1)}{P_p} < \varphi_{epr} < 1\right) \\ P_p A_t \sqrt{\frac{k}{R_g T_0}\left(\frac{2}{k+1}\right)^{\frac{k+1}{k-1}}} & \left(0 < \varphi_{epr} < \frac{P(\lambda_1)}{P_p}\right) \end{cases} \quad (1)$$

$$P_b = \frac{P_s}{\pi_{m2}}\left[\varphi_{epr}\pi_{p0}\frac{A_e}{A_m} + \pi_{s1}\left(1 - \frac{A_e}{A_m}\right) + C\frac{k\varphi_{epr}}{\varphi_3}\pi_*\frac{A_t}{A_m}\right] \quad (2)$$

$$C = \varphi_1\varphi_2\varphi_3\lambda_{p0} + \varphi_2\varphi_3\varphi_4\mu\lambda_{s1} - (1+\mu)\lambda_{m2} \quad (3)$$

Eq. (1) calculates primary mass flow under both critical and subcritical state of working nozzle. Eq. (2)-(3) are equations of ejector's performance curve based on the conservation of mass and momentum in mixing chamber.

RESULTS AND DISCUSSION

Seen in Fig.2(a), when ejector's backpressure is higher than the back-flow pressure P_{bf}, ejector works in back-flow state and has no recirculation effect. When the backpressure gradually decreases, ejector becomes sub-critical and the entrainment ratio increases sharply. When the backpressure furtherly decreased to be lower than the critical pressure P_{cr}, ejector enters a stable critical state and the entrainment ratio is constant at maximum value μ_{hp}. Fig.2(b) demonstrates a good agreement between the model results and the experimental data of a 60kW fixed-nozzle ejector, based on which a pre-study of variable-nozzle scheme was carried out. Eq. (1) explains that shrinking nozzle's throat raises primary pressure. Therefore as shown in Fig.2(c), under the double effect of shrinking nozzle and raising primary pressure, a smaller throat results in bigger maximum entrainment ratio and higher critical backpressure. Whether ejector works in critical or subcritical state as marked by red lines, shrinking nozzle improves entraining performance.

A 120kW fixed-nozzle ejector was designed according to the operating conditions under 120kW stack load, and the variable-nozzle scheme was later proposed to reach the target entrainment ratio. λ_t and λ_{m2} are superficial isentropic velocity at the throat and the exit of mixing chamber respectively. When λ equals 1, the working nozzle or the ejector itself become critical. Seen in Fig.3(a) and (b), with initial structure (D_t=2mm) ejector can't achieve required entrainment ratio when stack load is lower than 60kW and nozzle becomes subcritical (λ_t<1) when load is lower than 40kW. Shrinking throat improves ejector's performance, especially with low stack load. At a load of 8.9kW, if the throat diameter is less than 1.2mm, ejector starts to recirculate and nozzle enters critical state. When throat diameter furtherly decreases to 0.4mm, ejector reaches target performance. Because the primary pressure becomes too high under relatively high stack load with small throat, which is unacceptable considering the selection of pressure regulator, the final control methods of variable-nozzle and primary pressure is stated in Fig.3(c). When stack load is lower than 60kW, the throat diameter needs to shrink gradually to 0.4mm and the primary pressure needs to be raised accordingly to 1181kPa.

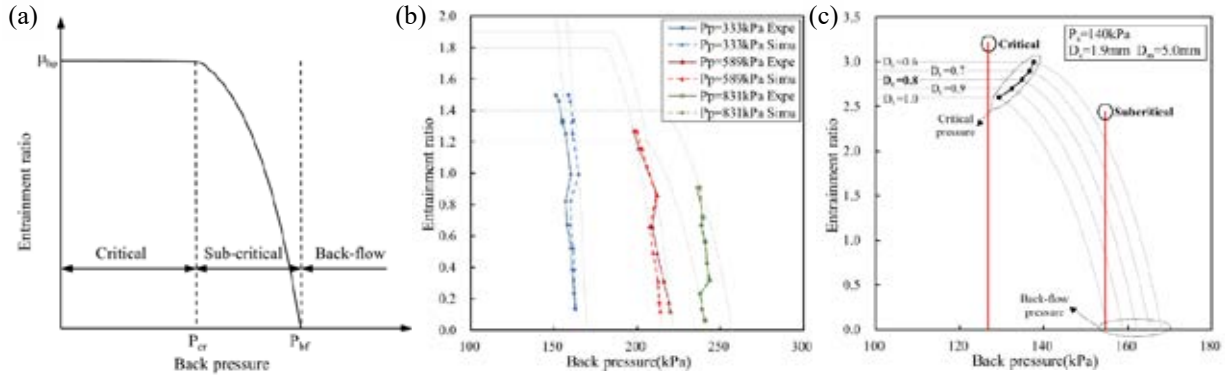


Fig.2 Characteristics of 60kW fixed-nozzle ejector: (a) typical performance curve, (b) model validation,

(c) performance with different throat diameter

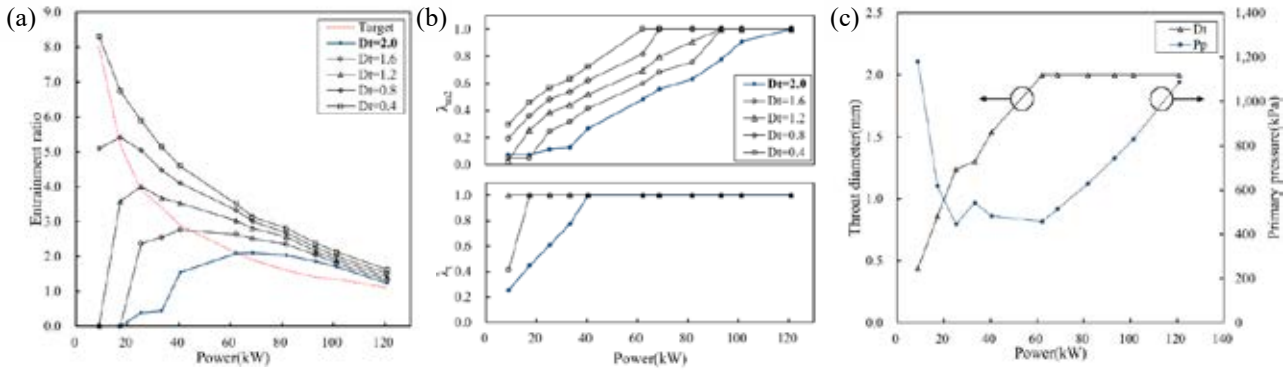


Fig.3 Characteristics of 120kW variable-nozzle ejector: (a) change of entrainment ratio, (b) change of superficial isentropic velocity,

(c) control method of throat and primary pressure

CONCLUSIONS

- A 1-D ejector model is built based on Soklov's theory with good accuracy. By shrinking nozzle's throat, the maximum entrainment ratio and critical backpressure can be raised, which is beneficial to entraining performance whether ejector works in critical or subcritical state
- A 120kW variable-nozzle ejector is designed. When stack load is within 60kW-120kW, ejector with maximum throat can provide required recirculation flow rate. When the load is smaller, throat needs to shrink gradually to a diameter of 0.4mm and the primary pressure needs to be raised accordingly to 1181kPa at the load of 8.9kW.

REFERENCES

1. Xue, H., et al., *Design and investigation of multi-nozzle ejector for PEMFC hydrogen recirculation.* International Journal of Hydrogen Energy, 2020. 45(28): p. 14500-14516.
2. Brunner, D.A., et al., *Design and characterization of an electronically controlled variable flow rate ejector for fuel cell applications.* International Journal of Hydrogen Energy, 2012. 37(5): p. 4457-4466.
3. Hosseinzadeh, E., et al., *Numerical analysis of transport phenomena for designing of ejector in PEM forklift system.* International Journal of Hydrogen Energy, 2014. 39(12): p. 6664-6674.
4. Sokolov, E., *Jet apparatuses*. second ed. " Energy" Publishing house. 1970, Moscow. 209.

WHEC-2022
23rd World Hydrogen Energy Conference
June 26-30, 2022 - Istanbul

#91

GIANTLEAP PROJECT: DEVELOPMENT OF A FUEL CELL RANGE EXTENDER FOR A BATTERY ELECTRIC BUS

[1]* *Frano Barbir,* [2] *Nadia Yousfi Steiner,* [3] *Federico Zenith*
[1]University of Split, Faculty of Electrical Engineering, Mechanical Engineering and Naval Architecture, Split, Croatia
[2] University of Franche-Comté, FEMTO-ST Institute, Belfort, France
[3] SINTEF Mathematics and Cybernetics, Trondheim, Norway

*Corresponding author e-mail: fbarbir@fesb.hr

ABSTRACT

Project Giantleap developed a fuel cell range extender for a battery electric bus. Several enhanced control functionalities were implemented to observe the state of health and to reduce the fuel cell stack degradation. The operation of the stack was remarkable. It showed very low degradation level in different operating conditions including some transient operations failures in coolant circuit. The range extender system was built in a trailer attached to a battery electric bus and successfully tested and demonstrated.

Keywords: Fuel cell, Range extender, Diagnostics and Prognostics, Control Unit

INTRODUCTION

City buses have long been considered an early market for the introduction of fuel cells, since a large deployment of fuel-cell buses is able to economically sustain its own hydrogen refuelling infrastructure. Several demonstration projects have demonstrated the feasibility of fuel-cell buses, in particular the long-running CHIC project, followed by the JIVE and JIVE2 projects. However, experience has also shown that availability and reliability of fuel cell buses is not mature yet: The project Giantleap addresses this challenge by improving the lifetime and reliability and reducing the total cost of ownership (TCO) of fuel cell systems in city buses. This is achieved through an advanced control system that includes novel diagnosis and prognosis approach. The system is, therefore, able to avoid or reduce faults and mitigate or slow down degradation.

THE GIANTLEAP PROJECT

The Giantleap project is a European project funded by the European Commission's public-private partnership Fuel Cell and Hydrogen 2 Joint Undertaking (FCH2JU). The Giantleap team consists of three research institutions SINTEF from Norway, Universite de Franche-Comte (UFC) from France, Faculty of Electrical Engineering, Mechanical Engineering and Naval Architecture (FESB) University of Split from Croatia, and 2 OEMs Bosch Engineering (BEG) and ElringKlinegr (EK) from Germany, and one end user – bus manufacturer, VDL Enabling Transport Solutions (VDL-ETS) from Netherlands. The team and interactions between the partners are shown in Fig. 1.

At the very beginning of the project the team has decided to develop and construct a prototype fuel cell range extender with built-in diagnostic and prognostic features into a control unit and demonstrate it by connecting it to a battery electric bus.

FESB in collaboration with SINTEF, has developed a method of quick and simple measurement of low-frequency intercept in the impedance spectrum (ELFIS) as an indicator of stack degradation. UFC has developed a PEMFC stack model using the Energetic Macroscopic Representation EMR formalism, that was used to predict both the fuel cell stack ageing and its interactions with the balance of plant (BoP), namely hydrogen line, air supply and the cooling subsystem. A voltage decay is observed with the stack ageing, and its trend is analyzed and confronted to the observed long-term testing results. The model integrates the stack ageing laws and is adapted for on-board prognostic and health management purposes. SINTEF in collaboration with BEG has developed the control logic which was used in the Fuel Cell Control Unit (FCCU) provided by BEG that ensures that the fuel cell and other BoP-components always are kept within safe operating conditions from startup to shut-down and during normal operation modes when the fuel cell delivers charging power to the bus. Several enhanced control functionalities were implemented to observe the state of health and to reduce the degradation.

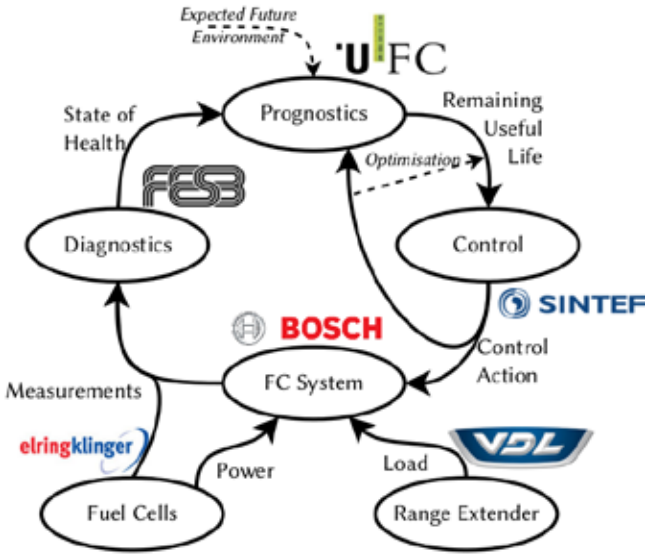


Fig. 1 The team and interactions between the partners

ElringKlinger has developed and provided full-size stack modules for laboratory experiments and for the integration into the fuel cell range-extender bus system. The NM5 stack platform suitable for mass production which is used in this project offers the possibility of realizing highly efficient systems due to a very low pressure drop on the cathode side. Patented structures within the metallic bipolar plate ensure a very homogeneous gas distribution and therefore operational stability especially in partial load at lower gas flow rates. Besides sensors, valves, droplet separators and bypass structures also the passive hydrogen recirculation unit as a major part of the anode sub-system is already integrated into the stack module. Hydrogen gas recirculation in general is important to maintain optimal gas distribution as well as humidification of the dry hydrogen supplied by the tank system of the trailer.

A robust fuel cell system including a reliable control system was designed by Bosch Engineering (BEG) and it is shown in Fig. 2. This system was assembled, tested on the test bench at BEG facilities before it was delivered for integration into the range extender, and brought into operation in a first demonstration prototype trailer at VDL-ETS facilities and on road.

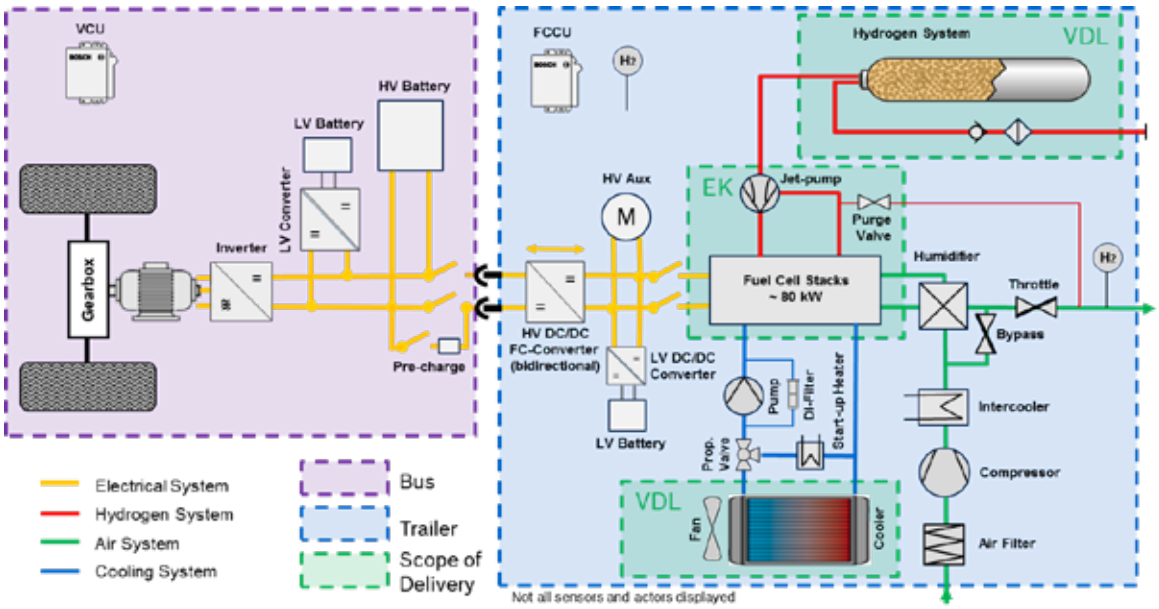


Fig. 2 Fuel cell system design

As part of the fuel cell system development, the BoP components were selected considering their robustness and expected lifetime. This applies to all BoP components, but in particular on the three main components that cause most system failures or have a large impact on system cost, i.e. air supply unit, pressure reducer and the cathode inlet humidifier. These components were evaluated separately on a test bench before being integrated in the system. In

general, the system was equipped with noninvasive sensors to perform prognostics and data evaluation to support the validation of the Prognostics and Health Management PHM control system during demonstrations and experiments.

VDL-ETS has facilitated and developed the mobile test platform as a trailer connected to an electrically driven VDL E-powered bus, shown in Fig. 3. The trailer includes the fuel cell system developed and tested by BEG and the hydrogen storage system holding 30 kg of hydrogen at 350 bar. The trailer is also equipped with vehicle lighting and brake subsystems for safe operation during testing. All electrical connections for high voltage power supply and communication have been provided. For software interfacing VDL-ETS assisted BEG and EK in communication for the safe start-up and shut-down of the system and linking signals to the vehicle.



Fig. 3. The trailer design (left) and the trailer built (right)

CONCLUSIONS

After three and a half years, the Giantleap project successfully concluded with a prototype demonstration in operational environment (i.e. on road, TRL 7) as opposed to the originally planned relevant environment (i.e. in a laboratory test bench, TRL 6). The bus and its range extender were tested while driving around VDL-ETS's premises in Valkenswaard, Netherland (Fig. 4).



Fig. 4. The trailer attached to the bus during test drive

Bosch Engineering has strengthened their activities in fuel-cell systems, and now offers balance-of-plant components specifically for such systems. While the project has been running, VDL-ETS has become the world's largest zero-emission bus manufacturer (outside of China), though most of these are battery buses., and over 90% of VDL-ETS's bus sales today are zero-emission. As the project concludes, the prototype developed in Giantleap has already evolved in a new generation ready to be demonstrated in passenger long-haul service between Rotterdam and Zeeland within the project 3-Emotion. Similar fuel cell range extender modules are being used in trucks.

ACKNOWLEDGEMENT

This project has received funding from the Fuel Cells and Hydrogen 2 Joint Undertaking under grant agreement No 700101. This Joint Undertaking receives support from the European Union's Horizon 2020 research and innovation programme and Hydrogen Europe and Hydrogen Europe Research.

WHEC-2022
23rd World Hydrogen Energy Conference
June 26-30, 2022 - Istanbul

#96
MULTI-OBJECTIVE OPTIMIZATION OF A TURBINE IMPELLER FOR FUEL CELL VEHICLES

[1] *Haoyu Mao,* [2] *Yuemeng Zhang,* [3*] *Sichuan Xu*
[1] School of Automotive Studies, Tongji University, 201804, Shanghai, China
[2] School of Automotive Studies, Tongji University, 201804, Shanghai, China
[3] School of Automotive Studies, Tongji University, 201804, Shanghai, China

*Corresponding author e-mail: scxutj@163.com

ABSTRACT

Turbines can effectively recover 25-40% of the power consumed by centrifugal compressors, which significantly improve the efficiency of the proton exchange membrane fuel cell system. In this paper, a turbine impeller for an 80kW fuel cell stack is optimal designed. A multi-objective optimization method for turbine impellers is presented via integrating uniform design, back-propagation neural network and multi-island genetic algorithm. The numerical results indicate a considerable improvement to total-static expansion ratio and isentropic efficiency of the turbine impeller by 4.2% and 6.8% at the design point, respectively. It is shown that reducing impeller outlet diameter ratio can improve the efficiency. A lower impeller inlet width and a higher outlet diameter ratio are beneficial to increase the expansion ratio.

Keywords: Turbine, Fuel cell vehicle, Uniform design, Back-propagation neural network, Multi-island genetic algorithm

INTRODUCTION

Fuel cell vehicles (FCVs) are characterized by zero emissions during driving, short fuel filling time and long driving distance, which are considered to be one of the ultimate clean energy vehicles. Among the various auxiliary parts of the FCS, air compressor is the most consuming component, accounting for about 10~20% of the output power of the fuel cell stack [1]. However, turbines can effectively recover 25-40% of the power consumed by compressors, which significantly improve FCS efficiency.

With the development of effective computational tools, there has been an increase in the use of coupling numerical simulations and optimization methods to release the impeller design process from depending on the designers' experience. However, the design process is a formidable optimization task involving computationally intensive models and multiple objectives. Thus, surrogate models have gained more and more attentions in the optimization of turbomachinery [2].

In this paper, a multi-objective optimal design method for turbine impeller is proposed via integrating uniform design (UD), back-propagation (BP) neural network and multi-island genetic algorithm (MIGA). The subsequent sections are organized as follows: First, detailed aerodynamic evaluation of turbines is carried out based on numerical model and validation by comparison with experimental results. Then, the flowchart of a multi-objective design optimization method is introduced. Impeller inlet width (b_1), impeller inlet lean angle (λ_1), impeller outlet width (b_2), impeller outlet angle (β_2) and impeller outlet diameter ratio (δ) and impeller axial length (L) are selected as optimal variables. Finally, the effect of geometric parameters of turbine impeller on the aerodynamic performance is evaluated.

MODELS AND METHODS

Numerical Model and Validation

To evaluate the aerodynamic performance of turbines, RANS equations coupled with the two-equation k-ω based shear stress transport (SST) turbulence model are applied. After the verification of grid independence, the number of grid nodes for impeller is 1,500,000. The aerodynamic performance curve is shown in Fig.1, which can be seen that the isentropic efficiency of the turbine based on the present model agree reasonably well with the experimental data.

Multi-objective Optimization Method

A turbine impeller for an 80kW fuel cell stack was designed via a multi-objective optimization method as shown in Fig. 2. It consists of three parts: UD, BP neural network and MIGA.

The UD method is one of DOE method developed by Fang and Wang, which is suitable for multi-objective and multi-level problems [3]. The entire experimental domain can be adequately explored with less arrangements. For DOE of five factors and ten levels, the UD method only needs 10 times, compared with 105 times by the general method and 102 times by the orthogonal method.

The BP algorithm is one of the most widely used in neural network training, which is improved by Rumelhart on the basis of neural network algorithm in 1989 [4]. It is a multilayer neural network model, including input layer, output layer and several hidden layers. Fig. 3 shows a three-layer model. It can realize the mapping from any M-dimension input to N-dimension output. BP neural network has a good nonlinear fast mapping ability. By studying the mapping relationship between the complex geometric parameters and the aerodynamic parameters, the time of 3D numerical simulation can be greatly reduced.

MIGA was proposed by Kaneko et al. based on improvements in parallel distributed genetic algorithms (PAGAs) . The main characteristic of MIGA is that each individual population is divided into several islands. Selection, crossover and mutation are carried out on each island separately. By using the roulette method, some individuals are selected from each island and moved to different islands on a regular basis.

Seven structural parameters are selected as optimal variables. b_1 influences inlet velocity and impeller flow capacity. λ_1 affects the distribution of inlet aerodynamic parameters in the circumferential and the span wise direction. b_2 determines the outlet flow area. It is closely related to the distribution of outlet aerodynamic parameters in the span wise direction. β_2 and δ affect the flow area and flow angle of the impeller outlet, thus they affect the outlet relative speed. The outlet relative speed determines the impeller internal flow loss. L determines the length and shape of the impeller passage, which affects the flow field distribution and the internal flow loss.

The turbine impeller is optimized for maximizing its total-static expansion ratio and isentropic efficiency with constraints on the averaged mass flow rate of impeller inlet and outlet. The corresponding mathematical expression for aerodynamic optimization of the impeller is as follows:

$$\begin{cases} \max\left(\pi_{ts}(x), \eta_{is}(x)\right), \\ x = (b_1, \lambda_1, b_2, \delta, \beta_{2s}, \beta_{2h}, L)^T \\ \text{s.t. } 0.99\dot{m}_{ave}(ref) \le \dot{m}_{ave}(x) \le 1.01\dot{m}_{ave}(ref) \end{cases} \quad (1)$$

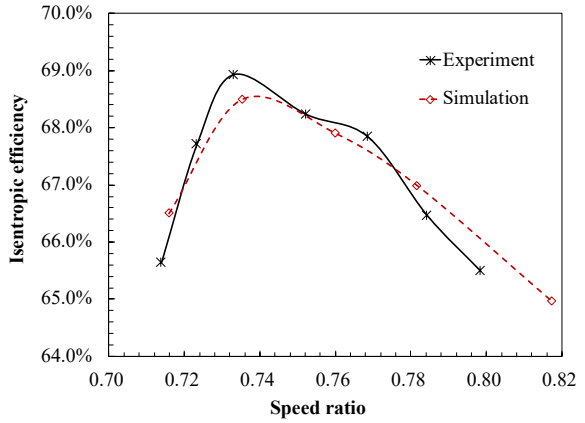


Fig. 1. Aerodynamic performance at 100,000 rpm speed for validation of the numerical model

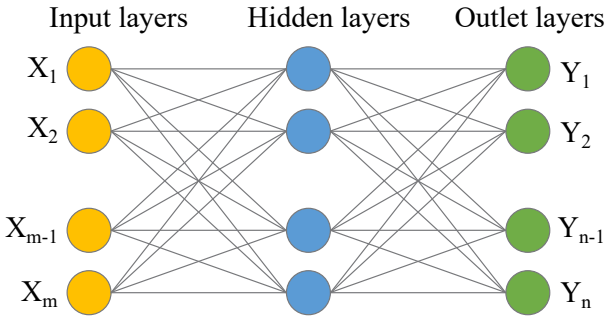


Fig. 3. BP neural network with one hidden layer and n outputs

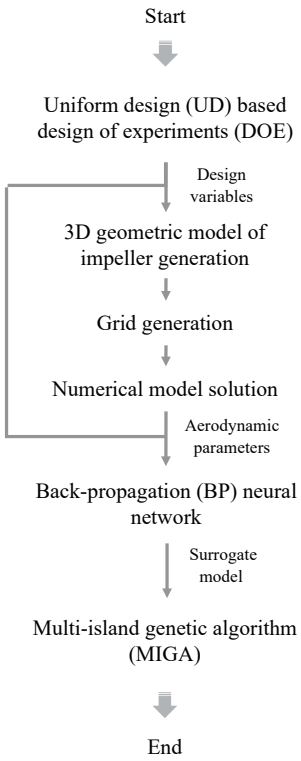


Fig. 2. Flow chart of the multi-objective optimization method

RESULTS AND DISCUSSION

The numerical results indicate a considerable improvement to total-static expansion ratio and isentropic efficiency of the turbine impeller by 4.2% and 6.8% at the design point, respectively. Fig. 4 shows the weight factors of geometric parameters in the aerodynamic performance of impellers. It can be seen that the impeller inlet width (X1)

and the outlet diameter ratio (X4) have a major impact on the aerodynamic performance. The weight factors of X1 and X4 in isentropic efficiency are 15.4% and 66.7%, respectively. The weight factors of X1 and X4 in expansion ratio is 44.5% and 38.2%, respectively. However, as the value of X4 increase, the value of expansion ratio increases, and the value of isentropic efficiency decreases at the same time. Similar phenomenon can be found for impeller inlet lean angle (X2). Therefore, there are trade-off relations between expansion ratio and isentropic efficiency, for larger expansion ratio is achieved by lowering its isentropic efficiency.

As the inlet width decreases, the inlet absolute velocity increases, which facilitates the conversion of pressure energy into kinetic energy. The increase of the inlet absolute velocity decreases the relative flow angle. As shown in Fig. 5, when the absolute angle of the entrance is constant, the inlet relative flow angle (incidence) is decreased (change from green flow condition to blue). According to the aerodynamic theory of turbomachinery, the decrease of the incidence is beneficial to improving the internal flow stability.

Although impeller outlet width and outlet angle have little influence on expansion ratio and isentropic efficiency, choosing a reasonable value can reduce the exit velocity loss and internal flow loss. Fig. 6 shows that the optimized impeller absolute flow angle is closer to zero, which indicates that the exit velocity loss is reduced. However, the absolute flow angle at 90% - 100% span wise increases. This is due to the mixing of the leakage flow and the transverse flow at the top of the suction section.

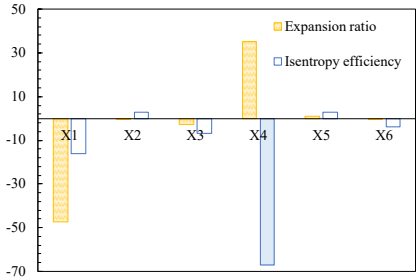


Fig. 4. Influence factors of geometric parameters on expansion ratio and isentropic efficiency of impeller

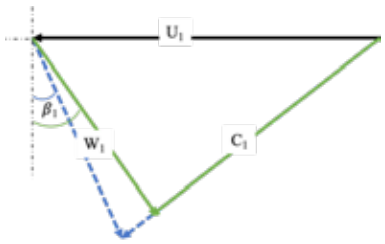


Fig. 5. The influence of impeller inlet width on the relative flow angle

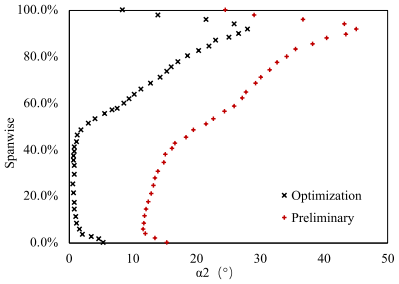


Fig. 6. Distribution of absolute flow angle at impeller outlet

CONCLUSIONS

A systematic method is established to analyze the influence of geometric parameters on the aerodynamic performance of turbine, and an appropriate geometry of small-scale turbine for fuel cell vehicle is obtained. The method can optimize the main parameters of the turbine, which considerably saves time and reduces cost, and can effectively improve the aerodynamic performance.

- The weight analysis of geometric parameters shows that impeller inlet width and outlet diameter ratio have a major impact on the turbine aerodynamic performance.
- Reducing outlet diameter ratio can improve the efficiency. A smaller impeller inlet width and a larger outlet diameter ratio are beneficial to increase the expansion ratio.

ACKNOWLEDGEMENT

This work was supported by Open fund of State Key Laboratory of Compressor Technology: Research on core key technologies of compressor for full power fuel cell, which is gratefully acknowledged.

REFERENCES

1. Ahluwalia, R. K. and Wang, X. 2015. “Fuel Cells Systems Analysis, 2015 DOE Hydrogen and Fuel Cells Program Review,”
2. Wang, G. G. and Shan, S. 2007. “Review of Metamodeling Techniques in Support of Engineering Design Optimization,” Asme International Design Engineering Technical Conferences & Computers & Information in Engineering Conference.
3. Yuan, W. and Fang, K. 1990. “Number theoretic method in applied statistics,” doi:10.1142/9789812701190_0038.
4. Rumelhart, D. E. 1986. Learning Representations by Back-Propagating Errors. Nature 23.

WHEC-2022
23rd World Hydrogen Energy Conference
June 26-30, 2022 - Istanbul

#103

SYNTHESIS AND CHARACTERIZATION OF MWCNT-SUPPORTED PBI MEMBRANES FOR HT-PEM FUEL CELLS

[1,2*] *Mehmet Turan Görüryılmaz,* [3]*Sibel Özenler,* [4]*Bihter Zeytuncu,* [1]*Nilgün Karatepe*
[1]Department of Energy Science and Technology, Energy Institute, Istanbul Technical University, Istanbul, Turkey
[2] Department of Energy Science and Technologies, Turkish-German University, Istanbul, Turkey
[3] Department of Material Science and Technologies, Turkish-German University, Istanbul, Turkey
[4] MEM-TEK Prof. Dr. Dincer Topacık National Research Center on Membrane Technologies, Istanbul Technical University, Istanbul, Turkey

*Corresponding author e-mail: mtgoruryilmaz@gmail.com

ABSTRACT

Polybenzimidazole (PBI) membranes are highly sought after for HT-PEMFCs due to their thermal stability, mechanical strength and protonic conductivity. In this study, PBI polymer and the membranes were synthesized for HT-PEMFC applications. Then, the polymer was characterized by using NMR and TG analyses. All the characteristic peaks were observed in the NMR results and PBI polymer decompose around 550 °C. After the synthesis, pristine and multi-walled carbon nanotube (MWCNT) supported membranes were prepared, doped with phosphoric acid and characterized by using TGA, FT-IR, XRD, SEM and EIS tests. The characteristic bonds of the polymer for both undoped and doped membranes were seen in FT-IR results. XRD results showed the semi-crystalline structure of the polymer. SEM results enabled to observe the homogeneous dispersion of the MWCNTs within the membrane. Finally, EIS tests were carried out in anhydrous conditions. The conductivities were obtained for pristine PBI membrane as 0.0518 S/cm, 0.0667 S/cm and 0.0895 S/cm, respectively. For the 0.5wt% PBI/MWCNT membrane, they were calculated as 0.0401 S/cm, 0.0586 S/cm and 0.0613 S/cm for 120 °C, 140 °C and 160 °C, respectively. For the 1wt% PBI/MWCNT membrane, slightly higher conductivities were obtained as 0.0429 S/cm, 0.0621 S/cm and 0.0655 S/cm for the temperatures 120 °C, 140 °C and 160 °C, respectively.

Keywords: PBI, MWCNT, PEM, fuel cell, membrane.

INTRODUCTION

PEMFCs use most commonly Nafion membranes and their working temperature is usually under 90 °C. However, the low working temperature is not enough for an efficient working condition due to low oxygen reduction kinetics and low tolerance towards gas impurity, as well as heat and water management problems. Thus, a new type of membrane, polybenzimidazole, was introduced [1]. Due to high working temperatures, the possibility of liquid water forming in the porous media is eliminated and a required low relative humidity does not need water management [2]. Since then, good mechanical strength, high conductivity and outstanding thermal stability up to 200 °C for this type of membrane have been presented [3]. Carbon-based fillers such as carbon nanotubes, carbon black, graphene oxide, etc., are observed to be used in PBI membranes to improve not only the physical but the conductive properties also [4]. Moreno et al. [5], showed that the MWCNT-supported PBI membranes produced by the spin coating method have higher tensile strengths, as well as higher protonic conductivity and open-circuit voltage (OCV). Similarly, other studies reported an increase in both tensile strength and ionic conductivity for the composite membranes prepared with functionalized MWCNTs [6-8]. Wu et al. [9], concluded that the functionalized MWCNTs decrease the gas permeability while increasing the ionic conductivity for direct methanol fuel cells. Shao et al. [10], introduced a new “one-pot” method to synthesize sulfonated MWCNT-supported PBI and demonstrated an increased tensile strength in the membranes.

In this study, both pristine and CNT doped PBI membranes were prepared by casting method and their properties were observed through characterization methods, such as NMR, SEM, FT-IR, TGA, XRD, EIS.

MATERIALS AND METHODS

3,3′-Diaminobenzidine tetrahydrochloride hydrate (DAB.4HCl.xH_2O, ≥96%, Sigma-Aldrich) and isophthalic acid (IPA, 99%, Sigma-Aldrich) were used as the monomers and polyphosphoric acid (PPA, reagent grade 115%, Sigma-Aldrich) was used as the solvent for the polymerization reaction. Calcium chloride (technical grade) was used as the drying agent and pure nitrogen gas was used to make the reactor inert. N,N-Dimethylacetamide (DMAc, ReagentPlus®, ≥99%, Sigma-Aldrich) is used for membrane preparation. The acid doping process was carried out

with o-phosphoric acid (PA, 85%, Sigma-Aldrich). Multi-walled carbon nanotubes (MWCNTs) were synthesized in Istanbul Technical University, Energy Institute, Material Production and Preparation Laboratory, by using the chemical vapor deposition method at 500 °C, using acetylene.

PBI Synthesis

A three-necked flask was chosen as the reactor. $CaCl_2$ was used as a drying agent and nitrogen gas was used to make the reactor inert. PPA was added to the reactor and heated to 140 °C. Then, DAB.4HCl (1/26.5 in weight of PPA) was added and stirred mechanically. After that IPA (equimolar amount of DAB) was added to the bubble and heated to 170 °C. Finally, the temperature was increased to 200 °C and the reaction carried on for 24 hours. The viscous polymer solution was filtered, washed and isolated.

Membrane Preparation

5wt% PBI/DMAc solution was prepared with ground polymer. The solution was stirred magnetically at 80 °C for 2 hours. The clean solution was cast on the petri dish and dried overnight. Thus, the pristine PBI membrane was obtained.

The MWCNT supported membrane preparation is not different from the pristine membrane preparation. The only difference is that PBI solution was mixed with 0.5wt% and 1%wt MWCNTs and homogenized ultrasonically for 6 hours. Then the solutions were cast into petri dishes and dried in the oven.

RESULTS AND DISCUSSION

The 1H-NMR results showed that the synthesized polymer had all the characteristic peaks of PBI, with imidazole protons at 13.421 ppm and aromatic protons between 9.2 ppm and 7.5 ppm.

The acid doping was carried out at room temperature for 5 days. At the end of 5 days, the membranes were dried thoroughly with a paper towel first, then in the vacuum oven at 90 °C for 5 hours. The doping levels were calculated as 14.3 mol PA/PBI for the pristine PBI, 5.9 mol PA/PBI for the 0.5wt% MWCNT/PBI membrane and 7.3 mol PA/PBI for the 1wt% MWCNT/PBI membrane

TGA analyses yielded excellent thermal stability for PBI polymer and the pristine membrane, with a decomposition temperature around 550 °C. A weight loss between 220-420 °C was observed for the composite membranes and it is attributed to the PBI coated MWCNT decomposition. All the membranes were thermally stable up to 220 °C, thus suitable for HT-PEMFC applications.

XRD analyses gave the semi-crystalline structure of the polymer with a broad peak around $2\theta = 25°$. The intensity of the peak increases with the increasing MWCNT amount.

FT-IR results of both doped and undoped membranes showed the peaks of the corresponding bonds of a PBI polymer. N-H stretching between 4000-2000 cm^{-1} and benzene/imidazole rings between 1700-1000 cm^{-1}. The peaks at 1620, 1530, 1440, 1280 and 790 cm^{-1} mean strong C=C/C=N stretch, the characteristic of 2-substitution, the characteristic of benzimidazole in-plane vibration, C-N stretch and C-H bending, respectively. The 2920 cm^{-1} peak signifies the N-H group, where the narrow peaks below 2000 cm^{-1} belong to phenyl groups. Acid doping gives a dramatically changed result. C-N, H-N and cycle deformations occur between 2000-1000 cm^{-1}. The phosphoric acid doping causes a shadowing over the visibility of the peaks due to hydrogen bonding and the vibrations of hydrogen phosphate groups. Doping also introduces a new peak at 1495 cm^{-1}, related to the C=N vibrations of the $C=NH^+$ group. The absorption bands of the MWCNTs are almost invisible for the composite membranes, due to the non-covalent π-π interactions.

SEM results yielded the morphological structure of the membranes. The tips of the MWCNTs were clearly visible as white dots. The lack of lumps indicates a good dispersion of the MWCNTs, along with the uniform distribution of the white dots.

EIS tests were carried out to measure the impedances and to calculate the ionic conductivities at different temperatures, 120 °C, 140 °C and 160 °C. While the conductivities of the pristine membrane were found as 0.0518 S/cm, 0.0667 S/cm and 0.0895 S/cm, the conductivities of the 0.5wt% PBI/MWCNT membrane were determined as 0.0401 S/cm, 0.0586 S/cm and 0.0613 S/cm for 120 °C, 140 °C and 160 °C, respectively. As expected from 1wt% PBI/MWCNT membrane, slightly higher conductivities were obtained. The temperatures 120 °C, 140 °C and 160 °C yielded 0.0429 S/cm, 0.0621 S/cm and 0.0655 S/cm, respectively.

CONCLUSIONS

PBI membranes with different amounts of MWCNTs were prepared and characterized in order to investigate the effect of MWCNTs. The polymer was synthesized via solution polymerization method and was characterized first by NMR, which ensured the characteristic peaks of PBI. Then FT-IR showed peaks that were clearly belong to PBI. Combined with the result of the TGA, it was concluded that the synthesized material was indeed PBI.

The polymer was dissolved in DMAc, to obtain mechanically strong and thermally stable membranes for HT-PEMFC applications. Then, the membranes were further tested with XRD and TGA. While XRD analyses showed the semi-crystalline structure of the polymer, TGA analysis yielded thermal stability up to 550 °C.

The surface morphology was investigated along with the MWCNT distribution within the membranes by using SEM analyses. It was concluded that the ultrasonic homogenization resulted in well-dispersed MWCNTs. It was also seen that the MWCNT-support increased the acid doping level for the composite membranes, due to acid retention.

The EIS results exhibited an increase in the ionic conductivity for all the membranes with the increasing temperature. Increasing MWCNT-support also showed an increase among the composite membranes.

REFERENCES

1. Wainright JS, Wang J-T, Weng D, Savinell RF, Litt M. 1995. Acid-Doped Polybenzimidazoles: A New Polymer Electrolyte. Journal of The Electrochemical Society. 142:121-123
2. Jensen JO, Li Q, Pana C, Vestbo AP, Mortensen K, Petersen HN, Sorensen CL, Clausen TN, Schramm J, Bjerrum NJ. 2007. High temperature PEMFC and the possible utilization of the excess heat for fuel processing. International Journal of Hydrogen Energy. 32:1567-1571
3. Li Q, Jensen JO, Savinell RF, Bjerrum NJ. 2009. High temperature proton exchange membranes based on polybenzimidazoles for fuel cells. Progress in Polymer Science. 34:449-477
4. Dey B, Ahmad MW, ALMezeni A, Sarkhel G, Bag DS, Choudhury A. 2020. Enhancing electrical, mechanical, and thermal properties of polybenzimidazole by 3D carbon nanotube@graphene oxide hybrid. Composites Communications. 17:87-96
5. Moreno NG, Gervasio D, Garcia AG, Perez Robles JF. 2015. Polybenzimidazole-multiwall carbon nanotubes composite membranes for polymer electrolyte membrane fuel cells. Journal of Power Sources. 300:229-237
6. Jheng LC, Huang CY, Hsu SLC. 2013. Sulfonated MWNT and imidazole functionalized MWNT/polybenzimidazole composite membranes for high-temperature proton exchange membrane fuel cells. International Journal of Hydrogen Energy, 38:1524–1534
7. Suryani, Chang, CM, Liu YL, Lee YM. 2011. Polybenzimidazole membranes modified with polyelectrolyte-functionalized multiwalled carbon nanotubes for proton exchange membrane fuel cells. Journal of Materials Chemistry, 21:7480.
8. Kannan R, Kagalwala HN, Chaudhari HD, Kharul UK, Kurungot S, Pillai VK. 2011. Improved performance of phosphonated carbon nanotube–polybenzimidazole composite membranes in proton exchange membrane fuel cells. Journal of Materials Chemistry, 21:7223
9. Wu JF, Lo CF, Li LY, Li HY, Chang CM, Liao KS, Hu CC, Liu YL, Lue SJ. 2014. Thermally stable polybenzimidazole/carbon nano-tube composites for alkaline direct methanol fuel cell applications. Journal of Power Sources, 246:39–48
10. Shao H, Shi Z, Fang J, Yin J. 2009. One pot synthesis of multiwalled carbon nanotubes reinforced polybenzimidazole hybrids: Preparation, characterization and properties. Polymer, 50:5987–5995

WHEC-2022
23rd World Hydrogen Energy Conference
June 26-30, 2022 - Istanbul

#110

DEVELOPMENT AND TESTING OF A PROTON EXCHANGE MEMBRANE FUEL CELL STACK ENVISIONING UNMANNED AERIAL VEHICLE APPLICATIONS

Diogo F.M. Santos, Rui B. Ferreira, D.S. Falcão, A.M.F.R. Pinto***
Transport Phenomena Research Center (CEFT), Chemical Engineering Department (DEQ), Faculty of Engineering of University of Porto (FEUP), Rua Dr. Roberto Frias, 4200-465 Porto, Portugal

*Corresponding author; E-mail address: rferreira@fe.up.pt
**Corresponding author; E-mail address: apinto@fe.up.pt

ABSTRACT

In this work, a 20 W 3-cell proton exchange membrane (PEM) fuel cell stack is developed and studied. This is an initial prototype for the future development of a 200 W stack to be used in an unmanned aerial vehicle (UAV). For this specific application, several considerations need to be made, such as size, weight and operation mode of the stack. The influence of several operating parameters on the stack performance is evaluated. The fans speed (air supply and temperature regulation) and the short-circuit (water production) are the most influential parameters due to their effect on the humidification state of the stack. H_2 purge and pressure do not significantly impact the performance. The purge, however, could be a more important factor in a larger stack.

Keywords: Proton exchange membrane, fuel cell stack, unmanned aerial vehicles

INTRODUCTION

The usage of unmanned aerial vehicles (UAVs) in both civil and military applications has increased in the last years [1]. Small UAVs are generally powered by electric batteries. However, they present some disadvantages, such as low energy density, resulting in short flight times, and long recharging periods. Fuel cells systems generally allow longer flight times [2] and faster refueling. Fuel cells directly convert the chemical energy in a fuel (generally H_2) in electric energy. Proton exchange membrane (PEM) fuel cells are the most common for small UAVs due to their high power density, high efficiency, fast dynamic response and fast start up time [3]. PEM fuel cells use solid polymer electrolyte membranes and a catalyst (generally platinum) to allow the generation of electricity at low temperatures. In this work, a small 3-cell PEM fuel cell stack was developed. This 20 W stack is an initial stage for the development of a 200 W PEM fuel cell stack, which will be tested as the power supply of a UAV commercialized by a partner company. The performance of the stack was evaluated and the influence of several operation parameters was investigated. This study will provide significant information for the future scale-up.

EXPERIMENTAL

Description of the stack

Fig. 1 contains a drawing of the fuel cell stack components. Due to the intended application, the size and weight of the stack are important parameters to consider. The end-plates were made of duralumin, a lightweight material, to give support to the rest to the stack components. The current collectors, made of gold coated copper, connect the stack to the test load/motor. Between these two components, a gasket is used to electrically isolate the end-plates. The bipolar plates, made of graphite, distribute the gas to the membrane electrode assembly (MEA) through their flow field. 25 cm^2 MEAs were used, having Nafion N212 membrane, Pt on carbon catalyst and carbon cloth gas diffusion layers (GDLs). The MEAs are surrounded by gaskets to avoid H_2 leakage. The stack operates with an open cathode with a parallel flow field. The air feed is accomplished by two fans (24 V / 6.9 W, PWM controlled), also responsible for the stack cooling. The stack also operates in a dead-end anode mode with a serpentine flow field. To remove excess water and N_2 that accumulate in the anode, periodical purges are performed. For the intended purpose of the stack, the humidification of the inlet gases is unfeasible, therefore, the stack humidification is facilitated by periodically short-circuiting the stack. The short-circuit momentarily increases the current of the stack, increasing the water production.

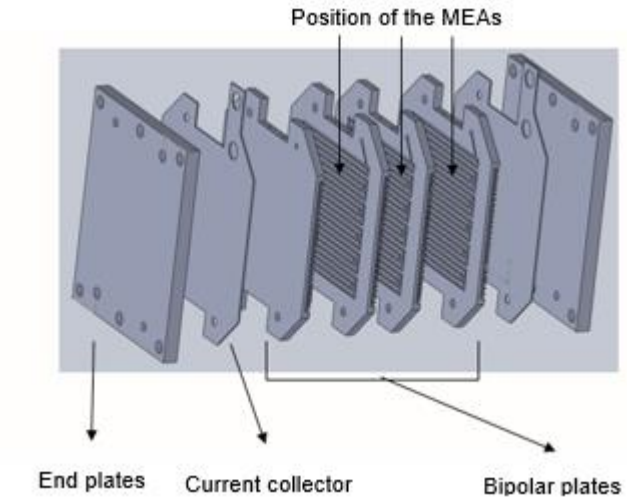


Fig. 1. Fuel cell stack components.

RESULTS AND DISCUSSION

Stack performance

The performance of the stack is shown in Fig. 2. These results were obtained with the fans at 50 % duty cycle, H_2 purge interval and duration of 15 s and 0.5 s, respectively, short-circuit interval and duration of 15 s and 0.1 s, respectively, and H_2 pressure of 50 kPa. As shown in Fig.2, the 3-cell stack reaches a power of 21 W at 15 A.

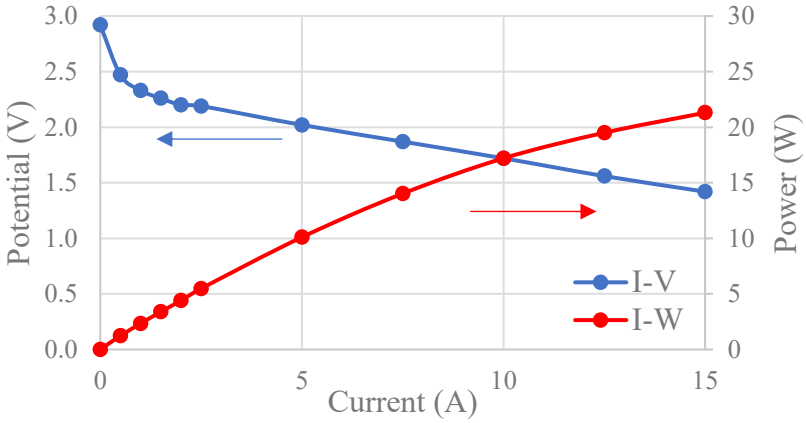


Fig. 2. Performance of the fuel cell stack.

Effect of operating conditions

The influence of operating parameters of the stack was studied. The results are presented in Table.1. For each current, a higher voltage represents a higher performance. The baseline operating conditions are the same as those indicated above when discussing the stack performance.

The fans speed was the most influential operation parameter for the stack performance. It was notorious that, for high currents (12.5 A), low fan speeds (<= 40%) are not capable of maintaining an appropriate temperature, leading to the drying of the membranes decreasing the stack performance.

The short-circuit presented a clear influence on the performance, especially the duration. A higher duration and frequency improve the humidification of the membranes improving the performance. However, the increase in current during the short--circuit may decrease the lifetime of the MEAs and affects the efficiency of the system. Nevertheless, these values may be used for maintenance/reconditioning of the stack in case of a long rest period or operation in dry conditions.

Besides the parameters indicated in Table 1, the effect of purge duration (0.1 to 1 s) and frequency (5 to 60 s) and H_2 pressure (10 to 60 kPa) were also evaluated. Both parameters did not have a relevant impact on the stack performance. In case of the purge, this may be due to the small amount of cells of the stack, allowing the complete removal of the

water (and possibly N_2) from the anode, even in the less favorable conditions (low purge duration and frequency). This parameter needs to be evaluated again in a larger stack as the total amount of water and N_2 to be removed will be considerably higher.
These results will be used to scale-up the stack for a 200 W output and to design the automatic control system so that the stack can be used as power supply for a small UAV.

Table 1. Effect of operating conditions on the stack performance.

		Potential (V) at a given current		
		1 A (0.04 A cm^{-2})	**5 A (0.20 A cm^{-2})**	**12.5 (0.50 A cm^{-2})**
Fans speed (%)	**20**	2.35	2.01	1.22
	40	2.39	2.05	1.44
	60	2.38	2.06	1.55
	80	2.40	2.09	1.56
Short-circuit duration (s)	**0.10**	2.37	2.05	1.55
	0.25	2.40	2.09	1.58
	0.50	2.43	2.15	1.65
Short-circuit frequency (s)	**5**	2.41	2.08	1.56
	30	2.37	2.03	1.52
	60	2.34	2.02	1.49

CONCLUSIONS

In this work, a PEM fuel cell stack was developed and the influence of the operation conditions on the performance was evaluated. A 3-cell stack was developed with specific materials and configuration to allow its application in an unmanned aerial vehicle. Of the operation parameters tested, the fans speed was the most influential. When the speed of the fans is low, at high currents the stack reaches a temperature sufficient to cause the drying of the membranes, decreasing the performance of the system. The short-circuit, related with the water production, also influences the humidification of the membranes, affecting the performance of the stack. A more frequent or long lasting short-circuit improved the performance due to a higher water production. H_2 purge and pressure did not significantly impact the performance of the system.

ACKNOWLEDGEMENTS

This work is a result of project ACE-Airborne Clean Energy systems (POCI-01-0247-FEDER-039863) co-funded by the European Regional Development Fund (ERDF), through COMPETE 2020 and LISBOA 2020 programmes. This work was also financially supported by: Base Funding - UIDB/00532/2020 and Programmatic Funding - UIDP/00532/2020 of the Transport Phenomena Research Center – CEFT - funded by national funds through the FCT/MCTES (PIDDAC).

REFERENCES

1. Boukoberine MN, Zhou Z and Benbouzid M. 2019. A critical review on unmanned aerial vehicles power supply and energy management: Solutions, strategies, and prospects. Applied Energy. 255:113823.
2. Gadalla M and Zafar S. 2016. Analysis of a hydrogen fuel cell-PV power system for small UAV. International Journal of Hydrogen Energy. 41:6422-6432.
3. Kurnia JC, Chaedir BA, Sasmito AP and Shamim T. 2021. Progress on open cathode proton exchange membrane fuel cell: Performance, designs, challenges and future directions. Applied Energy. 283:116359.

WHEC-2022
23rd World Hydrogen Energy Conference
June 26-30, 2022 - Istanbul

#124

EXPERIMENTAL DYNAMIC LOAD CYCLING AND CURRENT DENSITY MEASUREMENTS OF A PARALLEL SERPENTINE PEMFC DESIGN

[1*] *Baltasar Toharias,* [1] *Christian Suárez,* [1,2] *Alfredo Iranzo,* [3] *Artem Chesalkin,* [1] *Javier Pino,* [1] *Felipe Rosa*
[1] Thermal Engineering Group, Energy Engineering Department, School of Engineering, University of Seville, Spain
[2] AICIA, Andalusian Association for Research & Industrial Cooperation, Seville, Spain
[3] ENET Centre – Research Centre of Energy Units for Utilization of Non Traditional Energy Sources, VSB Technical University of Ostrava, Czech Republic

*Corresponding author e-mail: btoharias@us.es

ABSTRACT

In the present work, the behaviour of a parallel serpentine bipolar plate of a proton exchange membrane fuel cell (PEMFC) working under dynamic load cycling (FC-DLC) was experimentally studied. Current density and temperature distribution along the cell active area was examined at different stages for the dynamic load of the urban cycle representative of fuel cell electric vehicle applications. Experimental results showed uniform temperature distribution in the active area of the fuel cell at both low and high intensities, with temperature differences below 2 ºC. This homogeneity in temperature distribution supported the suitability of the proposed parallel serpentine design concept.

Keywords: Fuel cell, Bipolar plate, Dynamic load cycle, Current density measurement

INTRODUCTION

Currently there is a high demand for propulsion systems supported by renewable energy sources in the transport sector, one of them being PEMFCs. Due to their clean properties, high efficiency and low operating temperature, fuel cells are a good alternative and they have become a potential substitute for conventional combustion engines [1]. The application of PEMFCs to the transport sector requires that the design, testing and operation of PEMFCs should correspond to the specific operating conditions and loads of the dynamic load of the urban cycle. The methodology followed to examine the performance of MEAs under operating and stress conditions for automotive applications has already been described by the European Commission in the JRC Science Policy Report [2].

One of the key components in PEMFCs are the bipolar plates (BPs) as they represent a significant part of the volume, weight and cost. The material and design of the channels in the BPs have to ensure an appropriate water management within the cell and improve the performance of the cell at high current densities. Materials include graphite, coated metallic or composite plates, and different flow field designs such as parallel or serpentine, and alternatively also bioinspired designs have been proposed [3].

Different local conditions may exist in PEMFCs that lead to an inhomogeneous current production. Analysing the measurement of the current density and temperature distribution is important for a better understanding of PEMFC behaviour, efficiency and possible points for future improvements in the design of the BP. Previous works have studied the design of BP channels by measuring the polarisation curve [4], but fewer studies have also analysed the local phenomena from sensors that measure the current density and temperature distribution within the cell [5].

The objective of this research is to analyse the effect of the dynamic load of the urban cycle on the temperature and current density distributions of a PEMFC with a parallel serpentine channel design. Current density and temperature distribution were experimentally measured and PEMFC performance results were analysed.

EXPERIMENTAL SECTION

A fuel cell with an active area of 50 cm^2 was analysed. A parallel serpentine flow field design was proposed. Several previous experimental tests of the polarization curve IV were performed under different flow configurations, taking as a reference the following conditions: operating temperature of 65 ºC, pressure of 0.5 bar(a), anode stoichiometry of 1.3, cathode stoichiometry of 2.5 and anode and cathode relative humidity (RH) of 60%. Additional experiments were carried out modifying the inlet and outlet of the gas hose on the fuel cell test bench and the results in terms of the polarisation curve were compared with the conventional flow configuration.

A Current Density Measurement (CDM) sensor [6] was included in the PEMFC to measure both current density and temperature distribution during the experimental tests of a dynamic load of the urban cycle, representative of the real conditions to which the fuel cell is exposed in a driving cycle [2].

RESULTS AND DISCUSSION

To perform the dynamic load of the urban cycle, the IV hysteresis curve was obtained, including the increasing current part up to a maximum current value and the decreasing current curve part. The reference current value was calculated as the average of the two curves for a given voltage and this result was selected for the reference current value of 100 % in the dynamic load cycling test. In Fig. 1 load cycle and the corresponding cell voltage evolution can be observed, where the minimum voltage was kept above 0.3 V during the test.

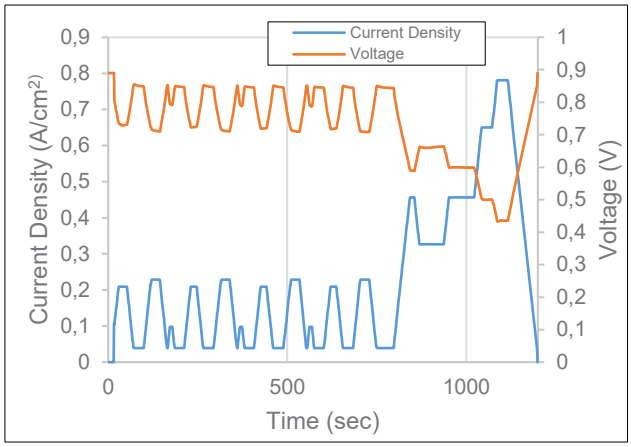


Fig. 1. Dynamic load cycling for operating conditions: P_{cell} = 0.5 bar, T_{cell} = 65 ºC, Relative Humidity at anode and cathode 60%, Stoichiometric factors at anode and cathode 1.3 and 2.5 respectively, and conventional flow configuration.

During the tests, temperature distribution transient data were obtained with the CDM sensor and local temperature distribution and the potential inhomogeneous zones were analysed. In Fig. 2, temperature distribution within the PEMFC active area is shown for both low and high intensities (left and right respectively). For low intensities the difference in temperature across the active area remained between 67 and 68 ºC, while for high intensities measured temperature differences were found to be higher, between 67.5 and 69 ºC.

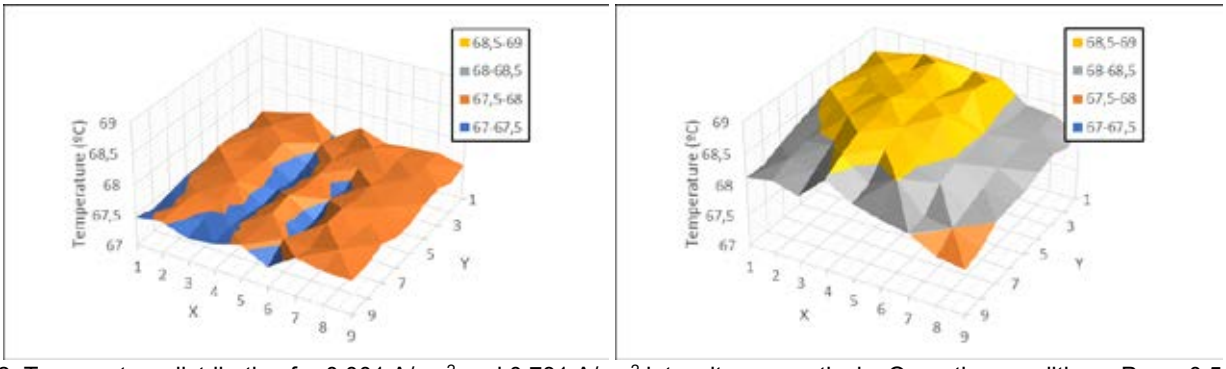


Fig. 2. Temperature distribution for 0.001 A/cm^2 and 0.781 A/cm^2 intensity, respectively. Operating conditions: P_{cell} = 0.5 bar, T_{cell} = 65 ºC, Relative Humidity at anode and cathode 60 %, Stoichiometric factors at anode and cathode 1.3 and 2.5 respectively, and conventional flow configuration.

CONCLUSIONS

The dynamic load of the urban cycle was tested with a parallel serpentine flow field PEMFC BP design. Both current density and temperature distribution were measured using a CDM sensor. Experimental results showed uniform temperature distribution in the active area of the fuel cell at both low and high intensities, with temperature differences below 2ºC. This homogeneity in temperature distribution supported the suitability of the proposed parallel serpentine design concept.

ACKNOWLEDGEMENTS

Grant PID2019-104441RB-I00 funded by MCIN/AEI/10.13039/501100011033, UNSE15-CE2962 and EQC2018-004258-P funded by MCIN/AEI, co-funded with ERDF funds.



Grant PY20 RE 026 AICIA funded by S.G. de Universidades, Investigación y Tecnología, PAIDI 2020 program by Junta de Andalucía, co-funded with ERDF funds.



REFERENCES

1. Reddy KJ and Sudhakar N. 2019. ANFIS-MPPT control algorithm for a PEMFC system used in electric vehicle applications. International Journal of Hydrogen Energy 44:15355–69.
2. Tsotridis G, Pilenga A, De Marco G and Malkow T. 2015. EU Harmonized Test Protocols for PEMFC MEA Configuration for Automotive Applications. EU Commission, JRC Science for Policy Report.
3. Iranzo A, Arredondo CH, Kannan AM and Rosa F. 2020. Biomimetic flow fields for proton exchange membrane fuel cells: A review of design trends. Energy 190:116435.
4. Iranzo A., Muñoz M, López E, Pino J and Rosa F. 2010. Experimental fuel cell performance analysis under different operating conditions and bipolar plate designs. International Journal of Hydrogen Energy 35:11437-11447.
5. Mingfu Y, Hong S, Tianyu Z, Qiang L, Jie L and Xiaochen Z. 2021. Current density distribution in an HT-PEM fuel cell with a poly (2, 5 – benzimidazole) membrane. International Journal of Hydrogen Energy 46:3022-3031.
6. http://www.splusplus.com. Accessed on December 09, 2021

WHEC-2022
23rd World Hydrogen Energy Conference
June 26-30, 2022 - Istanbul

#143

OPTIMIZING FUEL CELL MEMBRANES THROUGH THICKNESS AND CATION DOPING

Xiaoyan Luo[1], Adlai Katzenberg[1], A.R. Crothers[1], Victoria Ehlinger[1], A.Z. Weber[1], R.L. Borup[2], and A.Kusoglu[1,]*
[1] Lawrence Berkeley National Laboratory, Energy Technologies Area, 1 Cyclotron Rd, Berkeley, CA 94720, USA
[2] Los Alamos National Laboratory, Los Alamos, New Mexico 87545, USA

*Corresponding author e-mail: akusoglu@lbl.gov

ABSTRACT

Efforts towards improving performance and durability of polymer-electrolyte fuel cells (PEFCs) require an understanding and expansion of the design space for proton-exchange membranes (PEMs) in the presence of additives used to enhance their stability. One such additive utilized in PEMs is Cerium, due to its ability to act as radical scavenger to improve membrane stability. While showing promise in durability improvement, doping a multivalent cation such as Cerium into a proton-form PEM ionomer alters it structure and transport properties, the implications of which for membrane and cell performance remain relatively unexplored. In addition to the doping strategies employed for optimizing durability, membrane thickness is another factor for optimizing cost and performance. Thus, it is of interest to understand and quantify the extent to which membrane properties are dependent on these distinct factors that can be used as design parameters. This talk presents a summary of key aspects of doping and thickness effects in a membrane based on a comprehensive experimental study on PEM properties, including water uptake, conductivity and nanostructure characterization, which are then implemented into multi-physics fuel-cell models to demonstrate the expanded design space for PEMs that account for the materials and environmental parameters affecting both performance and durability.

Keywords: Fuel Cell, Ionomers, Cerium, Thickness, Durability

INTRODUCTION

Polymer electrolyte fuel cells (PEFCs), if optimized for durability, cost, and performance, have offer great prospects to revolutionize transportation in the form of fuel-cell vehicles (FCV) for automotive and heavy-duty applications.[1] In a PEFC, ion-conductive polymers, ionomers, primarily function as a selective proton-exchange membrane (PEM) facilitating ion transport between the catalyst layers (CLs), while also function as a electrolyte binder in CLs wherein they are mixed with the catalyst supports and particles (e.g., Carbon and Platinum) to improve mass transport of reactants to catalytic sites and remove product water. Perfluorosulfonic acid (PFSA) is the most widely used ionomer in PEFCs, due to their remarkable ion transport properties and mechanical stability.[2] However, PFSA-based PEMs still exhibit vulnerability to attacks by hydroxyl radical species during operation, which could possibly reduce their effectiveness as separators. During cell operation, chemical degradation occurs due to formation of hydrogen peroxide, H_2O_2, and its radicals that attack the ionomer and leads to its local decomposition.[3, 4] A popular strategy to combat this problem is to introduce scavengers, like cerium (Ce), into the membrane so that they can neutralize the radical species generated in and near the PFSA and improve chemical durability.[2-4] Such cation-doping, however, creates a complex multi-ion system (Fig. 1),[4, 5] thereby altering the mechanisms of transport understanding of which is extremely important for developing strategies for effective doping levels and utilization in membrane design. Thus, controlled Ce-doped PFSA provides a representative model system for studying the underlying origins of transport in cation-exchanged ionomers in PEM fuel cells (Fig. 1). While doping strategy is a design parameter employed for enhancing PEM durability, membrane thickness is another key factor for optimizing cost and performance.[6, 7] It is of interest to understand and quantify the extent to which membrane properties are dependent on these distinct factors that can be used as design parameters. The focus of this talks is to present an overview of two key factors impacting PEM properties, namely thickness[7] and Ce-doping,[4] based on a systematic experimental and theoretical investigation and demonstrate how they are utilized in cell models. The combinatory roles of operating conditions and doping-levels in membrane performance are also elucidated using multi-physics fuel cell simulations.[8, 9]

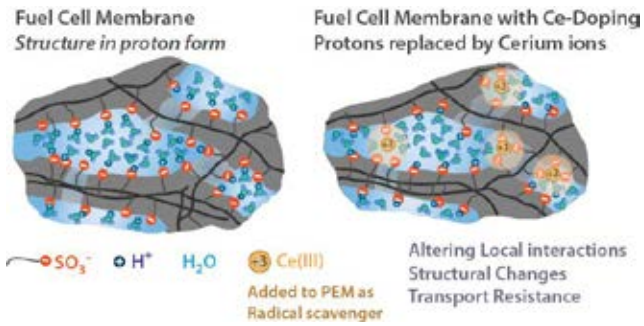


Fig. 1. Cerium added to Fuel-Cell proton-exchange membrane (PEM) as radical scavenger results in a complex structural state with implications for both transport (and performance) and durability.[4]

EXPERIMENTAL

Ce-doped Nafion membranes are prepared with various degrees of Ce(III) and Ce(IV) ion-exchange to obtain a mixed proton-cerium state in ionomer membrane. A systematic experimental investigation is carried out to measure water uptake and conductivity of Nafion-Ce membranes as a function of humidity and temperature, and the impact of Ce on nanostructural features of membranes are investigated using small- and wide-angle x-ray scattering (SAXS/WAXS). Collected data are modeled to examine how Ce-doping influences structure-hydration and conductivity-hydration relationships, which is analyzed using dilute-solution theory as well as concentrated solution theory. Moreover, the effect of thickness on fuel-cell membranes is investigated based on a PFSA membrane. Membrane structure and properties are measured as a function of thickness, in controlled environment. The impact of relative humidity and temperature on the proton transport was also investigated for selected membrane thicknesses, to provide insights towards membrane design for high-temperature fuel-cell operation. The acquired data are analyzed to identify to what extent thickness impacts properties and to provide insights on the extent to which thickness can be considered a design parameter for PEMs.

RESULTS AND DISCUSSION

In this study, hydration and conductivity measurements, along with small- and wide-angle X-ray scattering are employed to elucidate how structural and concentration changes due to cationic additives in controlled environments alter solvation behavior and meso/nano-scale morphology of Ce-doped PFSAs, and ultimately govern their ion transport.[4] Both water uptake and conductivity decrease with increasing Ce-doping, at all humidity levels, even though the magnitude of the reduced transport functionality intensifies at higher humidity values. Using the Nernst-Stokes-Einstein equation, the impact of Ce on the local solvation structure of water in the membrane can de delineated the from mesoscale changes in transport pathways, which were characterized using data from x-ray scattering experiments. SAXS/WAXS experiments reveal that nanostructural features, especially spacing and inter-connectivity of hydrophilic nano-domain decrease with increasing Ce-loading, in a nonlinear fashion. While the effects of Cerium on membrane uptake and nanostructure is relatively minimal below 10% Ce-exchange, this impact on structure-properties is exacerbated with increasing Ce-exchange up to 50%.

Exploration of the relationship between conductivity and hydration reveals universal correlations, which are validated by transport models based on dilute- and concentrated solution theory.[1, 9] The results indicate that conductivity diminished with doping level but different than expected by simple substitution of proton by another cation. Overall, Ce-doping tends to increase transport resistances in the membrane especially in dry-hot conditions, a critical finding for automotive fuel cells. Also, since Ce gradients form within the membrane during operation, which is confirmed by both experiments and simulations, low average Ce loadings can yield very high local Ce concentrations, thereby deteriorating membrane transport even more dramatically. This effect of the latter phenomenon is confirmed using a multi-physics model,[8] which is used to simulate cell performance with and without the acquired data on Ce-dependent properties.

Lastly, the collected dataset on thickness-dependent properties indicate transitions in certain structural features below 10 μm, accompanied by an increased anisotropy in swelling and conductivity. Many properties deviate within 10-20% without monotonic changes with thickness, however, linear correlations are observed between thickness and thermal-mechanical properties and gas permeability, although the latter is less significant.

CONCLUSIONS

The combined experimental and theoretical analysis reveals a decrease in hydration and a nonlinear decrease in conductivity with increasing cerium loading, which is driven by fundamental phenomena such as cation solvation at

molecular level and morphological changes. The implications of these structure-property changes on membrane performance and optimization are analyzed and simulated using membrane transport theories and cell-performance models, respectively. Experimental and theoretical results are used to generate a design map for PEMs with additives that account for various operation conditions (humidity and temperature) and material parameters (doping levels). These conclusions could also translate into other mixed-cation systems relevant to fuel-cells to model and examine not only other radical scavengers but also cations originated from other sources, such as contamination and cobalt leaching. These results have significant implications on the design of experiments and membranes for optimizing not only the ionomers as PEMs but also the ionomers in fuel-cell catalyst-layer design for an expanded investigation of polymer electrolyte fuel cell performance and durability. Additionally, identifying the thickness-dependence of PFSA properties could help expand the parameter window of PEMs, thereby enabling their optimization for automotive fuel cells, heavy-duty applications, and electrolyzers.

ACKNOWLEDGEMENT

This material presented herein is based on work performed by the Million Mile Fuel Cell Truck (M2FCT) Consortium (https://millionmilefuelcelltruck.org) technology manager Greg Kleen, which is supported by the U.S. Department of Energy, Office of Energy Efficiency and Renewable Energy, Hydrogen and Fuel Cell Technologies Office, under contract numbers No. DE-AC02-05CH11231. AK acknowledges the ECS-Toyota Fellowship.

REFERENCES

1 Cullen DA, Neyerlin KC, Ahluwalia RK, Mukundan R, More KL, Borup RL, Weber AZ, Myers DJ, and Kusoglu A (2021). New roads and challenges for fuel cells in heavy-duty transportation. *Jounal* 6, 462-474.
2 Kusoglu A, and Weber AZ (2017). New Insights into Perfluorinated Sulfonic-Acid Ionomers. *Jounal* 117, 987-1104.
3 Baker AM, Komini Babu S, Chintam K, Kusoglu A, Mukundan R, and Borup RL (2019). Ce Cation Migration and Diffusivity in Perfluorosulfonic Acid Fuel Cell Membranes. *Jounal* 92, 429-438.
4 Baker AM, Crothers AR, Chintam K, Luo XY, Weber AZ, Borup RL, and Kusoglu A (2020). Morphology and Transport of Multivalent Cation-Exchanged Ionomer Membranes Using Perfluorosulfonic Acid-CeZ+ as a Model System. *Jounal* 2, 3642-3656.
5 Shi SW, Weber AZ, and Kusoglu A (2016). Structure-Transport Relationship of Perfluorosulfonic-Acid Membranes in Different Cationic Forms. *Jounal* 220, 517-528.
6 Gittleman CS, Kongkanand A, Masten D, and Gu WB (2019). Materials research and development focus areas for low cost automotive proton-exchange membrane fuel cells. *Jounal* 18, 81-89.
7 Luo X, Lau G, Tesfaye M, Arthurs CR, Cordova I, Wang C, Yandrasits M, and Kusoglu A (2021). Thickness Dependence of Proton-Exchange-Membrane Properties. *Jounal* 168, 104517.
8 Ehlinger VM, Kusoglu A, and Weber AZ (2019). Modeling Coupled Durability and Performance in Polymer-Electrolyte Fuel Cells: Membrane Effects. *Jounal* 166, F3255-F3267.
9 Crothers AR, Darling RM, Kusoglu A, Radke CJ, and Weber AZ (2020). Theory of Multicomponent Phenomena in Cation-Exchange Membranes: Part II. Transport Model and Validation. *Jounal* 167, 013548.

WHEC-2022
23rd World Hydrogen Energy Conference
June 26-30, 2022 - Istanbul

#147

MODELING OF AN ASSISTED COLD START OF A PEMFC COUPLED WITH A METAL HYDRIDE REACTOR

Tom Gießgen, Thomas Jahnke*
German Aerospace Center (DLR), Institute of Engineering Thermodynamics,
Pfaffenwaldring 38-40, D-70569 Stuttgart, Germany

* Tom.Giessgen@dlr.de

ABSTRACT

One challenge for the automotive application of polymer electrolyte fuel cells (PEMFC) is the start-up at sub-zero temper-atures due to the freezing of water inside the cell. The temperature has to rise above 0 °C before the ice completely blocks the cathode pores and inhibits the oxygen reduction and species transportation. A promising solution to quickly increase the temperature of the fuel cell in a sub-zero environment is a metal hydride reactor. This thermochemical heater can exothermally absorb hydrogen and heat up the heat transfer fluid of a PEMFC stack.

This work presents a transient 2D numerical model of a single fuel cell thermally coupled to a metal hydride reactor via the heat transfer fluid. Both components are validated with experimental data. The simulation of the coupled system yields the necessary preheating time up to 0 °C to avoid any ice formation and potential damages due to ice in the cathode. Another cold start strategy is the potentiostatic start-up after a shorter preheating time, i.e. ice may be formed but a quicker cold start is possible. The criterion for a successful start in this work is an average temperature of 20 °C in the cathode catalyst layer, because the cold start can fail due to the blockage of the pores in the catalyst layer with ice but also with liquid water. For temperatures from - 5 °C to - 30 °C and cell voltages from 0.9 V to 0.1 V the preheating duration is varied to determine the optimum cold start procedure.

Keywords: PEMFC, Simulation, Cold start, Metal hydride, Preheating

INTRODUCTION

One challenge for the widespread application of polymer electrolyte fuel cells (PEMFC) is the start-up with temperatures below 0 °C. The water stored in the polymer electrolyte membrane and catalyst layer and produced during oxygen reduction reaction may freeze and block the electrode pores. This reduces the reaction sites and species transport which decreases the electrical power of the cell. If the frozen or liquid water blocks the pores completely the cold start fails.

A solution for this problem is the assisted cold start instead of a self start, i.e. external heating of the fuel cell. This can be achieved by heating up the coolant with an electrical heater [1, 2] or with a metal hydride reactor (thermochemical preheater). Such a device utilizes the pressure of the hydrogen tank and produces heat upon hydrogen absorption. After a successful cold start, the waste heat of the fuel cell during normal operation recharges the metal hydride reactor (desorption of hydrogen) [3, 4, 5].

MODELING

The simulation of the assisted cold start is performed with a 2D transient modeling framework called NEOPARD-X [6, 7] which is based on DuMux [8]. The governing model equations are described in references [6, 7,9, 10]. It includes following features:

- A 2D along-the-channel geometry (Fig. 1) with nine spatially resolved layers in the fuel cell (anode and cathode channels, GDLs, MPLs, CLs and the membrane) and three layers in the metal hydride reactor (heat transfer fluid, reactor shell and metal hydride bed)
- A multiphase Darcy model for the two-phase, multicomponent transport within the porous electrodes
- Phase change of water in the pores, membrane and ionomer (Fig. 1)
- A hydrogen absorption (and desorption) model in the metal hydride
- A membrane model including coupled water and proton transport as well as transport of dissolved gas species

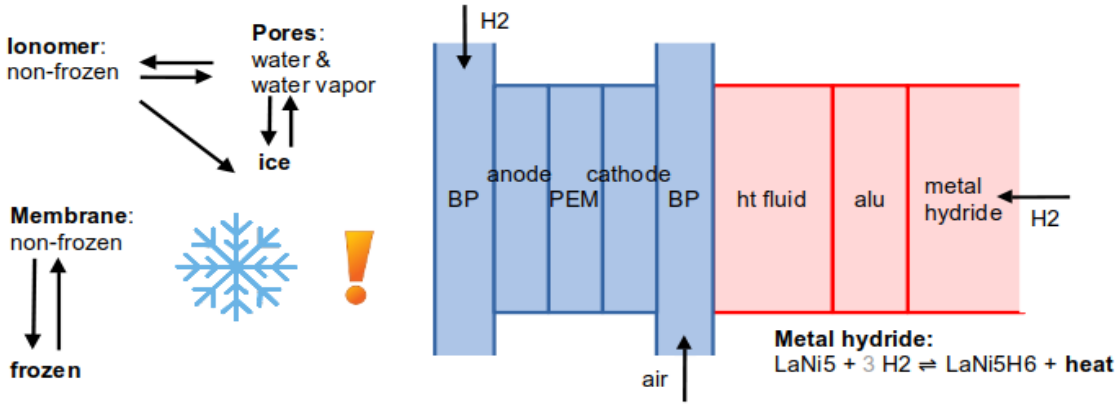


Fig. 1. Simulation domain of the fuel cell coupled to the metal hydride reactor.

- Proton transport through the ionomer within the CLs and electron transport through the support phase of the porous electrodes
- Butler-Volmer kinetics for the ORR and HOR reactions
- An ionomer film model describing the oxygen transport from the gas phase through the ionomer film to the cathode catalyst
- Energy transport through all layers of the cell

The fuel cell has a channel length of 10 cm and an active area of 73.8 cm². In the experimental setup, a fuel cell stack with 15 cells (end plates are neglected) is heated by one metal hydride reactor. One cell is then effectively heated by 20.7 g metal hydride (LaNi5) and thermally coupled by 31.1 g coolant (50 % Glysantin) and 19.7 g reactor shell (AlSi10Mg).

RESULTS AND DISCUSSION

One possible cold start strategy is the preheating until the mean temperature reaches 0 °C in the cathode catalyst layer (CCL) before starting the fuel cell to completely avoid ice formation and potential degradations in the CCL. According to the simulations, cold start without ice formation is possible from - 5 °C in 14.8 s, - 10 °C in 24.2 s, - 15 °C in 37.0 s and from - 20 °C in 61.1 s. However, the maximal temperature increase with external heating only is 24.3 K and takes longer time.

Another cold start strategy is the potentiostatic start-up when the CCL temperature is still below 0 °C. While ice formation is possible, this strategy allows for faster start-ups in colder environments. For example, the time for a successful cold start with - 20 °C is 142 s for 0.7 V cell voltage, 74.7 s for 0.5 V, 50.4 s for 0.3 V and 45.0 s for 0.1 V. The corresponding preheating times for - 20 °C are 15 s, 35 s, 30 s and 30 s for 0.7 V, 0.5 V, 0.3 V and 0.1 V, respectively. The criterion for a successful cold start is here defined as the CCL temperature reaching + 20 °C, since next to freezing also flooding of the CCL is a common cause for a failed cold start.

Lower cell voltages enable faster cold starts, because the overpotential, especially the concentration overpotential, is larger and, hence, the heat production higher. The cold starts at - 20 °C with 30 s preheating time with two different cell voltages are compared in Fig. 2. On the left, the start-up with 0.5 V fails due to the high saturation of frozen and liquid water in the CCL. While the mean temperature reaches + 3 °C, the temperature distribution is inhomogeneous and the areas closer to the gas inlet and outlet are still below 0 °C due to the thermal mass of the bipolar plate gas manifold. However, this failure is close and a 5 s longer preheating time yields a successful cold start.
By lowering the cell voltages, the waste heat is significantly increased [11, 12] (Fig. 2 right). Upon starting, the CCL temperature quickly increases from - 8.7 °C to 0 °C within 1.7 s. The cold start would then finish much quicker if the thermal mass of the coolant would be smaller. Hence, it is recommended to turn off the coolant circulation upon the potentiostatic start with a low cell voltage, because the CCL temperature is then higher than the coolant temperature.

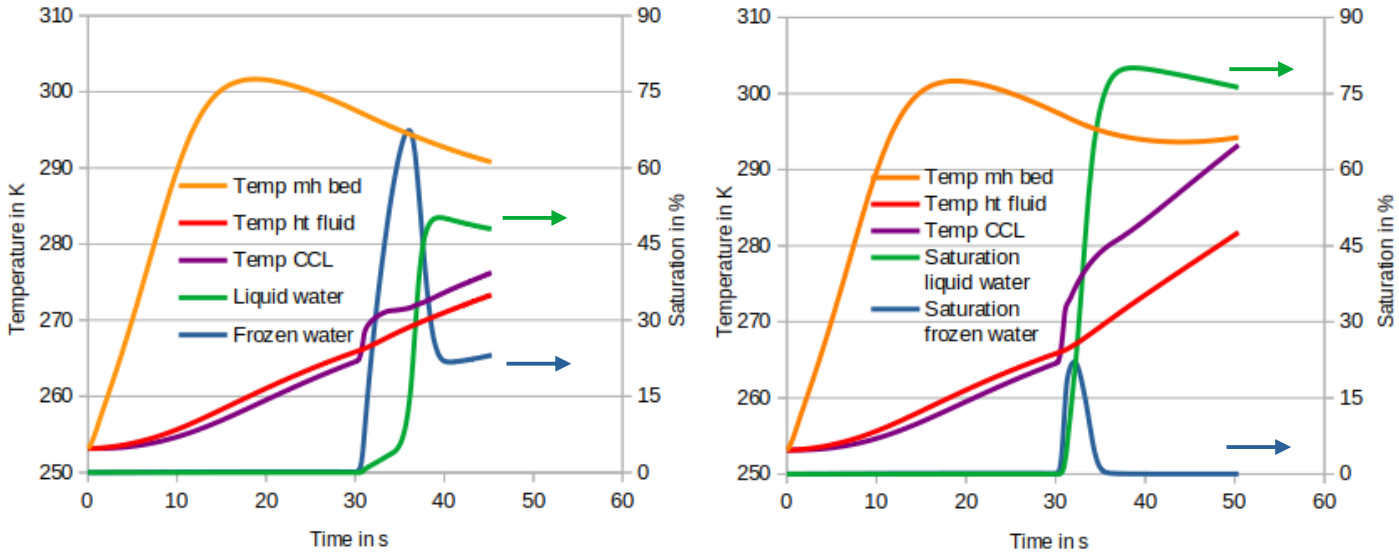


Fig. 2. Cold start from - 20 °C and 30 s preheating time. Left: cell voltage of 0.5 V results in a failed start due to high saturation of liquid and frozen water. Right: 0.3 V yields higher heat production and a successful start-up.

CONCLUSIONS

This work models the assisted cold start of a PEMFC with a thermochemical preheater (metal hydride reactor) and investigates effective start strategies for temperatures from - 5 °C to - 30 °C. The first strategy is the preheating of the cell up to 0 °C and then starting the cell. This procedure avoids ice formation and potential damages in the cathode, but is slow (e.g. 61 s from - 20 °C). A faster cold start strategy is heating the fuel cell up to about - 8 °C, switching off the coolant circulation and starting the cell with a low voltage (~ 0.1 V). Such a low voltage yields a high concentration overpotential and thus a high heat production.

REFERENCES

[1] Montaner Ríos G, Schirmer J, Gentner C and Kallo J. 2020. Efficient Thermal Management Strategies for Cold Starts of a Proton Exchange Membrane Fuel Cell System. Applied Energy 279: 115813.
[2] Luo M, Zhang J, Zhang C, Chin CS, Ran H, Fan M, Du K and Shuai Q. 2022. Cold Start Investigation of Fuel Cell Vehicles with Coolant Preheating Strategy. Applied Thermal Engineering 201: 117816.
[3] Dieterich M, Bürger I and Linder M. 2017. Open and Closed Metal Hydride System for High Thermal Power Applications: Preheating Vehicle Components. International Journal of Hydrogen Energy 42: 11469–11481.
[4] Kölbig M. 2018. „Coupled metal hydride reactions for preheating vehicle components at low temperature“, PhD thesis. Stuttgart, Germany.
[5] Bürger I, Sourmelis Terzopoulos VE, Kretschmer C, Kölbig M, Brack C and Linder M. 2021. Lightweight Reactor Design by Additive Manufacturing for Preheating Applications Using Metal Hydrides. International Journal of Hydrogen Energy 46: 28686–28699.
[6] Futter GA, Gazdzicki P, Friedrich KA, Latz A and Jahnke T. 2018. Physical Modeling of Polymer-Electrolyte Membrane Fuel Cells: Understanding Water Management and Impedance Spectra. Journal of Power Sources 391: 148–61.
[7] Jahnke T, Futter GA, Baricci A, Rabissi C and Casalegno A. 2020. Physical Modeling of Catalyst Degradation in Low Temperature Fuel Cells: Platinum Oxidation, Dissolution, Particle Growth and Platinum Band Formation. Journal of The Electrochemical Society 167: 013523.
[8] Flemisch B, Darcis M, Erbertseder K, Faigle B, Lauser A, Mosthaf K, Müthing S, et al. 2011. DuMux: DUNE for Multi-{phase,Component,Scale,Physics,...} Flow and Transport in Porous Media. Advances in Water Resources 34: 1102–12.
[9] Jiao K and Li X. 2009. Effects of Various Operating and Initial Conditions on Cold Start Performance of Polymer Electrolyte Membrane Fuel Cells. International Journal of Hydrogen Energy 4: 8171–8184.
[10] Gießgen T and Jahnke T. 2021. Modelling of PEMFC Cold Starts. EFCF 2021. Lucerne, Switzerland.
[11] Manabe K, Naganuma Y, Nonobe Y, Kizaki M and Ogawa T. 2010. Development of Fuel Cell Hybrid Vehicle Rapid Start-up from Sub-Freezing Temperatures. pp 2010-01–1092.
[12] Zhu Y, Lin R, Jiang Z, Zhong D, Wang B, Shangguan W and Han L. 2019. Investigation on Cold Start of Polymer Electrolyte Membrane Fuel Cells with Different Cathode Serpentine Flow Fields. International Journal of Hydrogen Energy, 44: 7505–7517.

WHEC-2022
23rd World Hydrogen Energy Conference
June 26-30, 2022 - Istanbul

#163

COMBINED NUMERICAL AND EXPERIMENTAL ANALYSIS OF LIQUID WATER DISTRIBUTION INSIDE PEMFCs

[1] Željko Penga, [1] Ivan Tolj, [1]Petar Bosnić, [1]Jure Penga, [1]Jakov Šimunović, [1]Gojmir Radica [1]Frano Barbir*
[1]Faculty of Electrical Engineering, Mechanical Engineering and Naval Architecture, University of Split, Croatia

*Corresponding author e-mail: zpenga@fesb.hr

ABSTRACT

The main objectives for the design of modern PEM fuel cells are to ensure minimize costs and size and ensure operation at elevated power densities with minimized accumulation of water inside the flow fields. Currently, number of authors are dedicated to increasing the flow field complexity, resulting in higher performance but also elevated manufacturing costs. By minimizing the complexity of the flow field and avoiding complex 3D structures, the main candidate still remains the serpentine flow field due to favorable characteristics of low pressure drop and good water removal. Due to discrepancies found in literature, in this work, the focus is on investigation of the liquid water accumulation inside the flow field of PEM fuel cell using up-to-date numerical model and full-scale single cell geometry with active area of 25 cm^2, experimentally and numerically using computational fluid dynamics modeling. The initial simulation model is calibrated using experimental data and later modified according to literature recommendations, outlining the influence of designs on water accumulation, resulting in significant performance improvement using simple geometry. The future goal of the research is upscaling the developed geometry for 50 cm^2 active area and comparing the numerical results with experimentally obtained locally resolved current density distribution.

Keywords: PEM Fuel Cells, Computational Fluid Dynamics, Experimental, Flow Fields

INTRODUCTION

PEMFCs are considered as the primary candidate for replacing internal combustion engines for transport applications in the near future due to high efficiency, clean and silent operation, compact size, capability of fast recharging, etc. Besides the MEA, the main influence on the performance of the cell is attributed to the flow field channels. The main objective of the flow field channels is to achieve uniform reactant distribution along the entire flow field of the cell with low pressure drop to avoid the requirement for pumping power for air. However, since PEMFC generates water and heat during operation, there are also two additional requirements – to ensure proper heat removal and avoid hot-spots which are detrimental to the health of MEA and to efficiently remove the generated water. Due to the reasons specified, it is not simple to design one-for-all flow field type. Due to complex relation between water and heat management inside PEMFC flow fields and MEAs, there are large number of different directions of flow field design, lately mostly oriented towards the development of flow fields which are highly complex and costly to produce, such as seen in first Toyota Mirai [1], resulting in designs which give high performance but at a very high financial cost and only for some narrow range of operating conditions. Also, evident by new Toyota Mirai, they have radically changed the flow field in the new Mirai and significantly decreased the complexity of the flow field and changed to simple zig-zag flow field, due to reasons specified. For this reason, we have decided to pursue the direction of simplifying the flow field design and reducing the cost while orienting towards achieving good dynamic performance, heavily dependent on the ability to remove the water from the cell. Highly accurate numerical model with advanced multiphase model is developed, shown in detail in Penga et al. [2], giving insight into the water distribution for different flow fields which can be produced using only a small CNC machine and tested in laboratory under different ambient conditions, with final goal in aim – to design a scalable flow field which may not give the highest performance under all circumstances, but will ensure good water removal even if we scale the cell to much larger size, but use the same number of serpentines, channel width, depth and land width, etc.

MODELING AND EXPERIMENTAL

The equations making up the numerical model are developed and shown in detail in a previous study by Penga et al. [2], while the experimental procedure regarding the polarization curve recording are described in another work by Penga et al. [3]. Numerical modeling is carried out using commercial software ANSYS Fluent v17.2 with PEM fuel cell add-on module. The geometry of the original flow field configuration is shown in Fig. 1., Model 1. The other geometries are adapted as a result of literature recommendations. Model 1 and 2 use triple serpentine, while Model 3 and 4 use quadruple serpentines. Model 2 is based on recommendations from Kerkoub [4]. The active area of the flow field is 25

cm^2, i.e. 50 mm x 50 mm. Mesh is fully structured with minimal orthogonal quality exceeding 0.99 and 4 subdivisions across the height of each MEA component and channel depth and width. Operating conditions are specified below in Table 1.

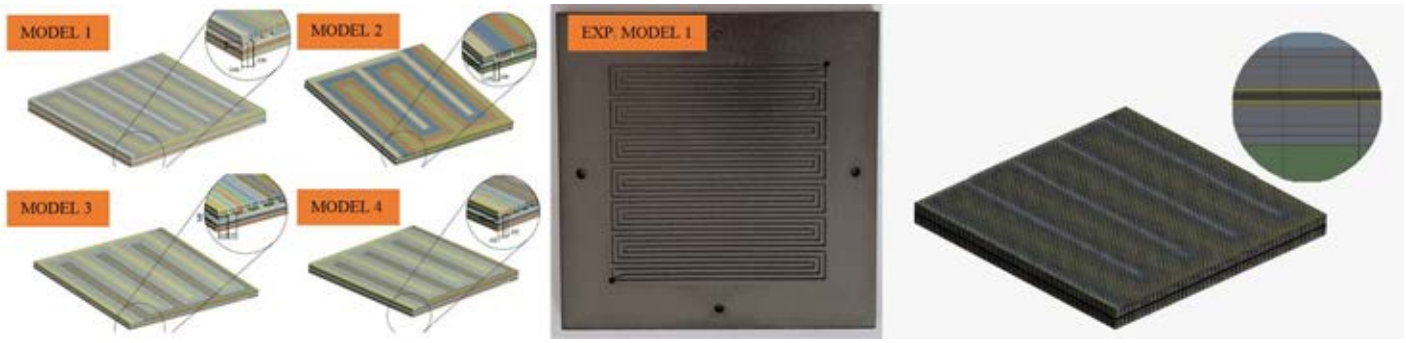


Fig. 1. Computational domains for different models (left), experimental flow field for Model 0 (middle) and mesh (right)

Table 1. Operating conditions, MEA and model geometrical parameters

Operating conditions				MEA geometrical parameters			Model geometrical parameters					
				Component	Units	Value		Units	Model 1	Model 2	Model 3	Model 4
	Units	Anode	Cathode	Current collector	mm	2 x Ch. depth	Active area	cm^2	25	25	25	25
Pressure inlet	kPa	100	100	Substrate	mm	0.155	Ch. width	mm	0.9	0.8	0.87	0.87
Relative humidity	%	50	50	Micro-porous layer	mm	0.02	Rib width	mm	0.9	2.4	0.87	0.87
Temperature cell	°C	80	80	Catalyst layer	mm	0.01	Ch. depth	mm	0.9	0.45	0.45	0.7
Flow	NLPM	0.4	80	Membrane	mm	0.015	No. serp.	/	3	3	4	4

RESULTS AND DISCUSSION

The resulting polarization curves are shown in Fig. 2. Model 1 was calibrated using the experimental polarization curve. The experimental polarization curve was recorded using 1 hour hold times at 4 different currents and low relative humidity operation to avoid accumulation of liquid water at higher currents. Such long hold times are necessary because the CFD analysis results in steady-state solution, and it is not possible to achieve steady-state with short hold times, as evident in a previous study [2]. The cathode and anode reference exchange current densities and concentration exponents are fine-tuned to result in good mutual agreement between the experimental and model polarization curve, evident from Fig. 2 (left). The fine-tuned values for Model 1 electrochemical parameters are used for all of the remaining models. Model 2 geometry was based on study of Kerkoub et al. [4], using channel to rib ratio of 0.33, which should result in increased performance. However, from Fig. 2. (left), it can be noted that the performance is almost identical to Model 0 regarding the operational efficiency, but it can also be noted in Fig. 2. (right) that the water removal is significantly improved vs. Model 1. Models 3 and 4 show higher performance along the entire range of operational current densities and significantly lower quantities of liquid water inside the flow fields, they both use 4 serpentines.

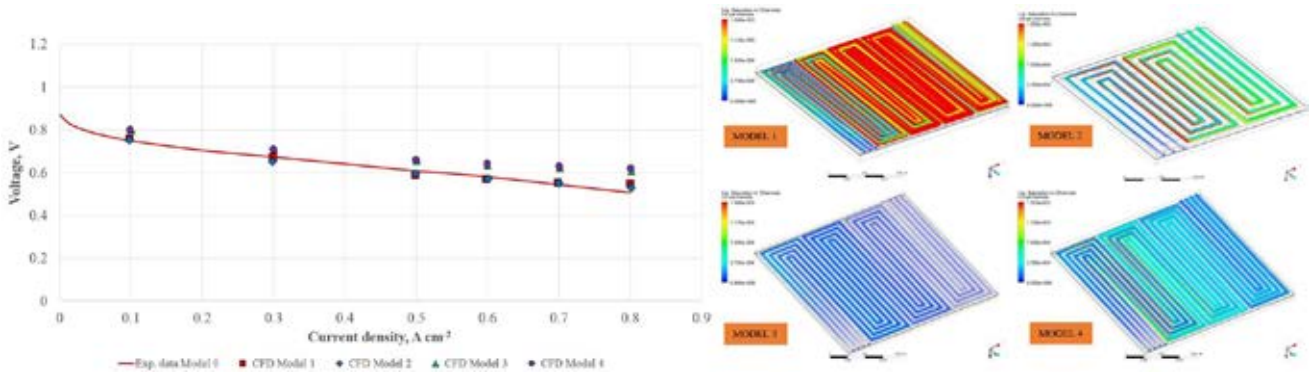


Fig. 2. Polarization curves (left) and liquid saturation inside channels (right)

Table 2 shows parameters of interest. It can be seen that performance related, Model 3 and 4 are the best. Model 3 shows lower quantities of liquid water inside the channels and CL, higher oxygen mass fraction in CL and lower overall temperature inside the cathode CL. For this reason Model 3 is chosen as the best and will be used for upscaling.

Table 1. Operating conditions, MEA and model geometrical parameters

Performance parameters					
	Units	**Model 1**	**Model 2**	**Model 3**	**Model 4**
Vol. ave. liq sat in cat. CL	/	0.285	0.277	**0.077**	0.166
Vol. ave. liq sat in cat. channels	/	0.002	0.001	**0.00008**	0.00038
Vol. ave. oxy mass fr. in cat. CL	/	0.223	0.212	**0.223**	0.219
Vol. ave. temp in cat. CL	K	344.35	346.33	**340.00**	342
Voltage at 0.8 A cm^{-2}	V	0.542	0.532	0.608	**0.618**

CONCLUSIONS

The objective of this work was to thoroughly analyze four different serpentine configurations of simple serpentine flow fields on a 25 cm^2 PEMFC using up-to-date numerical model and to outline which flow field is the most promising candidate for upscaling on 50 cm^2 size in a future study where the results of numerical model will also be compared with locally resolved current density distribution using current scan shunt. The most influencing parameters on the performance are namely number of serpentines and channel depth. Channel depth of 0.45 mm vs. 0.9 mm and 0.7 mm, was found as optimal as well as four serpentines vs. three. Although literature suggests that channel to rib ratio of ca. 0.33 would be beneficial, this was not the case as out study found out.

ACKNOWLEDGEMENT

This researchwas supported under the project STIM–REI (contract number: KK.01.1.1.01.0003), funded by the European Union through the European Regional Development Fund—the Operational Programme Competitiveness and Cohesion 2014-2020 (KK.01.1.1.01.) and Croatian Science Foundation project IP-2020-02-6249 “Efficiency Improvement, Emission Reductions and Hybridization of the Marine Power Systems”.

REFERENCES

1. Konno N, Mizuno S, Nakaji H, Ishikawa Y. 2015. Development of compact and high-performance fuel cell stack. SAE International Journal of Alternative Powertrains 4:123-129.
2. Penga Ž, Bergbreiter C, Barbir F, Scholta J. 2019. Numerical and experimental analysis of liquid water distribution in PEM fuel cells. Energy Conversion and Management 189:167-183.
3. Penga Ž, Pivac I, Barbir F. 2017. Numerical and experimental analysis of liquid water distribution in PEM fuel cells. International Journal of Hydrogen Energy 42:26084-26093.
4. Kerkoub Y, Benzaoui A, Haddad F, Ziari YK. 2018. Channel to rib width ratio influence with various flow field designs on performance of PEM fuel cell. Energy Conversion and Management 174:260-275.

WHEC-2022
23rd World Hydrogen Energy Conference
June 26-30, 2022 - Istanbul

#190
TOPOLOGY OPTIMIZATION OF RADIAL FLOW FIELD IN CIRCULAR PEM FUEL CELLS

[1*] *Fereshteh Razmara,* [1] *Luís Fernando Nogueira de Sá,* [1] *Jéssica Alves Nogueira,* [1] *Thiago Lopes,* [1] *Julio Romano Meneghini,* [1] *Emílio Carlos Nelli Silva*
[1] Research Centre for Greenhouse Gas Innovation, University of Sao Paulo, Escola Politecnica, Av. Prof Mello Moraes 2231, Sao Paulo, SP 05508030, Brazil

*Corresponding author e-mail: f.razmara@usp.br

ABSTRACT

This research applies the topology optimization method to propose an optimum radial flow field in polymer electrolyte membrane fuel cells with circular endplates. The cathode flow field is investigated in two dimensions, with the reactant gas modelled as a single-phase isothermal flow at steady-state. The gradient-based topology optimization approach is used, where the objective function is set to maximize the amount of power generated. The flow field evolves freely within the circular domain, and the resulting geometry is compared to a square endplate fuel cell with a single serpentine flow field. The results show that the optimized radial flow field significantly outperforms the serpentine flow field in power generation. Furthermore, the optimized radial flow field presents a lower pressure loss than the traditional serpentine flow field.

Keywords: PEM fuel cell, Topology optimization, Radial flow field, Circular endplate

INTRODUCTION

In Proton Exchange Membrane Fuel Cells (PEMFC), the performance can be further enhanced by modifying the geometry of the bipolar plates where the flow field channel structure plays a significant role. Several studies have been conducted on square endplates with different channel configurations such as parallel, serpentine, and interdigitated. In contrast, few studies have been undertaken on circular endplates with radial flow fields. In our research, the Topology Optimization Method (TOM) is employed to find an optimal radial flow field, and its performance is compared with a conventional serpentine flow field.

The flow field of PEMFC with square endplates has seen many improvements in the literature. For the time being, flow field topology optimization is the most robust design technique, primarily marked by Secanell et al. [1] in 2010 and recently applied on the flow field of PEMFCs with square endplates by Behrou et al. [2] in 2019. This research implemented a density-based topology optimization method, and the results demonstrate better power output, improved reactant distribution, and reduced pressure drop compared to classical flow fields. In contrast, fuel cells with circular flow fields have not been sufficiently developed over time. Perez-Raya [3] published a paper in 2010 on a radial design for circular endplates of PEMFCs. They placed the flow inlet in the center with four outlets on the perimeter and also added small rectangular ribs in the domain to better disperse the reactants. As a result, a serpentine configuration still had a better performance power than the suggested radial flow field; however, it required more pumping power. Their study demonstrated that channel design is a significant factor in designing radial flow fields to compete with conventional types. Later in 2012, Friess et al. [4] developed a novel radial flow field design for the cathode side of a PEMFC, which had a series of rings machined to various radii. They stated that the performance was increased compared to the parallel and serpentine flow fields and the pressure drop was at about half of the serpentine flow field. The performance of a radial flow field can be further improved by focusing on the ideal size of channels and ribs. In this way, the study by Wanchao et al. [5] in 2019 was carried out with a radial flow field in three cases. The flow field was modeled with eight independent sectors, each having ribs in the radial and angular directions. The results reveal that channel depth has a negligible effect while channel and rib widths directly impact radial flow field performance. Their comparison confirmed that the design with optimal dimensions yields a higher power density, improved water discharge, and lower pressure drop. This highlighted the significance of the channel structure in radial flow fields.

Studies in the literature lead us to conclude that significant improvements have been made in the channel configuration of fuel cells with square endplates. In contrast, circular endplates are limited to a few studies. Accordingly, radial flow fields can outperform flow fields in the square domain. Thus, our study aims at optimizing radial flow fields using a topology optimization approach to improve circular PEM fuel cells' performance.

NUMERICAL MODELING

The Finite Element Analysis is used to study the model numerically, and the Topology Optimization Method is applied to the design domain using COMSOL Multiphysics. The cathodic side of a PEM fuel cell consists of the bipolar plate (BPP), gas diffusion layer (GDL), catalyst layer, and membrane. Since the topology optimization method is computationally expensive, we reduced the simulation space from 3D to 2D using the depth-averaging procedure [2]. The 2D model is created by averaging the material properties of BPP and GDL to define equivalent porosity, permeability, and species diffusivity.

Governing Equations

A single-phase, steady-state, isothermal model is assumed, and the conservation equations can be summarized as follows.

$$\nabla \cdot \boldsymbol{u} = 0 \qquad \text{Conservation of mass} \tag{1}$$

$$\frac{1}{\epsilon^2}\rho \nabla \boldsymbol{u} \cdot \boldsymbol{u} = -\nabla p + \frac{1}{\epsilon}\mu \nabla^2 \boldsymbol{u} - \frac{12\,\mu}{H_{tot}^2}\boldsymbol{u} + \frac{\mu}{\kappa}\boldsymbol{u} \qquad \text{Conservation of momentum} \tag{2}$$

$$H_{tot}\,\rho\,\nabla \omega_k \cdot \boldsymbol{u} = H_{tot}\nabla j_k + R_k \qquad \text{Conservation of species} \tag{3}$$

In Eqs. (1,2), u is the velocity vector, ρ is the gas density, p is the relative pressure, μ is the dynamic viscosity, and H_{tot} is the sum of the heights of BPP and GDL. The third term on the right-hand side of Eq. (2) takes into account velocity gradients normal to the 2D plane. In Eq. (3), ω is the mass fraction of the species, k={O_2, N_2, H_2O}, and R_k is the reaction source term. The diffusion flux, j_k, is calculated from a mixture-averaged formula that includes the diffusivity factor f. Also, the porosity ϵ, permeability κ, and diffusivity f, are the design-dependent properties of the averaged materials. The local current density, i_{loc}, lies within the reaction source term and is calculated with the Butler-Volmer formulation.

Topology Optimization Method

An optimal radial flow field is derived using a density-based topology optimization method. The topology optimization formulation is defined as follows:

$$\underset{x}{Minimize} \quad -\int_{\Omega} V_{cell} \cdot i_{loc}\, d\Omega \tag{4}$$

$$Subject\ to \quad \frac{V(\boldsymbol{x})}{V_0} \le \overline{V}, \quad 0 \le x_i \le 1, \quad i=1,\ldots,N \tag{5}$$

Here, the objective function is defined as maximizing power generation and, in other words, minimizing the negative of the calculated power. V_{cell} is the cell voltage, V(x) is the final volume of the design, V_0 is the volume of the entire design domain, and $\overline{V}$ is the maximum volume fraction set at 50% to constrain the amount of material used in the optimization procedure. x_i is the independent design variable bounded continuously between zero and one, and N is the number of design variables. The design-dependent properties, $\epsilon(x_i)$, $\kappa(x_i)$, and $f(x_i)$ are interpolated with linear, modified RAMP, and SIMP material models respectively [2]. To eliminate checkerboard and mesh dependency issues, Helmholtz Filtering is used. Hyperbolic Tangent Projection is then applied to refine the unwanted grayscale areas. The discrete adjoint method is applied to analyze the sensitivities of the objective function and constraint with respect to design variables. Finally, the Globally Convergent Method of Moving Asymptotes (GCMMA) optimizer is used to solve the gradient-based optimization problem.

RESULTS AND DISCUSSION

In this work, the radial flow field in a circular fuel cell is optimized, aiming to maximize the power output. Different topologies are obtained with different constant values, and the results are compared to the serpentine flow field fuel cell with a single channel. To achieve comparable results, the two cells have the same active area and function under identical conditions. The circular cell domain and boundary conditions are shown in Fig. 1.

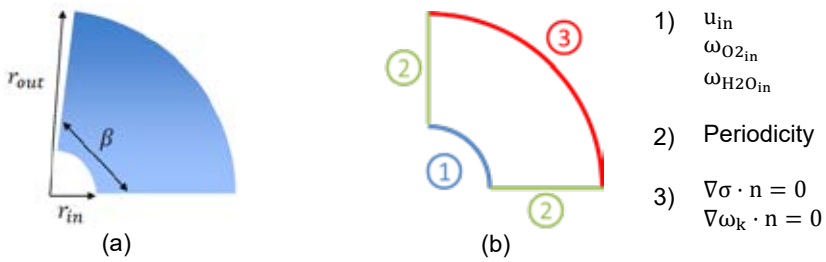
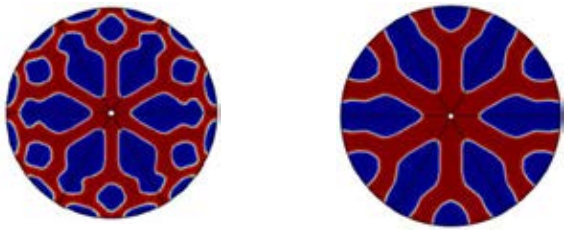


Fig. 1. (a) Domain and (b) boundary conditions for the circular fuel cell

Fig. 2 depicts the optimized topologies of the radial flow field. The ribs are shown in blue, and the flow fields are shown in red. The flow fields are mainly composed of radial channels with bifurcations which increase the reaction area. By comparing the final electrical power obtained by the cell with a traditional serpentine flow field, an improvement of around 20% is achieved. The results also reveal that the new optimized radial flow field has less pressure drop, which improves over a serpentine flow field.



Case 1 Case 2

Fig. 2. Optimized topologies of circular flow fields

CONCLUSIONS

A 2D numerical model has been investigated to simulate the cathodic side of PEMFCs with circular endplates. The 2D simulation appropriately represents the 3D model with the same transport conditions using the averaging procedure. The study is focused on designing circular fuel cells with an optimized radial flow field using the topology optimization method. The optimized topology is compared to a conventional fuel cell with a single serpentine flow field in the square domain. According to the results, the output power of the optimized cell is increased significantly compared to the serpentine flow field. Moreover, the optimized radial flow field has less pressure drop than a serpentine flow field, which is also advantageous.

ACKNOWLEDGEMENT

We gratefully acknowledge support of the RCGI – Research Centre for Greenhouse Gas Innovation, hosted by the University of São Paulo (USP) and sponsored by FAPESP – São Paulo Research Foundation (2014/50279-4 and 2020/15230-5) and Shell Brasil, and the strategic importance of the support given by ANP (Brazil's National Oil, Natural Gas and Biofuels Agency) through the R&D levy regulation. TL also thanks FAPESP under grant number 2014/22130-6.

REFERENCES

1. Secanell M, Wishart J and Dobson P. 2011. Computational design and optimization of fuel cells and fuel cell systems: A review. Journal Power Sources 196:3690–3704.
2. Behrou R, Pizzolato A and Forner-Cuenca A. 2019. Topology optimization as a powerful tool to design advanced PEMFCs flow fields. International Journal of Heat and Mass Transfer 135:72–92.
3. Perez-Raya I, Hernandez-Guerrero A, Elizalde-Blancas F, Juarez-Robles D and Almanza-Huerta L. 2010. 3D analysis of a new radial channel for pemfcs and comparison with a traditional channeled system. ASME's International Mechanical Engineering Congress & Exposition Proc 5:899–908.
4. Friess BR and Hoorfar M. 2012. Development of a novel radial cathode flow field for PEMFC. International Journal of Hydrogen Energy 37:7719–7729.
5. Zhu W and Zheng M. 2019. Radial flow field of circular bipolar plate for proton exchange membrane fuel cells. International Journal of Heat and Technology 37:733–740.

WHEC-2022
23rd World Hydrogen Energy Conference
June 26-30, 2022 - Istanbul

#222

INVESTIGATION ON AIRFLOW PERFORMANCE OF OPEN CATHODE PROTON EXCHANGE MEMBRANE FUEL CELL

[1,2*] *Ebubekir Pinar,* [1] *Gürsel Şefkat*
[1]Uludag University, Engineering Faculty, Mechanical Engineering Department, 16059, Bursa, Turkey
[2] B Plas A.Ş., R&D Center, 16369, Bursa, Turkey

*Corresponding author e-mail: ebubekirpinar@gmail.com

ABSTRACT

Fuel-cell systems have been considered as an alternative power source to replace internal combustion engines in future vehicles to reach zero emission transportation target. A trustworthy and straightforward fuel cell system is needed to adopt a fuel cell-based power unit successfully. Open cathode fuel cell offers a simple configuration where the ambient air is used directly to provide cooling and serve as an oxidant. Therefore, an open cathode fuel cell system eliminates the requirement for a complex air supply subsystem, minimizing accessory load and reducing the overall cost of the system. The main challenge with the open cathode design is the strong dependence of the stack performance on the ambient conditions. Numerous studies considering the performance of open cathode fuel-cell and various factors affecting them have been reported. This paper presents the investigation of the effects of the environmental parameters on open cathode fuel-cell.

Keywords: Open cathode PEM fuel cell, airflow management, forced convection.

INTRODUCTION

Fuel-cell systems have been considered as an alternative power source to replace internal combustion engines in future vehicles to reach zero emission transportation target. Fuel cells can operate at higher efficiencies than combustion engines and can convert the hydrogen to electrical energy with efficiencies capable of exceeding 60%. Among various types of fuel cells currently available [1], the proton exchange membrane/polymer electrolyte membrane fuel cell (PEMFC) is considered to be the leading candidate for mobile and portable applications, especially for the vehicle power unit. It offers unique features not available in other fuel cells, such as low operating temperature, high power density, quick start-up, fast response to load changes, easy scale-up and high efficiency [2].

In a typical PEM fuel cell, fuel (hydrogen) and oxygen (air) are supplied to the active area inside the cell a series of channels where electricity is generated by an electrochemical reaction, water and heat come out as by product.

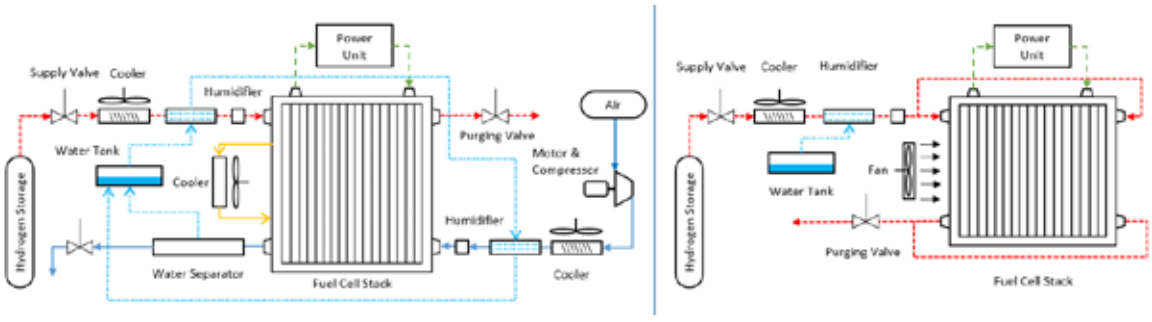


Fig. 1. Schematics representation of a) typical PEMFC and b) open cathode PEMFC system

Two configurations are commonly used for a fuel cell operating with air as an oxidant, i.e. closed cathode and open cathode. It is shown the general schematics of both configurations in Fig.1. The closed cathode PEMFC consists of an air supply, fuel delivery and circulation subsystem, cooling subsystem and fuel cell controller, as shown in Figure 1a. In contrast, an open cathode PEMFC is significantly less complex and less bulky, it is fed with ambient air directly (shown in Figure 1b).

This study evaluates the performance of the open cathode PEMFC system, including all the system components from those of fuel and air supply systems. Parameters such as; the cooling conditions, coolant flow rate, fan power rating in the natural and forced convection cooling at fuel cell stack are optimized to obtain efficient operating conditions. The performance of two different cooling strategies is then compared about the stack performance, complexity and polarisation.

System configuration of an open-cathode PEM fuel cell

The open-cathode PEM fuel cell has the unique merits of simple auxiliary subsystem and low cost; consequently, it can be an alternative power generation device for automobiles and other portable compact electric equipment [6].

As shown in Fig. 2, a 500 W open-cathode PEM fuel cell stack consists of 30 cells. There are many channels on the cells and electrically conductive separator plates between each pair of cells that function as the passageway of airflow and the conductor of electrons flow. The cells are all placed on top of each other and held together by intermediate plates with four blowers attached to the peripheral wallboard. The blowers feed in air consumed by the fuel cell and act as a forced coolant and take out the heat. The open-cathode fuel cell (selecting an H-500 fuel cell [7]) is fueled by hydrogen and oxygen-containing ambient air. The operating parameters of the 500 W open-cathode fuel cell are displayed in Table 1.

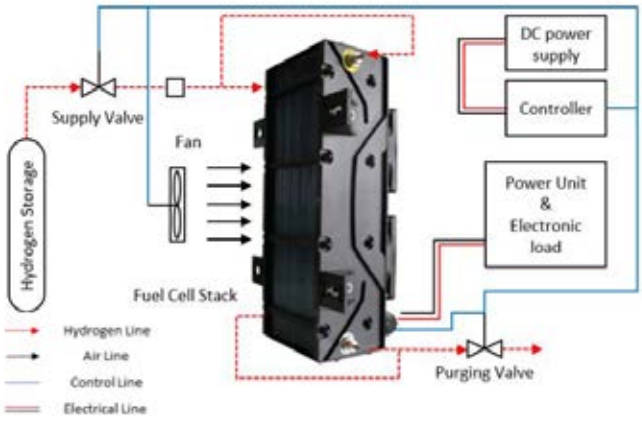


Fig. 2. Schematic diagram of a 500 W open-cathode fuel cell system

Table. 1: Operating parameters of the 500 W open-cathode fuel cell.

Descriptions	Values	Units
Over current shut down	*48*	*A*
Low voltage shut down	*12*	*V*
External power supply	*13/8*	*V/A*
Over temperature shut down	*63*	*°C*
Stack weight	*2500*	*g*
Voltage of blowers	*13*	*V*

Oxygen delivery mode in open cathode PEMFC

Oxygen delivery is an essential aspect in PEMFC operation. It directly affects the thermal performance and power of the fuel-cell stack. A uniform airflow distribution is crucial for the efficient operation of a PEMFC.

Cathode channels in the open cathode PEMFC system are exposed to the atmosphere, and hence the PEMFC operates at ambient pressure. As shown in Figure 1, this configuration simplifies the system, removing the need for a compressor, heater, and external humidifier. In general, there are two types of open-cathode fuel cells regarding the oxygen delivery method: natural convection and forced convection. In this study system, natural convection due to temperature and concentration difference drives air into the cathode channels. In forced convection system uses a fan to direct the ambient air to the cathode channel. Regarding the number of auxiliary devices used, free-breathing fuel cells offer superior simplicity relative to the forced convection counterparts. However, the airflow rate to the cathode might not be sufficient for the optimum reaction without the external fan.

MATERIALS AND METHODS

In this study, a fuel cell model (H-500XP Horizon) was utilized to measure the performances of the open cathode PEMFC stacks. Firstly, dry hydrogen was supplied to the anode side, at room temperature, and four fans supplied the forced ambient air to the open cathode channels. The ambient air is had a marked influence on the performance of an OC-PEMFC. Therefore, all experiment steps were carried out under the following conditions: a room temperature of 25.0 °C (±3.0 °C) and relative humidity of 40% (±15%). An additional voltage monitoring setup was attached to the fuel cell test station to measure the stack voltages of the 30-cell.

RESULTS AND DISCUSSION

A recorded current, voltage and temperature (temperature I-Forced convection, temperature II-Natural convection). values are shown in Tabel.2. As the increase of current, the output voltage of the stack continues to decline. Due to the increase of current, more and more heat is generated, and the average temperature of the fuel cell stack gradually increases. The stack temperature change can be seen for each fuel cell system.

The operating temperature of the PEMFC stack with forced convection is significantly lower than that of natural convection. When the current is equal to 28 A, the output voltage of the two is about 15 V, and the heat production is similar, but the average temperature difference between them is 7.8 °C. The control unit stops the system when the temperature is reached to 63 °C or more to protect the membrane from overheating. The output voltage of the stack with natural convection can be slightly lower than that of the stack with forced due to higher operating temperature [8].

Table. 2: Average voltage and temperature values for each current steps

Time (s)	Current (A)	Voltage (V)	Power (W)	Temp.-I (°C)	Temp.-II (°C)
0	0	27,90	0,00	24,2	24,2
240	4	21,40	85,60	26,5	26,6
480	8	20,00	160,00	30,9	31,5
720	12	18,70	224,40	34,5	35,9
960	16	17,70	283,20	39	41,5
1200	20	16,70	334,00	44	48
1440	24	16,00	384,00	48	53,7
1680	28	15,50	434,00	53	60,8
1920	32	14,40	460,80	55	-
2160	36	13,50	486,00	58	-
2400	40	12,50	500,00	58	-

CONCLUSIONS

The fundamental working principle, performance, technical challenges and potential applications of open cathode PEM fuel cells have been studied for both natural and forced air convection modes. Conclusions drawn from this study:

1. The forced convection open-cathode PEM fuel cell has a much better thermal, water and gas management as compared to the natural convection.
2. The fan selection and stack design need to be optimized to ensure high stack power.
3. Performance breakdown over time due to air quality is a significant issue in practical applications.
4. Seasonal temperature variations can affect the performance and durability of the stack. The environmental conditions, system design and material selection need to be carefully researched to ensure the stack can operate efficiently in all seasons.

ACKNOWLEDGEMENT

The authors wish to express their sincere gratitude to Professor Ali Sürmen for his valuable and constructive comments, which remarkably improved the paper.

REFERENCES

[1] Kurnia JC, Sasmito AP. Hydrogen Fuel Cell in Vehicle Propulsion: Performance, Efficiency, and Challenge. In: Sulaiman SA, editor. Energy Efficiency in Mobility Systems, Singapore: Springer; 2020. https://doi.org/10.1007/978-981-15-0102-9_2.

[2] Wang Y, Chen KS, Mishler J, Cho SC, Adroher XC. A review of polymer electrolyte membrane fuel cells: Technology, applications, and needs on fundamental research. Apply Energy 2011;88:981–1007. https://doi.org/10.1016/j.apenergy.2010.09.030.

[3] Štekl P, Kadlec P. Influence of oxygen content at the PEM fuel cell cathode. Advanced Methods of Theory of Electrical Engineering, Trebic, Czech Republic: Západočeská univerzita v Plzni; 2015, p. IV–6.

[4] Gaumont T, Maranzana G, Lottin O, Dillet J, Guétaz L, Pauchet J. In Operando and Local Estimation of the Effective Humidity of PEMFC Electrodes and Membranes. J Electrochem Soc 2017;164:F1535–42. https://doi.org/10.1149/2.0161714jes.

[5] Fournier M, Hamelin J, Agbossou K, Bose TK. Fuel Cell Operation with Oxygen Enrichment. Fuel Cells 2002;2:117–22. https://doi.org/10.1002/fuce.200290001.

[6] C. Mahjoubi, J.-C. Olivier, S. Skander-mustapha, M. Machmoum, I. Slamabelkhodja, An improved thermal control of open cathode proton exchange membrane fuel cell, Int. J. Hydrogen Energy 44 (22) (2019) 11332e113345.

[7] Horizon Fuel Cell Technologies Inc, H-500XP fuel cell stack user manual. https://www.horizonfuelcell.com/h-series-stacks

[8] B.S. Pivovar, An overview of electro-osmosis in fuel cell polymer electrolytes, Polymer 47 (2006) 4194–4202, https://doi.org/10.1016/j.polymer.2006.02.071.

WHEC-2022
23rd World Hydrogen Energy Conference
June 26-30, 2022 - Istanbul

#230

EFFECT OF PLATINUM PARTICLE GRADIENT DISTRIBUTION IN LOW PLATINUM LOADING CATHODE CATALYST LAYER ON MEA PERFORMANCE

* *Rui Lin, Shengchu Liu*
Tongji University, School of Automotive Studies, 4800 Caoan Road, Shanghai, China

*Corresponding author e-mail: ruilin@tongji.edu.cn

ABSTRACT
The durability and performance of membrane electrode assembly (MEA) compose the bottleneck of fuel cells industrialization. In this paper, the effects of gradient distribution of Pt particles in the catalyst layer of MEA are studied. Polarization curves are carried out to evaluate the performance of MEAs with different Pt gradient dispersion under different relative humidity. It is found that when the Pt content of the catalyst layer remains unchanged, and the Pt particles are distributed near the membrane, the MEA has better performance because of the smaller oxygen transport resistance.

Keywords: Proton exchange membrane fuel cells, Pt dispersion, MEA, Catalyst layer

INTRODUCTION
The proton exchange membrane fuel cell (PEMFC) is regarded as one of the most potential clean energy technologies due to its high energy conversion rate, environmental friendliness, and high reliability[1]. At present, although the high cost of fuel cell stacks stems from the lack of large-scale applications, the cost of its core material-platinum-based precious metal catalysts also needs to be resolved urgently. Therefore, the development of high-performance, long-life, and low-platinum-loaded membrane electrode assemblies has attracted increasing attention[2, 3].

There will be oxygen transport resistance in each part of MEA during the operation of PEMFC. The oxygen transport resistance can be measured and analyzed by the limiting current method commonly.[4] At present, there are two ways to control the distribution of Pt particles in the cathode catalyst layer. Nonoyama et al.[5] did two types of experiments. In one experiment, the weight ratio of Pt/C remains the same, and the thickness of the catalyst layer (CL) is decreased, and in another experiment, the weight of Pt/C is reduced while the thickness of the CL remains constant. He concluded that the increase in oxygen transport resistance of low Pt loading was related to the reduction in the ionomers on the surface of the Pt particles. Owejan et al.[6] studied the oxygen transport resistance under different platinum loading. He kept the thickness of the catalyst layer constant by changing the weight ratio of Pt/C and adding carbon dilution. The above studies discussed the influence of the thickness of the catalyst layer on the oxygen transport resistance. The first way is to change the thickness of the catalyst layer by changing the Pt/C ratio while keeping the catalyst layer loading unchanged. The second is to keep the Pt/C ratio unchanged and adjust the thickness of catalyst layer doping carbon particles. In the catalyst layer prepared by these two methods, the distribution of Pt particles in different positions in the catalyst layer is the same.[7, 8]

Moreover, in the low Pt loading catalyst layer, the gradient distribution of Pt particles in catalyst layer has not been studied by researchers. Therefore, it is necessary to further explore the influence of the catalyst distribution in the cathode catalyst layer on the performance of the fuel cell under low platinum loading.

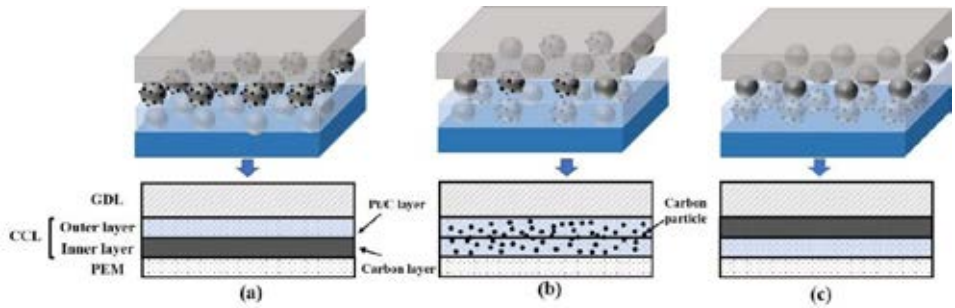


Fig. 1. Different structures of the cathode catalyst layer. (a) Add a carbon layer between CCL and GDL; (b) Add a carbon layer between CCL and PEM; (c) Mixing carbon powder into CCL.

EXPERIMENTAL
All MEA samples were manufactured by the decal transfer method. The catalyst ink was prepared by uniformly mixing 40 % Pt/C (Johnson Matthey), deionized water (DI Water), isopropanol (IPA), and 5 % Nafion solution. The cathode

catalyst layer (CCL) structure with different Pt dispersion positions is shown in Fig. 1. The structure was realized by mixing carbon powder into the CCL. The active area of the CCL and anode catalyst layer (ACL) was 25 cm^2, and the Pt loading was both 0.1 mg/cm^2.

Table 1. The composition of six types of CCL.

MEA-No	Total mass ratio Pt:C in CCL	Mass ratio Pt: C of CCL	
		Inner layer	Out layer
MEA-1	3:7	0	4:6
MEA-2	3:7	4:6	0
MEA-3	3:7	3:7	3:7

RESULTS AND DISCUSSION

The effect of relative humidity on the cell performance

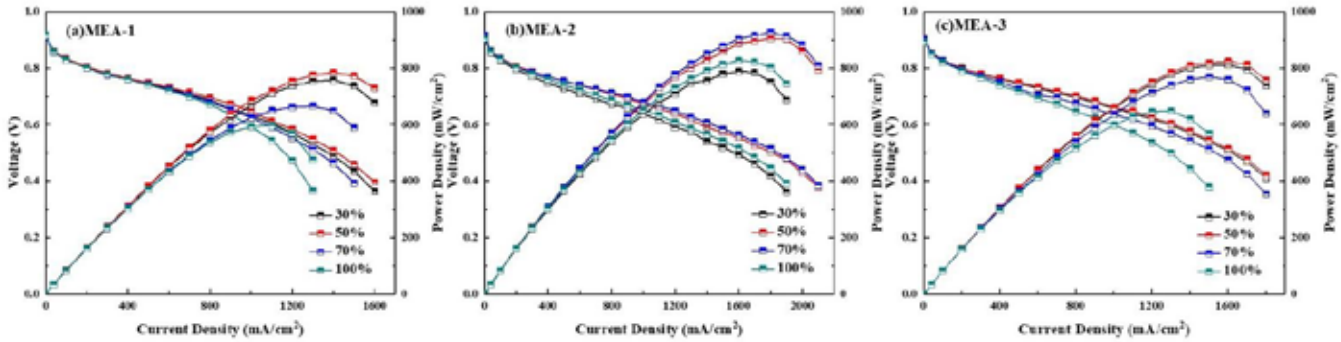


Fig. 2. Polarization curves under different relative humidity. Conditions: cell temperature of 80 °C, anode/cathode backpressure of 150/150 kPa, anode/cathode stoichiometry of 1.5/2.0.

Fig. 2 compared the polarization curves and power density curves under different relative humidity (RH) conditions. By comparing the performance of MEAs with different CL structures, it could be found that the MEA with structure (c) in Fig. 1 showed the best performance. Moreover, as shown in Fig. 2(b), when the RH was 50 %, the performance was almost the same as when the RH was 70 %. The maximum power density of MEA-2 was 905 mW/cm^2, and when the humidity was 30 % and 100 %, the performance of MEA was significantly reduced. This indicated that for the structure of Fig. 1(c), high RH would cause water flooding, and low RH would cause the membrane to dry and cause excessive internal resistance. The MEA-3 showed the second performance on the whole. It could infer from the performance curve that the structure (b) in Fig. 1 had better water retention capacity under low RH and inadequate drainage capacity under high RH. Therefore, the design was suitable for operation under low RH. And the MEA performance corresponding to structure (a) in Fig. 1 was the worst. As shown in Fig. 2(a), when the RH was 50 %, the maximum power density of MEA-1 was 785 mW/cm^2. When the RH was 100 %, the maximum power density was 599 mW/cm^2.

Oxygen transport resistance

The oxygen transport resistance can be measured by the limiting current method. When the absolute pressure was 0 kPa, the value of R_{total} was equal to the pressure-independent OTR (R_{PI}). And the pressure-independent OTR was mainly in the catalyst layer and micropores layer. As shown in Fig. 3, by extending the curve of R_{total}, when the curve intersected the vertical axis, the R_{total} can be obtained when the absolute back pressure was 0 kPa. The R_{PI} of MEAs with the structure in Fig. 1(c) was 10.88 s/m, which was smaller than that of MEAs with other structures. It meant that CCL with Fig. 1(c) was beneficial to oxygen transport.

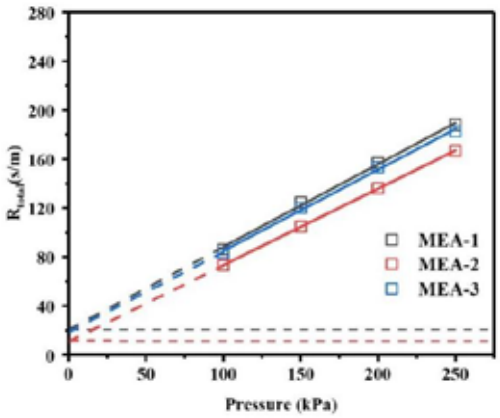


Fig. 3. The relationship between the back pressure and OTR of MEAs.

CONCLUSIONS

In this study, the low loading cathode catalyst layer with gradient dispersion of Pt particles was designed, and the influence of dispersibility on the performance of the MEAs was explored. When the cathode catalyst layer loading was 0.1 mg/cm^2, the maximum power density of MEA-2 can reach 0.927 W/cm^2. The result of the OTR test manifested that MEA-2 had the minimum gas transport resistance. A simple catalyst layer structure was successfully designed and applied to effectively improve the performance of MEAs.

ACKNOWLEDGEMENT

The authors gratefully acknowledge the financial support by National Natural Science Foundation of China (No.22178274) and the Shanghai Automotive Industry Science and Technology Development Foundation (No. 2004).

REFERENCES

[1] Lin R, Yu XT, et al. 2021. Structure majorization on the surface of microporous layer in polymer electrolyte membrane fuel cells to optimize performance and durability. Energy Conversion and Management. 243.
[2] Yang C, Han N, et al. 2020. A Novel Approach to Fabricate Membrane Electrode Assembly by Directly Coating the Nafion Ionomer on Catalyst Layers for Proton-Exchange Membrane Fuel Cells. Acs Sustainable Chemistry & Engineering. 8:9803-9812.
[3] Qiu YL, Zhang HM, et al. 2013. A novel cathode structure with double catalyst layers and low Pt loading for proton exchange membrane fuel cells. International Journal of Hydrogen Energy. 38:5836-5844.
[4] Wang H, Lin R, et al. 2021. Transition metal dissolution control in Pt-alloy catalyst layers for low Pt-loaded PEMFCs for improving mass transfer. International Journal of Heat and Mass Transfer. 178.
[5] Nonoyama N, Okazaki S, et al. 2011. Analysis of Oxygen-Transport Diffusion Resistance in Proton-Exchange-Membrane Fuel Cells. Journal of the Electrochemical Society. 158:B416-B423.
[6] Owejan JP, Owejan JE, et al. 2013. Impact of Platinum Loading and Catalyst Layer Structure on PEMFC Performance. Journal of the Electrochemical Society. 160:F824-F833.
[7] Cheng XJ, Wei GH, et al. 2021. Experimental probing of effects of carbon support on bulk and local oxygen transport resistance in ultra-low Pt PEMFCs. International Journal of Heat and Mass Transfer. 164.
[8] Wang C, Cheng XJ, et al. 2017. The Experimental Measurement of Local and Bulk Oxygen Transport Resistances in the Catalyst Layer of Proton Exchange Membrane Fuel Cells. Journal of Physical Chemistry Letters. 8:5848-5852.

WHEC-2022
23rd World Hydrogen Energy Conference
June 26-30, 2022 - Istanbul

#262

SURFACE TOPOGRAPHY EVALUATION DURING LONG-RUN MICRO-STAMPING OF BPPs AND ITS EFFECT ON CORROSION AND CONTACT RESISTANCE CHARACTERISTICS

[1] Mevlüt Fatih Peker, [2] Hasan Gedikli, [2,*] Ömer Necati Cora, [3] Muammer Koç*
[1] İSTAÇ, İstanbul Environment Management Industry and Trade Company, 34379, Şişli, İstanbul, Turkiye
[2] Karadeniz Technical University, School of Engineering, Department of Mechanical Engineering, Trabzon, Turkiye
[3] Hamad bin Khalifa University, College of Science and Engineering, Sustainable Development Division, Doha, Qatar

*Corresponding author e-mail: oncora@ktu.edu.tr

ABSTRACT

Long-run stamping of bipolar plates affects die life, and bipolar plate geometric accuracy, formability and surface quality characteristics. These characteristics, in turn, would affect the corrosion and contact resistance of BPPs, consequently the fuel cell performance. The aim of this study was to investigate the reasons and consequences of the interactions during the mass manufacturing of micro-stamped sheets, and establish correlations between surface interactions vs. corrosion and contact resistance of BPPs. In experimental part of this study, 10,000 SS316L sheet blanks with 51µm in thickness were micro-stamped under 175-225 kN stamping force levels with a constant stamping speed of 1mm/s. Surface inspections, corrosion and contact resistance tests were carried out on the BPPs, periodically. On the other hand, 3-D finite element model of micro-stamping process was established to determine the coefficient of friction at the contact interface of micro-stamping dies and BPPs, von-Mises equivalent stress, plastic strain and final sheet thickness distributions. The results revealed that the roughness values for die pairs and BPPs followed similar trends during 10,000 micro-stampings. The corrosion resistance variation as a consequence of long-run manufacturing was found to be statistically insignificant, and the relation between surface roughness and corrosion resistance was found to be indirect.

Keywords: Bipolar plates, stamping, surface topography, contact resistance, corrosion resistance

INTRODUCTION

PEM Fuel cells are appropriate for the portable power and transportation applications mainly due to their low operating temperature levels and relatively quick-start features. However, cost and durability issues prevent PEM fuel cells from widespread use [1]. If the mass manufacturing of PEM is considered, the cost issue becomes more critical. When the cost of fuel cell power is compared with the internal combustion engines, fuel cell power is 4-10 times more expensive ($30-$50/kW vs. $200-$300/kW) [1-4].

Bipolar plate stands for high volume and high cost component of PEM fuel cells (60-80% of stack weight, 30-45% of stack cost) [5]. Molded graphite material is widespread BPP material for PEM fuel cells due to their excellent electrical conductivity and chemical stability. However, graphite BPP is not competitive in the energy market because of high manufacturing cost and time which is $10.42 and 45 seconds per plate, respectively [6]. Formed thin metallic sheets are promising candidates for a PEM fuel cell stack with high efficiency and low cost [7]. In addition to these advantages, metallic BPPs offer high electrical and thermal conductivity, chemical stability, compatibility for mass production, mechanical strength, cold-start features which are crucial in long-term stability of fuel cell applications. Considering the corrosion resistance requirement of BPPs, stainless steel stands forward as the most appropriate material among the other metallic BPP materials such as Ni, Ti, and Al based alloys [8].

There are several forming methods proposed for different materials such as machining for graphite BPPs, stamping process for metal BPPs and molding for polymer-carbon composites [9-11]. Among these BPP fabrication methods, stamping is the most competitive process since high production rates and cost effectiveness are possible with this technique [9]. Geometric accuracy (thickness and flatness), shape accuracy (channel dimensions, shape and distribution) and surface quality requirements are satisfied by stamping process. Since the surface quality of BPPs is highly affected by tribological conditions and die wear, understanding of material behavior and die/BPP surface interactions in micro-scale is very critical. Previous studies also showed that friction conditions in micro-scale is more aggressive than that for macro-scale because of the higher surface to volume ratio so called “size effect” [12-13]. During the high volume production of BPPs, high contact pressures cause highly localized stresses which result in topographic and tribological changes. These changes, in turn, may influence the corrosion and contact resistance behavior of BPPs, consequently the fuel cell performance. Therefore, surface topography alterations should be monitored and kept in acceptable range throughout the long-run manufacturing conditions.

Previous investigations on the topography and tribological behavior in micro-forming were performed mostly with short-run processes. This study, on the other hand, aimed for monitoring the topographic and tribological changes, contact conditions and their effects on the BPP in long run manufacturing conditions to obtain more realistic results since in real production conditions micro-stamping of BPPs is supposed to take place for ten thousands, if not hundred thousands, of cycles. In the experimental part of the study, investigations of the surface topography and tribological changes on the die and BPP interface during long-run micro stamping process were performed. Furthermore, correlations between surface topography and corrosion/contact resistance characteristics of BPPs were examined. Finite element (FE) based models were also established to observe stress-strain conditions and thickness change distributions on the formed BPPs. The coefficient of friction during the long run micro-stamping process was obtained from finite element analyses and compared with experimental findings.

EXPERIMENTAL AND NUMERICAL ANALYSES

Material and Stamping Dies

SS316L metallic sheet alloy with a thickness of 51 μm was chosen as BPP material. Mechanical and chemical properties of SS316L were presented in Table 1 and Table 2. 10,000 of SS316L sheet blank samples were prepared in 70mm x 70mm dimensions. Figure 1 shows the schematic of the stamping process and micro-stamping dies employed.

Table 1. Mechanical Properties of SS316L (as provided, Brown Metals, Rancho Cucamonga, CA, USA)

Condition/Tempering	Annealed
Modulus of Elasticity (Tension)	193 GPa (28 x 10^6 psi)
Ultimate Tensile Strength	711 MPa (103,100 psi)
Yield Strength at 0.2% offset	341 MPa (49,400 psi)
Percent Elongation in 2 inches	56.00%
ASTM Grain Size	10

Table 2 Chemical composition of SS316L (as provided Brown Metals Company, Rancho Cucamonga, CA, USA)

C	Mn	P	S	Si	Cr	Ni	Mo	Cu	N	Fe
0.021	1.48	0.033	0.001	0.43	16.2	10.03	2.06	0.43	0.04	Bal

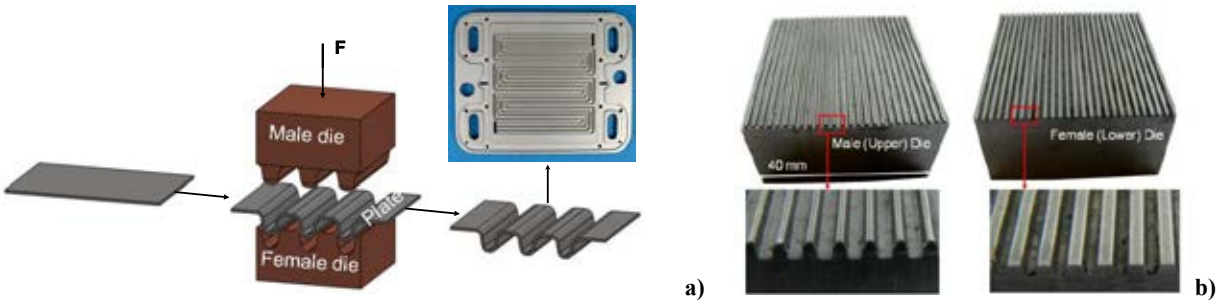


Fig. 1. a) Schematic of stamping process, b) Micro-stamping dies used to form SS 316L sheet blanks

Numerical Analysis

Commercially available explicit/implicit finite element code Ls-Dyna was employed to simulate the micro-stamping process. Due to the symmetry nature of the problem, a quarter 3-D model (Fig. 2) was established to reduce the simulation time. The blanks and blank holder were defined as deformable bodies and modeled with 4-node quadrilateral elements while female and male dies were assumed as rigid parts. The total number of elements used in the models was 52,338. In analysis, at least 11 different FEA were performed with different coefficient of friction values using Coulomb's friction model. In order to determine the range of coefficient of friction experienced in micro-stamping tests, first, a few FEA with the coefficient of frictions of 0, 0.1, 0.2, 0.3, 0.4 and 0.5 were applied and their corresponding channel height results were compared with the experimental results. Then, iterative finite element analyses were performed until the change in coefficient of friction value with respect to previous step is reduced under a level of 0.01. All contacting surfaces were specified as "contact forming one way surface to surface".available in Ls-Dyna. Blank holder force of 3 kN was applied on sandwiched sheet blank between upper

and lower die flat surfaces. Simulations were performed on a personal computer equipped with 2.8 GHz hyper-threading featured processor and 8 GB of RAM. Average computational time of 20 min. was recorded for analyses. This study investigated the effect of long-run manufacturing conditions on the surface topography, corrosion and contact resistance of micro-stamped BPPs. Several FEA analyses were conducted to estimate the coefficient of friction values occurred at contact interface.

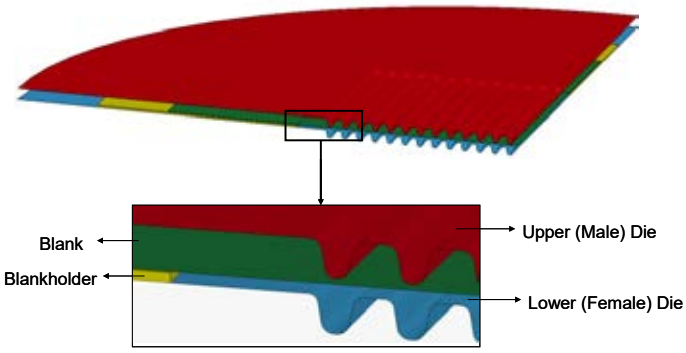


Fig. 2. 3D quarter FE model of stamping process used in fabrication of BPPs

CONCLUSION

Surface roughness analyses for forming die and BPPs demonstrated significant changes during the whole range of experiments. Although without patterned roughness changes was observed, the roughness trend between the microforming die parts (male, female dies) and micro-stamped BPPs was observed to be similar. Corrosion resistance test results showed that surface treatment is required to improve the corrosion resistance of plates to reach the DOE corrosion resistance targets. According to contact resistance tests, SS316L plates exhibited much higher contact resistance than DOE target levels. Contact resistance test results exhibited significant changes over 10,000 micro-stamping process. The correlation between surface roughness and contact resistance of BPPs was deemed to be direct.

The dimensional measurements of channel heights showed insignificant channel height changes at different stages of micro-stamping runs (i.e., 1st, 2000th, 4000th, 6000th, 8000th, 10000th). This implied to dimensional stability of formed products and repeatability of the process. Affected by these findings, coefficient of friction variation was negligibly small and was found to be between 0.18 and 0.19. Finite element analyses provided also useful information on the experienced stress, strain, thickness change magnitudes and valuable data for better die design and longer tool life.

REFERENCES

1. Brady MP, Yang B, Yang H, Turner JA, More KL, Wilson M and Garzon F. 2006. The formation of protective nitride surfaces for PEM fuel cell metallic bipolar plate. Journal of Materials 58:50-57.
2. Bar-On I, Kirchain R, Roth R. 2002. Technical Cost Analysis for PEM Fuel Cells. Journal of Power Sources 109:71-75.
3. Middleman E, Kout W., Vogelaar B, Lenssen J., Waal E. 2003. Bipolar Plates for PEM fuel cells. Journal of Power Sources 118: 44-46.
4. Cunningham B, Baird DG. 2006. The Development of Economical Bipolar Plates for Fuel Cells. Journal of Materials Chemistry 16: 4385-4388.
5. Herman A, Chaudhuri T and Spagnol P., 2005. Bipolar plates for PEM fuel cells: A review. International Journal of Hydrogen Energy 30:1297-1302
6. White RI. Modern aspects of electrochemistry. 2007. New York, Springer-Verlag
7. Peng L, Lai X, Yi P, Mai J, Ni J. 2011. Design, optimization, and fabrication of slotted-interdigigated thin metallic bipolar plates for PEM Fuel Cells. Journal of Fuel Cell Science and Technology 8:011002-1-8.
8. H. Wang, J.A. Turner, 2010, “Reviewing Metallic PEMFC Bipolar Plates”. Fuel Cells 2010: v.10, pp. 510-519.
9. Mehta V, Cooper JS. 2003. Review and analysis of PEM fuel cell design and manufacturing. Journal of Power Sources 114:3253

WHEC-2022
23rd World Hydrogen Energy Conference
June 26-30, 2022 - Istanbul

#276

HIGHLY EFFICIENT LOW METAL LOADING NANOSTRUCTURED ELECTROCATALYSTS

[1] A. M. Valenzuela-Muñiz, [2] H. Valenzuela-Ramos, [1] M. E. Zi-Chi, [3] M. Miki-Yoshida, [1*] Y. Verde-Gomez
[1]Tecnológico Nacional de México/IT de Cancún, Av. Kabah Km 3, Cancún, Q. Roo, México, 77500
[2] Tecnológico Nacional de México/IT de Chihuahua, Av. Tecnológico 2909, Chihuahua, Chih. México, 31310
[3] Centro de Investigación en Materiales Avanzados S. C., Av. Miguel de Cervantes 120, Chihuahua, Chih. México, 31136

*Corresponding author e-mail: jose.vg@cancun.tecnm.mx

ABSTRACT

In order to increase the utilization of PEM fuel cells, it is very important to develop alternatives that allow wider commercialization. It is well known that one of the most expensive components of the mentioned technology are the electrocatalysts [1] since they are based on scarce metals, such as Platinum. Diverse approaches have been taken to overpass this problem; different research works propose the combination of metals to achieve the required activity. Also, a variety of supporting materials have been studied to increase stability. However, a clear alternative there is still not available. This research work proposes to design and development of PEM fuel cell electrocatalysts with adequate activity and stability, but also optimizing the platinum loading. Multiwalled Carbon Nanotubes were obtained using a modified chemical vapor deposition method and used as support of Platinum particles deposited via a colloidal procedure. Low loadings were achieved. The obtained materials were physical and chemically analyzed with scanning and transmission electron microscopies. Also, an electrochemical evaluation towards the PEM fuel cell reactions was performed using cyclic and linear voltammetry, the proposed system exhibited higher current density per mg of Pt compared to a commercial material.

Keywords: PEM fuel cell, nanostructured electrocatalyst, low Pt loading, carbon nanotubes support

INTRODUCTION

Platinum base electrocatalysts are still monopolizing the PEM fuel cells market since they have the best activity. However, the scarcity of this metal impulses the research field to search for alternatives. The necessity of reducing the utilization of Pt for the PEM fuel cells electrocatalyst has been the motivation of diverse research works such as combining the Pt with other metals, decreasing the metal loading, using co-catalysts, testing different supporting materials, among others. On the other hand, during the last years, it has been established that the Multiwalled Carbon Nanotubes (MWCNT) exhibit great mechanical, chemical, and electrical properties. Hence, its utilization as a supporting material for PEM fuel cells electrocatalysts is currently being explored. The relevant surface characteristics allow the stabilization of metallic nanoparticles as well as promote the electronic transference during electrochemical reactions.

Hence, the main objective of this research work is to generate highly active low Pt loading electrocatalysts, optimizing the utilization of the Pt by creating very well distributed nanoparticles, as well as promoting the interaction with the support, MWCNT. A great advantage of the proposal is that the methodology used to obtain the MWCNT allows a semi-scale production (around 4 grams per batch) [2,3]. Also, the Pt nanoparticles deposition method is simple and accurate, allowing the low metal loading [4,5].

MATERIALS AND METHODS

Multi-Walled Carbon nanotubes (MWCNT) were obtained using a modified chemical vapor deposition methodology (M-CVD) already established and studied by the research group [2, 3]. In addition, a colloidal methodology was used to do the deposition of Platinum nanoparticles over the CNT surface [4,5]. Low Pt loadings were tested, to analyze the behavior of the electrocatalysts.
The structure of the obtained materials was analyzed using electron transmission microscopy (TEM). Also, scanning electron microscopy (SEM) studies were done to obtain the chemical properties and the morphology. On the other hand, the electrochemical evaluation was performed by cyclic and lineal voltammetry in a conventional three-electrode cell. The tests were done in acidic media using Ag/AgCl (KCl sat) as reference electrode, and Pt wire as a counter. To compare, the same analyzes were carried out on a commercial electrocatalyst, Vulcan carbon with Pt particles.

RESULTS AND DISCUSSION

Fig. 1 shows the typical tubular formation of the multi-walled carbon nanotubes (MWCNT) taken from transmission electron microscopy (TEM). In addition, it is possible to observe the Pt nanoparticles evincing that the used methodology is appropriated to achieve a very good particle distribution.

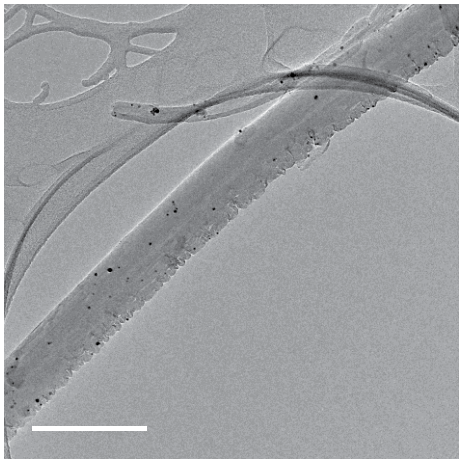


Fig. 1. Transmission Electron Microscopy micrograph of the low Pt loading material (LPt/CNT).

Table 1 shows the chemical elemental analysis performed by energy dispersion spectroscopy (EDS) using scanning electron microscopy (SEM). As can see, low metal loading was achieved around 2 wt%. Iron metal is attributed to the ferrocene catalyst used which remains inside the MWCNT.

Table 1. Chemical Elemental analysis by EDS

Element	Wt. %
Carbon	90.50
Iron	2.88
Oxygen	5.01
Platinum	1.17

The electrochemical results of the proposed material in the PEM fuel cell reactions is presented in Fig. 2. Regarding the hydrogen oxidation reaction (Fig. 2a) it is possible to observe that the Pt/CNT sample did not achieve a good activity compared to the commercial material (5%Pt over Vulcan). However, for the oxygen reduction reaction (Fig. 2b) the synthesized material demonstrates a higher limiting current. It is important to mention that as it is shown in Table 2, the Pt/CNT material has 4 times less Pt available to perform the reactions. However, the good distribution and size of the particles, as well as the interaction with the support (MWCNT) allows the material to provide better performance [6]. It is also noticed the onset potential is still low compared to the commercial material. Nevertheless, the behavior achieved opens a good opportunity to improve the design of the material with low Pt loading.

Table 2. Metal loading over the electrode

Sample	mg Pt/cm^2	Pt ratio
Low Pt CNT	0.016	1
5Pt Vulcan	0.067	4

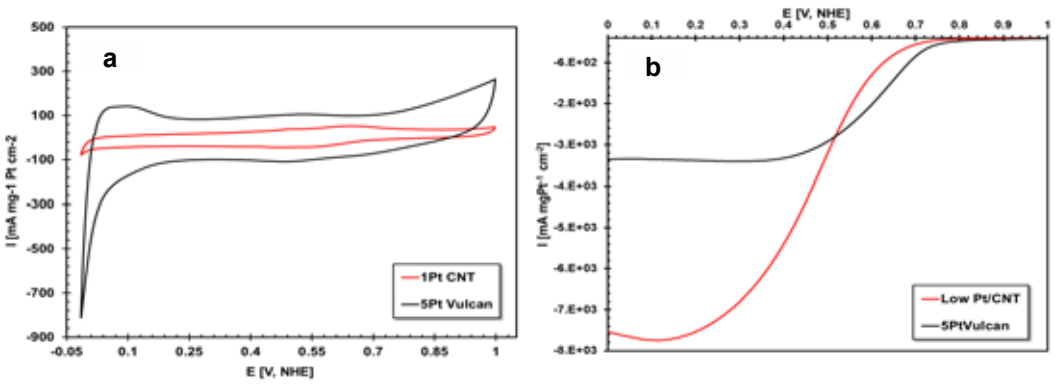


Fig. 2. Electrochemical evaluation using 0.5M H_2SO_4 as electrolyte: a) cyclic voltammetry, b) linear voltammetry

CONCLUSIONS

The Modified Chemical Vapor Deposition Method is suitable to produce MWCNT. The Low Pt/CNT system has shown a low activity (compared to commercial material) towards de hydrogen oxidation reaction. However, for the ORR low, Pt/CNT material exhibited a higher current density per mg of Pt, than the commercial material, this can be attributed to the good dispersion of Pt particles over the surface and the interaction with graphitic domains of carbon. Even though the onset potential is still lower, the behavior of the proposed materials opens a great opportunity for the development of affordable PEM-FC electrocatalyst with low Pt loading as well as good thermal and chemical stability. It is important to mention that different loading has been tested during the development of this research work, the complete set analysis will be presented at the conference.

ACKNOWLEDGEMENT

The authors acknowledge "CONACyT-SENER-Sustainability Energy" under grant No. 254667.

REFERENCES

1. Chen, Z. H. et al 2011. A review on non-precious metal electrocatalysts for PEM fuel cells. Energy & Environmental Science, 3167-3192.
2. Romero-Cano, G. Rosado-Ortiz, A.M. Valenzuela-Muñiz, L.C. Ordoñez, R. Gauvin, Y. Verde Gómez, 2019. Solvent effect in the synthesis of nanostructured PtSn/CNT as electrocatalysts for the electrooxidation of ethanol. International Journal of Hydrogen Energy, 44:12430-12438.
3. Rosado Ortíz, G. M., 2014. Síntesis y caracterización de nanopartículas Pt-Ni para aplicaciones en celdas de combustible tipo PEM. Tecnológico Nacional De México / Instituto Tecnológico de Cancún. Master's degree Thesis.
4. Rosado, G., Verde, Y., Valenzuela-Muñiz, A. M., Barbosa, R., Miki Yoshida, M., & Escobar, B., 2016. Catalytic activity of Pt-Ni nanoparticles supported on multi-walled carbon nanotubes for the oxygen reduction reaction. International Journal of Hydrogen Energy, 41:1-12.
5. Escobar, B. et al 2013. Carbon nanotubes as support of well dispersed platinum nanoparticles via colloidal synthesis. Journal of Power Sources, 243:88-94.
6. Jiwei Ma, Aurélien Habrioux, Cláudia Morais, Adam Lewera, Walter Vogel, Ysmael Verde-Gómez, Guadalupe Ramos-Sanchez, Perla B. Balbuena and Nicolas Alonso-Vante, 2013. Spectroelectrochemical Probing of the Strong Interaction between Platinum Nanoparticles and Graphitic Domains of Carbon. ACS Catalysis, 3:1940−1950.

WHEC-2022
23rd World Hydrogen Energy Conference
June 26-30, 2022 - Istanbul

#288

EFFECTS OF CATALYST LOADING ON THE PERFORMANCE IMPROVEMENT OF PEMFCS APPLYING A MAGNETIC FIELD

[1] *Wonseok Yang,* [1] *Jihyun Kim,* [1*] *Yongchan Kim*
[1]School of Mechanical Engineering, Korea University, 145, Anam-ro, Sungbuk-gu, Seoul, 02841, Republic of Korea

*Corresponding author e-mail: yongckim@korea.ac.kr

ABSTRACT

In this study, the performance improvement of a proton exchange membrane fuel cell (PEMFC) by applying a magnetic field was revealed according to the catalyst loading. A unit H_2-air PEMFC was tested at catalyst loadings of 0.5 mg_{pt} cm^{-2} and 0.03 mg_{pt} cm^{-2}. The performance of a PEMFC increased by applying a magnetic field in both high and low catalyst loading conditions. However, the increasing rate in the performance was significantly higher in the high catalyst loading than in the low loading. The magnetic field effectively increased the catalyst utilization, and the performance improvement as a result of increased catalyst utilization was more effective in high catalyst loading. In conclusion, it is more effective to apply a magnetic field to PEMFCs at high catalyst loading than at low catalyst loading.

Keywords: PEMFC, Catalyst loading, Magnetic field, Performance

INTRODUCTION

Proton exchange membrane fuel cells (PEMFCs) are next-generation energy converters as an essential component of a hydrogen economy. A PEMFC has many advantages to be a promising energy source such as zero emissions and high efficiency. However, the low activity of a cathode oxygen reduction reaction (ORR) deteriorates the performance of PEMFCs, which hinders the commercialization of PEMFCs [1]. Therefore, the improvement of ORR performance is important for the commercialization of PEMFCs.

Among many efforts to enhance the ORR performance of PEMFCs, recently, an ORR activity improvement method using a magnetic field has been studied by several research groups. Oxygen is affected by the force of a magnetic field because oxygen is a paramagnetic material [2]. Therefore, a magnetic field can have a positive influence on the ORR of PEMFCs by enhancing the movement and transport of oxygen on an electrode surface. Several studies were reported to reveal the performance improvement by a magnetic field. Abdel-Rehim [3] studied the performance enhancement of an open cathode PEMFC stack by a magnetic field controlling the fan power of the air inlet. Ruksawong et al. [4] reported the performance improvement of a PEMFC by a magnetic field, and the improvement increased with an increase in the magnetic field density. However, the electrode condition of cathode catalysts has not been mainly discussed as a critical variable for the study. The performance improvement of PEMFCs by a magnetic field is mainly caused by the improvement of ORR activity. Since the ORR occurs on the cathode electrode, the performance improvement by a magnetic field is naturally affected by the electrode condition of a cathode catalyst.

In this study, the effect of catalyst loading on the performance improvement of a PEMFC by a magnetic field was investigated using a unit cell. The performance of a PEMFC was tested by varying the Pt/C catalyst loading of a cathode with and without a magnetic field. Based on this experimental study, the effect of catalyst loading was revealed, and the optimal catalyst loading for best performance improvement by a magnetic field was determined.

EXPERIMENTAL

In this study, a unit PEMFC with an active area of 9 cm^2 was used to determine the performance. Hydrogen and air were supplied to the anode and cathode, respectively. The relative humidity of both hydrogen and air was 80%, and the stoichiometries were 1.5 and 2.5 for hydrogen and air, respectively, based on the current density of 2 A cm^{-2}. The operating temperature and pressure were 80 °C and atmospheric pressure, respectively.

A magnetic field of 0.2 T density was applied to the PEMFC. The magnetic field was created by five neodymium (Nd-Fe-B) magnets at each side of the PEMFC. The Pt/C catalyst loading of the cathode electrode in the PEMFC was varied as 0.03 mg_{pt} cm^{-2} and 0.5 mg_{pt} cm^{-2}. The catalyst loadings were selected as the representative of high and low loading. Based on the variation of catalyst loading, the effect of the catalyst condition on the performance improvement by a magnetic field was revealed.

RESULTS AND DISCUSSION

Fig. 1 shows the variation in voltage and power density as a function of current density with and without a magnetic field. The voltages and corresponding power densities increased by applying a magnetic field in both high (0.5 mg_{pt} cm^{-2}) and low (0.03 mg_{pt} cm^{-2}) loadings. However, the amount of increment was notably different. The performance improvement using a magnetic field was much larger in the electrode condition of high loading than in low loading.

Fig. 2 shows the increasing rate of the PEMFC performance by applying a magnetic field according to the catalyst loading. The performance increasing rate of high loading PEMFC was significantly larger than that of low loading in all voltages. The magnetic field aided the transport and movement of oxygen, so the oxygen was better adsorbed on the catalyst surface in the magnetic field. In other words, the magnetic field effectively increased the catalyst utilization, and the performance improvement as a result of the increased catalyst utilization was more effective in high catalyst loading condition. In summary, it is effective to apply a magnetic field to PEMFCs at high catalyst loading conditions.

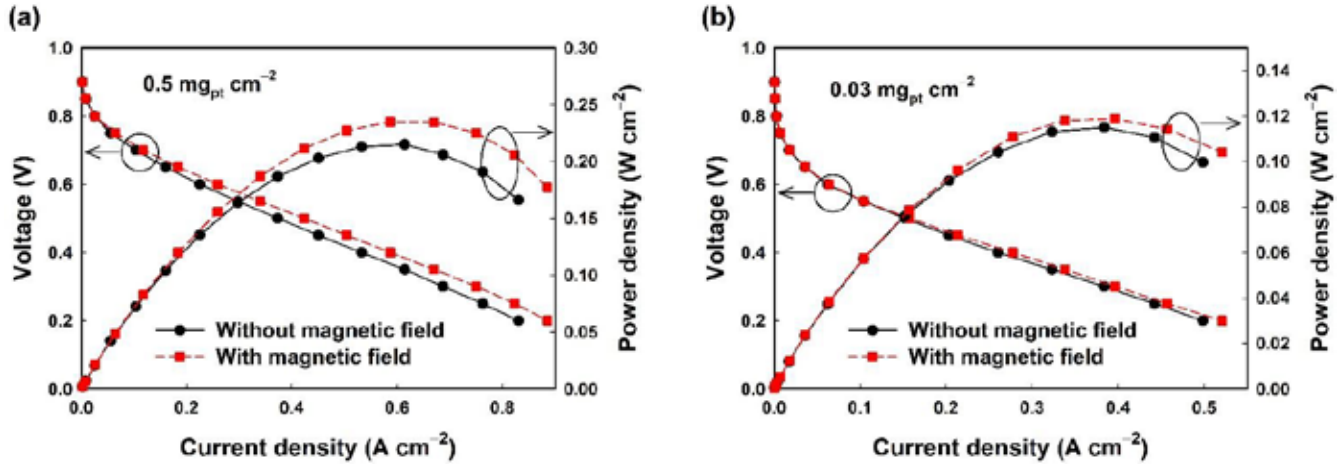


Fig. 1. Variation in voltage and power density as a function of current density according to the catalyst loading of (a) 0.5 mg_{pt} cm^{-2} and (b) 0.03 mg_{pt} cm^{-2} with and without a magnetic field.

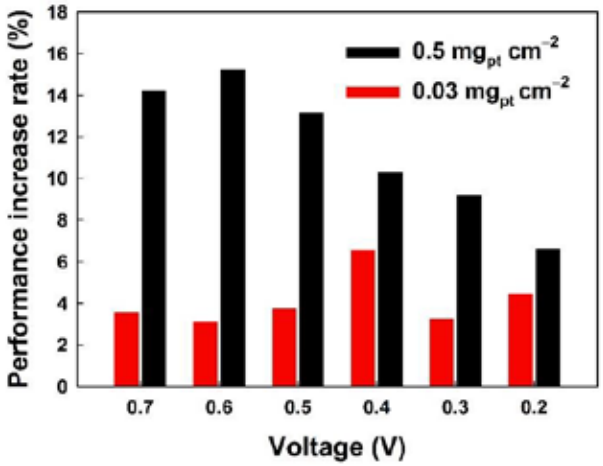


Fig. 2. The increase rate of PEMFC performance by applying a magnetic field according to catalyst loading.

CONCLUSIONS

In this study, the performance improvement of a PEMFC by a magnetic field was investigated according to the catalyst loading. The unit PEMFC tests were conducted at catalyst loadings of 0.5 mg_{pt} cm^{-2} and 0.03 mg_{pt} cm^{-2}. The performance of a PEMFC increased by applying a magnetic field in both high and low catalyst loadings. However, the amount of increment and increasing rate were much higher in the high catalyst loading than in the low loading because the magnetic field improved the catalyst utilization. In conclusion, the performance improvement by applying a magnetic field can be significantly increased with the increase in catalyst loading on an electrode.

ACKNOWLEDGEMENT

This work was supported by a National Research Foundation of Korea grant funded by the Korean Government (MSIT) (No. 2020R1A2C2008539).

REFERENCES

1. Barbir F. 2013. PEM fuel cells: theory and practice. 2nd ed. Academic press.
2. Spaldin NA. 2010. Magnetic Materials: Fundamentals and Applications. 2nd ed. Cambridge: Cambridge University Press.
3. Abdel-Rehim AA. 2019. The influence of electromagnetic field on the performance and operation of a PEM fuel cell stack subjected to a relatively low electromagnetic field intensity. Energy Conversion and Management 198:111906.
4. Ruksawong K, Songprakorp R, Monyakul V, David NA, Sui PC, Djilali N. 2016. Investigation of PEMFC under static magnetic field: temperature, relative humidity and performance. Journal of Electrochemical Society 164:F1.

WHEC-2022
23rd World Hydrogen Energy Conference
June 26-30, 2022 - Istanbul

#297

EFFECT OF CHITOSAN ON THE CORROSION INHIBITION FOR ALUMINIUM ALLOY IN H_2SO_4 MEDIUM

[1,3] I Gusti Ayu Arwati, [1]*Edy Herianto Majlan, [1]Loh Kee Shyuan, [1]Khuzaimah Ariffin , [1]Teuku Husaini,[2]Sagir Alva, [2] Wahyu Muhammad, [3]Nabilah Afiqah Mohd Radzuan
[1] Fuel Cell Institute, National University of Malaysia , 43600 UKM Bangi, Selangor Darul Ehsan, Malaysia
[2] Engineering Faculty, Mercu Buana University,11650, Indonesia
[3]Centre for Materials Engineering and Smart Manufacturing, Faculty of Engineering and Built Environment, Universiti Kebangsaan Malaysia, 43600 Bangi, Selangor, Malaysia.

* Corresponding author: edyhm71@gmail.com

ABSTRACT

Aluminum Alloy (AA 5052) is an inexpensive and lightweight metal that has been used in a variety of applications including as a bipolar plate in Proton Exchange Membrane Fuel Cells (PEMFC). The alloy has good electrical conductivity and low corrosion, corrosion rate will increase during PEMFC operation with increasing temperature. Inorganic dyes such as chromate are commonly used to reduce metal corrosion, unfortunately, they are toxic and have a negative impact on the environment. To solve this problem, chitosan as an organic solvent is green, cheap, non -toxic and environmentally friendly. Thickening electrophoresis (EPD) technique was used to coat the surface of AA 5052 with chitosan.. To measure the level of corrosion rate using electrochemical and weight los methods (in 0.5 M H_2SO_4 solution). Levels of AA 5052, with and without chitosan, were 0.1702 $mgcm^{-2}\ h^{-1}$ and 0.0552 $mgcm^{-2}\ h^{-1}$, respectively. Based on the polarization test, chitosan inhibitors can decrease the corrosion rate and will increase with increasing temperature.

Keywords: PEMFC, Inhibitor Chitosan, EPD, Corrosion rate

INTRODUCTION

Aluminum and its alloys have many advantages over other metals because of their high electrical conductivity, low cost and light weight [1]. The resistance of aluminum in a corrosive environment under certain conditions is due to the presence of an oxide layer on its surface [2]. Aluminum alloy 5052 (AA 5052) contains 97.2% - 97.8% aluminum (Al) and 2.2% - 2.8% magnesium (Mg). The addition of Mg to AA 5052 metal can increase its strength without reducing its ductility [1]. AA 5052 can be applied to aircraft, automotive, construction and bipolar plate components in Proton Exchange Membrane Fuel Cell (PEMFC) systems. The selection of AA 5052 as a bipolar plate is generally based on its properties namely, high conductivity, low cost and light metal) compared to other metals [3,4]. Generally PEMFCs are operated under acidic conditions at temperatures of 40 °C to 80 ° C (313 – 353 K) [5,6]. Yang, Guo & Liu [5] reported that acidic environmental conditions and relatively high operating temperatures can cause alloy AA 5052 to corrode [7].

In general, corrosion is defined as damage to metal surfaces caused by chemical reactions between the surface and the environment. Inorganic inhibitors such as chromate to combat corrosion. Unfortunately it has a negative impact on the environment due to its toxicity [9, 10]. Based on these facts, green organic inhibitors are the best alternative to prevent and reduce corrosion. Chitosan is an organic compound derived from chitin which has the potential as a corrosion inhibitor because it fulfills all the characteristics. Chitosan can be produced from chitin through hydrolysis and deacetylation processes containing amino (-NH2) and hydroxyl (-OH) groups both of which act as absorbents to inhibit the corrosion rate through the absorption process [11-14].

It is known that temperature plays an important role in the corrosion process, especially in PEMFC operation. Therefore, this study tried to explore the effect of temperature differences on the corrosion rate of AA 5052 alloy with and without chitosan in 0.5 M H_2SO_4 at different times and temperatures. The effects on corrosion rate and inhibition efficiency are discussed in detail along with the performance analysis (potentiodynamic polarization and activation energy analysis).

MATERIALS AND METHODS

Equipment and Materials

AA 5052 alloy with size of 20 mm x 10 mm x 2.5 mm was selected during this experiment. Chitosan (Merck, with standard analysis) was used as a green organic inhibitor. The corrosion rates of AA 5052 with and without chitosan were evaluated by using the potentiostate CorrTest CS350 to analyze the potentiodynamic polarization. The morphology and element compositions on the surface of AA 5052 with and without chitosan were analyzed by using a scanning electron microscope (SEM, Hitachi TM3000) equipped with energy dispersive X-ray spectroscopy (EDX,

Carl Zeiss EVO MA 10). Firstly, AA 5052 alloy was washed with acetone and polished by sand paper with grids of 200, 400, 600, 1000 and 2000. After that, AA 5052 alloy was washed with acid and base pickling solution, and then rinsed with deionized water. Cleaned AA 5052 alloy was perforated using a drill with a diameter of 2.5 mm. To hold the AA 5052 alloy, a polyvinyl chloride (PVC) cable was attached. Lastly, the AA 5052 alloy surface was smeared with epoxy, except for a 1.0 cm^{-2} of its surface. 0.5 % of chitosan solution was prepared using a total 0.15 g of chitosan that was diluted in 30 mL acetic acid (CH_3COOH). The mixed-solution was stirred until homogeneous by using a magnetic stirrer [14]. AA 5052 alloy was put into the electro phoresis deposition (EPD) cell that contained 0.5 % chitosan solution. The EPD process was performed at room temperature with AA 5052 as cathode and carbon felt as anode. The EPD process was conducted for 10, 20 and 30 minutes with an applied voltage of 20 V..Corrosion rate tests: Weight loss analysis AA 5052 with and without chitosan were immersed in 0.5 M H_2SO_4 for 72, 120 and 168 hours at room temperature [15].

Electrochemical method with potentiodynamic polarization

The corrosion rates of AA 5052 alloys with and without the chitosan was verified and analyzed using the potentiodynamic polarization method. This test was performed using the potentiostat CorrTest, model CS350 at temperature of 298 K, 313 K, 333 K and 353 K. Potentiodynamic polarization cell was arranged as three electrode configurations, in which theAA 5052 acted as the working electrode (WE), platinum (Pt) rod as the counter electrode (CE) and Ag/AgCl as the reference electrode (RE). The applied potential used was in the range of -0.9 V to -1.0 V with a scan rate of 2 mVs.

RESULTS AND DISCUSSION

Analysis of time effect on EPD process

The corrosion rate of AA5052 with and without chitosan increased with increasing immersion time in 0.5 M H2SO4 solution . The lowest corrosion rate without chitosan was obtained at 0.1491 mgcm-2h-1 at 72 hours. Meanwhile, after the EPD process, the lowest corrosion rate was found in the 20th minute (0.0181 mgcm-2h-1) followed by 10 minutes (0.0245 mgcm-2h) and 30 minutes (0.0398 mgcm-2h-1). This phenomenon can occur because the chitosan layer on the surface in the 10 minute EPD process has not yet been formed. Meanwhile, the chitosan layer is thicker in the 30 minute EPD process, so that the layer acts as an inhibitor that reduces current density; consequently, the absorption of chitosan is less homogeneous [16,17]. Overall, the corrosion rate of AA 5052 alloy with chitosan decreased at 120 hours to 168 hours of immersion time. In principle the protective layer reduces the contact between the alloy surface and the electrolyte [18].

Effect of temperature on corrosion rate and inhibition efficiency

The results showed that the corrosion rate of AA 5052 with and without chitosan increased with increasing temperature The corrosion rate of AA 5052 with chitosan-20 cm^{-2} $h^{-1}$was 0.25 mg cm^{-2} h^{-1}at 298 K then increased to 0.43 mg cm^{-2} h^{-1} (313 K), 0.62 mg cm^{-2} h^{-1} (333 K) and 1.38 mg cm^{-2} h^{-1} (353 K), increasing temperature accelerates anodic and cathodic reactions, reduces dissolved oxygen in solution, and also accelerates cathodic diffusion, consequently increasing the corrosion rate [19]. The highest inhibition efficiency was 42.31% at 298 K. As discussed above, the inhibition efficiency decreased with increasing temperature. This fact may be because the cathodic chitosan has physisorption properties [20] which reduce the electrostatic interaction between the chitosan and the surface of AA 5052; consequently, its inhibitory activity decreases.

Activation energy analysis

- Activation energy can be defined as the minimum amount of energy that is required to activate atoms or molecules to a condition in which they can undergo chemical reaction or physical conversion. Theoretically, the corrosion rate can also been analyzed using the activation energy (E_a) equation, as formulated by Arhenius [21]. AA 5052 whitout chitosan was lower (20.55 kJ mol^{-1}) compared to AA 5052 with chitosan (25.82 kJ mol^{-1}). The higher activation energy indicates that AA 5052 with chitosan was more difficult to corrode compared to AA 5052 without chitosan [21]. This fact showed that the corrosion in AA 5052 alloy can be reduced by using a chitosan inhibitor is as shown in Table 1.

-

Table 1. Values of activation energy (E_a) for AA 5052 alloys with and without chitosan

Sample AA 5052	Linear regression	$-E_a/R$	E_a (kJ mol^{-1})
Without Chitosan	y = -2471x + 7.457	-2471	20.55
With Chitosan	y = -3105x + 9.020	-3105	25.82

Potentiodynamic Polarization Analysis

Potentio-dynamic polarization tests provided the corrosion current density (I_{corr}) and the corrosion potential (E_{corr}) data. In general, the corrosion rates were determined based on the ASTM G102 standard. Firstly, the corrosion current density was tested through the electrochemical method [24], The potentiodynamic polarization can be transformed towards the corrosion potential to determine the corrosion current density. Table 2 shows the values of Tafel extra-polarization for AA 5052 with and without chitosan.

Overall, the Ecorr values for AA 5052 without chitosan were lower than those coated with chitosan at each temperature tested. For example, -0.4829 V vs Ag/AgCl Ecorr for AA 5052 without chitosan is lower than 0.5519 V vs Ag/AgCl Ecorr for AA 5052 with chitosan at the test temperature of 298 K. This fact reveals that chitosan predominantly protects the cathodic region [22]. The corrosion rate can be determined using the Icorr value. The higher the Icorr value, the higher the corrosion rate. Overall, the corrosion rate gradually increases with increasing temperature. The activation energy (Ea) of the particles increases with increasing temperature; consequently, the corrosion reaction becomes faster [19]. Furthermore, the highest IE of chitosan was observed at 95.12% at 298 K and then gradually decreased with increasing temperature tested [23]. This is due to the physisorption properties of chitosan, where the dominant adsorption reaction occurs on the cathodic side [24].

Table 2. Tafel of potentiodynamic polarization for AA 5052 with and without chitosan in 0.5 M H_2SO_4 at 298, 313, 333 and 353 K

Sample AA 5052	T (K)	E_{corr} (V vs Ag/AgCl)	I_{corr} (mA cm^{-2})	CR (mpy)	IE (%)
	298	-0.4829	144.8	62.96	-
Without Chitosan	313	-0.5880	490.0	213.12	-
	333	-0.6558	959.5	417.34	-
	353	-0.5925	2794.2	1215.31	-
	298	-0.5519	7.07	3.07	95.12
With Chitosan	313	-0.6277	88.29	38.40	81.98
	333	-0.6844	501.93	218.31	47.69
	353	-0.6345	2011.90	875.06	28.00

CONCLUSIONS

Chitosan has been successfully coated on aluminum alloy AA 5052 using the EPD method and the role of organic molecules as a green inhibitor to reduce the corrosion rate of the alloy has been studied. Based on the weight loss method, the optimum conditions for the EPD process were obtained at an exposure time of 20 minutes. Meanwhile, the corrosion rate for AA 5052 with and without chitosan at an immersion time of 168 hours was 0.0552 mg cm^{-2} h^{-1} and 0.1702 mg cm^{-2} h^{-1}, respectively. Increasing the temperature can decrease the inhibitory properties of chitosan.

ACKNOWLEDGEMEN

The authors would like to thank the financial support provided by the Universiti Kebangsaan Malaysia through the Petronas short project research grant and the University of Mercubuana for its good cooperation so that this research can be completed.

REFERENCES

1. Davis, J.R. 2001. Alloying: Understanding The Basics. USA: ASM International.
2. Ali, A.I,. & Foaud, N. 2012. Inhibition Of Alminium Corrosion In Hydrochloric Acid Solution Using Black Mulberry Extract. J. Mater. Environ. Sci, 3 , 917-924.
3. Yuan, X.Z., Wang, H., Zhangn, J., & Wilkinson, D.P. 2005. Bipolar Plates For PEM Fuel Cells-From Materials To Processing. Journal Of New Materials For Electrochemical Systems, 8, 257-267.
4. Taherian, R. 2014. A Review Of Composite Anda Metallic Bipolar Plates In Proton Exchange Membrane Fuel Cell: Materials, Fabrication, And Material Selection. Journal Of Power Sources, 265, 370-390.
5. Yang, Y., Guo, L., & Liu, H. 2011. Corrosion Characteristics Of SS316L As Bipolar Plate Material In PEMFC Cathode Environments With Different Acidities. International Journal Of Hydrogen Energy, 36, 1654-1663.
6. Barbir, F. 2013. PEM Fuel Cells (Second Edition). UK: Academic Press.
7. Chiang, A.U., Tsai, L.C., Sheu, H.H., & Lu, C.E. 2014. Corrosion Resistance Of 5052 Al-Alloy With A Zirconia-Rich Conversion Coating Used In Bipolar Plates In Pemfcs. International Journal Of Electrochemical Of Science, 9, 5850-5863.

WHEC-2022
23rd World Hydrogen Energy Conference
June 26-30, 2022 - Istanbul

#305

DESIGN, INTEGRATION, AND VALIDATION OF A TESTING SETUP FOR PEMFC STACK CHARACTERISATION AT HEAVY DUTY AND MARITIME LOAD PROFILES

* *Piotr Bujlo, Øystein Ulleberg*
Institute of Energy Technology (IFE), Department of Hydrogen Technology, 18 Instituttveien, 2007 Kjeller, Norway

*Corresponding author e-mail: piotr.bujlo@ife.no

ABSTRACT

This study presents the design, integration, and validation of a PEMFC stack testing setup, which was realized at the Hynor Laboratory – IFE. The design of the testing setup, which includes an anode/cathode loop and a cooling, power conditioning, and control system, is described in detail. The setup is used for fuel cell stack testing (up to 20 kW power) using a system-like configuration, fuel cell system testing (up to 135 kW power) and the characterisation of its components, and fuel cell system operation using a hybrid configuration with Li-ion battery modules (up to 100 kW power). The integrated fuel cell testing setup is planned to be used for research investigations related to the utilisation of fuel cell technology in heavy duty and maritime applications.

Keywords: fuel cell stack, testing setup, PEM fuel cell

INTRODUCTION

Hydrogen technology coupled with polymer electrolyte membrane fuel cells (PEMFCs) has been recognised as a key technology that enables decarbonisation of the transport sector [1]. Even though PEMFC technology has reached the high technology readiness level and is currently being commercialised, the application of this technology in heavy duty vehicles and maritime requires further research, which will allow for smooth deployment. Fuel cell stack testing is an important stage in the development process of new stack designs and in the development of new fuel cell system configurations and architectures [2].

The PEMFC stack testing setup developed at IFE is a response to the current needs for stack and system testing and it is an open platform configuration that enables testing of stacks, balance of plant components, and complete systems.

EXPERIMENTAL SETUP

The PEMFC stack testing setup was integrated according to the developed detailed piping and instrumentation diagram (P&ID), a simplified version is depicted in Fig. 1 (a). The real view of the fuel cell stack testing setup available at Hynor Laboratory - IFE, including control system, is shown in Fig. 1 (b).

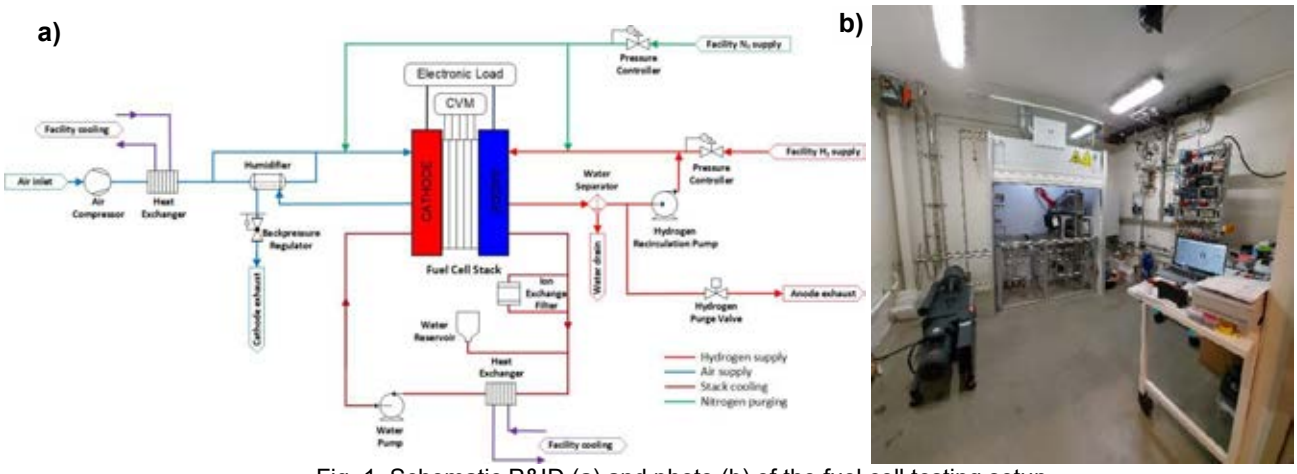


Fig. 1. Schematic P&ID (a) and photo (b) of the fuel cell testing setup.

Fuel cell stack

A PowerCell S2 type of fuel cell stack was integrated into the testing setup. Detailed technical specification of the applied fuel cell stack unit is presented in Table 1.

Table 1. Fuel cell stack technical specifications

Physical	Number of cells	150
	Electrode active area	195 cm^2
	Dimensions	148 x 484 x 293 mm (WxLxH)
	Weight	approx. 24.2 kg
Electrical	Nominal / maximum stack power	12.9 kW / 18.0 kW
	Nominal / maximum stack current	136.5 A (@ single cell voltage 0.63 V) / 195.0 A (@ single cell voltage 0.40 V)
	Minimum / nominal / maximum DC stack voltage	60.0 V / 94.5 V / 127.5 V (OCV @ 165.0-195.0 V)
Operating conditions	Anode	Hydrogen or reformate
	H_2 temperature / pressure / humidity	75 °C / 150-1200 $mbar_g$ / >40% RH
	Cathode	Air
	Air temperature / pressure / humidity	75 °C / 150-1000 $mbar_g$ / 60-80% RH
	Cooling	Liquid cooled (de-ionized water)
	Nominal stack temperature	70-75 °C
	Ambient operating conditions	2-70 °C / 0.8-1.5 bar_a / 0-100% RH (noncondensing)

Anode loop

The anode loop was operated in the dead-end mode with hydrogen recirculation. Hydrogen was supplied from the laboratory hydrogen storage to the setup at 5 barg pressure. The pressure was further reduced to the maximum of 1.2 barg before it was supplied to the stack. The pressure in the loop was regulated by a pressure controller (Bronkhorst). The parameters of the supplied hydrogen (humidity, pressure, temperature, and flow rate) were carefully controlled, and the stack outlet gas parameters (pressure and temperature) were carefully monitored. Recirculation of the anode gas was performed using a hydrogen pump (Busch). Gaseous impurities that may diffuse from the cathode side (e.g., nitrogen) and accumulate in the anode loop, as well as water vapour, were released using a purge valve. The valve was periodically opened to release the volume of gas enclosed in the fuel cell stack. The outlet gas was directed to the anode exhaust and evacuated outside laboratory building. For safety reasons the anode loop was flushed to remove residual air using nitrogen and hydrogen during system start-up and shutdown, respectively.

Cathode loop

The oxygen required for the reaction was obtained from air and delivered to the stack by an air compressor (Busch). Outlet air from the compressor was cooled to room temperature using a heat exchanger (AlfaNova) coupled with the facility's cooling system. The inlet air was humidified by a humidifier (FumaTech) before it reaches the stack, and the backpressure was controlled using a backpressure regulator (Equilibar). The parameters of the supplied air (humidity, pressure, temperature, and flow rate) were carefully regulated, and the stack outlet gas parameters (pressure and temperature) were precisely monitored. The cathode loop was flushed with nitrogen to remove potential gas impurities and liquid water during system start-up and shutdown, respectively.

Cooling loop

Heat is generated as a by-product during the operation of the fuel cell stack and used for stack self-heating and excess heat is transferred to the facility's cooling system via the cooling loop. The main component of the cooling loop was the water pump (DP-Pumps) that flows deionised water through the stack and heat exchanger (Alfa Nova), which connects the cooling loop of the stack to the facility's cooling system. The flow rate of the coolant was regulated, and its inlet/outlet conductivity, pressure, and temperature were measured to ensure suitable stack operating conditions, especially its temperature.

Power conditioning

The fuel cell testing setup was electrically connected to the DC-bus, which is part of the laboratory power conditioning system. The nonlinear stack DC voltage was regulated using a 20 kW DC/DC boost converter (Hot Platinum), which enables stack operation in the galvanostatic mode. Alternatively, the DC-bus was connected to the grid via a DC/AC inverter (Bitrode), which balances the DC-bus voltage. Another part of the power conditioning system is the cell voltage monitoring (CVM) unit (Smart Testsolutions), which was used to carefully monitor the voltage of each cell in the stack.

Control system

The operation of the testing setup components, signal measurements from integrated sensors, and control of the valves was performed using the control system. The system hardware is based on the cRIO chassis (National Instruments) equipped with digital/analog input/output modules and the software application used for communication and data logging was programmed using the LabView environment. The software application contains an embedded matrix with alarms and warnings, which ensures safe fuel cell stack operation and an immediate response in the case of operating parameters being out of range.

TESTING CAPABILITIES

The developed infrastructure was mainly used for PEMFC stack testing with a nominal power up to 20 kW in a system-like configuration. The instrumentation of the setup and its open platform configuration allows for the characterisation of various fuel cell system balance of plant components. The integration of the setup within the available laboratory power conditioning system facilitates the testing of fuel cell systems up to 135 kW and enables hybridisation with Li-ion battery modules with a power capacity up to 100 kW.

CONCLUSIONS

A PEMFC stack testing setup was successfully designed and integrated at IFE and is available in the Hynor Laboratory. The setup's validation process is ongoing, and the preliminary results obtained thus far are promising. These results confirmed that the design assumptions are correct, and the selection of the system components is appropriate to operate high power PEMFC stacks. The main setup specifications and functionalities are:

- PEMFC stack testing up to 20 kW nominal power in a system-like configuration.
- Characterisation of fuel cell system balance of plant components (e.g., air compressor/blower, humidifier, hydrogen recirculation pump, heat exchanger) and in situ system testing.
- Fuel cell system testing up to 135 kW power and system hybridisation with LI-ion battery modules with a power capacity up to 100 kW.

ACKNOWLEDGEMENT

This study was performed within MoZEES, a Norwegian Centre for Environment-friendly Energy Research, co-sponsored by the Research Council of Norway (Project no. 257653) including 40 partners from the research, industry, and public sectors. The financial support received from the Research Council of Norway (Project no. 294568) for the project "Hydrogen and Fuel Cell for Maritime Applications (H2Maritime)" is gratefully appreciated. The experimental study was partly executed in the national infrastructure Norwegian Fuel Cell and Hydrogen Centre and funded by the Research Council of Norway (Grant no. 245678/F50).

REFERENCES

1. Anandarajah G, McDowall W and Ekins P. 2013. Decarbonising road transport with hydrogen and electricity: Long term global technology learning scenarios. International Journal of Hydrogen Energy 38: 3419-3432.
2. https://www.avl.com/-/cell-stack-testing. Accessed on January 10, 2022.

WHEC-2022
23rd World Hydrogen Energy Conference
June 26-30, 2022 - Istanbul

#320

EXPERIMENTAL STUDY OF MODIFIED POLYBENZIMIDAZOLE/ PHOSPHONATED POLYVINYL ALCOHOL BLEND MEMBRANE FOR FUEL CELL OPERATIONS

[1*] *Aygun Cali,* [2] *Alpay Sahin,* [3] *İrfan Ar*
[1]Gazi University, Graduate School of Natural and Applied Sciences, Chemical Engineering Department, Eti Mah., Maltepe/Çankaya, Ankara, TURKEY
*Corresponding author e-mail: ayguncali@yahoo.com

ABSTRACT

Polybenzimidazole (PBI) is a high-temperature polymer that is used for many purposes in polymer technology since its high hydrophilic nature and mechanic stability. Polyvinyl alcohol (PVA) has advantages, such as its easily modifiable structure and high ionic conductivity features. Polybenzimidazole and polyvinyl alcohol polymers were used as blend membrane structures with different percentage ratios such as 90:10, 70:30, 50:50 for proton exchange membrane fuel cell (PEMFC) applications. Firstly, PBI was synthesized by the solution polycondensation method which means that polyphosphoric acid was applied as both condensation agent (catalyst) and monomer solvent. The H-Nuclear Magnetic Resonance (H-NMR) was applied to identify the structural formation of the polymer. PVA and synthesized PBI polymers were dissolved in different solvents separately and both polymers were mixed by sol-gel method to prepare the blend membrane. The blend membrane was treated with phosphoric acid which was used as a phosphonation agent. The PBI/Phosphonated-PVA (PPVA) blend membrane was examined for evaluating the suitability for proton exchange membrane fuel cell (PEMFC) operations. The characterization tests, i. e; water uptake capacity, FT-IR Analysis, Ion-exchange capacity, Thermal Gravimetric Analysis measurements were applied to the synthesized blend membrane. The synthesized PBI membrane has 2.12 meq gr^{-1} Ionic exchange capacity (IEC) while PBI/PPVA-90:10 blend membrane has 4.15 meq gr^{-1} IEC value.

Keywords: Polybenzimidazole (PBI) polymer, PBI/PVA blend membrane, polyvinyl alcohol, PEMFC, Fuel cell applications

INTRODUCTION

Polymer exchange membranes were attracted a great deal of interest for fuel cell applications since their high energy efficiency at low temperature and low emission output [1, 2]. The polybenzimidazole polymer is known as a highly chemically/mechanical stable polymer which was selected as a basis polymer to obtain PEM blend membrane. However, PBI polymer needs to be improved since its inefficient proton conductivity under medium-temperature conditions. To obtain higher proton conductivity and water uptake features of a membrane PVA polymer was added to the membrane structure since its high ability of conductivity [3, 4]. A wide range of modified PBI polymers was studied thoroughly for PEMFC. For the purpose of attributing the proton conductivity of PBI, the sulfonation/phosphonation procedure is applied mostly before/ after the membrane preparation [5,6]. The PBI based composite or crosslinked acid-base membrane production methods are other applied techniques for PEMFC's [7,8]. Kerres et. al., ionically crosslinked PBI polymer by adding different types of cation-exchange ionomers and compared the results in terms of chemical/ thermal stability and fuel cell performance [9]. PBI polymer was synthesized by using the solution polycondensation method. The PBI/PVA blend polymer was produced according to the sol-gel method and the membrane was obtained by the casting method. The prepared PBI/PVA membrane was treated with dilute phosphoric acid in order to phosphonate the blend membranes. The characterization tests, i. e; water uptake capacity, FT-IR Analysis, Ion-exchange capacity, Thermal Gravimetric Analysis measurements were applied to the synthesized blend membrane. The H-Nuclear Magnetic Resonance (H-NMR) was applied to identify the structural formation of the synthesized polybenzimidazole polymer.

MATERIALS AND METHODS

3, 3''-Diaminobenzidine (Anhydrous DAB, $(NH_2)_2C_6H_3C_6H_3(NH_2)_2$, M_w: 214.27), and Isophthalic acid (Anhydrous IPA, C_6H_4-1,3-$(CO_2H)_2$, M_w: 166.13) were used as monomers for PBI synthesis and purchased from Akerman Group, Ankara, Turkey. The polyphosphoric acid (PPA, 99%) was used as a solvent and poly-condensation agent. N, N-Dimethylacetamide (DMAC, $CH_3CON(CH_3)_2$, 99.8%, Mw: 87.12) and Dimethyl sulfoxide (DMSO, $(CH_3)_2SO$, 99.8%, Mw: 78.13) were used as solvents for PBI and PVA polymers.

Polybenzimidazole Polymer Synthesis

The PBI synthesis solution polycondensation method is described as follows: PPA was heated to 120 °C for 4 hours under a nitrogen atmosphere for the dehydration process. The monomers were dehydrated as well before the polymerization stage. DAB was added to the pre-heated PPA in a ratio of 1:26.5 (wt.) and mixed with PPA at 120 °C for an hour. IPA was added to the system (as an equimolar quantity of the DAB) and mixed at 175 °C until the monomers were properly dissolved. After 4 hours, the reaction temperature was heated up to 300 °C and held under the nitrogen atmosphere for 20 hours. Then, the homogenous mixture was poured into cold de-ionized water to obtain

a solid dark purple coloured polymer. The solid polymer was washed and filtered continuously to be neutralized. The polymer was held into 10% of $NaHCO_3$ solution for a day to neutralize the polymer. PBI was dried in a vacuum drying at 60 °C for 3 days.

PBI/PVA Blend Membrane Preparation

PBI polymer was dissolved in DMAC (99%) solvent at 100 °C for 2 days and 5 wt. % of LiCl was added as a stabilizer. Separately, PVA polymer was mixed in DMSO solvent at 80 °C for 2 hours and 5 % of PVA solution was prepared. The blend membrane sol-gel method and casting method were described by Cali et al. [2]. The dissolved polymers were poured into the glass flask at a different percentage of 90:10, 70:30 and 50:50, then mixed at 100 °C for 48 hours and then, an ultrasonic homogenizer device was applied for 1 hour to homogenize the solution. The polymer solution was cast into a glass petri dish and then dried at 50 °C for 4 days.

PBI/PVA Blend Membrane Phosphonation

The blend PBI/PVA membranes were extracted from the petri dish and then, dried in an oven at 100 °C for a day. The dilute phosphoric acid solution (0.1 M) was prepared for the process. The blend membranes were soaked in the phosphoric acid solution at room temperature and held for a day. The excess phosphoric acid was cleaned out of the membranes and finally, membranes were dried in an oven at 100 °C for a day. The phosphonated blend membranes were named PBI/PPVA-90:10, PBI/PPVA-70:30 and PBI/PPVA-50:50.

Characterization Methods

Prepared PBI/PPVA blend membranes were weighted (Wdry) and their thickness value was measured at different points (Tdry). The measured samples were plunged in distilled water and kept overnight at 30 °C and 80 °C. The thickness of the samples was measured using a Sheen thickness measurement device [2]. Equation (1) illustrates the water uptake calculation of the samples.

$$\%WaterUptakeCapacity = \frac{m_{wet} - m_{dry}}{m_{dry}} x100 \quad (1)$$

FTIR analysis was employed by using a Jasco FT / IR-480 + instrument to obtain information about the chemical structure of membranes. The measurements were executed at a wavelength from 4000 to 400 cm^{-1} and a scanning speed of 4 cm^{-1}.

The NaCl solution was used to examine the Ion exchange capacity (IEC) of the PBI/PPVA blend membranes. The samples were held in NaCl solution (2 M) for 2 days at room temperature and then the classic titration method was operated. The solution, where membranes held, titrated with stock NaOH solution and then, IEC results were examined.

$$IEC = (V_{NaOH} \cdot M_{NaOH}) / W_{dry} \quad (2)$$

The thermal gravimetric analysis method was applied to evaluate the thermal stability of the PBI/PPVA blend membranes. Perkin Elmer Pyris 1 Thermogravimetric Analysis Device suitable for TS ISO EN 11358-1 accredited method was used in Middle East Technical University Research Lab. The TGA heating rate is 10 °C $minute^{-1}$ from room temperature to 900°C in air conditions.

A liquid H-proton Nuclear Magnetic Resonance Ultrashield TM 300 MHz device having a superconductive magnet, digital Bruker Biospin AVANCE 300 MHz ~7 Tesla, was used to identify the synthesized polybenzimidazole polymer structure.

RESULTS AND DISCUSSION

Fig.1. illustrates the weight loss of synthesized blend membranes at different temperatures. The synthesized PBI

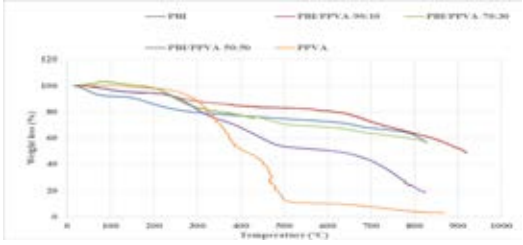


Fig. 1. TGA Results of the PBI/PPVA blend membranes

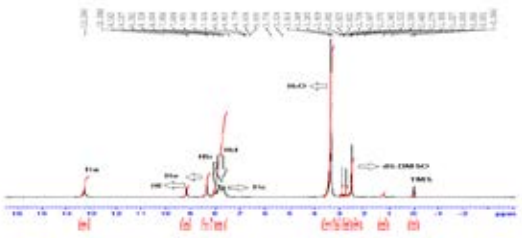


Fig. 2. H-NMR results of PBI polymer

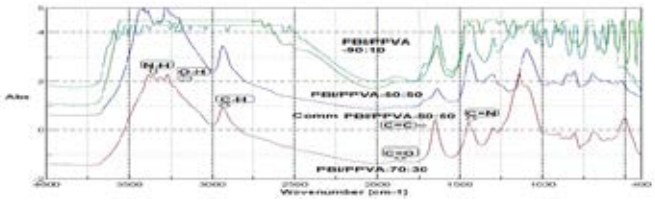


Fig. 3. FT-IR results of the synthesized membranes

membrane has the lowest weight loss (43%) amongst the blend membranes. PBI/PPVA-90:10 blend membrane has 51% weight loss after 700 °C. The dropping line around 100 °C is attributed to the water loss [10]. The phenyl group proton peaks of the synthesized polybenzimidazole polymer, which could be seen in Fig. 2., is at 7.42 and 9.16 ppm. The N-H proton absorption peak belonging to the PBI imidazole ring is at 13.266 ppm. The peaks at 2938 cm^{-1} at Fig.3 belongs to C-H asymmetric/ symmetrical vibration peaks of the PVA polymer. The characteristic phosphonation peak is at 1095 cm^{-1}. The Ion exchange capacity of the PBI membrane was found as 2.12 meq gr^{-1}. PBI/PPVA-90:10 and PBI/PPVA-50:50 membranes have the same IEC which found as 4.15 meq gr^{-1}. PBI/PPVA-70:30 blend membrane has 3.33 meq gr^{-1} IEC. Synthesized PBI membrane has no water uptake capacity at room temperature and 80 °C. PBI/PPVA-90:10 blend membrane has 5 % of water uptake capacity. The highest water uptake capacity (8 %) was calculated for PBI/PPVA-50:50 blend membrane.

CONCLUSION

Polybenzimidazole and polyvinyl alcohol polymers were used as blend membrane structures with different percentage ratios and blend membranes were phosphonated for proton exchange membrane fuel cell (PEMFC) applications. The ion exchange capacity of the PBI membrane was enhanced from 2.12 to 4.15 meq gr^{-1} by preparing PBI/PPVA-90:10 blend membrane. The highest water uptake capacity (8 %) was calculated for PBI/PPVA-50:50 blend membrane. The prepared PBI/PPVA blend membranes have great thermal stability according to TGA results. The structural formation of the PBI polymer was verified by H-NMR Analysis. Authors indicate that prepared PBI/PPVA blend membranes have greater properties compared to synthesized PBI membranes and they could be excellent candidates as proton exchange membranes.

ACKNOWLEDGEMENT

The authors would like to acknowledge the help of THE SCIENTIFIC AND TECHNOLOGICAL RESEARCH COUNCIL OF TURKEY (TUBİTAK) for their contributions to this study.

REFERENCES

1. Ibrahim A, Hossain O. 2020. GO-Nafion composite membrane development for enabling intermediate temperature operation of pemfc. International Journal of Hydrogen Energy 45:5526-5534.
2. Çalı A. Şahin A. 2019. Incorporating sepiolite and kaolinite to improve the performance of SPEEK composite membranes for proton exchange membrane fuel cells. The Canadian Journal of Chemical Engineering. 98:892-904.
3. Saito M, Naoko A. 2004. Mechanisms of Ion and Water Transport in Perfluorosulfonated Ionomer Membranes for Fuel Cells J. Phys. Chem. B. 108: 16064-16070.
4. Cali A, Yağızatlı Y. 2020. Highly durable phosphonated graphene oxide doped polyvinylidene fluoride (PVDF) composite Membranes. International Journal of Hydrogen Energy. 60: 35171-35179.
5. Zhang H, Li X. 2008. Composite membranes based on highly sulfonated PEEK and PBI:-Morphology characteristics and performance. Journal of Membrane Science. 308: 66-74.
6. Ergun D, Devrim Y. 2010. Phosphoric Acid Doped Polybenzimidazole Membrane for High-Temperature PEM Fuel Cell. Journal of Applied Polymer Science. 124: E267-E277.
7. Li Q, Pan C. 2007. Cross-Linked Polybenzimidazole Membranes for Fuel Cells. Chemical Materials. 19: 350- 352.
8. Peach R, Henning M. 2018. Novel cross-linked PBI-blended membranes evaluated for high-temperature fuel cell application and SO_2 electrolysis. Materials Today: Proceedings. 5: 10524-10532.
9. Kerres J, Atanasov V. 2015. Cross-linked PBI-based high-temperature membranes: Stability, conductivity and fuel cell performance. International Journal of Hydrogen Energy. 40:14723-14735.
10. N N. Krishnan, Joseph D. 2017. Phosphoric acid doped crosslinked polybenzimidazole (PBI-OO) blend membranes for high temperature polymer electrolyte fuel cells, Journal of Membrane Science. 544:416–442.

WHEC-2022
23rd World Hydrogen Energy Conference
June 26-30, 2022 - Istanbul

#321
INTELLIGENT MONITORING OF HYDROGEN/VANADIUM REDOX FLOW BATTERY

[1] Chi-Yuan Lee, [2] Chia-Hung Chen, [3] Chin-Lung Hsieh, [1] Yu-Chun Chen, [1] Siao-Yu Chen*
[1] Department of Mechanical Engineering, Yuan Ze Fuel Cell Center, Yuan Ze University, Taoyuan, Taiwan
[2] HOMYTECH Global CO., LTD, Taoyuan, Taiwan
[3] Institute of Nuclear Energy Research, Taoyuan, Taiwan

*Corresponding author e-mail: cylee@saturn.yzu.edu.tw

ABSTRACT

This work attempts to innovatively develop a hydrogen/vanadium redox flow battery stack and improve the previous vanadium redox battery encountered by our team when the electrolyte leaks easily and the strong acid corrosion environment may cause the vanadium redox battery and the micro sensor to age or fail. Utilize MEMS to innovatively develop hydrogen concentration and conductivity micro sensors, and integrate the flexible five-in-one (voltage, current, temperature, flow and pressure) micro sensors developed by our team. Corrosion-resistant, thinner and miniaturized flexible seven-in-one micro sensor embedded in the hydrogen/vanadium redox flow battery for real-time microsensing and diagnosis.

Keywords: Hydrogen/vanadium redox flow battery, Flexible seven-in-one micro sensor, Real-time microsensing and diagnosis.

INTRODUCTION

Vanadium redox battery system is an emerging energy storage technology, which has many advantages in application, such as high efficiency, long life, high power and high safety. The latest literature points out that the hydrogen (H_2)/vanadium(V) redox flow battery has better energy density and efficiency than the vanadium redox battery, and has the advantages of low cost and light weight. Weng [1] et al. indicated that the theoretical energy of the hydrogen/vanadium redox flow battery is 5 times that of the vanadium redox battery, and the discharge voltage of the hydrogen/vanadium redox flow battery is about 1.76V, which is higher than the discharge voltage of its control system. In addition, the hydrogen concentration, conductivity, voltage, current, temperature, electrolyte flow and flow channel pressure inside the hydrogen/vanadium redox flow battery will affect its performance and life.

RESEARCH METHODS

The development of the flexible seven-in-one micro sensor mainly focuses on the newly developed micro hydrogen sensor and micro conductivity sensor and integrates the micro voltage, current, temperature, flow and pressure sensors of the past core technologies of our team. The production process of the flexible seven-in-one micro sensor is shown in Fig. 1. Simultaneous and synchronous development of hydrogen/vanadium flow batteries. Although the design and key components of the hydrogen/vanadium redox flow battery is similar to those of the vanadium redox battery, the design and material selection of the hydrogen/vanadium redox flow battery also need to be redesigned. The biggest difference between the flow battery is that half of the storage space of the hydrogen/vanadium redox flow battery is hydrogen, and the other half is vanadium electrolyte. Therefore, it is necessary to find a container suitable for storing hydrogen, and the electrolyte is a strong corrosive solution. Containers of suitable material and improved according to past experience.

Sensing principle of micro hydrogen sensor

This micro hydrogen sensor is a semiconductor type sensor. The sensing principle is to use the oxygen adsorption between the reducing gas and the surface of the gas-sensitive film. After oxygen atoms (O) are adsorbed on the surface of the gas-sensitive film, the electrons inside the material will tend to oxygen atoms form oxygen ions (O^-), which reduces the number of electrons inside the gas-sensitive film, which increases the resistance of the sensing material; when the surface of the gas-sensitive film and the reducing gases in the environment (such as CO, H_2, etc.) When in contact, the reducing gas will react with oxygen ions on the surface of the gas-sensitive film, releasing electrons back into the gas-sensing film, thereby reducing the overall resistance of the material.

Sensing principle of micro-conductivity sensor

Conductivity measurements were investigated using Alternating Current Impedance. The AC impedance analysis method obtains the impedance value of the electrochemical system by calculating between the AC voltage and the AC current, and then substitute the impedance valued into the Eq. (1) to obtain the conductivity value (Conductivity, σ):

$$\sigma = L/R \times A \quad (1)$$

where σ is the conductivity (S/cm), R is the membrane impedance (Ω), L is the membrane thickness (cm), and A is the electrode area (cm^2).

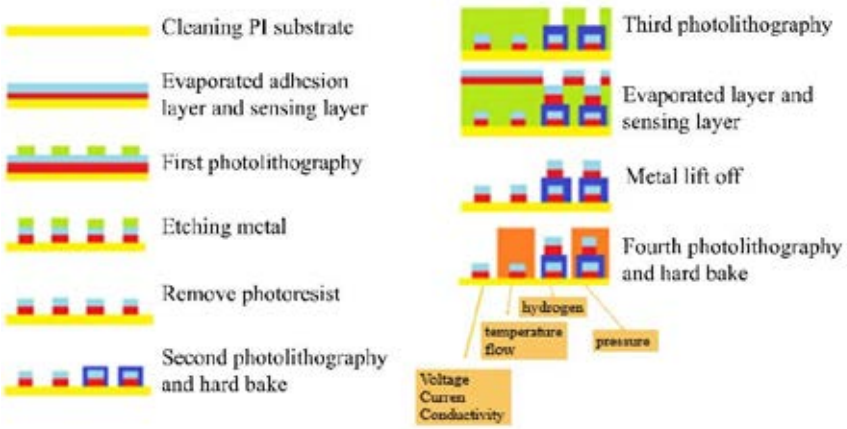


Fig. 1. Step diagram of the integration process of the flexible seven-in-one micro sensor.

RESULTS AND DISCUSSION

In this study, a flexible seven-in-one micro sensor was embedded in the hydrogen/vanadium redox flow battery of 100 hours of microscopic diagnosis of seven physical quantities, including hydrogen, conductivity, voltage, current, temperature, flow and pressure. The hydrogen/vanadium flow batteries of embedded microsensor and without embedded microsensor were tested separately, using the same reaction area size, the same flow channel design and the same operating conditions, and compared the performance difference between the two, and the long-term results were obtained. Effective real-time monitoring of local hydrogen, conductivity, voltage, current, temperature, flow and pressure distribution of the hydrogen/vanadium redox flow battery, and real-time feedback of internal information through a flexible seven-in-one micro sensor to analyze and discuss hydrogen, conductivity. The relationship between voltage, current, temperature, flow rate and pressure to allow users to instantly grasp the internal reaction and operating conditions of the battery, so that the hydrogen/vanadium redox flow battery can be quickly adjusted to the best operating parameters.

CONCLUSIONS

In response to the needs of real-time micro-diagnosis inside the hydrogen/vanadium redox flow battery, this work innovatively develops a flexible seven-in-one micro sensor using MEMS technology and embeds it inside the hydrogen/vanadium redox flow battery, so that it can real-time micro-sensing and diagnosis and real-time feedback of internal information, however, the hydrogen/vanadium redox flow battery can operate in the best condition, which can effectively improve the performance of hydrogen/vanadium redox flow battery and achieve the purpose of extending life.

ACKNOWLEDGEMENT

This work was accomplished with much needed support and the authors would like to thank for the financial support by Ministry of Science and Technology of R.O.C. through the grant MOST 110-2221-E-155-034, 111-2622-8-155-004-TM, 107-2622-E-155-001-CC2, 108-2221-E-155-049-MY2, 108-2622-E-155-011-CC3, 108-3116-F-155-001 and Institute of Nuclear Energy Research of R.O.C. through grants NL 1070289, 1061191, 1050770, 1040734. In addition, we would like to thank the YZU Fuel Cell Center and NENS Common Lab, for providing access to their research facilities.

REFERENCES

1. Weng GM, Li CYV, Chan KY. 2018. High-voltage pH differential vanadium-hydrogen flow battery. Materials Today Energy 10: 126-131.

WHEC-2022
23rd World Hydrogen Energy Conference
June 26-30, 2022 - Istanbul

#322

DEVELOPMENT OF MONITORING TOOL FOR HIGH VOLTAGE PROTON EXCHANGE MEMBRANE WATER ELECTROLYZE

[1*] *Chi-Yuan Lee,* [2] *Chia-Hung Chen,* [1] *Shan-Yu Chen,* [1] *Zhi-Yu Huang*
[1] Department of Mechanical Engineering, Yuan Ze Fuel Cell Center, Yuan Ze University, Taoyuan, Taiwan
[2] HOMYTECH Global CO., LTD, Taoyuan, Taiwan

*Corresponding author e-mail: cylee@saturn.yzu.edu.tw

ABSTRACT

Proton exchange membrane water electrolyzer (PEMWE) requires high operating voltage for hydrogen production, so it is easy to accelerate the decomposition of hydrogen molecules, and it is easy to cause PEMWE to age or fail. This research uses micro-electro-mechanical systems (MEMS) technology to innovatively develop the micro oxygen sensor inside PEMWE so as to know the oxygen production rate in real time. This information is one of the important information on PEMWE aging. The flexible six-in-one (voltage, current, temperature, humidity, flow and pressure) micro sensor developed by our team has been integrated into a flexible seven-in-one micro sensor. It embedded in the high voltage PEMWE to monitor oxygen, voltage, current, temperature, humidity, flow and pressure. And, we observe whether the high voltage PEMWE is aging or damaged so as to prolong its service life.

Keywords: MEMS, Flexible seven-in-one micro sensor, High voltage proton exchange membrane water electrolyzer.

INTRODUCTION

The seven important physical quantities of oxygen, voltage, current, temperature, humidity, flow and pressure inside PEMWE have a key impact on aging. As mentioned in [1], thermal stress has a significant effect on the degradation of polymer films. If the input voltage is higher, it is easy to generate a large amount of waste heat due to the resistance. The heat will increase the temperature of the system, which will accelerate the aging and performance degradation of PEMWE. Although increasing the operating temperature of PEMWE can improve performance. If the temperature is too high, it may cause damage to the membrane electrode assembly (MEA) and make water to evaporate into water vapor and cause aging. Therefore, how to find the best operating conditions and aging test and predict its life is the focus of this work.

RESEARCH METHODS

Process development and calibration of semiconductor-based flexible micro oxygen sensor

In the research, a semiconductor-based micro oxygen sensor was developed by using the MEMS technology. Use a sputtering machine sputtered tin dioxide (SnO_2) on the surface of the sensor as a gas-sensitive sensing layer, and sputtered platinum (Pt) as a catalyst layer afterwards. When the micro oxygen sensor is completed, the eight-channel fuel cell test machine is used for testing and calibration. The sensor is connected with precision data acquisition machine (NI PXI-1033). Then, the constant temperature and constant current oxygen is introduced, the resistance change is measured and captured.

Integrated process development of flexible seven-in-one micro sensor

(a) First, wash the PI film with acetone and methanol organic solutions respectively in order to increase the adhesion of metals. Then, use deionized water to remove residual methanol, remove surface dust and residual grease.
(b) Then use an E-beam evaporator to evaporate chromium (Cr) and gold (Au) as the adhesive layer and the sensing electrode layer.
(c) Use the photolithography processed to define the patterns of the micro oxygen, voltage, current, temperature, humidity, pressure and flow sensors.
(d) Use gold etching solution and chromium etching solution to wet etching.
(e) Coating photoresist, then defining the micro oxygen sensor pattern, sputtering tin dioxide and platinum on the micro oxygen sensor, and then cleaning off the photoresist mask.
(f) Coating LTC 9320 as a protective layer, and using the yellow light lithography process again to define the sensing area and pins of the micro voltage, current, humidity and pressure sensors so that they are exposed and not covered by the protective layer.
(g) Finally, coat LTC 9305 as the moisture-sensing film of the micro humidity sensor to complete the manufacturing process of the flexible seven-in-one micro sensor, as shown in Fig. 1.

Establish PEMWE technology

At present, parallel flow field is still one of the most common forms of PEMWE flow channel design. The advantages are that the deionized water is easy to enter and exit, the flow rate is faster and the piezoresistance is lower. The assembly pressure will affect the aging, and it is necessary to be careful to prevent the deformation and rupture of the bipolar plate and the collector plate due to uneven stress. On the other hand, the rotational speed of the external pump of PEMWE also has a great influence on its aging. When the performance is optimized, the flexible seven-in-one micro sensor, which is the focus on this research, is embedded to measure the internal physical quantities of PEMWE in real time.

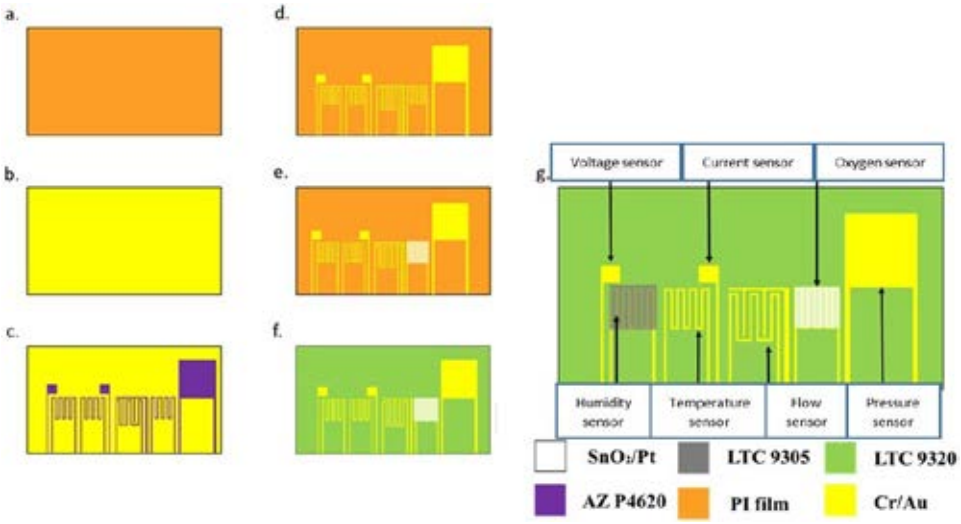


Fig. 1. Fabrication flowed chart of the flexible seven-in-one micro sensor.

RESULTS AND DISCUSSION

The flexible seven-in-one micro sensor is embedded in the PEMWE for 200 hours of accelerated aging test. Detect the distribution of oxygen, voltage, current, temperature, humidity, flow and pressure of PEMWE from activation to aging so as to know the relationship between these seven important physical quantities affecting each other.

CONCLUSIONS

In this research, a flexible seven-in-one micro sensor has been developed and embedded in PEMWE for 200-hour accelerated aging micro-monitoring, and the life prediction of PEMWE has been achieved. The sensor makes product development and application wider and verify its reliability at the same time.

ACKNOWLEDGEMENT

This work was accomplished with much needed support and the authors would like to thank for the financial support by Ministry of Science and Technology of R.O.C. through the grant MOST 109-2622-E-155-008,110-2622-E-155-014, 110-2622-E-155-001 and 111-2622-8-155-004-TM. The authors also like to thank Shih-Hung Chan, Guo-Bin Jung, Yu-Chun Chiang and Hsiu-Li Lin of Yuan Ze University for their valuable advice and assistance in the experiments. In addition, we would like to thank the HOMY Technology, YZU Fuel Cell Center and NENS Common Lab, for providing access to their research facilities.

REFERENCES

1. Ogumerem GS and Pistikopoulos EN. 2020. Parametric optimization and control for a smart Proton Exchange Membrane Water Electrolysis (PEMWE) system. Journal of Process Control 91:37-49.

WHEC-2022
23rd World Hydrogen Energy Conference
June 26-30, 2022 - Istanbul

#341

COMPARATIVE STUDY ON THE EFFECT OF SELECTED DISPERSION TECHNOLOGIES FOR FUEL CELL INK PREPARATION ON THE OVERALL PEMFC PROCESS CHAIN

[1*] Amin S. Amin, [1] Fatih Özcan, [1,2]Doris Segets
[1] Particle Science and Technology (IVG-PST)
[2] Centre for Nanointegration Duisburg-Essen (CENIDE)
University of Duisburg-Essen, Duisburg (UDE), Germany

*Corresponding author e-mail: amin.amin@uni-due.de

ABSTRACT

In this paper, we report on the influence of different dispersion technologies on fuel cell performance. We present the complete process chain from dispersing the dry powder components in a liquid phase to final performance testing on the electrode level in order to identify process-structure-property relations. For comparing different dispersion technologies, we use both an ultrasound-based batch-type method and a continuously operable wet impact milling device that can be operated at elevated hydrostatic pressures of up to 245 MPa. We use analytical centrifugation to analyse the sedimentation behaviour of concentrated inks and the surfaces of the electrode layers are characterised by means of Atomic Force Microscopy (AFM). The results of the ink characterisation were visualised in self-developed transmittograms in the working group. In addition, we spray the inks and prepare electrodes for a final evaluation in a fuel cell. We found that ink dispersion by wet impact millling ends up in more stable formulations than when dispersion by ultrasound is applied. This is also reflected in the performance of the fuel cells, i.e., the electrodes made from inks generated by wet impact milling did perform better with regard to polarization curves than those made from inks generated by ultrasonic Sonotrode.

Keywords: PEMFC, Ink Preparation, Wet Impact Milling, Sonication, Transmittograms

INTRODUCTION

In the context of climate change, increasing globalisation and mobility as well as the growing industrialisation of emerging countries such as India and China, environmental protection is taking on unprecedented importance. Therefore, there is an increasing shift in thinking towards alternative drive systems, which also includes the fuel cell technology. Fuel cells are regarded as efficient and climate-neutral energy converters and could be one alternative to thermal engines in the future. Among the fuel cell types, the Polymer Electrolyte Fuel Cell (PEMFC) has advantages in efficiency, quiet operation, good reaction dynamics and low environmental impact [1].
The biggest obstacle to the market breakthrough of polymer fuel cells is the high cost of materials mainly as a result of the use of precious yet highly active metals such as platinum. Therefore, the main concern is to reduce the platinum loading by simultaneously increasing the performance or without adverse effects on the performance at least. Because of this, a better and more efficient utilization of platinum in the electrode should be sought. One of the possibilities to address this angle includes an improved and well-controlled dispersion of the ink preparation process which can have a detrimental effect on the final electrodes. A poor dispersion can potentially lead to inhomogeneous distribution and agglomeration of catalyst particles and thus to an uneven distribution of platinum on the electrodes.

The overall aim of this work is to investigate the whole process chain in PEMFC production from preparing inks from powders over the production of electrodes to final performance tests. To this end, we are mainly focusing on the preparation of FC inks by applying two different dispersion methods (see Fig. 1). Here, we are interested in the influential factors of ink preparation on the general process chain.

MATERIALS AND METHODS

Dispersions were prepared by a continuous and a batch device. For a potential continuous preparation, we used a wet impact milling device (Sugino Corp, Japan) and for ink preparation in a batch mode we used an ultrasonic device (Branson SFX Digitaler Sonifier). In the wet impact mill the dispersion is homogenised by collision with a static ceramic ball using an adjustable hydrostatic pressure in the range of 100 -245 MPa. By this method, the particles in the dispersion are subjected to varying and controllable shear forces and are hence homogenised. Additionally, we can repeat the processing several times by running several cycles. The dispersion in the lab-scale sonotrode occurs through ultrasonic waves. Here, the controllable parameters are the amplitude resulting in different dispersion intensities and time. The inks were characterised with an analytical centrifuge (LUMisizer, LUM GmbH) and the results were visualised in self-developed transmittograms in the working group by Bapat et al. [2],[3]. After preparing

the ink, we spray it onto a Polytetrafluoroethylene (PTFE) foil with an ultrasonic spray coater (PRISM 400, Ultra-Coat). For layer characterization, we measured the surface roughness and topology of the electrodes using atomic force microscopy (AFM). All layers were analyzed at nine different locations on the coated electrodes.

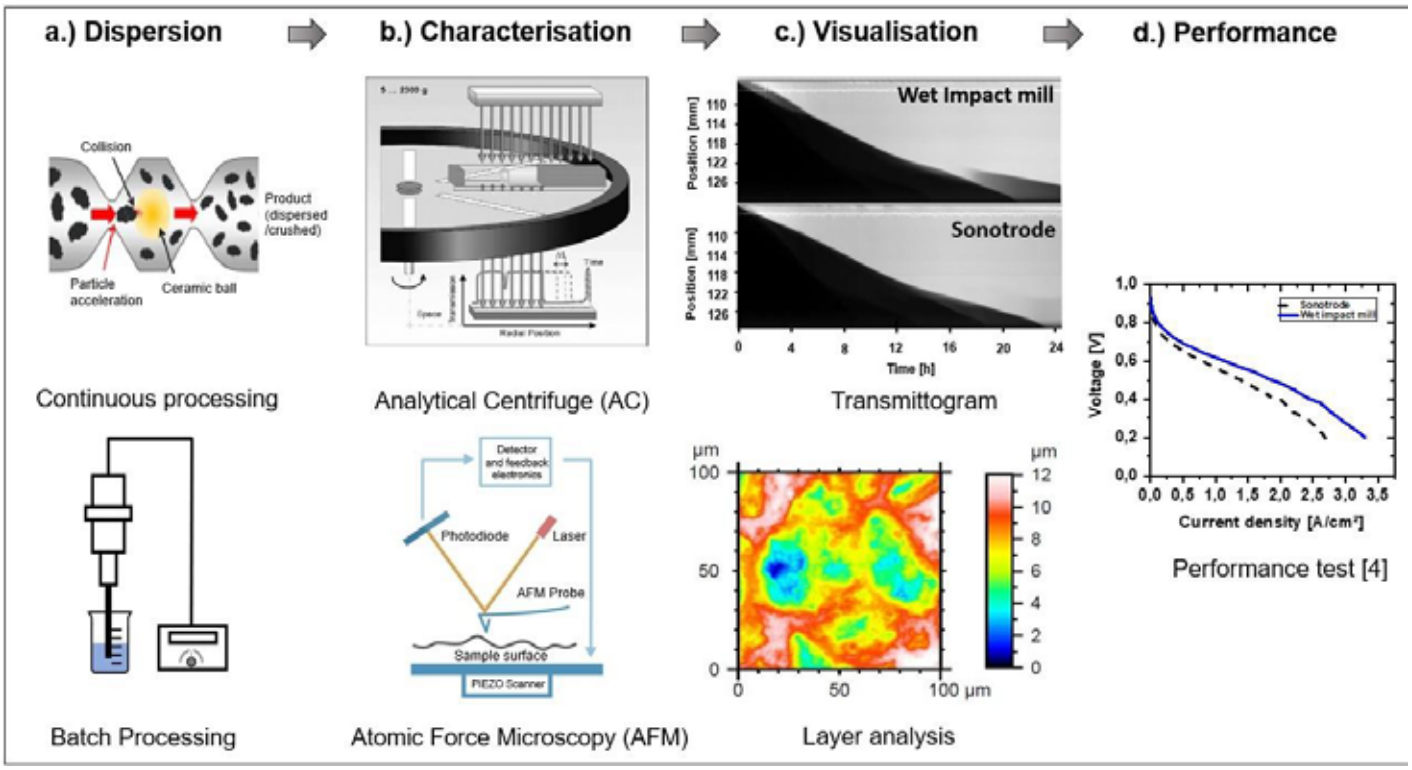


Fig.1: a.) Principle of the wet impact mill (particle acceleration at nozzle and collision at ceramic ball); principle of the ultrasonic sonotrode (dispersion by ultrasonic waves); b.) AC as the method of choice for characterising highly disperse FC inks; Atomic Force Microscopy (AFM) as a method to analyse the surface changes of the electrode layers; c.) Visualisation of the particle fractions via transmittograms after comminution/dispersion; resulting surface topography image after AFM analysis; d.) Performance test results on the fuel cell.

RESULTS AND DISCUSSION

As visualized by transmittograms (Fig. 1c.), we observed different sedimentation behaviour of the inks depending on the type of dispersion technology. The samples that were dispersed using both, the wet impact method and ultrasonic device show two distinguishable particle fractions which settle at different times. The fractions in the ink after wet impact milling are more pronounced than after using the ultrasound device. This is an indication that both devices crush and homogenise the particle agglomerations differently in the course of the dispersion procedure. While the wet impact milling seems to create a higher heterogeneity of particle assemblages suggesting a more intensive and efficient dispersion or comminution result, the ink after ultrasound treatment is more homogeneous with regard to particle assemblages. The number of particle assemblages and especially their settling time can be linked to size estimations. The longer the settling time for an assemblage is, the smaller are the particles within the settling fraction. As described previously by Bapat and Segets, transmittograms enable to deduce the behavior of particles in suspension. Moreover, they provide a size estimate. The sedimentation equivalent diameter of particles that reach the rotor position in a given time can be obtained from Stoke's law [3]. This is another hint towards a more efficient and intensive crushing by the wet impact milling.

Furthermore, from the transmittograms we can deduce that the dispersion with the wet impact method is more stable than the dispersion prepared via sonotrode. In the inks made by sonotrode, all particles settle completely shortly before about 24 hours, while for the inks made from the wet impact mill a full settling of all particles is not achieved, even within 24 hours (Fig. 1c).

Results of the layer analysis via AFM show that surfaces of both layers are uneven and inhomogeneous. The differences in height for both layers reach up to 10 micrometres (Fig. 2). One explanation for this observation are the features of the spraying process itself which is used for the generation of coated layers. The spray coater sprays in an X-Y grid with distinct spacing both in horizontal and vertical direction. This creates gaps between the coatings,

which leads to the observed differences in height and the surface roughness. In addition, we suspect that the spray coater does not spray constantly at the same rate, as there are slight blockages in the line. An additional factor is the point that the PTFE substrate material itself introduces an uneven and inhomogeneous surface which is to be coated during spray coating. This will be analyzed more quantitatively and systematically in future work but confirms the power of transmittograms derived from analytical centrifugation that are able to unravel clear changes of the ink properties with varying disperion procedures.

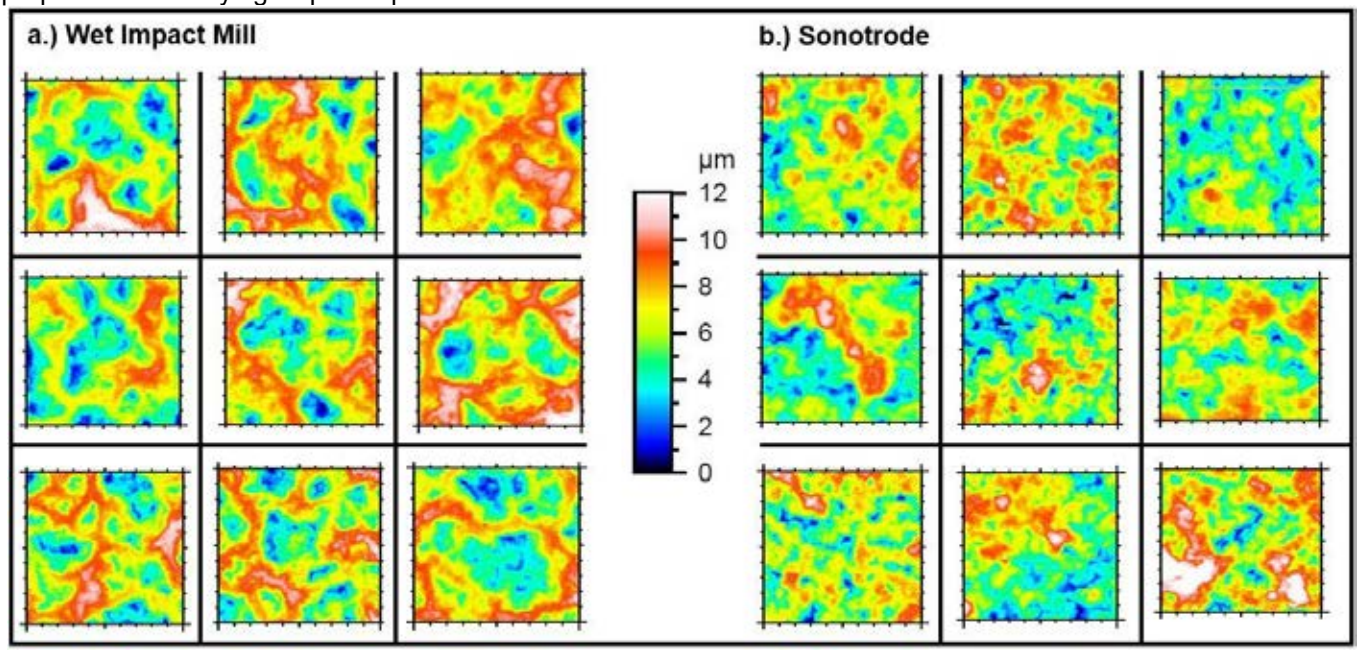


Fig.2 Investigation of the surface differences of the electrodes with AFM

However, compared to the dispersion produced by ultrasonic sonotrode, the MEA produced by wet-impact method delivers a comparable to slightly improved performance. Above all, the electrochemically active surface increases significantly. This can be recognised by the parallel shift of the characteristic curve (Fig. 1d).

In summary, with the help of transmittogram analysis we were able to link dispersion features with fuel cell performance data. We found that the stability of the inks is related to the performance which is a main outcome and feature of the respective dispersion technique applied. This is an outstanding starting point for establishing the initially mentioned process-structure-property relations and parameterize the PEMFC process chain. Individual process step interdependencies can be unravelled and used for a knowledge-driven and efficient production of FC electrodes while improving the environmental footprint through reduction of required amount of precious metals such as platinum.

REFERENCES

[1] Ulrich Mis; *Auswirkungen, Schädigungscharakteristik und Regenerationspotential von verkehrsbedingten Stickoxidemissionen bei PEM-Brennstoffzellen unter variablen Betriebsbedingungen*, PhD thesis (2018; University of Duisburg-Essen

[2] Bapat, Shalmali; Giehl, Christopher; Kohsakowski, Sebastian; Peinecke, Volker; Schäffler, Michael; Segets, Doris: *On the state and stability of fuel cell catalyst inks,* In: Advanced Powder Technology (2021) in press ISSN: 1568-5527; 0921-8831

[3] Bapat, Shalmali; Segets, Doris: *Sedimentation Dynamics of Colloidal Formulations through Direct Visualization: Implications for Fuel Cell Catalyst Inks*, ACS Applied Nano Materials Vol. 3 (2020) Nr. 8, pp. 7384 – 7391 ISSN: 2574-097

[4] Performance on the fuel cell was carried out by our project patner *The hydrogen and fuel cell center ZBT GmbH*

WHEC-2022
23rd World Hydrogen Energy Conference
June 26-30, 2022 - Istanbul

#371

INFLUENCE OF OPERATING PARAMETERS ON THE COLD START OF POLYMER ELECTROLYTE FUEL CELL SYSTEMS FOR TRANSPORTATION AND AEROSPACE APPLICATIONS

[1*] *Gema Montaner Ríos,* [2] *Johannes Schirmer*
[1] German Aerospace Center (DLR), Institute of Engineering Thermodynamics, Hein-Saß-Weg 22, 21129, Hamburg, Germany
[2] German Aerospace Center (DLR), Institute of Engineering Thermodynamics, Pfaffenwaldring 38-40, 70569, Stuttgart, Germany

*Corresponding author e-mail: Gema.MontanerRios@dlr.de

ABSTRACT

Understanding the influence of operating parameters on the cold start of polymer electrolyte fuel cell (PEFC) is essential for the development of improved cold start strategies for transportation and aerospace applications. The effects of different operating parameters on the cold start performance at temperatures down to -30°C have been investigated using a 4-kW PEFC system. The results showed that the start-up temperature, coolant volume flow rate, cell voltage, cathode excess ratio and gas, make a significant impact on the cold start time and performance. The PEFC system was able to self start-up at -30°C, though it led to a standard slow cold start performance with three stages. The results indicate that lowering the start-up cell voltage and operating with oxygen enhance the cold start since more current and heat are generated, thus reducing ice formation. In addition, increasing the cathode excess ratio assists to overcome flooding issues once ice melts.

Keywords: Cold Start, Ice Formation, Operating Parameters, Polymer Electrolyte Fuel Cell (PEFC)

INTRODUCTION

The start-up of PEFC systems in winter scenarios is a remaining challenge for transportation and aerospace applications. At temperatures below 0°C, the water produced by the cathode reaction freeze, which may lead to shut-down and cause several degradations to the fuel cell. Experimental studies have been mostly carried out on single-cells and the influence of operating parameters on the cold start performance mostly focused on cell voltage and temperature [1, 2]. In this study, the influence of the start-up temperature, coolant volume flow rate, cell voltage, cathode excess ratio and gas on the cold start performance of a 4-kW PEFC system, and the interrelationship between these parameters have been investigated. The aim is, to develop a rapid, energy-efficient, and reliable cold start procedure that meets the technical targets for transportation fuel cell systems [2-4]. Establishing operating parameters that generate more heat and assist to evacuate more water to avoid freezing once the membrane is hydrated, as well as flooding after reaching 0°C, is expected to improve the cold start performance.

EXPERIMENTAL

Test bench

This investigation was conducted in a test rig developed in-house for testing PEFC systems at freezing temperatures. The 4-kW stack used consisted of 40 cells with 200 cm² of active cell area, graphite bipolar plates and liquid-cooled. The system was run without humidifiers but with H_2 recirculation, and the test rig was equipped with a programmable electronic load and NI programmable controllers. A schematic outline of this test rig is shown in Fig. 1.

Operating parameters

This work investigates the influence on the cold start performance of PEFC system of the following operating parameters: start-up temperature, coolant volume flow rate, voltage, cathode excess ratio and cathode gas. The value ranges of the tested operating parameters are given in Table 1.

Test protocol

After a conditioning test, the stack was purged with dry gases for 3 min. Then, the stack was cooled down to the test temperature and kept for a defined time. Next, the cold start test was run with the small cooling loop under the investigated operating parameters values. Finally, a polarization curve was conducted at standard conditions.

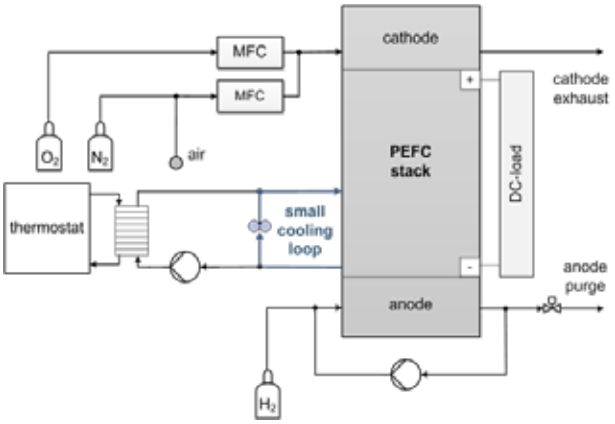


Fig. 1. Schematic outline of the 4-kW PEFC system developed test rig

Table 1. Operating parameters and value ranges tested

	Value
Start-up temperature (°C)	0 … -30
Coolant volume flow rate (g/s)	0 … 83.33
Cell voltage (V)	0.1 … 0.55
Cathode excess ratio	2.3 … 5.8
Cathode gas	air, oxygen

RESULTS AND DISCUSSION

As an example, the effects of start-up temperature, cell voltage, and cathode excess ratio on the cold start performance of the 4-kW PEFC system are briefly discussed below.

Effect of start-up temperature

The 4-kW PEFC system was able to start-up without external heat at temperatures down to -30°C. As expected, the lower the start-up temperature, the slower the cold start and less linear the performance was [5]. The cold start at -30°C led to a standard slow cold start performance with three stages: membrane hydration, ice formation, and ice melting and flooding [6].

Effect of cell voltage

Operating the fuel cell in potentiostatic mode can improve the cold start performance since the total heat generation rate depends nearly linearly on the current density [7]. The lower the cell voltage, the more current density and the more water is generated. Therefore, more heat is produced in the cells to warm up the stack more quickly, thus accelerating the cold start.

Effect of cathode excess ratio

Fig. 2 shows the effect of cathode excess ratio on the cold start performance of the 4-kW PEMFC system at -20°C. As illustrated in Fig. 2 (a), the higher the cathode excess ratio, the faster the cold start was. By increasing the cathode stoichiometry, the cold start performance is improved since higher oxygen excess ratio can generate more current and heat. Furthermore, a higher cathode excess ratio can remove more water, thus assisting to overcome the flooding phase that takes place once the ice formed melts, as shown in Fig. 2 (b).

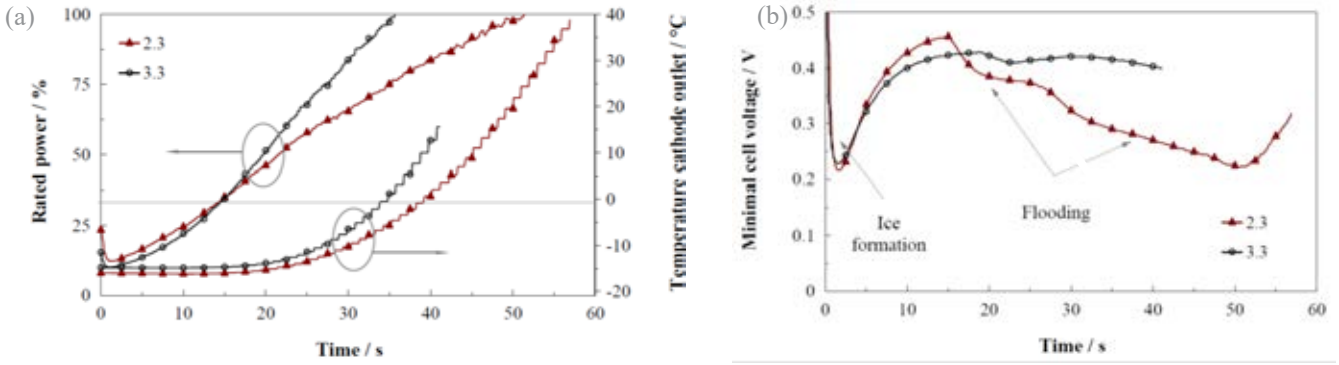


Fig. 2. Effect of cathode excess ratio (2.3 and 3.3) on the cold start of the 4-kW PEFC system performance at -20°C: (a) time-rated power and time-temperature cathode outlet; (b) time-minimal cell voltage

CONCLUSIONS

In this investigation, the effects of start-up temperature, coolant volume flow rate, cell voltage, cathode excess ratio and cathode gas on the cold start performance of PEFC fuel cell systems have been studied. The results of this experimental study can be summarized as follows:

- A self-start of the PEFC fuel cell systems was possible at temperatures down to -30°C. The startup temperature makes a significant impact on the cold startup time and on the cold start performance.
- The cell voltage has an enormous influence on the cold start time. Operating at lower cell voltage reduces the start-time since more waste heat is produced.
- Cold start performance can be improved by increasing the cathode excess ratio since more current and heat are produced, and more water is removed, thus assisting to overcome the flooding phase.

The remaining results obtained within this study will be presented and discussed in further detail during the conferences. Additionally, guidelines to optimize cold start strategies for transportation and aerospace applications will be provided.

ACKNOWLEDGEMENT

This work was financially supported by the Fuel Cells and Hydrogen 2 Joint Undertaking within the framework of the INN-Balance project (No 735969), and by the Federal Ministry of Transport and Digital Infrastructure of Germany within the framework of the BILBO project (No 03B10701C). This Joint Undertaking receives support from the European Union's Horizon 2020 research and innovation programme, Hydrogen Europe and Hydrogen Europe research. The authors would also like to thank Antonio Lozano, Felix Barreras, Florian Becker and Christoph Gentner for fruitful discussions.

REFERENCES

1. Rice CA. 2021. Review—Subzero Automotive Fuel Cells: Water Fill Tests vs Cold-Starts. J. Electrochem. Soc. 168:044513.
2. Luo Y, Jiao K. 2017. Cold start of proton exchange membrane fuel cell. Progress in Energy and Combustion Science 000:1-33.
3. https://www.fch.europa.eu/publications/programme-review-report-2018. Accessed on January 15, 2022
4. https://www.energy.gov/eere/fuelcells/doe-technical-targets-fuel-cell-systems-and-stacks-transportation-applications. Accessed on January 15, 2022
5. Jiang F, Fang W, Wang CY. 2007. Non-isothermal cold start of polymer electrolyte fuel cells. Electrochimica Acta 53:610-621.
6. Wang Y, Mukherjee PP, Mishler J, Mukundan R, Borup RL. 2010. Cold start of polymer electrolyte fuel cells: Three-stage startup characterization. Electrochimica Acta 55:2636-2644.
7. Jiang F, Wang CY. 2008. Potentiostatic Start-Up of PEMFCs from Subzero Temperatures. J. Electrochem. Soc. 155:B743-B751.

WHEC-2022
23rd World Hydrogen Energy Conference
June 26-30, 2022 - Istanbul

#372

INVESTIGATIONS ON THE MICRO-SCALE SURFACE INTERACTIONS AND TRIBOLOGICAL SIZE EFFECT IN MICRO-STAMPING OF SS316L SHEETS

[1*] *Mevlüt Fatih Peker,* [2] *Hasan Gedikli,* [2,*] *Ömer Necati Cora,* [3] *Muammer Koç*
[1] İSTAÇ, İstanbul Environment Management Industry and Trade Company, 34379, Şişli, İstanbul, Turkiye
[2] Karadeniz Technical University, School of Engineering, Department of Mechanical Engineering, Trabzon, Turkiye
[3] Hamad bin Khalifa University, College of Science and Engineering, Sustainable Development Division, Doha, Qatar

*Corresponding author e-mail: oncora@ktu.edu.tr

ABSTRACT

Micro-stamping is a convenient sheet-metal forming technology providing small tolerances, surface accuracy, low-cost and fast production of thin metallic sheets. Compared to macro-forming operations, tribological changes in micro-forming processes are harshened. Tribological size effect should be considered for a better understanding of surface interaction on micro-scale. The objective of this study is to establish numerical and experimental models for micro-stamping of stainless steel blanks regarding the tribological size effect and determine the effects of feature size of the dies and stamping force onto friction, von-Mises stress, plastic strain, part thickness changes. Numerical models of micro-stamping process for the dies with 3 distinct channel sizes (250 µm, 750 µm and 2500 µm) were established in FEA package Ls-Dyna. Several coefficients of friction values were imposed and runs were performed. Micro-stamping were also conducted to verify the established FE models. It was noted that the dies with different channel sizes showed different magnitudes and distributions of von-Mises stress and plastic strain. In addition, different friction coefficients were encountered for the micro-stamping dies with 250 µm, 750 µm and 2500 µm channel sizes. The lower channel size the higher coefficient of friction was observed as a result of tribological size effect.

Keywords: Bipolar Plates, Stamping, Surface Topography, Contact Resistance, Corrosion Resistance

INTRODUCTION

The demand for miniaturization is incessantly growing with the technological developments in micro-electromechanics, electronic health care and automobile industries. The global micro electromechanical systems (MEMS) market size was estimated as big as $48.7 billion in 2018, and is forecasted to surpass $122.8 billion by 2026 [1]. Specifically, the market size for MEMS devices in biomedical applications in which micro components and mechanisms are involved is expected to reach $ 27.38 billion, by 2026 [2]. As a result of this demand, the research and industrial activities on mass manufacturing of micro-scale parts such as micro-gears, pumps, connector pins, miniature screws, contact springs have been a trend. In this respect, metal forming methods are preferred and adapted to microforming since these methods are appropriate for high production rates, and can provide high quality final product surface, and high strength with a low cost [3-6]. On the other hand, it is challenging to produce form micro-scale parts in big quantities and very tight tolerances compared to macro-scale process. Some of these challenges that need to be properly addressed are as follows; (1) Influence of size effect on material behavior, (2) Unknowns in contact mechanics, surface interactions and macro-scale tribology, (3) Lack of reliable modeling and simulation of micro-forming processes, (4) Machine and equipment problems [6,7]. Different from macro forming, in micro forming the ratio of surface area to volume of workpiece is high that causes size effect [8,9]. In addition, due to the higher ratio of surface area to volume, an increased level of friction and wear issues at the contact interface are experienced [10,11]. The friction at the tooling/workpiece interface in sheet metal forming operations determined the formability level of the sheets [12-14]. Thus, the energy and force required for forming sheets can be minimized and longer tool life and better surface quality of tool-workpiece can be provided via reduction of friction [12, 15, 16]. Therefore, the determination of coefficient of friction is critical, particularly in micro-scale [17]. FE based models needs to be integrated to the experiments for more reliable friction analysis. Quite a few studies are available in literature on the Hall-Petch equation-based grain size effect, however; limited number of studies investigated the tribological size effect and determination of coefficient of friction. Hu and Vollertsen carried out strip drawing tests and FEA to identify the tribological size effect [18]. They concluded that friction increased with miniaturization. Bin et al. investigated tribological size effect through cylinder compression tests and found that as tribological size effect encountered in lubricated condition whereas it is not observed in dry condition [19]. In another attempt by Peng et al, micro-scale soft punch stamping process, a rigid die and rubber as a flexible medium involves in only, was investigated with experiments and simulations. They noted that sheet blanks with smaller grain size are prone to attain higher formability. They noted that friction forces increase with miniaturization that leading to reduce formability [22].

Compared to micro strip/deep drawing and micro extrusion, micro-stamping is more prevalent technique in producing micro-parts and has not been investigated in detail, thus far. Current paper is therefore, dedicated for investigating tribological size effect via performing micro-stamping experiments with thin metallic sheet blanks and establishing FE models and their validation. It aims also to establish FE models and their validation.

EXPERIMENTAL

SS316L metallic sheet alloy with a thickness of 51µm (0.051mm) was chosen as material of interest for forming of blanks since SS316L offers low cost, electrical and thermal conductivity and easy formability [23, 24]. Total number of 36 SS316L sheet blanks were prepared in 30mm x 70mm dimensions. Rectangular strip blanks were preferred in the current study based on the previous research noting that the die corners cause tangential pressure in the blank and causes problems in numerical calculations [18, 25]. 3 different die pairs with different channel heights, 250, 750 and 2500 µm (representing the scale factors of X, 3X, and 10X) shown in Figure 1 were used to stamp the sheet strips. Each die pair was made from H13 tool steel with the dimensions of 40mm X 40 mm X 20 mm and had 67, 26, 9 arrays of micro channels, respectively. Blank holders used in the test setup were made from rubber material. Rubber blank holders protected the strips against the possible micro-cracks during the forming process. The optimum dimensions of blank holders were determined regarding the highest channel height that can be attained while avoiding the micro-cracks on the blank. The variables in micro-stampings was the blank holder dimensions and channel sizes of the dies used while the same sheet strip and blank holders materials were used in all experiments. Dies and blanks with almost the same roughness values were employed in experiments to minimize the effect of surface quality on results.

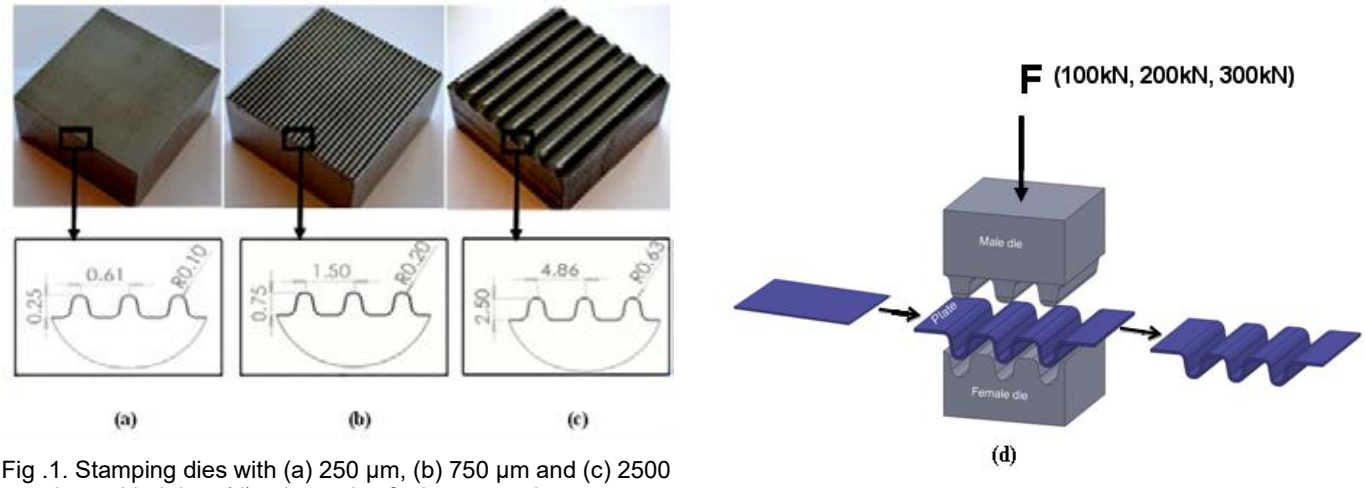


Fig .1. Stamping dies with (a) 250 µm, (b) 750 µm and (c) 2500 µm channel heights, (d) schematic of micro-stamping process

FE Model for Micro Stamping

The numerical simulations were preformed using commercial explicit/implicit finite element code Ls-Dyna for the micro-stamping processes employed three different channel sized dies (250 , 750 and 2500 µm). In order to simplify the analysis of stamping process and reduce the simulation time, 2-dimensional half models were built in Ls-Dyna. At first, die, blank, and blankholder geometries were prepared using SolidWorks CAD tool. Then, the models were prepared, as demonstrated in Figure 2 for finite element analyses. The FE models consisted of 37172, 28840 and 28613 4-node quadrilateral elements for the stampings with 250, 750 and 2500 µm channel height dies, respectively. Male and female dies were defined as rigid materials, whereas the blanks and blank holders were specified as deformable bodies. Elastic mechanical properties for blanks, male and female dies such as elasticity modulus, density and poisson ratio were acquired from literature as E=193 GPa, ρ = 7.99 g/m^3, υ = 0.31, respectively [27]. Power law material model with strength coefficient value (K) of 1058 and strain hardening exponent (n) of 0.28 were utilized for blanks. Blatz-Ko Rubber material model with mass density of 0.95 t/mm^3 and shear modulus of 28 N/mm^2 was used for blankholder. Coulomb friction model was defined for all contact surfaces. All contact conditions between upper (male) die and blank, lower (female) die and blank, blank and blankholder, blankholder and lower die (female) were selected as “2D Automatic Node to Surface” contact algorithm [28]. A very wide range of coefficients of friction values (µ= 0.001, 0.01, 0.02, 0.03, 0.04, 0.05, 0.1, 0.2 and 0.3) were employed in the simulations. The upper die was moved down with a constant stamping speed of 1 mm/s, and a blank holder force of 3000 N was applied on the blank holder. Finally, an implicit solver was imposed as a solution algorithm in the simulation due to allowing for much larger time steps.

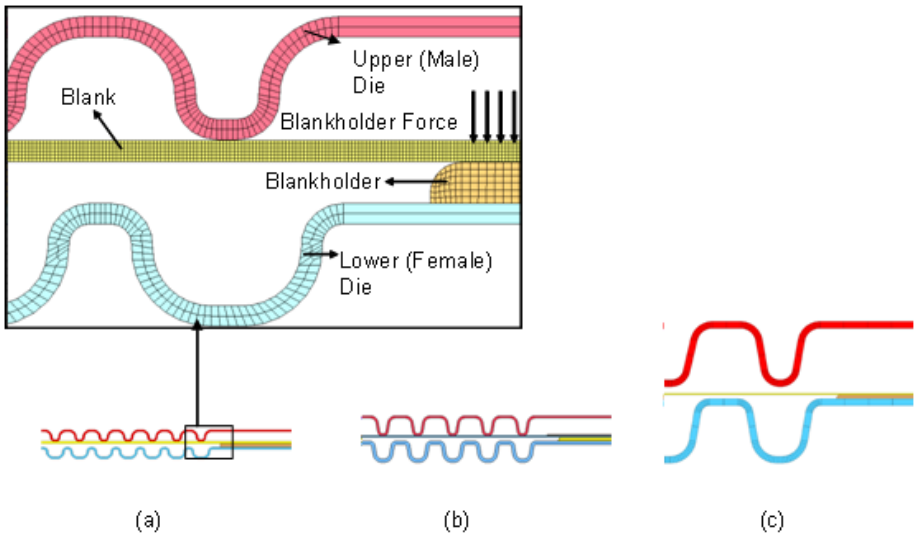


Fig.2. 2-D FE model of stamping process for the dies with the channel dimensions of (a) 250 µm, (b) 750 µm and (c) 2500 µm.

CONCLUSION

Formability and surface interactions between micro-stamped SS 316L sheet strips and micro-stamping dies were studied both experimentally and numerically. Channel height formation was taken as a measure for formability. Micro-stamping experiments were performed using three different dies with distinct channel height values (x, 3x, 10x) at different stamping force levels (100, 200, 300 kN) to investigate the tribological size effect. It was found that when the forming die dimensions get smaller the frictional conditions get harsher. Hence, tribological size effect was confirmed with the results. Interestingly, increasing force levels used in the experiments and simulations did not affect the coefficient of friction value in micro-forming of sheet strips with a certain die. On the other hand, plastic strain, equivalent stress so the formability levels were increased with increasing stamping force, as forecasted initially.

REFERENCES

1. Tewari D and Baul S. 2019. Microelectromechanical System (MEMS) Market by Type, and Application: Global Opportunity Analysis and Industry Forecast, 2019–2026, Allied Market Research.
2. Global MEMS devices for biomedical applications Market Research Report 2020, 360 Research Reports.
3. Koç M, Kim GY and Ni J. 2007. Modeling of the Size Effects on the Behavior of Metals in Microscale Deformation Processes. Journal of Manufacturing Science and Engineering v.129, pp.470-477.
4. Jeon J and Bramley AN, 2007. A friction model for micro-forming. International Journal of Advanced Manufacturing Technology 33: 125-129.
5. Geiger M, Geißdorfer S and Engel U. 2007. Mesoscopic model: advanced simulation of microforming processes. Journal of Production Engineering 1:79-84.
6. Trung ND, Nghe PV and Kien LT. 2008. Using Micro Forming Technologies for Production of Components in Electronic Industry. Proceeding of International Conference on Computational Solid Mechanics CSM2008, 27-30 November 2008, Ho Chi Minh City, Vietnam.
7. Engel U and Eckstein R. 2002. Microforming-from basic research to its realization. Journal of Materials Processing Technology 125-126:35-44.
8. Messner A, Engel U, Kals R and Vollertsen F. 1994. Size effect in the FE simulation of micro forming processes Journal of Materials Processing Technology 45:371-376.
9. Shimizu T, Murashige Y, Ito K and Manabe K. 2009. Influence of Surface Topography Interaction between Tool and Material in Micro-Deep Drawing. Journal of Solid Mechanics and Material Engineering 3:397-408.
10. Weidel S and Engel U. 2009. Characterization of the flattening behavior of modeled asperities. Wear 266:596-599.
11. Yao Z, Kim GY and Faidley L. 2011. Experimental study of high-frequency vibration assited micro/meso-scale forming of metallic materials. Proceeding of ASME 2011 International Manufacturing Science and Engineering Conference MSEC2011-50135, pp. 465-474.

WHEC-2022
23rd World Hydrogen Energy Conference
June 26-30, 2022 - Istanbul

#385

SYNTHESIS AND CHARACTERIZATION OF CATIONIC MEMBRANES WITH POLY(INDENE) SULPHONATED POLYELECTROLYTE FOR FUEL CELL APPLICATION

[1*] *Hannah Corrêa de M. M. Thomaz,*[1] *João Víctor M.R. de Souza,* [1] *Alexandre Furtado Ferreira*, [1] *Fábio José Bento Brum*
[1]Universidade Federal Fluminense, Avenida dos Trabalhadores, 420, Vila Santa Cecília, 27255-125 Volta Redonda, RJ, Brazil.

*Corresponding author e-mail: hannah_correa@id.uff.br

ABSTRACT

In this work, results of the synthesis and characterization of cationic hydrocarbon membranes with application in fuel cells will be presented. Semi-interpenetrating membranes based on PVA with sulfonated aromatic electrolyte polymer were prepared. In the polarization tests in a fuel cell prototype, the membrane with the best result obtained the value of open circuit potential and power equal to $0.8\,V$ and $7.5x10^{-2}\,W$, respectively, very close values when compared to Nafion®, an industrial membrane that reaches $0.8\,V$ and $9.0x10^{-2}\,W$, respectively, thus proving the applicability of the synthesized membrane in fuel cells.

Keywords: Electrolyte Polymers, Fuel Cells, Membranes, Polarization Curve

INTRODUCTION

Hydrocarbon electrolyte polymers have been good substitutes for the Nafion® membrane due to their low-cost synthesis, ease of insertion of hydrophilic groups, good proton conductivity and high chemical stability in some cases [1-4]. This work presents a new sulfonated indene-based electrolyte polymer applied in the synthesis of membranes with semi-interpenetrating structure, semi-IPNs, based on poly (vinyl alcohol) crosslinked with different crosslinking agents and tested in a fuel cell prototype.

MATERIALS AND METHODS

Poly (vinyl alcohol) - PVA Sigma Aldrich PM 130,000 g/mol and degree of hydrolysis 99% and ethanol Sigma Aldrich 98% were used in the synthesis of the membranes. The crosslinking agents used were Sigma Aldrich 99% citric acid, Sigma Aldrich 50% sulfosuccinic acid, Sigma Aldrich 50% 4-sulfophthalic acid. Poly(indene) sulfonated electrolyte polymer (SPInd) was synthesized as described by Brum and Colab [3–5]. Membranes were prepared by mixing 1.0 grams of PVA, 30% by weight of the crosslinking agents and 40% by weight of the SPInd polymer electrolyte [3,4]. For the characterization of the membranes, the following tests were performed: ion exchange capacity (IEC) at room temperature; degree of swelling at room temperature for 24 hours; degree of hydration; electrochemical impedance spectroscopy with humidified samples (sample area: 1.5 cm^2) [3,4]. In the fuel cell test, a hydrogen pressure of 1.5 psi and 3.0 psi of oxygen, cell area of 5.8 cm^2 and platinum catalyst 0.5 mg/cm^2 were used.

Units and Equations

Evaluation of the degree of swelling (WU): the degree of swelling measures the water absorption capacity of the membranes. The previously dried membrane sample is weighed and immersed in distilled water at room temperature for 24 hours, then it is removed from the aqueous medium, lightly dried to remove excess water, and weighed again. The value of the degree of swelling is calculated by the difference between then.

Ion exchange capacity (IEC): indicates the number of moles of the ion in 1.0 g of polymer. To perform this method, conventional titration is used, later the sample is placed in 1M NaCl solution for 24 hours. Then titrated with a 0.05M NaOH solution and using Eq. (1). Where V_{NaOH} is the volume of NaOH solution used to reach the equivalence point in the titration, M_{NaOH} is the molar concentration of the NaOH solution and M_{sample} is the mass of the sample, in grams:

$$IEC = (V_{NaOH} x M_{NaOH}) / M_{sample} \quad (1)$$

Hydration Degree (λ): indicates the degree of hydration of membranes, or number of H_2O molecules per an acidic hydrophilic group by Eq. (2).

$$IEC = (\%_{swelling})/(18/IEC) \quad (2)$$

Ionic conductivity (EIS): evaluates the resistance profile of isolated membranes and membranes in the prototype. It relates the ionic conductivity (δ) with the film thickness (l), the cross-sectional area (A) of the analyzed material, and the material resistance (R), the latter determined by electrochemical impedance spectroscopy (EIS), given by Eq.3. To perform this method, the membranes were conditioned in deionized water for 1h:

$$\delta = (1/R)x(1/A) \quad (3)$$

RESULTS AND DISCUSSION

Table 1 presents the values of ion exchange capacity, degree of swelling and hydration, and the description of each synthesized membrane. The only variation in the formulation of the membranes was the crosslinking agents. Membranes crosslinked with citric acid will be called M-AC, those with sulfophthalic acid (M-ASF) and sulfosuccinic acid (M-ASS).

Table 1. Values of ion exchange capacity, degree of swelling and hydration of synthesized membranes

Membranes	IEC (mEq/g)	Thickness (cm)	Swelling degree (%)	Hydration degree (λ)
M-AC	1.3	0.021	206	8.803
M-ASF	1.5	0.022	100	3,704
M-ASS	1.4	0.022	121	4.801

It can be seen that the IEC values were practically unchanged, but on the other hand, in the swelling values a significant variation is observed. This fact is attributed to the acidic character of the hydrophilic sulfonic groups (-SO_3H) having a strong influence as a catalyst in membrane esterification reactions, and crosslinking reactions [1,4]. The M-AC membrane has a hydrophilic carboxylic group (-COOH) and this fact explains the high swelling degree value, since the carboxylic acid group has a lower acidic character compared to the sulfonic group (BRUM, 2013). The values of the degree of hydration are almost double for the membrane with (-COOH), while those with group (-SO3H) had little difference. The M-ASF membrane has an aromatic group in its composition, and this group confers greater rigidity to the polymeric structure, which justifies the differences in swelling and hydration values of this membrane when compared to the M-ASF membrane.

Table 2 presents the results of the electrochemical impedance test. Citric acid and sulfosuccinic acid present a linear carbonic chain structure, with their major difference being the hydrophilic groups. This fact is observed by the proximity of the electrolyte resistance values, but with very different values in relation to conductivity.

Table 2. Resistance and conductivity values obtained by impedance

Membranes	Resistance (ohm)	Conductivity (S/cm)*
M-AC	9.20	$15.9x10^{-04}$
M-ASF	10.5	$5.77x10^{-04}$
M-ASS	3.47	$4.99x10^{-03}$
Nafion®	1.94	$5.529x10^{-03}$

*1.5 cm^2 area electrodes

From the resistance values it is observed that the M-ASS membrane presented the lowest value and, when compared to the M-AC membrane, the difference between the resistance values reaches more than 250%. This is due to the low ionic strength of the carboxylic groups, which is proven by the values of degree of hydration presented (Table 1). The M-ASF membrane, which presents only sulfonic hydrophilic groups in its composition, presented the highest resistance value and the lowest conductivity. This fact is associated with the presence of aromatic groups in the composition of this membrane from the structure of SPInd and the crosslinking agent sulfophthalic acid [1]. The aromatic groups tend to rearrange themselves in structures in the form of a half ladder and make the polymeric structure more rigid, thus impairing the ionic transport [3,4].

Figure 1 shows the polarization curves of the synthesized membranes obtained from the fuel cell performance test [2]. It can be seen that all the electrode/membrane/electrode sets presented the same open circuit value, around

0.8V, therefore, it is evident in the test only the influence of the tested membrane. The membrane that came closest to the Nafion® reference (power 9.20 x10^{-2} W) was the HC (power 7.49 x10^{-2} W) crosslinked with sulfosuccinic acid.

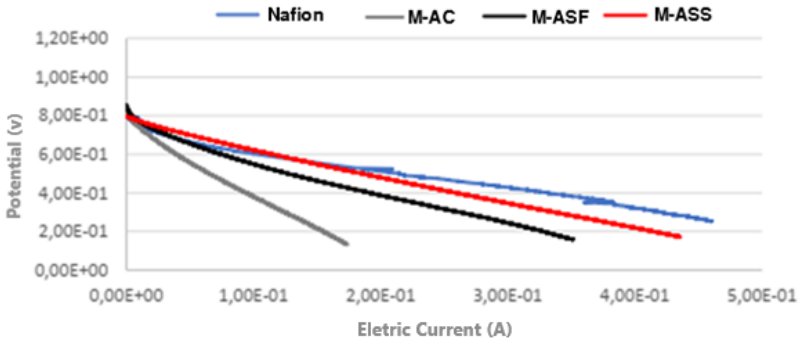


Fig.1. Polarization Curves of M-AC, M-ASF, M-ASS and Nafion® membranes

This result is corroborated by the conductivity values presented in Table 2. Although the HB membrane (power 5.56 x10^{-2} W) has in its composition only hydrophilic sulfonic groups, what may have influenced the reduction of proton transport was the presence of aromatic rings leaving the molecular structure of the semi-interpenetrating network more rigid, which impaired the transport of H_3O^+ species. Even with the presence of the polymer electrolyte SPInd, the HA membrane (power 2.31 x10^{-2} W) showed low performance compared to the other membranes.

CONCLUSIONS

Semi-interpenetrating PVA-based cationic membranes with poly(indene) sulfonated electrolyte polymer were prepared and presented homogeneous and stable films. The IEC values, degree of swelling and degree of hydration confirmed the esterification reaction and the structural differences between the membranes presented. Citric acid, sulfophthalic acid and sulfosuccinic acid were good crosslinking agents. The membrane that showed the best performance in a fuel cell test was the HC, crosslinked with sulfosuccinic acid.

REFERENCES

1. C.Y Wong et al., “Development of Poly(Vinyl Alcohol) – Based Polymecs as Proton Exchange Membranes and Challenges in Fuell Cell Application: A Review,” Polym. Rev., vol. 60, no.1, pp. 171-202, 2020, doi: 10.1080/15583724.2019.1641514.
2. Costa, L.A.T, Aguiar, L.C.V, Gomes, A. S, F.J.B. Brum. “Characterization of PVA and phenol salt modified tin dioxide cationic membranes” Inernational Journal of Hydrogen Energy, doi: 10.1016/j.ijhydene.2021.12.074.
3. F.J.B. Brum, F.G.Zanatta, E.S.Marczynski, M.M.C. Forte, and B. Pollet, “Synthesis and characterization of a new sulphonated hydrocarbon polymer for application as a solid proton-conducting electrolyte,” Solid State Ionics, vol. 263, pp. 62-70, 2014, doi: 10.1016/j.ssi.2014.05.009
4. F.J.B. Brum, “Membranas catiônicas a base de poli(indeno) sulfonado/PVA para uso como eletrolito em célula a combustível tipo PEMFC,” 2013.
5. F.J.B. Brum, F.N. Lau, and M.M.C. Forte, “Synthesis of hydrocarbon polymers by cationic polymerization and their thermal properties,” Des. Monomers Polym., vol.16, no. 0, pp. 291-301, 2013, doi: 10.1080/15685551.2012.747145

WHEC-2022
23rd World Hydrogen Energy Conference
June 26-30, 2022 - Istanbul

#386
USE OF TWO-PHASE COOLING FOR THE FUEL CELL SYSTEM

[1] *Thanyarak Bogdanske*, [2] *Andreas Sklarow*, [3*] *Johannes Gulden*
[1] University of Applied Sciences Stralsund (HOST), Fak. Mech. Eng., Zur Schwedenschanze 15, 18435 Stralsund, Germany
[2] University of Applied Sciences Stralsund (HOST), IRES, Zur Schwedenschanze 15, 18435 Stralsund, Germany
[3] University of Applied Sciences Stralsund (HOST), Fak. Elec. Eng. & IRES, Zur Schwedenschanze 15, 18435 Stralsund, Germany

*Corresponding author e-mail: Johannes.gulden@hochschule-stralsund.de

ABSTRACT

Hydrogen mobility is becoming increasingly important and is seen as an alternative to electric and conventional mobility. As a student project the ThaiGer-H2-Racing Team at the University of Applied Sciences Stralsund has been working on hydrogen propulsion since 2007 and is building ultra-light prototype vehicles with fuel cells. Within the fuel cell system cooling is a crucial problem to be solved for future applications. We report on an experiment with a two-phase cooling system, which was developed for the fuel cell stack. An engineered liquid Novec 7000 from 3M was used as the cooling medium. The cooling medium evaporates in the fuel cell stack at about 45 °C and thus transports the heat to the outside. The cooling circuit is driven by the evaporation of the cooling medium and thermosiphon effect and therefore does not require an additional cooling pump. Since the cooling circuit is operated at a slight overpressure, the membranes in the stack are more uniformly compressed by the metallic bipolar plates, which might increase the performance of the stack. The two-phase cooling system was successfully tested in the new vehicle on a track. By saving the cooling pump and reducing the consumption, the overall efficiency of the fuel cell system was significantly improved.

Keywords: Two-phase cooling, Thermosiphon, Cooling System, Fuel Cell, 3M Novec

INTRODUCTION

In recent years' automobile manufacturers are recognizing the potential of hydrogen mobility and are launching series-produced vehicles on the market. The biggest players are Toyota and Hyundai, but German manufacturers are also following this trend and developing hydrogen vehicles and their own fuel cell systems. For weight reasons, the bipolar plates in such fuel cells are made of thin metal sheets. These usually consist of two metal foils welded together, in which the channels for the media supply (H2 and air) are stamped. The coolant flows through the interstitial space and removes the waste heat. The coolant used is usually an ethylene glycol/water mixture with corresponding cation and anion exchangers, which must have low electrical conductivity in the FC stack (<5 µS/cm at 25 °C), otherwise the water molecules will be split in the fuel cell, because a high voltage is applied across the bipolar plates. [1]

The ThaiGer-H2-Racing Team is a student team at the University of Applied Sciences in Stralsund, Germany, which has been developing and building hydrogen-powered prototype vehicles for over 14 years. These vehicles have excellent aerodynamics and are designed for highest efficiency. The team competes annually in the largest efficiency competition Shell Eco-marathon Europe, and won 1st place in the hydrogen-powered prototype category in 2017, 2018 and 2019. In 2019, the team achieved their best performance of 1083 km/m^3 of hydrogen, the equivalent of 3295 km on one litre of gasoline.

For Shell Eco-marathon 2022, the team has developed a new vehicle - ThaiGer 7. Compared to the previous model, the weight, aerodynamics and design have been improved, but above all the fuel cell (FC) system has been optimised for higher efficiency. The diaphragm pumps for the air supply were replaced by efficient side channel blowers developed in-house. In contrast to the water cooling system used in the old vehicle, a new type of two-phase cooling system was developed for the FC stack.

The two-phase cooling system requires a cooling medium with a boiling temperature below the desired operating temperature of the fuel cell (40-45°C). The medium must have a very high electrical resistance and must compatible with the used materials. In addition, low viscosity and low surface tension are advantageous for the cooling medium.

The engineered liquids from the company 3M, which are sold under the brand name Novec, were shortlisted as suitable liquids. These are the fluorine-based liquids, which are similar in structure to hydrocarbons, but in which the hydrogen atoms are replaced by the fluorine atoms. These liquids are relatively inert, non-flammable, non-inflammable and non-toxic. Typical applications for these fluids are ORC systems, thermosiphon systems, ion implanters, plasma etching, two-phase pumping systems and fuel cells. [2]

RESULTS AND DISCUSSION

Of all the Novec fluids, three were considered for the cooling system. Decisive for the selection is the boiling temperature, which must either correspond to the operating temperature in an open two-phase system or be below the desired operating temperature for a closed two-phase cooling system. Since the Novec liquids are relatively volatile, only a closed cooling system can be used. Table 1 summarizes the essential properties of selected media. Only Novec 7000 has the boiling point (34 °C) below the desired operating temperature of 45 °C. The water, Novec 7100 and Novec 649 have a higher boiling points, but are thermally more stable. The Novec liquids can be mixed with each other, but they do not form an azeotropic mixture, so that only the liquid with the lower boiling temperature would evaporate first. For this reason Novec 7000 was chosen for the experiments with the cooling system of the fuel cell.

Table 1. Comparison of cooling liquids [2, 3, 4]

	Unit	Water	3M Novec 7000	3M Novec 649	3M Novec 7100
Boiling Point (@ 1 atm)	°C	100	34	49	61
Vapor Pressure	bar	1	0,646	0,404	0,268
Liquid Density	kg/m^3	998	1400	1602	1510
Surface Tension	mN/m	72.75	12.4	10.8	13.6
Volume Resistivity	Ω·cm	1·10^6	1·10^6	9,9·10^{11}	3,29·10^9
Coefficient of Expansion	1/K	0.00021	0.00219	0.002	0.002
Kinematic Viscosity	mm^2/s	1.004	0.32	0.39	0.38
Absolute Viscosity	mPa·s	1.001	0.45	0.63	0.58
Specific Heat	kJ/(kg K)	4.183	1.300	1.103	1.180
Latent Heat of Vaporization	J/g	2257	142	88	112
Thermal stability	°C	-	150	300	150
Thermal Conductivity	W/(m·K)	0.5984	0.075	0.059	0.0688

The fuel cell stack consists of 30 cells connected in series. The series connection is guaranteed by the metallic bipolar plates. The bipolar plates consist of two metallic stainless steel foils, in each of which the flow field for the hydrogen and the air are embossed. The interstitial space is filled with the cooling liquid, Novec 7000. When the liquid reaches boiling temperature, it boils at the hot spots occurring in the fuel cell during operation. The phase transition removes the heat from the bipolar plates. The warm cooling liquid rises together with the steam bubbles to the top of an expansion tank. There, the vapour condenses and releases the heat into the environment in a heat exchanger. Due to its higher density, the cooled medium sinks downwards through an aluminium tube to the inlet of the fuel cell stack. With the correct sizing of the plumbing the liquid in the cooling circuit is made to circulate by the evaporation and thermosiphon effect. This supersedes the circulation pump and reduces the system's self-consumption, thus increasing the efficiency.

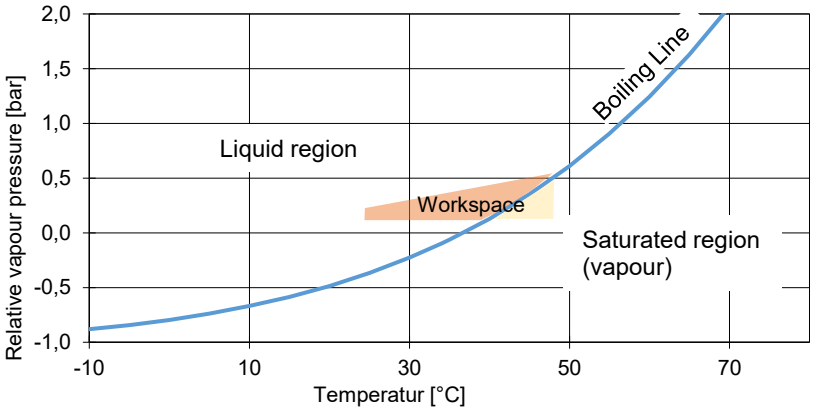


Fig. 1: Vapour diagram from Novec 7000 [5]

The steam curve of Novec 7000 is shown in the diagram (figure 1). The working area of the cooling system is shown in the diagram as a red area. The medium is present in the cooling system in two phases: liquid and as vapour. As the temperature rises, the volume of the cooling liquid increases significantly due to thermal expansion, since the

coefficient of expansion is about a factor of 10 higher than that of water. The expansion tank is equipped with a spring-loaded piston and has the task of compensating for the expansion, so that the pressure in the cooling system changes only in a very tight area and is about 0.4 bars. Due to this overpressure, the membranes in the stack are pressed more evenly by the metallic bipolar plates, which might increase the performance of the stack.

The assembled fuel cell system is shown in the figure 2. The expansion tank with spring-loaded piston is located above the FC stack. The expansion tank is made of an aluminium tube and serves together with the vertical recooling tube to dissipate the waste heat into the environment. The spring force, and thus the pressure in the cooling system, is adjusted by means of a screw. The pressure can be read on a digital pressure display (blue box on the top).

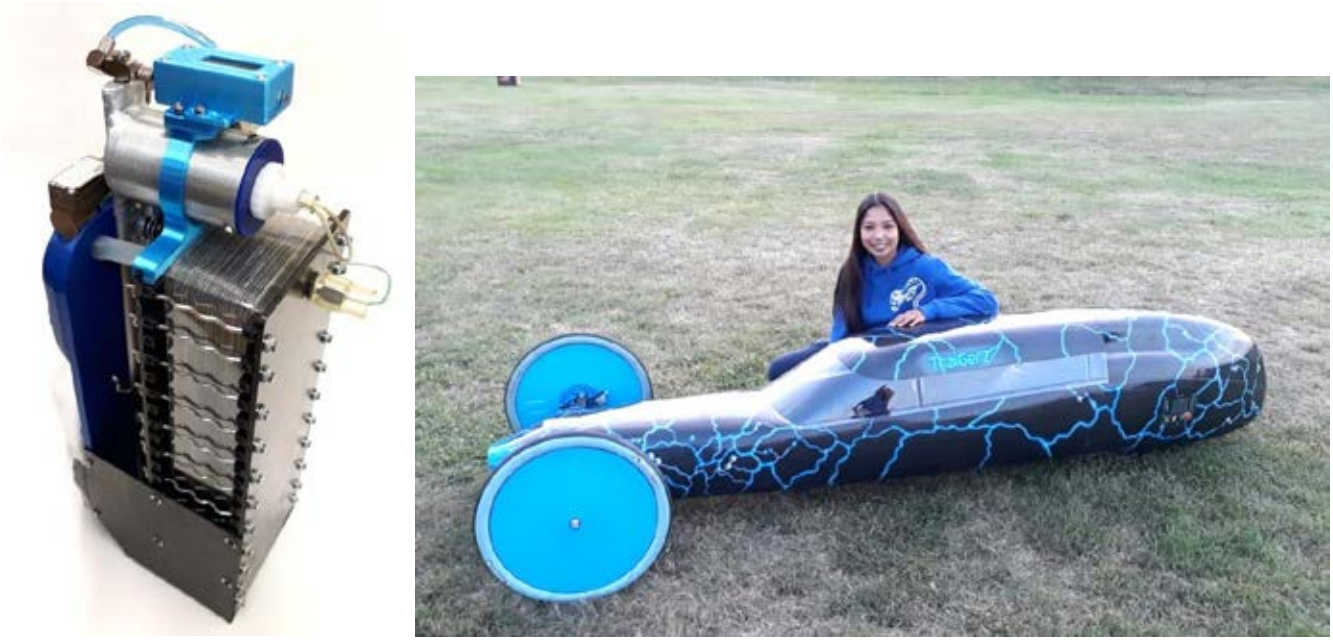


Fig. 2: Fuel cell system with the two-phase cooling (left); ThaiGer 7 vehicle with the author T. Bogdanske (right)

CONCLUSIONS

A passive two-phase cooling system was developed for the FC stack of an ultra-light vehicle. This is based on a light boiling liquid Novec 7000, which has a boiling temperature of 34 °C at ambient pressure. The overpressure in the cooling system of about 0.4 bar ensures an operating temperature of 45 °C. The overpressure ensures that the membranes in the fuel cell stack are compressed more evenly, which slightly increases the performance. Since the cooling circuit is driven by the evaporation and thermosiphon effect, no circulation pump is required for this closed cooling system. This saves power for the pump and increases system efficiency.

REFERENCES

1. P. Kurzweil. 2016. Brennstoffzellentechnik. ISBN 978-3-658-14935-2 (eBook). Wiesbaden, Springer.
2. https://www.3m.co.uk/3M/en_GB/p/d/b5005006004/, 3M™ Novec™ 7000 Engineered Fluid, Accessed on February 2, 2022
3. https://www.3m.co.uk/3M/en_GB/p/d/b5005005025/, 3M™ Novec™ 649 Engineered Fluid, Accessed on February 2, 2022
4. https://www.3m.co.uk/3M/en_GB/p/d/b40044867/, 3M™ Novec™ 7100 Engineered Fluid, Accessed on February 2, 2022
5. Th. Bogdanske. 2021. Aufbau einer 2-Phasen-Kühlung für einen Brennstoffzellenstack. Bachelor-Thesis. Hochschule Stralsund

WHEC-2022
23rd World Hydrogen Energy Conference
June 26-30, 2022 - Istanbul

#405

TWO-DIMENSIONAL SIMULATION OF COLD START PROCESS FOR PEMFC STACK WITH VARIOUS CURRENT LOADING MODES

*Jing Liu, * Tong Zhang*
School of Automotive Studies, Tongji University, Shanghai 201804, China

*Corresponding author e-mail: tzhang@tongji.edu.cn

ABSTRACT

Rapid cold start of proton exchange membrane fuel cell (PEMFC) stack is imperative for the widespread commercialization of fuel cell vehicles. In the present work, a two-dimensional transient cold start model of a PEMFC stack with coolant recirculation is developed to explore a fast start-up strategy and the corresponding required operating conditions. Five current loading modes are evaluated for the stack performance from – 20 °C, including three constant current loading modes and two current ramping loading modes. It is found that a linear current ramping strategy with a larger initial current density can generate more heat and facilitate rapid cold start without excessive voltage undershoot. Meanwhile, the cell voltage variation of the 20 cells during the cold start process is recorded and two end side cells show smaller output voltage due to lower cell temperature than that of the middle cells. In order to maintain cell voltage consistency, external heating or insulation is necessary for PEMFC stack cold start stably and successfully.

Keywords: PEMFC Stack, Cold Start, Current Loading Strategy

INTRODUCTION

Under the background of carbon neutrality, the development of proton exchange membrane fuel cell (PEMFC) obtained an unprecedented opportunity due to its characteristics of zero emission. However, the cold start problem brings a big challenge to PEMFC, which is one of the main obstacles to the promotion of fuel cell vehicles in cold zones [1]. During the cold start of PEMFC, the ice will block the diffusion path of reactant to the reaction site [2], which prevents electrochemical reactions from taking place and results in cold start failures.

In order to explore the multidisciplinary coupling process of PEMFC cold start, a number of cold start models of single cell or stack have been developed. Three-dimensional model is very useful to observe the ice distribution and temperature distribution. However, the computational domain is mainly limited in one single channel [3, 4] because of the limitation of computation resources [5]. Therefore, the characteristics of large-scale cell or stack can not be fully considered. One-dimensional models only consider through-plane direction of PEMFC stack without taking in-plane direction into account. Two-dimensional models are the extension of the one-dimensional models, which usually focus on the through-plane domain and long-the-channel domain. Comparatively speaking, the two-dimensional models require less computational cost, and the detailed transport phenomenon uniformity of ice distribution, consistency of voltage can also be taken into consideration. Thus, it can be an alternative way to investigate the cold start process of PEMFC stack. In addition, one of the most important parameters influencing the cold start process of PEMFC is coolant circulation. Nevertheless, rare multi-dimensional cold start model of PEMFC stack considers the coolant, and only the single cell model with straight flow channel has been studied to investigate the effect of coolant flow [3, 4]. Therefore, it is necessary to establish a two-dimensional large-scale cold start model considering coolant circulation, so as to study the cold start characteristics and evaluate various auxiliary start methods.

In this paper, a two-dimensional cold start model is developed for PEMFC stack. This study aims to investigate the effect of current loading strategies on the PEMFC stack cold start process with consideration of coolant circulation, which is closer to the actual working condition of PEMFC stack. Based on this model, an optimal current loading method is recommended.

MATHEMATICAL MODEL

A two-dimensional model for PEMFC stack cold start process with coolant circulation is established. Fig. 1 (a) shows the computational domain. N nodes is set along the channel and N is determined to be 5 in this study after the grid independency check. The cell number is set to be 20 to reflect the characteristics of the PEMFC stack [6]. The model is formulated based on the conservation equations of mass conservation, gas species transport, membrane water transport, liquid water transport, ice transport and energy [7]. Some basic assumptions are made as described in reference [7]. The coolant is assumed to be evenly distributed in each single cell.

$$\partial(\varepsilon(1-s_{\mathrm{lq}}-s_{\mathrm{ice}})\rho_{\mathrm{g}})/\partial t+\nabla\bullet(\rho_{\mathrm{g}}\vec{u}_{\mathrm{g}})=S_{\mathrm{m}} \quad (1)$$

$$\partial(\varepsilon(1-s_{lq}-s_{ice})\rho_g c_i)/\partial t=\partial^2(\rho_g D_i^{eff} c_i)/\partial x^2+S_i \quad (2)$$

$$[\rho_{MEM}/EW][\partial(\omega\lambda_{nf})/\partial t]=[\rho_{MEM}/EW][\partial^2(\omega^{1.5}D_{nf}\lambda_{nf})/\partial x^2]+S_{nmw} \quad (3)$$

$$[\rho_{MEM}/EW][\partial(\omega\lambda_f)/\partial t]=S_{fmw} \quad (4)$$

$$\partial(\varepsilon\rho_{lq}s_{lq})/\partial t=\partial^2(\rho_{lq}p_{lq}K_{lq}/\mu_{lq})/\partial x^2+S_{lq} \quad (5)$$

$$\partial(\varepsilon s_{ice}\rho_{ice})/\partial t=S_{ice} \quad (6)$$

$$\partial((\rho C_P)^{eff}T)/\partial t=\partial^2(k_T^{eff}T)/\partial x^2+S_T \quad (7)$$

In this model, the convective heat transfer rate between the end bipolar plate and environment is set as:

$$Q=h(T-T_{BP})A_{BP} \quad (8)$$

The inlet gas boundary condition is shown below:

$$u_{in,a}=(ST_aI_{ave}A_{cell})/(2Fc_{H_2}A_{ACH}),u_{in,c}=(ST_cI_{ave}A_{cell})/(2Fc_{O_2}A_{ACH}) \quad (9)$$

RESULTS AND DISCUSSION

Model validation

This two-dimensional model is validated by comparing the output voltage and temperature of coolant with experiment results of cold start process for PEMFC stack at -20 ºC [8]. The coolant inlet temperature is set as -17 ºC both in the experiment and the model. According to the Fig. 1(b) and (c), the output voltage, coolant inlet and outlet temperature of PEMFC stack model are in good agreement with the experiment data. And it is shown that this model can be used to predict the cold start performance of PEMFC stack reasonably.

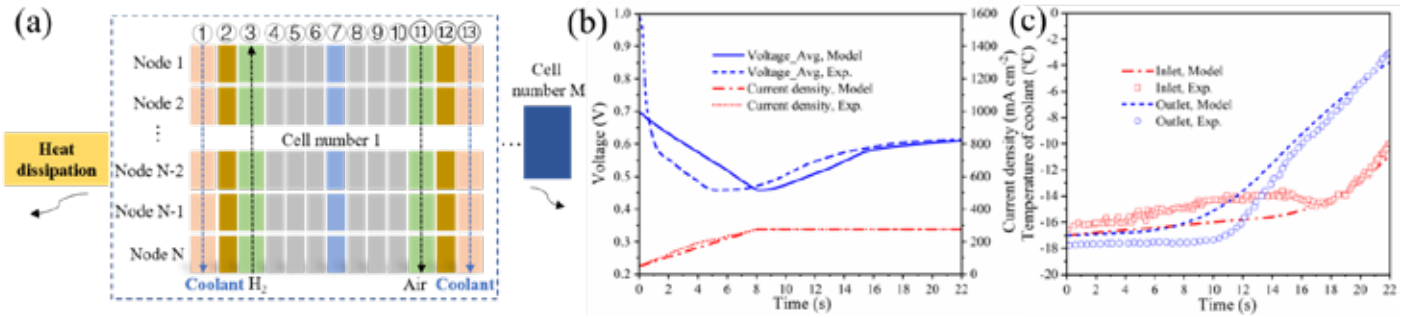


Fig. 1. (a) Schematic diagram of two-dimensional PEMFC stack model: ①ACF, ②ABP, ③ACH, ④AGDL, ⑤AMPL, ⑥ACL, ⑦MEM, ⑧CCL, ⑨CMPL, ⑩CGDL, ⑪CCH, ⑫CBP, ⑬CCF. (b) and (c) Comparison of model prediction with experimental results [8].

The output voltage and coolant inlet temperature of the PEMFC stack

This work aims to find out a proper current loading mode for rapid cold start process. Five different current loading modes are introduced in Table 1, including constant current and current ramping modes. The cell voltage and coolant inlet temperature are elucidating here to evaluate the effects of various current loading modes on PEMFC stack cold start process, as are shown in Fig. 2(a) and (b) respectively.

In regard to the three constant current cases, it is found that growth rate of the coolant inlet temperature in case 1 is the slowest. Because low current density can not provide sufficient heat to rise the PEMFC stack temperature rapidly. Increasing the start-up current density properly would favorable due to more heat generated. However, case 3 indicates that a large current density can result in too low output voltage to fail in cold start of PEMFC stack because of inadequate initial membrane water content. As to current ramping methods, case 4 shows lower cell voltage dropdown than that in case 2, which can avoid MEA degradation. Short cold start-up time and harmless to PEMFC stack are both imperative. Using a larger current ramping loading from 500 mA cm^{-2} to 700 mA cm^{-2}, the PEMFC stack can be successfully cold start-up in 19.5 s with the higher initial membrane water content.

Table 1. Detailed parameters of five current loading strategies.

	Current loading mode	Current density (mA cm^{-2})	Initial water content		Current loading mode	Current density (mA cm^{-2})	Initial water content
case 1	constant	100	3.2	case 4	ramping	50 – 400, 10 s	3.2
case 2	constant	400	3.2	case 5	ramping	500 – 700, 4 s	7
case 3	constant	500	3.2				

The cell voltage consistency of the PEMFC stack

Fig. 2(c) gives the output voltage variation of the 20 cells during the cold start of PEMFC stack in case 5, where the cell voltage is recorded when the coolant inlet temperature reaches 0 °C. It is obvious that the side cells (cell 1-4 and cell 17-20) have the lower output voltage than that of the middle cells. This is because the cells at both sides dissipate more heat to the environment, making it harder to warm up. Thus, it is necessary to make insulation or apply external heating to the cells at the both end sides of PEMFC stack to maintain cell voltage consistency and successful cold start-up.

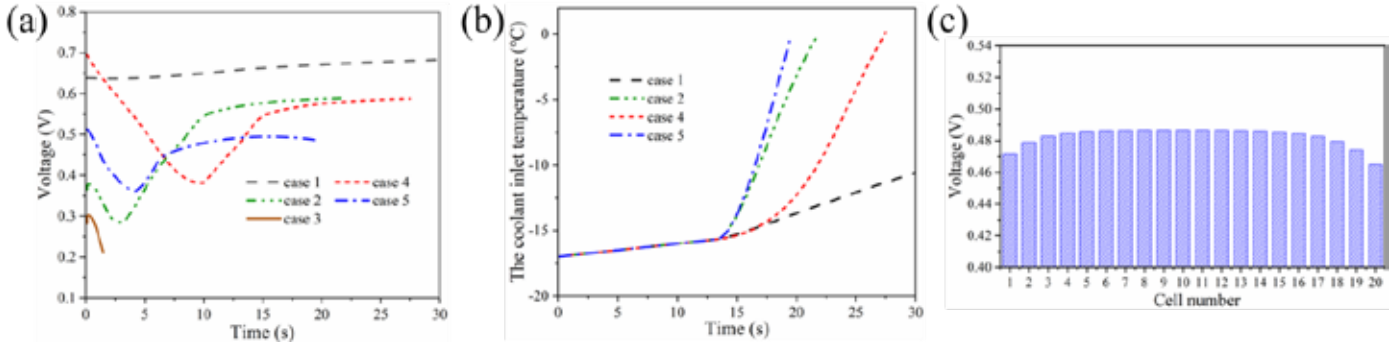


Fig. 2. (a) Average cell voltage for the five cases. (b) The coolant inlet temperature of PEMFC stack for the five cases. (c) Cell voltage variation of case 5 at start-up time t=19.5 s (the coolant inlet temperature T=0 °C).

CONCLUSIONS

A two-dimensional cold start model of the PEMFC stack with coolant recirculation is developed and a current ramping strategy is proposed for rapidly cold start-up. The constant current loading modes with a small start-up current density can not produce sufficient heat. Otherwise, the higher constant current density may cause too large voltage undershoot to cold start failure. As to current ramping mode, it can take advantage of sufficient heat generation and less voltage undershoot. The PEMFC stack mildly hydrated before cold start process can be successfully cold start-up in 19.5 s by using a current ramping loading from 500 mA cm^{-2} to 700 mA cm^{-2}. In addition, insulating or heating the cells at the both end sides of PEMFC stack is essential to retain voltage consistency and achieve cold starts.

REFERENCES

1. Luo Y and Jiao K. 2018. Cold start of proton exchange membrane fuel cell. Progress in Energy and Combustion Science 64:29-61.
2. Mishler J, Wang Y, Mukherjee PP, Mukundan R and Borup RL. 2012. Subfreezing operation of polymer electrolyte fuel cells: Ice formation and cell performance loss. Electrochimica Acta 65:127-33.
3. Wei L, Dafalla AM and Jiang F. 2020. Effects of reactants/coolant non-uniform inflow on the cold start performance of PEMFC stack. International Journal of Hydrogen Energy 45:13469-82.
4. Wei L, Liao Z, Suo Z, Chen X and Jiang F. 2019. Numerical study of cold start performance of proton exchange membrane fuel cell with coolant circulation. International Journal of Hydrogen Energy 44:22160-72.
5. Luo Y, Guo Q, Du Q, Yin Y and Jiao K. 2013. Analysis of cold start processes in proton exchange membrane fuel cell stacks. Journal of Power Sources 224:99-114.
6. Zhou Y, Luo Y, Yu S and Jiao K. 2014. Modeling of cold start processes and performance optimization for proton exchange membrane fuel cell stacks. Journal of Power Sources 247:738-48.
7. Wu K, Xie X, Wang B, Yang Z, Du Q and Xuan J, et al. 2020. Two-dimensional simulation of cold start processes for proton exchange membrane fuel cell with different hydrogen flow arrangements. International Journal of Hydrogen Energy 45:17795-812.
8. Wang F. 2017. -20 oC cold start of fuel cell engine. Shanghai Auto 8:3-6 (in Chinese).

WHEC-2022
23rd World Hydrogen Energy Conference
June 26-30, 2022 - Istanbul

#418

AIR SUPPLY MODULE FOR PRESSURIZING FUEL CELLS IN AIRBORNE APPLICATIONS

[1] Daniel Frank, [1] Jonas Schröter, [1] Christiane Bauer, [1*] Caroline Willich
[1]Ulm University, Institute for Energy Conversion and Storage, Albert-Einstein-Allee 47, 89081 Ulm, Germany

*Corresponding author e-mail: caroline.willich@uni-ulm.de

ABSTRACT

In order to obtain high power and efficiency while operating PEM fuel cells in airborne applications, pressurizing the inlet air is a prerequisite. An air supply module and its control strategy was developed in order to provide air at optimal conditions for different ambient conditions (low pressure, temperature and humidity) and varying power demand. The system was successfully tested statically and dynamically and afterwards connected to a fuel cell system.

Keywords: PEM Fuel Cell, Air supply, Aviation

INTRODUCTION

Using PEM fuel cells for propulsion in aircrafts has attracted much attention in the last years [1][2]. However, the performance of fuel cells decreases significantly with decreasing pressures [3][4], so the fuel cell will perform worse at high altitudes unless it is pressurized. The pressurization of the fuel cell air in an all-electric aircraft should be achieved by means of an electrically driven compressor. Both the characteristic of the fuel cell and the compressor change with inlet conditions; therefore, the components need to be carefully matched for optimal airborne operation. The dynamic behavior of the system is especially important since both the load requirement and the ambient conditions change and influence the behavior of the two main components, fuel cell and compressor.

SYSTEM DESIGN

In order to provide the required quality and amount of air-feed to the fuel cell at the optimal pressure, temperature and humidity, the air supply system has to incorporate an air filter, an electric compressor, an intercooler and a humidifier before it enters the fuel cell and a valve is required after the fuel cell. In previously presented work [5] a preliminary architecture was designed and suitable components were identified. An enhanced architecture is shown in Figure 1.

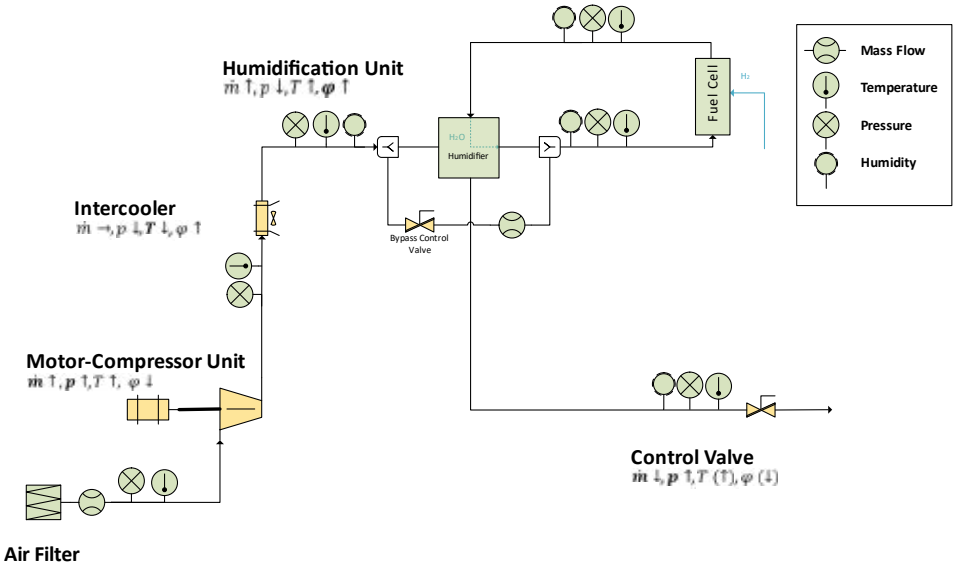


Figure 1: Enhanced Architecture of the developed air supply system

EXPERIMENTAL SETUP

After the design of the system, the air supply module was built up in a test-rig. Figure 2 shows the experimental installation. The setup uses a motor-compressor unit EK10AA (Rotrex, DK), a humidifier H50N (Fumatech, GER), an air filter FC F-0514-N (Freudenberg, GER) and two control valves APC (Hyundai Kefico, KOR) and was equipped with mass flow, pressure, temperature and humidity sensors.

The control of the air supply module was developed as well. With the help of the actuators compressor and throttle valve a decentralized control strategy for pressure and mass flow was developed, implemented and parameterized. The air temperature is controlled by means of intercooler coolant flow regulation. The humidity is controlled via the bypass control valve.



Figure 2: Experimental setup of the air supply module

RESULTS AND DISCUSSION

The compressor as the key component was in the first step tested inside an under-pressure chamber [6]. Figure 3 shows how the compressor characteristic shifts to lower outlet pressures and lower mass flow rates for low ambient pressures.

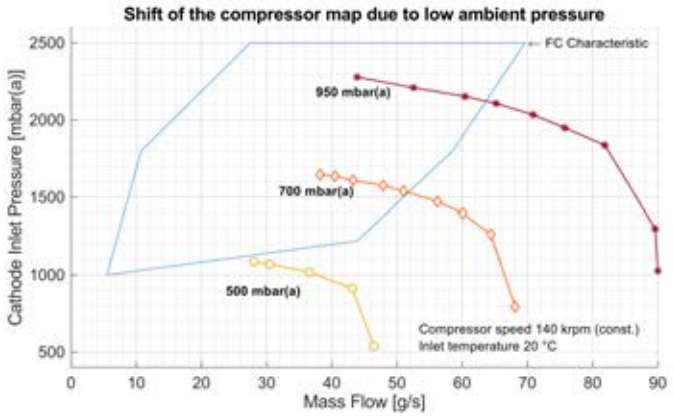


Figure 3: Shift of the compressor map due to low ambient pressure [5]

The dynamic behavior of the complete air supply system was then tested as well. Figure 4 shows an example of the pressure and mass flow provided by the system, where the air supply module performs a transition from a low power setpoint to a high power setpoint (1 → 6), as well as a transition from the high power setpoint to a setpoint with the minimum expected request (6 → 0). The figure shows the nominal operational characteristic of the fuel cell stack (300 cells, 68 kW peak), the compressor map and the trajectory of pressure and mass flow. It can be seen that the provided air stays within the preferred operational area, which is the overlap between the fuel cell map and the compressor map. In order to enable the system to perform transitions such as the beforehand mentioned (6 → 0), a surge avoidance strategy has been developed and implemented.

After successfully completing the tests, the air supply module was connected to a NM5 fuel cell stack (EKFC, GER) in cooperation with the German Aerospace Centre and the joint system was tested. The first coupled tests were successful, the functionality of the combined system was demonstrated, and measurement data will be presented.

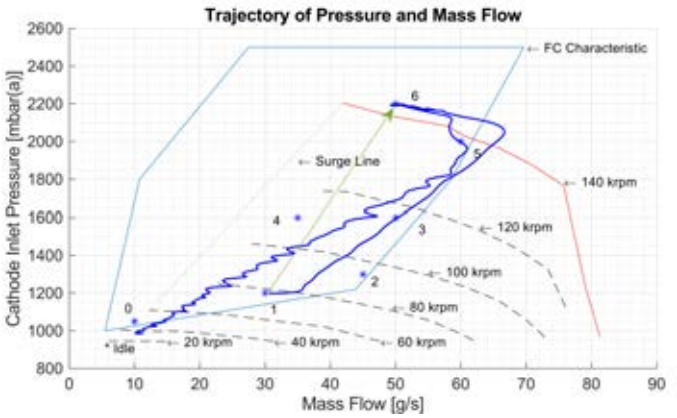


Figure 4: Exemplary transition between steady-state points of operation within the overlap between the fuel cell map and the compressor map at ambient pressure p_0 = 950 mbar

CONCLUSIONS

An air supply module for PEM fuel cells in airborne applications was designed, build and a control strategy was developed. The system was then successfully tested under static and dynamic operation. Afterwards the air supply module was connected to a fuel cell system and the combined system was tested as well.

ACKNOWLEDGEMENT

This work received funding from the German Ministry for Economic Affairs and Energy under grant number 20Y1701B, HighV, and grant number 20M1905D, Enable. The authors want to thank the German Aerospace Centre in Stuttgart for their support and cooperation with regard to the fuel cell.

REFERENCES

[1] “H2FLY.” hy4.org
[2] “ZeroAvia.” zeroavia.com
[3] C. Werner, F. Gores, L. Busemeyer, J. Kallo, S. Heitmann, and M. Griebenow, “Characteristics of PEMFC operation in ambient- and low-pressure environment considering the fuel cell humidification,” *CEAS Aeronaut. J.*, vol. 6, no. 2, pp. 229–243, 2015, doi: 10.1007/s13272-014-0142-z.
[4] M. Henke, C. Willich, C. Westner, F. Leucht, R. Leibinger, J. Kallo, and K. A. Friedrich, “Effect of pressure variation on power density and efficiency of solid oxide fuel cells,” *Electrochim. Acta*, vol. 66, pp. 158–163, 2012, doi: 10.1016/j.electacta.2012.01.075.
[5] J. Schröter, T. Graf, D. Frank, C. Bauer, J. Kallo, and C. Willich, “Influence of pressure losses on compressor performance in a pressurized fuel cell air supply system for airplane applications,” *Int. J. Hydrogen Energy*, vol. 46, no. 40, pp. 21151–21159, 2021, doi: 10.1016/j.ijhydene.2021.03.218.
[6] J. Schröter, D. Steinbarth, C. Bauer, U. Reichmann, J. Kallo, and C. Willich, “Climate and pressure chamber for simulation of flight conditions.” Open Access Repositorium der Universität Ulm und Technischen Hochschule Ulm, 2021. doi: http://dx.doi.org/10.18725/OPARU-38012.

WHEC-2022
23rd World Hydrogen Energy Conference
June 26-30, 2022 - Istanbul

#423

THE OPTIMISATION OF GRAPHENE-BASED MICROPOROUS LAYERS FOR POLYMER ELECTROLYTE FUEL CELLS

*F.C. Lee [a *], M.S. Ismail [a, b **], D.B. Ingham [a], K.J. Hughes [a], L. Ma [a], A. El-Kharouf [e], M. Pourkashanian[a,b].*
[a] Energy 2050, Department of Mechanical Engineering, Faculty of Engineering, University of Sheffield, Sheffield S3 7RD, United Kingdom.
[b] Translational Energy Research Centre, University of Sheffield, Sheffield S3 7RD, United Kingdom
[e] Centre for Fuel Cell and Hydrogen Research, University of Birmingham, B15 2TT, United Kingdom

* Corresponding author: fclee1@sheffield.ac.uk

ABSTRACT
The viability of graphene-based microporous layers for polymer electrolyte fuel cells is critically assessed through detailed characterisation of the morphology, microstructure, and transport properties. Microporous layer composition was optimised by the fabrication of several hybrid MPLs produced from various ratios of graphene to Vulcan carbon black. Single cell tests were performed at various operating conditions: between 25 % and 100% relative humidity, and at 80°C, in order to give a detailed understanding of the MEA performance over a range of conditions.

Keywords: Polymer Electrolyte Fuel Cells; Graphene; Gas Diffusion Layers; Hydrogen

INTRODUCTION
Polymer Electrolyte Fuel Cells (PEFCs) are electro-chemical energy conversion devices capable of providing sustainable transport, stationary and portable solutions, owing to their high-power density and fast start-up time and operation at relatively low temperatures [1]. Currently, liquid water management remains one of the largest barriers limiting fuel cell efficiency and the wide scale deployment of PEFC; this is due to the problem of liquid water accumulation in the electrode which limits reactant transport [2,3], and also membrane dehydration leading to ohmic losses [4,5]. The microporous layer (MPL) of PEFC is widely acknowledged as a crucial, performance enhancing component [6] largely due to enhancing the removal of liquid water and the subsequent reduction flooding. Moreover, the MPL may decrease ohmic losses by increasing the interfacial contact between the gas diffusion layer (GDL) and the catalyst layer, thus enhancing catalyst utilisation, and maintaining membrane hydration [7].
Although the MPL has significantly improved the conversion efficiency and performance of the fuel cell, it still requires optimisation to minimise potential losses from the MPL/catalyst layer interface and from inadequate oxygen mass transport. A recent trend has seen graphene being explored as an alternative to carbon black in the MPL. Graphene is a two-dimensional monolayer of graphitic carbon atoms, with good mechanical stiffness and elasticity, as well as extremely high electrical conductivity and thermal conductivity [8]. Graphene has previously been explored as an MPL material by a few researchers both as a freestanding MPL [9] and conventionally applied to carbon substrate [10,11,12,13]. Mixing graphene with carbon black, or a mixture of graphene with different morphologies has the potential for a synergetic effect on MPL morphology and microstructure, and thus optimising cell performance. The purpose of this research is to develop a greater understanding of how composition affects MPL microstructure and morphology, and ultimately identifying strategies to improve fuel cell efficiency. Here we present the fabrication and characterisation of novel MPLs produced from graphene-based materials. In this research, microporous layers were produced from Nanene (2D Tech, Cheltenham) which is a high-purity graphene, Vulcan XR72C carbon black, and a combination of the two materials.

METHODOLOGY
The fabricated dual-layer GDLs were used as the cathodic GDLs. Toray TGP H-60 carbon paper (10% wt. PTFE treated, Fisher Scientific) was used to produce the dual-layer GDLs. The carbon powder used in the MPL ink were Vulcan XC 72 R whereas the few-layer graphene (FLG) powder used in this study was Nanene provided by 2-DTech Ltd. The hydrophobicity was achieved from the addition of 60 wt. % polytetrafluoroethylene dispersion. Table 1 lists the MPL compositions following drying and thermal treatment. The carbon composition by weight and MPL loading was kept constant at 80 wt. % carbon and 20 wt. % PTFE and at 2.0 mg cm^{-2}.

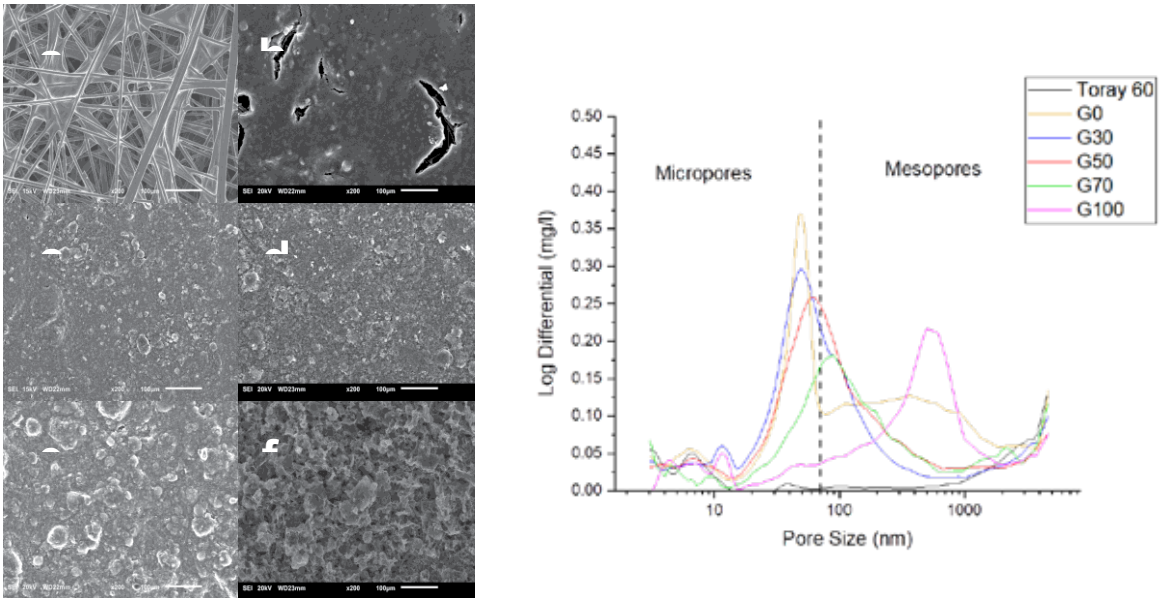
Table 1 Lists of the compositions of the microporous layer inks.

MPL	Vulcan Carbon black (wt.%)	Graphene nano-plates (GNP) (wt.%)	PTFE (wt. %)
G0	80	0	20
G30	56	24	20
G50	40	40	20
G70	24	56	20
G100	0	80	20

RESULTS AND DISCUSSION

Fig. 1a is a series of SEM micrographs showing the surface structure of the MPL coated and the uncoated Toray substrates; notable differences can be seen between the surface structure and morphology of the carbon black MPL and the graphene based.

The pore size distribution can be seen in Fig 1b, G0 (Vulcan MPL) has the typical pore profile of the conventional microporous layer: the majority of the pores are in the microporous region (50 nm). Conversely, G100 (GNP MPL) has a larger median pore size, with most pores occurring in the mesoporous region (500 nm). The inclusion of GNP to the MPL composition increases the average pore sizes in the MPL and leads to the formation of small mesopores in the layer. Interestingly, for the mixed composition MPLs, Vulcan is the dominant material in determining the average pore size. This is in line with the SEM micrographs which show that voids between the larger GNP are occupied by the smaller carbon black particles, and as such leads to the formation of micropores and reduction of mesoporous void space. G50 MPL has a desirable pore size distribution with a median pore size of 61nm, as it has an even distribution of micropores and mesopores. The adequate presence of micropores and mesopores may lead to enhanced performance at high relative humidity operation and current densities, thus enabling the simultaneous capillary wicking of liquid water to mitigate flooding at the cathode and improve reactant diffusion to the catalyst [14, 15].



(a) (b)

Fig. 1 (a) SEM micrographs of MPL coated and the uncoated GDLs (from top left): Toray H-060, G0, G30, G50, G70 and G100), (b) pore size distribution of the uncoated and coated GDLs by mercury intrusion porosimetry.

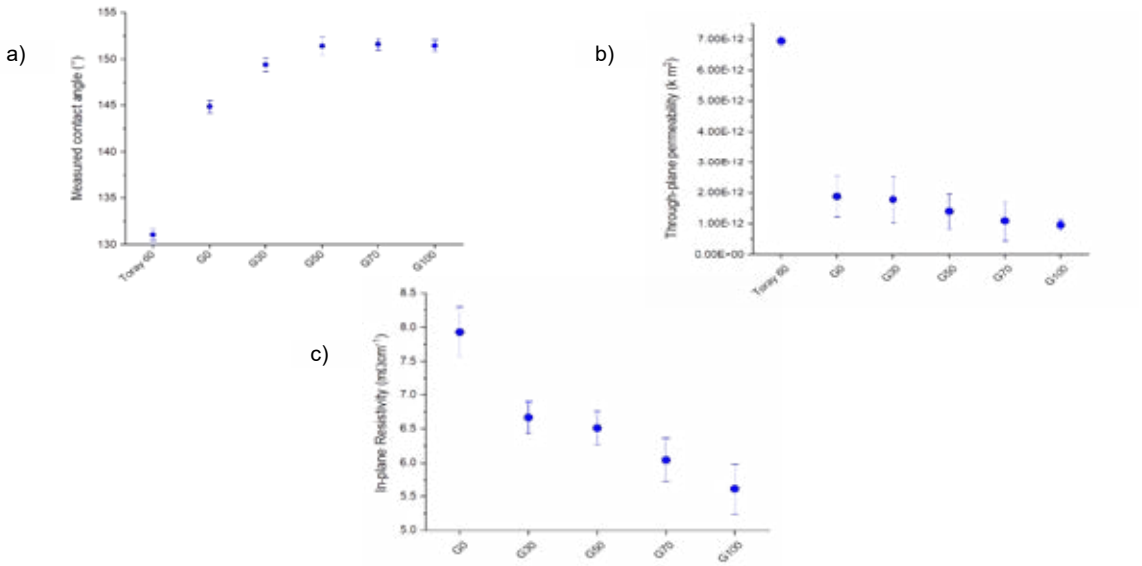


Figure 2: (a) The contact angle, (b) through-plane permeability and (c) in-plane electrical resistivity of the GDLs.

Fig 2(a) shows the contact angle measurements of the coated and uncoated GDLs. The uncoated carbon substrate is moderately hydrophobic (131˚) which is in good agreement with those reported in the literature (129 ± 9˚) [15]. Fig 2(a) indicates that G70 has the highest contact angle (~ 152˚). The inclusion of graphene in the MPL ink results in a higher contact angle; this is likely due to the horizontal stacking of the graphene nanoplates perpendicular to the water droplet. G0 has the lowest hydrophobicity with (145˚), although these values are not dissimilar and indicate that the determining factor in hydrophobicity is likely the PTFE (20 wt. %). The through-plane permeability decreases with graphene inclusion in the MPL; the graphene nanoplates lead to a greater resistance to air flow, this increase in resistance can be attributed to the morphology of the graphene flakes; their 2-dimenisonal geometry lends to dense, horizontal stacking of the graphene flakes in the MPL, which forms a sheet-like structure obstructing air flow in the through-plane direction. Similar findings are reported in [10].

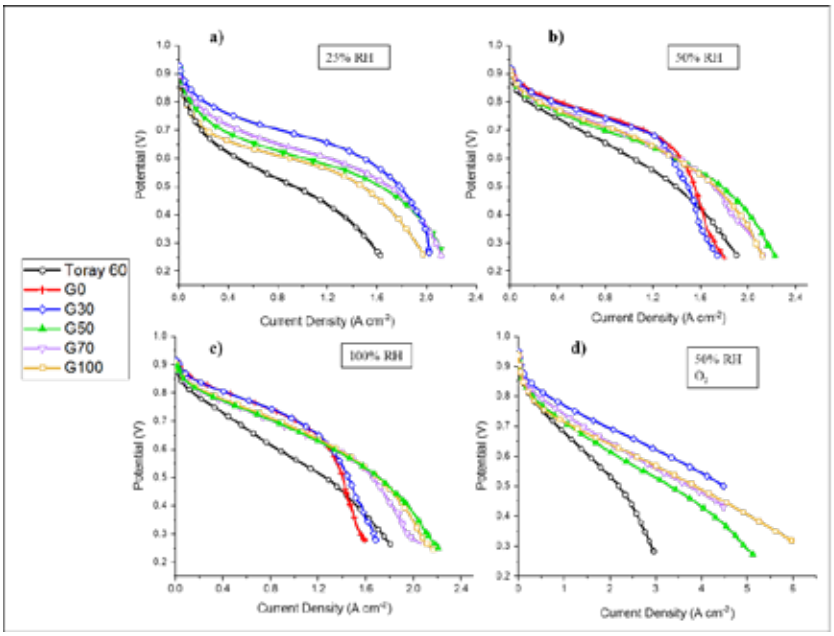


Figure 3: Polarisation curves of the MPL coated and uncoated GDLs at (a-c) 25%, 50%, and 100% relative humidity in air, and (d) 50% relative humidity in pure oxygen.

Polarisation curves were taken at 25%, 50% and 100% relative humidity in air, and 50% relative humidity in pure oxygen (Figs. 3a, b, c and d), at a constant cell temperature of 80°C. Fig 3a shows the polarisation curve of the GDLs at 25% relative humidity operation, where G30 MPL outperforms all the other MPLs. Under low humidity operating conditions, the ohmic losses caused by the membrane dry-out is the prevailing factor behind the degradation of the fuel cell. The high performance exhibited by G30 indicates that it is better than the other MPLs at retaining liquid water and preventing membrane dry-out. This is attributed to the larger proportion of micropores present in the G0 and G30 MPL that favour liquid water retention.

However, at 50% RH (fig 3b) G30 and the commercial G0 MPL start to experience significant potential drops at relatively high current density (> 1.2 A cm^{-2}). This is due to the inability of the above MPLs to reject excess liquid water produced at the cathode catalyst layer. This trend continues at 75% and 100% RH operation, where liquid water is more prevalent, thus it is clear that these performance losses are due to the inability of G0 and G30 to sufficiently divert liquid water away from the cathode catalyst layer. Larger inclusions of graphene in the MPL composition produce a higher limiting current density and greater power density in more humidified conditions (50%, 75% and 100% RH). Figs. 3b, c and d indicate that G50, G70 and G100 do not suffer the same potential drops that G0 and G30 experience in these conditions. It can be concluded that, under intermediate or high humidity conditions, the addition of 50% or above of GNP to the MPL has a positive impact on the fuel cell performance as evidenced from the lower mass transport losses and the increased limiting current density of the fuel cell.

CONCLUSIONS

Microporous layers were produced from graphene and carbon black, and a combination of the two materials in which the weight percentage of graphene was varied (0 %, 30%, 50%, 70% and 100%). The inclusion of graphene in the MPL was shown to increase the mean pore size, leading to the formation of mesopores in the layer. Polarisation curves were taken at different relative humidity operation. Inclusions of graphene at 50 wt. % and greater enhance fuel cell performance at higher relative humidity operation (50%, 75% and 100% RH), indicating that the addition of graphene in the microporous layer mitigates flooding and reduces mass transport losses.

REFERENCES

[1] B. C. H. Steele, “Materials technology in fuel cell development,” *Materials & Design*, vol. 11, no. 1, pp. 4–10, Feb. 1990, doi: 10.1016/0261-3069(90)90083-v.
[2] S.-J. Lee, S.-G. Kim, G.-G. Park, and C.-S. Kim, “Quantitative visualization of temporal water evolution in an operating polymer electrolyte fuel cell,” *International Journal of Hydrogen Energy*, vol. 35, no. 19, pp. 10457–10463, Oct. 2010, doi: 10.1016/j.ijhydene.2010.07.173.
[3] P. Deevanhxay, T. Sasabe, S. Tsushima, and S. Hirai, “In situ diagnostic of liquid water distribution in cathode catalyst layer in an operating PEMFC by high-resolution soft X-ray radiography,1`” *Electrochemistry Communications*, vol. 22, pp. 33–36, Aug. 2012, doi: 10.1016/j.elecom.2012.05.028.
[4] Q. Yan, H. Toghiani, and J. Wu, “Investigation of water transport through membrane in a PEM fuel cell by water balance experiments,” *Journal of Power Sources*, vol. 158, no. 1, pp. 316–325, Jul. 2006, doi: 10.1016/j.jpowsour.2005.09.013.
[5] V. Ramani, H. R. Kunz, and J. M. Fenton, “Investigation of Nafion®/HPA composite membranes for high temperature/low relative humidity PEMFC operation,” *Journal of Membrane Science*, vol. 232, no. 1–2, pp. 31–44, Mar. 2004, doi: 10.1016/j.memsci.2003.11.016.
[6] J. Zhou, S. Shukla, A. Putz, and M. Secanell, “Analysis of the role of the microporous layer in improving polymer electrolyte fuel cell performance,” *Electrochimica Acta*, vol. 268, pp. 366–382, Apr. 2018, doi: 10.1016/j.electacta.2018.02.100.
[7] J. P. Owejan, J. E. Owejan, W. Gu, T. A. Trabold, T. W. Tighe, and M. F. Mathias, “Water Transport Mechanisms in PEMFC Gas Diffusion Layers,” *Journal of The Electrochemical Society*, vol. 157, no. 10, p. B1456, 2010, doi: 10.1149/1.3468615.
[8] P. Avouris and F. Xia, “Graphene applications in electronics and photonics,” *MRS Bulletin*, vol. 37, no. 12, pp. 1225–1234, Nov. 2012, doi: 10.1557/mrs.2012.206.
[9] M. J. Leeuwner, D. P. Wilkinson, and E. L. Gyenge, “Novel Graphene Foam Microporous Layers for PEM Fuel Cells: Interfacial Characteristics and Comparative Performance,” *Fuel Cells*, vol. 15, no. 6, pp. 790–801, Sep. 2015, doi: 10.1002/fuce.201500031.
[10] A. Ozden, S. Shahgaldi, J. Zhao, X. Li, and F. Hamdullahpur, “Assessment of graphene as an alternative microporous layer material for proton exchange membrane fuel cells,” *Fuel*, vol. 215, pp. 726–734, Mar. 2018, doi: 10.1016/j.fuel.2017.11.109.
[11] A. T. Najafabadi, M. J. Leeuwner, D. P. Wilkinson, and E. L. Gyenge, “Electrochemically Produced Graphene for Microporous Layers in Fuel Cells,” *ChemSusChem*, vol. 9, no. 13, pp. 1689–1697, Jun. 2016, doi: 10.1002/cssc.201600351.
[12] M. J. Leeuwner, A. Patra, D. P. Wilkinson, and E. L. Gyenge, “Graphene and reduced graphene oxide based microporous layers for high-performance proton-exchange membrane fuel cells under varied humidity operation,” *Journal of Power Sources*, vol. 423, pp. 192–202, May 2019, doi: 10.1016/j.jpowsour.2019.03.048.
[13] M. Mariani, S. Latorrata, S. Patrignani, P. Gallo Stampino, and G. Dotelli, “Characterization of novel graphene-based microporous layers for Polymer Electrolyte Membrane Fuel Cells operating under low humidity and high temperature,” *International Journal of Hydrogen Energy*, vol. 45, no. 11, pp. 7046–7058, Feb. 2020, doi: 10.1016/j.ijhydene.2019.12.213.
[14] T. Tanuma, M. Kawamoto and S. Kinoshita, “Effect of properties of hydrophilic microporous layer (MPL) on PEFC performance,” *Journal of the Electrochemical Society*, vol. 161, no. 6, pp. F499- F503, Feb. 2017, doi: 10.1149/2.0371706jes.
[15] C. Fang and M. Chan, “Improving proton exchange membrane fuel cell performance with carbon nanotubes as the material of cathode microporous layer,” *International Journal of Energy Research,* vol. 40, no. 2, pp. 181- 188, Oct. 2015, doi: 10.1002/er.3445
[16] A. El-kharouf, T. J. Mason, D. J. L. Brett, and B. G. Pollet, “Ex-situ characterisation of gas diffusion layers for proton exchange membrane fuel cells,” Journal of Power Sources, vol. 218, pp. 393–404, Nov. 2012, doi: 10.1016/j.jpowsour.2012.06.099.

WHEC-2022
23rd World Hydrogen Energy Conference
June 26-30, 2022 - Istanbul

#1454

A STUDY ON CORROSION DURABILITY IMPROVEMENT OF CrAl COATED METAL BIPOLAR PLATE FOR PEMFC BY 3D LASER CLADDING METHOD

[1*] Ha Eun Kang, [1] Ji Hyeok Choi, [1] Hyeong Woo Min, [2*] Dong Joo Kim, [1*] Young Soo Yoon
[1]Department of Materials Science and Engineering, Gachon University, 1342 Seongnam-daero, Seongnam, Republic of Korea
[2] Department of Mechanical Engineering, Auburn University, Auburn, AL 36849, United States

*Corresponding author e-mail: benedicto@gachon.ac.kr

ABSTRACT

In the field of metallic bipolar plates for PEMFCs, since coating technology can achieve improved resistance and surface properties without changing the base material, numerous studies have been conducted. The cost of the vacuum coating process and corrosion resistance and electrical conductivity of the coating materials are still under discussion. In order to improve the corrosion resistance of metallic bipolar plates, we select materials and technologies that are in the spotlight at ATF and conduct convergence research. The 3D laser cladding method was applied to the base material as metallic bipolar plate and the CrAl binary alloy was coated to evaluate its performance.

Keywords: PEMFC, Bipolar Plates, Corrosion, 3D Laser Cladding, Coatings

INTRODUCTION

The proton exchange membrane fuel cells (PEMFCs) directly convert chemical energy into electrical energy, so the conversion efficiency is high, and the by-products after the reaction are clean and reliable power is produced [6]. The bipolar plate is one of the key components because it supplies and cuts off fuel and air to each pole, exhausts the reaction products from the cell, and exchanges heat generated in the electrochemical reaction. However, metallic bipolar plates, the surface is corroded in the fuel cell environment in an acidic environment, and metal ions are eluted, which contaminates the catalyst and membrane, thereby reducing PEMFC performance [2],[3]. On the other hand, 3D laser coating technology using CrAl alloy powder is considered and have been developed to enhance the oxidation resistance as accident tolerant fuel (ATF) under loss of coolant accident (LOCA) conditions [4],[5],[6]. This technology has the characteristics of forming a local molten area to minimize the heat-affected zone and to minimize deformation and damage of the base material. It is also evaluated as an efficient and economical protective coating technology compared to the vacuum coating process [5],[6],[7]. In addition, it has been reported that CrAl alloy coating was very effective in enhancing the oxidation resistance of metals at high temperatures [8]. Since Cr_2O_3 and Al_2O_3 can form on the surface of CrAl, so the possibility of further increasing oxidation resistance has been confirmed. [4],[6]. In this study, nuclear convergence technology and materials were implemented and evaluated to solve the corrosion problem of metallic bipolar plates.

COATING METHODS

The selection of the coating materials was based on the physical properties such as thermal conductivity and expansion, melting points and phase transformation behavior. For plate-shaped substrates, laser cladding parameters such as laser power, specimen velocity, powder injection and gas flow have been systematically discussed in previous studies [4],[5],[6]. The continuous wave (CW) diode laser (wavelength of 1062 nm) with a maximum power of 300 W (PF-1500F) and a power supply (Pwp14Y04K). The continuous wave (CW) laser (wavelength of 1062 nm) was applied with power ranged 80 to 250 W (PF-1500F), and the scanning speed ranged was adjusted 12 to 15 mm/s for the surface coating on stainless steels 316L (SS316L). To prevent any oxidation during the process, an inert gas (Ar) was continuously blowing into the melted surface of specimen. SS316L Bare plates were cut to a size of 60 mm × 60 mm × 0.1 mm. The substrates were molded using etching techniques. The CrAl coatings were deposited on the SS316L Bipolar plate using 3D Laser cladding coating method with CrAl powder (0.85Cr-0.15Al) and cleaned sonically in ethanol and acetone solution.

CORROSION TESTS

In the case of PEMFC system, it operates in the operating temperature range of 80–120 °C and the hydrogen ion concentration in the range of 2–4. In addition, a wet fuel injection environment promotes corrosion of the metal bipolar plates [6],[8]. Damage to the passivation film occurs due to various causes such as temperature, humidity, and pH, and eventually, ionic dissolution of the base material is derived. In response, potentiodynamic polarization test was conducted to confirm the corrosion behavior of bare SS316L and CrAl coated substrates in a sulfuric acid environment

in the PEMFC environment was simulated ex-situ conditions (0.5 M H_2SO_4, 80℃) [1],[8]. Potentiodynamic polarization is a method to test the corrosion reaction of fuel cell bipolar plates using the LSV technique. Measuring the current value in operating voltage range of the fuel cell, it is possible to know the active and the passivation region. The electrochemical process of corrosion potential and passivation behavior is determined by the Butler-Volmer equation and the Tafel plot. The Butler-Volmer equation is expressed for a current that varies with an applied voltage when the overall reaction rate is governed by the charge transfer process [1],[9].

$$I = I_0 \left[exp\left(\frac{-\alpha F\eta}{RT}\right) - exp\left(\frac{(1-\alpha)F\eta}{RT}\right)\right] \quad (1)$$

I : Electrode current density

α : Charge transfer coefficient

F : Faraday constant

H : Activation over potential (defined as $E–E_{eq}$)

R : universal gas constant

T : absolute temperature

RESULTS AND DISCUSSION

Fig 1. (a),(c) are the SEM images of the CrAl coated SS316L by 3D Laser cladding method. The coating layer appears 2.5 ㎛ thickness and no crack and void are observed on the surface. For a more detailed study of the coating layer, (b) and (c) confirmed the EDS profiles from the base substrate to the coating layer.These results indicate that the CrAl coating is composed of two compositions, Cr and Al, without elution of the base material on the surface. Moreover, in Fig 2, the XRD results of the surface can prove that there are no defects in the coating. Only Cr and CrAl components are detected on the surface. Aluminum is not identified here because the CrAl alloy is a Cr-based solid solution structure.

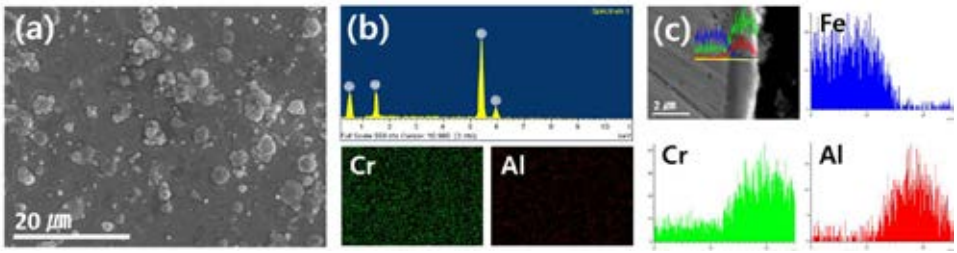


Fig 1. (a),(b) SEM image and EDS analysis of surface and (c) cross-sectional area

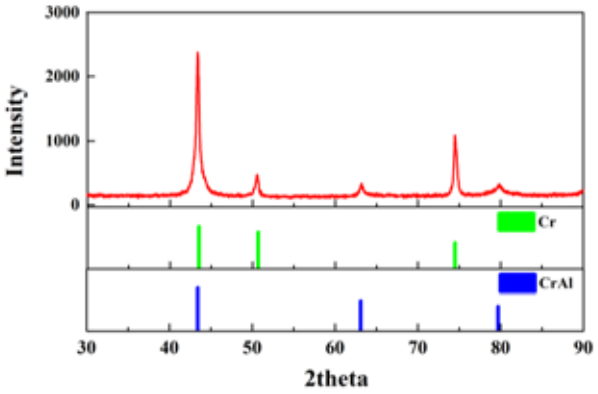


Fig 2. Surface XRD analysis of CrAl coated specimen

Potentiodynamic polarization curves of Bare SS316L (uncoated SS316L), CrAl on SS316L in the simulated acidic environment are shown in Fig 3. The corrosion behaviors of specimens are confirmed through the current value generated on the metal surface, and the potential at which the anode and cathode current become equal is expressed as the corrosion potential (E_{corr}). The corrosion potential means a potential value at which corrosion starts after the surface passivation film is formed. That is, the smaller the corrosion potential value, the greater the oxidation

tendency. the current density (I_{corr}) is larger, which means that the electron transfer due to the elution of ions is activated, which means that more corrosion occurs. In the LSV results, the corrosion potential value of the CrAl coated specimen was higher than that of stainless steel and the corrosion current was lower. These results showed that the CrAl coating had a positive effect on the corrosion inhibition properties compared to SS316L.

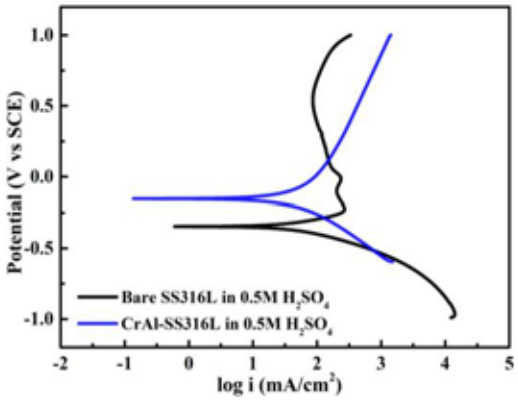


Fig 3. Polarization curves of bare SS316L and CrAl coated SS316L in 0.5 M H_2SO_4 solution at 80℃

CONCLUSIONS

3D Laser cladding coating technique is applied to CrAl on the surface of metal bipolar plates. The CrAl film as a protecting layer was successfully deposited on the SS316L bare substrate and uniform microstructure by laser cladding system. Moreover, In PEMFC acidic environment, CrAl coated SS316L was excellent high corrosion durability compared SS316L, which will form the basis for the electrochemical thin film process of the next generation of the bipolar plates for Fuel Cells. In this study, we demonstrated that ATF coating materials and coating Convergence techniques can also be applied in the fuel cell future industry. Especially, these studies could be open pathways to widely applied as bipolar plate and interconnector materials for fuel cells.

ACKNOWLEDGEMENT

This work was supported by Korea Institute of Energy Technology Evaluation and Planning(KETEP) grant funded by the Korea government(MOTIE)(2021400000690, GCU-AU Next-Generation Fuel Cell Development Program).

REFERENCES

1. Gür and Turgut M. 2018. Review of electrical energy storage technologies, materials and systems: challenges and prospects for large-scale grid storage. Energy & Environmental Science
2. Lynch and Benjamin and et al. 2020 Passivation-induced Cr and Mo enrichments of 316L stainless steel surfaces and effects of controlled pre-oxidation. Journal of The Electrochemical Society.
3. Olsson and C-OA. 2003. Dieter Landolt. Passive films on stainless steels chemistry, structure and growth. Electrochimica acta
4. Kim and Jeong-Min and et al. 2017. Microstructure and oxidation behavior of CrAl laser-coated Zircaloy-4 alloy. Metals
5. Lee and Kwan Geun, et al. 2017. Experimental Study of Pool Quenching with Zircaloy and CrAl-Coated Claddings.
6. Hyun-Gil Kim and et al. 2018. Out-of-pile performance of surface-modified Zr cladding for accident tolerant fuel in LWRs. Journal of Nuclear Materials
7. Hyun-Gil Kim and et al. 2015. Adhesion property and high-temperature oxidation behavior of Cr-coated Zircaloy-4 cladding tube prepared by 3D laser coating. Journal of Nuclear Materials
8. Chen and Cheng. 2016. Investigation of Cr–Al composite coatings fabricated on pure Ti substrate via mechanical alloying method: effects of Cr–Al ratio and milling time on coating, and oxidation behavior of coating. Journal of Alloys and Compounds
9. G. F. Knoll. 1999. Radiation Detection and Measurement, John Wiley & Sons, New York

WHEC-2022
23rd World Hydrogen Energy Conference
June 26-30, 2022 - Istanbul

#1455

INVESTIGATION OF WASTE HEAT RECOVERY FROM PROTON EXCHANGE MEMBRANE FUEL CELL USING ORGANIC RANKINE CYCLE WITH ZEOTROPIC

[1] Tahir Abdul Hussain Ratlamwala, [1] Muhammad Furqan Siddiqui, [1]Syed Muhammad Ali, [1]Muhammad Muneeb Vohra, [1]Abdul Sami, [1]Khurram Kamal*
[1]National University of Sciences and Technology, Islamabad, Pakistan

*Corresponding author e-mail: tahir.ratlamwala@pnec.nust.edu.pk

ABSTRACT

In view of the rapid depletion of fossil fuel sources and growing concerns on adverse environmental effects; including ozone depletion, global warming, sea-level rise and air-quality degradation. In last decade, there has been great endeavors to search for viable alternate energy resources. Fuel cells have shown great potential for energy production application because of their short start up time, low temperature operation and most importantly very little environmental cost of use. The present paper discusses the viability of using Organic Rankine Cycle (ORC) for waste heat recovery from Proton Exchange Membrane Fuel Cells (PEMFCs) is investigated. PEMFC and ORC system is modelled in Matlab® Simulink®. Thermodynamic property data of the working fluid is imported though Cool-Prop Python library. As the working fluid, suitability of multiple zeotropic mixtures is assessed. Finally, first law and second law thermodynamic analysis of the system is carried out. The developed ORC waste heat recovery system increased the overall power output of the system by 5.46 percent.

Keywords: PEMFC, Zeotropic, Matlab

INTRODUCTION

Polymer Electrolyte Membrane Fuel Cell (PEMFC) also called as Proto Exchange Membrane Fuel Cell (PMFC) are those fuel cells which were developed for the vehicles, and for the immobile fuel cell applications and transferable fuel cell applications. The thing that separate them from other cells are their low operating temperature and pressure and a specially made polymer electrolyte for the conduction of protons [1]. This technology will soon replace the old, alkaline type, batteries for the space shuttle application. These cells are clean energy as they have no impact on the environment. The wastage from these cells are water which is not harmful to the environment. Due to their high energy density these cells are now getting more and more sophisticated.

PMFC's are made of Built Electrode Assemblies also known as BEA which is composed of the electrolyte as medium for reaction, electrode (conductive material), catalyst to speed up the reaction and a diffused layer of gas. Catalyst, electrode and carbon are sprinkled or painted in the form of ink on to the solid electrolyte [2]. The hot pressing of the carbon paper is done on the inside to protect it and also to be used as an electrode. The TPB also known as the Triple Phase Boundary is a pivotal part, where all the part like catalyst, electrolyte and reactant mixes and thus the reaction starts [3]. The membrane of the cell should not be electrically conductive so that the half-cell reactions do not get mixed. The temperature of above 100 °C is desired, this to evaporate the water and management gets less critical.

SELECTION OF ZEOTROPIC MIXTURE

While selecting optimum zeotropic mixtures, not only thermodynamic properties are taken into account but the impact that they are going to inflict on environment is also considered. Some zeotropic mixture was befitting from the thermodynamic however they were rejected due to their hostile effect on environment. For thermodynamic viability, factor such as critical pressure and temperature were considered and for the environmental impact factors such as Global Warming Potential (GWP), toxicity, flammability and Ozone Depletion Potential (ODP) were taken into account. All the zeotropic mixtures were found to be non-flammable and nontoxic. [4].
The maximum temperature of the mixture on the turbine inlet is estimated around 343 K and pressure is estimated to be 3.0 MPa, therefore it is necessary to select those mixtures which fulfills this thermodynamic requirement because if the critical temperature of mixture is too high then it may not get become superheated. And further more compliance to the environmental safety standards is also considered necessary for selection. R-422 A and R-422 D were rejected due to their high GWP value. R-401 A was rejected due to its high ODP value. R-404 A was rejected due to its low critical temperature. A draw in terms of thermodynamic property is reached between R-407 C and 417 -A, but since 417-A had higher GWP value therefore final refrigerant selected is R-407C. Comparison summary is presented in Table 1.

Table 1 : Thermodynamic property and Environmental data of mixtures are shown.

Refrigerant	Critical temperature /K	Critical Pressure/MPa	Global Warming Potential (GWP)	Ozone Depletion Potential (ODP)
R 422 A	344	3.75	3144	0
R 404 A	345	4.9	2088	0
R 407 C	359	4.6	1774	0
R 417 A	361	4.03	2350	0
R 422 D	352.73	3.9	2730	0
R 401 A	380.4	4.6	1182	0.033

CONCLUSIONS

The use of Organic Rankine Cycle for waste heat recovery in PEMFCs is investigates in this paper. Models for the PEMFC and the Organic Rankine cycle were developed on Simulink and the performance of the system is studied under various input current values to the fuel cell.
As working fluid, zeotropic fluid R407C is used. The properties of the fluid at various stages of the cycle were calculated by implementing the Python Library of Cool Prop in MATLAB. The developed ORC waste heat recovery system increased the overall power output of the system by 5.46%.

REFERENCES

1. Erdinc O, Uzunoglu M., "Recent trends in PEM fuel cell-powered hybrid systems: Investigation of application areas, design architectures and energy management approaches," Renewable and Sustainable Energy Reviews, Elsevier, Vols. vol. 14(9), pages 2874.
2. P. Loyselle and K. Prokopius, "Teledyne Energy Systems, Inc., Proton Exchange Member (PEM) Fuel Cell Engineering Model Powerplant. Test Report: Initial Benchmark Tests in the Original Orientation," NASA, Glenn Research Center.
3. B. Millington, S. Du and B. G. (. Pollet, "The Effect of Materials on Proton Exchange Membrane Fuel Cell Electrode Performance," Journal of Power Sources. 196(21): 9013–017.
4. "Designation and Safety Classification of Refrigerants," ANSI/ASHRAE 34, 2001.

WHEC-2022
23rd World Hydrogen Energy Conference
June 26-30, 2022 - Istanbul

#1457

NUMERICAL INVESTIGATION ON THE EFFECTS OF INHOMOGENEOUS GAS DIFFUSION LAYER AND IMPACT OF INTERFACIAL CONTACT RESISTANCE ON PERFORMANCE OF POLYMER ELECTROLYTE FUEL CELLS

[1] *Umesh Shinde,* [1] *Pranav Padavu,* [1*] *Poornesh Kumar Koorata*
[1] Electrochemical Energy System Design Lab, Department of Mechanical Engineering,
National Institute of Technology Karnataka, Surathkal, Mangalore – 575 025, India

*Corresponding author e-mail: kpkoorata@nitk.edu.in

ABSTRACT

A three-dimensional single-channel is modeled numerically to simulate homogeneous and inhomogeneous gas diffusion layer (GDL). The effect of interfacial contact resistance (ICR) between flow field ribs and GDL is also studied. The present study involves GDL being considered as a single component (homogeneous) in one case while in another case, GDL being considered with varying porosities to depict the inhomogeneity. The inhomogeneity in GDL is assumed to occur due to localized deformation induced due to non-uniform contact pressure. The study reveals increased availability of reactants at higher current loads in the case where ICR is assumed negligible. This study explains how the presence and absence of ICR impact reaction concentrations, water concentration, current density and polarization curve of polymer electrolyte fuel cells. It is observed in polarization curve that the presence of ICR has effect both in ohmic and mass transport region. This work involves considering 4 cases viz: homogeneous GDL, inhomogeneous GDL, homogeneous GDL with ICR and inhomogeneous GDL with ICR.

Keywords: PEM Fuel Cell, Gas Diffusion Layer, Interfacial Contact Resistance, Porosity, Cell Performance.

INTRODUCTION

Among the several components in PEMFC, gas diffusion layer (GDL) is a crucial component which facilitates the transportation of reactant gases and water and supports the catalyst layer (CL). It also provides electronic contact with the flow fields in fuel cells [1,2]. The behaviour of gas diffusion layer is known to change based on various physical properties like interfacial contact resistance (ICR) with flow field ribs, permeability, porosity and bulk resistance [3–6]. It is observed that inhomogeneous GDL has localized variations on these properties, impacting the performance of PEMFC. The GDL is a porous material and it often undergoes high compression during assembly, leading to variation in material and geometrical properties.

Various studies have been carried out on the transport behaviour and performance of PEM fuel cells [7–10]. However, it is observed that limited studies have been carried out while considering transport behaviour when taking the interfacial contact resistance into effect. The ohmic losses occurring due to interfacial contact resistance between GDL and the flow field plays a significant role in fuel cell performance. To this end, the numerical study by Chen et al. [11] showed the impact of interface contact resistance on a three-dimensional, single-cell, single serpentine flow channel fuel cell model. It is revealed that with the increase of ICR the polarization curves affects both the ohmic and concentration region at lower voltages. Li et al. [12] numerically investigated a two-dimensional, two-phase flow fuel cell model considering the effect of electrical contact resistance. They observed that cell performance significantly decreased when interfacial contact resistance was considered. Hence it is observed that ICR does impact on the performance and various properties in fuel cell. Thus it is necessary to consider ICR effect while conducting numerical investigation on PEMFC.

Studies related to homogeneous and inhomogeneous GDL occurring majorly during assembly operation have been carried out earlier. Wang et al. [9] developed 3D numerical model of PEM fuel cell considering inhomogeneous compression effects of GDL. The results revealed that higher compression is helpful in heat removal but reduces cell performance in contrast. Hence, it becomes evident to have optimum compression that can improve fuel cell performance. Padavu et al. [13] studied the transport behaviour of depth-dependent flow channels considering GDL as inhomogeneous. They illustrated that inhomogeneous GDL has slight reduction in performance of fuel cell compared to homogeneous GDL. This behaviour is predicted to occur due to improved hydrogen oxidation reaction and reduced oxygen reduction reaction in inhomogeneous GDL case. Jha et al. [8] studied the effect of varying GDL porosity of fuel cells, considering it to be as inhomogeneous GDL. Their results revealed that GDL with porosity of 0.5-0.6 provides better performance, while it is seen to reduce at higher current densities when porosity exceeds 0.6

Based on the aforementioned brief literature, numerical studies on transport characteristics and fuel cell performance have been investigated, with GDL considered as either homogeneous or inhomogeneous. Few other studies considered the impact of ICR in their numerical investigation. However, the effects of inhomogeneous GDL and ICR

are not considered together in the numerical investigation as observed from the available literature. Hence this study focuses on bridging the gap between the two cases.

NUMERICAL METHODOLOGY

A three-dimensional single channel, multiphase, steady state with homogeneous and inhomogeneous GDL has been considered in the present study. Table 1 lists the various geometrical parameters. The grid size considered along the x direction is 20, in y direction is 55 (through plane), and in z direction (along channel) is 480.

Table 1. Single channel geometrical parameters

Parameter	Value	Parameter	Value
Fuel Cell Length	50 mm	BPP Height	1.5 mm
Fuel Cell Width	2 mm	GDL Thickness	0.3 mm
Flow Channel Width	1 mm	Catalyst Thickness	0.015 mm
Rib Width	1 mm	Membrane Thickness	0.05 mm

The properties for homogeneous and inhomogeneous GDL like porosity, permeability and ICR values have been imported from ref [4]. The governing equations considered in present work are conservation of mass, momentum, species, energy and charge (both ionic and electronic). The present numerical investigation is carried out in ANSYS Fluent (2020 R2). The stoichiometry at anode is 1.5 and cathode is 2. The gas flow inlet at anode and cathode is calculated using the mentioned stoichiometry. Reference current density considered is 1.0 A/cm^2.

RESULTS AND DISCUSSION

The performance of PEMFC with four different cases viz; homogeneous GDL, inhomogeneous GDL, homogeneous GDL with ICR and inhomogeneous GDL with ICR has been depicted in Fig. 1(a) The current densities for all the four cases coincide with each other above 0.65 V cell voltage. It is shown that the current densities at 0.2 V for homogeneous GDL is 1.1886 A/cm^2, inhomogeneous GDL is 1.1637 A/cm^2, homogeneous GDL with ICR is 1.1725 A/cm^2 and inhomogeneous GDL with ICR is 1.1551 A/cm^2.

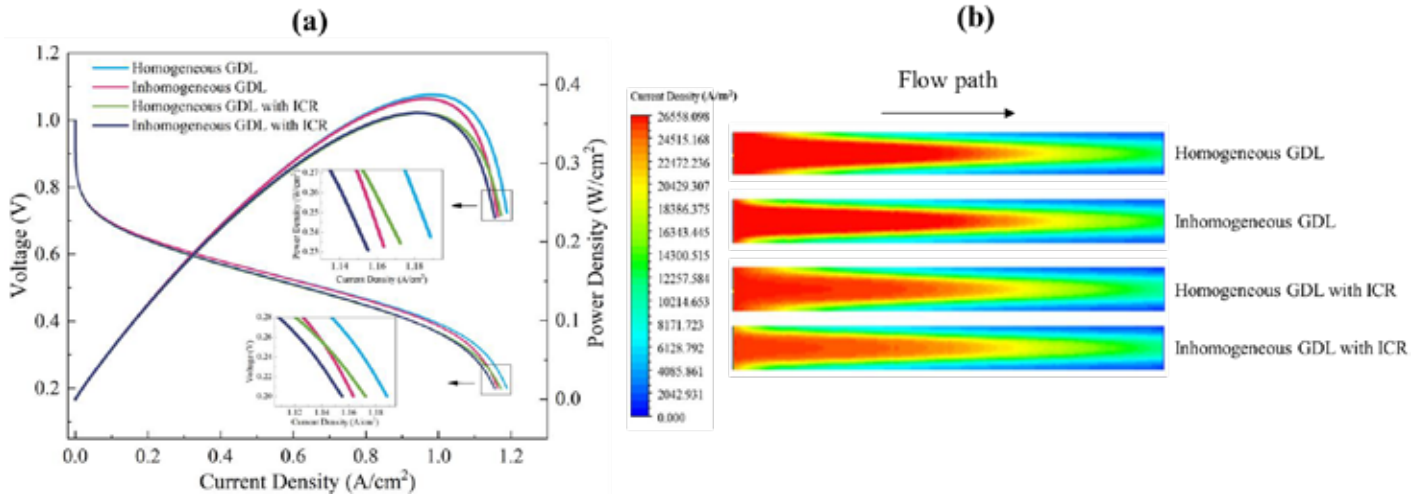


Fig. 1. (a) Cell performance of PEMFC at different cases, (b) Local current density at mid-section of membrane.

Similarly, power density at 0.2 V cell voltage for homogeneous GDL is 0.2377 W/cm^2, inhomogeneous GDL is 0.2327 W/cm^2, homogeneous GDL with ICR is 0.2345 W/cm^2 and inhomogeneous GDL with ICR is 0.2310 W/cm^2. Hence it is observed that the homogeneous GDL without ICR has maximum current density and power density. Whereas, inhomogeneous GDL with ICR has minimum current and power densities. The difference between considering ICR and absence of ICR is clearly visible in ohmic loss region and concentration loss region.

Results with respect to distribution of hydrogen mass fraction at anode, oxygen mass fraction at cathode, water mass fraction at cathode and current density at membrane show similar behavior (for reference local current density distribution is as shown in Fig. 1(b)). That is homogeneous GDL without ICR yields higher concentration of these species while inhomogeneous GDL with ICR yields lower. Therefore, it can be said that investigating transport

behaviour without ICR numerically is not the correct approach which can be considered as ideal case. In reality investigating with the effects of ICR and inhomogeneous GDL yields the correct results.

CONCLUSIONS

In this study, the impact of interfacial contact resistance with homogeneous and inhomogeneous GDL is investigated numerically. It involves investigating three-dimensional, steady state, multiphase, single flow channel transport behaviour. A PEFC with homogeneous without ICR provides best performance while PEFC with inhomogeneous with ICR results lower performance. Literature studies show that most of the numerical investigation are carried without considering ICR which is not the ideal approach since fuel cell performance is affected by resistance. Hence it is evident to consider ICR effects which helps in predicting realistic PEFC performance.

REFERENCES

[1] Zhang J, Zhang H, Wu J, Zhang J. 2013. PEM Fuel Cell Testing and Diagnosis.
[2] O'Hayre R, Cha S-W, Colella WG, Prinz FB. 2016.Fuel cell fundamentals.
[3] Sow PK, Prass S, Kalisvaart P, Mérida W. 2015. Deconvolution of electrical contact and bulk resistance of gas diffusion layers for fuel cell applications. Int J Hydrogen Energy 40:2850–61.
[4] Shinde U, Koorata PK. 2021. Numerical investigation on the sensitivity of endplate design and gas diffusion material models in quantifying localized interface and bulk electrical resistance. Int J Hydrogen Energy 46:17358–73.
[5] Qiu D, Peng L, Yi P, Lai X. 2017. A micro contact model for electrical contact resistance prediction between roughness surface and carbon fiber paper. Int J Mech Sci 124–125:37–47.
[6] Mukherjee M, Bonnet C, Lapicque F. 2020. Estimation of through-plane and in-plane gas permeability across gas diffusion layers (GDLs): Comparison with equivalent permeability in bipolar plates and relation to fuel cell performance. Int J Hydrogen Energy 45:13428–40.
[7] Hashemi F, Rowshanzamir S, Rezakazemi M. 2012. CFD simulation of PEM fuel cell performance: Effect of straight and serpentine flow fields. Math Comput Model 55:1540–57.
[8] Jha V, Hariharan R, Krishnamurthy B. 2020. A 3 dimensional numerical model to study the effect of GDL porosity on high temperature PEM fuel cells. Int J Heat Mass Transf 161:120311.
[9] Wang J, Yuan J, Sundén B. 2016. Modeling of inhomogeneous compression effects of porous GDL on transport phenomena and performance in PEM fuel cells. Int J Energy Res.
[10] Li S, Yuan J, Xie G, Sunden B. 2017. Numerical investigation of transport phenomena in high temperature proton exchange membrane fuel cells with different flow field designs. Numer Heat Transf Part A Appl 72:807–20.
[11] Zhou Y, Jiao K, Du Q, Yin Y, Li X. 2013. Gas diffusion layer deformation and its effect on the transport characteristics and performance of proton exchange membrane fuel cell. Int J Hydrogen Energy 38:12891–903.
[12] Li S, Wei R, Qi Y, Yang G, Shen Q. 2019. Effect of Electrical Contact Resistance on Performance and Transport Characteristics of Proton Exchange Membrane Fuel Cells. Int J Electrochem Sci 14:11367–78.
[13] Padavu P, Koorata PK, Bhat SD. 2021. Numerical investigation on the improved reactant mass transport with depth-dependent flow fields in polymer electrolyte fuel cell under inhomogeneous gas diffusion layer compression. Int J Heat Mass Transf 180:121796.

WHEC-2022
23rd World Hydrogen Energy Conference
June 26-30, 2022 - Istanbul

#1461

PERFORMANCE EVOLUTION OF PEM FUEL CELLS WITH STRAIGHT AND WAVY PARALLEL FLOW CHANNELS OF VARIOUS WAVELENGTHS USING CFD SIMULATION

[1] *Rashed Kaiser,* [1] *Gyu-Mok Jeon,* [1*] *Jong-Chun Park*
[1] Pusan National University, Dept. of Naval Architecture and Ocean Engineering, Busan, South Korea

*Corresponding author e-mail: jcpark@pnu.edu

ABSTRACT

Polymer electrolyte membrane fuel cell (PEMFC) is one of the emerging fuel sources which have the potential to replace the conventional fossil fuels continuously endangering the earths climate system. The purpose of this paper is to evaluate the performance and the reliability of PEMFCs with straight channel in comparison to three wavy channels in the basis of polarization curve, pressure drop and velocity on cathode channel. The higher pressure drop of wavy channels facilitates the water removal and improve the cell efficiency. Eventually the wavy channel with short wavelengths showed the best performance.

Keywords: Fuel Cell, Flow Channel, Wavelength, Pressure Drop, Water Accumulation.

INTRODUCTION

The performance of the PEMFCs mostly depends on the design of the flow channels as it determines the supply of adequate amount of oxygen and hydrogen on the diffusion layers while keeping the back pressures as low as possible for both flow channels for the sake of cell efficiency [1]. There exist a number of experiments [2-4] and simulations [5,6] to investigate the effect of flow field using various channel designs. Anyanwu et al. [2] compared the performance of a serpentine, interdigitated, parallel with straight and 2 wavy channels under different relative humidity and found that the high relative humidity enhanced the cell performance while wavy parallel channels showed the best performance considering pressure drop, cell performance and structural integrity. Cooper et al. [3] changed the dimensions of flow channel for an interdigitated and a parallel flow in order to obtain a design guideline for both configurations using statistical analysis. The effect of flow channel on water flooding and hydrodynamics also investigated experimentally [4], where serpentine flow channel showed more stable cell performance, less water accumulation and high pressure drop compared to an interdigitated and a parallel flow channel. The numerical analysis carried out by Atyabi et al. [5] showed that the higher-pressure drops lead to more uniform distribution of oxygen and better water management for wavy flow channel in comparison to straight parallel channel which results in high power densities. In the present study, as shown in Fig. 1, the flow characteristics and performance are investigated and compared for the PEMFCs with 1 straight channel and 3 wavy channels with different wave lengths, in terms of the cell performance, pressure drop and velocity of gas.

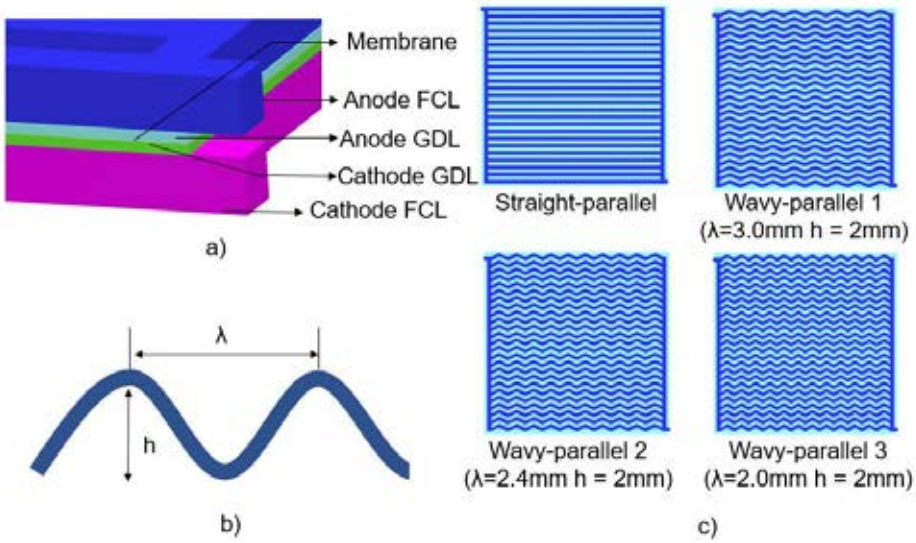
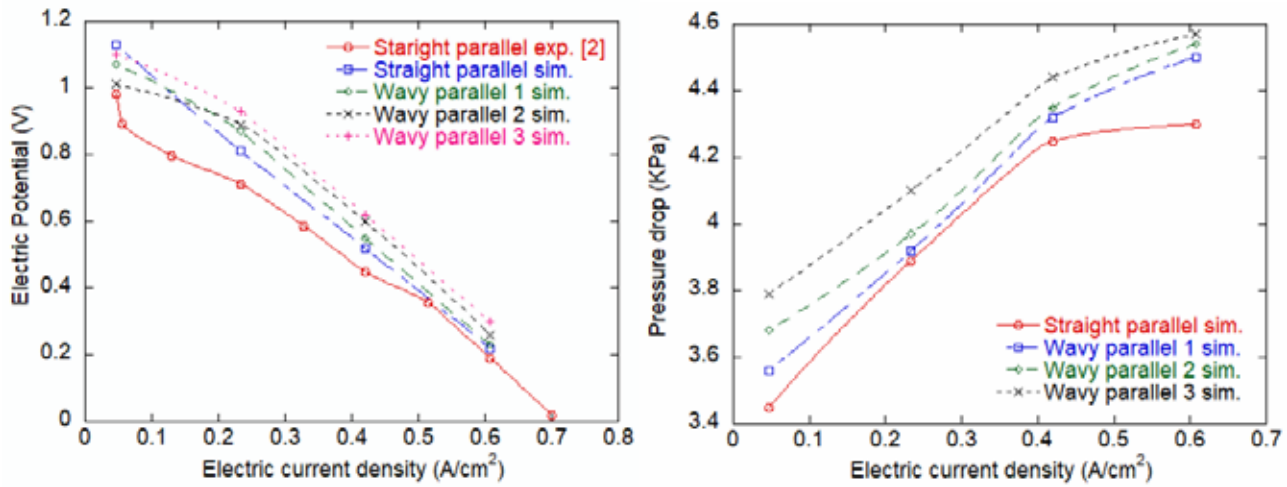


Fig. 1. a) Schematic view of PEMFC, b) parameters of wavy channel and c) front view of 1 straight and 3 wavy channels.

GEOMETRY AND MODEL IMPLEMENTATION

Fig. 1(a) shows the schematic view of PEMFC with parallel or sinusoidal flow field including gas flow channel layers (FCLs), gas diffusion layers (GDLs) and membrane, in which the area of the fuel cell is 25cm^2 (5cm×5cm) and channel dimension is 1 mm x 1mm. And (b) and (c) illustrate the parameters of sinusoidal wavy channel and the front view of 1 straight and 3 wavy channels, respectively. A mixture multiphase model of steady and laminar flow, which can solve simultaneously electrochemical reaction and heat transfer, was employed for gas flow channel and porous diffusion layers while solid membrane with ionic transport was considered in the membrane part. SIMCENTER STAR-CCM+ 16.04 was used for 3-D modeling and simulation of PEMFCs. A structured and directed mesh was generated (quadrilateral for straight channel and polygonal mesh for wavy channel). Catalyst layers were assumed as an infinite thin layer and not included in the mesh system, as suggested in previous research [7]. The relative humidity of the fuel cell was set to be maintained at 40%, and accordingly the mole fraction of hydrogen, oxygen, nitrogen and water vapor were reflected in the simulation conditions.

RESULTS AND DISCUSSION



a) b)

Fig. 2. a) Polarization curve and b) pressure drop at cathode channel at different current densities

The polarization curve along the electric current density for four different shapes of flow channel as shown in Fig. 2(a), where only the case of straight channel is validated through comparison with the experiment [2]. Although the overall trend of the slope looks similar to the experiment, the overestimation of the electric potential related to lack of bipolar plate seems to be made in the present simulation. Regardless of the higher conductivity, it has been observed that bipolar plates tend to decrease the potential of the entire cell by increasing ohmic losses. The case of wavy parallel 3 indicates the best performance among the flow channels. Fig. 2(b) shows the pressure drop on the cathode flow channel for different current densities. The pressure drop contributes the enhancement of cell performance by increasing the convective flow and removing the resultant water efficiently [2, 5]. It is understood that the pressure drop increases as the wavelengths decreases, and thus the velocity of gas also becomes high as shown in Fig.3. Therefore, it is seen that the diffusion through GDL is higher for wavy channels with short wavelength [5].

CONCLUSIONS

In this study, 4 different flow fields (1 straight and 3 wavy) in the channel of PEMFC were investigated using CFD simulation. The numerical result for the straight parallel channel was validated with the experiment. The wavier channel (wavy channel 3) showed the overall best performance while conventional straight channel acted as the worst candidate for large fuel cell stacks. The adequate pressure drops and relatively high velocity helps the wavier flow channel to increase the reaction rate and avoid water flooding inside the channel.

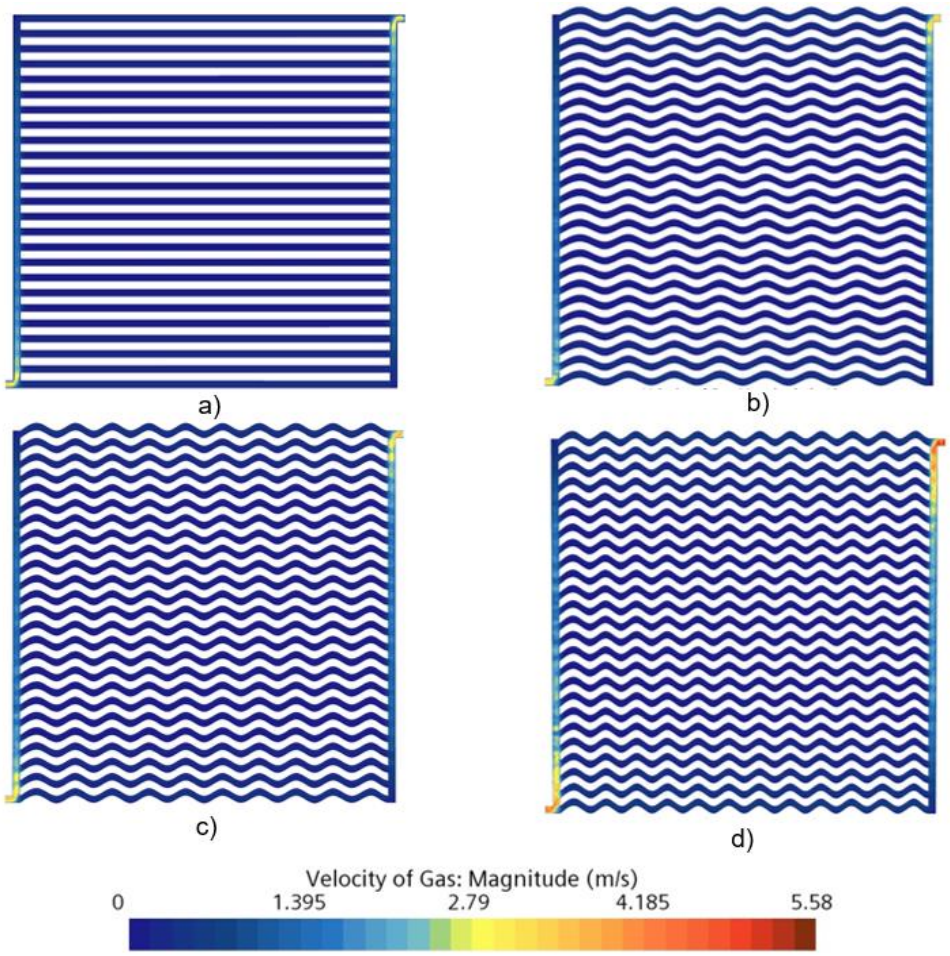


Fig. 3. a) Velocity distribution along the cathode channel for a) straight parallel, b) wavy parallel 1, c) wavy parallel 2 and d) wavy parallel 3

REFERENCES

1. Marappan, M., Palaniswamy, K., Velumani, T., Chul, K.B., Velayutham, R., Shivakumar, P. and Sundaram, S., 2021. Performance Studies of Proton Exchange Membrane Fuel Cells with Different Flow Field Designs–Review. The Chemical Record, 21(4), pp.663-714.
2. Anyanwu, I.S., Xie, X., Liu, Z. and Jiao, K., 2021. Experimental investigation and optimization of proton exchange membrane fuel cell using different flow fields. Energy, 217, p.119313.
3. Cooper, N.J., Smith, T., Santamaria, A.D. and Park, J.W., 2016. Experimental optimization of parallel and interdigitated PEMFC flow-field channel geometry. international journal of hydrogen energy, 41(2), pp.1213-1223.
4. Spernjak, D., Prasad, A.K. and Advani, S.G., 2010. In situ comparison of water content and dynamics in parallel, single-serpentine, and interdigitated flow fields of polymer electrolyte membrane fuel cells. Journal of Power Sources, 195(11), pp.3553-3568.
5. Atyabi, S.A. and Afshari, E., 2019. A numerical multiphase CFD simulation for PEMFC with parallel sinusoidal flow fields. Journal of Thermal Analysis and Calorimetry, 135(3), pp.1823-1833.
6. Anyanwu, I.S., Hou, Y., Xi, F., Wang, X., Yin, Y., Du, Q. and Jiao, K., 2019. Comparative analysis of two-phase flow in sinusoidal channel of different geometric configurations with application to PEMFC. International Journal of Hydrogen Energy, 44(26), pp.13807-13819.
7. d'Adamo, A., Riccardi, M., Borghi, M. and Fontanesi, S., 2021. CFD Modelling of a Hydrogen/Air PEM Fuel Cell with a Serpentine Gas Distributor. Processes, 9(3), p.564.

WHEC-2022
23rd World Hydrogen Energy Conference
June 26-30, 2022 - Istanbul

#1464

SUPERHYDROPHOBIC FLUORINATED CARBON FOR IMPROVED MICROPOROUS LAYERS IN POLYMER ELECTROLYTE FUEL CELLS

[1*] *Enes M.CAN*, [2,3] *Kazunari Sasaki*, [1,3,] **Stephen M. Lyth*
[1]Department of Automotive Science, Kyushu University, Fukuoka, Japan
[2] Next-Generation Fuel Cell Research Center (NEXT-FC), Kyushu University, Fukuoka, Japan
[3] International Research Center for Hydrogen Energy, Kyushu University, Fukuoka, Japan

* *Stephen M. Lyth*: lyth@i2cner.kyushu-u.ac.jp

ABSTRACT

Flooding is one of the major issues in polymer electrolyte fuel cells (PEFCs), especially under high current density operation. Therefore, gas diffusion layers (GDLs) coated with hydrophobic microporous layers (MPLs) are usually employed to decrease water saturation at the cathode side of the cell. In this study, fluorinated carbon powders are synthesized to create superhydrophobic microporous layers to facilitate water management and prevent flooding. Fluorinated carbons are synthesized by a solvothermal method and characterized by various technics techniques. Then, either fluorinated carbon or commercially available carbon black are formed into a slurry and screen printed onto a commercial GDL to form MPLs. These MPLs are then characterized by water contact angle measurements, air permeability tests, and oxygen transport resistance measurement. Furthermore, their performance in a PEFC is evaluated using I-V measurements in a PEFC under various conditions. The results indicate that fluorinated carbon based MPLs are superhydrophobic, leading to lower oxygen transport resistance and significantly higher fuel cell efficiency compared to conventional carbon black.

Keywords: PEFC, Microporous Layer, Fluorinated Carbon Powder, Superhydrophobicity

INTRODUCTION

Polymer electrolyte fuel cell systems (PEFCs) running on hydrogen are one of the most promising clean energy conversion technologies for a carbon-neutral society. Gas diffusion layers (GDLs) are employed at both electrodes to transport reaction gases and remove the products. At the cathode side of the PEFC, under the high current density operation, excessive water accumulation inside of the gas diffusion media hinders the transportation of oxygen to the catalyst layer [1,2]. This phenomenon decreases the PEFC performance significantly. To overcome this, GDLs are usually coated with a hydrophobic microporous layer (MPL) comprising carbon black and a polytetrafluoroethylene (PTFE) binder [3,4]. However, the use of PTFE can negatively impact the conductivity and gas diffusion properties of the MPL. In this study, we synthesize superhydrophobic fluorinated carbon (SHFC) as an alternative MPL material with a view to improve the water-repelling properties of the MPL.

EXPERIMENTAL

Superhydrophobic fluorinated carbon powder was synthesized by reacting fluorinated alcohol with sodium metal at elevated temperature in a sealed PTFE crucible [5]. After the reaction, the product was already carbonized. The product powder was washed in an ethanol / water mixture for 24 hours. The product was then vacuum-filtered and dried at 65°C. The yield was ~20%. Superhydrophobic fluorinated carbon was characterized by X-ray photoelectron spectroscopy (XPS, PHI 5000 Versa probe (II) ULVAC) to prove fluorination of carbon and morphologic structure of carbon was observed by scanning electron microscopy (FE-SEM, JSM-7900F). Furthermore, thermal stability of SHFC was analyzed by thermogravimetric analysis (Rigaku Thermo plus EVO2 TG8121) under the air

RESULTS AND DISCUSSION

Fig 1. shows a scanning electron microscopy (SEM) image of the fluorinated carbon. The morphology comprises spheroidal nanostructures with an average particle size of around 100 µm.

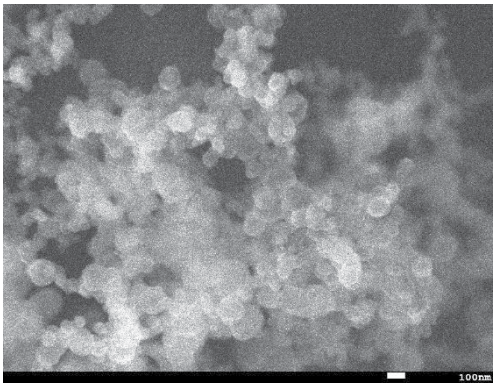


Fig. 1. SEM images of superhydrophobic fluorinated carbon

X-ray photoelectron spectroscopy (XPS) revealed an atomic concentration of ~89 at% carbon, ~10 at% fluorine, and ~1 at% oxygen, with trace amounts of sodium contamination. XPS also indicated that the fluorine atoms are mainly covalently bonded to carbon. Energy dispersive X-ray analysis (EDX) revealed lower fluorine content (2 at%) compared to XPS, suggesting that fluorination occurs mainly near the surface of the particles. X-ray diffraction (XRD) showed that SHFC is largely non-crystalline. From the XRD, EDX and TEM results, it is concluded that small amounts of sodium fluoride are trapped in the structure of the SHFC, which could not be removed by extensive washing in water and ethanol.

The synthesized SHFC powder was then coated onto a GDL substrate and employed as an MPL material, using PTFE as a binder. Water contact angle measurement results revealed that superhydrophobic fluorinated carbon based MPL has a water contact angle of around 151° while the identically prepared carbon black based MPL has a water contact angle of 130°.

Single fuel cell performance tests were conducted at 100% relative humidity conditions and two different cell temperatures (45° and 80°) (Fig.2). Compared to carbon black, the SHFC-based MPLs showed significantly higher I-V performance in the high current density region, suggesting improved water management due to the hydrophobic nature of the MPL material.

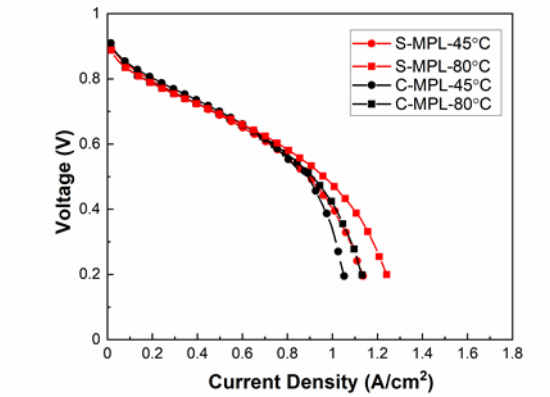


Fig.2. Single fuel cell performance test results of superhydrophobic fluorinated carbon (S-MPL) and conventional carbon black based MPL (C-MPL)

CONCLUSIONS

In this paper, fluorinated carbon was synthesized with a solvothermal method and used as MPL material to create superhydrophobic MPL with low PTFE loading. Its performance was evaluated and compared with conventional carbon black based MPL. Results indicate that it is possible to increase the hydrophobicity of the MPL by employing fluorinated carbons as an MPL material. Superhydrophobic fluorinated carbon based MPL with 5 wt% PTFE binder shows a much higher hydrophobicity than conventional carbon black based MPL. Due to the superhydrophobicity of superhydrophobic fluorinated carbon based MPL, its water-repellent characteristic increased significantly, which has led to higher fuel cell performance under high relative humidity conditions.

ACKNOWLEDGEMENT

The authors gratefully acknowledge the support of Ministry of National Education of Republic of Türkiye. This study was partially supported by NEDO (Contract No. JPNP20003).

REFERENCES

[1] H. Li, Y. Tang, Z. Wang, Z. Shi, S. Wu, D. Song, J. Zhang, K. Fatih, J. Zhang, H. Wang, Z. Liu, R. Abouatallah, A. Mazza, A review of water flooding issues in the proton exchange membrane fuel cell, J. Power Sources. 178 (2008) 103–117. https://doi.org/10.1016/j.jpowsour.2007.12.068.
[2] J.T. Gostick, M.A. Ioannidis, M.W. Fowler, M.D. Pritzker, On the role of the microporous layer in PEMFC operation, Electrochem. Commun. 11 (2009) 576–579. https://doi.org/10.1016/j.elecom.2008.12.053.
[3] M.S. Ismail, T. Damjanovic, D.B. Ingham, M. Pourkashanian, A. Westwood, Effect of polytetrafluoroethylene-treatment and microporous layer-coating on the electrical conductivity of gas diffusion layers used in proton exchange membrane fuel cells, J. Power Sources. 195 (2010) 2700–2708. https://doi.org/10.1016/j.jpowsour.2009.11.069.
[4] T. Kitahara, H. Nakajima, Microporous layer-coated gas diffusion layer to reduce oxygen transport resistance in a polymer electrolyte fuel cell under high humidity conditions, Int. J. Hydrogen Energy. 41 (2016) 9547–9555. https://doi.org/10.1016/j.ijhydene.2016.04.117.
[5] S.M. Lyth, W. Ma, J. Liu, T. Daio, K. Sasaki, A. Takahara, B. Ameduri, Solvothermal synthesis of superhydrophobic hollow carbon nanoparticles from a fluorinated alcohol, Nanoscale. 7 (2015) 16087–16093. https://doi.org/10.1039/c5nr03484a.

WHEC-2022
23rd World Hydrogen Energy Conference
June 26-30, 2022 - Istanbul

#1489

INVESTIGATING THE WATER FLOODING EFFECTS ON THE PERFORMANCE OF LOW-TEMPERATURE PROTON EXCHANGE MEMBRANE FUEL CELLS

[1] *Akshaykumar N. Desai,* [2] *Surajeet Mohanty,* [1*] *Venkatasailanathan Ramadesigan,* [1] *Suneet Singh,* [2] *Shaneeth M.*
[1] Department of Energy Science and Engineering, Indian Institute of Technology Bombay, Mumbai, 400076, India
[2] Fuel cell development division, Vikram Sarabhai Space Centre, ISRO, Thiruvananthapuram, 695022, India

*Corresponding author e-mail: venkatr@iitb.ac.in

ABSTRACT

Liquid water flooding in low-temperature proton exchange membrane fuel cells (LT-PEMFCs) is one of the key issues, significantly reducing its performance. This study investigates the impact of water flooding on the reactant transport across the porous domain, active surface area of the catalyst layer (CL), and membrane water content. The main objective of this work is to estimate the LT-PEMFC performance in the mass transport region using a 3-D, multiphase, non-isothermal, physics-based model. The model is validated using the data obtained from experiments performed on a 32 cm^2 area LT-PEMFC with the hybrid flow configuration. The results show that the multiphase model with a root mean square current density error of 39 mA/cm^2 is in good agreement with the experimental results compared to the single-phase model with an RMS current density error of 60 mA/cm^2. The substantial drop in O_2 mass fraction from 0.95 at the flow channels to 0.14 at the CL at 0.4 V cell potential indicates a reduction in reactant transport due to the liquid water. On the other hand, water generation helps to improve water content inside the membrane, which increases the membrane's ionic conductivity from 1.5 to 5.3 S/m with a decrease in cell potential.

Keywords: Low-Temperature Proton Exchange Membrane Fuel Cell, 3-D Physics-Based Model, Multiphase Flow, COMSOL Multiphysics

INTRODUCTION

Low-temperature proton exchange membrane fuel cells (LT-PEMFCs) have emerged as a clean energy solution in the transportation sector and as backup power generators in deep space missions. For higher current density operations, the mass transport limitation is one of the major hurdles in the LT-PEMFC performance enhancement. It arises from the liquid water generated during the electrochemical reactions, which hinders the reaction sites of the catalyst layer (CL) and oxygen transport in the gas diffusion layer (GDL) [1]. The liquid water flooding may accelerate the degradation of the membrane electrode assembly (MEA) due to the hydrophobic material loss and platinum dissociation [2]. Though 1-D [3] and 2-D [4] models are quite simplified and quick, they are not useful for understanding water dynamics inside the cell while altering the flow configurations. Meng et al. [5] observed that the single-phase model over-predicts the cell performance by 20% compared to the multiphase single-channel model. However, this performance disparity requires a detailed analysis from the experimental and a detailed modeling perspective. In most of the studies, the full-fledged multiphase model containing the flow configuration is not studied and validated with the experimental results.

The current study aims at estimating the LT-PEMFC performance in the mass transport region considering multiphase phenomena. Using the governing equations and correlations from the numerical and experimental studies in the literature, we develop a comprehensive 3-D, multiphase, non-isothermal, steady-state physics-based model of the LT-PEMFC that can closely predict the experimental results. A hybrid flow configuration is used for the anode and cathode sides of the LT-PEMFC. The simulations are performed using the COMSOL Multiphysics, and the experiments are conducted on the LT-PEMFC to validate the model. The cell performance is characterized through the polarization curve, concentration profile, and water content across the flow channel, GDL, and CL.

MATHEMATICAL MODEL OF THE LT-PEMFC

The computational domain of the LT-PEMFC is comprised of the membrane, GDL, CL, and flow channels on the cathode and anode sides. The physics-based model is developed coupling the fundamental phenomena such as electrochemical reactions, transport of reactant species, porous media flow, heat generation, liquid water transport, and charge transfer. Fig. 1 shows the computational domain and cross-section of the LT-PEMFC. The total area of the cell is 32 cm^2, with a channel length of 55 mm and a channel width of 1 mm. The thickness of the GDL, CL, and membrane is 0.4 mm, 0.02 mm, and 0.127 mm, respectively. Primary operating parameters used in the experiments and physics-based model are shown in Table 1. The remaining parameters like diffusivity, relative permeability, active surface area, ionomer water diffusion and water drag coefficient are calculated from the liquid water saturation correlations [3, 4].

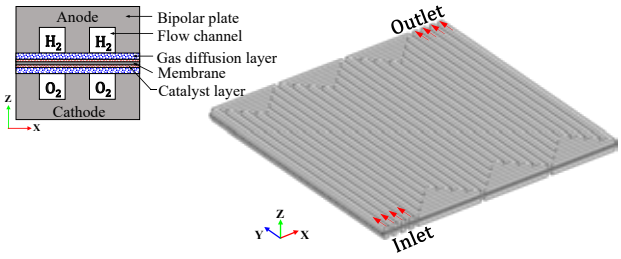


Table 1 Parameters used for the LT-PEMFC model

Parameter	Symbol	Value
Operating temperature, pressure	*T, P*	40[°C], 1[atm]
Relative humidity	*RH*	75 %
Porosity of GDL, CL	ε	0.4, 0.3
Inlet mass flow rate of H_2 and O_2	$\dot{m}$	2, 3 [lpm]

Fig. 1 Computational domain and cross-section of the LT-PEMFC

Governing Equations

For brevity, equations are not included in the text. However, they are described here with relevant references. Porous media flow using the Brinkman equation and gaseous species transport using Fick's law of diffusion are implemented for the GDLs, CLs, and flow channels [3]. The ionic conductivity of the Nafion® membrane is calculated using the power-law with Arrhenius temperature correction [6]. The current conservation equations are used for the ionic and electronic phases with the modified Butler-Volmer equation to obtain the I-V relation and mass transportation losses [4]. The heat transfer in various components of the HT-PEMFC is computed through the energy equation, including the heat generation due to electrochemical reaction and internal resistance. The water transport across the membrane is modeled combining the back diffusion due to concentration gradient and electro-osmotic drag due to potential gradient [3]. Darcy's law with the differential relation between the capillary pressure and saturation is implemented for the liquid water transport inside the cathode [3].

RESULTS AND DISCUSSION

Based on the computational geometry and operating parameters, the actual cell with a hybrid flow configuration is manufactured and assembled in the lab. Fig. 2(a) compares the polarization curve of the present multiphase model, single-phase model, and the experiments. The validation study suggests that the present multiphase model with an RMS current density error of 39 mA/cm^2 estimates the LT-PEMFC performance better than the single-phase model with an RMSE of 60 mA/cm^2. The maximum relative error in the current density is 4% with multiphase model and 12.5% with single-phase model. The results show that the multiphase model closely approximates the mass transport region identified between 0.6 and 0.4 V cell potential. An increment in water content inside the membrane is observed in Fig. 2(b) with a decrease in cell potential due to rapid electrochemical reactions and resultant water generation. The rise in water content enhances the ionic conductivity of the membrane from 1.5 S/m at 1 V to 5.3 S/m at 0.4 V cell potential, lowering the ohmic overpotential of the cell. At the same time, the increased water generation adversely affects the overall cell performance by impeding the reactant transport.

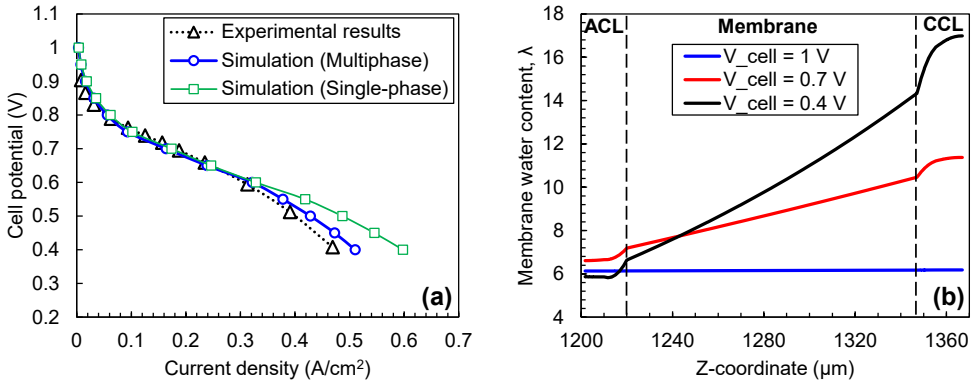


Fig. 2 (a) Validation of the present multiphase model with experimental results (b) Water content across the MEA at different potentials

The O_2 mass fraction and liquid water saturation on the cathode side of the LT-PEMFC are shown in Fig. 3. It is observed that the oxygen mass fraction substantially drops from 0.95 at the flow channels (Fig. 3(a)) to 0.14 at the CL (Fig. 3(b)) at 0.4 V cell potential. At lower cell potential (higher current density), the rapid electrochemical reactions consume a large quantity of oxygen and generate water. Some water moves towards the anode side due to back-diffusion. The remained liquid water floods the porous media and covers the reaction sites of the CL, as shown in

Fig. 3(c), which leads to performance deterioration of the LT-PEMFC. AA' line shows the central portion of the cell at which the water saturation is depicted.

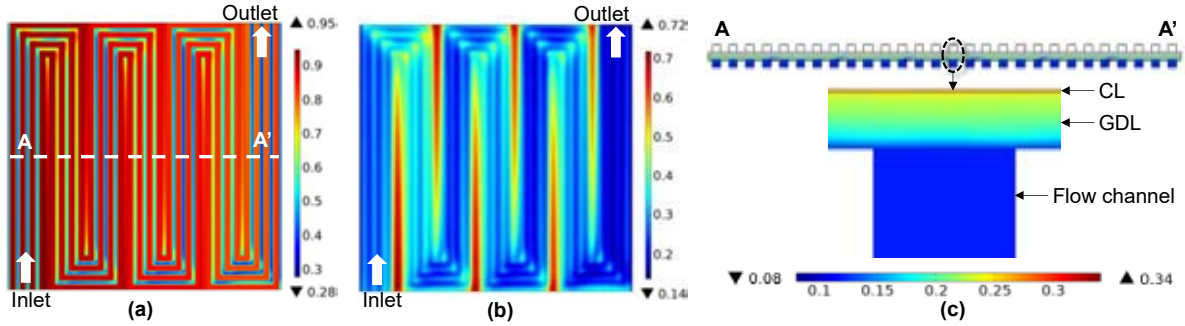


Fig. 3 (a) O_2 mass fraction at the flow channel-GDL interface (b) O_2 mass fraction at the GDL-CL interface (c) liquid water saturation at AA' section for 0.4 V cell potential

CONCLUSIONS

In the present study, a 3-D, non-isothermal, multiphase, steady-state physics-based model of the LT-PEMFC is developed to study the performance in the mass transport region considering the electrochemical reactions, transport phenomena, porous media flow, heat generation, liquid water transport, and charge transfer. The effect of liquid water flooding is analyzed on the crucial parameters like the active surface area of CL, porosity, permeability, water content, and diffusivity of the reactants. The validation study confirms that the present model estimates the LT-PEMFC performance with greater accuracy than the single-phase model. A significant reduction in the O_2 mass fraction from the flow channels (0.95) to the CL (0.14) suggests the liquid water impeding the reactant transport and deteriorating the LT-PEMFC performance. The liquid water can be effectively removed from the cell by implementing different flow configurations, increasing the hydrophobicity of GDL, and raising the operating temperature and reactant flow rate. The findings from this work can be used to design an efficient flow configuration, which enhances the LT-PEMFC performance. The developed model will be used to study the membrane deformation due to the shrinking-swelling under the humidification and thermal cycling and GDL-CL deformation due to clamping force.

ACKNOWLEDGEMENT

This work has been funded by the Indian Space Research Organization (ISRO) in collaboration with the Indian Institute of Technology Bombay (IITB) under ISRO-IITB Space Technology Cell grant no. RD/0120-ISROC00-008.

REFERENCES

1. Wang XR, Ma Y, Gao J, Li T, Jiang GZ, Sun ZY. 2021. Review on water management methods for proton exchange membrane fuel cells. International Journal of Hydrogen Energy 46(22):12206–12229.
2. Pan Y, Wang H, Brandon NP. 2021. Gas diffusion layer degradation in proton exchange membrane fuel cells: Mechanisms, characterization techniques and modelling approaches. Journal of Power Sources 513:230560.
3. Vetter R, Schumacher JO. 2019. Free open reference implementation of a two-phase PEM fuel cell model. Computer Physics Communications 234:223–234.
4. Zhang H, Rahman MA, Mojica F, Sui P, Chuang PA. 2021. A comprehensive two-phase proton exchange membrane fuel cell model coupled with anisotropic properties and mechanical deformation of the gas diffusion layer. Electrochimica Acta 382:138273.
5. Meng H, Wang C-Y. 2005. Model of Two-Phase Flow and Flooding Dynamics in Polymer Electrolyte Fuel Cells. Journal of The Electrochemical Society 152(9):A1733–A1741.
6. Weber AZ, Newman J. 2004. Transport in Polymer-Electrolyte Membranes II. Mathematical Model. Journal of The Electrochemical Society 151(2):A311–A325.

WHEC-2022
23rd World Hydrogen Energy Conference
June 26-30, 2022 - Istanbul

#1493

MICROWAVE-ASSISTED SYNTHESIS OF POROUS CARBON FROM PEANUT SHELLS

[1]Hilal Doğan, [1]Tuğba Meşeli, [1*]Gamze Genç, [1]Gülşah Elden
[1]Erciyes University, Engineering Faculty, Department of Energy Systems Engineering, 38039 Kayseri, Turkey

*Corresponding author e-mail: gamzegenc@erciyes.edu.tr

ABSTRACT

Porous carbon materials have been more attractive and promising ones since their outstanding properties such as high surface area, accessible active sites, mass transport, diffusion. This study aims to synthesize bio-carbon based catalysts via the microwave method and KOH activation agent. By the reason of the abundant of Peanut shells in Turkey besides being an important agricultural by-product, they were used as a carbon source in this study. The obtained carbon was analyzed by Brunauer - Emmett - Teller (BET), X-ray diffraction (XRD), Raman spectroscopy.

Keywords: Porous Carbon, Electrocatalyst, Biomass, Peanut Shell.

INTRODUCTION

Peanut shell has an important potential in the world (6.49 million tons/year) and in Turkey (24.50 thousand tons/year) [1]. Considering that the values are high, it can be evaluated that peanut shell is an important waste plant biomass resource. Peanut shells have a high carbon content and are a suitable raw material for carbon synthesis [2]. Carbon materials play an important role in the development of alternative, clean and sustainable energy technologies. Bio-carbon-based materials can be a good alternative to commercial carbon materials when used as catalysts in various fields because of their high surface area, abundant porous structure, low cost, and environmentally friendly nature [3-9].

Although there are a lot of methods used in the synthesis of biomass-derived carbon materials, the microwave-assisted chemical activation method is commonly preferred in recent times due to its important advantages such as high carbon yield, improved porous carbon quality and high energy efficiency. Furthermore, it is an environmentally friendly method because of minimizing the formations and emissions of hazardous materials [10]. The objective of this research is to develop carbon-based catalysts with less expensive and simple experimental methods by employing peanut shells as a natural carbon source instead of fossil sources. Microwave assisted chemical activation method was applied as method.

EXPERIMENTAL

Materials and Chemicals

Peanut shells (PS) belonging to Osmaniye region in Turkey were used. Potassium hydroxide (KOH), isopropanol, hydrochloric acid (HCl) and sulfuric acid (H_2SO_4) Sigma-Aldrich and Merck Chemicals brands were used.

Synthesis of Porous Carbon

The experimental scheme for synthesis of porous carbon from peanut shells is given in Figure 1. After the peanut shell was washed with copious amounts of distilled water (DW) as firstly, it was dried at 105°C. The particle sizes were reduced by grating, and then pulverized in a mortar. The obtained peanut powder was mixed with a H_2SO_4 solution having a volume of 50 ml and molarity of 9 in a magnetic stirrer at room temperature during 48 hours. At the end of this duration, powder is filtered and was washed with DW. The filtered sample was mixed with the sample (1:3 - sample:KOH) and it was kept in the microwave at 700 W for 5 minutes. It was finally washed with hot and cold DW and 2M HCl until pH neutral. The resulting product was named PS-PC1. In order to reveal the effect of sonication process, it was further PS-PC1 sample was washed with isopropanol and distilled water and probe sonication having a time of 60 min was applied in solution of 10% H_2SO_4. This resulting product was named PS-PC2.



Fig 1. Synthesis of porous carbon from peanut shells

RESULTS AND DISCUSSION

The PS-PC samples properties obtained from PS were investigated by various characterizations. Firstly, the carbon content of the peanut shell was found as 48.19% via elemental analysis. Raman spectroscopy, XRD and BET analysis were used to show and compare the sonication and microwave treated porous carbon structures. Fig. 2a and b shows the Raman spectra and XRD pattern of both types of porous carbons (PS-PC1 and PS-PC2), respectively.

According to the Raman spectroscopy, as the D-band shows the C–C bond stretching vibrations (sp^3 vibrations) in the structure, the G band shows C=C bond in-plane stretching vibrations (sp^2 vibrations). The default peak values for carbon structures are 1340 and 1580 cm^{-1} for D and G bands, respectively. As is apparent from Fig.2a, while the low-intensity peak values in the D-band for PS-PC1 and PS-PC2 are 1340 and 1343 cm^{-1}, respectively, the peak values in G band are 1584 and1580 cm^{-1}. It is seen that these results are corresponded with literature [11]. The results of XRD patterns shown in Fig. 2b confirm the amorphous nature. Fig. 2b shows XRD spectrum peaks that are around 22.6°, indicating the lower graphitization degree of the sample. 43°4 indicates the availability of honeycomb-like structures formation in PS-PC carbons [12-13].

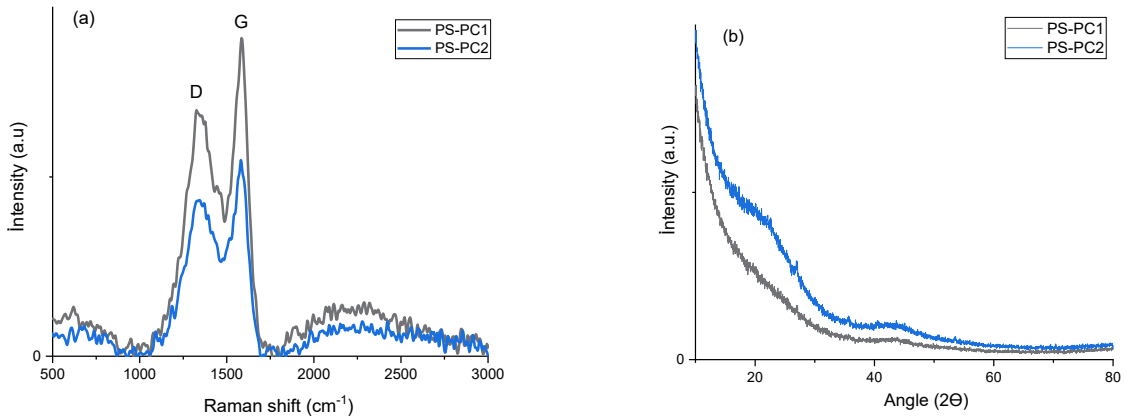


Fig 2. (a) Raman spectra; and (b) XRD pattern of PS-PC1 and PS-PC2

The specific surface area, porosity volume and pore size for PS-PC1 and PS-PC2 are given in Table 1. The surface area of PS-PC2 was higher than PS-PC1. It can be said that the sonication process has positive effect on the surface area.

Table 1. BET surface area, total pore volume and pore size of PS-PC1 and PS-PC2.

Sample Name	Surface Area [m^2g^{-1}]	Total Pore Volume [cm^3g^{-1}]	Pore Size [Å]
PS-PC1	1052.66	0.70	26.4
PS-PC2	1155.81	0.76	26.3

CONCLUSIONS

In the presented study, it was aimed to obtain a carbon source from peanut shell with two different techniques. Porous carbons were successfully synthesized using peanut shells by acid-treatment and chemical activation methods. The main conclusions can be given briefly as follows:

- Porous carbons with a high surface area were synthesized.
- The probe ultrasonication process had a significant effect on the specific surface area of porous carbon.
- Materials with rich porosity have an elevated specific surface area (SBET) leading to high active place density.

Consequently, the porous carbons obtained from peanut shells, which are a renewable biomass source, can be used in fuel cells and energy storage devices.

ACKNOWLEDGEMENT

The authors would like to thank the Scientific Research Projects Unit of Erciyes University for funding and supporting the project under the contract numbers: FDK-2021-11005. The first named author Hilal DOĞAN thanks the Scientific and Technological Research Council of Turkey for their scholarships under the “2211-C Priority Areas Ph.D. Scholarship Program (grant number 1649B032100138).” Hilal DOĞAN and Tuğba MEŞELİ also thanks the Turkish Higher Education Institution YÖK 100/2000 Ph.D. Scholarship Program.

REFERENCES

1. Gül, Ü. D., & Yıldız, Y. 2020. Yüzey Aktif Madde ile Modifiye Edilmiş Atık Yer Fıstığı Kabuğunun Tekstil Boyası Biyosorpsiyonu Kapasitesinin Belirlenmesi. Turkish Journal of Agricultural and Natural Sciences, 7(3), 533-539.
2. Boyluca, M. 2019. Yer fıstığı kabuğundan hazırlanan karbon türevi malzemelerin hidrojen depolama kapasitelerinin belirlenmesi. Balıkesir Üniversitesi Fen Bilimleri Enstitüsü.
3. Yadav, N., et al. 2018. High performance quasi-solid-state supercapacitors with peanut-shell-derived porous carbon. Journal of Power Sources. 402: p. 133-146.
4. Murali, G., et al. 2019. Hierarchically porous structured carbon derived from peanut shell as an enhanced high rate anode for lithium ion batteries. Applied Surface Science. 492: p. 464-472.
5. He, X., et al., 2013. Facile preparation of mesoporous carbons for supercapacitors by one-step microwave-assisted $ZnCl_2$ activation. Materials Letters, 94: p. 158-160.
6. Volperts, A., Plavniece, A., Dobele, G., Zhurinsh, A., Kruusenberg, I., Kaare, K., ... & Norkus, E. 2019. Biomass based activated carbons for fuel cells. Renewable Energy, 141, 40-45.
7. Wang, H., Yu, W., Shi, J., Mao, N., Chen, S., & Liu, W. 2016. Biomass derived hierarchical porous carbons as high-performance anodes for sodium-ion batteries. Electrochimica Acta, 188, 103-110.
8. Kaur, P., Verma, G., & Sekhon, S. S. 2019. Biomass derived hierarchical porous carbon materials as oxygen reduction reaction electrocatalysts in fuel cells. Progress in Materials Science, 102, 1-71.
9. Varathan, P., Akula, S., Moni, P., & Sahu, A. K. 2020. Natural aloe vera derived Pt supported N-doped porous carbon: A highly durable cathode catalyst of PEM fuel cell. International Journal of Hydrogen Energy, 45(38), 19267-19279.
10. Ao, W., Fu, J., Mao, X., Kang, Q., Ran, C., Liu, Y., ... & Dai, J. 2018. Microwave assisted preparation of activated carbon from biomass: A review. *Renewable and Sustainable Energy Reviews*, *92*, 958-979.
11. Wang, K., Cao, Y., Wang, X., Kharel, P. R., Gibbons, W., Luo, B., ... & Metzger, L. 2016. Nickel catalytic graphitized porous carbon as electrode material for high performance supercapacitors. Energy, 101, 9-15.
12. Xu, Wenjie, et al. 2017. "Optimization of organic pollutants removal from soil eluent by activated carbon derived from peanut shells using response surface methodology." Vacuum 141 : 307-315.
13. Purkait, T., Singh, G., Singh, M., Kumar, D., & Dey, R. S. 2017. Large area few-layer graphene with scalable preparation from waste biomass for high-performance supercapacitor. Scientific reports, 7(1), 1-14.

WHEC-2022
23rd World Hydrogen Energy Conference
June 26-30, 2022 - Istanbul

#1494

FACILE SYNTHESIS FOR POROUS CARBON FROM BIOMASS SUGARCANE BAGASSE

[1] Tuğba Meşeli, [1] Hilal Doğan, [1*] Gülşah Elden [1] Gamze Genç
[1]Erciyes University, Engineering Faculty, Department of Energy Systems Engineering, 38039 Kayseri, Turkey

Corresponding author e-mail: gulsah@erciyes.edu.tr

ABSTRACT

This study presents the synthesis of porous carbon from the sugarcane bagasse precursor. Carbon material obtained from sugarcane bagasse was synthesized by two different methods. In the first method, Sugarcane was carbonized without pretreatment and then impregnated with KOH. In the second method, It was activated with KOH. The surface areas of the prepared carbon materials were determined by Brunauer Emmet-Teller and the vibrational modes of the material properties were examined by Raman Spectrum analysis. The specific surface area of porous carbons was found at 646.96 m^2/g and 566.96 m^2/g, respectively.

Keywords: Biomass, Sugarcane Bagasse, Porous Carbon

INTRODUCTION

The interest in materials obtained from renewable resources is constantly increasing owing to the search for new materials in the energy sector and the increasing environmental awareness of both the industry and the public. More efficient and environmentally friendly energy solutions stand out with the use of renewable energy sources. Among renewable energy sources, biomass is a renewable resource that covers a wide variety of materials with significant energy potential [1,2]. Moreover, biomass-derived carbon materials show unique chemical, mechanical and thermal stability with high surface area. Sugarcane Bagasse *(Saccharum officinarum) (SB)* is biomass that plays an important role in the development of sustainable processes and the production of value-added materials due to its diversity of biomass composition and high carbon content.

SB is fibrous lignocellulosic biomass that consists of a cheap and very rich carbon source [3]. SB composes of approximately 48% cellulose, 29% hemicellulose, 24% lignin, moisture and less than 2% ash [4,5,6]. The cellulose-hemicellulose-lignin complex is degraded during pretreatment. Therefore, pretreatment of lignocellulosic materials is necessary. With the pyrolysis process, functional groups containing large amounts of oxygen in cellulose and hemicellulose are easily converted to H_2O, CO and CO_2, producing microporous carbon [7,8]. Thus, biobased carbon materials can be produced efficiently from this material. However, the production of material from sugarcane can be highly variable due to several factors such as local farming conditions, harvesting practices (i.e. equipment type, process, season, sunlight, harvest time, fertilizers and weather), storage conditions, age, environmental problems and pretreatment processes [9].

In this study, it is aimed to compare some similarities and differences affecting the properties of both pre-treated and untreated carbon materials obtained from SB precursors.

MATERIALS AND METHODS

Materials and Sample Preparation

In the experimental studies, sugarcane supplied from Kocaeli was used. After the sugarcane was firstly peeled and shredded, it was dried at a temperature of 105°C for 1 week in the oven in order to remove the water and unwanted volatile components. The dried product was sifted to obtain at average particle size of 1 mm. The obtained samples finally were stored in glass bottles at the room temperature and dry place.

Carbon Material Synthesis from Sugarcane Precursor

The synthetic scheme of porous carbon from sugarcane biomass employed to produce the target carbon is shown in Fig. 1. SB was firstly carbonized with a tube furnace at 400 °C for 2 h with an increment in temperature of 5 °C/min under the N_2 atmosphere at 0.2 L/min. The obtained biochar precursor was impregnated with KOH solution (C: KOH, 1:3 wt%) by stirring at 25 °C for 12 h, and then the mixture was treated under the hydrothermal condition at 120 °C for 6 h. After this process, the mixture was dried, which was followed by pyrolysis at 750 °C with a temperature rise of 5 °C/min under N_2 atmosphere at 0.2 L/min for 2 hours. The final product (SB-PC-1) was washed several times separately with HCl solution (0.1 M) and deionized water until the pH value was approximately 7. Carbon material was also

synthesized under the same conditions after SB fiber was further purified by a three-step acid-alkali-acid technique to compare (SB-PC-2).

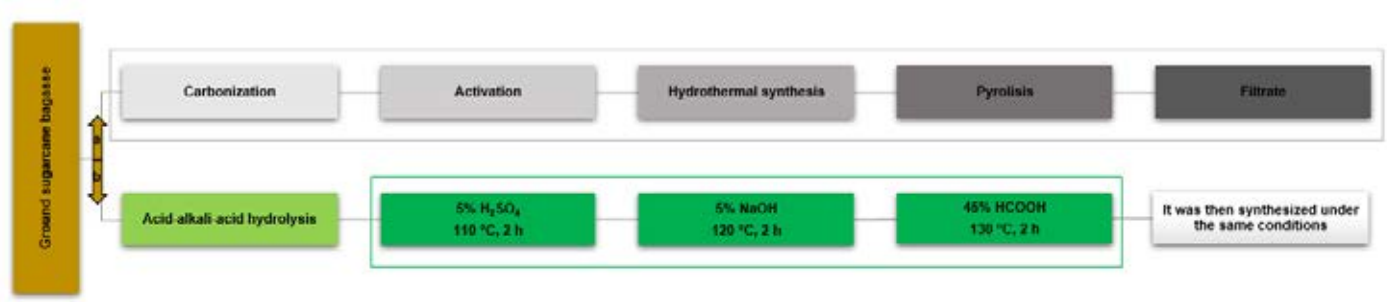


Fig. 1. Illustration of the synthesis scheme of porous carbon from sugarcane biomass a) SB-PC-1 b) SB-PC-2

RESULTS AND DISCUSSION

In this study, elemental analysis was firstly performed to evaluate the composition, properties and suitability of SB biomass. The carbon content of the crude SB biomass was 40.49%. A porosity was occurred on the carbon materials because of Chemical activation using KOH. SB-PC-1 and SB-PC-2 samples were characterized by Raman analysis to exhibit the vibration modes of material characteristics. Raman spectra of the prepared SB-PC samples are shown in Fig. 2. As is apparent from the Fig. 2, the samples have the sharpness band in value of 1576-1584 cm^{-1}, and this is known as G band been composed of sp^2 bonded carbon. Also in Fig. 2., it can be seen a distinct band around 1335-1355 cm^{-1}. This band shows a D band that is composed of sp^3 bonded carbon. Moreover, I_D/I_G value reflects the level of disorder in graphitic structure. A higher I_D/I_G value signifies a higher disorder, whereas a lower value shows less disorder in the graphitic plane [10]. The I_D/I_G ratio of SB-PC-2 is higher than SB-PC-1, indicating that the pre-treatment increases the defect of the material. The specific surface areas of SB-PC-1 and SB-PC-2 were found to be 648 m^2/g and 566.96 m^2/g, respectively, using BET analysis.

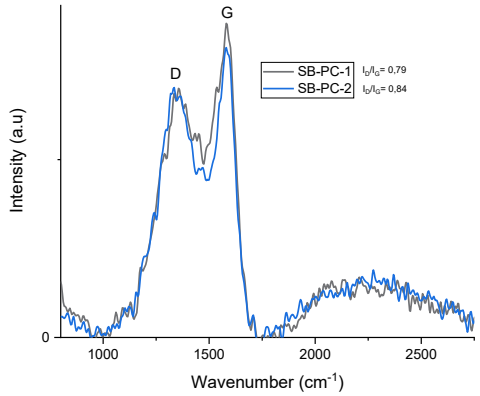


Fig. 2. Raman spectra of SB-PC-1 and SB-PC-2 samples

CONCLUSIONS

In the presented study, a simple and cost-effective hydrothermal assisted way to prepare porous carbon from sugarcane bagasse has been developed. This study highlights the benefit of pre-treatment for the preparation of porous carbon with a tuned surface chemistry that improves biochar properties. Sugarcane raw fiber was hydrolyzed by a three-step acid-alkaline-acid technique and so disorder in graphitic structure increased. The presence of defects aids in the transmission of electrolyte ions and increases transmission efficiency. In conclusion, the synthesized carbon materials can be applied in fuel cells and energy storage devices as a renewable, cost-effective and environmentally friendly electrocatalyst material.

ACKNOWLEDGEMENT

The authors would like to thank the Scientific Research Projects Unit of Erciyes University under the contract numbers: FHD-2021-11141 for funding. The first named author Tuğba MEŞELİ thanks the Scientific and Technological Research Council of Turkey for their scholarships under the “2211-C Priority Areas Ph.D. Scholarship Program (grant

number 1649B032103050).” Tuğba MEŞELİ and Hilal DOĞAN also thanks the Turkish Higher Education Institution YÖK 100/2000 Ph.D. Scholarship Program.

REFERENCES

1. Tsamba, A. J., Yang, W., & Blasiak, W. (2006). Pyrolysis characteristics and global kinetics of coconut and cashew nut shells. Fuel Processing Technology, 87(6), 523-530.
2. Tang, X., Liu, D., Wang, Y. J., Cui, L., Ignaszak, A., Yu, Y., & Zhang, J. (2021). Research advances in biomass-derived nanostructured carbons and their composite materials for electrochemical energy technologies. Progress in Materials Science, 118, 100770.
3. Miranda, N. T., Motta, I. L., Maciel Filho, R., & Maciel, M. R. W. (2021). Sugarcane bagasse pyrolysis: a review of operating conditions and products properties. *Renewable and Sustainable Energy Reviews*, *149*, 111394.
4. Yao, S., Nie, S., Yuan, Y., Wang, S., & Qin, C. (2015). Efficient extraction of bagasse hemicelluloses and characterization of solid remainder. *Bioresource Technology*, *185*, 21-27.
5. Mahmud, M. A., & Anannya, F. R. (2021). Sugarcane bagasse-A source of cellulosic fiber for diverse applications. *Heliyon*, *7*(8), e07771.
6. Kumar, A., Kumar, V., & Singh, B. (2021). Cellulosic and hemicellulosic fractions of sugarcane bagasse: Potential, challenges and future perspective. *International Journal of Biological Macromolecules*, *169*, 564-582.
7. de Moraes Rocha, G. J., Nascimento, V. M., Goncalves, A. R., Silva, V. F. N., & Martín, C. (2015). Influence of mixed sugarcane bagasse samples evaluated by elemental and physical–chemical composition. *Industrial Crops and Products*, *64*, 52-58.
8. Um, J. H., Ahn, C. Y., Kim, J., Jeong, M., Sung, Y. E., Cho, Y. H., ... & Yoon, W. S. (2018). From grass to battery anode: agricultural biomass hemp-derived carbon for lithium storage. *RSC advances*, *8*(56), 32231-32240.
9. Singh, S. P., Jawaid, M., Chandrasekar, M., Senthilkumar, K., Yadav, B., Saba, N., & Siengchin, S. (2021). Sugarcane wastes into commercial products: Processing methods, production optimization and challenges. *Journal of Cleaner Production*, *328*, 129453.
10. Yu, K., Wang, J., Wang, X., Liang, J., & Liang, C. (2020). Sustainable application of biomass by-products: Corn straw-derived porous carbon nanospheres using as anode materials for lithium ion batteries. Materials Chemistry and Physics, 243, 122644.

WHEC-2022
23rd World Hydrogen Energy Conference
June 26-30, 2022 - Istanbul

#1498
EVALUATION OF ETHANOL MICROFLUIDIC DEVICE AT LOW ELECTROCATALYSIS LOADING

*A. Martínez-Lázaro[1], J. Ledesma-García[1], L.G. Arriaga[2] and A. Arenillas[3]**
[1]División de Investigación y Posgrado, Facultad de Ingeniería, Universidad Autónoma de Querétaro, 76010, Querétaro, México.
[2]Centro de Investigación y Desarrollo Tecnológico en Electroquímica, 76703, Santiago de Querétaro, México.
[3]Instituto de Ciencia y Tecnología del Carbono, INCAR-CSIC. Francisco Pintado Fe, 26. 33011 Oviedo, Spain.

*Corresponding author e-mail: aapuente@incar.csic.es

ABSTRACT

Microfluidic fuel cells (MFCs) have received a great deal of attention in the last two decades for their high utility and versatility in portable electronics devices. Microfluidic-fuel cell technology used a liquid electrolyte, which show a great advantage compared to cells that include conventional polymer membranes (physical barrier). To date, different MFC configurations have been designed, in which ethanol have been used as fuel, however the implementation of high electrocatalysts materials is still the key for improvement performance of real devices applications.

The present work shows high performance in a MFC with ethanol as fuel, the excellent performance is due to use Pd-M (M= Co) based aerogels anode electrode, within the configuration of a microfluidic cell system. The use of hybrid aerogels allows the use of low catalyst masses of just 0.1 mg/cm^2 to generate current densities close to 400 mA cm^{-2}.

Keywords: Unsupported Aerogel, Microwave Heating, Microfluidic Fuel Cell, Nanotechnology, Electrocatalyst.

INTRODUCTION

Microfluidic fuel cells have the advantage of being portable and of carrying out small-scale processes what it offers high efficiency of energy conversion. The development of this type of devices allows to incorporate the ethanol oxidation (EO) for diverse technological applications on a small scale. Miniaturizing the cell may reduce fabrication costs. A study has recently presented a novel microfluidic fuel cell (MFC) that incorporates the innovation of using a laminar flow instead of the conventional solid membrane to separate the fuel and oxidant. Hence, the membrane-related issues are eliminated in this new MFC, which also offers savings in the manufacturing costs. However, it is still necessary to develop effective materials for this type of small devices [1].

Catalysts for different fuels have been continuously developed to optimize their power output and fuel utilization, with notable improvements achieved. Noble metals are potential hydrogen-storage materials that have been extensively studied due to its high efficiency, non-toxicity and stability. Particularly, Pd is widely used in anodes for EO [2]. The synergistic effect of metallic phase and oxyphilic properties of the Pd surface provides active sites for adsorption and dissociation of formic acid besides providing promoters of oxygen-containing species at low potentials [3]. There are a great number of Pd-based catalysts in the bibliography, however improving its activity is still a matter of fact to be implemented in fuel cells. Mesoporous materials with low density and greater number of active sites such as aerogels would allow to use less mass of catalyst and, at the same time, to provide a high catalytic activity [4]–[7]. Noble metal aerogels have approximately 90% air and very low content of the active metal which reduces the cost of the catalysts [8]. These innovative materials are commonly obtained by sol gel process and supercritical drying , however other techniques such as lyophilization allows promising aerogel qualities.

In this work, Pd-Co aerogels are synthetized by means of a totally innovative methodology based in microwaved heating during the sol-gel process, followed by lyophilization drying. The optimization of the synthesis process of the aerogels is performed to obtain the best performance in a microfluidic fuel cell for ethanol electrooxidation.

EXPERIMENTAL

Aerogels samples were obtained by a sol-gel methodology by microwave heating and lyophilization drying. The electrocatalytic activity of the Pd-Co aerogels towards EO were tested by Cyclic Voltammetry (CV) in a 0.5 M of ethanol in 0.5 M KOH as electrolyte. As for the electrocatalytic activity in half-cell configuration, at potential range between 0 and 1.4 V vs RHE was explored. The results were also compared with the electrocatalytic activity of a commercial reference (Pd/C 20%, Sigma Aldrich). For the MFC, Pd-Co aerogel samples were deposited on Toray carbon paper-060 (TCP) with a transversal area of 0.02 cm^2.The electrocatalyst loading was 0.1 mg for cm^2 anode and cathode electrode. Linear Sweep Voltammetry (LSV) was performed injecting 0.5 M ethanol with KOH as electrolyte in the anode with the evaluated catalyst; and 0.5 M H_2SO_4 in the cathode with commercial Pt/C as previous studies reported its best performance. A flow rate of 200 µL min-1 was used in the tests.

RESULTS AND DISCUSSION

A microfluidic fuel cell (Figure 1) was used for testing samples to verify their real activity under real operating conditions, using 0.5 M ethanol with 0.5 M KOH as electrolyte for the anodic reaction. Pd-Co materials have been tested and compared with the commercial Pd/C catalysts used as reference material in order to put into perspective the effectiveness of the best catalyst obtained using this novel methodology. LSV is a specific electrochemical protocol to discriminate the catalytic activity of the materials present in the anode surface. The microcell works by pumping 200 µL min^{-1} of the electrolyte fuel into the anode, and 200 µL min^{-1} of only 0.5 M H_2SO_4 into the Pt/C cathode. The polarization curves were obtained for stable open circuit voltage (OCV) and values registered for the samples were until 0.9 V. The power density obtained shows favourable results for the aerogel obtained by microwaved assisted sol-gel process. Small bubbles could be detected on the anode during the experiment, corresponding to the generation of hydrogen. The current density of the aerogel is up to almost three times higher than the commercial Pd/C catalyst, thus corroborating again the superior performance of the aerogels obtained in this work.

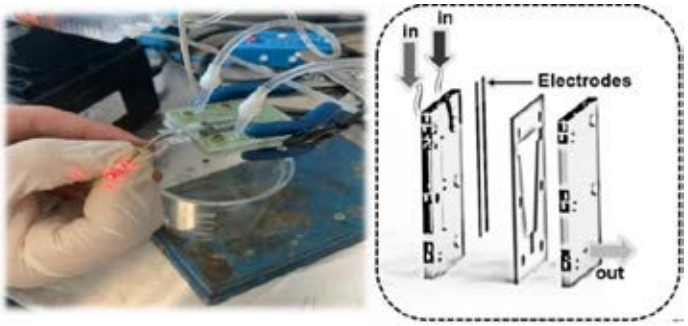


Figure 1. Scheme of the microfluidic system using the Pd-Co aerogels obtained in this work.

CONCLUSIONS

The use of microwave heating during the synthesis, followed by lyophilization as the drying step, allows obtaining Pd-Co aerogels with particle size smaller than 10 nm in anchored chains, favouring the ethanol oxidation. The Pd-Co aerogel sample showed a three times superior performance in a microfluidic fuel cell than a commercial Pd/C catalyst, reaching current densities of up to 118.3 mA cm^{-2}.

REFERENCES

1. Rupa, P., Harivignesh, R., Sung, Y. & Kalai, R. 2020. Polyol assisted formaldehyde reduction of bi-metallic Pt-Pd supported agro-waste derived carbon spheres as an efficient electrocatalyst for formic acid and ethylene glycol oxidation. *J. Colloid Interface Sci.* **561**, 358–371.
2. Wang, H., Chen, H., Wang, H., Ou, C. & Li, R. 2020. Synthesis of ultrafine low loading Pd e Cu alloy catalysts supported on graphene with excellent electrocatalytic performance for formic acid oxidation. *Int. J. Hydrogen Energy* **45**, 10735–10744.
3. Gharib, A. & Arab, A. Electrodeposited 2020. Pd , PdCd , and PdBi nanostructures : Preparation , characterization , corrosion behavior , and their electrocatalytic activities for formic acid oxidation. **866**.
4. Bao, Y., Liu, H., Liu, Z., Wang, F. & Feng, L. 2020. Pd/FeP catalyst engineering via thermal annealing for improved formic acid electrochemical oxidation. *Appl. Catal. B Environ.* **274**.
5. Bi, Y. *et al. 2015.* Investigation on gelation process and microstructure for copper-based aerogel prepared via sol-gel method. *J. Non. Cryst. Solids* **425**, 195–198.
6. Vareda, J. P., Lamy-Mendes, A. & Durães, L. 2018. A reconsideration on the definition of the term aerogel based on current drying trends. *Microporous Mesoporous Mater.* **258**, 211–216.
7. Maleki, H. 2016. Recent advances in aerogels for environmental remediation applications: A review. *Chem. Eng. J.* **300**, 98–118.
8. Du, R., Fan, X. & Jin, X. 2019. Emerging Noble Metal Aerogels : State of the Art and a Look Forward. 39–56.

WHEC-2022
23rd World Hydrogen Energy Conference
June 26-30, 2022 - Istanbul

#1507

GRAPHITE BASED-POLYMER COMPOSITE BIPOLAR PLATES FOR PEM FUEL CELLS

*Miquel Gamón Rodríguez, * Alina Madalina Darabut, Yevheniia Lobko, Yurii Yakovlev, Iva Matolínová, Vladimír Matolín*
Charles University, Faculty of Mathematics and Physics, Department of Surface and Plasma Science, V Holešovičkách 747/2, 180 00 Prague 8, Prague, Czech Republic

*Corresponding author e-mail: alinadarabut@gmail.com

ABSTRACT

The polymer composite bipolar plates based on commercially available and self-prepared graphite and epoxy resin were obtained. The electrical conductivity, gas permeability, and other characteristics of materials were measured. The percolation behavior of the composites was analyzed. The own-designed bipolar plates were prepared using compression molding technique. The in-situ tests in fuel cells' stations were performed.

Keywords: Bipolar Plates, Polymer Composites, Thermally Expanded Graphite, Electroconductive Fillers, PEM Fuel Cells

INTRODUCTION

Recently the European Commission proclaimed the new hydrogen strategy to reach the climate-neutrality in Europe (basically by reducing CO_2 emissions) by 2050 by using renewable energy [1]. Hydrogen fuel cells (FCs) are one of the key alternative, eco-friendly, zero-emission, and effective energy sources [2]. Among important components of fuel cells such as membrane, catalysts, gas diffusion layers, and the bipolar plates (BPs) play a significant role in the fuel cells' operation (homogeneous distribution of gases, current collection, prevention of water flooding, heat management, etc.) [3]. Consequently, such often mutually exclusive requirements for BPs as high electrical and thermal conductivity, flexural strength, toughness, high electrochemical stability, low gases permeation, and lightness are indispensable [4], [5]. In light of that, the polymer composites BPs have undeniable advantages over graphite and metal BPs [6]–[8]. They are lightweight and corrosion-resistant as graphite BPs and yet have a reduced thickness, high conductivity, and mechanical properties as metal ones. To overcome the disadvantage of low performance, the developing of effective nonporous materials for BPs with high electrical and thermal conductivity, high mechanical and chemical resistivity, etc., is an actual challenge nowadays. In the present research efforts were made to obtain bipolar plates based on polymer composites by hot compression molding to achieve the demanded goals. Moreover, the properties of polymer composites series filled with different graphite fillers, are analysed.

MATERIALS AND METHODS

Polymer composite bipolar plates preparation

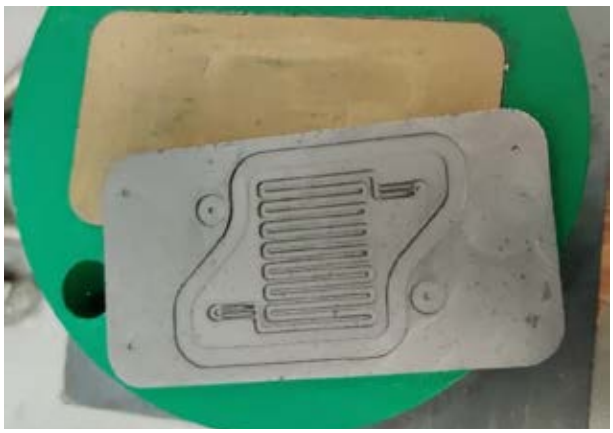


Fig. 1. Polymer composite bipolar plate based on carbon-filler obtained by hot compression molding.

Polymer BPs based on carbon fillers and epoxy resin were obtained using compression molding technique. The different materials as own-prepared thermally expanded graphite (TEG) (size particles ~500 μm), natural graphite (NG) (size particles ~17 μm), and synthetic graphite (SG) (size particles ~55 μm), were used as fillers. The filler content was varied from 2 to 60 vol.%. In order to obtain a good interface between the matrix and the fillers, among of increasing the quantity of latter, obtain the uniform dispersed materials, and, as a results, improve the mechanical characteristics of composites the filler particles were covered with epoxy resin in the dispersion. The pellets (with diameter 3 cm and thickness 0.1-0.3 cm), as well as bipolar plates (Fig. 1) were formed at 100 ºC at the 80 kN. The polymer composite with the best properties will be used for the manufacturing of the bipolar plates (Fig. 1).

Characterization of the polymer composite bipolar plates

The electrical conductivity of polymer composites was characterized using the impedance spectroscopy. Gas permeability of the materials were analyzed with electrochemical method and tested using linear sweep voltammetry. The bulk density and surface tension of the composites were measured.

The prepared polymer composite bipolar plates were characterized in a single cell with active area of 5 cm^2. Membrane electrode assembly consist of Nafion membrane, and two gas diffusion electrodes with 0.3 (mgPt cm^{-2}). The operating conditions for all experiments were: temperature 70 ºC; 0.5/0.5 bar of O_2 /H_2 or air/H_2 (piston pressure 8 bar), and 100 % relative humidity.

RESULTS AND DISCUSSION

The fillers' content affects the final materials' properties, such as the electrical conductivity, mechanical characteristics, etc. The influence of different carbon fillers (own-prepared TEG, synthetic and natural graphite) and variable content of them on the polymer composites' electrical conductivity is analyzed (Fig. 2). Moreover, the percolation behavior of such fillers in the bulk of epoxy resin matrix is studied (Fig. 2b).

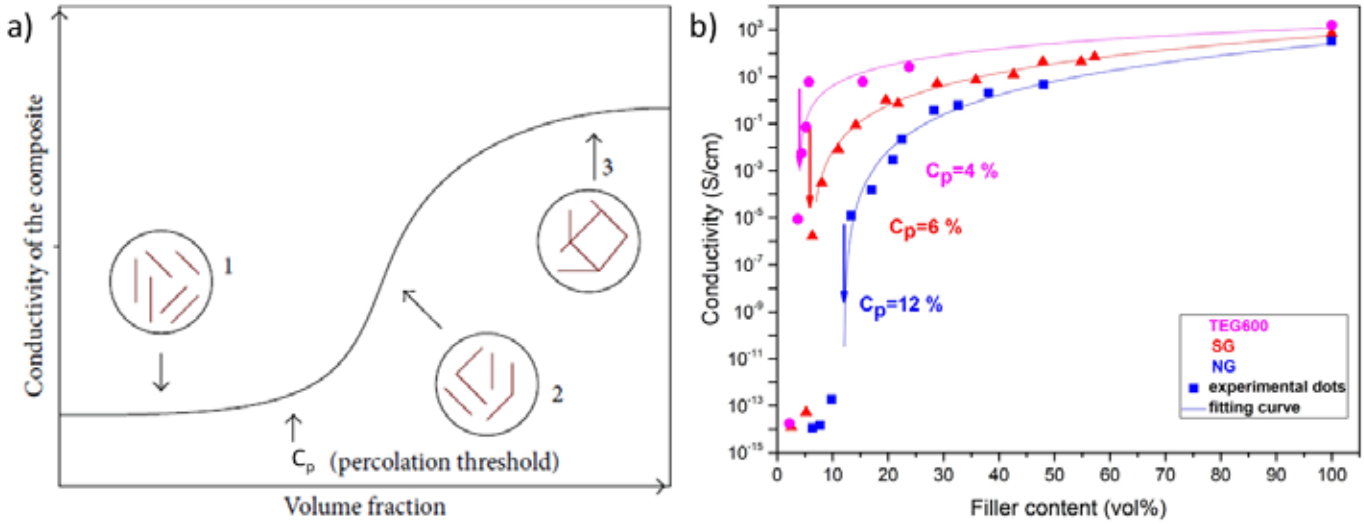


Fig. 2.Schematic percolation curves (a) [9], and experimental and fitted percolation curves for three different series (b).

Fig. 2a shows schematic percolation curves with 3 different regions of the fillers' particles packing [9]. The percolation threshold (C_p) is the critical filler volume fraction, where the electrical conductivity starts to increase due to the direct contact between the fillers' particles. Fig. 2b demonstrates that at the filler content around 60 vol.% the level of the electrical conductivity increases to 100 S/cm. The percolation threshold for the epoxy resin composites with TEG, SG, and NG are equal to 4.0, 6.0 and 12.0 vol.%, respectively. This effect shows that the TEG already forms electrically conductive percolation cluster at 4.0 vol.%. The critical index of electrical conductivity (t), calculated from the scaling relation derivate from Kirkpatrick's equation [10], are equal to 2.0, 4.4, and 3.6 for TEG, SG, and NG, respectively. The critical indexes from 1.6 to 2 correspond to standard 3D fillers' percolation [11]. The critical indexes higher than 2 indicate, on the electrical conductivity, which is realized due to the tunneling effect. It could mean that the SG and NG has less direct contact between the particles and covered with the thin polymer layer.
The polymer composites bipolar plates with own design of flow fields are prepared using epoxy resin and different carbon fillers (Fig. 1). The prepared BPs reaches the DOE target in terms of electrical conductivity (>100 S cm^{-1}) and gas permeability (<1.3x10^{-14} Std cm^3 s^{-1} cm^{-2} Pa^{-1}) with values of 150 (S cm^{-2}) and 2.8x10^{-14} (cm^3 s^{-1} cm cm^{-2} Pa^{-1}), respectively. The performance of membrane electrode assemblies in prepared BPs is tested in-situ in the fuel cell station. The tests' results are comparable to the literature.

CONCLUSIONS

The epoxy resin composites with different carbon-based fillers were obtained. The polymer composites BPs were formed using compression molding. The electrical conductivity, gas permeability, bulk density, etc., of the materials were analyzed. The percolation behavior of the different fillers in the bulk of the polymer matrix were studied. The critical filler volume fraction and the critical index of conductivity were calculated. The prepared BPs were tested in the fuel cell station.

ACKNOWLEDGEMENT

This study was financially supported by the grant CZ.02.1.01/0.0/0.0/16_025/0007414 OPVVV PaC-NG.

REFERENCES

1. https://ec.europa.eu/energy/sites/ener/files/hydrogen_strategy.pdf. Accesed on January 15, 2022.
2. Hoogers, G. 2003. Fuel Cell Technology Handbook. New York, CRC Press LLC.
3. Singh, R., Oberoi, A. S., and Singh, T. 2021. Factors influencing the performance of PEM fuel cells: A review on performance parameters, water management, and cooling techniques. International Journal of Energy Research, 1–33.
4. Alo, O. A., Otunniyi, I. O., Pienaar, H., and Iyuke, S. E. 2017. Materials for bipolar plates in polymer electrolyte membrane fuel cell: performance criteria and current benchmarks. Procedia Manufacturing, 7:395–401.
5. Cunningham, B. D., Huang, J., and Baird, D. G. 2007. Review of materials and processing methods used in the production of bipolar plates for fuel cells. International Materials Reviews, 52(1):1–13.
6. Phuangngamphan, M., Okhawilai, M., Hiziroglu, S., and Rimdusit, S. 2019. Development of highly conductive graphite-/graphene-filled polybenzoxazine composites for bipolar plates in fuel cells. Journal of Applied Polymer Science, 136(11):1–10.
7. Blunk, R., Abd Elhamid, M. H., Lisi, D., and Mikhail, Y. 2006. Polymeric composite bipolar plates for vehicle applications. Journal of Power Sources, 156(2):151–157.
8. Zarmehri, E. 2014. Construction of Composite Polymer Bipolar Plate for Pem Fuel Cell. Iranica Journal of Energy and Environment, 4(4):357–360.
9. Vargas-Bernal, R., Herrera-Pérez, G., Calixto-Olalde, M. E., and Tecpoyotl-Torres, M. 2013. Analysis of DC electrical conductivity models of carbon nanotube-polymer composites with potential application to nanometric electronic devices. Journal of Electrical and Computer Engineering, 1-14.
10. Kirkpatrick, S. 1973. Percolation and Conduction. Reviews of Modern Physics, 45(4):574–588.
11. Nan, C.-W., Shen, Y., and Ma, J. 2010. Physical Properties of Composites Near Percolation. Annual Review of Materials Research, 40:131-151.

WHEC-2022
23rd World Hydrogen Energy Conference
June 26-30, 2022 - Istanbul

#1510

HIGHLY POROUS Pt-CeO_2-C THIN FILM CATALYST PREPEARED BY MAGNETRON CO-SPUTTERING FOR PROTON EXCHANGE MEMBRANE FUEL CELLS

Xianxian Xie, Yurii Yakovlev, Peter Kúš, Jaroslava Nováková, Kateřina Veltruská, Yevheniia Lobko, Vladimír Matolín, Ivan Khalakhan, Iva Matolínová**
Charles University, Faculty of Mathematics and Physics, Department of Surface and Plasma Science, V Holešovičkách 2, 18000 Prague, Czech Republic

*Corresponding author e-mail:khalakhan@gmail.com

ABSTRACT

The Pt-CeO_2-C thin film catalyst was prepared by magnetron co-sputtering in Ar+O_2 atmosphere. The electrochemical surface area (ECSA) of thin film catalysts was tested in half-cell rotating disk electrode (RDE) system and showed 2.5 times higher than that for pure platinum. When Pt-CeO_2-C deposited directly on polymer-electrolyte membrane, creates a porous structure. The Pt-CeO_2-C catalyst coated membrane (CCM) was further measured in single-cell and exhibited only 21% power density loss during the accelerated stress test (AST).

Keywords: Thin Film, Catalyst, Porous Structure, Fuel Cell

INTRODUCTION

In order to reduce global dependency on fossil fuels, many renewable energy sources are being widely developed, such as wind, rain and solar energies [1]. Among them, hydrogen represents one of the most prospective forms because it is easier to store and it can be simply generated through electrolysis of water. One of the most efficient methods of utilizing hydrogen is through the proton exchange membrane fuel cells (PEMFCs) [2].
At the present stage of PEMFCs technology, platinum catalyst shows the highest performance for both anode and cathode. However, the high cost together with a rare resource of Pt severely limits the widespread fuel cell commercialization. It is thus urgent to reduce the Pt content in a cathode catalyst while maintaining its high performance. There are two major strategies for cost-effective and high-performance catalysts. One is to lower Pt content in the catalysts through doping other low-cost elements, without compromising performance. The other one is to increase the active area of Pt catalyst through the development of highly porous nanostructures.
CeO_2 has been studied for years due to its unique feature – the Ce^{3+}/Ce^{4+} redox couple ability. This makes CeO_2 a prospective substance either as a support or as an active catalyst. In our previous studies, we showed that we are able to produce high surface area catalyst by sputtering CeO_2 into carbon support in Ar+O_2 atmosphere [3]. During the sputtering process, the nuclei of CeO_2 form islands on the carbon-based substrate. The substrate surface area between those islands is etched with oxygen by forming gaseous products such as CO and CO_2. The carbon below CeO_2 nuclei is prevented from oxygen etching, resulting in the formation of porous columnar structure.
Herein, we investigate the thin film catalysts prepared by simultaneous co-sputtering of Pt, CeO_2 and C in Ar+O_2 atmosphere as cathode catalyst for PEMFCs. The catalyst thin films were deposited directly onto the polymer-electrolyte membrane in order to achieve a highly porous surface structure. Thus, the catalyst combines both strategies for cost-effective fuel cell catalysts i.e. it contains a low amount of platinum and has a high surface area. Except for high activity, such catalyst showed high stability.

MATERIALS AND METHODS

Magnetron sputtering

Pt-CeO_2-C and Pt thin film catalysts with 70 nm thickness were prepared using magnetron co-sputtering. The Pt (SAFINA, 99.99%,101.6 mm x 2 mm) target and C target (Kurt J. Lesker, 99.99%, 4.00" Dia. x 0.250" Thick) were faced the substrate under the angle of 45° (target-to-substrate distance is 15.5 cm). In turn, the CeO_2 target (Kurt J. Lesker, 99.99%, 4.00" Dia. x 0.250" Thick) is mounted in front of the substrate holder. The sputtering pressure was kept constant at 0.15 Pa with the Ar:O_2 ratio of 100:1. Powers on Pt, C, and CeO_2 magnetrons were set at 20 W, 300 W, and 65 W, respectively.

Structure characterization

The thickness and roughness of the as-deposited catalysts were determined by atomic force microscope (AFM, Bruker MultiMode 8) operated in tapping mode. SCANASYST-AIR probes (Bruker) were used with a nominal tip radius of 2 nm. Image processing was carried out using the NanoScope 1.5 software.
The microstructure of thin film catalyst coated membrane (Nafion® NR-212, Fuel Cell Store) was measured by scanning electron microscopy (SEM, Tescan MIRA III) operated at 30 keV beam energy. The cross-sections were prepared by focused ion beam (FIB, Tescan LIRA).

Half-cell electrochemical measurements

Thin film Pt and Pt-CeO_2-C catalysts were deposited on a glassy carbon electrode (Dia.5mm, 0.196cm^2). Cyclic voltammetry was done in an electrochemical cell with a typical three-electrode setup containing the sample as a working electrode (WE), a platinum wire (Safina, 99.99%) as a counter electrode (CE) and a saturated Hg/Hg_2SO_4 (Monokrystaly, RME 122) as a reference electrode (RE). Cyclic voltammograms (CV) were captured between 0.05-1 V_{RHE} at a scan rate of 50 mV/s in N_2 saturated 0.5 M H_2SO_4 solution. Electrochemically active surface area (ECSA) was calculated from the H_2 desorption/adsorption peaks.

Single-cell membrane electrode assembly (MEA) measurements

The membrane electrode assembly (MEA) contained thin film catalyst deposited on a Nafion membrane (20 × 20mm, Fuel Cell Store) as the cathode and commercially available gas diffusion layers (GDL) supported Pt catalyst (FuelCellStore, 0.3 mg/cm^2 40% Platinum on Vulcan) as the anode. Measurements were performed at 80 °C, 50 kPa gas backpressure and with the 1.2:2 constant ratio of H_2/O_2 flow. Accelerated stress test (AST) was performed at 500 mV/s scan rate in the range of 1-1.5 V_{RHE}.

RESULTS AND DISCUSSION

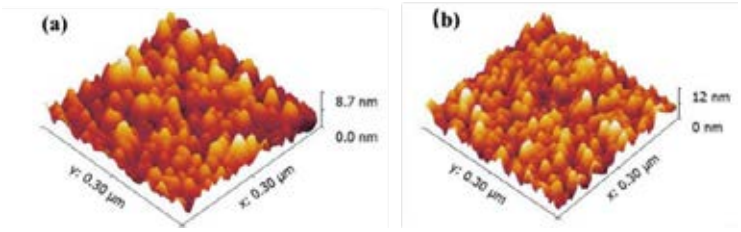


Fig.1 AFM images of (a) pure Pt and (b) Pt-CeO_2-C thin films

Fig.1 represents 3D AFM images of as-deposited Pt and Pt-CeO_2-C thin films. The average roughness (Ra) parameters calculated from the corresponding images are 1 nm and 1.5 nm for Pt and Pt-CeO_2-C, respectively. One can also observe that the Pt-CeO_2-C film surface is composed of smaller grains than the pure Pt film, which can be attributed to the CeO_2 and C doping effect.

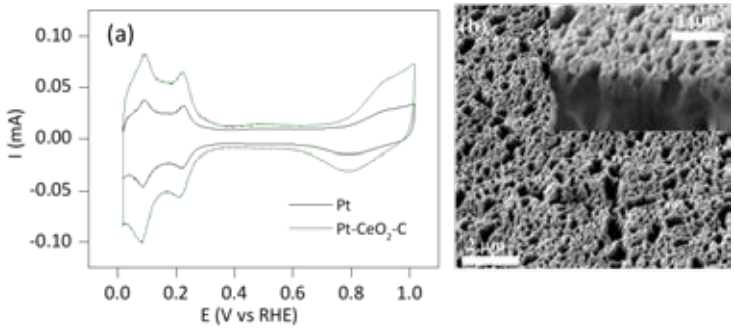


Fig.2. (a) Cyclic voltammetry curves of Pt and Pt-CeO_2-C catalysts. (b) Top and cross-section view SEM images of Pt-CeO_2-C catalyst deposited on Nafion membrane

Cyclic voltammetry (CV) was then applied to determine an electrochemically active surface area (ECSA) of the investigated samples. The CV curves of pure Pt and Pt-CeO_2-C thin film catalysts are shown in Fig 2a. Both CVs consist of the hydrogen oxidation/reduction and the platinum oxidation/reduction regions separated by the double layer potential region which is typical for polycrystalline platinum [4]. The ECSA of Pt-CeO_2-C thin film calculated from corresponding CV is 2.5 times higher than that for the pure Pt thin film. The higher ECSA for Pt-CeO_2-C can be explained by the formation of the so-called Pt-skeleton structure with higher concentration of low-coordinated Pt atoms due to CeO_2 leaching from the surface [5]. Fig. 2b shows SEM image of CCM. The highly porous surface of deposited layer can be explained by simultaneous membrane etching during the sputtering process [6]. The cross-section view from the inset of Fig. 2b, indicates that co-sputtering thin film deposited on membrane creates pores with about 1µm depth.

The Pt-CeO_2-C thin film with 21 µg·cm^{-2} Pt loading was then deposited on the Nafion membrane as cathode and commercial Pt/C catalysts with 300 µg·cm^{-2} as anode for testing in single cell. The commercial catalyst for both cathode and anode side were tested as reference. Polarization curves together with the power density (PD)

characteristics of investigated cathode catalyst are shown in Fig. 3. The specific power density of catalysts during 4000 cycles of AST are summarised in Table 1.

Table 1. The specific power density of catalysts during ADT

	Specific Power Density ($W \cdot g^{-1}$ Pt)	
Cycles	Commercial Pt/C	Pt-CeO_2-C
0	3.3	9.8
1000	1.8	8.9
2000	1.3	8.6
3000	1.0	8.5
4000	0.9	8.0

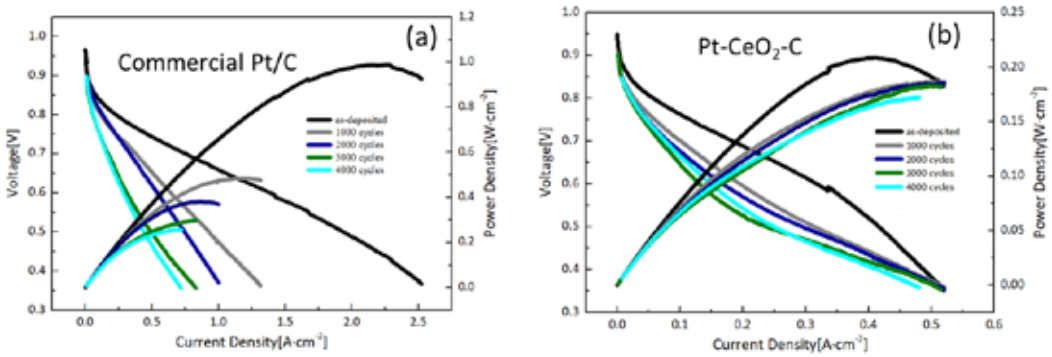


Fig.3. Polarization curves together with the power density of catalyst during AST

CONCLUSIONS

In this study, we developed Pt-CeO_2-C thin film catalyst prepared by magnetron co-sputtering in Ar+O_2 atmosphere. It showed 2.5 times higher ECSA than the pure Pt thin film catalyst. When deposited directly onto Nafion membrane, the porous structure with about 1 μm depth pores was achieved. Moreover, such catalyst showed only 21% power density loss after 4000 cycles durability test. Overall, the described results confirm the potential of using Pt-CeO_2-C catalyst as cathode in PEMFCs.

REFERENCES

[1]. Dudley, B. 2018. BP statistical review of world energy. BP energy economic.
[2]. Lykhach, Y.; Bruix, A.; Fabris, S.; Potin, V.; Matolínová, I.; Matolín, V.; Libuda, J.; Neyman, K. M. 2017. Oxide-based nanomaterials for fuel cell catalysis: the interplay between supported single Pt atoms and particles. Catalysis Science & Technology 7 (19):4315-4345.
[3]. Dubau, M. 2016. Preparation and Characterization of Porous Cerium Oxide/Carbon Bilayers on Silicon Substrates. Charles University in Prague.
[4]. Napporn, T. W.; Holade, Y.; Kokoh, B.; Mitsushima, S.; Mayer, K.; Eichberger, B.; Hacker, V. 2018. Electrochemical Measurement Methods and Characterization on the Cell Level 175-214.
[5]. Khalakhan, I.; Vorokhta, M.; Kúš, P.; Dopita, M.; Václavů, M.; Fiala, R.; Tsud, N.; Skála, T.; Matolín, V. 2017. In situ probing of magnetron sputtered Pt-Ni alloy fuel cell catalysts during accelerated durability test using EC-AFM. Electrochimica Acta, 245:760-769.
[6]. Yakovlev, Y. V.; Nováková, J.; Kúš, P.; Dinhová, T. N.; Matolínová, I.; Matolín, V. 2019. Highly developed nanostructuring of polymer-electrolyte membrane supported catalysts for hydrogen fuel cell application. Journal of Power Sources 439: 227084.

WHEC-2022
23rd World Hydrogen Energy Conference
June 26-30, 2022 - Istanbul

#1530

EXPERIMENTAL VALIDATION OF A 2-D MULTI-LAYER MODEL FOR FUEL CELL DIAGNOSIS USING MAGNETO-TOMOGRAPHY

[1] Antony Plait, [1] Frédéric Dubas*
[1]FEMTO-ST Institute, FCLAB, Univ. Bourgogne Franche-Comté, CNRS, 90000, Belfort, France

*Corresponding author e-mail: antony.plait@gmail.com

ABSTRACT

This paper focuses on the fuel cell (FC) diagnosis by using the magneto-tomography, which involves mapping the magnetic field produced by any electric device. Since the magnetic field and the current density are directly related, this study could describe the (ab)normal operation of a FC. For this purpose, a two-dimensional (2-D) multi-layer model based on the Maxwell-Fourier methods is developed. In order to validate the model developed for the FC diagnosis, an experimental bench was set up to emulate the FC operating mode. The purely analytical model is validated since the average difference between analytical results and experimental measurements is about 7%.

Keywords: Fuel Cell, Magnetic Field, Magneto-Tomography, Experimental Validation, Diagnostic.

INTRODUCTION

Many factors (e.g., obstruction of the gas diffusion layers, temperature hotspot, ...) can affect the current density distribution inside the FC and thus its performances. A bipolar plate of a FC stack, exposed in Fig.1, consists of a central active part (i.e., electrochemical active cell) and a peripherical inactive part (i.e., seal). Both invasive and non-invasive methods were developed to diagnose a FC. Magneto-tomography consists of measuring the magnetic field distribution around a FC. This interesting non-invasive method allows achieving an efficient study of FC health state. Hauer *et al.* (2005) [1] were the first to use this method for the FC diagnosis. To estimate the FC life state using magneto-tomography, the Biot-Savart's law [1]-[5], varying-network magnetic circuit [5] or the heuristic search method [6]-[7] are used. Recently, Plait *et al.* (2020) [8] developed a novel analyzer device of the magnetic field to increase the diagnostic performance.

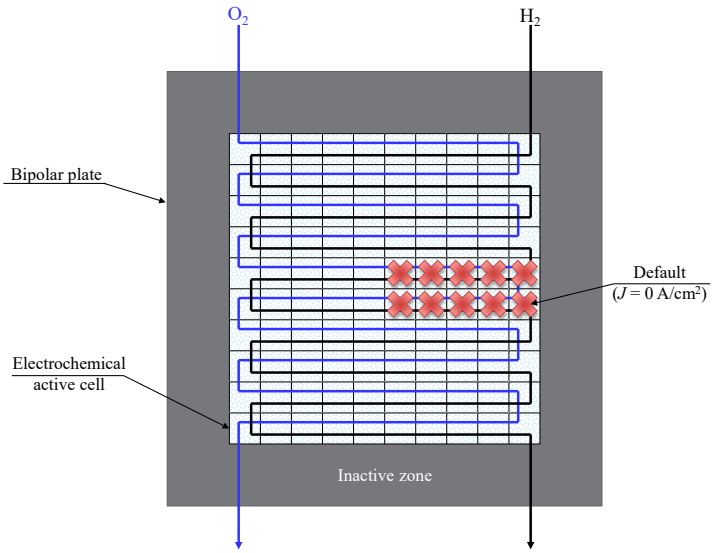


Fig. 1. Scheme of a FC bipolar plate

In this paper, an innovative magnetostatic model for the FC diagnosis is developed and validated by experimental measurements. The used experimental emulator, consisting of 100 aluminum bars and different switches, reproduces the behaviour of a FC that will have different types/locations of failure and reflects the current density distribution. Around the FC, the generated magnetic field is measured for a healthy FC and a FC failure with the default as indicated by the red cross in Fig. 1.

ANALYTICAL PREDICTIONS

The 2-D magnetic field distribution of the FC bipolar plate was studied from multi-layer model by solving magnetostatic Maxwell's equations in Cartesian coordinates (x,y). Knowing the current density distribution inside the FC, it's possible to accurately estimate the magnetic field distribution generated around the FC, or vice versa (by solving an inverse problem). The bipolar plate modeling is decomposed into 3 regions, viz., (R1) and (R3) similar to vacuum and (R2) the electrochemical active cell, as shown in Fig. 2.

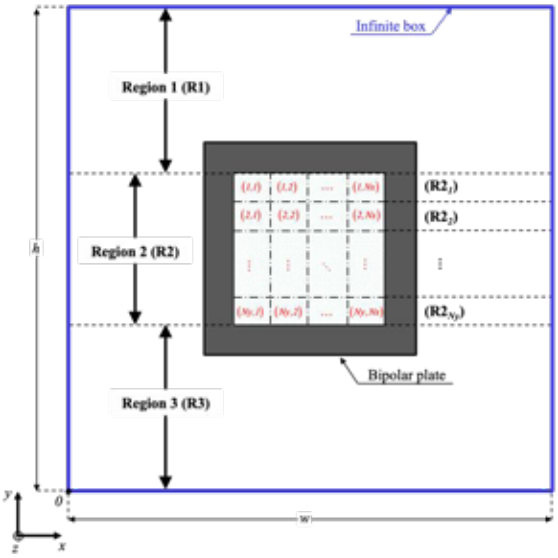


Fig. 2. FC bipolar plate modeling with 3 regions

The partial differential equations of magnetostatic in terms of magnetic vector potential ***A*** are defined by the Laplace's equation in (R1) & (R3) and the Poisson's equation in ($R2_i$) whose the electromagnetic source is the (in)homogeneous distribution of current density inside the FC stack. By using the separation of variables, the 2-D general formal solution of A in each region is defined by Fourier's series. The integration constants of series are determined analytically from a linear matrix system satisfying the classic boundary conditions [9].

EXPERIMENTAL FUEL CELL EMULATOR

To evaluate the capacity and efficiency of the developed 2-D multi-layer model, an experimental bench that reproduces the current density in operating condition is developed. The active part of this FC bipolar plate is emulated by multiple aluminum conductor bars supplied by DC current (white grid in Fig.1). A picture of the developed experimental bench is shown in Fig. 3. The emulator is surrounded by a non-magnetic support (3-D printed in white PLA in Fig.3), necessary for the installation of micro-Hall effect sensors. Both components of the magnetic field (viz., H_x and H_y) are measured at regular intervals around the FC emulator. A DC current of 100 A is distributed in the total surface of 100 cm^2.

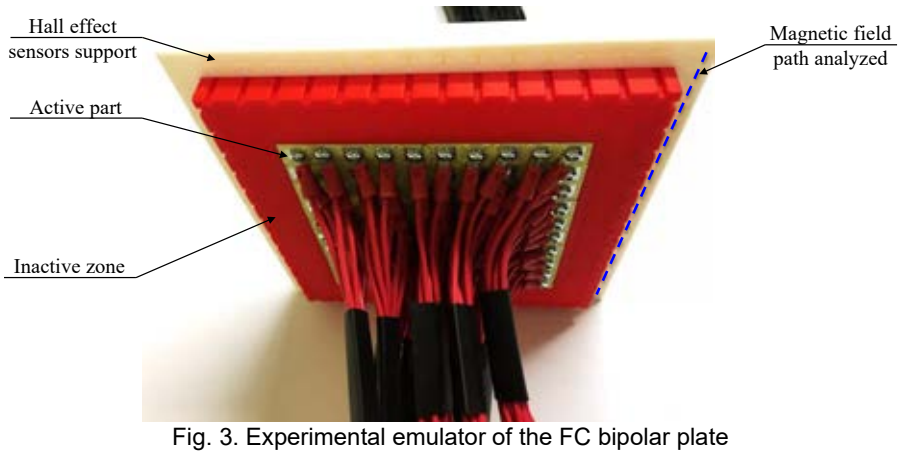


Fig. 3. Experimental emulator of the FC bipolar plate

RESULTS AND DISCUSSION

In this section, the analytical predictions are compared to experimental measurements. The focus is on the magnetic field waveform of the path shown in Fig. 3. The comparison is realized for a healthy FC (homogenous

current density of 1 A/cm^2) in Fig.4(a). Concerning an inhomogeneous distribution: a failure of 10% of the total active part as presented in Fig. 1 is considered. In case of failure the current density of the damaged part is zero and for the rest of the FC is equal to 1.11 A/cm^2. The analytical results and experimental measurements are shown in Fig. 4(b).

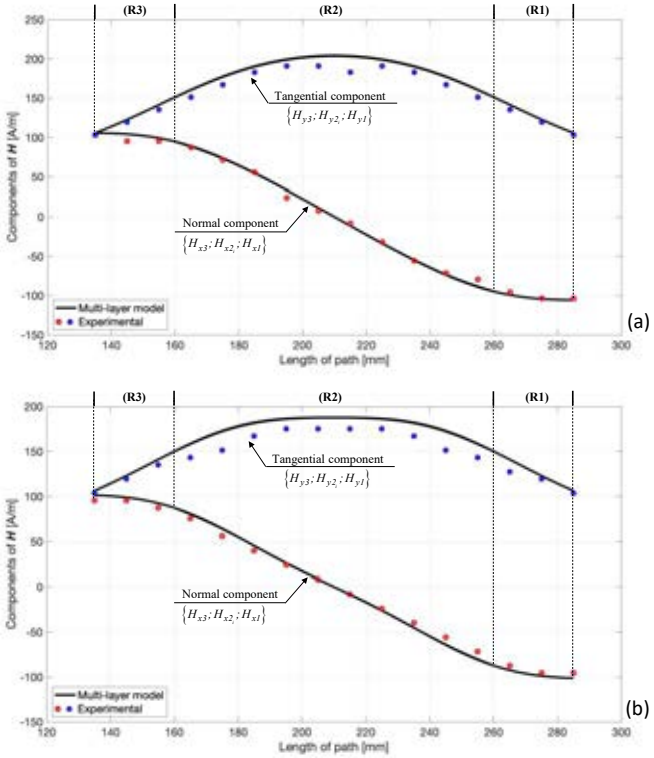


Fig. 4. Results comparison for (a) a healthy FC and (b) a FC failure

A current density fault (failure of 10%) results in a decrease of the magnetic field near the damaged zone and an increase away from it. A good accuracy between analytical results and experimental measurements allows the validation of the 2-D analytical model for both normal and abnormal FC operations.

CONCLUSIONS

In this paper, the analytical model is presented and the experimental setup is detailed. The analytical results and the experimental measurements are compared in order to validate the 2-D multi-layer model based on the Maxwell-Fourier methods. The validation is confirmed as the average difference is about 7%. The development of a fast and efficient multi-layer model is the first step. An inverse model is under development for the determination of the current density distribution in the FC from the measured magnetic field distribution.

ACKNOWLEDGEMENT

This work has been supported by the EIPHI Graduate School (contract ANR-17- EURE-0002) and the Region Bourgogne Franche-Comté.

REFERENCES

1. Hauer KH, Potthast R, Wüster T and Stolten D. 2005. Magneto-tomography-a new method for analysing fuel cell performance and quality. J. Power Source. 143:67-74.
2. Lustfeld H, Reißel M, Schmidt U and Steffen B. 2009. Reconstruction of electric currents in a fuel cell by magnetic field measurements. J. Fuel Cells Sci. Technol. 6:Art. ID 021012.
3. Nasu T, Matsushita Y, Okano J and Okajima K. 2012. Study of current distribution in PEMFC stack using magnetic sensor probe. Journal of International Council on Electrical Engineering. 2:391- 396.
4. Le Ny M, Chadebec O, Cauffet G, Dedulle JM, Bultel Y, Rosini S, Fourneron Y and Kuo-Peng P. 2013. Current distribution identification in fuel cell stacks from external magnetic field measurements. IEEE Trans. Magn. 49:1925-1928.
5. Ifrek L, Chadebec O, Rosini S, Cauffet G, Bultel Y and Bannwarth B. 2019. Fault identification on a fuel cell by 3-D current density reconstruction from external magnetic field measurements. IEEE Trans. Magn. 55:Art. ID 6200705.
6. Katou T, Gotoh Y, Takahashi N and Izumi M. 2012. Measurement technique of distribution of power generation current using static magnetic field around polymer electrolyte fuel cell by 3D inverse problem FEM. Materials Transactions. 53:279-284.

7. Yamanashi R, Gotoh Y, Izumi M and Nara T. 2015. Evaluation of generation current inside membrane electrode assembly in polymer electrolyte fuel cell using static magnetic field around fuel cell. ECS Trans. 65: 219-226.
8. Plait A, Giurgea S, Hissel D and Espanet C. 2020. New magnetic field analyzer device dedicated for polymer electrolyte fuel cells noninvasive diagnostic. Int. J. Hydrogen Energy. 45:14071-14082.
9. Dubas F and Boughrara K. 2017. New scientific contribution on the 2-D subdomain technique in Cartesian coordinates: Taking into account of iron parts. Math. Comput. Appl. 22:p17.

WHEC-2022
23rd World Hydrogen Energy Conference
June 26-30, 2022 - Istanbul

#1551

NUMERICAL ANALYSIS OF LIQUID WATER PERMEATION PROCESS THROUGH THE DEFORMED GAS DIFFUSION LAYER OF PEM FUEL CELL

[1*] *Yingxu Liu,* [1] *Yinming Du,* [1] *Maximilian Wick,* [1] *Stefan Pischinger*
[1]Chair of Thermodynamics of Mobile Energy Conversion Systems,
RWTH Aachen University, Forckenbeckstrasse 4, Aachen, Germany

*Corresponding author e-mail: liu@tme.rwth-aachen.de

ABSTRACT

This research studies the impact of the gas diffusion layer (GDL) deformation on liquid water diffusion. A GDL model of a solid microstructure with randomly dispersed fibers is built parametrically. The Finite Element Method (FEM) is used to simulate the fiber deformation and porosity change at the rib's border area under different stresses. Finally, the deformed GDL's liquid water diffusion and dispersion are examined with the help of the Lattice Boltzmann Method. According to the findings of this study, the assembly pressure and radius of the rib corner has a crucial role in the liquid water penetration process.

Keywords: PEM Fuel Cell, Liquid Water, Gas Diffusion Layer, Lattice Boltzmann Method, Rib Corner

INTRODUCTION

Proton Exchange Membrane Fuel Cells (PEMFC) are considered a promising alternative to internal combustion engines, as they do not cause harmful emissions and have high efficiency [1]. The gas diffusion layer (GDL) is one of its key components, being a porous substance composed of many layers of carbon fibers. The primary function of GDL is to deliver hydrogen and oxygen to the electrical extremities where an electrochemical reaction occurs. At the same time, to transport water out of the fuel cell [2]. Assembly pressure on the contact surfaces between GDL and bipolar plates (BPP) directly determines the shape of GDL, and thus the liquid water permeation behavior, which further influences its performance [3]. Therefore, it is necessary to study the effect of GDL deformation on the flow process of liquid water within GDL. Under this background, in this paper, a GDL model consisting of randomly distributed carbon fibers was firstly generated. The deformation of the GDL model was then simulated for different pressures and BPP rib corner radii. The compressed GDL model is used to analyze the liquid water permeation process with the Lattice Boltzmann method (LBM). At last, the effect of compression and rib corner radii is evaluated.

METHODS

3-D parametric GDL model

With the help of ANSYS APDL, a 3-D parametric GDL model is firstly created, as shown in Fig.1.

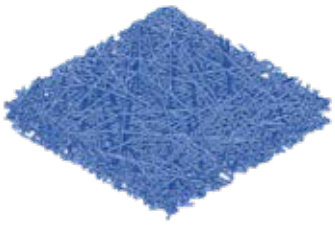


Fig 1. GDL produced with parametric modeling

The carbon fibers are the essential element to form this model. The geometric parameters utilized in the configuration of the GDL model are listed in Tab. 1.

Table 1. Geometric parameters of the 3-D parametric GDL model

Symbol	Quantity	Value
d_{f}	Fiber diameter	0.01 mm [4]
l_{f}	Fiber length	0.6 mm [4]
$\varepsilon_{\mathrm{GDL}}$	Porosity	0.78 [5]
H_{GDL}	Thickness	0.14 mm [5]

In this study, ideal hexagonal prisms are used to represent carbon fibers. This is based on three main reasons: firstly, using hexagonal prisms for the simulation saves computational resources compared with using cylinders; secondly, hexagonal prisms are promised with a better meshing process, which makes the model more suitable for finite element

analysis; thirdly, the contact area between a cylindrical body and a flat face is infinitely small, which can lead to an infinitely large pressure in the static stimulation.

GDL deformation

In the simulation, the pressure is loaded normally to the top surface of the bipolar plate. Due to the symmetrical and repetitive structure of the fuel cell cross-section, half of the ribs and half of the gas channels are presented in the geometric model.

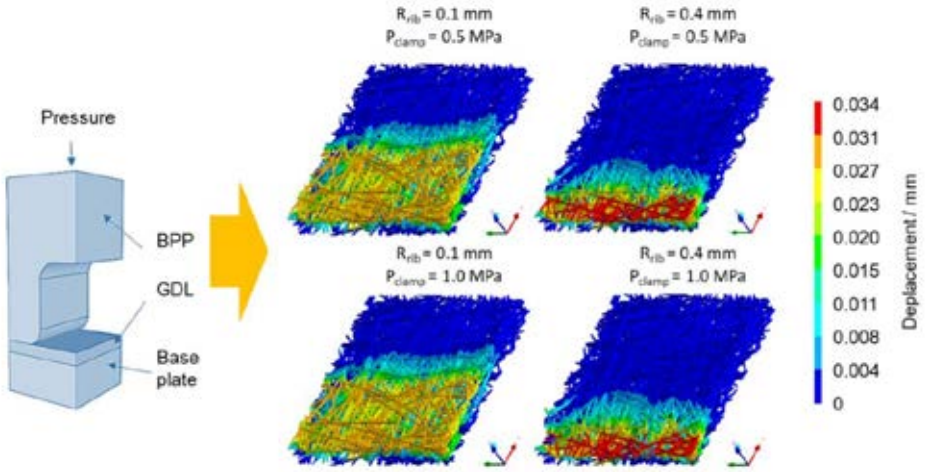


Fig 2. GDL deformation under compression of BPP rib

In the direction of the z-axis, the deformation of carbon fibers in the upper layer is more significant than in the lower layer. The maximal deformation is always found in the top layer. Besides, overlapped fiber nodes can transmit pressure and cause deformation to the fibers in lower layers. As a result of the rib intrusion into the fiber layer, the deformation of carbon fibers in the region under the rib is more significant compared with the region under the gas channel.

Liquid water permeation process

The water permeation process through compressed GDL is simulated via commercial LBM software X-Flow. The boundary conditions are presented in Tab. 2. It is worth noting that the simulation is based on the isothermal assumption, so temperature variations, as well as phase changes, are not considered.

Table 2. Geometric parameters of the 3-D parametric GDL model

Symbol	Quantity	Value
ρ_w	Water density	983.20 kg/m^3
ρ_a	Air density	0.98 kg/m^3
μ_w	Dynamic viscosity of water	0.466 mPa·s
μ_a	Dynamic viscosity of air	0.0184 mPa·s
v_w	Water inlet velocity	0.1 m/s

Simulation results are displayed in Fig. 3. As a result of GDL compression, the water in the cases with more considerable pressure will first break through GDL and contact the bipolar plate. After the water has flowed into the gas channel, the water flow is more random as fewer obstacles in the gas channel can constrain the flow.

Fig.3 also reveals that various rib corner radii significantly impact GDL water distribution. The water beneath the rib with a 0.4 mm corner radius comes into touch with the rib earlier than in other circumstances. This phenomenon is caused by the GDL thickness compressed under GDL, resulting in a significantly shorter distance for water to diffuse.

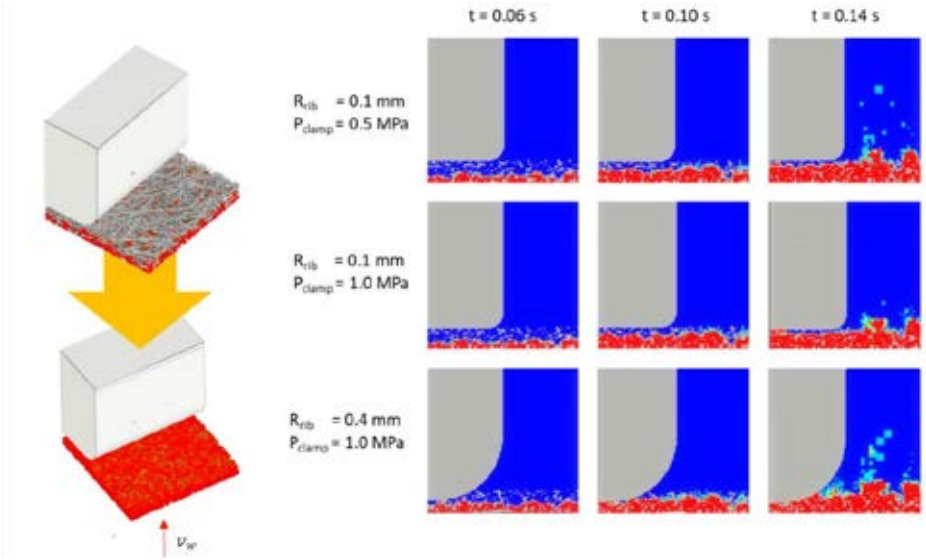


Fig 3. Water permeation process

The simulation also showed that in the event of a larger rib corner radius, the obstructed air bubbles might be released more quickly. This is because, compared to the case with a lower rib corner radius, the flat bottle surface takes up a more tremendous amount of the bottle, which is not favorable for the ejection of blocked air bubbles.

CONCLUSIONS

The microstructure GDL model is utilized in this thesis to simulate GDL deformation and examine the influence of deformation on liquid water diffusion. A parametrically generated solid microstructure GDL model with randomly distributed fibers was created. Fiber deformation at the rib's border region and the porosity change under various stresses were simulated using the Finite Element Method (FEM). Finally, the Lattice Boltzmann technique investigated the liquid water diffusion rate and distribution.

The simulation findings indicate that the radius of the rib corner plays a critical role in the liquid water penetration process inside the GDL. The distortion of the carbon fiber in GDL is more prominent when the rib corner radius is significant. Meanwhile, a big rib corner radius aids in water permeability. It is feasible to expect an ideal rib corner radius that balances the displacement of GDL and the rate of water penetration.

Further study on a series of chosen rib corner radii may be beneficial. Carbon fibers are modeled in this simulation as continuous entities bent but not broken. Carbon fiber's irreversible deformation may be explored in future studies. Additionally, the computational domain can be sufficiently enlarged to model the actual process.

FUNDING

This work is funded by Deutsche Forschungsgemeinschaft (DFG, German Research Foundation) [grant number GRK 1856].

REFERENCES

[1] Wang Y, Chen KS, Mishler J, Cho SC and Adroher XC. 2011. A review of polymer electrolyte membrane fuel cells: Technology, applications, and needs on fundamental research. Applied Energy 88: 981–1007.
[2] Mathias MF, Roth J, Fleming J and Lehnert W. 2010. Diffusion media materials and characterisation. Handbook of Fuel Cells.
[3] Lee W, Ho CH, Van Zee JW and Murthy M. 1999. The effects of compression and gas diffusion layers on the performance of a PEM fuel cell. Journal of Power Sources 84: 45–51.
[4] Liu Y, Tang C, Kohrn M, Shi B, Wang ZY, Wick M, Pischinger S and Andert J. 2022. A numerical study of the polarization effect of liquid water in the gas diffusion layer of a proton exchange membrane fuel cell. Journal of Power Sources 529: 231221
[5] Zhang Z, He P, Dai YJ, Jin PH and Tao WQ. Study of the mechanical behavior of paper-type GDL in PEMFC based on microstructure morphology. International Journal of Hydrogen Energy. 45: 29379–29394.

WHEC-2022
23rd World Hydrogen Energy Conference
June 26-30, 2022 - Istanbul

#1558

THE IMPACT OF AMBIENT TEMPERATURE ON HIGH-TEMPERATURE PEM FUEL CELL

[1] *Phil-Jacques Alphonse,* [1] *Mert Taş,* [1,2*] *Gülşah Elden*
[1] Erciyes University, Engineering Faculty, Energy Systems Engineering Department, 38039, Kayseri, Turkey
[2] Erciyes University, Energy Conversions Research and Application Center, 38039, Kayseri, Turkey

*Corresponding author e-mail: gulsah@erciyes.edu.tr

ABSTRACT

The temperature management and temperature distribution in the fuel cell are important issues in terms of improving reaction kinetics. To examine the impacts of the different ambient temperatures on the heat transfer occurring inside a high-temperature PEM fuel cell, two dimensional and steady-state model is developed by using Comsol 5.5 Multiphysics. While the operating temperature is kept constant at 150 °C, the different ambient temperatures (10 °C, 20 °C, 30 °C and 40 °C) are applied to the model. The obtained results show that the fuel cell performance is improved with lower ambient temperatures. Moreover, the highest cell temperature is found in the $T_{ambient}$= 40°C case, which is around 425 K.

Keywords: HTPEM Fuel Cell, Modeling, Temperature Distribution, Reaction Kinetics

INTRODUCTION

High-temperature polymer electrolyte fuel cell (HT-PEMFC) systems have attracted a lot of attention in recent years with their features such as energy efficiency and power density. It is used in fixed systems such as portable and charging stations such as land, air, and sea vehicles, and uninterrupted power systems. Unlike polymer electrolyte membrane fuel cells (PEMFCs) operating at low temperatures (50°C-80°C), HT-PEMFCs can operate in the range of 120°C-180°C. This is possible by using polybenzimidazole (PBI) instead of Nafion as a membrane. Since the water is in the vapor phase at operation temperature, the water management problem is eliminated. However, cell temperature management and temperature distribution are much more important in terms of improving reaction kinetics and maintaining the single phase in HT-PEMFC.

A 3D physical model is used to investigate several ways of investigating heat management of an HT-PEMFC. It is observed that for the combined gas channel and reaction heating, the cell temperature can exceed the highest temperature limit [1]. Similarly, the effect of the ultrathin vapor chamber (UVC) on the output performance of a conventional PEMFC stack is studied [2]. Experimentation and simulation are used to investigate thermal management and operating stability. It is found that the UVC can significantly increase output voltage and thermal management under high current density. The heat, mass, and charge transport processes of fuel cells are analyzed at different stoichiometric ratios (1, 2, and 3). For the case with a stoichiometric ratio of 1, the temperature decreases along the flow direction [3]. The rib design of a HT-PEMFC is investigated by Xia et al [4]. They revealed that the temperature of the MEA is higher than the temperature of bipolar plates and gas channels due to entropy change and overpotential losses. The aim of this study is to examine the effects of the change in ambient temperatures on the thermal behaviour of the high-temperature PEM fuel cell.

MODELING

The 2D HT-PEMFC model is developed with Comsol 5.5 Multiphysics. The model geometry is illustrated in Figure 1.a. As is shown in this figure, the numerical model consists of two gas diffusion layers and membrane. The catalyst layers are reactive boundaries. While the cell operating temperature is kept constant at 150 °C, the ambient temperature is varied from 10°C to 40 °C (stepping by 10°C). The following assumptions are considered to simplify and minimize the complexity of the model. Also, the model parameters are listed in Table 1.

1. The process is in a steady state.
2. The gas flows in the flow channels are compressible and laminar.
3. All gas mixtures are considered to be ideal gases, including the fuel, oxidant, and generated water.
4. The porous structure of the GDLs and membrane ensures that they are isotropic and homogeneous in all directions.
5. Thermal conductivities of all materials are assumed not to change with temperature.

$$\nabla.(\vec{u}) = 0 \quad (1)$$

$$\frac{\mu}{K}\vec{u} = -\nabla P \quad (2)$$

$$\nabla(\vec{u}c_i)\text{-}\nabla(D_i^{eff}\nabla c_i)=S_i \quad (3)$$

$$\nabla\vec{\imath_s} = \sigma_s\nabla\phi_s \quad (4)$$

$$\nabla\vec{\imath_l} = -\sigma_m\nabla\phi_l \quad (5)$$

$$\nabla.(\varepsilon\rho c_p\vec{u}T)=\nabla.(k\nabla T) + S_E \quad (6)$$

Table 1. Model parameters

Parameters	Symbols	Values
GDL height	L	2e-2 [m] [5]
Catalyst thickness	H_catalyst	5e-5 [m] [5]
GDL thickness	H_gdl	380E-6 [m] [5]
Membrane thickness	H_membrane	100e-6 [m] [5]
GDL porosity	eps_gdl	0.4
GDL permeability	kappa_gdl	5e-13 [m^2]
GDL electric conductivity	sigma_gdl	222 [S/m]
Acid Doping Level	X_dop	6.2 [6]
Membrane conductivity	sigma_m	(100/T[1/K])*exp(8.0219-((2605.6-70.1*X_dop)/T[1/K]))[S/m] [6]
GDL permeability	kappa_gdl	5e-13 [m^2]
GDL electric conductivity	sigma_gdl	300 [S/m]
Cell temperature	T	150+273.15 [K]
Cell voltage	V_cell	0.9
Permeability (electrode)	kappa_cl	0.4
Hydrogen molar mass	MH2	0.002[kg/mol]
Nitrogen molar mass	MN2	0.028[kg/mol]
Water molar mass	MH2O	0.018[kg/mol]
Oxygen molar mass	MO2	0.032[kg/mol]
Ref. concentration of H2	c_H2_ref	40.88 [mol/m^3]
Ref. concentration of O2	c_O2_ref	40.88 [mol/m^3]
Inlet water molar fraction	x_H2O_in	0.0236
Inlet hydrogen molar fraction	x_H2_in	0.743
Inlet oxygen molar fraction	x_O2_in	0.228

RESULTS AND DISCUSSION

The change in the temperature difference between the ambient and the cell affects the temperature distributions within the cell. As is shown in Fig. 1.b, the model results are compatible with the experimental data [6]. Fig. 1.c. presents the polarization curves for four different ambient temperatures. It is shown that the performance of the fuel cell is improved with lower ambient temperatures. Fig.1.d demonstrate the maximum cell temperature change according to ambient temperatures. It is found that the cell temperature increased with the increase of ambient temperature.

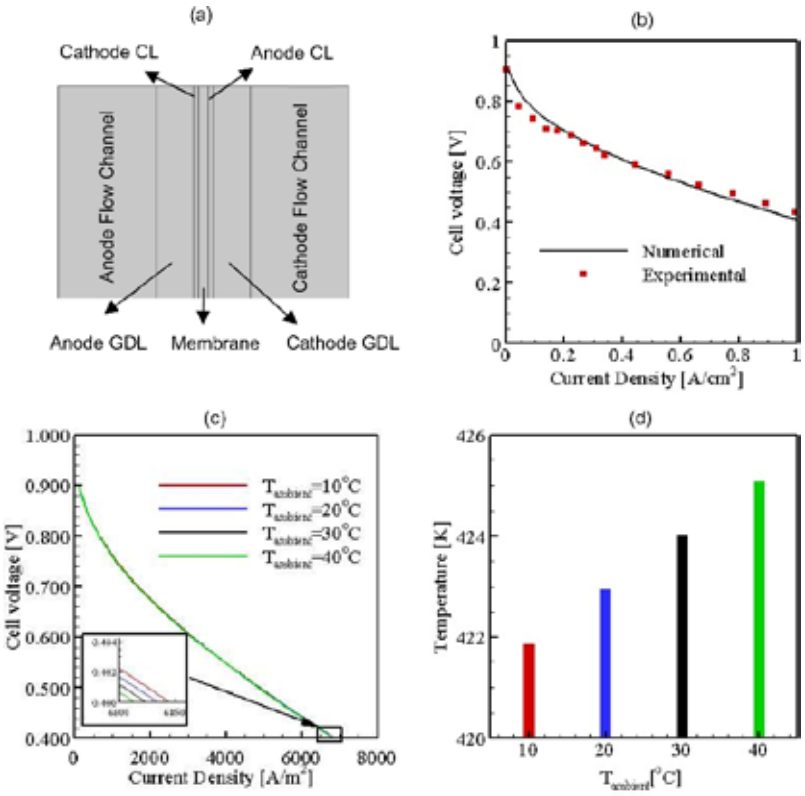


Fig. 1. (a) Model geometry, (b) Comparison of model results with experimental data [5], (c) The variation of polarization curves depending on ambient temperature, (d) Maximum cell temperature distribution for four different ambient temperatures at cell voltage of 0.4V.

CONCLUSIONS

The effects of ambient temperature on the performance and temperature distribution of HT-PEMFC are numerically analyzed. As a result of the analysis, it is revealed that the performance and temperature distribution of HT-PEMFC are affected by the change in ambient temperature.

REFERENCES

[1] Wang Y, Sauer DU, Koehne S, Ersöz A. Dynamic modeling of high temperature PEM fuel cell start-up process. Int J Hydrogen Energy 2014;39:19067–78. https://doi.org/10.1016/j.ijhydene.2014.09.095.
[2] Chen Y, Jian Q, Huang Z, Zhao J, Bai X, Li D. Improvement of thermal management of proton exchange membrane fuel cell stack used for portable devices by integrating the ultrathin vapor chamber. Int J Hydrogen Energy 2021;46:36995–7006. https://doi.org/10.1016/j.ijhydene.2021.08.185.
[3] Li S, Wei R, Lv X, Ye W, Shen Q, Yang G. Numerical analysis on the effect of stoichiometric ratio on fuel utilization and performance of high temperature proton exchange membrane fuel cells. Int J Electrochem Sci 2020;15:7407–16. https://doi.org/10.20964/2020.08.51.
[4] Xia L, Xu Q, He Q, Ni M, Seng M. Numerical study of high temperature proton exchange membrane fuel cell (HT-PEMFC) with a focus on rib design. Int J Hydrogen Energy 2021;46:21098–111. https://doi.org/10.1016/j.ijhydene.2021.03.192.
[5] Ubong EU, Shi Z, Wang X. Three-Dimensional Modeling and Experimental Study of a High Temperature PBI-Based PEM Fuel Cell. J Electrochem Soc 2009;156:B1276. https://doi.org/10.1149/1.3203309.
[6] Elden G, Çelik M, Genç G, Yapici H. The effects of temperature on transport phenomena in phosphoric acid doped polybenzimidazole polymer electrolyte membrane fuel cell. Energy 2016;103:772–83. https://doi.org/10.1016/j.energy.2016.02.137.

WHEC-2022
23rd World Hydrogen Energy Conference
June 26-30, 2022 - Istanbul

#1567
MODELING OF H_2/Br_2 REDOX FLOW BATTERY IN FUEL CELL MODE

[1,2]*Anil Can Turkmen, [1]Kursat Can Ata, [1]Cenk Celik
[1]Kocaeli University Faculty of Engineering, Department of Mechanical Engineering, Kocaeli 41380, Turkey
[2]ACT Scientific Ltd., Budotek Teknopark, Istanbul, 34776, Turkey

*Corresponding author e-mail: anilcan.turkmen@hotmail.com

ABSTRACT

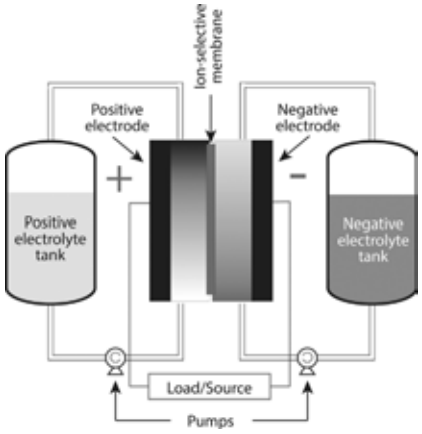
A single-channel H_2/Br_2 redox flow battery is modeled in this study. Within the scope of the modeling, the use of the redox flow battery only in the discharge mode has been studied. In this context, Nafion 115 was used as the membrane and SGL 34BC was used as the diffusion layer. The highest power density obtained in this context was reached at 0.8 V, and this value was obtained as 0.62 W/cm^2.

Keywords: Hydrogen, Bromide, Redox Flow Battery

INTRODUCTION

The issue of energy storage has gained importance, especially with the increase in the use of renewable energy sources. Unstable sources, predictably due to the nature of wind and sunlight, are a challenging problem for modern power distribution networks that draw power. By far the most efficient storage method is systems based on mechanical principles. Two of the best are pumped storage hydropower and compressed air [1]. However, to achieve high efficiency, these systems require large-scale deployment and thus significant initial investment. Not every location is suitable for the construction of these systems, and it is not always feasible or even desirable to build a large-scale system. Therefore, storing the excess energy produced in electrochemical cells (batteries) is a necessary choice and perhaps even the most practical method. The challenge, however, is to find batteries that are reliable, widely available, effective, and cost-effective [1]. Due to various problems with lithium-based batteries, which are frequently used today, studies on redox flow batteries have increased.

Flow redox cells differ from more common electrochemical cells in that the reactive material is not part of the structure but is supplied from external storage tanks in the form of a liquid phase during cycle transitions from the storage vessels. The total energy capacity of the system is then proportional to the amount of electrolyte in the external containers while the output power depends on the electrode arrangement (the electrode area of the system). The schematic diagram of the flow cell system is given in Figure 1 [2].



Şekil 1. Schematic diagram of the Redox battery.

It is thought that hydrogen will be in our lives in the future. For this reason, it will be possible to produce in high quantities and access it at low prices. However, bromine is a very cheap mineral and can be obtained at approximately 6 times more cost-effective than vanadium. Commercialization of H_2/Br_2 redox flow batteries has started quite recently and has not reached its full capacity. The main reason for this is the limited research on it. Some of the studies in the literature are summarized below.

Oh et al. [3] developed a three-dimensional model for H_2/Br_2 redox flow batteries, meticulously taking into account the species and charge transfer that occurs via redox reactions of hydrogen and bromine species and various cell

components. First, the H_2/Br_2 redox flow batteries model was validated experimentally against the measured discharge and charge voltage curves over a wide range of current densities up to 1.4 A/cm^2. Overall, the model predictions compare well with the experimental data. Particular emphasis was placed on analyzing the cross-membrane crossover of bromine species at detailed levels where the model calculates electro-osmotic and diffusive fluxes through the membrane; The relative sizes were compared at various charging and discharging stages. Additionally, a parametric study was performed to examine the effects of two important design variables on cell performance and migration behavior, namely the thickness of the membrane and bromine porous media. This fully 3D model of H_2/Br_2 redox flow batteries can be applied to realistic large-scale cell geometry for grid-scale energy storage applications and can be directly used to determine the optimum design and operating conditions for H_2/Br_2 redox flow batteries.

Chinannai et al. [4] developed a kinetic model of the chemical reaction by comprehensively taking into account the detailed reaction steps and incorporating a three-dimensional, time-dependent H_2/Br_2 flow battery model. First, the H_2/Br_2 flow cell model containing BrO^{-3} was validated according to experimental data in which cell voltage recovery was observed until the BrO^{-3} was completely consumed. The model successfully reproduced the voltage evolution data measured during discharge, thus accurately obtaining the transient behavior of an H_2/Br_2 cell affected by the bromate-bromide chemical reaction. In addition, H_2/Br_2 cells were simulated with and without BrO^{-3}, and model predictions revealed that the reversible voltage, ohmic overpotential at the membrane, and activation overpotential of the Br_2 reduction reaction was improved due to the use of BrO^{-3} in the catholyte. The current model for the H_2-Br_2-BrO^{-3} system has provided a quantitative analysis of the beneficial effects of using the redox-mediated bromate anion, thus making it a useful tool for the design and optimization of the H_2/Br_2 cell with BrO^{-3}.

In his master's thesis, Haile [5] aimed to perform a system architecture, dynamic behavior analysis, component selection, and experimental work to develop the control system of a commercial company Elestor's hydrogen bromine flow battery. To achieve this goal, different aspects of system architecture design have been proposed. In addition, components such as a current sensor and an electrolyte pump were selected and tested for the Elestor H_2/Br_2 flow battery. In addition, the first experimental study was conducted on the performance of the first Elestor H_2/Br_2 flow battery at different hydrogen pressure and electrolyte pump speed. In the theoretical analysis, the transfer function for both open and closed-loop electrolyte subsystems is investigated from dynamic mass balance, and step responses are also preplanned. From the theoretical analysis, it is found that the open-loop step response of the electrolyte subsystem behaves as a pure capacitive operation. The result of the analysis also showed that the closed-loop step response of the electrolyte subsystem behaves as a first-order system.

This limitation arises from the fact that experimental studies are not sufficient to ensure optimum reactions in all electrochemical energy conversion systems. For a better understanding of the system, H_2/Br_2 redox flow batteries are modeled in a computer environment and the performance of the cell's behavior in discharge mode is examined.

MODELING

H2/Br2 redox flow batteries are a promising system today. The reactants of this system are gaseous hydrogen on the negative side, and aqueous bromine and HBr solution on the positive side. During discharging, if the cell electrode loses the electrode and the proton passes through a proton-conducting membrane to the other solution, the gaseous hydrogen on the surface reacts with bromine to produce positive electrode HBr [6].Bu sistem için yarı reaksiyonlar aşağıda gösterilmiştir:

Positive electrode $2Br^-(aq) \leftrightarrow Br_2(aq) + 2e^-$ (2.1)

Negative electron $2H^+(aq) + 2e^- \leftrightarrow H_2(g)$ (2.2)

Total reaction $Br_2(aq) + H_2(g) \rightarrow 2Br^-(aq) + 2H^+(aq)$ (2.3)

The general standard potential for this system is E_0 = 1.09 V.

In the studies, heat transfer equations were excluded from the modeling scope and an isothermal model was developed. The model was prepared using diffusion equations, flow equations in a porous material (Briggmann equations), and electrochemical equations.

For the electrochemical reactions in the system, firstly the Nernst equation was used to determine the output voltage, and the modified Butler-Volmer equation was used for the modeling of the electrochemical reactions.

RESULTS AND DISCUSSION

The polarization curve of the modeling study is given in Figure 2. As can be seen from the polarization curve, the highest cell performance was obtained at 0.8 V. The power density produced at this point was obtained as 0.62 W/cm^2.

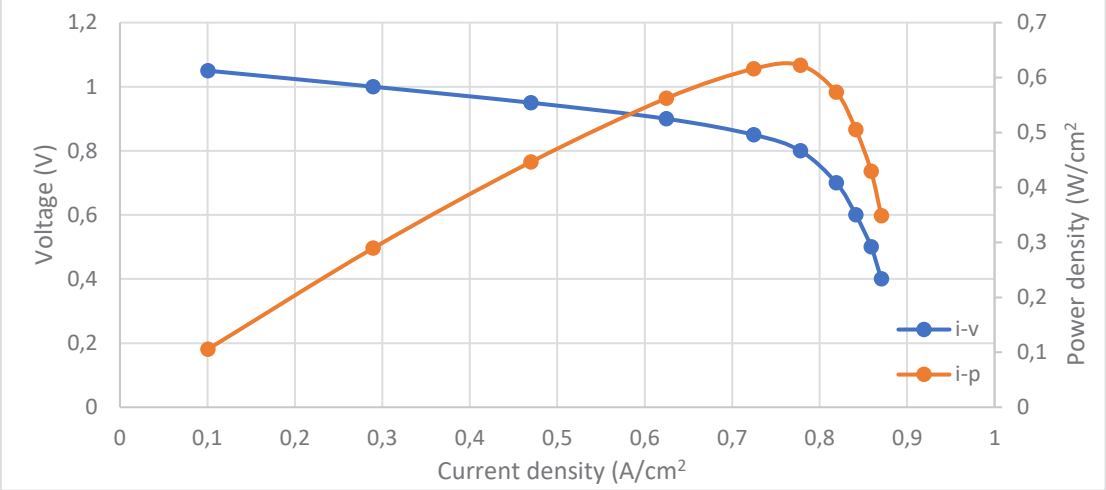


Figure 2. Polarisation curve

In Figure 3, the hydrogen concentration distribution on the anode side, and the bromide concentration distribution in Figure 4 are given.

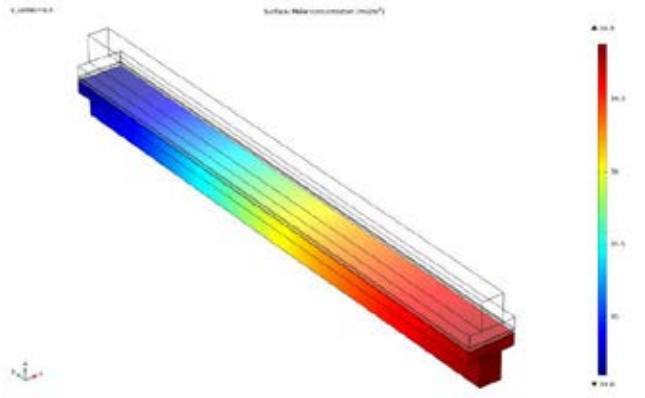


Fig. 3. Hydrogen concentration distribution

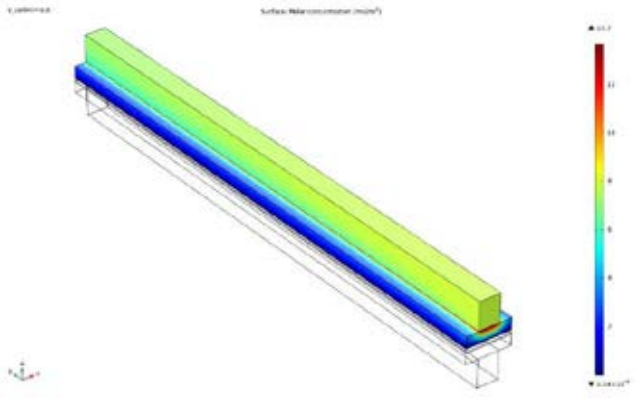


Fig. 4. Bromide concentration distribution

CONCLUSIONS

In this study, an isothermal model of a single-channel h2/br2 redox flow battery was studied. Within the scope of the modeling study, the polarization curve was created and it was determined that the maximum power density of 0.8V was reached. In this context, it is seen that all of the hydrogens are used, but the bromide concentration does not decrease too much. In this case, it is seen that the cell included in the scope of the study can also achieve higher performances.

REFERENCES

[1] Vanýsek P Chladil L Dvořák P. 2015. Velké srovnání metod a systémů uchovávání energie. Dostupně a schůdně. HW server 10:1-8.
[2] Vanýsek P Novak V. 2017. Redox flow batteries as the means for energy storage. Journal of Energy Storage 13:435-441.
[3] Oh K Weber AZ Ju H. 2017. Study of bromine species crossover in H2/Br2 redox flow batteries. International Journal of Hydrogen Energy, 42:3753-3766.
[4] Chinannai MF Ju H. 2021. Analysis of performance improvement of hydrogen/bromine flow batteries by using bromate electrolyte. International Journal of Hydrogen Energy. 46:13760-13774.
[5] Haile EG. 2015. H_2/Br_2 Flow Battery System Architecture and Control System Analysis. Master Thesis. Tecnico Lisboa.
[6] Tucker MC Cho K Weber AZ Lin G Van Nguyen T. 2015. The Influence of Electric Field on Crossover in Redox-Flow Batteries. Journal of The Electrochemical Society.

WHEC-2022
23rd World Hydrogen Energy Conference
June 26-30, 2022 - Istanbul

#1569

DEVELOPMENT OF HYDROGEN RANGE EXTENDER FOR A SPECIALIZED MULTIPURPOSE VEHICLE

[1*] *Ing. Lukáš Polák, Ph.D.* [1] *Ing. Aleš Doucek, Ph.D.,* [1] *Ing. Stanislav Kříž*
[1]ÚJV Řež, a.s., Department of Hydrogen Technologies and Innovations in Energetics, Hlavní 130, 250 68 Husinec-Řež, Czech Rep.

*Corresponding author e-mail: lukas.polak@ujv.cz

ABSTRACT

The scope of the project is a research and development of a hydrogen range extender by implementing a hydrogen fuel cell, high pressure cylinders and other supporting components in a commercial battery-based multipurpose vehicle. In the final phase, the long term real-operation testing of the prototype vehicle will be carried out. The documentation for a small serial production will be prepared after a final optimisation of the whole electric power train system.

Keywords: Hydrogen, Fuel Cell, Multipurpose Vehicle, Range Extender

INTRODUCTION

The aim of the project is to develop a hybrid powertrain for a commercial multipurpose vehicle that will enable emission-free operation with comparable performance to conventional internal combustion engine vehicles. At present, the development of clean mobility mainly focuses on electric vehicles using battery energy. The range of electric vehicles is limited by the size and the battery capacity, which is limited due to weight and size, resulting in a shorter range. This problem is not so obvious for conventional cars, since analysis of traffic statistics shows that most journeys are made within a distance between 30 - 80 kilometres. Commercial vehicles, unlike passenger cars, are used in shifts that typically last 8 hours and it is therefore preferred that the vehicle does not have to be recharged for a longer period during the shift. Due to the higher investment costs of commercial vehicles, there is a desire to use them as much as possible. The research and development of a hydrogen range extender for commercial multipurpose vehicles allows the benefits of emission-free operation to be combined with the required operating time and comparable refuelling times to existing internal combustion engine vehicles.



Fig. 1. Preliminary tests of protype vehicle with hydrogen range extender

EXPERIMENTAL WORK

The use of hybrid powertrains in passenger cars faces space challenges. Commercial vehicles using an electric motor, on the other hand, have more space for battery storage, but weight is still a limiting factor. Hybridising the vehicle with hydrogen can ensure sufficient range.

The research and development of hybrid propulsion system is divided into three stages:

- Stage 1 - Technical design of the hydrogen fuel cell system integration
- Stage 2 - Implementation of hydrogen range extender into the prototype multipurpose vehicle
- Stage 3 - Optimization and testing of the prototype multipurpose vehicle

Technical design

Mathematical modeling for energy balance was carried out with goal to double a range of a battery electric vehicle. This modeling with a market research led to a design of fuel cell range extender present on Figure 2.

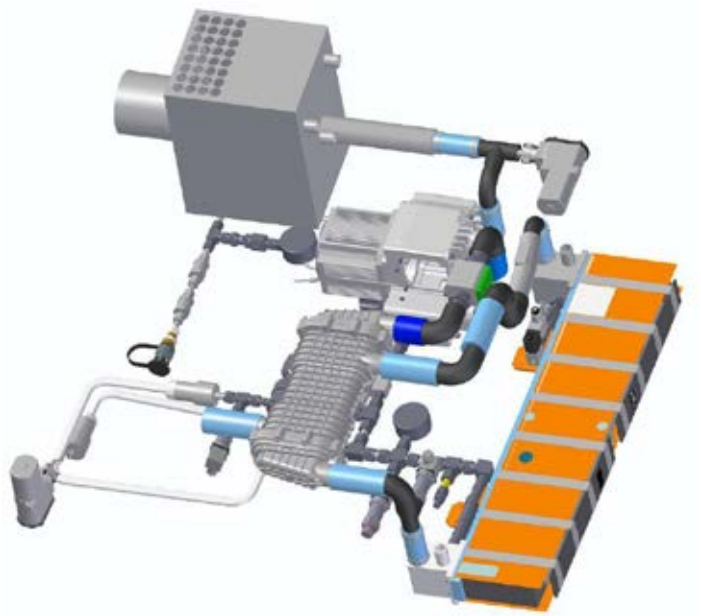


Fig. 2. 3D model of fuel cell range extender (excluding high-pressure cylinders)

Implementation of hydrogen range extender into the vehicle

In the second year of project, the all component including fuel cell, DC/DC converter, pressure cylinders etc. were implemented in a complex system and embedded on the vehicle platform. The own control system was developed and install and help to modify operating conditions of main component as well as safe operational data for later evaluation and optimisation. The complete prototype of vehicle with the implemented range extender is shown on Figure 3.



Fig. 3. The prototype of vehicle with fuel cell range extender via testing

CONCLUSIONS

In the first two years of project, the research team focused on the modeling, design and development of fuel cell range extender for multipurpose vehicle. Also, an analysis of the individual risks associated with the hydrogen range extender was prepared and the severity of their consequences and the level of risk were evaluated. Furthermore, the control philosophy of the vehicle as well as the design of the actual control electronics was completed.

The research team has mainly focused on the assembly of the hydrogen technology, verification of its complex functionality, installation of the technology into a prototype vehicle, development of the control unit and implementation of safety measures. First preliminary operational tests are underway with focus on efficient energy usage and control of heat distribution in colling system. A possible partial design modification resulting from the continuously evaluated test operation will be implemented in the following months.

ACKNOWLEDGEMENT

The development and research work is supported by Czech Ministry of Industry and Trade within the TRIO programme under project number FV40096.

WHEC-2022
23rd World Hydrogen Energy Conference
June 26-30, 2022 - Istanbul

#1570

TRANSIENT CHARACTERISTICS OF IN-PLANE WATER TRANSPORT IN THE GAS DIFFUSION LAYER OF PEM FUEL CELLS

[1] *Sung Yong Jung,* [2*] *Mehdi Mortazavi*
[1]Department of Mechanical Engineering, Chosun University, 309 Pilmun-Daero, Dong-gu, Gwangju, 61452 Republic of Korea
[2] Department of Mechanical Engineering, Western New Englan University, Springfield, Massachusetts, 01119 USA

*Corresponding author e-mail: mehdi.mortazavi@wne.edu

ABSTRACT

Understanding about water transport in gas diffusion layer (GDL) is important for the water management of proton exchange membrane fuel cells (PEMFC). In this study, the in-plane water transport in a commercial GDL was visualized to investigate the transient characteristics using an optical imaging system providing a high spatial resolution. Previously proposed non-dimensional scaling model and specific interfacial area were obtained from measured wetted area, perimeter, and percolation pressure. In addition, the wetted area with time is graphically presented by spatiotemporal maps. It is newly found that the transition of flow characteristics including flow pattern and transport mechanism occurs. Results indicate that at higher compressions, the transition occurs earlier under lower saturation, and water invades along a more complex path through pores that are altered by compression.

Keywords: In-Plane Water Transport, Proton Exchange Membrane Fuel Cells, Gas Diffusion Layer

INTRODUCTION

The water management for the correct water content ranges is required for reliable proton exchange membrane fuel cells (PEMFC) operation because the proton conductivity of the polymeric membrane is directly related to the humidification levels [1]. Water produced by the electrochemical reactions is invaded into pores in the gas diffusion layer (GDL), and the occlusion of the GDL pores by water can lead to worse cell performance [2]. Although it is known that water transport through the GDL pores is mainly caused by the capillary effects [3], the mechanism of water transport through GDL pores is not fully understood.

To better understand water transport in the porous structure of the GDL, many studies focused on visualizing water percolation in this layer. The direct optical visualization technique, which is an affordable and easy-to-implement technique, is commonly employed to investigate water flows through GDL pores [4-6]. Most studies with an optical visualization method focused on the transports across the thickness of the GDL (in through-plane direction). While the through-plane transport is a realistic scenario of transport phenomena in an actual PEM fuel cell, both time and length are limited to observe fingering patterns due to the thin thickness of the GDL.

Several studies employed the optical method to visualize in-plane water transports through GDL pores to overcome the limitations of the through-plane observation [7, 8]. Compared to the through-plane transport, the in-plane percolation occurs over a longer time, increasing the experimental precision and providing more opportunity to identify flow patterns. The visualization of in-plane percolations with an optical method was employed to validate the drainage phase diagram [7] and an analytical scaling model [9]. In those studies, fluid evolutions through GDLs were observed only under the steady-state condition in a relatively larger displacement than the pore-scale due to the limitation of a spatial resolution. In the present study, the transient characteristics of the ex-situ in-plane water transport in GDL pores were observed by obtaining the pore-scale spatiotemporal variations of wetted regions with a measurement of percolation pressure.

EXPERIMENTAL APPARATUS

The schematic of the experimental set-up for the visualization of in-plane water transport is shown in Fig. 1. In order to obtain high-resolution images, a digital single-lens reflex (DSLR) camera (EOS REBEL T4i, Canon) was attached to a stereo-microscope (SMZ645, Nikon). This imaging system provided the corresponding field of view was 1.5 mm × 1.0 mm (5184 × 3456 pixels), and the equivalent spatial resolution was 0.289 μm/pixel. GDL sample was cut into 1.5 cm wide (W) square and placed between two transparent polycarbonate plates, and liquid water was injected from the bottom plate through a 250 μm diameter stainless steel capillary (U-111, Upchurch) with a syringe pump (NE-300, New Era Pump Systems Inc) at a flow rate (Q) of 100 μL/hour (inlet velocity v = 0.566 mm/s). The variations of the percolation pressure were monitored simultaneously using a pressure transducer (PX163-120D5V, Omega Engineering).

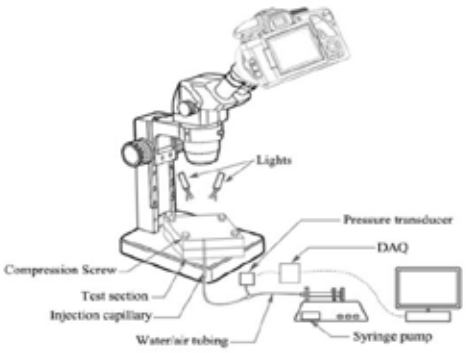


Fig. 1. Schematics of (left) the experimental set-up for visualization of in-plane water transport

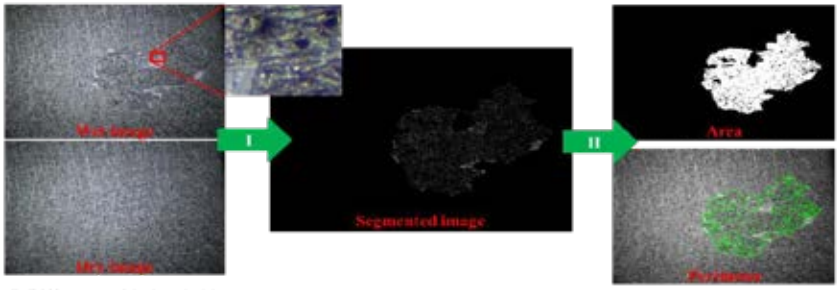


Fig. 2. Procedure of image processing. Wetted regions are segmented by subtracting wet and dry images with a threshold value. Area and perimeter of wetted regions are obtained after applying connected component analysis with methods of noise reduction and filling small holes

The digital image processing technique with an in-house-developed MATLAB code was applied, and the procedure of the image processing is shown in Fig. 2. As shown in the inset of Fig. 2, the spatial resolution of the employed imaging system is high enough to classify wet and dried regions on a pore scale. Wetted regions were segmented from difference images between wet and dry images with a threshold. Information on the wetted area and perimeter was obtained by applying connected component analysis after noise reduction and filling small holes.

RESULTS AND DISCUSSION

GDLs are generally compressed in practical applications, and different degree of compression leads to changes in flow inside the porous structure [8]. The effect of GDL compression with commercial GDL (Sigracet 29 BA having a thickness of 190 μm) on the water transport was investigated. The degree of compression was controlled with stainless steel shims having different thicknesses (δ). Temporal variations in wetted area normalized with the GDL sample width ($A^*=A/W^2$) during water transport are shown in Fig. 3(a). A* in all cases continuously increases, and the lowest compression (δ of 150 μm) had the largest A*.

A Non-dimensional scaling model for percolations in porous media was proposed by combining the time evolutions of pressure and the wetted area [9]. In the model, energy ratio ($Ce=p\delta^3A/Q\mu W^2$) and non-dimensional time ($t^*=t\sigma\delta^2/\mu W^3$) were defined where p is the pressure, μ is the dynamic viscosity, t is time, and σ is the surface tension. It was found that the Ce and t* have a linear relationship. Ce is plotted against t* in Fig. 3(b). Different from the previous observation of Ce-t* having a linear relationship with a single slope during the entire percolation process, Ce had two slopes where Ce linearly increased with a lower slope at a steady state after the rapid increase at initial states. Ce indicates the degree of energy dissipation or pressure-wetted area state. Both the time and Ce for the transition to the steady-state were decreased as the compression becomes higher. Therefore, the decreases of t* and Ce with the increase of compression represent that the transition occurs earlier under lower saturation.

The specific interfacial area defined as a ratio of the wetted perimeter and area (P/A) is commonly employed to investigate the fingering flow pattern, and normalized specific interfacial areas (P*/A*) are shown in Fig. 3(c). P*/A* rapidly decreased until at a specific time, thereafter it kept almost constant. P*/A* curve shifts to the upper left as the compression increases. Higher P*/A* indicates that more fingers or branches occur. Therefore, it is confirmed that the flow pattern is changed over time and water transport occurs along a more complicated path through pores split by compression.

The Ce variation for δ of 50 μm is compared to the variation of P*/A* in Fig. 3(d). It is known that P*/A* is strongly related to Ce, and the water transport pattern is changed when the phase of water transport changes to the steady-state. In order to compare wetted patterns with time, the distributions of the wetted area as time evolution are represented with spatiotemporal maps in Fig. 3(e). At the initial state, most of water comes from regions separated from previously wetted locations. In contrast, water mostly emerges from neighboring spots connected to already wetted regions.

Two typical mechanisms of transport were proposed by Nam and Kaviany [10] and Litster et al [5]. In the first mechanism, the flow is distributed like tree branches where both micro- and macro-transports simultaneously occur. In the second mechanism, the water transport is dominated by fingering and channeling which caused the formation of dead ends and breakthrough locations. Figs. 3(d) and (e) indicate that two different transport mechanisms are dominated in each state. Water transport is dominated by fingering and channeling at the initial state or lower saturation. In contrast, macro transport occurs along a preferential path at the steady-state or higher saturation.

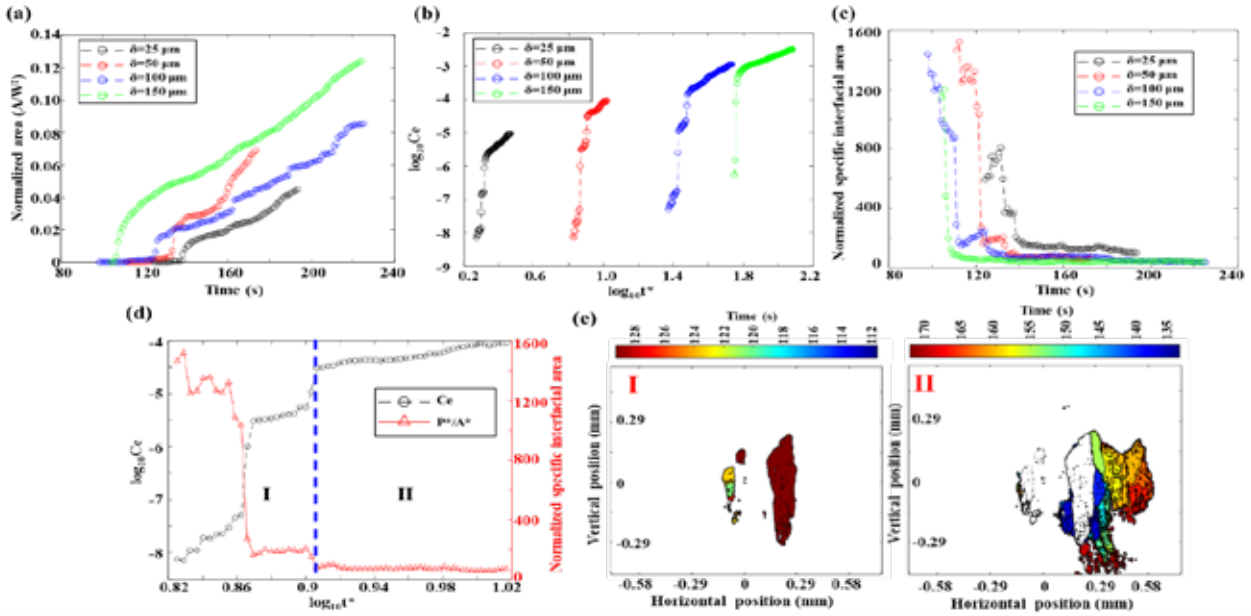


Fig. 3. Comparisons of (a) normalized wetted area (b) Ce, and (c) normalized perimeter with various compressions (16.7, 33.3, 52.6, and 78.9 % for shim thicknesses of 25, 50, 100, and 150 μm, respectively). (d) Time variations of Ce and P*/A* and (e) spatiotemporal maps at initial (left) and steady (right) states for shim thickness of 50 μm.

CONCLUSIONS

In the present study, the transient characteristics were investigated by visualizing the in-plane water transport in GDL. Ce-t* and P*/A* were analyzed, and the wetted area with time is graphically observed by spatiotemporal maps. It is confirmed that the transition of flow characteristics including flow pattern and transport mechanism occurs. As the compression becomes higher, the earlier transition with lower saturation level occurs, and water moves through pores broken by compression.

ACKNOWLEDGEMENT

This study was supported the Technology Innovation Program (20011633) funded by the Ministry of Trade, Industry & Energy (MOTIE, Korea).

REFERENCES

1. Okonkwo PC and Otor C. 2021. A review of gas diffusion layer properties and water management in proton exchange membrane fuel cell system. International Journal of Energy Research 45: 3780-3800.
2. Li H, Tang Y, Wang Z, Shi Z, Wu S, Song D, Zhang J, Fatih K, Zhang J, Wang H. 2008. A review of water flooding issues in the proton exchange membrane fuel cell. Journal of Power Sources 178: 103-117.
3. Allen J, Son S, Collicott S. 2010. Proton exchange membrane fuel cell (PEMFC) flow-field design for improved water management. Handbook of Fuel Cells.
4. Kim SG, Lee SJ. 2013. A review on experimental evaluation of water management in a polymer electrolyte fuel cell using X-ray imaging technique. Journal of power sources 230: 101-108.
5. Litster S, Sinton D, Djilali N. 2006. Ex situ visualization of liquid water transport in PEM fuel cell gas diffusion layers. Journal of Power Sources 154: 95-105.
6. Bazylak A, Sinton D, Djilali N. 2008. Dynamic water transport and droplet emergence in PEMFC gas diffusion layers. Journal of Power Sources 176: 240-246.
7. Medici E, Allen J. 2009. Existence of the phase drainage diagram in proton exchange membrane fuel cell fibrous diffusion media. Journal of Power Sources 191: 417-427.
8. Mortazavi M, Santamaria AD, Chauhan V, Benner JZ, Heidari M, Médici E. 2020. Effect of PEM fuel cell porous media compression on in-plane transport phenomena. Journal of Power Sources Advances 1: 100001.
9. Medici E, Allen J. 2011. Scaling percolation in thin porous layers. Physics of Fluids 23: 122107.
10. J.H. Nam, M. Kaviany, Effective diffusivity and water-saturation distribution in single-and two-layer PEMFC diffusion medium, International Journal of Heat and Mass Transfer 46(24) (2003) 4595-4611.

WHEC-2022
23rd World Hydrogen Energy Conference
June 26-30, 2022 - Istanbul

#1579

GDL DEGRADATION EFFECT ON FLOWS INSIDE FLOW CHANNEL ON POLYMER ELECTROLYTE MEMBRANE FUEL CELL

[1] *Jong Woon Moon,* [1] *Seong Keun kim,* [1*] *Sung Yong Jung*
[1]Chosun University, Department of Mechanical Engineering, 309 PILMUN-DAERO, DONG-GU, GWANGJU 61452, Rep. of KOREA

*Corresponding author e-mail: syjung@chosun.ac.kr

ABSTRACT

Performance reduction of polymer electrolyte membrane fuel cell caused by the degradation of gas diffusion layer (GDL) is hydrodynamically analyzed by comparing visualized two-phase flows in flow channels. GDL was chemically degraded using hydrogen peroxide, and the degree of GDL degradation was controlled by changing soaking time. The I-V curves for fresh and aged GDLs were compared using a commercial single cell, and the behavior of water in the cathode flow channel was visualized using a specially designed single cell having a transparent window. Two-phase flow characteristics were quantitatively compared after applying image processing technique to captured images. As a result of the experiment, it was confirmed that the hydrophobicity of GDL decreases as it degrades, absorbing the water generated inside, and reducing the efficiency by blocking the supply of reactants.

Keywords: Proton Exchange Membrane Fuel Cell, Gas Diffusion Layer Degradation, Flow Visualization, Reduced Hydrophobicity, Mass Transport Loss

INTRODUCTION

Hydrogen is regarded as an eco-friendly alternative energy source that can replace fossil fuels, and polymer electrolyte membrane fuel cell (PEMFC), which convert hydrogen to electric power has been widely studied in various fields because of its high energy efficiency. PEMFC has a fatal disadvantage in its long-term durability. Water management is critical to the suitable water content for the reliable operation of PEMFC, and poor water management causes reducing durability and performance by aging internal components [1]. GDL (Gas Diffusion Layer) plays a role in the fuel diffusion and electric and heat transfers, and it also effectively manages the water inside the PEMFC. It is known that GDL is degraded due to hydrogen peroxide and electrochemical oxidation during the practical operation of PEMFCs, and the GDL degradation leads to the increase of mass transport losses resulting in the performance reduction of PEMFCs.

The accumulation of liquid water accumulation causes performance degradation such as voltage instability, and many researchers have studied water distributions inside PEMFCs. Donggun Ko et al. investigated water accumulation inside PEMFC using X-ray imaging technique [2]. Juliane Kätzel et al. studied the relationship between the degrading time and droplet size distribution of GDL through neutron radiographs [3]. Although several studies have been conducted to quantify the liquid water in the cathode flow channel, the effect of flow patterns inside the flow channel on mass transfer is still not clear and systematic studies about the GDL degradation effect on flows are still lacking.

In this study, cell performances for pristine and aged GDLs were measured, and corresponding two-phase flow in the cathode flow channel was visualized using optical high-speed imaging. The relationship between flow pattern and cell performance was analyzed.

MATERIALS AND METHODS

To degrade GDL (SGL 39BB), it was immersed in a 35 wt% hydrogen peroxide solution at 90 °C. Three degradation GDLs with different degradation degrees were prepared by changing the immersion time to 4, 12, and 24 hours. Degraded samples were soaked in DI water for 24 hours to remove residual hydrogen peroxide and then dried in an oven. For the performance test, hydrogen and oxygen were supplied to the cell. The temperature of the cell was set higher than the supply pipe to prevent the condensation of the fully humidified gas. The polarization curves for fresh and aged GDLs were measured using a commercial unit cell with a 25 cm2 active area. For accurate performance comparison, the degraded GDLs were placed only at the cathode side, and fresh GDLs were used in the anode side. To investigate the direct effect of the GDL degradation on the mass transport loss PEMFC, two-phase flows inside the cathode flow channel were visualized using a specially manufactured single cell. End plate was changed with a transparent plate mead of quartz. Images of flows were captured for 8 seconds using a high-speed camera at a current of 1.0 A/cm2 where mass transport losses significantly occur.

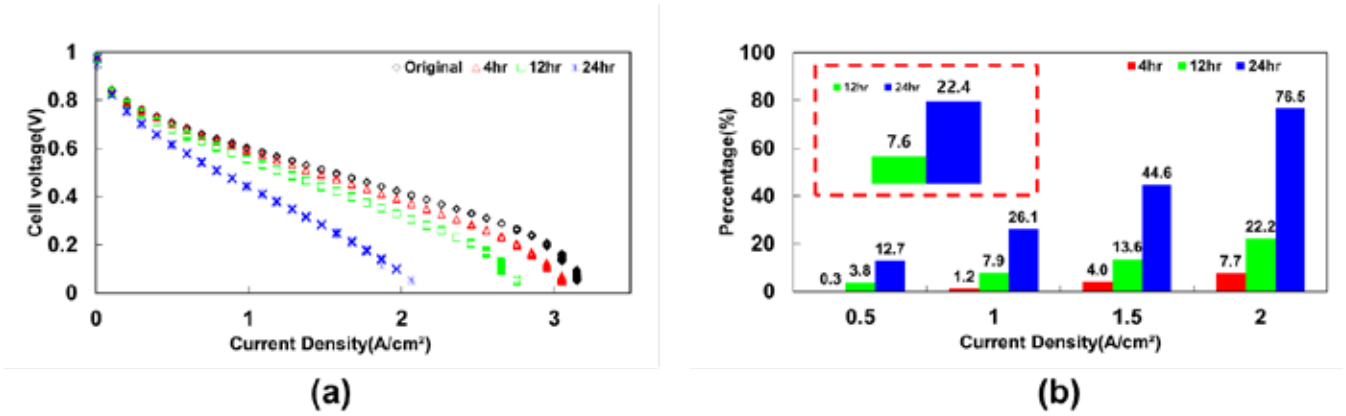


Figure. 1. (a) Comparison of the I-V curves and (b) The voltage decay ratio for degradation GDLs compared to the pristine GDL at various current densities (voltage decay ratio at 1.0A/cm^2 with the visualization cell is represented in red dashed box).

RESULTS AND DISCUSSION

Fig. 1(a) compares the I-V curves with various degradation GDLs. The voltages in all GDLs gradually decreased as the current density increased, and decreased rate of voltages with the increase of current became higher as the degradation time increased. Compared to voltages in the fresh GDL, the voltage reduction ratios in each GDL at various current densities are quantitatively calculated in Fig. 1(b). The voltage reduction rapidly increased as the degrading time was longer. The 4 hr degraded GDL had a small voltage reduction rate, and the maximum reduction was 7.7 %. Whereas, the performance reductions significantly occurred for the 12 and 24 hr GDLs, and the reductions reached to 22.2 % and 76.5 % at a current density of 2.0 A/cm^2, respectively. This means that the degradation of GDL strongly affects the performance of the cell, and it is important to understand the relationship between water transport and cell performance because the degradation of GDL mainly leads to the change of mass transport.

In order to confirm the similarity of operations in the visualization cell, the voltage reduction at 1.0 A/cm^2 was also calculated in Fig. 1(b). The voltage reduction was almost identical to that of the commercial cell. Therefore, the operations in the visualization cell are similar to those in the commercial cell. In addition to the operating condition, material properties (particularly the wettability of flow channels) strongly affect flows inside flow channels. Contact angles on Teflon film on the transparent plate side in contact with the gas channel in the visualization cell were measured, and both surfaces had similar contact angles. Fig. 2(a) shows the procedure of image processing with Matlab and Image J software to obtain information of two-phase flows. Flat field correction was firstly applied to captured images based on a background image obtained before operations, Thereafter, liquid water and gas were finally distinguished after performing threshold correction and noise reduction. Void fractions were calculated using areas of liquid and gas from 1000 images and compared in Fig. 2(b). Liquid water covered 5.9 % channel area in the fresh GDL. The degradation GDLs represented higher void fractions, and GDLs with the degradation time of 12 and 24 hours had 14.1 % and 21.2 %, respectively. This indicates that as the degradation time of the GDL increases, the liquid water remains in the gas channel longer.

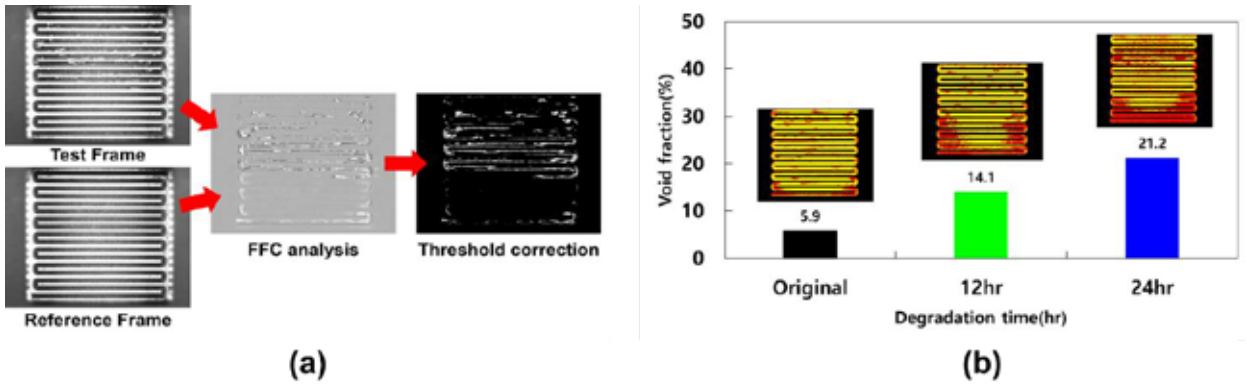


Figure. 2. (a) Procedure of image processing and (b) comparison of void fractions in the flow channel

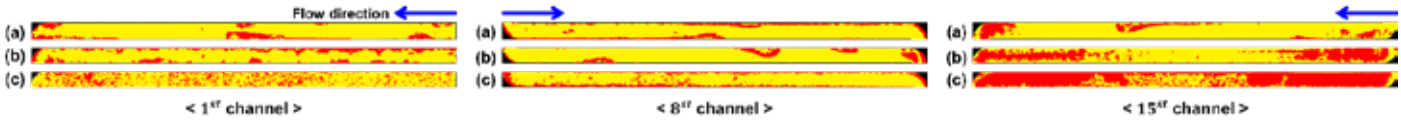


Figure. 3. Typical flows in channels near inlet, middle, and outlet for (a) pristine, (b) 12 hr, and (c) 24 hr degradation GDLs.

To compare flows more clearly, typical liquid and gas distributions are represented in Fig. 3. Yellow and red regions represents the gas and liquid phases, respectively. From inlet to outlet, the amount of liquid water increased and gas flow velocity decreased because gas supplied to MEA through GDL and produced water by a chemical reaction uniformly discharged from GDL and coalescence of droplets occurred. Therefore, flow characteristics vary according to channel locations, and images in three channels at different locations near inlet, midstream, and outlet are represented in Fig. 3. Slug flows where dropwise liquid water moved were observed near the inlet. Almost liquid water removed for the pristine GDL when droplet passed. Whereas, water remained on surfaces for degradation GDLs because the hydrophobicity of GDL surface decreased with GDL degradation, and the amount of remaining water was increased with the increases of the degradation time. As liquid water flows further, continuous liquid columns are formed due to droplet merging. Near the midstream, stratified-wavy flows with long liquid columns were observed, and the width of liquid columns increased as the degree of GDL degradation was higher. When liquid columns have a large width comparable to the channel width, severe channel flooding having liquid films completely covering GDL surfaces and moistures on the transparent plate occurs. When the severe flooding occurs, it is difficult to distinguish liquid and gas phases from optical images of liquid flows. Therefore, liquid continuously flows although no liquid region is distinguished in processed images. Near the outlet where severe flooding occurred, distributions of only remained water were mainly observed from image processing as shown in Fig 3, and liquid water accumulated at curved locations. The number of channels having a high accumulation of liquid water at bended location indicates the number of flooding channels, and the flooding channels increased with the increase of degradation time. These results show that more surface areas of GDL were blocked by liquid water which caused the reduction of supplying gas to chemical reaction sites resulting in the voltage drop.

CONCLUSIONS

In this study, the deterioration of PEMFC performance cause by GDL degradation was analyzed in terms of mass transport loss by visualizing two-phase flows in cathode flow channels. The reduction of hydrophobicity in degradation GDLs leads to the increase of water fractions because water was not completely removed from GDL surfaces when droplets passed. As liquid water flows further, continuous liquid columns are formed, and the width of those liquid columns gradually increased. Liquid column having large width caused the severe channel flooding, and the flooding region increased with the increase of the degradation time. More flooding channels with the GDL degradation leaded the increase of mass transport losses resulting in the decrease of PEMFC performance.

ACKNOWLEDGEMENT

This study was supported the Technology Innovation Program (20011633) funded by the Ministry of Trade, Industry & Energy (MOTIE, Korea)

REFERENCES

1. Ijaodola, O., et al. (2019). "Energy efficiency improvements by investigating the water flooding management on proton exchange membrane fuel cell (PEMFC)." Energy 179: 246-267.
2. Ko, D., et al. (2019). "The effects of water accumulation at the interface between gas diffusion layer and gas supplying channel on the water distribution in polymer electrolyte membrane fuel cells." International Journal of Hydrogen Energy 44(45): 24947-24953.
3. Kätzel, J., et al. (2016). "Effect of ageing of gas diffusion layers on the water distribution in flow field channels of polymer electrolyte membrane fuel cells." Journal of Power Sources 301: 386-391.

WHEC-2022
23rd World Hydrogen Energy Conference
June 26-30, 2022 - Istanbul

#1585

A SCALABLE ANALYTICAL MODEL FOR RAPID MULTIPHYSICAL ANALYSIS AND STRUCTURAL OPTIMIZATION OF PEM FUEL CELLS

[1*] *Markus Kohrn,* [1] *Yingxu Liu,* [1] *Maximilian Wick,* [1] *Stefan Pischinger*
[1]Chair of Thermodynamics of Mobile Energy Conversion Systems,
RWTH Aachen University, Forckenbeckstrasse 4, Aachen, Germany

*Corresponding author e-mail: kohrn@tme.rwth-aachen.de

ABSTRACT

To further improve the overall marketability of fuel cell vehicles, improves are necessary in particular on the durability of the employed proton exchange membrane fuel cells. A key factor in durability is the distribution of mechanical stresses within the cells, which can be reduced by optimization of the bipolar plate rib structure. However, this optimization should not be performed without taking into account further physical quantities such as porosity and electric resistivity, as these have a direct impact on the cell performance. Therefore, this study presents a multiphysical simulation model based on a new analytical approach, which, in addition to the stress and strain distribution can also compute a variety of relevant physical quantities. The model's capability is demonstrated on an exemplary fuel cell layout. Compared to FEM models, the computation time can be reduced by a factor of up to 1000. Thus, extensive simulation studies with multi-criterial optimization can be implemented with reasonable computational effort.

Keywords: PEM Fuel Cell, Analytical Model, Gas Diffusion Layer, Mechanical Stresses, Physical Properties

INTRODUCTION

PEM fuel cell stacks consist of two main components, the solid bipolar plates (BPP) and the soft membrane electrode assemblies (MEA), which are alternately stacked and clamped. BPPs conduct the electric current between the cells, dissipate the waste heat from the stack, and distribute the reaction gases over the cell surface via the integrated gas channels. MEAs in turn consist of a proton exchange membrane (PEM) in the center, which is enclosed by a catalyst layer (CL) and a gas diffusion layer (GDL) on each side. The GDLs, which may account for up to 95 % of the MEA's overall thickness, are composed of carbon fiber fabrics [1]. Because of its physical structure, GDLs exhibit highly anisotropic mechanical properties. The carbon fibers conduct electricity and heat and provide mechanical support for the fragile membrane. Through the pores, gas and liquid water are transported.

One of the main reasons for early-stage failure of fuel cells is mechanical damage [2]. This risk can be reduced by optimizing the BPP rib structure with respect to the mechanical stress distribution. But changing the flow field may affect other relevant physical properties including the GDL's porosity and electrical resistance, both of which have a direct impact on cell performance. However, multicriterial optimization of the BPP structure is rare in the literature. The aim of this study is to address this research gap.

In this study, a novel analytical model (AM) is utilized. In contrast to the traditional finite element method (FEM), the equations are not solved interactively for defined grid nodes. Instead, explicit analytical formulations are established for each quantity. The computational speed is thus increased by a factor of up to 1000, with an average inaccuracy of less than 5 % [3]. Thus, instead of small segments, entire flow fields can be optimized with reasonable computational effort.

MODELING

Firstly, the general modelling approach of the AM is explained. Then the geometrical build-up and solving algorithm for the mechanical properties are introduced, followed by an extension of the model for other significant physical properties.

Analytical Modelling Approach

The modeling approach has been described in detail in our previous work Liu et Al. [3]. Therefore, only the basic assumptions and equations will be presented here: 1) The MEA is approximated as 100 % GDL; 2) The GDL is significantly stiffer in in-plane direction than in through-plane direction, thus, the in-plane strain can be neglected; 3) the BPP is assumed to be rigid; 4) only forces in the principal stress direction (y) are considered.

For an infinitesimal element, the force balance is as follows:

$$\frac{\partial \sigma_y(x,y)}{\partial y} = -\frac{\partial \tau_{xy}(x,y)}{\partial x} \quad (1)$$

The shear stress τ_{xy} on the GDL surfaces is directly related to the 2nd derivative of the GDL surface curve $h(x)$. With the shear modulus G_{xy} and the Timoshenko coefficient k, it holds:

$$\tau_{xy,surf}(x) = kG_{xy}\,\frac{\partial^2 h(x)}{\partial x^2} \tag{2}$$

For the sub-surface shear stress distribution, the following relationship is proposed:

$$\tau_{xy}(x,y) = \tau^{Top}_{xy,surf}(x)\left(0.5+\frac{y}{H_{GDL}}\right)^{n^{Top}} + \tau^{Bot}_{xy,surf}(x)\left(0.5-\frac{y}{H_{GLD}}\right)^{n^{Bot}} \tag{3}$$

n^{Top} and n^{Bot} are parameters fitted against FEM simulations and dependant on the rib radius R_{rib} and the initial GDL thickness H_{GDL}. The relation between GDL deformation and normal stress is governed by Hook's law:

$$\frac{h^{Top}(x)-h^{Bot}(x)}{H_{GDL}} = \frac{1}{E_y}\int_{y=-\frac{H_{GDL}}{2}}^{\frac{H_{GDL}}{2}} \sigma_y(x,y)dy \tag{4}$$

From these basic equations, by applying the specific boundary conditions, analytical equations for normal and shear stress as well as displacement and deformed height can be derived.

Model build-up and solving algorithm

Starting from pre-designed anode and cathode flow fields, one (or more) characteristic cross-sections are placed across a single fuel cell (Fig. 1a). Then, based on symmetry, recurring segments are identified (Fig 1b), which are subsequently divided into distinct regimes depending on the clamping state (Fig. 1c). In each regime, the top and bottom surfaces are each subjected to either the flat BPP bottom, the BPP edge, or are free under the channel. Some of the regime boundaries are geometrically determined and thus fixed, whereas others depend on the GDL deformation and are thus movable. The specific boundary conditions that apply in each regime simplify the set of analytical equations and ultimately the coupling conditions of the regimes allow the system to be solved. The moving boundaries are determined iteratively by setting the adjacent shear stresses equal.

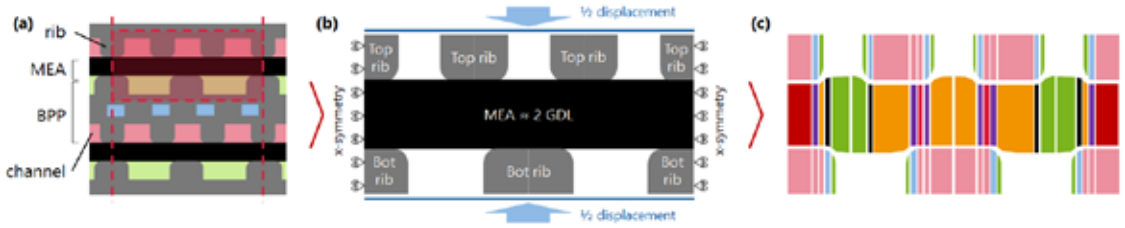


Fig. 1. Model build-up (a) cross-section through single cell (b) recurring segment (c) subdivision in regimes

The obtained simulation results are continuous and differentiable on the surfaces, but not in the interior of the GDL. This is because the model does not take into account the y-direction Therefore, the model employs a smoothing algorithm, that preserves the GDL surface curve and the y-force balance. Thus, continuous normal and shear stress distribution maps are obtained for the whole fuel cell cross section. This also enables further relevant physical quantities to be derived.

Muliphysical extension

The strain ε of a perfectly-elastic material can be determined from the normal stress by Hook's law. From the strain, distribution, the porosity ϵ (fraction of pore volume V_{pore} in total GDL volume V_{tot}) can be calculated:

$$\epsilon = \frac{V_{pore}}{V_{tot}} = 1-\frac{1-\epsilon_0}{1+\varepsilon} \tag{5}$$

From the porosity, further quantities are derived, e.g. the diffusivities of the individual gases and liquid water. Another quantity is the volumetric resistivity ρ , which can be determined from the effective conductivity κ_{eff} using the Bruggemann approximation, where κ_s is the bulk conductivity and m is the Bruggemann coefficient:

$$\rho_V = \frac{1}{\kappa_{eff}} = \frac{1}{\kappa_S\,(1-\epsilon)^m} \tag{6}$$

The contact resistance is mainly dependant on the pair of materials, the surface textures, and the contact pressure. It is usually measured experimentally. The overall material resistance results from the combination of volumetric resistivity and surface resistance.

MODEL DEMONSTRATION

To demonstrate the model's capability, an exemplary GDL is investigated multiphysically. The geometrical and physical input parameters are listed in Table 1 and reflect typical values for automotive fuel cells.

Table 1. Simulation Parameters

	Para	Description	Value / Unit			Para	Description	Value / Unit	
Geometrical	d_{rib}	Rib width (anode / cathode)	1000 / 600	µm	Physical	E_y	Young's Modulus of GDL	8.79	MPa
	d_{ch}	Channel width (anode / cathode)	500 / 400	µm		G_{xy}	Shear Modulus of GDL	8.55	MPa
	R_{rib}	Rib edge radius (anode / cath.)	150 / 200	µm		ϵ_0	Bulk porosity of GDL	0.5	-
	H_{gdl}	Thickness of gas diffusion layer	400	µm		κ_s	Bulk conductivity of GDL	1000	S/m

The geometrical conditions result in a recurrent segment of 3000 µm width with 2 channels on the top side and 3 on the bottom side. The simulation results for normal y-stress, porosity and volumetric resistivity are depicted in Fig. 2a-c. With the resistivity and the contact resistance interpolated from experimental data by Zamel et Al [4] and an assumed voltage of 1 V between the BPPs, an electrical potential field is (Fig. 2d).

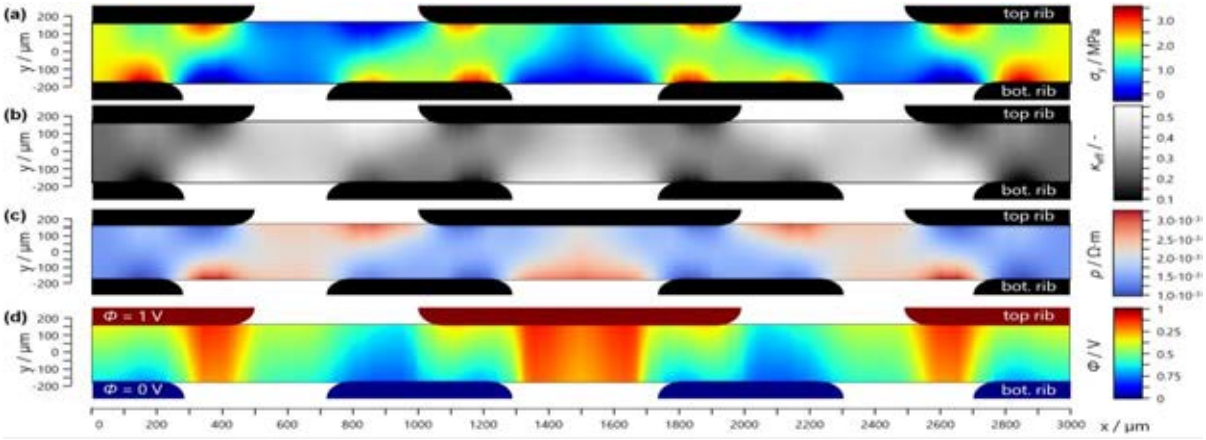


Fig. 1. Multiphysical analysis of a 400 µm thick GDL between 2 nonequal BPPs
(a) through-plane stress, (b) porosity, (c) volumetric resistivity, (d) electric potential.

CONCLUSIONS

In this study, a scalable simulation tool based on a novel analytical method for multiphysical analysis of PEM fuel cells is presented. Due to the high computational speed compared to FEM, extensive simulation studies of entire flow fields can be performed. In addition to shear and normal stresses, other relevant physical quantities, such as porosity and electrical resistance can also be calculated. Hence, the model is highly suited for multicriterial optimization tasks of BPP structures.

FUNDING

This work is funded by Deutsche Forschungsgemeinschaft (DFG, German Research Foundation) [grant number GRK 1856].

REFERENCES

1. Lee T, Yang C. 2020. A parametric study on the deformation of gas diffusion layer in PEM fuel cell. J Mech Sci Technol 34:259-68.
2. Qiu D, Peng L, Lai X, Ni M, Lehnert W. 2019. Mechanical failure and mitigation strategies for the membrane in a proton exchange membrane fuel cell. Renewable and Sustainable Energy Reviews 113:109289
3. Liu Y, Kohrn M, Wick M, Pischinger S. 2022. Optimization of the bipolar plate rib structure in proton exchange membrane fuel cells with an analytical method. International Journal of Hydrogen Energy. [accepted manuscript]
4. Zamel N, Xianget L, Shen J. 2012. Numerical estimation of the effective electrical conductivity in carbon paper diffusion media. Applied Energy 93:39-44.

WHEC-2022
23rd World Hydrogen Energy Conference
June 26-30, 2022 - Istanbul

#1590

STUDY OF CATALYST LOADING AND GDL POROSITY GRADIENT VARIATION EFFECT TO PEMFCs PERFORMANCE THROUGH RECURRENT NEURAL NETWORK (RNN) DATA-DRIVEN ASSISTED MODELLING

Hanhui Lei
Northumbria University, UK

*Corresponding author e-mail: hanhui.lei@northumbria.ac.uk

The required electrochemical activities and mass transport rates of polymer electrolyte membrane fuel cell (PEMFCs) is different owing to the inhomogeneous distributions of reactants and products within the membrane electrode assemblies (MEAs). The graded distributions of Pt loading in the catalyst layer (CL) and porosity of gas diffusion layer (GDL) along the in-plane and through-plane directions significantly affect the spatial distributions of electrochemical reaction and mass transport rates, thus influence the cell performance, i.e., the limiting current density. Herein, we developed a two-dimensional (2D), multi-physics, two-phase flow model to investigate the gradients of linear change of two design parameters, i.e., platinum loading and GDL porosity at the cathode. Both the profiles of platinum loading and GDL porosity obey an elliptic function, leading to the linear variations of these two design parameters along the in-plane and through-plane directions (see Fig. 1a and 1b). Six parameters were selected, and their interaction was numerically studied by the recurrent neural network **(**RNN) model, including the 1). platinum loading at the CL-GDL interface at the cathode inlet, 2). platinum loading gradient along the in-plane direction (from inlet to outlet), 3). Platinum loading gradient along the through-plane direction (from CL-GDL interface to PEM-CL interface), 4). GDL porosity at the CL-GDL interface at the cathode inlet, 5). GDL porosity gradient along the in-plane direction (from inlet to outlet), and 6). GDL porosity gradient along the through-plane direction (from CL-GDL interface to GDL-channel interface). The combination of these parameters will generate 5000 permutations at the accuracy of 0.1. To reduce the computational time and resources of solving the mechanistic model, a data-driven surrogate model is developed based on RNN algorithm, which is used to assist the identification of the relationship between the chosen parameters and the objective function (current density at 0.1V).

Initial data acquisition was conducted using COMSOL Multiphysics for training and testing the surrogate model. Then Latin hypercube sampling method is used to guarantee the uniformity of sampling data. Random nodes are selected to train the RNN algorithm to accelerate the acquisition of simulation results. The RNN model achieved > 97% prediction accuracy (Fig. 1d).

The separate studies of platinum loading and GDL porosity indicated that the highest current density of 3.627 A cm^{-2} was achieved when 0.2 mg cm-2 platinum loading was implemented at the membrane-CL interface at the cathode inlet (point A in Fig. 1c) and at the CL-GDL interface at the cathode inlet (point B in Fig. 1c), while the platinum loading at the membrane-CL interface at the cathode outlet (point F in Fig. 1c) was 0.3 mg cm-2 and the GDL porosity was uniformly maintained at 0.7. On the contrary, the impact of GDL porosity on current density is monotonous - the current density increases with the increase of GDL porosity. When the inhomogeneous distribution of GDL porosity is simultaneously considered, the maximum current density of 3.820 A cm-2 was obtained when the platinum loading was 0.1, 0.2, and 0.8 at A, B and F in Fig. 1c, and the GDL porosity is 0.8, 0.8, and 0.8 at B, C and E, respectively. It also showed that machine learning algorithm could effectively assist the optimal design of PEMFCs.

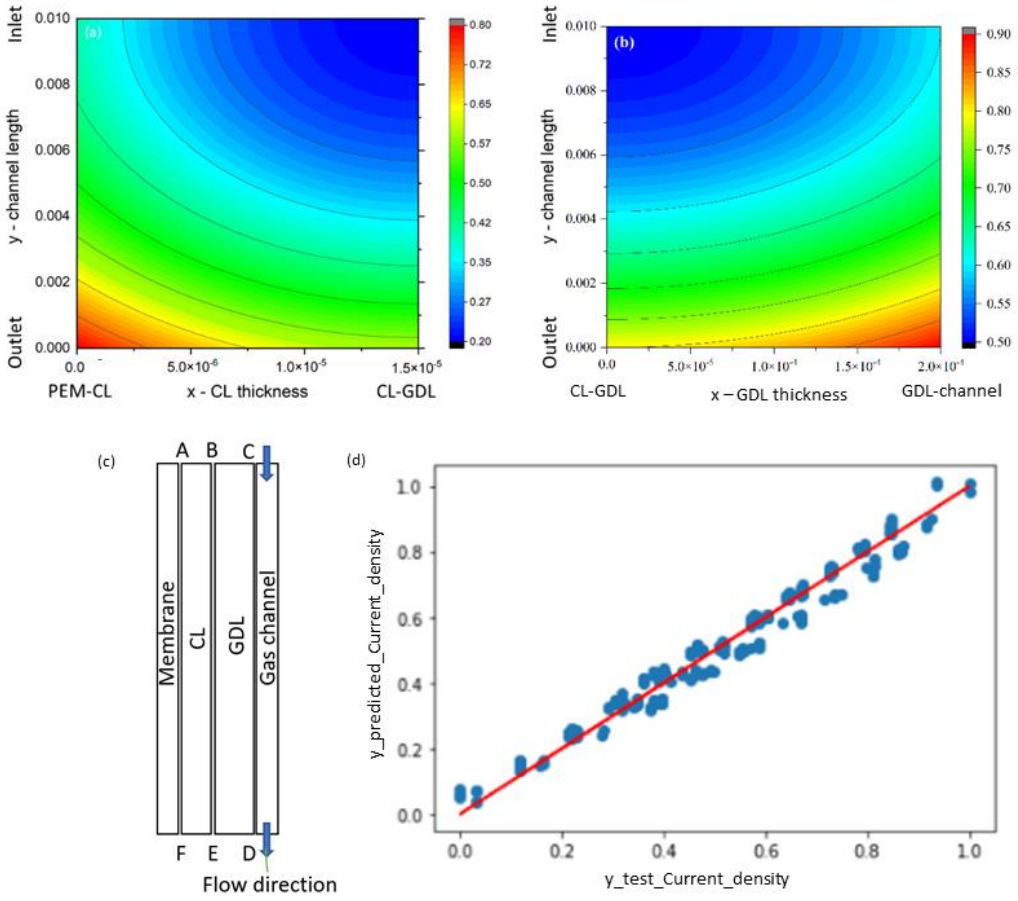


Fig. 1 Profiles of platinum loading (a) and GDL porosity (b) with $m_{Pt,0}$ = 0.2 mg cm^{-2}, $m_{Pt,1}$ = 0.4 mg cm^{-2}, $m_{Pt,2}$ = 0.6 mg cm^{-2}; and $\varepsilon_{GDL,0}$ = 0.5, $\varepsilon_{GDL,1}$ = 0.6, $\varepsilon_{GDL,2}$ = 0.8. Structure of device (c), AD edge is inlet, CB edge is outlet. Comparison of fitting results between prediction set and test set (d)

WHEC-2022
23rd World Hydrogen Energy Conference
June 26-30, 2022 - Istanbul

#1591

SULFONATED SILICA/NAFION® BASED COMPOSITE ELECTROSPUN MEMBRANES FOR PEM FUEL CELLS

[1*] *Naeimeh Rajabalizadeh,* [1] *Ahmet Can Kırlıoğlu* [1,2] *Selmiye Alkan Gürsel and* [2]*Begüm Yarar Kaplan*
[1] Sabancı University, Faculty of Natural Science and Engineering, 34956, Istanbul, Turkey
[2] Sabancı University Nanotechnology Research and Application Center(SUNUM), 34956, Istanbul, Turkey

*Corresponding author e-mail: nrajabaliazdeh@sabanciuniv.edu

ABSTRACT

In this study, dual electrospinning were employed to fabricate proton conducting membranes comporising sulfonated silica, Nafion® and PVDF or P(VDF-TrFE) as the carrier polymers. Firstly, dual electrospinning was carried out to obtain dual fiber-based mats and converted into compact membranes via hot-pressing. After obtaining compact membranes, effect of various amounts of Nafion and type of carrier polymers were investigated. FTIR, ionic conductivity, ion exchange capacity (IEC), water uptake measurments and mechanical test were conducted for these membranes. Finally Membrane-electrode-assemblies (MEAs) were prepared via composite electrospun membranes and sprayed electrodes and fuel cell performance tests were performed. The fuel cell test showed that presence of sulfonated silica in the composite membranes improved the performance at lower humidity conditions. The P(VDF-TrFE)-Nafion®/S-SiO_2 membranes with 60/30 wt% Nafion®/S-SiO_2 compositon showed the best ionic conductivity and fuel cell performance.

Keywords: Dual Electrospinning, Sulfonated Silica, Sol-Gel, Membranes, PEM Fuel Cells

INTRODUCTION

Growing demand for clean energy, global warming issues and depletion of fossil fuel resources are highligheted the urgent need for developing alternative energy conversion systems in recent years. Among various clean energy technologies polymer electrolyte (PEMFC) fuel cells have received a lot of interest due to thier exceptional merits such as compact set-up, rapid start-up, and high efficiency [1]. However, significant design and component innovations are required to address the drawbacks and high cost of existing systems. In PEM fuel cells hydrogen and oxygen or air are fed into to anode and cathode side respectively as fuel to generate electricity, heat and water are being the only by products of this electrochemical reaction. The central part of a PEMFC is a proton conducting membrane, which is responsible for proton conduction from the anode to cathode as well as preventing of water and oxygen to diffuse back into anode side [2]. Perfluorosulfonic acid-based membranes (Dupont's Nafion®) are the most common membrane material for PEM fuel cell applications; but their proton conductivity is limited to fully humidified conditions, and they are expensive. As a result, research into finding a cost effective membrane material that can match the fundamental features of high proton conductivity, chemical stability and mechanical property under harsh cell operating conditions and efficient system performance is a hot issue [3].

Due to the this fact sulfonated silica-based composite proton exchange membranes for PEMFC applications were prepared via dual electrospinning method. Incorporation of hydrophilic sulfonated silica network to reduce the Nafion® amount results in minimizing excess water swelling problems of Nafion® membranes while maintaining ionic conductivity at low humidity levels, mechanical properties and fuel cell performance.

MATERIALS AND METHODS

Sulfonated silica was prepared via sol gel method using tetraethyl orthosilicate (TEOS) as silica precursor. PVDF and P(VDF-TrFE) were used as carrier polymers mixed with Nafion® solution. The prepared solutions were loaded in two different syringes. Sulfonated silica solution was electrospun from one side and PVDF-Nafion® or P(VDF-TrFE)-Nafion® from opposite side on to the rotating drum. The obtained mats were hot-pressed and annealed to convert dual fiber mats to the compact membranes. Figure 1 shows schematic of electrospinning set up and dual fiber-based membrane preparation steps.

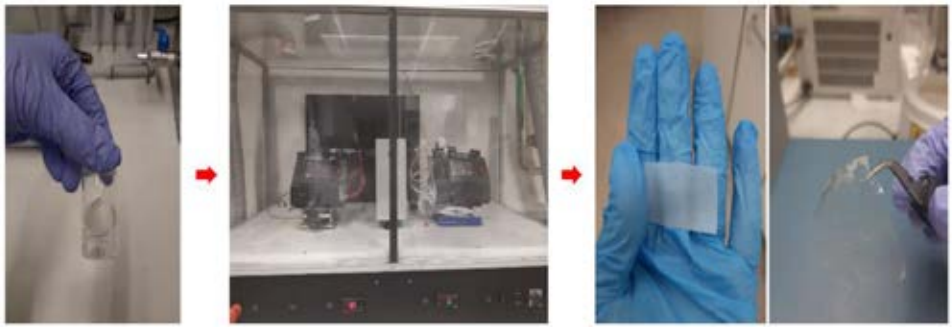


Figure 1. Schematic of dual-electrospuning setup and preparation steps of the membrane

Scanning Electron Microscopy (SEM) were conducted to investigate the morphology of resultant electrospun mats before and after hot pressing. Tensile tests were performed to analyzed mechanical properties such as Young's modulus and maximum elongation. Ion exchange capacity (IEC), water up-take (%) at room temperature were conducted prior to conductivity test. The conductivity tests at room temperature and 80°C were performed. The composite membranes with promising characteristics were selected for fuel cell test.

RESULTS AND DISCUSSION

Figure 2 shows the SEM images of resultant electrospun membrane prior to hot-pressing as well as hot-pressed compact membrane that reveals a homogenous fibrous morphology for resultant mats and uniform dense membrane without pores and cracks after further manipulations.

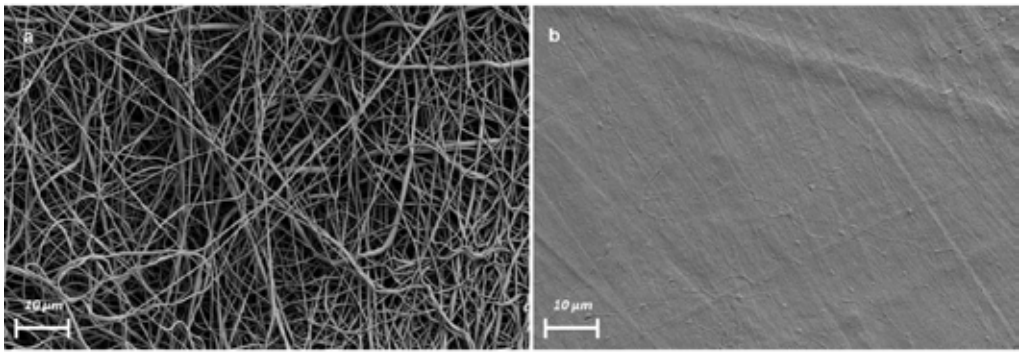


Figure 2. SEM images of P(VDF-TrFE)-Nafion/S-SiO_2 electrospun mat a) before hot-pressing and b) after hot-pressing

CONCLUSIONS

In this work, dual electrospinning method were used to synthesize sulfonated silica Nafion®-based composite membranes. P(VDF-TrFE) as the reinforcing polymer was used for the first time for this purpose in the literature. The obtained proton exchange membranes were characterized to find out the promising membrane for PEM fuel cell application at low relative humidity condition. The water-uptake and ionic conductivity of the membranes is reduced with decreasing the amount of Nafion in membrane composition for either using PVDF or P(VDF-TrFE) as carrier polymers. The highest ionic conductivity of 132 mS/cm was achieved for P(VDF-TrFE)- Nafion®/S-SiO_2 membranes with 60/30 wt% Nafion®/S-SiO2 at 80°C and 100% relative humidity. Furthermore, unlike to prinstine Nafion membranes, these membranes showed no significant reduction in ionic conductivity or fuel cell performance when relative humidity was reduced up to 60%. Therefore, we can conclude that these membranes can be considered as promising candidate for low humidity PEM fuel cell applications.

REFERENCES

[1] Wang Y, Ruiz Diaz DF, Chen KS, Wang Z, Adroher XC. Materials, technological status, and fundamentals of PEM fuel cells – A review. Mater Today 2020;32:178–203. doi:10.1016/j.mattod.2019.06.005.
[2] Sood R, Cavaliere S, Jones DJ, Rozière J. Electrospun nanofibre composite polymer electrolyte fuel cell and electrolysis membranes. Nano Energy 2016;26:729–45. doi:10.1016/j.nanoen.2016.06.027.
[3] Banerjee S, Curtin DE. Nafion® perfluorinated membranes in fuel cells. J Fluor Chem 2004;125:1211–6. doi:10.1016/j.jfluchem.2004.05.018.

WHEC-2022
23rd World Hydrogen Energy Conference
June 26-30, 2022 - Istanbul

#1596

PREPARATION OF KAOLIN AND BENTONITE ADDED NAFION COMPOSITE MEMBRANES

[1] *Fahriye Dönmez,* [2*] *Nezihe Ayas*
[1]Eskişehir Technical University, Engineering Faculty, Department of Chemical Engineering, Eskişehir, Turkey

*Corresponding author e-mail: nazcan@eskisehir.edu.tr

ABSTRACT

Clay (kaolin, bentonite) doped Nafion composite membranes are considered as an alternative material for proton exchange membrane fuel cell (PEMFC). In this study, 10% clay (wt./wt.) doped Nafion membranes were prepared by solution casting method and characterized by water uptake capacity, ion exchange capacity (IEC), X-Ray diffractometry (XRD) and Fourier transform infrared spectrometry (FT-IR). The results showed that kaolin and bentonite doped Nafion membranes can be evaluated for PEM fuel cells.

Keywords: Nafion, Kaolin, Bentonite, Membrane, Fuel Cell

INTRODUCTION

The membrane is considered the key component for the operation of Proton exchange membrane (PEM) fuel cells [1]. The main function of PEM is to transfer protons from the anode to the cathode and to prevent mixing of reactants (H_2 and O_2). Therefore, an ideal PEM should have high proton conductivity, low permeability to fuel, excellent mechanical and chemical stability, and high durability [2]. Nafion is the most widely used electrolyte in PEM fuel cells due to its chemical and electrochemical stability and high proton conductivity [1,3]. However, the proton conductivity of Nafion above 80 °C is significantly reduced as it depends on the hydration level of the membrane [3]. In order to improve the thermal stability and water uptake properties of the membrane, hygroscopic particles such as SiO_2, ZrO_2, TiO_2, ZrP and clays with high SiO_2 content are included in the structure of the membrane [4]. Composite membranes are of interest because most of the additives used can operate at much higher temperatures than pure polymers. The main roles of fillers in composite membranes are to retain water within the membrane to improve proton conductivity and ion exchange capacity while maintaining good mechanical and thermal stability [5]. Although there are studies in the literature with sepiolite, laponite and zeolite doped composite membranes, no studies have been found with kaolin and bentonite. In this study, composite membranes containing kaolin and bentonite added to Nafion were prepared by solution casting method and characterized by water uptake capacity, IEC, XRD and FTIR.

MATERIALS AND METHODS

Materials: In membrane synthesis, Nafion solution (Ion Power, D2021, 20% polymer content) was used as a polymer and N-N Dimethylformamide (DMF, 99%, Sigma Aldrich) was used as a solvent. Sulfuric acid (H_2SO_4, 95%, Merck), hydrogen peroxide (H_2O_2, 30%, Merck), sodium chloride (NaCl) and sodium hydroxide (NaOH, 85%, VWR Chemicals) was used without further purification. The bentonite and kaolin were supplied from a commercial company in Turkey.

Membrane preparation: Nafion/clay composite membranes were prepared by the solution casting method. The solution is prepared with a 1:2.5 ratio of Nafion solution:DMF is mixed for 30 minutes. The specified amount of clay is added to the mixture and homogenized for 1 hour by ultrasonic. The solution is poured into a glass petri dish and dried at 80 °C for 20 hours, then at 100 °C for 4 hours, then membrane was removed using deionized water. Composite membranes containing 10% kaolin and bentonite were labeled as Nafion-K10 and Nafion-B10 respectively. For comparison, recast Nafion and commercial Nafion-212 were used. Recast Nafion was prepared from a 20 wt.% Nafion solution by the same steps without the addition of any clay and labeled as Nafion. Then, as a protonation process, all membranes were treated with hydrogen peroxide, deionized water, sulfuric acid and deionized water at 80 °C for 1 hour. Each membrane was stored in deionized water.

Characterization techniques: The water uptake of the membrane was calculated from the weight difference between the dry and wet weight of the membrane. The membrane was dried at 105 °C until it reached a constant weight. The dried membrane was kept in deionized water at room temperature for 24 hours. Eq. 1 was used to calculate the water uptake capacity of the membranes. Where W_u, W_w and W_d are the water uptake capacity, wet and dry weight of the membrane, respectively.

$$W_u = \frac{W_w - W_d}{W_d} \times 100 \quad (1)$$

IEC of the membranes were measured by the acid-base titration method. Membrane samples (0.05 g) were kept in 10 mL of 3 M NaCl solution for 24 hours to exchange H^+ with Na^+ ions. NaCl solution containing H^+ ions were titrated using 0.01 M NaOH by adding phenolphthalein indicator. The IEC of the membrane samples was calculated using Eq. 2.

$$IEC = \frac{Volume\ of\ NaOH\ Consumed\ x\ Molarity\ of\ NaOH}{Weight\ of\ dry\ membrane} \quad (2)$$

The crystal properties of the membranes were investigated with the Rigaku Rint 2200 brand XRD device operating with 40 kV voltage and 30 mA current. Cu-Kα radiation was used as the X-ray source. XRD analyzes were performed at a scanning angle of 0.02° and a scanning speed of 2°/min and a Bragg angle of 2-70°.
Thermo Science Nicolet IS10 FT-IR device was used to detect the chemical functional groups of the membranes at 64 scan rates and 4 cm^{-1} resolutions and 525-4000 cm^{-1} scanning range.

RESULTS AND DISCUSSION

The proton conductivity of the membrane is highly dependent on the water uptake of the membrane. Clays are an extremely hygroscopic material, and these properties affect the water uptake. The water uptake capacity of the membranes at room temperature was calculated according to Eq. 1 and is presented in Fig. 1. When the results are examined, the water uptake of the Nafion membranes is clearly higher than that of the recast Nafion. With the addition of kaolin and bentonite, the water uptake capacity increased 2.7 and 2.4 times. This increase may be related to the water affinity between the additive and the polymer. Another reason is that the high water content facilitates the conduction of protons across the membrane [6].
The IEC values of the membranes were calculated by Eq. 2. Looking at Fig. 2, the IEC value of recast Nafion and Nafion-212 is higher than composite membranes. Compared with Nafion, the decrease in IEC in the composite membrane can be attributed to the interaction of the clay nanoparticles with the sulfonic groups of the polymer matrix. Despite the reduction of available sulfonic sites after the addition of additives, the conductivity values of such membranes may not be affected. This is due to the fact that the incorporation of clays into the Nafion matrix increases water uptake and thus proton conductivity in composite membranes [9].

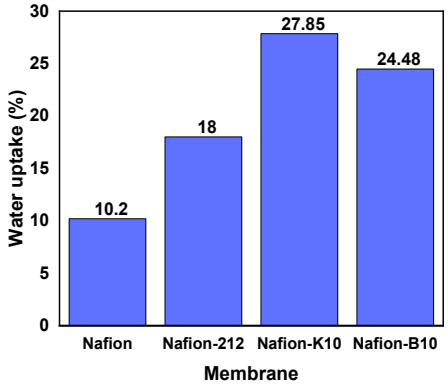


Fig. 1. The water uptake of the membranes

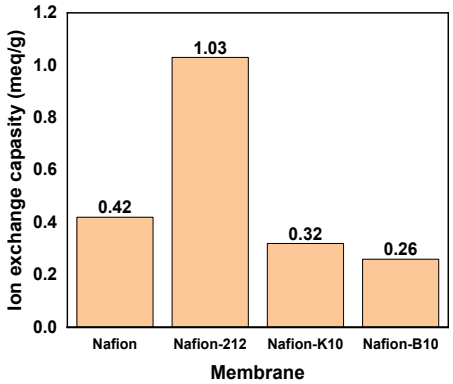


Fig. 2. Ion exchange capacities of membranes

Recast, commercial and composite Nafion membranes were characterized by FTIR to confirm changes in Nafion groups. Fig. 3 shows the spectra of Nafion 212 membrane and recast Nafion and composite membranes in the 525–4000 cm^{-1} range. In the FTIR spectrums, symmetrical O–S–O bending at 512 cm^{-1}, stretching of C-S groups at 632 cm^{-1}, C–O–C stretching at 976 cm^{-1}, symmetrical S–O stretching at 1060 cm^{-1}, symmetrical C–F stress bands at 1145 cm^{-1} and C–F stretch bands at 1201 cm^{-1} are seen. It also shows O–H stretching vibration at 3456 cm^{-1}, which corresponds to physically adsorbed water, and at 1630 cm^{-1}, which is attributed to the O-H bending vibration of free water molecules. It is seen that the Nafion-B10 membrane is more prominent than the other membranes. This may be due to clay doping, which increases the water content in composite membranes [7]. Due to the tensile bands of S=O and the tensile bands of the C-F bonds, it showed very strong and wide absorption bands characteristic of Nafion around 1200 and 1145 cm^{-1}. These bands were observed in the same IR region of the main and intense bands of the phosphonate compounds, and hence the Nafion bands overlap with the characteristic phosphonic acid bands [1]. The spectra of the composite membranes show all characteristic bands attributed to Nafion without shifts or modifications. The absence of characteristic bands of additives occurs due to the low concentration of clays in the polymeric matrix [3].
XRD analyzes were performed to determine the crystal phases of the membranes (Fig. 4). It was also used to confirm whether the clay particles were indeed incorporated into the membrane by the casting process. Nafion has a semi-

crystalline structure and shows two peaks, one at 19-20° (large crystalline) and 39-40° (small amorphous peak) [2]. Two main peaks observed at 17.6° and 38.8° appear in all membranes and are attributed to the characteristic peaks of Nafion [2,4,5,7]. It was observed that the positions of these diffraction peaks changed slightly, and the intensity decreased with the clay.

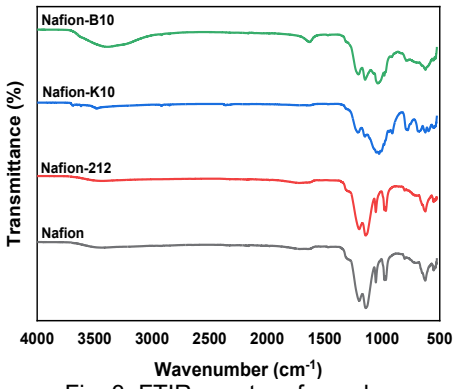


Fig. 3. FTIR spectra of membranes

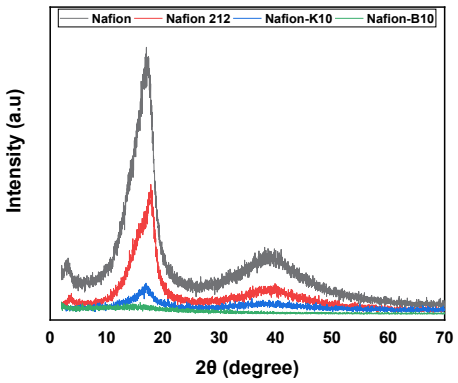


Fig. 4. XRD pattern of membranes

CONCLUSIONS

Kaolin and bentonite doped composite membranes were prepared by solution casting method and characterized by water uptake capacity, ion exchange capacity, FTIR, and XRD. Depending on the found results, it was determined that the clays were successfully added to the membrane structure. The results of XRD and FTIR show that clays be added to the structure. Although the ion exchange capacity (0.26-0.32 meq/g) values of composite membranes are not in the expected results range, the water uptake capacity (24.48%-28.85%) results are compatible with the literature. Since the proton conductivity in the membranes is provided by two different mechanisms, it is planned to make a comparison by making proton conductivity and cell performance characterizations in the future study for a more accurate result.

ACKNOWLEDGEMENT

This study was supported by Eskişehir Technical University Scientific Research Projects Commission (Project no. 21DRP138) and the Council of Higher Education (YÖK) 100/2000 Doctoral Scholarship Program.

REFERENCES

[1] Teixeira FC, de Sá AI, Teixeira APS, Rangel CM. Nafion phosphonic acid composite membranes for proton exchange membranes fuel cells. Appl Surf Sci 2019;487:889–97.
[2] Altaf F, Gill R, Batool R, Drexler M, Alamgir F, Abbas G, vd. Proton conductivity and methanol permeability study of polymer electrolyte membranes with range of functionalized clay content for fuel cell application. Eur Polym J 2019;110:155–67.
[3] Charradi K, Ahmed Z, Cid RE, Aranda P, Ruiz-Hitzky E, Ocon P, vd. Amelioration of PEMFC performance at high temperature by incorporation of nanofiller (sepiolite/layered double hydroxide) in Nafion membrane. Int J Hydrogen Energy 2019;44:10666–76.
[4] Devrim Y, Albostan A. Enhancement of PEM fuel cell performance at higher temperatures and lower humidities by high performance membrane electrode assembly based on Nafion/zeolite membrane. Int J Hydrogen Energy 2015;40:15328–35.
[5] Devrim Y, Erkan S, Baç N, Eroglu I. Improvement of PEMFC performance with Nafion/inorganic nanocomposite membrane electrode assembly prepared by ultrasonic coating technique. Int J Hydrogen Energy 2012;37:16748–58.
[6] Çalı A, Şahin A, Ar İ. Incorporating sepiolite and kaolinite to improve the performance of SPEEK composite membranes for proton exchange membrane fuel cells. Can J Chem Eng 2020;98:892–904.
[7] Sigwadi R, Dhlamini MS, Mokrani T, Ṇemavhola F, Nonjola PF, Msomi PF. The proton conductivity and mechanical properties of Nafion®/ ZrP nanocomposite membrane. Heliyon 2019;5:e02240.

WHEC-2022
23rd World Hydrogen Energy Conference
June 26-30, 2022 - Istanbul

#1617

MODELING OXYGEN TRANSPORT IN CARBON SUPPORT MICROSTRUCTURE OF PROTON EXCHANGE MEMBRANE FUEL CELL ELECTRODES USING PORE NETWORKS

[1,2,3*] *Alper Can Ince*, [3,4]*Mustafa Fazil Serincan*, [3]*Hasnain Hafiz*, [5]*Edward F. Holby*, [6]*J. S. Spendelow*, [1,2]*U. Pasaogullari*, [3]*Wilton J. M. Kort-Kamp*

[1] Center for Clean Energy Engineering, University of Connecticut, Storrs, CT, USA
[2] Department of Mechanical Engineering, University of Connecticut, Storrs, CT, USA
[3] Theoretical Division, Los Alamos National Laboratory, MS B262, Los Alamos, NM, USA
[4]Gebze Technical University, Faculty of Engineering, Mechanical Engineering Department, Gebze, Kocaeli, Turkey
[5] Sigma Division, Los Alamos National Laboratory, Los Alamos, NM, USA
[6] Materials Physics and Applications Division, MS D429, Los Alamos National Laboratory, Los Alamos, NM, USA

*Corresponding author e-mail: alper_can.ince@uconn.edu

ABSTRACT

The structural morphology of high surface area carbon (HSC) on which both the platinum catalyst and ionomer are dispersed is very complex and critical for understanding the transport of oxygen (O_2). This study aims to develop a model to simulate O_2 transport in the cathode catalyst layer of proton exchange membrane fuel cells fabricated using HSCs. A stochastic two-dimensional multiscale domain, including micro and mesopores, and connecting throats is constructed. Steady state coupled transport and electrochemical reaction models are then implemented into using transport properties estimated using in-house atomistic level calculations. This study provides a multi-scale approach by relating the pore-scale approach with the atomistic level model, allowing to represent a large modeling domain at higher detail. Oxygen concentration in HSC surfaces is predicted for dry and flooded cases. Results show an effective diffusivity of $8.752 \cdot 10^{-8}$ m^2/s and $4.851 \cdot 10^{-8}$ m^2/s for the flooded case and non-flooded case, respectively. Oxygen concentration drops significantly when micropores are flooded, consequently Pt utilization decreases.

Keywords: Pore-scale modeling, PEMFC, catalyst layer, transport phenomena, multiscale modeling, high surface carbon area

INTRODUCTION

Proton exchange membrane fuel cells (PEMFCs) are a competitive power technology because of their benefits such as low-temperature operation, low-carbon emission, and rapid start-up. However, the wide commercialization of this technology still depends on cost and lifetime, which must become competitive with traditional power technology (e.g., internal combustion engine) [1]. Here, the critical component is the Pt group metal (PGM) catalyst that contributes to a significant portion of the cost of fuel cells. The development of the PGM catalyst layer has progressed towards enhancing Pt utilization. High surface area (HSA) carbon support is a promising material to enhance the reaction area due to its high porosity (i.e., three times greater than typical carbon support [2]). HSA carbon consists of the hierarchical microstructure of the carbon support upon which the Pt-alloy particles are dispersed, as shown in Figs. 1a and 1b. This HSA carbon support is bounded by an ion-conducting polymer (ionomer). Microtomography studies reported that up to 85% of Pt particles can be inside the micropores of the carbon particles, which are in the range of 2-10 nm [3]. Oxygen typically needs to pass first through the ionomer film and transport through these micropores to reach the catalyst inside of the HSA. In a typical HSA carbon support, the carbon particles have macropore regions of dimension ~20 nm in diameter that could be only accessible by means of the micropore openings of dimensions ~2 nm on its surface.

Cetinbas et al. [4] investigated the effects of carbon microstructure and relative humidity (RH) on the local oxygen transport resistance. Porous carbon agglomerate was reconstructed using a hybrid approach that combines a nano-CT image with statistical information from TEM images and porosimetry techniques. Direct simulation was then performed on the reconstructed geometry to determine local oxygen transport resistance (R_{O2}) for different structures. When the primary pores are filled with condensed water at various levels of RH, the agglomerate size and shape become significant factors determining R_{O2}. If primary pores are on the other hand dry, ionomer resistance becomes more dominant on R_{O2}. Ramaswamy et al. [2] studied the effect of carbon structure on the high current density transport losses in PEMFC cathode under various relative humidities. They compared Ketjen Black® - a high surface area carbon - and Vulcan - a medium surface area (MSA) carbon. Measured H_2/O_2 polarization curve showed that HSA (Ketjen Black®) is superior in terms of kinetic activity of the catalyst even though micropores lead to the additional resistance.
Pore network model (PNM) is an effective method for describing transport phenomena inside porous media due to its capability to resolve even nanopores in the simulation [5]. We utilize PNM approach here to investigate O_2

transport in the HSA carbon microstructure considering transport through the ionomer and micropores for flooded and non-flooded cases.

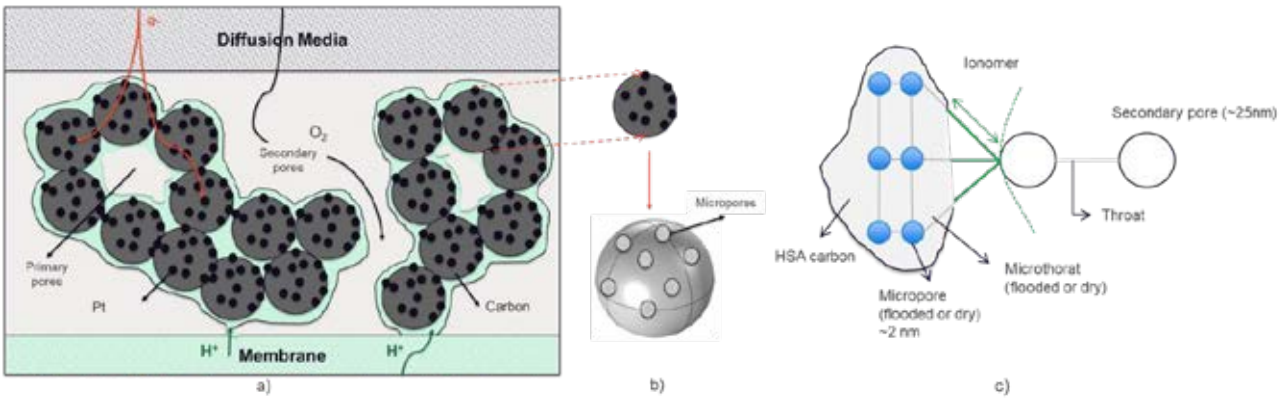


Fig. 1. a) Schematic description of a typical PGM electrode b) HSA carbon support c) PNM representation considered in this study

MODELING APPROACH

PNM is an alternative modeling approach to the volume-averaged approach (e.g., CFD model) to model porous media. In PNM, the porous domain is idealized as interconnected pores and throats. Therefore, the transport is modeled as a resistor network. Capillary transport in porous media can also be described similarly using the percolation theory concept to investigate multiphase transport [6,7]. This approach can be used for complex transport phenomena in many engineering applications (e.g., fuel cells, batteries, CO_2 storage, electrolyzers).

In this study, the PNM approach is used for the understanding of O_2 transport in a multiscale porous cathode structure including secondary pores, primary pores, micropores, and ionomers. To obtain a multiscale structure, first the secondary pores are constructed based on statistical distributions. Then some secondary pores are replaced by micro domains, which include micro-pores and throats. Here, the micropores and throats represent narrow porous region inside carbon, where Pt particles are embedded, as displayed in Fig. 1c. The O_2 transports from the secondary pore region passing through the ionomer and reaches the micropores. Therefore, the ionomer resistance is implemented between micro- and secondary pores. The steady-state reactive transport model is implemented into this domain considering transport properties estimated using in-house atomistic DFT level calculations. For this purpose, the diffusion coefficient due to binary and Knudsen is calculated for secondary pores, while atomistic level calculations are used for estimation of the diffusion coefficient in micropores (as shown in Fig 2). Therefore, the conductance which is a function of geometry and diffusion coefficient for each pore-throat-pore assembly is calculated. The kinetic is modeled using the form of Butler-Volmer equations for cathode reactions. Here, one of the important assumptions is that the reaction terms are assigned for only micropores.

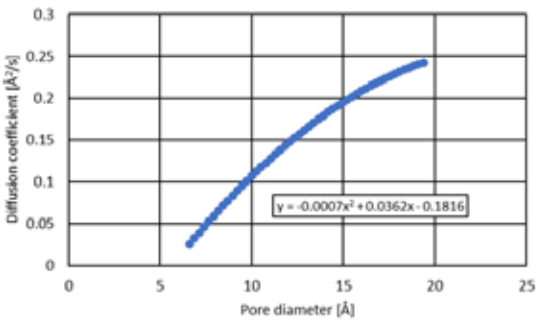


Figure 2 Diffusion coefficient in flooded micropores based on atomistic DFT level calculations

RESULTS AND DISCUSSION

The O_2 transport simulation is performed for a 4x4 μm^2 multiscale electrode domain, as illustrated in Fig 3a (dark black regions → micro domain with 10x10 micropores). The arbitrary pore and throat size distribution for secondary pore domain ~20 nm) micro domain (~2 nm) is assigned. In the geometry considered in this study, outlet of the geometry is bound to membrane, while inlet is bound with the gas diffusion layer.

The effective diffusivity is calculated as $8.752 \cdot 10^{-8} m^2/s$ and $4.851 \cdot 10^{-8}$ m^2/s for flooded and non-flooded case, respectively, that are three order magnitude smaller than binary diffusion coefficient of O_2 in N_2. The reason can be explained with geometry effect (Knudsen effect due to micropores) and additional phase resistant (e.g., ionomer, water). The structural characterization shows that the micropore volume fraction (which is the ratio of the volume of micro domain to bulk domain) is 1 %. Micro domain area is found as $1.21 \cdot 10^{-13}$ m^2 in an electrode volume of $1.6 \cdot 10^{-18}$ m^3. The concentration distribution is shown in Figs. 3b and 3c for non-flooded and flooded micropores, respectively. As expected, the O_2 concentration is consumed dramatically under the flooded case that is subjected to the reaction in micropores and drops to almost 0. These results also shows that utilization of interior Pt decreases significantly after ~ 1 μm distance from the membrane because the O_2 concentration is not satisfied for the non-flooded micropore case. On the other hand, 2 μm distance from the membrane is an ineffective in terms of Pt utilization for the flooded micropore case even though effective diffusivity increases for in this case. It is because of that the reaction sink term specified for microdomain consumes O_2 concentration significantly in this case.

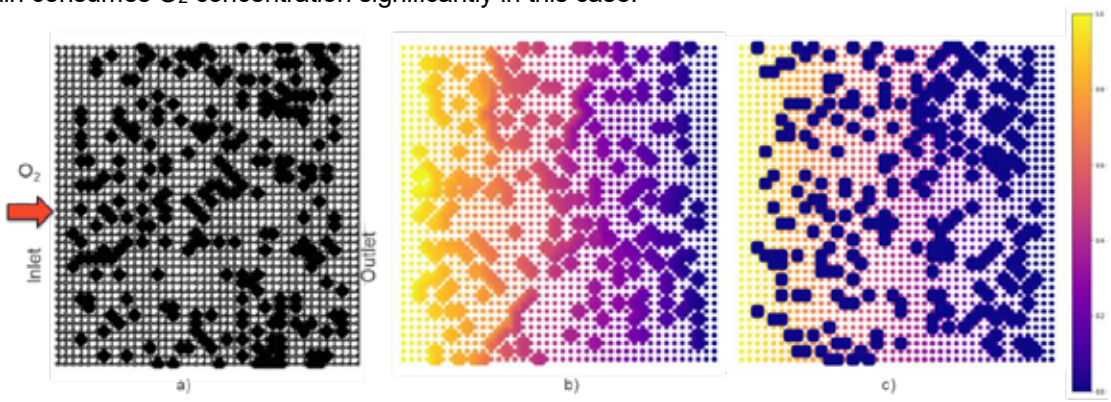


Figure 3 a) the multiscale structure considered in this simulation, b) O_2 concentration distribution for non-flooded case, c) O_2 concentration for flooded case

CONCLUSIONS

PNM is used to describe O_2 transport in a multiscale catalyst layer constructed stochastically. The model is incorporated with atomistic level calculations. The effective diffusion coefficient is found as $8.752 \cdot 10^{-8}$ m^2/s and $4.851 \cdot 10^{-8} m^2/s$ for flooded and non-flooded cases, respectively. The simulation is performed for dry and flooded scenarios. The oxygen concentration drops significantly when micro domain is flooded as the reaction is specified for micropores even though effective diffusivity in flooded case is greater than non-flooded case, and thus the Pt utilization decreases.

REFERENCES

[1] F.C. Cetinbas, R.K. Ahluwalia, N. Kariuki, V. De Andrade, D. Fongalland, L. Smith, J. Sharman, P. Ferreira, S. Rasouli, D.J. Myers. 2017. Hybrid approach combining multiple characterization techniques and simulations for microstructural analysis of proton exchange membrane fuel cell electrodes, Journal of Power Sources. 344 62–73. https://doi.org/10.1016/j.jpowsour.2017.01.104.

[2] N. Ramaswamy, W. Gu, J.M. Ziegelbauer, S. Kumaraguru. 2020. Carbon Support Microstructure Impact on High Current Density Transport Resistances in PEMFC Cathode, J. Electrochem. Soc. 167 064515. https://doi.org/10.1149/1945-7111/ab819c.

[3] Y.-C. Park, H. Tokiwa, K. Kakinuma, M. Watanabe, M. Uchida. 2016. Effects of carbon supports on Pt distribution, ionomer coverage and cathode performance for polymer electrolyte fuel cells, Journal of Power Sources. 315 179–191. https://doi.org/10.1016/j.jpowsour.2016.02.091.

[4] F.C. Cetinbas, R.K. Ahluwalia, N.N. Kariuki, V. De Andrade, D.J. Myers. 2020. Effects of Porous Carbon Morphology, Agglomerate Structure and Relative Humidity on Local Oxygen Transport Resistance, J. Electrochem. Soc. 167 013508. https://doi.org/10.1149/2.0082001JES.

[5] M. Aghighi, M.A. Hoeh, W. Lehnert, G. Merle, J. Gostick. 2016. Simulation of a Full Fuel Cell Membrane Electrode Assembly Using Pore Network Modeling, J. Electrochem. Soc. 163 F384–F392. https://doi.org/10.1149/2.0701605jes.

[6] J. Hinebaugh, A. Bazylak. 2010. Condensation in PEM Fuel Cell Gas Diffusion Layers: A Pore Network Modeling Approach, J. Electrochem. Soc. 157 B1382. https://doi.org/10.1149/1.3467837.

[7] L. Chen, A. He, J. Zhao, Q. Kang, Z.-Y. Li, J. Carmeliet, N. Shikazono, W.-Q. Tao. 2022. Pore-scale modeling of complex transport phenomena in porous media, Progress in Energy and Combustion Science. 88 100968. https://doi.org/10.1016/j.pecs.2021.100968.

WHEC-2022
23rd World Hydrogen Energy Conference
June 26-30, 2022 - Istanbul

#1623

OPTIMIZATION OF CHARACTERIZATION ROUTINES FOR CARBON BLACKS USED IN ENERGY RELATED APPLICATIONS

[1*] *Fatih Özcan,* [1] *Amin S. Amin,* [1,2] *Doris Segets*
[1] Particle Science and Technology (IVG-PST), University of Duisburg-Essen (UDE), Duisburg, Germany
[2] Centre for Nanointegration Duisburg-Essen (CENIDE), Duisburg, Germany

*Corresponding author e-mail: fatih.oezcan@uni-due.de

ABSTRACT

Here, we report on characterization routines for carbon blacks both in terms of their intrinsic properties resulting from their synthesis history and process-related quality parameters. We establish characterization methods based on analytical centrifugation which work fast, reliable and at low cost and were developed in-house. We apply them to analyze CB particle properties (particle size distribution, morphology, surface properties) and link them with ink properties. First results indicate that small deviations in feed quality can be determined by our stability trajectories. By the same methods, we found out that mixing parameters in the course of ink preparation greatly influence stability parameters which are important in the subsequent process chain of electrode production.

Keywords: Carbon Black, PEMFC, Stability Trajectories, Analytical Centrifugation, Hansen Solubility Parameters

INTRODUCTION

In recent years, technical carbon blacks (CB) increasingly become a valuable and attractive material in the context of various energy related applications. Due to their low cost, abundance, favorable intrinsic properties (e.g. conductivity, specific surface area) and flexibility regarding mentioned intrinsic properties, they are heavily used as conductive additives in battery electrodes or as conductive support for electrocatalysts in fuel cells [1]. Usually, they are produced via incomplete combustion of carbon sources (oil or gas) and possible post-processing steps (e.g. surface functionalization). The flexibility in their properties is a direct result of the variety in production and post-processing steps that are applied by the numerous manufacturers. Although initially seen as an advantage, the broad range in material properties can at the same time raise problems for users in the subsequent value chain who focus on large-scale production of proton exchange membrane fuel cells (PEMFC) or lithium-ion batteries (LIB). Possibly facing fluctuations in product quality, they seek fast, reliable and standardized measures for CB characterization in order to keep control over their processes which eventually define final electrode properties.

So far, characterization of commercial CB involves several techniques including N_2 physisorption and determination of sulfur content. For an additional characterization, specialized techniques for distinct questions play a role. For example, thermogravimetric analysis or Boehm titration can be used to identify surface functional groups [2]. These methods have in common that they are quite time-consuming and costly. Additionally, they are not optimized for the targeted electrochemical application fields. To this end, we report on standardized characterization routines for CB materials designed for fuel cell and battery application. By mainly applying analytical centrifugation (AC), we identify parameters like particle size, morphology and surface properties that are influential for the overall value chain in electrode manufacturing. This helps to minimize the effects of material inherent property fluctuations as well as process related fluctuations on final electrochemical performance.

MATERIALS AND METHODS

The primary use of analytical centrifugation has the advantage that CB powder properties can be assessed in liquid / dispersed state. Since formulation investigations play a major part in the mentioned electrochemical applications, AC measurements enable investigations under real process conditions with technically relevant solid concentrations [3,4]. For a first assessment, we investigated the dispersibility of CB in 14 probe liquids at diluted solid concentrations in order to deduce Hansen solubility / dispersibility parameters (HSP, Table 1) [5].

We derived stability trajectories and S scores (Fig. 1a & 1b) [3,4] based on the sedimentation behavior of CB in the listed PL measured via AC. In subsequent considerations, we used S scores for ranking the PL, calculated HSP based on this ranking and compared this HSP derivation with the standard method by Süß et al. [6].

Table 1: Overview on selected probe liquids (PL) for dispersibility tests of CB.

No.	Probe liquid	Abbreviation
1	2-propanol	IPA
2	methanol	MeOH
3	acetonitrile	ACN
4	ethyl acetate	EA
5	acetone	Ace
6	dimethyl sulfoxide	DMSO
7	dimethylformamide	DMF
8	tetrahydrofuran	THF
9	1-methyl-2-pyrrolidone	NMP
10	1,4 dioxane	Diox
11	2-(butoxyethyl)-acetate	BAc
12	triethylamine	TEA
13	p-xylene	Xyl
14	n-hexane	Hex

Furthermore, our investigations were expanded towards full inks. We determined the effects of mixing intensity variation during ink preparation by applying stability trajectories as well as rheological characterization. The initial investigations predominantly consisted of lab-scale mixing techniques using simple magnetic and / or sonication methods. Other methods are planned for future studies.

RESULTS AND DISCUSSION

Since we aim at developing robust and reliable routines for CB characterization, our first investigations entailed reproducibility tests. Not only repeated measurements at the AC for the same batch of a selected CB were conducted but different batches of the same material were measured under identical conditions. Fig. 1a & 1b illustrate the results in this context. A very good reproducibility of dispersion stability analysis for two Vulcan XC72 batches in selected PL is displayed. With minor deviations in the stability trajectories, it can be stated that with this method changes in material properties can be detected in a fast way.
For full fuel cell inks, it is apparent that the type of mixing technique as well as the mixing intensity have a large influence on the stability of the obtained inks (Fig 1c & 1d). Simple magnetic stirring produces the least stable inks. Stability increases with the use of sonication methods, but probe sonication at high intensities seems to be disadvantageous for FC ink preparation in terms of stability. Rheological data confirm these findings by showing a comparable, yet not identical trend with the applied mixing techniques. From MS (magnetic stirring) → UB (ultrasonic bath) → UB+S20 (ultrasonic bath + 20% probe sonication intensity) → UB+S70 (ultrasonic bath + 70% probe sonication intensity), a general decrease in dynamic viscosity within a small range is observed for the mainly Newtonian inks. The effect on particle size by the applied mixing method is one factor that can describe the trend in viscosity where breakage of aggregates/agglomerates possibly enhances flow properties. Similarly, possible effects on the chemical stability of other additives like the ionomer can be used as explanation. A degradation and shorter chain length of the polymeric ionomer due to critical intensity applied by sonication might change the overall flow properties as well.

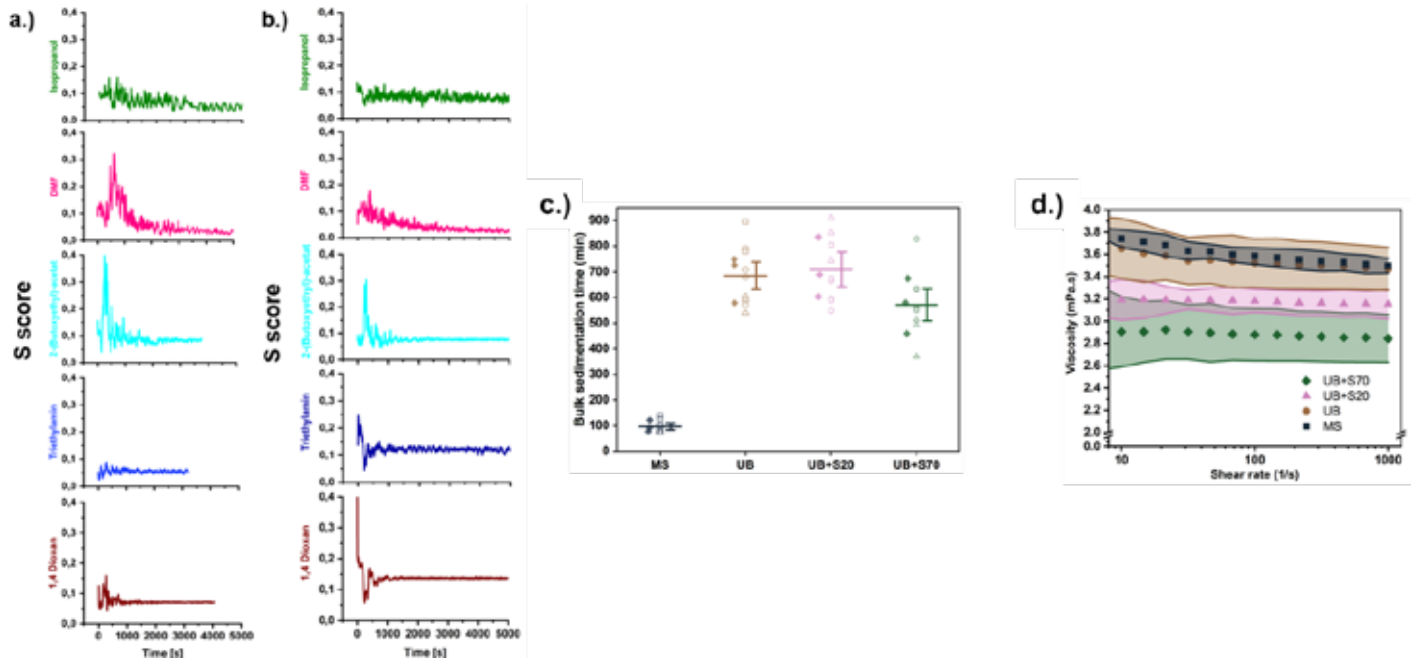


Fig. 1: Stability trajectories for two different batches of Vulcan XC72 in five selected probe liquids (a.) and b.)); bulk sedimentation times for full inks as function of applied mixing techniques (MS: magnetic stirring; UB: ultrasonic bath; S20: probe sonication at 20% intensity; S70: probe sonication at 70% intensity) and intensity derived from stability trajectories (c.)) and dynamic viscosities of same inks as function of the same applied mixing conditions and shear rate (d.)).

CONCLUSIONS

In conclusion, we were able to identify differences in CB materials by applying AC-based characterization. Those differences play a huge part in the overall process chain of electrode production as they are decisive in formulation considerations mainly, but also in the subsequent processing steps. We were able to link both intrinsic material properties and processing parameters to formulation properties. In future, we will focus on closing the process chain and try to apply our characterization routines for an efficient identification of decisive process parameters at every stage of production. Additionally, we want to transfer gained knowledge from lab-scale techniques (e.g. sonication methods) to industrially relevant mixing procedures. By this, we want to give electrode manufacturers tools at hand for a fast characterization of the feed materials to save costly and lengthy adjustment of processes due to quality fluctuations. An accelerated implementation of green energy solutions is sought by this approach.

REFERENCES

[1] L. M. Roen, C. H. Paik, and T. D. Jarvi: *Electrocatalytic Corrosion of Carbon Support in PEMFC Cathodes*, Electrochem. Solid-State Lett., vol. 7, no. 1, p. A19, 2004.
[2] A. Kalijadis, M. Vukcevic, Z. Jovanovic, Z. Lausevic, M. Lausevic, *Characterisation of surface oxygen groups on different carbon materials by the Boehm method and temperature-programmed desorption* J. Serb. Chem. Soc., 76, 757, 2011.
[3] S. Bapat, D. Segets: *Sedimentation Dynamics of Colloidal Formulations through Direct Visualization: Implications for Fuel Cell Catalyst Inks*, ACS Applied Nano Materials, Vol. 3 Nr. 8, pp. 7384 – 7391, 2020.
[4] S. Bapat, C. Giehl, S. Kohsakowski, V. Peinecke, M. Schäffler, D. Segets: *On the state and stability of fuel cell catalyst inks*, Advanced Powder Technology, 32, 3845-3859, 2021.
[5] C. M. Hansen, Chemische Technik, 2, 547-553, 1972.
[6] S. Süß, T. Sobisch, W. Peukert, D. Lerche, and D. Segets, *Determination of Hansen parameters for particles: A standardized routine based on analytical centrifugation,* Adv. Powder Technol., 29, 1550–1561, 2018.

WHEC-2022

23rd World Hydrogen Energy Conference

TRACK 8.
FUEL CELLS: SOFC AND OTHER TYPES

TRACK 8. FUEL CELLS: SOFC AND OTHER TYPES

#7 DEVELOPMENT OF HIGHLY DURABLE AND DENSE GDC BUFFER LAYER FOR ANODE-SUPPORTED PLANAR SOFC	829
#107 NUMERICAL INVESTIGATION OF NI MIGRATION IN SOC FUEL ELECTRODE USING PHASE FIELD MODEL AND LATTICE BOLTZMANN MODEL	832
#173 EFFICIENT REGENERATIVE HYDROGEN/VANADIUM FUEL CELL USING TRICHOME-LIKE ELECTRODES FOR ENHANCED VANADIUM ELECTROLYTE UTILIZATION AND ITS SYSTEM INTEGRATION	833
#273 COMBINATORIAL DEVELOPMENT OF LSF/rp-LSF/ScSZ COMPOSITE CATHODE FOR INTERMEDIATE TEMPERATURE SOLID OXIDE FUEL CELLS	836
#294 IDENTIFICATION OF OXYGEN ION CONDUCTIVITY OF TWO LAYERS YTTRIA STABILIZED ZIRCONIA MATRIX IMPREGNATED BY LITHIUM/POTASSIUM ELECTROLYTE FOR MOLTEN CARBONATE FUEL CELLS	839
#325 OPTIMIZATION OF LOW-GRADE CGO TRANSPORT PROPERTIES FOR SOFC APPLICATIONS	842
#326 ELECTRICAL CONDUCTIVITY OF Y-DOPED CGO BASED MATERIALS SINTERED BY HOT PRESS	845
#327 OPTIMIZATION OF LOW-GRADE TETRAGONAL ZIRCONIA BY PRASEODYMIUM OXIDE ADDITIONS	848
#366 ACCELERATED STRESS TESTING OF SOLID OXIDE FUEL CELLS VIA EX-SITU CHEMICAL REDOX CYCLING OF Ni-CGO FUEL ELECTRODES	851
#1452 THEORETICAL AND EXPERIMENTAL ANALYSES OF ETHANOL-FUELED SOFC MICRO-COGENERATOR	855
#1467 A HIGHLY STABLE COBALT SPINEL-GDC NANOCOMPOSITE CATHODE FOR INTERMEDIATE-TEMPERATURE SOLID OXIDE FUEL CELLS	858
#1499 EFFECT OF A REDUCTION OF THE CATALYST LOADING ON THE PERFORMANCE OF A MINI PASSIVE DIRECT METHANOL FUEL CELL	861
#1501 DEVELOPMENT OF LSF-LSM COMPOSITE CATHODES FOR IT-SOFC	864
#1503 A NEW CLASS OF AMOURPHOUS/NANOCRYSTALLINE (La,Sr)CoO_3 BASED CATHODES FOR IT-SOFCs	867
#1511 EFFECT PARTIAL SUBSTITUTION OF LANTHANUM ON THE THERMAL PROPERTIES OF PEROVSKITES	870
#1564 INVESTIGATION OF PALLADIUM COATED NICKEL FOAM ANODE ELECTRODE APPLICATION FOR DIRECT ETHANOL FUEL CELLS	873
#1572 DEVELOPMENT OF NOVEL MEMBRANE STRUCTURES VIA RADIATION INDUCED GRAFTING AND ELECTROSPINNING TECHNIQUE FOR ANION EXCHANGE MEMBRANE FUEL CELLS	876
#1581 DEVELOPMENT OF BROMINE RESISTANT ANODE CATALYST FOR HYDROGEN OXIDATION AND REDUCTION REACTIONS IN HYDROGEN BROMINE FLOW BATTERIES	879
#1609 A NEW METHOD FOR MANUFACTURING ANODE SUPPORTED SOLID OXIDE FUEL CELLS WITH AFL	882
#1621 EXPERIMENTAL AND EXERGY ANALYSES OF INTERNAL REFORMING SOLID OXIDE FUEL CELL FED WITH REFORMATE GAS	886

WHEC-2022
23rd World Hydrogen Energy Conference
June 26-30, 2022 - Istanbul

#7
DEVELOPMENT OF HIGHLY DURABLE AND DENSE GDC BUFFER LAYER FOR ANODE-SUPPORTED PLANAR SOFC

Amjad Hussain[1,2], Muhammad Zubair Khan[1], Rak-Hyun Song[1,2], Dong Woo Joh, Jong-Eun Hong[1], Seung-Bok Lee[1,2], Tak-Hyoung Lim[1,2]*
[1]Fuel Cell Research Center, Korea Institute of Energy Research, Korea
[2]Department of Advanced Energy and System Engineering, University of Science and Technology (UST), Korea

Corresponding author e-mail*: rhsong@kier.re.kr

ABSTRACT

Solid oxide fuel cells (SOFCs) are highly efficient, low emission and fuel flexible (H_2, CH_4, and CO) future energy device that can also operate in reverse as co-electrolysis cell, converting the CO_2 and H_2O into useful fuel (H_2). However, among numerous sources of electrochemical degradation, the inter-diffusion between electrolyte and cathode has been identified as pre-dominant factor in long run operation, facile method for manufacturing GDC buffer layer should be accomplished for long-term stability and cost effectiveness. Herein, established a highly reliable durable buffer layer that exclusively suppresses the detrimental elemental diffusion at high temperature. This buffer layer is manufactured via tape casting film approach, in which both electrolyte and buffer layer films are laminated by warm iso-static press (WIP) to control the interfacial and bulk properties. The simple approach for electrolyte and buffer layer enables to manufacture a desired thin film structure. Subsequently, the formation of harming insulating phases and decomposition of cathode are effectually prevented, resulting in a remarkably enhancement in electrochemical performance and long-term stability. The scalability and feasibility of mass production are confirmed via the fabrication of large area cells.

Keywords: Solid oxide fuel cell, Thin film SOFC, WIP (Warm iso-static pressing), Buffer layer, Interfacial

INTRODUCTION

Solid oxide fuel cell (SOFC) technology is capable and adaptable energy next-generation design. SOFC is widely used in variety of applications to offer compensations of fuel flexibility, high-energy conversion efficiency and environmentally friendliness. It has much higher conversion efficiencies than the conventional combustion method. However, the major challenges in SOFCs have been associated with elevated temperature and its impact on long-term reliability. High temperature degradation is a crucial factor in SOFC commercialization because it leads to performance deterioration. Cathode and electrolyte are reacted at high temperature, resulting in La and Sr diffusions from state of art perovskite cathode (LSCF and LSC) to form a detrimental secondary phase such as $La_2Zr_2O_7$ and $SrZrO_3$ [1, 2]. The conductivity of these secondary phases is very lower than electrolyte. The universal approach to address this challenge is to insert the buffer layer between the cathode and electrolyte.

To overcome the above challenge, a facile method for fabrication of GDC buffer layer is developed and the very thin, dense and adherent interfacial properties are achieved. The GDC films are engineered to complete densification for control of interfacial properties and to suppress elemental diffusion from cathode using tape casting approach.

EXPERIMETATION

Commercial powders of NiO (Nickelous oxide green, kojundu, Japan), coarse YSZ (TZ-8Y, TOSOH, Japan), Scandia stabilized zirconia ScCeSZ (Fuel cell material, USA and gadolinium-doped ceria GDC (Fuel cell material, USA were used as raw materials for anode NiO-YSZ, Anode functional layer NiO-ScCeSZ, ScCeSZ electrolyte and GDC buffer layer. The raw materials were first mixed and ball-milled for 24hr to form a homogenous slurry. Tape-casting was performed using a tape casting machine (Hansung system, Korea), by which slurry was coated on a Si- coated polyethylene (PET) carrier film at a rate of 1 cm s − 1 at 50 ◦C. The film thicknesses of the green tapes produced were 40 μm for the anode (Figure1), 15-10 μm for the AFL, 6-5μm for the electrolyte and 2-3μm for buffer layer (GDC) respectively. The anode-supported electrolytes were laminated with several anode sheet, AFL sheet, electrolyte sheet and GDC buffer film. The specimens were laminated using WIP by means of a non-directional method. The GDC film-laminated green cell put into the furnace for burning organic substances and co sintering were carried out by heat treatment at 25°C to 1400 ◦C for 60 hr

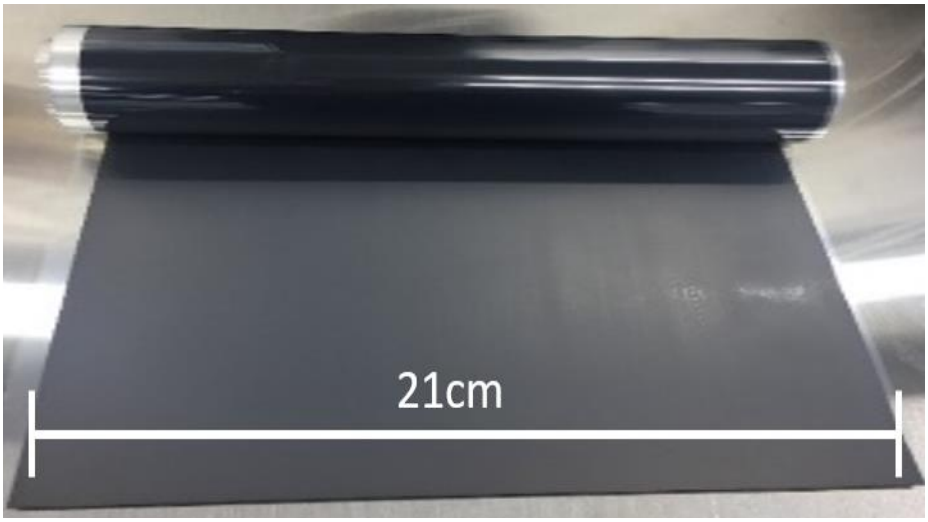


Figure 1. Fabrication of anode support film by tape casting

RESULTS AND DISCUSSION

To examine the effects of buffer layer on electrochemical performance and long-term stability, a large area anode supported planar type cell was fabricated by multi-layer structure (Figure 2). Dense and Defects free buffer layer successfully was fabricated via tape casting approach. Electrolyte and buffer layer have incredibly interfacial adhesion bonding state, which can be clearly recognised. Although few small pores are observed, and all of them are isolated and not connected so that they do not contribute to elemental diffusion and migration from cathode to electrolyte. The advantages of this GDC fabrication method are its scale up capability. To demonstrate the feasibility and scalability of this method for real applications, it was applied on the 12cm×12cm large area anode supported planar cell. The large cell was successfully fabricated. Also the long-term test of the cell was carried out, and there were no delamination between cathode and GDC buffer layer during long-term test. Stability of their interface is confirmed by elemental diffusion and microstructure analysis.

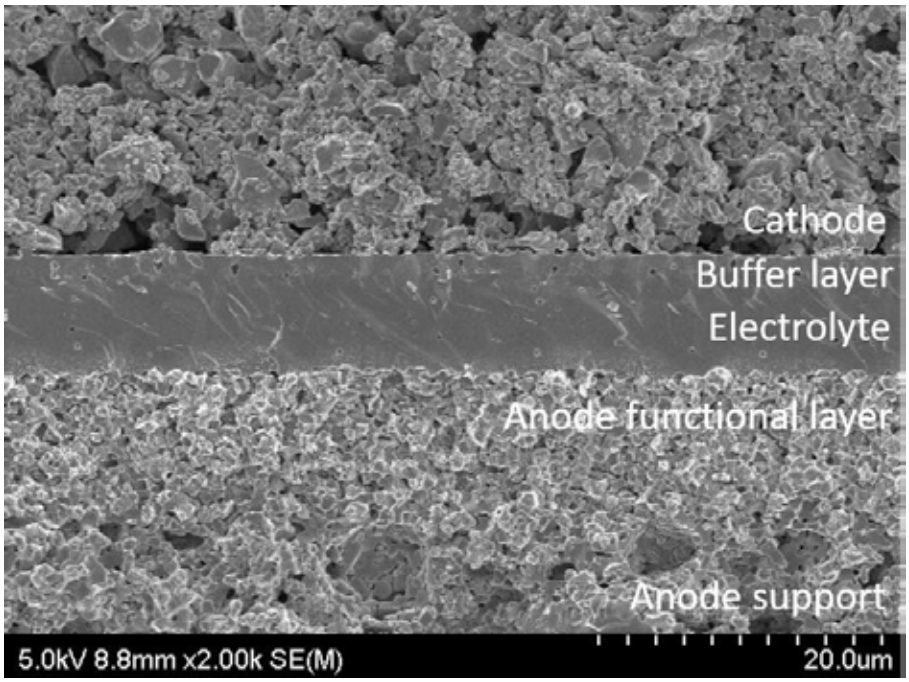


Figure 2. Cross sectional SEM morphology of multi-layer film structure (NiO-YSZ/NiO-ScCeSZ/ScCeSZ/GDC) of large area anode supported planar type SOFC.

CONCLUSIONS

Thin film structure GDC buffer layer are successfully fabricated by tape casting and multi-layer lamination approach. The highly reliable buffer layer suppressed efficiently the secondary phases between cathode and electrolyte, and prevented the performance losses during long-term operation.

ACKNOWLEDGEMENT

This work was supported by the Technology Development Program to Solve Climate Change under a National Research Foundation (NRF) grant funded by the Korean government (Ministry of Science and ICT) (NRF-2020M1A2A2080867).

REFERENCES

1. Yokokawa H, Sakai N, Horita T, Yamaji K, Brito ME and Kishimoto H. 2008. Thermodynamic and kinetics consideration on degradation in solid oxide fuel cell cathode. Journal of alloys and compounds 452:41-47.
2. Duan Z, Yang M, Yan A, Hou Z, Dong Y, Chong Y, Cheng M and Yang W. 2006. $Ba_{0.5}Sr_{0.5}Co_{0.8}Fe_{0.2}O_{3-\delta}$ as a cathode for IT-SOFCs with a GDC interlayer. Journal power sources 160: 57–64.

WHEC-2022
23rd World Hydrogen Energy Conference
June 26-30, 2022 - Istanbul

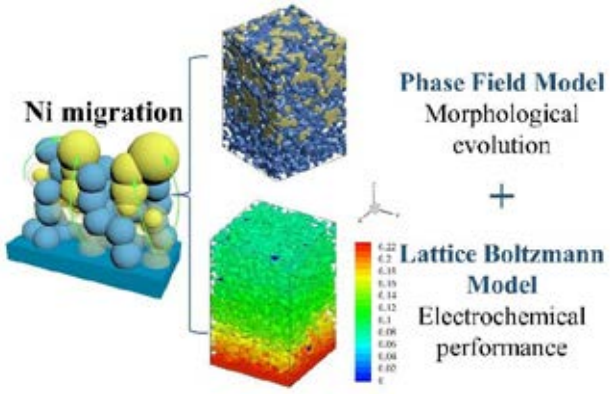
#107
NUMERICAL INVESTIGATION OF Ni MIGRATION IN SOC FUEL ELECTRODE USING PHASE FIELD MODEL AND LATTICE BOLTZMANN MODEL

[1,2] *Yang Wang,* [2] *Siyuan Zhao,* [2] *Zengjia Guo,* [1] *Qing Du,* [1] *Kui Jiao,* [1,3*] *Bingfeng Zu,* [2**] *Meng Ni*
[1]State Key Laboratory of Engines, Tianjin University,
135 Yaguan Road, Tianjin, China
[2] Department of Building and Real Estate, Research Institute for Sustainable Urban Development (RISUD) & Research Institute for Smart Energy (RISE), Hong Kong Polytechnic University, Hung Hom, Kowloon, Hong Kong, China
[3] Internal Combustion Engine Research Institute, Tianjin University, 92 Weijin Road, Tianjin, China

*Corresponding author e-mail: zbf@tju.edu.cn (B. Zu)
**Corresponding author e-mail: meng.ni@polyu.edu.hk (M. Ni)

ABSTRACT

The long-term stability of Solid Oxide Cells (SOCs) is seen as one of the key obstacles hindering commercialization. The effects of morphological changes in fuel electrodes account for a large part of the cell performance degradation during long-term operation. The morphological changes refer to the migration processes of the Ni phase in Ni-based composite electrode at high operating temperature (600-1000 ℃). The initial smaller Ni particles will agglomerate to reduce the surface energy and form larger particles, and this is the Ni coarsening process which will occur in both fuel cell and electrolysis mode. The Ni coarsening will reduce the density of three-phase boundaries (TPBs) and increase the cell overpotential. Another Ni migration process may be quite destructive, which refers to the redistribution of the Ni phase from one location to another. The redistribution of the Ni phase usually occurs in the electrolysis mode. A series of experimental studies have revealed that the Ni phase will migrate away from the most active functional layer close to the dense electrolyte, which greatly aggravates the performance degradation process. In this study, we conduct a numerical investigation on the Ni migration process in SOCs using an integrated model. First, a phase field model is established to track the morphology evolution of Ni-based electrodes. After experimental validation, the phase field model provides a good characterization of the Ni migration process. Then a lattice Boltzmann model is used to evaluate the electrochemical performance of the fuel electrode at different operating times. The results show that severe Ni depletion can cause an increase of the total overpotential by 0.081 V at high operating current density. Besides, the effects of initial microstructure and operating conditions are also investigated.



Keywords: Solid Oxide Cells, Ni migration, Numerical simulation, Phase field model, Lattice Boltzmann method

REFERENCES

1. Hauch A, Küngas R, Blennow P, et al. 2020. Recent advances in solid oxide cell technology for electrolysis, Science 370: 6513.
2. Wang Y, Wu C, Zu B, et al. 2021, Ni migration of Ni-YSZ electrode in solid oxide electrolysis cell: An integrated model study. Journal of Power Sources 516: 230660.
3. Trini M, Hauch A, De Angelis S, et al. 2020. Comparison of microstructural evolution of fuel electrodes in solid oxide fuel cells and electrolysis cells. Journal of Power Sources 450: 227599.

WHEC-2022
23rd World Hydrogen Energy Conference
June 26-30, 2022 - Istanbul

#173

EFFICIENT REGENERATIVE HYDROGEN/VANADIUM FUEL CELL USING TRICHOME-LIKE ELECTRODES FOR ENHANCED VANADIUM ELECTROLYTE UTILIZATION AND ITS SYSTEM INTEGRATION

[1*] *Barun K. Chakrabarti,* [2] *Yashar S. Hajimolana,* [3] *Mengzheng Ouygang,* [4] *J. Rubio-Garcia,* [2] *Abhishek K. Singh,* [3] *Yuhua, Xia,* [1] *Nigel P. Brandon,* [5] *Vladimir Yufit*

[1] WMG, Warwick, Electrochemical Engineering Group, Energy Innovation Centre, University of Warwick, Coventry CV4 7AL, United Kingdom; RFC Power Ltd., London SW7 2PG, United Kingdom

[2] Department of Thermal and Fluid Engineering, University of Twente, Enschede 7500 AE, The Netherlands

[3] Department of Earth Science and Engineering, Imperial College London, London SW7 2AZ, United Kingdom

[4] SweetGen Limited, London SW7 2PG, United Kingdom

[5] Addionics Ltd., London W12 0BZ, United Kingdom

*Corresponding author e-mail: Barun.Chakrabarti@warwick.ac.uk

ABSTRACT

In this work we explore an in-house made carbon metal fabric (CMF) electrodes for enhanced performances in regenerative hydrogen/vanadium fuel (or flow) cells. CMF is manufactured via a sophisticated electrospinning method followed by carbonization that leads to the development of carbon nanotubes and trichome-like structures with iron nanoparticles that improve the vanadium electrolyte utilization in the RHVFC significantly. The long-term storage costs of the RHVFC are reduced when CMF is used as electrodes, and this leads to a successful systems integration for water desalination and/or solar energy storage plants.

Keywords: Hydrogen, Regenerative fuel cell, Electrospinning, Levelized cost, System integration

INTRODUCTION

Hydrogen as a zero-emission fuel has shown significant promise, as it possesses the highest gravimetric energy density in comparison to any other known substances [1]. It has mainly been applied as direct fuel and its application in fuel cell technology is well documented [2-4]. Both VRFBs (all-vanadium redox flow batteries) and PEMFCs are well known technologies in their own rights but have drawbacks that limit their complete acceptance by end users [5,6]. On their own, both technologies seem to suffer from incompatible material platforms. Therefore, researchers have looked at developing a strong materials-based platform by combining both of these technologies that has the potential to affect a major step change in the stationary energy storage market [7]. This involves the simple replacement of the OER/ORR reaction with the VO^{2+}/VO_2^+ couple that not only lowers cost but also promises a system, known as the regenerative hydrogen vanadium fuel cell (RHVFC), that can almost eliminate capacity fade issues related with the VRFB [8].

In this investigation, we have compared the performance of the RHVFC using several positive electrodes for enhancing the vanadium half-cell reactions. The initial study involved comparing several commercially sourced electrodes to determine the best one as a platform for depositing or modifying with carbonaceous catalysts. Electrophoretic deposition was then used to deposit reduced graphene oxide (rGO) and nitrogen doped graphene (N-G) to compare with a specially synthesized carbon paper catalyst that was fabricated by means of a combination of electrospinning and carbonisation. The RHVFC operation is briefly illustrated in Fig. 1, which also displays the electrochemical reactions occurring in the system.

MATERIALS AND METHODS

Vanadium (IV) oxide sulfate (hydrated) was purchased from Sigma-Aldrich (purity > 99%). Sulfuric acid (5 M) was obtained from Fluka. Electrode modification via electrophoretic deposition is given in detail in our earlier publications [10]. Electrospinning followed by carbonisation was employed to prepare carbon metal fabric electrodes as detailed elsewhere [11]. Vanadium sulfate electrolyte solutions were prepared at a concentration of 0.8 M dissolved in 5 M sulfuric acid based on previously utilized electrolytes for VRFBs, some of which provided high power densities (in excess of 1 W cm^{-2}) [12]. The volume of electrolyte used was 60 ml. A peristaltic pump (Cole Parmer Masterflex Model 77200-50) was used to circulate the vanadium electrolyte between the cell and the reservoir at a constant flow rate of 50 ml min^{-1}. The humidified hydrogen (was passed through the anodic side at a constant flow rate of 100 ml min^{-1} for polarization experiments or 30 ml min^{-1} for charge and discharge, while a glass reservoir was connected to the hydrogen outlet to collect any vanadium electrolyte cross-over [13]. The galvanostatic tests were performed using a Bio-Logic

potentiostat (VSP-300). For all tests, the RHVFC system was allowed to reach an upper cut-off voltage of 1.4 V and a lower cut-off voltage of 0.4 V.

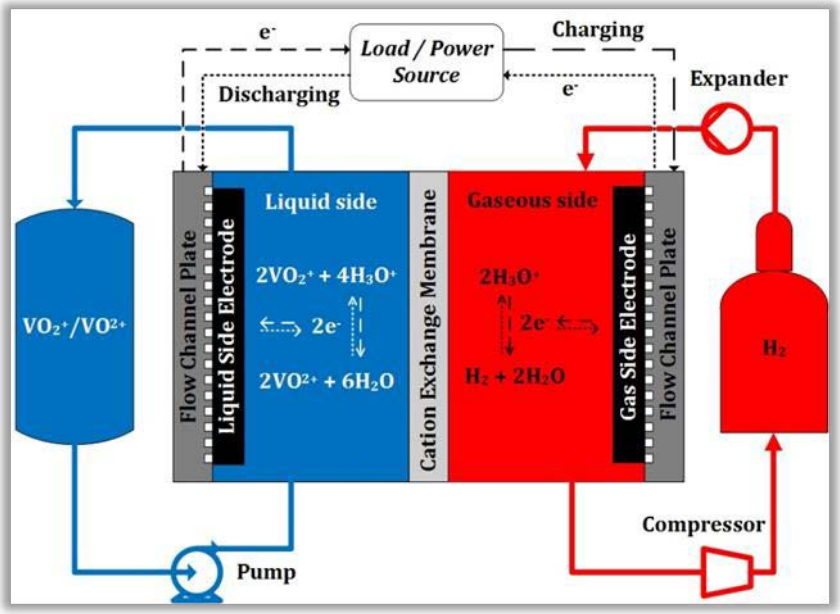


Fig. 1. RHVFC operation showing the key electrochemical reactions occurring in each half-cell. Electrode modification was performed on the liquid side. Reproduced with permission from ACS [9]

RESULTS AND DISCUSSION

Three commercially sourced electrodes - SGL (hydrophobic gas diffusion layer carbon paper), Freudenberg (hydrophilic flexible carbon paper) and ELAT (hydrophilic carbon cloth), all sourced from Fuel Cell Stores Ltd. - were modified with rGO and their power densities were compared in the RHVFC (Fig. 2a). The ELAT cloth gave best performance (even better than the nitrogen doped graphene SGL or N-G_SGL) and was used along with a single layer of CMF as the positive electrode (labelled CMF_ELAT) in an RHVFC. The power density noted was exceptional for a non-optimised system as reported elsewhere [10]. A comparison of the fifth cycle electrolyte capacity utilisation displayed much better performance for CMF_ELAT when compared to pristine ELAT (Fig. 2b).

A cost analysis of the RHVFC (for 8 h of storage) has been performed to rationalize the use of the carbon fabric electrode as catalyst layer (along with carbon cloth) for potentially scaling-up this system in comparison to the standard VRFB [16]. Although the levelized cost of VRFB and RHVFC appears similar at the same continuous discharge power density, RHVFC becomes cheaper with increased current density (hence power density) and this cost can be further reduced in comparison to VRFB if the system is operated at higher power densities (see Fig. 3).

CONCLUSIONS

The positive electrode for a regenerative hydrogen/vanadium fuel cell was modified with reduced graphene oxide and carbon metallic fabrics (CMFs) to enhance the vanadium-based liquid electrochemistry of the system. This not only resulted in higher power densities, but also higher capacities were generated, especially when using CMF as electrodes. Levelized cost of storage was lower when applying CMF.

REFERENCES

1. Møller, K. T.; Jensen, T. R.; Akiba, E.; Li, H.-w., Progress in Natural Science: Materials International 2017, 27 (1), 34-40.
2. Gambini, M.; Stilo, T.; Vellini, M., International Journal of Hydrogen Energy 2019, 44 (29), 15118-15134.
3. Dincer, I.; Acar, C., International Journal of Hydrogen Energy 2015, 40 (34), 11094-11111.
4. Güllü, E.; Mert, B. D.; Nazligul, H.; Demirdelen, T.; Gurdal, Y., International Journal of Energy Research 2021, https://doi.org/10.1002/er.7502.
5. Minke, C.; Turek, T., Journal of Power Sources 2018, 376, 66-81.
6. Staffell, I.; Scamman, D.; Velazquez Abad, A.; Balcombe, P.; Dodds, P. E.; Ekins, P.; Shah, N.; Ward, K. R., Energy & Environmental Science 2019, 12 (2), 463-491.
7. Dowd, R. P.; Verma, A.; Li, Y.; Powers, D.; Wycisk, R.; Pintauro, P. N.; Van Nguyen, T., Journal of The Electrochemical Society 2017, 164 (14), F1608-F1614.

8. Pino-Muñoz, C. A.; Chakrabarti, B. K.; Yufit, V.; Brandon, N. P. Characterization of a Regenerative Hydrogen-Vanadium Fuel Cell Using an Experimentally Validated Unit Cell Model. Journal of The Electrochemical Society 2019, 166, A3511−A3524.
9. Chakrabarti, B.; Yufit, V.; Kavei, A.; Xia, Y.; Stevenson, G.; Kalamaras, E.; Luo, H.; Feng, J.; Tariq, F.; Taiwo, O.; Titirici, M.-M.; Brandon, N. P. International Journal of Hydrogen Energy 2019, 44 (57), 30093-30107.
10. Chakrabarti, B. K.; Feng, J.; Kalamaras, E.; Rubio-Garcia, J.; George, C.; Luo, H.; Xia, Y.; Yufit, V.; Titirici, M.-M.; Low, C. T. J.; Kucernak, A.; Brandon, N. P., ACS Applied Materials & Interfaces 2020, 12, 53869−53878.
11. Chakrabarti, B. K., et al., ACS Applied Nano Materials 2021, 4, 10754−10763.

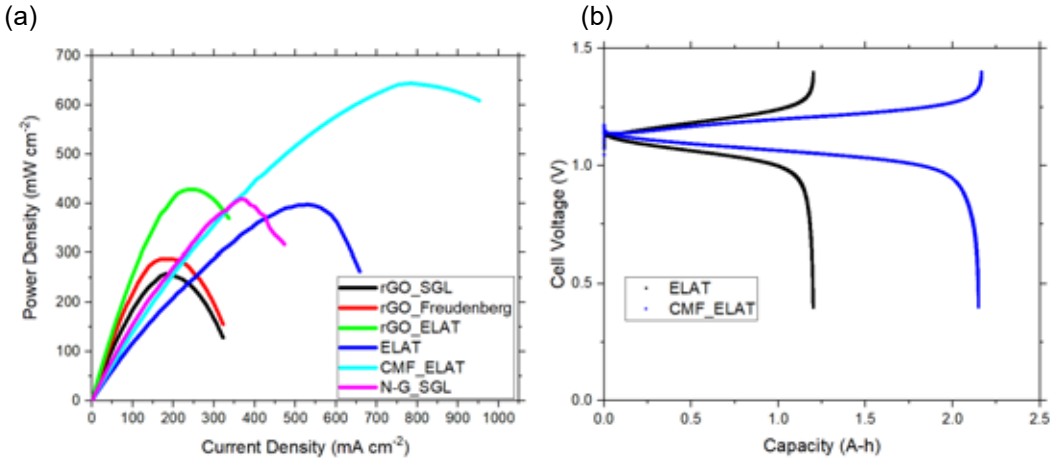


Fig. 2. (a) Evaluation of rGO modified commercial electrodes against ELAT modified CMF. (b) Capacities for CMF and CMF_ELAT at 150 mA cm^{-2}. RHVFC conditions for testing: 50 mA cm^{-2} current density, vanadium flow rate of 50 ml min^{-1}, H2 flow rate of 30 ml min^{-1}, [V] = 0.8 M, [H_2SO_4] = 5 M, room temperature, 5 charge/discharge cycles. 60 ml V electrolyte. With permission from ACS [10,11]

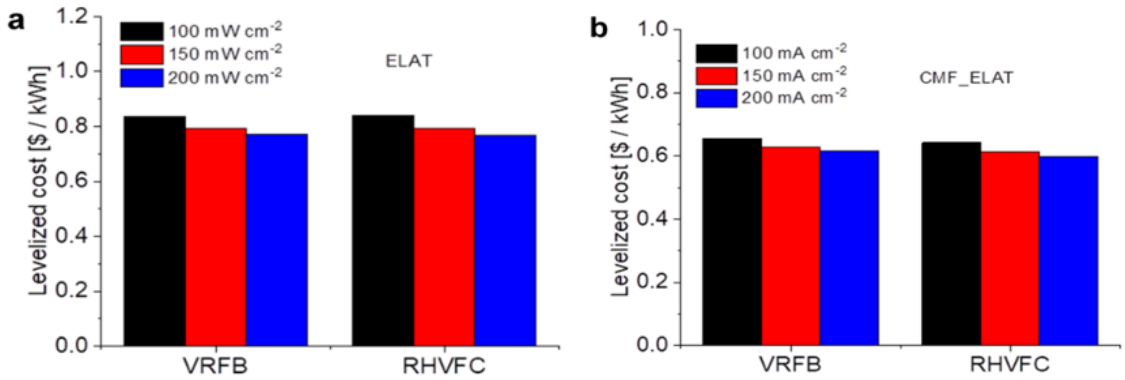


Fig. 3. Levelized cost comparison at three different current densities and 8 h of storage between RHVFC and the standard VRFB (a) for ELAT; (b) for CMF_ELAT

WHEC-2022
23rd World Hydrogen Energy Conference
June 26-30, 2022 - Istanbul

#273

COMBINATORIAL DEVELOPMENT OF LSF/rp-LSF/ScSZ COMPOSITE CATHODE FOR INTERMEDIATE TEMPERATURE SOLID OXIDE FUEL CELLS

[1*] *Fahrettin Kılıç,* [1,2] *Tayfur Öztürk*
[1]Middle East Technical University, Metallurgical and Materials Engineering, Ankara, Turkey
[2] ENDAM, Center for Energy Storage Materials and Devices, Middle East Technical University, Ankara, Turkey

*Corresponding author e-mail: fahrettinkkilic@gmail.com

ABSTRACT

This study focuses on the synthesis, characterization, and processing of LSF based composite cathode for solid oxide fuel cells. The cathode comprises three oxides; LSF, rp-LSF and ScSZ which are synthesized by co-sputtering using combinatorial approach. The electrolyte was Scandia doped Zirconia (ScSZ), as it has attractive ionic conductivity at lower temperatures. Having chosen the electrolyte ScSZ as electrolyte. After detailed analysis regarding conductivity and thermal expansion for each oxide, the compositions selected were $La_{0.8}Sr_{0.2}FeO_{3-\delta}$, $LaSr_3Fe_3O_{10-\delta}$, and $Sc_{0.15}Zr_{0.85}O_{2-\delta}$ LSF, rp-LSF, ScSZ respectively. A total of 21 composite cathodes were deposited on electrolytes, each with a different composition. The performance of cathodes was characterized via EIS measurements on symmetric cells. A temperature ranges from 600 ^{0}C up to 800 ^{0}C was covered at 50 ^{0}C interval. LSF-rpLSF-ScSZ ternary diagram was mapped in terms of area specific resistance (ASR). The ASR values at 600 ^{0}C varied from 2.159 to 34.68 ohm.cm^2. At 800 ^{0}C the values were significantly better which ranged from 0.1649 to 0.85 ohm.cm^2.

Keywords: SOFC cathodes, Electrochemical impedance spectroscopy, Magnetron sputtering

INTRODUCTION

SOFC is a fuel cell technology that operates at high temperatures. They are useful in large, high-power applications such as industrial stations and large-scale power plants. The electrolyte in a SOFC system is typically solid ceramic, and the system run at high temperatures (600-1000 ^{0}C). This high working temperature facilitates quick electro-catalytic reactions with non-precious materials and generates heat as byproduct for cogeneration. The efficiency of this type of fuel cell can be as high as 70%.

Because of its relatively large activation energy for the oxygen reduction process, the cathode electrode is the primary contributor to the overall resistance of a SOFC, especially at intermediate and low operating temperatures. One of the most significant methods for improving cell performance in SOFCs is to reduce the polarization resistance of the cathode electrode. As a result, substantial research has been conducted on the modification and improvement of SOFC cathodes to lower oxygen reduction reaction (ORR) activation energy and resistance of the electrode. For the cathode in SOFC, LSF is an often-used oxide in composite cathodes. LSF has a perovskite type structure, and because it has good oxygen ion conductivity and does not react with a zirconia-based electrolyte, it has been employed as the cathode electrode for SOFCs by numerous studies. Furthermore, because of its oxygen nonstoichiometry at high temperatures, Ruddlesden-Popper type layered perovskite, $LaSr_3Fe_3O_{10}$, has been described as a viable cathode material for solid oxide fuel cells. $LaSr_3Fe_3O_{10}$ has been found to have nearly no overpotential at the air electrode when used as an electrocatalyst for rechargeable metal-air batteries.

EXPERIMENTAL PROCEDURE

For the synthesis of active powders, Pechini method was followed. Precursors used for the synthesis of active powders were nitrates of La, Sr, Fe, Mn, Sc and Zr elements. Nitrates were mixed with deionized water in a large beaker at the intended stoichiometry with the aid of a magnetic stirrer. After the cations were dissolved in water, three times the total number of moles of cations, citric acid was added to the mixture and the solution was mixed for 20 minutes at 100 ^{0}C. Subsequently, four times the molar number of citric acid, ethylene glycol was added to the solution and the temperature was gradually increased to 150 ^{0}C and then to 200 ^{0}C. Mixing was continued at this temperature until foam formation occurred. The gel, which dries after the foam formation, is kept in a 250 ^{0}C oven for 12 hours to be purified from organic compounds. As the last process, the dry gel was calcined at the appropriate temperature.

The production of target discs was carried out by pressing followed by sintering. Deformable Teflon dies were used for this purpose. Initially, the powders were compacted to high density using a small die and subsequently sintered at different temperatures.

Thin film cathodes were sputter deposited on electrolytes. For this purpose, a prismatic chamber with dimensions of 500x500x500 mm was used which incorporates three peripheral sputter guns placed in a diameter of 350 mm, Fig. 1. In this study, the substrates are ¾ inch diameter electrolyte discs and there are total of 21 discs on the substrate holder on triangular distribution. What makes this system special is the ability to produce 21 different compositions at the same time.

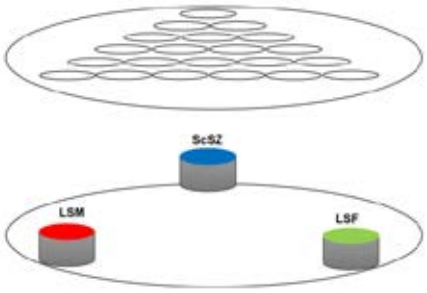


Figure 1. Drawing of samples in the substrate holder with guns in the gun holders

All the fabricated materials in this thesis were characterized by X-ray diffractometer (XRD). The D/MAX-2200 Rigaku X-ray Diffractometer with Cu-Kα radiation with 2^0/min scan rate was used. Rietveld analysis were applied to refine the X-ray patterns using Maud software. Fabricated samples were characterized using SEM. For this purpose, FEI Nova NanoSEM 430 were used. Where necessary, the use was also made of EDX attachment in SEM for elemental analysis of the synthesized powders.

Electrochemical characterization of cathodes produced with combinatorial approach was performed by symmetrical cell measurements. The symmetrical cell prepared for electrochemical characterization was place at the end of an alumina tube with an inner diameter of 14mm and an outer diameter of 24mm, and sealing was provided with AREMCO ceramic adhesive. The setup created is shown in Figure 3.6 as placed in a split oven. The produced symmetrical cells were subjected to EIS measurements at different temperatures.

RESULTS AND DISCUSSION

All the results obtained should be discussed in detail.
EIS measurements were conducted via Gamry ref. 3000 Potentiostat/Galvanostat. As perturbation voltage and frequency, 10mV and 0.1Hz-0.3Mhz were used respectively. Results were obtained between 400-800 ^{0}C with 50 ^{0}C intervals. Some examples of Nyquist plots obtained is given in Fig. 2. Nyquist plots were used to obtain the total cathode resistance.
Results are given as area specific resistance (ASR). This value is obtained from multiplying area of the cathode with the cathode resistance divided by 2 since there are cathodes on both sides of the cell. Obtained ASR results were mapped, Fig. 3.

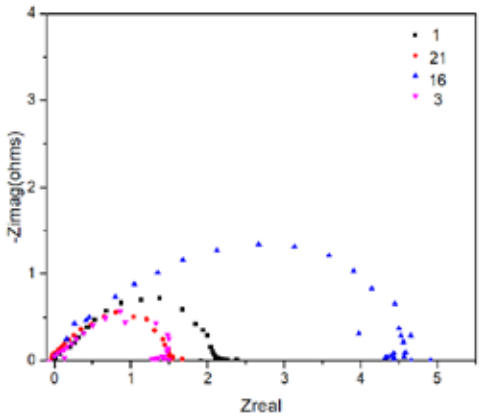


Figure 2. Nyquist plots of sample number 1,21,16 and 3 at 800 ^{0}C.

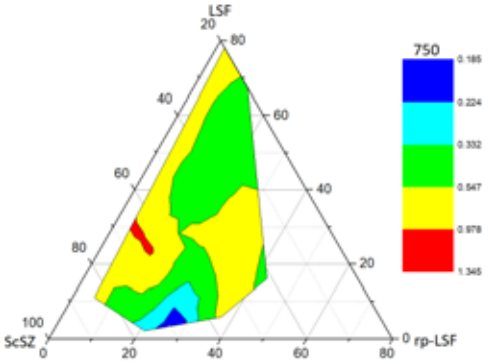


Figure 3. Contour mapping of ASR results of all 21 cells at 800 ^{0}C.

CONCLUSIONS

In this study, a combinatorial study was carried out to develop new cathode materials based on for LSF-rpLSF-ScSZ ternary system. A total of 21 cathode compositions were sputter deposited each with different compositions and were screened using symmetric cell via electrochemical impedance spectroscopy as a measure of their ORR performance. It can be determined from the study that; combinatorial approach is very useful for determining the optimum composition in the composite cathode system.

ACKNOWLEDGEMENT

This study was financially supported by the Scientific and Technological Research Council of Turkey (TUBITAK) under Grant No. 217M628.

WHEC-2022
23rd World Hydrogen Energy Conference
June 26-30, 2022 - Istanbul

#294

IDENTIFICATION OF OXYGEN ION CONDUCTIVITY OF TWO LAYERS YTTRIA STABILIZED ZIRCONIA MATRIX IMPREGNATED BY LITHIUM/POTASSIUM ELECTROLYTE FOR MOLTEN CARBONATE FUEL CELLS

[1*] *Jaroslaw Milewski*
[1]Warsaw University of Technology, Faculty of Power and Aeronautical Engineering, Institute of Heat Engineering, 21/25 Nowowiejska street, Warsaw, Poland

*Corresponding author e-mail: Jaroslaw.milewski@pw.edu.pl

ABSTRACT

It is proposed that dual conductive electrolytes have the potential to improve the performance of Molten Carbonate Fuel Cells by using oxygen ion conductors as matrix material, creating what is termed composite electrolyte. This paper presents the results of testing of a composite electrolyte layer based on Yttria Stabilized Zirconia and Lithium/Potassium carbonates for its electrochemical performance as a matrix for MCFC. The voltage–current density curves were collected for a range of temperatures: 500–800°C. Without very accurate measurements it is not easy to determine the additional electric charge provided by oxygen ions ($O^{=}$). We tried to build a mathematical model which takes into account both conductivities and, based on the model, estimated the ratio of electric charge provided by oxygen ions and carbonate ions.

Keywords: MCFC, Composite electrolyte, Dual conducting; YSZ, Li/K

INTRODUCTION

The efficiency of energy production has a major impact on operation costs and pollution. Molten carbonate fuel cells (MCFCs) [1–4] are approaching commercialization, mostly as megawatt (MW) scale systems. MCFC can operate on biofuels and hydrocarbons with negligible pollution and high efficiency of fuel conversion due to the absence of Carnot cycle efficiency restraints. This obviates the need for hydrogen, which is quite difficult to generate and store. One way of boosting the performance of these fuel cells is to improve the ionic conductance of the electrolyte matrix, a component that is exclusive to cells with a liquid electrolyte and needed to withhold the carbonate melt in its fine open-porous structure. Therefore, alternative matrix materials that have additional oxygen ionic conductivity (like yttrium stabilized zirconia – YSZ) [5] at 500–800°C have been developed for use in MCFCs.

Recently, a paper was published [6] which is very critical about the interpretation of dual conductivity provided by Li [7]. It is interesting that the arguments Nafe gives are only supported by his own papers (8 of 11 papers in the references) and he ignores other investigations made in the field (as presented in this chapter). Additionally, Nafe suggests that Li misunderstood the experimental results on the conductivity of carbonate-based composites due to disregarding electrode polarization and making the purely speculative assumption that the nature of ions mobile in the conducting media is determined by the surrounding species. Finally, Nafe concludes that composites do not distinguish themselves by enhancing ionic conductivity, but they can enjoy better performance due to their ability to reduce the extent of electrode polarization. In fact, we too do not understand why Li et al. claim that there is double “protonic” and “oxide ionic” conductivities of the electrolyte made from SDC (oxygen ion conductor, two electrons charge) and Li/Na carbonates (carbonate ion conductors, two electrons charge as well).

We believe we could try to contribute to the discussion by trying to estimate the oxygen ion conductivity of composite electrolyte indirectly by introducing the additional conductance to a fuel cell model. A few years ago, the reduced order model was proposed for describing fuel cell voltage [8]. The model is based on a combination of electric laws, gas flow relationships, solid materials properties, and electrochemical correlations. An adequate equation for cell voltage estimation was derived and commented on. The model contains only physically explained parameters (with the minimum possible number of required factors) and considers all important thermal flow as well as architecture parameters. The model assumed that fuel cell electrolyte is a conductor of one type of ions ($CO_3^{=}$). This paper presents the upgraded model of the Molten Carbonate Fuel Cell which is used for estimating the additional conductivity caused by using YSZ as the matrix material.

The experimental database composed of about 3,000 experimental points was used to validate the model and to identify the oxygen ion conductivity of the electrolyte.

Table 1: The parameters obtained by using the model

	Li/K	YSZ
Electrolyte thickness, δ, mm	2.32	1.73
Pre-exponential factor, σ_0 , S/cm	14.6*	391*
Activation energy, E_{act} , J/kmol	18.1*	87.8*
Electric resistance, r_e, Ω·cm^2	154	13
*fixed parameters as per literature data		

The model was created in Excel®. The factors which were found are set out in Table 1. It was assumed that the structure of the composite electrolyte does not change the temperature characteristics of the individual materials (YSZ and Li/K), thus the area specific resistance values are provided (r_e, Ω·cm^2). Additionally, the temperature dependent conductivity of anode and cathode was also found by fitting to the experimental data, and is given by the following equation:

$$\sigma_{anode+cathode} = 29.5 \cdot \exp(-0.895/R/T)$$

The oxygen ion conductivity of the composite electrolyte was found by mathematical modeling. The conductivity is expressed by the equivalent thickness of the YSZ matrix at a value three times greater than the electrolyte layer itself. Surprisingly, the simulated path for carbonate ions is even longer, but finally the favorable temperature characteristics of the molten salts give lower specific resistance.

DISCUSSION OF THE OBTAINED RESULTS

Based on the mathematical modeling and experimental investigations, we tried to identify the oxygen ion conductivity of the composite electrolyte. To do so, the reduced order model of MCFC was modified to include additional conductivity of the oxygen ion by a matrix prepared from YSZ.

Path length of oxygen ions (δ_{YSZ}) was found at a value of 3.8 times greater than the physical thickness of the electrolyte. This indicates that there is visible oxygen ion conductivity through the composite electrolyte. If no oxygen conductivity is found, the length should be very high (infinite in theory). On the other hand, for pure solid electrolyte as used in SOFC, the oxygen ion path length is equal to the physical thickness of electrolyte.

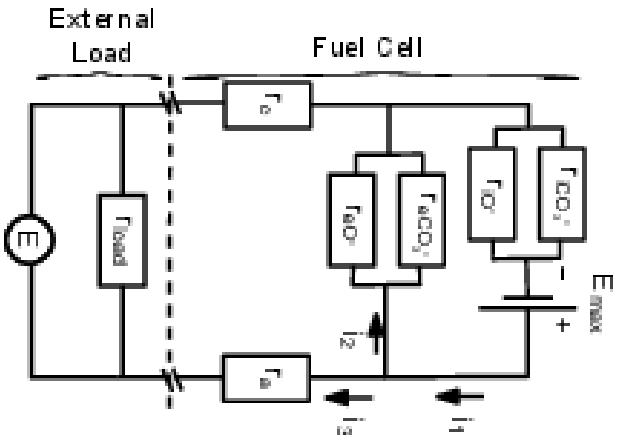


Figure 1: The equivalent electric circuit for dual conductivity MCFC

Surprisingly, the free path of carbonates ions is even longer than with oxygen ions: 5 times thicker than the electrolyte layer. This issue merits further studies and experiments. The free paths of the ions are not directly translated into the internal current which flows through composite electrolyte. The ionic conductivity of the material is strongly dependent on temperature. The average value of internal current density (i_1 in Figure 1) is the sum of oxygen and carbonate ions charges. Based on the results obtained, the average internal current caused by carbonates is 0.0936 against 0.000509 A/cm^2 made by oxygen ions, thus the oxygen ionic conductivity can be described as marginal (about 0.5% of the total internal current density). The value obtained is close to the measurement and modeling inaccuracies, thus cannot be seriously used as proof of oxygen ionic conductivity.

Presumably, if we raise the operating temperature, the part of total internal current caused by additional ionic conductance will play a larger role.

There were additional two fitting parameters: internal electric resistance of both materials used for constructing the composite electrolyte. In fact, here we do have an opposite effect: lower conductivity (higher resistivity) means better fuel cell performance. The internal electric resistance of molten salts is found to be 11.9 times higher than the solid material used. This can be explained by reference to the different mechanisms that apply to charge transfer in the two materials.

CONCLUSIONS

In this paper we provide insight into the oxygen ionic conductivity of composite electrolyte through using a mathematical model fitted to more than 3000 experimental points. The original impulse for this work came from a paper published by Nafe [6] which was very critical about work done by Li [7]. We modified the reduced order model to include hypothetical additional conductivity caused by solid material of the matrix manufactured from oxygen ion conductors (YSZ). Then the model was fitted to the experimental data, and we indicated that oxygen ion conductivity is not so evident. The obtained values of internal current density produced by oxygen ions are very small, approximating to the level of inaccuracies of experiments and modeling.

To resolve this issue, we intend to carry out – soon – an accurate analysis of cathode off gas during operation of a fuel cell that is based on composite electrolyte.

ACKNOWLEDGEMENT

The project is co-financed by Polish National Center for Research and Development of Polish-Taiwanese/Taiwanese-Polish Joint Research Call granted by decision number DZP/PL-TWIII/16/2016 and by the Norway Grants 2014-2021 via the National Centre for Research and Development under the grant number NOR/POLNORCCS/MOLCAR/0017/2020-00.

REFERENCES

1. Davoodi AH, Pishvaie MR. Plant-Wide Control of an Integrated Molten Carbonate Fuel Cell Plant. J Electrochem Energy Convers Storage 2018;15:21005. https://doi.org/10.1115/1.4039043.
2. Frattini D, Accardo G, Moreno A, Yoon SP, Han JH, Nam SW. A novel Nickel-Aluminum alloy with Titanium for improved anode performance and properties in Molten Carbonate Fuel Cells. J Power Sources 2017;352:90–8. https://doi.org/10.1016/j.jpowsour.2017.03.112.
3. Lee D, Cheon Y, Ryu J-H, Lee I-B. An MCFC operation optimization strategy based on PID auto-tuning control. Int J Hydrogen Energy 2017;42:25518–30. https://doi.org/10.1016/j.ijhydene.2017.08.184.
4. Wu M, Zhang H, Liao T. Performance assessment of an integrated molten carbonate fuel cell-thermoelectric devices hybrid system for combined power and cooling purposes. Int J Hydrogen Energy 2017;42:30156–65. https://doi.org/10.1016/j.ijhydene.2017.10.114.
5. Nadar A, Banerjee AM, Pai MR, Pai R V, Meena SS, Tewari R, et al. Catalytic properties of dispersed iron oxides Fe2O3/MO2 (M = Zr, Ce, Ti and Si) for sulfuric acid decomposition reaction: Role of support. Int J Hydrogen Energy 2018;43:37–52. https://doi.org/10.1016/j.ijhydene.2017.10.163.
6. Näfe H. Cause of “Multi-Ionic Conduction” and “Ionic Conductivity Enhancement” in Carbonate-Based Composite Electrolytes. Electrochim Acta 2017;248:250–7. https://doi.org/10.1016/J.ELECTACTA.2017.07.127.
7. Li C, Zeng Y, Wang Z, Xu F, Ye Z, Shi R. An Investigation of Protonic and Oxide Ionic Conductivities at the Interfacial Layers in SDC-LNC Composite Electrolytes. Electrochim Acta 2016;212:583–93. https://doi.org/10.1016/J.ELECTACTA.2016.07.015.
8. Milewski J, Wołowicz M, Miller A, Bernat R, RafałBernat. A reduced order model of molten carbonate fuel cell: A proposal. Int J Hydrogen Energy 2013;38:11565–75. https://doi.org/10.1016/j.ijhydene.2013.06.002.

WHEC-2022
23rd World Hydrogen Energy Conference
June 26-30, 2022 - Istanbul

#325

OPTIMIZATION OF LOW-GRADE CGO TRANSPORT PROPERTIES FOR SOFC APPLICATIONS

Eduarda.Gomes[1], Devaraj Ramasamy[1], António A.L. Ferreira[1], João C.C. Abrantes[1,2,]*
[1]proMetheus, Instituto Politécnico de Viana do Castelo, 4900-347 Viana do Castelo, Portugal
[2] CICECO, Aveiro Institute of Materials, Universidade de Aveiro, 3810-193 Aveiro, Portugal

*Corresponding author e-mail: jabrantes@estg.ipvc.pt

ABSTRACT

Grain boundaries are frequently responsible for a poor performance of gadolinium-doped ceria-based electrolytes, due to a low ionic conductivity, orders of magnitude smaller than the bulk conductivity. Silica, the dominant impurity in many low-grade ceramics, namely, in ceria-based materials, has a detrimental effect on grain boundaries conductivity. Several previous works had explored the silica-scavenging effect. In the present work, we exploit an alternative approach using the addition of 5% (w/w) of Y_2O_3, as silica scavenging agent, and sintering by hot pressing at low temperature to minimize bulk dissolution of yttrium in the CGO lattice. Gadolinium-doped ceria-based powders were co-fired with additions of 1% (w/w) of silica, and silica and yttrium oxide to test the silica scavenging role of yttrium. The samples were prepared by hot press at low temperature (1000ºC) and were characterized by impedance spectroscopy as a function of temperature in air, in order to de-convolute different microstructural contributions to the overall electrical behaviour. Combined information obtained from structural, microstructural, and electrical characterization allowed one to study the impact of new phases on the resulting ceria-based solid electrolytes.

Keywords: Ceria, Yttria, Scavenge effect, Heterogeneities, Hot press.

INTRODUCTION

The threat of global warming due to burning fossil fuels and clean-up challenges from using nuclear power have resulted in rise of environmental consciousness and tremendous efforts on seeking alternative power sources in the whole world. The fuel cell is one attractive alternative that can produce clean and efficient electricity to meet the environmental challenges and is a radically different way of making electrical power from a variety of fuels. The major requirement for current carrying devices like solid oxide fuel cell (SOFCs) is the fast ion conduction in solid electrolytes, which is the combined result of large concentrations of ionic defects and high ionic mobility. Materials with the fluorite-type structure are amongst the most effective oxygen-ion conductors. The fluorite structure shows comparatively high oxygen-ion mobility and accepts high levels of anionic disorder, which can be introduced to compensate for aliovalent metal doping [1,2]. One of the most used fluorite-type oxides is yttria stabilized zirconia (YSZ), which, due to the relatively low ionic conductivity, requires an operating temperature range reasonably high, and consequently the use of expensive complementary materials. Reducing the operating temperature allows the use of cheaper construction materials and more reliable seals. Thus, new materials have been investigated to lower the operating temperature to 500/700ºC, which includes new electrolyte materials [3] with higher ionic conductivity. The recommended use of low-grade ceramics, much cheaper than the high purity oxides, has silica as predominant constituent of the grain boundary region. Doped ceria is one of the most recognized electrolytes in the intermediate temperature range (IT-SOFCs), and shows much higher ionic conductivity than that of the well-established yttria-stabilized zirconia (YSZ) [4, 5]. However, the grain boundary behaviour usually dominates the total conductivity of ceria-based electrolytes in intermediate temperature range [4-6]. Due to the presence of thin siliceous films, the grain boundary has a blocking effect to the transport of oxygen ions across the electrolyte. In the well-established stabilized zirconia system, there have been many studies [7–13] aimed at improving grain-boundary conduction by engineering the grain-boundary phase. The principal approaches are the scavenging of the siliceous phase by the addition of Al_2O_3 [7–11], the gathering of a Si-containing phase into a discrete configuration [11,12] and the dewetting of the intergranular phase by crystallization [13]. However, alumina additions to CGO ceramics showed a detrimental effect attributed to the formation of another non-conductive phase, $GdAlO_3$ [14]. Another attempt with CGO ceramics involved additions of lanthanum oxide, as scavenging agent, which proved to be effective on removing the siliceous phases from the grain boundaries [15].

In the present work, we exploit an alternative approach to optimize the total conductivity of CGO electrolytes, using the addition of 5% (w/w) of Y_2O_3, as silica scavenging agent, and sintering by hot pressing at low temperature to minimize bulk dissolution of yttrium in the CGO lattice and hence promoting the formation of heterogeneous microstructures.

EXPERIMENTAL

Ceramic samples were prepared using commercially high purity powders as starting materials (Table 1). CGO5 was used as a reference material to compare with the prepared compositions. All samples were prepared using conventional ceramic solid state processing route. To obtain dense ceramics, the powders were sintered by hot press (HP) at 1000ºC for 2 h with 65 MPa. To study the temperature effect, a posterior thermal treatment was done at 1100ºC and 1400°C for 2h. The density was calculated using Archimedes method. The samples were analysed by x-ray diffraction (XRD) and SEM/EDS. The relative density (RD) was obtained using the density from Archimedes method and from XRD The bulk and grain boundary resistances were obtained by ac impedance spectroscopy in air, using HP Impedance Analyzer. The electrical measurements were performed in air between 1000ºC and 300ºC, in the frequency range of 20 -10^6 Hz. The same analyser was used to assess the oxygen partial pressure (pO_2) dependence of the total conductivity, during isothermal measurements carried out between 800 and 1000°C, with pO_2 changing from about 10^{-15} Pa to air, using a gas mixture of 5%H_2 and 95% of N_2.

RESULTS AND DISCUSSION

Structural characterization by XRD confirms a CGO single phase material with the fluorite type structure, without detection of silica and yttrium oxide. SEM/EDS analysis also show a homogeneous distribution of Si and Y over all the samples, suggestion an incorporation of this elements into the CGO lattice. Slight increase of the lattice parameter (Table 1) also suggests the formation of solid solution.

Table 1. Prepared samples notation, composition, thermal treatment, and obtained relative density (RD) and lattice parameter (a_0).

Sample	Composition	Thermal treatment	RD (%)	a_0 (Å)
CGO5	$Ce_{0,95}Gd_{0,05}O_{2-\delta}$	HP	92.42	5.416535
CGO5 Si	$Ce_{0,95}Gd_{0,05}O_{2-\delta}$ +1%(w/w) SiO_2	HP	77.56	5.4176936
CGO5 Si 1100	$Ce_{0,95}Gd_{0,05}O_{2-\delta}$ +1%(w/w) SiO_2	HP + 1100ºC 2h	93.36	5.4157112
CGO5 Si 1400	$Ce_{0,95}Gd_{0,05}O_{2-\delta}$ +1%(w/w) SiO_2	HP + 1400ºC 2h	95.97	5.4139509
CGO5 Si 5Y	$Ce_{0,95}Gd_{0,05}O_{2-\delta}$ +1%(w/w) SiO_2+5% (w/w) Y_2O_3	HP	83.97	5.417249
CGO5 Si 5Y 1100	$Ce_{0,95}Gd_{0,05}O_{2-\delta}$ +1%(w/w) SiO_2+5% (w/w) Y_2O_3	HP + 1100ºC 2h	85.44	5.41408
CGO5 Si 5Y 1400	$Ce_{0,95}Gd_{0,05}O_{2-\delta}$ +1%(w/w) SiO_2+5% (w/w) Y_2O_3	HP + 1400ºC 2h	93.44	5.412672

Silica addition significantly decrease the specific grain boundary conductivity, which suggests the presence of this impurity on the grain boundary (Fig.1A). Specific grain boundary conductivity partially recovers with the addition of yttria for all temperatures of thermal treatment. This effect on the specific grain boundary conductivity denotes that Si and Y have a preferential effect on grain boundaries.

The oxygen partial pressure dependence of the total conductivity shows the well-known behaviour of CGO based materials, with an ionic plateau for high oxygen partial pressures and an onset of n-type conductivity for low oxygen partial pressure. Silica as a negative effect on both types of conductivities, while yttria addition reveals some recover of the ionic conductivity and no significative effect on the n-type conductivity.

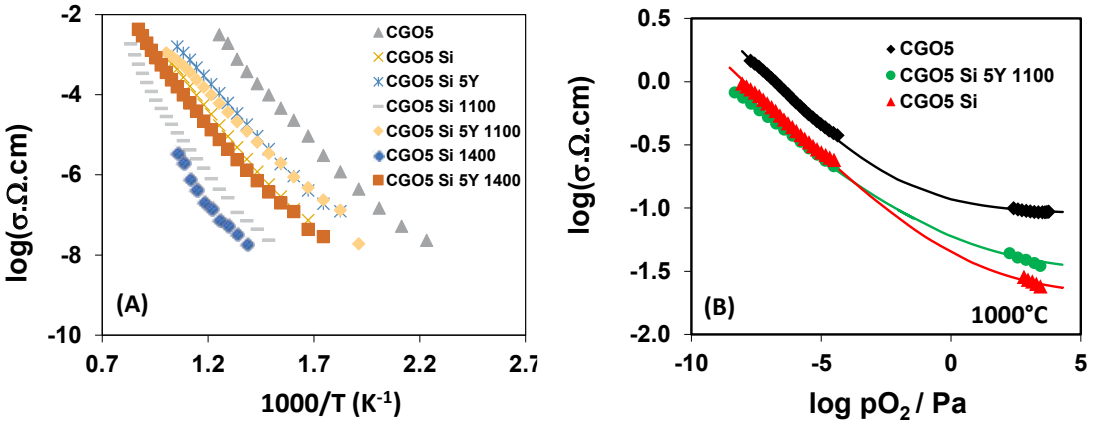


Fig. 1. Arrhenius plot of specific grain boundary conductivity (A) and oxygen partial pressure dependence of total conductivity (B).

CONCLUSIONS

Samples of gadolinium-doped ceria-based electrolytes were thermal treated at different temperatures (1100 and 1400ºC) after hot press at 1000ºC. High density (≥90%) was achieved with almost all the samples.
Addition of small amounts of impurity of silica reduces the total conductivity when compared with pure ceramic sample. However, addition of yttria increases total conductivity when compared with samples without yttria. This effect is related with the partial recover of specific grain boundary conductivity, suggesting a preferential location of Si and Y cations on grain boundaries.

ACKNOWLEDGEMENT

This work was supported by the projects HEALING (POCI-01-0145-FEDER-032036) and within the scope of the project proMetheus – Research Unit on Materials, Energy and Environment for Sustainability, FCT Ref. UID/05975/2020, financed by national funds through the FCT/MCTES.

REFERENCES

1. Steele BCH, Powell BE and Moody PMR. 1968. Anionic Conduction in Refractory Oxide Solid Solutions Possessing the Fluorite, Pyrochlore and Perovskite Structures. Proc. Brit. Ceram. Soc., 10:87-102.
2. Kharton VV, Marques FMB, Atkinson A. 2004. Transport properties of solid oxide electrolyte ceramics: a brief review. Solid State Ionics 174:135– 149.
3. Tuller HL. 2000. Solid State Ionics 131:143_.
4. Anjaneya KC, Nayaka GP, Manjanna J, Govindaraj G, Ganesha KN. 2013. Solid State Sci. 26:89-96.
5. Zhang TS, Ma J, Chan SH, Kilner JA.2005. Solid State Ionics 176: 377-384.
6. Zhang TS, Ma J, Leng YJ, He ZM. 2005. J. Cryst. Growth 274:603-611.
7. Feighery AJ, Irvine JTS, Solid State Ionics.1999. 121:209.
8. Rajendran S, Drennan J, Badwal SPS.1987. J Mater Sci Lett 6:1431.
9. Butler EP, Drennan J. 1982. J Am Ceram Soc, 65:474.
10. Lee JH, Mori T, Li JG, Ikegami T, Komatsu M, Haneda H, J Am Ceram Soc 83 (2000), 273.
11. Lee JH, Mori T, Li JG, Ikegami T, Komatsu M, Haneda HJ. 2000. Electrochem Soc 147:2822.
12. Lee JH, Mori T, Li JG, Ikegami T, Drennan J, Kim DY. 2002. J Electrochem Soc 149:J45.
13. Jung YS, Lee JH, Kim DY. 2003. J Electrochem Soc 150:J49.
14. Zhang T, Zeng Z, Huang H, Hing P, Kilner J. 2002. Effect of alumina addition on the electrical and mechanical properties of Ce0.8Gd0.2O2-δ ceramics. Materials Letters 57:124-129.
15. Ivanova D, Kovalevsky A, Kharton VV, Marques FMB. 2008. Silica-scavenging effects in ceria-based solid electrolytes. Boletin de la Sociedad Española de Cerámica y Vidrio 47:201-206.

WHEC-2022
23rd World Hydrogen Energy Conference
June 26-30, 2022 - Istanbul

ELECTRICAL CONDUCTIVITY OF Y-DOPED CGO BASED MATERIALS SINTERED BY HOT PRESS

[1]Devaraj Ramasamy, [1]Eduarda Gomes, [1]António A.L. Ferreira, [1,2*]João C.C. Abrantes
[1]proMetheus, Instituto Politécnico de Viana do Castelo, 4900-347 Viana do Castelo, Portugal
[2]CICECO Aveiro Institute of Materials, Universidade de Aveiro, 3810-193I Aveiro, Portugal

*Corresponding author e-mail: jabrantes@estg.ipvc.pt

ABSTRACT

Commercial ceria–gadolinia powders were used to prepare dense CGO (5 mol% Gd) samples, by hot press method at relatively low temperature (1000°C). To study the effect of post-sintering, further the as-sintered bodies were subjected into different thermal treatments 1100ºC-1400ºC. The sintered samples were characterized by impedance spectroscopy as a function of temperature in air, in order to identify each microstructural contribution to the overall electrical behaviour. Scanning electron microscopy shows that the increase in the temperature of thermal treatment leads to grain growth. Electrical properties were studied with different oxygen partial pressures and ion blocking methods. Y_2O_3 (5 wt%) additions were used to seek the grain boundaries heterogeneities effects in CGO material, prepared by hot press and subjected into post sintering thermal treatments. Electrical conductivities of CGO samples were analysed with and without Y_2O_3 additions.

Keywords: SOFC, Hot press, CGO, Electrical conductivity, Heterogeneities.

INTRODUCTION

The electrolyte is a crucial component of solid-state electrochemical systems, in which ions must diffuse between electrodes. Gadolinium doped cerium oxide (CGO) electrolytes have an extraordinary range of applications, which include solid oxide fuel cells (SOFC), electrolysers, oxygen sensors, oxygen permeation membrane systems, oxygen storage capacitors, pumps and photo catalysts, mostly, due to its unique properties, such as high electrical conductivity (high mobility of oxygen ions) and catalytic activity (large oxygen storage capacity) compared to those of conventional zirconia-based electrolytes. However, a high material cost or insufficient performance of CGO may prevent commercial success in some of these applications [1-3]. It is noted that the contribution of grain-boundary resistivity to the overall resistivity of CGO based materials are known to be 2-3 orders of magnitude higher than the grain-interior resistivity, due to the depletion of oxygen vacancies near the grain-boundary, due to the formation of a space charge layer. Though, promising properties of CGO can be obtained by selecting the proper concentration of oxygen vacancies in the crystal structure, as well as the fitting microstructure, since both have a direct and decisive effect on functional properties [4-5]. However, it is challenging to obtain homogeneous microstructures with full densification for ceria-based materials, since CGO has a poor sinterability due to its high refractoriness. It is also expected that ionic conductivity of ceria-based electrolytes might be optimized by engineering core–shell microstructures, with higher contents of trivalent additive at the shell [6].

In this work, we assess and correlate the sinterability, microstructural evolution, and electrical properties of CGO samples with and without addition of Y_2O_3, prepared by hot press method.

MATERIALS AND METHODS

Commercially available $Ce_{0,95}Gd_{0,05}O_{2-\delta}$ (Praxair) and Y_2O_3 (Alfa Aesar) high purity powders were used as starting materials. Doped Y_2O_3 (5 wt%) into $Ce_{0,95}Gd_{0,05}O_{2-\delta}$ powder was prepared using conventional solid-state reaction method. The $Ce_{0,95}Gd_{0,05}O_{2-\delta}$ powders with and without Y_2O_3, were sintered by hot-press method in an alumina die under 60 MPa at 1000ºC for 2h, 5˚C/min heating and 10ºC/min cooling rate were used. The sintered samples are labelled CGO5 and CGO5 5Y. In order to study the effect of post-sintering, further the as-sintered bodies were subjected into different thermal treatment at 1100˚C and 1400˚C for 2h. The samples were named CGO5-1100˚C, CGO5 5-1100˚C and so on. Scanning electron microscopy was used to characterize microstructure features of sintered ceramic samples. The total conductivity measurements were performed on dense pellets prepared by hot-press and post thermal treatment, using an AC impedance spectroscopy in air HP Impedance Analyzer. The pellets were painted on both sides with porous platinum electrodes and fired at 900ºC. All measurements were carried out from 1000 to 100°C with 25°C steps, in the frequency range of 20 -10^6 Hz. In order to obtain the n-type conductivity, a dense CGO based samples were painted with a Pt electrode and then sealed against a dense alumina disk with glass ceramic seal, to achieve gas tightness required for ion blocking measurements. This electrode was polarized cathodically, at different values of applied voltage and the corresponding current was measured.

RESULTS AND DISCUSSION

The morphology of CGO samples sintered at 1000˚C by hot press and with post thermal treatment at 1100˚C and 1400˚C are presented in Fig.1. The ceramics sintered at 1000˚C show relatively small grains and a further increase in temperature of thermal treatment leads to grain growth. Along with, CGO ceramic thermal treated at 1400ºC achieved large grains.

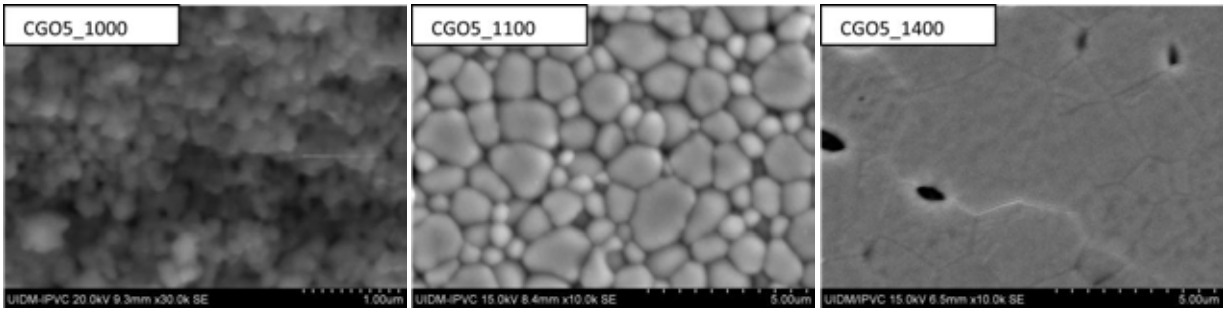


Fig. 1. SEM micrographs of CGO ceramics: sintered at 1000ºC, 1100ºC and 1400ºC.

Specific grain boundary conductivity of selected samples was determined and is showed in Fig. 2. In order to understand the effect of hot press approach, CGO sample prepared by conventional sintering at 1400˚C is also included. Sample prepared by hot press at 1000ºC with and without Y_2O_3 shows higher specific grain boundary conductivity than CGO from conventional sintering. Thermal treatments of the samples between 1100°C and 1400ºC have a negative effect on specific grain boundary conductivity, with the worst value observed at the temperature of 1400ºC, which suggest a degradation of properties of the grain boundary with the increase of the thermal treatment temperature. The thermal treatment temperature effect it is much evident for Y-doped samples than for the pure CGO, which suggest a dissolution of Y into the grain interior for higher temperatures.

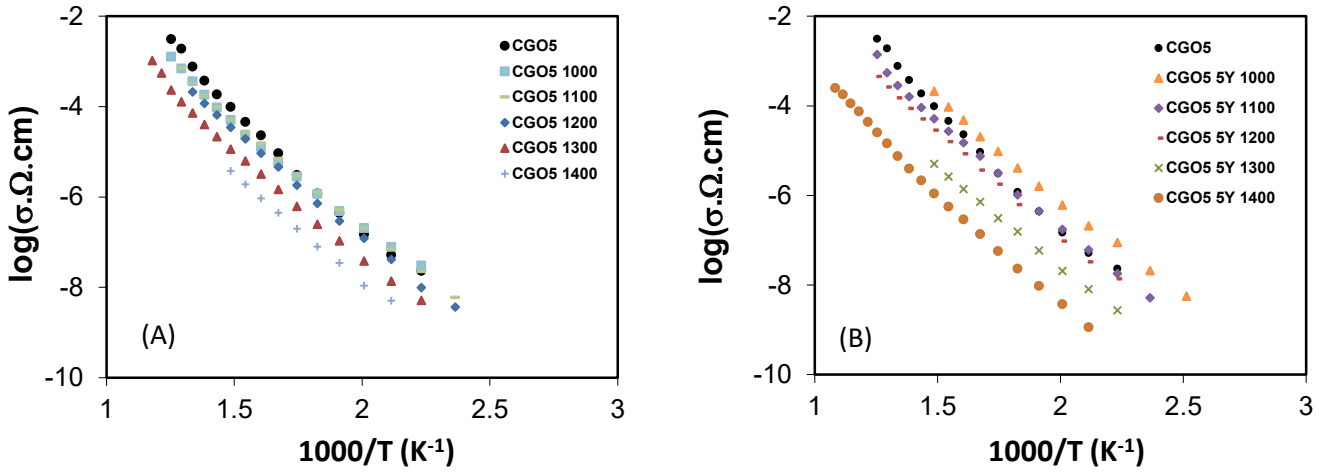


Fig. 2. Arrhenius plot of specific grain boundary conductivity of CGO (A) and CGO 5Y; (B) ceramics with post thermal treatment 1100ºC and 1400ºC.

The oxygen partial pressure dependence of the total conductivity and ion blocking measurements, shows the well-known behaviour of CGO based materials, with an ionic plateau for high oxygen partial pressures and an onset of n-type conductivity for low oxygen partial pressure (Fig.3).

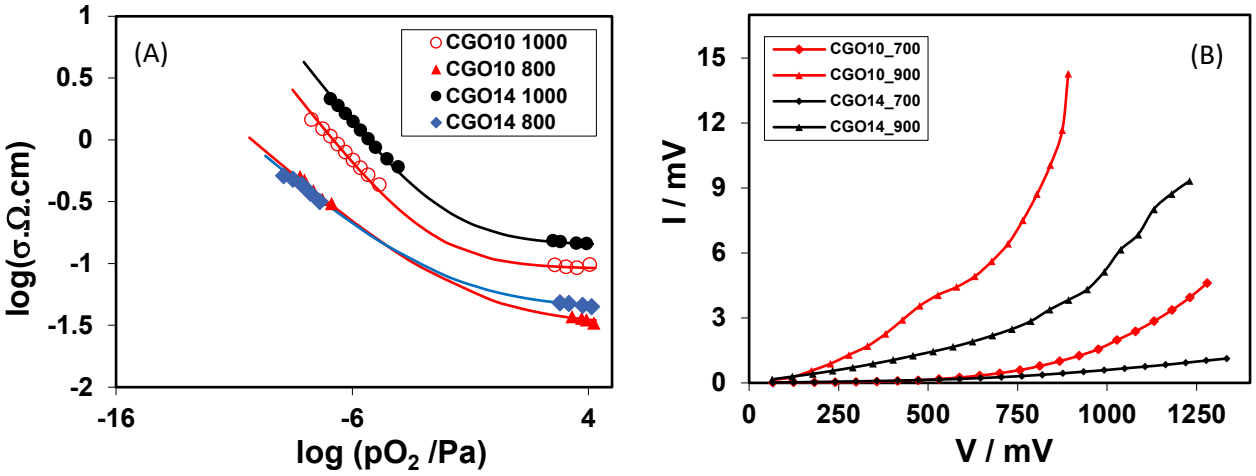


Fig. 3. Electrical conductivity as a function of the oxygen partial pressure(A) and ion blocking results (B) for of CGO based ceramics sintered at 1000˚C and 1400°C.

CONCLUSIONS

The present studies have shown that, using hot press sintering method, the widely used gadolinia doped ceria (CGO) electrolyte ceramics could be densified at relatively lower temperature 1000°C-1100°C with favourable performance, namely with higher electrical conductivities of the grain boundaries, when compared with traditional materials obtained at higher sintering temperature (≥1400˚C).

ACKNOWLEDGEMENT

This work was supported by the project HEALING (POCI-01-0145-FEDER-032036) and within the scope of the project proMetheus – Research Unit on Materials, Energy and Environment for Sustainability, FCT Ref. UID/05975/2020, financed by national funds through the FCT/MCTES.

REFERENCES

1. Inaba H, Tagawa H. 1996. Ceria-based solid electrolytes. Solid State Ionics. 83:1–16.
2. Steele BCH. 2000. Appraisal of Ce1-yGdyO2-y/2 electrolytes for IT-SOFC operation at 500°C. Solid State Ionics. 129:95–110.
3. Guo X, Zhang ZL.2003. Grain size dependent grain boundary defect structure: case of doped zirconia, Acta Mater. 51:2539–2547.
4. Tian CY, Chan SW. 2000. Ionic conductivities, sintering temperatures and microstructures of bulk ceramic CeO2 doped with Y2O3. Solid State Ionics. 134:89–102.
5. Cho YH, Cho PS, Auchterlonie G, Kim DK, Lee JH, Kim DY, Park HM, Drennan J.2007. Enhancement of grain-boundary conduction in gadolinia-doped ceria by the scavenging of highly resistive siliceous phase, Acta Mater. 55:4807-4815.
6. Tanaka R, Oliveira WS, Brandão A, Abrantes JCC, Frade JR.2012. Grain boundary conductivity of heterogeneous ceria gadolinia, Electrochimica Acta 85:116-121.

WHEC-2022
23rd World Hydrogen Energy Conference
June 26-30, 2022 - Istanbul

#327

OPTIMIZATION OF LOW-GRADE TETRAGONAL ZIRCONIA BY PRASEODYMIUM OXIDE ADDITIONS

[1] António A.L. Ferreira, [1] Devaraj Ramasamy, [1] Eduarda Gomes, [1,2*] João C.C. Abrantes
[1] proMetheus, Instituto Politécnico de Viana do Castelo, 4900-347 Viana do Castelo, Portugal
[2] CICECO, Aveiro Institute of Materials, University of Aveiro, 3810-193 Aveiro, Portugal

*Corresponding author e-mail: jabrantes@estg.ipvc.pt

ABSTRACT

Zirconia-based materials are still the state of art electrolyte for high temperature electrochemical systems, and for non-electrochemical applications. Their purity is known to affect performance, thus requiring high-grade expensive precursors and additional concerns about contamination during high temperature processing and/or during long term applications at intermediate temperatures, as found for contamination by silica. Thus, the purpose of this work was to demonstrate the scavenging ability of praseodymium oxide to minimize or suppress the impact of contamination by silica.

In the present work, one used TZP precursor powders from Tosoh and Innovnano. Starting materials of both powders contained significant fractions of monoclinic phase, coexisting with tetragonal zirconia, and yielded highly dense samples after sintering at 1450°C/2h. Praseodymium oxide and/or silicon oxide additions did not affect significantly the sintering behaviour. Additions of Pr and Si yielded co-existing tetragonal and cubic phases, as revealed by XRD and Rietveld refinements, with an impact on lattice parameters of the cubic phase.

The electrical characterization showed the expected severe decrease in conductivity after the addition of silicon oxide addition and also showed that this negative impact is at least partially reverted by additions of praseodymium oxide.

Keywords: solid electrolyte, yttria-stabilized zirconia, praseodymium oxide, scavenging, silica impurity

INTRODUCTION

Growing environmental concerns force the search and development of alternative energy technologies. However, the buoyancy in renewable energy production and the mismatch between energy production and demand point to the need for energy storage systems. Therefore, the importance of the study and development of solid electrochemical systems is relevant in deepening the knowledge of solid oxide fuel cells (SOFC), solid oxide electrolysis cells (SOEC) and, more recently, solid oxide reversible cells (rSOC) [1]. The growing importance of the latter cells is related to the finding that the degradation that occurs at the oxygen electrolyte/electrode interface can be delayed with the cell operating in a reversible SOEC/SOFC regime and the degradation that occurs in the SOEC regime can be partially recovered when the cell works in SOFC mode, properly controlling cycle duration [2-4]. One possible approach might be to introduce active components into the reduction. To achieve greater chemical and thermomechanical compatibility, these components can be based on zirconia with the addition of yttria and additions of cations of varying valence such as manganese and praseodymium [5].

MATERIALS AND METHODS

Commercially available Tosoh and Innovnano tetragonal zirconia powder (3% molar percentage of Y_2O_3) (TZP), Pr_2O_3 and SiO_2 high purity powders were used as starting materials. Doped powders were prepared using the conventional solid-state reaction method. The powder mixtures were weighed and mixed through ball milling in ethanol medium using zirconia balls. The prepared slurry was dried in and grounded using agate mortar and pestle until a fine powder was obtained. To study the effect of SiO_2 as impurity and Pr_2O_3 as a scavenging solution, pellets of undoped and doped TZP were unidirectionally pressed at 125 MPa and then sintered at 1450°C for 2 hours with heating and cooling rates of 10°C/min. The densities of sintered samples at various temperatures were calculated by the Archimedes method. X-ray diffraction was used to characterize the phase composition of the as-prepared and thermally treated ceramics, also the lattice parameters were calculated after Rietveld refinements. Scanning electron microscopy and EDS were used to analyse microstructure characterization of sintered ceramic samples. The total conductivity measurements were performed on dense pellets, using an AC impedance spectroscopy in an air atmosphere by HP Impedance Analyzer. The variation of the total conductivity with oxygen partial pressure at a fixed temperature was also made.The pellets were painted on both sides with porous platinum electrodes and sintered at 900°C. All measurements were carried out in the direction of decreasing temperature, from 1000 to 200°C with at 25°C steps in the frequency range of 20 -10^6 Hz.

RESULTS AND DISCUSSION

The high densification of the samples of all compositions is achieved for the sintering conditions used, see Table 1. There are no remarkable differences in densification with the additions of silica or praseodymium oxide. The high densification is confirmed by SEM, Figure 1, where is also evident the small size of the grains. It is also clear some bimodal distribution of the grain sizes.

Table 1. Sample identification, density and relative density (RD) of the different compositions sintered at 1450°C for 2h.

Notation	TZP provider	at% SiO_2	at% Pr_2O_3	Density	RD (%)
T	Tosoh	0	0	5.962	98.7
3PT	Tosoh	0	3	5.828	96.5
ST	Tosoh	1	0	5.904	97.7
S3PT	Tosoh	1	3	6.028	99.8
I	Innovnano	0	0	5.818	96.3
3PI	Innovnano	0	3	5.730	94.9
SI	Innovnano	1	0	5.882	97.4
S3PI	Innovnano	1	3	5.546	91.8

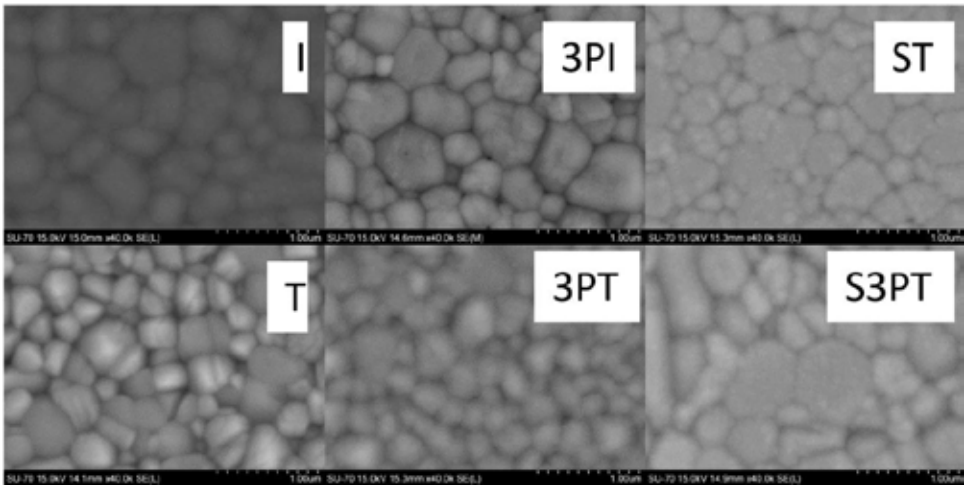


Fig. 1. SEM micrographs of the different studied compositions.

The overall conductivity of the samples is strongly affected by the presence of silica, but not so much with the additions of praseodymium oxide. It is also noticeable that the addition of praseodymium oxide to samples with silica benefits the samples, the conductivity decrease is not so relevant. By the analysis of the bulk and the grain boundary conductivities, it is clear that the more significant variations are seen on the grain boundary conductivity, as illustrated in Figure 2.

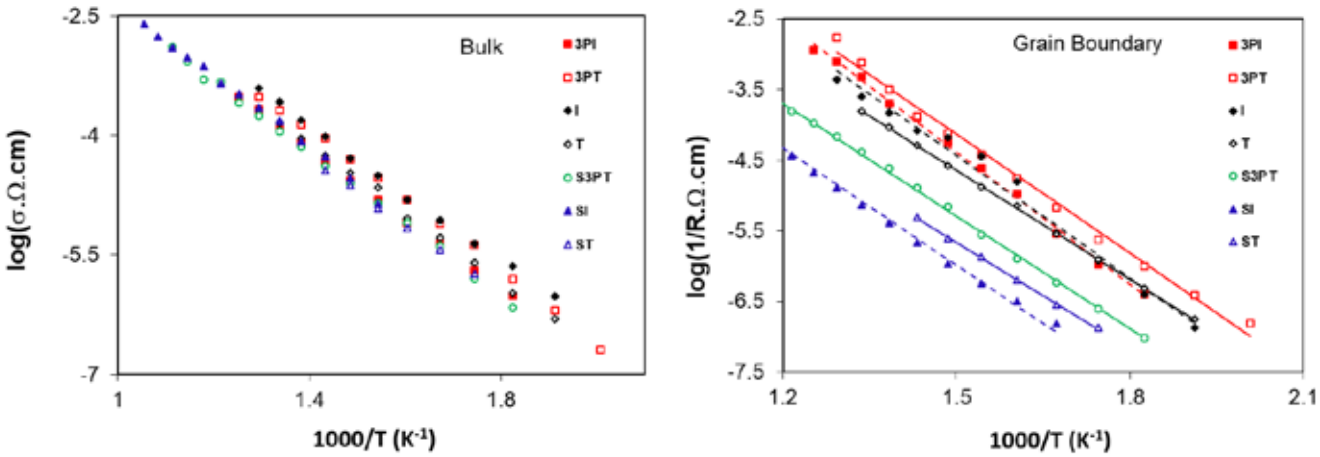


Fig. 2. Bulk and grain boundary conductivities as a function of temperature for the studied compositions.

CONCLUSIONS

The addition of praseodymium oxide to TZP to prevent or diminish the prejudicial results of the impurity silica is a viable hypothesis. The degradation in the conductivity is attenuated and further studies should be carried on to preview the right amount of praseodymium to be added to obtain the maximum effect to correct the deviations promoted by silica and not to alter the properties by itself.

ACKNOWLEDGEMENT

This work was supported by the project HEALING (POCI-01-0145-FEDER-032036) and also within the scope of the project proMetheus – Research Unit on Materials, Energy and Environment for Sustainability, FCT Ref. UID/05975/2020, financed by national funds through the FCT/MCTES.

REFERENCES

1. Mogensen MB, Chen M, Frandsen HL, Graves C, Hansen JB, Hansen KV, Hauch A, Jacobsen T, Jensen SH, Skafte TL.2019. Reversible solid-oxide cells for clean and sustainable energy. Clean Energy. 3:175–201.
2. Chen K., Jiang SP.2016. Review-Materials degradation of solid oxide electrolysis cells. J. Electrochem. Soc. 163: F3070–F3083.
3. Khan MS, Xu X, Knibbe R, Zhu Z. 2021. Air electrodes and related degradation mechanisms in solid oxide electrolysis and reversible solid oxide cells. Renew. Sustain. Energy Rev. 143: 110918.
4. Graves C, Ebbesen SD, Jensen SH, Simonsen SB, Mogensen MB. 2015. Eliminating degradation in solid oxide electrochemical cells by reversible operation. Nat. Mater. 14: 239–244.
5. Natoli A, Frade JR, Bamburov A, Zurawska A, Yaremchenko A. 2021. Impact of Praseodymia Additions and Firing Conditions on Structural and Electrical Transport Properties of 5 mol.% Yttria Partially Stabilized Zirconia (5YSZ); Appl. Sci. 11:5939.

WHEC-2022
23rd World Hydrogen Energy Conference
June 26-30, 2022 - Istanbul

#366

ACCELERATED STRESS TESTING OF SOLID OXIDE FUEL CELLS VIA EX-SITU CHEMICAL REDOX CYCLING OF Ni-CGO FUEL ELECTRODES

[1] *Massimiliano Della Pietra,* [1*,2] *Andrea Monforti Ferrario,* [1] *Davide Pumiglia,* [1] *Livia Della Seta* [1] *Stephen McPhail*
[1] ENEA, Laboratory of Energy Storage, Batteries and Hydrogen Production & Use, Department of Energy Technologies and Renewable Sources (TERIN-PSU-ABI), C.R. Casaccia, Via Anguillarese 301, 00123 Rome, Italy
[2] Department of Industrial Engineering and Mathematical Sciences (DIISM), Università Politecnica delle Marche, Via Brecce Bianche 12, 60131 Ancona, Italy

*Corresponding author e-mail: andrea.monfortiferrario@enea.it

ABSTRACT

Although Solid Oxide Fuel Cells (SOFC) are key for the energy transition, current lifetimes represent a critical barrier for deployment and a full understanding of the degradation mechanisms is yet to be reached. In this work an innovative testing approach has been implemented to evaluate an Accelerated Stress Test (AST) via chemical redox cycling as stressor for electrolyte supported SOFC Ni-CGO fuel electrodes. The fuel electrodes were aged with an *ex-situ* approach by exposing half-cells to alternating redox cycles (up to 12 cycles). Successively, fresh oxygen electrodes were screen-printed and the resulting full-cells with pre-aged anodes were electrochemically tested (comparing IV curves and EIS spectra with a virgin full-cell) and characterized with SEM post-test imaging. Preliminary results show that chemical redox cycling seems a viable AST pathway, showing a coherent performance degradation (both in terms of voltage and impedance) with increasing number of cycles. The accelerated degradation ascribed to the anode processes (both charge and mass transfer) by the impedance analyses is confirmed by SEM observations which show Ni particle agglomeration within the fuel electrode. However, full-cell stability with high number of redox cycles might represent a limiting factor in terms of AST replicability and testing performance, since recurrent cathode detachment is observed.

Keywords: Solid Oxide Fuel Cells, Accelerated Stress Tests, Redox Chemical Cycling, Electrochemical Testing, SEM

INTRODUCTION

Solid Oxide Fuel Cells (SOFC) are a key technology for the energy transition, due to high conversion efficiency and fuel flexibility, among other features, especially in the perspective of hydrogen as future energy vector. However, the high temperature operating conditions (500-800 °C) in relation to current material properties result in high degradation rates, leading to low lifetimes with respect to competing technologies, which represent a major criticality [1].
The determination of the degradation phenomena of a SOFC is extremely complex since multiple processes and reactions occur simultaneously in different components of the SOFC, which can be affected in several ways. Cell degradation occurs both in normal operating conditions over very long periods of operation time (several thousand hours) and in the occurrence of events (on-off cycles, thermal cycles, etc.) which can trigger soft or hard failures. The cell degradation trend is typically non-linear, and its direct observation is time-consuming since significant data is obtained only after long testing periods under several different operating conditions and occurrences [2].
The development of Accelerated Stress Tests (AST) is a prominent trend which aims to replicate the spontaneous degradation obtained in long periods of time by performing tests of shorter duration in which one or more operating parameters, named stressor (e.g. thermal, chemical, electrochemical, mechanical, etc.), are set to a harsher condition respect to standard operation. In this way the degradation mechanisms can be studied over shorter periods of time, providing meaningful information to understand the trend and evolution of each specific performance loss in order to ultimately develop suitable mitigation strategies (i.e. cell design or cell operation strategies) [2–4].
In this work an innovative combined *ex-situ* and *in-operando* testing approach has been implemented to evaluate chemical redox cycling as stressor, thus developing an AST protocol with particular focus on accelerating degradation phenomena occurring at SOFC fuel electrodes during both standard ageing and fuel-lacking events, in which Ni re-oxidation might occur such as on-off procedures, hot standby or fuel leakages/starvation.

MATERIALS AND METHODS - EXPERIMENTAL

The first step of this work is related to the *ex-situ* pre-ageing of the fuel electrodes via chemical redox cycling. Figure 1 illustrates the main features of the experimental setup.
Commercial Electrolyte Supported Cell (ESC) half cell samples have been provided by Sunfire for the study composed of State-of-Art materials. The cells present a square geometry with a YSZ supporting electrolyte layer (3x3

cm; ≈85 µm) and a single 3-layer Ni-CGO fuel electrode (1x1 cm; ≈25 µm in reduced phase). The other side of the electrolyte is bare.
The cells are mounted in a 10x10 cm single-cell metallic cell holder, in which a customized sealing geometry is designed to ensure single atmosphere at the target electrode for up to four housed samples. The gas distribution system is adapted to provide alternating reducing (H_2 and N_2) and oxidizing (air) atmospheres to all samples by two three-way non-return valves fitted on the inlet/outlet pipes. The samples are placed in a temperature-controlled furnace which is operated at fixed temperature (850°C, nominal ESC temperature) with ≈50 kg applied spring load.
After the initial heat-up procedure, the chemical redox cycles are composed of: *i)* reduction step [3 h; 400 ml/min; 25/75% H_2/N_2]; *ii)* purge phase [1 h; 400 ml/min; N_2]; *iii)* oxidation step [1 h; 400 ml/min; Air]. The duration, flow rates and compositions of each step have been selected to ensure full reduction or oxidation of the Ni particles [5,6]. When the n redox cycles are completed a final reduction step is performed before cooling down the cell under reducing conditions to fix structural variations induced by the redox cycling in typical operating conditions (reduced fuel electrode).



(a) **(b)** **(c)** **(d)**

Fig. 1. Experimental setup for *ex-situ* artificial pre-ageing of fuel electrodes via redox cycling. **(a)** Custom gas sealing; **(b)** Cell holder configuration; **(c)** Test rig configuration; **(d)** Redox cycling procedure scheme

Once the *ex-situ* artificial pre-ageing of the fuel electrode is completed, a fresh LSCF cathode layer (1x1 cm; 30-35 µm) was applied by screen-printing & sintering on the bare side of YSZ electrolyte, resulting in full cells with pre-aged anode. In this way any performance loss is ascribed to the degradation of the fuel electrode since the oxygen electrode did not undergo the pre-ageing chemical treatment (it is assumed that the YSZ electrolyte is chemically stable).
The second step of this work is related to the *in-operando* characterization of the full cells with pre-aged fuel electrode. Figure 2 illustrates the complete experimental workflow procedure which was followed.
The electrochemical characterization is carried out in a standard ceramic button-cell test setup [7]. The cells are tested at 850°C with stationary fuel and oxidant feeds of [100 ml/min; 60/40% H_2/N_2] and [200 ml/min; air], respectively. The electrochemical characterization is performed in OCV both at t=0 h and at t=100 h after a stabilization under a current load of 0.25 A/cm^2 to ensure stationary conditions of the performed following measurements:

- Polarization curves (galvanostatic mode, stepwise current sweep from OCV up to 0.5 A/cm^2) from which the average Area Specific Resistance (ASR) parameter is obtained from the average slope of the IV curve;
- Electrochemical Impedance Spectroscopy (EIS) spectra [OCV; ΔV_{AC} 10 mV; f=2x10^{-3}-10^5 Hz; 12 points/decade].
    - The deconvolution of the EIS data is elaborated via Distribution of Relaxation Times (DRT) technique. The trend of each process contribution is assessed by analysing the shifts in the DRT spectra with respect to the physico-chemical process mapping previously obtained by EIS testing of the virgin cell and from literature review [8].

Finally, the samples are characterized with post-test imaging via Scanning Electron Microscopy (SEM) to detect morphological and structural modifications.

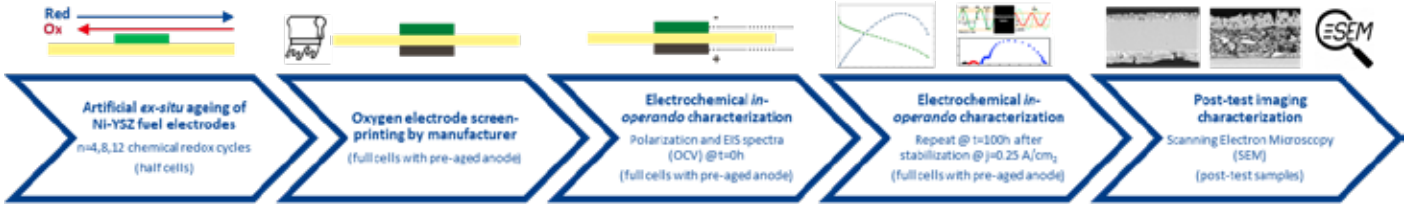
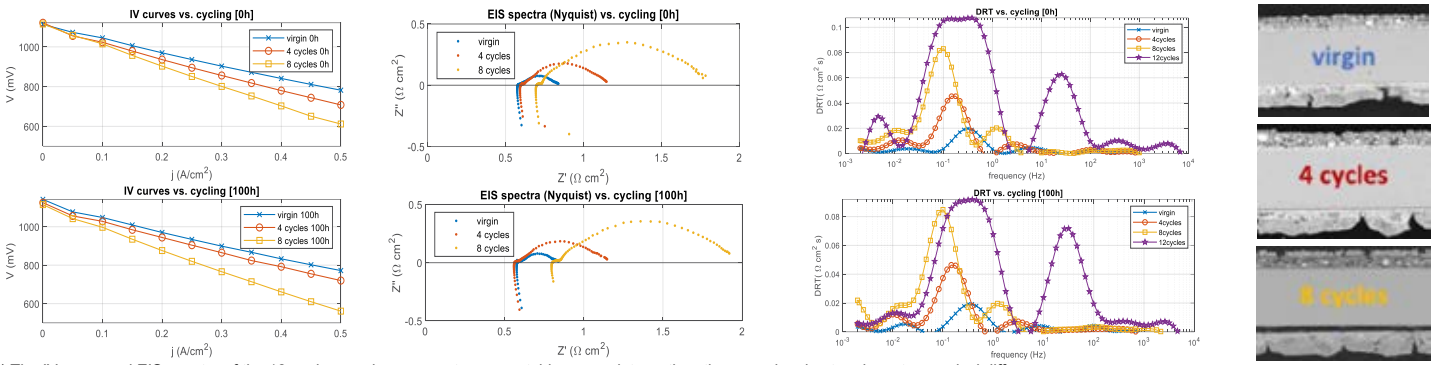


Fig. 2. Integrated experimental workflow

RESULTS AND DISCUSSION

In the following section the preliminary cell characterization results are presented for samples which have performed 4, 8 and 12 redox chemical cycles. The results – illustrated in Figure 3 – are compared with a

benchmark full cell (virgin), manufactured with the same 2-step approach starting from a half cell which has not undergone the pre-ageing procedure. The full benchmark characterization and process mapping via DRT analysis of the virgin cell are not here reported for sake of brevity.



* The IV curve and EIS spectra of the 12-cycle samples were not representable same plots as the other samples due to relevant numerical differences.

(a) **(b)** **(c)** **(d)**

Fig. 3. Summary of preliminary results vs. cycling: **(a)** IV polarization curves; **(b)** EIS spectra; **(c)** DRT spectra; **(d)** SEM images

From the IV curve the ASR is gradually increasing with increasing n (0.72 Ωcm², 0.83 Ωcm² and 1.01 Ωcm² for the virgin, 4- and 8-cycle samples respectively). Despite several repetitions the 12-cycle samples did not reach acceptable performances, suggesting a stability issue for high n (also slightly observed for the 8-cycle sample).
In terms of EIS parameters, R_0 is unaffected for the 4-cycle sample, only slightly increased for 8-cycle sample and dramatically increased for the 12-cycle samples. On the other hand, R_{pol} seems to follow a gradual increasing trend with increasing n. The DRT analysis confirms that the most impacted processes are the anode ones (both charge and mass transfer, which are convoluted between 0.01-10 Hz due to the Ni-CGO properties [8]). The result is consistent with structural variations in the cermet network caused by the alternating Ni-NiO phase transitions ($\Delta V/V \approx 40\%$ [6]), as seen in [5,6,9]. Thermal cycling during the various procedures could also have an impact [3]. In addition, an increase of the cathode charge transfer impedance (1-10 and 30-100 Hz [8]) is observed for the 8- and 12-cycle sample.
The post-test SEM images show a progressive Ni particle agglomeration with increasing n, which matches with worsened anodic performance (both mass and charge transfer). The coalescence of Ni particles seems to induce μ-cracks in the Ni-CGO substrate, modifying its porosity and particle distribution [6]. Delamination of the external layer is observed with regions where the anode bulk thickness is sensibly reduced due to lost material. Furthermore, the 8- and 12-cycle samples show an important cathode detachment, which - together with loss of electronic continuity of the external Ni contact layer - is responsible for the dramatic increase of R_0 and for increased cathode impedance. Both aspects lead to instability issues, which could limit the replicability of the AST protocol. A possible cause of detachment is related to mechanical surface degradation of the bare side of the YSZ electrolyte during redox cycling, leading to unsuccessful screen-printing. This could be avoided with an *in-situ* approach, carrying out the AST protocol on full-cells which should allow more stable performances albeit unavoidable cathode degradation during chemical redox cycling.

CONCLUSIONS

A preliminary assessment of accelerated testing of SOFC Ni-CGO fuel electrodes via chemical redox cycling with an integrated experimental approach has been carried out. Full cells with *ex-situ* pre-aged anodes show coherent results in terms of performance degradation (IV curves, EIS spectra, DRT analysis) with increasing number of redox cycles, suggesting that chemical redox cycling could be a viable AST pathway. The correlation of electrochemical results and post-test SEM images suggest that the main accelerated phenomena are related to Ni particle agglomeration within the fuel electrode, which affects both charge and mass transfer processes. The application of the cathode layer on pre-aged half cells led to detachment, especially for samples with higher numbers of cycles (8 and 12 cycles), which – together with anode delamination – could represent a strong limitation for the analysed Accelerated Stress Test protocol.

ACKNOWLEDGEMENT

This research is financed by the EU project AD ASTRA (FCH-JU; Grant ID 825027) which is kindly acknowledged.

REFERENCES

1. Sreedhar I, Agarwal B, Goyal P, Agarwal A. J Solid State Electrochem 2020;24:1239–70. doi:10.1007/s10008-020-04584-4.
2. Ploner A, Hagen A, Hauch A. J Power Sources 2018;395:379–85. doi:10.1016/j.jpowsour.2018.05.034.
3. McPhail SJ, Pumiglia D, Laurencin J, Hagen A, Leon A, Van herle J, et al. ECS Trans 2019;91:563–70. doi:10.1149/09101.0563ecst.
4. Hagen A, Høgh JVT, Barfod R. J Power Sources 2015;300:223–8. doi:10.1016/j.jpowsour.2015.09.054.
5. Vladikova D, Burdin B, Sheikh A, Piccardo P, et al. E3S Web Conf 2022;334:04015. doi:10.1051/e3sconf/202233404015.
6. Laurencin J, Delette G, Sicardy O, Rosini S, Lefebvre-Joud F. J Power Sources 2010;195:2747–53. doi:10.1016/j.jpowsour.2009.10.099.

7. Pumiglia D, Della Pietra M,, Monforti Ferrario A, McPhail S, Pylypko S. E3S Web Conf 2022;334:04021. doi:10.1051/e3sconf/202233404021.
8. Padinjarethil AK, Bianchi FR, Bosio B, Hagen A. Front Energy Res 2021;9:1–19. doi:10.3389/fenrg.2021.668964.
9. Faes A, Hessler-Wyser A, Zryd A, Van Herle J. J Solid State Electrochem (2020) 24:1239–1270

WHEC-2022
23rd World Hydrogen Energy Conference
June 26-30, 2022 - Istanbul

#1452

THEORETICAL AND EXPERIMENTAL ANALYSES OF ETHANOL-FUELED SOFC MICRO-COGENERATOR

[1] Alberto Coralli, [1] Selma Aparecida Venâncio, [1] Paulo Emílio Valadão de Miranda*
[1]Laboratório de Hidrogênio, PEMM-PET/Coppe, Universidade Federal do Rio de Janeiro, Rua Moniz Aragão 207, Cidade Universitária, Ilha do Fundão, 21941-594, Rio de Janeiro (RJ), Brazil

*Corresponding author e-mail: alberto.coralli@coppe.ufrj.br

ABSTRACT

In Brazil, bioethanol is produced from sugarcane on a large scale and with high process efficiency. Characterized by simple logistics, low toxicity and small environmental impact, it represents a convenient fuel for Solid Oxide Fuel Cells (SOFCs). This perspective motivated the present research that aimed at developing theoretical and experimental analyses of ethanol-fueled SOFC micro-cogenerator. It included a stack designed for hydrogen and bearing conventional materials, running on ethanol under internal reforming regime, and a Balance of Plant (BoP) specifically designed to allow direct ethanol supply, avoiding carbon deposition on the BoP tubing. To validate the project and the components, the stand-alone system was tested with hydrogen and an ethanol/water mixture, demonstrating the capability of conveniently producing electricity and heat under such conditions. After determining the BoP efficiency, possible actions to improve it were identified and the projected efficiency that can be reached applying them was calculated, resulting close to pre-established targets. In addition, electrochemical performance results obtained with proprietary developed nickel-free anodes were promising for the direct utilization of anhydrous ethanol in an SOFC.

Keywords: Solid oxide fuel cells, Balance of plant, Micro-cogeneration, Direct utilization of ethanol, Nickel-free multifunctional SOFC.

INTRODUCTION

Solid Oxide Fuel Cells (SOFCs) directly convert the chemical energy of a fuel into electricity, with high efficiency and low environmental impact. Single cells are typically arranged in stacks, which work coupled to a Balance of Plant (BoP), the ensemble of all auxiliary devices that allow the operation of the stack and the conditioning of the energies produced. SOFCs run at high temperature and present fuel flexibility, being capable of operating with hydrogen and simple hydrocarbons: therefore, they are particularly suitable for stationary cogeneration [1]. An interesting biofuel in the Brazilian context is sugarcane bioethanol: characterized by low toxicity and small environmental impact. It is produced on a large scale and with high process efficiency [2], without competing with food production. Moreover, it is easily storable with simple logistics. Its use in SOFC-based micro-cogeneration systems would guarantee high efficiency and low pollutant emissions in a variety of applications: thus, this technology can help to expand Brazilian electrical generation capacity, further increasing the present high share of renewables in the energy mix. In this perspective, the present research concerns the development of theoretical and experimental analyses of a SOFC-based electricity generator fueled with ethanol. To use ethanol in a SOFC system, major technological modifications are required, particularly in the fuel supply line [3] and in the stack [4], which are otherwise designed to operate with gaseous fuels and utilize materials that are prone to carbon deposition. Numerical simulations evaluated the performance of SOFC operation with pure ethanol, as well as mixed with water [5]. This paper's content involves the conception of a BoP designed, built and tested with a conventional nickel-based anode stack designed for hydrogen, operated using an ethanol/water mixture as fuel, as well as the design and testing of multifunctional single SOFC cells bearing nickel-free anodic electrocatalyst that allow the direct utilization of anhydrous ethanol. The BoP materials, devices and operating conditions, as well as the nickel-free multifunctional SOFC single cells were designed to resist carbon coking and clogging upon the direct utilization of a carbonaceous fuel such as ethanol. The tests performed permitted to collect data regarding the real-life operation of a conventional SOFC stack in ethanol internal reforming regime, about the BoP needed for such operation and also on the direct utilization of ethanol in an SOFC with multifunctional anode. Similar data are not available in the literature.

MATERIALS AND METHODS

The SOFC stack employed had a nominal power of 700 W. One stack unit was tested in a test rig in order to characterize it and to identify its optimal operation point and another one was integrated to and tested in the BoP. The stacks were initially tested with hydrogen, to activate the catalyst and to ensure that they were functioning properly. Using data from the literature, computational simulations of the system and bench tests of the stacks, the characteristics of the stand-alone system and its components were defined. For multifunctional SOFC single cell

development, ceramic suspensions with different compositions were obtained from the following precursors: 8%$_{mol}$ yttria stabilized zirconia (8YSZ) catalyst powder; CeO_2-Al_2O_3 nanostructured ceramic electrocatalyst powder, synthesized through the amorphous citrates' method [6]; cornstarch pore former; terpineol-based vehicle. The anode was screen printed over an 8YSZ button-type electrolyte support with 20 mm in diameter and approximately 170 µm thick. Subsequently, the ceramic suspension was sintered at 1500 °C for three hours. After that, over the other electrolyte side, the ceramic suspension of lanthanum Strontium-doped Manganite, $La_{0.8}Sr_{0.2}MnO_3$, cathode was screen printed and sintered at 1100 °C for two hours. An aqueous solution of (Cu $(NO_3)_2.3H_2O$) was produced and cautiously dropped onto the anodes porous surfaces in order to attain 20 wt% of Cu inside the Cu-($Zr_xCe_{1-x}Y_{0.2}O_{2-\delta}$-$Al_2O_3$) system.

RESULTS AND DISCUSSION

The first SOFC stack unit bench tests were initially ran using hydrogen and air. After that, the stack was fueled with an ethanol/water mixture, maintaining the same fuel excess. The second unit was also initially tested in the test rig, only with hydrogen to avoid any damage prior to the installation in the stand-alone system. After that, the stack was coupled with the BoP and tested both with hydrogen and an ethanol/water mixture. Fig. 1a shows the best polarization and power curves obtained for the two stacks in the test bench and in the stand-alone system, with hydrogen and ethanol. Using the collected data, it was possible to estimate the power that the BoP components would consume if the stack produced 500 W of net power with ethanol. Moreover, possible actions to improve the BoP performance were determined, leading to a projection of BoP power consumption after such additional developments. The experimental power consumption of the BoP components is reported in Fig. 1b, together with the estimated and projected values.

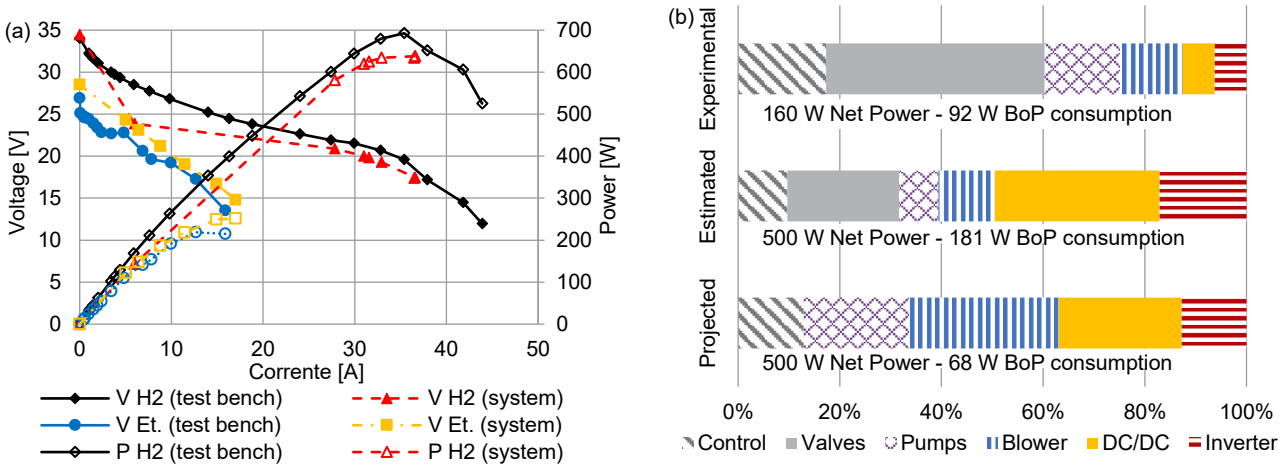


Fig. 1. Polarization and power curves of the stacks (a) and BoP power consumption with ethanol (b).

Data analysis supplied valuable information about the system operating modalities and the interdependence of the different parameters, evidencing some critical relationships between them that is important to consider in the design of the control system. This includes: the air flow should be as low as possible, to improve stack efficiency and make the system thermal management easier, but needs to be high enough to completely burn the excess fuel, unreacted in the stack; a fuel flow increase makes the stack power higher but reduces overall system efficiency and is associated to a higher water flow and consequent possible evaporation problems; a higher operation temperature increases the stack efficiency but needs a higher fuel flow to be sustained; battery charge at system start-up and shut-down must be above values that permits the safe conclusion of the transients. Using the test data, it was also possible to calculate the BoP electrical efficiency and to identify the devices responsible for most of the power consumption, as well as the actions necessary to improve the energy efficiency of the system. The projected overall BoP efficiency that can be reached applying conclusions of the theoretical analyses made reaches 88.1 %, very close to the industry target of 90 %. This confirms the validity of the BoP design and of the actions considered to reduce its power consumption.

Encouraging results were obtained with Cu-($Zr_xCe_{1-x}Y_{0.2}O_{2-\delta}$-$Al_2O_3$) nickel-free single cell anode materials (Fig. 2). Preparation and sintering procedures that promotes a high degree of interaction between CeO_2 and 8YSZ to form $Zr_xCe_{1-x}Y_{0.2}O_{2-\delta}$-$Al_2O_3$ resulted in anodes that exhibit redox properties highly favorable for direct utilization of anhydrous ethanol in SOFCs. In this material, Cu acts as electronic conductor, while the solid solution $Zr_xCe_{1-x}Y_{0.2}O_{2-\delta}$-$Al_2O_3$ is active for electrochemical oxidation of ethanol and/or of the products obtained from its thermal decomposition, while Al_2O_3 phase acts against thermal degradation, avoiding the coarsening of the solid solution at the high operating temperatures.

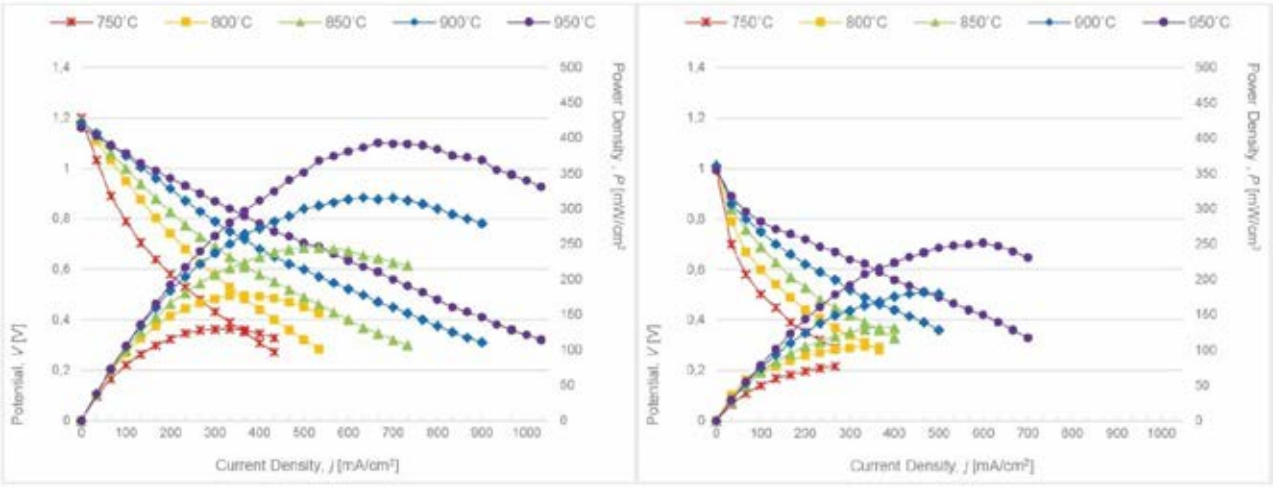


Fig. 2. Polarization and power curves for the nickel-free SOFC anode operated with hydrogen (a) and ethanol (b).

CONCLUSIONS

SOFC stacks designed for hydrogen were tested with hydrogen and with an ethanol/water mixture: one stack was tested only in a test rig, and a second one was also tested in a stand-alone system integrated to a complete BoP. Stack performance was similar in the test rig and in the stand-alone system, confirming the validity of the BoP system design. During operation with hydrogen the desired net electrical power of 500 W was reached, while the performance obtained with ethanol was considerably lower, due to the fact that the stack is a model designed to operate exclusively with hydrogen. Using the test data, it was also possible to calculate the BoP electrical efficiency, and to identify the devices responsible for most of the power consumption, as well as the actions necessary to improve the energy efficiency of the system. Key advances of this work with respect to the state of the art include: monitoring of real-life operation of a commercial SOFC stack with conventional nickel-based anode, fed with an ethanol/water mixture and working in internal reforming regime; design, construction and operation of a BoP for an ethanol-fueled SOFC-based generation system; elaboration of activation, steady state operation and deactivation routines for the stand-alone system. The results obtained confirmed the feasibility of the construction of an ethanol-fueled SOFC-based micro-cogenerator, which can be conveniently used for various applications in Brazil and worldwide.

REFERENCES

1. Coralli A, Sarruf BJM, Miranda PEV, Osmieri L, Specchia S and Minh NQ. 2019. Fuel Cells. In Science and Engineering of Hydrogen-Based Energy Technologies. Edited by Miranda PEV. Academic Press, pp. 39-122.
2. Empresa de Pesquisa Energética. 2021. Balanço energético nacional 2021: Ano base 2020. Rio de Janeiro, EPE.
3. Miranda HV, Miranda PEV, Coralli A, Silva JFR. 2014. Patent Application INPI - BR 102014026190-7 A2.
4. Venâncio SA, Miranda PEV. 2017. Direct utilization of carbonaceous fuels in multifunctional SOFC anodes for the electrosynthesis of chemicals or the generation of electricity. International Journal of Hydrogen Energy 42:3927-3938.
5. Coralli A, Miranda HV, Monteiro CFE, Silva JFR, Miranda PEV. 2014. Mathematical model for the analysis of structure and optimal operational parameters of a solid oxide fuel cell generator. Journal of Power Sources 269:632-644.

WHEC-2022
23rd World Hydrogen Energy Conference
June 26-30, 2022 - Istanbul

#1467

A HIGHLY STABLE COBALT SPINEL-GDC NANOCOMPOSITE CATHODE FOR INTERMEDIATE-TEMPERATURE SOLID OXIDE FUEL CELLS

[1] *Saeed Ur Rehman, Muhammad Haseeb Hassan,[1] Hye-Sung Kim,[1,2] Rak-Hyun Song,[1,2] Tak-Hyoung Lim,[1] Jong-Eun Hong,[1,2] Seok-Joo Park,[1,2]* Seung-Bok Lee*

[1] High Temperature Energy Conversion Laboratory, Korea Institute of Energy Research, 152 Gajeong-ro, Yuseong-gu, Daejeon 34129, Republic of Korea

[2] Department of Advanced Energy and System Engineering, University of Science and Technology, 217 Gajeong-ro, Yuseong-gu, Daejeon 34113, Republic of Korea

*Corresponding author e-mail: sblee@kier.re.kr

ABSTRACT

Cobalt spinel oxide (Co_3O_4) and gadolinium-doped ceria (GDC) nanocomposite were prepared via sol-gel processing and were studied as cathode material for intermediate-temperature solid oxide fuel cells (SOFCs). XRD analysis confirmed separate precipitation of Co_3O_4 and GDC phases during the calcination process thus, producing a nanocomposite. Various nanocomposite compositions were tested for their electrical property where a nanocomposite having a Co to GDC mole ratio of 1 (CGC1) showed the highest electrical conductivity. Electrochemical impedance spectroscopy and DC polarization measurements were conducted to study the performance of SOFC consisting of CGC1 cathode. The SOFC showed an initial maximum power density of 484 mW cm^{-2} at 800 °C however, the cell performance gradually increased, and a maximum power density of 1380 mW cm^{-2} was observed after a 168 h operation.

Keywords: Solid oxide fuel cell, Cathode, Nanocomposite, Cobalt, Spinel.

INTRODUCTION

Solid oxide fuel cell (SOFC) is a promising green energy conversion technology that can convert fuel directly into electricity through electrochemical reactions across the interfaces [1]. However, to make the SOFC technology reliable and cost-effective it is imperative to reduce its operating temperature to an intermediate range i.e., ≤800 °C. However, SOFC shows a decreased performance at low operating temperatures due to the slow kinetics of its cathode for the oxygen reduction reaction (ORR). Hence, a highly active and stable cathode is required for low-temperature operation [2].

Researchers have made extensive efforts with the aim to acquire new cathode materials with high catalytic activity. In this regard, cobalt-doped perovskite materials have been one of the most famous topics in SOFC cathode research. This is because the cobalt-doped cathode materials show high electrical conductivity and outstanding electrocatalytic activity for the ORR. However, cobalt-doped perovskite oxides show high values of thermal expansion coefficient (TEC) (14.5–20 × 10^{-6} K^{-1}), producing high thermal expansion mismatch with the state-of-the-art electrolyte materials (12 × 10^{-6} K^{-1}). Therefore, there is a risk of structural instability that can cause high-performance degradation during the thermal cycling of the SOFCs [3].

Spinel oxide with cubic structure has attracted high attention as an alternative cathode material in the SOFCs due to its appropriate electrical conductivity, high ORR activity as well as compatible values of thermal expansion coefficient (11–12.5 × 10^{-6} K^{-1})[4,5]. Spinel oxides are also attractive because they do not contain rare-earth elements and therefore, reduce the material cost. Previously, various authors have reported spinel oxide as cathode materials for the SOFC consisting of two or more transition elements. In this work, we present a simple and cost-effective approach to produce a Co_3O_4 spinel-GDC nanocomposite. SOFC consisting of the newly developed nanocomposite cathode was tested for its electrochemical performance and durability at 800 °C.

MATERIALS AND METHODS

For the synthesis of Co_3O_4-GDC nanocomposites, nitrate salts ($Co(NO_3)_2 \cdot 6H_2O$, $Ce(NO_3)_3 \cdot 6\ H_2O$, and $Gd(NO_3)_3 \cdot 6H_2O$) and citric acid were purchased from Sigma-Aldrich in South Korea. Nanocomposites were prepared by using Co to GDC molar ratio of 0.05, 0.1, 0.25, 0.5, 0.75, and 1. The nanocomposites were named CGC0.05, CGC0.1, CGC0.25, CGC0.5, CGC0.75, and CGC1 according to the molar ratio Co and GDC. To synthesize a nanocomposite, stoichiometric amounts of metal nitrates and citric acid were dissolved in de-ionized water and stirred onto a hot plate until a gel was formed. The gel was then burnt and calcined at 250 and 800 °C, successively and finally a black powder, Co_3O_4-GDC nanocomposite, was obtained.

The phase composition of nanocomposites was characterized by X-ray diffraction (XRD, 2500 D/MAX, Rigaku) using Cu*Kα* radiation. The electrical conductivity of the nanocomposites was measured by standard 4probe technique using rectangular bar prepared by compacting and sintering of nanocomposite powders at 1050 °C. For the electrochemical performance measurement, a nanocomposite cathode (CGC1) was fabricated onto an in lab prepared anode-supported half cell. The fabrication process of the anode-supported half cells can be found elsewhere. To fabricate the nanocomposite cathode, an ink paste was prepared by centrifugal mixing of CGC1 powder with appropriate amounts of α-terpinol and ethyl cellulose. The CGC1 ink paste was screen printed onto the fully dense YSZ electrolyte of the anode supported half cell and sintered at 1050 °C for 1 h in air. After sintering, the nanocomposite cathode had an active area of 1 cm^2. For cell tests, Ag and LT-CCC (kceracell, South Korea) pastes were used to create electrical contacts for the anode and cathode, respectively. Ag mesh and wire were used for current collection from the electrodes. The electrochemical performance was recorded by measuring the current-voltage (*I–V*) and electrochemical impedance data at 800 °C using hydrogen as a fuel and air as an oxidant. A DC load device was used to gather the *I–V* data.

RESULTS AND DISCUSSION

In this work, Co_3O_4-GDC nanocomposites were acquired by sol-gel processing and calcination at 800 °C. The resulting black powders were characterized by XRD to observe the phase composition as shown in Fig. 1b. Although Co, Ce, and Gd were initially dissolved together as nitrate salts, Co_3O_4 and GDC phases were separately crystallized during calcination at 800 °C thus, producing the required nanocomposite. It can be observed from Fig. 1a that the peak intensity of the Co_3O_4 has continuously increased as the molar ratio of Co is increased in the precursor. Fig. 1b shows the electrical conductivity plots of various CGC nanocomposites. The electrical conductivity of the nanocomposite showed a decline as initially the amount of Co_3O_4 increased in the nanocomposite from CGC0.05 to CGC0.25. However, the electrical conductivity increased rapidly after that as it went from 2.5 to 23 S cm^{-1} for CGC0.5 and CGC1, respectively, at 800 °C. The reason for the initial decrease observed in the electrical conductivity even though the amount of conductive phase was increased is not known at this point, but it is under investigation. Due to its highest electrical conductivity, CGC1 was selected to be employed as cathode material for performance measurement in a SOFC.

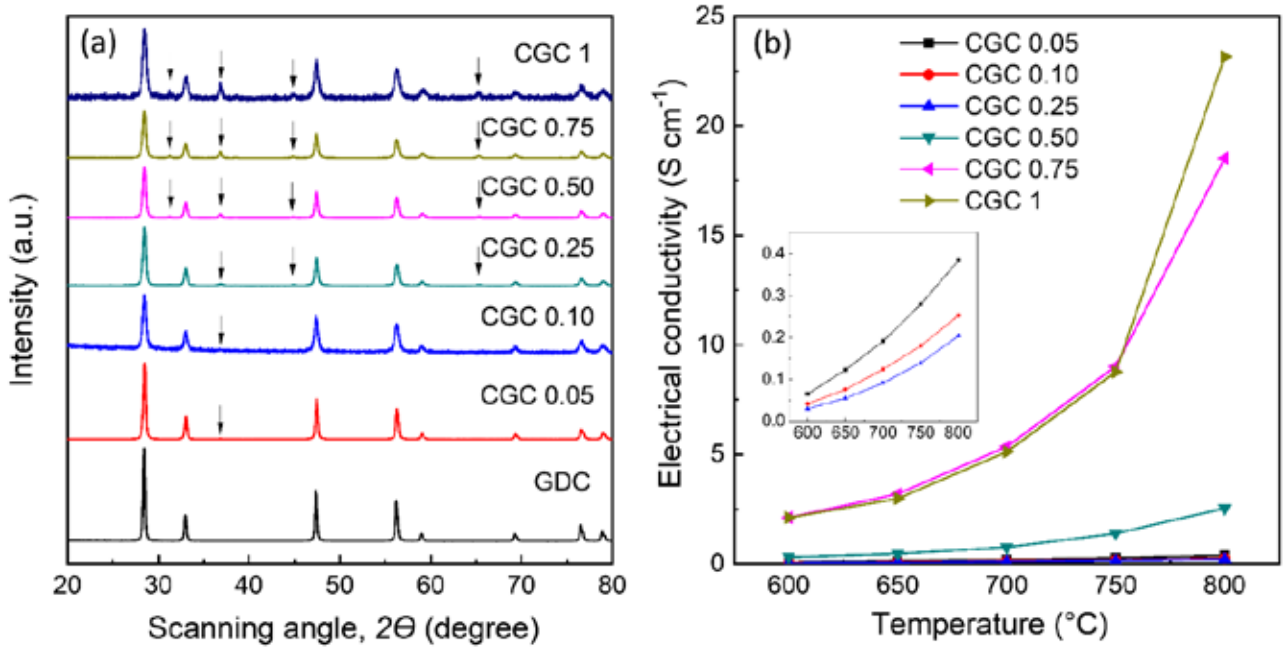


Fig. 1. (a) XRD analysis of various Co_3O_4-GDC (CGC) nanocomposites obtained after calcination at 800 °C. (b) Electrical conductivity plots of CGC nanocomposite rectangular bar samples obtained by 4probe method.

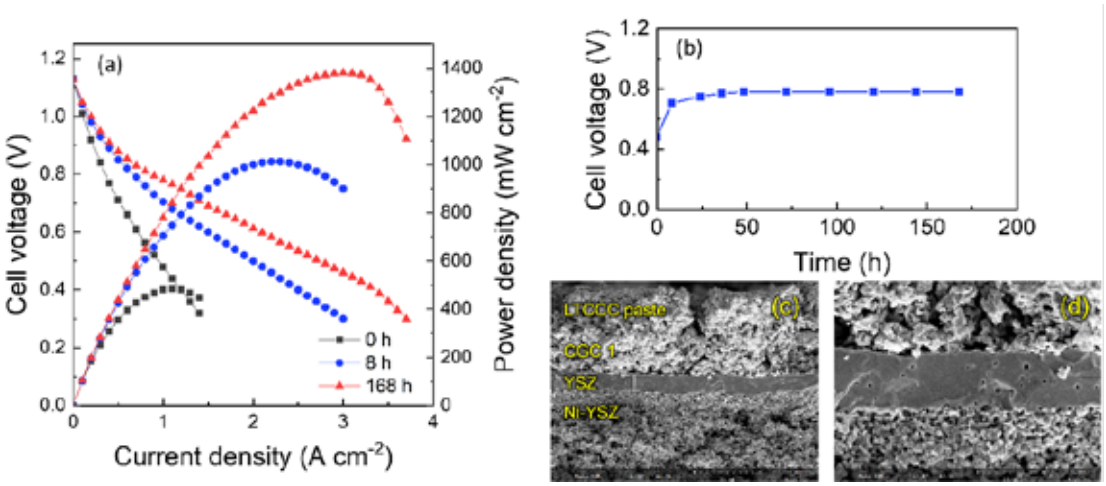


Fig. 2. (a) *I–V–P* plots obtained at 800 °C at different times for the SOFC consisting of CGC1 nanocomposite cathode while using hydrogen as a fuel and air as an oxidant. (b) long term stability data acquired at 800 °C while operating under a galvanostatic load of 1 A cm^{-2}. (c, d) Cross-sectional SEM images of the anode supported SOFC after stability test.

Anode-supported SOFC consisting of a nanocomposite CGC1 cathode was tested for its electrochemical performance (Fig. 2). Fig. 2a shows the *I–V–P* plots of the anode supported SOFC indicating high open-circuit voltage observed at different times while operating at 800 °C. Initially, the SOFC showed a relatively low maximum power density of 484 mW cm^{-2}. However, the SOFC was operated at a high current density of 1 A cm^{-2} and the performance was noticed to increase rapidly and a maximum power density of 1012 mW cm^{-2} was observed after an 8 h of operation. The SOFC was kept under a high current density of 1 A cm^{-2} continuously for 168h at the end of which the SOFC showed a high power density of 1380 mW cm^{-2}. Performance of the SOFC consisting of CGC1 nanocomposite cathode increased by 185% during the 168 h operation. Fig. 2b shows the stability data obtained during the 168 h operation which indicates a highly stable performance obtained even in such extreme operating conditions. Fig. 2c and d show the microstructure of the SOFC after the stability test illustrating a typical SOFC morphology. Electrochemical performance and stability results indicate that the new nanocomposite is promising as high performing and durable SOFC cathode material, and it should be explored for more exciting results.

CONCLUSIONS

A simple and cost effect Co_3O_4-GDC nanocomposite was synthesized by sol-gel processing and was evaluated for its electrochemical performance as a SOFC cathode material. A SOFC consisting of the nanocomposite cathode initially showed a low performance (484 mW cm^{-2}) at 800 °C however, a continuous operation under a high current resulted in rapid performance enhancement, and finally, after a 168 h operation, the SOFC showed a high power density of 1380 mW cm^{-2}. The results indicate that the new nanocomposite shows potential for fabricating high-performing and robust SOFC cathodes and it should be further matured for industrial-scale applications.

REFERENCES

1. Minh NQ. 2004. Solid oxide fuel cell technology–features and applications. Solid State Ionics 174(1-4): 271-277.
2. Wachsman ED and Lee KT. 2011. Lowering the temperature of solid oxide fuel cells. Science 334(6058): 935-939.
3. Kumar RV and Khandale AP. 2022. A review on recent progress and selection of cobalt-based cathode materials for low temperature-solid oxide fuel cells. Renewable and Sustainable Energy Reviews 156: 111985.
4. Shao L, Wang Q, Fan L, Wang P, Zhang N and Sun K. 2016. Copper cobalt spinel as a high performance cathode for intermediate temperature solid oxide fuel cells. Chemical communications 52(55): 8615-8618.
5. Zhong F, Li Z, Luo Y, Fang H, Chen K, Zhou C, ... and Jiang L. 2022. Direct ammonia solid oxide fuel cells based on spinel ACo_2O_4 (A= Zn, Fe, Ni) composite cathodes at intermediate temperature. International Journal of Green Energy: 1-10.

WHEC-2022
23rd World Hydrogen Energy Conference
June 26-30, 2022 - Istanbul

#1499

EFFECT OF A REDUCTION OF THE CATALYST LOADING ON THE PERFORMANCE OF A MINI PASSIVE DIRECT METHANOL FUEL CELL

[1,2] C.S. Moreira, [1,2] A.M.F.R. Pinto, [1,2 *] V.B. Oliveira
[1]CEFT - Transport Phenomena Research Center, Faculty of Engineering, University of Porto, Rua Dr. Roberto Frias, 4200-465 Porto, Portugal
[2]ALiCE - Associate Laboratory in Chemical Engineering, Faculty of Engineering, University of Porto, Rua Dr. Roberto Frias, 4200-465 Porto, Portugal

*Corresponding author e-mail: vaniaso@fe.up.pt

ABSTRACT

Passive direct methanol fuel cells (pDMFCs) appear as a promising alternative for power portable electronic devices, since they use a liquid fuel, which is easy to handle, storage and distribute and have a quick refuelling, high efficiency and low environmental impacts. However, some issues need to be solved before the introduction of this technology in the market, such as methanol and water crossover through the membrane, low lifetime and high costs. In this way, the present work studies the effect of reducing the catalyst loadings, on both anode and cathode sides, on the performance of a mini passive DMFC towards a reduction of these systems costs. Moreover, the different phenomena that affect the cell performance were identified based on the polarization measurements and quantified using the electrochemical impedance spectroscopy (EIS) technique. The main goal of this study was to reduce the costs of these systems without a significant lost on their performance and analyse in detail the different losses that negatively affect the cells under the light of the EIS technique. Therefore, it was proposed an innovative equivalent electric circuit (EEC) that reproduces with accuracy the system under study.

Keywords: Passive direct methanol fuel cell, Catalyst loading, Power output, Electrochemical impedance spectroscopy, Equivalent electric circuit

INTRODUCTION

Alternative power sources with low environment impacts are urgent in the society. Additionally, the growing interest in portable electronic devices motivate the research on finding alternative technologies to overcome the batteries limitations. The passive direct methanol fuel cells (pDMFCs) appear as a promising solution to achieve that due to their low environmental impacts, high efficiency, simplicity and quick refuelling. Nevertheless, these fuel cells present some limitations, such as slow anode kinetics, methanol and water crossover through the membrane, high costs and low lifetime [1]. The pDMFC catalysts, where the electrochemical reactions occur, are responsible for a major fraction on these systems costs since the most common used catalysts are noble metals, such as Platinum and Ruthenium. The present work studies the effect of a significant decrease on both anode and cathode catalyst loadings, to reduce the cell costs, without a significant decrease on these systems efficiency. The performance is evaluated through the polarization and power density curves and the electrochemical impedance spectroscopy data. The EIS technique provide useful information to identify and quantify the different phenomena that occur on the fuel cell and have a negative impact on its performance [2]. As the methanol concentration has a clearly impact on the pDMFC performance, the effect of the methanol concentration for the different loadings used at both sides was also evaluated. The methanol concentration that leads to a higher performance results in a balance between the negative effect on the methanol crossover rate that increases with an increase of the methanol concentration, and the positive effect on the anode oxidation reaction rate that increases with the methanol concentration. Another target of this work was to identify the different losses that negatively affect the system (ohmic, activation and mass transfer) at the anode and cathode sides under the light of the EIS measurements.

MATERIALS AND METHODS

The mini passive DMFC (mini pDMFC) used in this work has an active area of 2.25 cm^2, two acrylic end plates (opened at the cathode side and with a fuel reservoir at the anode side (1.8 cm^3)), two isolating plates, two stainless steel current collectors (with an open ration of 28% at the anode and 17% at the cathode), carbon cloth with a microporous layer (MPL) as anode and cathode diffusion layers (thickness of 0.410 mm and a porosity of 0.8), a Nafion 117 membrane, Pt-Ru as anode catalyst and PtB as cathode catalyst (Fig. 1).

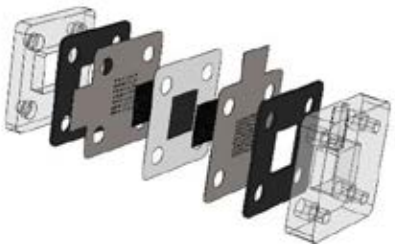


Fig. 1. Schematic representation of the mini pDMFC

The experimental tests were performed at ambient conditions, with different methanol concentrations and different anode and cathode catalyst loadings, setting a loading on one side of the cell and using different loadings at the other side, towards a cost reduction without a significant decrease on the cell performance.
The cell performance was evaluated by polarization curves and electrochemical impedance spectroscopy data. The experimental tests were performed with a commercial fuel cell test station, Zahner Elektrik GmbH &Co. kG. The EIS measurements were conducted at different fuel cell voltages, with an amplitude of 10 mV and a frequency range between 0.01 Hz to 100 kHz. The impedance results were fitted to an equivalent electric circuit (EEC).

RESULTS AND DISCUSSION

As the Nafion membrane is permeable to methanol and due to the alcohol concentration gradient between the anode and the cathode side, the cell suffers from methanol crossover leading to an open circuit voltage much lower that the ideal one (1.21 V). This methanol loss to the cathode side leads to a decrease of the available fuel on the anode side, decreasing the methanol oxidation rate and increasing the anode losses. Additionally, the methanol that reaches the cathode is oxidized at this side, poisoning the cathode catalyst by the intermediate compounds of the incomplete methanol oxidation reaction, as Platinum (the cathode catalyst) is not the most proper one to this reaction. Consequently, a mixed potential is formed at the cathode side increasing the cathode losses and decreasing the overall fuel cell efficiency. Even though higher methanol concentrations lead to a higher methanol concentration gradient between the anode and cathode side, increasing the methanol crossover, it also increases the availability of methanol at the anode side, favouring the methanol oxidation reaction at this side. Therefore, the optimal methanol concentration arises from a balance between these two phenomena, the negative effect on the methanol crossover rate and the positive effect on the anode oxidation reaction. Figure 2 shows the effect of methanol concentration on the mini pDMFC performance using 4 mg/cm^2 Pt-Ru as anode catalyst and 4 mg/cm^2 PtB as cathode catalyst.

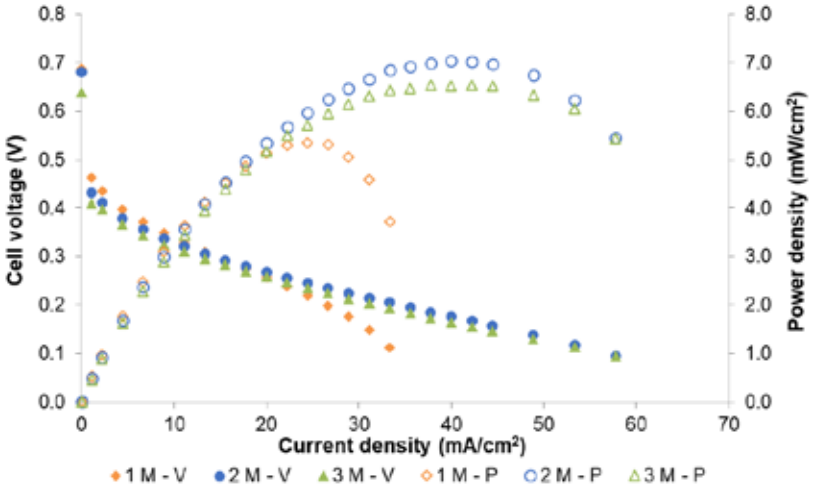


Figure 2. Effect of the methanol concentration on the mini pDMFC performance

Table 1 presents the different resistances of the EEC for the different methanol concentrations and voltages tested using an anode catalyst loading of 4 mg/cm^2 Pt-Ru and a cathode catalyst loading of 4 mg/cm^2 PtB.

Table 1. Values of the different resistances of the EEC for the different methanol concentrations and voltages tested.

		Methanol Concentration		
	Voltage (V)	1 M	2 M	3 M
Rohm (Ω)	0.40	0.45	0.41	0.41
	0.30	0.45	0.41	0.41
	0.20	0.45	0.41	0.41
R1 (Ω)	0.40	2.4	1.1	0.79
	0.30	1.9	0.92	0.75
	0.20	-	0.76	0.49
R2 (Ω)	0.40	6.5	8.0	11
	0.30	2.2	2.1	2.2
	0.20	3.6	1.2	1.2
Power Density (mW/cm^2)		5.3	7.0	6.5

As can be seen in Fig. 2 and Table 1, the best methanol concentration, the one that leads to a higher performance and consequently lower losses (lower resistances) was 2 M.
This work allowed studying the effect of methanol concentration and the anode and cathode catalyst loadings on the performance of a mini passive DMFC and the identification of the different system losses. An EEC was proposed showing a good agreement with the experimental EIS data, which allowed the quantification of each loss that negatively affects the cell performance.

CONCLUSIONS

Costs and lifetime are key challenges to overcome towards the introduction of the pDMFC in the market to replace the lithium batteries in portable applications. A mini passive DMFC with an active area of 2.25 cm^2 was studied through polarization curves and EIS. A reduction of the catalyst loadings on both anode and cathode layers was evaluated in order to reduce the fuel cell costs and analyse the different losses that affect its performance. The system allowed working with high methanol concentrations and the EEC proposed showed a good agreement with the experimental results.

ACKNOWLEDGEMENT

This work was financially supported by: Project PTDC/NewPortCell-POCI-01-0145-FEDER-032116 - funded by FEDER funds through COMPETE2020 - Programa Operacional Competitividade e Internacionalização (POCI) and by national funds (PIDDAC) through FCT/MCTES. This work was financially supported by LA/P/0045/2020 (ALiCE), UIDB/00532/2020 and UIDP/00532/2020 (CEFT), funded by national funds through FCT/MCTES (PIDDAC).

REFERENCES

1. Braz BA, Moreira CS, Oliveira VB and Pinto AMFR. 2019. Effect of the current collector design on the performance of a passive direct methanol fuel cell. Electrochimica Acta 300: 306-315.
2. Siracusano S, Trocino S, Briguglio N, Baglio V and Aricò AS. 2018. Electrochemical impedance spectroscopy as a diagnostic tool in polymer electrolyte membrane electrolysis. Materials 11 (8): 1368.

WHEC-2022
23rd World Hydrogen Energy Conference
June 26-30, 2022 - Istanbul

#1501

DEVELOPMENT OF LSF-LSM COMPOSITE CATHODES FOR IT-SOFC

[1,2*] *Ramin Babazadeh Dizaj,* [1,2] *Fahrettin Kılıc,* [1,2] *Tayfur Öztürk*
[1] Dept. of Metallurgical and Materials Engineering, Middle East Technical University, Dumlupınar Blv., Ankara, Turkey
[2] ENDAM, Center for Energy Storage Materials and Devices, Middle East Technical University, Ankara, Turkey

Corresponding author e-mail*: ramin.dizaj@metu.edu.tr

ABSTRACT

Following a pioneering study on (La,Sr)CoO_3- (La,Sr)$_2CoO_4$ amorphous cathodes which was synthesized via sputter deposition, a similar work was carried out for (La,Sr)FeO_x – (La,Sr)MnO_3 composite cathodes to see if the cathode can be used in amorphous form with acceptable ORR. First a thorough search was made in LSM/LSF/ScSZ ternary system to identify most favorable compositions. Unfortunately, even in most favorable cathode composition, an acceptable ASR value of 0.15 ohm cm^2 was obtained at temperature not lower than 800 ^oC where the cathode, was already crystalline. This study however showed that a thorough investigation is needed in LSM-LSF binary system where a more favorable results may be obtained. Accordingly a set of 6 cathodes were sputter deposited in combinatorial geometry using LSM and LSF sputter targets where the cathode make-up varied over a wide range. Electrochemical performance of the cathodes were measured using symmetric cell. The tests were performed starting from 450 ^oC at 50 ^oC interval and stopped when ASR <=0.15 ohm *cm^2. Cathodes which were amorphous in the deposited state were monitored so as to determine the temperature of crystallization. The aim is to identify compositions where the cathode is still amorphous with an acceptable ASR values. The role of ScSZ addition in improving the stability of amorphous cathode was also investigated.
Keywords: SOFC, Cathode, LSM, LSF, Magnetron sputtering.

INTRODUCTION

There is a considerable interest in the reduction of operating temperature of solid oxide fuels cell (SOFC). Thus, numerous studies have been conducted to develop the so-called intermediate temperature SOFCs [1,2]. The bottle neck in IT-SOFCs is the cathode material as there are suitable alternatives for anode and electrolyte that could operate with acceptable kinetics at temperatures as low as 600 °C. In the case of cathode materials, the main problem is oxygen reduction reaction (ORR) which becomes unacceptably slow at reduced temperatures.

Although there are various strategies in reducing the operation temperature of SOFC, one notable approach is based on the use of a MIEC oxide in polyamorphous cathode [2]. This was illustrated in composite (laSr)CoO3- (La Sr)2CoO4 cathode synthesized via sputter deposition in amorphous form. The cathode had an acceptable ORR performance at temperatures as low as 570°C . In addition the structure was still amorphous/nanocrsytalline at these temperature with added benefit contributing to the stability of the cathode [3].

The current work was undertaken to develop cathode material of improved ORR performance to be used with scandia stabilized zirconia(ScSZ) as electrolyte. Based on thermal mismatch consideration, two oxides were selected, namely $(La_{0.8}Sr_{0.2})FeO_3$ (LSF), a well known MIEC oxide and $La_{0.5}Sr_{0.5}MnO_{3-\delta}$ (LSM). The purpose is to see if an amorphous cathode could be synthsized with improved ORR and stability. A third oxide, namely $Sc_{0.15}Zr_{0.8}5O_{2-\delta}$ (ScSZ) may also be added to this system, though the fraction of this oxide will not be more than 0.15.

MATERIALS AND METHODS

Active materials $(La_{0.8}Sr_{0.2})FeO_3$ ($La_{0.5}Sr_{0.5}MnO_{3-\delta}$) and $Sc_{0.15}Zr_{0.8}5O_{2-\delta}$ were synthesized using Pechini method. by mixing their nitrates in stoichiometric proportions. Having synthesized the powders and checked their composition, they were compacted and sintered at elevated temperature in the form of discs to be used as target for sputter deposition.

The sputter deposition were carried out in a prismatic vacuum chamber in 500X500X500 mm dimension. Sputter targets were 300 mm apart with an inclination of approximately 45^o. Schematic representation of the sputter deposition is given in Fig. 1. Distances and inclination of sputter targets were adjusted in such a manner that thickness of sputter deposited cathode were almost the same. Deposition was carried out with a duration that cathodes were approximately 500 nm thick.



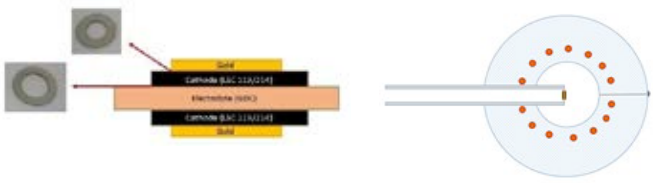
(a) (b)

Fig. 1 Sputter deposition of cathodes inn combinatorial geometry a) photograph of the deposition unit in operation- 3 sputter guns are in operation. b) Geometry of deposition used in the current work using two sputter targets

Two sets of substrates were deposited; one set was borosilicate glass discs for structural investigation and the other set was ScSZ electrolyte. Both had a diameter of 18 mm. The latter, i.e. electrolyte was in the form of 4 mm thick discs. EIS measurements were carried out on symmetric cell, dimensions of which are given in Fig. 2. Thus as shown in the figure, both sides of the electrolyte was coated with cathodes of diameter less than the electrolyte disc, on which a smaller diameter gold was coated for connection purposes.

RESULTS AND DISCUSSION

First, a ternary study was carried out using three sputter targets; LSF, LSM and ScSZ. A total of 21 cathodes were deposited covering a wide compositional range. Fig.2 taken from the work of Kılıç[4] shows the most promising compositions in this ternary system. The figure shows the temperature at which the cathodes would have an ASR value of 0.15 Ω cm^2 via extrapolation. It is seen that the best cathode had a composition of $LSM_{0.77}$ $LSF_{0.11}$ $ScSZ_{0.12}$ with an expected operational temperature of 805 oC. It was further found that the cathodes which were amorphous in the as-deposited state crsytallized when the the symmetric cell was heated to 800^{o}C.



(a) (b)

Fig. 2 Schematic presentation of symmetric cell used in EIS measurement. a) cell , b) cell mounted on alumina tube in a furnace for measurement

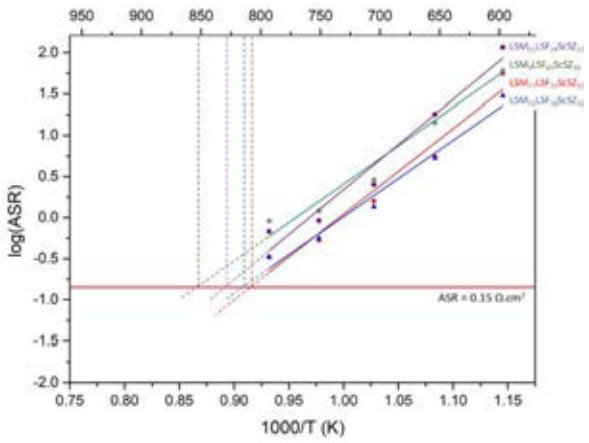


Fig. 3 log(ASR) vs 1000/T determined for cathodes in ternary LSM-LSF-ScSZ system. The best cathode (red) yields an operating temperature of 805 oC (ASR=0.15 Ω cm^2 and has a composition of $LSM_{0.77}$ $LSF_{0.11}$ $ScSZ_{0.12}$ [4]

The work is currently in progress where the binary LSM-LSF cathodes are deposited in two sets one on glass substrate to examine the maximum temperature at which they can be exposed without crystallization and the second set of deposition will be used for the symmetric cell to determine lowest ASR values in terms of composition while the cathodes were amorphous.

ACKNOWLEDGEMENT

The support was provided by the Scientific and Technological Research Council of Turkey (TÜBİTAK) with a project number 217M628, which the authors gratefully acknowledge.

REFERENCES

1. ZÇ Torunoğlu, D Sarı, O Demircan, YE Kalay, T Öztürk, Y Kuru,2018, One pot synthesis of (La, Sr) CoO3/(La, Sr) 2CoO4 for IT-SOFCs cathodes International Journal of Hydrogen Energy 43 (40), 18642-18649.

2. D Sari, F Piskin, ZC Torunoglu, B Yasar, YE Kalay, T Ozturk, 2018, Combinatorial development of nanocrystalline/amorphous (La, Sr) CoO3-(La, Sr) 2CoO4 composite cathodes for IT-SOFCs, Solid State Ionics 326, 124-130.
3. D Sari, B Yaşar, F Pişkin, YE Kalay, T Öztürk Segregation Resistant Nanocrystalline/Amorphous (La, Sr) CoO3-(La, Sr) 2CoO4 Composite Cathodes for IT-SOFCsJournal of The Electrochemical Society 166 (15), F1157.
4- F Kılıç, M. Sc. Thesis, 2021 Middle East Technical University .

WHEC-2022
23rd World Hydrogen Energy Conference
June 26-30, 2022 - Istanbul

#1503

A NEW CLASS OF AMORPHOUS/NANOCRYSTALLINE (La,Sr)CoO_3 BASED CATHODES FOR IT-SOFCs

[1,2]Dogancan Sari, [1,2]Ziya Çağrı Torunoğlu,[1,2]Bengisu Yaşar[1,2] Yunus Eren Kalay [1,2]Tayfur Öztürk*
[1]ENDAM, Center for Energy Materials and Storage Devices,METU, Ankara Turkey
[2]Department of Metallurgical and Materials Engineering, METU, Ankara,Turkey

* Corresponding author e-mail: ozturk@metu.edu.tr

ABSTRACT
In this study, we report results of an investigation carried out on (La,Sr)CoO_3- (La,Sr)$_2CoO_4$ dual phase oxides as cathode for IT- SOFCs. Cathodes were produced via sputter deposition where the volume fraction varied over a wide range from 0.10 <(La,Sr)$_2CoO_4$ < 0.90 and screened electrochemically using symmetric cells. The study showed that the compositions with volume fractions in the range 0.40 < (La,Sr)$_2CoO_4$ < 0.60 were particularly significant in yielding cathodes of improved performance. Refocusing the combinatorial screening to this range yielded (La,Sr)CoO_3-(La,Sr)$_2CoO_4$=0.45:0.55 as the most favorable composition. Taking ASR=0.15 Ω · cm2 as a useful benchmark, the study showed that cathodes in this range may be used at temperatures as low as 575 °C. It was further shown that composite cathodes have amorphous structures in co-sputtered conditions and could remain so when used at reduced temperatures. At temperatures close to 700 °C the amorphous cathode turns into nanocrystalline two phase structure with grains not more than 10 nm in size. Moreover, these refined cathodes were extremely stable and resistant to Sr segregation. The results imply a new class of LSC based amorphous/nanocrystalline cathodes for IT-SOFCs.

Keywords: IT- SOFCs, ORR Catalysts, Amorphous cathodes, (La,Sr)CoO_3- (La,Sr)$_2CoO_4$ dual phase oxides,

INTRODUCTION
Increasing demand to energy and limited existence of fuels have directed investigations to find out new and novel routes for alternative and efficient energy conversion systems. Solid oxide fuel cells (SOFCs) as a more efficient alternative fall into this category in consequence of their ability to convert chemical energy directly into electricity in highly efficient way with fuel flexibility and without the limitation of Carnot cycle. However, this is at the cost of high operating temperatures (>800^{o}C) dictated by the requirement of sufficiently fast oxygen reduction rate, occurring at cathode side and constituting the main source of rate limitation in overall SOFC operation. High operating temperature not only constitutes a problem in terms rapid degradation of cell, i.e., reduction in lifetime of SOFC, but it also severely restricts the choice of interconnect materials. Difficult sealing conditions at high temperatures is another major source of stimulus for intermediate temperature SOFCs. Accordingly, there is a strong motivation in reducing operating temperature of the cell down to 700-500^{o}C, i.e., IT-SOFC, at which oxygen reduction kinetics becomes quite critical.

The introduction of mixed electronic and ionic conductive (MIEC) oxides has opened a new era in pursuit of realizing IT-SOFCs [1]. The impact of MIEC oxides in catalyzing the oxygen reduction reaction (ORR) and achieving temperature reduction have been well recognized. Furthermore, following the work of Sase et al. [2] on (La,Sr)CoO_3/(La,Sr)$_2CoO_4$ (LSC113/214), there has been considerable interest in dissimilar interfaces as a way of further accelerating ORR at cathode. The improvement that occurred by 3-4 orders of magnitude in oxygen exchange coefficient at the hetero-interface have focused studies on composite cathodes [2,3]. Studies, therefore, have concentrated on maximization and utilization of the dissimilar interface in SOFC cathodes [3,4]. By maximizing the dissimilar interfaces, the resulting accelerated ORR, could lead to lower polarization resistance in the cathode which in turn could lead to a lower SOFC operating temperatures. Studies aiming for maximization of dissimilar interfaces has mainly relied on thin film work [e.g., 3].

In maximizing the interfacial regions, the volume fraction is an important parameter as well as the scale of structure. Therefore, the current study was undertaken to investigate how the cathode performance is affected by the phase fractions, while keeping the structure at nanoscale. For this purpose, we adopt a combinatorial approach where the volume fraction of (La,Sr)$_2CoO_4$ varied from 0.10 to 0.90.

MATERIALS AND METHODS
LSC-113 as well as LSC-214 powders were synthesized using Pechini method [5]. Details regarding the preparation of the sputter targets from the synthesized powders were described by Sari et al. [6]. Thin film cathodes of mixed oxides were produced via sputter deposition in a specially designed vacuum deposition system. Detailed description of the deposition system and method used combinatorial sputtering were described in Ref [6]. Fig.1 illustrates the

combinatorial sputtering where 6 samples each with different cathode compositions were obtained simultaneously by co-sputtering of (La,Sr)CoO3 and (La,Sr)2CoO4 targets . EIS responses of the thin film cathodes were measured on symmetric cells. Schematic drawing of the symmetric cell used in this study is given in Fig. 2. Here, it is seen that the symmetric cell is made up of three layers. Top and bottom layers were cathodes which were deposited on the mid-layer, i.e., electrolyte. The electrolyte used was gadolinium doped ceria (GDC) typically 1mm in thickness and 19 mm in diameter. Two sets of masks were used to control the surface area of the cathodes and the current collectors. These masks were stainless steel flat rings with 12mm (cathode) and 10mm (current collector) in inner diameter.

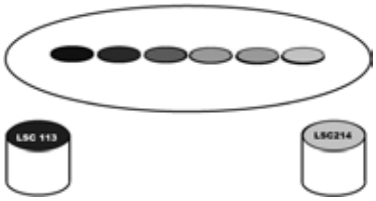


Fig.1 Schematic representation of combinatorial sputter deposition geometry used to obtain a library of thin film cathodes.

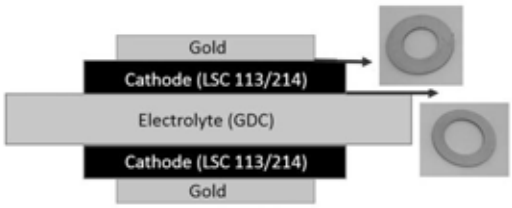


Fig.2 Schematic representation of symmetric cell used in electrochemical impedance spectroscopy measurement.

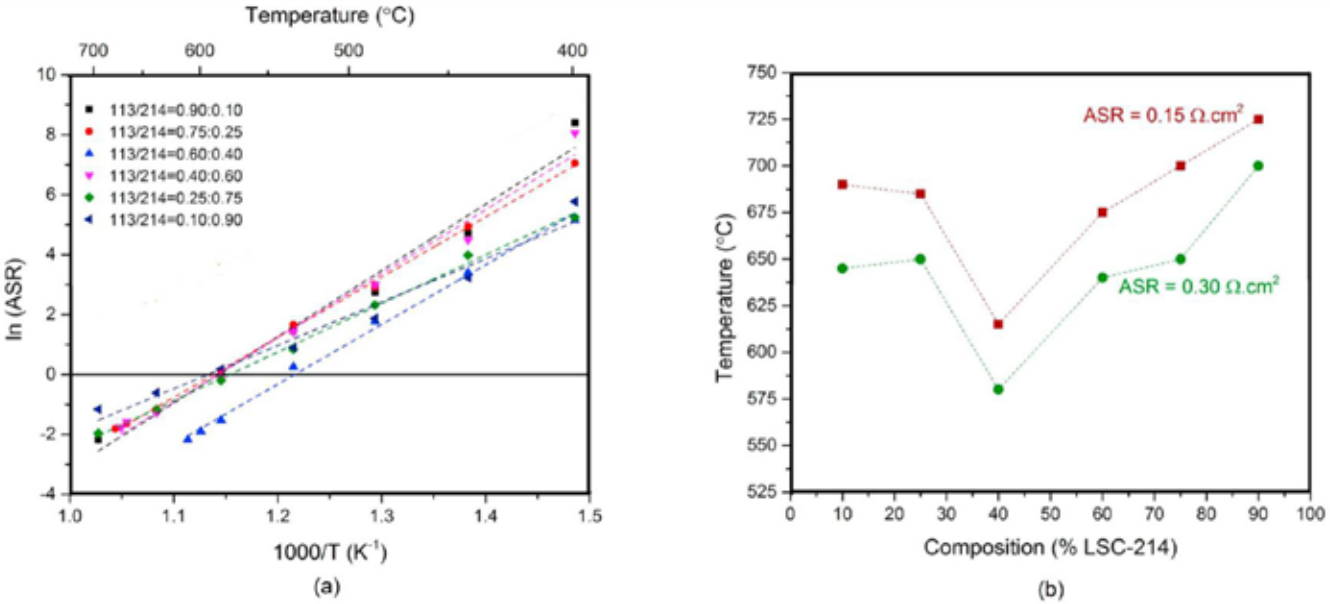
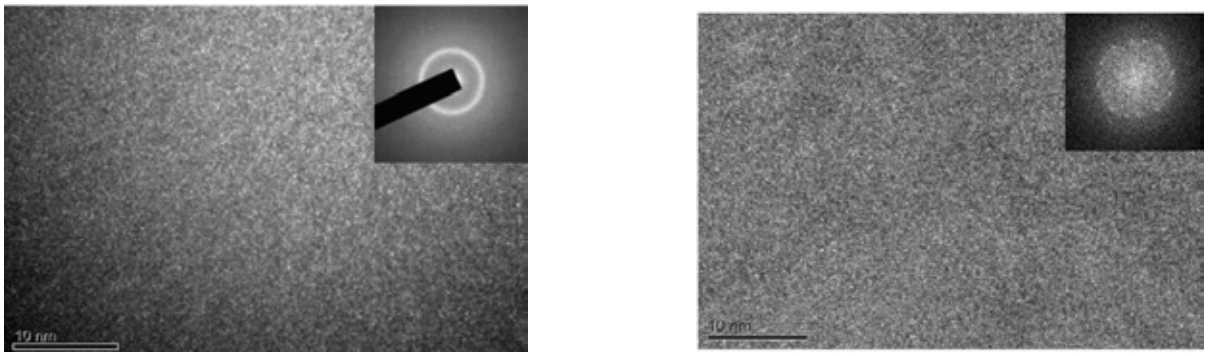


Fig. 3 a) The relationship between ln (ASR) vs 1/T [K−1] for the co-sputtered cathode library in the composition range of LSC-113:LSC-214=0.90:0.10–0.10:0.90. b) Temperatures at constant values of ASR as a function of cathode compositions. Temperatures refer to ASR values of 0.15, and 0.30 Ω·cm2. Note that minimum operating temperatures occur at mid-compositions.

RESULTS AND DISCUSSION

Area specific resistance values determined from symmetric cell are shown platted as a function of temperature in Fig.3. Figure 4 is derived from Fig. 3 where temperature at which specific values of ASR are shown plotted as a function of the cathode composition. ASR= 0.15 ohm cm^2 is usually taken as a benchmark for cathode. Using this value it is seen that the temperatures are quite low at compositions close to $(La,Sr)_2CoO_4$ = 0.4-0.5 Refocusing the compositions onto this range yields a dual phase cathode (La,Sr)2CoO4 = 0.45 where the temperature reaches its lowest value, namely 575°C.

Structural examination showed that the cathodes in as deposited conditions were amorphous.Fig. 4(a). When used at elevated temperature e.g., 700°C, the structure is quite stable. As shown in Fig.4(b), the cathode tends to crystallize at. 700°C forming two phase structure but it is ill defined and clear crystallized grains cannot be seen.



(a) (b)

Fig.4 High resolution transmission electron microscope (HRTEM) image of co-sputtered cathode with composition (La,Sr)CoO_3: (La, Sr)$_2CoO_4$=0.50:0.50. a) the cathode in as sputtered condition and b) the cathode sputtered and annealed 700 °C for 10 days.

CONCLUSIONS

Results reported above imply that the improved cathode performance in mid-compositions as reflected to favorable ASR values may be due to the refined homogenous structure arising from co-sputtering of (La,Sr)CoO_3 and (La,Sr)$_2CoO_4$. This structure when used at elevated temperatures, e.g., 700°C, is in the form of refined crystalline structure of extremely small grain size. The improved performance might, then, originate from interfacial maximization. Overall, the current study implies LSC based cathodes of amorphous/ nanocrystalline structure as a new class of cathode material for IT SOFCs.

ACKNOWLEDGEMENT

The work reported in this paper was carried out within EU FP7 ERAfrica program with the project title HENERGY. The support was provided by the Scientific and Technological Research Council of Turkey (TUBITAK) with a project number 114M128 and 217M628 which the authors gratefully acknowledge. Authors are also thankful to Serkan Yılmaz for his help with TEM analysis.

REFERENCES

1. C. Niedrig, S.F. Wagner, W. Menesklou, S. Baumann, E. Ivers-Tiffee, Oxygen equilibration kinetics of mixed-conducting perovskites BSCF, LSCF, and PSCF at 900 °C determined by electrical conductivity relaxation, Solid State Ionics 283 (2015) 30–37.
2. Sase M, Yashiro K, Sato K, Mizusaki J, Kawada T, Sakai N, et al. Enhancement of oxygen exchange at the hetero interface of (La,Sr)CoO3/(La,Sr)2CoO4 in composite ceramics. Solid State Ionics 2008;178:1843-52.
3. Crumlin EJ, Mutoro E, Ahn SJ, La OGJ, Leonard DN, Borisevich A, et al. Oxygen reduction kinetics enhancement on a heterostructured oxide surface for solid oxide fuel cells.J Phys Chem Lett 2010;1:3149-55.
4. Ma W, Kim JJ, Tsvetkov N, Daio T, Kuru Y, Cai Z, et al. Vertically aligned nanocomposite La0.8Sr0.2CoO3-d/(La0.5Sr0.5)2CoO4±d cathodes e electronic structure, surface chemistry and oxygen reduction kinetics. J Mater Chem A 2015;3: 207-19.
5. Torunoğlu Z., Sarı D., Demircan O., Kalay Y. E., Öztürk T., and Kuru Y. 2018. One pot synthesis of (La,Sr)CoO3/(La,Sr)2 CoO4 for IT-SOFCs cathodes, J. Hydrogen Energy., 43, 18642.
6. Sari D., Piskin F., Torunoglu Z. C., Yasar B., Kalay Y. E., and Ozturk T. (2018). Combinatorial development of nanocrystalline/amorphous (La,Sr)CoO3-(La,Sr)2CoO4 composite cathodes for IT-SOFCs, Solid State Ionics., 326, 124.
7. Sari D, Yaşar B, Piskin F, Kalay Y. E., Öztürk T, (2019), Segregation Resistant Nanocrystalline/Amorphous (La, Sr)CoO3-(La,Sr)2CoO4 Composite Cathodes for IT-SOFCs, Journal of The Electrochemical Society, 166 (15) F1157-F1163.

WHEC-2022
23rd World Hydrogen Energy Conference
June 26-30, 2022 - Istanbul

#1511

EFFECT PARTIAL SUBSTITUTION OF LANTHANUM ON THE THERMAL PROPERTIES OF $La_{0.7-X}Ln_XCa_{0.3}MnO_3$ (Ln = Pr or Sm) PEROVSKITES

Jessica Ramírez-Hernández[1], Aidé M. Torres-Huerta[2], Silvia B. Brachetti-Sibaja[1], Miguel A. Domínguez-Crespo[2], Diana Palma-Ramírez[3], Wencel de la Cruz[4], Francisco Gutiérrez-Galicia[2].
[1]Tecnológico Nacional de México, IT de Ciudad Madero, D.E.P.I., Cd. Madero, Tamps., C.P. 89440, México.
[2]Instituto Politécnico Nacional, UPII-Hidalgo, San Agustín Tlaxiaca, Hidalgo, C.P. 42162, México.
[3]Instituto Politécnico Nacional, CMPL, Cd. de México, C.P. 07340, México.
[4]UNAM, Centro de Nanociencias y Nanotecnología, Ensenada, B.C, C.P. 22860, México.

jess_6_11@hotmail.com, +52 8333006919; atorresh@ipn.mx, +5257296000; bbrachetti@hotmail.com,+52 8333574820

ABSTRACT

$La_{0.7-x}Ln_xCa_{0.3}MnO_3$ (Ln = Pr or Sm) perovskites synthesized by Pechini method with different stoichiometries (x = 0.1, 0.3, 0.5 and 0.6) were analyzed in order to evaluate the effect of cationic substitution and final composition on thermal properties; specific heat, thermal conductivity and thermal diffusivity at different temperatures are specifically reported. The results are discussed in terms of the potential use as a cathode material to be applied in solid oxide fuel cells (SOFCs) applications at intermediate temperatures (600 to 800°C). The results showed that thermal conductivity decreases as Pr doping increases; but a different trend is observed with samarium: first, a decrease is observed from x = 0.1 to x = 0.3, and then, from x = 0.3 to x = 0.6, an increase is determined. Also, thermal diffusivity presents a marked behavior when Sm-based perovskites display a high cation substitution (x = 0.6). Thermal expansion coefficient studies are in progress.
Keywords: ABO_3 perovskites, thermal conductivity, solid oxide fuel cells.

INTRODUCTION

Solid oxide fuel cells (SOFCs) are electrochemical energy conversion devices that can produce electrical energy through oxidation and reduction reactions and are considered a clean and renewable solution for the electric energy generation from hydrogen, providing higher efficiencies than conventional systems [1 - 5]. Due to high operating temperatures (800-1000°C) produce structural changes in the electrode material, the development of materials with a perovskite-type structure (ABO_3) has been encouraged, establishing that by doping the A-site with rare earths (praseodymium and samarium, in this case), the overpotential at the cathode could be reduced, and the electrocatalytic activity, increased. Several authors have studied doping at the A-site and found that substitution with Ca increases the electrical conductivity by more than three orders of magnitude, while at the same time the thermal conductivity is reduced; therefore, the reduction in thermal conductivity is due to the heavier mass of dopant ions [6, 7]. However, one of the major issues to be evaluated during operation of perovskites (as cathode in SOFCs) is the mismatch in the thermal properties that cause thermal stress. Temperature gradients and thermal expansion coefficients can provoke hot spots and curling of the components. Although its importance is evident, few studies are related to evaluating the changes in the thermal properties of ABO_3 perovskites depending on the cation-type or composition at intermediate temperatures, particularly of $La_{0.7-x}Ln_xCa_{0.3}MnO_3$ perovskites (Ln=Pr or Sm, x = 0.1, 0.3 0.5 and 0.6) which is the goal of this research.

MATERIALS AND METHODS

The $La_{0.7-x}Ln_xCa_{0.3}MnO_3$ perovskites were prepared using the Pechini method from metal nitrates. Lanthanum (III) nitrate hexahydrate ($La(NO_3)_3*6H_2O$, 99.99% purity), praseodymium (III) nitrate hexahydrate ($Pr(NO_3)_3*6H_2O$, 99.9% purity), samarium(III) nitrate hexahydrate ($Sm(NO_3)_3*6H_2O$, 99.9% purity), calcium nitrate tetrahydrate ($Ca(NO_3)_2*4H_2O$, 99.0% purity) and manganese(II) nitrate tetrahydrate ($Mn(NO_3)_2*4H_2O$, 97.0% purity), were acquired from Sigma Aldrich and stoichiometric amounts were weighed according to desire final nominal composition (x = 0.1, 0.3 0.5 and 0.6).The precursors were mixed with citric acid, CA, (3:1 CA/metal cations) and ethylene glycol, EG, (2:1 EG/CA) in molar ratios. The salt mixture was dissolved in deionized water by heating to 90°C to 110°C and kept under stirring for 4 to 5 hours, until removing excess solvent, forming an intermediate resin. Continuing with a calcination stage of 3 h at 450°C obtaining a dark powder, to finally take it to a heat treatment at 1000°C.

Thermal Properties Measurements

The thermal properties of synthesized perovskites were determined by a laser flash technique obtaining specific heat, thermal conductivity, density and thermal diffusivity measurements from room temperature to 800°C.

RESULTS AND DISCUSSION

Table 1 and 2 list the results obtained through laser flash analysis of all the samples at two different temperatures. It can be observed that thermal conductivity is reduced while the doping increases, according to work reported in literature, where A-doped samples has a tendency to reduce this parameter. Thermal conductivity (k) is correlated to the availability in oxygen vacancies and is determined from the measurement of thermal diffusivity (α), specific heat (Cp), and density (ρ) of the sample using the relation $\kappa = Cp\alpha\rho$ [6, 7]. The thermal conductivity values obtained are those expected for a crystalline solid, since they are above the range reported for non-crystalline. A low value of this parameter could be originated from the distortions of the lattice resulting in high degree of disorder. In case of manganites such scenario may be attributed to the Jahn-Teller distortion of the MnO_6 octahedra [8].

To praseodymium, the thermal diffusivities increase with the rise in temperature and decrease in relation to the cation amount. On the other hand, with samarium the diffusivity decreases when a rise in the temperature its applied and even when the tendency in 0.1, 0.3 and 0.5 it seems to be reduced, highest value is observed in x = 0.6, which means that the site substitution increases the thermal diffusivity, also according to previous reports the substitution of Ca in La site slightly increases the measurement. The thermal changes in the SOFC components occur due to differences in thermal properties of them. Especially, the heat diffusivity plays an important role during transient heat production and local heat transference [9].

New cathode materials must have matched thermal expansion coefficients (TEC) and sufficient chemical stability. These two characteristics are influenced by the concentration of oxygen vacancies within the perovskite lattice, according with the literature. The TEC of the perovskites decreased with increasing Ca content up to 20 mol-% and then increased. $LaMnO_3$ perovskite with highest TEC, can be explained by either of the two following reasons, the loss of oxygen and the accompanying decrease in the cation vacancy concentration led to a larger thermal expansion in $LaMnO_{3+\delta}$ or, the average ionic radius of B-site metals in the perovskites increases due to the change from Mn^{4+} to Mn^{3+} [10].

Table 1. Laser flash technique results to $La_{0.7-x}Pr_xCa_{0.3}MnO_3$

	$La_{0.7-x}Pr_xCa_{0.3}MnO_3$							
	Room temperature				120 °C			
	0.1	0.3	0.5	0.6	0.1	0.3	0.5	0.6
Thermal diffusivity (cm^2/s)	0.0033	0.0032	0.0023	0.0021	0.0036	0.0038	0.0025	0.0022
Specific heat (J/gK)	0.9364	0.4106	0.5000	0.4368	0.6568	0.4058	0.4648	0.4498
Density (g/cm^3)	2.69	2.76	3.20	3.19	2.69	2.76	3.2	3.19
Thermal conductivity (W/mK)	0.8358	0.3630	0.3656	0.2866	0.6448	0.4218	0.3762	0.3212

Table 2. Laser flash technique results to $La_{0.7-x}Sm_xCa_{0.3}MnO_3$

	$La_{0.7-x}Sm_xCa_{0.3}MnO_3$							
	Room temperature				120 °C			
	0.1	0.3	0.5	0.6	0.1	0.3	0.5	0.6
Thermal diffusivity (cm^2/s)	0.0030	0.0026	0.0027	0.0061	0.0026	0.0025	0.0020	0.0051
Specific heat (J/gK)	0.9310	0.4150	0.5010	0.4400	0.6842	0.3880	0.4408	0.4276
Density (g/cm^3)	3.05	2.8	3.03	2.98	3.05	2.8	3.03	2.98
Thermal conductivity (W/mK)	0.8572	0.3054	0.4116	0.7990	0.5410	0.2700	0.2744	0.6542

CONCLUSIONS

In the praseodymium samples, a reduction in thermal conductivity is observed when the value of x increases, but it shows a small increase with respect to the change in temperature. The diffusivity measurements have a similar trend, maintaining the lowest values when x = 0.6. On the contrary, with the samarium doping and with the same value of x, a higher conductivity is observed even though the first trend of this value seems to be reduced. The thermal diffusivity presents the same behavior giving us the highest value in a higher doping of the sample. Evaluation of thermal properties is still ongoing to confirm these observations.

ACKNOWLEDGEMENTS

Jessica Ramírez-Hernández is grateful to CONACYT for her fellowship, Tecnológico Nacional de México, Instituto Tecnológico de Ciudad Madero. The authors are thankful for the financial support provided by Instituto Politécnico Nacional through the SIP projects: 2022-0668, 2022 0671, 2022-1153, 2022-1155, 2022-0244 and COFAA. This work has been also founded by CONACyT through the CB-2015-252181 project and SNI-CONACyT.

REFERENCES

[1] A.B. Stambouli, E. Traversa, Solid oxide fuel cells (SOFCs): a review of an environmentally clean and efficient source of energy, Renew. Sustain. Energy Rev. 6 (2002) 433e455.
[2] M. Sharifzadeh, N. Shah, Chapter 6 - Synthesis, Integration, and Intensification of Solid Oxide Fuel Cell Systems: Process Systems Engineering Perspective, in: M. Sharifzadeh (Ed.), Design and Operation of Solid Oxide Fuel Cells, Academic Press, 185-215 (2020).
[3] M.K. Rath, K.-T. Lee, Investigation of aliovalent transition metal doped La0.7Ca0.3Cr0.8X0.2O3d (X¼Ti, Mn, Fe, Co, and Ni) as electrode materials for symmetric solid oxide fuel cells, Ceram. Int. 41, 10878-10890 (2015).
[4] W. Li, C.Y. Xiong, L.C. Jia, J. Pu, B. Chi, X. Chen, J.W. Schwank, J. Li, Strontium doped samarium manganite as cathode materials for oxygen reduction reaction in solid oxide fuel cells, J. Power Sources 284, 272-278 (2015).
[5] L.S. Mahmud, A. Muchtar, M.R. Somalu, Challenges in fabricating planar solid oxide fuel cells: A review, Renew. Sustain. Energy Rev. 72, 105-116 (2017).
[6] A. Mishra, S. Bhattacharjee, Effect of A- or B-site doping of perovskite calcium manganite on structure, resistivity, and thermoelectric properties, Journal of the American Ceramic Society, 100(10), 4945-4953 (2017)
[7] Y. Miyazaki, D. Abe, T. Kajitani, Preparation, Crystal Structure and Thermoelectric Properties of La2-2xCa1+2xMn2O7. In 26th International Conference Thermoelectric. Piscataway, NJ: Institute of Electrical & Electronics Engineers (IEEE); pp. 129-132 (2007).
[8] M. Battabyal, T. K. Dey, Thermal conductivity of silver doped lanthanum manganites between 10 and 300K, Journal of Physics and Chemistry of Solids, 65(11), 1895–1900 (2004).
[9] Y. Ohno, Y. Ishizuka, Y. Hatoh, N. Oikawa, Investigations of Heat Diffusivity of SOFC Components by a Laser Flash Method, ECS Proceedings Volumes, Vol. 40, 937 (1997).
[10] M. Mori, Y. Hiei, N. Sammes, G. Tompsett, Thermal-Expansion Behaviors and Mechanisms for Ca- or Sr-Doped Lanthanum Manganite Perovskites under Oxidizing Atmospheres. Journal of The Electrochemical Society, 147(4), 1295 (2000).

WHEC-2022
23rd World Hydrogen Energy Conference
June 26-30, 2022 - Istanbul

#1564

INVESTIGATION OF PALLADIUM COATED NICKEL FOAM ANODE ELECTRODE APPLICATION FOR DIRECT ETHANOL FUEL CELLS

[1*] Cansu Kılıç, [2]Kürşat Can Ata, [2]Anıl Can Türkmen [1]Sibel Demirel,[2]Cenk Çelik
[1]Chemistry Dept., Kocaeli University, Umuttepe Campus, İzmit/Kocaeli
[2]Mechanical Eng. Dept., Kocaeli University, Umuttepe Campus, İzmit/Kocaeli

*Corresponding author e-mail: kursatcanata@gmail.com

ABSTRACT

Direct ethanol fuel cell (DEFC) is a subcategory of proton exchange membrane fuel cell (PEMFC). Ethanol as a fuel for DEFC is easier to obtain, store and transport than hydrogen. Additionally, ethanol has advantages over methanol due to lower toxicity, easier usability, and renewability. Therefore, DEFC is more suitable for mobile and portable power supplies if the disadvantages such as low efficiency and high total operating costs are resolved in the future. In this study, the use of Pd coatings on nickel foam in DEFC was investigated. SEM and EDS analyzes were performed for the characterization of the foam coatings. Also, the effect of Pd coatings made on nickel foam on the efficiency will be investigated by using highly-sulfonated SPEEK membranes in DEFC, the anode electrode for DEFC will be developed and its performance parameters will be examined in detail.

Keywords: Direct ethanol fuel cell, Electrocoating, Metal foam, SPEEK membrane, Hydrogen energy

INTRODUCTION

Fuel cell is a power generation element that is efficient, quiet, environmentally friendly and converts fuel energy into electrical energy in the electrochemical principle. Fuel cells do not contain fuel and combustors like batteries. Instead, it constantly receives these two chemicals from an external source where they are stored. Fuel cells can be operated continuously as long as the source flow is provided, and batteries contain their fuel and burners in their own internal structure. As one of the promising portable batteries, the direct ethanol fuel cell (DEFC) has attracted great attention due to the impressive properties of high-power and renewable, non-toxic ethanol fuel. Much of the work in recent years has focused on anode and cathode catalysts. Many new precious metal-free carbon-containing and low-cost transition metal-based ORR electrocatalysts have been developed for the cathodic oxygen reduction reaction (ORR). However, their electrocatalytic activity or durability still did not surpass the noble metal (Pt-based) catalysts. For the most effective Pt-based ORR catalysts, using various effective Pt carriers such as heteroatom-doped carbon nanomaterials or adding transition metals to reduce the amount of Pt and increase the Pt activity, studies have been carried out to reduce the high cost of the Pt catalyst [2,3]. Direct ethanol fuel cells (DEFCs) have been predicted to be strong candidates to compete with advanced batteries, with advantages such as the use of clean fuel, abundant biomass resources, high efficiency, large energy density, small design, compactness, quietness and low temperature operation [4]. However, the performance and stability of DEFC in particular, and fuel cells in general, face many hurdles and challenges in commercialization. One of the most important factors affecting the effectiveness of DEFC is the electrochemical catalysts for the oxidation and reduction processes taking place at the anode and cathode, respectively. Pd-based electrocatalysts offer similar conversion properties to Pt and are therefore widely used for the oxidation of EOR and other alcohols, but in alkaline medium, Pd-based electrocatalysts have shown better results than Pt-based electrocatalysts. Therefore, Pd-based electrocatalysts are a good alternative for use in alcohol oxidation-based fuel cells [5]. However, despite their respective activity on a DEFC, important structure-activity relationships are still not well understood in such bimetallic systems, and much progress is required to tailor DEFC performance. Moreover, given that electrocatalytic reactions usually involve the adsorption process of reactants, intermediates and products, the role of electronic effects as a function of catalyst microstructure is of great importance for understanding the overall electrochemical behavior [6,7].

MATERIALS AND METHODS

PEEK has some thermal and chemical stability problems at high degree of sulfonations (DS). Concentrated sulfuric acid was used as the sulfonating agent. All membranes were prepared by solvent-casting method by using dimethylacetamide (DMAc). In this study, membranes prepared by different degree of sulfonation processes [1]. The membranes were characterized for their proton conductivity. The anode electrode coating process was carried out with the following process steps. With 20 g degreasing chemical and 350 ml degreasing solution prepared with pure water cause the surface of the foam material had to purified from oils and chemicals. The positive end of the DC power supply in the stainless-steel anode, the negative end is connected to the foam material and degreasing is

performed by giving 3 V voltage from the power supply for 20 seconds. After the degreasing process, the metal foam is cleaned from the degreasing bath by washing with pure water. Then the metal foam part is dried with the help of heater and compressor and made ready for the next process. Ni foam is removed from the oxide layer on its surface by immersing in 11,2 gr Ammonium bifluoride, 175 ml Nitric acid and 350 ml etching bath prepared with pure water for 20 seconds. After the etching process, the metal foam is washed with pure water and purified from the etching bath. Then the metal foam part is dried with the help of heater and compressor and made ready for the next process. Before proceeding to another stage, the foam material is weighed to determine the weight before coating. The platinum anode immersed in the Pd solution between 50-55 ° C is connected to the positive end of the DC power supply, and the foam material is connected to the negative end of the power supply, and Ni foam is coated at different coating times by applying 3 V voltage from the power supply. After the coating process, the metal foam is cleaned from the coating bath by washing with pure water. The metal foam is then dried with the help of a heater and a compressor and weight measurement are taken after coating. Coating amounts are given in Table 1.

Table 1. Coating Measurement Results

Sample No:	Before Coating: (g)	After Coating (g)	Coating Time (in sec.)
1	5,00	5,16	60
2	5,48	5,57	45
3	6,68	6,84	75
4	5,57	5,73	90
5	6,41	6,57	120

RESULTS AND DISCUSSION

Figures 1a and b show SEM images of the fabricated electrode. Figure 1 shows that the catalyst on the surface of the approximately 1 cm nickel foam electrode is evenly supported on the nickel foam skeleton, taking full advantage of the unsupported noble metal catalyst. Uniform coupling of the catalyst and nickel foam skeleton can also increase the rate of electron transfer. Electrons released by the ethanol oxidation reaction (EOR) on the outer surface of the catalyst particles can be quickly transferred through the metal foam skeleton, reducing the resistance of electron transfer. In the SEM image for Sample 2 (Figure 1a&b), it is seen that there is a smooth coating on the surface. Thanks to the roughness on the surface, the active area is increased. It is coated at 3V and the coating weight is low due to the low current it draws. EDS analysis is a point analysis and by measuring the radiation (Figure 2), it is possible to determine the element or elements K alpha L alpha et al. It encounters the values and tells which element it is. As can be seen from the peaks in the figure, Pd was successfully coated on the nickel foams. In the sample, the coating appears to be homogeneous in the both micro and macro scales.

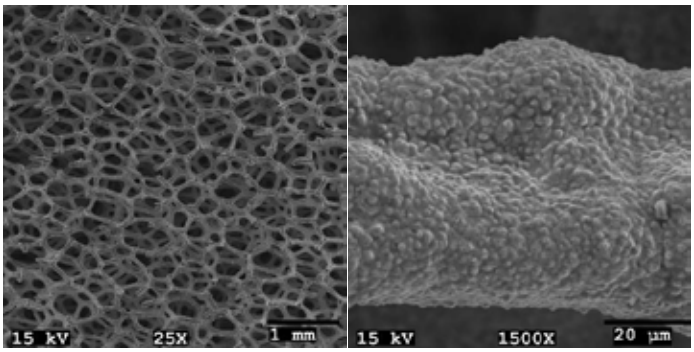


Fig 1. SEM image for sample 2 in (a)1 mm and (b)20 µm diameter

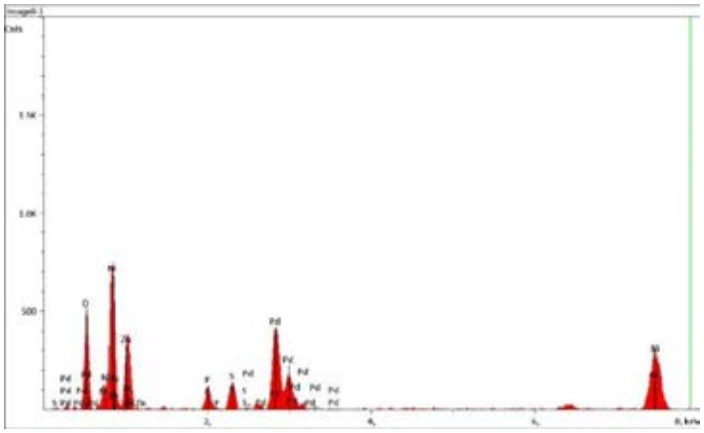


Fig 2. EDS analysis for Sample 2

Membrane's ionic conductivities were determined in potentiostatic mode using the "4-probe through-plane" ionic conductivity system by electrochemical impedance spectroscopy (EIS) method. In this study, measurements were made at 80% humidity at room conditions and at the same humidity level at 80 °C. SPEEK with a high degree of sulfonation was measured as 0.309 mS/cm. The thickness of the membrane used is 45 micrometers.

CONCLUSIONS

As a result of the studies, SPEEK polymers with desired sulfonation degrees were obtained. It was made into a membrane and various characterizations were carried out. As a result of these characterizations, it was confirmed that the produced membrane was produced with or very close to predetermined properties both electrochemically and morphologically. In addition, a literature study was conducted on the preparation of system and MEA. The catalysts and MEA components to be used ultimately have been precisely determined. SPEEK membrane prepared with a high degree of sulfonation (~80%) will be used in single cell tests. Foams with high coverage ratios will be used in MEA production. When the Pd coated foams prepared using different coating times were examined, it was seen that the coating time did not show a significant difference in the use of constant voltage, since sufficient coating saturation was provided. In future studies, handles will be made at different voltage values and different parameters.

ACKNOWLEDGEMENT

This study was supported by Kocaeli University Scientific Research Projects (BAP) Unit (Grant Id: BAP-FHD-2021-2755). The support and fundings of these institutions are gratefully acknowledged.

REFERENCES

1. Ata KC, Kadıoğlu T, Türkmen AC, Çelik C, Akay RG, 2019. Investigation of the effects of SPEEK and its clay composite membranes on the performance of Direct Borohydride Fuel Cell. International Journal of Hydrogen Energy 45(8):5430-37.
2. Lamy C, Belgsir EM, Leger JM, 2001. Electrocatalytic oxidation of aliphatic alcohols: application to the direct alcohol fuel cell (DAFC). Journal of Applied Electrochemistry 31:799-809.
3. An L, Zhao TS, Li YS, 2015. Carbon-neutral sustainable energy technology: direct ethanol fuel cells, Renewable and Sustainable Energy Reviews 50:1462–1468.
4. An L, Zhao TS, 2017. Transport phenomena in alkaline direct ethanol fuel cells for sustainable energy production. Journal of Power Sources 341:199-211.
5. Lv H, Sun L, Lopes A, Xu D, Liu B, 2019. Insights into compositional and structural effects of bimetallic hollow mesoporous nanospheres toward ethanol oxidation electrocatalysis, Journal of Physical Chemistry Letters 10:5490–5498.
6. Amin RS, Abdel Hameed RM, El-Khatib KM, Elsayed Youssef M, 2014. Electrocatalytic activity of nanostructured Ni and Pd–Ni on Vulcan XC-72R carbon black for methanol oxidation in alkaline medium, International Journal of Hydrogen Energy 39:2026–2041.
7. Antolini E, 2011. An empirical model to evaluate the contribution of alloyed and non-alloyed tin to the ethanol oxidation reaction on Pt-Sn/C catalysts based on the presence of SnO2 and a Pt(1-x)Snx solid solution: application to DEFC performance. International Journal of Hydrogen Energy 36:11043-7.

WHEC-2022
23rd World Hydrogen Energy Conference
June 26-30, 2022 - Istanbul

#1572

DEVELOPMENT OF NOVEL MEMBRANE STRUCTURES VIA RADIATION INDUCED GRAFTING AND ELECTROSPINNING TECHNIQUE FOR ANION EXCHANGE MEMBRANE FUEL CELLS

[1*] *Ahmet Can Kırlıoğlu,* [1] *Naeımeh Rajabalizadeh,* [1,2] *Selmiye Alkan Gürsel and* [2]*Begüm Yarar Kaplan*
[1]Sabancı University, Faculty of Natural Science and Engineering, 34956, Istanbul, Turkey
[2] Sabancı University Nanotechnology Research and Application Center(SUNUM), 34956, Istanbul, Turkey

*Corresponding author e-mail: kirlioglu@sabanciuniv.edu

ABSTRACT

Development and commercialization of fuel cells, as an alternative to fossil fueled engines, are at its highest importance and urgency due to global climate change crisis. Proton Exchange Membrane Fuel Cells (PEMFC) made a huge technological leap with the breakthrough of development of Nafion® membranes however its high catalysts and membrane costs hinders further developments. Anion Exchange Membranes Fuel Cells (AEMFC) doesn't require expansive Pt group catalysts to be efficient which can solve the cost problem, but it is still needed to develop a cheap, durable membrane with high anion conductivity and ion exchange capacity. Membranes with radiation-induced grafted polymers can provide good ion exchange capacity and conductivity while weakens the mechanical robustness. Therefore, we used dual electrospinning technique to fine tune mechanical properties without sacrificing the functionality. We have prepared anion conducting membranes for AEM fuel cells by a dual-electrospinning technique using inert poly(vinylidene fluoride) (PVDF) powders and radiation induced grafted PVDF with vinyl benzyl chloride (VBC) with various compositions. The dual fiber-based mats are hot-pressed, aminated and ion exchanged in this order. We have investigated and optimized the grafting levels, mechanical properties and morphologies of the duel electrospun membranes.

Keywords: Electrospinning, Radiation induced grafting, Anion exchange membrane, Fuel cells

INTRODUCTION

Climate change crisis is the new generations' doom and gloom unless greenhouse effect due to carbon dioxide emissions are hindered or at least slowed down. One of the main contributor of carbon dioxide emissions is the fossil fuel usage, especially in transportation and energy sectors in which we need a feasible alternative to fossil fueled engines. PEM Fuel cells are the main competitors of the fossil fuels engines but acidic media in which only expensive catalysts can work efficiently, and cost of membrane made PEMFC lose its competitive edge financially. Alkaline medium of AEMFC can solve the bottleneck cost problem due to opening up more alternative and cheaper catalysts as long as an ideal membrane is developed. The requirements of an ideal membrane for AEMFC are as follows:

i) High ion conductivity and high ion exchange capacity;
ii) High mechanical and chemical stability;
iii) Low water absorption and swelling.

If these requirements can be made without sacrificing any one of them, one can obtain high performance and efficient AEMFCs. Because sacrificing any aspect of an ideal membrane would result in either very low durability or low efficiency. In order to solve the problems mentioned above, first, we radiation induced grafted the PVDF powders in an optimized reaction with VBC to control the ion exchange capacity and the ion conductivity of the final membrane, however, radiation-grafting is generally decreasing the mechanical robustness of the membranes because of the chain scissions of the backbone polymer [2]. Hence, we have used the electrospinning technique and fabricated dual-fiber-based electrospun mats which include the inert and grafted PVDF powders to control the mechanical properties of the final membrane by adjusting the ratio without a dramatic decrease in ion conductivities. Firstly, the characterizations of the grafted PVDF-g-VBC to understand the grafting levels of the PVDF powder with VBC such as NMR, FT-IR, FT-Raman; and SEM and EDS to investigate morphologies and elemental analysis of the electrospun fibers as well as the ion exchange capacities and ion conductivity of the aminated mats are provided in this work.

MATERIALS AND METHODS

Figure 1 shows the experimental procedure steps. First, the commercial PVDF powders are irradiated with 50 kGy gamma rays and grafted with VBC to prepare PVDF-g-VBC powders while changing the parameters such as temperature, reaction duration, mixing rate to optimize the grafting levels which are calculated by before-after weight change of the powders. Using these powders and inert commercial PVDF, two different solutions is prepared and

used at the dual-spin setup which can be seen in the 4th inset of Figure 1. In order to reduce the permeability of fuels, these electrospun fibers are hot-pressed to the thickness of 50 µm and confirmed a non-porous structure by SEM and aminated with trimethylamine solution for one day, and finally alkanizated with potassium hydroxide.

Nuclear magnetic resonance spectroscopy (NMR), Fourier-transform infrared spectroscopy (FT-IR), and Fourier-transform Raman spectroscopy are used to the characterization of the molecular structure of the PVDF-g-VBC and its grafting levels.

Additionally, scanning electron microscopy (SEM) and energy dispersive spectroscopy (EDS) are conducted with electrospun mats to investigate the morphology and elemental mapping of the fibers. The mechanical tensile test, ion exchange and ion conductivity tests are done for the mats after the hot-pressing and amination, and alkalization steps.



Figure 1. Schematic of dual fiber-based mat production setup

RESULTS AND DISCUSSION

Figure 2A shows the successful grafting of the VBC into the PVDF backbones with FT-Raman peaks at the 1450 cm^{-1} shows the CH_2 scissor mode of vibration for the inert PVDF powder. The VBC grafted powders were showing additional peaks at 1001 cm^{-1} and 1611 cm^{-1} which were due to aromatic peaks of VBC. Additionally, the peak at the 1266 cm^{-1} the broad peaks between 600-800 cm^{-1} are showing the C-Cl bonds.

In Figure 2B. we can observe 2 different fiber structures with different morphologies (inset) One type of the fibers showed more wrinkled surface morphology while the others showed less wrinkled surface but more porous fiber morphology. We have speculated that two fiber types are due to inert PVDF and PVDF-g-VBC. In order to confirm these two fiber types are indeed has different chemical structure we have used EDS to investigate Cl presence on each fiber types.

In figure 3 the SEM micrographs of the electrospun fibers are given at the 5000X magnification as well as their elemental analysis is shown with the spectrums that are obtained from the single points on top of the two fibers with different morphologies. The images indicate a good fibrous structure without any beads and homogenous distribution of the dual-fibers which were confirmed by the elemental analysis of the fibers with EDS. EDS results indicated that there are two types of fiber with and without Cl atoms which resulted in different morphologies.

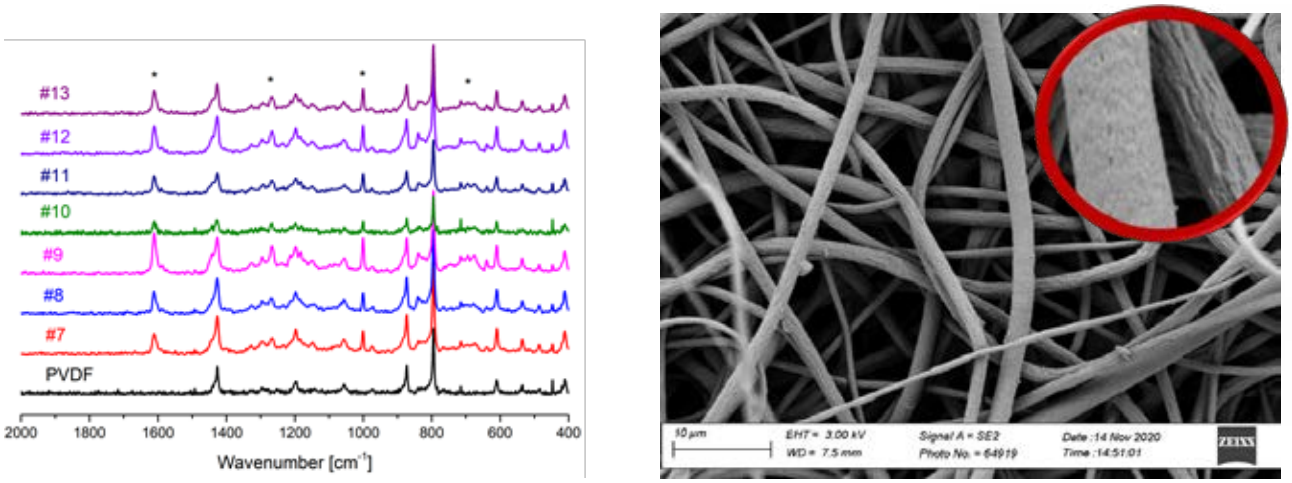


Figure 2. A. FT-Raman results of the PVDF-g-VBC and B. SEM images of dual fiber structures.

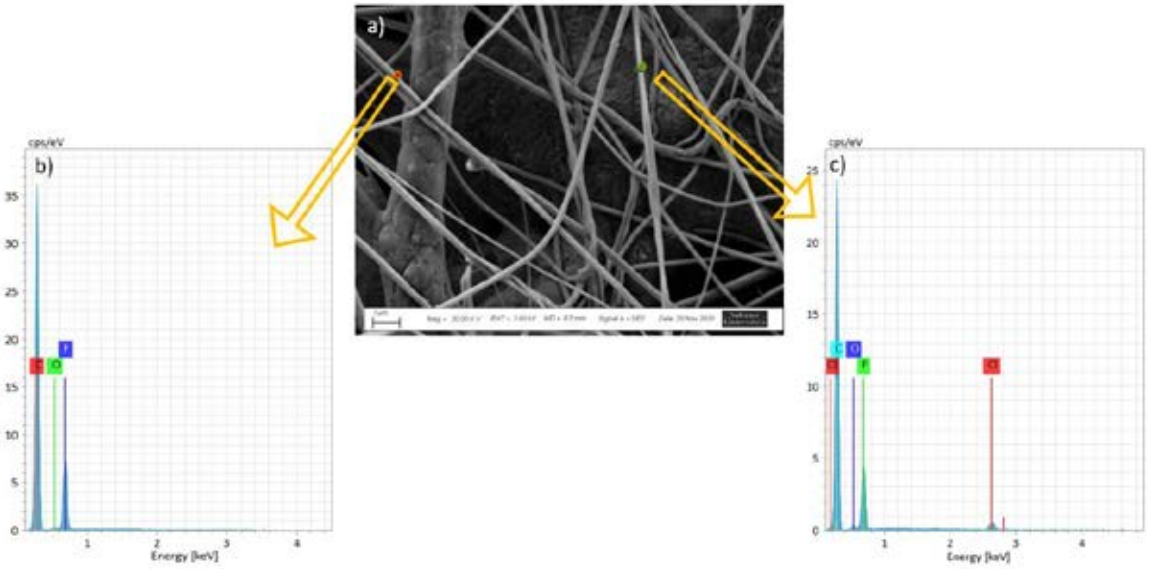


Figure 3. SEM micrographs of the two different fiber structures and their corresponding EDS results

CONCLUSIONS

In this study, radiation-induced grafting and electrospinning techniques were used to fabricate dual fiber-based electrospun anion exchange membranes. These membranes were characterized and prepared to be used in a fuel cell for the first time in literature. To fabricate anion exchange membranes with promising ionic conductivity and mechanic strength, we have developed a two-step procedure: First, VBC monomers were grafted into irradiated PVDF powders. Then, the grafted and inert PVDF powders were solved and electrospun into dual-fiber mats which were later aminated and alkalized into the anion exchange membrane forms. Characterization techniques such as NMR, FT-Raman and FT-IR were conducted to show the grafting steps were successful. SEM imaging and EDS spectroscopy were used to indicate homogenous morphologies with a good distribution of dual-fiber structures. After the hot-pressing and compacting the membrane, amination and alkalization steps are conducted, the ionic conductivity and the ion exchange capacity measurements of the dual-fiber-based electrospun anion exchange membranes showed promising results.

ACKNOWLEDGEMENT

The authors gratefully acknowledge the financial support of The Scientific and Technological Research Council of Turkey (TÜBİTAK) (Grant Number: 119M059)

REFERENCES

1. He, Qinggang, and Elton J. Cairns. "Recent progress in electrocatalysts for oxygen reduction suitable for alkaline anion exchange membrane fuel cells." Journal of The Electrochemical Society 162, no. 14 (2015): F1504.
2. Bürger, W., K. Lunkwitz, G. Pompe, A. Petr, and D. Jehnichen. "Radiation degradation of fluoropolymers: Carboxylated fluoropolymers from radiation degradation in presence of air." Journal of applied polymer science 48, no. 11 (1993): 1973-1985.

WHEC-2022
23rd World Hydrogen Energy Conference
June 26-30, 2022 - Istanbul

#1581

DEVELOPMENT OF BROMINE RESISTANT ANODE CATALYST FOR HYDROGEN OXIDATION AND REDUCTION REACTIONS IN HYDROGEN BROMINE FLOW BATTERIES

[1*] *Burcu Kirtoklu,* [2] *Berker Fiçicilar*
Ondokuz Mayıs University, Faculty of Engineering, Chemical Engineering, Turkey, Samsun

Corresponding e-mail*: burcukirtoklu@gmail.com

ABSTRACT

Hydrogen-bromine flow cell system is considered a highly advantageous electrical energy storage system due to its high energy capacity, high charge-discharge efficiency, and low cost. The hydrogen oxidation reaction (HOR) that takes place on the anode side of the hydrogen-bromine flow cell is generally catalyzed by high-activity (platinum) catalysts. The bromine reduction reaction (BRR) on the cathode side can be catalyzed with platinum-based high-performance catalysts to obtain high power density, while it can also be directly catalyzed by carbon structures. Bromine ions passing from the cathode to the anode side via the ion-permeable membrane poison the anode catalyst, causing a decrease in anode kinetics and thus battery performance. A new anode catalyst resistant to the bromine environment needs to be developed to eliminate this crossover problem, which significantly reduces the catalyst performance and lowers the hydrogen oxidation reaction (HOR) kinetics. This project, it is aimed to improve the kinetics of the hydrogen oxidation reaction by developing bromine resistant anode electrocatalysts with high catalytic activity.
Keywords: Bromine tolerant electrocatalyst, hydrogen bromine flow batteries

INTRODUCTION

The increasing energy demand in recent years has significantly increased the interest in renewable energy sources. Most renewable energy sources (such as solar, wind) are intermittent by nature and cannot provide the necessary continuity in meeting the need. This has increased the need for large-scale, low-cost, and durable electrical energy storage systems. Hydrogen/bromine flow cell systems, one of the electrochemical energy conversion systems, are advanced and innovative energy conversion systems because they both produce electrical energy and can store the generated electrical energy [1]. Flow batteries are a promising technology as an energy storage system because they are scalable, long-lasting, and do not pose a safety risk. Flow cells such as zinc/bromine, vanadium/redox, polysulfide/bromine, hydrogen/bromine are among the important flow batteries that have been researched and studied in recent years [2]. Hydrogen bromide flow batteries are a liquid-gas system. It is an electrochemical system in which electrolytes containing gaseous hydrogen (negative side), aqueous Br_2, and HBr (positive side) are fed from storage tanks to the battery cell. The hydrogen bromine flow system is shown below.

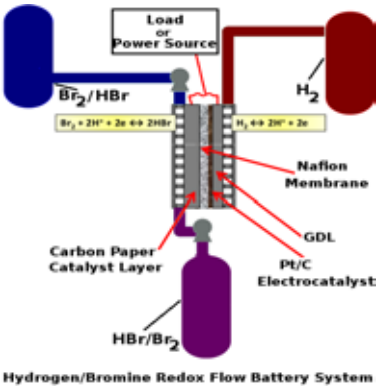


Fig 1. Hydrogen/Bromine Redox Flow Battery System

Despite all these positive aspects of hydrogen bromine flow batteries, several challenges must be overcome to become more widely available. One of the main problems of this flow battery is that as a result of the crossover of bromine chemicals, the performance of hydrogen oxidation and evolution catalysts on the anode side is significantly reduced and the anode electrode kinetics becomes unstable. This problem can be solved by using membranes to reduce crossover or by developing an anode catalyst with bromine-type stability and high catalytic activity. Another problem arises from the need for relatively low-cost catalysts as an alternative to noble high-cost metal-based catalysts with electrode kinetics during the reduction and oxidation reactions on the cathode side of bromine, which

has a corrosive effect. To overcome the problem here, carbon structures with high surface area and mesopores are used at the cathode [3]. Wei et al. examined a series of Ir alloy nanoparticles and it was found that IrNi had the highest HOR activity [6]. Satsuma et al. It showed that the Ir-Ru alloy catalyst has higher HOR activity than Ru, Ir, and Pt single metal catalysts, which is comparable to the state-of-the-art Pt-Ru alloy catalyst [7]. Abruna et al. It was found that $Ir_3Pd_1Ru_6$ / C exhibited high activity and durability for HOR in the alkaline environment [8]. Recently, Shao et al. an IrNi@PdIr core-shell was prepared, showing superior HOR activity than commercial Pt/C [9]. However, there is still room to further improve the HOR activity of Ir-based catalysts, and this can be achieved by fine-tuning the structure of the catalysts. Based on these studies, IrNi @ Ir core-shell nanoparticles with high HOR activity in alkaline electrolytes were developed. The core-shell nanoparticle will be synthesized by a simple one-pot synthesis using two Ir sources with different reactivities. The HBE of the Ir shell will be weakened by the IrNi core [5]. In another study, carbon nanotubes (SWCNTs) were tried to be grown by CVD technique using a few nanometer-sized Ir particles as catalysts and they were able to grow vertically aligned SWCNTs with small diameters less than 1.2 nm [10]. The syntheses of the catalysts synthesized for these different methods and situations will be designed and developed.

MATERIALS AND METHODS

$IrCl_6.6H_2O$ and $NiCl_2.6H_2O$ salts with carbon consumption iridium and nickel core nanoparticles in equal molars will be used. It will be mixed with high surface area XC-72 carbon black to achieve 20% total metal loading. After washing with pure water, it will be purified in an ultrasonic bath and under gas. Sodium borohydride ($NaBH_4$) is added to reduce the salts. After ($NaBH_4$) is added, it is washed again with distilled water and dried. The samples obtained are purchased in a tube furnace under Ar gas at 600°C for 2 hours [11]

RESULTS AND DISCUSSION

In the development of the bromine resistant anode catalyst for the hydrogen bromine flow cell, carbon-supported IrNi/C bimetallic was first used. IrNi/C bimetallic was obtained by the core-shell method, which is one of the determinant synthesis methods. The electrochemical characterization of IrNi/C bimetallic synthesized by the core-shell method was investigated in cyclic voltammetry analysis. Cyclic voltammograms of Ir@Ni/C bimetallic synthesized by the core-shell method at scanning rates of 10mV/s and 25 mV/s, respectively, in the potential region of 0.0-1.1V are shown in the figure.

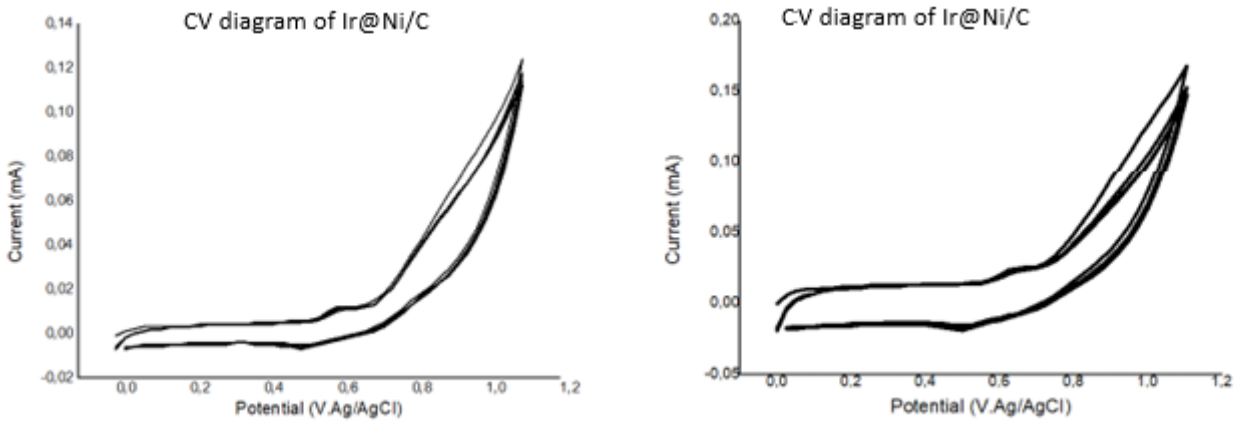


Fig 2-3. CV diagram of Ir@Ni/C catalyst at a sweep rate of 10-30 mV/s respectively, in the 0.0-1.1V potential region

The obtained CV was taken from a voltage peak of 0.4-0.6 from the voltammogram at a rate of 10 mV according to the scan/s scan. A voltammogram date to 25 mV/s scanning rate was observed as 0.6-0.8 potential. Other electrochemical and physical characterizations of IrNi/C catalyst will be presented at the congress.

REFERENCES

1. Y. Liu,Q. Chen,P. Sun,Y. Li,Z. Yang,T. Xu, 2021, Organic electrolytes for aqueous organic flow batteries, Materials Today Energy, 20, 100634
2. Luo X., Wang J., Dooner M., & Clarke J., 2015, Overview of current development in electrical energy storage technologies and the application potential in power system operation, Applied Energy, 137, 511-536
3. Zhao L., Liu Y., Han X., Ding Y., Kong W., Tong Y., Xu J., Xing W., 2021, Theoretical study of the alkaline hydrogen oxidation reaction on Ni-Based nanocluster Catalysts: Effects of graphene supports and dopants, Applied Surface Science, 567,150895

4. Jianhua Liao,Wei Ding,Sicheng Tao,Yao Nie,Wei Li,Guangping Wu,Siguo Chen,Li Li,Zidong Wei,2016, Carbon supported IrM (M = Fe, Ni, Co) alloy nanoparticles for the catalysis of hydrogen oxidation in acidic and alkaline medium, Chinese Journal of Catalysis, 7, 37, 1142-1148.
5. D.Liu,S.Liu et al 2019, One-pot synthesis of IrNi@Ir core-shell nanoparticles as highly active hydrogen oxidation reaction electrocatalyst in alkaline electrolyte, NANO ENERGY, 59, 26-32/10.1016/j.nanoen.2019.01.070
6. J. Liao, W. Ding, S. Tao, Y. Nie, W. Li, G. Wu, S. Chen, L. Li, Z. Weil, 2016 Carbon supported IrM (M = Fe, Ni, Co) alloy nanoparticles for the catalysis of hydrogen oxidation in acidic and alkaline medium, CHIENESE JOURNAL OF CATALYST, 37,1142 – 1148/10.1016/S1872-2067(15)61064-6
7. J. Ohyama, D. Kumada, A. Satsuma J. Mater. Chem. A, 2016, Improved hydrogen oxidation reaction under alkaline conditions by ruthenium–iridium alloyed nanoparticles, JOURNAL OF MATERİALS CHEMİSTRY A, 41,15980 – 15985/10.1039/C6TA05517F
8. H. Wang, HD Abruna, 2017, IrPdRu/C as H_2 Oxidation Catalysts for Alkaline Fuel Cells, JOURNAL OF THE AMERİCAN CHEMİCAL SOCİETY,139, 6807-6810/ 10.1021/jacs.7b02434
9. B. Qin, H. Yu, J. Jia, C. Jun, X. Gao, D. Yao, X. Sun, W. Song, B. Yi, Z. Shao, 2018A novel IrNi@PdIr/C core-shell electrocatalyst with enhanced activity and durability for the hydrogen oxidation reaction in alkaline anion exchange membrane fuel cell, NANOSCALE,10,4872-4881/ 10.1039/C7NR09452C
10. T.Maruyama,T.Odada et al. 2020, Vertically aligned growth of small-diameter single-walled carbon nanotubes by alcohol catalytic chemical vapor deposition with Ir catalyst,APPLİED SURFACE SCİENCE, 509,145340/ 10.1016/j.apsusc.2020.145340
11. Kotaro Sasaki, Kurian A. Kuttiyiel, Laura Barrio, et al “Carbon-Supported IrNi Core-Shell Nanoparticles: Synthesis, Characterization, and Catalytic Activity’’ The Journal of Physical Chemistry C, 115, 20, 9894-9902, 2011.

WHEC-2022
23rd World Hydrogen Energy Conference
June 26-30, 2022 - Istanbul

#1609

A NEW METHOD FOR MANUFACTURING ANODE SUPPORTED SOLID OXIDE FUEL CELLS WITH AFL

[1*] *Osman Yağız Akduman,* [2] *Mehmet Sinan Uyanık,* [1,3] *Elif Kabakcı,* [2] *Ali Murat Soydan*
[1] Gebze Technical University, Engineering Faculty, Department of Material Science and Engineering, Gebze, Kocaeli, Turkey
[2] Gebze Technical University, Institute of Energy Technologies, Gebze, Kocaeli, Turkey
[3] Canakkale 18 Mart University, Engineering Faculty, Department of Material Science and Engineering, Gebze, Kocaeli, Turkey

*Corresponding author e-mail: oakduman@gtu.edu.tr

ABSTRACT

In this study, a new method to manufacture anode supported SOFCs (solid oxide fuel cells) with AFL (anode functional layer) is proposed. To manufacture the anode supports, anode mixture with polyethylene glycol (PEG) is prepared and anode mixture is fed into a twin screw extruder and extruded in the shape of tubes. PEG in the anode tubes is selectively removed to by water debinding and sweat debinding methods and AFL layer is obtained with different microstructure and porosity. SEM (Scanning electron microscope) images of the manufactured SOFCs show AFL layers with the thickness of approximately 7 µm, which is akin to the values given in the literature. Electrolyte and cathode layers are added to the anode tubes using dip coating. Effects of AFL on performance of the manufactured cells are tested.

Keywords: Solid oxide fuel cells, Anode functional layer, Anode supported SOFCs

INTRODUCTION

There are problems regarding usage of the fossil fuels as the main energy source for power generation. The most important problems regarding fossil fuels are high environmental impact and the possibility of depletion of the said fuel sources. These problems make the usage of renewable energy and clean energy sources more appealing, ultimately causing development of systems and devices which uses renewable energy and clean energy sources. Solid oxide fuel cells (SOFCs) are one of the many promising systems which generates electricity with electrochemical processes at high efficiencies.

SOFCs are energy conversion devices, they can use a variety of fuels (hydrogen, natural gas etc.) to generate electricity with electrochemical processes. These systems have a plethora of advantages such as high efficiency, modularity, fuel flexibility, operation with low noise and without vibration, low emission of pollutants. Main drawbacks of SOFCs are high manufacturing costs, high unit cost of energy, long start-up times and high operating temperature [1,2]. The high operating temperature problem of the SOFCs can be solved by employing a thinner electrolyte in the SOFC, thus reducing the ohmic loss caused by the electrolyte. To employ a thinner electrolyte, anode supported designs have been investigated [3,4].

In anode supported SOFCs, thickness of the anode support must be sufficient to ensure the required the mechanical strength to the cell. Because of the increased thickness of the anode support, the concentration polarization resistances are also increased, which in turn limits the power density of the cell. In literature, it has been shown that employing an anode functional layer (AFL) between anode and the electrolyte of the cell overcomes this problem. AFL can be described as an anode layer with specially tailored microstructure [5,6].

Triple phase boundary (TPB) is the juncture of electrons, oxygen ions and gaseous species where the electrochemical reactions of the SOFC occur. AFLs increase the performance of the SOFC by enlarging the TPB thus lowering the activation polarization resistance of the anode, the enlargement of the TPB is achieved by the decreased porosity of the AFL. In addition to increase in performance, employing AFL causes matching thermal expansion coefficient between electrolyte and anode which in turn increases the stability of the SOFC [7–10]. The properties and performance effects of the AFL have been a topic of interest and thoroughly investigated. Chen et al. have manufactured an anode supported SOFC with AFL and concluded that the optimal thickness of the AFL is 7,6 µm. The reported a peak power density of 0,906 Wcm^{-2} at 700 °C [8].

Yamaguchi et al. have investigated the effect of AFL on performance at 650 °C. They constructed 3 anode supported cells, one without AFL and two with AFL. They reported a power density value of 0,18 Wcm^{-2} in the cell without AFL, 0,22 Wcm^{-2} and 0,27 Wcm^{-2} in the cells with 4 µm and 10 µm AFL thicknesses, respectively. They concluded that the increased thickness of the AFL increases the power density and decreases ohmic resistances. They also reported enhanced area specific resistance (ASR) which suggests an increase of the triple-phase boundaries (TPBs) at the electrolyte-anode interface [11].Suzuki et al. have investigated the effect of AFL on energy efficiency of a fuel cell. They reported an energy density increase from 0,27 Wcm^{-2} to 0,45 Wcm^{-2} and 0,35 Wcm^{-2} to 0,52 Wcm^{-2} at 650

°C and 700 °C respectively by employing AFL in the fuel cell. They also reported an increase in the energy efficiency [12]. Kagomiya et al. have prepared cells with AFL thicknesses varying from 5 μm to 100 μm by using tape casting method. They reported that the AFL thickness of 10 μm had the best electrochemical properties and the highest power density [13].

In literature, several methods for forming AFL have been investigated. Kong et al. developed AFL with sub-layers using dry pressing, Kim et al. used dip coating to NiO-YSZ particles, Reitz and Xiao used spray coating. Methods such as slurry spin coating, vacuum slip casting and tape casting are also used. In this study a new method to develop AFL in anode supported SOFCs is investigated [14–16].

MATERIALS AND METHODS

The pilot-scale SOFC manufacturing line in the Institute of Energy Technologies in Gebze Technical University was used in the production of anode supported tubular SOFC.

Materials

In the extrusion process, Nickel Oxide - 8YSZ composite powder (Fuel Cell Materials), Polymethylmethacrylate (PMMA, Alfa Aesar) powder and polyethylene (PE) powder with a low density (Petkim - Turkey) were used as anode pore former and binder, respectively. Additionally, PEG 400 (Alfa Aesar) was used as plasticizer.

Extrusion

The anode powder, binder and pore former were mixed in ethanol via a turbula mixer (TM-100, DMR – Turkey) for 4 hours. Nalgene jars were used as container and one third of the jar was filled with zirconia beads. After the mixing, the solvent was evaporated at 70°C under stirring. The dried powder was sieved and fed to a twin screw extruder (Rondol Technology, UK) to produce small granules. PEG 400 was continuously added during the extrusion of the anode mixture. The extrudate, which was in the form of filament, were granulated by a rotating cutter. Then, the granules were fed into a single screw extruder (Rondol Technology, UK) and extruded in the form of a tube. The extrusion system had 4 different temperature controllers in total; 3 zone with separate temperature control unit along the screw and barrel, and an external temperature controller unit was used for the extrusion die.

The extruded tubes were separated into two sets. Set 1 was subjected to additional water debinding before firing in a container at 30°C. Both ends of the tubes were sealed by Parafilm plugs from the inside of tube to protect the inner walls of the tubes from water. Water soluble PEG 400 is removed in this step to prevent the deformations during the thermal debinding by using water solubility of PEG 400. Set 2 was subjected to a waiting period at 25 °C in open atmosphere. The PEG was ejected from the green body by sweating mechanism. The weight loss of the samples was recorded before and after for both treatment methods.

The pre-sintering temperature was selected as 1000°C. The half of the pre-sintered tubes were sintered consequently at 1400°C to mimic the effect of electrolyte layer sintering. Sintering profiles were determined by TG analysis. The effects of temperature and debinding methods on the microstructure and mechanical properties of the pre-sintered and sintered anode supports were investigated using SEM (Philips XL30 SFEG) and a universal mechanical tester (Instron 5569). The porosity rates of the anode tubes were determined using the Archimedes method performed in an aqueous environment.

RESULTS

The investigation on the debinding types suggested that water debinding is more effective as the final mass change is higher than the sweat debinding.

The extrudates of Set 1 and Set 2 were investigated via TGA for determination of the sintering profiles. For both sets, the rates of the mass loss were low before ~215°C, then, accelerated until the burnout process was completed. The dwelling temperature was selected as 210°C to avoid cracking due to the fast burning of the polymeric content within the samples.

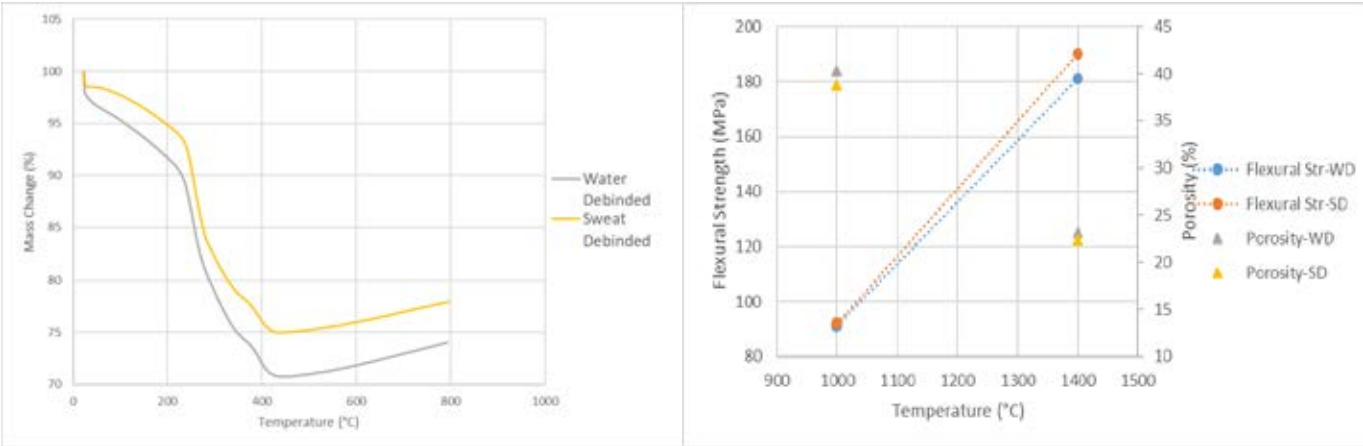


Fig 1. Results of TGA (a), and flexural strength-porosity measurements.

It was evident that the outer layer of both sample types had a different microstructure compared to the main body could act as anode functional layer (Fig 2). The AFL of Set 1 differed from Set 2 in terms of microstructure. The different debinding processes were resulted in different microstructures. A sponge like structures can be seen in Fig 1 for Set 1. Water debinding resulted in thicker AFL and lesser density was observed compared to the AFL of Set 2. On the other hand, the AFL of sweat debinded sample had needle like structures with higher density compared to the water debinded sample. The dissolution of the PEG was enhanced by the presence of the water; thus, the layer structure was preserved due to the absence of the contraction. Contrarily, the sweat debinding caused mechanical stress, the green density was thought to be increased even during the debinding phase. The density of measurements indicated that water debinding resulted in higher porosity (Fig 1b). The mechanical strength of the samples was almost inseparable (Fig 1b).

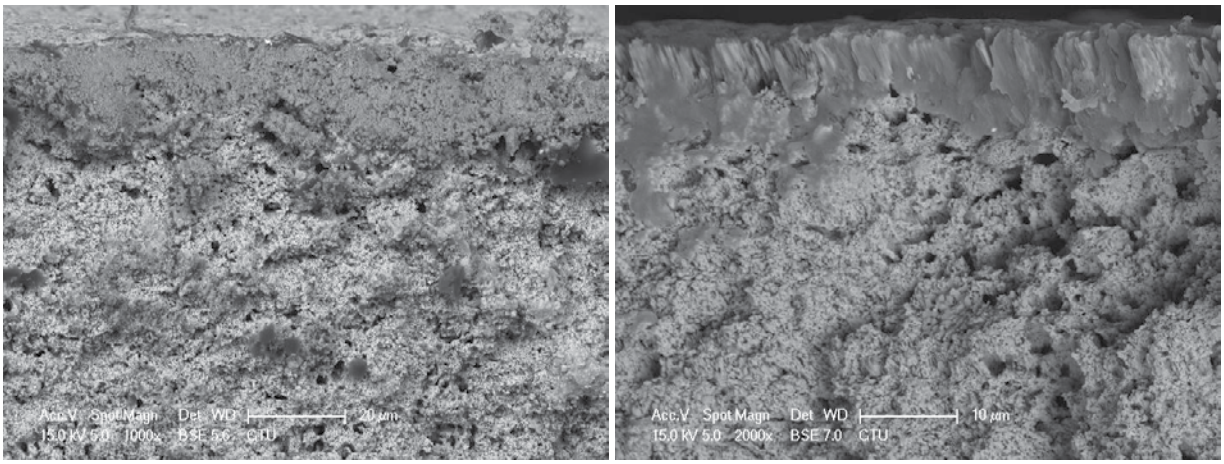


Fig 2. The micrographs of water debinded sample (a) and sweat debinded sample (b).

CONCLUSIONS

Two different debinding methods were used to obtain anode supports with two different microstructures. The mechanical properties of both types were similar. The water debinding resulted in deeper penetration compared to the sweat debinding method, hence, the thickness of the AFL was higher for the Water debinded anodes. The thickness of 7-8 micron AFL was attained by sweat debinding, which was in accordance with the optimum AFL thickness given in the literature. The AFL thickness for water debinding can be controlled by dwelling time and bath temperature. A more detailed study should be conducted to optimize the water debinding process. The cell performances of both types were comparable to the literature results for the given thicknesses.

REFERENCES

1. Badwal SPS, Foger K. Solid oxide electrolyte fuel cell review. Ceramics International 1996;22:257–65.
2. Singhal SC. Advances in solid oxide fuel cell technology. Solid State Ionics 2000;135:305–13.
3. Kim SD, Hyun SH, Moon J, Kim JH, Song RH. Fabrication and characterization of anode-supported electrolyte thin films for intermediate temperature solid oxide fuel cells. Journal of Power Sources 2005;139:67–72.
4. Brett DJL, Atkinson A, Brandon NP, Skinner SJ. Intermediate temperature solid oxide fuel cells. Chemical Society Reviews 2008;37:1568–78.
5. Chen K, Chen X, Lü Z, Ai N, Huang X, Su W. Performance of an anode-supported SOFC with anode functional layers. Electrochimica Acta 2008;53:7825–30.
6. Yang S, Chen T, Wang Y, Peng Z, Wang WG. Electrochemical analysis of an anode-supported SOFC. International Journal of Electrochemical Science 2013;8:2330–44.
7. Kong W, Zhang M, Han Z, Zhang Q. A theoretical model for the triple phase boundary of solid oxide fuel cell electrospun electrodes. Applied Sciences (Switzerland) 2019;9.
8. Chen X, Lin J, Sun L, Liu T, Wu J, Sheng Z, et al. Improvement of output performance of solid oxide fuel cell by optimizing the active anode functional layer. Electrochimica Acta 2019;298:112–20. https://doi.org/10.1016/j.electacta.2018.12.078.
9. Jeong HG, Kim D, Sharma B, Noh JH, Lee KT, Myung J ha. Surface decorated La0.43Ca0.37Ni0.06Ti0.94O3−d as an anode functional layer for solid oxide fuel cell applications. Korean Journal of Chemical Engineering 2020;37:1440–4.
10. Wang Z, Zhang N, Qiao J, Sun K, Xu P. Improved SOFC performance with continuously graded anode functional layer. Electrochemistry Communications 2009;11:1120–3.
11. Yamaguchi T, Sumi H, Hamamoto K, Suzuki T, Fujishiro Y, Carter JD, et al. Effect of nanostructured anode functional layer thickness on the solid-oxide fuel cell performance in the intermediate temperature. International Journal of Hydrogen Energy 2014;39:19731–6.
12. Suzuki T, Sugihara S, Yamaguchi T, Sumi H, Hamamoto K, Fujishiro Y. Effect of anode functional layer on energy efficiency of solid oxide fuel cells. Electrochemistry Communications 2011;13:959–62.
13. Kagomiya I, Kaneko S, Yagi Y, Kakimoto K ichi, Park K, Cho KH. Dependence of power density on anode functional layer thickness in anode-supported solid oxide fuel cells. Ionics (Kiel) 2017;23:427–33.
14. Kong J, Sun K, Zhou D, Zhang N, Mu J, Qiao J. Ni-YSZ gradient anodes for anode-supported SOFCs. Journal of Power Sources 2007;166:337–42.
15. Kim SD, Hyun SH, Moon J, Kim JH, Song RH. Fabrication and characterization of anode-supported electrolyte thin films for intermediate temperature solid oxide fuel cells. Journal of Power Sources 2005;139:67–72.
16. Reitz TL, Xiao H. Characterization of electrolyte-electrode interlayers in thin film solid oxide fuel cells. Journal of Power Sources 2006;161:437–43.

WHEC-2022
23rd World Hydrogen Energy Conference
June 26-30, 2022 - Istanbul

#1621

EXPERIMENTAL AND EXERGY ANALYSES OF INTERNAL REFORMING SOLID OXIDE FUEL CELL FED WITH REFORMATE GAS

[1,2*] *Anil Erdogan,* [2] *Federico Capotondo,* [2] *Anke Hagen,* [3] *C. Ozgur Colpan*
[1]The Graduate School of Natural and Applied Sciences, Dokuz Eylul University, Buca, Izmir, Turkey
[2]Department of Energy Conversion and Storage, Technical University of Denmark (DTU), DK-2800 Kgs., Lyngby, Denmark
[3]Faculty of Engineering, Department of Mechanical Engineering, Dokuz Eylul University, Buca, Izmir, Turkey

*Corresponding author e-mail: anilerdogan1992@hotmail.com

ABSTRACT

In this study, a thermodynamic and mathematical model for an internal reforming and anode-recirculated SOFC fed with reformate gas is developed. Experimental testing of SOFC fed with reformate gas is also performed in order to validate the model. A parametric analysis is conducted to study the effect of the SOFC operating temperature, current density, and steam-to-carbon ratio (S/C) on the the exergy destruction of the SOFC. In addition, XRD and EIS analyses results for SOFC obtained from the experimental studies are presented.

Keywords: Experimental test, Mathematical modeling, SOFC, Anode recirculation, Reformate gas

INTRODUCTION

Solid oxide fuel cell (SOFC) is a highly efficienct electrochemical system operating at high temperatures (typically between 600°C to 850°C). As shown in Fig. 1, SOFC consists of two electrodes separated by an electrolyte made of ceramic material. Oxygen fed from the cathode is reduced to oxygen ions thanks to the presence of free electrons coming from an external circuit. The oxygen ions can move between the electrodes through the electrolyte. At the anode side, reformed hydrogen combines with oxygen ions from the cathode generating water vapor and electrons. The movement of electrons through a load, connecting the anode and the cathode of the SOFC, generates electricity.

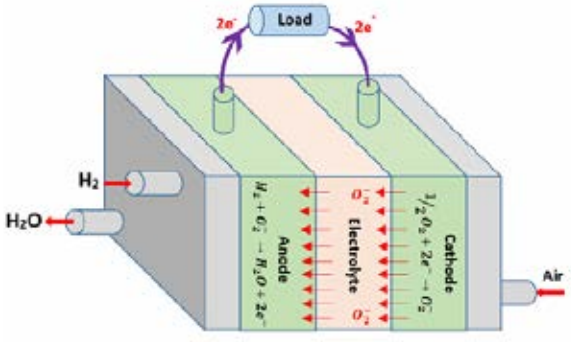


Fig. 1. The schematic of a SOFC

SOFCs have many advantages over other types of fuel cells [2–5]. These are (1) water management problems do not occur due to the operation at high temperature levels; (2) cheap materials and production methods can be used; (3) SOFCs can be thermally integrated with other systems (e.g. Rankine cycle, Brayton cycle, gas turbine, and biomass gasifiers) thus increasing the system efficiency from the thermodynamic point of view; (4) SOFCs have a wide range of fuel types such as hydrogen, hydrocarbons, methanol, biomass produced gas mixtures called syngas, and reformate gas mixtures; (5) carbon-containing fuels pass on chemical transformation inside the SOFC and are converted into hydrogen/CO, which are converted into electricity. Some challenges for the SOFCs are: (1) the mechanical robustness of ceramics that is limited and (2) in case of carbon-containing fuels, the anode can be deactivated by carbon deposition that might occur and also by impurities like sulfur. The main application of these fuel cells is combined power and heat generation. SOFCs are also used in other areas such as transportation, military, stationary, and portable applications [6,7].

EXPERIMENTAL TESTING OF SOLID OXIDE FUEL CELL

Experimental studies on SOFC were performed in the Electrochemistry Laboratory of the Technical University of Denmark (DTU), Department of Energy Conversion and Storage using state-of-the-art (SoA) SOFC. Detailed information and test protocol of SOFC are explained in Refs. [8,9]

MODELING OF SOLID OXIDE FUEL CELL

The diagram of SOFC used in the model is given in Fig. 2. In the analysis of the SOFC, firstly, electrochemical equations (Eqs. (1) and (2)) and the energy balance equation (Eq. (3)) enclosing the control volume of the SOFC are combined

to determine the inlet and exit streams of SOFC. Then, to determine the exergy destruction of the SOFC, the exergy balance (Eq.(4)) is applied to the control volume of the SOFC [10,11].

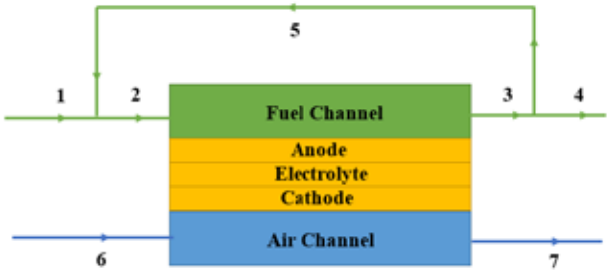


Fig. 2. The schematic of the SOFC used in the model

$$V_{cell} = V_{Nernst} - V_{ohm} - V_{act} - V_{conc} \quad (1)$$

$$\dot{W}_{SOFC} = i_{cell} \cdot A_{cell} \cdot V_{cell} \quad (2)$$

$$0 = -\dot{W}_{SOFC} + \left(\left(\dot{n}_1 \cdot \bar{h}_1\right) + \left(\dot{n}_6 \cdot \bar{h}_6\right)\right) - \left(\left(\dot{n}_4 \cdot \bar{h}_4\right) + \left(\dot{n}_7 \cdot \bar{h}_7\right)\right) \quad (3)$$

$$0 = -E\dot{x}_W + \left(\dot{n}_1 \cdot \left(\overline{ex}_{PH,1} + \overline{ex}_{CH,1}\right) + \dot{n}_6 \cdot \left(\overline{ex}_{PH,6} + \overline{ex}_{CH,6}\right)\right) - \left(\dot{n}_4 \cdot \left(\overline{ex}_{PH,4} + \overline{ex}_{CH,4}\right) + \dot{n}_7 \cdot \left(\overline{ex}_{PH,7} + \overline{ex}_{CH,7}\right)\right) - E\dot{x}_D \quad (4)$$

RESULTS AND DISCUSSION

Validation Results

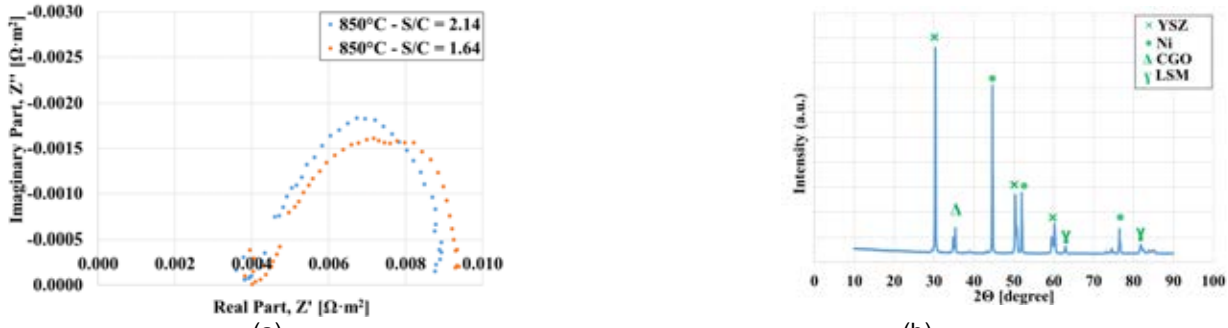
In this section, the results obtained from the study are discussed. The developed model is validated through experimental study. The validated results are given in Table 1. As can be seen in Table 1, the values obtained from the odelling study are agreeable with the experimental study.

Table 1. The comparison of cell voltage and power values between the experimental and the modelling studies

Current Density [A/cm²]	Voltage Experiments [V]	Voltage Model [V]	Power Experiments [W]	Power Model [W]
0	0.95	0.98	0	0
0.1	0.94	0.93	1.50	1.49
0.2	0.93	0.92	2.96	2.94
0.3	0.91	0.90	4.38	4.31
0.4	0.90	0.89	5.76	5.68

Experimental Study Results

The obtained electrochemical impedance spectroscopy (EIS) results as function of the S/C ratios and XRD results for cell testing in order to analyze the structure of crystalline materials, and its phases are presented in Figs. 3(a) and 3(b), respectively. As the S/C ratio increases, the polarization resistance, as well as the total cell resistance decreases.This happens because steam enhances the cathalityc activity on Nickel. It was found from the EIS that there is an important presence of Ni, and indeed the polarization resistance is affected by the steam/carbon ratio considerably.



(a) (b)

Fig. 3. Experimental study results (a) EIS according to the different S/Cs at 850°C, (b) XRD pattern for cell used in the experimental (compounds were labeled according to the Ref. [12])

Parametric Study Results

In this subsection, the parametric study results obtained from the model are presented. The effect of the current density on the exergy destruction rate according to the different S/C ratios is shown in Fig. 4(a). Increasing the S/C

ratio has a positive effect on the SOFC performance. It was obtained that under the same current density (e.g. 1.6 A/cm^2), the exergy destruction rate decreases by 19.71% when the S/C changes from 1.5 to 2.5. Fig. 4(b) shows the effect of current density on the exergy destruction rate of SOFC according to the different operating temperatures. When the operating temperature varies between 750°C to 850°C, the exergy destruction rate decreases for all current densities.

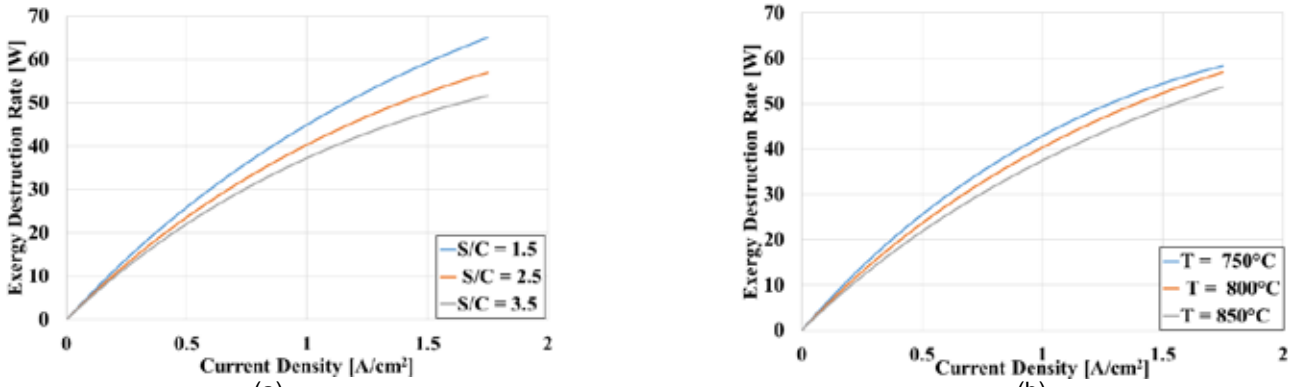


Fig. 4. The effect of current density on the exergy destruction rate according to the (a) different S/Cs, (b) different operating temperatures

CONCLUSIONS

In this study, an experimental test for SOFC is conducted in order to validate the model and assess the cell used in the study. Then an exergy analysis is conducted for SOFC to find the magnitude of the exergy destruction of the SOFC. The results derived from the study conducted are given as follows.

- According to the EIS study, increasing the S/C ratio decreases the total cell resistance.
- As the S/C ratio increases, the exergy destruction rate decreases.
- As the operating temperature increases, the exergy destruction rate decreases.

ACKNOWLEDGEMENT

The first author would like to thank the 2214-A program (Grant Number: 1059B142000598) of The Scientific and Technological Research Council of Turkey (TUBITAK) for providing financial support to his research at the Technical University of Denmark.

REFERENCES

1. Ormerod RM. Solid oxide fuel cells. Chem Soc Rev 2003;32:17–28. https://doi.org/10.1039/b105764m.
2. Ferrari ML, Damo UM, Turan A, Sánchez D. Hybrid Systems Based on Solid Oxide Fuel Cells. Chichester, UK: John Wiley & Sons, Ltd; 2017. https://doi.org/10.1002/9781119039044.
3. Colpan CO, Dincer I, Hamdullahpur F. A review on macro-level modeling of planar solid oxide fuel cells. Int J Energy Res 2008;32:336–55. https://doi.org/10.1002/er.1363.
4. Bove R, Ubertini S, editors. Modeling Solid Oxide Fuel Cells: Methods, Procedures and Techniques. Springer; 2008.
5. Huang K, Goodenough JB. Solid Oxide Fuel Cell Technology: Principles, Performance and Operations. CRC Press; 2009.
6. Braun RJ, Kazempoor P. Application of SOFCs in Combined Heat, Cooling and Power Systems. In: Zhao TS, Ni M, editors. Solid Oxide Fuel Cells From Mater. to Syst. Model., UK: 2013.
7. Singhal S. Solid oxide fuel cells for stationary, mobile, and military applications. Solid State Ionics 2002;152–153:405–10. https://doi.org/10.1016/S0167-2738(02)00349-1.
8. Hagen A, Langnickel H, Sun X. Operation of solid oxide fuel cells with alternative hydrogen carriers. Int J Hydrogen Energy 2019;44:18382–92. https://doi.org/10.1016/j.ijhydene.2019.05.065.
9. Christensen JO, Hagen A, Sudireddy BR. Performance of Metal Supported SOFCs Operated in Hydrocarbon Fuels and at Low (<650˚C) Temperatures. ECS Trans 2021;103:713–24. https://doi.org/10.1149/10301.0713ecst.
10. Colpan CO, Hamdullahpur F, Dincer I, Yoo Y. Effect of gasification agent on the performance of solid oxide fuel cell and biomass gasification systems. Int J Hydrogen Energy 2010;35:5001–9. https://doi.org/10.1016/j.ijhydene.2009.08.083.
11. Moran, M. J., Shapiro, H. N., Boettner, D. D., & Bailey MB. Fundamentals of Engineering Thermodynamics. USA: John Wiley & Sons, Ltd.; 2010.
12. Tong X, Hendriksen PV, Hauch A, Sun X, Chen M. An Up-scalable, Infiltration-Based Approach for Improving the Durability of Ni/YSZ Electrodes for Solid Oxide Cells. J Electrochem Soc 2020;167:024519. https://doi.org/10.1149/1945-7111/ab6f5c.

WHEC-2022

23rd World Hydrogen Energy Conference

TRACK 9. INTEGRATED HYDROGEN ENERGY SYSTEMS

TRACK 9. INTEGRATED HYDROGEN ENERGY SYSTEMS

#9 DEVELOPMENT OF INNOVATIVE HYDROGEN COMBUSTION SYSTEMS FOR INDUSTRIAL GAS TURBINES	893
#18 REACTOR EVALUATION FOR ALTERNATIVE FUEL SYNTHESIS OF METHANOL AND DIMETHYL ETHER (DME) FROM CO2 AND RENEWABLE HYDROGEN	896
#33 OPTIMAL TRACKING OF GRID OPERATED LOAD DEMAND WITH HYDROGEN BASED STORAGE SYSTEM USING MODEL BASED PREDICTIVE CONTROL	899
#37 COKE OVEN GAS AS POTENTIAL FUEL FOR STATIONARY SI ENGINES	902
#46 GREEN HYDROGEN PRODUCTION FROM GEOTHERMAL POWER PLANTS: KIZILDERE (DENIZLI-TURKEY) GEOTHERMAL POWER PLANT CASE STUDY	905
#47 THERMAL BALANCE IN FUEL CELL VEHICLES WITH LIQUID HYDROGEN UTILISATION	908
#64 OPTIMIZATION OF ENERGY MANAGEMENT STRATEGY FOR FUEL CELL-RANGE EXTENDED ELECTRIC VEHICLE	911
#69 DESIGN OF A NEW HYDROGEN DRIVEN INTEGRATED POWERING SYSTEM FOR FERRY APPLICATIONS	915
#89 THE ULTRA-EFFICIENT FC-ICE HYBRID CYCLE WITH THERMOCHEMICAL RECOVERY OF THE WASTE HEAT - FINITE-TIME AND FINITE-SPEED THERMODYNAMICS ANALYSIS	919
#92 THE ROLE OF HYDROGEN FOR THE DEFOSSILISATION OF THE GERMAN CHEMICAL INDUSTRY	922
#98 TSUKUBA GREEN HOLONISM TOWN (II)—EXAMINING A PRELIMINARY ENERGY DEMAND–SUPPLY OUTLOOK	925
#100 TSUKUBA GREEN HOLONISM TOWN (I)—BUILDING A CARBON-NEUTRAL COMMUNITY	928
#108 DESIGN AND OPTIMIZATION OF GREEN HYDROGEN-BASED HYBRID ENERGY SYSTEM	931
#121 OPTIMAL CONFIGURATION OF ENERGY STORAGE AND HYDROGEN PRODUCTION AT RENEWABLE ENERGY SITES IN A POWER SYSTEM WITHOUT FOSSIL FUELS IN JAPAN	934
#146 THE ROLE OF HYDROGEN FOR A GREENHOUSE GAS-NEUTRAL GERMANY BY 2045	937
#148 INTEGRATION OF A RENEWABLE METHANOL PRODUCTION PROCESS WITH A LOW CO_2 EMISSIONS CRGT POWER PLANT	940
#172 VERTICALLY INTEGRATED PROJECTS AS A TRANSFORMATIVE PEDAGOGY FOR GREEN HYDROGEN STUDY ABROAD PROGRAMS	944
#175 FUEL CELL-BATTERY HIBRIDIZATION FOR AN UNMANNED SURFACE VEHICLE POWERPLANT	947
#176 NUMERICAL INVESTIGATION OF THERMAL PERFORMANCE OF HYDROGEN -FUELLED MICRO-COMBUSTOR WITH TRAPEZOIDAL RIB	950
#179 PERFORMANCE ANALYSIS AND COMPARISON ON ENERGY STORAGE DEVICES IN HYDROGEN-BASED INTEGRATED ENERGY SYSTEMS	953
#186 ANALYSIS OF TRANSPORT OPTIONS FOR LIQUID HYDROGEN IN GERMANY	957
#201 NOVEL TEG HEAT EXCHANGER IN Cu-Cl CYCLE OF HYDROGEN PRODUCTION	960
#204 INTEGRATION OF PEM ELECTROLYZER AND FUEL CELL TO A SOLAR-GEOTHERMAL COMBINED SYSTEM FOR A ZERO-ENERGY BUILDING: AN EXERGYECONOMIC ANALYSIS	964
#210 EVALUATION OF HYDROGEN PRODUCTION PROCESSES FOR USE IN AUTOMOTIVE SECTOR	967
#212 THE ROLE OF RENEWABLE HYDROGEN-BASED SYSTEMS TO ACHIEVE LOW-CARBON STATIONARY POWER APPLICATIONS	972
#237 CONTROL STRATEGIES FOR THERMAL COUPLING SYSTEM OF FUEL CELL AND METAL HYDRIDE TANK: A REVIEW	975
#270 GREEN MILITARY SITE SUPPORTING PUBLIC HYDROGEN MOBILITY	978
#286 PREDICTION OF HYDROGEN COMBUSTION USING DATA-DRIVEN APPROACH	981
#289 PERFORMANCE ANALYSIS ON THE NOVEL PEMFC ASSISTED GROUND SOURCE HEAT PUMP SYSTEM	984
#293 IMPROVED REACTOR DESIGN FOR A METAL HYDRIDE REFRIGERATION SYSTEM IN HYDROGEN POWERTRAINS	987
#302 PILOT-SCALE HYBRID SYSTEM FOR CO_2/H_2 MIXTURE PRODUCTION – FIRST EXPERIENCES IN THE “TENNESSEE” PROJECT	990

#309 THERMODYNAMIC ANALYSIS OF AN INTEGRATED SYSTEM WITH SOLAR METHANE CRACKING AND CO-ELECTROLYSIS OF CO_2/H_2O FOR METHANOL AND ELECTRICITY PRODUCTION	993
#318 THERMODYNAMIC CONSIDERATIONS OF THE COX HYDROGENATION REACTION TO LIGHT OLEFINS USING CARBON-NEUTRAL FEEDSTOCK MIXTURES	996
#330 PROCESS SIMULATION AND ASSESSMENT OF AN INTEGRATED POWER SYSTEM COMBINING OLIVE KERNEL PYROLYSIS, GASIFICATION AND SOLID OXIDE FUEL CELL	999
#348 SYSTEM INTEGRATION AND VALIDATION OF HYDROGEN FUEL CELL NICHE VEHICLES AND RELATED REFUELLING INFRASTRUCTURE AT HySA SYSTEMS / SOUTH AFRICA	1002
#352 MODELING AND DESIGN OPTIMIZATION OF CARBON-FREE HYBRID ENERGY SYSTEMS WITH THERMAL AND HYDROGEN STORAGE	1005
#373 OFFSHORE WIND ENERGY PROSPECTS FOR POWER-TO-DIRECT AIR CAPTURE AND POWER-TO-GAS	1008
#379 EXERGY ANALYSIS OF REVERSIBLE SOFC COUPLED WITH ORGANIC RANKINE CYCLE AND HYDROGEN STORAGE FOR RENEWABLE ENERGY STORAGE	1011
#389 SCIENTIFIC AND TECHNOLOGICAL SYNERGIES CONNECTING ELECTROLYSERS, FUEL CELLS AND ELECTROCHEMICAL COMPRESSORS FOR HYDROGEN USE	1014
#398 PRELIMINARY ASSESSMENT OF THE GREEN HYDROGEN PRODUCTION POTENTIAL IN KAZAKHSTAN	1017
#401 OPTIMIZATION OF A STAND-ALONE PV SYSTEM FOR EFFICIENT HYDROGEN PRODUCTION USING AN ALKALINE WATER ELECTROLYZER	1020
#411 EFFECT OF THE ADDITION OF HYDROGEN-CONTAINING GAS ON INDICATED AND EFFECTIVE PARAMETERS OF A GASOLINE ENGINE	1023
#412 HYDROGEN AND OXYGEN (HHO) GAS INFLUENCE ON ENGINE CHARACTERISTICS WHILE FUELED ON PETROL ANT BIOETHANOL LEAN MIXTURES	1026
#428 EXPERIMENTAL STUDY ON SPRAY CHARACTERISTICS OF INTERNAL MIXED HYDROGEN-ASSISTED FUEL INJECTION SYSTEM	1029
#435 ANALYSIS OF AN INTEGRATED GAS TURBINE-LOCOMOTIVE ENGINE USING SUSTAINABLE FUEL BLENDS WITH HYDROGEN	1032
#1443 AN APPLICATION AND EVALUATION OF BLENDING BIOGAS AND HYDROGEN INTO THE NATURAL GAS FOR COMBUSTION APPLICATIONS	1035
#1456 COMPARATIVE ANALYSIS OF A MULTI-GENERATION SYSTEM USING DIFFERENT CONVENTIONAL AND NANO-BASED WORKING FLUIDS	1038
#1476 CO-GENERATION OF ELECTRICITY USING WASTE HEAT FROM HYDROGEN FUEL CELL IN A VEHICLE: A SIMULINK MODEL	1041
#1479 PERFORMANCE ASSESSMENT OF A CALCIUM-IRON BROMIDE CYCLE BASED MULTIGENERATION SYSTEM	1042
#1504 HYDROGEN POWERED VESSELS AT SEA: FUEL CELL & BATTERY UPSCALING	1044
#1522 THERMODYNAMIC ANALYSIS OF A NEW GEOTHERMAL ENERGY BASED INTEGRATED PLANT FOR COMPRESSED HYDROGEN PRODUCTION	1048
#1523 MODELING OF A SUSTAINABLE INTEGRATED PLANT wıth S-CO_2 and T-CO_2 CYCLES FOR HYDROGEN GENERATION	1052
#1550 ENERGY MANAGEMENT OF GREEN HYDROGEN-BASED POWER-TO-POWER GENERATION SYSTEMS	1056
#1553 HYDROGEN AND FRESHWATER PRODUCTION FROM TIDAL ENERGY	1059
#1555 DEEP LEARNING-BASED BINARY CLASSIFICATION OF ISLANDING CONDITIONS IN A HYDROGEN ENERGY-BASED DISTRIBUTED GENERATION SYSTEM	1063
#1556 THD MINIMIZATION OF VEHICLE-TO-GRID (V2G) IN FUEL CELL EVs WITH A DEVELOPED ELLIPTIC IIR FILTER	1066
#1568 PV-FUEL CELL HYBRID SYSTEM MODELING AND ANALYSIS	1069
#1587 EXPERIMENTAL STUDY ON HYDROGEN ENRICHED NATURAL GAS COMBUSTION IN INDUSTRIAL BURNER	1072

#1597 INVESTIGATION OF SIMULTANEOUS HYDROGEN PRODUCTION AND DESALINATION OF SALINE WATER VIA ELECTRODIALYSIS PROCESS	1075
#1604 MATHEMATICAL MODELING AND DYNAMIC SIMULATION OF A PV-BASED HYDROGEN GENERATION AND STORAGE SYSTEM	1078
#1606 A NEWLY DEVELOPED BRAYTON CYCLE-BASED COMBINED PLANT INCLUDING HYDROGEN PRODUCTION AND COMPRESSION: ENERGY AND EXERGY ANALYSES	1081
#1607 THERMODYNAMIC ANALYSIS OF A NEW COMPRESSED AIR ENERGY STORAGE-BASED COMBINED PLANT FOR MULTIGENERATION WITH HYDROGEN PRODUCTION	1084
#1608 A SYSTEM MODEL FOR SIMULATING A FUEL CELL RECREATIONAL BOAT	1087
#1610 MULTI-OBJECTIVE OPTIMIZATION OF AN INTEGRATED DOWNDRAFT BIOMASS GASIFIER AND SOLID OXIDE FUEL CELL SYSTEM	1091
#1618 A STUDY ON EXERGETIC SUSTAINABILITY INDICATORS OF SOLAR METHANE CRACKING	1095
#1620 SOLAR ASSISTED HYDROGEN PRODUCTION VIA PV/T ASSISTED SMALL SCALE TRANSCRITICAL POWER CYCLE WITH DIRECT STEAM GENERATION	1098
#1622 DEVELOPMENT AND PERFORMANCE ASSESSMENT OF INTEGRATED RENEWABLE ENERGY SYSTEM WITH HYDROGEN STORAGE FOR AUTONOMOUS AND MOBILE 3D PRINTING SYSTEM	1101
#1625 THERMODYNAMIC ASSESSMENT OF A NEW SMALL MODULAR REACTOR FOR HYDROGEN AND ELECTRICITY	1104
#1626 DESIGN OF A NEW HELICAL METHANE FIXED BED- REACTOR	1107

WHEC-2022
23rd World Hydrogen Energy Conference
June 26-30, 2022 - Istanbul

#9

DEVELOPMENT OF INNOVATIVE HYDROGEN COMBUSTION SYSTEMS FOR INDUSTRIAL GAS TURBINES

[1*] *Nurettin Tekin,* [2] *Atsushi Horikawa,* [3] *Mitsugu Ashikaga,* [4] *Harald Funke*
[1]Project Manager, Kawasaki Gas Turbine Europe, Nehringerstr. 15, 61352 Bad Homburg, Germany
[2] Researcher, Kawasaki Heavy Industries, LTD. Technical Institute Akashi, 673-8666 Japan
[3] Project Manager, Kawasaki Heavy Industries, LTD. Technical Institute Akashi, 673-8666 Japan
[4] Professor for Gas Turbines and Aircraft Engines, Aachen University of Applied Sciences, Hohenstaufenallee 6, 52064 Aachen

*Corresponding author e-mail: n.tekin@kge-gmbh.com

ABSTRACT

Combined with the use of renewable energy sources for its production, hydrogen represents a possible alternative gas turbine fuel within future low emission power generation.
Kawasaki Heavy Industries, LTD. (KHI) has research and development projects for future hydrogen societies; production of hydrogen gas, refinement and liquefaction for transportation and storage, and utilization with gas turbines / gas engines for the generation of electricity.
Due to the large difference in the physical properties of hydrogen compared to other fuels such as natural gas (NG), well established gas turbine combustion systems cannot be directly applied for Dry-Low-Emission (DLE) hydrogen combustion. Thus, the development of DLE hydrogen combustion technologies is an essential and challenging task for the future of hydrogen fueled gas turbines.
The DLE Micro-Mix combustion principle (MMX) for hydrogen fuel has been in development for many years to significantly reduce NOx emissions. This combustion principle is based on cross-flow mixing of air and gaseous hydrogen which reacts in multiple miniaturized flames. The major advantages of this combustion principle are the inherent safety against flashback (stable flame) and the low NOx-emissions due to a very short residence time of the reactants in the flame region of the micro-flames.

Keywords: Hydrogen gas turbine, Micro-mix combustion, Dry low mission (DLE), Carbon free

INTRODUCTION

Within the last decade the global demand for renewable energy has increased rapidly, which leads to new challenges for conventional power generation systems. For nuclear and coal power plants it will be very difficult to be part of the future power generation, especially in Europe. In case of overcoming the new challenges, the gas turbine technology has realistic chances to solidify and expand its role in future power generation. Thus, future gas turbines must offer more operational flexibilities, such as a higher number of starts, lower emissions at partial load, hot start capability, short start time, low maintenance and fuel flexibility to meet the requirements of the renewable energy market.

To enhance fuel flexibility, hydrogen has great potential as a renewable and sustainable energy source derived from wind or solar power and gasification of biomass and therefore substituting the limited resources of fossil fuels. It represents a possible alternative gas turbine fuel within future low emission and carbon free power generation. Due to the large differences in the physical properties of hydrogen compared to other fuels such as NG, the combustion of hydrogen gases is a very challenging task, especially for the DLE combustion. Nevertheless, KHI overcame these challenges and developed 3 different H2-combustion systems, which are illustrated in Fig.1.

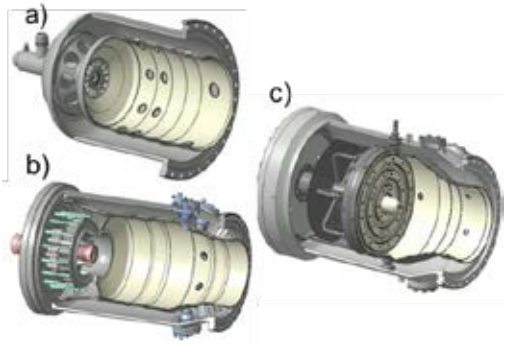


Fig. 1. Different hydrogen combustion systems: a) Diffusion flame-, b) Supplemental-, c) Micro-Mix-Combustor (MMX)

The diffusion flame combustor (Fig. 1a) can operate with 100% hydrogen and 100% natural gas and also with mixtures of both. Water injection is used to achieve low emissions. The first gas turbine with this diffusion flame combustor has been used in the project “Development of smart community technology by Utilization of Hydrogen CGS (Co-Generation System)”. This project is subsidized by NEDO (New Energy and Industrial Technology Development Organization). The successful commissioning took place on the 19th and 20th of April 2018 in a demonstration plant in Kobe. Fig. 2 shows the process control interface, during the 100% hydrogen fuel operation mode. The electrical power output is approx. 1.5MW. The amount of measured NOx emission during 100% hydrogen combustion is 50ppm (16%Vol.O2).

In total, three different fuel modes are available at the touch of a button, which leads to very high flexible operation. The first fuel mode “Natural Gas Only” is the conventional operation with natural gas. The second mode “Blend Gas” is the operation with mixture ratios of natural gas and hydrogen. The mixture ratio can vary from 1%-99% hydrogen. The third mode “H2 Gas Only” is the innovative pure hydrogen fuel mode, as visualized below.

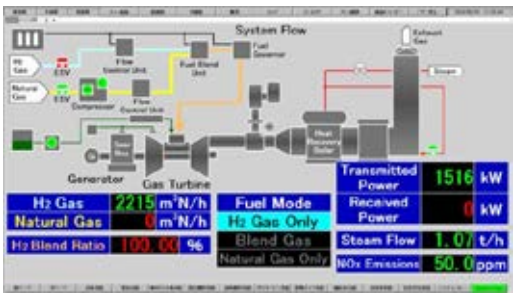


Fig. 2. Process controlling interface of Kobe plant

The second development in Figure 1b is the so-called M1A-17 DLH combustor. It based on a conventional DLE combustor with hydrogen injection over the supplemental burner up to 60Vol% hydrogen, which corresponds to 30% of the total thermal input. Basically, the DLE combustor of KHI has pilot, main and supplemental burners. And usually natural gas is supplied from the supplemental burners. Within this combustor, it can be switched from natural gas to hydrogen or natural gas and hydrogen mixing gas fuel via the supplemental burner. The NOx emission can be kept below the 25 ppm (O2-15%) guaranteed level. This combustor has also been tested successfully at Akashi Works.
Using hydrogen in conventional DLE combustors increase the NOx emission values as well as the risk of flashbacks. The established gas turbine combustion systems cannot be directly applied. Thus, the development of DLE-H2 combustion technologies is indispensable for pure hydrogen (100Vol%) combustion. Therefore, the innovative DLE-MMX combustion chamber (Fig. 1c) has been developed.

THE DLE-MMX COMBUSTION PRINCIPLE FOR HYDROGEN

Kawasaki Heavy Industries, Ltd. has developed in cooperation with the Aachen University of Applied Science and B&B-AGEMA, the DLE-MMX combustion principle for hydrogen fuel to significantly reduce NOx emissions [1]. This combustion principle is based on cross-flow mixing of air and gaseous hydrogen which reacts in multiple miniaturized “diffusion-type” flames with a usual size of 5-10mm in length. Within the development and optimization process the number of holes was reduced from 1600 flames to 410 flames with fuel injector diameters of 0.3-0.8mm. The multiple micro flames at the test burner are visualized in Fig. 3 (left). The H2-injection holes and the air guiding panels are also visible.

On the right side, the prototype of the combustion chamber and MMX burner with its three ring segments is shown. Each ring is supplied with hydrogen from the center and can be individually controlled depending on the power load. The major advantages of this combustion principle are the inherent safety against flashback and the low NOx-emissions due to a very short residence time of the reactants in the flame region of the micro-flames.

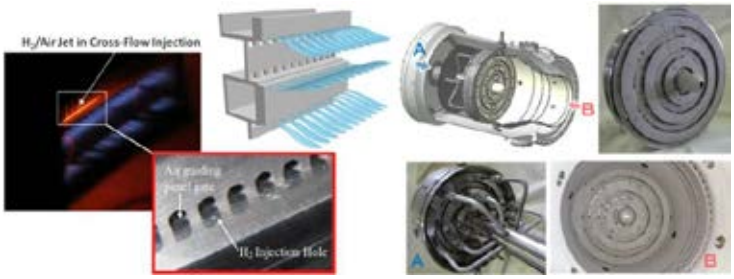


Fig. 3. H2-Micro-Mix test burner (left) and prototype (right) [2]

Fig. 4 shows the NOx emission and the total pressure loss ratio (TPLR) distribution for two different prototype combustors under operating pressure. From idle to 30% load, the inner hydrogen rings were used and from 30% load to full load, all rings were used. It can be seen, that low NOx values are also achievable at partial load. The NOx values are below the project target value of 35ppm over the whole load range only for 0.55MMX. The TPLR project target level is achieved for both configurations.

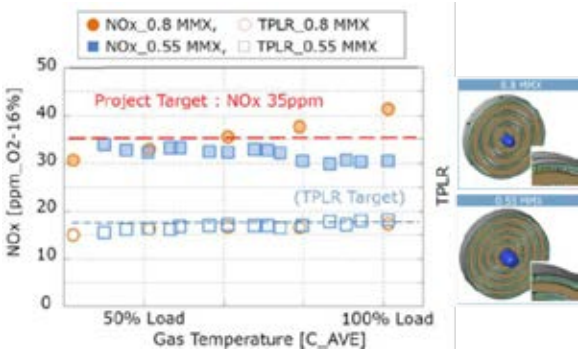


Fig. 4. NOx and TPLR distribution over load for prototype combustor under operation pressure [3]

Figure 5 shows an innovative future power plant with combined heat and power (CHP) and integrated renewable energy supply. The system consists of a H2/NG fueled gas turbine with integrated hydrogen production and storage. The surplus energy from the renewable sources such as wind and solar is used for hydrogen production via an electrolyzer. This is temporarily stored and can be used for generating power and heat via the hydrogen gas turbine anytime as needed, with low NOx emissions and zero carbons.

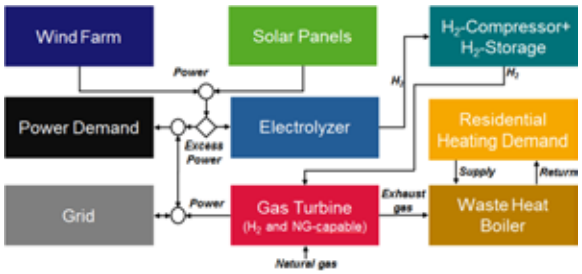


Fig. 5. Innovative CHP power plant with renewable energy supply

CONCLUSION

The commissioning of the world's first diffusion flame combustor with a 100% hydrogen fueled gas turbine has been carried out successfully in Kobe, Japan.
In addition, the hydrogen fueled DLE Micro-Mix Prototype combustor has been tested successfully under atmospheric and pressurized conditions and has proven its dry low NOx ability over a wide operating range. The Micro-Mix combustion principle leads to significantly reduced NOx emissions due to the miniaturized micro flames with inherent safety against flashback.
The MMX-Technology is a technological breakthrough for hydrogen combustion within gas turbines. It ensures, that gas turbines have realistic chances to solidify and expand their roles in future CHP generation. Thus, with this innovative and unique technology the gas turbine is ready for the upcoming energy transition.

REFERENCES

1. Funke, H. H.-W., Keinz, J., Börner, S., Kusterer, K., Haj Ayed, A., Tekin, N., Kazari, M., Kitajima, J., Horikawa, A., K. Okada, „Experimental and Numerical Characterization of the Dry Low NOx Micromix Hydrogen Combustion Principle at Increased Energy Density For Industrial Hydrogen Gas Turbine Applications“, ASME Turbo Expo 2013, GT2013-94771, San Antonio/Texas, USA, June 2013.
2. H. H.-W. Funke, J. Dickhoff, J. Keinz, A. Haj Ayed, A. Parente, P. Hendrick "Experimental and Numerical Study of the Micromix Combustion Principle Applied for Hydrogen and Hydrogen- Rich Syngas as Fuel with Increased Energy Density for Industrial Gas Turbine Applications", The 6th International Conference on Applied Energy – ICAE 2014-863.
3. Horikawa, A., Wirsum M., Funke H. H.-W., Kusterer K., „Application of Low NOx Micro-Mix hydrogen combustion for industrial gas turbine and DLN combustor developments for 2MW class gas turbine". WHTC 2019, Tokyo

WHEC-2022
23rd World Hydrogen Energy Conference
June 26-30, 2022 - Istanbul

#18

REACTOR EVALUATION FOR ALTERNATIVE FUEL SYNTHESIS OF METHANOL AND DIMETHYL ETHER (DME) FROM CO_2 AND RENEWABLE HYDROGEN

Stefan Weiske[1], Nils Beltermann[1], Rafael Becka[1], Remzi Can Samsun[1], Ralf Peters[1], Detlef Stolten[2,3]*
[1]Forschungszentrum Jülich GmbH, Electrochemical Process Engineering (IEK-14), 52425 Jülich, Germany
[2] RWTH Aachen, Chair for Fuel Cells, 52072 Aachen, Germany
[3]Forschungszentrum Jülich GmbH, Techno-economic Systems Analysis (IEK-3), 52425 Jülich, Germany

*Corresponding author e-mail: s.weiske@fz-juelich.de

ABSTRACT

In this contribution different reactor types are evaluated in the context of the synthesis of alternative fuels like methanol and dimethyl ether (DME) from carbon dioxide and renewable hydrogen produced via water electrolysis. The evaluation is based on a theoretical approach, which combines computational fluid dynamics (CFD) simulations of the synthesis reactors with ANSYS Fluent® and process analyses with ASPEN PLUS®. Multiple optimization strategies were applied to the synthesis reactors to increase the productivity. A membrane reactor setup could show a maximal increase of 181 % in space time yield for the direct synthesis of DME form CO_2. By this result the significance of tailor-made reactors and processes for fuel synthesis from CO_2 and renewable hydrogen are highlighted.

Keywords: Power-to-fuel, Hydrogenation, Methanol, Dimethyl ether (DME), Reactor engineering

INTRODUCTION

To counter the effects of anthropogenic climate change and in line with the process of energy transition and the climate protection goals of the German government, higher amounts of renewable energy generation capacities are installed and more renewable energy is introduced into Germany's energy supply grid [1]. To reach the defined climate protection goals, it is necessary not only to change the ways of power generation, but also the supplying infrastructure. Especially in the transport sector it is hard to reach the goals for the emission of greenhouse gases and pollutants, since in the last decade there have been no or only slight reductions [2, 3]. One promising approach to connect the renewable energy generation and the transport sector is the concept of power-to-fuel [4]. According to this concept chemical energy carriers are synthesized from hydrogen and carbon dioxide. In this approach, the power, industry and transport sectors are connected via sector coupling and thereby the emissions of greenhouse gases and pollutants are reduced significantly [6]. Hydrogen is produced by water electrolysis and carbon dioxide can be supplied from carbon capture from industrial sources (multiple use of carbon dioxide) or the ambient air (full carbon recycling). The described reference frame shows a fully sustainable supply chain for the production of synthetic fuels and therefore a defossilization of the transport sector [7]. In terms of alternative electro fuels chemicals like alcohols, ethers and advanced synthetic fuels e.g. $OME_{3\text{-}5}$ [8], synthetic diesel or kerosene (MtG/ MtK/ MtD-processes) are promising [9, 10]. The aim of this work is to analyse the production pathways of methanol and DME among other possibilities with the focus on the reactor development.

MATERIALS AND METHODS

The two fuel alternatives mentioned above are evaluated regarding their technical feasibility and energy efficiency using process simulation with Aspen Plus®. The process models of these production processes are based on the determination of the chemical equilibrium for the given boundary conditions. The reactors are therefore modeled as Gibbs-reactors, which determine the chemical equilibrium by minimizing the Gibbs energy. The boundary conditions of these reactors can be extracted from the process simulations and be used in the CFD-simulations of the reactors (with ANSYS Fluent®). This approach supports the design of innovative reactors for methanol and DME synthesis. Since the aim is to produce bulk materials like fuels, these reactors need to be scaled to industrial sizes within great production capacities.

The modeling approach for the CFD simulations is based on a pseudo-homogeneous modeling of the fixed bed catalyst zone. In these regions kinetic models can be applied to describe the reaction rates in detail. Various kinetic models have been published for both methanol and DME synthesis. The most suitable models are selected on the basis of consistency and best agreement with literature. An important aspect in the modeling process is the integration of mass transport limitations, which are not included in the kinetic models. The limitations of mass transport come from the diffusive flux through the diffusive boundary layer and within the catalyst particle. The internal and external catalyst effectiveness factors are derived from physics to model these limitations. According to Lommerts et al. [11] the modified Thiele-modulus is used to calculate the internal catalyst effectiveness. The external catalyst effectiveness factor refers to the usage of the second Damköhler number [12]. All these different aspects (kinetics, mass transport) have to be integrated into the CFD simulations by self-developed user-defined-functions (UDF).

RESULTS AND DISCUSSION

The simulation results are divided into the different pathways and modeling approaches that have been presented in the methods part. The very first step is to determine the overall potential of the production processes based on the process analysis. This evaluation includes the carbon dioxide-based production of methanol and DME synthesis. Methanol and DME show high efficiencies (52-59 %) and therefore offer a very effective way to store hydrogen-based renewable energy. Thus, a more detailed look into the mechanism of syntheses should be done by CFD simulations. Since methanol synthesis is the basis for DME synthesis, this process is investigated first. Kinetic models from Graaf [13], Bussche and Froment [14] as well as Seidel et al. [15] are tested. The model of Graaf [13] is selected to be the base model. In case of methanol synthesis, a broad study of various reactor types determines the reactor types with the greatest potential. In this simulation study, reactors that are classified as quasi-adiabatic (e.g. quench reactors (QR)) and quasi-isothermal (e.g. Lurgi-type reactor (LR) and Mitsubishi Superconverter (MSC)) are included. In addition, an innovative membrane reactor (MR) is designed on the basis of MSC and LR. With the help of simulations the previously described modeling approach was validated using data from an industrial scale reactor [16]. Finally, the quasi-isothermal reactor types show far more potential for the application in hydrogenation of carbon dioxide. The study of methanol synthesis can be seen as a starting point of the analysis of DME synthesis. There are two different ways to synthesize DME. The first one is called indirect synthesis where methanol is used as an educt. The second one is called the direct synthesis and it starts with hydrogen and carbon dioxide. Both production pathways need to be included and compared in this analysis.

For the indirect synthesis of DME different models or parameter settings have been extracted from literature and tested against experimental data. Most relevant models are updated parameter sets for low temperature DME synthesis [17-20] of the original kinetic model by Bercic [21]. These modified parameters lead to an increased conversion in a lowered temperature regime in comparison to the original model by Bercic [21]. In conclusion to that, these adapted parameter sets lead to a far better agreement with the experimental data and thus the adapted version is chosen for the further study. Parameter studies on weight hourly space velocities (WHSV), temperatures, pressures and catalyst properties show the effects of the mentioned parameters on the DME synthesis. Boundary conditions like inlet temperature (260 °C), wall temperature (300 °C) and WHSV (1-5 1/h) are results from this study that can be transferred to the direct synthesis. A first look at the results is shown on the left side of Figure 1.

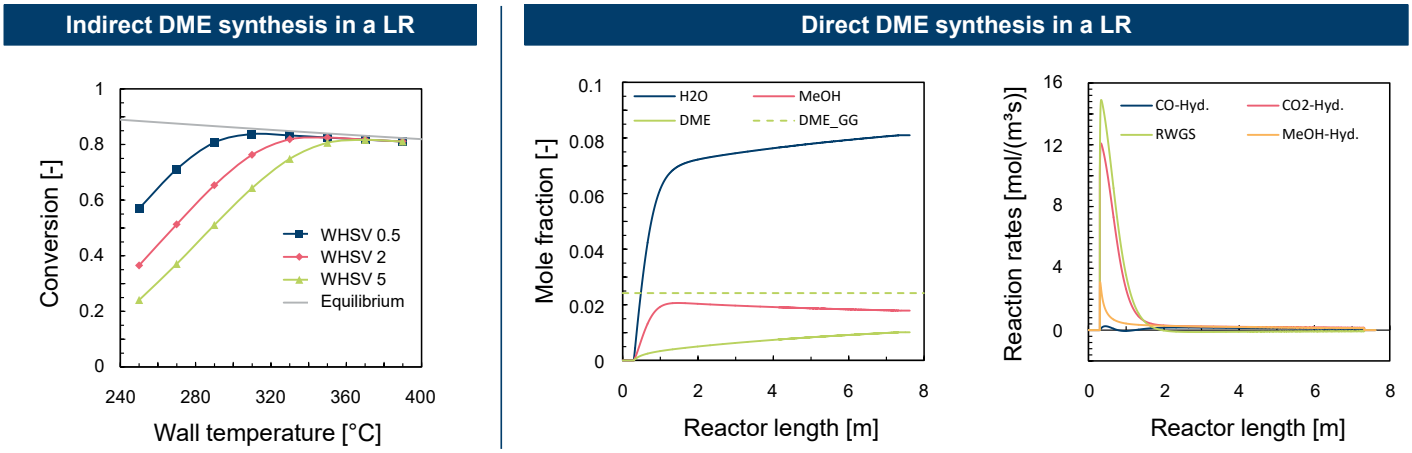


Fig. 1. Simulation results of direct DME synthesis in a lurgi-type reactor (LR)

Most of the simulations of the direct synthesis of DME are carried out by the Lurgi-type reactor model. Exemplary results are presented in the middle and on the right side of Figure 1. As a first result it can be seen that the DME synthesis is much more affected by product inhibition due to the formation of water in comparison to the CO_2-based methanol synthesis. This mechanism is pointed out by the rapidly decreasing reaction rates on the right side of Figure 1. After just 2 m within the reactor the reaction rates drop to nearly 0 mol/(m³s). Process simulations are carried out and used to determine the equilibrium conversion for the given boundary conditions. These equilibrium conversions (marked DME_GG) in the middle of Figure 1 indicate the limitations of the direct synthesis. From this starting point, the analysis of the direct synthesis of DME has to show the optimization potential by various methods. This includes operating conditions like wall temperatures/ cooling, pressures and feed compositions as well as spacial distributions of the two active catalyst sites. These analyses show that a tight temperature control of the reactor is crucial for an effective synthesis of DME. Furthermore, an increased CO ratio of the feed gas improves the reaction conditions significantly.

Nevertheless, in order to overcome the observed limitations for the CO_2-based DME synthesis, innovative technologies have to be applied. For that reason, a CFD-simulation model of a membrane reactor was implemented. The membrane reactor offers an in-situ water removal. The in-situ water removal is a counter technique to the product inhibition and enables better kinetics and higher performances of the synthesis reactor. The performance of the membrane regarding mass transport is the key element within this theoretical study and is also analyzed by a detailed parameter variation. All the mentioned studies will be discussed in detail in the oral presentation.

CONCLUSIONS

As it can be seen from the simulation results the overall crucial aspect of hydrogenation of carbon dioxide is the depletion of product water. The effect of in-situ water removal by a semi-permeable membrane is shown for both, methanol and DME synthesis and will be highlighted in the oral presentation as well as an enhancements by increased CO feed ratio. As a result, the membrane reactor concept enables far higher conversion rates than the conventional fixed bed reactors. In case of methanol synthesis this potential is limited by reduced space-velocities. In contrast to this, the direct DME synthesis from CO_2 is far more challenged by product inhibition and the membrane reactor concept increases the conversion and the space time yield as well. Nevertheless, the direct synthesis of DME shows in addition to the pointed-out challenges in the synthesis further challenges in terms of product separation and overall process design. The resulting conclusion from process and reactor analysis is to optimize the 2-step process or develop completely new direct synthesis route for example via reactive distillation.

ACKNOWLEDGEMENT

Parts of this publication are products of the ERA-ACT project ALIGN CCUS. The ALIGN CCUS Project is funded by RVO (NL), FZJ/PtJ (DE), Gassnova (NO), UEFISCDI (RO), BEIS (UK) and the European Commission. The ALIGN CCUS project is part of the Horizon 2020 program.

REFERENCES

1. German Environment Agency (UBA), *Zweiter Fortschrittsbericht zur Energiewende - Die Energie der Zukunft*. 2019.
2. German Environment Agency (UBA), *Zahlen und Fakten Energiedaten - Nationale und Internationale Entwicklung*. 2019.
3. German Environment Agency (UBA), *Nationale Trendtabellen für die deutsche Berichterstattung atmosphärischer Emissionen*. EU-Submission:15/01/2020. 2020, Dessau.
4. Schemme, S., et al., *Power-to-fuel as a key to sustainable transport systems - An analysis of diesel fuels produced from CO2 and renewable electricity.* Fuel, 2017. **205**: p. 198-221.
6. Buttler, A. and H. Spliethoff, *Current status of water electrolysis for energy storage, grid balancing and sector coupling via power-to-gas and power-to-liquids: A review.* Renewable & Sustainable Energy Reviews, 2018. **82**: p. 2440-2454.
7. Kramer, U., et al., *Defossilisierung des Transportsektors – Optionen und Voraussetzungen in Deutschland.* 2018.
8. Held, M., et al., *On the energetic efficiency of producing polyoxymethylene dimethyl ethers from CO2 using electrical energy.* Energy & Environmental Science, 2019.
9. Keil, F.J., *Methanol-to-hydrocarbons: process technology.* Microporous and Mesoporous Materials, 1999. **29**(1): p. 49-66.
10. Yang, M., et al., *Recent Progress in Methanol-to-Olefins (MTO) Catalysts.* Advanced Materials, 2019.
11. Lommerts, B.J., G.H. Graaf, and A.A.C.M. Beenackers, *Mathematical modeling of internal mass transport limitations in methanol synthesis.* Chemical Engineering Science, 2000. **55**(23): p. 5589-5598.
12. Cussler, E.L., *Fundamentals of Mass Transfer*, in *Diffusion: Mass Transfer in Fluid Systems*, E.L. Cussler, Editor. 2009, Cambridge University Press: Cambridge. p. 237-273.
13. Graaf, G., *The Synthesis of methanol in Gas-Solid and Gas-Slurry Reactors - PhD Thesis, 1988*. 2015.
14. VandenBussche, K.M. and G.F. Froment, *A steady-state kinetic model for methanol synthesis and the water gas shift reaction on a commercial Cu/ZnO/Al2O3 catalyst.* Journal of Catalysis, 1996. **161**(1): p. 1-10.
15. Seidel, C., et al., *Kinetic modeling of methanol synthesis from renewable resources.* Chemical Engineering Science, 2018. **175**: p. 130-138.
16. Samimi, F., M.R. Rahimpour, and A. Shariati, *Development of an Efficient Methanol Production Process for Direct CO2 Hydrogenation over a Cu/ZnO/Al2O3 Catalyst.* Catalysts, 2017. **7**(11).
17. Ng, K.L., D. Chadwick, and B.A. Toseland, *Kinetics and modelling of dimethyl ether synthesis from synthesis gas.* Chemical Engineering Science, 1999. **54**(15): p. 3587-3592.
18. Farsi, M., A. Jahanmiri, and R. Eslamloueyan, *Modeling and Optimization of MeOH to DME in Isothermal Fixed-bed Reactor.* International Journal of Chemical Reactor Engineering, 2010. **8**.
19. Lee, S.B., et al., *Simulation of fixed bed reactor for dimethyl ether synthesis.* Korean Journal of Chemical Engineering, 2006. **23**(4): p. 522-530.
20. Song, D., et al., *Numerical analysis of a pilot-scale fixed-bed reactor for dimethyl ether (DME) synthesis.* Industrial & Engineering Chemistry Research, 2008. **47**(13): p. 4553-4559.
21. Bercic, G. and J. Levec, *Catalytic Dehydration of Methanol to Dimethyl Ether - Kinetic Investigation and Reactor Simulation.* Industrial & Engineering Chemistry Research, 1993. **32**(11): p. 2478-2484.

WHEC-2022
23rd World Hydrogen Energy Conference
June 26-30, 2022 - Istanbul

#33

OPTIMAL TRACKING OF GRID OPERATED LOAD DEMAND WITH HYDROGEN BASED STORAGE SYSTEM USING MODEL BASED PREDICTIVE CONTROL

[1] Muhammad Bakr Abdelghany, [1]Muhammad Sheshzad, [1]Valerio Mariani, [2]Davide Liuzza, [1]Luigi Glielmo*
[1] Affiliation (University of Sannio, Department of Engineering), Piazza Roma, 82100, Benevento, Italy
[2] Affiliation (ENEA Fusion and Nuclear Safety Department, Via Enrico Fermi 45, 00044 Frascati (Rome), Italy

*Corresponding author e-mail: bmuhammad@unisannio.it

ABSTRACT

It has become imperative for the power and energy engineers to look out for the renewable energy sources such as sun, wind, geothermal, ocean and biomass as sustainable, cost-effective and environment friendly alternatives for conventional sources. However, since they are inherently unreliable, during the last decades the scientific community addressed research efforts to their integration with the main grid by means of properly designed energy storage systems (ESSs). However, due to the complexity of the involved systems in terms of number of inputs, number of outputs, number of decision variables, constraints and costs this topic is still open. In particular, advanced control strategies for the management of ESSs in order to take into account all the reported aspects need to be designed.
In this paper we present a model predictive controller (MPC) which operates a hydrogen-based ESS (HESS) within a wind farm fence. The controller is derived in order to minimize the operating and economical costs of the HESS and the difference between the available power and that required by the grid operator through a suitable reference, while satisfying physical constraints and considering the dynamics of the system. In order to capture both continuous/discrete dynamics and transitions among different operating modes, the plant is modelled as a mixed logic dynamic system. The study has been developed within the EU-FCH 2 JU funded project HAEOLUS aiming at building and integrating advanced control strategies for a ESS within a wind farm. Numerical simulations show the feasibility and the effectiveness of the proposed approach.

Keywords: Hydrogen-based energy storage systems, Energy management, Model predictive control.

INTRODUCTION

Nowadays, renewable energy resources are subject to considerable attention as being in principle possible replacement of fossil fuel. In this regard, wind and solar resources are commonly considered the most promising options. Many studies have been carried out to improve the technologies aiming at easing their exploitation in real scenarios and to overcome their limitations.

With regard to the wind, energy production and consumption mismatches due to its inherent stochastic nature and possibly high capital and operational costs, are the main hurdles for its utilization at large scales [1]. Further, the use of specific and advanced technological solutions, such as electrolysers and fuel cells, increases the complexity of actual plants which then require well-designed management strategies. For this reason, control algorithms for energy management systems (EMSs) are addressed in relevant works, e.g., in Valverde et al. [2] a supervisory MPC for a HESS with optimal power market management is implemented.

According to the authors' knowledge, relevant aspects of HESSs with electrolyser, tank and fuel cell peculiarities, such as degradations, operating modes transitions and stand-by consumptions, have not been modelled in the literature. Our paper develops preliminary operational models with constraints for a HESS to be integrated in a wind farm fence under the EU-FCH 2 JU funded project HAEOLUS-Hydrogen-Aeolic Energy with Optimized eLectrolysers Upstream of Substation [3].

Specifically, the plant is modelled considering mixed logic constraints and switching dynamics. Depreciation costs when switching among on, off and stand-by operating modes are also taken into account. Then, a controller whose goal is to track and meet a reference demand with the available system power in the most economical and effective way is derived.

SYSTEM DESCRIPTION AND MODELING

The electrolyser and the fuel cell can be operated in 3 different physical modes, namely the on, the off and the stand-by mode. Specifically, as shown in Fig. 1, each machine can be modeled as an automaton of 5 states: ON, OFF and STB correspond to the on, the off and the stand-by modes, respectively, while CLD and WRM are added in order to account for cold and warm starts when switching among the three different modes.

DISCRETE OPERATIONAL STATES OF THE ELECTROLYZER AND THE FUEL CELL

The discrete operational states of the devices are presented in this section. As shown in Fig. 1, each node represents a particular state and the edges represent transitions among them. The states and the edges are linked to

corresponding mutually exclusive binary variables $\delta_i^{\alpha}(k)$ and $\sigma_{\alpha,i}^{\beta}(k)$, respectively, with $\alpha, \beta \in$ {OFF, CLD, STB, WRM, ON} and $i \in \{e, f\}$, that are used in order to translate the models of the electrolyser and the fuel cell into mixed logic constraints to be included into an optimization based controller. The overall system assumes the so-called form of a mixed logic dynamical (MLD) system.

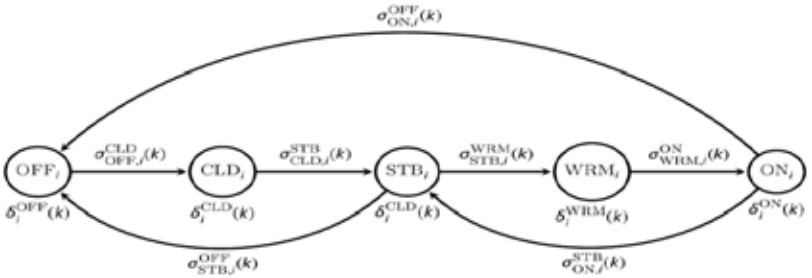


Fig. 1 Automaton of the electrolyser (i=e) and the fuel cell (i=f).

Mathematical Model and Constraints Formulation of the States

The states OFF,CLD,STB,WRM and ON of each automaton are characterized by the product of one logical variable and one power, which is relevant for that state, to be different from zero. For instance, whenever the electrolyser is in the ON state, the corresponding input power is limited within the range $[P_e^{min}, P_e^{max}]$. Thus, by defining $P_e(k)\delta_e^{\mathrm{ON}}(k) = P_e^{\mathrm{in}}$ and since in this case we set $\delta_e^{ON} = 1$ it results $P_e(k) = P_e^{\mathrm{in}} \in [P_e^{min}, P_e^{max}]$. On the other hand, whenever the electrolyser is in the STB state, the relevant power to be considered is the stand-by power P_e^{STB}. Therefore, by defining $P_e(k)\delta_e^{\mathrm{STB}}(k) = P_e^{\mathrm{STB}}$ it follows that $P_e(k) = P_e^{STB}$ and, accordingly, $\delta_e^{\mathrm{STB}}(k) = 1$, while all other logical variables δ_e^{α}, $\alpha \neq$ STB are again null. Similar considerations apply in case of WRM and CLD states. Finally, when the electrolyser is in OFF state, its corresponding input power along with the power consumption are null, resulting in $P_e(k) = 0$.

Mathematical Model and MLD Constraints Formulation of the State Transitions

In principle, each automaton depicted in Fig. 1 enables the referred device to 20 possible transitions. However, only those reported concur to the corresponding operational costs, while the others are unfeasible for either practical or technological considerations and will be constrained to zero in the proposed controller. The state transitions can be defined in terms of logical states and logic connectives as

$$\sigma_{\alpha_i}^{\beta}(k) = \delta_i^{\alpha}(k-1) \wedge \delta_i^{\beta}(k), \tag{1}$$

with $\sigma_{\alpha_i}^{\beta} \in [0,1]$, $\alpha, \beta \in$ {OFF,CLD,STB,WRM,ON} and $\alpha \neq \beta$. Then, based on the formulation in [4], (1) is recast into inequalities that are included as constraints into the proposed MPC.

State Space Model of the Hydrogen Storage Dynamics

Hydrogen dynamics are given in terms of the hydrogen level $H(k)$ in the tank, the efficiencies of the electrolyser and of the fuel cell η_e and η_f, their respective power in the on state P_e and P_f, and the corresponding logic variables δ_e^{ON} and δ_f^{ON}. The resulting formula is

$$H(k+1) = H(k) + \eta_e P_{\mathrm{e}}(k)\delta_e^{ON}(k)\, T_s - P_{\mathrm{f}}(k)\delta_f^{ON}(k)T_s/\eta_f, \tag{2}$$

where $\boldsymbol{T_s}$ is the sampling period.

Power Balance Equation

The power balance

$$P_w(k) - P_{\mathrm{e}}(k)\delta_e^{ON}(k) + P_{\mathrm{f}}(k)\delta_f^{ON}(k) - P_{\mathrm{avl}}(k) - P_{\mathrm{dump}}(k) = 0, \tag{3}$$

achieved through operating the HESS, is included as constraint into the proposed MPC algorithm. Eq. (2) highlights that the available power P_{avl} depends on the power P_w achieved through wind generation, the balancing action of the HESS and the dumping load.

RESULTS

Simulations have been carried out for a horizon of 24 hours. We wish to emphasize that the main contribution of this paper relies in the derivation of the preliminary operating models useful for running the hydrogen-based storage plant according to the project Haeolus [3].

In our numerical examples, the wind power production and the reference power demand are such that both surplus and deficit powers are considered, with a power flow towards or from the storage.

Fig. 2(a) and 2(b) show the power by wind generation P_w and the reference P_{ref} provided by the grid operator, respectively. It can be seen that the difference between the wind power and the reference demand is positive for the first 5 hours, so that the reference demand is met through the wind power only and the surplus power is shunted to

the electrolyser for hydrogen production. Accordingly, changes to the current level of hydrogen occurs, while the physical constraints regarding the storage are fulfilled, as depicted in Fig. 2(f). Fig. 2(e) shows the fuel cell power. It can be clearly observed that during the daily hours the available power P_{avl} is less than the reference demand P_{ref} and the fuel cell provides power to the grid through re-electrification (hours 9, 10, 14, 17 and 21).

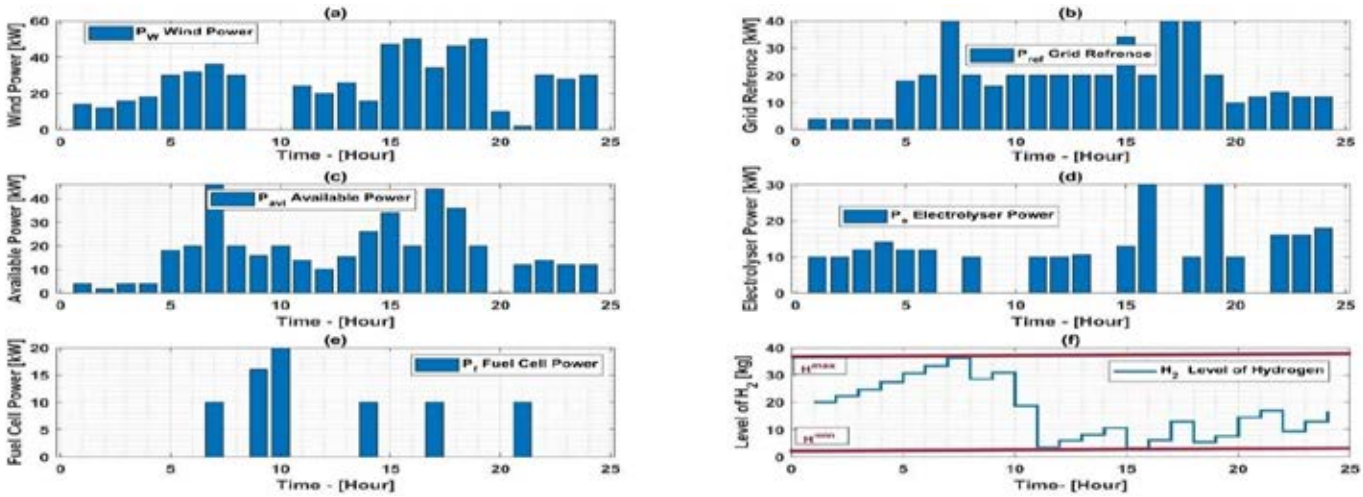


Fig. 2. Numerical results: (a) Forecasted wind power. (b) Grid operator reference. (c) Available power. (d) Electrolyser power. (e) Fuel cell power. (f) Hydrogen level.

CONCLUSION

In this work we developed models for operating, with optimal control strategies, an ESS to be coupled to a wind farm. The models of both the electrolyser and the fuel cell encode discrete logical states representing the devices operating modes while the continuous dynamics refer to the hydrogen level in the tank.

The proposed MPC scheme considers the cost that the electrolyser and the fuel cell introduce each time they switch between different operating modes, thus decreasing the corresponding number of life cycles and efficiencies. Furthermore, all other physical constraints and costs, such as the power consumption in stand-by, cold and warm starts, are considered, among the others.

The costs related to the operations of each device and the developed mixed logic dynamic models have been included in an MPC scheme. Simulations have been carried out by tracking a reference power provided by the grid operator, over an optimization horizon of 24 hours. Numerical results show the correct behaviour of the devices and their commutations among the different operating modes. The power is correctly stored or injected via hydrogen conversion to help the wind production in determining the total available power complying with the operator requirements.

ACKNOWLEDGEMENT

This work received founding from the Fuel Cells and Hydrogen 2 Joint Undertaking under the project HAEOLUS, grant agreement No. 779469.

REFERENCE

1. J. O. G. Tande, "Exploitation of wind-energy resources in proximity to weak electric grids," *Applied Energy,* vol. 65, pp. 395--401, 2000.
2. L. Valverde, C. Bordons and F. Rosa, "Power management using model predictive control in a hydrogen-based microgrid," in *IECON 38 Conference on Industrial Electronics Society*, 2012.
3. "Hydrogen-Aeolic Energy with Optimized eLectrolysers Upstream of Substatio Project," [Online]. Available: http://www.haeolus.eu/.
4. A. Bemporad and M. Morari, "Control of systems integrating logic, dynamics, and constraints," *Automatica,* vol. 35, no. 3, pp. 407--427, 1999.

WHEC-2022
23rd World Hydrogen Energy Conference
June 26-30, 2022 - Istanbul

#37

COKE OVEN GAS AS POTENTIAL FUEL FOR STATIONARY SI ENGINES

*Rafael Ortiz-Imedio, * Alfredo Ortiz, Daniel Gorri, Inmaculada Ortiz*
Chemical and Biomolecular Engineering Department, University of Cantabria, Av. Los Castros 46, 39005, Santander, Spain

*Corresponding author e-mail: ortizal@unican.es

ABSTRACT

Internal combustion engines (ICE) can be fuelled with hydrogen rich waste streams coming from industry providing good performance and low emissions. Coke oven gas (COG), a by-product of coke manufacture, has a high volumetric percentage of H_2 and CH_4 and can be used as auxiliary support for electric generation. Computational fluid dynamics (CFD) simulation tool has been used to assess the combustion and performance of COG compared to pure H_2 and pure CH_4. Simulations were validated with experiments in a Volkswagen Polo 1.4 L port-fuel injection spark ignition (SI) engine varying engine speed from 2000 to 5000 rpm at wide open throttle (WOT), optimum spark advance for maximum brake torque (MBT) and air-fuel ratios (λ) between 1 and 2. Comparison is made through power, heat release, pressure and temperature combustion variables. Results show that COG combines benefits of both pure fuels, widening the operation range, with good performance and low wall heat transfer at intermediate λ values. Furthermore, the energy content of an industrial waste stream can be harnessed for the industrial plants where is produced.

Keywords: Coke oven gas, Hydrogen, Internal combustion engine, Computational fluid dynamics (CFD), Methane

INTRODUCTION

Facing climate change, alternative cleaner fuels in ICE are being studied, predominating H_2 and CH_4 [1]. As each of these fuels has different advantages, they can be used complementary in mixtures with interesting properties. However, industrial waste streams with high percentages of H_2 are also very attractive, as they can provide good performance and low emissions, harnessing the energy content and being converted into electricity for auxiliary support to industries. Clean COG, a by-product of coke manufacture with the typical composition shown in Table 1, is sometimes flared in periods of low energy consumption within the coke plant [2]. Some studies with this gas have been carried out in SI engines [3–5]; however, a comprehensive analysis of the combustion of COG compared with its main components (H_2 and CH_4) in a SI engine through CFD at a wide range of engine speeds (2000 – 5000 rpm), different λ values (1 to 2) at WOT and MBT lacks in the literature and is carried out in this work. Combustion is assessed with power, heat release, pressure and temperature variables to understand deeper the behavior and advantages of this waste stream.

Table 1. Composition of synthetic COG in percentage by volume and by weight used in this study.

Composition	H_2	CH_4	CO	N_2	CO_2
vol%	57	30	6	5	2
wt%	11.6	48.5	16.9	14.1	8.9

MODELLING

A CFD model of a symmetrical single cylinder (Fig. 1) from a Volkswagen Polo naturally aspirated port-fuel 1.4 L SI engine converted to work with gases [6] has been developed with Ansys® Forte® to study the combustion of COG, pure H_2 and pure CH_4.

Simulations were conducted at the same operating conditions as a previous work [5], varying the engine speed between 2000 and 5000 rpm, λ between 1 and 2 and optimum spark timing to obtain MBT. The detailed Gri-Mech 3.0 mechanism was selected to compare the three fuels. Gaseous fuels were injected with a time-varying velocity profile, assuming the fuel density at 3 bar and mass flow rates according to the fuel (0.6 g/s for H_2, 1.4 g/s for COG and 2 g/s for CH_4). A mechanical efficiency correlation was applied, decreasing linearly with the engine speed: 90% at 2000 rpm and 75% at 5000 rpm.

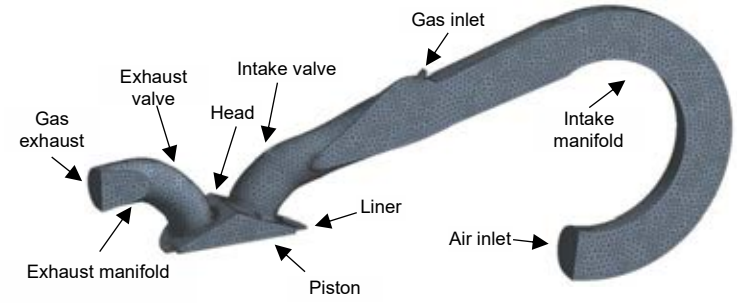


Fig. 1. 3D symmetric mesh of the CFD model of a single cylinder from the engine.

RESULTS AND DISCUSSION

In Fig. 2, the experimental and simulated brake power values of COG, CH_4 and H_2 are graphed at different λ values and in the entire speed range, confirming a good agreement. In addition, Fig. 3 shows the chemical heat release (CHR) and wall heat transfer (WHT), both in J, at the same operating conditions. As the mixture becomes richer (lower λ), the power increases due to higher CHR, though higher WHT is also produced. At λ values of 1 and 2, similar performance is achieved with COG compared to CH_4 and H_2, respectively, widening the operation range. However, at λ=1.5, COG delivers similar CHR than CH_4 and H_2, but produces the lowest LHV values (Fig. 3b), increasing the resulting brake power. The main reason is the reduction of the maximum in-cylinder temperature (Fig. 4b) because COG has a higher flame growth speed than CH_4, delaying the spark timing. At 5000 rpm, COG releases 40.1% of WHT less than CH_4 and 14.3% of WHT less than H_2. At higher engine speed, higher power is achieved because the total amount of mass dragged into the cylinder increases.

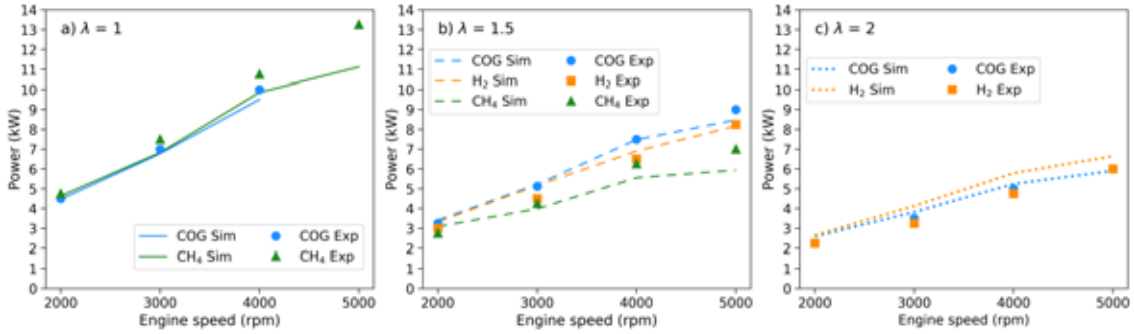


Fig. 2. Experimental (discrete values) and simulated (lines) brake power (kW) of COG, CH_4 and H_2 vs engine speed at a) λ=1, b) λ=1.5 and c) λ=2.

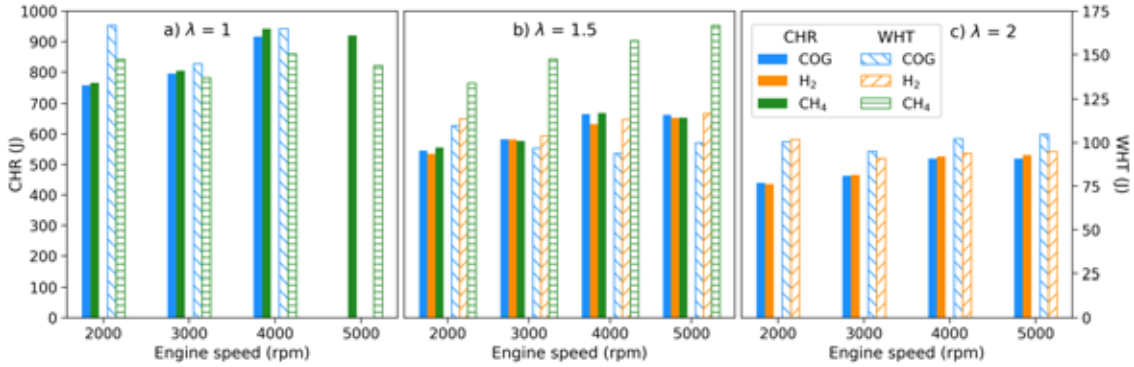


Fig. 3. CHR (solid bars) and WHT (dashed bars) of COG, CH_4 and H_2 vs engine speed at a) λ=1, b) λ=1.5 and c) λ=2.

Fig. 4 shows the evolution of the average in-cylinder pressure, temperature and the apparent heat release rate (AHRR, in J/CAD) graphed at 3000 rpm and different λ values for COG, H_2 and CH_4. Leaner mixtures reduce the maximum values due to lower CHR. Higher H_2 contribution in fuel reduces the combustion duration increasing the slope of pressure and temperature curves. CH_4, with the highest spark advance, increases the maximum values of pressure and temperature. H_2 has the highest AHRR values due to high flame speed, increasing the temperature and the WHT. Suitable pressure peak but lower temperature maximum values of COG reduce WHT but increase brake power.

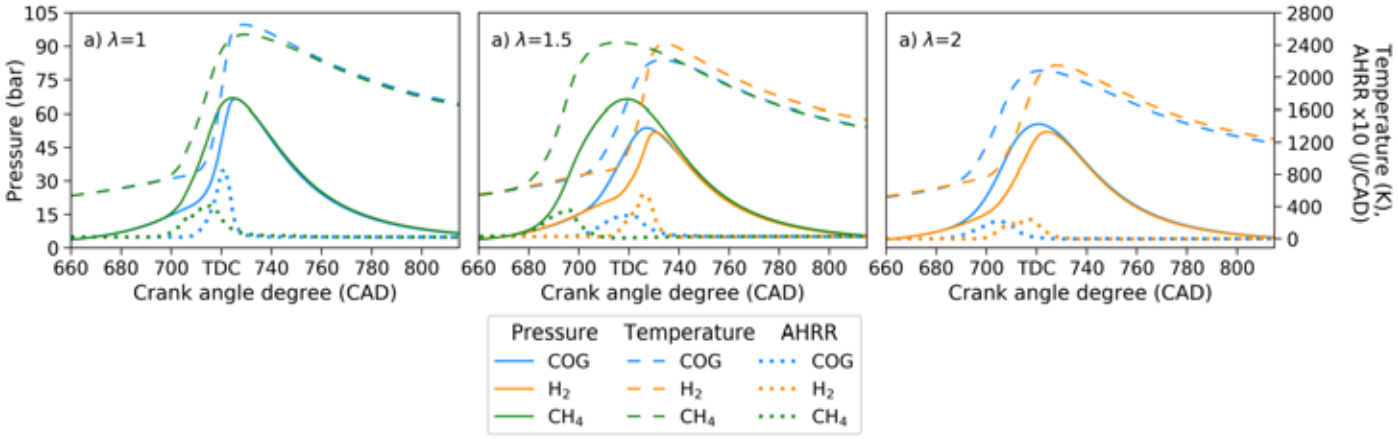


Fig. 4. Pressure (bar), temperature (K) and AHRR (J/CAD) of COG, CH_4 and H_2 inside the cylinder at 3000 rpm and at a) λ=1, b) λ=1.5 and c) λ=2.

CONCLUSIONS

A CFD model of a port-fuel 1.4L SI engine at WOT, MBT, engine speeds between 2000 and 5000 rpm and λ values between 1 and 2 has been developed. A comparison of COG, pure H_2 and pure CH_4 gaseous fuels with combustion variables was carried out, analyzing the performance.

- Leaner mixtures reduce the pressure, temperature, CHR and WHT values inside the cylinder.
- COG delivers the highest power at λ=1.5 due to high pressure and intermediate spark advance, decreasing WHT.
- CH_4 requires high spark advance due to lower flame speed, increasing the peaks of pressure and temperature and maintaining high values for a longer time, raising the WHT and NO emissions.

COG combines advantages of pure H_2 and pure CH_4, increasing the operation range, with higher power performance and lower emissions, becoming an interesting fuel for ICE in industry plants coupled to generator systems as auxiliary support for electricity production.

ACKNOWLEDGMENT

This research is being supported by the Projects “SUDOE ENERGY PUSH SOE3/P3/EO865” and “HYLANTIC”-EAPA_204/2016 and, which are co-financed by the European Regional Development Fund in the framework of the Interreg Sudoe and Atlantic programs. Rafael Ortiz-Imedio thanks the Concepción Arenal postgraduate research grant from the University of Cantabria and the Santander Supercomputación support group who provided access to the supercomputer Altamira Supercomputer at the Institute of Physics of Cantabria (IFCA-CSIC).

REFERENCES

1. Yan F, Xu L, Wang Y. Application of hydrogen enriched natural gas in spark ignition IC engines: from fundamental fuel properties to engine performances and emissions. Renew Sustain Energy Rev 2018;82:1457–88. doi:10.1016/j.rser.2017.05.227.
2. Ball M, Wietschel M. The Hydrogen Economy. Opportunities and Challenges. New York: Cambridge University Press; 2009.
3. Feng H, Zhang W, Zhang J, Wang X, Zhang X. Availability analysis of a coke oven gas fueled spark ignition engine. Int J Hydrogen Energy 2018;43:1835–45. doi:10.1016/j.ijhydene.2017.11.125.
4. Szwaja S. Hydrogen rich gases combustion in the IC engine. J KONES Powertrain Transp 2009;16:447–54.
5. Ortiz-Imedio R, Ortiz A, Urroz JC, Diéguez PM, Gorri D, Gandía LM, et al. Comparative performance of coke oven gas, hydrogen and methane in a spark ignition engine. Int J Hydrogen Energy 2021;46:17572–86. doi:10.1016/j.ijhydene.2019.12.165.
6. Sopena C, Diéguez PM, Sáinz D, Urroz JC, Guelbenzu E, Gandía LM. Conversion of a commercial spark ignition engine to run on hydrogen: Performance comparison using hydrogen and gasoline. Int J Hydrogen Energy 2010;35:1420–9. doi:10.1016/j.ijhydene.2009.11.090.

WHEC-2022
23rd World Hydrogen Energy Conference
June 26-30, 2022 - Istanbul

#46

GREEN HYDROGEN PRODUCTION FROM GEOTHERMAL POWER PLANTS: KIZILDERE (DENIZLI-TURKEY) GEOTHERMAL POWER PLANT CASE STUDY

[1] Raziye Şengün[1,2] Füsun S. Tut Haklıdır[2]
[1]Zorlu Energy Company, Sarayköy Denizli-Turkey
[2] İstanbul Bilgi University, Santral Campus Istanbul-Turkey

*Corresponding author e-mail: raziye.sengun@zorlu.com

ABSTRACT

The widespread use of especially solar, wind, geothermal and biomass investments for electricity generation coincides with the Paris Climate Agreement and the European Green Deal Act decarbonization targets and is supported by the whole world now. Green hydrogen can produce from renewable energy sources; it has been attracting attention recently because it is more environmentally friendly and in line with decarbonization targets. Geothermal power plants have the highest capacity factor among renewable energy plants, and they are systems that can produce electricity all day long without interruption.

In this study, a perspective towards green hydrogen production from geothermal power plants is discussed with the Kızıldere geothermal power plant (GPP) in Denizli, Turkey. This concept study is proposed for hydrogen production by Proton Exchange Membrane (PEM) type fuel cell at multi-flash geothermal power plants.

Keywords: Green hydrogen, hydrogen production, PEM, geothermal energy, Kızıldere GPP

INTRODUCTION

Geothermal energy is a substantial indigenous energy resource on the earth, which is believed to originate in geo-nuclear activity. Geothermal fluids consist of three phases such as brine, steam, and non-condensable gases like CO_2, H_2S, CH_4, H_2 and trace gases at liquid-dominated systems. The chemical composition of geothermal fluids changes with heat source, fluid rock interaction and reservoir temperature. Electricity generation is dependent on the geothermal reservoir temperature and if temperatures higher than >150°C it is used for flash and combined cycle, while it is lower than 150°C is suitable for binary cycle. The Western Anatolia is rich in medium-high geothermal sources for electricity production and there are large graben systems which have good geothermal energy potential such as Büyük Menderes Graben, Gediz Graben and Simav Graben [1]. In addition to required energy for H_2 production, which is not found alone in nature, from renewable energy sources [2, 3], it is possible to produce H_2 from H_2S by different methods such as thermochemical, photo-catalytic, biological and membrane technologies in geothermal systems. Especially, steam-reforming process is one of the important options to produce H_2 and the reaction of H_2S with CH_4 can be thought of as sulphur analogue of steam-methane reforming process. The process is represented by the overall reaction above will produce carbon disulphide and it can be used to produce sulfuric acid (and carbon tetrachloride H_2S-methane reformation is more suitable for utility type of operation with large-scale production rates [4]. H_2 production is from H_2S can be converted into electricity generation with proton exchange membrane (PEM) type fuel cell, which is integrated with the PEM electrolyser, and will be in storable purity and the end member sulphur can also be used for the industrial purposes.

There are more than 60 numbers of geothermal power plants in Aydin, Denizli, Manisa cities at the Western Anatolia (Turkey). 98.5-99 % of the non-condensable gases emitted from the geothermal power plants are CO_2. Due to the structure of the geological formation in Aydin city, these gases of organic origin, enriched by the paleo-sea effect, pH of the reservoir and hydrocarbon effects [1] and it attracts the attention of local people and researchers due to the obvious smell and toxic effects of H_2S. Due to its toxic effect, H_2S may cause negative environmental effects besides CO_2 and to solve this problem, H_2S (20.4 kJ/mol), which requires a lower decomposition enthalpy than water (286 kJ/mol) and methane (75 kJ/mol), can be used for H_2 production by consuming less energy or using electro-chemical energy. Non-condensable gas production at the values given in Table 1 for the Western Anatolia that shows there is a potential that can contribute to the hydrogen economy in the region in future.

The second option is to use only geothermal energy to produce hydrogen. PEM electrolyzers can generate hydrogen (and optionally oxygen) at pressures up to 200 bar, with very little additional power consumption, which may be attractive for the application where hydrogen needs to be stored or used at elevated pressure. PEM type electrolyzers produce hydrogen with very high purity (up to 99.999), which may be used in a fuel cell (Fig.1).

Table 1 The amount of non-condensable gas production in Aydın and Denizli provinces geothermal power plants (Gas amounts are calculated from [1])

Location	CO2 (kg)	H2S (kg)	CH4 (kg)	N2 (kg)
Kızıldere (Denizli)	25	0.0105	0.06	0.15
Salavatlı (Aydın)	9.8	0.0112	0.025	0.091
Germencik (Aydın)	14	0.0315	0.105	0.066

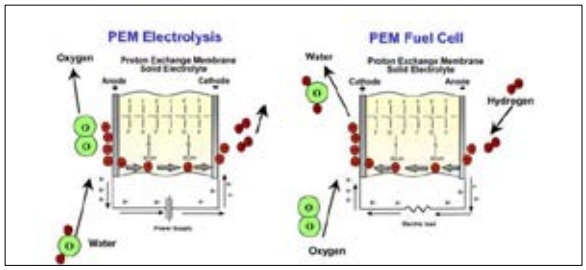


Fig.1 The working principles of PEM electrolysis and PEM fuel cell [5]

THE CASE STUDY

Kızıldere (Denizli) geothermal field was the first discovered high temperature system in the Western Anatolia (Turkey). The first power plant was established as single flash cycle in 1984 and the capacity expeanding studies continued between 2008-2018 years and the total installed geothermal power is reached to 260 MWe with a one single, three flash and combined three binary organic Rankine cycles in the field [6].

In this study, it is assumed that one of the triple flash geothermal power units in the field can be used for hydrogen production. The proposed design for hydrogen production from the flash cycle GPP is given in Fig.2. Since there is no vacuum process in the flash system, the utilizable energy is re-injected back to the ground. In the system, the temperature is reduced to the extent of mineral saturations allow, mostly amorphous silica saturation is used for energy extraction limits. In proposed case, geothermal water, which is re-injected to the ground at 109 ^{0}C, can be reduced to 80 ^{0}C with the help of a heat exchanger and ORC integrated into the main geothermal power plant and extra energy can be produced. The required energy for the hydrogen production will be provided from the additional geothermal power unit. This provides 1.3 MWe for roughly 1000 tph geothermal fluid. While it is sufficient to use resources such as low pH condensed steam, electricity, and heat from geothermal fluid to produce H_2 in the electrolyzer, chemical or biological integrated methods may be required to produce H_2 from H_2S.

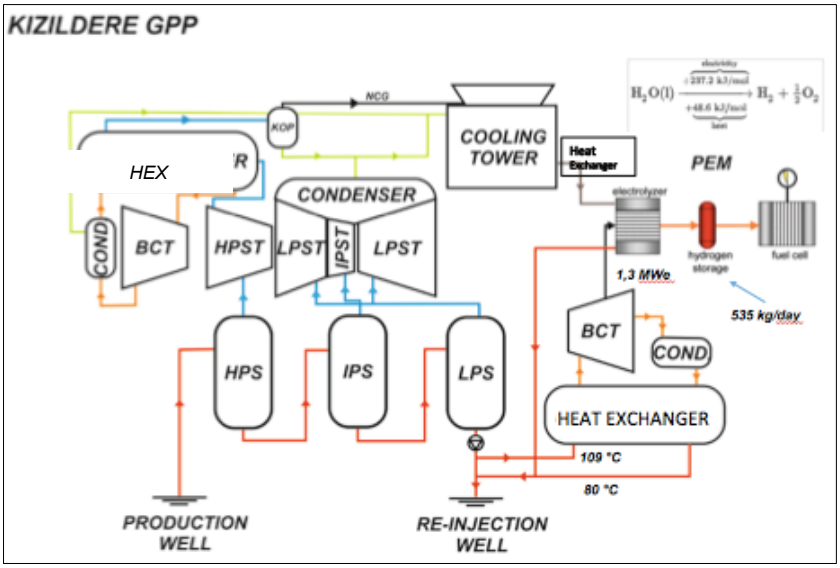


Fig. 2 Hydrogen production by PEM at Kızıldere triple flash geothermal power plant (HPST: High pressure steam turbine, LPST: Low pressure steam turbine, IPST:Intermediate pressure steam turbine, Cond: Condenser, HPS: High pressure seperator, IPS: Intermediate pressure seperator, LPS: Low pressure separator, HEX: Heat exchanger, NCG: Non-condensible gas, BCT: Binary Cycle Turbine , KOP:Knock-out Pot

CONCLUSION

It is expected that the global decarbonization targets will enable more widespread use of hydrogen energy. Considering decarbonization targets while producing hydrogen requires evaluating options for green hydrogen production, geothermal power plants being one of these options.

Green hydrogen production There are two main alternatives to produce hydrogen from geothermal power plants. The first one is to use H_2S gas, which is emitted from cooling towers at geothermal power plants, and the second way is to use only geothermal power to electrolysis.

In this study, it is preferred to decrease the reinjection water temperature and gain additional energy and use this energy for H_2 production in PEM type electrolyser. The required pure water is provided from cooling tower for hydrogen production and 535 kg/day H_2 is produced by this system in the selected geothermal power plant with a specific condition.

REFERENCES

1. Tut Haklıdır F.S. and Şengün, R. [2020] “Hydrogeochemical similarities and differences between high temperature geothermal systems with similar geologic settings in the Büyük Menderes and Gediz Grabens of Turkey”, Geothermics, v. 83, 101717.
2. Balta, T.M., Dincer, İ., Hepbasli, A. [2009] “Thermodynamic assessment of geothermal energy use in hydrogen production”, International Journal of Hydrogen Energy 34; 2925-2939.
3. Akrami, E., Chitsaz, A., Nami, H., Mahmoudi, S.M.S., [2017] “Energetic and exergoeconomic assessment of a multi-generation energy system based on indirect use of geothermal energy”. Energy,124:625-39.
4. Haklıdır, M. Tut Haklıdır F.S. [2010] Hydrogen production from geothermal sources in Turkey. Proceedings of World Geothermal Congress, 24-30 April 2010, Bali, Indonesia.
5. H2 Generating and Fueling Station for Vermont https://www.greencarcongress.com/2005/03/hsub2sub_genera.html
6. Tut Haklıdır F.S. and Şengün R, Aydın, H. [2021] "Characterization and Comparison of geothermal fluids geochemistry within the Kızıldere Geothermal Field in Turkey: New findings with power capacity expanding studies". Geothermics, v. 94: 102110.

WHEC-2022
23rd World Hydrogen Energy Conference
June 26-30, 2022 - Istanbul

#47

THERMAL BALANCE IN FUEL CELL VEHICLES WITH LIQUID HYDROGEN UTILISATION

[1]Anatoliy Unitsky, [2] Ilya Kavalcuk, [3] Irina Skitsunova, [4] Vera Yanchuk, [4] Sergey Artyushevskiy,
[1] CEO, Unitsky String Technologies Co., Minsk, Belarus
[2] Head of Epectricap Engineering Department, Alasala University, Dammam, Saudi Arabia
[3] Department of thermal power technologies, JSC "Belgorkhimprom, Minsk, Belarus
[4] Advanced R&D Department, Unitsky String Technologies Co., Minsk, Belarus

*Corresponding author e-mail: s.artyushevskiy@unitsky.com

ABSTRACT

Hydrogen storage and its efficiency is one of the key challenges, which has been developed in line with the popularity of the fuel cell systems. However, fuel cells operation is linked with intensive heat release, which should be utilised by the cooling system to prevent membrane damage. With on-board cooling system, the overall efficiency of the vehicle decreases further. This paper provides design of a novel system to utilise heat of the fuel cells, drivetrain elements and ventilation system to vaporize liquid hydrogen and reach higher efficiency of the system with cooling system capacity decrease.

Keywords: Fuel cells, Liquid hydrogen, Thermal balance

INTRODUCTION

Hydrogen fuel cells (FC) has been seen as one of the balanced solutions for electric vehicles (EVs), including cars and rail-based systems due to its refuelling time, energy density and self-discharge rate in comparison with batteries and capacitors [1]. The key challenges of FC EVs are storage weight and size, reliability concerns regarding leakages and heat utilisation from the FC due to its efficiency [2].

There have been several solutions developed to meet certain technical objectives of the storage. Absorbent-based canisters prevent leakages, but have excessive mass, in comparison with alternatives and it requires very high purity of the hydrogen. Compressed gas bottles are easy to refuel and have relatively low weight, but their leakage characteristics prevent their application for long-term storage solutions. One of the alternatives can be seen in the cryogenic compressed hydrogen systems, however, storage cost and manufacturing process are very expensive [2, 3].

Alternative solution is to store hydrogen in liquid form [4]. This helps to reduce leaks in comparison with gaseous storage systems, and doesn't require complex expensive canisters to prevent high pressure explosions. Manufacturing process is not cheap, as for the compressed gas, however, it has comparable cost with the cryogenic compressed gas production. Considering better technical performance, it provides balanced solution for the FC EV. Operation of liquid storage requires additional system to be put in EV – evaporating and heating system for the hydrogen. Heating system should increase temperature of the gas to meet requirements of the FC and its efficiency range [4,5]. Overall, hydrogen storage systems have been combined in Figure 1.

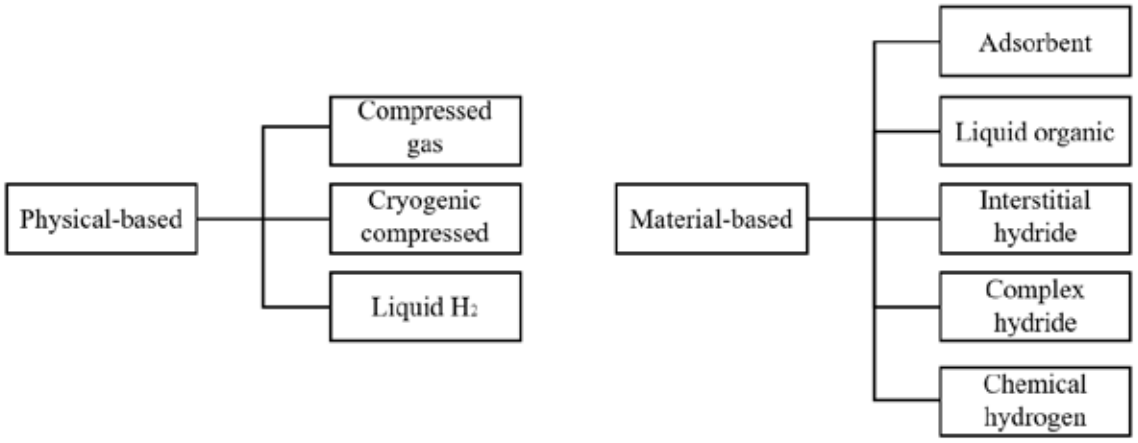


Figure 1. Hydrogen Storage Technologies

Another issue with FC EV is thermal management in the vehicle. FC has relatively low efficiency, in comparison with the battery and capacitors, and generate significant amount of heat, which can damage components of the system, including membranes, which can further reduce the production of electricity. Complex cooling systems have been

proposed in [6] to decrease thermal loading of FC. In comparison with battery-based EV, cooling losses in FC-based vehicles are significantly higher and can be compared with the sizes of cooling systems in conventional vehicles with internal combustion engines [4,6]. Large-scale cooling system requires larger FC to be installed, increases overall vehicle's mass and further impacting efficiency of the solution. In most proposed solutions, such system is combined with the cooling system of the drivetrain, however these two systems have different operating temperatures and different heat generation rates, so efficiency of such solutions is not high.

Furthermore, EVs have significant challenges in organisation of ventilation of the cabin due to the limited available resources and complex control strategies over the storage systems. Intensive use of ventilation system leads to the significant decrease in the operating range of EV. Utilisation of the heat, generated by the occupants, specially in the public transport, is a technical challenge [7].

This paper proposes a novel system, which utilises heat, developed in the drivetrain, cabin and FC of high speed train, to heat up liquid hydrogen from the relative storage system. Developed solution allows to reduce cooling system power consumption, organise effective cabin ventilation system and remove pre-heater for the liquid storage, based on the calculated thermal energy balance.

ENERGY BALANCE ANALYSIS

In the project, remotely moving high-speed stings-rail operating vehicle was developed. Such system has lower power consumption during the motion in comparison with the road vehicles [8]. The key savings come from the decreased rolling resistance in the contact couple rail – steel wheels in comparison with the rubber tires with high hysteresis losses. With the growth of speed, the required power in significantly smaller, even for the vehicles with higher capacity of passengers and goods. Remote access to the power was developed to reduce air drag of the contactors, which significantly increase power consumption of the current trains [9].

Developed solution on the operating speed has power consumption of 800 kW due to the high operating speed, dimensions and its capacity. As efficiency of the drivetrain system, including electric motors, power electronics and control system, is around 90% and all losses are generating heat, the heat generation rate was calculated as 80 kW. Based on the health standards and passengers' numbers, ventilation and air conditioning system was designed with the power rating of 5 kW.

Based on the power requirements, the power of the FC was chosen as 900 kW, to meet all requirements of auxiliary loads, maintain high speed and operate with the cooling system. The heat developed in FC, can be calculated using method from [10], and in the efficient range, FC heat generation is 612 kW.

In total, developed system shows the heat generation power of 697 kW of heat, including ventilation, drivetrain cooling and FC temperature maintenance. The flow of the hydrogen was calculated as in (1):

$$G_{H_2} = N \cdot g_{H_2} = 0.0194 \text{ kg/s} \quad (1)$$

Where G_{H_2} – mass consumption of the hydrogen, N – number of used cells, g_{H_2} – balanced consumption of one cell in the efficiency range.
The heat capacity of the liquid hydrogen can be assessed with equation (2), considering that the hydrogen is stored in Dewar vessels at 0.1 MPa at saturated state with the enthalpy h_1 and then is heated to gas with enthalpy of h_2:

$$Q = h_1 - h_2 = 4.1 \text{ MJ/kg} \quad (2)$$

Then for the given flow rate in the system, the heat capacity of the system is equal to 79 kW. This energy has constant flow requirements and doesn't change, depending on the environmental conditions.

RESULTS AND DISCUSSION

The heat exchange system was developed, as shown on Figure 2.

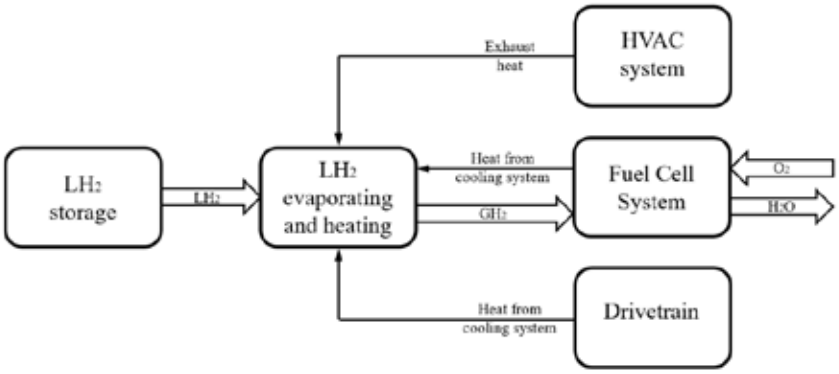


Figure 2. Designed Heat Exhchange System

As it can be seen, the heat generated in various parts of the vehicle, is re-directed to the evaporating chamber of the liquid hydrogen system. The heat dissipation rate in the chamber is 79 kW, however the total required size of the cooling system should have combined capacity of 697 kW. Developed system allows to scale down the required size of the cooling system by 12.9%, with the folloowing gain in the power consumption. Developed system allows to reduce overall complexity of the system, as there is no heating system required for the liquid hydrogen, as the heat is taken from the other systems of the vehicle. This solution can be scaled up or down, depening on the application.

CONCLUSIONS

The paper presents a novel system design, which utilises heat, generated in the various systems of FC EV, including FC, drivetrain and ventilation system, to heat up liquid hydrogen storage system. Developed solution allows to reduce power consumption of the cooling system by 12.9%, which leads to the higher efficiency of the overall system.

REFERENCES

1. Hu, Z., Li, J., Xu, L., Song, Z., Fang, C., Ouyang, M., ... & Kou, G. (2016). Multi-objective energy management optimization and parameter sizing for proton exchange membrane hybrid fuel cell vehicles. *Energy Conversion and Management*, *129*, 108-121.
2. Arlt, M. L., Cardoso, G. F., & Weng, D. (2017, November). Hydrogen storage applications in industrial microgrids. In *2017 IEEE Green Energy and Smart Systems Conference (IGESSC)* (pp. 1-6). IEEE.
3. Gambini, M., Stilo, T., & Vellini, M. (2019). Hydrogen storage systems for fuel cells: Comparison between high and low-temperature metal hydrides. *International Journal of Hydrogen Energy*, *44*(29), 15118-15134.
4. Zohuri, B. (2019). Cryogenics and Liquid Hydrogen Storage. In *Hydrogen Energy* (pp. 121-139). Springer, Cham.
5. Fierro, V., Ramirez-Vidal, P., Sdanghi, G., Schaefer, S., Maranzana, G., & Celzard, A. (2019). Hydrogen adsorption in cryogenic conditions: relationship between the porous texture and the parameters of the Modified Dubinin-Astakhov equation.
6. De las Heras, A., Vivas, F. J., Segura, F., Redondo, M. J., & Andújar, J. M. (2018). Air-cooled fuel cells: Keys to design and build the oxidant/cooling system. *Renewable Energy*, *125*, 1-20.
7. Kavalchuk, I., Arisoy, H., Oo, A. T., & Stojcevski, A. (2014, January). Challenges of electric power management in hybrid and electric vehicles. In *2014 Australasian Universities Power Engineering Conference (AUPEC)* (pp. 1-7). IEEE.
8. Юницкий, А. Э. (2017). *Струнные транспортные системы: на Земле и в космосе*. Belaruskaianavuka.
9. Pombo, J., Ambrósio, J., Pereira, M., Rauter, F., Collina, A., & Facchinetti, A. (2009). Influence of the aerodynamic forces on the pantograph–catenary system for high-speed trains. *Vehicle System Dynamics*, *47*(11), 1327-1347.
10. Niknam, T., Bornapour, M., & Gheisari, A. (2013). Combined heat, power and hydrogen production optimal planning of fuel cell power plants in distribution networks. *Energy conversion and management*, *66*, 11-25.

WHEC-2022
23rd World Hydrogen Energy Conference
June 26-30, 2022 - Istanbul

#64

OPTIMIZATION OF ENERGY MANAGEMENT STRATEGY FOR FUEL CELL-RANGE EXTENDED ELECTRIC VEHICLE

[1*] *Yan Sun*, [1] *Changgao Xia*
[1] School of Automotive and Traffic Engineering, Jiangsu university, Zhenjiang, 212013, China

*Corresponding author e-mail: 1360118360@qq.com

ABSTRACT

For the fuel cell-range extended electric vehicle (FC-REEV), the fuel cell system can work at a fixed output power point and have a good durability. However, the differences in output power and start-stop threshold can lead to a significant difference in energy loss and degradation of power sources. Based on the thermostat control strategy (TCS), the economy of vehicle is considered in the evaluation function. Furtherly, the artificial bee colony (ABC) optimization algorithm is used to increase driving range, in order to improve the durability of fuel cell, a penalty factor is added in the performance index function, and a novel optimized ABC-TCS (OABC-TCS) is proposed. Different strategies are tested under FTP-72 and WLTC drive cycle respectively, result shows that compared with TCS, the optimized driving range proportion of OABC-TCS is about 10.59% and 10.3%.

Keywords: Fuel cell vehicle, Range extend, Artificial bee colony algorithm, Thermostat control strategy

INTRODUCTION

In order to solve the problem of excessive greenhouse gas emissions of vehicles, the technology of electric vehicles (EVs) was proposed. However, limited driving range and slow charging problems cannot be fundamentally solved so far [1]. The plug-in hybrid electric vehicles (PHEVs) which is powered by internal combustion engines (ICE) can effectively solve the problems, but it still has a considerable amount of pollutant emissions [2]. Therefore, fuel cell-range extended electric vehicle (FC-REEV) is developed as an effective solution [3]. In this system, the battery works as the main power source, and the fuel cell works as an auxiliary power source. Energy management strategies (EMS) of multiple power sources has become a key problem in FC-REEV. Fuel economy is an important optimization goal of EMS. The performance of fuel cell will degrade gradually in long-term operation [4]. Therefore, it is important to balance fuel economy and component durability when formulating the EMS.

In this paper, a novel EMS for FCEV is proposed, and it considers the hydrogen consumption, lifespan of fuel cell. The SOC range of battery and output current of fuel cell are also considered in the strategy. The proposed strategy is an online strategy with the idea of offline optimization. The start-stop times of the fuel cell are taken into consideration as a key constraint, which is ignored by others.

POWER SOURCES MODELS

The battery uses the “RINT” model. The relationship among battery power, output current, internal resistance and SOC is shown in Eq. (1) and (2).

$$P_{bat} = U_{oc} I_{bat} - I^2_{bat} R_{bat} \tag{1}$$

$$\Delta SOC = \eta_c \frac{\int_{t0}^{t1} I_{bat} dt}{C_{bat}} \tag{2}$$

where, P_{bat} is the output power of battery. U_{oc} is the open circuit voltage. I_{bat} is the output current of battery. R_{bat} is the battery resistance. η_c is the coulomb efficiency of battery. C_{bat} is the max capacity of battery. The degradation of fuel cell is the key factor to be considered. In addition, the fuel cell degradation model is established, which mainly includes four parts: load changing cycles, start-stop cycling, idle and high-power load condition [5]. The fuel cell degradation model is as follows:

$$D_{fc} = \sum_{i=1}^{n} [d_{change}(i) + d_{on-off}(i) + d_{idl}(i) + d_{high}(i)] \tag{3}$$

where, D_{fc} is the total degradation of fuel cell. d_{change} is the fuel cell degradation caused by load change cycles. d_{on-off} is the fuel cell degradation caused by start/stop cycles. d_{idl} is the fuel cell degradation caused by idling/low power conditions. d_{high} is the fuel cell degradation caused by high power conditions.

The efficiency of fuel cell is related to the hydrogen consumption rate, the hydrogen consumption rate has a nonlinear proportional relationship with the output current of fuel cell. It is necessary to build the relationship among hydrogen consumption, output current and efficiency of fuel cell, as shown in Eq. (4) and (5).

$$m_{fc} = \left(N \cdot I_{fc} \cdot M_{\mathrm{H2}}\right) / 2F \tag{4}$$

$$\eta_{fc} = P_{fc} / (m_{fc} \cdot LHV_{\mathrm{H2}}) \tag{5}$$

where: m_{fc} is the instantaneous hydrogen consumption rate of the system. N is the number of single cells in the stack. I_{fc} is the output current of fuel cell. M_{H2} is the hydrogen molar mass. F is the Faraday constant. η_{fc} is the working efficiency of fuel cell. LHV_{H2} is the low calorific value of hydrogen.

ENERGY MANAGEMENT STRATEGY

TCS is mainly used in this paper, and five states are defined according to the SOC and the driving/braking state of the vehicle. Control rules and trigger conditions are shown in Fig. 1.

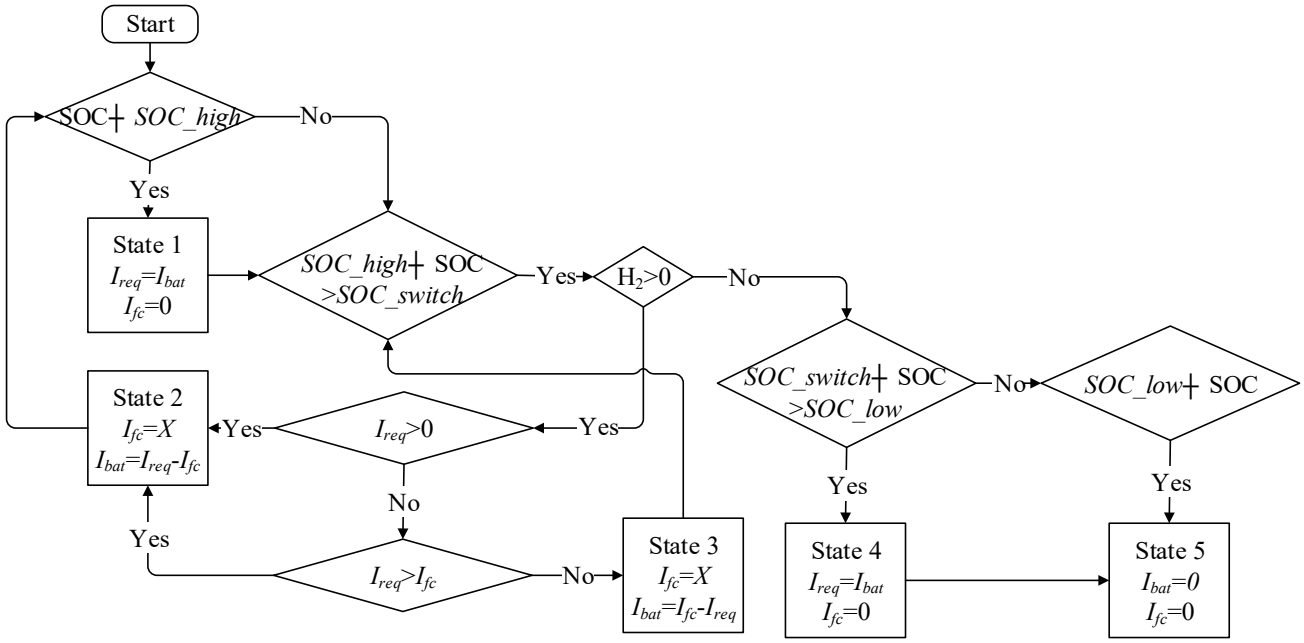


Fig. 1. TCS Process

State 1: The battery SOC ≥ *SOC_high*, the battery meets the energy requirements of the vehicle alone, $I_{req} = I_{bat}$, $I_{fc} = 0$. State 2: When *SOC_high* ≥ SOC > *SOC_switch*, $H_2>0$ (hydrogen is not exhausted), and $I_{req} > 0$(braking mode). Or, *SOC_high* ≥ SOC > *SOC_switch*, $H_2>0$, and $0 \geq I_{req} > I_{fc}$ (driving mode), $I_{fc} = X$ (constant value), $I_{bat} = I_{req} - I_{fc}$. State 3: When *SOC_high* ≥ SOC > *SOC_switch*, $H_2>0$, and $I_{req} > 0$(braking mode), $I_{fc} = X$ (constant value), $I_{bat} = I_{fc} - I_{req}$. State 4: When *SOC_switch* ≥ SOC > *SOC_low*, $H_2=0$ (hydrogen is exhausted). $I_{req} = I_{bat}$, $I_{fc} = 0$. State 5: When *SOC_low* ≥ SOC, $H_2=0$ (hydrogen is exhausted). $I_{bat} = I_{fc} = 0$. *SOC_switch* and I_{fc} are the key parameters to be determined, the economy of vehicle and degradation of power sources are affected by these parameters seriously. The determination and optimization of parameters are shown below.

For TCS strategy, the start-stop frequency is the most important factor affecting the degradation of fuel cell. Based on TCS, this paper takes the number of start-stop cycling as a penalty factor in the evaluation function, and an optimized ABC-TCS (OABC-TCS) is proposed. The optimization parameters are *SOC_ switch* and *I_ fc*. The objective function of ABC algorithm is replaced by the actual running cost. In this way, the multi-objective optimization problem is transformed into a single objective optimization problem, and the optimization objective is the minimum value of the evaluation function. The evaluation function is as follows.

$$P = (con_{\mathrm{H2}} \cdot P_{\mathrm{H2}} + D_{fc} \cdot P_{fc} \cdot W_{fcmax} / 30\% + 90\% \cdot P_{ele} \cdot Q_{bat}) / mile \tag{6}$$

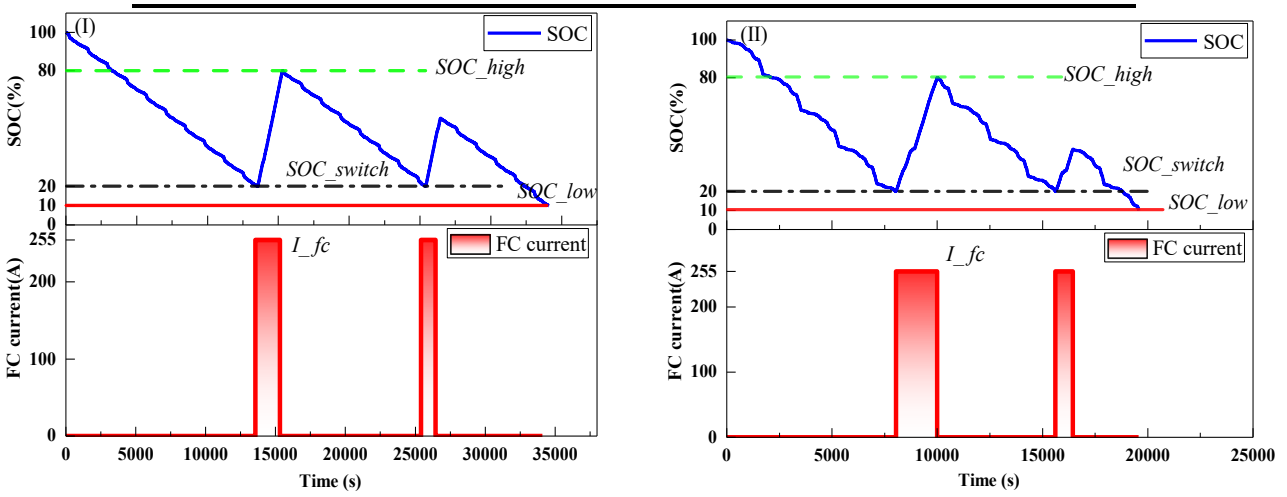
where, P is the equivalent cost per kilometer, W_{fcmax} is the maximum power of fuel cell. 30% represents the allowed degradation of fuel cell used in this paper. P_{fc} is the price of fuel cell.

RESULTS AND DISCUSSION

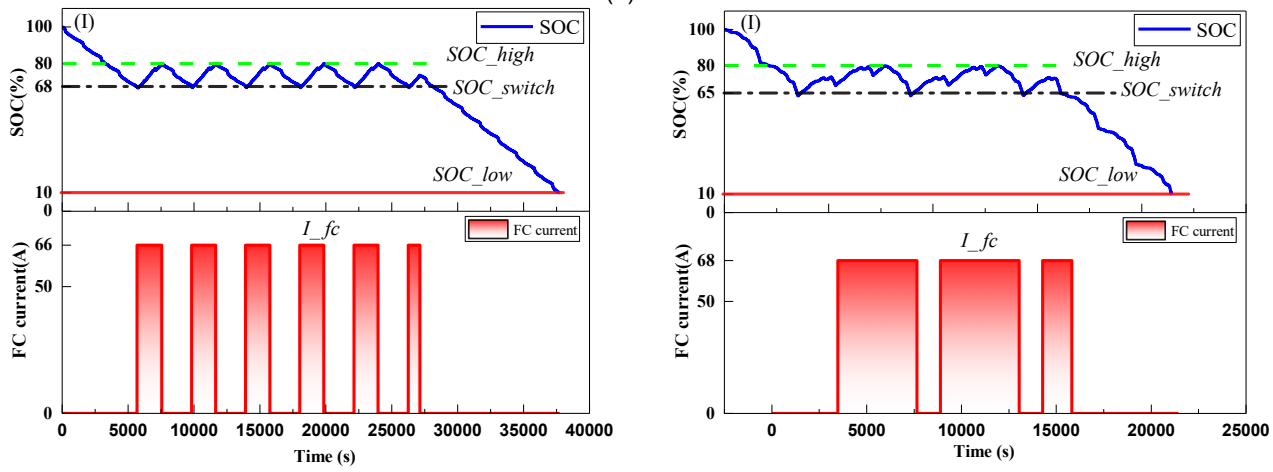
The strategy parameters and algorithm optimization results are shown in Table 1. $N_{on\text{-}off}$ is the start-stop times of fuel cell. Results shows that the start-stop times of original TCS is 4 times (2 start and 2 stop), but due to the large output current of fuel cell and the long time in the high resistance region of battery, the overall energy loss of the battery is large, the battery energy loss of FTP-72 and WLTC are 4632 kJ and 6523 kJ respectively. On the premise of reasonable start-stop times, OABC-TCS decreases the start-stop times to 12 times and 6 times under FTP-72 and WLTC. The energy loss caused by internal resistance of battery is decreased too, the battery energy loss of FTP-72 and WLTC is 2574 kJ and 4416 kJ. Fig. 2 shows the simulation results of FTP-72(Ⅰ) and WLTC(Ⅱ) drive cycle under TCS(a), OABC-TCS(b) respectively. The results include the SOC curve of battery and the output current curve of fuel cell.

Table 1 Strategy parameters

		SOC_ switch	*I_ fc* /(A)	$N_{on\text{-}off}$	Energy loss of battery /(kJ)
TCS	**FTP-72**	20%	254.6	4	4632
	WLTC	20%	254.6	4	6523
OABC-TCS	**FTP-72**	67.57%	66.4	12	2574
	WLTC	65.23%	68.2	6	4416



(a)



(b)

Fig.2. Battery SOC, FC current under FTP-72(Ⅰ) and WLTC(Ⅱ) with TCS(a), OABC-TCS(b)

CONCLUSIONS

In this paper, Two EMS considering the economy of vehicle and the degradation of fuel cells are proposed. It can also satisfy the energy management requirements very well. Firstly, the power sources models are built, including degradation model of fuel cell. secondly, a new EMS is designed, which uses TCS to decompose the required power into output power of two power sources. Thirdly, in order to improve the economy of vehicle, the OABC-TCS is compared with TCS under FTP-72 and WLTC drive cycle. It is shown that the OABC-TCS can improve the durability of fuel cell with a slight increase in fuel consumption, and the service life of fuel cell can be effectively improved.

Compared with TCS, the driving range proportion of OABC-TCS in FTP-72 and WLTC conditions is increased by 10.59% and 10.3% respectively.

REFERENCES

1. Zhou Y and Li H. 2020. An integrated predictive energy management for light-duty range-extended plug-in fuel cell electric vehicle. Journal of Power Sources 451: 227780.
2. Zaouche F and Rekioua D. 2017. Supervision and control strategy for photovoltaic generators with battery storage. International Journal of Hydrogen Energy 42(30): 19536-19555.
3. Liu Y and Li J. 2019. Research on a multi-objective hierarchical prediction energy management strategy for range extended fuel cell vehicles. Journal of Power Sources 429: 55-66.
4.Caux S and Gaoua Y. 2017. A combinatorial optimisation approach to energy management strategy for a hybrid fuel cell vehicle. Energy 133: 219-230.
5. Song K and Chen H. 2018. A comprehensive evaluation framework to evaluate energy management strategies of fuel cell electric vehicles. Electrochimica Acta 292:960-73.

WHEC-2022
23rd World Hydrogen Energy Conference
June 26-30, 2022 - Istanbul

#69

DESIGN OF A NEW HYDROGEN DRIVEN INTEGRATED POWERING SYSTEM FOR FERRY APPLICATIONS

Ali Erdogan Karaca, Ibrahim Dincer
Clean Energy Research Laboratory (CERL), Faculty of Engineering and Applied Science, Ontario Tech. University, 2000 Simcoe Street North, Oshawa, Ontario L1H 7K4, Canada

* Corresponding author's email: ali.karaca@ontariotechu.net

ABSTRACT

In the current study, a new hydrogen energy-based integrated powering system is designed and analysed for ferry applications. The system comprises photovoltaic (PV) solar cells and Darrieus type wind turbines mounted on the ferry's body to harness renewable energy and produce the required hydrogen on-board. A proton exchange membrane (PEM) electrolyzer, a PEM fuel cell, a thermal seawater desalination unit and a heat pump are some other major sub-components of the integrated system. The system offers green hydrogen, fresh water, heating, cooling and electricity as useful outputs. In the scope of the study, the system is evaluated energetically and exergetically. Impact of the primary design and operational parameters, e.g. solar irradiance and wind speed, on the system performance are investigated by conducting parametric studies. The system is capable of producing the required hydrogen on-board while operating with energy and exergy efficiencies of 26.75% and 18.20%, respectively.

***Keywords*:** Sustainability; Solar energy; Wind energy; Hydrogen; Hydrogen vehicles; Thermodynamic analysis.

INTRODUCTION

As the world moves towards green energy, hydrogen era is coming closer and faster than expected. Hydrogen allows to store, transport and distribute green energy effectively. It has a significantly higher energy density than batteries and even all other fossil fuels, which makes hydrogen a very attractive candidate to achieve an environmentally-benign transportation sector in all kinds. It should be highlighted that the technology to use hydrogen as fuel for transportation applications is already existing [1] [2]. Short charging times, low weights, zero harmful emissions on tailpipe, suitability for scale up projects and domestically production are some of many advantages that hydrogen promises to the global transportation sector and all others. CO_2 emission-dense conventional productions and the cost are the two main concerns with hydrogen in the current state. On the other hand, it is foreseen that the cost of hydrogen will decline dramatically decline from 16 US$ per kilogram at present to 6 US$ by 2025 [3]. It should also be noted that producing hydrogen from fossil fuels with carbon capturing and storing, so-called blue hydrogen, decreases the emission from production process of hydrogen by up to 95% [4]. Thus, low emission, cost-effective and a reliable hydrogen sector is even possible with existing hydrogen production and distribution infrastructures. However, development of hydrogen-based effective energy systems is crucial to diversify and enlarge the use of hydrogen.

In this study, a new hydrogen-based integrated power system is developed and analyzed for sea transportation. The system is configurated in a manner where the required hydrogen to generate power is produced by utilizing from renewable solar and wind energy on-board to achieve a green hydrogen-based nature friendly operation. The performance of the system evaluated from energy and exergy points of view by using thermodynamic approaches. The impact of primary design and operational parameters on the system's performance is investigated through parametric studies.

SYSTEM DESCRIPTION

Within the scope of the current study, a new hydrogen energy-based integrated power system is developed analyzed for ferry applications. The system comprises PV solar panels and wind turbines to harness renewable energy, a PEM electrolyzer to produce hydrogen, a PEM fuel cell to generate power, a single-stage thermal seawater desalination unit to produce fresh water, and a heat pump to provide space cooling. The thermal energy occurring during the operation of the PEM fuel cell is captured and utilized for seawater desalination and space heating. Table 1 summarizes the power need and design characteristics of the system. Figure 1 presents the developed hydrogen energy-based integrated power system.

Table 1: Integrated system characteristics.

Vessel length	30 m
Vessel Width	8 m
Engine power	60 kW
Heating load	4-6 kW
Cooling load	6-7 kW
Appliances (including lighting, tv and media units, fan, fridge and power supply)	4-6 kW

ANALYSIS

The main equations used in the energy and exergy efficieny analyses of the proposed system are summarized as follows:

$$\dot{W}_{Net} = \dot{W}_{FC} - \dot{W}_{Comp_{HP}} - \dot{W}_{Booster} - \dot{W}_{pumps} \quad (1)$$

$$\dot{W}_{Wind} = \frac{1}{2} \times \rho_{air} \times A_{WT} \times V_{Wind}^3 \quad (2)$$

$$\dot{Q}_{Solar} = I_{solar} \times A_{PV} \quad (3)$$

$$\eta_{overall} = \frac{(\dot{W}_{Net} + \dot{Q}_{Heating} + \dot{Q}_{Cooling} + \dot{Q}_{Dis})}{\dot{Q}_{Solar} + \dot{W}_{Wind}} \quad (4)$$

$$\psi_{overall} = \frac{(\dot{W}_{Net} + \dot{E}x_{Heating} + \dot{E}x_{Cooling} + \dot{E}x_{Dis})}{\dot{E}x_{\dot{Q}_{solar}} + \dot{W}_{Wind}} \quad (5)$$

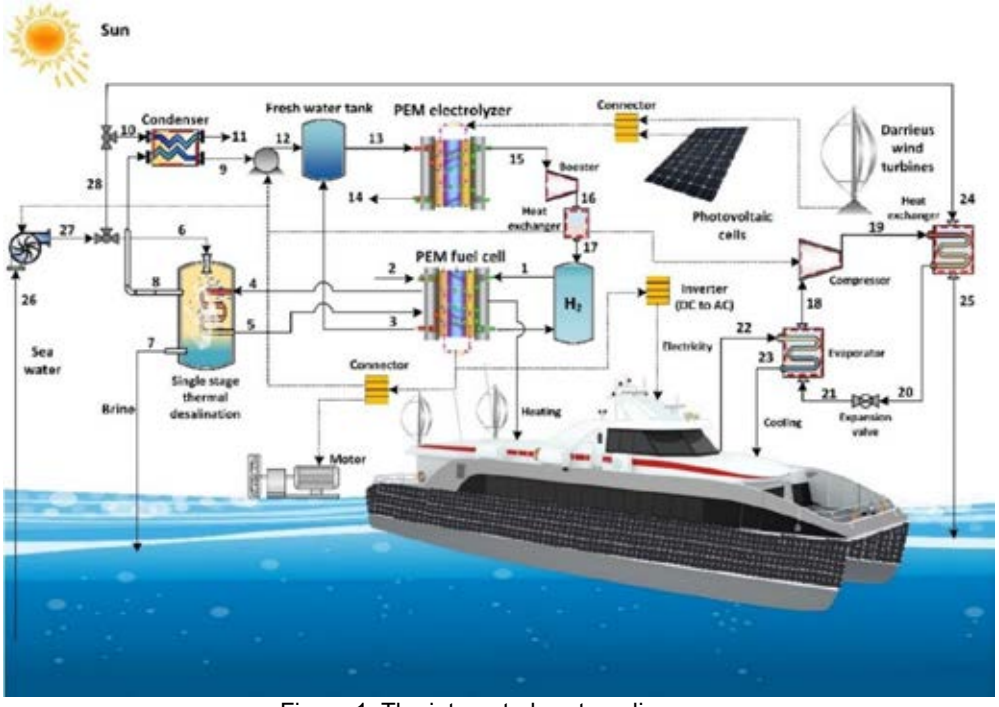


Figure 1. The integrated system diagram.

RESULTS AND DISCUSSION

The required hydrogen mass flow rate for the PEM fuel cell to power the system is evaluated as 1.085 g/s. For an on-board hydrogen production, the system requires 260 m^2 of PV cells and two Darrieus wind turbines with 20 m height and 3 m width. The energy harnessed from wind and solar is used to generate hydrogen via PEM electrolysis unit. The freshwater required for the electrolysis process is produced from seawater by a single-stage desalination unit. The required thermal energy for the desalination unit is evaluated as 28 kW, which is provided by the heat occurring during the operation of the 71-kW fuel cell stack with 98 cells. The fuel cell stack is also capable of providing the required heating load of 4 kW. The required cooling load (7.8 kW) is generated by employing a heat pump using the sea as heat sink. With the power consumption of 1.615 kW in its compressor, the coefficient performance of the heat pump is evaluated as 5.87. The performance of the proposed system evaluated energetically and exergetically through thermodynamic approaches. According to this the system's energy and exergy efficiencies are calculated as

26.75% and 18.20%, respectively. The system performance is further evaluated with parametric studies conducted on the primary design and operational parameters. Figure 2 presents the results of the parametric study investigating the impact of wind speed on the hydrogen production and overall system efficiency. As it can be seen from the figure, the increase in wind speed impacts the performance of the system in a positive manner. Figure 2 shows the results of another parametric study where the impact of solar irradiance on the system's energy and exergy efficiencies is evaluated. It can be seen that, increase in the solar energy input overwhelms the useful outputs from the system; thus, both energy and exergy efficiencies slightly decrease with increasing solar irradiance.

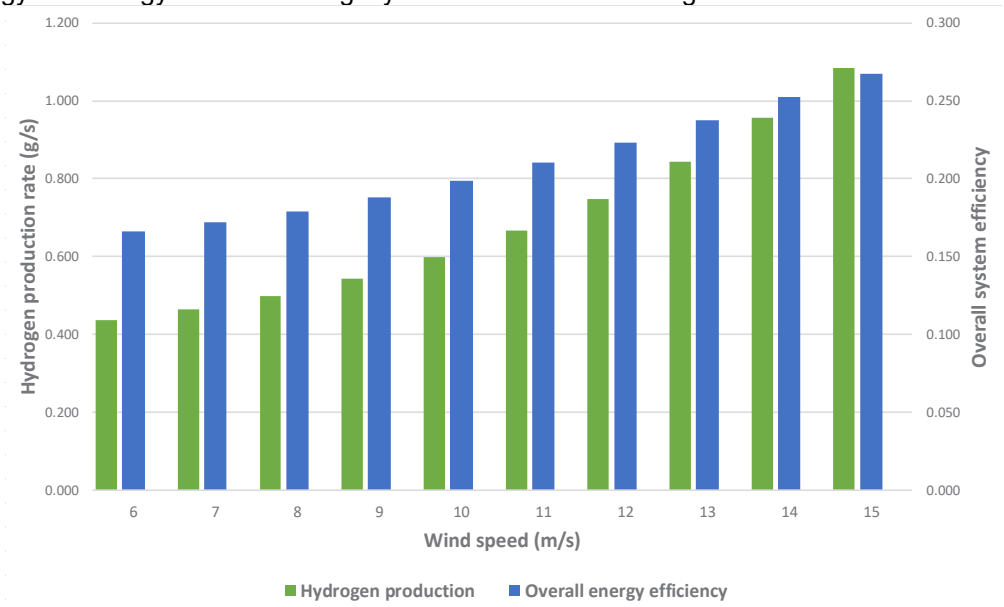


Figure 2. Impact of wind speed on the integrated system performance.

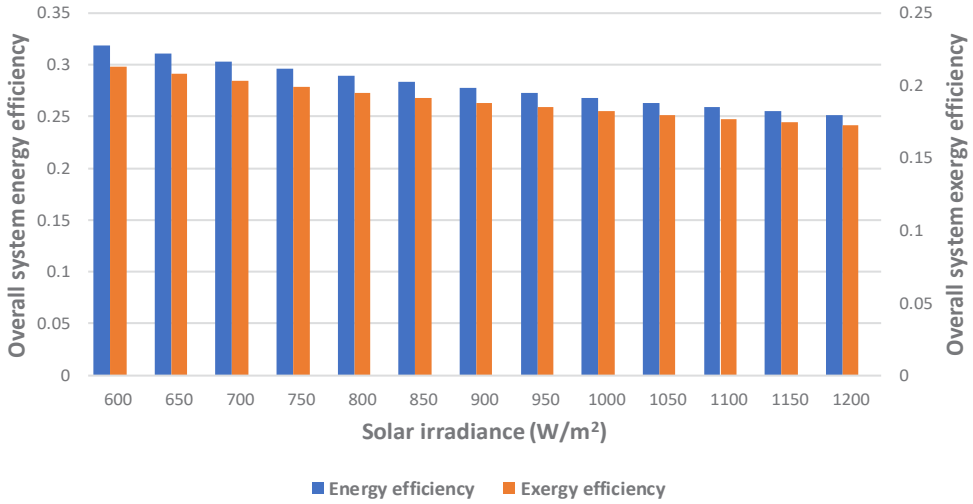


Figure 3. Impact of solar irradiance on the system performance.

CONCLUSIONS

In the current study, a new wind and solar driven integrated power system is investigated for self-sufficient ferry applications. The harnessed renewable energy is used to generate hydrogen on-board to fuel the ship. Electricity, heating, cooling, freshwater and green hydrogen are the useful outputs that the system provides. The system performance is evaluated through energy and exergy approaches as well as various parametric studies. According to the results, the system operates with an energy efficiency of 26.75% and exergy efficiency of 18.20%. The conducted parametric studies show that eventhough the hydrogen production rate increases increase in the solar irradiance, the overall system energy and exergy efficiencies decrease since the input energy becomes much greater than the useful output.

REFERENCES

1. "Sustainable Mobility: Renewable Hydrogen in the Transport Sector | Belfer Center for Science and International Affairs." [Online]. Available: https://www.belfercenter.org/publication/sustainable-mobility-renewable-hydrogen-transport-sector.

[Accessed: 08-Nov-2021].
2. “Energy Observer.” [Online]. Available: https://www.energy-observer.org/. [Accessed: 08-Nov-2021].
3. J. Reed et al., “Roadmap for the Deployment and Buildout of Renewable Hydrogen Production Plants in California,” 2020. Available at: https://cafcp.org/sites/default/files/Roadmap-for-Deployment-and-Buildout-of-RH2-UCI-CEC-June-2020.pdf
4.“Hydrogen from SMR and CCS | Climate Solutions.” [Online]. Available: https://www.frompollutiontosolution.org/hydrogen-from-smr-and-ccs. [Accessed: 08-Nov-2021].

WHEC-2022
23rd World Hydrogen Energy Conference
June 26-30, 2022 - Istanbul

#89

THE ULTRA-EFFICIENT FC-ICE HYBRID CYCLE WITH THERMOCHEMICAL RECOVERY OF THE WASTE HEAT - FINITE-TIME AND FINITE-SPEED THERMODYNAMICS ANALYSIS

[1] *David Diskin,* [2]* *Leonid Tartakovsky*
[1,2]Technion – Israel Institute of Technology, Mechanical Engineering, Technion City, Haifa, Israel

*Corresponding author e-mail: tartak@technion.ac.il

ABSTRACT

Efficiency and power of the hybrid cycle combining fuel cell (FC) and internal combustion engine (ICE) was analyzed using finite-time and finite-speed thermodynamics (FTT and FST). The study shows that at high efficiencies beyond 70% the hybrid cycle has the potential of a significant power gain (up to 35%) over FC or ICE operation alone. Power-efficiency maps of the hybrid cycle are obtained for various conditions and properties of the selected FC and ICE. Thermochemical recuperation (TCR) was suggested for heat recovery from the FC & ICE, and onboard hydrogen production. TCR is found to be the favorite choice for waste heat recovery in the hybrid cycle. Vehicle weight, size and the travel range are functions of the specific power and the efficiency of the propulsion system. Hence, the results of the reported study are of high importance for transportation.

Keywords: Electrochemical reaction, Combustion, Finite-time thermodynamics, Finite-speed thermodynamics, Fuel cell

INTRODUCTION

Fuel cells (FCs) produce electrical work by electrochemical reaction between fuel and oxygen. FC operation produces heat, as irreversible processes occur in the electrochemical reaction. Hybrid cycles that consist of FC and heat engine aim at using the waste heat to produce additional work, and by that to increase efficiency. Hybrid cycles with this configuration have been studied since 1990s [1]. Lately, internal combustion engines (ICEs) gained attention as the bottoming heat cycle, enabling the re-use of the FC anode off-gas on the one hand, and on the other hand enabling parallel work extraction by independent combustion cycle. Chuahy and Kokjohn [2] performed detailed analysis of a hybrid powertrain with a solid-oxide fuel cell (SOFC) and ICE and reported a 70% thermal efficiency of the system. Both SOFC and ICE can use the same fuel, and fuel reforming using thermochemical recuperation (TCR) can be employed as the waste heat recovery method from both FC and ICE.

Efficiency has a mutual relationship with power output due to their both dependency on the cycle driving forces. Therefore, power-efficiency analysis is of high importance and it is in the focus of this work. The analysis of heat engines that undergo irreversible interactions with its reservoirs was performed for the first time by Novikov in 1957 [3] and later by Curzon-Ahlborn in 1975 [4]. They were able to express the efficiency at maximum power of a heat engine. Petrescu et al. [5] developed a method called Finite-Speed Thermodynamics (FST) to evaluate the internal irreversible processes of the cycle. Sayyaadi et al. [6] applied the FST approach to ICEs. In [7,8], we have developed analytical expressions for efficiency at maximum power of the hybrid FC-ICE cycle. In the current study, we perform a detailed analysis of the hybrid cycle, using FTT and FST models for FC and ICE. An effect of TCR integration for waste heat recovery is analyzed also, and power-efficiency relationship of the cycle at various conditions and for various configurations is discussed.

MODEL

The hybrid system is composed of a FC, an ICE and a fuel reformer as shown in Fig 1. The system is fed with air and fuel. FC produces electrical work by an electrochemical reaction and the ICE produces mechanical work by gas expansion. FC waste heat is recovered by expansion of the hot FC exhaust gases in the ICE, and/or by thermochemical recuperation (TCR) in the reformer. Solid-oxide fuel cell (SOFC) was chosen due to its high working temperatures, and its power-efficiency characteristics were analyzed by a zero-dimensional model, with the following assumptions: 1. Uniform temperature across the whole fuel cell at steady state 2. Zero-dimensional channel representation 3. No bypass side reactions occur, and no crossover reactions occur 4. Negligible cells connection effects.

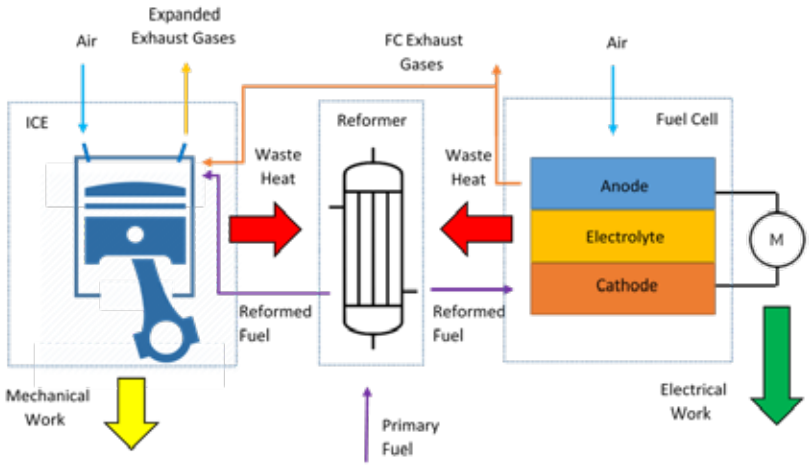


Figure 1. Hybrid ICE-FC scheme with TCR.

ICE model is built using the FST and FTT principles, which enable evaluation of the power-efficiency relation of a piston engine. ICE efficiency depends on the cycle duration and cylinder dimensions through several parameters. Piston speed has effect on pressure losses due to pressure gradient in the cylinder, throttling losses, and friction losses. The temperature after combustion is a function of the waste heat expelled from the FC (Eqs. 1,2).

Without TCR:

$$T_{cycle,\max} = T_{comp} + \frac{c_{v,23}\dot{m}_{ICE,parralel}\cdot(T_{\max} - T_{comp}) + c_{v_{FC,exhaust}}\dot{m}_{FC,series}\cdot(T_{FC} - T_{comp})}{c_{v,23}\dot{m}_{ICE,parralel} + c_{v_{FC,exhaust}}\dot{m}_{FC,series}} \quad (1)$$

With TCR:

$$T_{cycle,\max} = T_{comp} + \frac{c_{v,23}\dot{m}_{ICE,reformate,mix}\cdot(T_{\max,reformate} - T_{comp}) + c_{v_{FC,exhaust}}\dot{m}_{FC,series}\cdot(T_{FC} - T_{comp})}{c_{v,23}\dot{m}_{ICE,reformate,mix} + c_{v_{FC,exhaust}}\dot{m}_{FC,series}} \quad (2)$$

where T_{comp}, $T_{\max}$ and T_{FC} are the temperatures after compression, after combustion and FC working temperature respectively. $\dot{m}$ and c_v are the corresponding mass flow rates and heat capacities. $T_{\max,reformate}$ is the combustion temperature of the reformed fuel.

RESULTS AND DISCUSSION

Fig. 2 shows a power-efficiency map (Left) and power-efficiency curves (Right) of the hybrid cycle. The ICE-FC maximal power-to-weight ratio was set to 2, the compression ratio of the ICE is 15 and the working temperature of the FC is 850^{O}C. Methanol was selected as the primary fuel due to the compatibility for SOFC and ICE and its low-temperature reforming process. Two reforming methods were examined: Methanol Decomposition (MD) and Methanol Steam Reforming (MSR). It can be seen that the Hybrid cycle has a clear power-to-weight ratio advantage over the FC operation for a range of efficiencies, however, ICE operation alone is superior in terms of specific power. Without TCR, FC is superior for high efficiencies over 60%. Waste heat recovery through TCR is beneficial and provides the widest range of power gain in the efficiency axis, and efficiency over 70% can be achieved with a significant power gain (approx. 20%) compared to FC. The benefit of TCR waste heat recovery is because it is restricted only by the amount of waste heat and is not limited by the energy conversion efficiency of isentropic expansion.

An additional analysis of power-efficiency relation was performed in the study for different compression ratios, FC working temperatures and for different power-to-weight ratios of FC and ICE. The latter factor was discovered as a key parameter affecting the hybrid cycle performance.

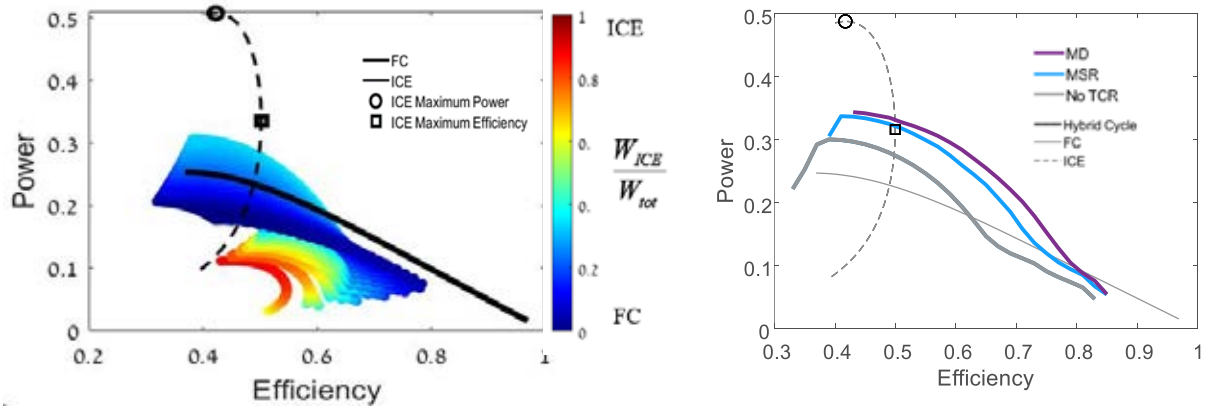


Figure 2. Power-efficiency relation of the hybrid ICE-FC cycle compared to the power and efficiency of the SOFC and ICE alone. Left: power-efficiency map without TCR, Right: power-efficiency curves with TCR.

CONCLUSIONS

Hybrid FC-ICE cycle performance was examined. Power-efficiency relation was analyzed for different FC and ICE properties and cycle configurations. It was found that the hybrid cycle is inferior in terms of maximum power compared to the ICE operation alone for almost all conditions - as our prior works suggest. However, for higher efficiency levels that cannot be achieved with ICE operating alone, the hybrid cycle performance is superior, and there is a range of efficiencies where a power gain is obtained compared to the FC. TCR was suggested for waste heat recovery from both the FC and the ICE, and power-efficiency relationship of a hybrid cycle with TCR was obtained and analyzed. The analysis shows that TCR is the beneficial method of waste heat recovery from the FC and ICE, and power gain is obtained for a wider range of efficiencies. Notably, the efficiency levels above 70% can be reached in the hybrid cycle with a significant power gain.

REFERENCES

1. Zabihian F and Fung A. 2009. A Review on Modeling of Hybrid Solid Oxide Fuel Cell Systems. International journal of engineering 3.2:85-119.
2. Chuahy FD and Kokjohn SL. 2019. Solid oxide fuel cell and advanced combustion engine combined cycle: A pathway to 70% electrical efficiency. Appl. Energy 235:391–408.
3. Novikov II. 1957. Efficiency of an atomic power generating installation. Sov. J. At. Energy 3:1269–1272.
4. Curzon FL and Ahlborn B. 1975. Efficiency of a Carnot engine at maximum power output. Am. J. Phys. 43:22–24.
5. Petrescu S, Stanescu G, Iordache R, and Dobrovicescu A. 1992. The first law of thermodynamics for closed systems, considering the irreversibilities generated by the friction piston-cylinder, the throttling of the working medium and finite speed of the mechanical interaction. Proc. of ECOS. 92:33-39.
6. Barjaneh A and Sayyaadi H. 2015. A new closed-form thermodynamic model for thermal simulation of spark ignition internal combustion engines. Energy Conversion and Management 105:607-616.
7. Diskin D and Tartakovsky L. 2020. Efficiency at Maximum Power of the Low-Dissipation Hybrid Electrochemical–Otto Cycle. Energies 13.15: 3961.
8. Diskin D and Tartakovsky L. 2021. Power and Efficiency Characteristics of a Hybrid Electrochemical-ICE Cycle. SAE Technical Paper 2021-01-0230.

WHEC-2022
23rd World Hydrogen Energy Conference
June 26-30, 2022 - Istanbul

#92

THE ROLE OF HYDROGEN FOR THE DEFOSSILISATION OF THE GERMAN CHEMICAL INDUSTRY

[1*] *Felix Kullmann,* [1] *Peter Markewitz,* [1] *Leander Kotzur,* [1,2] *Detlef Stolten*
[1] Institute of Techno-Economic Systems Analysis (IEK-3), Forschungszentrum Jülich GmbH, Wilhelm-Johnen-Str., 52428 Jülich, Germany
[2] Chair for Fuel Cells, RWTH Aachen University, c/o Forschungszentrum Jülich (IEK-3)

*Corresponding author e-mail: f.kullmann@fz-juelich.de

ABSTRACT

Within the European Green Deal, the European industry is summoned to transform towards a green and circular economy in order to reduce CO_2-emisisons and reach climate goals. Special focus is on the chemical industry to boost recycling processes for plastics, exploit resource efficiency potentials, and switch to a completely renewable feedstock (defossilisation). Despite common understanding that drastic changes have to take place it is yet unknown how the industrial transformation should be accomplished. How does a cost-optimal defossilisation of the chemical industry in the context of national greenhouse gas (GHG) mitigation strategies look like? The central part of this investigation is based on a national energy system model to optimize the future energy system design of Germany. A replacement of fossil-based feedstocks by renewable feedstocks leads to a significant increase in hydrogen demand by +40% compared to a reference scenario. Without the import of hydrogen-based energy carriers, the entire hydrogen demand, including the demand for renewable raw materials, must be produced domestically. This leads to cumulative additional costs of the transformation that are 72% higher than those of the reference scenario. Fischer-Tropsch synthesis and the methanol-to-olefins route can be identified as key technologies for the defossilisation of the chemical industry.

Keywords: Energy systems analysis, Defossilisation, Industrial transformation, Chemical industry, Climate targets

INTRODUCTION

The central concept of this work deals with non-energetic demand. This demand describes energy carriers that are not used as fuels or for conversion into other energy carriers, but as raw material inputs in processes [1]. The largest share of German non-energetic consumption is accounted for by mineral oil derivatives and natural gas which are used in basic chemicals, e.g., to produce methanol, ammonia, or plastics. Initially, no direct emissions are emitted through non-energetic demand. However, energy-related emissions can arise from the use of electricity or fuel for the manufacturing processes, as well as process-related emissions from the conversion of the non-energetic sources into end products. Worldwide, non-energetic consumption is responsible for about 15% of industrial CO_2-emissions [2]; the exact share of German CO_2-emissions is not recorded statistically. Since 1990, non-energetic consumption has remained constant at between 250 and 310 TWh [3]. Even though a slight drop in demand has been observed in the last three years, the chemical industry expects demand to increase in the future [4]. In recent national energy scenarios for Germany (e.g. [5-7]), showing possible transformation paths towards a low-carbon energy system in 2050, defossilisation is not at all or insufficiently considered. An assessment of the extent to which defossilisation measures are part of cost-optimal and efficient greenhouse gas reduction strategies and what effects their absence implies for the German energy system as a whole has not yet been made [8].

MODELLING

The *National Energy System model with SecTor coupling* (NESTOR) covers all system-relevant technologies of the German energy system, which are described by nodes and edges and set up a large interacting network [9]. The nodes describe all energy and material sources, conversion technologies, energy and material storage, and energy and material sinks, whereas the edges describe energy and material flows between the nodes. The energy system model analyses the future energy system design of Germany. Under greenhouse gas reduction restrictions, the model derives the energy system design and the transformation pathway based on cost-optimality. The cost comparison of the transformation is carried out on the basis of a reference scenario. This ensures that, among other things, autonomous developments of the energy system can also be taken into account. The model maps the German industrial final energy demand on a detailed process level. This allows processes for defossilisation of the chemical industry to be analysed and evaluated based on cost-efficiency and effectiveness.

A reference scenario is created (*REF95*), in which CO_2 emissions are reduced by 95% by 2050 compared to 1990 levels. Apart from the phase-out of coal and nuclear power generation, no other limitation is placed on the model. Recycling rates are fixed at today's levels in the individual industrial sectors until 2050. Novel recycling processes (e.g., chemical recycling of plastic waste) are only available from 2040. Otherwise, no further restrictions are

applied. Another scenario is calculated to analyze the effects of a switch in the chemical industry from a fossil-based to a fully renewable use of raw materials (*GreenCheem*).

RESULTS AND DISCUSSION

Fig. 1 shows the development of primary energy consumption of the *GreenChem* scenario and the change compared to the reference scenario *REF95.* In 2050, no major absolute change in primary energy consumption can be seen; additional 80 TWh primary energy are required in the *GreenChem* scenario, and it can be observed that non-energetic crude oil and natural gas are completely substituted by hydrogen.

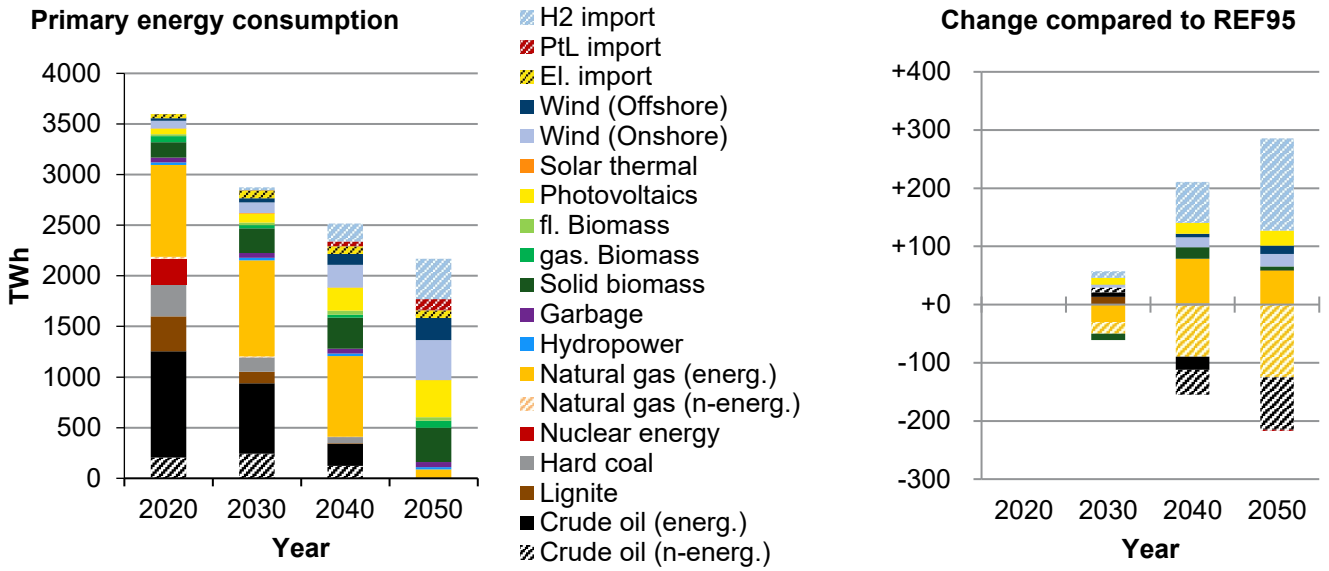


Fig. 1 Development of the primary energy demand of the *GreenChem* scenario until 2050 (left) and the change compared to reference scenario *REF95* in TWh (right)

In 2050, about 160 TWh hydrogen is needed more compared to the reference scenario, substituting 91 TWh crude oil and 125 TWh natural gas, resulting in a total demand of 560 TWh hydrogen for the whole energy system. In addition, there is a small additional consumption of natural gas used for electricity generation (59 TWh). This can be explained by the released CO_2 budget in the chemical industry. By forcing the chemical processes to switch to renewable raw materials, fewer CO_2-emissions are generated in this sector, which can be emitted more in other sectors, e.g., power generation, and still meet the overall GHG-reduction target.

A deeper dive in the model results of the chemical industry reveals that of the 16.5 Mt of plastics produced in 2050, 50% will be supplied via the methanol-to-olefins route and the other half via the use of green naphtha in steam crackers. This feedstock switch also implies a change in naphtha production. In 2050, about 10 Mt of naphtha will be produced. Of this, more than 3 Mt (30%) is based on pyrolysis oil from chemical recycling and about 7 Mt from Fischer-Tropsch synthesis. Compared to *REF95,* the introduction of Fischer-Tropsch synthesis in this way replaces the entire crude oil input for naphtha production in 2050. For the energy demand for naphtha production, this results in an additional demand of 94 TWh hydrogen in 2050 compared to *REF95* (Fig. 2). Together with methanol production (+89 TWh), these two areas are mainly responsible for the increase in hydrogen demand in the industrial sector. The chemical industry uses more than 250 TWh hydrogen in 2050.

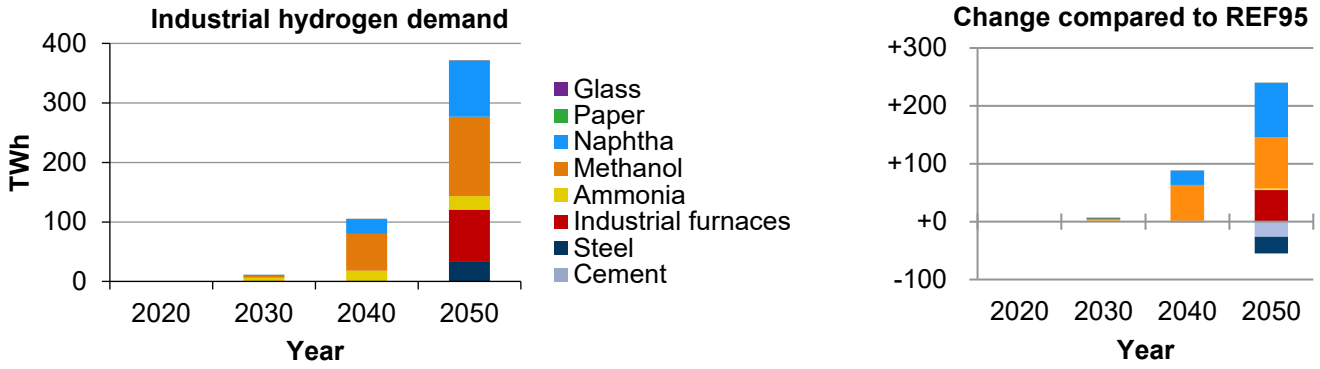


Fig. 2 Industrial hydrogen demand of the *GreenChem* scenario (left) and the change compared to scenario *REF95* (right).

CONCLUSIONS

Through the implementation of new and innovative industrial processes, it is now possible to evaluate the effects of defossilisation on the German energy system design. This also includes the analysis of suitable defossilisation strategies. The following results can be stressed:

- Defossilisation is an additional stringent constraint in addition to GHG mitigation itself.
- There is a significant impact on the overall energy system.
- The majority of non-energetic demand is replaced by hydrogen and its derivatives (green hydrogen is essential).
- Chemical recycling and the methanol-to-olefins route can be identified as critical technologies.
- Methanol production in 2050 will require additional 89 TWh hydrogen compared to a reference scenario, in which only GHG emissions are reduced. 19 Mt methanol is used for the production of highly refined chemicals.
- The industrial hydrogen demand is more than 185 TWh above that of the reference scenario. Overall, the hydrogen demand of the total energy system increases by 160 TWh.

A 95% reduction in CO_2 emissions in 2050 with additional defossilisation of the chemical industry leads to increased additional costs. In contrast to the reference case, the cumulative costs of the transformation increase by an additional 32%, or €212 billion. This additional cost is mainly due to the increased hydrogen import. In the course of a holistic consideration of the transformation of the energy system, the defossilisation of the chemical industry should be taken into account. In particular, the future supply of hydrogen is decisive for the associated additional costs.

REFERENCES

1. Federal Ministry for Economic Affairs and Energy (BMWi). Energieeffizienz in Zahlen: Entwicklungen und Trends in Deutschland 2019; 2020. https://www.bmwi.de/Redaktion/DE/Publikationen/Energie/energieeffizienz-in-zahlen-2020.html (accessed on 06.12.2021, German only)
2. Daioglou V, Faaij APC, Saygin D, Patel MK, Wicke B, van Vuuren DP. Energy demand and emissions of the non-energy sector. Energy Environ. Sci. 2014;7(2):482–98.
3. AG Energiebilanzen e.V. Auswertungstabellen zur Energiebilanz Deutschland: Daten für die Jahre von 1990 bis 2019; 2020. https://ag-energiebilanzen.de/10-0-Auswertungstabellen.html (accessed on 06.12.2021, German only)
4. Geres R, Kohn A, Lenz SC, Ausfelder F, Bazzanella A, Möller A. Roadmap Chemie 2050: Auf dem Weg zu einer treibhausgasneutralen chemischen Industrie in Deutschland eine Studie von DECHEMA und FutureCamp für den VCI. Frankfurt am Main: DECHEMA Gesellschaft für Chemische Technik und Biotechnologie e.V; 2019.
5. Ariadne Projekt. Deutschland auf dem Weg zur Klimaneutralität 2045. 2021. www.ariadneprojekt.de/publikation/deutschland-auf-dem-weg-zur-klimaneutralität-2045-szenarienreport (accessed on 06.12.2021)
6. AGORA. Klimaneutrales Deutschland 2045. 2021. www.agora-energiewende.de/veroeffentlichungen/klimaneutrales-deutschland-2045 (accessed on 06.12.2021, German only)
7. dena. Leitstudie Aufbruch Klimaneutralität. 2021. www.dena.de/newsroom/publikationsdetailansicht/pub/abschlussbericht-dena-leitstudie-aufbruch-klimaneutralitaet (accessed on 06.12.2021, German only)
8. Kullmann F, Markewitz P, Stolten D, Robinius M. Combining the worlds of energy systems and material flow analysis: a review. Energ Sustain Soc 2021;11(1).
9. Lopion, Markewitz, Stolten, Robinius. Cost Uncertainties in Energy System Optimization Models: A Quadratic Programming Approach for Avoiding Penny Switching Effects. Energies 2019;12(20):4006.

WHEC-2022
23rd World Hydrogen Energy Conference
June 26-30, 2022 - Istanbul

#98

TSUKUBA GREEN HOLONISM TOWN (II)—EXAMINING A PRELIMINARY ENERGY DEMAND–SUPPLY OUTLOOK

[1*] *Ichiro Sugimoto,* [2] *Kenji Morita,* [2] *Hiroyuki Mitsuishi,* [3] *Masayoshi Ishida*
[1] Laboratory of Energy & Human Life Science Inc., 3-6-2, Asahigaoka, Ikeda-city, Osaka, Japan
[2] Japan Automobile Research Institute, Environment Research Division, 2530, Karima, Tsukuba, Ibaraki, Japan
[3] University of Tsukuba, Faculty of Engineering, Information and Systems, 1-1-1, Tennoudai, Tsukuba, Ibaraki, Japan

*Corresponding author e-mail: ichiro@energy-and-humanlife.com

ABSTRACT

This study proposes a draft system design for a solar photovoltaic (PV)-based energy community as an example of "Tsukuba Green Holonism Town" in Japan, as described in the previous report, "Building A Carbon-Neutral Community," and examines a preliminary energy demand-supply outlook in 2030. The energy outlook includes an allocation plan of zero-emission energy sources in the Ibaraki Prefecture and a set of residential electricity and heat demands estimated in winter, summer, and the other seasons. Japan decided to increase renewable energy sources (RES) from 18% in 2019 to 36%-38% energy mix in 2030, thus we are urged to deploy a considerable amount of RES in each region. The preliminary outlook identifies a particular problem in the PV-based energy community in Japan. Furthermore, an example of solving this problem is also suggested.

Keywords: Energy community, Renewable energy resource, Solar photovoltaic, Power-to-hydrogen and fuel cell

INTRODUCTION

Japan fixed the sixth strategic energy plan on October 22, 2021, and decided to increase renewable energy sources (RES) from 18% in 2019 to 36%-38% energy mix in 2030 [1], therefore we are urged to install a considerable amount of RES in each region. Since 2013, the Tsukuba 3E Forum's workgroup has been discussing a low-carbon community in Tsukuba City [2] and developing a concept called "Tsukuba Green Holonism Town," which aims to implement a carbon-neutral community in harmony with its residents and workers by 2030 [3]. This study proposes a draft system design of an example of Tsukuba Green Holonism Town in Japan, which is a solar photovoltaic (PV)-based energy community, and examines the community's preliminary energy outlook for 2030. The preliminary outlook identifies a specific problem that PV dominant systems in Japan have, and a rational solution to this problem.

PV–BASED ENERGY COMMUNITY

This is an example of Tsukuba Green Holonism Town. A draft system design of this community, an allocation plan of zero-emission energy sources near and in the community, and a preliminary energy supply and demand outlook in 2030, including discussion are described below.

A Draft System Design

Fig. 1 shows a draft system design for a PV-based energy community. The energy community is expected to be equipped in an existing city area, in Tsukuba City, Ibaraki Prefecture, with about a hundred households. It consists of community facilities that are powered by PV plants and a nuclear power plant, common facilities which are installed in public buildings near the community, vehicle-to-microgrid integration (VmGI) facilities that are charging and discharging stations for electric vehicles (EV) and fuel cell vehicles (FCV), household demand-installed fuel cells (FC) and PVs, and household demand with only appliances.

An Allocation Plan of Energy Sources

Excluding hydroelectric generation, PV accounts for over 90% of RES capacity as of 2019 in Japan, and will account for over 50% in 2030. In 2030, the Ibaraki Prefecture will have two types of zero-emission energy sources: utility PV plants with a generation capacity of 399 kW for the energy community and a generated energy of 1192 kWh per day which is simulated based on solar insolation in the Tsukuba City for a year, and a nuclear power plant, Tokai No.2 Power Station with a capacity of 46 kW and generated electricity of 628 kWh per day based on its capacity factor 56.9%.

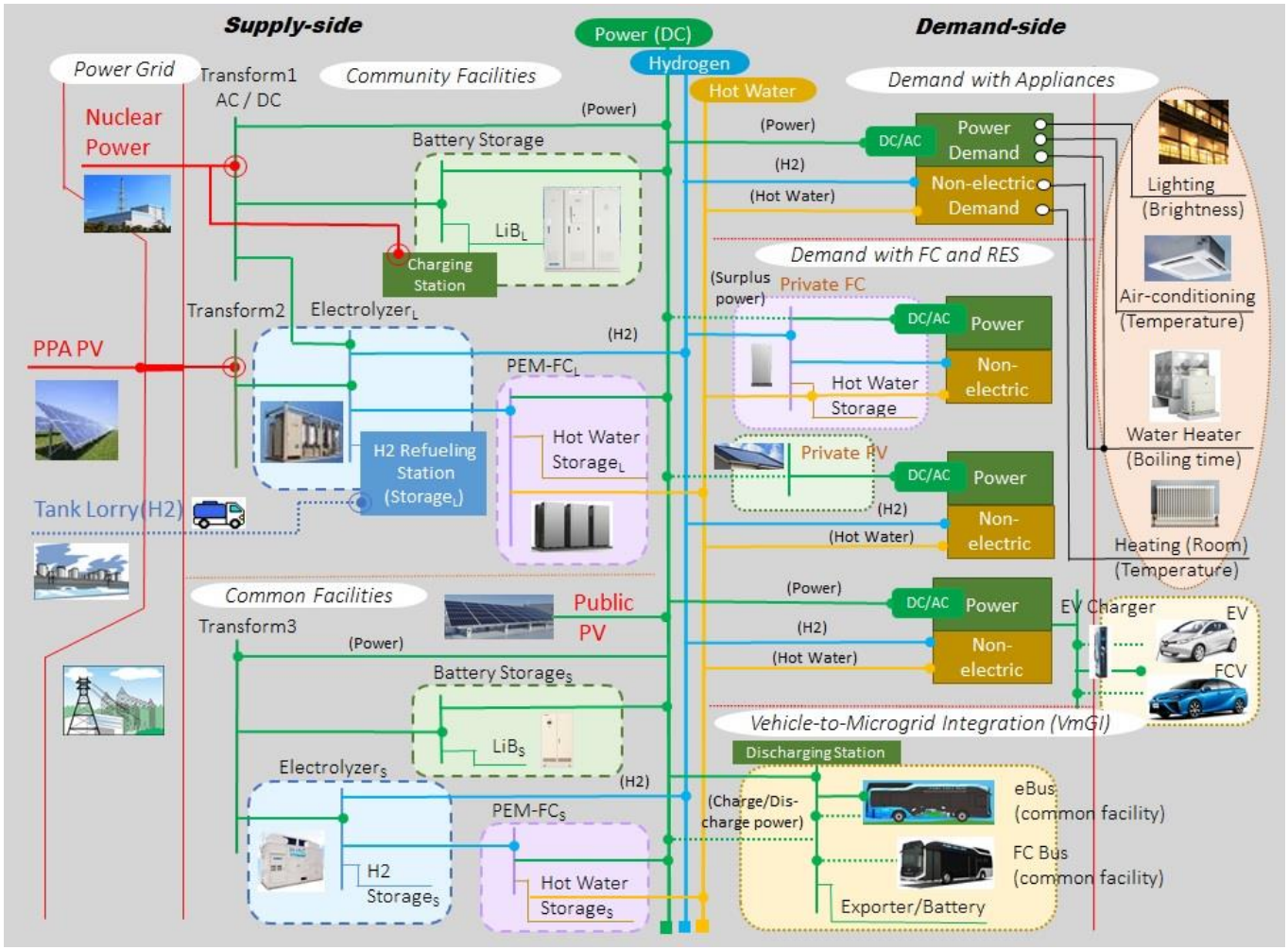


Fig. 1. System design for a PV–based energy community as an example of Tsukuba Green Holonism Town (draft)

A Preliminary Energy Outlook

According to reference [4], a set of residential electricity and heat demands in the Ibaraki Prefecture is designed in winter, summer, and other seasons. The residential demand is consistent with the electricity demand in 2010 in the Tokyo area, therefore it is necessary to consider the effects of energy efficiency and conservation (EE) in 2030. In comparison to the final energy consumption in 2013, Japan forecasts two types of EE in 2030: 10.2% and 22.9% of EE in the fifth and sixth strategic energy plans respectively [1]. In 2030, two types of EE in 2030 will lead the efficient demand, saving 10.2% and 22.9% of energy, respectively. The allocation plan and two types of energy demand, including energy-saving, indicate a preliminary energy outlook in 2030 in the PV-based energy community. Fig. 2 shows the preliminary energy outlook, which includes a preliminary energy supply from PV plants and nuclear power plants, and two types of energy demand with 10.2% and 22.9% of EE, and solar insolation in Tsukuba City in the terms of every three months. Notably, this energy outlook excludes conversion losses of AC-DC converters, power-to-hydrogen, and hydrogen-to-power, storage loss of batteries and hot water tanks, transmission loss of energy networks, and auxiliary power of the community facilities.

Discussion

Based on the allocation plan, PV accounts for over two-thirds of the energy supply, therefore solar insolation affects the amount of electric power supply in the energy community. Fig. 2 shows that energy supply varies by plus or minus 20% seasonally compared to the annual average, energy demand with 22.9% of EE varies from -15% in spring and autumn to +40% in winter compared to the annual average, and a demand-supply rate is calculated as 1.45 in winter, 0.59 in spring, 0.69 in summer, and 0.86 in the autumn.

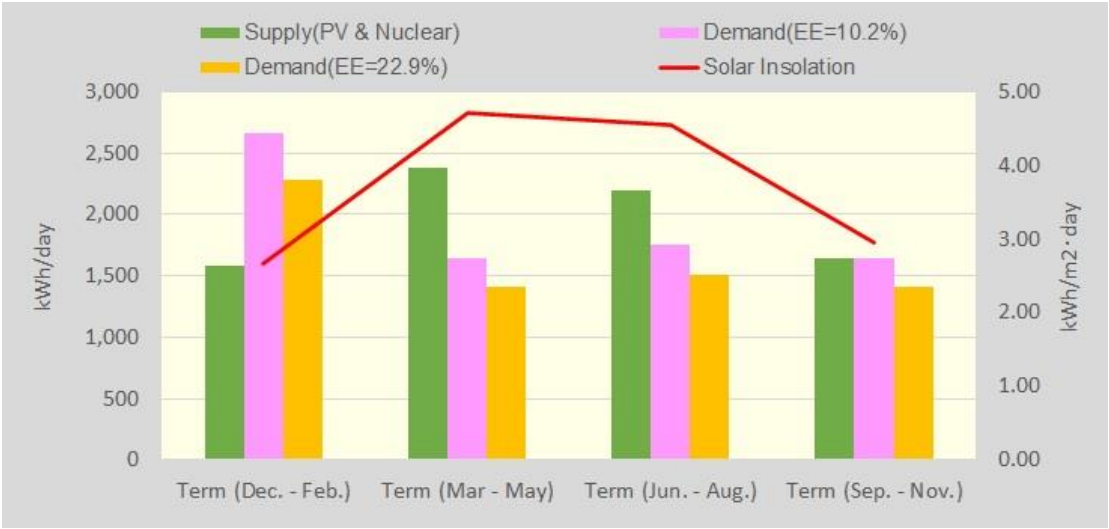


Fig. 2. Energy outlook of the PV–based energy community from December to November (preliminary)

The seasonal energy gap between supply and demand in winter is remarkably different from the other seasons in the PV-based energy community in Japan. These results show that the draft system combined with a demand response (DR) can balance energy in the spring, summer, and autumn if capacities of the facilities are fixed properly, but an additional system and backup mechanism is essential for the winter. An example of solving the winter energy gap is suggested, such as FCVs dispatching power at charging stations to the electric network as the VmGI facilities and an adaptive hydrogen distribution for hydrogen refueling stations (HRS), and FC cogeneration plants supplied by HRSs as the community facilities in the winter.

CONCLUSIONS

This paper proposed a draft system design of a PV-based energy community as an example of Tsukuba Green Holonism Town, and examined a community's preliminary energy demand-supply outlook for 2030. The outlook suggests that a hybrid hydrogen-battery storage and energy network mechanism combined with DR is expected to apply to the energy community effectively in the spring, summer, and autumn. As a gateway to solve the seasonal energy gap in Japan, an additional system such as FCVs for power dispatching to the community and FCs supplied by HRSs, and a backup mechanism, such as flexible hydrogen distribution for HRSs, are necessary for the winter.

NOMENCLATURE

DR	*Demand Response*	*EE*	Energy Efficiency and conservation	*EV*	Electric Vehicle
FC	Fuel Cell	*FCV*	Fuel Cell Vehicle	*HRS*	Hydrogen Refueling Station
PV	Solar Photovoltaic	*RES*	Renewable Energy Source	*VmGI*	Vehicle-to-Microgrid Integration

REFERENCES

1. Ministry of Economy, Trade and Industry Press Release, Cabinet Decision on the Sixth Strategic Energy Plan, Agency for Natural Resources and Energy, October 22, 2021.
2. Tsukuba 3E Forum brochure, Tsukuba Environment-Energy-Economy Forum - Reduce CO2 emissions by 50% in Tsukuba by 2030, August 27, 2013.
3. K. Morita, I. Sugimoto, M. Ishida, et al.: Tsukuba Holonism Town—Building A Carbon Neutral Community, The 11th International Symposium on Solar Energy and Efficient Energy Usage (SOLARIS), Proceedings, September 2021, Tokyo, Japan.
4. I. Sugimoto, H. Aki: CHP-based Demand Response for controlling Electricity Load Profile, The 6th International Conference on Integration of Renewable and Distributed Energy Resources (IRED2014), Nov. 20, 2014, Kyoto, Japan.

WHEC-2022
23rd World Hydrogen Energy Conference
June 26-30, 2022 - Istanbul

#100

TSUKUBA GREEN HOLONISM TOWN (I)—BUILDING A CARBON-NEUTRAL COMMUNITY

[1] Kenji Morita, [2] Ichiro Sugimoto, [1] Hiroyuki Mitsuishi, [3] Masayoshi Ishida*
[1] Japan Automobile Research Institute, Environment Research Division, 2530, Karima, Tsukuba, Ibaraki, Japan
[2] Laboratory of Energy & Human Life Science Inc., 3-6-2, Asahigaoka, Ikeda-city, Osaka, Japan
[3] University of Tsukuba, Faculty of Engineering, Information and Systems, 1-1-1, Tennoudai, Tsukuba, Ibaraki, Japan

*Corresponding author e-mail: kmorita@jari.or.jp

ABSTRACT

This study illustrates a concept of “Tsukuba Green Holonism Town” in Japan, comprising three basic policies: achieving carbon neutrality in the community, balancing the energy demand and supply, and changing the lifestyle, work style, and mobility style of residents and workers. Furthermore, this community is constituted of five functional categories: community facilities with nearby renewable energy sources (RES), energy dispatching station and energy networks, common facilities equipped with fuel cells (FC), vehicle-to-microgrid integration facilities, household demand installed RES or FC, household demand with both controllable and uncontrollable appliances. Japan and other OECD countries are taking on the considerable challenge of reducing greenhouse gas emissions to zero by 2050, thus we must push for more robust green policies and decarbonization breakthroughs immediately. The workgroup of Tsukuba 3E Forum has been developing the concept of Tsukuba Green Holonism Town, which implements a carbon-neutral community using demand response methods in harmony with residents, workers, household FCs, and electric vehicles. An example of cooperative scenarios among the functional categories for a rainy week is also described.

Keywords: Carbon-neutral community, Balancing the energy demand and supply, Hydrogen and demand response

INTRODUCTION

Japan decided on October 26, 2020, to achieve a decarbonized society by 2050, and to reduce its greenhouse gas (GHG) emissions by 46% in 2030 compared to 2013 levels [1], therefore we should push for more robust green policies and lower-carbon breakthroughs. The Tsukuba 3E Forum’s workgroup has been discussing a low-carbon community in Tsukuba city [2] and is developing a concept of “Tsukuba Green Holonism Town,” which aims to implement a carbon-neutral community in harmony with its residents and workers by 2030 [3]. This study illustrates the community concept, which consists of three basic policies and five functional categories. An example of cooperative scenarios among the functional categories for a rainy period is also described.

TSUKUBA GREEN HOLONISM TOWN

This is a community concept based on three basic policies with five functional categories according to the capacity of available renewable energy sources (RES), household quantity, population, and energy demand in the community. The basic policies, functional categories, and an example of cooperative scenarios are described below. Fig. 1 shows a concept image of Tsukuba Green Holonism Town.

Basic Policies

The concept comprises three basic policies: environmental, energy demand and supply, and energy consumption behavior policies as follows.

- Achieving carbon neutrality in the community.

As shown in Fig. 1, the community attains and maintains net-zero carbon dioxide (CO_2) using RES, nuclear power, energy conversion, and CO_2 recycling technologies, such as solar photovoltaic (PV), power-to-hydrogen, hydrogen storage and transport, and fuel cells (FC).

- Balancing the energy demand and supply in the community.

The community supplies clean and variable energy depending on the weather through PV power plants located in and near the community. According to the demand response (DR), the energy demand meets the community supply.

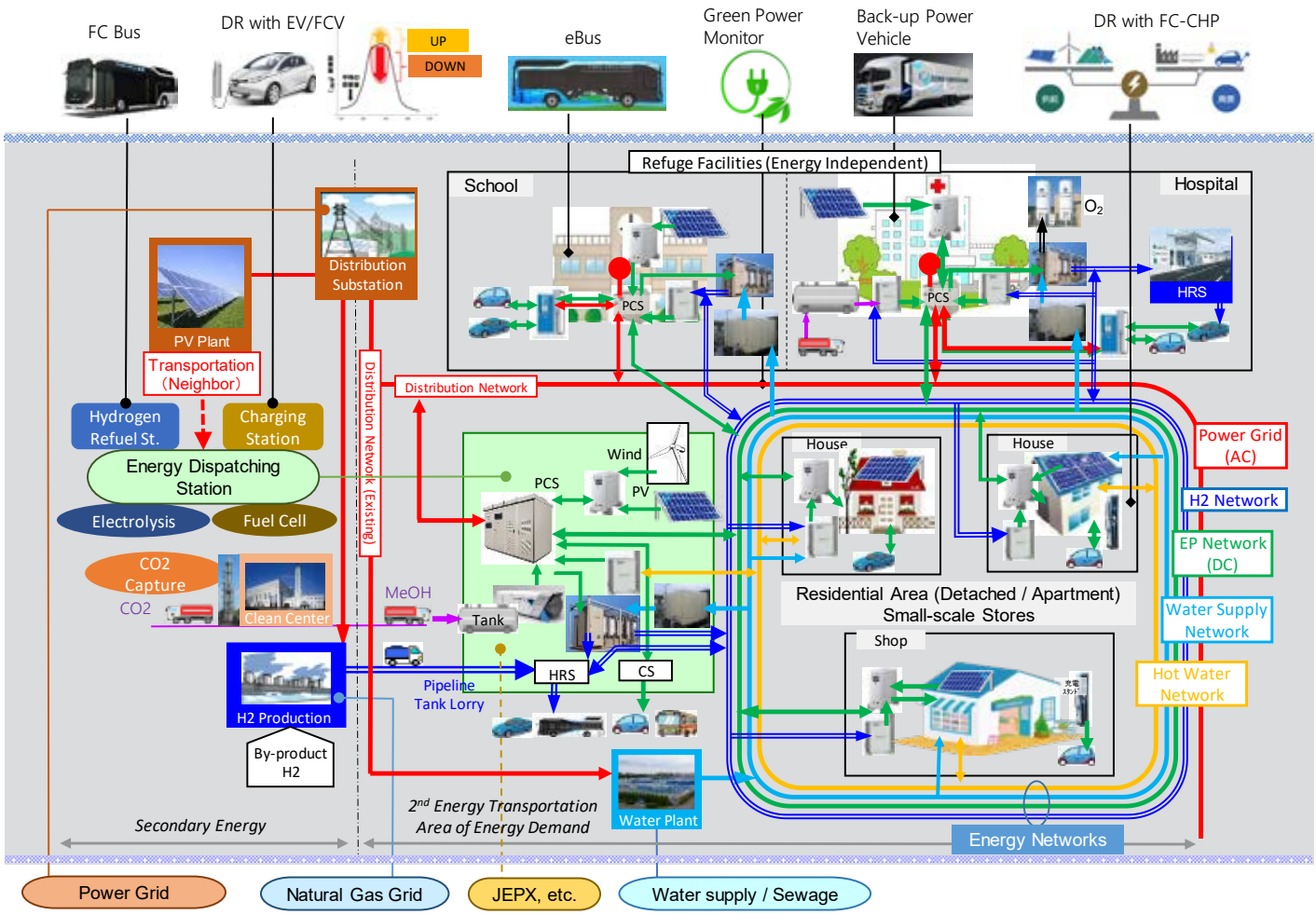


Fig. 1. A Concept Image of Tsukuba Green Holonism Town

The DR applications are, for example, water electrolysis and FC, and electric vehicle (EV) charge and discharge in Fig. 1.

- Changing lifestyle, work style, and mobility style of the community residents and workers.

The residents and workers in the community change their lifestyles, work styles, and their mobility styles in accordance with the energy production forecast, such as daylight savings time and remote work.

Functional Categories

The basic policy, carbon neutrality by 2030, means that zero-emission energy sources (e.g., PV, nuclear power) near the community should be introduced into the grid, and the generation capacity for the community should be shared rationally. The policy, balancing the energy demand and supply, means that the supply is estimated based on the weather in a given period, and the demand should meet the energy supplied to the community through water electrolysis, hydrogen storage, and network transport, FC regeneration, and vehicle-to-microgrid integration (VmGI). The changing lifestyle, work style, and mobility style means that the demand curve ought to be reshaped and fit to the energy supply by increasing the power generation of household FCs, discharging power from household EVs, and reducing the energy consumption of household appliances automatically or manually. Community facilities, common facilities, VmGI facilities, household demand with FC or RES, and household demand with appliances are the five functional categories that constitute the community. Table 1 shows the Tsukuba Green Holonism Town's functional categories and system configuration.

Table 1. Functional Categories and System Configuration in Tsukuba Green Holonism Town

Functional categories	System Configuration	
	Supply side	Conversion and Demand side
Community Facilities	Neighboring RES (PPA*2)	Energy Dispatching Station, including Electrolyzer, Fuel Cell, and Storage Tank Hydrogen Refueling Station and FCV, Charging or Discharging Station and EV
	Neighboring Nuclear Power (PPA*2)	
	Energy Networks (Power, Hydrogen, and Hot water)	
Common Facilities	RES deployed in the community	Conversion and Storage Equipment deployed in the community
VmGI*1 Facilities	Charging or Discharging Station, EV, FCV	Energy Network (Power)
Household Demand with FC or RES	Household FC and RES	Household FC and EV. Appliances (Controllable / Uncontrollable)
Household Demand with Appliances		Appliances (Controllable / Uncontrollable)

(*1) VmGI: Vehicle-to-Microgrid Integration (*2) PPA: Power Purchase Agreement

An Example of Cooperated Scenarios

Assuming that the neighboring RES power supply of the community facilities is primarily PV, power generation is dependent on solar insolation and weather-related temperature. If the weather forecast predicts rain for a week, this means the power supply will be drastically reduced for a week, then FCs both in the community facilities and in the household demand, and EVs in the VmGI facilities will generate and supply electric power to the community systematically for a week. Synchronously, energy consumption in the household demand will be curtailed by changing the lifestyle (e.g., disuse of vehicles), and the work style (e.g., remote work).

CONCLUSIONS

This study proposed a community concept of the Tsukuba Green Holonism Town, including three basic policies and five functional categories. A distinctive feature of this community is that the demand in collaboration with its residents, workers, and EVs meets the energy supply and varies based on weather conditions. Furthermore, it described an example of cooperative scenarios between common facilities and household demand against a dark period.

ACKNOWLEDGMENT

The authors gratefully acknowledge the Tsukuba 3E Forum Task Force workgroup members for discussing and clarifying the concept of Tsukuba Green Holonism Town.

NOMENCLATURE

EV Electric Vehicle
FCV Fuel Cell Vehicle
GHG Greenhouse Gas
PV Solar Photovoltaic
RES Renewable Energy Source

REFERENCES

1. Ministry of Foreign Affairs of Japan Press Release, Intended Nationally Determined Contributions (INDC): Greenhouse Gas Emission Reduction Target in FY2030, July 26, 2021.
2. Tsukuba 3E Forum brochure, Tsukuba Environment-Energy-Economy Forum - Reduce CO_2 emissions by 50% in Tsukuba by 2030, August 27, 2013.
3. K. Morita, I. Sugimoto, M. Ishida, et al.: Tsukuba Holonism Town—Building A Carbon Neutral Community, The 11th International Symposium on Solar Energy and Efficient Energy Usage (SOLARIS), Proceedings, September 2021, Tokyo, Japan.

WHEC-2022
23rd World Hydrogen Energy Conference
June 26-30, 2022 - Istanbul

#108

DESIGN AND OPTIMIZATION OF GREEN HYDROGEN-BASED HYBRID ENERGY SYSTEM

[1,2] *Ceren Ceylan, Yılser Devrim*[2]
[1] Yıldız Technical University, Mechanical Engineering-Energy, Istanbul, Turkey
[2] Atılım University, Energy System Engineering Department, Ankara, Turkey

*Corresponding author e-mail: yilser.devrim@atilim.edu.tr

ABSTRACT

Hydrogen (H_2) is widely used in many industries because it can be used as a chemical raw material with its high mass-energy density and can be converted back into electricity via fuel cells. H_2 energy systems seem to be one of the most effective solutions for providing a better environment and sustainability. Green H_2, produced by renewable energy-assisted electrolysis without greenhouse gas emissions, has been of great importance in recent years. In this study, a hybrid energy system including Photovoltaic (PV), Wind Turbine (WT), Proton Exchange Membrane Fuel Cell (PEMFC), and electrolyzer is compared for grid-connected and off-grid operating conditions. In the grid-connected system, electricity generated from PV and WT is used directly to meet electricity demand, while excess electricity is used for green H_2 production. In the off-grid connected system, electricity generated from PV and WT was used for H_2 production. Produced H_2 and O_2 were used to generate electricity by PEMFC. While 20186 kWh energy & 3273 m^3 H_2 were generated in an on-grid connected system, 95145 kWh energy & 17942 m^3 H_2 and 83511 kWh energy & 14370 m^3 H_2 were generated in two different configurations in the off-grid connected system. The Levelized Cost of Energy (LCOE) for the on-grid connected system and the off-grid system for two different designs were determined as 0.307 $/kWh, 0.341 $/kWh and 0.349 $/kWh**,** respectively. The hybrid system design was simulated using MATLAB software and it was examined which hybrid energy system configuration would be the most economical to meet the load.

Keywords: Green hydrogen, Hydrogen production, Hybrid energy system, Renewable energy

INTRODUCTION

Nowadays, besides the fossil fuels, such as oil and natural gas, that are endangered, renewable energy sources (solar, tidal, geothermal, etc.) are alternative for those because of suitable for use and are everywhere [1]. Renewable energy means that never-ending energy sources or self-renewing and found in nature such as solar, wind, H_2, etc. All renewable energy sources, solar and wind energy have been widely used. Nevertheless, weather conditions, daily solar cycle, and seasonal variations affect the undesirable performance of PV and WT systems [2]. In addition, the storage of electricity is more difficult progress than its production. H_2 could be produced and stored by electrolysis with the generated electricity from renewable energy sources [3]. Thus, either all of the produced electricity or the excess electricity after use is stored as H_2. In this study, to meet the 25kWh electricity demand, on-grid and off-grid renewable hybrid energy systems were designed. The cost analysis was made and compared by calculating how many PV panels and WT were used and the power of electrolyzer and PEMFC.

MATERIALS AND METHODS

By obtaining hourly solar radiation, ambient temperature, and wind speed data from Atilim University Meteorology Station, hybrid energy systems were designed to supply 25 kWh energy connected as on-grid and off-grid applications.

Proposed On-grid and Off-grid Hybrid Systems

Fig. 1. (a) shows the on-grid hybrid energy system design. In this system electricity produced from PV panels and WT is fed to the grid and sent to the consumer. When the consumption is less than production; the excess of electricity is sent to the electrolyzer to produce H_2 and O_2. Produced H_2 and O_2 are stored in tanks with the help of compressors. Thus, excess electricity is not stored in batteries, but as H_2 and O_2.

Fig.1. (b) shows the off-grid hybrid energy system design. In this system, the electricity produced from PV panels and WT operates the electrolyzer to produce H_2 and O_2. Produced H_2 and O_2 are stored in tanks and fed to the PEMFC that generates electricity to meet the 25 kWh energy need of the system.

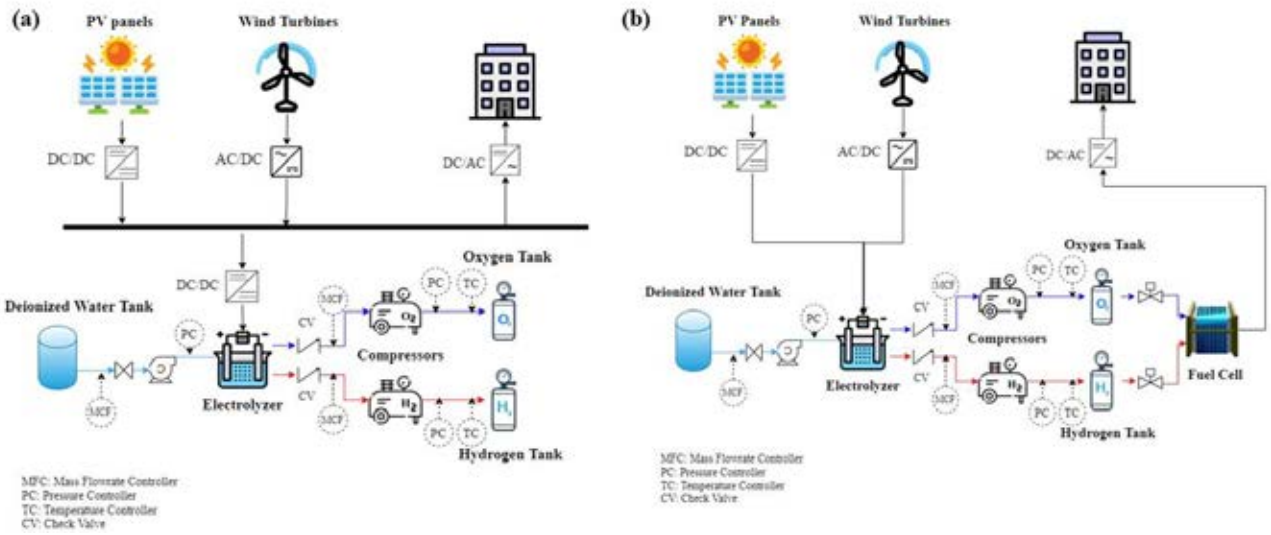


Fig. 1. (a) On-grid connected hybrid energy system design, (b) Off-grid connected hybrid energy system design

Optimal Design Strategy of the Proposed On-grid and Off-grid Hybrid System

On-grid hybrid system: Firstly, the number of PV panels and WT that meet the 25 kWh energy need is calculated. By using solar radiation, ambient temperature and wind speed data, the total energy produced from PV panels and WT are calculated. If the produced energy does not meet the entire consumed energy, energy need is met by using produced energy from PV panels and WT and grid. In case the produced energy is greater than the consumed energy, it is checked whether the excess energy is sufficient to operate the designed electrolyzer or not. When it is sufficient, excess energy is fed into the grid; in the other case, the electrolyzer is operated by using excess energy, H_2 and O_2 are produced and stored.

Off-grid hybrid system: The H_2 requirement of the PEMFC, which operates at 5 kW power for 5 hours, has been determined. According to the H_2 requirement, the power of the electrolyzer to be used to meet it, the number of PV panels and WT that will produce the energy for operating the electrolyzer are calculated. By using solar radiation, ambient temperature and wind speed data, the total energy produced from PV panels and WT are calculated. The produced energy is sent to the electrolyzer, then H_2 and O_2 are produced and stored. The stored H_2 and O_2 are sent to the PEMFC to produce electricity and the 25-kWh electricity need of the system is met.

RESULTS AND DISCUSSION

Table 1. Comparison of the grid-connected and off-grid hybrid system by annual produced energy stored H_2 and LCOE

Components		On-grid	Off-grid	
			Design 1	Design 2
PV	Number of Panels	30	140	105
	Installed Power (kW)	11.1	51.8	38.85
WT	Number of Turbines	1	1	1
	Installed Power (kW)	4	4	10
Electrolyzer	Number of Electrolyzer	1	1	1
	Power of Electrolyzer (kW)	7	20	20
PEMFC	Number of PEMFC	-	1	1
	Power of PEMFC (kW)	-	5	5
H_2 Tank	Temperature of Tank (°C)	25	25	25
	Pressure of Tank (bar)	150	150	150
Annual Produced Energy (kWh)		20186	95145	83511
Annual Stored H_2 (m^3)		3273	17942	14370
LCOE ($/kWh)		0.307	0.341	0.349

Table 1 illustrates the components of the on-grid and off-grid connected hybrid systems. Figure 2 shows the amount of the produced and stored H_2 of on-grid and off-grid systems. The levelized cost of energy for the grid-connected system and the off-grid system for design 1 and design 2 was determined as 0.307 $/kWh, 0.341 $/kWh and 0.349 $/kWh, respectively.

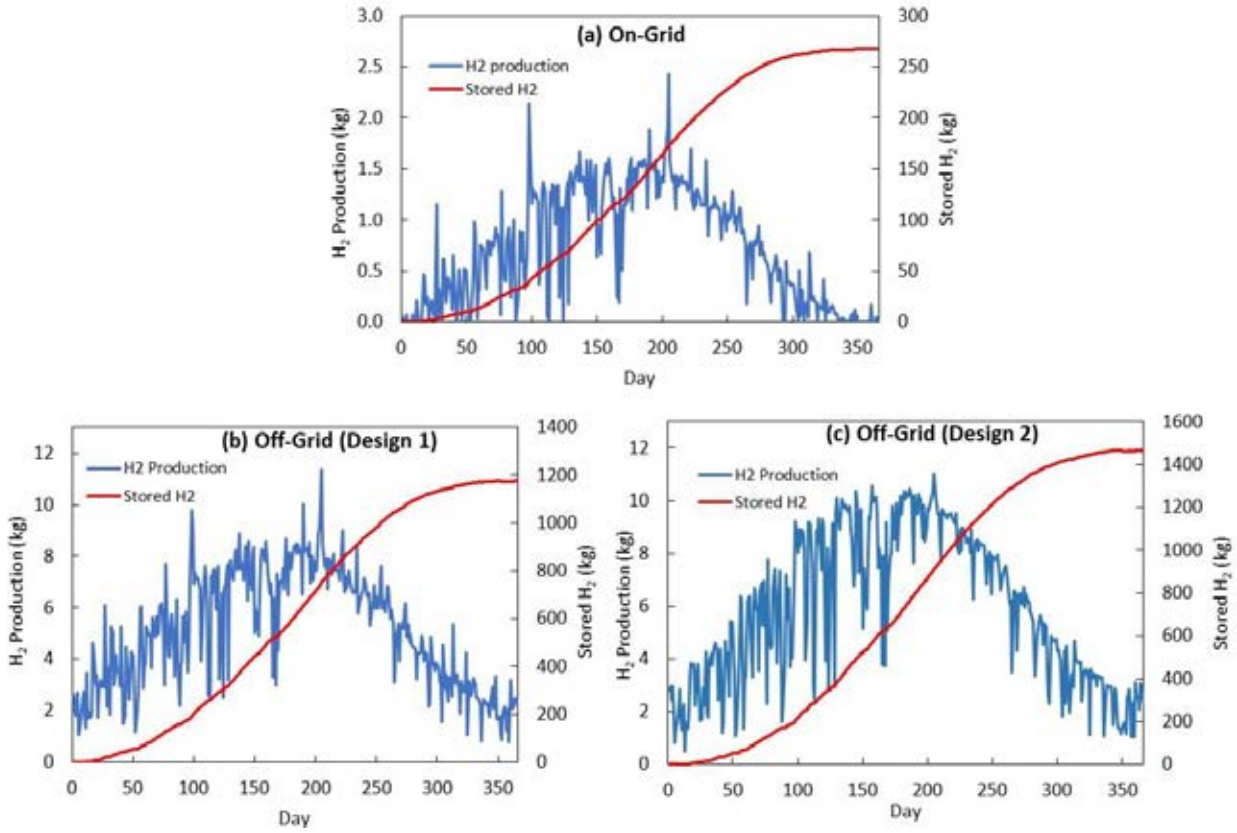


Fig. 2. The amount of produced and stored H_2 in (a) on-grid system, (b) off-grid system (Design 1) and c) off-grid system (Design 2)

CONCLUSIONS

In this study, renewable energy systems based on-grid and off-grid connected hybrid systems were examined. According to solar irradiation, ambient temperature, and wind speed, the number of PV panels and WT's, the power of electrolyzer, and PEMFC were calculated to meet the 25-kWh energy requirement. When the LCOE is examined, although the most suitable system seems to be the on-grid system, there is not much difference between it and other designs. This makes the idea that the entire system to be installed will consist of a renewable energy system more attractive.

ACKNOWLEDGEMENT

This study was supported by The Scientific and Technological Research Council of Turkey (TUBITAK) 1001 (Grant number: 119F182) Project.

REFERENCES

1. Q. Zhao, X. Guo, H. Zhang, M. Ni, and S. Hou, "Performance evaluation of a novel photovoltaic-electrochemic hybrid system," *Energy Convers. Manag.*, vol. 195, pp. 1227–1237, Sep. 2019, doi: 10.1016/J.ENCONMAN.2019.05.097.
2. Z. Qadir *et al.*, "Predicting the energy output of hybrid PV–wind renewable energy system using feature selection technique for smart grids," *Energy Reports*, vol. 7, pp. 8465–8475, Nov. 2021, doi: 10.1016/J.EGYR.2021.01.018.
3. O. Posdziech, K. Schwarze, and J. Brabandt, "Efficient hydrogen production for industry and electricity storage via high-temperature electrolysis," *Int. J. Hydrogen Energy*, vol. 44, no. 35, pp. 19089–19101, Jul. 2019, doi: 10.1016/J.IJHYDENE.2018.05.169.
4. B. Frano, *PEM Fuel Cells | Sigma-Aldrich*. 2013.

WHEC-2022
23rd World Hydrogen Energy Conference
June 26-30, 2022 - Istanbul

#121

OPTIMAL CONFIGURATION OF ENERGY STORAGE AND HYDROGEN PRODUCTION AT RENEWABLE ENERGY SITES IN A POWER SYSTEM WITHOUT FOSSIL FUELS IN JAPAN

[1,2*] *Kosuke Harada,* [2] *Kuniaki Yabe,* [2] *Yasuhiro Hayashi*
[1] ENEOS, 8 Chidori-cho, Yokohama-shi, Kanagawa, Japan
[2] Waseda University, Address, City, Japan

*Corresponding author e-mail: harada.kosuke@eneos.com

ABSTRACT

In an electric power system consisting solely of non-fossil power sources, the capacity of storage batteries and hydrogen production facilities that should be attached to renewable energy power plants depends on the cost of these facilities and the cost of connecting them to the grid. In this study, assuming that a large amount of renewable energy will be introduced into the Japanese power system in 2050, the capacity and annual operation of storage batteries, water electrolysis equipment, hydrogen tanks, and transmission facilities that minimize costs were investigated. The results showed that solar photovoltaic (PV) plants require more variability mitigation equipment than wind farms. At a transmission cost of 1.2 JPY/kW/h, the optimal Li-ion battery capacity and transmission capacity for PV are 9.1 times and 0.18 times that for wind farms, respectively, and only PV is equipped with a 5 MW hydrogen production unit and 15 kNm^3 of hydrogen storage.

Keywords: Renewable energy, Hydrogen, Carbon neutrality, Sector coupling, Linear programming

INTRODUCTION

The decarbonization of energy supply is being promoted worldwide. One of the major challenges in increasing the introduction of renewable energy in Japan is that there are few suitable locations for renewable energy, and they are far from demand areas. Large-scale introduction of offshore wind power plants is expected, but the power grid needs to be significantly strengthened in order to transmit electricity to the demand areas.

Storage batteries and hydrogen production facilities attached to renewable energy site can be expected to reduce the capacity of power transmission facilities by shaving off the peak of renewable energy, and to improve the average unit price of electricity sold through time shifting. As a previous study on the optimization of storage batteries and hydrogen production facilities attached to renewable energy site, the cost of hydrogen supply by water electrolysis equipment (WE) attached to photovoltaic power generation systems has been analyzed in combination with and suppression of storage batteries [1]. Yamamoto et al. have shown that electricity supply costs can be reduced by an energy storage system that optimally combines storage batteries and hydrogen storage while also optimally combining photovoltaic and wind power generation [2]. However, since these models cannot represent electricity supply and demand on a nationwide scale, it is not possible to properly evaluate the effects of time shifting to control the timing of transmission. Therefore, in this study, we developed a model to determine the optimal configuration of ancillary facilities for local renewable energy power plants based on the optimized energy supply and demand in Japan in 2050, when renewable energy has been introduced.

MODELING

In this study, the equipment configuration shown in Figure 1 is investigated. The grid node (G-node) is a huge grid that covers the whole country, and the additional renewables node (AR-node) is a single power plant with 100 MW of photovoltaic (PV) or wind power. Each node is equipped with Li-ion batteries (LIB), water electrolyzer (WE), hydrogen combined-cycle plant (H2CC), and hydrogen tank. AR-node is connected to G-node by the transmission line. The configuration that minimizes the total cost is obtained by linear programming. In order to reduce the amount of computation, the solution is divided into the following two steps. In both steps, the optimal capacity and the hourly energy flow (power flow and hydrogen flow) that gives the minimum total cost are determined by linear programming.

- Step 1: Optimize G-node without AR-node.
- Step 2: Fix the capacity of facilities in G-node and optimize the entire model including the transmission system.

This model can consider the start-up and shutdown costs and partial load efficiency of the H2CC. It can simultaneously optimize 8760 hours of operation because it does not include integer variables and can be calculated quickly. This is particularly effective when considering long-term storage technologies such as hydrogen. The analysis period was one year, and the time resolution was set to one hour. GAMS was used as the calculation tool and CPLEX as the solver.

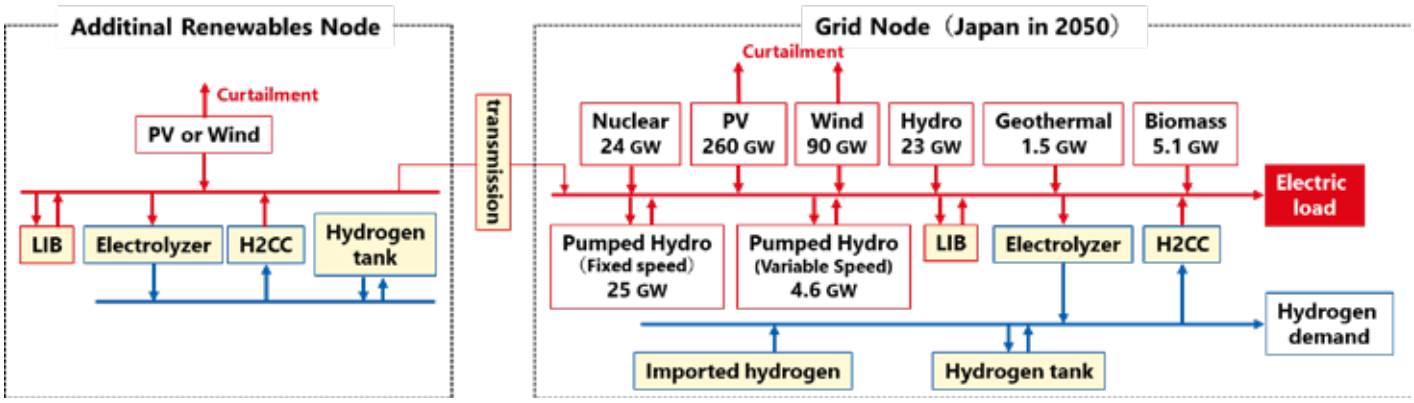


Fig. 1. Electricity-Hydrogen Model. The capacities of the facilities with yellow backgrounds were optimized.

Objective Function and constraints

The objective function *obj* to be minimized is shown in Eq. (1). It represents the sum of the equipment cost for each facility and the imported hydrogen cost.

$$\text{minimize: } obj = \sum_{node}\sum_{j} FC_{node,j} \cdot x_{node,j} + FC_{\text{tie}} \cdot x_{\text{tie}} + \sum_{i} HP \cdot u_{\text{imp},i} \quad (1)$$

The model includes constraints such as simultaneous equalization (electricity and hydrogen), supply and demand adjustment power, reserve power, output upper and lower limits, and storage upper and lower limits.

Exogenous variables

Electricity demand and generation curves were set based on the actual values in Japan in 2020. Hydrogen demand is assumed to be 16.7 million tons per year. Imported hydrogen was assumed to be available at 30 JPY/Nm^3 per hour in any quantity. The specifications of each power source and energy storage facility were set as shown in Table 1. It was assumed that no additional compression power is needed during storage since hydrogen is stored at low pressure.

Table 1. The specifications of each power source and energy storage facility.

Facility	Capital cost	kWh/kW ratio	Roundtrip efficiency
Pumped water	-	8	70 %
LIB	43,000 JPY/kWh	2	88 %
H2CC	161,000 JPY/kW	-	57 %
Water Electrolyzer (WE)	50,000 JPY/kW	-	79 %
Hydrogen tank	4,700 JPY/Nm^3	-	100 %

CASE STUDY

Parameters

In order to investigate the impact of transmission costs on the optimal installed capacity, the unit cost of power transmission (including cost of installation and maintenance of transmission and transformation facilities and power lines) between AR-node and G-node was set in the range of 0.3-1.8 JPY/kW/h for the case study.

Results and discussion

The optimization of G-node in step 1 resulted in the installation of 34 GW of WE and 55 GW of LIB. The capacity utilization of WE are 16 %, and domestic hydrogen production is mainly done when surplus electricity is generated. Out of the total PV and wind power generation of 557 TWh, 531 TWh that is not curtailed cover 62 % of the electricity demand.

In Step 2, AR-node was optimized. Figure 2 (a) and (b) shows the results of the optimal installed capacity in AR-node when the transmission unit price is changed. In the case of PV, even when the transmission unit price is 0.3 JPY/kW/h, the output is leveled by LIB. In the case of PV, output equalization by LIB is performed even when the

transmission unit price is 0.3 JPY/kW/h, but in the case of wind, it is not performed until 1.2 JPY/kW/h. In addition to the fact that PV has a smaller capacity utilization ratio than wind power, it also has a strong cannibalization effect, which lowers the value of electricity transmitted to the national grid when it is generated, because the generation period is concentrated in the daytime nationwide. Therefore, the effect of time shifting and transmission leveling to improve the utilization rate of transmission facilities can be considered to have been more significant.

Figure 2 (c) shows the supply and demand profile within AR-node from July 11 to 13 in the case where the transmission cost is 1.2 JPY/kW/y and the additional renewables is 100 MW of PV. In this case, the optimal transmission capacity is only 17 MW, and most of the power generate by PV is charged by 66 MW of LIB and discharged in the evening (time-shifting). Hydrogen production using surplus electricity will also be implemented by 5 MW of WE. The stored hydrogen in 15 kNm^3 of hydrogen tank will be used to generate electricity when renewable energy is in short supply nationwide. The optimal capacity of a hydrogen tank is 15 hours of rated hydrogen production for WE, which is used for longer term energy storage than LIB, so that LIB and hydrogen storage are introduced in coexistence. The optimal utilization rate of WE at renewables node is only 20.1%.

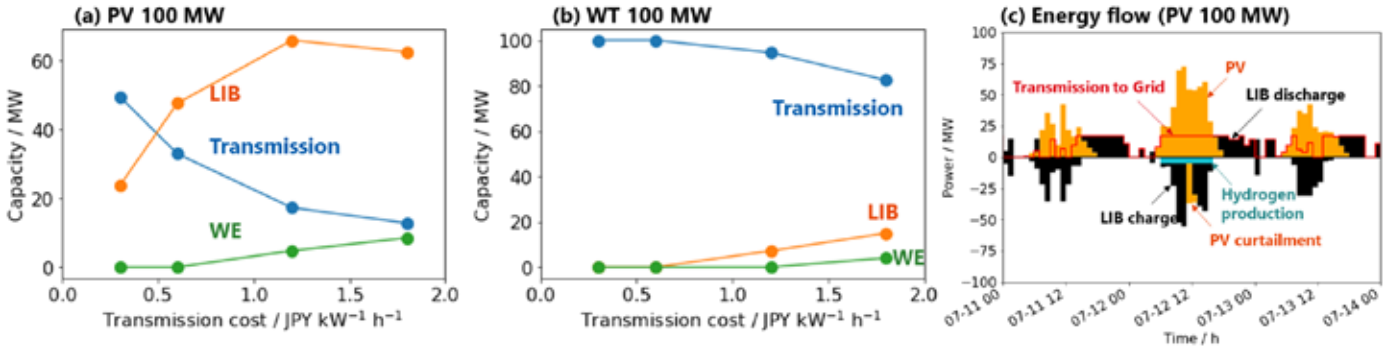


Fig. 2. (a) (b) Optimal installed capacity in AR-node when the transmission unit price is changed when the additional renewables is (a) PV or (b) wind. (c) The supply and demand profile within AR-node from July 11 to 13 in the case where the transmission cost is 1.2 JPY/kW/y and the additional renewable energy is 100 MW of PV.

CONCLUSIONS

In this study, the optimal configuration of ancillary facilities for renewable energy power plant was discussed in Japan in 2050, assuming a configuration that does not use fossil fuels, and the following suggestions were obtained.

- For the same transmission unit price, more electricity storage and hydrogen storage facilities will be required for PV than for wind power on the renewable energy side. This is due to the low utilization rate of PV facilities and the high value of time-shifting due to the strong cannibalization effect.
- In the market environment around the year 2050, for example, when the transmission unit cost is 1.2 JPY/kW/h, the optimal configuration with a 100 MW PV power plant is 66 MW, 132 MWh of LIB and 4.8 MW of WE.

NOMENCLATURE

node	Node (Grid / Additional Renewables)
j	Type of facility to be optimized (LIB, WE, H2CC, hydrogen tank)
i	time ($1 \leq i \leq 8760$)
FC_j	Fixed cost unit price of facility j, JPY/MW/y (JPY/Nm^3/y when j = tank)
x_j	Installed capacity of facility j, MW (kNm^3 when j = tank)
HP	Price of imported hydrogen, JPY/Nm^3
$u_{imp,i}$	hydrogen import volume at time i , Nm^3/h

REFERENCES

1. Kikuchi Y, Ichikawa T, Sugiyama M and Koyama M. 2019. Battery-assisted low-cost hydrogen production from solar energy: Rational target setting for future technology systems, International Journal of Hydrogen Energy, 44:1451-1465.
2. Yamamoto H, Fujioka H and Okano K. 2021. Cost analysis of stable electric and hydrogen energy supplies derived from 100% variable renewable resources systems, Renewable Energy, 178:1165-1173.

WHEC-2022
23rd World Hydrogen Energy Conference
June 26-30, 2022 - Istanbul

#146

THE ROLE OF HYDROGEN FOR A GREENHOUSE GAS-NEUTRAL GERMANY BY 2045

[1*] Thomas Schöb, [1] Peter Markewitz, [1] David Franzmann, [1] Heidi Heinrichs, [1] Leander Kotzur, [1] Jochen Linßen, [1,2] Detlef Stolten
[1] Forschungszentrum Jülich GmbH, Institute of Energy and Climate Research, Techno-economic Systems Analysis (IEK-3), Wilhelm-Johnen-Straße, 52425 Jülich, Germany
[2] RWTH Aachen University, Chair for Fuel Cells, c/o Forschungszentrum Jülich GmbH, Institute of Energy and Climate Research, Techno-economic Systems Analysis (IEK-3), Wilhelm-Johnen-Straße, 52425 Jülich, Germany

*Corresponding author e-mail: t.schoeb@fz-juelich.de

ABSTRACT

Germany's transition to greenhouse gas-neutrality by 2045 requires a dynamic change in all sectors of its energy system. Despite several studies already depicting possible pathways for this transformation, the role of hydrogen in this process remains unclear. In this study we utilize a combination of energy system models to examine the usage and production of hydrogen during this transition in detail. Our results show that 412 TWh of hydrogen are needed in the year 2045, mostly in the industry and transport sector. Particularly, the use of hydrogen in industry is essential as there are no cost-effective alternatives for achieving greenhouse gas neutrality. Furthermore, we illustrate that domestic hydrogen production through electrolysis provides 53% of the needed hydrogen in 2045 and the remaining share is imported from other European countries or Northern Africa via pipelines or ships. Additionally, seasonal storage of hydrogen and hydrogen gas turbines play an important role in balancing the intermittent nature of variable renewable energy sources. In summary, hydrogen usage and production are crucial for a greenhouse gas-neutral Germany and should be integral part of the transformation strategy.

Keywords: Energy system modeling, Greenhouse gas-neutrality, Germany, Hydrogen demand, Hydrogen imports

INTRODUCTION

In 2021 Germany adapted its Federal Climate Change Act [1] and committed itself to become greenhouse gas-neutral by 2045. Furthermore, greenhouse gas emissions shall be reduced by at least 65 percent by the year 2030 compared to 1990 levels. Thus, a rapid transformation of the entire German energy system is necessary. Besides a large expansion of renewable energy sources like wind energy and photovoltaics, energy efficiency measures and a direct electrification in the end use sectors, hydrogen can play an important role in a greenhouse gas-neutral energy system.

However, recently conducted studies show a wide range for the expected German hydrogen demand in 2045. Moreover, the share of hydrogen imports differs significantly in the various scenarios. Prognos et al. [2] expect a hydrogen demand of 265 TWh in 2045, which is mostly used for electricity and heat production. Additionally, they state that 64% of the hydrogen is imported, but without mentioning of the import countries and costs. In contrast, the German energy agency [3] predicts a higher demand of 458 TWh hydrogen in 2045, where the largest consumption originates from the industry sector. Furthermore, they forecast that only 13% of the hydrogen is produced domestically and most of the hydrogen is imported from other European countries, North Africa, Russia, or Turkey. The scenarios conducted by the Fraunhofer Institute for Solar Energy Systems [4] show a range of 120 to 330 TWh hydrogen demand in 2045, but do, in contrast to other studies, not include the usage of hydrogen as a feedstock in industry. Depending on the investigated scenario most of the hydrogen demand stems either from the transport or the industry sector. In the Ariadne-Report [5] a wide range for the hydrogen demand from 100 to 600 TWh in 2045 is given, as different scenarios are investigated, and different energy system models are utilised. While the largest hydrogen demand is consistently based in the industry sector, the hydrogen demand in all sectors varies significantly between the scenarios and models. Moreover, the import share of hydrogen greatly differs between the scenarios and models, but import countries and costs are not given.

This study provides a holistic analysis of the hydrogen demand, production, and imports in a greenhouse gas-neutral Germany. We apply an integrated energy system model which includes all energy demand sectors and the demand for hydrogen as a feedstock. Furthermore, we discuss in detail sources and costs for hydrogen imports to Germany. Additionally, we show the role of long-term hydrogen storage for providing supply security in periods with low energy supply by wind energy and photovoltaics. While the previously mentioned studies investigate some of these aspects as well, to the best of our knowledge no study for a greenhouse gas-neutral Germany by 2045 discusses all aspects in detail and provides a complete view of the future role of hydrogen.

MODELING

In this study we use the model family ETHOS (Energy Transformation Pathway Optimization Suite), which was developed at the Institute for Techno-economic System Analysis (IEK-3) of the Forschungszentrum Jülich [6]. This model suite consists of models which represent energy systems in a high temporal and spatial resolution. The center of this analysis is the optimisation model FINE-NESTOR [7], which depicts the German energy system and analyses cost optimal transformation pathways to greenhouse gas-neutrality. This integrated energy system model represents the sectors energy, industry, buildings, and transport in detail through an hourly resolved network of energy sources, transformation processes, storages and energy demands. The central boundary condition for this analysis are the emission reduction targets from the Federal Climate Change Act, which must be met by the optimisation model. Hydrogen import sources and costs are determined with the simulation model InfH2 [8], which models worldwide energy supply chains. It includes the entire value chain for hydrogen imports from electricity production, electrolyzers and ship transport to Germany. The resulting cost-quantity curve is then passed to the FINE-NESTOR model, which decides if it is cheaper to produce hydrogen in Germany or import it.

RESULTS AND DISCUSSION

Our results show that hydrogen plays an important role for a greenhouse gas-neutral Germany. Fig. 1 displays that already in the year 2030 104 TWh of hydrogen are used. This demand increases by 2045 to 412 TWh. Thereby, the industry sector is with 267 TWh the main consumer of hydrogen. A main demand arises from the usage of hydrogen as a feedstock in the chemical industry, where 112 TWh of hydrogen are used to produce methanol. This methanol in turn is converted to high-value chemicals, which are used in the plastics production. Moreover, 86 TWh of hydrogen are used in the steel industry to produce iron via direct reduction of iron ore. Sensitivity analyses show that the industrial hydrogen demand is robust, as there are no cost-effective alternatives to the usage of hydrogen in this sector.

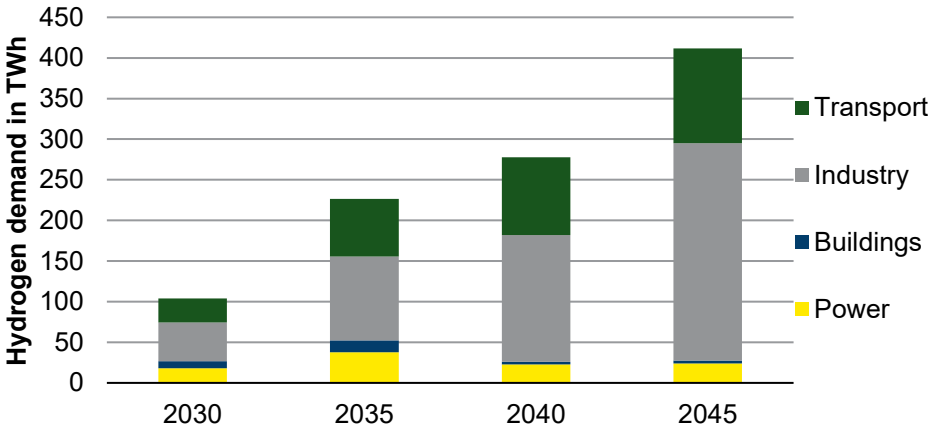


Fig. 1. Hydrogen demand by sectors in the transition to greenhouse gas-neutrality

In the transport sector 117 TWh of hydrogen are used, mainly for heavy trucks with fuel cells. Furthermore, hydrogen is used in the power sector to produce electricity in hydrogen gas turbines. This is especially important during dark doldrums, which describe periods with little energy generation from wind and solar power. In this study we consider a dark doldrum of two weeks in January, where only 10% of the capacity of wind energy turbines and photovoltaic plants is available for electricity production. To overcome this, period controllable power plants like hydrogen gas turbines or biomass power plants are used for meeting the electricity demand. Therefore, about 35.4 TWh of long-term hydrogen storage is needed to supply the hydrogen for the gas turbines and compensate for the seasonal variation of energy production from renewable sources. For this hydrogen storage salt caverns are used, which can mostly be created by conversion of existing natural gas storages.

Another source of flexibility for the energy system are the installed electrolyzers with a production capacity of 71 GW in the year 2045. They adjust their hydrogen production based on the available electricity produced by renewable sources and thereby help to balance the electricity production and demand. In the course of the transition, the full-load hours of centrally installed electrolyzers increase from about 2000 h in the year 2030 to about 2800 h in the year 2045. Fig. 2 shows that in the year 2045 electrolyzers produce 219 TWh of green hydrogen, the remaining 47% of hydrogen is imported from other European countries or Northern Africa via pipeline or ship. It must be noted, that in the year 2030 still about 26 TWh of hydrogen are produced by steam reforming, which is not depicted in Fig. 2.

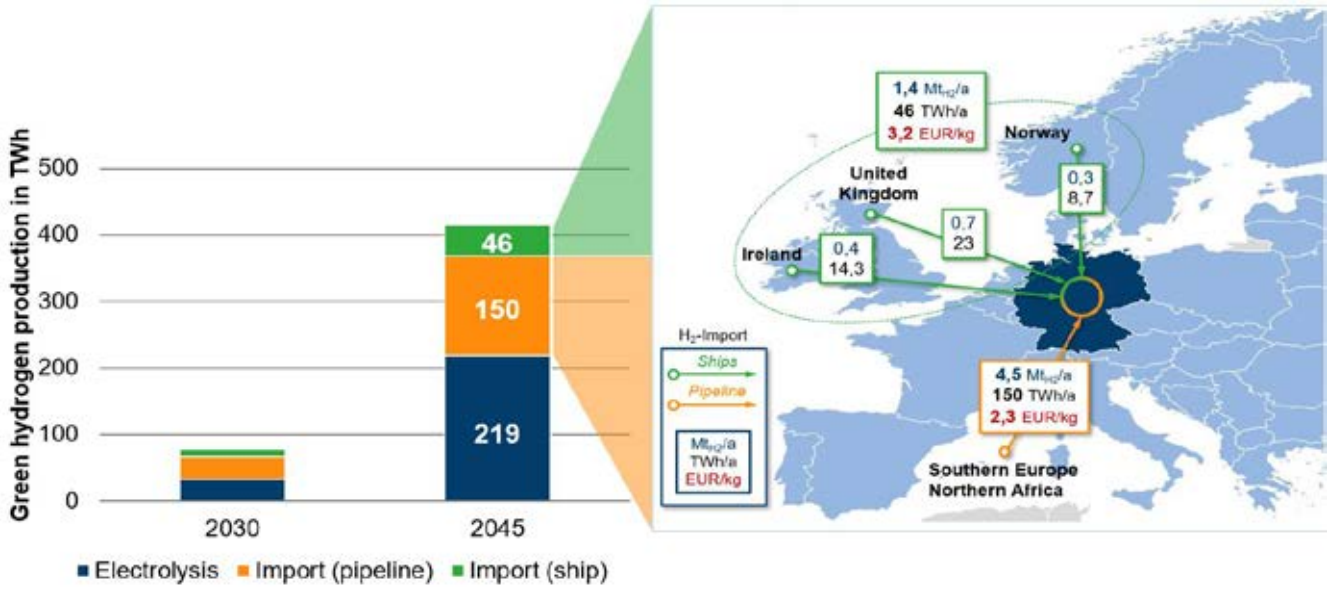


Fig. 2. Green hydrogen production and imports into a greenhouse gas-neutral Germany in the year 2045

With 150 TWh most of the hydrogen is imported via pipelines from Southern Europe or Northern Africa using mainly converted natural gas pipelines. Thus, the import costs of 2.3 €/kg are significantly lower than the average import costs of 3.2 €/kg for hydrogen imports from Northern Europe. This cost difference is mainly caused by the assumption that hydrogen from Northern Europe must be liquefied, transported by ship and then regasified in German harbors. If pipelines could be used to transport the hydrogen to Germany, the price difference would be smaller and more hydrogen could be imported.

CONCLUSIONS

Our study demonstrates that hydrogen is a central aspect of Germany's transition to greenhouse gas neutrality. Hydrogen is mainly used in the industry and transport sector, but also helps to balance the intermittent nature of photovoltaics and wind energy through long-term storage and flexible hydrogen gas turbines. Furthermore, this study shows that the target of the new German Federal Government of 10 GW electrolyzer capacity in 2030 [9] is not sufficient for the transformation, as according to our model results about 15 GW of electrolyzer capacity are needed in 2030. Thus, additional efforts must be made to meet 71 GW electrolyzer capacity in 2045, which is needed to produce 53% of the hydrogen domestically.

REFERENCES

1. Federal Climate Change Act of 12 December 2019 (Federal Law Gazette I, p. 2513), as last amended by Article 1 of the Act of 18 August 2021 (Federal Law Gazette I, p. 3905)
2. Prognos, Öko-Institut, Wuppertal-Institut. 2021. Klimaneutrales Deutschland 2045. Wie Deutschland seine Klimaziele schon vor 2050 erreichen kann. Study on behalf on Stiftung Klimaneutralität, Agora Energiewende and Agora Verkehrswende
3. Deutsche Energie-Agentur GmbH (Ed.). 2021. dena-Leitstudie Aufbruch Klimaneutralität
4. Brandes J, Haun M, Wrede D et al. 2021. Wege zu einem klimaneutralen Energiesystem. Die deutsche Energiewende im Kontext gesellschaftlicher Verhaltensweisen. Update November 2021: Klimaneutralität 2045. Freiburg. Fraunhofer Institute for Solar Energy Systems ISE
5. Luderer G, Kost C, Sörgel D (Eds.). 2021. Ariadne-Report. Deutschland auf dem Weg zur Klimaneutralität 2045 – Szenarien und Pfade im Modellvergleich. Potsdam. Potsdam Institute for Climate Impact Research
6. Stolten D, Markewitz P, Schöb T, Kullmann F et al. 2021. Strategien für eine treibhausgasneutrale Energieversorgung bis zum Jahr 2045 (Kurzfassung). Forschungszentrum Jülich GmbH
7. Lopion P, Markewitz P, Stolten D, Robinius M. 2019. Cost Uncertainties in Energy System Optimization Models: A Quadratic Programming Approach for Avoiding Penny Switching Effects. Energies, Vol. 12, no. 20, p. 4006
8. Heuser P. 2020. Weltweite Infrastruktur zur Wasserstoffbereitstellung auf Basis erneuerbarer Energien. Schriften des Forschungszentrum Jülichs, Reihe Energie & Umwelt, Vol. 532
9. Sozialdemokratische Partei Deutschlands (SPD), Bündnis 90 / Die Grünen, Freie Demokraten (FDP). 2021. Coalition Agreement 2021-2025: Mehr Fortschritt wagen. Bündnis für Freiheit, Gerechtigkeit und Nachhaltigkeit

WHEC-2022
23rd World Hydrogen Energy Conference
June 26-30, 2022 - Istanbul

#148

INTEGRATION OF A RENEWABLE METHANOL PRODUCTION PROCESS WITH A LOW CO_2 EMISSIONS CRGT POWER PLANT

[1*] *Vittorio Tola*, [1] *Francesco Lonis*
[1]University of Cagliari, Department of Mechanical Chemical and of Materials Engineering, Via Marengo 2, Cagliari, Sardinia, Italy

*Corresponding author e-mail: vittorio.tola@dimcm.unica.it

ABSTRACT

Power-to-liquids (PtL) technologies are an interesting way for storing the excess of renewable electricity into liquid fuels. Methanol is well-known as hydrogen carrier and energy feedstock, since it can be stored, transported and used more easily than hydrogen. The renewable methanol produced in PtL processes through the CO_2 hydrogenation process can feed a chemically recuperated gas turbine (CRGT) where the exhaust heat recovery boosts the plant performance. The hydrogen required for PtL is produced in an alkaline electrolyser, while the CO_2 is captured from the CRGT exhausts

Keywords: Methanol, CO_2 hydrogenation, Alkaline electrolysis, Chemically recuperated gas turbine, CO_2 capture

INTRODUCTION

One of the most interesting options to boost the performance of a gas turbine relies on exhaust heat recovery trough thermochemical recuperation (chemically recuperated gas turbine, CRGT). Many CRGT solutions are based on methane steam reforming, characterised by significant drawbacks, due to its high reforming temperature (600–800 °C), higher than the exhaust temperature of commercial gas turbines. On the contrary, methanol can be more suitable for CRGT plants owing to its lower reforming temperature (250–300 °C) [1]. Moreover, methanol can be easily stored, transported and used without significant changes in the existing infrastructure [2]. Typically, methanol is produced from fossil fuels, but renewable methanol can be produced via the application of power-to-X technologies [3], such as the catalytic conversion of hydrogen, from the excess of renewable energy sources (RES), and recycled CO_2 [4].

In this paper a performance assessment of an integrated plant based on a power-to-liquids system and a CRGT fuelled by methanol is presented. Methanol is produced in a synthesis section (MSS) via catalytic CO_2 hydrogenation, it is stored and reused by producing electricity via the CRGT to level out peak demand. The required H_2 is produced in an alkaline electrolyser (AEL) fed by excess of electricity from RES, whereas the CO_2 is captured from the CRGT exhausts. Heat recovery and thermal integration of the overall system are performed to obtain optimal operating conditions and energy savings in each section. Performance energy indexes were also defined for the single sections and the overall system. Functional schemes and dedicated simulation models were implemented using the Aspen Plus commercial software.

SYSTEM CONFIGURATION

Figure 1 shows the functional scheme of both the overall system and the CRGT.

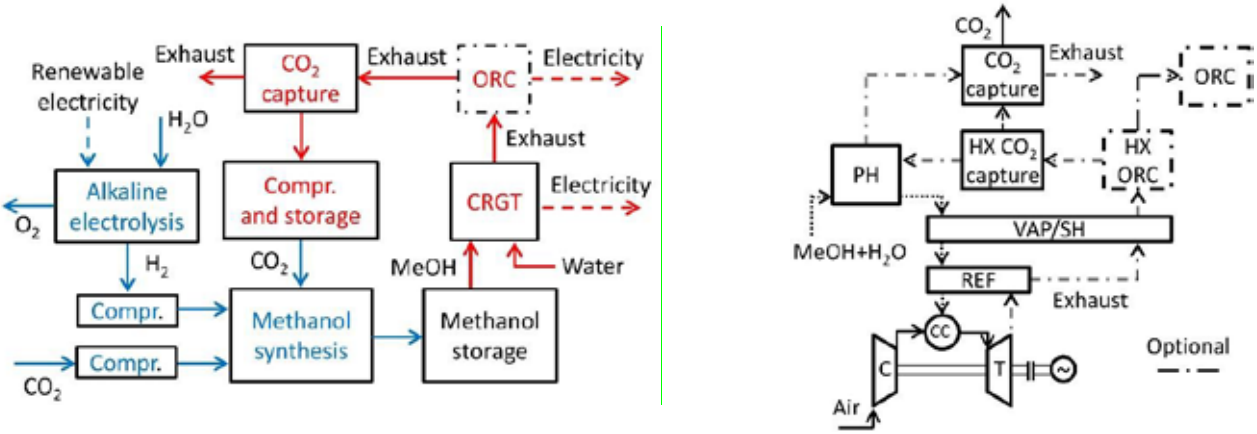


Fig. 1. Functional scheme of the overall system (left) and of the CRGT (right)

In case of excess electricity from RES, an AEL produces hydrogen, that is compressed and feeds, together with CO_2, a synthesis section to produce methanol in a catalytic reactor (charge phase). Methanol is stored at ambient conditions for feeding the CRGT in case of higher electricity demand (discharge phase). The CRGT exhaust firstly feeds the reforming section (vaporization, superheating and reforming of the mixture water-methanol), then is used to regenerate the MEA in the CO_2 removal section and finally, it is absorbed by the water-methanol preheating. To better exploit the residual heat released by the CRGT, the integration between the overall system and an organic Rankine cycle (ORC) was also studied.

The overall system was sized with reference to a 3.2 MW commercial AEL, leading to a H_2 production of 800 Nm^3/h and generating 350 kg/h of methanol in the MSS (about half of the only existing commercial renewable methanol plant [5]). Assuming the same duration for the charge and discharge phases, a power production of about 750 kW was calculated.

Alkaline electrolyzer

The chosen AEL is characterized by a H_2 production of 800 Nm^3/h (about 72 kg/h), requiring a water flowrate of about 640 kg/h. The electrolysis process is performed at a pressure of 5 bar and 65 °C, since under these conditions the efficiency reaches the highest value. The model of the AEL was adapted from the electrochemical model developed by Ursua and Sanchis [6] for simulating commercial water AELs. A specific energy consumption of about 4 kWh/Nm^3_{H2} was found [6].

Methanol synthesis section

CO_2 catalytic hydrogenation takes place in an adiabatic reactor operating at 65 bar and 210 °C [7]. H_2 and CO_2 are compressed and preheated to the reactor inlet temperature. Due to the exothermicity of the CO_2 hydrogenation a reactor outlet temperature of about 290 °C is obtained. Thermal energy from the reactor exhaust cooling is used to preheat the reactor feeding and the crude methanol upstream of the distillation column. Unreacted gases are separated and recycled back to the reactor. Assuming the stoichiometric conditions, a H_2 production of 72 kg/h requires about 520 kg/h of CO_2 to produce 350 kg/h of methanol. An extensive description of the MSS can be found in Lonis et al. [8].

Chemically recuperated gas turbine

The CRGT power plants is based on a small-size gas turbine characterized by a maximum temperature of 1100 °C and a pressure ratio equal to 8. The CRGT is fuelled by the reformed gas, which composition (mainly hydrogen, water and CO_2) strictly depends on the water-to-methanol molar ratio “n” entering the reforming section. The CRGT is integrated with a post-combustion CO_2 removal section based on a mixture of water and monoethanolammine (MEA) (30%wt). Assuming a CO_2 removal efficiency equal to 90%, a thermal power of about 425 kW is required for the regeneration of the MEA.

ORC section

An ORC plant was considered to increase the power output of the system by exploiting the residual heat of the CRGT exhausts. Benzene was chosen as working fluid and the regenerated ORC operates between 0.218 and 46.5 bar, and between 25 and 290 °C. The ORC shows a global efficiency equal to 0.26.

Performance indexes

Several performance indexes were defined to establish the performance of the subsystems and of the overall plant. The electrolysis efficiency is defined as the ratio between the chemical power of the hydrogen $\dot{m}_{H_2} \cdot LHV_{H_2}$ and the electric power consumed in the electrolysis process including auxiliaries $P_{AEL} + P_{BOP,AEL}$, as shown in Eq. (1):

$$\eta_{AEL} = \frac{\dot{m}_{H_2} \cdot LHV_{H_2}}{P_{AEL} + P_{BOP,AEL}} \quad (1)$$

From the methanol chemical power. an actual overall efficiency η_{MSS} and a chemical energy conversion efficiency $\eta_{MSS,C}$ of the MSS can be defined as reported in Eq. (2), considering or not the MSS auxiliaries $P_{BOP,MSS}$ contribution:

$$\eta_{MSS} = \frac{\dot{m}_{MeOH} \cdot LHV_{MeOH}}{\dot{m}_{H_2} \cdot LHV_{H_2} + P_{BOP,MSS}} \; ; \; \eta_{MSS,C} = \frac{\dot{m}_{MeOH} \cdot LHV_{MeOH}}{\dot{m}_{H_2} \cdot LHV_{H_2}} \quad (2)$$

WHEC-2022
23rd World Hydrogen Energy Conference
June 26-30, 2022 - Istanbul

An efficiency of the power-to-liquids process η_{PtL}, is obtained considering the efficiency chain of the electrolysis and MSS (Eq. (3)), where φ_{AEL} represents the fraction of power entering the AEL with respect to the total power (Eq. (4)):

$$\eta_{PtL} = \frac{\dot{m}_{MeOH} \cdot H_{i,MeOH}}{P_{AEL}+P_{BOP,AEL}+P_{BOP,MSS}} = \eta_{AEL} \cdot \varphi_{AEL} \cdot \eta_{MSS,C} \quad (3) \; ; \quad \varphi_{AEL} = \frac{P_{AEL}+P_{BOP,AEL}}{P_{AEL}+P_{BOP,AEL}+P_{BOP,MSS}} \quad (4)$$

The efficiency of the electricity production, defined as the ratio between the net power and the methanol chemical power, taking into account or not the ORC, is shown in Eq. (5):

$$\eta_{CRGT} = \frac{P_{CRGT}-P_{BOP,CRGT}}{\dot{m}_{MeOH} \cdot LHV_{MeOH}} \; ; \; \eta_{CRGT+ORC} = \frac{P_{CRGT}+P_{ORC}-P_{BOP,CRGT}-P_{BOP,ORC}}{\dot{m}_{MeOH} \cdot LHV_{MeOH}} \quad (5)$$

Globally, the power-to-power efficiency of the overall system η_g can be defined as the ratio between the net power produced and the total power entering the overall system, as shown in Eq. (6):

$$\eta_g = \frac{P_{CRGT}-P_{BOP,CRGT}}{P_{AEL}+P_{BOP,AEL}+P_{BOP,MSS}} = \eta_{PtL} \cdot \eta_{CRGT} \; ; \; \eta_g = \frac{P_{CRGT}+P_{ORC}-P_{BOP,CRGT}-P_{BOP,ORC}}{P_{AEL}+P_{BOP,AEL}+P_{BOP,MSS}} = \eta_{PtL} \cdot \eta_{CRGT+ORC} \quad (6)$$

RESULTS AND DISCUSSION

The proposed power-to-liquids system is characterized by an efficiency η_{PtL} slightly lower than 0.57, due to an electrolysis efficiency η_{AEL} of about 0.72 and an actual efficiency of the methanol synthesis section η_{MSS} of about 0.765.

Different sizes for the ORC were considered, varying the thermal power available from the CRGT exhaust. An increase of the ORC thermal input reduces the heat available in the reformer, leading to a lower value of “n”. A reference value of 300 kW was set, leading to a n value higher enough to avoid carbon formation. The introduction of the ORC causes a reduction of the CRGT efficiency, due to the lower flowrate in the gas turbine, while boosting the efficiency of the electricity production from 0.366 to 0.372. Globally, an overall power-to-power efficiency η_g slightly lower than 0.22 can be obtained. Tables 1 and 2 summarize the main results of the proposed system in terms of performance indexes and net power of the electricity production sections.

Table 1. Performance indexes of the AEL and MSS

Performance index	Value
η_{AEL}	0.722
φ_{AEL}	0.934
η_{MSS}	0.766
$\eta_{MSS,C}$	0.841
η_{PtL}	0.567

Table 2. Parameters of the CRGT and ORC sections

Parameter	CRGT	CRGT+ORC
P_{CRGT}	703.3 kW	656.9 kW
P_{ORC}	-	56.6 kW
η_{CRGT}	0.3662	0.3420
$\eta_{CRGT+ORC}$	0.3662	0.3716
η_g	0.2149	0.2180

Finally, a parametric analysis of the CRGT in function of the maximum temperature and pressure ratio was carried out.

CONCLUSIONS

A power-to-methanol energy storage system based on an AEL, a methanol synthesis section and a CRGT power plant was analysed, with and without the integration with an ORC. CRGT systems can be an interesting option to use the methanol produced through a CO_2 hydrogenation process, especially if integrated with an ORC and a CO_2 removal section. Indeed, despite an overall power-to-power efficiency slightly higher than 0.21, the proposed system can store renewable energy surplus and then producing electricity with very low CO_2 emissions. The introduction of the ORC allows a better use of the heat released by the CRGT, improving the global efficiency by 0.3 ppts, from 0.215 to 0.218.

REFERENCES

1. Cocco D, Tola V, Cau G. 2006. Performance evaluation of chemically recuperated gas turbine (CRGT) power plants fuelled by di-methyl-ether (DME). Energy 31: 1446-1458
2. Olah GA, Goeppert A, Prakash GKS. 2009. Beyond oil and gas: the methanol economy. 2nd ed. Weinheim, Germany: Wiley-VCH Verlag GmbH & Co. KGaA
3. de Vasconcelos BR, Lavoie JM. 2019. Recent advances in power-to-X technology for the production of fuels and chemicals. Front Chem 7:1–24.
4. Galindo Cifre P, Badr O. 2007. Renewable hydrogen utilisation for the production of methanol. Energy Conversion Management 48:519–27.

5. Atsonios K, Panopoulos KD, Kakaras E. 2016. Investigation of technical and economic aspects for methanol production through CO2 hydrogenation. International Journal of Hydrogen Energy 41:2202–14
6. Ursua A, Sanchis P. 2012. Static-dynamic modelling of the electrical behaviour of a commercial advanced alkaline water electrolyser. International Journal of Hydrogen Energy 37:18598–614
7. Van-Dal ÉS, Bouallou C. 2013. Design and simulation of a methanol production plant from CO2 hydrogenation. Journal of Cleaner Production 57:38–45.
8. Lonis F, Tola V, Cau G. 2019. Renewable methanol production and use through reversible solid oxide cells and recycled CO_2 hydrogenation. Fuel 246: 500-515.

WHEC-2022
23rd World Hydrogen Energy Conference
June 26-30, 2022 - Istanbul

#172

VERTICALLY INTEGRATED PROJECTS AS A TRANSFORMATIVE PEDAGOGY FOR GREEN HYDROGEN STUDY ABROAD PROGRAMS

[1*]Stewart F. Bauserman, [2]Johnny Nahui Ortiz, [3]Jose Cesar Ramos Saravia, [1]John W. Sheffield, [4]Matteo J. Mereu
[1] Purdue University, School of Engineering Technology, West Lafayette, IN, U.S.A.
[2] Universidad Nacional de Ingeniería, Facultad de Ingeniería Ambiental, Lima, Peru
[3] Universidad de Ingeniería y Tecnología, Ingeniería de la Energía y Ingeniería Mecánica, Lima, Peru
[4] Purdue University, Mechanical Engineering Technology, West Lafayette, IN, U.S.A.

*Corresponding author e-mail: stew@purdue.edu

ABSTRACT

The introduction of transformative pedagogy provides for active learning in the incentivized, faculty-led, study abroad programs focused on green hydrogen projects. These study abroad programs utilize Purdue's Hydrogen Learning HUB, which is comprised of the Vertically Integrated Projects, Collaborative Online International Learning, Hub of Intercultural Learning, and Strategic Doing educational programs. Two faculty-led study abroad programs have been developed, one in Peru during Spring Break and one in Europe during a 4-week summer term. The Peruvian program is focused on two open-pit mines, the Falchani Lithium and the Quellaveco Copper projects, for green hydrogen technology integration into the mining operations. American Lithium Corporation is developing the Falchani mine located in the Andes Mountains. The Falchani mine is the world's sixth-largest hard rock lithium deposit. The Quellaveco mine, which is being developed by Anglo American Perú, in partnership with the Mitsubishi Corporation, is one of the world's largest copper deposits. The summer study abroad focuses on remote island communities, such as the Orkney Islands, as an ideal candidate for evaluation of green hydrogen technology integration into remote communities on islands. Currently, the community-based renewable energy systems on the Orkney Islands generate more than 130% of the electric energy consumed.

Keywords: Green hydrogen, Transformative pedagogy, Vertically integrated projects

INTRODUCTION

The Hydrogen Insights 2021 report [1] published by the Hydrogen Council [2-4] in collaboration with McKinsey & Company notes that, with the scaling up of hydrogen projects and the falling renewable energy costs, the Total Cost of Ownership (TCO) of green hydrogen could be the most competitive solution in more than 20 applications by 2030, including heavy-duty mining trucks. Purdue University introduced a Green Hydrogen Study Abroad program targeting the earliest breakeven Total Cost of Ownership (TCO) of Fuel Cell Electric Vehicles (FCEV) in the transport sector, i.e. heavy-duty, haul trucks in open-pit, surface mining operations [5]. Purdue University introduced a second Green Hydrogen Study Abroad program targeting remote [6], small-island communities as early net-zero winners in the Race-to-Zero, such as the Orkney Islands. The first Study Abroad program focuses on two open-pit mines, the Falchani Lithium and the Quellaveco Copper projects, for green hydrogen technology integration into the mining operations. American Lithium Corporation is developing the Falchani mine located in the Andes Mountains. The Falchani mine is the world's sixth-largest hard rock lithium deposit. The Quellaveco mine, which is being developed by Anglo American Perú in partnership with the Mitsubishi Corporation, is one of the world's largest copper deposits. The second study abroad focuses on remote island communities, such as the Orkney Islands, as an ideal candidate for evaluation of green hydrogen technology integration into remote communities on islands. Currently, the community-based renewable energy systems on the Orkney Islands generate more than 130% of the electric energy consumed.

First introduced by Georgia Tech, the Vertically Integrated Projects (VIP) [7] program provides a transformative mindset to enhance educational outcomes by engaging undergraduate and graduate students in ambitious, long-term, global, interdisciplinary project teams that are led by faculty. VIP programs are now active in over 40 universities across the globe. The VIP program extends project-based learning with the inclusion of innovative study abroad programs. These Purdue University study abroad programs [8] utilize a Hydrogen Learning HUB, which is comprised of the VIP, Collaborative Online International Learning (COIL), Hub of Intercultural Learning (HubICL), and Strategic Doing [9] educational programs.

The Green Hydrogen Study Abroad program focused on mining trucks at two open-pit mines in Peru as ideal candidates for evaluation of green hydrogen technology integration into the mining operation. The mining projects are known as the Falchani Lithium Project and the Quellaveco Copper Project. The first surface mine is being developed by American Lithium Corporation and is known as the Falchani Lithium Project and located on the

Macusani Plateau in the Andes Mountains of the south-eastern part of Peru. It is estimated that the Falchani Lithium deposit to be the world's sixth-largest hard rock lithium deposit. The Falchani Lithium Project incorporates many green initiatives, including the recycling of up to 90% of process water, a self-sufficient, high-efficiency green energy on-site acid plant, and goals of adding future "green energy" initiatives. The second surface mine is the Quellaveco Copper Project and is being developed by Anglo American Perú, in partnership with the Mitsubishi Corporation near Moquegua in southern Peru, as one of the world's biggest undeveloped single porphyry copper deposits with a reserve base of more than 1.3 billion tonnes. ENGIE Energía Perú and Anglo American Perú signed an agreement to convert the total electricity supply for the Quellaveco mines (187 MW) to 100% green energy. ENGIE Energía Perú will source the renewable energy from its Punta Lomitas wind power plant, an in-development wind farm with a joint nominal capacity of 260 MW located in Ocucaje-Ica and a 60 km transmission line connecting the plant with the National Interconnected Electric System. Figure 1 illustrates a solar PV microgrid for the Falchani Lithium mine utilizing a hybrid battery/hydrogen energy storage system to provide both electricity and hydrogen for the fleet of fuel cell, electric-drive mining trucks equipped with trolley assist.



Fig. 1. Solar PV Microgrid integration into the Falchani Lithium Mining Operation

A four-week summer study abroad program focuses on remote island communities, known as the Orkney Islands, was selected as an ideal candidate for evaluation of green hydrogen technology integration into remote communities on islands. Orkney is an archipelago in the Northern Isles of Scotland. Orkney has about 70 islands, of which 20 are inhabited with a total population about 22,000. Since the Orkney Islands have an abundance of wind, waves and tides energy resources, they have become a green hydrogen hub for R&D projects demonstrating the use of hydrogen to decarbonize electric power, heat and transport applications. Currently, these community-based renewable energy systems generate more than 130% of the electric energy consumed on the islands, even with the growing number of plug-in cars on the islands. The largest of these green hydrogen projects is the Flotta Hydrogen Hub powered by offshore wind turbines.

TRANSFORMATIVE PEDAGOGY

Transformative pedagogy provides for active learning through incentivized, faculty-led, study abroad programs. It is imperative that faculty members in a faculty-led program [1] focus on learning outcomes and the assessment of those outcomes. Example of Transformative pedagogy at Purdue include (a) Team Project-Based Learning [10], (b) Global and Cultural Immersions, and (c) Innovative Teaching Methods. *Team Project-Based Learning* allows for learning through the lens of a project, along with exposure to real-world team dynamics, problem-solving and deadlines, which prepares graduates for success. *Global and Cultural Immersions* allows students to gain insights into cultures other than their own, broadening their perspectives and becoming more marketable to employers. *Innovative Teaching Methods* allows for a shift away from lectures to active-learning such as faculty-led study abroad programs.

CONCLUSIONS

Using Transformative Pedagogy in the VIP faculty-led study abroad programs in green hydrogen provides for active and engaged learning. The faculty-led study abroad program relies on creating a student-centered learning environment where innovative skills such as applying new green hydrogen technologies to the greening of mining fleets and integrating hydrogen energy systems for net zero communities are learned. The world economy and energy needs are in the throes of transformation, Transformative Pedagogy in a faculty-led study abroad program provides a high-impact approach for the application of green hydrogen energy systems.

ACKNOWLEDGEMENT

The authors would like to acknowledge the financial support from Dr. Michael A Brzezinski, Dean of International Programs at Purdue University; Elizabeth Barajas, Purdue Polytechnic's Director of Globalization; and Dr. Julien Noel, Director de Carrera - Ingeniería de la Energía e Ingeniería Mecaníca y Director de Operaciones y Servicios Académicos, Universidad de Ingeniería y Tecnología; and Dr. Carla B. Zoltowski, Director of the Vertically Integrated Projects (VIP) Program at Purdue University.

REFERENCES

1. https://hydrogencouncil.com/wp-content/uploads/2021/02/Hydrogen-Insights-2021.pdf Accessed on December 15, 2021.
2. https://hydrogencouncil.com/wp-content/uploads/2017/11/Hydrogen-Scaling-up_Hydrogen-Council_2017.compressed.pdf Accessed on December 15, 2021.
3.https://hydrogencouncil.com/wp-content/uploads/2021/11/Hydrogen-for-Net-Zero.pdf Accessed on December 15, 2021.
4. https://hydrogencouncil.com/wp-content/uploads/2020/01/Path-to-Hydrogen-Competitiveness_Full-Study-1.pdf Accessed on December 14, 2021.
5. Kalantari H, Ghoreishi-Madiseh SA, and Sasmito AP. 2020. Hybrid Renewable Hydrogen Energy Solution for Application in Remote Mines. Energies 13(23), 6365.
6. Dawood F, Shafiullah GM, Anda M. 2020. Stand-Alone Microgrid with 100% Renewable Energy: A Case Study with Hybrid Solar PV-Battery-Hydrogen. Sustainability 2020, 12(5): 2047.
7. https://www.vip.gatech.edu/node/491 Accessed on November 28, 2021.
8. Brzezinski M, Acheson-Clair K and Cox R. (n.d.). Incentivizing Faculty-led Study Abroad and Intercultural Learning Outcomes: A Grant Program Model. Purdue University.
9. Morrison E, Hutcheson S, Nilsen E, Fadden J, and Franklin N. 2019. Strategic Doing. Wiley.
10. Strachan SM, Marshall S, Murray P, Coyle EJ, and Sonnenberg-Klein J. 2019. Using Vertically Integrated Projects to embed research-based education for sustainable development in undergraduate curricula. International Journal of Sustainability in Higher Education, 20(8), 1313–1328.

WHEC-2022
23rd World Hydrogen Energy Conference
June 26-30, 2022 - Istanbul

#175

FUEL CELL-BATTERY HIBRIDIZATION FOR AN UNMANNED SURFACE VEHICLE POWERPLANT

[1*]Diego Tejada-Guzmán, [1]Laura Vargas, [1]Eduardo M. López, [1]Fernando Isorna, [2]Víctor García, [2]Alberto Giménez, [2]Manuel Martínez, [2]Luis Domenech, [2] Fernando Sánchez, [2]Jordi Renau

[1] Instituto Nacional de Técnica Aeroespacial (INTA), Área de Energías Renovables, Ctra. S. Juan- Matalascañas, km. 34, 21130 Mazagón-Moguer (Huelva), Spain

[2] Cardenal Herrera University – CEU Universities, C/ San Bartolomé 55, Alfara del Patriarca (Valencia), Spain

*Corresponding author e-mail: dtejguz@inta.es

ABSTRACT

Remote Piloted Vehicles are in the aim of the experts because of its wide usability. The main disadvantage of battery based technologies are their low endurance operation time due to high energy demand coming from propulsion system. This paper proposes a way to overcome this problem by means of a fuel cell (FC) and batteries hybrid system. The hybrid system designed consists in a 500W fuel cell and a 3S-3P battery in active configuration to deliver enough energy to feed the different loads onboard during at least 7h mission. The final target system increase of the total mission time and reliability of the whole system.

Keywords: Hybrid system, Fuel cell, Batteries, Hydrogen, Stack

INTRODUCTION

Unmanned vehicles begin to gain attention as they can be used in a wide range applications as repetitive or unpleasant tasks, those tasks that involve danger to an operator, between others. Electric propulsion systems become a good option due to their high performance and low emissions compared to internal combustion engines. Despite of achieve power requirements, only battery-based systems present disadvantages as short life cycle and long charging periods, etc. [3-5] a Fuel cell (FC) and batteries hybrid systems are intended to combine advantages of both technologies. Such as increase the operating range of the vehicle, reliability, life cycle and performance. There are two possible configurations for the interaction between fuel cells and batteries, which depend on the energy regulation, namely, passive or active configuration. Passive configuration uses passive electronics like diodes to couple the devices, it is a higher specific (W kg^{-1}) power powerplant which means simplicity in the end, but require to match voltages between FC and batteries which is not possible sometimes. Active configuration regulates the energy flows with energy electronics like DC/DC converters to adapt the operation point to optimize the efficiency, although it does not require the voltage matching between batteries and FC, but control electronics become more complex as additional sensors and actuators must be used [6].

This paper details the development and testing of a hybrid power plant, designed to be integrated in an unmanned surface vehicle (USV) for environmental monitoring. Systems such as hydrogen storage, electricity production by means of a FC and Li-ion batteries, monitoring system, navigability, positioning and propulsion subsystems will be onboard. Energy system will work in an active configuration, i.e., a DC/DC converter will fix the optimal operating point of the FC to achieve the energy demand. Nevertheless, usability of the whole platform will be extensive and will depend on the payloads onboard.

MATERIALS AND METHODS

The hybrid system will be mounted in the hull of a ship, and it is designed specifically for this purpose depending on the power requirements of the platform. The whole system can be divided in four well differentiated parts, and they will interact between each other:

Hydrogen subsystem

This system includes hydrogen piping from the gas storage tank until consumption point at FC. It also includes devices such a pressure regulator at 0.5bar, security devices (press release device PRD) and solenoid valves to control gas inlet and venting in the stack. A DC/DC converter fixes the best performance of the system depending on the energy demand. And finally, the proper hydrogen storage tank, which depending on its size, the operating time will be rise or decreased.

Battery subsystem

A battery bank is mounted as main power supply for the whole vehicle. Additionally, battery bank act as an energy buffer so the different system will simultaneously input and draw the energy. The initial conception of the system is

that batteries will assume high peak consumptions during short periods while hydrogen system supply energy to cover average demand as well as charging the battery bank. A battery bank consists in a number of cells in series (S) and a number of arrays in parallel (P). The association in series set the working voltage level and the number of parallel arrays set the capacity and the maximum instant demand from the rest of the platform. This way, as propulsion system admits up to 3 cells in series (3S), probably, the battery bank would be 3S and at least 3P. Parallel number is only limited by the maximum affordable weight of the ship.

Energy monitoring and management system (EMMS)

As a part of the above systems, the ship will be equipped with an Energy Monitoring and Management System (EMMS). EMMS consist of voltage, current, temperature and pressure sensors which allows the user to know the energy status of the platform. Those measurements let us to know where the energy is coming from and where it is spent. In addition, EMMS can decide to switch off a power source (FC or the whole system) when some maximum admissible limits are reached such as low battery, low voltage of the stack, low pressure at gas storage, etc. This is possible thanks to electronic switches (MOSFETS, transistors, etc) driven by the microcontroller in the EMMS. In active configurations, EMMS plays a special role due to it is in charge to control the DC/DC converter to couple FC to the rest of the power supply system.

Navigation and propulsion subsystem

This subsystem is responsible for moving, maneuvering and positioning the ship. By means of a flight controller board based on Ardupilot and Mission Planner software, the vessel will be able to control directional surfaces (rudder), the main motor, GPS communication for positioning as well as IMU communication for knowing the situation of the ship. Final user would schedule a trajectory to execute autonomously or would follow the route manually by means of a Radio Control (RC) transmitter. The device will increase complexity of the whole system as it needs sensors, the knowledge of the software, there are a lot of parameters to configure, etc. However, a lot of functionalities will be added, and it allow extra safety and reliability to the platform. Some of those functionalities are the return to home in case of failure, path planning, real time telemetry, payload control, video streaming, between others.

An electronic speed controller will manage the energy for the brushless three-phase motor wide used in RC field and RC servos ensure enough power to keep steering over the vessel during the whole mission.

Figure 1 shows a diagram of the whole system and the interaction between subsystems above explained.

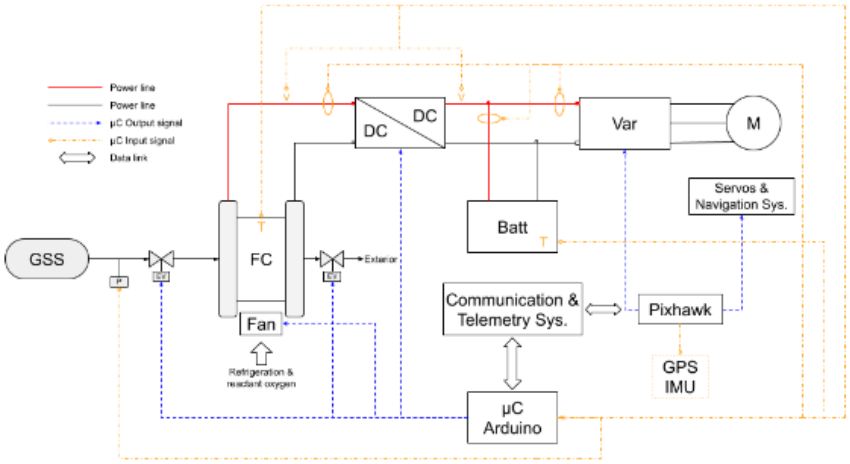


Fig. 1. Block diagram

RESULTS AND DISCUSSION

To analyze feasibility of the installation of the hybrid system, the first test consists in measuring the energy consumptions of the vehicle in a target mission, in this case the monitoring of physical, chemical and biological parameters in a lake. During this test, the vehicle was equipped with a 30A Electronic Speed Controller (ESC) and a brushless motor as a propulsion system, a Pixhawk with standard M8n GPS device as onboard computer and the very early version of the energy monitoring and management system to serve as a data-logger. The vessel was

tested at 2 knots of constant speed in a swell under 0.3 m in height. These real data serve to obtain different load profiles, which are used in test benches to evaluate the hybrid power systems configuration.

Although the power system has been designed for a higher demanding applications, for this particular mission and application of the USV, which no high speed nor sudden movements are required, the consumption is around 300 W. Energy strategy to be pursued will be that the fuel cell will cover the average consumption while battery will supply energy during power peaks in the demand due to proper fluctuations over it. In this case, the proposed hybrid system includes a 500W fuel cell, 4.7 L and 300 bar hydrogen tank and 3S-3P, 27Ah LiPo Battery. It is important to mention that the fuel cell is intended to cover a higher demand than required for this application if it means necessary.

Considering the performance of the fuel cell and converter and power density of the hydrogen at 300 bar –45 and 96% respectively and 0.7 kWh/l– available energy will be 1.37 kWh. The battery voltage and current meet ESC and motor specifications given by manufacturers. Preliminary characterization of the main components of the systems is done, and the results of the testing of the hybrid power system will be presented at the conference.

CONCLUSIONS

After several tests carried over a prototype of the USV platform, a profile of the energy demand has been obtained, and a hybrid system has been proposed to extend its operating time. The prototype vessel, powered currently by batteries would operate for 3 h in the best conditions and an average 300 W load. The hybrid system proposed will allow to increase the operating time up to 7 h, depending on the features of the hydrogen storage system, weather conditions, etc. In terms of energy density, if the vessel works with the same weight in batteries, it will reach 258 Wh/kg. By means of the hybrid system, the energy density decreases to 205 Wh/kg. Despite of its lower energy density, dead time due to recharge the system will be significantly reduced as refueling the hydrogen system only last for a few minutes. Now, tasks to integrate hybrid FC and batteries energy system in a specific test bench, in order to subject the system to a load profile similar to the one obtained previously under real conditions. Once carried a successfully test at the test bench, the hybrid system will be mounted in the real platform to assess it in a real operation.

ACKNOWLEDGEMENT

This work has been funded by the Spanish ministry of science and innovation under the project DOVELAR (Ref.: RTI2018-096001-B-C33).

REFERENCES

1. https://www.iea.org/reports/world-energy-outlook-2021, World energy outlook 2021. Accessed on December 12, 2021.
2. https://www.roadmap2050.eu/ European Climate Foundation. Roadmap 2050. Accessed on December 12, 2021.
3. E. López González, R. Rengel Gálvez, L. Vargas Vázquez, J. Sáenz Cuesta, M.A. Ridao, E. Hernández, J. Brett, HYCELTEC 2019, Design, development and testing of fuel cell systems for an autonomous underwater vehicle.
4. M.A. Hannan, M.M. Hoque, A. Mohamed, A. Ayob, Review of energy storage systems for electric vehicle applications: Issues and challenges, Renewable and Sustainable Energy Reviews 69, (2017) 771-789.
5. B. Scrosati and J. Garche, “Lithium batteries: Status, prospects and future”, Journal of Power Sources, vol. 195, no. 9, pp. 2419–2430, 2010.
6. Y.-S. Chen, S.-M. Lin, B.-S. Hong, Experimental Study on a Passive Fuel Cell/Battery Hybrid Power System, Energies 2013, 6, 6413-6422; doi:10.3390/en6126413.

WHEC-2022
23rd World Hydrogen Energy Conference
June 26-30, 2022 - Istanbul

#176

NUMERICAL INVESTIGATION OF THERMAL PERFORMANCE OF HYDROGEN -FUELLED MICRO-COMBUSTOR WITH TRAPEZOIDAL RIB

[1*] *Abdelbasset Lachraf,* [2] *Mohamed Si Ameur*
[1]Laboratory of the Industrials Energy Systems Studies, Mechanical Engineering Department, Faculty of Technology, University of Batna 2, Batna 05000, Algeria
[2] Laboratory of the Industrials Energy Systems Studies, Mechanical Engineering Department, Faculty of Technology, University of Batna 2, Batna 05000, Algeria

*Corresponding author e-mail: a.lachraf@univ-batna2.dz

ABSTRACT

The miniaturization movement in the recent years motivated the development of micro-combustion-based power generators. The micro-thermophotovoltaic (MTPV) relies on converting the heated micro-combustor radiation into electricity using PV cells. Enhancement of heat transfer and wall temperature distribution in a MTPV combustor is strongly influenced by the combustor structure. In this regard, a novel planar micro-combustor geometrical configuration based on creating a stable recirculation zone near the chamber wall using trapezoidal rib, is proposed. This work numerically investigated the flow and flame behavior in the proposed micro-combustor. It also studied the effect of hydrogen to air mixing ratio and the inlet velocity on the wall temperature distribution. The results shows that the wall temperature is increased by 3.4% to 9.24% with the increase of the inlet velocity and decreases for lean and rich hydrogen/air mixture by 0.33% to 3.92%. The average outer wall temperature is higher than that without ribs. The chemical reaction products locked in the recirculation zones formed around the ribs that acts just like an igniter and the flame is more stable and continuous. The proposed structure is found to have a better performance in terms of the thermal parameters of mean weighted average and non-uniformity index.

Keywords: Micro-combustion, Heat transfer enhancement, Hydrogen, Temperature distribution.

INTRODUCTION

The miniaturization movement in the recent years motivated the development of a variety of Micro Electro Mechanical Systems (MEMS) devices. Meanwhile, the conventional power supplies sources met their limits [1]. Proceeding from the urgent need, a revolutionizing alternative combustion-based micropower generator system was proposed by Epstein and Santuria in 1997 [2]. The trigger is to get advantage of the higher power density per unit of weight offered by the hydrogen combustion. In this regard, numerous of systems that vary in geometrical configuration have been developed. Such as the micro thermoelectric generator (MTEG) and the micro thermophotovoltaic (MTPV) system [3]. However, the Micro Thermophotovoltaic (MTPV) relies on converting the heated micro-combustor radiation into electricity using PV cells. Therefore, the effectiveness of the MTPV system passes basically through the improvement of the combustion efficiency and the combustor thermal performance. Which is strongly influenced by the combustor structure. So far, several experimental and numerical studies have been conducted by different researchers in order to analyse and optimize the geometrical configuration effects. Different approaches are extensively being proposed and employed. For example, Saad Akhtar et al. [4] has discussed the impact of different cross-section backward facing step on the flow and flame behavior. The results shows that the trapezoidal and triangular cross-sections are found to have the better performance. Aikun Tang et al. [5] developed a micro-combustor with a multi-mode heat transfer passages in the combustion channel. The numerical study proves the enhancement of heat transfer and the effect of the plates number and length on the uniformity of the external wall temperature distribution. Siliang Ni et al. [6] studied the effect of different rib shapes based on the mean temperature as a parameter to measure the thermal performance. It found that the two ribs perform generally better than that with a single rib and the round shape to be the optimum shape. Besides, Xiao Yang et al. [7] numerically investigated the thermal performance on proposed converging diverging combustor configuration. Results show the increase of the wall temperature by 82.39 K and the emitter efficiency by 6.59 %. Hai Chen et al. [8] proposed an improvement to the micro-combustor with wall cavity by adding a rectangular rib. The configuration is investigated under various operating conditions. Results prove that the enlargement of recirculation zone enhances the energy conversion. On this basis, this study proposed an improved micro-combustor with a backward facing step and 4 trapezoidal shaped ribs. Different operating conditions were investigated numerically using Ansys Fluent software. The mean wall temperature, the wall temperature difference and the non-uniformity of wall temperature are used as parameters of gage.

MODELIING

Physical Model

In contrary to previous studies, we introduce 4 ribs instead of single rib. The ribs have a novel shape which consist of a trapezoidal cross-section; the micro planar combustor dimensions are detailed in the Fig. 1.

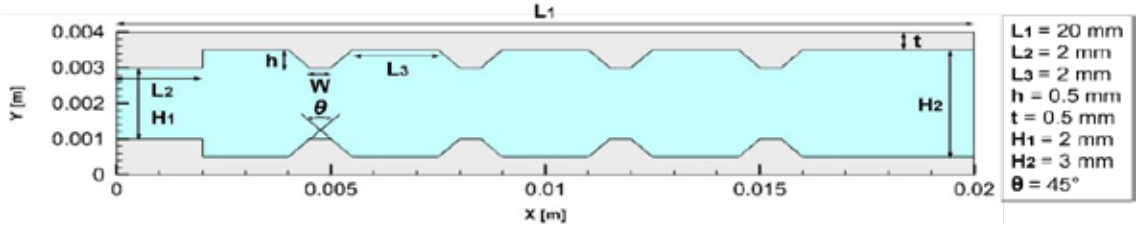


Fig 1. Schematic diagram of the proposed micro-combustor general configuration

Mathematical Model

The steady-state conservation equation of mass, momentum, energy, and species in the fluid zone can be written as:

$$\nabla \cdot (\rho \vec{v}) = 0 \quad (1)$$

$$\rho(\vec{v}.\overrightarrow{\nabla v}) = -\nabla p + \nabla \cdot (\mu[(\nabla \vec{v} + \vec{v}^T) - \frac{2}{3}\nabla \cdot \vec{v} I] \quad (2)$$

$$\nabla \cdot \vec{v}(p + \rho E_f) = \nabla \cdot \left[k_{eff}\nabla T - \left(\sum_i h_i \vec{J_i}\right)\right] + S_h \quad (3)$$

$$\nabla(\rho \vec{u} Y_i) = -\nabla \vec{J_i} + R_i \quad (4)$$

The heat along the solid zone transport purely by steady-state conduction following the Fourier's law, expressed as:

$$\nabla \cdot (k_w \cdot \nabla T) = 0 \quad (5)$$

RESULTS AND DISCUSSION

Validation of model and effect of the geometry

The results of the numerical model and the experimental data measured by Aikun Tang et al. [9] were compared as shown in Fig. 2(a). It is indicated that there is some disagreement at the inlet from 0 to 2 mm. Beyond that the maximum relative error is only around 1.06% and 1.78%. This confirms the reasonable accuracy and the model is applicable. The effects of introducing the novel ribs appears clearly by the increases of the overall outer wall temperature profile in comparison to the combustor without ribs, as shown in Fig. 2(b). We note that the introducing of ribs results an important increase of outer wall average temperature (T_{ave}) by 3.46%. Besides, temperature difference (ΔT) and non-uniformity index (Y) of the temperature distribution decreases by 15.27% and 26.86%, respectively.

Effect of inlet velocity and equivalence ratio

Fig. 2(b) show the significant effect of inlet velocity for 5 different velocities. These values were chosen based on the limitations of flash back and acoustic emission. The results show the parallel increment of temperature with the inlet velocity. The results show the increment of the average temperature with the velocity. While, decrement of temperature difference and non-uniformity up to 10 m/s and then rise again. Besides, Fig. 2(c) show the effect of 5 different H_2/air mixing ratio varies from 0.8 to 1.2, as the inlet velocity is set to 6 m/s. It can be seen that the temperature profiles decrease from 0.8 to 1.0, then slightly overlap for 1.0 and 1.1, and decrease again for 1.2. While, the non-uniformity decreases from 0.8 to 1.0 then balance.

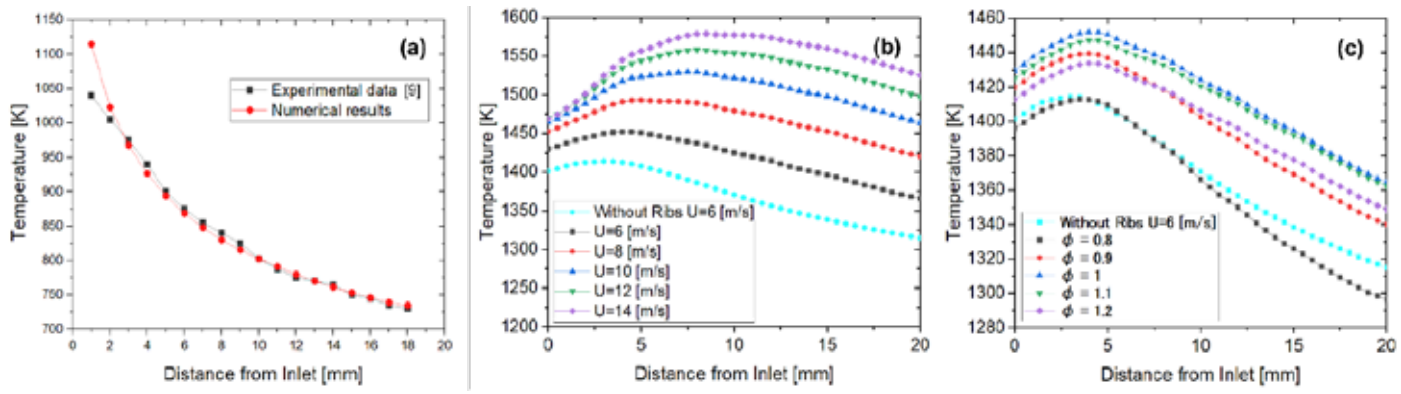


Fig. 2 The outer wall temperature distribution profiles, (a) Validation of model, (b) Effect of the ribs and the inlet velocity (c) Effect of the ribs and the equivalence ratio Φ

CONCLUSION

Compared to the micro-combustor without ribs, micro-combustor with trapezoidal ribs owns higher and more uniform outer wall temperature. Results an important increase of outer wall average temperature by 3.46% and ***decreases temperature difference and non-uniformity by 15.27% and 26.86%, respectively***. In a second step, we deduced that the wall temperature is increased by 3.4% to 9.24% with the increase of the inlet velocity and decreases for lean mixture by 0.33% to 3.92%. The temperature profile increment for inlet velocity is more uniform and the highest in magnitude. This reflects the important enhancement of heat transfer due essentially to the stable recirculation zones formed by the trapezoidal ribs. Furthermore, the equivalence ratio is found to have a slightly better performance only for rich mixture.

REFERENCES

1. Jianlong Wan and Aiwu Fan. 2021. Recent progress in flame stabilization technologies for combustion-based micro energy and power systems. Fuel. Volume 286. Part 2:119391.
2. Yiguang Ju and Kaoru Maruta. 2011. Microscale combustion: Technology development and fundamental research. Progress in Energy and Combustion Science 37:669-715.
3. Wei Wang, Zhengxing Zuo, Jinxiang Liu. 2019. Experimental study and numerical analysis of the scaling effect on the flame stabilization of propane/air mixture in the micro-scale porous combustor. Energy 174:509-518.
4. Saad Akhtar, Jundika C. Kurnia, Tariq Shamim. 2015. A three-dimensional computational model of H2-air premixed combustion in non-circular micro-channels for a thermo-photovoltaic (TPV) application. Applied Energy 152:47-57.
5. A. Tang, P. Jianfeng, W.M. Yang, Xu Yiming, Hou Zhiyong. 2015. Numerical study of premixed hydrogen/air combustion in a micro planar combustor with parallel separating plates. International Journal of Hydrogen Energy 40(5):2396-2403.
6. Q Q, N. Siliang, Zhao Dan, Sun Yuze, E Jiaqiang. 2019. Numerical and entropy studies of hydrogen-fuelled micro-combustors with different geometric shaped ribs. International Journal of Hydrogen Energy 44:7692-7705.
7. Yang Xiao, He Zhihong, Dong Shikui, Tan Heping. 2018. Enhancement of thermal performance by converging-diverging channel in a micro tube combustor fueled by premixed hydrogen/air. International Journal of Hydrogen Energy.
8. Chen Hai and Liu Wei-qiang. 2019. Numerical Investigation of the Combustion in an Improved Microcombustion Chamber with Rib. Journal of Chemistry 2019:1-12.
9. A. Tang, X. Yiming, S. Chunxian, P. Jianfeng, L. Yangxian. 2015. A comparative study on combustion characteristics of methane, propane and hydrogen fuels in a micro-combustor. International Journal of Hydrogen Energy 40.

WHEC-2022
23rd World Hydrogen Energy Conference
June 26-30, 2022 - Istanbul

#179

PERFORMANCE ANALYSIS AND COMPARISON ON ENERGY STORAGE DEVICES IN HYDROGEN-BASED INTEGRATED ENERGY SYSTEMS

[1] *Ke Shao,* [1*] *Xiangxiang Dong,* [2] *Jie Zhang,* [1] *Zhanbo Xu,* [1] *Jiang Wu*
[1] MOE KLINNS Lab of Xi'an Jiaotong University, Xi'an, Shaanxi Province 710049, China
[2] Tongfang Co., Ltd., Beijing 10083, China

*Corresponding author e-mail: gavin1014@stu.xjtu.edu.cn

ABSTRACT

Storage devices play a very important role in the efficient utilization of renewable supply, since energy can be flexible scheduled by storage in time horizon and thus improve the energy utilization efficiency. It is important to plan, schedule, and coordinate storage devices together with other energy devices in energy systems. This paper proposes a bi-level planning and operation optimization problem of hydrogen-based integrated energy systems. The optimal combination and capacities of storage devices can be obtained at the upper-level. The optimal scheduling strategy of the system is obtained at the lower-level, and a scenario tree-based algorithm is used to solve the lower-level problem with the system uncertainty. The effectiveness of the developed method is demonstrated using numerical case studies. It is also found that the combination of hydrogen and water tanks is most efficient in saving cost.

Keywords: Hydrogen-based integrated energy system, Storage devices, Bi-level programming problem

INTRODUCTION

Hydrogen is well known as the ultimately conventional energy media in the 21st century due to its cleanness and sustainability [1]. Since hydrogen can be produced by the renewable supply and stored into hydrogen tanks, and then converted to electrical and thermal energy through fuel cells, hydrogen coordinated with the renewable supply is considered as a potential way to improve the utilization efficiency of renewable supply [2]. And it has attracted a lot of attention. Li et al. [3] developed an operation optimization method for coordinating the hydrogen and heating energy generated from the renewable energy sources with district heating networks to meet the demand loads. Liu et al. [4] optimized the planning of a distributed hydrogen-based energy system under several cases with different characteristics of renewable supply and demand. Dong et al. [2] studied the coordination of a hydrogen-based integrated energy system (HIES), and the utilization efficiency of renewable supply was improved through the coordinated scheduling of the HIES.

Although the above innovative results lay the foundation for the application of hydrogen coordinated with the renewable supply, the impact and performance of energy storage devices is rarely analyzed in the HIES. Storage devices play a very important role in the efficient utilization of renewable supply, since energy can be flexible scheduled by storage in time horizon and thus improve the energy utilization efficiency. However, there are many types of storage devices, how to select the appropriate storage devices is very important for maximizing the utilization efficiency of renewable supply based on quantitative performance analysis and comparison. In this paper, we focus on planning, scheduling, and coordinating different storage devices together with other energy devices in a HIES. A bi-level optimization problem for the integrated planning and scheduling of the HIES is thus presented. With the proposed formulation, the best combination and optimal capacities of storage devices can be obtained at the upper-level. The optimal scheduling strategy of the HIES can be obtained at the lower-level. And a scenario tree-based algorithm is used to address the uncertainty in both the renewable supply and demand profiles.

MATERIALS AND METHODS

Problem Statement

The focus of this paper is to study the performance analysis of different energy storage devices by investigating the integrated planning-and-scheduling problem with other devices in the HIES. The problem is formulated as a bi-level mixed integer programming problem. The investment decisions of the storage devices are determined by the upper-level problem, and it will affect the scheduling strategy in the lower-level problem. And the scheduling strategy of the HIES is determined by the low-level problem by minimizing the operation cost, and it will affect the investment decisions in the upper-level problem. As shown in Fig. 1, the HIES consists of the distributed power grid, hydrogen market, renewable energy sources such as photovoltaic (PV) panels and solar thermal collectors (STC), electrolyzer, compressor, fuel cell CHP unit, absorption chiller, heat pump, battery, hydrogen tank, and water tanks. The objective function is to minimize the annual overall planning cost of the storage devices and operation cost of the HIES over the

scheduling horizon with the time of use (TOU) electricity price. While satisfying the electrical, heating and cooling demand. A set of scenarios of renewable supply and demand profiles is used to describe the system uncertainties.

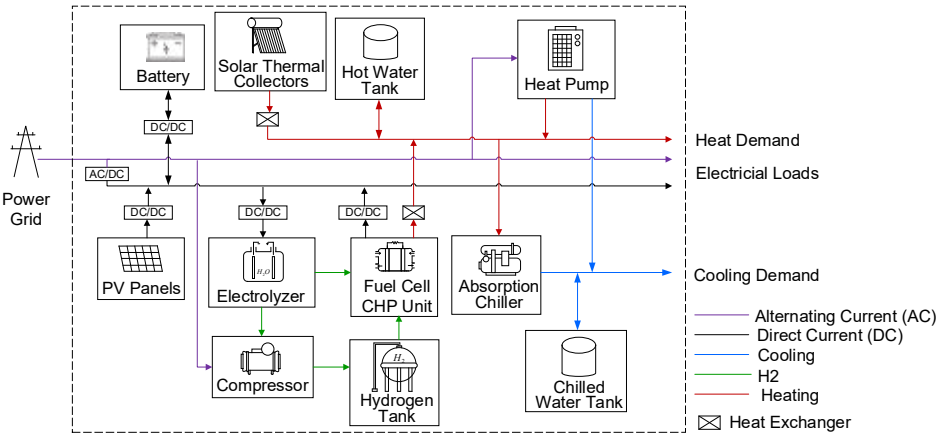


Fig. 1. Hydrogen-based integrated energy system (HIES)

Problem Formulation

At the upper-level, the objective function of the problem is to minimize the annual investment cost of energy storage devices (CPEX) and the annual operation cost of the HIES as following:

$$\min J = CRF^{ct} \cdot Q^{ct} \cdot c^{ct} + CRF^{wt} \cdot G^{wt} \cdot c^{wt} + CRF^{ht} \cdot M^{ht} \cdot c^{ht} + CRF^{bat} \cdot E^{bat} \cdot c^{bat} + OPEX \tag{1}$$

where CRF is the capital recovery factor [4]. Capacity decision variables are $Q^{ct}, G^{wt}, M^{ht}, E^{bat}$. c is unit investment cost. Upper indexes ct, wt, ht, bat represent the chilled water tank, hot water tank, hydrogen tank and battery, respectively. $OPEX$ is the annual operation cost of the HIES.

At the lower-level, considering the uncertainty of renewable energy and demand profile, a stochastic optimization problem is constructed to minimize the average operation cost of all scenarios in the scheduling horizon. Therefore, we have the following objective function:

$$\min OPEX = \sum_{i}^{I} \pi_i \sum_{j}^{J} \pi_j \sum_{t=1}^{T} \left[\lambda^{G}_{i,j,t} p^{G}_{i,j,t} \cdot \tau + \lambda^{B} m^{B}_{i,j,t} \right] \tag{2}$$

where i, j are the scenario index of the demand profile and solar radiation, respectively. t is the time period index. π is the scenario probability. λ is the price. p is power. m is mass of hydrogen. τ is the period span. Upper indices G, B represent the electricity purchased from power grid and hydrogen purchased from hydrogen market respectively. Note that the subscripts i, j indicating the scenario indices are omitted in following constraints for simplicity.

$$e^{io}_{t+1} = e^{io}_{t} + p^{bat}_{t}, x_0 = x_T, \underline{x} \cdot E^{bat} \le e^{io}_{t} \le \bar{x} \cdot E^{bat}, z^{in}_{t} + z^{out}_{t} \le 1, z^{in}_{t} \cdot \underline{p}_{bi} - z^{out}_{t} \cdot \bar{p}_{bo} \le p^{bat}_{t} \le z^{in}_{t} \cdot \bar{p}_{bi} - z^{out}_{t} \cdot \underline{p}_{bo} \tag{3}$$

$$m^{io}_{t+1} = m^{io}_{t} + m^{in}_{t} - m^{out}_{t}, m^{io}_{t} + m^{in}_{t} \le M^{ht}, z^{in}_{t} + z^{out}_{t} \le 1, 0 \le m^{out}_{t} \le z^{out}_{t} \cdot M^{ht}, 0 \le m^{in}_{t} \le z^{in}_{t} \cdot M^{ht} \tag{4}$$

$$g^{io}_{t+1} = g^{io}_{t} + g^{in}_{t} - g^{out}_{t} - g^{loss}_{t}, g^{io}_{t} + g^{in}_{t} \le G^{wt}, q^{io}_{t+1} = q^{io}_{t} + q^{in}_{t} - q^{out}_{t} - q^{loss}_{t}, q^{io}_{t} + q^{in}_{t} \le Q^{ct} \tag{5}$$

where e is electrical energy in the battery. Upper indices $io, in, out, loss$ represent the remaining, input, output and loss energy of the storage devices, respectively. Upper index bat represent the battery. x is the state of charge of battery. z is the binary variable. Subscripts bi and bo represent charge and discharge of the battery respectively. g is the heating energy. q is the cooling energy. Eqs. (3)-(5) represent the dynamics and operating constraints of battery, hydrogen tank and water tank respectively, as similar to our previous work [2], [5]. The constraints of energy balance and operating constraints of other energy devices such as the fuel cell, absorption chiller are excluded in this paper, which are similar to our previous work [2].

In this paper, a particle swarm optimization algorithm [6] is used to iteratively solve the bi-level problem, and thus obtain the optimal investment decisions of the energy storage devices. In addition, a scenario tree-based algorithm [2] is used to address the system uncertainty in the lower-level problem.

RESULTS AND DISCUSSION

The bi-level problem is tested based on an office building with 3000 m^2 at Beijing, Yinchuan, Shanghai, Guangzhou and Chongqing, China. The developed HIES includes a fuel cell CHP unit (with a rated power of 250 kW), an absorption chiller (with a rated power of 500 kW), an electrolyzer (with a rated power of 500 kW), a compressor (with

a rated power of 100 kW), a heat pump (with a rated power of 50 kW), PV panels (laying area of 1000 m^2) and solar thermal collectors (laying area of 500 m^2). The unit investment cost of battery, hydrogen tank (HT) and water tanks (WT) are assumed to be 1600 RMB/kWh, 3600 RMB/kWh and 35 RMB/kWh, respectively [4].

The optimal combination and capacities of storage devices of different locations are shown in Fig. 2. The results show that the optimal capacities of storage devices vary with locations due to the demand and solar radiation. The performances of different combinations of storage devices are tested, and the results are shown in Table 1. The results show that the combination of hydrogen and water tanks can save the overall cost by 42.6%, which is the most significant among all combinations. A winter day in Yinchuan is used as an example to demonstrate the characteristics of scheduling strategies, and the result are show in Fig. 3. It can be seen that there is a mismatch between renewable energy supply and demand. However, with the hydrogen tank, hydrogen can be converted from the renewable supply and stored into the hydrogen tank, such hydrogen can be converted to electrical and heating energy to meet the demand at other periods. Thus, the utilization efficiency of the renewable supply can be improved. During the off-peak periods (1:00-7:00), a large amount of electricity can be purchased to produce hydrogen and stored in the hydrogen tank. A part of hydrogen is consumed to produce heating energy and stored in hot water tanks. During the peak periods, the fuel cell consumes the hydrogen, which stored in the hydrogen tank, to produce heating and coordinating with the hot water tank to jointly meet the heating demand. It is beneficial to achieve the energy balance and improve the energy utilization efficiency.

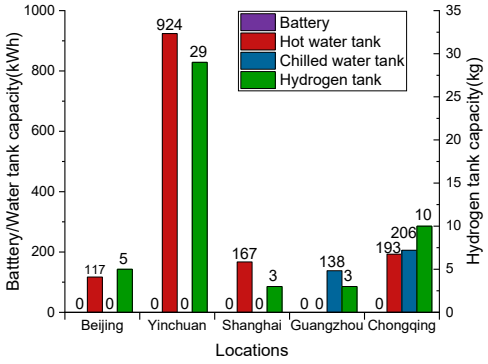


Fig. 2. Capacities of storage devices

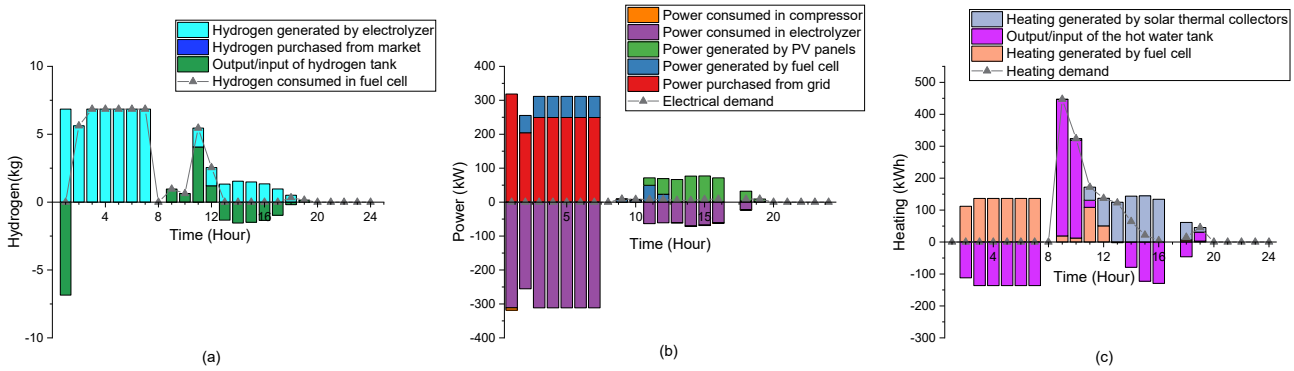


Fig. 3. Operation strategies about (a) hydrogen (b) electrical power (c) heating energy

Table 1. Overall cost with different combinations of storage devices in Yinchuan

Cost (RMB)	Include all devices	Without storage	Battery	HT	WT	Battery + HT	Battery + WT	HT + WT
CPEX	14411	0	7391	22733	4167	22366	4167	14411
OPEX	45114	103764	89976	46903	59500	47131	59500	45114
CPEX+OPEX	59525	103764	97367	69636	63667	69497	63667	59525

CONCLUSIONS

In this paper, we study the performance analysis and comparison of different storage devices in the HIES. A bi-level decision problem for planning and scheduling is established. In the lower-level, a stochastic optimization problem is proposed to minimize the operation cost of the HIES and solved by the scenario tree-based algorithm. In the upper-level, the optimal combination and capacities of storage devices are obtained to minimize the annual investment cost of storage devices with the annual operation cost of the HIES. The numerical results show that the developed method can effectively select the optimal combination and capacities of energy storage devices, and obtain the optimal

scheduling strategy of the HIES, as well as improving the utilization efficiency of the renewable supply. It is also found that the combination of hydrogen and water tanks is most efficient in saving cost.

REFERENCES

1. Mazloomi K and Gomes C. 2012. Hydrogen as an energy carrier: Prospects and challenges. Renewable and Sustainable Energy Reviews 16(5):3024 – 3033.
2. Dong X, Wu J, Xu Z, Liu K and Guan X. 2022. Optimal coordination of hydrogen-based integrated energy systems with combination of hydrogen and water storage. Applied Energy 308: 0306-2619.
3. Li J, Lin J, Song Y, Xing X and Fu C. 2019. Operation optimization of power to hydrogen and heat (P2HH) in ADN coordinated with the district heating network. IEEE Transactions on Sustainable Energy 10(4):1672–83.
4. Liu J, Xu Z, Wu J, Liu K and Guan X. 2021. Optimal planning of distributed hydrogen-based multi-energy systems. Applied Energy 281: 0306-2619.
5. Xu Z and Guan X. 2012. Performance analysis and comparison on energy storage devices for smart building energy management. IEEE Transactions on Smart Grid 3(4):2136-2147.
6. Wang Z, Chen Y, Mei S, Huang S and Xu Y. 2017. Optimal expansion planning of isolated microgrid with renewable energy resources and controllable loads. IET Renewable Power Generation 11(7):931-940.

WHEC-2022
23rd World Hydrogen Energy Conference
June 26-30, 2022 - Istanbul

#186

ANALYSIS OF TRANSPORT OPTIONS FOR LIQUID HYDROGEN IN GERMANY

[1, 2*] *Toni Busch*, [1] *Theresa Groß*, [1] *Jochen Linßen*, [1, 2] *Detlef Stolten*
[1] Forschungszentrum Jülich GmbH, IEK-3, 52425 Jülich, Germany
[2] RWTH Aachen University, Templergraben 55, 52056 Aachen, Germany

*Corresponding author e-mail: t.busch@fz-juelich.de

ABSTRACT

A wide range of studies have analyzed the transportation of liquid hydrogen (LH_2) over long distances. This study aims to investigate the role of LH_2 in the downstream process of a greenhouse gas neutral energy supply system. The high volumetric energy density and high level of purity are two features that distinguish LH_2 from gaseous pipeline transport. An integrated energy system model covering the sectors electricity, hydrogen, and methane for Germany in a carbon neutral scenario for 2045 has been enhanced by means of liquid hydrogen transportation via inland vessel, truck, and rail.

The results of the energy systems optimization highly depend on the amount and spatial distribution of the LH_2 demands: LH_2 demands can be either served by imports and the distribution by single means of transportation as well as combination of multiple means of transportation (intermodal) or even by the inland liquefaction of gaseous hydrogen (GH_2). The promising applications of LH_2 transportation in future energy systems are currently underrepresented in the discussion around options for hydrogen distribution.

Keywords: Liquid hydrogen, Hydrogen transportation, Integrated infrastructure analysis, transportation costs, Domestic hydrogen distribution

INTRODUCTION

For the first time, a comprehensive analysis of the LH_2 transportation options by inland vessels, truck and rail is carried out within this study. These means of transport are embedded in an integrated optimization model of a national energy system including grid-bound infrastructure for electricity, gas, hydrogen, and heat.

In the current state of the literature trucks are the LH_2 transportation option featured most often in the field of energy system analyses [1–6]. Vessels for the transportation of LH_2 are primarily analysed in the context of intercontinental transport [1, 4, 5, 7]. No studies could be identified that investigate inland vessels and only in one study LH_2 transportation by rail has been investigated [4].

This work aims to shine light on mostly underrepresented means and modes of hydrogen transportation as hydrogen is expected to play a significant role in future climate neutral energy systems. From this level of importance, the need to evaluate potential usecases and applications of LH_2 transportation is derived.

MATERIALS AND METHODS

The energy systems analysis in this paper is based on the ETHOS Framework developed by the Institute for Techno-Economic System Analyses of the Forschungszentrum Jülich. ETHOS incorporates an energy system optimization model with high spatial (80 regions) and temporal resolution (8760 timesteps per year). The sectors electricity, gas and GH_2 and its corresponding components for storage, transmission, conversion as well as sources and sinks of the respective energy carriers make up the optimization model. Key objective is the minimization of the total annual costs (TAC) to obtain the cost optimal energy system design and its operation. The methodology is applied to the energy system of Germany for a climate neutral scenario in 2045 as a case study.

For the year 2045, the optimization results to demands for electricity (727 TWh/a), natural gas (39 TWh/a) and GH_2 (378 TWh/a) based on a single-region model for Germany [8]. These demands are distributed among 80 regions for Germany (derived from Voronoi regions around the nodes of the national electricity transmission grid).

The current implementation of the hydrogen domain in ETHOS includes GH_2 and its import via locations in the west and southwest of Germany, its transmission via pipeline (newly built and converted), its storage (e.g., in salt caverns) and its demands (in the transportation, industry and building sector). This paper describes the modeling of the liquid hydrogen transportation. The key aspects supply, distribution, and demand are highlighted in the following.

Supply: LH_2 can either be produced within the energy system (liquefaction of GH_2) or be imported via oversea vessels. The harbors Wilhelmshaven, Stade, and Brunsbüttel in northern Germany which are currently considered as potential LNG terminals serve as import locations for LH_2 in this 2045 case study.

Demand: Four different scenarios of LH_2 demands (cp. figure 1) are considered to identify potential use cases and modes of transportation of LH_2.

Reference Scenario: LH_2 options for transportation are introduced in the model without introducing any dedicated LH_2 demand. This shall determine whether the transportation of LH_2 is an economical option to serve GH_2 demands.

Scenario Aviation: Additional 33 TWh/a of LH_2 are introduced as a kerosene replacement for emission-free air travel. This accounts to a third of the energy content of today´s kerosine consumption in aviation. The LH_2 is spatially distributed based on the location and the passenger volume of the 24 largest airports in Germany. In two other scenarios parts of the projected GH_2 demands for 2045 are assumed to be served by LH_2 of equivalent energy content instead.

Scenario Industry: 30 % of the projected GH_2 demands in the industry sector (predominantly in the chemical sector) are replaced with LH_2 demands. This results in LH_2 demands of 78 TWh/a that are distributed according to major ammonia and methanol production sites and their production volume.

Scenario Transportation: Due to the low temperature of LH_2, contaminating gases with higher liquefaction temperatures than hydrogen are separated during the liquefaction process. This results in high levels of hydrogen purity, which is required for fuel cell applications e.g., in vehicles. In this scenario the largest fueling stations for high duty vehicles are considered to receive LH_2 instead of GH_2 resulting in a total LH_2 demand of 62 TWh/a.

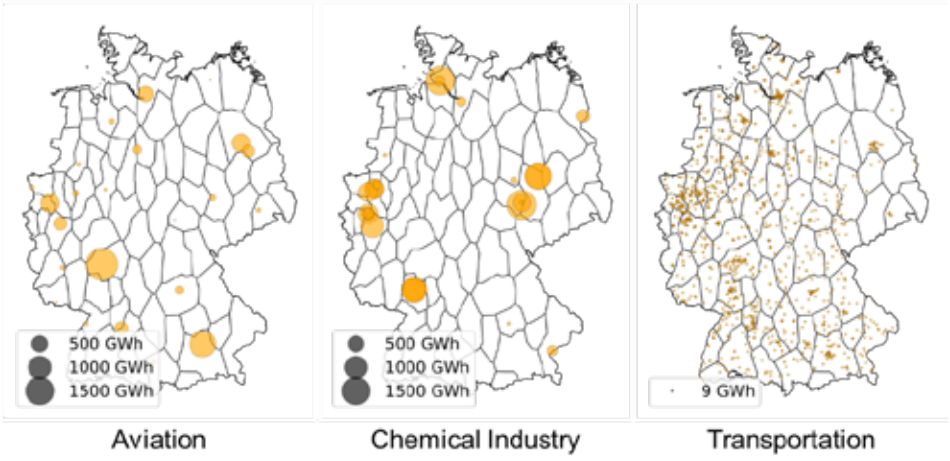


Figure 1: Amount and spatial distribution of LH_2 demands in the different scenarios.

Transportation: Rail, truck, and inland vessel are eligible candidates for LH_2 transportation as their applications in the past (rail and inland vessel transport for NASA space missions [9]) and present (truck and oversea vessels [10, 11]) demonstrate. Roads, railroads, and federal waterways serve as possible transport routes [12–15]. Using Dijkstra's algorithm, the shortest path between the region centroids is calculated for the different means of transportation [16]. Capital and operating costs are calculated á priori for each combination of regions as a function of distance and fed to the model. Due to the high rate of utilisation of the rail network and already congested route sections the transportation of LH_2 via rail is limited to two trains (each carrying 25 Waggons) per day that can be loaded and unloaded in every region. The techno-economic parameters for the three means of transportation are based on the studies [3, 7, 17].

RESULTS AND DISCUSSION

From the first results, four main observations can be made: **No LH_2 transmission is used to serve GH_2 demands when there are no LH_2 demands.** The import and distribution of GH_2 via pipeline in the reference scenario is economically more efficient than the import of LH_2 and the distribution via rail despite its higher energy density.

The ranking in terms of economic efficiency of LH_2 transportation options is rail, ship, truck. More expensive transportation option are drawn when cheaper options reach capacity limits. For railway transport, the limiting factor is the number of train deliveries per day. The limiting factor of inland vessels is the course of the waterways not connecting all regions. Regions that can not be reached by waterways are likely to be served by trucks.

A combination of transport technologies is carried out to bypass constrains of transportation options. This can be observed in the aviation scenario where the *import limit* for liquid hydrogen by rail is exceeded in the region of the Munich airport in southern Germany. For example, to overcome this limitation, LH_2 is transported to Munich neighboring region by rail then reloaded onto more expensive trucks for the last kilometers. Bypassing the *export limitation* can be observed in the transportation scenario. Only in two regions in northern Germany LH_2 can be obtained by oversea vessel imports. To extend the amount of LH_2 distributed by rail in this scenario, inland vessels are deployed to carry LH_2 to neighboring regions further inland. From there it is loaded to trains and distributed within the country.

Inland liquefaction of GH_2 can be preferred to the import and distribution of LH_2. This occurs in the industry and the transportation scenario in regions in the southwest and in the east of Germany. Reasons for preferring liquefaction over import and distribution of LH_2 lie in the high overall LH_2 demand in these scenarios and the capacity limits of rail transportation. The reasons why especially these regions rely on liquefaction can bee seen in the proximity to a GH_2 import location in the southwestern regions and the high availability of renewable energy sources in the eastern regions.

CONCLUSIONS

The results of the optimization show that LH_2 inland transportation represents a promising alternative to pipeline transportation. It can be a use case when high purity levels of hydrogen are required, when hydrogen is demanded in liquid form and when regions cannot be connected to the pipeline network. The lack of comprehensive studies on this topic shows that LH_2 transportation (especially the role of railways) is still underrepresented in the discussion of future hydrogen infrastructures.

REFERENCES

1. Niermann M, Timmerberg S, Drünert S, Kaltschmitt M. Liquid Organic Hydrogen Carriers and alternatives for international transport of renewable hydrogen. Renewable and Sustainable Energy Reviews. 2021;135:110171. doi:10.1016/j.rser.2020.110171.
2. Lahnaoui A, Wulf C, Dalmazzone D. Optimization of Hydrogen Cost and Transport Technology in France and Germany for Various Production and Demand Scenarios. Energies. 2021;14:744. doi:10.3390/en14030744.
3. Reuß M, Dimos P, Léon A, Grube T, Robinius M, Stolten D. Hydrogen Road Transport Analysis in the Energy System: A Case Study for Germany through 2050. Energies. 2021;14:3166. doi:10.3390/en14113166.
4. Almansoori A, Betancourt-Torcat A. Design of optimization model for a hydrogen supply chain under emission constraints - A case study of Germany. Energy. 2016;111:414–29. doi:10.1016/j.energy.2016.05.123.
5. Teichmann D, Arlt W, Wasserscheid P. Liquid Organic Hydrogen Carriers as an efficient vector for the transport and storage of renewable energy. International Journal of Hydrogen Energy. 2012;37:18118–32. doi:10.1016/j.ijhydene.2012.08.066.
6. YANG C, Ogeden J. Determining the lowest-cost hydrogen delivery mode. International Journal of Hydrogen Energy. 2007;32:268–86. doi:10.1016/j.ijhydene.2006.05.009.
7. Ishimoto Y, Voldsund M, Nekså P, Roussanaly S, Berstad D, Gardarsdottir SO. Large-scale production and transport of hydrogen from Norway to Europe and Japan: Value chain analysis and comparison of liquid hydrogen and ammonia as energy carriers. International Journal of Hydrogen Energy. 2020;45:32865–83. doi:10.1016/j.ijhydene.2020.09.017.
8. Lopion PM. Modellgestützte Analyse kosteneffizienter CO2-Reduktionsstrategie. Jülich: Forschungszentrum Jülich GmbH, Zentralbibliothek, Verlag; 2020.
9. Narson S, Larson R. LNG on the Rails - Precursor to LH2 on the Rails?; 2019.
10. Linde. H2-Distribution und -Speicherung. 2021. https://www.linde-gas.de/h2_distribution_and_storage/index.html. Accessed 5 Aug 2021.
11. Kawasaki. World's First Liquefied Hydrogen Carrier SUISO FRONTIER Launches Building an International Hydrogen Energy Supply Chain Aimed at Carbon-free Society | Kawasaki Heavy Industries, Ltd. 2019. Accessed 23 Nov 2020.
12. DB Netz AG. Strecken und Bauwerke nach INSPIRE. 2019. https://data.deutschebahn.com/dataset/data-streckennetz.html.
13. Eurostat. Verkehrsnetze. 2019. https://ec.europa.eu/eurostat/de/web/gisco/geodata/reference-data/transport-networks.
14. Wasserstraßen- und Schifffahrtsverwaltung des Bundes. Verkehrsnetz Bundeswasserstraßen. 2020. https://www.gdws.wsv.bund.de/DE/service/karten/03_VerkNet-BWaStr/VerkNet-BWaStr_node.html.
15. European Commission. Straßennetz - INSPIRE Geoportal; 2020.
16. Dijkstra EW. A note on two problems in connexion with graphs. Numer. Math. 1959;1:269–71. doi:10.1007/BF01386390.
17. Amos WA. Costs of Storing and Transporting Hydrogen; 1998.

WHEC-2022
23rd World Hydrogen Energy Conference
June 26-30, 2022 - Istanbul

#201

NOVEL TEG HEAT EXCHANGER IN Cu-Cl CYCLE OF HYDROGEN PRODUCTION

[1*]*Amir Mohammadi* [1]*Ehsan Armoudli,* [1]*Ofelia A. Jianu*
[1]Mechanical Automotive and Materials Engineering, University of Windsor, 401 Sunset Avenue, Windsor, Canada

*Corresponding author e-mail: mohamm63@uwindsor.ca

ABSTRACT

The looming threat of global warming has elicited efforts to develop reliable sustainable energy resources. Hydrogen as a clean fuel is deemed an appealing solution to problem of the storage of power from renewable energy technologies. Among current thermochemical hydrogen generation methods, the thermochemical copper-chlorine (Cu-Cl) cycle is of high interest owing to lower temperature requirements. However, this method faces challenges such as scaling up. Therefore, it is crucial to improve the performance of the cycle in terms of designing more efficient heat exchangers to surmount such obstacles. Present study investigates a novel heat exchanger comprising a thermoelectric generator (TEG) within the Cu-Cl cycle. This configuration enables electric power production, which could be utilized in the electrolysis step of the cycle. There are several heat recovery spots within Cu-Cl cycle where conventional heat exchangers could be superseded by TEGs. The performance of the proposed heat exchanger is numerically examined using commercially available finite element software, COMSOL Multhiphysics. Impact of operational conditions on the performance of TEG has been assessed to provide insights for better understanding of the design. Results indicate that maximum generated power is 41.3 W at the matching current. Average deviation from anticipated friction factor and Nusselt number are 0.31% and 16.77%, respectively.

Keywords: Thermoelectric generator, Hydrogen, Thermolysis, Heat transfer, Copper-chlorine cycle.

INTRODUCTION

Global warming as an existential threat entails mitigation of greenhouse gas emissions resulting from the consumption of fossil fuels. Hydrogen, as a carbon free fuel, could play a pivotal role in our transition toward finding a more sustainable energy resource. Furthermore, excess energy of power plants as well as curtailed power, due to intermittent nature of most renewable and green energy sources, could be stored through hydrogen generation. Nevertheless, most of the existing methods for hydrogen production emit carbon dioxide themselves. Therefore, it is crucial to develop more sustainable hydrogen methods for substantial hydrogen generation at affordable costs [1]. Among hydrogen generation methods thermochemical cycles, especially copper-chlorine (Cu-Cl) cycle, have shown ample potential regarding zero carbon emission [2]. Cu-Cl cycle employs several reactions to split water into its constituent compounds, hydrogen and oxygen. In comparison with other thermochemical counterparts, Cu-Cl cycle possesses lower temperature requirements [1,3] although maintaining high temperature levels, near 530°C, is still inevitable for this cycle to some extent. The common 4-step Cu-Cl cycle consists of electrolysis, thermolysis, and hydrolysis reactors and emerged in response to the pressing need for surmounting concerns regarding exergoeconomic and exergoenvironmental concerns [4]. The decomposition of water into its constituent elements occurs through several intermediate stages and reactors. Previous studies aimed at investigating heat exchangers in five-step and four step Cu-Cl cycle in attempt to improve the cycle performance [3,5]. Results indicate that more effective heat exchangers would lead to better energy and exergy performances. Therefore, a shrewd approach would include design and use of efficient heat exchangers to improve the overall performance of the cycle.
TEGs, as direct energy conversion devices, produce electricity due to Seebeck effect [ref]. Key attributes such as low-cost, long life cycle, no emissions and absence of moving parts have turn them into decent low grid energy recovery devices [2, 6]. Several n-type and p-type semiconductor junctions, which are connected electrically in series and thermally in parallel form a thermoelectric module. Applying a temperature gradient to a TEG would lead to an electric current [7]. Employing TEGs alongside other energy systems, predominantly as heat exchangers and for heat recovery purposes, has been extensively studied [2, 6, 8, 9]. In the realm of hydrogen generation, TEG has been considered as a Rankine cycle condenser and the generated power has been transferred to PEM electrolyzer for hydrogen production. Results delineate that the integrated system could enhance the overall performance satisfactorily in terms of exergy efficiency and reducing total cost [2]. Thermal efficiency is usually determined using the widely accepted but rather simple approach non-dimensional figure of merit (ZT). ZT has been introduced to compare various thermoelectric materials since thermoelectric performance is highly dependent on material properties. For available TEGs in the market, ZT is approximately 1 leading to an energy conversion efficiency of around 5% [10]. Manufacturers mainly use bismuth telluride (Bi2Te3) for thermoelectric semiconductors, hence TEGs with same properties are adopted in the present study. The efficiency values of TEG based heat exchangers might seem very low; however, such devices harvest electric energy from waste heat increasing the system's overall

efficiency. Regardless of appealing aspects of Cu-Cl cycle, scaling up and improving the efficiency of the cycle remains as an inextricable challenge. Thus, methods to enhance the overall efficiency of the cycle are of high interest. There are various points in the Cu-Cl cycle where the TEG heat exchangers could be used such as steam and HCl separation unit, condenser after the dryer and/or the thermolysis. The overarching goal of the present work is to introduce a thermoelectric based heat exchanger to improve heat recovery from this cycle. Hence, a novel TEG heat exchanger within the Cu-Cl cycle is proposed and its power generation efficiency will be examined via a numerical approach. To maintain a temperature difference throughout the TEG module, the molten salt leaving the thermolysis is used to serve as the heat source while heat is dissipated from the other side of the TEG to water. In this study, a three-dimensional steady state compact model is proposed to model the thermoelectric module. Heat and electric fields for the TEG elements considered to be coupled and pertinent equations are solved numerically using COMSOL Multiphysics software. A cooling tube using water as the coolant is attached to the upper side of TEG. Another tubular chamber carrying molten Cu-Cl is attached to the lower side of TEG serving as the heat source. Boundary conditions will be applied regarding the existing data for the Cu-Cl cycle. In the quest of better understanding of the designed heat exchanger, both molten salt and water fluid fields are also modeled.

METHODOLOGY AND BASELINE CASE DESCRIPTION

TEG elements consist of two different semiconductor materials which are connected thermally in parallel. By applying a temperature gradient to the junctions, two electromotive forces will be formed, i.e., Thomson and Peltier. To gain higher levels of voltage, a series of semiconductor junctions connected electrically in series is required [11, 12]. The two main approaches to model thermoelectric devices comprise energy balance (zero-dimensional) model and heat transfer (differential form) model. In this research, a three-dimensional, steady state compact TEG model is considered to simulate the TEG unit. Owing to extreme reduction of the computational domain, this approach, i.e., compact model, reduces the computational costs substantially while maintaining acceptable error levels [12,13,14]. The fully coupled temperature and electric potential fields are solved using COMSOL Multiphysics software. Bismuth telluride-based semiconductors are considered as TEG materials. The melting temperature for bismuth telluride is about 585 ℃ [12]. In this study, working temperatures of the TEG block are kept below this value to ensure satisfactory performance of the TEG unit. The conservation of energy equations for the TEG, water circuit and molten salt circuit are solved in a steady state analysis. Moreover, conservation of mass and conservation of momentum equations have been employed to visualize fluid flow fields for both cold and hot fluids.
A schematic representation of the TEG unit and the propounded boundary conditions are depicted in Fig. 1. Top (cold) end of TEG block is attached to a tubular circuit for water flow as heat dissipating heat sink. TEG side boundaries are assumed to be adiabatic while bottom (hot) end of the unit is attached to another circuit containing molten salt. The results must be independent of number of employed grid. Thus, grid independence test is performed to examine the generated mesh for the heat exchanger. As an indispensable part of the analysis, the proposed computational model is compared with the reported results in the literature. The utilized thermoelectric model has been collated with the compact model introduced in [15]. Results demonstrate an agreement between the reported data in [15] and current investigation. Additionally, the adopted laminar fluid flow model for both molten salt and water circuits have been compared with existing results and experimentally validated formulation for such flows. Friction factor and Nusselt number are considered to verify the flow field and the thermal solutions, respectively. Average deviation of the present model results from anticipated friction factor is only 0.31% and 16.77% for the Nusselt number in laminar regime. One concern regarding the configuration of the heat exchanger is to prevent CuCl molten salt from solidification due to heat loss to the cold heat sink. Therefore, inflow Reynolds number of molten salt ought to be above 190 to ensure a continuous fluid flow.

RESULTS AND DISCUSSION

As demonstrated in Fig. 2, temperature and velocity flow fields for both circuits have been solved using a CFD analysis. Moreover, output power of the TEG unit over effective applied electric current is presented in Fig. 3. Identical to other electric generators, maximum produced power occurs at the matching electric resistance equal to internal electric resistance of the TEG itself and for the applied boundary conditions this value is about 41.3 W, at I=4.5 A. An assorted range of boundary conditions including various inlet velocities and temperatures for water and molten salt have been considered in the present work. It is expected that power generation fall behind maximum amount for higher hot inlet temperatures, owing to domination of conduction heat transfer. To compensate for conduction heat transfer due to higher temperatures, increasing the inlet velocity of water will facilitate the TEG element to have a better performance at higher temperatures, although the outlet temperature of water will decrease.

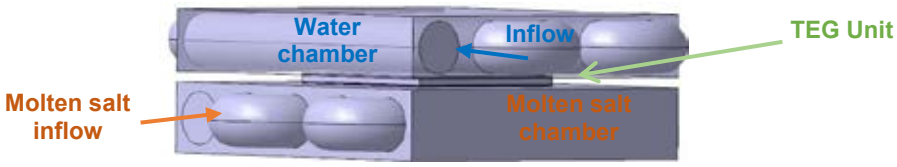


Fig. 1. Schematic of the heat exchanger

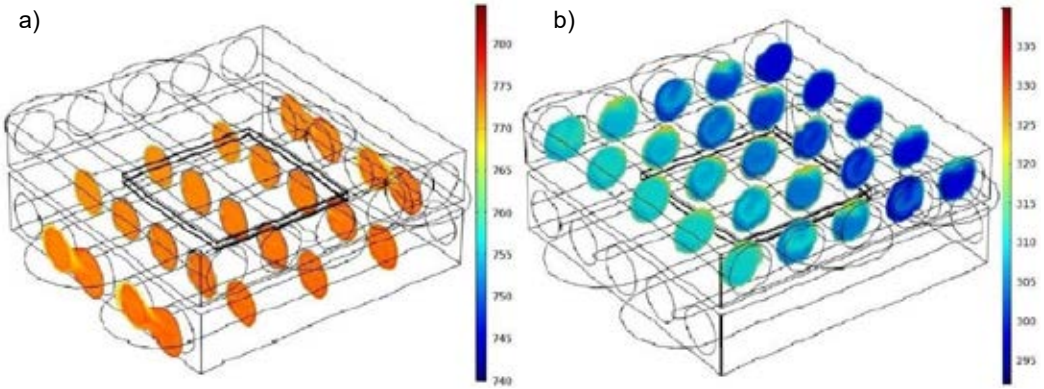


Fig. 2. a) Temperature distribution of molten CuCl within the heat exchanger b) Velocity field of cooling water

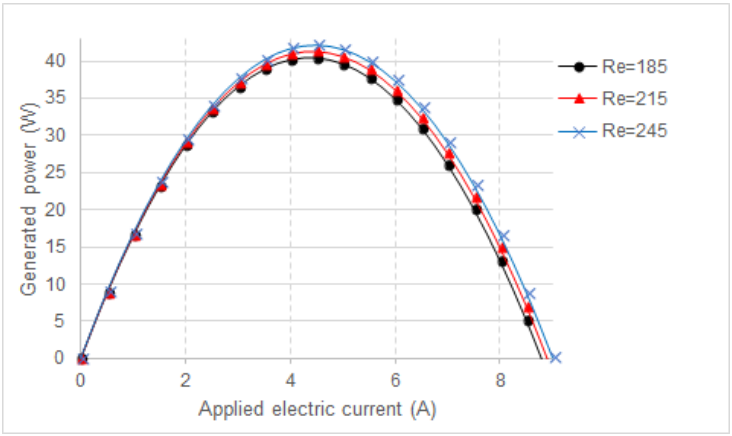


Fig. 3. Temperature distribution of the reactant inside the heat exchanger

CONCLUSIONS

A TEG heat exchanger for heat recovery purpose within the copper-chloride cycle can generate electric power which can be used in other Cu-Cl reactors, namely the electrolysis reactor. This could increment the overall efficiency of the Cu-Cl cycle. This study aimed at investigating of the thermal performance of a TEG heat exchanger operating under Cu-Cl cycle working conditions. The focus of current study has been on modelling a novel thermoelectric heat exchanger numerically.

Results are within acceptable error levels comparing with existing data. Average deviation of present model results from anticipated friction factor and Nusselt number are 0.31% and 16.77%, respectively. The generated power shows a parabolic behavior with respect to the applied electric current. Maximum power occurs at the I_{max} corresponding to matching resistance. An exhaustive analysis of thermal and exergy performance of the hybrid heat exchanger could be subject of future works. Considering the exergy destruction in the heatsink is necessary to investigate the capability of the novel hybrid heat exchanger. Although applied temperatures in this study were below the melting point of TEG materials, these devices should not operate at such temperatures. Certain types of TEGs for high temperatures have been developed which could be used for empirical investigations. The model-based framework employed in the present paper could be translated to improve the design and performance of other heat exchangers for hydrogen production applications as well.

REFERENCES

1. Naterer G, Suppiah S, Lewis M, Gabriel K, Dincer I, Rosen MA, Fowler M, Rizvi G, Easton EB, Ikeda BM, Kaye MH. 2009. Recent Canadian advances in nuclear-based hydrogen production and the thermochemical Cu–Cl cycle. International Journal of Hydrogen Energy. 34:2901-17.

2. Habibollahzade A, Gholamian E, Ahmadi P, Behzadi A. 2018. Multi-criteria optimization of an integrated energy system with thermoelectric generator, parabolic trough solar collector and electrolysis for hydrogen production. International journal of hydrogen energy. 43:14140-57.
3. Ozbilen A, Dincer I, Rosen MA. 2016. Development of a four-step Cu–Cl cycle for hydrogen production–Part I: Exergoeconomic and exergoenvironmental analyses. International Journal of Hydrogen Energy. 41:7814-25.
4. Ishaq H, Dincer I. 2019. A comparative evaluation of three CuCl cycles for hydrogen production. International Journal of Hydrogen Energy. 44:7958-68.
5. Ozbilen A, Dincer I, Rosen MA. 2014. Development of new heat exchanger network designs for a four-step Cu–Cl cycle for hydrogen production. Energy.77:338-51.
6. Gao, X., Chen, M., Snyder, G. J., Andreasen, S. J., and Kær, S. K. 2013. Thermal management optimization of a thermoelectric-integrated methanol evaporator using a compact CFD modeling approach. Journal of Electronic Materials. 42: 2035–2042.
7. Shittu, S., Li, G., Zhao, X., and Ma, X. 2020. Review of thermoelectric geometry and structure optimization for performance enhancement. Applied Energy. 268:115075.
8. Niu, Z., Yu, S., Diao, H., Li, Q., Jiao, K., Du, Q., Tian, H., and Shu, G. 2015. Elucidating modeling aspects of thermoelectric generator. International Journal of Heat and Mass Transfer. 85:12-32.
9. Kim TY, Negash A, Cho G. 2017. Experimental and numerical study of waste heat recovery characteristics of direct contact thermoelectric generator. Energy Conversion and Management. 140:273-80.
10. Rodriguez, R., Preindl, M., Cotton, J. S., and Emadi, A. 2019. Review and trends of thermoelectric generator heat recovery in automotive applications. IEEE Transactions on Vehicular Technology. 68: 5366–5378.
11. Meng, J.-H., Zhang, X.-X., and Wang, X.-D. 2015. Characteristics analysis and parametric study of a thermoelectric generator by considering variable material properties and heat losses. International Journal of Heat and Mass Transfer, 80: 227–235.
12. Chen, W.-H., Wu, P.-H., Wang, X.-D., and Lin, Y.-L. 2016. Power output and efficiency of a thermoelectric generator under temperature control. Energy Conversion and Management. 127:404–415.
13. Wang, X.-D., Huang, Y.-X., Cheng, C.-H., Ta-Wei Lin, D., and Kang, C.-H. 2012. A three-dimensional numerical modeling of thermoelectric device with consideration of coupling of temperature field and electric potential field. Energy. 47:488–497.
14. Wang, C.-C., Hung, C.-I., and Chen, W.-H. 2012. Design of heat sink for improving the performance of thermoelectric generator using two-stage optimization. Energy. 39: 236–245.
15. Chen M, Snyder GJ. 2013. Analytical and numerical parameter extraction for compact modeling of thermoelectric coolers. International Journal of Heat and Mass Transfer. 60:689-99.

WHEC-2022
23rd World Hydrogen Energy Conference
June 26-30, 2022 - Istanbul

#204

INTEGRATION OF PEM ELECTROLYZER AND FUEL CELL TO A SOLAR-GEOTHERMAL COMBINED SYSTEM FOR A ZERO-ENERGY BUILDING: AN EXERGYECONOMIC ANALYSIS

[1*] *Ehsan Baniasadi,* [1] *Masoud Ziaei-Rad,* [1] *Mohammad Amin Behvand,* [2] *Nader Javani*
[1]University of Isfahan, Department of Mechanical Engineering, Faculty of Engineering, Hezar Jerib Ave., Isfahan, Iran
[2] Yildiz Technical University, Department of Mechanical Engineering, Yildiz Campus, Istanbul, 34349 Yildiz, Turkey

*Corresponding author e-mail: e.baniasadi@eng.ui.ac.ir

ABSTRACT

In this study, a novel system which generates cooling effect, heat, electricity, hot water and distilled water simultaneously for a green building is analyzed which operates based on solar and geothermal heat pump, proton exchange membrane (PEM) electrolysis, proton exchange membrane (PEM) fuel cell, photovoltaics, desalination system along with pressure exchanger. The results demonstrats that energy and exergy efficiencies in cooling mode are 13.27% and 32.44% respectively, and in heating mode are also 17.25% and 42.4%, respectively. The largest exergy destruction occurs in the photovoltaics and organic Rankine cycle. It is also worth noting that turbine and vaporizer have the highest portion in exergy losses of organic Rankine cycle. The unit exergy cost of cooling, and hot water, and the cost of produced distilled water and 84.5 $/GJ, 64 $/GJ and 67.63 c$/m^3, respectively.

Keywords: Zero energy building, CCHPW System, Geothermal energy, Solar energy, Exergy-economic analysis

INTRODUCTION

Solar energy and geothermal energy are two important sources of renewable energy that can be used for a variety of constructional applications, such as electricity generation, heating and cooling of buildings, and consuming water. Ezzat et al. [1] investigated the energy and exergy analysis of a new hybrid system powered by geothermal and solar energy. The results showed that total energy and exergy efficiencies are 69.9% and 42.8%, respectively. Ozturk et al. [2] studied thermodynamic analysis of a hybrid system based on solar energy, which produces electricity, heating, cooling, hot water, and hydrogen. They found that the exergy efficiency of total system is 57.35%, while it is 44.88%, 19.62%, 14.31% and 20.32%, respectively, for Rankine cycle, Rankine organic cycle, cooling/heating, and hydrogen production. Islam et al. [3] presented an analysis and evaluation on a hybrid system based on solar and geothermal energies for simultaneous production. Their results indicated that energy and exergy efficiencies are increased by the mass flow rate, while turbine inlet pressure has reverse effect on the efficiencies. Boyaghchi et al. [4] studied the optimization of a new combined cooling, thermal and power cycle containing water-CuO nanofluid based on geothermal and solar energies. The maximum daily thermal coefficient and minimum rate of price for R1234ze are 39.940% and $5819 per year, respectively.

In present study, we investigate a hybrid system with more comprehensive objectives than previously studied ones. In this combined system, photovoltaic system, Rankine cycle, heat pump, fuel cell, and water desalination system are integrated and used together for the first time to meet all energy and fresh water requirements of a residential building based on renewable energies. Economic exergy analysis of the system evaluates its implementation feasibility from the perspective of second law of thermodynamics, as well as its economic justification. Furthermore, the performance of the system is surveyed at different working conditions and the optimal values are obtained.

SYSTEM DESCRIPTION

Figure 1 depicts the flowchart of a hybrid system based on solar and geothermal renewable energies which supplies electricity, cooling and heating, hot water, and fresh water for a zero-energy building. The system includes an organic Rankine cycle, fuel cell, photovoltaic system (PV) with energy storage tank, heat pump with geothermal energy source, and reverse osmosis (RO) desalination system with energy recovery. The electrical power, heating and cooling loads, hot water consumption and fresh water demand in the residential building are 142 kW, 27.8 kW, 32.4 kW, 93.4 kW and 2.6 m^3/h, respectively.

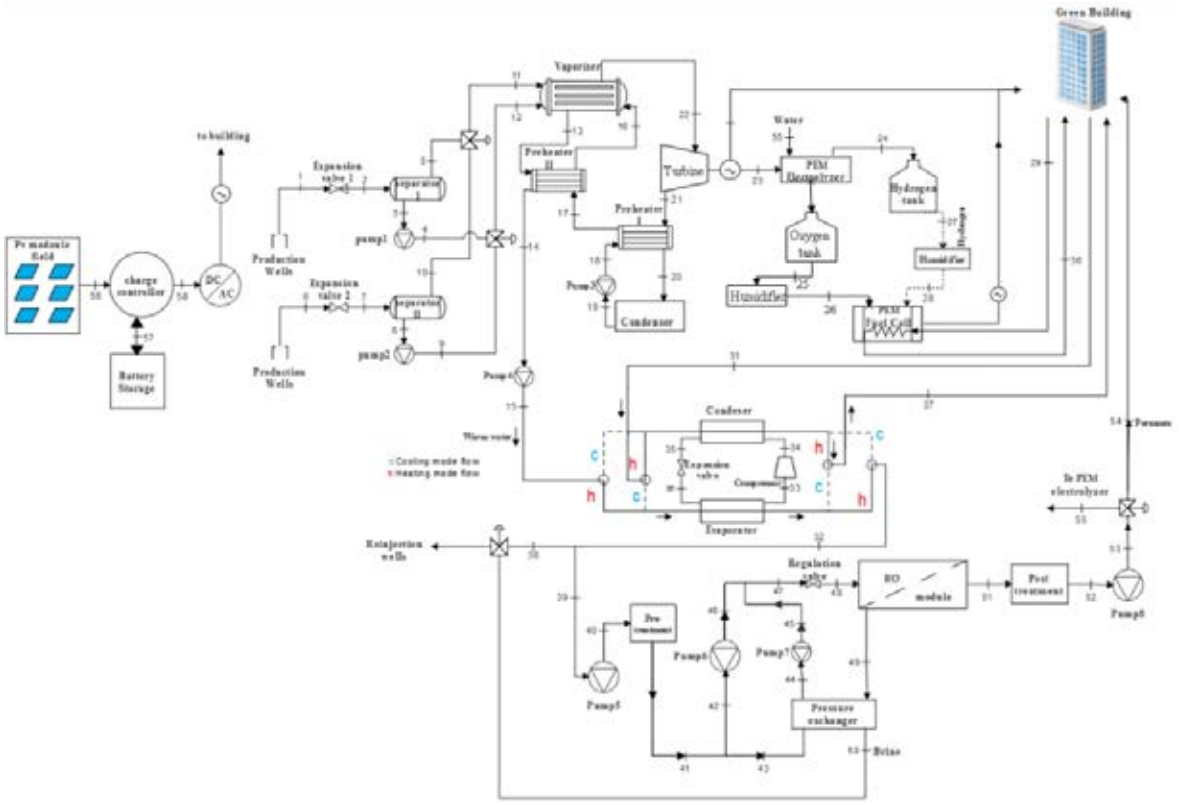


Fig. 1. Flow diagram of the simultaneous cooling, heating, electricity and water production system

ENERGY, EXERGY AND EXERGYECONOMIC ANALYSES

The governing equations for the analysis of intended cogeneration system include mass balance, energy balance, and exergy balance and cost balance. The exergy balance is written as follows [3,4]:

$$\dot{E}x_Q + \sum_{in} \dot{E}x_{in} = \sum_{out} \dot{E}x_{out} + \dot{E}x_W + \dot{E}x_{des} \quad (1)$$

The exergy destruction in the electrolyzer can be calculated using the following equation:

$$\dot{N}_{H_2O.in}\dot{E}x_{H_2O.in} + \dot{W}_{PEM} + \dot{E}x_{heat.PEM} = \dot{N}_{H_2}\dot{E}x_{H_2} + \dot{N}_{O_2}\dot{E}x_{O_2} + \dot{N}_{H_2O.out}\dot{E}x_{H_2O.out} + \dot{E}x_{des.PEM} \quad (2)$$

The PEM fuel cell voltage is consisting of ohmic, activation and concertation overpotentials and it is calculated as follows:

$$V_{cell} = E_{Nernst} - V_{act} - V_{ohm} - V_{cons} \quad (3)$$

The exergy of solar radiation is calculated as follows:

$$\dot{E}x_{solar} = I_s A\left(1 - \frac{4}{3}\left(\frac{T_0}{T_{solar}}\right) + \frac{1}{3}\left(\frac{T_0}{T_{solar}}\right)^4\right) \quad (4)$$

The energy and exergy efficiencies of the overall cycle are written as follows:

$$\eta_{en.total} = \frac{(\dot{m}_{37}h_{37} - \dot{m}_{31}h_{31}) + (\dot{m}_{30}h_{30} - \dot{m}_{29}h_{29}) + (\dot{m}_{60}h_{60} - \dot{m}_{59}h_{59}) + \dot{W}_{gen} - \dot{W}_{cons}}{\dot{m}_1 h_1 + \dot{m}_6 h_6 - \dot{m}_{RW}h_{RW} + \dot{Q}_{Solar}} \quad (5)$$

$$\psi_{ex.total} = \frac{(\dot{E}x_{37} - \dot{E}x_{31}) + (\dot{E}x_{30} - \dot{E}x_{29}) + (\dot{E}x_{60} - \dot{E}x_{59}) + \dot{W}_{gen} - \dot{W}_{cons}}{\dot{E}x_1 + \dot{E}x_6 - \dot{E}x_{RW} + \dot{E}x_{Solar}} \quad (6)$$

The cost balance equation for each component of the system is presented as:

$$\sum \dot{C}_{out.k} + \dot{C}_{w.k} = \sum \dot{C}_{in.k} + \dot{C}_{q.k} + \dot{Z}_k \quad (7)$$

Each component has it own cost equation that is used to estimate the investment cost. The main assumptions in the exergy-economic analysis are summarized in Table 1. The total cost rate includes investment, operation, maintenance, and exergy destruction costs. The cycle utilizes electrical energy storage therefore the operation hours is 7600 h.

Table 1. Summary of main assumptions

Parameter	Quantity
Annual interest rates, i_r	14 (%)
Lifetime (n)	15 (year)
Maintenance factor, ∅	1.06
Annual operation hours	7300 (h)
Hydrogen cost, c_{H_2}	10 ($/GJ)
Geothermal saline water cost, c_{GW}	1.3 ($/GJ)

RESULTS AND DISCUSSION

Herein, the results of thermodynamic analysis of the integrated system in cooling and heating modes are presented. Then, the results of exergy-economic assessment are discussed. Figure 2 shows the effect of current density on the exergy efficiency of the organic Rankine cycle in cooling and heating modes. increasing the current density, the amount of voltage and power required by the electrolyzer increase and the exergy efficiency of the Rankin organic cycle decreases. It is observed that increase of current density from 1000 A/m^2 to 5000 A/m^2 lead to almost 10% decrease in the exergy efficiency of the ORC.

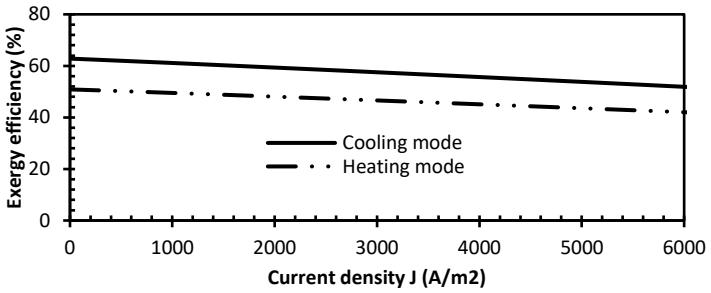


Fig. 2. The effect of electrolyzer current density on the exergy efficiency of the ORC

Figure 3 presents the effect of solar irradiation on energy and exergy efficiencies of the overall system in cooling mode. Increase of solar intensity from 200 to 800 W/m^2 cause 36% increase in the exergy efficiency. Increase of solar radiation intensity leads to higher input exergy of which large portion is wasted due to heat dissipation in different subsystems.

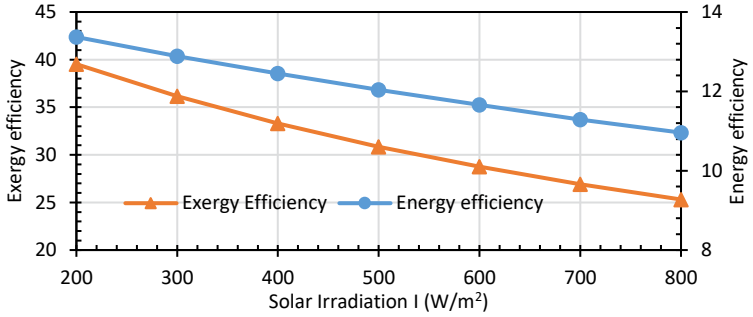


Fig. 3. Energy and exergy efficiency of the overall system in cooling mode versus solar intensity

Table 2 presents the unit exergy cost of system products. It is concluded that cooling has the highest cost per unit of exergy and electricity has the lowest cost per unit of exergy, i.e., 84.5 and 9.23 $/GJ, respectively. In this system, the fuel cell uses hydrogen (at a high exergy unit cost) as fuel for its operation; this causes a high cost per unit of exergy hot water.

Table 2. Exergy unit cost of output commodities in cooling mode

	Electric power	Cooling	Hot Water
Exergy unit cost ($/GJ)	9.23	84.5	64.06

CONCLUSIONS

- Energy and exergy efficiency of the overall system in cooling mode are 13.27% and 32.44%, respectively, and in heating mode are 17.24% and 42.4%.
- The photovoltaic panels and organic Rankine cycle cause the highest exergy destruction. Also in the ORC, the highest exergy loss take place in the turbine and steam generator.
- Increase of current density by 5 times leads to increase of exergy unit cost of the produced electricity by 11%.

REFERENCES

1. Ezzat M. F., Dincer I. 2016. Energy and exergy analyses of a new geothermal-solar energy-based system. Solar Energy,134: 95-106.
2. Ozturk M., Dincer I. 2013. Thermodynamic analysis of a solar-based multi-generation system with hydrogen production. Applied Thermal Engineering, 51: 1235-1244.
3. Islam S., Dincer I. 2017. Development, analysis and performance assessment of a combined solar and geothermal energy-based integrated system for multigeneration. Solar Energy, 147: 328-343.
4. Boyaghchi F. A., Chavoshi M., Sabeti V., 2015. Optimization of a novel combined cooling, heating and power cycle by geothermal and solar energies using the water/Cuo (copper oxide) nanofluid, Energy, 91: 685-699.

WHEC-2022
23rd World Hydrogen Energy Conference
June 26-30, 2022 - Istanbul

#210
EVALUATION OF HYDROGEN PRODUCTION PROCESSES FOR USE IN AUTOMOTIVE SECTOR

[1]Francisco Edvan Bezerra Feitosa, [2]Antonella Lombardi Costa
Universidade Federal de Minas Gerais, Departamento de Engenharia Nuclear, Campus UFMG, Escola de Engenharia, Av. Antônio Carlos, 6627, Belo Horizonte, MG, Brasil.

*Corresponding author e-mail: [1] feb.feitosa@gmail.com, [2] antonella@nuclear.ufmg.br

ABSTRACT

This article identifies and evaluates large-scale hydrogen production processes - those capable of providing hydrogen for an eventual automotive hydrogen program in a community and along highways - to answer the following research question: which of the production processes of hydrogen is more attractive for an eventual automotive hydrogen program? To answer this question, the MACBETH method – Measuring Attractiveness by the Category-Based Assessment Technique Method and the computational code M-MACBETH 3.2.O are used. The MACBETH is a method to support complex decision making, which allows evaluating alternatives or options, taking into account multiple criteria. Thus, this work used the computational code M-MACBETH 3.2.0 to evaluate ten hydrogen production processes and build some Rankings of attractiveness of hydrogen production processes, considering the following criteria: economic (invested capital and production cost), technical (the purity of the hydrogen produced) and environmental (the amount of energy used to produce one kilogram of hydrogen and the CO2 emissions to produce one kilogram of hydrogen). In the end, MACBETH built three Rankings considering three scenarios, which allow to conclude that: a) the hydrogen production process from natural gas reforming with CCS is the most attractive alternative when economic and financial aspects prevail over environmental aspects and technicians; b) the hydrogen production process by the electrolysis process using photovoltaic solar energy becomes more attractive when the environmental aspects prevail over the economic and financial aspects; c) the process of producing hydrogen by the electrolysis process using photovoltaic solar energy is also the most attractive process when using balanced weights of economic, financial, technical and environmental aspects, in the analysis taken for decision making in relation to hydrogen.

Keywords: Hydrogen, Gasification, Steam Reforming, Electrolysis

INTRODUCTION

The hydrogen is the most abundant element in the universe; however, it is rarely found in its elemental form on Earth. So, it must be produced, which is made from some industrial processes using raw materials containing it, such as water, coal, biomass, natural gas and oil and its derivatives, using an energy source [1]. In this context, this article carried out a structured bibliographic research in order to identify the processes of large-scale hydrogen production - capable of producing quantities of hydrogen for a highway, a city, a state and even an entire nation - and at the end answers the following research question: Which of the hydrogen production processes is the most attractive for an eventual hydrogen program for the automotive transport sector, considering as criteria, the capital needed to produce, the cost of production, the purity of the hydrogen produced, the depletion in the energy matrix and in greenhouse gas emissions resulting from the production process? Thus, this work aims to evaluate the hydrogen production processes to select the most attractive process for an eventual hydrogen program for use in the automotive sector in conjunction with a cell, which has as an essential requirement the purity of the hydrogen that is supplied as fuel. The minimum hydrogen purity required is established by the International Organization for Standardization ISO 14687:2019 as 99.97%. In addition, the aforementioned standard specifies the limits for the presence of several other contaminants [2], as some of them are considered poison for a fuel cell.

There are several processes capable of producing hydrogen on large-scale for supporting a hydrogen program for the automotive sector of a city, a state and a nation. Among them, the following stand out: a) gasification; b) steam reforming; and c) the electrolysis of water.

In Gasification process, raw materials such as biomass and coal are transformed in gas in equipment called a gasifier, through a process that involves drying, pyrolysis, oxidation reduction, producing a gas composed of CO, CO_2, CH_4, H_2, H_2O. Furthermore, in the case where the raw material is coal, S, sulfur is produced. After the process of capturing CO2 and eliminating impurities, it turns synthesis gas (syngas) [3, 4].

The steam reforming process, consists of the reforming of liquid and gaseous fuels, such as ethanol and natural gas, which are transformed into hydrogen in an equipment called a steam reformer [1]. In the methane gas reformer, the CH_4 reacts with water steam. This process, after a series of reactions, produce a gas containing H_2, CO, CO_2 and ash (C) [3,4]. The ethanol reforming process, on the other hand, takes place in equipment called an ethanol reformer. This process begins when the C_2H_5OH reacts with steam water followed by a series of reactions that result in a gas composed from H_2, CO_2, CH_4, H_2O and ash (C) [3,4].

As can be seen, the synthesis gas produced by the gasification and steam reforming processes does not contain pure hydrogen and, therefore, needs to go through cleaning processes, which include the capture of contaminants and the capture of carbon compounds before storage as vehicle hydrogen, which here will be identified as CCS. There are several mature CCS processes, which make the gases produced acquire, in the end, the hydrogen content and purity necessary so that they can be burned in a fuel cell that drives a hydrogen vehicle [3,4].

In the electrolysis process, water molecules are split into hydrogen and oxygen by the electric current [3,4]. The research identified three electrolysis technologies: alkaline electrolysis, proton exchange membrane electrolysis, and solid oxide electrolysis, all of which use a reactor called an electrolyzer, which are respectively called an alkaline electrolyzer (AEC), proton exchange membrane (PEM or PEMEC) and the solid oxide electrolyzer (SOEC) [4].

MATERIALS AND METHODS

To answer this research question, the computational code M-MACBETH 3.2.0 is used, and it was developed based on the MACBETH method - Measuring Attractiveness by Categorical Based Evaluation Technique Method, which is a method to support complex decision making, which allows evaluating existing alternatives or options, taking into account multiple criteria, developed by two researchers in the 1990s [5,6]. At the end of the evaluation, MACBETH builds Rankings in descending order of attractiveness, and the alternative that presents the best score is considered the most attractive alternative.

The computational code M-MACBETH 3.2.0 was developed to be used as an interactive method to support complex decision-making and was mathematically modeled in four linear programs called Mc1, Mc2, Mc3 and Mc4. The Mc1 program analyzes the consistency of the data presented as a performance of the alternatives being analyzed. The Mc2 program suggests and builds a numerical scale of attractiveness of the alternatives, calculates the differences in attractiveness, interacts with the analyst doing the analysis and, in the end, generates reports and graphs. The Mc3 and Mc4 programs identify and reveal inconsistencies, interact with the analyst by accepting or rejecting judgments, validating or changing data [5, 6]. The MACBETH mathematical modeling will not be presented, in order not to lose the necessary objectivity in this work, however, it is very well detailed in [5,6].

The research identified several production processes, however, it was selected for analysis in this work, only those that are capable of producing hydrogen on a large scale, capable of supplying hydrogen to a city, a state or even a nation.

The selected processes were coded and registered in M-MACBETH 3.2.0 and are as follows: 1) Coal gasification without CCS **-** Primary gasification of coal producing hydrogen as synthesis gas without capture of CO_2 and without removal of impurities; 2) Coal gasification with CCS **-** Primary gasification of coal producing hydrogen as synthesis gas with capture of CO_2 and with removal of impurities; 3) Biomass Gasification without CCS - primary gasification of biomass producing hydrogen as synthesis gas without capture of CO_2 and without removal of impurities**;** 4) Biomass Gasification with CCS - primary gasification of biomass producing hydrogen as synthesis gas with capture of CO_2 and removal of impurities**;** 5) Natural Gas reforming without CCS- synthesis gas resulting from the steam reforming process of natural gas or Methane without capture of CO_2 and without removal of impurities; 6) Natural Gas reforming with CCS- synthesis gas resulting from the steam reforming process of natural gas or Methane with capture of CO_2 and with removal of impurities; 7) Ethanol reforming - synthesis gas resulting from the steam reforming of ethanol without capture of CO_2 and without removal of impurities; 8) On grid electrolysis - hydrogen gas product of electrolysis powered with energy from the electrical grid; 9) wind electrolysis - hydrogen gas product of electrolysis powered with electricity from wind generators off grid; and 10) Solar PV electrolysis - hydrogen gas product of electrolysis powered with electricity from photovoltaic generators off grid.

The research also identified several indicators that could be used as criteria in the evaluation of hydrogen production alternatives, however, it was selected and used only five criteria: 1) Purity (%) - considers the purity of the hydrogen produced measured in percentage of hydrogen contained in the gas that will be delivered to vehicle filling stations; 2) Depletion (Btu/kgH_2) - considers the amount of energy removed from the energy matrix in the form of raw material and energy; 3) Emissions (kgCO_2/kgH_2) - considers the amount of carbon dioxide that is emitted per kilogram of

hydrogen produced; 4) Costs (U$/kg$H_2$) - evaluates the cost of producing hydrogen for the alternative under analysis; and 5) Capital (US/kWH_2) - evaluates the capital needed to produce an equivalent kW of hydrogen. The performance indicators of the selected processes and object of this evaluation are shown in Table 1.

Table 1. Performance indicators

Options	Capital (U$/kg$H_2$)		Costs (U$/kg$H_2$)		Depletion (Btu/kgH_2)		Purity (%)		Emissions (kgCO_2/kgH_2)	
Coal gasification wo CCS	2,670	[8]	1.34	[3]	223,253	[7]	20	[1]	20.2	[8]
Coal gasification with CCS	2,780	[8]	1.63	[3]	223,253	[7]	95	[1]	2.1	[8]
Biomass gasification wo CCS	2,670	[8]	1.77	[3]	259,226	[7]	40	[1]	0	[8]
Biomass gasification w CCS	6,320	[8]	2.07	[3]	259,226	[7]	95	[1]	0	[8]
Natural gas reforming wo CCS	910	[8]	2.08	[3]	158,191	[7]	37	[1]	8.9	[8]
Natural gas reforming w CCS	1,680	[8]	2.27	[3]	160,595	[7]	99	[1]	1	[8]
Ethanol reforming	910	[*]	1.63	[3]	168,910	[7]	95	[1]	11	[*]
On grid electrolysis	900	[8]	4.3	[1]	170,607	[7]	99.999	[1]	1	[*]
Wind electrolysis	2,120	[1]	5.96	[3]	0	[7]	99.999	[1]	0	[1]
Solar PV electrolysis	2,000	[1]	13.0	[1]	0	[1]	99.999	[1]	0	[1]

[*] Estimated by the authors; wo=without; w=with; CCS= CO_2 capture and storage.

The performance data presented in Table 1 were entered into M-MACBETH 3.2.0, which, after judgments and validation, generated several reports and graphs, including Rankings of attractiveness of hydrogen production processes. Three scenarios were considered and analyzed: scenario A considers that the decision maker has a preference for economic and financial criteria; scenario B considers that the decision maker has no preference for any of the criteria and scenario C considers that the decision maker has a preference for criteria that consider sustainability aspects. The results are shown in Figure 1 and analyzed below.

RESULTS AND DISCUSSION

Scenario A – focus on economic aspects

In this scenario, it was informed in the MACHBETH judgment matrix that the decision maker decides with a focus on economic and financial aspects. For this, they were assigned, with a weight of 30% being assigned to the capital criterion, 30% to the cost criterion, 10% for hydrogen purity, 15% for energy matrix depletion, and 15% for CO2 emission. The ranking for this scenario is shown in Figure 1, where it can be seen that the most attractive process is NG reform with CCS with a rating of 86.52 and that the second most attractive process is solar PV electrolysis with a rating of 85.54. This ranking also shows that the worst processes are those without CCS.

Scenario B – Balanced

In this scenario, it was informed in the MACHBETH judgment matrix that the decision maker has no preference for any of the criteria. For this, equal weights were assigned to each of the criteria. Thus, a weight of 20% was assigned to the capital criterion, 20% to the cost criterion, 20% to hydrogen purity, 20% to energy matrix depletion and 20% to CO2 emissions. The classification for this scenario is presented in Figure 1, where it can be seen that the most attractive process is photovoltaic solar electrolysis with a rating of 90.36. The second most attractive process is Wind Electrolysis with a rating of 90.06. This ranking shows that the worst hydrogen production processes are those without CCS.

Scenario C – Focus on sustainability

In this scenario, it was informed in the MACHBETH judgment matrix that the decision maker decides with a focus on sustainability. For this, they were assigned, with a weight of 30% being assigned to the CO2 emissions criterion, 30% to the energy matrix depletion criterion, 10% for hydrogen purity, 15% for capital, and 15% for costs. The ranking for this scenario is shown in Figure 1, where it can be seen that the most attractive process is solar PV electrolysis with a rating of 92.77. The second most attractive process is Wind Electrolysis with a rating of 92.54. This ranking also shows that the worst processes are those without CCS.

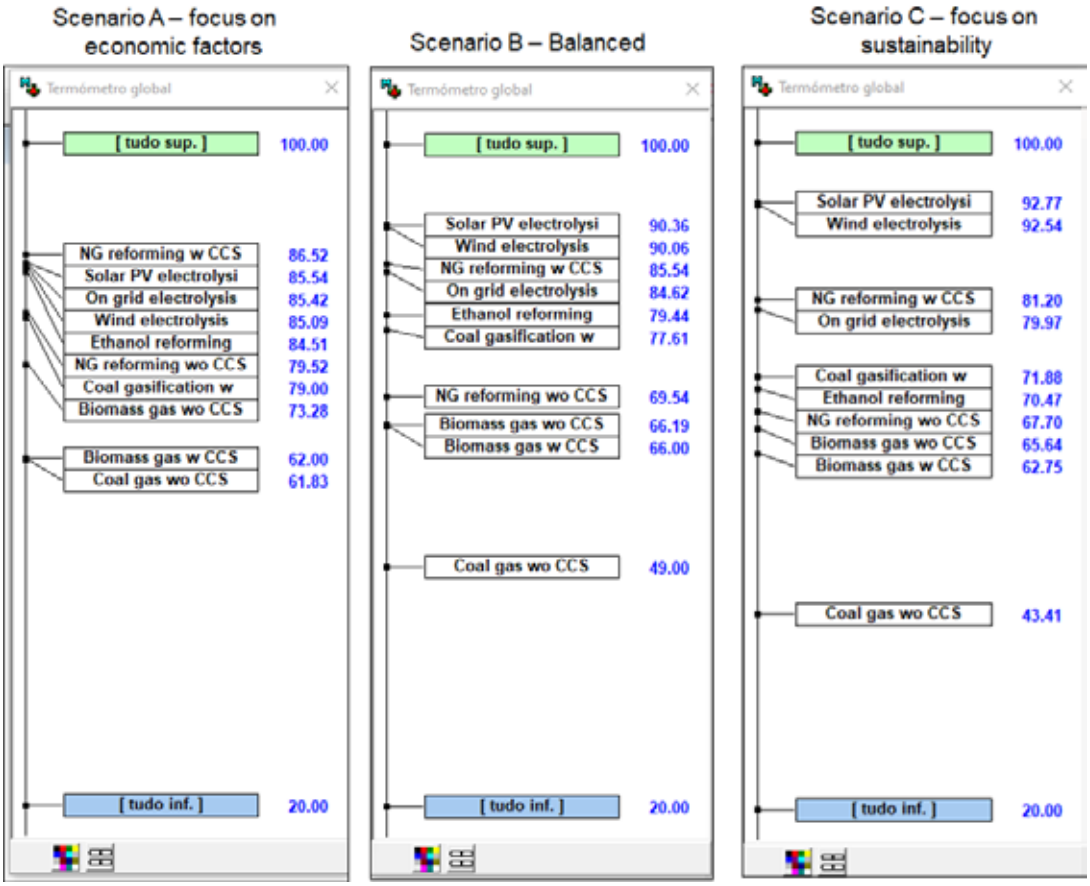


Fig. 1. Attractiveness rankings built by MACBETH

CONCLUSIONS

This work carried out a structured bibliographic research and identified ten processes capable of producing hydrogen on a large scale for an eventual hydrogen program for the transport sector. These ten processes were evaluated by the MACBETH method through the M-MACBETH 3.2.0 computational code considering economic, technical and environmental criteria. The MACBETH built three Rankings considering three scenarios, which allow us to conclude that: a) the process of producing hydrogen from the reform of natural gas with CCS is the most attractive alternative, when, in the decision-making, economic and financial aspects prevail over environmental and technical aspects; b) the hydrogen production process by Solar PV electrolysis becomes more attractive when, in decision-making, environmental aspects prevail over economic and financial aspects. This conclusion is completely in line with the current reality, since most of the hydrogen currently produced in the world is through the reform of natural gas, despite the fact that NG is a fossil fuel, finite, polluting and contributes to increase the greenhouse effect. Furthermore, this work is in line with scientists around the world, as they believe that hydrogen produced by electrolysis from renewable sources will be the energy solution of the future for the transport sector, when necessary capital and its costs come down.

ACKNOWLEDGEMENT

The authors are grateful to Brazilian research funding agencies: Conselho Nacional de Desenvolvimento Científico e Tecnológico (CNPq), Coordenação de Aperfeiçoamento de Pessoal de Nível Superior (CAPES) and Fundação de Amparo à Pesquisa do Estado de Minas Gerais (FAPEMIG).

REFERENCES

[1] https://www.hydrogen.energy.gov. Accessed on December, 2021.
[2] https://standards.iteh.ai. Accessed on December, 2021.
[3] Nikolidis P and Poullikkas A. 2017. A comparative overview of hydrogen production processes. Renewable and Sustainable Energy Reviews. 67:597-611
[4] Xing, L Y and HINO R. 2011. Nuclear Hydrogen Production Handbook. Ohio: CRC Press Book, 2011.

[5] https://www.m-macbeth.com. Accessed on November, 2021.
[6] Costa C A B and Vansnick J C. 1999. The MACBETH Approach: Basic Ideas, Software, and an Application. In: Meskens N., Roubens M. (eds) Advances in Decision Analysis. Mathematical Modelling: Theory and Applications, vol 4. Springer, Dordrecht.
[7] https://h2tools.org. Accessed on December, 2021.
[8] https://www.iea.org. Accessed on December, 2021.
[9] Feitosa F E B and Costa A L. 2021. Application of a multicriteria methodology for evaluation of energy alternatives for hydrogen production for the automotive sector e Case study. International Journal of Hydrogen Energy, 46:20799-20814.

WHEC-2022
23rd World Hydrogen Energy Conference
June 26-30, 2022 - Istanbul

#212

THE ROLE OF RENEWABLE HYDROGEN-BASED SYSTEMS TO ACHIEVE LOW-CARBON STATIONARY POWER APPLICATIONS

[1] *Víctor Manuel Maestre,* [1*] *Alfredo Ortiz,* [1,] *Inmaculada Ortiz*
[1] Chemical and Biomolecular Engineering Department, University of Cantabria, Av. Los Castros 46, 39005, Santander, Spain

*Corresponding author e-mail: ortizal@unican.es

ABSTRACT

Increasing the contribution of renewable energy sources (RES) to the final energy consumed is fundamental to achieving a low-carbon economy. In this context, the use of hydrogen as an energy carrier offers a clean and versatile alternative to boost RES penetration and ensure an uninterrupted energy supply. Moreover, stationary applications account for almost 75% of greenhouse gases (GHG) emissions globally associated with power generation. This study thoroughly analyzes the state of the art and presents an overview of the evolution of renewable hydrogen-based systems (RHS) from simulated case studies to pilot plants and commercial systems for large power generation, industrial parks, buildings, and critical infrastructures. Relevant techno-economic parameters such as levelized cost of energy (LCOE), loss of power supply probability (LPSP), self-sufficiency ratio (SSR), hydrogen roundtrip efficiency (HRE), or renewable fraction (f_{RES}) are evaluated. Subsequently, the main techno-economic barriers and challenges for the deployment of RHS are identified and discussed. Finally, a pilot plant implemented in the north of Spain in the frame of the SUDOE ENERGY PUSH project is presented as a case study of the application of RHS in buildings.

Keywords: Renewable hydrogen, Stationary applications, Fuel cell, Technical feasibility, Cost-competitiveness.

INTRODUCTION

Governments, policymakers, private companies, and stakeholders are coordinating different measures to fight the unsustainable climate change situation and to ensure the required energy transition. In this context, more than 2,500 GW of RES capacity is already installed worldwide, with solar photovoltaic (PV) and wind energy predominating. However, a six-fold increase in the contribution of RES to the energy mix is required to comply with the Paris agreement [1]. To enable a higher RES penetration, hydrogen has emerged as a promising and feasible energy carrier. Accordingly, countries are focusing R&D activities on the generation of “green hydrogen” obtained through water electrolysis and renewable energy as an alternative to hydrogen produced by steam methane reforming that represents almost 95% of hydrogen generated globally [2]. Green hydrogen is an emissions-free and versatile solution that can be employed as a bulk energy storage system (ESS) or for small dispatchable backup power generation, with a fast response and long periods of full-load operation.

This study provides an in-depth overview of RHS and their deployment in the stationary sector, exploring the green hydrogen generation and power retrieval by different FC technologies. First, the different topologies and ways of integrating the components that make up each of the configurations are also evaluated. Furthermore, a global market status, trends, and main barriers beyond techno-economic ones are highlighted from a comprehensive perspective [3]. Finally, a case study of RHS pilot plant within the framework of the SUDOE ENERGY PUSH project is analyzed.

MATERIALS AND METHODS

Renewable hydrogen-based systems (RHS) are designed depending on the type of load to be supplied, the meteorological conditions of the location, the type of technologies to be used, or the budget available for the execution of the installation. Therefore, their evaluation requires a deep understanding of energy balances within the system, implemented control strategies, and load characteristics. Figure 1 depicts a general schematic diagram of an RHS that is divided into three main parts: 1) power generation, 2) energy storage and supply, and 3) load demand [4].

Renewable energies represent the primary power supply sources and their surpluses are then employed to charge the ESS (consisting of batteries, supercapacitors, etc.) and to run the electrolyzer. The generated hydrogen can be stored in vessels, pressurized tanks (needing an intermediate compressor), salt caverns, etc. The stored energy is released via direct electricity or hydrogen re-electrification in an FC system when RES is not enough to cover the demand. Besides, diesel generators and grid connections can be used as dispatchable backup energy sources to avoid power shortages, but they may imply CO_2 emissions. Microgrids with properly sized RHS and grid-tied converters may be remunerated for back feeding the power utility grid in compliance with the local legislation for self-consumption.

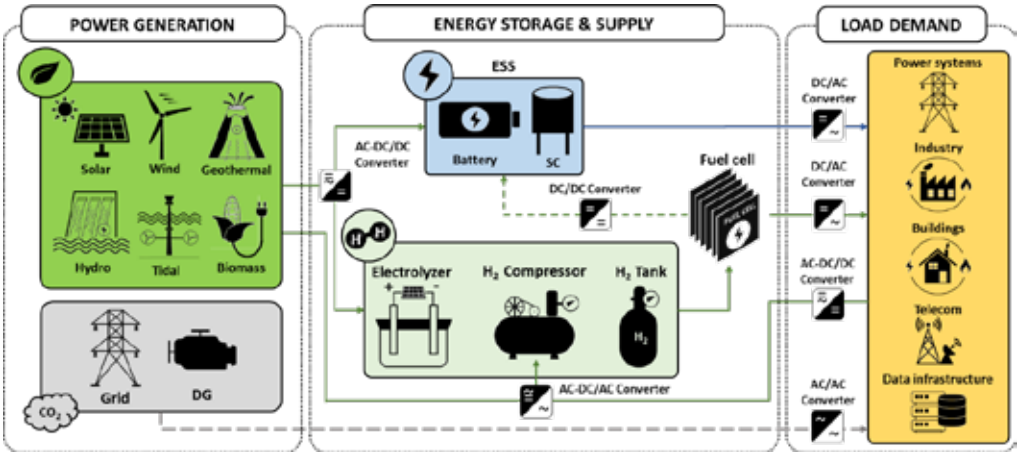


Fig. 1: Schematic diagram of an RHS including RES and fossil fuel-based power generation (through grid and DG), energy storage and supply (through hydrogen-based technologies and other ESS), and load demand (considering required power converters).

To evaluate the performance of RHS in a uniform and harmonized manner, the following techno-economic parameters are selected as the most reported ones in the literature: levelized cost of energy (LCOE), hydrogen roundtrip efficiency (HRE), loss of power supply probability (LPSP), self-sufficiency ratio (SSR), and renewable fraction (f_{RES}).

$$LCOE = C_{ann,tot} / E_{load} \quad (1)$$

$$HRE = \eta_{EL} \cdot \eta_{FC} \quad (2)$$

$$LPSP = \Sigma(E_{load}(t) - E_{gen}(t)) / \Sigma(E_{load}(t)) \quad (3)$$

$$SSR = 1 - E_{grid,imp} / E_{load} \quad (4)$$

$$f_{RES} = 1 - E_{non,RES} / E_{load} \quad (5)$$

Where $C_{ann,tot}$ is the total annualized cost of the system in US$, E_{load} is the total load consumption in kWh, η_{EL} and η_{FC} are the electrolyzer and FC efficiencies respectively, $E_{load}(t)$ and $E_{gen}(t)$ are the consumed and generated energy in every time step in kWh, $E_{grid,imp}$ is the total energy imported from the grid in kWh and $E_{non,RES}$ is the total non-renewable energy consumed in kWh.

RESULTS AND DISCUSSION

The literature reflects a predominance of PV as the main RES over wind turbines (WT) for buildings as roofs and facades can be exploited for PV energy harvesting. However, WT represent a good opportunity in remote areas without grid access and limited surface availability. The combination of PV panels and WT would reduce the energy storage needs. In addition, the reduction of loss of power supply probability (LPSP) and the increase of the renewable fraction (f_{RES}) and self-sufficiency ratio (SSR) enlarge the system size and investment needed. Reduced hydrogen roundtrip efficiencies have the same impact on the configuration dimensions and economics. Finally, despite the current high CAPEX of hydrogen-related technologies in comparison with fossil fuels, off-grid hybrid schemes may present a competitive levelized cost of energy (LCOE) in mid and long-term scenarios.

Concerning real implemented systems, large-scale pilot projects focus on the decarbonization of the utility grid and industrial applications using multi-MW fuel cells to get heat and power and benefiting from waste streams with high hydrogen content or biofuels. The waste heat produced can be used for district heating or within industrial processes. At lower scales, RHS schemes contribute to the decarbonization of micro-grids, residential communities, and other remote applications; while micro-cogeneration and stationary FC systems are the main alternatives for buildings due to the lower complexity and space requirements. These trends are also reflected in commercial devices that are paving the way towards carbon neutrality by 2050. However, different barriers apart from techno-economic boundaries arise to achieve broader deployment of hybrid systems. Thus, hybrid systems require focused, consistent and specific policies to establish a solid legal framework to create a robust hydrogen infrastructure.

CASE STUDY SUDOE ENERGY PUSH PROJECT

The SUDOE ENERGY PUSH project proposes an innovative solution for the overall management of social housing located in the regions of southwestern Europe as a reference to increase the energy efficiency of public buildings and improve the quality of life of disadvantaged citizens. Through the combination of passive renovation, RES, and

BIM methodology, it aims at reducing the consumption and emissions of buildings and at improving the comfort of the inhabitants, overcoming the risks of energy poverty [5]. In this context, a pilot plant combining RES and hydrogen technologies will be implemented in social housing in Cantabria (Spain) to demonstrate the feasibility and benefits of the system depicted in Figure 2. This demonstration is aimed at achieving energy self-sufficiency of the house without needing neither electricity from the grid nor fossil fuel-based ancillary gensets during the year. In addition, further RES surpluses that cannot be stored will be re-injected into the grid so that the inhabitants can obtain extra remuneration.

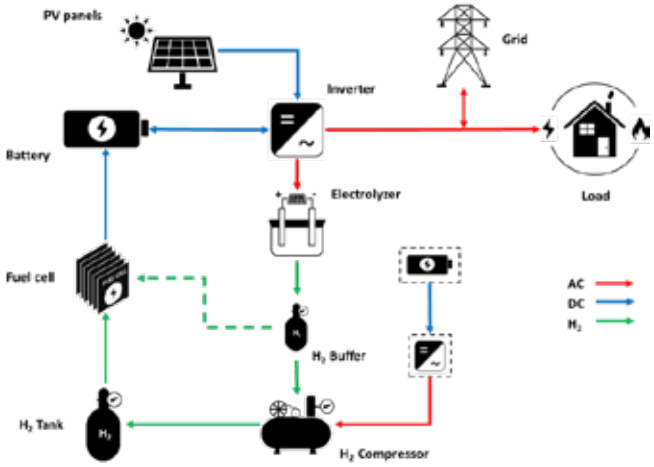


Fig. 2: Schematic diagram of the hybrid renewables hydrogen-based system in Cantabria (Spain)

CONCLUSIONS

The combination of RES and emerging hydrogen technologies is continuously evolving as a solution to achieve the required energy transition of the stationary sector. Both are well-known technologies, but their integration is in an early stage of development. Thus, several studies have been conducted, and a variety of pilot plants from few kW to multi-MW systems deployed to assess their potential. Despite the successfully implemented systems worldwide, there are still pending challenges to overcome for a broader deployment of RHS in the stationary sector. Apart from the lack of dedicated infrastructure, defining proper regulation, codes, and standards for safe hydrogen management combined with dialogue, education, and experience is crucial to encourage end-users awareness. Therefore, the SUDOE ENERGY PUSH project aims at improving energy efficiency management, combating energy poverty, and achieving greater social acceptance of hydrogen-based technologies among the most disadvantaged inhabitants by implementing a pilot plant.

ACKNOWLEDGEMENT

This research is being supported by the Project ENERGY PUSH SOE3/P3/E0865, which is co-financed by the European Regional Development Fund (ERPF) in the framework of the INTERREG SUDOE Programme and the Spanish Ministry of Science, Innovation, and Universities (Projects: RTI2018-093310-B-I00 and PLEC2021- 007718).

REFERENCES

1. Salvia M, Reckien D, Pietrapertosa F, Eckersley P, Spyridaki NA, Krook-Riekkola A, et al. 2021. Will climate mitigation ambitions lead to carbon neutrality? An analysis of the local-level plans of 327 cities in the EU. Renewable and Sustainable Energy Reviews 135:110253.
2. https://hydrogencouncil.com/wp-content/uploads/2021/01/Hydrogen-Council-Report_Decarbonization-Pathways_Part-2_Supply-Scenarios.pdf. Accessed on October 20, 2021.
3. Maestre VM, Ortiz A, Ortiz I. 2021. Challenges and prospects of renewable hydrogen-based strategies for full decarbonization of stationary power applications. Renewable and Sustainable Energy Reviews 152:11628.
4. Maestre VM, Ortiz A, Ortiz I. 2021. The role of hydrogen-based power systems in the energy transition of the residential sector. Journal of Chemical Technology and Biotechnology.
5. https://www.sudoe-energypush.eu/. Accessed on October 20, 2021.

WHEC-2022
23rd World Hydrogen Energy Conference
June 26-30, 2022 - Istanbul

#237
CONTROL STRATEGIES FOR THERMAL COUPLING SYSTEM OF FUEL CELL AND METAL HYDRIDE TANK: A REVIEW

[1] Jiaxuan Liu, [1*] Fusheng Yang, [1] Zhen Wu, [1] Zaoxiao Zhang
[1]School of Chemical Engineering and Technology, Xi'an Jiaotong University, Xi'an, China

*Corresponding author e-mail: yang.fs@mail.xjtu.edu.cn

ABSTRACT

The utilization of hydrogen storage unit in distribute energy system (DES) attracts wide attentions, and storing hydrogen with metal hydrides (MH) have been explored as a promising way considering the high volumetric density and relative safety. To improve system efficiency and compactness, the thermal coupling of fuel cell (FC) and MH tank is proposed. However, the strong interactions in the system introduces challenges for meeting the power demand satisfactorily, thus various control strategies have been proposed. The aim of this study is to review the control strategies of thermal coupling system in multiple scenarios comprehensively. The literature survey illustrates that the traditional linear controller e.g. PID can realize a good tracking performance in some application, but the output may fluctuate with fast-changing signal, and nonlinear multi-input-multi-output (MIMO) controller is hence recommended in this case.

Keywords: Thermal coupling, Metal hydride, Fuel cell, Control strategies

INTRODUCTION

To integrate large amounts of renewable energy like solar and wind power, the distributed energy systems (DES) has gained a lot of interest in recent years [1]. However, the inherent randomness and intermittence of renewable energy source (RES) hampers the development of DES. On the other hand, the energy storage system (ESS) has been proven as a feasible solution to alleviate this problem and becomes a necessary component for DES [2].
Hydrogen is set to become a promising energy carrier for long-term energy storage due to high gravimetric energy density and convenient transportation [3]. Compared with the conventional hydrogen storage technologies e.g. compressed gas and liquefaction, storing hydrogen with metals hydride (MH) has seen rapid development in recent years due to its high volumetric density, relative safety and wide range of operating temperatures and pressures [4].
In MH storage tank, the mechanism of hydrogen absorption/desorption is reversible reactions between MH and hydrogen. However, large amounts of heat need to be removed or provided to maintain the desired reaction rate. For this sake, a variety of thermal management solutions have been proposed, as reviewed by Nguyen et. al [5]. On the other hand, the heat generated by FC system is also need to be dissipated to avoid overheating, thus the removed heat can be recovered by MH storage tank during desorption, and the feasibility of this thermal coupling system (TCS) has been first confirmed by Jiang et. al [6]. Although the TCS is projected to be of great benefit for system compactness and efficiency, the heat provided by FC will influence the desorption rate of MH significantly. In addition, the output of FC is often irregular due to the unpredicted power demand. Thus, a higher requirement for control strategy of TCS is put forward.
Actually, Lototskyy et. al [7] reviewed developments in hydrogen storage systems integrated with fuel cells. Particular emphasis was laid on the MH material selection and container design. Various control strategies for individual PEMFC subsystems were discussed by Wu et. al [8]. However, there is a lack of review associating with control strategies of TCS. This paper is dedicated to summarize the control strategies of TCS focusing on system structure and control method. The discussion starts with a brief introduction of thermal coupling approaches and then is followed by a critical review of control strategies distinguished by linear and nonlinear controller. Finally, several gaps and search directions are addressed.

THERMAL COUPLING APPROACHES

The thermal coupling approaches can be divided into passive and active types based on the controllability, as shown in Fig. 1. The passive approaches include direct contact heat transfer and heat pipes. Kang et al. [9] proposed a direct heat exchange method, and the FC in TCS shows a 31% increase in maximum power compared with single one. The feasibility of TCS utilizing heat pipes was proven by Tetuko et al. [10], and the simulation results showed the maximum hydrogen flow rate of each tank increases by additional heat significantly with low maintenance. In addition, the heat transfer effect can be adjusted based on the equilibrium pressure and boiling point of liquid in heat pipes.

The active types include air-cooled and liquid-cooled approaches. Zhu et al. [11] analyzed a mathematic model of air-cooled TCS considering the degradation of FC and MH, and the exhaust air from FC stack is blown to the external surfaces of the MH tank. The results demonstrated that for a stable operation of 1000 h, the voltage degradation of PEMFC is reduced from 6.8% to 4.5% by thermal coupling, and this kind of TCS has been proven to be effective for small size FC (< 2 kW) due to low convection heat transfer coefficient of the exhaust air and thermal conductivity of the MH tank [12,13]. Førde et al. [14] investigated a liquid-cooled TCS by experiment. The exhaust heat from FC was recovered through a U-tube heat exchanger embedded into the MH tank. The results indicated that the MH tank can supply the hydrogen demand for 3h at the maximum power of FC, and about 25% of total cooling load of the PEMFC is sufficient for MH desorption.

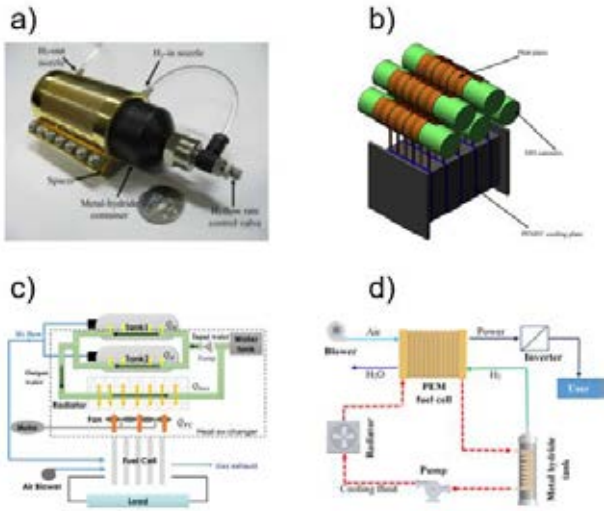


Fig. 1. Thermal coupling approaches; a) direct heat exchange [9]; b) heat pipes [10]; c) air-cooled [11]; d) liquid-cooled [14].

CONTROL STRATEGIES OF TCS

One of the major concerns of control strategies is controller design. Mostly, the linear controller is developed by approximate linearization, while nonlinear controller is integrated with intelligent algorithm. Table 1 summarizes part of the control strategies of TCS based on different controller and control variable. It can be seen that most of the control variables for TCS focused on the thermal management system, and mainly linear controller is adopted.

What's more, from the recent simulation research of TCSs, the lumped model is often adopted whose error between experiment is non-negligible for large-scale system. On the other hand, it's hard to analyze a TCS using the multi-dimensional model due to high computational expense. Thus, it is necessary to propose a novel analysis method with both acceptable accuracy and efficiency for TCS.

Table 1. Summary of control strategies of TCS.

Research method	Control variable	Controller	Ref
Simulation and experiment	Fan power	PID controller	[11]
Experiment	Water mass-flow rate	On/off-switching controller	[14]
Experiment	Gas mass-flow rate	NI-PXI control system	[15]
Experiment	Fan power	PID controller	[16]
Simulation	Water mass-flow rate and fan speed	Two PI controller	[17]
Simulation	Water mass-flow rate	Rule-based controller	[18]
Simulation	Water mass-flow rate	PI controller	[19]

CONCLUSIONS

The paper presented an extensive review on control strategies of TCS. One of the main technical challenges of system control are irregular power demand and nonlinearity of MH reaction. The thermal coupling approaches can be divided into passive and active types base on the controllability. The enhancement of convection heat transfer and thermal conductivity of the MH tank should be taken into account for the air-cooled method, whereas the liquid-cooled method is more compact in large-scale system. For system control, linear controller is often used in research whereas the output may fluctuate with rapid power change. Two separate controllers are adopted for better control effect but a coordination operation for controllers should be considered. Thus, a multivariable nonlinear controller is required.

Furthermore, an analysis method with both acceptable accuracy and efficiency for TCS remains an open issue to be addressed by future studies.

ACKNOWLEDGEMENT

Financial support from National Natural Scientific Foundation of China under grant no. 52076178 and National Key Research& Development Program (2018YFE0202000) were greatly acknowledged.

REFERENCES

1. Nastasi B and Lo Basso G. 2016. Hydrogen to link heat and electricity in the transition towards future Smart Energy Systems. Energy 110:5-22.
2. Wolsink M. 2020. Distributed energy systems as common goods: socio-political acceptance of renewables in intelligent microgrids. Renew Sustain Energy Rev 127:109841.
3. Mao J, Jafari M and Botterud A. 2022. Planning low-carbon distributed power systems: Evaluating the role of energy storage. Energy 238:121668.
4. Abe JO, Popoola API, Ajenifuja E and Popoola OM. 2019. Hydrogen energy, economy and storage: review and recommendation. Int J Hydrogen Energy 44:15072-86.
5. Nguyen HQ and Shabani B. 2021. Review of metal hydride hydrogen storage thermal management for use in the fuel cell systems. Int J Hydrogen Energy 46:27.
6. Jiang Z, Dougal RA, Liu S, Gadre SA, Ebner AD and Ritter JA. 2005. Simulation of a thermally coupled metal-hydride hydrogen storage and fuel cell system. J Power Sources 142:92-102.
7. Lototskyy MV, Tolj I, Pickering L, Sita C, Barbir F and Yartys V. 2017. The use of metal hydrides in fuel cell applications. Progress in Nat Sci: Mater Int 27(1):3-20.
8. Wu D, Peng C, Yin C and Tang H. 2020. Review of System Integration and Control of Proton Exchange Membrane Fuel Cells. Electrochem. Energy Rev 2020; 3:466-505.
9. Kang IL, Chung DK and Min SP. 2013. The development of a cylindrical proton exchange membrane fuel cell with an integrated metal-hydride container. International Journal of Precision Engineering & Manufacturing, 14(6), 1065-1070.
10. Tetuko AP, Shabani B and Andrews J. 2016. Thermal coupling of PEM fuel cell and metal hydride hydrogen storage using heat pipes. Int J Hydrogen Energy 41:4264-77.
11. Zhu D, Ait-Amirat Y, N'Diaye A and Djerdir A. 2019. Active thermal management between proton exchange membrane fuel cell and metal hydride hydrogen storage tank considering longterm operation. Energy Convers Manag 202:112187.
12. Omrani R, Nguyen HQ and Shabani B. 2019. Open-cathode PEMFC heat utilisation to enhance hydrogen supply rate of metal hydride canisters. Energy Procedia 160:542-9.
13. Omrani R, Nguyen HQ and Shabani B. 2020. Thermal coupling of an open-cathode proton exchange membrane fuel cell with metal hydride canisters: an experimental study. Int J Hydrogen Energy 45(53):28940-50.
14. Førde T, Eriksen J, Pettersen A, Vie P and Ulleberg Ø. 2009. Thermal integration of a metal hydride storage unit and a PEM fuel cell stack. Int J Hydrogen Energy 34:6730-9.
15. Khayrullina AG, Blinov D and Borzenko V. 2019. Novel kW scale hydrogen energy storage system utilizing fuel cell exhaust air for hydrogen desorption process from metal hydride reactor. Energy 183:1244e52.
16. Khaitan SK and Raju M. 2012. Discharge dynamics of coupled fuel cell and metal hydride hydrogen storage bed for small wind hybrid systems. Int J Hydrogen Energy 37:2344–52.
17. Chabane D, Iqbal M, Harel F, et al. 2021. Coupling a metal hydride tank with a PEMFC for vehicular applications: A simulations framework. Int. J. Energy Res. 45(11):16511-16523.
18. Pedrazzi S, Zini G and Tartarini P. 2012 Modelling and simulation of a wind-hydrogen CHP system with metal hydride storage. Renew Energy 46:14-22
19. M. Cavo, E. Gadducci, D. Rattazzi, M. Rivarolo and L. Magistri. 2021. Dynamic analysis of PEM fuel cells and metal hydrides on a zero-emission ship: A model-based approach. Int J Hydrogen Energy 46(64): 32630-32644,

WHEC-2022
23rd World Hydrogen Energy Conference
June 26-30, 2022 - Istanbul

#270
GREEN MILITARY SITE SUPPORTING PUBLIC HYDROGEN MOBILITY

[1] Mitja Mori, [1] Urban Ž. Baškovič, [1] Boštjan Drobnič, [2] Robert Šipec, [1*] Tomaž Katrašnik*

[1] University of Ljubljana, Faculty of Mechanical Engineering, Aškerčeva 6, Ljubljana, SI-1000, Slovenia
[2] Ministry of Defense of the Republic of Slovenia, Vojkova cesta 55, Ljubljana, SI-1000, Slovenia

*Corresponding author's e-mail: mitja.mori@fs.uni-lj.si and tomaz.katrasnik@fs.uni-lj.si

ABSTRACT

To support the energy transition in the defence sector, transport, and power generation sector at the local level simultaneously, a detailed virtual analysis was conducted with an aim to convert military sites from a conventional consumer of external energy vectors to an energy positive hub and at the same time ensure independent operation in case of emergency circumstances. This was achieved by coupling of green energy sources, where geographic conditions favour solar energy, and zero emission storage devices with the main energy storage being hydrogen, which is supported by the batteries. This approach enables multiple shifts of paradigms: a) development of a stand-alone green energy system for military sites, b) converting military sites to energy positive hub for powering military and civil vehicles with green energy vectors (cumulative on-site production of electricity and hydrogen exceeds the electricity consumption by over 50 %), c) achieving autonomous energy operation for several days or weeks depending on the sizing of the system and concept of operation (with normal energy consumption the site can be autonomous for 30 straight days during 60 % of the year and with some reduction in energy consumption 30 day autonomous operation can be achieved throughout the entire year), and d) achieving, on the yearly basis, low or in some cases net negative carbon footprint of military barracks including support of the mobility sector (carbon footprint can be reduced by as much as 70% with respect to grey H_2 production). Such an approach ensures higher robustness of energy supply and storage, construction of hydrogen mobility infrastructure, and the support of local communities through green hydrogen production.

Keywords: Green hydrogen, Military site, Mobility, Sector coupling, Carbon footprint

INTRODUCTION

Military site in the study represents an island energy system (energy hub), which is required to operate independently from external energy sources in emergency situations. For normal operation the system is also connected to the grid and can offer it's resources to community. Self-sufficient military sites are planned to form a network of energy hubs across Slovenia and EU forming Defence RESilience HUB Network in Europe [1]. This is important direction in the energy transition of the EU defence sector based on renewable energy sources (RES) with low carbon footprint (future decarbonization), energy storage systems (hydrogen, battery) and the possibility to act like a prosumer (producer and consumer) in the EU energy system. The basic topology of the energy hub (Fig. 1), in which solar panels, battery, PEM electrolyzer, hydrogen tanks, and PEM fuel cell are the main components, was designed based on the strict military energy requirements, considering the basic energy balance and the 3-, 10-, and 30- days autonomy and predictions of hydrogen mobility in military environment and local community. As a prosumer, energy hub transfers PV electricity to electricity grid and the hydrogen provided also for public mobility sector (sector coupling). The military energy hubs represent an important building block in the hydrogen road map of the EU in the transition to more sustainable energy sources [2].

METHODOLOGY

A numerical model of the observed energy system was developed to evaluate the operational characteristics of the system based on various input parameters, including onsite available RES, power consumption, and component's characteristics. Topology of the energy system allows to achieve predefined goals of the study, designed to fulfil military standards and to achieve high share of renewable energy within the energy system: (i) PV electricity production should be maximized and used to produce green hydrogen; (ii) Hydrogen is stored in storage tanks to enable off-grid operation of the site; (iii) Hydrogen is primary used for mobility, alternatively it is used in PEMFC during off-grid operation of the site; (iv) Battery should be utilized for day-night storage; (v) Electricity production on a yearly basis should be higher than electricity consumption; (vi) Hydrogen and electricity can be supplied from external source or grid.

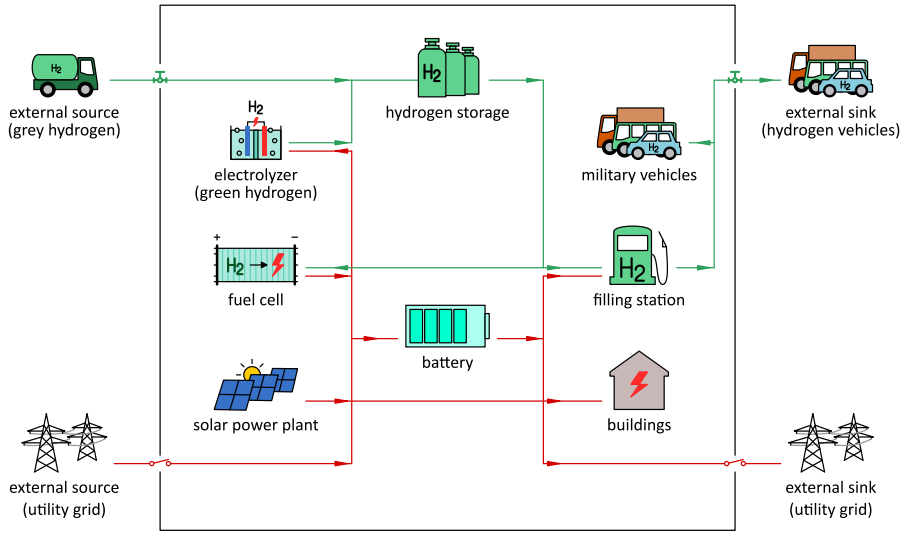


Fig. 1: Topology of the military energy hub for Peter Petrič barracks in Kranj, Slovenia.

The operation of the proposed system was evaluated monthly, considering electricity consumption profile of the barracks, the available RES (solar radiation), the required hydrogen consumption at the refuelling stations, and the characteristics of the power system components (efficiencies, performance, and capacity). Electricity consumption of the site is based on measured consumption over several years while estimations were made regarding hydrogen consumption and additional electricity consumption for hydrogen production, storage and further use. Availability of RES was estimated with respect to available data for typical meteorological year (TMY).

RESULTS AND DISCUSSION

Operating characteristics of the designed energy system are presented in Fig 2a, which summarizes integral values on a yearly basis, and in Fig. 2b, which summarizes results on a monthly basis. The thin columns represent electricity consumption, and the thick columns represent electricity generation or transfer from the grid.

a) b)

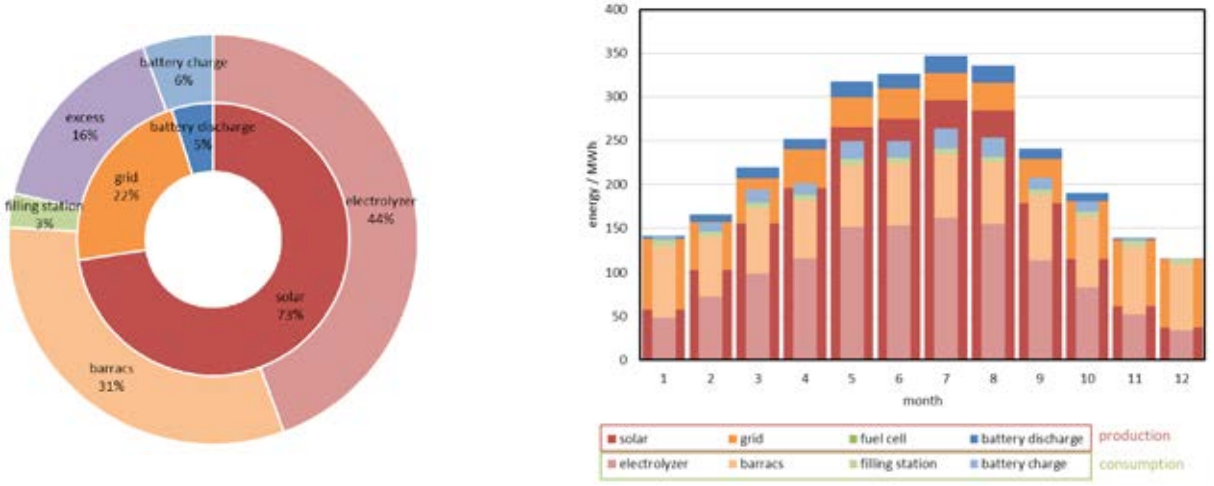


Fig. 2: Monthly (a) and yearly (b) generated and consumed electricity in Peter Petrič barracks in Kranj, Slovenia.

The largest consumer of electricity (44 %) is the electrolyzer, which produces hydrogen for the refuelling stations, and the second largest (31 %) are the barracks. The rest of the electricity is used to recharge batteries during the day and to power refuelling stations. About 16 % of the electricity produced by PV is transferred into the grid as green electricity, reducing the carbon footprint of the energy hub and generates avoided environmental impacts in the electricity grid of the region or country. On the production side, most electricity is generated by PV system (73 %), followed by the electricity grid (22 %). The military energy hub is not completely independent in baseline operational regime (no crisis, no natural disasters, etc.), since 6 % of the electricity still must be transferred from the grid. But when crisis occurs the military energy hub is capable of autonomous operation for a longer period relying just on

internal energy sources without being connected to the grid or outside hydrogen source. To further evaluate the operation of the energy hub monthly integral data are analysed in Fig. 2b. During the warmer months with higher solar radiation (May through August) PV electricity can power all the loads, providing complete independence. Nevertheless, a certain amount of electricity from the grid is needed for the operation, as the battery capacity is not sufficient for the night-time operation and on days with lower solar radiation intensity. During the summer the hydrogen storage state of charge (SOC) increases, so the energy system can operate into the fall without additional hydrogen from external sources. During the rest of the year, electricity consumption is higher than PV electricity generation resulting in the need for additional electricity from the grid even during the day.

In Fig. 3 three cases of the carbon footprint for the military energy hub are presented. "*H2 grey in*" is the case where all H_2 (grey) is distributed to the military energy hub from the outside distributor and "*H2 onsite*" is the case, where hydrogen is produced onsite with PEM electrolyser using electricity from the grid that is in the case of Slovenian Ministry of Defence low carbon electricity with 131 $gCO_2eq./kWh$. The *"model case"* carbon footprint consist of H_2 that is distributed to the military place from outside, the electricity that is provided from grid and the electricity for onsite H_2 production (mobility, PEMFC) and consumption which is generated with the PV system. However, the green electricity distributed to grid presents negative carbon footprint since it reduces the need for electricity from non-renewable sources, so the combined effect is much lower than in other two cases. Further, if in the "model case" the green H_2 would be distributed to the military energy hub the carbon footprint reduction would be even bigger, and we would approach near zero carbon footprint.

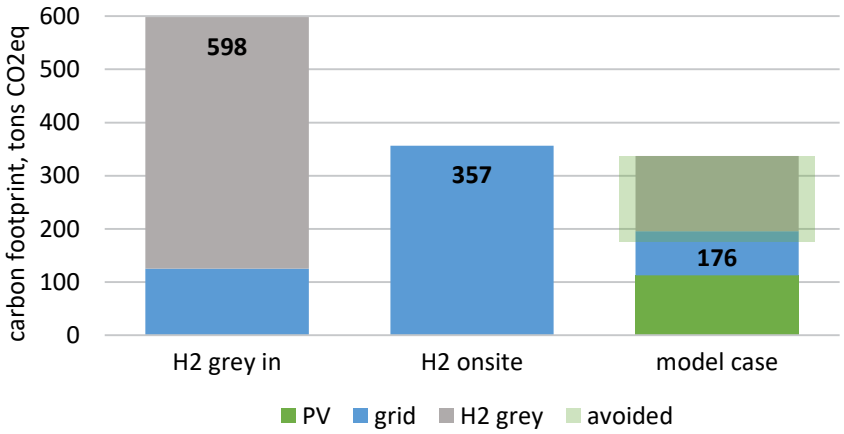


Fig. 3: Carbon footprint of the electricity generation and hydrogen for mobility.

Results show we can expect carbon footprint to be much lower in the "Model case" (-70.6 %) than in the case of distributing grey H_2 to the site or even producing H_2 onsite with low carbon electricity (-40.4 %). The main reason for that is the generation of green electricity that is transferred to the grid, therefore avoided impacts occur relative to the normal electricity production scenario in the grid. Although the need for electricity from the grid is necessary to operate the barracks, the proposed energy system has a significantly lower environmental footprint than the current energy system that relies solely on electricity from the grid, and most importantly, the proposed energy system allows to produce 17.2 tonnes of green hydrogen per year to support hydrogen mobility.

CONCLUSIONS

The designed system model provides the basis for transition to green technologies by coupling different sectors and could be further optimized in terms of component characteristics based on additional input parameters, including the requirements for autonomous operation of the military site and the change in energy performance of the buildings within the military site after optimizing their energy consumption. Further, if the energy hub is a part of a Defence RESilience HUB Network in Europe it can use the green hydrogen not only from its own production, but green hydrogen can be transported from other military energy hub to enable sustainable energy supply.

REFERENCES

1. SiEnE - RESHUB Project Available online: https://siene.teces.si/en/reshub-project/ (accessed on Jan 14, 2022).
2. Report on Hydrogen Valleys shows development of hydrogen economies around the world | www.fch.europa.eu Available online: https://www.fch.europa.eu/news/report-hydrogen-valleys-shows-development-hydrogen-economies-around-world (accessed on Jan 14, 2022).

WHEC-2022
23rd World Hydrogen Energy Conference
June 26-30, 2022 - Istanbul

#286

PREDICTION OF HYDROGEN COMBUSTION USING DATA-DRIVEN APPROACH

[1*] Kazuma Kunihara, [1*] Rahmat Waluyo, [2*] Muhammad Aziz
[1]Department of Mechanical Engineering, The University of Tokyo, 7-3-1 Hongo, Bunkyo-ku, Tokyo 113-8656, Japan
[2]Institute of Industrial Science, The University of Tokyo, 4-6-1 Komaba Meguro-ku, Tokyo 153-8505, Japan

*Corresponding author e-mail: kunihara@iis.u-tokyo.ac.jp, maziz@iis.u-tokyo.ac.jp

ABSTRACT

A data-driven simulation approach is proposed in this study to minimize the development process and efforts of hydrogen combustion-based energy systems. For this purpose, both reacting and non-reacting large-eddy simulation of a turbulent diffusion type burner is conducted to generate the data, which will be trained further using an artificial neural network that predicts the reacting field from a cold flow field. The training data consists of a non-reacting flow field as an input value, from which the neural network should predict the reacting flow, and a reacting flow field is treated as the true value. In the training phase, the prediction of the reacting flow from the former non-reacting flow is compared with the latter reacting flow. In addition, a governing equation is considered in the comparison.

Keywords: Hydrogen combustion, Large eddy simulation, Reacting flow, Non-reacting flow, Artificial intelligent

INTRODUCTION

Hydrogen combustion is considered the next-generation power source, which is carbon-free and energy-efficient. In addition, its utilization is also economically sustainable since the existing conventional combustion technologies can be applied to it. Currently, hydrogen-fueled combustion systems are in active development by many companies [1-3]. However, the development of hydrogen-combustion technologies requires more effort than conventional combustion because of its properties, such as the higher flame speed and temperature, resulting in a high-cost experiment or higher simulation effort.

The development of a combustion chamber requires an interactive optimization cycle starting from prototyping a combustion chamber, then a numerical investigation followed by experimental investigation, and finally a system validation [4]. If this optimization process can be achieved by utilizing a model-based numerical study, as it is done in the automobile industry, the development cost could be reduced drastically. Currently, the usage of combustion simulation in the industry is still not widely adopted, compared to a computational fluid dynamics or structural simulation. The non-reacting flow can be easily utilized to design the rough dimension of the chamber. However, this must always be validated through any experiment, which leads to a longer optimization cycle and higher cost.

A numerical simulation of hydrogen combustion is not widely performed because it consumes a very high calculation power than conventional fuels like methane because of its higher flame speed. In addition, compared to the reacting simulation of conventional fuel, the spatial and temporal resolution must be higher in order to get a valid result. Moreover, while it requires a calculation power of many-core processors in high-performance computers, they are often located in highly-advanced research facilities, in which the companies cannot run large numbers of simulations.

To overcome the problem of limited computational resources, a coupling of a reaction-free flow field and reacting combustion flow field by a physics-informed neural network is proposed. This work aims to use a small number of large-scale simulations to train a network, which will then emulate many numbers of reacting flow under different conditions. As a result, it can increase the number of numerical investigations instead of experiments, leading to a shorter development cycle and total cost.

NUMERICAL SETUP AND METHODS

Figure 1 shows the whole main concept developed in this research. In general, two main research steps are conducted, including combustion data generation and data training. In the former, a large-eddy simulation (LES) is conducted in this study to generate both reacting and non-reacting combustion data. The generated data is then validated using the experimental data from the German Aerospace Center (DLR).

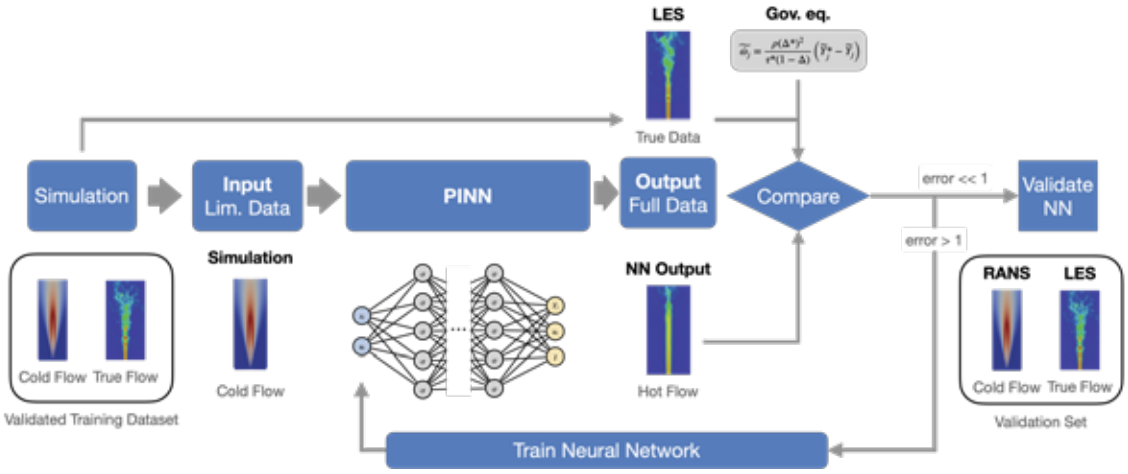


Fig. 1. Illustration of the research concept.

The study case of this research is an $H_2/CH_4/N_2$ Jet Diffusion Flame (= DLR Jet Flame)[5, 6]. The fuel consists of 33.2% H_2, 22,1% CH_4, and 44,7% N_2, and it is supplied from a tube having an internal diameter of 8 mm velocity of 42 m/s. Around the fuel inlet, the co-flow air is supplied from a nozzle having an internal diameter of 140 mm and velocity of 0.3 m/s.

The numerical simulation is conducted using the open-source software OpenFOAM[7], with the reactingFoam solver. The numerical setup is based on the previous paper by Mitani et al. [8]. For this study, a cylindrical computational domain has been used. The non-dimensionalized sizes based on the fuel tube diameter are 17.5D in the radial direction and 62.5D in the axial direction. This has been divided into 75 cells in a radial direction, 60 cells in a circumferential direction, and 500 cells (Fig. 2).

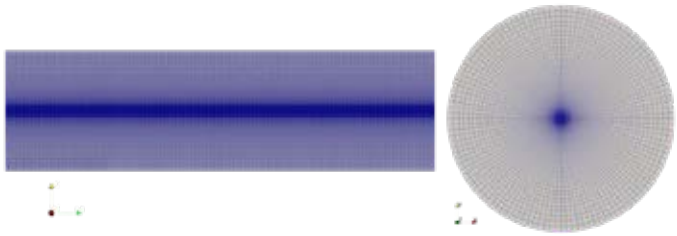


Fig. 2: Computational domain: side view (left) and top view (right)

The boundary condition is set according to Mitani et al. [8]. The fuel inlet velocity profile is according to the 1/7-th law of the turbulent pipe flow.

$$V_{axial} = V_{\max}\left(1 - \frac{r}{1.01R}\right),$$

with $V_{max} = 49\ [m/s]$.

The co-flow air is assumed to have a uniform velocity of 0.3 m/s. The domain is under atmospheric pressure, whereby the inlet has a zero gradient pressure condition. The surrounding hull of the domain is considered as free-boundary, to prevent unwanted pressure vibration. For the turbulent and combustion turbulent modelings, the Smagorinsky and eddy dissipation models have been adopted.

After obtaining the result of the simulations, the training of the artificial neural network is conducted. The cold flow field is fed into the neural network, and by comparing it with the true combustion field and the governing equation, the parameter of the network is adjusted. Once the error of the output has reached the tolerance value, the network is validated by new data that differs from the training data set.

RESULTS

As the preliminary results of the study, an LES for non-reacting flow has been conducted, continued with the reacting flow. Fig. 3 shows the instantaneous velocity and the pressure field obtained in this study. In general, the fuel is distributed well starting from from the fuel nozzle to the outlet, and has an intereaction with the air which is fed from

its surrounding. The pressure across the combustion chamber is also distributed uniformly. These preliminary results (non-reacting simulations) are very important for further simulation and data training.

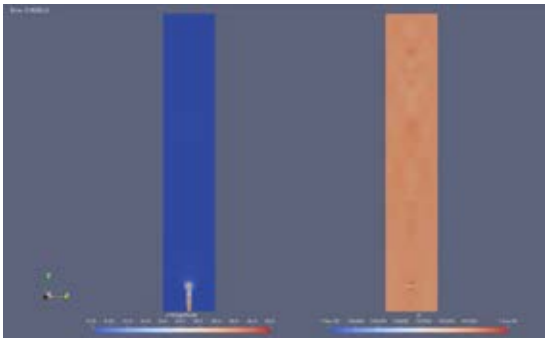


Figure 3: Preliminary result of the velocity (left) and pressure (right) field of the non-reacting flow.

CONCLUSIONS AND FUTURE OUTLOOK

This research aims to shorten the development process of the hydrogen combustion chamber. The number of optimization iterations can be decreased by emulating the combustion field by inputting a cold flow field. The emulation is performed by a neural network; hence, the result can be obtained in a very fast manner and significantly cost-effective. Nevertheless, a beforehand training of a neural network is necessary, but considering the universal applicability, the merit like the development process enhancement exceeds the cost. Besides the development process, it is also expected to function as a digital twin. By changing the input for the neural network to real-time data instead of simulation data, an actual combustion field can be emulated. This can be used for monitoring or failure prediction in the after-market.

ACKNOWLEDGEMENT

This research was conducted using the FUJITSU Supercomputer PRIMEHPC FX1000 and FUJITSU Server PRIMERGY GX2570 (Wisteria/BDEC-01) in the Information Technology Center, The University of Tokyo.

REFERENCES

1. Bohan, K., et al., *White paper | Hydrogen power with Siemens gas turbines*. 2020: Siemens Gas and Power GmbH & Co. KG.
2. Nose, M., et al., *Hydrogen-fired Gas Turbine Targeting Realization of CO2-free Society.* Mitsubishi Heavy Industries Technical Review, 2018. **Vol. 55**(No. 4).
3. Horikawa, A., et al., *Hydrogen Utilization — Development of Hydrogen Fueled Power Generation Technologies.* Kawasaki Technical Review, 2021. **No. 182**: p. 41-46.
4. Ayed, A.H., et al., *CFD based exploration of the dry-low-NO x hydrogen micromix combustion technology at increased energy densities.* Propulsion and Power Research, 2017. **6**(1): p. 15-24.
5. Bergmann, V., et al., *Application of spontaneous Raman and Rayleigh scattering and 2D LIF for the characterization of a turbulent CH 4 /H 2 /N 2 jet diffusion flame.* Applied Physics B: Lasers and Optics, 1998. **66**(4): p. 489-502.
6. Meier, W., et al., *Raman/Rayleigh/LIF measurements in a turbulent CH4/H2/N2 jet diffusion flame: experimental techniques and turbulence–chemistry interaction.* Combustion and Flame, 2000. **123**(3): p. 326-343.
7. Weller, H.G., et al., *A tensorial approach to computational continuum mechanics using object-oriented techniques.* Computers in Physics, 1998. **12**(6).
8. Mitani, M., Y. Ito, and N. Yamasaki, *Large eddy simulation of methane non-premixed flame using the laminar flamelet model.* Journal of Thermal Science, 2011. **20**(6): p. 534-542.

WHEC-2022
23rd World Hydrogen Energy Conference
June 26-30, 2022 - Istanbul

#289

PERFORMANCE ANALYSIS ON THE NOVEL PEMFC ASSISTED GROUND SOURCE HEAT PUMP SYSTEM

[1] *Jinyoung Kim,* [2*] *Yongchan Kim*
[1]1Graduate School of Mechanical Engineering, Korea University 145 Anam-ro, Seongbuk-gu, Seoul, 02841 Republic of Korea
[2]Department of Mechanical Engineering, Korea University 145 Anam-ro, Seongbuk-gu, Seoul, 02841 Republic of Korea

*Corresponding author e-mail: yongckim@korea.ac.kr

ABSTRACT

In this study, the novel PEMFC-assisted ground source heat pump system (PAGSHPs) was investigated by transient simulation. The mathematical model was developed and simulated in TRNSYS software. The annual performance and ground temperature degradation during the 5 years were analyzed by the simulation results. The heating and cooling COP were evaluated as the annual performance of PAGSHPs. The performance of GSHPs was compared with that of PAGSHPs. As a result, the average heating COP of PAGSHPs was enhanced by 26.5% compared to the conventional system. However, the average cooling COP of PAGSHPs was degraded by 7.65% owing to high ground rise.

Keywords: Proton exchange membrane fuel cell, Ground source heat pump, Waste heat recovery.

INTRODUCTION

Ground source heat pump system (GSHPs) is an efficient system that can efficiently supply heating and cooling energy [1,2]. Since the fluctuation of underground temperature is more stable than the outdoor temperature, GSHPs can achieve higher heating and cooling coefficient of performance (COP) than conventional heat pumps. However, in a heating dominant region, there is a critical issue that the underground temperature decreases when the GSHPs are used for a long time [3].

In order to mitigate this issue, solar-assisted ground source heat pump systems (SAGSHPs) have been studied for decades [4]. SAHGSHPs are the combined system of GSHPs and solar collectors [5]. By utilizing high-temperature solar energy, they can mitigate the long-term ground temperature degradation issue and enhance the COP [6]. However, SAGSHPs require a large space to install solar collectors and complex control logic to use solar energy with severe temperature fluctuations [7]. These shortcomings have become a major hindrance to the use of SAGSHPs.

Further efficient way to resolve this issue is the integration of proton exchange membrane fuel cells (PEMFC) and GSHPs. PEMFC waste heat can be used as an auxiliary heat source for GSHPs. Therefore, the underground temperature degradation could be relieved by the integration of these two systems.

In this study, the novel PEMFC assisted ground source heat pump system (PAGSHPs) was proposed and analyzed. To analyze the operating characteristics and performance of PAGSHPs, transient simulation during the 5 years was performed through the mathematical model. Mathematical modeling was developed in TRNSYS software. The simulation was performed under the meteorological conditions of Sam Cheok, the heating dominant region in Korea. As a result, both heating and cooling COP, and the underground temperature degradation over 5 years were analyzed and compared with GSHPs through the simulation results.

SYSTEM DESCRIPTION

Fig. 1 shows the Schematic diagram of PAGSHPs. The system can be divided into a power line and a thermal line. The power line consists of PEMFC, DC/AC inverter (DAI), and energy storage system (ESS). DC power produced by PEMFC is stored in ESS through DC/AC Inverter or converted into AC and used for RES. The thermal line consists of PEMFC, heat exchanger-1 (HEX-1), heat exchanger-2 (HEX-2), ground heat exchanger (GHEX), heat pump (HP), and heat storage tank (HST). The waste heat recovered from the PEMFC can be stored directly in the ST or exchanged with an ethylene-glycol water mixture (EGW) from the underground heat exchanger through HEX-1. EGW, which has undergone heat exchange with deionized water (DIW), is used as a heat source for heating in a heat pump or is injected into GHEX to prevent a decrease in underground temperature.

PEMFC waste heat is used in various ways to increase energy efficiency. In summer, the heat pump supplies cooling energy, so when a hot water supply energy load is required, the PEMFC waste heat directly supplies heat to the HST through the HEX-2. On the other hand, when there is no hot water energy load, the HEX-1 reduces the temperature of the dielectric water returning to the PEMFC and stores heat in the ground simultaneously. In winter, another operating

strategy is available in addition to the above two methods. When the heat pump is heating, the COP of the heat pump can be enhanced by increasing the temperature of the heat source through HEX-1. Through the above operation method, it is available to enhance the overall energy efficiency of the system and decrease the coolant of the PEMFC simultaneously.

RESULTS AND DISCUSSION

Fig. 2 (a) shows the change in the geologic temperature of GSHPs and PAGSHPs over 5 years. For both GSHPs and PAGSHPs, the underground temperature decreased over the years. For GSHPs, the average underground temperature decreased by about 2.36°C for 5 years. On the other hand, for PAGSHPs, the underground temperature decreased by

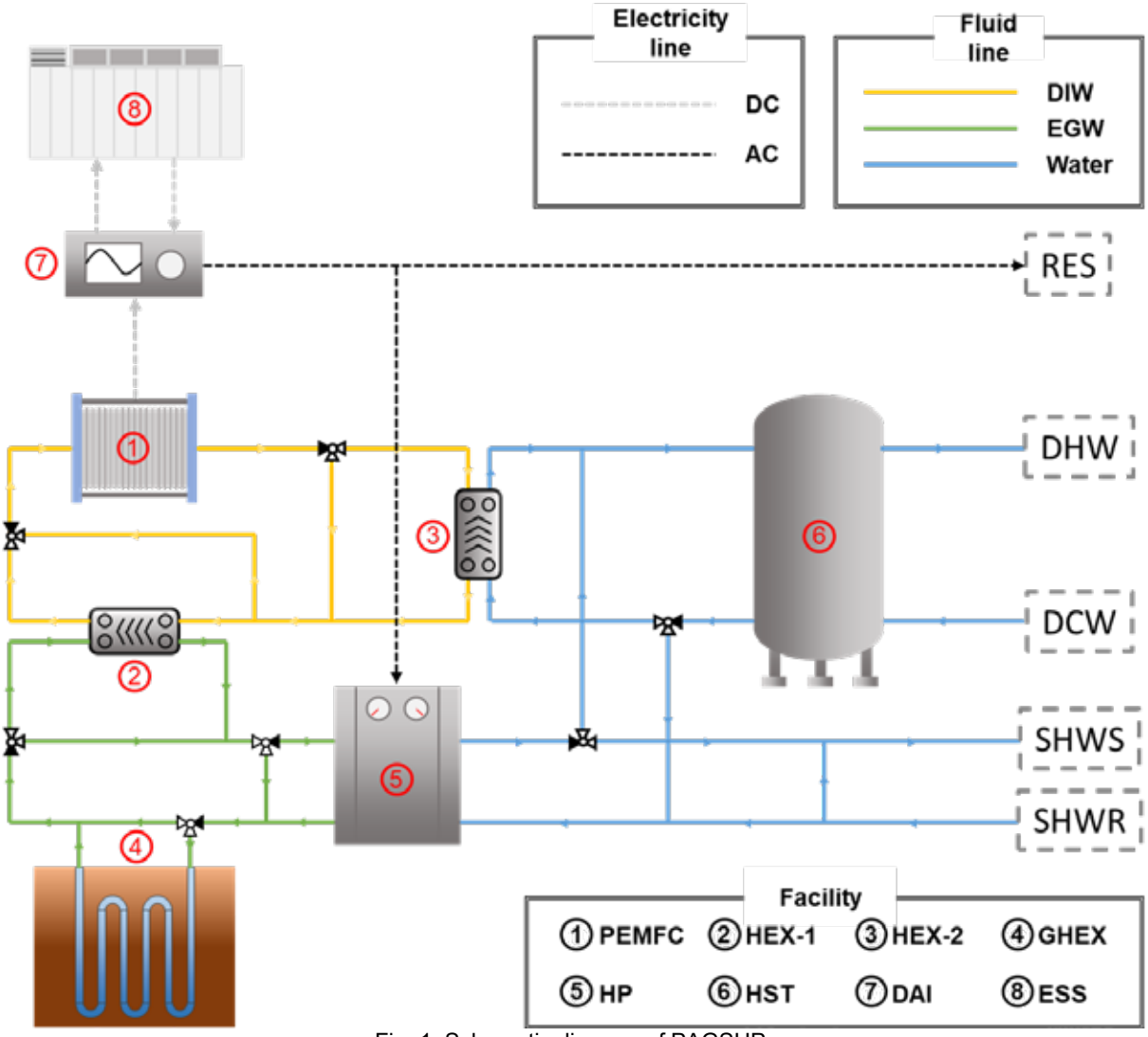


Fig. 1. Schematic diagram of PAGSHPs

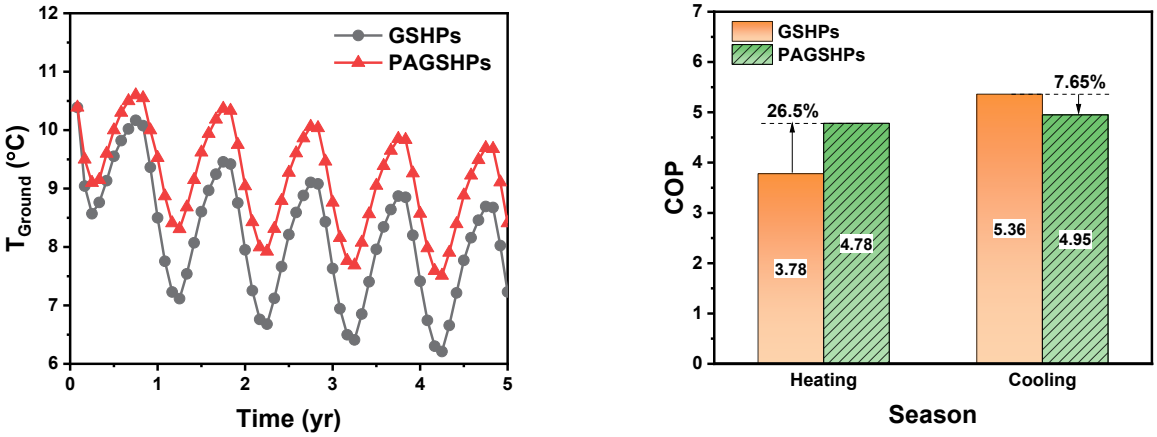


Fig. 2. (a) Variation of the average ground temperature and (b) average heating and cooling COP

1.59 for 5 years. Therefore, PAGSHPs could mitigate the ground temperature decrease by about 32.7% compared to GSHPs.

Fig. 2 (b) shows the average heating and cooling COP of GSHPs and PAGSHPs over 5 years. PAGSHPs had a heating COP of 4.78, which was improved by about 26.5% compared to GSHPs. This indicates that the temperature increase of the heat source of the heat pump was very effective by recovering the fuel cell waste heat. However, in the case of Cooling COP, it was 4.95, which decreased by about 7.65% compared to GSHPs. This is because the underground temperature of PAGSHPs was higher than that of GSHPs, so the heat source temperature increased.

CONCLUSIONS

In this study, the performance of PAGSHPs was analyzed by transient simulation. By the simulation results, the variation of average ground temperature was investigated during the 5 years. The heating and cooling COP was evaluated as the final performance. As a result, the average ground temperature degradation was relieved by 32.7% compared to GSHPs. Furthermore, the Heating COP was enhanced by 26.5%. However, the cooling COP was slightly decreased by 7.65% owing to the higher ground temperature.

In conclusion, the heating COP degradation issue by the ground temperature decrease of GSPHs could be supplemented by the integration of PEMFC. Thus, PAGSHPs could be considered as another attractive option for prospective renewable energy systems. However, the cooling temperature degradation issue has remained as future work.

REFERENCES

1. Zou S, Xie X. 2017. Simplified model for coefficient of performance calculation of surface water source heat pump. Applied Thermal Engineering 112:201-207
2. Lee M, Cha D, Yun S, Yoon SM, Kim Y. 2020. Comparative heating performance evaluation of hybrid ground-source heat pumps using serial and parallel configurations with the application of ground heat exchanger. Energy Conversion and Management 229:113743.
3. BniLam N, Al-Khoury R. 2020. Analysis of short-to-long term heat flow in GSHP systems based on heat pump power. Applied Thermal Engineering 173:114561.
4. Lee M, Lee D, Park MH, Kang YT, Kim Y. 2022. Performance improvement of solar-assisted ground-source heat pumps with parallelly connected heat sources in heating-dominated areas. Energy 240:122807.
5. Nouri G, Noorollahi Y, Yousefi H. 2019. Solar assisted ground source heat pump systems – A review. Applied Thermal Engineering 163: 114351.
6. Weeratunge H, Aditya GR, Dunstall S, de Hoog J, Narsilio G, Halgamuge S. 2021. Feasibility and performance analysis of hybrid ground source heat pump systems in fourteen cities. Energy 234:121254.
7. Badiei A, Golizadeh Akhlaghi Y, Zhao X, Shittu S, Xiao X, Li J, et al. 2020. A chronological review of advances in solar assisted heat pump technology in 21st century. Renewable and Sustainable Energy Reviews 132:110132.

WHEC-2022
23rd World Hydrogen Energy Conference
June 26-30, 2022 - Istanbul

#293

IMPROVED REACTOR DESIGN FOR A METAL HYDRIDE REFRIGERATION SYSTEM IN HYDROGEN POWERTRAINS

[1] Alexander Wimmer, [1] Steffen Feierfeil, [1*] Inga Bürger, [1] Marc Linder
[1]German Aerospace Center (DLR), Department of Engineering Thermodynamics, Pfaffenwaldring 38-40, Stuttgart, Germany

*Corresponding author e-mail: inga.buerger@dlr.de

ABSTRACT

By means of metal hydrides the so far unused potential energy of compressed hydrogen in a hydrogen powertrain can be utilised for air condition of the cabin. The main problem in the latest development is the low power to mass ratio of the reactor component. That is why in this work a new reactor design is proposed, which shows mayor improvements in the key factors for high power to mass ration. Special focus is set on the outer heat transfer to a heat transfer fluid. By numerical simulation optimal design and operations points could be identified for the new reactor design.

Keywords: Metal hydrides, Unused energy, Refrigeration, Power to mass ratio

INTRODUCTION

To bring renewable energy in to the transport sector, hydrogen powered power trains are a promising technology especially for heavy duty vehicles with high range requirements. State of the art on-board storage is realised with high pressure tanks. For the compression work roughly 15% of the energy content is needed [1] and during unloading not recovered in any way. This so far unused potential energy from the compressed gas can be utilised by means of a reversible gas-solid reaction of hydrogen with metal hydrides. The exothermic and endothermic reaction can be used to generate refrigeration power for instance for the cabins air conditioning. A functional demonstration of this machine in an application relevant configuration is published in [2]. However, to reach the requirements of a mobile system in the automotive environment a significant higher power output with a lower system weight has to be realised. The focus on this work is to design a reactor which can achieve a higher thermal power density.

WORKING PRINCIPLE OF THE METAL HYDRIDE REFRIGERATION SYSTEM

Two reactors are arranged in the hydrogen flow path between a high-pressure tank and a hydrogen consumer (fuel cell or internal combustion engine). They are operating in anticyclic mode: One reactor exothermically absorbs hydrogen on medium pressure level releasing heat to the ambient. The second reactor endothermically desorbs hydrogen at low pressure level producing cold. After the specific hydrogen capacity of the metal hydride in the reactors is reached, the first reactor switches from absorption to desorption and the second from desorption to absorption. In this way a quasi-continuous hydrogen flow from a medium to a low pressure side is realised where heat is pumped quasi-continuously from a cold temperature level to the ambient level. A more detailed system description can be found in [2].

NEW REACTOR CONCEPT

The overall requirements for the new reactor concept are specified as modular scalable, manufacturable through conventional processing (suitable for mass production) and easy adjustable in the main dimension to allow future improvements. Due to the systems alternating working principle, in each half cycle a part of the reaction heat is used to heat or cool down the respective reactor to the temperature level, where the heat or cold should be generated. Consequently, this part of the reaction heat does not contribute to the refrigeration or heating output off the system and therefore is denoted as internal temperature switching loss. From this intrinsic behaviour of a metal hydride refrigeration system, one can deduce a key requirement for its reactor component: The heat capacity of the empty reactor structure should be as low as possible. An indicator to evaluate a specific reactor design can be defined as the ratio of the heat capacity from all reactor parts to the heat capacity of the metal hydride (MH) material inside.

$$k_c = \frac{\sum_i C_i}{C_{MH}} \quad (1)$$

With the below described metal hydride pellets and a thin walled double tube geometry the achieved ratio k_c is 4.9.

A second key requirement is a good heat transport behaviour. Most reactor configurations are limited in their thermal power, due to bad heat transport properties. This means the intrinsic reaction kinetics could reach higher rates and consequently higher thermal power, but the high occurring temperature difference causes the material to reach reaction its equilibrium temperature very fast and as a consequence the reaction stops early.

In order to reach a high inner heat conductivity, the metal hydride is not used as loose powder, which exhibits values of around 1 W/mK [3], but compacted in a graphite matrix [4]. In this work the fabricated ring pellets showed a radial heat conductivity of 30 W/mK. With an outer diameter of 26 mm and an inner diameter of 20 mm the ring thickness corresponds to a maximum heat transfer distance of only 3 mm, confer with fig. 1. The pelletized metal hydride powder has the additional advantage that it can be easily handled and filled into the reactor during the assembly process.

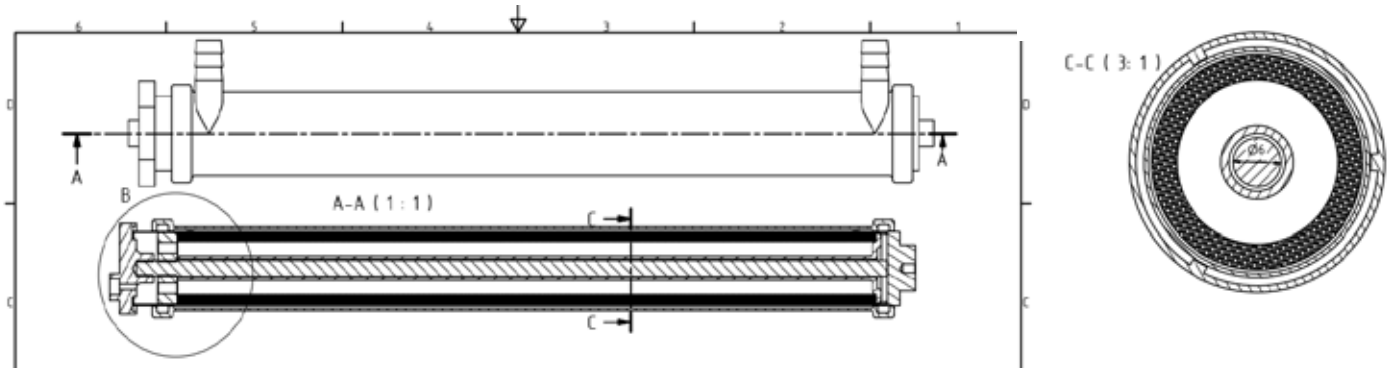


Fig. 1: Technical drawing reactor design

On the outer surface of the reactor, the heat is transferred to a heat transfer fluid (HTF), which flows in an annular gap. This channel should have a small height for two reasons. Firstly, a smaller channel height reduces the fluid volume and therefore the heat capacity of the reactor's fluid part leading to a lower value of k_c, according to eq. (1). Secondly a lower channel height, which is two times the hydraulic diameter d_h, increases the heat transfer coefficient h according to the definition of the Nusselt number. The heat transfer coefficient can be calculated by appropriate correlations [5]. For example, for a gap height of 0.5 mm and a fluid rate of 1 L/min the heat transfer coefficient is 2000 W/(m^2K). To sum up, the new reactor has a low value of k_c and good heat transport properties when compared to similar studies in the literature [2]. Thus, an improved thermal power density especially at higher temperature differences between hot and cold side is expected. When considering the pressure drop in the fluid gap, the question for the optimal gap height and flow rate occurs. Therefore, a simulation model in combination with an evaluation method is applied and descripted in the following section.

SIMULATION MODEL

The reactor is described as 2-dimensional rotary symmetric domain discretized with the finite element method for a time-resolved simulation. For the reaction behaviour of the metal hydride detailed information on kinetics and pressure-temperature-concentration properties of a real measured material are implemented. The outer heat transfer to the HTF is implemented with a local heat transfer coefficient [6] and a one-dimensional differential equation in flow direction instead of a discretized flow simulation in the gap. A more detailed description and its successful validation is published in [7]. The initial conditions are the absorbed metal hydride at equilibrium conditions of 30 °C and 35 bar representing the condition at finished absorption. As boundary conditions the HTF inlet temperature is set to a constant value of 20 °C, and the constant outlet hydrogen mass flow to 75 standard liter per minute. Considering the parasitic loss of electricity needed for the fluid pump, an evaluation parameter is defined. In this the resulting mean thermal power is reduced by a fictive thermal power that a state-of-the-art refrigeration machine could generate with the respective electrical power at a usual Coefficient of Performance (COP):

$$\dot{Q}_{eff} = \bar{\dot{Q}} - COP\ P_{Pump} \quad (3)$$

RESULTS AND DISCUSSION

Figure 1 shows the effective thermal power normalized to one kilogram of MH material over the gap's hydraulic diameter. It can be seen that for each flow rate there is an optimal gap height for which the effective thermal power reaches its maximum. This is due to the two opposing trends: If d_h decreases, on the one hand the heat transfer coefficient is higher and hence the thermal power increases. On the other hand, the smaller channel induces a higher pressure loss, increasing the negative right hand term in eq. (3). On the opposite, if d_h increases, the pressure loss decreases, but also the heat transfer coefficient and thus the thermal power is reduced.

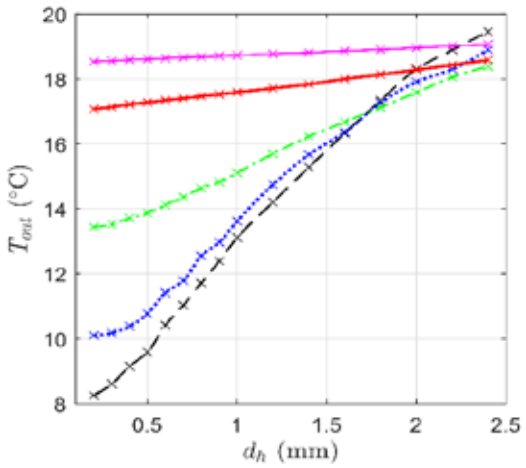


Fig. 2. eff. therm. Power for diff. hydraulic diameters and flow rates

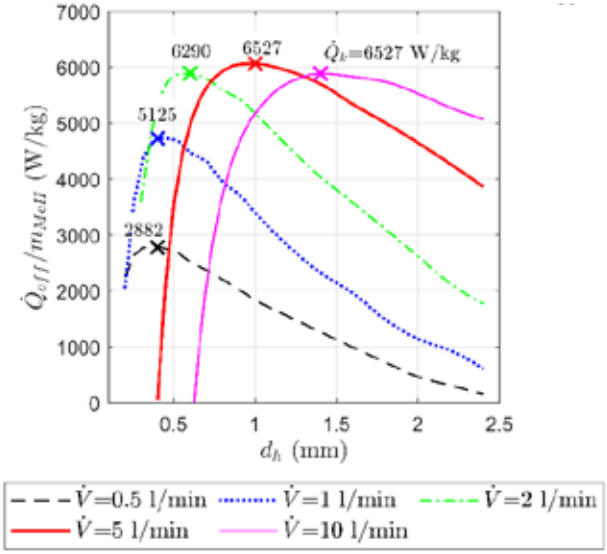


Fig. 3. Mean outlet temperature for diff. hydraulic diameters and flow rates

Moreover, it can be seen, that higher flow rates result in higher eff. thermal power. This is obvious as higher flow rates enhance the heat transfer coefficient. But a second reason is due to the fact, that higher flow rates lead to less fluid cooling, seen by the higher outlet temperatures for higher flow rates in fig. 3. A higher HTF temperature implies a higher temperature difference between the HTF and the equilibrium temperature, which in turn induces a higher reaction rate according to the kinetic equation [7]. Right hand side of the optimum the eff. thermal power decreases again at higher flow rates, caused by the dominating pressure loss. From fig. 3 it can be seen that for higher flow rates the cold is generated at higher outlet temperatures. From the two figures it also can be recognized: If the cold is required on lower temperature, lower thermal power is possible, which is physically feasible.

CONCLUSIONS

A new lightweight reactor design for the use of metal hydrides in a refrigeration machine is proposed. Based on a simple double tube configuration it enables easy filling, easy adjustment of the main dimensions and modular scaling. The important ratio of the reactors heat capacity (empty) to the metal hydrides heat capacity is 4.9 and 22% better than reported in the literature. Higher heat conductivity of the MH bed and higher heat transfer coefficient are reached through pressed MH-graphite pellets and a thin fluid channel. With the reduced value k_c and the enhanced heat transfer properties, the design improves both factors, which allow higher thermal power densities than demonstrated in other published works. For selecting an appropriate fluid channel height and fluid flow rate simulations based on a validated and published model where performed. Considering the pressure drop it could be shown that for every flow rate there exists one optimal channel thickness. The maximal thermal power density of the given reactor depends on the temperature level, where the cold is generated.

REFERENCES

1. Klell M, Eichlseder H and Trattner A. 2018. Wasserstoff in der Fahrzeugtechnik. Wiesbaden, Springer Vieweg.
2. Weckerle C, Nasir M, Hegner R, Bürger I, Linder M. 2020. A metal hydride air-conditioning system for fuel cell vehicles – Functional demonstration. Applied Energy 259:114187.
3. Suda S, Komazaki Y, Kobayashi N. 1983. Effective thermal conductivity of metal hydride beds. J Less Comm Metals 89:317-324
4. Pohlmann C, Röntzsch L, Heubner F, Weißgärber T, Kieback B. 2013. Solid-state hydrogenstorage in Hydralloy-graphite composites. Journal of Power Sources 231:97-105.
5. Gnielinski V. 2013. Wärmeübertragung im konzentrischen Ringspalt und im ebenen Spalt. In VDI-Wärmeatlas, Ed. 11. Edited by VDI e.V. Springer Vieweg.
6. Hatton A. P. und Quarmby A. 1962. Heat transfer in the Thermal Entry Length with Laminar Flow in an Annulus. International Journal of Heat and Mass Transfer 5:973–980.
7. Weckerle C, Bürger I, Linder M. 2019. Numerical optimazation of a plate reactor for a metal hydride open cooling system. International Journal of Hydrogen Energy 44:16862-16876.

WHEC-2022
23rd World Hydrogen Energy Conference
June 26-30, 2022 - Istanbul

#302

PILOT-SCALE HYBRID SYSTEM FOR CO_2/H_2 MIXTURE PRODUCTION – FIRST EXPERIENCES IN THE "TENNESSEE" PROJECT

[1] Łukasz Bartela, [2] Janusz Zdeb, [3] Jarosław Milewski, [3] Aliaksandr Martsinchyk, [2] Wojciech Smółka, [2] Łukasz Rybak*
[1]Silesian University of Technology, Department of Power Engineering and Turbomachinery, 18 Konarskiego Street, Gliwice 44-100, Poland
[2] Tauron Wytwarzanie S.A., 51 Promienna Street, Jaworzno 43-603, Poland
[3] Warsaw University of Technology, Institute of Heat Engineering, 21/25 Nowowiejska Street, Warsaw 00-665, Poland

*Corresponding author e-mail: lukasz.bartela@polsl.pl

ABSTRACT

Currently, in the Tennessee project realized by the Polish energy group Tauron Polska Energia, work on the construction of an installation that integrates MCFC modules with SOE modules is nearing completion. The installation is to enable highly effective production of the CO_2/H_2 mixture based on the process of high-temperature electrolysis and process of CO2 separation carried out in MCFC modules from flue gases generated in the coal-fired unit. The article summarizes the results of analytical work and describes the first experiments on the first trial runs of the installation.

Keywords: Solid oxide electrolyzer, Molten carbonate fuel cell, CO_2 separation, Hydrogen, Synthetic natural gas

INTRODUCTION

In Poland, as in many European countries, many activities have been initiated in recent years to contribute to the development of the hydrogen economy. Objectives in this respect were set out in the "Polish Hydrogen Strategy until 2030 with an outlook until 2040" [1] adopted in 2021. Although the country is the third largest producer of hydrogen in the European Union (production amounts to over 1 Mt of hydrogen per year), there is a need to organize green hydrogen production systems, and in the transition period, also to implement technologies for its economic use, as well as conversion to energy carriers that can now be transported, stored and used safely and efficiently. One such product of the chemical synthesis of hydrogen is synthetic natural gas (SNG). Large chemical and petrochemical companies as well as energy groups are involved in these activities. Among them is the Tauron Polska Energia Group - the second largest producer of electricity in Poland. Tauron Polska Energia also conducts activities aimed at launching the first systems representing the CCUS technology [2,3]. These two directions of technological development identified in Poland significantly correspond to the urgent need to decarbonize the economy, which is at the forefront of world economies most heavily dependent on coal (nearly 70% of electricity is produced from this fuel). One of the activities in both technological areas is the initiation and launch of the Tennessee project by the Tauron Group, which involves the demonstration of the technology of producing a CO_2/H_2 gas mixture that is compatible with the needs of the generation of synthetic natural gas, which is, according to the assumptions, to be carried out in reactors enabling the Sabatier reaction. The Sabatier reaction is a simple reaction of hydrogen with carbon dioxide taking place at moderate temperatures and pressures in the presence of metallic catalysts, leading to formation of methane and water.

Hydrogen and carbon dioxide necessary for the Sabatier reaction are obtained most often in separate processes, but nowadays, due to the ecological nature, it is most often proposed to use the popular low-temperature PEM or alkaline electrolyzers to generate hydrogen. In turn, for the obtaining of carbon dioxide, separation processes from flue gases or process gases are proposed. The separation process itself can be carried out with the use of adsorption, absorption, membrane separation or cryogenic processes. Both the production of hydrogen, which is not in free form on Earth, and the extraction of carbon dioxide from gas mixtures, regardless of the methods used, are related to the need to use electricity and/or thermal energy for this purpose. For this reason, the production of synthetic natural gas is associated with the need to incur high operating costs. In addition, technologies enabling the separation of carbon dioxide, based, for example, on the methods of chemical absorption, physical adsorption, or oxygen combustion, are intended for large-scale applications, which excludes their implementation in small distributed systems. The technology that is being prepared to be demonstrated as part of the Tennessee project will allow for the reduction of energy demand and is intended for applications with a wide range of capacity.

PILOT-SCALE SOE-MCFC HYBRID SYSTEM

The diagram of the installation built in the Tennessee project is shown in Fig. 1. MCFC modules, along with SOE modules, are the basic elements of an integrated system, which is to demonstrate how to improve the process of storing energy in chemical form through the production of synthetic natural gas (SNG). MCFCs proved their usefulness in capturing carbon dioxide from coal power plant flue gases without energy penalty for host power plant, and even they generate additional power. This feature is very welcome in power-to-gas systems, where hydrogen needs to be mixed with carbon dioxide. Anode outlet gases contain a mixture of carbon dioxide (captured from flue gases) and hydrogen (depleted fuel) what meets the inlet requirements of the Sabatier reactor for methane synthesis [4]. In pilot installation the hydrogen will be generated within two modules of SOE. The reference technology for the technology being the subject of the project, which is also a reference for estimating the effects of the improvement, is the power-to-SNG technology demonstrated by Tauron, also at the Łaziska Power Plant, in which the production of gases required for the Sabatier process, i.e., hydrogen and dioxide carbon, takes place due to the operation of the alkaline electrolyzer and the installation using chemical absorption.

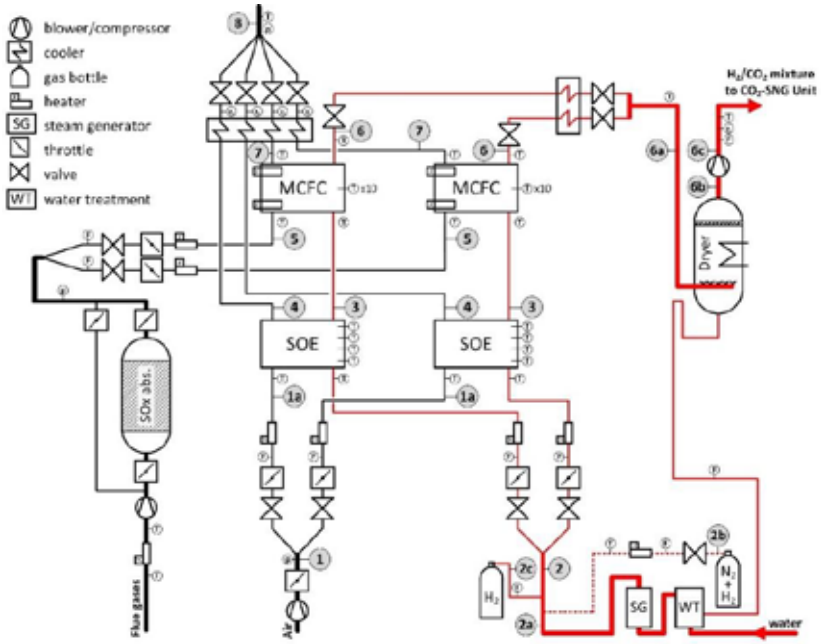


Fig. 1. Diagram of pilot-scale SOE-MCFC hybrid system

The power to gas system can be improved by the following three key novelties which will be introduced in the existing power–to–gas installation:

- Using Solid Oxide Electrolysis for generating hydrogen
- Using Molten Carbonate Fuel Cells for capturing carbon dioxide from coal fired boiler flue gas
- The electric and thermal integration of MCFC with SOE for thermal and power support of electrolysis by fuel cells

It is possible to integrate both MCFC and SOE for thermal management, to produce hydrogen and carbon dioxide at adequate temperature level for the methanation process (200–400 °C). The heating by using the electric heaters will be avoided, what increases effectiveness of the installation. Additional value—MCFC can be combined with SOE by Direct Current to support electrolysis.

RESULTS

The development of the concept of a prototype installation, for which the diagram is shown in Fig. 1, was accompanied by analytical works, aimed mainly at determining the structure of the system, which would enable the conduct of widely profiled research works. A very important issue was the design the measuring equipment of the installation that will allow to determine the performance characteristics of individual components under various load conditions, including the identification of their degradation. For a specific structure, on the basis of simulation analyzes, the parameters of factors at characteristic points of the installation were selected. The results of these analyzes, which are presented in Table 1, became the basis for the development of the detailed design of the installation.

Table 1. Parameters in characteristic points of installation

No.	Composition, %							Temperature, °C	Pressure, mbar	Mass flow, kg/h	Specific heat, kJ/kgK
	N_2	O_2	H_2	H_2O	CO	CO_2	CH_4				
1	79.0	21.0	-	-	-	-	-	20	1030	18.25	1.01
1a	79.0	21.0	-	-	-	-	-	687	1020	9.13	1.13
2	-	-	5.0	95.0	-	-	-	570	1020	6.66	2.26
2a				100.0				150	2000	6.63	2.07
2b	95.0	-	5.0	-	-	-	-	20	1500	11.27	1.09
2c	-	-	100.0	-	-	-	-	20	1500	0.04	14.24
3	-	-	81.0	19.0	-	-	-	710	1020	0.98	6.20
4	63.0	37.0	-	-	-	-	-	704	1020	11.48	1.13
5	66.5	7.5	-	12.5	-	13.5	-	380	1020	17.70	1.17
6	-	-	43.1	39.8	5.5	11.0	0.6	646	1020	3.34	2.54
6a	-	-	43.1	39.8	5.5	11.0	0.6	200	1010	6.68	2.31
6b	-	-	70.2	2.0	9.0	17.9	0.9	20	1000	3.63	2.49
6c	-	-	70.2	2.0	9.0	17.9	0.9	90	14000	3.63	2.61
7	73.7	5.0	-	13.8	-	7.5	-	646	1010	15.34	1.25
8	69.3	18.3	-	8.0	-	4.4	0	60	1000	53.64	1.07

By applying the proposed novelties, a several goals will be reached. First of all, power necessary to hydrogen generation will be decreased by ca. 25%. This makes the system more competitive to the other technologies for energy storage and makes the substitute of natural gas cheaper. Based on the experimental investigations, the achievable CO_2 separation rate was determined at above 90% by adjusting the cathode inlet flow. In this way, potentially consumption of heat from host coal fired power plant for CO_2 capture will be eliminated. Thus, there will be no energy penalty for the host power plant what makes the power plant efficiency and power at the desired level. Thirdly, the whole installation will be more simple, compact, and modular—thus any scale–up procedure can be done without any technological difficulties.

CONCLUSIONS

The conducted analytical works indicate the possibility of obtaining satisfactory technical effectiveness indicators for the installation, and thus a potential reduction of costs ultimately incurred to produce SNG. The analytically identified effects of the integration of SOE modules with MCFC modules will be confirmed only after the research campaign on the prototype installation is carried out. The work will be focused on the evaluation of the flexibility of changing the loads of individual components of the installation, the impact of changes in the composition of the flue gases fed to MCFC modules, and the impact of the electrical load on the respective modules. Ultimately, as part of the project, guidelines for scaling the technology for industrial requirements will be developed. Preparatory work for the formation of fuel cell stacks is currently underway at the Tennessee Project. Corrections are also being made at the installation for the identified leaks within the SOE modules. The commissioning of the installation, which will start the research phase, is scheduled for the first half of 2022.

ACKNOWLEDGEMENT

The project is co-financed by Polish National Center for Research and Development of Operational Programme Smart Growth, 2014-2020 Application for project co-funding within Sectoral Programme PBSE Priority Axis Priority Axis I: Supporting R&D carried out by enterprises, Application no.: POIR.01.02.00-00-0281/16.

REFERENCES

1. Polish Hydrogen Strategy until 2030 with an outlook until 2040. Ministry of Climate and Environment. 2021, October.
2. Chwoła T., et al., Pilot plant initial results for the methanation process using CO2 from amine scrubbing at the Łaziska power plant in Poland. Fuel 2020;263:116804.
3. Stec M., et al., Pilot plant results for advanced CO2 capture process using amine scrubbing at the Jaworzno II Power Plant in Poland. Fuel 2015;151:50-56.
4. Milewski J., Lewandowski J., Separating CO_2 from flue gases using a Molten Carbonate Fuel Cell. IERI Procedia 2012;1:232-237.

WHEC-2022
23rd World Hydrogen Energy Conference
June 26-30, 2022 - Istanbul

#309

THERMODYNAMIC ANALYSIS OF AN INTEGRATED SYSTEM WITH SOLAR METHANE CRACKING AND CO-ELECTROLYSIS OF CO_2/H_2O FOR METHANOL AND ELECTRICITY PRODUCTION

[1*] *Aliya Banu*, [1] *Yusuf Bicer*
[1] Division of Sustainable Development, College of Science and Engineering, Hamad Bin Khalifa University, Qatar Foundation, Doha, Qatar

*Corresponding author e-mail: alba34159@hbku.edu.qa

ABSTRACT

Due to zero greenhouse gas emissions, hydrogen fuel production from methane cracking is a cleaner pathway than steam methane reforming. Co-produced carbon black is valuable and can be used in other industries. Using solar energy for the high-temperature requirement can further improve the sustainability of the process. This paper evaluates an integrated solar methane cracking where its products are utilized in fuel cells to generate electricity. The CO_2 produced in the system is co-electrolyzed with water to produce syngas which is further converted to methanol. The process is simulated in Aspen Plus®, and its energy and exergy efficiencies are evaluated by conducting a detailed thermodynamic analysis. The proposed system has an energy and exergy efficiency of 37.4% and 31.2%, respectively

Keywords: Methane cracking, Turquoise hydrogen, Solid oxide electrolyzer, Synthetic fuel, Methanol

INTRODUCTION

Hydrogen fuel is a clean energy carrier that can meet the decarbonization targets of increasing energy demand. However, alternative processes need to be considered that lower the environmental impact during its production [1]. Industrially, hydrogen is produced via steam methane reforming (SMR). The hydrogen produced using SMR is termed 'gray hydrogen' because it has high CO_2 emissions. When carbon capture and storage (CCS) are added to the process, the hydrogen derived is termed as 'blue hydrogen'. A cleaner pathway is methane cracking at high temperatures termed 'turquoise hydrogen' where carbon black is formed as a by-product that can be useful in several industries [2]. Solar energy can reach the required high temperatures making it a cleaner process utilizing renewable energy [3].

Integrated systems increase efficiencies, minimize losses and reduce costs [4]. Both products from methane cracking can generate electricity in fuel cells. Moreover, the produced hydrogen needs to be converted to a suitable energy form to make it more easily transportable. With these in mind, an integrated system shown in Fig. 1 is proposed for cleaner utilization of methane resources with carbon management and the production of clean energy carriers.

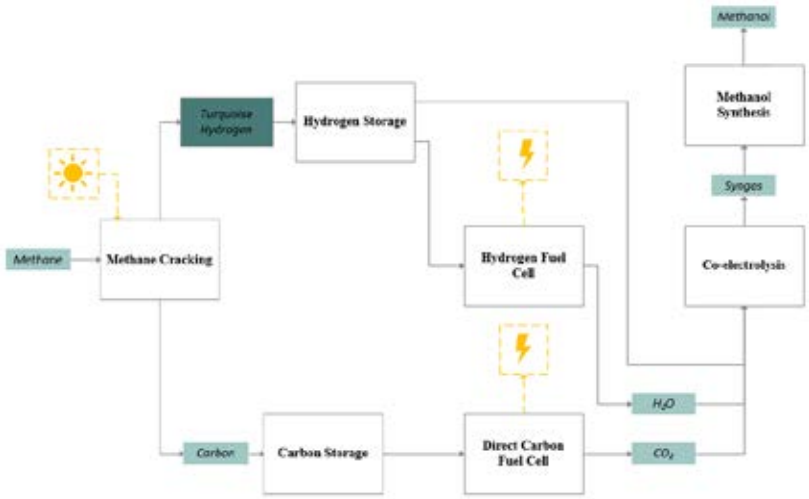


Fig. 1. Block flow diagram of the process

SYSTEM DESCRIPTION

The system consists of a solar methane cracking subsystem (SMC) that decomposes methane into turquoise hydrogen and carbon in the presence of concentrated solar energy, as shown in Fig. 1. The hydrogen produced is stored and used in a proton exchange fuel cell (PEMFC) to generate electricity. The carbon is also used in a direct carbon fuel cell (DCFC) to generate electricity with an exhaust stream consisting of pure CO_2. The CO_2 that is produced then undergoes co-electrolysis with water to produce syngas in a solid oxide electrolyzer (SOEC) using electricity generated using solar PV. Syngas can be used to produce a variety of other chemicals. This system converts syngas to methanol (MEOH), a suitable liquid hydrogen carrier.

THERMODYNAMIC ANALYSIS

A detailed thermodynamic analysis was conducted for the proposed integrated system. Aspen plus® was used to simulate the process and obtain the thermodynamic properties of the state points of the process. The developed model is shown in Fig. 2. The fuel cells are simulated using a Gibbs reactor and separator as the electrodes. Similarly, the co-electrolyzer is modelled using three reactors in series based on the model reported in [5].

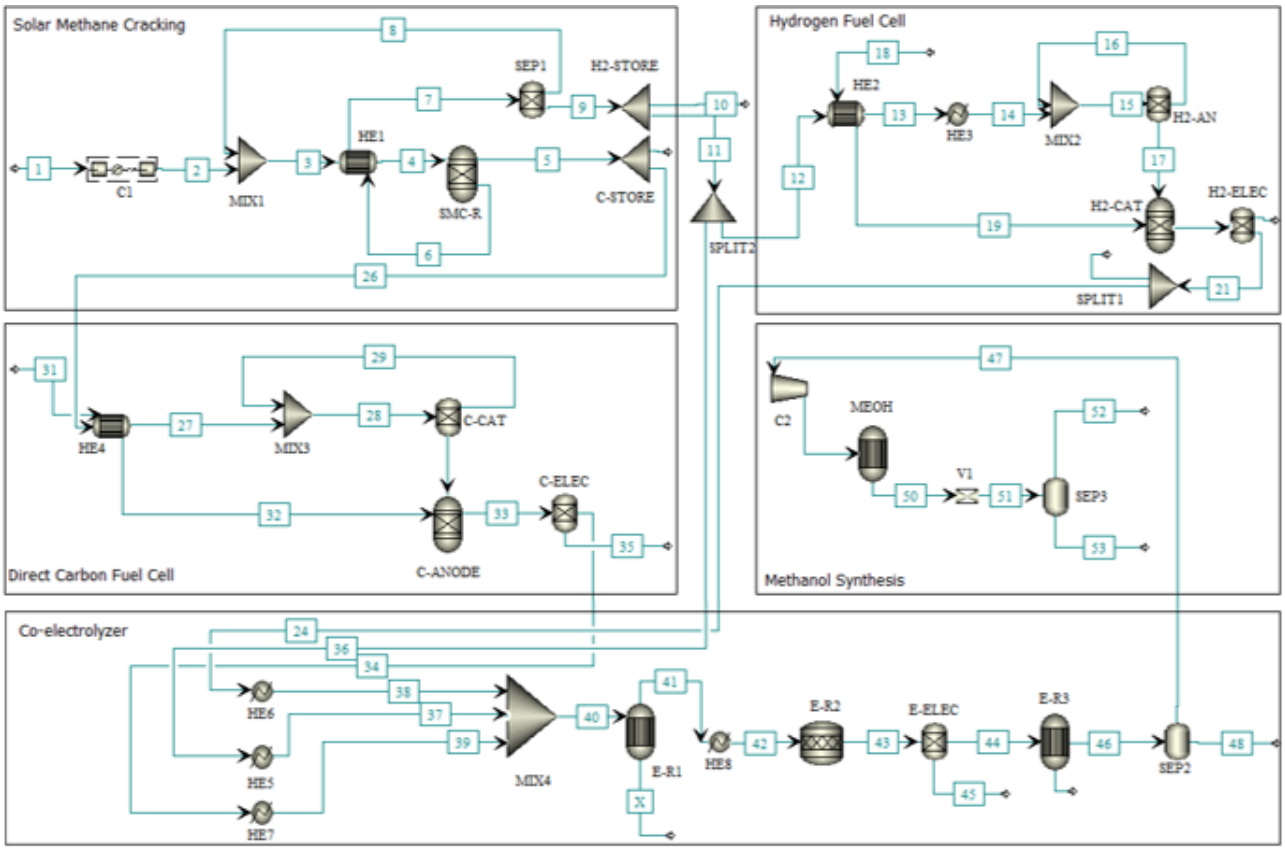


Fig. 2. Aspen flowsheet of the entire processes

Mass, energy, entropy, and exergy balances were carried out over each unit of the system. The entropy generation and exergy destruction rates of the components were found. In addition, the energy and exergy efficiencies of the overall system and the subsystem were calculated. The general balance equations are as follows:

$$\sum_{in} \dot{m}_\iota = \sum_{out} \dot{m}_\iota \quad (1)$$

$$\dot{Q}_{in} + \dot{W}_{in} + \sum_{in} \dot{m}_\iota h_i = \dot{Q}_{out} + \dot{W}_{out} + \sum_{out} \dot{m}_\iota h_i \quad (2)$$

$$\frac{\dot{Q}_{in}}{T_s} + \dot{S}_{gen} + \sum_{in} \dot{m}_\iota s_i = \frac{\dot{Q}_{out}}{T_s} + \sum_{out} \dot{m}_\iota s_i \quad (3)$$

$$\dot{E}x_{Q_{in}} + \dot{E}x_{W_{in}} + \sum_{in} \dot{m}_\iota ex_i = \dot{E}x_{Q_{out}} + \dot{E}x_{W_{out}} + \sum_{out} \dot{m}_\iota ex_i + \dot{E}x_D \quad (4)$$

RESULTS AND DISCUSSION

The thermodynamic properties were obtained for each stream from Aspen Plus, and the balances were performed. The efficiencies were calculated, and the results are displayed in Fig. 3. The process utilizes a 0.5 kg/s feed of pure

methane, cracked in a Gibbs reactor block operating at 1200℃ and 10 bar giving a methane conversion rate of 95%. 5.3 MW of solar thermal power is required with an efficiency of 75% to crack the methane feed.

Due to the intermittency of solar energy, the produced hydrogen and carbon produced during the day are stored. 5.4 tonne/day of H_2 and 16.1 tonne/day of carbon are produced that are used in fuel cells to generate an overall 7.71 MW of electricity. Co-electrolysis of CO_2/H_2O in the SOEC is performed using electricity generated in a solar PV system with an efficiency of 20%.

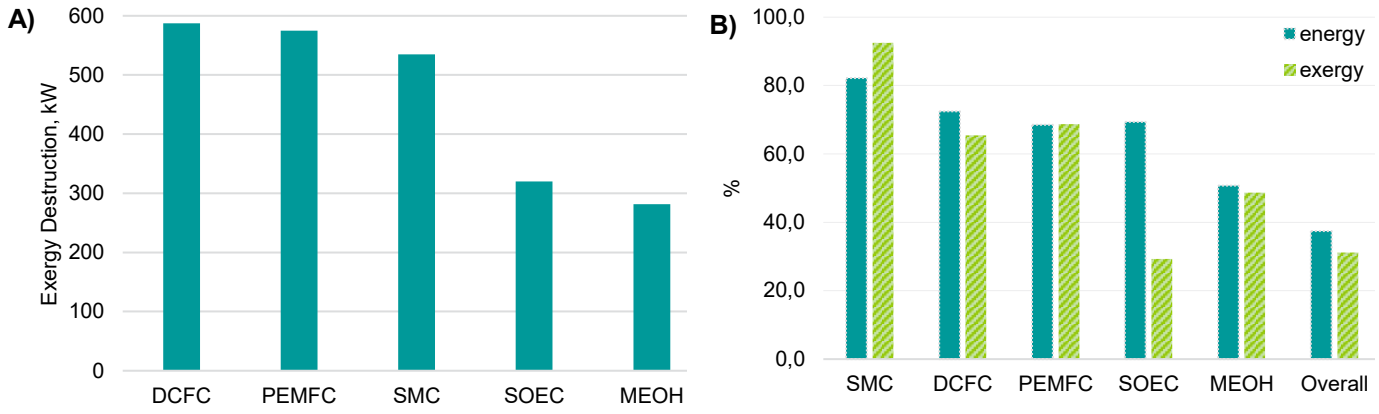


Fig. 3. A. Exergy destruction rates of the subsystems B. Energy and Exergy Efficiencies of the systems

Fig. 3A shows the exergy destruction rates from the different subsystems; it can be noted that the highest exergy destruction occurs in the direct carbon fuel cell followed by the hydrogen fuel cell. Fig. 3B shows obtained efficiencies. The overall system has an energy and exergy efficiency of 37.4% and 31.2%, respectively.

CONCLUSIONS

This study outlines the thermodynamic analysis of a methane cracking system for clean hydrogen production. The products are utilized in fuel cells to generate electricity. The CO_2 exhaust from the DCFC is pure and can be further co-electrolysed with water to efficiently produce syngas and then converted to methanol. The proposed system was modelled on Aspen plus to obtain the thermodynamic properties of the streams. Balances were carried out over each component to identify the losses within the system. The solar methane cracking subsystem has energy and exergy efficiency of 82.2% and 92.5%, respectively. It was found that the overall system produces electricity and methanol with an energy and exergy efficiency of 37.4% and 31.2%, respectively.

ACKNOWLEDGEMENT

This publication was made possible by Graduate Sponsorship Research Award (GSRA7-2-0427-20025) from the Qatar National Research Fund (a member of Qatar Foundation). The findings herein reflect the work, and are solely the responsibility, of the authors.

REFERENCES

1. Koroneos C, Dompros A, Roumbas G and Moussiopoulos N. 2004. Life cycle assessment of hydrogen fuel production processes. International journal of Hydrogen Energy.
2. Muradov N, Smith F, T-Raissi A. 2005. Catalytic activity of carbons for methane decomposition reaction. Catalysis Today.
3. Acar C and Dincer I. 2019. Review and evaluation of hydrogen production options for better environment. Journal of Cleaner Production.
4. Dincer I and Bicer Y. 2019. Integrated energy systems for multigeneration. Elsevier.
5. Redissi Y and Bouallou C. 2013 Valorization of carbon dioxide by co-electrolysis of CO2/H2O at high temperature for syngas production. Energy Procedia.

WHEC-2022
23rd World Hydrogen Energy Conference
June 26-30, 2022 - Istanbul

#318

THERMODYNAMIC CONSIDERATIONS OF THE CO_X HYDROGENATION REACTION TO LIGHT OLEFINS USING CARBON-NEUTRAL FEEDSTOCK MIXTURES

Evridiki Mandela[1], Georgios Varvoutis[1,2], Athanasios Lampropoulos[1], Eleni Papista[1], Costas Athanasiou[3], Dimitris Ipsakis[4], Michalis Konsolakis[4], George Marnellos[1,2]*

[1] Department of Mechanical Engineering, University of Western Macedonia, Kozani, Greece
[2] Chemical Process and Energy Resources Institute, CERTH, Thessaloniki, Greece
[3] Department of Environmental Engineering, Democritus University of Thrace, Thrace, Greece
[4] School of Production Engineering and Management, Technical University of Crete, Chania, Greece

*Corresponding author e-mail: e.mandela@uowm.gr

ABSTRACT

Light olefins are considered the backbone of chemical industry, and a broad variety of derivatives, used in our daily lives, are produced from these building blocks. Notably, it is estimated that the $C_{2-4}^{=}$ demand will face an annual growth of 3.5% by 2030, as a combined result of global population growth and rising living standards. The current leading technology for light olefins production is the steam cracking of natural gas and/or crude oil fractions but this process is linked with a high carbon footprint. Concerns associated with the depletion of fossil fuels and the threat of global warming have recently initiated efforts to explore alternative pathways and feedstocks to produce light olefins through CO_X hydrogenation by employing either excess RES-powered electrolytic hydrogen combined with captured CO_2 industrial emissions or syngas mixtures generated through biomass gasification or biofuels reforming. Therefore, the present work aims to examine the thermodynamic aspects of the CO_X hydrogenation to light olefins at a range of temperatures and pressures of industrial practice by feeding several carbon-neutral CO_X-H_2 mixtures. For this end, the Aspen Plus software and the Gibbs free energy minimization method have been compiled in a series of simulation scenarios.

Keywords: Thermodynamic analysis, CO_X hydrogenation, Light olefins production, Industrial CO_2 capture, Bio-syngas

INTRODUCTION

Light olefins, $C_{2-4}^{=}$, are the top chemicals in terms of global production rates with an annual ethylene and propylene capacity of ca. 150 million tons [1], and are deemed as the key building blocks for a range of products, such as plastics, gels, fibers, pharmaceuticals, cosmetics, etc. Olefins are industrially produced by the steam cracking of naphtha or the thermal ethane cracking, both highly energy intensive processes that charge each ton of olefin with 0.75 up to 11.5 tons of CO_2 emissions, depending on the employed production route, raw materials and energy sources (usually 2 – 5 $tnCO_2/tnC_{2-4}^{=}$ for oil and natural gas) [2]. EU Green Deal recognizes the necessity to detach chemical industries from fossil carbon towards the transition to complete decarbonisation at 2050. Recently, new approaches to generate light olefins by neutral carbon sources and renewables have been proposed including among others the employment of syngas by biofuels reforming and biomass gasification, as well as, the hydrogenation of industrially captured CO_2 emissions by renewable electrolytic hydrogen.

CO_2 to $C_{2-4}^{=}$ olefins is a catalysis benchmark and includes a complicated reaction system due to i) the multiple reaction pathways of CO_2 hydrogenation to various products (CO, CH_4, light olefins, higher hydrocarbons, methanol, etc.) and ii) its sensitivity to operational conditions (e.g., temperature, pressure, $H_2/CO_2/CO$ feed ratio, presence of other substances) and catalyst properties (e.g., active phases, dispersion, acidity-basicity). The challenges of this process highlight the importance of obtaining a thorough understanding of the reaction's thermodynamics prior to catalytic studies. To the best of the authors knowledge, there are only a few relevant works in literature thermodynamically exploring the effect of operational temperature, pressure and feed composition on conversion, selectivity and light olefins/paraffins product distribution [3], [4].

In the present study, an extensive thermodynamic analysis of industrially relevant CO_X hydrogenation reaction systems to light olefins is conducted, using the Aspen Plus software and the Gibbs free energy minimization method. More specifically, carbon-free and renewable H_2/CO_X upstream industrial feed mixtures were considered and the performance in terms of conversion, selectivity and yields to light olefins was explored over a wide range of operational parameters (i.e., temperature, pressure, H_2/CO_X reactants ratio). Moreover, the methodology took into consideration the presence of other chemical substances (CH_4, H_2O) existing in practical feedstock mixtures.

METHODOLOGY

For the current thermodynamic analysis, the ASPEN Plus software was used to calculate the equilibrium compositions, utilizing the Gibbs reactor (R_{Gibbs}). The non-ideal behavior in Gibbs energy values was introduced by the Soave-Redlich-Kwong thermodynamic package in order to calculate the substantial properties per component and per reaction mixture. Ethylene, propylene, butylene, hydrogen and carbon dioxide were considered as the only products of the aforementioned reaction system. It is highlighted that paraffins were excluded from the study since the aim was to identify the pathway towards olefins (in other words, paraffin production is thermodynamically favoured and masks the production of olefins through a tailor-made catalytic system). The equations that define the conversion of CO_2, the selectivity and yields of light olefins (C_nH_m) are presented as follows:

$$X_{CO_2}(\%) = \frac{\mathrm{CO_{2\ inlet}} - \mathrm{CO_{2\ outlet}}}{\mathrm{CO_{2\ inlet}}} \times 100 \quad (1)$$

$$S_{C_nH_m}(\%) = \frac{nC_n\mathrm{H_{m\ outlet}}}{\sum_1^n nC_n\mathrm{H_{m\ outlet}}} \times 100 \quad (2)$$

$$Y_{C_nH_m}(\%) = \frac{X_{CO_2} \times S_{C_nH_m}}{100} \quad (3)$$

RESULTS AND DISCUSSION

For the thermodynamic calculations a reacting mixture consisting of captured CO_2 and electrolytic hydrogen by excess RES power is initially considered. Figure 1 depicts the effect of operational temperature on the CO_2 conversion and light olefins selectivity at various pressures ranging from 10 to 30 bar and for a stoichiometric H_2/CO_2 = 3. The increase of the temperature leads to lower CO_2 conversions for all employed pressures, as expected due to the exothermic nature of the investigated reactions. Butylene is the main olefin product at low temperatures following a decreasing trend with temperature. On the other hand, ethylene starts to formulate at ca. 300 °C and increases with temperature and appears to be the prevailing olefin at higher temperatures. The corresponding selectivity profile for propylene follows a volcano behavior showing a maximum at approximately 500 °C. In general, higher pressures favour butylene selectivity, whereas ethylene/propylene selectivities decrease with pressure.

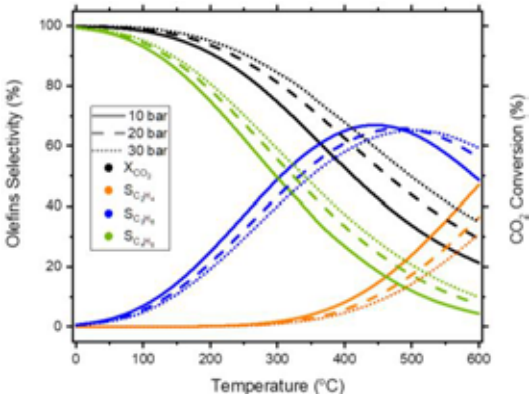


Figure 1: Effect of temperature on $C_{2\text{-}4}^{=}$ selectivity and conversion at 10, 20 and 30 bar for a stoichiometric H_2:CO_2 feed

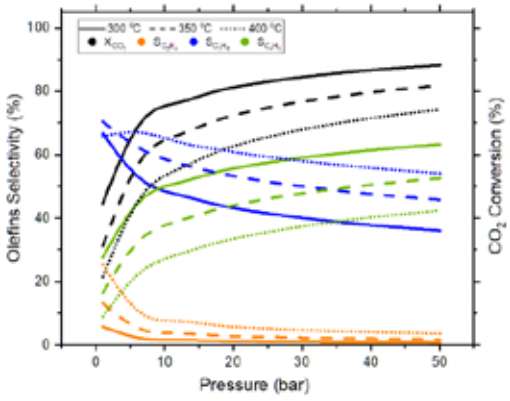


Figure 2: Effect of pressure on $C_{2\text{-}4}^{=}$ selectivity and conversion at 300, 350 and 400 °C for a stoichiometric H_2:CO_2 feed

As a volume-reducing reaction system, the conversion of CO_2 is expected to increase with pressure according to the Le Chatelier's principle. This is confirmed in Figure 2, which presents the effect of pressure (1 – 50 bar) at three different temperatures (300, 350 and 400 °C) and at stoichiometric feed ratio H_2/CO_2 = 3. The selectivities for ethylene and propylene decrease with pressure, whereas butylene exhibits an increasing trend with the operating pressure being the main product for pressures higher than 10 bar and T= 300 °C. At 400 °C, propylene exhibits the highest selectivity in the whole pressure range. At 350 °C, propylene's selectivity is higher than butylene's for pressures up to 30 bar, while above 30 bar an inverse behavior is observed. Figure 3 shows the effect of H_2:CO_2 molar feed composition from sub- to over-stoichiometric ratios (1 – 9) at three different temperatures (300, 350 and 400°C) and for the pressures of 20 and 30 bar. It is clearly observed that the CO_2 conversion linearly increases with the feed ratio increase, while the corresponding effect on olefins selectivity is essentially negligible. Finally, in the case of upstream derived syngas mixtures from biomass gasification or biofuel reforming containing CO_2, CO, H_2, CH_4 and H_2O, the results revealed that CO_2-rich syngas mixtures favor the selectivities of ethylene and propylene, while the corresponding values for butylene are suppressed.

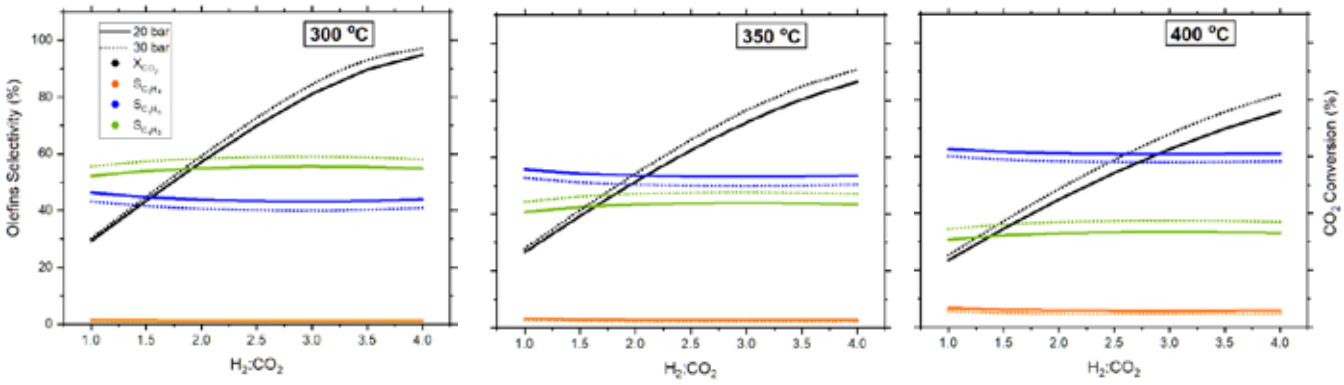


Figure 3: Effect of H_2:CO_2 feed molar ratio on $C_{2-4}^{=}$ selectivity and CO_2 conversion at 300, 400 and 500 °C and for 20 and 30 bar pressures

CONCLUSIONS

A detailed thermodynamic analysis of CO_X hydrogenation to light olefins was conducted and the effect of the operation temperature, pressure and feed composition on the conversion and selectivity to light olefins was thoroughly investigated. As an exothermic and mol-reducing reaction, the conversion is favored at low temperatures and high pressures, while the increase in H_2 feed concentration shift the reaction equilibrium to the right. In the case of syngas mixtures derived by upstream biomass gasification or biofuel reforming processes with high CO_2 contents, the selectivities to ethylene and propylene are enhanced at the expense of butylene formation.

ACKNOWLEDGEMENT

This research has been co-financed by the European Union and Greek national funds through the Greece 2.0 National Recovery and Resilience Plan, under the call RESEARCH-CREATE-INNOVATE (project code: T2EDK-01378) and the project “Development of New Innovative Low Carbon Footprint Energy Technologies to Enhance Excellence in the Region of Western Macedonia” (MIS 5047197) which is implemented under the Action “Reinforcement of the Research and Innovation Infrastructure”, funded by the Operational Programme "Competitiveness, Entrepreneurship and Innovation" (NSRF 2014-2020) and co-financed by Greece and the European Union (European Regional Development Fund).

REFERENCES

1. Z. Ma and M. D. Porosoff, “Development of Tandem Catalysts for CO 2 Hydrogenation to Olefins,” *ACS Catal.*, vol. 9, no. 3, pp. 2639–2656, 2019, doi: 10.1021/acscatal.8b05060.
2. M. Ghanta, D. Fahey, and B. Subramaniam, “Environmental impacts of ethylene production from diverse feedstocks and energy sources,” *Appl. Petrochemical Res.*, vol. 4, no. 2, pp. 167–179, 2014, doi: 10.1007/s13203-013-0029-7.
3. C. Jia, J. Gao, Y. Dai, J. Zhang, and Y. Yang, “The thermodynamics analysis and experimental validation for complicated systems in CO2 hydrogenation process,” *J. Energy Chem.*, vol. 25, no. 6, pp. 1027–1037, 2016, doi: 10.1016/j.jechem.2016.10.003.
4. B. Yao, W. Ma, S. Gonzalez-Cortes, T. Xiao, and P. P. Edwards, “Thermodynamic study of hydrocarbon synthesis from carbon dioxide and hydrogen,” *Greenh. Gases Sci. Technol.*, vol. 7, no. 5, pp. 942–957, 2017, doi: 10.1002/ghg.1694.

WHEC-2022
23rd World Hydrogen Energy Conference
June 26-30, 2022 - Istanbul

#330

PROCESS SIMULATION AND ASSESSMENT OF AN INTEGRATED POWER SYSTEM COMBINING OLIVE KERNEL PYROLYSIS, GASIFICATION AND SOLID OXIDE FUEL CELL

Athanasios Lampropoulos[*,1], *George Varvoutis*[1,4], *Evridiki Mandela*[1], *Stavros Spyridakos*[1], *Dimitris Ipsakis*[2], *Costas Athanasiou*[3], *Michalis Konsolakis*[2], *George E. Marnellos*[1,5]

[1] Department of Mechanical Engineering, University of Western Macedonia, Kozani, Greece
[2] School of Production Engineering and Management, Technical University of Crete, Chania-Crete, Greece
[3] Department of Environmental Engineering, Democritus University of Thrace, Xanthi, Greece
[4] Chemical Process & Energy Resources Institute, Centre for Research & Technology Hellas, Thessaloniki, Greece

*Corresponding author e-mail: alabropoulos@uowm.gr

ABSTRACT

The adverse impact of fossil fuels' on the environment and the increasing concerns regarding climate change, have intensified research efforts towards the exploitation of renewable energy sources (RES). Biomass can be utilized as a CO_2-neutral fuel in several energy conversion technologies. For instance, biomass gasification converts solids to syngas, which can be directly used as a fuel or as a valuable building-block toward synthetic liquid fuels and/or chemicals. The scope of the present study is the simulation of a combined process that exploits olive kernel (OK, 833 kg/day) for the production of electrical power and bio-oil. The integrated process includes: a) the slow pyrolysis of the olive kernel at 500 ^oC to solids (biochar, 252 kg/hr), liquids (336 kg/hr) and non-condensable gases (245 kg/hr), b) the autothermal gasification of biochar to syngas (1126 kg/hr) and c) the direct utilization of syngas in a solid oxide fuel cell (SOFC), for the cogeneration of electrical (1.35 MW_{el}) and thermal (1.1 MW_{th}) power. The combined process approaches a 50 % electrical efficiency, upon the raw biomass lower heating value (LHV). The integrated process was simulated using Aspen Plus® software and based on the experimental results of a previous study.

Keywords: Olive kernel, Pyrolysis, Gasification, SOFC, Co-generation of electricity and io-oil

INTRODUCTION

In 2019, the European Commission announced the European Green Deal to direct the EU economy on a pathway towards climate neutrality by 2050 [1]. The increase of renewables share in gross energy consumption and the adoption of the circular economy principles through innovative and efficient processes constitute crucial actions for this direction. Biomass is a cheap and widely available renewable form of energy. Agricultural and industrial activities are the main sources of residual biomass that could be used as renewable feedstock, thus enhancing local economies and minimizing problems of waste handling. Greece has a biomass potential of 3.5-5 Mtoe, with agro-industrial residues constituting 70% of the available capacity. Specifically, olive kernel and olive prunings account for almost 20% of the exploitable potential of agricultural residues, in Greece. In specific, Greece represents the third largest olive oil industry worldwide with an annual capacity of approximately 400,000 tons of olive kernel waste [2]. Despite the positive impacts of bioenergy on the way to combat climate change, biomass has lower energy density compared to fossil fuels and high logistic costs comprising harvesting and collection, storage, pretreatment and transportation. The biomass combustion route, in typical steam turbines, obtains a net efficiency of ca. 30% of biomass low heating value (LHV) [3]. The present work aims on increasing the energy efficiency through the thermochemical conversion of residual biomass to electricity and high added-value energy products (bio-oil). Considering the system as a combination of three technologies (Pyrolysis-Gasification-SOFC), a technical assessment is conducted and simulated using Aspen Plus® software and the experimental results from our previous study [4].

SYSTEM DESCRIPTION AND ASSUMPTIONS

The proposed system, based on the biomass pyrolysis reactor, the gasifier and the SOFC sub-systems, is demonstrated in Fig. 1. The biomass feedstock is olive kernel (OK) with physicochemical characteristics as presented in our previous work [4]. The OK feedstock enters the pyrolysis reactor (RYield) at ambient conditions (e.g. 20 ^oC / 1 bar) through a solid conveyor belt. For this study, the throughput of biomass was set at 20 tn/d (or 833 kg/h) and the endothermic pyrolysis takes place at 500 ^oC. Two streams exit the pyrolysis reactor: a) a solid phase stream rich in carbon (biochar) that enters the gasification reactor (RGibbs, 800 ^oC) and b) a gaseous stream that refers to a mixture of non-condensable gases and tar-oil. The gaseous stream is flash-cooled at 45 ^oC in heat exchanger 1 (HX1) in order to separate the constant gases (H_2, CO, CO_2, CH_4) from the tar-oil. The bio-oil is separated from the aqueous phase of the tar-oil and is a readily marketable-product of low oxygen content. The aqueous phase of the tar-oil is sent to the gasifier, whereas the pyrolysis gases are mixed with the syngas from the gasifier. The latter is then cleaned (in a cyclone) in order to remove the ash content and the syngas stream is preheated at 800 ^oC (HX2) prior entering the Solid Oxide Fuel Cell's (SOFC) anode.

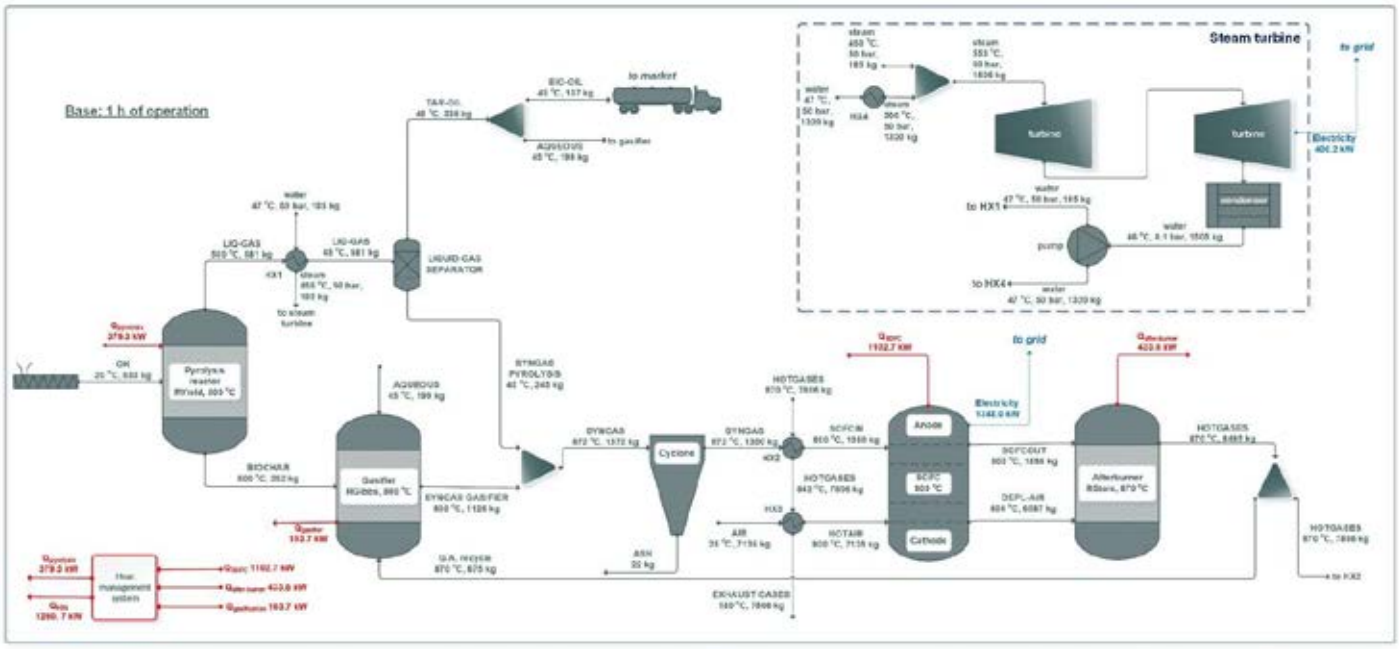


Fig.1 Process flow diagram of the olive kernel-to-power/bio-oil configuration.

In the SOFC, a combined heat and electrical energy production takes place and the anode/cathode effluents are sent to a series-connected burner (RStoic, 870 °C). The hot effluent gases from the burner split and an 8 % fraction is recycled back to the gasifier as the gasification agent. Finally, The residual heat of the SOFC and the after-burner is directed to a Rankine cycle for additional power generation.

RESULTS AND DISCUSSION

Regarding the mass balances of the integrated process, Table 1 summarizes the main input and output streams of the three sub-processes.

Table 1. Stream flowrates (kg/hr) and temperatures

	OK	pyrolysis gas	bio-oil	tar-oil aqueous	biochar	syngas	$anode_{in}$	gasification agent	exhaust gases
T, °C	20	45	45	45	500	800	800	870	180
H_2,	45	3.7	14	17	5.8	29	33	0	0
O_2	309	0	34	123	8.7	0	0	78	902
N_2	5.4	0	0	3.4	2	479	479	474	5476
H_2O	66	0	7	47	12	20	20	28	325
CO	0	110	0	0	0	506	616	0	0
CO_2	0	110	0	0	0	67	178	95	1095
CH_4	0	14.7	0	0	0	1.7	16.4	0	0
C	385	0	82	9	201	0	0	0	0
Ash	22	0	0	0	22	22	0	0	0
Total	**833**	**245**	**137**	**199**	**252**	**1126**	**1350**	**675**	**7806**

The simulation of the olive kernel slow pyrolysis was based upon our previous work [4], regarding the elemental composition of pristine olive kernel and of the produced biochar, as well as the yields towards solid, liquid and gaseous products. For these yields and elemental compositions, a typical gaseous products' composition was assumed, in agreement to slow pyrolysis literature [5], allowing the calculation of the elemental composition of the liquid products, by the elemental mass balances. The elemental composition of the aqueous and bio-oil phases were calculated assuming that a) the 40 wt. % of liquids corresponds to the organic phase (bio-oil) and the 60 wt. % to the aqueous phase and b) the 90 wt. % of the liquids' elemental carbon content, the 55 wt. % of hydrogen and the 40 wt. % of oxygen end up to the d.a.f. bio-oil phase (5 wt. % moisture), in agreement to slow pyrolysis literature [6,7]. The pyrolysis heat requirements were calculated at 1.83 MJ/kg of d.a.f OK biomass, which corresponds to the 9.8 % of its HHV_{daf} (18.80 MJ/kg), which is in accordance to literature [8]. Concerning the solid stream of pyrolysis (biochar, 252 kg/hr), it is driven to a fixed-bed gasifier (RGibbs) where the total char gasification takes place at 800 °C and

atmospheric pressure. The gasification-syngas was then mixed with the syngas derived from pyrolysis, and the total syngas is driven to the anode of the solid oxide fuel cell (SOFC) for the co-generation of electricity (1.35 MW_{el}) and heat (1.1 MW_{th}). The air inlet to the SOFC's cathode was adjusted so that the oxygen utilization factor to be 0.8, according to the literature [9]. Depleted air, as well as the non-utilized fuel from the SOFC, were sent to the afterburner, the exhaust-gases of which (N_2, O_2, H_2O, CO_2) were split and partially recycled as gasification agent. The exhaust-gases recycle percentage (8 %) was selected in order to almost sustain the autothermal operation of the gasifier at complete bio-char gasification.

Regarding the heat management of the integrated process, the heat generated at the SOFC and the after-burner (1.55 MW_{th}), was found adequate to cover the pyrolysis endothermic operation and the preheating of both air and cleaned syngas at the SOFC's inlets. The residual heat of the SOFC and the after-burner (after the coverage of internal heat requirements) generates high-pressure steam (1505 kg/h, 50 bar, 553 ^oC), for the steam turbines to produce additional electricity (0.40 MW_{el}). The total electrical power produced equals to 1.75 MW_{el}, corresponding to an efficiency of 49 %, with respect to the lower calorific value of the raw olive kernel.

CONCLUSIONS

The overall simulation showed that, despite the valorization of the 16.4 % of biomass feed as bio-oil, the remaining 83.6 % generates 1.75 MW_{el}, compared to the 1.07 MW_{el} of the total biomass feed, in a potential biomass combustion and steam turbine process. Thus, the integrated biomass pyrolysis/gasification/SOFC process can contribute to the economic sustainability of either the bioelectricity generation in SOFCs (by the cogeneration of high added-value bio-oil) or the bio-oil production (by the highly efficient co-generation of electricity). The economic assessment of the integrated process is currently under progress.

ACKNOWLEDGEMENT

This research has been co-financed by the European Union and Greek national funds through the Operational Program Competitiveness, Entrepreneurship and Innovation, under the call ERA-NETS 2018 (project code: T8EPA2-00005).

REFERENCES

1. Directorate-General for Research and Innovation (European Commission). Europe's 2030 climate and energy targets. Research & innovation actions 2021:3.
2. Aravani VP, Sun H, Yang Z, Liu G, Wang W, Anagnostopoulos G, et al. Agricultural and livestock sector's residues in Greece & China: Comparative qualitative and quantitative characterization for assessing their potential for biogas production. Renew Sustain Energy Rev 2022;154:111821. https://doi.org/10.1016/j.rser.2021.111821.
3. Brigagão GV, de Queiroz Fernandes Araújo O, de Medeiros JL, Mikulcic H, Duic N. A techno-economic analysis of thermochemical pathways for corncob-to-energy: Fast pyrolysis to bio-oil, gasification to methanol and combustion to electricity. Fuel Process Technol 2019;193:102–13. https://doi.org/10.1016/j.fuproc.2019.05.011.
4. Lampropoulos A, Kaklidis N, Athanasiou C, Montes-Morán MA, Arenillas A, Menéndez JA, et al. Effect of Olive Kernel thermal treatment (torrefaction vs. slow pyrolysis) on the physicochemical characteristics and the CO2 or H2O gasification performance of as-prepared biochars. Int J Hydrogen Energy 2020. https://doi.org/10.1016/j.ijhydene.2020.11.230.
5. Amini E, Safdari MS, DeYoung JT, Weise DR, Fletcher TH. Characterization of pyrolysis products from slow pyrolysis of live and dead vegetation native to the southern United States. Fuel 2019;235:1475–91. https://doi.org/10.1016/j.fuel.2018.08.112.
6. Christoforou EA, Fokaides PA, Banks SW, Nowakowski D, Bridgwater A V., Stefanidis S, et al. Comparative Study on Catalytic and Non-Catalytic Pyrolysis of Olive Mill Solid Wastes. Waste and Biomass Valorization 2018;9:301–13. https://doi.org/10.1007/s12649-016-9809-5.
7. Hani FFB, Hailat MM. Production of Bio-Oil from Pyrolysis of Olive Biomass with/without Catalyst. Adv Chem Eng Sci 2016;06:488–99. https://doi.org/10.4236/aces.2016.64043.
8. Crombie K, Mašek O. Investigating the potential for a self-sustaining slow pyrolysis system under varying operating conditions. Bioresour Technol 2014;162:148–56. https://doi.org/10.1016/j.biortech.2014.03.134.
9. Athanasiou C, Vakouftsi E, Coutelieris FA, Marnellos G, Zabaniotou A. Efficiencies of olive kernel gasification combined cycle with solid oxide fuel cells (SOFCs). Chem Eng J 2009;149:183–90. https://doi.org/10.1016/j.cej.2008.10.017.

WHEC-2022
23rd World Hydrogen Energy Conference
June 26-30, 2022 - Istanbul

#348

SYSTEM INTEGRATION AND VALIDATION OF HYDROGEN FUEL CELL NICHE VEHICLES AND RELATED REFUELLING INFRASTRUCTURE AT HySA SYSTEMS / SOUTH AFRICA

Vladimir Linkov, Mykhaylo Lototskyy, Sivakumar Pasupathi*
University of the Western Cape, South African Institute for Advanced Materials Chemistry, HySA Systems Centre of Competence, Robert Sobukwe Road, Private Bag X17, Bellville 7535, South Africa

*Corresponding author e-mail: vlinkov@uwc.ac.za

ABSTRACT

An overview of HySA Systems activities related to the development, demonstration and implementation of hydrogen fuel cell vehicles and their refuelling infrastructure is presented. The activities are focused on the integration, prototyping and validation of niche vehicles, including forklifts and scooters, as well as their hydrogen refuelling infrastructure.

Keywords: Hydrogen South Africa, Niche vehicles, Refuelling infrastructure, System integration, Testing and validation

INTRODUCTION

A long-term (15-year) Hydrogen and Fuel Cell (HFC) Technologies Research, Development, and Innovation Strategy "Hydrogen South Africa" (HySA) was officially launched in September 2008 by the Department of Science and Technology (DST; Department of Science and Innovation / DSI since 2019). HySA Systems, a Systems Integration and Technology Validation Centre of Competence, was established in 2007 at the South African Institute for Advanced Materials Chemistry (SAIAMC) at the University of the Western Cape (UWC). The main objective of HySA Systems is to perform system integration and validation of HFC technologies, including hydrogen fuel cell vehicles (HFCVs) [1,2].

Hydrogen mobility and related refuelling infrastructure is a significant component in further implementation of HFC technologies in South Africa according to the Hydrogen Society Roadmap (HSRM) approved by the Cabinet on September 14, 2021 [3] and prepared on the basis of contribution of the DSI, in collaboration with the South African governmental institutions (SANEDI) and business (Anglo American, Bambili Energy, Engie) [4]. The HFCV-related activities are focused on the heavy-duty vehicles (buses, trucks, trains), as well as some operational niche vehicles for underground mining and materials handling.

This presentation overviews HySA Systems activities related to the development, demonstration and implementation of HFC niche vehicles and their refuelling infrastructure.

INTEGRATION OF NICHE VEHICLES AT HYSA SYSTEMS

The R&D on the integration of HFCVs at HySA Systems is focused on some niche vehicles including light vehicles (golf cart, bi- and tricycles, scooters), as well as forklifts. Common features of the integration solutions on the basis of commercial electric vehicles include:

(a) Hybrid "battery + fuel cell" powertrain where the battery is used for the start-up and compensating peak loads, and the fuel cell provides the electric power during the main driving cycle. The use of range extender configuration along with careful balancing of the battery capacity and the fuel cell power allows to minimise consumption of hydrogen fuel and to maintain the optimal state of the charge of the battery [5].
(b) Use of metal hydrides for the compact on-board hydrogen storage which requires lower H_2 refuelling pressures and, in turn, allows to use less complicated and expensive and more safe and reliable refuelling infrastructure as compared to conventional H_2 refuelling stations with dispensing pressures of 350 and 700 bar.

Table 1 presents list of the related prototypes developed by HySA Systems during the period 2010–2019. Some recent examples are shown in Fig.1. As mentioned above, due to low-pressure on-board H_2 storage in MH, refuelling of HySA Systems HFCVs takes place at the lower dispensing pressures, below 150 bar for the forklifts and below 40 bar for the cartridge-type hydrogen storage canisters for the light vehicles. It allowed us to develop simple, inexpensive and reliable hydrogen refuelling stations (## 7, 10 in Table 1; Fig. 2).

Table 1. Summary of HFCV prototypes and their refuelling facilities developed by HySA Systems

#	Year	Description	Funders	Collaborators
1	2010	*Ahi Fambeni* tricycle with HT-PEMFC range extender and MH H_2 storage tank	DST	Tshwane University of Technology (TUT)
2	2013	Electric golf cart with FC range extender and hybrid H_2 storage tank utilising MH [6]	Impala Platinum, DST	–
3	2013	Electric scooter with FC range extender and MH H_2 storage tanks	DST	–
4	2014	Electric bicycle with FC range extender and MH H_2 storage tank	DST	–
5	2014	Pedicab vehicle with FC range extender and MH H_2 storage tank	DST	–
6	2016	Fuel cell forklift with MH H_2 storage extension tank [7,8]	Impala Platinum, DST	TF Design (Pty) Ltd
7	2016	H_2 refuelling station with integrated MH H_2 compressor [9]	Impala Platinum, DST	TF Design (Pty) Ltd
8	2018	Locally developed FC power module with integrated MH H_2 storage for electric forklift [10]	DST, Impala Platinum	Hot Platinum (Pty) Ltd
9	2019	Trial series of FC scooters with cartridge-type MH H_2 storage tanks	South African Post Office (SAPO)	TF Design (Pty) Ltd
10	2019	SAPO FC scooters refuelling station	SAPO	TF Design (Pty) Ltd



Fig. 1. Left – operation of 3-ton forklift with HySA Systems fuel cell power module. Right – trial series of HySA Systems scooters with fuel cell range extenders.

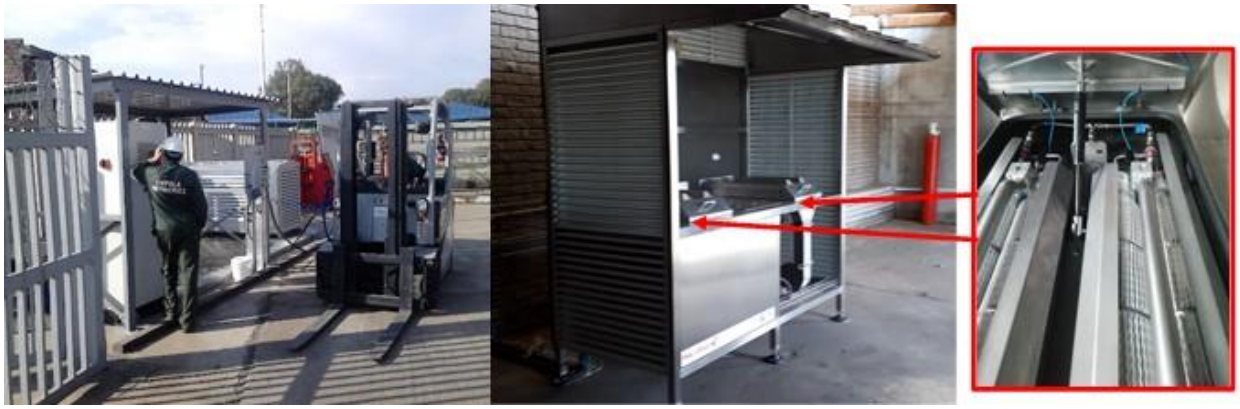


Fig. 2. HySA Systems hydrogen refuelling stations for FC forklift (left) and MH cartridges for FC scooters (right).

For the refuelling which requires hydrogen compression, HySA Systems solutions use thermally driven hydrogen compression utilising MH. Realisation of this approach is particularly beneficial for the industrial customers who possesses necessary services, first of all, low-pressure hydrogen and waste heat (low-grade steam) in their infrastructure. Along with MH compressors for low-pressure refuelling stations (150 bar; see Fig. 2(left)), HySA

Systems presently develops MH technology for high-pressure (up to 1000 bar) H_2 compression to be further used in conventional hydrogen refuelling stations with dispensing pressures of 350 and 700 bar [11].

CONCLUSIONS

HySA Systems activities in hydrogen and fuel cell technologies for mobile applications are focused on the integration, prototyping and validation of niche vehicles, including forklifts and scooters, as well as their hydrogen refuelling infrastructure. The integration is carried out on the basis of commercial electric vehicles by introducing hybrid power train where fuel cell plays a role of the range extender. Another feature of the developed prototypes is in the use of metal hydride on-board hydrogen storage which provides compactness, safety, as well as less stringent requirements for the refuelling infrastructure due to the lower refuelling pressure.

ACKNOWLEDGEMENT

The work described was carried out at HySA Systems and funded by the Department of Science and Innovation of South Africa, as well as by South African business partners including Impala Platinum Ltd. and South African Post Office. The international collaboration activities started in 2018 and related to the development of fuel cell forklifts and their refuelling infrastructure utilising metal hydrides were supported by the EU Horizon 2020 Program; Grant Agreement 778307 – HYDRIDE4MOBILITY – H2020-MSCA-RISE-2017.

REFERENCES

1. Pollet BG, Pasupathi S, Swart G, Lototskyy M, Williams M, Bujlo P, Ji S, Linkov V and Bladergroen BJ. Hydrogen and Fuel Cell Technologies at the Hydrogen South Africa (HySA) Systems Competence Centre. 2014. Platinum Metals Review 58: 68-81.
2. Pollet BG, Pasupathi S, Swart G, Mouton K, Lototskyy M, Williams M, Bujlo P, Ji S, Bladergroen BJ and Linkov V. Hydrogen South Africa (HySA) Systems Competence Centre: Mission, objectives, technological achievements and breakthroughs. 2014. International Journal of Hydrogen Energy 39: 3577-3596.
3. Hydrogen Society Roadmap to guide South Africa's hydrogen rollout. 2021. https://www.engineeringnews.co.za/article/hydrogen-society-roadmap-to-guide-south-africas-hydrogen-rollout-nzimande-2021-10-22
4. South Africa Hydrogen Valley: Final Report. 2021. https://www.dst.gov.za/images/2021/Hydrogen_Valley_Feasibility_Study_Report_Final_Version.pdf
5. Radica G, Tolj I, Markota D, Lototskyy MV, Pasupathi S and Yartys V. Control strategy of a fuel-cell power module for electric forklift. 2021. International Journal of Hydrogen Energy 46: 35938-35948.
6. Lototskyy M, Tolj I, Davids MW, Bujlo P, Smith F and Pollet BG. "Distributed hybrid" MH–CGH2 system for hydrogen storage and its supply to LT PEMFC power modules. 2015. Journal of Alloys and Compounds 645: S329–S333.
7. Lototskyy MV, Tolj I, Davids MW, Klochko YV, Parsons A, Swanepoel D, Ehlers R, Louw G, van der Westhuizen B, Smith F, Pollet BG, Sita C and Linkov V. Metal hydride hydrogen storage and supply systems for electric forklift with low-temperature proton exchange membrane fuel cell power module. 2016. International Journal of Hydrogen Energy 41: 13831-13842.
8. Lototskyy MV, Tolj I, Parsons A, Smith F, Sita C and Linkov V. Performance of electric forklift with low-temperature polymer exchange membrane fuel cell power module and metal hydride hydrogen storage extension tank. Journal of Power Sources 2016. 316: 239-250.
9. Lototskyy M, Davids MW, Swanepoel D, Louw G, Klochko Y, Smith F, Haji F, Tolj I, Chidziva S, Pasupathi S and Linkov V. Hydrogen refuelling station with integrated metal hydride compressor: Layout features and experience of three-year operation. 2020. International Journal of Hydrogen Energy 45: 5415-5429.
10. Lototskyy M, Tolj I, Parsons A, Klochko Y, Khan I, Naylor E, Shenker M, Brey A, Pasupathi S and Linkov V. 2019. Fuel cell power module for electric forklift with integrated metal hydride hydrogen storage system. In: mESC-IS2019 4th International Symposium on Materials for Energy Storage & Conversion, September 11-13, 2019, p. 103.
11. Yartys V, Lototskyy MV, Linkov V, Pasupathi S, Davids MW, Tolj I, Radica G, Denys RV, Eriksen J, Taube K, Bellosta von Colbe J, Capurso G, Dornheim M, Smith F, Mathebula D, Swanepoel D and Suwarno S. HYDRIDE4MOBILITY: An EU HORIZON 2020 project on hydrogen powered fuel cell utility vehicles using metal hydrides in hydrogen storage and refuelling systems. 2021. International Journal of Hydrogen Energy 46: 35896-35909.

WHEC-2022
23rd World Hydrogen Energy Conference
June 26-30, 2022 - Istanbul

#352

MODELING AND DESIGN OPTIMIZATION OF CARBON-FREE HYBRID ENERGY SYSTEMS WITH THERMAL AND HYDROGEN STORAGE

[1]Jacob Bryan, [1] Aiden Meek, [1] Seth Dana, [1] Md Sajedul Islam Sakir, [1*] Hailei Wang
[1]Utah State University, Mechanical and Aerospace Engineering, 4130 Old Main Hill, Logan, UT, USA

*Corresponding author e-mail: hailei.wang@usu.edu

ABSTRACT

The study is focused on replacing all coal and natural gas electricity generation in the state of Texas with solar, wind, and nuclear power. As an integral part of the designed hybrid energy system, both thermal and hydrogen storages are used to minimize overproduction and allow for load following. The Dymola system model uses wind speed and solar irradiation data for 2020 to meet the real load data for Texas in 2020. An optimization algorithm is developed to find an optimum design point, aiming to minimize the system's levelized cost of electricity (LCOE) while meeting the demand at all times of the year. The optimized LCOE of the system was $73.04/MWh, which results from 61 Natrium nuclear power plants, 5317 3.2-MW wind turbines, and 307.9 km2 of solar panels. Most of the demand is met by nuclear power with the rest being a near even split between wind and solar. While this optimized LCOE is greater than the current LCOE, it provides carbon-free electricity for the entire state of Texas. Although the stored hydrogen in salt caverns contributed only to a small portion of the total electricity production, it provides a large amount of green hydrogen to future clean energy markets.

Keywords: Hydrogen, Hybrid energy system, Nuclear, LCOE, Dymola/Modelica

INTRODUCTION

Continuing to rely on fossil fuels for our energy needs results in further carbon emissions and increased CO2 levels in the atmosphere. Society faces the problem of reducing fossil fuel consumption, while maintaining the power generation required to maintain our way of life. Texas has installed significant numbers of wind turbines to help reduce its dependence on fossil fuels. However, Texas still has a significant dependence on fossil fuels that needs to be reduced. The goal of this study is to determine an economically optimized hybrid energy system (HES) that can provide Texas' energy needs while eliminating the need for fossil energy. By increasing solar production, installing more wind turbines, building nuclear reactors, and incorporating energy storage, Texas could become carbon-free in its electricity production. The HES design would be capable of meeting Texas' energy demands while minimizing the cost of electricity in the new system. The HES would be built in, and provide power for, Texas (specifically for the ERCOT power company that provides electricity for nearly all of Texas). Solar would be installed in the west of Texas; additional wind production would likely be installed in the north of Texas. The nuclear reactors could be located anywhere in the state. Thermal energy storage, which allows nuclear reactors to follow load, would be installed on site next to the nuclear reactors. Additional energy storage, in the form of hydrogen, could be installed salt caverns in the north or east of Texas.

Texas is a state of both significant energy production, with abundant wind and solar natural resources, and energy consumption, consuming more energy than other state [1]. Despite these natural resources and having two large nuclear energy facilities, Texas still derives 63.7% of its energy from fossil fuel sources via a combination of coal and natural gas, as of 2020 [2]. With the goal to replace these coal and natural gas generation facilities with carbon-free alternatives – namely a combination of wind, solar, nuclear, and hydrogen fuel cells – the demand profile which the new HES must meet is determined by subtracting the energy generated from green energy sources from the total demand. This section will examine this demand profile and consider the wind and solar potential of the state through a look at the wind speed and solar irradiance at multiple locations in the state.

The demand profile which the HES is required to meet is equal to the total demand from the ERCOT data, minus the energy generated from existing carbon-free energy sources. The residual demand profile has several interesting characteristics. First, the demand increases significantly over the summer months, peaking in August. The demand is often 50-100% higher during the summer compared to the rest of the year. This seasonal variation poses a significant difficulty when trying to design a HES with a significant portion of nuclear power, as sizing the system to meet summer demand peaks will invariably result in significant energy overproduction during the winter, spring, and fall. Alternatively, extreme levels of seasonal energy storage may be required to meet the demand during summer if the HES is sized more appropriately (i.e. smaller) for the remainder of the year. The difference in demand profile during each season is further illustrated in Fig. 1, which shows

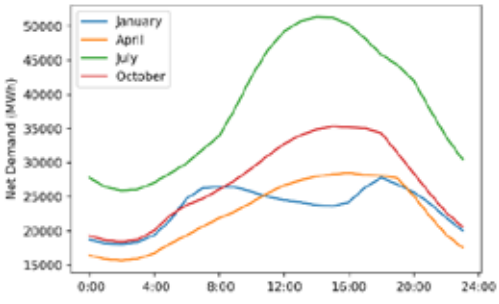


Figure 1: Average hourly demand profile for January, April, July, and October.

hourly average demand profiles for January, April, July, and October. Energy consumption in July is significantly higher than that in the other three months. Also, the January profile is bimodal with peaks around 7:00 am and 6:00 pm, while the other months are unimodal.

Wind speed and solar irradiance data were collected from NASA POWER, using the 50-m height (parameter "WS50M") for wind speed and all-sky surface shortwave downward irradiance (parameter "ALLSKY SFC SW DWN") for global horizontal irradiance (GHI) [3]. To make the data collected for wind speed and GHI less dependent on a specific location and more representative of a region, data from several locations were sampled from the regions of interest for each resource and averaged. The hourly averaged profiles for wind speed and GHI are shown in Fig. 2. As shown, wind speed at 50 meters has significant seasonal variation. First, wind speed tends to be higher at night than during the day. This is advantageous, as wind production will typically increase at night, when solar energy is no longer producing electricity. However, the average wind speed in the plot is lowest for July when demand is at its highest, potentially increasing the effective seasonal variation in demand that must be met by other resources.

Hydrogen, as a great energy carrier, have been drawn substantial interests in recent years to be produced using carbon-free energies such as nuclear. It is typically stored in artificial salt caverns. According to Ahluwalia, et al. [4], it holds up to 6000 metric tons of hydrogen with pressure between 50 and 150 bar. In this study, up to 20 artificial caverns is considered for hydrogen storage. Given Texas has large salt deposits in the north and the east of the state, these salt deposits could be used as geologic hydrogen storage. This is expected to be included in future works.

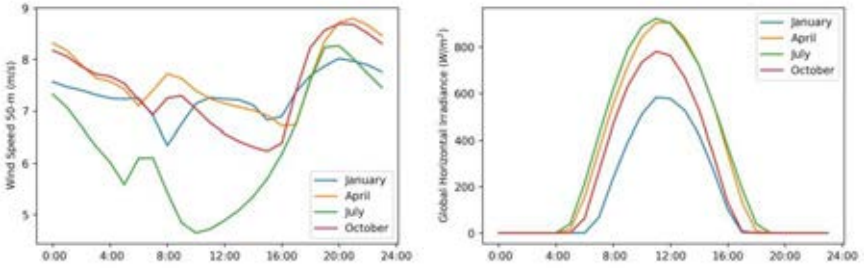


Figure 2: Hourly averaged wind and solar data for January, April, July, and October.

SYSTEM DESIGN, MODELING AND OPTIMIZATION

Given the significant wind and solar resources present in Texas, the proposed HES design includes both wind turbines and photovoltaic solar panels. However, these resources are intermittent and non-dispatchable; the HES uses nuclear power to complement these renewables. Specifically, the Natrium system developed by GE Hitachi Nuclear and TerraPower is used here due its ability to vary power output through its integrated molten salt thermal storage system. This thermal storage is useful short-term energy storage. Hydrogen storage is used for long-term storage. The proposed HES is modeled using Dymola, a software for modeling dynamic systems using the Modelica language. Models for each subsystem - Natrium, wind, photovoltaic solar, hydrogen storage, and hydrogen fuel cells - were developed and integrated in this software. This hybrid energy system (HES) is shown in Fig. 3.

The Natrium system operates a 840-MWt sodium fast reactor as its primary heat source. The reactor is cooled by molten nitrate salt, which is stored in a two-tank storage system. The molten salt can be drawn from the hot storage tank through a salt-steam heat exchanger to drive a steam cycle, outputting 345 MWe at steady state operation. The salt storage capacity allows to boost the power output to 500 MWe for up to 5.5 hours. The wind power production is based on the power curve for the GE 3.2 MW wind turbines, while the solar panels are modeled with 15% efficiency.

The high-temperature steam electrolyser (HTSE) is used to convert excess power to hydrogen with an efficiency of 0.83, which can be obtained by a Solid Oxide Electrolysis Cell (SOEC) [5]. When meeting peak energy demand, a Solid Oxide Fuel Cell (SOFC) with 60% efficiency is modeled to generate electricity. The power output of the fuel cell was capped at 35.5 GW with 2556 GWh of storage, which allows the storage to deliver electricity for 3 days at its full capacity. The excess hydrogen produced by the current optimal HES design needs to be sold for other markets in producing chemicals such as diesel, ammonia, and methanol. In the current model, green hydrogen is priced between $2.50-6.80/kg in calculating the system LCOE. Given the global hydrogen demand is 98.8 billion kg per year and a hydrogen market report predicts

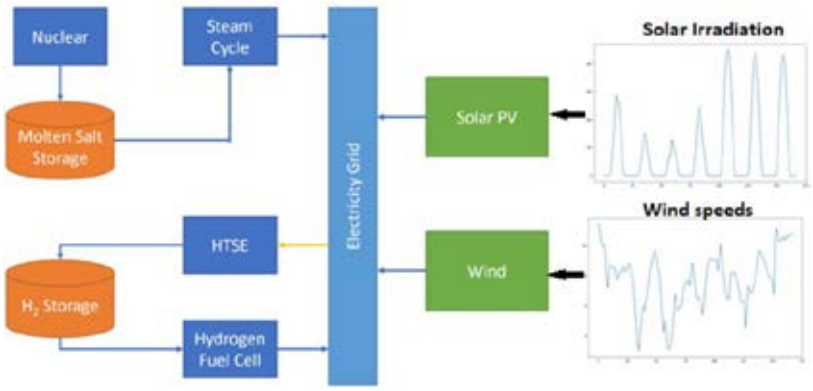


Figure 3: The schematic diagram of the HES design

the world demand for hydrogen to more than double in the next 10 years [6], the green hydrogen produced in the current HES could contribute significantly to those growing needs.

The optimal HES design is defined as the one which minimizes the LCOE of the system. To calculate this system-level LCOE, a weighted sum of the subsystem LCOEs is taken according to the amount of energy produced by each subsystem [4,5,7]. Then, the revenue from sold hydrogen is subtracted from the annual cost, and the difference is normalized by the total annual energy demand.

RESULTS AND DISCUSSION

The optimized HES consists of 61 Natrium reactors, 5317 3.2-MW wind turbines, and 307.9 km2 of solar panels. Given the significant amount of hydrogen being sold, the effective LCOE of the system is very sensitive to the hydrogen price. The estimated LCOE of the system is $73.04/MWh given the green hydrogen price being $6.80/kg. Figure 4 shows how the HES subsystems work together to meet the residual demand for summer 202 in a 10-day period. As shown, both wind and solar output are lower than demand. Besides the nuclear power is modulating significantly to try to match the peaks and valleys of the demand, the hydrogen storage and fuel cell systems are utilized heavily during these periods. Stored hydrogen is consumed at nights to mee the peak demand while during the day the excess energy is converted to hydrogen to replenish the hydrogen storage.

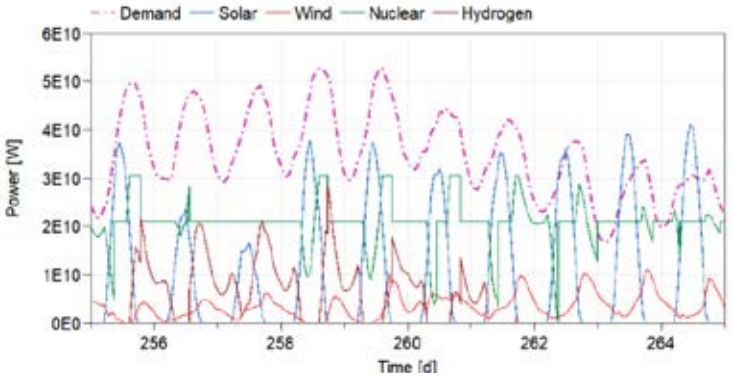


Figure 4: Simulation of 10-day operation of the HES (summer 2020)

CONCLUSIONS

The hybrid energy system presented in this report successfully meets the electricity demand in Texas without using fossil fuels by using a combination of wind, solar, nuclear, and hydrogen power, while also producing significant amounts of green hydrogen for growing industrial needs. However, it does not accomplish this goal particularly economically. The system has an overall LCOE of $73.04/MWh when adjusting the subsystem LCOEs for their respective capacity factors. Additionally, this study only considered the demand and weather data for one year. A more robust system design would need to account for the volatility more directly in wind speed, solar irradiance, temperature, demand, and the correlations between these variables. This could be accomplished by using synthetic time histories and a stochastic optimization to find robust designs with quantified uncertainty. Nevertheless, the proposed HES could be a design which can flexibly grow with the population and adapt to changes in demand with minimal modifications while avoiding carbon emissions.

REFERENCES

1. U.S. Energy Information Administration (EIA). Texas - State Energy Profile Overview.
2. ERCOT. Hourly Load Data Archives.
3. NASA. NASA POWER | Prediction of Worldwide Energy Resources.
4. R.K. Ahluwalia, D.D. Papadias, J-K Peng, and H.S. Roh. System Level Analysis of Hydrogen Storage Options. 2019 Annual Merit Review and Peer Evaluation Meeting, page 42, April 2019.
5. Konor L. Frick, Paul W. Talbot, Daniel S. Wendt, Richard D. Boardman, Cristian Rabiti, Shannon M. Bragg-Sitton, Mark Ruth, Daniel Levie, Bethany Frew, Amgad Elgowainy, and Troy Hawkins. Evaluation of Hydrogen Production Feasibility for a Light Water Reactor in the Midwest. Technical Report. INL/EXT-19-55395-Rev000, Idaho National Lab. (INL).
6. Grand View Research. Global Hydrogen Generation Market Size Report, 2021-2028, March 2021.
7. U.S. Energy Information Administration. Levelized Costs of New Generation Resources in the Annual Energy Outlook 2021.

WHEC-2022
23rd World Hydrogen Energy Conference
June 26-30, 2022 - Istanbul

#373

OFFSHORE WIND ENERGY PROSPECTS FOR POWER-TO-DIRECT AIR CAPTURE AND POWER-TO-GAS

* *Muhammad Faisal Shehzad, Haris Ishaq, Curran Crawford*
Institute for Integrated Energy Systems at University of Victoria (IESVic), Department of Mechanical Engineering, University of Victoria, BC V8P 5C2, Canada

*Corresponding author e-mail: mshehzad@uvic.ca

ABSTRACT

Direct air capture of carbon dioxide (CO_2) is technically a feasible solution for reducing atmospheric CO_2 concentrations at scale, building on decades of global research. However, powering such systems even partially with CO_2-intensive fossil fuels results in more CO_2 emissions. This paper presents a novel energy management strategy (EMS) to further explore modular offshore wind energy off Canada's West Coast via power-to-direct air capture and power-to-gas systems. The system architecture includes a 15MW wind turbine paired with a hydrogen energy storage system, i.e. hydrogen production and storage, and direct air capture (DAC) units. Hydrogen production from wind generation is stored and used to deliver the thermal loads of the DAC system. In addition to meeting DAC thermal loads, any excess produced hydrogen is used to meet hydrogen demand for external consumers, such as hydrogen as a fuel for fuel cell vehicles. The effectiveness of the proposed EMS is shown through extensive simulations with different seasonal conditions.

Keywords: Offshore wind energy, Direct air capture, Hydrogen storage, Power-to-gas, Energy storage system

INTRODUCTION

It is now well recognized that climate scenarios for the Earth to stay within the limits set by the Paris Agreement [1] must include negative emission technologies (NETs) on a large scale. In the past, there has been concern that these technologies would be viewed as a replacement for actions to directly stop greenhouse gas emissions, but that view has changed. A recent report from the U.S. National Academy of Sciences [2] concluded that "NETs (removing CO_2 from the atmosphere and sequestering it) are best viewed as a component of the mitigation portfolio, rather than a way to decrease the atmospheric concentration of CO_2." Among all CO_2 capture strategies, it is understood that the net flow of CO_2 out of the atmosphere must be positive. However, powering CO_2 capture by fossil fuel, even fractionally, results in additional CO_2 emissions [3]. A potential replacement for powering a CO_2 capture system is to use CO_2-free power, such as wind or solar [4]. In this paper, conventional fossil energy is replaced by offshore-wind energy to power a system of CO_2 capture from air. The main entities of the scenario under investigation are offshore-wind energy, the electrolyzer (hydrogen production and storage), and DAC units.

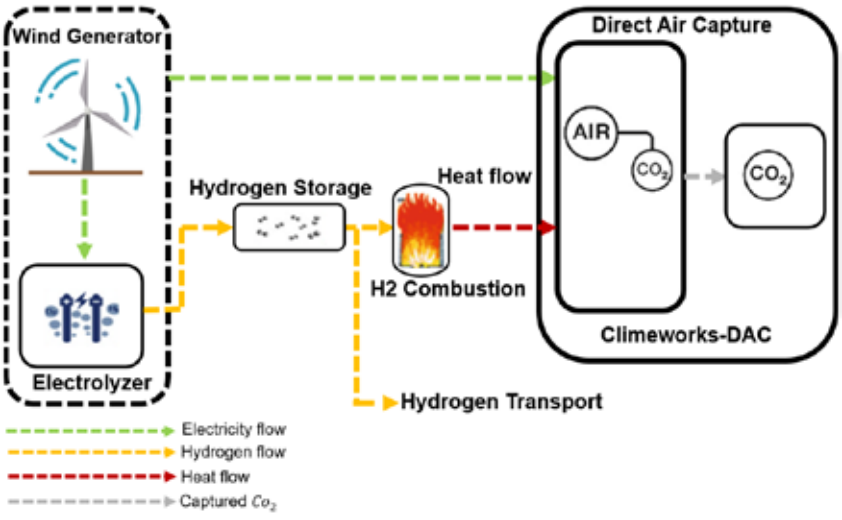


Fig. 1. The overall schematics of the proposed offshore wind-DAC system

In order to achieve the proposed research study goals, this paper presents a novel EMS as a carbon-free nearly zero emission-based solution. In particular, the EMS developed has to fulfill the following:

- to maximize the amount of CO_2 capture via DAC;
- to produce hydrogen for meeting DAC thermal loads (to avoid further CO_2 production in the process);

- to sell any excess of hydrogen produced (after meeting DAC thermal loads) to external consumers, such as hydrogen as a fuel for fuel cell vehicles.

DIRECT AIR CAPTURE SYSTEM MODEL

In order to efficiently utilize the logical dispatch behavior of the DAC units, the system is modeled employing a mixed logic dynamic framework. Two decision variables, namely, the DAC energy requirement (E), and its working state are determined at each time step interval. There is a linear relation between the energy required to operate the DAC and the total amount of CO_2 captured, as shown in Eq. 1. The energy requirement of the whole system for capturing 1kg of CO_2 per unit time is defined as μ, in kWh/kg [5].

$$E = \mu C_T \tag{1}$$

where C_T denotes the total amount of captured CO_2, and E represents both the electric ($P_{DAC}(k)$) and thermal energy requirements ($\dot{Q}_{DAC}(k)$) of the DAC system at each time interval.

HYDROGEN PRODUCTION SYSTEM MODEL

The dynamics of the stored hydrogen H at the next step $k+1$ depends on the level of hydrogen at each time step, on the hydrogen production/consumption efficiencies η and the power P of the electrolyzer. Therefore, we have:

$$H(k+1) = H(k) + \eta P_{elc}(k) T_s - H^{ext} - \sigma_c \dot{Q}_c(k) T_s \tag{2}$$

where T_s denotes the sampling period, H^{ext} is the hydrogen produced for external consumers, $\dot{Q}_c$ is the heat supply to the DAC from the H_2 combustor, σ_c is the heat conversion factor. Notice that, according to Eq. 3, the electrolyzer produces hydrogen whenever the input power is within the electrolyser's acceptable rates only.

POWER BALANCE CONSTRAINTS

The essence of the optimization model is to meet the electrical and thermal demands with renewable generation and hydrogen combustion. The following power balance equations must be satisfied at each time-step k:

$$P_{DAC}(k) \leq P_w(k) - P_{elc}(k) \tag{3}$$

$$\dot{Q}_{DAC}(k) \leq \dot{Q}_c(k) \tag{4}$$

NUMERICAL RESULTS

Parameters of the major components of the proposed modular power-to-DAC and power-to-gas system include a wind turbine with a rated output of 15 MW, and 28 units of CO_2 capture containers (126 kW of each unit and a total of 3.884 MW). These components could all fit on a single floating platform to form a modular, mass-produced architecture. The parameters of the major components are summarized below in Table 1.

Table 1. Parameters of the major components of the wind power-driven CO_2 capture system

Parameters	**CO_2 Capture system (Power-to-DAC)**	
	Adsorption	**Desorption**
Power requirements $E(k)$	44kW per DAC container	82kW per DAC container
$\mu(kWh/kg)$	0.98	1.82
Power consumption ratio	35%	65%
Total amount of the captured CO_2		
	Simulation Week Starting March 13	
C_T	292.34 t-CO_2/week	
Electrolyser (Power-to-gas)		
Efficiency $\eta = 0.23$kg/kW	$P_{elc}^{min} = 300kW$	$P_{elc}^{max} = 3000kW$

In this section, we validate via numerical simulations the proposed control strategy based on west coast Cascadia region wind profiles. In order to show the correct working and capabilities of the devices, week-long power production profiles are considered. As will be clear in what follows, the numerical results show that the proposed EMS is able to correctly satisfy both the electric and thermal demands of the DAC system. In particular, the thermal demands have been met via hydrogen combustion, and any excess of hydrogen is sold to the external consumers for meeting hydrogen as fuel demand for transportation purposes. Further, the system overall constraints are always respected.

The simulations have been conducted over a T=168h simulation horizon with $T_s = 1h$ sampling time. Fig 2(a) shows a typical week-long power production profiles, along with the DAC adsorption (Electric) and desorption (thermal) loads. The details of both the adsorption and desorption energy requirements are reported in Table 1.

It is worth noticing that the hydrogen production objectives in this study are two-fold: meting DAC thermal demand, and hydrogen as a fuel for meeting hydrogen vehicles' demand. Fig. 2(b) shows the excess hydrogen production and storage after meeting the thermal demands with the highest priority.

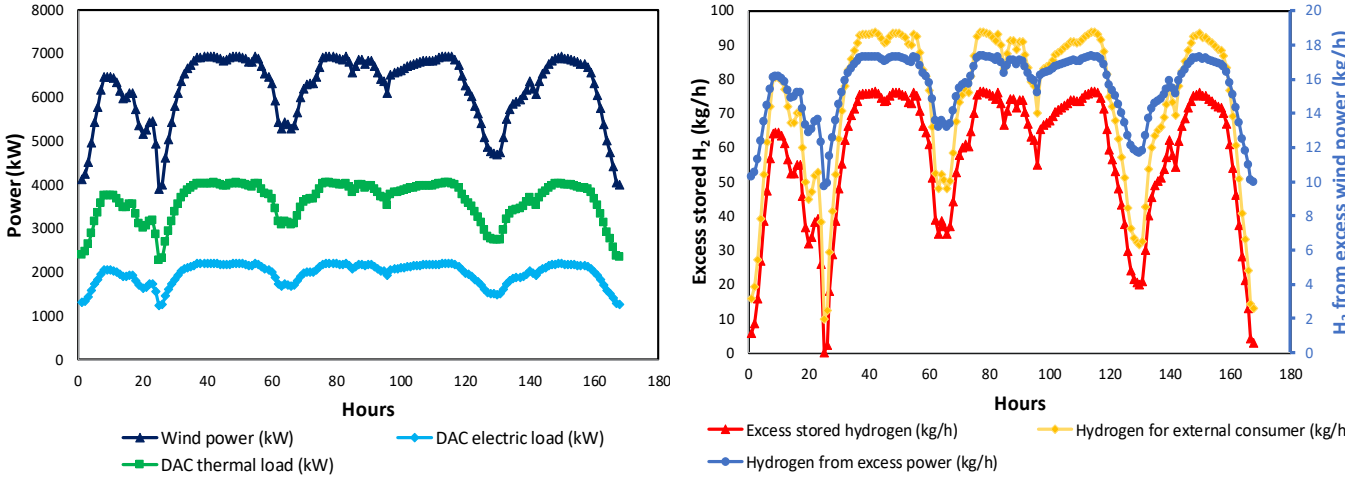


Fig. 2(a). Power production profiles, DAC adsorption and desorption loads (b) Excess hydrogen production and storage

CONCLUSIONS

In this paper, we proposed an EMS within the perspectives of offshore wind energy-driven power to DAC and power to gas. Offshore wind energy is employed with the highest priority to capture the maximum CO_2 by the DAC system. The hydrogen is produced and stored with the objectives of meeting DAC thermal demands (for the desorption phase of the DAC process) as well as hydrogen as a fuel for external consumers. Future works will investigate the proposed results in real-time to produce hydrogen for DAC process as well as for commercialization purposes according to the project goals and also the integration of battery storage system to capture CO_2 for shorter sub-hourly scale variations.

ACKNOWLEDGEMENT

The authors acknowledge the support provided by the Pacific Institute of Climate Solutions (PICS) for the Solid Carbon project and private donor.

REFERENCES

.
1. Agreement, P. (2015, December). Paris agreement. In Report of the Conference of the Parties to the United Nations Framework Convention on Climate Change (21st Session, 2015: Paris). Retrieved December (Vol. 4, p. 2017). HeinOnline.
2. National Academies of Sciences, Engineering, and Medicine. (2018). Negative emissions technologies and reliable sequestration: a research agenda. Negative emissions technologies and reliable sequestration: a research agenda.
3. Jacobson, M. Z. (2019). The health and climate impacts of carbon capture and direct air capture. Energy & Environmental Science, 12(12), 3567-3574.
4. TechnipFMC. Energy Transition, Deep Purple. 2022. Available from https://www.technipfmc.com/en/what-we-do/subsea/energy-transition-deep-purple/.
5. Li, C., Shi, H., Cao, Y., Kuang, Y., Zhang, Y., Gao, D., & Sun, L. (2015). Modeling and optimal operation of carbon capture from the air driven by intermittent and volatile wind power. Energy, 87, 201-211.

WHEC-2022
23rd World Hydrogen Energy Conference
June 26-30, 2022 - Istanbul

#379
EXERGY ANALYSIS OF REVERSIBLE SOFC COUPLED WITH ORGANIC RANKINE CYCLE AND HYDROGEN STORAGE FOR RENEWABLE ENERGY STORAGE

[1] *Uday Raj Singh,* [1*] *Satya Sekhar Bhogilla*
[1] Department of Mechanical Engineering, Indian Institute of Technology Jammu, Jammu, 181221, India

*Corresponding author e-mail: satya.bhogilla@iitjammu.ac.in

ABSTRACT

A novel renewable energy storage system based on reversible solid oxide fuel cell (SOFC) with integrated organic Rankine cycle (ORC), metal hydride hydrogen storage (MHHS) and absorption refrigeration cycle are proposed in the present study. The system utilizes the waste heat generated from the SOFC unit into the ORC evaporator to produce power using the turbine. After that, the rejected heat is being used for heating application and produces a cooling effect by implementing the single-effect absorption chiller. A part of high-quality exhaust heat from SOFC is transferred to the MHHS for the desorption process to facilitate the release of hydrogen. Exergy analysis of the trigeneration system and evaluation of the exergy destruction rates of system components is carried out. Furthermore, a detailed parametric study is conducted to study the influence of critical parameters such as current density, SOFC temperature and turbine inlet pressure on exergy efficiency and exergy destruction rates. It has been observed that the maximum value of trigeneration energetic efficiency of 74% is obtained at SOFC temperature of 800°C and current density of 0.8 A/cm². Moreover, maximum net electrical exergy efficiency is 67.39%, maximum heating exergy efficiency is 73.1%, maximum cooling exergy efficiency is 66.48%, and maximum ORC exergy efficiency obtained is 16.63%.

Keywords: Solid oxide fuel cell, Exergy analysis, Trigeneration, Organic Rankine cycle, Metal Hydride

INTRODUCTION

As fossil fuels are decreasing with time, efficient power systems are becoming an important subject. As a result, there is an increased focus on developing technologies that will provide better energy conversion efficiencies. SOFC is one such attractive technology that can be used to generate power. SOFC has a great advantage to working on multiple fuels as input such as hydrogen, biomass, hydrocarbons, etc. Also, reversible SOFC produces hydrogen by electrolysis and alternatively generating power output using hydrogen input while working in the fuel cell mode [1]. In addition, multiple concepts to use high-quality waste heat from SOFC have been proposed and investigated. Al-Sulaiman et al. has performed various studies on trigeneration system where they have investigated the biomass-based system and performed energy and exergy analysis [2]. One more study by Al-Sulaiman et al. explored the possibility of using solar energy to drive a trigeneration system [3,4]. Similar studies on SOFC driven trigeneration systems were proposed wherein the SOFC was driven by methane fuel, and the exhaust heat was utilised by ORC and single-effect absorption chiller [2, 5, 6].

The present study is focused on exergy analysis of the system novel energy storage system. The energy analysis of the proposed system is already performed in our previous study [7]. In order to utilize the waste heat from SOFC effectively, various heat recovery units are integrated with the system. The exergy destruction rates of various components of the system are also computed. A parametric study is also performed wherein the current density, SOFC temperature, and inlet turbine pressure are varied to observe the influence on the trigeneration system's exergy efficiency and exergy destruction rates.

System Description

The illustration of a conceptual renewable energy storage unit is shown in Fig. 1. The system comprises a SOFC, MHHS, ORC, heating process and absorption chiller. The operation takes place in two modes, i.e., SOFC and reversible SOFC or solid-oxide electrolyser cell (SOEC) modes. In the SOEC mode, hydrogen is produced by utilising renewable sources and is stored in the metal hydride tank. In the next phase, i.e., the SOFC mode, the stored hydrogen is fed to the SOFC, generating power and exhaust heat. This exhaust heat is further utilised to generate power and enhance the overall power output. The waste heat coming out from SOFC is provided to the H1 heat exchanger, where turbine power output is achieved. The exhaust heat from the turbine is thereafter used in heating applications using H_2 and to produce a cooling effect using the vapour absorption cycle.

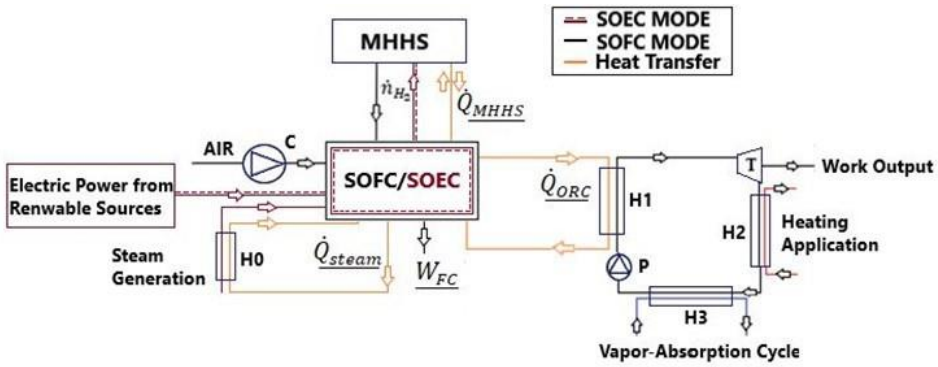


Fig. 1. Schematic representation of a Trigeneration plant with reversible SOFC, MHHS, ORC and vapour absorption cycle.

MODELLING AND ANALYSIS

The rate of exergy destroyed for each component considered in the system can be given by Eq. (1)

$$\dot{E}_{x_d=}\sum_j\left(1-\frac{T_0}{T_j}\right)\dot{Q}_j-\dot{W}_{cv}+\sum_i\dot{m}_i ex_i-\sum_e\dot{m}_e ex_e \tag{1}$$

where $\dot{E}_{x_d}$ and ex represents exergy destruction and exergy per flow rate. Exergy related with any stream can be defined as the sum of chemical and physical exergy per mass flow rate and can be given by Eq. (2).

$$ex_{total}=ex^{ph}+ex^{ch} \tag{2}$$

where ex^{ph} and ex^{ch} can be given by Eq. (3) and Eq. (4)

$$ex^{ph}=(h-h_0)-T_0(s-s_0)+\frac{V^2-{V_0}^2}{2}+g(z-z_0) \tag{3}$$

$$ex^{ch}=x_i ex_i^{ch,0}+RT_0x_i ln(x_i) \tag{4}$$

The SOFC exergy efficiency is given by Eq. (5)

$$\eta_{ex,SOFC}=\frac{W_{SOFC}}{Ex_{f,H_2}} \tag{5}$$

where Ex_{f,H_2} is the input exergy. The electrical exergy efficiency can be given by Eq. (6)

$$\eta_{ex,el}=\frac{W_{net}}{Ex_{f,H_2}} \tag{6}$$

The cooling exergy efficiency can be expressed using Eq. (7)

$$\eta_{ex,cog,c}=\frac{W_{net}+\left(1-\frac{T_0}{T_{evp}}\right)Q_{evp}}{Ex_{f,H_2}} \tag{7}$$

The heating cogeneration exergy efficiency is expressed as Eq. (8)

$$\eta_{ex,cog,\mathrm{h}}=\frac{W_{net}+\left(1-\frac{T_0}{T_{hp}}\right)Q_{hp}}{Ex_{f,H_2}} \tag{8}$$

The tri-generation exergy efficiency is given by Eq. (9)

$$\eta_{ex,\mathrm{tri}}=\frac{W_{net}+\left(1-\frac{T_0}{T_{hp}}\right)Q_h+\left(1-\frac{T_0}{T_{evp}}\right)Q_{evp}}{Ex_{f,H_2}} \tag{9}$$

RESULTS AND DISCUSSION

It is evident from Fig. 2 that the trigeneration exergy efficiency decreases as the SOFC current density increases. Also, the electrical exergy efficiency tends to reduce with increasing current density. As the current density rises, the voltage tends to decrease. As a result, less power is produced from the SOFC. The highest SOFC exergy efficiency value of 57.92% takes place at 0.6 A/cm² which drops down to 50.37% at 1 A/cm². As shown in Fig. 2, the cooling co-generation energetic efficiency is 1.5% more than the electrical exergy efficiency, which is attributed to the comparatively small amount of cooling effect being provided from the cooling cycle. On the contrary, the trigeneration exergy efficiency is also observed to be more than heating co-generation exergy efficiency by 1.5%. This is because of the small addition in the exergy efficiency due to cooling.

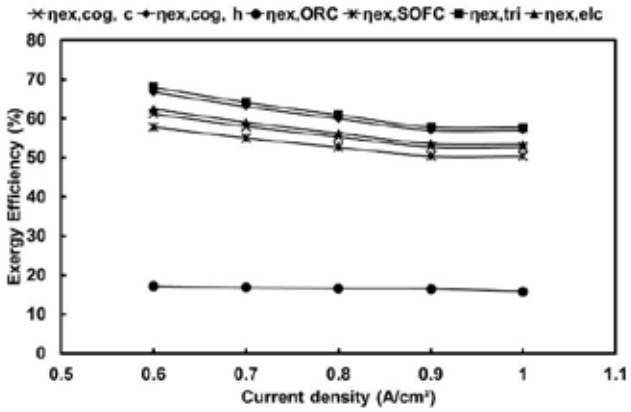


Fig. 2. Effect of current density on exergy efficiency at SOFC temperature=650°C, turbine inlet pressure=1600kPa.

CONCLUSIONS

The proposed study presents a novel design for renewable energy storage using reversible SOFC. Two modes, i.e., SOFC and SOEC, are described, and exergy analysis is performed. In SOFC mode, the maximum SOFC exergy efficiency of 57.92% is achieved at 0.6 A/cm². The electrical exergy efficiency is low at higher current density values. The ORC efficiency is found to decrease from 17.14% to 15.84% as the current density value changes from 0.6 to 1 A/cm². With SOFC temperature shift, the trigeneration exergy efficiency reaches its maximum value of 73.98%. However, the exergy efficiency of the system is observed to remain unaffected by the variation in the turbine inlet pressure.

REFERENCES

1. Lototskyy M, Nyamsi SN, Pasupathi S, Wærnhus I, Vik A, Ilea C and Yartys V. 2018. A concept of combined cooling, heating and power system utilising solar power and based on reversible solid oxide fuel cell and metal hydrides. International journal of hydrogen energy. 43:18650-63.
2. Lototskyy M, Nyamsi SN, Pasupathi S, Wærnhus I, Vik A, Ilea C and Yartys V. 2018. A concept of combined cooling, heating and power system utilising solar power and based on reversible solid oxide fuel cell and metal hydrides. International journal of hydrogen energy. 43:18650-63.
3. Al-Sulaiman FA. 2014. Exergy analysis of parabolic trough solar collectors integrated with combined steam and organic Rankine cycles. Energy Conversion and Management 77:441-9.
4. Al-Sulaiman FA, Dincer I and Hamdullahpur F. 2011. Exergy modeling of a new solar driven trigeneration system. Solar Energy 85:2228-43.
5. Al-Sulaiman FA, Dincer I and Hamdullahpur F. 2010. Exergy analysis of an integrated solid oxide fuel cell and organic Rankine cycle for cooling, heating and power production. Journal of power sources 195:2346-54.
6. Al-Sulaiman FA, Dincer I and Hamdullahpur F. 2010. Energy analysis of a trigeneration plant based on solid oxide fuel cell and organic Rankine cycle. International Journal of Hydrogen Energy 35:5104-13.
7. Singh UR, Kaushik AS and Bhogilla SS. 2022. A novel renewable energy storage system based on reversible SOFC, hydrogen storage, Rankine cycle and absorption refrigeration system. Sustainable Energy Technologies and Assessments 51:101978.

WHEC-2022
23rd World Hydrogen Energy Conference
June 26-30, 2022 - Istanbul

#389

SCIENTIFIC AND TECHNOLOGICAL SYNERGIES CONNECTING ELECTROLYSERS, FUEL CELLS AND ELECTROCHEMICAL COMPRESSORS FOR HYDROGEN USE

[1*] *Sonya Calnan,* [1,2] *Rutger Schlatmann*
[1]PVcomB, Helmholtz-Zentrum Berlin für Materialien und Energie GmbH, 12489 Berlin, Germany
[2] Hochschule für Technik und Wirtschaft Berlin, Wilhelminenhofstraße 75A, 12459 Berlin, Germany

*Corresponding author e-mail: sonya.calnan@helmholtz-berlin.de

ABSTRACT

Electrolysers, electrochemical compressors and fuels cells will be crucial to supporting the role of green hydrogen in the energy, transport and manufacturing sectors. In this contribution we discuss several scientific and technological synergies between these three types of electrochemical cells and their benefits towards fostering the wider deployment of these devices are outlined. The identified synergies can also be extended to the same type of electrochemical cells based on different dual use (energy and materials) chemicals for example ammonia.

Keywords: Hydrogen, Fuel cell, Electrolyser, Electrochemical compressor

INTRODUCTION

The green house emission targets set by the global community to mitigate the adverse effects of climate change require a massive reduction in the contribution of fossil-based fuels to the energy, transport and manufacturing sectors [1]. Thus, the contribution of renewable energy sources such as solar, wind, hydro- and geothermal energy is increasing to compensate the gradually reducing supply from fossil fuels. Despite the geographically wide dispersion of wind and solar energy resources, unlike hydro and geothermal sources, they are intermittent and thus need storage when electricity supply outstrips demand. Hydrogen (H_2) is the ideal chemical energy carrier because it can be produced and used with little or no green house gas emissions if electrochemical conversion processes are used.

Electrolysers (EC) use electrical energy to split water into oxygen and hydrogen, thus providing storage of excess electricity for later use. Electrochemical hydrogen compressors (EHC) operate by simultaneously compressing and purifying hydrogen supplied to the anode to a purer higher pressure H_2 stream at the cathode, thus increasing the volumetric energy density of stored hydrogen. Lastly, hydrogen fuel cells (FC) convert hydrogen into electricity and thus provide a route to recover stored energy from intermittent primary energy sources. All three devices use and/or produce only water, oxygen and hydrogen which are environmentally benign and sustainable. Thus, in a closed sustainable zero carbon hydrogen-energy cycle, the hydrogen would be generated by an electrolyser driven by either solar or wind energy, compressed using an electrochemical compressor driven by the same energy sources and then re-converted back to electricity in a hydrogen fuel cell. These technologies must be of low cost, operate efficiently and have a long service life to be established in the global energy system.

Since the underlying principal of operation of electrolysers, fuel cells and electrochemical compressors is similar, synergies between them can be leveraged to accelerate the transition to zero carbon or carbon neutral energy pathways. Although there is an implicit awarenes of these synergies in the interested community, e.g. in unitary reversible fuel cells [2] and for fuel cells and EHCs, the development of each of the technologies is largely mutually exclusive. Moreover in recent years, the attention to and advances in fuel cells have exceeded those for electrolysers with EHCs lagging far behind. This unbalanced interest and rate of development of the technologies may lead to missed opportunities of knowledge transfer accross the technologies and unnecessary re-inventions since relevant new insights may be overlooked. This contribution serves to identify and create an overview, that is till now missing in the contemporary publications, of aspects of these devices in which useful scientific and technological synergies may exist. A comprehensive catalogue of such synergies would accelerate the elimination of the barriers that hinder the widespread adoption and deployment of hydrogen based electrochemical devices in the global energy system.

POSSIBLE SYNERGIES AND THEIR BENEFITS

Identification of synergies

The layout and relevant half-reactions, assuming a proton exchange membrane (PEM) electrolyte, of a fuel cell, an electrochemical compressor and an electrolyser, indicating the essential components are shown in Fig 1. The architecture of electrochemical cells such as fuel cells, electrolysers and electrochemical compressors is similar in

that a membrane (which may also act as a solidstate ionic electrolyte) is sandwiched between a pair of oppositely charged electrodes. Electrochemical half reactions that take place at the interface of the electrolyte and each of the electrodes affect the conversion of energy to a chemical and vice-versa. Also, the backbone hardware of all the devices is essentially the same although slight modifications. particularly of the flow field geometry and microporosity of the catalyst interfaces may be required, to enhance functionality that is distinctive to the specific device reactions. The similarity of the fundamental electrochemical principles and device architecture also provides a platform enabling the use of similar numerical models for accelerated optimisation. These devices use similar auxillary hardware for the management of the flows of reactants, products and cooling water, control and safety monitoring, as well as for temperature management. Thus, there would be clear synergies in the development of component manufacturing processes and plants, as well as in the circular economy and recycling of these systems.

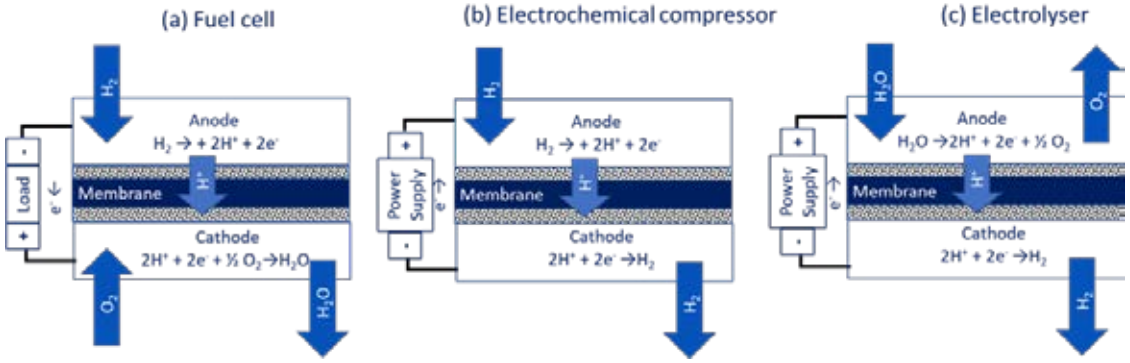


Fig. 1. Schematics of proton exchange membrane (PEM) electrolyte based hydrogen electrochemical cells (a) fuel cell, (b) electrochemical compressor (EHC) and (c) electrolyser. Notice that the anode and cathode, of the EHC, are exactly the same as those of the fuel cell and the electrolyser, respectively. For anion exchange membrane (AEM) based devices, the half reactions are slightly different but the overall reactions are the same.

An inspection of the cell schematics in Fig 1. reveals that the electrodes (electrocatalysts) may be interchanged between the devices. For instance, the EHC uses the hydrogen oxidation reaction (HOR) at the anode to split hydrogen molecules like the fuel cell and uses the hydrogen evolution reaction (HER) at the cathode to generate hydrogen as in the electrolyser. Additionally, the operation of unitary reversible fuel cells depends on availability of highly active, highly selective and stable bifunctional oxygen reduction/evolution reaction (OER/ORR) catalysts and bifunctional HER/HOR catalysts [3]. Indeed the synergies that enable unitary reversible fuel cells play a role in increasing the capacity factor of such devices and thus accelarating their amortisation thereby reducing the total cost of ownership when deployed for electrolysis driven by intermittent primary energy sources. EHCs also depend on the availability of bifunctional HER/HOR catalysts and platinum already shows significant activity in both acidic and alkaline conditions [4]. However, in view of the anticpated demand for platinum, the research community is actively searching for alternative bifunctional catalysts based on transition metals. This in turn drives the development of electrochemical cells employing anion exchange membrane AEM electrolytes, both for OER/ORR [5] and HER/HOR [6].

Additionally, the operational and performance behaviour of these electrochemical cells shows common patterns. For instance, increasing the operating temperature increases the performance but only to a certain extent, since high currents may lead to self-limitation caused by mass transport issues. Suboptimal removal of reaction products and/or delivery of reactants, under high current density, from the electrolyte-catalyst interface increases the internal resistance of the system thus reducing the power density with time. Increased operating pressure also increases membrane cross-over creating a safety risk for fuel cell and electrolysers and also increases back diffusion across the membrane in EHCs ultimately reducing the compression ratio.

For all device technologies, water management is becoming increasingly important because of the trend towards using PEM/AEM that are wetted using humidity supplied via one electrode. Thus, dehydration of the ionomer and membrane which reduces the membrane conductivity and thus the current density, must be avoided. Although electrolysers have previously been run with continuous loading, the majority are, in the future, likely to be operated using fluctuating renewable energy sources. Thus, insights from fuel cells, whose largest area of deployment will be in transportation characterised by high load variability, frequent starts and stops as well as steep ramps, will be useful to improve the durability of electrolysers and ultimately of EHCs in renewable energy cycles. For temperate climates, this also means that such devices may be required to work with „cold“ starts to save energy used to keep the device warm during idle times. Thus, learnings from the control regimes for operating one type of device, may

with some adjustments, be used to improve the operability of the others. All devices suffer from issues with durability mainly attributed to (electro)-chemically induced degradation namely, corrosion in oxidising conditions and embrittlement in hydrogen-rich conditions. For these, reliable analytical testing and stressing procedures are required to identify the causes and mechanisms of degradation which would be useful to prolong the economic service life.

Benefits of identified synergies

A comprehensive awareness of synergies may offer routes to innovative solutions to existing challenges (cost, performance and durability) in all devices. Researchers would then be able to select the priority research areas from which all the technologies may benefit. Research and discovery may benefit from combined efforts channelled to select the most promising material classes for catalysts and membranes, among others. All concerned parties would benefit from the development of test protocols and facilities hinging on common requirements for safety, plant control strategies and balance of plant. Electrochemical cell manufacturers would benefit from a quicker achievement of a critical mass, for economies of scale, to become an attractive market for raw materials supply. Synergies in device architecture and balance of plant may foster the development of common quality assurance practices, norms and standards for common components/subsystems. In turn, the end-users and operators of the electrochemical cells would benefit from reduced costs of ownership because of standardized common components/sub systems and a wider pool of maintenance and servicing providers. Research laboratories and electrochemical cell manufacturers may use synergies to widen their competences and product offerings, respectively. Lastly, collaboration between researchers and industry may be initiated, increasing knowledge transfer and spillover effects across applications.

CONCLUSIONS

Electrochemical cells namely, electrolysers, electrochemical compressors and fuel cells have the potential to contribute to the decarbonisation of the global energy supply by using hydrogen as a chemical energy vector. Commonalities in the device architecture, catalyst materials, electrolyte (and membranes), standards and balance of plant equipment may enable synergetic scientific and technological advancements in fuel cells, electrolysers and electrochemical hydrogen compressors. The benefits of these synergies would best be realised when the attention to, and pace of development of the three technologies is more equally balanced than at present where electrochemical compressors lag electrolysers which in turn lag behind fuel cells. These insights may also be relevant for the equivalent set of electrochemical cells based on other dual use (energy and material) chemicals such as ammonia.

ACKNOWLEDGEMENT

The authors gratefully acknowledge the support from the German Federal Ministry of Education and Research in the framework of the project CatLab (03EW0015A).

REFERENCES

1. “Global Warming of 1.5°C: An IPCC Special Report on the impacts of global warming of 1.5°C above pre-industrial levels and related global greenhouse gas emission pathways, in the context of strengthening the global response to the threat of climate change, sustainable development, and efforts to eradicate poverty”, Intergovernmental Panel on Climate Change (IPCC), World Meteorological Organization, Geneva, Switzerland, 2018.
2. Klingenhof M, Hauke P, Brückner S, Dresp S, Wolf E, Nong HN, Spöri C, Merzdorf T, Bernsmeier D, Teschner D, Schlögl R., and Strasser P. 2021. ACS Energy Letters 6 (1):177-183.
3. Elbert K, Hu J, Ma Z, Zhang Y, Chen G, An W, Liu P, Isaacs HS, Adzic RR and Wang J. X. 2015. ACS Catalysis 5 (11):6764-6772.
4. Lambert TN, Vigil JA, White S, Davis DJ, Limmer SJ, Burton PD, Coker EN, Beechem TE and Brumbach MT. 2015. Chem. Commun. 51, 9511-9514.
5. Chen W, Jin Y, Zhao J, Liu N, and Cui Y. 2018. Proceedings of the National Academy of Sciences Nov 2018, 115 (46):11694-11699.

WHEC-2022
23rd World Hydrogen Energy Conference
June 26-30, 2022 - Istanbul

#398
PRELIMINARY ASSESSMENT OF THE GREEN HYDROGEN PRODUCTION POTENTIAL IN KAZAKHSTAN

[1] *Saniya Danenova,* [2] *Yerdaulet Abuov,* [2]*Akmaral Tleubergenova,*[2,3,*]*Woojin Lee*
[1] Department of Mechanical and Aerospace Engineering, School of Engineering and Digital Sciences, Nazarbayev University, Nur-Sultan 010000, Republic of Kazakhstan
[2] Department of Civil and Environmental Engineering, School of Engineering and Digital Sciences, Nazarbayev University, Nur-Sultan 01000, Republic of Kazakhstan
[3] Green Energy and Environment Laboratory, National Laboratory Astana, Nazarbayev University, Nur-Sultan 01000, Republic of Kazakhstan

*Corresponding author e-mail: woojin.lee@nu.edu.kz

ABSTRACT

Hydrogen has been considered a clean energy source, playing a crucial role in the energy transition. Due to its low-carbon intensity, green hydrogen appears to be an exciting solution to reduce greenhouse gas (GHG) emissions and increase secure energy supply. This study is the first attempt to evaluate the green production of hydrogen in Kazakhstan. At this stage, we have used the GIS tool to quantify solar, wind, and biomass resources in Kazakhstan. Most prospective areas for solar-based hydrogen include Jambyl, Kyzylorda, and Turkestan with hydrogen potential of 3800-4100 t/km^2/year, while Jambyl, Kyzylorda, and Central Kazakhstan regions favored the production of wind-based hydrogen with a hydrogen potential of 16 000-18 800 t/km^2/year. Southern Kazakhstan is also prospective for biomass-based hydrogen energy production (up to 47 t/km^2/year). Based on the hydrogen production estimated from the regions, Kazakhstan could be a supplier of new energy carriers globally, significantly contributing to future hydrogen energy system development.

Keywords: Renewable sources, Electrolysis, Gasification, Hydrogen energy systems

INTRODUCTION

Hydrogen as a part of future energy sources experiencing recognition from both industries and governments, with 39 countries recently announcing their hydrogen strategies [1]. There are multiple pathways to produce hydrogen, with principal production routes informally defined as gray, blue, and green, with the latter having the least carbon intensity. The future of hydrogen energy systems is closely linked with a rapid increase in green hydrogen production in the net-zero world, despite the currently prevailing role of gray hydrogen production (96% as of 2019) [2]. Kazakhstan can play a significant role in future hydrogen energy systems due to its considerable renewable resources and its will to expand renewable energy deployment in the future [3]. This study estimated the amount of potential green hydrogen production from Kazakhstan's wind, solar, and biomass resources using GIS tools.

METHODOLOGY

We consider three types of renewable resources for green hydrogen production: solar, wind, and biomass. We assume that electricity generated from solar and wind energy produces hydrogen from water splitting via electrolysis. Electrical potential obtained from sun and wind goes through AC output to convert it into DC voltage used in the electrolyzer within the AC/DC converter. The geographic distribution of electricity generated by wind turbines and solar panels was assessed using GIS-based average wind speed and global horizontal irradiation data respectively. PEM electrolyzers used electricity to generate hydrogen [4], which was modeled in our work. Wind turbine, solar panel, and electrolyzer parameters are shown in Table. For biomass hydrogen, our work modeled biomass feedstock as agricultural crop residues, which undergo a gasification process to produce hydrogen. Gasification of biomass has a Technology Readiness Level (TRL) value of > 7, which implies that the technology can be demonstrated in the operational environment [5]. Biomass feedstock and gasification parameters are shown in Table 1.

The data for wind and solar resources of Kazakhstan was obtained from the NREL database [6]. Agricultural crop production data for analysis was obtained from the Kazakhstan Agency of Statistics (KAS).

Table 1. Model assumptions for green hydrogen production

Hydrogen production methods	Operating strategy	
	Solar panel/wind turbine parameters [7]	***Electrolyzer parameters [4]***
Solar hydrogen	ElySun Monocristallin 250 Wc Solar Panel [7] PV module: mono-crystalline Efficiency of module conversion:15.28%	Electrolyzer type: PEM Hydrogen delivery pressure: 13.8 bar Power consumption (equivalent of 75% efficiency): 52.5 kWh/kg H_2
Wind hydrogen	Enercon E82 Wind Turbine [8] Hub Height: 82 m Rotor Diameter: 82 m Coefficient of performance of the wind turbine: 0.45	
	Biomass feedstock properties (KAS)	***Gasification parameters [9]***
Biomass hydrogen	Agricultural residues: grains, wheat, sugar beet, cotton, oil seeds and sunflower Moisture content: assumed to be 16% Crop residue to product ratios: specific for each crop type	Conversion rate of agricultural residues: 13.8 kg dry weight/kg H_2 Gasification pressure: 1.6 bar Gasification temperature: 870°C

RESULTS AND DISCUSSION

Estimated solar, wind, and biomass-based hydrogen production results are given in the unit of t/km^2/year, referred to as hydrogen production potential hereinafter.

The geographic analysis of solar electricity gave us the distribution of hydrogen potential across Kazakhstan: the lowest values were observed in the northern part of the country, whereas the highest ones were found in the southern Kazakhstan (Fig. 1). This pattern occurs due to higher horizontal solar irradiation in Shymkent, Turkestan, and Kyzylorda regions and is significantly lower in Petropavlovsk, Kostanay, and Aktobe. The former regions are located relatively closer to the equator, where the solar irradiation meets its peak. Thus, solar panels in South Kazakhstan can result in a hydrogen production potential of 3 800 to 4 100 t/km^2/year.

Overall hydrogen production potential from wind energy sources was similarly high across the country, ranging mainly from 10500 to 19000 t/km^2/year (Fig. 2). The tendency of average wind speed remaining at high levels comes from the continental climate in Kazakhstan and could be a promising energy source. However, the southern-eastern region is relatively lower at hydrogen production potential varying from 1900 to 6400 t/km^2/year. Such a difference occurs due to mountain landscapes that prevent the long flat ranges for developing high wind speed.

Fig. 3 depicts hydrogen production potential from gasification of residues of grain and legume, sugar beet, cotton, and oilseeds. High hydrogen production potential values up to 48 t/km^2/year resulted from cotton residues in South Kazakhstan. Oilseeds resulted in the hydrogen production potential of 11-19 t/km^2/year in numerous regions (Zhambyl, Northern Kazakhstan, Pavlodar, Almaty, Eastern Kazakhstan, Southern Kazakhstan). The hydrogen production potential of grain and legume and oilseed crop residues remains moderate (5-15 t/km^2/year) across the country.

Besides the growing interest in the deployment of renewable energy, hydrogen energy is also gaining momentum in Kazakhstan. Recently, German-Swiss company Svevind Energy GmbH announced the construction of a huge hydrogen production project in the Mangistau region that would launch in 2027-2031 [10]. Svevind Energy is willing to construct facilities that would benefit from wind and solar power stations for an estimated 30 GW capacity, which will produce 2 million tons of green hydrogen annually [10].

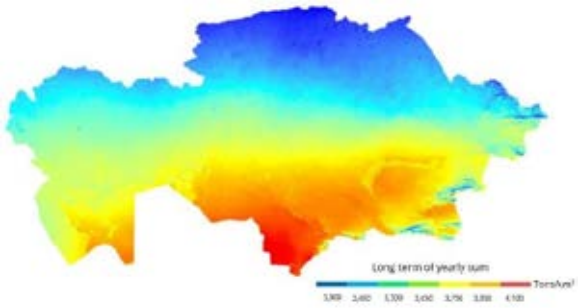


Figure 1. Solar hydrogen production per area

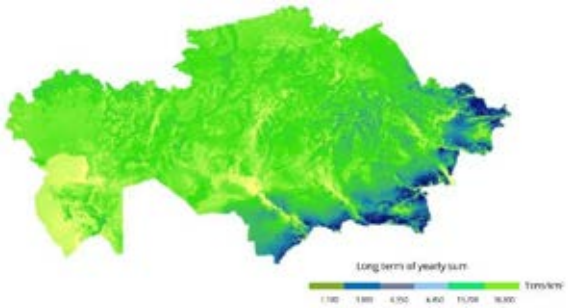


Figure 2. Wind hydrogen production per area

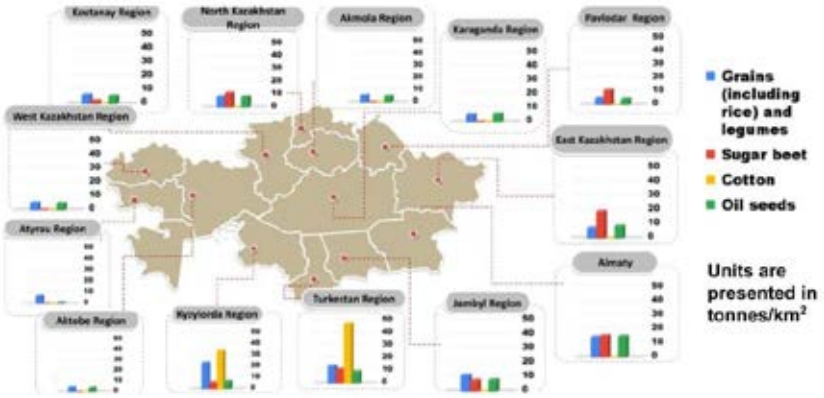


Figure 3. Biomass hydrogen production per area (biomass here refers to agricultural crop residues only)

ACKNOWLEDGEMENT

The study was supported by the Research Grants of Nazarbayev University (091019CRP2106 and 021220FD1051) and the Ministry of Education and Science of the Republic of Kazakhstan (APO9260229).

REFERENCES

1. Hydrogen Council and McKinsey. 2021. Hydrogen for Net-Zero: A critical cost-competitive energy vector.
2. World Energy Council. 2019. New hydrogen economy – hope or hype?
3. Karatayev, M. and Clarke, M.L., 2016. A review of current energy systems and green energy potential in Kazakhstan. *Renewable and Sustainable Energy Reviews*, *55*, pp.491-504.
4. Rahmouni S, et al. 2016. Prospects of hydrogen production potential from renewable resources in Algeria. International Journal of Hydrogen Energy 42:1383-1395.
5. Lepage, T., Kammoun, M., Schmetz, Q. and Richel, A., 2021. Biomass-to-hydrogen: A review of main routes production, processes evaluation and techno-economical assessment. Biomass and Bioenergy, 144, p.105920.
6. https://www.nrel.gov/gis/. Accessed on March 6, 2021
7. http://www.elysun.fr/pdf/elysun_250w_hr.pdf . Accessed on December 5, 2021
8. https://www.enercon.de/en/products/ep-2/e-82/. Accessed November 12, 2021
9. NREL, 2007. Potential for hydrogen production from key renewable resources in the United States.
10. https://kursiv.kz/news/otraslevye-temy/2021-08/kazakhstan-mozhet-stat-krupneyshim-proizvoditelem-vodoroda-v-mire-k . Accessed on December 29, 2021

WHEC-2022
23rd World Hydrogen Energy Conference
June 26-30, 2022 - Istanbul

#401

OPTIMIZATION OF A STAND-ALONE PV SYSTEM FOR EFFICIENT HYDROGEN PRODUCTION USING AN ALKALINE WATER ELECTROLYZER

[1*] *Victor Arturo Martinez Lopez,* [2] *Hesan Ziar,* [3] *Miro Zeman,* [4] *Olindo Isabella*
[1, 2, 3, 4] Delft University of Technology, Faculty of Electrical Engineering, Mathematics and Computer Science, Photovoltaic Materials and Devices, Mekelweg 4, 2628CD, Delft, The Netherlands

*Corresponding author e-mail: V.A.MartinezLopez@tudelft.nl

ABSTRACT

We present the analysis of the size and angle configuration of a solar photovoltaic (PV) plant connected to an alkaline electrolyzer without electrical storage nor support from the grid. Our approach is based on using the available energy in the most efficient way. To reach our objective, we allocated the available PV power to the stack and auxiliary components, then determined the produced hydrogen in one year. By defining 4 indicators, we determine that the PV plant should be oversized 1.6 times the rated power of the electrolysis stack. The orientation analysis of the PV modules shows that the optimal angles determined for maximum PV yield are not the same if other indicators are used and many of them are in conflict.

Keywords: Optimization, Energy efficiency, Green hydrogen

INTRODUCTION

Of all the production methods for hydrogen, water electrolysis is still a minority. In The Netherlands, water electrolysis contributed to only 1% of the produced hydrogen during 2021 [1]. If the country were to shift all of its production to electrolysis, a considerable amount of extra electricity is needed. To put things in context, the country needs 3.7 times more electricity than its goal for renewable energy set for 2030. For this reason, it is essential to ensure an energy efficient production of hydrogen. Previous studies have analyzed the optimization of PV-electrolysis systems targeting sizing of batteries, but ignoring the Balance-of-Plant[2]; optimizing grid connected systems [3], or optimizing the PV size for off-grid systems aiming at reducing the cost of hydrogen [4].

Our study contributes to the previous research by defining operation indices that describe the energy use of the electrolysis system. Our analysis leads to an optimization of the PV array. As we omit electric storage, the daytime available energy must be used as efficient as possible. We included the extra power needed to power the pumps, instrumentation and other equipment required to support the production of hydrogen. The PV array must meet the power demand of the electrolyzer and these additional components.

MODELLING METHODOLOGY

We modelled a PV-electrolyzer system to study the effect of plant size (in terms of nameplate power) and module angle configuration on the hydrogen production. We consider a fictitious horizontal PV plant located in Cabauw, The Netherlands. This system receives uniform irradiance and is connected to the electrolyzer by ideal power converters. Hence, we considered that the modules are always operating at maximum power point (MPP). All the generated power (P_{pv}) is consumed by the electrolyzer (P_{ele}) and Balance-of-Plant (P_{BoP}) (Eq. (1)). PV power that would violate the operating limits of the electrolyzer is curtailed.

$$P_{pv} = P_{ele} + P_{BoP} \quad (1)$$

The electrolyzer considered is a 100 kW, alkaline type and 186 cells (n_{cells}) in series. The stack voltage (V_{ele}) is modelled as a function of the applied current density (i) using Eq. (2) [5]. The operating limits lie within 20% of nominal current and 100% of nominal power. We assumed a constant operating temperature of 60 °C, considering that the power needed to keep this condition is absorbed by the Balance-of-Plant.

$$V_{ele} = n_{cells}(1.29 + 4.0468 \cdot i + 0.1803\, log(2.2709 \cdot i + 1)) \quad (2)$$

To support the operation of the electrolyzer, auxiliary components (pumps, power electronics) are included as Balance-of-Plant. These components consume power that is a percentage of the power demanded by the stack as in Eq. (3) [6].

$$P_{BoP} = 0.19276 \cdot P_{ele}^{0.249} \quad (3)$$

The performance of the system is measured using 4 indicators: (i) total produced hydrogen (kgH_2), (ii) system energy usage per kilogram hydrogen produced (kWh/kgH_2), (iii) wasted energy (kWh) and (iv) the utilization factor, defined as a ratio of the monthly energy used by the stack to the energy used if it was operated at nominal power during the same period.
The irradiance data was obtained from the Royal Meteorological Institute of the Netherlands (KNMI) and corresponds to the measurements of 2013 with a resolution of one minute.

RESULTS AND DISCUSSION

We first analyzed the oversizing of the PV-electrolyzer system. We kept the electrolyzer nominal power fixed while changing the PV nameplate capacity (kW) as a fraction of the electrolyzer's power. As seen in Figure 1, downsizing the electrolyzer (i.e., increasing the PV plant peak power) results in an improvement of all indices. The hydrogen production (Figure 1 (a)) benefits the most from an increased PV plant, in part due to a higher utilization of the electrolyzer (Figure 1 (d)). However, there is a limit in the PV plant size at which the energy is best utilized. This limit corresponds to a PV plant rated power that exceeds by 1.6 times the nominal power of the electrolyzer (Figure 1 (b)). The minimum wasted energy is achieved with a PV size that is 1.2 times larger in power than the electrolyzer (Figure 1 (c)).

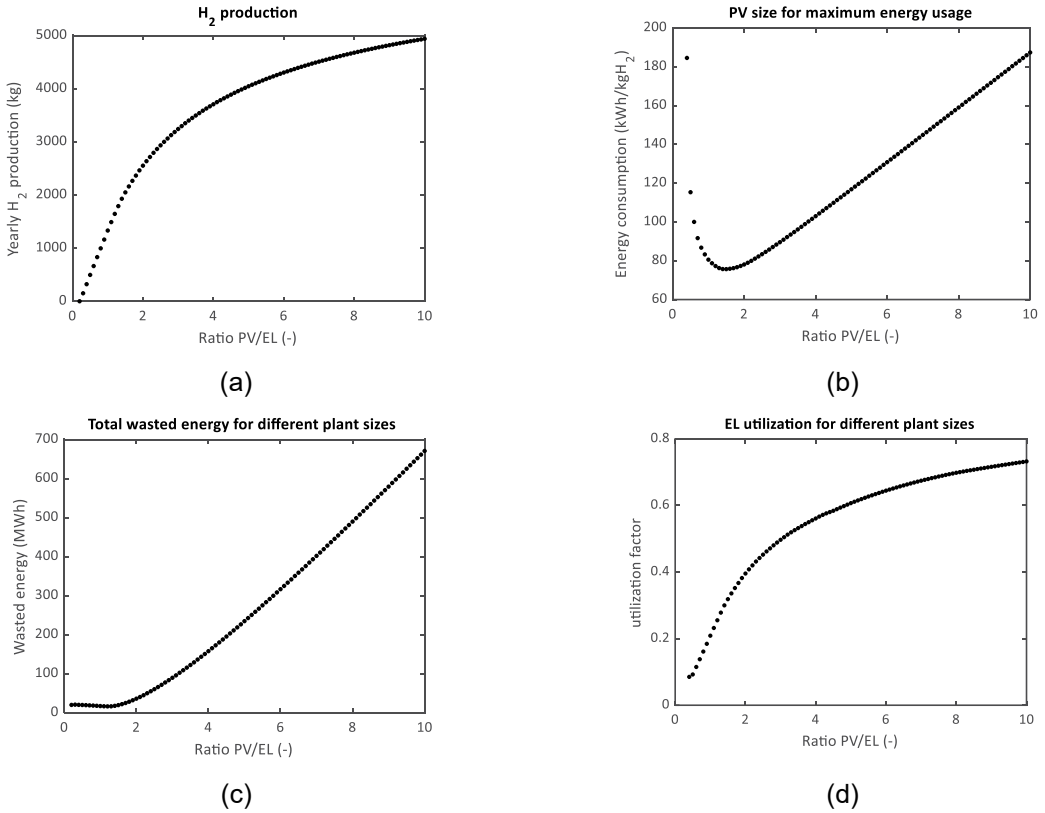


Figure 1. Analysis of PV rated power with respect to the electrolyzer nominal power. The horizontal axis shows a ratio of the two powers. Different indicators are analyzed. (a) hydrogen production, (b) the system efficiency expressed as a measure of the energy needed to produce 1 kg of hydrogen; (c) the energy that cannot be used for exceeding or not being enough to power up the process and (d) the amount of time the electrolyzer operates at nominal power .

We chose the ratio PV/electrolyzer that minimizes the utilization of energy (Figure 1 (b)) and studied the effect of different module orientations (azimuth and tilt) on the 4 indicators. Figure 2 shows the optimal module angles for each indicator. From the figure, it becomes clear that the indicators compete. In particular, setting the array at an optimal angle for minimizing the energy use can potentially reduce the produced hydrogen, but results also in lower wasted energy.

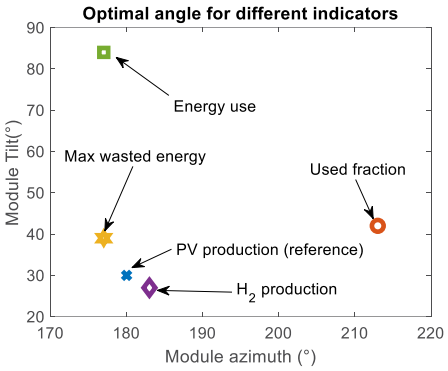


Figure 2. Optimal angles of the different indicators. The 'x' is the optimal angle for maximum PV production at the site and is included as a reference. Note that none of the indicators coincides with this configuration.

Even when increasing the PV size leads to an improved hydrogen production, the analysis of wasted energy imposes a limit on the oversize of the system. Note that this indicator never drops to zero even for very small PV systems as low power levels are not enough to start the electrolyzer, which remains off and hence curtailment is unavoidable. At an oversize ratio (PV power/electrolyzer rated power) of 1.2 the wasted energy is minimized. Interestingly, this is not the point for highest efficiency (oversize ratio of 1.6). At low power, the auxiliary components demand more energy, making the process more inefficient. The most efficient point occurs then when the correctly allocated to produce hydrogen, instead of supporting the Balance-of-Plant, at a cost of more energy spilled.

CONCLUSIONS

We presented an analysis and method for sizing a PV system connected to an alkaline electrolyzer and its auxiliary components. Our approach gives priority to a best utilization of the available energy from the Sun, trying to reduce the amount of unused energy. We found that spilling is unavoidable without storage. Further, minimizing the wasted energy can be detrimental for a high-efficiency process mainly due to the Balance of Plant. We found an optimal ratio of PV peak power to rated power of electrolyzer equal to 1.6.
We concluded a module orientation analysis concluding that the PV system should not be oriented aiming at maximum PV production but to a specific target. The selection of this target needs to be selected carefully as the module orientations are different for each one.

REFERENCES

1. https://www.energieinnederland.nl/ Accessed on:17-06-2021.
2. Gutiérrez-Martín, F., L. Amodio, and M. Pagano 2020 Hydrogen production by water electrolysis and off-grid solar PV. International Journal of Hydrogen Energy.
3. Karacavus, B. and K. Aydın 2020 Hydrogen production and storage analysis of a system by using TRNSYS. International Journal of Hydrogen Energy. 45: 34608-34619.
4. Yates, J., et al. 2020 Techno-economic Analysis of Hydrogen Electrolysis from Off-Grid Stand-Alone Photovoltaics Incorporating Uncertainty Analysis. Cell Reports Physical Science. 1: 100209.
5. Ulleberg, O. 2003 Modeling of advanced alkaline electrolyzers: a system simulation approach. International Journal of Hydrogen Energy. 28: 21-33.
6. Fragiacomo, P. and M. Genovese 2019 Modeling and energy demand analysis of a scalable green hydrogen production system. International Journal of Hydrogen Energy. 44: 30237-30255.

WHEC-2022
23rd World Hydrogen Energy Conference
June 26-30, 2022 - Istanbul

#411

EFFECT OF THE ADDITION OF HYDROGEN-CONTAINING GAS ON INDICATED AND EFFECTIVE PARAMETERS OF A GASOLINE ENGINE

[1*] *Jonas Matijošius,* [2] *Yurii Gutarevych,*[2] *Yevheniy Shuba,* [1] *Alfredas Rimkus,*[2] *Oleksander Syrota,*
[1]Vilnius Tech, J. Basanavičiaus str. 28, Vilnius, Lithuania
[2] National Transport University, Mykhaila Omelianovycha-Pavlenka Str. 1, Kyiv 01010

*Corresponding author e-mail: jonas.matijosius@vilniustech.lt

ABSTRACT

The article presents the results of a study of the effect of the addition of hydrogen-containing gas on the indicator and effective indicators of a gasoline engine. Experimental and numerical analysis studies of the combustion process in a gasoline engine when operating without additives and with the addition of different quantities of hydrogen-containing gas have been carried out. As a result, it was found that the addition of a hydrogen-containing gas leads to a reduction in the duration of the combustion process and an improvement in engine performance. The addition of hydrogen-containing gas leads to an increase in the indicated efficiency of the engine, the heat utilization factor and an increase in the indicated power. As a result of bench tests, an increase in the effective power and a decrease in the brake specific fuel consumption of the engine were found.

Keywords: hydrogen, hydrogen-containing gas, H_2/O_2, combustion process, indicated parameters, gasoline engine.

INTRODUCTION

Decreasing global oil reserves and pollution of the environment with exhaust gases from vehicle engines are prompting scientists around the world to look for ways to reduce the consumption of petroleum-based fuels and reduce the negative impact on the environment [1]. One of the promising areas is the use of additives obtained from renewable sources to improve the combustion of traditional fuels. The most promising additive is hydrogen, which is the most abundant substance in the universe [2]. In addition, the combustion of hydrogen produces water that does not have a negative impact on the environment.

It was found that with the addition of H_2/O_2 to a gasoline engine, which operates with an excess air coefficient λ = 0.92 - 0.94, the thermal efficiency of the engine increases by 1.2 - 5.6%. CO_2 and HC emissions are reduced by 30 and 40%, respectively. CO and NOx emissions are practically unchanged. When the engine is operating with an excess air ratio λ = 1.18 - 1.2, the thermal efficiency of the engine increases by 3 - 17%. HC, CO and CO_2 emissions are reduced by 67, 54 and 18%, respectively. In addition, the scientific novelty is the method of calculating the indicated parameters of the engine, taking into account the addition of hydrogen-containing gas.

RESEARCH METHOLOGY

Experimental studies were carried out in the engine testing laboratory of the Department of Engines and Heat Engineering of the National Transport University (Kyiv, Ukraine.). The object of research is Opel C30 NE engine with a working volume of 3.0 liters, with a gasoline injection system, on which a system for adding hydrogen-containing gas H2/O2 to the intake manifold is installed. To substantiate the improvement of fuel efficiency and environmental performance of a gasoline engine when using a hydrogen-containing gas as an additive, an indexing of the working process was carried out at various values of H_2/O_2 additives. A measuring device was developed to record gas pressure in the cylinder. The main element of the device is a high-temperature strain gauge pressure transducer 6 MIDA-DI-12P-081. Hydrogen-containing gas was obtained using an ATW-1000 electrolysis unit, which operates from an external current source with a voltage of 220 V. The amount of hydrogen-containing gas added to the air charge was varied in the range from 0 to 7.88% of the mass fuel consumption (the H_2/O_2 flow rate was varied from 0 to 9.5 l/min). To confirm the reliability of the obtained characteristics, the characteristic of fuel burnup was calculated according to the expression of Vibe [3]:

$$x = 1 - e^{-6.908 \cdot \left(\frac{\varphi - \varphi_{s.c.}}{\Delta \varphi_c} \right)^{m+1}} \quad (1)$$

where φ – angle corresponding to the moment of ignition crank angle, deg.;
$\varphi_{s.c.}$ – start of combustion, deg;
φ_z $\varphi_{c.d.}$ – combustion duration, deg;

m – an indicator of the nature of combustion, is determined by enumerating numerical values in order to obtain a theoretical characteristic of heat release as close as possible to the experimental curve of the characteristic of fuel burnup.

RESULTS AND THEIR ANALYSIS

In fig. 1 shows indicated parameters diagrams when the Opel C30NE engine is running on gasoline and when the engine is running with the addition of 7.88% hydrogen gas based on the mass fuel consumption. Also, the dependences of changes in pressure, temperature, characteristics of heat release and heat utilization on the angle of rotation of the crankshaft are shown. As can be seen from Fig. 2, when the engine switches to a power supply with the addition of a hydrogen-containing gas, the total duration of the combustion process is reduced from 73.35 deg to 69.4 deg. In this case, the main phase (phase II) has the main effect on the duration of the combustion process, which decreases by 3.36 deg. The initial combustion phase (phase I) and the later burning phase on the expansion line (phase III) decrease relatively insignificantly: by 0.085 and 0.026 deg., respectively.

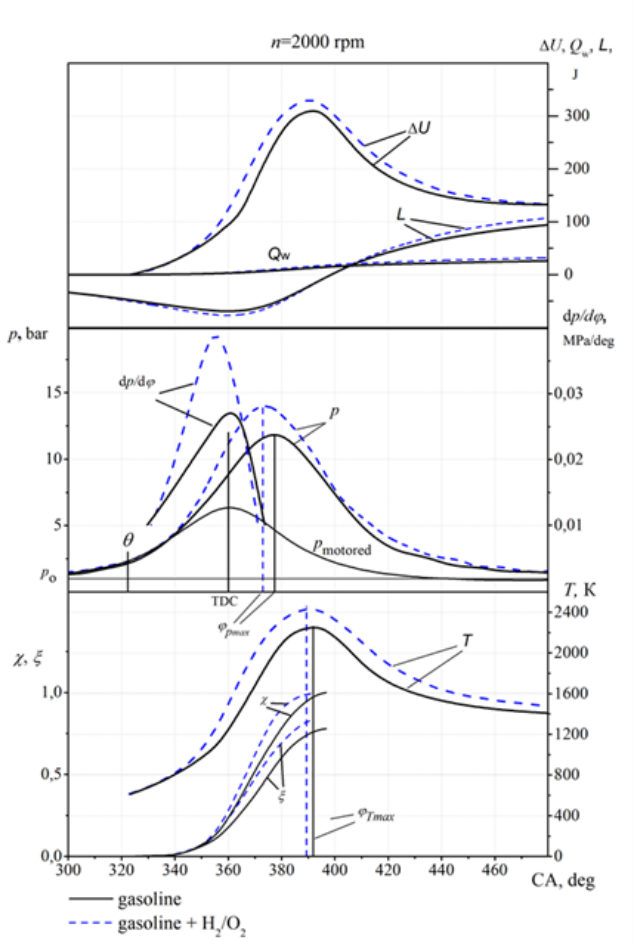


Fig. 1 Indicated parameters of the engine Opel C30NE when the engine is running only on gasoline and on gasoline with the addition of hydrogen-containing gas

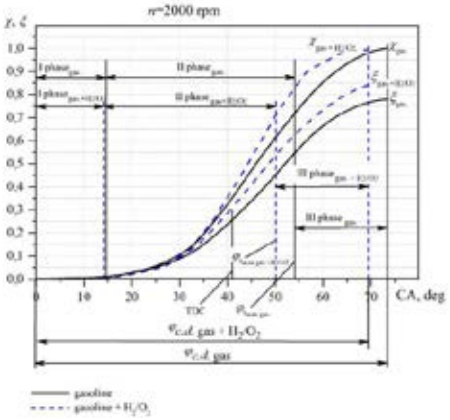


Fig. 2 Characteristics of heat release and heat use of the engine Opel C30NE when the engine is running on gasoline and with the addition of hydrogen-containing gas H_2/O_2

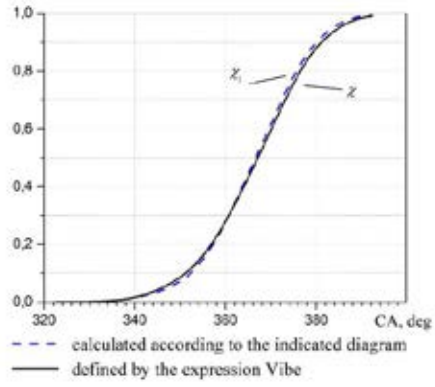


Fig. 3 Characteristics of heat release of the engine Opel C30 NE with the addition of hydrogen-containing gas; χi – calculated according to the indicated diagram, χ – defined by the expression Vibe

An example of the calculated characteristics of fuel burnup according to the expression Vibe when the engine is running with the addition of a hydrogen-containing gas, it is shown in Fig. 3. As can be seen, the curves of heat release characteristics obtained by different methods differ insignificantly, which indicates the reliability of the results of calculation studies.

The results of processing the indicated parameters diagrams of the working process of the Opel C30 NE engine when the engine is running on gasoline and with the addition of hydrogen-containing gas are given in Table 1.

Table 1. The results of processing the indicated parameters diagrams of the working process of the engine Opel C30 NE when running on gasoline and with the addition of hydrogen-containing gas

Workflow parameters	**Gasoline**	**Gasoline+ H_2/O_2**
Vacuum in the intake manifold Δp_m, kPa	59	59
Ignition advancing angle θ, deg. before TDC	41	41
The maximum pressure p_{max}, bar	11.82	13.98
The maximum temperature T_{max} , K	2260.3	2456.5
Duration of the initial phase of combustion φ_I, deg.	14.7	14.1
Duration of the second (main) combustion phase φ_{II}, deg.	39.4	36.0
Coefficient of active heat release in TDC, χ_0	0.24	0.26
Active heat release coefficient at p_{max}, χ_{pmax}	0.72	0.715
Active heat dissipation coefficient at T_{max}, χ_{Tmax}	0.97	0.99
Heat utilization coefficient in TDC, ξ_0	0.175	0.215
Heat utilization coefficient at p_{max}, ξ_{pmax}	0.55	0.55
Heat utilization coefficient at T_{max}, ξ_{Tmax}	0.755	0.82
The angle of rotation of the crankshaft from TDC to p_{max}, deg.	17.37	13.0
The angle of rotation of the crankshaft from TDC to T_{max}, deg.	31.85	29.4
The duration of the combustion process $\varphi_{c.d}$, deg.	73.35	69.4
Maximum rate of pressure rise $dp/d\varphi$, MPa / deg	0.0272	0.04

CONCLUSIONS

It was found that the addition of hydrogen-containing gas H_2/O_2 has a positive effect on the indicated parameters of a gasoline engine. When the engine is running with 7.88% hydrogen-containing gas added to the fuel mass flow rate, the maximum cycle pressure increases from 11.82 bar to 13.98 bar (~15%). This was due to the higher rate of hydrogen combustion and the more complete oxidation process of the fuel.

The duration of the combustion process is reduced from 73.35 degrees to 69.4 degrees. In this case, the second (main) phase has the largest influence on the duration of the combustion process, which decreases by 3.36 deg. The first (initial) and third (later) combustion phases are reduced comparatively slightly. At the moment of maximum pressure, there is an increase in the heat utilization coefficient at the end of the third combustion phase from 0.78 to 0.84 due to the optimization of the combustion process.

REFERENCES

[1] Bereczky, A., 2017. The Past, Present and Future of the Training of Internal Combustion Engines at the Department of Energy Engineering of BME, in: Jarmai, K and Bollo, B (Ed.), VEHICLE AND AUTOMOTIVE ENGINEERING, Lecture Notes in Mechanical Engineering. pp. 225–234. https://doi.org/10.1007/978-3-319-51189-4_22

[2] Gutarevych, Y., Shuba, Y., Matijošius, J., Karev, S., Sokolovskij, E., Rimkus, A., 2018. Intensification of the combustion process in a gasoline engine by adding a hydrogen-containing gas. Int. J. Hydrog. Energy 43, 16334–16343. https://doi.org/10.1016/j.ijhydene.2018.06.124

[3] Vibe, I., 1962. Novoe o rabochem tsikle dvigatelei : skorost' sgoraniia i rabochii tsikl dvigatelia [Новое о рабочем цикле двигателей. Скорость сгорания и рабочий цикл двигателя- New about the duty cycle of engines. Combustion rate and engine duty cycle.

WHEC-2022
23rd World Hydrogen Energy Conference
June 26-30, 2022 - Istanbul

#412

HYDROGEN AND OXYGEN (HHO) GAS INFLUENCE ON ENGINE CHARACTERISTICS WHILE FUELED ON PETROL ANT BIOETHANOL LEAN MIXTURES

[1*] *Gabrielius Mejeras,* [1,2] *Alfredas Rimkus,* [1,2] *Jonas Matijošius*
[1]Vilnius Tech, J. Basanavičiaus str. 28, Vilnius, Lithuania
[2]Vilnius College of Technologies and Design, Antakalnio str. 54, Vilnius, Lithuania

*Corresponding author e-mail: gabrielius.mejeras@vilniustech.lt

ABSTRACT

As ecological requirements getting stricter and the new manners of decreasing emissions of pollutants are being researched. One of them is to focus the usage none or small count of carbon fuels as a fuel for internal combustion engine. Therefore, usage perspective of bioethanol with HHO gas as an additive fuel to petrol lean mixtures, is presented in this research. Ecological (CO, CO_2, HC, NO_x) and energetic (M_B, B_f, BTE) parameters were measured when using petrol ant bioethanol mixtures (E10 and E70) enriched with HHO gas. Experimentation was done by using spark ignition engine changing the ignition timing from 16° to 42° BTDC and changing stoichiometric mixture (λ = 1.0) to a lean (λ = 1.1; 1.2; 1.3; 1.4). Hydrogen and oxygen gases are produced using mobile electrolysis unit – HHO gas generator. It was concluded that for all air / fuel ratios tested the maximum torque was reached with 70% bioethanol additive to petrol, HHO gas has positive effect when mixtures are lean. The NO_X emission has increased, however CO, CH and CO_2 were lower when HHO was supplied.

Keywords: petrol, bioethanol, HHO, hydrogen, combustion.

INTRODUCTION

Modern development trends in motoring are focused on the greening of vehicles - the promotion of less polluting vehicles, but also the substitutability of vehicles and the economic aspect of their use. These issues call for alternatives to be sought in transforming the current fleet of vehicles from fossil fuels to alternatives that generate less CO_2. Various new generation fuels, such as Hythane (a mixture of hydrogen and natural gas) and biomethane, serve this purpose (“Biomethane CNG hybrid,” 2011). Thus, there remains a need to use more affordable alternative fuels such as methane (Biomethane) (Abdul Rahman and Ramesh, 2017), hydrogen (can be used pure or in the form of HHO)
Another product used in spark ignition engines is bioethanol. Its use is currently widespread and is regulated as a mandatory additive to petrol (up to 10%) throughout the European Union (AEE., 2019). As a fuel, bioethanol in a spark ignition engine increases combustion efficiency, cylinder pressure, cylinder temperature and flame rate. It also reduces combustion time, combustion rate, combustion temperature and maximum heat release rate (HRR)(Thangavelu et al., 2016).

In summary, the additional supply of HHO gas without the need for additional modifications to the engine systems is very promising in trying to address some aspects of engine performance when it comes to the use of bioethanol and gasoline blends. These would be ecological aspects like reducing the emissions of PN cells. On the other hand, a decrease in the burning rate with lean bioethanol and gasoline blends has been found in the literature, and low levels of HHO should address this issue. An analysis of the literature shows that the use of such fuel blends (bioethanol and gasoline blends and in addition to HHO gas) is still poorly researched, but the topic is very promising.

RESEARCH METHOLOGY

The experiment investigates the effect of hydrogen and oxygen (HHO) gas on the energy and environmental performance of a spark ignition (SI) engine, when conventional fuels E10 (90% petrol / 10% ethanol by volume) is replaced by E70 (30% petrol / 70% ethanol by volume). The test was performed using a Nissan Qashqai SI engine HR 16DE.
Engine is controlled by MoTeC M800 programmable electronic control unit (ECU), the engine load is created using AMX 200/100 load stand.

Fuel mixtures E10, E70 are prepared by mixing pure petrol (produced at the ORLEN Lithuania refinery) and bioethanol (produced at the JSC Kurana bioethanol plant).
A constant flow of (3.8 l / min) HHO gas is additionally supplied to the engine trough the intake manifold. HHO gas is produced using an electrolysis unit that uses an external energy source. The electrolyte consists of 4% KOH alkali and distilled water mixture. The unit uses 700 W of power, this power is evaluated to determine the brake thermal

efficiency of the engine. Specific electrical power for HHO gas production 184 W / (l / min). HHO gas consists of a stoichiometric mixture of H_2 and O_2 gases, which the volume of hydrogen occupies 2/3 and oxygen 1/3 of the total volume in the mixture (https://doi.org/10.1016/j.energy.2018.03.087). An anti-backfire device was installed in the gas supply system to protect the HHO unit from the reverse flame from the intake manifold. The low density of hydrogen (ρ_{H2} = 0.09 kg / m^3) compared to oxygen (ρ_{O2} = 1.43 kg / m^3) results in a mass fraction of H_2 and O_2 in the HHO gas mixture of 0.111 and 0.889, respectively. With HHO gas flow of 3.8 l / min, H_2 and O_2 gas are supplied at ~ 0.0137 kg / h and 0.1087 kg / h, respectively. After estimating the H2 flow and the LHV, the additional energy supplied to the engine is 1,642 MJ / h, which corresponds to a power of 456 W. This means that the efficiency of the HHO generator used is ~ 0.65.

RESULTS AND THEIR ANALYSIS

Engine power indicators

Break thermal efficiency (*BTE*) was highest running E10 when λ = 1.1 (1.9% more compared to E10 when λ = 1.0) (Fig.1). Using E10 when λ = 1.0–1.2 the HHO gas did not have a major impact on BTE, when λ = 1.3–1.4 a positive effect of HHO gas is observed, but the BTE remains lower compared to E10 when λ = 1.1. We only see a better result when using lean high ethanol mixture E70 with HHO gas. Oxygen in ethanol and hydrogen and oxygen in HHO gas increased the burning rate of the lean mixture. The maximum positive effect of HHO is when E70 + HHO and λ = 1.4. In this case, the BTE increases by ~ 2% compared to E70 when λ = 1.0, and increases by ~ 3.1% compared to E10 when λ = 1.0.

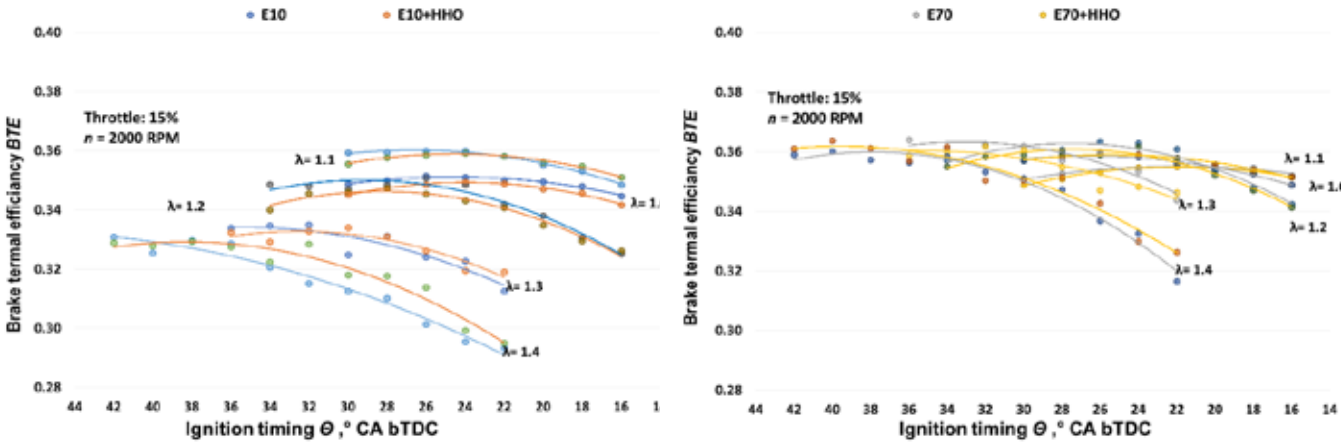


Fig. 1 Brake thermal efficiency running on different fuel blends, changing spark timing

Engines ecological indicators

The ecological performance of the engine is calculated by looking at the specific emissions (g / kWh), changing the fuel and excess air ratio changes the engine power.

Changing E10 fuel to E70 and changing the air excess ratio from 1.0 to 1.4 reduces CO_2 emissions by 1–3% (Fig. 2). This is due to the lower C / H ratio and higher BTE of the E70 fuel. The additional use of carbon-free HHO reduces CO_2 emissions by 0.3-1.5% and is close to the share of hydrogen energy in fuels.

Lowest CO_2 emissions are achieved with the engine running E70 + HHO at λ = 1.4, as these fuels have the lowest C / H ratio and the highest BTE (Fig. 1), but the brake torque achieved by the engine is reduced. The next best option is to use E70 + HHO when λ = 1.0. In this case, CO_2 emissions are up to 2.7% lower compared to E10, optimal ignition timing is similar to E10, and brake torque increases by 2.2%.

CONCLUSIONS

Experimental tests on SI engines running on petrol-bioethanol mixtures of E10 and E70 were performed at 2000 rpm with the throttle open at 15%, changing the ignition timing and the air excess ratio (λ = 1.0, 1.1; 1.2; 1.3; 1.4). Adding an additional 3.8 l / min HHO gas to the intake manifold. The share of hydrogen energy in the fuel during leaning of the mixture varies from ~ 1.2% to ~ 1.8%.

Increasing bioethanol concentration in the fuel mixture from 10% to 70% decreases the C / H ratio by 22%, increases the oxygen concentration by 6.7 times, increases the stoichiometric air to fuel ratio by 24.5%, decreases the lower heating value by 24.0% (mass) and 20.7% (volume) the octane number of the fuel increases, and the evaporation of

bioethanol cools the intake fuel mixture better. Hydrogen in HHO gas reduces the C / H ratio, increases lower heating value and burns.

With the engine running at the set air excess ratio, the E70 injects 18 to 20% more fuel than the E10. Depending on the operating conditions, the torque was 2… 10% higher using E70. For E10 fuel, the maximum thermal efficiency is reached when λ = 1.1 and leaning the mixture efficiency decreases. The BTE of E70 does not decrease even in the case of very lean mixtures (λ = 1.3; 1.4). In the case of E70 + HHO (λ = 1.4), HHO gas accelerates combustion and BTE increases by ~ 2% compared to E70 when λ = 1.0, and by ~ 3.1% compared to E10 when λ = 1.0.

E70 fuel CO_2 emissions are 1–3% lower compared to E10, and the addition of HHO additive lowers it by 0.3–1.5%. In regard to CO_2 emissions it is more rational to use E70 with HHO, when λ = 1.0, since without changing ignition timing CO_2 emissions are reduced by 2.7% and brake torque is increased by 2.2%, while comparing with E10.

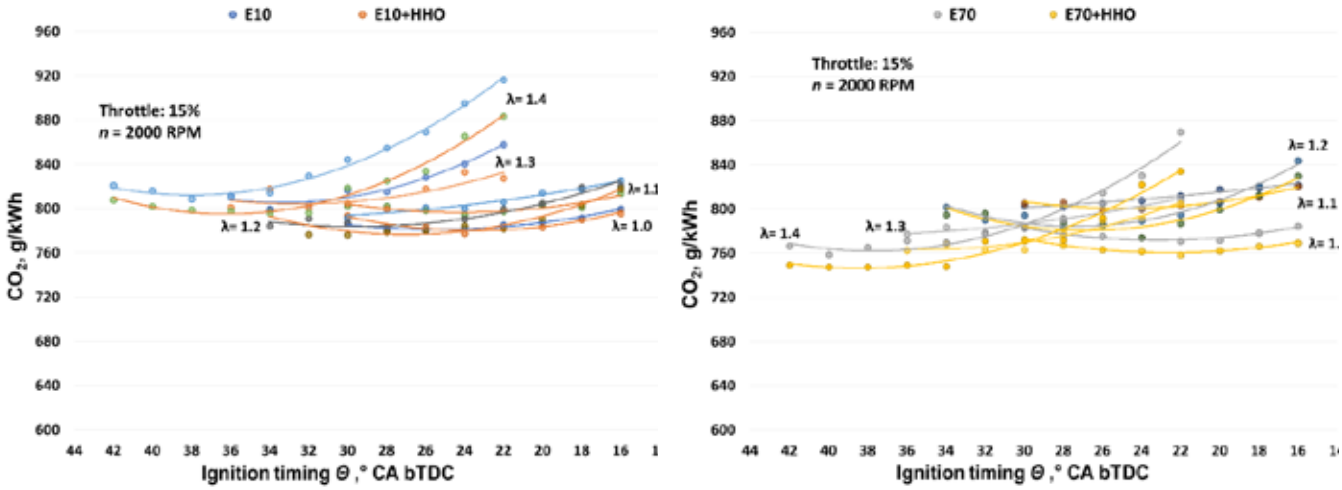


Fig. 2 CO_2 emission running on different fuel blends, changing spark timing

REFERENCES

Abdul Rahman, K., Ramesh, A., 2017. Effect of reducing the methane concentration on the combustion and performance of a biogas diesel predominantly premixed charge compression ignition engine. Fuel 206, 117–132. https://doi.org/10.1016/j.fuel.2017.05.100

AEE., 2019. The European environment: state and outlook 2020 : knowledge for transition to a sustainable Europe. Publications Office, LU.

Biomethane CNG hybrid: A reduction by more than 80% of the greenhouse gases emissions compared to gasoline, 2011. . J. Nat. Gas Sci. Eng. 3, 617–624. https://doi.org/10.1016/j.jngse.2011.07.007

Thangavelu, S.K., Ahmed, A.S., Ani, F.N., 2016. Review on bioethanol as alternative fuel for spark ignition engines. Renew. Sustain. Energy Rev. 56, 820–835. https://doi.org/10.1016/j.rser.2015.11.089

WHEC-2022
23rd World Hydrogen Energy Conference
June 26-30, 2022 - Istanbul

#428

EXPERIMENTAL STUDY ON SPRAY CHARACTERISTICS OF INTERNAL MIXED HYDROGEN-ASSISTED FUEL INJECTION SYSTEM

[1] Zenghui Liu , [1*] Tao Qiu , [1] Yan Lei
[1] Department of Automotive Engineering, Beijing University of Technology, Beijing 100124, China

*Corresponding author e-mail: qiutao@bjut.edu.cn

ABSTRACT

Hydrogen-assisted diesel injection is suitable for low-power and high-power-to-weight ratio in-cylinder piston direct injection engines. The jet characteristics of hydrogen-assisted diesel direct injection have an important effect on engine performance. The effects of fuel injection duration and mixture duration, hydrogen pressure and fuel/hydrogen premix time on spray penetration distance and diffusion area were qualitatively analyzed by high-speed photography on a constant volume chamber test bench. The results show that increasing the fuel injection duration increases the penetration distance and decreases the spray projection area. Increasing hydrogen pressure will increase both penetration distance and spray projection area. Increasing the duration of air injection will increase the penetration distance and decrease the spray area. The spray area increases with the increase of fuel/hydrogen premixing time, and tends to be stable when the premixing time is 3ms, which has no effect on the spray penetration distance.

Keywords: Piston engine, Hydrogen-assisted injection system, Direct injection, Diesel, Spray characteristics

INTRODUCTION

The development of high-altitude small aircraft has received unprecedented attention worldwide due to the demand of future information warfare[1]. Gas-assisted fuel injection is suitable for high-altitude small aircraft [2]. Hydrogen is considered as the most ideal clean energy because of its high calorific value per unit mass, fast combustion rate and no pollution to the environment[3,4]. Hydrogen-assisted fuel injection can help improve fuel atomization effect and combustion performance, improve engine performance and reduce exhaust emissions.The experimental research by Wu et al.[5] showed that the air-assisted spray tends to produce smaller droplet size and more uniform distribution. Bai et al.[6] studied the influence of injection duration on spray characteristics and pointed out that increasing air injection volume could improve fuel atomization effect and significantly reduce the sauter mean diameter (SMD) of spray.

In this paper, hydrogen/fuel internal mixture injector is designed, and experimental research is carried out under different control parameters. Diesel spray penetration distance and spray projection area are used for quantitative analysis, which provides a certain theoretical basis for the application and parameter matching of hydrogen-assisted injection in practical engines.

EXPERIMENTAL SETUP AND METHODOLOGY

As shown in Fig. 1, the experimental apparatus for hydrogen-assisted fuel spray characteristics mainly include visual constant volume chamber system, hydrogen-assisted fuel injection system, intake and exhaust system, schlieren imaging system, high-speed camera and image acquisition system.

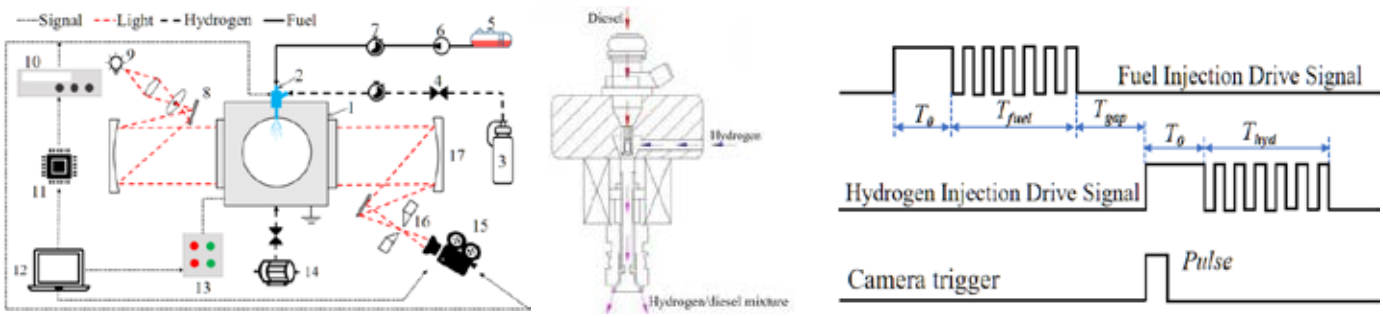


Fig. 1. Schematic diagram of test bench, fuel and air assisted signal control timing. (1) constant volume chamber, (2) gas-assisted nozzle, (3) hydrogen container, (4) relief valve, (5) fuel tank, (6) fuel pump, (7) pressure gage, (8) minor reflector, (9) light source, (10) synchronizing signal generator, (11) ECU, (12) computer, (13) temperature controller, (14) exhaust system, (15) high-speed camera, (16) knife edge, (17)main reflector.

Fig. 1 illustrates the timing phase diagram of the nozzle of the hydrogen-assisted fuel injection system and the driving signal of the high-speed camera. Nozzle signal T_{fuel} is the fuel injection duration, T_{gap} is the fuel/hydrogen premix time, and mixture nozzle opening signal T_{hyd} is the mixture injection duration.

In order to quantitatively analyze the spray morphology of hydrogen assisted injection, the parameters of spray penetration distance and spray diffusion area were introduced. Spray penetration distance refers to the distance from the nozzle to the furthest end of spray, and spray diffusion area refers to the total distribution area of spray in space (longitudinal section), as shown in Fig. 2. The test was repeated 5 times for each test condition and the average was used to determine the penetration distance and diffusion area. Through MATLAB programming software, the spray images are binarized. Diesel was used as fuel in this study, and the test conditions are shown in Table 1.

Table 1. Experiment conditions

Parameter (unit)	Value
Ambient pressure (MPa)	0.1
Fuel injection pressure (MPa)	1
Fuel injection duration (ms)	2/3/4/5
Hydrogen injection pressure (MPa)	0.6/0.7/0.8/0.9
Hydrogen injection duration (ms)	2.5/3.5/4.5/5.5
Interval of fuel and hydrogen (ms)	1/2/3/4

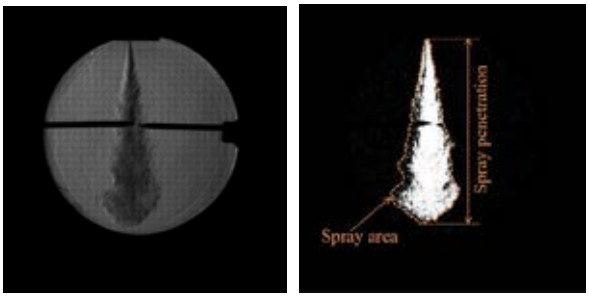


Fig. 2. Spray picture, spray characteristic definition.

RESULTS AND DISCUSSION

Fig. 3 shows that the increase of fuel injection duration will lead to the decrease of spray penetration distance and the increase of spray area. Because a large amount of gas kinetic energy is converted into fuel droplet kinetic energy and surface energy in the premixed chamber, the first atomized fuel is accelerated in this process. The increase of single injection amount leads to the increase of hydrogen fuel ratio in the premixed chamber, and the increase of fuel content in the mixture reduces the motion capacity of compressed hydrogen, which reduces the jet kinetic energy of the mixture to a certain extent. Increasing the fuel injection duration weakens the atomization effect of compressed hydrogen on fuel in the premix chamber, and the spray particle size will increase. The edge of the fuel vapor spray field that is not easy to be vaporized and gasified will be easier to identify, and the spray area will also increase.

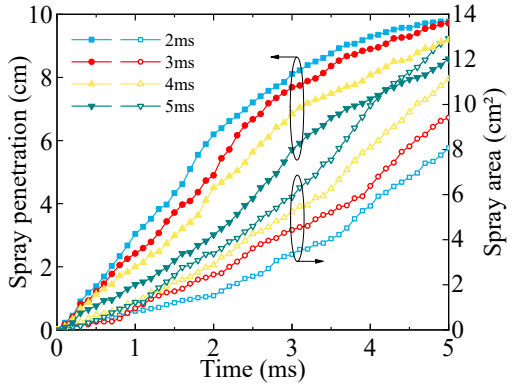


Fig. 3. Different duration of fuel injection.

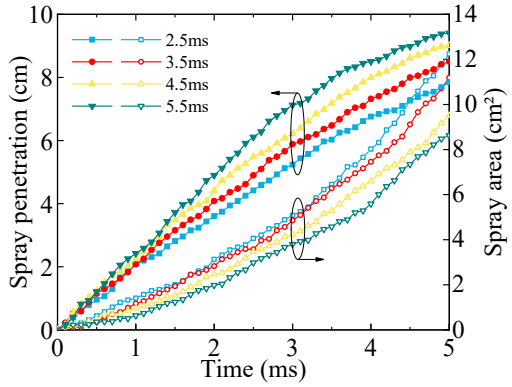


Fig. 4. Different fuel/hydrogen mixture injection duration.

As shown in Fig. 4, the spray penetration distance increases with the increase of injection mixture duration, while the spray area is on the contrary. This is because the mixture duration increases, the amount of high-pressure hydrogen injected into the cylinder increases, and the interaction time between droplet and compressed hydrogen increases, which accelerates the droplet movement and increases the penetration distance. At the same time, the time for hydrogen to flow through the nozzle is prolonged, which increases the capacity of spray expansion and breakage and reduces the spray particle size, which is conducive to the rapid evaporation of fuel. After the evaporation and vaporization of fuel, the spray width will be reduced, which leads to a smaller spray area.

Fig. 5 shows that under different hydrogen pressures, spraying is divided into two different stages: in the first stage, the spraying speed is large and the spray penetration distance increases rapidly; In the second stage, the spray speed decreases obviously and the spray development becomes slow. The higher the hydrogen pressure is, the greater the initial kinetic energy will be when entering the constant volume indoor spray. In the case of the same environmental pressure, the resistance will be the same and the through-distance will be larger. The projection area of spray increases linearly with time under different air injection pressures. The spray projection area is mainly affected by two factors: the axial distance (that is, the through-distance) along the spray and the radial development distance. As the air injection pressure increases, the axial distance increases, and the radial development generally shows an increasing trend, so the spray projection area also increases.

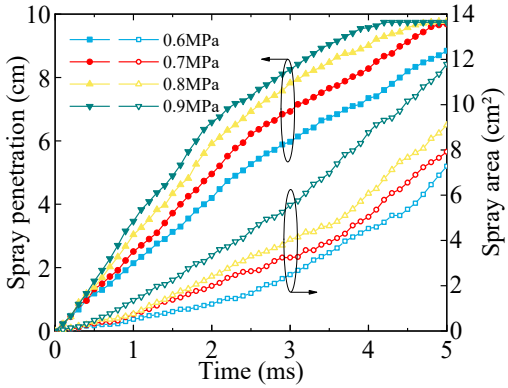


Fig. 5. Different hydrogen injection pressures.

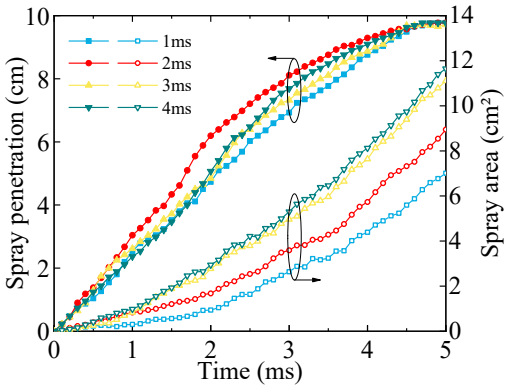


Fig. 6. Different fuel/hydrogen mixing times.

According to the comparison in Fig. 6, the mixing time of fuel/hydrogen hardly affects the spray penetration distance, because the pressure difference at both ends of the mixture nozzle is not changed, and the initial spray velocity does not change, and the penetration distance does not change significantly under the same environmental back pressure. If the mixture nozzle is opened immediately after fuel injection, the atomization effect of spray is relatively poor. With the increase of mixing time, the spray area increases, but when the interval time is more than 3ms, the change of spray area slows down. In other words, the spray area increases and tends to be stable with the increase of mixing time.

CONCLUSIONS

In this paper, the spray characteristics of hydrogen-assisted fuel were experimentally studied, including the effects of fuel injection duration, mixture injection duration, hydrogen pressure and fuel/hydrogen premix time on spray characteristics. From the results, it can be concluded that:

- When the fuel/hydrogen premix time is 3ms, the liquid fuel and compressed hydrogen can be fully mixed and the atomization effect is the best.
- The hydrogen assisted injection penetration distance is similar to the traditional single fuel injection. The spray penetration distance presents a two-stage development trend, and the spray projection area mainly presents a linear growth trend. Increasing hydrogen pressure and mixture injection duration can improve spray penetration and fuel atomization.
- Reducing the injection pulse width or increasing the injection pulse width can promote the ability of the oil beam to run through the direction of the injection hole. At the same injection time, the spray penetration distance tends to increase, which helps the mixture of liquid fuel and compressed hydrogen to be completely ejected by the mixture ejector.

REFERENCES

1. Boukoberine MN, Zhou ZB, Benbouzid M. 2019. A critical review on unmanned aerial vehicles power supply and energy management: Solutions, strategies, and prospects. Appl Energy 255:113823.
2. Ning L, Duan QM, Wei YH, et al. 2019. Effects of injection timing and compression ratio on the combustion performance and emissions of a two-stroke DISI engine fuelled with aviation kerosene. Appl Therm Eng 161:114124.
3. Abe JO, Popoola API, Ajenifuja E, Popoola OM, et al. 2019. Hydrogen energy, economy and storage:review and recommendation. International Journal of Hydrogen Energy 29:15072-15086.
4. Wang MJ, Wang GZ, Sun ZX, et al. 2019.Review of renewable energy-based hydrogen production processes for sustainable energy innovation. Global Energy Interconnection 5:436-443.
5. Bai HL, Hu CM, Li ZJ, et al. 2016. Effect of air injection quantity on spray characteristics of an air-assisted direct injector. Journal of Tianjin University 49:206-212.
6. Wu H, Zhang FJ, Zhang ZY, et al. 2021. Fundamental spray characteristics of airassisted injection system using aviation kerosene. Fuel 286:119420.

WHEC-2022
23rd World Hydrogen Energy Conference
June 26-30, 2022 - Istanbul

#435

ANALYSIS OF AN INTEGRATED GAS TURBINE-LOCOMOTIVE ENGINE USING SUSTAINABLE FUEL BLENDS WITH HYDROGEN

[1*] *Shaimaa Seyam,* [1] *Ibrahim Dincer,* [1] *Martin Agelin-Chaab*
[1] Clean Energy Research Laboratory (CERL), Faculty of Engineering and Applied Science Ontario Tech University 2000 Simcoe Street North, Oshawa, Ontario, L1H 7K4, Canada

*Corresponding author e-mail: Shaimaa.seyam@ontariotechu.net

ABSTRACT

Greenhouse gas emissions have led to the imminent global warming crisis, which has motivated scientists and engineers to search for creative solutions for this problem. Rail transportation is known to emit greenhouse gases because of its reliance on fossil fuels. This paper investigates an integrated design of a locomotive engine to replace the traditional internal combustion engines. The integrated system consists of a gas turbine with double compressors and double turbines, two fuel cells, and an energy recovery system including two thermoelectrical generators and an absorption refrigeration system. The proposed engine is analyzed thermodynamically to examine its performance using methane and hydrogen fuel blends. It was found that the integrated engine can generate 9 MW of total power, which is threefold of the traditional locomotive engines with 70.6% of thermal efficiency and 42% of exergetic efficiency.

Keywords: Locomotive engine, Fuel cells, Energy recovery system, Thermodynamic analysis.

INTRODUCTION

The COVID-19 pandemic alerted the world to the severe impact of global warming, and a major contributor to this impact is the transportation sector due to its dependency on fossil fuels [1]. Tremendous efforts are made to develop and redesign transportation engines in different sectors in order to reduce carbon emissions and improve engine performance. Hybridization and new design engines are introduced to rail transportation, including fuel cells, batteries, new efficient engines instead of internal combustion engines (ICE), and alternative fuels. For example, Akhoundzadeh et al. [2] studied a hybridized train operated by lithium-ion battery and proton exchange membrane fuel cell (PEMFC). They utilized a blend of diesel and hydrogen fuels at various ratios for diesel multiple unit (DMU) rail commuters. Seyam et al. [3] proposed a hybridized locomotive engine, which involves ICE, gas turbine, and molten carbonate fuel cell with clean fuels such as hydrogen and hydrocarbons. The overall engine power is increased by 25%, with 43% and 55% of energetic and exergetic efficiencies, respectively. Moreover, Locomotive engines release massive heat as heat loss, which reduces the overall thermal efficiency. A convenient approach is to apply an energy recovery system by converting thermal energy into electrical energy using thermoelectric generators (TEG). For instance, Ma et al. [4] constructed a platform of 32 TEG units around an exhaust pipe of a truck. The inlet mass flow rate varied from 12 to 24 kg/h, and inlet temperature changed from 100 ℃ to 300℃. The units can produce 0.66 to 3.17 W of electricity with an efficiency of 0.67%. The main objective of the current paper is to propose a new powering system for locomotives consisting of a gas turbine with two compressors and three turbines, fuel cells such as high-temperature proton exchange membrane fuel cell (PEMFC) and solid oxide fuel cell (SOFC), an energy recovery system including two thermoelectric generator (TEG) and an absorption cooling system (ARS). The proposed new engine design uses a methane and hydrogen blend and is investigated thermodynamically to examine its performance and compare it with the EMD 16-710G3 of 3355 kW traditionally used for Canadian rail transportation.

SYSTEM DESCRIPTION AND ANALYSIS

The proposed locomotive engine design is presented in **Error! Reference source not found.**. This design consists of an intercooled gas turbine system, an energy recovery system, and a fuel cell system. The gas turbine comprises two compressors (C1 and C2), two turbines (T1 and T2), an intercooler (IC), a combustion chamber (CC), and an afterburner (BR). The fuel cell system involves a high-temperature proton exchange membrane (PEMFC) and solid oxide fuel cell (SOFC). The energy recovery system contains two thermoelectric generators (TEG1 and TEG2) and an absorption refrigeration system (ARS). The ARS consists of a generator (AGN), condenser (ACN), evaporator (AEV), absorber (ABS), and heat exchanger (AHX).

The intake air passes through the first compressor C1, which is pressurized in the intermediate compressor. Then the air is cooled by IC and split into two parts; the main part is passed through the second compressor to be pressurized to a high pressure, the secondary part passes through the high-temperature PEMFC. Then the fuel blend is burnt with compressed air in the CC to reach its high temperature producing exhaust gases. These gases are expanded by the high-pressure turbine (T2) to generate electricity. After that, some of the exhaust gases is utilized in the SOFC to produce electricity, while the remaining is recombusted in the afterburner (BR) with the exhaust of SOFC to ensure the

complete combustion of the fuel blends before expanding in the low-pressure turbine (T1) to be released to the atmosphere. The exhaust gases leave the engine at high temperature with large thermal waste energy, which can be recovered by the energy recovery system (ERS) by transferring thermal energy into electric power using TEG1 and TEG2 and into a cooling load for air conditioning the trains by the ARS, which is operated using an ammonia-water refrigerant.

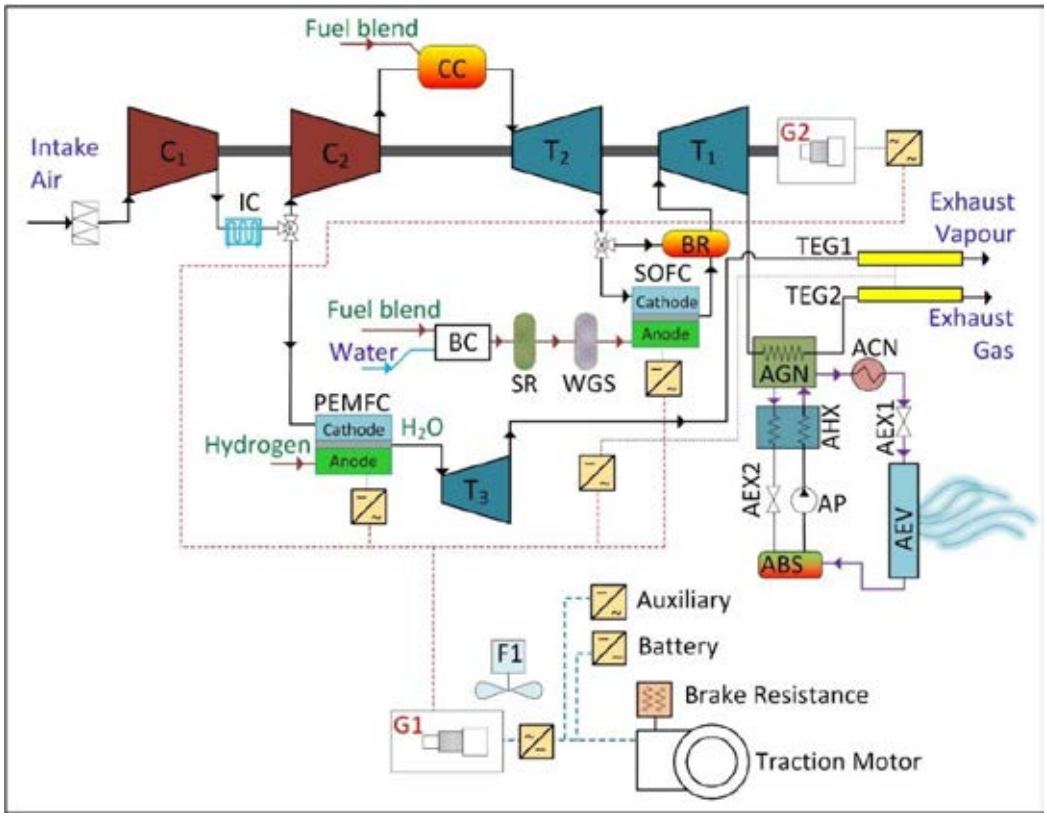


Fig. 1. Schematic layout of the hybridized gas turbine based locomotive engine

The engine power ($\dot{W}_{eng}$) and heat required ($\dot{Q}_{eng}$) are given as follows:

$$\dot{W}_{eng} = \dot{W}_{GT} + \dot{W}_{TEG1} + \dot{W}_{TEG2} + \dot{W}_{SOFC} + \dot{W}_{PEMFC} \quad (1)$$

$$\dot{Q}_{eng} = \dot{Q}_{CC} + \dot{Q}_{BR} \quad (2)$$

The overall performance of the hybrid locomotive engine can be measured using thermal efficiency (η_{eng}) and exergetic efficiency (ψ_{eng}) of the engine, which are written below:

$$\eta_{eng} = \frac{\dot{E}_{out,eng}}{\dot{E}_{in,eng}} = \frac{\dot{W}_{eng} + \dot{Q}_{AEV}}{\dot{Q}_{eng}} \quad (3)$$

$$\psi_{eng} = \frac{\dot{E}x_{out,eng}}{\dot{E}x_{in,eng}} = \frac{\dot{W}_{eng} + \dot{E}x^{Q}_{AEV}}{\dot{E}x^{Q}_{CC} + \dot{E}x^{Q}_{BR}} \quad (4)$$

RESULTS AND DISCUSSION

The newly designed engine is modelled and analyzed thermodynamically to present the energetic efficiency and exergetic efficiency using the Aspen Plus software package. The equation of state is selected to be the Peng-Robinson. The highest power is gained by the high-pressure turbine (T2) (8978 kW). The total generated power of the turbines is 13978.1 kW, and the total required power of the compressors is 10320.8 kW. The heat from the combustion chamber (CC) and afterburner (BR) is 5759.3 kW and 7632.7 kW, respectively. The exergy destruction rate reaches its high value for the BR then CC because of the extreme temperature differences and chemical reactions of the substances. The fuel cells of PEMFC and SOFC release heat losses of about 9 MW and produce a total power of 6 MW. The released heat rates from the SR and WGS are 414 kW and 29 kW, respectively. The intercooler (IC) releases heat from the air after pressurization by C1 by 880 kW to drop 50℃. The waste heat from the engine after the turbine T1 is 3638 kW, and that of after T3 is 184 kW. This waste energy has been transferred to two useful forms of energy: electric power by using TEG1 (9 kW) and TEG2 (16 kW), and cooling load by the AEV (615 kW) by the ARS. Therefore, the total useful energy is 623 kW (excluding the pump power), which increases the efficiency by 16.3%. The integrated engine has an overall thermal efficiency of 70.6% and an exergetic efficiency of 42%. The gas turbine only engine can produce a power of 3181 kW, while the integrated one can produce 9166 kW, which is about threefold the traditional engine. In addition, the engine can produce 1.09 kg/s of CO_2, meaning an 80% drop in carbon emissions compared to any fossil fuel-operated engines [5]. Also, the performance of traditional gas turbine engines using methane and hydrogen blend is 25.4% and 31.6% energetic and exergetic efficiency, respectively.

CONCLUSIONS

The proposed integrated locomotive engine consists of a gas turbine, two fuel cells, and an energy recovery system. This engine is investigated thermodynamically using the Aspen Plus simulation to address its performance. The integrated engine is operated using 75% methane and 25% hydrogen blend as a replacement for fossil fuels. The proposed engine can produce a total power of 9 MW, which is threefold the value of traditional locomotive engines with 70.6% of thermal efficiency and 42% of exergetic efficiency. The proposed engine has a promising potential as the future of locomotive engines because of its great performance and environmentally benign fuels.

NOMENCLATURE

$\dot{Q}$	Heat rate, kW
T	Temperature, ºC
$\dot{W}$	Work rate, kW
Greek Letters	
η	Energy efficiency
ψ	Exergy efficiency
Subscripts	
eng	overall engine
Acronyms	
PEM	Proton exchange membrane
SOFC	solid oxide fuel cell
TEG	thermoelectric generator

REFERENCES

1. M. I. Shah, F. F. Adedoyin, and D. Kirikkaleli, “An evaluation of the causal effect between air pollution and renewable electricity production in Sweden: Accounting for the effects of COVID-19,” *Int. J. Energy Res.*, vol. 45, no. 13, pp. 18613–18630, 2021.
2. M. Haji Akhoundzadeh, S. Panchal, E. Samadani, K. Raahemifar, M. Fowler, and R. Fraser, “Investigation and simulation of electric train utilizing hydrogen fuel cell and lithium-ion battery,” *Sustain. Energy Technol. Assessments*, vol. 46, no. August 2020, p. 101234, 2021.
3. S. Seyam, I. Dincer, and M. Agelin-Chaab, “Development and assessment of a cleaner locomotive powering system with alternative fuels,” *Fuel*, vol. 296, no. February, p. 120529, Jul. 2021.
4. X. Ma, S. Hu, W. Hu, Y. Luo, and H. Cheng, “Experimental investigation of waste heat recovery of thermoelectric generators with temperature gradient,” *Int. J. Heat Mass Transf.*, vol. 185, p. 122342, 2022.
5. S. Seyam, I. Dincer, and M. Agelin-Chaab, “Development and assessment of a cleaner locomotive powering system with alternative fuels,” *Fuel*, vol. 185, no. March, p. 120529, 2021.

WHEC-2022
23rd World Hydrogen Energy Conference
June 26-30, 2022 - Istanbul

#1443

AN APPLICATION AND EVALUATION OF BLENDING BIOGAS AND HYDROGEN INTO THE NATURAL GAS FOR COMBUSTION APPLICATIONS

[1*] *Merve Ozturk*, [2,1] *Ibrahim Dincer*
[1] Yildiz Technical University, Faculty of Mechanical Engineering, Mechanical Engineering Department, Istanbul, Turkey
[2] Clean Energy Research Laboratory, Ontario Tech. University, Faculty of Engineering and Applied Science, Ontario, Canada

*Corresponding author e-mail: merveoz@yildiz.edu.tr

ABSTRACT

In this study, an integrated system is developed for environmentally benign and efficient combustion of natural gas in domestic applications. For this purpose, natural gas is blended with biogas and renewable hydrogen to combat fossil fuel usage and greenhouse gas emissions released to the environment. Different blending ratios are analyzed with Aspen Plus software and combustion emissions are investigated. While CO_2 emission and reactor heat rate are 6.48 kg/h and 27 kW when using only natural gas. These values decrease to 6.35 kg/h and 22 kW for 60%-40% natural gas-biogas blend and 5.06 kg/h and 18 kW for 40%-40%-20% natural gas-biogas-hydrogen blend, respectively. In the case of this triple blending, the natural gas consumption reduces from 2.46 kg/h to 0.98 kg/h.

Keywords: Hydrogen, Renewable energy, Biogas, Natural gas, Blend, Emissions, Performance assessment

INTRODUCTION

Although natural gas (NG) resources are still receiving high attention for use, high carbon dioxide emissions are unavoidable when burned. For this reason, researchers show great interest in studies on blending cleaner fuels such as renewable hydrogen and biogas into natural gas. Benaissa et al. [1] studied the combustion specifications of the biogas-hydrogen blend at several blending ratios for a non-premixed swirling flame in a combustor of the gas turbine, numerically. The hydrogen ratio was changed from 0% to 50% by volume. They revealed that CO_2 and CO emissions reduced with higher hydrogen addition. Ozturk and Dincer [2] proposed a geothermal based system for hydrogen and power production and blending hydrogen into natural gas for combustion applications. Hydrogen was blended into the natural gas network with blending ratios up to 20% by volume. The overall exergy and energy efficiencies of the investigated system were calculated as 77.9% and 46.8%, respectively. Gómez Montoya et al. [3] studied several strategies for spark-ignition engine performance. In their experimental study, biogas was blended with natural gas, hydrogen and propane to enhance combustion specifications. As a result, the power output and production efficiency were found out higher than the original operation of the diesel engine. Zhao et al. [4] investigated the effect of renewable gas ratio on the performance of operating for a residential room furnace. The results of their study showed that 15% hydrogen and 5% carbon dioxide by volume could be mixed with natural gas separately without substantial effects. The flashback and blow-off risks are the limiting factors for above these amounts. The main goal of this study is to propose a novel system for efficient and environmentally friendly combustion of natural gas with the help of blending biogas and renewable hydrogen in it. In this system, biogas is produced from biomass while hydrogen is produced from an alkaline electrolyzer fed by renewable sources of energy such as wind and solar. Several blending rates are utilized to analyze the effect of hydrogen and biogas amounts on combustion performance.

SYSTEM DESCRIPTION

The proposed system for the blending of biogas and hydrogen into natural gas is shown in Fig. 1. While biogas is generated from biomass in a biogas plant, hydrogen is produced by an alkaline electrolyzer. The required electricity for the electrolyzer unit is provided by renewable sources such as photovoltaic (PV) panels and wind turbines. Produced hydrogen and biogas are blended into natural gas in a blending unit at the same pressure of 4 bar. The generated blend has a volumetric flow rate of 3.5 Nm^3/h is fed to the household appliances.

METHODOLOGY

The proposed system is simulated with the Aspen Plus software [5]. The worksheet of the Aspen Plus simulation is shown in Fig. 2. Several blending rates are utilized for biogas and hydrogen as changed from 0% to 40 and 0% to 20%, respectively. For the analyses, natural gas and biogas content are taken as given in Table 1.

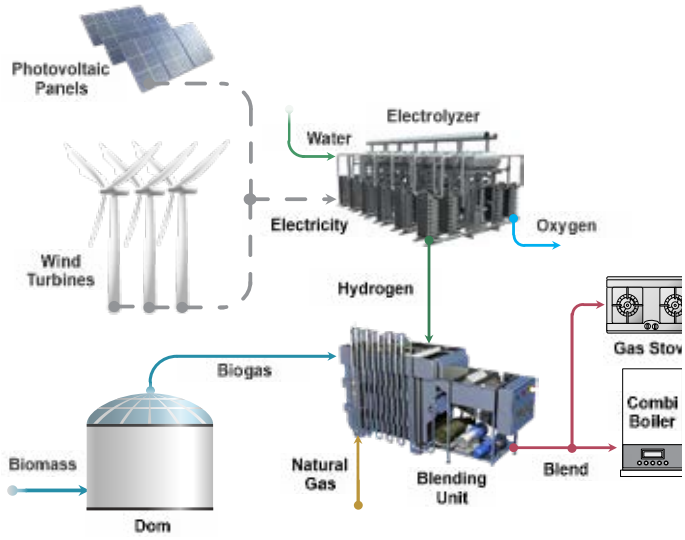


Fig. 1. The proposed system for blending of biogas and renewable hydrogen into natural gas

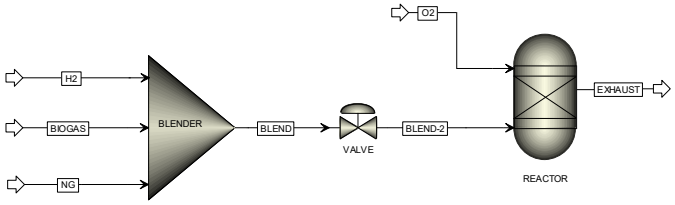


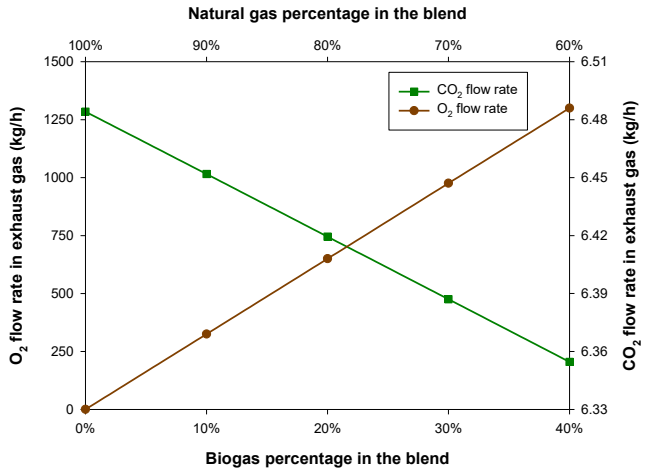
Fig. 2. The simulation flowsheet of the blending and combustion of the blend

Table 1. Natural gas [6] and biogas [7] compositions

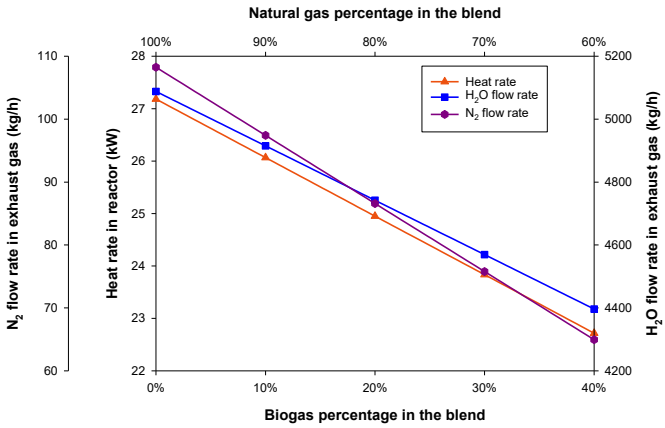
Gas	Composition	Fraction (%)
Natural gas	Carbon dioxide	0.38079
	Nitrogen	2.76014
	Hexane+	0.02362
	n-Pentane	0.05342
	i-Pentane	0.07035
	n-Butane	0.31704
	i-Butane	0.23230
	Propane	1.13812
	Ethane	3.48796
	Methane	91.5363
Biogas	CO_2 + CH_4	35 + 65

RESULTS AND DISCUSSION

The effect of biogas addition into the NG on combustion performance is shown in Figs. 3a and 3b. When biogas content in the NG changed from 0% to 40%, O_2 and CO_2 flow rates in the exhaust stream is changed from 0.19 kg/h to 1300 kg/h and from 6.48 kg/h to 6.35 kg/h, respectively. Moreover, the heat rate, N_2 and H_2O flow rates are decreased from 27 kW, 108 kg/h and 5088 kg/h to 22 kW, 64 kg/h and 4396 kg/h, respectively.



(a)



(b)

Fig. 3. The effect of biogas addition into the NG on a) O_2 and CO_2 flow rates b) N_2, H_2O flow rates and heat rate

The effect of both hydrogen and biogas blending into the NG on combustion performance is shown in Figs. 4a and 4b. When pure natural gas is employed for the combustion process, CO_2, O_2, N_2, H_2O flow rates and heat rate in the exhaust stream are 6.48 kg/h, 0.19 kg/h, 108 kg/h, 5088 kg/h and 27 kW, respectively. On the other hand, when 40%-40%-20% NG-biogas-hydrogen blend is available, these values are changed to 5.05 kg/h, 2700 kg/h, 43 kg/h, 3883 kg/h and 18 kW, respectively.

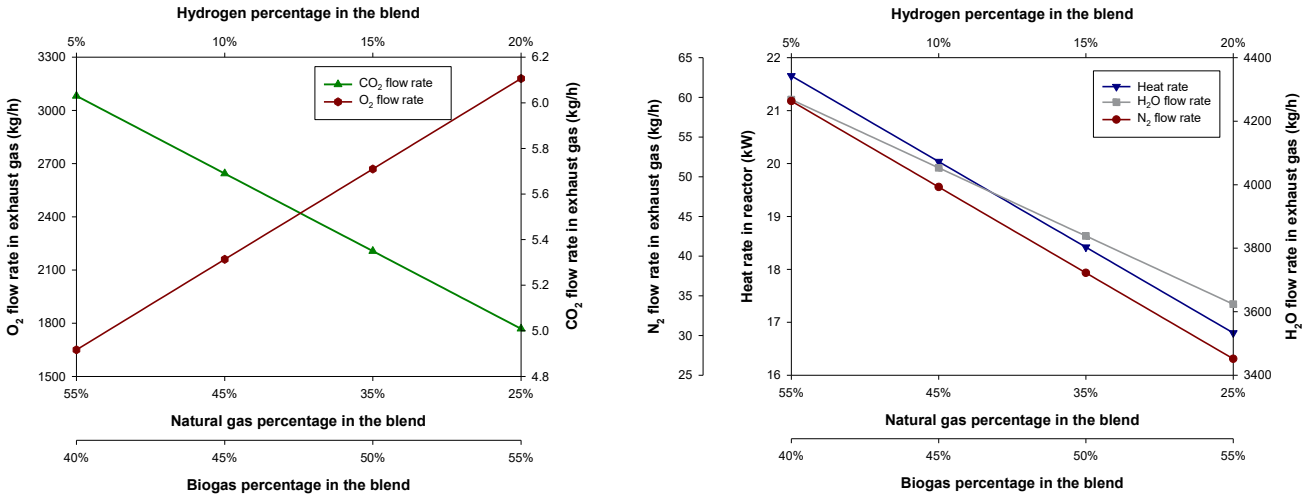


Fig. 4. The effect of biogas and H_2 addition into the NG on a) O_2 and CO_2 flow rates b) N_2, H_2O flow rates and heat rate

CONCLUSIONS

Some of the main conclusions are derived from this particular study as follows:

- With the triple blending, the natural gas consumption is decreased from 2.46 kg/h to 0.98 kg/h.
- When biogas addition rate into the NG varied from 0% to 40%, O_2 and CO_2 flow rates in the exhaust is changed from 0.19 kg/h to 1300 kg/h and from 6.48 kg/h to 6.35 kg/h, respectively. Also, the heat rate, N_2 and H_2O flow rates are reduced from 27 kW, 108 kg/h and 5088 kg/h to 22 kW, 64 kg/h and 4396 kg/h, respectively.
- When 40%-40%-20% NG-biogas-hydrogen blend is employed, CO_2, O_2, N_2, H_2O flow rates and heat rate in the exhaust stream are varied to 5.05 kg/h, 2700 kg/h, 43 kg/h, 3883 kg/h and 18 kW, respectively.

REFERENCES

1. Benaissa S, Adouane B, Ali SM, Rashwan SS and Aouachria Z. 2022. Investigation on combustion characteristics and emissions of biogas/hydrogen blends in gas turbine combustors. Thermal Science and Engineering Progress 27:101178.
2. Ozturk M and Dincer I. 2021. Development of a combined flash and binary geothermal system integrated with hydrogen production for blending into natural gas in daily applications. Energy Conversion and Management 227:113501.
3 Gómez Montoya JP, Amell AA, Olsen DB and Amador Diaz GJ. 2018. Strategies to improve the performance of a spark ignition engine using fuel blends of biogas with natural gas, propane and hydrogen. International Journal of Hydrogen Energy 43:21592–602.
4. Zhao Y, McDonell V and Samuelsen S. 2020. Assessment of the combustion performance of a room furnace operating on pipeline natural gas mixed with simulated biogas or hydrogen. International Journal of Hydrogen Energy 45:11368–79.
5. https://www.aspentech.com/en/products/engineering/aspen-plus. Accessed on March 14, 2022.
6. http://www.gazmer.com.tr/. Accessed on March 14, 2022.
7. Sganzerla WG, Tena-Villares M, Buller LS, Mussatto SI and Forster-Carneiro T. 2022. Dry Anaerobic Digestion of Food Industry by-products and Bioenergy Recovery: A Perspective to Promote the Circular Economy Transition. Waste Biomass Valor 2022.

WHEC-2022
23rd World Hydrogen Energy Conference
June 26-30, 2022 - Istanbul

#1456

COMPARATIVE ANALYSIS OF A MULTI-GENERATION SYSTEM USING DIFFERENT CONVENTIONAL AND NANO-BASED WORKING FLUIDS

[1*] *Tahir Abdul Hussain Ratlamwala,* [1] *Hafsa Javed,* [1] *Sana Naseem,* [1] *Khurram Kamal*
[1]National University of Sciences and Technology, Islamabad, Pakistan

*Corresponding author e-mail: tahir.ratlamwala@pnec.nust.edu.pk

ABSTRACT

The aim of the research is to study a system that uses both non-renewable and renewable energy sources, fulfilling the energy requirements by using fossil fuels but also reducing the use of fossil fuels which are damaging the environment in hindsight by the introduction of a renewable energy system. The system provides a total of six different outputs, which are Electricity Generation, Desalination of Water, Heating of space, Cooling of space, Heating of Water and Waste Heat for Industrial Purposes. The performance of the system is studied through detailed energy and exergy analyses. Further the effects of variation in geothermal fluid's mass flow rate, pressure and quality on system outputs are evaluated. Additionally, multiple fuels including nano-based fuels with varying calorific values are evaluated and it is found that the fuels with highest calorific values provide the best possible system outputs.

Keywords: Nano fluids, Multigeneration, Exergy

INTRODUCTION

Energy crisis in the world is real and the difference between demand and supply is increasing day by day. The energy crisis is being dealt with using various non-renewable and renewable energy sources. These include fossil fuels, wind energy, solar energy, geothermal energy, biomass, etc. Among these, the most easily available ways to fulfill the power needs are fossil fuels in the form of Coal, Oil and Gas. Fossil fuels have been the major source of power generation for a long time as they have concentrated energy and the energy extraction methods are cheaper. According to Global Status Report 2018, about 77.9% of electricity is generated using fossil fuels [1].

However, the impact of fossil fuels on the environment cannot be ignored. Fossil fuels have been a big source of pollution in the environment and have contributed a lot towards Global Warming [2], a phenomenon of increasing average temperature of the planet due to the highly increased concentration of greenhouse gases in the atmosphere. These greenhouse gases chiefly consist of Carbon dioxide which is the prime product of combustion of fossil fuels. Greenhouse gases capture heat in the atmosphere and prevent it from escaping the Earth's grasp [3] which increase the overall heat content of the atmosphere and cause a heating effect more commonly known as Global Warming.

The only sensible way to counter the effects of fossil fuels on the environment is to introduce Renewable and Green energy sources. These sources can cater to two-thirds of global energy demands and can play a major role in the reduction of greenhouse gas emissions required to limit the global surface temperature increase to 2°C by the year 2050 [4]. As per research conducted on 38 countries with renewable energy consumption around the world, a positive impact was witnessed on the economic growth for about 58% of these countries from the year 1990 to 2018 [5]. Hence, it wouldn't be wrong to say that renewable energy is the way forward for a brighter and safer future.

The energy crisis in the world can effectively be dealt with by incorporating such systems in our everyday usage and expanding these to cater the needs of more and more people. The six outputs are all necessary for human life and are needed for a comfortable living anywhere. These could be achieved by using the conventional systems only that use fossil fuels as the prime source of energy. However, that would cause more damage to the environment and the atmosphere if fossil fuels and other conventional methods are solely used.

SYSTEM DESCRIPTION

The designed system consists of 2 Genset engines, which are a major source of electricity generation as shown in Fig. 1. The engines operate on natural gas and have a rated efficiency of 45.5%, resulting in power production of 3 MW.
In Genset engines, waste heat in the form of flue gases is produced as a by-product. Energy is recovered from these flue gases to be used mainly to operate Waste Heat Recovery Boiler and as a source of heat input to geothermal fluid, converting saturated vapor to superheated vapor before it enters the steam turbine. This reduces the fuel consumption cost.
Standard Gensets are available in market with fixed emission rates. The 1.5 MW Genset produces flue gases at a flow rate of 2.10 kg/s and releases energy of 650 kW. Since two Gensets are installed in the proposed system, flue gases from both the engines provide 1300 kW of energy.

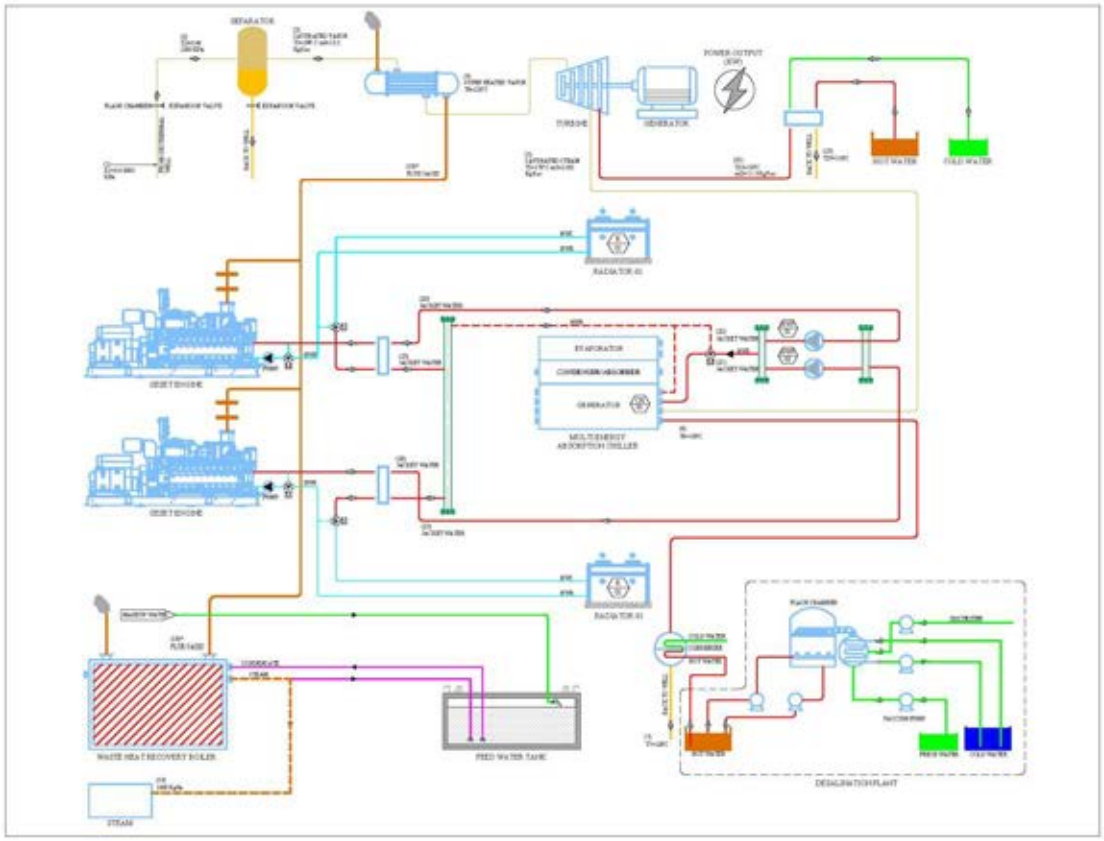


Fig. 1. Schematic of multigeneration system.

RESULTS AND DISCUSSION

The effect of fuel input was studied by performing calculations and plotting their results. Apart from the original fuel considered for the system, i.e., natural gas, twenty-one other fuels were considered including nano-based fuels. The variation in the system outputs due to change in the type of fuel was studied in detail. The overall effect of different fuels on system's energetic efficiency were also studied and as per the results shown in the Fig. 2, Boron with the highest calorific value provides the highest system efficiency of 40.79% and Ethanol with the lowest calorific value provides the lowest system efficiency of 40.42%. The variation in system efficiency, however, is not substantial as all the other system inputs are kept constant.

CONCLUSIONS

The multi-generation system proposed in this paper utilizes both renewable and non-renewable energy sources, keeping in mind the merits and demerits of both. This system is sufficient and capable enough to cater to the energy needs of an industry and the community within the premises of an industry. This industry is obviously located near a geothermal source which provides the geothermal fluid continuously to meet the requirements of the system. In addition, the industry location allows the supply of fuel required for Genset system.

Analyses of the multi-generation system working on Geothermal energy and Gensets has been done. Six outputs are generated which are Power Generation, Space Heating, Space Cooling, Heating of Water, Waste Heat Recovery, and Desalination of Water. The outputs of the system at general conditions are 6.7 MW of electricity, 650kW for Waste Heat Recovery Boiler, desalinated water at a rate of 10.54 kg/s, hot water at a rate of 41 kg/s, heated space at 30oC and 331.7 kW and cooled space at 5o C and 314.1kW.
Effects of variation in input conditions on the outputs and system efficiency have been studied. The plotted results show that an increase in geothermal water's quantity, quality, and pressure all result in an increase in system outputs. Similarly, an increase in the calorific value of fuel results in greater system outputs and efficiencies. This has been concluded after studying the impact of 21 different fuels on system outputs.
Hence, this system not only contributes to the renewable energy sector and greener earth narrative but also fulfills all the energy requirements. It does utilize fossil fuel which is contributing to global warming and has several other negative impacts on the environment but it derives the maximum possible energy out of the fuel by reusing or redirecting the

energy of flue gases and jacket water to either support the geothermal processes or to recover waste heat for other industrial purposes.

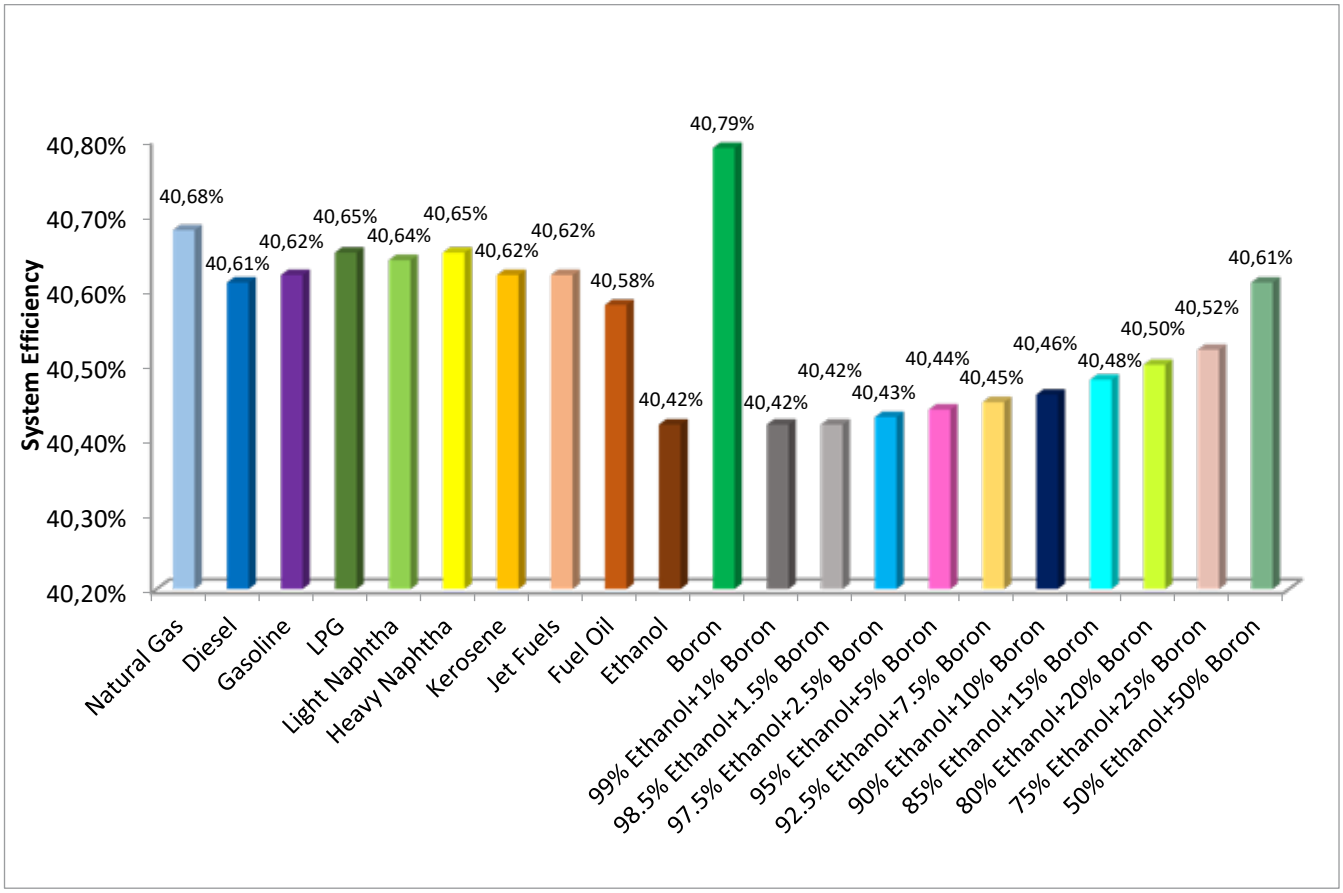


Figure 5: Effect of Fuel Variation on System's Energetic Efficiency

REFERENCES

1. A. H. Bagdadee and L. Zhang, "Electrical power crisis solution by the developing renewable energy based power generation expansion," Energy Rep., vol. 6, pp. 480–490, Feb. 2020, doi: 10.1016/j.egyr.2019.11.106.
2. U. Shahzad, "Global Warming: Causes, Effects and Solutions," vol. 1, no. 4, p. 8, 2015.
3. D. Kweku et al., "Greenhouse Effect: Greenhouse Gases and Their Impact on Global Warming," J. Sci. Res. Rep., vol. 17, no. 6, pp. 1–9, Feb. 2018, doi: 10.9734/JSRR/2017/39630.
4. D. Gielen, F. Boshell, D. Saygin, M. D. Bazilian, N. Wagner, and R. Gorini, "The role of renewable energy in the global energy transformation," Energy Strategy Rev., vol. 24, pp. 38–50, Apr. 2019, doi: 10.1016/j.esr.2019.01.006.
5. M. Shahbaz, C. Raghutla, K. R. Chittedi, Z. Jiao, and X. V. Vo, "The effect of renewable energy consumption on economic growth: Evidence from the renewable energy country attractive index," Energy, vol. 207, p. 118162, Sep. 2020, doi: 10.1016/j.energy.2020.118162.

WHEC-2022
23rd World Hydrogen Energy Conference
June 26-30, 2022 - Istanbul

#1476

CO-GENERATION OF ELECTRICITY USING WASTE HEAT FROM HYDROGEN FUEL CELL IN A VEHICLE: A SIMULINK MODEL

[1] Khurram Kamal, [1] Adeem Ahmed Shaikh, [1]Muhammad Usama Shaikh, [1]Samita Khan, [1]Azka Jawed, Ammad Yousuf Tariq, [1] Tahir Abdul Hussain Ratlamwala, [2]Asad Ali Zaidi*

[1]National University of Sciences and Technology, Islamabad, Pakistan

[2]Department of Mechanical, Faculty of Engineering Science and Technology, Hamdard University, Pakistan

*Corresponding author e-mail: khurram.kamal@pnec.nust.edu.pk

ABSTRACT

This paper discusses the use of Proton Exchange Membrane Fuel Cell (PEMFC) as the source of energy for installation in vehicles. The paper includes a Simulink model for a vehicle with a Thermo-Electric Generator (TEG), also showing the fuel cell and the method used for a stable energy output from it.

Considering the parameters for an automobile, especially weight and dimensional constraints, the paper is the study of waste heat recovery from a 50 to 70°C temperature difference produced by the fuel cell. The study has been done for a generalized scalable model of PEMFC, containing 20 cells per stack. The stacks are connected in parallel to keep the output voltage at a constant level. It was observed that under dynamic conditions an average of 10.85% power regeneration occurred. This regeneration percentage is directly proportional to the number of cells TEG modules used. Therefore, the study can be scaled to a variety of PEMFC models. However, increasing the number of cells does not affect the stack temperature significantly but provides a large area for heat transfer.

Keywords: Fuel cells, PEMFC, Simulink, TEG

INTRODUCTION

Figure 1 shows the Simulink model of the proposed system

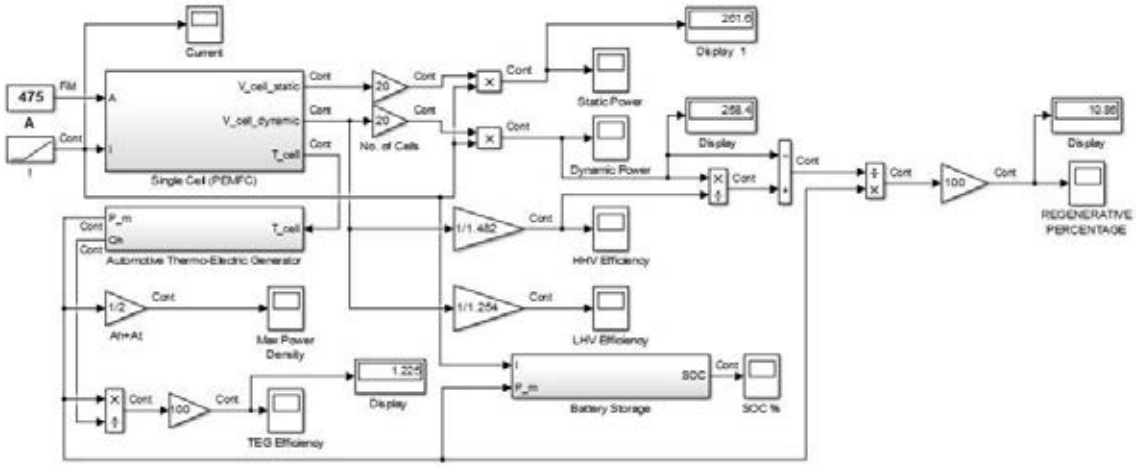


Fig. 1. Simulink model of the proposed system

WHEC-2022
23rd World Hydrogen Energy Conference
June 26-30, 2022 - Istanbul

#1479

PERFORMANCE ASSESSMENT OF A CALCIUM-IRON BROMIDE CYCLE BASED MULTIGENERATION SYSTEM

Fatih Sorgulu[1] and Ibrahim Dincer[2,1]*
[1]Faculty of Mechanical Engineering, Yildiz Technical University, Besiktas, Istanbul, Turkey
[2]Faculty of Engineering and Applied Science, Ontario Tech. University, Oshawa, Ontario, Canada

*Correspondence e-mail: fatihs@yildiz.edu.tr

ABSTRACT

In this study, a performance assessment of a novel solar energy-based multigeneration system integrated with a thermochemical cycle is performed. A steam generator is also integrated to reach high temperatures which are required for the thermochemical cycle. While 550 °C is reached with solar tower, the temperature is increased to 750 °C, which is the maximum temperature of the cycle, with the steam generator. Hydrogen is produced by a calcium-iron bromide cycle and is blended with natural gas. The blend is supplied both to the boiler of the organic Rankine cycle and a community to utilize in combi boiler and gas cooker. The reverse osmosis and multi-effect distillation units are integrated to produce fresh water for the community which consists of one thousand houses. 9.3 MWh electricity is supplied by organic Rankine cycle with 41.27 million m^3 hydrogen and natural gas blend. Furthermore, a total of 7.2 million m^3 of the blend is utilized for household appliances including gas cookers and combi boilers.

Keywords: Efficiency, Hydrogen, Natural gas, Renewable energy, Solar tower

INTRODUCTION

Novel solutions and newly developed systems are required to provide technically, economically, environmentally sustainable energy. It is vital to overcome the increasing electricity, heat, and freshwater demand by supplying various fuels and integrating systems. Although fossil fuel-based systems are mainly used all over the world, environmental awareness is more significant than ever. CO, CO_2, SO_2, NOx emissions which are emitted due to fossil fuel usage are recognized as the primary environmental problems. Fossil fuel-based systems should be integrated with renewable energy-based systems and energy storage subsystems to utilize them wisely. Hydrogen is a promising solution to utilize natural gas resources effectively and to reduce emissions. This study presents energy, exergy, and environmental assessments on hydrogen injection into natural gas pipelines.

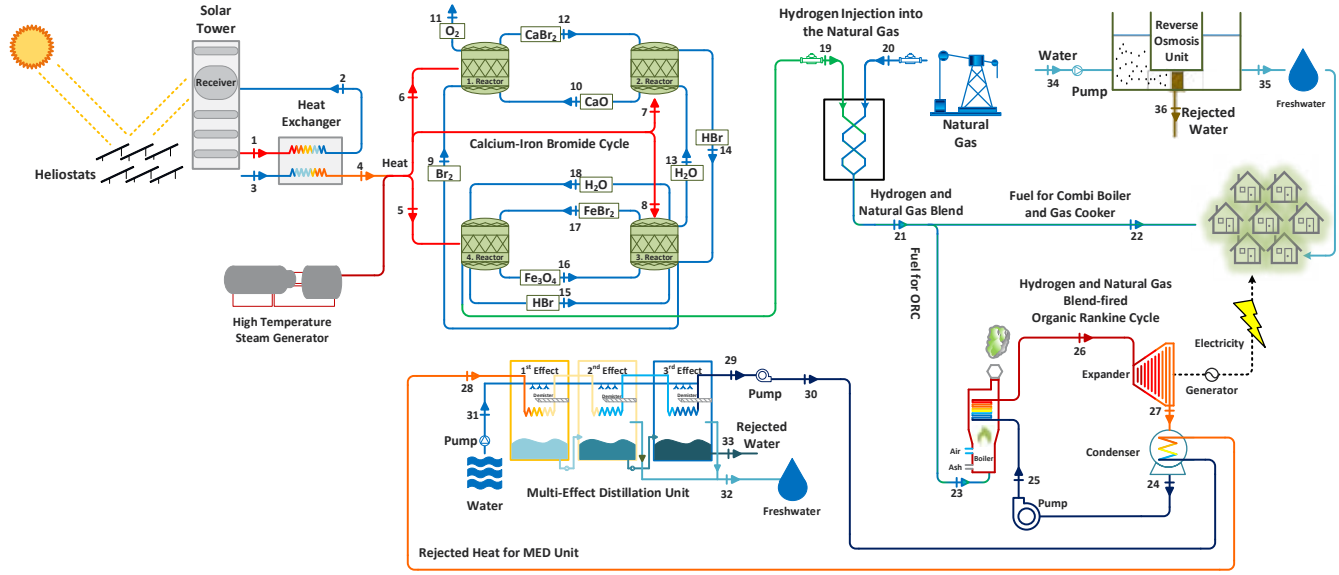


Fig. 1: Schematic illustration of the multigeneration system.

SYSTEM DESCRIPTION AND ASSESSMENT

A solar heliostat field, high-temperature steam generator, organic Rankine cycle (ORC), combi boilers, multi-effect distillation unit, and reverse osmosis units are utilized to produce electricity, heat, and freshwater. A schematic illustration of the multigeneration system is given in Fig. 1. Hexamethyldisiloxane (MM) is considered as the working fluid of the organic Rankine cycle [1]. The calcium-iron bromide cycle is considered to produce hydrogen. Hydrogen is injected into natural gas and utilized in the boiler of the ORC, gas cooker, and combi boilers. The average daily electricity consumption is considered as 8.38 MWh [2]. In addition to the electricity requirement for the community,

300 m³ freshwater is supplied by the reverse osmosis and multi-effect distillation subsystems. The requirements for electricity and freshwater for the community are given in Fig. 2. Mainly during sunny hours, hydrogen is produced by the thermochemical cycle. High temperatures, which are 600 °C for the first and fourth reaction and 750 °C for the second step of the cycle and high flow rates are required for the calcium-iron bromide cycle. Thermodynamic and environmental impact assessments of the integrated system are performed by utilizing the Engineering Equation Solver (EES) and Aspen Plus software.

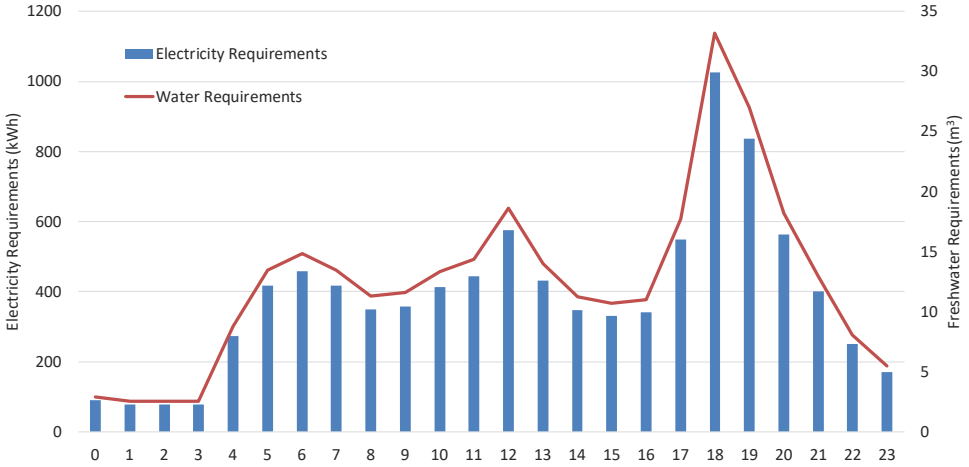


Fig. 2: Hourly electricity and freshwater amounts required for the selected community.

RESULTS AND DISCUSSION

In this study, solar tower, steam generator, organic Rankine cycle, thermochemical cycle, multi-effect distillation and reverse osmosis subsystems are considered for electricity, hydrogen, heat, and freshwater production. Here, hydrogen and natural gas blend is utilized as fuel for the gas cooker, combi boiler, and the boiler of ORC. The amounts of CO_2 and CO emissions are, as expected, decreased with the use of hydrogen. Here, a 20% of the blend consists of hydrogen. The hydrogen and natural gas requirements both for the household appliances and organic Rankine cycle are presented in Fig. 3.

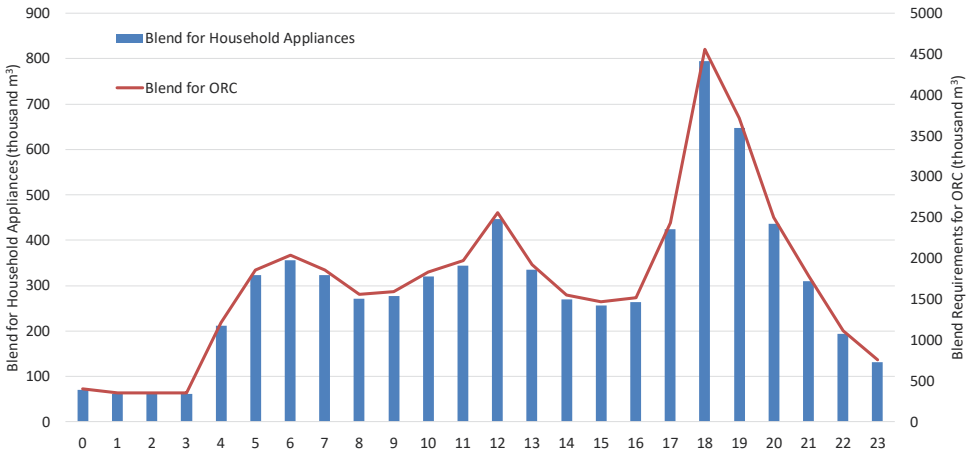


Fig. 3: Hourly hydrogen and natural gas requirements both for the household appliances and organic Rankine cycle.

CONCLUSIONS

In this particular study, a hydrogen and natural gas blend-based multigeneration system is studied in terms of energy, exergy, and the environment. The main findings obtained in this study are listed as follows:

- 41.27 million m³ hydrogen and natural gas blend, with a fraction of 20% hydrogen and 80% natural gas, is supplied to the boiler of the organic Rankine cycle.
- 7.2 million m³ blend with the same ratios is required for the household appliances of the selected community with 1000 houses.

REFERENCES

1. Sorgulu, F., Akgul, M.B., Cebeci, E., Yilmaz, T.O. and Dincer, I., 2021. A new experimentally developed integrated organic Rankine cycle plant. *Applied Thermal Engineering*, 187, p.116561.
2. Mepas Energy. Available at: https://www.mepasenerji.com (Accessed on: 02/08/2021).

WHEC-2022
23rd World Hydrogen Energy Conference
June 26-30, 2022 - Istanbul

#1504

HYDROGEN POWERED VESSELS AT SEA:FUEL CELL & BATTERY UPSCALING

[1*] *Christer Helleland,* [2] *Fionn Iversen,* [3]*Svein Olav Halstensen*
[1]NORCE, Nygårdsgaten 112, 5008, Bergen, Norway
[2]NORCE, Nygårdsgaten 112, 5008, Bergen, Norway
[3]NORCE, Sørhauggata 128, 5527, Haugesund, Norway

*Corresponding author email: chel@norceresearch.no

ABSTRACT

There is today a strong effort in developing fuel cell / battery systems for ship propulsion to achieve zero-emission maritime transport, in accordance with UN sustainability goals and the Fit For 55 plan to achieve the climate goals agreed by the EU Council and the European Parliament. Critical for successful implementation of fuel cell / battery systems are system design and control during operation. Fuel cells and batteries have ideal operating ranges. Use outside of this range will cause degradation, impacting system lifecycle. Fuel cell / battery systems are used for transport today but applying such systems for maritime transport requires significant upscaling. Cars typically have a power of 100 to 300 kW, while ocean going ships require tens of MW of power to handle the loads required. To achieve such system capacity, systems are assembled with multiple fuel cells and batteries in stacks. A better understanding of the effect of such upscaling, and system dynamics with respect to load, is therefore required for successful implementation of fuel cell / battery systems for maritime transport. This paper discusses fuel cell types, methods and models applicable for this purpose.

Keywords: PEM fuel cell, Battery, Upscaling, Marine vessel hybrid system.

HYBRID FUEL-CELL/BATTERY DRIVEN SHIP

A hydrogen fuel cell is an electrochemical cell using hydrogen and oxygen as fuels to convert chemical energy to electrical energy. Commercial solutions for hydrogen-based transport using fuel cell systems, generally combined with batteries acting as an energy buffer, has existed for a couple of decades. The use in cars manufactured in series started in the late 2000s, and the first passenger-ship running on a hybrid FC/batteries system was put into service in 2008 [1]. With the national and global green transition, there is today a strong incentive for increasing the use of such technology in maritime transport. This technology transfer requires upscaling of both fuel cell and battery technology to cover the increase in power requirements [2], which for large ships can be several MW when in transit. The operational properties of individual battery and fuel-cell components are normally known. However, for an upscaled system such as a large ship with an integrated fuel cell as the main power generator, the system requires the consideration of fuel cell stacks and battery packs, but the properties of scaled systems with multiple elements are not necessarily proportional [3]. The energy / power requirements will vary with time, these load variations depend on such factors as ship schedules, speed/current, waterline (cargo), wind, and waves, making it challenging to predict system power and energy requirements. Poor predictability means that systems must have the capacity to deal with a large variability in load. This introduces a challenge with respect to systems engineering and systems control. Additionally, reliable and predictable upscaling of fuel cell technology remains a challenge, with respect to the system performance of a fuel cell which are characterized by durability, reliability and robustness [4]. So, uncertainty in systems performance, or degradation of system components, must also be considered in engineering. Relevant characteristics of ships and ship components are illustrated in Fig. 1.

The type of fuel cell and battery technology also impacts system performance. Oxide fuel cells provide high energy efficiency and fuel versatility but are unsuitable for rapidly varying loads [5]. Polymer Electrolyte Membrane (PEM) fuel cells, more suited to maritime application, are also limited with respect to fast current transients [6]. To accommodate for load transients on a PEM fuel cell and quick upstarts/shutdowns, a battery pack is integrated to minimize such transient behavior. Such a power splitting between a fuel cell and a battery requires a fuel cell-battery management strategy and system (FCBMS). Recent advances in autonomy, connectivity and machine learning have given rise to methods for predictive power management systems but has not yet been applied to large-scale ships in transit at sea. Also, recent health-conscious power management strategies have been considered for fuel cell-battery hybrid systems for on ground vehicles [7], however these advances do not properly account for the thermal dynamics which are strongly connected to fuel-cell/battery aging.

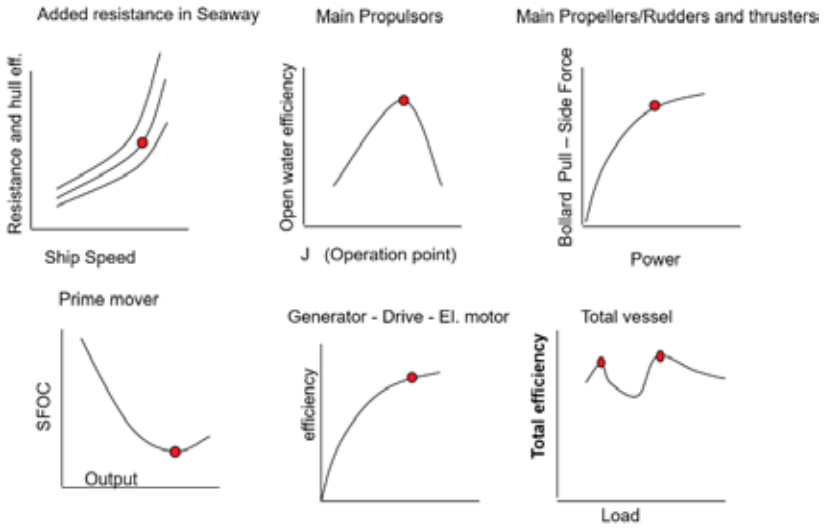


Fig. 1. Typical ship characteristics

For fuel cells, power output is constrained by compressor saturation limits. Exceeding these limits cause oxygen starvation, increase in temperature, fuel cell degradation, and reduced stack lifetime. Sufficient hydrogen and oxygen, provided by the compressor, must always be available at the cathode for the required power output to avoid oxygen / hydrogen starvation and subsequent stack degradation. It is well-known that load variations induce temperature changes in a fuel cell, and that temperature has an impact on both degradation (thermal degradation) of the membrane and on its performance. However, the temperature dynamics involve on a faster timescale than that of degradation. This imposes challenges on how to capture instantaneous effects of degradation on the fuel-cell/battery by implementing the thermal dynamical behavior. Most research in literature has not been focused on such instantaneous effects [8]. Ideally instantaneous effects of degradation should be described in terms of power requirements over time [9]. The performance of a PEM fuel cell can be classified into four processes, the membrane, catalyst layers, GDL/MPL and the channels. Each of these can further be described by the internal dynamics of the fuel cell including transport phenomena. In fact, in order to achieve realistic and detailed accounts of system degradation then atomic and system scale coupled models must be constructed [10]. For a PEM fuel cell ideal operating temperature is close to $80°C$, for which thermal degradation can be completely neglected. Therefore from this perspective, it is crucial to develop a temperature control strategy to avoid thermal cycling and induced stress on the fuel cell and other related components [10], [11]. For a battery its health indicators often use the charge capacity as a characteristic parameter which is a fixed value, while for a fuel cell the charge capacity is not fixed since it depends on the fuel supply. This induces issues on how to properly define the SOH of a fuel cell, in the literature health indicators that have been considered include voltage and impedance-based indicators. However, most research done has been for steady-state systems, thus for a dynamical system where load variations occur and change rapidly i.e., for actual operating conditions, estimating the SOH of a PEM fuel cell has not been considered [8].

The charge capacity for batteries fades over time. How the battery is used affects this degradation. Batteries have a minimum state of charge where further discharge will cause permanent damage [12], so this should be avoided. Further, depending on the cell chemistry, both high and low state of charge may deteriorate performance and shorten battery life. Subsequently, the state of charge of a battery should vary as little as possible around its ideal state of charge. Deviation from this state of charge increases battery degradation. On a ship simultaneously the SOH and SOC of both the fuel cell and battery must be estimated along with possibly other relevant states of their domain, this is referred to as multi-state joint estimation. This type of estimation is challenging, since there is often a coupling between states and even for a single battery, most multi-state joint estimation that has been described in the literature are for two-state joint estimation. There is also a challenge with respect to upscaling, in the sense of how state estimation algorithms developed for a single fuel-cell/battery can be generalized to a fuel cell stack respectively battery pack [13]. This issue strongly depends on the modeling complexity of the fuel cell stack/battery pack needed for the system-level estimation requirements, i.e., lumped vs distributed configurations.

Models exist for predicting battery lifetime, and capacity, as a function of state of charge history [3]. There is a comparison issue that needs to be addressed between modeling types, particularly towards upscaling, a proper analysis in literature comparing lumped models versus distributed models is lacking. For a PEM fuel cell, lumped parameter models are the most common ones explored in the literature, from static to dynamic, and in some cases they are represented as an electrical equivalent circuit [14]–[16]. However, to implement degradation into a dynamical

model, which strongly depend on the internal dynamics including mass, water and heat transport, then one needs to consider more spatial dimensions, i.e., distributed parameter models. The latter model types are more complex to work with from the computational and simulation aspect, in the sense that their state spaces are infinite dimensional and involve PDEs which are highly non-linear. They also come with a high number of parameters to estimate, and discretizing methods must be applied which pose numerical challenges [15]. In contrary to lumped models they are not naturally suited for control because of their computational complexity, and model order reduction techniques need to be applied. In literature distributed parameter models have also been considered, for example model order reduction techniques have been applied to a single PEMFC distributed parameter model, for which a model suitable for control and simulation was found [17].

It may be concluded that batteries have operational sweet spots or zones, while fuel cells have upper operational limits: Operating outside of these zones will cause component degeneration, impacting both system capacity and life cycle. To ensure staying within battery and fuel cell limits, process management requires intelligent systems control with predictive capability (or equivalent manual systems management). There must always be sufficient power to drive the vessel with respect to required loads, while the fuel-cell and battery systems should ideally operate within their ideal operating limits. Through model prediction, future energy demand, through the current sailing leg, needs to be estimated. Ideally the fuel cell / battery system should be regulated so that the combined power supply of both will provide the power needed at any time while still working within ideal component operating limits. For full power, electricity from both battery and fuel-cells can be directed to the ships electric drive system, but battery charge will run out in such a mode, so such operation is unsustainable. Further, if required, it should be possible to run the system at full capacity, overriding any possible limitation with respect to ideal operational limits. However, such operation will cause significant increase in component degradation, having a high impact on the lifetime of fuel cells and batteries. Subsequently, operational management of the fuel cell / battery system needs to cover not only the current sailing leg, but the entire life cycle of the system, where choices in systems engineering impact operational constraints. Constraints in optimization with respect to lifetime are subsequently maintenance / upgrading cost, ship/system lifetime expectancy, and fuel cell / battery energy density and available system space – impacting total possible capacity.

Further knowledge of system behavior is subsequently required for optimization, including such properties as fuel cell and battery degradation as a function of power load and time [9], battery discharge rate as a function of load [18], and also load capacity for system components as a function of degradation [19]. There may also be a question with respect to properties of scaled systems. Gains in energy efficiency, and time spent, may be gained by integrating dynamic models with the ships control systems for optimizing dynamic operational sequences such as ship accelerations – both building and reducing speed, and for ship maneuvering in general. A good analogy in drilling process control is optimization of drill pipe movement and starting of pumps for drilling fluid circulation [20], where automation must account for available power, operational constraints, and specific sequence requirements.

Finally, if optimal operation is to be achieved using continuous predictive models, enforcing limits, accounting for breach of limits, and always ensuring optimal combined use of fuel cell / battery system, then a certain degree of automation is needed. Automation / semi-automation using model prediction, enforcing constraints, and continuous model updating, has been applied in other domains, such as for control of petroleum drilling operations [18]. Technology transfer from such development is therefore highly relevant.

CONCLUSIONS

Designing hydrogen driven hybrid fuel cell battery power systems for ships requires systems upscaling from today's hydrogen powered systems to meet power demands. A better understanding of the effects of upscaling on individual battery and fuel cell components is required for systems design and control.
Degradation of battery and fuel cells as a function of load and other operating conditions impacts system lifecycle. Such effects must be understood and accounted for in systems control. Automated control can help optimize and prolong system lifetime.
Predicting operational loads as a function of weather, waves, ship routes and schedules enables improved systems control. Efforts should be made to improve such prediction, thereby improving operating reliability and system lifetimes.

ACKNOWLEDGEMENT

The authors wish to acknowledge Geir Nævdal for discussions and input on battery technology and estimation methods for optimization.

REFERENCES

1. A. Alaswad, A. Baroutaji, H. Achour, J. Carton, A. Al Makky, and A. G. Olabi, “Developments in fuel cell technologies in the transport sector,” *Int. J. Hydrog. Energy*, vol. 41, no. 37, pp. 16499–16508, Oct. 2016, doi: 10.1016/j.ijhydene.2016.03.164.
2. L. Birk, *Fundamentals of Ship Hydrodynamics: Fluid Mechanics, Ship Resistance and Propulsion*, 1st ed. Wiley, 2019. doi: 10.1002/9781119191575.
3. A. Perez, V. Quintero, H. Rozas, F. Jaramillo, R. Moreno, and M. Orchard, “Modelling the degradation process of lithium-ion batteries when operating at erratic state-of-charge swing ranges,” in *2017 4th International Conference on Control, Decision and Information Technologies (CoDIT)*, Barcelona, Apr. 2017, pp. 0860–0865. doi: 10.1109/CoDIT.2017.8102703.
4. J. Wang, “Barriers of scaling-up fuel cells: Cost, durability and reliability,” *Energy*, vol. 80, pp. 509–521, Feb. 2015, doi: 10.1016/j.energy.2014.12.007.
5. L. Kistner, A. Bensmann, and R. Hanke-Rauschenbach, “Optimal Design of Power Gradient Limited Solid Oxide Fuel Cell Systems with Hybrid Storage Support for Ship Applications,” *Energy Convers. Manag.*, vol. 243, p. 114396, Sep. 2021, doi: 10.1016/j.enconman.2021.114396.
6. A. Vahidi, A. Stefanopoulou, and H. Peng, “Current Management in a Hybrid Fuel Cell Power System: A Model-Predictive Control Approach,” *IEEE Trans. Control Syst. Technol.*, vol. 14, no. 6, pp. 1047–1057, Nov. 2006, doi: 10.1109/TCST.2006.880199.
7. Y. Wang, S. J. Moura, S. G. Advani, and A. K. Prasad, “Power management system for a fuel cell/battery hybrid vehicle incorporating fuel cell and battery degradation,” *Int. J. Hydrog. Energy*, vol. 44, no. 16, pp. 8479–8492, Mar. 2019, doi: 10.1016/j.ijhydene.2019.02.003.
8. X. Hu and T. Zhang, “Review on State of Health Definition in Relation to Proton Exchange Membrane Fuel Cells in Fuel Cell Electric Vehicles,” Apr. 2021, pp. 2021-01–0735. doi: 10.4271/2021-01-0735.
9 J. Wu *et al.*, “A review of PEM fuel cell durability: Degradation mechanisms and mitigation strategies,” *J. Power Sources*, vol. 184, no. 1, pp. 104–119, Sep. 2008, doi: 10.1016/j.jpowsour.2008.06.006.
10. T. Jahnke *et al.*, “Performance and degradation of Proton Exchange Membrane Fuel Cells: State of the art in modeling from atomistic to system scale,” *J. Power Sources*, vol. 304, pp. 207–233, Feb. 2016, doi: 10.1016/j.jpowsour.2015.11.041.
11. F. Barbir, *PEM fuel cells: theory and practice*. Amsterdam; Boston: Elsevier/Academic Press, 2013. Accessed: Feb. 23, 2022. [Online]. Available: http://public.ebookcentral.proquest.com/choice/publicfullrecord.aspx?p=1032957
12. C. Bordin and O. Mo, “Including power management strategies and load profiles in the mathematical optimization of energy storage sizing for fuel consumption reduction in maritime vessels,” *J. Energy Storage*, vol. 23, pp. 425–441, Jun. 2019, doi: 10.1016/j.est.2019.03.021.
13 .X. Hu, F. Feng, K. Liu, L. Zhang, J. Xie, and B. Liu, “State estimation for advanced battery management: Key challenges and future trends,” *Renew. Sustain. Energy Rev.*, vol. 114, p. 109334, Oct. 2019, doi: 10.1016/j.rser.2019.109334.
14. BEI. N. GOU and B. WOONKI. DIONG, *FUEL CELLS: dynamic modeling and control with power electronics applications, second edition.* S.l.: CRC PRESS, 2020.
15. M. Guarnieri, P. Alotto, and F. Moro, “Distributed and Lumped Parameter Models for Fuel Cells,” in *Thermodynamics and Energy Engineering*, P. Vizureanu, Ed. IntechOpen, 2020. doi: 10.5772/intechopen.89048.
16. S. M. C. Ang, E. S. Fraga, N. P. Brandon, N. J. Samsatli, and D. J. L. Brett, “Fuel cell systems optimisation – Methods and strategies,” *Int. J. Hydrog. Energy*, vol. 36, no. 22, pp. 14678–14703, Nov. 2011, doi: 10.1016/j.ijhydene.2011.08.053.
17. M. L. Sarmiento-Carnevali, C. Batlle, M. Serra, and I. Massana, “Distributed parameter PEMFC model order reduction,” 2014, p. 4.
18. J. Zhang, S. Ci, H. Sharif, and M. Alahmad, “Modeling Discharge Behavior of Multicell Battery,” *IEEE Trans. Energy Convers.*, vol. 25, no. 4, pp. 1133–1141, Dec. 2010, doi: 10.1109/TEC.2010.2048904.
19. Y. Wu, Z. Liu, J. Liu, H. Xiao, R. Liu, and L. Zhang, “Optimal battery capacity of grid-connected PV-battery systems considering battery degradation,” *Renew. Energy*, vol. 181, pp. 10–23, Jan. 2022, doi: 10.1016/j.renene.2021.09.036.
20. F. Iversen, E. Cayeux, E. W. Dvergsnes, R. Ervik, M. Welmer, and M. K. Balov, “Offshore Field Test of a New System for Model Integrated Closed-Loop Drilling Control,” *SPE Drill. Complet.*, vol. 24, no. 04, pp. 518–530, Dec. 2009, doi: 10.2118/112744-PA.

WHEC-2022
23rd World Hydrogen Energy Conference
June 26-30, 2022 - Istanbul

#1522

THERMODYNAMIC ANALYSIS OF A NEW GEOTHERMAL ENERGY BASED INTEGRATED PLANT FOR COMPRESSED HYDROGEN PRODUCTION

[1*]Fatih Yilmaz, [1]Murat Ozturk
[1]Isparta University of Applied Sciences, Faculty of Technology, Department of Mechatronics Engineering, Isparta, TURKİYE

*Corresponding author e-mail: fatiyilmaz7@gmail.com

ABSTRACT:
The main aim of this newly designed geothermal energy-based combined plant is to conduct the thermodynamic performance investigation for clean and sustainable power, hydrogen, heating, cooling, and hot water. For this aim, the Kalina cycle, an ORC, a double effect cooling system, two thermoelectric generators, a hot water generator, and finally, a hydrogen generation and storage unit are thermally integrated with a geothermal source. Each subsystem is examined in detail from the thermodynamic point of view and parametric analyzes are carried out. According to the analysis findings, the energy and exergy efficiency of the whole system is determined as 39.63% and 36.14%.

Keywords: Energy, Hydrogen, Multigeneration, Geothermal.

INTRODUCTION

With the rapid increase in energy demand in the world, the creation of suitable energy options for countries has become an important issue. Therefore, various energy sources have started to be preferred. Consequently, multigeneration systems (MG) have become one of the most important main alternatives [1]. Other important alternatives are renewable energy sources and hydrogen energy. The use of hydrogen by producing it from renewable energy sources is also indispensable in the fight against global warming and environmental problems. Geothermal energy has an important position among renewable energy sources and recently many studies have been presented to obtain different useful outputs in combined systems.

Mehdikhani et al. [2] proposed the two geothermal wells based combined plant in terms of thermodynamic and exergoeconomic analysis. According to the results they obtained, they stated that the thermal efficiency is improved by 3.18% compared to similar studies. Koc et al. [3] examined a geothermal energy-based combined plant system in which the energy and exergy efficiency of the overall plant is determined as 60.14% and 58.37%, respectively. Li et al. [4] studied an innovative flash-binary geothermal energy-based MG plant for power, hydrogen, freshwater and cooling. Their modeled plant has optimum exergy efficiency is 46.44%. As a result of a short literature review, it is seen that many useful outputs such as power and hydrogen can be obtained with geothermal energy-supported MG systems. The main purpose of this designed study, thermodynamic analysis of geothermal energy supported plant that is generated power, hydrogen, heating, cooling, and hot water production is carried out. One of its innovative parts is the storage of hydrogen and the other is the use of TEG instead of a condenser. Moreover, a comprehensive parametric study is carried out to examine the effects of some system elements on efficiency.

SYSTEM DESIGN AND ANAYSIS

The newly designed geothermal energy-based MG system, mainly consists of a Kalina cycle, an ORC plant, a double effect absorption cooling system, two thermoelectric generators, a domestic hot water generation unit, and a hydrogen generation and storage system, as illustrated in Fig.1.
Before applying a comprehensive thermodynamic analysis to this designed study, the general mass, energy, exergy, and entropy equilibrium equations are applied to each component separately, as stated below, according to the first and second laws of thermodynamics [5-7]

$$\sum \dot{m}_i = \sum \dot{m}_e \quad (1)$$

$$\sum \dot{m}_i h_i + \sum \dot{Q}_i + \sum \dot{W}_i = \sum \dot{m}_e h_e + \sum \dot{Q}_e + \sum \dot{W}_e \quad (2)$$

$$\dot{S}_{gen} = \sum \dot{m}_e s_e - \sum \dot{m}_i s_i - \sum \frac{\dot{Q}_{cv}}{T} \quad (3)$$

$$\dot{E}x_{Des} = \sum \dot{m}_e \dot{e}x_e + \sum \dot{E}x_e^Q + \sum \dot{E}x_e^W - (\sum \dot{m}_i \dot{e}x_i + \sum \dot{E}x_i^Q + \sum \dot{E}x_i^W) \quad (4)$$

where i and e subscripts determine the inlet and exits of the component. $\dot{Q}$ and $\dot{W}$ display the heat power, power transfer rate, respectively. For overall plant, the performance ratio of the whole system should be specified as;

$$\eta_{WS} = \frac{\dot{W}_{net} + \dot{Q}_{cooling} + \dot{Q}_{heating} + \dot{Q}_{hotwater} + LHV_{H_2}\dot{m}_{H_2}}{\dot{m}_1 h_1 - \dot{m}_7 h_7} \quad (5)$$

$$\psi_{WS} = \frac{\dot{W}_{net} + \dot{E}x^{\dot{Q}}_{cooling} + \dot{E}x^{\dot{Q}}_{heating} + \dot{E}x^{\dot{Q}}_{hotwater} + ex_{H_2}\dot{m}_{H_2}}{\dot{m}_1 ex_1 - \dot{m}_7 ex_7} \quad (6)$$

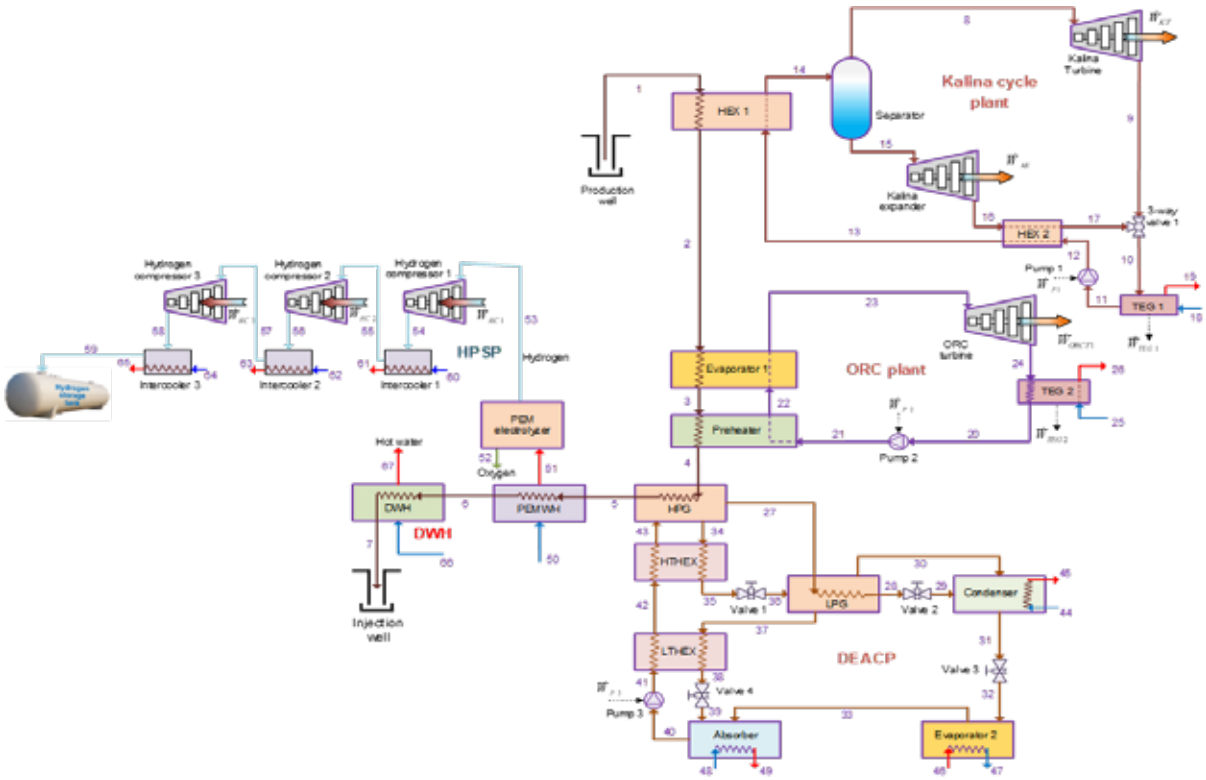


Fig. 1. Schematic illustration of geothermal MG plant

RESULTS AND DISCUSSION

In this proposed study, thermodynamic analysis is performed theoretically. There are some assumptions made and these are that the whole system is steady-state flowing, there is no temperature change between the system and the environment, kinetic and potential energy changes are neglected, and 25 ℃ ambient temperature and 101.325 kPa ambient pressure are assumed. As a result of the assumptions made, the results of the thermodynamic analysis findings are presented in Table 1 and Table 2 below. While Table 1 illustrates the useful outputs and consumed electrical power values in the system, Table 2 shows the energy and exergy efficiencies of the main subsystems.

Figs. 2 and 3 show the change of the reference temperature and the geothermal water temperature (T1) on the useful outputs obtained from the system. That is clearly seen that a positive effect of these two parameters on the system performance.

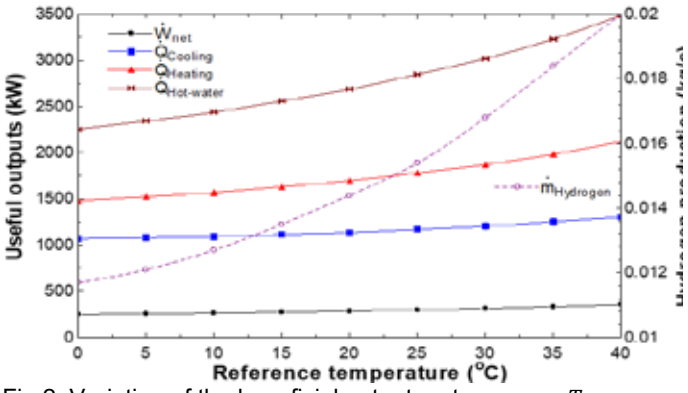


Fig.2. Variation of the beneficial outputs rates versus T_0

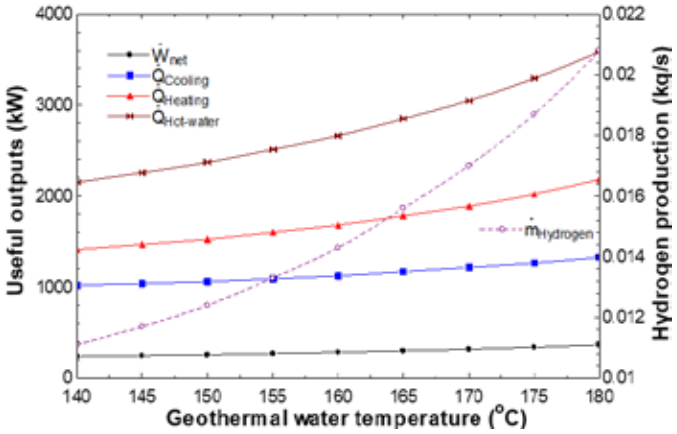


Fig.3. Variation of the beneficial outputs rates versus T_1

Figs. 4 and 5 display the increase in energy and exergy efficiency of the overall system and subsystems against different T1 temperatures. With the increase of the geothermal water outlet temperature from 140 ℃ to 180 ℃, the

useful outputs are obtained as the system reaches higher heights and the thermodynamic performance with flour increases.

CONCLUSION

The newly designed geothermal energy-based combined plant is proposed and analyzed for power, hydrogen, heating, cooling, and hot water. The proposed plant comprised a Kalina cycle, an ORC, a double-effect absorption cooling system, a domestic hot water generator, and hydrogen generation and storage. By applying a detailed thermodynamic analysis method, system efficiencies, namely energy and exergy efficiencies, are investigated for sub-systems and the whole system. It can highlight the most important points that come to the fore in the analysis results as follows;

- The power generation rate of the Kalina cycle and ORC are 358.2 kW and 160.4 kW. Also, TEG power generation rate is 182.62 kW. Furthermore, heating and cooling loads of this modeled plant are 1783 kW and 1169 kW, respectively. In conclusion, total hydrogen generation rate is 0.0156 kgs^{-1}
- The proposes MG plant's energy and exergy efficiency is computed as 39.63% and 36.14%, respectively.
- It is reported that with the goes up the reference and geothermal water temperature, the proposed system and subsystem performance clearly increase.

Table 1. Thermodynamic analysis results of the combined plant

Products	
Kalina turbine ($\dot{W}_{KT}$)	189.1 kW
Kalina expander ($\dot{W}_{KE}$)	169.1 kW
ORC turbine ($\dot{W}_{ORCT}$)	160.4 kW
TEG 1 ($\dot{W}_{TEG1}$)	70.82 kW
TEG 2 ($\dot{W}_{TEG2}$)	111.8 kW
Cooling ($\dot{Q}_{Cooling}$)	1169 kW
Heating ($\dot{Q}_{Heating}$)	1783 kW
Hot water ($\dot{Q}_{Hot_water}$)	2850 kW
Hydrogen ($\dot{m}_{H_2}$)	0.0156 kgs^{-1}
Oxygen ($\dot{m}_{O_2}$)	0.1232 kgs^{-1}
Consumptions	
Pump 1 ($\dot{W}_{P1}$)	17.76 kW
Pump 2 ($\dot{W}_{P2}$)	10.22 kW
Pump 3 ($\dot{W}_{P3}$)	30.88 kW
PEM electrolyzer ($\dot{W}_{PEM}$)	83.98 kW
Hydrogen compressor 1 ($\dot{W}_{HC1}$)	42.17 kW
Hydrogen compressor 2 ($\dot{W}_{HC2}$)	54.72 kW
Hydrogen compressor 3 ($\dot{W}_{HC3}$)	163.1 kW

Table 2. Energy and exergy efficiency of the main sub-plants

	Energy efficiency (%)	Exergy efficiency (%)
Kalina cycle plant	21.04	18.23
ORC plant	24.31	20.96
Double effect absorption cooling plant	18.28	10.24
Hydrogen production and storage plant	58.93	55.31
Domestic water heater	78.24	74.09
Overall plant	39.63	36.14

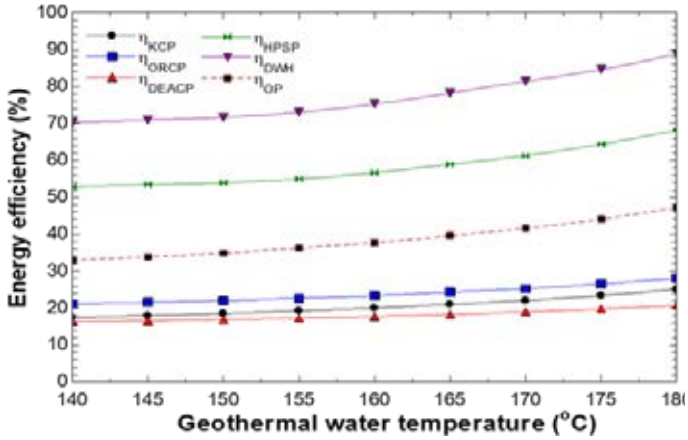


Fig.4. The picture of the energy efficiency of the sub-component and overall system vs different T_1.

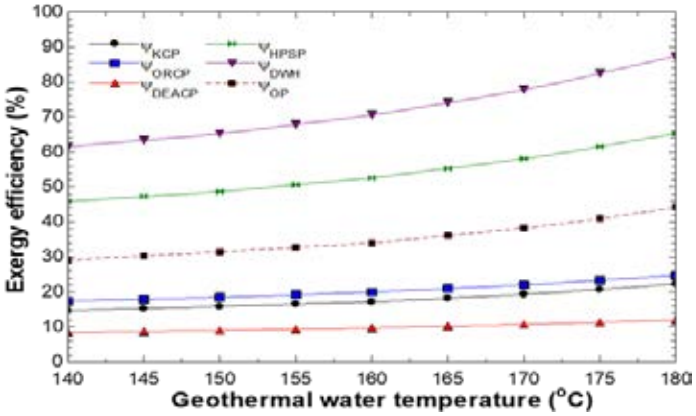


Fig.5. The picture of the exergy efficiency of the sub-component and overall system vs different T_1.

REFERENCES

1. Bicer, Y., & Dincer, I. (2016). Development of a new solar and geothermal based combined system for hydrogen production. *Solar Energy*, *127*, 269-284.
2. Mehdikhani, V., Mirzaee, I., Khalilian, M., & Abdolalipouradl, M. (2022). Thermodynamic and exergoeconomic assessment of a new combined power, natural gas, and hydrogen system based on two geothermal wells. *Applied Thermal Engineering*, 118116.
3. Koc, M., Yuksel, Y. E., & Ozturk, M. (2022). Thermodynamic assessment of a novel multigenerational power system for liquid hydrogen production. *International Journal of Hydrogen Energy*.
4. Li, K., Ding, Y. Z., Ai, C., Sun, H., Xu, Y. P., & Nedaei, N. (2022). Multi-objective optimization and multi-aspect analysis of an innovative geothermal-based multi-generation energy system for power, cooling, hydrogen, and freshwater production. *Energy*, 123198.
5. Çengel YA, Boles MA. Thermodynamics : an engineering approach. 8th ed. Mc. New York: McGraw-Hil;2015; 2015
6. Kotas TJ. The exergy method of thermal plant analysis. 1st ed. London: Butterworth-Heinemann; 1985
7. Dincer I. Thermodynamics: A Smart Approach. USA: John Wiley & Sons Ltd; 2020

WHEC-2022
23rd World Hydrogen Energy Conference
June 26-30, 2022 - Istanbul

#1523

MODELING OF A SUSTAINABLE INTEGRATED PLANT WITH sCO_2 AND tCO_2 CYCLES FOR HYDROGEN GENERATION

[1*]Fatih Yilmaz, [1]Murat Ozturk, [2]Resat Selbas
[1]Isparta University of Applied Sciences, Faculty of Technology, Department of Mechatronics Engineering, Isparta, TURKİYE
[2]Isparta University of Applied Sciences, Faculty of Technology, Department of Mechanical Engineering, Isparta, TURKİYE

*Corresponding author e-mail: fatiyilmaz7@gmail.com

ABSTRACT:
The primary goal of this proposed work is to examine the solar energy-combined multigeneration model in order to produce heating, power, hydrogen, and clean water in a comprehensive way from the thermodynamic aspect. This plant consists of mainly five sub-unit that is heliostat field, supercritical Brayton cycle, transcritical Rankine cycle, multi-effect desalination unit, and PEM electrolyzer. Looking at analysis results, the amount of the hydrogen rate of this combined plant is 0.001179 kgs^{-1}. Also, the capacity of the electrical power is 1194 kW. To finish, the whole energetic and exergetic performance of the modeled plant is 44.63% and 13.74%, respectively.

Keywords: Energy, Exergy, Hydrogen, Thermodynamic, Solar

INTRODUCTION

Currently, to meet the energy demand in our global, fossil-based fuels have still widely usage proportion. That is, it is mean that environmental problems caused by fossil fuels have linearly increased. One of the main and important solve these complications, the widespread usage of non-fossil energy sources that are solar, wind, geothermal, biomass and etc., in almost every field. However, it can be stated that the production and use of hydrogen in clean and sustainable ways is another effective method. In this respect, renewable energy, especially solar, assisted multigeneration systems and obtaining hydrogen from them, has become a subject of interest and researched by many researchers in recent years.

Dincer and Zamfirescu [1] modeled a multigeneration plant that generates a number of outputs. Their modeled plant' exergy efficiency is determined between 55% and 65%. Yilmaz [2] evaluated a new solar heliostat supported multigeneration plant. The modeled plant energy and exergy performance is computed as 78.93% and 47.56%, respectively. El-Emam and Dincer [3] developed a combined plant driven by solar heliostat system. They performed a comprehensive thermodynamic evaluation and then the amount of the hydrogen rate is found as 1.25 kgh^{-1}. Izadi et al. [4] conducted a comprehensive optimization of the trigeneration system driven by a solar tower unit and a hydrogen generation unit. Further, in 2021, thermodynamic and environmental analysis as well multiobjective optimization of a multigeneration plant are conducted by Colakoglu and Durmayaz [5]. Their suggested plant's energy efficiency is modeled at 55.57%, in the light of analysis results. Again in 2021, the authors [6] designed and thermodynamically examined a solar-assisted trigeneration plant for the purpose of electricity, ammonia, and fresh water production. The whole exergy efficiency of their suggested system is 12.1%.

The key difference of this paper from other works is the use of environmentally friendly CO_2 fluid in sub-power generation cycles. The significant purpose of this study is to examine the thermodynamic analysis of power, heating, freshwater, and hydrogen production by integrating solar heliostat supported, supercritical Brayton cycle ($sCO_2 - BC$), and transcritical Rankine cycle ($tCO_2 - RC$) subsystems.

SYSTEM DESIGN AND ANALYSIS

In this research, solar heliostat-based $sCO_2 - BC$ and $tCO_2 - RC$ sub-power plants are integrated to generate power, hydrogen, freshwater, and heating, as illustrated in Fig.1.

Thermodynamic performance analysis is applied to this integrated system that is above-mentioned. For thermodynamic modeling, mass, energy, entropy, and exergy balance equations in their general form are written for each component and then modeled with the EES package program. This equilibrium equation can be expressed as [7–9]:

$$\sum \dot{m}_i = \sum \dot{m}_e \quad (1)$$

$$\sum \dot{m}_i h_i + \sum \dot{Q}_i + \sum \dot{W}_i = \sum \dot{m}_e h_e + \sum \dot{Q}_e + \sum \dot{W}_e \quad (2)$$

$$\dot{S}_{gen} = \sum \dot{m}_e s_e - \sum \dot{m}_i s_i - \sum \frac{\dot{Q}_{cv}}{T} \quad (3)$$

$$\dot{E}x_{Des} = \sum \dot{m}_e \dot{e}x_e + \sum \dot{E}x_e^Q + \sum \dot{E}x_e^W - (\sum \dot{m}_i \dot{e}x_i + \sum \dot{E}x_i^Q + \sum \dot{E}x_i^W) \quad (4)$$

where i and e subscripts determine the inlet and exits of the component. $\dot{Q}$ and $\dot{W}$ display the heat power, power transfer rate, respectively. For overall plant, the performance ratio of the whole system should be specified as;

$$\eta_{WS} = \frac{\dot{W}_{net} + \dot{Q}_{heating} + LHV\dot{m}_{H_2} + \dot{m}_{fw}h_{fw}}{\dot{Q}_{solar}} \quad (5)$$

$$\psi_{WS} = \frac{\dot{W}_{net} + \dot{Ex}_{Q_{heating}} + ex_{H_2}\dot{m}_{H_2} + \dot{m}_{fw}ex_{fw}}{\dot{Ex}_{Q_{solar}}} \quad (6)$$

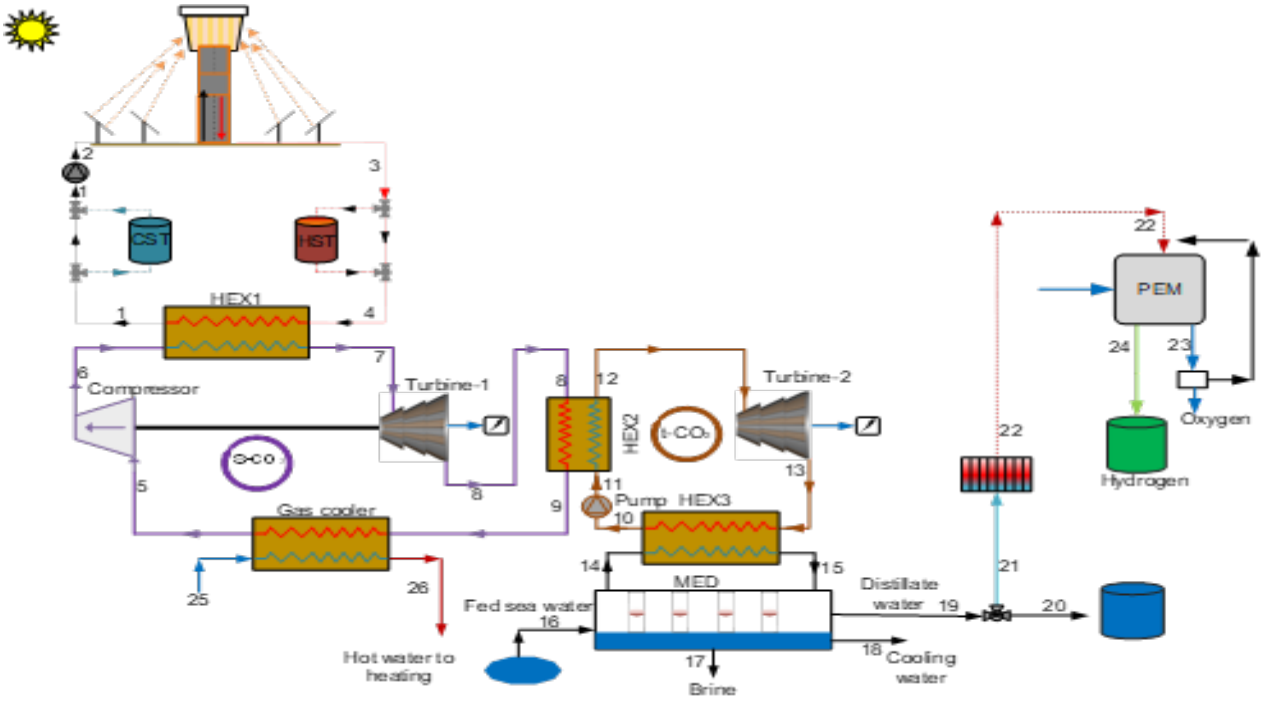


Fig. 1. Schematic representation of solar energy-based plant

RESULTS AND DISCUSSION

This examined work is carried out with a complete thermodynamic modeling of the solar multigeneration system that generates hydrogen, electricity, heating, and clean water production. The assumptions made to perform this analysis are presented in Table 1. In the light of Table 1, the analysis results applied are highlighted in Table 2.

Figure 2 shows the rise in useful output from the plant with the change of solar energy flux. Figure 3 plots the linear increase in energy and exergy performance of the total plant with increasing solar flux. Moreover, the effect of ambient temperature on the energy and exergy efficiency and total exergy destruction of the entire plant is presented in Figure 4.

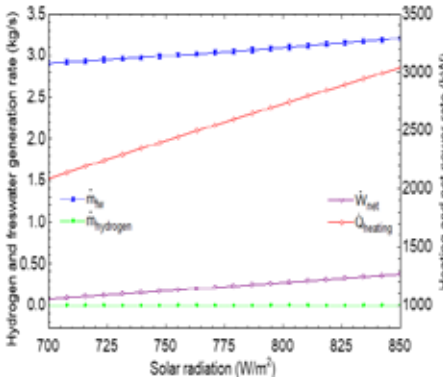


Fig.2. Effect of solar flux on the beneficial products from the suggested plant

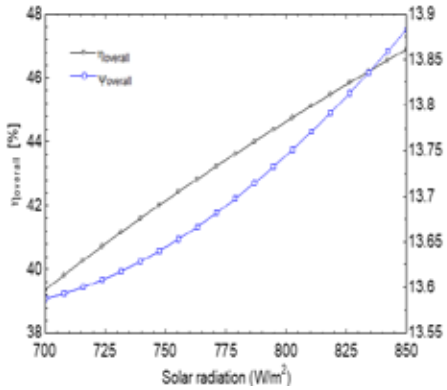


Fig.3. Impact of solar flux on the suggested plant's performance

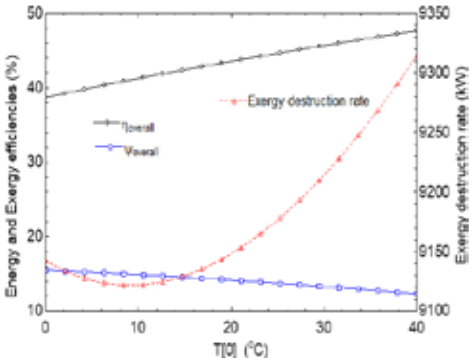


Fig.4. Performance and total exergy destruction rate versus reference temperature

Table 1. Assumptions for the thermodynamic modeling of the plant

Parameters	Unit	Value
Solar radiation	$\dot{W}/_{m^2}$	800
Heliostat are	m^2	11*11
Heliostat efficiency	%	76.5
Mass flow rate of solar cycle	kgs^{-1}	50
Solar cycle working fluid	-	Salt(68KCl_32MgCl2)
Compressor inlet pressure	kPa	$P_{critic} * 1.5$
Compressor pressure rate	-	2.5
Pump inlet pressure of RC	kPa	6300
Turbine inlet pressure of RC	kPa	9450
Desalination effect number	-	4
Sea water's salinity	ppm	42,000
Brine's salinity	ppm	47,000
Reference point temperature	℃	25
Reference point temperature	kPa	101.325

Table 2. Thermodynamic analysis results of the examined plant

Parameters		Value
Net power generation rate		1194, kW
Hydrogen generation capacity		0.001179, kgs^{-1}
Clean water generation capacity		3.095, kgs^{-1}
Heating capacity from hot water		2728, kW
$sCO_2 - BC$	Energy efficiency	14.7, %
	Exergy efficiency	41.69, %
$tCO_2 - RC$	Energy efficiency	6.41, %
	Exergy efficiency	30.78, %
Overall plant	Energy efficiency	44.63, %
	Exergy efficiency	13.74, %

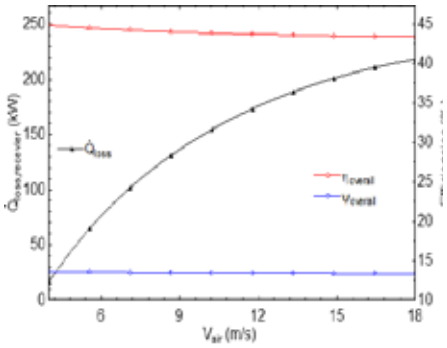


Fig.5. Performance and total heat loss rate versus air velocity

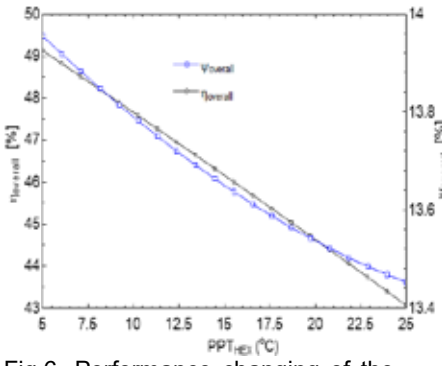


Fig.6. Performance changing of the overall plant versus different PPT_{HEX}

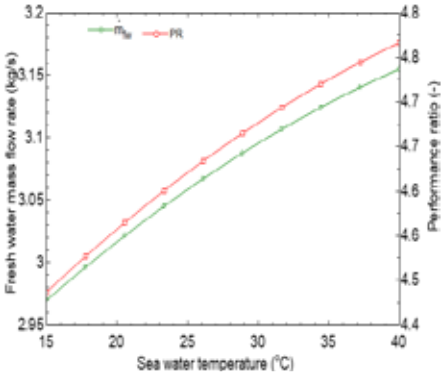


Fig.7. Impact of the seawater temperature on the performance rate of MED and amount of fresh water

Also, Figure 5 shows the impact of air velocity variation on overall system performance and heat loss. As the air velocity rises, the system performance decreases as the loss on the heliostat surface increases. The energy and exergy efficiency of the whole plant with the increase of pinch point temperature of HEX (PPT_{HEX}) is presented in Figure 6. In conclusion, increment in the seawater temperature give rise to an increase in the MED performance and fresh water generation rate, as shown in Fig. 7.

CONCLUSION

The proposed combined work that generates hydrogen, power, heating, and freshwater, is investigated and thermodynamically analyzed. For this aim, to examine energetic and exergetic performance and exergy destruction rate of the overall plant, parametric analysis is also applied. As a coming to the analysis results, some important points can be presented as below;

- The power and hydrogen generation capacity of this designed model is 1194 kW and 0.001179 kgs^{-1}. In addition, 3.095 kgs^{-1} of clean water was produced in this system.
- The total energetic and exergetic performance is calculated as 44.63% and 13.74%.
- With the increase of solar flux, the valuable productions obtained from the plant and the efficiency of the whole system increased.
- It is noted that with the increase of air velocity, the thermal loss on the heliostat surface increased and there is a low decrease in system performance due to this.

REFERENCES

1. Dincer I, Zamfirescu C. Renewable-energy-based multigeneration systems 2012. https://doi.org/10.1002/er.2882.
2. Yilmaz F. Thermodynamic performance evaluation of a novel solar energy based multigeneration system. Appl Therm Eng

2018;143:429–37. https://doi.org/10.1016/j.applthermaleng.2018.07.125.
3. El-Emam RS, Dincer I. Development and assessment of a novel solar heliostat-based multigeneration system. Int J Hydrogen Energy 2018;43:2610–20. https://doi.org/10.1016/j.ijhydene.2017.12.026.
4. Izadi A, Ahmadi P, Bashiri Mousavi S, Fakhari I. A comparative optimization of a trigeneration system with an innovative integration of solar Heliostat towers and Hydrogen production unit. Sustain Energy Technol Assessments 2021;47:101522. https://doi.org/10.1016/j.seta.2021.101522.
5. Colakoglu M, Durmayaz A. Energy, exergy and environmental-based design and multiobjective optimization of a novel solar-driven multi-generation system. Energy Convers Manag 2021;227:113603. https://doi.org/10.1016/j.enconman.2020.113603.
6. Demir ME, Dincer I. Development and assessment of a solar driven trigeneration system with storage for electricity, ammonia and fresh water production. Energy Convers Manag 2021;245:114585. https://doi.org/10.1016/j.enconman.2021.114585.
7. Çengel YA, Boles MA. Thermodynamics : an engineering approach. 8th ed. Mc. New York: McGraw-Hil;2015; 2015.
8. Kotas TJ. The exergy method of thermal plant analysis. 1st ed. London: Butterworth-Heinemann; 1985.
9. Dincer I. Thermodynamics: A Smart Approach. USA: John Wiley & Sons Ltd; 2020.

WHEC-2022
23rd World Hydrogen Energy Conference
June 26-30, 2022 - Istanbul

#1550

ENERGY MANAGEMENT OF GREEN HYDROGEN-BASED POWER-TO-POWER GENERATION SYSTEMS

[1,3*] *Alexandros Kafetzis,* [2] *Stella Chatzigavriel,* [1] *Panos Seferlis,* [3] *Kyriakos Panopoulos*
[1]Aristotle University of Thessaloniki, Department of Mechanical Engineering, Thessaloniki, Greece
[2] Horizon S.A., Serres, Greece
[2] Centre for Research and Technology Hellas, Chemical Process and Energy Resources Institute, Thessaloniki, Greece

*Corresponding author e-mail: akafetzi@certh.gr

ABSTRACT

Post-2030 decarbonization targets, enable energy storage as a key element in the energy mix of future sustainable energy systems in Europe. Storage is supported by the high penetration of renewable energy sources (RES) in the European energy landscape. One of the most efficient, zero emission fuels is hydrogen produced by RES via electrolysis. Hydrogen production and storage is combined with fuel cells and batteries to comprise an integrated Power-to-Power (P2P) system. Such systems offer efficient, reliable, and cost-effective energy delivery that is quick in release and of high density, aspects that are necessary to counter the RES power intermittency. Stochastic RES profiles, dynamic response of sub-components, and multiple decisions inside a constantly changing environment are major challenges in P2P systems' operation. The Energy Management Strategy (EMS) developed in this work and employed in the control framework of the P2P systems ensures their efficient operation. The EMS supervises the optimal distribution of power production and consumption. A series of applications of pilot P2P systems with different characteristics showcase the system's performance, resilience and replicability potential through certain key performance indicators (KPIs).

Keywords: Energy storage, Green hydrogen, Control, Renewable energy, Energy management

INTRODUCTION

Electricity generation, in general, is heavily dependent on fossil fuel generators that burn diesel, gas, or heavy fuel oil. Such fuels are extremely pollutant, expensive and uncertain due to high greenhouse gas emissions and challenges regarding transportation and availability [1]. Governments around the world are investing in infrastructure to provide an efficient, cost-effective, and cleaner alternative to electricity generation. Power generation through RES such as solar, wind, hydroelectric, and biomass is a viable solution to this task. The highly unpredictable and intermittent nature of RES power generation systems requires that the produced energy is converted and stored, like hydrogen or electricity in battery banks. Green hydrogen-based power-to-power systems integrated with fuel cells (FC), electrolyzers (EL), and batteries (BAT) provide medium to long-term storage capabilities by exploiting the available RES [2]. This work describes the formulation of a generalized control strategy that was built in parallel with the formulation of a decision-making algorithm in the form of operating rules that constitute an energy management strategy. This algorithm, namely finite state machine or finite state automata, integrates a propositional-based rationale that seeks to determine the status of each plant's subsystem and lead in the transition to a new status in compliance with the operational standards of the integrated framework [3]. This technique provides a robust and easily expandable systemic approach to the energy management of P2P systems in comparison to the widely used heuristic approaches. This approach is replicated to be implemented in different case studies and highlight its advantages. The main objectives and contributions of this study are the:

- Formulation of a generic control strategy based on the developed EMS.
- Operation analysis and comparison of performance among the case studies.
- Showcase the replicability of the EMS and overall system design.

SYSTEM DESCRIPTION AND METHODOLOGY

Three different motivating cases which are located in the north and south of Europe are selected, two are islanded microgrids and the third one is at a remote location at the edge of the electrical network [4]. The power supply subsystems are illustrated in Fig. 1. The primary energy source is local renewable systems from various sources (solar, wind, biomass). Moreover, the short-term load demands and energy storage is governed by batteries. Finally, hydrogen energy storage ensures the P2P system's long-term ability to satisfy load demands (days/weeks/months). Hydrogen is produced at 30 bars by electrolysis without any further compression stage. Low-pressure hydrogen storage comes with higher round-the-year efficiency, longer durability, improved reliability, and lower maintenance. The main characteristics of the subsystems and the overall configuration are given in Table 1. In this study, the operation of the hybrid energy storage system is realized with the use of Hybrid Automata (HA) which is described in detail in [3]. The interaction

between discrete and continuous operating dynamics motivates the use of HA which appears as a suitable formulation for the realization of a systemic EMS. The system requirements are transformed into propositional-based logic realizing a set of operating rules. The dynamics exhibited in such a system are predominantly of two kinds: a) specific actions such as start-ups and shutdowns of the FC and b) continuous dynamics (state of charge (SOC) of BAT). The application of the aforementioned systematic methodology to the power distribution between the subsystems is targeted within this work. To this end, the developed EMS is employed to achieve this objective using linear system-level models. The general objectives of the P2P energy storage system are:

- Optimal exploitation of RES power regarding load satisfaction and energy stored.
- Safe operation within the safety limits of every subsystem
- Preservation of battery life expectancy

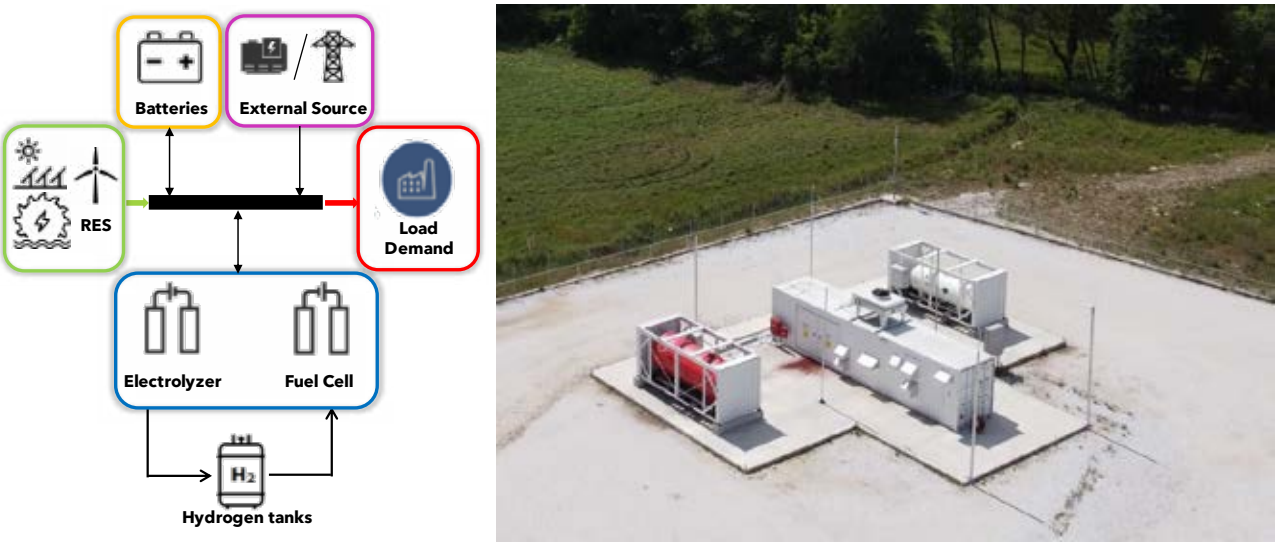


Fig. 1. (left) General layout of the P2P system, (right) Pilot demonstration of the P2P system [4]

Table 1. Main characteristics of the case studies

	Case 1	Case 2	Case 3
Remoteness	Off-grid	Micro-grid	Off-grid
Load	Residential	Residential, fish industry	Residential
RES	Solar (170kW)	Solar (85kW), Wind (225kW)	Solar (40kW), Biomass (50kW)
Storage	Hydrogen (1800kWh) Battery (600kWh)	Hydrogen (3700kWh) Battery (550kWh)	Hydrogen (500kWh) Battery (30kWh)
Fuel Cell	Proton Exchange Membrane (50kW)	Proton Exchange Membrane (100kW)	Proton Exchange Membrane (50kW)
Electrolyzer	Alkaline (50kW)	PEM (55kW)	Alkaline (25kW)

In this study, the battery, the fuel cell, the available RES in each site, and the external power (EXT) source are considered energy sources. Whether the energy that is produced by the RES is adequate to cover the load or another power source (FC, BAT, EXT) is necessary, it is defined by the size of the load demand. Therefore, the operation of the individual subsystems is determined by the energetic surplus or deficit between load and RES production occurring in each time step. When there is a RES surplus, the excess energy is stored. Depending on the level of fulfillment of the hydrogen tanks and battery banks, the battery is charged first up to the desired SOC, and then the electrolyzer will operate to produce and store hydrogen. If there is still a surplus of energy after both the tanks and batteries are full, then the energy is curtailed. When there is a RES deficit, the amount of energy to cover the remaining load comes from one of the power sources. First, the battery covers the load until it reaches its lower SOC limit and then the FC takes over the load demand. In case the system's stored energy is depleted then the external power source operates as backup.

RESULTS AND DISCUSSION

Each examined case integrates different RES technologies, exhibits variable load demands depending on the location, and incorporates the same control strategy with some minor adjustments. A set of metrics, or performance indicators, allows the assessment of the effects that each technology has on the integrated case. Each control formulation and its application to each case study is examined using these KPIs, which are defined as ratios of the cumulative energy (kWh) of each subsystem divided by the total RES surplus (kWh) or total demand (kWh) for a year. The first three metrics depict the conversion of the available RES surplus energy. Excess energy can either be stored or curtailed. Battery utilization is favored against hydrogen, resulting in a big difference between the converted surplus to hydrogen energy storage percentage and the electricity storage percentage. However, when a larger hydrogen storage unit is employed in combination with greater RES production, hydrogen storage is favored. The rest of the metrics refer to the distribution of the total load demand among the subsystems. The satisfaction of the load is mainly met by RES in all three cases, while the battery's involvement is governed by its capacity. When analyzing the overall performance, the KPI that best reflects the ability of the system to be resilient and emission-free is the "Total load satisfied by EXT". It is within the goals of the EMS to minimize the utilization of EXT. Overall, the issues that arise from the simulation of the three case studies are the large amounts of curtailed RES energy and the need for EXT intervention to cover the load. These issues can be dealt with in the designing process of the P2P plant by optimizing the storage capacities of both electricity and hydrogen storage. Larger hydrogen tanks or the addition of more battery stacks or both are the solutions to utilize as much RES energy as possible and fully curtail the use of fossil fuels.

Table 2. KPI comparison of the case studies

KPI	Equation	Case 1	Case 2	Case 3
RES surplus to electricity	$\frac{\text{RES surplus energy to battery}}{\text{RES surplus energy}}$	41%	15%	17.6%
RES surplus to hydrogen	$\frac{\text{RES surplus energy to battery}}{\text{RES surplus energy}}$	10%	18.8%	58.2%
RES surplus to curtailment	$\frac{\text{RES surplus energy to battery}}{\text{RES surplus energy}}$	49%	66.2%	24.2%
Total load by FC	$\frac{\text{Fuel cell energy to load}}{\text{Total load}}$	4.7%	4.6%	5.8%
Total load by EXT	$\frac{\text{External source energy to load}}{\text{Total load}}$	4.5%	0.8%	4.4%
Total load by BAT	$\frac{\text{Battery energy to load}}{\text{Total load}}$	43.6%	25.7%	4.2%
Total load by RES	$\frac{\text{RES energy to load}}{\text{Total load}}$	47.2%	68.9%	55.6%
Total load by BIO	$\frac{\text{Biomass energy to load}}{\text{Total load}}$	-	-	30%

CONCLUSIONS

This work developed and implemented a supervisory control algorithm based on the formulated generic EMS. The same EMS was implemented in different case studies with varying conditions and contexts, showing the replicability and performance that can be achieved. Future work will include the incorporation of additional and multiple energy sources and the integration of a greater number of subsystems.

ACKNOWLEDGEMENTS

This work has received funding from the European Union HORIZON 2020 project REMOTE - Remote area Energy supply with Multiple Options for integrated hydrogen-based TEchnologies, under Grand Agreement Number: 779541.

REFERENCES

1. Hirsch A, Parag Y, Guerrero J. 2018. Microgrids: A review of technologies, key drivers, and outstanding issues. Renewable and Sustainable Energy Reviews 90:402–11.
2. Tschiggerl K, Sledz C, Topic M. 2018. Considering environmental impacts of energy storage technologies: A life cycle assessment of power-to-gas business models. Energy 160:1091–100.
3. Kafetzis A, Ziogou C, Panopoulos KD, Papadopoulou S, Seferlis P, Voutetakis S. 2020. Energy management strategies based on hybrid automata for islanded microgrids with renewable sources, batteries, and hydrogen. Renewable and Sustainable Energy Reviews 134:1364-0321.
4. REMOTE - Remote area Energy supply with Multiple Options for integrated hydrogen-based Technologies. https://www.remote-euproject.eu. Accessed 10 Apr 2022.

WHEC-2022
23rd World Hydrogen Energy Conference
June 26-30, 2022 - Istanbul

#1553

HYDROGEN AND FRESHWATER PRODUCTION FROM TIDAL ENERGY

[1*] Cihad Çelik, [2] Murat Emre Demir
[1,2]İstanbul Technical University, Faculty of Naval Architecture and Ocean Engineering, Maslak, İstanbul, Turkey

*Corresponding author e-mail: celikciha@itu.edu.tr

ABSTRACT

This study presents a concept of a renewable energy system based on hydrogen generation by coupling of an electrolyser to a tidal generator. The proposed energy conversion system has two main energy requirements. The first one is for the electrolyser and the other is for the reverse osmosis unit. High-fidelity CFD simulations are performed on whether the preliminary designed turbine would provide sufficient power in OpenFOAM open-source package. Results show the importance of detailed design to understand the hydrodynamics characteristics of tidal turbines. Considering the maximum C_p at 3.5 TSR, the output power calculated as $44.67\ kWh$. The selected turbine's parameters do not meet the required power. In this case, the preliminary turbine design should be updated by increasing the swept area of it.

Keywords: Tidal power, Hydrogen storage, CFD, Reverse osmosis

INTRODUCTION

Tides are very long waves that move back and forth in the same direction in response to the forces of the moon and sun. Tidal energy is a type of renewable energy most prevalent along ocean coasts. Therefore, countries with this type of coastal area are interested in utilizing and improving the efficiency of tidal energy. There are three leading technologies, namely tidal turbines [18], barrages and lagoons based on their physical configurations that utilize tidal energy. Lopez and his colleagues [10] investigated the hydrokinetic energy conversion systems in detail and their current status in terms of energy conversion schemes and structural installation. As with all renewable energy conversion systems, tidal energy devices should be divided into three stages: design, operation, and end use. In design stage, requirements have to be defined carefully to be able to decide the size of tidal energy convergence system. Then, the system layout is prepared according to the direction of flow, mass flow rate and so on. In operation, tidal devices generally work back and forth in the same direction regarding the tides' directions [14]. The stored energy in the form of pumped, compressed air or in batteries is directly consumed by the user in end-use stage. Tidal turbines are classified in two main categories according to their rotor configuration, horizontally and vertically. Both of them have advantages and disadvantages concerning design simplicity, generator coupling, floating equipment, noise emission, skewed flow, knowledgebase, performance, control, which are clearly described by [10].

DESIGN OF THE ENERGY CONVERSION SYSTEM

Fig. 1 (a) shows a concept of a renewable energy system based on hydrogen generation by coupling an electrolyser to a tidal generator in the first line. This type of system can be used to store hydrogen and operate a polymer electrolyte membrane (PEM) fuel cell to provide power at times when renewable energy cannot meet the load demand and to compensates for the power oscillations of the production units. The other line of the system occurs the freshwater from the seawater with the help of Reverse Osmosis (RO) unit [6]. The tidal turbine powers the high-pressure pump which moves and pressurizes water from the sea to the RO unit. An electrolysis unit is a system that utilizes electricity to break water into hydrogen and oxygen. Produced hydrogen is directly stored in an undersea storage unit. The hydrogen storage system is designed to be underwater in order to take advantage of the tidal turbine operating beneath the free surface and thereby keep away from most of the significant effects of storms and waves. The storage system has a buoyant balloon suspended in deep-sea water and connected by an anchor [12]. Freshwater supply has always been critical to sustainability. In this context, the generated tidal power is used to generate freshwater by utilizing the coastal area within the scope of this study. Studies [2],[11] showed that RO is one of the best desalination methods which can be coupled with tidal energy. In the RO process, the pressurized seawater passes through a semipermeable membrane which, separates freshwater from the seawater.

System Energy Requirement

The proposed energy conversion system has two main energy requirements. The first one is for the electrolyser and the other is for the RO unit. There are many analyzes [1],[13] that show the energy consumption of a RO unit. According to [4], an energy efficient RO unit's consumption is assumed to be $2.4\ kWh$ for $1\ m^3$ fresh water.

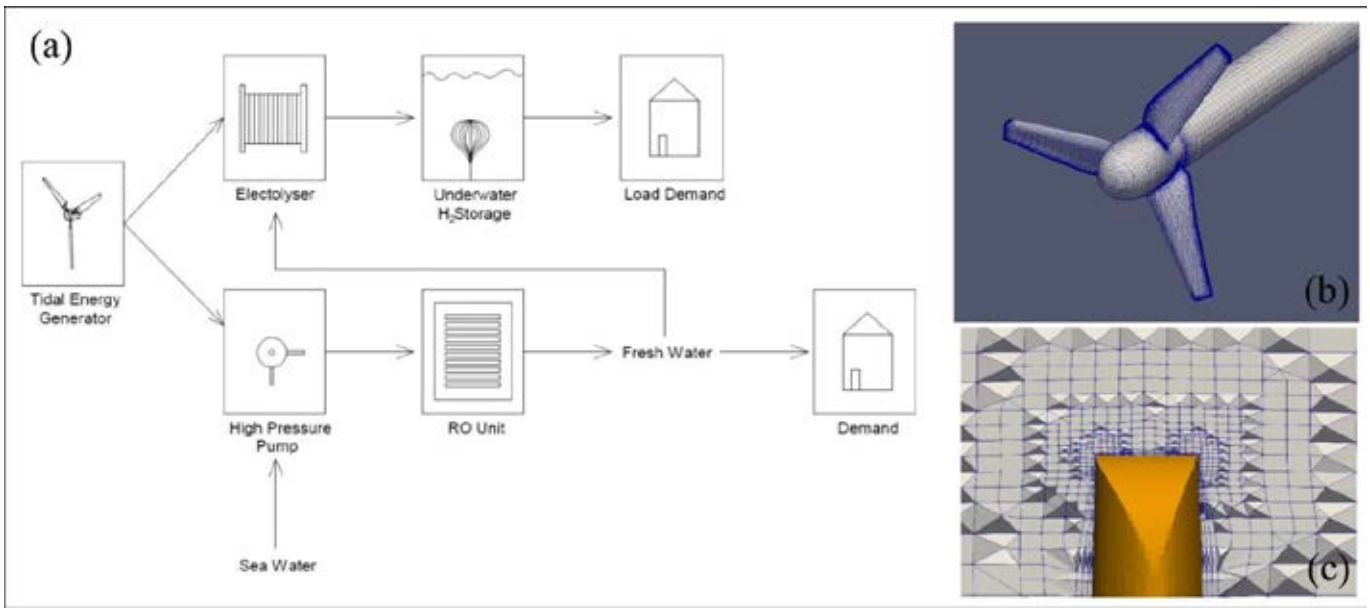


Fig. 1. Tidal energy conversion scheme (a), mesh structure on the turbine geometry (b) and detailed view of mesh layers in boundary layer at tip of the blade (c)

1 kg of hydrogen is ideally produced from 8.9 liters of water by supplying $39\ kWh$ of electricity at $25℃$ and 1 atmosphere pressure. Typical electrolyser units are being used with an efficiency of between approximately 56% and 80% which corresponds to between $70\ kWh$ and $50\ kWh$. The required power for the selected Proton Exchange Membrane (PEM) type electrolyser is $55\ kWh$ to produce 1 kg of hydrogen gas [9],[8]. The rest of the fresh water after the electrolyzes process is consumed by the community.

Considering the real state of a wind turbine, there are environmental and structural effects such as biofouling around the turbine, turbine's hydro-elastic behavior and so on that consume the produced power. Therefore, an additional 10% margin is considered, and the turbine's total energy is estimated as $63.14\ kWh$.

PRELIMINARY DESIGN OF THE HORIZONTAL AXIS TIDAL TURBINE

In this study, the steady flow condition is assumed to design and implement the horizontal axis tidal turbine energy conversion system. An approach is presented to determine of the tidal turbine dimensions with respect to the load demand. Firstly, the required power is determined and then an initial tidal turbine [6] is selected to carry out CFD analysis which computes the torque (Q) and output power (P_{out}) relatively. CFD simulations are performed by changing the rotational speed (ω) of the tidal turbine, which give the results of C_p in equation (1). The curve of the tip speed ratio (TSR) versus C_p is drawn to determine the maximum power of the characteristic tidal turbine and corresponding TSR value. The output power is directly related to the design parameters of a tidal turbine such as diameter of the rotor area, number of blades, section profiles of blades, sections' twist angle, hub geometry and so on. It has a dominant importance to determine the diameter of the rotor area among other parameters. In the second stage of the design, it is checked whether the output power provides the required power of the energy conversion system. The rotor diameter decreased or increased depending on the result from the CFD within the scope of this study.

Power coefficient is defined as follows;

$$C_p = \frac{P_{out}}{P_{in}} = \frac{Q\omega}{\frac{1}{2}\rho A V_{in}^3} \quad (1)$$

Here, ρ is the density of water, A is the blade swept area, V_{in} is the inlet velocity, Q is the turbine torque, ω is the turbine angular velocity (rad/s).

The mean flow velocity of tides is assumed as $2\,m/s$. In the preliminary design of the horizontal axis turbine, the maximum C_p is considered to be 0.4 before the high-fidelity CFD simulations. Then, the initial radius of the swept area is calculated as $3.5\ m$.

Turbine Geometry

There are different types of tidal turbines based on the number of blades and section geometry. Three blade and S814 section type tidal turbine investigated experimentally [16] in Emerson Cavitation Tunnel is selected to produce the power. The model scale turbine has $0.4m$ diameter utilized instead of using the full scale one in this study. There is a critical phenomenon that should be pointed out about the scale effect of the tidal turbine. Song and his colleagues [15] have carried out numerical analysis on both model and full scale to show the difference in terms of C_p. They presented that there is a slight difference on C_p curve between 1 and 5 TSR.

CFD SIMULATION AND VALIDATION

In this work, the viscous flow around the tidal turbine is solved with the open-source software, OpenFOAM. Three dimensional, incompressible, unsteady RANS equations as momentum equations are solved by the method of finite volume discretization. The other governing equation is the conservation of mass in the problem. The first-order implicit (Euler) scheme is applied to discretize the unsteady term in Navier-Stokes equations. PIMPLE Algorithm, a combination of PISO (Pressure Implicit Split Operator) and SIMPLE (Semi Implicit Methods Pressure Linked Equations) algorithms, is used to solve the pressure-velocity coupling. Inlet, bottom, top and side boundaries are located 10 times diameter (D) of the turbine away from the turbine model and the outlet boundary is placed 20 times D downstream direction. The snappyHexMesh utility is executed to create a three-dimensional mesh. The number of mesh is around 2.5 M and the average $y+$ value of turbine blades is 12.6. (see Fig. 1 (a) and (b))

RESULTS AND DISCUSSION

CFD simulations have been performed by changing the rotational speed (ω) of the tidal turbine. The curve of the tip speed ratio (TSR) versus C_p was obtained to determine the maximum power of the characteristic tidal turbine and corresponding TSR value. The maximum C_p is 0.283 achieved at around 3.5 TSR, which shows good agreement with the experimental data provided by [16]. The power into turbine P_{in} is $157.85\ kWh$ on full scale condition. Considering the maximum C_p at 3.5 TSR, the output power calculated as $44.67\ kWh$. It should be noted that the selected turbine's parameters do not meet the required power. In this case, the preliminary turbine design should be updated by increasing the swept area of it.

Pressure distribution around the turbine has been shown in Fig. 3 at 3.5 TSR. Tip vortex formation starts from TSR3 and then grows gradually up to TSR4.

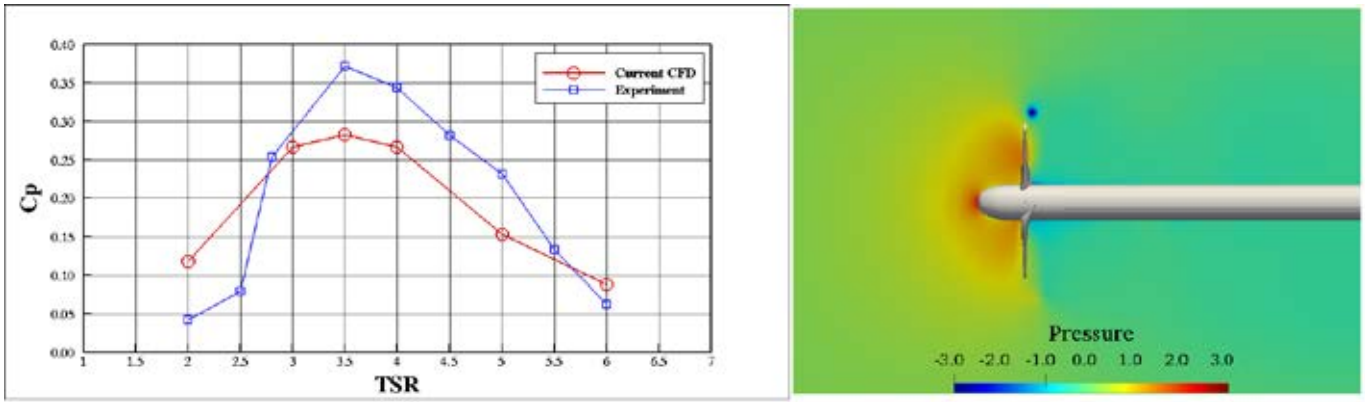


Fig. 3. Variation of C_p with TSR and pressure distribution at 3.5 TSR

CONCLUSIONS

Performing CFD simulations play a critical role to understand the hydrodynamics characteristics of tidal turbines. This study shows the miscalculation points at the preliminary design stage. The maximum C_p at 3.5 TSR, the output power calculated as $44.67\ kWh$. The output power of the designed horizontal axis tidal turbine at the preliminary design stage does not meet the required power according to the high-fidelity CFD simulations. Therefore, the swept area of the tidal turbine should be increased to generate enough torque.

REFERENCES

1. Amy, G., Ghaffour, N., Li, Z., Francis, L., Linares, R. V., Missimer, T., & Lattemann, S. (2017). Membrane-based seawater desalination: Present and future prospects. *Desalination*, *401*, 16-21.
2. Delgado-Torres, A. M., García-Rodríguez, L., & del Moral, M. J. (2020). Preliminary assessment of innovative seawater reverse osmosis (SWRO) desalination powered by a hybrid solar photovoltaic (PV)-tidal range energy system. *Desalination*, *477*, 114247.
3. Gu, Y. J., Liu, H. W., Li, W., Lin, Y. G., & Li, Y. J. (2018). Integrated design and implementation of 120-kW horizontal-axis tidal current energy conversion system. *Ocean engineering*, *158*, 338-349.
4. Karabelas, A. J., Koutsou, C. P., Kostoglou, M., & Sioutopoulos, D. C. (2018). Analysis of specific energy consumption in reverse osmosis desalination processes. *Desalination*, *431*, 15-21.
5. Khan, M. J., Bhuyan, G., Iqbal, M. T., & Quaicoe, J. E. (2009). Hydrokinetic energy conversion systems and assessment of horizontal and vertical axis turbines for river and tidal applications: A technology status review. *Applied energy*, *86*(10), 1823-1835.
6. Khanjanpour, M. H., & Javadi, A. A. (2021). Optimization of a Horizontal Axis Tidal (HAT) turbine for powering a Reverse Osmosis (RO) desalination system using Computational Fluid Dynamics (CFD) and Taguchi method. *Energy Conversion and Management*, *231*, 113833.
7. Kim, J., Park, K., Yang, D. R., & Hong, S. (2019). A comprehensive review of energy consumption of seawater reverse osmosis desalination plants. *Applied Energy*, *254*, 113652.
8. Kroposki, B., Levene, J., Harrison, K., Sen, P. K., & Novachek, F. (2006). Information and Opportunities for Electric Power Utilities.
9. Kumar, S. S., & Himabindu, V. (2019). Hydrogen production by PEM water electrolysis–A review. *Materials Science for Energy Technologies*, *2*(3), 442-454.
10. López, A., Morán, J. L., Núñez, L. R., & Somolinos, J. A. (2020). Study of a cost model of tidal energy farms in early design phases with parametrization and numerical values. Application to a second-generation device. *Renewable and Sustainable Energy Reviews*, *117*, 109497.
11. Ling, C., Lou, X., Li, J., & Zhang, Y. (2018, October). Experimental investigation of a novel tidal supercharger driven by tidal energy for reverse osmosis seawater desalination. In *Advances in Renewable Energies Offshore: Proceedings of the 3rd International Conference on Renewable Energies Offshore (RENEW 2018), October 8-10, 2018, Lisbon, Portugal* (p. 191). CRC Press.
12. Morgan, J. P. (2010). *U.S. Patent Application No. 12/614,183*.
13. Park, K., Kim, J., Yang, D. R., & Hong, S. (2020). Towards a low-energy seawater reverse osmosis desalination plant: A review and theoretical analysis for future directions. *Journal of Membrane Science*, *595*, 117607.
14. Rourke, F. O., Boyle, F., & Reynolds, A. (2010). Tidal energy update 2009. *Applied energy*, *87*(2), 398-409.
15. Song, S., Demirel, Y. K., Atlar, M., & Shi, W. (2020). Prediction of the fouling penalty on the tidal turbine performance and development of its mitigation measures. *Applied Energy*, *276*, 115498.
16. Uşar, D. (2015). *Sualtı akıntı türbinlerinin hidrodinamik analizi* (Doctoral dissertation, Fen Bilimleri Enstitüsü).
17. Wang, Y., Seo, B., Wang, B., Zamel, N., Jiao, K., & Adroher, X. C. (2020). Fundamentals, materials, and machine learning of polymer electrolyte membrane fuel cell technology. *Energy and AI*, 100014.
18. https://www.conserve-energy-future.com/tidalenergy.php

WHEC-2022
23rd World Hydrogen Energy Conference
June 26-30, 2022 - Istanbul

#1555

DEEP LEARNING-BASED BINARY CLASSIFICATION OF ISLANDING CONDITIONS IN A HYDROGEN ENERGY-BASED DISTRIBUTED GENERATION SYSTEM

[1] *Alper Yılmaz,* [2*] *Gökay Bayrak*
[1,2] Bursa Technical University, Smart Grid Laboratory, Department of Electrical and Electronics Engineering, 16300, Bursa, Turkey

*Corresponding author e-mail: gokay.bayrak@btu.edu.tr

ABSTRACT

This paper presents a deep long short-term memory (DLSTM) with a binary-label classifier method proposed for binary classification of islanding and non-islanding events in a hydrogen energy-based distributed generator (DG) system. Deep learning (DL)-based method eliminated the lack of performance of conventional intelligent islanding detection methods that uses feature extraction, feature selection, and event classification. Besides, the proposed method has provided the need for a processing-intensive filtering process to reduce noise from the signal. The proposed islanding detection method has a 98.33% accuracy rate under no-noise, and 97.66% high-level noise conditions. In the proposed method, the non-detection zone (NDZ) is almost zero, and the detection time is under the defined IEEE 929-2000 standards. Experimental and simulative data results show that the LSTM-based islanding detection method outperforms the algorithms in recent studies in terms of noise immunity and accuracy.

Keywords: Hydrogen energy, Islanding detection, Long-short-term memory, Deep learning, Microgrid.

INTRODUCTION

The use of distributed generators (DGs) is becoming more common worldwide and hydrogen energy (HE) is the most promising renewable energy source for DGs with their advantages [1]. The adoption of Fuel Cell (FC) technology can eliminate the weather dependence on renewable energy resources (RES) such as wind farms and, photovoltaic (PV) systems [2]. Besides, the rapid advancement of FC technology has increased the popularity of grid-connected FC systems. The rapidly growing number of grid-connected FC systems must meet some electrical connection standards. As a result, connecting FC systems to the main grid is a major concern for DGs [1]. One of these criteria and the most important is islanding detection. Islanding as defined by IEEE standards [3]: The condition in which a distribution system becomes is electrically isolated from the grid yet continues to be energized by one or more local DG through the associated point of common coupling (PCC). Detecting unplanned islanding conditions in FCs improves system stability and allows consumption-side equipment to operate more consistently for longer periods [4].

Islanding detection methods can be classified as remote, local, and intelligent methods. However, local methods have several drawbacks, including difficulty in determining a threshold value, uncertainty due to operating conditions, and susceptibility to noise [5]. Also, they contain a large non-detection zone (NDZ) [6]. NDZ is low in remote methods, but the cost is quite high [6]. To eliminate the drawbacks of conventional methods, intelligent methods including signal analysis and classifier are proposed [6]. Previous research divided automatic islanding identification into three stages: signal processing [7], feature selection [8], and event classification [9]. In the signal analysis step, all methods have a heavy computation burden and are affected by noise. Besides, the feature filtering optimization process is time-consuming and tedious. Deep learning (DL) methods have automatic feature extraction capability, eliminate human involvement, it has closed-loop feedback. These methods can automatically extract t features without the need for any conventional signal analysis method.

In this study, the DL-based islanding detection method using long short-term memory (LSTM) is proposed for binary classification of islanding and minor disturbances such as sags, swells, and frequency deviations in a hydrogen energy-based DG system. Besides, high penetration of PV and wind energy in the micro-grid with hydrogen energy-based DG is examined in the scenarios. The motivation for using LSTM in this model is to extract the dependencies between each row of features from the network model. Deep LSTM (DLSTM) is used for feature extraction and classification, unlike the conventional three-stage process. The proposed islanding detection method has a 98.33% accuracy rate under no-noise, and 97.66% high-level noise conditions. In the proposed method, the NDZ is almost zero, and the detection time is under the IEEE standards.

DATA GENERATION AND TEST SYSTEM

Islanding conditions with different real/reactive power mismatches and minor disturbances are generated using the MATLAB/SIMULINK model in Ref. [9] for hydrogen energy-based DG connected microgrid. The fundamental frequency and the sampling frequency are selected 50 Hz, and 10 kHz, respectively. Besides, the number of cycles for each

sample is selected 10 cycles.1000 samples are generated for each event for the training proposed model. The number of training sets reached 7000 samples. Generated test samples for islanding and non-islanding classes are shown in Table 1.

Table 1. Generated test samples for islanding and non-islanding classes using a simulated test system [9]

Class	Events	Number of Test Samples
C1	Islanding in different power mismatches (at the PCC of the Hydrogen energy-based DG)	300
C2	Voltage sag (switching on loads and switching off capacitor banks)	100
	Voltage swell (switching offloads and switching on capacitor banks)	100
	Induction motor starting	100
	Presence of drive systems	100
	PV disconnection	100
	Line-to-ground (LG), two line-to-ground (LLG), and three line-to-ground (LLLG) faults	200

DLSTM-BASED ISLANDING DETECTION METHOD

The proposed DL-based model is shown in Fig. 1. LSTM models are a type of recurrent neural network (RNN) to overcome the vanishing gradient problem. LSTM models are formed by sequential use of the LSTM units [10]. Models using multiple LSTM layers are called deep LSTM (DLSTM). In the proposed method, there is a dropout layer, which can be used once or several times between layers to prevent overfitting problems. At the output of the LSTM layers, there is a traditional neural network layer containing an activation function for classification. This layer is called a fully connected (FC) layer. FC layer uses the features extracted from the previous layers. As a result of this, it is possible to say that the DLSTM model includes feature extraction in itself. In islanding and minor disturbances classification, we used a softmax layer with a softmax activation function at the end of FC layers. The softmax means the probability of the input sample. That is, the class with the highest probability will be determined as the output. Utilizing the softmax activation function given by

$$P(y = j\,|x) = \frac{e^{x^T w_j}}{\sum_{k=1}^{K} e^{x^T w_k}} \tag{1}$$

where, x represents the input vector, and w is the weight matrix.

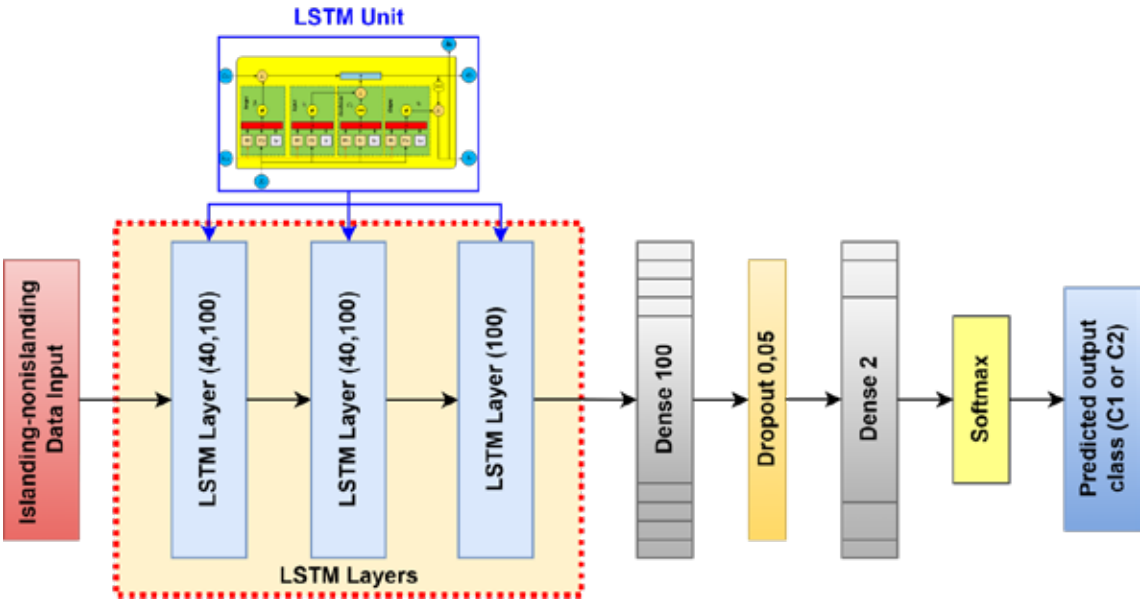


Fig. 1. Proposed DL-based islanding detection model

RESULTS

The classification test results of the proposed method have shown in Table 2. Accuracy performance is very high for test data containing noise at different signal-to-noise ratio (SNR) values and covering all scenarios. The proposed approach classifies islanding conditions caused by CB opened and minor disturbances caused by the presence of drivers with industrial equipment, short circuit faults, motor starting, RES disconnection, and, loads/capacitors switching in microgrids.

Table 2. Classification results for DLSTM

Class	Number of test samples	Corrections	Accuracy rate (%)
C1	300	294	98.0
C2	700	687	98.14

The performance comparison of DLSTM and convolutional neural network (CNN)-based method at different noise levels is given in Table 3. DLSTM provides better performance than CNN in accuracy and noise immunity. LSTM is to extract the dependencies between each row of features from the model. With this advantage, the proposed model shows performance superiority in automatic feature extraction.

Table 3. Comparison with CNN

	Accuracy rate (%)		
Model	**Under no-noise**	**Under low level noise (SNR:40 dB)**	**Under high level noise (SNR:30 dB)**
CNN	98.37	97.89	96.47
Proposed DLSTM	98.33	98.01	97.66

CONCLUSIONS

In this study, the LSTM-based DL method is proposed for binary classification of islanding and minor disturbances in hydrogen energy-based DG-connected microgrid. DLSTM eliminated the lack of performance of conventional intelligent islanding detection methods. The LSTM-based method is analyzed under different load conditions on the simulated test system. The accuracy results are also compared with the CNN-based method. DLSTM has 98.33% accuracy under no-noise, and 97.66% high-level noise conditions. The NDZ is almost zero, and the detection time is under the IEEE standards for DLSTM with binary classifier.

REFERENCES

1. Lin, R. H., Zhao, Y. Y., and Wu, B. D. 2020. Toward a hydrogen society: Hydrogen and smart grid integration. International Journal of Hydrogen Energy 45.39: 20164-20175.
2. Wang, F. C., Lin, K. M., Yang, Y. Z., and Liu, H. W. 2021. Fuel-cell sharing for a distributed hybrid power system. International Journal of Hydrogen Energy 46(1), 1174-1187.
3. IEEE Std. 929-2000, IEEE Recommended Practice for Utility Interface of Photovoltaic (PV) Systems, Institute of Electrical and Electronics Engineers, Inc., New York, NY.
4. Bayrak, G. and Cebeci, M. 2014. A novel anti-islanding detection method for grid-connected fuel cell power generation systems. International Journal of Hydrogen Energy 39(16), 8872-8880.
5. Bayrak, G. 2018. Wavelet transform-based fault detection method for hydrogen energy-based distributed generators. International Journal of Hydrogen Energy, 43(44), 20293-20308.
6. Khan, M. A., Haque, A., Kurukuru, V. B., and Saad, M. (2022). Islanding detection techniques for grid-connected photovoltaic systems-A review. Renewable and Sustainable Energy Reviews, 154, 111854.
7. Yılmaz, A., and Bayrak, G. 2022. A new signal processing-based islanding detection method using pyramidal algorithm with undecimated wavelet transform for distributed generators of hydrogen energy. International Journal of Hydrogen Energy.
8. Hussain, A., Kim, C. H., and Admasie, S. 2021. An intelligent islanding detection of distribution networks with synchronous machine DG using ensemble learning and canonical methods. IET Generation, Transmission & Distribution, 15(23), 3242-3255.
9. Yılmaz, A., Küçüker, A., and Bayrak, G. 2022. Automated classification of power quality disturbances in a SOFC&PV-based distributed generator using a hybrid machine learning method with high noise immunity. International Journal of Hydrogen Energy.
10. Özcanlı, A. K., & Baysal, M. 2022. A novel multi-LSTM-based deep learning method for islanding detection in the microgrid. Electric Power Systems Research, 202, 107574.

WHEC-2022
23rd World Hydrogen Energy Conference
June 26-30, 2022 - Istanbul

#1556

THD MINIMIZATION OF VEHICLE-TO-GRID (V2G) IN FUEL CELL EVs WITH A DEVELOPED ELLIPTIC IIR FILTER

[1*]Gökay Bayrak, [2]Alper Yılmaz
[1,2] Bursa Technical University, Smart Grid Laboratory, Department of Electrical and Electronics Engineering, 16300, Bursa, Turkey

*Corresponding author e-mail: gokay.bayrak@btu.edu.tr

ABSTRACT

The popularity of fuel cell electric vehicles (FCEVs) and plug-in electric vehicles (PEVs) is a key factor in addressing the electricity demand. With vehicle-to-grid (V2G) applications, these vehicles can act as distributed generators. Total harmonic distortion (THD) in the connection of electric vehicle charge stations (EVCSs) capable with V2G technology with the grid should be fulfilling the values specified by international electrical standards. Although V2G topologies are improved, the use of a suitable filter is necessary to improve the power quality (PQ) of the system. Since analog filters bring additional losses to power losses caused by inverter and converter, software-based digital filters are also needed. Due to the implementation of the infinite impulse response (IIR) filter includes fewer parameters, it requires less memory and has less computational complexity. In this study, a low-pass elliptical IIR filter design is realized in real-time with the converter using LabVIEW infrastructure. When imbalances occur in the grid voltage, reducing bandwidth using phase locked loop (PLL) will not be enough to keep the system stable. This problem solved by adding a proposed low-pass elliptical IIR filter to the system.The results obtained by using the filter are presented in the paper and the THD value was obtained as 0.82% for converter capable V2G.

Keywords: Vehicle-to-grid (V2G), Fuel cell electric vehicles (FCEVs), IIR filter design, THD minimization, Power quality

INTRODUCTION

Today, limited fossil fuel sustainability, environmental concerns, and increasing energy demand are universal issues that are widely addressed to find appropriate solutions. Fuel cell electric vehicles (FCEVs) and plug-in electric vehicles (PEVs) with vehicle-to-grid (V2G) support stand out in solving these problems [1,2]. Here, it is an important criterion to connect the electric vehicle charging stations (EVCS) with V2G technology to the grid following the grid code requirements. Besides, V2G topologies have improved, and a proper filter is required to increase the system's power quality (PQ) and THD minimization.

A digital filter used in converters is a method or algorithm that works on digitized analog signals, converting the input signal to the desired output signal. Among the main design purposes of the filters, which have a wide application area, are to separate the interfering signals from each other, to increase the signal quality by reducing the noise in the signal, and to recover the distorted signal. In the frequency selective filters, desired filter properties are defined in the frequency region in terms of desired amplitude and phase response. In the filter design filter, we determine the desired frequency response characteristics, and the response coefficients to provide the causal finite impulse response (FIR) [3] or infinite impulse response (IIR) filter [4] most closely. Digital filter design depends on the nature of the problem and the characteristics of the desired frequency response.Due to the implementation of the IIR filter includes fewer parameters, it requires less memory and has less computational complexity. Because of its advantages, the IIR filter is used in this study.

In a study on this subject [5], an adaptive IIR digital filter design has been implemented for inverter output. In this way, it is aimed to prevent harmonic distortions in the output voltage. In another study using a narrow band in IIR filter design [6], harmonic distortions in the output current and voltage were tried to be prevented. Especially by developing different control methods for LCL filters, is aimed to reduce the effects of DG systems on grid power quality and preventing total harmonic distortion (THD). Some of these studies [7, 8] performed digital IIR filter designs to increase the stability of the inverter and DC / DC converter. Through IIR filter design, both the grid and the converter system are operated stable, and the power system quality is between the defined threshold values by the international grid codes. Today, the design of FIR and IIR digital filters can be carried out by a large number of computer software programs. Thus, designing an accurate digital filter with a high-efficiency converter is a significant issue for PV-based distributed generators to avoid power quality disturbances (PQDs).

In this study, elliptical IIR filter design is realized using LabVIEW infrastructure for THD minimization on the V2G side. The results obtained by using the filter are presented in the paper and the THD value was obtained as 0.82%. In this

way, a high-efficiency converter structure with a low THD value has been obtained following the values determined by the grid code.

THEORETICAL BACKGROUND

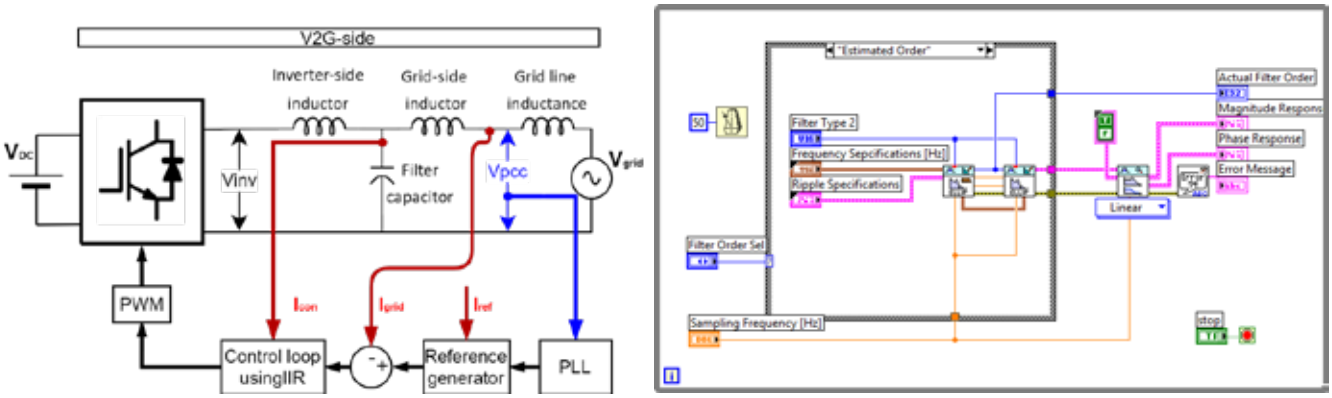
Describe the problem/system being studied and the methodology applied. Avoid footnotes at the bottom of the page within the frame. In many converter applications, the digital filter is designed in the frequency domain. To define the frequency response in the digital filter, it is necessary to define the phase response, target magnitude response, and the allowable deviation for them. Stopband edge frequencies, passband gain, passband edge frequencies, maximum passband ripple, and minimum stopband attenuation are the selected parameters in our filter design. Considering these parameters, the z transform of an IIR filter is defined as:

$$H(z) = \frac{\sum_{k=0}^{N} b_k z^{-k}}{1+\sum_{i=1}^{M} a_i z^{-i}} = K \frac{\prod_{k=1}^{N}(1-z_k z^{-1})}{\prod_{k=1}^{M}(1-p_k z^{-1})} \quad (1)$$

where z_k and p_k are the roots of the H(z).

PROPOSED METHOD

A general schematic of the developed IIR filter and phase-locked-loop (PLL) structure is shown in Fig. 1 (a). In the loop filter design of PLL, fast locking of the obtained phase angle to the phase angle of the grid and showing a good filtering characteristic is very important for the dynamic performance of the system. In ideal conditions, the high bandwidth of the filter enables the amplitude and phase angle of the grid voltage to be determined quickly and accurately and high order harmonics of the grid voltage. In case of failure, the stable operation of the PLL is provided by reducing the bandwidth, but in this case, the synchronization time increases. When imbalances occur in the grid voltage, reducing the bandwidth cannot stabilize the system. This problem can be solved by adding a low-pass IIR filter to the system. The changes that occur with the addition of a low pass filter improve the stability of the system, while significantly reducing the dynamic response of the system. The signal acquired was then processed in digital IIR filter design software developed with LabVIEW filter tools shown in Fig. 1 (b).

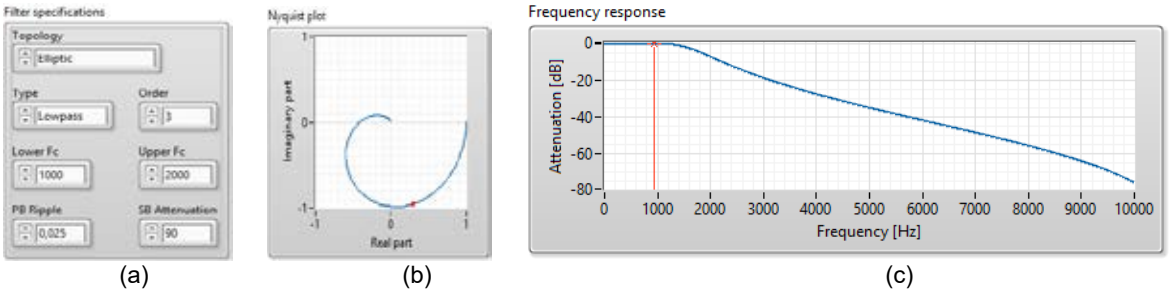


(a) (b)

Fig. 1. (a) Block diagram of the proposed method and, (b)developed software for designed IIR filter in LabVIEW environment

RESULTS

As shown in Fig. 2a, 3rd order low-pass elliptical IIR filter design was realized by selecting the lower cut frequency 1 kHz, uppercut frequency 2 kHz, switching frequency 10 kHz, SB Attenuation 90, and PB ripple 0.025. The Nyquist plot and frequency response of the proposed IIR filter is also indicated in Fig. 2a and Fig 2b, respectively.



(a) (b) (c)

Fig. 2. (a) 3rd order low-pass elliptic filter specifications, (b) Nyquist plot, (c) frequency response

The amplitude and phase responses of the proposed filter are also shown in Figures 3a and 3b. 3rd order low-pass elliptical IIR filter design is observed in the figures, and the proposed filter has a stable response. Thanks to LabVIEW filter tools and other software developments, it is aimed to filter the inverter output voltage and comply with the grid connection conditions required by international standards (IEEE 519 and 1547, IEC 61000-3-2, and IEC 61000-3-12). Especially disturbing signals and electrical noise caused by harmonic distortions caused by inverter and converter are largely eliminated by the developed 3rd order low-pass elliptical IIR filter.

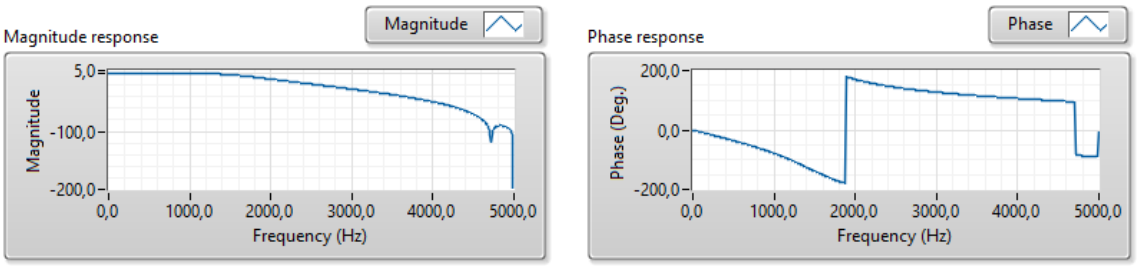
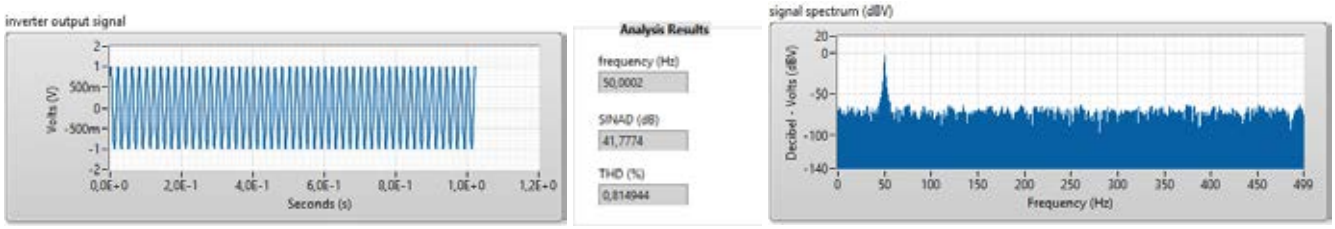


Fig. 3. (a) Magnitude, (b) Phase response of proposed filter

As can be seen from Figures 4a, 4b, and 4c, the THD value is calculated as approximately 0.82% according to the waveform at the inverter output with a single phase 50 Hz frequency. Considering that the allowable THD value should be less than 5%, it is seen that the result obtained is a quality output close to pure sinus. This shows that the developed filter can be used for V2G applications. The developed filter is software-based and provides great convenience both in terms of development and in terms of allowing the search for suitable solutions by easily testing different types of filters.



(a) (b) (c)

Fig. 4. (a) Inverter output signal, (b) THD result, (c) signal spectrum

CONCLUSIONS

In this study, a low-pass elliptical IIR filter design is realized with the V2G converter using LabVIEW infrastructure. The results obtained by using the filter are presented in the paper and the THD value was obtained as 0.82% for a converter. In this way, a low THD value is obtained for the V2G converter under the values determined by the grid code.

REFERENCES

1. Li, H., Sun, B., Hao, J., Zhao, J., Li, J., and Khakichi, A. 2022. Economical planning of fuel cell vehicle-to-grid integrated green buildings with a new hybrid optimization algorithm. International Journal of Hydrogen Energy, 47(13), 8514-8531.
2. Shobana, S., Praghash, K., Ramya, G., Rajakumar, B. R., and Binu, D. 2022. Integrating renewable energy in electric V2G: Improved optimization assisting dispatch model. International Journal of Energy Research, 1- 18.
3. Olyaee, S., Abadi, M. S. E., Hamedi, S., & Finizadeh, F. 2011. Refractive index determination in fuel cells using high-resolution laser heterodyne interferometer. international journal of hydrogen energy, 36(20), 13255-13265.
4. Brunner, D. A., Marcks, S., Bajpai, M., Prasad, A. K., and Advani, S. G. 2012. Design and characterization of an electronically controlled variable flow rate ejector for fuel cell applications. International journal of hydrogen energy, 37(5), 4457-4466.
5. Ye, J., Liu, L., Xu, J., and Shen, A. 2020. Frequency Adaptive Proportional-Repetitive Control for Grid-Connected Inverters. IEEE Transactions on Industrial Electronics, 68(9), 7965-7974.
6. Celis, S., Farhat, M., Almansouri, A. S., Bagci, H., and Salama, K. N. 2020. Simplified Modal-Cancellation Approach for Substrate-Integrated-Waveguide Narrow-Band Filter Design. Electronics, 9(6), 962.
7. Yang, L., Yang, J., Gao, M., Chen, Y., and Zhang, X. 2020. A Systematic Approach via IIR Filters for Enhancing the Robustness of LCL-Type Shunt Active Power Filters to Grid Impedance. IEEE Transactions on Industry Applications, 56(5), 5095-5107.
8. Y. Xiong, Y. Ye, Y. Cao, and Y. Wu. 2020. Separate-Structure UDE-Based Current Resonant Control Strategy on LCL-Type Grid-Tied Inverters With Weighted Average Current Method for Improved Injected Current Quality and Robustness. IEEE Transactions on Power Electronics, vol. 35, no. 12, pp. 13641-13651.

WHEC-2022
23rd World Hydrogen Energy Conference
June 26-30, 2022 - Istanbul

#1568

PV-FUEL CELL HYBRID SYSTEM MODELING AND ANALYSIS

[1]Bihter Anlamaz, [1,2]*Anil Can Turkmen, [1]Kursat Can Ata, [1]Cenk Celik
[1]Kocaeli University Faculty of Engineering, Department of Mechanical Enginlerini, Kocaeli 41380, Turkey
[2]ACT Scientific Ltd., Budotek Teknopark, Istanbul, 34776, Turkey

*Corresponding author e-mail: anilcan.turkmen@hotmail.com

ABSTRACT

In this study, an analysis of the use of photovoltaic (PV) and fuel cell (FC) systems as a combined (hybrid) system is presented. unified system; It consists of a PV panel, electrolysis unit, hydrogen tank, and fuel cell. The electrical energy supplied from the PV panel is used for hydrogen production in the electrolysis unit. The stored hydrogen then drives the fuel cell, providing a regular supply of electricity. Fuel cell stack efficiency was found to be 65% in Antalya region and 58% in Sinop region.

Keywords: Photovoltaic, Fuel cell

INTRODUCTION

The use, transportation, and storage of energy, which is the most important factor in a sustainable environment, society, and economy, must also be sustainable. However, the depletion of fossil energy resources, environmental problems due to energy consumption, greenhouse gas emissions and global warming, the increase in foreign dependency on energy and economy, and the rapid decrease in natural and local resources cause the social and economic order to change rapidly. Due to their low environmental impact, PV hybrid systems using fuel cells as energy storage devices are one of the most promising renewable energy sources.

Renewable sources of vitality, for example, photovoltaic and wind, do not transmit a constant power, but due to their complementarity, their combination provides more uninterrupted electrical output.[1] The reason for the hybrid power system is to provide as much energy as possible from renewable energy sources to guarantee the load demand. The increase in power demand and the growth in fuel prices are among the solar energy sources that we need to develop alternative energy technologies.[1]

Variable renewable energy (RE) and power conditioning units such as hydrogen, alkaline water electrolyzer, storage hydrogen tank, solar and wind PEM fuel cell (PEMFC) can be used to store its energy [2].

METHODS

Hydrogen, the lightest element in the world, was created technologically for its storage. Hydrogen is a very efficient and clean fuel. Hybrid energy systems design mainly depends on the performance of the individual system. To predict performance, individual components must be modeled first.

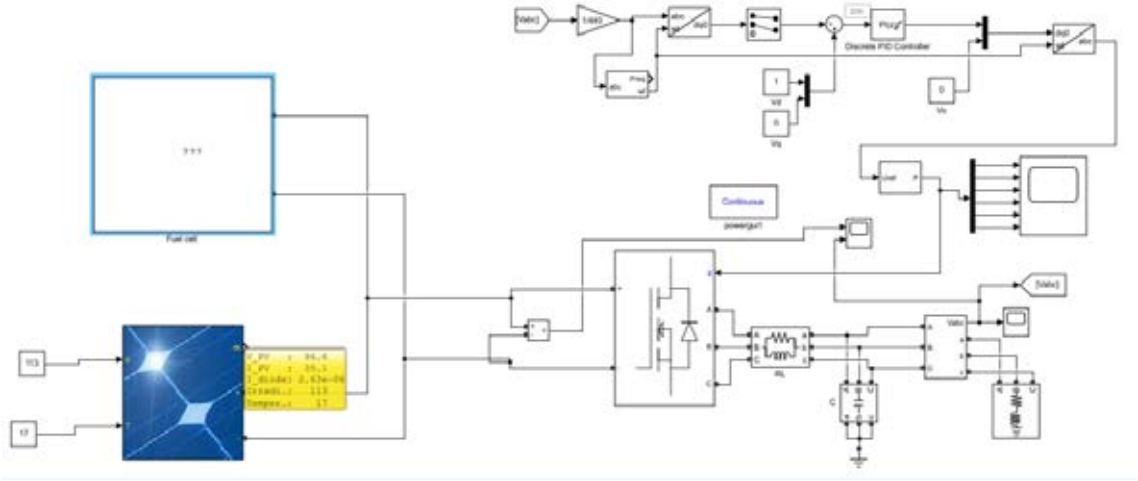


Fig. 1. Photovoltaic (PV) and fuel cell (FC) hydrid model

In Fig. 1, the photovoltaic (PV) and fuel cell (FC) hydride model is simulated in Matlab/Simulink environment. By running Matlab simulation, the voltages and fuel cell usage depending on the varying amount of radiation were investigated in the cities of Antalya and Sinop in April, on the same day and time, using the same panel and cell.



Fig. 2. Antalya Radiation Values [3]

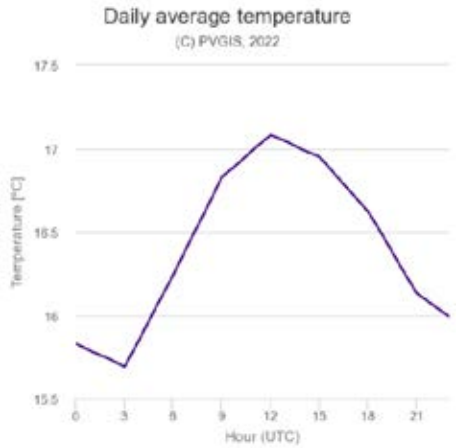


Fig. 3. Antalya Temperature Values in April 2022 [3]



Fig. 4. Sinop Radiation Values [3]

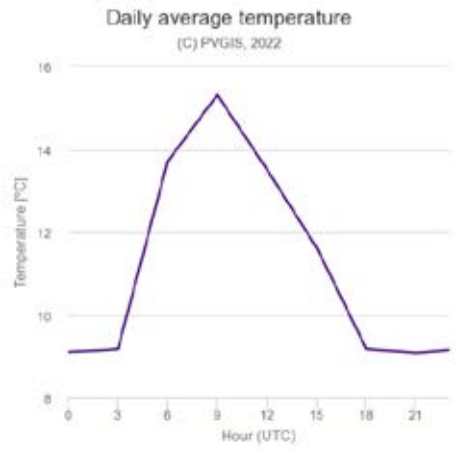


Fig. 5. Antalya Temperature Values in April 2022 [3]

The model given in Fig.1 consists of a photovoltaic and a dc-dc converter activated by the fuel cell. Power from the DC link is supplied to the electrical grid via the converter. A fuel cell works like a battery by converting a chemical reaction into electricity. The dependence of operating continuity on the supplied hydrogen and oxygen separates the fuel cell from the battery. The operation of the fuel cell depends on the chemical reaction of hydrogen with oxygen. In this study, a module was created by using a 6 kW 45V DC PEMFC and 10 serial and 40 parallel solar panel modules. The dc voltages produced were converted to ac voltages using the inventor. In the case of insufficient sunlight, the voltage was generated from the insulating cell by the electrolysis reaction.

By using the created module, the radiation and temperature values of April in two cities were taken and run on Matlab simulation. In the simulation, the voltages and the changes in the fuel cell depending on the radiation values falling on the solar panel were read.

RESULTS AND DISCUSSION

When the created module is run with simulation, the voltage values obtained for the cities of Antalya and Sinop are shown in Fig.6 and Fig.7. The radiation value measured in April in Antalya is 218.69 kWh/m^2, and the radiation value measured in Sinop in April is 159.99 kWh/m^2. Taking these values as a reference, when the photovoltaic and fuel cell hybrid generation system was operated for 0.45 seconds using Matlab simulation, it was observed that the voltage values formed in April in the two cities were very close to each other.

However, when we look at the fuel cell usage values shown in Fig.8 and Fig.9 in the Matlab simulation made concerning the April radiation data of Antalya and Sinop cities, the fuel cell of the hybrid module in Sinop city needs to work much more to produce almost the same voltage. Figures 8 and 9 also show A: Fuel flow (increase); B: The

usage percentages of hydrogen and oxygen are shown (Fixed after a certain period of time); A: Hydrogen and oxygen flow rates of the stack are shown (increase over time); D: Shows the efficiency of the stack (Minimum decreases are observed over time).

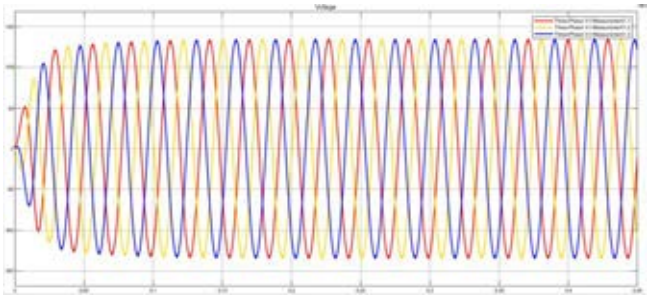


Fig. 6. Antalya April Produced Voltages (Voltage-seconds)

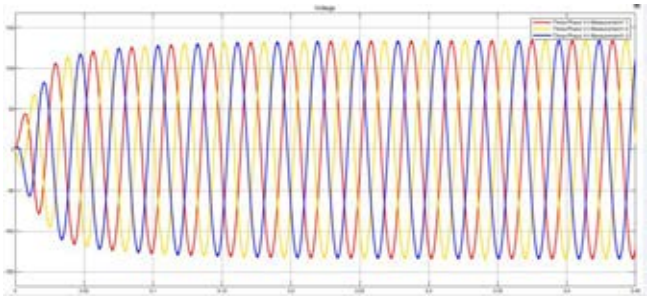


Fig. 7. Sinop April Produced Voltages (Voltage-seconds)

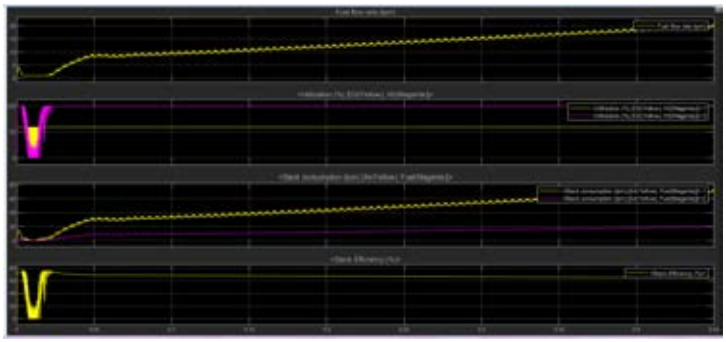


Fig. 8. Antalya April Fuel Cell Usage

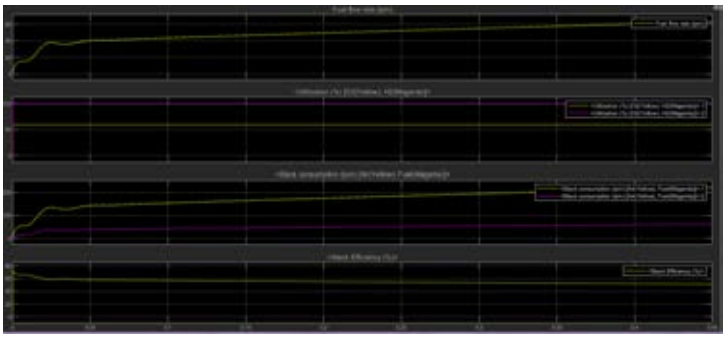


Fig. 9. Sinop April Fuel Cell Usage

In this study, the use of fuel cells was investigated to produce approximately the same voltage in the determined period by using the hydride module created in two cities with different temperatures and radiation values. It has been observed that the need for the use of fuel cells is much less to reach the desired voltage in a city with a high radiation value.

CONCLUSIONS

The photovoltaic and fuel cell hybrid power system powered by Matlab Simulation works flexibly by utilizing maximum solar energy and optimum energy from the fuel cell. The studies conducted using the information of two different cities in the south and north were quite close to each other. This result shows that the system from north to south can be used in Turkey.

REFERENCES

1. Shekhawat OS Singh P Singh AK Sharma J Chauhan V Dhariwal S. 2017. Photovoltaic and Fuel Cell Hybrid Generating System Grid Simulation and Harmonics Analysis. International Journal of Engineering Research & Technology 6:237-241.
2. Mehrpooya M and Daviran S. 2013. Dynamic Modeling of a Hybrid Photovoltaic System with Hydrogen/Air PEM Fuel Cell, Iranica Journal of Energy & Environment 4 (2): 104-109.
3. https://re.jrc.ec.europa.eu/pvg_tools/en/tools.html Accessed on February 5, 2022

WHEC-2022
23rd World Hydrogen Energy Conference
June 26-30, 2022 - Istanbul

#1587

EXPERIMENTAL STUDY ON HYDROGEN ENRICHED NATURAL GAS COMBUSTION IN INDUSTRIAL BURNER

[1,2]*Sean Byrne,*[2]*Qarib Ullah,*[2*]*Dipal Patel*
[1]BMM Heaters Ltd, Dormanstown, Redcar, United Kingdom
[2] Teesside University, School of Computing Engineering and Digital Technologies, Middlesbrough, United Kingdom

*Corresponding author e-mail: d.patel@tees.ac.uk

ABSTRACT

The effects of hydrogen enrichment with natural gas have been experimentally investigated in an industrial burner for heat production. The hydrogen content was varied from 0%, 30%, and 50% by vol in the fuel blend (hydrogen + natural gas) to examine the burner's performance, combustion, and emission characteristics. The emission characteristics were analysed by using a flue gas analyser and verified with a mass spectrometer. The experiments were performed on HEC (High Efficiency Combustion) range – TMG fully condensing industrial heater. The experimental study shows that flame thermal runaway occurs in the burner when deploying higher amount of hydrogen (i.e. ≥30% by vol.) in the blend and combustion instability increases. The required fuel flow rate for hydrogen blend increased to achieve the same power output as for natural gas. The most important influence of using hydrogen blend in combustion for industrial burner is the reduction of both CO and NOx. The study shows that CO, NO and NOx are reduced up to two times and more for 30% by vol. hydrogen blend with natural gas. The study also shows that the higher amount of hydrogen blend (i.e. ≥50% by vol.) will require a significant amount of modification to the burner's control.

Keywords: Industrial burner, Hydrogen, Emission,Combustion instability, Flames

INTRODUCTION

Hydrogen has been identified as one of the new, low (or zero) carbon solutions that will be critical for many countries' transitions to net zero [1]. Stringent regulations on emissions from industrial heat production and applications have motivated researchers and engineers of various low emission technologies, including decarbonised industry, carbon capture, and flexi-fuel systems allowing the use of carbon-free fuel such as ammonia and hydrogen. Ultra-lean and low emission (ULLE) combustion has traditionally been one of the most common technology used to reduce emissions from industrial burners. The HEC (High Efficiency Combustion) fully condensing industrial heater (gas fired warm air heaters) provides 101% efficiency on high fire and 109%+ on low fire [2]. Such industrial heaters range from 12 to 1000 kW. This ULLE combustion is reliant on a highly controlled mixing of mixture composition (i.e. air and fuel) to achieve ultra-lean premixed combustion. This premixed combustion supports reducing the flame temperature and ultimately reducing the NOx formation. The control system of this heater ensures that the combustion does not promote an unnecessary level of unburnt hydrocarbons, carbon monoxide, and combustion instabilities. It is important to note that these burners face other challenges when deploying hydrogen blend fuel – e.g. higher burning velocities, higher flame temperature, flashbacks etc. These challenges require careful design optimization via heater's control system. The properties of hydrogen and natural gas (methane) are outlined in Table 1.

Table 1. Characteristics of hydrogen and natural gas (methane)

	Hydrogen	Natural gas (methane)
Density	0.084 kg/m^3 (much lighter than air 1.225 kg/m^3)	0.651 kg/m^3
Energy of Combustion	141.8 MJ/kg	55.5 MJ/kg
Flame temperature	2045 °C	1957 °C
Flammability limits (ϕ*)	0.1 – 7.1	0.4 – 1.6
Ignition temperature	585 °C	800 °C
Flame velocity	1.85 m/s	0.38 m/s

* equivalence ratio is defined as the ratio of the stoichiometric air-to-fuel ratio to the actual air-to-fuel ratio

The effects of constant velocity and constant residence time scaling on the local NOx emissions and flame characteristics of complex partial premixed hydrogen burners have been previously investigated [3]. Additionally, the

conversion of natural gas jet flame burners to hydrogen was also studied [4] and found that to retain the same heat release in burners as with CH_4, H_2 would require an approximately three fold increase in jet velocity [4]. Moreover, an experimental study on potential natural gas/hydrogen blends as fuel for industrial heat treatment furnaces was investigated and both technological and economical aspects were considered with the possibility of CO_2 reduction [5]. However, there is a gap in the literature for the study on hydrogen blend fuel with natural gas in an industrial burner for heating application which has not been done for emission aspect, where the aim is to meet same power output as natural gas while lowering the emission. This study aims to address this gap by conducting an experimental study on hydrogen enriched natural gas combustion in industrial burner.

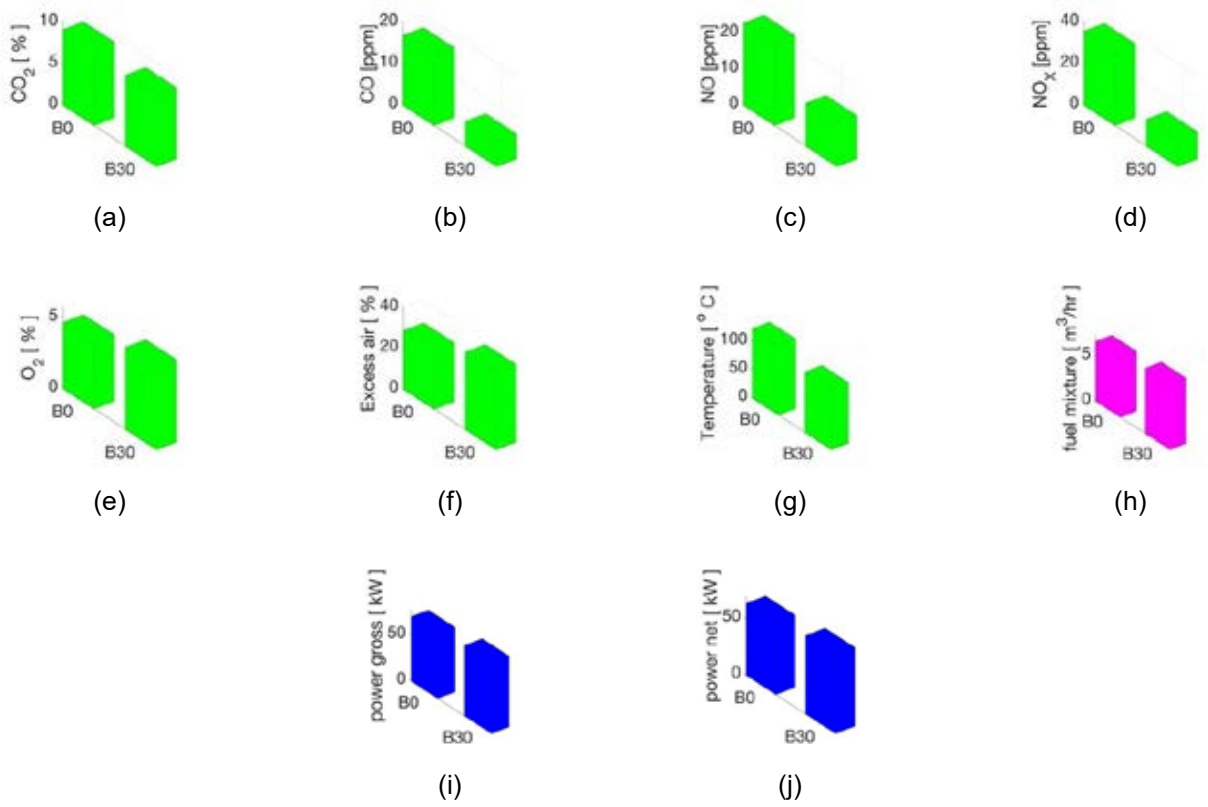


Fig. 1. The emissions ((a), (b), (c), (d), (e), (f), (g)) and performance ((h), (i), (j)) characteristics of TMG module burner for B0 and B30 blend cases

EXPERIMENTAL SETUP

The experiments were carried out using the TMG range of fully condensing gas module burner unit from BMM Heaters Ltd. The various hydrogen blends were obtained and supplied from Air Products UK. The accuracy of such hydrogen blend with natural gas was %mole = $\pm$0.5 and calculated calorific values were recorded for power output and required fuel flow rate calculations. The composition of the combustion products was measured using a flue gas analyser which then further verified with the ESS quadrupole mass spectrometer [6]. The mass spectrometer measures mass-to-charge ratio (m/z) of gas-phase ions. It has three main components: an ion source, a mass analyser, and a detector. The ion source converts analyte molecules into gas-phase ions, the mass analyser separates the ionised analytes according to their m/z, and the detector records the number of ions at each m/z value. An advantage of mass spectrometers over other analytical instruments is that it affords a high degree of accuracy and sensitivity. The various missions were captured using ESS quadrupole mass spectrometer. Here B0, B30, and B50 case represent hydrogen contents in blend fuel of 0%, 30%, and 50% by vol. respectively.

RESULTS AND DISCUSSION

The emissions, combustion, and performance characteristics of the TMG module burner have been captured, calculated, and shown in fig 1. The emissions characteristics includes CO_2 (%), CO (ppm), NO (ppm), NOx (ppm) and O2 (%) are show in fig 1 (a), (b), (c). (d) and (e) respectively. The combustion characteristic includes excess air (%) and flue temperature (^oC) are shown in fig 1 (f) and (g) respectively. And finally, the performance characteristics including fuel mixture inflow (m^3/hr), power gross (kW) and power net (kW) are shown in fig 1(h), (i) and (j)

respectively. It can be seen from fig 1(b) that the CO (ppm) for B30 case is significantly lower compared to B0 case due to that the fuel contains 30% less carbon content in the combustible mixture to start with. Both NO and NOx levels are expressively lower in 30% hydrogen blend case (i.e. B30) compared to pure natural gas (i.e. B0). The ultra-lean combustion was successfully obtained for the hydrogen blend case using the burner's control unit by allowing more excess air (please see fig 1(e) and 1(f)), which further supports the reduction in combustion flue temperature (please see fig 1(g)). It is worth noting that the flow rate for hydrogen blend case mixture was higher compared to that of natural gas case to achieve the same power output. This finding is in consistent with experimental study from [4]. The performance characteristics of TMG module burner show that more comparative (if not higher) power output results can be obtained for hydrogen blend cases without any modification to the existing burner. Both the gross and net power output for 30% hydrogen blend cases were more advanced than natural gas. It is important to mention that much higher hydrogen blend cases (i.e. $\geq 50\%$ by vol.) impose combustion instability, thermal runaway, and flashbacks. A more control optimization for burner is required for flame initiation and self-sustained combustion. The higher mass diffusivity of hydrogen coupled with a higher mixture inflow rate tends to move combustible mixture away from the ignition point – leaving misfire and unsuccessful combustion. Hence the hydrogen blends with 50% by vol. results are not shown here because TMG module burner's control system was modified to accommodate higher hydrogen blend fuel to achieve the same performance output.

CONCLUSIONS

The current study presents an experimental investigation on hydrogen enriched natural gas combustion in an industrial burner for heat production applications. The TMG module burner from BMM heaters was used for the experiments. And emissions data were captured using a flue gas analyser and further verified with an ESS quadrupole mass spectrometer. The experimental study shows very promising results for accommodating hydrogen blend fuel for an industrial burner application. A recent report [7] on hydrogen blending and the gas commercial framework suggests that interim use of hydrogen blend is required before the commercial gas network is ready for 100% hydrogen. Moreover, this report shows that hydrogen blend up to 20% by vol. in the gas commercial framework can be demonstrated in the upcoming near future (early 2023) and the industrial burner market requires to be ready for such change. The main findings are listed below:

- B30 case shows two to three times reduction in CO, NO, and NOx emission as compared with 100% natural gas case.
- Consistent and comparative (if not more) power output can be achieved with a 30% hydrogen blend case without any modification to the existing burner.
- An ultra-lean and low emission combustion can be successfully initiated and self-sustained with a 30% hydrogen blend.
- The TMG module burner is well-suited and supports the UK government's plan for blending up to 20% hydrogen by vol into the existing gas network.

ACKNOWLEDGEMENT

The authors gratefully acknowledge the support of the European Regional Development Fund (ERDF) – Tees Valley Hydrogen Innovation Project and BMM Heaters Ltd.

REFERENCES

1.UK Government, UK Hydrogen Strategy, August 2021 www.gov.uk/official-documents. Accessed on April 15, 2022.
2.BMM Heaters Ltd. https://www.bmmheaters.co.uk. Accessed on April 05, 2022.
3.Meraner, C, Li T, Ditaranto M, Lovas T. 2020. Effects of scaling laws on the combustion and NOx characteristics of hydrogen burners. Combustion and Flame 214:407-418.
4.Palacios A and Bradley D. 2021. Conversion of natural gas jet flame burners to hydrogen. International Journal of Hydrogen Energy 46:17051-17059.
5.Mayrhofer M, Koller M, Seemann P, Prieler R, Hochenauer C. 2021. Assessment of natural gas/hydrogen blends as an alternative fuel for industrial heat treatment furnaces. International Journal of Hydrogen Energy 46:21672-21686.
6.European Spectrometry Services Ltd. https://www.essco.com. Accessed on April 10, 2022.
7.Frontier Economics Ltd. https://www.frontier-economics.com/media/4201/hydrogen-blending-commercial-framework.pdf. Accessed on April 10, 2022.

WHEC-2022
23rd World Hydrogen Energy Conference
June 26-30, 2022 - Istanbul

#1597

INVESTIGATION OF SIMULTANEOUS HYDROGEN PRODUCTION AND DESALINATION OF SALINE WATER VIA ELECTRODIALYSIS PROCESS

[1]Ragad AlShebli, [*1,2]Burak Yuzer, [1]Yusuf Bicer
[1]Division of Sustainable Development, College of Science and Engineering, Hamad Bin Khalifa University, Qatar Foundation, Doha, Qatar
[2] Department of Environmental Engineering, Engineering Faculty, Istanbul University-Cerrahpasa, Istanbul, Turkiye
*Corresponding author e-mail: byuzer@hbku.edu.qa

ABSTRACT

Electrodialysis (ED) is an efficient process that desalinates brackish and saline water under the influence of the electrical field. The ions that present inside a solution moves through ion exchange membranes to the adjacent compartments called concentrate compartment. The main purpose of the ED process is to desalinate brackish water; besides this, a valuable energy carrier gas, hydrogen is generated at the cathode side of the ED cell in this study. However, due to the internal recirculation of the electrolyte solution from anode to cathode compartment, hydrogen gas reacts with oxygen gas and reforms water. In this study, the potential of hydrogen gas generation in an ED system while treating saline/brackish water, is experimentally investigated. The ion removal efficiencies are 68% and 67% for combined and separated processes, respectively. The hydrogen production rates of the ED system are 2.42 and 3.28 mL/h.cm^2 for combined and separated processes, respectively.

Keywords: Cogeneration, Energy Carrier, Hydrogen, Ion-exchange Membrane, Seawater

INTRODUCTION

Water and energy are the most essential needs of the humanity. The energy and water demand increase by the increasing world population and urbanization, however the earth has limited natural sources. Available fresh water sources are getting polluted by human applications and getting depleted due to the insufficient precipitation triggered by the climate change. The main cause of the climate change is the increase of the burning of the carbon-based fossil fuels to generate energy. Also, the fossil fuels are getting depleted day by day thus, the usage of the alternative energy sources should be expanded for a more sustainable life. In this case, hydrogen gas, which is a crucial energy carrier, is an important alternative fuel. Recently, integrated processes that produce hydrogen gas from saline water has gained importance. Tufa et al. [1] have integrated reverse electrodialysis and alkaline polymer electrolyte water electrolysis to produce hydrogen gas. They have reported maximum hydrogen production rate as 50 mL/h.cm^2. Similar research has been conducted by Zhang et al. [2] by using serial reverse electrodialysis stacks for hydrogen production. They have reported the maximum hydrogen production rate of 2.652 mL/h.cm^2. On the other hand, in conventional electrodialysis process, hydrogen gas is also produced during desalination process of the saline water on the cathode electrode of the ED cell, however, mostly the catholyte solution recycled to the anode compartment. By this way, the pH, electrical conductivity, and the total dissolved solids concentration of the electrolyte solution remain same in the ED cell. However, this prevents collection of the hydrogen gas. In this study, the hydrogen gas that is generated in a conventional electrodialysis process has been collected by separating anolyte and catholyte solutions. The effects of the separated electrolyte solutions on the ED desalination efficiency and hydrogen production rate are examined.

MATERIALS AND METHODS

The conventional electrodialysis (ED) process has been set up as given in Fig. 1. The ED cell was supplied from PCCELL company from Germany (GmbH, 2021) [3]. The system was composed of three solution containers for the electrolyte, dilute, and concentrate solutions. Two peristaltic pumps with three mounted apparatus to circulate the solutions have been used. Electricity was supplied to the ED system by using Gamry Potentiostat “Interface 1000 E model 12016”, and two reference electrodes have been used to conduct the electrochemical analysis. During the running of ED process, hydrogen gas is generated at the cathode compartment. A volumetric cylinder has been used to collect the generated hydrogen gas. The hydrogen production rate was calculated according to the area of the electrodes. The area of the electrodes was 64 cm^2. The ED system is tested in batch mode and solutions are circulated until desired conductivity levels of the solutions are obtained.

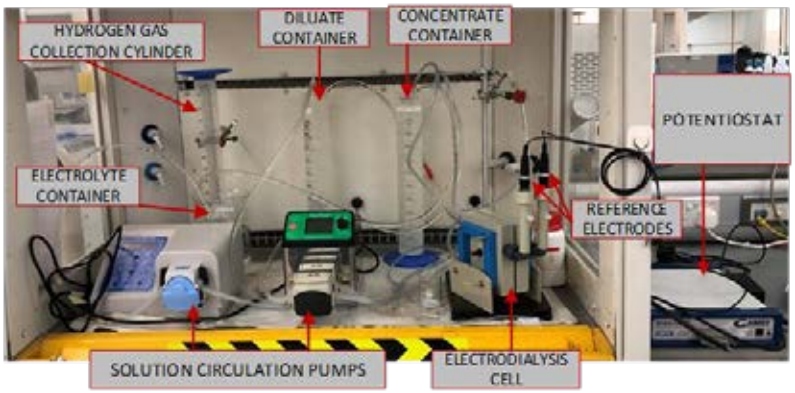


Fig. 1. Electrodialysis system setup.

Hydrogen gas has been collected during electrodialysis process in two different ways. First, anolyte and catholyte compartments have been separated. A graduated cylinder with gas vent has been utilized to collect H_2 gas. The tip of a curved piped was placed inside the cylinder from its open end as shown in Fig. 2. The effluent of the cathode compartment has been returned to the catholyte vessel by using this pipe. Here, the solution was pumped back to the cathode compartment while the hydrogen gas was rising inside the cylinder. The amount of the collected hydrogen gas was recorded in every 5 minutes.

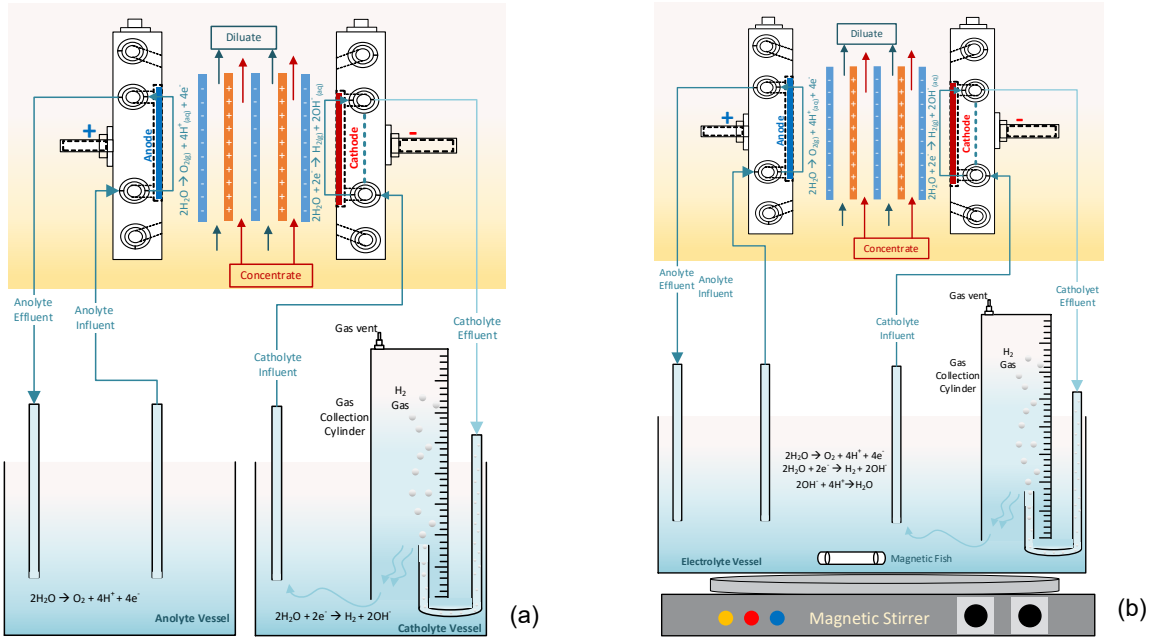


Fig. 2. Schematic representation of hydrogen gas collection alternatives. (a) Hydrogen gas is collected at separated catholyte vessel and (b) hydrogen gas is collected at combined anolyte and catholyte vessel.

RESULTS AND DISCUSSION

The saline waters with 21 and 14 mS/cm initial conductivity values are desalinated by using the ED process at batch mode. The results reflect that when the initial conductivity value of the saline water is higher, the resistance is getting lower and more current could pass through the ED system. The ion removal rates of the ED system can be compared by the slopes of the lines given in Fig. 3. (a) and (b). It is obvious that the ion removal rate is at its peak when the initial conductivity value of the saline water is 21 mS/cm. In addition, the ED process is run in two different modes (separated and combined anolyte and catholyte). The desalination time is adjusted as 60 min for 500 mL saline water to make comparison. The conductivity values of the dilute solutions reach to 7 and 4.3 mS/cm with separated and combined electrolyte solutions, respectively as given in Fig. 3. (a) and (b). The average power consumption of the ED cell is calculated as 4 kWh/m^3 according to Ohm's law. Nassrullah et al. [4] have reported energy requirement for seawater desalination as 2.58-8.5 kWh/m^3 by using different kinds of treatment processes and the required energy increases with increasing total dissolved solids (TDS) concentrations. The current densities of the ED cell show slight changes between 6.9 – 8.08 mA/cm^2 for separated electrolyte and 4.8-5.6 mA/cm^2 for the combined electrolyte solutions due to the change in the conductivity of the solutions (Fig. 3. (c)). Finally, the hydrogen production rates of

the ED process have been calculated as 3.28 and 2.42 mL/h.cm^2 for separated and combined electrolyte solutions, respectively. Since, the main problem of the application of ED process for desalination of high salinity waters is the power consumption and energy cost, the recovery of the energy as the hydrogen gas will lead to increase of the ED process for waters with high salinity.

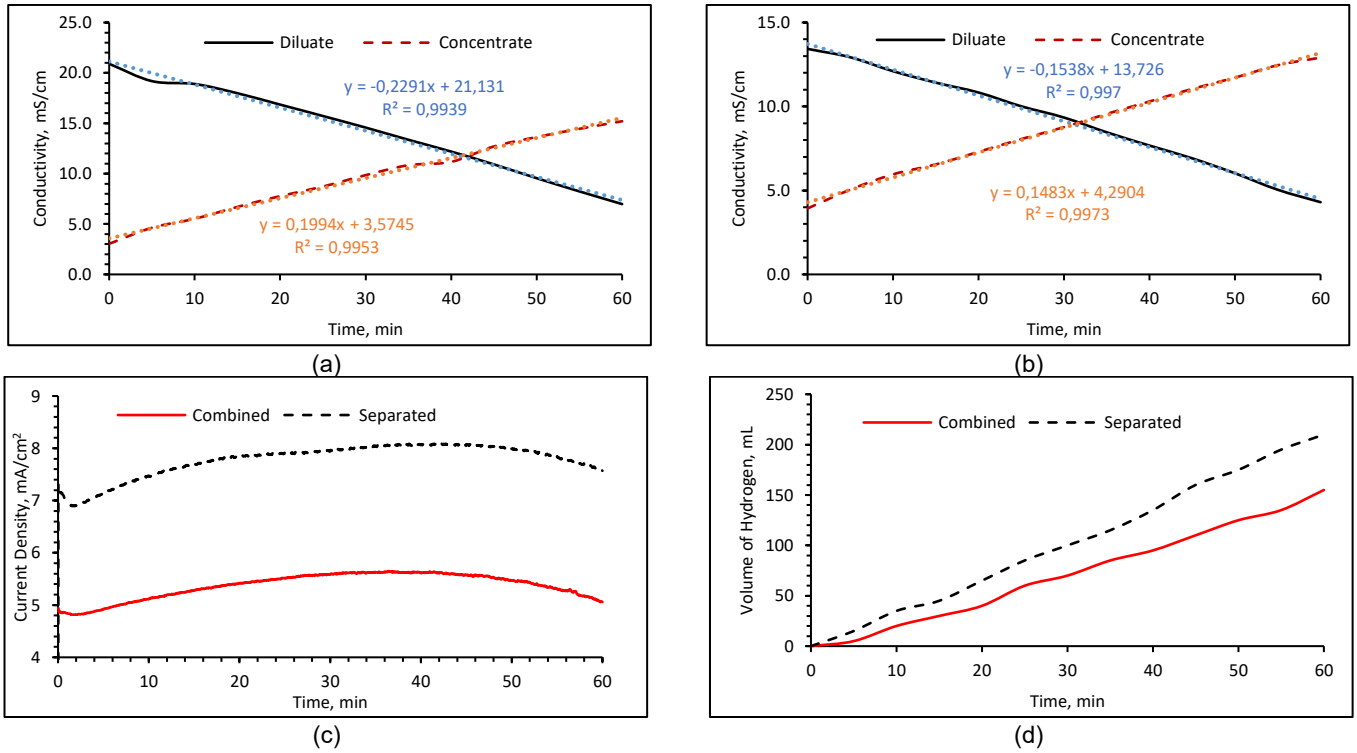


Fig. 3. Results of the desalination of the saline water by using the ED process (a) conductivity vs time graph “separated anolyte and catholyte”, (b) conductivity vs time graph “combined anolyte and catholyte”, (c) current density vs time graph, (d) volume of the hydrogen gas vs time graph.

CONCLUSIONS

The applicability of the recovery of the hydrogen gas generated during the desalination of saline waters by using the ED process is investigated. It is by separation of the anolyte and catholyte solutions in the ED process, the generated hydrogen gas can be collected from the ED system. The ion removal efficiencies are 68% and 67% for combined and separated processes, respectively. The hydrogen production rates of the ED system are 2.42 and 3.28 mL/h.cm^2 for combined and separated processes, respectively. The recovery of the hydrogen gas from the ED process may increase the ED applications for high salinity waters such as sea water.

REFERENCES

1. Tufa RA, Hnat J, Nemecek M, Kodým R, Curcio E, Bouzek K. 2018. Hydrogen production from industrial wastewaters: An integrated reverse electrodialysis - Water electrolysis energy system.Journal of Cleaner Production 203:418-426.
2. Zhang Y, Wu X, Xu S, Leng Q, Wang S. 2022. A serial system of multi-stage reverse electrodialysis stacks for hydrogen production. Energy Conversion and Management 251:114932
3. GmbH, Pcc. (2021). Electrodialysis Systems and Ion Exchange Membranes - PCCell GmbH. https://www.pccell.de/en/BED1-3-Compact-S_27_content2_BED-1-Complete-Lab-Scale-Systems_84_Produktdetail.html
4. Nassrullah H, Anisa SF, Hashaikeha R, Hilal N. 2020 Energy for desalination: A state-of-the-art review. Desalination 491:114569.

WHEC-2022
23rd World Hydrogen Energy Conference
June 26-30, 2022 - Istanbul

#1604

MATHEMATICAL MODELING AND DYNAMIC SIMULATION OF A PV-BASED HYDROGEN GENERATION AND STORAGE SYSTEM

[1*]Gamze Soyturk, [1]Onder Kızılkan, [2]Mehmet Akif Ezan, [2]Can Ozgur Colpan
[1]Isparta University of Applied Sciences, Faculty of Technology, Department of Mechanical Engineering, 32200, Isparta, Turkey
[2]Dokuz Eylul University, Faculty of Engineering, Department of Mechanical Engineering, Tinaztepe Campus, 35397, Izmir, Turkey

*Corresponding author e-mail: gamzeyildirim@isparta.edu.tr

ABSTRACT

Energy storage becomes a more critical issue for humanity to maintain a sustainable integration of renewable-based energy resources with the demand side. As an energy carrier, hydrogen can provide a large amount of energy storage with minimal loss over long periods. The current work focuses on designing and modeling a hybrid renewable energy-based system comprised of Photovoltaic (PV) cells, a battery bank, a PEM Electrolyzer for hydrogen generation, a compressor, and a pressurized hydrogen tank to meet the electricity demand of an off-grid house in Izmir. In the proposed system, solar energy was utilized to produce electricity through PV arrays. The produced energy was either used in the PEM electrolyzer for Hydrogen (H_2) production or stored in the batteries to meet the required energy during low solar radiation or nighttime. An energy management strategy was developed for the proposed hybrid system using the MATLAB software for carrying out the above-mentioned purposes. For the system component modeling, a one-dimensional mathematical approach was applied to investigate the dynamic behavior of the integrated system. The hydrogen generated by the electrolyzer was pressurized with a compressor and stored in pressure tanks at a pressure of 350 bar.

Keywords: PV, PEM electrolyzer, Energy management, Hydrogen storage.

INTRODUCTION

The dramatic increase in energy demand and the adverse environmental effect of fossil fuels in recent years have led some countries to meet their energy needs using alternative clean energy resources. Renewable energy resources such as wind, solar and geothermal are inexhaustible and harmless to the environment. In addition, these sources are intermittent and discontinuous energy sources due to hourly, daily, and seasonal differences. For this reason, it is necessary to store the energy to ensure the continuity of the energy obtained from these sources. When the demand is low, the energy produced is stored and used when the demand is high, allowing the existing resources to be used more effectively. Renewable energy coupled with energy storage will supply better system dependability, making it appropriate for off-grid applications as well [1]. Hydrogen produced by water electrolysis combined with solar energy creates an appealing energy pathway that can balance the intermittent nature of renewable energy resources as a storage medium and an energy carrier for electricity generation [2]. Previous research has mostly focused on improving solar electrolyzer technology for hydrogen generation, progressing hydrogen storage technology, lowering costs, assessing and optimizing off-grid hydrogen production, and hydrogen safety concerns. Toghyani et al. [3] investigated the performance of a hydrogen refueling system consisting of an integrated PEM electrolyzer with PV cells and a compressor to raise the hydrogen pressure. Nasser et al. [4] examined the use of wind turbines and PV cells in a hybrid renewable energy system for hydrogen generation and storage in various climatic conditions of five different Egyptian cities from a techno-economic perspective.

MATERIALS AND METHODS

Fig.1 shows the schematic representation of the PV-based hydrogen generation and storage system. After the power produced by the set of PV arrays supplies the dwelling's electricity needs, the remaining power is passed to the electrolyzer, decomposes water, and generates hydrogen and oxygen. When sufficient power cannot be supplied from the PV panels, lithium-ion batteries are used to meet the electricity needs of the house and to power the electrolyzer. The hydrogen produced by the PEM electrolyzer is sent to the compressor, the pressure is increased, and high-pressure hydrogen is stored in the tank. The design parameters of the integrated system used in this study are given in Table 1. Fig. 2 shows the annual solar radiation and electrical load profile for the province of İzmir.

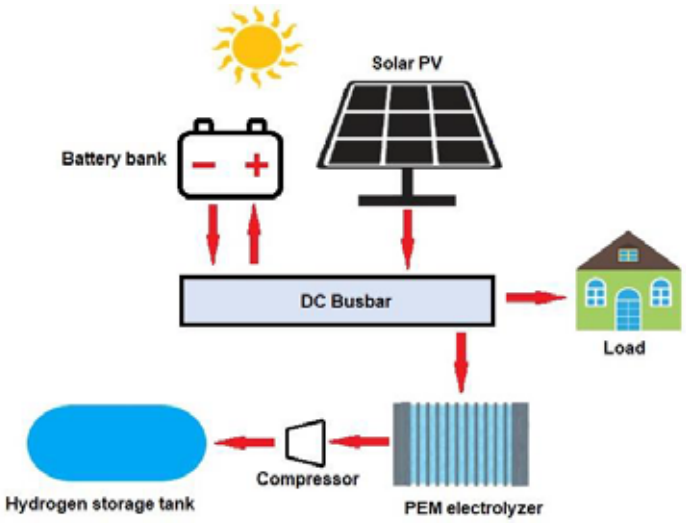
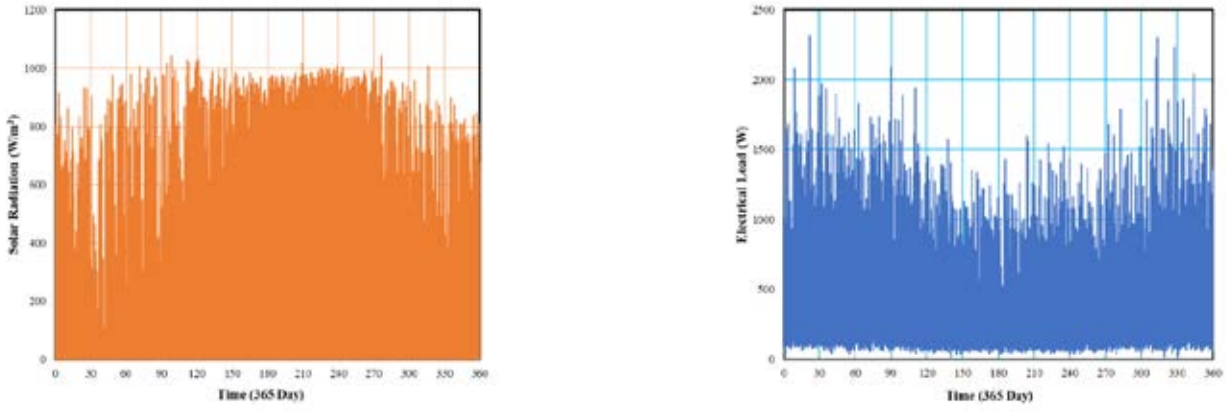


Fig. 1. Schematic diagram of the PV based hydrogen generation and storage system

Table 1. Input parameters of hybrid system

Parameter	**Value**	***Parameter***	**Value**
PV		***Electrolyzer***	
Length, [m]	1.649	Current density, [A/cm^2]	2
Width [m]	0.992	Voltage, [V]	1.78
Number of PV [-]	20	Active area, [cm^2]	100
Reference electrical efficiency	0.14	Rated power, [W]	400
Temperature coefficient, [1/K]	0.0046		
Battery bank		***Compressed hydrogen storage tank***	
Minimum state of charge, [-]	0.35	Pressure, [bar]	350
Maximum state of charge, [-]	0.85	Temperature, [K]	300
Battery capacity, [Wh]	24000		

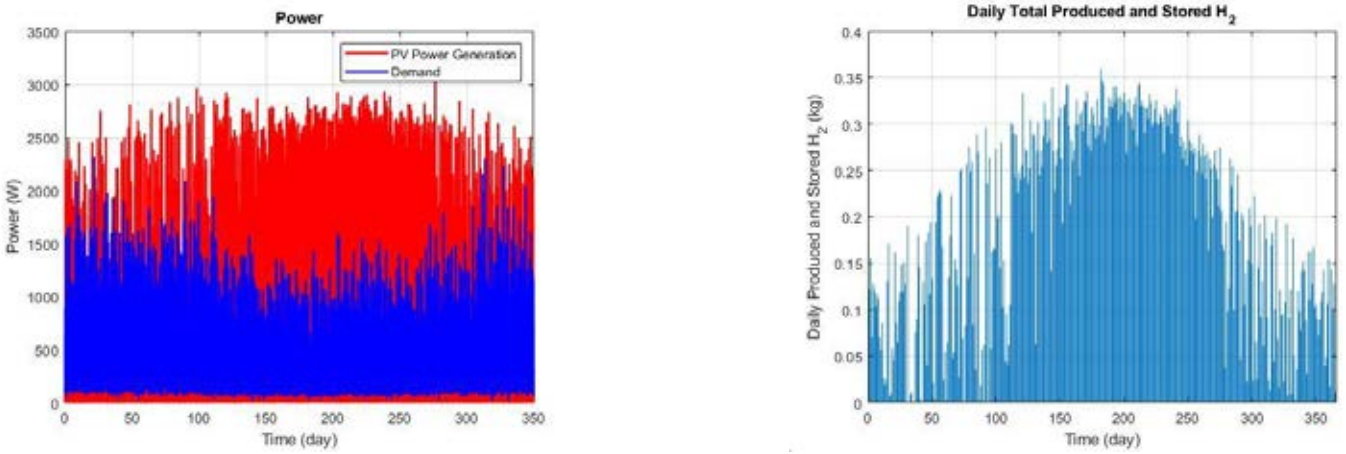


(a) (b)

Fig. 2. Variations in annual (a) solar radiation and b) electrical load

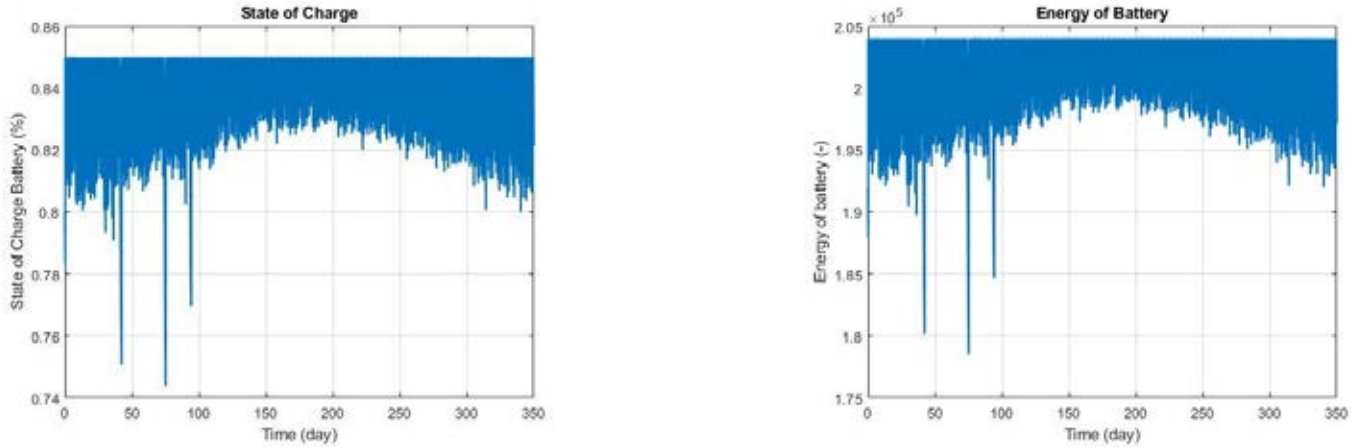
RESULTS AND DISCUSSION

Mathematical modeling of the hybrid system consisting of PV solar panels, battery, PEM electrolyzer, compressor, and hydrogen storage tank was made in MATLAB software. Modeling of PV solar panel is taken from Ref. [5] work, and battery modeling is from Ref. [6] study. In addition, PEM electrolyzer modeling is taken from Ref. [7] study, and hydrogen storage tank from Ref. [8] study. Fig.3. and Fig. 4. show variations in annual power and stored hydrogen production, battery state of charge, and energy variations, respectively.



(a) (b)

Fig. 3. Variations in annual (a) PV power production and electrical demand (b) daily total produced hydrogen



(a) (b)

Fig. 4. Variations in annual (a) battery state of charge (b) energy of a battery

ACKNOWLEDGEMENT

This research was supported by TUBITAK with project number 220N405.

REFERENCES

1. Shiroudi A, Taklimi SRHT, Mousavifar A and Taghipour P. Stand-alone PV-hydrogen energy system in Taleghan- Iran using HOMER software: optimization and technoeconomic analysis. 2013. Environment Development Sustainable 15:1389-1402.
2. Naseri N, Hani SE, Aghmadi A, Medionui H and Aboudrar I. 2019. Solar photovoltaic energy storage as hydrogen via PEM fuel cell for later conversion back to electricity.
3. Toghyani S, Baniasadi E and Afshari E. 2021. Performance assessment of an electrochemical hydrogen production and storage system for solar hydrogen refueling station. International Journal of Hydrogen Energy 46:24271-24285.
4. Nasser M, Megahed TF, Ookawara S and Hassan H.2022. Techno-economic assessment of clean hydrogen production and storage using hybrid renewable energy system of PV/Wind under different climatic conditions. Sustainable Energy Technologies and Assessments 52:102195.
5. Duffie JA, Beckman WA. 2013. Solar engineering of thermal processes (4th ed.). New York: Wiley.
6. Arun P. Banerjee R. and Bandyopadhyay S. 2008. Optimum sizing of battery-integrated diesel generator for remote electrification through design-space approach. Energy 33:1155-1168.
7. Ceylan C, Devrim Y. 2021. Design and simulation of the PV/PEM fuel cell-based hybrid energy system using MATLAB/Simulink for greenhouse application. International Journal of Hydrogen Energy 46:22092-22106.
8. Toghyani S, Ehasn B, Afshari E. 2021. Performance assessment of an electrochemical hydrogen production and storage system for solar hydrogen refueling station. International Journal of Hydrogen Energy 46:24271-24285.

WHEC-2022
23rd World Hydrogen Energy Conference
June 26-30, 2022 - Istanbul

#1606

A NEWLY DEVELOPED BRAYTON CYCLE-BASED COMBINED PLANT INCLUDING HYDROGEN PRODUCTION AND COMPRESSION: ENERGY AND EXERGY ANALYSES

[1]*Yunus Emre Yuksel, [2]Murat Ozturk, [3]Ibrahim Dincer
[1] Afyon Kocatepe University, Kirkgoz Campus, Afyonkarahisar, Turkey
[2] Isparta University of Applied SciencesCunur West Campus, Isparta, Turkey
[3] Ontario Tech. University, 2000 Simcoe Street North, Oshawa, Ontario, Canada

*Corresponding author e-mail: yeyuksel@aku.edu.tr

ABSTRACT
In this study, a novel multigeneration energy system based Brayton cycle is designed to generate power, compressed hydrogen, heating, drying and fresh water. The multigeneration system consists of the Brayton cycle, regenerative Rankine cycle, s-CO_2 power cycle, t-CO_2 power cycle, hydrogen production and compression plant, fresh water production plant and drying plant. In the evaluation part, energy and exergy analyses have been performed with a parametric analysis. The overall power production capacity of the system has been found as 13029 kW, and hydrogen production rate is 0.0624 kg/s. According to the thermodynamic analysis results, the overall energy and exergy efficiencies of the plant are 55.62% and 51.28%.

Keywords: Hydrogen production, Brayton cycle, Multigeneration, Thermodynamic analysis, Energy, Exergy, Efficiency

INTRODUCTION
During past several decades, there have been increasing environmental concerns and energy supply issues where bring out a necessity for more efficient, more cost effective and more environmentally-sound solutions implemented in various sectors. There are numerous researchers concentrating on tri-generation or multigeneration systems because of their high efficiencies compared to single generation systems, recently [1]. Santiago et al. [2] have performed a thermodynamic analysis and optimization of a tri-generation system. The products are cooling, heating and power which are used in a medium-sized hospital. They have compared different combinations of the tri-generation system and as a result, they have found the best energy efficiency at 81% while exergy efficiency is 42%. Kerme et al. [3] have designed a solar energy-based poly-generation system. Numerous configurations and combinations in various viewpoints of the system have been evaluated. The results of the study reveal that solar thermal collector and desalination unit are two main exergy destruction sources. Also, they have found that the overall energetic improvement potential of the system is 64.8%.

In this study, a novel multigeneration system is designed using the Brayton cycle as a prime source of the system and producing power, compressed hydrogen, heating, drying and fresh water. The energy and exergy analyses supported by parametric analyses are performed in order to determine the system performance and how some parameters affect the system performance.

SYSTEM DESCRIPTION
In this multigeneration energy system design, the Brayton cycle, regenerative Rankine cycle, s-CO_2 power cycle, t-CO_2 cycle, hydrogen production and compression plant, multi-effect desalination unit and drying plant are used. Compressed air and fuel mix in the combustion chamber and drive the gas turbine to produce power. Then the heat energy of the turbine is transferred into the heat exchanger (HEX) 1. Here, the regenerative Rankine cycle produces power by using heat energy. The waste heat energy of the regenerative Rankine cycle goes to HEX 2 with stream 5. In this part of the multigeneration system, s-CO_2 and t-CO_2 power cycles produce power by using heat energy. On the other part of the system, sea water enters the multi-effect desalination unit with stream 30. Here brine is separated, produced fresh water is sent to either tank or PEM electrolyzer with stream 36. PEM electrolyzer separates the water into oxygen and hydrogen, and hydrogen is sent to hydrogen compressors' series. Then, compressed hydrogen is stored in the tank. Finally, air enters HEX 5 to gain heat energy and the hot air can be used in drying applications. The related design and working parameters of the multigeneration plant are presented in Table 1.

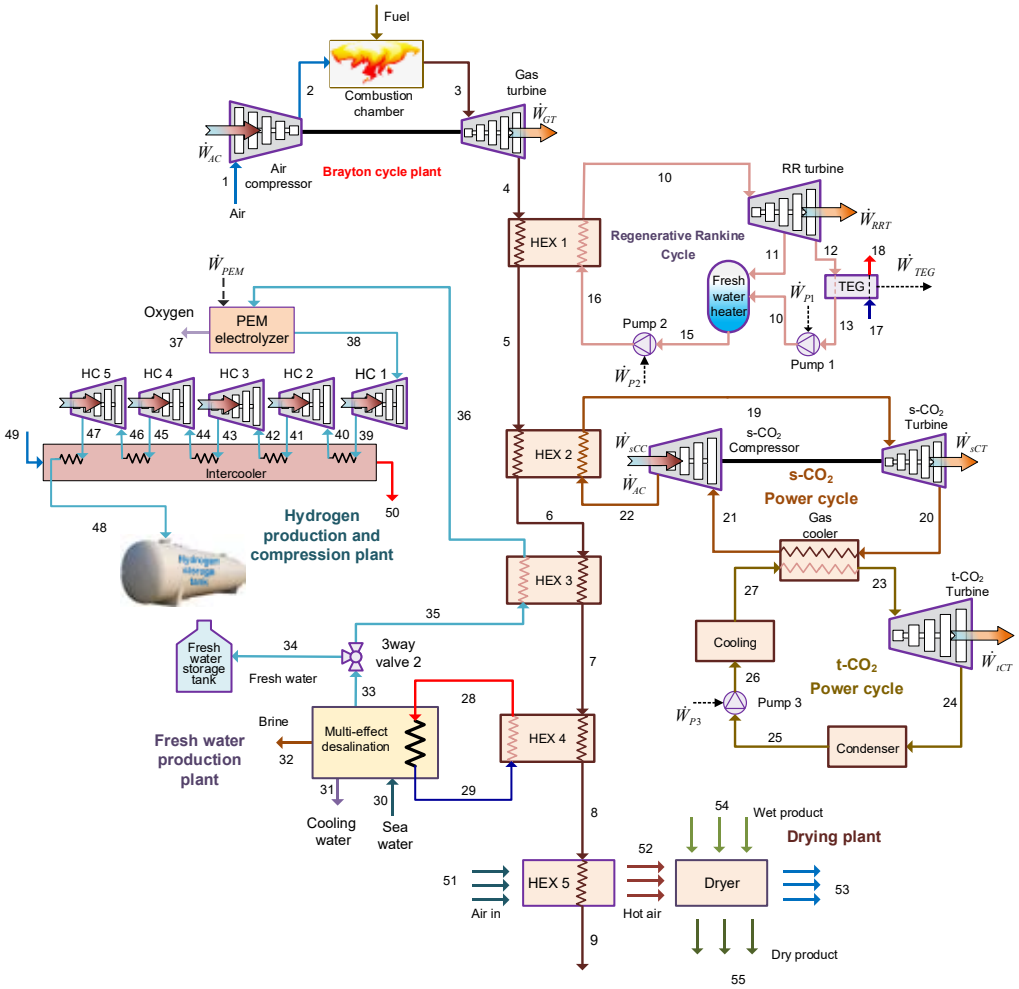


Figure 1. The schematic representation of the modeled multigeneration system

Table 1: Design and working parameters of the multigenerational plant.

Descriptions	**Values**
Ambient temperature, T_o	25°C
Ambient pressure, P_o	101.3 kPa
Isentropic efficiency of turbines	88%
Isentropic efficiency of pumps and compressors	85%
Combustion chamber temperature	890°C
Gas turbine inlet pressure	1500 kPa
RR turbine inlet temperature	356°C
RR turbine inlet pressure	4500 kPa
s-CO_2 turbine inlet temperature	237°C
s-CO_2 turbine inlet pressure	20000 kPa
t-CO_2 turbine inlet temperature	88°C
t-CO_2 turbine inlet pressure	20000 kPa
Mass flow of inlet air	23.5 kg/s

ANALYSIS

In this part, the thermodynamic analysis used to determine the system performance is described briefly. Calculations are made via EES software to determine energy and exergy efficiencies with exergy destruction rates of sub-plants and the overall plant. The general assumptions accepted for the calculations are listed as follows:

- A steady-state mechanism is assumed for the system units.
- The HEXs, pumps, and turbines are adiabatic.
- The changes in kinetic and potential exergetic terms are negligible.
- The reference temperature and pressure are constant (i.e., T_o=25°C and P_o=101.3 kPa)
- The ideal gas characteristics are chosen for air to make an assessment.
- The pressure losses are negligible.

To perform the thermodynamic assessment, the general mass, energy, entropy, and exergy balance equalities can be written as

$$\sum \dot{m}_i = \sum \dot{m}_e \quad (1)$$

$$\sum \dot{m}_i h_i + \sum \dot{Q}_i + \sum \dot{W}_i = \sum \dot{m}_e h_e + \sum \dot{Q}_e + \sum \dot{W}_e \quad (2)$$

$$\sum \dot{m}_i s_i + \sum \left(\frac{\dot{Q}}{T}\right)_i + \dot{S}_{gen} = \sum \dot{m}_e s_e + \sum \left(\frac{\dot{Q}}{T}\right)_e \quad (3)$$

$$\sum \dot{m}_i ex_i + \sum \dot{E}x_i^Q + \sum \dot{E}x_i^W = \sum \dot{m}_e ex_e + \sum \dot{E}x_e^Q + \sum \dot{E}x_e^W + \dot{E}x_d \quad (4)$$

where i and e show inlet and exit conditions, respectively, $\dot{Q}$ represents heat transfer rate, $\dot{W}$ is the work rate, s and h show entropy, and enthalpy, respectively, $\dot{m}$ is the mass flow rate, $\dot{S}_{gen}$ and $\dot{E}x_d$ show entropy generation and exergy destruction rate, respectively.

RESULTS AND DISCUSSION

The designed multigeneration plant has the capacity of producing 13029 kW power, 5132 kW heating, 4194 kW drying and hydrogen and fresh water production rates are 0.0624 kg/s and 16.53 kg/s. Thermodynamic analyses also reveal that energy and exergy efficiencies of sub-plants and the overall plant which are listed in Table 2. Also, parametric analyses show that as reference temperature increases from 0 °C to 40 °C, both energy and exergy efficiencies of sub-plants and the multigeneration plant increase. Another parameter investigated in this study is the air mass flow rate of the Brayton cycle altered from 21 kg/s to 25 kg/s. As air mass flow rate increases energy and exergy efficiencies of sub-plants and the overall plant increase.

Table 2. Energy and exergy efficiencies of sub-plants and the overall plant

Overall plant and sub-plants	η	ψ
Brayton cycle plant	0.4831	0.4498
Regenerative Rankine cycle	0.3283	0.2871
s-CO_2 power cycle	0.1718	0.1485
t-CO_2 power cycle	0.1325	0.1032
Fresh water production plant	0.4546	0.3893
Hydrogen production and compression plant	0.6938	0.6527
Drying plant	0.7416	0.6946
Overall plant	0.5662	0.5128

CONCLUSIONS

In this study, a novel Brayton cycle-based multigeneration system is designed and analyzed both thermodynamically and parametrically. The results of this study show that the overall energy and exergy efficiencies of the system are 55.62% and 51.28%. An increase in the reference temperature or the air mass flow rate has a positive impact on the hydrogen generation rate. Some key results of the study can be listed as follows:

- The lowest exergy efficiencies occur in t-CO_2 and s-CO_2 power cycles with 10.32% and 14.85%.
- The highest energy and exergy efficiencies belong to the drying plant with 74.16% and 69.46%.
- As the reference temperature goes up from 0 °C to 40 °C, the exergy efficiency of the overall plant increases from 48.07% to 53.31%.
- As the air mass flow rate increases from 21 kg/s to 25 kg/s, the overall exergy efficiency improves from 47.60% to 53.62%.

REFERENCES

1. I. Dincer and C. Zamfirescu, "Renewable-energy-based multigeneration systems," *International Journal of Energy Research,* vol. 36, no. 15, pp. 1403-1415, 2012.
2. T. S. Santiago, A. E. Achiles and J. V. H. Dangelo, "Thermodynamic performance analysis and optimization of a trigeneration system with different configurations applied to a medium-sized hospital," *Energy,* vol. 239, p. 122195, 2022.
3. E. D. Kerme, J. Orfi, A. S. Fung, E. M. Salilih, S. U. D. Khan, H. Alshehri and M. Alrasheed, "Energetic and exergetic performance analysis of a solar driven power, desalination and cooling poly-generation system," *Energy,* vol. 196, p. 117150, 2020.

WHEC-2022
23rd World Hydrogen Energy Conference
June 26-30, 2022 - Istanbul

#1607

THERMODYNAMIC ANALYSIS OF A NEW COMPRESSED AIR ENERGY STORAGE-BASED COMBINED PLANT FOR MULTIGENERATION WITH HYDROGEN PRODUCTION

[1] *Murat Koc,* [2*] *Yunus Emre Yuksel,* [3] *Murat Ozturk*
[1]Isparta University of Applied Sciences, Technical Sciences Vocational School, Electricity and Energy Department, Cunur West Campus, Isparta, Turkey
[2]Afyon Kocatepe University, Bolvadin Vocational School, Electricity and Energy Department, Kirkgoz Campus, Afyonkarahisar, Turkey
[3]Isparta University of Applied Sciences, Faculty of Technology, Department of Mechatronics Engineering, Cunur West Campus, Isparta, Turkey

*Corresponding author e-mail: yeyuksel@aku.edu.tr

ABSTRACT

In this study, a novel compressed air energy storage-based combined plant for hydrogen production and other utilities is designed. Wind turbines and solar photovoltaic modules are the main drivers of the plant to compress the air. The multigeneration system is able to produce power, hydrogen, heating, and cooling. In the design step, each flow is enumerated and assigned thermodynamic balance equations. In order to evaluate the system performance, energy and exergy analyses are used. Then parametric analyses were performed in order to see the effects of the reference temperature and the charge-discharge pressure ratio. The study results show that the overall energy and exergy efficiencies of the multigeneration plant are 27.52% and 24.83%.

Keywords: Compressed air energy storage, Hydrogen production, Multigeneration, Energy, Exergy

INTRODUCTION

The increase in the world's population and the demand for more energy result in the depletion of fossil fuel reserves and environmental problems [1]. In order to overcome such problems, renewable energy sources such as solar, wind, biomass, and geothermal have been used in recent years [2]. Although solar and wind are good alternatives to meet the energy demand, their unstable and intermittent nature causes problems in their widespread use. One of the best ways to overcome such challenges is to use energy storage systems [3]. Ji et al. proposed a new hybrid wind-solar compressed air energy storage system. They have also integrated the organic Rankine cycle (ORC). Energy, exergy, and parametric sensitivity analyzes were performed for the proposed system. They showed that an increase in ambient temperature has a negative effect on system performance, while an increase in turbine inlet temperature has a positive effect [4]. Another study by Alirahmi et al. proposes an integrated system that offers a combination of compressed air energy storage with solar heliostat and multi-effect thermal vapor compression desalination units providing power and clean water. By performing energy, exergy, and exergoeconomic analyzes for the whole system, round-trip efficiency and total cost rate were calculated as 48.7% and 3056 $/hr, under the optimum conditions, respectively [5]. Another study emphasizing that the energy sector can be converted from fossil fuel to renewable energy sources and that energy can be used effectively with compressed air energy storage (CAES) systems was conducted by Xia et al. [6]. The literature clearly shows the importance of stored energy from intermittent renewable sources such as wind and sun. This proposed system is a new integrated system that air energy storage for electricity and hydrogen production from renewable energy sources. This study aims to evaluate the performance of the air storage system associated with power and hydrogen production from solar and wind from a thermodynamic point of view.

SYSTEM DEFINITION

The air heated by the energy obtained from the sun (PV modules) and the wind is passed through a three-stage compressor and sent to the air cave, and the compressed air storage cycle is completed (streams 1-7). The air entering the HEX 2 by stream 8 is included in the power production process. The air out of the Hex 2 passes through the high-mid-low heaters, and then the high-medium-low pressure air generates power in the turbines, respectively. The oil from stream 41 is used in the single-acting absorption refrigeration cycle to create a cooling effect. On the other hand, the water heated in HEX1 is sent to the PEM electrolyzer by stream 59. Here, water is decomposed into oxygen and hydrogen. While the oxygen is sent to be used in the health sector, the hydrogen is sent to the hydrogen liquefaction facility to liquefy. Some of the produced hydrogen passed through the heat exchangers is sent to the storage tank. The remainder is passed through the helium turbo expander to generate power. Thus, the integrated system cycle is completed.

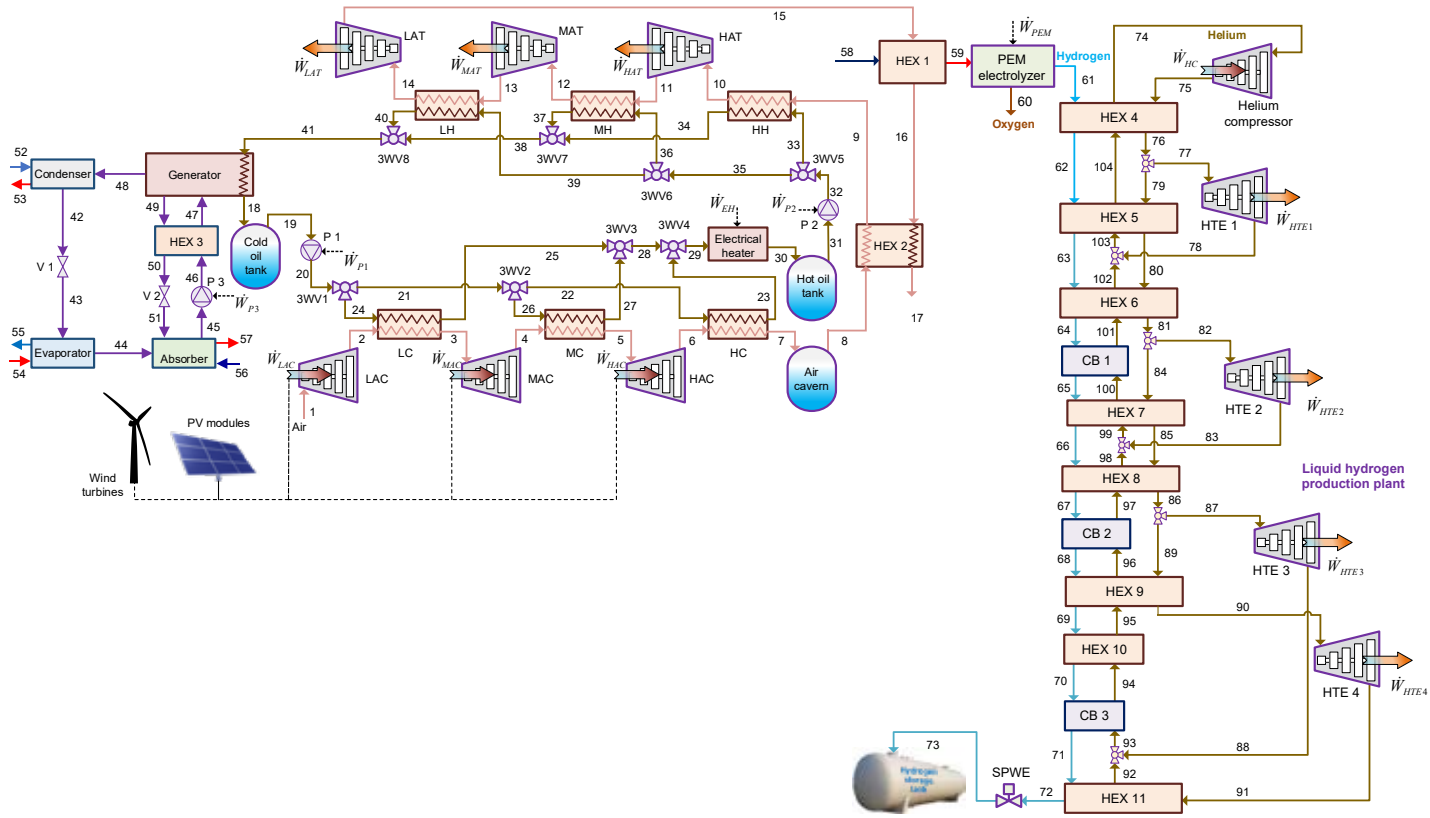


Fig. 1. Schematic diagram of the combined plant for compressed hydrogen production

THERMODYNAMIC ANALYSIS

In this subpart, the thermodynamical assessment utilized to determine the plant's effectiveness is defined briefly. View-points are analyzed using the Engineering Equation Solver (EES) program to determine energetic and exergetic performances with exergy destruction rates of the combined plant and its sub-plants. The general assumptions can be defined with:

- Steady-state and steady-flow mechanisms are assumed.
- The HEXs, compressors, pumps, and turbines are adiabatic.
- Kinetic and potential energy and exergy terms are neglected.
- The reference temperature and pressure are taken as 25°C and 101.3 kPa, respectively.
- The ideal gas characteristics are chosen for air to make an assessment.
- The pressure losses for connections and components are negligible.

To perform the thermodynamical analysis, the general mass, energy, entropy, and exergy balance equalities are written as given below;

$$\sum \dot{m}_i = \sum \dot{m}_e \tag{1}$$

$$\sum \dot{m}_i h_i + \sum \dot{Q}_i + \sum \dot{W}_i = \sum \dot{m}_e h_e + \sum \dot{Q}_e + \sum \dot{W}_e \tag{2}$$

$$\sum \dot{m}_i s_i + \sum \left(\frac{\dot{Q}}{T}\right)_i + \dot{S}_{gen} = \sum \dot{m}_e s_e + \sum \left(\frac{\dot{Q}}{T}\right)_e \tag{3}$$

$$\sum \dot{m}_i ex_i + \sum \dot{E}x_i^Q + \sum \dot{E}x_i^W = \sum \dot{m}_e ex_e + \sum \dot{E}x_e^Q + \sum \dot{E}x_e^W + \dot{E}x_D \tag{4}$$

where i and e give the inlet and exit conditions, respectively, $\dot{Q}$ shows the heat transfer rate, $\dot{W}$ illustrates the work rate, s and h are the specific entropy and enthalpy, respectively, $\dot{m}$ shows the mass flow rate, $\dot{S}_{gen}$ and $\dot{E}x_D$ are the entropy generation and exergy destruction rate, respectively.

RESULTS AND DISCUSSION

In this part of the study, the thermodynamic and parametric analysis results are presented. According to the findings, the multigeneration plant's overall energy and exergy efficiency are 27.52% and 24.83. Energy and exergy efficiencies of other sub-plants are listed in Table 1.

Table 1. Energy and exergy efficiencies of the multigeneration plant and its sub-systems

Overall plant and its sub-plants	η	ψ	$\dot{E}x_D$ (kW)
Compressed air storage plant	0.4554	0.4187	13839
Power production plant	0.3474	0.3196	8721
Hydrogen production and liquefaction plant	0.5827	0.5154	794
Cooling plant	0.2306	0.1935	1023
Overall plant	0.2752	0.2483	24377

On the other hand, the heating, cooling, and hydrogen amounts are 1921 kW, 1183 kW, and 0.0513 kg/s, respectively. Parametric analyses reveal that as the reference temperature increases from 0 to 50 °C, the energy efficiencies of sub-plants, except for the cooling plant, increase. For this increase in the reference temperature, the overall energy efficiency goes up from 26.31% to 28.78%. As focused on the exergy efficiencies, a similar trend with the energy efficiency can be seen. The overall exergy efficiency increases from 23.51% to 26.23% as the reference temperature increases.

Additionally, an increase in the reference temperature from 0 to 50 °C has a positive impact on the hydrogen production such that it improves from 0.0474 kg/s to 0.0555 kg/s while the exergy destruction rate of the multigeneration plant decreases. The second parameter investigated in this study is the charge-discharge pressure ratio from 1.2 to 2. When the charge-discharge ratio increases from 1.2 to 2, the energy efficiencies of sub-systems and the multigeneration system improve. Similarly, the exergy efficiencies of sub-plants and the overall plant increase as the charge-discharge pressure ratio increases. This parameter change increases the overall exergy efficiency from 24.24% to 25.63%.

CONCLUSIONS

In this study, a novel design is done with a multigenerational aim using compressed air storage. Thermodynamic and parametric analyses are performed to evaluate the multigeneration system's efficiencies. According to the results, the hydrogen production and liquefaction plant operate with the best efficiency among other sub-systems. Other concluding remarks are as follows:

- The highest exergy destruction rate occurs in the compressed air storage plant with 13839 kW.
- The energy and exergy efficiencies of the power production plant are 34.74% and 31.96%.
- The increase in the reference temperature positively impacts the sub-plants efficiencies except for the cooling plant.
- The overall energy and exergy efficiencies improve as the charge-discharge pressure ratio increases from 1.2 to 2.

REFERENCES

1. Ibrahim NI, Al-Sulaiman FA, Saat A, Rehman S, and Ani FN. 2020. Charging and discharging characteristics of absorption energy storage integrated with a solar driven double-effect absorption chiller for air conditioning applications. Journal of Energy Storage, 29, 101374.
2. Bull SR. 2001. Renewable energy today and tomorrow. Proceedings of the IEEE, 89(8), 1216-1226.
3. Dong L, Xing T, Song J, and Yousefi A. 2021. Performance analysis of a novel hybrid solar photovoltaic-pumped-hydro and compressed-air storage system in different climatic zones. Journal of Energy Storage, 35, 102293.
4. Ji W, Zhou Y, Sun Y, Zhang W, An B, and Wang J. 2017. Thermodynamic analysis of a novel hybrid wind-solar-compressed air energy storage system. Energy conversion and management, 142, 176-187.
5. Alirahmi SM, Mousavi SB, Razmi AR, and Ahmadi P. 2021. A comprehensive techno-economic analysis and multi-criteria optimization of a compressed air energy storage (CAES) hybridized with solar and desalination units. Energy Conversion and Management, 236, 114053.
6. Xia T, Li Y, Zhang N, and Kang C. 2022. Role of compressed air energy storage in urban integrated energy systems with increasing wind penetration. Renewable and Sustainable Energy Reviews, 160, 112203.

WHEC-2022
23rd World Hydrogen Energy Conference
June 26-30, 2022 - Istanbul

#1608

A SYSTEM MODEL FOR SIMULATING A FUEL CELL RECREATIONAL BOAT

[1,2*] S. Aykut Korkmaz, [1] Sera Ayten Çetinkaya, [3] Burak Göksu, [2] Olgun Konur, K. Emrah Erginer, [4] C. Ozgur Colpan
[1] The Graduate School of Natural and Applied Sciences, Dokuz Eylul University, Izmir, Turkey
[2] Department of Marine Engineering, Faculty of Maritime, Dokuz Eylul University, Izmir, Turkey
[3] Department of Marine Engineering, Faculty of Maritime, Bulent Ecevit University, Zonguldak, Turkey
[4] Department of Mechanical Engineering, Faculty of Engineering, Dokuz Eylul University, Izmir, Turkey

*Corresponding author e-mail: aykut.korkmaz@deu.edu.tr

ABSTRACT

Fuel cell vehicles' low environmental impacts, current technological advancements, and commercial manufacturing have opened the path to their employment in a variety of areas. The usage of fuel cell technology in marine transport has increased as the International Maritime Organization's (IMO) environmental regulations have been tightened. A simulation of a fuel cell propulsion system for use on boats is constructed in this study. A fuel cell, a metal hydride hydrogen tank, a battery pack, and an electric motor are represented as part of the system. The speed-power curve of the hull is obtained for the design draft using a computational fluid dynamics tool. The field data from the ongoing project are used to verify this system model.

Keywords: PEMFC, System Simulation, Recreational Boat, Fuel Cell Vehicles, CFD

INTRODUCTION

The marine transportation volume is growing at a rapid pace with the advancement of technology and the growth of the population. The number of ships in the oceans and, accordingly, the pollution in the seas have increased significantly. Shipping accounts for 3% of worldwide CO_2 emissions, according to the International Maritime Organization (IMO), with that percentage anticipated to climb up to 6% by 2050 [1]. As a result, ship transportation regulations have been strengthened. Following the tightening of regulations, efforts have been undertaken to reduce emissions in maritime transportation. One of them is to use fuel cells to meet the shipboard power requirements.

Because of the high cost of the fuel cell systems, it is important to understand the performance of the fuel cell vehicle with an accurate model. There are several studies on the fuel cell maritime vehicle system model. Honn-Choi et al. [2] developed and installed a hybrid proton exchange membrane fuel cell (PEMFC)/battery system for a 20-meter tourist boat with an output power of approximately 85 kW and a speed of 6.6-7.8 knots. Rivarolo et al. [3] compared the energy efficiency, CO_2 emissions, and other fuels for the fuel cell system to be used in a ferry. Software was created at the University of Genoa to study the design and cost of a 200-passenger capacity ferry operating on the artificial lake of Itaipu. Boudjabar and Khooban [4] suggested a zero-emission hybrid fuel cell/battery/cold-ironing system and used real data from a ferry to examine hull design and energy resources. Balestra and Schjolber [5] created a simulation tool that evaluates a user-selected configuration in a battery and fuel cell power plant for marine applications that can produce the electricity required by the energy management system realistically. Dall'Armi et al. [6] carried out simulations using different types of compressed hydrogen storage tanks (Type 1,3,4) to analyze the peak shaving point of the low temperature (LT)-PEMFC/battery system used for propulsion of a small-sized RoRo vehicle and passenger ferry.

In this study, the mathematical model of a 5.6-meters recreational boat with a hybrid PEMFC/battery system was modeled using the MATLAB/Simulink software in an ongoing project. The required engine power equation was deployed to the simulation as a velocity-power curve by curve fitting method using the gathered results from the computational fluid dynamics (CFD) tool. The batteries supply the boat's primary propulsion power. The fuel cell is used to charge the batteries as a range-extender. A Horizon H1000XP PEMFC with 1 kW rated power output and two pouch-type lithium-ion batteries with 3.3 kWh energy capacity produced by Farasis were selected. Two different configurations of the boat's propulsion system were evaluated at various service speeds, acceleration times, and ranges to find an optimized service speed versus energy consumption.

MATHEMATICAL MODEL AND SYSTEM DESCRIPTION

Assumptions

- Acceleration and deceleration rates were considered equal.
- The overall delivered efficiency (losses such as propeller and electric motor) was assumed to be 50%.

- The Froude number was assumed to be at most 0.4, due to the displacement type boat, even keel, and calm water condition.
- The batteries were operated between 20 - 80% state of charge (SoC).
- The electric motor efficiency was assumed to be 90%.
- The DC/DC converter efficiency was assumed to be 95%.
- The SoC of batteries and the battery efficiency were initially accepted as 100% and 92%, respectively.
- It was assumed that the fuel cell is constantly operating at its most efficient power point (500 W - 56.82%).
- The fuel cell was added to the system as a range extender.

The mathematical modeling of the ship was conducted in MATLAB/Simulink environment. The model includes three subsystems, which are a fuel cell model, a vehicle dynamic model, and a battery model. The design parameters of the battery, fuel cell, and boat are given in Table 1.

Table 1. Design Parameters of the Boat

Battery Parameters	***Values***	***Fuel cell Parameters***	***Values***	***Boat Parameters***	***Values***
Nominal Voltage	51.1 [V]	Voltage	30 [V]	Length	5.6 [m]
Rated energy	3.3 [kWh]	Current	0- 33.5 [A]	Beam	1.76 [m]
Weight	18 [kg]	Weight	7 [kg]	Hull Weight	500 [kg]
Energy Density	183 [Wh/kg]	Number of Cell	50 [-]	Design Draft	0.475 [m]
Cell Configurations	14S2P	Rated Power	1,100 [W]	Design Service Speed	5.5 [knot]
Dimensions (W x H x L)	168 mm x 248 mm x 200 mm	Max. Efficiency	0.56	Length of Water Line	5.1 [m]

Fuel Cell Subsystem

The fuel cell model was deployed as a subsystem to Simulink by integrating the data from the manufacturer's datasheet to the simulation environment as 1-D lookup tables for the H1000XP fuel cell [7]. The net power of the fuel cell system was calculated as follows,

$$P_{net} = P_{fc} - P_{BoP} \quad (1)$$

where P_{fc} is the fuel cell power and P_{BoP} is the power of the balance of plant components. MyH2 7000 was chosen as the onboard storage tank (produced by H2planet), which has more energy storage capacity per unit weight than the battery [8]. The specifications of the metal hydride (MH) tank are given in Table 2.

Table 2. Specifications of the MyH2 7000 [8]

Weight (kg)	**External Volume (liters)**	**Refilling Pressure (bar)**	**Max. Pressure (bar)**	**Storage Capacity (liters)**	**Energy Consumption (Wh/kg)**
47	16.7	5-12	30	7,000	218.67

Vehicle Dynamic Subsystem

The boat's power requirements are given as inputs to the model. The third order speed-power curve equation was obtained based on the design draft of the boat on a particular route (8.8 km, Urla-Izmir) using the results of the CFD at different service speeds corresponding to Froude numbers between 0.25 to 0.4.

The boat was designed to carry safely a total of 1,500 kg with four passengers. According to the Froude number of 0.4, which is critical for the boat's effective cruising, the boat's service speed was selected as 1.769 m/s [9]. Using multiple speeds (1.769, 1.9455, 2.122, 2.2985, 2.475, 2.6515, 2.828 m/s) and varied fixed acceleration values, the best cruising speed and acceleration time with the least amount of travel time and energy usage were obtained using multi-criteria decision-making method with TOPSIS (Technique for Order of Preference by Similarity to Ideal Solution). Ten associated academicians and boat owners were interviewed about the weighting criteria utilized in this procedure, and the average of their responses was obtained as 0.73 for energy usage and 0.27 for cruising time.

Battery Model Subsystem

In the model, the batteries are planned to provide the main propulsion power. The characteristics of the batteries to be used are given in Table 1. Battery current and power are calculated by Equations (2) and (3).

$$I_{battery} = {V_{OCV} - \sqrt{V_{OCV}^2 - 4 \cdot R_{int} \cdot P_{load}}}\Big/{2 \cdot R_{int}} \quad (2)$$

$$P_{battery} = I_{battery} \cdot V_{OCV} \quad (3)$$

where V_{OCV} is the open-circuit voltage (V), R_{int} is the internal resistance of the battery, and P_{load} is the power required by the electric motor.

RESULTS AND DISCUSSION

After applying the curve fitting tool of MATLAB, the power equation was obtained as:

$$P = 83.573 \cdot V^4 - 137.54 \cdot V^3 - 26.365 \cdot V^2 + 185.72 \cdot V \quad (3)$$

TOPSIS multi-criteria decision-making method was applied to find an optimum value for speed by using a weighting factor between acceleration time and service time. Some of the findings were given in Table 3 to give a better understanding. It can be seen that scenarios with high service speeds have worst ranks in the TOPSIS ranking according to the specified weight factors of 0.73 for energy usage and 0.27 for cruising time. The results in Table 3 were derived based on the boat's only one round (roundtrip) on the selected route. Except for the first two instances when the service speed is low, a short acceleration time has a negative impact on the TOPSIS result since it generates higher energy consumption and has a limited effect on the entire cruise duration.

Table 3. Pre-Design Calculations for the Ship Power and Energy Requirements

Service Speed [m/s]	Power @ Service Speed [W]	Acceleration Time [s]	Total Time [s]	Required Energy [kWh]	Rank from TOPSIS
1.8	303	30	5049	0.4218	1
		5010	10029	0.3072	1210
1.9	446	30	4594	0.5640	906
		4560	9124	0.3391	1013
2.1	656	30	4214	0.7560	1654
		4180	8364	0.3905	802
2.3	950	30	3893	1.0152	2090
		3860	7723	0.4642	945
2.5	1349	30	3617	1.3377	2420
		3580	7167	0.5634	1259
2.7	1874	30	3379	1.7341	2639
		3340	6689	0.6908	1553
2.8	2549.	30	3170	2.2106	2753
		3140	6290	0.8513	1838

The significant constraint of a boat design is the weight consideration. The desired passenger capacity of the boat has been planned as four passengers. The load capacity that the boat can carry in the design draft was found to be 1,500 kilograms. In the absence of a fuel cell, MH tanks, and batteries, the total weight of the lightship and equipment was calculated as 1,164 kilograms. Accordingly, the weight limitation for the fuel cell and batteries was determined as 336 kilograms. In Figure 1, the cost and range of the vehicle for different situations were given. The battery-only (with 18 batteries), fuel cell-only (with 7 MH tanks), and 6 different hybrid systems as Case 1 (15 batteries and 1 MH tank), Case 2 (12 batteries and 2 MH tanks), Case 3 (10 batteries and 3 MH tanks), Case 4 (7 batteries and 4 MH tanks), Case 5 (5 batteries and 5 MH tanks) and Case 6 (2 batteries and 6 MH tanks) were determined according to weight limitations. When the system is dimensioned according to the weight limitations, it can be seen that the fuel cell-only case yields the longest range. In the cost analysis, the battery-only case gave the lowest cost. In hybrid cases, it can be seen that while the MH tank number increases, the range of the boat increases. In this case, the fuel cell-only situation is the most advantageous case. It was shown that the best case among hybrid systems is Case 6.

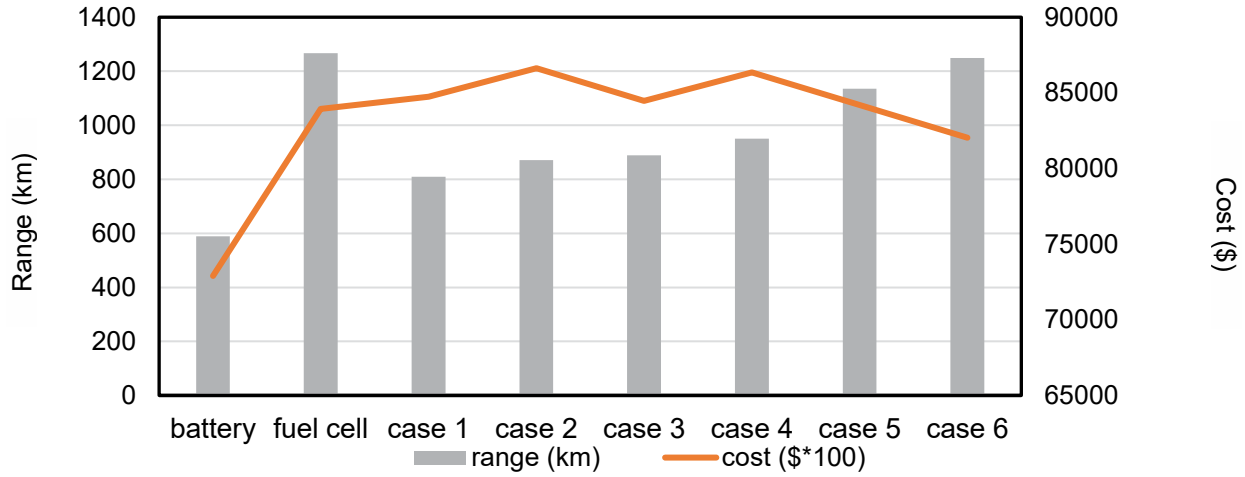


Fig. 1. Range and cost analysis for different cases

CONCLUSION

In this study, using the CFD method, a speed-power curve was obtained for four different service speeds of the boat at the design draft. By using this curve, the power values required by the boat were obtained on the route determined. Service times and total energy consumption were calculated by using different acceleration time values for the same cruise speed and the same acceleration time values for different service speeds. The best acceleration time (30 s) and service speed (1.769 m/s) values were determined with the multi-criteria decision-making method with TOPSIS using the obtained cruise times and energy consumption amounts. These values were simulated for different scenarios in the system model created with MATLAB/Simulink. Considering the weight constraint, range and cost analyzes were carried out. As a result, it was observed that only the fuel cell situation gave the longest range, and the cost of Case 6 was found minimum.

ACKNOWLEDGEMENTS

This research was supported by the Dokuz Eylul University's Scientific Research Projects with the project number 2020.KB.MLT.012.

REFERENCES

1. International Maritime Organization, https://www.imo.org/ Accessed: 05.18.2022.
2. Choi, C. H., Yu, S., Han, I. S., Kho, B. K., Kang, D. G., Lee, H. Y., ... & Kim, M. (2016). Development and demonstration of PEM fuel-cell-battery hybrid system for propulsion of tourist boat. International Journal of Hydrogen Energy, 41(5), 3591-3599.
3. Rivarolo, M., Rattazzi, D., Lamberti, T., & Magistri, L. (2020). Clean energy production by PEM fuel cells on tourist ships: A time-dependent analysis. International Journal of Hydrogen Energy, 45(47), 25747-25757.
4. Rafiei, M., Boudjadar, J., & Khooban, M. H. (2020). Energy management of a zero-emission ferry boat with a fuel-cell-based hybrid energy system: Feasibility assessment. IEEE Transactions on Industrial Electronics, 68(2), 1739-1748.
5. Balestra, L., & Schjølberg, I. (2021). Modelling and simulation of a zero-emission hybrid power plant for a domestic ferry. International Journal of Hydrogen Energy, 46(18), 10924-10938.
6. Dall'Armi, C., Micheli, D., & Taccani, R. (2021). Comparison of different plant layouts and fuel storage solutions for fuel cells utilization on a small ferry. International Journal of Hydrogen Energy, 46(26), 13878-13897.
7. Horizon Educational, H-1000 PEM Fuel Cell - 1kW. https://www.horizoneducational.com/h-1000-pem-fuel-cell-1kw/p1355 Accessed: 20.05.2022.
8. H2planet, MyH2 7000, https://www.h2planet.eu/en/detail/myh2%C2%AE_7000_1 Accessed: 20.05.2022.
9. Göksu, B., Korkmaz, S. A., & Erginer, K. E. Ship Wind Resistance Prediction: A Case-Based Approach. Engineering and Architectural Sciences, 1-22.

WHEC-2022
23rd World Hydrogen Energy Conference
June 26-30, 2022 - Istanbul

#1610

MULTI-OBJECTIVE OPTIMIZATION OF AN INTEGRATED DOWNDRAFT BIOMASS GASIFIER AND SOLID OXIDE FUEL CELL SYSTEM

[1*] *Beyza Dursun,* [1] *Anil Erdogan,* [2] *C. Ozgur Colpan* [3] *Azize Ayol*
[1]The Graduate School of Natural and Applied Sciences, Dokuz Eylul University, Buca, Izmir, Turkey
[2] Faculty of Engineering, Department of Mechanical Engineering, Dokuz Eylul University, Buca, Izmir, Turkey
[3] Faculty of Engineering, Department of Environmental Engineering, Dokuz Eylul University, Buca, Izmir, Turkey

*Corresponding author e-mail: beyzanisandursun@gmail.com

ABSTRACT

In this study, a mathematical model is developed for an integrated downdraft biomass gasifier and solid oxide fuel cell (SOFC) system. The models for the SOFC as well as the other components are developed in Matlab environment. Regarding the mathematical modelling, energy and exergy analyses are conducted to assess the system's performance. Then thermo-economic analysis is performed in order to find the electricity production cost. After that, a multi-objective optimization study using TOPSIS method is conducted in order to find the optimum operating conditions.

Keywords: *Thermo-economic analysis, Biomass Gasifier, Solid Oxide Fuel Cells, Multi-Objective Optimization*

INTRODUCTION

Recently, energy demand has increased as a result of the increasing population and developing technology. In the coming years, it is predicted that fossil energy resources will be insufficient compared to the population. This situation has created the need for alternative energy resources. One of these resources is biomass, which is made up primarily of carbon-based materials and organic chemical combinations. Some examples of biomass can be listed as rice husk, wood chips, agricultural waste, and municipal solid waste [1]. One of the methods used to convert biomass into usable energy is gasification. Gasification is one of the processes for turning biomass into useable energy. Biomass is fed into the gasifier with air, oxygen, or steam, and then transformed into syngas via a thermochemical process. Updraft and downdraft gasifiers are the most typical fixed bed gasifiers. As both the biomass and the air move downstream in the downdraft gasifier, the biomass is fed from above and the syngas generated leaves from the bottom. The biomass is still fed from above in an updraft gasifier, but the biomass moves downwards, the supplied air goes upwards, and the produced syngas leaves from the top of the gasifier. The gasification process is divided into four steps. In the downdraft gasifier, the biomass is first fed to the dryer (>150°C) in order to reduce its moisture content. Then, in the pyrolysis step (between 200°C and 500°C), dry biomass is separated into components such as coal, and. During the oxidation process (between 700°C and 1500°C), carbon dioxide and water are produced as a result of the reactions with oxygen. The reduction process takes place in the absence of oxygen, under high temperatures (between 650°C and 900°C) and syngas is formed [2].

Solid oxide fuel cells (SOFCs) are thermochemical systems that operate at high temperatures (800-1000℃). Solid oxide fuel cells are made up of two electrodes which are separated by a ceramic electrolyte. The oxygen fed from the cathode chamber is reduced to the oxygen ion. In the anode chamber, on the other hand, hydrogen combines with the oxygen ions coming from the cathode chamber and electrons from the external load, and water is released [3].

Evaluations of integrated systems on an economic basis can be evaluated by calculating some economic indicators such as the cost of useful products over the active life of the facility and the payback period. Thermo-economic and techno-economic analysis methods are generally used in the cost analysis of these systems. In this study, energy and exergy analyses are conducted to find the state properties and the component's irreversibilities, respectively. After that, thermoeconomic analysis is used to calculate the operating cost of the system and to make economic improvements in the system. Finally, a multi-objective optimization (using TOPSIS method) is used to find the optimum operating parameters of the integrated system.

MATERIAL AND METHOD

In this study, thermo-economic analysis of a hybrid system as shown in Fig. 1, which consists of a downdraft biomass gasifier, a SOFC, an afterburner, and heat exchangers was investigated. Firstly, energy balance equation (Eq. (1)) is applied in order to find the state properties. Then, exergy balance equation (Eq. (2)) is used to find the flow exergies of each states and irreversibilities of system's components. After applying the energy and exergy balances, the cost of exergy flows for each

component k^{th} is calculated. The general equation used for thermo-economic analysis is written as Eq. (3) shown below. Details of the equations used for economic analysis can be found in the literature [4]. By means of these equations, the effect of the gasifier temperature and power produced by the SOFC on the cost of the electricity produced was examined and a parametric study was carried out via MATLAB.

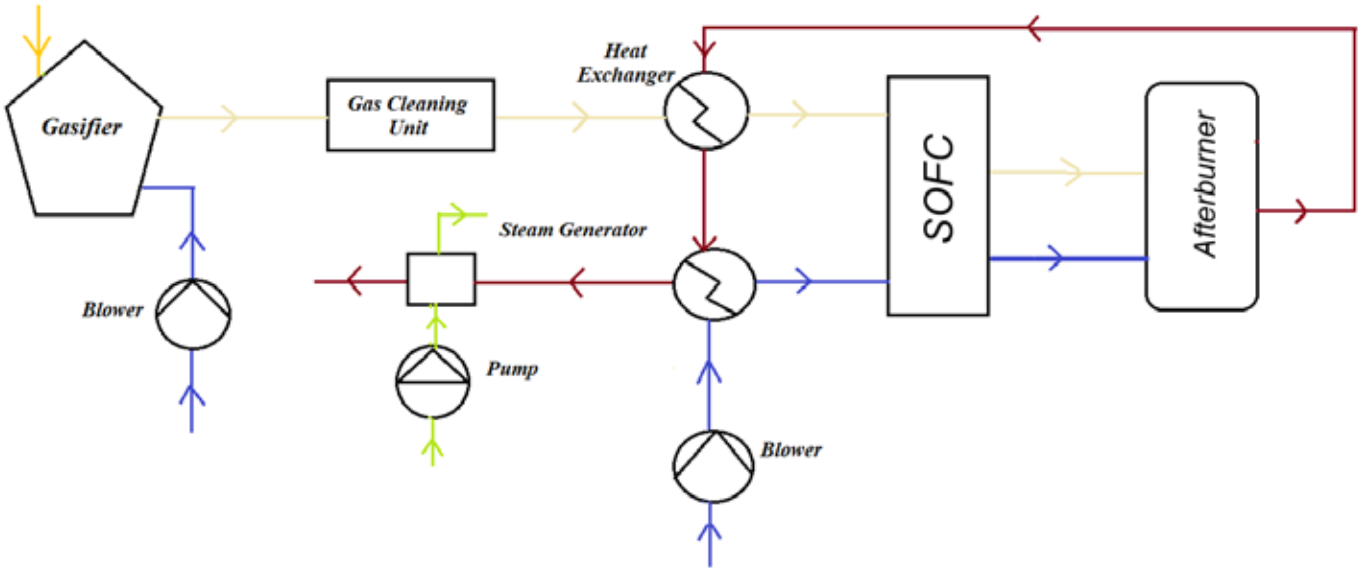


Fig. 1. The schematic of the integrated down-draft biomass gasifier and SOFC system

$$0 = \dot{Q} - \dot{W} + \sum_i(\dot{n}_i \cdot \bar{h}_i) - \sum_e(\dot{n}_e \cdot \bar{h}_e) \quad (1)$$

$$0 = \dot{E}x_Q - \dot{E}x_W + \sum_i \dot{n}_i \cdot (\bar{e}_{f,i}{}^{PH} + \bar{e}_{f,i}{}^{CH}) - \sum_e(\bar{e}_{f,i}{}^{PH} + \bar{e}_{f,i}{}^{CH}) - \dot{E}x_D \quad (2)$$

$$\sum \dot{C}_{out,\ k} + \dot{C}_{W,\ k} = \sum \dot{C}_{in,k} + \dot{C}_{q,\ k} + \dot{Z}_k \quad (3)$$

After finding the thermodynamic and thermo-economic performance parameters, an optimization study using TOPSIS method is carried out to find the optimal operating conditions for the system studied. The main equations used this method are presented as follows.

$$r_{i,j} = \frac{a_{i,j}}{\sqrt{\sum_{k=1}^{m} a_{k,j}{}^2}} \quad (4)$$

$$S_i{}^+ = \sqrt{\sum_{j=1}^{n}(v_{i,j} - v_j{}^+)^2} \quad (5)$$

$$S_i{}^- = \sqrt{\sum_{j=1}^{n}(v_{i,j} - v_j{}^-)^2} \quad (6)$$

$$C_i{}^* = \frac{S_i{}^-}{(S_i{}^+ - S_i{}^-)} \quad (7)$$

Regarding the optimization study, the range for operating parameters are given as follows. The aim of optimization study is to maximize the exergy efficiency and the fuel utilization efficiency and to minimize the cost of produced electricity.

Table 1. Parameter ranges for the optimization study

Parameter Name	Range
Gasifier Temperature	800°C - 940°C
SOFC Power	10 kW – 100 kW

RESULTS AND DISCUSSION

In this section, the results derived from the study are presented and discussed. Fig. 2 shows that the effect of gasifier temperature on the electrical efficiency and fuel utilization. As the gasifier temperature increases, the electrical efficiency increases. This trend mainly due to the slightly increase of net power output of the integrated system. On the other hand, when the gasifier temperature increases, the fuel utilization efficiency decreases due to the decrease

of useful heat from the steam. In addition, it can be observed that if the gasifier temperature increases from 800°C to 980°C, the electrical efficiency decreased by 7.69%; whereas FUE decreased by 22.5%.

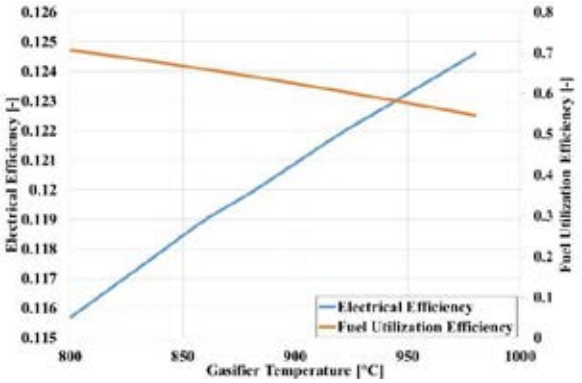
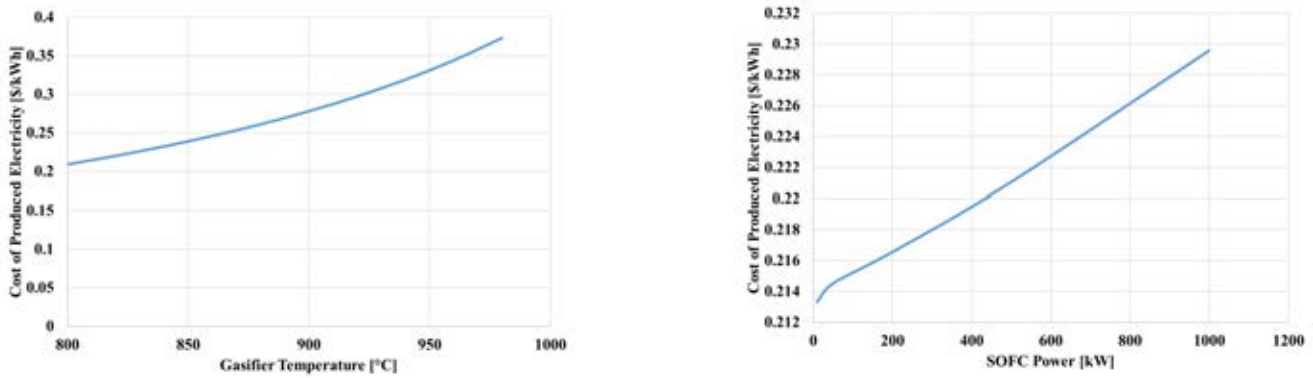


Fig. 2. The effect of gasifier temperature on the electrical efficiency (left axis), and fuel utilization efficiency (right axis).

Fig. 3(a) illustrates the effect of gasifier temperature on the cost of produced electricity of the system. As the gasifier temperature increases, the cost of power produced increases. Fig. 3(b) shows the effect of number of SOFC stack on the electricity cost. As the number of stack increases, the electricity cost increases. However, it should be noted that this parameter could be optimized in order to increase the system's performance and decrease the cost.



(a) (b)

Fig. 3. (a) The effect of gasifier temperature on the cost of produced electricity of the system. (b) The effect of the number of SOFC stack on the cost of produced electricity.

Table 2 shows that the results for optimization study. For the analysis, the weighting factor for the performance parameters are taken as 25% for the exergy efficiency, 25% for the fuel utilization efficiency, and 50% for the cost of power produced.

Table 2. Results of the optimization study

Gasifier Temperature (°C)	Power of SOFC (kW)	Exergy Efficiency	Fuel Utilization Efficiency	Cost of Power Produced ($/kWh)	Rank
800	99	0.225536	0.411	0.171	1
800	92	0.225567	0.398	0.170	2
800	95	0.225341	0.395	0.175	3

CONCLUSION

In this study, thermodynamic and thermo-economic analyses of a biomass gasifier integrated with solid oxide fuel cell was conducted in order to assess the performance in terms of thermodynamic and economic point of view. Then, a multi-objective optimization using TOPSIS method was performed to indicate the optimum operating parameters. The results derived from the study conducted are listed as follows.

- As the gasifier temperature increases, electrical efficiency increases. However, the fuel utilization efficiency decreases.

- As the gasifier temperature increases, the cost of electricity increases.
- In order to assess the system's performance in terms of environmental point of view, as the gasifier temperature increases, the rate of CO_2 impact keeps stable.
- As the number of stack increases, the electricity produced cost increases. However, this parameter should be optimized in order to reduce the electricity cost.
- The optimization study results show that when the gasifier temperature 800°C, the SOFC power is 99 kW, the exergy efficiency, the FUE, and the cost of power produced are found as 22.55%, 41.1%, and 0.171 $/kWh, respectively.

ACKNOWLEDGMENT

This study was supported by the Scientific and Technological Research Council of Turkey (TUBITAK) 1001 (Grant number: 119R029) Project. In addition, the first two authors would like to thank Suleyman Aykut Korkmaz and Okan Gok for their technical advice on the optimization studies.

REFERENCES

1. 2019 AEO. Annual Energy Outlook 2019 with projections to 2050. Annu Energy Outlook 2019 with Proj to 2050 2019;44:1–64.
2. Basu P. Biomass Gasification and Pyrolysis. 1st ed. 2010.
3. Ormerod RM. Solid oxide fuel cells. Chem Soc Rev 2003;32:17–28. https://doi.org/10.1039/b105764m.
4. Cheng, C., Cherian, J., Sial, M. S., Zaman, U., & Niroumandi, H. (2021). Performance assessment of a novel biomass-based solid oxide fuel cell power generation cycle; Economic analysis and optimization. *Energy*, *224*, 120134.

WHEC-2022
23rd World Hydrogen Energy Conference
June 26-30, 2022 - Istanbul

#1618

A STUDY ON EXERGETIC SUSTAINABILITY INDICATORS OF SOLAR METHANE CRACKING

[1,2*] *Aliya Banu,* [2] *Adnan Midilli,* [1] *Yusuf Bicer*

[1] Division of Sustainable Development, College of Science and Engineering, Hamad Bin Khalifa University, Qatar Foundation, Doha, Qatar

[2] Division of Hydromechanics and Hydraulic Machines, Department of Mechanical Engineering, Yildiz Technical University, Istanbul, Turkey

*Corresponding author e-mail: alba34159@hbku.edu.qa

ABSTRACT

In this study, exergetic sustainability indicators of solar methane cracking for hydrogen production have been analysed. For this purpose, solar methane cracking system is considered a cleaner process for production of hydrogen fuel from natural gas. To evaluate the system comprehensively, a detailed exergy analysis is performed, and indicators based on exergetic sustainability are defined and calculated. The system has an exergy efficiency of 53% and a recoverable exergy ratio of 34%. Further improvements to the system can lead to enhanced sustainability.

Keywords: Exergetic sustainability indicators, Turquoise hydrogen, Thermodynamic modelling, Methanol, DME

INTRODUCTION

Hydrogen is a clean fuel, but the production process plays a crucial role in determining the level of environmental impact [1]. Currently hydrogen is produced from natural gas using steam reforming. An alternate pathway for cleaner hydrogen production is methane cracking. At high temperatures methane can be decomposed into pure hydrogen and solid carbon black. The process produces carbon black instead of CO/CO_2 as a by-product and the hydrogen produced is termed as 'turquoise hydrogen'. The carbon black is easier to manage and has several applications in other industries [2]. Nevertheless, carbon utilization can lead to CO_2 emissions. Therefore, it needs to be ensured that the CO_2 is captured and utilized.

Hydrogen due to its low energy density is difficult to transport or store, therefore it is suggested to convert it to other suitable energy carriers such as methanol and dimethyl ether (DME). This study proposes an integrated system for hydrogen production from natural gas, along with cleaner utilization of carbon product and conversion of hydrogen into a suitable energy carrier. The systems performance is studied by calculating indicators for exergetic based sustainability.

SYSTEM DESCRIPTION

An integrated system was designed to utilize the products of methane cracking in fuel cells. Concentrated solar power is used to provide the high temperatures required for methane cracking. Hydrogen and carbon black are used in a hydrogen fuel cell and direct carbon fuel cell (DCFC) respectively to generate electricity. The DCFC produces a pure CO_2 waste exhaust stream that is further utilized to produce fuels. CO_2 hydrogenation subsystem uses CO_2 from the DCFC and hydrogen to produce methanol and DME in a single step. The sources of this system are methane, solar energy, air to provide electricity, methanol and DME. The proposed process is summarized in Fig. 1.

ANALYSIS

The overall system was modelled on Aspen Plus® to obtain the thermodynamic properties of the streams. An exergy analysis is performed, and the input and output exergy flows were determined. Exergetic sustainability indicators were calculated using equations from the literature [3-4]. The following main indicators were computed for the proposed system:

$$Exergy\ efficiency\ (EE) = \frac{Useful\ exergy\ output}{Total\ exergy\ input} \quad (1)$$

Where the useful exergy outputs are determined based on the desired outputs from the overall system which are electricity, DME and methanol.

$$Waste\ exegy\ ratio\ (WER) = \frac{Total\ waste\ exergy\ output}{Total\ exergy\ input} \quad (2)$$

Where total waste exergy output includes all exergy outputs from the overall system to reference environment except the desired output. This also includes the total exergy destruction.

$$Exergy\ destruction\ ratio\ (EDR) = \frac{Total\ exergy\ destruction}{Total\ exergy\ inputs} \quad (3)$$

The total exergy destruction is calculated using the exergy balance.

$$Exergy\ recoverability\ \text{ratio}\ (ERR) = \frac{Total\ recoverable\ exergy\ output}{Total\ exergy\ inputs} \quad (4)$$

Exergy flows from the waste exergy outputs that can be reused for the same system are considered as recoverable exergy outputs.

$$Environmental\ effect\ \text{ratio}\ (EEF) = \frac{Waste\ exergy\ ratio}{Exergetic\ efficiency} \quad (5)$$

$$Exergetic\ sustainabilty\ index\ (ESI) = \frac{Exergetic\ efficiency}{Waste\ exergy\ ratio} \quad (6)$$

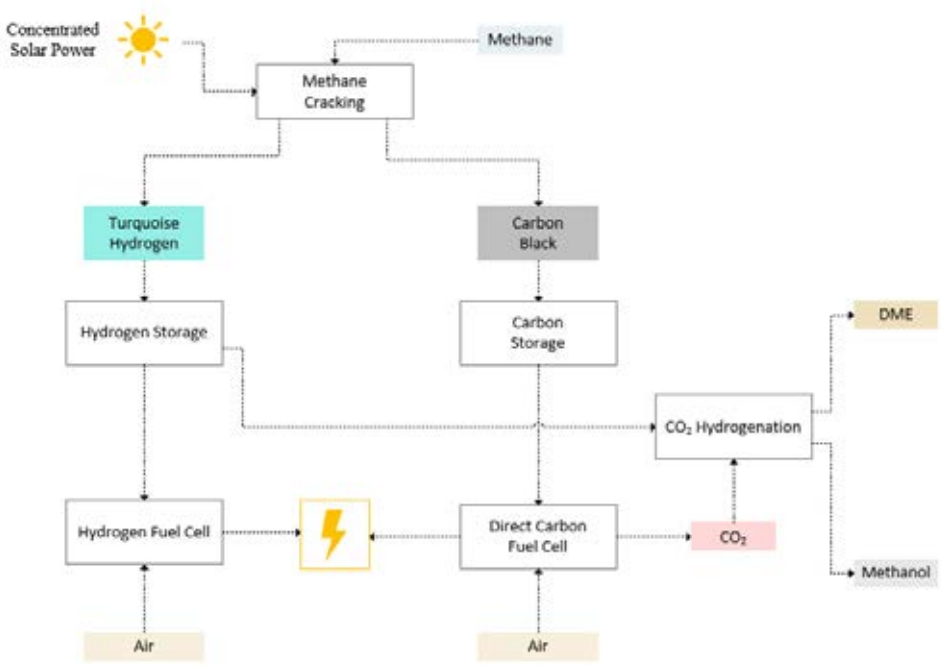


Fig. 1. Block flow diagram of the proposed integrated system

RESULTS AND DISCUSSION

The exergy flows of all streams in the process were obtained using the Aspen plus simulation. Exergy balances were performed over each unit and the overall system exergy inputs and outputs were determined. The exergetic sustainability indicators were calculated and the results are presented in Table 1. The exergy efficiency of the overall system is 53%. The system has an ESI greater than 1 and a high EEF. This system can be further improved by recovering the waste exergy outputs to increase its sustainability.

Table 1. Results of the exergy analysis

Exergetic sustainability indicator	Value
Exergy efficiency (EE)	0.53
Waste exergy ratio (WER)	0.47
Exergy recoverability ratio (ERR)	0.30
Exergy destruction ratio (EDR)	0.09
Environmental effect factor (EEF)	0.89
Exergetic sustainability index (ESI)	1.12

CONCLUSIONS

An integrated system for solar methane cracking is proposed and evaluated using exergetic sustainability indicators. The system has an exergy efficiency of 53% and ESI of 1.11. it was also noted that the exergy recoverability ratio is high indicating that system can be further improved. The addition of other technologies can recover waste exergy outputs to decrease the level of environmental impact and achieve higher overall efficiencies. Future work includes evaluating each subsystem to determine the areas that need improvement and comparisons with other alternate utilization pathways for produced hydrogen and carbon.

ACKNOWLEDGEMENT

This publication was made possible by Graduate Sponsorship Research Award (GSRA7-2-0427-20025) and Researchers Exchange and Mobility Program (REMP3-2-0207-21004) from the Qatar National Research Fund (a member of Qatar Foundation). The findings herein reflect the work, and are solely the responsibility, of the authors

REFERENCES

1. Koroneos C, Dompros A, Roumbas G and Moussiopoulos N. 2004. Life cycle assessment of hydrogen fuel production processes. International journal of Hydrogen Energy.
2. Muradov N, Smith F, T-Raissi A. 2005. Catalytic activity of carbons for methane decomposition reaction. Catalysis Today.
3. Midilli A, Dincer I. 2009. Development of some exergetic parameters for PEM fuel cells for measuring environmental impact and sustainability, International Journal of Hydrogen Energy.
4. Ozsaban M, Midilli A, Dincer I. 2011. Exergy analysis of a high pressure multistage hydrogen gas storage system, International Journal of Hydrogen Energy.

WHEC-2022
23rd World Hydrogen Energy Conference
June 26-30, 2022 - Istanbul

#1620

SOLAR ASSISTED HYDROGEN PRODUCTION VIA PV/T ASSISTED SMALL SCALE TRANSCRITICAL POWER CYCLE WITH DIRECT STEAM GENERATION

[1*]Gamze Soyturk, [1]Onder Kızılkan, [2]Mehmet Akif Ezan, [2]Can Ozgur Colpan
[1]Isparta University of Applied Sciences, Faculty of Technology, Department of Mechanical Engineering, 32200, Isparta, Turkey
[2]Dokuz Eylul University, Faculty of Engineering, Department of Mechanical Engineering, Tinaztepe Campus, 35397, Izmir, Turkey

*Corresponding author e-mail: gamzeyildirim@isparta.edu.tr

ABSTRACT

The objective of the proposed study is to examine the performance of an integrated hydrogen generation system based on solar energy. For this purpose, CO_2, a natural fluid that does not harm the environment, was used as the working fluid. The system is comprised of the Photovoltaic/thermal (PV/T) panels, a pump, a condenser, a turbine, a Proton Exchange Membrane Electrolysis Cell (PEM-EC), and hydrogen and oxygen storage tanks. MATLAB and EES software programs are utilized to perform the performance assessment of the system. According to the analysis made on data for 17th August of İzmir, the net power generation from the PVT panels was calculated as 2696 W, the net power generation from the transcritical C02 Rankine cycle was 73.03 W, and the hydrogen production was 0.514 g/h.

Keywords: PV/T, CO2, Transcritical CO_2, Hydrogen, PEM electrolyzer,

INTRODUCTION

Because of the significant growth in population and industrial development, global energy demand continues to rise. Fossil fuels are the most widely used energy resource on the planet. These traditional energy resources have serious negative environmental consequences, such as global warming, greenhouse impact, and air pollution. As a result, replacing fossil fuels with sustainable fuels like hydrogen is unavoidable if our ecosystem is to remain clean and green. Hydrogen as an energy carrier facilitates sustainable energy systems. Hydrogen fuel has several benefits over fossil fuels, comprising a reduced carbon footprint. As a result, efforts to develop and deploy sustainable energy and fuel technologies are underway [1]. One of the most prevalent hydrogen generating techniques is the PEM-EC [2]. The PEM-EC consumes electrical energy to break water molecules into hydrogen and oxygen gas [2]. The quantity of electrical input to the PEM-EC has a nearly linear relationship with the amount of hydrogen produced [3]. Consequently, the presence of a stable and sustainable energy supply to meet the PEM-EC's electricity demand is required. In order to produce hydrogen by the green method, this energy resource must also be renewable and environmentally friendly. Because of its abundance, solar energy is the most potential renewable energy resource. It must, however, be turned into power or heat. PV/T systems are the most common combined solar systems. Thermal collectors and PV modules combine to produce both thermal and electrical energy in this system. In recent years, energy production technologies using sCO_2 based on solar energy have attracted the attention of important research. The sCO_2 power generation cycles use environmentally friendly and non-toxic CO_2 as the working fluid. Also, the thermophysical characteristic of CO_2 presents sharp changes near the critical state, which diminishes the compression power consumption and consequently promotes its cycle efficiency. Integrated PV/T modules with transcritical CO_2 Rankine cycle is a promising way of energy production with solar energy. These systems convert low-grade thermal energy into electricity. Salari and Hakkari-Fard [1] investigated the performance of a PV/T-ORC system coupled with a PEM-EC and developed a combined numerical/theoretical model of the system. The performance of a combined PVT-ORC system was theoretically explored by Tourkov and Schaefer [4]. The effects of numerous design parameters on PVT-ORC performance, for instance, ORC configuration, ORC working fluid, and working fluid mass flow rate, were explored in this study. Hosseini et al. [5] designed the PVT/ORC cycle to produce hydrogen with the aim of energy storage. They concluded that the integrated system could generate 2.378 kW of electrical power. The objective of this study is to explore the performance of an integrated solar-based hydrogen production system to decrease environmental damage using carbon dioxide, a highly natural liquid. When the studies in the literature are examined, no low-temperature operating systems integrated with PVT using CO2 as the working fluid have been found. It is thought that this study will contribute to the literature.

MATERIALS AND METHODS

Fig.1 shows the schematic representation of solar-assisted hydrogen production system by PV/T assisted transcritical power cycle with direct steam generation. The PV/T system converts solar energy into electricity and heat energy. The output thermal energy of the PV/T system drives the transcritical sCO2 cycle to generate more electricity. Thus, the total electricity generation from solar input is increased by combining the PV/T system with the

transcritical sCO_2 cycle. Lastly, the generated electrical energy is transmitted to a PEM-EC to produce hydrogen, which is the main objective of this work.

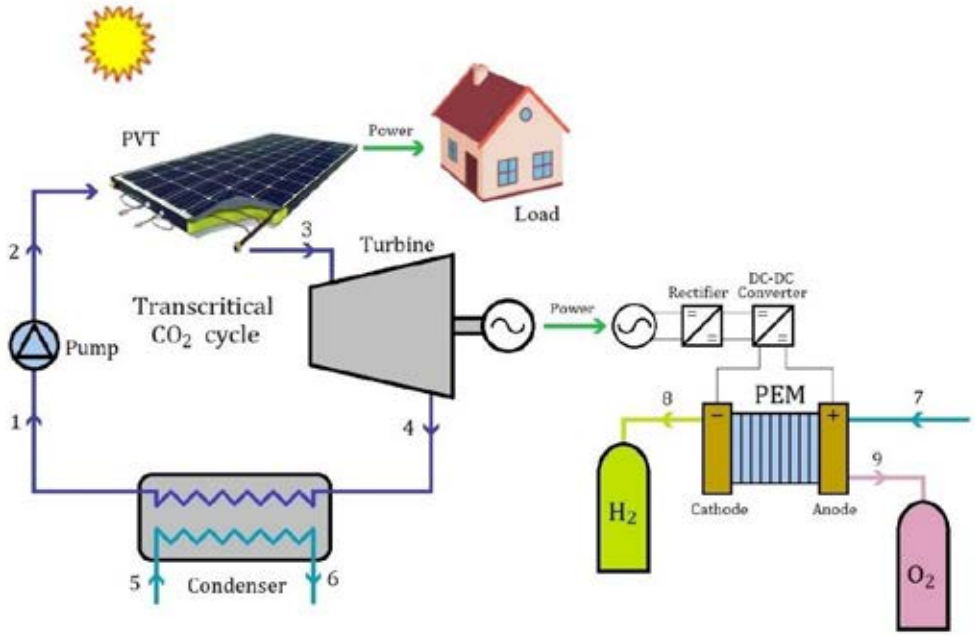


Fig. 1. Schematic representation of the PV/T based hydrogen generation system with transcritical sCO_2 cycle

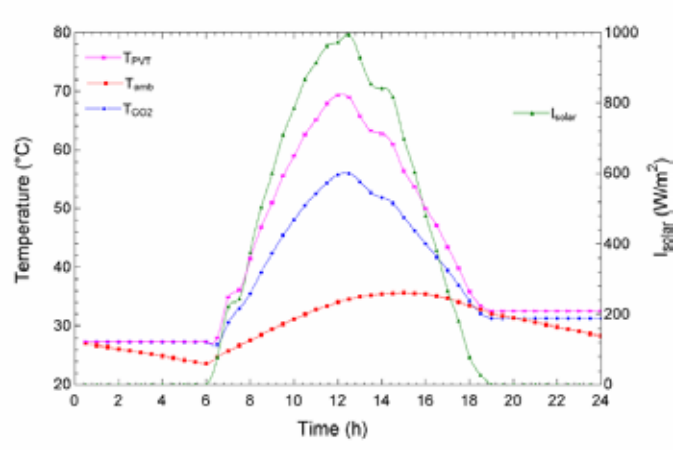
The design parameters of the integrated system used in this study are given in Table 1.

Table 1. Design parameters for the proposed multi-generation system

Design Parameters	**Values**	***Design Parameters***	**Values**
PVT		***PEM Electrolyzer***	
Length, [m]	1.649	Freshwater temperature, [℃]	25
Width [m]	0.992	PEM electrolyzer temperature, [℃]	79
Number of PV [-]	20	E^{a}_{act} , [kJ/mol]	76
Reference electrical efficiency	0.14	E^{c}_{act} , [kJ/mol]	18
Temperature coefficient, [1/K]	0.0046	λ_a [-]	14
Transcritical sCO_2 Rankine		λ_c [-]	10
Turbine inlet pressure, [kPa]	9000	D, [μm]	100
Turbine outlet pressure, [kPa]	600	J^{a}_{ref} , [A/m^2]	1.7×10^5
Compressor isentropic efficiency [-]	0.90	J^{a}_{ref} , [A/m^2]	4.6×10^3
Turbine isentropic efficiency [-]	400	F, [C/mol]	96486

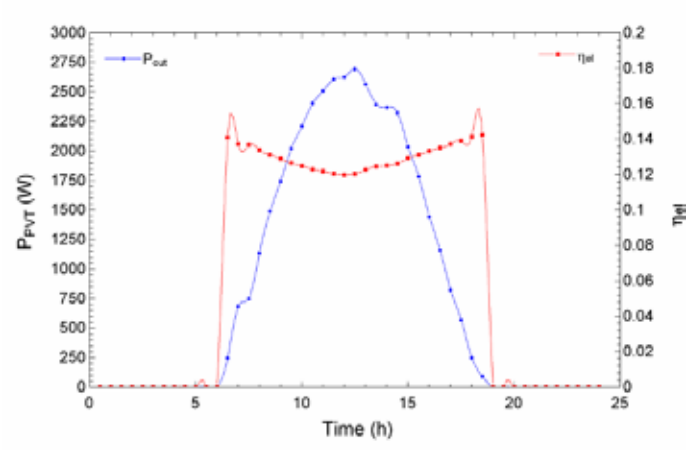
RESULTS AND DISCUSSION

This part gives the results of the analysis. As indicated before, mathematical modeling of the integrated system consisting of PV/T solar panels, turbine, condenser, pump, PEM electrolyzer, and hydrogen and oxygen storage tank was made in MATLAB and EES software. For the modeling of the PV/T solar panel, Ref. [6] is used, while the PEM electrolyzer modeling is adapted from Ref. [7]. In Fig. 2, the variation of solar radiation, PV/T temperature, ambient temperature, and CO_2 temperature with the time is given. As can be seen from the figure, changes in solar radiation and temperature changes are compatible with each other. Fig. 3 shows the change in PV/T power generation and electrical efficiency with time. As can be seen from the figure, the electrical efficiency decreases with the rise in the power supplied from the PV/T panels. Fig. 4 shows that the net power generated from the transcritical cycle increases with time since solar radiation increases. After noontime, it starts to decrease. Besides, the right-hand side of the figure indicates that the cycle efficiency reaches a maximum value of nearly 5 %. Finally, the hydrogen production amount by the time is given in Fig.5. As seen from the figure, the produced H_2 amount reaches 0.514 g/h. It seems very low; however, it must be noted that the energy requirement for the PEM electrolyzer was only supplied from power generated by the transcritical cycle. Also, to increase the generated amount, additional power could be used from PV/T, yet, in this study, this condition has not been taken into account since all electricity produced from PV/T was considered to be used for the residential house.



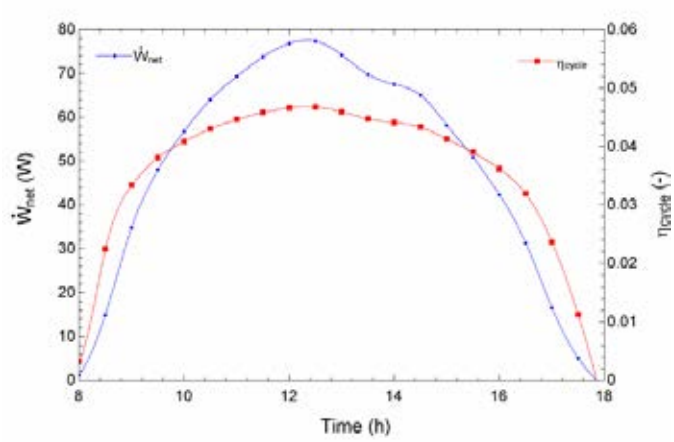
(a)

Fig. 2. Variation of PVT temperature, ambient temperature, CO_2 exit temperature, and solar radiation by the time



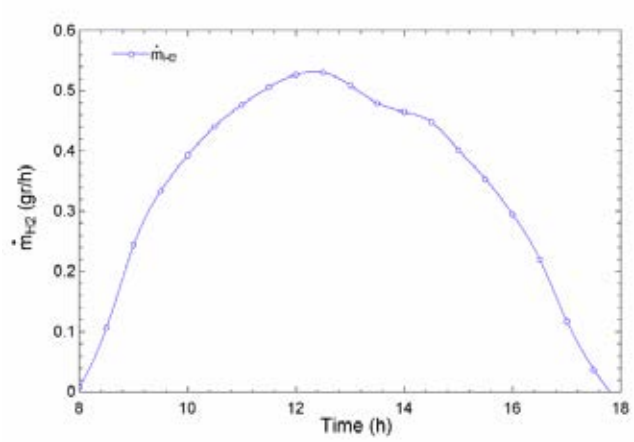
(b)

Fig. 3. Hourly power generation from PV/T and efficiency



(a)

Fig. 4. Variation of power production from CO_2 cycle and efficiency by the time



(b)

Fig. 5. Hourly hydrogen production with time

REFERENCES

1. Salari A and Fard-Hakkari A. Thermodynamic analysis of a photovoltaic thermal system coupled with an organic Rankine cycle and a proton exchange membrane electrolysis cell. 2021. International Journal Hydrogen Energy.
2. Ma Z, Witteman L, Wrubel JA and Bender G. A comprehensive modeling method for proton exchange membrane electrolyzer development. 2021. International Journal Hydrogen Energy 46:17627-43.
3. Wang H, Liu M, Kong H and Hao Y. Thermodynamic analysis on mid/low temperature solar methane steam reforming with hydrogen permeation membrane reactors. 2019. Applied Thermal Engineering 152:925e-36.
4. Tourkov K, Schaefer L. Performance evaluation of a PVT/ORC (photovoltaic thermal/organic Rankine cycle) system with optimization of the ORC and evaluation of several PV (photovoltaic) materials. 2015. Energy 82:839-49.
5. Hosseini SE, Butler B and Wahid MA. Hydrogen as a battery for a rooftop household solar power generation unit. 2020. International Journal of Hydrogen Energy 45:25811-26.
6. Duffie JA, Beckman WA. 2013. Solar engineering of thermal processes (4th ed.). New York: Wiley.
7. Toker SC, Soyturk G and Kizilkan O. Development of a sustainable multi-generation system with re-compression sCO_2 Brayton cycle for hydrogen generation. 2021. International Journal of Hydrogen Energy.

WHEC-2022
23rd World Hydrogen Energy Conference
June 26-30, 2022 - Istanbul

#1622

DEVELOPMENT AND PERFORMANCE ASSESSMENT OF INTEGRATED RENEWABLE ENERGY SYSTEM WITH HYDROGEN STORAGE FOR AUTONOMOUS AND MOBILE 3D PRINTING SYSTEM

*Shoukat Alim Khan, *Muammer Koc[1,2]
[1]Division of Sustainable Development (DSD), Hamad Bin Khalifa University (HBKU), Qatar Foundation (QF), Education City, Doha, Qatar
[2] University of Karabük, Turkey

*Corresponding author e-mail: shoukat.alimkhan@gmail.com; mkoc@hbku.edu.qa

ABSTRACT

3D concrete printing technology provides an ideal solution for resilient infrastructure development in critical and emergency situations; however, access and energy are critical challenges in such conditions. This study presented the design of an integrated renewable energy system with hydrogen storage for a unique mobile and autonomous 3D printing system for construction printing. The system has been designed to fulfil the off-grid energy requirement, such as material synthesis, printing, computation, communication, and surveillance/monitoring. The designed energy system has been analysed to produce a 3D printed structure with two different local materials; Construction and Demolishing Waste (CDW) based geopolymer concrete and direct printing of local materials. Due to the energy-intensive process and higher energy requirement for the pre-processing of waste to produce geopolymers, the designed system is more favourable for the direct printing of local materials. With the designed steady-state standard operating conditions the designed integrated system of 5.36kW can print 2.86m^3 of the final structure from direct printing of local material and 0.22m^3 of geopolymer based concrete structure in 24 hours. The analyse feasibility and production capacity of the designed system, and the overall performance of the system are also analysed for varying solar irradiance (I) conditions.

Keywords: 3D construction, Integrated renewable energy system, Hydrogen storage, Mobile 3D printing.

INTRODUCTION

The Provision of fast, inexpensive, durable and resilient solutions is a tremendous and urgent need during climate change emergencies, disasters, etc. However, such solutions are slow, expensive, and insufficient and leads to further problems and technical barriers, causing the lack of decent and humanitarian solutions for oppressed people in need. 3D Printing (3DP) technology could provide a stronger and more resilient solution to several basic human needs of the built environment in these conditions. 3D construction printing technology provides an ideal solution for resilient infrastructure development in critical and emergency situations such as wars, floods etc. However, due to damaged infrastructure in such situations, the access, printing materials and energy solutions for the printing technology are major challenges. An integrated renewable energy system provides more sustainable, off-grid and clean energy solutions in such conditions even in remote locations. In literature, researchers have designed integrated renewable energy-based integrated systems for energy electrical and thermal energy requirements [1–3]. However, the varying availability of renewable energy systems at different locations is one of the challenges which can be overcome with the design of suitable integrated renewable energy systems and energy storage [4]. In the previous publication of the research group various studies have been performed on the development of recycled demolishing and construction waste-based geopolymers [5]. This study proposed the development of an integrated multigeneration system for mobile and autonomous 3D concrete printing systems that can be used for the development of critical infrastructures such as bridges, shelters, water and health facilities etc. development in disaster and emergency conditions. The specific objectives of the design system are off-grid energy system, renewable, portable for easy mobility and cable of energy storage. The study also focused to know the building capacity of such a mobile 3D printing system installed on the truck.

SYSTEM DESIGN AND DESCRIPTION

The system is designed to fulfil the off-grid energy requirement of material synthesis, computational, communication and surveillance energy and printing energy requirements of the mobile concrete 3D printing system. The proposed integrated renewable energy system for mobile 3D printing systems is illustrated in Figure 1. In the designed system solar PV and wind turbines have been considered for the electrical energy requirement of the system. The generated electrical energy is designed to be used for direct printing and material synthesis, computational and communication and surveillance system energy. Electrical energy from the generated system is designed to be stored in the form of hydrogen and oxygen in conditions when the system is in pause mode during travelling or nighttime. The generated hydrogen and oxygen will be used for the electrical energy requirement in conditions when not enough renewable energy is available such as low wind conditions, nighttime, and bad weather for solar energy. The generated hydrogen

will also be used for the communication balloon system. The related cost of the components, subsystem or overall system is not considered.

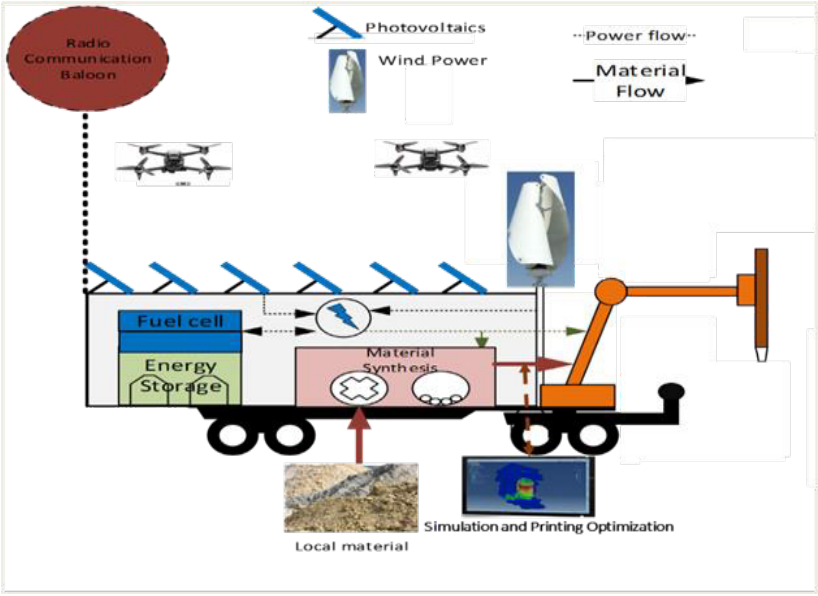


Figure 1. Designed mobile 3D printing system with integrated renewable energy, storage, material synthesis and 3D printing system.

RESULTS AND DISCUSSION

Comprehensive energy analysis has been performed for the design and performance analysis of the system at steady conditions. The initial design is considered at standard steady states of solar and wind turbines, the total Electrical energy produced has been considered as a combination of solar and wind energy during the daytime. EES software has been used for analytical modelling and calculation of the designed system. The design conditions of the installed system at a steady state are summarised in Table 1.

Table 1. Energy input requirement and the production capacity of different sub-systems at standard operating conditions.

System	Description
Solar PV	I=850 kW/m^2 at Standard operating conditions, installed at 80% of the total considered truck area. The capacity of 1.36 kW with an efficiency of 20%. Considered working hours of eight per day.
Wind Turbine	The standard wind turbine of 2 kW. Two wind turbines are installed within the available space of the considered truck of [4x 2.5]m^2 of surface area.
Energy storage	Proton Exchange Membrane Fuel Cell (PEMFC) with hydrogen and oxygen storage. The system is considered to at least store 60% of the total energy capacity of the system at standard conditions.
Printing Energy for m^3 final printed material.	The total energy required to produce material synthesis is 484.18 kWh for 1 m^3 of production of the final material. For geopolymer based concrete material the overall energy required is from the previous paper. This includes grinding, crushing, mixing and curing energy, for detail [5]
Communication, surveillance, and computation energy	The overall energy is 5% of the total required energy from material synthesis and printing.
Building Units	Considered a 3D building unit of [7x7x4] m with a double-wall structure of 10 cm thickness.

For the installed capacity and standard working conditions, the designed system can produce 106 kWh of energy per day which can print 2.86m^3 of final 3D printed volume of local material and 0.22 m^3 of the considered geopolymer concrete structure, including all the material synthesis, printing, computational and communication and surveillance energy.

The system has been analysed for the varying installed capacity and the corresponding number of possible 3D building units of [7x7x4] m^2 of the wall structure, shown in Figure 2. An installation capacity of higher than 200kWh may not be feasible to be installed on the moving system due to limitations of the installed area on the moving vehicle.

For higher such cases the system can be moved by moving vehicle and can be installed in the desired location conditioned to the feasibility of working.

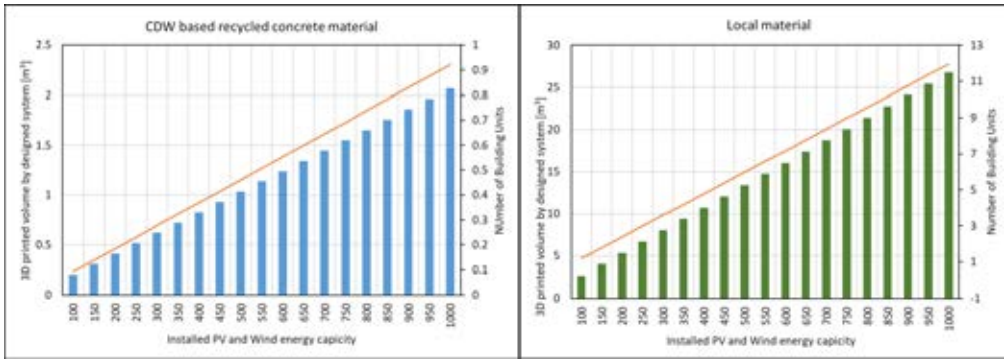


Figure 2. The capacity of the designed system for the produced 3D printed structure volume and number of building units as a function of installed integrated renewable energy system.

The output of renewable energy systems varies due to the varying availability of energy at different locations. The proposed system is intended to work at different locations depending upon the needs. Hence the final production capacity of the overall system is analysed for varying I value. For the varying value of I from 850 kW/m^2 to 1200 kW/m^2 the overall portion of solar energy varied from 10.88 to 15.36 kWh, considering 8 hours of production time. This leads to an increase in the production volume of the final 3D printed material from 2.86 m^3 to 2.98 m^3, Figure 3.

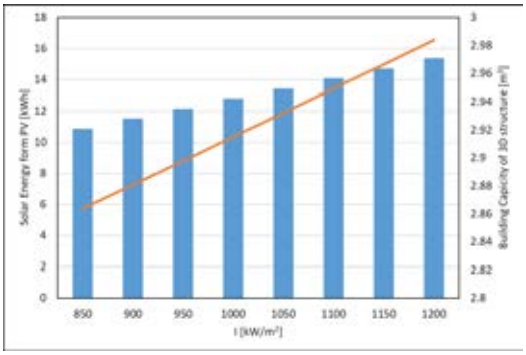


Figure 3. Solar energy production and the overall building capacity as a function of I.

CONCLUSION AND FUTURE DIRECTION

An integrated renewable energy system has been designed for an autonomous, mobile 3D printing system that can be used for the 3D construction of critical infrastructure in disaster and emergency conditions. The performed analysis verified the feasibility of the designed system for the energy requirement of the targeted system. The designed PV and wind energy integrated system of 5.36 kW with the energy production of 106.8 kWh per day has been proven up to produce 2.86 m^3 of final 3D printed material. In future studies, the detailed effect of the metrological conditions including humidity and temperature on the installed PV, wind, and storage system will be analysed using exergy and energy analysis of the designed system. A parametric study to different locations efficiency of different components cost and LCA analysis could be considered.

REFERENCES

1. Khalid F, Dincer I, Rosen MA. Techno-economic assessment of a renewable energy based integrated multigeneration system for green buildings. Applied Thermal Engineering 2016;99:1286–94. https://doi.org/10.1016/j.applthermaleng.2016.01.055.
2. Dincer I, Bicer Y. Integrated energy systems for multigeneration. Joe Hayton; 2020.
3. Khan SA, Al-Ghamdi SG. Renewable and Integrated Renewable Energy Systems for Buildings and Their Environmental and Socio-Economic Sustainability Assessment, 2021, p. 127–44. https://doi.org/10.1007/978-3-030-67529-5_6.
4. Sodiq A, Baloch AAB, Khan SA, Sezer N, Mahmoud S, Jama M, et al. Towards modern sustainable cities: Review of sustainability principles and trends. Journal of Cleaner Production 2019;227. https://doi.org/10.1016/j.jclepro.2019.04.106.
5. Ulugöl H, Kul A, Yıldırım G, Şahmaran M, Aldemir A, Figueira D, et al. Mechanical and microstructural characterization of geopolymers from assorted construction and demolition waste-based masonry and glass. Journal of Cleaner Production 2021;280:124358. https://doi.org/10.1016/j.jclepro.2020.124358.

WHEC-2022
23rd World Hydrogen Energy Conference
June 26-30, 2022 - Istanbul

#1625

THERMODYNAMIC ASSESSMENT OF A NEW SMALL MODULAR REACTOR FOR HYDROGEN AND ELECTRICITY

[1] Ieeba Khan, [2] Farrukh Khalid*
[1]Indian Institute of Technology, Delhi, India
[2] Department of Mechanical Engineering, Istinye University, Topkapi Kampüsü, Teyyareci Sami, Sk. No.3, 34010, Zeytinburnu, Istanbul, Turkey

*Corresponding author e-mail: farrukh.khalid@ontariotechu.net

ABSTRACT

In this paper, a technological assessment of a small modular nuclear reactor system for hydrogen and electricity is presented. Energy and exergy analyses are being used to make the technological assessment by evaluating the efficiencies namely, energy and exergy efficiencies. A three-step thermochemical cycle based on aluminum is being used for hydrogen production. Heat and electricity from the nuclear reactor are being used to run the thermochemical cycle. Simulation results show that one can produce 2.2 tonnes of hydrogen daily with an electric input of 190 MW.

Keywords: Energy, Hydrogen, Thermochemical, Integrated system, Thermodynamic

INTRODUCTION

Global energy data show that the conventional energy sources like oil and coal is leading the list of energy consumption. The fossil fuel usage is related to deleterious effects on the environment like increase in the greenhouse gases/increase in carbon footprint. With the growing energy demand researchers are investigating reliable non-conventional energy sources with minimum environmental impact. Efforts are being put in place to develop non-conventional energy-based systems. Renewable energy power generation increased by a percentage of 12.5 from 2789.2 TWh to 3147.0 TWh in the years 2019 to 2020 [1]. This finding suggests that renewable energy will play a considerable role in the future energy scenario, implying that a symbolic increase in renewable energy sources could significantly contribute to meeting future energy demand in a viable manner. To stimulate and support the use of renewable energy various countries have implemented effective programs and other critical policies. In Germany, policies have been implemented which forecast the growth of renewable energy by 40% between 2021 and 2026 [2]. It is also expected that by 2040, the consumption of renewable energy will nearly double. In spite of all these crucial characteristics and advantages, there are a number of shortcomings linked with renewable energy sources. For instance, they are recurrent in nature and are not obtainable through the year consistently [3,4]. However, integration of renewable energy with nuclear energy may act as one of the sustainable solutions for this intermittency. Hydrogen can act as an excellent connection among renewable and nuclear energies. Many techniques are being investigated to produce hydrogen in a sustainable way and thermochemical cycles are considered one of them [5].

SYSTEM DESCRIPTION

A small modular reactor based integrated energy system for hydrogen and electricity is being presented schematically in Figure 1. The system comprises of a nuclear reactor and an aluminum based thermochemical cycle. The presented thermochemical cycle comprised of three chemical reactions namely Reactions 1, 2 and 3. Reaction 2 is the electrolysis process run by the electricity (provided by nuclear reactor) while reaction 1 is the endothermic reaction (absorbing the heat from the helium at state 1 coming out of the nuclear reactor core) and reaction 3 is the exothermic reaction. In the considered thermochemical cycle all the reagents are recycled except water. After giving the heat to the reaction 1 of the thermochemical cycle, the helium stream (state 2) enters the turbine and produce the required electricity. The helium stream coming out of gas turbine at state 3 is being cooled down using a recuperator. The cooled helium gets pressurized in the compressor and its temperature gets further increase (state 6) with the help of recuperator before entering the reactor core.

ANALYSIS

Thermodynamic assessment of the presented system is done via the exergy and energy analyses. Several reasonable assumptions have been invoked to facilitate the analyses. Technical feasibility of the proposed three step aluminum-based cycle for hydrogen production is made via thermodynamic analysis and following assumptions are made:

- Pressure for all the chemical reactions assumed to be ambient i.e., 101.3 kPa.
- Chemical reactions are assumed to be as stoichiometric.

- Steady state is assumed for all chemical reactions.

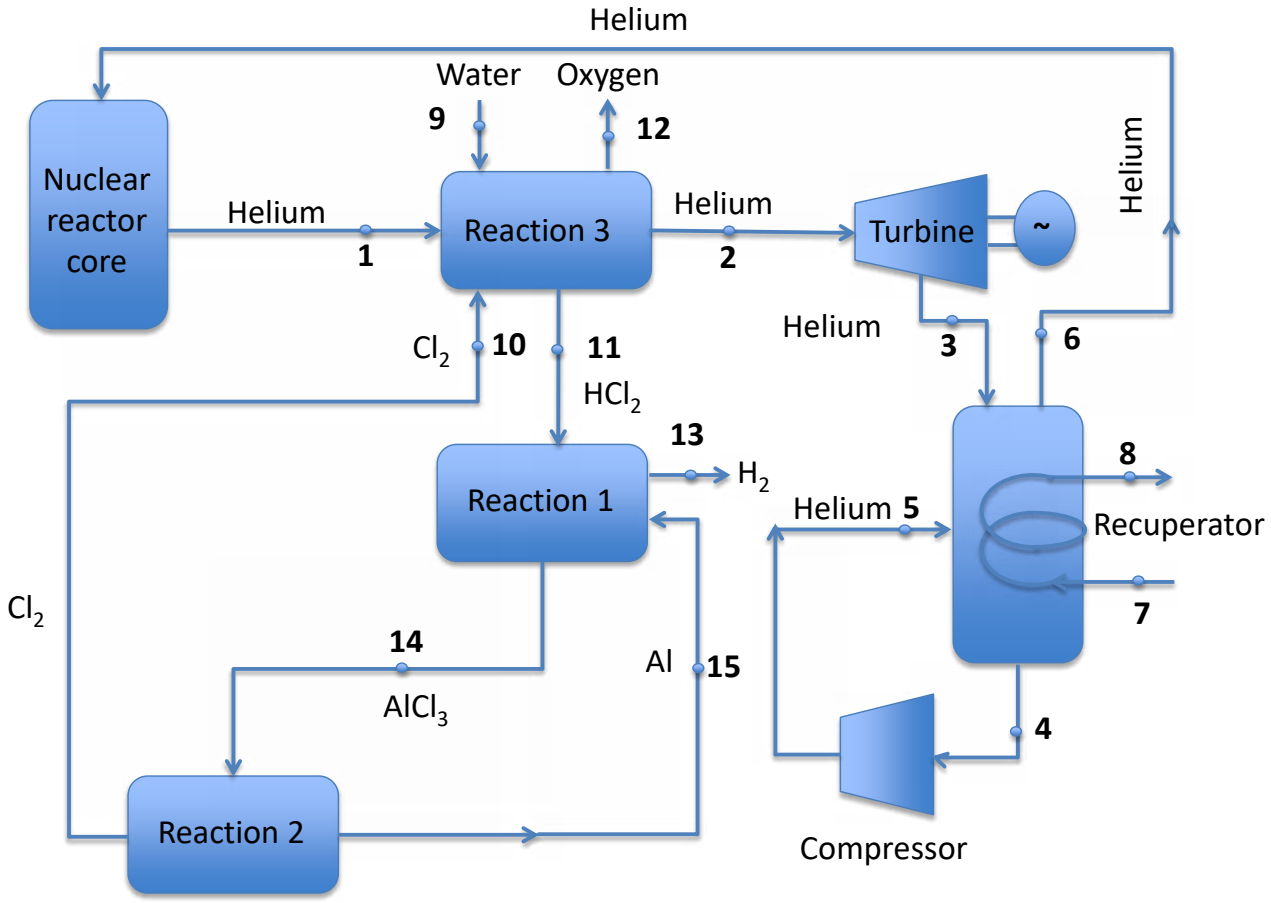


Figure 1 Schematic diagram of a small modular reactor for hydrogen and electricity

The energetic input to the electrolyser has been evaluated as follows:

$$\dot{W}_{\text{in,elec}} = \dot{m}_{H_2} \Delta g_{rxn} \quad (1)$$

RESULTS AND DISCUSSION

The presented system in the figure 1 has been analyzed via the principle of thermodynamics and results are tabulated in Table 1. To produce 0.26 kg/s of hydrogen, 190 MW of electric work has been utilized in the given thermochemical cycle.

Table 1. Parameters obtained from the study

Parameter	Value
Mass flow rate of helium (kg/s)	439
Mass flow rate of hydrogen produced (kg/s)	0.26
Work input of the electrolyser (MW)	190
Coolant Inlet Temperature (℃)	850
Maximum Operating Temperature of the Cycle (℃)	630

CONCLUSIONS

A new nuclear energy based integrated energy system for co-production of hydrogen and electricity is developed and presented. In the presented system, hydrogen is produced via a thermochemical cycle utilizing heat and electricity. Simulation is being carried out in the software called Engineering Equation Solver and results show that 0.26 kg/s of hydrogen can be produced in a sustainable manner using the heat and electricity from the small modular reactor.

NOMENCLATURE

g	Specific Gibbs' free energy kJ/kg
$\dot{m}$	Mass flow rate, kg/s
$\dot{W}$	Work rate, MW

Greek Letters

ρ	Density, kg/m^3

Subscripts

elec	Electrolyser
rxn	Reaction

REFERENCES

1. BP Statistical Review of World Energy 2021. 70th Edition, London, United Kingdom. https://ourworldindata.org/energy-mix Accessed on May 15, 2022
2. IEA. 2021. Renewables 2021:Analysis and forecast to 2026. International Energy Agency, France. https://iea.blob.core.windows.net/assets/5ae32253-7409-4f9a-a91d-1493ffb9777a/Renewables2021-Analysisandforecastto2026.pdf Accessed on May 15, 2022
3. Khalid F, Dincer I and Rosen MA. 2015. Energy and exergy analyses of a solar-biomass integrated cycle for multigeneration. Solar Energy 112: 290-299.
4. Khalid F, Dincer I and Rosen MA. 2017. Thermoeconomic analysis of a solar-biomass integrated multigeneration system for a community." Applied Thermal Engineering 120: 645-653
5. Dincer I. 2007. Energy and sustainability aspects of hydrogen and fuel cell systems. International Journal of Energy Research 31: 29-55

WHEC-2022
23rd World Hydrogen Energy Conference
June 26-30, 2022 - Istanbul

#1626

DESIGN OF A NEW HELICAL METHANE FIXED BED- REACTOR

*Andre Bolt, Ibrahim Dincer and Martin Agelin-Chaab
Clean Energy Research Laboratory (CERL), Faculty of Engineering and Applied Science, Ontario Tech. University, 2000 Simcoe Street North, Oshawa, Ontario L1H 7K4, Canada

* Corresponding author's email: Andre.Bolt@ontariotechu.ca

ABSTRACT
In this study, the design of a new fixed-bed reactor is proposed and examined through computational fluid dynamics. The design follows a unique helical design to maximize the amount of surface area that is exposed and to reduce the need for gas recycling. The heat distribution through the reactor is measured using the surface temperature before and after cooling takes place. Additionally, the mole ratio of all of the species used in the reaction is measured along the length of the reactor. The numerical simulations reveal that less than 1 kW of cooling is sufficient to significantly reduce the temperature of the reactor and that an H_2 conversion of approximately 84% can be achieved.

Keywords: Hydrogen, Natural Gas, Methane, CFD, Reactor analysis.

INTRODUCTION
As issues revolving around climate change and the growing global energy demand continues to rise, scientists and engineers look for sustainable solutions such as using hydrogen as an energy carrier. Hydrogen as an energy carrier has tremendous potential given its high energy density [1], and non-polluting effects [2]. However, the use of hydrogen is not limited to being an energy carrier; it can also be used to synthesize many other essential gases such as CH_4 or natural gas. CH_4 can be produced through the Sabatier reaction as follows [3]:

$$CO_2 + 4H_2 \rightarrow CH_4 + 2H_2O(g) \quad -164\ kJ\ mol^{-1} \tag{1}$$
$$CO + 3H_2 \rightarrow CH_4 + H_2O(g) \quad -206\ kJ\ mol^{-1} \tag{2}$$

The CH_4 used in the reaction has the potential to be produced renewably if the hydrogen is produced through processes such as wind/ solar electrolysis and if the CO_2 or CO are produced through biomass gasification. The CH_4 produced from these chemical reactions can be used for a multitude of applications such as fuel for transportation, as well as in residential applications (water heaters, and stoves), and industrial applications (boilers and burners). Furthermore, the methane produced can also be used to synthesize acetic acid, which is used to produce plastic, textiles, rubber, and paint. Also, natural gas has the benefit of being a cleaner hydrocarbon, considering it produces 45%, 15%, and 30% less CO_2 compared to coal, wood, and crude oil, respectively [4]. Additionally, 6 -11% less greenhouse gases are emitted by natural gas compared to gasoline during their respective fuel life cycles [5].

In order to synthesize natural gas, fixed bed reactors are most commonly used, where the typical fixed bed reactor shape comprises a cylindrical catalyst bed. A major barrier in the production of methane is attributed to the chemical reactions being highly exothermic. The reaction is most effective at 200°C, however, due to the heat being released from the chemical reaction, it elevates the temperature of the reactor and the feed gas [6]. Therefore, it is important to incorporate effective reactor cooling.

This study presents the design of a novel fixed bed reactor, which uses a helical design rather than a conventional straight cylindrical path. The helical design will increase the amount of surface area exposed within the reactor to facilitate cooling and mitigate the need for recycling a portion of the gases.

MODEL DESCRIPTION
The proposed chemical reactor geometry and boundary conditions are presented in Figures 1a and 1b respectively.

ANALYSIS
The reactor's measured H_2 mole ratio at the entrance and exit of the reactor was used to determine the amount of H_2 that was successfully converted into CH_4. Furthermore, the H_2 conversion value was calculated using concentrations along the reactor. Additionally, the CH_4 yield was used to provide a measure of the CH_4 successfully produced. The general form of the mole fraction of each respective specie is defined as follows:

$$x_i = \frac{n_i}{n_{total}} \tag{1}$$

where n_i represents the mole of a specific specie at a specific stage within the reactor, and n_{total} represents the total amount of all the species within the gas mixture.

The H_2 conversion in the reaction can be defined as follows:

$$X_{H_2} = \frac{n_{H_2 in} - n_{H_2 Out}}{n_{H_2 in}} \quad (2)$$

where $n_{H_2 in}$ represents the moles of H_2 which enters the reactor and $n_{H_2 out}$ represents the moles of H_2 leaving the reactor. Additionally, the CH_4 yield can be defined as follows:

$$Y_{CH_4} = \frac{n_{CH_4 out(actual)}}{n_{CH_4 out(theoretical)}} \quad (3)$$

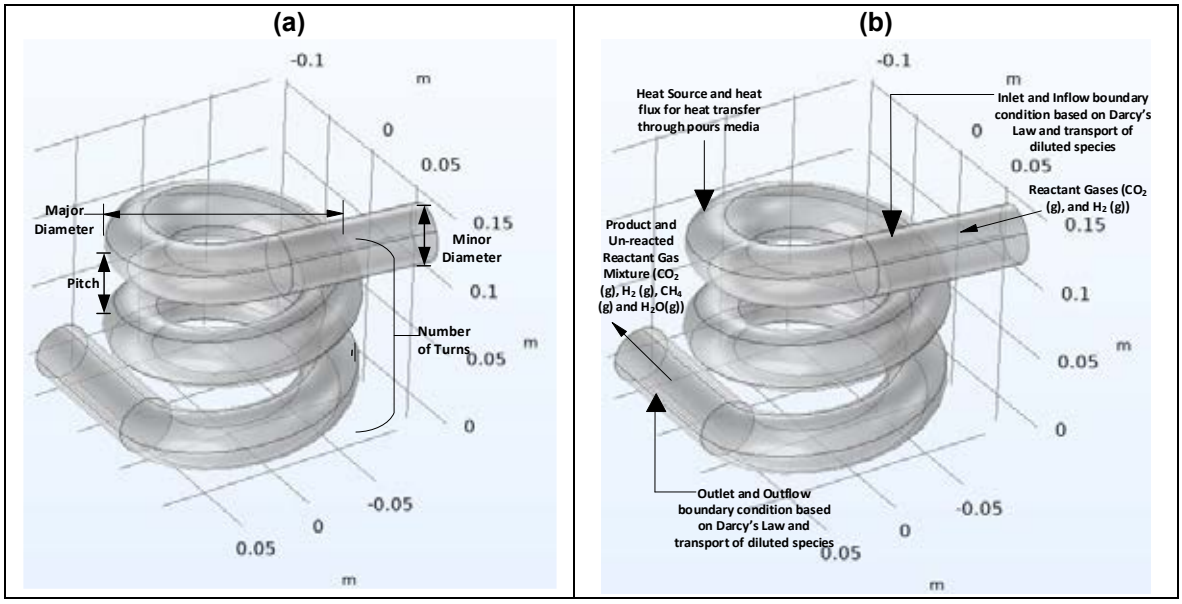


Fig.1. (a) Reactor Geometry, with the (b) Reactor Boundary Conditions

Table 1. Reactor Dimensions and Operating Conditions

Reactor Dimensions	
Parameter	**Value**
Reactor Length (m)	1.2
Reactor Major Diameter (m)	0.125
Reactor Minor Diameter (m)	0.0381 (1.5 inches)
Pitch (m)	.06
Number of Turns	2.23
Catalyst Bed Volume (m3)	.001
Operating Conditions	
Conditions	**Value**
Reactant Gas Inlet Velocity (m s^{-1})	0.45
Reactant Gas Flow Rate ($m3s^{-1}$)	5.7005E-4
Reactant Gas Inlet Pressure (bar)	10
Reactant Gas Inlet Temperature (°C)	200

4. RESULTS AND DISCUSSION

Given the exothermic nature of the reaction, effective reactor cooling is essential. Figure 2a presents a model of the reactor without the presence of external cooling. Whereas Figure 2b depicts a significantly improved version of the reactor's temperature distribution after providing 800 W of cooling along the external surface of the reactor after the inlet section.

Additionally, the mole fraction of the various species from the inlet of the reactor to the exit is presented in Figure 3. The results show that a substantial portion of the reactants used in the reactor model was successfully converted into the targeted products. At the start of the process, the observed mole fraction of H_2 was 0.8, however, it sharply decreased to 0.13. Whereas the mole fraction for H_2 started at 0 and was elevated to 0.28. The values obtained in

Fig. 3 correspond to an H_2 conversion and CH_4 yield of 84% and 93%, respectively. Additionally, the trends presented were consistent with various other research works [7].

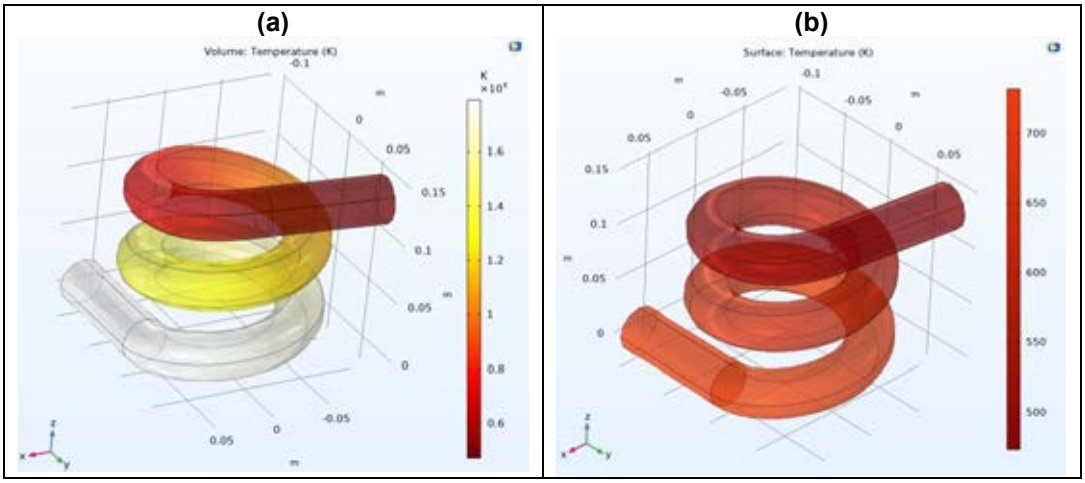


Fig.2. (a) Reactor Temperature Distribution without Cooling, (b) Reactor Temperature Distribution with 800W of Cooling

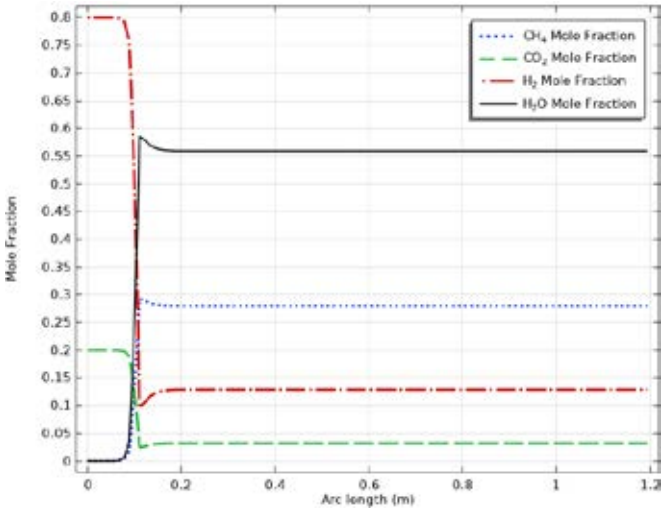


Fig.3. Species Mole Fraction Along the Length of the Reactor

CONCLUSIONS

This study has reported a new configuration for a fixed bed methane reactor which used CO_2 and H_2 as reactants. As shown earlier the proposed reactor was able to provide effective reactor cooling with less than 1kw of energy supplied to the system. Additionally, the reactor was able to achieve high H_2 conversion and CH_4 yield of 84 and 93%, respectively. The helical design presented in the system also has the potential to remove the need for reactor gas recycling and multiple passes as used in the HICOM and TREMP.

REFERENCES

1. Office of Energy Efficiency & Renewable Energy, “Hydrogen Storage,” 2019. https://www.energy.gov/eere/fuelcells/hydrogen-storage.
2. U.S. Department of Energy, “Alternative Fuels Data Center (Hydrogen Benefits and Consideration),” 2020. https://afdc.energy.gov/fuels/hydrogen_benefits.html.
3. S. Rönsch *et al.*, “Review on methanation - From fundamentals to current projects,” *Fuel*, vol. 166, pp. 276–296, 2016, doi: 10.1016/j.fuel.2015.10.111.
4. Enbridge, “Is natural gas environmentally friendly?,” 2021. https://www.enbridge.com/energy-matters/energy-school/natgas-enviro-friendly.
5. U.S. Department of Energy, “Natural Gas Vehicle Emissions.” https://afdc.energy.gov/vehicles/natural_gas_emissions.html.
6. T. Schaaf, J. Grünig, M. R. Schuster, T. Rothenfluh, and A. Orth, “Methanation of CO2 - storage of renewable energy in a gas distribution system,” *Energy. Sustain. Soc.*, vol. 4, no. 1, pp. 1–14, 2014, doi: 10.1186/s13705-014-0029-1.
7. S. Matthischke, S. Roensch, and R. Güttel, “Start-up Time and Load Range for the Methanation of Carbon Dioxide in a Fixed-Bed Recycle Reactor,” *Ind. Eng. Chem. Res.*, vol. 57, no. 18, pp. 6391–6400, 2018, doi: 1.

WHEC-2022

23rd World Hydrogen Energy Conference

TRACK 10.
POWER TO GAS

TRACK 10. POWER TO GAS

#66 FUTURE ECONOMIC PERSPECTIVE OF POWER-TO-GAS SYSTEM BASED ON MOLTEN CARBONATE ELECTROLYZER	1112
#111 TOWARDS ELECTRIFYING CEMENT PRODUCTION BY ELECTROCHEMICALLY ENHANCED DISSOLUTION OF $CaCO_3$ DURING WATER ELECTROLYSIS UNDER A PH-GRADIENT	1115
#125 BUTADIENE PRODUCTION VIA THE DIRECT DEHYDROGENATION OF N-BUTANE IN MEMBRANE REACTORS: A TECHNO-ECONOMIC ANALYSIS	1118
#141 NOVEL EMERGENCY GAS-TO-POWER MH-STORAGE AND FUEL CELL SYSTEM: MODELING AND EXPERIMENTAL VALIDATION	1121
#188 PROCESS IMPLICATIONS OF ELECTRIFYING AMMONIA PRODUCTION	1124
#207 SENSITIVITY ANALYSIS OF INDEPENDENT PARAMETERS FOR FORMATION OF NO_x EMISSION IN HYDROGEN ENRICHED COMPRESSED NATURAL GAS ALONG WITH EXHAUST GAS RECIRCULATION BY SUPPORT VECTOR MACHINE	1127
#229 CO_2 METHANATION OVER BIMETALLIC NICKEL-NOBLE METAL CATALYSTS	1130
#249 HYDROGEN AS ENERGY STORAGE FOR RESOLVING ELECTRICITY GRID ISSUES IN INDONESIA	1133
#343 AN MINLP-BASED OPTIMAL DESIGN AND SCHEDULING OF A POWER TO GAS SYSTEM INTEGRATED MICROGRID: A CASE STUDY FROM TURKEY	1136
#359 HEAT SOURCE FREE CO_2 METHANATION OVER HYDROGEN STORAGE ALLOY	1139
#402 INTEGRATED PLANNING TOOL FOR COST AND 3D STRUCTURAL PLANNING FOR OFFSHORE WIND FARMS FOR THE GENERATION OF H_2	1142
#406 METHANATION OF CO_2 OVER $LaNi_5$/V LAYERED FILM	1146
#407 CO_2 METHANATION OVER SURFACE MODIFIED $LaNi_5$ FILMS WITH PD	1149
#417 PRELIMINARY DESIGN AND FLOWSHEETING OF A SABATIER BASED POWER-TO-GAS SYSTEM WITH INTEGRAL HEAT RECOVERY AND DOWNSTREAM SYNGAS CLEANING	1152
#1536 INFLUENCE OF BIOGAS COMPOSITION TO CATALYTIC METHANATION PROCESS	1155
#1616 TECHNO-ECONOMIC PERFORMANCE ASSESSMENT OF A REACTOR SYSTEM USED FOR POWER-TO-METHANE PLANT	1158

WHEC-2022
23rd World Hydrogen Energy Conference
June 26-30, 2022 - Istanbul

#66

FUTURE ECONOMIC PERSPECTIVE OF POWER-TO-GAS SYSTEM BASED ON MOLTEN CARBONATE ELECTROLYZER

*[1]Dayan Monzer, [1]*Chakib Bouallou*
(MINES ParisTech, PSL - Research University, CES - Centre d'Efficacité Energétique des Systèmes), 60 Boulevard Saint Michel, 75006 Paris, France

*Corresponding author e-mail: chakib.bouallou@mines-paristech.fr

ABSTRACT

A Power-to-gas system based on high-temperature electrolysis is a feasible and environmental approach to convert low-carbon electrical energy into chemical energy stored in the form of synthetic gas (H_2 & CO). The most desirable application is to convert the syngas into synthetic fuel. The overall process is currently being studied using two different electrolyzers: Solid Oxide Electrolyzer and Molten Carbonate Electrolyzer. This work focuses on the Power to Methane technology using high-temperature Molten Carbonates electrolysis cells (MCEC). It aims to investigate the economic feasibility of the overall process in the methane production. For this purpose, a rigorous parametric study is conducting by developing a VBA excel code to acquire a better knowledge of the cost drivers of the methane production cost. This overall study revealed that if more effort is put into reducing cell and operating costs, this technology might become competitive with conventional methane production technologies. A perspective towards the future revealed that the operating cost, mainly represented by the renewable electricity cost, could attain the required target. However, estimating the time required to have an economically competitive power-to-gas plant is challenging due to the lack of data on the MCEC cell cost and its roadmap.

Keywords: Power-to-gas, Molten carbonate electrolysis cell, Economic assessment

INTRODUCTION

Power to Gas is a promising technology that is capable of resolving two main issues. This approach addresses the need for energy storage associated with renewable energy integration in the power grid. Besides, it has the potential to be a viable technique for the sequestration and the re-use of the captured CO_2 as synthetic fuels.

This technology is now encountering some economic implementation challenges that necessitate in-depth research. A series of studies were performed to investigate the economic aspect of the Power-to-Gas. They are mainly based on alkaline, proton membrane (PEM), and Solid Oxide electrolyzers. For instance, Gotz et al., 2015 [1] examined the existing electrolysis and methanation technologies in terms of the technical and economic requirements of the power-to-gas chain. Peters et al., 2019 [2] analyzed the techno-economic features of the power-to-gas system using the three existing technologies and evaluated the ecological aspects of using methane as a transport fuel. Lately, Szima & Cormos, 2021[3] assessed the techno-economic aspects of synthetic methane production from renewable hydrogen obtained from different renewable resources and captured CO_2. All studies revealed that synthetic natural gas produced from renewables is still non-competitive with conventional natural gas at the current stage.

On the other hand, Power-to-gas systems that use Molten Carbonate electrolyzers are not currently in the field of economic research. This technology is in the research and development stage, so all research focuses on the technical rather than the economic aspects. An economic study of the power-to-gas system using Molten carbonate Electrolyzer was firstly addressed in our earlier research [4]. However, this work aims to assess the economic feasibility of such technology based on the previous study outcomes and provide a future perspective on being competitive with conventional natural gas.

METHODOLOGY

The economic assessment was performed based on a developed process simulation consisting of the electrolyzer and all the balance of plant equipment, presented in [4]. This assessment evaluated the capital and operating expenses of the process at the current conditions, as well as investigated the impact of both CAPEX and OPEX on the final methane production cost by a limited sensitivity analysis. The sensitivity analysis involved the variation of different parameters, such as cell cost, lifetime, CO_2 and electricity cost within a finite margin. In this work, a profound parametric study is performed by developing a VBA excel code. It includes all the previously stated parameters and the operating hours of the plant.

RESULTS AND DISCUSSION

As inspired by the parametric study in [4], it was declared that the best conditions for having an approximate competitive methane selling price with the current market price are to have a 45000 h cell lifespan, 30€/MWh electricity cost, 20€/tonne CO_2 cost, and 1000 €/kW cell cost. The future perspectives for having these conditions depend on several criteria. The cell lifetime of MCFC has reached over 40000h lifespan in the fuel cell mode [5]. Besides, Hu et al., 2014[6] proved that the cell exhibited better electrochemical performance in MCEC mode than in MCFC mode, which leads to a higher lifetime of the MCEC. According to this information, it can be deduced that the lifetime of MCEC can easily attain 45000 hours of operation.

Based on the fact that the cell has reached 40000h lifetime, the impact of both CAPEX (cell cost) and OPEX (CO_2 and electricity cost) together on the methane selling price is simultaneously examined assuming that the plant operates for 8000 h per year. The outcomes are illustrated in Figure 1. The diagram displays an alternating repetitive pattern, where the trend changes with the variation in cell lifetime and cost, CO_2 cost, and electricity cost. It can be classified into three categories. The first category is the cell cost zone that is identified by two consecutive repetitive patterns. The second category is the cell's lifetime zone that is represented by a single pattern within the cell cost zone. The last category corresponds to the CO_2 and electricity cost zone that is expressed within each pattern. In this zone, there are two complementary trends. The first trend is the methane price with an increase in Electricity cost (green arrow), and the second one is the methane price with an increase in CO_2 cost (orange arrow).

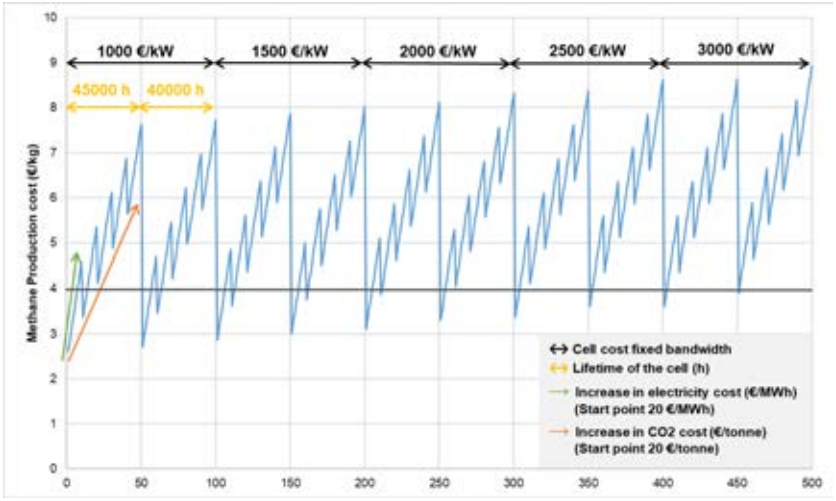


Figure 1. Impact of both CAPEX and OPEX on the methane production cost

The assessment results highly coincide with the expected ones. It can be observed that methane production cost decreases with the decrease in cell cost. However, the additional improvement in lifetime of the cell after reaching 40000 h has no significant impact on the methane selling price. Although the methane cost is highly affected by the cell capital cost, it can't reach a competitive price with the conventional ones without reducing the operating cost. To have a competitive methane price, the methane production cost must drop below 4€/kg. According to the graph, the methane price is below 4€/kg when the CO_2 cost is low (20-40€/tonne CO_2), and the electricity cost is between 20-80€/MWh at a cell cost below 2000€/kW. The selection of the maximum cost values of CO_2 and electricity highly relies on the cost values of one and the other as well as the cell cost to have methane production cost below 4€/kg. For instance, a cell with a cost of 3000€/kW requires a CO_2 cost of 20€/tonne and electricity cost of 20€/MWh, whereas a cell with a cost of 1500€/kW requires either a CO_2 cost of 20€/tonne and electricity cost ranging between 20-80€/MWh or a CO_2 cost of 40€/tonne and electricity cost between 20-30€/MWh. Therefore, it can be deduced that the operating cost combined with the cell cost considerably influence the final methane selling price. A comparable study conducted at a plant operating hours of 5000 h per year revealed a similar trend with an average increase of 6% in the methane cost compared to 8000h; whereas, at a plant operating hours of 3000h, the methane price seems unlikely to reach below 4€/kg based on the studied range of variables. In conclusion, the target of methane price below 4€/kg can be attained if the operating costs are low, the cell cost is below 3000€/kW, and the operating hours of the plant are higher than 5000 hours per year.

The parametric study outcomes encourage profound research on the operating and capital costs situation. First of all, the electricity is driven by the cost of the renewable energy source since MCEC is the most electric energy consumer. The International Renewable Energy Agency (IRENA) [7] has reported the decreasing trend of the Levelized Cost of the different renewable energy sources from the year 2010 to 2019. According to their outcomes,

the cost of onshore wind turbine electricity was 50$/MWh (~42€/MWh) and that of PV electricity was 68$/MWh (~57€/MWh) in 2019. These costs are expected to reach below 50$/MWh in the coming years. On the other hand, the CO_2 cost depends on the carbon capture technology used. Each technology has a different investment and operating cost, thus the selling price of the produced CO_2 will change. The MCEC cost is determined by the technology improvements and the manufacturing capacity, which will be reflected in an increase in the cell market causing a reduction in the cell cost per installed capacity. In 2003, MTU (a former fuel cell manufacturing company in Germany, that transferred its assets to Fuel Cell Solution Gmbh in 2012, a subsidiary of the FuelCell energy USA) expected that the commercial MCFC cost will attain a value <1250 €/kW once the production volume reaches 160 to 200 systems per year [8]. However, there is still no public available information on the current status of the MCEC cost and its roadmap.

CONCLUSION

The power-to-gas system based on Molten carbonate electrolyzer is an intriguing concept of storing energy and reusing CO_2. However, significant advances in terms of cost feasibility are required. Based on our economic study, this process might be economically competitive with other technologies if the operating costs are low, the cell cost is below 3000€/kW, and the operating hours of the plant are higher than 5000 hours per year. The vision for the future on these targets appears optimistic in terms of operating cost; nevertheless, there are still some challenges due to a lack of the cell cost forecast in the upcoming years.

REFERENCES

1. M. Götz *et al.*, “Renewable Power-to-Gas: A technological and economic review,” *Renew. Energy*, vol. 85, pp. 1371–1390, Jan. 2015, doi: 10.1016/J.RENENE.2015.07.066.
2. R. Peters, M. Baltruweit, T. Grube, R. C. Samsun, and D. Stolten, “A techno economic analysis of the power to gas route,” *J. CO_2 Util.*, vol. 34, pp. 616–634, Dec. 2019, doi: 10.1016/J.JCOU.2019.07.009.
3. S. Szima and C. C. Cormos, “CO_2 utilization technologies: A techno-economic analysis for synthetic natural gas production,” *Energies*, vol. 14, no. 5, 2021, doi: 10.3390/en14051258.
4. D. Monzer, R. Rivera-Tinoco, and C. Bouallou, “Investigation of the Techno-Economical Feasibility of the Power-to-Methane Process Based on Molten Carbonate Electrolyzer,” *Front. Energy Res.* | *www.frontiersin.org*, vol. 1, p. 650303, 2021, doi: 10.3389/fenrg.2021.650303.
5. M. Cassir, S. J. McPhail, and A. Moreno, “Strategies and new developments in the field of molten carbonates and high-temperature fuel cells in the carbon cycle,” *Int. J. Hydrogen Energy*, vol. 37, no. 24, pp. 19345–19350, 2012, doi: 10.1016/j.ijhydene.2011.11.006.
6. L. Hu, I. Rexed, G. Lindbergh, and C. Lagergren, “Electrochemical performance of reversible molten carbonate fuel cells,” *Int. J. Hydrogen Energy*, vol. 39, no. 23, pp. 12323–12329, Aug. 2014, doi: 10.1016/j.ijhydene.2014.02.144.
7. IRENA, “RENEWABLE POWER GENERATION COSTS IN 2019,” Abu Dhabi, 2019.
8. W. Krewitt and S. Schmid, “Fuel Cell Technologies and Hydrogen Production/Distribution Options,” 2005. [Online]. Available: http://www.dlr.de/fk/Portaldata/40/Resources/dokumente/publikationen/2005-09-02_CASCADE_D1.1_fin.pdf.

WHEC-2022
23rd World Hydrogen Energy Conference
June 26-30, 2022 - Istanbul

#111

TOWARDS ELECTRIFYING CEMENT PRODUCTION BY ELECTROCHEMICALLY ENHANCED DISSOLUTION OF $CaCO_3$ DURING WATER ELECTROLYSIS UNDER A PH-GRADIENT

[1*]*Rémy Rouxhet,* [1]*Renaud Delmelle,* [1]*Joris Proost*
[1]Université catholique de Louvain, Division of Materials and Process engineering, 1348 Louvain-La-Neuve, Belgium

*Corresponding author e-mail: remy.rouxhet@uclouvain.be

ABSTRACT

The cement industry, which accounts for 7-8% of worldwide CO_2 emissions, is essential to decarbonize but challenging especially due to its high process emissions, high temperature heat requirements and low maturity of decarbonization solutions. A new electrochemical path to produce calcium hydroxide, a precursor of cement, has been proposed recently. This technology is based on a new design of a water electrolyser working in tri-phase environment. It has the potential to electrify cement production while at the same time producing valuable gases, but is still at a very early stage of development (TRL-3). In this paper, lab-scale experiments in a 200mL cell were performed to have a better understanding of the electrochemical system. The development of a pH gradient between the anode and the cathode has been quantified for different electric charges applied. Due to acidification of the anode side, the dissolution of calcium carbonate is enhanced. A solubility ten times higher than at neutral pH has been observed. At the same time, the migration of Ca^{2+} and OH^- ions to respectively the cathodic and anodic side has been demonstrated as well, thereby opening the way for an electrochemically-enhanced $Ca(OH)_2$ precipitation.

Keywords: Electrolysis, Electrification, Cement, Hydrogen

INTRODUCTION

In the race to decarbonize our society, reducing emissions from the industrial sector (32% of total greenhouse gas emissions [1]) appears as one of the major challenges to take on. The industry is known as a “hard-to-abate emission” sector due to high-temperature heat requirements, process emissions, long-lived capital assets and trade considerations [2]. This paper focuses on the decarbonization of cement production - one of the three main industries along with steel and chemicals. The cement sector accounts alone for about 7-8% of total CO_2 emissions, so that cutting these emissions is essential to tackle climate change [3-5, 7]. Among these emissions, around two third are due to the calcination reaction of limestone. These process emissions make it more challenging to achieve carbon neutrality [4-7]. Several decarbonization technologies are being studied such as carbon capture, electrification, fuel and raw material substitution [2-4].

In 2019, Ellis *et al.* proposed a new electrochemical path for cement synthesis. By taking advantage of the pH gradient established during water electrolysis in an initially neutral medium, limestone ($CaCO_3$) can be decarbonated and the dissolved Ca^{2+} further precipitated as hydrated lime ($Ca(OH)_2$). This calcium hydroxide can then be used directly for its own industrial applications or to produce alite, the major phase of conventional cement. The concentrated gaseous carbon dioxide produced can be easily collected at the outlet while hydrogen and oxygen can be used to generate power for other steps or valued in their respective markets. With the emergence of low-cost renewable energy, this new technology could allow for the production of calcium hydroxide and cement with nearly zero emissions and at a competitive cost [8].

The aim of the current paper is to go further in the understanding and optimization of this new electrolyser design in a triphase environment in order to evaluate its potential on an industrial scale.

ELECTROCHEMICAL SYSTEM

The electrolyser is divided into three compartments. At the anode, the oxidation of water (reaction 1 in Fig.1A) produces oxygen and H^+ ions. Solid calcium carbonate inserted at the anode has a low solubility (14.31mg/L at 25°C [9]). Its decomposition (reaction 4) in neutral water is weak. Thanks to the generated H^+ ions in the anodic environment, the carbonate dissolution equilibrium is modified (cf Fig.1B) and CO_3^{2-} ions react to stabilize as CO_2 (reaction 5) for a pH lower than 6.4 [10]. The chemical dissolution of $CaCO_3$ is thereby further enhanced by the release of gaseous CO_2 and by the migration of Ca^{2+} ions towards the cathode. Besides CO_2, also O_2 is being collected at the anodic side. At the cathode, hydrogen gas and hydroxide ions are produced by water reduction (reaction 2). The hydroxide ions will make the medium alkaline and will naturally migrate towards the anode. In the

central compartment, the different migrated ions (H^+, Ca^{2+} and OH^-) react together (reaction 3 and 6),calcium hydroxide precipitation being favoured at pH >12.5 [8].

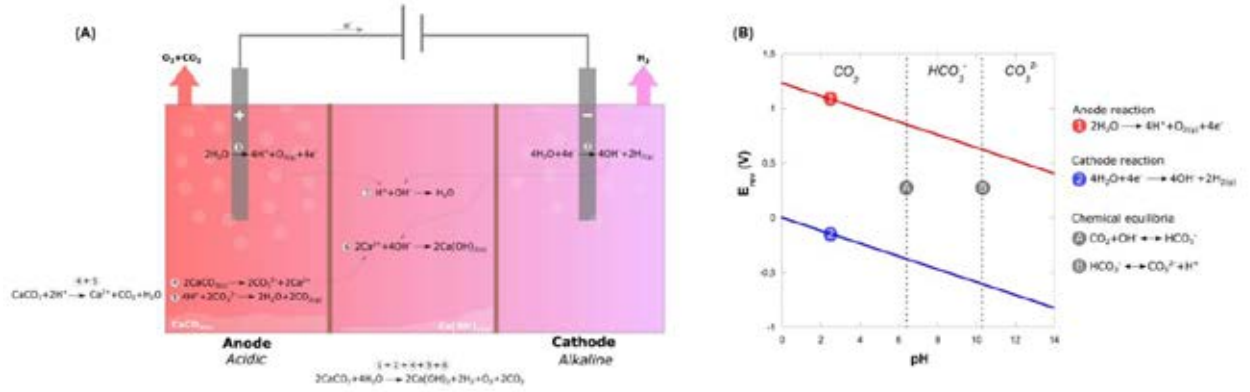


Figure 1. (A) Electrochemical system and chemical reactions (B) Pourbaix diagram for water electrolysis and carbonate equilibria

MATERIALS AND METHODS

Experiments were performed in an H-type cell (200mL, Adams & Chittenden Scientific Glass) at room temperature. The electrolyte used is a 1M $NaNO_3$ (Sigma-Aldrich BioXtra, >99%) solution in ultra-pure water (18.2MΩ/cm). The physical separations used to divide the three compartments are paper filters (VWR, 516-0818). Electrodes are platinum foils. The potentiostat used (AUTOLAB, Methrom) is equipped with a booster (allowing to go up to 10A) and two continuous pH readers. Two types of one-hour experiments have been carried out: a galvanostatic set of 6 experiments between 2.5-4.5V and a potentiostatic set of 7 experiments between 0.007-0.06A. For each experiment, 50mg of calcium carbonate (Sigma-Aldrich BioXtra, <99%) are initially inserted on the anodic side. ICP-AES analysis were performed to quantify the Ca^{2+} ions in solution.

RESULTS AND DISCUSSION

Figure 2A clearly illustrates the establishment of a pH gradient between the anodic and cathodic compartments. The higher the electric charge, the more the gradient becomes important. The theoretical pH value shown in Figure 2B is obtained as the value for which all the current applied is converted into H^+/OH^- while assuming that none of these ions will react or move from their respective compartments. As it can been seen, the difference between the theoretical and real pH is more pronounced on the anode side, essentially since H^+ are being consumed by reaction with CO_3^{2-} (reaction 5 in Fig. 1A).

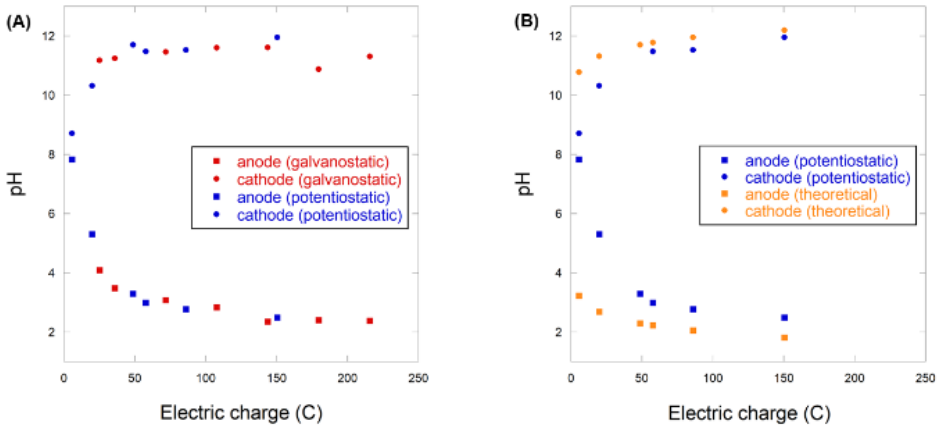


Figure 2. (A) Final pH obtained in anodic and cathodic compartments for a defined electric charge applied in one hour (B) Comparison between final pH obtained and theoretical value expected (potentiostatic experiments only)

Figure 3A shows the amount of Ca^{2+} in solution at the end of the experiments as a function of electric charge. Although all calcium is initially inserted at the anode as $CaCO_3$, a small quantity is found at the cathode as well due to its electrical field induced migration. The total amount increases as a function of the applied electric charge until it reaches a plateau. Indeed, the higher the charge, the lower the pH will be at the anode (cf Fig. 2A). A lower pH will ease the dissolution of $CaCO_3$ due to carbonate equilibrium modification as explained previously. This is illustrated on Figure 3B. The maximum amount found in solution is 13 mg out of a total of 20mg initially inserted. This amount

corresponds to a solubility of 126mg/L in the anodic side, which is almost ten times higher than the solubility at neutral pH [9]. The remaining 7mg can be either in the form of undissolved $CaCO_3$ or in the form of $Ca(OH)_2$.

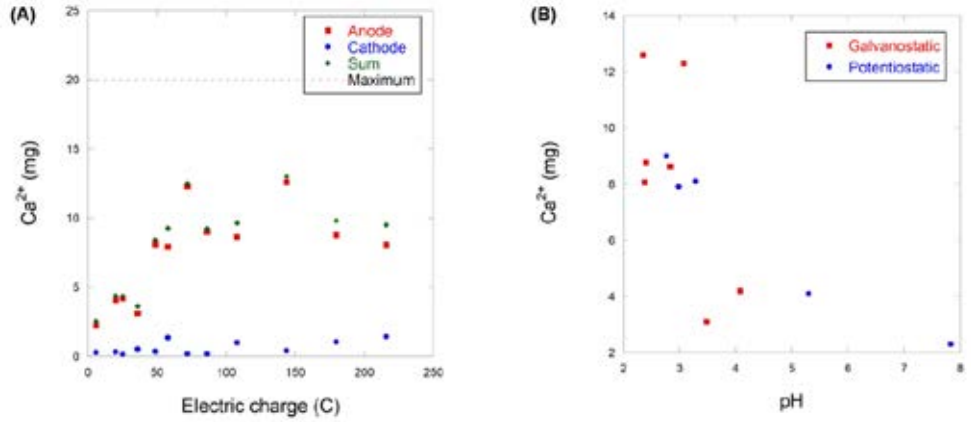


Figure 3. (A) Final mass of Ca^{2+} ions in solution in anodic and cathodic compartments for a defined electric charge applied in one hour (B) Final mass of Ca^{2+} ions in solution in anodic side vs anodic final pH

CONCLUSIONS

During neutral water electrolysis, the development of a pH gradient between anode and cathode has been demonstrated and quantified. This gradient increases with the electric charge applied. The gradient observed is lower than expected due to ion migration, reaction between H^+ and CO_3^{2-} and other potential side reactions. Due to acidification of the anodic compartment, the dissolution of calcium carbonate is favored until a maximum observed solubility of 126mg/L, ten times the value in neutral water at 25°C [9]. The migration of Ca^{2+} and OH^- ions towards the central compartment has been demonstrated as well. This migration is necessary for the production of calcium hydroxide.

ACKNOWLEDGEMENTS

We acknowledge funding from the Walloon Region (Contract number 8512).

REFERENCES

1. Intergovernemental Panel on Cimate Change. 2014. AR5 Climate Change 2014: Mitigation of Climate Change.
2. International Energy Agency. 2020. Energy Technology Perspectives 2020.
3. Lehne J. and Preston F. 2018. Making Concrete Change. Chatham House.
4. Favier A. et al. 2018. A sustainable future for the European Cement and Concrete Industry. ETH Zurich.
5. International Energy Agency and Cement Sustainability Initiative. 2018. Technology Roadmap: Low-Carbon Transition in the Cement Industry.
6. Davis J. Steven et al. 2018. Net-zero emissions energy systems. Science 360:1419.
7. Rissman J. et al. 2020. Technologies and policies to decarbonize global industry: review and assessment of mitigation drivers through 2070. Applied Energy 266:114848.
8. Ellis D. Leah et al. 2019. Toward electrochemical synthesis of cement – An electrolyzer-based process for decarbonating CaCO3 while producing useful gas streams. Proceedings of the National Academy of Sciences 117:12584-12591.
9. Kendall J. et al. 1912. XCVI The solubility of calcium carbonate in water. The London, Edinburgh, and Dublin Philosophical Magazine and Journal of Science 23:958-976.
10. Herranz J. et al. 2020. Co-electrolysis of CO_2 and H_2O: From electrode reactions to cell-level development. Current opinion in Electrochemistry 23:89-95.

WHEC-2022
23rd World Hydrogen Energy Conference
June 26-30, 2022 - Istanbul

#125

BUTADIENE PRODUCTION VIA THE DIRECT DEHYDROGENATION OF N-BUTANE IN MEMBRANE REACTORS: A TECHNO-ECONOMIC ANALYSIS

[1]*Camilla Brencio,* [1,2]*Martina Maruzzi,* [2]*Giampaolo Manzolini,* [1,3*]*Fausto Gallucci*
[1]Inorganic Membranes and Membrane Reactors, Sustainable Process Engineering, Department of Chemical Engineering and Chemistry, Eindhoven University of Technology, De Rondom 70, Eindhoven, 5612 AP, The Netherlands
[2]Group of Energy Conversion Systems, Department of Energy, Politecnico di Milano, Milano, Italy
[3]Eindhoven Institute for Renewable Energy Systems (EIRES), Eindhoven University of Technology, PO Box 513, Eindhoven 5600 MB, the Netherlands

*Corresponding author e-mail: F.Gallucci@tue.nl

ABSTRACT

The direct dehydrogenation of butane (BDH) is emerging as an attractive on-purpose technology for the direct production of 1,3-butadine. However, its product yield is hindered by the high rate of carbon deposition associated to the high temperature required for the highly endothermic reaction. In this work, we evaluated the use of membrane reactor with H_2-selective membranes, to increase the yield of the dehydrogenation process at milder operating conditions. The novel proposed membrane reactor (MR)-assisted BDH technology is compared from a techno-economic point of view with the benchmark technology. The results of this analysis reveal that the membrane reactor technology allows to maintain same production capacity as the benchmark technology, working at milder operating conditions and most importantly lowering the required shale gas-based feedstock; this will result in an overall plant efficiency almost 20% higher in the MR-assisted plant, being equal to 37.7% with respect to the one of the benchmark case, which is 50.92%. This work demonstrates that MR-assisted technology is a valuable alternative to the conventional BDH technology, reducing of almost 20% the final cost of production of 1,3-butadiene, due to the lower installation costs and the higher energy efficiency.

Keywords: Butane dehydrogenation process, Butadiene production, Membrane reactors, Hydrogen removal, Techno-economic analysis

INTRODUCTION

The direct dehydrogenation of butane (BDH) is a promising process to meet the increasing global butadiene demand by using shale gas-derived feedstock. However, this “on-purpose” technology, already commercialized and installed worldwide, is limited by rather low product yields and high energy demands, as the dehydrogenation reaction is highly endothermic and limited by the thermodynamic equilibrium [1]. In addition to that, cracking and other side reactions are thermodynamically and kinetically enhanced at the designated reaction conditions, leading to the need of periodic regenerations of the catalyst. Most of the scientific research on BDH technology is based on the development of improved catalyst formulations to increase the reactor performance [2][3].The effect of metals, the nature of supports, the nature of ligands and the polarity of active species have been investigated to better understand the structure-reactivity relationship and to develop catalysts with higher activity at lower operating temperatures. In this way, it is possible to overcome one of the main limitations for the dehydrogenation process, which is the high coking rate. Another interesting strategy to increase the yield of the dehydrogenation process at lower temperatures is the use of the membrane reactor technology with integrated H_2-selective membranes [4][5]. The selective removal of H_2 from the catalytic bed shifts the equilibrium beyond the thermodynamic restriction of the conventional process, leading to an increase of butadiene production. In this way, it would be possible to achieve same conversions of butane as in the conventional process but working at milder operating conditions. The opportunity to lower the operating temperature will reduce the rate of coke formation on the catalyst increasing the catalyst deactivation timespan. Additionally, the heat duty of the reactors is expected to be drastically reduced, making the overall process more energy efficient [6]. Therefore, the present work aims at assessing the techno-economic feasibility of the membrane reactor integrated process for the dehydrogenation of butane, and this process is compared to the benchmark technology. In this work, the potential application of the membrane reactor technology for BDH, widely used experimentally, is investigated for the first time at industrial level from a process performance point of view. The membrane reactor configuration will be compared with the conventional BDH, which uses packed bed reactors, highlighting the consequent changes in the overall process configuration and the influence of these modifications from a techno-economic point of view.

METHODOLOGY

Two different technologies for the direct dehydrogenation of n-butane into 1,3-butadiene have been simulated with Aspen Plus. The first technology, represented in Fig. 1a, is based on the benchmark CATADIENE process. In the second technology, the conventional reactor is replaced by the membrane-assisted fixed-bed reactor. The goal of this new reactor technology is to reduce the operating reaction temperature, while maintaining the same performance, in terms of conversion, as the benchmark reactors. Due to the lower operating conditions of the reaction zone, the configuration of the Membrane Reactor-Assisted BDH plant (MR-BDH) has few modifications compared to the benchmark, as shown in Fig. 1b.

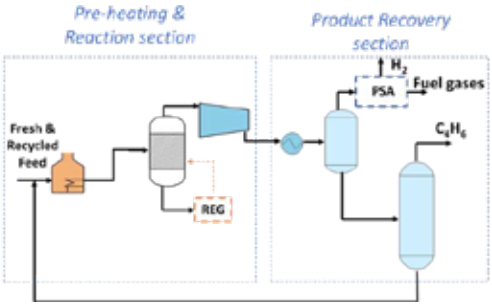


Fig. 1a: Benchmark BDH process scheme.

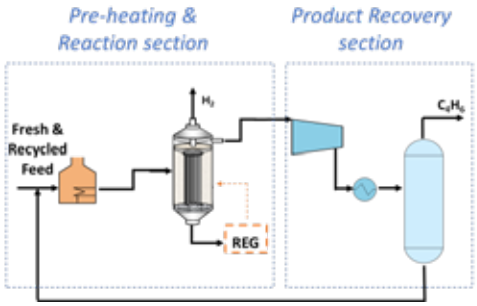


Fig. 2b: Membrane Reactor-Assisted BDH process scheme.

To allow for a fair comparison, both the technologies have been designed with a fixed plant size, equal to a target production of 11,2 kg_{C4H6}/s, which is equivalent to 320 kiloton per year (KTA) of 1,3-butadiene. The analysis of both configurations is performed under the assumptions that the overall reactions are kinetically controlled, and the heat released by the regeneration is used to keep the reactor under isothermal conditions.
Several performance indicators are used to enable a fair comparison of the technical and environmental performance of the processes. The plant performance is calculated using two main types of indexes: one, known as Feedstock-to-Chemical efficiency, accounts for the production of valuable products (i.e. 1,3-butadiene and hydrogen), and the other, known as Overall Energy Efficiency, evaluates the production/consumption of energy.
The economic analysis is performed applying the NETL (National Energy Technology Laboratory) method which differentiates the expenditures of an industrial plant into capital (CAPEX) and operational (OPEX) costs, used to determine the final cost of production of butadiene (COP), according to the following Eq. (1):

$$COP\left[\frac{€}{ton_{C_4H_6}}\right] = \frac{OPEX_{variable} + OPEX_{fixed} + CAPEX}{\dot{m}_{C_4H_6,year}} \quad (1)$$

RESULTS AND DISCUSSION

The results obtained comparing the benchmark and the MR-assisted BDH technologies, reveal that the implementation of membranes for the selective removal of H_2 from the reaction ambient allows to maintain same production capacity as in the benchmark case by lowering the required feedstock of almost 25%. This is mostly due to the more efficient reaction zone, characterized by a lower selectivity to the undesirable cracking products (CH_4, C_2H_6 and C_2H_4), going from 14.4wt% to 13.6wt%, and a higher achievable selectivity to 1,3-butadiene, going from 64.7wt% to 73.3wt%, which allows to have a more efficient downstream separation section. As a result, the overall η_{FTC} can be increased from 57.4% in the benchmark to 74.5% in the novel MR-assisted process. The energy balances of both the technologies, obtained after a detailed heat integration strategy, show that the electricity consumption is three times higher in the benchmark process, which presents a net electricity consumption equal to 1.09 MW_{el}/ton_{C4H6}, compared to 0,31 MW_{el}/ton_{C4H6} in the novel technology. In addition, the total thermal duty per unit of product results to be 62% lower in the MR-assisted plant than in the benchmark, mostly due to the more energy efficient downstream separation section. These three advantages make the MR-assisted technology to have a higher overall plant efficiency, being equal to 66.82%, with respect to the benchmark case, which can reach a total efficiency as low as 50.92%. The reduced energy consumptions in the MR-assisted BDH process allows to improve the carbon footprint of the plant, with a reduction of the total CO_2 emission per unit of product of 20% with respect to the benchmark case, as shown in Fig. 2.

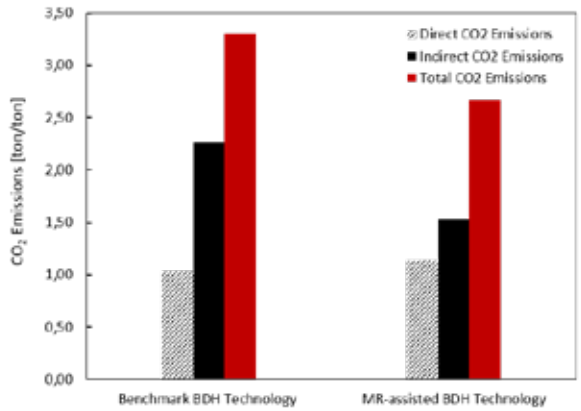


Fig. 2: CO_2 Emissions of the BDH plants.

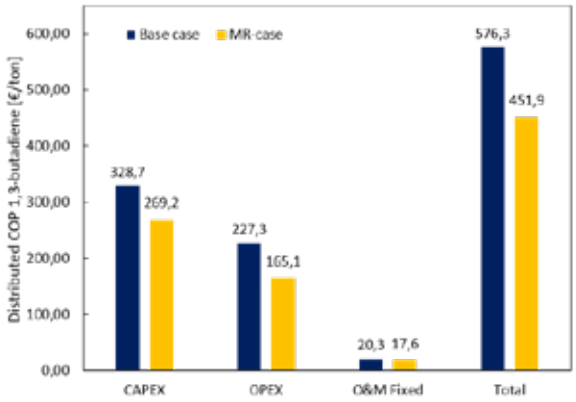


Fig. 3: Distributed COP of the BDH plants.

The MR-assisted technology allows to reduce the specific OPEX per unit of product by 26.5%. This is mostly due to the main savings associated with the feedstock, which has the major impact on the variable costs, and with the utilities. The cost for utilities is higher in the benchmark technology, both due to the larger electricity demand for the turbomachines and due to the higher amounts of cooling water and refrigerant for the condensers and steam for the reboilers of the distillation columns. These costs account for the 21.3% of the total OPEX in the benchmark technology, while for only the 9.6% in the MR-assisted case. At the same time, the better environmental performance of the MR-assisted technology results in a reduced CO_2 emission tax (4.30€/ton), compensating the additional costs associated to the membrane modules. Moreover, the implementation of the membrane reactor technology made the whole plant less intensive, and this can lead to the abolition of a few process equipment and to the reduction in size of some process components. As a result, the CAPEX reduces from 2598.5 M€ in the benchmark to 2130.2 M€ in the novel process. As a main result, the final COP of 1,3-butadiene can be reduced of almost 22%, from 576.3 €/ton$_{C4H6}$ in the benchmark process to 451,9 €/ton$_{C4H6}$ in the MR-assisted process.

CONCLUSIONS

The techno-economic analysis conducted in this work reveals that the implementation of the membrane reactor technology to produce 1,3-butadiene makes the BDH process more cost efficient and environmentally friendly than the benchmark technology. The use of a membrane reactor technology allows to reduce the final COP by 21.6% with respect to the commercial technology, maintaining the same plant production capacity. Thus, the MR-assisted BDH technology shows great potential to be implemented in the petrochemical industry.

ACKNOWLEDGEMENT

This project has received funding from the European Union's Horizon 2020 research and innovation program under grant agreement No 814671 (BiZeolCat).

REFERENCES

1. B. R. Jermy, B. P. Ajayi, B. A. Abussaud, S. Asaoka, and S. Al-khattaf, "Oxidative dehydrogenation of n -butane to butadiene over Bi – Ni – O / ⇗ -alumina catalyst," *"Journal Mol. Catal. A, Chem.*, vol. 400, pp. 121–131, 2015.
2. M. Shao, C. Hu, X. Xu, Y. Song, and Q. Zhu, "Pt/TS-1 catalysts: Effect of the platinum loading method on the dehydrogenation of n-butane," *Appl. Catal. A Gen.*, vol. 621, no. April, p. 118194, 2021.
3. A. Dejoz, J. M. López Nieto, F. Márquez, and M. I. Vázquez, "The role of molybdenum in Mo-doped V-Mg-O catalysts during the oxidative dehydrogenation of n-butane," *Appl. Catal. A Gen.*, vol. 180, no. 1–2, pp. 83–94, 1999.
4. C. Téllez, M. Menéndez, and J. Santamaría, "Oxidative Dehydrogenation of Butane Using Membrane Reactors," *AIChE J.*, vol. 43, no. 3, pp. 777–784, 1997.
5. M. Farsi, A. Jahanmiri, and M. R. Rahimpour, "Optimal operating condition of membrane reactors to enhance isobutene production, selectivity and hydrogen production," *J. Ind. Eng. Chem.*, vol. 18, no. 5, pp. 1676–1682, 2012.
6. B. V. Vora, "Development of dehydrogenation catalysts and processes," *Top. Catal.*, vol. 55, no. 19–20, pp. 1297–1308, 2012.

WHEC-2022
23rd World Hydrogen Energy Conference
June 26-30, 2022 - Istanbul

#141

NOVEL EMERGENCY GAS-TO-POWER MH-STORAGE AND FUEL CELL SYSTEM: MODELING AND EXPERIMENTAL VALIDATION

[1,*]David Michael Dreistadt, [1,2]Julián Puszkiel, [1]José M. Bellosta von Colbe, [1]Giovanni Capurso, [3]Gerd Steinebach, [3]Stefanie Meilinger, [1]Thi Thu Le, [2]Myriam Covarrubias Guarneros, [1,2]Thomas Klassen, [1,2]Julian Jepsen
[1]Institute of Hydrogen Technology, Helmholtz-Zentrum hereon GmbH, Max-Planck-Straße 1, D-21502 Geesthacht, Germany
[2]Helmut Schmidt University, Holstenhofweg 85, 22043 Hamburg, Germany
[3]Hochschule Bonn-Rhein-Sieg, Institut für Technik Ressourcenschonung und Energieeffizienz, Grantham-Allee 20, 53757 Sankt Augustin, Germany

*Corresponding author e-mail: David.Dreistadt@hereon.de

ABSTRACT

A gas-to-power (GtoP) system for power outages is digitally modeled and experimentally developed in this work. The design includes a solid-state hydrogen storage system based on TiFeMn as a hydride forming alloy (5 tanks, total capacity: 110 g H_2) and an air-cooled fuel cell (maximum power: 1.6 kW). In an emergency use case of the system, hydrogen is supplied to the fuel cell, and the waste heat coming from the exhaust air of the fuel cell is used for the endothermic dehydrogenation reaction of the metal hydride. This GtoP system shows fast, stable, and reliable responses from 149 W to 596 W under constant and dynamic conditions. The developed model is based on a network approach, and it is validated under static and dynamic power load scenarios, showing excellent agreement with the experimental results.

Keywords: Gas to power, Hydrides, Hydrogen storage, Fuel cell, Modeling, Hydrogen

INTRODUCTION

In today's society, fossil fuels are becoming an increasing problem, due to the high environmental impact, so the call for alternative energy sources is becoming louder [1-3]. In the last 20 years, much effort has been put into developing systems to integrate renewable sources into the current energy system [4]. The developed experimental integrated systems (renewable energy source + electrolyzer + storage system + fuel cell) present relatively low efficiency and high costs [4]. Therefore, improving the overall efficiency of these integrated systems is demanding.

This work investigates the application of low-temperature metal hydride (TiFeMn) for GtoP systems for stationary emergency power supply. The herein-developed GtoP system (“MH2-Powerbank”) consists of 5 TiFeMn powder-filled MH-tanks with a total weight of 6.7 kg, to supply hydrogen to an air-cooled 1.6 kW fuel cell. This GtoP system is experimentally tested and simulated by applying a novel network simulation approach. The simulation model was implemented in the MATLAB/Simscape environment based on conservation equations. The overall GtoP system efficiency is optimized by utilizing the waste heat of the air-cooled fuel cell as the heat supply for the desorption process of the hydride tanks. Based on the system simulation, the efficiency can be optimized in future work.

MATERIALS AND METHODS

Description of the experimental set-up

Figure 1 shows the basic design of the MH2-Powerbank test stand: a detailed sketch of the system (Figure 1 a) and a photograph of the experimental set-up (Figure 1 b). An amount of 6.7 kg of TiFeMn powder with a theoretical maximum capacity of 1.73 wt.% [5], produced by GKN Powder Metallurgy GmbH and developed within the HyCare project (Hydrogen Carrier for Renewable Energy Storage) was used [6]. The TiFeMn powder was distributed in 5 tanks (each tank of 500 cm^3 made of 316L Stainless Steel, from the company Swagelok), as seen in Figure 1 a. This low-temperature hydride was able to operate at pressures below 50 bar and loaded hydrogen at room temperatures. The 1.6 kW PEM (proton exchange membrane) Fuel Cell was from the type "DBX2000 power backup module" produced by Dantherm Power and needed a hydrogen supply of Grade 3.0 (99.9 %) or higher (Figure 1 a). The fuel cell was cooled with forced convection using a fan that provided airflow at room temperature (Figure 1 a). The heated air entered an air duct and reached the hydride storage tanks (”red arrows”). In this way, the hydride storage tanks were heated with air to carry out the endothermic hydrogen desorption. In order to reduce the thermal losses, the whole system was placed in a closed and isolated cabinet. Several sensors were integrated into the shown experimental set-up to gather data to evaluate the system performance. The temperatures of the MH-tanks (T1-5), the inlet temperature (T6) of the cooling air stream, and the air stream outlet temperature after warming up (AN) were measured. The hydrogen pressure and hydrogen flow from the MH-tanks to the fuel cell were measured by a pressure transducer (P2) and a flowmeter (between the valves V11 and V12), respectively. The air speed from the fuel cell stack to the MH-tank was measured by an anemometer (AN).

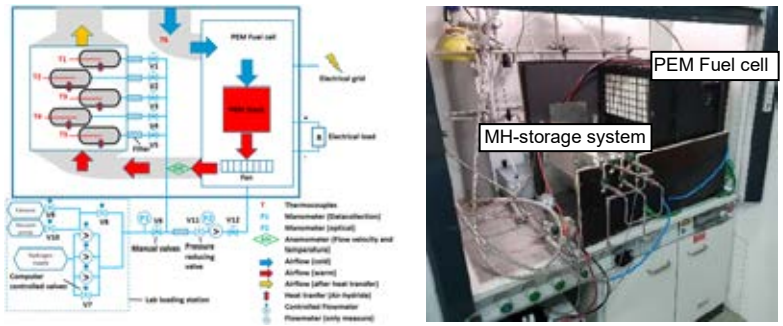


Fig. 1. a) Detailed sketch and b) photo of the MH2-Powerbank [7].

Mathematical model

The system simulation model was developed in the environment MATLAB/Simulink. Utilizing the MATLAB/Simulink included the additional component library Simscape, which contained several mathematical component models. This approach allowed the coupled simulation to form a network. The MH-tanks are modeled in 0D geometry by using the following mass and energy conservation equations (1) and (2), respectively:

$$\epsilon \frac{d\rho_s}{dt} = \dot{m}_{R.rate} \qquad (1)$$

and

$$\frac{d\left(\left(\rho_m c_p\right)_e T_m\right)}{dt} = \dot{Q}_{HE} + \frac{\dot{m}_{R.rate}}{M_{H_2}} \cdot \Delta H \qquad (2)$$

with

$$\left(\rho_m c_p\right)_e = \left(\epsilon \rho_g c_{p,g} + (1-\epsilon)\rho_s c_{p,s}\right)$$

where $\rho_s \left[\frac{kg}{m^3}\right]$ is the density of the solid, $\epsilon\,[-]$ is the porosity of the powder bed and $\dot{m}_{R.rate} \left[\frac{kg}{m^3\,s}\right]$ is the reaction rate per unit volume. In the conservation of energy $\rho_g \left[\frac{kg}{m^3}\right]$ is the density of the gas, $T_m[K]$ is the equilibrium temperature of the gas and solid phases, $c_{p,g} \left[\frac{J}{kgK}\right]$ or $c_{p,s} \left[\frac{J}{kgK}\right]$ is the specific heat capacity of gas or solid, $\dot{Q}_{HE} \left[\frac{J}{m^3\,s}\right]$ is the volume-based heat flow between the heat exchanger (HE) and the hydride, $\Delta H \left[\frac{J}{mol}\right]$ is the molar-based reaction enthalpy, and $M_{H_2} \left[\frac{kg}{mol}\right]$ is the molar mass of hydrogen. These equations provide the basis for the system simulation of MH2-Powerbank in Simscape.

Figure 2 describes the conceptual implementation of the 0D model in the platform MATLAB/Simscape. According to mass and energy conservation, the grey cylinders represent the MH-tanks modeled in Simulink. The yellow boxes represent the heat exchange between the tanks and the airstream coming from the fuel cell. The MH-tanks are assembled via a gas reservoir interphase of Simscape (blue box). As seen, the pipes (Figure 2: blue cylinders) are also represented and interconnected. The air velocities around each tank and coming from the exhaust of the fuel cell are represented by $v_{T1-T5}(t)$. $T_A\,(t)$ and $v_A(t)$ represents the temperature and velocity measured in the anemometer (Figure 1 a). These values were used as the boundary conditions.

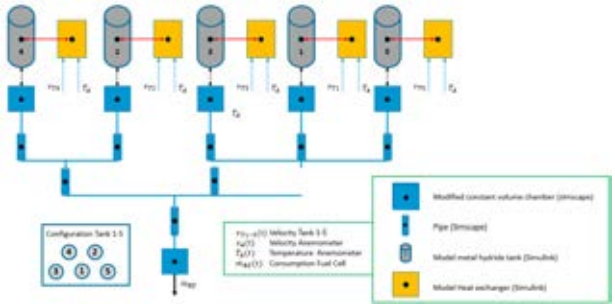


Fig. 2. Implementation of MH2-Powerbank in MATLAB Simulink/Simscape [7]

RESULTS AND DISCUSSION

As one of the main results of this investigation, the integrated MH-storage and fuel cell system was tested in a daily dynamic load. This scenario is essential to test the system for emergency power supply purposes. Thus, a representative household scenario on Saturday afternoon in winter from 5:00 p.m. with an annual power consumption of 1000 kWh/year was chosen. Figure 3 shows the results of the temperature profiles from tanks 1 and 3 (Figure 3 c), the system pressure drop (Figure 3 a) and fuel cell power (Figure 3 b). As seen, the power requirements vary in small steps, from 149 W to a maximum of 215 W every 15 min (Figure 3 b).

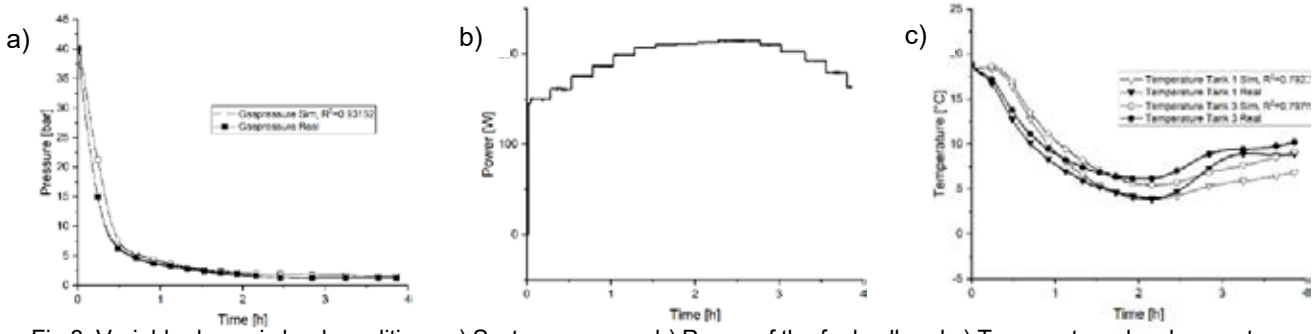


Fig 3. Variable dynamic load conditions a) System pressure b) Power of the fuel cell and c) Temperature development.

The observed substantial pressure drop (Figure 3 a) is mainly due to the hydrogen removal from the gas phase of the tanks. As soon as the pressure drops below the dehydrogenation equilibrium pressure of the hydride material, the pressure driving force increases further. Hence, a more significant hydrogen amount is desorbed from the hydride, strongly reducing the pressure curve slope. Minimum temperature values of 3.57 °C after 1.9 h and 5.68 °C after 1.8 h are reached in tanks 1 and 3, respectively (Figure 3 c). The temperature drop to the minimum value is due to the endothermic desorption reaction. In tank 1, the reached minimum temperature level is lower because the heat exchange with the waste heat airflow of the fuel cell is not as effective as in tank 3. In this regard, the temperature profiles in the last measurement stage (Figure 3 c) do not present the same behavior. For both tanks, the temperature rises after 3 h: 8.9 °C for tank 1 and 9.0 °C for tank 3. The observed temperature increase is caused by the reduced consumption of the fuel cell. The system model shows a good agreement with the experimental results, particularly for the pressure profile, and the small differences between the experimental and simulated temperature profiles (Figures 3 a and c).

CONCLUSIONS

The digital and experimental development of a gas-to-power system (GtoP) for power outages has been successfully demonstrated. Such GtoP system, called MH2-Powerbank, is composed of a 1.6 kW air-cooled PEM fuel cell and a TiFeMn based MH-system. The MH2-Powerbank can provide energy under different scenarios in a power range between 149-596 W. The waste heat from the air-cooled fuel cell is effectively utilized as a heat source for the dehydrogenation process of the MH-system. The dynamic consumption scenario, shown here, demonstrates that the concept of the MH2-Powerbank system is suitable for the emergency power supply of households, due to its fast and reliable response to the power load changes. The novel developed 0D model, using the MATLAB/Simscape library, shows the advantages of low computational cost and full coupling between the fuel cell and the MH-system. This work presents an experimental and digital strategy for integrating MH-systems in any hydrogen network for GtoP system applications and potential dimensioning.

ACKNOWLEDGEMENT

The authors thank Mr. Jürgen Stolzenberger for the great support with the programming in Labview. Thanks to the colleagues from the workshop at the HZ-hereon, who helped with the construction of MH2-Powerbank.

REFERENCES

1. G. Forest and A. Markova, The road to carbon-free society. Climate Change Energiy and Environment, 2021.
2. M. Chitanava, et al., *The impact of climate change mitigation policy on employment*. Climate Basics.
3. M. Munta, *The European Green Deal*. Climate Change Energiy and Environment, 2020.
4. T. Egeland-Eriksen, A. Hajizadeh, and S. Sartori, Hydrogen-based systems for integration of renewable energy in power systems: Achievements and perspectives. International Journal of hydrogen energy, 2021. 46: p. 31963-31983.
5. E. M. Dematteis, et al., Fundamental hydrogen storage properties of TiFe-alloy with partial substitution of Fe by Ti and Mn. Journal of Alloys and Compounds, 2021. 874.
6. HyCare. Hydrogen CArrier for Renewable Energy Storage. Available from: https://hycare-project.eu/
7. D. M. Dreistadt, et al., Novel emergency gas-to-power system based on efficient and long-lasting solid-state hydride storage system: Modeling and experimental validation. *Energies* (Preprint submitted), 2021

WHEC-2022
23rd World Hydrogen Energy Conference
June 26-30, 2022 - Istanbul

#188
PROCESS IMPLICATIONS OF ELECTRIFYING AMMONIA PRODUCTION

[1*]Antoine Dechany, [2]Vladimir Galvita, [2]Kevin Van Geem, [1]Joris Proost
[1] Université catholique de Louvain, Division of Materials and Processes Science, Place Ste Barbe 2, Louvain-la-Neuve, Belgium
[2] Universiteit Gent, Laboratory for Chemical Technology, Technologiepark 125, B-9025, Ghent, Belgium

*Corresponding author e-mail: antoine.dechany@uclouvain.be

ABSTRACT

The current ammonia production plants - Steam Methane Reforming (SMR) and Haber-Bosch (HB) - are responsible for 1.2% of global CO_2 emissions. As more sectors are shifting to electrification, so does the NH_3 industry as shown by the amount of studies focusing on electrolysers and Pressure Swing Adsorbers (PSA) to replace SMR. Haber-Bosch itself is being questioned as a new alternative technology is emerging: Chemical Looping (CL). Such transformations imply changes to the current process. This work assesses such implications by comparing 2 alternative scenarios with the conventional case. In terms of emissions, the electrification is clearly benefic with a cut of 74-95% when using wind energy. The replacement of SMR by electrolysers and PSA also improves the energy efficiency, as >60% of the energy consumption in conventional plants originates from the compressors and heat integration. Finally, the combination of Alkaline Electrolysers (AE) and CL is determined as the most suitable for small-scall flexible and economical installations.

Keywords: Ammonia synthesis, Hydrogen production, Electrolysis, Electrification, Green hydrogen

INTRODUCTION

There is no doubt that the climate crisis is the number one issue the world has to tackle. As a consequence, paradigm shifts are happening globally to reduce greenhouse gas emissions, be it on small scales such as in individuals' routines, or on larger scales such as in the transport, building, power and industrial sector. Looking closer at the chemical sector, it was responsible for 1.4 $GtCO_2$ in 2019, which is equivalent to 4.2% of global CO_2 emissions [1][2]. Within those 4.2%, 1.2% are attributable to ammonia production and its methane-based Haber-Bosch (HB) process, making it one of the largest greenhouse gas emitters within the chemical sector [3][4]. Solutions to reduce its carbon footprint could therefore have quite a significant impact on global emissions. Lately, electrification has been one of the main focuses when assessing decarbonizing solutions for different sectors [5], and the chemical industry is one of them. Several studies have assessed the electrification of NH_3 production by replacing the standard Steam Methane Reforming (SMR) by water electrolysis [3][4][6]. Implementing such a change in technology implies changes in the process. The main objective of this work is to review these implications by comparing three scenarios. Scenario 0 is the current situation of NH_3 production: the combination of SMR and HB. Scenario 1 replaces SMR by a Solid Oxide Electrolyser (SOE). Finally, Scenario 2 replaces SMR by an Alkaline Electrolyser (AE) and HB by Chemical Looping (CL).

SCENARIOS DESCRIPTION

Scenario 0: SMR + HB

Scenario 0 is the reference scenario as it describes the current situation. Ammonia is produced through a Haber-Bosch process which is fed with a H_2/N_2 mix produced by Steam Methane Reforming (Fig. 1a). The combination of SMR and HB currently represents the Best Available Technique (BAT) for NH_3 production as it yields the highest efficiency and lowest carbon emissions while being the most economical route for large scale NH_3 production [3][4].

The SMR is composed of several units. It is first supplied with methane (CH_4) and air which enter a primary and secondary reforming reactor. The reforming is endothermal. Its primary reactor is thus heated by a methane-fed furnace while the secondary reactor is autothermal. The latter generates a gas mixture which comprises N_2, H_2, CO and unreacted steam and CH_4. It enters a water-gas shift reactor (WGS) where the CO reacts with steam to produce H_2. This reaction is exothermal, and heat should be removed to decrease the CO equilibrium concentration. The mixture at the output, stripped from most of the CO, successively goes through an acid gas removal unit and a methanator to respectively strip the remaining CO_2 and CO. The product mixture is sent to the HB loop. It is first compressed and pre-heated before entering the HB catalytic reactor. The resulting feed is then condensed to separate the NH_3 from the remaining reactants and inerts. The latter are partially purged and recycled to the reactants feed. Overall, this system works at high temperatures and pressures (550°C and 250 bar). [4][6]

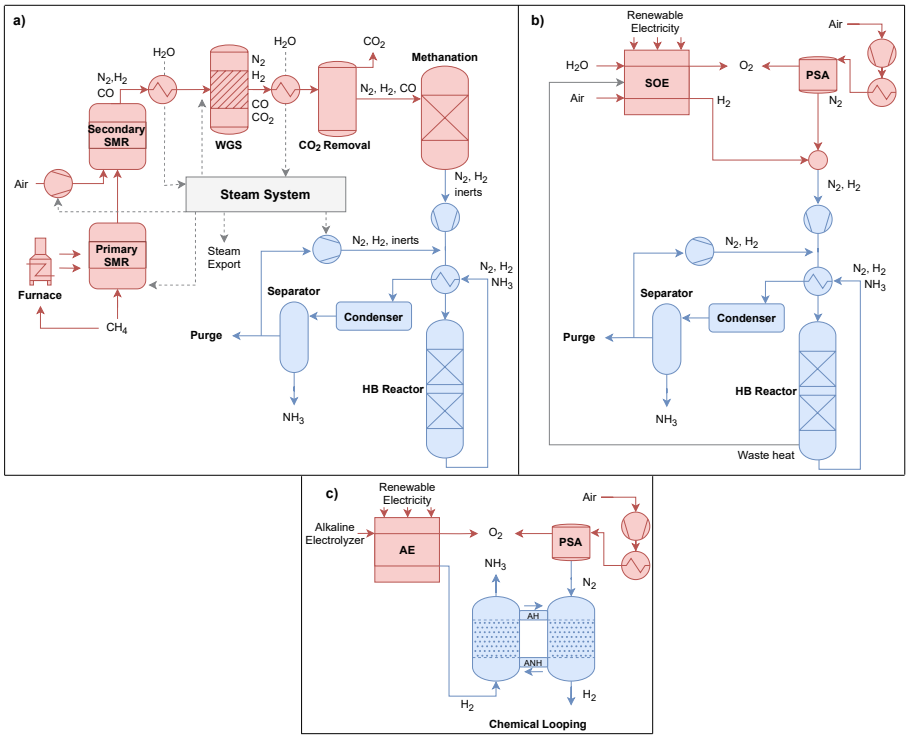


Fig. 1. Process diagrams of Scenario 0 (a), 1 (b) and 2 (c). Each has a H2/N2 production unit (red) and a NH_3 production unit (blue)

Scenario 1: SOE + HB

The first alternative scenario involves a change of technology by implementing a Solid Oxide Electrolyser (SOE) to replace the SMR process while keeping the HB loop (Fig. 1b). As the SOE only produces H_2, the N_2 feed is produced via Pressure Swing Adsorption (PSA). Both technologies are powered electrically. Assuming that the electricity comes from renewable sources, the hydrogen produced here can be qualified as Green H_2 [7]. The SOE unit can be represented as a single block, as opposed to the SMR process which is a succession of numerous units. It is fed with air and water and generates H_2. At the output, the H_2 is separated from the unreacted water and mixed with the N_2, which is produced through the PSA unit fed with air. The resulting mixture is then compressed and heated before being sent to the conventional HB loop. In terms of operating conditions, the SOE must operate at high temperature and pressure to match the HB conditions (650°C and 550 bar) and the HB reactor waste heat can therefore be recycled to the SOE. [6]

Scenario 2: AE + CL

The second alternative scenario implies a change in both hydrogen and ammonia production units. The SMR is replaced by an Alkaline Electrolyser (AE) for the H_2 production and a PSA for the N_2. The HB loop is replaced by a Chemical Looping (CL) unit (Fig. 1c). Just as in the first alternative scenario, the electrolyser is represented by a single block. This time, it is only fed with an alkaline electrolyte. In this scenario, however, the H_2 output is not mixed with the N_2 output. In fact, both are sent to two distinct entries in the CL reactor. The latter technology relies on a decoupling of the conventional catalytic reaction that normally takes place in a single HB reactor. The CL reactor is here composed of 2 separate reactors connected in a cycle and in which two sub-reactions are conducted. The CL process of interest in this case is the one proposed by Gao et al. which uses alkaline earth metal hydrides (AH) and imides (ANH). During the first step, N_2 is fed into the first reactor and reduced by the H in the AH catalysts, producing ANH intermediates. The latter are sent to the second reactor and undergo a hydrogenation by the H_2 feed. This last step produces the NH_3 but also regenerates the metal hydride which is recycled back to the first step. In terms of operating conditions, both AE and CL run at a relatively low temperature (~100°C) and pressure (1 bar) compared to the previous scenarios. [9]

COMPARISON AND DISCUSSION

To compare the three scenarios, four characteristics are examined: emissions, energy losses, scalability and flexibility. In terms of emission, it appears that the conventional process described in Scenario 0 is the most polluting. Specifically, it emits in average 2.0-2.5 ton $CO_{2,eq}$ per ton NH_3, and these numbers would be higher for smaller plants.

In comparison, only 0.12-0.53 ton $CO_{2,eq}$ are emitted for a wind powered plant in Scenario 1 and 2, which is 74 to 95% smaller [4][10].

This trend is comparable regarding energy intensity. In fact, the steam compressors alone account for 60% of the energy consumption in Scenario 0. In addition, the heat integration system and the HB purge also take part in decreasing the energy efficiency [4]. Considering the steam system would not be present anymore in both Scenario 1 and 2, this is a sensible optimisation in energy efficiency. The losses due to the purge in those scenarios are also negligible as almost no inerts are present in the feeds [6]. Furthermore, Chemical Looping in Scenario 2 allows an in-situ separation of the NH_3, which allows more energy savings as the separation system in HB is very energy-intensive [11].

The scalability aspect is directly linked to the latter observations. First, due to the absence of any steam management units (compressors and steam turbines) when using electrolysers, and due to the latter's compactness, both electrified scenarios are suitable for small-scale installations. Then, regarding pressure, the NH_3 production cost being affected by the operating pressure, Scenario 1 and its high-pressure conditions make it less favorable to be scaled down [12]. This makes Scenario 2 the best to build small and agile production plants at low capital costs and flexible operation to cope with the intermittent nature of renewable energy.

CONCLUSIONS

- The carbon intensity in the current NH_3 production can be cut by 70-95% by electrifying the process.
- Replacing the SMR by electrolysers and PSA allows energy savings of at least 60% and avoid the need of a purge.
- It also allows more compact and straightforward installations.
- Replacing HB by CL avoid the use of an energy intensive separation unit.
- Combining AE and CL allows ambient operating pressure, making it favorable for small-scale agile plants.

ACKNOWLEDGEMENTS

Funding from the Belgian Energy Transition Funds of the Federal Planning Service for Economy, S.M.E., Self-employment and Energy is gratefully acknowledged through the BE-HyFE project (Belgian Hydrogen Fundamental Expertise).

REFERENCES

1. International Energy Agency. 2021. Energy Technology Perspectives 2020. IEA. 182-187.
2. https://www.iea.org/articles/global-energy-review-co2-emissions-in-2020. Accessed on December 3. 2021.
3. Morlanés N, Katikaneni S, Paglieri S, Harale A, Solami B, Sarathy S M and Gascon J. 2021. A technology roadmap to the ammonia energy economy: current state and missing technologies. Chemical Engineering Journal. 408:127310.
4. Smith C, Hill A and Torrente-Murciano L. 2020. Current and future role of Haber-Bosch ammonia in a carbon-free energy landscape. Energy and Environmental Science. 13:331-344.
5. Sugiyama M. 2012. Climate change mitigation and electrification. Energy Policy. 44:464-468.
6. Cinti G, Frattini D and Jannelli E. 2017. Coupling Solid Oxide Electrolyser (SOE) and ammonia production plant. Applied Energy. 192:466-476.
7. IRENA. 2020. Green Hydrogen: a guide to policy making. 1:1-51.
8. Ghavam S, Vahdati M, Wilson I and Styring P. 2021. Sustainable ammonia production processes. Frontiers in Energy Research. 9:580808.
9. Gao W, Guo J, Wang P, Wang Q, Chang F, Pei Q, Zhang W, Liu L and Chen P. 2018. Production of ammonia via a chemical looping process based on metal imides as nitrogen carriers. Nature Energy. 3:1067-1075.
10. Wang M, Khan M A, Mohsin I, Wicks J, Ip A H, Sumon K Z, Dinh C T, Sargent E H, Gates I D and Kibbria M G. 2021. Can sustainable ammonia synthesis pathways compete with fossil-fuel based Haber-Bosch processes?. Energy and Environmental Science. 14:2535-2548.
11. Poelman H and Galvita V. 2021. Intensification of chemical looping processes y catalyst assistance and combination. Catalysts. 11:266
12. Lin B, Wiesner T and Malmali M. 2020. Performance of a small-scale Haber process: A techno-economic analysis. ACS Sustainable Chemistry and Engineering. 41:15517-15531.

WHEC-2022
23rd World Hydrogen Energy Conference
June 26-30, 2022 - Istanbul

#207

SENSITIVITY ANALYSIS OF INDEPENDENT PARAMETERS FOR FORMATION OF NO_x EMISSION IN HYDROGEN ENRICHED COMPRESSED NATURAL GAS ALONG WITH EXHAUST GAS RECIRCULATION BY SUPPORT VECTOR MACHINE

[1,2] *Anas Rao,* [1] *Yongzhen Liu,* [1*] *Fanhua Ma*
[1] State Key Laboratory of Automobile Safety and Energy, Tsinghua University, Beijing, 100084, China
[2]Department of Mechanical Engineering, University of Engineering & Technology Lahore, Pakistan

*Corresponding author e-mail: anasrao986@gmail.com

ABSTRACT:

The utilization of hydrogen fuel in internal combustion engine is one step towards the implementation of zero-carbon foot print. The main drawback is higher PPM of NOx emission. Numerous techniques are applied by different researchers to bring NOx emission under EURO-VI emission standards. The experiments have been performed at different spark timings (0 to 60°CA bTDC), hydrogen percentages (0 to 40%) in CNG fuel, EGR rates (0 to 35.8%), MAP (65 to 178 kPa), speed (700 to 2000 rpm) at ***lambda*** = 1.0. The simulation of NO_x emission has been conducted by support vector machine. The sensitivity analysis has been carried out for the selection of best combination of input variables for the formation of NOx emissions that are: controllable parameters (MAP, hydrogen fractions in CNG, EGR rate, spark timing & RPM) and combustion parameters (maximum pressure, IMEP, adiabatic flame temperature, HRR & COV). The minimum mean absolute percentage error is 7.6996% & MRE is 57.05 corresponding to the best combination (RPM-MAP-ST-EGR-P_{max}/T_{ad}).

Keywords: Hydrogen enriched compressed natural gas, NOx emission, Support Vector Machine.

INTRODUCTION

The global warming, depleting in hydrocarbons and emission hazards are the main factors that encourage the policy makers and scientists to look forward the other possible alternative resources. The hydrogen fuel is an alternative fuel to achieve the zero-carbon foot prints for transportation sector. Huang et al.[1] & Ma et al.[2] have performed an extensive work on hydrogen enriched compressed natural gas at different lean burn operations and EGR ratios in heavy duty spark ignition engine. Rao et al.[3–5] have simulated the quasi-dimensional combustion model of HCNG engine under a wide range of operating conditions. They have coupled the thermal NOx mechanism with quasi-dimensional combustion model of SI engine. They have also conducted the mathematical modelling of NO_x emission in HCNG engine under a wide range of operating conditions. Mehra et al. [6] have applied the artificial neural network for training of hydrogen enriched compressed natural gas at lean burn operations. Huang et al. [7] compared the quadratic polynomial, neural network, and support vector machine for tuning of engine torque, BSFC and NO_x emission of HCNG engine. They have concluded that support vector machine has better prediction accuracy as compare to the other two algorithms. Duan et al.[8–10] analyzed the particle swarm optimization (PSO), GRID and genetic algorithm of SVM in terms of engine torque, BSFC and NO_x emission at different operating conditions in HCNG engine. They have concluded that PSO optimization is the best one with respect to regression correlation = 0.97. They have also iterated the different factors such as: penalty factor, width and loss function for training of NOx emissions in HCNG engine. They have also studied the laminar burning speed and maximum in-cylinder pressures of HCNG engine at different hydrogen fractions in CNG fuel, equivalence ratios and electric fields in constant volume combustion chamber and support vector machine. The thermal NOx emission has a large prediction error. The main parameters in Zeldovich' mechanism are combustion pressure and temperature. The motivation of this research is to train the NOx emission of HCNG engine under EURO-VI emission standard by support vector machine. The other objective is to analyze the combination of different parameters such: hydrogen percentage in CNG fuel, spark timing, speed, MAP, EGR ratios, maximum pressure, indicated mean effective pressure, adiabatic flame temperature, heat released rate and coefficient of variance. The best combination is RPM-MAP-ST-EGR-P_{max}/T_{ad} with the combination of four controllable variables and one combustion parameter.

METHODOLOGY

The experiments have been conducted under a wide range of operating conditions to obtain PPM of NOx emission in HCNG engine at different spark timings (0 to 60°CA bTDC), hydrogen percentages (0 to 40%) in CNG fuel, EGR rates (0 to 35.8%), MAPs (65 to 178 kPa) and speed (700 to 2000 rpm) at lambda= 1. The maximum pressures, indicated pressures, heat released rates and coefficient of variances have been attained with aid of Kistler KIBOX combustion software. The adiabatic flame temperatures are calculated by balanced chemical equation. The total 666 sample points have been utilized for the training purpose and 59 operating conditions for the testing purpose. The PSO algorithm and radial based function have been applied for the optimization of support vector machine with tuning

of penalty kernel (c) and intensive loss function (g) at kernel width (p=0.01). The sensitivity analysis has been carried out with different combinations of independent variables.

RESULTS & DISCUSSION:

The support vector machine has been applied as a tool for sensitivity analysis of different independent variables related to the controllable parameters (MAP, hydrogen fractions in CNG, EGR rate, spark timing & RPM) and combustion parameters (maximum pressure, IMEP, adiabatic flame temperature, HRR & COV) as shown in figure 1. The best combination for the prediction of NO_x emission with respect to independent variables has been chosen on the basis of mean absolute percentage errors (MAPE), maximum regression errors (MRE) and squared regression (R^2). The PSO algorithm has been applied for tuning the penalty factor (c) & loss width (g) at function width (p=0.01). The first combination (IMEP-P_{max}-Tad-MAP-EGR) consists of three combustion variables (maximum pressure, indicated mean effective pressure & adiabatic flame temperature) and two controllable parameters (manifold absolute pressure & EGR rate). The MAPE=8.5215%, MRE=76.9089% and R^2=0.9859 with tuning factors c= 207.0429, g=6.5566 & p=0.01. The second combination (H_2-EGR-IMEP-P_{max}-T_{ad}) consists of three combustion parameters (indicated mean effective pressure, maximum pressure & adiabatic flame temperature) and two controllable factors (hydrogen fractions in CNG & EGR rate). The MAPE=10.3135%, MRE=94.1157% and R^2=0.9716 with optimized factors c= 814.909, g=9.0673 & p=0.01. The third combination (MAP-ST-EGR-H_2-P_{max}/T_{ad}) consists of one combustion factor. (Maximum pressure over adiabatic flame temperature) and four controllable factors (hydrogen fractions in CNG, EGR rate, manifold absolute pressure & spark timing). The MAPE=8.4497%, MRE=79.3387% and R^2=0.9906 with optimized factors c= 207.0429, g=6.5566 & p=0.01. The fourth combination (RPM-MAP-ST-EGR-P_{max}/T_{ad}) consists of one combustion variable (maximum pressure over adiabatic flame temperature) and four controllable parameters (speed, EGR rate, manifold absolute pressure & spark timing). The MAPE=7.6996%, MRE=57.04852% and R^2=0.9826 with tuning factors c= 276.0174, g=3.9427 & p=0.01. The fifth combination (RPM-ST-MAP-H_2-P_{max}/T_{ad}) consists of one combustion parameter (maximum pressure over adiabatic flame temperature) and four controllable variables (speed, manifold absolute pressure, hydrogen fractions & ignition timing). The MAPE=7.9125%, MRE=116.2818% and R^2=0.9753 with iterated constants c= 814.909, g=9.0673 & p=0.01. The sixth combination (RPM-ST-EGR-H_2-P_{max}/T_{ad}) consists of one combustion parameter (maximum pressure over adiabatic flame temperature) and four controllable variables (speed, EGR rate, hydrogen fractions & spark timing). The MAPE=14.8866%, MRE=116.2818% and R^2=0.9753 with tuning of variables c= 207.0429, g=6.5566 & p=0.01. The seventh combination (RPM-MAP-ST-EGR- P_{max}/(IMEP $_x$ T_{ad})) consists of one combustion parameter (maximum pressure over the product of adiabatic flame temperature and indicated mean effective pressure) and four controllable variables (speed, EGR rate, ignition timing and manifold absolute pressure). The MAPE=8.9920%, MRE=113.1708% and R^2=0.9900 with tuning of variables c= 276.0174, g=3.9427 & p=0.01. The eight combination (P_{max}-IMEP-COV-HRR-T_{ad}) consists of five combustion parameters that included (maximum pressure, indicated mean effective pressure, coefficient of variance, heat released rate & adiabatic flame temperature). The MAPE=15.1538%, MRE=172.0425% and R^2=0.9651 with tuning factors c= 737.4321, g=5.7792 & p=0.01

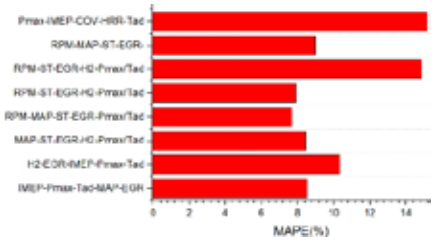


Fig 1(a) MAPE

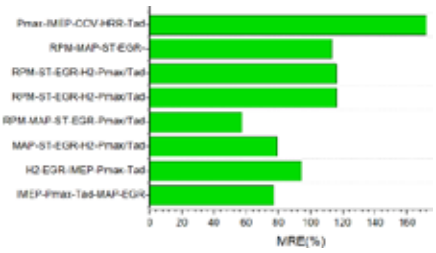


Fig 1(b) MRE

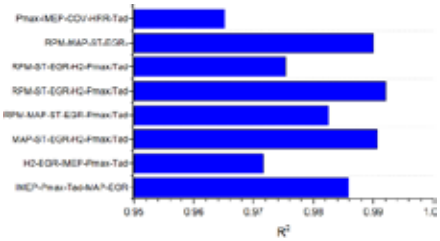


Fig 1(c) R^2

CONCLUSIONS

1) The best combination of input variables is RPM-MAP-ST-EGR-P_{max}/T_{ad} with respect to MAPE=7.6996 & MRE=57.04852 as shown in fig (2).

2) The best combination of independent parameters is RPM-ST-EGR-H_2-P_{max}/T_{ad} with respect to R^2=0.9920.

3) The order of combination in terms of NOx emission is as follows: (RPM-MAP-ST-EGR-P_{max}/T_{ad} > RPM-ST-EGR-H_2-P_{max}/T_{ad} > MAP-ST-EGR-H_2-P_{max}/T_{ad} > IMEP-P_{max}-Tad-MAP-EGR > RPM-MAP-ST-EGR-$P_{max}/(IMEP_x T_{ad})$ > H_2-EGR-IMEP-P_{max}-T_{ad} > RPM-ST-EGR-H_2-P_{max}/T_{ad} > P_{max}-IMEP-COV-HRR-T_{ad}.

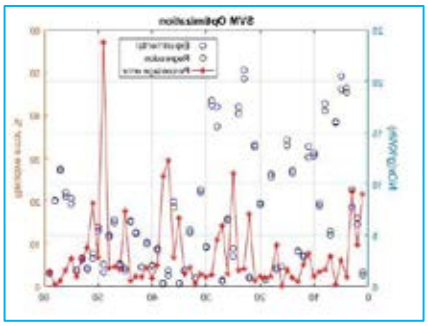


Figure 2. Best combination

NOMENCLATURE:

SVM: Support Vector machine
MRE: Maximum relative error
G: Loss width
MAPE: Mean absolute percentage error
C: Penalty factor
P: Function width

REFERENCES:

1. Huang Z, Wang J, Liu B, Zeng K, Yu J, Jiang D. Combustion characteristics of a direct-injection engine fueled with natural gas–hydrogen blends under different ignition timings. Fuel 2007;86:381–7. https://doi.org/https://doi.org/10.1016/j.fuel.2006.07.007.
2 Rao A, Wu Z, Kumar Mehra R, Duan H, Ma F. Effect of hydrogen addition on combustion, performance and emission of stoichiometric compressed natural gas fueled internal combustion engine along with exhaust gas recirculation at low, half and high load conditions. Fuel 2021;304:121358. https://doi.org/https://doi.org/10.1016/j.fuel.2021.121358.
3. Rao A, Gao H, Ma F. Study of laminar burning speed and calibration coefficients of quasi-dimensional combustion model for hydrogen enriched compressed natural gas fueled internal combustion engine along with exhaust gas recirculation. Fuel 2021;283. https://doi.org/10.1016/j.fuel.2020.119284.
4. Rao A, Mehra RK, Duan H, Ma F. Comparative study of the NOx prediction model of HCNG engine. Int J Hydrogen Energy 2017;42. https://doi.org/10.1016/j.ijhydene.2017.07.107.
5. Rao A, Mehra RK, Hao D, Fanhua M. Study of NOx Modelling of HCNG engine by applying the Gaussian function. IJSER 2018;9:644–9.
6. Mehra RK, Duan H, Luo S, Rao A, Ma F. Experimental and artificial neural network (ANN) study of hydrogen enriched compressed natural gas (HCNG) engine under various ignition timings and excess air ratios. Appl Energy 2018;228. https://doi.org/10.1016/j.apenergy.2018.06.085.
7. Huang Y, Ma F. Intelligent regression algorithm study based on performance and NOx emission experimental data of a hydrogen enriched natural gas engine. Int J Hydrogen Energy 2016;41:11308–20. https://doi.org/https://doi.org/10.1016/j.ijhydene.2016.03.204.
8. Duan H, Li Z, Wang B, Mehra RK, Luo S, Xu C, et al. Experimental study of premixed hydrogen enriched natural gas under an alternating-current (AC) electric field and application of support vector machine (SVM) on electric field assisted combustion. Fuel 2019;258:115934. https://doi.org/https://doi.org/10.1016/j.fuel.2019.115934.
9. Duan H, Huang Y, Mehra RK, Song P, Ma F. Study on influencing factors of prediction accuracy of support vector machine (SVM) model for NOx emission of a hydrogen enriched compressed natural gas engine. Fuel 2018;234:954–64. https://doi.org/https://doi.org/10.1016/j.fuel.2018.07.009.
10. Hao D, Mehra RK, Luo S, Nie Z, Ren X, Fanhua M. Experimental study of hydrogen enriched compressed natural gas (HCNG) engine and application of support vector machine (SVM) on prediction of engine performance at specific condition. Int J Hydrogen Energy 2020;45:5309–25. https://doi.org/https://doi.org/10.1016/j.ijhydene.2019.04.039.

WHEC-2022
23rd World Hydrogen Energy Conference
June 26-30, 2022 - Istanbul

#229
CO_2 METHANATION OVER BIMETALLIC NICKEL-NOBLE METAL CATALYSTS

[1]Anastasios I. Tsiotsias, [1]Nikolaos D. Charisiou, [2]Giovanni D. Ferrante, [2]Cristina Italiano, [2]Antonio Vita, [3]Victor Sebastian, [1*]Maria A. Goula*

[1] Laboratory of Alternative Fuels and Environmental Catalysis (LAFEC), Department of Chemical Engineering, University of Western Macedonia, GR-50100 Kozani, Greece

[2] CNR-ITAE, Institute for Advanced Energy Technologies "Nicola Giordano", Via S. Lucia sopra Contesse 5, 98126, Messina, Italy

[3] Chemical and Environmental Engineering Department, Instituto de Nanocienza de Aragón (INA) and Instituto de Cienza de Materiales de Aragón (ICMA), Universidad de Zaragoza-CSIC, Zaragoza, Spain

*Corresponding author e-mail: mgoula@uowm.gr; cristina.italiano@itae.cnr.it

ABSTRACT

The CO_2 methanation reaction was investigated over bimetallic Ni-NM catalysts supported on Pr-doped CeO_2, where NM represents a noble metal (NM = Ru, Pt, Rh, Pd and Ir). 10% Ni and 1% NM were loaded over a mesoporous Pr-CeO_2 support via co-impregnation and directly reduced at 400°C, without prior calcination. The prepared catalysts were characterized via XRD, N_2-physisorption and HAADF-STEM along with EDS mapping. The addition of 1% Ru and Rh was shown to improve the dispersion of the metallic Ni phase and reduce pore blockage upon impregnation. Catalytic activity evaluation revealed that the addition of 1% Ru led to a remarkable increase in the catalytic activity, especially at lower temperatures. Pt and Ir addition led to minor changes in activity, whereas Rh and Pd incorporation surprisingly reduced CO_2 conversion. The most active 1% Ru, 10% Ni/ Pr-CeO_2 catalyst was shown to be particularly stable over a 50h time-on-stream experiment at 325°C, with CO_2 conversion and CH_4 selectivity values at 80% and 99.5% respectively.

Keywords: Power-to-Gas, Synthetic natural gas, CO_2 methanation, Bimetallic catalysts, Noble metals

INTRODUCTION

Global warming induced by anthropogenic CO_2 emissions is increasingly becoming a major concern. On the other hand, the intermittency in renewable energy production and problems associated with the handling, storage and transportation of hydrogen undermine the efforts made to decarbonize the energy sector. The CO_2 methanation reaction attempts to tackle both problems by utilizing captured CO_2, as well as green hydrogen produced via water electrolysis, for the production of high energy density synthetic natural gas, in an overall carbon neutral process [1-3]. Ni-based catalysts are often favoured for the CO_2 methanation reaction due to their high activity and the low cost of Ni [1,3]. On the other hand, noble metal catalysts can offer a much higher activity at lower temperatures, as well as improved stability, but they are being held back from industrial implementation due to their prohibiting cost [3]. Thus, a lot of research has been focussed on the creation of bimetallic Ni-NM (NM=Noble Metal) catalysts with a very low noble metal content, aiming to exploit the Ni-NM synergy and achieve a high catalytic activity at low temperatures, without greatly increasing the material cost [1]. In this work, we prepared 1% NM, 10% Ni catalysts loaded over a mesoporous sol-gel prepared Pr-doped CeO_2 support with a tailored pore structure, to achieve improved metal dispersion. The active metals were introduced via co-impregnation and reduced directly in-situ without prior calcination. The prepared catalysts were characterized via XRD, N_2-physisorption and HAADF-STEM with EDS mapping, whereas their catalytic activity was evaluated for the CO_2 methanation reaction.

MATERIALS AND METHODS

The Pr-doped CeO_2 support ($Ce_{0.9}Pr_{0.1}O_{2-\delta}$) was prepared via a modified Pechini method. At first, citric acid and the corresponding metal nitrates ($Ce(NO_3)_3{\cdot}6H_2O$ and $Pr(NO_3)_3{\cdot}6H_2O$) were dissolved in ethylene glycol at 30 min intervals at 60 °C, under stirring. The molar ratio of ethylene glycol: citric acid: total metal cations was set at 15:1.5:1. The temperature was then increased under stirring to 130 °C for 2 h to promote polycondensation between citric acid and ethylene glycol. The polymer gel was then further dried at 130 °C and calcined at 400 °C for 1 h and 500 °C for 4 h. Ni and the noble metals (NM = Ru, Pt, Rh, Pd, Ir) were subsequently introduced to the supports via a single wet impregnation step (co-impregnation) using calculated amounts of $Ni(NO_3)_2{\cdot}6H_2O$ and a noble metal precursor salt ($Ru(NO)(NO_3)_x(OH)_y$, $[Pt(NH_3)_4](NO_3)_2$, $RhCl_3{\cdot}xH_2O$, $PdCl_2$, $IrCl_3{\cdot}xH_2O$) to obtain a final Ni loading of 10 wt% and final noble metal loading of 1%. The metal salts were first dissolved in 100 ml of d-H_2O, followed by the addition of the support powder and after water evaporation, the resulting slurry was dried at 90 °C overnight. The dried powders were

reduced under H_2 flow at 400 °C for 1 h and named as 1NM10Ni (NM = Ru, Pt, Rh, Pd, Ir). Following the synthesis, the catalysts were characterized via XRD, N_2 physisorption, TEM, HAADF STEM and EDS mapping.

Catalytic tests were carried out at atmospheric pressure in a continuous flow fixed-bed quartz reactor (I.D. = 0.9 cm). Evaluation of the catalytic activity as a function of reaction temperature was performed under Experimental Protocol #1. 0.24 g of the catalyst, diluted with quartz sand till 0.5 g, were initially loaded into the quartz reactor. The total gas flow rate was set at 100 ml min^{-1} (10% CO_2, 40% H_2 and 50% Ar), while the reactor temperature was varied between 200 °C and 400 °C, remaining for 30 min at each temperature step to achieve steady-state. In Experimental Protocol #2, the catalytic stability of the catalysts was evaluated during 50h time-on-stream at a constant temperature of 325 °C. The gas composition in the reactor outlet was analyzed online by gas chromatography.

RESULTS AND DISCUSSION

XRD patterns of the reduced catalysts (Fig. 1a) reveal the presence of diffraction peaks attributed to the fluorite lattice of CeO_2. The small diffraction peak at $2\theta \approx 44.5°$ is indicative of the presence of the crystalline metallic Ni phase, whereas diffraction peaks attributed to the noble metals could not be distinguished, either due to their low loading and high dispersion, or due to alloying with the Ni metal phase. The incorporation of Ru, and especially Rh, led to a broadening of the Ni^0 (111) peak (Fig. 1b), thereby leading to a reduced Ni crystallite size (17 nm and 12 nm for 1Ru10Ni and 1Rh10Ni respectively, compared to 19 nm for 10Ni), while the introduction of the other noble metals did not greatly affect the Ni dispersion. N_2 physisorption reveals a mesoporous structure for all catalysts (Fig. 1c, type IV isotherm with a hysteresis loop). 1Ru10Ni and 1Rh10Ni exhibit a higher surface area (47 m^2/g and 45 m^2/g, compared to 40 m^2/g for 10Ni), which could be attributed to reduced pore blockage via the higher active metal dispersion. Furthermore, HAADF-STEM coupled with EDS mapping for the 1Ru10Ni catalyst (Fig. 1d) shows the presence of medium-sized Ni nanoparticles, while Ru appears to be homogeneously dispersed over the catalyst.

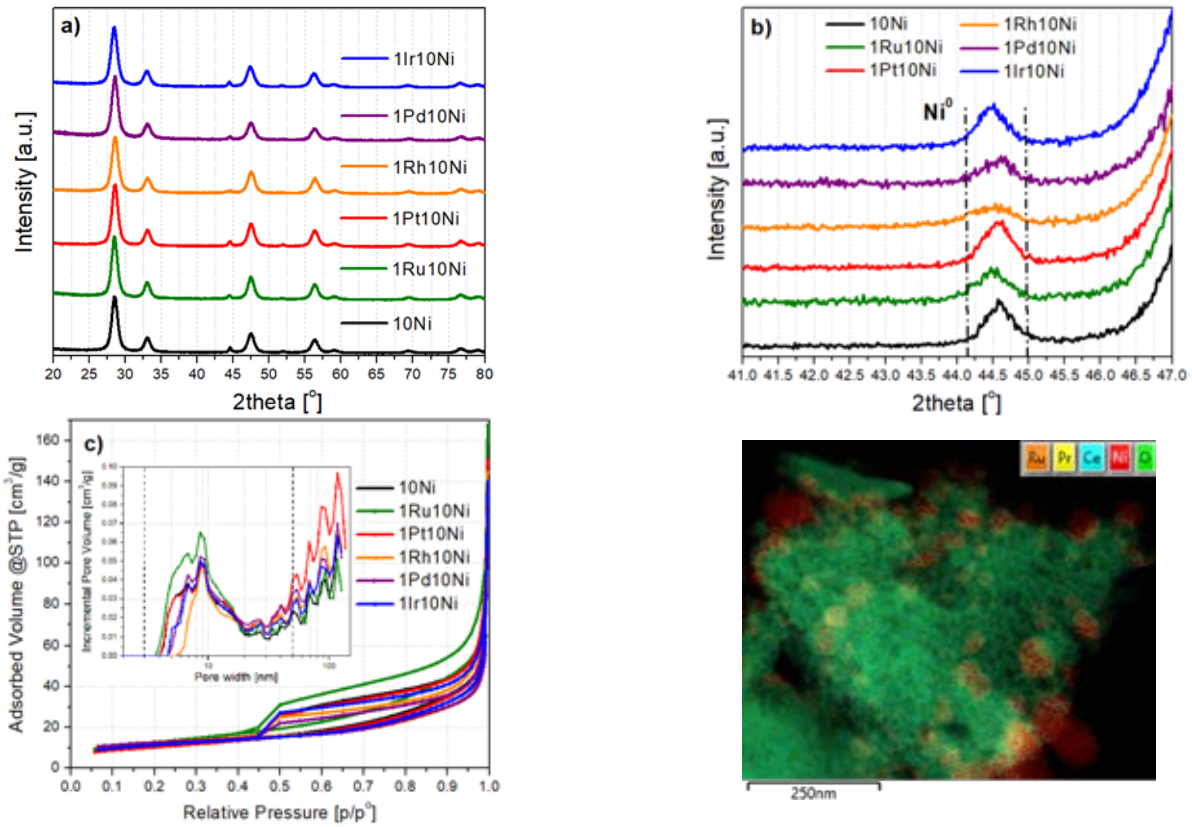


Fig. 1. (a,b) X-ray diffractograms with (b) focussing on the Ni^0 (111) reflection region. (c) N_2 physisorption isotherms and pore size distribution (inset) of the reduced catalysts. (d) HAADF-STEM and EDS elemental mapping image of the 1Ru10Ni reduced catalyst.

Fig. 2a shows the evolution of the catalytic performance as a function of reaction temperature. Among all the noble metal promoters, the addition of 1% Ru led to by far the best improvement in the catalytic activity, which was especially apparent at lower temperatures. As a result, the bimetallic 1Ru10Ni catalyst led to a drop in the

temperature for 50% conversion (T_{50}) by around 50 °C compared to the monometallic 10Ni catalyst, while also improving the low-temperature CH_4 selectivity (Fig. 2b). This can be attributed to a favourable Ni-Ru synergy, where Ru can greatly promote the reducibility, dispersion and CH_4 producing capability of the Ni phase, while also providing additional CO_2 methanation active sites [1,4]. The addition of Pt led to negligible differences in activity but favored the reverse water-gas shift reaction at low temperatures [4]. Interestingly, Ir promoted the low-temperature activity and CH_4 selectivity but hampered the catalytic activity at higher temperatures, indicating a major change in the reaction pathway. On the other hand, the introduction of Rh and Pd greatly decreased the catalytic activity but maintained a high CH_4 selectivity. In the case of Rh, this has also been reported by other works [1,4]. The 1Ru10Ni catalyst underwent a further 50h time-on-stream experiment at 325 °C (Fig. 2c), which showed a negligible drop in catalytic activity, with CO_2 conversion and CH_4 selectivity values stabilizing at around 80% and 99.5% respectively.

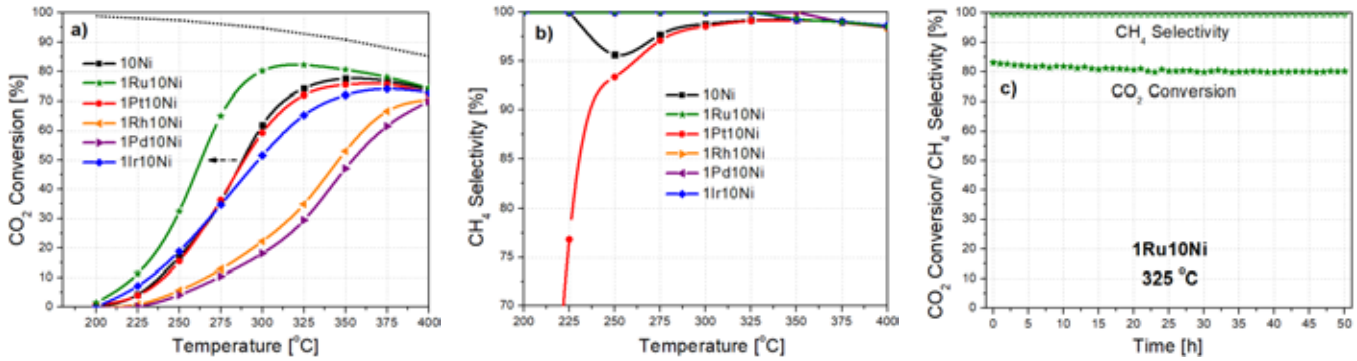


Fig. 2. (a) CO_2 Conversion and (b) CH_4 selectivity of the catalysts as a function of reaction temperature; Reaction conditions: Experimental Protocol #1. (c) CO_2 Conversion and CH_4 selectivity for the 1Ru10Ni catalyst at 325 °C as a function of reaction time; Reaction conditions: Experimental Protocol #2.

CONCLUSIONS

This study reported on the synthesis of bimetallic 1% NM, 10% Ni catalysts (NM = Ru, Pt, Rh, Pd and Ir) supported on Pr-doped CeO_2 for the CO_2 methanation reaction. The introduction of Ru and Rh could promote the dispersion of Ni and reduce pore blockage. Catalytic activity evaluation evidenced that Ru was the sole noble metal able to dramatically enhance the catalytic performance, by providing a 50 °C decrease in the T_{50} due to a favorable Ni-Ru synergy. The 1% Ru, 10% Ni/ Pr-CeO_2 catalyst could provide a stable catalytic performance with around 80% CH_4 yield at just 325 °C.

ACKNOWLEDGEMENT

We gratefully acknowledge support of this work by the project “Development of new innovative low carbon energy technologies to improve excellence in the Region of Western Macedonia” (MIS 5047197) which is implemented under the Action “Reinforcement of the Research and Innovation Infrastructure”, funded by the Operational Programme "Competitiveness, Entrepreneurship and Innovation" (NSRF 2014-2020) and co-financed by Greece and the European Union (European Regional Development Fund).

REFERENCES

1. Tsiotsias AI, Charisiou ND, Yentekakis IV and Goula MA. 2021. Bimetallic Ni-based catalysts for CO_2 methanation: A review. Nanomaterials 11:28.
2. Siakavelas GI, Charisiou ND, AlKhoori S, AlKoori AA, Sebastian V, Hinder SJ, Baker MA, Yentekakis IV, Polychronopoulou K and Goula MA. 2021. Highly selective and stable nickel catalysts supported on ceria promoted with Sm_2O_3, Pr_2O_3 and MgO for the CO_2 methanation reaction. Applied Catalysis B: Environmental 282:119562.
3. Keen FW and Tahir M. 2021. Recent trends in developments of active metals and heterogenous materials for catalytic CO_2 hydrogenation to renewable methane: A review. Journal of Environmental Chemical Engineering 9:105460.
4. Renda S, Ricca A and Palma V. 2021. Study of the effect of noble metal promotion in Ni-based catalyst for the Sabatier reaction. International Journal of Hydrogen Energy 46:12117-12127.

WHEC-2022
23rd World Hydrogen Energy Conference
June 26-30, 2022 - Istanbul

#249

HYDROGEN AS ENERGY STORAGE FOR RESOLVING ELECTRICITY GRID ISSUES IN INDONESIA

[1*]*Arif Darmawan,* [2]*Muhammad Huda,* [1] *Eniya Listiani Dewi,* [1]*Abdul Hamid Budiman,* [1]*Abdul Hadi,* [1]*Kurniawan,* [3]*Muhammad Aziz*
[1]National Research and Innovation Agency, Tangerang Selatan, Indonesia.
[2] The Center of Certification Indonesian State Electric Company (PT PLN) Jakarta Selatan, Indonesia.
[3] Institute of Industrial Science, The University of Tokyo, Japan.

*Corresponding author e-mail: arif.darmawan@brin.go.id

ABSTRACT

According to many studies, economic growth is closely correlated with energy consumption. Specifically, electricity is required in the regional development to support all residential, government, or private agencies and industrial sectors. Unfortunately, because of unexpected low demand due to a complex economic system, the increase in power generation is predicted to result in an oversupply. Power-to-Gas is a vital part of a future renewable energy system to convert water into hydrogen. Surplus electricity can be utilized by adopting this technology via the electrolysis of water to produce hydrogen; therefore, it can be stored or converted into other energy carriers. The pre-feasibility of investing in hydrogen production is investigated in the Java-Bali grid of the Indonesian power system, considering volatilities and future uncertainties in the region as background. Some scenarios are evaluated for different parameters such as electricity demand projection, electrolyzer cost and efficiency, including plant capacity factor. With a very large electrolyzer, operating with an efficiency of about 70% for about 8000 hours per year, the annual hydrogen production potential would be 600-900 Mt of hydrogen, assuming 50-80 kWh could produce 1 Kg of H_2. A proper approach to the cost reduction in raw material procurement, power generation, and related H_2 facilities should be taken and established. Therefore, the overall H_2 production cost can be minimized. Further investigation will be conducted for storage scenarios, including distribution strategies.

Keywords: Hydrogen, Power-to-Gas, Surplus electricity, Electrolyzer

INTRODUCTION

Rapid economic growth necessitates energy use, particularly electricity, for regional developments. Energy is required in all sectors, including residences, government agencies, offices, and industry, implying that the availability of electricity is critical for a better life and a rising economy. Unfortunately, because the available electricity continues to expand in significant quantities despite low demand, the increase in power generation is expected to result in an oversupply. Due to the mismatch between power supply and demand, a period of excess energy (or excess generation) arises as this increase in generation growth increases [1]. Keeping the power system dynamic is essential to export, absorb, or reduce surplus electricity as soon as possible.

Suppose it cannot be addressed with the correct approach. In that case, increasing the amount of excess energy from installed capacity undermines the reason for obtaining high penetration of renewable energy sources. In this context, it is necessary to widen the scope of decarbonization goals to include the absorption of excess energy from the grid for use in transportation and gas systems. PtG and PtL (Power-to-Gas and Liquids) are frequently mentioned as vital parts of a future renewable energy system [2]. Most PtG systems use electrolysis to convert water into hydrogen. Several excellent reviews have been conducted on general electrolysis technologies, including developments in alkaline electrolysis [3], PEM electrolysis [4], and solid oxide electrolysis [5]. The H_2 obtained can be used directly as a fuel or stored or converted into other carriers such as syngas, methane, or LPG. The generated gas can further be distributed, stored, and used without political or geographical constraints [6]. It can also act as power storage by converting the gas back into electricity.

The main objective of this study is to identify the operating profile of the electrolyzer required if an oversupply of electricity in the Java-Bali system is utilized and to estimate the contribution that this energy can make to the generation of hydrogen as storage or secondary form of energy. Indonesia has a very high penetration of coal power plants due to the 35 GW government program, some of which ignore the electricity demand. This excess electricity could be utilized via water electrolysis to satisfy the future carbon society.

MATERIALS AND METHODS

Java-Bali Grid Current System and Scenario

Indonesia's system planning is mainly island-based, such as Java-Bali, Sumatera, Kalimantan, Sulawesi, Nusa Tenggara, Maluku, Papua, and other minor systems, as it is the largest archipelago country. Economic growth, which is expected to be 6–7% per year, is one of the key aspects of demand forecasting; therefore, the load projection is relatively high. In 2020, the state electricity company (PLN) had a total installed capacity of 63.3 GW. For the next 10 years, the total new plan will be 40,6 GW, with renewable energy accounting for 20.9 GW or 51.6 %. The coal power plant will be retired at a capacity of 1.1 GW. With an installed capacity of roughly 41 GW in 2020, the Java-Bali system dominates the number of power plants (almost 65% of the national capacity). In this region, the additional generating capacity will be 13 GW in the next 10 years, dominated by coal power plants. The addition of new power plants with very large capacity combined with low demand growth may result in an oversupply in the near future.

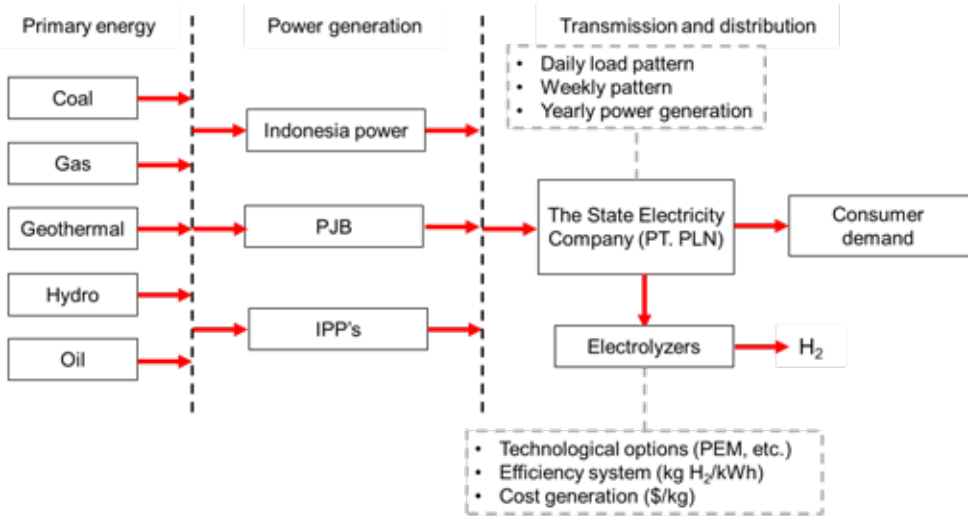


Fig. 1. Current Java-Bali power system

The electricity market model in Indonesia is a single buyer multi-seller in Indonesia, where PLN is the only buyer requiring a take-or-pay (TOP) contract to guarantee the IPP developer's return of investment (ROI) (see Fig. 1). However, in the current situation, the TOP contract is quite burdensome for PLN. The growth in electricity consumption has decreased, but PLN electricity from IPPs should not be reduced. Consequently, PLN is forced to reduce its electricity purchases from its power plants to reduce costs and avoid penalties (deemed dispatch) due to the TOP contract [7]

Modeling approach

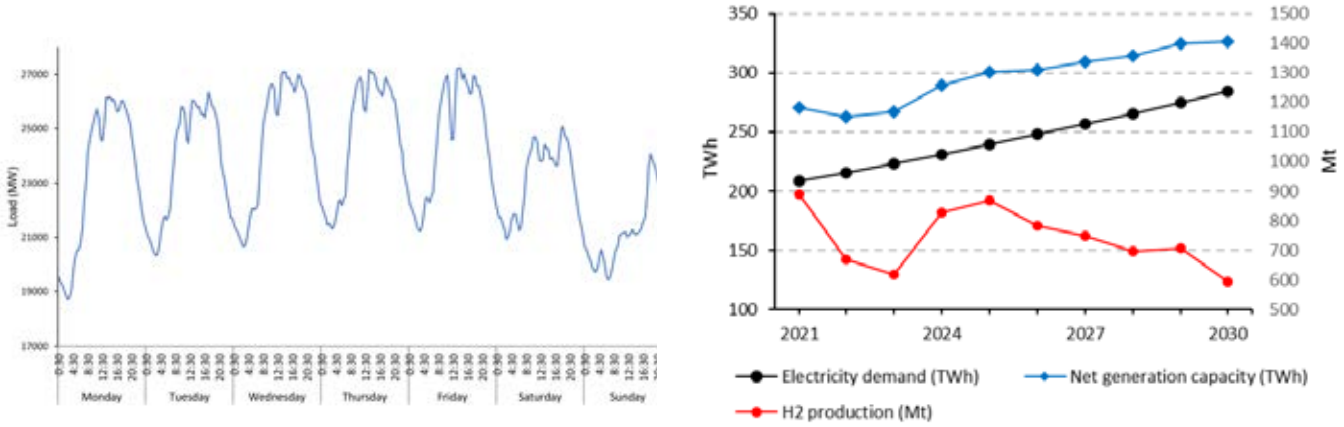
In order to estimate the effects of using P2G alternatives and capacities to absorb surplus electricity, the modeling and calculation are developed based on existing/future power plants, government plan until 2030, daily/weekly/annual power generation profiles, and some parameters of electrolyzer technology. Also, several assumptions are made, which are presented in Table 1.

Table 1. Modeling assumptions [8]

	Description
Scenario planning	2021-2030
Type of electrolyzer	PEM and Alkaline
Efficiency (system)	50-80 kWh/KgH_2
Lifetime	7-10 years
Capital costs estimate for large system	500-1000 USD/kW_{el} for Alkaline 700-1400 USD/kW_{el} for PEM

PRELIMINARY RESULTS AND DISCUSSION

The typical hourly electricity load profile for the Java-Bali power system is shown in figure 2a. The load data were recorded in December 2021 for one week to compare weekdays and weekends (Saturday-Sunday). The electricity consumption at night is higher than the day time. Due to residential activities, the peak load typically occurred at 26,000-27,000 MW from 18:00 to 19:00. Considering a very large electrolyzer, operating with an efficiency of about 70% for 8000 hours per year, the annual hydrogen production potential would be 600-900 Mt of hydrogen, as shown in Fig. 2(b).



(a) (b)

Fig. 2. (a) Weekly load profile in December 2021, (b) Hydrogen production potential

Hydrogen can be stored or converted into other energy carriers such as ammonia, methanol, methane, and liquid hydrocarbons once produced at scale and a competitive cost. Further investigation will be conducted for storage scenarios, including distribution strategies. A proper approach to the cost reduction in raw material procurement, power generation, and related H_2 facilities should be taken and established. Therefore, the overall H_2 production cost can be minimized.

CONCLUSIONS

White hydrogen production uses water as a key feedstock and surplus electricity as an energy source to separate hydrogen and oxygen from water in an electrolyzer. The annual hydrogen production potential for the Java-Bali system would be 600-900 Mt of hydrogen, assuming 50-80 kWh could produce 1 Kg of H_2. Further investigation will be conducted for storage scenarios, including utilization and distribution strategies.

REFERENCES

1. Toklu E, Coskun Avci A, Kaygusuz K, Gur M. A research on hydrogen production from industrial waste heat by thermal water splitting. Int J Hydrogen Energy 2016;41:10071–9. doi:10.1016/j.ijhydene.2015.12.131.
2. Buttler A, Spliethoff H. Current status of water electrolysis for energy storage, grid balancing and sector coupling via power-to-gas and power-to-liquids: A review. Renew Sustain Energy Rev 2018;82:2440–54. doi:10.1016/J.RSER.2017.09.003.
3. Zeng K, Zhang D. Recent progress in alkaline water electrolysis for hydrogen production and applications. Prog Energy Combust Sci 2010;36:307–26. doi:10.1016/j.pecs.2009.11.002.
4. Carmo M, Fritz DL, Mergel J, Stolten D. A comprehensive review on PEM water electrolysis. Int J Hydrogen Energy 2013;38:4901–34. doi:10.1016/j.ijhydene.2013.01.151.
5. Hansen JB. Solid oxide electrolysis - a key enabling technology for sustainable energy scenarios. Faraday Discuss 2015;182:9–48. doi:10.1039/C5FD90071A.
6. Sterner M, Specht M. Power-to-gas and power-to-x—the history and results of developing a new storage concept. Energies 2021;14:1–18. doi:10.3390/en14206594.
7. Huda M, Tokimatsu K, Aziz M. Techno Economic Analysis of Vehicle to Grid (V2G) Integration as Distributed Energy Resources in Indonesia Power System. Energies 2020, Vol 13, Page 1162 2020;13:1162. doi:10.3390/EN13051162.
8. IRENA. Green Hydrogen Cost Reduction. 2020.

WHEC-2022
23rd World Hydrogen Energy Conference
June 26-30, 2022 - Istanbul

#343

AN MINLP-BASED OPTIMAL DESIGN AND SCHEDULING OF A POWER TO GAS SYSTEM INTEGRATED MICROGRID: A CASE STUDY FROM TURKEY

[1,2] *Handan Akülker,* [2,3,4*] *Erdal Aydın*
[1]Ondokuz Mayıs University, Department of Chemical Engineering, Kurupelit,55139, Samsun,
[2] Boğaziçi University, Department of Chemical Engineering, Bebek, 34342, İstanbul, Turkey
[3] Koç University, Department of Chemical and Biological Engineering, Sarıyer, 34450, İstanbul, Turkey
[4] Koç University, Tüpraş Energy Center, Sarıyer, 34450, İstanbul, Turkey

*Corresponding author e-mail: eaydin@ku.edu.tr

ABSTRACT

A microgrid is a power network section including distributed generators, storage systems, and loads. A "*Power to Gas*" (PtG) system is a rising technology that produces synthetic methane (or similar gas) by using electricity and carbon dioxide extracted from the flue gases. Recently, Turkey has been preparing to make strict sanctions on energy producers to decrease the greenhouse gas emissions due to the Paris Agreement. Additionally, it is struggling with the outage of imported natural gas. Accordingly, PtG systems may handle both the problems of natural gas shortages and carbon dioxide emissions. This study aims to propose methods to optimally design and schedule a PtG system integrated microgrid by Mixed-Integer Nonlinear Programming (MINLP). PtG system is assumed to be installed, whereas other equipment, consisting of renewable and non-renewable sourced generators and a battery, is nominated as selection candidates. Two different integrated gasification combined cycle generators and one combined heat and power generator are selected to be installed. The model does not prefer to choose renewable sourced generators, such as wind turbines and solar panels, for the investigated location due to fixed and maintenance costs, weather conditions, and demand levels.

Keywords: Power to Gas, Microgrid, Carbon dioxide emission, MINLP, Optimal design and scheduling

INTRODUCTION

Today, Turkey is dependent on imported gas reserves. Although it has just found natural gas reserves in the Black Sea, the usage will have been possible in the upcoming seven to ten years, at the same time not securing the whole demand of the country [1]. Turkey's energy sector uses a high amount of natural gas. Hence, electricity outage linked to the natural gas shortage is a significant threat to Turkey's economy. In addition, the Paris Agreement dictates Turkey to reduce its carbon dioxide emission as soon as possible.

A PtG system is a technology that includes an electrolyzer, carbon capture and storage (CCS) unit, and a methanation reactor. Excess electricity produced by the microgrid is used to convert water into hydrogen. Obtained hydrogen and carbon dioxide are consumed to produce methane, and later synthetic natural gas. Therefore, PtG systems may be a nice solution for both the problems of natural gas shortages and the carbon dioxide emissions in Turkey.

Optimization of integrated microgrids with economically and environmentally promising technologies, such as Power to Gas (PtG) systems and Green Hydrogen, has frequently been studied in recent years [2,3]. Most studies include Mixed Integer Linear Programming (MILP) formulations to avoid computational complexity, but they underestimate the nonlinear nature of model equations [4,5]. On the other hand, MINLP-based studies mostly focus on optimal sizing of installed equipment in the grid or optimal scheduling of the grid without addressing optimal equipment selection and design [6,7]. In addition, some of those studies include only renewable sourced generators coupled with PtG systems [8]. There are also some studies that comprise wider equipment variety in addition to renewable strategies while not considering the optimal design level [6,7]. Yet, studies of equipment selection from candidates, rich in diversity, for optimal design and scheduling by MINLP are scarce in the literature, especially for coupled green hydrogen and synthetic methanation.

This study offers both optimal design and scheduling at the same level, in contrast to the aforementioned studies, of a PtG system integrated by deterministic MINLP based on carbon dioxide emission sanctions. Moreover, a candidate equipment pool is formed by considering the newest technologies and higher diversity compared to similar studies. Furthermore, the actual data belonging to Samandağ, Antakya, is used to obtain the results. Thus, this study can be claimed to provide more reliable decision-making structures compared to many other studies using MILPs including more detailed analysis.

MATERIALS AND METHODS

Description of the Optimization Problem

The deterministic MINLP is used to meet the electricity demand of Samandağ, Antakya. Each day is set to have the same data of hourly electricity demand, wind speed, solar irradiance, and air temperature through a year. Each day is divided into 24-hour intervals and each interval is assumed to be in the quasi-steady-state condition.

The candidate equipment pool consists of two wind turbine farms, two solar panel arrays, two bio-gasifier generators, one biomass generator, two coal-fired conventional generators, two natural gas-fired combined heat and power (CHP) generators, two coal-fired integrated gasification combined cycle generators (IGCC), one synthetic natural gas production system, and one battery.

Mathematical Formulation of the Optimization Model

The objective function of the problem is to minimize the total annualized cost (*TAC*) of the microgrid:

$$\min \quad TAC = (CRF)\, f^{Capital} + f^{O\&M} + f^{EC} - f^{SNG} \tag{1}$$

$f^{Capital}$ is the installation cost of the microgrid, and $f^{O\&M}$ presents the total operational and maintenance costs through a year. f^{EC} is the emission cost for carbon dioxide, and f^{SNG} is the income from the sale of synthetic natural gas (SNG) to the national grid. *K* is the life span of candidate equipment of the microgrid, and $|\mathcal{K}|$ is twenty for all of them. *CRF* is the capital recovery factor.

MINLP problem is solved by SCIP (Solving Constraint Integer Programs) in GAMS (General Algebraic Modeling System). SCIP is a global solver for nonconvex MINLP problems. OptCA (Absolute optimality criterion of solver) and OptCR (Relative optimality criterion of solver) are set to 0.001.

RESULTS AND DISCUSSION

Excess electricity production and the purchase of electricity from the national grid are not allowed in the optimization model. PtG system's working duration is limited to 8 hours a day. Spinning reserve is included in the model to compensate for possible shortages in each interval.

The optimization model selects two different integrated gasification combined cycle generators, whose rated powers are 50 MW, and one combined heat and power, whose rated power is 105 MW. IGCC generators consume coal but generate much lower carbon dioxide than conventional coal-fired generators. CHP units can produce only electricity within their tetragonal feasible regions. They emit more carbon dioxide than IGCC generators while releasing much lower carbon dioxide than conventional coal-fired generators. Even though bio-gasifiers and bio-generators emit much less carbon dioxide than IGCC and CHP generators, the MILNP model does not prefer to bio-gasifiers and bio-generators, because installation costs of bio-gasifiers and bio-generator are higher than them. In addition, they consume much more amount of wood fuel and biomass even though biomass and wood fuels are cheaper than coal and natural gas. Moreover, the model does not choose wind turbines and solar panels. The reason may be their intermittent production due to weather conditions. The PtG system uses 10 MW of electricity, which is produced inside the grid for all operating intervals.

The optimal TAC value is found as 2.06 billion ₺. The capital cost is 4.21 billion ₺, the maintenance cost is 163 million ₺, and the operational cost is 799 million ₺. The emission cost is calculated as 444 million ₺. The revenue coming from the sale of SNG is 14 million ₺. The PtG system consumes 1.414 tons of CO_2 in each interval. If the PtG system were not used, the emission cost of this amount of CO_2 would be 9.9 million ₺. In other words, installation of the PtG system to the microgrid decreases the total emission cost of the microgrid by using carbon dioxide. In addition, it reduces the total annualized cost by producing synthetic natural gas, at the same time satisfying the emission limits of the microgrid with respect to the Paris Agreement. Finally, the optimal energy production schedule is shown in Figure 1.

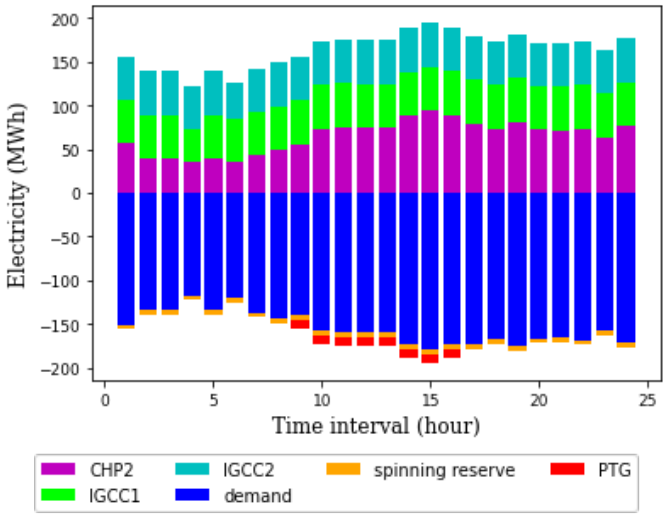


Figure 1. Energy balance of the microgrid over a day.

CONCLUSIONS

The aim of this study is to design a PtG system integrated microgrid and to schedule the energy production over a year. Candidate equipment pool includes renewable and non-renewable sourced generators. Results show that it is vital to design a microgrid, both from an economic and environmental perspective, to overcome greenhouse emissions and shortages of energy sources. PtG systems are state-of-the-art and preferable technologies producing a financially valuable energy source, SNG, while reducing the cost coming from environmental sanctions. Thus, integration of PtG systems into the microgrids by selecting the optimal interconnected equipment is critical for the energy producers.

Results also show that IGCC and CHP generators are selected by the decision-making model. They all produce a lower amount of carbon dioxide than conventional generators. Wind turbines and solar panels are not preferred due to their intermittent and insufficient production profile, although they generate the lowest amount of carbon dioxide. Therefore, installation of them is simply not economically feasible under current conditions. The PtG system provides a considerable amount of revenue, 14 million ₺, decreasing the emission cost by 9.9 million ₺ annually. When a multi-period design for the microgrid is considered and natural gas decreases year by year worldwide, PtG system integrated microgrids will be much more profitable in the upcoming future.

REFERENCES

1. https://www.reuters.com/article/us-turkey-energy-idUSKBN25G2A5. Accessed on February 11, 2022.
2. Mehrjerdi, H., Saboori, H., and Jadid, S. 2022. Power-to-gas utilization in optimal sizing of hybrid power, water, and hydrogen microgrids with energy and gas storage. Journal of Energy Storage, 45, 103745.
3. Salehi, J., Namvar, A., Gazijahani, F. S., Shafie-khah, M., and Catalão, J. P. 2022. Effect of power-to-gas technology in energy hub optimal operation and gas network congestion reduction. Energy, 240, 122835.
4. Yang, M., Li, J., Sun, J., Xu, J., and Li, J. 2022. Robust Optimal Scheduling of EHG-IES Based on Uncertainty of Wind Power and PV Output. International Transactions on Electrical Energy Systems, 2022.
5. Ju, L., Yin, Z., Zhou, Q., Li, Q., Wang, P., Tian, W.,and Tan, Z. 2022. Nearly-zero carbon optimal operation model and benefit allocation strategy for a novel virtual power plant using carbon capture, power-to-gas, and waste incineration power in rural areas. Applied Energy, 310, 118618.
6. Jalilian, F., Mirzaei, M. A., Zare, K., Mohammadi-Ivatloo, B., Marzband, M., and Anvari-Moghaddam, A. 2022. Multi-energy microgrids: An optimal despatch model for water-energy nexus. Sustainable Cities and Society, 77, 103573.
7. Ghanbari, A., Karimi, H., and Jadid, S. 2020. Optimal planning and operation of multi-carrier networked microgrids considering multi-energy hubs in distribution networks. Energy, 204, 117936.
8. Nastasi, B., Mazzoni, S., Groppi, D., Romagnoli, A., and Garcia, D. A. 2021. Solar power-to-gas application to an island energy system. Renewable Energy, 164, 1005-1016.

WHEC-2022
23rd World Hydrogen Energy Conference
June 26-30, 2022 - Istanbul

#359

HEAT SOURCE FREE CO_2 METHANATION OVER HYDROGEN STORAGE ALLOY

[1,2,3*] *Keito Sawahara,* [3,4] *Ryota Gemma,* [1,2] *Hajime Kawanami*
[1]University of Tsukuba, Degree Programs in Pure and Applied Sciences, 1-1-1 Tennodai, Tsukuba Ibaraki, Japan
[2]National Institute of Advanced Industrial Science and Technology (AIST), 1-1-1 Higashi, Tsukuba, Ibaraki, Japan
[3]Tokai University, Graduate School of Engineering, 4-1-1 Kita-kaname, Hiratsuka, Kanagawa, Japan
[4]Tokai University, Department of Applied Chemistry, 4-1-1 Kita-kaname, Hiratsuka, Kanagawa, Japan

*Corresponding author e-mail: k-saw@star.tokai-iu.jp

ABSTRACT

Recently, CO_2 methanation has gained attention for mitigating global warming. In our previous study, it has been demonstrated that the methanation of CO_2 takes place by mechanochemical reaction under H_2+CO_2 atmospheric conditions if a small amount of hydrogen storage alloys like $LaNi_5$ are present. It has also been found that the $LaNi_5$ partially decomposed into La-oxides, hydroxides, carbonate, and metallic Ni formed metal/oxide nanostructure complex during the reaction. However, the impact of this decomposed structure on the CO_2 methanation itself has not been revealed yet. In this study, we attempted *in-situ* measurements of gas composition during the mechanochemical CO_2 methanation using ball mill connected with quadrupole mass spectrometer (QMS).

Keywords: Methanation, CO_2, $LaNi_5$, Hydrogen storage alloys

INTRODUCTION

Recently, CO_2 concentration in the atmosphere has been increasing, which may enhance on-going global warming issue[1]. Thus, reduction of CO_2 emission and effective utilization of CO_2 have been considered inevitable measures for global sustainability. Methanation of CO_2 with green hydrogen is one of such approaches to utilize CO_2 with reducing atmospheric CO_2. This reaction (Sabatier reaction) is exothermic, but, requires high temperatures varied at 300 ~ 400 ^oC in the presence of catalysts like Ru, Rh, Ni etc. [2]. Indeed, Castellani et al. reported CO_2 methanation using hydrogen from renewable energy sources, e.g., solar energy[3]. They reported CO_2 conversion rate higher than 95 % at 2.0 MPa at reaction temperatures of about 400 ^oC using Ni supported catalysts, while the spent energy/stored energy marked around 0.4 in the process. Therefore, in view of energy saving and thermodynamic point of view, low temperature processes with high methane yield are preferred to further gain the energy profit. Previously, we demonstrated mechanochemical CO_2 methanation over La-Ni based hydrogen storage alloys using ball-milling method and reported CH_4 generation at room temperature without heat source [4]. It has also been found that the $LaNi_5$ alloy partially decomposes into Ni, La-oxides, hydroxides, and carbonates. However, its microstructural impact on the CO_2 methanation reaction is still unclear. Namely, following issues can be posed here: if such decomposed structure could be the origin of CO_2 methanation during the mechanochemical treatment and also, if hydrogen once absorbed in the hydrogen storage alloy ($LaNi_5$) could have activated the observed methanation reaction. In order to elucidate above mentioned aspects, we conducted *in-situ* measurements of gas composition during the mechanochemical CO_2 methanation by using ball-milling apparatus connected with high pressure Sieverts' type apparatus and mass spectrometer.

In the said process, H_2 dissociation reaction is necessary in the first place at the surface of the reaction site, i.e. the surface of alloy. If atomic H supply is sufficient due to hydrogen absorption reaction in the alloy powder, it is anticipated that the conversion of CO_2 to CH_4 would be enhanced. We, therefore, have chosen several Ni-based hydrogen storage alloys with different maximum hydrogen content to investigate the impact of atomic H supply on the mechanochemical CO_2 methanation. In addition, we studied possible influences of La compounds formed by the phase decomposition.

MATERIALS AND METHODS

A schematic picture of the experimental setup is shown in Figure 1. A vibratory ball-milling apparatus (Nissin-Giken, NEV-MA-8) is connected to homemade type Sieverts' apparatus and quadrupole mass spectrometer (QMS), allowing for control of H_2 gas and CO_2 gas introduction separately and *in-situ* gas composition analysis. $LaNi_5$ or Mg_2Ni powder together with ten balls (SUS304, diameter: 10 mm) were filled into the milling vial (SUS304, φ 54 mm x 43 mm). The vial interior was evacuated below 8.0×10^{-5} Pa by a turbo molecular pump, followed by the introduction of H2 and CO_2 from Sieverts' type apparatus. The ratio of H_2 and CO_2 was 4: 1 and initial total pressure was set at 2.0×10^{-2} Pa. The ball-milling was carried out at 11.7 Hz of vibration frequency, and the vial temperature was controlled at 20 °C by running water during the milling. The gas composition was continuously monitored by QMS.

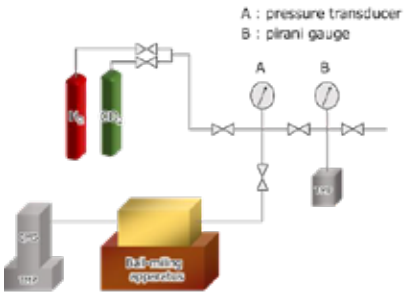


Figure 1 Experimental setup

RESULTS AND DISCUSSION

Figure 2 shows the time-course gas composition during $LaNi_5$ milling under continuous CO_2+H_2 flow. At the beginning, the ion current m/z = 2 (H_2^+) decreases rapidly and increases gradually. The rapid decrease is considered as a result of H-uptake into $LaNi_5$ alloy powder. The gradual increase indicates H desorption of once absorbed H, but this does not immediately mean that the amount of gaseous H_2 is increased compared to the initial state. Only after 4800s, the ion current of H_2^+ exceeds the initial level. This means that the desorbed H contributes to form H_2, with exceeding the initial amount of H_2 in the system. Notably, after 4800 s, continuous increase of CH_4 (ion current m/z = 15 (CH_3^+), fragment ion of CH_4) with gradual decrease of CO_2 (ion current m/z = 44 (CO_2^+),) was observed. This hints that the H supplied from $LaNi_5$ contributes to the methane generation. Results of XRD measurements of the powder sample milled for less than 4800 s showed H disordered structure. In case of the powder sample milled longer than 4800 s showed the decomposed structure of Ni and La oxides. This indicates that the desorption of H due to the phase decomposition might be responsible for the CH_4 generation. In the early stages of methanation, it was previously shown that the atomic hydrogen from sub-surface accelerates the methanation reaction, as reported by Kato et.al. [5,6].

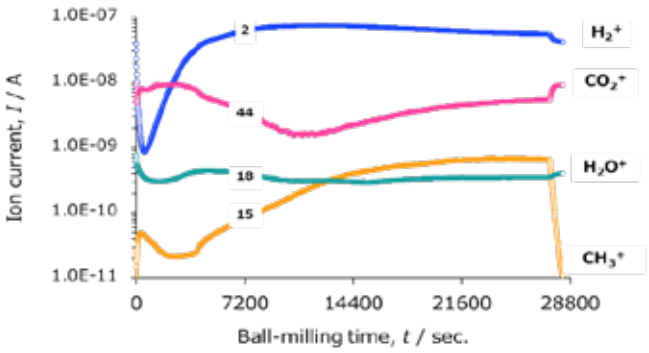


Figure 2. Result of gas composition analysis of $LaNi_5$ milling under CO_2 +H_2 atmosphere

After milling for 14400 s, we confirmed $LaNi_5$ phase completely disappeared and was changed to La-oxide, hydroxide, carbonate, and metallic Ni phases by XRD analysis. Also, it has been suggested that the formed La-compounds is effective for mechanochemical methanation [4]. We observed the methane generation continues even after 14400 s, as long as the ball-milling is carried out. It is suggested also here that a composite structure of Ni and La-compound formed as a result of the phase decomposition could be responsible as a catalyst for the mechanochemical methanation.

CONCLUSIONS

In this study, we reported *in-situ* monitoring results of CO_2 methanation over Ni based hydrogen storage alloy, $LaNi_5$, by mechanochemical methods with the mixture of CO_2 and H_2. The *In-situ* gas composition measurements revealed a rapid decrease of hydrogen until 4800 s by the absorption into $LaNi_5$. After then, once absorbed hydrogen was gradually desorbed, and methane was generated in this period. This indicates that the mechanochemical CO_2 methanation was caused by atomic hydrogen supply from sub-surface. We suggest that the observed methane generation occurred in two stages. The first stage was dominated by atomic hydrogen desorption from sub-surface, and the second stage of methanation involves Ni/Lanthanum compound formed by phase decomposition, which catalytically drives the methane generation.

REFERENCES

1. Manabe S, Stouffer RJ. Journal of Geophysical Research 1980;85:5529.
2. Tada S, Nagase H, Fujiwara N, Kikuchi R. Energy & Fuels 2021;35:5241–51.
3. Castellani B, Gambelli A, Morini E, Nastasi B, Presciutti A, Filipponi M, et al. Energies 2017;10:855.
4. Yatagai K, Shishido Y, Gemma R, Boll T, Uchida HH, Oguri K. International Journal of Hydrogen Energy 2020;45:5264–75.
5. Kato S, Matam SK, Kerger P, Bernard L, Battaglia C, Vogel D, et al. Angewandte Chemie - International Edition 2016;55:6028–32.
6. Kato S, Borgschulte A, Ferri D, Bielmann M, Crivello JC, Wiedenmann D, et al. Physical Chemistry Chemical Physics 2012;14:5518–26.

WHEC-2022
23rd World Hydrogen Energy Conference
June 26-30, 2022 - Istanbul

#402

INTEGRATED PLANNING TOOL FOR COST AND 3D STRUCTURAL PLANNING FOR OFFSHORE WIND FARMS FOR THE GENERATION OF H_2

Martin Hayduk [1], Romy Sommer [1], Oliver Kühn [2], Florian Beuß [2], Wilko Flügge [3], Johannes Gulden [1]*
[1] Affiliation: University of Applied Sciences Stralsund, Institute of Renewable Energy Systems (IRES),
Zur Schwedenschanze 15, 18435 Stralsund, Germany
[2] Affiliation: Fraunhofer Institute for Large Structures in Production Technology (IGP),
Albert Einstein Str. 30, 18059 Rostock, Germany
[3] Affiliation: University of Rostock, Chair of Manufacturing Technology,
Albert Einstein Str. 30, 18059 Rostock, Germany

* Corresponding author email: johannes.gulden@hochschule-stralsund.de

ABSTRACT

The planning of new offshore wind farms (OWP) is characterized by increasing complexity. In addition to technical factors like water depth, ground conditions, wind development, and others, there is also an increasing range of design options in the wind farm concept. This concerns in particular the integration of hydrogen into the value chain for offshore wind power. For the wind farm planner, the decision, whether a decentralized electrolysis is directly implemented at the wind farm or a centralized electrolysis is built at the harbor edge, is crucial. Again, the influencing factors are manifold. The cable length for shore connection, the potential storage and offtake of hydrogen close to the harbor edge, the hydrogen transport via pipelines or ships have to be considered.

To address this complexity, a planning tool is being developed that enables an evaluation of offshore wind farm options. The core of the tool is a holistic cost model for the installation of offshore wind farms for hydrogen production. Based on this, an interactive 3D planning tool is developed, which enables the flexible structural planning of new wind farms based on GIS data to be displayed in a VR environment. The interactive adjustment of the wind farm changes the cost drivers of the cost model. In addition, the land connection and associated transport routes are selected in the 3D model and transferred to the cost model. The wind farm planner directly sees the impact of changes on the total costs. Thus, the system helps in the design and structural planning of new offshore wind farms as well as the conversion planning of existing offshore wind farms for hydrogen generation. Here we present the first results of this ongoing project.

Keywords: Planning tool, Offshore wind farm, Hydrogen

INTRODUCTION

The use of hydrogen (H2) as an energy carrier is increasingly becoming the focus of public attention. The main focus has to be on the so-called green hydrogen, which is produced from wind energy [1]. The combination of offshore wind farms and integrated H2 generation has so far only been considered theoretically but is discussed as a promising future topic [2]. One reason for the low realization rate is the complexity of a holistic planning of offshore wind farms with an associated H2 generation. Up to now, no tools exist to support this highly complex process to advance towards the realization of environmentally friendly H2 generation on an industrial scale [3]. Therefore, this project aims to develop a planning tool that enables flexible cost and 3D structural planning of new OWPs with H2 generation from offshore electricity based on geographic information system (GIS) data. To simplify the complex and interdisciplinary planning process and the associated coordination, the implementation will be done in a VR-environment. Cost models will be integrated into the planning tool to calculate the prime costs for offshore hydrogen production depending on the location and the distance to the mainland as well as the associated logistics costs. The results of the project should thus drive the implementation of corresponding projects. The project is currently in the implementation phase and is expected to be completed by the end of this year. In this abstract, only an excerpt of the work done so far is presented.

METHODOLOGY

In the first step, the technical data of current electrolysis technologies were collected with a literature review as well as expert surveys with partners from the industry. The data was evaluated by means of a utility value analysis. This is followed by data collection of hydrogen storage technologies and a subsequent evaluation.

RESULTS AND DISCUSSION

The various data of the electrolysis technologies were collected, and the technical parameters were compared with each other. To evaluate the market maturity of the various water electrolysis processes for offshore use, a utility value analysis of existing technologies was carried out. Based on a point system from 1 (bad) to 10 (very good). A weighting of important parameters for the question of offshore suitability was made. The total score represents the comparative value of the technology. Proton Exchange Membrane (PEM) electrolysis is best suited for offshore use with a total score of 914, followed by by AEL with only 767 points.

Table 1: Utility value analysis of electrolysis technologies

	PEM	AEL	AEM	HTL	utility [%]
Power-to-weight ratio	10	5	10	6	4,76
Footprint	10	8	8	4	9,52
Efficiency LHV	7	8	7	10	9,52
Working pressure	9	8	8	9	4,76
Load dynamics	10	5	3	1	14,29
Lifetime (Stack)	8	10	3	4	14,29
Suitability (Offshore)	10	6	7	1	14,29
Market readiness in the MW range	9	10	7	6	14,29
Maintenance & Operating Costs	10	7	8	5	9,52
Cost per MW	8	9	8	7	4,76
Sum	**914**	**767**	**629**	**457**	**2.767**

The reason for the margin needs to be discussed. PEM electrolysis is already available on the market in the MW range and, if scaled accordingly, can even have similar or even lower acquisition costs than the other comparable technologies [4]. Although high-temperature electrolysis (HTL) offers the advantage of being able to use water in the form of hot steam for the manufacturing process and thus achieve significantly better efficiencies, this technology can hardly be operated dynamically so far [5]. This eliminates the possibility of adjusting performance to the volatile energy flows of a wind farm. Furthermore, the technology is still in the development phase and currently has a technology readiness level (TRL) between 6-7 [3,6] and has so far only been tested in pilot plants. Figure 1 compares the four electrolysis processes available on the market. The percentage represents the results of the sum (2767 points) in the utility value analysis for the applications in OWP. PEM water electrolysis has proven to be the reference technology for offshore use. This technology was able to clearly assert itself in important comparative values such as: power-to-weight ratio, footprint, load dynamics, service life, TRL and OPEX [7].

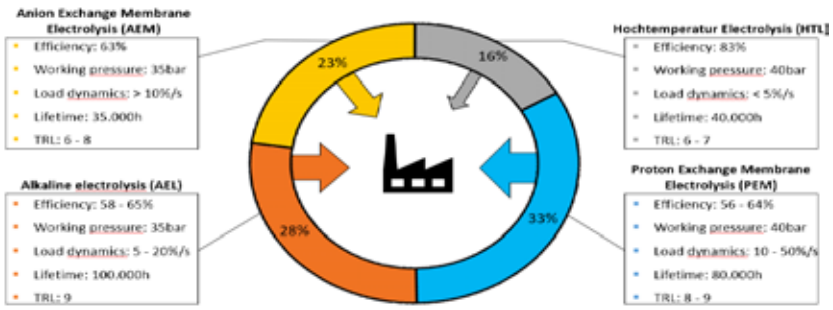


Figure 1. Comparison of ELY technologies

In the second phase of the project a comparative evaluation of different hydrogen storage technologies, their advantages and disadvantages were carried out showing the state of the art and suitability for different logistics systems in offshore applications. The focus was here on Tank & Bunker Systems such as (LH2 / CGH2 / MH / LOHC / CH4 / CH3OH / NH3), see Table 2.

Table 2: Utility value analysis of H2-storage technologies

	CGH2 (350bar)	LH2	MH	CH4 (liquid)	CH3OH	HCOOH	LOHC	NH3 (liquid)	Utility [%]
Energy per litre	1	4	9	10	7	3	3	7	9,52
Efficiency (provisioning)	9	5	8	8	5	3	6	6	9,52
Lifetime (storage)	9	8	9	8	10	10	10	9	4,76
Cycles (carrier medium)	10	10	5	10	10	10	2	10	4,76
Storage (carrier medium)	7	3	10	9	10	9	10	8	4,76
Dynamics (storage)	9	8	7	8	10	10	10	8	4,76
Dynamics (generation)	9	9	9	6	6	4	7	5	4,76
Market readiness (in the MW range)	10	7	7	10	8	3	2	10	14,29
Suitability (Offshore)	10	6	4	6	6	5	4	9	14,29
Environmental compatibility (carrier medium)	10	10	8	6	4	3	5	1	9,52
Cost (Storage)	9	6	4	7	10	10	7	8	4,76
Transport (in the MW range)	10	4	2	10	10	7	10	7	14,29
Sum	**871**	**633**	**633**	**829**	**762**	**552**	**581**	**733**	**5.595**

Here a summary of the second phase of the project will be presented. Surprisingly it turns out that gaseous hydrogen clearly prevails as the reference technology. A particularly high energy transfer potential was found for transmission via pipelines. Furthermore, in the utility analysis, compressed hydrogen had decisive advantages over liquid / chemical storage technologies in the following parameters: efficiency (supply), dynamics (storage & generation), market maturity (in the MW range), suitability (offshore), environmental compatibility (carrier medium), storage costs, and transportation (in the MW range). The total score for each storage technology is presented in figure 2, showing the significant margin of CGH2 to the alternatives.

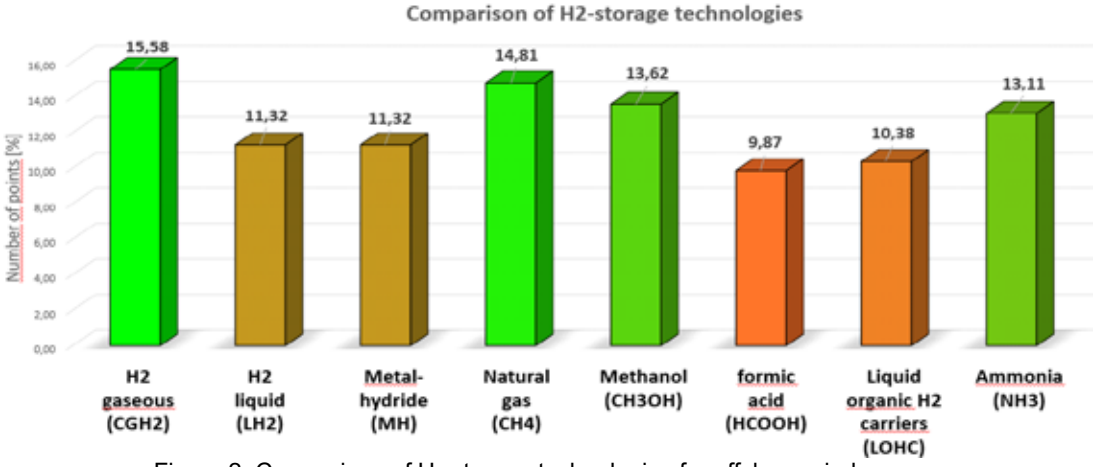


Figure 2: Comparison of H_2 storage technologies for offshore wind energy

Energy transfer in the form of gaseous hydrogen can enable a supply efficiency >90% depending on the transfer distance, which is currently not possible to the same extent with any other hydrogen carrier. As a storage option in this magnitude only salt caverns offer an economical option. For example, a cavern with a diameter of 60m, a height of 300m and a usable pressure range of 120bar can store about 100MNm³ of hydrogen. This corresponds to an energy quantity of 300GWh in relation to the LHV of H2. At the same time, loading and unloading can be performed at over 10t per hour, which corresponds to an output of more than 333MW per cavern. This enables direct operation with volatile renewable energy sources such as wind power [8]. The technology is already available and could make an important contribution to hydrogen storage. For Europe a total storage capacity in salt caverns is estimated to be of 84,8PWh (H2, LHV) [9]. Since hydrogen is a non-toxic gas, the impact on the environment and nature is significantly lower compared to the other storage technologies. In the event of a leak there is no poisoning of aquatic organisms (MeOH) or increased emissions of greenhouse gases (CH4). The storage costs per $MWh_{_H2}$ in a salt cavern are significantly below a standard hydrogen pressure storage up to 350bar [10]. The energy transport from the offshore wind farm can be easily implemented in a pipeline using gaseous hydrogen. Thus, a transmission capacity of more than $10GW_{_H2}$ can be realized in only one pipeline with a diameter of one meter.

CONCLUSIONS

PEM water electrolysis has emerged as the reference technology for offshore use. This technology was able to clearly prevail in important comparison values. Though the other technologies are not far off, and a future development might change the result. Especially AEM and HTL are still at a low TRL and will see further developments in the future.

Gaseous hydrogen has established itself as a reference technology for hydrogen storage. The utility value analysis of the various hydrogen storage technologies showed significant advantages in critical parameters for the connection to offshore wind farms. Storage on a TWh-scale could be implemented economically and safely by means of cavern storage.

In the next phase of the project, an economic evaluation of the location of an electrolysis plant will be carried out. The influencing parameters such as the distance of the OWP to the mainland and the power to be transmitted are compared with the transmission technologies available on the market and compared in a break-even analysis. The aim of this section is to find the most economical location for the hydrogen production plant. Subsequently, all data from the previous work packages will be incorporated into a cost tool and thus the production costs for the hydrogen supply will be determined. In the final step the model will be merged with the VR planning tool.

REFERENCES

1. Stratmann K: *Green Hydrogen: Politicians Discover the Alternative to Electricity*.
URL https://www.handelsblatt.com/politik/deutschland/energiewende-gruener-was-serstoff-politik-entdeckt-die-alternative-zum-strom/24856400.html?ticket=ST-9567294-SfkPANbu6JktDt90gpTp-ap5.
Update date: 2019-07-31 - Review date: 07. January 2022
2. Diermann R: *Offshore factories*: *The hydrogen of the future will be produced at sea*.
URL https://www.spiegel.de/wissenschaft/technik/offshore-wasser-stoff-wellen-wind-und-wasserstoff-a-24524291-ce70-4793-a322-5c1b8b1ae4f2.
Update date: 2020-06-10 - Review date: 07. January 2022
3. Hebling C., Ragwitz M., Smolinka T., et al. 2019. *A Hydrogen Roadmap for Germany*. Fraunhofer ISI, Fraunhofer ISE (Eds.), Karlsruhe & Freiburg. Available online at:
https://www.ise.fraunhofer.de/content/dam/ise/de/documents/publications/studies/2019-10_Fraunhofer_Wasserstoff-Roadmap_fuer_Deutschland.pdf, Retrieved January 07 2022
4. Smolinka T., et.al. 2018. Studie IndWEDe *Industrialisierung der Wasserelektrolyse in Deutschland*: Chancen und Herausforderungen für nachhaltigen Wasserstoff für Verkehr, Strom und Wärme. NOW GmbH P.43
5. Dincer I and Acar C. 2018. *Comprehensive Energy Systems* Hydrogen Production. Elsevier P.15
6. Lösch O., et.al. 2019. *Bewertung der Direktreduktion von Eisenerz mittels Elektrolyse-Wasserstoff* Technische Universität Darmstadt. Institut für Produktionsmanagement. Technologie und Werkzeugmaschinen (PTW) P. 21
7. Holst M., Aschbrenner S., Smolinka T., et al. 2021. *Cost forecast for low- temperature electrolysis* – technology driven bottom- up prognosis for PEM and alkaline water electrolysis. Fraunhofer ISE. P 08-33
8. Stolzenburg K., Hamelmann R., Wietschel M., Lehmann J., et al. 2014. *Integration von Wind-Wasserstoff-Systemen in das Energiesystem*. Abschlussbericht P. 115-155
9. D. G. Caglayan, et al. 2019 *Technical Potential of Salt Caverns for Hydrogen Storage in Europe* Institute of Energy and Climate Research, Techno-economic Systems Analysis (IEK-3), Forschungszentrum Juelich GmbH
10. Töpler J and Lehmann J. 2017. *Hydrogen and Fuel Cell* Technologies and Market Perspectives. Springer P. 28-29

WHEC-2022
23rd World Hydrogen Energy Conference
June 26-30, 2022 - Istanbul

#406
METHANATION OF CO_2 OVER $LaNi_5$/V LAYERED FILM

[1*]*Shuichi Kaneta,* [1]*Haruya Baba,* [2]*Sota Yamada,* [1,2]*Ryota Gemma*
[1] Graduate School of Engineering, Tokai University, 4-1-1 Kitakaname, Hiratsuka, Kanagawa, 259-1292, Japan
[2] Department of Materials Science, Tokai University, 4-1-1 Kitakaname, Hiratsuka, Kanagawa, 259-1292, Japan

* Corresponding author email: sh.knt99.udon.180315@gmail.com

ABSTRACT

In this study, the effect of underlying V film on the CO_2 methanation on $LaNi_5$ surface was investigated using a quadrupole mass spectrometer, using a stacked film of LaNi-based thin film as a catalyst layer on top of a V layer as a hydrogen supply layer. It was confirmed that CO_2 methanation over thin film samples can be experimentally observed. Also, the underlying V layer was found to absorb hydrogen, thereby possibly prevented severe oxidation of La and concomitant phase decomposition of the $LaNi_5$ upper layer in to La oxide and Ni.

Keywords: CO_2 methanation, Hydrogen, Hydrogen storage alloys

INTRODUCTION

In recent years, global warming has been progressing due to rapid increase in the concentration of carbon dioxide (CO_2) in the atmosphere triggered by massive consumption of fossil fuels. To mitigate this impact, the conversion of CO_2 into methane by the Sabatier reaction (Eq.1) has been proposed. For example, the generation of methane from renewable hydrogen and CO_2 has been considered [1].

$$CO_2 + 4H_2 \rightarrow CH_4 + 2H_2O \quad (1)$$

Even though this Sabatier reaction is exothermic ($\Delta H_{298\,K}$ = -165 kJ/mol), high temperatures of 300~400°C or higher and catalysts like Ni are necessary due to its high activation barrier. Thus, reducing the reaction temperature is desirable if coking on the catalyst surface can be avoided. In search of effective catalysts, various combinations of metal catalyst/support have been investigated [2].

According to our previous research, with using planetary ball-mill, it was found that mechanochemical process of La-Ni based alloys under the presence of CO_2 and H_2 generates CH_4 without any external heating [3]. But post-experimental sample analysis confirmed that the alloy decomposed into Ni and La compounds including carbonates. Even in this phase-separated state, Ni was dispersed on nanometer scale, suggesting that Ni acts as a catalyst and is involved in the Sabatier reaction. In addition, recent results of our research [4] and other reports [5,6] suggest possible impacts of atomic hydrogen supply on the methanation. It is suggested that hydrogen once stored in a hydrogen storage alloy, is discharged due to phase separation, atomic hydrogen is supplied to the reaction surface, which may directly/indirectly enhance the methanation [5].

In this study, the possibility of improving the methane generation rate by supplying atomic hydrogen was investigated by applying thin film technique. A catalytic layer was formed as a thin film on top of the hydrogen supply layer. Specifically, the effect of underlying V film on the methane generation reaction on $LaNi_x$ surface was investigated using a quadrupole mass spectrometer. The findings obtained in this study may be applied to the design of more efficient methanation catalysts.

EXPERIMENTAL

Film preparation

Thin film samples were prepared by a D.C. magnetron sputtering process. A glass substrate (18 mm × 18 mm × 0.2 mm) was used. As target materials, a disk-shaped La-Ni mosaic target and a disk-shaped V target were prepared. The sputtering conditions are shown in Table 1. The films with a total thickness of about 1.4 μm (LaNi: 400 nm, V: 1000 nm) were prepared in this study.

Sample analysis

Phase identification of the prepared films was carried out by X-ray Diffraction: XRD (MiniFlex600, Rigaku). Cross-sectional observation and elemental analysis of the samples were conducted by scanning electron microscopy (SEM) and energy dispersive X-ray spectroscopy (EDX) (JSM-7100F, JEOL), respectively.

Table1: Deposition conditions

Base pressure (Pa)		Sputtering power (W)		Ar gas flow rate (ccm)
8.0×10^{-5}		50		30
Ar gas pressure (Pa)		Time (min)		Substrate holder temperature (K)
$LaNi_5$	V	$LaNi_5$	V	623
3.6	1.2	10	50	

CO_2 methanation

Eleven film samples were placed in an homemade methanation equipment. The reaction chamber was evacuated below 5.33×10^{-5} Pa by rotary pump and turbo molecular pump. The reaction tube of the methanation equipment was heated up to 773 K by external heating using an electric furnace. Surface activation was carried out for 1 hour by flowing 10 ccm of H_2. After that, CO_2 was fed into the reaction tube at a flow rate of 2.5 ccm. Gas analysis inside the tube was carried out using quadrupole mass spectrometer (QMS: Prisma 200, Pfeiffer). A blank test without the film samples was also conducted under the same conditions.

RESULTS AND DISCUSSION

Results of EDX analysis showed that the composition of prepared films was 17.9 at% La and 82.1 at% Ni, which closely agreed with $LaNi_5$. Figure 1 shows the secondary electron image of the cross section of $LaNi_5$/V film. V and $LaNi_5$ were found to be stacked on the glass substrate. The thickness of the film was found to be about 1000 nm for the V layer and about 400 nm for the $LaNi_5$ layer. Figure 2 shows change in ion current of CH_2^+ ($LaNi_5$/V film vs. blank test). Figure 3 shows change in ion current of CH_3^+ ($LaNi_5$/V film vs. blank test). In this study, we focused on the behavior of CH_2^+ and CH_3^+, which are fragment ions of methane, because CH_4^+ overlaps with the peak of O^+. After initiating CO_2 gas flow, the ion current of methane fragment ions (CH_2^+, CH_3^+) increased. When the film samples were present, the ion current of CH_2^+ after CO_2 gas flow increased by 11 % compared to the ion current of blank test. Similarly, the ion current of CH_3^+ after CO_2 gas flow increased by 42 % compared to that of blank test.

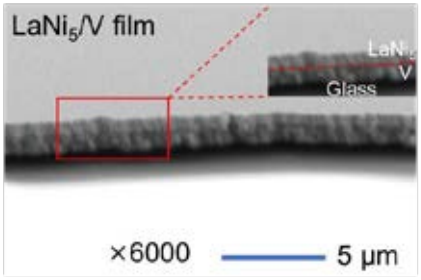


Figure1: Secondary electron image of the cross section of $LaNi_5$/V film.

Figure 4 shows the results of XRD measurements. Bragg peaks of $LaNi_5$ and V were found in as-received state, verifying the EDX results. The peak around 80° was close to the Ni reference pattern, suggesting the presence of Ni precipitates. After the methanation, peaks of La oxide, which has been reported to be formed after phase decomposition during the methanation [4], were not observed. This suggests that the $LaNi_5$ layer did not decompose in this case. Interestingly, the peaks of V shifted to the lower angle side after the methanation experiment, suggesting the V lattice being expanded. This could be due to hydrogen absorption in the V layer. Atomic hydrogen supplied from the V layer might have kept the $LaNi_5$ surface free from severe oxidation, as confirmed in our XRD results.

CONCLUSIONS

We found that the CO_2 methanation reaction over thin film samples can be monitored by using QMS. In the methanation of CO_2 using $LaNi_5$/V layered film, an increase in the ion current of methane was observed when compared to the results of blank tests. In addition, it was suggested that hydrogen was kept stored in the V layer even after the methanation, which might have avoided previously reported phase decomposition of $LaNi_5$ phase into Ni and La oxides.

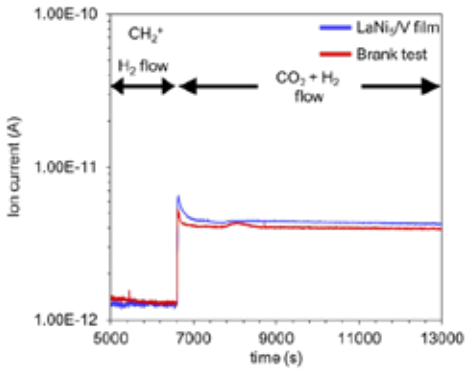


Figure 2: ion current of CH_2^+ ($LaNi_5$/V film vs. blank test)

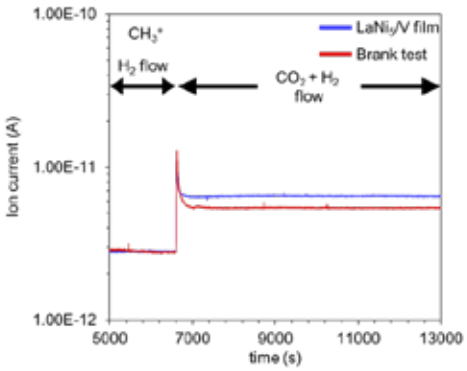


Figure 3: ion current of CH_3^+ ($LaNi_5$/V film vs. blank test)

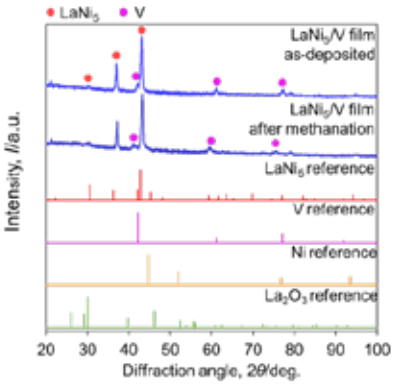


Fig.4: Results of XRD

ACKNOWLEDGEMENT

Technical support of Ms. Awano at Tokai University imaging Center for Advanced Research (TICAR) and technical support by staffs of the Technology Joint Management Office, Research Promotion Division, Tokai University are gratefully acknowledged.

REFERENCES

1. B. Castellani, A. M. Gambelliet, E. Morini, B. Nastasial, A. Presciutti, M. Filipponi, A. Nicolini, F. Rossi, Energies 10 (2017) 855.
2. S. Danaci, L. Protasova, J. Lefevere, L. Bedel, R. Guilet, P. Marty, Catalysis Today 273 (2016) 234-243.
3. K. Yatagai et al., J. Adv. Sci. 31 (2019) 31101.
4. K. Sawahara, K. Yatagai, T. Boll, A. Pundt, R. Gemma, *submitted*.
5. S. Kato, S. K. Matam, P. K. Kerger, L. Bernard, C. Battaglia, D. Vogel, M. Rohwerder, A. Züttel, Angew. Chem. Int. Ed. 55 (2016) 1-6.
6. R. Tsukuda, T. Kojima, D. Okuyama, S. Kameoka, C. Nishimura, A. Tsai, Int. J. Hydrog. Energy 45 (2020) 19226-19236.

WHEC-2022
23rd World Hydrogen Energy Conference
June 26-30, 2022 - Istanbul

#407

CO_2 METHANATION OVER SURFACE MODIFIED $LaNi_5$ FILMS WITH Pd

[1*]Haruya Baba, [1]Shuichi Kaneta, [2]Sota Yamada, [2]Ayataka Motoshige, [1,2]Ryota Gemma
[1] Graduate School of Engineering, Tokai University, Kitakaname 4-1-1, Hiratsuka City, Kanagawa, 259-1292, Japan
[2] Department of Material Science, Tokai University, Kitakaname 4-1-1, Hiratsuka City, Kanagawa, 259-1292, Japan

*Corresponding author e-mail: bbharukb@icloud.com

ABSTRACT

Recent increase in the concentration of carbon dioxide (CO_2) in the atmosphere has led to global warming. For mitigating the increase in atmospheric CO_2, CO_2 methanation using hydrogen (H_2) has been proposed. In this study, we attempted to convert CO_2 into methane using $LaNi_5$ alloy thin films prepared by DC magnetron sputtering. The surface was decollated with palladium (Pd) islands, which is known as a hydrogen dissociation catalyst. Monitoring of gas species in the reaction chamber by quadrupole mass spectroscopy revealed successful methane generation over the film sample. The findings from such thin film samples with artificially formed interfaces as attempted in this study can be translated to the design of catalysts in powder form, in search of more efficient methanation catalysts.

Keywords: Thin Film, $LaNi_5$, Methanation, Palladium

INTRODUCTION

Recently, the increase in the atmospheric concentration of carbon dioxide (CO_2) has caused serious global warming, and climate changes. Therefore, reducing the CO_2 emission is necessary, and hydrogen energy system has been attracting great attention. Hydrogen-based energy storage systems have proven to be one of the of the most promising energy storage techniques. [1] However, research on hydrogen technologies has been facing many challenges, including production, storage, and transportation infrastructure.[2] To mitigate the impact of CO_2 emission on climate change as soon as possible, it has been proposed to convert atmospheric CO_2 into methane (CH_4) using hydrogen (H_2), under the concept of carbon recycling. Methane is the main component of city gas and can be used with only simple modifications to existing infrastructure facilities. The Sabatier reaction is known as a reaction to produce methane, as shown in Eq. (1).

$$CO_2 + 4H_2 = CH_4 + 2H_2O \quad \Delta H_{298\,K} = -165\ \mathrm{kJ/mol} \tag{1}$$

The reaction generally proceeds at 300-400°C under the presence of catalysts like Ni or other precious metals supported by oxides. In our previous study [3,4], we confirmed the formation of methane by ball-milling without heating, using $LaNi_5$ powder as a catalyst precursor. It was also confirmed after the experiment that the phase decomposition of the powder into Ni and La compounds occurs at nanometer scale as confirmed by atom probe tomography (APT) analysis [5]. Our recent on-going investigation suggested that this phase-decomposed structure might also contribute to methane generation, strongly indicating a need for nano-structural investigation of the hetero interfaces in these powder samples. Meanwhile, thin film techniques enable fabrication of artificial interfaces and flat film samples are more advantageous than powder samples for the observation of such microstructures by surface analysis. In this study, we employed thin film deposition technique to investigate CO_2 methanation reaction over LaNi-thin films. In addition, we attempted to investigate the impact of surface modification of LaNi-film by Pd islands on the methane generation since Pd surface is known to dissociate H_2 easily [6]. The findings obtained from the thin film samples with artificially formed interfaces in this study might be applicable to the design of catalysts that are generally used in powder form.

MATERIALS AND METHODS

Film preparation

Film samples were prepared by DC magnetron sputtering system. Films were deposited on glass substrates. The substrates were first cleaned by ultrasonication in acetone and in ethanol for 5 minutes, respectively. For LaNi-based thin films, mosaic targets were prepared aiming for obtaining $LaNi_5$ films. The film thickness was about 400 nm. Pd was deposited in the form of islands through a mesh mask (#40) placed over the $LaNi_5$ films. Table 1 shows the deposition conditions. Films obtained were evaluated by XRD (Miniflex 600, Rigaku) and AFM (SPM-9700, SHIMADZU).

Table 1. Film forming conditions

Sample	$LaNi_5$	Pd
Base pressure (Pa)	7.51×10^{-5}	3.22×10^{-5}
Argon (Ar) gas flow rate (ccm)	30	
Ar gas pressure (ccm)	3.6	4.5
Substrate holder temperature (℃)	350	29
Power (W)	50	10
Sputtering time (min)	10	0.5~1

Methanation experiment

The prepared film samples were introduced into the self-made methanation system for thin film samples [7] as shown in the schematic diagram in Figure 1. The base pressure of the reaction chamber was 1.39×10^{-5}. Prior to the methanation experiment, the reaction tube was heated up to 500°C in an electric furnace attached to the outside of the tube, and H_2 was introduced up to 10 ccm with a flow meter to reduce the sample surface for 1 hour. Subsequently, the temperature was lowered to 400°C and 2.5 ccm of CO_2 was introduced with the flow ratio of H_2 : CO_2 = 4:1 to initiate the methanation. The gas composition in the reaction chamber was analyzed with a mass spectrometer (QMS: Prisma™, PFEIFFER VACCUM) to verify the methane generation. The amount of methane generated was confirmed by monitoring changes in the ion current values of CH_3^+ and CH_2^+ (fragment ions of CH_4). In order to investigate the impact of sample holder on methane generation, gas composition analysis was also conducted with only the sample holder in place (Blank test).

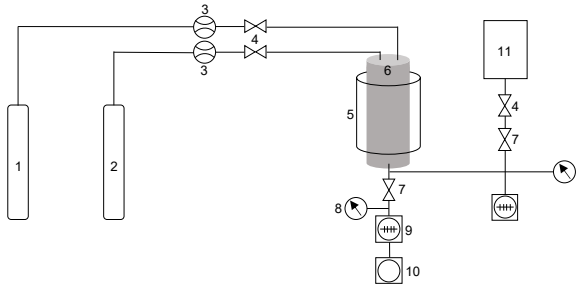


Figure.1 Schematic diagram of CO_2 methanation system for thin film samples
1: H_2 gas bottle 2: CO_2 gas bottle 3: Flow meter 4: Variable leak valve 5: Electric furnace 6: Reaction tube
7: Gate valve 8: Vacuum gauge 9: Turbo molecular pump 10: Oil rotary pump 11: Quadrupole mass spectrometer

RESULTS AND DISCUSSION

Figs. 2(a) and 2(b) show surface topography of Pd/$LaNi_5$ stacked films obtained by AFM. The Pd deposition time of (a) is 30 seconds, (b) is 60 seconds. It can be seen that Pd is distributed as islands on the area where the height is partially increasing. When the deposition time was 30 s, the average surface roughness (Ra) was 5.5 nm, whereas the average surface roughness marks 10.7 nm at 60 s. The histogram of the height distribution for 60 s shows that the maximum value of the scale is about twice as large as for 30 s. Likewise, the median value of the distribution is also about twice as large at 60 s compared to 30 s, suggesting that the desired island-like growth of Pd could be achieved on the surface.

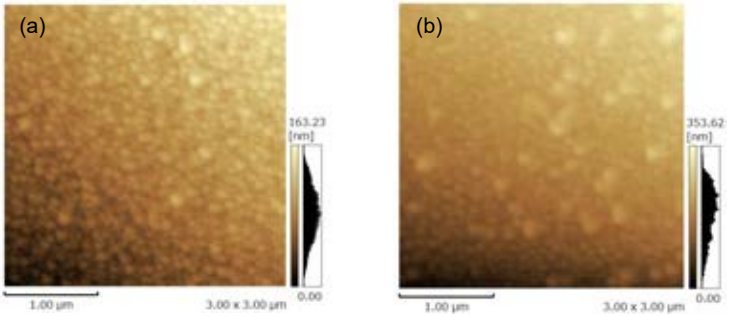
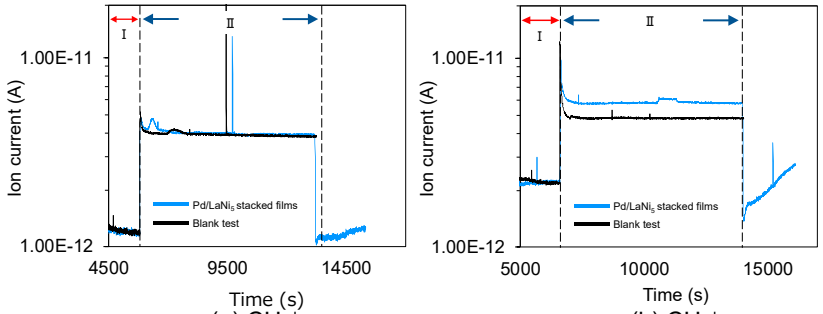


Figure.2 Sample surface scanning image in AFM

Figure 3 shows the results of CO_2 methanation experiments using Pd/$LaNi_5$ films (CH_3^+, CH_2^+). Region I depicts the reduction process using hydrogen and Region II means the period where CO_2 was introduced. The deposition time of Pd in this case was 60 s. The results are compared with the blank test. Compared to the blank test results, the Pd/$LaNi_5$ stacked film sample showed detectable increase in the ion current value of CH_3^+. The increase in the ion current value of CH_2^+ was negligible. It was also confirmed that the ion current value of CH_3^+ slowly increased after the CO_2 inflow was stopped. This is considered to be due to the gradual methanation process as the CO_2 adsorbed on the sample surface was released.



(a) CH_2^+ (b) CH_3^+

Figure.3 Gas composition analysis results (Pd/$LaNi_5$ stacked films vs. Blank test)

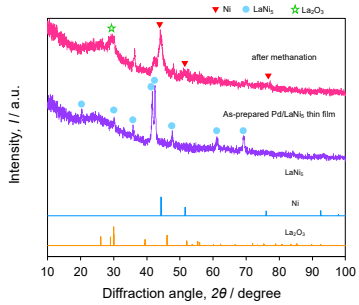


Figure.4 XRD measurement results

Figure 4 shows the results of XRD measurements. The results show that the underlying LaNi-based film has a structure similar to $LaNi_5$. Pd peaks were not clearly detected due to peak overlap and also probably because the thickness of Pd was too small. In the sample after the methanation experiment, Ni and La oxide were detected, suggesting previously reported phase separation [3,4] during the CO_2 methanation.

CONCLUSIONS

In this study, we have investigated CO_2 methanation behavior over Pd/$LaNi_5$ films using a thin film-oriented experimental setup. The use of a mesh mask allowed AFM to confirm the island-like deposition of Pd on $LaNi_5$. Methane generation the prepared thin films was successfully detected by mass spectroscopy. We confirmed that the phase decomposition of the $LaNi_5$ film occurs upon the methanation, which is a similar behavior to our previous findings on powder samples. This suggests that the methanation experiment using thin film samples can be a useful alternative to explore candidates of effective methanation catalysts in powder form.

ACKNOWLEDGEMENT

Technical support of Ms. Awano at Tokai university Imaging Center for Advanced Research (TICAR) and technical support by staffs of the Technology Joint Management Office, Research Promotion Division, Tokai University are gratefully acknowledged.

REFERENCES

1. Grigorios L. Kyriakopoulos et al., Electrical energy storage systems in electricity generation: Energy policies innovative technologies, and regulatory regimes, Renewable and Sustainable Energy Reviews, 56 (2016) 1044-1067.
2. Beatrice Castellani et al., Experimental Investigation on CO2 Methanation Process for Solar Energy Storage Compared to CO2-Based Methanol Synthesis, Energies, 10 (2017) 855.
3. Kohei Yatagai et al., Methanation of CO_2 by using $LaNi_5$ alloy with ball-milling method, Journal of Advanced Science, 31 (2019) 31101.
4. Keito Sawahara et al., In-situ monitoring of CO_2 methanation: pressure change upon ball-milling of $LaNi_5$ under CO_2 and H_2, Journal of Advanced Science, 33 (2021) 33107.
5. Kohei Yatagai et al., Mechanochemical CO_2 methanation over LaNi-based alloys, International Journal of Hydrogen Energy, 45 (2020) 5264-5275.
6. Koichi Sato, Materia (in Japanese), 50(1) (2011) 11-18.
7. Shuntaro Nakahiro, Observation of CH_4 formation from CO_2 and H_2 and microstructural changes in La-Ni alloy thin films, Tokai University, Diploma Thesis (2020).

WHEC-2022
23rd World Hydrogen Energy Conference
June 26-30, 2022 - Istanbul

#417

PRELIMINARY DESIGN AND FLOW SHEETING OF A SABATIER BASED POWER-TO-GAS SYSTEM WITH INTEGRAL HEAT RECOVERY AND DOWNSTREAM SYNGAS CLEANING

R.Capata[a], R.Melli[b], E.Sciubba[c,d]
a: roberto.capata@uniroma1.it; b: xpertsystems@mpessrl.it; c: enrico.sciubba@unicusano.it

ABSTRACT
The present global energy scenario -and the consequences of the invasion of Ukraine- forces researchers, designers and policymakers to face the technical and economic challenges of an unavoidable and urgent mitigation of global Greenhouse gas (GHG) emissions. Such emissions from anthropogenic sources have been continuously growing since the beginning of the industrial revolution. The perturbing potential of these GHG emissions on the natural atmospheric concentration cycle might trigger, or at least hasten, an amplification of the global climate change.
Besides continuous efforts to improve the efficiency of combustion processes and the recourse to "CO_2 neutral" secondary fuels, the only feasible path -at least in the so-called "transition phase" towards a less unsustainable energy scenario- is the implementation of CO_2 capture and storage solutions. Since Thermodynamics teaches us that in the energy conversion arena "there is no free lunch", technical feasibility must be combined with economical positive returns, and thus the energy community must address the problem of the high CO_2 sequestration costs.
Sabatier based power-to-gas systems are potential answers for this issue, and this paper describes the modelling, process design and simulation of a CO_2 methanation plant based on the Sabatier reaction. To cure one of the problems of this technology, namely its low overall conversion efficiency, an exergy-based optimization of the thermal recovery within the system boundary was introduced. The results of our study demonstrate the great technical and economic potential of this solution as an H_2-mediated "energy storage" and CO_2 capture facility.

Keywords: CO_2 methanation, Hydrogen Cyclic Storage, Energy Recovery, Sustainable Energy

INTRODUCTION
The present global energy scenario -and the consequences of the invasion of Ukraine- forces researchers, designers and policymakers to face the technical and economic challenges of an unavoidable and urgent mitigation of global Greenhouse gas (GHG) emissions. Such emissions from anthropogenic sources have been continuously growing since the beginning of the industrial revolution. The perturbing potential of these GHG emissions on the natural atmospheric concentration cycle might trigger, or at least hasten, an amplification of the global climate change.
Besides continuous efforts to improve the efficiency of combustion processes and the recourse to "CO_2 neutral" secondary fuels, the only feasible path -at least in the so-called "transition phase" towards a less unsustainable energy scenario- is the implementation of CO_2 capture and storage solutions. Since Thermodynamics teaches us that in the energy conversion arena "there is no free lunch", technical feasibility must be combined with economical positive returns, and thus the energy community must address the problem of the high CO_2 sequestration costs.
Sabatier based power-to-gas systems are potential answers for this issue, and this paper describes the modelling, process design and simulation of a CO_2 methanation plant based on the Sabatier reaction. To cure one of the problems of this technology, namely its low overall conversion efficiency, an exergy-based optimization of the thermal recovery within the system boundary was introduced. The results of our study demonstrate the great technical and economic potential of this solution as an H_2-mediated "energy storage" and CO_2 capture facility. While the insistence of public opinion, media and policymakers on the absolute necessity of reducing anthropic atmospheric emission of CO_2 into the atmosphere is obviously correct, and so is their urging to evolve into an alternative power generation with zero-emission to prevent future catastrophic effects, non-specialists are in general unprepared to understand the enormous technical problems connected with such a transition, and very often also unwilling to accept either the unavoidable economic effects on the cost of the final kWh or the efficiency measures that they perceive as attempts to "reduce their standard of life". It is therefore imperative for the scientific community to bring about substantial advances in GHG reduction that combine a satisfactory degree of technological feasibility (i.e. are reliable, efficient, safe and low-impact) with a sufficient economic return (in terms for example of payback and of low impact on the final kWh cost). Policymakers are well-aware of this in fact, and the incentivation campaigns are designed to facilitate such a transition.
All forecasts for the world global electricity consumption indicate that, in spite of the evermore stringent source-demand matching and energy recycles and recovery, the electricity demand will be on the rise. At the current state of affairs, it is impossible to cover this demand by renewable sources only, and therefore the recourse to fossil-fueled electricity generation is unavoidable. The main harmful pollutants are NO_x, SO_x, dust, CO_2, and wastewater from flue-gas treatment installations. Keeping in mind that carbon dioxide emissions are an unavoidable consequence of combustion, we shall address here a possible mitigation strategy.

There are several proposals for carbon capture, utilization and storage (CCS or CCUS). Their common goal is to capture CO_2 from industrial sources and either store it in underground structures or convert it into useful products. All this is happening while emissions from the industrial and energy sectors are reduced mostly thanks to the so-called Carbon Tax: the current fees related to CO_2 emissions in the European Union run in the range of 50 €/t_{CO2}, and there is an expected upward trend in the coming years.

MATERIALS AND METHODS – DESCRIPTION OF THE PROPOSED SYSTEM

In this study we examine a possible alternative solution to CCS, namely a chemical conversion: an attractive final product being *methane* (CH_4): through the well-known *Sabatier reaction* or *methanation*, exhaust CO_2 can be converted into a very valuable and easy-to-use fuel. In this way, CO_2 mitigation is achieved not only through carbon chemical storage, but also through a reduction of the final energy use, because the generated CH_4 is a perfect local substitute for natural gas.

Even though, contrary to geological sequestration, the captured CO_2 will be almost immediately released into the atmosphere by the combustion of CH_4, the methanation process provides a profitable CO_2 zero emission-cycle if it is fed by renewable energy sources. But since it requires the generation of H_2 -usually via an electrolytic process, it is also economically attractive if it uses a portion of the electricity generated in low-demand hours: in this sense, it is a sort of “chemical H_2 storage and reuse” system. When compared to competing capture systems, it combines a higher efficiency and an easily handled the final product (CH_4). In the process we are proposing, this methane can be burned on-site to generate the electricity required by the H_2 electrolysis and -in an economic but obviously not in a thermodynamics sense- “close” the loop.

The simplified scheme of the proposed process is shown in figure 1: electricity from renewable sources –or alternatively energy generated by fossil-fuelled power plants in low-demand hours-is used to generate H_2 in a standard electrolyser. The hydrogen is then injected into the Sabatier reactor together with combustion fumes. The final products are Steam, CH_4, NO_x (which is not affected by the catalytic conversion reaction) and, since the system is obviously not 100% efficient, a small amount of residual CO_2 (5-10%).

A first innovative feature of the proposed system is a carefully designed waste heat recovery (the Sabatier reaction is strongly exothermic) via a Heat Exchangers Network (HEN) that substantially improves the overall efficiency of the plant. The second innovative feature is a cryogenic separation of the NO_x from the CH_4 performed downstream of the process, that ensures a quality of the Syngas sufficient for it being burnt on-site in standard gas engines to generate electricity and reduce the overall primary consumption. To design the integrated system and analyze the plant performance a steady state simulation of the plant was performed with an open-source Process Simulator, COCO by AMSTERCHEM.

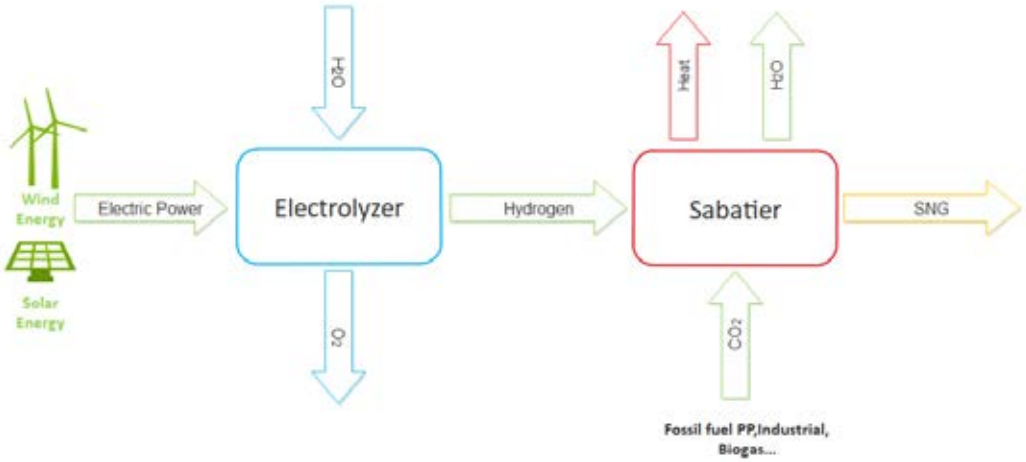


Figure 1 Sabatier Methanation scheme: the main processes

CONCLUSIONS

This paper presents and discusses the modelling and process design of a CO_2 methanation system. Heat Exchange Network (HEN) optimization techniques have been integrated in order to increase system efficiency. The Sabatier reactor treats the stack fumes, and thus no prior CO_2 separation is required: a cryogenic system is installed downstream to separate NO_x and SNG. A preliminary economic analysis demonstrates that the CH_4 costs are competitive with the current market situation.

REFERENCES

1. Bailera M, Lisbona P, Romeo LM, Espatolero S. *Power to Gas projects review: Lab, pilot and demo plants for storing renewable energy and CO_2*. Renewable and Sustainable Energy Reviews. 2017;69:292-312.
2. Genovese J, al. e. *Current (2009) State-of-the-Art Hydrogen Production Cost Estimate Using Water Electrolysis*. NREL; 2009.
3. Götz M, Koch AM, Graf F. *State of the Art and Perspectives of CO_2 Methanation Process Concepts for Power-to-Gas Applications*. International Gas Union Research Conference (IGRC). Copenhagen2014.
4. Gunnarsson G. *Icelandic CO2 Electrofuel cases*. CO2 Electrofuels seminar; 2013.http://www.carbonrecycling.is/.
5. Gutiérrez-Martín F, Rodríguez-Antón LM. *Power-to-SNG technology for energy storage at large scales*. International Journal of Hydrogen Energy. 2016;41:19290-303.
6. Han C, Graves K, Neathery J, Liu K.: *Simulation of the Energy Consumption of CO_2 Capture by Aqueous Monoethanolamine in Pilot Plant*, Energy and Environment Research. 2011;1:67-80.
7. Haszeldine RS. C*arbon capture and storage: how green can black be?* Science. 2009, 325:1647-52.
8. Commission IE. *Electric Energy Storage*. White Paper. 2011.
9. Heyne S., Harvey S. *Impact of choice of CO_2 separation technology on thermo-economic performance of Bio-SNG production processes*. International Journal of Energy Research. 2013; (wileyonlinelibrary.com).
10. G. Iaquaniello, S. Setini, A. Salladini, M. De Falco: *CO_2 valorization through direct methanation of flue gas and renewable hydrogen: A technical and economic assessment*, Int. J. Hydrogen Energy 43, 2018
11. IEA. CO_2 emissions from fuel combustion. International Energy Agency; 2013.http://unfccc.int/2860.php.
12. IEA. 20 Years of Carbon Capture and Storage. 2016
13. Jacquemin M, Beuls A, Ruiz P. *Catalytic production of methane from CO_2 and H_2 at low temperature: Insight on the reaction mechanism*. Catalysis Today. 2010;157:462-6.
14. Kopyscinski J, Schildhauer TJ, Biollaz SMA. *Production of synthetic natural gas (SNG) from coal and dry biomass – A technology review from 1950 to 2009*. Fuel. 2010;89:1763-83.
15. Le Treut H, et al.: *Historical Overview of Climate Change*, Cambridge University Press; 2007.
16. Ohya H, Fun J, Kawamura H, Itoh K, Ohashi H, Aihara M, et al. *Methanation of carbon dioxide by using membrane reactor integrated with water vapor permselective membrane and its analysis*. Journal of Membrane Science. 1997;131:237-47.
17. Petrakopoulou F.: *Comparative Evaluation of Power Plants with CO_2 Capture: Thermodynamic, Economic and Environmental Performance*, Ph.D. Thesis, Berlin, Germany: Technischen Universität Berlin; 2011.
18. Rahmani S, Rezaei M, Meshkani F. *Preparation of highly active nickel catalysts supported on mesoporous nanocrystalline γ-Al2O3 for CO_2 methanation*. Journal of Industrial and Engineering Chemistry. 2014;20:1346-52.
19. Re F., Toro C, Sciubba E. *Sabatier Based Cycle for CO2 Methanation: Exergy and Thermo-Economic Analysis*. 2017:V006T08A76.
20. Schlereth D, Hinrichsen O. *A fixed-bed reactor modeling study on the methanation of CO_2*. Chemical Engineering Research and Design. 2014;92:702-12.
21. Selamet ÖF, Becerikli F, Mat MD, Kaplan Y. *Development and testing of a highly efficient proton exchange membrane (PEM) electrolyzer stack*. International Journal of Hydrogen Energy. 2011;36:11480-7.
22. Simonis B, Newborough M. *Sizing and operating power-to-gas systems to absorb excess renewable electricity*. International Journal of Hydrogen Energy. 2017;42:21635-47.
23. Sudiro M, Bertucco A. *Synthetic Natural Gas (SNG) from Coal and Biomass: a Survey of Existing Process Technologies, Open Issues and Perspectives*. Natural Gas. 2010.
24. C.Toro, E.Sciubba: *Sabatier based power-to-gas system: Heat exchange network design and thermoeconomic analysis*, Applied Energy 229 (2018) 1181–1190
25. Ulleberg O. *Modeling of advanced alkaline electrolyzers: a system simulation approach*. International Journal of Hydrogen Energy. 2003;28:21-33.

WHEC-2022
23rd World Hydrogen Energy Conference
June 26-30, 2022 - Istanbul

#1536

INFLUENCE OF BIOGAS COMPOSITION TO CATALYTIC METHANATION PROCESS

[1,2*]Jan Kulas, [1]Lukáš Polák, [1]Aleš Doucek
[1] ÚJV Řež, plc., Department of Hydrogen Technologies, Hlavní 130, Husinec-Řež, Czech Republic
[2] University of Chemistry and Technology, Department of Gaseous and Solid Fuels and Air Protection, Technická 5, Prague, Czech Republic

*Corresponding author e-mail: jan.kulas@ujv.cz

ABSTRACT

It is expected that generation of electricity from renewable energy sources will significantly increase in the next decades. As a basic assumption for successful integration of renewable energy, any large-scale and long-term energy storage system will be needed. Power-to-Gas (P2G) technology is often mentioned as a promising solution. The surplus of electricity can be used for electrolytic hydrogen production. In the second step, the synthetic natural gas (SNG) is produced via catalytic hydrogenation of carbon dioxide. Experiments based on direct biogas methanation show, that this technology provides an effective way of production storable and transportable energy medium. Once national SNG quality requirements are met, the existing natural gas infrastructure give a massive energy storage system.

Keywords: Power-to-Gas, Methanation, Biogas, Synthetic natural gas, Biogas upgrading

INTRODUCTION

As share of renewable electricity has increased recent years, energy storage is more and more important. Balancing of power demand and supply is required at different time levels (hour, day, season) and scales. It results in different energy storage technologies suitable for various applications. It was observed [1,2] that there are many technologies suitable for short-term storage from minutes to hours. These technologies have limited capacities. When focused on large-scale or seasonal storage, the possibilities are limited to pumped hydro, compressed-air storage and P2G [3]. In the Czech Republic, the potential of pumped hydro has been already deployed and compressed-air storage is very limited by its specific geological requirements as well as significant thermal loss for long-term usage. Thus, P2G is consider as a technology capable to provide flexible large-scale storage solution from hours to months [4].

Nowadays, there are two basic approaches for methanation of carbon dioxide. The first one uses methanogenic microorganisms as biocatalysts, while the second is based on chemical catalytical synthesis [5]. Both conversions can be described by following reaction:

$$4\,H_2 + CO_2 \rightarrow CH_4 + 2\,H_2O \qquad (-165\ kj/mol) \qquad (1)$$

Nowadays carbon dioxide that is needed for the methanation reaction is usually separated with the use of several technologies based on physical or chemical absorption, adsorption, membrane or cryogenic separation. Carbon dioxide can be used from fossil fuel power plants, industrial processes or from biogas [5].

Biogas is an interesting source of carbon dioxide. Biogas consists mainly of carbon dioxide and methane, so it can be used directly as a source of carbon dioxide for the methanation reaction. However, biogas also contains many minor components (e.g. sulphane and other sulphur compounds) which must be removed before to methanation unity otherwise they could permanently deactivate the catalyst [6].

When biogas is directly used as a source of carbon dioxide, the reaction (1) can be rewritten by:

$$4\,H_2 + CO_2 + n\,CH_4 \rightarrow (n+1)\,CH_4 + 2\,H_2O \qquad (2)$$

While n can usually differ from 0.2 to 1.5 depending on biogas composition.

Catalytic methanation provides an alternative way to upgrade biogas without the need to separate carbon dioxide. The added benefit when compared to conventional methods is elimination of waste carbon dioxide and the possibility of storing electrical energy [7].

MATERIALS AND METHODS

For experimental evaluation of P2G technology in Czech Republic, chain of photovoltaic power plant, proton exchange membrane (PEM) electrolysis and chemical methanation has been selected. Main components of the system and its technical parameters are shown in Table 1.

Table 1. Technical parameters of P2G system

	Component	Technical parameters
Primary energy source	Photovoltaic power plant	13 kW(p), 60 polycrystalline panels
Hydrogen generation	PEM electrolyzer (HOGEN S40)	6.7 kW, 1.5 MPa, 1.05 $Nm^3/hr.$ H_2
P2G technology	Fixed-bed chemical reactor	0.4-1.2 MPa, Ni-based catalyst

Design of one-stage chemical reactor with fixed-bed of catalyst and external cooling is shown on Fig. 1. This configuration allows efficient heat management crucial for high conversion of methanation process. Also, a various composition of inlet gas can be introduced to study influence of biogas composition as well as influence of non-stoichiometric H_2/CO_2 ratio. Synthetic, organic oil Marlotherm LH has been used as a heat-transfer medium. Its boiling point set a limitation up to 380 °C.

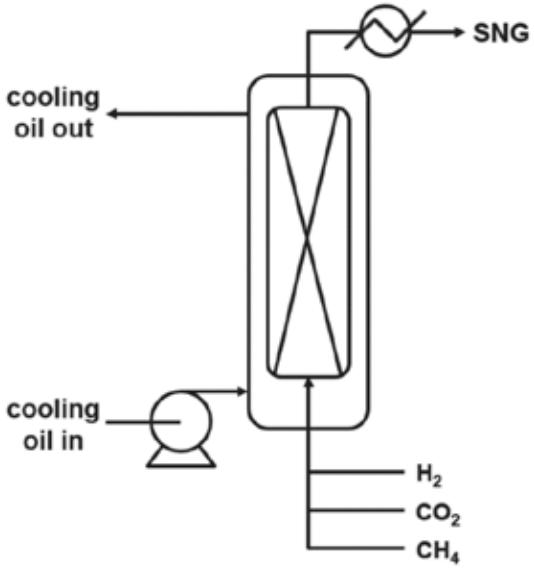


Fig. 1. Chemical reactor design

Series of experiments have been done with focus on influence of methane presence in inlet gas to carbon dioxide conversion. The applied nickel-based catalyst supported onto alumina has been developed in cooperation with University of Chemistry and Technology in Prague. This catalyst shows high selectivity for methanation and long-term stability. Constant pressure 0.5 MPa has been set for all experiments while various inlet gas composition has been introduced with methane content of 20 – 60 vol. %. The experimental unit has been coupled with on-line analysis of produced SNG to allowed evaluation of carbon dioxide conversion.

RESULTS AND DISCUSSION

At the beginning methanation of carbon dioxide with no methane has been carried out to set base for comparison. In next steps 20, 40 respectively 60 vol. % of methane have been introduced to carbon dioxide flow to simulate differ composition of biogas while H_2/CO_2 ratio has been fixed on stoichiometric value 4. When the methane concentration in produced SNG is influenced by its presents in inlet mixture, carbon dioxide conversion has been calculated for evaluation the methanation process. Carbon dioxide conversion within temperatures 250 – 370 °C for differ inlet gas composition is shown on Fig. 2.

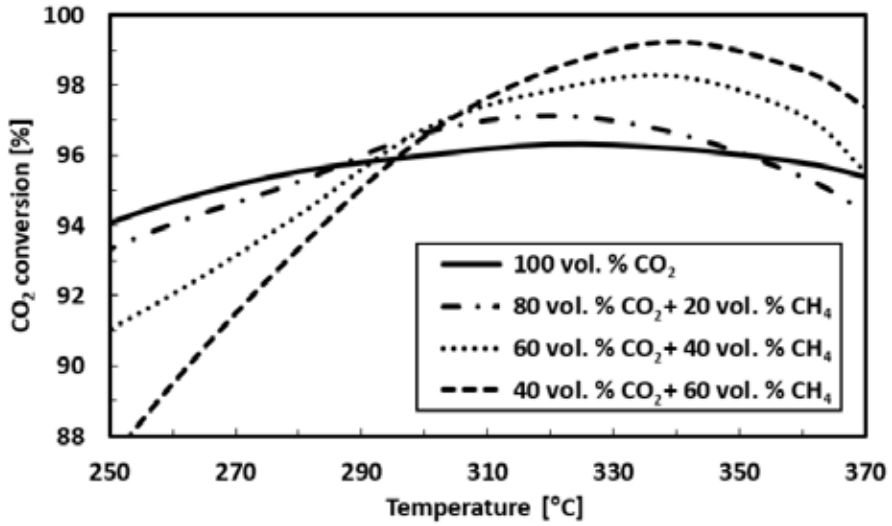


Fig. 2. Conversion of carbon dioxide within methanation process

The results show of significant increase in carbon dioxide conversion from 96 % to 99 % with increasing concentration of methane in inlet gas. Also, a slight shift in maximal conversion temperature is visible (310 – 340 °C). This phenomenon is probably caused by different thermal conductivity of carbon dioxide and methane and has not been described in previous works. More experiments will be needed for detail understanding of whole process.

CONCLUSIONS

P2G technology will play significant role as share of renewable energy sources will increase. The chemical catalytic reaction of hydrogen and carbon dioxide can provide a suitable, storable and transportable energy medium. While hydrogen can be produced via electrolysis, one of the main sources of carbon dioxide the biogas is considered.

This experimental work focuses on influence of methane presence in biogas to carbon dioxide conversion during methanation process. A phenomenon of increasing carbon dioxide conversion as well as optimal methanation temperature have been discovered. The presence of methane helps to convert carbon dioxide and reach SNG with a high heating value. Next experiments with nickel-cobalt and nickel-molybdenum catalysts will be carried out in future.

ACKNOWLEDGEMENT

This work has been supported by grant no. TH02020767 of Technological Agency of Czech Republic.

REFERENCES

1. Luo X., Wang J., Dooner M., Clarke J. 2015. Overview of current development in electrical energy storage technologies and the application potential in power system operation. Applied Energy 137:511–36.
2. Chen H., Cong TN., Yang W., Tan C., Li Y., Ding Y. 2009. Progress in electrical energy storage system: a critical review. Progress in Natural Science 19:291–312.
3. Hofstetter D., Battke B., Cox B., Hughes J. 2014. Power-to-Gas in Switzerland - demand, regulation, economics, technical potential. Erdgas Zürich, Elektrizitätswerk der Stadt Zürich (ewz), Swissgrid AG, Swiss Gas Industry Association (VSG), Electrochaea, Swiss Federal Institute of Technology Zurich.
4. Lehner M., Tichler R., Steinmüller H., Koppe M. 2014. Power-to-gas technology and business model. Austria: Springer
5. Götz M.., Lefebvre J., Mörs F., Koch AM., Graf F., Bajohr S., Reimert R., Kolb T. 2016. Renewable Power-to-Gas: A technological and economic review 85:1371-1390.
6. Walker S. B., Sun D., Kidon D., Siddiqui A., Kuner A., Fowler M., Simakov D. S.A. 2017. Upgrading biogas produced at dairy farms into renewable natural gas by methanation. Energy research. 1714-1728.
7. Hlinčík T., Tenkrát D., Šnajdrová V., Baraj E. 2017. Catalytic Methanization of Biogas using Nickel Catalyst. Paliva 9, 3, 93-98.

WHEC-2022
23rd World Hydrogen Energy Conference
June 26-30, 2022 - Istanbul

#1616

TECHNO-ECONOMIC PERFORMANCE ASSESSMENT OF A REACTOR SYSTEM USED FOR POWER-TO-METHANE PLANT

[1,2,3*]*Alper Can Ince*, [4]*C. Ozgur Colpan*, [5]*Ali Keles*, [1]*Mustafa Fazil Serincan*, [2,3]*Ugur Pasaogullari*
[1]Gebze Technical University, Faculty of Engineering, Mechanical Engineering Department, Gebze, Kocaeli, 41400, Turkey
[2]Center for Clean Energy Engineering, University of Connecticut, Storrs, CT 06269-5233, United States
[3]Department of Mechanical Engineering, University of Connecticut, Storrs, CT 06269-4602, United States
[4]Dokuz Eylul University, Faculty of Engineering, Mechanical Engineering Department, Buca, Izmir, 35397, Turkey
[5]GKE Energy R&D Center, Milas, Muğla, 48200, Turkey

*Corresponding author e-mail: alper_can.ince@uconn.edu

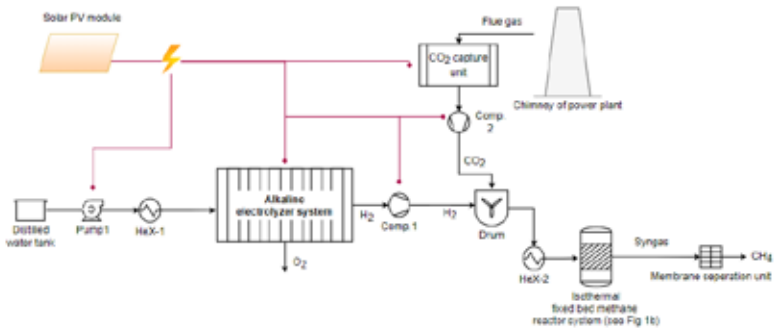
ABSTRACT

The interest in methane production from the utilization of electricity and hydrogen, also well-known as power-to-methane (PtM), has increased significantly in the last decades. A typical PtM system mainly consists of an electrolyzer (for hydrogen production) that is powered by a renewable power production technology, such as a solar PV module, a CO_2 source and a chemical reactor for methane production. In this study, the sizing of a PtM system is first performed based on the operating strategy that relies on the avoidance of hydrogen storage and selection of appropriate hydrogen content of syngas and catalyst loading in the reactor. Then, thermodynamic analysis is performed for this system. Finally, cost analysis is conducted for new reactor installation considering sizing and thermodynamic performance of the system. The combined simulation shows that the electrical efficiency is found as 50-55 % according to various operating conditions. The syngas production rate decreases even though the methane content of syngas increases when the operating pressure of the reactor decreases. Moreover, the total investment cost decreases from 4,354,200 $ to 3,470,200 $ when the reactor pressure increase from 1 bar to 7 bar.

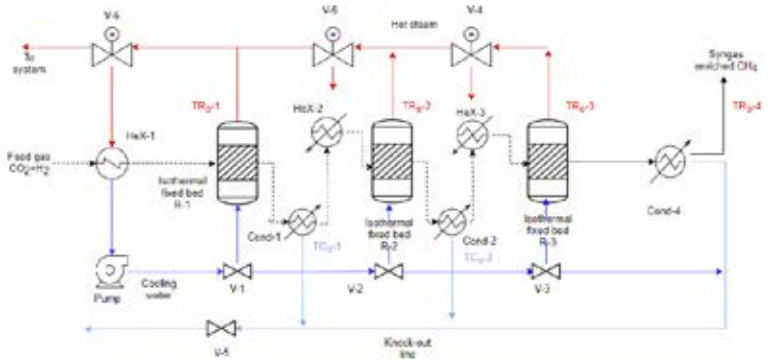
Keywords: Power-to-methane, Syngas, Cost analysis, Economic model, Methane reactor

INTRODUCTION

Storage of methane (or syngas) is easier compared to hydrogen because methane has readily available delivery infrastructure in many countries. This makes the synthetic methane production systems more attractive. Power-to-methane (PtM) is an effective concept to produce synthetic methane utilizing electricity and hydrogen through an eco-friendly pathway compared to the traditional methane production systems [1]. A typical PtM system mainly consists of an electrolyzer (for hydrogen production) that is powered by a solar PV module, CO_2 capture unit, and reactor system for methane production, as displayed in Figs. 1a and 1b. The financial feasibility of the PtM systems has been increased in the last decade, making these systems more cost-competitive [2–4]. Techno-economic assessment is an effective method to evaluate the PtM systems as the cost of the methane production, investment cost of the plant, and payback time, which show the economic competitiveness of the process, can be found using this method. In this study, a PtM system is sized based on the operating strategy. Then, a thermodynamic assessment for this system is performed. The cost analysis for the reactor system of the PtM plant based on the sizing and thermodynamic results is eventually conducted.



a)



b)

Fig 1. a) Schematic of the PtM system and b) the isothermal fixed bed methane reactor system of the PtM

SYSTEM DESCRIPTION AND MATHEMATICAL MODEL

The schematic of the PtM system considered in this study is displayed in Figs 1a and 1b. The required power for hydrogen production from the electrolyzer is provided by a solar PV module. The CO_2 capture unit is used to capture CO_2 from flue gas. However, the modeling of the CO_2 capture unit is neglected in this study. The hydrogen and CO_2 are fed to the methanation subsystem where Sabatier reactors and balance of plant components (e.g., pumps, valves, condensers, heat exchangers) are employed. The system sizing is first performed based on the operating strategy The thermodynamic assessment of the sized system is then done. Finally, an economic analysis is performed for this system based on the revenue requirement method [5].

Thermodynamic performance is evaluated by using energy efficiency:

$$\eta = \frac{\dot{n}_{CH_4} \cdot LHV_{CH_4} + \dot{n}_{H_2} \cdot LHV_{H_2}}{P_{total}} \quad (1)$$

The economic performance is evaluated for the methanation section by estimating investment cost and methane production cost. It is assumed that the total investment cost (TCI) is mainly composed of fixed capital investment (FCI) that covers direct and indirect costs neglecting other outlays (e.g., start-up costs, costs of licensing, research and development). For the calculation of FCI for main equipment, acquisition costs in the base state $\left(C_p^0\right)$ are needed to be calculated:

$$C_p^0 = 10^{K_1 + K_2 \log_{10}(Z) + K_3 [\log_{10}(Z)]^2} \quad (2)$$

where Z is the capacity or size parameter, and K represents the coefficient.

Since some cost data used in an economic analysis refers to the year 2001, they are needed to be brought to the same reference year:

$$C_{p,\$}^0(2022) = C_{p,\$}^0(2001) \cdot \frac{cost\ index\ (2022)}{cost\ index\ (2001)} \quad (3)$$

Purchased equipment cost of the methanation section (including pumps, heat exchangers, and reactors which are made of the higher quality material) considers the material factor F_M, and the pressure factor F_P as given in Eq (4).

$$C_{p,\$} = C_{p,\$}^0(2022) \cdot (2.25 + 1.82 \cdot F_M \cdot F_P) \quad (4)$$

Some simplified relations can be then used to predict the total capital investment required for a new methanation system. The relations can be found in the literature [6].

RESULTS AND DISCUSSION

In this study, a PtM system is first sized, and its thermodynamic performance is performed based on various operating strategies basically based on the avoidance of hydrogen storage and selection of appropriate hydrogen content of syngas and catalyst loading in the reactor. Economic analysis is then conducted. Sizing analysis shows that the methanation section has three serial reactors which have catalyst weights of 6800 g, 2990 g, and 1510 g,

respectively. Moreover, the number of cells at which an active area of 200 cm^2 in the stack is calculated as 180, while the number of solar PV panels which has an area of 2 m^2 is found as 120. This system is capable of producing 0.101 mol/s syngas (roughly 50 % methane, 30 % hydrogen, 12 % water, and 8 % carbon dioxide). Thermodynamic calculations show that the LHV-based system energy efficiency is found around 50-55% under various operating conditions. Moreover, the system has a capacity to generate around 10000 W of heat in these conditions. For this purpose, the hydrogen production flow rate and CO_2 flow rate used are calculated as 0.09221 and 0.02323 mol/s, respectively.

From the economic point of view, the investment costs for reactors in the methanation section are found as given in Table 1. To produce 50 tons of syngas per year, the total investment cost of new reactors is found as 2,397 M$ for the following reactor operating conditions: Pressure, temperature, the contact time in the first reactor (R1), and stoichiometric ratio (H_2/CO_2) are 1 bar, 498 K, 83 g·h/mol, 4, respectively. When the pressure increases from 1 bar to 7 bar while other parameters are taken the same, the sizing analysis shows that two reactors can be operated for the operating strategy. In this case, the system is capable of producing 26-ton syngas per year. Total investment cost decreases to 1.860 M$.

Table 1. Estimate of total capital investment costs for new reactor(s) installation in the PtM system

Equipment	Operating pressure of the reactor	The number of reactors	Syngas production rate	Methane content	FCI	TCI
R-1 R-2 R-3	1 bar	3	50 ton/year	50 %	2,960,000 $	4,354,200 $
R-1 R-2	7 bar	2	26 ton/year	70 %	2,360,700 $	3,470,2000 $

CONCLUSIONS

In this study, a power-to-methane (PtM) system is first sized based on operating strategies. Then, a thermodynamic simulation is performed on the system. Finally, the cost analysis for new reactor(s) installation in the PtM system is done. Sizing analysis shows that when the pressure of the methane reactor increases, the number of reactors decreases to meet the operating strategy. Based on this result, the syngas production rate decreases even though the methane content of syngas increases. Moreover, the total investment cost decreases from 4,354,200 $ to 3,470,200 $ when the pressure increase from 1 bar to 7 bar.

ACKNOWLEDGEMENT

Dilek Temel Saygan, Meltem Küs, and Meltem Ergin from GKE are gratefully acknowledged for fruitful discussions.

REFERENCES

1. Ince AC, Colpan CO, Hagen A, Serincan MF. Modeling and simulation of Power-to-X systems: A review. Fuel 2021;304:121354. https://doi.org/10.1016/j.fuel.2021.121354.
2. Blanco H, Nijs W, Ruf J, Faaij A. Potential of Power-to-Methane in the EU energy transition to a low carbon system using cost optimization. Applied Energy 2018;232:323–40. https://doi.org/10.1016/j.apenergy.2018.08.027.
3. Ghaib K, Ben-Fares F-Z. Power-to-Methane: A state-of-the-art review. Renewable and Sustainable Energy Reviews 2018;81:433–46. https://doi.org/10.1016/j.rser.2017.08.004.
4. Peters R, Baltruweit M, Grube T, Samsun RC, Stolten D. A techno economic analysis of the power to gas route. Journal of CO2 Utilization 2019;34:616–34. https://doi.org/10.1016/j.jcou.2019.07.009.
5. Turton R, Bailie RC, Whiting WB, Shaeiwitz JA. Analysis, Synthesis and Design of Chemical Processes. Pearson Education; 2008.
6. Bejan A, Tsatsaronis G, Moran MJ. Thermal design and optimization. New York: Wiley; 1996.

WHEC-2022

23rd World Hydrogen Energy Conference

TRACK 11.
HYDROGEN SAFETY

TRACK 11. HYDROGEN SAFETY

#8 COMPUTATIONAL INVESTIGATION OF PREMIXED HYDROGEN-AIR FLAMES STABILIZED IN DIVERGING ANNULAR CHANNEL	1163
#55 MESH-INDEPENDENT LARGE-EDDY SIMULATION WITH ANISOTROPIC ADAPTIVE MESH REFINEMENT FOR HYDROGEN DEFLAGRATION PREDICTION IN LARGE-SCALE VENTED VESSELS	1166
#252 FAULT ANALYSIS AND SAFETY PROTECTION OF ON-BOARD HYDROGEN SUPPLY SYSTEM	1169
#257 SAFETY STUDY AND CFD SIMULATION OF HYDROGEN LEAKS AND DISPERSION WITHIN SEMI ENCLOSED SPACE OF HYDROGEN FACILITY	1173
#280 TOWARD THE CONTINUOUS SENSING OF LEAKED HYDROGEN BY A QUAD-ROTOR DRONE	1176
#296 RISK EVALUATION OF HYDROGEN DISPERSION FROM COMPRESSED HYDROGEN (H_2) STORAGE VESSELS	1179
#384 INVESTIGATIONS ON THE DEFLAGRATION-TO-DETONATION PHENOMENA BY MEANS OF NUMERICAL SIMULATIONS WITH DETAILED CHEMISTRY AND AUTOMATED MESHING	1182
#429 FRETTING WEAR OF ELASTOMER MATERIALS IN HYDROGEN	1185
#436 METAL NANOPARTICLE DECORATED ZnO NANORODS FOR HYDROGEN SENSOR APPLICATIONS	1187
#1475 THE EFFECT OF CRYSTAL STRUCTURE AND METAL ELECTRODES ON GAS DETECTION IN TiO2 NANOTUBES H_2 SENSORS	1190
#1482 DETERMINATION OF SAFETY DISTANCE AND THE STRUCTURAL DAMAGE VULNERABILITY RESULTED FROM VAPOR CLOUD EXPLOSION (VCES)	1193
#1514 ASPECTS OF RISKS USING MAGNESIUM HYDRIDE FOR ZERO EMISSION MOBILITY	1196
#1519 HYDROGEN SENSING PROPERTIES OF ULTRATHIN Pt-Co ALLOY FILMS	1199
#1534 AN EXPERIMENTAL APPARATUS FOR IN-SITU STUDIES OF HYDROGEN INGRESS, DISSOLUTION AND PRECIPITATION AT CONTROLLED TEMPERATURE AND APPLIED TENSILE STRESSES	1202
#1560 NUMERICAL INVESTIGATIONS ON FLASHBACK LIMITS OF PREMIXED METHANE-HYDROGEN-AIR LAMINAR FLAMES	1206

WHEC-2022
23rd World Hydrogen Energy Conference
June 26-30, 2022 - Istanbul

#8

COMPUTATIONAL INVESTIGATION OF PREMIXED HYDROGEN-AIR FLAMES STABILIZED IN DIVERGING ANNULAR CHANNEL

* *Ali Cemal Benim, Björn Pfeiffelmann*
Duesseldorf University of Applied Sciences, Faculty of Mechanical and Process Engineering, Center of Flow Simulation (CFS), Muenstersrasse, 156, D-40476 Duesseldorf, Germany

*Corresponding author e-mail: alicemal@prof-benim.com

ABSTRACT

Atmospheric, laminar, premixed flames of hydrogen and air are computationally investigated in an annular diverging channel. This used configuration closely resembles the one that was recently used in a series of experimental studies to obtain the burning velocities and quenching distances for premixed flames of different fuels, including hydrogen. Three different equivalence ratios are considered. Global and detailed reaction mechanisms are adopted to describe the combustion process. For ensuring an adequately fine resolution of the flame fronts, local adaptive grid refinement techniques are applied to track the flame front. The goal of the current analysis is the validation of the applied prediction procedures by comparing them with the experimental results. To this purpose, the predicted burning speeds and quenching distances are compared with the measured values.

Keywords: Hydrogen combustion, Premixed flame, Flame speed, Quenching distance, Computational Fluid Dynamics

INTRODUCTION

Power generation by thermal machinery largely depends on the conversion of the chemically bound energy by the combustion process. Parallel to the exploitation of new energy sources and recovery techniques [1], combustion continues to play an important role in power generation. Combustion of H_2 and H_2-blend fuels plays an important role in clean and efficient energy supply. On the one hand, H_2 represents an attractive alternative to storing excess energy in renewable power generation [2]. On the other hand, instead of combustion [3,4] gasification of biomass and coal [5] is a good possibility for clean power generation. The synthesis gas contains, in addition to CO and small amounts of CH_4, significant amounts of H_2. Additionally, there is a growing interest in hydrogen production using nuclear power plants [6].

Use of H_2 in combustion systems represents a great challenge. In power generation, the state-of-the-art technology for gas turbines is the lean premixed combustion, due to its high potential for achieving very low NO_x emissions. A principal problem here is the so-called “flashback” [7]. This makes the use of H_2 containing fuels in premixed combustion to a great challenge, since its high reactivity increases the flame speed and flashback propensity. Thus, effective measures are needed to prevent flashback when using H_2 containing fuels in premixed mode. Combustion of H_2 has relevance also for safety engineering. H_2 has a high diffusivity and its leakage is more likely to be an issue compared to other gases. H_2 plays also a special role in conjunction with the safety of nuclear power plants on conjunction with the storage of the released slightly radioactive H_2-steam mix.

A measure against flashback is the “quenching mesh”. Here, a primary cause preventing flame propagation is heat loss to walls. A temperature decrease in the flame front retards the combustion, and, thus, flame propagation. A termination of the combustion reactions as result is “quenching”. The range, in which the flame is quenched is termed as “quenching distance”. Thus, a solid mesh in the flow path, with mesh sizes smaller than the quenching distance can prevent flashback. Although experimental values for quenching distances can be found in the literature, there is a need for a better understanding of the phenomenon with respect to the influence of different conditions [8]. Until recently a number of further experimental and theoretical studies were performed on the subject. Computational investigations are, however, still rare and bound to simplifications leaving room for further exploration.

A computational analysis of the flow, heat and mass transfer processes for a laminar hydrogen flame in the presence of a quenching mesh was presented by the present authors [9,10]. In that study several modelling aspects were investigated and conclusions were drawn for the modelling and for quenching mesh design. The results were found to be in agreement with the experimental observations in general, while a direct comparison with measurements was not performed. The present work is to be understood as a continuation of the previous work, where explicit comparisons of the predictions with the experimental data are aimed. In recent years, an experimental method based on a so-called “Annular Stepwise Diverging Tube” (ASDT) was applied to measure the burning velocities and quenching distances for premixed flames of different fuels [11,12]. The measurements for a premixed hydrogen flame

are taken as the experimental basis for the present paper. Computational investigations are performed for premixed hydrogen flames in this configuration and the results are compared with the measurements [13] for validation purposes.

The preliminary results of the present work were presented in a recent publication [14]. In that publication, the geometry of the analyzed diverging tube was, however, not very similar to the one used by Jung et al. [13] in their measurements. A planar diverging tube was used in the previous work [14] without a very close resemblance of the annular tube used by Jung et al. [13]. In the present study, a geometry with a closer similarity to the one used in the experiments is considered. Furthermore, lean and rich mixture compositions are additionally investigated, whereas a stoichiometric flame was considered in the previous work [14]. The prediction of burning velocities is also put into the focus of the investigation, whereas only the prediction of the quenching distance was addressed previously [14].

MODELING

The differential transport equations of the chemically reacting mixture are numerically solved, assuming a subsonic flow and an ideal gas behavior [15,16]. Buoyancy is neglected. The radiative heat transfer is also neglected. Laminar flames are considered. Thus, modelling errors with respect to the modelling of turbulence [17,18] and turbulence-chemistry interaction [19] are avoided. Considering the multi-component diffusion, the Soret and Dufour effects are neglected, in the species transport and energy equations. For the numerical simulations, ANSYS Fluent 18.0 [20] is used. As Navier-Stokes solver, the SIMPLEC [21] scheme is used. For discretizing the convective terms, a second-order upwind scheme [20] is applied. The chemical kinetics software Cantera [21], is also used 1D calculations for verifying different reaction mechanisms. Flame propagation depends on the material properties. Thus, their accurate modeling is attempted. The specific heat capacities as function of temperature are obtained using a pair of fourth order polynomials [15], for low and high temperature ranges. Transport properties are obtained from the kinetic theory [15]. Chemical kinetics rate coefficients are modeled by Arrhenius expressions [16]. A single-step mechanism a detailed reaction mechanism are considered. The single-step mechanism is that of Marinov et al. [22]. The detailed mechanisms is the mechanism of Conaire et al. [23].

RESULTS

The predicted distributions of temperature and OH mass fractions are displayed in Figure 1 for a stoichiometric hydrogen-air premixed flame stabilized in a planar diverging duct with cooled walls. The fresh mixture flows from left to right (Figure 1). The flame cannot propagate further upstream, since the flow velocity balances the propagation speed of the flame. The “tulip” like shape of the flame front is affected by the shape of the velocity profile of the fresh mixture approaching the flame in the duct. With a reduction of the flow speed, the flame would stabilize at a further upstream position. Since the duct height is getting smaller in the upstream, the quenching effects of the cold walls will affect the flame front more strongly. At a position, the flame cannot be sustained and gets completely quenched. Through this procedure, the quenching distance can be obtained.

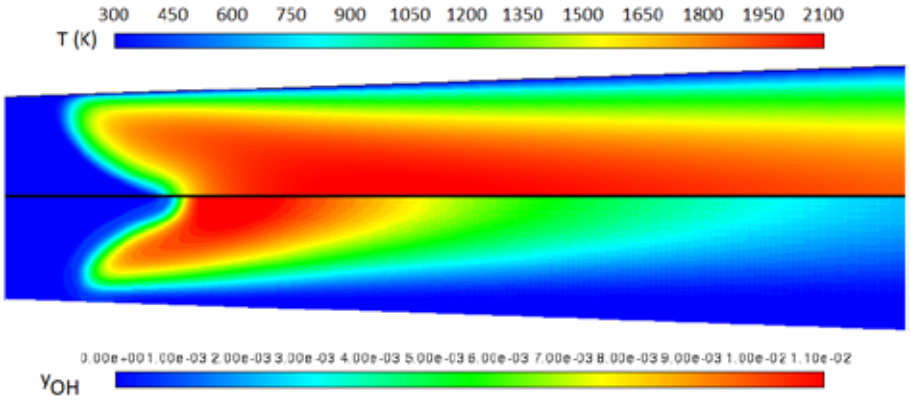


Fig. 1. Laminar stoichiometric hydrogen-air premixed flame stabilized in planar diverging duct with cooled walls, above: temperature distribution, below: distribution of OH mass fraction

CONCLUSIONS

Laminar premixed flames of hydrogen air mixtures in diverging ducts are numerically simulated for different equivalence ratios using different reaction mechanisms. For a given flow rate, the stabilization of the flame at an axial position along

the diffuser is predicted, allowing convenient means for the determination of the burning speed and quenching distance. The applied computational procedures are validated by comparing the predictions with the measurements of other authors.

REFERENCES

1. Pfeiffelmann B, Benim AC and Joos F. 2019. A finite volume analysis of thermoelectric generators. Heat Transfer Engineering 40(17-18): 1442-1450.
2. Götz M, Lefebvre J, Mörs F, McDaniel Koch A, Graf F, Bajohr S, Reimert R and Th. Kolb, Th. 2016. Renewable power-to-gas: a technological and economic review. Renewable Energy 85: 1371-1390.
3. Benim AC, Epple, B and Krohmer B. 2005. Modelling of pulverised coal combustion by a Eulerian-Eulerian two-phase flow formulation. Progress in Computational Fluid Dynamics – An International Journal 5(6): pp.345-361.
4. Epple B, Fiveland W, Krohmer B, Richards G and Benim AC. 2005. Models for the simulation of pulverized coal combustion. International Journal of Energy for a Clean Environment 6(3):267-287.
5. Benim AC and Kuppa K. 2016. Modeling of entrained-flow coal gasification by an equilibrium Eulerian-Eulerian two-phase flow formulation. Isi Bilimi ve Teknigi Dergisi / Journal of Thermal Science and Technology 36(2): 93-102.
6. IAEA. 2013. Hydrogen Production Using Nuclear Energy, IAEA Nuclear Energy Series No. NP-T-4.2, Int. Atomic Engy. Ag., Vienna.
7. Benim AC and Syed KJ. 2015. Flashback Mechanisms in Lean Premixed Gas Turbine Combustion, Cambridge, Academic Press.
8. Lewis B and von Elbe G. 1987. Combustion, Flames and Explosions of Gases, 3rd ed., Orlando, Academic Press.
9. Pfeiffelmann B and Benim AC. 2018. Numerical study of the quenching of a laminar premixed hydrogen flame. MATEC Web of Conferences 240:01031.
10. Benim AC and Pfeiffelmann. 2019. Computational investigation of laminar premixed hydrogen flame past a quenching mesh. International Journal of Numerical Methods for Heat & Fluid Flow. DOI: 10.1108/HFF-11-2018-20.
11. Liu Z and Kim NI. 2014. An assembled annular stepwise diverging tube for the measurement of laminar burning velocity and quenching distance", Combustion and Flame, 161, pp. 1499-1506.
12. Kim HY and Kim NI. 2018. Precise measurement if the length-scale effects on the flame propagation velocity using a compact annular stepwise-diverging-tube (ASDT). Combustion and Flame 191:210-212
13. Jung Y, Lee MJ and Kim NI. 2016. Direct prediction of laminar burning velocity and quenching distance of hydrogen-air flames using an annular stepwise diverging tube (ASDT). Combustion and Flame 164:397-399.
14. Benim AC and Pfeiffelmann. 2019. Prediction of burning velocity and quenching distance of hydrogen flames. E3S Web of Conferences 128:01012.
15. Turns SR. 2012. An Introduction to Combustion, 3rd ed., New York, McGrawHill.
16. Bird RB, Stewart WE and Lightfoot EN. 2002. Transport Phenomena, 2nd ed., New York, Wiley.
17. Benim AC, Cagan M, Nahavandi A and Pasqualotto E. 2007. Proceedings of the 5th IASME/WSEAS International Conference on Fluid Mechanics and Aerodynamics, Athens, Greece, August 25-27, 2007. pp. 232-237
18. Benim AC, Nahavandi A, Stopford P, Syed KJ. 2006. DES LES and URANS investigation of turbulent swirling flows in gas turbine combustors. WSEAS Transactions on Fluid Mechanics 5(1):465-472
19. Iqbal S, Benim AC, Fischer S, Joos F, Kluß D and Wiedermann A. 2016. Experimental and numerical analysis of natural bio and syngas swirl flames in a model gas turbine combustor. Journal of Thermal Science 25(5):460-469
20. www.ansys.com. Accessed on December 2, 2019
21. www.cantera.org. Accessed on November 6, 2019
22. Marinov NM, Westbrook CK, Pitz W. 1995. Detailed and global chemical kinetics model for hydrogen. Report No. UCRL-JC-120677, Lawrence Livermore National Laboratory, CA.
23. Conaire MO, Curran HJ, Simmie JM, Pitz WJ and Westbrook CK. 2004. A comprehensive modeling study of hydrogen oxidation. International Journal of Chemical Kinetics 36:603-622.

WHEC-2022
23rd World Hydrogen Energy Conference
June 26-30, 2022 - Istanbul

#55

MESH-INDEPENDENT LARGE-EDDY SIMULATION WITH ANISOTROPIC ADAPTIVE MESH REFINEMENT FOR HYDROGEN DEFLAGRATION PREDICTION IN LARGE-SCALE VENTED VESSELS

[1*] *Lucian Ivan*, [2] *Mohamad Khalil*, [2] *Clinton P.T. Groth*, [1] *Zhe Liang*
[1] Canadian Nuclear Laboratories, 286 Plant Road, Chalk River, Canada
[2] University of Toronto Institute for Aerospace Studies, 4925 Dufferin Street, Toronto, Canada

*Corresponding author e-mail: lucian.ivan@utoronto.ca

ABSTRACT

The use of high-fidelity simulation methods based on large-eddy simulation (LES) are proving useful for understanding and mitigating the safety hazards associated with hydrogen release in nuclear facilities. However, accurate modeling of turbulent premixed hydrogen flames via LES can require very high resolution to capture both the large-scale turbulence and its interaction with the flame fronts. Standard meshing strategies can result in impractically high computational costs, especially for thin hydrogen flame fronts. The use of a recently formulated integral length scale approximation (ILSA) subfilter-scale model in combination with an efficient anisotropic block-based adaptive mesh refinement (AMR) technique is examined herein for performing LES of hydrogen flames in large-scale vented vessels. The proposed LES methodology has already been applied to simulations within closed vessels. The anisotropic AMR method resolves the flame fronts. The grid-independent properties of the ILSA model ensure that numerical errors associated with implicitly-filtered LES techniques in regions with varying spatial resolution, and hence filter widths as well, are avoided and therefore, formally converged LES solutions are allowed. The final paper will provide a detail description of the computational framework along with an assessment of the capabilities of the combined approach based on comparisons between predictions and experimental data.

Keywords: large-eddy simulation, adaptive mesh refinement, integral length scale approximation, large-scale vented vessels, hydrogen release in nuclear plants

INTRODUCTION AND MOTIVATION

The accurate prediction of hydrogen flames in closed and vented vessels is beneficial in a number of safety related fields, including the assessment of the hazards of hydrogen combustion within the containment building of a nuclear reactor. The use of three-dimensional (3D) computational fluid dynamics (CFD) methods has proven useful in this regard, with many organizations and studies adopting such methods to perform high-fidelity detailed simulations of hydrogen release and combustion under postulated accident conditions [1].

The widespread application of large-eddy simulation (LES) to hydrogen combustion in nuclear containments has been limited by the high-resolution requirements for capturing the flame front and flame brush to accurately predict large-scale flame wrinkling and propagation. Unfortunately, computationally tractable, static, numerical meshes are usually not fine enough to sufficiently resolve the critical length scales associated with practical configurations. For instance, the computational cost incurred by static meshes is generally prohibitive to resolve the width of the flame brush (mili- or micro-meters) in a vessel on the order of meters. Therefore, the use of adaptive mesh refinement (AMR) [2, 3], wherein the mesh is dynamically refined and coarsened depending on the local solution content to accurately treat the required regions of the flow while reducing the overall computational cost, is an attractive alternative for LES of reactive flows. The use of AMR is especially attractive for large-scale facilities for which the mesh requirements to resolve solutions can vary significantly. However, the use of mesh-dependent LES subfilter-scale (SFS) turbulence models, such as the popular Smagorinsky model, can cause problems when used in conjunction with AMR or even with static meshes featuring varying cell sizes [4]. Specifically, mesh-dependent LES SFS models tie the SFS viscosity directly to the cell volume, which can lead to sharp changes in the unresolved fluctuating quantities with cells of largely different sizes. These undesirable sudden changes can introduce significant numerical error and even instabilities into the simulation [4], thereby negatively impacting the quality of the LES results.

In this study, a novel block-based anisotropic AMR scheme [2, 3] is applied in conjunction with a recently proposed mesh-independent integral length scale approximation (ILSA) SFS model [5] to the LES of turbulent premixed hydrogen flames in large-scale vented vessels. The application and evaluation of the proposed approach has been already considered for closed vessels [6] by performing simulations of a number of the well-studied THAI (Thermal-

hydraulics, Hydrogen, Aerosol, and Iodine) experiments [1], and it is extended here to include large-scale vented vessels.

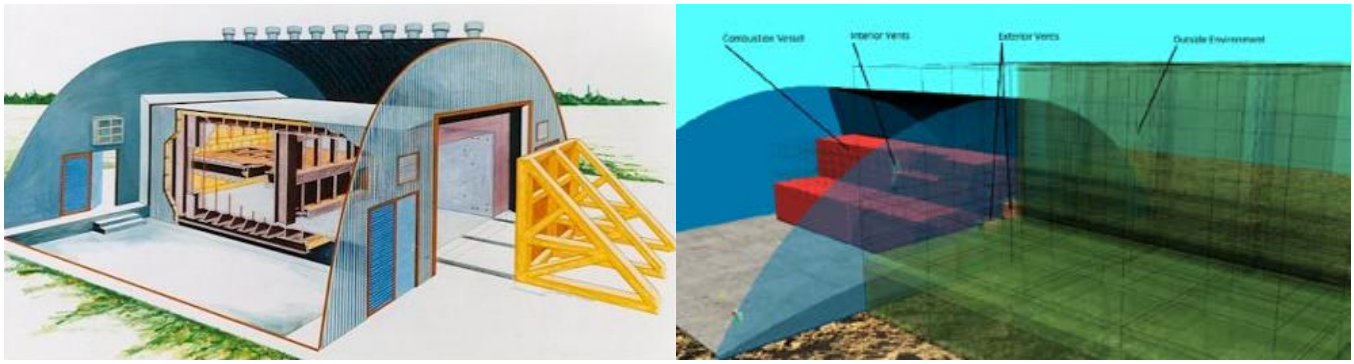
In what follows, a brief summary of the solution approach and numerical results to demonstrate the capabilities of the proposed approach are provided. The final paper will provide details of the proposed computational model for turbulent premixed hydrogen combustion flames, and the numerical discretization and solution procedure on anisotropically-refined grids. To illustrate the performance of the proposed approach, comparisons between the LES results and available experimental data are provided in this abstract. Simulation results for a range of experimental conditions for vented vessels will be provided in the final paper.

COMPUTATIONAL MODEL FOR PREMIXED LEAN HYDROGEN COMBUSTION

In this work, the Favre-filtered form of the Navier-Stokes equations governing compressible flows of a thermally perfect reactive gaseous mixture is solved to describe the turbulent premixed combustion processes. Dufour and Soret radiation effects are neglected. The partial differential equations governing the transport of the mixture mass, momentum, energy, and species concentrations are solved by applying a finite-volume discretization procedure in combination with a solution-driven anisotropic AMR procedure on 3D, multi-block, body-fitted, computational mesh consisting of hexahedral volume elements. The system of governing equations is closed by modelling the LES SFS turbulence stress tensor. The current work investigates the use of the ILSA model [5], which makes use of a similar eddy viscosity approach as the classical Smagorinsky model but differs in the evaluation of the SFS turbulent viscosity, to enable mesh-independent LES solutions to be achieved. To model the interaction between turbulence and chemistry and thermal-diffusive instabilities of the hydrogen flames, a multi-phenomena burning velocity combustion model is adopted here [6].

DESCRIPTION OF THE VENTED COMBUSTION EXPERIMENTAL FACILITY

The large-scale vented combustion test facility (LSVCTF) was operated at Canadian Nuclear Laboratories for over two decades. LSVCTF is a rectangular chamber with dimensions of 10-m long, 4-m wide, and 3-m high for an internal volume of 120 m^3. A schematic cutaway representation is shown in Fig. 1a. Two removable internal walls made of structural steel can divide the entire chamber into two or three rooms. For instance, the half chamber configuration is 4.5-m long. Both the front end and rear end walls are covered with rectangular steel plates bolted to the end wall structure. The vent area can be changed by removing an appropriate number of panels. During an experiment, the vent openings are covered with aluminum foil to prevent premature loss of pre-combustion gases; however, they can easily break open during combustion.



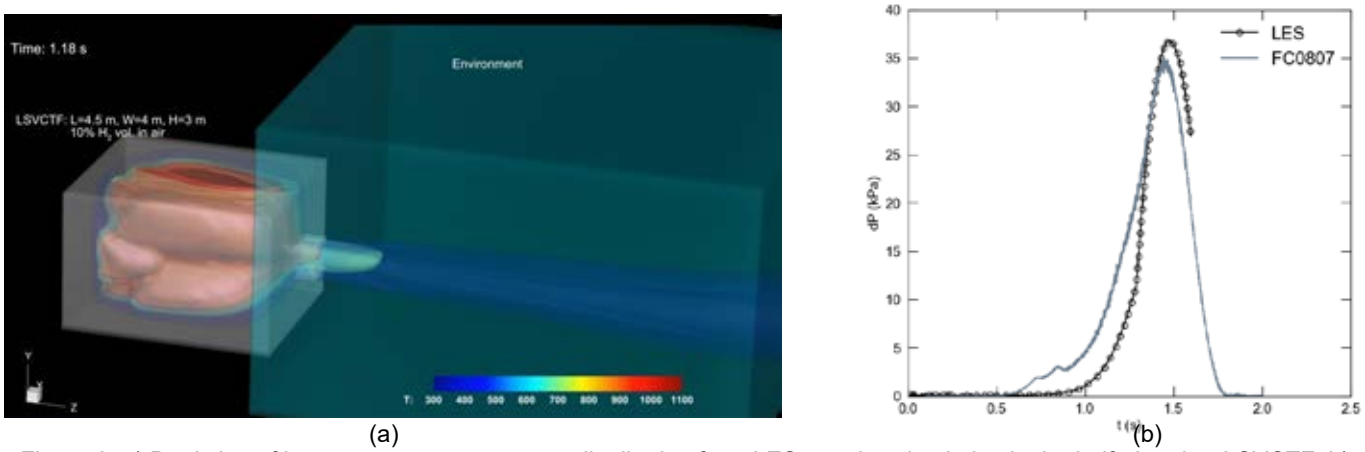
(a) (b)

Figure 1: a) Schematic representation of the Large-Scale Vented Combustion Test Facility (LSVCTF), b) cutaway of an initial multiblock structured mesh for the LSVCTF depicting the combustion vessel, interior and exterior vents, and the outside environment.

COMPUTATIONAL MODELLING OF THE LSVCTF

The LES modelling procedure for hydrogen deflagration described above is considered now for performing simulations of vented vessels. In particular, the conditions tested experimentally in the LSVCTF are considered. Figure 1b depicts an example of the computational mesh developed for the LSVCTF, in which the combustion vessel consists of two chambers separated by an interior vent. The two exterior vents that connect the combustion vessel with the outside environment are triggered to open dynamically if the wall pressure becomes greater than a desired vent burst pressure.

To demonstrate current capabilities of the computational framework, simulation results for the half-chamber configuration are depicted in Fig. 2. The instantaneous temperature distribution predicted by the LES framework at t=1.18 s is shown in Fig. 1a. The experimental conditions are for an initially quiescent mixture with 10% H_2 vol. in air. Figure 2b shows a comparison between the LES predicted and experimental time histories of the vessel overpressure at the location of a pressure sensor in the LSVCTF.



(a) (b)

Figure 2: a) Depiction of instantaneous temperature distribution for a LES reactive simulation in the half-chamber LSVCTF, b) comparison of predicted time history of the vessel overpressure to the LSVCTF measurements for the FC0807 experiment (9% H_2 vol. in air and an initially turbulent mixture).

Preliminary simulations with AMR indicate that the use of dynamically-adaptive grids is desirable to accurately capture the flow behaviour at vent interfaces. The final paper will present a full set of numerical results for a range of conditions studied in the LSVCTF and additional comparisons against the experimental data. Furthermore, the performance of the ILSA model for meshes with varying mesh resolution will be assessed.

REFERENCES

1. ISP-49 on Hydrogen Combustion. Nuclear Energy Agency, JT03314550, 2012.
2. M. J. Williamschen and C. P. T. Groth. Parallel Anisotropic Block-Based Adaptive Mesh Refinement Algorithm For Three-Dimsensional Flows. AIAA Paper 2013-2442, June 2013.
3. L. Freret and C. P. T. Groth. Anisotropic Non-Uniform Block-Based Adaptive Mesh Refinement Algorithm for Three-Dimensional Inviscid and Viscous Flows. AIAA Paper 2015-2613, June 2015.
4. S. B. Pope. Ten Questions Concerning the Large-Eddy Simulation of Turbulent Flows. New Journal of Physics, vol. 6, 2004.
5. U. Piomelli, A. Rouhi and B. J. Geurts. A Dynamic Subfiltre-Scale Stress Model for Large Eddy Simulation. Physical Review Fluids, vol. 766, 2016.
6. R. Taylor, C. P. T. Groth, Z. Liang and L. Ivan. Mesh-independent large-eddy simulation with anisotropic adaptive mesh refinement for hydrogen deflagration prediction in closed vessels. In Proceedings of the 8th International Conference on Hydrogen Safety, September 2019.

WHEC-2022
23rd World Hydrogen Energy Conference
June 26-30, 2022 - Istanbul

#252

FAULT ANALYSIS AND SAFETY PROTECTION OF ON-BOARD HYDROGEN SUPPLY SYSTEM

[1]Xiujuan Cao, [1]Xingzi Yu, [2]Donghai Hu, [1*] Caizhi Zhang
[1] School of Automotive Engineering; The State Key Laboratory of Mechanical Transmissions; Chongqing Automotive Collaborative Innovation Centre, Chongqing University, Chongqing, China, 400044
[2] School of Automotive and Traffic Engineering, Jiangsu University, Zhenjiang 212013, China

*Corresponding author e-mail: czzhang@cqu.edu.cn

ABSTRACT

Fuel cell vehicle hydrogen supply system is an important part of fuel cell vehicle driving. Ensuring the safety of hydrogen supply system is very important for fuel cell vehicles. At present, the main safety problems in hydrogen supply system of fuel cell include hydrogen leakage, overtemperature and overpressure. In this paper, the fault tree is used to analyze the explosion caused by internal faults in the hydrogen system, and the safety protection for the hydrogen supply system is carried out. As the monitoring equipment of hydrogen supply system, hydrogen controller plays an important role in ensuring the safety of on-board hydrogen supply system. The safety status of hydrogen supply system is verified by hydrogen controller test.

Keywords: Hydrogen Supply System, Hydrogen Controller, Solenoid Valve, Fault Tree, Labview

INTRODUCTION

With the emergence of new problems such as energy shortage and greenhouse gas emissions, more and more attention has pay to new energy. The emergence of new energy vehicles promotes the rapid transformation of traditional vehicles, and vigorously developing new energy vehicles has become the current industry trend. As an ideal energy source for new energy vehicles, fuel cell has become a research hotspot for its advantages of environmental protection, continuous power supply, good durability and no noise. At the same time, hydrogen plays an important role in the new energy system. As the world's largest hydrogen producer, China's annual output can reach 10 million tons, which has significant advantages in the development and utilization of hydrogen energy [1]. At present, environment and energy have become the global common concern. Therefore, as an important measure of energy structure adjustment, fuel cell vehicle is an important development direction of energy technology in the future[2]. As the power source of vehicles, on-board hydrogen supply system is an important part of fuel cell vehicles. To ensure the safety of hydrogen supply system is of great significance for fuel cell vehicles.

The hydrogen controller is mainly responsible for monitoring the temperature and pressure of the hydrogen bottle, the pressure of the hydrogen supply pipeline and the hydrogen leakage concentration in the hydrogen supply system, and then controlling the opening and closing of the electromagnetic valve. As the monitoring equipment, the controller plays an important role in ensuring the safety of on-board hydrogen supply system[3]. Therefore, it is necessary to conduct the fault test of hydrogen controller, in order to verify the safety state of hydrogen supply system.

Hydrogen Supply System

Structure And Composition of Hydrogen Supply System

Fuel cell vehicle hydrogen supply system is composed of hydrogen supply part, hydrogen safety part and system communication part. The hydrogen supply part is mainly composed of gas supply pipeline and related combined valves. The core of this part is to control and regulate the hydrogen pressure and flow in the hydrogen supply pipeline through key valves. The hydrogen safety part mainly includes various sensor components, which are responsible for monitoring the hydrogen concentration, pressure and flow, and reasonably distributing and installing the corresponding devices, so as to ensure the overall safety[4]. The communication part of the system is to establish CAN signal transmission and feedback control between the hydrogen supply system and the hydrogen system controller.

Working Principle of Hydrogen Supply System

When the hydrogen supply is supplied, the solenoid valve on the high-pressure hydrogen cylinder valve is opened, and then the fuel cell stack is supplied by the flow valve, the filter, the pressure reducing valve, the safety valve and the pipe solenoid valve. At the same time, the bottle vent solenoid valve in the whole system is

equipped with a PRD relief device, and there are safety protection devices such as over-current valve and safety valve on the pipeline, so as to ensure the safety of the whole system in use.

Failure Analysis of Hydrogen Supply System
Analysis Of Safety Hazards Based on Fault Tree

The purpose of analysis of safety hazards is to ensure the safety and reliability of hydrogen supply system and avoid dangerous accidents. Based on the above analysis of the structure and function of on-board hydrogen supply system, this paper summarizes the safety hazards, focuses on the analysis of faults in the hydrogen supply process, and puts forward the corresponding recovery conditions and protective measures.

The main safety hazards in the operation of the hydrogen supply system are: deflagration caused by hydrogen leakage in the hydrogen supply system, and rupture of the hydrogen storage bottle caused by overtemperature and overpressure. In the hydrogen supply system, the main components used for monitoring and protection are hydrogen supply controller and sensors. Therefore, according to the types of sensors, the faults in the hydrogen supply system are classified as follows: hydrogen leakage, high/low pressure fault, high temperature fault and component fault. Fault tree is used to analyze the faults in the hydrogen supply system.

Through analysis of fault tree, it can be concluded that the reason of deflagration caused by hydrogen leakage in the hydrogen supply system is that hydrogen gathering in the hydrogen supply system and reaches ignition energy[5]. Due to the characteristics of hydrogen, the ignition energy is extremely low when its concentration is in the range of 4%-75%, and it is easy to explode in open flame. Based on the large flammable concentration range and low ignition energy of hydrogen, there will be a great probability of deflagration when hydrogen leakage. The hydrogen pipeline includes many pipes and connections, which are the leakage sources (the probability of hydrogen leakage depends on the number of connected parts).

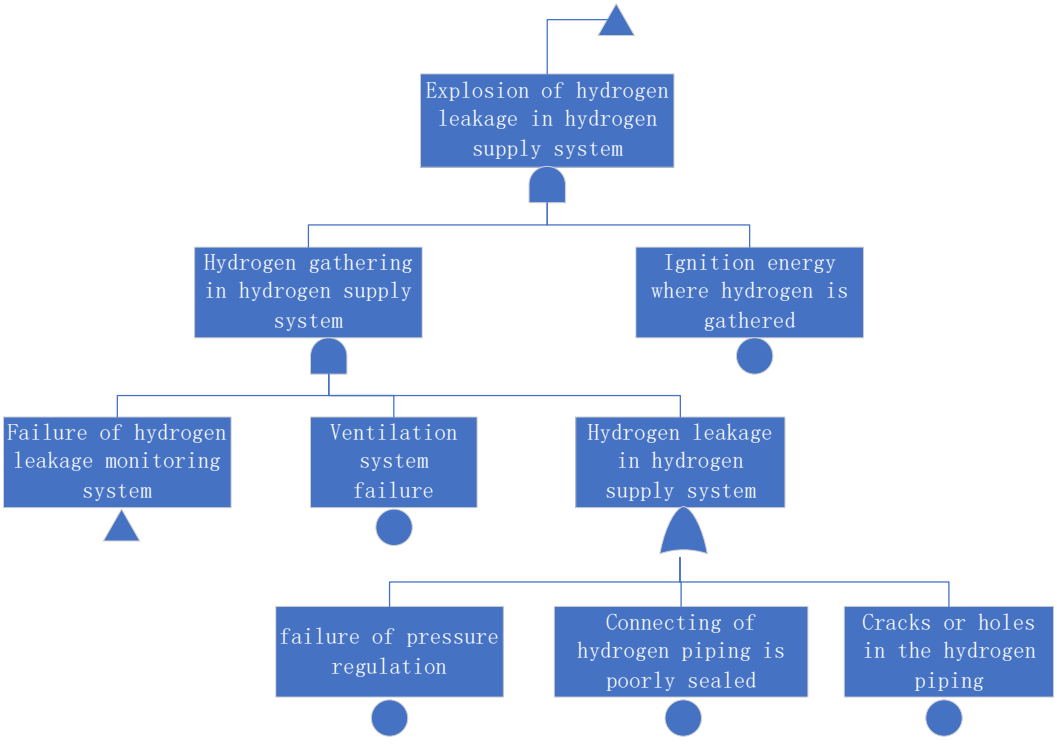


Fig. 1. Fault tree of deflagration caused by hydrogen leakage in hydrogen supply system

Through analysis of fault tree, it can be concluded that the reason for the rupture of the hydrogen storage bottle caused by the excessive temperature and pressure is the overpressure inside the tank[6]. In addition, the rupture spontaneously caused by external failures such as car accidents with collision and aging of the bottle that the safety valve can't protect will not be studied in this paper.

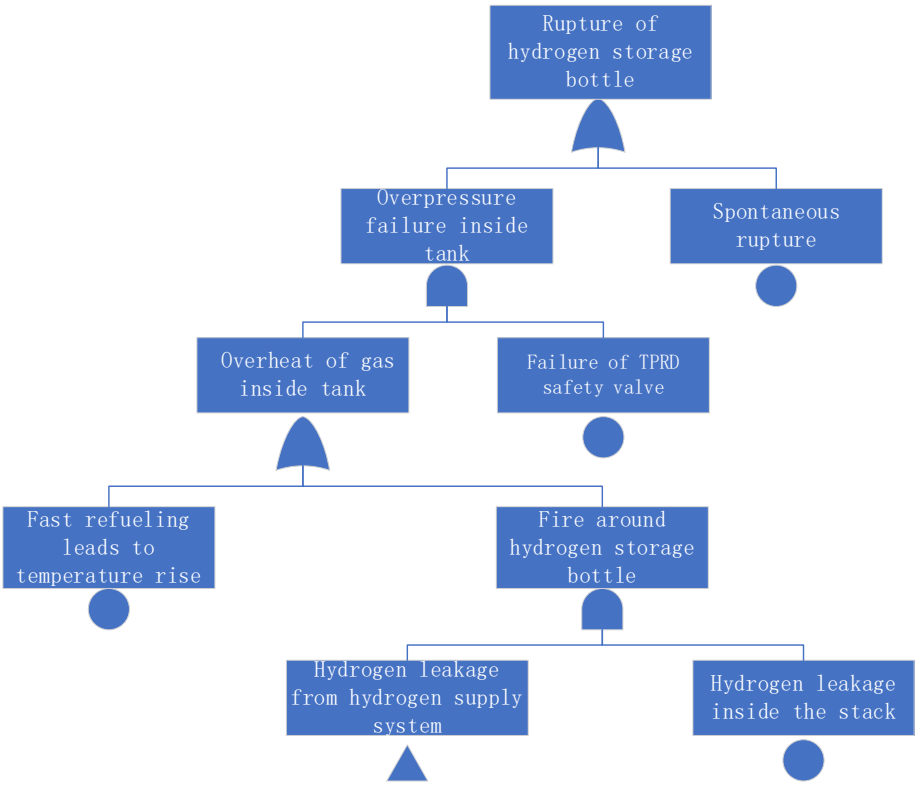


Fig. 2. Fault tree of hydrogen bottle rupture

Derivation of Fault Threshold

This part mainly introduces the composition, working range and fault threshold of the sensor.

Safety Protection of Hydrogen Supply System

Based on the above fault analysis results, the safety protection of hydrogen supply system is optimized. To ensure the reliability of on-board hydrogen system, it is necessary to protect the hydrogen supply system. Each hydrogen bottle mouth valve is equipped with a temperature sensor and a pressure sensor to measure the temperature and pressure of the bottle mouth. The pressure reducing valve in the hydrogen supply pipeline has a pressure sensor at the front and rear, which is used to measure the hydrogen pressure in the pipeline. In addition, the concentration sensor is distributed in the hydrogen supply pipeline, which is used to detect hydrogen leakage in the pipeline.

Fault Testing

In order to verify the safety monitoring function of hydrogen controller, it is necessary to carry out hardware-in-the-loop test on hydrogen controller. Test links mainly include the following: sensor signal acquisition, controller output execution command and CAN communication. The sensor signal is simulated in LabVIEW and sent it to the controller. The hydrogen controller responds after receiving the signal and transmits the response signal to the analog actuator in LabVIEW. Based on the output of actuator with different sensor signal input, judge whether the upper logic of hydrogen controller is correct. After the basic work is done, the entire in-loop test is debugged. Sensor signal input, actuator signal output and CAN communication are tested and verified.

CONCLUSIONS

Hydrogen supply system in the fuel cell vehicle is the core part of fuel cell system. In this paper, the fault tree is used to analyze the internal faults that may cause hydrogen explosion in the hydrogen supply system, and then the explosion risk assessment caused by internal faults can be obtained. Combined with the results of fault analysis, the safety protection system of hydrogen supply system is optimized. Among them, the hydrogen system controller plays an important role in ensuring the safety of the vehicle-mounted hydrogen supply system. Therefore, a test of hydrogen controller based on Lab VIEW is established, which can verify the safety status of hydrogen supply control system.

REFERENCES

1.C. San Marchi, E. S. Hecht, I. W. Ekoto, K. M. Groth, C. LaFleur, B. P. Somerday, R. Mukundan, T. Rockward, J. Keller, C. J. I. J. o. H. E. James, Overview of the DOE hydrogen safety, codes and standards program, part 3: Advances in research and development to enhance the scientific basis for hydrogen regulations, codes and standards, 42 (2017) 7263-74.
2. C. Zhang, X. Cao, P. Bujlo, B. Chen, X. Zhang, X. Sheng, C. J. J. o. E. S. Liang, Review on the safety analysis and protection strategies of fast filling hydrogen storage system for fuel cell vehicle application, (2021) 103451.
3. W. Jia, T. Ma, C. J. S. I. J. o. A. Ye, C. P. i. Mobility, Development of Hardware and Software for On-Board Hydrogen System, 1 (2019) 798-807.
4. W. Won, H. Kwon, J.-H. Han, J. J. R. E. Kim, Design and operation of renewable energy sources based hydrogen supply system: Technology integration and optimization, 103 (2017) 226-38.
5. S. Collong, R. J. i. j. o. h. e. Kouta, Fault tree analysis of proton exchange membrane fuel cell system safety, 40 (2015) 8248-60.
6.O. Rosyid, D. Jablonski, U. J. I. J. o. H. E. Hauptmanns, Risk analysis for the infrastructure of a hydrogen economy, 32 (2007) 3194-200.

WHEC-2022
23rd World Hydrogen Energy Conference
June 26-30, 2022 - Istanbul

#257

SAFETY STUDY AND CFD SIMULATION OF HYDROGEN LEAKS AND DISPERSION WITHIN SEMI ENCLOSED SPACE OF HYDROGEN FACILITY

[1] Daniel Prasetyo, [2] Alberto Costilla Alvarez, [3] Alberto Frisa Rubio, [4] Aurora Garcia Jimenez*
[1] CIRCE - (Research Centre for Energy Resources and Consumption), Avenida Ranillas, Edificio Dinamiza 3D, Zaragoza, Spain

*Corresponding author e-mail: dprasetyo@fcirce.es

ABSTRACT

Safety study and Computational Fluid Dynamics (CFD) simulation are conducted to analyze hydrogen leakage in semi -closed space of hydrogen facilities and installation in the framework of Cervera H24NEWAGE project. The goal of this study is to evaluate the hydrogen dispersion from release sources inside the building and to give detailed analysis of gas dispersion by using CFD in all areas, especially in some areas where there are highly potential leakages and inadequate flow ventilation due to some obstacles which could impede air recirculation in the zone. This study is useful to understand the dispersion of hydrogen release inside the building in order to implement best safety engineering practice for the new hydrogen facilities. In this study, hydrogen release is calculated by using UNE 60079-10 and considering other international standards such as API 505, and EIGA Doc 15/21. CFD simulations of different combinations of hydrogen release are done by varying pressure and opening area of release source with four air ventilation systems in operation. Velocity of air and concentration of hydrogen are calculated from the CFD model to hydrogen dispersion inside the building.

Keywords: Hydrogen safety, Hydrogen leakage, CFD simulation, Air ventilation

INTRODUCTION

Hydrogen (H2) is a clean energy source and has a great potential as a key element in the world economy due to its potential applications in basic sectors such as energy, industry and transportation. Hydrogen is foreseen as a key to the energy transition, due to its high potential contribution to the decarbonization of the economy and the reduction of fossil fuels use, which allows a greater integration of renewable energies in the energy mix and an important contribution to the circular economy. However, the maturity of hydrogen technology applications is still low and future development of its implementation is needed. Therefore, a new laboratory and facilities are needed to help us to understand and develop the best safety engineering practice of its applications.

Our study consists of safety study and CFD (Computational Fluid Dynamics) modelling of hydrogen leakage from equipment and piping installations in the new CIRCE hydrogen laboratory which is carried out in the framework of Cervera H24NEWAGE project. This building has a total effective volume of 6,434 m3 (49.4 m (L) x 16.28 m (W) x 8 m (H)) which are planned to be installed in 2022-2023. It consists of three working areas which are gasification, burner, and biomass reactor unit with hydrogen bottles installation located outside the building (Fig. 1).

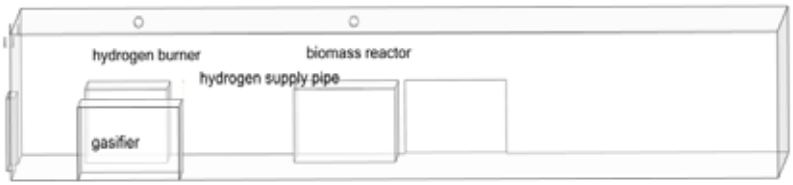


Fig. 1. 3D Model of Alfajarín Hydrogen Facilities

Hydrogen Leakage Analysis

The UNE-EN 60079-10-1 standard will be used to calculate hydrogen release from the system such as leak from piping connections, instruments, exhaust vent, safety valves considering its operating and design condition. Air recirculation and maximum hydrogen release in each block will be evaluated to guarantee that the total calculated hydrogen release in each block is below its maximum limit. Ventilation design criteria is evaluated carefully and is considered as a control measure to reduce the hydrogen gas hazard due to hydrogen release from the system. Hydrogen release from equipment and piping connections can create an explosive atmosphere if the concentration of the hydrogen exceeds 25% of the LEL which is 1% considering 4% LEL of Hydrogen. Six (6) air changes per hour is

considered as minimum requirement to guarantee adequate ventilation inside the enclosed building [1-2]. The minimum ventilation of the building will be 38604 Nm3/h (6434 m3 x 6 changes/h) and four exhaust fans of 10,000 Nm3/h will be in operation to guarantee the minimum requirement according to standard.

Release Rate and Release Characteristics

Release rate for gas (W_g) from hydrogen installation is calculated by using equations below for subsonic release (Eq.1) and sonic release (Eq. 2). Subsonic release is mainly considered in the calculation due to low discharge velocity of release rate of gas which is below the speed of sound. On the other hand, sonic release or release rate of gas with choked gas velocity is considered when the discharge velocity equal to the speed of sound which is the maximum theoretical discharge velocity [3]. Release characteristic is considered as maximum allowed concentration of hydrogen and is calculated by using Eq. 3 considering mass release of gas, density, LFL and safety factor.

$$W_g = C_d \, x \, S \, x \, p \, x \sqrt{\frac{M}{Z\,R\,T}\frac{2\gamma}{\gamma-1}\left[1-\left(\frac{P_a}{p}\right)^{(\gamma-1)/\gamma}\right]}\left(\frac{Pa}{p}\right)^{1/\gamma} \quad (1)$$

$$W_g = C_d \, x \, S \, x \, p \, x \sqrt{\gamma\frac{M}{Z\,R\,T}\left(\frac{2\gamma}{\gamma-1}\right)^{(\gamma+1)/(\gamma-1)}} \quad (2)$$

$$V_g = \frac{W_g}{\rho_g \, k \, LFL} \quad (3)$$

Variation of Hydrogen Release

The release and accumulation of hydrogen in semi-closed spaces is potentially dangerous as the hydrogen moves rapidly upwards due to the large difference of air and hydrogen density. Hydrogen dispersion in a semi-closed space with one open boundary, with uniform or nonuniform concentration distribution of hydrogen, depends on several factors such as hydrogen pressure, leak size, direction of release, and the enclosure parameters such as its volume and vent sizes [4]. Different combinations of hydrogen release pressure and source opening area are shown in Table 1.

Table 1. Variations of Hydrogen Release

Parameters	Unit	Case 1	Case 2	Case 3	Case 4	Case 5
Pressure	barg	0.10	5.00	10.00	50.00	6.00
Mass release (W_g)	kg/s/flange	1.404E-06	7.019E-05	1.404E-04	7.019E-04	8.422E-05
Volume release	L/s/flange	0.016	0.781	1.561	7.807	0.937
LFL	vol/vol	0.040	0.040	0.040	0.040	0.040
Gas density (ρ_g)	kg/m^3	0.0899	0.0899	0.0899	0.0899	0.0899
Safety factor (k)	-	0.500	0.500	0.500	0.500	0.500
Release characteristic (V_g)	m^3/h	0.0028	0.1405	0.2811	0.1686	1.4053

CFD Modeling

The CFD model has been developed with a commercial CFD software (Ansys Fluent) and consist in a 3 million polyhedric cells that reproduce the fluid volume. Boundary conditions have been defined by imposing an outlet mass flow in the extractors and a pressure inlet in the door openings. This approach realistically models the actual building conditions. For turbulence model, two model has been tested (standard k-ε and SST k- ω). In order to characterize the leaks in the pipe joints, an opening area is created which corresponds to leakage value of each case study.

RESULTS AND DISCUSSION

The result of the CFD numerical model is shown in Fig.2 which shows the volumetric concentration of hydrogen inside the building in the range of 0-1%. In this case, ventilation system performance is evaluated to ensure that the concentration in all areas is below the maximum limit (1%).

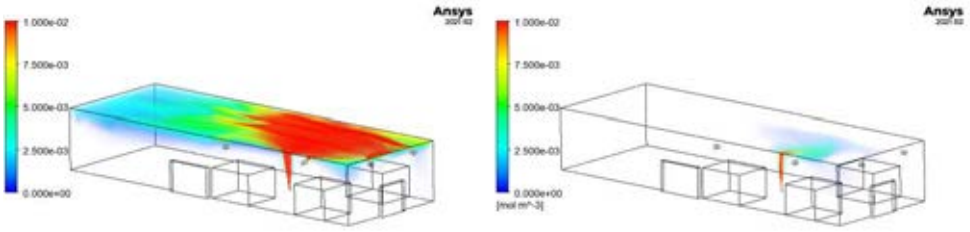


Fig. 2. Volumetric concentration of hydrogen in case 4 and 5

CONCLUSIONS

CFD is considered as a useful numerical model to evaluate air characteristics in all areas, such as velocity and gas concentration, especially in some areas where air dilution is inadequate which can't be measured easily by normal air measurement instrument. According to preliminary result of CFD model in Fig.2, hydrogen concentration inside the building is varied between 0-1% depends on number of air recirculation in each area, and in some particular areas is above than 1% which is the maximum limit off hydrogen according to UNE-EN 60079-10-1 standard. Therefore, the CFD model is useful to understand hydrogen distribution profile inside the building which will help us to design proper ventilation system in order to guarantee that hydrogen concentration inside the building in all areas less than 1%.

Moreover, a detailed study will be done with different variations of hydrogen release in order to give several recommendations concerning safety issues due to hydrogen release and to give the best recommendation based on good safety engineering practice.

NOMENCLATURE

W_g	Mass release of gas, kg/s
C_d	Discharge coefficient (dimensionless)
S	Cross section of the opening (hole), through which the fluid is released (m2) (Reference to EN 60079-10-1 2015 Table B.1)
M	Pressure inside the container, Pa
M	Molar mass of gas or vapour, kg/kmol
Z	Compressibility factor (dimensionless)
R	Universal gas constant, 8,314 J/kmol K
P_a	Atmospheric pressure, 101,325 Pa
T	Absolute temperature of the fluid, gas or liquid, K
V_g	Release characteristic, m^3/s
k	Safety factor attributed to LFL (dimensionless)
LFL	Lower Flammability Limit, vol/vol

Greek Letters

ρ_g	Gas density, kg/m^3

REFERENCES

1. API. 2003. API 505: Recommended Practice for Classification of Locations for Electrical Installations at Petroleum Facilities Classified as Class I, Zone 0, Zone 1, and Zone 2.
2. EIGA. 2021. EIGA Doc 15/21 Gaseous Hydrogen Installations
3. CEN-CENELEC. 2015. EN 60079-10-1 Explosive atmospheres - Part 10-1: Classification of areas - Explosive gas atmospheres
4. Malakhov AA, Avdeenkov AV, du Toit MH and Bessarabov DG. 2020.CFD simulation and experimental study of a hydrogen leak in a semi-closed space with the purpose of risk mitigation. International Journal of Hydrogen Energy 45:9231-9240.

WHEC-2022
23rd World Hydrogen Energy Conference
June 26-30, 2022 - Istanbul

#280

TOWARD THE CONTINUOUS SENSING OF LEAKED HYDROGEN BY A QUAD-ROTOR DRONE

[1]Takafumi SUGA and [1*]Kazuo MATSUURA*
[1]Ehime University, Bunkyo-cho, Matsuyama, Ehime, 790-8577, Japan

*Corresponding author e-mail: matsuura.kazuo.mm@ehime-u.ac.jp

ABSTRACT

Hydrogen is expected to leak in a variety of situations, from production to consumption. To realize a hydrogen sensing system that is more flexible and quicker than conventional systems, we have proposed a new drone-based system for hydrogen sensing with a small hydrogen sensor of the semiconductor type. Initially, quad-rotor drones were thought to be unsuitable for hydrogen leak detection because hydrogen is pushed away from the drone by propeller downwash. However, recent CFD (Computational Fluid Dynamics)-analyses and experiments detecting hydrogen at a drone have shown that hydrogen leak detection is possible even under the propeller downwash. In particular, it has been found that the flow rises from the leak source to the propeller outside the propeller downwash. In this study, we investigate the mechanism of hydrogen sensing by the quad-rotor drone through direct measurement of hydrogen dispersion around the drone. For this purpose, hydrogen leak experiments were conducted and the path of hydrogen dispersion around the drone was analyzed by twenty hydrogen sensors installed on a lattice constructed around the drone. These results substantiate, for the first time as long as the authors know, the hydrogen sensing mechanism mentioned above and support that reliable drone sensing can be achieved.

Keywords: Hydrogen safety, Sensing, Drone, CFD analysis, Smoke-visualization

INTRODUCTION

The use of hydrogen is becoming more and more widespread in our daily lives. From production to consumption, hydrogen leakage is anticipated in various situations. Generally speaking, hydrogen sensing can be categorized as fixed measurement, portable probing and laser measurement. In the fixed measurement, the location of a hydrogen sensor is fixed, therefore some time is required until hydrogen reaches the sensor from a leak source. In the portable probing, measurement becomes difficult in the places where human access is difficult. In the laser measurement, Raman scattering method based on an ultraviolet laser is known. In this method, optical system inevitably becomes expensive. To realize a hydrogen sensing system that is more flexible and quicker than conventional systems, we have proposed a system in which a small semiconductor-type hydrogen sensor is mounted on a drone [1]. Initially, it was anticipated that quad-rotor drones were unsuitable for hydrogen leak detection because the rise-up of hydrogen from a leak source is suppressed by the propeller downwash. However, recent-CFD analysis and smoke experiments have shown that hydrogen leak detection is still possible [2]. In this study, we will measure the process of hydrogen dispersion in order to clarify the mechanism of the successful hydrogen sensing.

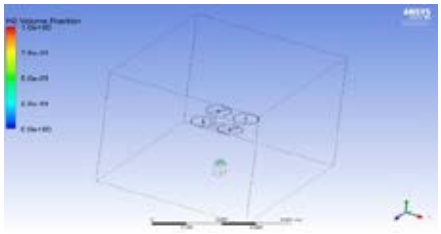
EXPERIMENTAL METHODS

Drone-based hydrogen sensing system

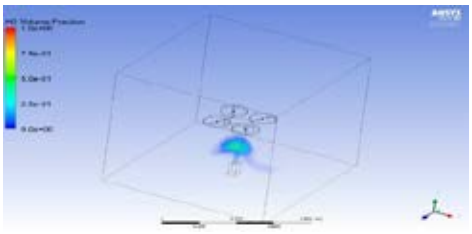
The sensor system is attached to a RC Logger's quad-rotor drone, RC EYE One Xtreme. The total length of the drone is 225 mm and the diameter of the propeller is 138 mm. The hydrogen sensor used in this project is an MQ-8 sensor from Zhengzhou Winsen Electronics Technology. This sensor is of semiconductor-type and its detection range is 100-10000 ppm. Its response time is less than 1s.

Hypothetical mechanism of the hydrogen sensing

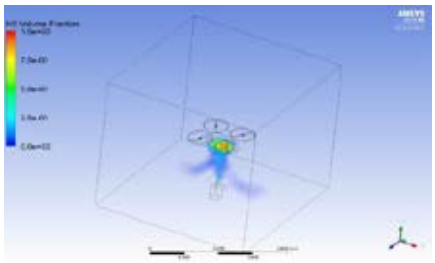
Drone sensing has been developed to enable easy detection of hydrogen leaks even in places where detection has been difficult by installing semiconductor-type sensors on drones. Initially, quad-rotor drones were thought to be unsuitable for hydrogen leak detection because the gas could not reach the sensor mounted on the drone due to the airflow of the propeller. However, the CFD analysis shown in Fig. 1 and the smoke experiment shown in Fig. 2 showed that it is feasible.



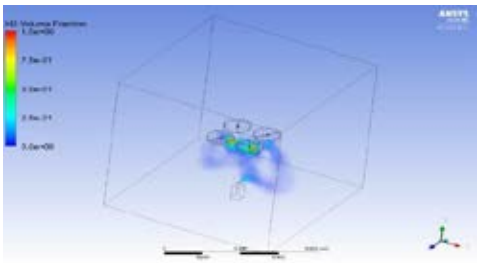
(a) t=3.5s (0.5s after the leak start of H2)



(b) t=5s (2s after the leak start of H2)



(c) t=6s (3s after the leak start of H2)



(d) t=7s (4s after the leak start of H2)

Fig. 1. Computed hydrogen distribution

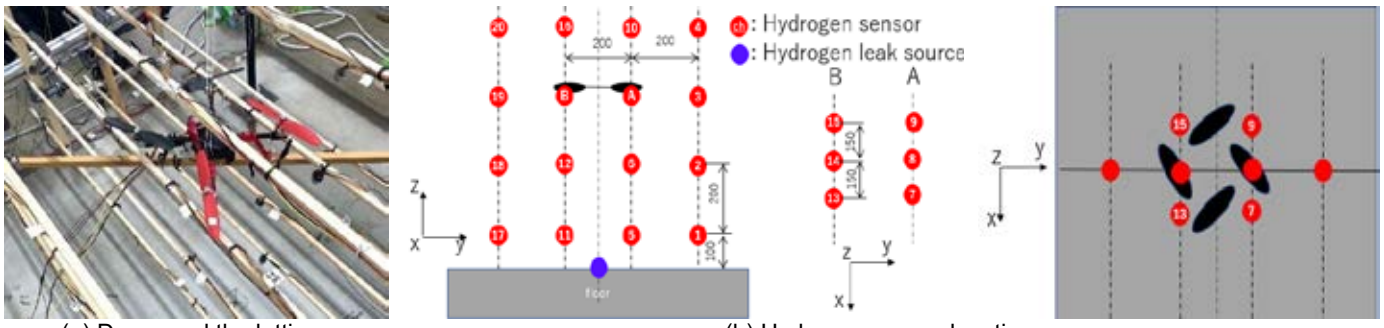


Fig. 2. Flow around the drone visualized by smoke experiment at the rotation speed of 1600 rpm (time evolves from left to right). Air stream circulation is created around the drone.

Figures 1 and 2 show CFD results of hydrogen dispersion around the drone and the flow around the drone visualized by a smoke experiment, respectively. In Fig. 1, computed hydrogen distribution for t=3.5-7 s is shown. Here, t=0 is the leak start. Hydrogen initially rises up from the leak source, and it is pushed down by downwash from the propellers. Hydrogen then passes outside the downwash and rises up again to the drone riding on circulating flows formed around the propellers. In Fig. 2, smoke is supplied from a pipe with small holes. For the purpose of clear visualization, smoke emission is terminated after a short time. Although smoke from the floor is diffused by the downwash of the propellers, flow circulation is formed due to suction from the upside of the propellers. From these results, it is considered that hydrogen from the leak source first rises to the propellers outside the region of propeller downwash, and then is sucked in and discharged from the propellers, which is the reason for the successful hydrogen detection by the present system.

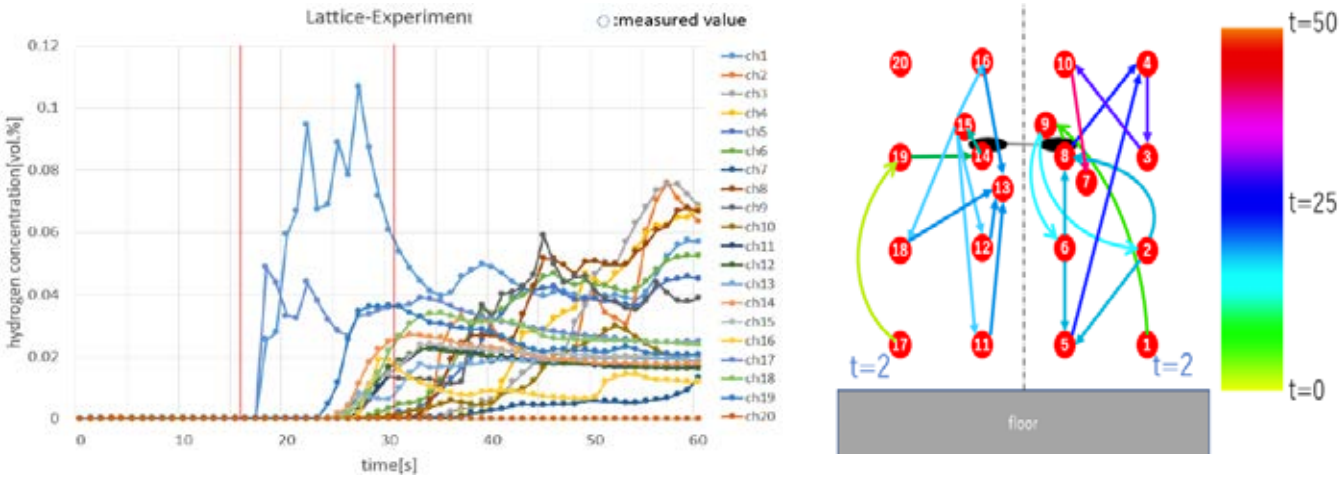
Direct measurement of hydrogen dispersion by a sensor array

In order to understand the actual path of hydrogen a sensor arrays was constructed as shown in Fig.3. A drone was placed at 50 cm directly above the leak source, and sensors were placed on the square bars held at 10 cm, 30 cm, 50 cm, and 70 cm from the floor. 100 vol.% hydrogen leaks from the leak source at the flow rate of 5 L/min for 15 s. The propeller rotation is 1600 rpm. Figure 4 shows the results. If we focus on the left side of Fig. 4, i.e., (b) detection order, the hydrogen arrive at Channel 17, 19 and 14, and then hydrogen diffuses to various regions around the drone.



(a) Drone and the lattice (b) Hydrogen sensor locations

Fig. 3. Experimental apparatus for the sensor array measurement



(a) Historical H2 concentration at each sensor (b) The path of hydrogen dispersion measured by the sensors

Fig. 4. Results of the sensor array experiment

CONCLUSIONS

A system called drone hydrogen sensing was proposed . The drone sensing was found to be feasible through the CFD analysis and smoke experiments, and a hypothesis was formulated about the detection mechanism. To corroborate the hypothesis, the process of hydrogen dispersion around an operating quad-rotor drone was measured by the sensor array consisting of twenty hydrogen sensors placed on a lattice constructed around the drone. Hydrogen from the leak source first rises to the propellers outside the propeller downwash and then is sucked in and discharged from the propellers. The present results, for the first time as long as the authors know, substantiate the previously-proposed mechanism of hydrogen sensing by a quad-rotor drone.

REFERENCES

1. Matsuura K. et al. 2018. Wireless high-speed continuous sensing of hydrogen leak by a quadrotor drone. Proc. of 3rd Int. Hydrogen Tech. Cong. (IHTEC-2018) March 15-18:1-3.
2. Matsuura K., Izawa N., Inoue M., 2021. Mechanism of continuous hydrogen sensing by a quadrotor drone. Proc. of 15th International Conf. on Heat Transfer. Fluid Mechanics and Thermodynamics. July 25-28:1-6.

WHEC-2022
23rd World Hydrogen Energy Conference
June 26-30, 2022 - Istanbul

#296

RISK EVALUATION OF HYDROGEN DISPERSION FROM COMPRESSED HYDROGEN (H_2) STORAGE VESSELS

* *Rafiziana Md.Kasmani,* *Arshad Ahmad, Norafneeza Norazahar , Aishah Abd.Jalil, Tuan Amran Tuan Abdullah, Mohd. Fadzhir Ahmad Kamaroddin*
Centre of Hydrogen Energy (CHE), Universiti Teknologi Malaysia, 81310 Johor Bahru, Johor, Malaysia.

*Corresponding author e-mail: rafiziana@utm.my, arshad@utm.my

ABSTRACT

Demand for hydrogen fuel increases with the introduction of fuel cell electric vehicles, giving increased pressure to minimize refueling station footprints and lower costs while maintaining safety and performance. Compressed gas hydrogen (H_2) storage is a viable approach to assuring sufficient hydrogen capacity at commercial fuelling stations. Due to the high pressure at which hydrogen is usually stored and dispensed, consequence analysis for risk assessment and power reduction is very crucial. In this regard, the present study aims at simulating hydrogen dispersion along with consequence analyses for such events as jet fire using ALOHA model. Dispersion consequence modeling was performed, followed by the evaluation of the effect of environmental (i.e., stability, ambient temperature, surface roughness, wind speed, and humidity) and process (i.e., vessel temperature and pressure, and leakage diameter) parameters on maximum size flammable vapor cloud and maximum level jet fire radiation on the ground. The size of flammable vapor cloud (consequence dispersion index) and the maximum flux of radiation were affected by process parameters more than ambient parameters. Leakage diameter was found to have the highest impact on the operational parameters.

Keywords: dispersion hydrogen, consequences, ALOHA

INTRODUCTION

Hydrogen is a promising energy carrier. However, hydrogen has a wide flammable range of 4–75 vol.% (in air) and a very low ignition energy of 0.019 mJ. The primary issue of hydrogen utilization is safety in various scenarios for the coming hydrogen economy. This work focuses on hydrogen leakage, which is typically induced by structural failure in refueling stations and transit vehicles, with attention to eliminate public concern and provide references for design, legislation, and standards. Rodionov et al. [1] presented a risk assessment of the hydrogen explosion related to a hydrogen-driven engine car. From the work, it stated that hydrogen explosion in open and semi-confined environments has a high level of risk with potential injuries to people and damage to cars and area of the hydrogen explosion. Hydrogen explosions in a confined environment have a low probability, but they can cause the most severe consequences to people, properties, and the area of the accident. For the safe design of retail facilities, through the development of appropriate codes, it is essential to understand all the hazards that could arise following an accidental release of hydrogen and to have data to allow the appropriate standards to be developed. These data can be also used to develop and validate models used in quantitative risk assessment tools [2-3] and tools based on computational fluid dynamics (CFD) [4] or tool based on integral models e.g. DEGADIS,SLAB, PHAST, HGSYSTEM, and ALOHA. The present study was formulated in order to determine the consequences caused by hydrogen dispersion, adopting ALOHA software. Variables such as wind speed and the leak hole diameter were selected as the factors to simulate the consequences of hydrogen storage leakage accidents. The impacts of each variable on accident consequences were analyzed for obtaining the reasonable and effective reference in actual accidents and conducting fire risk assessment.

SIMULATION METHODS

The model of dispersion chosen for the purpose of this research is the ALOHA model, which has been built upon the Gaussian dispersion model of continuous, buoyant air pollution flumes that capable to simulate the accidental release of hazardous substances and the dispersion of chemical vapor. For this work, hydrogen refueling station (HRS) facilities with storage involving compressed gas hydrogen have been chosen as the subjects of simulation. Suppose leakage occurred at Pasir Gudang highway, in Malaysia with longitude and latitude of 1.4825°N, 103.8811°E. The initial condition of the simulation and for the potential incidence of release, two hypothetical scenarios (I and II) have been created with environmental configurations as shown in Table 1.

Table 1 Initial condition and Potential incidence of release

Potential release	Scenario I: Rupture in tank at a refueling station (HRS)	Scenario II: Rupture of storage hydrogen tank in a car
Simulation scenarios	**a) Pipeline** • Diameter = 0.15, 0.20 and 0.30 m • Pipe length = 200 m • Pressure in pipe = 70 bar • Wind speed: 2 and 8 m/s from North • Ambient temperature = 33°C • Humidity = 46 % **b) For storage tank** • Direct source of hydrogen (worst case scenario) • Leak hole diameter of 15 cm • Volume: 300 litre • Uncongested area of hydrogen refueling station • Vessel pressure = 500 bar	Use Toyota Mirai as model for the simulation • Moving car – possible being hit at back (25-L hydrogen storage tank) • Possible rupture of all connected storage tanks (Total volume is 141 litre) • Storage pressure = 700 bar • Car moving in semi-confined area, e.g., tunnel • Car parked in a confined area and congested area, e.g., multilevel parking

RESULTS AND DISCUSSION

The main consequences of hydrogen leakage in this work are jet fire (radiation intensity) , flammable cloud and blast overpressure of vapor cloud explosion. Table 2 summarizes the maximum distance from the maximum jet fire, maximum flammable vapor cloud and blast overpressure when hydrogen leaks at different wind speeds i.e. 2 and 8 m/s. It can be depicted that the effect of the wind speeds on from the hydrogen leakage sources is minimum at the stable climate condition. However, when the leak hole diameter pipe increases in case of Scenario Ia, the maximum distance from flammable vapor cloud and maximum radiation level increase with a higher leakage diameter due to an increased release rate and an increased amount of hydrogen. For instance, from 15 to 30 cm leakage in pipe, the maximum distance from flammable vapor cloud and the thermal radiation jet fire increases ~ 2.3 – 2.8 times.

Table 3 Threat zones of hydrogen release computed in the ALOHA simulation at wind speed of 2 and 8 m/s.

8 m/s wind speed							
	Scenario Ia: Dispensing pipes at the HRS				Scenario Ib: Leaks from the storage tank		
Leak hole diameter	**Thermal radiation threat zone**			**Leak hole diameter**	**Thermal radiation threat zone**		
	10.0 kW/sq.	5.0 kW/sq.	2.0 kW/sq.		10.0 kW/sq.	5.0 kW/sq.	2.0 kW/sq.
15 cm	47 m	66 m	102 m	15 cm	12 m	16 m	25 m
20 cm	67 m	93 m	144 m				
30 cm	107 m	150 m	233 m				
	Flammable threat zone				**Flammable threat zone**		
	60 % LEL	10% LEL			60 % LEL	10% LEL	
15 cm	538 m	1600 m		15 cm	N.A	118 m	
20 cm	817 m	2500 m		Direct	N.A	110 m	
30 cm	1500 m	5000 m					
2 m/s wind speed							
Leak hole diameter	**Thermal radiation threat zone**		**Thermal radiation threat zone**				
	10.0 kW/sq.	5.0 kW/sq.	2.0 kW/sq.		10.0 kW/sq.	5.0 kW/sq.	2.0 kW/sq.
15 cm	47	65	101	15 cm	11	16	25
20 cm	66	92	143				

30 cm		107	149	231			
	Flammable threat zone				**Flammable threat zone**		
	60 % LEL	10% LEL			60 % LEL	10% LEL	
15 cm	5000 m	>10 km		15 cm	N.A	118 m	
20 cm	8900 m	>10 km		Direct	N.A	110 m	
30 cm	> 10 km	> 10 km					

For Scenario II, it can be said that the congested situation gave higher maximum distance of blast overpressure (0.55 bar) and 60% LEL flammable cloud i.e. 24 m and 97 m , respectively. It can be explained as; the multilevel parking and available cars can represent congestion and if engulfed by a vapour cloud, can lead to significant flame acceleration. The turbulent energy created by the congestion has a greater effect on explosiveness than does the total amount of leakage or premixed volume [6]. Hence the implication is that it is not necessary to release large quantities of hydrogen to obtain high overpressures on ignition. A release of relatively small quantities with rapid ignition may give a severe event.

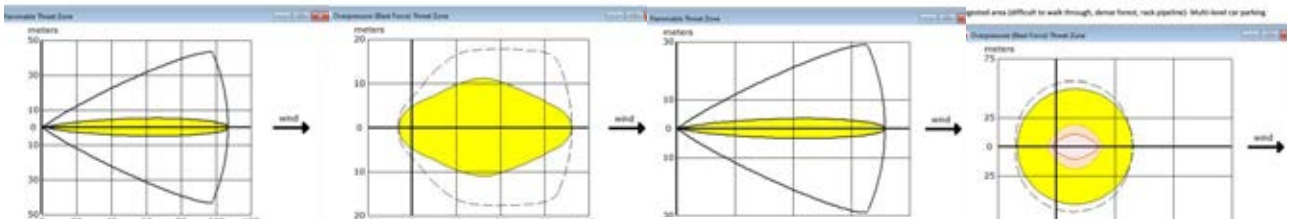


Fig. 2 Threat zones of hydrogen release from the vehicle storage leakage at total rupture for uncongested scenario (two from left) and congested area (two from right)

CONCLUSIONS

The current study evaluates parameters affecting the hydrogen dispersion and ignition using ALOHA model. It can be said that wind speed (climatic factor) gave a minimum change on maximum distances from the consequences scenario, however, the process condition i.e., leakage hole diameter showed a significant factor determining the maximum distance from the radiation intensity and blast overpressure. Likewise, congested area also plays vital impact on the resultant overpressure in case of total rupture of vehicle hydrogen storage.

ACKNOWLEDGEMENT

This work was supported by Malaysia of Higher Education (MOHE) under Research Excellence Consortium (REC) grant [R.J130000.7809.4L947] and Fundamental Research Grant Scheme (FRGS)[FRGS/1/2021/TK0/UTM/01/5].

REFERENCES

1. Rodionov, H. Wilkening, & P. Moretto, 2011. Risk assessment of hydrogen explosion for private car with hydrogen-driven engine. International Journal of Hydrogen Energy, 36, 2398–2406
2. Jin T, Liu Y, Wei J, et al. 2017. Modeling and analysis of the flammable vapor cloud formed by liquid hydrogen spills. Int J Hydrogen Energy. 42, 26762-26770.
3. Shao X, Pu L, Li Q, Li Y. 2018. Numerical investigation of flammable cloud on liquid hydrogen spill under various weather conditions. Int J Hydrogen Energy. 43, 5249-5260.
4. Dadashzadeh, M., Ahmad, A.,Khan F., 2016. Dispersion modelling and analysis of hydrogen fuel gas released in an enclosed area: A CFD-based approach, Fuel, 184, 192-201.
5. Sulaiman S.Z, Kasmani R.M, Mustafa A.B, Emami S.D, 2020. Flame propagation in a straight and 90-degree bend pipe for premixed hydrogen/air and methane/air, IOP Conference Series Materials Science and Engineering 736.

WHEC-2022
23rd World Hydrogen Energy Conference
June 26-30, 2022 - Istanbul

#384

INVESTIGATIONS ON THE DEFLAGRATION-TO-DETONATION PHENOMENA BY MEANS OF NUMERICAL SIMULATIONS WITH DETAILED CHEMISTRY AND AUTOMATED MESHING

[1] Pietro Scienza, [1] Marius-Gabriel Cojocaru, [2] Nitesh Attal, [2] Gaurav Kumar*
[1] Convergent Science GmbH, Hauptstrasse 10, 4040 Linz, Austria,
[2] Convergent Science Inc., Madison, WI, 53719, USA

*Corresponding author e-mail: pietro.scienza@convergecfd.com

ABSTRACT

When it comes to storing and transporting hydrogen, safety is key. Using Computational Fluid Dynamics (CFD) simulations in the design and verification of hydrogen storage and transportation devices has become the norm. Accurate CFD models for explosions and hydrogen venting involve complex meshing solutions applied in several iterations to refine and accurately capture the flame and shock positions. To this end, the current work builds on the study of the deflagration-to-detonation transition (DDT) phenomena by proposing and validating against experiments a novel simulation approach. This approach couples automated mesh generation and mesh refinement techniques with detailed chemistry to reduce the overall time to solution. The proposed method is coupled with different combustion modeling approaches, including the eddy dissipation concept and the homogeneous reactor model, as part of the validation study. The numerical simulations are centred around the analysis of DDT in hydrogen-rich enclosures that include a number of obstacles arranged in either a symmetrical or staggered manner. The influence of the layering of the gas species inside the enclosures that leads to homogenous or inhomogeneous conditions is discussed in parallel to the effects of the overall hydrogen fraction.

Keywords: Hydrogen Safety, Deflagration-to-Detonation Transition, CFD.

INTRODUCTION

The growing use of hydrogen as a viable source of energy in many sectors of our society puts greater demand on engineers to evaluate and design systems that have safety as one of the key criteria. In accordance with [1], the 1st priority of research topics related to "Accident Physics of Gaseous Hydrogen" is the "*premixed combustion associated with large scale problems with obstacles, flame acceleration and particularly deflagration-to-detonation-transition (DDT)*". DDT phenomena have long been of interest [2], and CFD is a valuable tool to analyze such complex physics. However, CFD often requires a high degree of expertise and several iterations for the user to build a model that is able to provide results with the desired accuracy. In order to address this issue, we propose and validate against experiments [3, 4 & 5] a novel simulation approach that reduces the number of mesh iterations and tuning model parameters. The DDT experimental setup used for validation consists of an enclosure (5400mm x 60mm x 300mm) that includes 7 rows of obstacles and an ignition source located at the center of the left-most wall; the obstacles produce a blockage ratio of 60% as shown in Fig. 1. The proposed method relies on automatic mesh generation and Adaptive Mesh Refinement [6] based on the local flow conditions. As shown by [4, 7 & 8], the combustion modelling and its related species reaction mechanism are other important aspects that enable the user to further improve the accuracy of the CFD model. To support this, two different combustion modelling approaches, the eddy dissipation concept (EDC) and the homogeneous reactor model (SAGE) [9, 10], are used. Following the validation of the proposed method, the effects of the existing gas layering and overall hydrogen concentration on DDT are analyzed. The last step involves the analysis of the geometrical layout of the obstacles for different blockage ratios and the effect on DDT [11].

CFD MODEL

The present work uses version 3.0.24 of CONVERGE CFD software, a cell-centered finite volume solver [6]. Here, CONVERGE solves the unsteady compressible Navier-Stokes equations using the Pressure-Implicit with Splitting of Operator (PISO) algorithm, coupling the energy, continuity, and species transport equations with the Redlich–Kwong equation of state. The momentum, continuity, species and energy equations are discretized using a second-order upwind scheme (MUSCL) based on the minmod limiter. The checker-boarding effect of the pressure-velocity coupling on collocated grids is mitigated through the use of the Rhie-Chow interpolation scheme. The turbulence is modelled with the Large Eddy Simulation (LES) approach using the Consistent Dynamic Structure model [12].

An automated mesh generation algorithm based on a modified Cartesian cut-cell approach is performed at runtime within the solver. In addition, the mesh is adjusted via an Adaptive Mesh Refinement (AMR) method during the simulation, introducing local on-the-fly grid refinements where gradients of selected variables exceed a certain user-specified threshold. This feature helps to remove the mesh generation iterations, which is particularly critical in cases dominated by strong gradients (e.g., shocks and flame front) and with a highly transient nature, as with DDT phenomena.

The combustion is modelled through different approaches: EDC and SAGE. The EDC model integrates the detailed chemistry into turbulent flows by assuming that reactions are happening at a scale based on the turbulence properties and that the reaction rate is controlled by the turbulence mixing. Therefore, the creation of new species and energy release/consumption source terms include turbulence quantities. For this reason, the Realizable k-epsilon turbulence model is used.

SAGE is a detailed chemical kinetics approach based on the homogeneous reactor model. With SAGE, the chemical reaction rates and the turbulent mixing directly determine the laminar and turbulent flame speeds. Adopting SAGE in the LES framework implies the usage of finer meshes to properly resolve the flame and turbulent structures. However, since these features are highly unsteady and localized, AMR proves to be an effective tool to limit the cell count [11].



Fig. 1. Model used for DDT simulation validation; ignition source shown in red.

RESULTS AND DISCUSSION

The validation geometry is shown in Fig. 1, and conditions are taken from [3, 4 & 5]. For the sake of brevity, only the results obtained with SAGE are shown here. In Fig. 3, the inhomogeneous and homogenous cases with 30% hydrogen molar fractions are computed and validated for the flame tip position and flame tip velocity. A reasonably good agreement with the experiments is observed for different hydrogen concentration and distribution, showing the transition from deflagration to detonation. As shown here, the transition from deflagration (where the flame tip proceeds with relatively low velocity) to detonation (where the front proceeds at few thousands meters per second) is happening sooner and more abruptly in the homogenous mixture, although higher flame tip velocities are obtained in the inhomogeneous mixture once the detonation is achieved. This seems to be in line with Chapman-Jouguet detonation speed [2, 4] and can be explained by the flame tip moving upwards in the channel, where the hydrogen mixture is higher on average than in the homogenous case with the same overall hydrogen concentration (see Fig. 2). In cases with a leaner hydrogen-air mixture (20% hydrogen concentration), the opposite trend has been observed. For reference, the theoretical Chapman-Jouguet detonation speed computed for a 30% hydrogen concentration is of the order of 2560 m/s. This seems to be well predicted by the simulation with the value of 2240 m/s. Gravity plays a larger role in the asymmetry of the burnt gas than in the flame front even in the homogenous mixture (Fig. 2). In these reacting flows with strong gradients, the numerical simulation is able to accurately account for the Richmeyer-Meshkov and Kelvin-Helmholtz instabilities. These are key ingredients in the shock-flame interaction, and this is where LES provides a more suitable modelling framework compared to URANS.

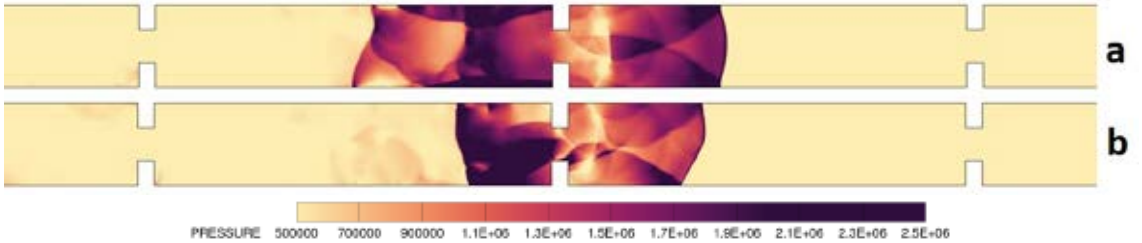


Fig. 2. Pressure [Pa] contours in the (a) homogeneous and (b) inhomogeneous mixture.

CONCLUSIONS

In this work, a novel simulation approach is proposed and validated against experiments for simulating hydrogen DDT phenomena with minimal user tuning required. Different combustion modelling approaches are investigated, as are the effects of the hydrogen-air mixture variation and the geometry modification on DDT.

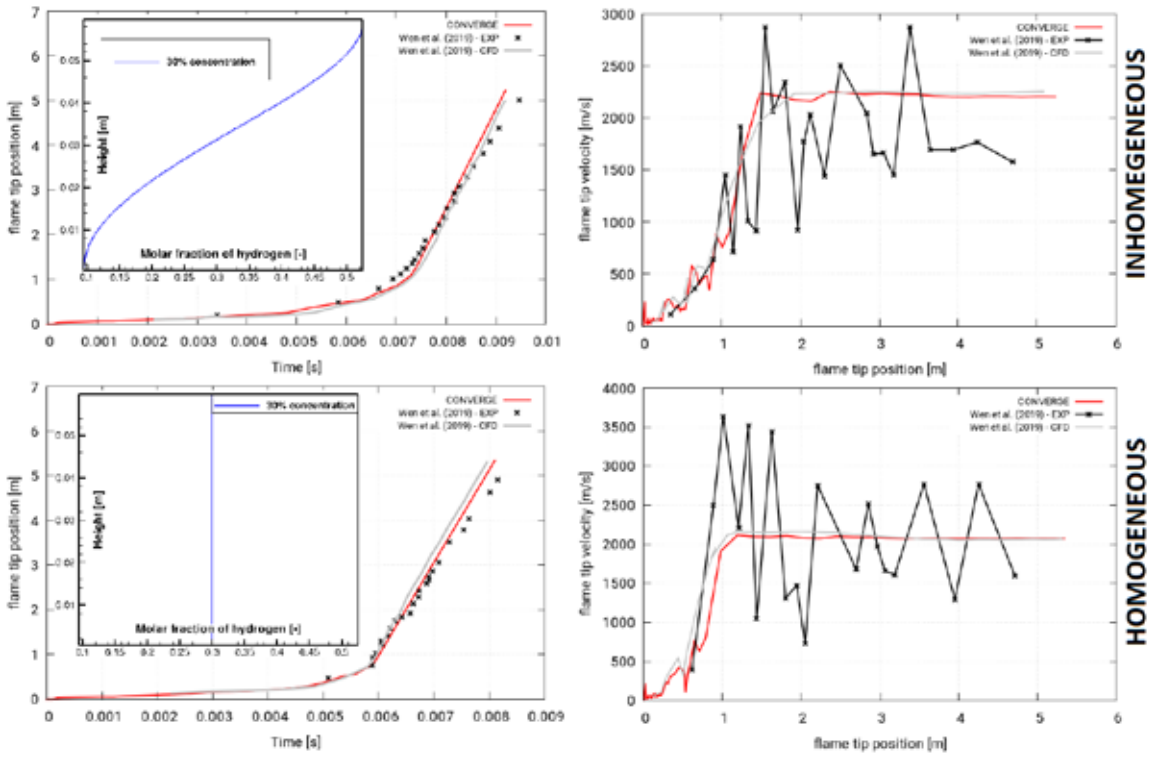


Fig. 3. Validation results against inhomogeneous and homogeneous hydrogen-air mixtures; experiments from [3, 4].

REFERENCES

1. Iñaki A, et al., 2018. International Association for Hydrogen Safety 'Research Priorities Workshop', Research Report RR1159.
2. Chue RS, Clarke JF and Lee JH, 1993. Chapman-Jouguet deflagrations. Proc. R. Soc. Lond. (1993): 607-623
3. Boeck LR, Katzy P, Hasslberger J, Kink A and Sattelmayer T, 2016. The "GraVent DDT Database". Shock Waves, 26:683–685
4. Wang CJ and Wen XJ, 2017. Numerical simulation of flame acceleration and deflagration-to-detonation transition in hydrogen-air mixtures with concentration gradients, International Journal of Hydrogen Energy, Vol. 42: 7657-7663.
5. Azadboni RK, Heidari A, Boeck LR and Wen XJ, 2019. The effect of concentration gradients on deflagration-to-detonation transition in a rectangular channel with and without obstructions – a numerical study, International Journal of Hydrogen Energy, Vol: 44; Issue13: 7032-7040.
6. Richards KJ, Senecal PK and Pomraning E, 2021. CONVERGE 3.0 Manual, Convergent Science, Madison, WI.
7. Dounia O, Vermorel O, Misdariis A and Poinsot T, 2019. Influence of kinetics on DDT simulations, Combustion and Flame, Vol. 200: 1-14.
8. Golub VV, Baklanov DB, Golovastov SV, Ivanov MF, Laskin IN, Saveliev AS, Semin NV and Volodin VV, 2008. Mechanism of high-pressure hydrogen gas self-ignition in tubes, Journal of Loss Prevention in the Process Industries 21: 185–198.
9. Senecal PK, Pomraning E and Richards KJ, 2003. Multi-Dimensional Modeling of Direct-Injection Diesel Spray Liquid Length and Flame Lift-off Length using CFD and Parallel Detailed Chemistry, SAE Paper 2003-01-1043.
10. Legier JP, Poinsot T and Veynante D, 2000. Dynamically thickened flame LES model for premixed and non-premixed turbulent combustion, Proceedings of the Summer Program, Center for Turbulence Research.
11. Nitesh OA and Gaurav K, 2022. Deflagration to detonation transition in two-dimensional obstructed channels, AIAA SCITECH 2022 Forum.
12. Pomraning E, 2000. Development of Large Eddy Simulation Turbulence Models, Ph.D. Thesis, University of Wisconsin-Madison, Madison, WI.

WHEC-2022
23rd World Hydrogen Energy Conference
June 26-30, 2022 - Istanbul

#429

FRETTING WEAR OF ELASTOMER MATERIALS IN HYDROGEN

[1*] *Géraldine Theiler,* [2] *Andreas Hausberger,*
[1]Bundesanstalt für Materialforschung und -prüfung (BAM), 12203 Berlin, Germany
[2] Polymer Competence Centre Leoben GmbH (PCCL), 8700 Leoben, Austria

*Corresponding author e-mail: Geraldine.theiler@bam.de

ABSTRACT

Safety and reliability are the major challenges to face for the development and acceptance of hydrogen technology. It is therefore crucial to study deeply material compatibility, in particular polymer materials that are directly in contact with hydrogen. This paper presents an experimental study on the fretting wear behavior of two types of cross-linked hydrogenated acrylonitrile butadiene rubbers against 316L steel ball in hydrogen environment. Furthermore, aging experiments were conducted for 7 days under static conditions in 100 MPa hydrogen. The influences of hydrogen pressure as well as the aging exposure on the fretting behavior are discussed by means of surface analyses and well as material properties.

Keywords: Fretting wear, elastomers, hydrogen, high-pressure

INTRODUCTION

The development of an infrastructure for the safe and reliable storage, handling and delivery of hydrogen is crucial for the expansion of hydrogen technology in the transport and industrial sector. Thereby, many polymeric materials that are directly in contact with hydrogen play a vital role in particularly in components such as seals, coupling systems and friction stressed surfaces in regulating and shut off valves [1]. It is therefore necessary to study the effects of hydrogen environment on friction and wear of polymers. Previous works on the sliding performances of polymeric materials pointed out the effect of polymer structure, fillers, temperature and counterface material in hydrogen environment [1-2]. Further studies in high-pressure hydrogen indicated the influence of fillers and fibers on the reciprocating behaviour of polymer and rubber materials [3-5]. For high pressure application, it is widely recognized that the main effects are swelling and blistering of rubbers due to rapid gas decompression. This can inevitably influence the tribological behavior of the polymers. Therefore, the focus of this study is to investigate the fretting behaviour of HNBR grades in hydrogen at different pressure up to 10 MPa compared to air and after hydrogen exposure in 100 MPa. For this purpose, aging experiments in 100 MPa hydrogen were conducted for 7 days under static conditions at the competence center H2safety@bam.

MATERIALS AND METHODS

Two different types of crosslinked elastomers provided from Arlanxeo Deutschland GmbH were investigated (Table 1). The mechanical properties of the rubber materials were examined before and after hydrogen exposure at 100 MPa, 120 °C and 7 days with dynamic mechanical analysis, tensile and hardness measurement.

Table 1. Composition of the HNBR investigated

Material	Fillers
HNBR 1	carbon black
HNBR 2	carbon black, polyamide

Friction tests were performed in a fretting tribometer developed at BAM for hydrogen environment up to 10 MPa. The upper specimen is a 316L stainless steel with a diameter of 6.0 mm. The lower specimen is the rubber fixed on a steel flat which is driven by a voice coil to make the reciprocating motion. The normal load was set to 5 N, the frequency 10 Hz and the stroke 2 mm. Before the tests, the elastomers were cleaned and exposed to dry heat at 60 °C for 48 hrs. This step is an essential pre-conditioning step for the removal of moisture content and outgassing of the samples that otherwise might have affected the properties of the hydrogen exposed samples. Tests were performed at room temperature in air and in hydrogen up to 10 MPa.

RESULTS AND DISCUSSION

Tribological tests revealed that hydrogen environment doesn't significantly affect the friction behaviour at normal pressure, but that the wear of the polymer decreases with increasing hydrogen pressure. Experiments performed

just immediately after hydrogen exposure at 100 MPa indicated however significant changes on the fretting behavior. Figure 1 show the friction curves of HNBR2 in air and at 10 MPa before and just after hydrogen exposure at 100 MPa. Comparing to air, the fretting behavior of HNBR2 in hydrogen is not affected by the environment. Before exposure, the fretting loop describe a slip motion between the steel ball and the polymer plate. After high pressure hydrogen exposure, the fretting process is characterized by increased adhesion due to elastic deformation, leading to partial slip. This could be explained by a decreased hardness of the elastomer measured immediately after high-pressure hydrogen exposure.

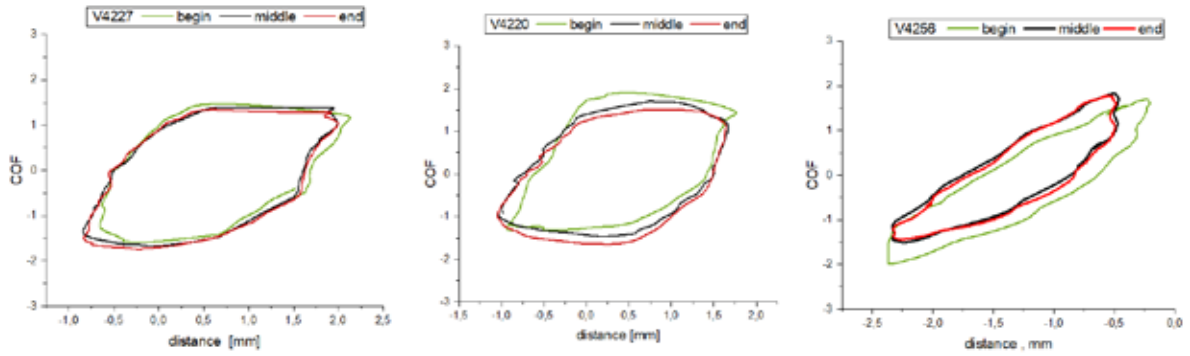


Fig. 1. Coefficient of friction of HBNR2 in air (a) and in H_2 at 10 MPa before (b) and after (c) H_2 exposure at 100 MPa

CONCLUSIONS

This paper presents an experimental study on the fretting wear behavior of two types of cross-linked hydrogenated acrylonitrile butadiene rubbers against 316L steel ball in hydrogen environment. Furthermore, aging experiments were conducted for 7 days under static conditions in 100 MPa hydrogen. Results reveal that hydrogen exposure has a significant influence on the fretting behavior of HNBR grades, changing the fretting process from gross slip to partial slip immediately after exposure at 100 MPa. This can be related to increased deformation due to decreased hardness of the elastomers.

ACKNOWLEDGEMENT

The research work was performed within the COMET-project “Polymers4Hydrogen“ (project-no.: 21647053) at the Bundesanstalt für Materialforschung und -prüfung (BAM) within the framework of the COMET-program of the Federal Ministry for Climate, Action, Environment, Energy, Mobility, Innovation and Technology and the Federal Ministry for Digital and Economic Affairs with contributions by Polymer Competence Center Leoben GmbH (PCCL, Austria), Montanuniversität Leoben (Department Polymer Engineering and Science, Chair of Chemistry of Polymeric Materials, Chair of Materials Science and Testing of Polymers), Technical University of Munich, Tampere University of Technology, Politecnico di Milano and Arlanxeo Deutschland GmbH, ContiTech Rubber Industrial Kft., Peak Technology GmbH, SKF Sealing Solutions Austria GmbH, and Faurecia.

REFERENCES

1. Theiler, G. and Gradt, T. 2015. Tribological characteristics of polyimide composites in hydrogen environment. Tribology International 92: 162-171
2. Theiler, G. and Gradt, T. 2016. Environmental effects on the sliding behaviour of PEEK composites. Wear 368: 278-286.
3. Theiler, G. and Gradt, T. 2021. Influence of counterface and environment on the tribological behaviour of polymer materials. Polymer Testing 93, 106912
4. Sawae, Y et al. 2021. Friction and wear of PTFE composites with different filler in high purity hydrogen gas. Tribology International 157, 106884
5. Duranty, E.R. et al. An in situ tribometer for measuring friction and wear of polymers in a high pressure hydrogen environment. 2017. Review of Scientific Instruments 88, 095114
6. Kuang, W. et al. (2021). In Situ Friction and Wear Behavior of Rubber Materials Incorporating Various Fillers and/or a Plasticizer in High-Pressure Hydrogen. Tribology International, 153, 106627

WHEC-2022
23rd World Hydrogen Energy Conference
June 26-30, 2022 - Istanbul

#436

METAL NANOPARTICLE DECORATED ZnO NANORODS FOR HYDROGEN SENSOR APPLICATIONS

[1*]Sadullah Öztürk, [2]Arif Kösemen, [3]Necmettin Kilinç, [4]Zafer Ziya Öztürk
[1]İstanbul University-Cerrahpasa, Institute of Nanotechnology and Biotechnology, İstanbul, TURKEY
[2]Mus Alparslan University, Department of Physics, 49100 Mus, TURKEY
[3]Inonu University, Department of Physics, 44280, Malatya, TURKEY
[4]Gebze Institute of Technology, Department of Physics, 41400, Kocaeli, TURKEY

*Corresponding author e-mail: sadullahozturk@iuc.edu.tr

ABSTRACT

In this study, ZnO nanorods, functionalized with Cr, Co, Ni and Cu metal nanoparticles are synthesized and the structural, electrical and hydrogen gas sensing properties are examined. ZnO nanorods with approximately 90 nm in diameter and 1 µm in length are produced by using hydrothermal method on ZnO seed layer coated glass substrate. Then Cr, Co, Ni and Cu metal acetate solutions are separately coated on ZnO nanorods by using spin coating method. It is obtained from structural characterization that the fabricated bare and metal functionalized ZnO nanorods are vertically aligned and have c–axis orientation. The FESEM images show metal nanoparticles with size below 20nm on ZnO nanorods. The electrical and hydrogen gas sensing characteristics of gold electrodes coated bare and metal functionalized ZnO nanorods are measured from room temperature to 200°C. The highest sensitivity and good selectivity were observed for Ni nanoparticles decorated ZnO nanorods.

Keywords: ZnO nanorods, Hydrogen, Gas Sensor, Nanoparticle, Decoration

INTRODUCTION

The increase in the amount of the using fossil fuels with the industrial revolution leads to the release of harmful gases to nature, negatively affecting the environment and human health. However, most of our energy today comes from fossil fuels. The use and dissemination of hydrogen gas as a primary energy source will enable both the elimination of the effects of global warming on humanity and the reduction of foreign dependency to meet the energy needs of countries. Fuel cells come to the fore in the use of hydrogen as an energy source. Hydrogen-based fuel cells generate electrical energy as a result of the chemical reaction between hydrogen molecules and oxidizing molecules. Although there are various studies and commercial applications on this principle from the past to the present, the energy shortages experienced reveal the value and necessity of using hydrogen energy. Despite its potential in the use of hydrogen as energy, it must be constantly monitored for gas leaks, as it is an odorless, tasteless and colorless gas and is explosive and flammable if it has a concentration above 4% in the air [1-3].Semiconductor metal oxide nanomaterials have been used as a sensing layer in the detection and monitoring of pollutants, inflammable and explosive, volatile organic compounds (VOCs), and toxic gases for many years due to maintaining stable structures against to harmful physical effects of ambient as temperature, humidity, pressure, and corrosion [4]. Zinc oxide (ZnO), tungsten oxide (WO_3), Tin oxide (SnO_2) and titanium dioxide (TiO_2) and have attracted the attention of researchers with their high sensitivity and fast response time, especially in sensor studies, due to their wide electronic band gap and d-symmetry of their valence orbits [5]. In gas sensor studies based on semiconductor metal oxide nanostructure, ZnO nanorods are frequently preferred because they can be synthesized with easy and low production cost techniques, and their electronic and chemical properties can be changed by the use of doping or heterostructure [6,7].

In this study, the changes in electrical and gas sensing characteristics of hydrothermally fabricated ZnO nanorods with metal nanoparticles were investigated. The selectivity properties of the sensor device developed with the decoration of metal nanoparticles differed. In addition, the gas sensing mechanisms of the developed metal-decorated nanorods are explained.

MATERIALS AND METHODS

The production of vertically oriented metal nanoparticle decorated ZnO nanorods on a glass substrate was carried out in three stages. The production steps are respectively forming the ZnO seed layer on the glass substrate, growing the ZnO nanorods, and decorating the metal nanoparticles with the sol-gel technique. Further information about ZnO nanorods fabrication with hydrothermal techniques was given in our previous works [8]. Fabricated ZnO nanorods were decorated with different metal nanoparticles as chromium (Cr), cobalt (Co), Nickel (Ni), and copper (Cu) for investigating selective detection of H_2 sensing with sol-gel techniques. For these purposes, acetate solution was prepared for each metal decoration and coated on the ZnO nanorods by using spin coating techniques at 2500 rpm for the 30s. The

coating process was repeated five times and then annealed at 300°C for 1h. The structural, morphological and composition of metal nanoparticle decorated ZnO nanorods were examined with X-ray diffractometer (D/MAX 2200) field emission scanning electron microscopy (FESEM, ZEISS ULTRA PLUS) and Energy Dispersive X-ray spectroscopy (EDX), respectively.
Gold (Au) interdigital transducers were coated on the surface of the metal nanoparticle decorated ZnO nanorods for electrical and gas measurements by using thermal evaporation systems. Current versus voltage measurements between -1V and +1V were realized for dc electrical characterization under dry airflow. Gas sensing measurements were realized in dry airflow in the homemade gas tight measurement cell. The fabricated ZnO nanorods were tested to the various concentration of the H_2, ethanol, and chloroform (1000 ppm to 5000ppm) for understanding sensing properties and especially selective detection of the H_2.

RESULT AND DISCUSSIONS

The morphologies of the ZnO nanorods and metal nanoparticle decorated ZnO nanorods were studied by using SEM. Fig 1a shows the SEM images of Cr nanoparticles decorated ZnO nanorods. All surfaces were covered with hexagonally shaped and vertically aligned ZnO nanorods and average diameters were approximately 90nm. Similar results were observed for all samples. To determine the decoration of the nanorods, cross-sectional SEM investigations were carried out at high magnification in Fig 1b. Facet surfaces of the ZnO nanorods were covered with the Cr nanoparticles. The content of the nanoparticle on the ZnO nanorods was investigated by EDX analysis (in fig 1c). In EDX spectra, Cr peaks with lower intensity were observed than Zn and O due to the concentration of the Cr atoms. Afterward, an XRD analysis was performed. Although there was no significant difference in the diffraction graph obtained from the analysis at first when the 002 peak was examined closely, the presence of a shift towards the right was detected. The presence of shifting in the diffraction angle is due to the effect of Cr and Co atoms placed around ZnO.

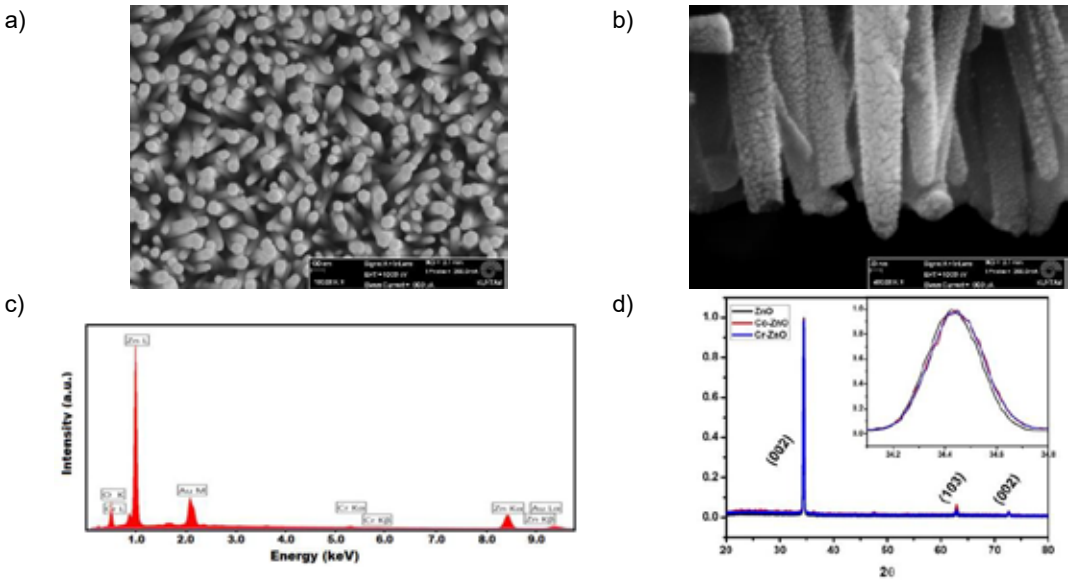
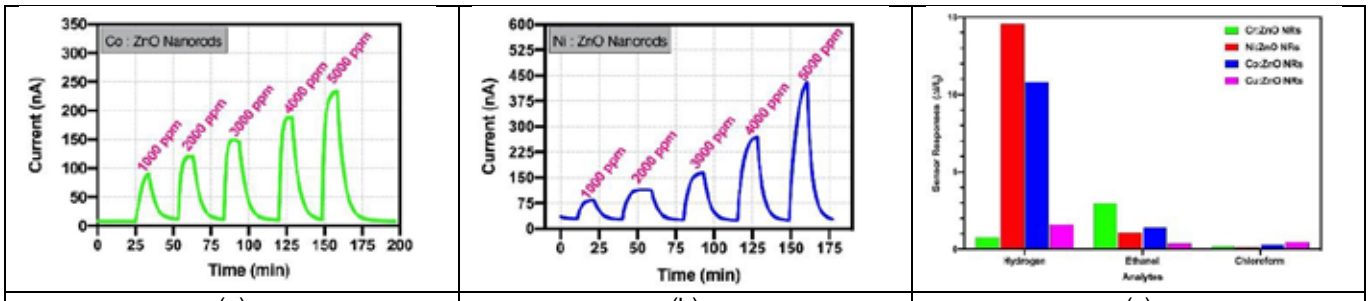


Fig. 1. a) SEM image of ZnO Nanorods, b) cross sectional and high magnificated SEM image of Cr nanoparticle decorated ZnO nanorods, c) EDX spectrum of Cr nanoparticle decorated ZnO nanorods and d) X-ray diffraction at 002 plane of bare ZnO Co and Cr decorated ZnO nanorods

Like all metal oxides with a wide electronic band gap and used as the gas sensing element, it produces a response against all analytes tested in ZnO. Although this provides a great advantage in sensor applications, it also leads to a decrease in selectivity. It is very important that the warning, which will indicate the dangerous situation, is reliable, especially when it is desired to be used in the monitoring of explosive and flammable gases. For this reason, the use of doping and heterostructures to increase the selectivity of metal oxides is a frequently encountered situation in the literature. Metal nanoparticle decorated ZnO nanorods were tested to the H_2, ethanol, and chloroform in various concentrations at 200°C under biased at 1V depending on increasing the sensitivity of the sensitive materials. The gas sensing mechanism of semiconducting metal oxide relies on a chemical reaction between oxygen ions absorbed on the metal oxide surface and target analyte molecules [3]. H_2, ethanol, and chloroform are reducing gases and therefore the current is expected to decrease or the resistance to increase. Current versus to time graphs of Co and Ni decorated ZnO nanorods were given in Fig 3a and 3b, respectively. When H_2 gas is purged into the measurement cell, the current of the sensing materials increases very rapidly and reached a steady-state level of nearly 6 min. Similar sensing responses were observed for other decorated sensor devices and also tested analytes. At this point sensor responses

are so important to understand selectively detection of the H_2 gas. Sensor responses of the metal nanoparticle decorated ZnO nanorods were tested to target analytes for 5000 ppm concentration in dry air ambient was given in Fig 3c. According to Fig. 3c, Ni nanoparticle decorated ZnO nanorods show better sensitivity for H_2. On the contrary, better ethanol sensor responses were observed for Cr decorated ZnO nanorods.



(a) (b) (c)

Fig. 1. Current vs time graphs of a) Co and b) Ni metal nanoparticle decorated ZnO nanorods exposed to H_2 and c) Sensor responses all fabricated samples versus to tested analytes for only 5000ppm

CONCLUSIONS

Gas sensing properties of ZnO nanorods decorated with metal nanoparticles were investigated in terms of selectivity and sensitivity properties. Among the decorated ZnO nanorods, it was determined that the sensitivity of Ni nanoparticles especially to hydrogen gas is higher than other metal nanoparticles. However, it was observed that the sensitivity values of the sensors developed by the exchange of metal nanoparticles differed against the other analytes tested, and it was determined that the selectivity was increased. On the other hand, it was observed that nanoparticle decoration was provided on the lateral surfaces of the nanorods with the sol-gel method, and an improvement in the physical properties of the base metal oxide was achieved.

ACKNOWLEDGEMENT

This study was partially supported by The Scientific and Technological Research Council of Turkey (TUBITAK) with a project number of 121M681 and Inonu University with a project number of FCD-2021-2587. The authors would like to thank Dr. Orhan Sisman for his valuable discussion and the authors also thank NOOR TEKNOLOJI Ltd for their support.

REFERENCES

1. Gopel W, Hesse J and Zeme JN. 1989. Sensors A Comprehensive Survey, 1st Edition, Wiley.,
2. Kilinc N. 2013. Resistive hydrogen sensors based on nanostructured metals and metal alloys, Nanosci. Nanotechnol. Lett. 5:825-841.
3. Hübert T, Boon-Brett L, Palmisano V and Bader MA. 2014. Developments in gas sensor technology for hydrogen safety. International journal of hydrogen energy 39(35):20474-20483.
4. Degler D, Weimar U and Barsan N. 2019. Current understanding of the fundamental mechanisms of doped and loaded semiconducting metal-oxide-based gas sensing materials. ACS sensors 4(9):2228-2249.
5. Eranna G, Joshi BC, Runthala DP and Gupta RP. 2004. Oxide Materials for Development of Integrated Gas Sensors—A Comprehensive Review. Critical Reviews in Solid State and Materials Sciences 29: 111–188.
6. Özgür Ü, Alivov YI, Liu C, Teke A, Reshchikov M, Doğan S, Avrutin V, Cho SJ and Morkoç AH. 2005. A comprehensive review of ZnO materials and devices. Journal of applied physics, 98(4): 11.
7. Choo TF, Saidin NU and Kok KY. 2018. Hydrogen sensing enhancement of zinc oxide nanorods via voltage biasing. Royal Society open science. 5(5): 172372
8. Öztürk S, Kılınç N, Taşaltın N and Öztürk ZZ. 2012. Fabrication of ZnO nanowires and nanorods. Physica E: Low-Dimensional Systems and Nanostructures. 44(6):1062-1065.

WHEC-2022
23rd World Hydrogen Energy Conference
June 26-30, 2022 - Istanbul

#1475

THE EFFECT OF CRYSTAL STRUCTURE AND METAL ELECTRODES ON GAS DETECTION IN TiO_2 NANOTUBES H_2 SENSORS

[1]Lutfi Bilal Tasyurek, [1]Esme Isik, [2]Ibrahim Isik [3]Necmettin Kilinc*
[1] Department of Optician, Malatya Turgut Ozal University, 44700, Malatya, Türkiye
[2] Department of Electrical Electronics Engineering, Faculty of Engineering, Inonu University, 44280, Malatya, Türkiye
[3] Department of Physics, Faculty of Science & Arts, Inonu University, 44280, Malatya, Türkiye

*Corresponding author e-mail: esme.isik@ozal.edu.tr

ABSTRACT

In this study, the effects of various metal electrodes and various crystal structures on hydrogen (H_2) gas sensors based on titanium dioxide (TiO_2) nanotubes were investigated. For the production of TiO_2 nanotubes, anodization method consisting of an electrolyte containing 0.5wt% NH_4F in 85% pure glycerol solution was applied. Scanning electron microscope (SEM) images of the obtained TiO_2 nanotubes were examined. In order to see the effect of different crystal structures of TiO_2, amorphous, anatase and rutile phases were obtained by annealing of samples. Each of the Ti/TiO_2 nanotubes/metal (Pd, Pt, Au, and Ag) gas sensors, obtained by coating with palladium (Pd), platinum (Pt), gold (Au) and silver (Ag) electrodes, was tested at room temperature at 1% H_2 concentration depending on three different phases.

Keywords: Titanium dioxide, nanotubes, hydrogen sensor, anodization, metal electrode

INTRODUCTION

Nowadays, H_2 has many industrial applications because it is environmentally friendly and low cost applications [1]. However, if the hydrogen concentration in the air increases, it can be flammable and explosive by mixing with oxygen. Therefore, there is a need to produce H_2 sensors with good sensitivity and selectivity to detect H_2 concentration before it reaches dangerous levels [2]. Many different technological methods such as catalytic, thermal conductivity, electrochemical, resistance based, work function based, mechanical, optical and acoustic are used in the production of H_2 sensor [3]. Titanium oxide (TiO_2), one of the metal oxides, has long been used in functional devices and gas mixture detection research due to its excellent thermal, synthetic and mechanical properties [4]. TiO_2 has three natural polymorphs: rutile, anatase and brookite [5]. TiO_2 can be produced in nanostructures (nanoparticles, nanorods, nanowires, nanotubes, etc.) with different surface-volume ratios and sizes [6]. TiO_2 nanotubes draw attention especially in gas sensor applications with their large surface-volume ratio and advantageous dimensions [7]. The fact that TiO_2 nanotubes can be easily produced by anodization method and their size can be adjusted depending on the anaodization parameters has enabled measurements at low temperatures and different gas concentrations in gas sensor research [8].

In recent years, TiO_2 nanotubes, which have been synthesized using various methods, have been shown to have different properties such as selectivity, response time, sensitivity, etc. against H_2 gas. The effects on the parameters are investigated. In order to produce TiO_2 nanotube-based H_2 sensors by anodization method, electrolytes consisting of hydrofluoric acid (HF) mixture, glycerol-based electrolytes, H_2SO_4-HF mixture solutions, NH_4F solutions in ethylene glycol (EG) were used [9]–[11]. Among these methods, TiO_2 nanotubes produced using glycerol-based electrolyte, high aspect ratio, arrangement, and response to H_2 gas attract attention.

To measure the current-voltage (I-V) change, metal electrodes such as Pt, Pd, Au, Ag etc. were coated on nanotubes. However, the sensing properties of these metals and various crystal structures against H_2 flow at different concentrations have not been compared.

MATERIALS AND METHODS

The high purity titanium foils with a thickness of 0.1mm, which we used to produce TiO_2 nanotubes, were cleaned by ultrasonic processes in acetone, isopropyl alcohol and deionized (DI) water in 15 minutes, respectively. Electrolyte solutions were prepared at 20 ^{0}C with 99.5wt% glycerol (85% purity) and 0.5wt% NH4F in a magnetic stirrer. In the anodizing process, a two-electrode system with DC power supply (20 V) and platinum gauze (99.9%, Sigma-Aldrich) as the cathode was applied for 120 minutes. After the production of TiO_2 nanotubes was cleaned and dried, SEM images (Fig. 1) were taken to examine their morphological structures. Then, TiO_2 nanotubes were annealed at 300 and 700 ^{0}C in dry air flow for 3 hours.

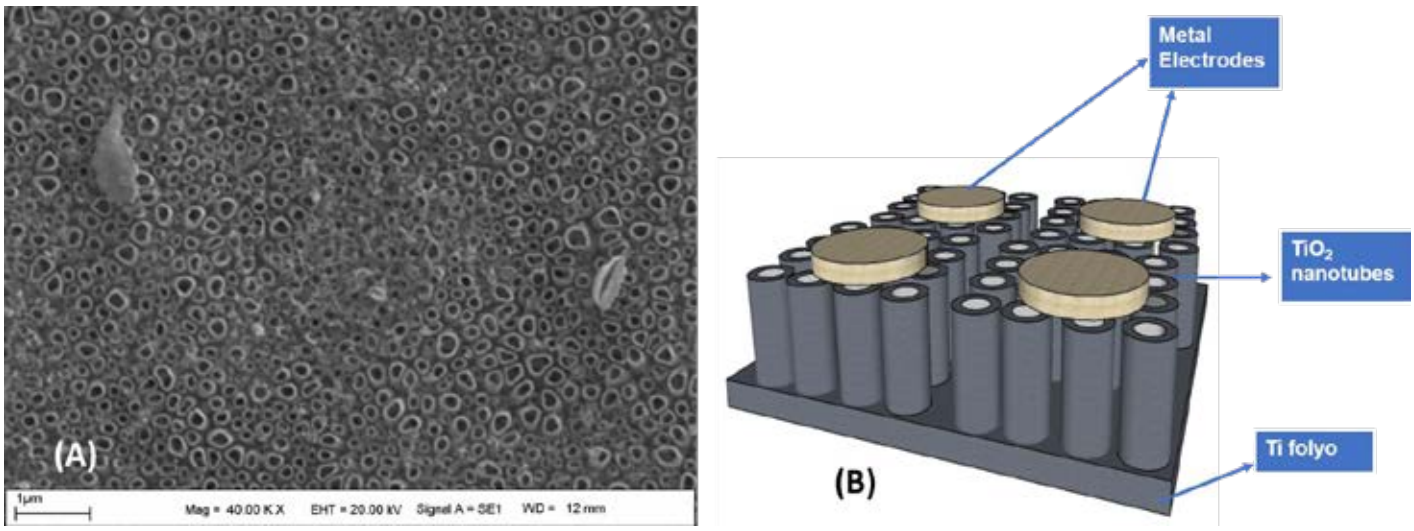


Figure 1. (A) SEM images of TiO_2 nanotubes, (B) schematic representation of TiO_2 nanotubes based gas sensors

Pd, Pt, Au and Ag electrodes were coated on unannealed, 300 and 700 ^{0}C unannealed TiO_2 nanotubes with 100 nm thickness by DC magnetron sputtering method using shadow mask. Thus, a total of 12 sensor structures were produced as in Fig. 2. Metal coatings of Pd/TiO_2 nanotube/Ti, Pt/TiO_2 nanotube/Ti, Au/TiO_2 nanotube/Ti and Ag/TiO_2 nanotube/Ti structures were used as upper electrode and Ti was used as lower electrode to take I-V measurements.

RESULTS AND DISCUSSION

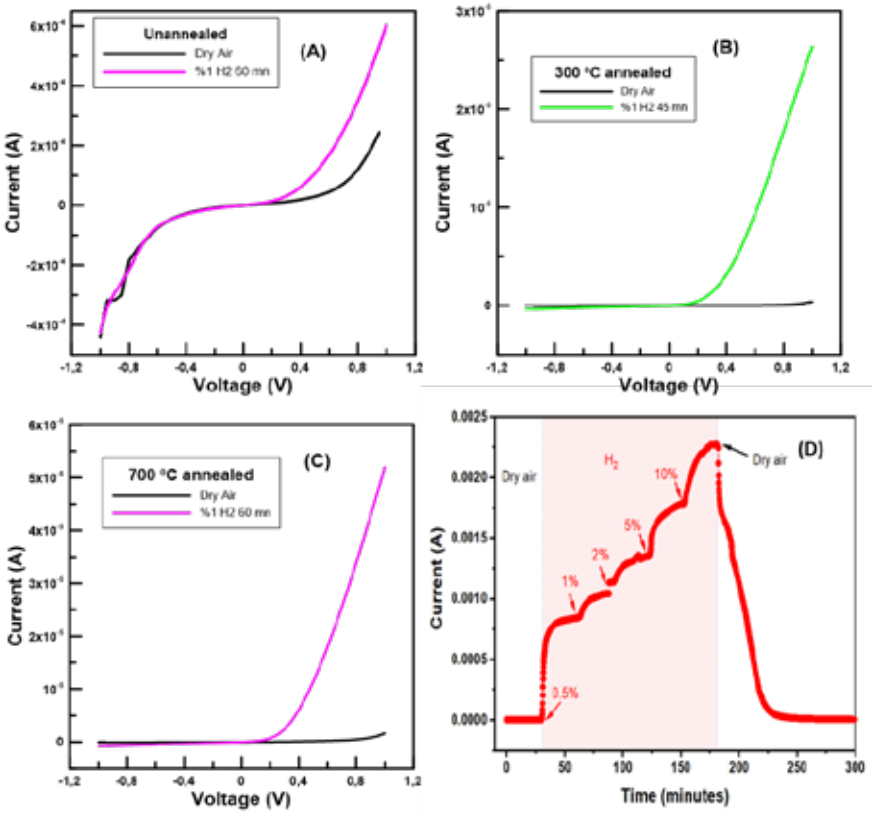


Figure 2. Current-voltage variation of Pt/TiO2 nanotubes/Ti devices (A) unannealed, (B) annealed at 300 and (C) 700 ºC (D) The current versus time for Pd/TiO2 nanotubes/Ti devices annealed at 300 ^{0}C by exposing various concentration of H_2

To explain the concentration due to H_2 gas sensing behavior on Pt/TiO_2 nanotubes/Ti sensor device structure, voltage applied current was measured in dry air and at a concentration of 1% H_2. Fig. 2A, B and C shows the current variation of the unannealed and annealed at 300 and 700 ºC of Pt/TiO_2 nanotubes/Ti devices. The response of the sensors to the gas can be calculated as follows;

$$\text{Sensor Response (R)} = \frac{\Delta I}{I_A} = \frac{I_H - I_A}{I_A} \quad (1)$$

where I_H is the current after the sensor is exposed to H_2, and I_A is the baseline value of the sensor exposed to dry air**.** The variation of the current as a function of time when exposed to various H_2 concentrations (1, 2, 5 and 10%) of Pd/TiO_2 nanotubes/Ti sensor device annealed at 300 ^{0}C is shown in Fig. 2D.

CONCLUSIONS

As a result, the production of TiO_2 nanotubes formed by anodic oxidation method on titanium foil has been completed. The effect of the crystal structure on the H_2 sensing properties of metal electrodes and TiO2 nanotube-based sensors was investigated. Unannealed, annealed at 300 and 700 ^{0}C, TiO_2 nanotubes exhibited Schottky-type behavior in I-V measurement in dry air condition and 1% H_2 environment. The measurements obtained show that the most ideal result belongs to the Pt electrode coated device annealed at 300 ^{0}C.

ACKNOWLEDGEMENT

This paper is based upon work from the European COST ACTION-Network for Research, innovation and product development on porous semiconductors and oxides CA20126 supported by COST (European Cooperation in Science and Technology). This paper was also funded by Inonu University Scientific Research Unit of Turkey (BAP, Project Number: FBA-2020-2315).

REFERENCES

[1] J. O. Abe, A. P. I. Popoola, E. Ajenifuja, and O. M. Popoola, “Hydrogen energy, economy and storage: Review and recommendation,” *International Journal of Hydrogen Energy*, vol. 44, no. 29, pp. 15072–15086, 2019, doi: https://doi.org/10.1016/j.ijhydene.2019.04.068.
[2] B. Sharma, A. Sharma, and J.-S. Kim, “Recent advances on H2 sensor technologies based on MOX and FET devices: A review,” *Sensors and Actuators B: Chemical*, vol. 262, pp. 758–770, 2018, doi: https://doi.org/10.1016/j.snb.2018.01.212.
[3] T. Hübert, L. Boon-Brett, G. Black, and U. Banach, “Hydrogen sensors–a review,” *Sensors and Actuators B: Chemical*, vol. 157, no. 2, pp. 329–352, 2011.
[4] C. M. Carney, S. Yoo, and S. A. Akbar, “TiO2–SnO2 nanostructures and their H2 sensing behavior,” *Sensors and Actuators B: Chemical*, vol. 108, no. 1–2, pp. 29–33, 2005.
[5] H. Kurban, M. Dalkilic, S. Temiz, and M. Kurban, “Tailoring the structural properties and electronic structure of anatase, brookite and rutile phase TiO2 nanoparticles: DFTB calculations,” *Computational Materials Science*, vol. 183, p. 109843, Oct. 2020, doi: 10.1016/J.COMMATSCI.2020.109843.
[6] P.-Y. Hsieh, Y.-H. Chiu, T.-H. Lai, M.-J. Fang, Y.-T. Wang, and Y.-J. Hsu, “TiO 2 Nanowire-Supported Sulfide Hybrid Photocatalysts for Durable Solar Hydrogen Production,” 2018, doi: 10.1021/acsami.8b17858.
[7] M. H. Seo, M. Yuasa, T. Kida, J. S. Huh, N. Yamazoe, and K. Shimanoe, “Detection of organic gases using TiO2 nanotube-based gas sensors,” *Procedia Chemistry*, vol. 1, no. 1, pp. 192–195, 2009, doi: 10.1016/j.proche.2009.07.048.
[8] N. Kılınç, E. Şennik, M. Işık, A. Ş. Ahsen, O. Öztürk, and Z. Z. Öztürk, “Fabrication and gas sensing properties of C-doped and un-doped TiO2 nanotubes,” *Ceramics International*, vol. 40, no. 1, Part A, pp. 109–115, 2014, doi: https://doi.org/10.1016/j.ceramint.2013.05.110.
[9] G. K. Mor, M. A. Carvalho, O. K. Varghese, M. V Pishko, and C. A. Grimes, “A room-temperature TiO2-nanotube hydrogen sensor able to self-clean photoactively from environmental contamination,” *Journal of Materials Research*, vol. 19, no. 2, pp. 628–634, 2004.
[10] C. Xiang *et al.*, “A room-temperature hydrogen sensor based on Pd nanoparticles doped TiO2 nanotubes,” *Ceramics International*, vol. 40, no. 10, Part B, pp. 16343–16348, 2014, doi: https://doi.org/10.1016/j.ceramint.2014.07.073.
[11] H. Liu, D. Ding, C. Ning, and Z. Li, “Wide-range hydrogen sensing with Nb-doped TiO2 nanotubes,” *Nanotechnology*, vol. 23, no. 1, p. 15502, 2011.

WHEC-2022
23rd World Hydrogen Energy Conference
June 26-30, 2022 - Istanbul

#1482

DETERMINATION OF SAFETY DISTANCE AND THE STRUCTURAL DAMAGE VULNERABILITY RESULTED FROM VAPOR CLOUD EXPLOSION (VCES)

Aminu Ismaila [a], *Rafiziana Md Kasmani* [b*], *Ahmad Termizi Ramli*
[a] Department of Physics, Ahmadu Bello University Zaria, Nigeria
[b] Energy Management Group, School of Chemical and Energy Engineering, Universiti Teknologi Malaysia, 81310 Skudai, Johor, Malaysia

*Corresponding author: rafiziana@utm.my

ABSTRACT

International Atomic Energy Agency (IAEA) specifies the principal requirements for the protection and mitigation strategies of safety-related plant components, within the vicinity of the nuclear plant. However, safety issues related to pressurized hydrogen release are of concern since a small leak in a hydrogen system could ignite easily, support a flame that is difficult to detect, and lead to catastrophic fire and explosion. In this work, three correlations used to determine the vapor cloud explosion prediction, i.e., Trinitrotoluene (TNT), TNO Multi-energy and Baker-Strehlow-Tang (BST) to estimate the failures and consequences of the accidental release of hydrogen in a hypothetical nuclear power plant. The data was compared to simulation results from FLACS dispersion model. It was shown that the consequential damage of explosion overpressure is strongly dependant on the global load of flammable gas volume and plant layout. In this work, 5000 m^3 of hydrogen explosion is sufficient to produce blast load wave for total plant destruction. It can be said that, for a safety consideration, a physical distance of 200 m between the explosion source and the target outer walls could be sufficient to protect against the explosion hazards.

Keywords: Blast Load Wave, Failure And Consequence Analysis, Hydrogen Explosion, Nuclear Plant, Safety Distance

INTRODUCTION

A large quantity of hydrogen gas is used in the nuclear plant to cool the unit generators and for binding the oxygen present in the exhaust gas systems. Hydrogen gas when is released under suitable conditions could form the dangerously explosive atmosphere in its vicinity. If ignited, could form a dangerously explosive atmosphere that could lead to catastrophic fire and explosion as evidently seen at the Muskingum River Power Plant in 2007 [1]. The consequences of VCEs on the nuclear island pose to substantial consequences on domino effect condition; high explosion overpressure, thermal radiation from the fireball, toxic gas dispersion and effect of explosion-generated fragments. The effect of overpressure is of greater interest rather than that of thermal radiation and the fragments. The explosion overpressure and blast waves could propagate several kilometres and could affect the functions of multiple redundant engineered safety systems. The severity of the resulting explosion is determined by the level of congestion and hence, the layout of structures in the plant, as a subsequent would give significant effect on the magnitude of severity in case of fire and/or explosion. Building structures, storage tanks and piping in the NPP will act as obstructing objects during explosion and tend to induce turbulent flow followed by the increase in pressure and impulse, capable of destructing nearby structures and causing the fatal damage. However, the sitting analysis of facilities is usually focused on the potential impacts of VCEs to building within the vicinity areas rather than the fatal damage. This study aims to investigate the physics and dynamic mechanism of hydrogen gas explosion as function of site distances by analysing the minimum standoff distance of central gas storage depot to other building structures, such that in an accidental release, the nearest building obstacles will not provide sufficient confinement that will generate higher explosion pressure and impulse that could lead to a progressive collapse of structures or pose serious threat to the safe operation of the plant. This is crucial particularly for multinuclear power plants that are under constructions around the world and the ones to be constructed in the feature. Therefore, in this work, energy-based analytical methods (Equivalent TNT mass method [2], TNO multi-energy method [2][3][4] and Baker-Strehlow-Tang method [2] and Computational Fluid Dynamics (CFD) FLACS simulation [5] were employed to estimate the blast load and impulsive loadings from VCEs. These methods were analysed and compared for the consequences analysis of explosion incident. The prime focus of this present paper is to determine the appropriate safety distance (as a countermeasure against the effects of explosion) such that an inherently safer operation of the NPP can be maintained during an explosion incident.

HYPOTHETICAL SCENARIO

In the accident scenario, it is considered that during delivery of hydrogen at a gas storage depot, a hydrogen relief device failed, causing a leak and ignition of the flammable cloud. Fig. 1. shows the plant layout for the multi-nuclear reactor site. A flammable hydrogen cloud of approximately 5003 m^3 is involved in a detonation type explosion. With the total of fuel dispersed, it is assumed that the overpressure produced would reach the surrounding building structures and the magnitude of explosion pressure received could challenge the safety functions of the components that were housed in such buildings.

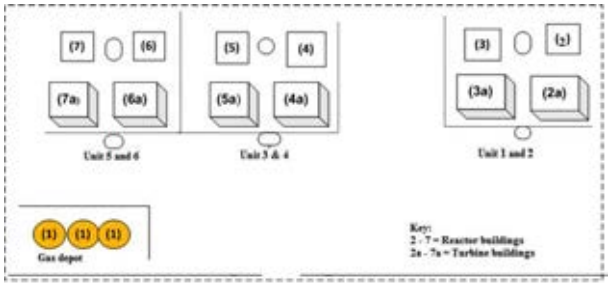


Fig. 1. The plant layout

RESULTS AND DISCUSSION

The effect of explosion overpressures and impulse loading as a function of separation distances

The functional relationship between overpressures and distance from the explosion position for the three empirical models is presented in Fig. 2a. The graph shows that TNT method predicts higher overpressure, as compared to that of TNO multi-energy and BST methods. The estimated overpressures shown in this graph are significantly higher, especially at a shorter distance (< 200 m) due to the deflagration to detonation transition alike phenomenon when hydrogen dispersed and exploded. The blast pressure measured at a detonation distance of 100 m for TNT, TNO, and BST were 2.19 bar, 0.17 bar, and 0.20 bar respectively. The damage corresponding to these overpressure levels are considered unbearable for most building structures. Accordingly, at a detonation distance of 150 m, the overpressures were 0.87 bar, 0.12 bar, and 0.14 bar, respectively.

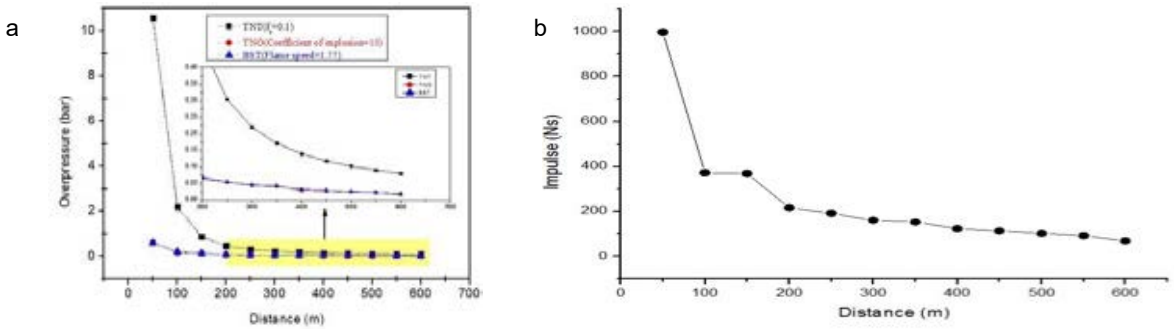


Fig. 2. (a) Overpressure and (b) impulse blast loading as a function of separation distance

Impulse load acting on structures may lead to the development of higher strain rates in reinforced concrete and its significant value may lead to substantial threat on structural integrity and safety function as indicated in [6]. At a longer distance of about 200 m, the impulsive loading is 215 Ns as shown in Fig. 2b. This value may not constitute much safety threats on surrounding buildings and relevant safety components exposed in the open.

Comparison of safety distance predicted by CFD and theoretical models

Table 3 presents a summary of overpressure estimation at some preselected locations by various models. As expected, the TNT method predicts higher overpressure loadings as compared to other two methods at the same distances. The discrepancies in the measurement between the TNT and other two models may be attributed to the differences in their formulation theories and assumptions adopted for a given scenario. It also indicates that FLACS CFD is grossly under-predicted explosion overpressure for the same detonation distances ~ 6 times lower than the computed data from the TNO and BST while an underprediction of ~59 – 79 is observed for the TNT measurements. The computed impulse from the TNO and BST measurements are ~2 times higher than that obtained with CFD technique [5].

Table 3: Overpressure estimation of VCE by various models

Method	Distance (m)	Overpressure (bar)	Impulse (Pa.s)
TNT	10	-	-
	60	7.10	-
	110	1.76	-
Baker–Strehlow–Tang	10	-	-
	60	0.50	970
	110	0.18	371
TNO (multi-energy)	10	-	-
	60	0.48	987
	110	0.18	360
CFD method	10	0.25	1240
	60	0.09	527
	110	0.03	220

CONCLUSION

This study presents the consequence analysis of VCE involving hydrogen gas dispersion in the vicinity of NPP, adapting the empirical correlations and FLACS CFD model. It can be said that empirical models predict higher value of impulse loading, however, the underpredicted values of FLACS model is not the preferred choice for the safety gaps studies, particularly at a far-field. It is also shown that the magnitude of explosion overpressure generated from the incident may affect other structural components and items exposed during VCEs within the radial distance of 100 m. Using a conservative value of 0.068 bar as the limiting overpressure on structures as in USNRC Regulation, the findings show that a minimum distance separation of 200 m between a gas storage depot and adjacent buildings could be sufficient to provide protection against the impact of explosion pressure waves from the postulated accident.

ACKNOWLEDGMENT

The work is partially sponsored by Ministry of Higher Education (MOHE) under Fundamental Research Grant Scheme (FRGS) vote no FRGS/1/2021/TK0/UTM/01/5. The authors greatly acknowledged the financial support to the postgraduate studentship of the first author by the Tertiary Education Trust Fund (TETFund), Nigeria.

REFERENCES

1. Angela, N. J. (2009). Lessons Learned from a Hydrogen Explosion (Vol. 2017).
2. Baker, W. E., Cox, P. A., Westine, P. S., Kulesz, J. J. and Strehlow, R. A. (1983). *Explosion Hazards and Evaluation*. (Vol. 5) Amsterdam, Natherlands: Elsevier Science.
3. Locking, P. M. (2011). The Trouble with TNT Equivalence. *Proceedings of the 2011 26th International Symposium on Ballistics*. 12 – 16 September 2011. Miami, 143-154.
4. van den Berg, A. C. (1985). The multi-energy method: A framework for vapour cloud explosion blast prediction *Journal of Hazardous Materials*. 12(1), 1-10.
5. Ismail, A., Kasmani, R.M., Ramli, A.T., (2019). Numerical evaluation of the severity of consequences of external fire and explosion incident at a nuclear power plant, Nuclear Engineering and Design, 355, 110314
6. Prugh, R. W. (1999). The Effects of Explosive Blast on Structures and Personnel. Process Safety Progress. 18 (1), 5-16.

WHEC-2022
23rd World Hydrogen Energy Conference
June 26-30, 2022 - Istanbul

#1514

ASPECTS OF RISKS USING MAGNESIUM HYDRIDE FOR ZERO EMISSION MOBILITY

[1*] *Bjørn Axel Gran,* [2] *Kjell Løvold,* [3] *Stefano Deledda,*
[1] Institute for Energy Technology, Norway
[2] Hydrogen Storage AS, Norway

*Corresponding author e-mail: bjorn.axel.gran@ife.no

ABSTRACT

The maritime sector has an increased focus on zero emission mobility solutions. One new initiative using hydrogen, is based upon storing hydrogen as magnesium hydride (MgH_2). Since in a such solution, continuous heating is required to desorb H_2, hydrogen storage in MgH_2 is considered a safer solution compared to compressed or liquified H_2. Indeed, if by accident there is a rupture of the metal container, the endothermic desorption of hydrogen will cool down MgH_2 and, as soon as heating is stopped, no hydrogen will be released. Institute for Energy Technology (IFE) was asked by a client to evaluate the safety benefits of magnesium hydride. This included to conduct a preliminary risk assessment and comparing the findings with similar risk assessments on the use of hydrogen and ammonia solutions related to use as a maritime fuel. The work also included compiling an overview of applicable rules and guidelines applicable in Norway, and an overview of relevant past incidents. This paper summarises on that work. One conclusion from the work is that the risk and safety assessments should not only include technical aspects, but also human, organisational and operational factors.

Keywords: Magnesium Hydride, Hydrogen Storage, Risk Assessment, Human Factors, Organisational Factors

INTRODUCTION

The regulator for most land facilities handling dangerous substances in Norway is the Directorate for Civil Protection (DSB) which provides guidance on how to address risk, vulnerability and emergency preparedness. Two main principles to follow are individual risk criteria defined through zones, and to apply the ALARP (As Low As Reasonably Practicable) principle. The ALARP principle says that the risk shall be reduced to the lowest level that can be achieved with reasonable effort. These principles are also applicable all over Europe.

When designing vessels fuelled by flammable gaseous fuels like hydrogen “the International Code of Safety for Ships using gas or other low-flashpoint fuels” (the IGF Code) gives the applicable rules [1]. The HyLaw Online Database [2] has a good overview of relevant legislation for most parts of Europe. The European pressure equipment directive (PED) applies to the design, manufacture and conformity assessment of stationary pressure equipment with a maximum allowable pressure greater than 0.5 bar [3]. There are no EU rules that describe exactly how one should conduct risk assessments, but the Your Europe Portal part for “Health and safety at work” recommends to [4]: (1) Collect the relevant information; (2) Identify the possible hazards; (3) Assess the risks arising from the hazards; for example, estimate the probability and severity of the consequences and decide whether the risk can be tolerated; (4) Plan actions to eliminate or reduce risk and (5) Document the risk assessment.

Lloyd’s Register Consulting issued in 2019 a report for DSB [5], providing guidance for performing facility risk assessments which is in line with the ISO 31000:2009 standard. In 2020 Lloyds Register Consulting issued a report for the Ocean Hyway Cluster on the use of hydrogen and ammonia infrastructure [6]. That report discusses risk aspects related to infrastructure, including production, transport, storage and bunkering, for zero emission fuels, such as hydrogen and anhydrous ammonia used as a maritime fuel. It also provides an overview of relevant historical accidents for the different fuels. For hydrogen and methane this is primarily explosion accidents, while for ammonia toxic exposure for people is the main concern. An increasing number of accidents has been seen in recent years. One pinpointed cause is the lack of experience in handling hydrogen. Another cause argued by Hydrogen Europe is that hydrogen is by many, non-technical stakeholders, considered to be safer than other fuels [7]. This is not in line with the very high reactivity of hydrogen.

Many hydrogen incidents can be found in the European Union HIAD database [8] and at the US DoE H_2 tools site [9]. Some accidents of interest are:

- The Hindenburg Disaster, 1937: 97 persons on board, filled with 15-20 tons of hydrogen, caught fire approaching the destination in New Jersey killing 36 people.

- Hydrogen explosion at the NI ammonia plant of Norsk Hydro (now Yara) at Herøya, Norway, 1985: damaging a larger plant building beyond repair and leading to severe window shattering within a 400m radius. This resulted in fatalities of two employees.
- Two explosions in pipelines at Herøya, 1986 and 1997: involved deflagration-to-detonation.
- The Challenger space shuttle disaster, 1986: besides killing all 7 astronauts, also led to the release and a fireball involving liquid oxygen and hydrogen from the failing fuel tanks.
- Hydrogen explosion accident at the Tesoro refinery near Seattle, WA, USA, 2010: high temperature hydrogen attack led to the burst of a heat exchanger during a start-up procedure, killing all 7 workers involved.
- Fukushima accident, 2011: explosions in hydrogen generated from meltdown represented steps in the chain of events.
- Uno-X Hydrogen refuelling station at Kjørbo in Sandvika, Norway, June 2019: A major release from a 950-bar tank containing less than 3 kg hydrogen ignited after 2-3 seconds resulting in a strong outdoor explosion [10]. An attempt to model possible release and explosion scenarios using computational fluid dynamics (CFD) indicates that an unconfined detonation of around 0.5kg hydrogen would be likely, and required, to explain observed effects [11].

To evaluate the safety benefits, IFE conducted a preliminary risk assessment of MgH_2 This included facilitating a Hazid meeting with stakeholders from academia and consultancy. Besides the case owner with insight in the solution, the team included an expert with insight on system and models and experts with insight in both technical and operational aspects of using hydrogen as a fuel in the maritime sector. 17 risks were identified, whereof 14 were classified in the yellow area of the ALARP and required us to evaluate mitigations. 26 mitigations were identified. If all 26 mitigations are implemented, only one risk “Exposure to heat (external fire) is not acceptable as this requires mitigations to systems outside of the scope of this assessment.

The DNV Handbook for Hydrogen-fuelled Vessels [12] points out that “*Hydrogen gas is flammable, highly explosive, and has different safety-related properties and behaviour compared with other gases including natural gas*”. Further it is also stated that “*As hydrogen is the smallest of all molecules, hydrogen gas is more challenging to contain than other gases; it has a wide flammability range, ignites easily, and may self-ignite. This combination of properties may lead to increased overall risk, unless applicable safety systems and practices concerning hydrogen are implemented*”. In view of this, the Hazid was considered to have taken an appropriate focus as it ended out with mitigations that are both technological (related to safety systems) and organisational (related to practises). The handbook also points to a number of maritime conditions, which are relevant for different solutions including magnesium hydride: (i) A ship is self-reliant on sea, (ii) Escape is not possible for crew or passengers, (iii) Safety distances are smaller on a ship than on land, (iv) Exposure to environmental conditions at sea (v) Power demand depends upon ship and operation at the ship; and (vi) Interface between storage and power generating system. It is therefore crucial to do specific risk assessments with the real volumes of potential released hydrogen, the actual safety systems and the actual safety distances on that ship. Compared to compressed gas storage, the potential volumes of hydrogen released from magnesium hydride stores are smaller. However, one question arises: is this volume small enough to not prompt unwanted consequences? When hydrogen gas can be stored in the open, it has several advantages since leakages can disperse in the open air. In the case of magnesium hydride, it might require that also the heating systems and interface to the power generating system needs to be designed on top of the ship. This may have negative impact on ship stability. In addition, there may over time be more leakages due to corrosion.

For compressed gas, there is a need of the following safety systems: tank, fuel lines, hydrogen vent systems, ventilation systems, pressure regulation unit(s), fire protection system, H_2 detection systems, safety systems (fire detection, firefighting systems, emergency shutdown systems); and structural fire protection.

Desorption of H_2 from magnesium hydride does not need any compression but requires heating. A high-pressure tank or a pressure regulation system is therefore not needed, but all the other safety systems need to be in place. In addition, there is a need of the following safety systems: heat protection systems and ignition control systems. One will in addition have a larger amount of potential leakage points that needs to be ventilated and monitored.

One observation from the Hazid is that many unwanted incidents ended in the yellow ALARP (as low as reasonably practicable) area. This could be an indication that there are uncertainties both for the frequency and the consequence assessments. Another observation from the Hazid is that all the unwanted incidents, including those that could lead to an explosion, could be mitigated. That made the risks acceptable. The identified mitigations were both related to technical aspects of the design as well as operational aspects of the use of magnesium hydride. This is at a first glance a good sign. However, the results could also be due to a misconception on the frequency estimations due to lack of

historical relevant experience and a wish of having the solution to work safe. The Hazid therefore recommended that all the risks were revaluated with specific leakage rates when concrete designs are available.

CONCLUSIONS

This paper has provided some background on rules, guidelines and historical incidents that are applicable for hydrogen-based solutions in Norway. The paper also discusses the results from a risk assessment on a magnesium hydride/based hydrogen storage solution with other risk assessments. Desorption of H_2 from magnesium requires the following safety systems: fuel lines, hydrogen vent systems, ventilation systems, pressure regulation unit(s), fire protection system, H2 detection systems, safety systems (fire detection, firefighting systems, emergency shutdown systems), structural fire protection, heat protection systems and ignition control systems. One will in addition have a larg amount of potential leakage points that needs to be ventilated and monitored. Findings from the Hazid are that there are uncertainties both for the frequency and the consequence assessments of the events, but also that all the unwanted incidents could be mitigated. That made the risks acceptable. The identified mitigations were both related to technical aspects of the design as well as operational aspects of the use of magnesium hydride. The conclusion from the Hazid supports the recommendation of doing holistic risk assessment when addressing the use of hydrogen-based solution for maritime mobility.

ACKNOWLEDGEMENT

The Hazid work was funded by the Regionale Forskningsfond Oslo via the project “Magnesiumhydrid for null-utslipp mobilitet i den maritime sector” (Project no. 321779).

REFERENCES

1 https://www.imo.org/en/OurWork/Safety/Pages/IGF-Code.aspx. Accessed on January 29, 2022
2 https://www.hylaw.eu/. Accessed on January 29, 2022
3 https://ec.europa.eu/growth/sectors/pressure-equipment-and-gas-appliances/pressure-equipment-sector/pressure-equipment-directive_en. Accessed on January 29, 2022
4 https://europa.eu/youreurope/business/human-resources/social-security-health/work-safety/index_en.htm. Accessed on January 29, 2022
5 Lloyd’s Register. 2019. *Guidelines for quantitative risk analysis of facilities handling hazardous substances*, Report no: 106535/R1 Rev A.
6 Lloyds Register. 2020, *Hydrogen and Ammonia Infrastructure, Safety and Risk Information and Guidance*, Report no: PRJ11100256122r1 Rev: 00.
7 https://hydrogeneurope.eu/hydrogen-safety. Accessed on January 29, 2022
8 https://odin.jrc.ec.europa.eu/giada/. Accessed on January 29, 2022
9 https://h2tools.org/lessons. Accessed on January 29, 2022
10 https://nelhydrogen.com/status-and-qa-regarding-the-kjorbo-incident/. Accessed on January 29, 2022
11 https://mozees.no/wp-content/uploads/2019/10/Hansen_Hydrogen-safety_Kjoerbo-incident-overview-and-perspectives.pdf. Accessed on January 29, 2022
12 DNV. 2021. Handbook for Hydrogen-fuelled Vessels.

WHEC-2022
23rd World Hydrogen Energy Conference
June 26-30, 2022 - Istanbul

#1519
HYDROGEN SENSING PROPERTIES OF ULTRATHIN Pt-Co ALLOY FILMS

[1,2]M Erkovan, [3]C. Deger, [1,2]S Cardoso, [4*]N. Kilinc
[1]Instituto de Engenharia de Sistemas E Computadores – Microsistemas e Nanotecnologias (INESC MN) Lisbon, 1000-029, Portugal
[2]Instituto Superior Tecnico (IST), Universidade de Lisboa, 1040 001 Lisbon, Portugal
[3]Marmara University, Physics Dept. 34722, Ziverbey, Istanbul, Türkiye
[4]Inonu University, Department of Physics, 44280, Malatya, Türkiye

*Corresponding author e-mail: necmettinkilinc@gmail.com

ABSTRACT

In the present work, ultrathin Pt_xCo_{1-x} (x=1, 0.75, 0.5 and 0.25) alloy films are fabricated using co-sputtering with approximately 2nm in thickness. The stoichiometry and structural characterization of the thin films are obtained from SEM, EDX and XPS measurements. The structural characterization of the thin films showed smooth coverage of the surface, in a fcc crystalline plane (111). The resistive properties of the films are tested towards a hydrogen gas sensor between 25 °C – 150 °C in the gas concentration ranging from 0.5% to 5%. The surface scattering phenomenon could explain the hydrogen gas sensing mechanism of ultrathin Pt_xCo_{1-x} alloy thin films. PtCo alloy thin films show better response time than bare Pt thin films.

Keywords: Platinum, Platinum-cobalt alloys, Thin films, Hydrogen sensor, Gas Sensor

INTRODUCTION

The use of hydrogen (H_2) as a clean, efficient, and sustainable energy source has been expanding into various fields since it will permit the reduction of the CO_2 gas generated by the combustion of fossil fuels. These fossil fuels are the main cause of the greenhouse effect [1]. Therefore, alternatives such as H_2 are seriously considered as an ideal energy source of the future [2] and will be critical enablers to achieve the European Green Deal's ambitious goals.

The H_2 has unusual properties such as a very low density, low boiling point and a high diffusion coefficient. It also possesses a low minimum ignition energy, a high combustion heat and a wide flammable range compared to other gases. The H_2 also acts as a robust reducing agent for many elements and has a high permeability through many materials, which demands special precautions in specific applications. For example, the H_2 is colorless, odorless, tasteless, and is a flammable gas, and it cannot be detected by human senses, unless it is present in high concentrations. In this regard, rapid and accurate H_2 gas measurement is essential to alert to the formation of potentially explosive mixtures with air, to help prevent the risk of an unexpected explosion. Until now, various types of H_2 sensors have been extensively studied and published [3-4], and are commonly classified into nine categories depending on their evident physical/chemical principles of detection mechanism: (i) catalytic, (ii) electrochemical, (iii) resistor based (semiconductor and metallic) (iv) work function based, (v) mechanical, (vi) optical, (vii) acoustic, (viii) thermal conductivity and more recently (ix) magnetic. One type of H_2 sensor, the resistive metallic H_2 sensor uses palladium (Pd), platinum (Pt) and their alloys as a sensitive layer. Pd based resistive metallic H_2 sensors have been intensively studied, but there are limited studies about Pt based resistive H_2 sensors [5], specially when combined with magnetic materials that can be integrated in sophisticated spintronic structures.

In this study, the changes in electrical resistivity and H_2 gas sensing properties of Pt_xCo_{1-x} thin films fabricated by the sputtering method are investigated depending on temperature, Co content in the alloy and H_2 concentration. In addition, the mechanisms of Pt_xCo_{1-x} thin films as gas sensors are explained.

MATERIALS AND METHODS

Ultrathin Pt_xCo_{1-x} films with approximately 2 nm were deposited onto Si/SiO2 100nm substrates using a Nordiko 2000 machine. The Nordiko 2000 is a magnetron sputtering system including a load lock for sample transfer and a high vacuum chamber (base pressure 4×10^{-8} Torr) with 6 targets. The Pt_xCo_{1-x} (x=1, 0.75, 0.5 and 0.25) thin films were grown by co-sputtering from pure Co and Pt targets, in a wave-mode deposition mode, where the alloy film is achieved through sequential deposition of N layers of Pt and Co, after deposition rate calibration at 1.15 Å/s and 0.44 Å/s for Pt and Co, respectively.

Structural characterization of the film was done by field emission scanning electron microscopy (ZEISS ULTRA PLUS), Energy Dispersive X-ray spectroscopy (EDX), X-ray diffraction (XRD, Rigaku D/MAX 2200), Rutherford backscattering spectrometry (RBS), X-ray photoelectron spectroscopy (XPS, Specs-Flex) techniques.
The electrical resistance of the sensor device was measured on the top of the thin films by two silver contacts. The resistance (R_H) of the films is continuously measured under different ambient conditions. The dry air is used as a carrier gas, the H_2 concentration is changed from 0.5% to 5%, and the temperature is varied between 25 °C and 150 °C by using a heater in the measurement cell.

RESULT AND DISCUSSIONS

Fig. 1a shows the SEM image of one $Pt_{0.5}Co_{0.5}$ film sample from where one can infer the surface of the film is smooth, with no segregation of $Pt_{0.5}Co_{0.5}$. The XRD spectra of Pt and $Pt_{0.5}Co_{0.5}$ thin films are seen in fig.1b. The peak near 40° comes from (111) plane reflection, and that corresponds to a face-centered cubic crystalline structure [6]. The chemical compositions of PtCo alloy films were investigated by the XPS technique. The XPS spectra of Pt and Co from $Pt_{0.75}Co_{0.25}$ thin film sample are shown in Fig. 1c and 1d, respectively. To analyze the chemical composition of PtCo alloys, high-resolution elemental XPS spectra for Pt 4f and Co 2p regions were taken within $Pt_{0.75}Co_{0.25}$ thin film sample and it is calculated as 73:27.

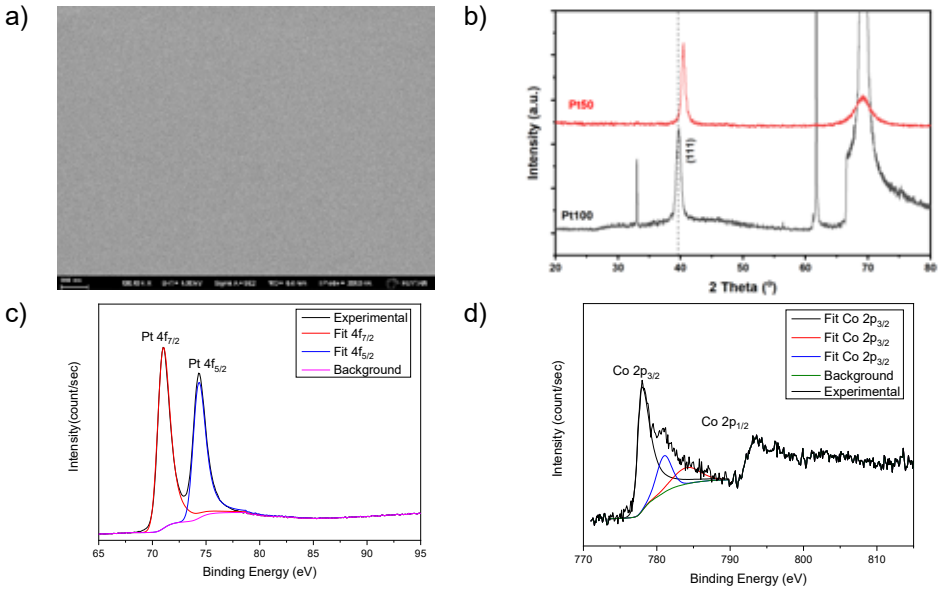
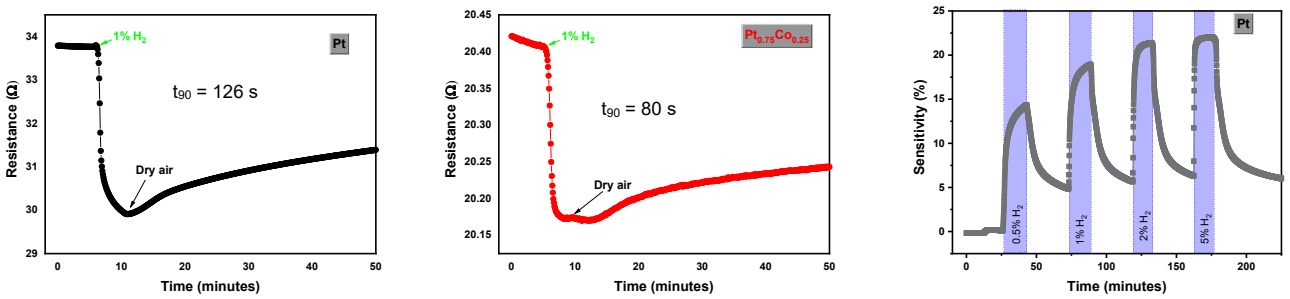


Fig. 1. a) SEM image of $Pt_{0.5}Co_{0.5}$ alloy thin film, b) XRD spectrum of Pt (Pt100) and $Pt_{0.5}Co_{0.5}$ alloy (Pt50) thin films c) $Pt_{0.75}Co_{0.25}$ alloy thin film's XPS spectra for photoemission of Pt 4f region and d) of Co 2p region.

Fig. 2a and 2b show the resistance change of Pt and $Pt_{0.75}Co_{0.25}$ thin film samples during exposure to dry air and 1% H_2 at room temperature. The resistances of both samples are decreased when the measurement cell is purged with 1% H_2. Similar behavior was reported for Pt nanowire [7,8] and Pt thin films [9,10]. After cleaning the measurement cell with dry air, the resistances of both samples increased slowly and remain larger than their baseline values for more than 40 minutes. During the resistance of Pt_xCo_{1-x} thin films measurement under dry air flow, the surface of the films is covered with adsorbed oxygen. While H_2 is exposed to the films, hydrogen atoms dislocate with oxygen atoms, and the number of electron surface scattering decreases. So the decrease in the resistances of Pt_xCo_{1-x} thin films could be elucidated with the surface scattering phenomenon. Fig. 2c shows sensitivity ($\frac{\Delta R}{R_H} x100$) as a function of time for Pt thin film sample under different H_2 concentrations at room temperature. The sensitivity is enhanced with increasing gas concentration.



(a) (b) (c)

Fig. 2. The resistance versus time graphs of a) bare Pt and b) $Pt_{0.75}Co_{0.25}$ thin film samples at room temperature. c) Sensitivity as a function of time for bare Pt thin film sample exposure to cycles of increasing H_2 concentration at room temperature

CONCLUSIONS

In this study, different chemical compositions of PtCo alloy films were prepared by sputtering deposition. XRD, XPS, SEM and RBS techniques were used to characterize for their structural and chemical compositions properties. H_2 sensing properties of the different PtCo alloys, the resistance of the films and sensitivity were measured under different hydrogen atmospheric conditions. The results were compared to pure Pt film. The hydrogen sensitivity decreases with the increasing Co ratio in the PtCo alloy films.

ACKNOWLEDGMENT

This study was supported by the research fund of TUBITAK with project number: 121M681. The authors also wish to acknowledge the Fundação para a Ciência e a Tecnologia for funding of the Research Unit INESC MN (UID/05367/2020) through plurianual BASE and PROGRAMATICO financing. The authors also thank to Inonu University (project number : FCD-2022-2864) for supporting conference attendance.

REFERENCES

1. Momirlan M and Veziroglu TN. 2002. Current status of hydrogen energy, Renewable and sustainable energy reviews. 6(1-2):141-179.
2. Armaroli N and Balzani V. 2011. The hydrogen issue, ChemSusChem. 4(1):21-36.
3. Hübert T, Boon-Brett L, Black G and Banach U. 2011. Hydrogen sensors–a review. Sensors and Actuators B: Chemical, 157(2):329-352.
4. Chauhan PS and Bhattacharya S. 2019. Hydrogen gas sensing methods, materials, and approach to achieve parts per billion level detection: A review. International journal of hydrogen energy, 44(47): 26076-26099.
5. Kilinc N. 2013. Resistive hydrogen sensors based on nanostructured metals and metal alloys, Nanosci. Nanotechnol. Lett. 5:825-841.
6. Chang I, Woo S, Lee MH, Shim JH, Piao Y and Cha SW. 2013. Characterization of porous Pt films deposited via sputtering. Applied surface science, 282:463-466.
7. Yoo HW, Cho SY, Jeon HJ and Jung HT. 2015. Well-defined and high resolution Pt nanowire arrays for a high performance hydrogen sensor by a surface scattering phenomenon. Analytical chemistry, 87(3):1480-1484.
8. Yang F, Donavan KC, Kung SC and Penner RM. 2012. The surface scattering-based detection of hydrogen in air using a platinum nanowire. Nano letters, 12(6): 2924-2930.
9. Patel SV, Gland JL and Schwank JW. 1999. Film structure and conductometric hydrogen-gas-sensing characteristics of ultrathin platinum films. Langmuir, 15(9):3307-3311.
10. Sennik E, Urdem S, Erkovan M and Kilinc N. 2016. Sputtered platinum thin films for resistive hydrogen sensor application. Materials Letters, 177:104-107.

WHEC-2022
23rd World Hydrogen Energy Conference
June 26-30, 2022 - Istanbul

#1534

AN EXPERIMENTAL APPARATUS FOR IN-SITU STUDIES OF HYDROGEN INGRESS, DISSOLUTION AND PRECIPITATION AT CONTROLLED TEMPERATURE AND APPLIED TENSILE STRESSES

[*] *Julien Lang, Michael Gharghouri, [3] Helmut Fritzsche*
[1]Canadian Nuclear Laboratories, 286 Plant Road, Chalk River, Canada

*Corresponding author e-mail: julien.lang@cnl.ca

ABSTRACT

This manuscript presents the design and utilisation of a unique environmental chamber allowing specimens to be heated and cooled, under tensile load and controlled atmosphere, while in a neutron beam, offering a unique opportunity for in-situ neutron diffraction experiments. The chamber was built to gain insight into the impact of parameters such as tensile stress, temperature and exposed atmosphere on the hydrogen solubility of materials and on the mechanisms relating to delayed hydride cracking, hydrogen embrittlement and hydrogen ingress.

The investigation presented in this work shows the chamber's performance up to 450°C and 275 MPa applied tensile stress. The effect of tensile stresses and temperature on hydrogen solubility in Zr-2.5Nb is presented for a sample nominally charged to a hydrogen concentration equivalent of 500 wppm (mg/kg). Due to kinetic factors, no significant effect of tensile stress on the hydrogen solubility of our samples was found for temperatures up to 300°C and at tensile stresses up to 275 MPa.

Keywords: Hydrogen, tensile stress, ingress, dissolution, precipitation

INTRODUCTION

It is well known that material degradation can lead to a weakening of mechanical and structural properties. In the nuclear industry, the use of zirconium-based materials that are exposed to hydrogen can lead to failure and cracking, compromising the system's safety and functionality. Indeed, when a zirconium alloy's hydrogen concentration exceeds its terminal solid solubility (TSS), it becomes susceptible to a crack initiation and propagation process called delayed hydride cracking (DHC). [1 - 3] Therefore, knowledge of the solubility limit as a function of temperature and applied stress is critical for the development of guidelines for fitness-for-service and reactor life-extension, advanced reactor designs, as well as, in the development and validation of DHC modeling.

Since the hydride volume fraction decreases as the result of hydride dissolution when the temperature increases, a neutron diffraction peak's intensity would decrease proportionally until, at the critical temperature for dissolution, T_{TSSD}, the peak would disappear completely into the background. Conversely, on cooling from a temperature at which all the hydrides are dissolved, the intensity of the hydride peak becomes non-zero at the critical temperature for precipitation, T_{TSSP}. Thus individual hydride diffraction peaks provide an unambiguous indication of changes to the hydrides as a function of temperature. [4 - 7]

It is known that applied stress influences hydride orientation [5, 8]. The influence of stress on hydrogen solubility though, has not been extensively investigated. The unique capabilities of our chamber allow such in-situ studies and a deeper understanding of hydrogen ingress/egress needed for both energy storage and materials performance studies. The chamber can also be used to determine the effect of hydrogen concentration, temperature, composition, microstructure, surface condition, and mechanical load on materials performance using in-situ neutron diffraction measurement.

The present study is a proof of concept of our controlled environment furnace. The effect of a tensile stress on the terminal solid solubility of deuterium via in-situ neutron diffraction was examined.

EXPERIMENTAL METHODS

Controlled Atmosphere Furnace

A custom controlled-atmosphere furnace for *in-situ* neutron diffraction studies of hydrogen ingress/egress and hydride precipitation/dissolution under load was designed, fabricated, and tested. Figure 1 shows a schematic of the assembled furnace. The furnace consists of two isolated chambers, one being an inner controlled-atmosphere specimen chamber and the other being an outer vacuum chamber. The chambers are isolated in such a way that a high vacuum can be maintained in the outer chamber while controlled gas is introduced as a static pressure or flowed in and out of the inner chamber.

The furnace's outer jacket is made of 3.175 mm thick 6061 aluminum alloy and has integrated water cooling jackets above and below the specimen position. This configuration provides neutron transparency at the height of the specimen and proper cooling to the rubber O-rings, keeping them within the specification temperatures. The inner sample chamber is made of high-performance alloy Nitronic 60, also known as alloy 218, with a wall thickness of 2.03 mm. The base of the inner chamber contains the gas inlet and outlet ports, which are also used to evacuate the chamber, and thermocouple feedthroughs. Conflat (CF) vacuum seals, which use a copper gasket and knife-edge flanges to achieve an ultra-high vacuum seal, are used at the top and bottom of the inner chamber to isolate it from the outer chamber. The CF seals proved effective up to an operating temperature of 450°C at the sample position.

The specimen is connected directly to the load frame base plate and actuator via steel pull rods and interchangeable grips, such that the furnace body is not subjected to, or does not affect, the loading during tests. The interchangeable grips allow different specimen geometries to be accommodated. Stainless steel bellows of 0.254 mm thickness are used to provide a vacuum seal between the pull rods and the top and bottom flanges of the inner chamber.

When connected to the load frame base plate, the lower pull rod is stationary. The upper pull rod, however, is moveable in the axial direction, with the bellows allowing ~20 mm of travel. The upper pull rod exits the outer chamber via a guard vacuum technology. Since the up and down movement of the rod through the guard vacuum piece implies that the hole's diameter must be bigger than the rod's diameter, there is a risk that air can leak into the chamber, causing oxidation on, and therefore compromising, the heating element. A guard vacuum is used to stop these gas molecules and protect the heating element. Standard commercial vacuum and gas fittings are used throughout the furnace.

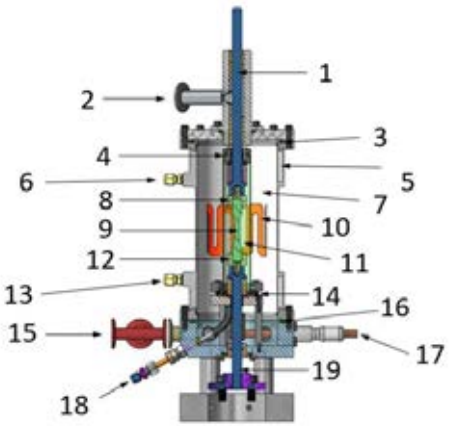


Figure 1: Schematic of controlled-atmosphere furnace. 1- upper pull rod, 2- guard vacuum pumping port, 3- upper body o-ring vacuum seal, 4- pull rod bellows CF copper gasket seal, 5- upper water cooling conduit, 6- water inlet, 7- high vacuum heater chamber, 8- upper sample jaw, 9- sample, 10- tantalum foil radiant heater, 11- sample chamber, 12- lower sample jaw, 13- water outlet, 14- sample chamber's CF copper gasket seal, 15- turbomolecular pump port, 16- lower body o-ring vacuum seal, 17- electrical feedthrough with CF copper gasket seal, 18- gas delivery to sample chamber, 19- lower pull rod

A high-current DC power supply driven by a custom temperature controller was used to operate the furnace. Feedback was provided by a thermocouple mounted adjacent to the specimen in the specimen chamber. The thermocouple was placed slightly below the neutron diffraction window to not obstruct the neutron beam.

Neutron diffraction and data analysis

Neutrons uniquely interact with hydrogen [6], scattering off the atoms strongly, both coherently, in the case of the deuterium isotope, and incoherently, in the case of hydrogen atoms. Due to this large contrast, the technique is therefore very sensitive to the presence of hydrogen and its isotopes in materials. Most neutron diffraction experiments use deuterium for crystallography purposes due to its strong coherent scattering abilities and hydrogen atoms for detection purposes due to its very large incoherent scattering cross-section, which leads to intensity loss and a higher background at very small concentrations [7, 9].

In the present context, diffraction peaks corresponding to hydride precipitates embedded in a zirconium alloy are easily distinguishable from the zirconium matrix peaks. The intensity of a given hydride diffraction peak depends on a number of factors, including the crystal structure factor, the Debye-Waller factor (related to thermal vibrations of atoms about their equilibrium positions), the crystallographic texture, the total volume of the specimen, and a variety of diffractometer parameters. [10] However, with all other parameters fixed, the intensity of a given hydride peak is predominantly a function of the hydride volume fraction in the sample.

The resulting changes in the pattern are attributable to changes in the volume fractions of the different phases present in the sample. In experiments involving changes in temperature, each pattern must first be corrected by subtracting out the changing thermal contribution to the overall level of the pattern.

Neutron diffraction measurements were performed using the L3 neutron diffractometer of the Canadian Neutron Beam Centre, located at the National Research Universal (NRU) reactor of Canadian Nuclear Laboratories in Chalk River, Ontario.

Material

The material presented in this work is a solid rod of Zr-2.5Nb having a diameter of 6.35 mm. The material specification sheet indicates that the room temperature yield strength at 0.2% offset is 485 MPa and the material's grain size is 12 μm. The crystal structure is a hexagonal close-packed structure which can change to a body-centered cubic crystal structure at temperatures over 860° C. Deuterium was introduced to different samples to equivalent hydrogen concentrations ([H_{eq}]) of 500 wppm using a gaseous technique not described here.

RESULTS

Zr-2.5Nb [H_{eq}] = 500 wppm

Specimen ZrNb02 was deuterated to a nominal equivalent hydrogen concentration of 500 wppm. The gamma hydride {202} and delta hydride {220} diffraction peaks [11], occurring at scattering angles of 89.3° and 89.6° respectively, were followed during thermomechanical cycling.

The integrated intensity vs temperature was plotted for the heating portion of cycles 2 (0 MPa), 3 (75 MPa), and 5 (150 MPa) in Figure . The intensity of the deuteride peak can be seen to shrink steadily with increasing temperature up to 420-440°C, where the peak disappears into the background. Increasing the applied stress did not appear to affect the curve significantly. This indicates that these stresses have little to no effect on the hydride dissolution temperature of Zr-2.5Nb. This experiment has demonstrated a successful preparation, operation and in-situ neutron diffraction study on a sample while simultaneously controlling the applied load, temperature and sample environment simultaneously.

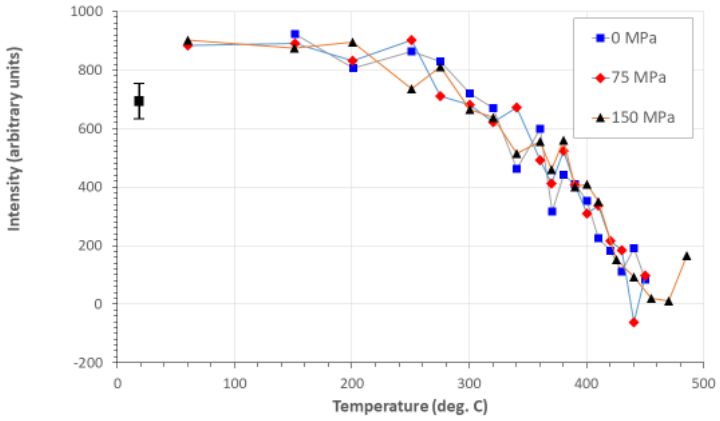


Figure 2: Hydride diffraction peak intensity as a function of temperature for specimen Zr-2.5Nb ([H_{eq}] = 500 wppm nominal) at 0 MPa, 75 MPa, and 150 MPa. The measurement uncertainty is represented by the error bar on the leftmost point.

CONCLUSIONS

Using a controlled-atmosphere furnace which allows specimens to be heated/cooled in the neutron beam while under a simultaneous tensile load, *in-situ* neutron diffraction measurements were performed on Zr-2.5Nb rods charged with deuterium to a nominal equivalent hydrogen concentration of 500 wppm.

An investigation of the effect of tensile stress on deuterium solubility, to obtain insights into the mechanism of hydrogen ingress as well as the mechanism behind DHC and hydrogen embrittlement, was performed. Samples were subjected to a series of thermomechanical cycles to investigate the effect of tensile stress on the dissolution of deuterides. No significant effect of tensile stress on the deuterium solubility of our Zr-2.5Nb rod samples was found for temperatures up to 300°C and at stresses up to 275 MPa. This is contrary to what can be found in literature [12] but it has to be noted that these temperatures are quite low for fast hydride dissolution and this result could be due to slow kinetics in this range of temperatures and applied stresses. The employment of a versatile controlled

atmosphere furnace was shown to be successful, exhibiting predictive behaviour and ease of use. The novel furnace design enables applied load control while maintaining the high vacuum seal and the sample's exposed environment.

ACKNOWLEDGEMENT

The authors gratefully acknowledge the expert advice of Jozef Mouris regarding the specimen hydriding process; the expert technical assistance of David Dean, Raymond Sammon, Derrick West, Shutao Li, and Jim Bolduc.

REFERENCES

1. B. P. Somerday, and P. Sofronis, 2013, Hydrogen-Materials Interactions. ASM International, Materials Park, OH
2. M. P. Puls, 2009, Review of the thermodynamic basis for models of delayed hydride cracking rate in zirconium alloys, Journal of Nuclear Materials, 393, 350-367
3. Y. S. Kim, 2010, Comments on 'The first step for delayed hydride cracking in zirconium alloys' by G. A. McRae et al., J. Nucl. Mater 396 130-143, Journal of Nuclear Materials, 396, 144-148
4. O. Zanellato, M. Preuss, J.Y. Buffiere, F. Ribeiro, A. Steuwer, J. Desquines, J. Andrieux, B. Krebs, 2012, Synchrotron diffraction study of dissolution and precipitation kinetics of hydrides in Zircaloy-4, J. Nucl. Mater., 420(1–3), 537-547
5. J. H. Root, R.W.L. Fong, 1996, Neutron diffraction study of the precipitation and dissolution of hydrides in Zr-2.5Nb pressure tube material, Journal of Nuclear Materials, 232, 11
6. A.J. Dianoux, G.H. Lander, 2003, Neutron Data Booklet, OCP Science
7. H. Fritzsche, J. Huot, D. Fruchart (Eds.), 2016, Neutron Scattering and Other Nuclear Techniques for Hydrogen in Materials, Neutron Scattering Applications and Techniques, Springer books
8. K. B. Colas, A.T. Motta, M.R. Daymond, J.D. Almer, 2013, Effect of thermo-mechanical cycling on zirconium hydride reorientation studied in situ with synchrotron X-ray diffraction, J. Nucl. Mater., 440(1), 586-595
9. G. Squires, 2012, Introduction to the Theory of Thermal Neutron Scattering, 3rd edn. Cambridge University Press, New York
10. H. M. Rietveld, 1969, A profile refinement method for nuclear and magnetic structures, Journal of Applied Crystallography 2 (2): 65–71
11. Inorganic Crystal Structure Database (ICSD) database, icsd.products.fiz-karlsruhe.de
12. P. Vizcaino, J.R. Santisteban, M.A. Vincente Alvarez, A.D. Banchik, J. Almer, 2014, Effect of crystallite orientation and external stress on hydride precipitation and dissolution in Zr2.5%Nb, J. Nucl. Mater., 447(1-3), 82-93

WHEC-2022
23rd World Hydrogen Energy Conference
June 26-30, 2022 - Istanbul

#1560

NUMERICAL INVESTIGATIONS ON FLASHBACK LIMITS OF PREMIXED METHANE-HYDROGEN-AIR LAMINAR FLAMES

*Tahsin Berk Kıymaz[a], Emre Böncü[a], Dilay Güleryüz[a], Mehmet Karaca[b], Barış Yılmaz[c], Christophe Allouis[d], İskender Gökalp[a,e]**
[a]Middle East Technical University, Mechanical Engineering Department, Ankara, Turkey
[b]Middle East Technical University, Aerospace Engineering Department, Ankara, Turkey
[c]Marmara University, Mechanical Engineering Department, İstanbul, Turkey
[d]STEMS-CNR, Naples, Italy
[e]ICARE-CNRS, Orléans, France

*Corresponding author Dr. Iskender Gökalp (igokalp@metu.edu.tr)

ABSTRACT

Premixed laminar methane-hydrogen combustion contains a potential flashback risk, which may be detrimental for home appliances. The present study investigates the effect of hydrogen addition to methane-air premixed laminar flames with two-dimensional transient computations performed by the CFD code OpenFOAM. The effect of wall temperature on flame flashback propensity is examined. After a stabilized flame is achieved, flashback conditions are approached by gradually decreasing the inlet premixture bulk velocity. At flame flashback velocities, flame symmetry is found to be broken because of the oscillations at the flame leading edge. Flashback tendency is found to be increasing with increasing wall temperature and increasing hydrogen addition rate. Flashback limits for 600K wall temperature case are calculated as 0.368 m/s, 0.62 and 0.99 m/s for 0 mol%, 10 mol% and 20 mol% of H_2 additions to CH_4-air mixture respectively. For 300K wall temperature case, they are calculated as 0.165 m/s, 0.265 m/s and 0.44 m/s for 0 mol%, 10 mol% and 20 mol% of H_2 additions to CH_4-air mixture respectively.

Keywords: Laminar premixed flames, Flame flashback, Hydrogen, Numerical simulations, OpenFOAM

INTRODUCTION

The global need to reduce CO2 emissions creates great interest in the utilization of hydrogen as an energy carrier in fuel cell and combustion applications. Hydrogen-enriched natural gas could be the preparatory step for using 100% hydrogen in combustion applications, because 100% hydrogen combustion still has immature aspects for designing the required changes in the infrastructure [1].

Adding hydrogen to CH_4-air premixed combustion alters he mixture laminar flame speed, flame thickness, flammability limits, and adiabatic flame temperature. Safe hydrogen injection limits are critical for determining hydrogen blending rates into the natural gas transmission networks to create safer combustion applications in households [2]. The hydrogen-methane-air premixture contains the risk of flashback, which is the flame propagation in the upstream direction into the unburned premixture. By modifying the laminar flame speed, hydrogen addition becomes one of the many parameters affecting flashback, including burner diameter and rim temperature, burner material, wall and premixture temperatures [3-7].

The present work investigates the flashback dynamics for CH_4-air and CH_4-H_2-air premixed flames with a numerical framework for a given combination of fuel composition and bulk inlet velocity, utilizing both isothermal walls at different wall temperatures and adiabatic wall temperature condition. The computed flashback limits are compared with the experiments of deVries et al. [5] and some experimental correlations proposed in earlier studies.

MATERIALS AND METHODS

The focus of the paper is on the boundary layer flashback phenomenon in Bunsen type burners. Flashback happens when the laminar flame speed exceeds the inlet mixture bulk velocity. This is an unwanted situation may cause severe damage to the combustion system.

In the numerical calculations, the transient reacting flow finite volume solver ‘reactingDNS’ is used [8]. The reactions are solved by the reduced GriMECH 3.0 mechanism, and chemical reactions are treated with the Tabulated Dynamic Adapted Chemistry method. The experiment is modelled as a two-dimensional burner to capture asymmetrical instabilities. The experimental details can be found in de Vries et al [5]. The cold flow inlet is a fully developed Hagen-Poiseuille velocity profile, with initial temperature and pressure being 300K and 100 kPa, respectively. Three different wall temperature conditions, Tw, are explored: adiabatic and constant temperatures of 300K and 600K.

RESULTS AND DISCUSSION

The changes in the equivalence ratio with hydrogen addition are considered in the numerical calculations mimicking the experiments. Laminar flame speeds are crosschecked with Cantera and OpenFOAM to test the solver's ability to calculate the correct laminar flame speeds. Flashback limits are numerically calculated for the same fuel composition, starting from a stable flame with varying bulk inlet velocities. Flashback is considered to take place when the flame front begins to enter the burner tube and travels in the upstream direction. The inlet velocity is gradually reduced by a percentage of the laminar flame speed until flashback is observed.

The flashback dynamics are represented in Fig. 1 for a CH_4-Air mixture at 1.3 equivalence ratio and 600K wall temperature. Normalized heat release rate, which is the ratio of heat release to its maximum value, is used to trace the flame front. The stable laminar flame with the bulk inlet velocity twice of laminar flame speed, which is 0.48 m/s, is shown in Fig 1a. Bulk inlet velocity is reduced gradually to 0.368 m/s where flashback is observed. Fig 1b shows that 0.195s after setting this inlet velocity, the flame front edges start to become parallel to the burner rim and in Fig 1c, the leading edge is formed travelling in the upstream direction. The figures demonstrate the quenching distance near the left wall, and the penetration distance emergence as the flame symmetry is broken in Fig 1c and 1d. Flashback velocity is about 53% higher than the laminar flame speed with 5% accuracy. Flashback onset times provided in Fig.1 are two orders of magnitude larger than the laminar flame characteristic chemical time, estimated to 0.005 s for this flame condition.

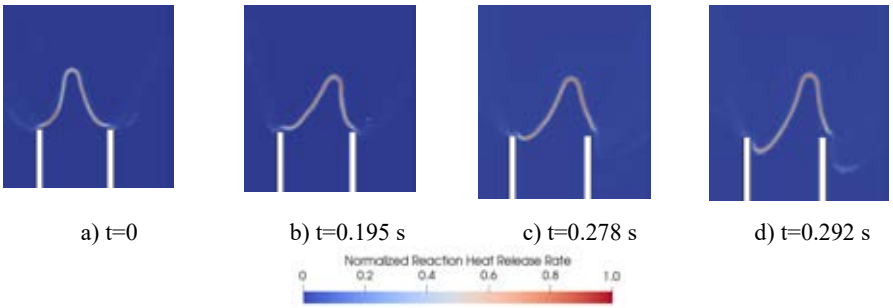


Fig. 1. Flashback dynamics represented with the normalized heat release rate contours for CH_4-air mixture at Φ=1.3 and T_{wall}=600K

Hydrogen addition impact is demonstrated in Fig.2. Fig. 2a. shows the stationary laminar premixed flame with 20% hydrogen addition (volume %) to the CH_4-Air mixture at 600K constant wall temperature. Flashback is observed with the decrease of bulk inlet velocity from 1.1 m/s to 0.99 m/s, which is 5% of the laminar flame speed. Flame symmetry is broken in Fig 2b and in Fig 2c, leading edge formation can be observed. The flame starts to travel upstream in Fig 2d.

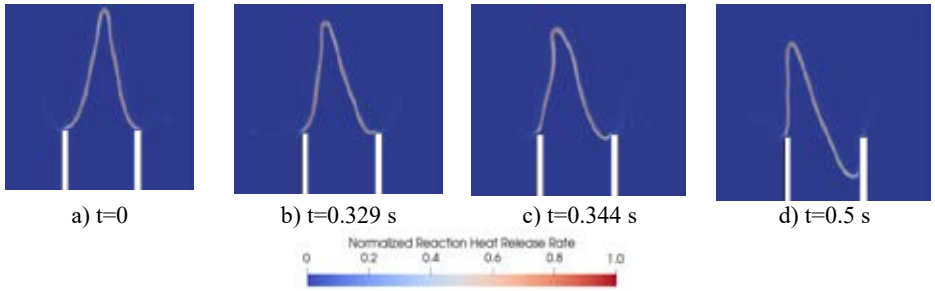


Fig. 2. Flashback dynamics represented with the normalized heat release rate contours for CH_4-air flame at Φ=1.216 with 20% H_2 addition for T_{wall} = 600K

Additional computations not presented here, show that the boundary layer flashback propensity is enhanced with increasing wall temperature. Also, when the adiabatic wall boundary condition is used, no quenching distance or leading-edge formation is observed, and the reactions occur almost at the wall. The computed flashback limits are compared in Figs. 3 with the measurements of deVries et al. [5] and with the correlations based on the critical gradient concept [3,6-7]. U_f is the experimental flashback limit that is observed when the flame just enters the burner tube.

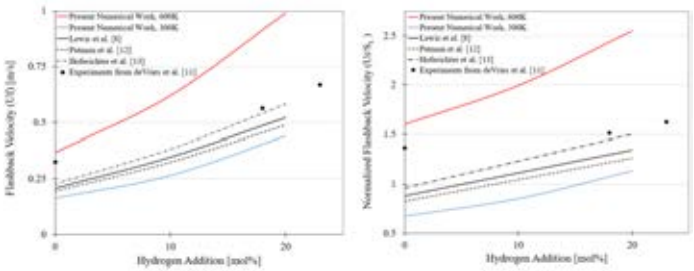


Fig. 3. Comparison of experimental and calculated flashback limits.

In Figs. 3, flashback is observed below the curves. Fig. 3a presents the absolute values of the critical flashback velocity while Fig. 3b represents the same data normalized by the computed laminar flame speed S_L for each mixture condition. With the addition of hydrogen to the premixture, flashback limit is increased for numerical, theoretical, and experimental results. Flashback velocity calculations are claimed to have an accuracy of 5%. For 600K wall temperature, the flashback velocity limits are calculated as 0.165 m/s for 0 mol% H_2, 0.265 m/s for 10 mol%H_2 and 0.44 m/s for 20 mol% H_2 addition to CH_4-air mixture. In the 300K wall temperature calculations, the limits are found as 0.165 m/s, 0.265 m/s and 0.44 m/s for 0 mol% H_2, 10 mol% H_2 and 20 mol% H_2, respectively. The experimental results lie in between our numerical results for constant wall temperatures set at 600K and 300K. The results of deVries et al. [5] are higher than the model predictions for all hydrogen addition rates for 300K wall temperature. This can be related to the quartz burner with low thermal conductivity used in the experiments. The normalized critical flame flashback velocity is above 1 for the experimental results and increases with the addition of hydrogen. All correlations and computations for 600K constant wall temperature show the same trend, especially above 10 % molar H_2 addition rate. The results imply that the simple interpretation of boundary layer flame flashback as only correlated to the laminar flame speed, should be further investigated for flames of methane-hydrogen mixtures.

CONCLUSIONS

Boundary layer flame flashback dynamics of hydrogen added methane-air laminar flames are investigated and flashback limits are determined numerically. The flashback limits are globally following the experiments and past correlations. The main contribution of the present full numerical simulation of the laminar flame flashback process in a simple burner configuration is the detailed information that can be obtained concerning the flashback dynamics without strong modelling hypotheses. For future work, the conjugate heat transfer approach should be included to model the burner wall temperature transiently since it affects the flashback limits substantially. Also, the Soret diffusion effect should be included in numerical calculations, especially for hydrogen mixtures.

ACKNOWLEDGMENTS

This work is supported by the TUBITAK Outstanding International Researchers program, projects no 118C287 and 118C233.

REFERENCES

1. Halter, F., Chauveau, C., Djebaili-Chaumeix, N., Gökalp, I. (2005) Characterization of the effects of pressure and hydrogen concentration on laminar burning velocities of methane-hydrogen-air mixtures. Proc. of the Combustion Institute 30: 201-208
2. Gökalp, I. (2019) A holistic approach to promote the safe development of hydrogen as an energy vector. Proceedings of the Ninth International Seminar on Fire and Explosion Hazards. Vol. 2: 21-26, 2019, DOI 10.18720/SPBPU/2/k19-127
3. Lewis, B., & von Elbe, G. (1943). Stability and structure of burner flames. The J. of Chemical Physics, 11(2), 75-97
4. Kalantari, A., & McDonell, V. (2017). Boundary layer flashback of non-swirling premixed flames: Mechanisms, fundamental research, and recent advances. Progress in Energy and Combustion Science, 61, 249-292.
5. De Vries, H. et al. (2017). The impact of natural gas/hydrogen mixtures on the performance of end-use equipment: interchangeability analysis for domestic appliances. Applied Energy 208: 1007-1019. https://doi.org/10.1016/j.apenergy.2017.09.049
6. Putnam, A. A., & Jensen, R. A. (1948). Application of dimensionless numbers to flash-back and other combustion phenomena. Symposium on Combustion and Flame, and Explosion Phenomena, 3(1), 89–98. https://doi.org/10.1016/s1062-2896(49)80011-0
7. Hoferichter, V., Hirsch, C., & Sattelmayer, T. (2018). Prediction of boundary layer flashback limits of laminar premixed jet flames. In Turbo Expo: Power for Land, Sea, and Air, https://doi.org/10.1115/GT2018-75546
8. Zhang, F., Bonart, H., Zirwes, T., Habisreuther, P., Bockhorn, H., & Zarzalis, N. (2014). Direct Numerical Simulation of Chemically Reacting Flows with the Public Domain Code OpenFOAM. High Performance Computing in Science and Engineering '14, 221–236. https://doi.org/10.1007/978-3-319-10810-0_16

WHEC-2022

23rd World Hydrogen Energy Conference

TRACK 12.
CODES, STANDARDS AND REGULATIONS

TRACK 12. CODES, STANDARDS AND REGULATIONS

#25 THE GERMAN HYDROGEN RCS ROADMAP	1211
#213 EUROPEAN REGULATORY FRAMEWORK FOR HYDROGEN UNDERGROUND STORAGE	1214
#258 TESTING OF BLENDED GREEN HYDROGEN IN GAS PIPELINES: CONSIDERING THE END-USERS LIMITS	1217
#338 HYDROGEN FUEL QUALITY FOR TRANSPORT: NPL ACCREDITATION ISO 17025, REFERENCE MATERIALS, PROFICIENCY TESTING AND NEW SAMPLING SYSTEM	1220
#368 METROLOGY FOR HYDROGEN VEHICLE 2: ACHIEVEMENTS AND PROGRESSES	1223
#1563 SAFE ENERGY RELATIONS: UNFOLDING THE PRECAUTIONARY PRINCIPLE WITH THE ADVENT OF HYDROGEN TECHNOLOGIES	1226

WHEC-2022
23rd World Hydrogen Energy Conference
June 26-30, 2022 - Istanbul

#25
THE GERMAN HYDROGEN RCS ROADMAP

[1] Elena Hof, [2] Reinhold Wurster*
[1]NOW GmbH, Fasanenstr. 5, 10623 Berlin, Germany
[2] Ludwig-Bölkow-Systemtechnik GmbH, Daimlerstr. 15, 85521 Ottobrunn, Germany

*Corresponding author e-mail: reinhold.wurster@LBST.de

ABSTRACT

In the exercise of developing a German Roadmap for Hydrogen Regulations, Codes and Standards (RCS), the identification of current developments and existing gaps and the preparation of recommendations has been performed. The following ongoing international RCS activities were reviewed: ISO, IEC, CEN, CENELEC, EU and UN ECE / WP29. Focus was primarily on hydrogen and fuel cell applications for road transport and stationary applications and to a lesser extent on trains / airports.

It became obvious that the development of standards and regulations and in particular the coordination between the two is complex and requires a concerted approach and substantial efforts. For this reason, a roadmap strategy paper has been prepared, in which a roadmap and timeline has been developed. As an appropriate instrument to achieve a successful implementation of all regulatory and normative requirements while involving all actors and stakeholders, the establishment of an H_2 RCS coordination platform has been considered.

Keywords: RCS Roadmap, RCS Platform, AFID, GTR13

INTRODUCTION

The efficient and cost-effective realization and implementation of hydrogen and fuel cell technologies in the existing energy and transport systems requires appropriate laws (regulations), standards and processes ("Regulations, Codes and Standards" - RCS). Almost all relevant regulations that are applicable to hydrogen and fuel cells in Germany today are based on or must be adapted to European legislation (directives or regulations). Likewise, the essential part of the standards used today is or will be harmonized with international (ISO, IEC) or European (EN) standards. New standards are essentially developed only within the framework of ISO, IEC or CEN, CENELEC. For example, in 2017, approximately 75% of the new standards relevant for Europe were international and only 20% European standards.

H_2 and FC technologies are developed worldwide, especially in Asia and North America. This influence is also reflected in important regulations and standards for hydrogen (H_2 RCS). Due to the path of regulatory development via the New Legislative Framework adopted by the European Commission in Europe, the relevant actors have to anticipate, synchronize and harmonize the development of standards and regulations and thus an increased representation of German experts is required in all relevant international standardization committees. In order to ensure the representation of Germany's interests in the future, consequently a more active participation in committee work is required, in particular by the EU, UNECE, ISO, IEC, CEN, CENELEC.

The development of standards and regulations and in particular the coordination between the two is complex and requires a concerted approach and substantial efforts. For this reason, a roadmap strategy paper has been prepared, in which a roadmap and timeline has been developed [1], how the necessary RCS coordination efforts will be implemented and then continuously pursued. The progress of this implementation must be regularly reviewed and, where appropriate, be adapted to changing requirements.

As the topics with the biggest needs for action have been identified the following ones:

- The revision and further development of the AFID, the GTR 13, the ADR as well international H_2 / fuel cell standards.
- Regarding the development of hydrogen and fuel cell standards international bodies of ISO/TC (197, 158, 58, 22), IEC/TC (105, 31) and the European technical committees of CEN / CENELEC are of special relevance for participation
- A stronger influence by or participation of Germany and Europe in these regulatory and standardization activities is urgently required.

In the following the most important needs for action as displayed in the *German H_2-Roadmap 2025* are visualized:

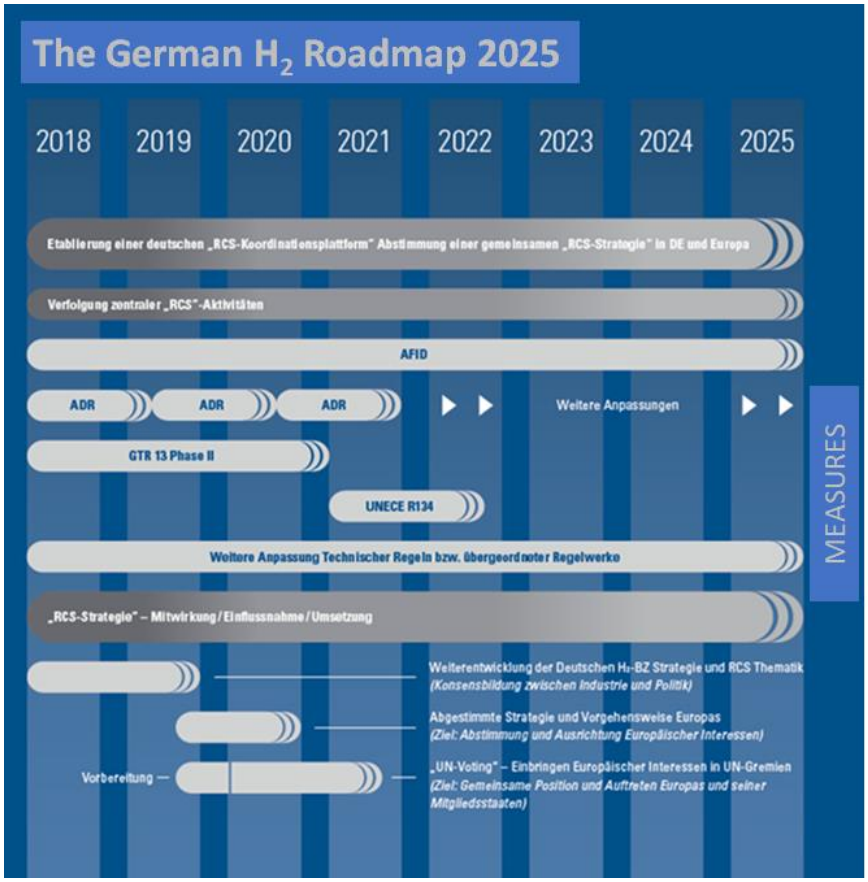


Fig. 1. Identified Need for Action in the German H_2-Roadmap 2025 [1]

The topological integration of the German legislation into the European and international regulatory framework is shown in Figure 2:

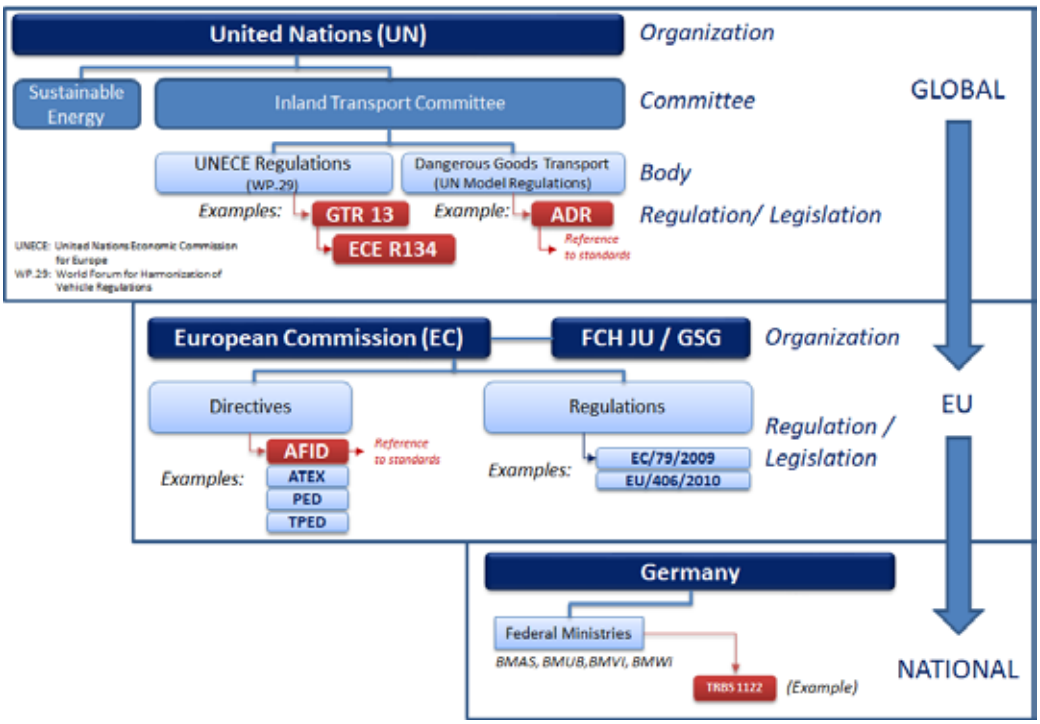


Fig. 2. Topological integration of the German legislation into the European and international [2]

Figure 2 indicates that according to Germany legislation technical rules for operational safety (TRBS) that reflect the state of the art and ensure the implementation of the Ordinance on Industrial Safety (BetrSichV as issued the German Federal Ministry of Labor and Social Affairs have to be complied with additionally to international and European framework legislation.

CONCLUSIONS

As an appropriate instrument to achieve a successful implementation of all regulatory and normative requirements while involving all actors and stakeholders, the establishment of an H_2 RCS coordination platform has been considered. Major tasks of this platform include, but are not limited to:

- Observation of priority developments & trends
- Development of a unified position / vote in RCS matters within Germany
- Regular consultation / harmonization with the actors in Germany (representatives of industry, relevant networks and other experts)
- Development of a unified position / vote in RCS matters within Europe
- Coordination of RCS activities with the FCH JU in Europe;
- Cooperation with the European Government Support Group (GSG) to achieve a agree on common positions among the EU member states
- Influence of/ participation in European (CEN / CENELEC) and international (ISO / IEC) standards development

NOMENCLATURE

AFID	*Alternative Fuels Infrastructure Directive (2014/94/EU)*
BetrSichV	*Betriebssicherheits-Verordnung (Ordinance on Industrial Safety)*
CEN	*Comité Européen de Normalisation (European Committee for Strandardization)*
CENELEC	*Comité Européen de Normalisation Électrotechnique (European Committee for Electrotechnical Strandardization)*
FC	*Fuel Cell*
FCH JU	*Fuel Cell and Hydrogen Joint Undertaking (a public private Partnership under participation of the European Commission)*
H_2	*Hydrogen*
IEC	*International Electrotechnical Committee*
ISO	*International Standardization Organization*
RCS	*Regulations, Codes and Standards*
TRBS	*Technische Regeln für Betriebssicherheit (technical rules for operational safety)*
UNECE	*United Nations Economic Commission for Europe*

REFERENCES

1 Wurster, R. Dey, R Elliger, T and Jungsbluth J. 2018. Die Deutsche H_2-RCS-Roadmap 2025, edited by the NOW GmbH, Berlin [https://www.now-gmbh.de/de/aktuelles/presse/now-broschuere-die-deutsche-h-rcs-roadmap-2025]

2 Zerta, M, Die Deutsche H_2-RCS Roadmap 2025, Presentation by Ludwig-Bölkow-Systemtechnik GmbH, Vollversammlung zum Nationalen Innovationsprogramm Wasserstoff- und Brennstoffzellentechnologie (NIP), Berlin, 6 December 2018,

WHEC-2022
23rd World Hydrogen Energy Conference
June 26-30, 2022 - Istanbul

#213

EUROPEAN REGULATORY FRAMEWORK FOR HYDROGEN UNDERGROUND STORAGE

[1*] *Sara Martínez,* [1] *Jesús Simón,* [2] *Arnaud Reveillere,* [2] *Flore Ostapoff*
[1]Foundation for the Development of New Hydrogen Technologies in Aragon (FHA), Parque Tecnológico Walqa
Ctra. N-330a, km. 56622197 Huesca, Spain
[2] Geostock, 2, rue des Martinets 92500 Rueil-Malmaison, Paris, France

*Corresponding author e-mail: smartinez@hidrogenoaragon.org

ABSTRACT

Renewable hydrogen, when combined with large-scale underground storage in aquifers, depleted fields, or salt caverns, enables energy transport over time while balancing the impacts of variable energy production from renewable sources. Although hydrogen storage in salt caverns has been practised since the 1970s in Europe, it has not yet been implemented anywhere in depleted fields or aquifers. The HyStories [1] project aims to provide technical developments applicable to depleted aquifers or fields, to conduct techno-economic feasibility studies and to provide information on underground hydrogen storage to decision-makers in administration and industry. In this context, the legal framework for underground hydrogen storage at European level was analysed in terms of the existence, or otherwise, of regulatory barriers, as well as the extent to which these barriers may affect the development of underground hydrogen storage projects. The starting point of this analysis of the legal framework for UHS was the existing national regulations for the mature underground natural gas storage industry and more than 39 experts from 17 different countries were involved in the project. Thus, this study compares the different country-specific approaches and offers a series of recommendations to avoid legal barriers to the deployment of UHS in geological formations across Europe.

Keywords: Hydrogen, Underground, Storage, Regulatory

INTRODUCTION

The Hystories project [1] aims provide insights on underground hydrogen storage (UHS) in aquifers and depleted fields for decision-makers in government and industry through technical developments, and techno-economic feasibility studies. This work has considered a geographical boundary of EU-27 + UK, and has shown that the regulation, legislation, standards, and permissions of the Member States involved in the HyStories project through partners, third parties and the Advisory Board [2].

Currently, there is no uniform set of laws on natural gas storage for most natural gas storage facilities located in Europe. The legal framework in different countries may be part of mining legislation, energy legislation, construction legislation, environmental legislation, labour protection legislation, health and safety regulations or similar associated legislation. Therefore, the starting point for the present analysis of the legal framework for large-scale hydrogen storage is therefore the existing rules for the advanced natural gas industry.

METHODOLOGY

Reviewing applicable legislation for UHS at the European scale is challenging since each country has its own, in its own language. To gather as much information as possible on the legal situation of underground storage of natural gas and hydrogen in the European context, a survey was launched to Hystories 7 partners and 17 third parties (so 24 institutions involved in hydrogen and/or underground storage from 17 countries), plus Hystories Advisory Board comprising 13 companies (large European gas storage operators, TSO, or manufacturers). From this survey, twenty-three entities provided relevant information for the study.

The survey consisted in 9 questions organised in 4 different sections: Survey Data, Regulatory framework, Standards related to the integrity of underground storages, and wells and Other related issues. Figure 1 shows the breakdown of the 39 responses per country (17 different countries).

Furthermore, to collect the complete list of permits required to develop an underground gas storage today, a questionnaire was developed, completed, and reviewed by experts from France, Germany, Spain, and Poland.

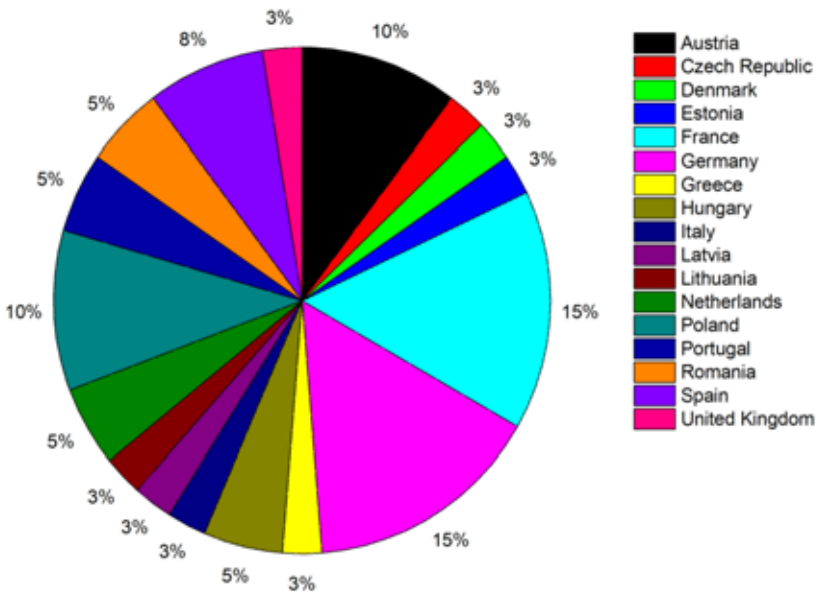


Figure 1.Percentage of responses obtained in the survey for each Member State. Source: FHA.

Regulation

R*egulation* is generally understood as a market concept in the natural gas sector: it is regulated in Europe by common directives that aim at unifying the natural gas market, specifically by the Directive 2009/73/EC [2] and the Regulation (EC) No 715/2009 [3]. The European Commission published the revision of both directives including hydrogen, called the "Hydrogen and Decarbonised Gas Market Package", at the end of 2021 [4].

Thus, the *Proposal for a Directive of the European Parliament and of the Council concerning common rules for the internal markets in natural and renewable gases and hydrogen* [5] in its measure 71 provides that hydrogen networks should be subject to third party access to ensure competition and a level playing field in the hydrogen supply market. Regulated third party access based on regulated access tariffs should be the default rule in the long term. To ensure the necessary flexibility for operators and to reduce administrative costs during the growth phase of the hydrogen market, Member States should have the option to allow the use of negotiated third-party access until 2030.

In addition, specifically for UHS in point 72, it is clarified that since the availability of large-scale underground hydrogen storage facilities is limited and unevenly distributed across the Member States and because of the potentially beneficial role for the functioning of the hydrogen transport and markets, access to such large-scale underground storage facilities should be access to such large-scale underground facilities should be subject to regulated third party access to ensure a level playing field for market participants.

Legislation

The starting point for the analysis of the UHS legal framework are the existing national laws for the natural gas storage industry. Depending on the country, the legal framework for underground natural gas storage in European countries is involving mining legislation, construction legislation, environmental legislation, labour protection legislation, health, and safety regulations and/or other similar associated legislation. This study compiles the detailed legislation for the seventeen countries shown in Figure 1 from the responses of national experts. In particular, the information provided concerns the legislation in force in each country for natural gas underground storage facilities, the bodies responsible for granting permits, the opinion on the need to adapt Directive 2012/18/EU [6] or other industrial safety standards applicable to hydrogen storage, as well as the existence of specific regulations for natural gas and, finally, the possible existence of hydrogen underground storage facilities that have gone through the permitting process.

Standards

Two different sets of standards related to the natural gas industry have been compiled. On the one hand, the standards developed by the International Organization for Standardization, ISO, for underground gas storage facilities, and on the other hand, different technical standards from usually international reference bodies or institutes, SMRI for instance, in relation to the operation and safety of underground gas storage facilities.

Permits

The current permitting requirements for developing underground gas storage were reviewed by experts from France (Geostock, Teréga), Germany (Uniper, Storengy Deutschland), Spain (FHa, Enagas), and Poland (MEERI-PAS, Gaz System) for these four countries. As a result, four tables with details of the procedures have been developed.

RESULTS AND DISCUSSION

Hydrogen is currently defined in most European regulations as a chemical product and not as an energy carrier, which raises legal barriers to developing business models based on renewable hydrogen as an energy carrier. In this respect, discrepancies at the European level on the approach and on the allowable concentration of hydrogen in the natural gas network are an inherent barrier to the development of hydrogen as an energy carrier, whether it is to be injected in the existing underground gas network, or in a new pure hydrogen one. On the other hand, regulatory barriers for underground hydrogen storage can be regional or national regulations that aim at curbing any activity in the underground, not only exploitation but also geological exploration or characterisation. In addition, it has been identified that in some Member States, the current legislation does not cover underground storage facilities for the power industry. Finally, the storage of natural gas in certain Member States can be decided independently of the claims of landowners. This is currently not possible for any other type of product, such as hydrogen, and represents a major barrier for underground hydrogen storage. Regulations that have enable Europe to have a natural gas transportation and storage network today need to be reviewed and adapted for hydrogen.

CONCLUSIONS

As a conclusion to this study, a ranking of countries according to the status of their UHS legislation at the time of this study, September 2021 has been elaborated.

The United Kingdom, Denmark, Germany, and Austria rank first for having UHS legislation in place. It should be noted that in the German case, the legislation in force is for underground storage of chemicals, not for specific UHS, and in the Austrian case only scientific research cases would be included.

Secondly, France and the Netherlands, are developing specific legislation for UHS.

Finally, Czech Republic, Estonia, Greece, Hungary, Italy, Latvia, Lithuania, Poland, Portugal, Romania, Spain do not have UHS legislation under development, although for the Portuguese and Spanish case, UHS is mentioned in their national hydrogen strategies.

REFERENCES

1. Hystories Project. Grant Agreement nº 101007176.
2. https://hystories.eu/partners-hystories/. Accessed on January 3, 2021.
3. Directive 2009/73/EC of the European Parliament and of the Council of 13 July 2009 concerning common rules for the internal market in natural gas and repealing Directive 2003/55/EC. OJ L 211, 14.8.2009, p. 94.
4. Regulation (EC) No 715/2009 of the European Parliament and of the Council of 13 July 2009 on conditions for access to the natural gas transmission networks and repealing Regulation (EC) No 1775/2005. OJ L 211 14.8.2009, p. 36.
5. https://ec.europa.eu/energy/topics/markets-and-consumers/market-legislation/hydrogen-and-decarbonised-gas-market-package_en. Accessed on January 3, 2021.
6. Proposal for a Directive of the European Parliament and of the Council on common rules for the internal markets in renewable and natural gases and in hydrogen. COM (2021) 803 final, 15.12.2021.
7. Directive 2012/18/EU of the European Parliament and of the Council of 4 July 2012 on the control of major-accident hazards involving dangerous substances, amending, and subsequently repealing Council Directive 96/82/EC. OJ L 197, 24.7.2012, p. 1–37.

WHEC-2022
23rd World Hydrogen Energy Conference
June 26-30, 2022 - Istanbul

#258

TESTING OF BLENDED GREEN HYDROGEN IN GAS PIPELINES: CONSIDERING THE END-USERS LIMITS

[1] Ali Ekhtiari, [2] Liam Nolan, [1] Eoin Syron*
[1]School of Chemical & Bioprocess Engineering, University College Dublin, Ireland
[2]Gas Networks Ireland, Dublin, Ireland

*Corresponding author e-mail: mohammad.ekhtiari@ucd.ie

ABSTRACT

Gas networks play a vital role in the global energy infrastructure. In Ireland, the natural gas transmission pipelines transport about 50 GWh, twice as much energy as power grids. The gas grids provide a reliable and secure energy supply for electricity generation as a backup when renewable energy is not available. The European Commission in the Green Target Plan set out the goal of net-zero carbon by 2050. The decarbonisation of gas networks incorporating hydrogen generated from surplus renewable power is a potential solution for the storage of excess renewable energy especially so in Ireland with huge available wind resources. The main objective of this research is to ensure a reliable and safe supply of adequate energy to residential end-users while decarbonising the gas network. Dealing with varying hydrogen blends poses significant challenges for gas network operators to ensure hydrogen concentration meets the limits of end-user devices. This experimental research investigates the effects of various hydrogen concentrations on common existing end-user devices found in the Irish gas network. The project examines the potential range of hydrogen blends that may be incorporated into the Irish gas network from 2-20% Hydrogen. This research work provides a detailed account of the tests and experiments carried out as part of this project in the UCD Integrated energy Lab and the Hydrogen Innovation Centre of Gas Network Ireland. This includes modelling of pressure drop in an example of distribution pipe rig, combustion and ignition temperature, and comparing the accuracy of meters before and after blending hydrogen through the pipelines. This study investigates how much the addition of hydrogen impacts the operation of appliances in the residential segment, also provides reference data for all relevant parties. The outcomes from this practical research allow for a complete costing of the necessary network and appliance upgrades to accommodate blended hydrogen in the gas network.

Keywords: Green Hydrogen, Gas Networks, Energy Storage, Hydrogen Blend

INTRODUCTION

In recent years, the development of renewables in energy systems has been targeted in many countries to support decarbonisation objectives. The European Green Deal frames Europe's response to climate change challenges and commits to delivering net-zero greenhouse gas emissions at the EU level by 2050 and an EU-wide GHG emissions reduction target of at least 55% for 2030 [1]. In line with EU ambition, the Irish Government's Programme, Our Shared Future commits to achieving a 51% reduction in Ireland's overall GHG emissions from 2021 to 2030, and to achieving net-zero emissions no later than 2050 [2]. A roadmap has been developed through Ireland's Climate Action Plan 2021 to put Ireland on a low-carbon trajectory to meet future targets in 2030 and 2050. These are challenging targets, in particular as Ireland has already missed targets for 2020. According to Ireland's Environmental protection Agency (EPA) report, since 2011 the rate of emissions has deviated upwards with an overall peak in 2018. However, this figure had a modest reduction from 2008 to 2011. Transport and industries are segments that represent 18% and 15% in generating emissions respectively in the same period.

Ireland's gas network provides almost one-third of all primary energy [3], 40% of heating and more than half of Ireland's electricity generation. Ireland's gas transmission system is among the most developed gas networks in EU countries and it can make a significant contribution to decreasing emissions by providing a more sustainable and secure transition to a clean energy future. Natural gas is a cleaner alternative to conventional hydrocarbons such as oil and coal and can replace these fuels in heat and power generation. The gas network can also transport renewable gas such as green hydrogen and biomethane for long-term energy sustainability and decarbonisation of the gas supply.

Hydrogen and decarbonising gas systems

The future decarbonised energy systems using hydrogen can be obtained in the following ways: 1. Using the process of steam methane reforming with a carbon capture unit to produce blue hydrogen, 2. Generating green hydrogen from renewable electricity through an electrolysis process that doesn't produce GHG emissions. Also, it can capture

the excess renewable energy which would be otherwise lost [4]. Hydrogen is flammable with a considerable calorific value which can be burned in different segmental of end-users. Hydrogen can be injected into the conventional gas pipelines usually in low percentages up to 20% volume. Ireland has one of the best wind resources in Europe and has significant potential for wind generation which can be expected to exceed end-users demands. With the current levels of wind generation on the island of Ireland, the power system operators sometimes curtail renewable power due to electricity grid limits and constraints. As the long term Irish target plan is to install more wind farms, this can increase the surplus renewable power. Therefore, finding an alternative use of this excess energy will improve the operation of the energy system. The production of hydrogen using electrolysers is a potential solution that provides an important opportunity to convert this excess renewable power to green hydrogen which can be injected into the gas pipelines.

Long term storage

The use of new technologies such as Power to Hydrogen (P2H) can be a potential solution to develop a more flexible energy system. Gas pipelines can play a key role in renewable energy storage by providing backup to fluctuate renewable power. The use of P2H means that large amounts of excess renewable energy can be converted to hydrogen stored within the gas network, providing long-term storage, and used at times of low availability of renewables replacing fossil fuels and reducing carbon emissions.

EXPERIMENTAL METHODS

The results from the computing analysis of the gas network system incorporating green hydrogen show that green hydrogen can be injected into the gas network without significant changes to its operation, as "pressure drop" and "flow rate" will not encounter big changes [2]. Also, by injecting green hydrogen, generated from excess renewable power, there is a reduction in flow rate from the natural gas supplier of up to 2%. This is approximately daily 200,000 cubic meters of natural gas reduction and consequently a decrease of CO_2 about 432 tonnes during the specific day. There are limitations in accepting hydrogen levels by different gas-based fuel devices. Concerning operating limits, such as the Wobbe index, as well as material compatibility, and safe permissible hydrogen concentration, the permissible upper hydrogen limit have been considered in practical standard projects. The gas distribution pipelines could convey up to 50% (even 100%) hydrogen concentration depending on the type of pipeline components and the designated standards; however, because of the end-users devices, the allowable hydrogen concentration is likely to be at a maximum blend of 20% in distribution networks. Figure (1) shows the current limits of hydrogen fraction in pipelines, considering the Wobbie index and calorific value limits. According to this plot, provided by European standards, The Red area relates to Common Business Practice (CBP) which is pointing to the gas quality criteria specification, used in Europe for Natural Gas. The hydrogen content should not exceed 15–20%. Since above 20%, there are technical concerns, due to safety perspective, metering and energy conversion.

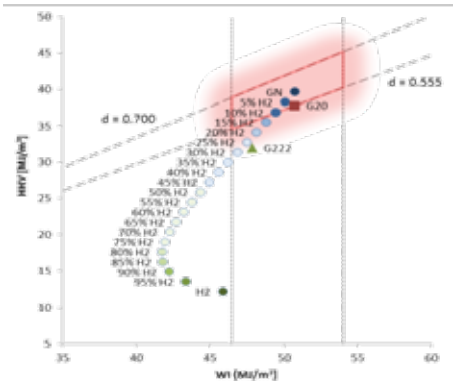


Figure 1. Admissible H2 considering the blends Wobbe index and heat value [5]

In the existing transmission gas system, the Wobbe index and the calorific value should not exceed the limits. As a consequence, natural gas may not meet the quality and safety requirements provided in the relevant standards. The current European standards which consider the gas quality of hydrogen blends are EN 437 for Test gases, Test pressures, and Appliance categories. This study is a collaboration between UCD Energy Institute and Gas Networks Ireland (GNI), Hydrogen Innovation Centre to ensure the safety and operability when blending hydrogen in the gas network. This looks at the feasibility of different volumes of green hydrogen being added to the gas network and the impact this will have on the operation of domestic appliances. Two main steps have been implemented by UCD and GNI for investigating the potential of gas networks for storing and transporting hydrogen. As a first step, the research

project started off by using modelling approaches to investigate how hydrogen impact the operation of the gas system when there are large variations of gas quality incorporating green hydrogen. The project will involve testing hydrogen blends in domestic appliances to make sure the designed computer models are valid and reliable in the real world. This will also test to ensure that the hydrogen is safe to be used by different appliances including (boiler, cooker, and heaters) also to determine how much does the addition of hydrogen impact the operation of gas pipelines in a distribution network.

CONCLUSIONS

Concerning operating limits, such as the Wobbe index, as well as material compatibility, and safe permissible hydrogen concentration, the permissible upper hydrogen limit has been considered in this practical project. The gas distribution pipelines could convey up to 50% (even 100%) hydrogen concentration depending on the type of pipeline components and the designated standards; however, because of the end-users devices, the allowable hydrogen concentration is likely to be at a maximum blend of 20% in distribution networks. The outcome of this research helps to inform the use and operation of gas networks as they move to decarbonise the energy systems to ensure that the hydrogen concentration meet the end-users limits and it can be a safe, secure and clean alternative fuel in the residential segment. Also, to help the National Standards Authority of Ireland (NSAI) which is following all the latest hydrogen standards developments to standardise the use of hydrogen blends.

ACKNOWLEDGEMENT

This work is supported by the Gas Networks Ireland Innovation Fund, by funding Ali Ekhtiari, Liam Nolan and Eoin Syron under Strategic Partnership Programme.

REFERENCES

[1] Xu, Xiaofeng and Wei, Zhifei and Ji, Qiang and Wang, Chenglong and Gao, Guowei, "Global renewable energy development: Influencing factors, trend predictions and countermeasures," *Resources Policy,* vol. 63, p. 101470, 2019.

[2] Ali Ekhtiari, Damian Flynn, Eoin Syron, "Investigation of the Multi-Point Injection of Green Hydrogen from Curtailed Renewable Power into a Gas Network," *Energies,* vol. 13, no. 22, p. 6047, 2020.

[3] Chiodi, Alessandro and Gargiulo, Maurizio and Rogan, Fionn and Deane, JP and Lavigne, Denis and Rout, Ullash K and Gallach, "Modelling the impacts of challenging 2050 European climate mitigation targets on Ireland's energy system," *Energy Policy,* vol. 53, pp. 169--189, 2013.

[4] Ali Ekhtiaria, Damian Flynnb, Eoin Syron, "Gas Networks, Energy Storage and Renewable Power Generation," *CHEMICAL ENGINEERING,* vol. 76, 2019.

[5] Jaworski, Jacek and Kuaga, Pawel and Blacharski, Tomasz, "Study of the effect of addition of hydrogen to natural gas on diaphragm gas meters," *Energies,* vol. 13, p. 3006, 2020.

WHEC-2022
23rd World Hydrogen Energy Conference
June 26-30, 2022 - Istanbul

#338

HYDROGEN FUEL QUALITY FOR TRANSPORT: NPL ACCREDITATION ISO 17025, REFERENCE MATERIALS, PROFICIENCY TESTING AND NEW SAMPLING SYSTEM

[1*]*Thomas Bacquart,* [1]*Abigail Morris,* [1]*Niamh Moore,* [1]*Mathew Hookham,* [1]*Yoana Hristova,* [1]*Robbie Wilmot,* [1]*Femi Omoniyi* [1]*Arul Murugan*
[1] National Physical Laboratory, Teddington, United Kingdom

*Corresponding author e-mail: thomas.bacquart@npl.co.uk

ABSTRACT

The enforcement of regulation on hydrogen fuel quality is a need supported by car manufacturer, policy makers and end users. Several laboratories in Europe and worldwide are becoming able to measure hydrogen fuel quality according to ISO 14687. However, it is currently difficult to evaluate the quality of these laboratories. Lack of gas calibrants, reference material and inter-laboratory comparison is a barrier for European commercial laboratory to prove their competences and obtain accreditation ISO 17025. National Physical Laboratory (NPL) has ISO 17025 accreditation and developed reference materials for hydrogen fuel quality. Based on experience in the previous proficiency testing on hydrogen fuel quality, NPL propose a new proficiency testing scheme and guidance on common issues. NPL will present new results on stability of contaminant in sampling container and advice for hydrogen fuel sampling. The presentation will provide advanced results and good practices to ensure reliability and accuracy of hydrogen quality analytical laboratory.

Keywords: Hydrogen Quality, Fuel Cell Hydrogen Vehicles, ISO14687, Gas Analysis, Proficiency Testing

INTRODUCTION

Deployment of FCEVs is a growing reality in Europe (i.e. 1600 Hyundai trucks in Switzerland by 2025 [1] or H2ME deploying 1400 FCEVs by 2022 [2]) with FCEVs production ramping up worldwide (i.e. Toyota increase from 3000 to 30000 FCEVs equivalent by 2020 [3] or Hyundai increase to 700000 FCEVs by 2030 [4]). At the same time, the number of refuelling stations is exponentially increasing with more than 152 stations currently in Europe. The enforcement of regulation on hydrogen fuel quality (European Directive 2014/94/EU [5]) is becoming a societal need supported by car manufacturer, policy makers and end users. Hydrogen fuel quality control is critical to meet the international regulations and recommendations and ensure the longevity of the vehicles (impacted by hydrogen fuel contaminants). Therefore, measurements of hydrogen fuel quality according to international standards (ISO 14687 [6], EN 17124 [7]) is required to demonstrate the actual fuel quality at the nozzle of the hydrogen refuelling stations. In order to support this need, European laboratories are developing the capability to measure the contaminants specified in ISO 14687 [6] and EN 17124 [7]. Several laboratories in Europe (as part of European project MetroHyVe, HYDRAITE or commercial laboratories) are becoming able to measure hydrogen fuel quality according to ISO 14687 [6]. The new challenges linked to the increase of analytical laboratories potentially capable of performing the analysis according to ISO 14687 [6] is to ensure that the results are accurate and agree between laboratories. There is a new requirement of cross check between laboratories or quality control check to ensure that the quality of the results is satisfying. Metrological tool (reference materials, proficiency testing) and accreditation requirements are the best strategy to promote better measurement agreement. The first inter-laboratory comparison led by EURAMET showed that several NMIs and analytical laboratories have good agreement on measurement of CO and H_2S in hydrogen [8]. However, this study was performed on gas standard not on real hydrogen fuel sample and the amount fraction level for H_2S was 250 time higher than ISO 14687 threshold [6]. Recent bilateral comparison organised by European projects (HyCoRa and HYDRAITE) showed discrepancies between laboratories results for hydrogen fuel quality especially for water and hydrocarbons [9]. Recently, MetroHyVe project organised an inter-laboratory comparison for 4 contaminants out of the 13 regulated in ISO 14687 [6]. Ensuring equivalence between analytical laboratories worldwide require that the metrological tools are available and recognised: reference materials, calibrants, proficiency testing schemes, accreditation. Lack of gas calibrants with sufficient uncertainty, reference material and inter-laboratory comparison is a barrier for European commercial laboratory to prove their agreement to ISO 21087 which is mandatory according to ISO 14687. The National Physical Laboratory (NPL) has successfully developed analytical methods and obtained ISO 17025 testing accreditation to measure accurately hydrogen contaminants according to ISO 14687 [6] at low amount fractions (i.e. 4 nmol/mol for total Sulphur, 100 nmol/mol for ammonia). Moreover, NPL has engaged in the development of new reference materials for most of the hydrogen fuel contaminants. The presentation will provide details information on contaminants reference materials in hydrogen and stability. Based on these developments and on knowledge on proficiency testing, NPL will present new proficiency testing scheme guidance for hydrogen fuel quality. Finally, an overview on different new sampling system developed and deployed

in the recent years to tackle sampling from production site, fuel cell vehicles or heavy duty will be provided with emphasis around the methodology. The presentation will be structured on four points: NPL accreditation scope for hydrogen fuel analysis, new hydrogen fuel reference materials, proficiency test and new sampling.

NPL ACCREDITATION SCOPE FOR HYDROGEN FUEL ANALYSIS

NPL achieved to validate method for most contaminant in hydrogen required in ISO 14687. Following method validation and quality control implementation, NPL obtained accreditation scope ISO 17025 and will extend it to complete ISO 14687 scope in 2020. NPL will present the different steps involved in method validation, the quality control tools implemented, and the final scope obtained (Table 1). Moreover, a perspective towards new analytical methods developed recently around picomol/mol of total sulphur and oil amount fraction will be mentioned with the first achievements from NPL.

Table 1. NPL hydrogen fuel quality analytical laboratory with ISO 17025 scope on December 2019.

Gas analysis	ISO 14687 EN 17124 [µmol/mol]	Analytical Method	Detection Limit [µmol/mol]	ISO 17025 testing	Required amount of gas [L]
Water	5	Quartz crystal microbalance CRDS	0.2 0.030	Yes No	30 30 - 60
Total Hydrocarbons	2	GC-Methaniser-FID	0.05	Yes	2
Methane	100	GC-Methaniser-FID	0.05	Yes	2
Oxygen	5	GC-PDHID	0.3	Yes	2
Helium	300	GC-TCD	10	Yes	2
Argon Nitrogen	300	GC-PDHID	0.3 1	Yes Yes	2 2
Carbon Dioxide	2	GC-Methaniser-FID	0.02	Yes	2
Carbon Monoxide	0.2	GC-Methaniser-FID	0.02	Yes	2
Total sulphur compounds	0.004	GC-SCD CryoGC-SCD	0.001 0.0002	Yes No	1 1
Formaldehyde	0.2	GC-Methaniser-FID SIFT-MS	0.05 0.02	No No	2 2
Formic Acid	0.2	FTIR SIFT-MS	0.05 0.02	No No	30 2
Ammonia	0.1	FTIR SIFT-MS	0.05 0.02	No No	30 2
Key halogenated compounds according to ASTM D7892-15	0.05	TD-GC-MS	0.016	No	1.5

NEW HYDROGEN FUEL REFERENCE MATERIALS

NPL developed new sets of multi contaminants in hydrogen gas mixture. The reference mixtures were prepared gravimetrically from the pure components in accordance with ISO 6142-1 [10] in different cylinders (aluminium, aluminium with passivation). Mixtures containing 7 to 12 contaminants have been prepared and studied over a period of several months to one year (example of composition presented in Table 2).

Table 2. Example of NPL reference materials for seven contaminants in hydrogen

Component	Amount fraction / [µmol/mol]
Helium	300
Argon	300
Nitrogen	300
Methane	100
Carbon dioxide	2
Ethane	1
Carbon monoxide	0.2
Hydrogen	Balance gas

NPL investigated reactive species and achieved to produce stable reference materials with low nmol/mol of reactive species including sulphur compounds (i.e. 15 nmol/mol of dimethyl sulphide in hydrogen for several months). NPL will present the new reference materials for hydrogen fuel with length life and uncertainty.

PROFICIENCY TESTING SCHEME

Based on NPL involvement in all the hydrogen fuel inter-laboratory comparisons, a review of the different good and bad practices will be presented involving the reference materials used (cylinder type, composition), the length of the proficiency testing (i.e. 3 months to 2 years), the scheme (shared cylinder versus batch). Following the state-of-the-art

review, NPL will present a new scheme trying to mitigate all the past issue encounter and allowing simpler proficiency testing using the new reference materials recently developed.

NEW SAMPLING SYSTEM

Based on the evolution of hydrogen economy, NPL has developed new sampling system to achieve sampling of hydrogen gas from various production facility, fuel cell electrical vehicles or heavy-duty application. The systems developed have been applied in real situation and hydrogen gas quality according to ISO 14687 was achieved. The presentation will highlight the different type of sampling system and the key points to achieve reliable sampling. The perspectives around these new sampling capabilities will be presented alongside the sector evolution and the need for standardisation.

CONCLUSIONS

The National Physical Laboratory has successfully obtained ISO17025 testing accreditation. New reference materials for a large part of the hydrogen fuel contaminants is available with sufficient length life. Therefore, it will allow to provide new proficiency testing scheme to assess analytical laboratory performance. Adherence to this new proficiency testing scheme will support higher degree of equivalence between laboratories and more reliable results of analysis on hydrogen quality. Finally, the complexity of hydrogen fuel sampling around new system and application will be highlighted and perspectives to support these new sectors will enhanced new research needs on material passivation, intercomparison and contaminants behaviour study. The results presented by NPL will highlight new critical issues to ensure adherence to regulation and international standard (ISO 14687) which seems highly challenging today.

REFERENCES

[1] Hampel C. (2019) Hyundai & H2E: 1,600 fuel cell trucks for Europe. Elecdrive.com https://www.electrive.com/2019/04/15/hyundai-h2e-1600-fuel-cell-trucks-for-european-market/ [accessed on the 29/09/2021]

[2] H2ME (09/08/2019) EU flagship project Hydrogen Mobility Europe (H2ME) reaches key milestone, with hydrogen-powered vehicles travelling over 8 million kilometres to date https://h2me.eu/2019/08/09/eu-flagship-project-hydrogen-mobility-europe-h2me-reaches-key-milestone-with-hydrogen-powered-vehicles-travelling-over-8-million-kilometres-to-date/ [accessed on the 30/09/2021]

[3] ToyotaNewsRoom (2018) Toyota moves to expand mass-production of fuel cell stacks and hydrogen tanks towards ten-fold increase post-2020. https://newsroom.toyota.eu/toyota-moves-to-expand-mass-production-of-fuel-cell-stacks-and-hydrogen-tanks-towards-ten-fold-increase-post-2020/ [accessed on the 29/09/2021]

[4] Hyundai Motor Group (2018) Hyundai Motor Group reveals 'FCEV Vision 2030. https://www.hyundai.news/eu/brand/hyundai-motor-group-reveals-fcev-vision-2030/ [accessed on the 29/09/2021]

[5] European Commission, Directive 2014/94/EU of the European Parliament and of the Council on the deployment of alternative fuels infrastructure Brussels, 2014.

[6] ISO 14687 Hydrogen fuel quality -- Product specification. Geneva, Switzerland: International Organization for Standardization.

[7] EN 17124, Hydrogen fuel. Product specification and quality assurance. Proton exchange membrane (PEM) fuel cell applications for road vehicles

[8] Bacquart T., Van der Veen A.M.H., Bartlett S., Ent H., Van Wijk J.I.T, Minarro M.D., Hill-Pearce R. E., Brewer P.J., Brown R.J.C., Brown A.S. Murugan A.M. (2017) EURAMET 1220: International comparison on hydrogen purity analysis. NPL REPORT ENV 16 https://www.euramet.org/research-innovation/search-research-projects/details/project/analysis-of-trace-level-impurities-in-hydrogen/?tx_eurametctcp_project%5Baction%5D=show&tx_eurametctcp_project%5Bcontroller%5D=Project&cHash=601e94eb98a69b77fc455b24ddd1b446, [accessed on the 29/09/2019]

[9] Aarhaug. T. (2017) Deliverable 6.7 Final report, HyCoRA – HydrogenContaminant Risk AssessmentGrant agreement no: 621223, http://hycora.eu/deliverables/D%206.7%20Final%20report_final.pdf [accessed on 29/09/2021]

[10] ISO 6142-1, Gas analysis - Preparation of calibration gas mixtures - Gravimetric method for Class I mixtures. 2015.

WHEC-2022
23rd World Hydrogen Energy Conference
June 26-30, 2022 - Istanbul

#368

METROLOGY FOR HYDROGEN VEHICLE 2: ACHIEVEMENTS AND PROGRESSES

[1*] *Thomas Bacquart,* [2] *Marc de Huu,* [3] *Karine Arrhenius,* [4] *Thor Anders Aarhaug,* [5] *Jaana Viitakangas,* [1] *Arul Murugan*
[1] National Physical Laboratory, Hampton Rd, Teddington Middlesex, TW11 0LW, United Kingdom
[2] Federal Institute of Metrology METAS, Lindenweg 50, 3003 Bern-Wabern, Switzerland
[3] RISE, Research Institutes of Sweden, Box 857, 501 15 Borås, Sweden
[4] SINTEF Industry, Richard Birkelandsvei 2B, 7034, Trondheim, Norway
[5] VTT Technical Research Centre of Finland, VTT, P.O. Box 1000, 02044, Finland

*Corresponding author e-mail: thomas.bacquart@npl.co.uk

ABSTRACT

Hydrogen fuel cells are an alternative power supply for electric drive trains and could represent 32 % of fuel demand by 2050. To deploy fuel cell electrical vehicles, there is current regulatory barriers (ISO 14687, OIML recommendations) that requires accurate measurements. The European funded project MetroHyVe has provided solutions and improvements in the four measurements challenges (flow metering, quality control, quality assurance and sampling). New challenges arised due to increase of hydrogen economy, therefore a new European project MetroHyVe 2 started in 2020 and its objectives will provide perspectives for the hydrogen economy to solve all regulatory barriers (ISO 14687, ISO 19880-8, ISO 19880-1, ISO 21087, OIML R139-1) and new measurement challenges (flow metering, quality control, sampling and fuel cell stack testing). The presentation will provide a comprehensive overview of the project achievements. The achievements around primary standard for flow metering (light and heavy duty), worldwide inter-laboratory comparison for hydrogen fuel quality, hydrogen sampling inter-comparison and fuel cell stack testing recommendations will be highlighted.

Keywords: Hydrogen fuel quality, ISO 14687, flow metering, metrology, regulations

INTRODUCTION

Climate change, air quality and reliance on imported fuels from non-renewable sources require immediate deployment of alternatives such as hydrogen to meet the 2050 Europe carbon neutral targets (net-zero emission from transport) [1]. Hydrogen fuel cells are an alternative power supply for electric drive trains and could represent 32 % of fuel demand by 2050 [2]. According to 78% of automotive executives polled, FCEVs are “the real breakthrough for e-mobility” [3]. To achieve mass implementation of hydrogen in transport, there is current regulatory barriers. European Directive 2014/94/EU [4] and OIML recommendations [5] must be met by all European hydrogen refuelling stations (HRS) and therefore requires accurate measurement and metrology support. European project MetroHyVe was the first metrological project funded by European metrology program for innovation and research (EMPIR) with focus on solving measurement challenges for fuel cell electrical vehicles. These measurement challenges are linked to the regulatory barriers and international standards (hydrogen quality: ISO 14687, hydrogen quality control: ISO 19880-8, flow metering: OIML R139-1, analytical methods: ISO 21087) ([5; 6; 7; 8; 9]. At the end of the project in 2020, it was evident that new measurement challenges arise in relation with the rapid growth of the hydrogen economy. Therefore, a new European project MetroHyVe 2 was funded by EMPIR around four measurement challenges:

- Flow metering: to develop and harmonise a metrological framework for testing hydrogen meters used to measure the mass of hydrogen dispensed from HRS using secondary standards for light-duty vehicles and primary or secondary standards for heavy duty FCEV).
- Hydrogen quality control (development quality control tool for analytical laboratory (reference materials and inter-laboratory comparison for all contaminants regulated in ISO 14687 and development of metrological guidelines for sensor and analyser at HRS over long period).
- Sampling (harmonization of hydrogen sampling methods at HRSs in Europe and worldwide with ASTM and Japan).
- Impact of contaminant on Fuel cell stack (reproducibility study with FC stack and inter-comparison evaluation, which will eventually result in a standardisation of automotive FC stack testing).

The presentation will highlight the achievement in the four measurement challenges: flow metering, quality control, sampling and Impact of contaminant on Fuel cell stack.

FLOW METERING

In Europe, the flow metering primary standards got developed as part of MetroHyVe and MetroHyVe 2 project. At least four primary standards are operational currently in Europe and two under approval by notified bodies. These mobile facilities are capable of calibrating or testing flow meters in the HRS at the operating conditions during

refueling (nominal working pressure of 700 bar) for light-duty vehicles [10]. The current primary standards are compliant for fuel delivery to light-duty vehicles according to the Society of Automotive Engineers (SAE) J2601 protocol but an international field comparison for clear acceptance by the HRS operators and notified bodies is missing. The MetroHyVe 2 project partners are currently undertaking the first key comparison of flow metering primary standards at EMPA HRS in Switzerland. The presentation will provide insight on the different primary standards in Europe and the status of the inter-comparison.

The implementation of heavy-duty vehicles such as buses and trucks into the hydrogen infrastructure requires primary standards that are capable of reaching higher flow rates and therefore require a dedicated standard, which is currently not available. The project partners are progressing with the development of two first primary standards for heavy-duty vehicle (35 and 70 MPa) with completion expected in summer 2022. The presentation will highlight the status of the two primary standards and will present the results of the uncertainty budget for these heavy-duty primary standards.

The project will also go beyond the state of the art by developing and demonstrating the traceability chain from primary standards to secondary standards for regular verification of small and light-duty vehicles as well as for heavy-duty vehicles. This method for field verification of HRS is using calibrated master meter and the outline of this new methodology will be presented. Finally, a summary of the finding of the project will be presented to support a revision of OIML R139-1 [**Error! Bookmark not defined.**].

HYDROGEN QUALITY CONTROL

European laboratories are developing the capability to measure the contaminants specified in ISO 14687 [6] and EN 17124 [11]. However, the current lack of gas calibrants with sufficient uncertainty, reference materials (RM) for validation and inter-laboratory comparison scheme is a barrier for European commercial laboratories to be able to prove their agreement to ISO 21087. The consortium published an open access report summarising the results of a survey on the requirements of gas calibrants for hydrogen fuel quality which highlights the industry needs. The partners have engaged in ambitious study to enhance gas calibrants stability. The study is evaluating stability of three new multi-contaminant (8 – 14 contaminants) gas mixtures in hydrogen in a large variety of gas cylinders. The stability study will last for at least 12 months and cover contaminants found in real hydrogen fuel samples and detailed in ISO 14687. The presentation will highlight and present the new interlaboratory scheme covering eight contaminants (specified in ISO 14687) in hydrogen fuel. It is the most ambitious interlaboratory comparison worldwide as it involves production of complex gas mixture in batch (14 equivalent gas mixtures), largest number of contaminants in gas cylinder (8 compounds) including reactive compounds at ISO 14687 threshold (i.e. 4 nmol/mol of sulphur compounds). Currently 13 laboratories (including commercial laboratories) from Europe, North America and Asia registered for the intercomparison that will take place in 2022. Finally, a presentation on the activity around validation of sensors in laboratory and at Hydrogen refuelling stations will highlight on the challenges for this new sensing requirement [12]. It will be based on recent study by the consortium on the performance of two sensors for water in hydrogen in laboratory condition and on the implementation of analysers at 3 HRS in Europe which is ongoing in 2022.

HYDROGEN FUEL SAMPLING

Hydrogen fuel sampling methods at HRS nozzle are currently not all validated or compared, which has raised concerns on sampling equivalence worldwide. Partners published an extensive peer-review article on sampling containers, sampling equipment and methodologies used for hydrogen fuel sampling [13]. The presentation will provide an overview on hydrogen fuel sampling system and methodology. To determine the degree of equivalence between hydrogen sampling method, the partners organised bilateral sampling intercomparison. The partners achieved bilateral sampling comparison between Europe and US approach (in collaboration with ASTM). Two joint samplings at HRS in USA were performed by US representative and project partner in 2021. The results of analyses will be presented alongside the status of the sampling inter-comparison in Europe and Asia.

FUEL CELL STACK TESTING

Harmonisation of automotive FC stack testing is needed for the assessment of their performance and durability under operating conditions (including reproducibility issues) and hence of their technological progress. Several European project (HyCoRA, HYDRAITE) has studied contaminant in fuel cell stack recirculation loop [14], however the protocol has not been standardised. The project objective is providing the first guideline for FC stack testing with a recirculation loop, highlighting the critical parameters for their performance, as well as harmonising the test protocol.

Based on an extensive literature review and state-of-the-art systems, the partners will be performed measurements on 4 different stacks. The measurements, comparison and evaluation are currently ongoing. The importance of reactive species behaviour in recirculation loop (temperature, humidity) are critical for the representativity of the results. Therefore, a study was dedicated on clean-up protocol of fuel cell pipes after exposure to contaminant (inert,

hydrocarbons, reactive species) in hydrogen. Further study on adsorption/desorption of reactive compounds (i.e. ammonia) will follow in hydrogen fuel cell system in correlation with online measurement (i.e. FTIR) at partner laboratories. The presentation will highlight the first results and the current progress of the studies.

CONCLUSIONS AND PERSPECTIVE

MetroHyVe 2 provided key studies for hydrogen fuel quality, fuel cell stack testing hydrogen flow metering at HRS and support to enforce regulation and international standards. Its impact is strong in the hydrogen community and support the quick expansion of hydrogen economy in Europe. The project is progressing significantly the measurement for hydrogen for transport however new needs and new activities are planned at European level and the link between MetroHyVe 2 project, the initiative of Clean Hydrogen partnership, the standardisation committees and more recent project will be highlights as perspective of this work.

ACKNOWLEDGEMENT

The Joint Research Project «Metrology for hydrogen vehicles 2» is supported the European Metrology Programme for Innovation and Research. The EMPIR initiative is co-funded by the European Union's Horizon 2020 research and innovation programme and the EMPIR Participating States.

REFERENCES

[1] European Commission - Press release, The Commission calls for a climate neutral Europe by 2050 http://europa.eu/rapid/press-release_IP-18-6543_en.htm Accessed on January 2, 2022

[2] https://ec.europa.eu/info/sites/info/files/ec-18-002-decarbonisation_booklet_27112018.pdf Accessed on September 2, 2022

[3] http://kpmg.com/GAES Accessed on September 29, 2022

[4] European Commission, 2014. Directive 2014/94/EU of the European Parliament and of the Council on the deployment of alternative fuels infrastructure. Brussels.

[5] OIML R 139-1. 2018. Compressed gaseous fuel measuring systems for vehicles. Part 1: Metrological and technical requirements. Paris, International Organization of Legal Metrology.

[6] ISO 14687. Hydrogen fuel quality -- Product specification. Geneva, Switzerland. International Organization for Standardization.

[7] ISO/DIS 19880-8. Gaseous hydrogen -- Fuelling stations -- Part 8: Fuel quality control. Geneva, Switzerland. International Organization for Standardization

[8] ISO 21087. 2019. Gas analysis -- Analytical methods for hydrogen fuel -- Proton exchange membrane (PEM) fuel cell applications for road vehicles. Geneva, Switzerland. International Organization for Standardization.

[9] ISO/DIS 19880-1 - Gaseous hydrogen -- Fuelling stations -- Part 1: General requirements. Geneva, Switzerland. International Organization for Standardization.

[10] de Huu, M; Tschannen, M; Bissig, H; Stadelmann, P; Büker, O; MacDonald, M; Maury, R; Neuvonen, P.T.; Petter, H.T; Rasmussen, K; Design of gravimetric primary standards for field-testing of hydrogen refuelling stations, Flow Measurement and Instrumentation, **2020,** 73.

[11] EN 17124, 2018. Hydrogen fuel. Product specification and quality assurance. Proton exchange membrane (PEM) fuel cell applications for road vehicles, British Standard Institution

[12] Arrhenius, K.; Bacquart, T.; Schröter, K.; Carré, M.; Gozlan, B.; Beurey, C.; Blondeel, C. Detection of Contaminants in Hydrogen Fuel for Fuel Cell Electrical Vehicles with Sensors—Available Technology, Testing Protocols and Implementation Challenges. Proces55ses **2022**, 10, 20. https://doi.org/10.3390/pr10010020

[13] Arrhenius, K.; Aarhaug, T.; Bacquart, T'; Morris, A.; Bartlett, S.; Wagner, L.; Blondeel, C.; Gozlan, B.; Lescornez, Y.; Chramosta, N.; Spitta, C.; Basset, E.; Nouvelot, Q.; Rizand, M.; Strategies for the sampling of hydrogen at refuelling stations for purity assessment, International Journal of Hydrogen Energy, 2021, 46(70), 34839-34853.

[14] Koski, P.; Viitakangas, J.; Ihonen, J. Dynamic Load Cycle Effects on PEMFC Stack CO Tolerance under Fuel Recirculation and Periodic Purge. Journal of The Electrochemical Society, 2022 169 014507

WHEC-2022
23rd World Hydrogen Energy Conference
June 26-30, 2022 - Istanbul

#1563

SAFE ENERGY RELATIONS: UNFOLDING THE PRECAUTIONARY PRINCIPLE WITH THE ADVENT OF HYDROGEN TECHNOLOGIES

[1*] *Ayşe Şehnaz Kart* [2]*İskender Gökalp*
[1] Middle East Technical University, Science and Technology Policy Studies, Ankara, Turkey
[2] Middle East Technical University, Mechanical Engineering, Ankara, Turkey
* sehnazkart@gmail.com , igokalp@metu.edu.tr

ABSTRACT

Proposals on the inclusion of hydrogen as an energy vector into the large-scale energy socio-technical system has gained considerable momentum along with the effects of the climate crisis and the COVID-19 pandemic. This study examines the conflict between various dimensions of decarbonization with hydrogen agenda within the conceptual framework of international environmental law and policies. Firstly, we carry out a general due diligence of the technical, economic, and legal aspects of the hydrogen economy particularly in Europe. Subsequently, via textual analyses of European Union's strategic documents, the incompatibility of the hydrogen risk chain with the hydrogen value chain is revealed. Finally, as one remedy to this incompatibility; the precautionary principle, its relation to science, technology and society studies, and its possible policy applications in the context of hydrogen technologies are discussed.

Keywords: Hydrogen, Decarbonization, Risk, Precautionary Principle, Environmental Law and Policy.

INTRODUCTION

The COVID-19 pandemic triggered the already existing volatility in the world's energo-political regimes to the point that the processes of sociotechnical change related to energy systems are more relevant than ever. Hydrogen is receiving unprecedented interest and investments as the post-fossil fuel world anticipates CO2-neutral chemical conversion of energy. This paper examines the conflict between various dimensions of decarbonization with hydrogen agenda within the conceptual framework of precautionary principle (PP).

EU is a pioneer in the promotion of a "hydrogen economy". The European Commission considers clean hydrogen as "a vital missing piece of the puzzle" to decarbonize heavy industries such as steel and help the EU achieve its 2050 climate neutrality goals. The 2020 EU Hydrogen Strategy [1]-flags up to €470 billion of investment. Hydrogen lobby declared €58.6 million expenditure in 2020 trying to influence Brussels policymaking [2]. On the other side of the coin, from Hindenburg to Fukushima, accidents involving hydrogen are fires and/or explosions with serious consequences for humans and the environment. Hydrogen value chain is more dynamic than ever before. In order to benefit from hydrogen's potential to reduce global and trans-national energy disputes and to solve environmental pollution and health problems; it should be used by minimizing the risk potential caused by its physical and chemical properties.

RESEARCH QUESTIONS

Research questions include: How can precautionary theory serve to explore the delicate balance between desires for a rapid advent of hydrogen energy technologies whilst keeping the highest safety level for the users? How to create value for policy-level research pursuing ecological complexity while analyzing the immature, complex, and differing nature of legal processes necessary for the deployment of hydrogen technologies? How to open hydrogen risk management to qualitative concerns? How to marry innovation and safety in terms of gas quality given that there is no present consensus and a future one is quite difficult to establish?

The answers to these questions are significant as hydrogen can play a crucial role in the transition to a new global sustainable energy regime. The decarbonization potential of hydrogen concerns almost all the economic spheres from industry, transport, services to household activities. In this context, PP offers trans-disciplinary expertise for safe and just energy transitions [3]. Implementation of precautionary theory requires continuous and holistic audit, where information and knowledge are always prone to revision and change [3]. PP can also encourage more open discussion of the value judgements underpinning methods of risk assessment and cost-benefit analysis. This makes policy-making more reasonable, scientific, and accountable.

The objectives of the research are examining the relationships between technical, economic, and legal aspects of «decarbonization with hydrogen» agenda; delving into the risk aspects of the hydrogen infrastructure for sound policy making and regulation as an integrated vision is in its infancy in the EU; contributing to scientific hydrogen policies

by offering extra transparency; suggesting hydrogen policies that enable more deliberative, participatory, democratic decision-making processes.

This study is novel as it tries to find ways for precaution and innovation to coexist. It is novel domain-wise regarding the intersection of energy studies with precautionary theory. Until now, hydrogen has not been the object of such study. It is also novel as one of the major findings reveal hydrogen risk chain – hydrogen value chain incompatibility; an issue yet "to be treated by the relevant literature. Finally, concrete policy recommendations are made in line with abstract principles as another novel feature of the study.

LITERATURE REVIEW

EU laws, official and strategic EU documents, EU directives, EU regulations, EU project reports consist of the first part of literature review. The second part of the literature includes readings of precautionary theory, its weak and strong versions from authors such as Sunstein, Morris, Marchant & Mossman, Fisher, Grant & Quiggin, Persson, Garnett & Parsons. The legal readings of PP are done in legally binding international agreements and treaties, case law, legal doctrine, customary international law and jurisprudence at the international level and state practice at the national level.

As one very successful example of PP, we focus on the Montreal Protocol in detail. It is the first Multilateral Environmental Agreement to set targets and timelines to phase out chemicals harmful to the atmosphere. It is designed in a way that protected the interests of producers and importers, preventing high price inflation or overproduction during the phase out period of the targeted gases [4]. Examination of this Protocol contributes to understanding the delicate balance between innovation and regulation.

METHODOLOGY

We used conceptual, analytical, and descriptive legal qualitative method. The research is conceptual as it doesn't involve conducting any practical experiments. It is related to abstract concepts or ideas. It is analytical as it involves critical thinking skills and the evaluation of facts and information relative to the research being conducted. It is descriptive, describing the characteristics of the phenomenon that is being studied. We also used discourse analysis on the relevant EU documents, conducting specified sets of research on precaution, safety, environmental principles, and energy transition. Legal discourse analysis enabled us to uncover/look at the social context and the political and cultural dynamics behind legislative processes or the policy implementation.

RESULTS

We found out that lack of consensus on hydrogen safety results in non-presence of references to safety. Use of discourse analysis of the latest official documents of EU revealed their perception of law as a "barrier", the absence of "safety" issues therein and loopholes allowing the gas industry to continue burning fossil fuels.

The existing framework for hydrogen in EU is ten years old and not clear enough to build up support schemes for hydrogen. Therefore, in terms of regulatory framework, the scenery is patchy and blurry. It was highly anticipated that the necessary regulations that will clarify the blurriness and reorganize the patchiness will come up with the new Hydrogen and Decarbonised Gas Markets Package [5,6]. This package was delayed for two years now due to the challenges of standardization and of patchwork features of the regulatory framework. The relevant Proposals published on December 15th, 2021, are now on scrutiny process at the European Parliament and European Council. These Proposals do not offer an exhaustive take on hydrogen in Europe. Rather, they add new pieces to a broad set of legislation puzzle including but not limited to the Renewable Energy Directive II, Energy Efficiency Directive (EED) and Emissions Trading Scheme (EU ETS) the proposal of the Carbon Border Adjustment Mechanism, the revised Climate, Energy and Environmental State Aid Guidelines, etc. This means that the regulatory patchwork problem is not solved, a multitude of legal acts will govern hydrogen.

In terms of standards for gas quality, currently Member States have discretion to set the hydrogen limit at the national level, including for gas interconnection points. Such a standard is difficult or perhaps impossible to establish given the diversity of conditions concerning the use of hydrogen, the resistance uncertainty of the pipelines to embrittlement, etc. The Proposals create an obligation for transmissions system operators to accept cross-border blended streams with up to 5% hydrogen content from 1 October 2025. There might be serious repercussions considering the variety of energy systems in different Member States, with different storage facilities and pipelines which cannot tolerate that amount of hydrogen.

DISCUSSION

a. Overall finding: Hydrogen risk chain – hydrogen value chain incompatibility

Hydrogen Value Chain (HVC) from generation to the end uses is well-appreciated. Hydrogen Risk Chain (HRC) appears not to receive the same attention. HVC goes hand in hand with HRC. Leakage, fire and explosion risks are present in all segments of HVC.

b. Policy and legal considerations for EU

We determined some preliminary precautionary policy action in light of the results of the study. They include,

- In terms of standards for gas quality, one solution is PP in its strong version: Do not store or transport hydrogen in its most dangerous gaseous form because the risk is not in the energy conversion of hydrogen by combustion or by fuel cells but in its storage and transport. Standards may then concern:

  1- In situ on demand generation (regulation: zero or minimal storage)
  2- Transport of hydrogen in a different form than gaseous: liquid, ammoniac, adsorbed in solids... (regulation: impose the different transport modes depending on distance, milieu, etc.)

- Incentivizing uses and users with already existing know-how to develop preventive measures
- Standardization for gas quality, but nuanced policies for different uses, users, countries, and regions
- Avoiding EU-level regulatory patchworking
- Accelerating ongoing EU safety assessment processes
- Developing regulatory sandboxes with varying precautionary levels
- Lower precautionary levels for industrial uses and dedicated pipelines
- Higher precautionary levels for general public end-users

c. Innovation Principle & Precautionary Principle as non-competing elements

Precautionary principle gives us room to genuinely shape and design our energy futures. It enables clean energy opportunities, provides “legitimacy” -so as to create an agency framework that is accepted to serve the common good. PP means policy that takes regulation back into real action. Regulation not in a strict sense, but a comprehensive one, one that uses hard and soft and mixed tools, directed at management of transitions via sound policy options, involving public participation in policy processes. We argue that innovation principle and PP are complementary, non-competing elements and the right implementation of PP can foster sustainable innovations. They can and should co-exist, to find innovative, safe and sustainable solutions to key societal challenges [7].

CONCLUSIONS

Considering the hydrogen risk chain, we introduced the concepts of precautionary theory developed to design the main ingredients of environmental laws. We also offered some preliminary considerations for the application of the precautionary principle to the safe development of hydrogen technologies. This study evokes significant research topics such as developing a general precautionary framework applicable to emerging technologies, ex-ante and ex-post impact analysis of precautionary applications, searching for various ways to implement PP in environmental cases, bibliometric studies on precaution, safety and energy transitions.

ACKNOWLEDGMENTS

This work is supported by the International Fellowship for Outstanding Researchers Program of TÜBİTAK (Project No: 118C287)

REFERENCES

1. COMMUNICATION FROM THE COMMISSION TO THE EUROPEAN PARLIAMENT, THE COUNCIL, THE EUROPEAN ECONOMIC AND SOCIAL COMMITTEE AND THE COMMITTEE OF THE REGIONS A hydrogen strategy for a climate-neutral Europe COM/2020/301 final
2. https://corporateeurope.org/en/hydrogen-hype accessed on April 13th, 2022
3. Whiteside, K. 2016. Precautionary Politics: Principle and Practice in Confronting Environmental Risk. Cambridge, Ma: MIT Press
4. https://www.unep.org/ozonaction/who-we-are/about-montreal-protocol Accessed on April 13th, 2002.

5. Proposal for a DIRECTIVE OF THE EUROPEAN PARLIAMENT AND OF THE COUNCIL on common rules for the internal markets in renewable and natural gases and in hydrogen COM/2021/803 final
6. Proposal for a REGULATION OF THE EUROPEAN PARLIAMENT AND OF THE COUNCIL on the internal markets for renewable and natural gases and for hydrogen (recast) COM/2021/804 final
7. European Political Strategy Centre. 2016. Issue 14: Towards an Innovation Principle Endorsed by Better Regulation.

WHEC-2022

23rd World Hydrogen Energy Conference

TRACK 13. HYDROGEN STRATEGIES AND POLICIES

TRACK 13. HYDROGEN STRATEGIES AND POLICIES

#95 HYDROGEN ROADMAP ASSESSMENT FOR COLOMBIA UNDER AN INTERNATIONALLY COMPARATIVE FRAMEWORK	1232
#104 CREATING A GLOBAL HYDROGEN ECONOMY: REVIEW OF INTERNATIONAL STRATEGIES, TARGETS, AND POLICIES WITH A FOCUS ON JAPAN, GERMANY, SOUTH KOREA AND CALIFORNIA	1235
#113 SUSTAINABILITY ANALYSIS OF HYDROGEN PRODUCTION PROCESSES	1239
#194 ASSESSING RENEWABLE HYDROGEN PRODUCTION CAPACITY ON A REGIONAL BASIS	1242
#226 BLUE H_2 PERSPECTIVE IN ENERGY TRANSITION OF COLOMBIA	1245
#228 COLOMBIA'S GREEN HYDROGEN: SOLAR AND WIND POWER CAPACITY SCENARIOS	1248
#267 HYDROGEN ENERGY RESEARCH AND DEVELOPMENT IN KAZAKHSTAN: CURRENT STATUS	1251
#298 DEVELOPMENT OF HYDROGEN ENERGY IN RUSSIA	1254
#304 FROM FOSSIL FUEL ENERGY TO HYDROGEN ENERGY: TRANSFORMATION OF FOSSIL FUEL ENERGY ECONOMIES INTO HYDROGEN ECONOMIES THROUGH SOCIAL ENTREPRENEURSHIP	1256
#329 WAYS TO IMPROVE THE COMPETITIVENESS OF CHINA'S HYDROGEN ENERGY INDUSTRY	1260
#377 H_2-INDEX FOR THE EVALUATION OF HYDROGEN PROJECTS IN MEXICO	1263
#392 HYDROGEN POTENTIAL AS VECTOR FOR A BIOMASS-BASED DECARBONISATION OF TRANSPORT IN BRAZIL	1266
#1478 ARGENTINE ACTIVITIES IN THE FIELD OF HYDROGEN	1269
#1535 COULD GREEN HYDROGEN AND ITS DERIVATIVE IMPROVE ENERGY SYSTEMS IN NORTH AFRICA, CASE OF MOROCCO, EGYPT AND TUNISIA	1273
#1599 GREEN AMMONIA TO ADVANCE THE ENERGY TRANSITION IN CHINA: AN ANALYSIS FROM A COMPLEX SYSTEM ENGINEERING PERSPECTIVE	

WHEC-2022
23rd World Hydrogen Energy Conference
June 26-30, 2022 - Istanbul

#95

HYDROGEN ROADMAP ASSESMENT FOR COLOMBIA UNDER AN INTERNATIONALLY COMPARATIVE FRAMEWORK

[1]Paula Riveros-Melo, [1]John Sanchez C., [1]Martha Cobo-Angel,[1*]Cesar Barraza-Botet
[1]Universidad de La Sabana, School of Engineering, Energy, Materials and Environment Laboratory, Km. 7 Autopista Norte de Bogotá, Chía, Cundinamarca, Colombia

*Corresponding author e-mail: cesar.barraza@unisabana.edu.co

ABSTRACT

Hydrogen roadmaps and national strategies have been used to evaluate scenarios and define pathways to include hydrogen as an energy vector in different countries. Aiming to become one of the early adopters of hydrogen in Latin America, Colombia has recently issued its hydrogen roadmap that sets goals for the near and long term. The aim of this study is to develop an assessment matrix to evaluate the hydrogen roadmaps of several countries and to propose a framework to compare them with Colombia's. To design the matrix, the key elements proposed by the International Energy Agency (IEA) were considered to evaluate the selected roadmaps. As an initial result, the analysis showed that the Colombian hydrogen roadmap contains several of the main aspects that a roadmap well-established should have. However, it should be improved by including more detailed information related to the use of the natural resources, setting milestones for the proposed goals, and designing policies aligned to the country's commitments to the Paris Agreement. As a result, the authors recommend the roadmap to be complemented by an actionable National Hydrogen Strategy containing the aspects identified in this work.

Keywords: Roadmap; Hydrogen, Policy, Comparative Assessment, National Strategy.

INTRODUCTION

Roadmaps are policy instruments used to establish actions and priorities to achieve expected outcomes and goals [1]. Such instrument is widely used to create momentum for the adoption of new technologies, and currently used to outline long-term transition pathways to net zero carbon emissions. Countries such as Australia, Republic of Korea, Japan, Russia and Colombia had recently published their hydrogen roadmaps to identify prospective technologies needed for the large-scale deployment of hydrogen as a novel clean energy vector [2].

In this study, we developed an assessment matrix to evaluate multiple key aspects that a comprehensive roadmap should have, based on the guide proposed by the IEA [1]. To our knowledge, there is not a comprehensive comparative analysis of multiple country's hydrogen roadmaps in the literature. Hence, as a first approach, this abstract presents the assessment matrix applied to the Colombian Hydrogen Roadmap [3]. By applying the same comparative methodology to the hydrogen roadmaps of the countries mentioned above, we will draw conclusion on how to improve Colombia's policies for hydrogen.

MATERIALS AND METHODS

To analyze national hydrogen roadmaps, we proposed a comparative methodology to assess technical, policy, legal, market, financial, environmental, and institutional aspects of the transition toward the hydrogen economy. The selected aspects were based on the guide for the development and implementation of roadmaps proposed by the IEA [1]. The methodology was initially applied to Colombia's hydrogen roadmap [3] and the analysis is presented in **Error! Reference source not found.**.

RESULTS AND DISCUSSION

Error! Reference source not found. shows the analysis of the Colombian roadmap following the key items proposed by the IEA [1]. According to **Error! Reference source not found.**, the main opportunities to reach the goals of the Colombian roadmap require actionable pathways to (i) identify available energy sources; (ii) establish economic policy commitments in both public and private sector, as well as the specific way to use those resources; (ii) define milestones for each of the goals; (iv) carry out technology assessments based on the current state of the art and the prospective technologies; (v) define indicators for each goal and milestone; (vi) identify and engage stakeholders in sectors with high adoption potential of production and end-use technologies to reduce GHG emissions. The assessment also shows that the lack of meaningful stakeholder participatory activities during the development of the roadmap may have affected the inclusion of detailed information. Hence, it is necessary to define methodological approaches for a stakeholder participatory strategy as a mean to fill these information gaps.

Table 1. Criteria matrix to compare the main subjects in roadmaps following the IEA guidelines [1].

Criteria	Assessment
Are there quantitative goals, milestones, gaps, and barriers defined to establish concrete actions?	The document presents quantitative goals for the production and demand of green and blue hydrogen. From a sustainability perspective, investment, job creation, and emission mitigation goals are established as well. However, no milestones associated with the goals were proposed. Regarding progress indicators, only 5 out of 6 have associated goals; and only 5 out of 9 goals have associated indicators.
Are the technologies to be used throughout the value chain and their development indicators defined?	Multiple technologies are mentioned in the roadmap, but none of them are prioritized for R&D or investment support. There is no technical or detailed information on main and enabling technologies applicable to different sectors. After assessing IEA's criteria, [1] the following aspects remain unanswered: Technology development status • Technology performance (e.g., conversion efficiencies) • Technology costs • Environmental impact (air, water, and land impacts) • Technology potential (saturation levels/other limitations) • Links to other technology areas The answer to all these technology aspects may require the development of detailed technology assessment studies and research agendas.
Are there defined policies that affect the development and establishment of hydrogen in the country?	The roadmap proposes policies to promote the use of hydrogen in Colombia in the residential, industrial, tertiary, land, maritime and air transport sectors, among others. However, the document does not establish quantitative goals nor describes a clear methodology to fulfill the purpose of the policy with a chronological priority of implementation, which is fundamental in policy measures associated with the objective [1].
Is there a detailed legal framework and is it enough?	The roadmap contains and describes the current and pertinent legislation for the implementation and development of the hydrogen economy in the country. In addition, it mentions the modifications and creation of necessary new legislation.
Are the hydrogen end-use sectors and their share of participation defined?	• Supply: 31.6 kt H_2 by 2040, and 37kt H_2 by 2050. • Industry demand: 112.8 kt H_2 by 2030, 387.1 kt H_2 by 2040, and 629 kt H_2 by 2050. • Transport demand: 7.2 kt H_2 by 2030, and 1184 kt H_2 by 2050. • Number of vehicles: 1500-2000 LDV, and 1000-1500 HDV by 2050. • There is not an indicator associated to green hydrogen demand, but the roadmap proposes a goal of a consumption of 40% of low emission hydrogen (green and blue) in the industry by 2050.
Is the installed capacity for hydrogen production projected in the national energy matrix?	Although the document presents these quantitative goals, it does not show any specific details on the project's locations, the sources that will be used, nor technical details related to the install capacity, size of the plants or specific milestones that should be accomplished. Related with these criteria the roadmap stablishes the following goals: • Electrolysis installed capacity: 1 - 3 GW by 2030 • Production volume: 50 kt H_2 by 2030 • Number of hydrogens fueling stations: 50 a 100 by 2030
Are the natural resources available for the generation of hydrogen established?	In terms of energy generation, the document does not propose the sources that will be designated to produce either green or blue hydrogen. One of the main opportunities to improve the roadmap is to identify and assign the energy sources and their contribution to hydrogen production.
Are the economic resources that will be used for the development and establishment of hydrogen in the country established?	An investment goal of the private sector of 2.5 to 5.5 billion USD is proposed, but there is not any information related to the sectors that will fund those investments or how they will be used. On the other hand, the government does not commit any economic resources. Related with these criteria, the roadmap stablishes the following goals: • Investment goal: 2.5 to 5.5 billion USD, this goal does not have a specific indicator. • Jobs creation: 7000 to 15000, this goal does not have a specific indicator.
Are hydrogen production cost (LCOH) targets set?	• Levelized cost of hydrogen (LCOH) goal: 1.7 USD /kg H_2 by 2030, this goal does not have a specific indicator. • Green hydrogen: LCOH of 1.5 USD/kg H_2 by 2050. • Blue hydrogen: LCOH of 2.4 USD/kg H_2 by 2050. • Grey hydrogen (Natural gas): LCOH of 2.9 USD/kg H_2 by 2050. • Grey hydrogen (Coal): LCOH of 4.4 USD/kg H_2 by 2050.

Criteria	Assessment
Are CO2 emission reduction targets defined?	• Greenhouse gases emission reduction goal: 2.5 to 3 Mt CO_{2eq} by 2050, this goal does not have a specific indicator. The document does not provide the information on how the GHG reductions was calculated or how it will be achieved.
Is it a governance model stablish and are the responsibilities and the members described?	The roadmap establishes a clear governance model linking the public and private institutions that will be a part of a steering committee and describes each member's responsibilities.

Since a roadmap should be credible, adaptable, and desirable [4], it should be tailored to each country's reality. Colombia is a country with a clean electricity mix—70% of the electricity is generated from hydropower [5]—as well as high potential for renewable energy, which represents a high potential source for low-carbon hydrogen production [3]. On the other hand, Colombian economy highly depends on fossil fuel—mainly coal and oil—since they represent over one third of exports [6]. Finally, recent mitigation commitments to the Paris Agreement in Colombia's NDC set a 51% GHG reduction goal by 2030 [7]. In the opinion of the authors, it is not clear how these key factors are accounted for in the hydrogen roadmap.

Even though a roadmap is a valuable instrument, is not enough to define the transition pathway to a low-carbon hydrogen economy. The roadmap is essential to set the aspirational goals, but it is also required to define the policies to achieve them [8]. For Colombia, a National Hydrogen Strategy should provide the set of policies aligned with the country's reality and environmental commitments to be implemented in the near, medium, and long terms.

CONCLUSIONS

A roadmap should be adaptable, and it would be susceptible to updates and improvements. The Colombian roadmap is an important framework to start with because it considers key elements proposed by the International Energy Agency. However, it is susceptible of improvements in the several aspects—i.e., technology assessments, milestones, and policies, which could be strengthen by the participation of relevant stakeholders. In this regard, the development of an actionable National Hydrogen Strategy that includes the missing aspects should define the pathways for the country to reap the benefits of deploying the hydrogen economy.

ACKNOWLEDGEMENT

The authors acknowledge the generous support of Universidad de La Sabana, the Colombian Ministry of Science, Technology and Innovation – Minciencias and the Colombian Mining and Energy Planning Unit – UPME via Contract No. 036-2021 (Universidad de La Sabana project code ING-272-2021).

REFERENCES

[1] International Energy Agency, "Technology Roadmap A guide to development and implementation," p. 27, 2014.
[2] International Renewable Energy Agency, "Green hydrogen a guide to policy making," 2020.
[3] Ministerio de minas y energía, "Hoja de ruta del hidrógeno en Colombia," 2021.
[4] W. McDowall, "Technology roadmaps for transition management: The case of hydrogen energy," *Technological Forecasting and Social Change*, vol. 79, no. 3, pp. 530–542, 2012, doi: 10.1016/j.techfore.2011.10.002.
[5] UPME, "Plan Energético Nacional 2020-2050," 2020.
[6] Ministerio de Comercio and Oficina de Estudios Económicos, "CONTEXTO MACROECONÓMICO DE COLOMBIA," 2021. Accessed: Dec. 01, 2021. [Online]. Available: https://www.mincit.gov.co/getattachment/1c8db89b-efed-46ec-b2a1-56513399bd09/Colombia.aspx
[7] Gobierno de Colombia, "Actualización de la Contribución Determinada a Nivel Nacional de Colombia (NDC)," p. 10, 2020.
[8] IEA, "Hydrogen in Latin America - From near-term opportunities to large-scale deployment," 2021. [Online]. Available: www.iea.org/t&c/

WHEC-2022
23rd World Hydrogen Energy Conference
June 26-30, 2022 - Istanbul

#104

CREATING A GLOBAL HYDROGEN ECONOMY: REVIEW OF INTERNATIONAL STRATEGIES, TARGETS, AND POLICIES WITH A FOCUS ON JAPAN, GERMANY, SOUTH KOREA AND CALIFORNIA

[1*] *Vishnu Vijayakumar, Lewis Fulton, Mahdi Shams, Daniel Sperling*
[1] Institute of Transportation Studies, University of California, Davis, California, US

*Corresponding author e-mail: vvijayakumar@ucdavis.edu

ABSTRACT

Motivated by increasing emphasis on decarbonization, hydrogen is enjoying unprecedented political and business momentum. This paper reviews the status of hydrogen strategies and progress in major global economies investing in hydrogen, and then focus on four jurisdictions (Japan, Germany, S. Korea and California) that have been among the most aggressive, though in different ways. Japan, Germany and S. Korea are more focused on developing a sustainable hydrogen supply chain. In contrast, California has been more focused on spurring hydrogen demand, especially in the transportation sector. Japan's strategy involves forging partnerships to import "blue" hydrogen while Germany has focused on "green" hydrogen production, along with plans to leverage its extensive natural gas pipelines for hydrogen distribution. Japan anticipates the power sector to be the largest consumer of hydrogen, while others expect the transportation and industry sectors to be the prime movers of future hydrogen demand. Japan, S. Korea and Germany will likely import a substantial portion of their future hydrogen supplies, while California has the potential for low-cost hydrogen production but establishing the distributional infrastructure continues to be a challenge. In all four jurisdictions, investments are still small and there exists huge opportunities for cooperation to develop a self-sustaining global hydrogen market.

Keywords: GHG Emissions, Sector Coupling, Blue and Green Hydrogen, Hydrogen Economy

INTRODUCTION

A concerted and coordinated effort to keep global warming well below 2°C, has become an urgent need. Achieving this target would mean an 85% reduction in global greenhouse gas (GHG) emissions by 2050 [1][2]. Decarbonization would be required across sectors such as transportation, buildings, and industry. Hydrogen is a potentially important option for decarbonization plans given its versatility to be used across different sectors. Hydrogen's versatility suggests that significant increases in hydrogen use, with accompanying economies of scale and cost reductions, will aid countries in achieving their carbon targets and eventually building a carbon-neutral energy system. But building up this hydrogen system is challenging and infrastructure intensive. Strong early investments, with a clear vision of where the hydrogen system buildout is going, are needed. While many countries have latched onto this opportunity to incorporate hydrogen in their long-term energy and transportation plan, they are not all approaching this in the same manner, and no country so far has put all the pieces together.

We begin the paper by reviewing policy activities, targets, and strategies in 8 of the world's most active economies, then focus on the "big four": Japan, Germany, South Korea and California. These four are among the world's largest economies, with a combined gross domestic product (GDP) greater than $15 trillion[3][4]. The sheer magnitude of these economies will be an enabling factor to undertake large scale capital investments necessary for the initial commercialization and adoption of hydrogen into the energy portfolio. Notwithstanding differing emphases and patterns, these four economies share common policy drivers for hydrogen development and deployment: achieving strong climate mitigation goals, energy supply diversification, energy storage for renewables-based grid, and attaining technology leadership. Differences in their policy emphases has led to varying levels of hydrogen adoption across these economies, in different sectors, with different levels of progress. The present study analyzes the policy framework of these four jurisdictions, considering the following aspects.

1. Carbon mitigation targets and the role of hydrogen envisaged by each jurisdiction.
2. Hydrogen in transportation: fuel-cell vehicles and hydrogen refueling infrastructure.
3. Differing policy emphasis on blue and green hydrogen along with supply chain development plans
4. Hydrogen demand projections and underlying policy drivers.

The study looks to draw policy parallels and contrasts, analyze the potential impacts, and provide plausible recommendations for the four jurisdictions to better align their decarbonization strategies using hydrogen. Since the

policies around hydrogen are still evolving, this work will keep pace with the latest announcements and suitable modifications in the analysis framework will be incorporated as and when necessary.

MATERIALS AND ANALYSIS

Worldwide, many countries are aggressively pursuing hydrogen policies and system developments. We start with a review of recent policy status and activities globally as of 2021. We then drill down to the four jurisdictions of interest. This study will draw from existing literature, announced policy targets and apply our own projections/extrapolations to draw plausible comparisons of these four jurisdictions. The ensuing analysis will try and compare carbon mitigation trends/targets extending until 2030(shown below), fuel cell vehicle and infrastructure deployment trends, hydrogen supply chain cost projections (production, distribution), hydrogen demand projections (sector wise) with detailed discussions of the possible impact of policies in each of the above.

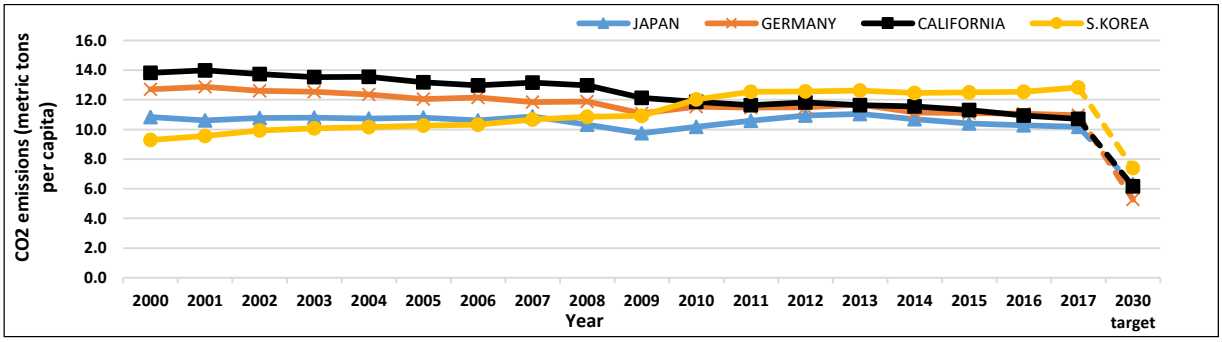


Figure 1 Per-capita GHG emissions from 2000 to 2017 and targets derived until 2030[5][6][7][8]

A big picture overview of the major policy/strategy developments of the four jurisdictions of interest are

Japan

Japan became one of the first countries to roll out a comprehensive hydrogen strategy in 2017, and it has since set out specific plans to become a “hydrogen society.” The strategy notably seeks to achieve cost parity with competing fuels, such as liquefied natural gas for power generation. In March 2019, the government released its third Strategic Roadmap for Hydrogen and Fuel Cells. Japan considers its domestic uptake of hydrogen as a viable way to increase its energy self-sufficiency; decarbonize its economy; increase industrial competitiveness; and position Japan as a fuel cell technology exporter. Japan is enroute to establishing a global supply chain for importing low-cost hydrogen mostly produced using fossil fuels and utilizing carbon, capture and storage (CCS) technology which is currently more economically competitive than renewable hydrogen. Japan is interested in importing green hydrogen if the price is competitive, and at least one Japanese company has signed an investment deal for green hydrogen projects in New Zealand[9].

Germany

In June 2020, Germany rolled out a national hydrogen strategy that eyes a 200-fold increase in electrolyzer capacity—of up to 5 GW by 2030. An additional 5 GW of capacity may be added by 2035 and no later than 2040. According to the IEA Future of Hydrogen report, as of 2030 German hydrogen demand is expected to increase significantly; about 340 TWh between 2015 and 2030, with industry (+164 TWh) and mobility (+70 TWh) being the main growth contributors. Germany has been focusing on establishing a strong supply chain, backed by import agreements as well as by bumping up the production capacity of green hydrogen domestically. The technology development for hydrogen systems have been historically funded and supported by the National Organization for Hydrogen and Fuel-cell Technology (NOW).

South Korea

In January 2019, Korea announced its Hydrogen Economy Roadmap. The roadmap outlines the goal of producing 6.2 million fuel-cell electric vehicles and rolling out at least 1,200 refueling stations by 2040. Additionally, the plan aims to roll out at least 35 hydrogen buses in 2019, ramping this number up to 2,000 by 2022 and 41,000 by 2040. Korea aims to become the world’s largest producer of hydrogen-powered vehicles and fuel cells by 2030, and to eventually also develop hydrogen ships, trains, and machinery. Of the total 6.2 million vehicles to be produced by 2040, 3.3 million would be exported. To achieve these targets, the government provides a subsidy of about 50% of the purchase price of a hydrogen passenger vehicle and subsidizes up to 50% of the installation cost of refueling stations. In 2018, demand for hydrogen was 130,000 tons and is estimated to increase to 470,000 tons by 2022, 1.94 million tons in 2030, and 5.26 Mt in 2040. Korea has a limited domestic capacity for eco-friendly hydrogen production, and it plans to establish overseas bases for hydrogen production. By 2040, South Korea aims to meet 70% of domestic demand through hydrogen from electrolysis and overseas production and 30% by reformed hydrogen.

California (US)

In June 2021, the US Department of Energy (DOE) launched the first “Hydrogen Energy Earth shot”, seeking to reduce the cost of producing green hydrogen by 80% to $1 per kilogram in one decade. This is the latest of the many initiatives taken by the US government to kick start the hydrogen economy. This is a combination of an R&D and deployment

initiative but without specific implementation policies. California has been leading the US efforts to deploy hydrogen with transportation-focused policies that have resulted in among the most fuel-cell vehicles in the world through 2020, only recently overtaken by S. Korea. California has over 90% of both the fuel-cell vehicles and hydrogen refueling stations in the country. Policies like the ZEV mandate, Low Carbon Fuel Standard (LCFS) and the recently announced Advanced clean truck rule have all encouraged uptake of hydrogen in the transport sector. However, the currently high retail costs of hydrogen (over $15/kg in many cases) have been a major impediment to the growth of fuel-cell vehicle sales.

RESULTS AND DISCUSSION

Figure 2 attempts to summarize the relative level of effort or success in different areas of the hydrogen market, and the emphasis and priority that each jurisdiction places on a range of strategies. The figure uses a simple low, medium, and high classification for each indicator listed, pertaining to the development of the hydrogen economy, based on current status and future targets. These ratings are not all encompassing and conclusive (owing to the dynamic nature of the hydrogen market) but provide some sense on progress and how the jurisdictions are similar and different from each other.

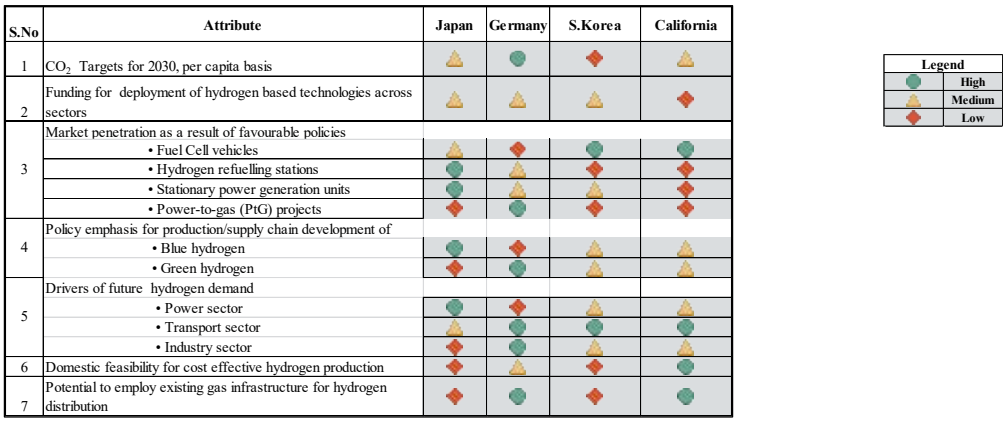


Figure 2 Summary of the relative areas of emphasis and progress for the four jurisdictions

CONCLUSIONS

Hydrogen is being increasingly promoted as a feasible decarbonizing tool by major economies. The current study investigated the policies and strategies of four prominent hydrogen economies: Japan, Germany, S. Korea and California.

- Japan's efforts have focused more on stationary demand side applications such as fuel-cell based off-grid power generation, whereas Germany has been the most proactive on developing hydrogen supply, mostly through the green hydrogen (electrolysis) route. California's hydrogen strategy has centered primarily around the demand side, specifically the transportation sector, by promoting fuel-cell vehicle sales. South Korea is bullish to become a global leader in the production and deployment of fuel cell electric vehicles and large-scale stationary fuel cells for power generation and has the third-largest public investment in hydrogen after Germany and Japan.
- Japan's major challenge will be to develop a self-reliant domestic hydrogen supply chain. Germany will need to incentivize a larger adoption of fuel-cell vehicles on road and look to diversify its low carbon hydrogen import basket. California should aim to increase the role of hydrogen in other sectors (apart from transportation), by incentivizing fuel-cell based power generation units, permitting blending of hydrogen into existing natural gas pipelines, and modifying the LCFS program to become more receptive towards hydrogen. South Korea has not yet focussed on the use of hydrogen in hard-to-decarbonize sectors (such as steelmaking and shipbuilding) which will be critical given its ambitious GHG reduction goals.

All four countries need to develop full hydrogen systems including supply, demand, and the infrastructure to move and store hydrogen in a cost-effective manner. This overall scaleup will be quite challenging, but the time to build it appears to have arrived.

REFERENCES

1. IPCC. 2014 Fifth Assessment Report of the IPCC. Geneva, Switzerland: IPCC.
2. United Nations. 2016 Framework Convention on Climate Change (COP21) Paris Agreement. See http://unfccc.int/paris_agreement/items/9485.php.
3. U.S. Gross Domestic Product (GDP), by state 2019 | Statista, https://www.statista.com/statistics/248023/us-gross-domestic-product-gdp-by-state/, Jun. 2020.
4. Countries by GDP: The Top 20 Economies in the World, https://www.investopedia.com/insights/worlds-top-economies/, Jun. 2020.
5. California Climate Policy Fact Sheet: Emission Reduction Policy., Center for law energy and the Environment; University of California; Berkeley.

6. Johnson, H., Mejia, M.C., and Hill, L., “Population California’s Future,” Public Policy Institute of California, 2018.
7. Eisenmenger, M., Pötzsch, O., and Sommer, B., “Germany’s population by 2050 Results of the 11th coordinated population projection,” 69, 2006.
8. National Institute of Population and Social Security Research, “Population Projections for Japan (2016 - 2065): Summary,” *Foreign Press Cent. Japan* 1–60, 2017.
9. New Zealand: Hiringa Energy And Mitsui & Co. Sign Strategic Alliance Agreement On Hydrogen - FuelCellsWorks, https://fuelcellsworks.com/news/new-zealand-hiringa-energy-and-mitsui-co-sign-strategic-alliance-agreement-on-hydrogen/, Jun. 2021.

WHEC-2022
23rd World Hydrogen Energy Conference
June 26-30, 2022 - Istanbul

#113

SUSTAINABILITY ANALYSIS OF HYDROGEN PRODUCTION PROCESSES

Andrea Mio[a,c], Elena Barbera[b], Alessandro Massi Pavan[a,c], Alberto Bertucco[b,d], Maurizio Fermeglia[a,c]*
[a] *Department of Engineering and Architecture, University of Trieste, Italy*
[b] *Department of Industrial Engineering (DII), University of Padova, Italy*
[c] *Center for Energy, Environment and Transport Giacomo Ciamician, University of Trieste, Italy*
[d] *Centro Studi "Levi Cases" for Energy Economics and Technology, University of Padova, Italy*

[*]*Corresponding author e-mail:* elena.barbera@unipd.it

ABSTRACT

Hydrogen is a versatile energy carrier and storage medium that may be employed in a variety of applications. It may be produced using different processes, each one generating a peculiar hydrogen identified by a color. In this work, process simulation is used to obtain material and energy balances for each process investigated, as well as for the evaluation of capital and maintenance costs. Process simulation outcomes are then used for to estimate three key performance indicators focusing on sustainability issues: the energy return of energy invested, the levelized cost of hydrogen and the life cycle assessment. We compared several hydrogen generation processes, each denoted by a unique color code: (i) green hydrogen, produced by electrolysis of water using electricity from renewable sources, (ii) yellow hydrogen, produced by electrolysis using grid electricity, (iii) grey hydrogen, produced from natural gas using steam reforming and (iv) blue hydrogen, like grey one, but with carbon capture and sequestration (CCS). From the results obtained it is possible to conclude that the most sustainable hydrogen production methods is the so-called green hydrogen, produced by water electrolysis.

Keywords: Hydrogen Production, EROEI, LCOH, LCA

INTRODUCTION

Human energy use has increased rapidly over the last few decades, putting growing strain on the energy industry. Per capita, primary energy use differs among countries and regions, and the global average has significantly increased from 2000 to 2019, of about 42%, passing from 122073 to 173340 TWh. Recent reports of IPCC [1] and EIA [2] indicates that a strong reduction in the usage of fossil fuels must be achieved in order to meet the 2030 greenhouse gases emission targets. Since energy production form renewable sources are not dispatchable due to their fluctuating nature, great attention is given to energy storage and energy carrier systems. Hydrogen is one of the most suitable energy carriers for several applications, mainly in heavy transportation and logistic.

Decisions in the energy sectors should be based on indicators able to summarise different aspects of the sector under study. There are several indicators available in the literature that are commonly employed by decision-makers. One of them is the Energy Return on Energy Invested (EROEI) [3], that relates the amount of net energy stored in the hydrogen produced to the total invested energy. It has recently been proposed as a benchmark tool by the international energy agency (IEA) in the guideline methodology for the net energy analysis [4].

Another key performance indicator, specific for hydrogen, is the Levelized Cost of Hydrogen (LCOH), which considers the cost of hydrogen production process and is calculated as the ratio between the net discounted costs over the amount of produced hydrogen [5]. Inputs to LCOH include cost of capital, investment costs and plant lifetime.

These two indicators focus on hydrogen productions in terms of energy consumption and economic analysis, however, they are insufficient for determining the overall environmental effect of the activities under consideration. We carried out a complete Life Cycle Assessment (LCA) study to achieve this goal.

This paper aims at providing reliable data for different hydrogen production processes in an early process design stage. In this paper we demonstrate how to use process simulation for the estimation of the performance indicators described above for hydrogen production processes. Specifically, we compare different methods of production of hydrogen each one defined by the appropriate color code: (i) green hydrogen, produced by electrolysis of water using electricity from renewable source, (ii) yellow hydrogen, produced by electrolysis using grid electricity, (iii) grey hydrogen, produced from natural gas using steam reforming, and (iv) blue hydrogen, like grey one, but with carbon capture and sequestration (CCS).

The paper considers as case study the production of hydrogen necessary for a medium size cruise ship to navigate for 8 hours full electric in the Adriatic Sea with an energy requirement of about 320 MWh. Considering an energy

content of hydrogen of 140 MJ/kg, and an efficiency of fuel cells of 60%, the quantity of hydrogen to be produced for a one-way trip is 13000 kg. The production of hydrogen will be set to consider 10 trips per day.

MATERIALS AND METHODS

Process simulation is used to perform material and energy balances, physical property estimations, design/rating calculations, process optimization, heat integration and economic analysis evaluation for a given hydrogen production process. The simulation starts with the definition of the problem and its objective. The process model consisting of process flow configuration and accompanying equations is then developed. Since in process simulators, constants and equations are already built-in to the system, it is only necessary to select the unit models, thermodynamic models and method of solution. Additional data is collected if data gaps were identified and required for the model: these may include stream data, equipment data/specification and operating data. The equations are solved and the results are then analyzed if further improvements can be made. The process is repeated until the whole process is finally optimized [6].

RESULTS AND DISCUSSION

The following processes have been simulated using Aspen plus™ 12.0: (i) water electrolysis (Figure 1), (ii) methane steam reforming (Figure 2 left) and carbon capture and storage (Figure 2 right).

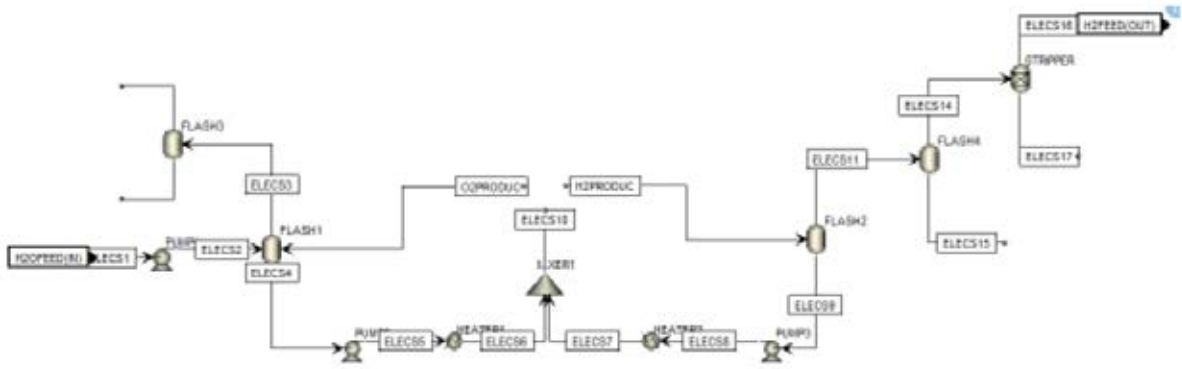


Figure 1. Water Electrolysis process flowsheet within Aspen Plus™..

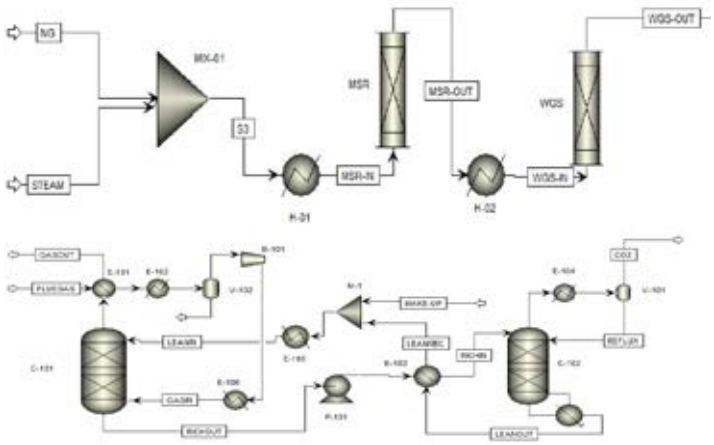


Figure 2. Methane steam reforming process flowsheet (left and MEA carbon capture process flowsheet (right) within Aspen Plus™..

Material and energy balance data coupled with cost estimation obtained by process simulation software are used to calculate the performance indicators: the detail of the data transferred from the process simulation are reported in Table 1.

The equation for the calculation of EROEI is:

$$EROEI = E_{out}/E_{in} \quad (1)$$

where E_{out} is the available energy that the process stores in the hydrogen (140 MJ/kg) and E_{in} is the total energy that is provided and consumed during the production and operations periods of the plant and is made up of three contributions: E_{cap} is the capital energy embodied in the materials and used for construction and decommissioning

of the plant; $E_{o\&m}$ is the energy needed for operating and maintaining the power plant; E_f is the energy needed for procuring and distributing the fuels, which includes also the energy used for extracting, refining and transporting the fuels from the production well to the power plant. All terms are expressed in GWh for consistency: the EROEI is thus dimensionless [7].

The LCOH is calculated as follows [7]:

$$LCOH = \frac{Total\ Costs - Electrical\ Revenue}{H_2 Annual\ production} \quad (2)$$

Table 1: Summary of data retrieved from process simulation for the estimation of EROEI, LCOH and LCA (cf = capacity factor).

		EROEI	LCOH	LCA
Installed capacity (P_{inst})	**kW_e**	x	x	x
Energy for auxiliary	**%**	x		x
Thermal energy	**%**	x		x
Net power output (P)	**kW_e**	x	x	x
Total plant cost (TPC)	**€**		x	
Share of investment costs due to operation and maintenance ($s_{o\&m}$)	**%**	x		
Fixed operation and maintenance costs (FO&MC)	**€/kW/year**		x	
Variable operation and maintenance costs (VO&MC), cf = 0.4	**€/kWh**		x	
Variable operation and maintenance costs (VO&MC) cf = 0.85	**€/kWh**		x	
Total amount of solvent	**kg**			x

The LCA procedure employs material and energy balances over the entire life cycle of the product system, taking into consideration the extraction of raw materials, manufacturing, use phase, end-of-life and the transportation between life cycle stages [8]. The results of life cycle assessments are depicted by means of several impact categories, which are able to represent the entire range of ecological burdens associated with the product system, avoiding shifting the impact among environmental compartments. The LCA procedure involves the implementation of four main phases: goal and scope; Life Cycle Inventory (LCI), Life Cycle Impact Assessment (LCIA) and interpretation.

CONCLUSIONS

Values of the key performance indicators, namely EROEI, LCOH and LCA, indicates that the best route for producing hydrogen in terms of global impact is the green hydrogen.

REFERENCES

1. https://www.ipcc.ch/report/sixth-assessment-report-cycle/ AR6 IPCC 2021 report. Accessed on December 7, 2021.
2. https://www.iea.org/reports/net-zero-by-2050 IEA (2021), Net Zero by 2050, IEA, Paris, Accessed on December 7, 2021.
3. Hall, C.A.S.; Lambert, J.G.; Balogh, S.B. 2014. EROI of different fuels and the implications for society. Energy Policy, 64, 141–152.
4. https://www.eia.gov/outlooks/aeo/pdf/electricity_generation.pdf in the Annual Energy Outlook 2021, Accessed on December 7, 2021.
5. Minutillo M., Perna A., Fprcina A., Di Micco S., Jannelli E. 2021. Analyzing the levelized cost of hydrogen inrefueling stations with on-site hydrogenproduction via water electrolysis in the Italianscenario. International Journal of hydrogen production, 46, 13667 – 13677.
6. Petrescu L., Burca S., Fermeglia M., Mio A,, Cormos C. 2021. Process simulation coupled with LCA for the evaluation of liquid - liquid extraction processes of phenol from aqueous streams. Journal of water process engineering 41: 102077.
7. Barbera, E., Mio, A., Massi Pavan, A., Bertucco, A., & Fermeglia, M. 2021. Fuelling power plants by natural gas: An analysis of energy efficiency, economical aspects and environmental footprint based on detailed process simulation of the whole carbon capture and storage system. Energy Conversion and Management.
8. EC-JRC. ILCD Handbook - General guide for Life Cycle Assessment. 2010.

WHEC-2022
23rd World Hydrogen Energy Conference
June 26-30, 2022 - Istanbul

#194

ASSESSING RENEWABLE HYDROGEN PRODUCTION CAPACITY ON A REGIONAL BASIS

[1,2] *Gonzalo Puig-Samper*, [1,3] *Felipe Campos-Carriedo*, [1] *Diego Iribarren*, [1,3*] *Javier Dufour*
[1] IMDEA Energy, Systems Analysis Unit, 28935, Móstoles, Spain
[2] Universidad Autónoma de Madrid, Chemical Engineering Department, 28049, Madrid, Spain
[3] Rey Juan Carlos University, Chemical and Environmental Engineering Group, 28933, Móstoles, Spain

*Corresponding author e-mail: javier.dufour@imdea.org

ABSTRACT

Local renewable hydrogen production is being promoted by European countries. In this sense, the deployment of renewable hydrogen requires evaluating whether countries or regions could achieve specific future hydrogen production and environmental targets. Within this context, this work proposes a linear optimisation model to find the most suitable production mix at the regional level in terms of costs, while respecting an exogenous environmental constraint. The model was applied to the case study of Spanish regions, analysing the potential contribution to meeting the Renewable Energy Directive II (RED II) target for the transport system in 2030. According to the results, production mixes would vary strongly depending on the region, and only one of the assessed regions would fail to meet the hydrogen demand from renewable sources. It was found that the overall national demand could be fulfilled using indigenous renewable sources, and renewable hydrogen hubs were identified with a regional scope.

Keywords: Environmental Impact, Levelised Cost, Linear Optimisation, Regional Assessment, Renewable Hydrogen

INTRODUCTION

Renewable hydrogen is foreseen as a key actor in decarbonising the economy across crucial sectors (in particular, energy, transport and industry). The EU Hydrogen Strategy structures the efforts that should be made to boost renewable hydrogen, setting a halfway target of 10 million tonnes of renewable hydrogen produced by 2030 [1]. This strategy emphasises the need for a decentralised hydrogen production mix to guarantee a good coupling with renewable energy systems and reduced transport distances. According to the expected economic and environmental benefits of this approach and the unequal distribution of renewable resources, territories will have to adopt different strategies in the near future. This new geopolitical scene can be observed in the hydrogen roadmaps of some European countries such as Germany and Spain, which start to contrast national hydrogen demands with potential indigenous resources for renewable hydrogen production [2].

Kakoulaki et al. [3] addressed the regional assessment of renewable hydrogen production for Europe considering the substitution of the current hydrogen demand. They identified potential hydrogen clusters and importers assuming that regional “grey hydrogen” is converted into “green hydrogen”. Other studies –focused on the quantification of renewable energy sources (RES)– estimate the potential hydrogen production from solar and wind energy by means of geographical information systems [4]. On the other hand, some studies place the focus on developing plans for hydrogen deployment [5]. These are generally based on linear programming optimisation models that minimise a cost-based objective function, considering an environmental constraint. Some of these works present models for regionalised hydrogen production networks [6,7]. However, none of them contrasts RES technical potential with current hydrogen roadmaps and projected hydrogen demands to answer questions on, e.g., the limits for renewable hydrogen production within a given territory and the hydrogen-related opportunities or gaps of a given region.

Within this context, this work aims to develop a model to estimate the potential of territories to generate renewable hydrogen. The objective of the study is twofold: (i) to establish regional production capacity of renewable hydrogen, and (ii) to quantify the required hydrogen and energy flows on a regional scale. The proposed methodology was applied to the case study of Spain, exploring the capacity of the Spanish regions to meet the RED II targets for the country as regards the final energy consumption of the transport sector.

MATERIALS AND METHODS

The methodology presented in this work requires three types of data: (i) RES technical potential at the regional level, (ii) techno-economic and environmental data of the hydrogen production technologies of interest, and (iii) hydrogen demand projections. The latter is implemented exogenously in the model, allowing the use of this methodology to evaluate different roadmaps and targets. Data regarding RES technical potentials were retrieved from ENergy Systems Potential Renewable Energy SOurces (ENSPRESO) [8] for solar, wind and biomass energy. This database presents normalised values for the period 2010-2050, defining the RES technical potential as the available technically-viable renewable resources regardless of whether they are already being exploited. The database has a maximum resolution

that corresponds to the Nomenclature of Territorial Units for Statistics no. 2 (NUTS 2), which was the one adopted in the proposed model. In addition to this dataset, the projected energy demand of other economic sectors (i.e., other than the one under study) can be included so as to quantify the available energy for hydrogen production. Furthermore, besides these RES (solar, wind, biomass), other renewable resources could be included (e.g., organic waste) if they are deemed relevant to the studied territory. For instance, domestic organic waste was considered in the case study shown in this work.

Techno-economic data on hydrogen technologies may be obtained from different sources (e.g., literature, industry) regarding parameters such as capital expenditure (CAPEX), operation and maintenance costs (OPEX), energy and feedstock consumption, and working hours. Since the model employs the levelised cost of hydrogen (LCOH) as the economic variable, LCOH values could also be directly fed to the model. Besides, environmental life-cycle impacts were included to evaluate specific targets (e.g., hydrogen carbon footprint reduction). In this regard, the calculation and implementation of harmonised life-cycle environmental indicators is recommended since they prevent inconsistent methodological choices in comparative studies. In particular, the proposed model employs the harmonised carbon footprints of hydrogen options calculated through the web-based software GreenH$_2$armony® [9]. Techno-economic and environmental values were then evolved and recalculated to 2030, respectively.

For each NUTS 2 region, the proposed model minimises the annual LCOH, which involves a set of n renewable hydrogen production technologies (k) with specific shares (x_k). The minimum cost is found while respecting some environmental constraints or targets as expressed in Eq. (1) and Eq. (2). In this case, the environmental constraint refers to a minimum relative carbon footprint reduction of 60% with respect to the global warming impact of conventional steam methane reforming in 2020 (GW_{SMR}). This reduction target was set to guarantee that the produced hydrogen is renewable according to the definition given by CertifHy [10]. It should be noted that the hydrogen demand (D) for each year (t) refers to the marginal value, meaning that only the annual increased demand is to be additionally produced. The model includes an iterative parameter γ that represents the fraction of the demand which can be fulfilled by indigenous resources. A γ value below 1 means that the region under assessment is not able to meet the corresponding hydrogen demand under the technical and environmental constraints implemented in the model. Further constraints were included in the model to contrast resource availability (R) from each RES (i) and regional hydrogen demand at each year as expressed in Eq. (3). Besides, a maximum share of 75% was imposed per year to production technologies based on the same renewable resource as expressed in Eq. (4), where x_j is the share of each technology based on the RES i and r stands for the total amount of technologies employing the RES i.

$$f(x)_t = (D \cdot \gamma \cdot \sum_{k=1}^{n} LCOH_k \cdot x_k)_t \quad (1)$$

$$\sum_{k=1}^{n} (GW_k \cdot x_k)_t \leq 0.6 \cdot GW_{SMR} \quad (2)$$

$$(D_i \cdot \gamma)_t \leq R_{i,t} \quad (3)$$

$$\sum_{j=1}^{r} x_{j,i,t} \leq 0.75 \quad (4)$$

The case study proposed was built upon current data for the final energy consumption of the transport sector in Spain [11]. Road transportation accounted for 77% of this final energy consumption, so the renewability target of the subsector was set to 10.7% of the final energy consumption of the transport sector. This assumption implies that other transport subsectors would also contribute to achieving the 14% sectoral target set by the RED II [12]. The hydrogen demand was regionalised considering that the necessary fossil-fuelled vehicles, both light-duty vehicles (LDV) and heavy-duty vehicles (HDV), are converted into hydrogen-fuelled vehicles. To this end, the 2019 distribution of fossil-fuelled vehicles by region was considered [13].

RESULTS AND DISCUSSION

The results include the regional hydrogen production mix evolution in Spain until 2030, identifying the export capacity or import needs of each region. The export capacity of each region was expressed relative to its accumulated hydrogen demand by 2030 (negative values meaning import needs). For reporting purposes, this score was then normalised to the highest value, resulting in the final indicator shown in Fig. 1. This indicator gives a clear picture of the capacity of a given region to satisfy its potential future hydrogen demand, as well as of the overall capacity of the analysed territories to fulfil the hydrogen demand by trade among regions.

For the case study of Spain (without Canary Islands, Ceuta, and Melilla), it was found that all of the regions under study, except for the Basque Country, could satisfy the projected regional hydrogen demand until 2030, while respecting the technical and environmental constraints implemented in the model. The unmet demand for hydrogen in the Basque Country could be fully satisfied by hydrogen produced in neighbouring regions. Finally, it should be noted that this picture would change if other hydrogen demand scenarios were fed to the model.

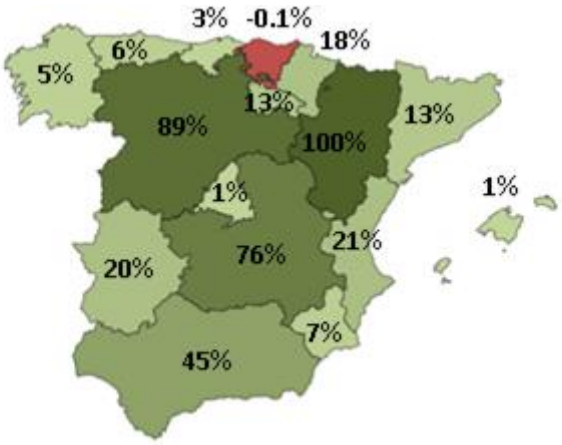


Fig.1. Resultant renewable hydrogen export capacity of Spanish regions (normalised to the highest score)

CONCLUSIONS

The proposed model serves to explore renewable hydrogen production capacity on a regional level, identifying potential hydrogen hubs and evaluating the feasibility of achieving hydrogen targets in terms of demand, cost, and environmental targets. According to the results, Spain would be able to achieve RED II targets by introducing renewable hydrogen in the road transport system. A significant export capacity was found for all of the regions under study except for the Basque Country, whose hydrogen demand could be fulfilled by neighbouring regions. The proposed approach could be implemented to explore other European countries and their potential relationships regarding renewable hydrogen trade.

REFERENCES

1. European Commission. 2020. Communication from the Commission to the European Parliament, the Council, The European Economic and Social Committee and the Committee of the Regions – A hydrogen strategy for a climate-neutral Europe. Brussels, European Commission.
2. Lambert M and Schulte S. 2021. Contrasting European hydrogen pathways: An analysis of differing approaches in key markets. Oxford, Oxford Institute for Energy Studies.
3. Kakoulaki G, Kougias I, Taylor N, Dolci F, Moya J and Jäger-Waldau A. 2021. Green hydrogen in Europe – A regional assessment: Substituting existing production with electrolysis powered by renewables. Energy Conversion and Management 228:113649.
4. Rahmouni S, Negrou B, Settou N, Dominguez J and Gouareh A. 2017. Prospects of hydrogen production potential from renewable resources in Algeria. International Journal of Hydrogen Energy 42:1383-1395.
5. Navas-Anguita Z, García-Gusano D, Dufour J and Iribarren D. 2020. Prospective techno-economic and environmental assessment of a national hydrogen production mix for road transport. Applied Energy 259:114121.
6. Hugo A, Rutter P, Pistikopoulos S, Amorelli A and Zoia G. 2005. Hydrogen infrastructure strategic planning using multi-objective optimization. International Journal of Hydrogen Energy 30:1523-1534.
7. Cho S and Kim J. 2019. Multi-site and multi-period optimization model for strategic planning of a renewable hydrogen energy network from biomass waste and energy crops. Energy 185:527-540.
8. Ruiz Castello P, Nijs W, Tarvydas D, Sgobbi A, Zucker A, Pilli R, Camia A, Thiel C, Hoyer-Klick C, Dalla Longa F, Kober T, Badger J, Volker P, Elbersen B, Brosowski A, Thrän D and Jonsson K. 2019. ENSPRESO - an open data, EU-28 wide, transparent and coherent database of wind, solar and biomass energy potentials. Brussels, European Commission.
9. Valente A, Iribarren D and Dufour J. 2020. Validation of GreenH$_2$armony® as a tool for the computation of harmonised life-cycle indicators of hydrogen. Energies 13:1603.
10. Velazquez Abad A and Dodds PE. 2020. Green hydrogen characterisation initiatives: Definitions, standards, guarantees of origin, and challenges. Energy Policy 138:111300.
11. https://sieeweb.idae.es/consumofinal/bal.asp?txt=Carretera&tipbal=s&rep=1. Accessed on December 21, 2021.
12. European Union. 2018. Directive (EU) 2018/2001 of the European Parliament and of the Council on the promotion of the use of energy from renewable sources. Official Journal of the European Union 328:82-209.
13. https://sedeapl.dgt.gob.es/WEB_IEST_CONSULTA/subcategoria.faces. Accessed on December 21, 2021.

WHEC-2022
23rd World Hydrogen Energy Conference
June 26-30, 2022 - Istanbul

#226
BLUE H_2 PERSPECTIVE IN ENERGY TRANSITION OF COLOMBIA

[1*] *Sara Domínguez Cardozo,* [2] *Bernay Cifuentes Vanegas,* [3] *Felipe Bustamante Londoño,* [4] *Néstor Sánchez,* [5*] *Martha Cobo*
[1,3] Universidad de Antioquia UdeA, Faculty of Engineering, Calle 70 No. 52-21, Medellín, Colombia
[2] Universidad de la Salle, Bogotá, Faculty of Engineering, Chemical Engineering Program, Carrera 2 No. 10-70, Bogotá, Colombia
[4,5] Universidad de La Sabana, Faculty of Engineering, Campus Universitario Puente del Común, Chía, Colombia
*Corresponding author e-mail: martha.cobo@unisabana.edu.co

ABSTRACT

Latin America is starting its transition towards sustainable energy alternatives. In particular, given its abundant natural resources and fossil fuel reserves, hydrogen (H_2) could play a leading role in Colombia. This contribution presents an analysis of the potential of blue H_2 in Colombia, considering it a possible promoter for the H_2 economy. The study focuses on the natural resources available to produce blue H_2 in the context of the recently launched H_2 Road Map and Energy Plan to 2050. Results indicate that the production of low-emission blue H_2 in Colombia, mainly from coal, besides allowing a more sustainable use of non-renewable resources would open the way to green H_2, and could supply up to 10% of global demand of blue H_2 by 2050. However, implementation of a clear public policy and a more detailed roadmap for the inclusion of blue H_2 in the energy matrix is required for the establishment of a H_2 economy in the country.

Keywords: Carbon Footprint, Blue Hydrogen, Coal, Gasification, Natural Gas.

INTRODUCTION

Energy demand keeps increasing due to economic growth, increasing population, and higher life-standards. Ensuring access to affordable, reliable, sustainable, and modern energy for all is indeed one of the 17 UN's sustainable development goals. However, the energy sector is an immense contributor to Greenhouse Gas (GHG) emissions, and the recent Intergovernmental Panel on Climate Change (IPCC) report has highlighted the urge for decarbonisation. For this, Latin American countries such as Chile, Uruguay, Brazil and Colombia are developing strategies to promote energy transition in the region.

While most of the attention has turned to solar and wind energy, the need to store electricity and integrate the locally available energy resources are smoothing the way for H_2 as an energy vector in Latin America. H_2 is a sought-after energy carrier because of its zero direct GHG emissions. Since pure H_2 is not found in nature, though, energy is required for its production, which usually results in indirect GHG emissions. Thus, the quest for clean energy has led to low-emission H_2 (< 5 gCO_2-eq/gH_2), either via water electrolysis using renewable energy sources (solar, wind, hydraulic and biomass), known as green H_2, or via fossil fuels (natural gas, coal, and oil) with carbon capture, utilization and/or storage (CCUS), known as blue H_2.

Currently, up to 98% H_2 produced worldwide comes from natural gas, oil, and coal, without CCUS (i.e., gray H_2) [1]. In this context, less than 2% of Latin American renewable energy projects involve green H_2 production, and at least a decade might be needed to see large-scale green H_2 production in the region. However, recent environmental policies and regulations call for low-emission H_2. This scenario has led to propose blue H_2 as a transitory solution to supply the low-emission H_2 demand in the region considering that the large fossil fuel industry infrastructure could favor the implementation of necessary CCUS technologies, while continuing to take advantage of the local natural resources, and reducing the impact of energy transition on employment in some countries. This could apply to Colombia, which has significant reserves of non-renewable resources and a strong economic dependence on the oil and coal industries.

This work presents an analysis of the potential for blue H_2 production in Colombia, examining mainly technical aspects.

METHODOLOGY

Calculations for potential blue H_2 production were based on fossil fuel reserves and annual production reported by Colombian official agencies [2]–[4]. The amount of coal available for H_2 production was calculated from the projected decrease in worldwide demand under conservative (Stated Policies), medium (Alleged Pledges), and optimistic (Net Zero Emissions) scenarios [5]. Given that most Colombian coal is exported, the underlying assumption was that coal not marketed due to the aforementioned decrease could be used in Colombia for H_2 production. A factor of 0.156 kg_{H2}/kg_{coal} was used, which includes gasification, water-gas shift, CO_2 absorption, and

pressure swing adsorption steps [6]. Demand and market projections were obtained from technical reports and international energy outlooks, Colombia's Energy Plan 2020-2050, and Colombia's National H_2 Road Map [5], [7], [8].

RESULTS AND DISCUSSION

Oil, natural gas, and coal industries represent about 35% of Colombian exports, generating more than 70,000 direct jobs. These non-renewable resources can be used to produce blue H_2 and energy through well-known processes. Figure 1 shows a general scheme of the conventional use of these resources and the potential technologies to produce H_2 instead. The standardized technologies for H_2 production differ only on the syngas production stage, and then follow a single path to H_2, while the emerging membrane reforming couples production and purification steps. Colombian fossil fuel reserves are included in the figure as a starting point for the potential transformations. Law 2099 of 2021 grants fiscal benefits for the production of green and blue H_2, aiming at a low-emission H_2 production of up to 120 kt/year by 2050 and making H_2 production pathways attractive for the fossil fuel industry [8]. In the following sections, the potential of each non-renewable resource available in Colombia to produce blue H_2 is reviewed.

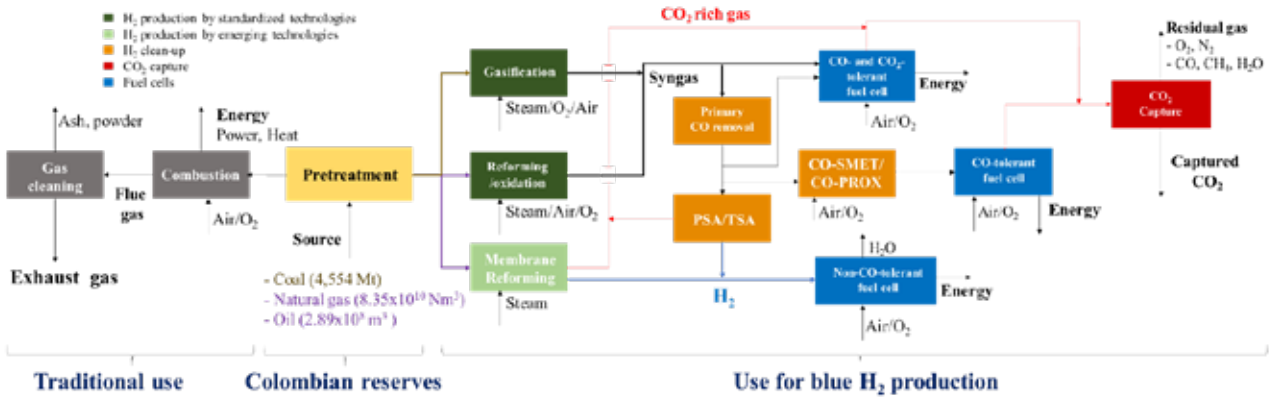


Figure 1. Conventional use (left) and H_2 production pathways (right) from fossil fuels. Simplified process diagram.

Blue H_2 from natural gas

H_2 from natural gas can be produced through the well-established Steam Methane Reforming (SMR), Autothermal Reforming (ATR) and Partial Oxidation (POX) processes, or the emerging Membrane Reforming (MR) process, as seen in Figure 1. SMR, ATR and POX all produce syngas (CO + H_2), which then passes through the H_2 clean-up stages shown in Figure 1, while MR directly produces high-purity H_2. H_2 in Colombia is produced through SMR without CCUS, solely for refinery consumption [8]. Nonetheless, the national H_2 strategy calls for 50 kt/year blue H_2 by 2030, either by replacement or retrofitting of current grey H_2 processes, and expects blue H_2 to be more competitive than grey H_2 by 2035 [8]. However, proven natural gas reserves in Colombia shown in Figure 1 translate into 7.7 years of self-sufficiency at the current annual consumption (1.09 x 10^{10} Nm^3) [4]. Thence, large-scale blue H_2 production from natural gas in Colombia would be a temporary option, unless reserves increase in the near future or gas imports are considered for H_2 production. Furthermore, H_2 from natural gas (e.g., for heating, Figure 1) may not be competitive with the direct use of natural gas.

H_2 from coal

H_2 from coal is produced through gasification processes, which produce syngas that then follows the H_2 clean-up pathway, Figure 1. Colombia is currently the lead coal producer in Latin America, and the third coke producer and fourth thermal coal producer worldwide [3]. Considering its proven coal reserves (Figure 1) and an annual production rate of 84.5 Mt [2], the country has coal for 54 years, whereas considering its estimated reserves (16,569 Mt in 2019) increases coal availability to 194 years, making it attractive as a H_2 feedstock. Most of this coal is exported, thus becoming the main mining export and a major contributor to the country's economy [2]. However, global warming and environmental agreements demand urgent decarbonisation of energy systems and production processes, envisioning a decrease in global coal consumption that could significantly affect the economy if sustainable alternatives are not considered. Table 1 shows Colombia's H_2 production potential if the coal not marketed internationally due to the projected decrease in worldwide consumption were to be used as feedstock. Results show that this production, even under conservative scenarios, could cover and exceed the projected internal demand as stated in Colombia's National H_2 Road Map [8]. With such surplus, Colombia could supply up to 10% of the global demand of blue H_2 by 2050 under an optimistic scenario. Thus, blue H_2 production from coal

could be a possibility for the mining sector to use such important reserves in a more sustainable way, while continuing to support the country's economy.

Table 1. Potential of H_2 production from coal not marketed due to expected decrease in worldwide consumption

Annual production Colombia (kt/year)	Decrease in world demand to 2050 (%)	Scenario	Available amount in 2050 (kt)	Potential H_2 (kt/year)	Ratio to projected demand Col. 2050
84500	25	STEPS [5]	21,125	3,296	1.78
	50	APS [5]	42,250	6,591	3.56
	90	NZE [5]	76,050	11,864	6.41

STEPS: Stated Policies Scenario; APS: Alleged Pledges Scenario; NZE: Net Zero Emissions.

H_2 from other fossil fuels

H_2 can be produced through reforming processes of light hydrocarbons or through partial oxidation of heavy hydrocarbons, Figure 1, but the use of fossil fuels different from coal and natural gas for H_2 production is yet only of interest in places with low availability of these resources or for the utilization of refinery residues. Still, the decarbonisation goals require a decline in the use of liquid fossil fuels that could set the conditions for their becoming H_2 feedstock and continuing to provide energy in a more sustainable way. However, Colombia's oil reserves (Fig. 1) yield 6.3 years of self-sufficiency at the current production rates (1.26×10^5 m^3/day) [4]. This short-term availability renders oil and its derivatives an unfeasible source for H_2 production unless, as in the case of natural gas, reserves increase in the near future and this matches a major decrease in fossil fuels direct use.

CONCLUSIONS

Energy transition to achieve decarbonisation has put H_2 in the spotlight as low-emissions energy carrier. Colombia, a growing economy with great dependence on fossil fuels, needs to find alternatives to use its resources in a sustainable way, and thus blue H_2 appears as an option to move towards a decarbonized economy. While blue H_2 production from oil is yet unfeasible, and from natural gas seems to be a temporary option and limited to the refinery sector, the abundance of coal makes it an attractive resource for H_2 production. Results of this work indicate that H_2 produced from not-marketed coal could cover and exceed the projected national demand, namely, the surplus could be exported and thus replace coal's current role to some extent. Introduction of blue H_2 to the energy matrix could promote H_2 use in the short to medium term and open the road to extended green H_2 uses.

ACKNOWLEDGMENTS

Authors are grateful to Ministerio de Ciencia Tecnología e Innovación (Minciencias) and Unidad de Planeación Minero Energética (UPME) for the financial support to this work (contract 036-2021, La Sabana' code ING-272-2021).

REFERENCES

[1] A. George, O. Siyaguna, A. Frank, and M. Le Floch, "H2 beyond CO2," 2021. [Online]. Available: https://regnan.com/literature/h2-beyond-co2-filling-the-gaps-in-the-environmental-case-for-hydrogen/.
[2] UPME, "Cifras sectoriales - Carbón," 2021. https://www1.upme.gov.co/simco/Cifras-Sectoriales/Paginas/carbon.aspx.
[3] Agencia Nacional de Minería, "El futuro del carbón en Colombia no termina, se fortalece con las ruedas de negocios," *Agencia Nacional de Minería*, Bogotá, Mar. 12, 2021.
[4] Agencia Nacional de Hidrocarburos, "Histórico de Reservas," Bogotá, 2020. [Online]. Available: https://www.anh.gov.co/Operaciones-Regalías-y-Participaciones/SiteAssets/estadisticas-del-sector/modulo-de-gestion-de-reservas/Histórico de Reservas 2020.pdf.
[5] "IEA – International Energy Agency." https://www.iea.org/.
[6] G. Li, P. Cui, Y. Wang, Z. Liu, Z. Zhu, and S. Yang, "Life cycle energy consumption and GHG emissions of biomass-to-hydrogen process in comparison with coal-to-hydrogen process," *Energy*, vol. 191, p. 116588, Jan. 2020, doi: 10.1016/J.ENERGY.2019.116588.
[7] UPME - Unidad de Planeación Minero-Energética, "Plan Energético Nacional 2020-2050," 2020, [Online]. Available: https://www1.upme.gov.co/DemandaEnergetica/PEN_2020_2050/Plan_Energetico_Nacional_2020_2050.pdf.
[8] Ministerio de Minas y Energía, "Hoja de Ruta del Hidrógeno en Colombia," Bogotá, 2021.

WHEC-2022
23rd World Hydrogen Energy Conference
June 26-30, 2022 - Istanbul

#228

COLOMBIA'S GREEN HYDROGEN: SOLAR AND WIND POWER CAPACITY SCENARIOS

*David Rodríguez-Fontalvo, Nelly M. Cantillo, Néstor Sánchez, Martha Cobo**
Universidad de La Sabana, Facultad de Ingeniería, Campus del Puente del Común, Chía, Cundinamarca, Colombia.

*Corresponding author e-mail: martha.cobo@unisabana.edu.co

ABSTRACT

Producing green hydrogen (H_2) with solar and wind energy as main sources is one of the main objectives in Colombia's national strategy for decarbonizing the national energy mix. This contribution studies the role of solar and wind H_2 projects in the Colombian energy mix to meet the H_2 demand for 2030, 2040 and 2050 established on the national H_2 strategy for different scenarios. For creating each scenario, different parameters such as installed capacity of each technology, the resource-to-H_2 efficiency and distribution of the electricity produced to generate H_2 (D_{H2}) were varied. Particularly in Scenario 3, which assumed a D_{H2} of 16.7 %, the solar and wind capacities will need to be 204,749 MW and 88,970 MW, respectively. This scenario was identified as a route to achieve the yearly goal proposed in Colombia's national strategy. This work exposes the implications that H_2 demand exerts on electricity supply and project installations from renewable sources, and is an approach to the green H_2 requirements within the Colombian context. Furthermore, this analysis can guide the required strategies and incentives to successfully integrate green H_2.

Keywords: Green Hydrogen, Installed Capacity, Onshore Wind Parks, Offshore Wind Parks, Photovoltaics.

INTRODUCTION

In 2020, Colombia's Government announced the goal for 2030 of cutting its greenhouse gas emissions to a maximum of 169.44 Mton CO_{eq} (which corresponds to a 51% reduction from a baseline projected scenario), as an updated strategy of the National Determined Contribution to meet Paris Agreements [1]. For doing so, the Ministry of Mines and Energy launched a national strategy. This strategy positions H_2 as the fuel for the transition in the energy mix that will allow to meet the emission goal [2]. This H_2 is specified to come from oil and coal industry including carbon capture technologies (blue H_2), and renewables energies such as hydric, solar, wind and biomass power (green H_2). Colombia's green H_2 demand is esteemed to be 1,850 ktn for 2050, and its main sources will be solar and wind driven electrolysis [2].

Nowadays, Colombia's solar and wind share in electricity production installed capacity is just of about 0.76 % and 0.10 % [3], respectively, and its green H_2 production rate is non-existent. In the years to come, it is expected to observe a growth in the installed capacity of each by electrolysis, and its efficiencies oscillate between 51-58 kWh/kg H_2. Yet, after electricity is produced, it cannot be assumed that it will all be employed to produce H_2. A parameter for its distribution to H_2 was established in this work, so it serves as a start-up to create policies that regulate the use of green energy to produce H_2. This work assesses different scenarios of solar and wind H_2 insertion to the Colombian energy mix by means of the year-to-year demand compliance according to the goals established on the national H_2 strategy.

METHODOLOGY

To comply with the H_2 demand specified in Colombia's national kind of renewable technology, and so the possibility of producing H_2 from the generated electricity. As a fact, according to the Mining and Energy Planning Unit (UPME) report of electricity generation projects, 220 of solar and 26 wind projects have been submitted to study and start operations between 2021 and 2026, with a total 11,210 MW and 4,871 MW installed capacity, for each technology [4]. Moreover, the few installed projects in Colombia report a capacity factor of 15% for utility photovoltaics [5] and 39% for the only wind park of the country [6]. Therefore, four different scenarios of solar and wind technologies insertion were assessed. For every scenario, UPME database was used to establish the potential installed capacity of both solar and wind technologies for the 2021-2026 period. After this period, each scenario comprehends a different calculation procedure. In each scenario, data from Table 1 was used for demand compliance reference and energy conversion efficiency. Eq. (1) was used to calculate H_2 production to meet demand.

Table 1. H_2 demand and supply prospective according to Colombia's national strategy

Year	H_2 demand (kton/yr)	CF_{Solar} (%)	CF_{Wind} (%)	PEMEC (MWh/ton_{H2})
2030	177	15	39	56.4
2040	790			53.2
2050	1,850			51.6

$$HpY = \frac{IC_R\,[MW] * h_{yr}\,[h] * CF\,[\%] * D_{H2}[\%]}{1000} \quad (1)$$

where HpY is the H_2 produced in a year, IC_R is the installed capacity by resource, h_{yr} the hours in a year, CF is the capacity factor to H_2 efficiency and D_{H2} the electricity distribution to produce H_2.

Scenario 1: Utility Photovoltaic and Onshore Wind parks.
For this scenario, an average growth of 1,868 MW and 812 MW of solar and wind energy projects were assumed to be installed year to year until 2050. This value corresponds to the average of year-to-year growth in installed capacity of the 2021-2026 period data from UPME database [4]. In this scenario, the response variable corresponds to D_{H2}, which, in addition, was constrained to be equal for every technology in the same year for each scenario.
Scenario 2: Urban and Utility Photovoltaics, and Onshore and Offshore Wind parks
For this scenario, installed capacity growth averages for utility scale photovoltaic farms and onshore wind farms projects remained the same as in Scenario 1. However, urban photovoltaics and offshore wind farms were included as other electricity sources. According to UPME, using 10 % of the urban roof surface of the 22 biggest cities from Colombia would represent an installed capacity of 1,886 MW [7]. Thus, it was considered a year-to-year growth in urban photovoltaics installed capacity of 65 MW for the 2022-2050 period. Alternatively, the share of offshore installations in the wind energy market was supposed to go from 6.5 % to 21 % [8] on the 2025-2030 period and maintained at 21 % from 2030 to 2050. For calculating the year-to-year growth in offshore installations, Eq. (2) was used. In this scenario the response variable was D_{H2}, which was set to be equal for every technology.

$$IC_{Offwind} = IC_{Onwind} * \frac{\%Share}{100\% - \%Share} \quad (2)$$

Scenario 3: Utility Photovoltaic and Onshore Wind parks with constant electricity distribution
This scenario consisted of fixing every year's D_{H2} to 16.7 %, which was the D_{H2}value obtained for 2030 in the first scenario. By doing so, the installed capacity year-to-year average growth became the response variable for this case, as every other variable was already defined. The ratio between utility photovoltaic and onshore wind (S:W) installed capacity was determined to be 2.3:1 in Scenario 1, therefore it was used as a parameter to maintain in this scenario, then Eq. (3) describes onshore wind installed capacity insertion as a function of solar installations:

$$IC_{Onwind} = \frac{IC_{UtilityPV}}{2.3} \quad (3)$$

Scenario 4: Urban and Utility Photovoltaics, and Onshore and Offshore Wind parks, with constant electricity distribution
This scenario consisted of fixing every year's D_{H2} to 15.6 %, which corresponds to the value obtained for D_{H2} for 2030 in the second scenario. Urban photovoltaics capacity was assumed to be the same as in Scenarios 2 and 3, the installed capacity year-to-year average growth became the response variable for this case. The 2.3 S:W ratio was maintained as parameter for Eq. (3).

RESULTS AND DISCUSSION

The summary of the data obtained for each scenario is presented in Table 2. Scenario 1 exhibits the lowest total installed capacity of all four scenarios. At 80,568 MW in 2050, the D_{H2} rises from 16.7 % in 2030 to 40.1 % in 2040 and 60.7 % in 2050. The values of installed capacity for utility PV and onshore wind parks rise to 56,170 MW and 24,399 MW each. Moreover, for solar power, the value for 2050 can be compared to Germany's 2020 PV installed capacity [9], and for wind power, the value can be contrasted to the 28,296 MW that Spain achieved in 2020 [8]. Less wind installations are needed to meet the same H_2 demand, due to onshore wind parks have higher capacity factors than PV farms.
On the other hand, the inclusion of urban photovoltaics and offshore wind parks in Scenario 2 increases the total installed capacity for 2050 to 87,471 MW, which relieves the D_{H2} to 53.5 % for the same year. Thus, Scenario 2 shows how diversification of an energy mix can lighten the burden of electricity demand for producing H_2. In this case, offshore wind parks installations reached 5,017 MW, comparable to Germany's 2020 offshore installed capacity of 7,728 MW [8], and urban photovoltaics did not represent a high participation in H_2 supply in any of the years, reason for which its implementation for H_2 production purposes may not be needed.
Alternatively, Scenario 3 presented a higher total installed capacity, reaching 293,719 MW, due to the constraint of maintaining the D_{H2} in 16.7 % through the years. In this case, utility PV and onshore wind parks reached 204,794 MW and 88,970 MW of installed capacity, respectively. The former value is comparable to China's 2020 PV installed capacity of 253,400 MW [10], while the latter can be compared to USA's 2020 total wind installations of 122,000 MW [8]. However, even if it seems plausible to achieve a goal that the biggest economies of the world achieved in 20 years, a technical assessment of Colombia's solar and wind energy potential must be done to assure this value can be attained in a country whose territorial surface is smaller than the countries previously mentioned.
Lastly, Scenario 4 presented a slight increase in total installed capacity compared to Scenario 3 (see Table 2) due to the addition of urban PV and offshore wind projects. The decrease in D_{H2} between Scenarios 4 and 3 does not

seem to be relevant for the efforts that must be done to install urban photovoltaics or offshore wind parks, at least at that level of insertion. Moreover, the feasibility of the level of insertion for offshore wind projects (20,433 MW in this case) could discard this scenario as 24,837 MW is the total installed capacity of offshore projects for the whole European Union [8].

Table 2. Annual installed capacities, H_2 supply share and electricity distribution by technology for each scenario.

Scenario	Year	Utility PV		Urban PV		Onshore Wind		Offshore Wind		Total		DH_2 (%)
		IC (MW)	H_2 supply (%)	IC (MW)	H_2 supply (%)	IC (MW)	H_2 supply (%)	IC (MW)	H_2 supply (%)	IC (MW)	H_2 supply (%)	
1	2030	18,803	47.0	0	0.0	8,159	53.0	0	0.0	26,962	100	16.7
	2040	37,486	47.0	0	0.0	16,279	53.0	0	0.0	53,765	100	40.1
	2050	56,170	47.0	0	0.0	24,399	53.0	0	0.0	80,568	100	60.7
2	2030	18,803	44.1	585	1.4	8,159	49.8	700	4.7	28,247	100	15.6
	2040	37,486	42.0	1,236	1.4	16,279	47.4	2,858	9.2	57,859	100	35.8
	2050	56,170	41.3	1,886	1.4	24,399	46.7	5,017	10.6	87,471	100	53.5
3	2030	18,803	47.0	0	0.0	8,159	53.0	0	0.0	26,962	100	16.7
	2040	90,153	47.0	0	0.0	39,167	53.0	0	0.0	129,320	100	16.7
	2050	204,749	47.0	0	0.0	88,970	53.0	0	0.0	293,719	100	16.7
4	2030	18,809	44.1	585	1.4	8,162	49.8	700	4.7	28,257	100	15.6
	2040	84,287	41.2	1,236	0.6	36,618	46.6	8,265	11.6	130,405	100	15.6
	2050	189,621	40.8	1,886	0.4	82,395	46.1	20,433	12.6	294,336	100	15.6

CONCLUSIONS

After evaluating the total installed capacity needed to meet the H_2 demand proposed in Colombia's national strategy, Scenario 3 can be analyzed as a route to achieve the yearly goal. In this case, the D_{H2} was set to 16.7 %, which implies that less than a fifth of the electricity produced by every renewable project would be used to produce H_2. Also installed capacity of solar and wind projects should reach 204,749 MW and 88,970 MW, respectively, to meet H_2 demand. This scenario seems to be feasible as countries like China and USA have already installed similar capacities of renewables into their energy mix. This study serves as a premise to know the effect that the diversification of the energy mix has on energy demand, the impact that H_2 demand has on the electrical generation from renewable sources, and in consequence, on the further investment and planning for total installed capacity of solar and wind projects that Colombia must embrace to ensure its energy mix transition.

ACKNOWLEDGEMENT

The authors acknowledge the support of Universidad de La Sabana, the Colombian Ministry of Science, Technology and Innovation – Minciencias and the Colombian Mining and Energy Planning Unit – UPME via contract no. 036-2021 (Universidad de La Sabana project code ING-272-2021).

REFERENCES

1. Gobierno de Colombia. 2020. "Contribución Prevista Determinada a Nivel Nacional de La República de Colombia."
2. Ministerio de Minas y Energía. 2021. "Hoja de Ruta Del Hidrógeno En Colombia." Ministerio de Energía de Colombia. Bogotá.
3. http://paratec.xm.com.co/paratec/SitePages/generacion.aspx?q=capacidad. Accessed on December 3, 2021.
4. Unidad de Planeación Minero Energética. 2015. "Integración de Las Energías Renovables No Convencionales En Colombia." http://www1.upme.gov.co/DemandaEnergetica/INTEGRACION_ENERGIAS_RENOVANLES_WEB.pdf.
5. https://www.eia.gov/electricity/monthly/epm_table_grapher.php?t=epmt_6_07_b. Accessed on December 3, 2021.
6. Pinilla A, Rodriguez L and Trujillo R. 2009. Performance evaluation of Jepirachi Wind Park. Renewable Energy 34:48-52.
7. Unidad de Planeación Minero Energética. 2015. "Integración de Las Energías Renovables No Convencionales En Colombia." Unidad de Planeación Minero Energética. http://www1.upme.gov.co/DemandaEnergetica/INTEGRACION_ENERGIAS_RENOVANLES_WEB.pdf.
8. Council, Global Wind Energy. 2021. "GWEC-Global-Wind-Report-2021.Pdf."
9. https://www.50hertz.com/Transparency/GridData/Production/Photovoltaics Accessed on December 6, 2021.
10. IEA. 2015. "Snapshot of Global PV Markets 2014." Www.Iea-Pvps.Org. http://www.iea-pvps.org/fileadmin/dam/public/report/technical/PVPS_report_-_A_Snapshot_of_Global_PV_-_1992-2014.pdf.

WHEC-2022
23rd World Hydrogen Energy Conference
June 26-30, 2022 - Istanbul

#267

HYDROGEN ENERGY RESEARCH AND DEVELOPMENT IN KAZAKHSTAN: CURRENT STATUS

[1*] *Saule Zholdayakova,* [1] *Botakoz Suleimenova*
[1] KMG Engineering LLP, D.Kunayev St, Nur-Sultan city, Republic of Kazakhstan

* Corresponding author e-mail: s.zholdayakova@niikmg.kz

ABSTRACT

Constant energy demand and environmental pollution have become a global concern. Central Asia Caspian countries are shifting their focus on alternative fuels, particularly hydrogen energy, while having significant fossil fuel resources. This study is a review of work and procedures done in Kazakhstan toward achieving a net zero emission future. Current studies and projects are summarized showing the condition of hydrogen production, storage and application. In this case, the organization of hydrogen supply chain and consumption, providing national funding, fruitful partnership, assessment of risks and outcomes should be taken into consideration, although it is the very first step of Kazakhstan to hydrogen energy.

Keywords: Hydrogen Energy, Central Asia Caspian Countries, Decarbonization Challenges

INTRODUCTION

Hydrogen is found as an attractive fuel not only for industrial applications but also for transportation and building sectors. The new promising energy carrier is expected to replace conventional fuel sources and provide cleaner energy supplied world. 17 governments have already released hydrogen strategies and policies, including Australia, Germany, Japan, and 20 more countries are developing new ones [1]. It is well known that Central Asia Caspian countries (CACs) have the energy structure, which is mainly based on fossil fuels. Kazakhstan has 58% of final energy consumption which is represented by 43 % of coal, 38% of gas and 18% of oil [2]. Consequently, it may cause challenges in the decarbonization pathway of the energy structure. The government of Kazakhstan has declared its goal to achieve a 15% reduction in GHG emissions in 2030. In order to achieve this extensive energy saving, the ratio is proposed to bring renewable energy in electricity generation to 6% by 2025, to 15% by 2030 and 50% by 2050 [3].

POTENTIAL OF HYDROGEN ENERGY IN KAZAKHSTAN

New Environmental Code is published, in line with international relations standards, from July 1, 2021. The Carbon neutrality Doctrine is being developed to achieve net zero carbon dioxide emission by 2060 strategies in the context of the Paris agreement and Agenda 2030 implementation. The realization of the carbon neutrality program is unattainable without innovative technologies such as carbon capture and storage (CCS) and hydrogen energy. Kazakhstan has potential of utilizing hydrogen as an energy carrier for spreading renewable energy and mitigating environmental problems as the hydrogen system can be considered as clean water source along with clean fuel source [4]. The proposed model consists of hydrogen generation by solar-powered electrolysis. However, political support is the most important factor in a sustainable hydrogen economy. A clear strategy with long-term policies, implementation of hydrogen energy standards and codes, providing hydrogen demand are key areas that should be considered to boost production, demand, and expand hydrogen energy deployment in the country.

Since 2021 Kazakhstan has started officially to talk about hydrogen. One of the largest projects which is about to be realized is a joint project of Kazakh Invest National Company JSC and the German-Swedish Svevind Energy. The full completion of the project is planned in 2026 generating electricity with a capacity of 2 million tons based on solar and wind energy (30 GW) [3]. The project will be implemented in the Mangystau region. Through development of green hydrogen production Kazakhstan may get its niche in the hydrogen market.

Secondly, the President of the Republic of Kazakhstan instructed the Ministry of Energy to interact with the Ministry of Ecology, Geology and Natural Resources, and JSC NC KazMunayGas to develop proposals for the development of hydrogen energy as part of the implementation of the Competence Center in new technologies. The company has launched a low carbon development program for the period of 2022-2031, which aims to envisage hydrogen energy as one of the additional measures for decarbonization of the company. JSC NC KazMunayGas, Atyrau Oil Refinery and Air Liquide Munai Tech Gases signed a Memorandum of understanding on the development of a mobile hydrogen refueling station in Atyrau city. It is also planned to purchase buses and cars running on hydrogen for the

transportation of plant employees [5]. JSC NC KazMunayGas has also signed a Memorandum of Understanding under the hydrogen project with Linde and ENI [6], [7].

Therefore, the company is in the stage of creating the Hydrogen Energy Competence Center at subsidiary company KMG Engineering LLP. The Hydrogen Energy Competence Center is a research hub which aims to develop environmentally friendly fuels, including hydrogen and chemical compounds from hydrogen. The development of the center will significantly expand the research and production potential of both the company and the country. It enables scientists and researchers to work together to implement projects for the production, storage, transportation and use of hydrogen and carbon capture and storage.

Several projects have an innovative role in the development of hydrogen energy in Kazakhstan. The hydrogen production projects cover different research areas. The project proposed by Nazarbayev University is aimed to synthesize titanium-carbide nanoplates of the Mxene type, which is being studied relatively recently around the world. Researchers from Kazakh National Research Technical University are studying the synthesis of energy-storage substances with the help of which it is possible to purify polluted water and at the same time obtain pure hydrogen as a fuel [8]. The topic of catalysts in the catalytic reforming of methane and synthesis gas has always remained relevant. In this regard, Institute of Fuel, Catalysis and Electrochemistry has proposed a technology for obtaining purified blue hydrogen on new inexpensive cluster catalysts without rare metals [9]. Projects on application of hydrogen are aimed at modeling low-temperature and high-temperature fuel cells at Eurasian National University named after L.N. Gumilyov [10], Kazakh-British Technical University [11], and Nazarbayev University [12].

The project on storage and transportation of hydrogen by KMG Engineering is going to be the first study, which proposes the use of Kazakhstani metals for the preparation of titanium-based alloys at a low cost for hydrogen storage. The idea of affordable transportation has been suggested using railway which is the main type of transport connecting the whole of Kazakhstan. It will allow transporting hydrogen in a safe and optimal way. In Kazakhstan, materials for hydrogen storage alloys are abundant and their prices are less expensive. For instance, Kazakhstan has 30 % of the global reserves of chrome ores, which is second globally, 25 % of manganese ores, 10 % of iron ores and is ranked tenth in the world in terms of titanium reserves [4]. Moreover, an increase to US$ 4,535.53 million in the hydrogen storage alloys market is forecasted according to market research on “Hydrogen Storage Alloys Market Forecast to 2028” [13].

However, there is a huge problem such as a lack of technologies, specialists, and experts in Kazakhstan. We believe these projects have a positive social and environmental impact by training new personnel and jobs, developing science and reducing the negative impact on the environment in Kazakhstan, where industry plays the main role of the economy.

CONCLUSION

Kazakhstan has great fossil fuel reserves that may sustain higher energy production. However, the global coalition for net zero emissions has not been avoided by Kazakhstan as the country is also significantly influenced by climate change. This study has reviewed current procedures toward the green economy. Indeed, political support is essential for demand generation, standardization and risk control for the growth of the hydrogen market in the country. Along with it, Kazakhstan is facing certain key challenges like formulation of regulating policies, standards and codes, implementation of R&D, etc. The country is at the very beginning of hydrogen energy deployment but overcoming these issues may bring a successful green economy and sustainable future.

REFERENCES

1. Global Hydrogen Review 2021, IEA report https://www.iea.org/reports/global-hydrogen-review-2021. Accessed on January 14, 2022
2. Yang X, Rocco DM, Gabriele C. 2021. Greening China's BRI in Central Asian Countries: The Role of Hydrogen Towards Net-Zero Future. Available at SSRN: https://ssrn.com/abstract=3858058 or http://dx.doi.org/10.2139/ssrn.3858058
3. Green Hydrogen developments in Central Asia. https://www.investinnet.com/energy-talks/. Accessed on December 9, 2021
4. Zholdayakova S, Uchida HH., Harada MR, Sato M, Gemma R, Matsumura Y. 2020. A Proposal for Water Transportation by a Hydrogen Energy System —A Feasibility Study for Kazakhstan. Proc. Schl. Eng. Tokai Univ., Ser. E 45: 1-6 DOI: 10.18995/24343641.45.1
5. KazMunayGas to launch first hydrogen filling station in Kazakhstan. https://www.kmg.kz/eng/press-centr/press-relizy/?rid=425&cid=0 Accessed on October 12, 2021
6. Linde, KazMunayGas ink hydrogen deal in Kazakhstan https://www.gasworld.com/linde-kazmunaygas-ink-hydrogen-deal-in-kazakhstan/2022092.article Accessed on November 1, 2021

7. Eni to partner with KazMunaiGas on energy transition projects in Kazakhstan. https://www.upstreamonline.com/energy-transition/eni-to-partner-with-kazmunaigas-on-energy-transition-projects-in-kazakhstan/2-1-1044809. Accessed on July 27, 2021
8. Sarmurzina RG, Boyko GI, Baigaziyev MT, Karabalin US, Lubchenko NP. 2018. New generation of energy accumulating substances on the basis of activated aluminum. Journal of Chemical Technology and Metallurgy 53(1):119-124.
9. Zhang X, Vajglova Z, Mäki-Arvela P, Peurla M, Palonen H, Murzin DY, Tungatarova SA, Baizhumanova TS, Aubakirov YA. 2021. Mono- and Bimetallic Ni−Co Catalysts in Dry Reforming of Methane. ChemistrySelect 6 (14): 3424-3434.
10. Solovyev AA, Kuterbekov KA, Nurkenov SA, Nygymanova AS, Shipilova AV, Smolyanskiy EA, Rabotkin SV, Ionov IV. 2021. Anode-supported solid oxide fuel cells with multilayer LSC/CGO/LSC cathode. Fuel Cells 21 (4):408-412.
11. Umirzakov AG, Mereke AL, Shaikenova AA, Rakhmetov BA, Yeleuov MA, Beisenov RE, Ebrahim R, Mansurov BA. 2021. Porous nickel based half-cell solid oxide fuel cell and thin-film yttria-stabilized zirconia electrolyte. Eurasian Chemico-Technological Journal 23 (1): 9-17
12. Kassenova N, Kalybekkyzy S, Kahraman MV, Mentbayeva A, Bakenov Z. 2022. Photo and thermal crosslinked poly(vinyl alcohol)-based nanofiber membrane for flexible gel polymer electrolyte. Journal of Power Sources 520: art. no. 230896.
13.Hydrogen Storage Alloys Market to Reach US$ 4,535.53 Million till 2027. https://www.digitaljournal.com/pr/hydrogen-storage-alloys-market-to-reach-us-4535-53-million-till-2027#ixzz7HwM4Iamh. Accessed on December 9, 2021

WHEC-2022
23rd World Hydrogen Energy Conference
June 26-30, 2022 - Istanbul

#298
DEVELOPMENT OF HYDROGEN ENERGY IN RUSSIA

[1,2*] *Dmitry Dunikov,* [1] *Vasily Borzenko*
[1]Joint Institute for High Temperatures of the Russian Academy of Sciences, Laboratory for Hydrogen Energy Technologies, 125412 Izhorskaya st. 13 bld. 2, Moscow, Russia
[2] National Research University "Moscow Power Engineering Institute", 111250 Krasnokazarmennaya 14, Moscow, Russia

*Corresponding author e-mail: h2lab@mail.ru

ABSTRACT

In August 2021 the Concept for the Development of Hydrogen Energy in Russia was released with a strategic goal to make Russia one of the global leaders in hydrogen production and export. It is a major step ahead, since from the collapse of the USSR there were no hydrogen energy program in Russia. The priorities for the development are low-carbon processes of hydrogen production from the fossils with CO_2-capture and water electrolysis using nuclear power. The Concept includes 3 stages with export targets at the end of each stage are 0.2 Mt H_2 in 2024, 2-12 Mt H_2 in 2035 and 15-50 Mt in 2050 H_2 depending on the development rate of the global low-carbon economy.

Keywords: Russian Federation, State policy, Concept for the Development of Hydrogen Energy

INTRODUCTION

Hydrogen is considered as a secondary energy carrier for energy accumulation, preferably for renewable energy sources. Development of hydrogen energy in Russia (as part of the USSR) has begun in 1970s. In 1975 the Academy of Sciences has established a Working Group on Hydrogen Energy, and in 1977 a Commission of Academy of Sciences on Hydrogen Energy was established, a concept of development of hydrogen energy in the USSR was created. Leaders of the Commission were academicians M.A. Styrikovich, V.A. Legasov and E.E. Shpilrain, base organizations were Institute for High Temperatures and Kurchatov Institute.

In the early 1980s the conception of hydrogen energy in the “purest” form considered production of hydrogen at large plants by water splitting by nuclear power, transportation of hydrogen to the centers of consumption and distribution with the next use as a fuel in that applications, which use natural gas, liquid or solid fuels [1]. There were many achievements in the field of hydrogen energy and fuel cells, including development of the first hydrogen aircraft Tu-155 and hydrogen airport infrastructure. In 1988 the 7th WHEC was held in Moscow.

After the collapse of the USSR in 1990-s the work of the Commission on Hydrogen Energy was stopped. Many efforts were made to revive activities, but until recently there were no Hydrogen Energy program in Russia. Research and development efforts were mostly concentrated in institutions of the Russian Academy of Sciences and universities, and were mostly supported within programs of the Russian Ministry of Science and Higher Education and grant programs of Russian Foundation for Basic Research and lately Russian Science Foundation. Nevertheless, the critical Technology “Novel and renewable energy sources, including hydrogen energy” was recognized within the “Energy efficiency and energy saving” top priority in science and technology development directions in Russia [2].

In the recent years, the understanding of the role of hydrogen as a clean and effective energy carrier has been increased. The G20 Osaka leaders' declaration published in June 2019 has recognized opportunities offered by further development of innovative, clean and efficient technologies for energy transitions, including hydrogen [3]. The declaration gave a new start for hydrogen in Russia, the interest has reached policymakers and on August 5, 2021 the Concept for the Development of Hydrogen Energy in Russia was released [4], with the two broad goals: increasing socioeconomic development and maintaining a commanding position in global energy, thus neutralizing future risks in a decarbonizing global economy for Russia as the major hydrocarbon producer.

CURRENT STATE

Today the global energy system is in transition, and the best available science and international cooperation are needed for deployment and dissemination of zero or low carbon emission and renewable technologies. While the share of renewables (RES) increases rapidly, the variable RES have the problem of low capacity factors and there’s a desperate need for energy storage. Hydrogen could contribute for a power system flexibility, as well as to a sector coupling with transport and industry. Russian energy sector relies mostly on cheap and abundant fossil fuels, nuclear and hydro energy. Renewables (excluding large hydro) contributes less than 1% of the total power generation and cannot compete with traditional generation within the Unified Energy System.

Nevertheless, Russian Federation actively supports international efforts in climate change reverse, conserving the environment and sustainable development, and has joined the Paris agreement (signed April 22, 2016 and adopted by the Russian government decree #1228 on September 21, 2019). Moreover, renewable energy sector is important for sustainable energy development of Russia, since 65% of the country are not covered by unified grids. Electricity in that regions is supplied mostly by diesel power stations (DPS). There are ca. 900 DPS generating 2.54 billion kWh/year (2% of total generation in Russia) with generation cost in the range 0.25-2 Euro/kWh. Power supply of isolated regions is heavily subsidized from the federal and regional budgets and causes significant environmental damage. Thus, the role of renewables in future energy systems is recognized, and Russia started to follow the global trend and introduce more RES generating capacities. For example, in 2020 there were commissioned 12 renewable power plants with total capacity 978.4 MW, an only 5 fossil and nuclear power plants with total capacity 957 MW [5]. Thus, research activities in hydrogen energy for the use in Russia have the goal of further socioeconomic development and include new technologies for low-carbon hydrogen production from traditional and renewable energy sources, fuel cells, hydrogen transport, hydrogen systems for electricity accumulation and for distributed power production, especially for isolated regions.

On the other hand, Russia is one of the major hydrocarbon producers and therefore faces future risks in the global economy decarbonization. The Concept has the strategic goal to make Russia one of the global leaders in hydrogen production and export. Today, the most economically efficient means of producing hydrogen are steam methane reforming and coal gasification, which contribute 75% and 23% of the global production, and low-carbon hydrogen production by water electrolysis with the use of renewables is only expected to reach the target of 2 USD/kg H_2 in 2050. Thus, and the criteria of success would be lowering carbon dioxide emissions for all the hydrogen technologies. Within the Concept the priorities for the development are the creation of low-carbon processes of hydrogen production from the fossils (e.g. pyrolysis) with CO_2-capture and water electrolysis using nuclear power. Potential markets are Europe and Asia Pacific region. The Concept includes 3 stages with export targets at the end of each stage are 0.2 Mt H_2 in 2024, 2-12 Mt H_2 in 2035 and 15-50 Mt in 2050 H_2 depending on the development rate of the global low-carbon economy.

The Concept proposes to use regional clusters to facilitate the development of export-oriented production of hydrogen and hydrogen-based energy mixtures, as well as production of hydrogen for domestic use. Three main clusters should be created: North-Western cluster for export in EU countries and development of low-carbon technologies, Eastern cluster for export to Asia and development of hydrogen technologies for transport and power production, and Arctic cluster to fulfill needs of Arctic regions for low-carbon energy and/or production of hydrogen and energy mixtures for export. Additional Southern cluster could be created for the use of resources of natural gas and renewables with base on the developed infrastructure of the Southern Russia. In October 2021 the Ministry of Industry and Trade of the Russian Federation presented Russian Atlas of low-carbon and carbon-free hydrogen and ammonia production projects [6], which includes 33 projects in 18 regions of Russia.

Realization of the Concept is expected with the participation of all organizations, including state institutions, Academia and universities, industry and business. The Ministry of Energy will present annual reports to the Government.

REFERENCES

1. Shpilrain EE, Malyshenko SP and Kuleshov GG. 1984. Introduction to hydrogen energy. Moscow, Energoatomizdat (in Russian).
2. Decree of President of Russian Federation #899 from 07/07/2011
3. https://www.mofa.go.jp/policy/economy/g20_summit/osaka19/en/documents/final_g20_osaka_leaders_declaration.html. Accessed on January 10, 2022
4. Concept for the Development of Hydrogen Energy in Russia (in Russian). http://static.government.ru/media/files/5JFns1CDAKqYKzZ0mnRADAw2NqcVsexl.pdf. Accessed on January 10, 2022
5. Shulginov NG. 2021. On the results of the Russian Ministry of Energy activities in 2020 and key goals for forthcoming period (in Russian). https://minenergo.gov.ru/node/20324 Accessed on January 10, 2022
6. https://minpromtorg.gov.ru/docs/#!russian_atlas_of_lowcarbon_and_carbonfree_hydrogen_and_ammonia_production_projects Accessed on January 10, 2022

WHEC-2022
23rd World Hydrogen Energy Conference
June 26-30, 2022 - Istanbul

#304

FROM FOSSIL FUEL ENERGY TO HYDROGEN ENERGY: TRANSFORMATION OF FOSSIL FUEL ENERGY ECONOMIES INTO HYDROGEN ECONOMIES THROUGH SOCIAL ENTREPRENEURSHIP

[1*] *Jossie Esteban Garzón Baquero,* [1] *Daniela Bellon Monsalve*
[1] Universidad de Santander, Facultad de Ingenierías y Tecnologías, Instituto de Investigación Xerira, Bucaramanga, Colombia

*Corresponding author e-mail: jos.garzon@mail.udes.edu.co

ABSTRACT

Social entrepreneurship plays a crucial role in global sustainable development, enhancing the quality of life and preserving environmental, human, and social capital. However, when it relates to the energy transition, it faces numerous challenges and experiences conflicts in terms of costs, technological innovation, public policies. This study seeks to illustrate one of the new alternative energy schemes which could replace fossil fuels in the future: hydrogen. This transformation would result in significant social impacts, leading to the question, “how should it be done?” Social entrepreneurship can integrate socio-economic actors and agents and help them to devise and implement new forms of energy innovation. Therefore, a descriptive qualitative methodology was designed, that allows us to analyze the process of building entrepreneurship with a social vision and to propose a model that enables the transition from fossil economies to the hydrogen economies. Among the most significant results, stands out the importance of the support of the three primary axes of each country and the role of social entrepreneurship as a key element for the transition. The discussion contributes to the debate on the path that academia should lead, and the fundamental role of entrepreneurship based on social conscience as a driver of change.

Keywords: Hydrogen Economy, Social Entrepreneurship, Hydrogen Energy, Sustainable Development, Innovation.

INTRODUCTION

For [1] the effort to find sustainable energy sources is driven by various factors: i) political stimuli from net energy importing nations, ii) environmental concerns, and iii) diminishing hydrocarbon reserves, especially of petroleum. In this context the development of hydrogen-based energy is logical. Hydrogen does not release carbon to the atmosphere, and the required technologies already exist and are experiencing gradual cost reductions, while the costs of discovering and extracting hydrocarbons continue to increase.

The aforementioned factors support the concept of a “Hydrogen Economy”, which has been theorized since the 19th century. In the novel “The Mysterious Island” penned by author Jules Verne in 1874, the author proposes separating the constituent elements of water by means of electricity and using them as fuel. Naturally, the concept has continued to evolve since then, but the basic transformation was envisioned long ago as humanity has sought to shift its energy matrix [2]. The term “hydrogen economy” can thus be taken to include the new business structure and system of socio-economic relationships that would be engendered by a move from fossil fuels to hydrogen [3], [4]. The question therefore arises as to how these socio-economic relationships can be created in a new business structure that is not only profitable, but also promotes projects of community interest that may encompass public works, volunteer involvement, or an array of other types.

In relation to the hydrogen economy, [5] propose that social entrepreneurship is the way to take advantage of the potential of clean energy sources existing in a territory, in this case, hydrogen; furthermore, it allows to raise the economic value of renewable energies, which as a new pattern, generates jobs and promotes the reactivation of other industries of local nature, which can act as suppliers of this. However, the cost of this new hydrogen-based economy is still too high, therefore, it must be supported by a social base, which implies the joint work of the industry through the social entrepreneur -as its goal is social rather than profit [6]-, the academy, and the state. Nevertheless, when an analysis of the state of the art on the subject is made, it is clear that the research gap between the hydrogen economy and social entrepreneurship is quite wide. Research has shown that collaboration between the hydrogen economy and social entrepreneurship is an essential condition for promoting innovation and improvement processes in the energy transition of any country; however, not all collaborative work stimulates substantial improvements in this type of transition if it is not accompanied by the key roles proposed in this research. This leads to questions such as: how is this transition going to be implemented? how to be an entrepreneur in the new hydrogen economy? what do we know about the theoretical-practical relationship between social entrepreneurship and the hydrogen economy? Why is the relationship between social entrepreneurship and hydrogen economy important?

In this context, the present study proposes a transformation of fossil fuel economies to a new model that uses hydrogen as an energy vector; and suggests that this transformation can best be undertaken through synergy with

social entrepreneurship, which aims for social and environmental development, and the resolution of socio-economic problems by means of sustainable strategies.

MATERIALS AND METHODS

The present research aims to generate a contribution to the theory on the process of transformation from fossil energy economies to hydrogen economies through social entrepreneurship using descriptive qualitative analysis. Qualitative research can be seen as an attempt to obtain a deep understanding of the meanings and definitions of the situation as people present it to us, rather than the production of a quantitative measure of their characteristics or behavior [7], in this particular case, the meanings and definitions of the relationship between social entrepreneurship and the hydrogen economy. To comply with this analysis, information is collected from various sources, mainly scientific, then critically analyzed and interpreted so that you finally realize the thematic development aimed at generating knowledge and understanding [8].

For the development of this research, a collection of documents on the subject was carried out through the search for scientific communications in different databases: Web of Science, Science Direct, Scopus, among others. Specifically, a document search is carried out using keywords such as “hydrogen economy,” “entrepreneurship”, “social entrepreneurship”, and “energy transition”. The search identified 710 documents. On applying inclusion/exclusion criteria shown in table 1, to title and abstract review 568 documents were excluded. Finally, 142 full texts were reviewed, and a further 66 were excluded. After reading the documents, a selection process is carried out and the information is analyzed following a tracking matrix.

Table 1 Inclusion and exclusion criteria

Parameters	Inclusion	Exclusion
Keywords: entrepreneurship, social entrepreneurship	The documents provide the pertinent guidelines or implications with regard to fields of social entrepreneurship, social enterprise management, social entrepreneur characteristics, and social entrepreneurial intention or orientation.	Non-relevant works and documents that only account for entrepreneurship activity from an income generation viewpoint were not considered.
Keywords: hydrogen economy, energy transition	The documents address issues pertaining to a hydrogen economy and energy transition from renewable energies under the social and environmental viewpoints.	Non-relevant works were excluded.
Type of publication	Due to the research scope itself, not only journal papers were included, but also books, book chapters, and reports of business success cases, that had passed through a peer-review process, ensuring quality criteria.	Documents that do not ensure a peer review process, and therefore, quality criteria.
Country of origin	Any country of origin	Geographical borders were not judged applicable.
Language	English and Spanish	Non-English or non-Spanish language studies were excluded due to the to resource constraints on translation.

RESULTS AND DISCUSSION

Geoffrey Edwin Hall Ballard, founder of Ballard Power Systems, supported the need for efforts together with the government, academia, and industry, for the transition of a fossil fuel economy to a hydrogen economy to be possible [9]. In this vision, where the government, academia, and industry are entrusted with the transition of a fossil fuel economy to a hydrogen economy, entrepreneurship must be prioritized as a key tool in the process, without forgetting that this entrepreneurship must emphasize the social aspect. In today’s world, all economic actors pursue their own ends, without considering the environment, and without considering the array of different types of companies; much less the previous work, experience, and knowledge provided by academia. Therefore, the current proposal links the hydrogen economy and social entrepreneurship in a manner that is pertinent, timely, and focused on innovative ideas from multidisciplinary sources from around the world. This allows for the structuring of business plans with higher chances of accessing public and/or private resources and converting them into sustainable companies with a greater impact upon any economy.

The proposal is based on the idea that it is possible to transform current fossil fuel economies using a multidisciplinary array of interdisciplinary ventures, an energy proposal that fits with the conditions of large economies and their ecosystems, the application of new technologies and good management practices, as well as the use of social networks and online learning communities as support strategies for knowledge diffusion between participants. The plan depends on support by the state (both its government and the population that benefits), industry (entrepreneur and intrapreneur), academia, and the environment (both the physical environment, as well as the social one) as a transversal axis. This proposal also considers the individual, in addition to corporations and the community.

The ecosystem that is suggested for this hydrogen economy must support the training of entrepreneurs and the creation of knowledge to improve the sustainability of start-up businesses over time. For [10], scientific and technological strategies must be implemented that revolve around human management, the creation of new knowledge, and dynamic and innovative social entrepreneurship that does not neglect productivity; all supported by robust institutions and the state, and a competitive environment conducive to business development. The current study is based upon this premise, as is shown in the following figure, where each one of the actors described above plays a fundamental role as explained in detailed in the final version of the research.

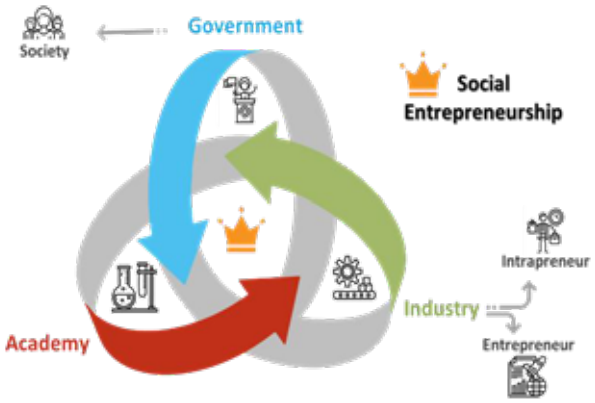


Fig. 1. Key players in the transition of a fossil fuel economy to a hydrogen economy. Source: Authors.

The proposed hydrogen economy, by means of social entrepreneurship, must meet the needs currently covered by the fossil fuel economy. The economy must be oriented towards those who are interested in creating firms with a social impact. According to [11], entrepreneurs who create firms are key agents of the economy, because they drive technological change, wealth generation, and job creation. Entrepreneurship is a way of life and is the ideal basis for the proposal in this study.

CONCLUSIONS

The current analysis is based on the transition of fossil fuel economies to hydrogen economies by means of social entrepreneurship and could be replicated for other types of clean energy. In this paper we analyzed the process of building an entrepreneurship with a social vision, however, social entrepreneurship can be studied in a world that is still in the process of constructing environmental protection scenarios and requires entrepreneurs who set forth and embody these values and propose new forms of environmental innovation [12].

Hydrogen economy represents a viable opportunity to replace that of fossil fuels in the medium to long term. The great powers of the world are showing considerable interest in implementing and enjoying the benefits thereof. Nevertheless, this will only be possible with the support of the three primary axes of each country; the state (including the government and society, as the ultimate end user), an industry which highlights the social entrepreneur as its principal agent, and of course academia, to lead and orient the required processes, interdisciplinary work, and collaborative networks.

In proposing such a drastic transition as that of a fossil fuel economy changing to hydrogen, it is necessary to give weight not only to the economic and financial costs of the projects that will make it possible, but also to consider other social costs, to make it a viable transition. It is in this sense that the role of social entrepreneurship plays a fundamental and essential role, which must be supported by academia, existing industry, and the state, in a joint effort for a sustainable economy that will guarantee the energy supply, decrease wealth inequality, and promote the efficient use of resources and an environment with lower levels of pollution.

REFERENCES

[1] P. Roberts, *The End of Oil: On the Edge of a Perilous New World*, vol. 9, no. 1. 2004.
[2] S. Berry, G & Aceves, “La Economía del Hidrógeno como Solución al Problema de la Estabilización del Clima Mundial,” *Acta Univ.*, vol. 16, no. 1, pp. 5–14, 2006, doi: 10.15174/au.2006.192.
[3] R. Moliner, M. J. Lázaro, and I. Suelves, “Analysis of the strategies for bridging the gap towards the Hydrogen Economy,” *Int. J. Hydrogen Energy*, vol. 41, no. 43, pp. 19500–19508, 2016, doi: 10.1016/j.ijhydene.2016.06.202.
[4] D. Sperling and J. Cannon, *The Hydrogen Energy Transition. Moving toward the post pretoleum age in transportation*, no. June. 2004.
[5] S. E. Sanabria A., P. A. Pedraza, and E. Hurtado A., “El emprendimiento como fuente de desarrollo y fortalecimiento de las capacidades endógenas para el aprovechamiento de las energías renovables,” *Rev. EAN*, no. 77, p. 152, 2014, doi: 10.21158/01208160.n77.2014.821.

[6] S. A. Zahra, E. Gedajlovic, D. O. Neubaum, and J. M. Shulman, “A typology of social entrepreneurs: Motives, search processes and ethical challenges,” *J. Bus. Ventur.*, vol. 24, no. 5, pp. 519–532, 2009, doi: 10.1016/j.jbusvent.2008.04.007.
[7] A. C. Salgado and S. Mart, “EVALUACIÓN DEL RIGOR METODOLÓGICO Y RETOS,” no. 2006, pp. 71–78, 2007.
[8] A. H. Garcia, *El arte de elaborar el estado del arte en una investigación*. 2014.
[9] G. Ballard, “Our History - Power to Change the World | Ballard Power,” 2008. https://www.ballard.com/about-ballard/our-history (accessed Jan. 16, 2020).
[10] H. J. Gómez R. and D. Mitchell, “Innovación y emprendimiento en Colombia: alcance, perspectivas y recomendaciones de política, 2014-2018,” *Cuad. Fedesarrollo*, p. 82, 2014.
[11] Gámez & Garzón, *Los emprendedores sociales y sus proyectos 1*. 2016. ISB: 978-958-763-301-6
[12] J. Gámez Gutiérrez *et al.*, “Nueva propuesta transversal de emprendimiento e innovación para programas educativos en el tercer nivel de educación,” *Contaduria y Adm.*, vol. 62, no. 1, pp. 239–261, 2017, doi: 10.1016/j.cya.2016.10.005.

WHEC-2022
23rd World Hydrogen Energy Conference
June 26-30, 2022 - Istanbul

#329

WAYS TO IMPROVE THE COMPETITIVENESS OF CHINA'S HYDROGEN ENERGY INDUSTRY

[1*] Xiangyu Meng, [2] Alun Gu, [1]Mingyun Chen,[1] Xinguo Wu, [2]Jian Zhou, [2]Bin Liu, [1,2**] Zongqiang Mao
[1]Tsinghua Innovation Center in Dongguan, Songshan Lake Hi-tech industrial Park, Dongguan, P.R. China
[2] Institute of Nuclear and New Energy Technology, Tsinghua University, Beijing, P.R.China

*Corresponding author e-mail: mengxy@tsinghua-dg.org
**Corresponding author e-mail: maozq@mail.tsinghua.edu.cn

ABSTRACT

At present, the development of China's hydrogen energy industry is beginning to take shape, and the high cost of hydrogen energy industry chain is the biggest obstacle to the development of hydrogen energy industry. Based on the analysis of the development background and current situation of hydrogen energy in China, this paper points out that the realization of economy of green hydrogen energy industry chain in China needs to start from the following four aspects: formulating policies, regulations and standards suitable for hydrogen energy; Promote the progress of hydrogen energy technology; Promote the localization and large-scale application of hydrogen energy technology, and strengthen international cooperation. The green hydrogen energy industry will also provide strong support for China to achieve the goal of carbon peak and carbon neutralization.

Keywords: Green Hydrogen, Economy, Sustainable Development

INTRODUCTION

In order to achieve the goal of carbon peak and carbon neutralization [1], a series of practical energy technologies are needed as support. Among them, hydrogen energy has gradually become the focus of international and domestic society because of its clean pollution, renewable and controllable safety. Hydrogen industry chain covers hydrogen energy production, storage and transportation, and downstream utilization. Currently, China's hydrogen industry chain has initially formed comprehensive pattern from basic research, application research to demonstration, and create a relatively complete hydrogen industry. According to the China Hydrogen Energy Alliance, hydrogen energy will account for at least 10% of China's final energy system by 2050, and hydrogen demand will be close to 60 million tons, of which the demand by transportation will be about 24.58 million tons, accounting for more than 40% of the total demand for hydrogen energy. Some researches also expect that China's demand for hydrogen energy in 2050 will reach to 80 million tons. It shows that hydrogen energy has a very broad development prospect in China. At present, most hydrogen energy comes from fossil energy (gray hydrogen). As a strategic emerging energy, it is necessary to promote and develop the production and application of green hydrogen. However, economy is the fundamental problem affecting the development of green hydrogen industry. Practical methods are needed to solve the economic problems in order to enhance the competitiveness of China's hydrogen energy industry.

CURRENT SITUATION AND DEVELOPMENT CHALLENGES OF CHINA'S HYDROGEN ENERGY INDUSTRY

China's hydrogen energy development policy

In April 2020, the Energy Law of the People's Republic of China (Draft for solicitation) issued by the National Energy Administration mentioned giving priority to the development of renewable energy [2], supporting the development and application of new fuels and industrial raw materials instead of oil and gas, and bringing hydrogen energy into the energy category. In December of the same year, the white paper "energy development in China in the new era" proposed to accelerate the development of hydrogen energy industry chains such as green hydrogen extraction, storage, transportation and application, and promote the development of hydrogen fuel cell technology chain and hydrogen fuel cell vehicle industry chain [3]. In September 2020, the Ministry of finance, the Ministry of industry and information technology, the Ministry of Science and Technology, the National Development and Reform Commission and the National Energy Administration issued the notice on starting the demonstration application of fuel cell vehicles. The notice proposed that the three urban agglomerations of Beijing, Shanghai and Guangdong become the key areas selected in the first batch of hydrogen fuel cell vehicle demonstration urban agglomerations, and the demonstration period is tentatively scheduled for four years [4]. In April 2021, the Ministry of science and Technology launched the "hydrogen into thousands of homes" science and technology demonstration project in Shandong Province [5]. The project will give full play to the advantages of infrastructure and hydrogen resources in Shandong Province, gradually promote the integrated development of innovation chain and industrial chain in the field of hydrogen energy, promote the application of hydrogen energy in terminal fields such as transportation, industry and household energy, accelerate the comprehensive utilization of hydrogen energy, promote the transformation of energy consumption to efficient and clean, and effectively reduce carbon emissions, Achieve "2030 carbon peak and

2060 carbon neutralization" and provide a demonstration model for building a "hydrogen energy society" in Shandong.

Challenges of green hydrogen industry development in China

At present, the development of China's hydrogen energy industry has started, but there are still some obstacles affecting competitiveness, such as high cost and insufficient infrastructure construction. Since China has strong infrastructure capacity, building hydrogen energy infrastructure is not a problem. Therefore, the high cost of hydrogen energy industry chain is the biggest obstacle. There are four reasons for the high cost of green hydrogen industry chain. First, China's existing policy system is not suitable for the development of renewable energy and hydrogen industry system, which increases the cost of green hydrogen industry chain. For example, the existing policy system treats hydrogen as a dangerous chemical. The hydrogen production plant must be built in the chemical park, and the hydrogen production plant and hydrogen refueling station should be built separately, which hinders the construction of integrated hydrogen production and hydrogenation station. In addition, it is required that the hydrogenation station must be built on commercial land, which also increases the construction cost of the hydrogenation station. Second, due to the limitation of renewable energy technology, the cost of hydrogen production from renewable energy is high. For example, the cost of hydrogen production from solar energy and wind energy is not competitive compared with that from fossil energy. Third, due to the low localization rate of hydrogen energy technology and the small industrialization scale of related products, it is difficult to reduce the cost of hydrogen industry chain. For example, in 2021, the output of fuel cell vehicles in China was only 1779, and hydrogen fuel cell vehicles were not popularized, resulting in high cost. Fourth, there is a gap between the existing green hydrogen industry technology and the international advanced level, indirectly pushing up the cost of the green hydrogen industry chain. For example, in terms of core technologies such as fuel cell stacks, the competitiveness of Chinese hydrogen energy enterprises is slightly insufficient.

MEASURES TO REALIZE THE ECONOMY OF CHINA'S HYDROGEN ENERGY INDUSTRY

Policy design

China's "14th five year plan" points out the specific direction for hydrogen energy, energy storage and other technology and industrial transformation fields, but it lacks strategic guidance and policy design for the development of hydrogen energy industry. Therefore, it is necessary to establish a special leading organization for hydrogen energy industry development planning at the national level to study and formulate China's hydrogen energy industry policy system according to the characteristics of hydrogen energy. For example, hydrogen can no longer be managed only as hazardous chemicals, but to strengthen the energy properties of hydrogen and formulate industrial, financial and tax policies to promote the development of hydrogen energy. Promote the research and development of hydrogen energy related specifications and standards, and promote the healthy development of hydrogen energy industry.

Promote the progress of hydrogen energy technology

To develop green hydrogen, key problems such as economy and technology maturity should be solved, and scientific and technological breakthroughs should be carried out to solve the technical bottlenecks of key materials and components. First of all, we need to promote the technological progress of renewable energy, so as to continuously reduce the electricity cost of renewable energy, so as to lay a foundation for the economy of green hydrogen. Secondly, we should strive to promote the development of hydrogen production technology from electrolytic water, increase the production capacity of electrolytic water equipment and reduce the cost of hydrogen production. Thirdly, we should promote the technological progress of fuel cell stack, increase the volume power density of fuel cell and reduce the cost of fuel cell. Fourth, we should pay attention to the application and progress of digital technology and intelligent manufacturing technology in the field of hydrogen energy, and improve the economy of the hydrogen energy industry chain. Developing green intelligent manufacturing is an important measure to develop China's hydrogen energy. Digital technology gives the hydrogen energy industry chain the ability to reduce production costs, reduce carbon emissions and realize green manufacturing by improving quality, reducing raw material consumption and shortening production cycle; Intelligent manufacturing improves production efficiency through automation, dynamic monitoring and control, and finally improves the economy of hydrogen energy industry chain.

Improve the localization and scale level of green hydrogen industrial chain

Generally, the unit product cost is negatively correlated with its output. The output increases and the unit product cost decreases. Improving the large-scale production of parts will promote cost reduction. China's domestic alkaline electrolytic cell technology leads the international advanced level. The capacity of a single electrolytic cell has

reached 1000 cubic meters of hydrogen / hour, and the cost has decreased to about 7000 yuan / kW, only half or even lower than that of developed countries. The localization of domestic upstream industry chain enterprises of fuel cell stack has achieved initial results: membrane electrode, proton exchange membrane and bipolar plate manufacturers have the localization ability, gas diffusion layer enterprises have begun small-scale production, catalyst enterprises are in the R & D stage, and metal bipolar plate enterprises have begun the localization stage. In the future, China should continue to strengthen the scale and localization of green hydrogen industrial chain, so as to bring more considerable economic benefits to the development of hydrogen energy industry.

Build standard system

Strengthening the research and formulation of standards and improving the precision of policy support will help the development of the hydrogen energy industry. In March 2020, the National Development and Reform Commission jointly issued the Opinions on Accelerating the Establishment of Legal and Policy System for Green Production and Consumption, studying and formulating standards and supporting policies for the development of hydrogen energy, marine energy and other new energy sources. By April 2021, there were 95 national standards related to hydrogen energy put into effect. But in order to further adapt to the rapid development of the hydrogen industry demand, it still need to accelerate the hydrogen standardization work, to further develop renewable energy hydrogen and high pressure hydrogen storage container inspection equipment, solid state hydrogen storage, hydrogen liquefaction and key equipment such as hydrogen station infrastructure level standard, at the same time as the hydrogen application in the field of innovation and development, the improvement of the relevant standard system construction.

Promote international cooperation

With the rapid advancement of global energy transformation, hydrogen energy is expected to become a new hotspot of international cooperation. From the perspective of resources and application scenarios, various conditions in China are relatively good. First, China should strengthen cooperation with hydrogen power countries (regions), such as Japan, South Korea, Canada, EU, etc. Meanwhile China should combine one belt, one road initiative and strengthen cooperation with the countries along the hydrogen industry, including leasing equipment, exporting hydrogen energy technology, producing green hydrogen, green ammonia, selling green hydrogen and green ammonia, and also sharing profits and realizing common prosperity with the countries along the route. Explore a green and low-carbon development path of win-win cooperation and common development, and make new contributions to promoting the global response to climate change and building a community with a shared future for mankind.

CONCLUSIONS

Improving the economy of the green hydrogen energy industry chain is the key to the development of China's green hydrogen industry. It is necessary to make a layout from the aspects of improving the policy system, promoting technological progress, improving the level of localization rate and strengthening international cooperation, so as to promote the healthy development of the hydrogen energy industry and provide support for China to achieve the goal of carbon peak and carbon neutralization.

ACKNOWLEDGEMENT

National Key R&D Program of China, No.2018YFE0202000 is great acknowledged.

REFERENCES

1. http://www.xinhuanet.com/2020-09/22/c_1126527652.htm. Accessed on September 20, 2020
2. http://www.nea.gov.cn/2020-04/10/c_138963212.htm. Accessed on April 20,2020
3. http://www.scio.gov.cn/zfbps/32832/Document/1695117/1695117.htm. Accessed on December 21,2020
4. http://www.china-nengyuan.com/news/173029.html. Accessed on September 1, 2021
5. http://www.most.gov.cn/dfkj/sd/zxdt/202104/t20210427_174380.html. Accessed on April 28, 2021

WHEC-2022
23rd World Hydrogen Energy Conference
June 26-30, 2022 - Istanbul

#377

H_2-INDEX FOR THE EVALUATION OF HYDROGEN PROJECTS IN MEXICO

[1] G. Ramos-Sánchez, [2] R.G. González Huerta*
[1]Universidad Autónoma Metropolitana- I IPH Department, Mexico City, Mexico
[2] ESIQIE-IPN, Mexico City, Mexico.

*Corresponding author e-mail: gramos@xanum.uam.mx

ABSTRACT

Hydrogen projects are being implemented all around the world, although at first sight all projects in which Hydrogen is involved appear appealing, in some cases other alternatives such as electrification and efficiency growth are better suited. In this work we have developed a methodology for the analysis of Hydrogen projects that assign a quantitative value to its implementation viability. The H2-index is based on the evaluation of 6 factors, social benefits, economic benefits, environmental benefits, national development, efficiency, and technical viability. A weighted factor will help to decide, in a simple manner, whether a project should be promoted and, moreover, what areas should be strength in order to make the project not only viable but worth to be financed.

Keywords: H2 Projects Evaluation, H2-Index, Positive Impact of Projects.

INTRODUCTION

Hydrogen is expected to play a substantial role in the following years, the immense advantages of its utilization such as null carbon footprint, flexibility to attend different uses and the possibility to decarbonize our society [1] make us think on Hydrogen as the only viable solution. Not only beginners, but specialized scientist and technologist tend to put Hydrogen as the first option in almost any energy project; however, in some cases Hydrogen does not represent a viable solution in front of other alternatives. In other cases, the Hydrogen project can represent serious disadvantages that make us think as an unviable option but strengthen in the weak areas can make it a viable alternative. The Mexican socio-politics this year is full of ideas for Hydrogen projects eager to be developed or to be financed. We must be aware that one of the main problems in the realization of projects is related to delusion, i.e., if a project is launched and implemented but the outcome results in more disadvantages than advantages Hydrogen might be discarded forever as a viable option in the society [2]. Viability analysis is a complex task that is performed by specialist in order to discern the main strengths and weakness of a project; however, the task is specialized and requires lots of data, while in some cases a simpler analysis is needed. The Mexican Hydrogen Society has launched a H2-index which intends to provide a simpler analysis of projects to decide whether a project is viable and represent advantages. Due to Hydrogen prices, in most of the cases to break market barriers the projects should be financed by government; thus, this strategy will allow evaluating the project viability and determine the existing opportunity areas to improve the project outcome.

METHODS

H2-Index is based on 6 factors which are listed in table 1, each project is weighted in a score based on the positive characteristics of the project. The factors evaluated, which are of interest for the Mexican sociopolitical characteristics are the following: 1) National benefits, this intends to evaluate if the project will benefit the growth of the economy, 2) Social impact, which measures the direct impact in society such as energy poverty elimination, jobs creation and wellness, 3) Economic, which evaluates if the project is economically viable in comparison to other options, 4) Technic viability, which evaluates if the technology is developed enough to be implemented or, if is expected to be developed in the future, 5) Efficiency, if the project represent advantages in efficiency in comparison to any other energy option, and 6) Environmental, if the project represent important improvements in comparison to the emissions of the system that is being replaced.

The specific scale for each factor goes from 0 to 5, at the end the score for all factors is averaged, resulting in the H2-index. If the project gets a 0 for each of the factors, the project is not viable; if the project receives an averaged H2-Index lower than 2.5 although not getting any zero, the project present serious limitations and most probably should be rejected. If the project receives an H2-index higher than 2.5 but lower than 4.0, the project is viable but should be revised to find opportunity areas that could make it increase its viability. If a project gets a 4.1-5.0 H2-Index the project is viable and should be promoted but also government financed. Table 1 shows each of the factors and its scale, to save space we have decided to include only the lowest and highest score.

Table 1. Factors and scores for the H2-Index, symbols and colors are included to make it visually appealing

	Minimum score	Maximum scoring
National	The project implies non-justified subsidies	Exist opportunities for the growth of the national industry and participation of several medium size companies
Social	The project represents a serious treat to civilians.	The project forecast a high number of new jobs, and academic opportunities.
Economic	The project is 30% more costly than the system that intends to replace.	The project saves at least 20% in production costs.
Technical	There are serious limitations in the technology at the present and, in the future.	Technology is ready to operate and does not exist another technology alternative.
Efficiency	The efficiency is lower than the system that intends to replace	Overall energy efficiency higher than 90%
Environment	Higher GHE than the system that intends to replace	Avoid GHE emissions in 100%

RESULTS AND DISCUSSION

H2-index was applied to two kinds of projects, the first is a barbeque hydrogen roaster (BH2) which has been proposed as and alternative to mitigate emissions in cities with cultural behaviours toward the use of charcoal to cook, while the other is Hydrogen forklifts (H2F) for industry indoor activities. The BH2 project has been promoted recently by local communities, the proposal sounds good as a great number of emissions could be avoided; however, other factors such as costs, technical viability and impact are serious treats to the viability. On the other hand, H2F have been long identified as one of the most viable projects for Hydrogen commercialization nowadays and their use is expected to be increased all around the world.

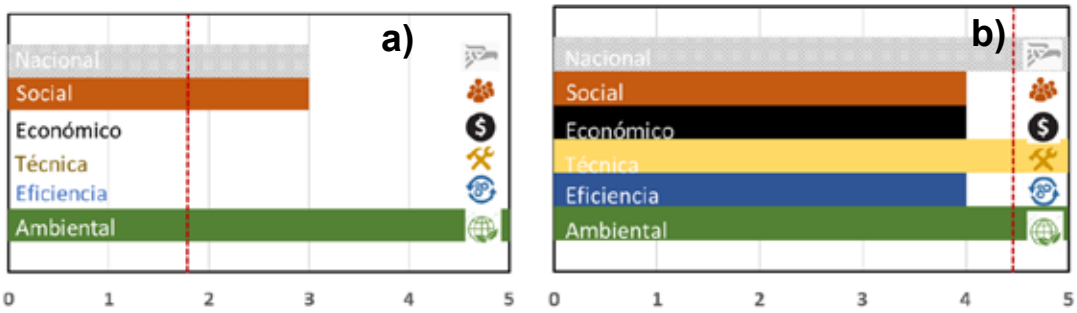


Fig. 1. H2-Index evaluation for a) BH2 projects and b) H2F projects

From the H2-index analysis, taking into account state of the art efficiencies, cost and technology status, we found that the main treat to the implementation of BH2 projects is the immense amount of efficiency lost, as the number of equipment is increased the efficiency is extremely lost; moreover the characteristics of Hydrogen make its flame not suitable for cooking as the radiative heat is lower; moreover the cost is unviable as small scale electrolysers are costly; although the environmental benefits are paramount, the overall H2-index indicates a value of 1.8 (red dotted line) which of course should rule out the implementation of such projects while electrification or sun cooking is becoming available. On the other hand, H2F present scores higher than four in most of the factors and a H2-index of 4.5 which indicates that the project is not only viable but represent important benefits, specially this represents the opportunity to create jobs and develop national technology to strength the value chain and enforce the realization of other projects.

CONCLUSIONS

H2-index was developed as a practical tool to evaluate Hydrogen projects, the multifactorial analysis which takes into account all the benefits and treats represents a simple but valuable tool to decide if a project should be promoted or financially supported. The analysis is being implemented for more complex systems and as a decidive tool to increment the impact of other hydrogen projects.

ACKNOWLEDGEMENT

This work was financially supported by project CONACYT A1-S-15770, the Mexican Hydrogen Society support is also acknowledged.

REFERENCES

1. Mohsin M, Rasheed AK, and Saidur R 2018. Economic viability and production capacity of wind generated renewable hydrogen. International Journal of hydrogen energy, 43: 2621-2630.
2. Meija J and D'Ulivo A 2008. Solution to nascent hydrogen challenge. Analytical and bioanalytical chemistry, 392: 771-772.

WHEC-2022
23rd World Hydrogen Energy Conference
June 26-30, 2022 - Istanbul

#392

HYDROGEN POTENTIAL AS VECTOR FOR A BIOMASS-BASED DECARBONISATION OF TRANSPORT IN BRAZIL

[1,2*] *Suani T. Coelho,* [1] *Antonio Stuchi,* [1,2] *Danilo Perecin,* [2,3] *Karen L. Mascarenhas,* [2] *Julio Meneghini*
[1] Institute of Energy and Environment, University of São Paulo, Av Prof Luciano Gualberto 1289, 05508-030, São Paulo, Brazil
[2] Research Centre for Greenhouse Gas Innovation, School of Engineering, University of São Paulo, Avenida Mello Moraes 2231, 05508-030, São Paulo, Brazil
[3] Institute of Psychology, University of São Paulo, Avenida Mello Moraes 1721, 05508-030, São Paulo, Brazil

*Corresponding author e-mail: suani@iee.usp.br

ABSTRACT

Hydrogen can be produced from biomass and eventually deliver largely needed negative emissions when combined with carbon capture and storage. The sugarcane industry in Brazil is well established and its main energy products – ethanol and electricity – are potential solutions but are still facing challenges related to decarbonisation. Aiming to contribute to the Brazilian matrix decarbonisation, this article estimates the hydrogen production potential for a current state-of-the-art sugarcane mill with an annexed distillery, based on 1G and 2G ethanol reforming, biogas reforming, and the use of surplus electricity for electrolysis-based process. This result is applied to the total sugarcane production in Brazil to compare the country's potential by using hydrogen in fuel cells to the equivalent in useful energy delivered by all fuels used in the transport sector. As a result, sugarcane-based hydrogen could deliver around 57% of total transport sector energy demand, compared to only 19% of current ethanol's contribution. In addition, ethanol is only used in passenger cars where pure electric vehicles are becoming increasingly competitive, and diesel oil consumption in the country is extremely high mainly for trucks; on another hand, hydrogen is more likely to play a role decarbonising these heavy vehicles. Hydrogen could become an option for the sugarcane industry to remain relevant under a battery electric-cars future and Brazil is well-positioned to develop a strategy around biomass-based hydrogen for heavy vehicles.

Keywords: Hydrogen, Biomass, Sugarcane, Transport Decarbonisation, Brazil

INTRODUCTION

Worldwide, hydrogen is expected to play an increasing role as a versatile energy carrier suitable to reducing greenhouse gas (GHG) emissions from different activities. The flexibility of hydrogen is the principle that creates the conditions for different hydrogen consumption and production models according to regional needs and resources. Low-carbon hydrogen can be produced from water electrolysis using clean energy sources, from fossil methane reforming or coal gasification with high carbon capture and storage rates, and from biomethane reforming or biomass gasification as well.

These last two routes involve biogenic carbon and can deliver negative emissions if CO_2 is captured and permanently stored. Technologies providing CO_2 removal from the atmosphere are key to achieving deep decarbonisation and keeping global temperatures below 1.5ºC and even 2ºC, as they provide a means to compensate for temperature overshoots and residual emissions from hard-to-decarbonise sectors.

Brazil's energy system relies on biomass from a diversity of feedstocks and for different purposes. The main product from biomass is ethanol used as fuel, covering more than 40% of the energy demand from passenger cars in 2020 [1]. Sugarcane is the feedstock used for over 90% of current ethanol production in the country, despite a recent growth in corn-based ethanol [2].

The sugarcane processing industry also generated around 37 TWh of electricity from bagasse-based combined heat and power (CHP) systems, with a net contribution for the Brazilian grid of around 20 TWh in 2020 [1].

A new product in this huge industry is biogas, produced from anaerobic digestion of ethanol processing residues such as vinasse and filter cake, which in some cases is being used for additional electricity generation. However, biogas upgrading to biomethane is receiving increasing attention due to the different energy uses such as diesel replacement, grid injection replacing natural gas and hydrogen production through reforming process.

However, the sugarcane sector's business model regarding its energy products is facing challenges.

First, vehicle electrification is a challenge to biofuel-based decarbonisation, threatening the projected ethanol's expansion over gasoline's market share. A distinguishing feature of electrification compared to internal combustion engines is increased energy efficiency, which can also be achieved by using hydrogen in fuel cells.

Secondly, auction-based long-term electricity contracts in Brazil are traditionally awarded based on a competition for the lower energy price, and bioelectricity has been struggling to compete with intermittent renewables such as solar and wind (which have strong subsidies) under this model.

Therefore, while it provides an alternative against the risks of its current business model based on electricity and ethanol, hydrogen is arguably an important way forward for the sugarcane industry to increase its contribution to transport decarbonisation without expanding sugarcane land area based on increased vehicle energy efficiency.

In addition, renewable electricity sources have the task of first decarbonising the electricity supply, and risk needing to be developed in a scale that could create challenges for the deployment of new projects if expected to also cover demand from other sectors. These challenges are linked to the intermittent characteristics of wind and PV-based electricity generation, exhaustion of the best available potentials, and public opposition to landscape impacts of large-scale wind and solar farms. Furthermore, by not possessing the capability of combining hydrogen production with negative emissions, hydrogen from solar and wind electrolysis may not be as desired as biomass-based hydrogen to deliver deep decarbonisation. These aspects create a demand for alternative forms of low- or negative-carbon hydrogen other than renewables-based electrolysis (i.e., green hydrogen), especially from biomass.

OBJECTIVES AND METHODOLOGY

In this context, the objective of this paper is to evaluate the potential for hydrogen production from products of a state-of-the-art sugarcane industry in Brazil. Additionally, we assess the impact of using hydrogen comparing it to the current contribution of ethanol considering the improvement in vehicle efficiencies. Based on the results, we discuss the role of switching to biomass-based hydrogen as a main fuel for decarbonising the Brazilian transport sector.

The feedstocks and processes considered for evaluating hydrogen production potential in sugarcane biorefineries are as follows:

- First- and second-generation ethanol reforming;
- Biomethane reforming;
- Water electrolysis from the biorefinery's surplus electricity generation.

We then use the hydrogen potential based on its conversion in fuel cells to assess the equivalent in energy and compare to the fuels it could replace in current internal combustion engine vehicles. The results are then used to discuss the increased contribution to decarbonising the Brazilian transport sector that hydrogen production combined with fuel cell vehicles can provide compared to the current system.

It is important to note that both ethanol and biomethane reforming can run all year around but surplus electricity generation for electrolysis can operate only during season, when 1G plant is in operation.

RESULTS AND DISCUSSION

The results of hydrogen production potential from sugarcane are provided in Table 1.

Table 1. Hydrogen potential from a state-of-the-art sugarcane industry using selected production pathways.

	Feedstock potential	Hydrogen potential from feedstock (kg/t)	Hydrogen potential per area (kg/ha)
Sugarcane	80 t/ha	-	-
Ethanol 1G	40 l/t	5.25 kg/t	420 kg/ha
Ethanol 2G	23 l/t	3.03 kg/t	242.4 kg/ha
Surplus electricity	49 kWh/t	0.89 kg/t	71.2 kg/ha
Biogas	8.9 Nm^3_{CH4}/t	0.92 kg/t	73.6 kg/ha
Total	-	10.09 kg/t	807.2 kg/ha

Based on the results from Table 1, the hydrogen potential from ethanol reforming, surplus electricity and methane in biogas can reach around 10.1 kg of hydrogen per ton of sugarcane (kg/t) or 807.2 kg per hectare (kg/ha), based on the average productivity for the state of Sao Paulo in the 2020/2021 harvest, according to [2].

Most of this contribution (52%) comes from first-generation (1G) ethanol, currently the main energy product in the sugarcane industry. The average sugarcane mill produces 1G ethanol and, therefore, this is not closely related to the potential from a state-of-the-art industry. This result considers the potential for 1G ethanol production in a typical

annexed distillery, i.e., when ethanol is produced in combination with sugar – the sugar content destination is around 50% for ethanol. Also, most mills also have surplus electricity produced during the season. However, biogas and second-generation (2G) ethanol are still produced by only a few of the nearly 400 mills currently in operation in Brazil, despite promising new projects being announced for starting production in the short-term.

The hydrogen potential can now be compared to the fuel use in Brazil, as in Table 2. It considers a total sugarcane production in Brazil of 654 million tons based for the 2020/2021 harvest [2].

Table 2. Fuel utilisation in the transport sector and the potential of hydrogen substitution in Brazil.

	Consumption (km^3, except H_2)	**Useful energy (GWh)**
Diesel	46,046	113,760
Gasoline	29,997	68,499
Hydrated ethanol (as E100)	19,385	28,771
Anhydrous ethanol (as E27)	10,214	15,881
CNG	2,210,770	14,431
Total	-	231,341
Hydrogen potential	6,598,860 t	132,260

Therefore, the hydrogen potential from sugarcane only could supply around 57% of total energy demand for transport in Brazil. Current ethanol's contribution is around 19% and could increase up to 30% if considered the production of 2G ethanol (as in the hydrogen case) but would still be short of what hydrogen could deliver.

CONCLUSIONS

Hydrogen can increase the useful energy delivered by sugarcane to the transport sector based on the combination of using the industry's main energy products (ethanol, electricity, and biogas) to produce a single energy carrier – i.e., hydrogen – but also due to a higher end-use efficiency in fuel cells. The contribution to decarbonisation is even more pronounced as currently ethanol is only used in passenger cars where pure electric vehicles are becoming increasingly competitive, while hydrogen is more likely to play a role decarbonising heavy vehicles which lacks large-scale, replicable solutions.

ACKNOWLEDGEMENT

The authors gratefully acknowledge the support of the RCGI – Research Centre for Greenhouse Gas Innovation, hosted by the University of São Paulo (USP) and sponsored by FAPESP – São Paulo Research Foundation (2014/50279-4 and 2020/15230-5) and Shell Brasil, and the strategic importance of the support given by ANP (Brazil's National Oil, Natural Gas and Biofuels Agency) through the R&D levy regulation.
Perecin and Mascarenhas are grateful to CNPq for the support during their visiting PhD period at Imperial College London, UK (Process numbers 200359/2019-3 and 202184/2019-6).

REFERENCES

1. https://www.epe.gov.br/pt/publicacoes-dados-abertos/publicacoes/balanco-energetico-nacional-2020. Accessed on January 30, 2022.
2. https://www.conab.gov.br/info-agro/safras/cana. Accessed on January 30, 2022.

WHEC-2022
23rd World Hydrogen Energy Conference
June 26-30, 2022 - Istanbul

#1535

COULD GREEN HYDROGEN AND ITS DERIVATIVE IMPROVE ENERGY SYSTEMS IN NORTH AFRICA, CASE OF MORROCO, EGYPT AND TUNISIA

[1*] *Amin Lahnaoui,* [1] *Wilhelm Kuckshinrichs*
[1]Forschungszentrum Jülich, Institute of Energy and Climate Research, Systems Analysis and Technology Evaluation, 52425 Jülich, Germany

*Corresponding author e-mail: a.lahnaoui@fz-juelich.de

ABSTRACT

North Africa constitutes a strategic point at the door of Europe and the corridor of West Asia. Some common cultural aspects could facilitate collaboration to strengthen its position in the region in the energy sector. Adding to that an increasing concern regarding the environmental impact of the current energy system, and a big renewable resources potential, the region could build a more sustainable economy around new energy resources. However, opportunities and potentials do not automatically translate into successful and radical changes and it is therefore important, now that the hydrogen economy and its derivatives its peaking speed, to not overlook the structural change that should be done in local energy systems in favour of export-based economy. Looking back to the last 28 years, hardly any change has been made to the way energy mixes are defined and the importance of carbon sources in it and the energy economy. Therefore, it is important to analyse first the energy supply and what drives energy consumption to define where future sustainable energy systems should intervene locally.

Keywords: Energy System, LMDI Decomposition, Energy Supply, Green Hydrogen.

INTRODUCTION

North Africa is still highly dependent on solid carbon and liquid sources as the main supply is driven by oil, natural gas, and coal. However, the different countries differ in the energy mix and energy security. Thus, while natural gas is the second energy source in the majority of countries, Morocco still relies on imported coal along with oil. The region shows as well disparity regarding conventional natural resources, as Algeria and Libya are oil and natural gas producers and therefore show a positive energy balance.
Looking at the change in energy supply, to a certain extent, the energy mix did not differ that much from how it was in 1991. This shows the impact limitation on new technologies to penetrate the existing energy system in the region. However, green hydrogen and its derivative have the potential not only to change the energy mix but as well to influence the economic structure and diversify it.
To spot where green hydrogen could play a role both on the supply and the demand side, it is important to study what has been driving energy supply and demand in the region. This is done by a decomposition analysis to define the adequate drivers.

METHODOLOGY

Index decomposition analysis has been widely used in energy to analyze the relative impacts of changes in a group of industrial activities, activity structure of the group, and activity energy intensities on energy consumption [1]. Among methodologies, the logarithmic mean Divisia index decomposition method became dominant in recent years [2] and produces decomposition results without leaving a residual term. A simple decomposition of total energy consumption (or total energy consumption for a given sector) into consumption at the subsectors in its basic form is shown in equation (1).

$$E = \sum_i E_i = \sum_i A\, S_i I_i \quad (1)$$

Where A is the total sectorial activity level, and Si and Ii are respectively the activity structure or share and energy intensity of sector i. The methodology has been adapted to analyze different sector's and sub-sector's consumption and emissions including for instance the metal industry in China [3], the manufacturing sector in Korea [4], and across country analysis in the EU-27 [5]. The methodology is adapted to analyse the drivers of primary energy generation PEG by ratios including, primary energy supply PES, final energy consumption FEC, and the gross domestic product GDP as expressed in equation (2).

$$E = GDP\, \frac{EG}{PES}\, \frac{PES}{FEC}\, \frac{FEC}{GDP} \quad (2)$$

This allows defining four effects to investigate:
- The activity one (GDP) that measures the economic activity growth impact on increasing energy production.
- Energy security effect (EG/PES) that measures the impact on energy trade balance on local generation.
- Transformation effect (PES/FEC) that measures the average efficiency of the energy system.
- Intensity effect ($FEC/\ GDP$) that captures changes in the structure of the economy.

As the final consumption is aggregated, an additive decomposition was more relevant [6], and a change in primary energy production can be decomposed on the change of the different effects as detailed in equation (3).

$$\{\Delta E = \Delta E_{activity} + \Delta E_{security} + \Delta E_{transformation} + \Delta E_{intensity} \quad (3)$$

The four effect changes $\Delta E_{\times}$ are defined by an additive logarithmic mean Divisia index decomposition method using the log men function $L({E_{i,j}}^{t}, {E_{i,j}}^{0})$ for a given initial and final year [2] expressed by equation (4).

$$\Delta E_{\times} = \sum_t L(E^t, E^0) \ln(\frac{\times^t}{\times^0}) \quad (4)$$

RESULTS AND DISCUSSION

Energy supply

Figure 1 show the results of primary energy production decomposition for Egypt, Morocco and Tunisia between 1991 and 2019, the main change in production in ktoe is represented as a change of the different effects represented in the vertical axis.

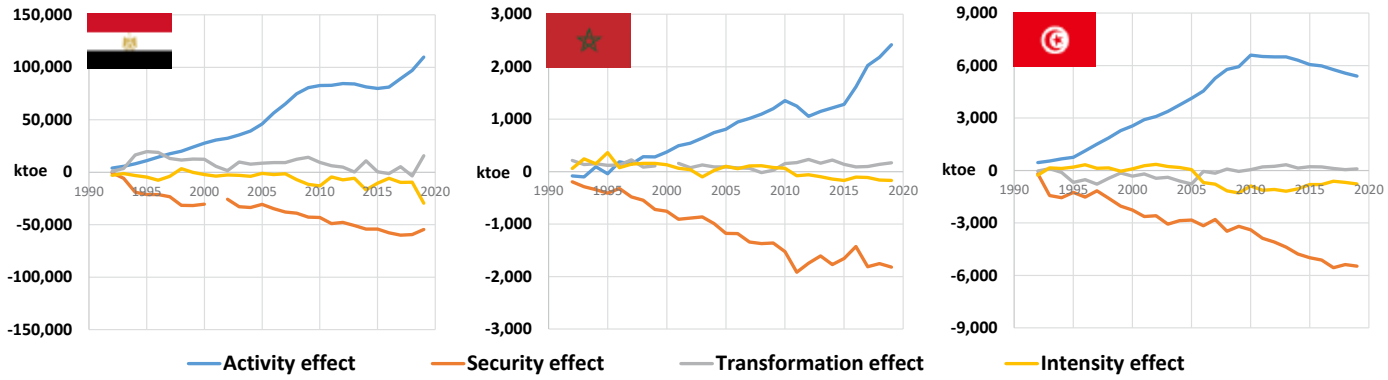


Fig. 1. Yearly additive LMDI decomposition results in ktoe for Egypt, Morocco and Tunisia between 1991 and 2019

Looking at the three countries, similarities can be deduced regarding the driver of primary energy consumption between 1990 and 2019, mainly economic growth has increased energy demand, but that was counterbalanced by an increase in net import, which limited the deployment of new sources of energy generation. The intensity effect reduction was negligible and didn't manage to reduce the demand and thus the supply, suggesting that hardly any change in economic structure was made, nor a substitutional transition to new sources was made. Finally, transformation gain was minimal as well, which suggests a slight improvement in energy efficiency.

However, a closer look at the case of Morocco and Tunisia, since 2010 shows divergences. Thus the Decomposition of changes for the two countries between 1991 and 2019 for two equal periods was done and the results shown in Figure 2.

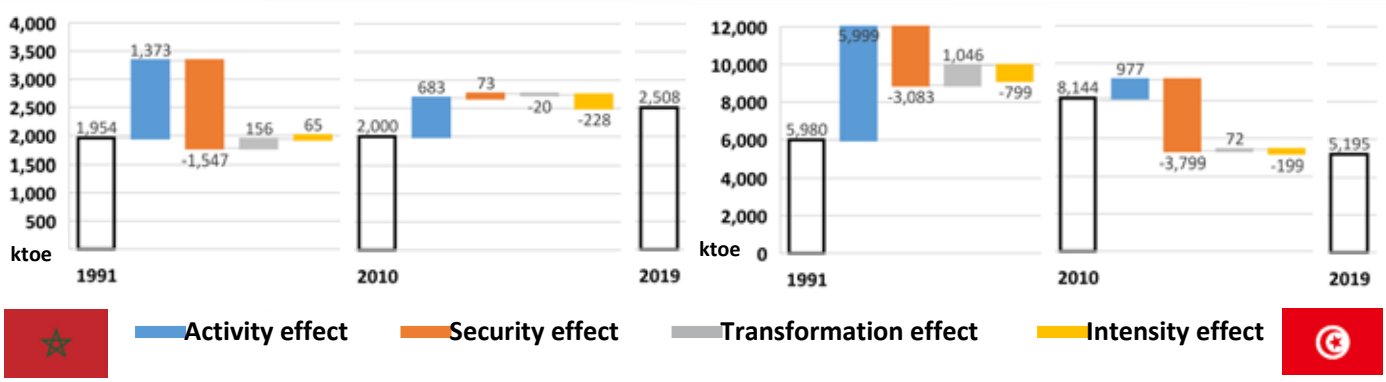


Fig. 2. Decomposition of changes in Moroccan and Tunisian primary energy production (ktoe) in 1991-2019 using the additive Logarithmic Mean Divisia Index approach (LMDI)

Fig. 2 shows that the impact of the spring Arab didn't go unnoticed in the case of Tunisia with the slowdown of the contribution of the activity effect to improve the energy system, which was worsened as well with an increase in imports translated by a negative effect of energy security on generation. Thus, all the gain between 1991 and 2010 on generated energy was canceled in the following 9 years.

The case of Morocco was to a certain extent less impacted by the Arab spring, more importantly, different policies that were taken to promote renewable energy reduced the balance deficit and reversed the energy security impact in favor of newly installed capacity. Moreover, this shift in technology as well allowed a noticeable reduction in energy intensity compared to the same previous period.

Energy demand

Concerning the final consumption balance per sector and source, Table 1 shows that oil demand is mainly driven by the transportation sector. However, differences could be noticed between the countries regarding the other sectors.
The industrial sector consumption is mainly fuelled respectively by electricity, oil, and natural gas.
For residential, services, and other sectors, the fuel mix priority highly diverges. Thus, it is mainly fuelled by electricity in Egypt, and oil in Morocco and Tunisia.
Finally comparing the final energy consumption and the total supply, energy efficiency averages 65.1 %, and varies to as high as 76.1 % in Morocco.

Table 2. *Energy final consumption balance for 2017*
** NG correspond to natural gas*
*** Other sectors include mainly household and services*

in ktoe		Final consumption balance for 2017					
		Electrcity	Biomass	Coal	Oil	NG*	Final demand
Egypt	Industrial	3,467	1,493	177	5,452	9,547	**59,206**
	Transport	50	0	0	17,900	283	
	Other**	6,436	0	0	0	0	
Morocco	Industrial	962	125	18	1,810	61	**15,091**
	Transport	30	0	0	5,511	0	
	Other**	900	0	0	0	0	
Tunisia	Industrial	466	0	0	881	786	**7,718**
	Transport	8	0	0	2,155	231	
	Other**	398	0	0	0	0	

CONCLUSIONS ON THE ROLE OF GREEN HYDROGEN

Looking back at the energy supply in the region for the last 28 years, oil has been and still is the main vector of the energy economy in Algeria and Libya, and the main imported source in Egypt, Morocco, and Tunisia.
So switching gradually to a sustainable energy vector-like hydrogen and its derivatives could be an economical added value for the last three countries, but as well a challenge for Algeria and Libya to transform their energy system, but as well adapt to their energy economy. However, its energy transformation could benefit mainly to increase lower efficiency

in the two countries. The sectoral analysis shows that importance should be given to decarbonizing the transportation sector as half of the oil and natural gas consumption is driven by transport. Thus, a first focus could be to finalize electrifying the rail system in the region and switching clean fuel alternatives in the public transport system. Most importantly, the focus is still first on the direct use of renewable electricity with alternatively hydrogen storage and thus upgrading and replacing existing coal and oil plants. Thus, a complementary analysis should focus on the power mix, and how to overcome the traditional centralized production without penalizing the level of access in the region. Moreover, an analysis of the industry sector-specific to each country should be undertaken to define the level of priority given to green hydrogen and the main used derivative (for instance ammonia for the fertilizer industry).

REFERENCES

1. Ang, B.W. Decomposition analysis for policymaking in energy: which is the preferred method? Energy policy 2004, 32, 1131-1139.
2. Ang, B.W. LMDI decomposition approach: a guide for implementation. Energy Policy 2015, 86, 233-238.
3. Wang, M.; Feng, C. Decomposing the change in energy consumption in China's nonferrous metal industry: An empirical analysis based on the LMDI method. Renewable and Sustainable Energy Reviews 2018, 82, 2652-2663.
4. Kim, S. LMDI decomposition analysis of energy consumption in the Korean manufacturing sector. Sustainability 2017, 9, 202.
5. Moutinho, V.; Moreira, A.C.; Silva, P.M. The driving forces of change in energy-related CO2 emissions in Eastern, Western, Northern and Southern Europe: The LMDI approach to decomposition analysis. Renewable and Sustainable Energy Reviews 2015, 50, 1485-1499.
6. Xu, X.; Ang, B. Analysing residential energy consumption using index decomposition analysis. Applied Energy 2014, 113, 342-351.

WHEC-2022
23rd World Hydrogen Energy Conference
June 26-30, 2022 - Istanbul

#1599

GREEN AMMONIA TO ADVANCE THE ENERGY TRANSITION IN CHINA: AN ANALYSIS FROM A COMPLEX SYSTEM ENGINEERING PERSPECTIVE

*Hanxin Zhao, Linda M. Kamp, Zofia Lukszo
Faculty of Technology, Policy and Management, Delft University of Technology, Jaffalaan 5, 2628BX Delft, the Netherland
*Corresponding author e-mail: h.zhao-1@tudelft.nl

ABSTRACT

This paper discusses the development of future green ammonia supply chains in China with the theory of complex system engineering, taking account of technical system, actors and institutions in future energy systems featured socio-technical systems as a whole. The energy condition in China identified features a spatial imbalance between renewable energy supply and demand, which cannot be fully addressed by the current power system-centric solution. This calls for hydrogen to make a concerted effort in the energy transition. By comparing major hydrogen delivery options, we argue that green ammonia can play a feasible role for large-scale energy distribution and long-term energy storage. The development of green ammonia supply chains and direct use of ammonia are proposed to avoid large uncertainties and initial investment in the early stage. The market creation will be key in the supply chain development. A long-term bilateral contract between buyer and seller and a joint investment in an integrated supply chain by several stakeholders are advised to share risks and ensure capital recovery. In addition, government participation is crucial in the early development phase by setting regulatory and financial institutions to support the market creation and supply chain development.

Keywords: Hydrogen Economy, Green Ammonia, Supply Chain, China, Complex System Engineering

INTRODUCTION

China pushes towards peaking emission by 2030 and reaching neutrality by 2060 [1]. Investments in wind and solar energy grew significantly and accounts for one-third of the world's total capacity [2]. However, the divergence between installed capacity and renewable power generation grows due to the gird inflexibility and insufficient transmission [3]. Lately, China step a move to green hydrogen produced from renewable energy. Mid and long-term targets was set for achieving carbon reduction goals and supporting the energy transition [4]. In the upcoming hydrogen economy, green ammonia increasingly draws attention as a reliable and efficient means to storing and transporting hydrogen [5, 6]. Therefore, an assessment of the development of future green ammonia supply chains is necessary.

A review of current literature reveals that recent studies have paid attention to assessments of green ammonia supply chains. Most of them have discussed cases beyond China (e.g. see [7-9]), and a limited number of studies are in the scope of China (e.g. see [10]). Moreover, these studies concentrate on the techno-economic evaluation. However, modern supply chains comprise of technical infrastructure, actors, interactions, etc. [11]. No research has discussed socio-technical supply chains. This paper aims to analyze the development of green ammonia supply chains in China with the theory of complex system engineering.

The remainder of this paper is arranged as follows: the methodology of complex system engineering is introduced in Section 2. Section 3 discusses green ammonia to advance the energy transition in China, while Section 4 presents our conclusions.

METHODOLOGY

Energy transitions are defined as long-term structural changes in energy systems [12]. Today's energy system is essentially a supply chain, known as a socio-technical system, as it is not only a technical matter, values of individual actors, policies, regulations and markets also shape the system [11, 13]. Complex system engineering addresses not only challenges in technical dimension, but also multi-actor complexity of socio-technical systems [14]. The framework proposed in works [14, 15], which is improved from previous works [16, 17], identifies three key pillars in handling complex socio-technical systems, including: technical system, actors and institutions, as shown in Fig. 1. In general, technical system refers to technical components in energy systems; institutions are the devised rules, while actors are the entities making decisions and participating in the process; the connections emphasizes the interactions between each other that should be considered simultaneously. Actors build and operate technical systems, which in turn influence actors' decisions. Institutions such as: norms, strategies influence actor behaviours, which in turn reshape institutions. The theory is used to view system behaviours as a results of interactions between social and technical components of energy systems.

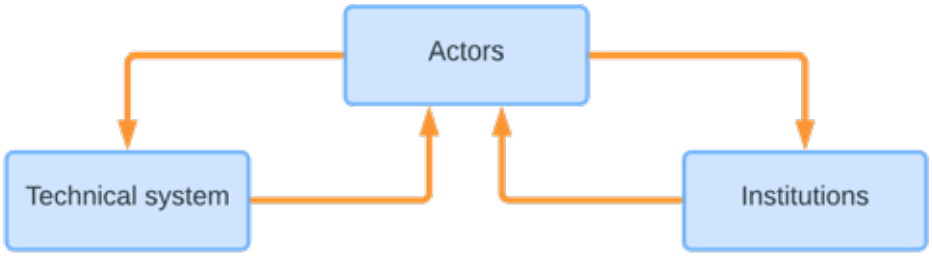


Fig. 1. Framework for analysing socio-technical systems

GREEN AMMONIA TO ADVANCE THE ENERGY TRANSITION IN CHINA

This section is discussed separately from the aspects of the energy condition in China, the current power system centered solution, and the development of green ammonia supply chains as follows.

The energy condition in China

China's economy still relies heavily on coal. The coal-dominant primary energy supply has made China the world's largest coal consumer and CO2 emitter [18]. The government targeted to phase out fossil fuel use by increasing the share of non-fossil energy in total energy consumption, in which, renewable energy is expected to play a key part [19]. China outpaces the rest of the world in wind and solar energy. The aggregate wind and solar generation capacity reached over 500 GW by 2020, and a massive renewable energy projects are in planning [20]. However, the energy condition in China presents an obvious spatial mismatch between renewable energy supply and potential demand, as shown in the Fig. 2. The aggregate wind and solar energy generation capacity in the north, northwest and northeast of China accounts for around 60% of the total capacity in China by 2020, thanks to the abundant renewable resources in these regions [20]. In contrast, economic clusters are generally located in the east and south of China. Therefore, large-scale and long-distance renewable energy distribution is fundamental to facilitating the energy transition in China.

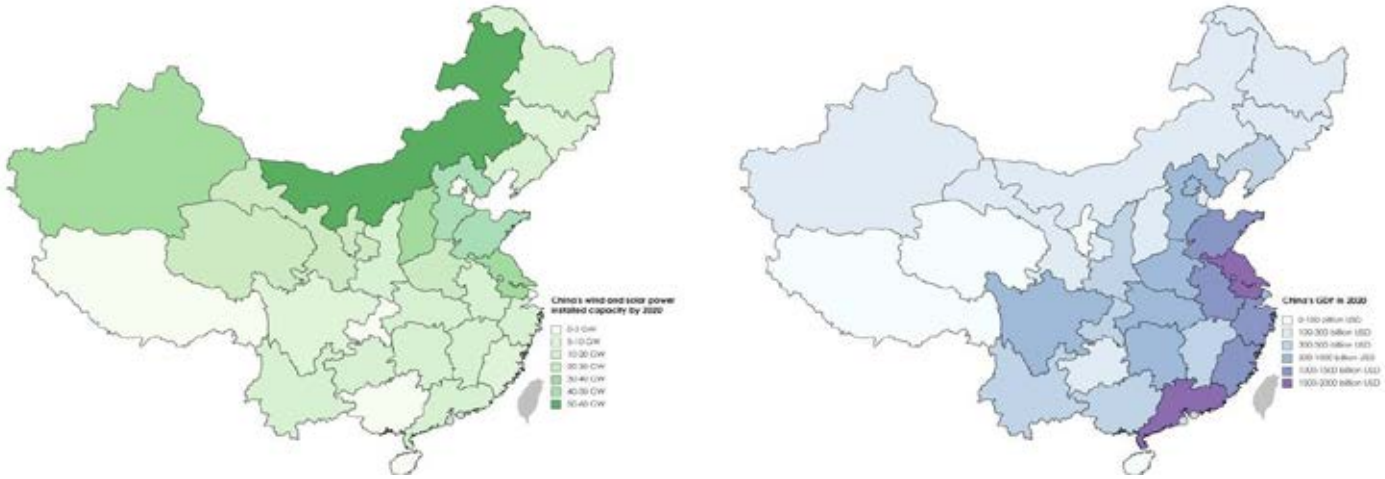


Fig. 2. Spatial mismatch between renewable energy supply and economic development

The power system centered solution

The spatial imbalance has led to serious renewable power curtailment, which declines the use of renewable energy. The further development of power system has been the focal point to address energy distribution and facilitate the energy transition declared in the 14th Renewable Energy Development Five Year Plan [21]. By 2020, China's national grid companies: China State Grid and China Southern Power Gird have built 20 ultra-high voltage lines to transmit renewable energy to load centers accounting for around 30% of total installed capacity of wind and solar energy, which is still not sufficient considering the fast expansion of renewable power bases in recent years [22]. Meanwhile, the intermittent power aroused challenges for grid integration that the overall operating rate of these lines was lower than 40% in 2019 [23]. Therefore, smarter power system is urgently needed by incorporating energy storage technologies. In addition, introducing market-based solutions is encouraged to eliminate institutional barriers.

The development of green ammonia supply chains

Meanwhile, these challenges also call for a concert effort. Revealed from the latest published 2021-2035 Hydrogen Development Plan of China, green hydrogen is expected to play a leading role for large-scale energy storage and long-distance energy distribution [4].

Fig. 3 shows hydrogen distribution costs we estimated for the most promising options. Although pipeline transportation appears to be the ultimate solution, distribution cost is influenced dramatically by volume and distance due to the high capital and operating expenses required. In contrast, liquid hydrogen and ammonia are more flexible options which have similar costs and limited influences by distance and volume. Ammonia defeats liquid hydrogen in terms of safe transportation and long-term storage due to much lower flammability and mild storage conditions [5, 6]. In addition, the transportation will be more efficient if ammonia can be directly used. Therefore, these advantages enable transporting hydrogen as ammonia a flexible, economical and safe option. Since infrastructure for ammonia is already in place due to a century of use in agriculture, the development of green ammonia supply chains and direct use of ammonia are proposed to avoid large uncertainties and significant initial investment in the early stage.

A supply chain comprises upstream production, midstream transportation and downstream wholesale and retail markets. The creation of green ammonia markets is essential in the development of future supply chains, given that green ammonia costs double that of grey ammonia [10]. Considering the large capital investments required in the infancy stage, the upstream and midstream with the participation of hydrogen producers, ammonia producers and ammonia transport operators can be operated with a joint investment to optimize the supply chain and reduce risks. Similar to the practices in renewable power generation [24], the creation of a long-term bilateral contracts between producer and consumer is proposed to share risks between both sides and guarantee investment recovery. Besides, government participation in the early stage is essential to support market creation and development of supply chains, e.g. incentivizing supply and demand, designing a clear and consistent regulatory framework, achieving ancillary policies, etc.

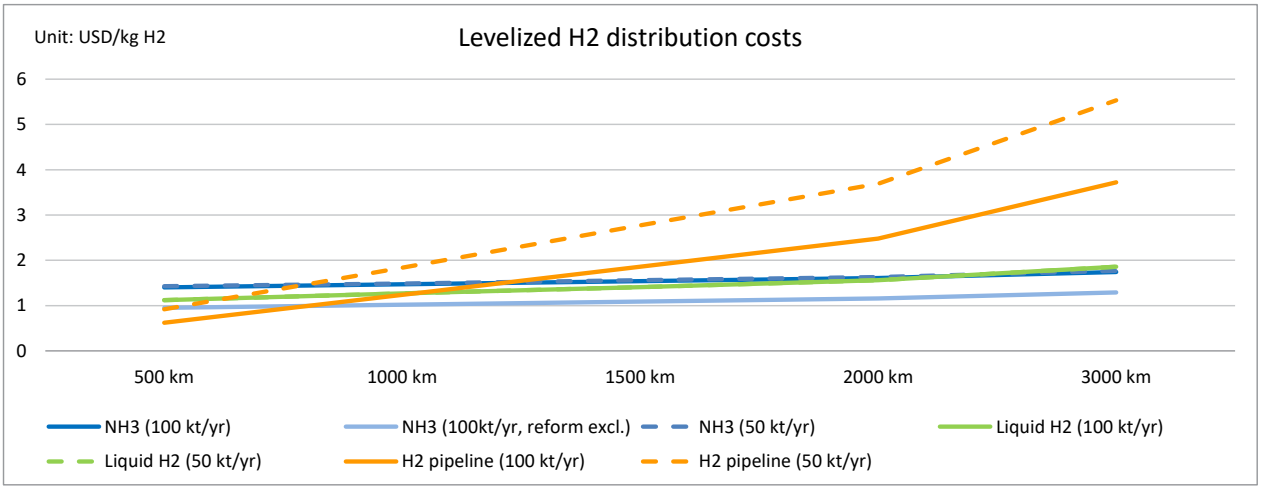


Fig. 3. Hydrogen distribution costs by distance and volume

CONCLUSIONS

Green ammonia is expected to play a key role in the transition to a hydrogen economy. The development of green ammonia supply chains to advance the energy transition in China was analyzed with the theory of complex system engineering. We considered the components of technical system, actors and institutions in the analysis of future energy systems featured socio-technical systems. We identified the spatial imbalance between future energy supply and consumption in China which cannot be fully addressed by the development of power systems. As a prospective hydrogen carrier, we argued that green ammonia can play a feasible role for large-scale energy distribution and long-term energy storage. The development of green ammonia supply chains and direct use of ammonia were proposed to avoid large uncertainties and significant initial investment in the early stage. Market creation will be key to the supply chain development. A joint investment in an integrated supply chain by several stakeholders and the creation of long-term bilateral contract between buyer and seller were also proposed to share risks and ensure capital recovery in the early phase. In addition, regulatory and financial institutions are essential to support supply chain development, which well requires government participation.

REFERENCES

[1] Zhao X, Ma X, Chen B, Shang Y, Song M. Challenges toward carbon neutrality in China: Strategies and countermeasures. Resources, Conservation and Recycling. 2022;176:105959.
[2] Ye Q, Lu J, Zhu M. Wind curtailment in China and lessons from the United States. China's Energy in Transition. 2018.
[3] Mengye Z, Ye Q, David B, Jiaqi L, Bart K. The China wind paradox: The role of state-owned enterprises in wind power investment versus wind curtailment. Energy Policy. 2019;127:200-12.
[4] NDRC. Mid and Long-term Hydrogen Development Plan of China (2021-2035). China: National Development and Reform Commission; 2022.
[5] Kakish N. Green ammonia: Opportunity knocks. Argus. 2020; https://www.argusmedia.com/en/blog/2020/may/28/green-ammonia-opportunity-knocks.
[6] The future of hydrogen. IEA. 2019; https://www.iea.org/reports/the-future-of-hydrogen.
[7] Guerra CF, Reyes-Bozo L, Vyhmeister E, Caparr MJ, Salazar JL, Clemente-Jul C. Technical-economic analysis for a green ammonia production plant in Chile and its subsequent transport to Japan. Renewable Energy. 2020;157:404-14.
[8] Smith C, Torrente-Murciano L. The potential of green ammonia for agricultural and economic development in Sierra Leone. One Earth. 2021;4:104-13.
[9] Bicer Y, Dincer I, Zamfirescu C, Vezina G, Raso F. Comparative life cycle assessment of various ammonia production methods. Journal of Clean Production. 2016;135:1379-95.
[10] Zhao H, Kamp LM, Lukszo Z. Exploring supply chain design and expansion planning of China's green ammonia production with an optimization-based simulation approach. International Journal of Hydrogen Energy. 2021;46:32331-49.
[11] Hoggett R, Bolton R, Candelise C, Kern F, Mitchell C, Yan J. Supply chains and energy security in a low carbon transition. Applied Energy. 2014;123:292-5.
[12] WEC. A Comparative Analysis of Key Countries and Implications for the International Energy Debat. Global Energy Transitions2014.
[13] Li FGN, Trutnevyte E, Strachan N. A Review of Socio-Technical Energy Transition (STET) Models. Technological Forecasting and Social Change. 2015;100:290-305.
[14] J.A.Moncade, Lee EHP, Guerrero GDCN, O.Okur, S.T.Chakraborty, Z.Lukszo. Complex Systems Engineering: designing in sociotechnical systems for the energy transition. Energy Web. 2017.
[15] Moncada JA, Lukszo Z, Junginger M, Faaij A, Weijnen M. A conceptual framework for the analysis of the effect of institutions on biofuel supply chains. Applied Energy. 2017;185:895-915.
[16] Williamson OE. Transaction cost economics: how it works; where it is headed. De economist. 1998;146:23-58.
[17] Ottens M, Franssen M, Kroes P, Van De Poel I. Modelling infrastructures as socio-technical systems. International journal of critical infrastructures. 2006;2:133-45.
[18] BP. Statistical Review of World Energy 2020. 2020.
[19] Ye Q. China's peaking emissions and the future of global climate policy. China's Energy in Transition. 2018.
[20] Renewable Capacity Statistics 2021. International Renewable Energy Agency; 2021.
[21] NDRC. The 14th Renewable Energy Development Five Year Plan. National Development and Reform Commission of China; 2021.
[22] Downie E. Sparks fly over ultra-high voltage power lines 2018.
[23] Xi J. Wind power transmission problem in the three North regions of China remains unsolved. 2020; https://www.jiemian.com/article/5263167.html.
[24] Price H, Mehos M, Kearney D, Cable R, Kelly B, Kolb G, et al. Chapter 20 - Concentrating solar power best practices. In: Lovegrove K, Stein W, editors. Concentrating Solar Power Technology (Second Edition): Woodhead Publishing; 2021. p. 725-57.

WHEC-2022

23rd World Hydrogen Energy Conference

TRACK 14. HYDROGEN INDUSTRY, COMMERCIALIZATION AND MARKETING, APPLICATIONS

TRACK 14. HYDROGEN INDUSTRY, COMMERCIALIZATION AND MARKETING, APPLICATIONS

#12 ANALYSIS OF THE HYDROGEN PURITY AT HYDROGEN REFUELLING STATIONS	1279
#80 INJECTION OF HYDROGEN INTO HIGH PRESSURE NATURAL GAS GRIDS: INVESTIGATION OF THE IMPACT ON MATERIALS AND EQUIPMENT AT RELEVANT ENVIRONMENT	1282
#118 SOLENCO POWER: HYDROGEN FOR THE DECARBONIZATION OF THE ENERGY SECTOR	1285
#200 AIR CARBON RECYCLING FOR AVIATION FUEL TECHNOLOGY	1286
#214 GREEN HYDROGEN PRODUCTION FOR FCEV TRUCKS AT A REMOTE OPEN-PIT COPPER MINE	1289
#285 CHIYODA'S APPROACH FOR HYDROGEN SUPPLY CHAIN BUSINESS WITH "SPERA HYDROGEN™" SYSTEM	1292
#350 OPTIMIZATION OF A PREMIXED CHARGE HYDROGEN ENGINE IN ARGON POWER CYCLE	1295
#365 MODIFIED WSGG GAS RADIATION MODEL FOR ANY MIXTURE OF H_2/CH_4 FUEL FOR HIGH-TEMPERATURE INDUSTRIAL FURNACES	1299
#387 HYDROGEN-METHANE MIXTURE STORAGE IN DEPLETED RESERVOIRS: AN OPTION FOR CONVERTING DECOMMISSIONED OFFSHORE PLATFORMS	1302
#388 REAL-WORLD ENERGY MEASUREMENTS AND LOCAL HYDROGEN COST AS INPUT PARAMETERS FOR REGIONAL VEHICLE FLEET OPTIMIZATION	1305
#442 FRAUNHOFER HYDROGEN LABS: UNIQUE TEST INFRASTRUCTURE FOR THE ENTIRE HYDROGEN VALUE CHAIN	1308
#1442 USE OF HYDROGEN FOR GREEN STEEL PRODUCTION	1311
#1448 GREEN HYDROGEN PRODUCTION USING GEOTHERMAL POWER GENERATION (1) PROJECT IN MOKAI, NEW ZEALAND	1314
#1451 GREEN HYDROGEN PRODUCTION USING GEOTHERMAL POWER GENERATION (2) PROJECT IN OITA, JAPAN	1316
#1468 ANALYSIS OF HYDROGEN COMBUSTION AS FUEL TO PREHEAT AIR IN POWER GENERATION PLANTS IN MICROMIX INJECTION TECHNOLOGY	1319
#1483 EXTENSION OF LEAN LIMIT USING HYDROGEN ADDITION FOR GASOLINE DIRECT INJECTION ENGINE AND EMISSION REDUCTION	1323
#1496 PROGRESS AND PERSPECTIVES IN USING HYDROGEN-ENRICHED BIOGAS FROM WASTE TO ENGINE IN AGRICULTURE	1326
#1513 A CFD STUDY ON HYDROGEN ADDITION TO THE METHANE-AIR MIXTURES	1329
#1531 PREDICTION OF CARBON DI OXIDE AND OTHER EMISSIONS CHARACTERISTICS OF LOW CARBON BIOFUEL-HYDROGEN DUAL FUEL ENGINE - A MACHINE LEARNING APPROACH	1332
#1552 EVALUATION OF KINETIC MODELS VIA COMPUTATIONAL OPTIMIZATION TECHNIQUES FOR DIRECT SYNGAS-TO-OLEFINS PROCESS	1335
#1577 ATOME: PURE-PLAY HYDROGEN PRODUCER	1338
#1595 DRIVE CYCLE SIMULATION OF A SMALL-SIZED FUEL CELL ELECTRIC VEHICLE	1341

WHEC-2022
23rd World Hydrogen Energy Conference
June 26-30, 2022 - Istanbul

#12

ANALYSIS OF THE HYDROGEN PURITY AT HYDROGEN REFUELLING STATIONS

[1, 2*] *Holger Janßen,* [1] *Michael Kröner,* [1] *Alexander Dyck,* [2] *Michael Wark,* [1] *Carsten Agert*
[1] German Aerospace Center (DLR), Institute of Networked Energy Systems, Carl-von-Ossietzky-Str. 15, 26129 Oldenburg, Germany
[2] Carl von Ossietzky University, Institute of Chemistry, Carl-von-Ossietzky-Str. 9-11, 26129 Oldenburg, Germany

*Corresponding author e-mail: Holger.Janssen@dlr.de

ABSTRACT

Contaminations in hydrogen have a strong impact on the long-term stability and thereby performance of proton exchange membrane (PEM) based fuel cells for mobile applications. While these influences have been intensively studied, particularly the purity of the hydrogen provided at public hydrogen refuelling stations (HRS) which is well-defined in ISO standards is rarely analyzed. We intend to take samples of hydrogen at HRS with a specially designed mobile refuelling module enabling the sampling at 70 MPa. With a method specifically developed and explicitly described in this paper, we seek to ensure that other sources of contamination can be excluded during the probe sampling. With analysis techniques able to determine concentrations of contaminants down to the parts per billion (ppb) level the hydrogen samples will be investigated in the laboratory. While single routes of contamination, such as the synthesis route, have been individually studied in detail elsewhere, the provision of hydrogen with different storage processes, as well as transport and compression at the HRS will be considered in these investigations as a holistic system. Finally, it can be stated whether the dispensed hydrogen meets the high-quality requirements of fuel cells for mobile applications.

Keywords: Contamination, Hydrogen Refuelling Station, Purity Analysis, Hydrogen Sampling

INTRODUCTION

Establishing sustainable and cost-optimized options for the energy supply is a key task during the energy transition process from fossil to renewable energy generation of the coming years. Particularly in the transportation sector, locally emission-free vehicles are attracting more and more attention in urban areas. In addition to battery electric vehicles (BEV), the fuel cell electric vehicle (FCEV) powered by hydrogen offers the option for zero emission driving with fast refuelling capability even for long range travels [1]. The needed hydrogen can be synthesized by a variety of methods; up to now it is produced mostly by steam reforming of natural gas. For emission-free fuel cell mobility, however, the production of hydrogen via electrolysis plants using renewable energy sources is needed [1]. For the provision of inter-seasonal energy storage of green hydrogen, salt caverns can be used to store relevant amounts of energy also for the other energy sectors. Stationary fuel cells can consequently use the chemically stored energy in hydrogen to balance seasonal fluctuating power generation sources as needed [2, 3]. It is known that contaminants or noxious gases in hydrogen are responsible for numerous degradation modes within the fuel cell [4, 5]. To avoid damage processes initiated by these compounds, international standards for the quality of hydrogen set precise limits for contaminations present in hydrogen. These are namely SAE J2719, ISO 14687 and EN 17124 [5, 6]. The simultaneous analysis of all contaminants in hydrogen is not trivial due to the very small concentrations in the low ppm and ppb range. The high purity requirements are not only barely measurable with a single method at the same time, but also the influences of the supply chain to the HRS or storage of hydrogen in salt caverns are little studied as an integral system.

For the investigation of hydrogen in the ppb range at HRS only a couple of devices for sampling at 70 MPa exist. Furthermore, there are also no general protocols available for the contamination-free sampling of hydrogen. Especially for sampling on a kilogram scale at 70 MPa, transport to the site of the analysis poses a challenge since no conventional gas cylinder can be used. In this study, a hydrogen sampling method was developed and used for hydrogen quality analysis. Extensive investigations on influencing parameters will be carried out and finally, estimated whether the hydrogen provided at public refuelling stations meets the purity requirements of the fuel cells.

EXPERIMENTAL

For the sampling of hydrogen at HRS a high-pressure hydrogen tank (shown in Photo 1) similar to that in fuel cell vehicles is used. With this tank, it is possible to use the standardized dispenser at public HRS to carry out a non-communicative refuelling according to the standard SAE J2601 [7]. With up to 70 MPa, this 37-liters carbon woven pressure vessel can be filled with hydrogen. Temperature, pressure and flow sensors are included to monitor these parameters. The fuel sampler does not contain an infrared communication interface and due to the small tank volume, the non-communication filling method specified in the mentioned protocol of the HRS is automatically used. A procedure has been developed to ensure that the refuelled hydrogen and the subsequent analyses of the contaminants are referable to the so-sampled hydrogen. In that regard, the first kilogram of hydrogen is fuelled and subsequently, the

tank is carefully emptied. We make sure that the hydrogen released to air is in a safe distance from possible ignition sources. The described procedure ensures that ISO 14687 and EN 17124 targeted constituents [5] will be removed from within the module and sampling lines [8]. Especially residues of water and sulfur components are avoided thereby. Finally, the module is refuelled with the amount of hydrogen necessary for the analysis.



Photo 1: Composite type IV high-pressure tank with receptacle for sampling of hydrogen at hydrogen refuelling stations.

For investigating the purity of hydrogen, a high-performance gas analyzer from the company V&F of the type AirSense will be used. The measurement principle is based on Ion-Molecule Reaction mass spectrometer (IMR-MS) and allows determining the concentrations of many contaminations in the parts per trillion (ppt) range. IMR means the use of an ion source for primary ions (e.g. Xe^+) with a particularly low energy level of 10 to 14 eV to completely ionize the gas sample. Without molecule fragments and interferences, the quadrupole mass filter separates the molecules for further detection at the fast pulse counter. [9] Even the smallest entrained impurities affect the actual quality of the hydrogen so any contamination of the sampled gas has to be avoided by an accurate selection of the materials and transport lines used. For the supply of hydrogen with concentrations of contaminants in the ppb range from the refuelling module to the gas analysis, conventional stainless steel tubes or PTFE lines cannot be used, as particularly contaminants with amounts of sulfur or ammonia adhere on the walls of the lines and tubes. Significantly more meaningful alternatives are hoses made of perfluoroalkoxy alkane polymer (PFA) or stainless steel tubes, which are coated with inert non-reactive silicon [10]. Due to the flat surface and the avoidance of interactions between the material of the tube and the contaminant, stable measurements of the concentrations are reached much faster [10].

RESULTS

Since we are still at the beginning with the investigations described above, results obtained are not presented in the following. Instead, an outlook on the results is depicted below. Selected HRS in Germany will be approached and hydrogen will be sampled with the mobile tank. Some HRS are supplied with hydrogen from steam reforming of natural gas via delivery by a trailer; others produce the hydrogen directly at the refuelling station by on-site electrolysis without necessary use of trailers. Thus, by investigating the hydrogen with the gas analysis in the laboratory a dependency of the manufacturing processes on the purity can be expected. Especially hydrogen produced by on-site electrolysis is likely to have only minor contaminations, e.g. in the form of water and oxygen [10, 11]. In contrast, hydrogen produced by steam reforming is expected to have significantly more contaminants, primarily considering the amount of total organic carbon (TOC) and inert gases, e.g. nitrogen [10, 11]. Since carbon dioxide and carbon monoxide are additional products in the steam reforming process, at least small concentrations in hydrogen after the mandatory purification with pressure swing adsorption are also anticipated here. By comparing the supply of hydrogen to the HRS, a negative impact from transport can probably be found. Further estimated influencing factors will also be identified, such as dependencies of the refuelling station's year of construction or the technology supplier (Linde, Shell, etc.) on the quality of hydrogen. The latter is also associated with a probably important parameter of the type of compression. Especially in reciprocating compressors and compressors working with ionic liquids an influence on the purity is expected.

Another factor influencing the purity of hydrogen is the inter-seasonal storage. In particular, the storage of hydrogen in salt caverns offers many unknown parameters, which give so far unconsidered possibilities of entrained contaminants. Due to the humid, alkaline environment with the brine present in the bottom of the cavern, the hydrogen stored under high pressure will come into contact with numerous ionic compounds. Besides, full saturation with water (designated contaminant in ISO 14687) is a reasonable consequence of the storage. Another path of contamination is the formation of methane by bacteria. These methanogenic bacteria convert carbon dioxide or carbon monoxide with hydrogen according to Sabatier’s reaction into methane and water [12].

Concerning all the above-mentioned paths of contamination, it is fairly obvious that examining the ongoing processes, e.g. synthesis route and compression separately is not an all-encompassing approach. Moreover, it is essential to consider the provision of hydrogen at the HRS with the numerous influencing factors as a holistic system.

CONCLUSIONS

By studying the quality of hydrogen provided at hydrogen refuelling stations, it will be estimated whether the purity of the hydrogen meets the high-quality requirements of mobile and stationary fuel cell applications. For this, extensive considerations for contamination-free sampling at 70 MPa with a specially designed mobile refuelling module were established. With a highly accurate trace gas analysis, the probed gas samples are to be investigated in the laboratory regarding critical components for fuel cells. Detection of contaminants in the ppb range is challenging but feasible by a reasonable selection of used materials (e.g. silicon-coated stainless steel tubes). As a result of the analyses, dependencies from the production process on the quality will be highlighted. Only minor contaminations are assumed to occur in hydrogen produced via PEM water electrolysis. However, further influences from the transport of hydrogen and the inter-seasonal storage in salt caverns will similarly be considered.

REFERENCES

1. Smolinka T, Wiebe N, Sterchele P, Palzer A, Lehner F, Jansen M, Kiemel S, Miehe R, Wahren S, Zimmermann F, 2018. Industrialisierung der Wasserelektrolyse in Deutschland: Chancen und Herausforderungen für nachhaltigen Wasserstoff und Verkehr, Strom und Wärme. Studie IndWEDe. 201. (In German)
2. VDMA Working Group Fuel Cells. 2018. German manufacturers well positioned in the growing global market. Fuel Cell Industry Guide Germany 2018.
3. Heinrich-Böll-Stiftung. Green European Foundation, European Renewable Energies Federation and Le Monde diplomatique. 2018. Daten und Fakten über die Erneuerbaren in Europa. Energieatlas. (In German)
4. Cheng X, Shi Z, Glass N, Zhang L, Zhang J, Song D, Liu Z, Wang H, Shen J. 2007. A review of PEM hydrogen fuel cell contamination: Impacts, mechanisms, and mitigation. Journal of Power Sources 165:739-756.
5. ISO. 2019. ISO 14687. Hydrogen fuel quality - Product specification.
6. Ohi JM, Vanderborgh N, Voecks G. 2016. Hydrogen Fuel Quality Specifications for Polymer Electrolyte Fuel Cells in Road Vehicles. Fuel Cell Technologies Office. U.S. Department of Energy.
7. SAE International Surface Vehicle Standard. 2016. SAE Standard J2601. Fueling Protocols for Light Duty Gaseous Hydrogen Surface Vehicles.
8. ASTM International. 2017. ASTM D7606-17. Standard Practice for Sampling of High Pressure Hydrogen and Related Fuel Cell Feed Gases.
9. http://www.vandf.com/en/. Accessed on September 22, 2021.
10. Bacquart T, Arrhenius K, Persijn S, Rojo A, Auprêtre F, Gozlan B, Moore N, Morris A, Fischer A, Murugan A, Bartlett S, Doucet G, Laridant F, Gernot E, Fernández T E, Gómez C, Carré M, De Reals G, Haloua F. 2019. Hydrogen fuel quality from two main production processes: Steam methane reforming and proton exchange membrane water electrolysis. Journal of Power Sources 444:227170.
11. Bacquart T, Murugan A, Carré M, Gozlan B, Auprêtre F, Haloua F, Aarhaug T A. 2018. Probability of occurrence of ISO 14687-2 contaminants in hydrogen: Principles and examples from steam methane reforming and electrolysis (water and chlor-alkali) production processes model. International Journal of Hydrogen Energy 43:11872-11883.
12. Panfilov M. 2016. Underground and pipeline hydrogen storage. In Compendium of Hydrogen Energy, Vol. 2: Hydrogen Storage, Transportation and Infrastructure. Edited by Gupta R B, Basile A, Veziroğlu T N. Woodhead Publishing Series in Energy.

WHEC-2022
23rd World Hydrogen Energy Conference
June 26-30, 2022 - Istanbul

#80

INJECTION OF HYDROGEN INTO HIGH PRESSURE NATURAL GAS GRIDS: INVESTIGATION OF THE IMPACT ON MATERIALS AND EQUIPMENT AT RELEVANT ENVIRONMENT

[1,2*] *Vanesa Gil,* [1] *Javier Sánchez-Laínez,* [3]*Alberto Cerezo-Alarcón,* [3,4] *María Dolores Storch de Gracia,* [5] *Ekain Fernandez,* [5] *Virginia Madina*

[1]Foundation for the Development of New Hydrogen Technologies in Aragón, Parque Tecnológico Walqa Ctra. N-330A, km. 566, Cuarte, Huesca, Spain

[2]ARAID Foundation, Avda. de Ranillas 1-D, 50018 Zaragoza, Spain

[3]Redexis, C/ Mahonia 2, 28043 Madrid, Spain

[4]Universidad Politécnica de Madrid, 28040 Madrid, Spain

[5]Tecnalia, Parque Tecnológico de Bizkaia, Astondo bidea, Edificio 700, E-48160 Derio, Bizkaia, Spain

*Corresponding author e-mail: vgil@hidrogenoaragon.org

ABSTRACT

This work addresses the potential of hydrogen injection into the transmission high pressure natural gas grid as way to decarbonise the gas system and gas uses. To achieve this potential, knowledge gaps have to be covered considering the current know-how on how different concentrations of hydrogen gas could affect the infrastructure and its components. The activities are developed within the frame of HIGGS (FCH 2JU funded project, No. 875091). An R&D platform working at high pressure has been developed in HIGGS to achieve advance the knowledge on operation of hydrogen admixtures in the high-pressure natural gas grid, simulating the operational conditions from selected equipment, gas quality, etc. The admixture levels consider various hydrogen concentrations until reaching pure hydrogen. So far, the impact of H_2/NG blends with up to 20 %vol H_2 on steels and equipment has been studied through a mechanical and chemical characterization after been exposed to the blend. Membrane technology has also been tested for hydrogen recovery, using a Pd-based membrane prototype installed in the platform.

Keywords: Admixture, H_2 Injection, Power to Gas, Gas Transmission, Decarbonisation.

INTRODUCTION

The Paris Agreement aims to limit global temperature increase and requires a global deep decarbonisation of many sectors of the economy. Nowadays, the European Union (EU) is updating its energy policy framework to facilitate the clean energy transition, introducing the national energy and climate plans, encouraging investments and empowering the EU consumers to become active players in the energy transitions. The new policies and the revised renewable energy directive [1] are fixing ambitious targets for 2030: renewable energy target of at least 32% and an energy efficiency target of at least 32.5%. When the policies are fully implemented, they will lead to a great reduction on emissions for the whole EU. The EU framework towards greenhouse gases (GHG) emissions reductions is based on six key areas of action, including the deployment of renewable energy production, decarbonising heating and cooling applications, and reducing the emissions on the transport sector. Therefore, the integrated energy markets in the EU shall allow important transformations to provide more flexibility and be better placed to integrate a greater share of renewable energies, allowing also a more independent energy system. In this context, hydrogen can play a pivotal role as energy vector allowing coupling the energy sectors and as an alternative fuel in hard to electrify sectors. To facilitate that a high amount of hydrogen is produced by renewable energies (RE), existing gas infrastructure could be a way of transporting hydrogen between production point and final use.

This is precisely the main goal of the HIGGS project “Hydrogen in Gas Grids: A systematic validation approach at various admixtures levels into high-pressure grids” The HIGGS project, which is funded by the Fuel Cells and Hydrogen Joint Undertaking (GA No. 875091) is a collaborative project involving four research institutions, a technical-scientific association and a transmission system operator (TSOs). HIGGS’ main objective addresses the potential of hydrogen injection into the transmission high pressure natural gas grid, as way to decarbonise the gas system and gas uses, and one of its most important tasks is the design and development of a R&D platform for the experimental validation of components of grid. To achieve this potential, knowledge gaps have to be covered considering the actual know-how on how different concentrations of hydrogen gas could affect the infrastructure and its components. Specific technical objectives are defined as intermediate goals in order to achieve the strategic objective:

1. Implement of an injection and admixture system.
2. Test gas separation systems based on membrane technology.
3. Design/execute a testing loop to validate components and materials identified.
4. Elaborate an impact assessment document (operation, maintenance procedures).

The present abstract explains the design and operation of this R&D platform (see Figure 1), an innovative system to advance the knowledge on operation of hydrogen admixtures in the high-pressure natural gas grid, with varying conditions, simulating the operational conditions from selected elements, components, gas quality, etc., to simulate conditions that differ at EU level. The first results of the tests performed with this platform are also explained, focusing on the characterization of materials after hydrogen exposure and gas separation tests with membrane technology.



Figure 1. Picture of the R&D platform developed in HIGGS

METHODOLOGY

HIGGS approach is based on implementing a project vision that allows the systematic validation systems and components, typically present in high pressure gas grids. The R&D platform consists in an admixture system, a testing platform (test loop) and a gas separation prototype. It is designed with a capacity of injecting over 5 kg/h H_2 at 80 bar to retrieve information on the impact of hydrogen in the transmission gas network equipment and deal with deblending issues to recover the injected hydrogen in end-uses. The admixture system produces the blend to study. Flow controllers and pressure regulators ensure the preparation of the blend with the desired composition at low pressure (15 bar), which is afterwards compressed up to 200 bar and stored in a buffer that feeds downstream the different parts of the testing platform (i.e. gas injection).



Figure 2. Pictures of the dynamic (left) and static section (right) of the testing platform

The testing platform allocates representative components that can be found in the transmission grid, as well as pipes of different API 5L steel grades. It considers two different sections: i) A static section, where leakages and hydrogen permeance is tested in components (valves of different nature) and connections (threaded joints, flanges, etc.) and ii) a dynamic section, where materials and components failure/degradation is investigated. In all cases the setup is pressurized up to 80 bar, a pressure level present in transmission gas grids. In the static section there is no flow of gas. The lines are pressurized and closed afterwards, and pressure drop and gas quality are then monitored during the tests. In the dynamic section, however, the gas flows through several branches in a closed-loop system using a compressor and a regulator to create the pressure difference in the setup (driven force). The different lines contain several steel grades, and typical components of the transmission gas grid (filters, flowmeters, flow regulators…). The steels considered for the tests range from API 5L X42 to X70. They are fresh materials incorporated in the platform as welded pipes and as strained specimens that will be allocated inside a pig trap for hydrogen exposure at high pressure.

During the experimental campaign, various hydrogen/natural gas admixtures will be investigated. The natural gas used is a “simplified gas” based on the use of methane as carrier mixed some common impurities in natural gas, such as

hydrogen sulfide or carbon dioxide. This simulated natural gas follows the gas quality according to the agreed standards in the trans-European gas grid. Pure hydrogen will also be injected in the setup, covering the most likely injection scenarios thought for the near future in the European gas grid. The testing campaign consists in exposing the testing material to the hydrogen blend at high pressure for several months. So far H_2/NG blends with up to 20 %vol H_2 have been studied and the effect of hydrogen on the steels and main elements of the equipment has been checked at the laboratory after dissembling them from the platform. Finally, to meet cases where users cannot accommodate the presence of hydrogen, test separation systems have been studied. In this regard, membrane technology has been tested for hydrogen recovery from H_2/CH_4 mixtures with a hydrogen content ≤ 20% and at a pressure of 40-80 bar, using a Pd-based membrane prototype installed in the R&D platform.

RESULTS AND DISCUSSION

HIGGS started 01/01/2020. The Project has a duration of 36 months and a budget of 2 million Euros from European Funding. To evaluate how different degrees of natural gas and hydrogen mixture behave in relation to the transport infrastructure, simulating different operating conditions by varying the flow, composition and quality of the gas, a testing platform has been developed at the facilities of the FHa where all the elements are tested up to 80 bar. The design and selection of components for the testing facility, the developed membrane technology and the preliminary project's results during the first months of the experimental campaign will be shown at the conference.

So far, 20 %vol H_2 blends in natural gas have been studied and the impact of hydrogen on steels and components have been ascertained. This has been achieved by disassembling the testing components in the platform (steel pipes, joints, seals, etc.) and performing characterization tests at the laboratory, including visual inspection for crack detection, mechanical tests (e.g. tensile strength test) and chemical characterization. The leakage rate of hydrogen through components has also been monitored, obtaining meaningful graphs that explain the tightness of the natural gas components for the new gas conditions. Results on gas separation consist in monitoring the composition of the permeate stream (i.e. the stream rich in hydrogen) by gas chromatography to asses the quality of the separation during the test.

CONCLUSIONS

HIGGS project, funded by the Fuel Cells and Hydrogen 2 Joint Undertaking (FCH 2JU) under Grant Agreement no. 875091, aims to pave the way to decarbonisation of the gas grid and its usage by hydrogen injection. The R&D platform developed in the project will help to perform experiments with materials and equipment present in the transmission gas grid to check their readiness for the transport of hydrogen in the near future. So far, blends with 20% vol hydrogen content has been tackled and the suitability of membrane technology to recover the hydrogen blended in end-uses has also been studied, showing promising results for understanding how prepared the natural gas grid is for the new tendencies of the market.

ACKNOWLEDGEMENT

This project has received funding from the Fuel Cells and Hydrogen 2 Joint Undertaking under Grant Agreement No. 875091. This Joint Undertaking receives support from the European Union's Horizon 2020 Research and Innovation programme, Hydrogen Europe and Hydrogen Europe Research.

REFERENCES

1. COM (2016) 767.2 Directive of the European Parliament and of the Council on the promotion of the use of energy from renewable sources (recast).
2. Sector Forum energy Management. 2016. Working Group Hydrogen Final Report, EUR 27641 EN, 10.2790/66386.

WHEC-2022
23rd World Hydrogen Energy Conference
June 26-30, 2022 - Istanbul

#118
SOLENCO POWER: HYDROGEN FOR THE DECARBONIZATION OF THE ENERGY SECTOR

[1] *Hugo Vandenborre*, [1*] *Francisco López*
[1]Solenco Power NV, Slachthuisstraat 112 box 2 - 2300 Turnhout, Belgium

*Corresponding author e-mail: francisco.lopez@solencopower.com

ABSTRACT

Solenco Power NV (SP) is a fast-growing Belgian SME active in the energy storage sector, with systems that combine generation, storage, and usage of pressurized hydrogen. SP was founded in 2015, as a spinoff of Vandeborre Energy Systems NV, company with an extensive career in the hydrogen sector. SP was launched having as a first objective, the commercialization of an integrated hydrogen solution capable of absorbing excess of a renewable energy sources, when available, for hydrogen generation, store that hydrogen in a pressurized form for unlimited periods and use that hydrogen for the cogeneration of electricity and heat, when needed. For reaching that objective, since its foundation SP has matured this concept towards a product called Solenco Powerbox (SPB) [1] and its certification.

Keywords: Renewable Energy, Energy Storage, Seasonal Storage, Hydrogen, Proton Exchange Membrane.

INTRODUCTION

The SPB is the first commercialized product of SP. It is targeting residential, commercial, and industrial installations. At is inception, the SPB was conceived as a system to be primarily integrated in households due to the growth of solar photovoltaic (PV) installations, coupled with homes, and the imperative need of both, electricity and heat. These characteristics and energy profiles of the residential sector made a perfect match with SPB's inputs and outputs. Electricity generated by the Solar PV will be directly consumed by the users. All the surplus of that production, instead of being injected to the grid, will be used for the electrolysis of water inside the SPB. Through that electrolysis process, water will split in oxygen, safely release to the atmosphere and hydrogen, which will be pressurized in certified cylinders as a renewable energy storage. When the users will require electricity, hydrogen will be used as a fuel for the fuel cell process, cogenerating electricity and heat. The complete process describes an installation with two main pillars, firstly the SPB or power unit and the renewable hydrogen storage or energy unit. Since power and energy are decoupled, SP installations based on the SPB can adapt their energy capacity in function of user requirements. This flexibility has allowed SP to mature the SPB not solely as home solution, but rather as product for the residential, commercial, and industrial sector.

MATERIALS AND METHODS

The process of shaping SPB's concept into a prototype, towards a commercialized product, has had as an outcome several generations of the same. Those intermediated steps were fundamental for the complete definition of the system, components, and processes part of the SPB. In general lines, all starts with renewable electricity and water as inputs for the SPB. The intermediate output is pressurized hydrogen, and the ultimate outputs are electricity and heat. Through out that chain, several processes like electrical rectification, inversion and conversion, water deionization, water heat exchange and electrochemical water and hydrogen oxidation. Moreover, those processes must be monitored and controlled for their optimal execution.

RESULTS AND DISCUSSION

During the development of the SPB, SP's team went through four generations where the processes mentioned above were steadily integrated across each generation for the completion of the technology readiness level (TRL) 9. Several of the described steps and milestones accomplished by the Solenco's team were supported by national and European projects [2] [3]. In the full paper, the four generations will be described, including field tests.

REFERENCES

1. Vandenborre, H. (2017) The Solenco Powerbox, ISBN 9789082551808
2. https://cordis.europa.eu/project/id/646463. Accessed on December 10, 2021
3. https://cordis.europa.eu/project/id/946442. Accessed on December 10, 2021

WHEC-2022
23rd World Hydrogen Energy Conference
June 26-30, 2022 - Istanbul

#200
AIR CARBON RECYCLING FOR AVIATION FUEL TECHNOLOGY

[1,2*] Vanesa Gil, [3] Kiyoharu Tadanaga, [4] Harald Gröger, [5,6] Stefan Wuttke, [7,2] Jonas Gurauskis, [8] Pedro Camargo, [9] Reinaldo Giudici, [10] Francesca Bonino, [11] Joke Hadermann
[1] Aragon Hydrogen Foundation, Parque Tecnológico Walqa Ctra. N-330A, km. 566, Cuarte, Huesca, Spain
[2] ARAID Foundation, Avda. de Ranillas 1-D, 50018 Zaragoza, Spain
[3] Division of Applied Chemistry, Faculty of Engineering, Hokkaido University, 060-8628Sapporo, Japan
[4]Chair of Industrial Organic Chemistry and Biotechnology, Faculty of Chemistry, Bielefeld University, Universitätsstr. 25, 33615 Bielefeld, Germany
[5] BCMaterials, Basque Center for Materials, UPV/EHU Science Park, 48940 Leioa, Spain
[6] Ikerbasque, Basque Foundation for Science, 48013 Bilbao, Spain
[7] INMA, Instituto de Nanociencia y Materiales de Aragón (CSIC-Unizar), 50018 Spain
[8] Department of Chemistry, University of Helsinki, 00560 Helsinki, Finland
[9] Escola Politécnica da Universidade de São Paulo, Av. Prof. Luciano Gualberto trav.3, no. 380, 05508-010 São Paulo, Brazil
[10] Department of Chemistry, NIS and INSTM Reference Centre, University of Turin, Via G. Quarello 15, I-10135 and Via P. Giuria 7, I-10125 Turin, Italy
[11] Department of Physics, EMAT, University of Antwerp, Groenenborgerlaan 171, B-2020 Antwerp, Belgium

*Corresponding author e-mail: vgil@hidrogenoaragon.org

ABSTRACT

The European Union and the Japan Science and Technology Agency awards 2.9M€ to 4AiCRAFT “Air Carbon Recycling for Aviation Fuel Technology”, for helping the aviation sector to reach the EU 2050 climate-neutrality targets.

4AirCRAFT, a H2020 funded project in International Cooperation with Japan for Research and Innovation on alternative renewable fuels, offers a novel cascade reactor for sustainable aviation fuel synthesised from H_2 and CO_2. The conversion to high-density hydrocarbons will be achieved at mild conditions and based on an intensified cascade reactor.

Key to the process is the combination of highly efficient electro-, chemo- and bio- catalysts. Synergy between hybrid catalysts which are selectively embedded within advanced porous carriers including hierarchical scaffolds are expected to raise selectivity and energy efficiency. In this project the technology readiness level is raised from TRL 2 to 3.

Keywords: Hydrogen-Based Fuels, Sustainable Fuel, Jet Fuel, Cascade Synthesis, Process Intensification.

INTRODUCTION

Climate change and the resulting global environmental threat are the main drivers for the efficient use of resources and transition to renewable energy sources. For this reason, researching alternative renewable fuels for transport sector by moving to a clean and circular economy constitutes, currently, one of the main priorities in Europe long-term ambitions for a better society. To achieve the overarching objective of “Climate neutrality” by 2050, the European Commission set up two years ago the Green Deal Commitment [1].

Aviation is a strong sector for the European Union’s economy and an increasingly important means of transport for EU citizens and businesses. However, as a capital-intensive industry characterised by a high-dependence on a global supply of energy-dense fuels, greenhouse gas (GHG) emissions due to aviation industry account for 13 % of the emissions for transport [2] emitting more than 900 million tons of CO_2 per year. [3] Therefore, energy transition should break the link between economic growth and GHG emissions. However, aviation is one of the most challenging sectors when it comes to reducing CO_2 emissions. One of the reasons it that common alternatives such as electrification or hydrogen propulsion are not expected to be a suitable substitute to kerosene for long haul flights in a short period of time. Therefore, sustainable production and use of low-carbon footprint alternative fuels produced from non-fossil resources could be a key skeleton to unlock “net zero” flying in the near term.

Alternative fuels synthesis by process intensification for hydrogen as feedstock and carbon dioxide conversion technologies along more energy-efficient processes can substantially contribute to mitigating the current and future impact of aviation on the environment. The combination of hydrogen production by renewable sources with recycling carbon dioxide from various sources leads to a renewable synthetic fuel with low carbon footprint, as illustrated in Figure 1.

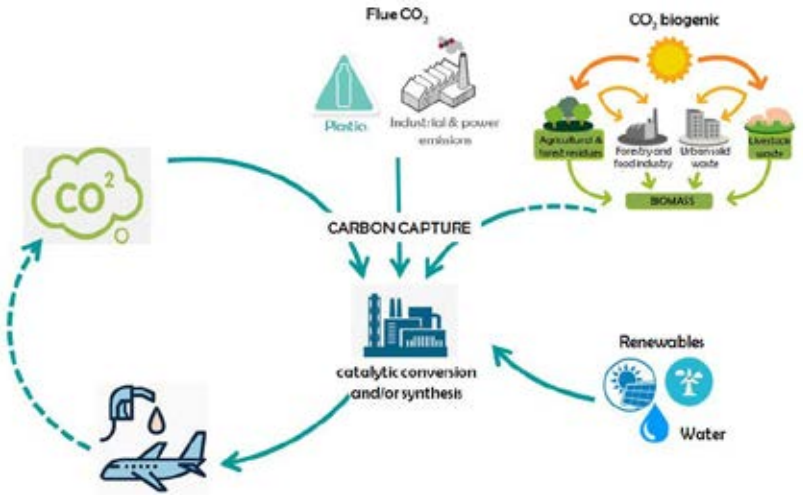


Fig. 1. CO_2 conversion cycle for sustainable production of jet fuel.

Launched in May 2021, the EU-JAPAN-BRAZIL cooperation will enable the development and prof of concept of the disruptive concept for jet fuel direct production.

4AirCRAFT's ultimate goal is to develop a next generation of stable and selective hybrid catalysts for the direct CO_2 and H_2 conversion into C_8-C_{16}. 4AirCRAFT will overcome the current challenges by combining three main reactions into one cascade reactor to increase the CO_2 conversion rate and simplifying the process. By achieving this we will be able to circumvent the need for further steps for hydrocracking or hydrorefining of Fischer–Tropsch waxes.

4AirCRAFT technology aims to deliver a highly innovative process which produces alternative fuel at mild conditions and high energy efficiency, reducing energy consumption and contributing to a circular economy, leading to a decrease in greenhouse gases emissions and reduced dependence on fossil fuel-based resources.

In summary, 4AirCRAFT combines hybrid catalytic conversion and process intensification to bring out an efficient, precise, flexible and scalable unique technology to direct convert water and recycled CO_2 into sustainable and clean liquid fuels, thus making flying carbon neutral.

RESULTS

4AirCRAFT moves beyond the state-of-the art by precisely integrating and taking advantage of biocatalysts, inorganic nanocatalysts, electrocatalysts, and their controlled spatial distribution within application tuned catalyst carrier structures. These catalyst carrier structures are based on metal-organic frameworks and engineered inorganic scaffolds with hierarchical porosity distribution. This will unravel the activity of catalytic active phases and materials based on earth-abundant elements allowing us to achieve high CO_2 conversion percentages and selectivity towards jet fuels.

In terms of inorganic catalysts, size and shape of metal NPs, metal clusters, and single atoms at the surface of catalyst carrier structures are being developed, and precise structure-performance-selectivity relationships will be established.

In terms of biocatalyst, special emphasis is given to assure the long-term stability of deployed enzymes through programmed anchoring and shielding from detrimental reaction conditions. Together application tuned catalyst carrier structures will be employed to steer selectivity towards C_8–C_{16} molecules.

CONCLUSIONS

4AirCRAFT project aims to pave the way to decarbonisation of aviation sector by developing alternative sustainable fuels. The 4AirCRAFT technology uses an innovative catalytic reactor which will be validated at lab scale to conduct the conversion in: a) precise synthesis and high yield of jet fuel and b) unprecedented low temperature.

ACKNOWLEDGEMENT

This project has received funding from the European Union's Horizon 2020 research and innovation programme under Grant Agreement No 101022633. This work is supported by Japan Science and Technology Agency (JST) under Grant Agreement No JPMJSC2102. This project is developed in the frame of a Mission Innovation Challenge.





REFERENCES

1. european-green-deal-communication_en.pdf (europa.eu). Accessed on December 15, 2021.
2. European Union Aviation Safety Agency, European Aviation Environmental Report (2019). ISBN: 978-92-9210-214-2 doi: 10.2822/309946.
3. International Air Transport Association, Fact sheet: climate change and CORSIA (2018). https://www.iata.org/pressroom/facts_figures/fact_sheets/Documents/fact-sheet-climate-change.pdf. Accessed on November 15, 2021.

WHEC-2022
23rd World Hydrogen Energy Conference
June 26-30, 2022 - Istanbul

#214
GREEN HYDROGEN PRODUCTION FOR FCEV TRUCKS AT A REMOTE OPEN-PIT COPPER MINE

[1*]*Stewart F. Bauserman,* [2]*Johnny Nahui Ortiz,* [3]*Jose Cesar Ramos Saravia,* [1]*John W. Sheffield,* [4]*Matteo J. Mereu*
[1] Purdue University, School of Engineering Technology, West Lafayette, IN, U.S.A.
[2] Universidad Nacional de Ingeniería, Facultad de Ingeniería Ambiental, Lima, Peru
[3] Universidad de Ingeniería y Tecnología, Ingeniería de la Energía y Ingeniería Mecánica, Lima, Peru
[4] Purdue University, Energy Engineering Technology, West Lafayette, IN, U.S.A.

*Corresponding author e-mail: stew@purdue.edu

ABSTRACT

This paper presents the results of an international collaboration on the analysis of the production of green hydrogen for a fleet of fuel cell electric vehicle mining trucks for use in a remote open-pit copper mine in Peru. For this research, HOMER Pro® microgrid software was used to simulate, optimize, and analyze the renewable energy system integration into the operation of fueling a fleet of 300-tonne mining trucks for the copper mine based on a 30-year life of the remote mine. The optimization results shows that the electrolyzer provided a mean output of 29.4 kg/h per truck for an operational schedule of 8,097 h/y with 46.4 kWh/kg specific energy. The system architecture of the green hydrogen production microgrid includes wind turbines, AC-DC bidirectional power converters, a battery energy storage system, electrolyzers, and compressed hydrogen storage tanks. The two loads were the electric load for the balance of plant and the hydrogen load to fuel the fleet of mining trucks. To meet the two loads, the optimized microgrid powered one 1,505 kW electrolyzer having a specific energy of 46.4 kWh/kg resulting in a mean hydrogen output of 29.4 kg/h to fuel one 300-tonne mining truck.

Keywords: Green Hydrogen, Microgrid, FCEV, Mining Trucks, GW Scale

INTRODUCTION

This paper presents the results of an international collaboration between Purdue University, the University of Engineering and Technology (UTEC), and the National University of Engineering (UNI) in Lima, Peru. The focus of this international research collaboration was on the production of green hydrogen to fuel cell electric vehicle (FCEV) powertrain for open-pit mining trucks [1] for use in a remote copper mine in Peru. The mining industry accounts for 60% of Peru's exports and Peru is the world's 2nd largest producer of copper, silver, and zinc. New to mining in Peru, Anglo American has the potential to help Peru transition to a hydrogen economy. To help the energy transformation needed by the mining industry in Peru, the authors are developing new workshops using Game Based Learning (GBL) to navigate the complexities of the emerging clean energy systems and understand the full potential of green hydrogen as a key enabler for the energy system transition to a sustainable future.

Recently the Hydrogen Council, a global CEO-led initiative of 120+ leading companies with a united vision and long-term ambition for hydrogen to foster the clean energy transition for a better and more resilient future, published their report *Hydrogen Insights* [2]. This report presented a Total Cost of Ownership (TCO) analysis of a 300-tonne open-pit mining truck used in operations in Chile with 6,200 operational hours per year and a lifetime of 12 years, based on the truck power requirements of approximately 2,000 kW comparing conventional diesel fueled engines, hydrogen fueled engines with mechanical drive and hydrogen fuel cell electric-drive powertrains. The *Hydrogen Insights* report showed that the FCEV mining truck has a TCO breakeven with both other powertrains before 2030. Hence, mining companies are transforming. For example, Anglo American, plans to replace their entire global fleet of 400 diesel-engine, mechanical-drive mining haul trucks with hydrogen fuel cell electric-drive mining trucks over a ten-year period as part of their ambition of achieving carbon neutrality by 2040.

For this paper, HOMER (Hybrid Optimization Model for Multiple Energy Resources) Pro® microgrid software was used to simulate, optimize, and analyze the renewable energy system integration into the operation of the hydrogen fueling of a fleet of 300-tonne mining trucks for the copper mine based on a 30-year life of the remote mine [3-4]. HOMER Pro® provides insight into the complexities and trade-offs of designing cost-effective, reliable microgrids. The renewable electricity for this copper mine is provided from the Punta Lomitas wind farm. The system architecture of the green hydrogen production microgrid modeled by HOMER Pro® includes land-based wind turbines [5-7], advanced AC-DC bidirectional power converters, advanced battery energy storage system, proton exchange membrane (PEM) electrolyzer, and compressed hydrogen storage tanks. The two loads were the electric load for the balance of the plant and the hydrogen load to fuel the fleet of FCEV mining trucks. To meet the two loads, the optimized microgrid powered one 1,505 kW electrolyzer having a specific energy of 46.4 kWh/kg resulting in a mean

hydrogen output of 29.4 kg/h to fuel one 300-tonne FCEV mining truck. Figure 1 illustrates a HOMER Pro® microgrid schematic diagram of the green hydrogen production for the fleet of FCEV mining trucks at the remote copper mine in Peru.

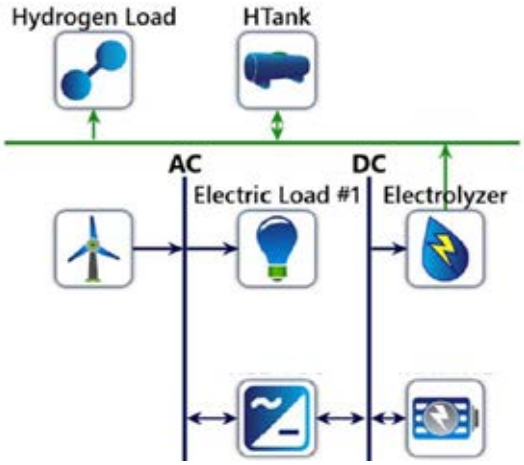


Fig. 1. HOMER Pro® microgrid schematic diagram of green hydrogen production for FCEV mining trucks

ANALYSIS

The HOMER Pro® microgrid software was used to analyze the feasibility of green hydrogen production using wind energy in Peru to support the fueling of a fleet of FCEV electric-drive mining trucks at a large, new, remote, copper mine. The results of this optimization analysis show the selected sizes of the microgrid components in Table 1.

Table 1. Microgrid Components

Component	Size	Unit
Li-Ion batteries	4.0	MWh
Punta Lomitas wind farm	260	MW
AC-DC converter	2,175	kW
Electrolyzer	1,505	kW
Hydrogen tanks	3,900	kg

Table 2 provides the performance parameters of the set of 1.5 MW PEM electrolyzers. Hence, each electrolyzer is dedicated to fuel a single 300-tonne mining truck. These electrolyzers have a specific power of 46.4 kWh per kilogram of hydrogen. The annual green hydrogen production per electrolyzer is over 250 tonne per year with a mean hourly production rate of 29.4 kg based on a 90.5% capacity factor.

Table 2. Electrolyzer Performance Parameters

Electrolyzer	Value	Unit
Mean output	29.4	kg/h
Minimum output	0	kg/h
Maximum output	32.4	kg/h
Total production	257,191	kg/y
Specific energy	46.4	kWh/kg
Rated capacity	1,505	kW
Mean input	1,362	kW
Minimum input	0	kW
Maximum input	1,505	kW
Total input energy	11,935,030	kWh/y
Capacity factor	90.5	%
Hours of operation	8,097	h/y

CONCLUSIONS

The conclusions of this optimization study show the feasibility of a microgrid powering the production of green hydrogen to fuel a fleet of FCEV mining trucks for use in a remote open-pit copper mine in Peru. HOMER Pro® microgrid software was used to simulate, optimize, and analyze the renewable energy system integration into the mining operations by selecting 1.5 MW PEM electrolyzers to fuel the fleet of the 300-tonne mining trucks. These electrolyzers have specific power ratings of 46.4 kWh per kilogram of hydrogen, each producing over 250 tonnes of green hydrogen annually.

ACKNOWLEDGEMENT

The authors would like to acknowledge the financial support from Dr. Michael A Brzezinski, Dean of International Programs at Purdue University; Elizabeth Barajas, Purdue Polytechnic's Director of Globalization; and Dr. Julien Noel, Director de Carrera - Ingeniería de la Energía e Ingeniería Mecaníca y Director de Operaciones y Servicios Académicos, Universidad de Ingeniería y Tecnología.

REFERENCES

1. Masrur M. 2021. Hybrid and electric vehicle (HEV/EV) technologies for off-road applications. Proceedings of the IEEE 109(6), 1077-1093.
2. Hydrogen Council. 2021. Hydrogen Insights: A perspective on hydrogen investment, market development and cost competitiveness, page 30.
3. Kalantari H, Ghoreishi-Madiseh SA and Sasmito AP. 2020. Hybrid renewable hydrogen energy solution for application in remote mines. Energies 13(23), 6365-6386.
4. Igogo T, Awuah-Offei K, Newman A, Lowder T and Engel-Cox J. 2021. Integrating renewable energy into mining operations: Opportunities, challenges, and enabling approaches. Applied Energy 300, 117375-117387.
5. Mansoor M, Stadler M, Auer H and Zellinger M. 2021. Advanced optimal planning for microgrid technologies including hydrogen and mobility at a real microgrid testbed. International Journal of Hydrogen Energy 46(37), 19285-19302.
6. Kumar K, Alam M and Dutta V. 2021. Energy management strategy for integration of fuel cell-electrolyzer technologies in microgrid. International Journal of Hydrogen Energy 46(68), 33738-33755.
7. Ayodele TR, Mosetlhe TC, Yusuff AA and Ntombela M. 2021. Optimal design of wind-powered hydrogen refuelling station for some selected cities of South Africa. International Journal of Hydrogen Energy, 46(49), 24919-24930.

WHEC-2022
23rd World Hydrogen Energy Conference
June 26-30, 2022 - Istanbul

#285
CHIYODA'S APROACH FOR HYDROGEN SUPPLY CHAIN BUSINESS WITH "SPERA HYDROGEN™" SYSTEM

[1] Osamu Ikeda, [2] Milesi Sara, [1] Masashi Nagai, [1,3] Takakazu Morimoto*
[1]Chiyoda Croporation, Hydrogen Business Department, 4-6-2 Minatomirai Nishi-ku, 2208765 Yokohama, Japan
[2] Chiyoda Corporation Netherlands BV, Parkstraat 83, 2514 JG Den Haag, Netherland
[3] Chiyoda Croporation, Frontier Business Devision, 4-6-2 Minatomirai Nishi-ku, 2208765 Yokohama, Japan

*Corresponding author e-mail: ikeda.osamu@chiyodacorp.com

ABSTRACT

Hydrogen is indispensable for decarbonisation through the expansion of renewable energy as its energy carrier. The organic chemical hydride method is key technology of hydrogen carrier to store and transport hydrogen under normal temperature and pressure in the liquid form by incorporating hydrogen atoms into the molecular structure of liquid organic hydrogen carrier (LOHC). Chiyoda started the development of innovative catalyst technology of LOHC method to establish hydrogen supply chain system since 2002, named "SPERA Hydrogen™" and the system has successfully demonstrated the international massive hydrogen supply chain from Brunei Darussalam to Japan in 2020. It is the only system that has completed the international demonstration of the entire value chain from production to utilization, and has moved to the commercialization stage. This system enable to storage and transport hydrogen safely, economically with its proven technology and existing petroleum infrastructure, and also has a high potential for cost reduction towards the future.

Keywords: Hydrogen, Storage, Transportation, LOHC, SPERA

INTRODUCTION

Expanding the use of renewable energy is essential for the decarbonization, and the role of hydrogen, which can be used as a clean energy and feedstock converted from primary energy including renewable energy, is indispensable. In order to expand the use of hydrogen, technologies that can "store" and "transport" hydrogen on a large scale are essential, as similar as fossil fuels such as oil and natural gas. The method of liquid organic hydrogen carrier (LOHC) enable to store and transport hydrogen under normal temperature and pressure in the liquid form by incorporating hydrogen atoms into the molecular structure of LOHC, with safe and lower risk .

Chiyoda started the development of innovative catalyst technology of LOHC method to establish hydrogen supply chain system since 2002, named the system "SPERA Hydrogen™" and the system has successfully demonstrated the international massive hydrogen supply chain from Brunei Darussalam to Japan in 2020[1)]. It is the only system that has completed the international demonstration of the entire value chain from production to utilization and has moved to the commercialization stage. In addition, the organic chemical hydride method, which uses LOHC as a hydrogen carrier, is a chemical method that allows for innovative technological improvements such as simplification of the process to integrate with hydrogen production or its demand applications. Those will lead the system to have a high potential of cost reduction towards the future. In this presentation, we will introduce the outline of this method, key features of "SPERA Hydrogen™" system as well as the efforts toward its commercialization.

SPERA HYDROGEN SYSTEM

Hydrogen is reacted with toluene (TOL) to produce methylcyclohexane (MCH), which is a liquid with hydrogen in its molecule enables that hydrogen to be "stored" and "transported" in a liquid form at normal temperature and pressure. Hydrogen can be generated at the place of use through dehydrogenation reaction. TOL is recycled and used repeatedly. Figure 1 shows scheme of SPERA Hydrogen System.

KEY FEATURES

TOL and MCH are used in household paints and correction pens, non-corrosive, low toxicity, and easy to operate. TOL and MCH are chemically stable substances, energy loss is extremely low even when stored in a large-scale for a long period of time since storage condition is under ambient temperature and pressure. Key features of this technology are,

i. **Safest method** for mass H2 storage and transportation, and easy to handle
ii. **Proven technology** and ready for commercialization
iii. **Largest cost reduction potentials**, including utilization of existing infrastructure and chemical process

Hydrogen can be also stored as national stockpiling. Using common MCH for both in large-scale and small-scale that makes it possible to establish a total and inexpensive hydrogen supply chain network.

Fig.2 shows an example of a comparison for hydrogen supply cost estimation by third party[2]. It shows the overall costs of producing green hydrogen in South America and shipping it to Rotterdam in different forms: liquefied Hydrogen, ammonia and two LOHC's. LOHC-MCH method is estimated around 3 €/kg-H_2.

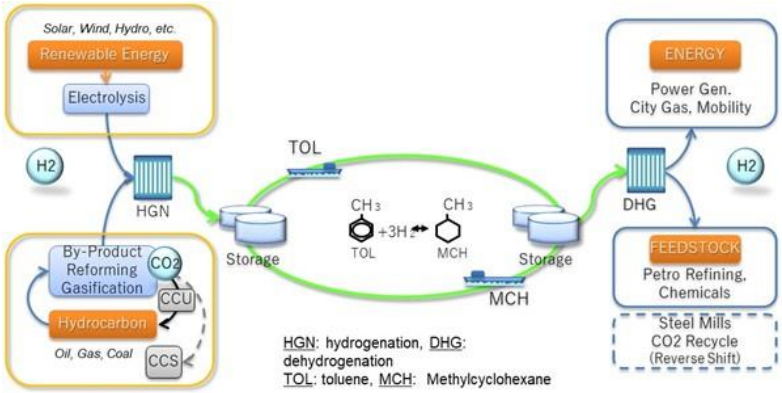


Fig. 1. Scheme of SPERA hydrogen system

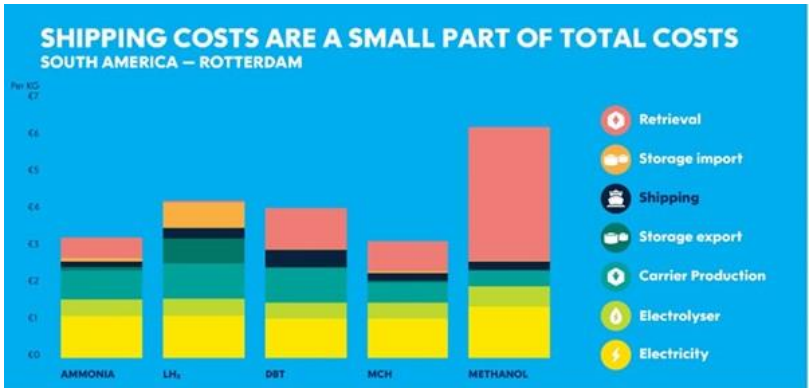


Fig. 2. Example of comparison for H_2 supply cost

COMMERCIALIZATION

Based on the success of global hydrogen supply chain demonstration project between Brunei Darussalam to Japan, SPERA Hydrogen System is in the process toward the commercialization.

Chiyoda joined the "Hydrogen Utilization Study Group in Chubu" to study the potential for large-scale hydrogen use, and construct a supply chain for stable utilization of hydrogen, in the Chubu region, Japan[3].

In South East Asia, Chiyoda has already started the collaboration with 5 Singapore partners since March 2020, and signed a MOU on 4 Oct. 2021 with Sembcorp industries (Singapore) and Mitsubishi Corporation for strategic partnership to explore the feasibility and implementation of a commercial scale supply chain to deliver decarbonized hydrogen to Singapore[4].
In addition, Chiyoda, Port of Rotterdam (PoR), Koole Terminals, Mitsubishi has signed MOU in July 2021 to conduct a joint study of importing hydrogen on a commercial scale to European market through Rotterdam by a MCH[5].

CONCLUSIONS

SPERA Hydrogen System has shifted to commercialization phase. It is the only system that has completed the international demonstration of the entire value chain from production to utilization at scale. The technology is ready to contribute to deliver hydrogen to the global society, "safely", "environmentally", "economically" and "stably". Chiyoda believe that we are ready to contribute the hydrogen business and economy through this technology globally.

ACKNOWLEDGEMENT

Part of this presentation is based on projects found by the Ministry of Economy, Trade and Industry (METI) and the New Energy and Industrial Technology Development Organization (NEDO). We express words of gratitude to METI and NEDO.

REFERENCES

1. Chiyoda Corporation, HP, https://www.chiyodacorp.com/en/service/spera-hydrogen/, Accessed on January 14, 2022
2. Allard Castelein, CEO Port of Rotterdam Authority, Keynote speech at the 2nd World Hydrogen Summit (2020)
3. Chiyoda Corporation, https://www.chiyodacorp.com/media/210409_e.pdf Accessed on January 14, 2022
4. Chiyoda Corporation, https://www.chiyodacorp.com/media/211004_e.pdf Accessed on January 14, 2022
5. Chiyoda Corporation, https://www.chiyodacorp.com/media/20210730_E.pdf Accessed on January 14, 2022

WHEC-2022
23rd World Hydrogen Energy Conference
June 26-30, 2022 - Istanbul

#350

OPTIMIZATION OF A PREMIXED CHARGE HYDROGEN ENGINE IN ARGON POWER CYCLE

[1*] *Taisei Chiba,* [2] *Taku Tsujimura,* [1] *Mihiro Kobayashi,* [2] *Yasumasa Suzuki,* [1] *Daisaku Swada,* [1] *Chen Zhili*
[1]Tokai University, Hiratsuka city. 259-1292, Japan
[2] National Institute of Advanced Industrial Science and Technology, Koriyama city. 963-0298, Japan

*Corresponding author e-mail: chiba-taisei@aist.go.jp

ABSTRACT

Hydrogen is attracting attention as a future fuel for automobiles and power generator because it does not emit carbon dioxide (CO_2) during the utilization phase. For example, when hydrogen is adapted as a fuel to a stationary engine generator, it is expected to be able to operate with higher thermal efficiency and cleaner exhaust emissions than those of conventional engines. Further improvement in efficiency is expected by adapting argon (Ar) gas with high specific heat ratio, to the working gas of hydrogen engines. The objective of this study is to optimize operating conditions of Ar power cycle of a spark ignition premixed hydrogen engine for achieving high efficiency and high power. In this study, the effect of Ar concentration added to the working gas on hydrogen combustion characteristics and engine performance was investigated with a single-cylinder test engine. The result shows that thermal efficiency was greatly improved as Ar concentration in the working gas was up to 40 mol% in comparison with the air cycle. On the other hand, some technical issues relating abnormal combustion were revealed.

Keywords: Hydrogen Engine, Argon Addition, High Thermal Efficiency

INTRODUCTION

Toward the realization of decarbonized society, hydrogen is attracting attention as the next generation of energy. Hydrogen has high expectations as a fuel for automobiles and power generator because it does not produce environmental load substances such as CO_2 in combustion process. When hydrogen is adapted as a fuel to a stationary engine generator, the excellent combustion properties of hydrogen are expected to be able to operate with higher thermal efficiency and cleaner exhaust emission than those of conventional engines. Theoretical thermal efficiency of Carnot cycle is defined in $\eta_{th} = 1 - (1/\varepsilon^{\kappa-1})$, so theoretical thermal efficiency improves with increases in the compression ratio ε and specific heat ratio κ. In other words, high thermal efficiency can be expected by using noble gases with a high specific heat ratio for the working gas of the engine. Argon (Ar) is monoatomic molecule so its high specific heat ratio is difficult to degrade even in high temperature combustion ambient. Namely, a significant improvement in thermal efficiency is expected by adapting argon gas as a part of the working gas. However, in previous studies of spark ignition hydrogen engines with Ar as the working gas, operation was limited by abnormal combustion, stable hydrogen combustion and improving thermal efficiency are supposed to be difficult [(1)].

This study aims to find the optimal operating conditions when adding Ar to a spark ignition premixed hydrogen engine for high efficiency and high power. In this study, the effect of Ar concentration on hydrogen combustion characteristics and engine performance is investigated with a single-cylinder test engine.

MATERIALS AND METHODS

A schematic diagram of the single-cylinder test engine apparatus used in this study is shown in Figure 1. The engine specifications and hydrogen supply conditions are shown in Table 1. The engine was modified from the base engine in terms of compression ratio, piston geometry and valve train, etc. A hydraulically actuated valve train system was installed to reproduce several kinds of engine system with changing timing of intake and exhaust valves, and the effective compression ratio and expansion ratio can be changed as desired. The engine speed is controlled by an AC electric dynamometer (HORIBA, DYNAS3 LI145), and fresh air is supplied by an electrical compressor. Ar and oxygen (O_2) are supplied from each cylinder to the intake pipe by controlling flow rate of each gas to reproduce desired compositions of the working gas. Hydrogen is supplied from cylinders to about 0.4 MPaG using a pressure reducing valve, and then supplied intermittently via a thermal mass flow meter (Bronkhorst, EL-FLOW) by an injector located near the intake port. Intake and exhaust gas components were measured by two types of gas analyzers (HORIBA: MEXA-ONE, Best Sokki: BOB-2000FT) with a time response speed of about 200 ms In-cylinder pressures of the test engine measured by a piezoelectric pressure transducer was recorded during 100 cycles for each condition by the combustion analyzer.

Table 1. Experiment condition

Engine Type		-	Water-cooled four-stroke
No. of cylinder		-	1
No. of valve		-	2
Bore×Stroke		mm	115×125
Displacement		cm^3	1298
Geometric compression ratio		-	12.9
Engine speed		rpm	1000
Intake gas boosting		-	Supercharger
Spark plug location		-	Center
H_2 injector	Gas injector		Nikki CNG injector
	Inj.pressure	MPaG	0.4
	Inj.timing	deg.CAaTDC	-360 ～ -270

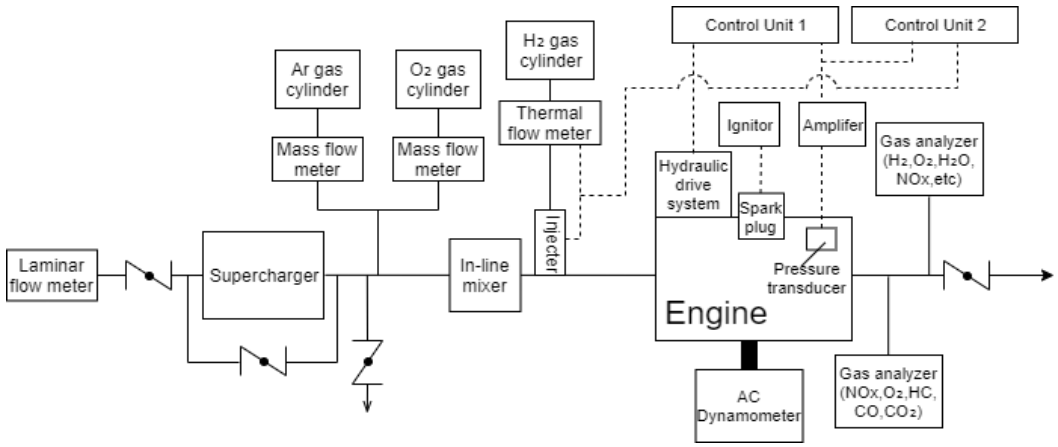


Fig. 1. Experimental apparatus for the single-cylinder engine test with hydrogen, Ar, and oxygen supply system

RESULTS AND DISCUSSION

Effect of effective compression ratio on maximum in-cylinder gas temperatures in motored cycles

Maximum in-cylinder gas temperatures in motored cycles is supposed to rise with increasing geometric compression ratio and Ar concentration. While an increase in maximum in-cylinder gas temperature due to Ar addition induces premature ignition, a higher geometric compression ratio is better from the viewpoint of thermal efficiency. Therefore, in order to improve thermal efficiency while reducing the risk of premature ignition due to the addition of Ar, it is considered to be effective to set the geometric compression ratio high and to vary the effective compression ratio depending on the timing of intake valve closing to suppress in-cylinder gas temperature.

Since there is a need to reduce in-cylinder temperature, the effect of changes in the intake valve closed timing (IVC), or effective compression ratio on the in-cylinder gas temperature was investigated in motoring experiments. In the experiments, the geometric compression ratio was set to 13 to keep high thermal efficiency. Figure 2 shows the relationship among the experimental conditions, IVC, effective compression ratio, and maximum in-cylinder gas temperature. Since the intake air flow rate varies with the change of IVC, it was kept by using the electrical compressor. As seen in Figue2, maximum in-cylinder gas temperature was reduced by advancing or delaying IVC from about IVC: -120deg.CAaTDC.

In addition, motoring experiments were conducted by changing Ar concentration in the working gas to investigate the effect of Ar addition on maximum in-cylinder gas temperature. The top-right corner of the dotted square is the maximum in-cylinder gas temperature of the engine in the air cycle (without Ar addition), which is about 750 K. The addition of Ar up to 60 mol.% increases maximum in-cylinder gas temperature by about 200 K compared to the air cycle. Therefore, it is necessity to optimize the in-cylinder temperature by changing the effective compression ratio in the actual test. Maximum in-cylinder gas temperature was lowered by decreasing the effective compression ratio. In

order to reduce the in-cylinder temperatures effectively, the IVC was set at an advanced crank angle from the bottom dead center of the intake stroke, and the single-cylinder engine experiments were conducted as described below.

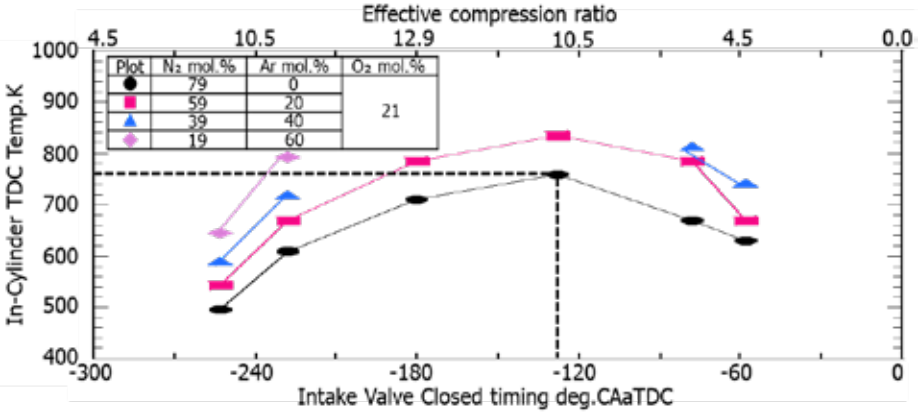


Fig. 2. Effect of IVC timing or effective compression ratio and Ar concentration on in-cylinder gas temperature

Effect of Ar concentration in the working gas

In this section, the effects of Ar concentration in the working gas on engine performance and combustion behavior are investigated. Fired engine experiments were carried out at constant hydrogen frow rate and IVC: -128 and -228 deg.CAaTDC with spark ignition timing as a variable. Figure 3 shows the experimental conditions and results. At IVC: -128 deg.CAaTDC, even with Ar: 20 mol.%, abnormal combustion with an intense heat release was observed with spark ignition timing at -20 deg.CAaTDC. It is supposed that the combustion temperature increases with an increase in Ar concentration. Moreover, the addition of Ar increases the laminar burning velocity with an increase in combustion temperature, that is thought to have led to shorted combustion period (CA10-90). The temperature of the unburned mixture including Ar increases more easily than that without Ar (the air cycle) duo to that the specific heat of Ar is small. It can be assumed that adiabatically compressed unburned gas during the combustion process could reach spontaneous ignition temperature of hydrogen during combustion process. Therefore, when IVC was at -128 deg.CAaTDC where the maximum in-cylinder gas was high as shown in Figure 2, the spark ignition timing could not be advanced due to frequent abnormal combustion. As a result, the amount of Ar added to the working gas was limited by the abnormal combustion and the thermal efficiency could not be improved.

Figure 4 shows the in-cylinder pressures and rate of heat release in case of IVC: -228 deg.CAaTDC and spark ignition timing: -36 deg.CAaTDC. In the air cycle, at IVC: -228 deg.CAaTDC, lowering maximum in-cylinder gas temperature slows down the combustion and prolongs the combustion period. On the other hand, as the Ar concentration increases, the rate of heat release became steeply and the combustion phasing was advanced with shortened combustion period. Even when Ar is increased to 40 mol.%, knocking does not occur. As shown in Figure 3, improvement of about 18 % in thermal efficiency was obtained in case of Ar: 40 mol.% compared with the air cycle. Although there was concern that the increase in Ar concentration would lead to an increase in NOx due to the rise in combustion temperature, there was almost no increase in NOx in any of the Ar concentration conditions with in the experiments.

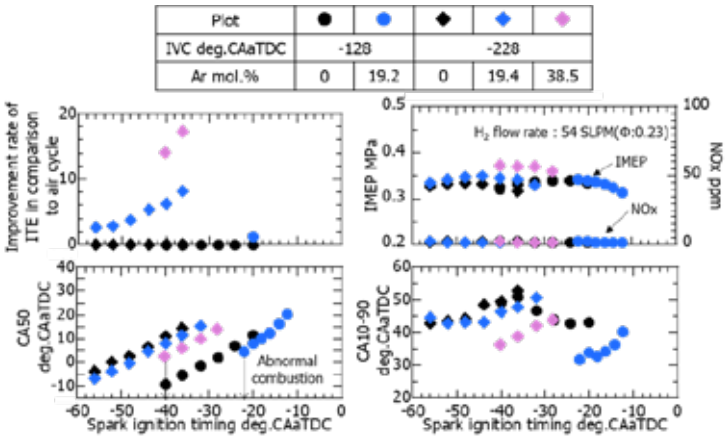


Fig. 3. Effects of IVC timings and Ar concentrations on engine performance

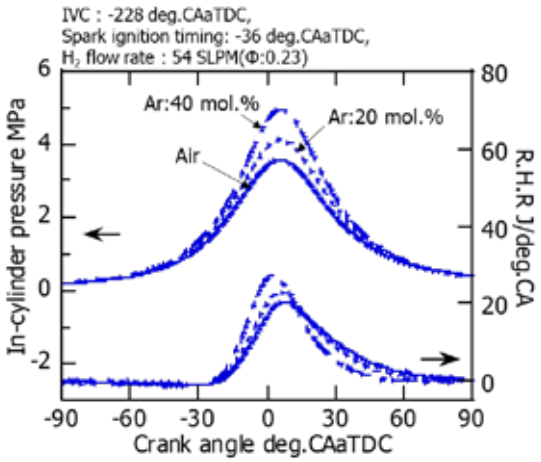


Fig. 4. In-cylinder pressures and rates of heat release with changing Ar concentrations

CONCLUSIONS

The effect of Ar addition to the working gas on the combustion characteristics of a spark ignited premixed hydrogen engine was investigated by the single-cylinder engine experiments.

- Increasing Ar concentration improves thermal efficiency of the test engine. On the other hand, the specific heat capacity becomes smaller, and the combustion temperature and burning velocity become higher. Then the rise of rate of heat release becomes steeper and the operative range is limited by knocking.
- Lowering maximum in-cylinder gas temperature with advanced IVC timing makes it possible to operate the engine system without premature ignition, and higher Ar concentration in the working gas could improve thermal efficiency more.

REFERENCES

1. Shinichi MITANI et al., A Study of Rising Thermal Efficiency using an Argon Circulated Hydrogen Engine, Transactions of Society of Automotive Engineers of Japan Vol.39 No.2 (2008)

WHEC-2022
23rd World Hydrogen Energy Conference
June 26-30, 2022 - Istanbul

#365

MODIFIED WSGG GAS RADIATION MODEL FOR ANY MIXTURE OF H_2/CH_4 FUEL FOR HIGH-TEMPERATURE INDUSTRIAL FURNACES

[1*] *Benjamin Le Creurer,* [1] *Fouad Ammouri*
[1]Air Liquide – Innovation Campus Paris, 1 Chemin de la Portes des Loges 78350, Les Loges-en-Josas, France

*Corresponding author e-mail: benjamin.le-creurer@airliquide.com

ABSTRACT

Energy transition will push more and more the use of hydrogen for mobility and to heat industrial furnaces with other fuels where radiation has the major contribution. Consequently, the need for adequate radiation model parameters to account for gas radiation from mixtures of hydrogen/methane combustion in high-temperature furnaces is of major importance. The proposed model is a modified weighted sum of grey gases (WSGG). The model validation is presented for a 1D gas column and also on a 2D domain with walls.

Keywords: Industrial Furnaces, H_2/CH_4 Mixture, Thermal Gas Radiation, Numerical Modelling

INTRODUCTION

In the coming years the role of hydrogen will become increasingly important not only for mobility but also for energy storage and for industrial applications. Hydrogen will be more used to heat industrial furnaces with a mixture of natural gas or other fuels. It should be noted that thermal radiation is the major contributor for total heat flux on the cold load for the different high-temperature industrial furnaces (steam methane reformer, glass furnaces, reheating steel furnaces...). Moreover, with the presence of combustion gases (*e.g.* H_2O, CO_2) one has to take into account these hot gases as a radiative participative medium. In order to do numerical simulations inside these furnaces, gas and wall radiation heat transfer should be calculated with enough precision and affordable computing time. For this purpose, the WSGG model is often used to carry out the radiative part of the heat transfer modeling inside the different industrial furnaces. For most applications [1][2], the WSGG absorption coefficients are constants with regard to the gas temperature.

The objective of this paper is to explain the method used for the determination of WSGG model parameters applied for hydrogen mixture combustion, which are all dependent of gas temperature. When dealing with high temperatures, radiative heat transfer has to be taken into account through the calculation of the radiative power in the energy balance equation, for participating media. This power mainly depends on the spectral absorption coefficient κ_ν ($atm^{-1}.m^{-1}$), the spectral directional intensity I'_ν ($W.m^{-2}.sr^{-1}$) and the spectral intensity for a black body I^0_ν ($W.m^{-2}.sr^{-1}$).

Solving the Radiative Transfer Equation (RTE) necessitates two integrations; a spatial one and a spectral one. This makes it very difficult and time consuming to solve, especially for real gases. Several spatial resolution methods are available (Monté-Carlo, zonal, Discrete-ordinates, ray tracing...). This part of the resolution is not the concern of this paper (in this work, the discrete transfer radiative (DTR) method [3] is used). Concerning spectral integration, mainly two kinds of models exist to compute radiative heat transfer for combustion matters; Spectral models and global ones. Spectral models are more accurate than global ones, since they take into account spectral dependency of the radiative parameters, but these models are also CPU time expensive, and thus hardly compatible with industrial requirements. The most accurate of these methods (Line-by-Line [1]) is used mainly by academics for creating benchmarks of reference results. The principal limitation of this method is its CPU cost since it computes absorption/emission coefficient every 10^{-2} cm^{-1}, leading to about 10^6 resolution of the RTE. Other spectral methods exist (*e.g.* Statistical-Narrow-Band SNB [1], correlated-K [4]), keeping the spectral dependency but for a wider discretization of the total spectrum ($\Delta\nu$=25 cm^{-1} or bigger), making them good candidates for almost affordable spectral models (about 360 RTE resolutions for the full spectrum). However, they are still highly computationally expensive for industrial furnaces. Despite a lower accuracy, global models (*e.g.* WSGG [2], spectral-line-based WSGG (SLW-WSGG) [5],[6]) have a reasonable time response, which makes them good candidates for multi physics approaches like the one treated for industrial processes.

MATERIALS AND METHODS

When dealing with gases as participating media, in industrial context, thermal radiation is often treated through the WSGG model. In this model, the real gas emissivity is expressed as a weighted sum of N_g grey gas emissivities. In

WHEC-2022
23rd World Hydrogen Energy Conference
June 26-30, 2022 - Istanbul

our case, one chooses N_g = 4 gases and a gas temperature dependence of $a_i(T_g)$ the weighted factor for gas i [-], but also for $\kappa_i^{H2O}(T_g)$ and $\kappa_i^{CO2}(T_g)$ the absorption coefficients for gas i [$atm^{-1}.m^{-1}$]. Thus, the total emissivity is written:

$$\varepsilon_g(T_g, x^{H2O}, x^{CO2}, \ell, p) = \sum_{i=1}^{N_g} a_i(T_g)\left[1 - e^{-\left(\kappa_i^{H2O}(T_g)\, x^{H2O} + \kappa_i^{CO2}(T_g)\, x^{CO2}\right)\ell p}\right], \quad (1)$$

with ℓ the gas column length [m], x^{H2O} and x^{CO2} the molar fractions of gas [mol_i/mol_{tot}] respectively for H_2O and CO_2 and p the total pressure [atm]. Moreover, the following conditions have to be respected:

$\sum_{i=1}^{N_g} a_i(T_g) = 1$ and considering the transparent gas $\kappa_4^{H20} = \kappa_4^{CO2} = 0$. (2)

The emissivity parameters (weighted factors and absorption coefficients) are sought as 5th order polynomials as $P(T_g) = \sum_{j=0,5} c_j\, T_g^j$ (where the c_j coefficients are the unknowns). Then, an optimization method is used to determine these c_j coefficients which minimizes the root-mean-square difference of the gas emissivity between the one calculated by the SNB model and the modified WSGG model, using a gradient descent method. Hence, a database for emissivity values is generated for 1D gas columns, thanks to a SNB model, as a function of the input parameters T_g, x^{H2O}, x^{CO2} and ℓ (in our case, p = 1 atm).

The following procedure has been followed:

1. Choose a range for each input parameters, and a sample rate for each range (this freezes the validation range of the final approximation for the emissivity)
2. Calculate the emissivity values ε^{SNB} for each value of the input parameters (according to the sampling rate used). This generates a database for training our model.
3. Use the database to fit the c_j coefficients for the expression of a_i, $\kappa_i^{H2O}(T_g)$ and $\kappa_i^{CO2}(T_g)$ and so for ε^{fit}.

A first validation is made using a gas emissivity database, different from the one used to train the modified WSGG model. The approximated values of emissivity ε^{fit} is compared to the one from the SNB model ε^{SNB}. A second validation uses a numerical code that solves the radiation in a 2D domain with walls, using either a SNB or a WSGG model. This will be presented in the final paper.

RESULTS AND DISCUSSION

A comparison between the fitted gas emissivity and the SNB gas emissivity over the temperature range is given on Fig. 1a, using the training set of data. The detailed comparison, for each temperature will be also presented. A validation has also been carried out, using the testing set of data, and is presented on Fig. 1b. Overall results, shown a good agreement with the SNB model, and an error under 10% on the range of interest (T_g > 1000K). Comparison with 2D modeling should be presented at the conference.

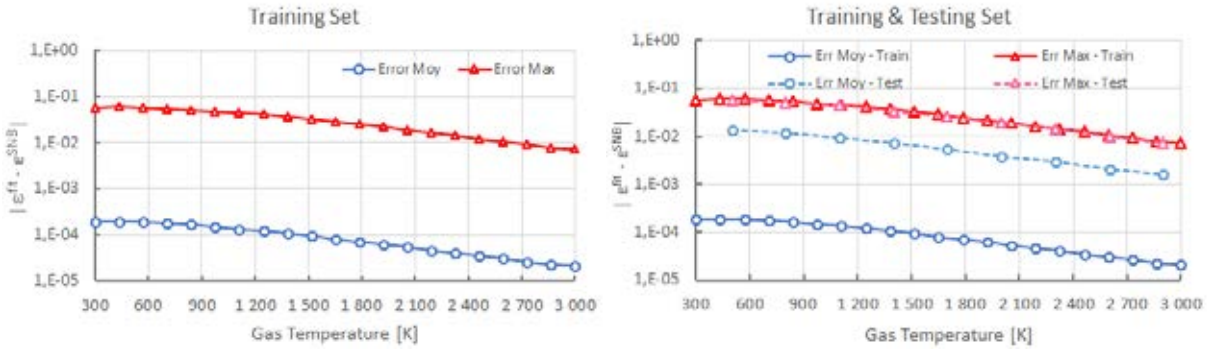


Figure 1: Error between fitted and SNB emissivity, for the training set on the left a), and on testing set on the right b).

CONCLUSIONS

A modified WSGG model is proposed with a set of new coefficients for the combustion of H_2/CH_4 mixtures. The mixing range admitted goes from 0% to 100% for H_2 and 100% to 0% for CH_4. Results show good agreement with the spectral model and a maximum error lower than 10% and an average error under 1%. This modified WSGG model has been implemented in a 2D numerical model. Next step should be to implement this model in a 3D software taking into account radiation, fluid dynamics and combustion for high-temperature industrial furnaces.

REFERENCES

1. Howell JR and Siegel R and Pinar Mengüç M. 2011. Thermal Radiation Heat Transfer, 5th Edition. CRC Press.
2. Hottel HC and Sarofim AF. 1967. Radiative Transfer.New York McGraw-Hill.

3. Lockwood, FC and Shah NG. 1981. A New Radiation Solution Method for Incorporation in General Combustion Prediction Procedures. 18th Symposium (International) on Combustion 1405-1414 (The Combustion Institute).
4. Lacis A and Oinas V. 1991. A description of the correlated k distribution method for modeling non gray gaseous absorption, thermal emission and multiple scattering in vertically inhomogeneous atmospheres. Journal of Geophysical Research 96:9027-9064
5. Denison MK and Webb BW. 1993. A spectral line-based weighted sum-of-gray-gases model for arbitrary RTE solvers. Journal of Heat Transfer 115:1004-1012.
6. Denison MK and Webb BW. 1995. The spectral line-based WSSG. Model in nonisothermal nonhomogeneous media. Journal of Heat Transfer 117:359-365.

WHEC-2022
23rd World Hydrogen Energy Conference
June 26-30, 2022 - Istanbul

#387

HYDROGEN-METHANE MIXTURE STORAGE IN DEPLETED RESERVOIRS: AN OPTION FOR CONVERTING DECOMMISSIONED OFFSHORE PLATFORMS

[1] Anna Chiara Uggenti, [1] Giorgio Rech, [1] Raffaella Gerboni, [1] Andrea Carpignano, [2] Amedeo Aliberti, [3] Andrea Tortora, [2] Gabriele Ballocco*
[1]Politecnico di Torino, Energy Department, Corso Duca degli Abruzzi 24, Torino, Italy
[2] RAMS&E s.r.l., Via Livorno 60, Torino, Italy
[3] Environment Park S.p.A. Via Livorno 60, Torino, Italy

*Corresponding author e-mail: raffaella.gerboni@polito.it

ABSTRACT

With several oil or natural gas offshore reservoirs depleting in different areas of the world, the producing platforms which insist on them are becoming a challenge for companies and governments: on one side they represent infrastructures that are ageing, and that most legislative frameworks impose to remove, while on the other side they represent a valuable opportunity for supporting the energy transition, thanks to their position, technical and structural characteristics.

The paper presents the outcomes of a basic design to reuse a natural gas production platform under decommissioning to inject and extract alternatively and seasonally a mixture of 10% hydrogen and methane in a depleted reservoir. The reuse brings along the idea of removing the equipment that are not useful anymore from the various platforms decks while preserving those major components that can still be fruitfully exploited: typical examples are represented by wellheads and separators. The exploitation of a depleted reservoir is a delicate matter and deep knowledge of the specific features of each reservoir is mandatory to dimension the single components. This paper focuses on the engineering philosophy of this kind of reconversion providing guidelines, included environmental and HSE safeguards to be considered.

Keywords: Reuse, H_2+CH_4 Mixtures, Platform Conversion, Safety, Temporary Storage

INTRODUCTION

The increasing attention devoted to hydrogen/methane mixtures is due to their role as “transition” fuels from a pure fossil infrastructure exploitation to a full hydrogen one. Criticalities linked to the fast approval, installation and exploitation of a full hydrogen network are well known but the 2050 decarbonisation targets cannot prevent from considering hydrogen in the mix. The entry point, thus, is the insertion of hydrogen in existing infrastructures. Percentage is the key as it is under demonstration that low percentages of hydrogen in the mixture do not pose significant challenges to materials and equipment in the network. The role of hydrogen as a storage option for intermittent renewable sources can be further coupled with the role of natural gas as a seasonal or strategic energy storage in underground deposits. The mix of the two represent a win-win solution when stored together in dedicated infrastructures.

At the same time, another energy related challenge is looming with Oil&Gas offshore platforms ageing as their reservoir become depleted. As an example, in Italy, of the existing 138 platforms, only 7 were built after 2010 which means that very soon companies and authorities will have to tackle the issue in a consistent way throughout the seas. It is evident, however, that these infrastructures offer a variety of opportunities also in the energy transition phase we are entering. Their position, the technical and the structural characteristics make them exceptional landmarks for hosting new and strategic energy systems. The Italian Ministerial Decree Feb. 15, 2019 [1] is an example of guideline for managing the transition of an aged platform toward a reused/revamped infrastructure, also considering the removal option when more appropriate. The Italian Ministry of Economic Development has also supported further research on specific options to reuse platforms, which include hosting desalination units supplied via PV electricity from panels installed onboard [2], or the option of hosting injection and extraction facilities for mixtures to be stored in the depleted reservoir the platforms are installed on. The paper presents a summary of concepts and solutions for this second option and an application on a sample platform, called GREEN1, which has the characteristics of an average Mediterranean platform.

METHODOLOGY

Design philosophy

This option foresees the installation on the representative GREEN1 platform of all the equipment necessary to exploit a reservoir to store temporarily a mixture of hydrogen and methane. The considered mixture contains a maximum of

10% of hydrogen, assumption taken after industrial tests have been performed as demo trial with success [3]. The mixture is stored to fulfil the needs during the cold season when the request is at its maximum; complementarily, the injection phase happens during the warmer period. The passage from the injection to the extraction phase is, then, alternated every six months.

To prepare the infrastructure to host the new equipment needed for the injection and extraction of the mixture, a fundamental criterion is the minimisation of interventions, adopting the following rules of thumb:

- The pre-existing equipment is dismissed only in case there is a clear need of more space or in case the sum of the old and new equipment is excessive for the stability of the platform
- Dismissing and removal of old equipment must be carried out in such a way to minimise environmental impacts and the risks connected to the operation
- All submarine interventions (e.g., wells inspections, structural integrity of the piles) must be reduced to a minimum, again to limit damages to the (submarine) ecosystem which has already developed around the structure.

An additional assumption for the reconversion is the conception of an unmanned platform, where the operators only get onboard for maintenance reasons. This choice is preferred under the safety and economic point of view, and it is also beneficial for the reduction of the loads onboard as the living quarter becomes an unnecessary structure. At the same time, a guiding principle is the maximisation of the availability of the system achieved by installing redundant equipment such as pumps and compressors and applying a preventive maintenance philosophy to reduce unplanned interventions. Onboard, only necessary equipment are installed, leaving to the onshore destination those which can fruitfully operate there: for example, electric power supply is achieved via a submarine umbilical avoiding onboard power generation and allowing easier renewable energy harvesting onshore. Also waste fluids are released onshore via an umbilical connection to a treatment plant which allows the reduction of loads onboard, reduces the possibility of accidental releases and eases the recovery of reusable fluids such as water.

Process design

The platform is converted to perform two activities:

- Injection in a reservoir of a hydrogen and methane mixture taken from the national grid. During this phase, the pressure in the reservoir increases as the volume of the gases injected increases and it is subjected to the petrographic and geo-structural characteristics of the reservoir and by the capacity of the onshore (grid connected) compression stations
- Production of a hydrogen and methane mixture taken from the reservoir and injected in the national grid. During this phase, the pressure in the reservoir decreases while the gas volumes are extracted. Again, the way the production takes places is influenced by the reservoir features.

During injection, the mixture from the national grid is pressurised by two centrifugal compressors which operate in parallel working each on 50% of the total flow. No gas treatment is needed in this phase as it is taken directly from the grid where the conditions are optimal. Compressors gas turbines are supplied by a small quantity of gas mixture taken form the total to be injected in the reservoir.

During production, there is no need to compress as the reservoir pressure is already enough for the grid, but the mixture must possess the quality required by the grid. This means the gas extracted from the reservoir has to be processed to remove any impurity. If not already existing on the original platform, some additional equipment must be installed for this purpose: a separator on top of the wellheads which removes most of the production water content, a MEG (Monoethylene Glycol) injection unit which improves the water separation, a demister which removes both water and MEG, a heater which increases the gas temperature needed by the following and last separation unit where a flow of TEG (Triethylene Glycol) absorbs the last drops of water. Water and MEG are shipped via umbilical onshore to be processed, while TEG is regenerated onboard.

CASE STUDY

The concept of reuse of an Oil&Gas platform to inject and extract a mixture of hydrogen and methane in the depleted reservoir has been applied to a sample platform GREEN1 composed of five decks (boat landing, lower, cellar, mezzanine and weather decks) and supported by four legs. The underlying reservoir maximum operating pressure has been assumed equal to 145 bar, based on average values of a family of reservoirs already assessed for reinjection [4,5]. After a first phase when the depleted reservoir must be filled in with the mixture in a regulated way, to maintain structural and fluid-dynamic stability of the reservoir, the extraction and injection volume of the mixture is calculated to be about 135 SMm^3 every six months. During the production phase, both pressure and flow rate

decrease in controlled intervals (e.g., the pressure drops from about 145 bar to about 80 bar). During injection, of course, the pressure increases, while the flow rate decreases as the filling completes.

The main additions to the platform are the couple of compressors on the weather deck, the demister and the heater on the mezzanine deck, dehydration unit and TEG regeneration units on the lower deck (Fig. 1). An estimation of the final variation of weight of the structure, after the removal of old equipment, when necessary, and the installation of the new ones is negative: the post-conversion platform would weight 60t less.

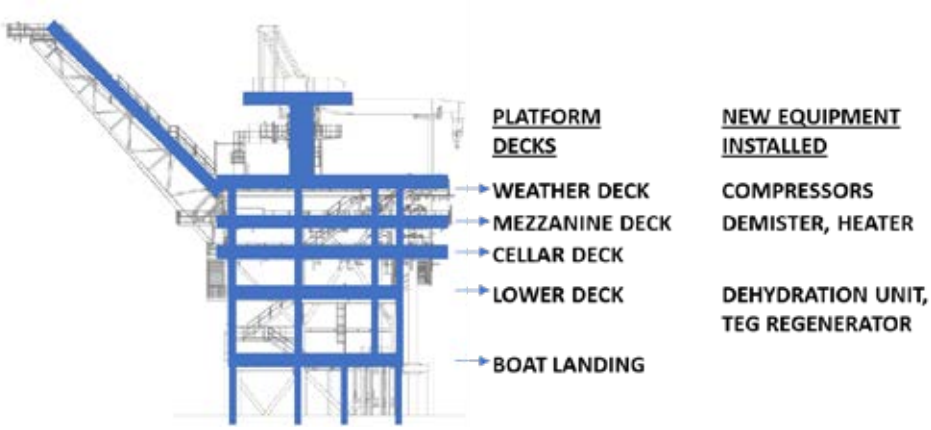


Fig.1 – Structure and interventions in the reconverted gas extraction offshore platform

An environmental assessment has been performed on this converted platform and the main preliminary finding is related to the use of compressors. They are the most important contributors to the emission of CO_2 in the atmosphere (as the heater has a very small capacity), but they operate only during the injection phase and the presence of hydrogen in the fuelling mixture helps abating the relative amount of CO_2. A HAZOP (HAZard and OPerability Analysis) has been performed to identify accidental initiating events and the preliminary outcomes show that there is no additional specific hazard posed by the presence of hydrogen (in comparison with traditional Oil&Gas installations) while recommendations can be implemented in the design phase to take care of the high pressure involved in the production phase so that any of the new equipment dedicated to dehydration may be affected.

CONCLUSIONS

The conversion of an Oil&Gas platform under decommissioning into a structure to store a mixture of hydrogen and methane mixture underground has been addressed. From the exercise performed, some guidelines on the philosophy which should drive this kind of intervention are drawn and can be fruitfully applied in several other similar installations. It is clear that the conversion is technically feasible once the data on the reservoir are known and a suitable platform is available but from the safety and environmental assessment risks can be maintained under control with usual safety systems and procedures and with conventional maintenance routines.

ACKNOWLEDGEMENT

The research presented in this paper has been sponsored by the Italian Ministry of Economic Development's Directorate General for Infrastructures and Energy Systems and Geo-Mining Safety.

REFERENCES

1. D.M. 15 February 2019. "Linee guida nazionali per la dismissione mineraria delle piattaforme per la coltivazione d'idrocarburi in mare e delle infrastrutture connesse". (in Italian)
2. Uggenti AC, Gerboni R, Carpignano A, Ballocco G, Tortora A and Aliberti A. 2022. Definition of a Basic Design for Conversion of an Offshore Fixed Platform on a Depleted Reservoir Into a Sustainable Plant. ASME J. Risk Uncertainty Part B. 8(4): 041101.
3. https://www.snam.it/en/Media/news_events/2020/Snam_hydrogen_blend_doubled_in_Contursi_trial.html. Accessed on February 13, 2022
4. Edison Stoccaggio S.p.A. 2011. Stoccaggio Gas Naturale Palazzo Moroni, Rapporto preliminare di Sicurezza.
5. Edison Stoccaggio S.p.A. 2007. Trasformazione a stoccaggio del giacimento di Bagnolo Mella - Studio di giacimento.

WHEC-2022
23rd World Hydrogen Energy Conference
June 26-30, 2022 - Istanbul

#388

REAL-WORLD ENERGY MEASUREMENTS AND LOCAL HYDROGEN COST AS INPUT PARAMETERS FOR REGIONAL VEHICLE FLEET OPTIMIZATION

[1] Rittmar von Helmolt, [1] Martin Rothbart, [2] Hans Beck, [2] Florian Bindges [3] Loic Lerminiaux*
[1]AVL List GmbH, 8020 Graz, Austria
[2] Strategy Engineers GmbH & Co. KG, 80335 Munich, Germany
[3] GÜRİŞ İNŞAAT & MÜHENDİSLİK A.Ş., 06830 GÖLBAŞI, ANKARA

*Corresponding author e-mail: rittmar.vonhelmolt@avl.com

ABSTRACT

When changing vehicle fleets from Diesel to a zero-emission alternative, the change involves the vehicle but also the fuel supply chain. For an informed decision on choosing vehicles fuelled by either hydrogen or direct electricity, this is a decisive factor which needs to be predicted as accurately as possible for a quite long time in the future, ideally for the lifetime of the intended infrastructure. For supply of green hydrogen, we have considered scenarios that incorporate either a local or domestic production or an import of hydrogen. The hydrogen is assumed to be transported in pressure vessels from the point of generation to the filling station. Also, possible alternative routes via Ammonia or LOHC are indicateded.

We furthermore describe a method for TCO optimization for a regional vehicle fleet, which is based on real-world measurements on the vehicle. Measurements have been done on a bus fleet in daily operation with focus on the thermal energy flow, and monitored for an extended period of 2 years in order to cover a wide range of climate and traffic conditions. These data are the basis for a simulation for an operation of battery electric as well as hydrogen vehicles, and the layout of respective infrastructures.

Keywords: Hydrogen Transport Cost, Hydrogen Bus Fleet, Regional Hydrogen Cost, Vehicle TCO, Fleet Monitoring and Simulation

INTRODUCTION

Vehicle fleets renewal will incorporate an increasing share of zero emission vehicles, primarily battery electric and hydrogen fuel cell. For public services and public procurement of vehicles, this transformation is mandatory, as laid out in the European Clean Vehicles Directive [1].

However, this change is not as easy as it seems since a zero-emission bus can not replace a Diesel bus 1:1. In particular, it is several times more expensive and in addition will require some significant infrastructure investment. Furthermore, in the near future, this will probably not, or at least not fully, be compensated by lower operating expenses.

We are describing our method to approach the main factors that are decisive for comparison of future vehicle fleet, infrastructure and energy scenario.

DEMAND CALCULATION

When changing from a Diesel vehicle to a zero-emission powertrain, there is no simple equation for correlating energy consumption. In a diesel vehicle, as well as in a fuel cell vehicle, energy for heating the passenger compartment comes “for free”, while in an electric vehicle, it has to be provided by the battery. On the other hand, energy for mass acceleration can be partly recuperated during deceleration in an electric vehicle, which is lost in a diesel vehicle.

As an example, we have measured a city bus fleet from Holding Graz over an extended period of time 2019-2021, operated on all lines, all days of week and all seasons, particularly all climate conditions of the year. Measurement focus was drivetrain energy as well as all anxilliaries, and, in particular, the cooling/heating circuits. Data from the measurement have been used for evaluating the energy demands.

Battery Electric Vehicles

Based on the calculated energy demand for propulsion, thermal requirements and anxilliaries, electric bus simulations have been performed and been “deployed” on particular routes of the day and days of the year. Electric energy demand and vehicle range has been determined, as well as potential recharging strategies anticipated.

Hydrogen Fuel Cell Vehicles

Similar considerations have been made for hydrogen fuel cell vehicles. For lack of real bus data, we are working from own assumptions as could be gained from fuel cell heavy duty powertrain integration.

For a first assessment of a vehicle fleet, not all vehicle measurements need to be performed. The data that have been obtained in Graz could be used for any other bus fleet that is operated in similar climate or profile, using a driving profile that is available e. g. from GPS data.

HYDROGEN COST

We did calculations of different scenarios for hydrogen supply to a filling station, including hydrogen production from an electrolyzer, conditioning for transport either by compression, or converting to Ammonia, or by hydrogenation of liquid organic carriers (LOHC), as well as re-conversion at the point-of-use. We however did not consider the cost for the hydrogen station itself (CAPEX and OPEX for the hydrogen filling station).

Local production

In the first scenario for hydrogen supply, we don't consider transportation cost at all. Assumed is the direct consumption of the on-site produced hydrogen, for supply to a hydrogen filling dispenser, underlying a 200 MW electrolyzer capacity. The levelized energy costs for green hydrogen are assumed with 100 €/MWh.

For a local production, with these assumptions, levelized costs of 5,51 €/kg CGH_2 have to be considered. As no conversion, filling or transportation is needed, the risk of dependencies is reduced. As operational costs equal for 94,2% of the levelized costs, fluctuation in energy costs must be observed closely.

Continental production

Beneficial use of reduced costs for green energy at the point of production is levered at the continental production scenario. Levelized energy costs from wind generated energy is assumed with 60 €/MWh, whereas for the re-conversion efforts still 100 €/MWh apply. Transportation is now needed and provided by trucking at a total of 520 km. We have considered transportation as compressed hydrogen gas, as well as conversion and re-conversion from ammonia and LOHC. For all three carriers, all cost categories are considered. Within the conversion CAPEX cost, the levelized initial investment for the LOHCs is included in accordance with the estimated shipping time. In the transportation cost, the return shipment of the de-hydrated LOHCs is considered.

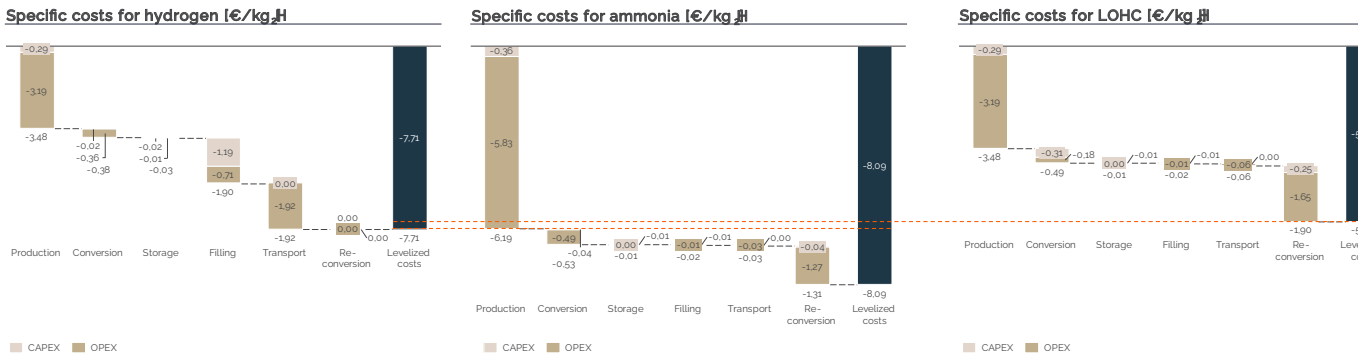


Figure 1. Levelized costs for hydrogen derivates at continental production [€/kg]

Intercontinental production

Further decrease of the levelized costs for energy by levering the intercontinental production scenario with 40 €/MWh, secured by either wind or solar generated electricity. Electricity used for re-conversion is again calculated with 100 €/MWh. Transportation is done by sea vessel port-to-port, covering 4080 km (2676 nm) and trucking, covering 520 km. Again, for all three carriers all cost categories are considered. Similar to the continental scenario, within the conversion CAPEX cost, the levelized initial investment for the unsaturated LOHCs, with the prolonged transportation time, is included. In the transportation cost, the return shipment of the de-hydrated LOHCs is considered, too.

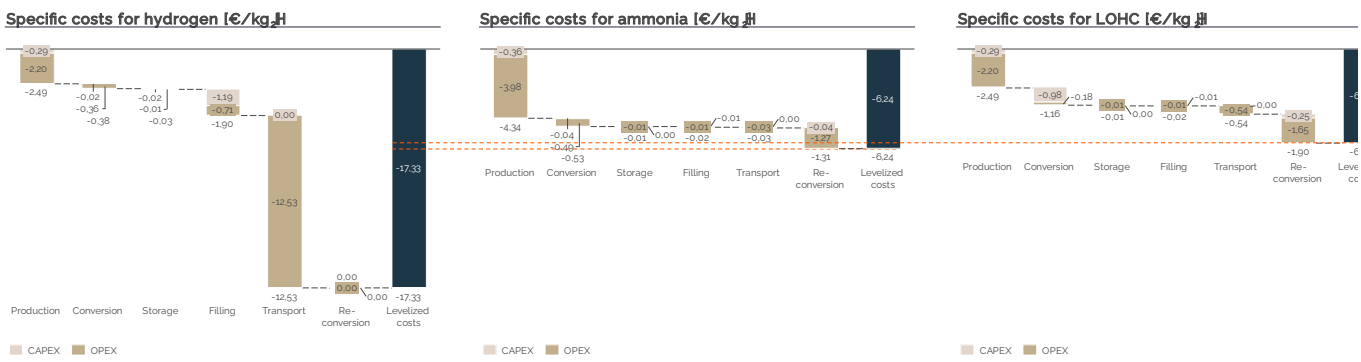


Figure 2. Levelized costs for hydrogen derivates at intercontinental production [€/kg]

RESULTS AND CONCLUSIONS

There is no general right answer for deciding on the right strategy for selecting and fueling a regional fleet of zero emission vehicles. While in general, longer operation times and distances and demanding climate conditions might exclude battery electric vehicles, the cost for hydrogen could be a no-go for fuel cell vehicles in some regions either. Analysis of existing fleet and simulation of alternative zero-emission vehicles can provide a good basis for further considerations on infrastructure. This is the basis for further detail planning on recharging scenarios, which is a complex issue on its own, i. e. combination of opportunity charging and depot charging, intelligent route planning and battery residual value monitoring.

Cheap green electricity could help both electric vehicles as well as local hydrogen production. Hydrogen transport is a major cost factor if local hydrogen production is not possible and no connection to a regional hydrogen pipeline network is available. This might gradually change in future, as scenarios and national strategies for decarbonization include hydrogen as a clean energy carrier for many other applications which are more cost sensitive that transportation.

ACKNOWLEDGEMENT

The authors acknowledge the fruitful discussions and project cooperation with the team around Andreas Solymos at Holding Graz.

REFERENCES

1. Directive 2009/33/EC of the European parliament and of the council of 23 April 2009 on the promotion of clean road transport vehicles in support of low-emission mobility, https://eur-lex.europa.eu/legal-content/EN/TXT/?uri=CELEX%3A02009L0033-20190801.

WHEC-2022
23rd World Hydrogen Energy Conference
June 26-30, 2022 - Istanbul

#442

FRAUNHOFER HYDROGEN LABS: UNIQUE TEST INFRASTRUCTURE FOR THE ENTIRE HYDROGEN VALUE CHAIN

[1,*] Vincent Köhler, M.Sc; [2] Kevin Schalk, M.Sc.; [3]Moritz Kühnel, Dr.-Ing.; [4,*] Johannes Höflinger, Dr. Ing.
[5] Sebastian Schmidt, Dr.-Ing.
[1,4] Fraunhofer Institute for Wind Energy Systems IWES, Hydrogn Lab Görlitz, Am Haupttor 06237 Leuna Germany
[2] Fraunhofer Institute for Wind Energy Systems IWES, Hydrogn Lab Bremerhaven, Am Seedeich 45, 27572 Bremerhaven, Germany
[3] Fraunhofer Institute for Wind Energy Systems IWES, Hydrogn Lab Bremerhaven, Am Haupttor 06237 Leuna Germany
[5]Fraunhofer Institute for Machine Tools and Forming Technology (IWU), Reichenhainer Str. 88, 09126 Chemnitz, Germany

*Corresponding author e-mail: vincent.koehler@iwes.fraunhofer.de; Johannes.hoeflinger@iwes.fraunhofer.de

ABSTRACT

The three Fraunhofer Hydrogen Labs in Bremerhaven, Leuna and Görlitz, aim to provide digitally cross-linked research infrastructure with testing capacities for hydrogen technologies with over 27 MW electrical power supply. The focus of the test fields is to investigate the efficiency and performance of electrolysers powered by renewable energy, building on the combined expertise of the Fraunhofer Institute for Wind and Energy Systems in collaboration with the Institute for Machine Tools and Forming Technology (IWU) and Center for Chemical-Biotechnological Processes (CBP). These integrated research facilities will enable evaluation and appraisal as the key basis for driving the market ramp-up of hydrogen technologies.

All three hydrogen Labs are digitally interconnected and cover the whole green hydrogen process: starting from renewable power generation with on- and offshore wind turbines, the optimization of electrolysis and manufacturing of electrolysers, as well as storage, transport, and electricity generation from green hydrogen. Therefore, the Fraunhofer Hydrogen Labs can offer a worldwide unique spectrum of pilot plants, covering the complete value creation chain of the hydrogen economy.

Keywords: Hydrogen, Electrolyser, Storage, Fuel Cell

INTRODUCTION AND MOTIVATION

The German government committed itself to limit the global warming to 1.5 K and therefore to reduce the carbon dioxide emissions to 20 percent in 2050 compared to the year 1990, with steps of 45% until 2030 and 30% until 2040. In order to fulfill this goal, all sectors, that is energy supply, mobility and transport, industry, housing and agriculture, need to contribute. Electrification is one of the solutions, using renewable hydrogen is another one. For both solutions a great amount of renewable energy is needed. [1, 2, 3]

The joint venture of the three Hydrogen Labs enables, for the first time, a cross-sector demonstration of wind-based energy generation towards the impact and modeling of the interplay of large regional energy generation, storage and consumer units. Plant and component manufacturers will have the opportunity to test new equipment developments on an industrial scale or to evaluate chemical processes and syntheses. Therefore, the Fraunhofer Institute for Wind and Energy Systems makes a significant contribution to the decarbonization of the sectors by mapping the entire value chain of green hydrogen, which can be studied at the Hydrogen Labs on the scale necessary for the success of the energy transition in Germany.

PROJECT OVERLOOK

To achieve a rapid market ramp-up of hydrogen technologies in all sectors and to establish corresponding value chains, research along the entire value chain of hydrogen production is needed. The three megawatt-scale Hydrogen Labs of the Fraunhofer IWES meet this requirement and have clear unique selling points: In Leuna, the electrolysis pilot plant is directly connected to the H_2 pipeline and infrastructure of the regional chemical industry. The Hydrogen Lab Leuna also enables the study of process chains of corresponding syntheses and Power-to-X (PtX) process on an industrial scale. In Görlitz, the focus is on the decarbonization of industrial processes, the consideration of components and systems along the entire value chain - generation, storage, and reconversion to electricity. The Lab also enables the research on production processes for system components. This aims to make automated production of high-performance electrolysers and fuel cells possible. In Bremerhaven, the special feature is the direct connection to an onshore wind turbine and a powerful grid emulator. Thereby the HLB focuses on coupling green electricity with

green hydrogen production. The laboratories are complemented by overarching competencies in the field of modelling and control of decentralized and local energy systems as well as materials science and diagnostics.

SCOPE OF PLANNED WORKS

Hydrogen Lab Bremerhaven (HLB)

Research with hydrogen technology (especially electrolysers) produces a large amount of hydrogen that should not remain unused. The HLB's task is also to adapt the technology to the location and to integrate it into the local economic conditions. This includes, on the one hand, the use of the generated green hydrogen, and on the other hand, the investigation of how the by-products of the processes - oxygen and heat - can be used sensibly. In this way, cross-sectoral solutions are created that can be used as a blueprint and transferred to other regions or other fields of application.

The focus is on combining the individual elements into an overall system. In the long term, all conventional power plants in Germany will be shut down and the energy system will be fundamentally changed. The changeover to a completely renewable energy system poses many challenges. One of them is the necessity of stability of the power grid, although the primary energy sources – wind and sun – cannot be switched on and off at will. Here, HLB is looking at the interaction of wind energy and hydrogen generation, as well as the reliability of the plants, even if a fault occurs in the power grid.

Another research topic at the IWES is offshore wind energy. This includes site assessment. For this purpose, so-called LiDAR buoys are used, which measure the wind conditions at any given offshore location. As part of the project, a fuel cell is being developed for the emergency power supply of the measuring buoy. In the future, it would be worthwhile to be able to produce or use hydrogen directly offshore. Here, however, there are other requirements than on land. In particular, the supply of ultra-pure water is an obstacle. The HLB will serve as a test and validation platform to test and then reliably establish the technology.

Hydropgen Lab Leuna (HLL)

At HLL, industrial-scale electrolysers of any type – polymer electrolyte membrane- (PEM), alkaline- (AEL) or solid oxide electrolyser (SOEC) – can be tested in continuous operation, by simulating dynamic load profiles when operating with electricity from photovoltaics and wind turbines, to investigate performance, cost-effectiveness and long-term behavior in real operation and time-accelerated aging tests.

The green hydrogen generated at HLL can be used on site in Power-to-X processes for the sustainable synthesis of chemical feedstocks, such as methanol. Due to the Integration of the HLL into the Leuna chemical site, model processes for sector coupling can thus be demonstrated directly at the chemical site and tested under realistic conditions, on an industrial scale.

Hydrogen Lab Görlitz (HLG)

The HLG will provide a research and development platform for the power-to-H2-to-power value chain, which is crucial for the energy and mobility sectors as well as industry. For this purpose, a multi-strand chain of electrolysers, pipeline systems, H2 storage and fuel cells with a total electrical capacity of 12.3 MW will be installed. In this chain, individual links can be replaced by test plants and prototypes to evaluate their real operation in the overall context of the hydrogen value chain - without having to rebuild the entire chain for individual development projects.

In addition to the development of production technologies for electrolysers and fuel cells suitable for large-scale production, the focus of research activities lies on the digitization of hydrogen technology. The modeling of individual components and their digital integration into a virtual overall model along defined interfaces allows distributed development of optimized plants, supported by modern database systems. At the same time, sensors for real-time monitoring of both production and operation of electrolysers and fuel cells will be developed to ensure quality and longevity and to detect faults at an early stage and initiate countermeasures by comparison with databases.

PRESENT STATUS AND OUTLOOK

HIB

At the start of operations at the end of 2022, the Hydrogen Lab Bremerhaven (HLB) will be able to produce up to one ton of hydrogen per day with two megawatt-scale electrolysers. By using a nearby wind turbine as a renewable energy source, green hydrogen will be produced. In the area of application technologies, a fuel cell and a hydrogen combined heat and power plant (CHP) will be constructed. In addition, the test field offers the possibility to connect further plants according to a modular principle. This will allow permanent extensions of the infrastructure or temporary test campaigns with industrial customers. In addition to the connection to wind energy, the HLB also has a connection to the virtual power grid of Fraunhofer IWES. Up to now, this realistic grid simulation has been used to test the electrical components of wind turbines for their grid compatibility and reactions to certain fault conditions in the power grid. At the HLB, this procedure can now also be applied to hydrogen technology to assess the performance of electrolysers under realistic 'green' operating conditions.

HLL

The Hydrogen Lab Leuna consists of an outdoor testing area as well as a laboratory and a technical center. The HLL is fully integrated within the chemical industry site Leuna and operates 24/7. The outdoor testing area was completed in May 2021 and comprises 4 separate test pads with 5 MW power supply each, designed for long-term system tests of all types of electrolysers (PEM, SOEC, AEL, AEM) as well as demonstrator systems for the utilization of hydrogen in chemical synthesis (PtX). Completion of the technical center including the laboratory is expected in spring 2022. The building will primarily be used for the performance and assessment of electrolysis system components on the kW scale as part of the H2Mare and H2GIGA projects. Fraunhofer IWES is currently developing a pilot process for producing methanol from CO2 and green hydrogen at the HLL together with "Total-Energies" and Sunfire in the eCO2Met project.

HLG

The Hydrogen Lab Görlitz will be constructed by the end of 2023 and will contain test facilities of industrial scale to generate, process, store and utilize hydrogen. Within the framework of research projects, the hydrogen production by PEM- and AEL-electrolysis as well as the development of an electrolyser design for fully automated mass production is addressed. Furthermore, characterizations on system-, stack-, cell- and component-level regarding performance and aging behavior under real conditions are planned. For hydrogen compression further development of electrochemical compressors towards systems with variably adjustable discharge pressures, exceeding 900 bar, are in progress. Chemical Storage for Hydrogen such as ammonia (NH3), Liquid Organic Hydrogen Carriers (LOHC) and metal hydrides are planned to be tested once the construction phase is finished. Additionally, physical storage of hydrogen for stationary use in high pressure tubular storage systems will be tested within the H2Mare project in Görlitz. Moreover, the test infrastructure in Görlitz is laid out for long-term testing and certification of hydrogen technologies.

REFERENCES

1. https://www.bmu.de/themen/klima-energie/klimaschutz/nationale-klimapolitik. Accessed on January 10, 2020
2. http://www.umweltbundesamt.de/publikationen/treibhausgasneutrales-deutschland-im-jahr-2050-0
3. Smolinka Tom et al., Lehner Franz et al. and Kiemel Steffen et al. 2018. Industrialisierung der Wasserelektrolyse in Deutschland: Chancen und Herausforderungen für nachhaltigen Wasserstoff für Verkehr, Strom und Wärme. Final study report. Berlin.

WHEC-2022
23rd World Hydrogen Energy Conference
June 26-30, 2022 - Istanbul

#1442
USE OF HYDROGEN FOR GREEN STEEL PRODUCTION

[1*] *Pablo Duarte*, [2] *Stefano Maggiolino*, [3] *Jorge Martinez*
[1]Sr. Consultant, Tenova, Castellanza, Italy
[2] President & CEO, Tenova HYL, Monterrey, Mexico
[3] Commercial director, Tenova HYL, Monterrey, Mexico

*Corresponding author e-mail: jorge.martinez@tenova.com

ABSTRACT

Among the various approaches for decarbonization of the steelmaking industry, two main routes should be considered, based on the intensive use of hydrogen (H_2) (CDA) and capture and use of CO_2 (CCU). One consists of the progressive conversion of the BF-BOF facilities to direct reduction-electric arc furnace (DRI-EAF). The second alternative is the production of hot metal (HM) by installing a gas-based direct reduction plant feeding DRI to an open slag bath furnace (DRI-OSBF). Schemes for liquid steel production with reduced or practically nil carbon input by using H_2, its equivalent cost for DRI production and the reduction of CO_2 emissions are analysed.

Keywords: Hydrogen, Direct Reduction, ENERGIRON process, Electric Arc Furnace, Open Slag Bath Furnace.

INTRODUCTION

The ENERGIRON DR process is the most flexible for sustainable production of suitable DRI quality for steel production via EAF or hot metal via OSBF using natural gas (NG) and/or H_2 as energy replacement of coal (Fig. 1).

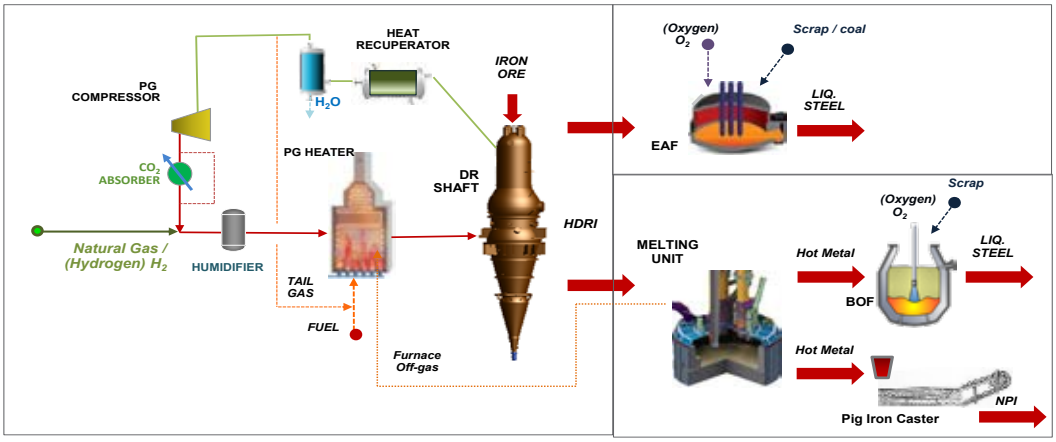


Fig. 1. Routes for Sustainable SteelmakingENERGIRON Process + EAF for Liquid Steel / OSBF for Hot Metal Production

The DR process consist of the reduction of iron oxides for production of direct reduce iron (DRI) using H_2 and CO as reducing gases. In general, the higher the temperature the faster the extent of the reduction process, whether the reducing agent is H_2 or CO. However, the reduction of iron ore with H_2 is more than 4 times faster as compared to CO. The ENERGIRON process is based on high operating temperature; >1,050°C with 100% NG and 950°C with 100% H_2, high operating pressure; 6-8 barA and selective CO_2 removal from the recycling gas. A unique feature of this technology is that when using 100% NG, ~62% of total carbon input to the process is selectively removed for CCU applications.

Although there is long lasting industrial experience of HYL/ENERGIRON plants with intensive use of H_2 for DRI production, typical H_2 concentration in the reducing gases is ~70% vol., using reformed gas as source of reducing gas through steam/NG reformer.

The approach for green steel production is based on the replacement of NG by fossil-free H_2, generated through electrolysers powered by renewable energy sources. In the 1990´s, Tenova HYL carried out extensive campaigns in its pilot plant using ~100% H_2 as reducing gas for production of highly metallised DRI. These tests provided all necessary information to define:

- Process and design parameters, mainly related to optimized flow-temperature correlation.
- DRI quality in terms of metallization and carbon content.

- Optimization of operating pressure, reactor L/D ratio, solids residence time (τ), to consistently achieve the DRI quality, determination of fluidization factor (f) to ensuring proper gas velocities and distribution through the solids bed, among others for the proper gas distribution and design of the scheme for H_2 utilization.

These campaigns at demonstration/pilot plant tests with high-H_2, simply reflect the fact that the ENERGIRON technology is already available for the use of 100% H_2. Main challenges when using 100%H_2 are related to the use of DRI with very low or 0%C in EAF and its energy equivalent cost in terms of electricity.

DRI-EAF SCHEME ANALYSIS

In general, the ENERGIRON ZR scheme provides a significant flexibility as compared to other DR technology. For the HYL/ENERGIRON DR technology, there are some characteristics which makes this process scheme the most suitable for H_2 use:

- The ZR process scheme is inherently suitable for any reducing gas make-up, specifically H_2.
- H_2 make-up directly replaces NG in the process. Same process/plant for any combination of NG/H_2 and reversible operation at any time. For H_2>70% (%energy), CO_2 removal is not required and can be by-passed.

In terms of DRI quality, the process is characterised by:

- Wider flexibility for significant %C in DRI with high concentrations of H_2. Using H_2 in the DRP to up to 35% (%energy) or ~70% vol. as process energy combined with NG, for achieving ~3.3%C in DRI.
- Efficient and safer high operating pressure (6-8 bar A) to better handle H_2-rich gases.

Energy consumption figures for DRI production and %C for different NG/H_2 ratios for the ENERGIRON process are presented in Fig. 2. The expected energy consumption for this process with H_2 is as low as 6.6 GJ/tDRI as H_2 for process plus 1.7 GJ/tDRI of fuel and about 55 kWh/tDRI for the core plant. This exceptionally low electricity consumption is not only because of the H_2 use but also due to the high operation pressure of the ENERGIRON system (≥6 barA @ top gas).

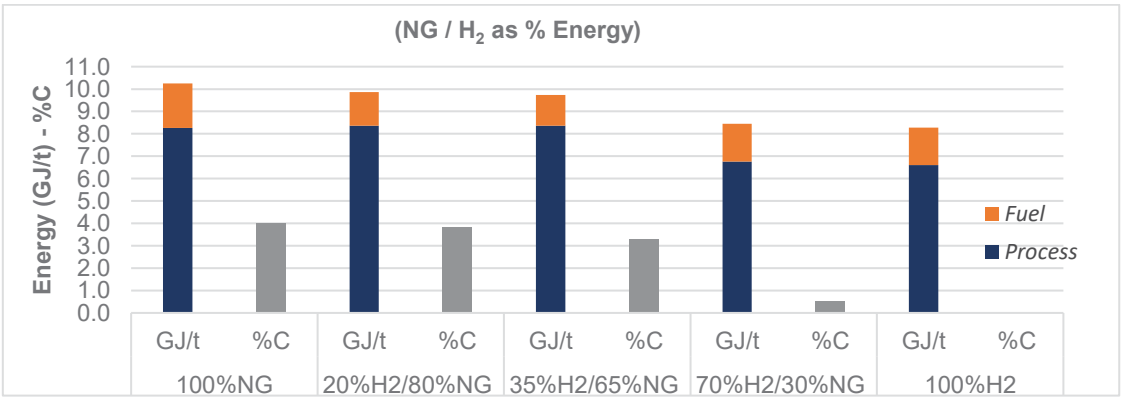


Fig. 2. DR Process schemes for different %NG/H_2

RESULTS AND DISCUSSION

In general, EAF's operations to melt DRI are based on certain DRI characteristics for reducing remaining FeO and promoting foaming slag. The optimum %C in DRI is based on the amount of DRI in the mix feedstock for certain steel quality, specific cost scenario, among others. H_2-based DRI will imply to feed low or 0%C DRI, which will require particular EAF melting practices. Fact: a minimum carbon content in DRI or carbon injected separately is required for EAF steel production operations.

Options:

1) To produce DRI from high Fe content premium iron ores, with the optimized/highest metallization (~96%), thus minimizing the FeO content. Considering the stoichiometric requirements for reduction of remaining FeO and minimum melting needs, the %C in DRI will be ~ 0.8 – 1.2%. This will imply certain NG injection to the DR plant, which is possible for the ENERGIRON process operating with ~90% (vol.) H_2, as already demonstrated in Tenova HYL pilot plant.

2) To produce DRI from selective iron ores chemistry with 100% H_2 and 0%C, which will be fed to an EAF, requiring a minimum carbon injection of 12-15 kg C/t steel, with particular melting operations and slag engineering practices.

While option 1) will result in emissions of about 150 kg CO_2/t steel, option 2) will represent just about 50 kg CO_2/t steel. In terms of overall decarbonisation, Option 2) would be the preferred choice for H_2-based steelmaking. However, longer tap-tap time and higher power consumption may be expected for option 2) as compared to option 1).

On the other hand, for OSBF, DRI with >3.0%C is possible with 70% vol. H_2 with the ENERGIRON technology as differentiating factor vs. other DR technologies. With this DRI carbon content, it is possible to produce hot metal in the OSBF with 4%C to be further processed in existing BOF's in integrated steelmaking facilities.

The analysis of CO_2 emissions for the schemes DRI-EAF/OSBF, as compared to BF-BOF, is presented in Fig. 3. Locations is carbon-neutral electricity, including CCU for CO_2 in DRP, which is selectively removed from the ENERGIRON DRP as inherent characteristic of the process. CO_2 emission factor for iron ore (typically Scope 3) is not included in this analysis; for all others inputs as per Scope 1, 2 and 3 as applicable (CO_2 Emissions Data Collection User Guide, Version 7. WSA). In case iron ore is included as Scope 3, all figures will be ~+10% vs. BF-BOF (100%).

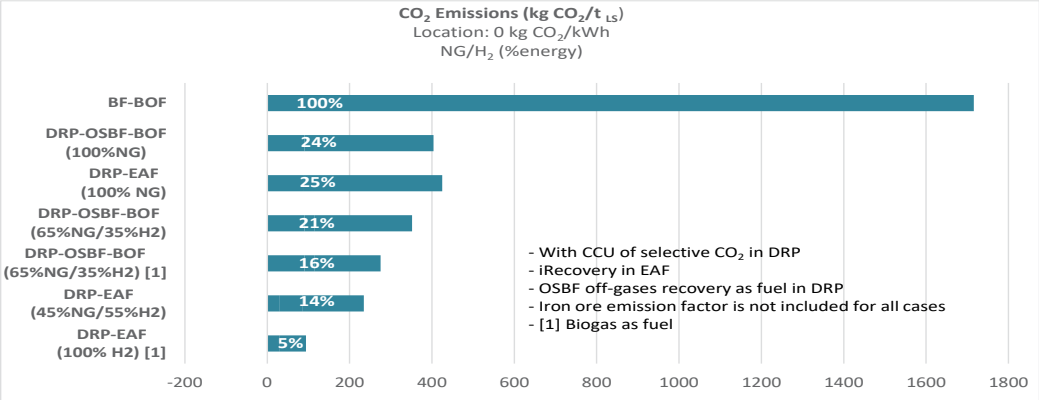


Fig. 3. CO_2 emissions for DRI-EAF/OSBF-BOF schemes

As related to fossil-free H_2 generation and supply, in general, the Alkali Electrolysis (AAE type) provides a cost-effective solution for large scale H_2-production based on an established supply chain. The largest module capacity is of 4,000 Nm^3/h H_2 with a total energy consumption of about 4.6 kWh/Nm^3 H_2. Lower consumption figures are expected with Proton Exchange Membranes (PEM) and High Temperature Electrolysers (HTE) type electrolysers.
As observed in below Fig. 3., H_2 cost, as compared to NG cost scenario, depends on the local electricity cost.
In general, to be competitive vs. NG, electricity cost for H_2-based DRI production shall be < $20/MWh.

CONCLUSIONS

The ENERGIRON DR technology is a very efficient process in terms of energy consumption and scheme simplicity. This scheme is the most flexible and proven technology for sustainable production of suitable DRI quality for steel production via EAF or hot metal with intensive use of H_2, up to 100% for the case of EAF.

Production of hot metal through DRI-OSBF with ~70%H_2 vol. allows the integrated mill steelmaker to optimise investment costs by keeping its downstream facilities in operation while replacing only the BF ironmaking installation.

WHEC-2022
23rd World Hydrogen Energy Conference
June 26-30, 2022 - Istanbul

#1448

GREEN HYDROGEN PRODUCTION USING GEOTHERMAL POWER GENERATION (1) PROJECT IN MOKAI, NEW ZEALAND

[1] *Kenichi Ando,* [1] *Toshihiro Hisaeda,* [1*] *Chiaki Nagai,* [1] *Nobuyoshi Sasaki,* [1] *Shoichi Ichikawa,* [1] *Yukio Mashimo,* [2] *Aya Inagaki*
[1]Obayashi Corporation, Green Energy Division, 2-15-2 Konan, Minato-ku, Tokyo, Japan
[2] Halcyon Power, 54 Tuwharetoa Street, Taupo, New Zealand

*Corresponding author e-mail: nagai.chiaki@obayashi.co.jp

ABSTRACT

For reducing greenhouse gases, the introduction of machines (Mobility and Power plants) that operate on hydrogen as a fuel has been under way. For hydrogen to be produced in a carbon-free way, water electrolysis using renewable energy is one of the methods implemented in the industry. Since continuous power generation is not committed from solar and wind power, stable production of hydrogen can be challenging as well. Therefore, we considered the efforts to stably produce green hydrogen by water electrolysis using geothermal power generation, and in 2021, New Zealand's first megawatt-class hydrogen production plant using geothermal power generation started its operation. This report describes the hydrogen production equipment, its operating conditions, and the utilization of hydrogen produced.

Keywords: Green Hydrogen, Geothermal Power Generation, Supply Chain

INTRODUCTION

For global warming countermeasures, it is important to use machines (Mobility and Power plants) that operate on hydrogen which does not generate any greenhouse gas in the production process. Water electrolysis using renewable energy can be considered and the efforts to stably produce green hydrogen by water electrolysis using geothermal power generation have been studied. As a result, in 2021, a green hydrogen production plant using geothermal power generation was put into operation at two locations in New Zealand and Japan. This report shows New Zealand's effort.

GREEN HYDROGEN PLANT

Fig. 1 shows a view of the hydrogen production plant. The plant is located near the MOKAI geothermal power plant in New Zealand, from which power lines are connected. Fig. 2 shows the system flow diagram of the plant. Using the green power generated at the MOKAI geothermal power plant, the water electrolyzer is operated to produce stable green hydrogen at approximately 22 kg/h. The produced hydrogen can be filled in gas curdles after being compressed to 20 to 45 MPa or 70 MPa for fuel cell vehicles. In addition, the system can grasp the amount of hydrogen produced by the Coriolis type flow meter.



Figure 1. View of the Hydrogen Production Plant

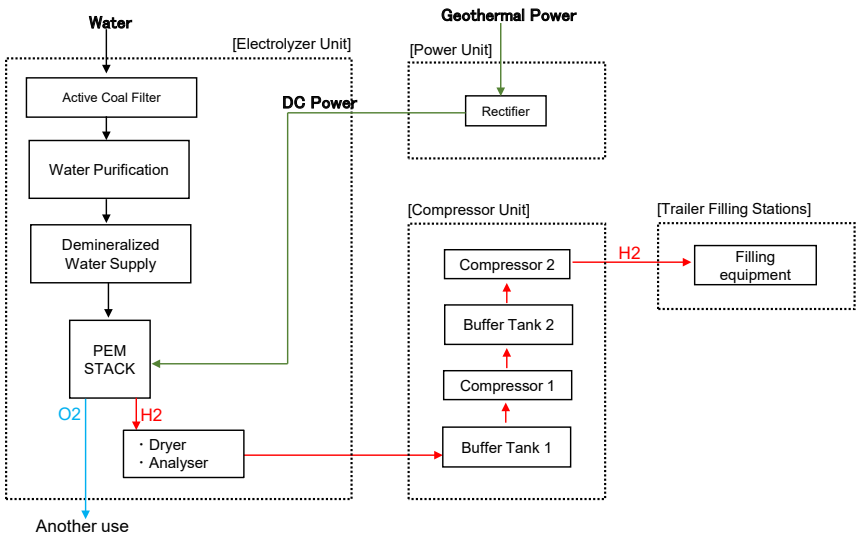


Figure 2. System Flow Diagram

PLANT OPERATION

At the plant shown in Fig. 1, stable green hydrogen production and compression to gas curdles are carried out. The produced hydrogen is supplied to fuel cell vehicles and leveraged for other use. The relations between the amount of hydrogen produced and that of electricity used are being investigated by actual measurement. Based on the measurement results, an economic evaluation of hydrogen production by geothermal power generation is being performed.

HYDROGEN SUPPLY CHAIN

We aim to build an overall hydrogen supply chain from production to supply to the off-takers. In this supply chain, green hydrogen, being stably produced from geothermal power generation, will be steadily supplied to each market shown in Fig. 3. We intend to maximize its economic efficiency by supplying hydrogen to fit the need of each market, by building a system that enables a producer/supplier(s) to grasp the market and transportation status with accuracy.

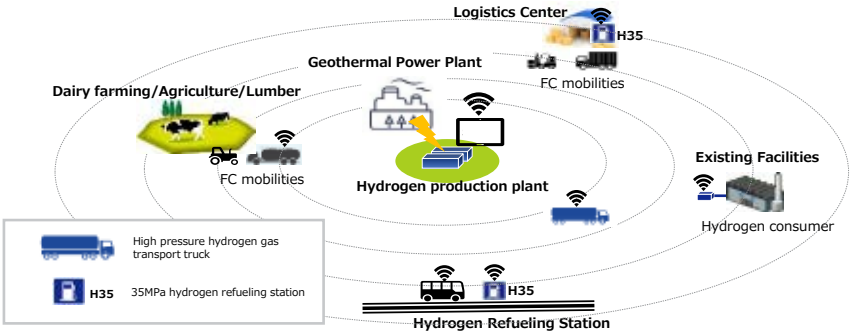


Figure 3. System Diagram

CONCLUSION

Water electrolysis produces green hydrogen using electricity from the Mokai geothermal power plant in New Zealand. This has made it possible to stably supply 200 tonnes of green hydrogen annually. Further, the amount of electric power required for hydrogen production and compression was successfully grasped through this plant operation, and the economic efficiency has been evaluated. We are thriving to build a consistent hydrogen supply chain from manufacturing to supply. This is how Obayashi can contribute to the prevention of global warming by converting geothermal energy into green hydrogen with stable and efficient operation.

WHEC-2022
23rd World Hydrogen Energy Conference
June 26-30, 2022 - Istanbul

#1451

GREEN HYDROGEN PRODUCTION USING GEOTHERMAL POWER GENERATION (2) PROJECT IN OITA, JAPAN

[1*] *Hitoshi Nagatsugu,* [1] *Kiyoshi Shima,* [1]*Tsuyoshi Ito,* [1] *Moriya Kajiki*
[1]Obayashi Corporation, Green Energy Division, 2-15-2 Konan, Minato-ku, Tokyo, Japan

*Corresponding author e-mail: nagatsugu.hitoshi@obayashi.co.jp

ABSTRACT

Japan has the third-largest geothermal resource in the world. Geothermal power generation is one of the renewable energy sources being an excellent energy source with a stable supply. Unfortunately, however, commercialization has been delayed due to several reasons. Because geothermal power generation facilities are in mountainous areas, the capacity of the power grid is often insufficient. In addition, since the development period is rather long, the capacity of the commercial power grid to apply for the feed-in tariff (FIT) gets filled earlier by other renewable energy projects which require a mere short development period. Accordingly, there exists difficulty for geothermal power to be connected to the transmission line. Therefore, we considered promoting the use of green hydrogen and establishing its economic efficiency along with the development of geothermal power generation. This project demonstrated a scheme in which hydrogen produced by geothermal power in Oita Prefecture is transported to various parts of Kyushu by land.

Keywords: Green Hydrogen, Geothermal Power Generation, EMS, Hydrogen Transport System, Supply Chain

INTRODUCTION

Japan's policy positions hydrogen as a key carbon-neutral technology that can be utilized in a wide range of applications, including power generation, industry, and transportation, and thus, the diverse policies and support are being implemented nationwide. The significance of hydrogen production using geothermal power generation with renewable energy is expected to be economical by using the electricity of solar and wind power, which will be introduced in large quantities in the future, and to contribute to stabilizing the grid power. We have challenged various hydrogen demonstrations to create new socially meaningful value in the view of carbon neutrality. This report shows Japan’s first demonstration project of hydrogen production and transportation using geothermal power generation.

FACILITY OVERVIEW

Fig. 1 shows the panoramic view of the plant. The plant is located in a mountainous area in Kokonoe Town, Oita, Japan. Table 1 shows the main facilities. The electrolysis unit operates with 100 kW of generated power from a binary turbine generator and produces 10 Nm3/h of hydrogen. The produced hydrogen is charged in a gas bundle with a pressure of 19.6 MPa and transported to neighboring areas by land.

Fig. 2 shows the system flow diagram of the plant. A mixed vapor blowing out of the 700-meter deep production well is separated into steam and hot water by the steam separator, which passes heat to the binary generator through each heat exchanger. The characteristic of binary generators is that the low potential source such as low temperatures of about 100°C can be applied. This system uses hot water for preheating to improve overall power generation efficiency.

ENERGY MANAGEMENT SYSTEMS(EMS)

The energy management systems (EMS) have the function of continuous operation efficiently without handling the plant systems according to a transportation schedule from the GPS terminal mounted on the hydrogen carriers. The operation pattern is calculated and instructed in Excel as needed so that hydrogen production, transportation and supply can be carried out without wasting time. E Operation modes (shown in Fig.3) are the inexpensive hydrogen production cost mode, prioritizing the Hydrogen greenness and maximizing the hydrogen production amount.

CONCLUSION

The green hydrogen produced at this demonstration plant is transported to nearby hydrogen stations and hydrogen research facilities for effective use as a local energy resource. In addition, by studying various ways to utilize the green hydrogen and geothermal power generated in this demonstration project, we will continue our challenge to make many people including local residents realize the use of renewable energy and the advent of a hydrogen

society. Based on the knowledge from the demonstration experiment, we conduct to establish the economic efficiency in the supply chain from production to supply of green hydrogen.

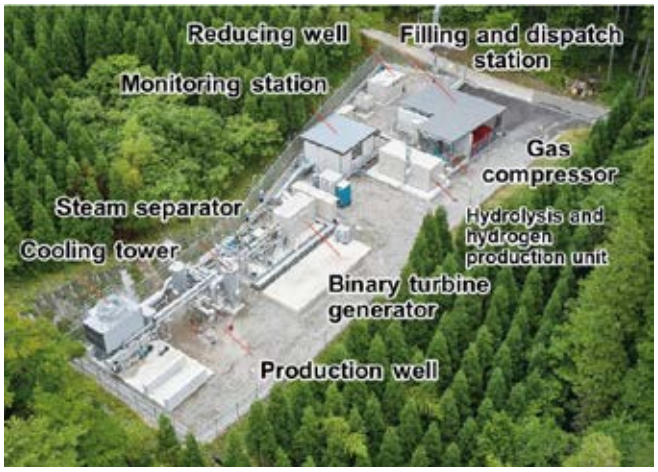


Figure 1. Panoramic View of the Plant

Table 1. Facility

Equipment	Capacity
1 binary turbine generator	Generator terminal: 125 kW Transmission terminal: 100 kW
1 hydrolysis unit	Rate: 10 Nm3/h Hydrogen purity: 99.999%
4 hydrogen bundles	180 Nm3 (19.6 MPa)/bundle

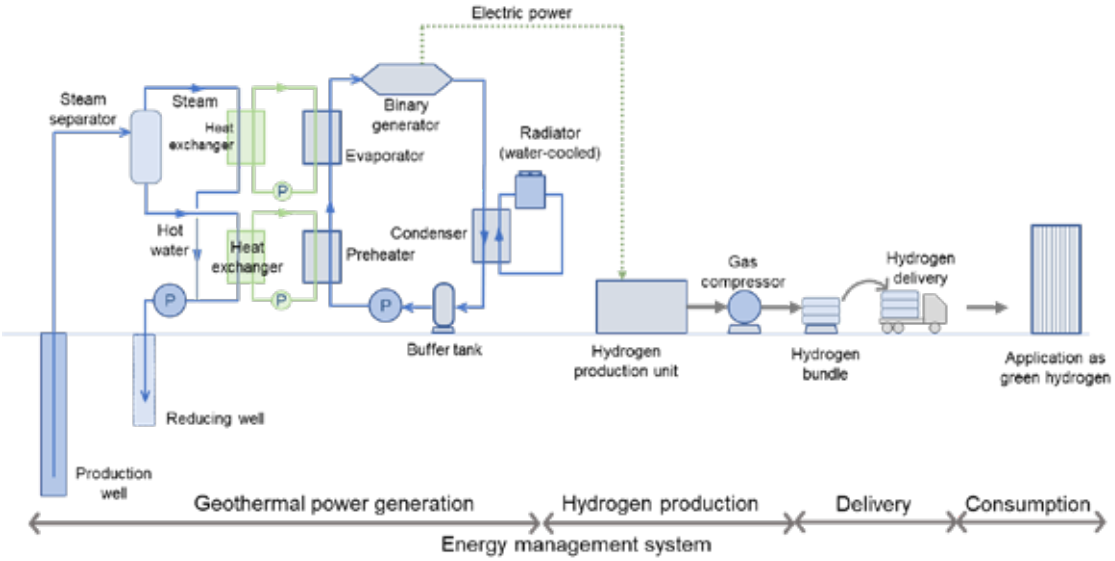


Figure 2. System Flow Diagram

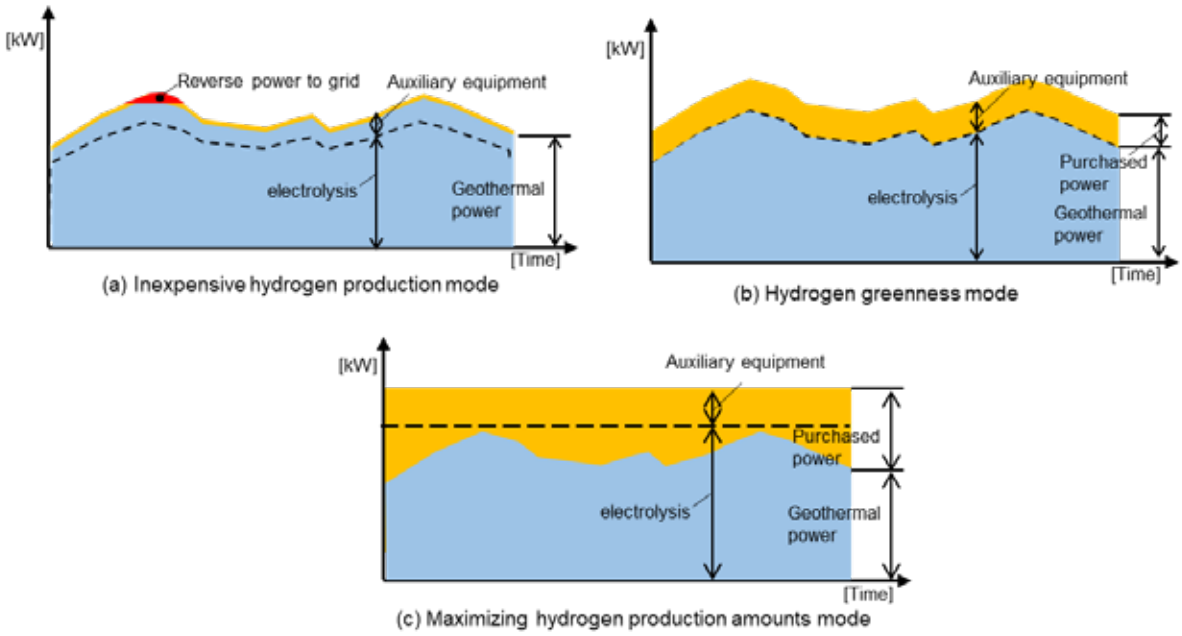


Figure 3. Hydrogen Operation Modes

WHEC-2022
23rd World Hydrogen Energy Conference
June 26-30, 2022 - Istanbul

#1468

ANALYSIS OF HYDROGEN COMBUSTION AS FUEL TO PREHEAT AIR IN POWER GENERATION PLANTS IN MICROMIX INJECTION TECHNOLOGY

[1] Germán Jiménez, [2] Ernesto Cantillo, [2] Ronald Howard, [1] Lesme Corredor, [1] Arturo González-Quiroga, [1*] Victor Pugliese
[1]Universidad del Norte, Mechanical Engineering Department, Barranquilla, Colombia
[2] Gecelca S.A., Barranquilla, Colombia

*Corresponding author e-mail: vpugliese@uninorte.edu.co

ABSTRACT

Hydrogen represents a viable alternative as fuel for future power generation plants. Different uses include but are not limited to partial substitution of coal in boilers, an energy source for preheating air, and fuel for starter-diesel boilers. The objective of power generations plants is to reduce emissions to fulfill national and international commitments before 2050. To speed up the use of hydrogen in established power plant generation systems, it is necessary to evaluate the current combustion technology and its flexibility to handle hydrogen due to the large difference in hydrogen thermophysical properties compared to other fuels such as natural gas or diesel. One of the main components that are calling the attention of researchers is the injection-mixing technology. The micromix hydrogen combustion injector allows a fast and intense mixing of hydrogen and air. As a result, micro flames are developed, and the residence time of the NOx-forming reactants is reduced. This study aims to evaluate the effect of air-fuel ratio on flame structure and stability in a micromix hydrogen combustion injector.

Keywords: Micromix Burner, Hydrogen, Combustion, Flame Temperature

INTRODUCTION

Advances in fuels such as hydrogen or mixtures of gaseous hydrocarbons with hydrogen have attracted attention in the scientific community. For example,Yilmaz investigated the effect of the air-fuel ratio, thermal energy produced, and the fuel composition in the combustion chamber using hydrogen-methane mixtures [1]. It was observed that the increase of hydrogen in the fuel mixture increased the temperature in the combustion chamber, while by increasing the air in excess, the temperature in the combustion chamber decreased. This behavior is crucial because it enables temperature control by manipulating the air mass flow rate.

The composition of the fuel mixture impacts the gases produced by the reaction. Increasing the amount of hydrogen in the fuel mixture reduces CO and CO_2 emissions; however, as the hydrogen share increases, the amount of H_2O and NO_x in the combustion gases increases [2], [3].

In the study presented by An et al. [4], the effect of hydrogen on the flame structure was analyzed in a low-swirl injector (LSI) burner. Depending on the design of the LSI and the operating conditions, the shape of the flame varies. The operating conditions that can be manipulated are volumetric flow, equivalent air-fuel ratio, and fuel composition; however, few studies exist. Carrying out this type of research is of vital importance in the context of the transition to clean, low-carbon energy, where the substitution of hydrogen for fossil fuels is a promising alternative. Furthermore, successful integration of H_2 in LSI-type burners requires a greater understanding of the role of hydrogen in flame stabilization.

The recent concept of Micro-mixing Combustion (MMC) is a combustion technology for hydrogen-enriched gas turbines. The objective is to achieve low NO_x emissions by reducing the size of the area in which the mixture between fuel and air occurs, thus achieving greater uniformity in the process reducing the residence time of combustion gases [5]. In this type of technology, conventional nozzles are replaced by numerous micro-nozzles, which evenly distribute fuel and air within each nozzle for mixing and subsequent injection into the combustion chamber.

Haj Ayed et al. [6], [7], studied the effect of various design parameters and combustion models on flame structure, hydrodynamics, and NO_x emissions in hydrogen combustion using micro-mixers. It had been reported that increasing the energy density in the burners produced more NOx emissions; however, a proper selection of the burner and injector geometry allows emissions to be reduced by approximately 80% through manipulating the shape of the flame and its stabilization. This is accomplished by adjusting the mixing length, the length of the flame, and the length of the shear boundary layer.

MODELING

The study aims to evaluate the potential use of a computational fluid dynamics (CFD) model as a tool for understanding the performance of a micro-mix burner. The CFD open-source software OpenFOAM v9 is used to simulate the combustion process using the reactingFoam solver.

The mass conservation is given by Eq. (1),

$$\frac{\partial \rho}{\partial t} + \nabla \cdot \left(\rho \vec{U}\right) = 0 \quad (1)$$

Eq. (2) gives the momentum balance equation,

$$\frac{\partial (\rho \vec{U})}{\partial t} + \nabla \cdot \left(\rho \vec{U} \times \vec{U}\right) = \nabla \cdot \left[\left((\mu + \mu_T)\left(\nabla \vec{U} + \nabla \vec{U}^T\right)\right) - \frac{2}{3}\nabla \cdot \vec{U}\,\bar{\bar{I}}\right] - \nabla p + \rho \vec{g} \quad (2)$$

where $\rho\,[kg/m^3]$ is the density, $\vec{U}[m/s]$ represent the local velocity components, $\vec{g}[m/s^2]$ the gravitational acceleration, $p[Pa]$ the pressure and $\mu[Pa \cdot s]$ and $\mu_t[Pa \cdot s]$ are respectively the dynamic and turbulence viscosity.

The energy balance equation, using the enthalpy form, is given by Eq. (3),

$$\frac{\partial (\rho h)}{\partial t} + \nabla \cdot \left(\rho h \vec{U}\right) + \frac{\partial (\rho k)}{\partial t} + \nabla \cdot \left(\rho k \vec{U}\right) - \frac{\partial p}{\partial t} = -\nabla \cdot q + \nabla \cdot \left(\tau \vec{U}\right) + \rho r + \rho g \vec{U} \quad (3)$$

where h is the total enthalpy, k is the kinetic energy, q is the heat flux, τ is the mechanical source, and r is the radiation.

The turbulent scale-resolving strategy used in the numerical simulation is Large-Eddy Simulation (LES). LES is based on unifying the phase averaging concept and the turbulent-scale filtering operation into one single process [8]. The eddy or turbulent viscosity μ_t in Eq. (2) is estimated using the Smagorinsky (1963) [9] turbulence model

The computational domain consists of a 2D simplified model of a micromix burner with the air-inlet at the left and the gas mixture outlet at the right. The hydrogen is injected vertically; thus, a proper mix with the air stream is accomplished. The mesh is composed of hexahedral cells with a level 0 size of 0.627mm, see Figure 1.

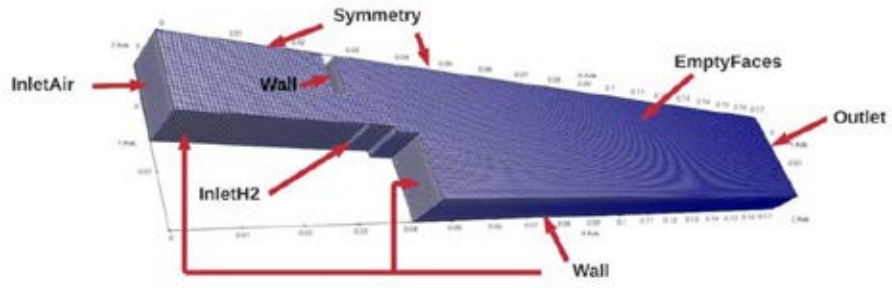


Figure 1 Computational domain. It is composed of hexahedral mesh with a level 0 size of 0.627mm.

During hydrogen combustion, Nitrogen Oxides (NO_x) are present in the emissions produced by the chemical reactions. NOx production is strongly related to high temperatures and the residence time of reactants in the combustion chamber. This study aims to assess the effect of the air and hydrogen velocity on the temperature and residence time of reactants. We use LES turbulence modeling to obtain a reliable velocity field; previous literature has only used Reynolds Average Navier Stokes (RANS) turbulence modeling. Table 1 presents the run cases.

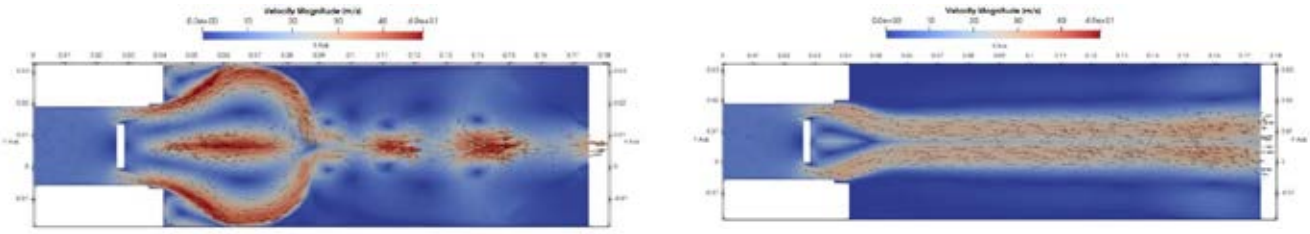
Table 1 Numerical Simulation Cases

Case ID	Air Flow Superficial Velocity [m/s]	Hydrogen Flow Superficial Velocity [m/s]	Air-Fuel Ratio
01	8.1	6.23	285.25
02	4.05	6.23	142.63
03	8.1	3.11	573.27

The computational time required by each case was approximately 24 h for 2 seconds of simulation. The actual CPU time depended on the velocity field because of the restriction imposed by the global Courant number [10]. The time step was adjusted continuously and was in the order of $1e^{-6}\,[s]$.

RESULTS AND DISCUSSION

Case 01 in Table 1 results are presented as follows. Air flows along the positive x-direction from the air inlet located on the left side. There is an obstruction to divert the flow and increase the gas velocity. In this high-speed zone, the hydrogen is injected vertically and is mixed with the air, see Figure 2a. It is essential to mention that this hydrodynamic behavior has not included the reaction between the species.



a) Velocity field at 0.3 seconds.

b) Velocity field at 1.5 seconds.

Figure 2. Velocity field before a), and after b), of ignition.

Once the flow was developed, a spark was implemented to promote the reaction between hydrogen and oxygen. This reaction increases the temperature to 2,300 K, and the gas mix is expanded. As a result, there is a zone of high-speed in the center of the micromix burner, see Figure 2b, and vortices are generated in the low-speed zone. Because of the high-speed zone, a large amount of air has a short residence time in the combustion chamber. In consequence, it is expected a relatively low NO_x generation.

Interaction between vortex and flame is an important mechanism for reducing NO_x formation. Vortex size determines the residence time of particles; therefore, a vortex of smaller diameter reduces NO_x formation. The geometry of the micromix burner used in this study promotes the generation of small vortices. This result explains why NO_x formation is lower than in larger flames. Figure 3 presents the Residence Time Distribution results for each case. The residence time for case 02, which uses a lower air flow rate, has a longer residence time.

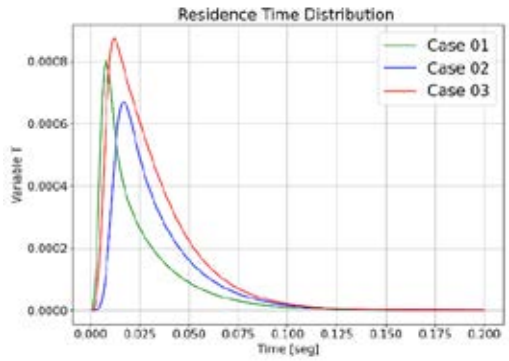


Figure 3 Residence Time Distribution for each simulation case.

CONCLUSIONS

- Increasing the amount of hydrogen increases the maximum temperature in the combustion chamber.
- There is a high-speed zone in the center of the micromix burner, and vortices are generated in the low-speed zone.
- Micromix geometry promotes a short residence time, expecting a reduced amount of NOx.
- It is necessary to evaluate the effect of hydrogen injection location on maximum temperature and residence time.

ACKNOWLEDGEMENTS

The authors gratefully acknowledge Gecelca S.A., Colombia (Contract Identification: UN-OJ-2021-50889) for the financial support.

REFERENCES

1. I. Yilmaz and M. Ilbas, "An experimental study on hydrogen–methane mixtured fuels," *International Communications in Heat and Mass Transfer,* vol. 35, pp. 178-187. DOI:10.1016/j.icheatmasstransfer.2007.06.004, 2008.
2. M. Ilbas and I. Yilmaz, "Experimental analysis of the effects of hydrogen addition on methane combustion," *International Journal of Energy Research,* vol. 36, no. 5, pp. 643-647. DOI:10.1002/er.1822, 2011.
3. I. Yilmaz, M. Tastan, M. Ilbas and C. Tarhan, "Effect of turbulence and radiation models on combustion characteristics in propane–hydrogen diffusion flames," *Energy Conversion and Management,* vol. 72, pp. 179-186. DOI:10.1016/j.enconman.2012.07.031, 2013.

4. Q. An, S. Kheirkhan, J. Bergthorson, S. Yun, J. Hwang, W. J. Lee, M. K. Kim, J. H. Cho, H. S. Kim and P. Vena, "Flame stabilization mechanisms and shape transitions in a 3D printed, hydrogen enriched, methane/air low-swirl burner," *International Journal of Hydrogen Energy,* vol. 46, pp. 14764-14779. DOI:10.1016/j.ijhydene.2021.01.112, 2021.
5. X. Liu, W. Shao, C. Liu, X. Bi, Y. Liu and Y. Xiao, "Numerical study of a high-hydrogen micromix model burner using flamelet-generated manifold," *International Journal of Hydrogen Energy,* vol. 46, pp. 20750-20764. DOI:10.1016/j.ijhydene.2021.03.157, 2021.
A. Haj-Ayed, K. A. Kusterer, H. H. Funke, J. Keinz, C. Striegan and D. E. Bohn, "Experimental and numerical investigations of the dry-low-NOx hydrogen micromix combustion chamber of an industrial gas turbine," *Propulsion and Power Research,* vol. 4, no. 3, pp. 123-131. DOI:10.1016/j.jppr.2015.07.005, 2015.
6. A. Haj-Ayed, K. A. Kusterer, H. H. Funke, J. Keinz and D. E. Bohn, "CFD based exploration of the dry-low-NOx hydrogen micromix combustion technology at increased energy densities," *Propulsion and Power Research,* vol. 6, no. 1, pp. 15-24. DOI:10.1016/j.jppr.2017.01.005, 2017.
7. D. Lakehal, "Status and future developments of Large-Eddy Simulation of turbulent multi-fluid flow (LEIS and LESS)," *International Journal of Multiphase Flow. Vol. 104,* pp. 322-337 DOI:10.1016/j.ijmultiphaseflow.2018.02.018, 2018.
8. J. Smagorinsky, "General circulation experiments with the primitive equations: I. The basic experiment," *Monthly Weather Review. Vol. 91,* pp. 99-163. DOI:10.1175/1520-0493(1963)091<0099:GCEWTP>2.3.CO;2, 1963.
9. R. Courant, K. Friedrichs and H. Lewy, "On the Partial Difference Equations of Mathematical Physics," *IBM Journal of Research and Development. Vol. 11,* pp. 215-234. DOI:10.1147/rd.112.0215, 1967.

WHEC-2022
23rd World Hydrogen Energy Conference
June 26-30, 2022 - Istanbul

#1483

EXTENSION OF LEAN LIMIT USING HYDROGEN ADDITION FOR GASOLINE DIRECT INJECTION ENGINE AND EMISSION REDUCTION

[1] *Jerome Stanley M,* [1] *Leenus Jesu Martin M,* [2*] *Edwin Geo Varuvel*
[1]Green Vehicle Technology Research Centre, Department of Automobile Engineering,
SRM Institute of Science and Technology, Kattankulathur, Tamilnadu, India.
[2*]Department of Mechanical Engineering, Faculty of Engineering and Natural Sciences,
Istinye University, Istanbul, Turkey

*Corresponding author e-mail: vedwingeo@gmail.com

ABSTRACT

The effect of hydrogen induction (0-5 liter per minute) in to the intake manifold of the small bore Gasoline Direct Injection (GDI) Engine is investigated experimentally. The intake manifold is slightly modified to accommodate the hydrogen induction system, where premixed mixture of hydrogen and air is formed in the intake manifold; attaining the excess air ratio of 1.0 to 1.2. With the increment of hydrogen fraction the fuel leaning (Gasoline) is attained and achieving economical fuel consumption rate. The decrement in torque characteristics is compensated with the increase of hydrogen fraction. The hydrogen induction improves the combustion rate and mean effective pressure; shortens the flame propagation, maximize the heat release rate and peak pressure attainment. On the emission side consistent decrease in CO and HC emission; and increase of NO_x emission since the mean gas temperature has increased. The cycle to cycle variation during the lean operating condition at 1.2 shows the combustion stability and effective flame propagation.

Keywords: Hydrogen Induction, Small Bore, Gasoline Direct Injection,

INTRODUCTION

The reputation of Internal Combustion Engine in recent days with fossil fuel as the working fuel has been has been in the downfall as the intense promotion of electric vehicle technology. The transportation sector contributes to 10% of the greenhouse gas (GHG) emission which makes it meager when compared to the energy sector [1]. The 100 years of scientific improvement in the engine technology makes it more mature than other recent alternative technologies. It is clear those alternatives to compete with IC engine do not cover the vast range of application. A lot of times the blame of the IC engine is about the source of the working fuel and not on the IC engine technology. Compared with the conventional fossil fuels hydrogen pose superior characteristic and more suitable for SI engine, where it offers wider flammability range with high diffusivity and low ignition energy. With the safety precaution and advancement towards the storage of hydrogen makes it viable option for alternate for fossil fuels. From the prior arts it is found that adding little quantity of hydrogen with the conventional fuels offers better heat release rate, stable lean mixture formation and improved combustion efficiency. Further it shortens the delay period and offers peak pressure attainment close to top dead center (TDC). The cycle to cycle variation of the engine operating behavior was also reduced with the addition of hydrogen with the gasoline. On the emission side significant reduction in CO and HC emission was noticed; with some penalty on NO_xemission, but particulate emission in the direct injection gasoline has consistent reduction with addition of hydrogen. The implementation of direct fuel injection technology in SI engine is one of the advancement that pushes the limits of SI engine in terms of its thermal efficiency, power performance, emission and lean operating limits [2]. The gasoline direct injection (GDI) engines are getting more robust since the research advancement was towards various combustion modes, alternate fuels, dual spark ignitions, plasma ignition, dilution techniques to treat emission, in-cylinder water injection, fuel injector study, dual fuel injection, combustion diagnosis and furthermore [3]. The Gasoline Direct Injection (GDI) Engine is known for its economical fuel consumption, improved thermal efficiency and better torque characteristic. Application of GDI technology for small bore engine increases the operating limits of the engine for the light commercial vehicles (LCV) and two wheeler segment; where this percentage of vehicles in Indian roads are higher in meeting the daily commutation. The GDI technology and the usage of Hydrogen as the primary/secondary fuel paves the path towards the lean combustion technology, wherein the real problems associated with the driving condition will be addressed [4]. On roads most of the engines are operated only at the partial load conditions, wherein the actual efficiency of the engine is poor due to the poor load characteristic, throttling effect and traffic conditions (start and stop). Leaning the gasoline by operating the engine under lean conditions leads to other technical issues like overheating engine misfire and unstable combustion [5]. Addition of hydrogen for the lean operating condition of GDI engine provides more stable combustion and significant reduction in the cycle to cycle variations will be attained. After accessing the prior literature, the author aims for hydrogen-gasoline lean burn

combustion for small bore GDI engine; with the performance, emission evaluation. The effect of lean burn combustion with addition of hydrogen in gasoline and the lean limit estimation with stable combustion is also investigated.

EXPERIMENTAL APPARATUS AND METHODS

Experimental Apparatus

The engine used for the present investigation is the 390 cm^3 small bore single cylinder air cooled GDI engine. The layout of the experimental setup is shown in Fig. 1. The engine was originally available as the carburetor engine, Honda make; it was later modified to direct injection gasoline engine. The engine head was modified to support the GDI injector, throttle control was replaced with the electronic actuator and to control the spark and injection timing, an Electronic Control Unit (ECU) was fitted. To make the close-loop system CAM and crankshaft position (CKP) sensors were additionally fitted with fuel rail pressure control. The modification details of the engine were not included since it is beyond the scope of the article. The engine details are listed in the Table 1. The spark plug location in the engine is at the sides with hemispherical type combustion chamber. The piston head was not modified, production type flat piston head was maintained throughout the investigation. The spray guided fuel injector was used and it was fitted near the spark plug. The details of the fuel injector and pump are listed in the Table 2. The water cooled eddy current type dynamometer was used to load engine for operating conditions. To measure the inlet air HFM (Hot Film) Type T-MAF Sensor was employed and the gravimetric type fuel flow measuring system was used to calculate the fuel consumption by the engine. Contact type encoder was coupled with the crankshaft, this was utilized to trigger the data acquisition system to record the various sensor data. Piezoelectric pressure transducer with the resolution of 0.1 crank angle degree (CAD) was employed to record the in-cylinder pressure data. Wideband Lambda sensor (from Bosch) LSU 4.9 was used to monitor the air fuel ratio and the exhaust gas temperature was monitored by K-type thermocouple. Di-gas analyser 444 (from AVL) was used to record the engine out emission.

Experimental Methods

The test condition for the investigation is 3000 rpm with 100% throttle opening, where the maximum brake torque was obtained for the given spark timing. The engine operating conditions are listed in Table 3. The hydrogen flow rates are estimated with the energy balance of not exceeding 50% by hydrogen and the maximum limit was set to 5 LPM. For the equivalence ratio of 1, the hydrogen flow rate was varied from 5 to 1 LPM and similarly the equivalence ratio was increased to 1.1 and 1.2. For the consistent increment in the equivalence ratio the subsequent gasoline leaning will be carried out.

Table 1. Engine Details

Particulars	Details
No. of Cylinders	1
No. of Valves	2
Type of CAM	Single Overhead
Ignition	Spark
Bore*Stroke (mm)	88*64
Displacement (cm^3)	390
Compression Ratio	8.2:1
Induction	Naturally Aspirated
Rated Torque	24 Nm @3000 rpm
Rated Power	8 hp @3600 rpm
Cooling system	Air

Table 2. Fuel Injector Details

Particulars	Details
Make	M/s. Bosch
No. of Nozzles	6
Configuration	Spray Guided
Operation	Peak & Hold- Solenoid
Make of pump and rail	M/s. Bosch
Pressure	180 bar

Table 3. Engine Operating Conditions

Particulars	Details
Speed (rpm)	3000
Mode	Constant Speed Mode
Throttle position	100%
Fuel Injection Pressure	80 bar

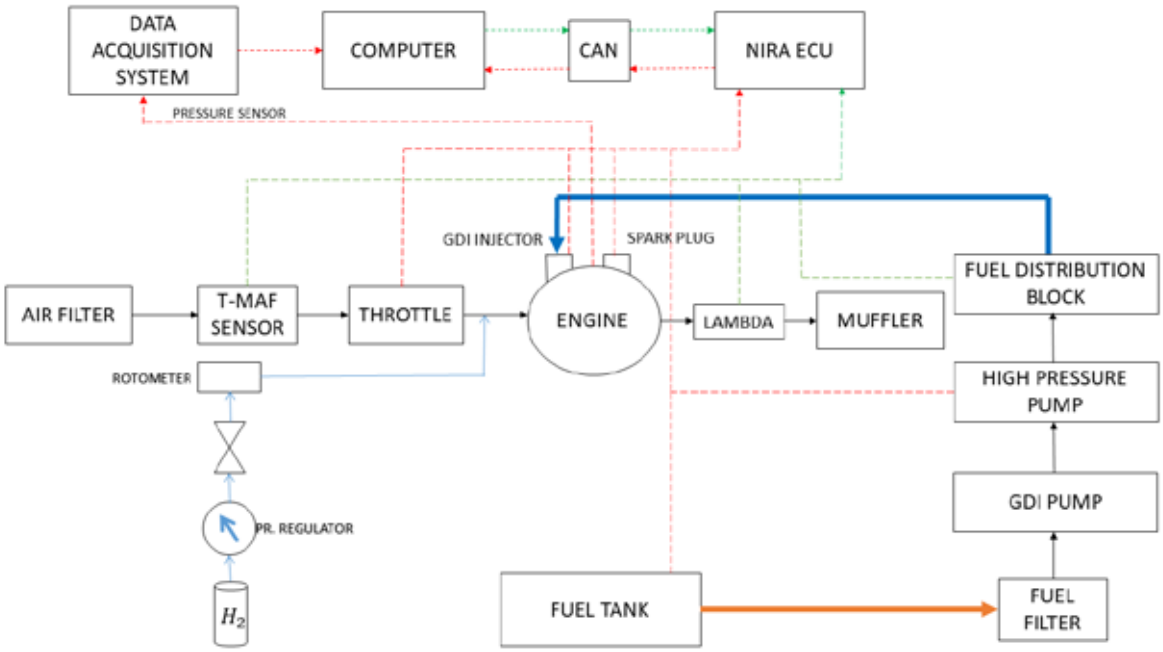


Fig. 1. Experimental Layout

CONCLUSIONS

1. Engine operation with 100% wide open throttle, equivalence ratio of 1, 1.1 & 1.2 and the varied hydrogen fraction of 1 to 5 LPM has the significant effect on the engine performance, combustion and emission characteristic. As the hydrogen fraction increases for the particular equivalence ratio significant increment in thermal efficiency and indicated mean effective pressure. At the equivalence ratio of 1.2 highest thermal efficiency was attained.
2. Engine operation with 100% wide open throttle, equivalence ratio of 1, 1.1 & 1.2 and with the increase in hydrogen fraction the combustion duration was shorten leading to peak pressure attained close to TDC. Keeping the hydrogen fraction constant and increasing the equivalence ratio improves the heat release rate and consistent reduction in the delay period.
3. Engine operation with 100% wide open throttle, equivalence ratio of 1, 1.1 & 1.2 and with the increase in hydrogen fraction CO and HC emissions decreases and increment in NO_x emissions. Keeping the hydrogen fraction constant and increasing the equivalence ratio, CO emission significantly reduces and HC emission reduces initially and increases in the later part. The NO_x emission has the adverse effect with the higher amount of hydrogen fractions.

REFERENCES

1. Reitz R.D, Ogawa H, Payri R and Fansler T. 2019. From IJER Editorial: The Future of the Internal Combustion Engine, International Journal of Engine Research. 21:3-10.
2. Liu Y, Pei Y, Peng Z, Qin J. 2017. From Spray Development and Droplet Characteristics of High Temperature Single Hole Gasoline Spray, Fuel. 191:97-105.
3. Eichhorn A, Lejsek D, Hettinger A, and Kufferath, A. 2013. From Challenge Determining a Combustion System Concept for Downsized SI-Engines - Comparison and Evaluation of Several Options for a Boosted 2-Cylinder SI-Engine, SAE Technical Paper. 2013-01-1730.
4. Gong C, Huang K, Jia J, Gao Q, Liu X. 2011. From Improvement of fuel economy of a direct-injection spark-ignition methanol engine under light loads, Fuel. 90:1826 to 1832.
5. Wang J, Huang Z, Tang C, Zheng J. 2010. From Effect of hydrogen addition on early flame growth of lean burn natural gas-air mixtures, International Journal of Hydrogen Energy. 35:7246 to7252.

WHEC-2022
23rd World Hydrogen Energy Conference
June 26-30, 2022 - Istanbul

#1496

PROGRESS AND PERSPECTIVES IN USING HYDROGEN-ENRICHED BIOGAS FROM WASTE TO ENGINE IN AGRICULTURE

[1*] *Sami Ayad,* [1] *Carlos Belchior,* [2] *Inoussa Tougri,* [3] *Robert Amoah,*[4] *Isaac Bryant*
[1] Department of Mechanical Engineering, Federal University of Rio de Janeiro, Rio de Janeiro, Brazil
[2] École Polytechnique de Ouagadougou (EPO), Ouagadougou, Burkina Faso
[3] Department of Agricultural Engineering, University of Cape Coast, Cape Coast, Ghana
[4] Department of Environmental Science, University of Cape Coast, Cape Coast, Ghana

*Corresponding author e-mail: samiayad@ufrj.br

ABSTRACT

This paper reviews the progress and perspectives in using hydrogen-enriched biogas, produced from agricultural wastes as fuel to power internal combustion engines. There is a direct link between a country's capacity for economic growth and its energy consumption, which in turn, is strongly correlated with its pollutant emissions. In response, many countries aim to exploit and include biofuels in their respective energy matrices to address energy insecurity and environmental concerns, foreign exchange savings, and fomenting growth in the rural sector. One way of realizing this potential is producing biogas through the fermentation or anaerobic digestion of organic, biodegradable waste. However, biogas has limitations when used as a fuel in internal combustion engines. In this context, hydrogen addition is one way of solving the drawbacks associated with biogas. Hydrogen enrichment of biogas has been shown to increase the engine's efficiency, mixture's lean operating limit, improving combustion stability, increase the mixture's laminar speed, and decrease carbon emissions. As a result, biological generation of hydrogen (biohydrogen) from renewable biomass presents the opportunity to simultaneously reduce fossil fuel dependence, decrease carbon dioxide emissions, and recover bioenergy. In addition, in some countries the thermal generation of hydrogen from renewable biomass is a viable option due to the abundance of solar energy.

Keywords: Biogas, Biohydrogen, Hydrogen Enrichment, Waste to Engine, Agriculture,

INTRODUCTION

There is a direct link between a country's capacity for economic growth and its energy consumption, which in turn, is strongly correlated with its pollutant emissions. In the context of a growing interest in finding ways to achieve sustainable economic growth, individual countries are obliged to meet the Nationally Determined Contributions (NDCs) of pollutant emissions agreed upon in the 2016 Paris Agreement. One such way is to replace fossil fuels, responsible for the majority of greenhouse gas (GHG) and carbon dioxide (CO_2) emissions in the energy sector [1,2], with alternatives. However, methane (CH_4) emissions, which were responsible for 20% of total GHG emissions in 2019, have a global warming potential that is 72 times higher than CO_2, and the energy sector is only the second-largest source of methane emissions [3]. The world's largest single source of methane emissions is agriculture, and in 2018, the agriculture and waste sectors accounted for 10% of Europe's and over 50% of New Zealand's GHG emissions [3]. This occurs because biomass such as animal manure and the organic fraction of municipal solid waste can produce methane [4].

Agricultural residues such as wheat straw, rice straw, bagasse, cotton stalk and wheat bran are rich in lignocellulose biomass (LCB) [5], which is the most abundant biomass resource on earth, and widely considered a potential feedstock for biofuels production that is mainly composed of three polymers: cellulose, hemicellulose and lignin, besides ash and extractives [6,7]. Cellulose consists of glucose and cellobiose as the basic coupling unit and is the most abundant polymer in LCB [6]. Hemicellulose is the second main polymer in LCB and is a short and highly branched polymer of pentoses, hexoses and uronic acids [6]. Finally, lignin is a large and complex molecular structure that contains crosslinked aromatic polymers of phenolic monomers and is disadvantageous due to its resistance to biodegradation [8].

In response, many countries aim to promote the use of biofuels in their respective energy matrices, to address energy insecurity and environmental concerns, foreign exchange savings, and fomenting growth in the rural sector [9]. Biofuel refers to a liquid or gaseous fuel that is predominantly produced from biomass. Examples of liquid biofuels include ethanol, methanol, biodiesel, Fischer-Tropsch diesel, while gaseous biofuels include hydrogen and methane [10]. Biofuels are readily available, represent a CO_2 cycle in combustion, are biodegradable, contribute to sustainability, and have a more environmentally friendly potential [11]. One way to explore this potential is by converting biomass to liquid and gaseous fuels, which is mainly done through thermochemical and biological routes [10]. Agricultural wastes are feedstocks that are particularly attractive because it is carbon neutral with low sulfur content and appear to have significant economic potential.

Within the context of the circular economy, one way of realizing this potential is the production of biogas by the fermentation or anaerobic digestion of organic, biodegradable waste [12]. Ref. [13] describes the typical molar composition of biogas as 50–75% CH_4, 25–45% CO_2,0–10% N_2,1–2% H_2, and 0–2% O_2, with a higher heating value of around 25 MJ/Nm^3. Not only composition, but also the production efficiency varies according to the raw material used as shown in Table 1 [14]. Biogas developed today is used mostly for power and heat, and a properly implemented biogas project not only helps to reduce emissions, but also promotes rural development and local job creation [4]. The presence of CO_2 in biogas leads to a narrow range of flammability limit, reduced laminar flame speed, and lower flame temperature, as well as flame quenching due to CO_2's lower reactivity [15]. Overall, direct use of biogas in engines designed for natural gas usually leads to a derating in power due to the lower HHV of biogas compared to natural gas' 39 MJ/m^3 [13].

Table 1. Amount of biogas produced from one kilogram of feedstock. Source: Ref [14]

Raw Material	Biogas Production (m3/kg)
Corn residues	0.563
Wheat straws	0.408–0.483
Rice straws	0.468–0.503
Sugarcane wastes	0.463
Lignocellulose biomass	0.178–0.402
Switch grass	0.208
Pine wood	0.033
Food wastes	0.683–0.725
Nonedible oil seed cakes	0.242
Bagasse	0.330
Dry leaves	0.118
Manure	0.129
Brewer's yeast	0.430
Dry maize	0.397
Cattle slurry	0.370
Maize silage, whole-crop rye silage	0.610

In this context, hydrogen addition is one way of solving the drawbacks associated with biogas use in internal combustion engines (ICE's). Although not a primary fuel, hydrogen is an alternative, odorless fuel with great potential as the energy carrier of the future [16]. It can be used in power generation applications, such as gas turbines, internal combustion engines, and fuel cells. The conversion of hydrogen's chemical energy into thermal energy or electricity is clean and generates only water vapor [17]. Hydrogen's high flame propagation speed and it's low minimum ignition energy facilitates combustion and formation of stable and self-sustaining flame cores, which reduces cyclic variation and accelerates combustion [18]. Also, hydrogen's short quenching distance contributes to reduced heat losses, due to less flame quenching in the vicinity of the combustion chamber walls [19], and its high auto-ignition temperature leads to knock resistance [20]. While it mostly generates non-toxic emissions, its high firing temperatures could increase thermal NO_x production in internal combustion engines [21], and its high diffusivity decreases volumetric efficiency and, depending on injection method, totally developed power due to air displacement [18,21]. Hydrogen enrichment of biogas has been shown to increase the engine's efficiency [14], mixture's lean operating limit [22], improving combustion stability [23], increase the mixture's laminar speed [15], and decrease in carbon emissions [12].

Although naturally occurring hydrogen has been found and reported, its exploration is still in its initial stages [17]. Consequently, the vast majority of hydrogen production worldwide is via extraction from fossil fuels, using methods such as steam reforming, thermal cracking of natural gas, partial oxidation of heavy fuels, and electrolysis of water [17,18,24,25]. In fact, hydrogen production through these processes is only economically viable in areas where electricity is cheap and can also cause significant emissions of CO_2. Alternatively, low-carbon hydrogen, which comprises less than 1% of current total hydrogen production [4], can also be produced from biomass, through thermochemical and biological processes. Thermochemical conversion processes, such as pyrolysis, gasification and steam gasification, are highly energy-intensive [16]. As a result, biological generation of hydrogen (biohydrogen) from renewable biomass presents the opportunity to simultaneously reduce fossil fuel dependence, decrease carbon dioxide emissions, and recover bioenergy [25]. Biohydrogen can be generated by direct or indirect biophotolysis, photo-fermentation, and dark-fermentation, or by a combination of these processes [16]. When by-products are not considered, the efficiencies of these products are lower than steam methane reform (SRM), despite more moderate non-renewable energy use and GHG emissions. However, the efficiencies of these processes increase significantly when by-products are considered. Among these biological processes, anaerobic hydrogen fermentation can yield

higher rates and at lower costs in degrading various organic wastes enriched with carbohydrates. Hydrogen fermentation could also be economical at less than stoichiometric yields by using the same hardware used for methane fermentation [26]. CONCLUSIONS

In conclusion, this paper reviews the potential of recycling agricultural waste and producing biogas and biohydrogen, and then combining these two fuels to improve engine performance of biogas. In summary, it can be concluded that:

- Biogas production from agricultural waste not only helps to reduce emissions, but also promotes rural development and local job creation;
- Biogas performance and emissions in internal combustion engines for waste to engine applications can be improved by hydrogen enrichment;
- Biohydrogen can be produced using the same feedstock used for biogas production;
- This application is a very promising way of offsetting methane and GHG emissions from agriculture and waste

ACKNOWLEDGEMENT

The authors would like to acknowledge the support of of Programa de Recursos Humanos da Agência Nacional do Petróleo, Gás Natural e Biocombustíveis – PRH8-ANP.

REFERENCES

1. I. IEA, Int. Energy Agency (2016).
2. P. IEA, in: IEA, 2016.
3. International Energy Agency, World Energy Outlook 2020, OECD, 2020.
4. IEA, (2021).
5. J.K. Saini, R. Saini, L. Tewari, 3 Biotech 5 (2015) 337–353.
6. J.F. Soares, T.C. Confortin, I. Todero, F.D. Mayer, M.A. Mazutti, Renew. Sustain. Energy Rev. 117 (2020).
7. D. Nagarajan, D.J. Lee, J.S. Chang, Int. J. Hydrogen Energy 44 (2019) 14362–14379.
8. R. Łukajtis, I. Hołowacz, K. Kucharska, M. Glinka, P. Rybarczyk, A. Przyjazny, M. Kamiński, Renew. Sustain. Energy Rev. (2018).
9. A. Demirbas, Prog. Energy Combust. Sci. 33 (2007) 1–18.
10. A. Demirbas, Energy Convers. Manag. 49 (2008) 2106–2116.
11. D. Puppán, Period. Polytech. Soc. Manag. Sci. 10 (2002) 95–116.
12. I. Amez, B. Castells, B. Llamas, D. Bolonio, M.J. García-Martínez, J.L. Lorenzo, J. García-Torrent, M.F. Ortega, Appl. Sci. 11 (2021).
13. X. Kan, D. Zhou, W. Yang, X. Zhai, C.H. Wang, Appl. Energy 212 (2018) 210–222.
14. S. Pukalskas, D. Kriaučiūnas, A. Rimkus, G. Przybyła, P. Droździel, D. Barta, Appl. Sci. 11 (2021) 1–17.
15. S. Benaissa, B. Adouane, S.M. Ali, A. Mohammad, Int. J. Hydrogen Energy 46 (2021) 18661–18677.
16. S. Manish, R. Banerjee, Int. J. Hydrogen Energy 33 (2008) 279–286.
17. P.E. Miranda, Science and Engineering of Hydrogen-Based Energy Technologies: Hydrogen Production and Practical Applications in Energy Generation, Academic Press, 2018.
18. S.M.M.E. Ayad, C.R.P. Belchior, G.L.R. da Silva, R.S.. Lucena, E.S. Carreira, P.E.V. de Miranda, Int. J. Hydrogen Energy 45 (2020).
19. M.O. Hamdan, M.Y.E. Selim, S.-A. Al-Omari, E. Elnajjar, Renew. Energy 82 (2015) 54–60.
20. I. Batmaz, Energy Sources, Part A Recover. Util. Environ. Eff. 35 (2013) 556–563.
21. H.M.Z. Rocha, R. da S. Pereira, M.F.M. Nogueira, C.R.P. Belchior, M.E. de L. Tostes, Int. J. Hydrogen Energy 42 (2017) 4530–4539.
22. S.Y. Jung, J. Park, Int. J. Hydrogen Energy 42 (2017) 16991–16999.
23. S. Lee, C. Park, S. Park, C. Kim, Int. J. Hydrogen Energy 39 (2014) 1086–1095.
24. R. Kothari, D. Buddhi, R.L. Sawhney, Renew. Sustain. Energy Rev. 12 (2008) 553–563.
25. J.J. Lay, Biotechnol. Bioeng. 74 (2001) 280–287.
26. S. Van Ginkel, S. Sung, J.J. Lay, Environ. Sci. Technol. 35 (2001) 4726–4730.

WHEC-2022
23rd World Hydrogen Energy Conference
June 26-30, 2022 - Istanbul

#1513

A CFD STUDY ON HYDROGEN ADDITION TO THE METHANE-AIR MIXTURES

[1-2*] *Eren Çolak, İlhami Karagül [2],*
[1]Hacettepe University, Mechanical Engineering Department, , Ankara, Turkey
[2] GKE Energy R&D Center, Muğla,Turkey

*Corresponding author e-mail: eren.colak@gke.com.tr

ABSTRACT

Hydrogen can be an alternative fuel to control the environmental affects of the hydrocarbon fuels. Since hydrogen flame temperature and, flame speed is higher than the methane flame it is an important alternative to the hydrocarbon fuels, which can replace hydrocarbon fuels fully or partially in near future. In this study CFD study of a reactive flow of the Hydrogen-Air-Methane mixture is investigated to understand the combustion characteristics of the mixture. 5-20% H_2 is added to the CH_4-Air mixture (16% CH_4) and temperature-specie fields are compared with the CH4-Air mixture combustion. Study conducted with turbulent flow conditions and with Eddy Dissipation Concept. It is found that hydrogen addition to the mixture increases the flame temperature, water production and decreases the CO_2 concentration along the flow in each H_2 percentage increase between 5-20% hydrogen addition.

Keywords: CFD, Methane, Hydrogen, Combustion, OpenFOAM.

INTRODUCTION

Hydrogen utilization is an important research subject that is getting heavy attention over last decades. Hydrogen can be produced locally and can be used in many applications; it is an outstanding research subject. Combustion of the hydrogen is one of the important topics in this sense. Since hydrogen is flammable substance with lower auto ignition temperature (500°C for H2 and 537°C for CH_4), higher flame temperature (2045°C for H2, 1947°C for CH_4, air as oxidant at 1 atm) [1] it is an alternative fuel to the hydrocarbons. Hydrogen can be used to partially or fully replace hydrocarbon fuels in future; therefore, it is important to understand the flow characteristics of the hydrogen included combustion. Many researchers studied CH_4,-Air- H_2 mixtures in the literature [2-5], and, recently researchers studying to develop novel technologies to mix the CH_4 and H_2 [6]. In this study, CFD simulations are conducted to understand the specie production (CH_4, H_2O) and, temperature field of the H2-CH4-Air mixtures.

PROBLEM DEFINITION AND GOVERNING EQUATIONS

2D cyclic replicate of the Sandia Flame-D case is used to model the reactive flow of the CH_4-Air-H2 mixture. OpenSource PDE solver, OpenFOAM [7] is used to calculate the corresponding fields (U, T, p, rho, etc.) with a reactive compressible solver.

Continuity, Momentum, transport equations for species, and energy equation is given in Eq. 1-4 [8]. These equations solved with PISO algorithm and with a pseudo time-step.1e-4 is chosen as convergence criteria for each field. For chemical reactions GRI 3.0 mechanism [9] used. Since the flow is turbulent, $k-\varepsilon$ model is used with EDC (eddy dissipation concept).

$$\frac{\partial \rho}{\partial t} + \rho\left(\nabla . \vec{U}\right) = 0 \quad (1)$$

$$\rho\frac{\partial \vec{U}}{\partial t} + \rho\vec{U}\left(\nabla . \vec{U}\right) = -\nabla \mathrm{P} + \mu\nabla^2\vec{U} + \rho\vec{g} \quad (2)$$

$$\rho\frac{\partial Y_k}{\partial t} + \rho\vec{U}(\nabla . Y_k) = \nabla(\rho D \nabla \mathrm{Y_k}) + \omega_k \quad (3)$$

$$\rho\frac{\partial h}{\partial t} + \rho\vec{U}(\nabla . h) = \nabla\left[\frac{\mu}{\sigma_h}\nabla . h + \mu(\frac{1}{S_{c_k}} - \frac{1}{\sigma_h})\sum h_k \nabla Y_k\right] + \frac{\partial \rho}{\partial t} + S_{rad} \quad (4)$$

Fuel inlet velocity is taken as 49.6 m/s and, pilot inlet velocity is taken as 11.4 m/s. Temperature of the pilot inlet is 1880 K and the fuel inlet temperature is 298 K. Total combustion chamber length is 0.5 m.

RESULTS AND DISCUSSION

Before starting to the simulations, a validation study and, a grid independency study is conducted. Fig. 2 shows the comparison with the Sandia Flame D records [10-12], CH4-Air combustion data and, the grid independence study. Our results shows that this case is grid independent after 46110 number of grids in 2D cyclic domain and, our data is close enough to the experimental values.

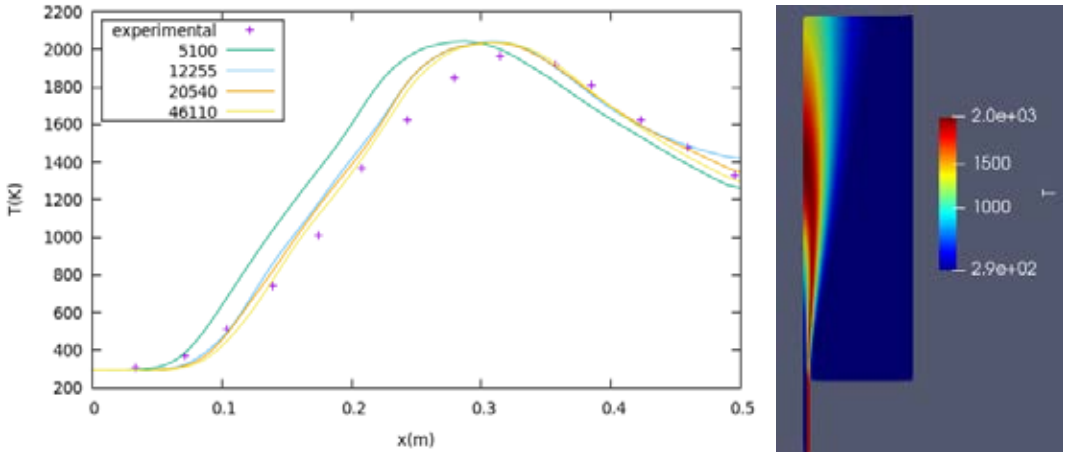


Fig. 2. Grid independency study and the temperature profile

Proceeding with the simulations, 5-20% H_2 addition to the CH_4-Air mixture effects on the computational fields are computed. Fig.3 shows the Temperature profile along the flow direction for different H_2 concentrations in the fuel. It is obvious that H_2 addition decreases the CO_2 concentration in flow path, because hydrocarbon concentration decreases as the fuel composition includes less CH_4. As a result, increase in H_2 concentration decreases the CO_2 concentration. H2O concentration is also influenced from the hydrogen addition. Since the hydrogen oxidation reaction results in H2O production, as the hydrogen fraction in the fuel increases, H2O production also increases. At 20% hydrogen fraction, this increase is around 30%.

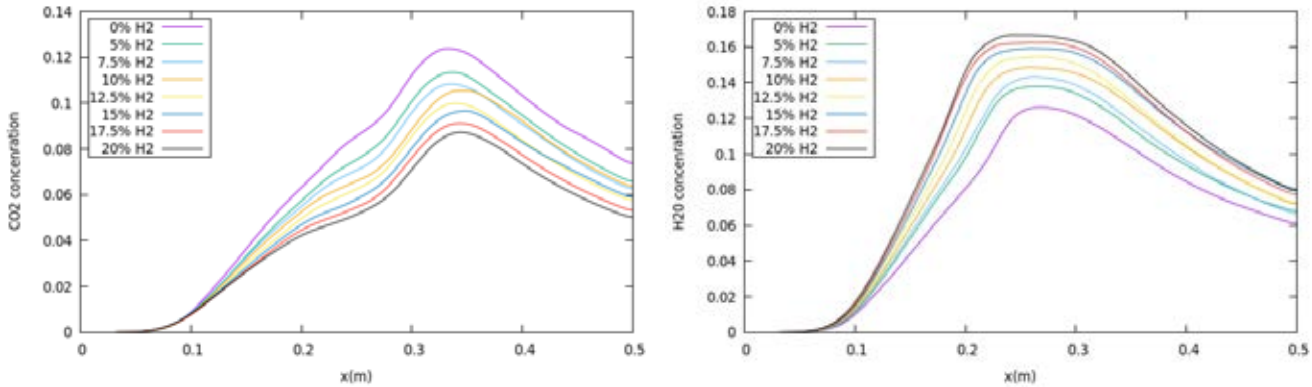
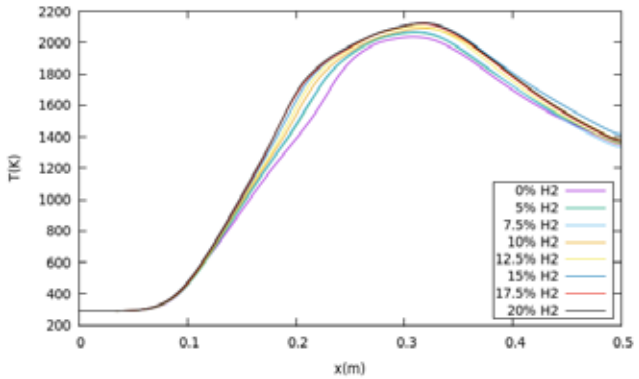


Fig. 3. CO2 and H2O concentration along the flow direction

Fig. 4 shows the temperature profile along the flow direction, as the H_2 addition percent increases, temperature along the flow direction increases. This increase caused by the radical reactions in GRI mechanism [9]. R10, R284, R52 has significant contribution to the heat release during combustion. Hydrogen addition boosts these reactions and the heat release. As result, temperature increases in the flow direction. Maximum temperature increase is 4.3% for 20% hydrogen addition and, position of the maximum temperature also increases with the hydrogen addition.



H2 (%)	T(K)	Position (m)
0	2036	0.308
5	2064	0.308
10	2090	0.318
15	2120	0.318
20	2123	0.318

Fig. 4. Temperature distribution along the flow direction

CONCLUSIONS

In this study hydrogen addition to the CH_4-Air mixture is numerically investigated under atmospheric pressure and, with 5-20% percent hydrogen addition under turbulent flow conditions. Study conducted with pseudo-transient solver, and steady-state solutions are compared. It is found that hydrogen addition increases temperature of the exhaust gas, and H2O production along the flow path and reduces the CO_2 production. This study will be extended to understand the flow behavior in different combustion chambers with transient LES modelling.

ACKNOWLEDGEMENT

Authors appreciates the funding from GKE Energy for this study.

REFERENCES

1. Kee, R., Coltrin, M. and Glarborg, P., 2010. *Chemically reacting flow*. New York: Wiley-Interscience.
2. Davazdah Emami, S., Kasmani, R., Hamid, M., Che Hassan, C. and Mokhtar, K., 2016. Kinetic and dynamic analysis of hydrogen-enrichment mixtures in combustor systems – A review paper. *Renewable and Sustainable Energy Reviews*, 62, pp.1072-1082.
3. Hu, E., Huang, Z., He, J. and Miao, H., 2009. Experimental and numerical study on lean premixed methane–hydrogen–air flames at elevated pressures and temperatures. *International Journal of Hydrogen Energy*, 34(16), pp.6951-6960.
4. Moccia, V. and D'Alessio, J., 2013. Burning Behaviour of High-Pressure CH4-H2-Air Mixtures. *Energies*, 6(1), pp.97-116.
5. Refael, S. and Sher, E., 1989. Reaction kinetics of hydrogen-enriched methane□air and propane□air flames. *Combustion and Flame*, 78(3-4), pp.326-338.
6. Ozturk, M. and Dincer, I., 2020. Development of renewable energy system integrated with hydrogen and natural gas subsystems for cleaner combustion. *Journal of Natural Gas Science and Engineering*, 83, p.103583.
7. Jasak, H., 2009. OpenFOAM: Open source CFD in research and industry. *International Journal of Naval Architecture and Ocean Engineering*, 1(2), pp.89-94.
8. Poinsot, T. and Veynante, D., 2012. *Theoretical and numerical combustion*. [S.l.]: T. Poinsot.
9. https://tnfworkshop.org/data-archives/pilotedjet/ch4-air/
10. Schneider, Ch., Dreizler, A., Janicka, J., "Flow Field Measurements of Stable and Locally Extinguishing Hydrocarbon-Fuelled Jet Flames," *Combust. Flame* 135:185-190 (2003).
11. Barlow, R. S. and Frank, J. H., *Proc. Combust. Inst*. 27:1087-1095 (1998)
12. Barlow, R. S., Frank, J. H., A. N. Karpetis, and Chen, J.-Y., "Piloted Methane/Air Jet Flames: Scalar Structure and Transport Effects," Combust. Flame 143:433-449 (2005).

WHEC-2022
23rd World Hydrogen Energy Conference
June 26-30, 2022 - Istanbul

#1531

PREDICTION OF CARBON DI OXIDE AND OTHER EMISSIONS CHARACTERISTICS OF LOW CARBON BIOFUEL-HYDROGEN DUAL FUEL ENGINE - A MACHINE LEARNING APPROACH

[1*]*Femilda Josephin Joseph Shobana Bai and* [2]*Edwin Geo Varuvel*
[1*]Department of Computer Engineering, Faculty of Engineering and Natural Sciences, Istinye University, Istanbul, Turkey
[2]Department of Mechanical Engineering, Faculty of Engineering and Natural Sciences, Istinye University, Istanbul, Turkey

*Corresponding author e-mail: femij80@gmail.com

ABSTRACT

The transportation sector is a major emitter of carbon dioxide emissions. It is a known fact that carbon dioxide is the cause of global warming which has resulted in extreme weather conditions as well as climate change. In this study a combination of different methods of expediting the CO_2 emission from a single cylinder common rail direct injection (CRDI) engine has been explored. The methods include use of low carbon content biofuels (lemon peel oil (LPO) and camphor oil (CMO), inducing hydrogen in the intake manifold and zeolite based after-treatment system. The emissions were found to reduce even further and at full load condition the lowest CO2 (39.7% reduction) and smoke (49% reduction) emissions were observed with LPO blend and hydrogen induction. The NO emission with hydrogen induction increases for both the blends, however, it was seen that the zeolite-based treatment system was effective in reducing the emission as well. As compared to baseline diesel, the maximum reduction in NO emission was 23% at full load with LPO blend, hydrogen induction and after-treatment system.

Unfortunately, a lot of experimental research in the engineering field takes a long time and costs a lot of money. The number of experimental trials can be minimized by applying predictions using the available experimental data. Machine learning approaches can aid in the development of rapid and reliable data-based models that can supplement a traditional physical model. The goal of this work is to investigate if a data-based model can help to predict engine emission characteristics including CO, NO_X, Smoke, BTE, and HC more accurately.

In machine learning, ensemble methods are strategies for creating numerous models and then combining them to obtain better results. In most cases, ensemble approaches provide more accurate results than a single model. In the present work, ensemble learning algorithms like XGBoost, LightGBM, CatBoost, Random Forest (RF) are used for the prediction of emissions. The brake power and BSEC are the input parameters to these algorithms from which CO, NO_X, Smoke, BTE, and HC are predicted under various combination of additives. The CatBoost model has produced high accuracy predictions which was followed by XGBoost, RF and LightGBM models. The predicted and actual values are compared each other and the performance of the algorithms were analysed using the evaluation metrics like R-Square(R^2), Mean Absolute Error (MAE), Mean Square Error (MSE) and Root Mean Square Error (RMSE).

Keywords: Hydrogen, Low Carbon Biofuel, After Treatment, Machine Learning, Ensemble Learning

MATERIALS AND METHODS

The experimental data generated were used to train the XGBoost, LightGBM, CatBoost, RF models. The dataset was split into two parts for training and testing purposes. 80% of the experimental data are used for training and 20% of data are used for testing the model with unknown data. The independent features that are given as input to the algorithms are brake power and BSEC values, whereas the dependent features that are generated as outputs are the corresponding engine emissions [1,2]. The Machine Learning (ML) model must first be trained with a set of known independent and dependent features. The model is ready to predict the output of any unknown input after it has been trained. Predictions were made for emissions characteristics like HC, NO_X, CO_2, smoke and BTE for diesel engines with different combination of low carbon biofuels and hydrogen with zeolite. The performance of the individual models is analysed with the evaluation metrics like R^2, MAE, MSE and RMSE. The best model was chosen based on the closeness between the predicted and the experimental values.

RESULTS AND DISCUSSION

The variation in CO_2 emission for CMO, LPO, with and without hydrogen along with after-treatment system from no load to full load condition is depicted in Figure 1. Both CMO and LPO blends have lower CO_2 emission than diesel

due to lower carbon content. The carbon dioxide emission at full load with diesel, CMO20 and LPO20 is 7.9%, 6.7% and 6.8%, respectively. The CO_2 emission at full load with hydrogen induction is 5.7% and 5.4%, with CMO20 and LPO20, respectively. Higher reduction in emission with LPO20 is caused by improvement in combustion and higher replacement of the fuel with hydrogen. When the zeolite based after-treatment is placed in the exhaust pipe, further reduction in CO_2 emission is observed. At full load, with LPO20 & hydrogen engine operation and with LPO20 & hydrogen & zeolite engine operation, the CO_2 emission reduced by 20.58% and 39.7%, respectively in comparison to neat LPO20 engine operation.

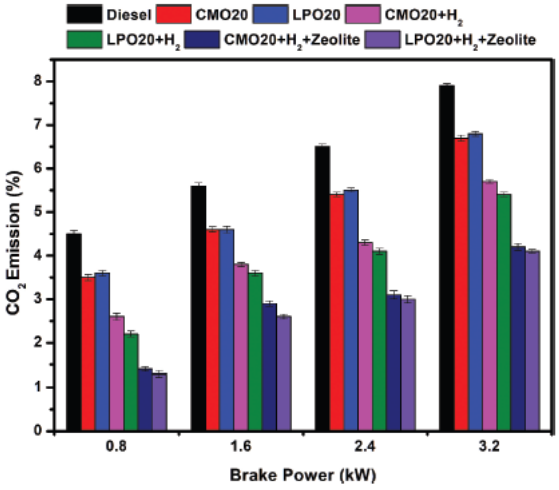


Fig. 1. Variation in CO2 emission with brake power.

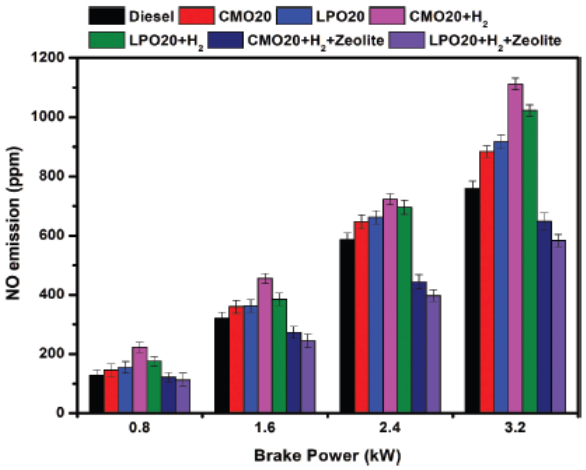


Fig. 2. Variation in NO emission with brake power.

The modulation in NO emission with load for diesel, CMO20, LPO20 and hydrogen and zeolite based after-treatment system is displayed in Figure 2. The NO emission was higher when the engine was operated with low carbon fuels in single fuel mode. At maximum load the NO emission is 759ppm, 884ppm, 917ppm with diesel, CMO20 and LPO20, respectively. With hydrogen induction the NO emission further increases. The NO emission at full load was 1112ppm and 1023ppm with CMO and LPO and hydrogen induction, respectively. The emission with CMO is higher than diesel because of higher substitution of hydrogen with the liquid fuel which increases the combustion temperature. With the after-treatment system in place, the NO emission was found to decrease at all the loads. The zeolite captures and stores the NO molecules in its porous structure, resulting in decrease in the emission.

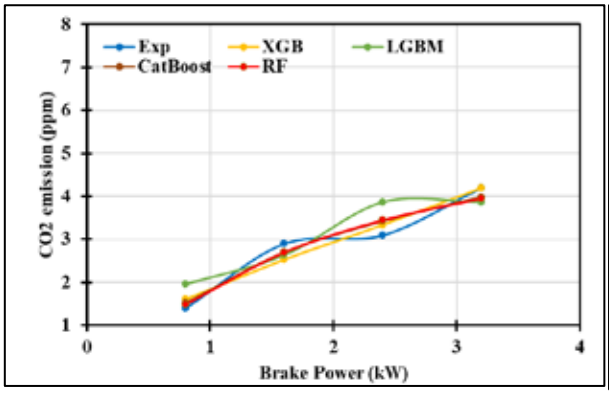


Fig. 3. Experimental and predicted CO2 in CMO20+H_2+Z

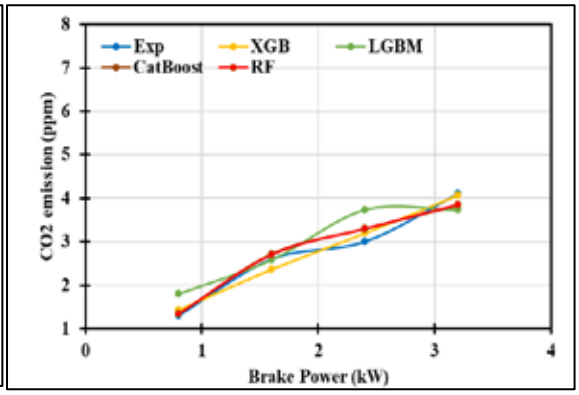


Fig. 4. Experimental and predicted CO2 LPO20+H_2+Z

Figures 3 and 4 illustrate a comparison of experimental findings and machine learning ensemble approaches for various brake power values against HC in the CM20+H+Z and LP20+H+Z, respectively. It is observed that the data-based models except the LGBM have predicted the NOX emission very close to the experimental results.

The comparison of experimental results and data-based models using ensemble techniques is shown in Figures 5 and 6. The various brake powers are represented on the major axis, while NOX emissions are represented on the minor axis. For both CM20+H+Z and LP20+H+Z, the graph depicts the proximity of the experimental data to the

projected data using various algorithms. It can be seen that XGBoost, CatBoost and RF algorithms have done predictions very close to experimental data.

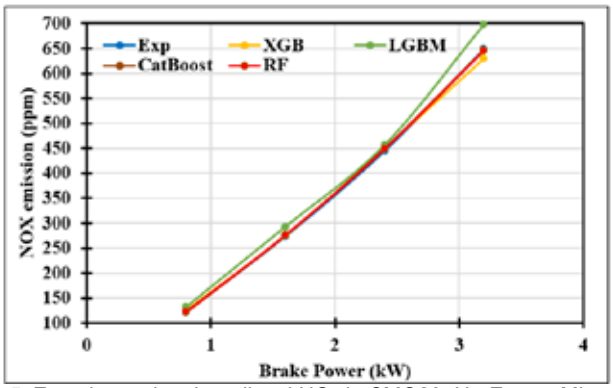


Fig. 5. Experimental and predicted NO_X in CMO20+H_2+Z w.r.t. ML

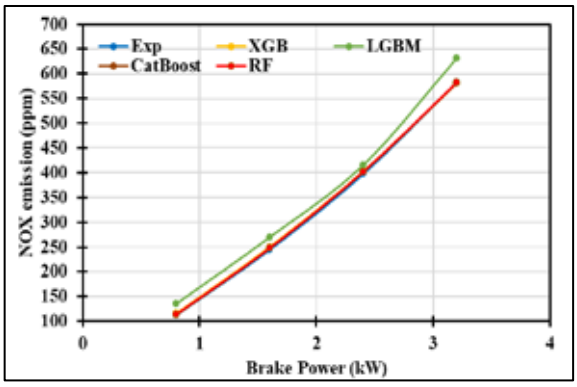


Fig. 6. Experimental and predicted NO_X LPO20+H_2+Z w.r.t. ML

CONCLUSIONS

In this study the CO_2 emission from a diesel engine was reduced by combining various techniques. Then these emissions were predicted using various machine learning algorisms.

- The CO_2 emission with blends of CMO and LPO was 15.19% and 13.94%, respectively, as compared to diesel. With induction of hydrogen the emission reduced by 27.8% and 20.6% for CMO and LPO in comparison to diesel. With the after-treatment system, the maximum reduction in emission was 39.7% for LPO blended fuel and hydrogen.
- The NO emission was found to increase for the blends in comparison to diesel on account of improvement in combustion and the presence of molecular oxygen. Hydrogen induction further improves the combustion thereby increasing the combustion temperature resulting in increase in NO emission. However, with after-treatment system in place the emissions were reduced drastically. The emissions with CMO+H_2 & LPO+H_2 with after-treatment system reduced by 41.72% and 43% as compared to the fuel combinations without after-treatment system.
- Ensemble learning algorithms were used to predict emission characteristics such as NO_X, CO_2, Smoke, BTE, and HC. 80% of the experimental data were used for training, whereas 20% of the data were used for testing purposes. The input parameters were braking power and BSEC, while the output parameters were emission characteristics.
- To predict emission characteristics with varied additive ratios, the XGBoost, LGBM, CatBoost, and RF algorithms were utilized as data-based models. To determine the prediction accuracy, each model was trained with input and output features and tested with unknown data.
- With the exception of LGBM, the other three algorithms have accurately predicted emission characteristics and were extremely closer to the experimental data.
- The percentage of prediction accuracies with respect to the models is analysed by the evaluation metrics R^2, MAE, MSE, and RMSE. It is seen that XGBoost, CatBoost, and RF algorithms have good R^2 value than LGBM. Better the R^2 value results with lesser MAE, MSE, and RMSE values.

REFERENCES

1. Ağbulut, Ü., Gürel, A.E. and Sarıdemir, S., 2021. Experimental investigation and prediction of performance and emission responses of a CI engine fuelled with different metal-oxide based nanoparticles–diesel blends using different machine learning algorithms. Energy, 215:119076.
2. Bilban, M. and Gökmen, M.S., 2020. Using of Support Vector Machine (SVM), Gradient Boosting (GB) and Artificial Neural Network (ANN) Techniques in Internal Combustion Engine Tests: A Review. Renewable Energy Sources Energy Policy and Energy Management, 2(1): 1-9.

WHEC-2022
23rd World Hydrogen Energy Conference
June 26-30, 2022 - Istanbul

#1552

EVALUATION OF KINETIC MODELS VIA COMPUTATIONAL OPTIMIZATION TECHNIQUES FOR DIRECT SYNGAS-TO-OLEFINS PROCESS

[1*] *Kerem Bülbül,* [2] *Abdullah Zahid Turan,* [1] *Alper Sarıoğlan,* [2] *Gamze Behmenyar,* [2] *Özlem Ataç*
[1]Istanbul Technical University, Faculty, Department of Chemical Engineering, ITU Ayazaga Campus, 34469, Maslak, Istanbul
[2] TUBITAK Marmara Research Center, Clean Energy Technologies, Kocaeli, Turkey

*Corresponding author e-mail: che.kerembulbul@gmail.com

ABSTRACT

In this study, the kinetics of Fischer-Tropsch (FT)-to-olefins was thoroughly investigated on activated carbon supported Fe-Cu-K catalyst. Among the evaluated methods, it was observed that the Runge-Kutta method gave better results. In general, the model that pertains to the study of Fernandes introduced fewer errors than Wang et al.'s model. In the simulations based on the Fernandes model, the H_2 values were estimated within error limits between 2% and 8% validated for 7 distinct experiments. CO, on the other hand, was estimated more accurately with the error limits in the ranges of 4-7% for high gas hourly space velocity (GHSV) values. However, error band of the model in the latter case was increased up to 30% for low GHSV values. Regarding hydrocarbon products, an average error value of 30% was obtained for ethylene while the best estimations were obtained for propylene with an error of 0.46% and 13.27%. However, Fernandes model neglects olefin re-adsorption, unlike the Wang's model, so Wang model seems more appropriated to estimate paraffin products. All in all, as per calculations on experimental analysis, both models need improvement in terms of product distribution.

Keywords: Kinetics, Fischer-Tropsch, Advanced optimization, Multi-objective generic algorithm

INTRODUCTION

Extensive kinetic studies on FT reaction, intended for the synthetic fuels, is widely available in literature. Yet in this study, the main interest is for light olefins. In order to implement a modelling study, the heterogeneous catalytic reaction taking place at gas-solid interface should be investigated by considering all steps of reaction, namely external diffusion, internal diffusion, adsorption, desorption along with the main catalytic surface reaction. All these steps should be accurately modeled for a sound computation of kinetics. However, adsorption and desorption are not considered in modeling calculations because they involve a complicated mechanism mostly dependent on the properties of the catalytic surface. Therefore, consideration of external and internal diffusion phenomena as per limitations is more applicable. In a study by Perego and Peratello [1], it has been pointed out that building a mathematical model describing all these limitations is a must to analyse the behaviour of a catalytic reactor. In this study, some assumptions have been made for the simplicity of modelling calculations such as sufficiently smaller size of catalyst diameter in order to omit internal diffusion limitations but would be in size enough with reasonable pressure drop. Since conversion changes with the presence of interphase limitations (external diffusion), operating conditions ensuring the free of external limitations have been determined with flow rate tests [1]. The kinetic experiments were performed under optimum operational conditions. Catalytic bed volume, flow rate and the like all those were selected according to this criterion. Next, a mathematical kinetic model was built fitting the experimental data. Finally, the model was tested with further experimental data that are beyond the ones used for building the model. Deviations from the model were reported with error values and the results were discussed.

EXPERIMENTAL AND MODELING STUDIES

Preliminary catalytic tests were conducted to find out the reaction-limiting conditions where kinetic experiments will be executed. In four consecutive tests, both reactant flow rate and the amount of catalyst were increased while keeping GHSV be constant at 2000 h^{-1}. Since the mass transfer across the boundary layer no longer limits the rate of reaction at sufficiently high velocities, the conversion will be constant at two consecutive flow rates in the reaction limited region. The results of reactant flow rate screening at constant GSHV value of 2000 h^{-1} are given in Figure 1. Reaction conditions were set to T=340℃, P=10 bar and H_2/CO = 0.65. The region where conversion becomes independent of flow rate was noticed for the amounts of catalyst in between 0.3 and 0.4 grams. Thus, the corresponding flow rates were taken as the limits ensuring the absence of external mass transfer limitations. Thereafter, kinetic experiments were executed in the flow rate corresponding to 0.35 gram of catalyst. In the next step, kinetic experiments were carried out in a fixed bed reactor under the reaction limited conditions and the obtained data were used for F-T reaction modelling. Different kinetic models have been evaluated recently by the authors of this manuscript [2]. Based on the previous work, the models that best describe the kinetic data were used in MATLAB R2021a. Driven differential equations were solved with two different methods. The differential equations were

presented in the derivative form of conversion per catalyst weight and Euler method was applied. Alternatively, ode45 function in MATLAB R2021a which uses the Runge-Kutta method was employed.

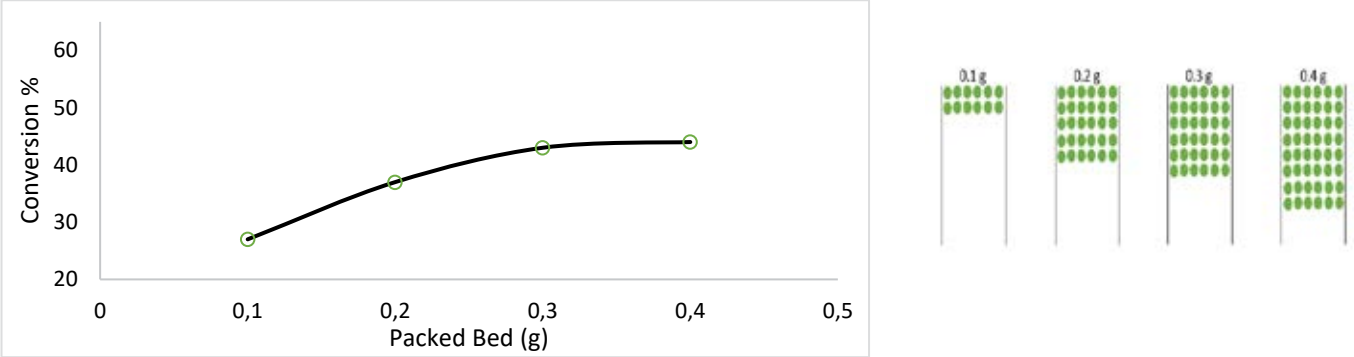


Fig. 1. Conversion versus constant space velocity with different catalyst bed amount

The objective functions for each method were determined as given in Eq. 1 where $N(z,i)_{exp}$ and $N(z,i)_{cal}$ were the experimental and calculated values of the i^{th} species for the z^{th} case. The minimization of these functions with multi-objective optimization led to the determination of kinetic parameters from experimental results. MATLAB multi-objective optimization helped in setting optimum parameters.

$$\mathrm{Fx(z)} = \sum_{i=1}^{n}\left(\left(N(z,i)_{exp} - N(z,i)_{cal}\right)/N(z,i)_{exp}\right)^2 \quad (1)$$

RESULTS AND DISCUSSION

In the experimental design study, an experimental matrix composed of 43 separate experiments was created for three different temperatures, three different pressures, three different GHSVs and two different H_2/CO, and the mathematical kinetic modeling study was carried out based on the experimental results. Experimental conditions and the main results were given in Table 1. Reasonable experimental results were obtained as such that conversion on carbon basis was improved with an increase in temperature and/or pressure and with a decrease in GHSVs and H_2/CO. It should be noted here that the calculated carbon error (%) was within acceptable limits.

Table 1. Experimental matrix and F-T reaction results

No	T (K)	P (Bar)	H_2/CO	GHSV (h^{-1})	X (%)	Carbon Error (%)	No	T (K)	P (Bar)	H_2/CO	GHSV (h^{-1})	X (%)	Carbon Error (%)
1	573.15	8	2	4037	9.11	1.21	**23**	573.15	8	1	5231	10.55	4.63
2	573.15	8	2	3000	12.33	2.25	**24**	573.15	8	1	4173	11.87	4.79
3	573.15	8	2	2000	16.57	2.3	**25**	573.15	8	1	2855	16.63	5.68
4	613.15	8	2	4037	34.5	3.61	**26**	613.15	8	1	5026	27.52	5.73
5	613.15	8	2	3000	44.54	3.96	**27**	613.15	8	1	3965	34.52	5.47
6	613.15	8	2	2000	57.35	5.76	**28**	613.15	8	1	2643	51.53	7.39
7	573.15	4	2	4037	5.73	0.07	**29**	573.15	4	1	5111	7.85	4.09
8	573.15	4	2	3000	7.97	0.97	**30**	573.15	4	1	4047	9.32	4.39
9	573.15	4	2	2000	11.49	0.89	**31**	573.15	4	1	2724	12.67	5.39
10	593.15	4	2	4037	9.02	1.05	**32**	593.15	4	1	3868	11.75	4.9
11	593.15	4	2	3000	12.14	1.8	**33**	593.15	4	1	2975	15.09	4.75
12	593.15	4	2	2000	18.15	2.23	**34**	593.15	4	1	1863	22.19	6.26
13	613.15	4	2	4037	18.09	2.61	**35**	613.15	4	1	4861	16	5.21
14	613.15	4	2	3000	23.99	3.16	**36**	613.15	4	1	3801	19.57	4.93
15	613.15	4	2	2000	36.01	3.23	**37**	613.15	4	1	2481	26.9	5.24
16	573.15	12	2	4037	15.23	2.76	**38**	573.15	12	1	4665	10.16	5.21
17	573.15	12	2	3000	19.72	3.56	**39**	573.15	12	1	3582	9.71	4.88
18	573.15	12	2	2000	25.69	5.27	**40**	573.15	12	1	2234	12.92	5.88
19	593.15	12	2	4037	17.74	3.14	**41**	613.15	12	1	5096	22.01	6.88
20	593.15	12	2	3000	20.28	3.98	**42**	613.15	12	1	4016	22.55	6.3
21	593.15	12	2	2000	26.89	4.51	**43**	613.15	12	1	2671	29.4	7.78
22	613.15	12	2	2000	45.68	7.09							

The results of kinetic experiments performed on carbon-supported iron catalyst were processed with the models proposed by A.N. Fernandes [3] and Y.N. Wang [4]. In addition, both Euler method, and Runge-Kutta method have been used in an effort to understand the convergence differences among them. The ode45 function was seen to be converged better for the model by A.N. Fernandes [3], therefore the results based on the model Y.N. Wang was calculated with this method. However, only the kinetic data calculated by the model by A.N. Fernandes were reported in Table 2 and Table 3. While activation energies were quite close whatever the method of calculation, rate constants varied considerably according to the method of calculation. Computed kinetic model parameters were validated experimentally. For validation, additional experiments outside the kinetic experimental matrix were conducted. It was seen that the results of models were in good agreement with the experimental results except the Euler method based on the model by A.N. Fernandes.

Table 2. Rate constants at 573.15 K

k_{fts} $\frac{mol}{h.g.MPa}$	b	k_{wgs} $\frac{mol}{h.g}$	k_i MPa^{-1}	k_p $g.mol^{-1}$	k_{par} $h^{-1}.MPa^{-1}$	k_{olef} $h^{-1}.MPa^{-1}$	$k_{methane}$ $h^{-1}.MPa^{-1}$	k_{ethane} $h^{-1}.MPa^{-1}$	$k_{etylene}$ $h.g^{2}.mol^{-1}$
2.02E+02	4.70E+03	5.16E+01	3.24E-03	4.17E+02	4.46E+01	3.12E+02	3.29E+02	5.99E+01	2.94E-05

Table 3. Activation and adsorption values of rate expressions

E_{ft} (kJ/mol)	$-\Delta H_b$ (kJ/mol)	E_w (kJ/mol)	E_i (kJ/mol)	E_p (kJ/mol)	E_{par} (kJ/mol)	E_{olf} (kJ/mol)	E_{met} (kJ/mol)	E_{eth} (kJ/mol)	E_{ety} (kJ/mol)
92.892	1.61E-03	162.682	91.001	77.361	107.703	91.525	108.707	119.869	113.819

CONCLUSIONS

Building a kinetic model is quite complex since Fischer-Tropsch reaction mechanism is not fully understood. Two models proposed by A.N. Fernandes and by Y.N. Wang were tested on the experimental data executed for carbon supported iron catalyst. These models were solved both Euler method and ode45 with the experimental results designed for the evaluation of kinetic models. Two of the mathematical kinetic models were observed to be in agreement with regard to hydrogen values. Even though kinetics parameters were akin to that was reported in literature, errors on the values for F-T products were relatively high. In general, whereas the model proposed by Y.N. Wang has been designated more valid to describe F-T mechanism, however, as per our experimental analysis, product distribution is still missing and needs to scrutinize.

REFERENCES

1. C. Perego and S. Peratello, “Experimental methods in catalytic kinetics,” Catalysis Today, vol. 52, no. 2–3, pp. 133 145, Sep. 1999, doi: 10.1016/S0920-5861(99)00071-1.
2. A. Z. Turan, Ö. Ataç, O. A. Kurucu, A. Ersöz, A. Sarıoğlan, and H. Okutan, “Kinetic modeling of Fischer–Tropsch-to-olefins process via advanced optimization,” International Journal of Chemical Kinetics, vol. 54, no. 1, pp. 3–15, Jan. 2022, doi: 10.1002/KIN.21536.
3. L. S. Fernandes and M. A. Peres, “Polymerization Kinetics of Fischer-Tropsch Reaction on Iron Based Catalysts and Product Grade Optimization,” Chemical Engineering & Technology, vol. 28, no. 8, pp. 930–938, Aug. 2005, doi: 10.1002/CEAT.200500036.
4. Y. N. Wang et al., “Kinetics modelling of Fischer–Tropsch synthesis over an industrial Fe–Cu–K catalyst,” Fuel, vol. 82, no. 2, pp. 195–213, Jan. 2003, doi: 10.1016/S0016-2361(02)00154-0.

WHEC-2022
23rd World Hydrogen Energy Conference
June 26-30, 2022 - Istanbul

#1577
ATOME: PURE-PLAY HYDROGEN PRODUCER

Mary-Rose de Valladares
ATOME Energy PLC, Carrwood Park, Selby Road, Leeds, LS15 4LG United Kingdom

Corresponding author e-mail: Mary-Rose.deValladares@atomeplc.com

ABSTRACT

ATOME Energy PLC (ATOME) was created to produce, market and distribute green hydrogen (H2) and ammonia (NH3). A pure-play company, ATOME was incorporated October 2020 in England and Wales and went public year end 2021 as the first green hydrogen and ammonia production company listed on the London Stock Exchange (LSE). ATOME has been awarded the LSE's prestigious Green Economy Mark. ATOME has deep expertise in H2 along with expert, globally experienced management. Shareholders include Trafigura, Schroders and President Energy PLC, its incubator. ATOME has foundation projects in two stable, democratic nations with market-based economies. The foundation projects – one in Paraguay and the other in Iceland -- are strategically situated and locally managed in attractive locations that feature renewable "green" baseload electricity available 24/7. Their combined capacity is conservatively estimated at 350 MW—250 MW Paraguay and 100 MW in Iceland. While an H2 mobility project will launch near-term in Paraguay, the first phase of foundation project production focusses on NH3, a global commodity that is urgently needed to meet market demand for fertilizer. Subsequent phases will expand H2 production. ATOME is laying the groundwork for a sustainable H2 and NH3 that serves the global energy and food systems.

Keywords: Hydrogen, Ammonia, H2, NH3, ATOME, Fertilizer

INTRODUCTION

Since COP 21 in 2015 and IEA release of *The Future of Hydrogen* in 2019, there has been an important global acceleration in adoption of national hydrogen (H2) strategies and dedication of associated national funding. As of July 2021 43 countries had or were about to release H2 strategies. Countries with H2 strategies have committed USD 100 billion to the development and deployment of H2 technologies. Innovative investment incentives are also expected. The cost of renewables and renewable electricity has declined in the recent past as has electrolyser technology, the cornerstone of the H2 value proposition. IRENA notes that electrolysers are poised to benefit from an additional 40% decline in the short term and an 80% decline by 2050.[1]

Heretofore, almost all H2 has been produced from fossil fuels, notably natural gas. However, surging natural gas prices are making green electrolytic H2 economically competitive. Green H2 is already the environmentally favored H2 production method. In response, the private sector has stepped up to participate in the H2 energy future. Included are established companies, some of them household names that are longstanding H2 proponents and others that have pivoted to H2 in recognition of commercial opportunity and climate concerns. Then there are newly formed companies responding to the marketplace and the climate change challenge. ATOME Energy PLC is one of these companies.

COMPANY OVERVIEW

ATOME Energy PLC (ATOME) was created to produce, market and distribute green H2 and ammonia (NH3) in response to the sustainable energy future challenge. A pure-play company, ATOME was incorporated in England and Wales in October 2021 and went public year end as the first green H2 and NH3 production company listed on the London Stock Exchange (LSE). ATOME has been awarded the LSE's prestigious Green Economy Mark. The company has solid Environmental, Social and Governance (ESG) credentials and addresses five (#s 7, 9, 11, 12 and 13) of the 17 United Nations (UN) Sustainable Development Goals. The ATOME team features expert, globally experienced management as well as deep expertise in H2. It holds a 75% Interest in Green Fuel elf in Iceland. Wholly owned subsidiary ATOME Paraguay S.A. operates in Paraguay. There is local management on the ground in both locations. ATOME shareholders include Trafigura, Schroders and President Energy PLC (President). President incubated ATOME and has an impressive track record of investment in Paraguay. ATOME plans to use project finance that combines debt, equity and possibly grants/concessional finance to fund execution of its foundation projects. Final Investment Decision (FID) is expected in late 2022 – early 2023.

MISSION AND MARKET: COMMITMENT TO GREEN HYDROGEN AND AMMONIA

ATOME is focused on green H2 and NH3 for all the reasons the H2 community well knows and appreciates. H2 is a fuel, energy carrier and a chemical base for fertilizers. It is a vital component of the world's toolkit to achieve net zero emissions by 2050. Estimates indicate that low carbon H2 will supply up to 25% of the world's energy by 2050, growing into a USD10 trillion market opportunity equivalent to removal of 20 mm bbl of oil from the market per day.[2]

Current uses of H2 are refining, chemicals, fertilizer, iron & steel and glass. Anticipated future uses include transport (road, rail and shipping), power, heat and renewable energy storage. H2 produced by electrolysis from renewable power is “green” with zero Scope 1 (direct), Scope 2 (indirect purchased) & Scope 3 (indirect all other) emissions.[3]

ATOME is committed to early market entry and fast production in order to scale up H2 and NH3 development in the 100s of MWs. Export markets for H2 and NH3 are expected to grow quickly in the EU and Asia. ATOME is focusing first on production of NH3, a global commodity, and then on production of H2 as its markets mature. ATOME has access to significant domestic and export markets with offtake possibilities through traders such as Trafigura, a shareholder. ATOME plans to produce and sell molecules - not only H2 and NH3 but also oxygen (O2). The shortage of O2 during the pandemic is proof positive of a medical market. As well, ATOME may be eligible to apply, obtain and trade carbon credits on the voluntary market by displacing polluting fuels. Current carbon pricing at approximately $110 per MT suggests that green H2 demand will continue to outstrip supply with a consequent effect on price.

Hydrogen (H2) – The installed global green H2 capacity has increased some 400% from 0.1 GW to .4 GW (March 2022.) However, installed capacity must ramp up to 465 GW by 2050 to meet Net Zero targets. The H2 market is expected to grow from USD755 million in 2020 to USD1.4 billion by 2026. IEA forecasts a sixfold increase in H2 demand (to 530 MT) by 2050.[4]

Ammonia (NH3) The second most widely produced chemical in the world, NH3 has heretofore been made exclusively from fossil fuels. In 2019 the total global NH3 production was 150 MT/ year. The NH3 market is expected to grow to 530 MT/year by 2050.[5] Green NH3 will help decarbonize key industries, include the fertilizer, chemical, refining and shipping fuel industries as well as the power industry. As an H2 carrier, NH3 has three times the energy density of H2 and liquefies at -33.3 C° or -27.27 F° — a much higher temperature than H2. NH3 is thus well suited for H2 storage and a logical choice for green H2 transport from exporting nations to importing nations.

Fertilizer Approximately 70% of all NH3 worldwide is used for fertilizers. In 2021, with the world population at 7.6 billion according to the UN, land use accounts for around 25% of global Greenhouse Gas (GHG) emissions. The UN population forecast is 8.6 billion by 2030 and 9.8 billion by 2050. Consequently, green fertilizer alternatives are imperative. The urgency surrounding fertilizer for food increased exponentially since the onset of the war that has consumed the bread basket of Europe and interrupted the production and export of fertilizer from Russia, the leading producer of urea fertilizer and a top producer of nitrogen fertilizer. This unexpected dynamic is making food and fertilizer for food immediate global priorities.

Marine The International Maritime Organization (IMO), the UN division that regulates shipping, adopted an Initial GHG Strategy in 2018 to reduce — by at least 50% -- GHG emissions from the global shipping sector by 2050 compared to 2008. Every maritime segment — including shipping, fishing, ports – falls within the IMO purview. Maritime transport emits 940 million MT of CO2 annually, equivalent to 2.5% of global GHG emissions. By 2050 the Ammonia Energy Association estimates that NH3 could comprise 25% of all maritime fuel, assuming all new ships operate on NH3 starting in 2044.

ENGINEERING AND TECHNOLOGY

Each project requires a Front End Engineering Design (FEED). The FEED process provides detailed plans and specifications for construction of the projects and their civil works. In order to produce green H2 and NH3 ATOME must procure, integrate and install equipment including electrolysers, air separation units, compressors and NH3 synthesis loops as well as storage. ATOME is agnostic as to technology and seeks to deploy the most efficient, state of the art appropriate and cost-effective technology available. In the early phase(s) ATOME is expected to utilize low temperature electrolysers. Discussions with original equipment manufacturers (OEMs) and engineering, procurement and construction (EPC) companies are well underway.

FOUNDATION PROJECTS

ATOME has foundation projects in two stable, democratic nations with market-based economies. Paraguay belongs to MERCUSOR (Mercado Común del Sur), the Southern Common Market. While not a European Union (EU) Member State, Iceland is part of the EU’s European Economic Area and Schengen Agreements. The foundation projects are strategically situated in attractive locations that feature green electricity available 24/7 as well as low cost water. ATOME’s teams in Iceland and Paraguay have made significant contributions to their respective countries’ H2 and sustainability roadmaps. Combined, the two foundation projects are conservatively sized at 350 MW—250 MW Paraguay and 100 MW in Iceland. Expected output: ~60,000 MT of H2; 333,000 MT NH3; and 476,000 MT of O2.

Paraguay

In Paraguay, hydropower produces renewable electricity. Paraguay’s electricity is sold to Paraguayan consumers at some of the lowest rates in the region. The preponderance of this electricity is produced at the Itaipu Dam, the world’s

second largest dam in terms of installed capacity. The Itaipu Binacional is jointly owned by Paraguay and Brazil which share equally in its hydroelectric output. While Brazil completely consumes its 50% share, Paraguay does not use its entire allocation and exports a substantial amount of hydroelectricity to Brazil or Argentina. Paraguay's energy policy seeks to reduce dependency on hydrocarbons and capitalize on hydroelectric capabilities to produce molecules for domestic consumption. ATOME has already entered into a Memorandum of Understanding (MOU) with ANDE, the national power company of Paraguay, to utilize its hydropower; the Power Purchase Agreement (PPA) is expected to follow shortly. ATOME also has an MOU with the Parque Tecnológico Itaipu (PTI), the Itaipu innovation arm, for a prime site as PTI's exclusive green hydrogen producer. In the first phase(s) ATOME is targeting domestic offtake markets for H2 and NH3 products for agriculture, industry and transport. Notably, agriculture is responsible for 20% of the country's total employment; all fertilizer (a USD470 million market) is currently imported. Paraguay is the world's fourth largest soybean exporter and also boasts the world's third largest fleet of barges, which are used to transport agricultural and industrial production in the absence of a national rail system. Heavy goods vehicles (trucks) are also used for industrial transport. Both road and barge systems need decarbonization. The initial H2, NH3 and O2 production plan for Paraguay comprises two phases and a total of 250 MW: 50 MW in Phase 1 - 2024 and 200 MW Phase 2 – 2025-26.

Iceland

Renewable energy — 75% hydropower and 25% geothermal -- accounts for Iceland's electricity production. This "green" nation, a true H2 pioneer, is in close proximity to Europe and its substantial export market. The maritime industry accounts not only for 25-30% of the country's GDP and 15-20% of its employment but also the majority of its GHG. Iceland's shipping and fishing industries, including vessels and vehicles (related to land transport), are subject to IMO decarbonization guidance. However, as of 2019 Iceland still imported USD605 million in oil so the nation's energy policy targets reduction of fossil fuels for transport and shipping sectors. PPA negotiations for geothermal electricity are underway. The initial identified power capacity is up to 100 MW.

HYDROGEN MOBILITY

In many parts of the world H2 demonstration projects over the past two decades have targeted the crucial transport sector that is responsible for some 20% of all CO2 emissions. While previous demonstrations have typically focused on buses and passenger cars, trucks and marine vessels are nowadays included in the mix. ATOME has created a new mobility division commencing operations in 2023 to produce green H2 for transport – initially road transport only — in Paraguay. Paraguay's *Hacia la Ruta del Verde en Paraguay* examines prospects for H2 road transport and identifies alternative energy possibilities for river transport. Paraguay's 2014 *National Development Plan 2014-2030* enshrines transport decarbonization as the central public policy recommendation, committing to a 60% increase of renewable energy consumption and a 20% reduction of fossil fuel consumption. Imported fuels such as diesel and gasoline cost Paraguay $1.3 billion USD in 2019. Growth is anticipated in the vehicle, motorcycle, truck and bus fleets. The bus fleet is effectively a public-private partnership. Consequently, in Paraguay's unique transport eco-system, which in 2019 introduced electric buses, a demonstration featuring trucks and buses has considerable promise. The mobility division will produce green H2 using a 1 MW electrolyser strategically located on a riverfront site in a prime industrial area.

CONCLUSION

ATOME is a first mover in the green H2 and NH3 production space. In the UK, it is actually the first listed pure-play H2 and NH3 producer. ATOME's foundation projects, beneficiaries of 24/7 baseload renewable power, constitute the groundwork for a sustainable, rewarding business that serves the planet, the global energy and food systems, and all our customers.

ACKNOWLEDGMENTS

The author would like to acknowledge the entire ATOME management team and Board of Directors, especially CEO Olivier Mussat and Director of Business Development Nikita Levine.

REFERENCES

[1] International Renewable Energy Agency (IRENA). 2020. Green Hydrogen Cost Reduction: Scaling up Electrolysers to Meet the 1.5°C Climate Goal. IRENA, Abu Dhabi.
[2] Goldman Sachs International. September 22, 2020. Green Hydrogen – the next transformational drive of the Utilities industry.
[3] https://ghgprotocol.org/sites/default/files/standards_supporting/FAQ.pdf Green House Gas Protocol World Resources Institute. Accessed on April 1, 2022.
[4] International Energy Agency. October 2021. Net Zero Emission by 2021 (net zero emissions scenario). Paris, France.
[5] World-first discovery could fuel the new green ammonia economy (phys.org). Monash University. 2021.

WHEC-2022
23rd World Hydrogen Energy Conference
June 26-30, 2022 - Istanbul

#1595

DRIVE CYCLE SIMULATION OF A SMALL-SIZED FUEL CELL ELECTRIC VEHICLE

[1,2*] *Eda Alpaslan,* [1] *Mustafa Umut Karaoğlan,* [1] *Can Ozgur Colpan*
[1]Mechanical Engineering Department, Dokuz Eylul University, Buca, Izmir, Turkey
[2] The Graduate School of Natural and Applied Sciences Dokuz Eylul University, Buca, Izmir, Turkey

*Corresponding author e-mail: edaa.alpaslann@gmail.com

ABSTRACT

Environmental concerns such as global warming and air pollution have increased mainly due to the high energy consumption all over the world. In order to reduce the greenhouse gas and pollutant emissions from transportation sector, fuel cell vehicles offer a clean and highly energy-efficient alternative. In fuel cell vehicles, an energy storage unit such as a battery and/or a supercapacitor (SC) is required in high power demands such as accelerating,uphill and start-up conditions. In this study, a mathematical model a fuel cell vehicle including both a supercapacitor and a battery was developed and its drive cycle simulation was conducted to determine the vehicle performance. As a result of the drive cycle simulation, FCEVs equipped with battery and supercapacitor as storage units, energy efficiency has increased according to the developed simulation algorithm.

Keywords: Fuel cell vehicle, drive cycle simulation, battery, supercapacitor

INTRODUCTION

Fuel cell electric vehicles (FCEV) can have various configurations including energy storage components such as supercapacitor, battery, etc. [1]. Due to the slow response time, narrow power generation range, and not being able to store regenerative energy during braking, fuel cells are used together with an energy storage unit in FCEVs [2] Among the energy storage technologies, supercapacitors are alternative to batteries in transportation with their high power density [3]; however, they have low energy densities. For this reason, a supercapacitor and a battery can provide a great advantage if used together in terms of performance and efficiency [4]. Supercapacitors are more useful in the short term power demands due to their high dynamic performance. Additionally, supercapacitors have a longer lifetime than the battery, so they can be used with batteries in vehicles [5]. In the literature, energy management algorithms and optimization studies have been conducted for hybrid vehicles equipped with fuel cells and supercapacitors. For example, a finite state machine strategy has been proposed for the energy management of the hybrid energy system [6] and a comparison between the proposed system and the system including only battery is done [7]. In this study, a simulation algorithm was determined for power outputs of the components and SOC of the battery with the developed algorithm to increase energy efficiency.

POWERTRAIN COMPONENT MODELS AND SIMULATION METHODS

An energy storage system consisting of a battery and a supercapacitor was modeled in Matlab/Simulink environment. The power requirement of the electric motor, which provides the current demand of a small-sized fuel cell electric vehicle, is calculated with the using the principles of vehicle dynamics. To calculate this requirement, as shown in Eq. 1, the vehicle must overcome total motion resistance forces during driving [8]. The motion resistances are F_R rolling resistance, F_L aerodynamic resistance, and F_a positive acceleration resistance for the vehicle. The regenerative braking effect caused by the negative acceleration due to braking is included in the calculation.

$$P_{EM} = \frac{\left(m.g.f_R + \frac{1}{2}.c_W.A.\rho_L.V^2 + m.a + m.a^-.i_{fr}.\eta_{EM}.\eta_M.\eta_B\right)}{\eta_{EM}.\eta_M}.V = \frac{(F_R+F_L+F_a+F_a^-.\eta_{EM}.\eta_M.\eta_B)}{\eta_{EM}.\eta_M}.V \quad (1)$$

In Eq. 1, m is the vehicle weight (500 kg), g is the gravitational acceleration (9.81 m/s^2), f_r is the rolling resistance coefficient (0.0015), C_w is the aerodynamic resistance coefficient (0.4), a is the vehicle projection area (2 m^2), ρ_L is the air density (1.2 kg/m^3), a is the positive acceleration, a^- is the negative acceleration, i_{fr} is the braking ratio, η_{em} is the electric motor efficiency (0.9), η_m *is the* mechanical efficiency (0.9), and η_b is the battery efficiency (0.92). Depending on the vehicle resistance forces, the power requirements of the motor have been calculated for the ECE 15 drive cycle. The speed profile of the drive cycle is given in Fig. 1.

$$SOC(t) = SOC_i - \frac{1}{Q_{bat}} \quad (2)$$

where Q_{bat} is the total capacity (3.3 [kWh]) of the battery, SOC_i is the initial battery charge (0.8).

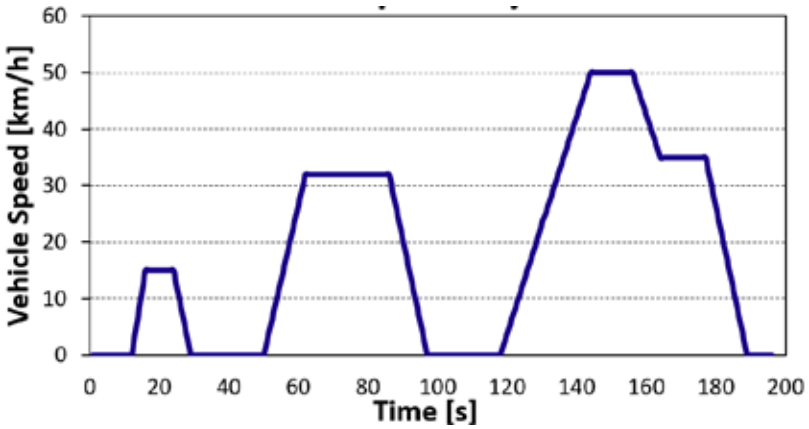


Fig. 1 Speed profile of ECE 15 drive cycle

A typical electrochemical zero-dimensional (0D) fuel cell stack model was conducted to simulate stack behavior under different operating and design conditions. It is generally assumed that every cell performs the same in a stack. The fuel cell operating voltage is generally calculated as follows[9],

$$V_{cell} = V_{Nernst} - \eta_{ohm} - \eta_{act} - \eta_{conc} - \eta_{other} \quad (3)$$

Where η_{ohm}, η_{act}, η_{conc} are the Ohmic, activation, and concentration polarizations, respectively; and η_{other} is the other losses.

In this study, a supercapacitor, as a high-power storage device, is added to the hybrid drive system configuration to provide full capacity. A supercapacitor submodel was built in Matlab/Simulink. The output of the model is the time-dependent supercapacitor energy stored in the SC pack. This energy (E_{SC}) is the value of SC relative to the pack voltage (U_{sc}) and is calculated by the following equation [10].

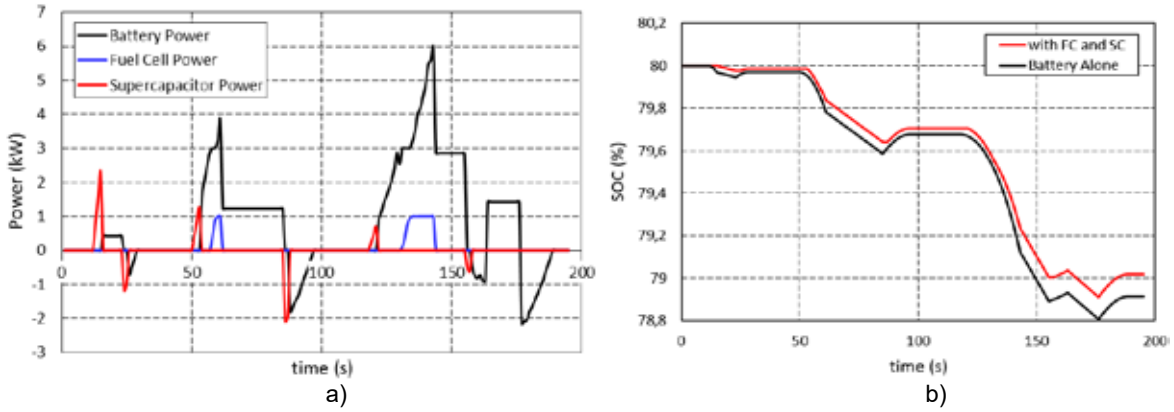
$$E_{sc} = \frac{1}{2} C_{eq} U_{sc}^2 = \frac{1}{2} \frac{N_{p_sc}}{N_{s_sc}} C_{sc} U_{sc}^2 \quad (4)$$

where C_{eq} is the equivalent capacity of the SC's pack, N_{p_sc} and N_{s_sc} are the number of parallel branches and the number of SC's series connections, respectively, and C_{sc} is the SC capacitance.

The battery, fuel cell, and supercapacitor power outputs are calculated according to the simulation algorithm that is developed depending on the vehicle speed, electric motor power, and acceleration time interval.

RESULTS AND DISCUSSION

The speed profile of the drive cycle and vehicle parameters are defined in the Matlab/Simulink model to calculate the power outputs of the fuel cell, supercapacitor, and battery, and the state of charge of the battery. The time-dependent results of the simulations are shown in Fig. 2. As a result of the increase in speed and acceleration due to the driving cycle, the energy required to be supplied to the electric motor also increases. Depending on the simulation algorithm defined for the model, energy is provided from the supercapacitor in regions where the speed increase is sudden, and from the fuel cell and batteries depending on the power requirement in other regions. As can be seen, the maximum battery power requirement of the vehicle is calculated as 6 kW when the fuel cell is also active (Fig 2a).



a) b)

Fig. 2. Simulation results of (a) the battery, fuel cell and supercapacitor power and (b) SOC of the battery

The SOC in the battery, which provides important information about the vehicle range, is calculated for the battery-only and hybrid cases of the vehicle propulsion (Fig. 2b). At the end of the drive cycle time, the SOC of the battery in hybrid configuration differs by 1.25% compared to the case of battery only.

CONCLUSIONS

The powertrain simulation of the fuel cell electric vehicle was carried out to determine the battery, fuel cell, and supercapacitor power with a selected energy management algorithm to investigate the effects of the characteristics of supercapacitor and battery on energy efficiency. The results showed that energy efficiency can be increased with a proper energy management algorithm in fuel cell electric vehicles equipped with battery and supercapacitor as an energy storage unit.

ACKNOWLEDGEMENT

This work has been supported by Dokuz Eylul University's Scientific Research Projects with the project number 2020.KB.MLT.012.

REFERENCES

1. Alpaslan, E., Çetinkaya, S. A., Yüksel Alpaydın, C., Korkmaz, S. A., Karaoğlan, M. U., Colpan, C. O., Erginer, K. E. & Gören, A. 2021. A review on fuel cell electric vehicle powertrain modeling and simulation. *Energy Sources, Part A: Recovery, Utilization, and Environmental Effects*, 1-37. (Article in Press)
2. Ellis, M. W., Von Spakovsky, M. R., & Nelson, D. J. 2001. Fuel cell systems: efficient, flexible energy conversion for the 21st century. *Proceedings of the IEEE*, *89*(12), 1808-1818.
3. Winter, M., & Brodd, R. J. 2004. What are batteries, fuel cells, and supercapacitors?. *Chemical reviews*, *104*(10), 4245-4270.
4. Du Pasquier, A., Plitz, I., Menocal, S., & Amatucci, G. 2003. A comparative study of Li-ion battery, supercapacitor and nonaqueous asymmetric hybrid devices for automotive applications. Journal of power sources, 115(1), 171-178.
5. Salmasi, F. R. 2007. Control strategies for hybrid electric vehicles: Evolution, classification, comparison, and future trends. IEEE Transactions on vehicular technology, 56(5), 2393-2404.
6. Wang, Y., Sun, Z., & Chen, Z. 2019. Energy management strategy for battery/supercapacitor/fuel cell hybrid source vehicles based on finite state machine. Applied energy, 254, 113707.
7. Djerioui, A., Houari, A., Zeghlache, S., Saim, A., Benkhoris, MF, Mesbahi, T., & Machmoum, M. 2019. Energy management strategy of supercapacitor/fuel cell energy storage devices for vehicle applications. International Journal of Hydrogen Energy, 44(41), 23416-23428.)
8. Ehsani, M., Gao, Y., Longo, S., & Ebrahimi, K. M. 2018. *Modern electric, hybrid electric, and fuel cell vehicles*. CRC press.
9. Chabane, D., Ibrahim, M., Harel, F., Djerdir, A., Candusso, D., & Elkedim, O. 2019. Energy management of a thermally coupled fuel cell system and metal hydride tank. *International Journal of Hydrogen Energy*, *44*(50), 27553-27563.
10. Lahyani, A., Venet, P., Guermazi, A., & Troudi, A. 2012. Battery/supercapacitors combination in uninterruptible power supply (UPS). *IEEE transactions on power electronics*, *28*(4), 1509-1522.

WHEC-2022

23rd World Hydrogen Energy Conference

TRACK 15. HYDROGEN ECONOMY, LOGISTICS, INFRASTRUCTURE

TRACK 15. HYDROGEN ECONOMY, LOGISTICS, INFRASTRUCTURE

#17 ASSESSMENT OF THE SOCIO-ECONOMIC COSTS AND BENEFITS OF INCREASED USE OF BIOMETHANE AND HYDROGEN IN EUROPE	1346
#62 THE HYDROGEN SCIENTIFIC ASPECTS IN ROMANIA	1349
#101 MUCILAGE IN THE MARMARA SEA VERSUS BLACK SEA's H_2S; HYDROGEN ENERGY PRODUCTION OPPORTUNITIES	1352
#112 FABRICATION OF PLATINUM-COBALT NANOWIRES BY CENTRIFUGAL ELECTROSPINNING METHOD AS ELECTROCATALYSTS FOR PEMFC	1355
#117 ECONOMICAL PREPARATION AND CHARACTERIZATION OF DUAL-IONS CONDUCTING FUEL CELL	1358
#132 ANALYSIS OF ECONOMIC EFFICIENCY ON INTERNATIONAL HYDROGEN SUPPLY CHAINS TO JAPAN	1361
#135 ON THE FUTURE ROLE OF HYDROGEN AS STORAGE FOR ELECTRICITY	1364
#153 NUMERICAL MODEL AND EXPERIMENTAL VALIDATION OF ULTRA-LEAN AIR-HYDROGEN COMBUSTION IN CATALYTIC MONOLITHS	1367
#185 OPTIMIZATION OF A HYDROGEN SUPPLY CHAIN: A CASE STUDY FOR ITALY	1370
#191 LIFE CYCLE COSTING APPROACHES OF FUEL CELL AND HYDROGEN SYSTEMS: A LITERATURE REVIEW	1373
#225 THE TECHNO-ECONOMIC EVALUATION OF HYDROGEN PRODUCTION COST TOWARDS ANION EXCHANGE MEMBRANE ELECTROLYZER	1376
#238 CHARACTERISTIC AND PERFORMANCE OF $Ce_{0.6}Mn_{0.3}Fe_{0.1}O_2$ FOR SOLID OXIDE FUEL CELLS ANODE ELECTRODE	1379
#241 SYNGAS PRODUCTION VIA CHEMICAL LOOPING DRY REFORMING OF METHANE USING IRON-BASED OXYGEN CARRIERS	1382
#243 MODELING FOR THE DEVELOPMENT OF HEAVY-DUTY REFUELING PROTOCOLS	1385
#260 INFLUENCE OF THE TURBULENCE MODEL IN THE CFD SIMULATION OF HYDROGEN TANK FILLING BY AN IMPINGING OBLIQUE JET	1388
#295 FORMABILITY AND PERFORMANCE TESTING OF STAINLESS-STEEL BIPOLAR PLATE FOR AIR-BREATHING PEMFC	1391
#310 PROTON-CONDUCTING SOLID OXIDE FUEL CELLS WITH NLSCF CATHODE	1394
#351 TRANSACTIVE MOBILITY WITH HYBRID ELECTRIC AND HYDROGEN CHARGING INFRASTRUCTURES	1397
#367 HYDROGEN TRANSPORTATION OPTIONS AND CHALLENGES	1400
#397 ECONOMIC AND ENVIRONMENTAL EVALUATION OF FUELING OPTIONS FOR HYDROGEN FUEL CELL HEAVY-DUTY VEHICLES	1403
#409 ANALYSIS OF THE DEMAND OF HYDROGEN AS FUEL FOR TRANSPORT IN THE UAE	1406
#439 GRID BASED RISK ASSESSMENT OF A HYDROGEN SUPPLY CHAIN	1409
#1458 ANALYSIS OF A HYDROGEN SUPPLY CHAIN WITH RANDOM DEMAND: A CASE STUDY	1412
#1470 ASSESSMENT OF HYDROGEN DELIVERY OPTIONS	1415
#1485 TECHNO-ECONOMIC AND PROCESS SIMULATION OF SMALL-SCALE HYDROGEN PRODUCTION FROM NH3 DECOMPOSITION	1418
#1525 TECHNO-ECONOMIC ANALYSIS OF 350 BAR LOHC-SUPPLIED HYDROGEN REFUELING STATIONS FOR HEAVY DUTY VEHICLE FLEETS	1421
#1562 EVALUATION OF POTENTIAL HYDROGEN PRODUCTION METHODS IN TURKEY BY USING A HYBRİD METHOD BASED ON PYTHAGOREAN FUZZY AHP AND INTERVAL TYPE-2 FUZZY TOPSIS	1424
#1632 WHAT IS THE KEY ROLE OF HYDROGEN ENERGY IN METAVERSE?	1428

WHEC-2022
23rd World Hydrogen Energy Conference
June 26-30, 2022 - Istanbul

#17
ASSESSMENT OF THE SOCIO-ECONOMIC COSTS AND BENEFITS OF INCREASED USE OF BIOMETHANE AND HYDROGEN IN EUROPE

Jan Michalski, Matthias Altmann, Ulrich Bünger, Jan Zerhusen*
Ludwig-Bölkow-Systemtechnik GmbH (LBST), Daimlerstr. 15, 85521 Ottobrunn, Germany

*Corresponding author e-mail: jan.michalski@lbst.de

ABSTRACT
This paper presents selected results from the study “Impact of the use of the biomethane and hydrogen potential on trans-European infrastructure” which has been conducted by Trinomics, Ludwig-Bölkow-Systemtechnik GmbH (LBST) and E3Modelling (E3M) for the European Commission. The major objective of the study was to analyse the impact of biomethane and hydrogen on the gas sector in Europe until 2050 from technical, economic and regulatory perspective. In general form the system perspective, the optimal system design strongly depends on the anticipated GHG emission reduction targets. Among the analysed cases the scenario with a strong focus on hydrogen technology appears to be a robust compromise where the advantages of higher system flexibility overcompensate the disadvantages of lower energy efficiency in comparison to the electricity-focused scenario. Based on the study’s results, strategies for fully decarbonized gas system by 2050 should be developed describing cost-effective transition pathways in the medium-term (2030) and towards the long-term (2050) target situation of full decarbonisation.

Keywords: Energy System, Gas Infrastructure, Decarbonization, Modelling

INTRODUCTION

Today the gas sector plays an important role in the existing energy system. It accounts for more than 200,000 km of transmission and 2 million km of distribution grids serving around 150 million customers from different sectors including heating and power sectors as well as industry [1], [2]. The overall natural gas consumption in European Union reached more than 4,800 TWh/a in 2017 out if which ca. 74% was imported mainly from Russia, Norway and Algeria [3]. In this context, natural gas is an important source for primary energy and feedstock for different end-users. It provides also adequate flexibility services to the energy system through the use of gas storage as well as flexible gas power plants. Nevertheless, the gas sector is subject to ambitious plans of the European Commission for deep decarbonization of the economy until 2050 by substituting the fossil natural gas by other green and GHG-free gases such as biomethane or hydrogen [4]. In this context, this paper presents selected results from the study “Impact of the use of the biomethane and hydrogen potential on trans-European infrastructure” which has been recently conducted by Trinomics, Ludwig-Bölkow-Systemtechnik GmbH (LBST) and E3Modelling (E3M) for the European Commission. The major objective of this study was to assess the socio-economic costs and benefits of increased use of biomethane and hydrogen in Europe until 2050 from technical, economic and regulatory perspective.

MODELLING ERUOPEAN ENERGY SYSTEM AND INFRASTRUCTRE

The quantitative analysis is carried out for three scenarios, each focusing on electricity, methane and hydrogen, respectively, as major energy carrier. Although all scenarios are of explorative character the economic value of the use of full potential of biomethane and hydrogen can be derived from comparison of the modelling results between the different scenarios for the time horizons 2030 and 2050. The analysis employs dedicated modelling of the European energy system with the objective to minimize the overall system costs by taking into account technical constraints of all system components. The model is formulated as a linear program and is subdivided into two steps. In the first step the cost-optimal energy supply for the predefined end-user sectors is calculated without any grid constraints. Based on these results in the second step the optimal energy flows and corresponding infrastructure capacities between the Member States for the three energy carries power, methane and hydrogen are analysed.

RESULTS AND DISCUSSION

Under the assumptions of this study the total gas demand in the end user sectors transport, residential, services, industry is expected to decrease from ca. 2,800 TWh/a in 2015 to 2,000-2,500 TWh/a, in 2030. In this context, the strong decline from residential, services, industry sectors due to building insulation and efficiency measures is partially compensated by the increase in gas demand from the transport sectors. Based on comparatively high carbon price of 84 €/t_{CO2} the power sector requires additional 1,000 TWh/a of methane supply (providing 600-730 TWh/a electricity) mainly due to the merit order switch from coal to gas. Hence, gas-fired power plants play an important role for the transition of the future energy system. Natural gas imports along the established routes from East to West

and from North to South are the major supply source in this time step whereas the use of biomethane and hydrogen due to comparatively high costs is limited.

In the long-term until 2050 the gas demand from the end user sectors increases in methane and hydrogen-focused scenarios due to additional gas consumption as fuel in the transport sector. However, since in 2050 gas-fired power plants provide only limited back-up power (25-190 TWh/a with a large capacity of 250-360 GW) to balance out intermittent electricity feed-in the overall gas demand decreases to ca. 2,500 TWh/a (in electricity and hydrogen-focused scenarios) or remains at the same level of approx. 3,500 TWh/a as in 2030 (in methane-focused scenario). Although in electricity and methane-focused scenarios the full potential of biomethane is used to decarbonise the energy system substantial amounts of synthetic methane from Power-to-Gas (200-1,500 TWh/a) are needed to satisfy the gas demand. In the hydrogen-focused scenario large amounts of hydrogen of more than 2,000 TWh/a are produced via water electrolysis which is mainly located in close proximity to renewable power feed-in. Therefore, the gas grid both for methane and hydrogen requires substantial enhancements to transport renewable gas from boundaries of Europe with large renewable energy potentials to demand clusters in Central Europe (Figure 1). The decarbonisation of the energy system and growing renewable power supply require additional flexibility measures to balance out the fluctuating electricity supply and demand. One of the major flexibility measures is represented by electrolysis as a flexible load with an installed capacity of 250-1,200 GW_{el} and utilisation rates of 2,000-3,000 full load hours in 2050.

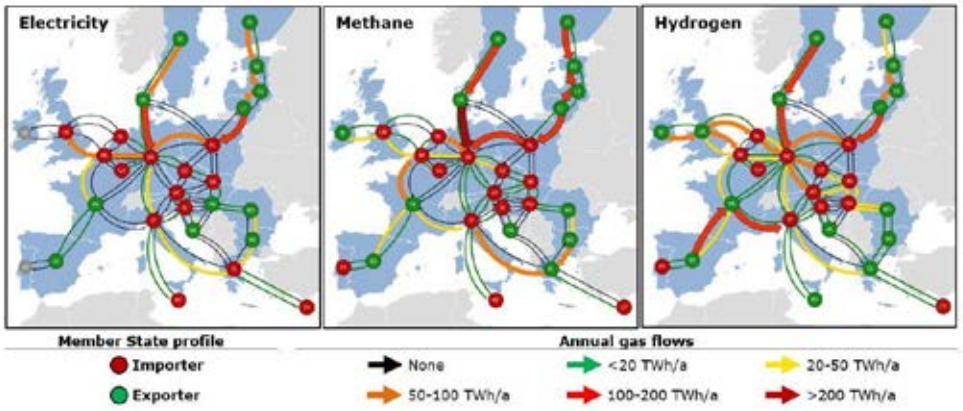


Fig. 1. EU28 cross-border annual gas flows in 2050 for the three scenarios

The comparison of the system costs for the three scenarios until 2030 reveals similar cost structure and magnitude with major contribution from fossil energy imports (Figure 2). In this context, bio methane and hydrogen supply have limited impact on the energy system costs. In the long-term until 2050 the system costs decrease due to cheap renewable power production and increasing sector integration between powers. The lowest system costs are achieved in hydrogen-focused scenario followed by electricity and methane-focused scenarios and can be viewed as a trade-off between renewables, system flexibility and gas supply. The system design with a strong focus on hydrogen technology appears to be a robust compromise where the advantages of higher system flexibility overcompensate the disadvantages of lower energy efficiency in comparison to the electricity-focused scenario. In the methane-focused scenario the lower efficiency of the end user applications makes this option less attractive than both other scenarios. At the interconnector level the gas transport costs are rather similar for all scenarios in 2030 and the electricity and methane-based scenario sin 2050 with approx. 1-2 B€/a. This is due to comparatively cheap existing methane infrastructure and limited investments in new capacities. In the hydrogen-focused scenario in 2050 the investments in new dedicated H2 pipelines as well as its maintenance drive the infrastructure costs at the international level up to 7 B€/a.

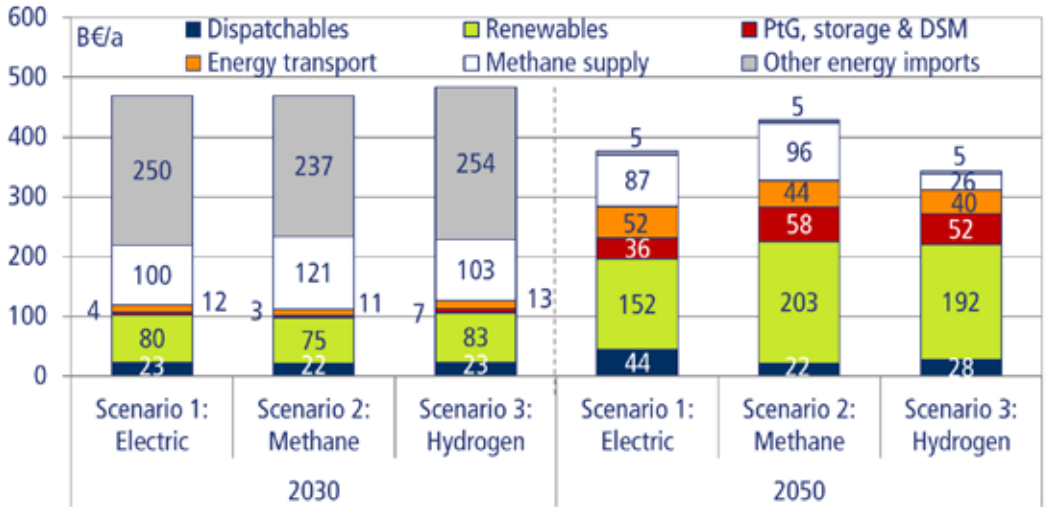


Fig. 2. Annual energy system costs in EU-28

CONCLUSIONS

In general form the system perspective the optimal system design strongly depends on the anticipated GHG emission reduction targets. Therefore, binding targets in particular in the long-term until 2050 are needed for a cost-effective transition of energy supply and transport infrastructures both for gas and power. In this way misinvestments and unfavourable lock-in effects can be avoided. Also, a coordinated development of power and gas infrastructures in line with the build-up of renewable energy and seasonal storage capacities is needed to minimize the system costs. In the context of system stability adequate market mechanism supporting the energy-only market should be considered in order to ensure the competitiveness of flexibility measures with low utilisation rates such as gas-fired power plants or electrolysis as a flexible load. Certification mechanism for renewable gases might help to establish fair competition between different players within the decarbonising gas market. Further analyses from the end user and business perspective would complement modelling exercises from a pure system perspective. Especially for the gas infrastructure the ongoing re-investments in aging assets should be assessed in more detail from the operator perspective to ensure positive business cases when comparing methane and hydrogen infrastructures.

Based on this study's results for 2030 and 2050 as spotlights of gas grid development scenarios, strategies for fully decarbonized gas system by 2050 should be developed describing cost-effective transition pathways in the medium-term (2030) and towards the long-term (2050) target situation of full decarbonisation. Notably for hydrogen, further analysis of possible development strategies and pathways for a stepwise development of 100% hydrogen grid "islands" growing into one large hydrogen grid with methane-based islands in the future is worth exploring for a roadmap for transitioning to a 2050 gas system with separate H_2 and CH_4 grid systems.

REFERENCES

1. CEER 2018. CEER Benchmarking Report 6.1 on the Continuity of Electricity and Gas Supply, Brussels
2. Marcogaz 2014. Technical statistics 01-01-2013, Brussels.
3. Eurostat 2019. Simplified energy balances. Brussels.
4. European Commission 2018. A Clean Planet for all A European strategic long-term vision for a prosperous, modern, competitive and climate neutral economy. COM(2018)773.

WHEC-2022
23rd World Hydrogen Energy Conference
June 26-30, 2022 - Istanbul

#62
THE HYDROGEN SCIENTIFIC ASPECTS IN ROMANIA

[1*] Ioan Iordache, [1] Mihai Varlam, [1] Elena Carcadea, [1] Dorin Schitea, [1] Mihaela Iordache
[1] National Research and Development Institute for Cryogenics and Isotopic Technologies -ICSI, Uzinei Str., Rm. Vâlcea, Romania

*Corresponding author e-mail: iordache.ioan@icsi.ro

ABSTRACT

This work presents the latest advances of hydrogen and fuel cell research and development from Romania.
The presentation focuses more on National Hydrogen and Fuel Cell Centre (NHFCC) researchers' activities as a part of national policy and program issues. This centre is a research and development facility with the mission to implement, develop and disseminate hydrogen-based technologies in Romania, as well as to support national priority policies in the field of energy and environment. It has an exceptional infrastructure for the entire process chain of the new energy revolution (production, storage, transport, and utilization). The researchers are focused on the development of technologies, products and services that contribute to achieve an "economy of hydrogen" in Romania.

Keywords: Romania, National Hydrogen and Fuel Cell Centre

INTRODUCTION

The national hydrogen and fuel cell technology strategies vary considerably from country to country due to different national specific and particular constraints. Two types of policies can be found at EU level: the policies of European Commission, supported by Fuel Cells and Hydrogen 2 Joint Undertaking (FCH2 JU), and the Members States' policies, including both national and regional.

In principle, the hydrogen economy is initiated by hydrogen communities as early adopters (cities, remote locations or islands, self-contained entities as airports, seaports, industrial complexes, etc., or distributed entities as hydrogen highways) of hydrogen and fuel cell technologies for energy proposes. The larger-scale adoption of such technologies within a coherent end-user grouping, is the next step that depend by the success of the initial demonstrative results. The hydrogen communities could be. In this context, it should be mentioned that Romania is a country that traditionally produces hydrogen [1].

In order to ensure Romania's energy security in the next period of time, there is necessary to understand the global perspective and the newest trends in energy. The implementation of new energy solutions depend on the co-operation of numerous public and private stakeholders. In this work authors intend to present and clarify this special situation in Romania. The authors hope that this work will be a useful tool in order to create an accurate picture about national specific situations in Romania.

HYDROGEN ASPECTS IN ROMANIA

National Hydrogen and Fuel Cell Centre

The National Hydrogen and Fuel Cell Centre (Fig. 1) is a research and development facility with the mission to implement, develop and disseminate hydrogen-based technologies in Romania, as well as to support national priority policies in the field of energy and environment. It has an exceptional infrastructure for the entire process chain of the new energy revolution. The human resource is focused on the development of technologies, products and services that contribute to achieve an "economy of hydrogen" in Romania [2].

NHFCC's milestones:

- 2009 – National Center for Hydrogen and Fuel Cells has been developed due to results, knowledge and expertise acquired in the research projects done in the renewable energy field.
- 2009 – the research center becomes a full member of the Joint Technology Initiative – Joint Undertaking on Hydrogen and Fuel Cell, a unique public-private partnership supporting research, technological development and demonstration in the field of fuel cells and hydrogen-based energy technologies in Europe.
- 2012 – the staff of research center leads to the foundation of the Romanian Association for Hydrogen Energy.

• 2012 the entire R&D has been completed both instrumentally and from human resources capabilities by developing two other facilities research: Low Temperature Laboratory - CRYO-HY and Energy Storage Laboratory - ROM-EST (in 2015).

• 2014 - National Center for Hydrogen and Fuel Cells becomes a national interest facility, being a support installation with experimental and testing equipment to address a wide range of research into the use of hydrogen for energy purposes.

• 2017 – NHFCC becomes a member of the Research infrastructure in Energy-Environment-Water-Systems – RENEWS, a Research Integrated Infrastructure active at national level.

The research activity carried out within this facility connects the Romanian research to the international scientific community in field of hydrogen based technologies. The research centre provides adequate scientific, technical and logistical support, being in the same time accessible to other users interested in conducting their own research activities or in collaboration.



Fig. 1. National Center for Hydrogen and Fuel Cell

Hydrogen and fuel cell research in Romania

Some more than 100 scientific articles in the field of fuel cell and hydrogen energy including topics such as: engineering, materials science, chemistry and chemical engineering, energy, environmental science and mathematics, have Romanian authors or affiliates of Romania since 2000.

The Romanian participation in EU co-financed projects is really modest. The National Center for Hydrogen and Fuel Cells has two participations and other four participations is realised by other four research or academic groups.

Here we provide three examples of this types of projects supported by the Fuel Cell and Hydrogen Joint Undertaking. The HyUnder project (FCH JU grant no. 303417) setting out the hydrogen underground storage potential from Romania and where was realised firs this type of study [3]. This project germinated new ideas and other scientific works referring to the hydrogen underground in salt caverns in Romania. The HyLaw (FCH JU grant no. 737977), it is referring to removal of legal barriers to the deployment of fuel cells and hydrogen applications. The results from this project are included in to a common database available on https://www.hylaw.eu/database. The HyLaw database is structured into nine categories with a relevant number of hydrogen applications and different legal and administrative processes. The last project, TeacHy (FCH JU grant no. 779730), strive to deliver a substantially improved teaching of hydrogen and fuel cell content across Europe.

Another important source for financing the projects was the National Plan for Research, Development and Innovation (PNCDI II), lunched by public authorities in period 2007-2013. It was a financing instrument based on competition between research groups. The program financed around 26 hydrogen and fuel cell research projects. The projects was created as a consortium led by research institutes, universities and research centers.

There are need early scientific, technical and business analysis in order to develop a future hydrogen infrastructure, which take years. The scientific studies ad researches are necessary for a better understand the role of hydrogen in Romania's future renewable energy based energy system.

Finally, but not at the end, the hydrogen community, concatenated the efforts and established the Romanian Association for Hydrogen Energy, in order to disseminate knowledge to the peoples and to press the decision makers. The association is a nongovernmental organization formed of individuals and legal entities.

CONCLUSIONS

The worldwide political requirements for reducing GHG-emissions and the EU's commitments and directives for the renewable energy are important aspects for the market penetration of the hydrogen and fuel cell in Romania. It has the opportunity to make the transition from the hydrocarbon power industry to a power sector utilizing hydrogen and renewable energy sources. The replacement of the actual technologies would offer the opportunity to implement hydrogen, fuel cell stacks and hybrid systems.

Above mentioned indices that mainly interest for hydrogen energy is in universities and research centers. This highlights the high level of the universities and research institutes. Unfortunately the industry is not so active and have avoided to participate in this very new sector.

REFERENCES

1. Ionescu C. 2005. Study on the implementation of fuel cell in Romania (in Romanian), in Ministry of Education and Research, Fuel Cell. Bucharest, Universul Energiei.
2. Iordache I, Gheorghe AV, Iordache M. Towards a hydrogen economy in Romania: Statistics, technical and scientific general aspects. International Journal of Hydrogen Energy 2013; 38:12231-40.
3. Iordache I., Schitea D., Gheorghe A., Iordache M.. Hydrogen underground storage in Romania, potential directions of development, stakeholders and general aspects. International Journal of Hydrogen Energy, 39, 11071-11081, 2014.

WHEC-2022
23rd World Hydrogen Energy Conference
June 26-30, 2022 - Istanbul

#101

MUCILAGE IN THE MARMARA SEA VERSUS BLACK SEA's H_2S; HYDROGEN ENERGY PRODUCTION OPPORTUNITIES

[1]* *Erhan Atay,* [2]*Sudi Apak,*
[1]Trakya University,Economics Department, Edirne,Türkiye.
[2]Istanbul Esenyurt University,Ind.Eng. Dept,Istanbul,Türkiye

*Corresponding author e-mail: erhanatay@trakya.edu.tr

ABSTRACT

Hydrogen energy is among alternative solutions to energy shortage regarding the aspects of being environmentally clean, economic and efficient. In this context, Turkey's energy demand, which cannot be met by our country and will not be able to be met by local resources in the 2020s. Therefore, Turkey should turn to renewable energy sources as soon as possible, especially hydrogen energy to be obtained from the Black Sea, as well as a new type of energy that can be obtained by turning the mucilage crisis in the Sea of Marmara into an opportunity. In addition, the conversion of these organic wastes in the Marmara Sea into hydrogen energy as a renewable energy source will be an innovative and high added value solution method.
Our aim in this study is to bring up the hydrogen energy potential in the Black Sea and Marmara Sea's mucilage crises to investigate the contribution of hydrogen energy to our economy by eliminating the energy deficit.

Keywords: Hydrogen economy, Marmara Sea, Mucilage, H_2S, Black Sea

INTRODUCTION

Hydrogen, as an energy carrier has some advantages with respect to fossil fuels on the environmental and economic bases. The fact that hydrogen fuel can be used in internal combustion engines, that is, in all vehicles such as buses, trucks, automobiles, tractors, and agricultural machinery, replaces petroleum products with limited reserves, and is an environmentally friendly energy, has attracted great interest of companies producing vehicles in recent years.

For instance, in the world's hydrogen energy usage practice as of September 2012, Coradia iLint, the world's first hydrogen powered train developed by Alstom, has passed the tests conducted in France. It was also tested in France at a ceremony in the presence of French Transport Minister Jean-Baptiste Djebarri.

Therefore, German state railways Deutsche Bahn and technology giant Siemens announced last year that they are developing hydrogen-powered trains as part of a plan to reduce emissions to zero by 2050.

On the other hand, the Black Sea is fed by the rivers coming from the countries around it. At the same time, all the polluted wastes of 21 countries in Europe and Asia are transported to the Black Sea. The fact that our Black Sea coasts are rich in hydrogen puts us among the lucky countries in the world in terms of reserves and is Turkey's hydrogen energy center. is mentioned by name.

The outline of the paper is as follows. Section 2 sets up Hydrogen economy and Hydrogen Energy Opportunity in the Black Sea while section 3 deal with as a new topic Marmara Sea's mucilage problem. Finally last section is conclusion.

FUTURE OF THE TURKEY'S HYDROGEN ENERGY POWER IN THE BLACK SEA

Hydrogen is the simplest of atoms. In its normal form in the universe, hydrogen contains an electron and a proton. In its rarer form, called heavy hydrogen, there are three particles. It is this structure of hydrogen that makes it the most active element in the 15-billion-year-old story of our universe (Rigden, 2002).

To achieve low carbon levels, hydrogen is well positioned in countries with a diversity of renewable energy sources, especially in the Middle East region, and some new projects are under development. However, the development of industrial strategies is not sufficient. If hydrogen-rich fuels such as ammonia, as well as critical minerals, gain importance in international energy-related trade, their total share is targeted to increase from 13% to 25% in APS by 2050 (IEA, 2021).

In this context, 90% of the water of the Black Sea is anaerobic and contains hydrogen sulfide (H_2S). 8ml at 1000m depth. The H_2S concentration, which is Lt-1, is 13.5 ml at the base. It reaches the level of Lt-1. There are technological studies on hydrogen production from H_2S using two reactors, such as an electrolysis reactor and an oxidation reactor.

Along the axis of the Black Sea, at a depth of 200 meters, there is a "fuel" layer, about 50 meters thick and yet untouched, between the oxygen-free and oxygenated water layers. The amount of hydrogen sulphate produced from the sediment layers of the sea is estimated to be around 10 thousand tons per day, and this amount is constantly increasing. This means a production potential of approximately 500 tons of hydrogen gas per day.

Producing hydrogen from hydrogen sulfide in the depths of the Black Sea is easier and cheaper than other methods, and R&D studies are also carried out in Russia, Georgia, Romania and Bulgaria in this area. Our Black Sea coasts have more hydrogen sulfide reserves since they are deeper than Russian side 90% of the water of the Black Sea is anaerobic and contains hydrogen sulfide (H_2S). 8ml at 1000m depth. The H_2S concentration, which is Lt-1, is 13.5 ml at the base. It reaches the level of Lt-1.

Another technology development study on this subject is hydrogen production by photocatalytic method using semiconductor particles. It is a scientific research in the literature for the production of hydrogen from the H_2S-containing water of the Black Sea by utilizing solar and wind energy, and Bulgaria is trying to develop a project. However, the presence of a natural hydrogen reservoir at the bottom of the Black Sea is an opportunity for Turkey's future. Hydrogen studies in our country should be developed by considering it consistently and seriously (Ültanır:1998)

In this regard, a PEM electrolyzer unit generates hydrogen from hydrogen sulfide that is available in the Black Sea deep water. The generated hydrogen and sulfur gas from hydrogen sulfide are stored in high-pressure tanks for later use. Hydrogen is blended with natural gas, and the blend is utilized for industrial and residential applications. The investigated system is modeled with the Aspen Plus software, and hydrogen production, blending, and combustion processes are analyzed accordingly (Öztürk, Midilli and Dinçer, 2021).

Therefore, at the international level, producing hydrogen from hydrogen sulfide in the depths of the Black Sea is easier and cheaper than other methods, and R&D studies are also carried out in Russia, Georgia, Romania and Bulgaria in this area. Our Black Sea coasts have more hydrogen sulfide reserves since they are deeper than the Russian side.

On the other hand, in order to activate the hydrogen energy reserves and make the necessary investments, Turkey, Bulgaria, Ukraine, Russia, It can be suggested to encourage the 'Black Sea Energy Cooperation' to be established by regional countries such as Georgia and Romania (Midilli et al., 2005).

Finally, the removal of H_2S from bottom of the Black Sea and separation into components undesirable harmful compound may turn into a useful energy resource. Hydrogen production from H_2S can be achieved by facilitating suitable hydrogen production methods in both the central and coastal regions of the Black Sea (Şeker, 2021).

MUCILAGE IN THE MARMARA SEA AND ITS UNKNOWN ENERGY OPPORTUNITIES

In aquatic environments that are under the influence of many environmental problems such as pollution, overfishing, invasive species, climate change. With the change of trophic conditions, harmful phytoplankton species multiply and become dominant. This harmful phytoplankton overgrowth of species is often referred to as harmful algae growth or algal bloom, and as a result aspect; A high amount of extracellular polymeric organic substance is secreted from the large number of living cells formed. These extracellular organic substances called mucilage; mostly by diatoms and dinoflagellates is produced (Eren, 2021).

Marine mucilage or sea sputum is one of the intense environmental problems that increases with global warming and pollution. Marine mucilage, which occurs especially interior in the waters and gulfs, has increased in recent years, its incidence and density in Turkish seas (Türkistanli, 2021).

Sea of Marmara, it is an important inland sea with traffic around Istanbul and Canakkale which their throats are tied dense sea with numerous industrial zones. In mid-spring of year 2021 appeared in the sea of Marmara The resulting mucilage has become a serious threat over time reachedup to kilometers in length mucilage, with its other names in the literature, “Sea The nature of the phenomenon of "snot" or "sea saliva" as gelatinous aggregates is defined (Kavzoğlu,T et al., 2021).

Another parameter of hydrogen energy is related to carbon dioxide in the atmosphere. It is estimated that the rate of carbon dioxide in the atmosphere will reach 520 ppm in 2050. It is estimated that this amount can be reduced with the widespread use of hydrogen energy (Erdener, 2007).

In sum, we can benefit from Marmara Sea’s mucilage problem as a new renewable energy in using microalgae isolated from marine mucilage. Accordingly, this opportunity should be take into account such as Black Sea’s H_2S hydrogen energy potential.

CONCLUSIONS

Coal is a type of rock formed by the transformation of plants and nature into fossils in swampy environments. Although there is no clear answer to the question of how oil is formed, it is assumed that oil was formed by the decomposition of plant and animal remains that lived millions of years ago.

It is clearly seen that hydrogen, which is an ideal fuel, will be widely used by solving the problems encountered in production, application and economic aspects. On the other hand, H_2S is a colorless, foul-smelling gas, heavier than air and flammable. It is possible to produce hydrogen energy by decomposition of H_2S such as Black Sea deep waters case.

Hydrogen energy from the Black Sea is not a single example in the worldwide .For example, historically, in the socialist period in Romania, former government wanted to build a hydrogen power plant by using the hydrogen sulfur from the deep waters of the Black Sea.

Therefore, if we take into account Marmara Sea's recent mucilage dilemma, hydrogen and photocurrent can be produced using microalgae isolated from marine mucilage. In this context, mucilage should be evaluated in green energy production studies on renewable energy as biological waste.

Consequently, it is suggested that the Black Sea region countries such as Turkey, Bulgaria, Ukraine, Russia, Georgia and Romania should encourage and invest to activate in renewable energy especially „"hydrogen energy" and this energy source can be transported to the European Union countries.

REFERENCES

1.Erdener,H et al. 2007. Sustainable Energy and Hydrogen,ODTÜ Toplum ve Bilim Merkezi Publ.,Ankara..
2.Eren, Z., (2021). The Relationship of Harmful Algae Bloom and Mucilage Outbreak in the Sea of Marmara, Journal of Environmental and Natural Studies, Volume, 3, Issue 2, Pages:182-192.
3.IEA ,2021 (International Energy Agency), World Energy Outlook .
4. Kavzoğlu,T et al.2021. Detection and Analysis of Marine Mucilage Bloom in the Sea of Marmara By A Machine Learning Algorithm from Multi-Temporal Optical and Thermal Satellite Images,
5.Midilli,A, and Ay M,Kale A,Veziroğlu,N.,2005. ''Hydrogen Enery Potential of Black Sea Deep Water Based on H2S and Importance of the Region'',IHEC 2005,Istanbul.
6.Öztürk,M,and Midilli,A, and Dinçer,İ. 2021. Effective use of hydrogen sulfide and natural gas resources available in the Black Sea for hydrogen economy,IJHE,vol:46,ıssue:18,pp. 10697-10707.
7.Rigden SJ. 2002. Hydrogen the essential element,Harvard College President and Fellows.
8.Şeker S, and Aydın N. 2021.Assessment of hydrogen production methods via integrated MCDM approach under uncertainty,International Journal of Hdyrogen Energy, Available online 20 August 2021.
9. Türkistanli TT et al.2021. Bibliometric Analysis of the Literature on Marine Mucilage, European Journal of Science and Technology Special Issue 28, pp. 947-958.
10.Ültanır,Mustafa Özcan. 1998. Evaluation of Turkey's Energy Strategy as We Enter the 21st Century,TÜSİAD Publ.,Istanbul .

WHEC-2022
23rd World Hydrogen Energy Conference
June 26-30, 2022 - Istanbul

#112

FABRICATION OF PLATINUM-COBALT NANOWIRES BY CENTRIFUGAL ELECTROSPINNING METHOD AS ELECTROCATALYSTS FOR PEMFC

[1]Chen-Yu Wu, [1*] Min-Hsing Chang
[1]Department of Mechanical and Materials Engineering, Tatung University, Taipei, 104, Taiwan

*Corresponding author e-mail: mhchang@gm.ttu.edu.tw

ABSTRACT

The centrifugal electrospinning method is employed to fabricate platinum-cobalt (PtCo) bimetallic nanowires as electrocatalysts for proton exchange membrane fuel cell (PEMFC). The influences of system parameters on the nanowire morphology are explored systematically including the rotating speed of spinneret, applied voltage, and atomic ratio of Pt and Co in the nanowires. The electrochemical performance of the PtCo nanowires is evaluated by performing cyclic voltammetry (CV) tests to characterize the electrochemical active surface area (ECSA). The accelerated degradation tests (ADT) are also conducted to examine the durability of the PtCo nanowires. The membrane electrode assembly (MEA) using PtCo nanowires as cathode electrocatalysts is also made and the fuel cell performance is tested and compared with conventional MEA using Pt/C catalysts. It is found that under the condition of rotating speed 1600 rpm, collecting distance 12 cm, applied voltage 13 kV, and atomic ratio of Pt:Co = 4:1, PtCo nanowires can be produced successfully with good morphology and the mean diameter is 76 nm. The corresponding ECSA is 11.69 $\mathrm{m^2 g^{-1}}$ and the ADT results show the resultant PtCo nanowires exhibit better durability than conventional Pt/C catalysts.

Keywords: Centrifugal electrospinning method, PtCo nanowires, Electrocatalyst, PEMFC

INTRODUCTION

Nowadays, the application of proton exchange membrane fuel cell (PEMFC) is still restricted due to the major barrier of precious platinum (Pt) catalyst. Because the slow reaction kinetics of oxygen reduction reaction (ORR) in the cathode, a high loading of Pt is usually used in the electrode which makes the cost reduction be difficult. In addition, traditional Pt/C catalysts exhibit poor performance in durability which is also a block for commercialization of PEMFC. Numerous studies have focused on the research of novel materials to lower the demand for precious Pt metal. In these efforts, Pt-based alloys have been thought a possible way to remove these barriers. Particularly, one-dimensional (1D) nanostructured Pt-based electrocatalysts have received much attention for their potential application in PEMFCs [1]. Many studies have found that 1D catalysts including nanowires and nanotubes can enhance electron transport performance, improve catalyst utilization efficiency, and increase catalyst activity and durability due to their structure characters. Several kinds of non-precious metals have been used to form Pt-based alloy and test their electrochemical performance. Cobalt is one of them that has been found the PtCo alloy nanowires can present a significant improvement in ORR activity and durability than Pt/C.

Considerable studies have devoted to the investigation of PtCo alloy nanowires in which various methods have been used to fabricate PtCo nanowires. In the work of Higgins et al. [2], they prepared PtCo nanowires by the electrospinning method and obtained an average diameter of 28 nm for the nanowires. They found the specific activity and durability could be enhanced significantly in comparison with commercial Pt/C catalyst. Accordingly, they suggested electrospinning is an attractive approach to prepare PtCo nanowires. While the flow rate of polymer solution was 0.25 ml per hour only, which is quite a low speed and severely restricts the production efficiency of nanowires. Recently, a novel method named centrifugal electrospinning method has been employed successfully to fabricate Pt nanowires [3]. This method takes the advantages of electrospinning and forcespinning together to make nanowires and the production rate can be improved greatly. In the present study, we first attempt to fabricate bimetallic PtCo alloy nanowires by the centrifugal electrospinning method. The morphology of nanowires is examined systematically by adjusting the system parameters including the rotation speed of spinneret, the applied voltage, and the atomic ratio of Pt and Co in the composition. The electrochemical properties of the prepared PtPd nanowires as electrocatalysts are tested by performing cyclic voltammetry (CV), linear sweep voltammetry (LSV), and accelerated degradation tests (ADT). The optimal condition to control the morphology and obtain high electrochemical performance of nanowires would be evaluated. Additionally, membrane electrode assemblies (MEA) using the PtCo nanowires as cathode electrocatalysts are made, and the fuel cell performance is measured and compared with the MEA using commercial Pt/C. The results show that 1D PtCo nanowires can be made efficiently by the centrifugal electrospinning method.

THE EXPERIMENTAL

The schematic of centrifugal electrospinning system can be found in the work [3]. The present study used the same apparatus to fabricate polymer nanofibers. The polymer solution containing precursors of Pt and Co was put inside the spinneret located at the center of the device. The collection distance from the tip of the nozzle to the collector is 12 cm. The rotating speed of spinneret can be controlled by a motor drive and a high voltage can be applied between the nozzle and collector. Once the spinneret rotates, both centrifugal force and electrostatic force exert on the polymer solution simultaneously and the solution would be ejected from the nozzles to form polymer jets. During the flowing process, the solvent would evaporate and the jets would be elongated to form polymer fibers with mean diameter less than one micrometer generally. Finally, the polymer fibers could be collected from the collectors. The polymer solution was prepared by of polyvinyl pyrrolidone (PVP, Mw = 1,300,000), ethanol, DI water, and $H_2PtCl_6 \cdot 6H_2O$ and $Fe(NO_3)_3 \cdot 9H_2O$ as precursors of Pt and Fe, respectively. The collected polymer fibers were calcinated in a high temperature oven. The heat treatment process is the same as the study [3] to burn off the polymer and other elements. The nanowires were then reduced in H_2 at 200 °C for one hour to form PtCo nanowires.

The morphology of the PtCo nanowires was observed by Scanning Electron Microscope (SEM) and the composition was analyzed simultaneously by the equipped energy dispersive X-ray spectroscopy (EDS). The mean diameter of the nanowires was estimated from the SEM image by the ImageJ software. The X-ray diffraction (XRD) patterns were also measured to observe the crystalline phase of nanowires. The measurement of cyclic voltammogram (CV) was conducted by the Autolab potentiostat with a three-electrode system to determine the electrochemical active surface area (ECSA), in which Ag/AgCl (in 3M KCl) was used as the reference electrode. The catalytic slurry of nanowires was prepared and micropipetted onto the polished GC electrode as the working electrode and dried to form a thin film on the GC surface. The tests were performed in N_2 saturated 0.5 M H_2SO_4 solution and scanned between −0.2 V and 1.0 V with a scan rate of 50 mVs^{-1}. The accelerated degradation test (ADT) was also implemented in the same way to evaluate the durability of PtCo nanowires while the potential was scanned repeatedly between 0.4 V and 1V and then the CV pattern was recorded to estimate the degradation of ECSA. Membrane electrode assemblies were also made by using the PtCo nanowires as the cathode electrocatalysts. The catalyst slurry was prepared by mixing PtCo nanowires, Nafion ionomer solution, and isopropanol. The catalyst slurry was brushed on the side of carbon cloth coated with microporous layer until the loading reached 0.5 mg cm^{-2}. The anode electrode was prepared using 20 wt% commercial Pt/C with the Pt loading of 0.5 mg cm^{-2}. A Nafion 115 membrane was sandwiched between the anode and cathode gas diffusion electrodes and then hot pressed to form the MEA with active geometric area of 5 cm^2. The fuel cell performance was measured using fully humidified hydrogen and air as reactants and the cell temperature was held at 70°C during the test.

RESULTS AND DISCUSSION

The effect of rotating speed of spinneret on the morphology of PtCo nanowires is examined as shown in Fig.1 (a)-(d), where the rotating speeds are 1400, 1600, 1800, and 2000 rpm, respectively. The other conditions in the collection of polymer fibers are 13 kV of applied voltage, 10 wt% of PVP concentration, 2 wt% of precursors, and 4:1 of atomic ratio Pt:Co. One can see that the nanowires can be made successfully under these conditions with various rotating speeds of spinneret. The mean diameters with standard deviations (SD) of these cases are 97±21, 76±14, 88±21, and 103±24 nm, respectively. Obviously, the case of 1600 rpm presents the minimum mean diameter with more uniform nanowire morphology. The results indicates that either of insufficient or excessive centrifugal force would result in higher mean diameter and SD. A lower rotating speed cannot provide sufficient centrifugal force to elongate the polymer jet, while a higher rotating speed will shorten the time for the solvent to evaporate during the flowing process since the collection distance is fixed. Hence, an appropriate rotating speed is very important for the evaporation of solvent and elongation of polymer jets during the fiber collection process.

The applied voltage is also a crucial factor that may affect the morphology of nanowires significantly. Two typical SEM images are shown in Fig. 2(a)-(b) for the cases of 12 and 14 kV, respectively, under the rotating speed of 1600 rpm. The mean diameters and SDs are respectively 100±18 nm and 91±24 nm. In comparison with the result of Fig. 1(b), it is observed that the applied voltage also may influence the morphology of the nanowires greatly. A smaller electrostatic force would not fully stretch the polymer jets while a larger electrostatic force may cause a higher flow rate from the Taylor cone at the tip of nozzle and then result in a larger mean diameter. The results of EDS and XRD patterns have shown that the Co can be integrated into the Pt-based alloy structure successfully as shown in Fig. 3 and Fig. 4. The results of CV as shown in Fig. 5 also reveal that PtCo nanowires made by the present method present excellent potential for the application in PEMFCs.

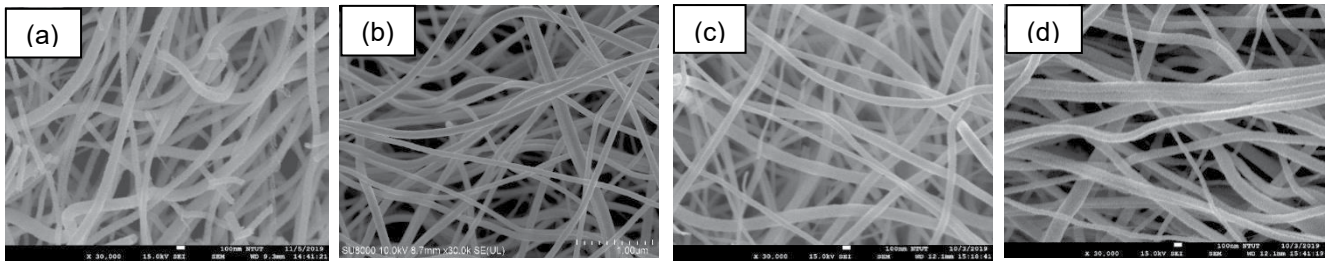


Fig. 1. The SEM images of PtCo nanowires collected at rotating speed of (a) 1400 rpm, (b) 1600 rpm, (c) 1800 rpm, and (d) 2000 rpm. The applied voltage is 13 kV.

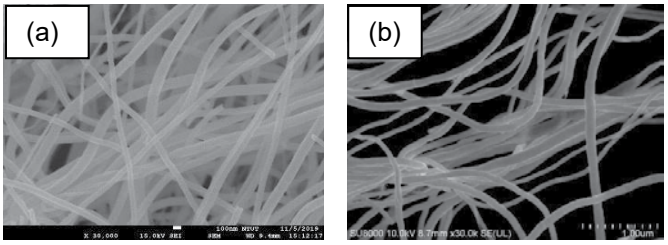


Fig. 2. The SEM images of PtCo nanowires collected at (a)12 kV and (b) 14 kV under rotating speed of 1600 rpm.

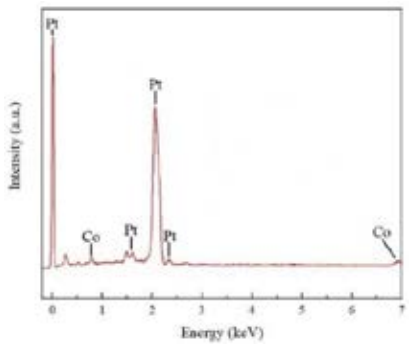


Fig. 3. The typical EDS pattern.

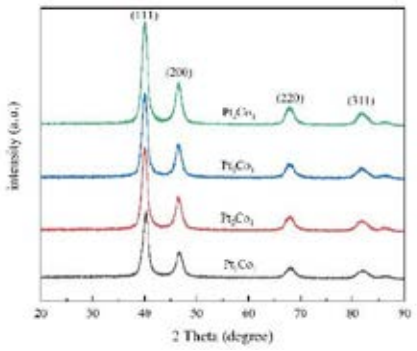


Fig. 4. The XRD patterns.

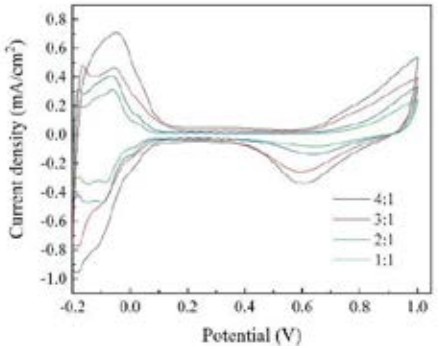


Fig. 5. The CV patterns.

CONCLUSIONS

The present results demonstrate that bimetallic PtCo alloy nanowires can be made successfully by the centrifugal electrospinning method. The prepared PtCo nanowires present excellent electrochemical performance which possess great potential to be used as electrocatalysts in PEMFCs. Further studies focusing on how to reduce the nanowire diameters would be helpful in the future.

ACKNOWLEDGEMENT

The financial supports for this work from Ministry of Science and Technology of Taiwan through the grant numbers MOST 108-2221-E-036-003 and MOST 110-2221-E-036-009 are gratefully acknowledged.

REFERENCES

1. Du S. 2021. Recent advances in electrode design based on one-dimensional nanostructure arrays for proton exchange membrane fuel cell applications. Engineering 7:33-49.
2. Higgins DC, Wang R, Hoque MA, Zamani P, Abureden S and Chen Z. 2014. Morphology and composition controlled platinum-cobalt alloy nanowires prepared by electrospinning as oxygen reduction catalyst. Nano Energy 10:135-143.
3. Huang CY and Chang MH. 2021. Fabrication of platinum nanowires by centrifugal electrospinning method for proton exchange membrane fuel cell. International Journal of Energy Research 45 12968-12979.

WHEC-2022
23rd World Hydrogen Energy Conference
June 26-30, 2022 - Istanbul

#117

ECONOMICAL PREPARATION AND CHARACTERIZATION OF DUAL-IONS CONDUCTING FUEL CELL

[1] *Yu-Tse Lu,* [1] *Wei-Cheng Huang,* [2] *Shing-Hoa Wang,* [1*] *Horng-Yi Chang*
[1] Department of Marine Engineering, National Taiwan Ocean University, Keelung 202301, Taiwan
[2] Department of Mechanical and Mechatronic Engineering, National Taiwan Ocean University, Keelung 202301, Taiwan

*Corresponding author e-mail: hychang@mail.ntou.edu.tw

ABSTRACT

The composite powders consisted of oxygen ion conductive $(La_{0.75}Sr_{0.2}Ba_{0.05})_{0.175}Ce_{0.825}O_{1.891}$ (LSBC) and proton conductive $BaZr_{0.1}Ce_{0.7}Y_{0.2}O_{3-\delta}$ (BZCY) were prepared by solid state reaction and sintered to be a composite membrane. The inter-diffusion was found between LSBC and BZCY. The conductivity of LSBC-BZCY single membrane exhibited slightly non-ohmic behavior in air but obviously non-ohmic diode behavior at 500°C in Ar/H_2. It indicated that the Schottky barrier could be designed at low to intermediate temperatures. The microstructure of sintered LSBC-BZCY surface fluctuated with convex and concave regions. The convex region was hard LSBC and the concave region was soft BZCY by micro-hardness and elemental measurement. The LSBC-30%BZCY let the two phases single membrane possess dual-ions conduction to obtain the power density of 20.51 mW/cm^2. The elemental distribution difference abruptly for Ba, Ce and O occurred at grain boundaries of LSBC/BZCY may correspond to the inter-diffusion and Schottky barrier results. The dual-ions composite membrane was proven single layer fuel cell possibly by this economical design process.

Keywords: Composite membrane, Dual-ions conduction, Schottky barrier, Economical design

INTRODUCTION

The intermediate solid oxide fuel cells (ITSOFCs) are economical and green power sources for large scale distributed power generation [1]. The energy conversion efficiency of sandwich-structured solid oxide fuel cell (SOFC), which consists of anode, electrolyte and cathode, is determined by interface, ohmic and diffusion impedances. Such interface and diffusion impedances result from triple-phase boundaries (TPBs), which are between electrode and electrolyte, and electrode internal structures (porosity, pore geometry and electrocatalytic sites etc.). The ohmic impedance originates from electrolyte and outer conducting interconnection materials [2]. Recently, the composite membrane composed of ionic and semi conductive characteristics is proposed to replace the conventional electrolyte layer to overcome the complex sandwich structure of fuel cells. This concept may avoid the interface polarization loss, lower the operation temperature and simplify the structure of a fuel cell [3,4] to achieve the simple synthesis process and economically in materials utility as well as environment friendly, sustainably.

Ceria-based materials such as Gd-doped ceria (GDC) and Sm-doped ceria (SDC) are well-known oxygen ion conducting electrolytes in ITSOFC [5]. Multiple elements doped ceria ($(La_{0.75}Sr_{0.2}Ba_{0.05})_{0.175}Ce_{0.825}O_{1.891}$ referred to LSBC) can exhibit high ionic conductivity at intermediate temperature (500-750°C) and anti-reduction at low partial oxygen pressure [6,7]. The nanodomain clusters resulted from oxygen vacancies by oxide doping in CeO_2 can be homogeneously distributed by multiple ions doping into CeO_2 structure thus increasing the ionic conductivity effectively [8,9]. To lower the operation temperature below 500°C is expected by using proton conducting electrolytes in SOFC [10]. Perovskite $BaZrO_3$ series materials are promise candidates due to chemically stable in steam and CO_2 atmosphere for proton conduction [11,12]. The yttrium (Y) doped $BaZrO_3$ such as $BaZr_{0.1}Ce_{0.7}Y_{0.2}O_{3-\delta}$ (BZCY) has been proven to be high proton conductivity [13,14].

The aim of this work is to develop economically single composite membrane consisted of LSBC and BZCY to replace the conventional sandwich SOFC structure. Such a LSBC-BZCY composite membrane behaves fuel cell characteristics. The BZCY conducts protons and is used as an electron blocking function for oxygen ion conducting LSBC material. The mixing LSBC-x mol% BZCY composite membranes are studied by dual-ions conduction behavior, Schottky barrier, elemental analyses and power density to characterize the performance of single membrane fuel cell.

MATERIALS AND METHODS

LSBC was prepared by ball milled La_2O_3, $SrCO_3$, $BaCO_3$ and CeO_2 in ethanol for 24 h and calcined at 1000°C/4h.

BZCY was also prepared by ball milled $BaCO_3$, ZrO_2, CeO_2 and Y_2O_3 in ethanol for 24 h and calcined at 1000°C/4h.

The two ball milled and calcined powders were ball-mixed again to obtain the LSBC – xBZCY (x=0, 10, 20, 30, 70,

80, 90 and 100 mol%) mixture and then calcined at 1000~1300°C for 4 h. Such calcined mixtures were pulverized and die-pressed into discs, then were sintered at 1500°C/6h to form composite membranes.

The crystal structures of the calcined powders and sintered bodies were characterized by X-ray diffraction (XRD). A field-emission scanning electron microscope (FESEM) equipped with energy dispersive X-ray spectroscopy (EDS) were used to determine their microstructures, morphologies and elemental analyses. The electric current-voltage (I-V) characteristic and the power density were measured using the Keithley 2400 source meter. Alternating current (AC) impedance analyses of the fuel cells were conducted with an electrochemical instrument (Zahner Zennium, Germany).

RESULTS AND DISCUSSION

The pure phases of LSBC and BZCY are still maintained after mixing LBSC-30BZCY, as shown in Fig. 1(a)(b). It can not detect the existence of secondary phase. The inter-diffusion between LSBC and BZCY is found in Fig. 1(c) by enlarged XRD patterns at 2θ=40°~43°. The diffusion resulted in the lattice distortion due to the diffraction angle shift. The LSBC-10BZCY after measured at 500°C in Ar/H_2 atmosphere by cyclic voltammetry method indicates the non-ohmic I-V behavior, as shown in Fig. 1(d). It revealed a diode behavior that the Schottky barrier may exist in the sample. The electron blocking effect was supposed in the LSBC-10BZCY composite membrane. Then the Schottky barrier may be further manipulated to accommodate the neutralization of proton – oxygen ion at low temperature of 500°C.

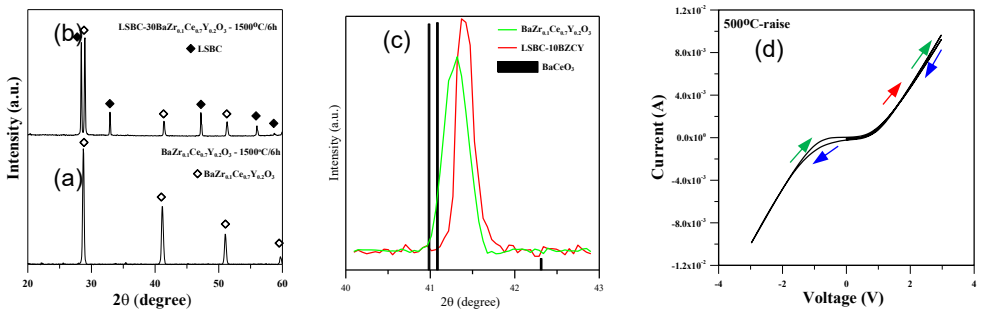


Fig. 1. XRD patterns of 1500°C/6h sintered (a) BZCY, (b) LSBC-30BZCY, and at (c) 2θ=40°~43°, and (d) I-V curve of LSBC-10BZCY measured by cyclic voltammetry in Ar/H_2 atmosphere at 500°C.

The polished LSBC-10BZCY surface fluctuated with convex and concave regions. The convex region was hard LSBC and the concave region was soft BZCY by micro-hardness and elemental analyses, as shown in Fig. 2(a). The EBDS analysis is further proof of the two phases with different hardness in Fig. 2(b). The EDS line scanning analysis presents the Ce, Ba and O elements (red, dark green and grass green color lines) distribution abruptly different at LSBC-BZCY grain boundaries, as shown in Fig. 2(c). The reasons may be originated from inter-diffusion and mechanical polishing stress. Elemental diffusion was more possible reason referred to the XRD results in Figs. 1(a) and 1(b).

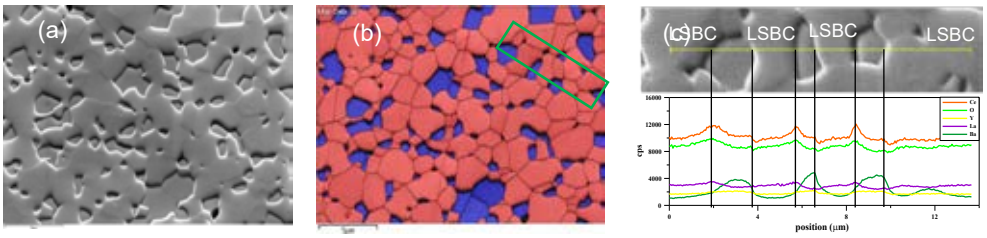


Fig. 2. Polished morphologies of LSBC-10BZCY, (a) FESEM, (b) EBSD, (c) elemental analyses (EDS line scanning) for the green rectangular region in (b).

The LSBC-BZCY composite membrane was realized as fuel cell by Pt||LSBC - xBZCY||Pt structure using H_2 in anode side and air in cathode side. The I-V curve and power density measured at 600 and 700°C are shown in Fig. 3 with different x values. Basically, LSBC-BZCY composite membrane can be used as a fuel cell even the power density is still spaces to improve. From the results, the highest power density is obtained at the LSBC-30BZCY about 20.51 mW/cm^2, as shown in Fig. 3(b). Such results prove the realization of dual-ions conducting single composite membrane as a fuel cell.

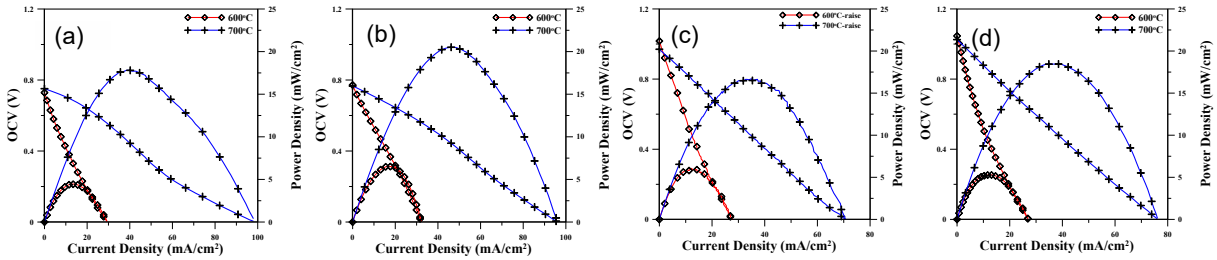


Fig. 3. The I-V and power density of Pt||LSBC - xBZCY||Pt composite membrane cells measured in H_2/air at 600~700°C, (a) x=0, (b) x=30, (c) x=90 and (d) x=100.

CONCLUSIONS

The conductivity of LSBC-BZCY single membrane exhibited slightly non-ohmic behavior in air but obviously non-ohmic diode behavior in Ar/H_2 atmosphere. It indicated that the Schottky barrier could be designed at low to intermediate temperatures. The LSBC-30BZCY let the dual phase single membrane possess dual-ions conduction to obtain the power density of 20.51 mW/cm^2. The dual-ions composite membrane was a single layer fuel cell possibly by this economical design process.

ACKNOWLEDGEMENT

The authors gratefully acknowledge the funding support by the Ministry of Science and Technology, Taiwan (Grant Nos. MOST108-2221-E-019-032-MY2 and MOST110-2221-E-019-054-MY3).

REFERENCES

1. Hayashi K, Yokoo M, Yoshida Y, Arai H. 2009. Solid oxide fuel cell stack with high electrical efficiency. NTT Technical Review 7(10):1-5.
2. Ogawa T, Takeuchi M and Kajikawa Y. 2018. Comprehensive analysis of trends and emerging technologies in all types of fuel cells based on a computational method. Sustainability, 10(2):458 (30 pp).
3. Zhu B, Raza R, Qin H, Fan L. 2011. Single-component and three-component fuel cells. Journal of Power Sources, 196(15):6362-6365.
4. Lu YZ, Mi YQ, Li JJ, Qi FH, Yan SL and Dong WJ. 2021. Recent progress in semiconductor-ionic conductor nanomaterial as a membrane for low-temperature solid oxide fuel cells. Nanomaterials 11:2290 (16 pp).
5. Dikmen S, Aslanbay H, Dikmen E, Şahin O. 2010. Hydrothermal preparation and electrochemical properties of Gd^{3+} and Bi^{3+}, Sm3+, La^{3+}, and Nd^{3+} codoped ceria-based electrolytes for intermediate temperature-solid oxide fuel cell. Journal of Power Sources 195(9):2488–2495.
6. Mori T, Drennan J, Lee JH, Li JG, Ikegami T. 2002. Oxide ionic conductivity and microstructures of Sm-or La-doped CeO_2-based systems Solid State Ionics 15:461–466.
7. Chang HY, Wang YM, Lin CH, Cheng SY. 2011. Effects of rapid process on the conductivity of multiple elements doped ceria-based electrolyte. Journal of Power Sources 196(4):1704-1711.
8. Ye F, Ou DR, Mori T. 2012. Microstructural evolution in a CeO_2-Gd_2O_3 system. Microscopy and Microanalysis 18(1):162–170.
9. Cajas Daza PC, Muñoz Meneses RA, de Almeida Ferreira JL, Alexander Araujo J, Martins Rodrigues AC, Moreira da Silva CR. 2018. Influence of microstructural characteristics on ionic conductivity of ceria based ceramic solid electrolytes. Ceramics International 44(2):2138–2145.
10. Lyagaeva J, Danilov N, Vdovin G, Bu JF, Medvedev D, Demin A and Tsiakaras P. 2016. A new Dy-doped $BaCeO_3$–$BaZrO_3$ proton-conducting material as a promising electrolyte for reversible solid oxide fuel cells. Journal of Materials Chemistry A 4:15390-15399.
11. Duan C, Tong J, Shang M, Nikodemski S, Sanders M, Ricote S, Almansoori A and OHayre R. 2015. Readily processed protonic ceramic fuel cells with high performance at low temperatures. Science 349:1321–1326.
12. Regalado Vera CY, Ding HP, Peterson D, Gibbons WT, Zhou M and Ding D. 2021. A mini-review on proton conduction of $BaZrO_3$-based perovskite electrolytes. Journal of Physics: Energy 3:032019 (13 pp).
13. Han D, Shinoda K, Sato S, Majima M and Uda T. 2015. Correlation between electroconductive and structural properties of proton conductive acceptor-doped barium zirconate. Journal of Materials Chemistry A 3:1243–1250.
14. Yamazaki Y, Hernandez-Sanchez R and Haile SM. 2009. High total proton conductivity in large-grained yttrium-doped barium zirconate. Chemistry of Materials 21(13):2755–2762.

WHEC-2022
23rd World Hydrogen Energy Conference
June 26-30, 2022 - Istanbul

#132

ANALYSIS OF ECONOMIC EFFICIENCY ON INTERNATIONAL HYDROGEN SUPPLY CHAINS TO JAPAN

[1*] *Yuki Ishimoto,* [1] *Michio Hashimoto,* [2] *Eiji Ohira*
[1] Kyoto University, Graduate School of Advanced Integrated Studies in Human Survivability, Higashi-Ichijo-kan, Yoshida-Nakaadachicho 1, Sakyo-ku, Kyoto, Japan
[2] New Energy and Industrial Technology Development Organization, Smart Community and Energy Systems Department, Fuel Cell and Hydrogen Technology Office, 1310 Omiya-cho, Saiwai-ku, Kawasaki City, Kanagawa 212-8554 Japan

*Corresponding author e-mail: ishimoto.yuki.4j@kyoto-u.ac.jp

ABSTRACT

In order to achieve carbon neutrality, hydrogen is one of the key technologies to decarbonize the whole energy system. Several countries especially Japan are planning to import low carbon hydrogen using international supply chains setting their hydrogen strategy. There could be a wide variety of combinations among the technology option to make the supply chains. LCOEs using the international hydrogen transport chains are analyzed in this study to consider economic efficiency and to find effective clues for cost reduction in the international hydrogen transport chains. As preliminary results, we have found that the transportation cost that includes liquefaction, storages and international seaborne transport is improved by about 40% considering the advantages of large-scale facilities and that lignite gasification technologies with carbon capture have a competitive edge under the current assumption. For the time being, blue hydrogen could be an affordable option until the cost of green hydrogen decreases to the similar level. (<200 words)

Keywords: Hydrogen carriers, International supply chains, Economic analysis

INTRODUCTION

At COP26 in Glasgow in 2021, it is confirmed that “Reaffirms the Paris Agreement temperature goal of holding the increase in the global average temperature to well below 2 °C above pre-industrial levels and pursuing efforts to limit the temperature increase to 1.5°C above pre-industrial levels”[1]. This will accelerate the movement toward greenhouse gas reduction. Japan firstly published their hydrogen strategy [2] and is planning to import low carbon hydrogen using international supply chains. There are already some studies on hydrogen imports from abroad [3-7]. Various hydrogen sources and hydrogen carriers are being studied, however in this research, we conducted an analysis that considers an unprecedented large-scale supply chain for energy applications, and various utilization technologies as well as incorporating the latest technology development.

METHODLOGY FOR ANALYSIS

Fig. 1 shows the scope of analysis in this study. An international hydrogen supply chain to be analyzed consists of a hydrogen production technology using primary energy resources that are low carbon emissions such as fossil fuels with CCS technologies and renewable energies, a storage and transport technology for long distance, and utilization technology in a wide variety of energy demand sectors. Utilization technologies considered are FCV, FC trucks, ships, CHP, hydrogen and ammonia as feedstock especially for chemical industries and power sector.

The procedure of analysis is as follows;

- Define an international supply chain for analysis considering facilities included;
- Set common assumptions such as year, system boundaries, the amount of energy transported, utilization factors, and distance;
- Set specific assumptions of facilities in the defined international supply chain;
- Carry out energy and mass balance analysis to set the capacities of the facilities included, the quantities of utilities used;
- Capital expenditures in the supply chain are estimated using the obtained results above;
- Levelized cost of hydrogen (or electricity) for the supply chain are obtained.

The Levelized cost method shown by the following equation is used to obtain the cost of hydrogen. This is a generic method to calculate the unit cost by dividing the total accumulated cost during the project period by the total hydrogen supply amount during the period. In order to consider the value of cash flow at different times, the cost and fuel supply amount are converted to the present value using the discount rate. This method is one of the standard cost analysis

methods used by the International Energy Agency [8]. As levelized cost of product (LCOP) in the equation is a generic expression, levelized cost of electricity (LCOE) is used as an indicator in this study.

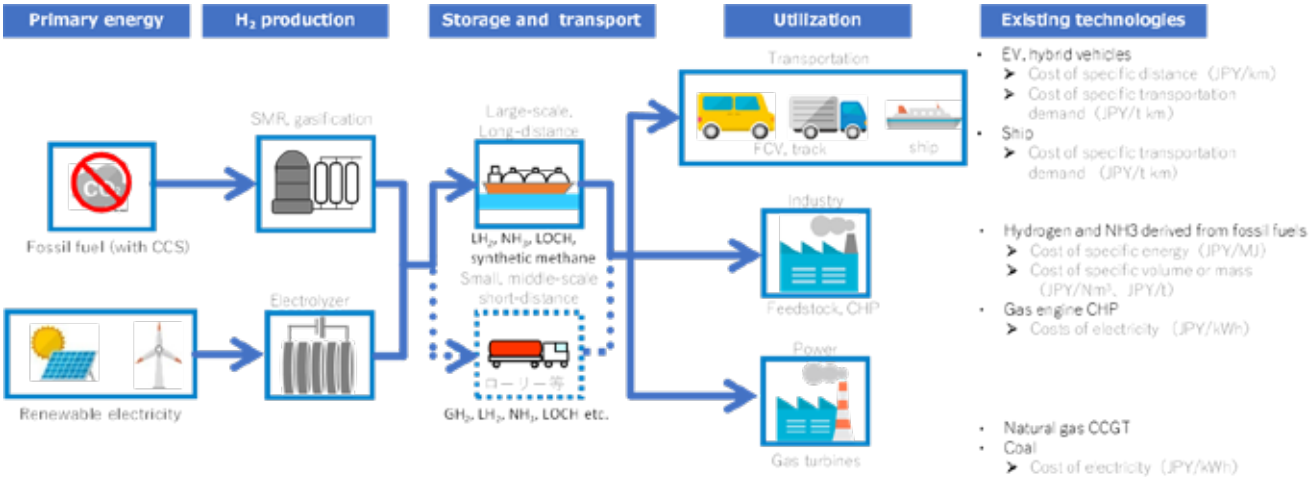


Fig. 1. The scope of analysis in this study

$$\mathrm{LCOP} = \sum_n \frac{\sum_t [(I_{n,t} + M_{n,t})(1+r)^{-t}]}{\sum_t (E_t (1+r)^{-t})} \quad (1)$$

where LCOP (Levelized Cost of Product), In,t: Capital related expenditure at term t and in facility n, Mn,t: operational expenditure, Et: production supply in term r , r: discount rate .

In order to evaluate the economic efficiency of the hydrogen supply chain, we have carried out a preliminary calculation of power generation cost using the imported hydrogen. The data for analysis are mainly based on literature. The capital expenditure of each facility in the supply chain is estimated using the scaling law and corrected by plant cost index and location factor as necessary. As operational and maintenance costs, fuel, electricity, labor, maintenance, insurance and general and administrative costs, are considered.

RESULTS AND DISCUSSION

Fig.2 shows preliminary results of levelized cost of electricity using hydrogen transported via the international liquefied hydrogen supply chain between Australia and Japan. Alkaline water electrolysis and lignite gasification in Australia are considered as hydrogen production technologies. The cost of renewable electricity from wind power for hydrogen production is 6.2 JPY/kWh. The cost of lignite is 12.7 AUD/t [9]. The transport capacity of the chain is 200 kt/year with technologies available in 2030 [10] and 2 Mt/year using advanced technologies in the future.

The most affordable case is lignite gasification with 2 Mt/year chain. The difference in LCOE with the chain of the same transport capacity is due to the cost difference in hydrogen production. The cost of both hydrogen production accounts for a large proportion of LCOE. The hydrogen cost of lignite gasification is about half of water electrolysis under the current assumption.

The transportation cost that includes liquefaction, storages and international seaborne transport is improved by about 40% considering the advantages of large-scale facilities. In this study hydrogen production and power generation did not anticipate economies of scale that changes from 200 kt/year to 2 Mt/year because the maximum unit capacities of these technologies are smaller than the capacity of supply chains. The assumed investment cost of electrolyzer of 200kt/year based on the scaling law is 29,000 JPY / kW which is in a similar range of the 2050 target of IRENA (< 200 USD/kW) considering the current status (500-1000 USD/kW) [11]. The number of lignite gasification reactor is more than one. The amount of hydrogen transport (2 Mt / year) is enough for several units of hydrogen fired gas turbine combined cycle power station. Even if water electrolysis is expected to have a quite good capital cost (the assumption are 29,000 yen / kW and capacity factor 35%), significantly inexpensive renewable energy power (1.6 JPY / kWh) is also required to compete hydrogen from lignite. For the time being, blue hydrogen could be an affordable option until the cost of green hydrogen decreases to the similar level.

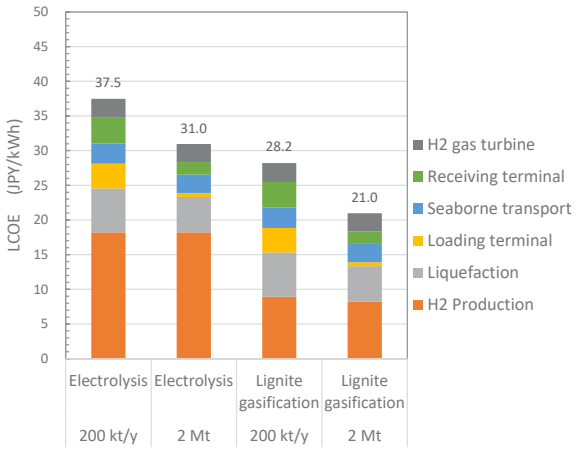


Fig. 2. Preliminary results of levelized cost of electricity using hydrogen transported via the international liquefied hydrogen supply chain between Australia and Japan

CONCLUSIONS

LCOEs using the international hydrogen transport chains are analyzed in this study to consider economic efficiency and to find effective clues for cost reduction in the international hydrogen transport chains. As preliminary results, we have found that the transportation cost that includes liquefaction, storages and international seaborne transport is improved by about 40% considering the advantages of large-scale facilities and that lignite gasification technologies with carbon capture have a competitive edge under the current assumption. For the time being, blue hydrogen could be an affordable option until the cost of green hydrogen decreases to the similar level. In the conference, another combination among hydrogen production, storage and transport (ammonia and liquid organic chemical hydrides) and demand technologies (FCVs, feedstock etc) will be discussed.

ACKNOWLEDGEMENT

This study is based on results obtained from a project commissioned by the New Energy and Industrial Technology Development Organization (NEDO).

REFERENCES

1. https://unfccc.int/sites/default/files/resource/cop26_auv_2f_cover_decision.pdf, Accessed on November 23, 2021
2. https://www.meti.go.jp/english/press/2017/pdf/1226_003b.pdf, Accessed on November 23, 2021
3. DNV GL. 2018. Hydrogen as an energy carrier. Oslo.
4. Wijayanta AT, Oda T, Purnomo CW, Kashiwagi T, Aziz M. 2019. International Journal of Hydrogen Energy 44:15026-44.
5. International Energy Agency. 2019. The future of hydrogen. Paris.
6. Heuser PM, Ryberg DS, Grube T, Robinius M, Stolten D. 2019. Techno-economic analysis of a potential energy trading link between Patagonia and Japan based on CO2 free hydrogen. International Journal of Hydrogen Energy 44: 12733-47.
7. Yuki Ishimoto, Mari Voldsund, Petter Nekså, Simon Roussanaly,David Berstad, Stefania Osk Gardarsdottir. 2020. Large-scale production and transport of hydrogen from Norway to Europe and Japan: Value chain analysis and comparison of liquid hydrogen and ammonia as energy carriers, International Journal of Hydrogen Energy 45:32865-32883.
8. International Energy Agency. 2020. Projected Costs of Generating Electricity 2020. Paris.
9. Mitsubishi Research Institute. Survey on Raw Coal Cost and Final Product Price FY2014 Annual Report. 2015.Kawasaki.
10. Kawasaki Heavy Industries.2015. Feasibility Study of a Project Promoting Utilization of Low Rank Coal Investigation of Improvement of a Value Chain of Hydrogen Production from Australian Low Rank Coal (FY2014) Final Report . Kawasaki .
11. International Renewable Energy Agency, 2021. MAKING THE BREAKTHROUGH Green hydrogen policies and technology costs. Abu Dhabi.

WHEC-2022
23rd World Hydrogen Energy Conference
June 26-30, 2022 - Istanbul

#135

ON THE FUTURE ROLE OF HYDROGEN AS STORAGE FOR ELECTRICITY

[1*] Reinhard Haas, [1] Marlene Sayer, [1]Amela Ajanovic
[1] TU Wien, Energy Economics Group, 1040 Wien, Austria

*Corresponding author e-mail: haas@eeg.tuwien.ac.at

ABSTRACT

Increasing electricity generation from variable renewable energy sources, such as wind and solar, has led to interest in additional short-term and long-term storage capacities. The core objective of this paper is to investigate the costs and the future market prospects of different electricity storage options, such as short-term battery storage, and long-term storage as pumped hydro, as well as hydrogen. The method of approach is based on formal economic framework with a dynamic component to derive scenarios up to 2040. The major conclusion is, that the economic prospects of storage are in general not very bright. For all market-based storage technologies it will become hard to compete in the wholesale electricity markets. The core problem of virtually all categories of storage are low full-load hours. However, any new storage capacity should be constructed only in a coordinated way and if there is a clear sign for new excess production, in this case from variable renewables.

Keywords: Storage, Hydrogen, Pumped hydro storage, Battery, Economics

INTRODUCTION

Increasing electricity generation from variable renewable energy sources, such as wind and solar, has led to interest in additional short-term and long-term storage capacities. One of these options is hydrogen. Since many decades hydrogen has been considered as a universal environmentally benign energy carrier. So far high production costs stated a major barrier for a broader market penetration, see e.g. Ajanovic (2008). With the current ambitious targets for increasing the share of renewable energy sources (RES) to 27% by 2030 set by the European Commission new prospects for hydrogen as energy storage for excess electricity from RES emerge. The reason is that an increasing share of these new RES comes from variable sources like wind and solar. This leads to the need for increased balancing activities between supply and demand, as well as flexibility measures in general, see e.g. Lund et al [1], including the demand for long-term electricity storages.

The core objective of this paper is to investigate the costs future market prospects of hydrogen as a storage for excess electricity and its possible more competitive use in the transport sector as a renewable fuel. Of specific relevance is the comparison with other possible storage such as traditional pumped hydro storage or looming new large batteries.

METHOD

Our method of approach on the electricity market side a fundamental approach is used where the intersection of supply and demand at every point-of-time gives the corresponding electricity market price. It is important to note that the quantity of storage has a feedback on the market price for charging storages as well as discharging. The method is based on cost calculation of different electricity storage technologies, see Hiesl [2] and Ajanovic [3]. In the following equation it is described how the storage cost C_{STO} are calculated:

$$C_{STO} = \frac{\frac{IC \cdot C.R.F + C_{OM}}{T} + C_E}{\eta_{STO}} \quad \text{(€/kWh)} \quad (1)$$

With:

C_{STO}… Cost of storing a kWh of electricity in hydrogen, in a pumped hydro storage or a battery (€/kWh)
IC …. Investment costs of a storage (€)
C.R.F. Capital recovery factor (1/year)
C_{OM} … O&M costs (€/year)
T ….. Full-load hours (hours per year)
C_E ….. Costs of electricity on the wholesale market (€/kWh)
η_{STO}… Efficiency of storage

Equation 1 shows the cost of storing one kWh. Whether a market-oriented storage is economically feasible decides the so-called price spread in the electricity market and the number of over-all operating hours, the full-load hours. The importance of full-load hours for the economic feasibility of storage facilities has already been discussed in Hiesl [2], Ajanovic [3] and Schill [4]. Along with the issue of the price spread this is the Alpha and Omega in every discussion on the future prospects of centralized storage as a market-based option from an economic point-of-view. Regarding the costs in the long-term the methodical approach used based on technological learning for the future development of investment costs of the storage technologies investigated, based on expected future quantities of these technologies.

RESULTS AND DISCUSSION

The major results of our investigations are: As shown in Fig. 1 for all types of storage the costs of storage depend very strongly on the yearly fullloadhours. E.g at 500 hours/year the capital costs are four times higher than at 2000 hours/yr. In Fig. 2 the total costs of hydrogen produced in large electrolyzers plants (10 MW) are shown depending on the yearly fullloadhours including also the costs of electricity on the market. E.g hydrogen can be used as storage for electricity from volatile RES, however efficiency of the whole energy supply chain including reelectrification of hydrogen is very low.

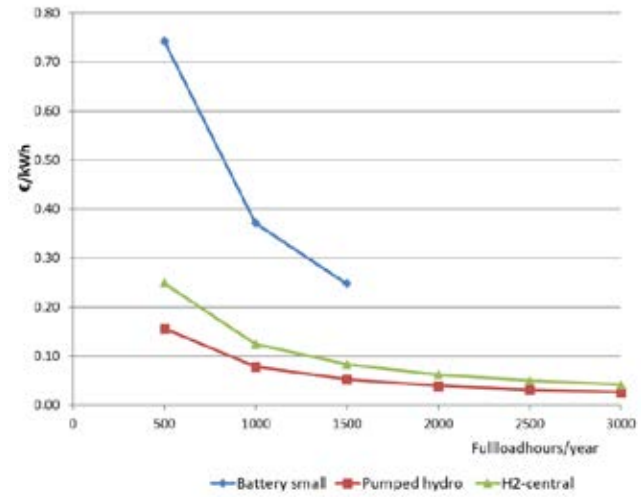


Figure 1. Dependency of the capital costs of various types of storage from the yearly fullloadhours

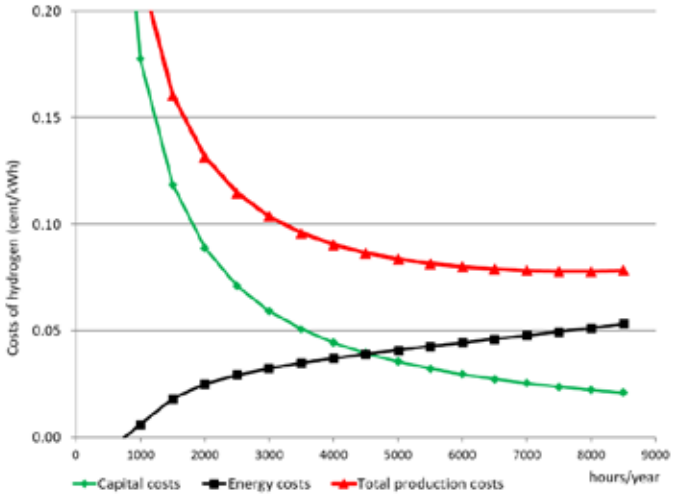


Figure 2. Dependency of the total costs of hydrogen produced in large electrolyzers plants (10 MW) on the yearly fullloadhours

However, over the period up to 2040 decreases in the costs of hydrogen production will take place mainly due to learning effects. In a dynamic market framework the costs of large centralized and smaller decentralized long-term hydrogen storage will finally be too high to become competitive in the electricity sector alone. By 2040 under most favourable learning conditions the investment costs of large electrolyzers will go down to about 1100 EUR/kW from currently about 1600 EUR/kW: The total production costs of hydrogen for 2000 fullloadhours per year will be about 0.09 EUR/kWh, see Fig. 4. For the same fullloadhours the price spread will be at the utmost about 0.08 EUR/kWh. For hydro pumped hydro storages (over a year) further investment costs will rather increase mainly due to a lack of sites with reasonable costs and lack of acceptance, Fig. 3. An additional reason for the unfavorable economic conditions of long-term storages is the self-cannibalism of storages in electricity markets. This means that every additional storage reduces the price spread and, hence, its own economic performance, Ehlers [5]. Other reasons are competition with demand response options, demand –side management, power-to-heat and decentralized storages. The costs of the latter will not decline significantly faster but they will compete on end-user price level which is (and will remain) remarkably higher.
To reduce the relatively high costs of hydrogen cheap surplus electricity from variable RES can be used for electrolysis. The major problem of the economics of all storage options are their low FLH. Currently, a figure of about 2000 hours per year is considered to be the minimum.

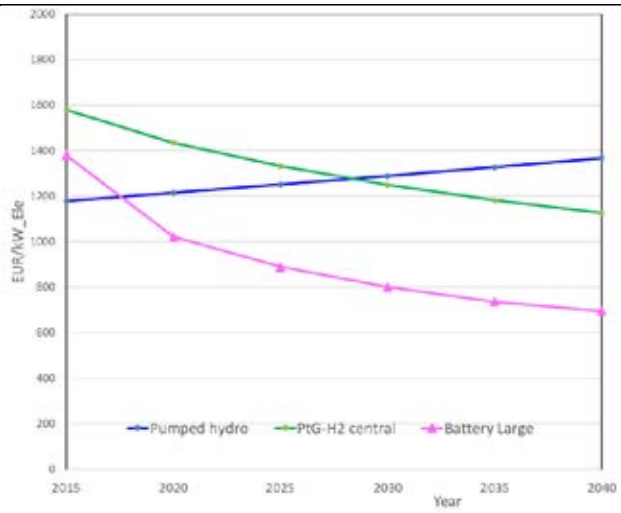


Figure 3. Development of the investment costs of hydrogen (electrolyzers), pumped hydro storage and batteries depending on Technological Learning over time up to 2040

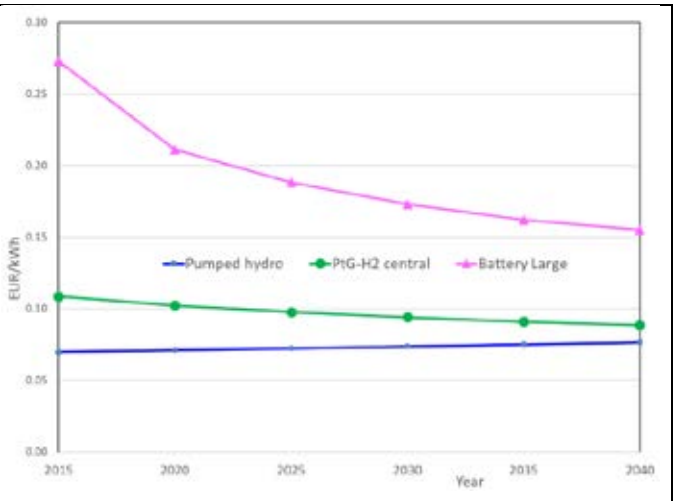


Figure 4. Development of the total storage costs of hydrogen, pumped hydro storage and batteries depending on Technological Learning of the technology over time up to 2040

CONCLUSIONS

The major conclusions are: (i) with respect to all centralized long-term storage technologies the future perspectives will be much less promising than currently indicated in several papers and discussions; (ii) For hydrogen it will also become very hard to compete in the electricity markets by means of re-electrification despite a high technological learning potential.

Finally, it has to be stated that storage is not the only flexibility option. It is in competition with grid extention, load management and other options. In addition, natural gas as storage and natural gas fired turbines for short-term generation are a flexibility alternative, however, not a fully carbon-free one. Hence, from an economic assessments point-of-view of electricity storage the possible competing options has to be considered simultaneously. However, any new storage capacity should be constructed only in a coordinated way and if there is a clear sign for new excess production, in this case from variable renewables. In addition, for hydrogen and methane there could be better economic prospects in the transport sector due to both, higher energy price levels as well as a general lack of low carbon fuel alternatives.

REFERENCES

1. Lund H. et al: Energy storage and Smart Energy Systems, Int. Journal of Sustainable Energy Planning, 11, 3-14, 2016.
2. Hiesl A., A. Ajanovic, R. Haas (2020). On current and future economics of electricity storage, Greenhouse Gases: Science and Technology 10 (6), 1176-1192
3. Ajanovic A., A. Hiesl, R. Haas (2020). On the role of storage for electricity in smart energy systems, Energy 200, 117473
4. Schill Wolf-Peter , Claudia Kemfert: Modeling Strategic Electricity Storage: The Case of Pumped Hydro Storage in Germany, The Energy Journal 2011.
5. Ehlers, N. 2011. Strommarktdesign angesichts des Ausbaus fluktuierender Stromerzeugung, Dissertation, Technische Universität Berlin 2011.

WHEC-2022
23rd World Hydrogen Energy Conference
June 26-30, 2022 - Istanbul

#153

NUMERICAL MODEL AND EXPERIMENTAL VALIDATION OF ULTRA-LEAN AIR-HYDROGEN COMBUSTION IN CATALYTIC MONOLITHS

[1]*Francesco Battistella*, [1]*Alessandro Donazzi*, [1]*Antonino Ravidà*, [1*]*Gianpiero Groppi*, [1]*Gianluca Valenti*
[1]Politecnico di Milano, Dipartimento di Energia, Via Lambruschini 4/A, 20156 Milano, Italy

*Corresponding author e-mail: gianpiero.groppi@polimi.it

ABSTRACT

Hydrogen plays an important role in the energy transition. The exploitation of hydrogen in gas turbines, as well as in other combustion processes, is promising but it may favor the formation of nitrogen oxides due to its high adiabatic flame temperature. The catalytic combustion of ultra-lean air-hydrogen mixtures solves the issue and improves the stability of the reaction at partial loads. The present work develops a numerical model for the design of catalytic combustors able to process ultra-lean air-hydrogen mixtures. The model simulates the catalytic combustion in a honeycomb monolith. Such tool is useful for the sizing of innovative combustors for micro-gas turbines for power generation. The numerical model solves mass and energy balances in a two-dimensional domain describing a single channel of the monolith. The channel is modelled as a cylinder, while the outer radius describes the catalyst surface. A validation of the numerical model is performed with experimental data obtained on a dedicated test bench at low inlet temperature and pressure. Comparing the simulated results with the experimental measurements, a 0.6% difference in outlet bulk temperature is obtained. Ultimately, useful recommendations are provided for combustor designers, based on the estimations of the numerical model in different operating conditions.

Keywords: Hydrogen, Catalytic combustion, Ultra-lean mixture, Numerical model, Micro-gas turbines

INTRODUCTION

Hydrogen economy is being deeply investigated for the process of decarbonization through the so-called energy transition. Such carrier allows an environmentally sustainable transport, storage, and usage of energy. Therefore, the exploitation of hydrogen for integrated power systems, as within gas turbines or via other combustion processes, is promising thanks to the avoidance of carbon dioxide emissions [1]. However, hydrogen high adiabatic flame temperature poses the issue of the formation nitrogen oxides. In this context, a feasible solution is the catalytic combustion of ultra-lean hydrogen mixtures, allowing for the combustion of hydrogen at low temperature without the production of any pollutant. This technology enables the development carbon and NO_x-free power production systems due to lower operating temperatures. Moreover, it offers an improved stability at partial load, when compared to traditional burners. Furthermore, ultra-lean hydrogen mixtures below the flammability limit are inherently safe.

The objective of the present work is the development and the validation of a tool for the design of the first stage of catalytic hydrogen combustors for micro-gas turbines. Such stage involves the combustion of an air-hydrogen mixture out of flammability limits. The tool allows the estimation of the main operational parameters of a honeycomb monolith catalytic combustor: the fuel conversion, the local maximum temperature, and the outlet bulk temperature. The inputs of the numerical model are the geometry of the catalyst, the inlet stream conditions and the reaction kinetics. Ultimately, inserting the inputs for a case study allowed the experimental validation of the tool.

Catalytic combustors for hydrogen-air mixtures are investigated in literature. Hayes and Kolaczkowski describe the modeling approach for honeycomb monolith catalysts adopting cylindrical coordinates in a book dedicated to the catalytic combustion [2]. The modeling of a single channel monolith honeycomb catalyst is performed also by Groppi et al. for the identification of the simplest representative model [3]. In a more recent work, Mantzaras describes the modeling of catalytic combustion of hydrogen focusing on hetero-homogeneous combustion for power generation applications [4]. The exploitation of hydrogen in micro-gas turbines is investigated in the last years. Devriese et al. developed a compressor and a combustor for a 100-kW hydrogen powered gas turbine [5]. The operation with alternative fuels as hydrogen of such systems is also considered in the review performed by Aslanidou et al. [6].

NUMERICAL MODEL AND EXPERIMENTAL VALIDATION

The current section describes the approach adopted for the numerical model and the setup for its experimental validation in the Laboratory of Energy Conversion and Storage of Politecnico di Milano. The aim is the development of a tool for the design of catalytic burners for ultra-lean air-hydrogen mixtures.

Numerical model methodology

The numerical model solves the mass and energy balances for a single channel of the monolith, eventual non-homogeneity in the feeding conditions should be addressed performing detached simulations for each region of the monolith. The channel of the monolith is described as a cylinder, and the two spatial coordinates indicate the axial and the radial position in the domain, respectively. Moreover, such model is based on simplifying assumptions for the calculation of fluid properties. The flow regime is laminar in the whole domain, neglecting the initial development of the velocity profile. The catalyst is placed on the outer radius of the monolith channel. It is described as a boundary condition of the domain. Such description is performed through a correlation containing the reaction kinetics and the thermal properties of the solid. Ultimately, mass diffusion is described as for a binary mixture for a first approximation of the problem [7]. Such assumption is feasible as more than the 75% of the mixture is nitrogen, on a molar basis.

The domain is discretized adopting finite differences in the axial direction and orthogonal collocations in the radial direction [**Error! Reference source not found.**]. The model is implemented in MATLAB and solved with a built-in solver for non-linear functions. After the solution, the model estimates the design parameters for the monolith catalyst. Among such parameters are included the maximum local temperature, the outlet bulk temperature and the unburnt hydrogen. The latter ones are exploited for the experimental validation of the tool.

Experimental setup for validation

The experimental validation of the estimation of the numerical model is performed on a dedicated test bench at ambient temperature and pressure. It features a monolith catalyst fed with an ultra-lean air-hydrogen mixture. Such mixture has a hydrogen molar fraction of 2.38% and is fed to the catalyst through a long intake duct. Therefore, the stream composition and velocity are uniform at the catalyst inlet for achieving the same feeding conditions on each channel of the monolith. This allows the reproduction of the condition simulated by the numerical model.

The tests are performed in steady state. The apparatus is switched on and the measurements are harvested when the outlet bulk temperature is stable. Such temperature is measured with a Pt1000 thermistor at the outlet of the monolith, close to the axis of the hollow cylinder containing the catalyst. The unburnt hydrogen is measured with a gas chromatograph with Argon as carrier gas. Such instrument analyzes samples gathered at the outlet of the catalyst. The measurements of concentration with the gas chromatograph are repeated three times, for statistical significance. The temperature readings are harvested continuously. Ultimately, the temperature reported in the results is the mean value of the readings in steady state.

RESULTS AND GENERAL RECOMMENDATIONS

The comparison between the estimations of the numerical model and the experimental measurement is reported in table 1. The estimated outlet bulk temperature is 0.6% higher than the experimental measurement. The estimated unburnt hydrogen is comparable with the experimental measurement and close to zero in the tested conditions. Such parameters validate the experimental model at low pressure and temperature. Therefore, the numerical model is exploited as a design tool of a catalytic combustor for micro-gas turbines.

Table 1. Parameters comparison for the validation of the experimental model.

Parameter	Numerical model estimation	Experimental measurement
Outlet bulk temperature [K]	486	483
Unburnt hydrogen [$\%_{mol}$]	0.016	0.022

After the experimental validation, the temperature trend and local hydrogen consumption are investigated for a first stage of combustion in a micro-gas turbine. This leads to some general recommendations for developers of catalytic hydrogen burners operating in ultra-lean conditions. The temperature trend shows an initial peak when the catalyst is operated at low pressure. This local overtemperature must be considered when designing the monolith. Increasing the operational pressure, the local peak is smoothed but not eliminated. The temperature distribution in the monolith channel is reported in figure 1. It shows an overtemperature on the outer radius of the channel. Hydrogen mass fraction is also reported in figure 1. It highlights the very effective diffusion of the component towards the outer radius of the channel.

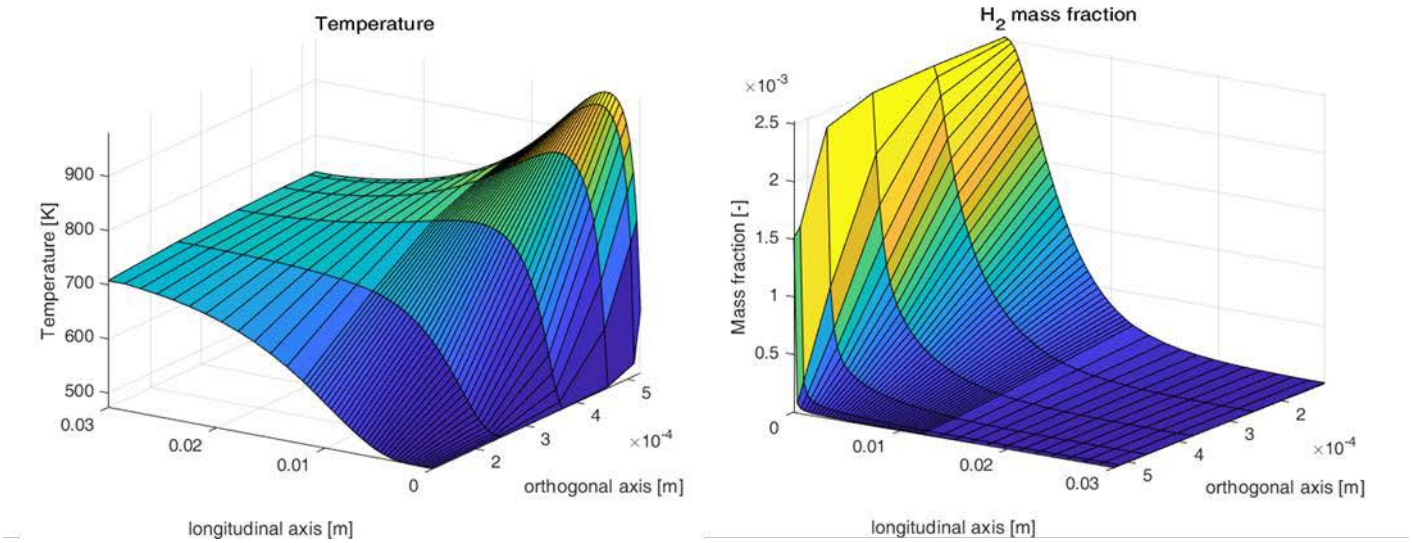


Fig. 1. Temperature and hydrogen distribution in the monolith channel for an inlet condition featuring a temperature of 473 K and an absolute pressure of 400 kPa as typical.

CONCLUSIONS AND FUTURE WORKS

The presented work develops a tool for the simulation of a hydrogen catalytic combustor. The simulation is performed with a numerical model implemented in MATLAB. The results are as follows.

- The numerical model is validated with the simulation of the operating conditions of a case study. The estimated bulk temperature is 0.6% higher than the experimentally measured one.
- The numerical model estimates overtemperatures on the catalyst wall related to the operation with hydrogen in the first 20% of the length of the channel.
- The hydrogen distribution allows an estimation of the unburnt hydrogen and of the fuel conversion. Consequently, the tool is exploitable for the convenient sizing of a catalytic combustor.

Future works will include a more detailed description of the hydrogen mass diffusion and the evaluation of the possible applications of the technology to other hydrogen end uses.

REFERENCES

1. https://www.nature.com/articles/d42473-020-00545-7, accessed on December 11, 2021
2. Hayes RE and Kolaczkowski ST. 1997. Introduction to catalytic combustion. London, Routledge.
3. Groppi G, Belloli A, Tronconi E and Forzatti P. 1995. Analysis of multidimensional models of monolith catalysts for hybrid combustors. AIChE Journal, Vol. 41, No. 10:2250-2260
4. Mantzaras J. 2014. Catalytic combustion of hydrogen, challenges, and opportunities. In Advances in Chemical Engineering Vol. 45, 2014, Pages 97-157. Edited by Anthony G. Dixon
5. Devriese C, Pennings W, de Reuver H, Bastiaans R and De Paepe W. 2019. The preliminary CFD design of a compressor and a combustor system towards a 100 kW hydrogen fuelled micro gas turbine. Proceedings of the ASME Turbo Expo 2019: Turbomachinery Technical Conference and Exposition. Volume 8: Microturbines, Turbochargers, and Small Turbomachines; Steam Turbines.
6. Aslanidou I, Rahman M, Zaccaria V and Kyprianidis KG. 2021. Micro gas turbines in the future smart energy system: fleet monitoring, diagnostics and system level requirements. Front. Mech. Eng 7:676853
7. Curtiss CF and Bird RB. 1999. Multicomponent diffusion. Ind. Eng. Chem. Res. 38:2515-2522
8. Finlayson BA. 1972. The method of weighted residuals and variational principles: with application in fluid mechanics, heat and mass transfer. New York, Academic Press.

WHEC-2022
23rd World Hydrogen Energy Conference
June 26-30, 2022 - Istanbul

#185

OPTIMIZATION OF A HYDROGEN SUPPLY CHAIN: A CASE STUDY FOR ITALY

[1,2*] *Renato Luise,* [1] *Annabelle Brisse,* [3] *Pietro Quaglia,* [2] *Catherine Azzaro-Pantel*
[1]European Institute for Energy Research, Emmy-Noether Straße 11, Karlsruhe 76131, Germany
[2] Université de Toulouse, Laboratoire de Génie Chimique, CNRS, INPT, UPS, 6 Allée Emile Monso, 31400 Toulouse, France
[3] Polytechnic of Turin, Corso Duca degli Abruzzi, 24, Turin, Italy

*Corresponding author e-mail: Renato.luise@eifer.eu

ABSTRACT

Although hydrogen has been identified as key for a zero-carbon energy system, the design and deployment of the hydrogen supply chain (HSC) is a challenging issue, in particular due to the various ways to produce, condition, store and transport hydrogen. Hydrogen demand is expected to increase rapidly as several new sectors (e.g. mobility, heat and buildings) in addition to the conventional industrial ones realize its applications.

The paper addresses the emerging issue of how to design, organize and size the HSC. The problem involves a single optimization framework, where the total cost of the HSC is minimized, with a multi-period (2020-2040) mixed-integer linear programming (MILP) formulation that is implemented in the General Algebraic Modelling System (GAMS) environment, using CPLEX as a solver. The superstructure used for HSC modelling is split into six echelons, i.e., primary energy source, H_2 production, conditioning and centralized storage, distribution, conditioning and decentralized storage, and finally usage.

A case study for Italy has been developed, leading to a final hydrogen cost of 4.6€/kg in 2045. Various key performance indicators (KPIs) have been identified for the optimal solution obtained: centralization degree of the HSC, form of hydrogen (i.e. liquified, compressed), transport mode (gaseous or liquid H_2 trucks, H_2 pipeline) and economic parameters (i.e. investment, operation and maintenance costs).

Keywords: Hydrogen supply chain, Optimization model, GAMS, Mixed integer programming, Decentralization

INTRODUCTION

Several authors have been tackling the problem of HSC optimization since more than 15 years. The work presented in [1] can be defined as one seminal contribution in HSC modeling which paved the way to other developments (e.g. [2], [3] and [4]). This work is the further development of the model previously developed in [3]. It consists in an optimization tool for the deployment and design the HSC, by minimizing the costs of the whole supply chain.

Hydrogen can be produced in either centralized (i.e. steam methane reforming with carbon capture and storage (SMR w. CCS) plants and large-size electrolysers) or decentralized sites (small size electrolysers) or imported from abroad. The solution includes centralized storage systems, which are linked to conditioning components such as compressors and liquefiers. The hydrogen produced and conditioned can be then transported either on road (i.e. by tankertruck for liquid H_2 by tube trailer for compressed H_2) or via H_2 pipeline. H_2 production must finally satisfy the H_2 demand coming from two different sectors, i.e., industry and mobility.

MODELING

In line with the majority of the works analysed in the literature, this formulation of the HSC design problem is based on a mixed-integer-linear-programming (MILP) approach. The model is developed in the General Algebraic Modelling System (GAMS) environment, using the CPLEX solver in a computer with Intel® Core™ i5-6200U processor with CPU @ 2.30GHz and 16GB RAM. A comprehensive explanation of all the parameters, formulas and constraints can be found in [2], [3], [4]. In this paper, only the new technological bricks and implementation done from [3] will be analysed in detail.

Availability of renewable energy sources (RES)

A parallel study has been carried out on the availability of RES in Italy. The available amount of energy for the production of electrolytic hydrogen has been calculated as the sum of the disincentivized RES electricity from 2020 up to 2045 and the 25% of RES production from the forecasted new installations.

Imported H_2

The model integrated the possibility of importation of hydrogen from abroad and its availability at the centralized storages. Once collected at the centralized storage, the hydrogen is then treated in a similar manner to the hydrogen produced in the system (i.e. conditioned and transported to the final user). Nevertheless, the priority has been given

to the National Italian H_2 production and for this reason the imported hydrogen has been seen only as secondary option and for this reason a high cost has been considered (i.e. 10€/kg).

H_2 transported via pipeline

The pipeline capital cost (PLCC) at each period t is evaluated as the product of the specific unit of pipeline capital cost (UPLCC) by the distance AD between grid g and g'.

$$PLCC_t = \sum_{g,g'} UPLCC \times AD_{g,g'} \times NTUgrid_{g,g',t} \quad ,\forall\, g \tag{1}$$

The pipeline operating cost (PLOC) is split into two parts: the first part is related to the pressure drops along the pipes, with the specific pipeline operating cost UPLOC multiplied by the amount of hydrogen transported via pipeline from g to g'. The second part is linked to maintenance costs, which are a percentage delta of the PLCC.

$$PLOC_t = \sum_{g,g'} UPLOC \times Q_{pipeline,g,g't} + delta \times PLCC(t) \quad ,\forall\, g \tag{2}$$

Overview on the HSC design

The HSC has been designed to satisfy the demand from two different sectors (i.e. mobility, industry) with the production of H_2 through SMR, electrolysis and imported H_2 from abroad. Storage and transport have been implemented in compressed and liquid forms. All the possible paths to satisfy the H_2 demand are shown in Fig. 1.

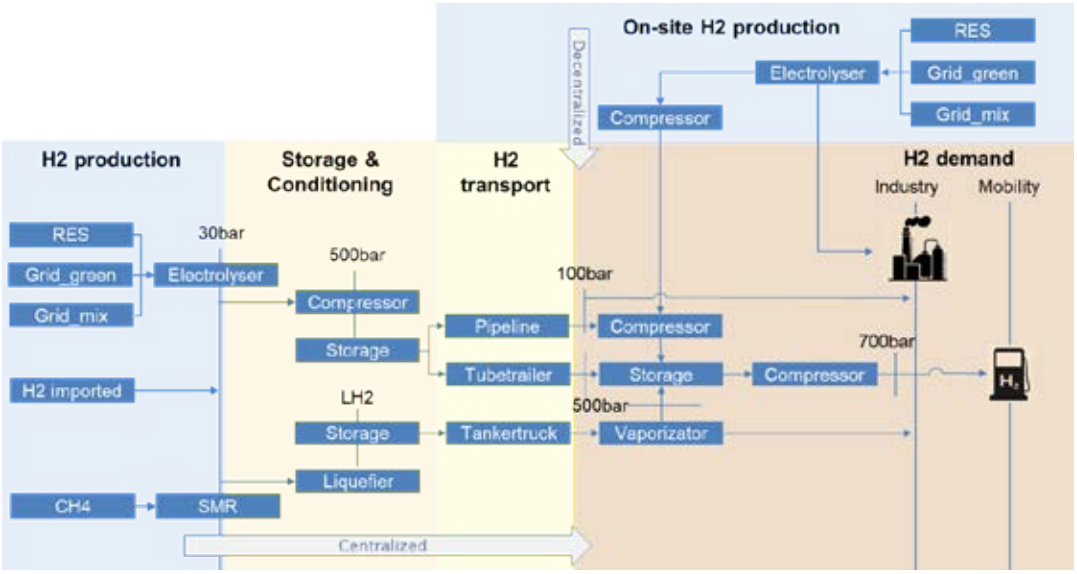


Fig. 1. Technologies and design of the HSC

CASE STUDY

To validate the new implemented model, a case study has been investigated where the system analysed is Italy divided into regions. Each Italian region represents a grid, which is centered in its own regional capital, excluding the islands, which would need different transport modes.

The hydrogen demand for mobility in each grid D_{MOB} has been calculated as the product of the number of vehicles NV registered in each region, the penetration rate PER of hydrogen vehicles, the average distance d traveled by each considered vehicle and the fuel consumption FC of each considered vehicle, as shown in Eq. 3.

$$D_{MOB_{g,t}} = NV_{g,t} \times PER_t \times FC \times d \quad ,\forall\, g,t \tag{3}$$

The hydrogen demand for mobility sector has been indeed calculated as a share of the current hydrogen demand in Italy coming from refinery and ammonia plants, which covers 91% of the Italian H_2 demand. Due to lack of information, the demand of H_2 for refinery has been equally split between the 12 identified plants (i.e. 35,300 ton/plant/year), while the whole H_2 demand for the ammonia sector (i.e. 80,200 ton/year) has been totally satisfied by the unique plant identified.

The resulting demand in average for mobility and industrial sector per each Region ranges from 3,400 ton/year in the first period, up to 11,800 ton/year in the last period.

RESULTS AND DISCUSSION

The optimization has been run to minimize the hydrogen costs along the HSC. Capital, operating and maintenance costs for each energy source and technological brick have been considered. All the economic parameters have been actualized with a discount rate of 2%.

The final cost of hydrogen along the whole analysed period amounts to 5.8€/kg. The costs are strongly influenced by the lack of infrastructures nowadays. Indeed, in the first analysed period (i.e. 2025-2030) the hydrogen has a cost of 9.3€/kg, which falls to 4.6€/kg in the last period (i.e. 2040-2045). Fig. 2 shows the final configuration of the HSC, which refers to the year 2045.

It must be emphasized that the optimization has found a solution with the installation of a steam methane reformer with carbon capture and storage (SMR w. CCS) needed only in the last period when the demand is higher. The H_2 demand in the first periods is indeed exclusively satisfied by electrolytic hydrogen production, with a distribution of 72% centralized rate and 28% decentralized. This ratio remains mainly constant also with the installation of the SMR w. CCS. The solution identified from optimization also includes in the first period only compressed hydrogen. Only in the last period indeed, liquid hydrogen enters the scene with a share of 35% (i.e. 6 liquefaction plants).

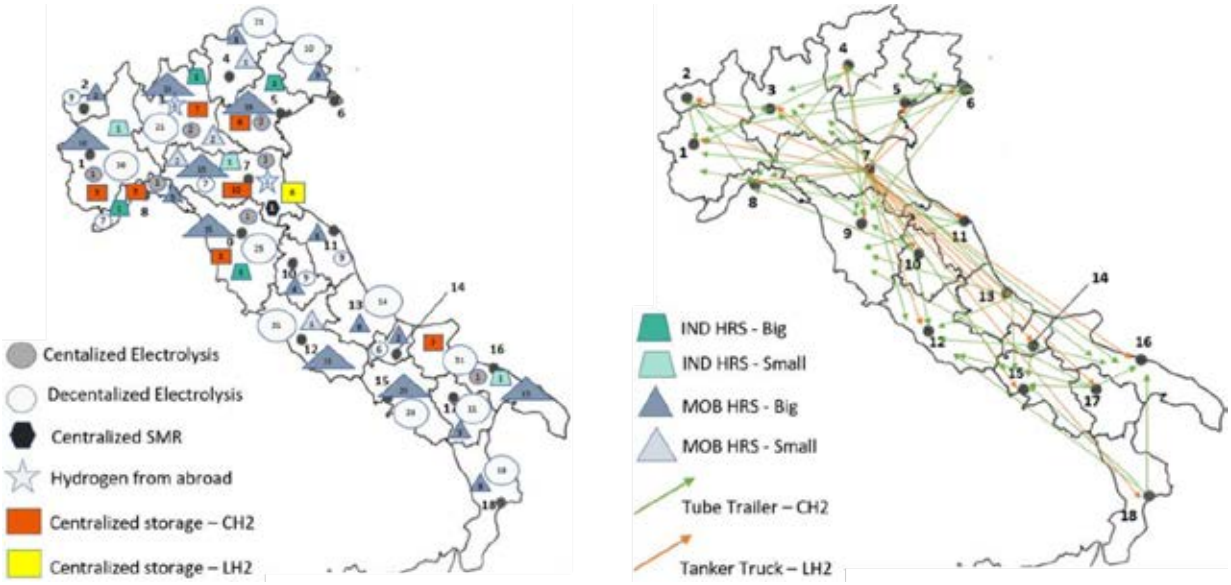


Fig. 2. Italian HSC design in 2045

CONCLUSIONS

When national hydrogen demand is greater than 200,000 tons per year, the model evaluate that the cheapest hydrogen cost for final consumer is achieved with centralised production via SMR w. CCS, the hydrogen being distributed in liquid form. With this H_2 supply chain, the cost for low carbon hydrogen is 5.8 €/kg The H_2 cost of 5.8 €/kg, obtained with this optimization results, is still not competitive with the H_2 produced through SMR at an industrial scale, especially if a margin on the top of the final H_2 cost is considered.

REFERENCES

1. Almansoori A, Shah N. 2006. Design and Operation of a Future Hydrogen Supply Chain. Chemical Engineering Research and Design. 84(6): 423-438.
2. Carrera Guilarte E., Azzaro-Pantel C.. 2020. A Methodological Design Framework for Hybrid “Power-to-Methane” and “Power-to-Hydrogen” Supply Chains: application to Occitania Region, France. Computer Aided Chemical Engineering. 48: 679-684.
3. Luise R., Brisse A, Azzaro-Pantel C.. 2021. Centralised vs. decentralised production and storage: optimal design of a decarbonised hydrogen supply chain with multiple end uses. Computer Aided Chemical Engineering.
4. De-León Almaraz S, Azzaro-Pantel C., Montastruc L., Domenech S.. 2014. Hydrogen supply chain optimization for deployment scenarios in the Midi-Pyrénées region, France. International Journal of Hydrogen Energy. 39(23): 11831-11845.

WHEC-2022
23rd World Hydrogen Energy Conference
June 26-30, 2022 - Istanbul

#191

LIFE CYCLE COSTING APPROACHES OF FUEL CELL AND HYDROGEN SYSTEMS: A LITERATURE REVIEW

[1*] *Yuki Ishimoto,* [2] *Christina Wulf,* [2] *Wilhelm Kuckshinrichs*
[1]The Institute of Applied Energy, Shimbashi SY Bldg., 1-14-2 Nishi-shimbashi, Minato-ku, Tokyo 105-0003, Japan
[2] Forschungszentrum Jülich, Institute of Energy and Climate Research—Systems Analysis and Technology Evaluation (IEK-STE), D-52425 Jülich, Germany

*Corresponding author e-mail: ishimoto@iae.or.jp

ABSTRACT

A comprehensive literature review on the papers using life cycle costing (LCC) approaches to fuel cell and hydrogen (FCH) related technologies was carried out as one task in the European project SH2E in order to develop an LCC guideline. The papers to be reviewed were extracted from two major literature databases, SCOPUS and Web of Science. The extracted papers were briefly reviewed to decide if the paper is to be reviewed later in detail. The numbers of papers to be reviewed in detail were finally 155. The selected papers were reviewed from the various viewpoints, in particular, the objectives, the scope, the entity of assessment, stakeholder involvement, depth of assessment, mass and energy balances of the systems, the facilities considered, calculation methods, discounting (social vs private) or EoL treatment etc. The overall trend of LCC approaches, methods and indicators will be clarified, in order to establish the LCC guidelines.

Keywords: Life cycle costing, Hydrogen, Fuel cell

INTRODUCTION

Fuel cell and hydrogen (FCH) related technologies are considered as an energy vector connecting low carbon and renewable resources and energy demand sectors for carbon neutrality [1, 2]. Many studies have been performed over the last decade analyzing the costs of FCH systems because costing evaluations are the backbone of all technology development. Companies only invest in new technologies if they see an economic advantage in the future. However, there is no standard methodology for cost calculations. When coming from the life-cycle-thinking perspective the SETAC has published a code of practice in 2011 for life cycle costing (LCC) [3]. Other studies might use the approach of 'Total Cost of Ownership', which also includes the full life cycle of a product from production, over the use phase and its disposal or end-of-life treatment. Regarding FCH systems, LCC is currently of utmost importance, because several FCH are on the edge of commercialization, e.g. water electrolyzers. Thus, in this study a comprehensive literature review was performed on LCC approaches for FCH systems to determine the most important methodological influencing factors and identify best practices.

This study is part of the Fuel Cell and Hydrogen 2 Joint Undertaking (FCH JU) funded SH2E project [4] where eventually guidelines for Lifecycle Sustainability Assessment (LCSA) for FCH technologies are being developed. LSCA consists of three assessment methods that are economy, environment and society and their integration.

This review aims to clarify the overall trend of LCC approaches, methods and indicators (including both conventional life-cycle economic indicators and life-cycle economic indicators based on externalities), identifying their main features and discussing their suitability for the assessment of FCH systems in order to establish LCC guidelines to be subsequently developed in the following task in the SH2E project. The review investigates the objectives, the scope, the entity of assessment, stakeholder involvement, depth of assessment, mass and energy balances of the systems, the facilities considered, calculation methods, discounting (social vs private) or EoL treatment etc.

So far, several review papers about FCH topics have been published. For example, a specific FCH technology is analyzed. Gigoriev et al. [5] are focussing in their paper on water electrolysis. They are mentioning costs, but only in absolute terms regarding the different technologies. Hydrogen supply chains is the technological topic of Fredershausen et al. [6]. On the example of hydrogen supply chains, they discuss already methodological aspects regarding sustainability evaluations. They classify the economic evaluations in four different types, i.e. macroeconomics, microeconomics, long-term competitiveness and innovation capability. However, they do not go further into methodological details, which was carried out in this study.

METHODS AND PRELIMINARY RESUTLS

Fig. 1 shows the procedure of the literature review on LCC papers. We extracted peer-reviewed papers on SCOPUS and Web of Science, dated from January 1st, 2010 to May 21st, 2021 with the search string in their titles, abstracts or

keywords. The number of extracted papers is 317 removing overlaps in both databases. The used search strings are as follows;

- For SCOPUS, PUBYEAR > 2010 AND TITLE-ABS-KEY(((hydrogen OR "fuel cells") AND ("life cycle" OR lifecycle)) AND ("sustainability assessment" OR lcsa OR costing OR lcc OR "economic analysis")
- For Web of Science, (AK=((((hydrogen OR "fuel cells") AND ("life cycle" OR lifecycle)) AND ("sustainability assessment" OR lcsa OR costing OR lcc OR "economic analysis")))) OR TI=(((hydrogen OR "fuel cells") AND ("life cycle" OR lifecycle)) AND ("sustainability assessment" OR lisa OR costing OR lcc OR "economic analysis")) OR AB=(((hydrogen OR "fuel cells") AND ("life cycle" OR lifecycle)) AND ("sustainability assessment" OR lisa OR costing OR lcc OR "economic analysis")) For a timespan from 2011-01-01 to 2021-05-21

Then, the papers were briefly checked based on their abstract, equations, figures, tables, and conclusion using the following criteria to choose the papers to be reviewed in detail;

- Include: Papers with peer review on LCC of FCH related facilities or equipment (production, storage, transport and utilization);
- Exclude: Conference papers, book chapters, review papers, paper that just refers another paper results, papers where hydrogen is minor operating agent, non-English written papers.

The number of the papers to be reviewed was 155. A difference in the scope of the cost items account for was observed in some papers we have reviewed. The overall trend and methodologies, indicators and other important aspects for LCC will be presented in the conference.

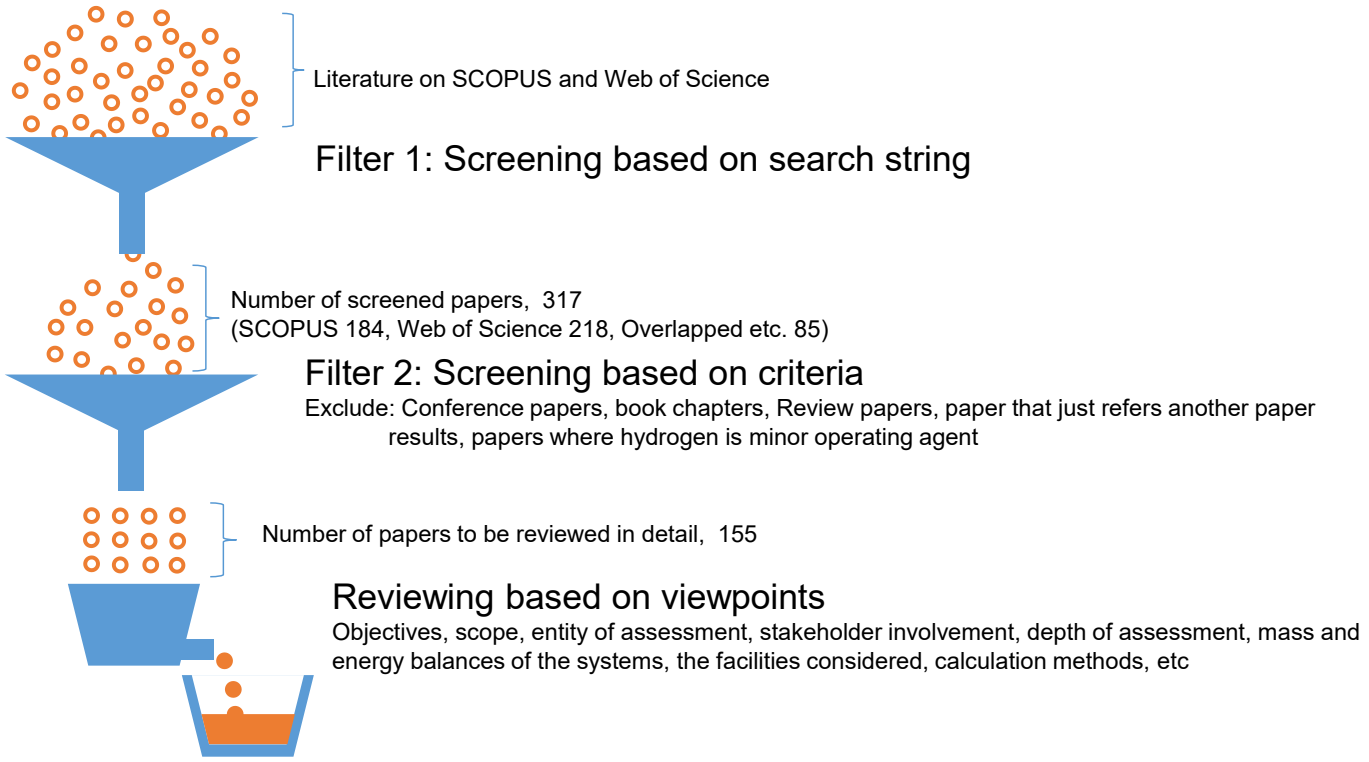


Fig. 1. Procedure of literature review on Life Cycle Costing (LCC) papers

Fig. 2 shows the number of the screened papers by published year. The number of LCC papers about hydrogen and fuel cells increases with time as observed. This could reflect the scientists' interests in these technologies.

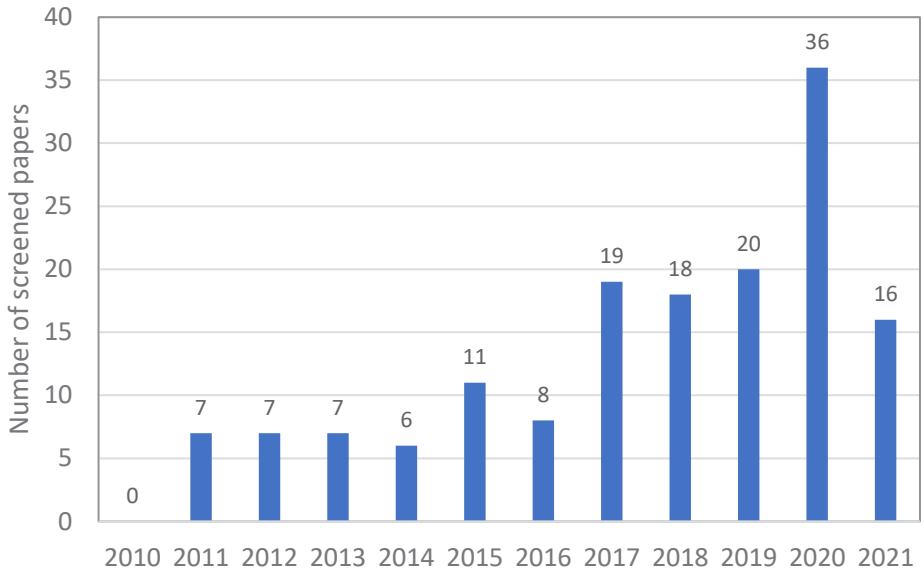


Fig. 2. Number of the screened papers by published year, until May 2021

CONCLUSIONS

A comprehensive literature review on the papers using LCC approaches to FCH related technologies was carried out as one task in the FCH JU funded SH2E project in order to develop an LCC guideline in the subsequent task. A total of 155 papers were extracted to be reviewed in detail. The number of the papers are soaring, which could reflect researchers' interests in this field. The selected papers are reviewed from the various viewpoints, in particular, the objectives, the scope, the entity of assessment, stakeholder involvement, depth of assessment, mass and energy balances of the systems, the facilities considered, calculation methods, discounting (social vs private) or EoL treatment etc. The overall trend of LCC approaches, methods and indicators will be clarified, in order to establish the LCC guidelines.

ACKNOWLEDGEMENT

This project has received funding from the Fuel Cells and Hydrogen 2 Joint Undertaking under grant agreement No 101007163. This Joint Undertaking receives support from the European Union's Horizon 2020 Research and Innovation programme, Hydrogen Europe and Hydrogen Europe Research.

REFERENCES

1. European commission. 2020. European Hydrogen Strategy, Brussels.
2. International Energy Agency. 2021. Global Hydrogen Review 2021, Paris.
3. Swarr TE, Hunkeler D, Klöpffer W, Pesonen H-L, Ciroth A, Brent AC, et al. 2011. Environmental life cycle costing: A code of practice. Pensacola, Brussels: SETAC.
4. https://sh2e.eu/. Accessed on December 3, 2021
5. Grigoriev SA, Fateev VN, Bessarabov DG, Millet P. 2020. Current status, research trends, and challenges in water electrolysis science and technology. International Journal of Hydrogen Energy 49: 26036-26058
6. Fredershausen S, Lechte H, Willnat M, Witt T, Harnischmacher C, Lembcke T-B, et al. 2021. Towards an Understanding of Hydrogen Supply Chains: A Structured Literature Review Regarding Sustainability Evaluation. Sustainability 13:11652.

WHEC-2022
23rd World Hydrogen Energy Conference
June 26-30, 2022 - Istanbul

#225

THE TECHNO-ECONOMIC EVALUATION OF HYDROGEN PRODUCTION COST TOWARDS ANION EXCHANGE MEMBRANE ELECTROLYZER

[1,2] *Bowen Yang,* [1,2] *Ruofan Zhang,* [1,2] *Cunman Zhang*
[1] School of Automotive Studies, Tongji University, Shanghai 201804, China
[2] Clean Energy Automotive Engineering Center, Tongji University, Shanghai 201804, China

*Corresponding author e-mail: zhangcunman@tongji.edu.cn

ABSTRACT

With the significant development of electrolyzer technology, blueprint of economical and long-run hydrogen production adopted by this technology inspires great interest. The economic competence of electrolyzer needs further investigation to answer their current and future viability with technology development of ultimate performance as well as the decisive impactor to affect hydrogen production cost. Economically and technically, this research is originally established with a combination of crucial technology features including current density, overpotential, and ohmic resistance, acquired from the polarization curve to make the techno-economic analysis of anion exchange membrane electrolyzer technology. A cell-stack-system level on materials and fabrication is performed based on the bottom-up study to give an optimal investigation. It reveals the possibility for future hydrogen cost reduction and points out how the internal technical factors act on achieving a more cost-competitive hydrogen production. With consideration of the service lifetime together, this research exhibits the potential economic benefits from multiple dimensions of technological progress.

Keywords: Hydrogen economy, Electrolyzer technology, Hydrogen production

INTRODUCTION

Hydrogen emerges promptly as a promising energy system to revolutionize the traditional power fuels[1]. Currently, H_2 production could be realized by advanced water electrolysis technology, which could be combined with the green renewable electricity[2,3]. Among the various electrolysis technology such as classical alkaline electrolyzer, progressive proton exchange membrane electrolyzer, the anion exchange membrane electrolyzer spurs as a burgeoning newbie which takes the advantage of both alkaline electrolyzer and proton exchange membrane electrolyzer. For instance, the usage of low-cost fabrication materials and high-quality electrolysis current density endow the anion exchange membrane electrolyzer significate competence to satisfy the low-cost hydrogen production demand. With the significant development of the anion exchange membrane electrolyzers technology in a foreseeable future, more economical hydrogen production cost could span the coming hydrogen society rapidly[4-6]. However, there remains critical questions toward the hydrogen production cost by anion exchange membrane electrolyzer technology under techno-economic perspective, including the near-term viability, long-term cost reduction from the key impactor consideration.

Previous hydrogen production cost investigation mainly established on the social market survey regarding capital investment and materials manufacture expansion, a separate economic consideration[7]. However, the greatest hydrogen production cost reduction stems from the technic character of electrolyzer ultimate performance such as electrolysis efficiency and service lifetime. The electrolyzer performance could be attributed by the technic breakoff of critical materials property, especially the catalyst activity, membrane conductivity and mass transfer in gas diffusion layer. Integrally, the special electrolyzer technology factor could be presented as current density and voltage potential, which will decide the electricity consumption. The electricity consumption cost occupies paramount of the final hydrogen production cost regarding to the electrolyzer manufacture costs. These technic impactors are few explored with the relationship of hydrogen production cost, whereas they act as favorable guidelines for the hydrogen production blueprint layout.

Herein, current density and voltage from polarization curve of electrolyzer performance is implemented into the electrochemical calculation and throughout to describe the technical character variation originally. Then, a techno-economic approach is established for the assessment of hydrogen production cost by application of anion exchange membrane electrolyzer technology. Current technology status and future potential of this technology are evaluated form cell-stack-system level.

MODELING

According to Faraday's law and independent efficiency of the anion exchange membrane electrolyzer, the techno-economic model was established for both the stack and system. Starting with the resultant hydrogen production cost, it should be calculated as the total cost divided by hydrogen production mass. Power consumption cost and electrolyzer manufacture contribute simultaneously to the total cost. Detail constructure is exhibited as the following equations and Fig. 1. Notably, the part of Balance of Plant (BoP) is customized rather than mass-produced, and it is viewed as proportion to the cost of the stack according to current Chinese market. Here the BoP is determined as 50% of the stack cost for anion exchange membrane. *C* stands for *Cost* and *P* stands for unit price here. The stack is designed as 1MW scale.

$$C_{stack} = n_{cell} \times \sum_{i=1}^{n} C_{materials,i} \quad (1)$$

$$C_{system} = C_{stack} + \sum_{i=0}^{n} C_{BOP,i} \quad (2)$$

$$C_{electricity} = P_{electricity} \cdot t \cdot n_{cell} \cdot (V_{cell} + R_{ohmic} \cdot i_o) \cdot i_o \cdot S_{cell} \quad (3)$$

$$m_{H_2} = t \times \frac{P_{total} - P_{loss}}{F} \quad (4)$$

$$C_{unit\ hydrogen\ production} = \frac{C_{system} + C_{electricity}}{m_{H_2}} \quad (5)$$

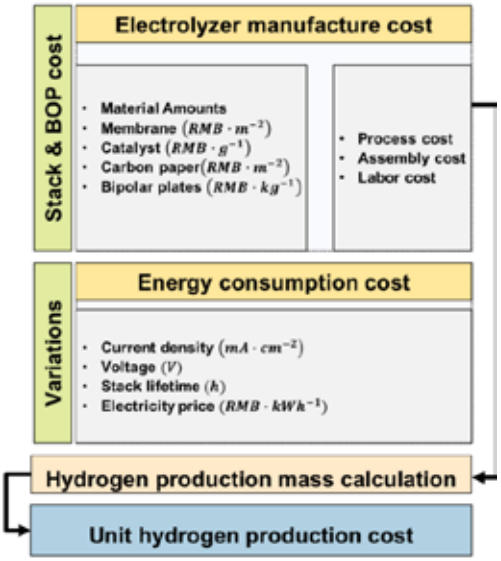


Fig. 1. Flow chart of the techno-economic modelling in which critical parameters are descripted in detail.

RESULTS AND DISCUSSION

Hydrogen production cost division towards anion exchange membrane electrolyzer technology

Generally, the hydrogen production cost decrease from 25.37 $(RMB \cdot kg^{-1})$ to 19.32 $(RMB \cdot kg^{-1})$ when the electrolyzer stack lifetime increases from 2 to 18 years, as shown in Fig. 2(a). To analyze the division of hydrogen production cost, it is mainly divided into manufacture cost and power consumption cost. In detail, the BoP and stack manufacture cost account for less section compared to the whole power consumption cost. And the BoP and stack manufacture cost are greatly diminished as the lifetime of electrolyzer increases. Since the power consumption cost domains, it could be divided into the electricity cost for directly hydrogen production according to Faraday's law, the electricity cost for over potential wastage, the electricity cost for ohmic loss wastage and the electricity cost for BoP support. Despite the electricity cost for directly hydrogen production exceeds largely to the electricity cost for over potential and ohmic loss cost, it should not be ignored that there exists considerable electricity not to be fully utilized.

Influence of voltage ad current density on hydrogen production cost

When the initial voltage starts at 1.43V, the hydrogen production cost decreases equally from 26 $(RMB \cdot kg^{-1})$ to 22 $(RMB \cdot kg^{-1})$ as the current density increases from 400 to 1400 $(mA \cdot cm^{-2})$, shown in Fig. 2(b). When the initial voltage decreases to 1.33V, a 0.1V deduction compared to 1.43V will cause a different change tendency of hydrogen production cost. Under this circumstance, the hydrogen production cost decreases from 25.5 $(RMB \cdot kg^{-1})$ to a minimum value of 21 $(RMB \cdot kg^{-1})$ firstly, whereas increases slightly to 21.5 $(RMB \cdot kg^{-1})$ as the current density increases from 400 to 1400 $(mA \cdot cm^{-2})$. That is to mean there exists an optimal current density point to realize a lowest hydrogen production cost. This current density value is 850 to 1300 $(mA \cdot cm^{-2})$. This

phenomenon could be ascribed to the higher electricity consumption at exorbitant current density. At the same time, the hydrogen production cost reduces rapidly at comparably lower current density of 400 to 600 ($mA \cdot cm^{-2}$), while it decreases slowly at higher current density of 700 to 1400 ($mA \cdot cm^{-2}$).

Sensitivity of hydrogen production cost reduction

As shown in Fig. 2(c), critical impactors including reduction in voltage, ohmic loss and electricity cost, increasement in stack lifetime are given simultaneously to consider the hydrogen production cost reduction degree. Among these factors, electricity cost shows as priority to others as the current density increases. Voltage takes the second place. The prolong of stack lifetime makes a positive reduction in hydrogen production cost at low current density but causes a slight increasement in hydrogen production at extra-high current density.

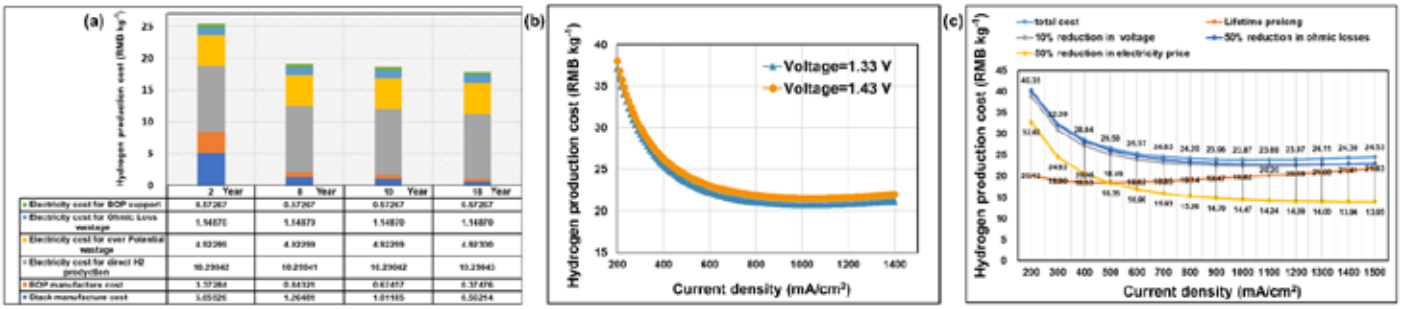


Fig. 2. (a) Hydrogen production cost division; (b) Hydrogen production cost reduction tendency under current density and voltage variation; (c) Sensitivity of hydrogen production cost reduction.

CONCLUSIONS

In summary, a techno-economic analysis of hydrogen production cost is investigated according to the critical technology character of anion exchange membrane at multiple dimensions. The hydrogen production cost division is given firstly to oversee the reduction tendency as electrolyzer lifetime prolongs. Subsequently, the influence of voltage and current density are discussed on hydrogen production cost, showing an optimal current density point for the lowest hydrogen production cost and significant hydrogen production cost triggered by a slight voltage decline. Sensitivity analysis reveals the electricity price as predominated factor and voltage reduction as secondary factor for hydrogen production cost reduction.

ACKNOWLEDGEMENT

The project was funded by the Plan of National Key Research and Development (2018YFB1503103).

REFERENCES

1. Mehrjerdi H. 2019. Optimal correlation of non-renewable and renewable generating systems for producing hydrogen and methane by power to gas process. International Journal of Hydrogen Energy. 44:9210-9219.
2. Peng Y, Jiang K, Hill W, Lu Z, Yao H, and Wang H. Large-Scale, 2019. Low-Cost, and High-Efficiency Water-Splitting System for Clean H_2 Generation. ACS Applied Materials&Interfaces.11:3971-3977.
3. Millet P, Ngameni R, Grigoriev SA, Mbemba N, Brisset F, and Ranjbari A. 2010. PEM water electrolyzers: From electrocatalysis to stack development. International Journal of Hydrogen Energy.35:5043-5052.
4. Lee H, Lee B, Byun M, and Lim H. 2020. Economic and environmental analysis for PEM water electrolysis based on replacement moment and renewable electricity resources. Energy Conversion Management.224:113477.
5. Locatelli G, Boarin S, Fiordaliso A, and Ricotti ME. 2018. Load following of Small Modular Reactors (SMR) by cogeneration of hydrogen: A techno-economic analysis. Energy.148:494-505.
6. Grigoriev SA, Fateev VN, Bessarabov DG, and Millet P. 2020. Current status, research trends, and challenges in water electrolysis science and technology. International Journal of Hydrogen Energy.45:26036-58.
7. Glenk G and Reichelstein S. 2019. Economics of converting renewable power to hydrogen. Nature Energy.4:216-222.

WHEC-2022
23rd World Hydrogen Energy Conference
June 26-30, 2022 - Istanbul

#238

CHARACTERISTIC AND PERFORMANCE OF $Ce_{0.6}Mn_{0.3}Fe_{0.1}O_2$ FOR SOLID OXIDE FUEL CELLS ANODE ELECTRODE

[1] *Ko-Yun Chao,* [1] *Deb"abrata Mohantya,* [1,2*] *I-Ming Hung,* [3] *Tai-Nan Lin*
[1] Department of Chemical Engineering and Materials Science, Yuan Ze University, Taoyuan, Taiwan
[2] Hierarchical Green-Energy Materials Research Center, National Cheng Kung University, Tainan, Taiwan
[3] Nuclear Fuels and Materials Division, Institute of Nuclear Energy Research, Taoyuan, Taiwan

*Corresponding author e-mail: imhung@saturn.yzu.edu.tw

ABSTRACT

The catalytic activity of $Ce_{0.6}Mn_{0.3}Fe_{0.1}O_{2-\delta}$ (CMF) for electrode reaction was reasonably high for SOFC anode application. In this study, we investigated the characteristic and electrochemical performance of CMF for solid oxide fuel cell (SOFC) anode in comparison with that of the conventional Ni-based anode. CMF anode powder was prepared by citric acid-EDTA complexing method with a fluorite structure and single phase, which was confirmed by XRD analysis. The average size of primary particle is about 200 nm, which was observed by SEM, and it sintered and aggregated to large secondary particle after calcination at 1000°C. The secondary particle size distribution, which was analysed by Dynamic Light Scattering (DLS), is in the range of 10-95 μm with D_{50} particle size of 27 μm.

Keywords: Solid oxide fuel cells (SOFC), Anode, Sol-Gel Method, Fluorite structure

INTRODUCTION

Solid oxide fuel cells (SOFCs) are the electrochemical conversion devices which generally operated at high temperatures. SOFC is a solid-state electrochemical device that converts the chemical energy into electrical energy. In comparison with other types of fuel cells, SOFC has high efficiency exceeding 80% when included the heat produced as a result of the conversion.
SOFCs includes three major components, i.e., anode and cathode two porous electrodes, and a dense solid oxygen ion conducting electrolyte membrane which separates the fuel and air compartments.
The operating principle of solid oxide fuel (Figure.1. [1])
(a) Cathode: the reduction reaction reduces oxygen to oxygen ions
(b) Electrolyte: transports oxygen ions to the anode
(c) Anode: Oxidizes hydrogen into water and releases electrons to provide electricity for the external circuit
The structure of the anode should exhibit good electronic conductivity and hydrogen catalysis ability, as well as chemical stability under reduction atmosphere.

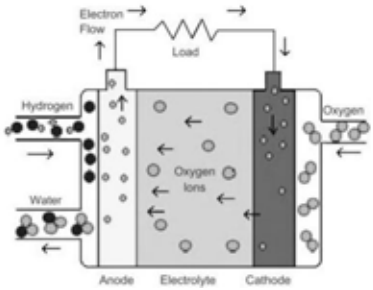


Fig.1. Operating principle of solid oxide fuel cell [1].

Ni-YSZ cermet has been generally used for the anode in SOFCs. However, Ni has the agglomerate problem on long-term operation at high temperatures, resulting in the degradation of anode performance. In order to solve these problems, many kinds of materials have been examined as replacements for Ni-YSZ. Additionally, these metal oxides, it is a mixed ionic-electronic conductor with high tolerance for coke deposition and high catalytic activity in the oxidation of fuels, such as ceria (CeO_2) has been an enhancing choice for anode materials. The catalytic activity of CMF for electrode reaction was reasonably high for SOFC anode application [2]. In this study, we further investigated the performance of CMF for SOFC anode in comparison with the property of the traditional Ni-based anode.

MATERIALS AND METHODS

$Ce_{0.6}Mn_{0.3}Fe_{0.1}O_{2-\delta}$(CMF) powder was prepared by citric acid-EDTA complexing method, $Ce(NO_3)_3 \cdot 6H_2O$, $Mn(NO_3)_2 \cdot 6H_2O$, $Fe(NO_3)_3 \cdot 9H_2O$ nitrate is dissolved in deionized water, EDTA metal chelate is dissolved in ammonia water, then two cups of solution are mixed, and citric acid is added to adjust the pH value to 6. The nitrate solution is under constant stirring, the solution will be configured on the heating stirrer, heated and stirred, and evaporated to dryness to a thick black gel, then put it into a high-temperature furnace and heat treatment at 250 °C for 2 hours to remove nitric acid, ammonia water with moisture. The heat-treated powder was ground in an agate mortar and sieved through a 200 mesh screen, and then calcined at 1100°C for 6 hours. The calcined powder is ground again in an agate mortar and sieved with a 200mesh sieve to obtain CMF powder. CMF powder process is shown in Figure.2.

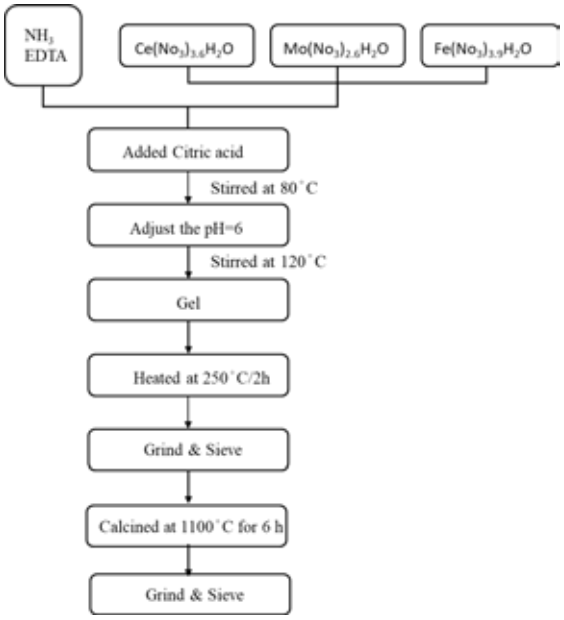


Fig. 2. The experiment procedure of CMF powders synthesis by the citric acid-EDTA complexing method.

RESULTS AND DISCUSSION

The X-ray diffraction (XRD) pattern of the CMF calcined at 1100°C for 6 hours was conducted as shown in Fig. 3. The pattern displays the peaks in agreement with the fluorite structure. There is no second phase was observed. This result indicated that the single phase of CMF powder with fluorite structure was successfully prepared by the citric acid-EDTA complexing method. The surface morphology and particle size of the CMF powder was observed by field-emission scanning electron microscope (FE-SEM) which was shown in Fig. 4. The SEM image shows that the average size of primary particle is about 200 nm, and it sintered and aggregated to large secondary particle after calcination at 1000°C. The secondary particle size distribution was analysed by Dynamic Light Scattering (DLS) which was shown in Fig. 5. The particle size distribution is in the range of 10-95 μm with D_{50} particle size of 27 μm.

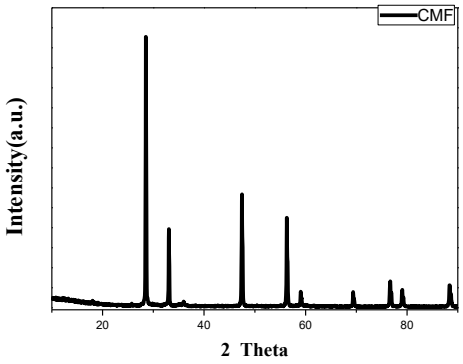


Fig. 3. The X-ray diffraction (XRD) pattern of the CMF powder calcined at 1100°C for 6 hours.

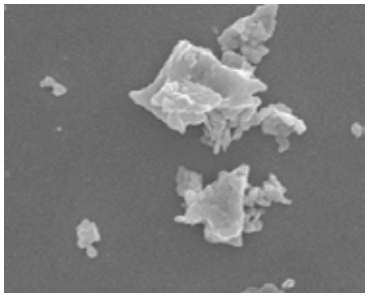


Fig. 4. The SEM image of the CMF powder calcined at 1100°C for 6 hours.

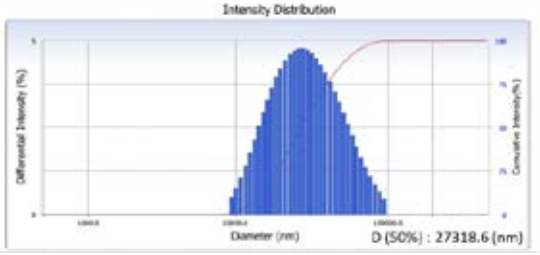


Fig. 5. The secondary particle size distribution of the CMF powder calcined at 1100°C for 6 hours.

CONCLUSIONS

In this experiment, single phase of CMF powder with fluorite structure was successfully prepared by the citric acid-EDTA complexing method. The primary particle is about 200 nm, and aggregated to large secondary particle with D50 particle size of 27 μm after calcination at 1000°C. The electrochemical performance of CMF based on SDC electrolyte will be investigated in the future.

ACKNOWLEDGEMENT

This study was funded by the Ministry of Science and Technology in Taiwan (MOST 107-2221-E-155-004-MY2 and MOST 110-2221-E-155 -011 -MY2).

REFERENCES

1. Kant R, Singh K, and Pandey OP. 2008. Synthesis and characterization of bismuth vanadate electrolyte material with aluminium doping for SOFC application, International Journal of Hydrogen Energy 33, 455-462.
2. Zhu C, Nobuta A, Ju YW, Ishihara T and Akiyama T. 2013. Solution combustion synthesis of $Ce_{0.6}Mn_{0.3}Fe_{0.1}O_2$ for anode of SOFC using $LaGaO_3$-based oxide electrolyte. International Journal of Hydrogen Energy 38, 13419-13426.

WHEC-2022
23rd World Hydrogen Energy Conference
June 26-30, 2022 - Istanbul

#241

SYNGAS PRODUCTION VIA CHEMICAL LOOPING DRY REFORMING OF METHANE USING IRON-BASED OXYGEN CARRIERS

[1]Po-Cheng Tsou, [1*]Rei-Yu Chein, [2]Wei-Hsin Chen
[1]Dept. of Mechanical Engineering, National Chung Hsing University, Taichung City, Taiwan
[2] Department of Aeronautics and Astronautics, National Cheng Kung University, Tainan, Taiwan

*Corresponding author e-mail: rychein@dragon.nchu.edu.tw

ABSTRACT

In this study, the iron-based oxygen carrier was used for the syngas production via chemical looping dry reforming of methane (CL-DRM). The effect of the content of F_2O_3 supported by Al_2O_3 on the reduction stage during the CL-DRM was examined for various reaction temperatures was experimentally studied. It was found that higher Fe_2O_3 content and reaction temperature were required to obtain high CH_4 and CO_2 conversions and avoid carbon deposition. The experimental results indicated that 100% CH_4 and CO_2 conversion can be obtained from 30wt% Fe_2O_3 oxygen carrier and reaction temperature of 1000°C. At lower Fe_2O_3 contents and temperatures, Fe_2O_3 has low reactivity and high carbon deposition leading to poor CL-DRM performance. The experimental results also indicated that iron-based oxygen carrier was suitable for reducing CO_2 into CO and carbon.

Keywords: Iron-based oxygen carrier, Syngas, Chemical looping dry reforming of methane (CL-DRM), CH_4 and CO_2 conversions

INTRODUCTION

As a new energy conversion technology, chemical looping reforming (CLR) can be used to produce syngas with desired H_2/CO ratio [1]. In CLR, an oxygen carrier is used for oxygen supply instead of air. It consists of an air reactor and a fuel reactor. In the fuel reactor, the oxygen carrier is reduced by the introduced fuel. The reduced oxygen carrier is circulated to the air reactor and re-oxidized with the injected air.

The oxygen carrier is one of the key components in CLR. Iron, nickel, copper, and manganese are the most promising oxygen carriers. As compared with others, the iron-based oxygen carriers are considered to have industrial application potential because of their low price, high reactive, high mechanical strength, and being environmentally-friendly. Many iron ores can be directly used as oxygen carriers after simple treatments. Meanwhile, environmental impact must be considered due to the increasing standards of the environmental protection. Iron has been considered to be a safe material as compared with other materials [2].

In addition to natural iron ore, iron-based oxygen can also be synthesized in the laboratory [3]. In this case, the Fe_2O_3 supported by Al_2O_3 is the most frequently used oxygen carrier. Although CLR using Fe_2O_3/Al_2O_3 as oxygen carriers have been studied extensively, systematic investigation on the weight percentage of Fe_2O_3 on the CLR performance was not reported. This study intended to examine this issue in detail via chemical looping dry reforming of methane (CL-DRM).

EXPERIMENTAL

The CLR was carried out using a conventional packed-bed tubular reactor operated at atmospheric pressure. A quartz tube with an inside diameter of 9 mm was used as the reactor. The oxygen carrier was loaded in the central section with the two ends fixed using quartz wool. The reactor is placed vertically in a temperature controllable electric furnace. A gas mixture of CH_4, CO_2, and N_2 was used as the reactant. The flow rate of each gas species was metered and regulated using mass flow controllers (Brooks 5850E, USA). In the reactant, N_2 was an inert gas and its volume flow rate was used as the basis for evaluating the flow rate of gas species in the product. After removing water using a condenser, the dried gas product was collected and analyzed using gas chromatography (Agilent 7890B, USA).

RESULTS AND DISCUSSION

The reaction temperature, reactant feed rate, reactant composition, oxygen carrier loading, and reaction time are the important factors that affect the CLR performance. In CLR, the chemical reactions involved in the reduction stage are more complicated than those in the oxidation stage. In this study, the reduction stage performance was studied in detail before carrying out the complete cyclic chemical looping processes. The reaction temperature and content of Fe_2O_3 were chosen as the primary parameters to examine the reduction reaction performance under fixed feed conditions and catalyst loading. The total feed rate of the reactant was a mixture of 15 sccm CH_4, 15 sccm CO_2, and 20 sccm N_2. The oxygen carrier loading was 2.5 grams.

Fig. 1 shows the reduction stage performance of CL-DRM using oxygen carriers with various Fe_2O_3 weight percentages for reaction temperature T=800°C. The reaction temperature is initially at room temperature and then gradually increases with the test time. At t=135 minutes, the reaction temperature reaches the designated reaction temperature and then keeps at this temperature beyond 135 minutes. Using 15wt%Fe_2O_3 as an example, the general variation trends of the gas species in the product as a function of test time are described as follows. During the heating period, the CH_4 conversion is almost zero as shown in Fig. 1(a) and negative CO_2 conversion due to CO_2 formation due to CH_4 oxidized by Fe_2O_3 can be found as shown in Fig. 1(b). For t=135 ~ 210 minutes, an abrupt increase in CH_4 and CO_2 conversions can be found indicating that Fe_2O_3 is reduced to Fe_3O_4. For test time is beyond 210 minutes, both CH_4 and CO_2 conversions decrease from maximum values. The decreases in CH_4 and CO_2 conversions may be caused by the deactivation of oxygen carrier due to carbon deposition. From Fig.1, Fe_3O_4 shows low reactivity with CH_4 and high reactivity with CO_2. For T=800°C, Fe_2O_3 content produces an insignificant difference in the reduction stage performance.

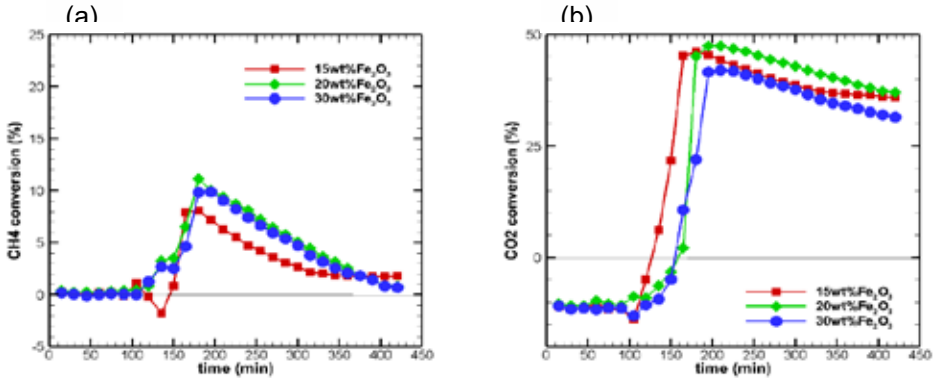


Fig. 1 Performance of reduction stage during CL-DRM for various Fe_2O_3 weight percentages. T=800°C. (a) CH_4 conversion, and (b) CO_2 conversion.

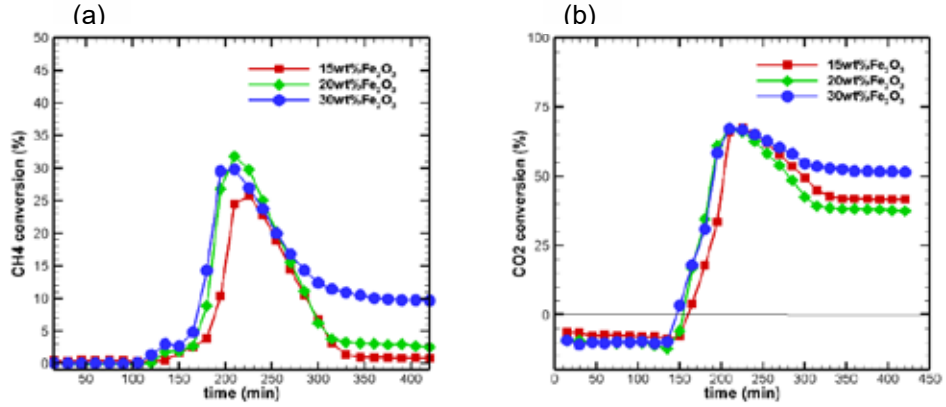


Fig. 2 Performance of reduction stage during CL-DRM for various Fe_2O_3 weight percentages. T=900°C. (a) CH_4 conversion, and (b) CO_2 conversion.

The reduction stage performance during CL-DRM for the T=900°C case is shown in Fig. 2. As compared with the T=800°C case, similar variation trends of CH_4 and CO_2 conversions were found. With increased reaction temperature, catalytic activity was enhanced and higher CH_4 and CO_2 conversions can be obtained. The carbon deposition also causes catalyst activity loss. Because the reactant flow rate has a fixed value, it is then expected that the carbon deposition becomes saturated as the test time increases further. Therefore, stable CH_4 and CO_2 were obtained time is beyond 300 minutes as shown in Fig. 2(a) and 2(b), respectively. Fig. 2 also shows that higher Fe_2O_3 content can enhance the reduction stage performance.

The same experiment was carried out except that reaction temperature is increased to T=1000°C. For the 15wt%Fe_2O_3 and 20wt%Fe_2O_3 cases, Fig. 3(a) and 3(b) show that the variation trends of CH_4 and CO_2 conversions are similar to those for the T=900°C case except that higher conversions can be obtained due to increased reaction temperature. For the 30wt%Fe_2O_3 case, almost 100% CH_4 and CO_2 conversions can be obtained. As a result, the H_2 and CO yields approaching to the theoretical limits were obtained as shown in Fig. 3(c) and 3(d), respectively.

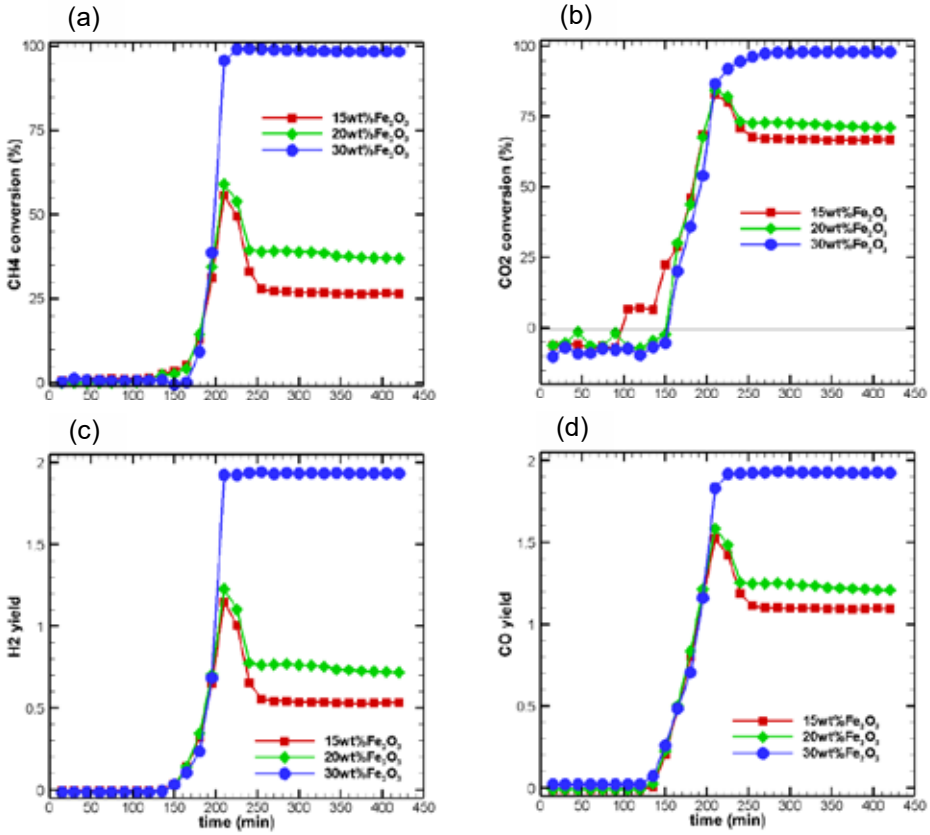


Fig. 3 Performance of reduction stage during CL-DRM for various Fe_2O_3 weight percentages. T=1000°C. (a) CH_4 conversion, (b) CO_2 conversion, (c) H_2 yield, and (d) CO yield.

CONCLUSIONS

As compared with nickel-based oxygen carrier, iron-based oxygen carrier has a lower reactivity for the reduction stage in CL-DRM. A higher reaction temperature is required to obtain the comparable CH_4 and CO_2 conversions. The study indicated that the Fe_2O_3 weight percentage should be high enough to obtain high CH_4 and CO_2 conversions. It was also found that iron-based oxygen carrier is suitable for reducing CO_2 into CO. Future studies on the examining the performance using lowering reaction temperature and higher Fe_2O_3 content are to be carried out.

ACKNOWLEDGMENT

This work was funded by the Ministry of Science and Technology, Taiwan, under the contracts MOST 109-2221-E-005-009-MY3.

REFERENCES

1. Lyngfelt A. Chemical Looping Combustion: Status and Development Challenges. Energy & Fuels. 2020;34:9077-93.
2. Tang M, Xu L, Fan M. Progress in oxygen carrier development of methane-based chemical-looping reforming: A review. Applied Energy. 2015;151:143-56.
3. Yu Z, Yang Y, Yang S, Zhang Q, Zhao J, Fang Y, et al. Iron-based oxygen carriers in chemical looping conversions: A review. Carbon Resources Conversion. 2019;2:23-34.

WHEC-2022
23rd World Hydrogen Energy Conference
June 26-30, 2022 - Istanbul

#243

MODELING FOR THE DEVELOPMENT OF HEAVY DUTY REFUELING PROTOCOLS

[1] Arnaud Charolais, [1] Fouad Ammouri, [1] Elena Vyazmina, [2] Alexander Grab[2], [2] Antonio Ruiz, [3] Alexander Kvasnicka*
[3] Christian Spitta, [4] Rony Tawk, [4] Quentin Nouvelot, [4] Nicola Benvenuti, [4] Thomas Guewouo
[1]Air Liquide, R&D, Jouy-en-Josas, France
[2]Nikola Corporation, Phoenix, Arizona, USA
[3]ZBT GmbH, Duisburg, Germany
[4]Engie, Stains, France

*Corresponding author e-mail: arnaud.charolais@airliquide.com

ABSTRACT

The road transport sector is in need of new technologies to help it emit less greenhouse gases, as the world's emissions should be halved before 2030 and ultimately be part of a net-zero society. To that goal, hydrogen is envisioned to be used as the fuel powering road vehicles, in particular for heavy duty (HD) applications. To achieve the replacement of the current fossil fuel vehicle fleet, a network of hydrogen refueling stations (HRS) should be installed, with the ability to provide safe and rapid fillings to ensure the widest adoption of this clean technology worldwide. The FCH JU project PRHYDE aims to develop a dedicated HD refueling protocol for type III and IV tanks with 350, 500 and 700 bar nominal working pressures (NWP). For this purpose, the SOFIL code, modeling the physical variables in the tanks during filling, is used in the frame of the project. The current paper compares SOFIL to experimental data for HD type IV tanks.

Keywords: Heavy duty, Hydrogen, Refueling, Protocol, Modeling

INTRODUCTION

Greenhouse gas emissions should be lowered in the next decade to help meet the emission targets. This can only be achieved, for the transport sector, with hydrogen as energy carrier, combined with fuel cells. To achieve mass adoption of this new technology, it needs to be safe, affordable and easy-to-use. This is the goal of refueling protocols, standardizing the process across different companies, systems and geographies. Existing LD (Light Duty) refueling protocols, such as the SAE J2601, provide table-based process requirements to ensure a safe filling. The PRHYDE project [1-3] is dedicated to help developing a HD (Heavy Duty) hydrogen refueling protocol. For this purpose, modeling tools, estimating the gas temperature and pressure evolution during fillings, are essential. In particular, SOFIL [4, 5] by Air Liquide and Hyfill by Engie, 0D-gas/1D-wall modeling software, are used in HD protocol development in PRHYDE. This paper is dedicated to their validation in real conditions.
Two different type IV tanks have been used for experimental validation. A first tank, with a volume of 165 L, will be used by Nikola in their vehicles, and was therefore tested in a variety of experimental conditions. The second tank, with a volume of 240 L, has been chosen by Toyota for their vehicles, and was tested by ZBT in different conditions.

RESULTS AND DISCUSSION

The first tank, 165 L type IV tank, was used for experimental testing. A thermocouple tree was placed inside the tank to measure the gas temperature at several locations, denoted as 'TinX' as shown in Figure 1. Thermocouples were also applied to the exterior of the tank, denoted as 'TsX'. The OTV (On Tank Valve) gas temperature is denoted as 'Totv', and the tank pressure 'Ptank' was recorded at the tank. Table 1 shows the different test conditions that have been run with the 165L type IV tank. Figure 2 shows the evolution of gas temperature and pressure in the first test case with the 165 L tank.

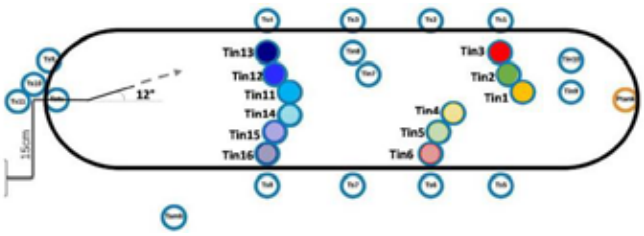


Fig. 1. Locations of thermocouples inside the 165L type IV tank during the testing.

Table 1. List of all tests for the 165L type IV tank.

Test number	Characteristics
#1 (ref)	Initial pressure 2 MPa. Ambient temperature 15 °C. Dispenser temperature -40 °C. Constant pressure ramp rate 8 MPa/min.
#2	Same as #1, but changing ambient temperature to 50 °C.
#3	Same as #1, but changing ambient temperature to 40 °C.
#4	Same as #1, but changing ambient temperature to -30 °C.
#5	Same as #1, but changing ambient temperature to -15 °C.
#6	Same as #1, but changing ambient temperature to 0 °C.
#7	Same as #1, but changing dispenser temperature to -33 °C.
#8	Same as #1, but changing dispenser temperature to -26 °C.
#9	Same as #1, but changing dispenser temperature to -17.5 °C.
#10	Same as #1, but changing initial pressure to 5 MPa.
#11	Same as #1, but changing initial pressure to 25 MPa.
#12	Same as #1, but changing the constant pressure ramp rate to 5 MPa/min.
#13	Same as #1, but changing the constant pressure ramp rate to 16 MPa/min.
#14	Same as #1, but changing the constant pressure ramp rate to 20 MPa/min.
#15	Same as #1, but changing the pressure ramp rate to 20 MPa/min for 3.85 minutes, then 1 MPa/min.
#16	Same as #1, but changing the pressure ramp rate to 20 MPa/min for 3.85 minutes, then 3 MPa/min.
#17	Same as #1, but changing the pressure ramp rate to 20 MPa/min for 3.33 minutes, then 1 MPa/min with pulse of 8 MPa/min for 10 seconds every 30 seconds.
#18	Same as #1, but changing ambient temperature to 40 °C and dispenser temperature to -17.5 °C.

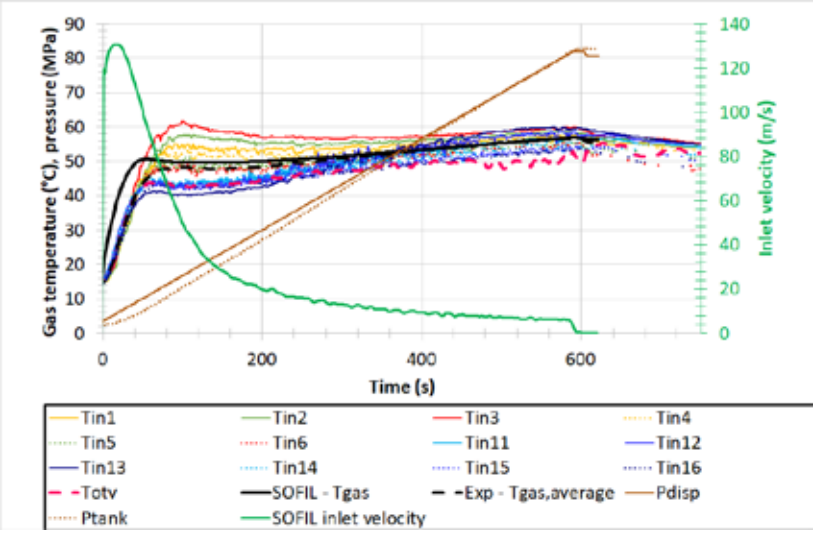


Fig. 2. Comparison of SOFIL model prediction with experimental data from 165 L tank testing. Case #1: Initial pressure 2 MPa, ambient temperature 15 °C, dispenser temperature set point -40 °C, pressure ramp rate 8 MPa/min, with a 165 L type IV tank.

The second tank is also a type IV tank, with a 240 L volume. Another thermocouple tree was placed inside to measure the gas temperature at several locations, as shown in Figure 3. Similar to the first set of tests, for the 240 L tank the tests varied the dispenser temperature (from -40 °C to ambient) and the pressure ramp rate (from 1 MPa/min to 16 MPa/min). Figure 4 shows the evolution of gas temperature and pressure in the reference test case with the 240 L tank.

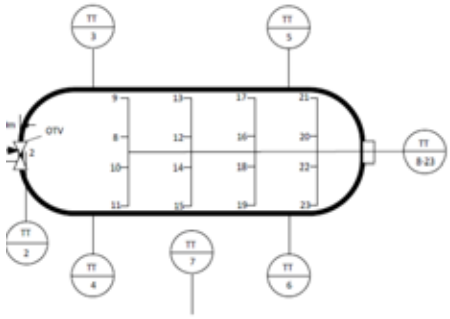


Fig. 3. Locations of thermocouples inside the 240 L type IV tank for testing.

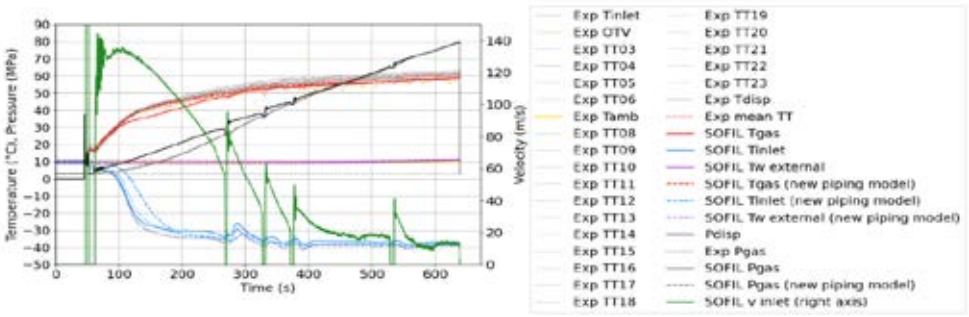


Fig. 4. Comparison of SOFIL model prediction with experimental data from 240 L tank testing. Initial pressure 2 MPa, ambient temperature 10 °C, dispenser temperature set point -40 °C, pressure ramp rate 8 MPa/min, with a 240 L type IV tank.

CONCLUSIONS

The modeling software used in the project is able to correctly estimate the gas temperature during the fillings. The validated software will be used to look into dynamic methods for the HD protocol.

ACKNOWLEDGEMENT

This project has received funding from the Fuel Cells and Hydrogen 2 Joint Undertaking under Grant Agreement No 874997. This Joint Undertaking receives support from the European Union's Horizon 2020 Research and Innovation program, Hydrogen Europe and Hydrogen Europe Research. We thank all partners of the PRHYDE project for their contribution to this work, namely: Air Liquide, CEA, ENGIE, ITM, NEL, Nikola, Toyota Europe and Toyota North America, Shell, ZBT, and LBST. Further contribution has been received by NREL and FirstElement Fuel.

REFERENCES

1. PRHYDE. FCH JU project protocol for heavy-duty hydrogen refuelling 2020-2021. https://prhyde.eu/progress/
2. Sinding, C.D. et al. 'Safety and other considerations in the development of a hydrogen fueling protocol for heavy-duty vehicles', *ICHS 2021: 9th international conference on hydrogen safety*, online conference, 21-24 September 2021
3. Charolais, A. et al. 'Protocol for heavy duty hydrogen refueling: a modeling benchmark', *ICHS 2021: 9th international conference on hydrogen safety*, online conference, 21-24 September 2021
4. Bourgeois T., et al. Optimization of hydrogen vehicle refuelling requirements. International Journal of Hydrogen Energy 2017;42:13789–809
5. Bourgeois T., et al. Evaluating the temperature inside a tank during a filling with highly-pressurized gas. International Journal of Hydrogen Energy 2015;40:11748-55

WHEC-2022
23rd World Hydrogen Energy Conference
June 26-30, 2022 - Istanbul

#260

INFLUENCE OF THE TURBULENCE MODEL IN THE CFD SIMULATION OF HYDROGEN TANK FILLING BY AN IMPINGING OBLIQUE JET

Julien MARTIN[1], Quentin Nouvelot [1], Vincent Ren [2], Guillaume Lodier [2], Pierre Carrere [2], Arnaud Charolais [2], Fouad Ammouri [2], Elena Vyazmina [2], Alexander Grab[3], Antonio Ruiz[3]*

[1]ENGIE LAB Crigen,4 Avenue Joséphine Baker, 93240 Stains, France
[2] Air Liquide, Innovation Campus Paris, 1, Chemin de la Porte des Loges, 78350 Jouy-en-Josas, France
[3] Nikola Corporation, Phoenix, Arizona, USA

*Corresponding author e-mail: julien.martin2@engie.com

ABSTRACT

During a hydrogen tank filling, high temperatures can be generated inside the vessel with a vertical or/and horizontal thermal stratification that can potentially further increase the temperature of the gas and the tank wall. European funded project PRHYDE study this phenomena as it can have an influence on the choice made during refueling protocol development. CFD tools can help predict this thermal stratification within the tank by providing complete and detailed 3D information on the flow characteristics and temperature distribution. The eddy viscosity turbulence model (Boussinesq hypothesis) approach is most often used since it gives the best compromise between the number of grid cells and equation solving time. This hypothesis is reasonable for turbulent shear flows without big curvature and swirl. These models show their limitations when the anisotropy of the turbulence significantly affects the mean flow. This paper compares several turbulence models (Eddy viscosity and RSM model) for the case of hydrogen tank filling with a turbulent tilted impinging jet and compare simulation results with experimental results generated in the European funded project PRHYDE.

Keywords: Hydrogen storage, Tank filling, Turbulence model, Impinging jet, Stratification

INTRODUCTION

In a context of global awareness of environmental issues, a revolution in production methods is challenging the current operation of the conventional energy system. Hydrogen is widely seen as an energy carrier that could help to overcome issues such as greenhouse gas emission, air pollution and safe energy supply. Compressed hydrogen is the technology of choice for on-board storage in hydrogen vehicles in the automotive industry. Due to the low density of hydrogen at atmospheric conditions, high pressures are required inside the fuel tanks to achieve a range comparable to conventional vehicles. The large pressure increases during refuelling, the gas temperatures inside the tank increase inside the vessel with possible stratification phenomena that can locally increase the high temperature areas. The maximum allowed temperature of 85°C inside the composite tank walls is specified by the international standards.

MATERIALS AND METHODS

In the frame of the FCH JU funded project (PRHYDE), aiming at defining a hydrogen tank filling protocol, a series of experimental tests was performed on several type IV tanks with various filling conditions. The tanks were instrumented with thermocouples trees monitoring the temperature evolution of the gas inside the tank. Some experimental cases presented new physical results, which are difficult to explain, such as horizontal stratification. These cases have been used for the 3D numerical simulation modeling. The 3D computational domain consists of two subdomains: one for the fluid part (hydrogen) and another for the thermal transfer with the solid (tank material). This type of 3D simulation solves Navier-Stokes equations. Real gas model (NIST tables) is essential for the pressure range considered in the experiments. The solved equations are of the form:

$$\frac{\partial}{\partial t}\int_V \rho\Phi dV + \int_A \rho\Phi V dA = \int_A \Gamma_\Phi \nabla\Phi . dA + \int_V S_\Phi dV \qquad (1)$$

instationnaire | Convection | Diffusion | Generation

After decomposing the velocity into mean and instantaneous parts, the transient Navier-Stokes equations can be rewritten as the Reynolds-Averaged Navier-Stokes (RANS) equations with the Reynolds stress tensor as additional unknowns:

$$\left(\rho\frac{\partial \bar{u}_i}{\partial t} + \bar{u}_k\frac{\partial \bar{u}_i}{\partial x_k}\right) = -\frac{\partial \bar{P}}{\partial x_i} + \frac{\partial}{\partial x_j}\left(\mu\frac{\partial \bar{u}_i}{\partial x_j}\right) + \frac{\partial R_{ij}}{\partial x_j} \qquad (2)$$

Reynolds stress tensor

Previous work ([4],[5],[6],[7]) used k-epsilon or k-omega SST and SAS turbulence models (Boussinesq hypothesis). Several publications ([1],[2],[3]) have demonstrated the limitations of models that use Boussinesq hypothesis when anisotropy of turbulence significantly affects the mean flow. This type of limitation can be reached in the case of an impacting jet on concave surfaces, which is the case when the injector is not aligned with the tank.

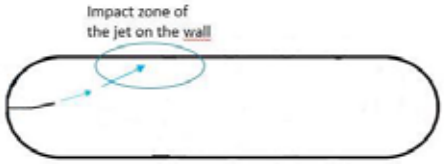


Fig. 1 Illustration of an impinging oblique jet on the tank wall during the filling stage.

To overcome this issue the RSM (Reynolds Stress Model) turbulence model could be used. A crucial step for the application of numerical modelling is the validation of the model against the corresponding experimental measurements. Several numerical simulations were performed to get a qualitative and quantitative comparison of several turbulence models available in ANSYS Fluent and more specifically to compare RSM and Boussinesq turbulence models (like k-epsilon) and SAS. Mass conservation has been verified for all simulations.

RESULTS AND DISCUSSION

Experimental results in the selected cases show horizontal stratification, probably due to a recirculation of the cold jet at the front of the tank and a local overheating at the back due to a limited propagation of the cold jet at the rear of the tank (fig 2).

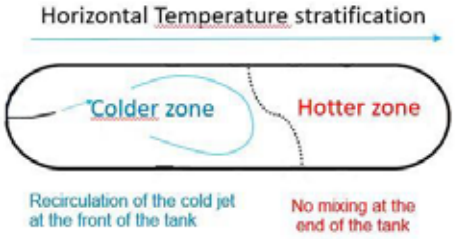


Fig. 2 Diagram of the fluid behaviour observed experimentally

With k-epsilon model, the flow does not behave as in the experiment: no horizontal temperature stratification is numerically observed. As shown on the figure below (fig. 3), the model only predicts vertical temperature stratification.

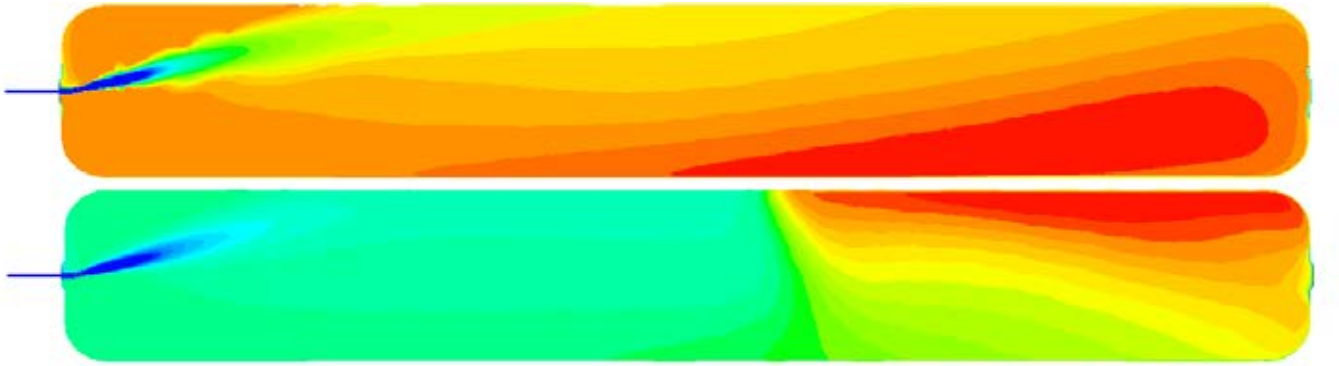


Fig. 3 Temperature field found using k-epsilon model (top frame) and RSM model (bottom frame) for the same time

The results of the two turbulence models show completely different temperature fields. The RSM model clearly demonstrates a horizontal stratification. In order to verify the jet recirculation hypothesis, we have analyzed the

velocity fields of both simulations. Comparisons with experimental measurements have also been performed. They show that the RSM model is better adapted for the impacting jets.

CONCLUSIONS

The impact of the jet on the tank wall is a complicated phenomenon to solve numerically. It shows the limit of Eddy viscosity turbulence models. In order to keep horizontal stratification, RSM turbulence model has been tested and allows highlighting this horizontal thermal stratification.

ACKNOWLEDGEMENT

This project has received funding from the Fuel Cells and Hydrogen 2 Joint Undertaking under Grant Agreement No 874997. This Joint Undertaking receives support from the European Union's Horizon 2020 Research and Innovation program, Hydrogen Europe and Hydrogen Europe Research. We thank all partners of the PRHYDE project for their contribution to this work, namely: Air Liquide, CEA, ENGIE, ITM, NEL, Nikola, Toyota Europe and Toyota North America, Shell, ZBT, and LBST. Further contributions have been received by NREL and First Element Fuel.

REFERENCES

1. Aillaud P.2017. Simulation aux grandes échelles pour le refroidissement d'aubages de turbines haute-pression
2. Taghinia, Rahman, Siikonen. 2015. CFD study of turbulent jet impingement on curved surface. Chinese journal of chemical engineering
3. Behnia, Ooi, Gregory. 2006. Prediction of turbulent heat transfer in impinging jet geometries
4. Miguel, Acosta, Moretto,Ortiz Cebolla. 2016. Influence of the gas injector configuration on the temperature evolution during refueling of on-board hydrogen tanks
5. Melideo, Baraldi, Galassi,Ortiz Cebola, Acosta Iborra, Moretto. 2013. CFD model performance benchmark of fast filling simulations of hydrogen tanks with pre-cooling.
6. Galassi, Papanikolaou, Heitsch, Baraldi, Acosta Iborra, Moretto. Validation of CFD models for hydrogen fast filling simulations
7. P. Carrere, G. Lodier, E. Vyazmina, F. Ammouri, A. Charolais, R. Gonin, CFD simulations of the refuelling of long horizontal H2 tanks, ICHS, Edinburgh, UK, September 21−23, 2021

WHEC-2022
23rd World Hydrogen Energy Conference
June 26-30, 2022 - Istanbul

#295

FORMABILITY AND PERFORMANCE TESTING OF STAINLESS STEEL BIPOLAR PLATE FOR AIR-BREATHING PEMFC

[1] Chen-Yu Chen, [2] Nai-Hsien Wu, [3] Kuan-Jen Huang*
[1]National Chiayi University, College of Science and Engineering, Department of Mechanical and Energy Engineering, No.300, Syuefu Rd., Chiayi City 60004, Taiwan (R.O.C.)
[2]National Cheng-Kung University, College of Engineering, Department of Aeronautics and Astronautics, No.1, Ta-Hsueh Rd., East District, Tainan City 701, Taiwan (R.O.C.)
[3]National Cheng-Kung University, College of Engineering, Department of Aeronautics and Astronautics, No.1, Ta-Hsueh Rd., East District, Tainan City 701, Taiwan (R.O.C.)

*Corresponding author e-mail: aeroshower@msn.com

ABSTRACT

In this study, the formability of the metallic bipolar plates for PEMFCs were studied via DYNAFORM software and LS-DYNA and the performance and the electrochemical impedance the air-breathing PEMFC with the stamped metallic bipolar plates were tested analyzed. The simulation results show that the optimum stamping parameters for the SS316L are the flow channel depth of 0.8 mm, punch and die radius of 0.4 mm, stamping speed of 250 mm/s, blank thickness of 0.2 mm and the binder pressure of 200 kN. The maximum error between the real stamped flow channel depth and the target depth is 12.8%. With the stamped SS316L bipolar plate, which has an active area of 150×54 mm^2, the air-breathing in this work has the maximum power density of 187.19 mW/cm^2 at an operating temperature of 45°C, a torque of 30 kgf-cm, a hydrogen stoichiometric ratio of 1.5 and a relative humidity of 100%.

Keywords: Proton exchange membrane fuel cell, Stainless steel bipolar plate, Stamping fabrication process, Performance test

INTRODUCTION

In recent years, due to the extensive use of fossil energy, the greenhouse effect and air pollution caused by burning the fossil fuels become more and more serious. Thus, the development of non-polluting energy becomes inevitable. The fuel cell is considered an option for the non-polluting energy technology because of its zero pollution. Proton exchange membrane fuel cells have the advantages of rapid start, low operating temperature, low noise, low pollution level and high efficiency. Thus, it is a good candidate for future transportation or portable energy sources and it is one of the most fully developed fuel cell type. To reduce the cost of PEMFCs, developing metallic bipolar plate becomes a trend, because replacing traditional graphite bipolar plate by metallic bipolar plates can significantly reduce the material and fabrication cost the bipolar plates. Among all kinds of metal, stainless steel is the most common material for bipolar plates [1-3]. As a result, the formability of the SS316L bipolar plate is the focal subject. To verify the performance of the PEMFC with metallic bipolar plates, we as well assembled an air-breathing PEMFC with stamped SS316L bipolar plates and tested its performance.

RESEARCH METHODS

In the first part of study, the DYNAFORM software and LS-DYNA are used to study the effects of flow channel geometry and stamping parameter on the formability of the metallic bipolar plate. The forming limit, thinning ratio and springback of the bipolar plates under various conditions are analyzed to obtain the optimum design and process parameters. In addition, the simution results are verified by the measurement of the real forming depth of the flow channel on the stainless steel bipolar plates which are performed via scanning electron microscopy (SEM). In the second part of study, an air-breathing single cell with our stamped stainless steel bipolar plates is assembled and tested. The performance and practicability of the fuel cell is evaluated by the polarization curve and electrochemical impedance spectroscopy.

RESULTS AND DISCUSSION

The research results indicate that the optimal flow channel geometry and stamping parameters for the SS316L bipolar plate are the flow channel depth of 0.8 mm, the radiuses for punch and die of 0.4 mm, the stamping speed of 250 mm/s, the blank thickness of 0.2 mm and the binder force of 200 kN. Through the SEM observation, it is verified that the real sealant groove channel depths and the design sealant groove channel depths are slightly different. The maximal forming error is 13.6%, and the maximal difference of the sealant groove depths is 0.075 mm. In addition, the flow channel depth measurements indicates that the maximal forming error is 12.8%, and the maximal difference of the real and design flow channel depths is 0.103 mm. Moreover, the error between the simulated spring back value

and the experimental value without the binder is 3.67%. The comparison between simulation and experiments presents a good reliability of the simulation. The simulation results as well show that the formability of the bipolar plate is not good as the flow channel depth is too shallow or too deep, and the probability of wrinkle and crack may occur. When the radius of the die and punch is increased, the fluidity of the material increases and this leads to decreasing the thinning ratio and spring back of the bipolar plate (Fig. 1). When the stamping speed is lower than 250 mm/s, the bipolar plate is prone to wrinkle and crack. When the stamping speed increases from 250 mm/s to 10000 mm/s, the amount of spring back increases by about 31.4%. In addition, increasing the thickness of the blank causes a significant increase in the thinning ratio of the blank because the material fluidity becomes lower at elevated thickness. As the thickness is higher than a critical value, cracks may occur. Moreover, increasing the binder force effectively improves the spring back of the bipolar plate.

The air-breathing fuel cell with the stamped SS316L bipolar plates is assembled and tested. The experimental results show that the maximum power density is 187.19 mW/cm^2 with a forced air convection at an operating temperature of 45 ^{o}C, a clamping torque of 30 kgf-cm, a hydrogen stoichiometric ratio of 1.5 and a relative humidity of 100% (Fig. 2). Among all of the operating parameters, the clamping torque, operating temperature and the voltage of fan have greater influence on the performance of the air-breathing fuel cell than other parameters.

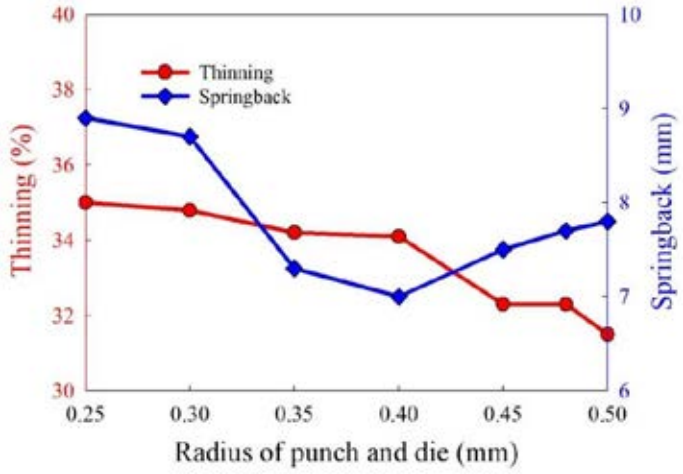


Figure 1 Effects of radius of punch and die on the spring back and thinning of the stamped SS316L bipolar plate

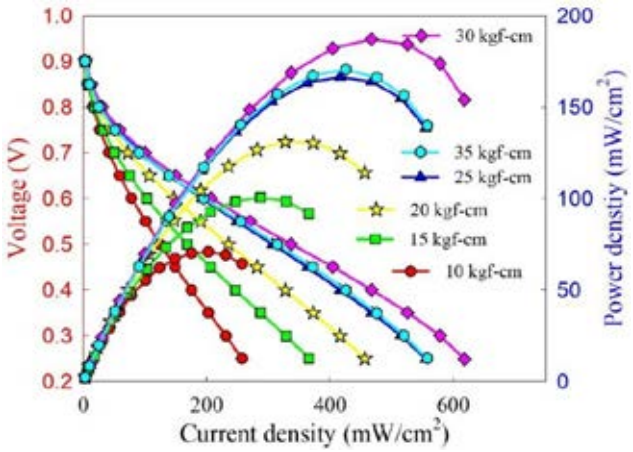


Figure 2 Effects of assembly torque on the PEMFC performance (T_{cell}=45℃，T_{d,H_2}=45℃，St_{H_2}=1.5，V_{fan}=15V)

CONCLUSIONS

An air-breathing single cell with the stamped SS316L bipolar plates of 150×54 mm^2 is successfully developed in this work. In this study, the results can be summarized into the following conclusions:

1. The peak power density of the air-breathing fuel cell with stamped SS316L bipolar plates is 187.19 mW/cm^2 at a cell voltage of 0.4 V with forced air convection at operating temperature of 45℃, torque of 30 kgf-cm, hydrogen stoichiometric ratio of 1.5 and relative humidity of 100%.
2. The simulation results show that when the channel depth increases, then the thinning ratio and springback both increase. When the radiuses of the die and punch increase, the fluidity of the material becomes smoother, leading

to decreasing the thinning ratio and springback of the bipolar plate. When the stamping speed increases, the springback of the bipolar plate increases. When the binder force increases, the springback is also improved effectively.

3. The simulation results show that the optimal flow channel geometry and stamping parameters for the stainless steel 316L bipolar plates are the flow channel depth of 0.8 mm, the radiuses for punch and die of 0.4 mm, the stamping speed of 250 mm/s, the blank thickness of 0.2 mm and the binder force of 200 kN.
4. For the bipolar plate formability, the maximal difference between the design depth of the flow channel and the measured flow depth on the stamped bipolar plate is 0.103 mm, which is equal to 12.8% of the design depth. The error between the simulated springback value and the experimental value without the binder is 3.67%.

ACKNOWLEDGEMENT

This work is financial supported by the Ministry of Science and Technology, Taiwan (Taiwan MOST) under the grant number of MOST 110-2622-8-006-020 and MOST 109-2221-E415-007-MY3. The authors appreciate the funding support from MOST.

NOMENCLATURE

T_{cell}	Operating temperature of the PEMFC
T_{d,H_2}	Dew point temperature of H_2
St_{H_2}	Stoichipmetric ratio of H_2
V_{fan}	Operating fan voltage

REFERENCES

1. E. Dur, Ö.N. Cora, M. Koç. 2014. Effect of manufacturing process sequence on the corrosion resistance characteristics of coated metallic bipolar plates. Journal of Power Sources 246:788-799.
2. C.K. Jin , J.Y. Koo , C.G. Kang. 2014. Fabrication of stainless steel bipolar plates for fuel cells using dynamic loads for the stamping process and performance evaluation of a single cell. International Journal of Hydrogen Energy 39:21461-21469.
3. F.A. Khatir, M. Elyasi, H.T. Ghadikolaee, M. Hosseinzadeh. 2017. Evaluation of effective parameters on stamping of metallic bipolar plates. Procedia Engineering 183:322-329.

WHEC-2022
23rd World Hydrogen Energy Conference
June 26-30, 2022 - Istanbul

#310
PROTON-CONDUCTING SOLID OXIDE FUEL CELLS WITH NLSCF CATHODE

[1*]S. W. Lee, [2]W. Y. Huang, [3]Y. C. Huang, [4]C. J. Tseng
[1] Institute of Materials Science and Engineering, National Central University, Taoyuan, Taiwan
[2] Department of Mechanical Engineering, National Central University, Taoyuan, Taiwan

*Corresponding author e-mail: swlee@g.ncu.edu.tw

ABSTRACT
The electrochemical performances of the solid oxide fuel cells (SOFCs) fabricated with Nd-doped LSCF (NLSCF) perovskite cathodes, thin BCZY electrolytes, and BCZY–Ni anodes by tape casting, spin coating, and co-firing are evaluated at 600–800 ℃. Material analysis, such as SEM, TEM, and XRD, confirmed that no detectable second phase remains in the NLSCF cathode, indicating that the calcined NLSCF nanopowders have good compatibility with the fabrication of anode-supported fuel cells in this study. It can be clearly seen that the NLSCF cathode is highly porous and adhered well to the BCZY electrolyte. Fuel cell testing with the NLSCF cathode exhibits a maximum power density of ~407.6 mW/cm^2 at 800 ℃, which is significantly higher than those of cells with a powder-derived LSCF cathode. The significantly lower polarization resistance elements extracted from electrochemical impedance spectroscopy (EIS) further suggested that the NLSCF cathode has superior catalytic activity for the oxygen reduction reaction and better oxygen ionic transport in the cathode reactions. The performance improvement of NLSCF cathode can be explained in terms of trade-off between electrocatalytic activity, oxygen ionic and electronic conductivity of the NLSCF. This study shows that NLSCF nanopowder would be a promising cathode material for proton-conducting SOFCs.

Keywords: Nd-doped LSCF, Nanopowder, Cathode, Oxygen reduction reaction, P-SOFC

INTRODUCTION

Solid oxide fuel cells (SOFCs) are electrochemical devices that can convert chemical energy directly into electricity and have attracted growing attention in recent years due to their superior efficiency to other energy conversion systems, fuel flexibility, use of non-precious metal/metal oxide catalysts, and low pollutant emissions [1]. All these advantages make SOFCs well suited for clean and distributed power generation [2]. In recent years, extensive efforts have been devoted to developing proton-conducting SOFCs (P-SOFCs) that operate in the low-to-intermediate temperature range (400 - 800 ℃). Compared to the conventional oxygen ion-conducting SOFCs (O-SOFCs) that require high operating temperature, this scheme enables more reliable sealing, use of cheaper materials for interconnect, and a better control of electrode/electrolyte interactions, thus prolonging the operational lifetime of SOFCs. One important factor in achieving high-efficiency P-SOFCs is to develop highly conductive proton-conducting electrolytes with sufficient chemical stability under operation condition. In addition, it is well known that oxygen reduction reaction (ORR) at the cathode is responsible for much of the loss in cell performance, especially when a thin electrolyte is used. The reduction in the cathode kinetics with decreasing fuel cell operation temperature could be more detrimental to the cell performance than the drop in the electrolyte conductivity. Therefore, an adequate material selection and microstructure optimization for the cathode are critical since the polarization resistance of the cathode could dominate the fuel cell performance. For O-SOFCs, relatively low cathode polarization in the intermediate temperature range could be achieved by using mixed ionic and electronic conductors (MIEC) such as LSCF, SSC, and PNO as cathode materials. However, simply applying the well-established cathode materials for O-SOFCs to P-SOFCs is insufficient because the cathode processes involved are not completely the same between O-SOFCs and P-SOFCs. Besides the elementary reaction steps occurring in the O-SOFC cathode, the proton migration and vapor formation also have to be considered in a P-SOFC cathode, both of which make the cathode kinetics more complex and bring about demands on purposely tailored cathode composition and microstructure. Hence, tailoring the cathode composition and microstructure to improve charge carrier transport, oxygen gas diffusion, and water removal is essential to achieving high-performance P-SOFCs [3]. In this research, the NLSCF nanopowder is used as the air electrode for PCFCs. The cell with Nd doped LSCF cathode can effectively promote the performance. The smaller cation radius of Nd^{3+} than that of La^{3+} causes a difference in the average A-site ion radii that has a relationship with lattice strain during oxygen hopping to oxygen vacancy.

MATERIALS AND METHODS

To characterize the electrochemical behavior of the NLSCF cathodes, anode-supported thin-BCZY-electrolyte single cells were fabricated and the process flow is illustrated in Fig. 1. Green cermet anode supports were prepared by tape casting and hydrostatic pressing. The slurry for tape casting was prepared by ball-milling BZCY, NiO, and starch

powders in a mixture of binder (polyvinyl butyral) and dispersant (toluene, alcohol, and menhaden fish oil). The height of the doctor's blade during tape casting was set to give 150-μm-thick green tapes. A stack of three BCZY-NiO-starch green tapes was uniaxially pressed at 5000 psi and then punched to produce 35-mm-diameter discs. The disc anode supports were then pre-sintered to attain sufficient mechanical rigidity required for the subsequent spin coating process. To form a stable colloidal electrolyte slurry for spin coating, BCZY powders were planetary-milled in a mixture of ethanol and polyvinylpyrrolidone (PVP). 50 wt% NiO nanometric powders were additionally added into the slurry for the deposition of anode functional layer (AFL). The AFL slurry and the electrolyte slurry were sequentially spin-coated over the pre-sintered anode support. The spin-coated substrate was then heat-treated at 1000 ℃ for 1 h to remove the organics. The electrolyte-coating processes were repeated twice to achieve the desired electrolyte thickness of ~8 μm. Finally, the half cells consisting of BCZY electrolyte, BCZY-NiO AFL, and BCZY-NiO anode support were co-sintered at 1500 ℃ for 10 h in ambient environment. LSCF, NLSCF, and NSCF nanopowders were separately mixed with the organic vehicle by using a high-speed homogenizer to obtain a homogeneous cathode ink. The ink was then screen-printed through a 200-mesh silk screen of 10 μm thickness. The sample was air-dried to remove bubbles. Afterwards, it was heat-treated at 1100 ℃ for 1h to obtain an NLSCF cathode via evaporation/pyrolysis of the organics and sintering between NLSCF particles.

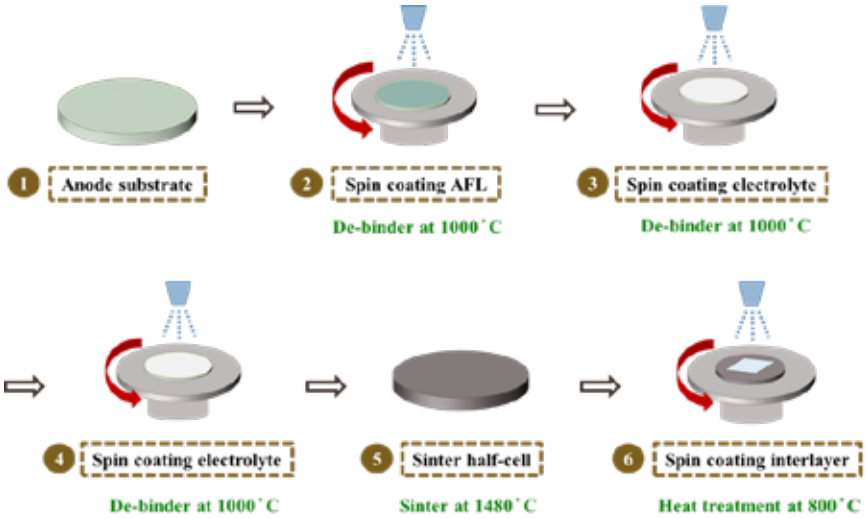


Fig. 1. The process flow anode-supported thin-BCZY-electrolyte single cells.

RESULTS AND DISCUSSION

Fig. 2 show the I-V and power density curves of the fuel cells with LSCF, NLSCF, and NSCF cathodes in the temperature range between 500 ℃ and 800 ℃. ALL cells exhibit open circuit voltages (OCVs) in the range of 0.98 to 1.0 V at 800 ℃, approaching the theoretical Nernst potential and indicating there is no obvious cracks in the thin electrolyte that could cause fuel or current leakage. In addition, no obvious change in the slope of the I-V curves at high current densities is observed, showing that no concentration polarization effect occurs in the electrodes. Furthermore, the cell with NLSCF cathode exhibits a peak power density of 407.6 mW/cm^2 at 800 ℃, which is higher than that of the cell with LSCF and NSCF cathodes. The short-term durability of the cell with NLSCF cathode is also investigated where the current density and power density were monitored as a function of time with a constant voltage of 0.7 V at 800 ℃. The cell power output was considerably stable during the short-term durability test.

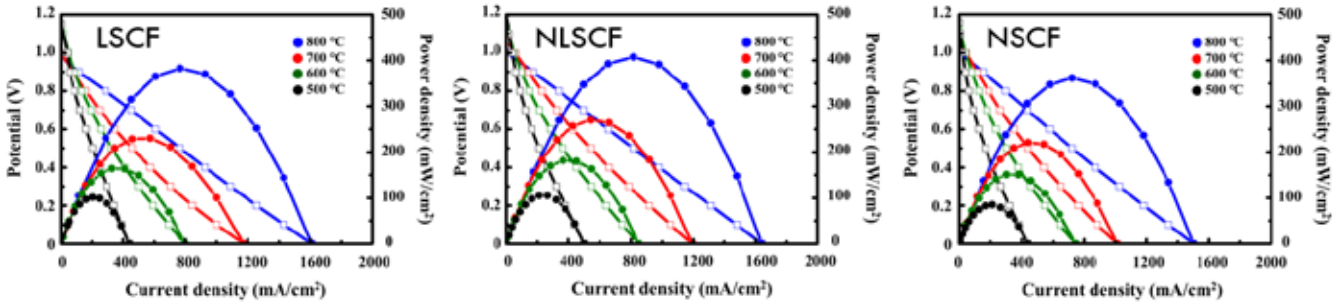


Fig. 2. I-V and power density curves of the fuel cells with LSCF, NLSCF, and NSCF cathodes at 500 - 800 ℃.

To reveal the underlying mechanisms for the greatly enhanced cathode performance and the dependence on added PS amount, electrochemical impedance spectroscopy (EIS) was performed on all these fuel cells at 800 ℃ under open circuit condition, and the results are shown in Fig. 3. The intercept with the real axis at high frequency represents the total ohmic resistance of the cell contributed from protonic resistances in the electrolyte and the anode, transfer of protons to TPBs, and electronic resistances in various fuel cell components. The difference between the high- and low-frequency intercepts on the real axis of impedance spectra gives the electrode polarization resistance. Since these fuel cells use the same BCZY-Ni anode and BCZY electrolyte, the difference in their polarization and ohmic resistances should come from their cathode properties. It is observed that the polarization resistance was improved as the NLSCF cathode was incorporated, which was also comparable to the numbers from similar electrode configurations in other studies. This improvement can be explained in terms of trade-off between electrocatalytic activity, oxygen ionic and electronic conductivity of the NLSCF.

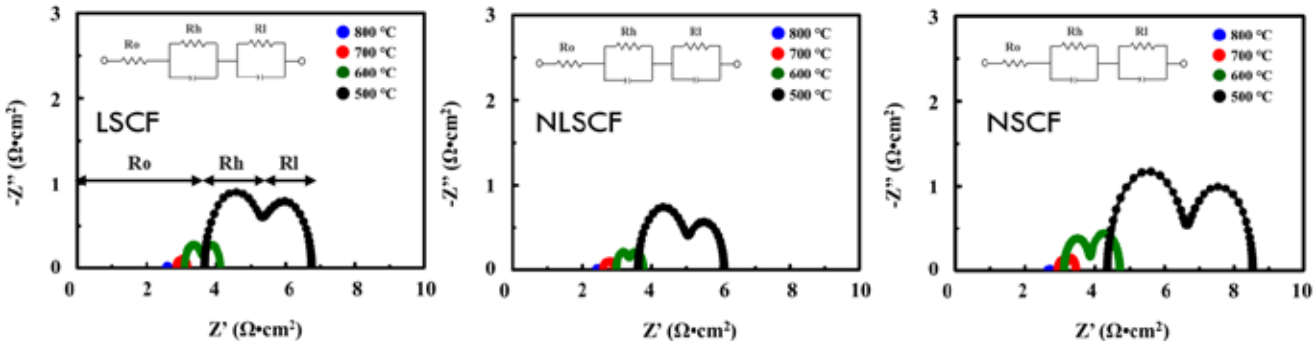


Fig. 3. Impedance spectra of fuel cells using LSCF, NLSCF, and NSCF cathodes at 800 ℃.

CONCLUSIONS

In this study, the NLSCF nanopowders were successfully used as the air electrode for PCFCs. The cell with Nd doped LSCF cathode can effectively improve the performance. The smaller cation radius of Nd^{3+} than that of La^{3+} causes a difference in the average A-site ion radii that has a relationship with lattice strain during oxygen hopping to oxygen vacancy. This improvement can be explained in terms of trade-off between electrocatalytic activity, oxygen ionic and electronic conductivity of the NLSCF.

REFERENCES

1. S.M. Haile, Fuel cell materials and components, Acta Mater. 51 (2003) 5981-6000.
2. K.D. Kreuer, Proton-conducting oxides, Annu. Rev. Mater. Res. 33 (2003) 333-359.
3. R.R. Peng, T.Z. Wu, W. Liu, X.Q. Liu, G.Y. Meng, Cathode processes and materials for solid oxide fuel cells with proton conductors as electrolytes, J. Mater. Chem. 20 (2010) 6218-6225.

WHEC-2022
23rd World Hydrogen Energy Conference
June 26-30, 2022 - Istanbul

#351
TRANSACTIVE MOBILITY WITH HYBRID ELECTRIC AND HYDROGEN CHARGING INFRASTRUCTURES

[1,2*] *Hossam A.Gabbar*
[1]Faculty of Energy Systems and Nuclear Science, Ontario Tech University, 2000 Simcoe St. North, Oshawa L1G0C5, ON, Canada
[2]Faculty of Engineering and Applied Science, Ontario Tech University, 2000 Simcoe St. North, Oshawa L1G0C5, ON, Canada

*Corresponding author e-mail: hossam.gaber@ontariotechu.ca

ABSTRACT

Mobility is supported by transportation infrastructures based on energy networks to meet mobility demands. Transportation electrification enables mobility with more penetration of electric vehicles (EVs) and hydrogen-based fuel cell vehicles (HVs), besides internal combustion vehicles. The charging infrastructures should support mobility based on hybrid transportation technologies. The complex and expensive transition to transportation electrification infrastructures can be alleviated by implementing transactive mobility, which will provide cost management of different layers within the mobility services infrastructures. This paper presents an integrated framework for transactive mobility in view of hybrid charging infrastructures. The interface between transactive energy and charging infrastructures will be modeled and formulated by the transactive mobility model.

Keywords: Transactive mobility (TM), transactive energy (TE), hybrid charging stations (HCSs), hydrogen vehicle (HV), transportation electrification

INTRODUCTION

Transactive energy (TE) offers a marketplace for peer-to-peer energy trading and exchange. It is essential to identify the specified zone or portion of the energy distribution network that will be served [1]. The transactive energy approach will enable consumers and prosumers to benefit from collaboration. Transactive energy can also support the deployment of microgrids with an evaluation of energy costing in view of internal costs within each microgrid [2]. The evaluation of different scenarios and trade parameters and constraints are evaluated with simulation to examine options prior to actual execution [3]. The selection and evaluation of constraints to couple electricity and gas networks are also discussed to show balanced electricity and gas networks in normal and emergencies [4]. Transactive energy is applied to charging infrastructures with different configurations. Transactive energy is applied on charging of EV in buildings with local PV where cost framework is applied considering energy supply from the grid, local PV energy generation, and local energy storage [5]. Transactive energy is applied on PV-based EV charging in parking lots [6]. Scheduling of EV charging can be optimized based on a collaborative cost model using transactive energy [7]. Energy management should incorporate charging schedules based on cost models from the transactive energy framework [8]. There are several applications where energy trade is developed and implemented, such as simultaneous wireless information and power transfer (SWIPT) [9]. The trade mechanism is essential to achieve fair transactive energy, while reducing CO2 emissions in the energy production and supply chain [10]. Energy trade can be implemented across countries. In Europe, energy trade between different countries, such as Turkey, is presented to show negotiation mechanisms to ensure a satisfying energy supply [11]. Energy is coupled with water networks. The trade can be applied to the energy-water nexus, where coupling and value exchange is represented in the trade process [12]. Similar approach is applied on fuel hydrogen vehicles (HVs) with fuel cells [13].

The proposed hybrid transportation and charging infrastructure is shown in Fig. 1. The charging infrastructure includes local hydrogen generation and hydrogen supply infrastructure as integrated with hybrid energy system with renewable and storage energy technologies. The hybrid energy system in the charging station includes PV, wind turbine, fuel cell, nuclear reactor, and hybrid energy storage, including battery, flywheel, and ultra-capacitor. Trade agents are defined to allow bidirectional energy flow between EV/HV, charging station units, renewable energy resources, and the grid. Trade agents will manage negotiation between incoming electric vehicles, hydrogen vehicles, internal combustion vehicles, and the different components within the station and the supply chains. Energy cost models are defined and communicated among trade agents and each component to ensure fair and profitable to each unit and the corresponding investor. The cost model includes cost parameters for energy generation units, storage units, station facilities, and energy supply chains. Key parameters include levelized energy cost, and minimum and maximum price limits for each component and system. The investment model is proposed to allow multiple investors for each component in the charging infrastructure. The bidding process between incoming vehicles and charging units will be managed based on power transfer, energy flow, and cost parameters. Bidding requests will be received and analyzed to ensure profitable mobility with charging infrastructures.



Fig. 1. Hybrid Transportation and Charging Infrastructures for Transactive Mobility

Transactive energy is applied on charging station with local energy resources from renewable energy sources and energy storage. The concept of transactive energy and transactive charging must be coupled to ensure robust strategies for supplying energy from the grid, energy resources, and energy storage. The flow of energy and charging requests are shown in Fig. 1. EV-T is the trade agent for the incoming EV for charging. HV-T is the trade agent for hydrogen vehicle. CU-T is the trade agent for the charging unit for EV. HF-T is the agent for the hydrogen fueling unit. FC-T is the trade agent linked with the trade agent for fuel cell charging and discharging. PV-T is the trade agent for energy supplied by PV.

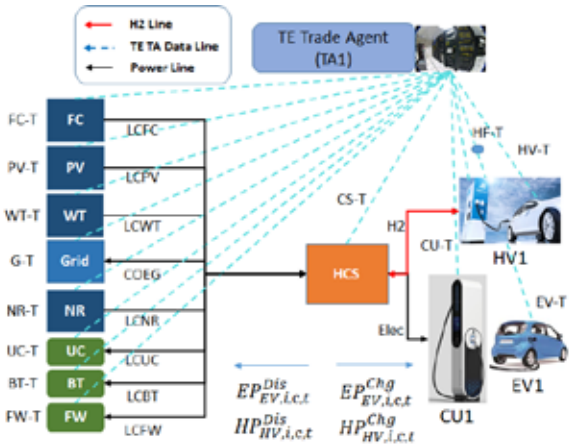


Fig. 2. Transactive Mobility Infrastructure

Similarly, WT-T is wind turbine trade, G-T is grid trade, NR-T is nuclear reactor trade, UC-T is ultra-capacitor trade, BT-T is battery trade, and FW-T is flywheel trade. The levelized energy costs are defined for each component. LCFW is the levelized cost of energy of FW. Similarly, LCBT is the levelized cost of the battery. LCUC is the levelized energy cost of the ultra-capacitor. LCNR is the levelized energy cost of the nuclear reactor. COEG is the cost of energy of the grid. LCWT is the levelized energy cost of wind turbine. LCPV is the levelized energy cost of PV. LCFC is the levelized energy cost of fuel cell.

CONCLUSIONS

This short paper presented a framework for transactive mobility to support hybrid transportation infrastructures with electric vehicles and hydrogen vehicles. Hybrid charging stations are designed based on local hydrogen generation with hybrid energy systems from renewables, small nucleal reactor, and the grid. The station can be implemented in different scales to support electrification of buses, trucks, marine, and railways. Transactive mobility trade agents are defined as supporting the bidding between incoming electric and hydrogen vehicles and the station while considering grid supply and the hydrogen supply chain. Cost models are based on lifecycle cost of each component in the charging station. The proposed transactive mobility model supports multi-investors for components to control profit operation of the charging infrastructures. The proposed transportation infrastructure supports different business models of shared

services, battery swaps, and V2G from EVs and HVs. Detailed research and solution are demonstrated in the extended publication.

Acknowledgement

This research is supported by NSERC Discovery Grant (#210320), CUTRIC (#234109) and Mitacs (#215433). Thanks to the support from all members at the Smart Energy Systems Lab (SESL) at Ontario Tech University, Canada.

Nomenclature

$EP^{Chg}_{EV,c,i,t}$ Energy Price of Charging EV i, at Charging Unit c, at Time t [$/kWh]

$EP^{Dis}_{EV,c,i,t}$ Energy Price of Discharging EV i (V2G) at Charging Unit c, at Time t [$/kWh]

$HP^{Chg}_{EV,c,i,t}$ Hydrogen Price of Charging HV i, at Fueling Unit c, at Time t [$/kg]

$HP^{Dis}_{HV,c,i,t}$ Energy Price of Discharging HV i (V2G) at Fueling Unit c, at Time t [$/kg]

REFERENCES

1. Bokkisam, Hanumantha Rao; M.P, Selvan, Effective community energy management through transactive energy marketplace, Computers & electrical engineering, 2021-07, Vol.93, p.107312.
2. Weijia Liu; Junpeng Zhan; Chung, C. Y, A novel transactive energy control mechanism for collaborative networked microgrids, IEEE transactions on power systems, 2019-05, Vol.34 (3), p.2048-2060.
3. Huang, Qiuhua; McDermott, Thomas E; Tang, Yingying; Makhmalbaf, Atefe; Hammerstrom, Donald J; Fisher, Andrew R; Marinovici, Laurentiu Dan; Hardy, Trevor, Simulation-Based Valuation of Transactive Energy Systems, IEEE transactions on power systems, 2019-09, Vol.34 (5), p.4138-4147.
4. Daneshvar, Mohammadreza; Mohammadi-Ivatloo, Behnam; Abapour, Mehdi; Asadi, Somayeh; Khanjani, Rashed, Distributionally Robust Chance-Constrained Transactive Energy Framework for Coupled Electrical and Gas Microgrids, IEEE transactions on industrial electronics (1982), 2021-01, Vol.68 (1), p.347-357.
5. liu, zhaoxi; Wu, Qiuwei; Shahidehpour, Mohammad; Li, Canbing; Huang, Shaojun; Wei, Wei, Transactive Real-Time Electric Vehicle Charging Management for Commercial Buildings With PV On-Site Generation, IEEE transactions on smart grid, 2019-09, Vol.10 (5), p.4939-4950.
6. Mohammad, Asaad; Zamora, Ramon; Lie, Tek Tjing, Transactive Energy Management of PV-Based EV Integrated Parking Lots, IEEE systems journal, 2021-12, Vol.15 (4), p.5674-5682.
7. Liu, Zhaoxi; Wu, Qiuwei; Ma, Kang; Shahidehpour, Mohammad; Xue, Yusheng; Huang, Shaojun, Two-Stage Optimal Scheduling of Electric Vehicle Charging Based on Transactive Control, IEEE transactions on smart grid, 2019-05, Vol.10 (3), p.2948-2958.
8. Wu, Zhouquan; Chen, Bo, Distributed Electric Vehicle Charging Scheduling with Transactive Energy Management, Energies (Basel), 2021-12-27, Vol.15 (1), p.163.
9. Kudathanthirige, Dhanushka; Shrestha, Rajan; Aruma Baduge, Gayan Amarasuriya, Max-Min Fairness Optimal Rate-Energy Trade-Off of SWIPT for Massive MIMO Downlink, IEEE communications letters, 2019-04, Vol.23 (4), p.688-691.
10. Zhang, Hongwei; Wang, Ying; Zhu, Xuehong; Guo, Yaoqi, The impact of energy trade patterns on CO2 emissions: An emergy and network analysis, Energy economics, 2020-10, Vol.92, p.104948.
11. Sakal, Halil Burak, Turkey's energy trade relations with Europe: The role of institutions and energy market, Energy & environment (Essex, England), 2021-11, Vol.32 (7), p.1243-1274.
12. Duan, Cuncun; Chen, Bin, Energy–water nexus of international energy trade of China, Applied energy, 2017-05-15, Vol.194, p.725-734.
13. Guo, Qun; Zhou, Hui; Lin, Wang; Nojavan, Sayyad, Risk-based design of hydrogen storage-based charging station for hydrogen and electric vehicles using downside risk constraint approach, Journal of energy storage, 2022-04, Vol.48.

WHEC-2022
23rd World Hydrogen Energy Conference
June 26-30, 2022 - Istanbul

#367

HYDROGEN TRANSPORTATION OPTIONS AND CHALLENGES

[1,2*] *Mohammad Anwar Omid,* [3] *Muammer Koç ,* [2*] *Ömer Necati Cora*

[1] Kabul Polytechnic University, Faculty of Electromechanics, Department of Auto-Mechanical Engineering, Kabul, Afghanistan
[2] Karadeniz Technical University, School of Engineering, Department of Mechanical Engineering, Trabzon, Turkey
[3] Hamad bin Khalifa University, College of Science and Engineering, Sustainable Development Division, Doha, Qatar

*Corresponding author e-mails: ma.omid@kpu.edu.af; oncora@ktu.edu.tr

ABSTRACT

In this study, different types of hydrogen transportation and delivery options have been evaluated comparatively. Various kinds of hydrogen transportation options including cryogenic tankers, tube trailers, ships, trains, novel transportation options, in addition to existing pipelines have been reviewed. Major findings such as cost-efficiency, technical and logistic challenges and problems, advantages and solutions of each option are outlined along with the further research and development needs.

Keywords: Hydrogen energy, Transportation, Hydrogen infrastructure, Hydrogen pipeline, Hydrogen delivery

INTRODUCTION

Hydrogen (H_2) is an odorless, colorless, light-weight, highly flammable, high permeable, small diatomic gas element that has a high gravimetric density of 120 MJ/kg, and low volumetric density of 0.0107 MJ/L compared to other types of fuels [1-3]. H_2 is the most abundant element in nature yet it cannot be found freely. It is available in different chemical compound for in other materials. H_2 is an emission-less energy carrier, but fossil-based production sources and technologies, and transportation of H_2 are causing high carbon emissions. As it is reported, 900 MT carbon dioxide (CO_2) emitted into the atmosphere to produce 90 MT H_2 solely in 2020 [4]. Luckily, there is a solution for producing clean/green hydrogen with zero emissions instead of grey hydrogen which generating hydrogen from fossil based resources. In green option, H_2 is produced from renewable sources through electrolyzing water molecules to its component H_2 and O_2 [5-7]. Therefore, solar, wind, and hydropower play a crucial role for producing green hydrogen. Nevertheless, this method of production is still at a high cost [2,4,8].

Another vital aspect of hydrogen energy is the transportation and delivery of H_2, and related infrastructure (such as power generation centers, fuel stations), from the production point to the end-use points [3]. Transportation of H_2, building new infrastructures, and installation of new equipment can impose extra costs to the final cost per unit of hydrogen energy for the end-users. Therefore, further research is needed to reduce the cost, increase energy efficiency, safety, and reliability with a focus to reduce environmental impacts in transportating of H_2. On the other hand, the current and future policies of the governments for the energy, economy, and environment are other matters that need attention. Therefore, this paper aims to overview the recent studies on the transportation of hydrogen, current and future policies of governments for hydrogen energy to find out the challenges, possible solutions, and policies in hydrogen transportation and delivery in different parts of the world.

HYDROGEN TRANSPORTATION AND DELIVERY

A variety of hydrogen transportation options can be adopted based onthe service type, demands, and the form of hydrogen to be transferred. Hydrogen either can be transported in gaseous form (at a pressure of 180 bar or even higher) through tube trailers, trains, ships, and pipelines or it can be transported in liquid form (liquefaction temperature -252.8 °C) through cryogenic tankers, ships, and trains. The pipelines are deployed mostly for long-distance, substantial demands (hundreds of tons per day) to remain stable for decades. Liquid cryogenic tankers and tube trailers, on the other hand, are deployed for smaller-scale demands [9]. For example, gaseous form of hydrogen can be delivered in bottles and transported by semi-trailers from 3000 to 6000 m^3 at 200 bar for demands below 50 m^3/h [10].

Based on an estimation by European Hydrogen Backbone (EHB), the pipeline is the most cost-efficient transportation method for importing hydrogen into EU+UK. This study reports that transportation of hydrogen through pipelines costs €0.11–€0.21/kg H_2/1000 km. However, the shipping of hydrogen from Saudi Arabia and North Africa costs 3 to 5 times more expensive than pipeline, around €1/kg of H_2 [11]. It is important to note that the cost of transportation is highly condition-dependent. For example, transporting hydrogen from Australia to the EU and UK is not cost-efficient through the underwater pipeline, due to high-cost infrastructure and safety matters [2] [11]. Figure 1 shows the cost comparison of different hydrogen transportation options at different distances. This is an advantage that the natural gas infrastructures can be repurposed for hydrogen, which makes it more cost-efficient than the new pipeline as is shown

in Figure 1. Also, the recen studies reveal that inland gaseous hydrogen pipeline is preferable to any other methods of transportation for the transportation of bulk amount of pure pressurized hydrogen for a long-distance [12].

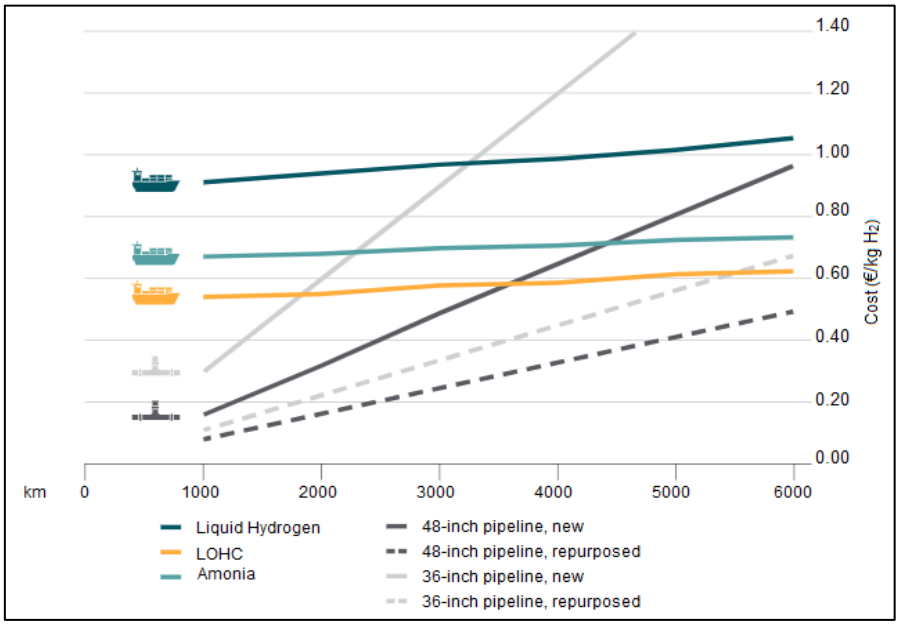


Figure 1. Cost comparison of different hydrogen transportation options at different distances [11]

According to a report by Lebrouhi, *et al*., countries including Australia, Canada, the USA, Morocco, Norway, and Chile are regarded as the top exporter of hydrogen energy while Japan, South Korea, EU are possible major importers based on the policies and projections regarding with hydrogen. China and Saudi Arabia are water-constrained producers of hydrogen. Saudi Arabia has the potential to produce green hydrogen 696 Mt/year which is 24% of the world energy demand in 2050. The report also shows that Spain, Thailand, and Turkey are self-sufficient producers; but India, Russia, Italy, Portugal are infrastructure-constrained producers. Germany, France, the UK, Netherlands, and South Africa are the major importers of hydrogen for their needs to meet NZE scenarios by 2030, and by 2050 [10].

Among the above countries, Turkey has an excellent geographical and geopolitical location that can play a pivotal role in the hydrogen market as it is surrounded by seas and is located close to the EU. Turkey needs to invest around $45 bn investment to produce green hydrogen, installation of electrolyzers, repurpose the current natural gas pipeline for hydrogen transportation, build dedicated hydrogen infrastructures, and so on [13]. Figure 2 shows the key regions for production and transportation of hydrogen.

Material based hydrogen delivery

The idea behind the material-based hydrogen delivery is based on the storage of hydrogen in the form of a solid chemical compound through hydriding a material or chemical compound at the site of hydrogen production, and then dehydriding it at the end-use point or delivery point. Metal-Organic Frameworks (MOFs), complex hydrides such as $NaAlH_4$, NH_3BH_3, and interstitial hydrides such as $LaNi_5H_6$ can be mentioned as a possible material based transportation of hydrogen solutions in the future [14]. This method is in its crawling stage and the studies are mostly concentrated on the storage of hydrogen, no reported projection of transportation yet [9].



Regions	1	2	3	4	5	6
Port Availability	+++	++	+++	+	+++	-
Industry (Refineries)	+++	-	+++	--	++	---
Renewable proximity	++	+++	+++	+++	-	+++
Water resources	+	++	+	++	-	+++
Demand centers	++	+	+++	+	+++	---
Infrastructure	++	-	+++	++	+++	+
Marine Safety	Med	Med	Med	Med	B.Sea	B.Sea

Figure. 2. Key regions for the production and export of green hydrogen in Turkey [13].

CONCLUSIONS

Currently, different types of hydrogen transportation infrastructure are commercially available worldwide, and some others are either under investigation or development stages. Undoubtedly, the transportation of hydrogen requires high-cost infrastructure, safety precautions, etc. Nevertheless, the geopolitical stability in the countries along the pipeline, bilateral tensions between countries will also play a critical role in realizing the green hydrogen delivery.

REFERENCES

1. Mazloomi, K. and C. Gomes, *Hydrogen as an energy carrier: Prospects and challenges.* Renewable and Sustainable Energy Reviews, 2012. 16(5): p. 3024-3033.
2. Omid, M.A., M.E. Şahin, and Ö.N. Cora, *Challenges and Future Perspectives on Production, Storage Technologies and Transportation of Hydrogen* in *6th International Hydrogen Technologies Congress (IHTEC-2022)*. 2022: Çanakkale Onsekiz Mart University, Çanakkale, Turkey.
3. US Department of Energy. *Hydrogen Storage*. 2021; Available from: https://www.energy.gov/eere/fuelcells/hydrogen-storage.
4. IEA, *Global Hydrogen Review 2021*. 2021.
5. Eljack, F. and M.-K. Kazi, *Prospects and Challenges of Green Hydrogen Economy via Multi-Sector Global Symbiosis in Qatar.* Frontiers in Sustainability, 2021. 1.
6. Rebecca L., B., *Hydrogen and Fuel Cells: A Comprehensive Guide*. 2005: PennWell Corporation 1421 South Sheridan Road Tulsa, Oklahoma 74112. P.445.
7. Dincer, I., *Green methods for hydrogen production.* Internatıonal Journal of Hydrogen Energy, 2012. 37: p. 1954-1971.
8. EIA, *International Energy Outlook 2021 Narrative*. 2021.
9. US-Department-of-Energy. *Hydrogen Delivery*. [cited 2022 30 January]; Available from: https://www.energy.gov/eere/fuelcells/hydrogen-delivery.
10. Lebrouhi, B.E., et al., *Global hydrogen development - A technological and geopolitical overview.* International Journal of Hydrogen Energy, 2022. 47(11): p. 7016-7048.
11. Wang, A., et al., *Analysing future demand, supply, and transport of hydrogen EUROPEAN HYDROGEN BACKBONE Executive summary.* 2021.
12. Okunlola, A., et al., *Techno-economic assessment of low-carbon hydrogen export from Western Canada to Eastern Canada, the USA, the Asia-Pacific, and Europe.* International Journal of Hydrogen Energy, 2022. 47(10): p. 6453-6477.
13. Çolak, E., H. Aksoy, and B. Sanlı, *Techno Economic Study on Turkey's Prodcution and Export Potential for Green Hydrogen*. 2021, SHURA: Turkey.
14. Shet, S.P., et al., *A review on current trends in potential use of metal-organic framework for hydrogen storage.* 2021. 46: p. 11782-11803.

WHEC-2022
23rd World Hydrogen Energy Conference
June 26-30, 2022 - Istanbul

#397

ECONOMIC AND ENVIRONMENTAL EVALUATION OF FUELING OPTIONS FOR HYDROGEN FUEL CELL HEAVY-DUTY VEHICLES

[1*] *Amgad Elgowainy,* [1] *Krishna Reddi*
[1]Argonne National Laboratory, 9700 S Cass Ave, Lemont, IL 60439, USA

*Corresponding author e-mail: aelgowainy@anl.gov

ABSTRACT

Hydrogen fuel cell electric vehicles have the advantage of faster fueling and longer driving range compared to battery electric vehicles, especially for medium and heavy-duty vehicles (M/HDVs). Argonne National laboratory developed cost and energy/emissions estimates of various options for fueling hydrogen fuel cell HDV fleets, considering various hydrogen supply chain (e.g., gaseous vs. liquid). In general, liquid hydrogen sourcing provides a significant cost advantage for large fleets with high fueling rates, compared to gaseous hydrogen supply to fueling stations. However, the hydrogen liquefaction is an energy intensive process that affects life-cycle energy use and greenhouse gas emissions, depending on the electricity generation mix used for liquefaction. The contribution of refueling station to total hydrogen cost at dispenser is between \$2-5/kg_{H2}, depending on daily and hourly fueling demand and speed, but can be reduced to \$1/kg_{H2} when considering large fleets and high production volume of fueling components. The fueling station cost contribution can be further reduced to <\$1/kg_{H2} by considering low-pressure liquid hydrogen storage onboard the fuel cell M/HDVs.

Keywords: Hydrogen, Fuel cell, Refueling cost, Greenhouse gas, Heavy-Duty vehicle

INTRODUCTION

Medium/heavy-duty vehicles (M/HDVs) class is the fastest growing and second largest energy consumer in the U.S. transportation sector, accounting for significant energy use and air emissions in the United States. There are about 11 million M/HDVs, representing only about 4% of the total on road vehicles in the United States. However, NOx emissions of M/HDV fleet are comparable to emissions from the much larger light-duty vehicle (LDV) fleet. Energy consumption share of M/HDVs is expected to increase to represent 30% of total U.S. transportation energy use by 2040. To mitigate the impact of M/HDVs on energy use and air emissions, several states developed plans to gradually increase the share of zero emissions vehicles (ZEV), such as battery electric vehicles (BEVs) and fuel cell electric vehicles (FCEVs) in their efforts to electrify on-road transportation sector. Hydrogen fueling station contributes significantly to the total dispensing cost of hydrogen. Such cost can be mitigated by appropriate choice of hydrogen supply chain (e.g., gaseous vs. liquid). Furthermore, the choice of hydrogen storage onboard the vehicle strongly impacts the fueling station equipment, and therefore the levelized cost of hydrogen dispensing.

MATERIALS AND METHODS

Techno-economic models are needed to estimate hydrogen delivery and refueling costs for various delivery and refueling technology options, considering both near-term and long-term markets. Additionally, techno-economic models can inform infrastructure deployment plans by incorporating important factors such as market demand, capacity utilization in early markets, manufacturing volume of fueling components, and hydrogen sourcing (e.g., delivered vs. onsite production, and liquid vs. gaseous). This study evaluates the cost and life cycle environmental impacts of various hydrogen supply chains for fueling MHDVs. The Heavy-Duty Refueling Station Analysis Model (HDRSAM)[1], shown in Figure 1, is a techno-economic model developed by Argonne National Laboratory (ANL) that was used to evaluate the cost of fueling fuel cell MHDVs.

Environmental life cycle analysis models provide consistent basis to compare the environmental performance of various hydrogen pathways. In particular, the carbon intensity of hydrogen is an important metric to evaluate the greenhouse gas emissions reduction associated with using hydrogen in FCEVs compared to the use of conventional fuels in internal combustion engine vehicles. The Greenhouse gas, Regulated Emissions, and Energy use in Technologies (GREET®)[2], also developed by ANL, was used to evaluate the environment impacts of various hydrogen production, delivery and fueling pathways. The trade-off between cost and environmental performance of various hydrogen pathways is evaluated to inform infrastructure deployment for various vehicle classes and vocations.

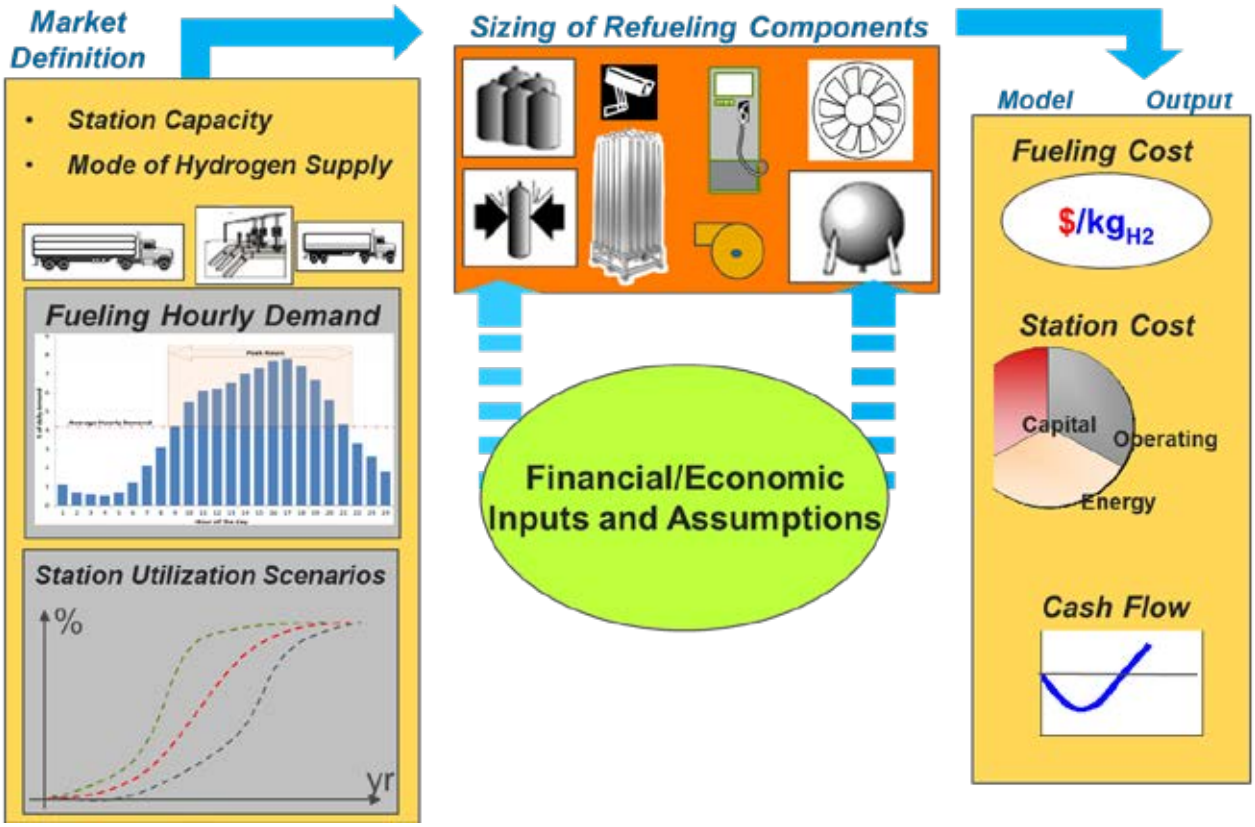


Figure 1. The Heavy-Duty Refueling Station Analysis Model (HDRSAM) framework

RESULTS AND DISCUSSION

ANL conducted a life cycle analysis of hydrogen use in M/HDV to evaluate the economic and environmental impacts of key fueling parameters, including vehicle onboard storage technology, fleet size, fueling amount per vehicle, fueling pressure, fueling rate, precooling requirement, and fleet fueling strategy. In this analysis, ANL presents cost and energy/emissions estimates of various options for fueling hydrogen fuel cell M/HDV fleets, considering various hydrogen sources (e.g., gaseous vs. liquid). In general, liquid hydrogen sourcing provides a significant cost advantage for large fleets with high fueling rates (> 3kg/min), compared to gaseous sources of hydrogen. However, liquefaction of hydrogen is an energy intensive process that affects the dispensing cost of hydrogen and the life-cycle energy use and greenhouse gas emissions, depending on the carbon intensity of the electricity generation mix used for the hydrogen liquefaction process, and its energy efficiency. The contribution of refueling station to total hydrogen cost at dispenser is between \$2-5/kg$_{H2}$ with gaseous hydrogen supply, depending on fueling demand and speed, but can be reduced to ~\$1/kg$_{H2}$ when considering liquid hydrogen supply and high production volume of fueling components (Figure 2). The fueling station cost contribution is also impacted by choice of hydrogen onboard storage option. Compressed hydrogen tanks (350 and 700 bar) require high capital investment in compressors and high-pressure storage to accommodate fast fueling of FCEVs, which impacts the levelized cost of hydrogen at the dispenser. Low-pressure, vacuum jacketed cryogenic hydrogen tanks require less capital investment at fueling station, which may contribute <\$1/kg$_{H2}$ to the hydrogen dispensing cost (Figure 2). However, the carbon intensity of liquid hydrogen supply can be significant if the electricity for liquefaction is sourced from a carbon intensive grid.

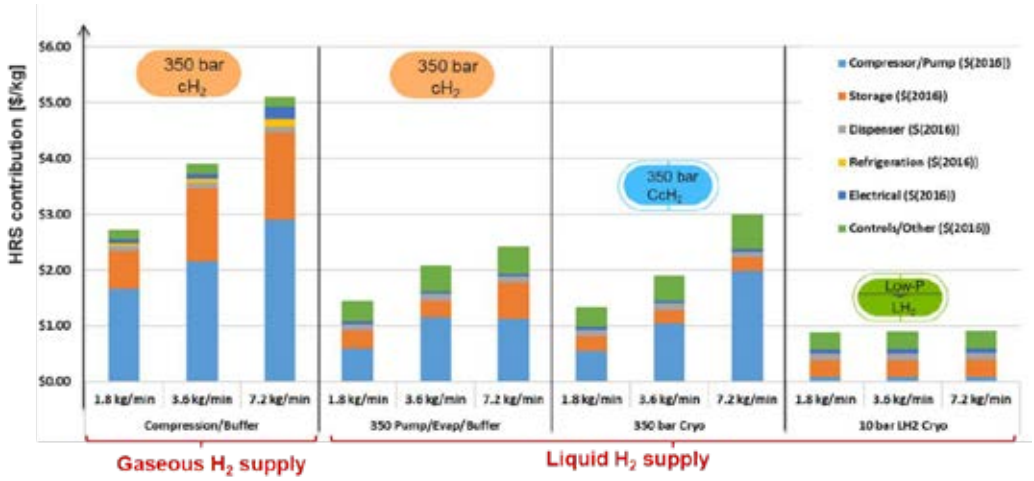


Figure 2. Hydrogen Refueling Station (HRS) contribution to the cost of fueling a fleet of 30 fuel cell buses, with 35 kg fill per bus, for various hydrogen supply modes and onboard storage technologies

CONCLUSIONS

The contribution of refueling station to total hydrogen dispensing cost is between \$2-5/kg_{H2}, depending on daily and hourly fueling demand and speed, but can be reduced to \$1/kg_{H2} when considering large fleets and high production volume of fueling components. The fueling station cost contribution can be reduced further to <\$1/kg_{H2} by considering low-pressure liquid hydrogen storage onboard fuel cell M/HDVs. It is important to use low-carbon electricity for hydrogen liquefaction to realize both the economic and environmental benefits of liquid hydrogen supply for fueling FCEVs.

ACKNOWLEDGEMENT

This study was supported by the Hydrogen and Fuel Cell Technologies Office under the Energy Efficiency and Renewable Energy Office of the United States Department of Energy under Contract Number DE-AC02-06CH11357. The views and opinions of the authors expressed herein do not necessarily state or reflect those of the U.S. Government or any agency thereof. Neither the U.S. Government nor any agency thereof, nor any of their employees, makes any warranty, expressed or implied, or assumes any legal liability or responsibility for the accuracy, completeness, or usefulness of any information, apparatus, product, or process disclosed, or represents that its use would not infringe privately owned rights.

REFERENCES

1. https:/hdsam.es.anl.gov/. Accessed on February 15, 2022
2. https:/greet.es.anl.gov/. Accessed on February 15, 2022

WHEC-2022
23rd World Hydrogen Energy Conference
June 26-30, 2022 - Istanbul

#409

ANALYSIS OF THE DEMAND OF HYDROGEN AS FUEL FOR TRANSPORT IN THE UAE

[1,2] *Maram Awad,* [3] *Ali Bouabid,* [3] *Andrei Sleptchenko, Ali* [1,2] *Ali Almansoori,* [1,2*] *Ahmed Alhajaj*
[1] Research and Innovation Centre on CO2 and H2, Khalifa University of Science and Technology, PO Box 127788, Abu Dhabi, United Arab Emirates
[2] Department of Chemical Engineering, Khalifa University, P.O. Box 127788, Abu Dhabi, United Arab Emirates
[3] Department of Industrial and Systems Engineering, Khalifa University, P.O. Box 127788, Abu Dhabi, United Arab Emirates

*Corresponding author e-mail: ahmed.alhajaj@ku.ac.ae

ABSTRACT

With the growing emphasis on building a green economy with low carbon footprint, UAE is gradually building a hydrogen economy through introducing hydrogen fuel for transport. Although hydrogen sources are abundant in the UAE, the supply-chain model is not in place. Given the cost sensitivity of hydrogen in relation to volumes produced, large consumption is essential to reduce the cost. In this work, we developed a system dynamics model that allow us to design a roadmap for deployment of hydrogen network in the UAE. We examined different policy incentives that inaugurate hydrogen fuel stations at a reasonable price in the UAE market.
Keywords: Hydrogen network, Green transport, System dynamics, Analysis, Demand

INTRODUCTION

Global economies, including UAE, have set strategies to comply with international commitment of reducing emissions by setting targets to develop and implement clean energy technologies [1]. The UAE Vision 2021 National Agenda emphasizes implementing green strategies and increasing reliance on clean energy. The vision is to reach a target of 27% share of clean energy and 15% reduction of CO_2 emissions, while maintaining strong economic growth. Additionally, UAE's 'Energy Strategy 2050' aims to increase the contribution of power generation from renewable energy to 50 percent, while reducing carbon emissions by 70 percent. The roadmap to achieving this ambitious yet realistic target is through diversifying energy sources, shifting from heavy reliance on oil and gas to a mix of 44 per cent clean energy, 38 per cent gas, 12 per cent clean coal, 6 percent nuclear. [2] The global shift to renewables has shed light on the abundance of hydrogen making it a core energy source of the future. Hydrogen energy is clean, storable, transportable and inexhaustible. Due to these attractive qualities, its applications are versatile [3]. With the prominent emphasis on building a green economy with low carbon footprint, UAE is gradually building a hydrogen economy by introducing hydrogen fuel for transport. Although hydrogen sources are abundant in the UAE and the applications are numerous, the supply-chain model is not in place. Given the cost sensitivity of hydrogen in relation to volumes produced, large consumption is essential to reduce the cost. This can be kickstarted through deployment of fuel cell vehicles (FCVs) that will justify the inauguration of hydrogen fuel stations and eventually reduce the price of H_2 fuel to an economically attractive price in the UAE.

Therefore, a roadmap for the development of hydrogen infrastructure is required with clear direction on commencing this transition to hydrogen as fuel for transport. Investors, industry and government need to coordinate to achieve this transition. As with any energy shift, communication is a key especially in the UAE, where it is heavily dependent on oil and gas for energy production. Therefore, it is essential to develop a tool that provides a clear path on fuel cell market penetration and communicate it to authorities and policymakers. Accordingly, a comprehensive vision could be established to reach the emission reduction targets set in the UAE. Deployment of hydrogen FCVs not only results in environmental benefit but also creates a sustainable economic growth through a new market of employment, sales and revenues. This ongoing research aims to analyze potential future demand for hydrogen as a fuel for transport in UAE. This facilitates the development of a roadmap for the utilization of hydrogen as transportation fuel in the UAE, as it provides a forecasting tool for hydrogen demand. This is accomplished through analyzing the incentives and factors that contribute to a successful penetration of hydrogen-powered vehicles in the market and the factors that inhibit its growth. By studying the complex interactions between these dynamic factors, it provides concrete data to commence and establish a hydrogen supply demand network with a site-specific roadmap to employ hydrogen

applications in UAE. This work will contribute to the reduction in carbon emissions and achieving the vision of low carbon economy.

The objectives of the research are to: (1) examine potential market to promote penetration of fuel cell vehicles in the UAE; (2) evaluate factors that would drive hydrogen fuel demand and analyze their effects through causal-loop approach; (3) analyze and quantify the effect of hydrogen fuel cell vehicles on development of hydrogen infrastructure; (4) analyze quantitative models produced to develop reliable hydrogen utilization road-map.

MATERIALS AND METHODS

Several modelling approaches in literature have been used to explore the future of hydrogen market in transportation. Mostly, scenario-based approaches and historical analogy were used to examine hydrogen adoption rate [4]. Key factors

that contribute to the penetration of fuel cell vehicles (FCVs) in the market such as technology economics, political regulations, and consumer behavior should be considered when analysing the demand of hydrogen for transport. Political regulatory interference, in terms of subsidies to support the hydrogen market, taxation on diesel powertrains, and incentives, plays a significant role in the initial diffusion process. Moreover, technology maturity and availability affect the economics, which consequently impact consumer behavior. Given that these factors are dynamic, their interactions and impact on the system as a whole is also dynamic, and hence complex to interpret. In this work, a systems dynamics model is developed to examine the market and study the complex interactions between the factors based on UAE context. The elements that contribute to FCV diffusion are modeled in a causal-loop diagram to analyze the relations between the multivariable system. Following the work done in a German study led by Keles et al (2008) on FCV market penetration, factors affecting the car system can be modeled in four modules: demand and supply, attractiveness, filling stations, and balance of payments [5]. By running different scenarios of policy combinations, the results of the causal-loop diagram demonstrate the real drivers of future hydrogen fuel demand, and the effect of different stakeholders' inputs on the system. Figure 1 demonstrates the main aspects considered in the study. The focus of the model is to estimate hydrogen fuel demand, which translates into fuel cell vehicles deployed annually. Accordingly, it is feasible to quantify the reduction of carbon dioxide emissions from transport achieved by adoption of fuel cell vehicles. Further analysis will be conducted to quantify the approximate governmental funding required and policies necessary for successful market penetration. Based on the results, a reliable hydrogen utilization roadmap will be developed.

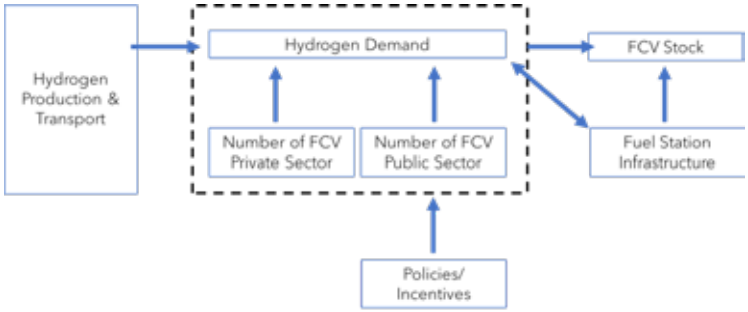


Fig. 1. Linkages between modules of FCV market

RESULTS AND DISCUSSION

The optimum market for preliminary FCV penetration in the UAE transport is through deploying fleets of medium and heavy-duty vehicles. The barriers to entry into medium and heavy-duty markets are easier to overcome relative to passenger FCV markets. Thus, in the near-future, taxi, bus, and truck fleets are more likely to be converted to hydrogen fuel cells. Fleet operators would require long term refueling contracts, as opposed to private users, resulting in consumption of large and predictable quantities of hydrogen fuel. Scaling up hydrogen production to supply the large demand would eventually reduce the cost of hydrogen. Moreover, fleets usually have fixed routes and refuel at base, which translates into fewer refueling stations. Also, the population density centralized in Abu Dhabi and Dubai allows for less infrastructure required to cover nationwide demand. Preliminary penetration of hydrogen in this market paves the way for a wider diffusion into mass market and comprehensive infrastructure. The pilot phase of FCV penetration in

the UAE commenced by importing 55 Toyota Mirais by Al Futtaim Motors, the exclusive distributor of Toyota in UAE. The vehicles refuel at the first hydrogen refueling station in the UAE installed by Air Liquide. Deploying the Mirais is a strategic attempt to demonstrate potential hydrogen market in the UAE, while managing to connect source to application and establishing a hydrogen supply chain. Fuel cells are already gaining momentum in UAE, as Dubai Taxi Corporation is test driving the Mirai for its fleet. Abu Dhabi police announced conversion of entire fleet from fossil fuel powertrain to fuel-cells by 2057. Successful market penetration can be achieved through a combination of FCVs subsidies, sufficient installation of hydrogen fuel stations, and tax-free hydrogen fuel. Subsidies and tax allowances are essential to reach cost parity with diesel vehicles, and hence increasing consumers acceptance to FCVs. Also, financial support from governmental entities is recommended to install hydrogen fueling stations [5].

CONCLUSIONS

A system dynamic model was developed as a tool to forecast the demand of hydrogen as a fuel for transportation in the UAE. The key factors that contribute to the penetration of fuel cell vehicles (FCVs) in the market such as technology economics, political regulations, and consumer behavior were investigated in details in this study using system dynamics approach. We found that the best strategy to close the gap between the demand and economies supply of hydrogen is thorough adoption of large operators such as taxi, bus, and truck fleets

ACKNOWLEDGEMENT

We acknowledge the fund received from Khalifa University of Science and Technology under project RC2 2019 007.

REFERENCES

1. Singh, S., Jain, S., PS, V., Tiwari, A., Nouni, M., Pandey, J. and Goel, S. (2015). Hydrogen: A sustainable fuel for future of the transport sector. *Renewable and Sustainable Energy Reviews*, 51, pp.623-633.
2. “National Climate Change Plan of the United Arab Emirates 2017 - 2050” *United Arab Emirates Ministry of Climate Change and Environment.* [Online]. Available: www.moccae.gov.ae [Accessed: 24- Mar- 2019].
3. Sims R., R. Schaeffer, F. Creutzig, X. Cruz-Núñez, M. D’Agosto, D. Dimitriu, M.J. Figueroa Meza, L. Fulton, S. Kobayashi, O. Lah, A. McKinnon, P. Newman, M. Ouyang, J.J. Schauer, D. Sperling, and G. Tiwari, 2014: *Transport. In: Climate Change 2014: Mitigation of Climate Change.* Cambridge University Press, Cambridge, United Kingdom and New York, NY, USA.
4. McDowall, W. (2016). Are scenarios of hydrogen vehicle adoption optimistic? A comparison with historical analogies. *Environmental Innovation and Societal Transitions*, 20, pp.48-61.
5. Keles, D., Wietschel, M., Most, D. and Rentz, O. (2008). Market penetration of fuel cell vehicles – Analysis based on agent behaviour. *International Journal of Hydrogen Energy*, 33(16), pp.4444-4455.

WHEC-2022
23rd World Hydrogen Energy Conference
June 26-30, 2022 - Istanbul

#439

GRID BASED RISK ASSESSMENT OF A HYDROGEN SUPPLY CHAIN

[1*]Ebru Geçici, [1]Mehmet Güray Güler, [1]Ahmet Erdoğan
[1]Department of Industrial Engineering, Faculty of Mechanical Engineering, Yıldız Technical University, Istanbul, Turkey

*Corresponding author e-mail: egecici@yildiz.edu.tr

ABSTRACT

Today's energy recourses are not supposed to be sufficient to fulfill increased energy demand in the near future, thus researchers and governments look forwards to alternative energy sources. Hydrogen energy is one of these alternative energies. To increase the use of hydrogen energy, it is essential to establish a good hydrogen supply chain (HSC), which provides the transmission of hydrogen from production facilities to the users. There are several key issues which must be addressed in establishing a good HSC like capital cost and operating costs, environmental effects like CO_2 emission, and risks. Although minimizing the total costs or total CO_2 emissions can be appropriate for a country, minimizing the cumulative risk may result in an unbalanced risk load between cities or grids of a country. In this study we analyze establishing the HSC of Turkey and showed that minimization of total risk yields low risks in grids with low population and grids with higher populations have to cope with larger risks.

Keywords: Hydrogen Supply Chain, Risk Analysis, Multi-objective Supply Chain

INTRODUCTION

Growing population and developed technology increase the energy consumption day by day. In addition to this, today's main energy sources, which are fossil fuels such as petroleum, natural gas, etc., will not be enough to fulfill energy need. For this reason, researchers seek alternative energy sources. Hydrogen energy is one of these alternative energy sources to meet the increasing energy demand. It is a low pollutant fuel [1, 2], efficient [2], and improves the security of primary energy supply [3]. Through these advantages although it is costly in today's technology, its use has become widespread. However, to retain its expansion in the future, the design of the hydrogen supply chain (HSC) has an essential role. An HSC provides the spread of the hydrogen energy from production facility or storage to the end users by appropriate transportation system. An HSC should be optimally designed to get proper flow from the starting point to the final consumption point with minimum cost in economic, environmental and social terms. Therefore these studies in the literature proposes HSC design by minimizing costs, CO2 emissions and/or environmental risks. One of the first studies in the literature, Almansoori and Shah [3], proposes a mixed integer programming (MIP) model by minimizing the capital and operating cost of the HSC for Great Britain as a single period model. This snap-shot MIP model is later extended to multi-period [4] and multi-objective models [5] by the authors. In the former, the objective function is the minimization of the total daily cost with the same as the main model, whereas, in the latter, the authors consider different objectives as CO2 emission and risk minimization. Carbon emission is directly proportional to the production method (Steam Methane Reforming (SMR), Electrolysis, etc.), the amount of production and the number of transports between the networks. However, in the risk analysis, besides the factors used in the CO2 analysis, it is affected by many different parameters such as the population density of the grid where the production facility will be established, and the route of transportation. For this reason, risk analysis become a significant point of view of the HSC in recent studies.

Almaraz et al. [6] propose a MIP model for the HSC of the Great Britain. Like Almansoori and Shah [5], the authors examine HSC of Great Britain with a multi-objective model (minimization of cost, CO2, and risk). Another multi-objective study is conducted by Bique et al. [7] where the authors examine HSC for Germany in 2030. Han et al. [8], on the other hand, create a multi-objective MIP model for the South Korea. Finally, Geçici et al. [9] propose a MIP model for Turkey's HSC for 2050. In all of the multi-objective studies, the aim is to minimize the total risk together with the total cost and/or the CO2 emission. However, this may result in unbalanced risks in terms of the grids. In another words, trying to minimize the total risk of a country may end up in very high risks in some grids. The subject of this study is minimizing the risk in the HSC on a grid basis rather than the total risk to ensure that all grids share the total risk in a balanced way. In this context, we propose a multi-objective MIP model, which minimize the total risk by taking into account the risk of each individual grid.

MATHEMATICAL MODEL AND CASE STUDY

In this study, we use the HSC model of Almansoori and Shah [5], Almaraz et al. [6], Bique et al. [7] and Geçici et al. [9]. We change the objective function given in (1) and added the constraints given in (2)-(6).

$$\sum_{g \in G} D_g^{risk} \quad (1)$$

$$PR_g \leq \frac{TPR}{NG} + D_g^{risk} \qquad g \in G \quad (2)$$

$$TDC \leq \varepsilon_1 \quad (3)$$

$$TDE \leq \varepsilon_2 \quad (4)$$

$$TR \leq \varepsilon_3 \quad (5)$$

$$D_g^{risk} \geq 0 \qquad g \in G \quad (6)$$

Our aim is to assign the risk to the grids as equally as possible. In order to ensure this, we assign the risk of each grid to the average of the total risk, allow the risk of the grid to deviate from the grid using a deviation variable (D_g^{risk}) and then minimize these deviations in the objective function. Eq. (1) gives the objective function, and it provides the minimization of the risk deviation D_g^{risk}. The constraint in Eq. (2) ensures that production risk of each grid should be smaller than or equal to the average risk as much as possible through the deviation variables. Here, PR_g shows the production risk of grid g. TPR is the total production risk, whereas NG is the number of grids. The constraints in Eq. (3)-(5) keep the other objectives of the model at a certain level, which are total daily cost (TDC), total daily emission (TDE), and total risk (TR), respectively. Keeping the levels at a certain level is a technique used by epsilon constraint method in multi objective problems. The constraint in Eq. (6) is for non-negativity of the decision variable D_g^{risk}.
In this study, the case study of Turkey in Geçici et al. [9] is analyzed. Turkey, which consists of 81 cities, is divided into 33 grids by combining the cities according to the population density. Here, two cases are analyzed: (i) multi-objective model and (ii) minimization of the deviation risk "D_g^{risk}". In the first case (base case), the model is solved as a multi-objective problem (minimization of cost, carbon emission and risk, respectively) by using the ε-constraint method. In the second case, the cost, carbon emission and risk values ($\varepsilon_1, \varepsilon_2, \varepsilon_3$) obtained in the first case are added to the model as constraints, and D_g^{risk}, which is defined to balance the distribution of production risk to the grids, is minimized.

RESULTS AND DISCUSSION

In this part, we examine the effect of the model via the results of two cases. As observed Table 1, in case 1, two different production plants are established in 33 different grids: 286 small-scale, 25 medium-sized electrolysis production plants, and 3 large-scale and 7 medium-sized SMR production plants. According to the open facilities and their effects over production risk distribution of each grid, it is seen that only 3 cities constitute 44% of the total production risk (Table 2).

Table 1. Results

Objectives	Number of production plants			
	Steam Methane Reforming		Electrolysis	
	Medium	Large	Small	Medium
Case 1 (Total)	7	3	286	25
Case 2 (Total)	8	4	274	36
Case 1 (İstanbul)	0	2	16	0
Case 2 (İstanbul)	0	0	2	11

In Case 2 (minimizing the grid-based risk), on the other hand, 274 small-scale, 36 medium-sized electrolysis production plants and 4 large-scale and 8 medium-sized SMR production plants are established (Table 1). The results show slight differences in the total number of established facilities compared to the first case. In both solutions, production facilities are established on all grids. However, while the production risk of 3 cities covers 44%of the total production risk in the first case, it decreases to 34% in the second case, as seen in Table 2. In order to reduce the production risk distribution in this way, 11 medium-sized electrolysis facilities were established in İstanbul instead of 2 large-sized SMR plants and 14 Electrolysis plants. Therefore, as seen in Table 1 although the total number of production plants, total cost, total risk, and total carbon emission values are very close to each other in both cases, there are serious differences in the type, size and number of plants established in some grids such as İstanbul.

Table 2. Distribution of Production Risk

Grid No	Grid Name	Case 1		Case 2	
		Production Risk	Rate	Production Risk	Rate
1	İstanbul	406	26%	273	19%
2	Ankara	150	9%	123	9%
3	İzmir	135	9%	90	6%
Total			**44%**		**34%**

CONCLUSIONS

One must address several objectives like cost, risk and environmental effect when designing efficient HSC. The general approach is to minimize the total of these objective over a particular region. In this study we show that such an approach may lead to unbalanced risks, i.e., very high risks in some parts of the regions. We proposed a model which tries to keep the risk of each grid at the average as much as possible and showed that the results are promising. This model can be improved to get more balanced risk values for each grids.

NOMENCLATURE

g, G	Indice and set of grids
PR_g	Decision variable of the production risk of grid g
D_g^{risk}	Deviation variable of grid g for the risk
HSC	Hydrogen supply chain
MIP	Mixed integer programming
NG	The number of grids
STR	Steam methane reforming
TDC	Total daily cost
TDE	Total daily emission
TPR	The total production risk
TR	Total risk
$\varepsilon_1, \varepsilon_2, \varepsilon_3$	The cost, carbon emission and risk values

REFERENCES

1. Acar, C., & Dincer, I. 2014. Comparative assessment of hydrogen production methods from renewable and non-renewable sources. *International journal of hydrogen energy*, *39*(1), 1-12.
2. Dincer, I. (2002). Technical, environmental and exergetic aspects of hydrogen energy systems. *International journal of hydrogen energy*, *27*(3), 265-285.
3. Almansoori, A., & Shah, N. 2006. Design and operation of a future hydrogen supply chain: snapshot model. *Chemical Engineering Research and Design*, *84*(6), 423-438.
4. Almansoori, A., & Shah, N. 2009. Design and operation of a future hydrogen supply chain: multi-period model. *International journal of hydrogen energy*, *34*(19), 7883-7897.
5. Almansoori, A., & Shah, N. 2012. Design and operation of a stochastic hydrogen supply chain network under demand uncertainty. *International journal of hydrogen energy*, *37*(5), 3965-3977.
6. Almaraz, S. D. L., Azzaro-Pantel, C., Montastruc, L., Pibouleau, L., & Senties, O. B. 2013. Assessment of mono and multi-objective optimization to design a hydrogen supply chain. *international journal of hydrogen energy*, *38*(33), 14121-14145.
7. Bique, A. O., Maia, L. K., La Mantia, F., Manca, D., & Zondervan, E. 2019. Balancing costs, safety and CO2 emissions in the design of hydrogen supply chains. *Computers & Chemical Engineering*, *129*, 106493.
8. Han, J. H., Ryu, J. H., & Lee, I. B. 2013. Multi-objective optimization design of hydrogen infrastructures simultaneously considering economic cost, safety and CO2 emission. *Chemical Engineering Research and Design*, *91*(8), 1427-1439.
9. Geçici, E., Erdoğan, A., & Güler, M. 2021. Design of Future Hydrogen Supply Chain: A Multi-Objective Model for Turkey. *TUBA World Conference on Energy Science and Technology (TUBA WCEST – 2021), İstanbul, ss.208-209.*

WHEC-2022
23rd World Hydrogen Energy Conference
June 26-30, 2022 - Istanbul

#1458

ANALYSIS OF A HYDROGEN SUPPLY CHAIN WITH RANDOM DEMAND: A CASE STUDY

[1*] *Busenur Türkali Özbek,* [1] *Mehmet Güray Güler*
[1] Department of Industrial Engineering, Faculty of Mechanical Engineering, Yıldız Technical University, İstanbul, Turkey

*Corresponding author e-mail: busenur.turkali@std.yildiz.edu.tr

ABSTRACT

Today, energy sources that are used intensively especially in vehicles are generally non-renewable energy sources and they are on the verge of depletion with increasing demand. To cope with this, countries have turned to hydrogen, which is seen as a clean and renewable energy source. However, due to the uncertain future demand, it is also difficult to design a good hydrogen supply chain. To overcome this, a stochastic hydrogen supply chain model is proposed in this study and the Marmara region of Turkey is used as a case study.

Keywords: Hydrogen supply chain, Stochastic, Renewable energy source

INTRODUCTION

Fossil fuels have become very popular in the 20th century with the increasing energy need and have been the savior of people for a while. Fossil fuels pioneered the industrial revolution and increased social and economic welfare [1]. But fossil fuels are not renewable and are bound to run out over time. However, the damage they cause to the environment is one of the main causes of global warming threatening the world in recent years.

Since the need for energy has increased with the increase in the world population, renewable energy sources have been preferred considering the depletion of fossil fuels and their damages. The oil crisis in 1973 also plays an important role in this regard [2]. However, although the use of renewable energy sources has become widespread today, the consumption of fossil fuels is still at a very high level.

Along with these, there is another energy source that has become widespread in recent years: hydrogen energy. Hydrogen energy is known as renewable energy, but it differs from renewable energy sources in some aspects. Especially being storable is one of the biggest advantages of hydrogen energy. In addition to this, it is a low pollutant fuel [3, 4], efficient [4], and improves the security of primary energy supply [5].

In recent years, governments of almost all countries have been working on infrastructure for the use and transportation of hydrogen as energy. In Turkey, steps are being taken in this regard. Finally, within the scope of the "Glasgow Agreement for Zero Emission Vehicles" signed by 33 countries, including Turkey, in 2021, it is foreseen that gasoline and diesel engine vehicles will be replaced by zero emission vehicles in the automobile markets until 2035. This means that vehicles working with hydrogen energy will increase.

In order to that countries can plan the hydrogen supply chain (HSC) correctly, various studies are carried out. In 2009, Almansoori and Shah designed a multi-period deterministic HSC model for Great Britain [5], and extended this model to a stochastic model in 2012 [6]. Dayhim et al. developed a stochastic model for New Jersey [7]. Camara et al. have similarly studied for Portugal [8].

In this study, it is aimed to make HSC planning with stochastic modeling within the scope of the Marmara region of Turkey. Under the study, it has been planned in which regions and in which capacities hydrogen production and storage facilities should be opened according to the hydrogen demands in the cities of Marmara region. Stochastic modeling was used to reflect demand uncertainty to the model.

MATERIALS AND METHODS

In this study, hydrogen supply chain planning has been made for the Marmara Region of Turkey for the year 2035, which is considered a milestone in the use of diesel and gasoline vehicles. To model demand uncertainty in the transition to hydrogen vehicles, a two-stage scenario-based stochastic programming framework, in which discrete control variables (here-and-now) are generated first for all generation units, and then the continuous dispatch variables (wait-and-see) are generated using a scenario-based technique is used [9]. In this problem, three different scenarios according to demand is considered. The first stage variables are the number of production and storage facilities to be opened regardless of the scenarios, and the second stage variables are the amount to be produced and stored at each facility and the amount of hydrogen to be transported between cities. In the scenarios, the ratio of hydrogen vehicle use

to the total number of vehicles is assumed to be 35%, 25%, and 15%, and the scenario probabilities are determined as 30%, 50% and 20%, respectively.

The demands in 2035 are given in Table 1 according to the provinces and scenarios in the Marmara Region. While determining the demands, the data of Güler et al.'s [10] study is used. The aim of the model is to determine the locations of the production facilities and warehouses that should be established in each province by minimizing the cost in a way that will meet these demands. It is assumed that the demand in one province can also be met by the production facilities in other provinces, and the flow between these provinces is also determined.

Table 1: Demands of the provinces in scenarios

Code	Name of Region	Demand		
		Scenario 1	Scenario 2	Scenario 3
1	İstanbul	2,176,994	1,554,996	932,998
2	Tekirdağ	469,410	335,293	201,176
3	Çanakkale	34,305	24,504	14,702
4	Balıkesir	376,574	268,982	161,389
5	Bursa	251,852	179,894	107,937
6	Yalova	120,161	85,829	51,498
7	Kocaeli	140,032	100,023	60,014
8	Edirne	83,489	59,635	35,781
9	Kırklareli	69,348	49,534	29,721
10	Sakarya	149,608	106,863	64,118
11	Bilecik	35,835	25,596	15,358

In the model, in order to be compatible with real life, it has been considered that hydrogen can be produced with 3 different methods (steam methane reforming, biomass gasification, electrolysis) and it can be stored with 2 different storage methods (compressed gaseous, liquid gaseous). In addition, three different plant capacities as small, medium and large scales are modeled for production and storage facilities in the model, but for the sake of ease of calculation, the capacities of all of them are considered equally for this study. Minimum capacities of production and storage facilities are considered as 10.000 liter and maximum capacities are considered as 960.000 and 540.000 liter respectively.

RESULTS AND DISCUSSION

In Table 2, the number of production and storage facilities that should be opened in each city to meet the demands in all scenarios and the production and storage rate of these facilities according to the scenarios are given.

Table 2:Results of the Stochastic Model

Code	Name of Region	PF	SF	Scenario 1 (%35)		Scenario 2 (%25)		Scenario 3 (%15)	
				PR (kg)	SR (kg)	PR (kg)	SR (kg)	PR (kg)	SR (kg)
1	İstanbul	1	21	960,000	10,884,972	960,000	7,774,980	932,998	4,664,988
2	Tekirdağ	1	5	960,000	2,347,051	445,028	1,676,465	201,176	1,005,879
3	Çanakkale	0	1	0	171,525	0	122,518	14,702	73,511
4	Balıkesir	1	4	410,879	1,882,871	268,982	1,344,908	161,389	806,945
5	Bursa	1	3	616,729	1,259,260	286,757	899,471	107,937	539,683
6	Yalova	0	2	0	600,806	0	429,147	51,498	257,488
7	Kocaeli	1	2	960,000	700,161	830,383	500,115	60,014	300,069
8	Edirne	0	1	0	417,443	0	298,174	35,781	178,904
9	Kırklareli	0	1	0	346,739	0	247,671	29,721	148,603
10	Sakarya	0	2	0	748,039	0	534,313	64,118	320,588
11	Bilecik	0	1	0	179,175	0	127,982	15,358	76,789
Total		**5**	**43**	**3,907,608**	**19,538,042**	**2,791,149**	**13,955,744**	**1,674,689**	**8,373,447**

The results show that the construction of only one generation facility in each of the 5 cities is sufficient to meet the demands in all scenarios. According to the scenarios, the production rates of these production facilities change, and all demands are met by transferring from the opened production facilities to other cities. In order to minimize the cost, it is observed that the cities where production facilities are opened are more centrally located compared to other cities. In storage, the situation is different. In each city, storage of hydrogen up to 5 times of its own demand is mandatory in the model. In the results, it is seen that the number of production facilities opened is suitable for this. The total cost for stochastic model is found as $7,456,550,181.

In order to make comparisons, the model was also run deterministically by considering all scenarios and the results are given in Table 3 where PF and SF denote number of production facilities and number of storage facilities respectively, and cost infer the total cost.

Table 3: Deterministic Model Results

Scenario 1			Scenario 2			Scenario 3		
PF	SF	Cost	PF	SF	Cost	PF	SF	Cost
8	43	7,657,653,280	5	31	5,537,647,495	4	21	3,614,969,962

Deterministic model results show that in scenario 1, where the demand is the highest, the number of production facilities opened is higher than the stochastic model. This is due to the fact that demand is certain to be high, and facilities are opened in various cities to reduce transportation costs as well. In the other scenarios, the number of facilities opened and the cost are unsurprisingly lower than in the stochastic model.

CONCLUSIONS

Hydrogen stands out as a clean energy source today. It is envisaged that this energy source will primarily be used as fuel in vehicles, but there is still uncertainty about what the rate of this will be. These uncertainties affect the investments of countries in hydrogen plant. In order to eliminate these uncertainties, a stochastic hydrogen supply chain has been developed for the Marmara region of Turkey. Although not used in this case, three different sizes of production and storage facilities are discussed in the model. In addition, the model has the capacity to be adapted to the whole of Turkey and it is aimed to do this in future studies.

REFERENCES

1. Ritchie H. and Roser M. 2017. Fossil Fuels. https://ourworldindata.org/fossil-fuels
2. Momirlan M. and Veziroglu TN. 2002. Current status of hydrogen energy. Renewable and sustainable energy reviews 6(1-2):141-179.
3. Acar C. and Dincer I. 2014. Comparative assessment of hydrogen production methods from renewable and non-renewable sources. International journal of hydrogen energy 39(1): 1-12.
4. Dincer I. 2002. Technical, environmental and exergetic aspects of hydrogen energy systems. International journal of hydrogen energy 27(3): 265-285.
5. Almansoori, A. and Shah N. 2009. Design and operation of a future hydrogen supply chain: multi-period model. International journal of hydrogen energy 34(19):7883-7897.
6. Almansoori, A. and Shah N. 2012. Design and operation of a stochastic hydrogen supply chain network under demand uncertainty. International journal of hydrogen energy 37(5):3965-3977.
7. Dayhim M., Jafari M. A. and Mazurek M. 2014. Planning sustainable hydrogen supply chain infrastructure with uncertain demand. International Journal of Hydrogen Energy 39(13):6789-6801.
8. Câmara D., Pinto-Varela T. and Barbósa-Povoa AP. 2019. Multi-objective optimization approach to design and planning hydrogen supply chain under uncertainty: A Portugal study case. Computer Aided Chemical Engineering 46:1309-1314.
9. Ruiz PA., Philbrick CR. and Sauer PW. 2009. Modeling approaches for computational cost reduction in stochastic unit commitment formulations. IEEE Transactions on Power Systems 25(1): 588-589.
10. Güler M. G., Geçici E.and Erdoğan A. 2021. Design of a future hydrogen supply chain: A multi period model for Turkey. International Journal of Hydrogen Energy, 46(30): 16279-16298.

WHEC-2022
23rd World Hydrogen Energy Conference
June 26-30, 2022 - Istanbul

#1470
ASSESSMENT OF HYDROGEN DELIVERY OPTIONS

[1*] *Eveline Weidner,* [2] *Francesco Dolci,* [3] *Rafael Ortiz Cebolla,* [4] *Alessandro Arrigoni*
[1-4] European Commission Joint Research Center, Westerduinweg 3, 1755 LE Petten, Netherlands

*Corresponding author e-mail: Eveline.Weidner@ec.europa.eu

ABSTRACT

The transport of hydrogen will be a key enabler for the widespread use of renewable hydrogen in Europe. To achieve the goals of the European Hydrogen Strategy [1] it is important to understand whether it is cost effective to produce renewable hydrogen where renewable electricity is cheap and then to transport the hydrogen to the customer, or it is better to produce the renewable hydrogen close to the demand location. JRC has performed a comprehensive study regarding the transport of hydrogen, in terms of costs and energy demand. The study reveals that there is no single optimal hydrogen delivery solution across every transport scenario. The most cost effective way to deliver renewable hydrogen depends on distance, amount, final use, and whether there is infrastructure already available. For distances compatible with the European territory, compressed and liquefied hydrogen solutions, and especially compressed hydrogen pipelines, offer lower costs than chemical carriers do. Chemical carriers become more competitive the longer the delivery distance (due to their lower transport costs) and open up import options from suppliers located, for example, in Chile or Australia.

Keywords: Hydrogen delivery, Hydrogen export, Hydrogen import

INTRODUCTION

The European Hydrogen strategy recognises the important role [1] the transport of hydrogen will have in enabling the penetration of renewable hydrogen in Europe in the future, and explicitly mentions the import of hydrogen from outside Europe. JRC is assessing the costs and energy demand of hydrogen transport and distribution for various volumes and distances, allowing for a semi-quantitative ranking of transport options for hydrogen within the chosen set of assumptions [2]. The study considers transport of compressed or liquefied hydrogen, but also by means of liquid hydrogen carriers such as ammonia, methanol or liquid organic hydrogen carriers (LOHC). Each option offers different advantages, for example a good hydrogen storage density (e.g. NH3, MeOH or LOHC) or better round-trip efficiency (e.g. compressed or liquefied gas). The assessment covers the transport of hydrogen to the demand location through various means, the main options being pipelines, ships, trains or trucks.

GOAL AND SCOPE

The goal of this study is to answer the question whether it is more convenient to produce renewable hydrogen close to the demand location or to transport it from a location where renewable hydrogen production is cheaper. A second point we looked into is how long the transport route can be for the cost of hydrogen to still be cost competitive. To provide these answers a comprehensive analysis of the energy demand and costs involved in the delivery chain for the supply of renewable hydrogen has been performed.
A case study (Case A) investigated the cheapest option to transport hydrogen for the delivery of one million tonnes of green hydrogen per year to an industrial plant in Northern Europe. The transport distance considered for shipping is 2,500 km. The end-user site is assumed to be close to the port. A second case study (Case B) assessed a more complex delivery route, involving trucks and rails transport, and a lower amount of hydrogen to be transported (100 000 tH2/a). The delivery is expected to take place in a timeframe of 2030+.

This study considers that the delivery chain comprises the key processes and equipment necessary for the delivery of hydrogen from the production site to the demand/use location(s) (see Figure 1). The delivery chain can be divided in three main segments: i) the “packing”, where hydrogen is prepared for its transport; ii) the transport itself; and iii) the “unpacking”, where hydrogen is prepared for its final use. Across each step of the delivery chain, a storage facility is assumed to enable a smooth transition. Since the focus of this study is the delivery stage, the production of hydrogen and its final use are considered to be outside of the scope.

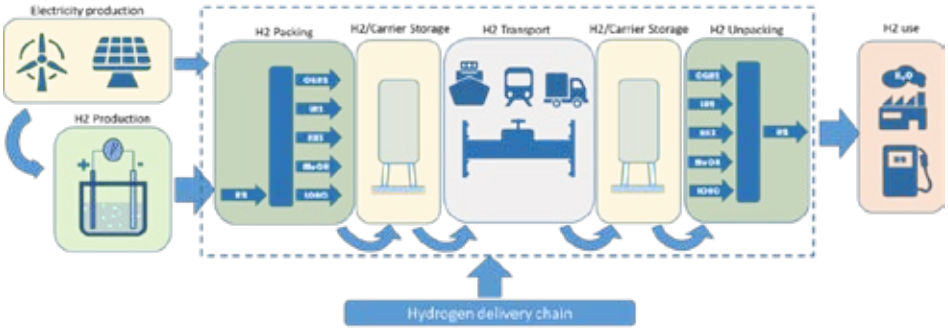


Fig. 1. Delivery chain elements

Figure 1 depicts the delivery chain elements considered in our study. Our analysis refers only to the elements within the dotted line.

The delivery chain options considered for this study are strictly related to the form in which hydrogen is transported (i.e., the 'packaging' mode). Five packaging modes are considered: compressed hydrogen (CGH2), liquefied hydrogen (LH2), ammonia (NH3), methanol (MEOH), with CO2 from Direct Air Capture (DAC), and Liquid Organic Hydrogen Carrier (LOHC) in the form of dibenzyltoluene (DBT). For LOHC, electricity, waste heat and hydrogen for providing the heat for dehydrogenation were assessed.

METHODOLOGY

The starting point of this analysis was gathering information regarding costs and energy demand coming from public literature and in some cases private companies. For several components and technologies of the hydrogen delivery chain, industry experts were consulted to provide information regarding costs and other key parameters.

The figures from literature sources are complemented by assumptions and extrapolations required to model large capacities, or a technology not characterized well enough by the sources collected. Calculations have been performed when the information available in literature was insufficient. One example is pipelines, where literature sources often were in disagreement and provided a wide range of costs.

To assess what difference electricity costs make, two scenarios are explored: (1) Low price (Lo), with a production site electricity cost of EUR 10/MWh and a consumption site electricity cost of EUR 50/MWh; (2) High price (Hi), with a production site electricity cost of EUR 50/MWh and a consumption site electricity cost of EUR 130/MWh. For case A (industrial use of hydrogen), waste heat at 300°C is assumed to be available, at a cost of EUR 20/MWh.

Any hydrogen delivery pathway is broken down into simple constituent individual steps (see Figure 1, i.e. hydrogen storage, hydrogen transport, conversion plants at production and delivery points, purification, compression), and the energy demand and costs assessed for each.

RESULTS

Hydrogen delivery costs obtained for case A (see Figure 2) indicate that transport options based on compressed gas (by ship or by pipeline) are the most cost competitive solution, alongside LOHC by ship if waste heat is available at the assumed price. Liquefied hydrogen transported by ship has a similar cost, within the margin of error. A more distributed delivery scenario involving smaller quantities of hydrogen (case B) leads to different conclusions. Transport and storage costs increase significantly in this scenario, in particular penalising the packaging solutions with lower gravimetric density (i.e. compressed hydrogen). Liquefied hydrogen therefore appears as the cheapest option for the scenario considered here.

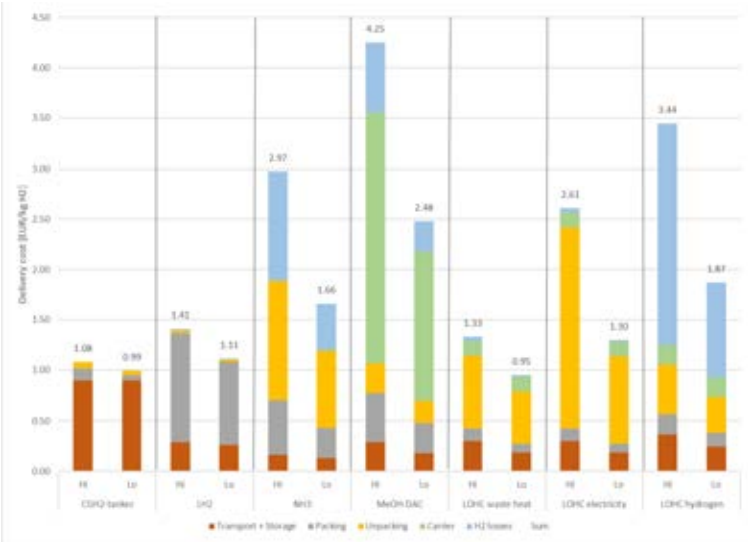


Figure 2 Hydrogen delivery costs. Hi(gh) and Lo(w) electricity prices are shown for each carrier.

CONCLUSIONS

The outcome of the study is that there is no single optimal hydrogen delivery solution across every transport scenario. The most cost effective way to deliver renewable hydrogen depends on distance, amount, final use, and whether there is infrastructure already available.

For distances compatible with the European territory, compressed and liquefied hydrogen solutions, and especially compressed hydrogen pipelines, offer lower costs than chemical carriers do. By contrast, chemical carriers become more competitive the longer the delivery distance (due to their lower transport costs) and open up import options from suppliers located, for example, in Chile or Australia.

Unpacking chemical carriers accounts for a significant share of their total cost, mostly due to the processes' high energy demand and the fact that unpacking plants are likely to be placed in locations with a relatively high electricity price. Optimization of unpacking processes has a key role to play in increasing the competitiveness of the chemical carrier pathways.

REFERENCES

1. "Communication COM/2020/301: A hydrogen strategy for a climate-neutral Europe," 2020.
2. R. Ortiz Cebolla, F. Dolci, and E. Weidner, "Assessment of Hydrogen Delivery Options," JRC124206, 2021.

Views expressed are those of the authors and do not reflect an official position of the European Commission

WHEC-2022
23rd World Hydrogen Energy Conference
June 26-30, 2022 - Istanbul

#1485

TECHNO-ECONOMIC AND PROCESS SIMULATION OF SMALL-SCALE HYDROGEN PRODUCTION FROM NH_3 DECOMPOSITION

[1]*Mostafa El-Shafie
[1] Gifu University, Environmental and Renewable Energy Systems Division, Graduate School of Engineering, 1-1 Yanagido, Gifu, 501-1193, Japan.

*Corresponding author e-mail: mostafaelshafie81@gmail.com

ABSTRACT

In this study, two proposed configuration plants were designed and simulated for the production of high-purity hydrogen at a rate of 25 kg_{H2}/day from blue ammonia. In configuration A, hydrogen was generated in a membrane reactor, while in configuration B, NH_3 decomposition and H_2 separation were carried out in an integrated catalytic membrane reactor. The performance of both hydrogen production plants was evaluated under different operating conditions. A pure palladium membrane with a thickness of 20 µm was utilized for pure hydrogen production. Configuration B was more energy efficient than configuration A. The hydrogen flow rate was evident with the increase in feeding pressure from 0.1 MPa to 0.3 MPa. The total H_2 production cost of configuration A was 5.33 €/kg_{H2} and that of configuration B was 5.05 €/kg_{H2}. Since the proposed plant configurations generated hydrogen and nitrogen, the total cost of production was distributed between them. The final H_2 and N_2 separation costs of configuration A was 4.21 €/kg_{H2} and 0.95 €/kg_{H2}, and configuration B was 3.94 €/kg_{H2} and 0.90 €/kg_{H2}. It can be also considered that the ammonia synthesis pathway controlled the ammonia prices and subsequently the hydrogen production cost.

Keywords: Hydrogen separation, Ammonia decomposition, Energy efficiency, Permeation rate

INTRODUCTION

Renewable energy sources combined with traditional ones are garnering interest because of their lower average prices. It is expected that in the upcoming years, renewable energy utilization trend will continue to increase [1]. However, the higher productivity and reliability of the application must be investigated to ensure its stability. Hydrogen can be generated by different technologies, such as water electrolysis and steam reforming [2, 3]. Hydrogen production from water electrolysis offers green products that overcome several compelling issues. Hydrogen is considered to have a unique potential for decarbonising different energy-consuming sectors. Indeed, hydrogen can be seen as a potential renewable energy vector that can be transferred to high demand sites [4]. In this study, a small-scale (25 kgH_2/day) hydrogen production plant using catalytic NH_3 decomposition was evaluated. Two ammonia decomposition systems (pre-catalytic and integrated ammonia decomposition systems) were designed to investigate the best method for hydrogen production at a low cost. The decomposition process of blue ammonia was carried out at low-pressure of 0.3 MPa and maximum temperature of 500°C. Pure hydrogen was separated using palladium membrane and PSA unit was used for nitrogen (N_2) gas separation. NH_3 decomposition processes were simulated using the CHEMCAD program. The effects of operating parameters, such as feeding pressure, NH_3 flow rate, and temperature, were analyzed. Techno-economic evaluation studies were conducted and compared for both systems.

Proposed NH_3 decomposition systems

Two ammonia decomposition system configurations were designed to evaluate small-scale hydrogen production. A good ammonia cracker system should include heat and mass transfer as well as process materials. A detailed blue ammonia cracker design is important for total heat duty calculations, which also results in a more accurate economic assessment. Blue ammonia is decomposed in the catalytic reactor, and the resulting hydrogen is separated using a Pd- membrane foil in another membrane reactor. The palladium and palladium-based alloys membranes have the ability to separate H_2 with high purity.

Configuration A

In this process simulation, the catalytic ammonia and membrane separation reactors were simulated using the CHEMCAD program. Two separate reactors were used for pure hydrogen production in the current ammonia configuration cracker. The process flow layout of the pre-catalytic system, named configuration A, is shown in Figure 3. The first reactor was utilized to decompose ammonia into hydrogen and nitrogen gases, while the second reactor was a membrane reactor used for hydrogen separation. The required heat is generated from the NH_3 combustion reactor (7), and ammonia and hydrogen were utilized as fuel. Combustion air, feeding NH_3, non-reactive ammonia, and hydrogen were mixed before being injected into the combustion reactor. The decomposition process of ammonia was performed at a low temperature and pressure of 500°C and 0.3 MPa, respectively. Heat exchangers were used for preheating the combustion air and ammonia before feeding into the catalytic reactor. In addition, the product

gases from the ammonia decomposition reactor were cooled to 350°C before entering the membrane reactor. The hydrogen permeance of the Pd- membrane thickness of 20 μm was adjusted at 2 × 10^{-6} mol/m²/s/Pa. The operating pressure was 0.3 MPa on the retentate side while the permeate pressure was 100 mbar. The separation process of hydrogen gas from the membrane reactor was operated at a temperature of 350°C and a vacuum pump was used to generate the driving force for the permeation. Nitrogen (N_2) gas was separated using a PSA unit, while the remaining non-reactive ammonia and hydrogen were mixed with ammonia fuel. The reason for decomposing ammonia in a separate reactor is to exploit the total membrane surface area for higher permeability of hydrogen gas. However, the ammonia decomposition and hydrogen separation processes are combined in one reactor, which is expected to lead to a decrease in the hydrogen permeation rate because of the presence of catalytic materials and a high ammonia decomposition temperature.

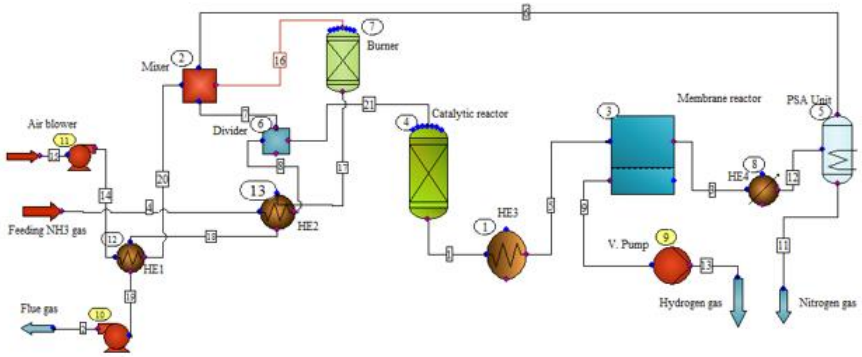


Fig. 1. Configuration A process flow layout.

Configuration B

Figure 2 depicts the integrated NH_3 decomposition system, named configuration B. In this simulation analysis, the decomposition of NH_3 gas was carried out at atmospheric pressure and a temperature of 450°C. The Pd- membrane was designed to be installed in the same ammonia catalytic reactor. Configuration B shows two separate reactors designed to operate under the same conditions as those for the simulation analysis. Indeed, both reactors were combined as integrated reactors that include both reactor functions. The retentate pressure was adjusted to 0.3 MPa, while a vacuum pump was installed at the hydrogen permeation side to generate a pressure of 100 mbar. Hydrogen separation and purification occurred inside the integrated catalytic reactor, while the retentate stream was cooled down and then passed to the PSA unit for nitrogen separation. The outlet gas flow stream from the PSA unit was fed to mix with the NH_3 fuel and then passed into the combustion reactor. The combustion air was preheated by the outlet high-temperature combustion product gases.

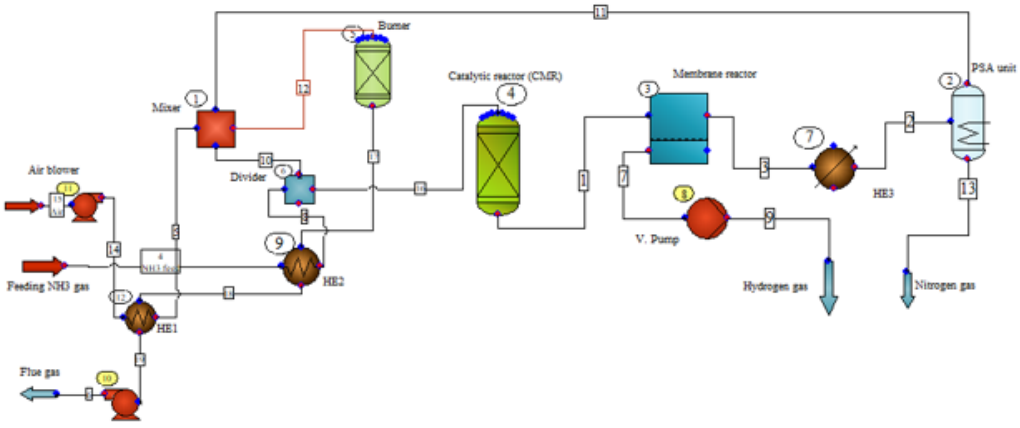


Fig. 2. Configuration B process flow layout.

RESULTS AND DISCUSSION

The hydrogen and nitrogen production costs for both configurations are shown in Figure 3. The results showed that the total hydrogen production cost of configuration A is greater than that of configuration B. Although the energy consumption is an important factor in cost estimation, the total cost of configuration B is high. The cost of blue ammonia as the main feedstock is considered as the main parameter controlling the hydrogen production cost. The total H2

production cost of the proposed hydrogen production system using configuration A was 5.33 €/kgH2, while that of configuration B was 5.05 €/kgH2. The hydrogen production cost using different ammonia types are compared in Figure 4. The results of the H_2 production cost from using gray ammonia as a raw material has lower economic results than the blue and green ammonia. The hydrogen production cost from the advanced NG steam reforming process with CCUS is higher than the NH_3 synthesis without the CCUS because the ammonia price is influenced by NH_3 as raw material cost.

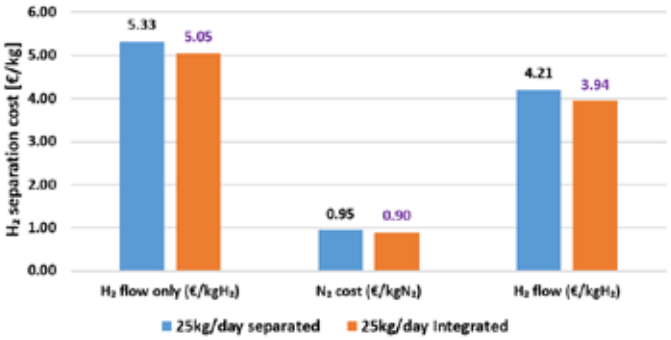


Fig. 3. Comparison of hydrogen separation cost of both systems.

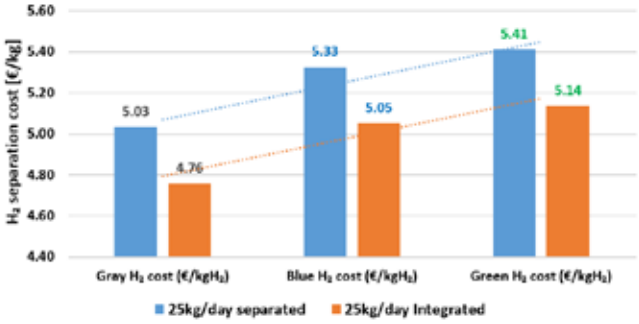


Fig. 4. The 25 kg/day hydrogen production cost from different NH_3 types.

CONCLUSIONS

A techno-economic analysis of pure hydrogen production from green ammonia was performed. Two proposed configuration systems were successfully designed and simulated for small-scale hydrogen production (25 kgH_2/day). It was found that the energy efficiency of the integrated system was higher than that obtained from separated system configuration A. The produced hydrogen flow rate and energy efficiency were enhanced with the increase in pressure from 0.1 to 0.3 MPa. A metal-based membrane was utilized to produce high-purity hydrogen. A techno-economic assessment was carried out for both suggested small-scale hydrogen production from blue ammonia. It was found that the total H_2 production cost of the proposed hydrogen production system using configuration A was 5.33 €/kgH_2, and that of configuration B was 5.05 €/kgH_2. The proposed plant configurations generated hydrogen and nitrogen; therefore, the total cost was distributed for hydrogen and nitrogen production. The H_2 and N_2 costs of configurations A and configuration B are 4.21€/kgH_2 and 0.95€/kgH_2, and 3.94€/kgH_2 and 0.90€/kgH_2, respectively.

REFERENCES

1. Average auction price by project commissioning date, 2012- 2022 e charts e Data & Statistics. IEA, https://www.iea.org/ data-and-statistics/charts/average-auction-price-by-projectcommissioning-date-2012-2022.
2. M. El-Shafie, S. Kambara, Y. Hayakawa, Hydrogen Production Technologies Overview. Journal of Power and Energy Engineering 7(2019) 107-154.
3. J. D. Holladay, J. Hu, D. L. King, Y. Wang, An overview of hydrogen production technologies, Catal. Today 139 (2009) 244-260.
4. Christensen CH, Johannessen T, Sørensen RZ, Nørskov JK. Towards an ammonia-mediated hydrogen economy? Catal Today Jan. 2006;111(1):140-4.

WHEC-2022
23rd World Hydrogen Energy Conference
June 26-30, 2022 - Istanbul

#1525

TECHNO-ECONOMIC ANALYSIS OF 350 BAR LOHC-SUPPLIED HYDROGEN REFUELING STATIONS FOR HEAVY DUTY VEHICLE FLEETS

[1*] *Stefan Aschbrenner,* [2] *Tobias Eissler,* [3] *Marius Schneider,* [4] *Christopher Voglstätter*
[1,2,3,4] Fraunhofer Institute for Solar Energy Systems ISE, Heidenhofstrasse 2, 79110 Freiburg, Germany

*Corresponding author e-mail: stefan.aschbrenner@ise.fraunhofer.de

ABSTRACT

The cost of hydrogen at a refueling station depends mostly on two factors, the hydrogen production itself and the hydrogen supply chain. For both there are different options with LOHC that are in the focus of several scientific discussions. The aim of this work is to contribute to this discussion a techno-economic comparison of a 350 bar Liquid Organic Hydrogen Carrier (LOHC)-supplied hydrogen refueling station (HRS) with a standard HRS. The analysis was focused on supplying hydrogen for a fleet of busses or trains with a total daily hydrogen demand of around 1.2 t/d. A dehydrator required to release the hydrogen from the LOHC as well as other standard components of an HRS were dynamically modelled and optimised depending on various demand profiles of the vehicle fleets using the inhouse simulation software H2ProSim. The results show specific refueling costs (HRS only) of between 2.1 €/kg and 3.3 €/kg for the LOHC-HRS scenarios investigated and a minimum of 0.89 €/kg can be obtained for a standard HRS. This cost difference is mainly caused by the high energy cost of the dehydrator and the added CAPEX. Furthermore, a smart demand management on the vehicle side can lead to significant cost reductions for the HRS infrastructure.

Keywords: Hydrogen Refueling Station, LOHC, Compressed Hydrogen, Refueling Cost

INTRODUCTION

To the present day more than 90% of the energy used in the mobility sector in germany is fossil based [1]. Solutions for the conversion of this sector to low-or zero carbon energy carriers need to be provided promptly to meet the ambitious CO_2 reduction targets for vehicle fleets. Electric batteries, hydrogen and synthetic fuels take up the challenge to replace fossil fuels in transportation. Hydrogen offers a compromise in terms of energy density and tank-to-wheel efficiency. Adding a given predictability in fuel demand especially Heavy Duty Vehicles (HDV), such as regional fuel-cell buses and trains are promising first applications [2]. For these applications, hydrogen refueling stations are required. With almost one hundred stations up and running in Germany alone, the most common HRS design is based on the supply of CGH2 for passenger cars, and consequently with small capacities (kg/d) [3]. To supply HDV fleets an upscaling of the HRS in terms of capacity is crucial. In this context, hydrogen transport via CGH2 trailer is facing capacity limitations. The use of Liquid Organic Hydrogen Carriers (LOHC) is analysed to be economically advantageous, regardless of distance, especially for the transport and storage of quantities of up to 10 tH2/d [4]. In this context the objectives of this publication are to provide novel insights into cost structures of a LOHC-HRS, identifying cost drivers and technical limitations, evaluating economical feasibility and analyse the footprint of such HRS infrastructures – all analysis in comparison to CGH2-HRS as the current standard approach to hydrogen refueling. The work was carried out as part of the Kopernikus P2X project, which aims to create a synergy between industry, academia and civil society on the subject of energy transition, whereby the subproject P2X includes research on the conversion of renewable electricity into gaseous or liquid energy carriers, plastics and chemicals.

MODELING APPROACH

First of all, a basic design of a LOHC-supplied hydrogen refueling station for a fleet of buses or trains with a tank pressure of 350 bar and a daily demand of 1200 kg_{H2} was created. A process flow schematic of the design is displayed in Figure 1.

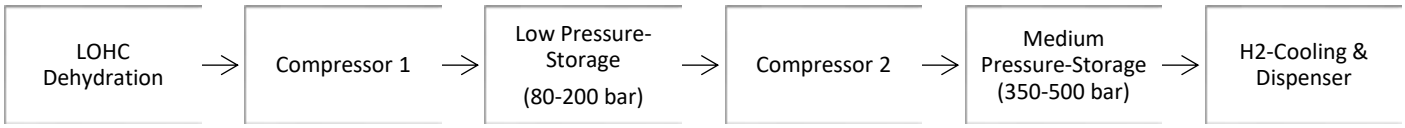


Figure 1. Process flow schematic of the basic LOHC-HRS design

According to this basic design, a dehydrator required to release the hydrogen from the LOHC as well as other HRS components, such as compressors, storage tanks and dispensers were modelled using the inhouse simulation software H2ProSim. Additionally, several refueling profile scenarios of the vehicle fleets were created (Table 1).

Table 1. Overview of the refueling profile scenarios

	Busses 1	Busses 2	Trains	Trains & Busses	Busses 3	Busses 4
H2 demand [kg/d]	1200	1200	1320	1210	~853	~494
Refueling profile	20x busses backtoback, two time slots / day	2x busses backtoback / 72 min	1x train / 8 h	1xTrain / 12 h + 1xBus / 2 h	Real dynamic profile, 7 days	Real dynamic profile, 28 days

Following a bottom-up cost approach depending on the optimized design parameters of the HRS components, the CAPEX and OPEX are determined via a cost model based on own cost data and functions, which is based on quotations from manufacturers. The technological part of the model is based on a dynamic thermodynamical simulation of the main components. (see Figure 1); for each demand scenario rated compression capacity of the compressors and volume of the storage tanks were optimized via a genetic algorithm with the optimisation objective minimum specific refueling cost for the whole HRS model. The calculation of the hydrogen refueling costs is carried out using the annuity method. The gas price was assumed at 0.045 €/kWh and the electricity price at 0.178 €/kWh. For one of the scenarios, rough footprints of the LOHC-HRS and a classic HRS design were calculated by a foot printanalysis tool of H2ProSim by utilizing footprint data of the individual components including German regulations concerning hazard zones and fire safety measures.

RESULTS AND DISCUSSION

The results in Figure 2 show specific refueling cost for the 350 bar CGH_2 trailer supplied HRS of 0.89 €/kg_{H2} and significantly higher cost of 2.39 €/kg_{H2} for the LOHC based solution, both for the same vehicle fleet and demand profile. For the LOHC-supplied HRS (left), OPEXs are dominated by energy costs (approx. 85-90 %), followed by maintenance costs of the dehydration system (approx. 5-10 %). As a result, energy supply costs also account for almost 50 % of the specific refueling costs. Thereby, half of the energy supply cost comes from heating the dehydrator and the other half is from the required electrical energy for the compression. Two other cost drivers are the LOHC dehydrator and compressor CAPEX (both 18% share). The high share of the H2 storage costs in the 350 bar trailer supplied HRS reflects the need for large storage volumes to supply the demand of the vehicle fleet at all time, which is chosen by the optimization algorithm due to the low part load capability of the dehydrator and its high costs.

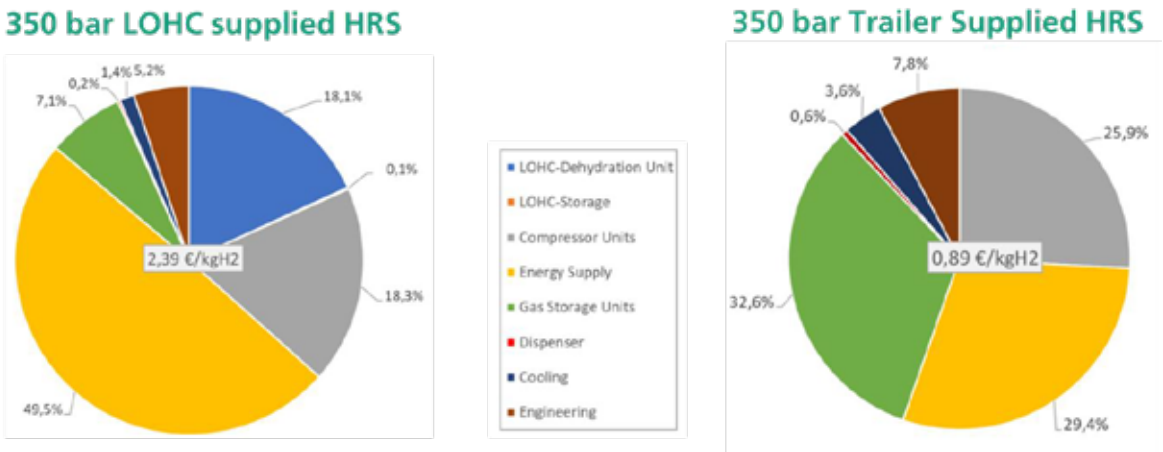


Figure 2. Comparison of the specific refueling cost [€/kgH2] and cost structure of LOHC supplied HRS (left) and conventional supply by CGH2 trailer (right), 1200 kg_{H2}/d

A total footprint of 738 – 1005 m² depending on the placement of fire protection walls for the 350 bar LOHC refueling station and data from literature states a footprint of 734 – 894 m² for the CH2 trailer supplied HRS [5]. From both values it could be deduced that the benefit of placing LOHC-storage tanks underground could be reduced or nullifiedby the space requirements for the dehydrator system. However, it must be mentioned that the footprint calculations represent a rough estimation and is not based on a detailed installation plan. Figure 3 displays the results of a sensitivity analysis of different refueling profiles, based on the investigated vehicle fleets, for the LOHC-HRS.
Figure 3 shows the impact of different refuelling profiles on hydrogen refuelling costs for the LOHC based refuelling stations. A more evenly distribution of the refuelling processes over time instead of concentrating the refuelings in two time slots results in lower CAPEX, since the HRS components can be dimensioned smaller, their utilization can be increased and thus the coupling with the rather continuous H_2 release from the LOHC dehydration process

improved. This CAPEX advantage reflects in the specific refuelling costs and can reach a difference of up to 0.5 €/kg_{H2} between scenarios with the same daily H_2 demand. The train scenario or a combination of trains and bus fleet offers slight cost advantages compared to the bus fleet scenarios due to better utilization of the LOHC-HRS components and smaller compressors required. It also causes higher costs for 500bar storage due to the large tank sizes (up to 2 x 94kg) compared to busses (roughly 34 kg) which required large storage for refueling in the required time.

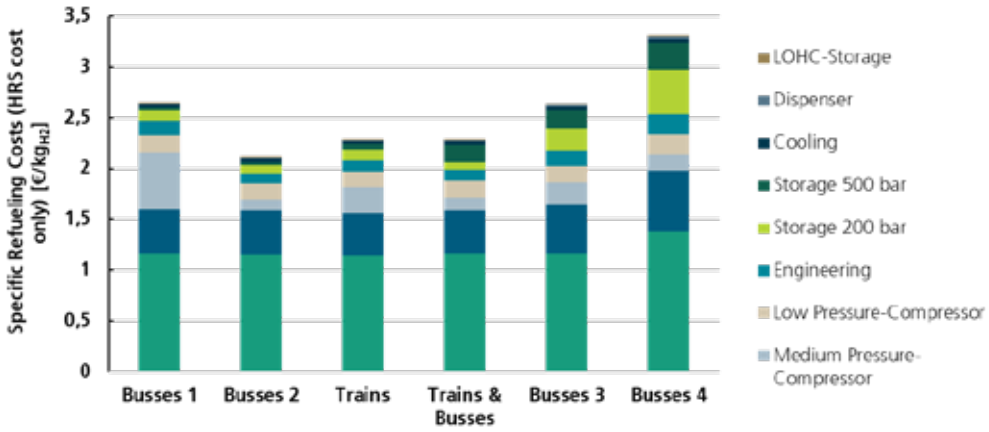


Figure 3. Results of the sensitivity analysis of different refueling profiles for a LOHC-based HRS

CONCLUSIONS

Looking only at the cost of a 350 bar HRS, a solution based on H_2-supply via LOHC is not economically competitive to a CGH_2-trailer supplied HRS in the assumed scenarios. However, the picture can change if the whole H_2 supply chain including preconditioning and transport would be part of the scope as well. Furthermore, it becomes clear that measures to reduce the energy demand for dehydration are crucial. Research activities in this direction are being undertaken and include the usage of LOHC materials with improved properties, such as Benzyltoluene (BT) and heat integration solutions. A smart refuelling strategy of a vehicle fleet can have a significant impact on the specific refuelling costs of a LOHC-HRS. Considering the estimated footprints and the fact that bus depots are preferably placed in inner city locations with high prices for land, costs for their expansion by adding HRS infrastructure can be significant.

ACKNOWLEDGEMENT

This work was funded by the German Federal Ministry of Education and Research (Bundesministerium für Bildung und Forschung - BMBF) in the framework of the Kopernikus P2X Project.

REFERENCES

1. https://www.umweltbundesamt.de/publikationen/erneuerbare-energien-in-deutschland-2021 Accessed on April 13, 2022
2. https://h2.live/. Accessed on April 14, 2022
3. McBain S, Teter J: https://www.iea.org/reports/tracking-transport-2021 Accessed on April 13, 2022
4. Reuss, ME: Techno-economic analysis of hydrogen infrastructure alternatives. Jülich: Zentralbibliothek, Verlag, 2019
5. Kupferschmid S, Hof E: Einführung von Wasserstoffbussen im ÖPNV. URL https://www.now-gmbh.de/wp-content/uploads/2018/12/NOW-Broschuere_Wasserstoffbusse-im-OePNV.pdf – Accessed on April 13, 2022

WHEC-2022
23rd World Hydrogen Energy Conference
June 26-30, 2022 - Istanbul

#1562
EVALUATION OF POTENTIAL HYDROGEN PRODUCTION METHODS IN TURKEY BY USING A HYBRID METHOD BASED ON PYTHAGOREAN FUZZY AHP AND INTERVAL TYPE-2 FUZZY TOPSIS

[1]Aytaç Yıldız, [2] Yunus Demir, [3] Gürkan Işık*
[1,2] Department of Industrial Engineering, Bursa Technical University, 16310, Bursa, Turkey
[3] Department of Business Development, Valuable Touch Energy Services, 41275, Kocaeli, Turkey

*Corresponding author email: yunus.demir@btu.edu.tr

ABSTRACT

Hydrogen is a promising energy storage and generation alternative to ensure that renewable energy sources are available to meet all energy needs in the long term. Many factors should be considered for sustainability of the environment while designing a hydrogen supply chain which consists of different production, storage, and transportation methods. Hydrogen energy is a new and innovative area especially for developing countries, so there can be high uncertainty during the decision process because of lack of expertness. In this study, available hydrogen production alternatives of Turkey are evaluated by using an integrated Pythagorean fuzzy AHP and interval type-2 fuzzy TOPSIS based methodology by considering technical, economic, environmental, and social aspects.

Keywords: AHP, Hydrogen production, Interval type-2 fuzzy set, Pythagorean fuzzy set, TOPSIS.

INTRODUCTION

Energy consumption overall the world is increasing day by day. Therefore, renewable energy (RE) sources gained importance for providing sustainable environment. However, the energy production capacity of the RE power plants are fluctuating because of the environmental dependencies of them. This issue hinders to trust the RE sources to handle the basal electricity demand. Hydrogen is a promising energy storage alternative that gives ability to transport with different techniques to use for different purposes. Hydrogen energy can be produced from multiple clean sources. It can also be produced from fossil fuels, which is an important advantage in making the hydrogen a sustainable energy storage method for the gradual transition to clean energy sources.

In recent years, research on hydrogen energy (HE) has gained momentum in Turkey as well as in the world [1]. As a comprehensive study, Hydrogen Technologies Association published a hydrogen technology (HT) roadmap report in 2021 explaining hydrogen production, storage and transportation techniques and presenting a future projection for potential usage area in Turkey [2]. Turkey has high potential for rapid dissemination of hydrogen energy because Turkey holds 72% of the total boron reserves of the world and the boron minerals can be used for carrying hydrogen [3] and has the largest geothermal energy resources in Europe [4]. There are several studies investigating the natural resources of Turkey in the direction of hydrogen production capabilities. Karayel et al. analyzed the green hydrogen production potential of the cities of Turkey with solar energy [5] and wind energy [6]. Genç et al. [7] evaluated four locations in terms of their hydrogen production capacities via electrolysis (ELE) systems supplied by wind energy. Uysal et al. [8] focused on the hydrogen production from the ELE of water by comparing the potential of the coastal seas, biggest lakes, and rivers. Coşkun et al. [9] examined the annual biogas and hydrogen production potential of Turkey from a milk-processing wastewater. Eroğlu et al. [10] conducted a comparative study with four olive mill wastewater types to investigate the hydrogen gas production amounts of them.

Hydrogen energy investments should be made by considering the accordance with multiple factors such as international standards and the environmental effects, cost, and technical restrictions. The expertness and the operating experience about HT are not sufficient in Turkey so the decisions about HT investments include high uncertainty. The traditional uncertainty modeling approaches may not yield applicable decisions about the HT investments because of the high uncertainty. In this study, the best hydrogen production alternative is decided by using a hybrid Pythagorean fuzzy AHP and interval type-2 fuzzy TOPSIS based methodology to be able to model high certainty in MCDM process.

MATERIALS AND METHODS

Decisions about HE investments include high uncertainty because of lack of expertness and environmental factors. FST is the most popular approach for modeling the uncertainties of real-life problems. In FST, the uncertainty is modeled with the membership degree concept. A set element can be both member and non-member of the set partially at the same time [11]. It should be noted that the use of Fuzzy Set Theory (FST) in multi-criteria decision making (MCDM) has provided important breakthroughs [12]. The study aims to decide the best hydrogen production method in Turkey by considering the uncertainty. An integrated two-stage methodology has been developed to

evaluate the hydrogen production alternatives depending on multiple criteria. Steps of the methodology are seen in Fig. 1. In the first stage of the methodology, weights of the criteria are decided by using Pythagorean fuzzy AHP and the alternatives are ranked by using interval type-2 fuzzy TOPSIS in the second stage.

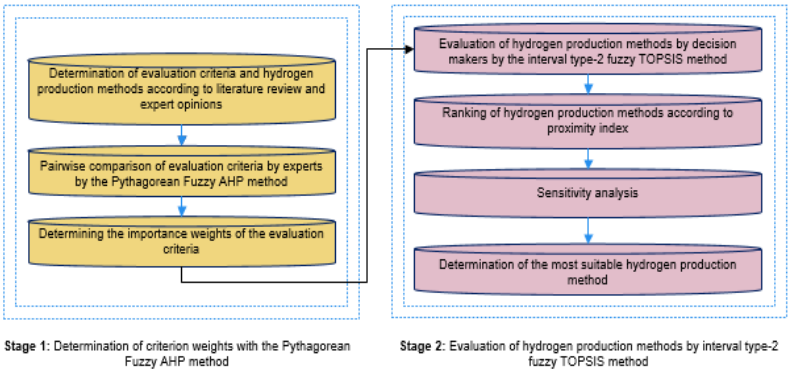


Fig. 1. Methodology

Pythagorean Fuzzy AHP

Traditional Fuzzy Sets (FSs) may not fully address the uncertainties related to decision making. Pythagorean FS (PFS), proposed by Yager [12] as an extension of Intuitionistic FS (IFS) to handle the uncertainties having indeterminacy and inconsistency about the evaluations. Owing to these advantages, it has begun to be applied to MCDM problems [13, 14]. AHP is brought to the literature by Thomas L. Saaty [15] as one of the MCDM methods. AHP facilitates the decision-making process by systematizing the assessment of alternatives' suitability to the criteria. In this way, decision makers can determine the best alternative in terms of satisfying the criteria. It also increases the decision maker's understanding and knowledge of the problem definition and components [16]. However, there are some limitations about the full reflection of human thoughts to the decision process in AHP. Fuzzy AHP has emerged by combining a concept of AHP and FST to eliminate this limitation. Instead of the deterministic evaluations of traditional AHP, the comparison ratios are determined as a series of values in fuzzy AHP. Then, PFSs were also integrated to AHP to gain the advantages of PFS theory to the decision process. In this methodology, decision makers use linguistic terms that are representing Pythagorean fuzzy numbers, which provide the ability to make more flexible assessments, rather than just assigning a precise number for evaluations [17].

Interval Type-2 Fuzzy TOPSIS

If the parameters of the uncertainty are determined faultlessly, traditional FSs can be preferred for modeling. However, the characteristics of the uncertainty can be complicated, and its parameters may not be determined easily in some real case problems such as decision making in a highly innovative field. Zadeh proposed Type- 2 FSs (T2FSs) to make it possible to model high uncertainties in which the uncertainty parameters are also uncertain variables [18]. Traditional FSs have two-dimensional membership function, while type-2 fuzzy sets are three-dimensional, and this third dimension provides additional flexibility in uncertainty modeling [21]. Nevertheless, the difficulty of making evaluations and calculations with such detailed data increases significantly. Therefore, Mendel et al. [19] extended the T2FS concept by integrating with interval-valued numbers to reduce the complexity of the operations, and proposed Interval Type-2 Fuzzy Sets (IT2FSs) whose membership function parameters are interval-valued numbers. Membership degrees are defined by a subrange in [0, 1] interval, rather than a single value as T1FS so the decision maker has more flexibility while assigning membership degrees. In this way, flexibility is almost preserved, while providing ease of operation compared to T2FS [20]. Because of these advantages, IT2FSs are widely used in MCDM problems in the literature. One of the most popular MCDM techniques is fuzzy TOPSIS in the literature that was developed by Hwang and Yoon [22]. Fuzzy TOPSIS also has limitations about representing the uncertainties because of being developed based on traditional fuzzy sets [23]. Chen and Lee [24] proposed interval type-2 fuzzy TOPSIS method to enable more realistic and flexible evaluations [25]. Decision makers have the opportunity to make assessments more freely without being too constrained by the method. Such a relaxation allows obtaining more reliable results in the cases where uncertainty is high.

Evaluation of Hydrogen Production Methods

As a preliminary step of the study, success factors for evaluation of hydrogen production methods were decided based on the literature review and the opinion of 3 experts and the criteria set was decided as shown in Fig. 2.

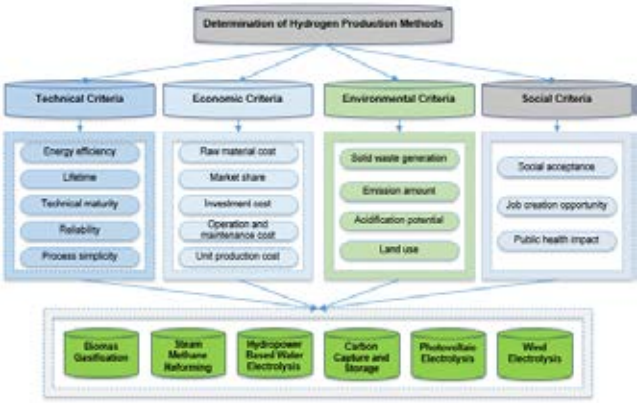


Fig. 2. Evaluation Model

The criteria were evaluated by the experts via Pythagorean fuzzy AHP method and the importance weights of the criteria were obtained. These importance weights were used as criteria weights in the decision process of interval type-2 fuzzy based TOPSIS method. According to the results yielded by the methodology and the sensitivity analysis, wind electrolysis has been decided as the most suitable hydrogen production method for Turkey within the current conditions.

CONCLUSIONS

Turning to renewable energy sources is essential for a sustainable environment. However, the energy production capacities of the renewable energy-based power plants are not stable because of the environmental conditions. Hydrogen is an effective energy storage alternative with low storage cost and the ability to transport with different techniques for the renewables. Hydrogen can also be produced from fossil fuels, which is an important advantage in making hydrogen a sustainable energy storage method for the gradual transition to clean energy sources. Turkey has high a potential for proliferation of hydrogen energy owing to the rich natural resources. Depending on this, hydrogen energy related studies gained attention in Turkey. Because of being an innovative field, the expertness about hydrogen technologies is inadequate in Turkey, therefore hydrogen energy related decision processes include high uncertainty. Traditional uncertainty modeling approaches may not produce beneficial results because of the lack of expertness-related high uncertainty. In this study, the best hydrogen production alternative is decided by using an integrated hybrid Pythagorean fuzzy AHP and Interval type-2 fuzzy TOPSIS methodology. As a future study, the best production, storage, and transportation combination can be decided to build the most effective hydrogen energy supply chain.

REFERENCES

1. Arat, HT., Baltacıoğlu, MK., Tanç, B., Sürer, MG. and Dinçer, İ. 2020. A perspective on hydrogen energy research, development and innovation activities in Turkey, International Journal of Energy Research, 44(2):588-593.
2. Dinçer, İ. and Eroğlu, İ. 2021. Türkiye için Hidrojen Teknolojileri Yol Haritası. [Online]. Available: https://www.hidrojenteknolojileri.org/HTD/Turkiye_icin_Hidrojen_Teknolojileri_Yol_Haritasi_Raporu_2021.pdf. Accessed on April 01, 2022
3. Kar, Y., Şen N. and Demirbaş, A. 2006. Boron minerals in Turkey, their application areas and importance for the country's economy, Minerals & Energy-Raw Materials Report, 20(3-4):2-10.
4. Apak, S., Atay, E. and Tuncer, G. 2017. Renewable hydrogen energy and energy efficiency in Turkey in the 21st century, International Journal of Hydrogen Energy, 42(4):2446-2452.
5. Karayel, G. K., Javani, N. and Dinçer, İ. 2021. Green hydrogen production potential for Turkey with solar energy, International Journal of Hydrogen Energy, (InPress).
6. Karayel, G. K., Javani, N. and Dinçer, İ. 2022. Green hydrogen production potential in Turkey with wind power, International Journal of Green Energy, (InPress):1-10.
7. Genç, M. S., Çelik, M. and Karasu, İ. 2012. A review on wind energy and wind–hydrogen production in Turkey: A case study of hydrogen production via electrolysis system supplied by wind energy conversion system in Central Anatolian Turkey, Renewable and Sustainable Energy Reviews, 16(9): 6631-6646.
8. Uysal, S., Kaya, MF., Demir, N., Hüner, B., Özcan, RU., Erdem, ÖN. and Yılmaz, M. 2021. Investigation of hydrogen production potential from different natural water sources in Turkey, International Journal of Hydrogen Energy, 46(61):31097-31107.
9. Coşkun, C., Bayraktar, M., Oktay, Z. and Dinçer, İ. 2012. Investigation of biogas and hydrogen production from waste water of milk-processing industry in Turkey, International Journal of Hydrogen Energy, 37(21):16498-16504.
10. Eroğlu, E., Eroğlu, İ., Gündüz, U. and Yücel, M. 2009. Comparison of physicochemical characteristics and photofermentative hydrogen production potential of wastewaters produced from different olive oil mills in Western-Anatolia, Turkey, Biomass and Bioenergy, 33(4):706-711.

11. Zadeh, LA. 1965. Fuzzy sets, Information and Control, 8:338-353.
12. Yager, R. R. 2013. Pythagorean membership grades in multicriteria decision making. IEEE Transactions on Fuzzy Systems, 22(4):958-965.
13. Xiao, F. and Ding, W. 2019. Divergence measure of Pythagorean fuzzy sets and its application in medical diagnosis. Applied Soft Computing, 79:254-267.
14. Ejegwa, PA. 2021. Generalized triparametric correlation coefficient for pythagorean fuzzy sets with application to MCDM problems. Granular Computing, 6(3):557-566.
15. Işıklar, G. and Büyüközkan, G. 2007. Using a multi-criteria decision-making approach to evaluate mobile phone alternatives. Computer Standards & Interfaces, 29(2):265-274.
16. Alkan, N. 2019. Yalın tedarik zinciri kapsamında sanayi 4.0 için sektörel önceliklendirmenin bulanık çok kriterli karar verme yaklaşımıyla analizi. Master's thesis, YTÜ Fen Bilimleri Enstitüsü
17. Yıldız, A., Ayyıldız, E., Gümüş, AT. and Özkan, C. 2019. Ülkelerin yaşam kalitelerine göre değerlendirilmesi için hibrit pisagor bulanık AHP-TOPSIS metodolojisi: Avrupa Birliği örneği. Avrupa Bilim ve Teknoloji Dergisi, 17:1383-1391.
18. Zadeh, LA. 1975. The concept of a linguistic variable and its application to approximate reasoning—I, Information sciences, 3(8):199-249.
19. Mendel, JM., John, RI. and Liu, F. 2006. Interval type-2 fuzzy logic systems made simple. IEEE transactions on fuzzy systems, 14(6):808-821.
20. Meniz, B. 2021. An advanced TOPSIS method with new fuzzy metric based on interval type-2 fuzzy sets. Expert Systems with Applications, 186:115770.
21. Kiracı, K. and Akan, E. 2020. Aircraft selection by applying AHP and TOPSIS in interval type-2 fuzzy sets. Journal of Air Transport Management, 89:101924.
22. Hwang, CL. and Yoon, K. 1981. Methods for multiple attribute decision making. In Multiple attribute decision making, 58-191. Springer, Berlin, Heidelberg.
23. Yildiz, A., Karakoyun, F. and Parlak, IE. 2018. The most suitable mobile RFID reader selection by using interval type-2 fuzzy topsis method. Sigma Journal of Engineering and Natural Sciences, 36(3):717-729.
24. Chen, SM. and Lee, LW. 2010. Fuzzy multiple attributes group decision-making based on the ranking values and the arithmetic operations of interval type-2 fuzzy sets. Expert Systems with applications, 37(1):824-833.
25. Lee, LW. and Chen, SM. 2008. A new method for fuzzy multiple attributes group decision-making based on the arithmetic operations of interval type-2 fuzzy sets. In 2008 International Conference on Machine Learning and Cybernetics, 6:3084-3089. IEEE.

WHEC-2022
23rd World Hydrogen Energy Conference
June 26-30, 2022 - Istanbul

#1632

WHAT IS THE KEY ROLE OF HYDROGEN ENERGY IN METAVERSE

[1*] *Feride Cansu İskenderoğlu,* [2] *Hüseyin Turan Arat,* [3] *Mustafa Kaan Baltacıoğlu*
[1] İskenderun Technical University, Faculty of Engineering and Natural Science, Mechanical Engineering Department, Hatay, Turkey
[2] Sinop University, Faculty of Engineering and Architecture, Mechanical Engineering Department, Sinop, Turkey
[3] İskenderun Technical University, Faculty of Engineering and Natural Science, Mechatronics Engineering Department, Hatay, Turkey

*Corresponding author e-mail: mkaan.baltacioglu@iste.edu.tr

ABSTRACT

With the increase in digitalization, the demand for energy is increasing day by day. Web 3 version, IoT technologies, social media platforms, rapidly increasing online worlds with online games and the popularization of crypto technologies make people dependent on energy. One of the most important problems of crypto and metaverse technology is the insatiable use of electricity. The current research uses a PEM fuel cell system as a renewable energy source to meet the electricity demand required for crypto mining. The required amount of hydrogen and equipment for the fuel cell system are explained.

Keywords: Metaverse, Coin mining, Cryptocurrency, PEMFC, Hydrogen

INTRODUCTION

In the rapidly digitalizing and virtualizing age, the world's energy demand is increasing significantly. Since its rebranding as "Meta," Facebook has come up with the idea of an immersive virtual reality world. To create a world where traditional money is replaced by encrypted alternatives and where each user can shape everything according to their own purposes. This world is fundamentally reimagined as something physical, three-dimensional, with the internet and all its services, a reality that our digital avatars can navigate. In this digital world universe, you can instantly teleport as a hologram from your commute to the office, to a concert with your friends, or to be in your parents' living room to catch up. There will be many different technologies that enable this greater vision of the metadatabase as a convergence of physical and digital, or our digital lifestyles that capture our physical lives. Some technologies are currently in use, such as virtual reality glasses and blockchain. In order for the digital world to approach reality, many technologies such as haptic technologies need to be developed. This means that internet speeds still need to be greatly improved for the metadata store to function fully. It will require incredible connectivity and internet speed of 5G and beyond.

A digital currency was created to be developed with a technology that can prevent duplication of documents as well as modern digital communication. Although technologies were developed to make this currency safe, it was not enough to create digital money [1-2]. The biggest impact on this technology has occurred with the publication of the Bitcoin whitepaper [3]. The effort to write data to Bitcoin's blockchain is rewarded with transaction fees paid by users and the emission of newly minted digital currencies. Anyone can try to write a valid block of transactions to the distributed ledger, but the network will only accept it if they are the first to create a digital signature, known as a hash. An effort to generate a hash is an energy-intensive process called cryptocurrency mining, which, in the case of the Bitcoin network, requires the use of custom-built computational hardware known as ASICs (Application-Specific Integrated Circuits). The higher the mining capacity or hash rate a participant has, the higher the chance of being the first to find the right digital signature for the next block of transactions. The current proof-of-work infrastructure relies heavily on electrical power [4]. According to the University of Cambridge's bitcoin electricity consumption index, bitcoin miners are expected to consume roughly 130 Terawatt-hours of energy (TWh), which is roughly 0.6% of global electricity consumption. This consumption was 75 TWh in January 2020 [5].

Due to Metaverse and digital money technologies, which are rapidly increasing in popularity and use, as well as social media platforms, a high amount of energy is required to ensure both the protection of the emerging big data and the existence of the virtual world uninterruptedly. Today, the largest energy source for the world is still fossil fuels with high carbon footprints. Although the development in renewable technologies is visible, it is not sufficient to store and maintain energy. For this reason, Hydrogen energy, which is an alternative energy source, is an efficient energy carrier and storage that has been defined so far and can be obtained from both renewable and non-renewable sources.

In this study, a general point of view is discussed in terms of providing the energy that needs to be provided continuously for Metaverse and crypto money technologies from renewable hydrogen production sources. Necessary calculations were made by considering some critical factors such as the absence of a value chain for clean hydrogen, storage and transportation of hydrogen, high production costs, lack of international standards and investment risks.

MATERIALS AND METHODS

The general method applied in the present research is to first determine the number of mining units according to the size of the operation being decided; Then, based on this number, the power required to run these miners is calculated. The next step is to calculate the amount of hydrogen gas required for the PEMFC module to generate the required electricity. The massive computing power required for the Bitcoin network has been calculated with CPUs and GPUs, FPGAs and ASICs [7-8]. While the energy efficiency of these units increases over time, their “energy consumption” ” and its results still remain the determining factor in miners' decision to operate in this market and their profit or loss margins [9]. Bitcoin mining hardware and cost are summarized in Table 1.

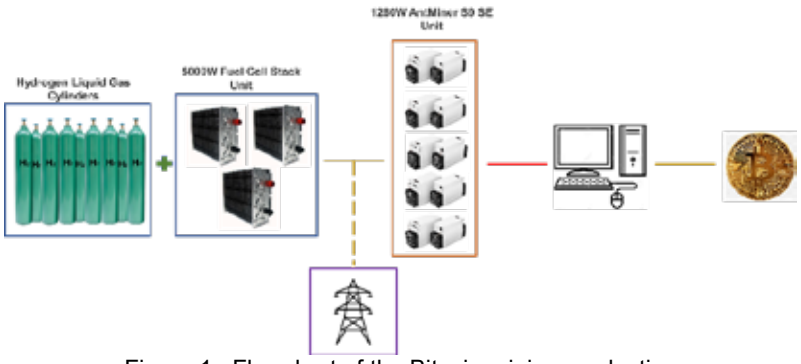


Figure 1. Flowchart of the Bitcoin mining production

There are several factors to consider when choosing the appropriate hardware and software for mining. The first is the cost of mining equipment, which depends on the hash rate and lead time; this cost is usually measured in terms of GHs. The second factor is energy costs; miners will prefer the equipment with the lowest power consumption as they are the most efficient and their heat emissions are relatively low. The third factor is the difficulty, an arbitrary dimensionless value that measures how problematic it is to find a hash below a given target. The difficulty would be recalculated every 2016 blocks, based on the assumption that if everyone was mining at this difficulty level, the 2016 blocks would be resolved in exactly 2 weeks [10].

Table 1. List of the Bitcoin mining equipment

Hardware generation	Device	Hash rate (Mhash/s)	Energy efficiency (Mhash/J)	Price ($)
Central Processing Unit (CPU)	Core i7 950 Atom N450	18.9 100	0.12 0.31	86 $
Graphics Processing Unit (GPU)	ATI 4850 ATI 5770	101 214.5	0.92 1.95	25 $
Field Programmable Gate Array (FPGA)	The Single Rig Box	832 50,000	10.40 20.40	140 $
Application-Specific Integrated Circuit (ASIC)	AntMiner S9i	14×1012	10,606	351 $
PEMFC	Hydrogen Fuel Cell 6000W Pem Electricity Generator	-	-	658 $
Hydrogen Gas	-	-	-	4.23 €/kgH2

RESULTS AND DISCUSSION

In this situation, the Bitcoin Blockchain's difficulty is increased by 1% per month for a period of four years, calculating an average difficulty value for each year. Then the BTC production of that year is calculated from these average difficulties. In PEMFC-based cases, electrical energy consumption, the CAPEX consists of; the Cost of the AntMiner S9 SE ($351 for each unit), the cost of an adequate power supply unit ($86 for each unit], the OPEX includes; Operation & Maintenance costs of mining and power supply units which are calculated as 5% of the corresponding CAPEX, electricity cost which is calculated by multiplying the electricity consumption (kWh) by the price of electricity

($/kWh) in each country. The cost of Hydrogen gas produced by grid-connected electrolysis has been calculated as approximately 4 €/kgH2 in Europe. Scenario-based analyzes of the current markets have shown that the system can make a profit if the products are fully purchased at prices above 20 €/kgH2. All of the system prices are 6020 $.

CONCLUSIONS

Cryptocurrency mining appears to be playing an increasing role in the transition to a clean, modern and more decentralized energy system. Miners can provide grid balancing and flexible demand response services and improve renewable energy integration. Cryptocurrency mining around the world is done with energy from hydroelectric, coal and natural gas. In order to meet the increasing demand day by day, cleaner and sustainable energy technologies are sought. In this study, the place that hydrogen energy can take in this production is discussed. It should be proven that the amount of carbon footprint, which is expected to increase with digitalization, can be reduced with renewable energy technologies. The energy industry, especially intermittent power producers based on natural energy sources, will be able to benefit from this hedging mechanism. Cryptocurrency mining may be preferred due to the simplicity of mining infrastructure construction, maintenance and cost-free migration. The findings of this paper could create incentives for the production and sale of cryptocurrency issued by energy producers, encouraging more timely completion of planned renewable power units. Investors in renewable power plants also benefit from this transition strategy, as they can generate higher returns with lower risk on their capital. Such a transition option can increase profitability while reducing risk, and its widespread use could stimulate the growth of the construction of new renewable energy sites globally.

REFERENCES

1. Back A. 2002. Hashcash - a denial of service counter-measure. http://www.hashcash.org/papers/hashcash.pdf Accessed on May 17, 2022
2. Finney H. 2004. Reusable proofs of work (rpow). http://web.archive.org/web/20040820070815/http://rpow.net/, Accessed on May 17, 2022 [22]
3. Nakamoto S. 2008. Bitcoin: a peer-to-peer electronic cash system. https://bitcoin.org/bitcoin.pdf Accessed on May 17, 2022
4. Krause M.J. and Tolaymat T. 2018. Quantification of energy and carbon costs for mining cryptocurrencies. Nature Sustainability, 1 (11): 711-718.
5. University of Cambridge. 2020. Cambridge Bitcoin Electricity Consumption Index.https://www.cbeci.org/cbeci/comparisons Accessed on May 17, 2022
6. Taylor M. B. 2017. The Evolution of Bitcoin Hardware. Computer (Long Beach Calif). 50:58–66. doi:10.1109/MC.2017.3571056.
7. Taylor MB. 2013. Bitcoin and the age of Bespoke Silicon.Int. Conf. Compil. Archit. Synth. Embed. Syst. CASES 2013. IEEE 2013: 1–10. doi:10.1109/CASES.2013.6662520.
8. Malone D. and O'Dwyer K. J. 2014. Bitcoin Mining and its Energy Footprint. 25th IET Irish Signals Syst. Conf. 2014/ China-irel. Int. Conf. Inf. Communities Technol. (ISSC 2014/CIICT 2014), Institution of Engineering and Technology; 2014, 280–5. doi:10.1049/cp.2014.0699.
9. Cocco L and Marchesi M. 2016. Modeling and simulation of the economics of mining in the Bitcoin market. PLoS One. 11:1–42. doi:10.1371/journal.pone.0164603.
10. Bhaskar N. D. and Chuen D. L. K. 2015. Bitcoin Mining Technology. Handb. Digit. Curr. Elsevier. 45–65. doi:10.1016/B978-0-12-802117-0.00003-5.

WHEC-2022

23rd World Hydrogen Energy Conference

TRACK 16. ENVIRONMENTAL IMPACT AND SUSTAINABLE DEVELOPMENT

TRACK 16. ENVIRONMENTAL IMPACT AND SUSTAINABLE DEVELOPMENT

#21 DESULFURIZATION PERFORMANCE OF SBA 15 SUPPORTED CALCIUM BASED MIXED METAL OXIDE SORBENTS	1433
#36 LIFE CYCLE GHG EMISSIONS OF A GASOLINE AND FUEL CELL VEHICLE WITH VARIOUS HYDROGEN PRODUCTION PATHWAYS	1436
#38 STEAM METHANE REFORMING INTEGRATION AND INCREASE OF CARBON DIOXIDE PRODUCTION	1439
#59 A PARAMETRIC NUMERICAL ANALYSIS OF LAMINAR HYDROGEN DIFFUSION FLAMES	1443
#115 HYDROGEN CERTIFICATION OF ORIGIN IN COLOMBIA	1446
#137 PROSPECTS OF RENEWABLE HYDROGEN IN TRANSPORT	1449
#151 HYDROGEN PRODUCTION FROM OLIVE OIL MILL WASTEWATER THROUGH STEAM REFORMING IN MULTIFUNCTIONAL REACTORS	1452
#266 SUSTAINABILITY ASSESSMENT OF A PROTON-EXCHANGE MEMBRANE FUEL CELL STACK AS A BASIS FOR THE DEVELOPMENT OF ECO-DESIGN GUIDELINES	1455
#283 THE ENERGY-ENVIRO-ECONOMIC EVALUATION AND MULTI-OBJECTIVE OPTIMIZATION OF THE HYDROGEN PRODUCTION PROCESS FROM COAL-BIOMASS CO-GASIFICATION CONSIDERING UNCERTAINTY IN CARBON PRICES	1458
#315 LCA AND CRITICALITY ANALYSIS OF WATER ELECTROLYSIS TECHNOLOGIES	1461
#1444 A COMPARATIVE LIFE CYCLE ASSESSMENT OF HYDROGEN PRODUCTION USING THE SPECTRUM OF HYDROGEN COLORS	1464
#1480 REDUCTION OF HYDROGEN CARBON FOOTPRINT IN EUROPE VIA INTERNATIONAL SHIPPING	1467
#1492 HOT GAS DESULFURIZATION PERFORMANCE OF SBA-15 SUPPORTED/MIXED METAL OXIDES (Cu, Fe, Mn, and Zn)	1470
#1516 THE EFFECT OF HYDROGEN AND AMMONIA COMBUSTION ON PERFORMANCE AND EMISSIONS	1473
#1549 LIFE CYCLE ASSESSMENT OF DIFFERENT HYDROGEN CONVERSION TECHNOLOGIES FROM BIOMASS GASIFICATION	1476
#1589 LIFE CYCLE AND ECONOMIC ASSESSMENT OF HYDROGEN FUEL CELL BUSES	1479
#1611 TOWARDS ETHICAL ENERGY STORAGE MATERIALS – COBALT FREE CATHODE ACTIVE MATERIAL LKMNO	1482

WHEC-2022
23rd World Hydrogen Energy Conference
June 26-30, 2022 - Istanbul

#21

DESULFURIZATION PERFORMANCE OF SBA 15 SUPPORTED CALSIUM BASED MIXED METAL OXIDE SORBENTS

[1]Arzu Kanca, [1]Zeynep Koseoglu, [1]Osman Nuri Ata*
[1] Ataturk University, Engineering Faculty, Chemical Engineering Department, 25240, Erzurum, Turkey

*Corresponding author e-mail: akanca@atauni.edu.tr

ABSTRACT

Syngas is a mixture of CO and H_2 formed during the gasification process of coal and biomass. Additionally, H_2S is undesired gasification products of fossil fuels with high sulfur content. H_2S causes serious problems, such as catalyst poisoning and pipeline corrosion during production process of fuel from syngas. Hot gas desulfurization (HGD) enables to reduce the sulfur contents of the gasification products by eliminating thermal losses of endothermic syngas processes. This study aims to develop regenerable sorbents to remove H_2S from hot flue gas. Unsupported and SBA 15 supported Ca-based binary mixed metal oxides (CaO-CuO, CaO-FeO, CaO-MnO, CaO-ZnO) were synthesized as sulfur sorbents by wet impregnation method. The crystal structure of sorbents was determined by X-ray diffraction (XRD), while BET analysis was used to determined the surface area and pore size distribution of the Ca based mixed metal oxide sorbents. The initial results of the XRD and BET analysis revealed the mixed metal oxide formation and high surface area of SBA 15 supported sorbents, respectively. Desulfurization performance of the sorbents was examined by gas chromatography analyzer equipped with Flame Photometric Detector. The best desulfurization performance with breakthrough sulfur capacity of 22.72 g S/100 g sorbent and 46.65% capacity usage ratios was obtained for CaO-CuO adsorbent.

Keywords: Desulfurization, Ca-Based Sorbents, SBA 15, Mixed Metal Oxide

INTRODUCTION

The increasing fuel consumption in the world leads to serious environmental problems. Gasification is one of the important alternative technologies for the environmentally friendly energy production. However, H_2S which is highly toxic and corrosive, is a gasification product of fossil fuels with high sulfur. Furthermore, since fuel production from syngas is endothermic process, H_2S should be removed from the hot gases without cooling. As a result, hot gas desulfurization (HGD) enables to reduce the sulfur contents of the gasification products by eliminating thermal losses.

Metal oxides are thermodynamically favorable sorbents for sulfur removal [1, 2]. Ca oxide is one type of sulfur sorbents having a high sulfur capture ability. Since it is both accessible easily and economical, Ca based adsorbents were preferred in this study. In a previous review study, Meng et al. was reported that naturally available Ca based sorbents such as dolomite and limestone can be used to remove sulfur [5]. Abbasian et al. found that sulfur capture efficiency is independent on temperature and it is higher for dolomite than limestone due to the difference in pore structure. The presence of $MgCO_3$ in dolomite allows the higher porosity and less sintering of CaS [6]. Compared to limestone and dolomite, calcium acetate and calcium magnesium acetate were reported as more effective sulfur sorbents due to their higher surface area and porosity [3-5]. One of the main drawbacks of the Ca based sorbent utilization is defined as the $CaSO_4$ formation during sorbent regeneration. Since $CaSO_4$ is very stable, sorbent regeneration becomes unfavorable [5]. The utilization of support materials and mixed metal oxides can be considered as alternative solution to solve the $CaSO_4$ formation. Yang et al. studied sulfur removal performance of calcium silicates and the silica supported lime as regenerative sorbents. They reported that the most of calcium silicates and silica supported calcium oxide are more reactive than pure calcium oxide. The regeneration rates of these sorbents were found higher than that of calcium oxide [7]. At that point, the utilization of silica based SBA 15 and Ca based mixed metal oxides can be considered as sulfur sorbent alternates.

In this study, unsupported and SBA 15 supported CaO-CuO, CaO-FeO, CaO-MnO, CaO-ZnO were selected as sorbents. Their preparation methods, characterization, and sulfur removal performance results are summarized in the following parts.

MATERIALS AND METHODS

Synthesis and characterization of Ca based mixed metal oxides sorbents

Wet impregnation method was used to prepare the Ca based mixed metal oxides. After Ca $(NO_3)_2{\cdot}4H_2O$ was dissolved in deionized water, other metal (Cu, Fe, Mn, and Zn) nitrates were added in 1/1 (wt/wt) ratio. The metal nitrate precursors were mixed by magnetic stirrer for 2 hours. The solution was dried at 105°C over night. The dried solid mixture was calcined at 550°C under air stream for 5h. SBA 15 was used as a support material synthesized in our laboratory, and Ca-based metal oxides were loaded on SBA 15 by again wet impregnation method.

Crystal structure of Ca based mixed metal oxides were determined by X-ray diffraction (XRD) (Panalytical Empyrean model, Anode material, Cu 1.56 A wavelength). Micromeritics 3Flex 3-port BET device was employed to analyze the surface structure of the sorbents in the presence and absence of SBA 15.

Desulfurization testing of Ca based mixed metal oxides sorbents

Sulfidation performance of Ca based sorbents is tested by using Agilent 6890N model gas chromatography analyzer equipped with Flame Photometric Detector.

RESULTS AND DISCUSSION

BET Results

BET results of unsupported and SBA 15 supported Ca based sorbents are presented in Table 1. As seen in Table 1, surface area and pore volume of the Ca based sorbents are significantly higher in the presence of SBA 15 than in the absence of SBA 15. The BET findings revealed the metal oxide deposition inside SBA 15 hexagonal channels.

Table1. BET results of supported and unsupported Ca based metal oxides.

Sorbent	Surface area (m^2/g)	Pore size (nm)	Pore volume (cm^3/g)
CaO-CuO	3.94	11.58	0.011
CaO-FeO	2.51	6.77	0.004
CaO-MnO	5.07	15.07	0.019
CaO-ZnO	3.21	6.59	0.005
SBA 15	763.20	6.38	1.217
CaO-CuO on SBA 15	143.21	10.34	0.370
CaO-FeO on SBA 15	151.58	9.99	0.378
CaO-MnO on SBA 15	152.64	10.56	0.403
CaO-ZnO on SBA 15	139.80	10.46	0.365

When the pore size distribution of unsupported and SBA15 supported sorbents is compared, the expanding pore size distribution in the presence of SBA 15 can be interpreted as the stable metal oxide loading on SBA 15.

XRD Results

In order to determine the metal oxide formation, the specific Bragg angle values of metal oxides were employed. The crystal structure of SBA 15 supported sorbents is shown in Figure 1. As seen in the figure, XRD patterns of metal oxides indicate the metal oxide formation.

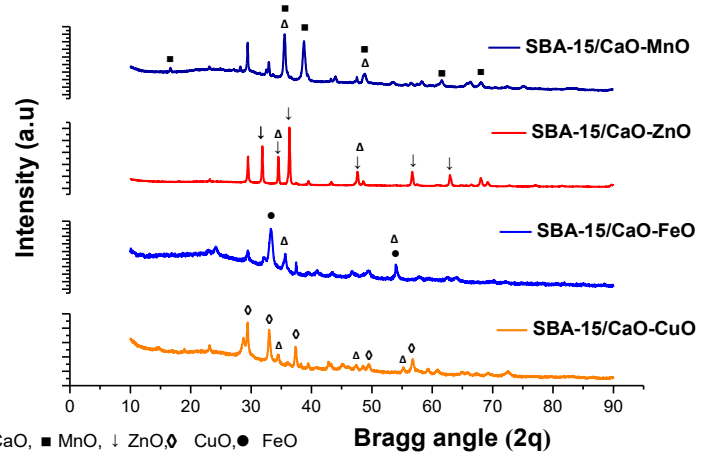


Figure 1. XRD patterns of SBA 15 supported CaO-ZnO [8, 9], CaO-FeO [8, 10], CaO-MnO [8, 11] and CaO-CuO [8, 12] mixed metal oxides.

Sulfur Sorption

Desulfurization test results of the unsupported and SBA 15 supported CaO based sorbents revealed that CaO-CuO has the highest breakthrough sulfur capacity of 22.72 and 46.65% Capacity Usage Ratios (CUR) among the unsupported Ca based mixed metal oxides. The maximum sulfur capacity was also determined as 11.57 with the CUR of 47.49% for the SBA 15 supported CaO-CuO. The sulfur sorption performance of Ca based mixed metal oxides is compared in Figure 2a for unsupported CaO-MeO and Figure 2b for SBA 15 supported CaO-MeO sorbents.

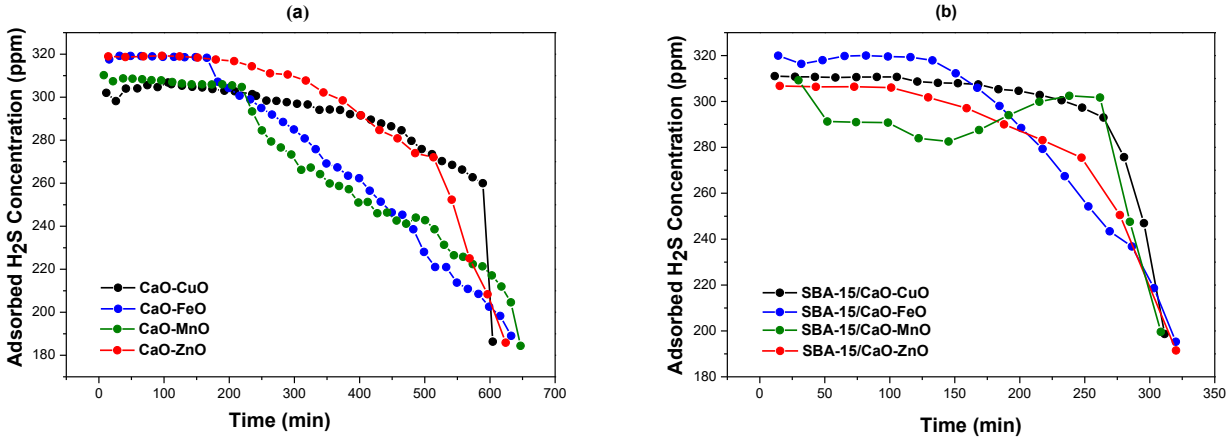


Figure 2. The sulfur sorption performance of Ca based mixed metal oxides. (a) unsupported CaO-MeO and (b) SBA 15 supported CaO-MeO sorbents.

CONCLUSIONS

New sorbents are developed using mixed metal oxides for the removal of H2S from gases at high temperature (800°C). BET results reveal that the presence of SBA 15 increases the surface area of metal oxides. Undefined peaks in XRD patterns can be interpreted as Ca based mixed metal oxides formation. Among the CaO based sorbents, unsupported and SBA 15 supported CaO-CuO mixed oxide show the best desulfurization performance with the sulfur capture capacity of 22.72 g S/100 g and 11.57 g S/100 g sorbent, respectively.

ACKNOWLEDGEMENT

Authors thank to The Scientific and Technological Research Council of Turkey (TUBITAK) for financial support. They are also grateful for DAYTAM for their help on sorbent characterization.

REFERENCES

1. Westmoreland PR and Harrison DP. 1976. Evaluation of candidate solids for high-temperature desulfurization of Low-Btu gases. Environmental Science & Technology, 10:659-661.
2. Westmoreland PR, Gibson JB, and Harrison DP. 1977. Comparative kinetics of high-temperature reaction between hydrogen sulfide and selected metal oxides. Environmental Science & Technology, 11 (5), 488-491.
3. Meng XM, De Jong W, Pal R and Verkooijen AHM. 2010. In bed and downstream hot gas desulphurization during solid fuel gasification: A review. Fuel Processing Technology, 91:964-981.
4. Abbasian J, Rehmat A, Leppin D and Banerjee DD. 1990. Desulfurization of fuels with calcium-based sorbents. Fuel processing technology, 25:1-15.
5. Garcia-Labiano F, De Diego LF and Adanez J. 1999. Effectiveness of natural, commercial, and modified calcium-based sorbents as H_2S removal agents at high temperatures. Environmental Science & Technology, 33:288-293.
6. Adanez J, Garcia-Labiano F, De Diego LF and Fierro V. 1999. Utilization of calcium acetate and calcium magnesium acetate for H_2S removal in coal gas cleaning at high temperatures. Energy & Fuels, 13:440-448.
7. Yang RT and Shen MS. 1979. Calcium silicates: A new class of highly regenerative sorbents for hot gas desulfurization. AICHE journal, 25:811-819.
8. Kesić Ž, Lukić I, Brkić D, Rogan J, Zdujić M, Liu H, and Skala D. 2012. Mechanochemical preparation and characterization of CaO· ZnO used as catalyst for biodiesel synthesis. Applied Catalysis A: General, 427, 58-65.
9. Mazhdi M. and Tafreshi MJ. 2018. The effects of gadolinium doping on the structural, morphological, optical, and photoluminescence properties of zinc oxide nanoparticles prepared by co-precipitation method. Applied Physics a-Materials Science & Processing. 124(12): p. 863.
10. Sharma SK, Vargas JM, Pirota KR, Kumar S, Lee CG and Knobel M. 2011. Synthesis and ageing effect in FeO nanoparticles: Transformation to core-shell FeO/Fe_3O_4 and their magnetic characterization. Journal of Alloys and Compounds, 509:6414-6417.
11. Zhang QT, Dai QQ, Li M, Wang XM and Li A. 2016. Incorporation of MnO nanoparticles inside porous carbon nanotubes originated from conjugated microporous polymers for lithium storage, Journal of Materials Chemistry A, 4:19132-19139.
12. Ye Q, Chen X, Yang J, Wu D, Ma J, and Kong Y. 2019. Fabrication of CuO nanoparticles-decorated 3D N-doped porous carbon as electrochemical sensing platform for the detection of Sudan I. Food chemistry, 287, 375-381.

WHEC-2022
23rd World Hydrogen Energy Conference
June 26-30, 2022 - Istanbul

#36

LIFE CYCLE GHG EMISSIONS OF A GASOLINE AND FUEL CELL VEHICLE WITH VARIOUS HYDROGEN PRODUCTION PATHWAYS

[1] *Samane Ghandehariun, [1]Shayan Sadeghi, [2]Amir Mohammad Ghandehariun
[1]Sustainable Energy Research Group (SERG), School of Mechanical Engineering, Iran University of Science and Technology, Tehran, Iran
[2]Faculty of Engineering, Ferdowsi University of Mashhad, Mashhad, Iran

*Corresponding author e-mail: samane_ghandehariun@iust.ac.ir

ABSTRACT

Moving towards a cleaner transportation is necessary for a more sustainable future. Hydrogen, as a clean energy carrier, can play an important role. It can be used in fuel cell vehicles (FCV) or in internal combustion engines. In this paper, a life cycle assessment of a FCV with 5 different fuel cycles including steam methane reforming (SMR), coal gasification, photovoltaics, solar thermal and grid electrolysis is conducted for Iran. Also, the FCV is compared with a conventional gasoline vehicle. It is concluded that for all of the considered pathways, the FCV is more environmentally benign than the gasoline vehicle, except when its hydrogen is produced from the electrolysis of water using national grid electricity. The total greenhouse gas (GHG) emissions of the FCV with grid electrolysis are found to be 0.465 kg CO_2 eq./km, which is 56% higher than those of a gasoline vehicle. It is also shown that the material production and manufacturing phase of the FCV's vehicle cycle is the main contributor to the total GHG emissions of the vehicle. The glider, hydrogen tank and fuel cell stack manufacturing have the most impacts on the environment. A FCV powered by clean hydrogen produced from electrolysis of water with the electricity produced from photovoltaics produces 0.135 kg CO_2 eq./km which is less than half of the emissions associated with a gasoline vehicle.

Keywords: Fuel Cell Vehicle, Hydrogen Production, Life Cycle Assessment, Greenhouse Gas Emissions

INTRODUCTION

Iran is a country rich in fossil fuels, but as these resources are depleting and the concerns about the environment is intensifying, their use must be limited. Transport sector is one of the most important sectors of a country's economy and welfare with huge energy requirement. Based on Iran's Ministry of Energy report, the transport sector devours an amount of 318 millions barrel of oil equivalent which is more than 17% of the country's total energy demand per year [1]. About 85% of Iran's transport sector energy use is based on petroleum products and less than 15% is from natural gas [1]. In 2016, about 590 million tonnes of carbon dioxide equivalent was emitted to the atmosphere of which 24% associated to transport sector [1,2]. Therefore, by utilization of more environmental benign vehicles and fuels, the amount of produced pollutants can be affected significantly. Fuel cell vehicles and hydrogen fuel can help us achieve this aim.

Evangelisti et al. [3] conducted a life cycle assessment study for a FCV and compared it to a battery electric vehicle and an internal combustion engine vehicle (ICEV). The focus of the study was on the manufacturing phase of the fuel cell system itself. It was concluded that most of the emissions produced from a FCV are related to its manufacturing phase while its total life time emissions are about 32% less than that of the ICEV [3].

Yoo et al. [4] conducted an LCA study for a FCV in South Korea with the GREET Model. It was shown that if the hydrogen is produced from Korea's grid with electrolysis, the GHG emissions associated with the total lifetime of the vehicle are more than 2 times higher than that of a conventional gasoline vehicle [4].

No publication has been found on an LCA of a FCV with various hydrogen production methods specific to Iran. The objective of this paper is to evaluate the GHG emissions of a FCV and a conventional gasoline vehicle which is currently used in Iran with the life cycle assessment methodology. Various hydrogen production pathways are considered. The vehicle manufacturing, operation and disposal as well as the fuel cycles are investigated and various scenarios are compared in this paper.

METHODOLOGY

A life cycle assessment (LCA) consists of four phases [5]: The goal and scope definition, including the reasons for performing the study, the functional unit, and the system boundary, inventory analysis, including data collection and

the quantifying inputs and outputs of each unit operation, impact assessment, in which the significance of potential environmental impacts is evaluated, and interpretation where the findings from the inventory analysis and the impact assessment phases are considered together to present consistent results based on the goal and scope definition phase of the study. The vehicle cycle studied includes raw material extraction, vehicle component fabrication, vehicle assembly, vehicle operation, vehicle disposal/recycling. The fuel cycle includes raw material extraction, feedstock transportation, fuel production, fuel transport and distribution. The functional unit is 1 km of driving and the lifetime of the vehicle is 150,000 km.

SYSTEM DESCRIPTION

The fuel cell vehicle considered in this study is similar to Toyota Mirai 2019. It is a proton exchange membrane fuel cell vehicle which is a 4 door family sedan. The total power of the fuel stack considered here is 113 kW with a fuel consumption of 0.76 kg H_2 per 100 km. Also, the net weight of the vehicle is 1850 kg [6].

Five pathways are considered for the production of hydrogen. The first one is the steam reforming of natural gas. In this pathway the natural gas is extracted from the Asaluyeh gas field in the southern Iran and is transported by a 0.6 m pipeline to the hydrogen production facility located in Tehran. The second pathway is the coal gasification in which the coals are extracted from an underground coal mine in Kerman province and transported by rail to the hydrogen production facility. The other three pathways include alkaline water electrolysis using photovoltaic, parabolic trough solar collector power plants, and the national grid.

Hydrogen is transported 30 km in tube trailers to the fueling station.

RESULTS AND DISCUSSION

Figure 1 shows the GHG emissions associated with the manufacturing of the FCV components. The manufacturing of the glider, hydrogen tank and fuel cell stack emits 0.0337, 0.0151, and 0.0135 kg CO_2 eq./km, respectively. The total GHG emissions of the fuel cell vehicle cycle are 0.0942 kg CO_2 eq./km.

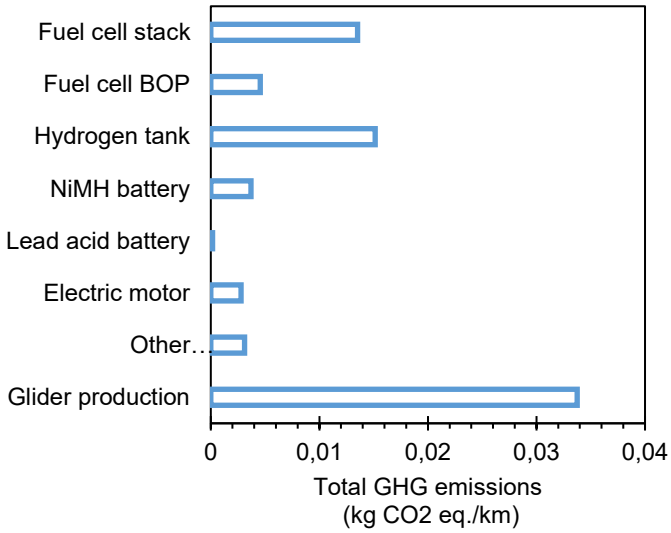


Fig.1. GHG emissions associated with FCV component fabrication

Figure 2 shows a comparison between GHG emissions associated with each fuel cycle and vehicle cycle of various scenarios considered in this paper.

The total life cycle GHG emissions of the gasoline vehicle are 0.297 kg CO_2 eq./km. The total GHG emissions of the FCV with grid electrolysis are 0.465 kg CO_2 eq./km which are significantly higher than those of the gasoline vehicle. Other FCV scenarios have lower GHG emissions than the gasoline vehicle.

Among the scenarios studied in this paper, FCV with PV electrolysis hydrogen has the lowest total life cycle GHG emissions equal to 0.135 kg CO_2 eq./km.

It is noted that even the FCVs with fossil-fuel-based hydrogen production have lower total GHG emissions than the gasoline vehicle. As Iran is rich in natural gas resources, SMR is suggested as an appropriate method for hydrogen production. The total life cycle GHG emissions of a fuel cell vehicle with SMR hydrogen production is about 36% lower than those of a gasoline vehicle in Iran.

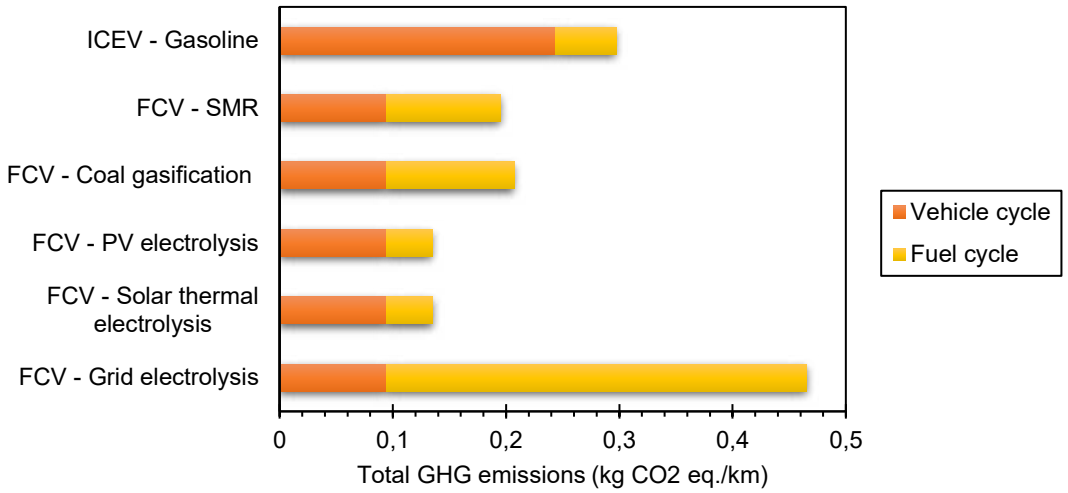


Fig. 2. GHG emissions of fuel and vehicle cycles of various scenarios

CONCLUSIONS

A life cycle GHG emissions assessment is conducted for a fuel cell vehicle in Iran using alternative hydrogen production methods. It is shown that the material production and manufacturing phase of the vehicle contributes significantly to the life cycle emissions. GHG emissions associated with a fuel cell vehicle with grid electrolysis hydrogen are 0.465 kg CO_2 eq./km, which are 56% higher than those of a gasoline vehicle. Among the scenarios studied in this paper, FCV with PV electrolysis hydrogen production has the lowest total life cycle GHG emissions equal to 0.135 kg CO_2 eq./km.

REFERENCES

1. Ministry of Energy, "Energy Balance Sheets for 2016", http://pep.moe.gov.ir. Accessed on December 4, 2019.
2. Statistical Center of Iran, "Total Emissions from Pollutant and Greenhouse Gases 2016", www.amar.org.ir. Accessed on December 4, 2019.
3. Evangelisti, S., Tagliaferri, C., Brett, D. J., & Lettieri, P. (2017). Life cycle assessment of a polymer electrolyte membrane fuel cell system for passenger vehicles. Journal of cleaner production, 142, 4339-4355.
4. Yoo, E., Kim, M., & Song, H. H. (2018). Well-to-wheel analysis of hydrogen fuel-cell electric vehicle in Korea. International Journal of Hydrogen Energy, 43(41), 19267-19278.
5. International Organization for Standardization. (2006). Environmental Management: Life Cycle Assessment; Principles and Framework (No. 2006). ISO.
6. Toyota, "Toyota Mirai Fuel Cell Electric Vehicle 2019 Full Specification Brochure". https://ssl.toyota.com/mirai/fullspecs.html, Accessed on July 17, 2019.

WHEC-2022
23rd World Hydrogen Energy Conference
June 26-30, 2022 - Istanbul

#38

STEAM METHANE REFORMING INTEGRATION AND INCREASE OF CARBON DIOXIDE PRODUCTION

[1*] *M. Tagliabue*
[1] Air Liquide Argentina S.A., Av. Larrabure 115, Campana (2804), Bs. As., Argentina

*Corresponding author e-mail: marcelo.tagliabue@airliquide.com

INTRODUCTION

The present work is a study of the efficiency optimization of a H_2 production plant through natural gas reforming, and contributes to preserving the environment. In recent years, H_2 has been attracting great interest as a clean fuel for combustion engines and fuel cells. H_2 can be produced using several routes. The main route is the catalytic reforming of methane, which includes, among others, steam-methane reforming (SMR) and dry-methane reforming (DMR) [1]. In recent times, the Refineries of the world have considerably increased the demand for H_2, in order to be able to hydrogenate their different fuels in order to fit within the legislation of each country regarding the maximum limits of contaminants in each of them. Currently one of our business units to produce H_2 (which is sent to a Refinery) has two SMRs. One of them is side fire (SMRI) and the other one is top fire (SMRII). The first is designed to be fed with NG, and the second can work with both NG and ROG. The business unit on the other hand has a CO_2 absorber unit of the syngas stream of the first SMR, which uses an aqueous solution of MDEA additive with Piperazine as absorbent agent. In addition, a CO_2 absorber uses an aqueous solution of MEA. In this way, the business unit markets food grade CO_2 that leverages the entire project. The typical reactions that are involved, both when running NG and ROG, are shown below. The only difference is that the plant that ROG treats has a pre reformer, to transform CH_4+ hydrocarbons into H_2, CO, CO_2 and CH_4.

SMR reactions [2, 5]:

$$CH_4 + H_2O \rightarrow CO + 3H_2 \qquad \Delta H°298 = 206\ KJ/mol \tag{1}$$

$$CO + H_2O \rightarrow CO_2 + H_2 \qquad \Delta H°298 = -41\ KJ/mol(WSR) \tag{2}$$

DMR reaction [3, 6]:

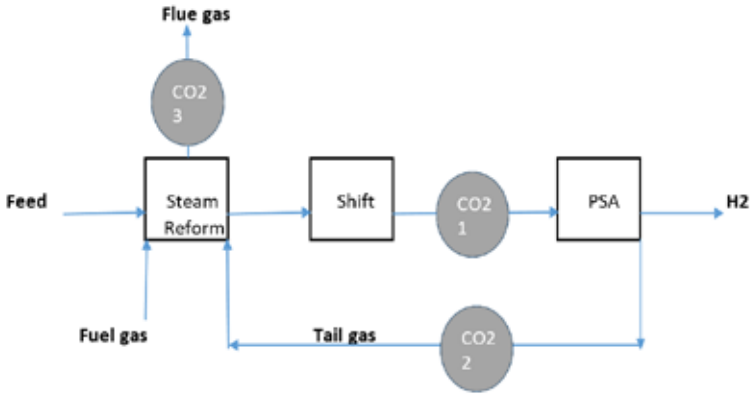
$$CH_4 + CO_2 \rightarrow 2CO + 2H_2 \qquad \Delta H°298 = 247\ KJ/mol \tag{3}$$

These reforming reactions (1, 3) are strongly endothermic, while the concomitant reaction of water displacement is moderately exothermic (2). This process therefore requires a reactor in which heat management is extremely important.
In practice, an SMR unit can contain from 40 to 1000 tubes, each of which is typically 6-13 m long, 70-160 mm in diameter, and 10-20 mm in wall thickness. In our case, the SMR I consists of 52 tubes of ID 86.2 mm, and a length of 13 m. The number of burners is 72 and they are arranged on the sidewall.

The SMR II consists as main difference the inclusion of a pre reformer of 1,300 mm ID, and a height of 3,320 mm, without MDEA unit. The reactor consists of 46 tubes of ID 125 mm and 18 burners, which are arranged at the top of the home.
These pipes are arranged vertically in a household or rectangular combustion chamber, the so-called radiant section. The reactor tubes contain a nickel-based catalyst, usually in the form of small cylinders or rings.

If our interest is not only the production of hydrogen, but also reduce CO_2 emissions, and produce it for sale in the industries that use it, there are several points in the scheme of an SMR for recovery.

In a modern steam reforming hydrogen plant fed by natural gas, up to approx. 60% of the total CO_2 produced is contained in the shifted gas (and then in the PSA tail gas), while the remaining 40% is the product of the combustion of the additional fuel gas required by the steam reformer. In our case to recover CO_2, we use points 1 and 3 shown in Figure 1.



Fiq. 1. Flowchart of recover CO_2

EXPERIMENTAL, THEORY AND/OR CALCULATIONS

The plant used to develop this study is the first reformer a side fire type, with a feeding of natural gas. This SMR plant consists of a high temperature shift plant (HTS), a CO_2 capture plant through an absorption process with activated amines, and a CO_2 liquefaction plant (for its later sale). This work was a theoretical and practical study with the objective to see how a stream of non-condensable usually vented to the atmosphere (rich in CO_2 and H_2) and coming from the stripper of the CO_2 liquefaction plant could be added to the feed of the SMR plant, in order to reduce the emissions of CO_2 and other compounds responsible of the greenhouse, and to reduce the consumption of natural gas, keeping hydrogen production. In the second stage, once made the theoretical study of the impact on the SMR when this feed is added, it was decided to proceed to the experimental work to learn how the major variables of the process were affected [4]. In the fieldwork, a line was built to link the non-condensable pipe, coming from the CO_2 liquefaction, whose pressure was 17.0 barg with the suction line to the natural gas compressor whose pressure was 7 barg. Additionally, the use of H_2 from non-condensable was considered to supplant part of the recycled H_2 (extracted from the flow of H_2 produced) usually necessary to eliminate sulfur from natural gas in the hydro treatment, which consists of a reactor with two beds, the first one filled with CoMo catalyst, to transform the possible organic sulfur compounds into SH2 and then an OZn bed that is responsible for absorbing SH2 through the following chemical reaction:

$$SH_2 + OZn \rightarrow SZn + H_2O \quad (4)$$

The practical results of the test were very encouraging. As dry reforming is more endothermic than the conventional reforming, the natural gas consumption increases initially because of the necessity of a bigger input of combustible and a lower flow of Off Gas from the pressure swing adsorption (PSA) due to the bigger conversion of CH_4. When the tubes wall cool down the excess air could be diminished (which in addition to provide the O_2 for the complete combustion is used to cool down the tubes), and so could be reduced the consumption of natural gas.

STAGE 3

In a third stage, in order to increase the profits of the business unit and mainly to continue reducing the emissions of CO_2 to the environment, a non-utilized active (a CO_2 production plant burning natural gas to produce it) was used to capture CO_2 from the SMR flue gases vented into the atmosphere. Thus, about 25 tons/day of CO_2 are recovered for the CO_2 local market, reducing emissions into the atmosphere in the same amount. For this, the stack of the combustion gases of the SMR was linked to the absorber (of the plant previously disused) by means of a duct and two blowers, one hot next to the fireplace and one cold after having reduced the temperature to the flow of flue gas after the exchange with cooling water. Absorber and stripper were operated at low pressure, and an 18% vol MEA solution was used. The liquefaction of CO_2 was carried out at 17 barg, using a refrigeration circuit with NH_3. This technique is very favorable for the industry since the stream rich in CO_2 is a waste. However, the practical use of this technique has some disadvantages, which must be known in advance to do not commit costly errors. As is well known, when the SMR already incorporates a sequestration of CO_2 in the syngas stream (MDEA), the flue gases are poor in CO_2 (4-8% v), and the separation is more difficult. On the other hand, the current in question has a high concentration of NOx, even using low NOx burners, which needs to the inclusion of a purification unit. Additionally, depending on the charge to the SMR, the stack gases may have an O_2 concentration, which may be in the range of 1 to 2% v, for 100% charge and 8% v for 50% charge. This last situation can lead to the degradation of solutions capable of absorbing CO_2, causing serious corrosion problems. To try to mitigate this situation, it is very important to choose the indicated amine for each process, its concentration, pressure and operating temperature. It is also advisable but not imperative to use stainless steel in key places of the process, and use an O_2 sequestrant to alleviate

corrosive problems. It is also advised to place before the absorber entry into the poor MEA solution, activated carbon filter to retain degradation products of the MEA solution which should be changed between three and six months of operation depending on the load at the unit. Normally when using MEA a good “reclaimer” is required, which should be in service as long as possible to partially reverse the degradation and recover the MEA.

STAGE 4

As the rules on clean fuels are increasingly demanding, the consumption needs of H_2 by refineries continues to increase. In this sense, our company installed a new SMR very close to the first. In this case, the technology is a Top fired, which has no units to recover CO_2.

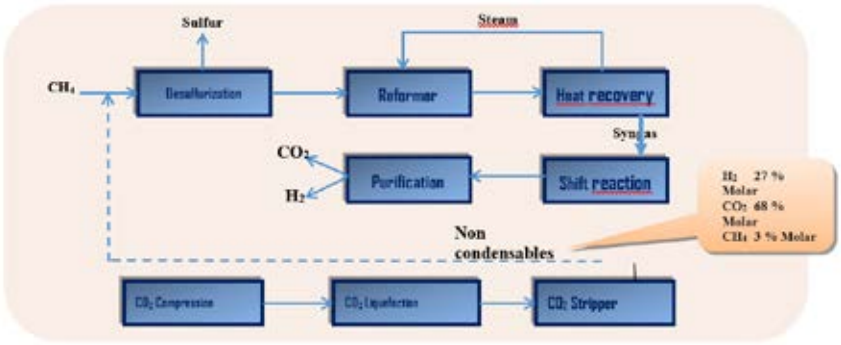
To try to mitigate as much as possible the CO_2 emissions to the atmosphere, and taking into account that the flue gas vented has about 19% vol of CO_2, it was decided to change the location of the chimney outlet to this second SMR, to add a Stripper to the absorption plant, and use an old liquefaction plant with NH_3 refrigerant circuit to recover in total about 80 Tn/day of CO_2. In this case, as the second reformer operates almost to its design capacity, the degradation problems of the MEA solution disappeared because the concentration of O_2 in the flue gas is in the order of 2 to 3% vol.

RESULTS AND DISCUSSION

Stages 1 and 2 show us very satisfactory results, since we managed to maintain H_2 production by reducing CO_2 emissions, and reducing the consumption of natural gas.

In stage 3, we had process complications caused by the composition of the raw material (flue gas), which made the absorption/desorption process difficult. Fundamentally, we had to take many precautions to abolish the corrosive processes in the derivative MEA solution of the high amount of O_2 present. Fortunately, with an exhaustive study of the problems, we were solving them one by one and we achieved the objective of reducing emissions and increasing CO_2 production.

In stage 4, since the composition of the flue gas was much friendlier, the operation of the absorption plant was much easier, achieving our final objective without any inconvenience, reducing emissions, significantly increasing the production of CO_2, reducing the consumption of natural gas, maintaining H_2 production and using disused assets of our company. In the scheme shown in **Figure 2**, the process of producing H_2 and CO_2 from natural gas can be visualized, and in a dotted line the injection of non-condensable.



Fiq. 2. The process of producing H_2 and CO_2 from natural gas

In the **Figure 3**, you can see the installation of the old plant not previously used to which a revamping was carried out and some equipment was added to adapt it to the recovery of CO_2 from the flue gas stream. In a yellow circle, you can see the flue gas outlet in the steam-reforming stack.



Fiq. 3. The installation of the old plant

CONCLUSIONS

The aforementioned possible drawbacks were solved by adding a suitable NOx filter as well as a formulation of the MEA solution suitable for O_2 present. As a result, production could be increased by around 25 Tn/day of CO_2. With the addition of SMRII, the amount of CO_2 recovered was increased and when taking another quality of flue gas with a much higher percentage of CO_2 and O_2 much lower under the absorption process, it was much easier to operate. In total, the amount of CO_2 that was avoided to be sent to the atmosphere was 82 Tn/day, and the reduction in natural gas consumption was 6,500 Nm^3/day. Our next step will be to send the non-condensable of these liquefaction units to the SMRII, to continue lowering the polluting emissions and reducing the consumption of fossil fuels (natural gas).

REFERENCES

1. C.N. Ávila-Neto, S.C. Dantas, F.A. Silva, T.V. Franco, L.L. Romanielo, C.E. Hori, A.J. Assis. *Hydrogen production from methane reforming: Thermodynamic assessment and autothermal reactor design*. Journal of Natural Gas Science and Engineering, 1(6), 205-215 (2009)
2. J.L.G. Fierro. *Tecnologías de producción masiva de Hidrógeno*. 1, 1-10 (2004)
3. M. Andrew Crews and B. Gregory Shumake. *Hydrogen Production and Supply - Meeting Refiners' Growing Needs*. Practical Advances in Petroleum Processing, 25, 771-817 (2006)
4. P. van Beurden, *On the catalytic aspects of steam-methane reforming: A literature Survey*. Technical report, ECN-I-04-003, ECN Energy Innovation, Netherlands (2004)
5. Yong-Seog Seo, Dong-Joo Seo, Yu-Taek Seo, Wang-Lai Yoon. *Investigation of the characteristics of a compact steam reformer integrated with a water-gas shift reactor*. Journal of Power Sources. 161(2), 1208–1216 (2006)
6. Vasant R. Choudhary, Kartick C. Mondal, *CO_2 reforming of methane combined with steam reforming or partial oxidation of methane to syngas over $NdCoO_3$ perovskite-type mixed metal-oxide catalyst.* Applied Energy, 83(9), 1024-1032 (2006)

WHEC-2022
23rd World Hydrogen Energy Conference
June 26-30, 2022 - Istanbul

#59

A PARAMETRIC NUMERICAL ANALYSIS OF LAMINAR HYDROGEN DIFFUSION FLAMES

Ayse Korucu [1], Ali Cemal Benim [2]*
[1]Izmir Institute of Technology, Faculty of Mechanical Engineering, Gülbahçe 35430 Urla / İzmir, Turkey
[2]Duesseldorf University Appl. Sci., Mech. & Process Eng., Center of Flow Simulation (CFS), Muensterstr., 156, 40476 Duesseldorf, Germany

*Corresponding author e-mail: alicemal@prof-benim.com

ABSTRACT

Atmospheric, laminar, diffusion flames of hydrogen and air are numerically investigated. A detailed hydrogen combustion reaction scheme, in combination with the extended Zeldovich mechanism for the thermal nitrogen oxide formation are used. For comparison purposes, a global mechanism is also applied. The numerical procedure is first validated by comparisons with results of other authors. Subsequently, parametric studies are performed to find optimal solutions with respect to the related to the operation parameters of such flames to achieve minimum low nitrogen oxide emission levels. The question that are addressed include the Reynolds number effect on nitrogen emissions, and the interaction of neighbouring flames, when they are applied in an array. For ensuring an adequately fine resolution of the flame fronts, local adaptive grid refinement techniques are applied to track the flame front. For preliminary results the radiative heat loses has assumed to be insignificant however it should be taken into the account for the further analyses. The maximum temperature is predicted to be ~2040 K which is higher than the reported adiabatic stoichiometric flame temperature, 2023K for the exit velocity of 0.5 m/s. The radial mole fractions of N2 and H2 at the centerline are observed to be 0.66 and 0.41 respectively at the axial distance of 10 mm. Furthermore, the width of the high temperature region of the flame is observed to be ~6.5 mm.

Keywords: Hydrogen combustion, Laminar diffusion flame, Thermal nitrogen oxide formation, CFD

INTRODUCTION

Power generation largely depends on the conversion of the chemically bound energy by the combustion process. Parallel to new energy sources and recovery techniques [1], combustion continues to play an important role in power generation. Combustion of H_2-blend fuels enable clean energy supply. On the one hand, H_2 represents an attractive alternative to storing excess energy in renewable power generation [2]. On the other hand, instead of combustion [3,4] gasification [5] is a good possibility for clean power generation, synthesis gas containing, in addition to CO and small amounts of CH_4, significant amounts of H_2. Additionally, there is a growing interest in hydrogen production using nuclear power plants [6].

In power generation, the state-of-the-art technology for gas turbines is the lean premixed combustion, due to its high potential for achieving very low NO_x emissions. A principal problem here is the so-called “flashback” [7]. This makes the use of H_2-blend fuels to a great challenge, since their high reactivity increases the flame speed and flashback propensity. Combustion of H_2 has relevance also for safety engineering. H_2 has a high diffusivity, and its leakage is more likely to be an issue compared to other gases. H_2 also plays a special role in conjunction with the safety of nuclear power plants on conjunction with the storage of the released slightly radioactive H_2-steam mix.

To circumvent the problem of flashback, many researchers started to revert to the more conventional non-premixed combustion technology and explore means of reducing NO_x emissions within this framework, with some success. In such applications that can be found in different areas, such as power generation [8], or domestic boilers [9], the main principle utilized to reduce the thermal nitrogen oxide formation is the reduction of the residence time in the hot flame zone. Principally, this is achieved by designs that utilize arrays of a large number of micro-scale diffusion flames. Due to the small sizes of the injectors, the resulting flames may turn out to be laminar, as e.g., observed in Ref. [9], which brings the combustion in the laminar flow regime again in focus of investigation as a relevant flow mode for certain applications.

Although the main principle of using micro diffusion flames is declared to be the reduction of the residence time of the combustion gases in the flame zone, there still is a need for further studies on the quantification of the various effects and optimization of the configuration. This constitutes the focus of the present contribution.

Hydrogen diffusion flames will be numerically analyzed. The thermal NO_x formation will be investigated. Due to the relevance to the present context, laminar flames will be considered at the present stage of the investigation. The study consists out of several stages. In the first stage, a detailed validation study will be performed, using the published data of other authors on H_2 flames [10]. Upon this basis, the question will be addressed, within the

framework of parametric studies. First, the combined role of the jet velocity and diameter for a power will be investigated. The question to be answered here is, if there is an optimum point for a given power, or in other words, if there is an optimal Reynolds number leading to lowest NOx emissions for a given power. Secondly, the $EINO_x$ scaling of H_2 diffusion flames will be addressed for the laminar flow, as the existing $EINO_x$ data [11] is mainly referring to the turbulent regime. A further question to be addressed is the interaction of neighboring flames in an array. In the known applications [8, 9] the number of micro-diffusion flames are applied in an array. To spare space, close arrangement of the flames is advantageous, where, however, the interaction between the flames may cause negative effects (eventual positive effects are to be identified). This point, which has not been numerically investigated for H_2 flames so far, will be studied to suggest an optimal spacing, allowing a minimum distance between neighboring flames, without a substantial performance deterioration.

MODELING

The differential transport equations of the chemically reacting mixture are numerically solved, assuming a subsonic flow and an ideal gas behavior [12], considering multi-component diffusion [13]. The specific heat capacities as function of temperature are obtained using a pair of fourth order polynomials [13], for low and high temperature ranges. Transport properties are obtained from the kinetic theory [13]. Chemical kinetics rate coefficients are modeled by Arrhenius expressions [13]. Laminar diffusion flames in a generic co-axial configuration are considered. Thus, modelling errors with respect to the modelling of turbulence [14] and turbulence-chemistry interaction [15,16] are avoided. For the numerical simulations, ANSYS Fluent 19.0 [17] is used. As Navier-Stokes solver, the SIMPLEC [17] scheme is used. For discretizing the convective terms, a second-order upwind scheme [17] is applied. The chemical kinetics software Cantera [18], is also used for verification purposes. As the reaction mechanism for H_2 combustion, the detailed mechanism of Conaire et al. [19] is used. For comparison purposes, the global mechanism of Marinov et al. [20] is also be considered. Thermal nitrogen oxide formation is modelled using the extended Zeldovich mechanism [12]. For coping with the high grid resolution requirements dictated by the small length scales of the flame front, adaptive gridding techniques are used. The radiative heat transfer has not been considered for the initial simulations however Toro et. al. has considered optically thin radiation model. The dimension of the computational domain is 60 cm in axial and 9.5 cm in radial directions meshed with 13500 quadrilaterals cells. Species Transport has been activated along with the Volumetric Reactions adopting the Finite-Rate/No TCI for the Turbulence -Chemistry Interaction in order to model laminar diffusion flames. Diffusion Energy Source, Full Multicomponent and Thermal Diffusion are all activated for the sake of the complete mathematical modeling.

RESULTS

Figure 1 shows the species radial mole fraction profiles at the axial distance of 10 mm for the fuel feeding speed (V) of 0.5 m/s, while Figure 2 contains the contour plot of flame temperature. Similar results have been obtained in comparison to Toro et.al.'s reported profiles in their work [10] for detailed mechanism of H2/Air laminar microdiffusion flames, which implicates that such flames may be analyzed with detailed chemistry for gaining a better understanding on the pollutant preventions in gas turbines adopting micromix layout for fuel feeding system. The radial mole fractions of N2 and H2 at the centerline are observed to be 0.66 and 0.41 respectively while they are reported to be 0.57 and 0.43 in Ref. [10]. In the current study the maximum temperature is predicted to be ~2040 K which is higher than the reported adiabatic stoichiometric flame temperature, 2023K for the maximum stream velocity considered in the study of 0.5 m/s as seen in Figure 2. Furthermore, the width of the high temperature region of the flame is observed to be ~6.5 mm in the current study being wider than the reported value which is ~4.5 mm in Ref. [10]. The differences for the mole fractions, flame temperature width and the maximum flame temperature between the current study and Ref. [10] might be explained by the adopted detailed chemical mechanism adopted in the current study as well as the lack of a radiation model for the initial simulations.

CONCLUSIONS

Laminar hydrogen-air diffusion flames are numerically investigated with emphasis on thermal nitrogen oxide formation. Results are validated by comparisons with calculations and measurements of other authors. The detailed H2/Air chemical mechanism is adopted and tested the validity of the laminar diffusion flame predictions in comparison to the existing literature. The preliminary results are promising which is able to extend the literature adopting detailed H2/Air chemical mechanism for laminar diffusion flames. The predicted maximum flame temperature has been observed to be higher than the reported adiabatic temperature, and the high temperature region's width is seen to be wider than the reported value in Ref. [10] which can be explained by the adopted chemical mechanism in the current study and lack of radiation modeling in the current study. For the future works, the grid independency of the CFD analyses must be ensured as well as the optimum Re number leading to the possible NOx emissions for a predetermined power.

Additionally, interaction between the flames in array and optimizing the spacing which will allow the minimum interval dimension between neighboring flames while preventing a substantial deterioration of performance.

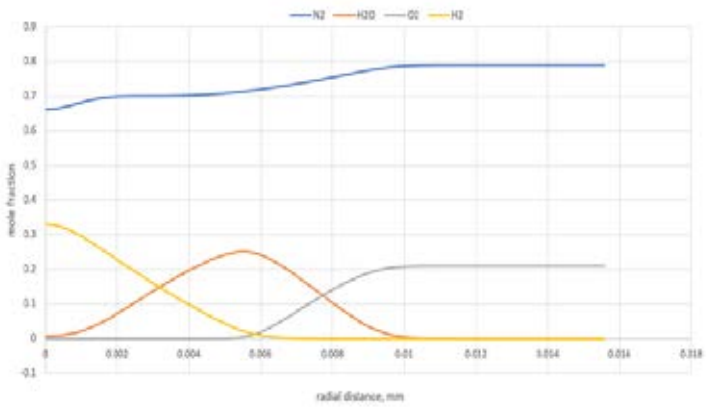


Figure. 1: Species mole fraction profiles at z = 10mm (V=0.5 m/s)

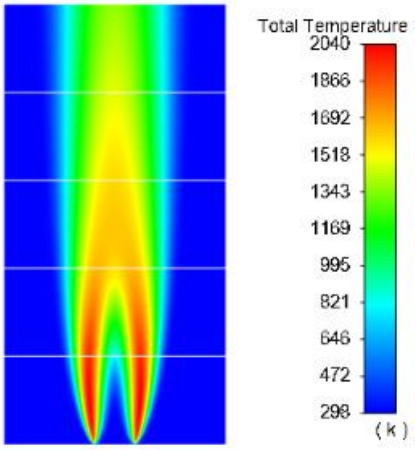


Figure 2: 2D Temperature contour plot (V=0.5 m/s).

REFERENCES

1. Pfeiffelmann B, Benim AC and Joos F. 2019. A finite volume analysis of thermoelectric generators. Heat Transfer Engineering 40(17-18): 1442-1450
2. Götz M, Lefebvre J, Mörs F, McDaniel Koch A, Graf F, Bajohr S, Reimert R and Th. Kolb, Th. 2016. Renewable power-to-gas: a technological and economic review. Renewable Energy 85: 1371-1390
3. Benim AC, Epple, B and Krohmer B. 2005. Modelling of pulverised coal combustion by a Eulerian-Eulerian two-phase flow formulation. Progress in Computational Fluid Dynamics – An International Journal 5(6): pp.345-361
4. Epple B, Fiveland W, Krohmer B, Richards G and Benim AC. 2005. Models for the simulation of pulverized coal combustion. International Journal of Energy for a Clean Environment 6(3):267-287
5. Benim AC and Kuppa K. 2016. Modeling of entrained-flow coal gasification by an equilibrium Eulerian-Eulerian two-phase flow formulation. Isi Bilimi ve Teknigi Dergisi / Journal of Thermal Science and Technology 36(2): 93-102.
6. IAEA. 2013. Hydrogen Production Using Nuclear Energy, IAEA Nuclear Energy Series, No. NP-T-4.2, International Atomic Energy Agency, Vienna, Austria
7. Benim AC and Syed KJ. 2015. Flashback Mechanisms in Lean Premixed Gas Turbine Combustion, Cambridge, Academic Press.
8. Haj Ayed A, Kusterer K, Funke HHW, Keinz J and Bohn D. 2017. CFD based exploration of the dry-low-NOx hydrogen micromix combustion technology at increased energy densities. Propulsion and Power Research 6(1):15-24
9. Lopez-Ruiz G, Fernandez-Akarregi AR, Diaz L, Urresti I, Alava I and Blanco JM. 2019. Numerical study of a laminar hydrogen diffusion flame based on the non-premixed finite-rate chemistry model; thermal NO_X assessment
10. Toro VV, Mokhov AV, Levinsky HB and Smooke MD. 2005. Combined experimental and computational study of laminar, axisymmetric hydrogen-air diffusion flames. Proceedings of the Combustion Institute 30:485-492
11. Oh J, Hwang J, Yoon Y. 2010. EINOx scaling in a non-premixed turbulent hydrogen jet with swirled coaxial air. International Journal of Hydrogen Energy 35(16): 8715-8722
12. Turns SR. 2012. An Introduction to Combustion, 3rd ed., New York, McGrawHill
13. Bird RB, Stewart WE and Lightfoot EN. 2002. Transport Phenomena, 2nd ed., New York, Wiley
14. Benim AC, Cagan M, Nahavandi A and Pasqualotto E. 2007. Proceedings of the 5th IASME/WSEAS International Conference on Fluid Mechanics and Aerodynamics, Athens, Greece, August 25-27, 2007. pp. 232-237
15. Benim AC, Nahavandi A, Stopford P, Syed KJ. 2006. DES LES and URANS investigation of turbulent swirling flows in gas turbine combustors. WSEAS Transactions on Fluid Mechanics 5(1):465-472
16. Iqbal S, Benim AC, Fischer S, Joos F, Kluß D and Wiedermann A. 2016. Experimental and numerical analysis of natural bio and syngas swirl flames in a model gas turbine combustor. Journal of Thermal Science 25(5):460-469
17. www.ansys.com. Accessed on December 2, 2019
18. www.cantera.org. Accessed on November 6, 2019
19. Conaire MO, Curran HJ, Simmie JM, Pitz WJ and Westbrook CK. 2004. A comprehensive modeling study of hydrogen oxidation. International Journal of Chemical Kinetics 36:603-622
20. Marinov NM, Westbrook CK, Pitz W. 1995. Detailed and global chemical kinetics model for hydrogen. Report No. UCRL-JC-120677, Lawrence Livermore National Laboratory, CA

WHEC-2022
23rd World Hydrogen Energy Conference
June 26-30, 2022 - Istanbul

#115
HYDROGEN CERTIFICATION OF ORIGIN IN COLOMBIA

[1] Juan Camilo Moreno, [1] Martha Cobo, [1] Nestor Sanchez*
[1]Group of Energy, Materials, and Environment. Universidad de La Sabana, Faculty of Engineering, Department of Chemical and Biochemical Processes. km 7 Autopista Norte Bogotá-Chía, Campus Universitario Puente del Común. Chia, Colombia

*Corresponding author e-mail: nestor.sanchez1@unisabana.edu.co

ABSTRACT

Hydrogen (H_2) has been widely recognized as a crucial alternative regarding an imminent energy transition, due to its use as an energy vector and its environmental innocuousness at usage. Steam Methane Reforming (SMR) is the most common H_2 production method, and standardizing its emissions is key to ensure long term benefits from using H_2. This work aims at comparing several existing standards and proposing an emission reduction target for Colombia. SMR has an average carbon footprint of 10.74 kg CO_2-eq/kg H_2. Additionally, it was found that existing standards concur on an emission reduction target of 60%. Factoring Colombia's low emission factor in energy production, as well as its existing piping system, it was concluded that this target is achievable and, due to the advantages of complying with international standards, it is recommendable to institute it in future regulations.

Keywords: Greenhouse Gases, Hydrogen, Life Cycle Assessment, Steam Reforming

INTRODUCTION

Climate change has turned into one of the most afflicting concerns in modern society, and the evolution of energy production is a key challenge in mitigation and reversion of its effects [1]. Using conventional energy sources, such as fossil fuels, provoke greenhouse gases (GHG) emissions [2]. Fossil fuels are responsible of about 65% of GHG emissions [3], and the fact that their sources will face scarcity in the future creates the need for an energy transition where renewable energies, such as solar power, wind power, geothermal, among others, play a key role.

In Colombia, hydrogen (H_2) has been identified as an ideal energy carrier that will allow the distribution of renewable energy since it can be stored and transported [4]. It is expected that the use of H_2 will allow the country to take advantage of the renewable energy potential located in the north Caribbean region, especially regarding solar and wind power, by supplying the whole country with low emission energy. Several countries, such as Canada, Japan, and members of the European Union, have identified the same opportunity, since H_2 is an energy vector that can be produced, stored, transported, and recycled. Besides, H_2 oxidation in fuel cells will produced water as by product, and consequently, mitigating carbon footprint [5]. By incorporating H_2 into the energy grid of a country, emission reduction and energy availability targets, (e.g., reducing 20% of CO_2) could be achieved [4]. Furthermore, moving towards H_2 will contribute significantly to the fulfillment of the Sustainable Development Goals proposed by the United Nations [6]. Specifically, goal 7 (i.e., affordable and clean energy), goal 11 (sustainable communities), and goal 13 (climate change action) will be the main targets on the use of H_2 to fulfill the aforecited goals. To warrant the benefits that H_2 could be offered, it is important not only to promote H_2 use but also to guarantee clean H_2 production through its entire life cycle. Currently, H_2 is produced either from fossil fuels through SMR, partial oxidation of hydrocarbons, and coal gasification, or from renewable energies through the electrolysis boosted by solar, wind, or hydropower [7]. All processes must be regulated to guarantee a minimum emission reduction when compared with conventional energy sources. Guarantees of origin (GO) have been commonly used to evaluate alternative energies, and they constitute a viable option for H_2. Countries such as Germany, United Kingdom, United States, France, and Australia have been developing standards for H_2 GO, by establishing emission reduction targets [8]. Hence, the aim of this research is to propose a GO scheme under Colombia scenario.

METHODOLOGY

To determine an appropriate requirement for low-emission H_2 in Colombia, it is important to identify current emission levels regarding the method of interest (SMR). Through literature review, common emission levels for this technique were retrieved. Then, following current regulation proposals, and considering Colombia's current energy grid, raw material obtention, and availability, a suitable level of emission reduction target was fulfilled.

SMR common emission levels and reduction target

Several studies have performed Life Cycle Assessment (LCA) processes regarding H_2 production through SMR. LCA determines environmental impacts of processes or products, contemplating not only their final uses, i.e., energy production using H_2, but also considering related processes, such as raw material extraction, plant decommissioning, waste disposal, among others [9]. By comparing existing LCA information from H_2 producing countries, common emission levels were verified, and differences between them were weighed. As aforementioned, several countries

have defined minimum emission reduction levels required to consider H_2 as low emission. Existing regulations were compared. Following this comparison and considering differences in the energy infrastructure, a fitting minimum reduction level for Colombia were proposed.

RESULTS AND DISCUSSION

SMR comparison using LCA

Table 1 presents the reported LCA results for SMR across several countries, considering systems without carbon capture and storage (CCS) or other emission reduction alternatives. According to Table 1, the average carbon footprint is 10.74 kg CO_2-eq/kg H_2, which is close to the value reported for the GO scheme proposed for the European Union (i.e., 10.92 kg CO_2-eq/kg H_2). Aside from the information presented in Table 1, relevant studies showed that CCS could reduce SMR emissions to 3.45 kg CO_2-eq/kg H_2 [10], while alternative technologies may improve the process, e.g., using chemical looping combustion (CLC) as a heat source for SMR can reduce emissions to 3.01 kg CO_2-eq/kg H_2 [12].

Table 1. Emissions and yield of SMR for current hydrogen producers.

Country	Emissions (kg CO_2-eq/kg H_2)	Yield (kg H_2/kg natural gas)	References
Spain	10.57	0.32	[10]
Canada	11.89	0.34	[11]
China	10.76	0.36	[12]
United States	11.88	0.34	[13]
Germany	8.59	0.15	[14]

Reduction target

Several countries are currently developing H_2 regulations, and some have already established their emission reduction requirements. Existing and developing standards and their requirements are presented in Table 2. All emission reduction requirements are based on SMR average emission levels, since it is the most common H_2 production method. A consensus can be observed in Table 2: Most countries expect reductions of about 60% CO_2-eq emissions to classify H_2 as “green” or “low emission”. While organizations like California Air Resources Board (United States) and the Department of Energy and Climate Change (United Kingdom) present higher and lower targets, respectively, there seems to be a global agreement on a 60% emission reduction.

Table 2. Emission reduction requirements in existing and developing hydrogen regulations.

Country	Current emission factor (kgCO_2-eq/kWh)	Status	Organization	Maximum emissions (kgCO_2-eq/kgH_2)	Other requirements
United States	0.38 [15]	Active	California Air Resources Board [16]	3.6 (67% reduction)	None
European Union	Not applicable	Active	CertifHy [17]	4.37 (60% reduction)	Renewable energy sources for green hydrogen label
United Kingdom	0.4 [18]	In process	Department of Energy and Climate Change [19]	3.33-8.33 (in discussion)	None
Germany	0.48 [20]	Active	TÜV SÜD [21]	4.37 (60% reduction for conventional sources) 2.73 (75% reduction for electrolysis)	None
Canada	0.79 [22]	Proposal	Natural Resources Canada [23]	4.37 (60% reduction)	None

When analysing Table 2, it is important to consider the emission factor in each country, since this value could limit a country’s ability to reach emission reduction targets. From Table 2, Canada has the highest emission factor, 0.79 kg CO_2-eq/kWh. Germany, with 0.48 kgCO_2-eq/kWh, United Kingdom, with 0.4 kgCO_2-eq/kWh and United States, with 0.38 kgCO_2-eq/kWh has similar emission factors. Colombia has a substantial advantage in the emission factor subject: in 2020, Colombia’s emission factor was only 0.16 kg CO_2-eq/kWh [24], which is substantially inferior when compared with current H_2 producers and prospects. Since Colombia has a well functioning pipeline, which could be

adapted for H_2 transport, it is reasonable to adopt current world trend and establish a 60% emission reduction target with respect to the average emission level of SMR processes, considering the future advantages that doing so would present, including exportation possibilities and international protocol compliance.

CONCLUSIONS

Natural Gas Steam Reforming is a suitable technology as starting point into a H_2 oriented energy grid. Thanks to the fact that it is currently used worldwide, and that technologies like CCS and CLC allow it to meet emission reduction targets, its viability for low emission H_2 production is evident. Current pipeline system, emission factor and natural gas availability position Colombia as a country with immense potential to adopt H_2 as a solution for energetic transition. Current H_2 leaders agree on a 60% emission reduction target, and Colombia's circumstances and advantages will allow the country to level with them and become a H_2 leader in Latin America. With an appropriate strategy and investment, this emission reduction target is reasonable, achievable and a potential driving force to fulfill energetic, environmental, and socio-economic targets.

ACKNOWLEDGEMENT

The authors acknowledge the generous support of Universidad de La Sabana, the Colombian Ministry of Science, Technology and Innovation – Minciencias and the Colombian Mining and Energy Planning Unit – UPME via contract no. 036-2021 (Universidad de La Sabana project code ING-272-2021).

REFERENCES

1. Edwards PP, Kuznetsov, VL and David WIF. 2007. Hydrogen energy. Philosophical Transactions of the Royal Society A 365:1043-1056.
2. Wuebbles DJ and Jain AK. 2001. Concerns about climate change and the role of fossil fuel use. Fuel Processing Technology 71:99-119.
3. Covert T, Greenstone M and Knittel CR. 2016. Will We Ever Stop Using Fossil Fuels?. Journal of Economic Perspectives 30:117-138.
4. https://www1.upme.gov.co/DemandaEnergetica/PEN_documento_para_consulta.pdf. Accessed on December 1, 2021.
5. Rosen MA and Koohi-Fayegh S. 2016. The prospects of hydrogen as an energy carrier: an overview of hydrogen energy and hydrogen energy systems. Energy, Ecology and Environment 1:10-29.
6. https://www.undp.org/sustainable-development-goals. Accessed on December 1, 2021.
7. Kothari R, Buddhi D and Sawhney RL. 2006. Comparison of environmental and economic aspects of various hydrogen production methods. Renewable and Sustainable Energy Reviews 12:553-563.
8. Velazquez A and Dodds PE. 2020. Green hydrogen characterisation initiatives: Definitions, standards, guarantees of origin, and challenges. Energy Policy 138:111300.
9. Hauschild MZ, Rosenbaum RK and Olsen SI. 2018. Life Cycle Assessment. Theory and Practice. Cham, Springer.
10. Dufour J, Serrano DP, Gálvez JL, Moreno J and García C. 2009. Life cycle assessment of hydrogen production. Environmental feasibility and reduction of greenhouse gases emissions. International Journal of Hydrogen Energy 34:1370-1376.
11. Cetinkaya E, Dincer I and Naterer GF. 2012. Life cycle assessment of various hydrogen production methods. International Journal of Hydrogen Energy 37:2071-2080.
12. Wang Z, Li L and Zhang G. 2018. Life cycle greenhouse gas assessment of hydrogen production via chemical looping combustion thermally coupled steam reforming. Journal of Cleaner Production 179:335-346.
13. https://www.nrel.gov/docs/fy01osti/27637.pdf. Accessed on December 2, 2021.
14. Schreiber A, Peschel A, Hentschel B and Zapp P. 2020. Life Cycle Assessment of Power-to-Syngas: Comparing High Temperature Co-Electrolysis and Steam Methane Reforming. Frontiers in Energy Research 8:533850.
15. https://www.eia.gov/tools/faqs/faq.php?id=74&t=11. Accessed on December 3, 2021
16. https://theicct.org/sites/default/files/publications/California%20Contracts%20for%20Difference_white-paper_ICCT_102016.pdf. Accessed on December 2, 2021.
17. https://www.certifhy.eu/go-labels/. Accessed on December 3, 2021.
18. https://assets.publishing.service.gov.uk/government/uploads/system/uploads/attachment_data/file/972583/2020_Provisional_emissions_statistics_report.pdf. Accessed on December 3, 2021.
19. https://assets.publishing.service.gov.uk/government/uploads/system/uploads/attachment_data/file/454538/Green_Hydrogen_Standard_CfE_Government_Response_v1_0.pdf. Accessed on December 3, 2021.
20. https://www.umweltbundesamt.de/en/press/pressinformation/co2-emissions-per-kilowatt-hour-of-electricity-in. Accessed on December 3, 2021.
21. https://www.tuvsud.com/en/press-and-media/2020/february/tuev-sued-provides-greenhydrogen-certification. Accessed on December 3, 2021.
22. https://www.cer-rec.gc.ca/en/data-analysis/energy-commodities/electricity/report/2017-canadian-renewable-power/canadas-renewable-power-landscape-2017-energy-market-analysis-ghg-emission.html. Accessed on December 3, 2021.
23. https://www.nrcan.gc.ca/sites/www.nrcan.gc.ca/files/environment/hydrogen/NRCan_Hydrogen-Strategy-Canada-na-en-v3.pdf. Accessed on December 3, 2021.
24. https://www.larepublica.co/especiales/colombia-potencia-energetica/en-colombia-el-factor-de-emision-de-co2-por-generacion-electrica-es-de-16438-gramos-por-kwh-2966236. Accessed on December 3, 2021.

WHEC-2022
23rd World Hydrogen Energy Conference
June 26-30, 2022 - Istanbul

#137
PROSPECTS OF RENEWABLE HYDROGEN IN TRANSPORT

[1*] *Amela Ajanovic,* [1] *Reinhard Haas,* [1] *Marlene Sayer*
[1]Vienna University of Technology (TU WIEN), Energy Economics Group, Gusshausstr. 25-27/370-3,1040 Vienna, Austria

*Corresponding author e-mail: ajanovic@eeg.tuwien.ac.at

ABSTRACT

Hydrogen is often discussed as an energy carrier of the future. In this paper economic and environmental benefits of hydrogen use in passenger car mobility are analysed in comparison to the conventional vehicles. In spite of many hypes over the last decades, fuel cell vehicles are still a rarity on the streets. However, with the pressing environmental problems and possibility to use hydrogen as a fuel for mobility as well as storage for surplus electricity from renewable energy sources, role of hydrogen in the future energy and transport system is becoming more important.

Keywords: hydrogen, fuel cell vehicles, mobility, costs, emissions

INTRODUCTION

With the growing environmental problems, rise a need for low-carbon fuels and technologies. The transport sector, which is still almost completely dependent on fossil fuels, is a huge challenge for decarbonization. Although, currently major focus is put on electrification of mobility, hydrogen and fuel cell vehicles (FCV) are very often seen as a long-term solution for the transport sector. Hydrogen and fuel cells vehicles have already a long history. The major milestones of hydrogen use in the transport sector are presented in Fig. 1. There were many hypes in the history of hydrogen. The new one is driven by the increasing use of volatile renewable energy sources (RES), which leads to a need for the additional storage options. The advantage of hydrogen is that it can be used as a fuel, feedstock or energy storage.

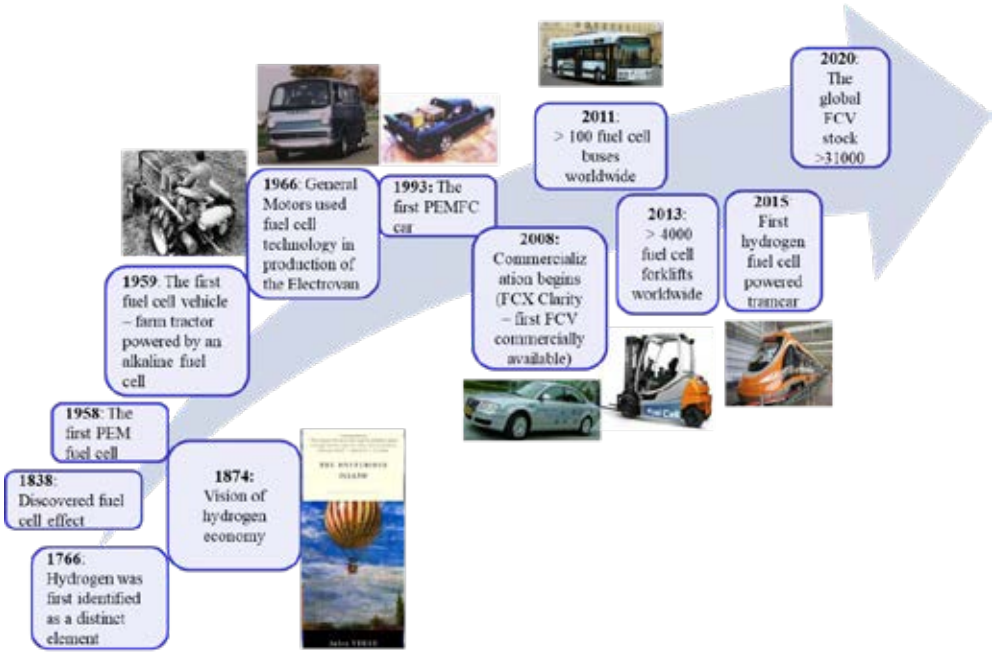


Fig. 1. Major milestones in the deployment of fuel cell vehicles (adapted from [1])

In the transport sector, besides battery electric vehicles, fuel cell vehicles powered by hydrogen are the only zero-emission options currently available.

The core objective of this paper is to discuss the economic and environmental performances of hydrogen and fuel cell passenger vehicles in comparison to conventional internal combustion engine (ICE) vehicles.

This topic has been already discussed by several authors [2-4], however, in this paper most recent data are included.

METHOD OF APPROACH

Since the future perspective of hydrogen and fuel cell vehicles is very dependent on their economic performance, total mobility costs per kilometer driven are calculated considering current energy and vehicles prices. These costs are calculated using following equation:

$$TMC = \frac{IC \cdot CRF}{skm} + P_e \cdot EC + \frac{C_{o\&m}}{skm} \quad (1)$$

Moreover, future investment costs are calculated considering possible technological learning through the increasing production of fuel cell vehicles:

$$IC(x_t) = IC(x_{t0}) \cdot (\frac{x_t}{x_{t0}})^{-b} \quad (2)$$

Environmental assessment is conducted considering well-to-tank (WTT) and tank-to-wheel (TTW) emissions, as well as emissions caused during car manufacturing and disposal ($CAR_{emissons}$). Total emissions caused by vehicles are calculated as:

$$CO_{2\ total\ emissions} = WTT_{emissions} + TTW_{emissions} + CAR_{emissions} \quad (3)$$

RESULTS AND DISCUSSION

Currently, fuel cell vehicles are economically not competitive with conventional ICE vehicles, mostly due to high investment costs. However, these costs are continuously decreasing. In the future, through the technological learning as well as increasing CO_2 taxes, which should better reflect the environmental costs of fossil fuels, it can be expected that fuel cell vehicles in combination with green hydrogen could become competitive with other automotive technologies. Figure 2 shows current and future mobility costs with fuel cell vehicles in comparison to conventional cars. As it can be seen, currently mobility cost with FCV is about 55% higher than those of conventional cars. In 2050, the cost difference could be just about 3%.

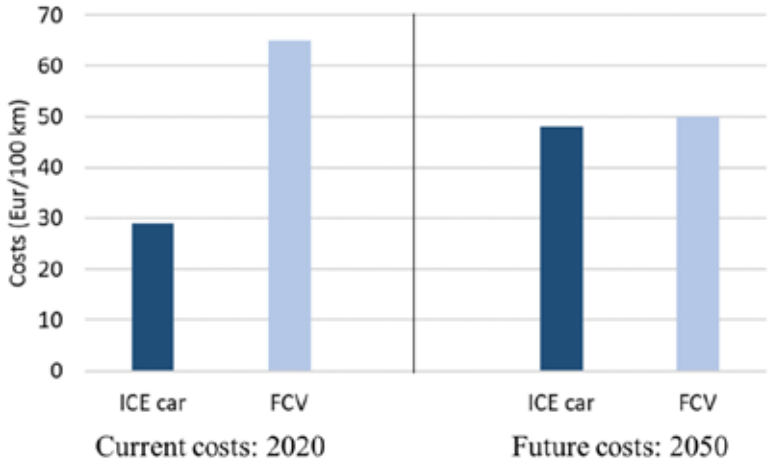


Fig. 2. Current and future mobility costs, FCV vs ICE vehicles

In opposite to poor economic performance, fuel cell vehicles have already now significant environmental benefits in comparison to conventional cars, see Fig. 3. Currently, the largest emission saving can be reached in the case that hydrogen is produced from RES (e.g. wind- and solar energy), so called green hydrogen. In such case total emissions of FCV are about four time lower in comparison to ICE vehicles. However, hydrogen is mostly produced by steam reforming of natural gas (NG) due to the lowest hydrogen production costs, and in this case, emission reduction is much lower. It is obvious that in the case of FCV, the largest contributor to the total emissions are WTT emissions, which are very dependent on the kind of primary energy sources used for hydrogen production.

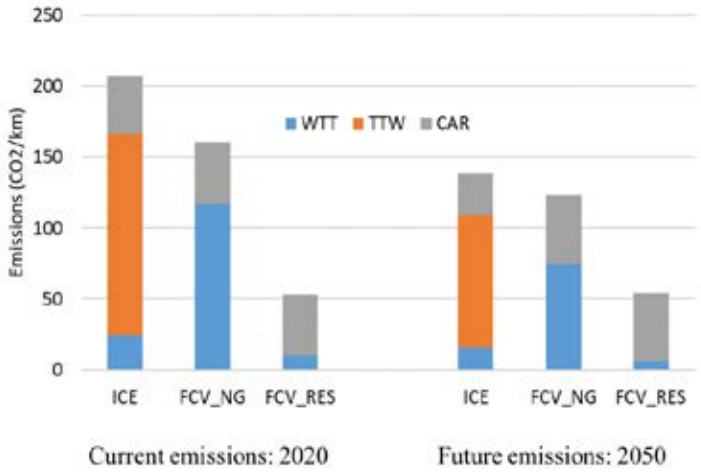


Fig. 3. Current and future emissions, FCV vs ICE vehicles

CONCLUSIONS

Hydrogen and fuel cell vehicles can contribute to the decarbonisation of the transport sector, especially if hydrogen is produced from RES. However, major current challenges are high investment costs of fuel cell vehicles and lack of necessary infrastructure. Future role of hydrogen and FCV is very dependent on policy framework. To reduce investment risks, it is important to have clear targets and long-term vision. With the increasing use of RES, interest in hydrogen which can be used also as a storage for the surplus electricity from RES, is growing every day.

NOMENCLATURE

TMC	Total mobility costs, EUR/100km
IC	Investment costs, EUR
CRF	Capital recovery factor
skm	specific number of kilometers driven, km/year
P_e	Energy price, EUR/kWh
EC	Energy consumption, kWh/km
$C_{o\&m}$	Operating and maintenance costs, EUR/year
x	Number of vehicles
b	learning index

REFERENCES

1. Ajanovic A. and Haas R. 2021. Prospects and impediments for hydrogen and fuel cell vehicles in the transport sector, International Journal of Hydrogen Energy, 46: 10049-10058
2. Ahmed A, Al-Amin AQ, Ambrose AF. And Saidur R. 2016. Hydrogen fuel and transport system: a sustainable and environmental future. Elsevier Int J Hydrogen Energy, 41:1369-1380
3. Yoo E, Kim M. and Song H. 2018. Well-to-wheel analysis of hydrogen fuel-cell electric vehicle in Korea. International Journal of Hydrogen Energy , 43:19267-19278.
4. Ajanovic A. 2015. The future of electric vehicles: prospects and impediments. WIREs Energy Environment. 4: 521-536

WHEC-2022
23rd World Hydrogen Energy Conference
June 26-30, 2022 - Istanbul

#151

HYDROGEN PRODUCTION FROM OLIVE OIL MILL WASTEWATER THROUGH STEAM REFORMING IN MULTIFUNCTIONAL REACTORS

*Cláudio Rocha, Miguel Angel Soria, Luís Miguel Madeira**
LEPABE, Dept. of Chemical Engineering, Faculty of Engineering-University of Porto, Rua Dr. Roberto Frias s/n, 4200-465 Porto.

*Corresponding author e-mail: mmadeira@fe.up.pt

ABSTRACT

Steam reforming technology integrating a membrane reactor and/or CO_2 capture for H_2 production from olive mill wastewater (OMW) was developed. The objective is to use a multifunctional reactor combining OMW reforming (using a stable/active catalyst) and the simultaneous products removal from the reaction zone in a single device: H_2 through an H_2-selective membrane and CO_2 through a CO_2 sorbent. Thus, the benefits of using different multifunctional reactors (sorption-enhanced reactor (SER), membrane reactor (MR) and sorption-enhanced membrane reactor (SEMR)), comparatively to the traditional reactor (TR), were assessed in this work in terms of H_2 production through the steam reforming of OMW (OMWSR). Using a SEMR, an H_2 yield enhancement of ≈ 44 % was observed compared to the TR – H_2 production of ≈ 11.5 mol_{H2}/mol_{OMW} in the SEMR.

Keywords: Olive mill wastewater; Steam reforming; CO_2 sorbent; H_2-selective membrane; Multifunctional reactors.

INTRODUCTION

Olive oil production is a major activity in the economy of Mediterranean countries, but also one of the agro-industrial sectors with major destructive environmental impacts. For instance, the OMW is a pollutant by-product of this process [1]. This effluent has a high pollutant organic load and is mainly composed of water, polyphenols, fatty acids and sugars. To decrease the environmental impact of this sector, it was suggested the application of the OMWSR, which can treat and economically valorize this waste (production of green H_2). A new multifunctional reactor configuration combining the OMWSR with H_2 and/or CO_2 selective removal is proposed herein for the 1st time, due to its potential to overcome some restrictions like the thermodynamic limit of the reversible reaction(s). In this work, it will be studied and compared the performance of a TR, a SER (with a CO_2 sorbent), a MR (with an H_2-selective membrane) and the SEMR (integrating both separations in the same device).

MATERIALS AND METHODS

The thermodynamic analysis of OMWSR was done employing the Aspen Plus V8.8® software [2]. The simulations were made at different temperatures, pressures and removal fractions of H_2 and CO_2 to identify the best operational conditions. Also, CO_2 equilibrium isotherms and breakthrough curves were obtained through static and dynamic tests, respectively, with both commercial sorbents and prepared doped-hydrotalcites (HTCs) at 300 ºC [3]. Further, a catalytic screening study (@ 350/400 ºC and 1 bar) was performed with commercial and prepared catalysts in a TR. After that, stability tests (24 h of time-on-stream) were performed with the best catalysts to be subsequently used in the above-mentioned multifunctional reactors [4]. The physicochemical characterization of all these samples was realized through several techniques (XRD, TPO, TPD, etc.). Finally, different multifunctional reactors (SER vs. MR vs. SEMR) were tested and compared to a TR (@ 350 and 1 bar, or 400 ºC and 4 bar) [5]. In all reactor configurations, a prepared Ni-Ru/Ce-SiO_2 catalyst was used, combined in the SERs with an HTC-based sorbent to capture CO_2. Additionally, in the MR and SEMR configurations, a Pd-Ag membrane was utilized to separate H_2 from the reaction medium.

RESULTS AND DISCUSSION

The optimum operating conditions for the OMWSR in a SEMR were determined in the thermodynamics analysis [2]. The H_2 yield increases with the H_2 and/or CO_2 removals – see Fig. 1a) for the hydrogen removal. It was also verified that the advantages of the SEMR are more perceptible at lower temperatures (300-400 ºC), and so this reactor configuration can be operated under milder conditions, which favor CO_2 sorption by the HTCs and membrane stability.

Among the prepared HTCs, the one modified with gallium and doped with potassium (HTC-CO_3(Ga)_K) presents the highest CO_2 sorption capacity (1.45 $mmol \cdot g^{-1}$, @ p_{CO2}= 1 bar and 300 ºC) in comparison with the other synthesized HTCs and even commercial sorbents – see Fig. 1b) [3].

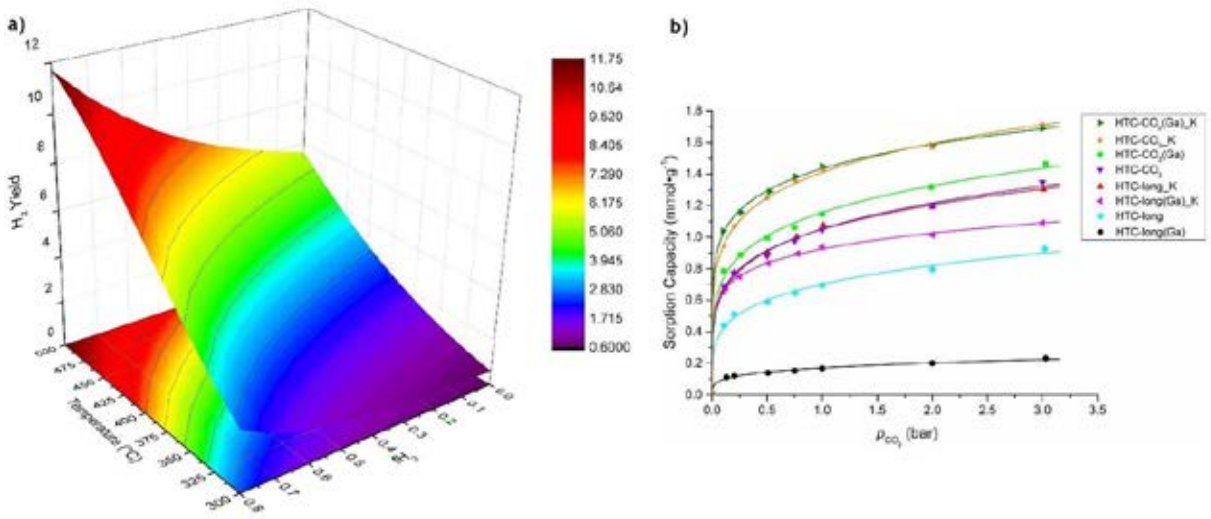


Fig. 1. a) Yield of H_2 as function of temperature and H_2 removal fraction at 1 bar in a MR – thermodynamic analysis. b) H_2 yield obtained using commercial and prepared catalysts. c) CO_2 equilibrium isotherms of prepared HTCs at 300 ºC.

Regarding the catalysts screening study, the Rh-based, as well as the Ni/SiO_2-Al_2O_3 and Ni-Ru/SiO_2 samples, reached the highest values of H_2 yield among the 10 commercial and 5 prepared catalysts tested (materials with different active phases/support and distinct metal loadings). Among them, the Rh/Al_2O_3 and Ni/SiO_2-Al_2O_3 catalysts presented a high and relative stable H_2 yield (ca. 9 mol_{H2}/mol_{OMW}) during 24 h of time-on-stream – Fig. 2.

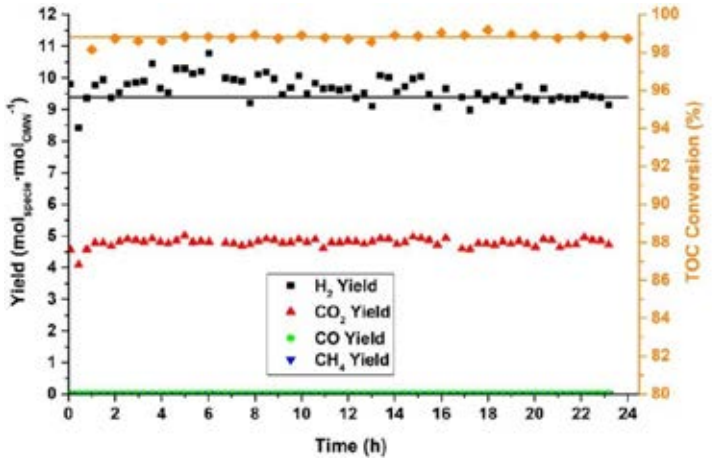


Fig. 2. Gaseous species yield and TOC conversion during 24 h time-on-stream for the Rh/Al_2O_3 catalyst at 400 ºC and 1 bar.

The removal of H_2 and CO_2 allowed reaching higher and stable H_2 yields in the SEMR (c.a. 11 mol_{H2}/mol_{OMW}) during the pre- and pos-breakthrough time in comparison with the TR (see Fig. 3a-b)) [5]. This allows the simultaneous production of highly pure H_2 in the retentate and ultra-pure H_2 on the permeate side. A higher improvement in terms of H_2 yield was observed when the MR and particularly the SEMR was applied (see Fig. 3c) - H_2 yield enhancement of ≈ 44 % was noted compared to the TR). It was also demonstrated that the steam reforming process, when implemented in a SEMR, can efficiently handle real OMW effluents, with high productions of H_2, with practically complete removal of the pollutant load. Considering the limit emission values of several parameters for the discharge of wastewater in Portugal, it was also observed that the condensable samples (liquid effluent) obtained during the tests present suitable physicochemical characteristics, namely in terms of pH (between 6.0 and 9.0), color (no visible color after a 1:20 vol dilution), smell (no smell after a 1:20 vol. dilution), total organic carbon (<55 $mg_C \cdot L^{-1}$ - removal of ≈ 100 %) and chemical oxygen demand (<150 $mg_{O2} \cdot L^{-1}$ – removal of ≈ 100 %).

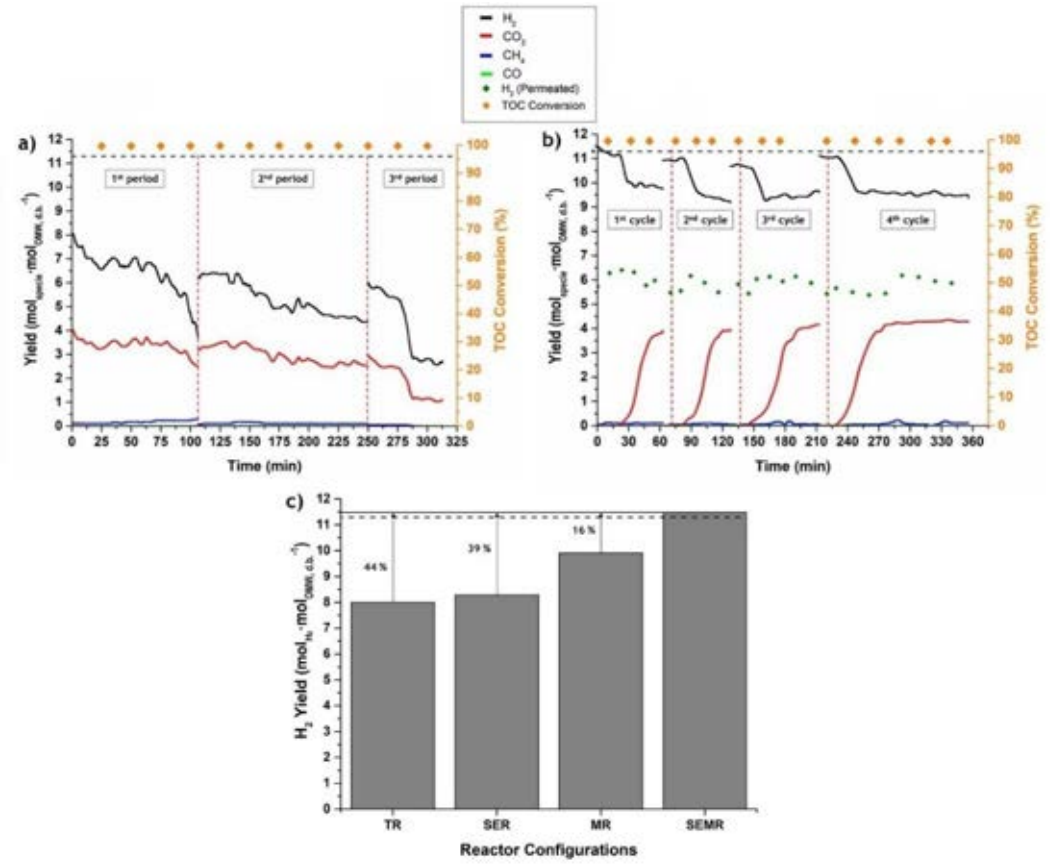


Fig. 3. Gaseous species yield and TOC conversion using a Ni-Ru/CeO_2-SiO_2 catalyst in a) TR or b) SEMR at 400 °C and 4 bar. c) H_2 yield with the different reactor configurations at 400 °C and 4 bar.

CONCLUSIONS

Thermodynamic analyses showed that the SEMR has several advantages in comparison with other reactor configurations. An HTC was prepared (HTC-CO_3(Ga)_K) showing high CO_2 sorption capacity under conditions suitable for a SEMR. Several commercial and new catalysts have shown high catalytic performance for OMWSR, some of them with high stability during 24 h of reaction (e.g. Rh/Al_2O_3). It was demonstrated that the use of multifunctional reactors in the OMWSR allows reducing considerably the pollutant load of such effluents, while economically valorizing this waste with the production of green H_2.

ACKNOWLEDGEMENT

This work was financially supported by: Base-UIDB/00511/2020 and Programmatic-UIDP/00511/2020 Funding of LEPABE, funded by national funds through FCT/MCTES (PIDDAC) and by the Project NORTE-01-0247-FEDER-39789, funded by European Regional Development Fund (ERDF) through the Programa Operacional Regional do Norte (NORTE 2020). C. Rocha acknowledges FCT for the PhD grant (SFRH/BD/120179/2016). M.A. Soria thanks FCT for the financial support of his work contract through the Scientific Employment Support Program (Norma Transitória DL 57/2017).

REFERENCES

[1] Dermeche S, Nadour M, Larroche C, Moulti-Mati F and Michaud P. 2013. Olive mill wastes: Biochemical characterizations and valorization strategies. Process Biochemistry 48 (10): p. 1532-1552.
[2] Rocha C, Soria MA, Madeira LM. 2017. Steam reforming of olive oil mill wastewater with in situ hydrogen and carbon dioxide separation – Thermodynamic analysis. Fuel 207: p. 449-460.
[3] Rocha C, Soria MA, Madeira LM. 2020. Doping of hydrotalcite-based sorbents with different interlayer anions for CO_2 capture. Separation and Purification Technology 235: p. 116140.
[4] Rocha C, Soria MA, Madeira LM. 2021. Screening of commercial catalysts for steam reforming of olive mill wastewater. Renewable Energy 169: p. 765-779.
[5] Rocha C, Soria MA, Madeira LM. 2022. Olive mill wastewater valorization through steam reforming using hybrid multifunctional reactors for high-purity H_2 production. Chemical Engineering Journal 430: p. 132651.

WHEC-2022
23rd World Hydrogen Energy Conference
June 26-30, 2022 - Istanbul

#266

SUSTAINABILITY ASSESSMENT OF A PROTON-EXCHANGE MEMBRANE FUEL CELL STACK AS A BASIS FOR THE DEVELOPMENT OF ECO-DESIGN GUIDELINES

[1*] Mitja Mori, [2] Diego Iribarren, [3] Julie Cren, [3] Elise Monnier, [1] Rok Stropnik, [1] Andrej Lotrič, [1] Mihael Sekavčnik, [4] Darío Cortés, [4] Lara Giménez, [5] Laurent Rey, [2,6] Gonzalo Puig-Samper, [2,7] Felipe Campos-Carriedo, [2] Eleonora Bargiacchi, [2,7] Javier Dufour, [3*] Emmanuelle Cor

[1] University of Ljubljana, Faculty of Mechanical Engineering, Aškerčeva 6, Ljubljana, SI-1000, Slovenia
[2] IMDEA Energy, Systems Analysis Unit, E-28935 Móstoles, Spain
[3] Univ. Grenoble Alpes, CEA, LITEN, F-38054 Grenoble, France
[4] Aragon Hydrogen Foundation, E-22197 Huesca, Spain
[5] SYMBIO, F-73370 Le Bourget-du-Lac, France
[6] Universidad Autónoma de Madrid, Chemical Engineering Department, E-28049 Madrid, Spain
[7] Rey Juan Carlos University, Chemical and Environmental Engineering Group, E-28933 Móstoles, Spain

*Corresponding author e-mail: emmanuelle.cor@cea.fr

ABSTRACT

The eGHOST project is the first milestone for the development of eco-design criteria in the European hydrogen sector. In the framework of this project, a life cycle sustainability assessment (LCSA) of a proton-exchange membrane fuel cell (PEMFC) stack was performed to estimate its potential environmental, economic, and social impacts. This assessment supports the identification and development of future sustainable design criteria that could be incorporated at early stages of the product development. The methodologies applied in the framework of the LCSA include environmental life cycle assessment (LCA), life cycle costing (LCC), and social life cycle assessment (S-LCA). Environmental (climate change, acidification, eutrophication, and resource use), economic (e.g., total production cost) and social (child labour, contribution to economic development, health expenditure, etc.) life-cycle indicators are evaluated for the product at the manufacturing phase, leading to the identification of sustainability hotspots. The results will support the development of future eco-design guidelines adapted to current and future fuel cells and hydrogen (FCH) technologies.

Keywords: eco-design, hydrogen, proton exchange membrane fuel cell, life cycle assessment, life cycle cost, social impacts

INTRODUCTION

Increasing concerns on climate change and natural resource depletion have raised interest in renewable energy sources and low-impact technologies. Among other solutions, fuel cells and hydrogen (FCH) technologies look promising provided that sustainable technologies for hydrogen production and use are effectively implemented. Therefore, the sustainability performance of FCH systems must be assessed in a holistic approach embracing environmental, economic, and social aspects [1]. The European project eGHOST involves a full life cycle sustainability assessment (LCSA) of a proton-exchange membrane fuel cell (PEMFC) stack, a rather mature technology for which the focus of researchers in the field of energy systems analysis has been mainly placed on its environmental life cycle assessment (LCA), while rarely on its life cycle costing (LCC) and almost never on its social life cycle assessment (S-LCA).

METHODOLOGY FOR LIFE CYCLE SUSTAINABILITY ASSESSMENT

The evaluated reference product for the PEMFC technology is a 48 kW_{el} PEMFC stack that can be used in light fuel cell electric vehicles (FCEV; single or multiple stack units). The detailed specifications and bill of materials (BoM) were provided by the industrial partner SYMBIO. The automotive PEMFC stack consists of 280 MEA (membrane electrode assembly) units with an active area of 200 cm^2 each. The amount of platinum in the 48 kW_{el} PEMFC stack is 0.5425 g/kW.

Environmental Life Cycle Assessment framework

For the environmental evaluation of the PEMFC stack, a conventional life cycle assessment (LCA) was applied considering international standards [2,3] and ILCD guidelines [4]. The functional unit was defined as “the manufacturing of one PEMFC stack of 48 kW electrical power output (balance of plant excluded)”. The data for the inventory of the PEMFC stack was collected by a manufacturer company, SYMBIO. In addition, for background processes, the ecoinvent database and extended databases for precious metals and critical materials were used. The Environmental Footprint 3.0 method was used to evaluate a set of environmental life-cycle indicators: climate change, acidification, eutrophication, resource use linked to minerals and metals, and resource use linked to energy carriers.

Life Cycle Costing framework

Conventional life cycle costing (LCC) is a method for evaluating all relevant costs over the lifetime of a product. It takes into consideration all costs including first costs, such as manufacturing costs, purchase, and installation costs; future costs, such as energy costs, operating costs, maintenance costs, capital replacement costs, financing costs; and any resale, salvage, or disposal cost, over the lifetime of the product. The LCC study applied was conducted following the same scope as the LCA study.

$$C = MP + P + D \quad (1)$$

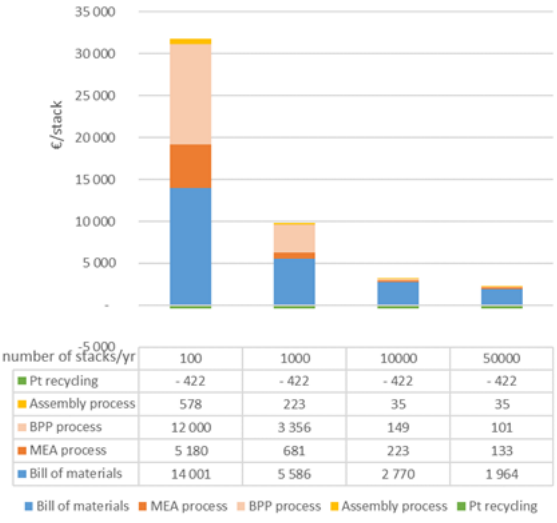
In Eq. (1) *C* is the cost of the stack, *MP* cost of raw materials and consumables, *P* cost of production involving tool depreciation, labour, energy and consumables, and *D* miscellaneous cost (premises, facilities, etc.).

Social Life Cycle Assessment framework

Updated guidelines for S-LCA of products have been developed within the framework of the United Nations Environment Programme [5] and were considered in this case. As in the case of environmental LCA, an S-LCA comprises four phases: goal and scope definition, social life cycle inventory, social life cycle impact assessment, and interpretation. The system boundaries were set according to the supply chain definition. Spain was considered as the stack manufacturing country. The supply chain of the product involves three tiers: tier 1 for the stack manufacturing plant itself, tier 2 for the plants related to the production of the components and energy flows required by the stack manufacturing plant, and tier 3 for the plants related to the material and energy flows required by the components manufacturing plants. The identification of the countries involved was carried out according to Martín-Gamboa et al. [6]. The inventories used for LCA and LCC, together with the working hours associated with each manufacturing plant considered, constitute the main source of data for the social life cycle inventory. PSILCA was used as both an auxiliary database and an assessment method [7]. Child labour, forced labour, and fair salary were selected as indicators within the stakeholder category “workers”, while health expenditure and contribution to economic development were considered within the stakeholder category “society” [8].

RESULTS AND DISCUSSION

Among the environmental results, the carbon footprint of one manufactured 48 kW PEMFC stack was estimated at 1200 kg $CO_{2eq.}$, which corresponds to 25 kg $CO_{2eq.}$ per kW_{el}. Platinum and, to a lesser extent, electricity production were found to have the highest contribution to the carbon footprint, namely platinum would represent 74% and electricity 14% of the total climate change impact.



number of stacks/yr	100	1000	10000	50000
Pt recycling	- 422	- 422	- 422	- 422
Assembly process	578	223	35	35
BPP process	12 000	3 356	149	101
MEA process	5 180	681	223	133
Bill of materials	14 001	5 586	2 770	1 964

Fig. 1. LCC of the 48 kW PEMFC stack according to production scale

The cost (LCC results) was found to be very dependent on the production rate (Fig. 1). The transition from laboratory to industrial scale could enable to divide the cost more than three times acting on both process and material costs. For 50,000 units produced per year, a cost of 2233 €/stack was calculated, and the main contributor comes from the bill of material and in particular the uncompressible cost of platinum. Finally, the results of the Social-LCA emphasizes that platinum production in South Africa was found to be the main social hotspot, arising –despite the limited amount

used– as the major contributor to all the social life-cycle indicators with a negative connotation (Fig. 2). The social risks associated with energy flows were found to be negligible.

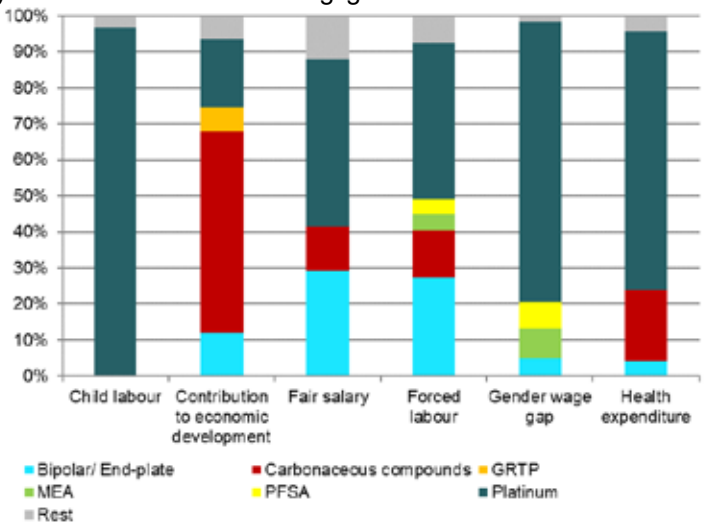


Fig. 2. Contribution to the potential social impacts for the 48 kW PEMFC stack

CONCLUSIONS

Even though platinum accounts only for 0.074% of the total mass of the stack, it is the main environmental and social hotspot, which highlights the importance of using low platinum loading and the new end-of-life possibilities to recover Pt from FCH technologies. Costs are highly dependent on the production rate: a transition from laboratory to industrial scale could allow a cost reduction of more than three times. Assuming a production capacity of 50,000 units, the estimated costs reach 2233 € per PEMFC stack. The sustainability assessment presented in this work arises as a key input to improve the life-cycle sustainability profile and provide eco-design guidelines for FCH product and supports the identification and development of future sustainable design criteria that could be incorporated at early stages of the product development.

ACKNOWLEDGEMENT

This work was carried out within the context of the project eGHOST. This project has received funding from the Fuel Cells and Hydrogen 2 Joint Undertaking under Grant Agreement No 101007166. This Joint Undertaking receives support from the European Union's Horizon 2020 Research and Innovation programme, Hydrogen Europe and Hydrogen Europe Research.

REFERENCES

1. Guinée, J. 2016. Life Cycle Sustainability Assessment: What Is It and What Are Its Challenges? In Taking Stock of Industrial Ecology. Edited by Clift R and Druckman A. Cham: Springer.
2. International Organization for Standardization. 2006. ISO 14040:2006 Environmental management - Life cycle assessment - Principles and framework. Geneva, ISO.
3. International Organization for Standardization. 2006. ISO 14044:2006 Environmental management - Life cycle assessment - Requirements and guidelines. Geneva, ISO.
4. European Commission - Joint Research Centre - Institute for Environment and Sustainability. 2010. International Reference Life Cycle Data System (ILCD) Handbook - General guide for Life Cycle Assessment - Detailed guidance. Luxembourg, European Union.
5. United Nations Environment Programme. 2020. Guidelines for social life cycle assessment of products and organizations 2020. Paris, UNEP.
6. Martín-Gamboa M, Dias AC, Arroja L and Iribarren D. 2020. A protocol for the definition of supply chains in product social life cycle assessment: application to bioelectricity. Sustainable Energy & Fuels 4:5533-5542.
7. Maister K, Di Noi C, Ciroth A and Srocka M. 2020. PSILCA database v.3 documentation. Berlin, GreenDelta.
8. Bargiacchi E, Campos-Carriedo F, Iribarren D and Dufour J. 2022. Social life cycle assessment of a proton exchange membrane fuel cell stack. E3S Web of Conferences 334:09001.

WHEC-2022
23rd World Hydrogen Energy Conference
June 26-30, 2022 - Istanbul

#283

THE ENERGY-ENVIRO-ECONOMIC EVALUATION AND MULTI-OBJECTIVE OPTIMIZATION OF THE HYDROGEN PRODUCTION PROCESS FROM COAL-BIOMASS CO-GASIFICATION CONSIDERING UNCERTAINTY IN CARBON PRICES

[1] Han Yang, [1] Min Dai, [1*] Fusheng Yang, [1]Yunsong Yu, [1]Zhen Wu, [1]Zaoxiao Zhang
[1] School of Chemical Engineering and Technology, Xi'an Jiaotong University, Xi'an, Shaanxi, China

*Corresponding author e-mail: yang.fs@mail.xjtu.edu.cn

ABSTRACT

Hydrogen has attracted more and more attention due to its advantages of low environmental impact and high energy density. However, the current hydrogen production process based on coal is usually accompanied by high energy consumption and CO_2 emission. Therefore, it is particularly important to develop efficient and clean hydrogen production technology. Based on this, a poly-generation system based on the co-gasification of coal and biomass coupled with carbon capture was proposed. Carbon dioxide emissions pricing is employed as an approach to mitigate climate change. Therefore, the impact of carbon prices on co-gasification system is analyzed, and the energy-enviro-economic evaluation of the system is carried out. Besides, the trade-off between exergy efficiency, annual gross profit and annual carbon emissions is conducted by multi-objective optimization. The results show that the system can be operated successfully under the optimum settings, achieving green and efficient hydrogen production while obtaining high economic benefits.

Keywords: Hydrogen production, Carbon price, Multi-objective optimization, Co-gasification

INTRODUCTION

Hydrogen is regarded as one of the most promising energy sources due to its high energy density, environmentally friendly and renewable characteristics [1]. Hydrogen production from coal gasification will lead to the consumption of fossil energy and damage to the environment. Biomass is renewable, clean and carbon neutral. Unfortunately, biomass cannot completely replace coal for power generation because it is seasonal and has low heat density [2]. The co-gasification of coal-biomass provides a better alternative for hydrogen production, and the system is often evaluated from the perspective of energy-enviro-economic(3E) [3]. However, the traditional method based on fixed price cannot precisely reflect the actual situation due to the fluctuation of carbon prices. The main purpose of the current paper is to figure out the impact of carbon prices on performance of co-gasification system based on the energy-enviro-economic evaluation and multi-objective optimization.

MATERIALS AND METHODS

Fig. 1 shows the basic contents of this paper. Firstly, a process model for hydrogen production from co-gasification is established by using Aspen Plus software, as shown in Fig. 2. This system is mainly divided into four units: gasification, purification, water gas shift, carbon capture and pressure swing adsorption (PSA). Gasification unit decomposes coal and biomass according to their composition as described through cracking module, and then the gasification process is implemented through RGIBBS module. The purification unit adopts the rectisol process to remove sulfide. Afterwards, purified syngas converts CO into CO_2 and H_2 through water gas shift [4]. Next the hydrogen is purified through PSA [5], attaining a purity of more than 99.999%. Then a quantitative sustainability evaluation method was introduced for the performance analysis of this system, including an energy model aiming at improving the exergy efficiency, a dynamic econometric model considering the fluctuation of carbon prices, and an environmental assessment model based on annual CO_2 emissions (ACE). Finally, the multi-objective optimization method was adopted based on the energy, economy and environment (3E) of the system.

RESULTS AND DISCUSSION

Model validation

Table 1 shows the comparison between the data under actual working condition and the simulated data of this study. Good consistency is achieved with the mean relative error of less than 7%, which indicates that the model can be used to analyze and optimize the process.

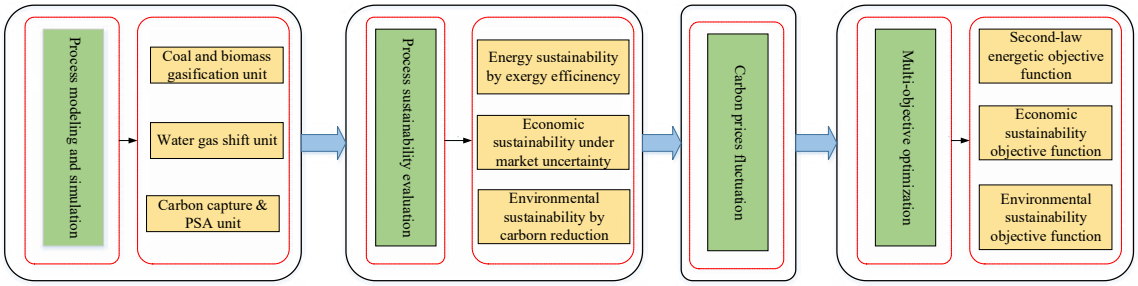


Fig. 1. The analysis procedure of the proposed system

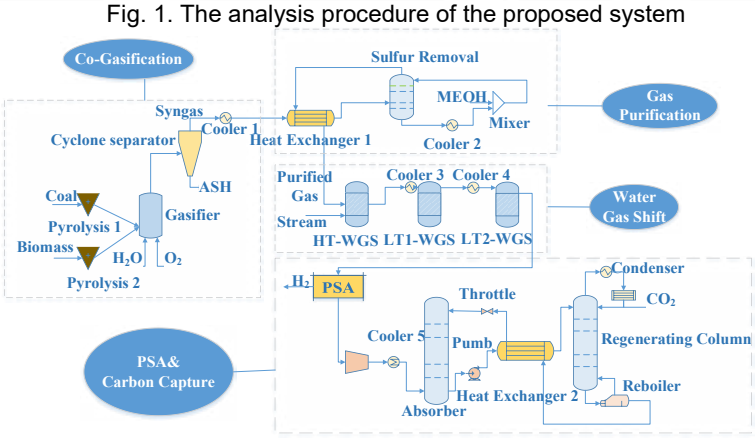


Fig. 2. Aspen plus flow sheet for co-gasification simulation

Table 1 Model validation

	Condition	Literature [6]	Simulation
Gibbs Reactor	Temperature (℃)	1074℃	1074℃
	Pressure (bar)	28.5bar	28.5bar
Initial Stream Data	Coal (kg/h)	21600	21600
	Biomass (kg/h)	14400	14400
	Stream (kg/h)	10800	10800
	O_2 (kg/h)	14400	14400
Syngas Component	H_2 (%)	0.31	0.33
	CO (%)	0.44	0.42
	H_2O (%)	0.14	0.14

Analysis of optimization results

Fig. 3 shows the Pareto-optimal fronts obtained by NSGA-II and the ultimate optimum solutions selected by TOPSIS. From Fig. 3, the optimum value of exergy efficiency changes from 40.86% to 48.80%, annual gross profit is between 7.130×10^7 \$/year and 1.161×10^8 \$/year, and accordingly, annual carbon emissions changes from 5.703×10^5 t/year to 8.488×10^5 t/year. Compared with the actual operating condition, the exergy efficiency and annual gross profit can be increased by 7.60% and 12.71% when the CO2 emission reduces by 1.50%. Further, the main decision variables corresponding to this Pareto front are shown in Figure 4. As can be seen from Fig. 4(a), exergy efficiency and carbon emission of the system decrease with the increase of oxygen content. This is because increasing the oxygen content will promote the combustion reaction, leading to the gradual rise of the internal temperature of the gasifier, thus increasing the exergy destruction caused by the temperature difference. At the same time, high temperature promotes the conversion of fuel, thus the CO_2 content decreases. As for the annual gross profit of the system, it increases with the growth of oxygen content because of promoted transformation of C and thus increasing total H_2 product. From Fig. 4(b), with the increase of steam, 3E index presents an upward trend, and the optimal range of the above three is [7500,12750], [8000,12000] and [2500,9500], respectively. The reason is that the increase of mass flow for steam will reduce the gasification temperature, thus reducing the exergy destruction caused by the temperature difference. Meanwhile, when the steam increases, the exothermic water-gas shift reaction intensifies, and a large amount of CO is converted into H_2 and CO_2. In this case, hydrogen production increases, thus increasing the system profit [6]. In addition, increasing carbon emissions are also generated.

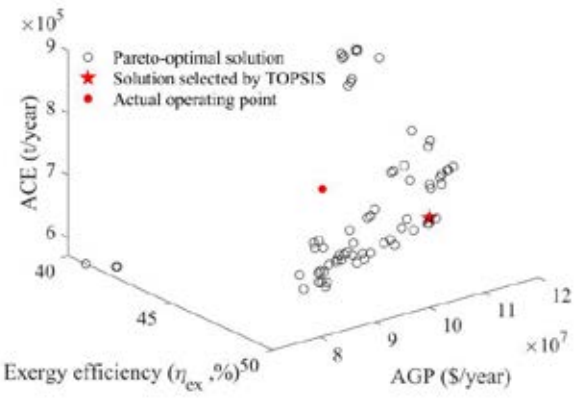


Fig. 3. Pareto front and the final optimal solution selected by TOPSIS for the H_2 production process

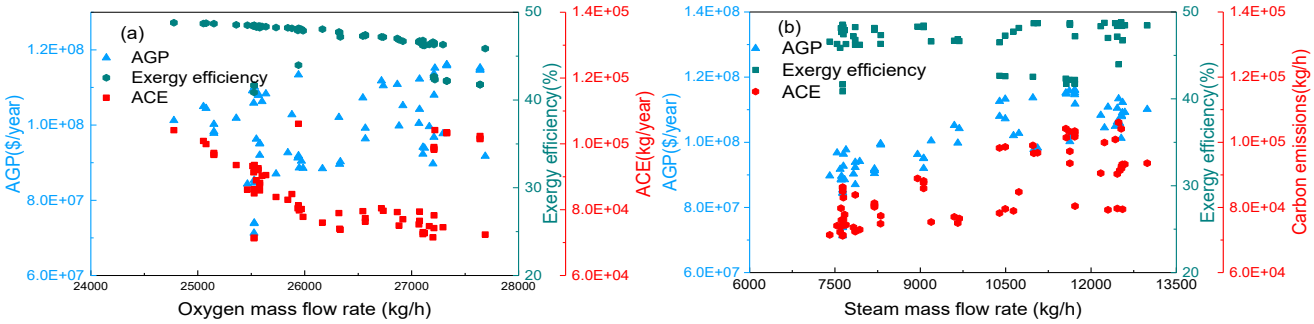


Fig. 4. Optimal values corresponding to the Pareto-optimal front, (a) Effect of oxygen flow (b) steam flow on 3E index.

CONCLUSIONS

In this paper, a process model for hydrogen production from coal-biomass co-gasification with carbon capture, is proposed and evaluated by 3E multi-objective optimization. The simulation results show exergy efficiency and carbon emission of the system decreased with the increase of oxygen content, meanwhile the annual gross profit of the system will increase. With the increase of steam, 3E indices present an upward trend, and the optimal range of the above three is [7500,12750], [8000,12000] and [2500,9500], respectively. The follow-up work is dedicated to discussion on the impact of carbon prices on economy and the analysis of other parameters.

ACKNOWLEDGEMENT

Financial support from National Natural Scientific Foundation of China (No. 21736008 & 52050027) are acknowledged.

REFERENCES

1. Momirlan M and Veziroglu T. 2005. The properties of hydrogen as fuel tomorrow in sustainable energy system for a cleaner planet. International Journal of Hydrogen Energy 30(7): 795-802.
2. Yan LB, Yue GX and He BS. 2016. Thermodynamic analyses of a biomass-coal co-gasification power generation system, Bioresource Technology 205:133-141.
3. AlNouss A, McKay G and Al-Ansari T. 2020. Enhancing waste to hydrogen production through biomass feedstock blending: A techno-economic-environmental evaluation. Applied Energy 266.
4. Gradisher L, Dutcher B, Fan M. 2014. Catalytic hydrogen production from fossil fuels via the water gas shift reaction. Applied Energy 139: 335-349.
5. Voldsund M, Jordal K, Anantharaman R. 2016. Hydrogen production with CO2 capture. International Journal of Hydrogen Energy 41(9): 4969-4992.
6. Fan J, Hong H, Jin H. 2018. Biomass and coal co-feed power and SNG polygeneration with chemical looping combustion to reduce carbon footprint for sustainable energy development: Process simulation and thermodynamic assessment. Renewable Energy 125: 260-269.

WHEC-2022
23rd World Hydrogen Energy Conference
June 26-30, 2022 - Istanbul

#315

LCA AND CRITICALITY ANALYSIS OF WATER ELECTROLYSIS TECHNOLOGIES

[1*] Jan Christian Koj, [2] Ansgar Taubitz, [2] Ole Zelt [2], [1] Wilhelm Kuckshinrichs, [3] Klaus Görner
[1]Forschungszentrum Jülich, Institute of Energy and Climate Research - Systems Analysis and Technology Evaluation (IEK-STE), 52425 Jülich, Germany
[2] Wuppertal Institute for Climate, Environment and Energy – Division Future Energy and Industry Systems, 42103 Wuppertal, Germany
[3] Gas- und Wärme-Institut Essen, 45356 Essen, Germany

*Corresponding author e-mail: j.koj@fz-juelich.de

ABSTRACT

Water electrolysis technologies enable the decarbonization of the industry, energy and transport sectors. Significant increases of electrolysis deployment are expected and will cause extensive material requirements. The current study investigates to which extent prospective electrolysis deployment affects raw material demand in relation to production volumes and reserves as well as environmental impacts related to further construction materials. The methods life cycle assessment and criticality analysis are used to exploit sustainability potentials of three water electrolysis technologies (AEC, PEMEC, and SOEC). LCA revealed minor contributions to climate change caused by materials required for plant construction. Clear changes of environmental impacts up to the year 2050 are given for SOEC as their life time significantly increases and material demand decreases. The work on the criticality analysis identified nine different raw materials, which are considered potentially critical and are required for water electrolysis plant construction. The expected demand for iridium and platinum, nickel, lanthanum and yttrium are particularly critical. Graphite, potassium, titanium and zirconium, on the other hand, do not exhibit raw material criticality. Results show different electrolysis technologies are likely to be used in parallel. Possible risks in the future raw material supply will thus be spread and mitigated overall.

Keywords: Hydrogen, water electrolysis, Power-to-Gas, Life Cycle Assessment, criticality analysis

INTRODUCTION

Climate protection is currently one of the greatest global challenges. Against the background of the Paris Climate Agreement, the EU aims at climate neutrality by 2050. Achieving this will require, in particular, a move away from the use of fossil fuels and their substitution with renewable energies. Water electrolysis technologies are seen as a technical solution to improve the integration of renewable energies and to replace fossil-based energy carriers. These technologies convert electricity into gaseous energy carriers, applicable in different sectors and can also be referred to as Power-to-Gas technologies. Therefore, water electrolysis is considered an important tool for the transformation and decarbonization of the industry, energy and transport sectors [1]. However, in order to contribute to the decarbonization of sectors in Europe in the long term, they must be technologically mature and sustainable in terms of their raw material requirements [2]. Thus, technological development of water electrolysis technologies supported by studies using life cycle assessment (LCA) and criticality analyses is needed to exploit sustainability potentials. A former review dealing with water electrolysis revealed that data about plant construction and materials used for it are mostly left out or the level of detail is rather low [3]. There is only a limited number of LCAs with a higher level of detail about the materials required for electrolyser construction (e.g. [4]) and those assessments typically focus on only one water electrolysis technology. Furthermore, the combination of LCA and in-depth criticality analysis rarely takes place. As significant increases of water electrolysis deployment is expected, detailed knowledge about environmental impacts and criticality of applied (raw) materials have to be obtained as early as possible to identify sustainable manufacturing pathways.

Due to this research need, this study presents detailed assessments and comparisons of three different electrolysis technologies, using the LCA and criticality analysis methods. The study aims to answer if and to which extent the expected multiplying water electrolysis deployment affects the demand for raw material in relation to their respective production volumes and reserves as well as environmental impacts provoked by further construction materials. Transparent life cycle inventories and environmental impacts, especially provoked by material use for electrolyser construction, and raw material criticalities are presented up to the year 2050 to show how even material use for hydrogen production can be as green and sustainable as possible.

MATERIALS AND METHODS

Objects of the current investigation are water electrolysis technologies. Following three water electrolysis technologies are currently under intense discussion for large-scale production and deployment [5] and consequently assessed within the current study: Alkaline Electrolysis Cell (AEC), Proton Exchange Membrane Electrolysis Cell (PEMEC), and High

Temperature Steam Solid Oxide Electrolyzer Cell (SOEC). All three technologies have in common that they split water into hydrogen and oxygen under supply of electrical energy. However, they use different reaction mechanisms, cell structures, and electrolytes as well as diverse raw materials and further materials required for their construction. To assess their impacts and to compare them the two sustainability-oriented methods LCA and criticality assessment are applied. Both assessment methods consider European and prospective conditions up to the year 2050. For the presented assessments, results of the centre of excellence “Virtual Institute - Power to Gas and Heat” project framework are considered.

The established method of LCA is applied for the environmental assessment on the different electrolysis technologies. Material, energy, emissions, and further flows occurring along the entire chain from raw material extraction, production, distribution, operation up to its final use are initially quantified and hereafter evaluated in terms of environmental impacts. This procedure as well as the consideration of the four typical LCA phases is based on the ISO standards 14040 and 14044. To compare life cycle impact assessment results they are based on a functional unit of 1 kg hydrogen. Beside foreground data, generic data is taken from the ecoinvent database. Special attention is paid to the analyses of the impact category global warming potential (GWP). In addition to this indicator, further impact categories were analyzed according to the established ReCiPe methodology. The LCA is limited to the construction and operation phase. The end of life phase is not included due to lack of information and standardization not yet fully completed.

Main objective of the criticality analysis is to examine whether future capacity additions of electrolyzer technologies may result in bottlenecks with regard to individual raw materials. To this end, the critical raw materials and their specific demands were first determined for each technology. In order to identify the total raw material requirements for Germany and Europe, these specific demands were extrapolated in a second step using modeled capacities of the technologies in 2050 derived from energy scenarios of the underlying project. Total demands were then compared to the annual production volumes and global reserves of the respective materials. An extensive literature research of potential critical raw materials, their used quantities (e.g. in g/kW_{el}) as well as the lifetime of the technology took place. A range from the minimum to the maximum researched raw material demand is considered in the criticality analyses. This range represents the "optimistic" and "pessimistic" estimates of the literature and underlines the fact that a large proportion of the technologies are still in development with uncertainties regarding actual future raw material requirements. Classification of raw materials as critical for the purposes of this study is primarily based on the European Commission's list of critical raw materials [6]. The two central parameters for compiling this list are the economic importance and the supply risk of the raw materials analyzed. In addition, classifications according to existing studies on the use of critical mineral raw materials in specific individual technologies or different technology groups are also considered (e.g. [7]).

RESULTS AND DISCUSSION

The LCA revealed minor contributions of materials required for plant construction to the GWP. Plant operation clearly dominates the GWP in case of operation with wind energy with contributions clearly above 80 %. This is mainly caused by upstream impacts of the electricity used for hydrogen production. A comparison of GWP results of the electrolysis technologies shows advantages for PEMEC as illustrated in Table 1. However, SOEC reveals the best performance for further environmental impact categories. Materials with noteworthy effects on further environmental impacts are e.g. chromium steel and polytetrafluoroethylene (PTFE) used for gaskets in AEC stacks. Chromium steel shows the highest individual contributions on several environmental impact categories for SOEC.
The work on the criticality analysis illustrates in Table 1 that nine different raw materials, which are considered potentially critical in the literature, are generally required for the construction of the assessed water electrolysis capacities. From the extrapolation of cumulative raw material requirements caused by water electrolysis utilisation in Germany and Europe in the long term up to 2050, only some of these nine raw materials investigated are likely to be deployed to a critical extent. The expected demand for iridium and platinum (PEMEC), nickel (primarily for AEC), and lanthanum and yttrium (SOEC) are particularly critical. Graphite, potassium, titanium and zirconium, on the other hand, do not exhibit raw material criticality based on applied criteria and assumed future installed electrolysis capacities.

Previously mentioned results of LCA and criticality analysis to compare the three water electrolysis technologies are summarized in Table 1.

Table 1. Qualitative comparison of LCA and criticality results for the three considered water electrolysis technologies (green: uncritical or lowest impacts, yellow: possibly critical or increased impacts, red: critical or significantly higher impacts, dark gray: raw material is not needed for the respective technology)

		AEC	PEMEC	SOEC
Criticality analysis results	*Graphite*			
	Iridium			
	Potassium			
	Lanthanum			
	Nickel			
	Platinum			
	Titanium			
	Yttrium			
	Zirconium			
LCA results	*GWP*			
	Further impacts			

With regard to the research objective, it can be seen that different electrolysis technologies (AEC, PEMEC, and SOEC) are likely to be used in parallel. Possible risks in the future raw material supply of the pathways will thus be spread and mitigated overall. Concerning environmental aspects a lower developed technology like SOEC should be part of the electrolysis deployment as this will lead to technological learning with effects on life time and environmental impacts.

CONCLUSIONS

Future research can build on the data and results presented and take into account new findings and further technologies. In addition, further methods and indicators can be used to compare water electrolysis technologies. One example is Life Cycle Costing, where levelised costs of hydrogen production are only one possible indicator. The classification of raw material criticalities needs to be verified by a more detailed analysis of previously used and additional indicators. Examples include a stronger focus on competitive applications and megatrends beyond water electrolysis deployment, and a comprehensive consideration of circular economy aspects. As shown a combined deployment of water electrolysis can lower the criticality to individual critical raw materials. Suchlike combination can also be reasonable from a technological or economic point of view as the electrolysis technologies have different strengths depending on operation strategies (e.g. flexible operation or heat integration).

ACKNOWLEDGEMENT

Funding of the center of excellence “Virtual Institute - Power to Gas and Heat” (EFRE-0400151 and EFRE-0400154) by the “Operational Program for the promotion of investments in growth and employment for North Rhine- Westphalia from the European fund for regional development” (OP EFRE NRW) through the Ministry of Economic Affairs, Innovation, Digitalization and Energy of the State of North Rhine-Westphalia is gratefully acknowledged.

REFERENCES

1. Sterner M. 2016. Power-to-Gas. In Handbook of Climate Change Mitigation and Adaptation. Edited by Chen WY, Suzuki T and Lackner M, Editors. New York, Springer.
2. Arnold K and Fischer B. 2018. „No regret Einstiegsmärkte“ – Power-to-Gas. gwf Gas + Energie 5:24-31.
3. Koj JC, Wulf C and Zapp P. 2019. Environmental impacts of power-to-X systems - A review of technological and methodological choices in Life Cycle Assessments. Renewable and Sustainable Energy Reviews, 112:865-879.
4. Bareiß K, de la Rua C, Möckl M and Hamacher T. 2019. Life cycle assessment of hydrogen from proton exchange membrane water electrolysis in future energy systems. Applied Energy 237: 862-872
5. Wulf C, Zapp P, Schreiber A. 2020. Review of Power-to-X Demonstration Projects in Europe. Frontiers in Energy Research 287:1-17
6. Blengini GA et al. 2020. Study on the EU's list of Critical Raw Materials (2020) - Final Report. Luxembourg, Publications Office of the European Union.
7. Viebahn P et al. Assessing the need for critical minerals to shift the German energy system towards a high proportion of renewables. Renewable and Sustainable Energy Reviews, 49: 655-671

WHEC-2022
23rd World Hydrogen Energy Conference
June 26-30, 2022 - Istanbul

#1444

A COMPARATIVE LIFE CYCLE ASSESSMENT OF HYDROGEN PRODUCTION USING THE SPECTRUM OF HYDROGEN COLORS

Huseyin Karasu, Ibrahim Dincer
Clean Energy Research Laboratory (CERL), Faculty of Engineering and Applied Science, Ontario Tech. University, 2000 Simcoe Street North, Oshawa, Ontario L1H 7K4, Canada

*Corresponding author e-mail: huseyin.karasu@ontariotechu.net

ABSTRACT
In this study, a comparative life cycle assessment (LCA) of hydrogen production is presented using the spectrum of hydrogen colors. The main hydrogen colors are studied depending on their varying energy sources and hydrogen production processes. The aim of the study is to investigate the environmental impacts of main hydrogen colors. The study results are illustrated in 6 different impact categories namely; global warming potential (GWP), ozone layer depletion potential (ODP), human toxicity potential (HTP), photochemical oxidation potential (POP), acidification potential (AP), and eutrophication potential (EP). The results show that brown hydrogen is the opposite of green hydrogen in the hydrogen spectrum, and it is the most environmentally harmful hydrogen type. Brown hydrogen emits 0.325 kg of CO_2 eq per 1 kg of hydrogen production while green hydrogen produce only 0.0072 kg of CO_2 eq per 1 kg of hydrogen production. Grey hydrogen is the second most harmful hydrogen type after brown hydrogen, with a value of 0.178 kg of CO_2 eq per 1 kg of hydrogen production. Turquoise hydrogen with a value of 0.079 kg of CO_2 eq per 1 kg of hydrogen production. Green hydrogen is the most environmentally friendly and sustainable option among the studied hydrogen production options.

Keywords: Hydrogen production, Life cycle assessment, Hydrogen colors, Environmental impact, Global warming.

1. INTRODUCTION
An intimate relationship exists between energy, the environment, and sustainable development. Ideally, a community pursuing sustainable development would only use energy products that do not have any environmental impacts. However, because all energy resources have some impact on the environment, it is fair to say that some of the concerns about the constraints placed by environmental emissions on sustainable development and their harmful impacts can be partially resolved by increasing energy efficiency. Clean, boundless, and highly competitive energy sources are renewable energy sources. They differ primarily in their variety, availability, and capacity for use anywhere on the planet from fossil fuels, but primarily in that, they generate neither greenhouse gases nor polluting emissions that cause climate change. Their expenditures are also declining and at a sustainable rate, despite their current uncertainty, the general cost trend for fossil fuels is in the opposite direction [1]–[3]. Due to the constantly falling cost of renewable energy generation, "green" hydrogen (i.e. hydrogen produced via electrolysis using renewable energy) is considered as a promising energy carrier for a variety of applications.

The main objectives of this study are listed as follows:

- conducting a cradle-to-grave LCA of hydrogen production methods considering hydrogen colors.
- determining the critical hot spots in the system for their environmental loads, and
- comparing the LCA results of hydrogen colors.

2. MATERIALS AND METHODS
Green Hydrogen
Green hydrogen is the color of hydrogen produced with no damaging greenhouse gases (GHGs) in the spectrum of hydrogen colors. Green hydrogen is created by electrolyzing water with clean electricity generated from surplus renewable energy sources such as solar or wind power. Electrolysis divide water into hydrogen and oxygen via an electrochemical reaction, producing no carbon dioxide in the process. Green hydrogen currently accounts for a small percentage of total hydrogen due to the high cost of generation. Green hydrogen will become more affordable as it becomes more widely available, just as wind energy has.

Blue Hydrogen
The most common source of blue hydrogen is natural gas, which is produced through a process known as steam reforming, which combines natural gas and heated water in the form of steam. Hydrogen is produced, but carbon dioxide is produced as a by-product. To catch and store this carbon, carbon capture and storage (CCS) is required. Because the steam reforming process does not actually avoid the generation of GHGs, blue hydrogen is sometimes referred to as "low-carbon hydrogen."

Turquoise Hydrogen
This is a new addition to the hydrogen color wheel, and scale manufacturing has yet to be confirmed. Turquoise

hydrogen is created using the methane pyrolysis process, which produces hydrogen and solid carbon. Turquoise hydrogen could be regarded as a low-emission hydrogen in the future, assuming that the heating process is supplied by renewable energy and that the carbon is permanently stored or utilized

Grey Hydrogen
This is currently the most frequent method of hydrogen synthesis. Grey hydrogen is manufactured from natural gas or methane, and by steam methane reformation, but without capturing the greenhouse gases produced.

Brown Hydrogen
This brown hydrogen is the complete opposite of green hydrogen in the hydrogen spectrum and the most environmentally harmful. They are produced using black coal or lignite (brown coal) in the hydrogen-making process. To add to the confusion, any hydrogen produced by the 'gasification' of fossil fuels is sometimes referred to as black hydrogen. [4]. The major hydrogen colors differ depending on the energy source and the hydrogen synthesis process, as shown in Fig. 1.

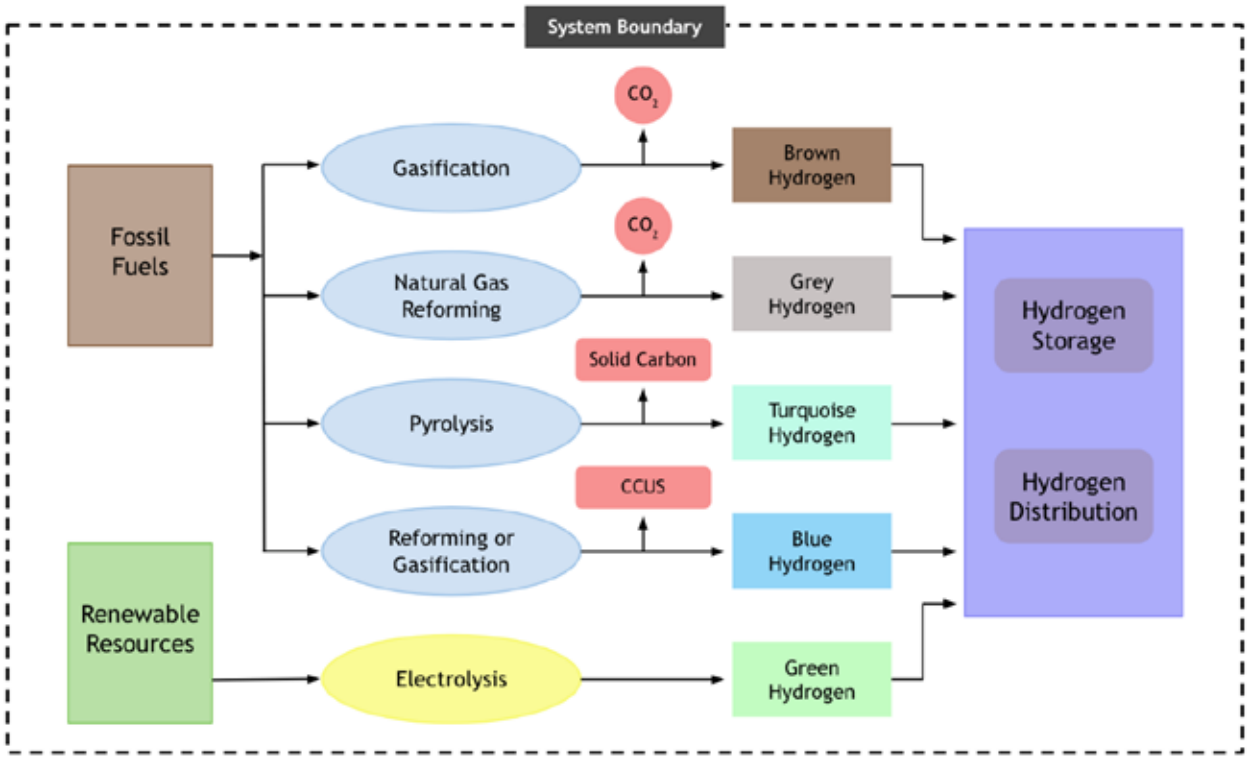


Fig. 1: Simplified layout of the proposed system boundary and major life cycle stages considered in this study

3. RESULTS AND DISCUSSION

A comparison of LCA results for hydrogen production methods using the spectrum of hydrogen colors is presented with Table 1. Impact assessment results displays five different hydrogen colors based on the hydrogen production sources and processes. The results shows that the brown hydrogen is opposite of green hydrogen in the hydrogen spectrum and it is the most environmentally harmful hydrogen type. Brown hydrogen is produced using black coal or lignite (brown coal) in the hydrogen-making process. Brown hydrogen emits 0.325 kg of CO_2 eq per 1 kg of hydrogen production while green hydrogen produce only 0.0072 kg of CO_2 eq per 1 kg of hydrogen production. Grey hydrogen is the second most harmful hydrogen type after brown hydrogen with value of 0.178 kg of CO_2 eq per 1 kg of hydrogen production, followed by turquoise hydrogen with a value of 0.079 kg of CO_2 eq per 1 kg of hydrogen production. Blue hydrogen is the most environmentally friendly option among the fossil-based hydrogen production options. This is because hydrogen is produced, but carbon dioxide is produced as a by-product. To catch and store this carbon, carbon capture and storage (CCS) is required. However, the steam reforming process does not actually avoid the generation of GHGs.

The impact assessment results show that grey hydrogen has the highest ozone layer depletion impact among the hydrogen production methods. Grey hydrogen is manufactured from natural gas or methane, and by steam methane reformation, but without capturing the greenhouse gases produced. The absence of capturing the greenhouse gases in the blue hydrogen production method results in higher emission values. The depletion of the ozone layer is primarily caused by nitrogenous chemicals such as NO_2, NO, and N_2O. Turquoise hydrogen production has the second highest

ozone layer depletion value, and then followed by brown hydrogen and blue hydrogen. Green hydrogen production techniques emerge as the most promising and sustainable hydrogen production method. As a result, using clean energy production techniques is crucial for achieving lower environmental impacts in the long term.

Table 1: Life cycle impact assessment results of the hydrogen colors

Impact category	Unit	Brown Hydrogen	Green Hydrogen	Turquoise Hydrogen	Grey Hydrogen	Blue Hydrogen
Global warming (GWP100a)	kg CO_2 eq	0.325	0.0072	0.079	0.178	0.0198
Ozone layer depletion	kg CFC-11 eq	3.09E-09	9.57E-10	1.02E-08	2.32E-08	1.97E-09
Human toxicity	kg 1,4-DB eq	0.126	0.0147	0.0317	0.0179	0.0526
Photochemical oxidation	kg C_2H_4 eq	2.49E-05	2.76E-06	7.89E-06	1.37E-05	5.21E-06
Acidification	kg SO_2 eq	0.00078	2.75E-05	9.55E-05	0.00015	6.67E-05
Eutrophication	kg PO_4 eq	0.00067	1.96E-05	3.17E-05	3.28E-05	4.68E-05

4. CONCLUSIONS

This paper deals with environmental impacts of hydrogen production methods using the spectrum of hydrogen colors. The main hydrogen colors are studied depending on their varying energy sources and hydrogen production processes. The key concluding remarks of this study can be summarized as follows:

- The results show that the brown hydrogen is the opposite of green hydrogen in the hydrogen spectrum and it is the most environmentally harmful hydrogen type.
- Brown hydrogen emits 0.325 kg of CO_2 eq per 1 kg of hydrogen production while green hydrogen produces only 0.0072 kg of CO_2 eq per 1 kg of hydrogen production.
- Blue hydrogen is the most environmentally friendly option among the fossil-based hydrogen production options.
- The impact assessment results shows that grey hydrogen has the highest ozone layer depletion impact among the hydrogen production methods.
- The LCA calculation results indicate that brown hydrogen produces the highest human toxicity during hydrogen production process.
- Brown hydrogen and grey hydrogen have the highest acidification potential impacts.
- Brown hydrogen has the highest eutrophication values in comparison to all other hydrogen production techniques with a value of 0.00067 kg of PO_4 equivalent per 1 kg of hydrogen production.

REFERENCES

1. C. Turkson, A. Acquaye, W. Liu, and T. Papadopoulos, “Sustainability assessment of energy production: A critical review of methods, measures and issues,” *J. Environ. Manage.*, vol. 264, no. January, p. 110464, 2020, doi: 10.1016/j.jenvman.2020.110464.
2. E. Baniasadi, I. Dincer, and G. F. Naterer, *Causes, Impacts and Solutions to Global Warming*. 2013.
3. C. Acar, “A comprehensive evaluation of energy storage options for better sustainability,” *Int. J. Energy Res.*, vol. 42, no. 12, pp. 3732–3746, 2018, doi: 10.1002/er.4102.
4. “The hydrogen colour spectrum | National Grid Group.” https://www.nationalgrid.com/stories/energy-explained/hydrogen-colour-spectrum (accessed Dec. 14, 2021).

WHEC-2022
23rd World Hydrogen Energy Conference
June 26-30, 2022 - Istanbul

#1480

REDUCTION OF HYDROGEN CARBON FOOTPRINT IN EUROPE VIA INTERNATIONAL SHIPPING

[1*] *Alessandro Arrigoni,* [1] *Eveline Weidner,* [1] *Francesco Dolci,* [1] *Rafael Ortiz Cebolla,* [2] *Umberto Eynard,* [2] *Fabrice Mathieux*
[1] European Commission Joint Research Center, Westerduinweg 3, 1755 LE Petten, Netherlands
[2] European Commission Joint Research Center, Via E. Fermi, 2749, 21027 Ispra, Italy

*Corresponding author e-mail: alessandro.arrigoni-marocco@ec.europa.eu

ABSTRACT

Green hydrogen is expected to play an important role in European decarbonisation efforts. This work investigates whether shipping green hydrogen within Europe could be a better climate solution than producing it locally. Three options for delivering hydrogen are analysed: hydrogen compression, liquefaction, and chemical bonding to other molecules (i.e., using ammonia, liquid organic compounds, methanol, or synthetic natural gas as hydrogen carriers). A distance compatible with the European territory was considered: i.e., production in Portugal and end-use in the Netherlands. The life cycle greenhouse gas emissions of shipped hydrogen are compared to the emissions arising from producing hydrogen locally, via either steam methane reforming or electrolysis powered by the electric grid. Preliminary results show that all the delivery options would guarantee in 2030 a supply of hydrogen with a lower global warming potential than locally produced hydrogen. Liquefaction appears to be the least greenhouse gas intense delivery solution, thanks to the lower volumes transported and the lack of an energy intensive transformation process at the delivery site. Nevertheless, much of the infrastructure for large scale hydrogen delivery does not yet exist, and therefore assumptions on technologies and emissions are subject to a high degree of uncertainty. Different delivery conditions (e.g., distances, means of transportation) can also alter the GHG emission ranking. Moreover, the present analysis was limited to the global warming impact, but an assessment of the overall environmental consequences is necessary to avoid shifting the burden from one environmental issue to another.

Keywords: Hydrogen delivery; Greenhouse gas emissions; Life cycle assessment

INTRODUCTION

Hydrogen transportation is included in the European Hydrogen strategy as an enabler of green hydrogen penetration in the European market [1]. The Joint Research Centre (JRC) of the European Commission is assessing the costs and energy demand of hydrogen transport and distribution to find the most advantageous economic and energetic solution [2]. This work aims at integrating the previous assessment with a life cycle greenhouse gas (GHG) analysis. The goal is to understand whether the cheapest option is also the best in terms of climate change mitigation. Results should provide new information to policymakers, stakeholders, and the public on the potential global warming impact of shipping hydrogen.

MATERIALS AND METHODS

The attributional life cycle assessment (LCA) methodology [3] is applied to compare the GHG emissions of eight different hydrogen delivery pathways: two on-site hydrogen productions (steam methane reforming and electrolysis powered by the electrical grid mix), and six pathways including green hydrogen shipping. These pathways assume that hydrogen is produced via renewable electricity in a location where solar energy is cheap, and subsequently packed in suitable forms for shipping by sea. The packing modes considered are: compressed hydrogen (CH_2), liquefied hydrogen (LH_2), ammonia (NH_3), a liquid organic hydrogen carrier (LOHC), methanol (MeOH), and synthetic natural gas (SNG).

Scope of the assessment

The system boundaries are the raw material extraction to produce hydrogen (e.g., to manufacture the electrolyser and to generate electricity), storage and its delivery to the end user: i.e., from cradle to gate. A simplified flow chart with the main processes included in the assessment is presented in Fig. 1.



Fig. 1. System boundaries of the assessment

The functional unit considered for the assessment is the delivery of 1 kg of hydrogen (30 bar, 99.97% purity) at an industrial site in the Netherlands, assuming that 1 Mt of hydrogen need to be delivered each year from 2030.
Data from the JRC techno-economic assessment [2] are combined with inventories found in the literature and the version 3.7 of the ecoinvent database for the life cycle inventory. The cut-off system model from ecoinvent is used as background database.
The analysis is limited to the global warming potential of the different options, considering a 100-year time horizon. The characterization factors for the different greenhouse gases are taken from the fifth assessment report of the IPCC: e.g., 30.5 kg CO_2e/kg fossil methane, 27.75 kg CO_2e/kg biogenic methane, and 265 kg CO_2e/kg nitrous oxide. Moreover, a global warming potential for hydrogen emissions of 5.8 kg CO_2e/kg H_2 was considered [4].

Main assumptions

Shipped green hydrogen is assumed to be produced via water electrolysis (50 kWh/kg H2), assuming an emission factor for photovoltaic electricity of 20 g CO_2e/kWh [5]. As for the average grid emissions in the Netherlands, the emission factor for electricity in Europe in 2030 estimated by the European Commission for the EUCO3232.5 scenario (150 g CO_2e/kWh) was considered [6].
To guarantee a constant supply of hydrogen, a storage facility is assumed to be available both at the production and use sites. Ships are assumed to travel on biodiesel, since large electric or hydrogen-powered ships will not likely be available yet in 2030. Greenhouse gas emissions from the combustion of biodiesel are taken from the inventory of the United States Environmental Protection Agency: 2.84 kg CO_2, 42.0 mg CH_4, and 150 g N_2O per kg of biodiesel [7]. When carbon is necessary to transport hydrogen (i.e., methanol and SNG pathways), CO_2 sourced via direct air capture is assumed to be used. When processes require external heat (e.g., direct air capture, unpacking stage for LOHC), extra green hydrogen is assumed to be produced and delivered to the processing plant (via the carrier considered for that pathway). The direct air capture unit is assumed to be at the green hydrogen production site.

RESULTS AND DISCUSSION

The comparison of the life cycle GHG emissions arising from the delivery of 1 kg of hydrogen at 30 bar is presented in Fig. 2. Based on our assumptions, in 2030 the delivery of hydrogen from a location where renewable energy is cheaper would emit less GHG than producing it on site from either steam methane reforming (SMR) or electrolysis powered by the grid mix. Despite the reduction in carbon intensity expected from the electricity grid mix of European countries, the residual fossil component in the mix would lead to significant GHG emissions when producing electrolytic hydrogen (i.e., more than more than 7 kg CO_2e). Although better than hydrogen produced via SMR, electrolytic hydrogen produced via the electricity grid mix is not expected to meet the taxonomy criterion for climate change mitigation of 3 kg CO_2e/kg hydrogen. On the other hand, our results show that the delivery of hydrogen from other parts of Europe where electrolytic hydrogen can be produced via renewable sources at a lower cost would likely meet the criterion in 2030. In our baseline scenario, the life cycle GHG emissions for the different carriers varied from a minimum of 1.4 kg CO_2e/kg H_2 delivered for liquefied hydrogen to a maximum of 2.8 kg CO_2e/kg H_2 delivered for SNG. The transportation advantage of packing hydrogen into a more manageable carrier does not seem to translate in a GHG advantage. On the contrary, the energy required to pack the carrier at the hydrogen production site and unpack it at the delivery site significantly increase the impact with respect to the compressed and liquefied hydrogen options. Compressed hydrogen results in higher emissions compared to liquefied hydrogen, mainly due to the higher transportation impact. However, more information is needed on the greenhouse gas effect resulting from the emissions of hydrogen in the atmosphere. In the reference scenario, a global warming potential over 100 years of 5.8 kg CO_2e per kg of H_2 was used; a higher value could change the ranking proposed here due to the boil-off from shipping liquefied hydrogen. As for the other carriers, results were very similar: the options emitting less GHG resulted to be ammonia and methanol, with a total impact of 2.3 kg CO_2e/kg H_2 delivered.

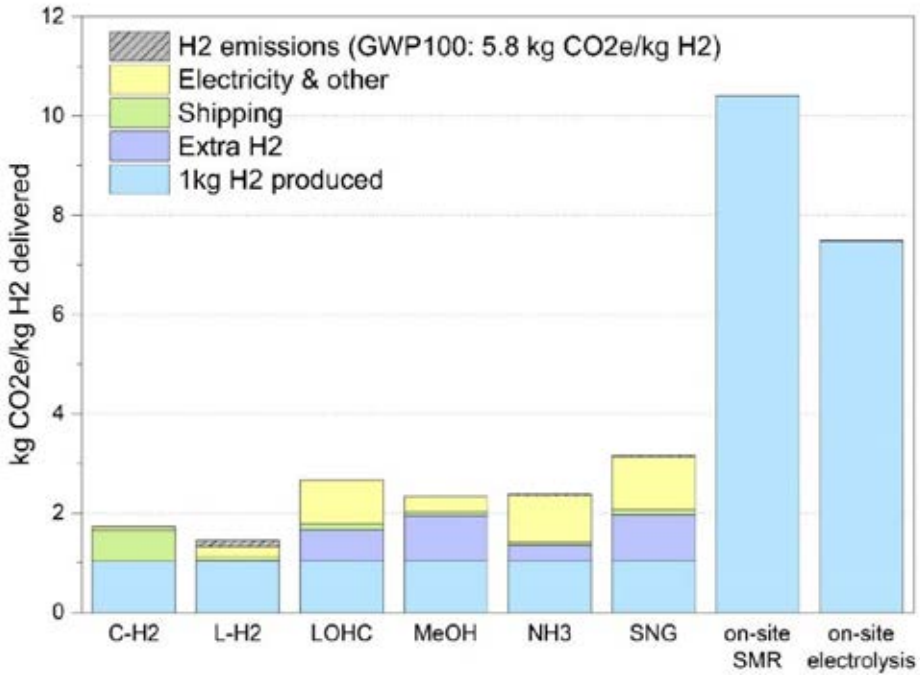


Fig. 2. Life cycle greenhouse gas emissions from hydrogen delivery

CONCLUSIONS

This analysis aimed at investigating the global warming impact of delivering hydrogen to an industrial site, comparing on-site production to hydrogen delivery from a location where renewable electricity is cheaper. Based on our assumptions, the least GHG intense option is to ship liquefied hydrogen. Energy required to pack and unpack hydrogen into more suitable carriers for shipping (i.e., ammonia, LOHC, methanol, and SNG) makes this option less attractive in terms of global warming potential.

The results presented here are subject to a high level of uncertainty, based on the numerous assumptions made throughout the assessment. A thorough sensitivity analysis is planned to ascertain the robustness of the results. Moreover, different delivery conditions (e.g., distances, means of transportation) may alter the GHG emission ranking. Finally, the present analysis was limited to the global warming impact, but an assessment of the overall environmental consequences is necessary to avoid shifting the burden from one environmental issue to another.

REFERENCES

1. European Commission. 2020. Communication COM/2020/301: A hydrogen strategy for a climate-neutral Europe
2. R. Ortiz Cebolla, F. Dolci and E. Weidner. 2021. Assessment of Hydrogen Delivery Options
3. ISO. 2006. ISO 14040:2006 Environmental management -- Life cycle assessment -- Principles and framework, International Organization for Standardization (ISO)
4. R. Derwent, P. Simmonds, S. O'Doherty, A. Manning, W. Collins, and D. Stevenson. 2006. Global environmental impacts of the hydrogen economy, International Journal of Nuclear Hydrogen Production and Applications 1:57-67.
5. Hydrogen Council. 2021. Hydrogen decarbonization pathways. A life-cycle assessment
6. European Commission. 2019. Technical Note. Results of the EUCO3232.5 scenario on Member States
7. US EPA. 2021. Emission Factors for Greenhouse Gas Inventories

Views expressed are those of the authors and do not reflect an official position of the European Commission.

WHEC-2022
23rd World Hydrogen Energy Conference
June 26-30, 2022 - Istanbul

#1492

HOT GAS DESULFURIZATION PERFORMANCE OF SBA-15 SUPPORTED/MIXED METAL OXIDES (Cu, Fe, Mn, and Zn)

[1*] *Arzu Kanca,* [2] *Gülcan Korkmaz*
[1, 2] Ataturk University, Engineering Faculty, Chemical Engineering Department, 25240, Erzurum, Turkey

*Corresponding author e-mail: akanca@atauni.edu.tr

ABSTRACT

The main components of the synthesis gas formed during gasification is H_2 and CO. In addition to these gases, it contains H_2S due to the sulfur contents of organic matters. Since H_2S causes corrosion of system equipment and catalyst poisoning, it should be removed from flue gas stream. Furthermore, since fuel production from synthesis gas is an endothermic process and cooling of syngas causes energy loss, desulfurization should be carried out at high temperature. This study aims to determine the hot gas desulfurization performance of unsupported and SBA-15 supported MeO-MeO (Me: Cu, Fe, Mn, and Zn) sorbents. Sorbents prepared by wet impregnation method were characterized by X-ray diffraction (XRD) technique and Brunauer, Emmet ve Tellere (BET). In the characterization part, metal oxide formation was indicted by XRD findings, while BET results showed that SBA-15 supported CuO-ZnO sorbent has the largest surface area. Finally, desulfurization performance of sorbents was analyzed by gas chromatography equipped with a fixed bed quartz reactor at 800°C. Ar balanced simulated coal gas including 330 ppm H_2S, 9% H_2, 13.5% CO, and 4.5% CO_2 was used as the flue gas. The results of the desulfurization experiments revealed that the sorbents including MnO indicated the similar good sulfidation performance among the unsupported sorbents, while the best desulfurization performance was obtained for FeO-MnO among SBA 15 supported sorbents.

Keywords: Hot gas desulfurization, SBA 15, mixed metal oxide

INTRODUCTION

Gasification is the process of producing synthesis gas as a result of partial oxidation of organic materials. In addition to CO and H_2, syngas gas contains H_2S due to the sulfur contents of organic matters. Since fuel production from syngas is an endothermic process, H_2S should be removed at the highest possible temperature to protect process equipment and catalysts [1]. In thermodynamic and kinetic studies, Westmoreland et al.[2] indicated that Fe, Zn, Mn, Ca, and Cu oxides are suitable sorbents for hot gas desulfurization. However, single metal oxides used as adsorbents cause problems of sintering, evaporation, pore blockage, capacity, loss in surface areas, and mechanical disintegration. In order to overcome these problems, metal oxides can be either mixed with each other or they can be loaded on support materials. Al_2O_3, TiO_2, ZrO_2, SiO_2 and zeolites are the most commonly used support materials to provide the sorbents with high surface area. In the desulfurization study performed with SBA-15 supported CuO, it was noted that the surface area and pore structure of SBA-15 did not change, but the capacity of the sorbent decreased during the 3 repetitive reduction and oxidation cycles of the sorbent [1]. A zeolite with a high silica content supported CuO and MnO were used as active sulfur sorbents. The results of the studies revealed that these metals significantly increased the sulfur holding capacity of the material and the presence of Mn increased its mechanical resistance [3, 4]. Hong et al. [5] tested the SBA-15 supported Cu−Mn mixed oxide for the hot flue gas desulphurization process at 800°C. The best desulfurization activity of was obtained for the sorbent with 1Cu-9Mn/SBA-15 as 13.8 g per 100 grams of sorbent. Iron oxide (FeO) based sorbents have been extensively preferred to remove H_2S due to their good regenerability, high reactivity, and cheapness. However, since iron oxide converts to iron carbide at temperatures higher than 550°C in the presence of the CO and H_2, its desulfurization potential is lower compared to other metal oxides [1, 3]. Wang et al.[6] studied on sulfidation of SBA-15 supported Fe_2O_3 sorbents. The highest sulfur capture capacity of 7.01g S/100g sorbent was recorded for the sorbent with 31.3 wt.% Fe content. Desulfurization performance of Mn-Zn loaded SiO_2 was examined at 873 K by Ko et al. in 2007 [7]. It was reported that the increasing amount of sorbent increased the metal sulfide formation, but the rapidly formed metal sulfide layer made the mass transfer of H_2S difficult. In the light of literature summarized above, the aim of this study is to prepare SBA-15 supported MeO-MeO (Me: Fe, Cu, Zn, Mn) sorbents by wet impregnation method and to investigate their desulfurization performance.

MATERIALS AND METHODS

Unsupported and SBA-15 supported binary metal oxides were synthesized by wet impregnation method. Ar balanced simulated coal gas including 330 ppm H_2S, 9% H2, 13.5% CO, and 4.5% CO_2 was used as the flue gas. H_2S removal from simulated coal gas was tested in the presence of unsupported and SBA 15 supported mixed metal oxides. Agilent 6890N gas chromatography analyzer was used to follow exit H_2S concentration.

Synthesis and characterization of unsupported and SBA-15 supported sorbents

In order to prepare mixed metal oxides, nitrate salts of Cu, Fe, Mn, and Zn were mixed by wet impregnation method. SBA-15 supported mixed metal oxides were prepared at a mass ratio of 1/1 wt/wt (MeO/MeO, Me: Cu, Fe, Mn, Zn). After SBA-15 was wet with 1-2 drops of water, it was added to mixed metal oxides solutions. Calcination at 600°C for 6 hours followed the overnight drying.

Crystal structure of CuO, FeO, MnO, and ZnO were determined by X-ray diffraction (XRD) (Panalytical Empyrean model, Anode material, Cu 1.56 A wavelength). Micromeritics 3Flex 3-port BET device was employed to analyze the surface structure of the sorbents in the presence and absence of SBA 15.

Sulfidation performance of unsupported and SBA-15 supported sorbents

Sulfidation performance of mixed metal oxide based sorbents was tested by using Agilent 6890N model gas chromatography analyzer equipped with Flame Photometric Detector. The simulated gas mixture flow rate was 100 cm^3/min. The outlet sulfur concentration 100 ppm was defined as the breakthrough point.

RESULTS AND DISCUSSION

Sorbents were characterized by PANalytical Empyrean model XRD device. In order to define the metal oxide and metal sulfide formation, specific Bragg angle values of metal oxides and sulfides are given in Table 1. SBA-15 supported MeO-MeO and MeS formations were shown in Fig. 1. CuO [8], FeO [9, 10], MnO [5, 7-9, 11], ZnO [10] were characterized in the left hand side of Fig. 1, while CuS [12, 13], FeS [14], MnS [15], ZnS [16].

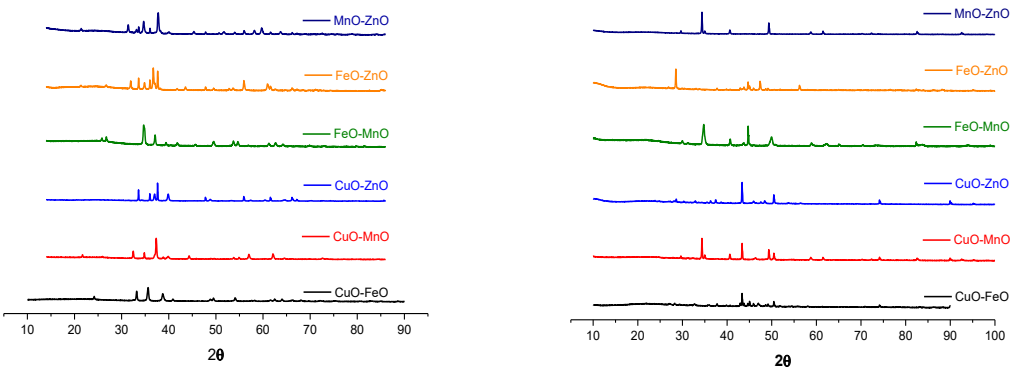


Fig. 1. SBA 15 supported MeO (left) and MeS formation (right).

The presence of SBA-15 increases the surface area of metal oxides. BET results showed that unsupported CuO-FeO (37.1 m^2/g) and SBA 15 supported CuO-ZnO (313 m^2/g) sorbents have the largest surface area. In Fig. 2, sulfidation performance of unsupported and SBA 15 supported MeO-MeO was indicated with respect to H_2S emitted to atmosphere at 800°C. As seen in Fig. 2, the unsupported sorbents including MnO show the better sulfidation than that of the other sorbents. Furthermore, the most important improvement on the sulfidation performance was recorded for SBA 15 supported FeO-MnO.

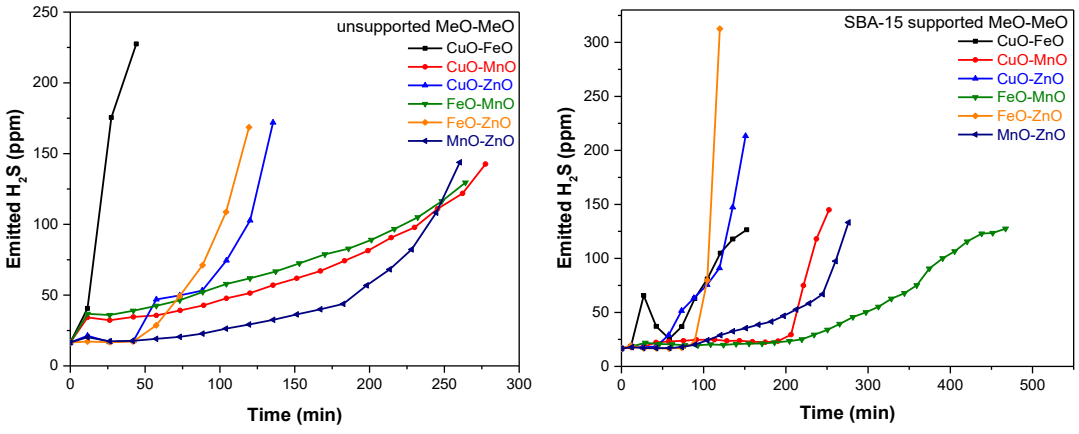


Fig. 2. The amount of H_2S emitted to atmosphere at 800°C.

CONCLUSIONS

BET results showed that SBA 15 supported FeO-ZnO sorbent has the largest surface area of 313 m^2/g. CuO-MnO, FeO-MnO, and MnO-ZnO were reported the best sulfidation performance among the unsupported sorbents, while the best desulfurization performance was obtained for FeO-MnO among the SBA 15 supported sorbents.

ACKNOWLEDGEMENT

Authors thank to The Scientific and Technological Research Council of Turkey (TUBITAK) under the project with Grant Number 118M613 for financial support. They are also grateful for DAYTAM for their help on sorbent characterization.

REFERENCES

1. Meng XM, de Jong W, Pal R, Verkooijen AHM. In bed and downstream hot gas desulphurization during solid fuel gasification: A review. Fuel Processing Technology. 2010;91:964-81.
2. Westmoreland PR, Gibson JB, Harrison DP. Comparative kinetics of high-temperature reaction between H_2S and selected metal-oxides. Environmental Science & Technology. 1977;11:488-91.
3. Atimtay AT, Gaspergalvin LD, Poston JA. Novel supported sorbent for hot gas desulfurization. Environmental Science & Technology. 1993;27:1295-303.
4. Gasper-Galvin LD, Atimtay AT, Gupta RP. Zeolite-supported metal oxide sorbents for hot-gas desulfurization. Industrial & Engineering Chemistry Research. 1998;37:4157-66.
5. Hong YS, Sin KR, Pak JS, Kim CJ, Liu BS. Kinetic Analysis of H_2S Removal over Mesoporous Cu-Mn Mixed Oxide/SBA-15 and La-Mn Mixed Oxide/KIT-6 Sorbents during Hot Coal Gas Desulfurization Using the Deactivation Kinetics Model. Energy & Fuels. 2017;31:9874-80.
6. Wang XH, Jia JP, Zhao L, Sun TH. Mesoporous SBA-15 supported iron oxide: A potent catalyst for hydrogen sulfide removal. Water Air and Soil Pollution. 2008;193:247-57.
7. Ko TH, Chu H, Liou YJ. A study of Zn-Mn based sorbent for the high-temperature removal of H_2S from coal-derived gas. Journal of Hazardous Materials. 2007;147:334-41.
8. Xue M, Chitrakar R, Sakane K, Ooi K. Screening of adsorbents for removal of H_2S at room temperature. Green Chemistry. 2003;5:529-34.
9. Sharma SK, Vargas JM, Pirota KR, Kumar S, Lee CG, Knobel M. Synthesis and ageing effect in FeO nanoparticles: Transformation to core-shell FeO/Fe_3O_4 and their magnetic characterization. Journal of Alloys and Compounds. 2011;509:6414-7.
10. Chow L, Lupan O, Chai G, Khallaf H, Ono LK, Roldan Cuenya B, et al. Synthesis and characterization of Cu-doped ZnO one-dimensional structures for miniaturized sensor applications with faster response. Sensors and Actuators a-Physical. 2013;189:399-408.
11. Zhang QT, Dai QQ, Li M, Wang XM, Li A. Incorporation of MnO nanoparticles inside porous carbon nanotubes originated from conjugated microporous polymers for lithium storage. Journal of Materials Chemistry A. 2016;4:19132-9.
12. Chaki SH, Tailor JP, Deshpande MP. Covellite CuS – Single crystal growth by chemical vapour transport (CVT) technique and characterization. Materials Science in Semiconductor Processing. 2014;27:577-85.
13. Riyaz S, Parveen A, Azam A. Microstructural and optical properties of CuS nanoparticles prepared by sol–gel route. Perspectives in Science. 2016;8:632-5.
14. Xia H, Liu B, Li Q, Huang Z, Cheung AS-C. High capacity Mn-Fe-Mo/FSM-16 sorbents in hot coal gas desulfurization and mechanism of elemental sulfur formation. Applied Catalysis B: Environmental. 2017;200:552-65.
15. Mi L, Chen Y, Zheng Z, Hou H, Chen W, Cui S. Beneficial metal ion insertion into dandelion-like MnS with enhanced catalytic performance and genetic morphology. RSC Advances. 2014;4:19257-65.
16. Soltani N, Saion E, Hussein MZ, Erfani M, Abedini A, Bahmanrokh G, et al. Visible light-induced degradation of methylene blue in the presence of photocatalytic ZnS and CdS nanoparticles. International journal of molecular sciences. 2012;13:12242-58.

WHEC-2022
23rd World Hydrogen Energy Conference
June 26-30, 2022 - Istanbul

#1516

THE EFFECT OF HYDROGEN AND AMMONIA COMBUSTION ON PERFORMANCE AND EMISSIONS

[1*] *Kubilay Bayramoğlu,* [2]*Abdullah Bahlekeh,* [3]*Kemal Masera*
[1]Dokuz Eylul University, Maritime Faculty, Marine Engineering Department, Buca, Izmir, Turkey
[2]Ege University, Mechanical Engineering Department, Bornova, Izmir, Turkey
[3]Aston University, Mechanical Biomedical and Design Engineering Department, Birmingham, UK

*Corresponding author e-mail: kubilay.bayramoglu@deu.edu.tr

ABSTRACT

The co-combustion of traditional methane gas and alternative fuels importance to reduce emissions in combustion has been increased in recent years. In this study, the effects of the combustion of methane-hydrogen and methane-ammonia-hydrogen fuel mixture on system performance and emissions were numerically investigated. Firstly, the effects of methane and 5%, 10% and 15% hydrogen mixture were investigated. Then, methane and 5% fixed hydrogen ratio with 5% ammonia, 10% ammonia and 15% ammonia mixtures were examined. As a result of the study, combustion chamber temperature, carbon and NO_X emissions are presented comparatively for each case. In addition, the Sandia D model used in the study is presented by verifying with the literature data. The findings obtained in the study showed that increasing hydrogen and ammonia increased NO_X emissions while decreasing CO_2 emissions.

Keywords: Hydrogen, Ammonia combustion, Flame, Emissions

INTRODUCTION

The depletion of fossil fuels and the formation of greenhouse gases that cause global warming because of combustion makes it necessary to use clean fuels in combustion engines. Hydrogen and ammonia are used as clean fuels to reduce carbon emissions. These fuels are currently used in combination with conventional fossil fuels to reduce carbon emissions [1].

Ammonia is one of the most likely fuels to be used as an alternative in the future due to having carbon-free and being obtained from renewable sources [2]. Therefore, it can be used to reduce greenhouse gas (GHG) emissions. In the last two decades, many experimental and numerical studies have been carried out on the use of ammonia as an alternative fuel. In the previous studies, various parameters such as ammonia production, ignition mode, combustion mode were investigated. However, it has several disadvantages when compared to a fossil source fuel. Studies have shown that ammonia has higher ignition energy due to its low flammability [3].

Hydrogen as a fuel is expected to be widely used due to its high energy potential and its feature of being a clean fuel. However, various problems such as the storage and safe transportation of hydrogen remain unresolved [4]. Hydrogen is secondary energy that acts as a carrier between different sources. Hydrogen is produced in nature from basic raw materials such as water. The fact that it is so easy to produce and is one of the renewable energy sources has enabled hydrogen to be included in the energy planning of most countries. The lower energy consumption of hydrogen simultaneously reduces emissions in various fields such as transport and industry. Compared to wind, solar and geothermal energy, whose uses are limited due to their volatility and stability, hydrogen's high cleanliness and efficiency make it of great value for use in future energy systems [5].

In this study, parametric studies were carried out based on the Sandia D model, which was previously validated experimentally and numerically in the literature [6]. The effect of the mixture of hydrogen, ammonia and methane on the combustion chamber temperature and emissions on the validated model was numerically investigated. Thus, the effect of ammonia and hydrogen fuels that do carbon-free on the emission and performance parameters have been investigated.

MATERIALS AND METHODS

The study was carried out on the methane-air flame pilot model by the Sandia National Laboratory. As demonstrated in Fig. 1, the model consists of three inlets: the jet, where the fuel is supplied with the air, the pilot, where the burnt gases are supplied at high temperature, and the airflow [6].

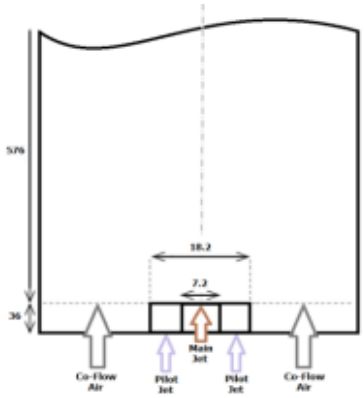


Fig. 1. Sandia flame model

Methane, hydrogen and ammonia were used as jet fuel on the model and a total of seven parametric studies were carried out. The boundary conditions used for numerical analysis are presented in Table 1.

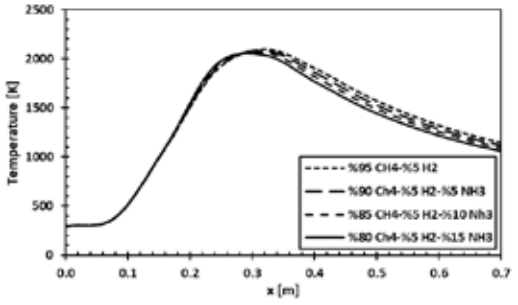
Table 1. Boundary conditions

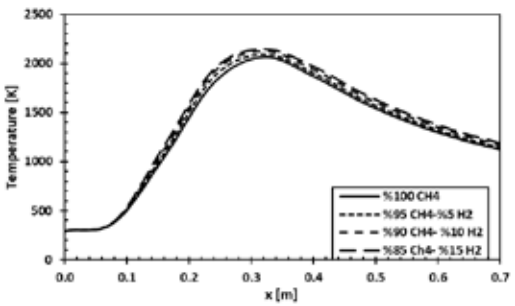
Jet	Mixture fraction [% mass]	0.156
	Velocity [m/s]	49.6
	Temperature [k]	294
	Gases	CH_4, H_2, NH_3
Pilot	Velocity [m/s]	11.4
	Temperature [K]	1880
	Gases	CO_2, H_2O, N_2, O_2
Co-flow	Velocity [m/s]	0.9
	Temperature [K]	294

The study was carried out numerically with computational fluid dynamics. Combustion was carried out in steady-state conditions using GRI-Mech 3.0 mechanism [7]. The numerical model was solved with the *k-ε* turbulence model, and the solution was also provided with species transport model using volumetric reactions. The experimental results were compared with numerical analysis and it was observed that the results were compatible [8].

RESULTS AND DISCUSSION

In this study, temperature, NO_X and CO_2 emissions were determined as a result of the mixture of clean alternative fuels such as hydrogen and ammonia with methane gas. It was determined that the combustion chamber temperature values increased with increasing hydrogen addition. However, the addition of ammonia lowers the combustion chamber temperature. This is due to the potential for higher combustion energy of hydrogen. In addition, NO_X emissions increase only with the addition of hydrogen. The increase in NO_X emissions with hydrogen addition is due to the formation of thermal NO_X with the effect of temperature. However, the increase in NO_X emissions with the addition of NH_3 is due to the conversion of N atoms in its structure to NO due to the unstable structure of NH_3. The carbon-free of both hydrogen and ammonia fuel has reduced CO_2 emissions. Fig. 2 shows the combustion chamber temperature, NO_X and CO_2 emissions formed by the combustion of hydrogen, methane and ammonia mixture at different rates.





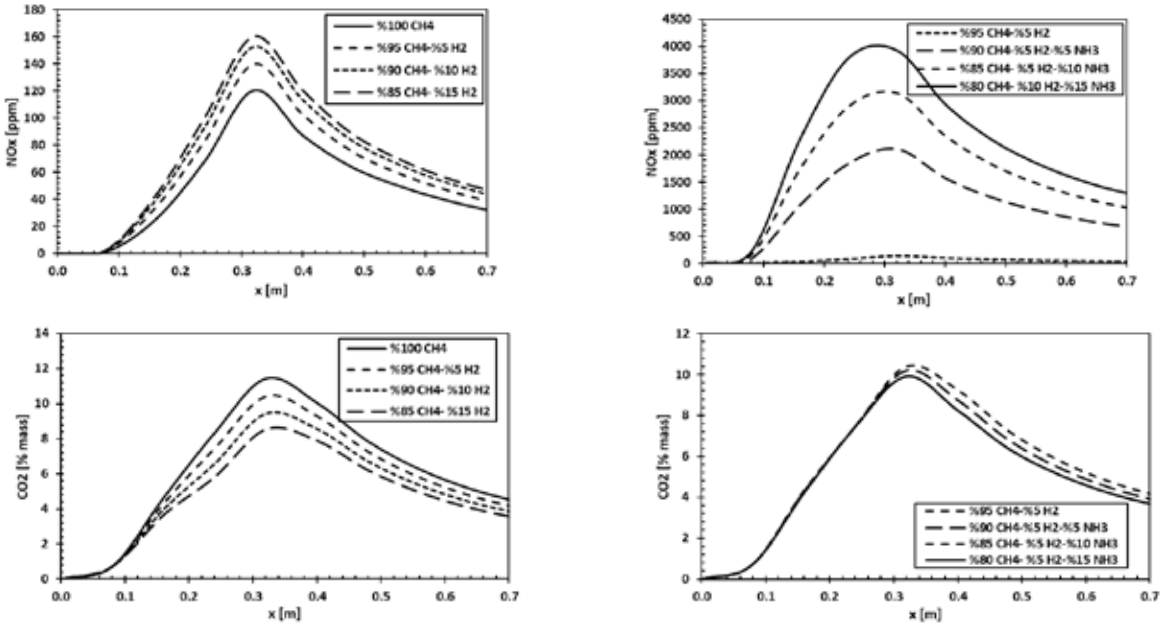


Fig. 2. Combustion chamber temperature and emissions

CONCLUSIONS

In this study, the effect of the use of alternative fuels on the emission and combustion temperature based on the Sandia Flame D model, from which literature data was taken, was investigated numerically. As a result of the study, it was determined that the combustion chamber temperature increased with the addition of hydrogen and decreased with the addition of ammonia. Another parameter determined is that NO_x emissions increase with increasing hydrogen and ammonia amount. Finally, the fact that hydrogen and ammonia do carbon-free ensures a reduction in CO_2 emissions because of combustion.

REFERENCES

1. Bioche, K., Bricteux, L., Bertolino, A., Parente, A., and Blondeau, J. 2021. Large Eddy Simulation of rich ammonia/hydrogen/air combustion in a gas turbine burner. Int. J. Hydrogen Energy *46*, 39548–39562.
2. Elbaz, A.M., Wang, S., Guiberti, T.F., and Roberts, W.L. 2022. Review on the Recent Advances on Ammonia Combustion from the Fundamentals to the Applications. Fuel Commun., 100053. Available at: https://doi.org/10.1016/j.jfueco.2022.100053.
3. Liu, L., Wu, Y., and Wang, Y. 2021. Numerical investigation on the combustion and emission characteristics of ammonia in a low-speed two-stroke marine engine. Fuel *314*, 122727. Available at: https://doi.org/10.1016/j.fuel.2021.122727.
4. Yang, W., Dinesh, K.K.J.R., Luo, K.H., and Thevenin, D. 2022. ScienceDirect Direct numerical simulation of turbulent premixed ammonia and ammonia-hydrogen combustion under engine-relevant conditions. Int. J. Hydrogen Energy, 1–18. Available at: https://doi.org/10.1016/j.ijhydene.2022.01.142.
5. Cohce, M.K., Dincer, I., and Rosen, M.A. 2011. Energy and exergy analyses of a biomass-based hydrogen production system. Bioresour. Technol. *102*, 8466–8474.
6. Magnussen, B.F., and Mjertager, B.H. 1976. Effects on Turbulence on Species Mass Fractions in Methane/Air Jet Flames. Proc. Sixt. Symp. Combust., 719–727.
7. Smith, G.P., Golden, M.D., Frenklach, M., Moriarty, N.W., Eiteneer, B., Goldenberg, M., Bowman, C.T., Hanson, R.K., Song, S., Gardiner Jr., W.C., *et al.* GRI Mech 3.0. Available at: http://combustion.berkeley.edu/gri-mech/ [Accessed November 30, 2021].
8. Rassoulinejad-Mousavi, S.M., Mao, Y., and Zhang, Y. 2018. Reducing greenhouse gas emissions in Sandia methane-air flame by using a biofuel. Renew. Energy *128*, 313–323. Available at: https://doi.org/10.1016/j.renene.2018.05.079.

WHEC-2022
23rd World Hydrogen Energy Conference
June 26-30, 2022 - Istanbul

#1549

LIFE CYCLE ASSESSMENT OF DIFFERENT HYDROGEN CONVERSION TECHNOLOGIES FROM BIOMASS GASIFICATION

[1] Mehmet Utku Öztürk, [2*] Azize Ayol, [1] Özgün Tezer[1]*
[1] Dokuz Eylul University, The Graduate School of Natural and Applied Sciences, Buca, 35390, Izmir, Turkey
[2] Dokuz Eylul University, Faculty of Engineering, Department of Environmental Engineering, Buca, 35390, Izmir Turkey

*Corresponding author e-mail: azize.ayol@deu.edu.tr

ABSTRACT

Gasification of different types of biomass in a lab scale up-draft fixed bed gasifier is evaluated from the environmental effect perspective through Life Cycle Assessment (LCA). Biomass is an energy source which has a lot of potential for electricity generation, and it is considered as an environmentally friendly renewable energy source. Gasification of the biomass has been considered as a significant renewable energy production alternative to fossil fuels. Biomass through gasification forms a syngas which includes H_2, CH_4, CO and as a solid by-product biochar is produced at high temperatures. In this study, LCA is used as a tool for assess the different environmental impact categories of the energy production from green waste and biological treatment sludge gasification studies, with the cradle to grave approach. Different hydrogen conversion technologies via LCA have been also assessed. LCA calculations were performed by using SimaPro 9.1 software and experimental data collected from LCA database and a lab scale gasifier operated in Dokuz Eylul University, Turkey.

Keywords: Life Cycle Assessment, Biomass, Gasification, Green Waste, Treatment Sludge, Hydrogen Conversion

INTRODUCTION

Biomass gasification has been considered as an important renewable energy alternative to deal with the environmental problems originating from fossil fuels and climate change effects. Biomass has the potential for electricity generation and biofuels, and it is considered as one of the most important renewable energy sources for the future and now [1]. In this study, two different biomass has been used: green waste, and biological treatment sludge. First biomass used in this study is green waste and collected from urban parks and gardens. It is a lignocellulosic-rich resource and can be obtained in large quantities at low cost [2]. Green waste is basically a composition of branches, grasses, and leaves. Green waste can be a good choice for biomass gasification because it can be easily gathered, it is economically affordable, and its water content can be easily reduced by drying. Other biomass kind used in this study is the biological sludge, which is produced in huge amounts at different treatment stages in wastewater treatment plants. The organic content of the treatment sludge is very high and if it is considered as a waste then it will create a lot of environmental problems. However, treatment sludge can be used as a feedstock to the gasification process because it has high calorific value and at the same time, using treatment sludge as a feedstock to the gasification process reduces the waste sludge amount.

Gasification process converts carbon containing materials to a syngas which is a combustible gas includes H_2, CH_4, CO. This syngas can be used as a fuel for electricity generation [3]. Gasification process is known as an environmentally friendly power system although to see its positive affect to the environment assessing its environmental impacts are very important. There are several hydrogen conversion technologies are available. In this study, three of the existing hydrogen to energy conversion technologies' environmental impacts are evaluated. The technologies are internal combustion, electrochemical electricity generation (fuel cells), and syngas fermentation. Hydrogen is a fitting fuel for internal combustion engines and turbines. Hydrogen engines as the same way of gasoline used in engine, burns hydrogen in an internal combustion engine, and hydrogen powered internal combustion engines are approximately 20% more efficient than gasoline powered engines [4]. Other hydrogen conversion technology is electrochemical electricity generation (fuel cells), with this technology, the hydrogen can combine with oxygen in an electrochemical reaction, where this reaction takes place is called the fuel cell [4]. And the last one is syngas fermentation. Syngas fermentation is a microbial process, and in this process, syngas used as a carbon source, and through the agency of microorganisms, syngas converted into fuel and chemicals such as ethanol [5].

LCA is an assessment of the environmental impacts of any product or process and includes the procurement of its raw material, production, transportation, use, recycling or end of life treatment, and final disposal furthermore it is not only assessing the chosen process or products environmental impact, but also considers the energy production [6]. It is evaluated as a powerful tool for analyzing the environmental impacts of a process throughout its life cycle [1].

In this study, it is aimed to assess the environmental effects of green waste and treatment sludge gasification applications for the energy production in three different routes, applying a LCA approach, as shown in Fig 1. First stage includes the different types of biomass, their production, and their shipment to the gasifier. Second stage represents the gasification of feedstock biomass, and it includes the cleaning of the synthetic gas. The third stage shows the hydrogen conversion technologies.

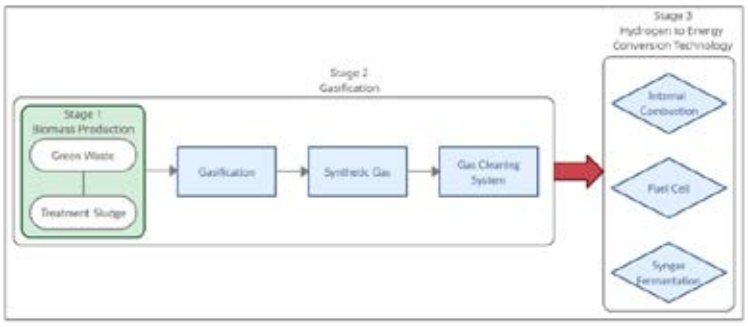


Fig. 1. LCA stages of the process

Six different scenarios are created to compare the LCA of the process. There are two different types of biomass and three different types of hydrogen conversion technology exist in this study, with the combination of them six scenarios have created. Through these six scenarios, which biomass gasification and which kind of hydrogen conversion technology have better impact on the environment will be determined. Data for green waste gasification and treatment sludge gasification were collected from a lab scale gasifier in Dokuz Eylul University, Turkey. LCA calculations were performed by using SimaPro 9.1 software according to the cradle-to-grave approach for different impact categories.

MATERIALS AND METHODS

In this study, it is aimed to assess the environmental effects of green waste and treatment sludge gasification for the energy production through three different hydrogen conversion technologies, applying a LCA approach and following the recommendations of the ISO 14040 series. LCA calculations were performed by using SimaPro 9.1 software. Calculations were made according to the cradle to grave approach for every scenario. The “Ecoinvent 3 – allocation, cut-off by classification” and Center of Environmental Science of Leiden University (CML)-IA Baseline V3.06 / EU25 have been chosen as the main database and the calculation method, respectively. CML-IA Baseline calculates eleven different impact categories from the environmental aspect: abiotic depletion, abiotic depletion (fossil fuels), global warming, ozone layer depletion, human toxicity, fresh water aquatic ecotoxicity, marine aquatic ecotoxicity, terrestrial ecotoxicity, photochemical oxidation, acidification, and eutrophication. Functional unit is a quantified definition of a products function and it is the reference for all calculations through the impact assessment. The objective of the biomass gasification process is producing energy therefore the functional unit defined as the produced energy amount. The functional unit is defined as 20 kW of energy produced from gasification, and since this study was conducted for a laboratory-scale gasifier, the energy production amount was chosen relatively low. After defining the functional unit, scenarios can be created on this base. The six different scenarios were determined considering the defined functional unit through the objectives of the study. To compare the different biomass types as a feedstock to the gasification process and to compare the three different hydrogen conversion technologies these scenarios were created based on the above considerations

RESULTS AND DISCUSSION

Table 1 is the results of the calculated LCA of the scenarios for different impact categories. Results show that the treatment sludge gasification is more harmful to the environment than the green waste gasification. But the treatment sludge’s environmental harm as a waste is much higher than the waste scenario of the green waste. So, the gasification of treatment sludge is still an environmentally friendly energy production way. This scenario compares only the biomass difference of the process. Fig 2 also shows that the gasification of green waste is much healthier than the other scenarios from the aspect of environmental harm level; also, treatment sludge gasification is by far the most harmful gasification scenario. In addition, LCA calculations includes long-term effects of every process.

Table 1. Impact values for each scenario, associated with the functional unit, 20 kW energy obtained from the gasification

Impact category	Unit	Green Waste Gasification	Treatment Sludge Gasification
Abiotic depletion	kg Sb eq	0,003126013	0,01219133
Abiotic depletion (fossil fuels)	MJ	355,40519	1922,3803
Global warming (GWP100a)	kg CO_2 eq	34,380321	216,73917
Ozone layer depletion (ODP)	kg CFC-11 eq	2,22E-06	1,43E-05
Human toxicity	kg 1,4-DB eq	397,21431	703,35112
Fresh water aquatic ecotox.	kg 1,4-DB eq	79,794189	196,26212
Marine aquatic ecotoxicity	kg 1,4-DB eq	95588,03	268207,86
Terrestrial ecotoxicity	kg 1,4-DB eq	0,49900227	1,8775595
Photochemical oxidation	kg C_2H_4 eq	0,007630562	0,056628938
Acidification	kg SO_2 eq	0,36993483	0,87700717
Eutrophication	kg PO_4--- eq	0,14416724	0,349306

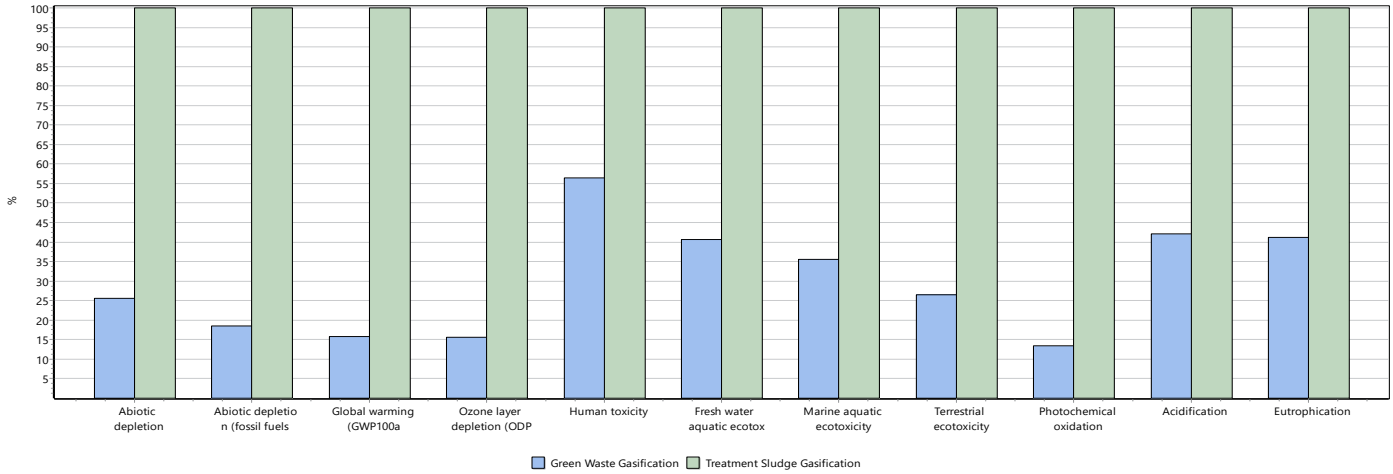


Fig 2. Impacts percentages for each scenario, associated with the functional unit, 20 kW energy obtained from the gasification

CONCLUSIONS

This study shows that the green waste gasification is more optimal than the treatment sludge gasification in the aspect of environmental pollution level. However, green waste takes up a lot of space in volume and therefore it is more difficult to transport and store. The study is still in progress, remaining scenarios will be discussed in detail. Three different hydrogen conversion technology's life cycle analysis will be evaluated and other than all six scenarios and also there will be another comparison with fossil fuels.

ACKNOWLEDGEMENT

This study was funded by TÜBİTAK-ÇAYDAG "Sustainable Energy Recovery from Treatment Plant Sludge, Green Wastes, and Olive Pomace via Gasification Process: Investigation of Beneficial Usage Alternatives of Gasification Products" Research Project (under grant #119R029).

REFERENCES

1. Zang, G., Zhang, J., Jia, J., Lora, E. S., & Ratner, A. 2020. Life cycle assessment of power-generation systems based on biomass integrated gasification combined cycles. *Renewable Energy*, *149*, 336-346.
2. Viretto, A., Gontard, N., & Angellier-Coussy, H. 2021. Urban parks and gardens green waste: A valuable resource for the production of fillers for biocomposites applications. *Waste Management*, *120*, 538-548.
3. Midilli, A., Dogru, M., Howarth, C. R., Ling, M. J., & Ayhan, T. 2001. Combustible gas production from sewage sludge with a downdraft gasifier. Energy Conversion and Management, 42(2), 157-172.
4. Barbir, F. 1999. Review of hydrogen conversion technologies. Hemijska Industrija, 53(12), 426-433.
5. Ayol, A., Peixoto, L., Keskin, T., & Abubackar, H. N. 2021. Reactor designs and configurations for biological and bioelectrochemical C1 gas conversion: a review. International Journal of Environmental Research and Public Health, 18(21), 11683.
6. Keoleian, G. A., & Volk, T. A. 2005. Renewable energy from willow biomass crops: life cycle energy, environmental and economic performance. BPTS, 24(5-6), 385-406.

WHEC-2022
23rd World Hydrogen Energy Conference
June 26-30, 2022 - Istanbul

#1589

LIFE CYCLE AND ECONOMIC ASSESSMENT OF HYDROGEN FUEL CELL BUSES

[1*] *Alireza Khoshnevisan,* [1] *Pouria Ahmadi,* [2] *Nader Javani*
[1]School of Mechanical Engineering, College of Engineering, University of Tehran, P.O. Box 11155-4563, Tehran, Iran
[2]Faculty of Mechanical Engineering, Yildiz Technical University, 34349, Istanbul, Turkey

ABSTRACT

Converting Intercity buses to hydrogen buses is an effective approch for a sustainable public transportation systems. In the current study, a life cycle analysis of hydrogen fuel cell and diesel buses are conducted, using real-world driving cycles. In this study, hydrogen buses are compared to diesel buses in terms of both life cycle emissions and life cycle cost. The results indicate that hydrogen buses can be economically comparable to diesel buses. Meanwhile, teing environmentally benign, makes them a promising solution for the considered situations in Canada.

Keywords: Life cycle assessment, Fuel cell, Electric Vehicles, Hydrogen

INTRODUCTION

Transportation is Canada's second-largest energy consumer, accounting for approximately 30% of total energy consumption [1]. Transportation is one of the most reasons for air pollution. Consumption of fossil fuels is also rising dramatically as global transportation grows. The increased use of fossil fuels accelerates the air pollution process and the depletion of oil resources. One of the main public transportation systems is intercity buses. Therefore, reducing the pollution caused by these buses, or using sustainable energy will significantly help to improve the air quality and to reduce reliance on fossil fuels. Vehicles with internal combustion engines currently have the largest market share in the transportation sector. Hydrogen buses use non-combustible electrochemical reactions to generate electricity with wateras the byproduct. . As a result, these buses provide a type of transportation system that has the potential to emit no greenhouse gas (GHG) at the point of use. Hydrogen vehicles can use up to 60% of the energy stored in hydrogen fuel due to the high efficiency of the electrochemical reaction in the fuel cell. On the other hand, internal combustion engine buses consume approximately 20% of the fuel energy [2]. Energy conversion in fuel cells has a thermodynamic efficiency that exceeds the Carnot efficiency limit for internal combustion engines [3]. The issue with using hydrogen buses is that pure hydrogen is not available for use in these buses, so other methods such as steam methane reforming (SMR) and water electrolysis should be considered, which, in turn, result in GHG emissions.

The life cycle assessment (LCA), also recognized as cradle-to-grave assessment, evaluates the environmental impacts of all stages of a product's life cycle [4]. The bus and its fuel are evaluated at each stage of the LCA analysis, from raw material extraction to production and recycling, and their environmental impacts are assessed. The LCA analysis for different buses can vary greatly depending on the type of fuel and how it is prepared, especially for hydrogen buses. Although hydrogen vehicles have received much attention in recent years, no comprehensive study has been conducted to examine their environmental and economic impacts. Therefore, a comprehensive life cycle assessment and economic analysis of fuel cell buses are conducted in this study, and they are compared with diesel buses from various perspectives.

MATERIALS AND METHODOLOGY

The fuel consumption of each bus is considered for the pollutant estimation. The Simcenter Amesim software is used to model the buses. This software offers a high level of accuracy when simulating a vehicle in real driving situations. Amesim software is used for this investigation. A real driving cycle in Vancouver is considered in the study to increase the accuracy of the analysis. The primary purpose of the LCA analysis performed in this study is to make a comparison between hydrogen-powered buses and buses working with diesel. In this study, Afleet LCA software is utilized to perform LCA analysis. AFLEET (Alternative Fuel Life-Cycle Environmental and Economic Transportation) is a software for Clean Cities stakeholders to calculate fuel use, air pollutant emissions, GHG emissions, and the ownership costs of different vehicles. For a vast range of fuels and vehicles, this software can integrate driving cycles, engine efficiency, and vehicle parameters. Aside from the amount of pollution, the purchase price and the costs of operating and maintaining the bus are all significant considerations when selecting the type of city bus. As a result, the life cycle emissions can be mentonized, resulting in the same unit for all primary factors, simplifying the analysis. This study considers two types of emissions: GHG emissions and air quality emissions. The greenhouse gases in this study are CO_2, CH_4, and N_2O, and the air quality emissions are

Volatile organic compounds (VOCs), carbon monoxide (CO), particulate matter (PM), and Nitrogen oxides (NO_X). The Air quality external cost is calculated as [5]:

$$C_{AQ} = \sum_i P_i e_i \quad (1)$$

where the pollutant emission and external cost of i are denoted by P_i and in e_i, respectively. Also, the air pollutants external cost is indicated by C_{AQ}. The external cost of greenhouse gases is then calculated as follows:

$$C_{GHGs} = \sum P_j e_j \quad (2)$$

The pollutant emission and external cost of j are shown by P_j and in e_j, respectively. Moreover, C_{GHGs} denote the greenhouse gas external cost. The damage costs for all pollutants are available in reference [6].

RESULTS AND DISCUSSION

The most popular method for hydrogen production worldwide, steam methane reforming (SMR), is considered for hydrogen production in this study. The amount of GHG emissions from fuel cell buses are compared with diesel buses in Figure 1(a). As depicted, the amount of GHG emissions from intercity buses can be reduced up to 30% in Canada by employing hydrogen buses. The amounts of air pollutants from both diesel and hydrogen buses are shown in Figure 1(b). Using hydrogen buses decrease the amount of carbon monoxide (CO), Volatile organic compounds (VOCs), and Nitrogen oxides (NO_X). Also, the amount of particulate matter (PM) is almost the same in both buses.

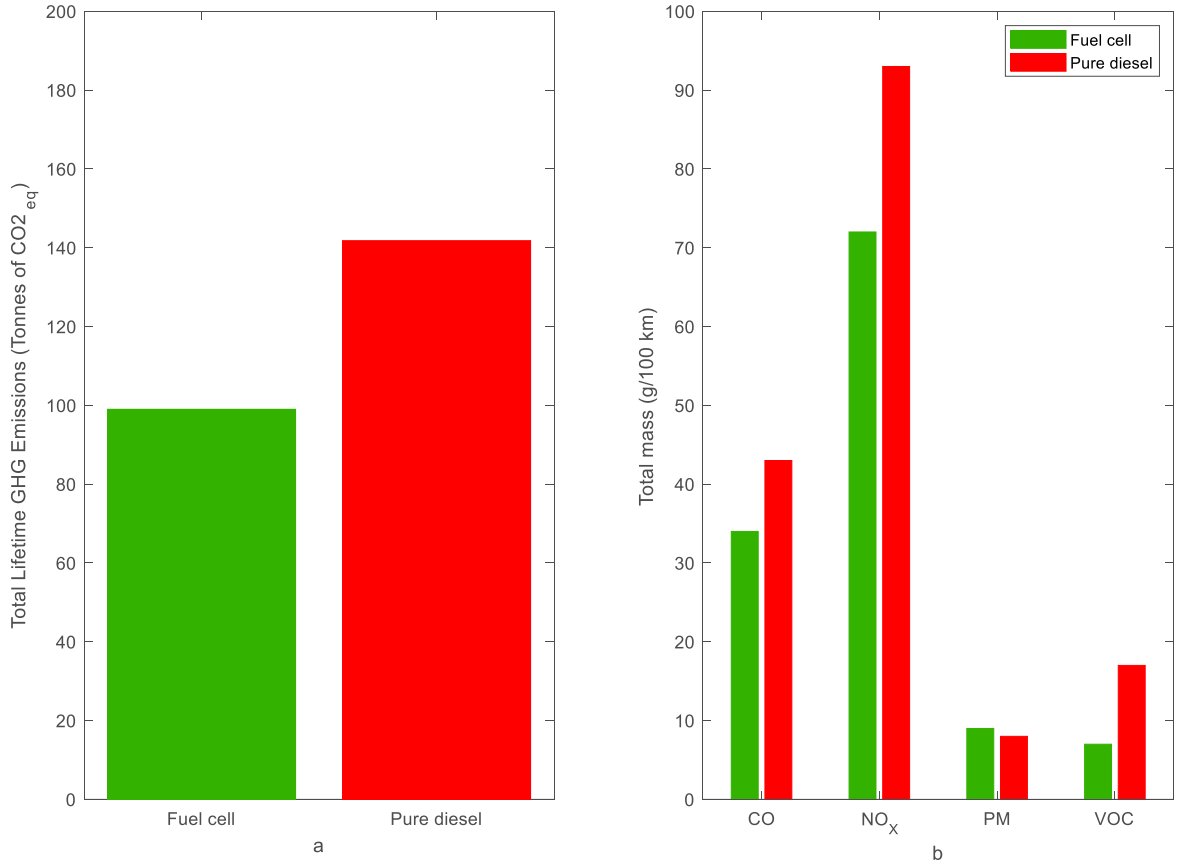


Figure 1. The emissions from fuel cell bus and diesel bus (a): the amount of GHG emissions; (b): the amounts of air pollutants

Both buses can be compared in the same unit since pollutants can be converted to costs. The life cycle costs of hydrogen and diesel buses are shown in Figure 2. Because the cost of producing hydrogen buses has decreased in the recent years, it can be seen that the lifetime costs of fuel cell buses have decreased as well, and if more than 400 of these buses are produced each year for Canada, the lifetime cost will be lower than diesel buses. Furthermore, with the costs of GHG and air pollution emissions rising each year, the use of fuel cell buses appears to be more important than ever.

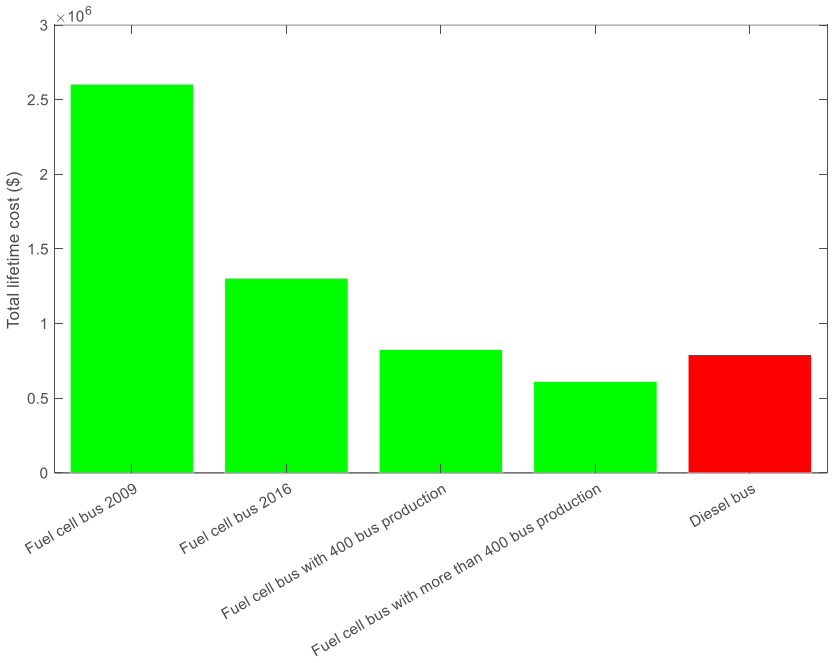


Figure 2. Lifetime cost comparison over the years

CONCLUSIONS

Dynamic models of hydrogen and diesel buses are developed in this study, and the amount of fuel consumption for both buses is computed in the real driving cycle and considering actual conditions. A comprehensive life cycle assessment of both buses was conducted, and it was observed that GHG emissions from fuel cell buses are 30% less than diesel buses. Moreover, comparing the amounts of air pollutants in the buses revealed that using hydrogen buses is more environmentally friendly. Furthermore, an economic study was conducted, and it was discovered that increasing the production of hydrogen buses reduces their lifetime cost; additionally, emission costs are rising, making fuel cell buses more cost-effective than diesel buses.

REFERENCES

1. Motasemi F, Afzal MT, Salema AA, Moghavvemi M, Shekarchian M, Zarifi F, et al. Energy and exergy utilization efficiencies and emission performance of Canadian transportation sector, 1990-2035. Energy 2014;64:355–66. https://doi.org/10.1016/j.energy.2013.09.064.
2. Ahmadi P, Kjeang E. Comparative life cycle assessment of hydrogen fuel cell passenger vehicles in different Canadian provinces. Int J Hydrogen Energy 2015;40:12905–17. https://doi.org/10.1016/j.ijhydene.2015.07.147.
3. Ahmadi P, Kjeang E. Realistic simulation of fuel economy and life cycle metrics for hydrogen fuel cell vehicles. Int J Energy Res 2017;41:714–27. https://doi.org/10.1002/er.3672.
4. Raeesi M, Changizian S, Ahmadi P, Khoshnevisan A. Performance analysis of a degraded PEM fuel cell stack for hydrogen passenger vehicles based on machine learning algorithms in real driving conditions. Energy Convers Manag 2021;248. https://doi.org/10.1016/j.enconman.2021.114793.
5. Prevedouros P, Mitropoulos L. Life Cycle Emissions and Cost Study of Light Duty Vehicles. Transp Res Procedia 2016;15:749–60. https://doi.org/10.1016/j.trpro.2016.06.062.
6. Ahmadi P. Environmental impacts and behavioral drivers of deep decarbonization for transportation through electric vehicles. J Clean Prod 2019; 225:1209–19. https://doi.org/10.1016/j.jclepro.2019.03.334.

WHEC-2022
23rd World Hydrogen Energy Conference
June 26-30, 2022 - Istanbul

#1611

TOWARDS ETHICAL ENERGY STORAGE MATERIALS – COBALT FREE CATHODE ACTIVE MATERIAL LKMNO

* *Karolina Charzewska, Olga Surma, Gabriel Moskal, Agnieszka Węgrzyn, Marcin Molenda*
Jagiellonian University, Faculty of Chemistry, Department of Chemical Technology, Gronostajowa 2, 30-387 Kraków, Poland

*Corresponding author e-mail: karolina.charzewska@student.uj.edu.pl ; k.charzewska55@gmail.com

ABSTRACT

The replacement of fossil fuels by renewable energy sources will require batteries capable of storing significant amounts of energy. The effects of scientific studies on this subject are not limited to the research sphere, but have real economic, political and social consequences: independence from the supply of raw materials from distant areas or reduction of human rights violations in the case of conflict elements. Ethical and ecological supply of the elements is regulated by the EU and the US, among others – all of this must be taken into the consideration when proposing new materials for Li-ion cells. Based on these premises, this article is focused on the production of cobalt free and low-nickel lithium-ion cells using improved cathode material LKMNO. Its 3D spinel structure is capable of fast cation-mediated anionic redox reaction making it stable, reversible and efficient cathode material to use.

Keywords: energy storage; Li-ion batteries; cobalt-free cathode materials; defect spinel; green chemistry

INTRODUCTION

Due to the rapid technological development in recent years, the production and demand for devices using portable energy sources is increasing. Consequently, there is a high demand for inexpensive and durable cells with stable charge/discharge cycles, high energy capacity and high operating potential. Recently popular Li-ion batteries are meeting those requirements. However, there are still many venues to explore, improving its parameters and lessening the environmental impact of this product.

The energy produced by wind power, hydroelectric power or photovoltaic panels is dependent on the environment, and is not always delivered in a uniform and sustainable manner. In order to use its full potential in periods of increased production dependent on natural conditions, the energy produced should be stored safely so that these resources are available in case of periods of stagnation or reduced production. The same assumption applies to the production of green hydrogen. Its main advantage is that it can be produced from water or from any hydrocarbon fuel. Water electrolysis combined with renewable electricity is considered the most beneficial for the environment and it is expected to make a significant contribution to the future hydrogen production. There is continuous research on improving this process [1,2]. The most efficient process for providing energy to a hydrogen-powered grid using electrolysis assumes continuous operation of the electrolyser. As above, power consumption from the grid is not constant, excess of unused energy should be stored in battery cells to make it more sustainable.

This green approach to battery components is our main concern. Currently, the majority of the elements used in the production of lithium batteries is sourced in a few limited areas, often plagued with military conflicts. This can have an impact on the economic dependencies and political issues, driving up prices and limiting material availability. The biggest problem in the production of popular cathode materials is the price and availability of cobalt ore [3]. Substitution of cobalt with less pricey metals like manganese in cathode materials is an opportunity to answer rising market demand for energy storages for lesser cost.

LKMNO ($Li_{0.98}K_{0.01}Mn_{1.86}Ni_{0.11}O_4$) is a derivative of LMO ($LiMn_2O_4$) spinel which has limited applications due to low specific capacity and capacity retention. Modification of its chemical composition with Ni and K leads to the stabilization of spinel structure, higher speed and reversibility of electrochemical reaction. Performance and capacity was also boosted significantly in comparison to LMO [4].

MATERIALS AND METHODS

In this study we were focusing on sol-gel synthesis of cobalt free cathode material $Li_{0.98}K_{0.01}Mn_{1.86}Ni_{0.11}O_4$ and influence of calcination step on the structure and its function.

Synthesis of LKMNO

The sol-gel method was used. Aqueous solutions of lithium acetate, manganese acetate, nickel acetate, and potassium nitrate were combined under constant flow of argon to prevent oxidation of the mixture. Concentrated

ammonia solution (25%) was added as an alkalizing agent. After thorough mixing, the suspension was left in the air oven for 3 days at 90°C.
Obtained xerogel was calcined in two steps, first at the temperature of 300°C for 24h (heating rate of 1 °C min^{-1}) and second at temperature of 650°C for 6h (heating rate of 5 °C min^{-1}) in the air atmosphere using muffle furnace [4,5,6].
The second sample was calcined at 800°C instead of 650°C.

Infra-Red Spectroscopy (FTIR)

Sample before calcination (LKMNO), after calcination in 650°C (LKMNO 650), after calcination in 800°C (LKMNO 800) were measured. Additionally, cathode material LKMNO 650 supported on Al-foil has been characterized. Results can be seen in Fig.1.

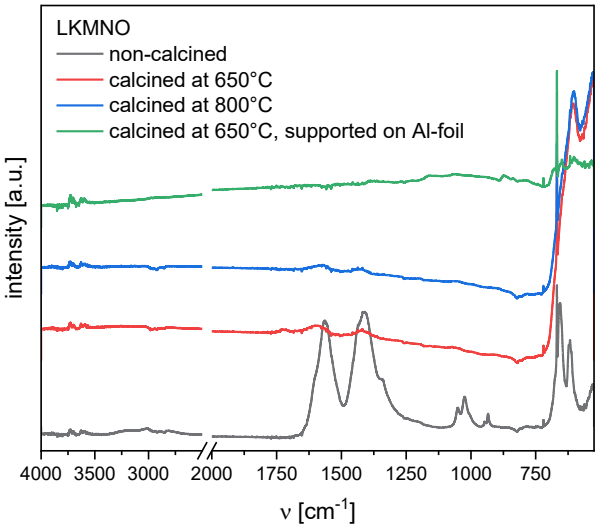


Fig1. FTIR results for the samples LKMNO, LKMNO 650, LKMNO 800 and LKMNO 650 electrode.

X-ray powder diffraction (XRD)

The same samples as listed above have been studied using x-ray powder diffraction. Recorded patterns are shown in Fig.2.

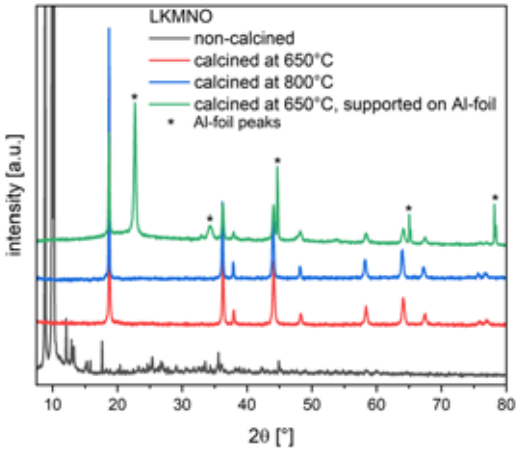


Fig.2 XRD results for the samples LKMNO, LKMNO 650, LKMNO 800 and LKMNO 650 electrode.

The size of the crystallites was measured after calcination and it was determined as 28 nm for LKMNO 650 and 43 nm for LKMNO 800, respectively.

RESULTS AND DISCUSSION

Sol-gel synthesis of LKMNO allowed for the preparation of material containing very small amounts of K and Ni. Samples were homogenous and the method was adhering to green chemistry principles. The analysis of FTIR spectrum measurements after calcination showed the disappearance of bands representing organic ligands introduced in the precursor. The XRD method also confirmed the occurring change in structure of the precursor and its transformation into spinel LKMNO. The size of crystallites is also an important parameter that can help in choice of calcination conditions, providing that we wish to produce cathode material with large active surface area and lower diffusion limitations.

CONCLUSIONS

Synthesis of LKMNO is effective and provides us with properly constructed 3D spinel structure. Calcination temperature does not have significant influence on the obtained results, so calcination in 650°C consumes less energy which is a preferable solution because of the environmental impact and maintenance cost. The size of crystallites also tells us that LKMNO calcined at 650°C has better properties for use as a cathode material. Lesser size of grains provides better diffusion in substance.

ACKNOWLEDGEMENT

Financial support of the project Priority Research Area Anthropocene (Talent Management) created by the Jagiellonian University is kindly acknowledged (K.Charzewska).

REFERENCES

1. Qiu, Z., Martín-Yerga, D., Lindén, P.A., Henriksson, G., and Cornell, A. 2022. Green hydrogen production via electrochemical conversion of components from alkaline carbohydrate degradation. *International Journal of Hydrogen Energy*. 47 (6), 3644–3654.
2. Hu, Y., Xiong, T., Balogun, M.S.J.T., Huang, Y., Adekoya, D., Zhang, S., et al. 2020. Enhanced metallicity boosts hydrogen evolution capability of dual-bimetallic Ni–Fe nitride nanoparticles. *Materials Today Physics*. 15.
3. U.S. Geological Survey, M.C.S. 2021. Cobalt.
4. Bakierska, M., Chudzik, K., Świętosławski, M., Klejna, S., Kubicka, M., Marciszko-Wiąckowska, M., et al. 2022. Reversible Cation-Mediated Anionic Redox in Defect Spinel Structure for High Power Batteries. *Advanced Functional Materials*. 32 (4),.
5. Molenda, M., Dziembaj, R., Podstawka, E., and Proniewicz, L.M. 2005. Changes in local structure of lithium manganese spinels (Li:Mn=1:2) characterised by XRD, DSC, TGA, IR, and Raman spectroscopy. *Journal of Physics and Chemistry of Solids*. 66 (10), 1761–1768.
6. Bakierska, M., Molenda, M., Świętosławski, M., Bielecka, P.; „LKMNO cathode materials and method of production thereof”; PAT. 235260; US 10,978,707 B2; EP 3464186; KR 10-2355068; IN 38422.

WHEC-2022

23rd World Hydrogen Energy Conference

TRACK 17.
SOCIAL DIMENSIONS

TRACK 17. SOCIAL DIMENSIONS

#71 TEACHY - A FLAGSHIP PROJECT FOR TEACHING FUEL CELL AND HYDROGEN TECHNOLOGY	1487
#193 SOCIAL LIFE CYCLE ASSESSMENT OF A SOLID OXIDE ELECTROLYSIS CELL STACK	1490
#239 ASSESSING PUBLIC ACCEPTANCE ON HYDROGEN ECONOMY IN JAPAN: A COMPARISON OF PAST SURVEY IN 2015	1493
#1473 GREEN HYDROGEN, AN ECONOMIC PARADIGM SHIFT – NEW PERSPECTIVES FOR THE GLOBAL SOUTH?	1497
#1474 GREEN HYDROGEN IN COSTA RICA – PERSPECTIVES OF AN ECONOMIC PARADIGM SHIFT FOR A SMALL DEVELOPING COUNTRY	1501
#1477 TURKEY'S POTENTIAL TO PRODUCE GEOTHERMAL-BASED GREEN HYDROGEN: INSIGHTS FROM INSIDE	1505
#1631 EFFECTS OF SOCIAL MEDIA PLATFORMS ABOUT ATTENDANCE TO WHEC 2022 CONFERENCE	1508

WHEC-2022
23rd World Hydrogen Energy Conference
June 26-30, 2022 - Istanbul

#71

TEACHY - A FLAGSHIP PROJECT FOR TEACHING FUEL CELL AND HYDROGEN TECHNOLOGY

[1, 2]*Ioan Iordache,* [2]*Virgil Dumbrava,* [3]*Robert Steinberger-Wilckens,* [3]*Naser Al-Mufachi,* [4]*Aravind Purushothaman Vellayani* [5]*Massimo Santarelli,* [6]*Yegor Brodnikovskyi,* [7]*Lars N. Cleeman,* [8]*Karel Bouzek,* [9]*Jan Van Herle,* [10]*Jean-Luc Delplancke* [11]*Florence Druart,* [12]*Vladimir Molkov,* [13]*Olaf Jedicke*

[1] The National R&D Institute for Cryogenic and Isotopic Technologies – ICSI, Str. Uzinei 4, Rm. Valcea, Romania
[2] University POLITEHNICA of Bucharest, Spl. Independentei Str. 313, Bucharest, Romania
[3] Centre for Fuel Cell and Hydrogen Research, School of Chemical Engineering, University of Birmingham, Edgbaston B15 2TT, UK
[4] University of Groningen, 9700 AB Groningen, the Netherlands
[5] Politecnico di Torino, Str. Corso Duca degli Abruzzi 24, Torino, Italy
[6] National Technical University of Ukraine 'Kyiv Polytechnic Institute', Str. Prosp. Peremohy 37, Kyiv, Ukraine
[7] Denmark Technical University, Str. Anker Engelunds Vej 1, Lyngby, Denmark
[8] University of Chemistry and Technology, Prague; Technická 5; 16628 Prague 6; Czech Republic
[9] Ecole Polytechnique Federale de Lausanne, Rte Cantonale, 1015, Lausanne, Switzerland
[10] Universite libre de Bruxelles, Av. Franklin Roosevelt 50, 1050 Brussels, Belgium
[11] Grenoble Institute of Technology, Av. Félix Viallet 46, Grenoble, France
[12] Ulster University, St. York 25-51, Belfast, United Kingdom
[13] Karlsruhe Institute of Technology, Karlstraße 6, Karlsruhe, Germany

*Corresponding author e-mail: iordache.ioan@icsi.ro

ABSTRACT

The TeacHy project (Teaching Fuel Cell and Hydrogen science and engineering across Europe) is funded by the Fuel Cell & Hydrogen Joint Undertaking (FCH2 JU), as part of the Horizon 2020 Programme. The TeacHy educational material and MSc course modules have been developed for blended learning delivery and will be available through the partnering universities. 12 partners from 11 European countries have contributed to the successful development of 20 modules.

Keywords: TeacHy, Hydrogen, Master of Science, Blended learning

INTRODUCTION

The TeacHy project is designed as a tool that can be used for universities where they intend to teach a master's programme based on the hydrogen economy, the benefits of implementing hydrogen and fuel cells technology, correlations with other engineering disciplines, etc. The project aims to be a way of increasing the number of postgraduate students in the technical labour market who have the necessary knowledge and skills to implement hydrogen in the field of renewable energy and alternative fuels, providing essential tools to academics in European universities who are active in the field of fuel cell and hydrogen (FCH) technology. The project supports the need for qualified personnel that will grow as the hydrogen industry gradually develops, evolving from a niche concept to a mature market.

Training of personnel to support the emergence and growth of the FCH industry will become a critical component with multi-sectoral implications in ensuring the competitiveness of human and professional resources in the coming decades.

PROJECT DESCRIPTION

The TeacHy project aims to create teaching materials necessary for the training of students pursuing a master's qualification in the field of FCH technology, along with identifying all the steps, difficulties, and solutions necessary to accredit such a master's programme. Obviously, other forms of postgraduate training are included.
The project consortium is comprised of 12 partners from 11 countries (Fig 1): University of Birmingham – UBHAM (UK), University of Groningen (Netherland), National Technical University of Ukraine 'Kyiv Polytechnic Institute' – KPI (Ukraine), Politecnico di Torino – POLITO (Italy), Karlsruhe Institute of Technology – KIT (Germany), University of Chemistry and Technology, Prague – UCTP (Czech Republic), École Polytechnique Fédérale de Lausanne – EPFL (Switzerland), Grenoble Institute of Technology - Grenoble INP (France), Denmark Technical University – DTU (Denmark), Ulster University – UU (UK), Université libre de Bruxelles – ULB (Belgium) and University “Politehnica” of Bucharest in partnerships with ICSI Rm. Vâlcea (both from Romania).

The consortium was created around this group of experienced institutions that also collaborate with other relevant partner networks (universities, professional associations, professional groups, etc.). Through this consortium, partners can access educational materials and use the master's course modules available on the project website [1].



Fig. 1. The TeacHy consortium

The above described educational institutions have a strong pedagogical background in the field of FCH technologies, having numerous similar projects, that include educational components, co-financed by the FCH JU, such as HySafe, TrainHy, HyProfessionals, HyFacts, KnowHy, and HyResponse [2].

RESULTS AND DISCUSSION

The TeacHy educational material and MSc course modules have been developed for blended learning delivery and will be available through the partnering universities. 12 partners from 11 European countries have contributed to the successful development of 20 modules. Within the project, the partners have developed seven modules that are mandatory, another eleven that are optional, and two additional ones.

The content of the teaching material includes slides, relevant multimedia materials, diagrams, graphs, figures, or videos, as well as summative evaluations of the modules (tests and exams). Content developers also evaluate and review content produced by other members of the consortium to ensure the delivery of a high-quality and fit-for-purpose educational programme. Where appropriate, the content developers have translated the teaching material into various spoken European languages so that the national language from the respective educational institution can be used.

TeacHy has the ambition to offer interested parties strong support for conducting and accrediting FCH courses. Support will be provided to a large number of European educational institutions, in the academic field, as well as vocational training institutions. These entities will be able to deliver an FCH master's programme locally, using only 20% of their own resources and the remaining 80% will be the support provided by the TeacHy project. In this way, a significant number of institutions will have the chance to offer high-quality FCH courses across Europe.

Parts of the course content have been delivered and will continue to be delivered to students at partner universities. This is done in order to follow and analyse feedback from students and target groups. The implications of the

pandemic required that in addition to the classical approach, virtual pedagogical tools have to be considered in terms of both teaching courses and evaluating students.

CONCLUSIONS

The TeacHy project is an innovative approach that allows the partner institutions (12 universities from 11 European countries) to offer educational courses on FCH technology. This type of pedagogical content is not yet available in many universities. The project partners carry out a series of activities through which they can make available to any educational institution in Europe didactic content that covers FCH technology that meets the highest quality standards.

ACKNOWLEDGEMENT

The TeacHy project is a Coordination and Support Action funded by the European Union's H2020 programme through the Fuel Cells and Hydrogen 2 Joint Undertaking under grant agreement no. 779730.

REFERENCES

1. http://www.teachy.eu/. Accessed on November 15, 2021.
2. Tretsiakova-McNally S., Maranne E., Verbecke F., and Molkov V., Mixed e-learning and virtual reality pedagogical approach for innovative hydrogen safety training of first responders. International Journal of Hydrogen Energy 42:7504-7512.

WHEC-2022
23rd World Hydrogen Energy Conference
June 26-30, 2022 - Istanbul

#193

SOCIAL LIFE CYCLE ASSESSMENT OF A SOLID OXIDE ELECTROLYSIS CELL STACK

[1,2] *Felipe Campos-Carriedo,* [1,3] *Gonzalo Puig-Samper,* [1] *Eleonora Bargiacchi,* [1] *Diego Iribarren,* [1,2*] *Javier Dufour*
[1] IMDEA Energy, Systems Analysis Unit, 28935, Móstoles, Spain
[2] Rey Juan Carlos University, Chemical and Environmental Engineering Group, 28933, Móstoles, Spain
[3] Universidad Autónoma de Madrid, Chemical Engineering Department, 28049, Madrid, Spain

*Corresponding author e-mail: javier.dufour@imdea.org

ABSTRACT

The relevance of Fuel Cells and Hydrogen (FCH) systems as decarbonisation solutions has grown significantly during the past decade. However, a sustainable life-cycle performance of FCH systems should be guaranteed. In this sense, while the focus is typically placed on their economic and environmental performance, scarce attention is usually paid to the social dimension, which should be assessed to avoid burden shifting. In this work, a Social Life Cycle Assessment (S-LCA) of a 5 kW Solid Oxide Electrolysis Cell (SOEC) stack was carried out within the context of the eGHOST project. The system boundaries include the extraction of materials, the manufacturing of components and the final assembly of the stack parts (balance of plant excluded). Design parameters such as current density, degradation and lifetime were defined considering 2030 targets, when this type of electrolysers is expected to be commercially mature. Inventory data (including working hours) were adapted accordingly from literature sources, while trade information from the UN Comtrade database was used for the regionalisation of the supply chain. Modelling and evaluation were performed using openLCA and the PSILCA database and method. Overall, stainless steel production in Spain arose as the main social hotspot under most of the evaluated indicators.

Keywords: Hydrogen, Life Cycle Assessment, Solid Oxide Electrolysis, Social Impact, Sustainability

INTRODUCTION

In December 2020, the European Union updated its Nationally Determined Contributions (NDC) to the 2015 Paris Agreement. This update increased the greenhouse emission reduction commitment from 40% to at least 55% by 2030, relative to 1990 levels [1]. In this context, the FCH sector has been identified as crucial for the expected energy transition. Ambitious targets have been set for its short-, medium- and long-term deployment. It is expected that up to 40 GW of water electrolysis capacity will be installed across Europe by 2030, enabling the production of hydrogen at a cost lower than 3 €/kg [2]. High-temperature electrolytic processes present advantages in terms of efficiency when compared to more mature options such as alkaline electrolysis [3], but they need to be further developed in order to reach technology maturity and cost-competitiveness.

The deployment of FCH technologies needs to be supported by a holistic approach that ensures a suitable economic and environmental performance while preventing burden shifting to social impacts. Within the context of the EU-funded project eGHOST (https://eghost.eu/), this work aims to comprehensively assess the social life-cycle performance of a 5 kW SOEC stack, a high-temperature electrochemical device for hydrogen production. Although Social Life Cycle Assessment (S-LCA) has scarcely been applied to FCH systems, it is an effective and increasingly used methodology to thoroughly assess the potential social impacts of product systems [4,5].

MATERIALS AND METHODS

Goal and scope definition

The assessed product is a 5 kW SOEC stack, one of the two reference cases selected in the eGHOST project for the development of eco-design guidelines for FCH technologies. The stack specifications and bill of materials were originally retrieved from literature sources [6]. Current density, active surface, degradation and lifetime parameters were defined to meet 2030 EU targets [2], resulting in a higher unitary power per cell and thus a lower number of total cells in the stack.

The goal of the present work is to identify social hotspots of the product under study. The functional unit (FU) was defined as one SOEC stack (balance of plant excluded). Due to the lack of prospective S-LCA databases, the assumption underlying this study refers to the assessment of social risks associated with manufacturing the SOEC stack in 2030 but assuming current social risk levels (at the level of country-specific sectors) and working hours. The system boundaries comprise materials production processes, the manufacturing of components and the final assembly of the stack (including the involved energy flows). Hence, the supply chain involves three tiers: tier 1 for the stack manufacturing plant itself, tier 2 for the plants related to the production of the components and energy flows required by

the stack manufacturing plant, and tier 3 for the plants related to the material and energy flows required by the components manufacturing plants.

Countries were identified along the supply chain following available protocols used for S-LCA [7]. Spain was set as the manufacturing country of the final product and thus established as the initial declarant entity. Global trade data for each stack component were obtained from the UN Comtrade database. If the Spain's monetary export-import balance for a component results positive, then the component was determined to be manufactured also in Spain. If the balance results negative, the principal exporter was targeted. A similar procedure was used to determine the origin of the materials within the third tier: each component manufacturing country was designated as declarant for every material flow involved in the component and its trade balance was characterised similarly (but, when looking for relevant exporters, the set of those accounting for more than 50% of world exports to the declaring country was considered, not being necessarily limited to the top one as in the second tier).

The social indicators under evaluation were selected based on the eGHOST project specific purpose as well as on previous S-LCA studies in the field of energy and hydrogen. Regarding the stakeholder category "workers", the indicators “child labour”, “forced labour” and “fair salary” were examined. Moreover, “health expenditure” and “contribution to economic development” were evaluated within the stakeholder category "society".

Data implementation

The software used to implement the inventory data was openLCA. PSILCA [8] was used as an additional source of data (mainly regarding working hours per economic unit for items without specific information available, as well as country- and sector-specific risk levels) and as the evaluation method.

RESULTS

The social life-cycle profile of the SOEC stack was calculated. The S-LCA results are shown in Fig. 1 in terms of process plant contribution to the selected social indicators. As a key finding, stainless steel production in Spain arouse as the main social hotspot in every impact category except for "child labour". This finding was found to be closely linked to the high mass rate of stainless steel in the SOEC stack. Furthermore, the materials totally or partially manufactured in China (zirconium dioxide, iron oxide, and lanthanum oxide) were also found to account for relevant social risk values, especially under the “child labour” indicator.

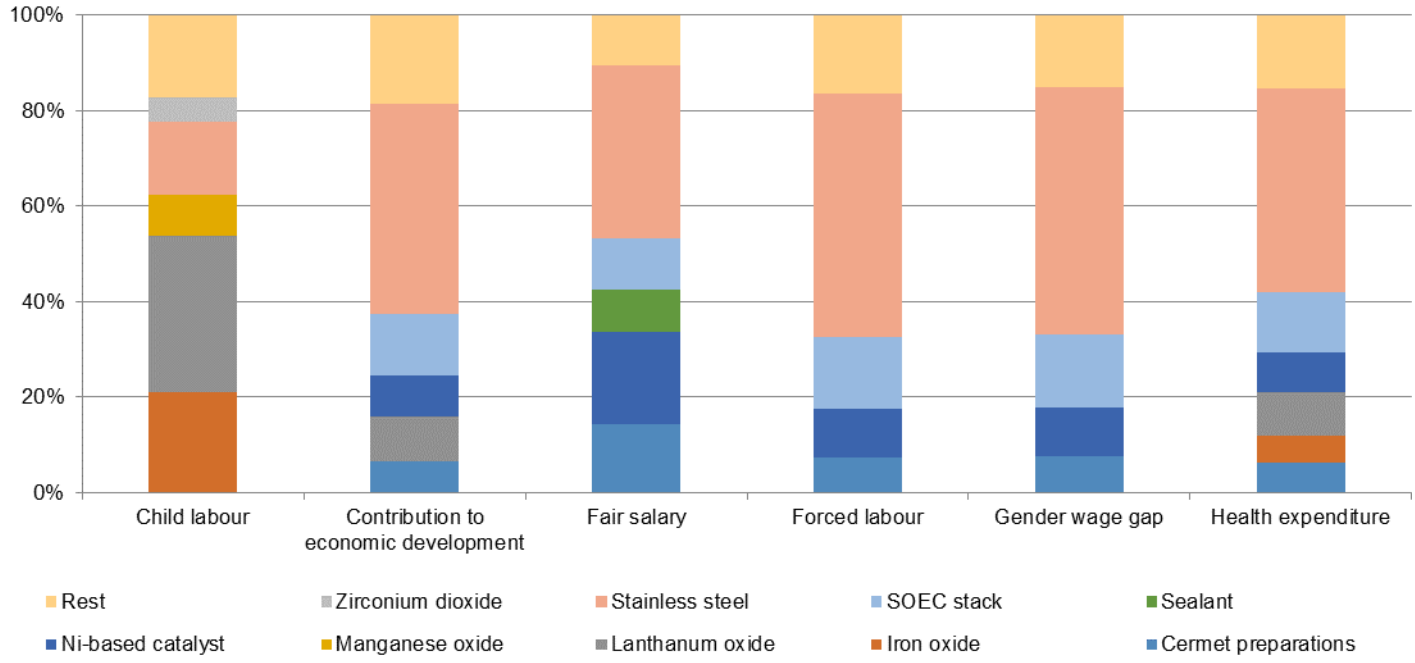


Fig. 1. Process plant contribution to the evaluated social risks of the SOEC stack under study

Overall, manufacturing processes at the level of materials were found to involve larger potential social impacts than manufacturing processes at the level of components and final product. It should also be noted that electricity flows across tiers were found to account for minor contributions.

CONCLUSIONS

In this study, an S-LCA of a 5 kW SOEC stack was performed. Stainless steel production in Spain generally arose as the main social hotspot, primarily due to the high mass rate of stainless steel in the stack. The materials manufactured in China also arose as a relevant source of social risk, mainly in terms of child labour. These results will serve as a relevant source of information for the development of eco-design guidelines for FCH technologies within the context of the eGHOST project.

ACKNOWLEDGEMENT

This work was carried out within the context of the project eGHOST. This project has received funding from the Fuel Cells and Hydrogen 2 Joint Undertaking under Grant Agreement No 101007166. This Joint Undertaking receives support from the European Union's Horizon 2020 Research and Innovation programme, Hydrogen Europe and Hydrogen Europe Research.

REFERENCES

1. https://ec.europa.eu/clima/eu-action/climate-strategies-targets/2030-climate-energy-framework_en. Accessed on December 15, 2021.
2. Hydrogen Europe. 2020. Strategic research & innovation agenda. Brussels, Hydrogen Europe.
3. Keçebaş A, Kayfeci M and Bayat M. 2019. Electrochemical hydrogen generation. In Solar Hydrogen Production. Edited by Calise F, D'Accadia MD, Santarelli M, Lanzini A and Ferrero D. London: Academic Press.
4. Ramos Huarachi DA, Piekarski CM, Puglieri FN and de Francisco AC. 2020. Past and future of Social Life Cycle Assessment: Historical evolution and research trends. Journal of Cleaner Production 264:121506.
5. United Nations Environment Programme. 2020. Guidelines for social life cycle assessment of products and organizations 2020. Paris, UNEP.
6. Battelle Memorial Institute. 2017. Manufacturing cost analysis of 1, 5, 10 and 25 kW fuel cell systems for primary power and combined heat and power applications. Columbus, Battelle Memorial Institute.
7. Martín-Gamboa M, Dias AC, Arroja L and Iribarren D. 2020. A protocol for the definition of supply chains in product social life cycle assessment: application to bioelectricity. Sustainable Energy & Fuels 4:5533-5542.
8. Maister K, Di Noi C, Ciroth A and Srocka M. 2020. PSILCA database v.3 documentation. Berlin, GreenDelta.

WHEC-2022
23rd World Hydrogen Energy Conference
June 26-30, 2022 - Istanbul

#239

ASSESSING PUBLIC ACCEPTANCE ON HYDROGEN ECONOMY IN JAPAN: A COMPARISON OF PAST SURVEY IN 2015

[1*] *Jiazhen Yap,*[1] *Benjamin McLellan*
[1]Graduate School of Energy Science, Kyoto University, Kyoto, 606-8501, Japan

*Corresponding author e-mail: yap.jiazhen.76z@st.kyoto-u.ac.jp

ABSTRACT

Hydrogen and Japan have a long, shared history, dating back to 1974 with the start of a green initiative known as the Sunshine Project. Since then, the Japanese government has actively sought to realise a hydrogen society by using hydrogen as an energy carrier in transportation, residential power systems, and industrial applications. Despite the continuous effort by the Japanese government, it remains to be seen whether hydrogen can achieve large-scale deployment. Assessing society's acceptance of a hydrogen economy is important to understanding social support and ultimately avoiding unwillingness for hydrogen technology and infrastructure deployment. This study aims to analyze the current attitude of Japanese society towards the realization of a hydrogen economy through a community survey. Given recent global interest, the results will be compared with a similar survey conducted in 2015 to see if there has been any recent changes. The questionnaire survey was designed to analyze responses under four main aspects: awareness of various energy resources and environmental policy; perception of hydrogen economy; knowledge of hydrogen technology and infrastructure; and acceptance towards the establishment of hydrogen infrastructure in the community.

Keywords: Hydrogen Economy, Survey, Public Acceptance, Japan

INTRODUCTION

The hydrogen economy refers to a vision of utilizing hydrogen (H_2) as a transition pathway to an equitable energy system that is clean, low carbon-intensive, and beneficial to society. Hydrogen is an energy carrier that can be produced by a variety of energy resources and support a multitude of end-use applications, including energy storage, transportation fuel, industrial processes, and more. Historically, the hydrogen economy has attracted the attention of many and resulted in multiple surges of interest over the years [1]. The hydrogen economy is a dynamic system that consists of economic, technological, and social structures that are constantly evolving. This dynamic system is affected by endogenous factors by stakeholders with different agendas and exogenous factors outside of a hydrogen economy's system boundary. The diversity of hydrogen as an energy solution allows people to interpret it based on their own perspectives and agendas, resulting in competing interpretations of what a future hydrogen economy may look like. This has created a gap between the public and scientific community understanding of the status of hydrogen economy and raised false expectations in the past [2]. It is widely accepted in socio-economics that the success of emerging technology depends to a great extent on public acceptance [3][4]. Emerging technologies such as hydrogen technology have received increased general coverage through the media [5], but public acceptance is still relatively unknown [6].

Literature Review

Over the past few decades, various studies have investigated the technical and economic aspects of hydrogen as a promising energy carrier to solve global climate issues and increased concerns in the fossil fuel-based energy economy [7][8]. However, studies on public perception of hydrogen have been significantly less common [9]. Country-specific studies such as in Germany [3][10], USA [11][12], UK [13], and Spain [4] have investigated the acceptance and implementation of H_2 technology. Although they use varying survey designs, the results concluded that the public seems to have a positive impression toward H_2 technology. However, the studies also reveal that the public is largely unaware of hydrogen beyond the automotive sector, and most individuals do not have firsthand experience with H_2 technology. Aside from perception, personal experience with H_2 technology can greatly influence the acceptance of hydrogen in daily life [10].

Given the long history of Japan with hydrogen [14], there have been few studies focusing on public perception of hydrogen to date. The few studies are available in Japanese and carried out by NEDO and Mizuho Information & Research Institute. The nationwide survey was conducted in 2008 [15] and 2009 [16], investigating the social acceptance of hydrogen. Their results indicated that the public perspective of H_2 technology is relatively high, although most respondents do not have experience using H_2 technology. Itaoka et al. [6] conducted an updated survey in 2015, comparing results to previous surveys and focusing more on hydrogen in the transportation sector.

The study concluded that public awareness of hydrogen energy, hydrogen infrastructure, and fuel cell vehicles had increased significantly compared to previous surveys.

In addition, there have been many hydrogen demonstrations or pilot projects involving different sectors and technology types. In some cases, the projects have been conducted in parallel with a community survey to evaluate public reactions in experiencing hydrogen in action or as a preliminary assessment of public acceptance for future investment of hydrogen technology. Notable projects include Clean Urban Transport for Europe (CUTE), the largest demonstration project of fuel cell buses in nine different cities within Europe [17][18], and Ecological City Transport System (ECTOS), a demonstration project in Reykjavik, Iceland, also using fuel cell buses [19]. However, the respondents of these studies are typically introduced to hydrogen and its benefits, thus not representing a random sampling of the entire population with regards to existing perspectives.

At present, the majority of studies focus on a single aspect of hydrogen, mainly transportation, often overlooking aspects such as production and storage, which also form the basis of a hydrogen-based society. This is partly because hydrogen technologies are not widely available yet, and most are at prototype or pilot stages, which leads to lower public engagement. Furthermore, the potential transition to a hydrogen economy is predominantly discussed among the scientific community [20]. Although hydrogen has been covered by media over the years, the interest has been a recurring hype, often associated with futuristic technology, environmental issues, and most recently COVID-19 post-economy recovery in the energy sector [21].

Aim

This study aims to analyze the current attitude of Japanese society towards the realization of a hydrogen economy through a community survey. The questionnaire survey is designed to evaluate the public perception, knowledge, and acceptance of hydrogen as an energy carrier, hydrogen infrastructure, and fuel cell technologies in Japan. This community survey is part of a parallel study with an expert panel survey that aims to quantify the different yet overlapping interpretations of hydrogen economy among different society groups, mainly academic, industry, government, and the general public, through an in-depth survey. It is crucial to understand the various interpretations of society and bring them together to exploit the diversity of hydrogen fully.

METHODS

This study was conducted from a social-economic perspective. The questions and structure of the survey were designed to allow comparison with a previous survey conducted in 2015 [6], using some of the same key questions but also adapted to the specific objectives of the current study. In total, 22 closed-ended questions were formulated under four main aspects: (i) awareness of various energy resources and environmental policy; (ii) perception of hydrogen economy; (iii) knowledge of hydrogen technology and infrastructure; and (iv) acceptance towards the establishment of hydrogen infrastructure in the community. In addition, social-demographic variables were included in determining the general characteristic of respondents and influences towards acceptance of hydrogen. The survey will be conducted in February 2022 using an internet-based survey, where respondents are panelists of a Japanese marketing research company. The respondents will be selected using a stratified random sampling method to ensure our results represent the Japanese population.

RESULTS AND DISCUSSION

Based on an earlier social acceptance study on hydrogen [9], a theoretical model was adapted to guide the formulation of the survey questions. The following model in Fig.1 was designed to evaluate and visualize various aspects that influence an individual's opinions toward the acceptance of a hydrogen economy. The three aspects are described as follow:

a. Value
   Personal values represent individual beliefs that guide everyday life, motivate actions, decision-making, and ultimately improves the quality of life [22]. Everyone holds various values with varying degrees of priority. As such, individuals with a stronger sense of environmental value would be expected to play a more active role in solving climate issues.

b. Knowledge
   The literature review has indicated the discussion of hydrogen is still novel among the general public. The level of knowledge is a good indicator to measure public understanding of hydrogen as individual opinions may be vulnerable to media hype reporting when access to hydrogen-related knowledge is still limited.

c. Perception

The nuances of a "Hydrogen Economy" provide potential points for disagreement and alternative perspectives. For example, the concept of a "Hydrogen Economy" is often referred as "Hydrogen Society" in Japan. This simple change of wording can also affect an individual perspective as the terminology of "Economy" is different to the Japanese term. Hydrogen is typically regarded as an energy carrier, not an energy source, in scientific literature (while this specific nuance is likely to be unclear to the general public). Hydrogen needs to be produced, stored, and distributed to the end-user, similar to electricity. Each stage of the hydrogen supply chain has significant implications in terms of public perception. Hydrogen can be produced from fossil fuels, renewable energy, or nuclear energy. Would people equally accept each production method as each has advantages and disadvantages? Similar questions can be asked concerning different stages in the hydrogen supply chain. Therefore, a specific image must be established to consider the acceptance of hydrogen in daily life. The association of hydrogen with everyday life can serve as an indicator of how the public perceives the issues with the system and technology.

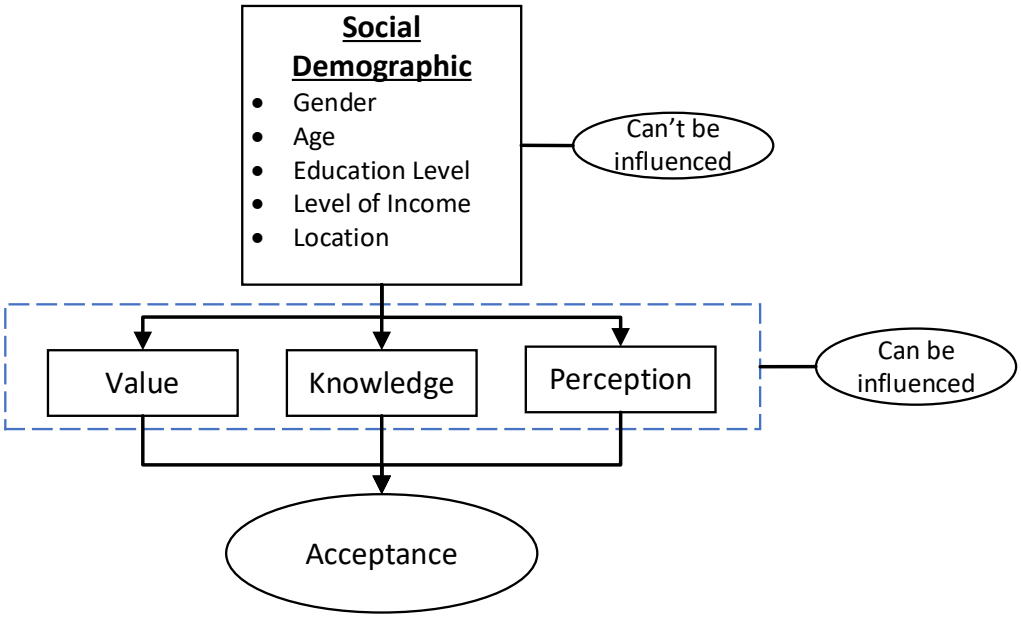


Fig. 1: Theoretical Model of Acceptance of Hydrogen Economy

CONCLUSIONS

This study offers a different perspective to the current body of knowledge as social aspects of a hydrogen economy are often discussed to a lesser extent in related reports or roadmaps. A theoretical model was developed, and a community survey will be conducted in February 2022 to evaluate the acceptance of a hydrogen economy in the Japanese community. Survey results and implications are expected to be presented in the conference presentation. The results from this study are expected to improve the current state of knowledge and serve as basic information in establishing a strategy for a future hydrogen economy transition and improving public acceptance.

REFERENCES

1. Khalilpour, K.R.; Pace, R.; Karimi, F. Retrospective and prospective of the hydrogen supply chain: A longitudinal techno-historical analysis. *Int. J. Hydrogen Energy* 2020, doi:10.1016/j.ijhydene.2020.02.099.
2. IEA The Future of Hydrogen. 2019.
3. Zimmer, R.; Welke, J. Let's go green with hydrogen! the general public's perspective. *Int. J. Hydrogen Energy* 2012, *37*, 17502–17508, doi:10.1016/j.ijhydene.2012.02.126.
4. Iribarren, D.; Martín-Gamboa, M.; Manzano, J.; Dufour, J. Assessing the social acceptance of hydrogen for transportation in Spain: An unintentional focus on target population for a potential hydrogen economy. *Int. J. Hydrogen Energy* 2016, *41*, 5203–5208, doi:10.1016/j.ijhydene.2016.01.139.
5. Hultman, M.; Nordlund, C. Energizing technology: Expectations of fuel cells and the hydrogen economy, 1990-2005. *Hist. Technol.* 2013, *29*, 33–53, doi:10.1080/07341512.2013.778145.
6. Itaoka, K.; Saito, A.; Sasaki, K. Public perception on hydrogen infrastructure in Japan: Influence of rollout of commercial fuel cell vehicles. *Int. J. Hydrogen Energy* 2017, *42*, 7290–7296, doi:10.1016/j.ijhydene.2016.10.123.

7. Nejat Veziroğlu, T. Quarter century of hydrogen movement 1974–2000. *Int. J. Hydrogen Energy* 2000, *25*, 1143–1150.
8. Nicoletti, G. The hydrogen option for energy: A review of technical, environmental and economic aspects. *Fuel Energy Abstr.* 1996, *37*, 182, doi:10.1016/0140-6701(96)88528-6.
9. Schulte, I.; Hart, D.; Van der Vorst, R. Issues affecting the acceptance of hydrogen fuel. *Int. J. Hydrogen Energy* 2004, *29*, 677–685, doi:10.1016/j.ijhydene.2003.09.006.
10. Schmidt, A.; Donsbach, W. Acceptance factors of hydrogen and their use by relevant stakeholders and the media. *Int. J. Hydrogen Energy* 2016, *41*, 4509–4520, doi:10.1016/j.ijhydene.2016.01.058.
11. Schmoyer, R.L.; Chew, A. Results of the 2004 knowledge and opinions surveys conducted for the U.S. department of energy hydrogen program. 2009.
12. Schmoyer, R.L.; Truett, T.; Cooper, C.; Chew, A. Results of the 2008/2009 knowledge and opinions surveys conducted for the U.S. department of energy hydrogen program. *Oak Ridge Natl. Lab.* 2010, 1–299.
13. O'Garra, T.; Mourato, S.; Pearson, P. Analysing awareness and acceptability of hydrogen vehicles: A London case study. *Int. J. Hydrogen Energy* 2005, *30*, 649–659, doi:10.1016/j.ijhydene.2004.10.008.
14. MITI Japan *JAPAN ' S SUNSHINE PROJECT SOLAR ENERGY R & D PROGRAM*; 1981;
15. Information, M.; Institute, R. Suiso shakaijuyousei ni kansuru chousa [Hydrogen's social acceptance research]. 2008.
16. Information, M.; Institute, R. Nenryoudenchi, suiso ni kansuru shakaijuyouseichousa [PEFC, Hydrogen's social acceptance research]. 2009.
17. O'Garra, T.; Mourato, S.; Pearson, P. Investigating attitudes to hydrogen refuelling facilities and the social cost to local residents. *Energy Policy* 2008, *36*, 2074–2085, doi:10.1016/j.enpol.2008.02.026.
18. Haraldsson, K.; Folkesson, A.; Saxe, M.; Alvfors, P. A first report on the attitude towards hydrogen fuel cell buses in Stockholm. *Int. J. Hydrogen Energy* 2006, *31*, 317–325, doi:10.1016/j.ijhydene.2005.11.008.
19. Maack, M.H.; Skulason, J.B. Implementing the hydrogen economy. *J. Clean. Prod.* 2006, *14*, 52–64, doi:10.1016/j.jclepro.2005.05.027.
20. Ricci, M.; Bellaby, P.; Flynn, R. What do we know about public perceptions and acceptance of hydrogen? A critical review and new case study evidence. *Int. J. Hydrogen Energy* 2008, *33*, 5868–5880, doi:10.1016/j.ijhydene.2008.07.106.
21. van Renssen, S. The hydrogen solution? *Nat. Clim. Chang.* 2020, *10*, 799–801, doi:10.1038/s41558-020-0891-0.
22. Kheirandish, S.; Funk, M.; Wensveen, S.; Verkerk, M.; Rauterberg, M. A comprehensive value framework for design. *Technol. Soc.* 2020, *62*, 101302, doi:10.1016/j.techsoc.2020.101302.

WHEC-2022
23rd World Hydrogen Energy Conference
June 26-30, 2022 - Istanbul

#1473

GREEN HYDROGEN, AN ECONOMIC PARADIGM SHIFT – NEW PERSPECTIVES FOR THE GLOBAL SOUTH?

[1*] *Andreas Stamm,* [1] *Rita Strohmaier,* [1] *Ece Oyan,* [1] *Katharina Thoms*
[1]German Development Institute – Deutsches Institut für Entwicklungspolitik (DIE), Bonn, Germany

*Corresponding author e-mail: andreas.stamn@die-gdi.de

ABSTRACT

Hydrogen is a key element for the energy system of the future. International experts and organizations [1] forecast a rapidly increasing demand for green hydrogen in the coming decades, especially in Europe and Japan. This opens new opportunities for developing countries to position themselves beneficially in a new international division of labour. Costa Rica has locational advantages for the production of hydrogen with renewable energies. It makes sense for the country not to focus exclusively on opportunities to develop a new export sector, which may not generate very good income and employment opportunities in the future. Rather, more comprehensive strategies should be developed combining export revenues and

Keywords: Green Hydrogen, Developing Countries, Development Potentials, Decarbonisation, Employment Creation

INTRODUCTION

Since the early 1970s, the notion of a global “hydrogen economy” was launched as a concept for a visionary future. 50 years later, it seems that the future has arrived. There is an international consensus that mitigating climate change is an urgent need and that hydrogen will play a crucial role in decarbonisation efforts. Following projections of the International Energy Agency (IEA), the global green hydrogen market is going to grow from 0.3 billion USD in 2020 by exponential rates and reach the threshold of 10 billion USD in 2028. In 2050, hydrogen could cover 24% of global energy demand [1]. Substituting fossil fuels by green hydrogen implies far-reaching shifts in the global economic geography. Countries of the Global South, often well endowed with renewable energy potentials, may become mayor exporters of green hydrogen (GH2) the “oil, gas and coal” of a climate-friendly future energy systems. This paper explores the developmental potential of the paradigm shift in the global energy and industrial resource system and sketches some basic open research questions.

MATERIALS AND METHODS

The paper analyses the development potentials of GH2 for the Global South. It is based on a thorough literature review and expert interviews.

RESULTS AND DISCUSSION

The fact that hydrogen can be used as an energy carrier is not at all new. Already in the 1870s, French novelist Jules Vernes envisaged a future, when hydrogen would be employed as a powerful source of heat and light, powering steam ships and locomotives [2]. The abundance of cheap and easier-to-handle fossil fuels and electricity as energy carrier explains, why this hydrogen vision was not pursued for around a century. Only in the 1970s, the fact, that fossil energy resources are limited and that their combustion may have detrimental effects on the global climate reached the international discourse [3]. The notion of a hydrogen economy was suggested in 1970 by the U.S. electrochemist John Bockris [1]. It took another half century until concrete commitments were made to start a determined transition towards a hydrogen economy. This can mainly be attributed to the fact that very significant technological and systemic advancements have been made, since around the turn of the century, in renewable energy deployment, mainly offshore and onshore wind and solar PV. Cost reductions in renewable energies and in electrolysis turned many ambitious projects into feasible options. Clear commitments to climate action also triggered the drafting and adoption of hydrogen strategies in Europe and beyond.

A milestone was the adoption of the trillion-dollar European Green Deal Package in 2019 and the subsequent EU Hydrogen Strategy. Green hydrogen is deemed to be the key driver of the EU’s carbon neutrality target by 2050. Both the European and the German hydrogen strategies are very ambitious in terms of building up domestic capacities for green hydrogen production. The technology of choice is clearly electrolysis, powered by electricity generated without or with very small amounts of GHG emissions. European hydrogen strategies envisage 40 GW of electrolysis capacity by 2030, with France (6.5), Germany and Italy (5 GW each) having the largest shares. Just how ambitious this is becomes clear when you consider that, according to the German Aerospace Center; Germany currently has a total electrolysis capacity of 30 megawatts, powered by renewable energy. Even if the ambitious plans will be implemented, it still implies that only a minor share of the hydrogen demand will be covered by local

production. What is a rather blind spot in both the European and the German hydrogen strategies are the expected trade flows in the future. The strategies stay rather vague about where the huge amounts of green hydrogen will be produced and how they will be transported to Europe. Within Europe, a certain share will be produced via solar PV in countries like Spain and by offshore wind in the riparian states of the Northern and Baltic seas. However, large part of the demand be covered by extra-regional imports.

DIRECT BENEFITS FOR DEVELOPING COUNTRIES FROM INTEGRATION INTO A GREEN HYDROGEN ECONOMY

Countries best prepared to produce GH2 at relatively low costs are those endowed with rich renewable energy potentials. Most high potential locations are located in the Global South, most of them, with the exception of Australia Low to Middle Income Countries (LIC/MIC). What has not yet been discussed is, why and under which conditions developing countries would be willing to export GH2 to the Global North. We briefly discuss four ways, how developing countries might benefit from integration into an international division of labour in a global GH2 economy:

- Export revenues can improve the national balance of payments and generate government revenues that can be invested, for example, in social transfers or in improving the country's human capital through education.
- The direct employment effects of hydrogen projects can reduce underemployment and stimulate the economy through multiplier effects.
- With the production of large quantities of climate-friendly hydrogen, the country has a completely new type of raw material at its disposal.
- Related to this is the fact that the establishment of hydrogen projects in developing countries goes hand in hand with the transfer of technological knowledge and international cooperation in research and development.

Whether the *export revenues* developing countries may obtain for selling GH2 on the markets of Europe or Japan will be attractive or not is difficult to predict. Given the starting conditions and the clear willingness of industrial countries to promote the market launch of a global GH2 economy it is likely that countries able to supply significant quantities of GH2 in the near future may benefit from first mover advantages. In the long run, however, with an increasing number of suppliers entering the market and technologies and systems becoming more and more standardized, it is very likely that the prices will go down. Whether or not being an exporter of GH2 remains attractive then depends on the combination of prices free on board (FOB) and international transport costs, which are still very difficult to predict.

Among the socio-economic challenges, most developing countries face is the urgent need to bring young people into productive *employment*. This is especially the case for regions, often seen as quasi-natural partners of Europe in a GH2 strategy. In most countries of sub-Saharan Africa, Northern Africa and the Middle East, youth unemployment is in the range of 20% to 30% and this tends to raise governance problems of different types. Currently, there are no reliable data about the employment, which GH2 projects generate. Drawing on analogies from large utility-scale energy projects in developing countries, it is reasonable to state that significant numbers of employment are created during the building of the facilities but that a limited number of jobs in operation, maintenance and repair remain, once they are up and running.

IMPORTANT CO-BENEFITS FOR DEVELOPING COUNTRIES

Even if the direct benefits of developing countries entering a global GH2 economy might be limited, there are other benefits with huge potentials to even become game changers for sustainable development on the ground. However, this requires a change in strategies from a mere export-oriented to a multipurpose and comprehensive model of GH2 economy. Availability of GH2 in significant quantities may open new pathways for value creation and innovation.

Hence, countries may also consider the mid and long-term benefits from implementing the green H2 economy within their national borders: First, an absence of legacy energy systems and path dependencies makes it comparatively easy to leapfrog to new and environmentally friendly energy technologies that reduce dependence from international fossil fuel supply chains. Second, hydrogen is a powerful technology for storing and transporting these energy sources and thus for solving the intermittency problem and overcoming the systems integration challenge related to VRE technologies by carbon-free load balancing [7]. Furthermore, decentralized hydrogen production based on solar energy does not entail expansive infrastructure and can therefore push rural electrification, thereby also contributing to social well-being and stability. It furthermore can be used either pure, as a feedstock or as a heating source in many different pathways and in various sectors. In addition to direct use in the transport sector or as a heating source, hydrogen may also be used as a feedstock in the chemical industry (e.g. copper, steel, solvents) or in the production of derivatives (e.g. synthetic fuels, ammonia, methane and methanol) in a wide range of industries such as the transport sector, agriculture or the building sector. Thus, reduces existing import dependencies and/or emissions.

Beyond the advantages related to the energy transition, green H2 production also opens strong opportunities regarding job and economic growth. This effect works through two channels: (1) the co-benefits associated with the exploitation of renewable energy; (2) co-benefits associated with the expansion of value chains into different sectors and energy-intensive industries. Major co-benefits are related to economic performance, as the renewable energy systems create jobs (8,9,10,11), increase economic activities and diversification [12,13,14,15,16], and lead to significant savings in terms of energy [17,18] and time [19].

RE expansion also bear social co-benefits, linked to health [20, 21, 22] due to the reduction of air pollution, educational opportunities and knowledge transfer [9,21], poverty reduction [23,24] as well as to an improvement in overall welfare and resilience [14], social equity [25], better inclusion of woman [19] as well rural and indigenous communities [16,10]. Furthermore, the advantages of RES regarding decentralized power supply improves energy access and security [26, 21, 27]. Environmental co-benefits associated with the energy transition are the reduction of GHG emissions [16,22] better air quality [see, e.g., 23,25], improved biodiversity, reduced deforestation and [19], less freshwater ecotoxicity and eutrophication [8], and waste disposal reduction [16].

CONCLUSIONS

For Europe, the vision of a rapid market ramp-up for green H_2 in order to decarbonise industry and transport faces challenges in terms of the sheer quantities involved. NationAL strategies like the German NWS need to be complemented by a European and a multilateral agenda that views H_2 as an opportunity to overcome global challenges and focus on benefiting all parties. For example, the countries of North Africa are exigently dependent on creating jobs for young people in particular. However, international ventures such as the Ouarzazate solar project in Morocco, which has been supported by Germany, demonstrate that these employment opportunities are often modest once large-scale systems have finished their construction phase and enter regular operation. Germany and Europe should reach out to potential exporter countries in the spirit of partnership and scope out what mutual benefits can be achieved in order to increase the political will and local acceptance for joining an international hydrogen economy. Knowledge sharing and scientific cooperation are essential if developing countries are to be empowered to develop their own H_2-based solutions, including switching their fertiliser production from fossil fuels to H_2 or decarbonising their (petro-)chemical industries. More technologically advanced countries such as South Africa or Brazil could supply core components for electrolysers. The least-developed countries could use H_2 as an energy storage medium in power grids supplied by intermittent renewable energy sources.

REFERENCES

1. Sadik-Zada ER. 2021. Political Economy of Green Hydrogen Rollout: A Global Perspective. Sustainability 2021, 13, 13464. https://doi.org/10.3390/su132313464
2. Vernes, J. 1874. L'Île mystérieuse. Paris. Chapter 11
3. Meadows DH et al 1970: Limits to Growth. Report to the Club of Rome. Washington DC
4. Griffiths S., Sovacool BK., Kim J., Bazilian M. and Uratani, JM. 2021. Industrial decarbonization via hydrogen: A critical and systematic review of developments, socio-technical systems and policy options. Energy Research & Social Science 80:102208
5. ESMAP (Energy Sector Management Assistance Program). (2020). Green Hydrogen in Developing Countries. Washington DC
6. https://www.greenindustryplatform.org/blog/green-hydrogen-fuelling-industrial-development-clean-and-sustainable-future. Accessed on Mach 15, 2021
7. van de Graaf, T., Overland, I., Scholten, D., & Westphal, K. (2020). The new oil? The geopolitics and international governance of hydrogen. Energy Research & Social Science, 70, 101667. https://doi.org/10.1016/j.erss.2020.101667
8. Lema, R., Bhamidipati, P. L., Gregersen, C., Hansen, U. E., & Kirchherr, J. (2021). China's investments in renewable energy in Africa: Creating co-benefits or just cashing-in? World Development. 141. 105365. https://doi.org/10.1016/j.worlddev.2020.105365
9. Müller, F., Neumann, M., Elsner, C., & Claar, S. (2021). Assessing African Energy Transitions: Renewable Energy Policies, Energy Justice, and SDG 7. Politics and Governance, 9(1), 119– 130. https://doi.org/10.17645/pag.v9i1.3615
10. Pittock, B. (2011). Co-benefits of large-scale renewables in remote Australia: energy futures and climate change. The Rangeland Journal. 33(4). 315. https://doi.org/10.1071/RJ11012
11. Wang, C., Zhang, W., Cai, W., & Xie, X. (2013). Employment impacts of CDM projects in China's power sector. Energy Policy, 59, 481–491. https://doi.org/10.1016/j.enpol.2013.04.010
12. IRENA. (2017a). Renewable energy benefit: Leveraging local capacity for solar PV. International Renewable Energy Agency (IRENA).
13. IRENA. (2017b). Renewable Energy Benefits: Leveraging local capacity for onshore wind. International Renewable Energy Agency (IRENA).
14. IRENA. (2017c). Renewable energy benefits: Understanding the socio-economics. International Renewable Energy Agency.https://www.irena.org/media/Files/IRENA/Agency/Publication/2017/Nov/IRENA_Understanding_Socio_Economics_2017.pdf?la=en&hash=C430B7EF772BA0E631190A75F7243B992211F102
15. Makešová, M., & Valentová, M. (2021). The Concept of Multiple Impacts of Renewable Energy Sources: A Critical Review. Energies. 14(11). 3183. https://doi.org/10.3390/en14113183

16. Röder, M., Mohr, A., & Liu, Y. (2020). Sustainable bioenergy solutions to enable development in low- and middle-income countries beyond technology and energy access. Biomass and Bioenergy. 143. 105876. https://doi.org/10.1016/j.biombioe.2020.105876
17. Bößner, S., Devisscher, T., Suljada, T., Ismail, C. J., Sari, A., & Mondamina, N. W. (2019). Barriers and opportunities to bioenergy transitions: An integrated, multi-level perspective analysis of biogas uptake in Bali. Biomass and Bioenergy. 122. 457–465. https://doi.org/10.1016/j.biombioe.2019.01.002
18. Dell'Anna, F. (2021). Green jobs and energy efficiency as strategies for economic growth and the reduction of environmental impacts. Energy Policy. 149. 112031. https://doi.org/10.1016/j.enpol.2020.112031
19. Kattumuri, R., & Kruse, T. (2019). Renewable technologies in Karnataka, India: jobs potential and cobenefits. Climate and Development. 11(2). 124–137. https://doi.org/10.1080/17565529.2017.1410085
20. Buonocore, J. J., Luckow, P., Fisher, J., Kempton, W., & Levy, J. I. (2016). Health and climate benefits of offshore wind facilities in the Mid-Atlantic United States. Environmental Research Letters. 11(7). 74019. https://doi.org/10.1088/1748-9326/11/7/074019
21. Simpson, N. P., Rabenold, C. J., Sowman, M., & Shearing, C. D. (2021). Adoption rationales and effects of off-grid renewable energy access for African youth: A case study from Tanzania. Renewable and Sustainable Energy Reviews. 141. 110793. https://doi.org/10.1016/j.rser.2021.110793
22. Haghi, E., Fowler, M., & Raahemifar, K. (2019). Co-benefit analysis of incentives for energy generation and storage systems; a multi-stakeholder perspective. International Journal of Hydrogen Energy. 44(19). 9643–9671. https://doi.org/10.1016/j.ijhydene.2018.08.150
23. Jacques, D. A., Guan, D., Geng, Y., Xue, B., & Wang, X. (2013). Inter-provincial clean development mechanism in China: A case study of the solar PV sector. Energy Policy. 57. 454–461. https://doi.org/10.1016/j.enpol.2013.02.019
24. Lo, K., & Castán Broto, V. (2019). Co-benefits, contradictions, and multi-level governance of low-carbon experimentation: Leveraging solar energy for sustainable development in China. Global Environmental Change, 59, 101993. https://doi.org/10.1016/j.gloenvcha.2019.101993
25. Chapman, A. J., McLellan, B. C., & Tezuka, T. (2018). Prioritizing mitigation efforts considering co-benefits, equity and energy justice: Fossil fuel to renewable energy transition pathways. Applied Energy. 219. 187–198. https://doi.org/10.1016/j.apenergy.2018.03.054
26. Murata, A., Liang, J., Eto, R., Tokimatsu, K., Okajima, K., & Uchiyama, Y. (2016). Environmental co-benefits of the promotion of renewable power generation in China and India through clean development mechanisms. Renewable Energy. 87. 120–129. https://doi.org/10.1016/j.renene.2015.09.046
27. Sovacool, B. K., Baker, L., Martiskainen, M., & Hook, A. (2019). Processes of elite power and low-carbon pathways: Experimentation, financialisation, and dispossession. Global Environmental Change. 59. 101985. https://doi.org/10.1016/j.gloenvcha.2019.101985
28. Gibon, T., Arvesen, A., & Hertwich, E. G. (2017). Life cycle assessment demonstrates environmental co-benefits and trade-offs of low-carbon electricity supply options. Renewable and Sustainable Energy Reviews. 76. 1283–1290. https://doi.org/10.1016/j.rser.2017.03.078

WHEC-2022
23rd World Hydrogen Energy Conference
June 26-30, 2022 - Istanbul

#1474

GREEN HYDROGEN IN COSTA RICA – PERSPECTIVES OF AN ECONOMIC PARADIGM SHIFT FOR A SMALL DEVELOPING COUNTRY

[1*] *Andreas Stamm,* [1] *Katharina Thoms,* [2] *Fernando Lizana*
[1]German Development Institute – Deutsches Institut für Entwicklungspolitik (DIE), Bonn, Germany
[2] Instituto Costarricense de Electricidad (ICE), San José, Costa Rica

*Corresponding author e-mail: andreas.stamn@die-gdi.de

ABSTRACT

Hydrogen is a key element for the energy system of the future. International experts and organizations [1] forecast a rapidly increasing demand for green hydrogen in the coming decades, especially in Europe and Japan. This opens new opportunities for developing countries to position themselves beneficially in a new international division of labour. Costa Rica has locational advantages for the production of hydrogen with renewable energies. It makes sense for the country not to focus exclusively on opportunities to develop a new export sector. Rather, Costa Rica should actively seek to create additional benefits domestically through the usage of hydrogen. In transport and certain industries, there are opportunities to lower greenhouse gas emissions while significantly reducing the import of fossil resources and creating job opportunities.

Keywords: Green Hydrogen, Developing Countries, Development Potentials, Decarbonisation, Employment Creation

INTRODUCTION

Green hydrogen (GH2) is a crucial element of any strategy aiming at reconciling socio-economic prosperity with the planetary boundaries, especially keeping climate change under control. The transition towards a green hydrogen economy will lead to significant shifts in the global economic geography. Developing countries, often well endowed with renewable energy resources, may be future focal points of GH2 production. The paper discusses the development potentials for Costa Rica of getting involved in the emerging GH2 economy. It argues for an integrated strategy, combining the export of GH2 or derivatives with actions outlined in the country's decarbonisation plan for lowering greenhouse gas (GHG) in the transport and industry sectors. This can contribute to import substitution and the building up of labor-intensive activities especially in underprivileged areas of Costa Rica.

MATERIALS AND METHODS

The paper analyses the development potentials of GH2 for a small developing country. It is based on a thorough literature review and interviews with core stakeholders of Costa Rica's energy sector.

RESULTS AND DISCUSSION

Costa Rica in a Global GH2 Economy: On Locational Advantages

Economic geography and regional economics analyse the likelihood of an industry locating in a country or region using the concept of locational advantages; such as access to raw materials, important markets, low wages and taxes. In traditional manufacturing, Costa Rica does not have major locational advantages, as the country is poor in natural resources, relatively far from major markets and has relatively high labour costs. Over the last four decades, however, it has managed to penetrate knowledge-intensive niches of the world market, from high-value agricultural exports to IT-enabled services and manufacturing and exporting medical equipment. In a coming GH2 world economy, the locational advantages will continue to shift:

- Renewable energy are "coal and oil", the most important resources of a post-fossil energy system.
- Water is the second most important resource, as current technologies require large quantities of pure water to produce GH2.
- Skilled personnel and advanced governance capacities will be crucial in the near future, as some elements of the hydrogen economy are still in flux and will require active efforts to make them work as a system under the specific conditions of each country.

In this new economic geography, Costa Rica has the opportunity to move from a rather peripheral position further into the centre. The country has excellent renewable energy potential. Hydropower, geothermal and wind power have accounted for about 98% of the country's total electricity generation in recent years. However, data from the International Energy Agency (IEA) shows that in 2019, still around 50% of the total energy consumed in the country came from oil, mainly in the transport sector and the fertilizer industry. This means that Costa Rica's energy transition

is far from complete and must now address sectors that are more difficult to decarbonise compared to electricity generation, especially passenger and freight transport and some industries.

Although water scarcity is an issue for some regions at certain times of the year, overall we can expect Costa Rica to have abundant water resources for the foreseeable future. Some high-altitude areas on the Atlantic slope are among the rainiest regions in the world, reaching about 6000 mm of precipitation per year.

Market access is a challenge for all GH2 producing countries, which are too far away to be connected to consuming regions via pipelines. The distance from Costa Rica to potential GH2 markets, e.g. Europe, is large, but not greater than potential competitors. The transport distance between, for example, Puerto Moin on the Caribbean coast and Rotterdam as the main import port for Europe can be estimated at 20 days, similar to the transport time from Namibia to Europe, shorter compared to Chile and at least ten days shorter compared to any port in Australia.

Finally, other, less quickly grasped locational advantages can be particularly important at an early stage in the development of a global GH2 economy. This is when technologies and processes are not yet fully standardised and need to be adapted to changing conditions and new knowledge in the course of the implementation process: The country has a highly skilled workforce and good institutions for academic research and education and for vocational training. The country's governance is considered capable and efficient, both in the political sphere and in terms of implementing agencies in investment promotion, export promotion and in the energy sector. In recent decades, Costa Rica has learned to negotiate and deal with large international companies that invest in free trade zones, industrial parks and agricultural exports. Despite relatively high labour costs, Costa Rica remains an attractive investment destination. There are thus good reasons to believe that Costa Rica has a good chance of positioning itself as a potentially important production location in a global GH2 economy.

Indeed, most recently, the Australia-based industrial corporation Kadelco announced its interest to establish a facility in Costa Rica to annually produce up to 50.000 tons of GH2. Investment could be as high as US$3 billion and 2600 jobs might be created. The Costa Rica government announced that at least two additional foreign companies have declared their interest in producing GH2 in Costa Rica.

Costa Rica National Decarbonization Plan

In January 2019, Costa Rica announced to "go beyond the usual" in the global efforts and commitments to aspire to become a modern, green, emission-free, resilient, and inclusive economy" and approved its National Decarbonization Plan [2]. This plan capitalizes on important environmental advances in previous decades, including an electricity network free of emissions in more than a 95% and very low rates of deforestation with a forest cover that exceeds 52% of the territory. It defines ten goals, among them ambitious targets for decarbonizing transport, housing and industry.

Possible Socio-Economic Benefits of the Country Entering the Emerging GH2 Economy

For a small developing country hosting "coal and oil" of a post-fossil energy system (renewables and water), there are four ways to benefit from these clean technology efforts.

- Export revenues can improve the balance of payments of the national economy and generate government revenues that can be invested, for example, in social transfers or in developing the country's human capital through education and training.
- The direct employment effects of hydrogen projects can reduce underemployment and stimulate the economy through multiplier effects.
- With the production of large quantities of climate-friendly hydrogen, the country has a completely new type of raw material at its disposal.
- Related to this is the fact that the establishment of hydrogen projects in developing countries goes hand in hand with the transfer of technological knowledge and international cooperation in research and development.

The latter two points open up perspectives for developing new value creation potentials and new social applications locally. The paper discusses the four potential benefits in the case of Costa Rica. We analyse this against the backdrop that the country has two major socio-economic problems to deal with. First, ways must be found to bring more people, especially youth, into productive employment. Second, the huge disparities between urban and rural areas, especially between Central High Valley and coastal areas, must be reduced when it comes to development opportunities for individuals and communities.

In terms of export revenues, it is difficult to assess the potential net benefits Costa Rica may derive from entering the emerging global green hydrogen economy. If the country acts fast and comes into a position to offer reasonable amounts of green hydrogen in the coming years, the economic prospects are good, as a large demand meets a barely developed supply (seller's market). In the long term, the conditions are less favourable, as other countries

probably have lower prime costs, due to even better ecological conditions for producing renewable energies and larger territories allowing to generate economies of scale.

There are currently now reliable data on the employment creation of a green hydrogen economy. Conclusions by analogy (large-scale renewable energy projects) indicate that positive effects on the labor markets will be generated during the construction phase, while in the long run, operation, maintenance and repair activities will only keep limited numbers of people in productive employment. For Costa Rica, large-scale investment in GH2 could be an important way to reduce the unemployment rate, which has risen from 8% to 17% (2017-2020) in the wake of the COVID-19 pandemic and from 20% to 40% in the youth unemployment sector. However, in the long run indirect and co-benefits may be structurally more important.

In Search of the Co-Benefits of GH2 Production

GH2 can be used in many ways. In some African countries, pilot projects are underway to use hydrogen as a storage medium in mini-grids fed by intermittent renewable energy sources. Energy storage can enable a 24-hour power supply. Mini grids are an important bridging technology to provide reliable electricity to communities beyond the reach of the national grid. Since almost 100 % of the population in Costa Rica has access to the grid, this benefit is not broadly relevant for the country. It may be an option, for instance, to assure reliable electricity supply for clinics or storage facilities for agricultural produce in some remote areas of the country.

Two options are important for Costa Rica and are already being explored by the national utility ICE: GH2 as a fuel for passenger and freight transport [3] and as a feedstock for industries, such as metal processing and fertilizer production. Both sectors together are largely responsible for the remaining GHG emissions of Costa Rica. In addition, they depend on imported fossil energy carriers and derivatives, such as ammonium for the fertilizer industry. United Nations data shows that in the years prior to the Corona pandemic, in 2016-2019, Costa Rica imported "mineral fuels, mineral oils and products of their distillation" worth between US$1.2 billion and US$1.7 billion, which represented about 10% of the total value of all imports in the country. Imports of fertilisers are much lower, but still represent a significant cost, amounting to US$60-70 million per year over the same period. Using GH2 to decarbonise industry is a viable option for sectors that require large amounts of process heat [4]. ICE is already working with a company that produces reinforcing steel from imported metal for the construction industry. The heat needed to melt the steel is obtained from GH2. The country's fertiliser and cement industries should be the next candidates, as imported intermediates could be saved while greenhouse gas emissions would be significantly reduced. Globally, the cement industry alone contributes an estimated 8% of greenhouse gas emissions, and the production of synthetic nitrogen fertilisers another 2.4%.

Economic Impulses for Underprivileged Areas

Costa Rica could benefit from the investment and job creation in infrastructure and facilities in the initial phase. This also has an important regional economic dimension, as the best location for a GH2 plant with an important export component (with a view to Europe) would be close to the export ports of Limon or Moin and thus in a structurally weak region compared to the Central High Valley. The creation of jobs on the Atlantic coast and possibly the demonstration effects of a "visible" future-oriented clean technology plant could help to counteract the frustration of the population in the Atlantic region. This feeling of regional marginalization has expressed itself in past elections in abstentions and high rates of support for right-wing populism.

A boost in economic activity and employment triggered by GH2 could help Costa Rica and the Atlantic coast recover from the impact of the COVID-19 pandemic. However, as large renewable energy projects in other parts of the world have shown, the high number of jobs created during the construction phase does not last once the infrastructure and equipment are up and running. This needs to be taken into account in the country's GH2 strategy. To avoid a new wave of frustration, part of the revenue generated by GH2 exports should be invested in creating labour-intensive follow-up activities, not in the Central Valley, but in the peripheral regions, especially on the Atlantic coast. One possible option, for example, would be to set up workshops to convert buses and trucks from combustion engines to fuel cell propulsion.

CONCLUSIONS

Green hydrogen is an important opportunity for developing countries to create new competitive advantages and sustainable employment in promising sectors. Costa Rica is a small developing country at a great distance from the likely major future hydrogen markets. However, the country might be well positioned to exploit first-mover advantages. The country has advanced governance capacities, an educated workforce and research and development institutes, which might collaborate with international investors in the early phase of the emerging global GH2 economy. It is fundamental that the government not only envisages large-scale export of a green commodity but also pursues an integrated strategy, which combines exports with the usage of GH2 for decarbonisation of local

industries and modes of transport, import substitution and the development of labor-intensive industries based on a new raw material in line with a future-proof climate-friendly economic development.

REFERENCES

1. World Energy Council 2020. International Hydrogen Strategies. Ottobrunn
2. Government of Costa Rica 2019: National Decarbonization Plan 2018-2055. San José, Costa Rica
3. Godínez-Zamora G et al. 2020. Decarbonising the transport and energy sectors: Technical feasibility and socioeconomic impacts in Costa Rica. Energy Strategy Reviews 32 (2020) 100573
4. Griffiths S, Sovacool BK, Kim J, Bazilian M and Uratani, JM. 2021. Industrial decarbonization via hydrogen: A critical and systematic review of developments, socio-technical systems and policy options. Energy Research & Social Science 80:102208

WHEC-2022
23rd World Hydrogen Energy Conference
June 26-30, 2022 - Istanbul

#1477

TURKEY'S POTENTIAL TO PRODUCE GEOTHERMAL-BASED GREEN HYDROGEN: INSIGHTS FROM INSIDE

[1*] *Ece Oyan*
[1]German Development Institute - Deutsches Institut für Entwicklungspolitik (DIE)
Tulpenfeld 6 53113 Bonn, Germany

*Corresponding author e-mail: ece.oyan@die-gdi.de

ABSTRACT

As a country with high renewable energy potential but still very much dependent on fossil fuel imports, green hydrogen can yield many opportunities to the Turkish economy. This study aims to examine Turkey's potentials in producing geothermal-based green hydrogen. For such an analysis, different stakeholders like private sector, scholars, policymakers, civil society organizations and locals will be interviewed and the results will be analyzed based on techno-economic, political-economic, environmental and societal impacts argued by the interviewees.
Keywords: Green hydrogen, Geothermal, Turkey

INTRODUCTION

Paris Agreement and its goal to keep the average global warming at 1.5°C made various countries announce long-term national roadmaps to either partially or completely decarbonize their economies. To reach such targets, the application and the use of green hydrogen as an energy carrier have been gathering attention for the last couple of years. Countries like United Kingdom (U.K.), the United States of America (U.S.A.), Germany, Japan, Australia, France or Italy have already published their national hydrogen strategies and shared their estimated demand for green hydrogen in the coming decades. Therefore, it can be claimed that the global market for green hydrogen will be expanding exponentially in the near future. In such a rapidly changing environment, countries with high renewable energy potential have the chance to produce and export green hydrogen.

As a country with highly diverse renewable energy potential, Turkey has been working on increasing the share of renewable energies in its power mix. In 2021, renewables constituted 35% of the electricity generated in the country [1]. Especially the installed geothermal capacity has been increasing steadily. Although as of 2020 geothermal represents only the 3.25% (1.6 GW) of the total power generation in Turkey [2], that year Turkey was the world leader in terms of additional installed geothermal energy capacity with 98.3 MW [3]. Given the fact that Turkey consumes more energy than it generates, which makes it highly dependent on fossil fuel imports, further increasing its share of renewables can decrease the country's dependency on other energy suppliers. Additionally that can provide a greater possibility to be a net green hydrogen producer and also help decarbonize its own economy [4].

Although in the literature the major attention has been given so far to the green hydrogen production from solar and wind power, we believe that as a base-load energy, geothermal may provide additional advantages, as it is not affected by ambient conditions. Moreover, multi-generation geothermal power plants where both hydrogen and electricity are produced offer more feasible and efficient production systems [5]. Besides, it is also possible to combine geothermal energy and solar power in places where both sources are available. In this case, both efficiency and flexibility of the system increases [5]. Given these benefits of geothermal energy, this study will analyze Turkey's potential to produce geothermal-based green hydrogen. For such an analysis the following research questions will be addressed:

- Which role can geothermal energy play for future green hydrogen production in Turkey for both exports to Europe but also for local usage?
- Which factors and risks might act as barrier against its use?
- What policy instruments could help overcome these barriers?

MATERIALS AND METHODS

In order to answer these research questions, the main methodology of this study will be conducting interviews with various actors of the Turkish innovation system like private sector, policymakers, universities, scholars, civil society organizations. Additionally a detailed literature review will also support this analysis by looking at both academic and non-academic research on the subject. Both interviews and the literature review will be conducted based on the criteria matrix represented in the Table 1.

Table 1. Analysis criteria

Stakeholders	Techno-economic impacts	Political-economic impacts	Environmental impacts	Societal impacts
Private sector (large)				
Private sector (medium)				
Private sector (small, start-ups)				
Policymakers				
University research				
Non-university research				
Civil society (national level)				
Civil society (local/regional)				
Public				

Such an analysis will help us identify the capacities, positions and interest of diverse stakeholders. By doing so, it will also depict a picture of the geothermal energy sector in Turkey and its potential to support green hydrogen production.

RESULTS AND DISCUSSION

As this is a research that is still at its early stages, the results are not yet complete. However, from the literature and some already established contacts, we know that there is an interest in Turkey to explore its potential in geothermal-based green hydrogen production.

Techno-economic impacts

SHURA Energy Transition Center together with some other research partners completed two studies on priority areas for a national hydrogen strategy [4] and also a techno-economic analysis on Turkey's production and export potential [6]. According to these studies, Turkey has the potential to produce 3.4 million tonnes of green hydrogen by 2050 [6]. They forecast that by 2050 1.9 million tonnes of this potential will cover the annual domestic demand, whereas annual 1.5 to 1.9 million tonnes of green hydrogen can be exported by 2050 [6]. The estimated total annual gross benefit is between 6 to 8 billion dollars to the Turkish economy in 2050 [6].

Although in these reports, the potential of green hydrogen production from Turkey's geothermal resources has not been studied, we have already contacted some private sector actors who engage in green hydrogen production from large scale geothermal power plants. It is to our knowledge that these projects are now in the R&D phase and were able to mobilize finance for this aim. That means there is an interest from the private sector and a vision that geothermal-based green hydrogen production is expected to be a profitable business.

Political-economic impacts

As mentioned above, in terms of fossil fuels Turkey is highly dependent on imports. In 2020 the 33% of the natural gas imports came from Russia, whereas the 11% and 24% of the remaining imports were supplied by Iran and Azerbaijan, respectively [7]. Although compared to 2010 (46.2%), Turkey was able to reduce its imports from Russia and managed to diversify its suppliers to a certain extent, current international developments like Russia's invasion in Ukraine prove that further diversification of suppliers and not being highly dependent on one country in terms of energy supplies is important. For example blending green hydrogen to the natural gas pipelines can reduce the import demand. That would allow Turkey to eliminate 2.5 billion m^3 imported natural gas per year, equivalent of US$0.6 billion per year [4].

Moreover, as part of the European Green Deal, Carbon Measuring at the Border (CMAB) will be implemented as of 2026. This application aims to create an economic incentive for the trade partners of the EU to phase out coal and decarbonize their economies. Since the EU is Turkey's biggest export destination, decarbonizing especially the heavy industry through green hydrogen applications would bring Turkey competitive power.

Environmental impacts

In October 2021 Turkey ratified the Paris Climate Agreement and announced its goal to be carbon neutral by 2053. In order to achieve this goal, hard-to-decarbonize sectors like heavy industries (e.g. steel and iron, cement, petro-

chemical industry) should be addressed with certain priority. Green hydrogen can be utilized in these sectors both as an energy carrier as well as a feedstock. This would support the phasing out coal and eliminate the devastating environmental harm coal power plants have been causing for decades.

Societal impacts

Especially in the recent years, the number of news about the protests against geothermal power plants and their construction sites have been increasing [8, 9, 10]. Locals from western cities of the country announce their disapproval and they get organized to raise their voices. Like many protests, these groups are not always homogenous. Some of them are not very well informed about the geothermal energy and its effects, whereas others are informed and have still big concerns. However, in both cases, this shows that public engagement in the decision making process is not achieved. Hence, conflicts between firms, who hold licenses to build and operate geothermal power plants, and locals, who live and work on these lands, arise very quickly. In order to be able to resolve these conflicts and achieve a mutual understanding, state can act as a mediator and maybe set the rules better, by leaving no room for violation of the locals' rights.

Also from the contacts that we were able to establish so far, we know that in some cities there is no major issue simply due to the fact that geothermal energy is utilized in many diverse ways and not just in power plants. For example, via district heating systems public have access to very affordable and sustainable residential heating. Also, thermal water enables the public to engage in tourism activities and provide them economic benefit and job opportunities. Moreover, since Turkish private firms also engage in the R&D and want to found their own business models and techniques, there might be high added value employment opportunities for engineers, architects, chemists etc.

CONCLUSION

As an energy carrier, green hydrogen offers many opportunities to countries like Turkey who are rich in renewable energy sources and look for new global markets to engage. Actively utilizing all possible renewable energy sources would increase the country's green hydrogen production capacity. Geothermal energy offers great potential as it is not effected by ambient conditions and provide a base-load power generation. Given the fact that storing and transporting hydrogen pose some technical challenges, as a close neighbor to Europe, Turkey has the geographical advantage to reach that market relatively easily through pipelines. Being able to cover the domestic demand and export green hydrogen to Europe can provide economic, political, environmental and societal benefits to Turkey.

REFERENCES

1. https://ourworldindata.org/energy/country/turkey#what-sources-does-the-country-get-its-electricity-from Accessed on March 13, 2022
2. https://enerji.gov.tr/eigm-yenilenebilir-enerji-kaynaklar-jeotermal Accessed on March 13, 2022
3. https://ourworldindata.org/grapher/installed-geothermal-capacity Accessed on March 13, 2022
4. Saygin D, Gencer E and Sanli B. 2021. Priority areas for a national hydrogen strategy for Turkey. Istanbul, Sabanci University https://shura.org.tr/en/priority-areas-for-a-national-hydrogen-strategy-for-turkey/
5. Mahmoud M, Ramadan M, Naher S, Pullen K, Abdelkareem MA and Olabi AG. 2021. A review of geothermal energy-driven hydrogen production systems. Thermal Science and Engineering Progress. 22
6. Colak E, Aksoy H and Sanli B. 2021. Techno-economic study of Turkey's production and export potential for green hydrogen. Istanbul, Sabanci University https://shura.org.tr/en/techno-economic-study-of-turkeys-production-and-export-potential-for-green-hydrogen/
7. https://www.petform.org.tr/dogal-gaz-piyasasi/turkiye-dogal-gaz-piyasasi/ Accessed on March 14, 2022
8. https://www.birgun.net/haber/aydin-da-jes-lere-karsi-buyuk-protesto-263717 Accessed on March 14, 2022
9. https://www.sesgazetesi.com.tr/haber/8189593/aydinda-jes-protestosu Accessed on March 14, 2022
10. https://www.cumhuriyet.com.tr/haber/seferihisarda-jes-protestosu-1855759 Accessed on March 14, 2022

WHEC-2022
23rd World Hydrogen Energy Conference
June 26-30, 2022 - Istanbul

#1631

EFFECTS OF SOCIAL MEDIA PLATFORMS ABOUT ATTENDANCE TO WHEC 2022 CONFERENCE

[1*] *Feride Cansu İskenderoğlu,* [2] *Mustafa Kaan Baltacıoğlu,* [3] *Hüseyin Turan Arat*
[1] İskenderun Technical University, Faculty of Engineering and Natural Science, Mechanical Engineering Department, Hatay, Turkey
[2] İskenderun Technical University, Faculty of Engineering and Natural Science, Mechatronics Engineering Department, Hatay, Turkey
[3] Sinop University, Faculty of Engineering and Architecture, Mechanical Engineering Department, Sinop, Turkey

*Corresponding author e-mail: mkaan.baltacioglu@iste.edu.tr

ABSTRACT

In recent years, it has become very important to examine the positive or negative factors affecting participation in Scientific Conferences and to determine the right strategies. In this study, it is aimed not only at academic research focusing on the motivating and hindering factors in the literature, but also to expand the existing academic knowledge in terms of social media platforms, together with the data obtained from the social media platforms of the WHEC2022 conference. In addition to new and established factors affecting conference attendance, an interactive management and organizational strategies are proposed. An increase of 3.2% was observed in the WHEC2022 conference participation with the social media strategy used. Research findings are important for conference administrators in addressing the higher-importance social media strategies that affect conference attendance and the factors that affect them.

Keywords: Social Media, Hydrogen Energy, Attractions, Effects, Conference

INTRODUCTION

Today, internet versions and virtual universes are developing rapidly with digitalization. The importance of social media platforms, whose popularity and usage areas have increased in a short time, and their use by researchers is in line with the interest in "big data" in the literature [1]. These social media platforms are being developed with new updates and become more suitable for the use of different communities [2].

Scientists also want to benefit from these web-based social media platforms both for their work and their own social circles. Shares made using these platforms can reach people all over the world in a short time. It is possible to quickly engage in discussions with other researchers on a topic of interest, participate in science conversations and exchange ideas. Many researchers can easily share the summary of their research findings, which they disseminate through official scientific channels such as peer-reviewed journals, by providing sufficient information in a shorter time, both with people in the scientific field and other people who are interested in this field, and increase their visibility [1-3].

Social media tools offer a new way for scientists to strengthen their professional profiles and to express and reach the public more easily. Studies show that public visibility and constructive speech on social media platforms are beneficial for scientists and can positively impact research. Although the type of online chats and shared content can vary greatly, scientists use social media to share journal articles, promote their thoughts and scientific views, and benefit from conferences and meetings. They are increasingly using it as a way to post updates and distribute information about professional opportunities and upcoming events. In addition, with the conferences and webinars that have started to be held in the virtual world, researchers save both financially and morally, they can increase their networks and participate in science conversations without leaving their place [3].

The increased use of online resources can eventually transform and expand the culture of science as a whole. Blogs and social media tools provide an ideal setting for extended scientific conversations and allow for fast-paced discussion of topics that scientists "want and need to discuss". Online platforms will increase researchers' productivity and research efficiency. Platforms such as Facebook, Twitter, LinkedIn help academics to be up-to-date on new research developments, prepare teaching materials, and guide students using the platform [4].

Other researchers use online activities as a way to organize thoughts and research notes, or as a way to encourage creativity and improve writing skills. Online communities are particularly useful for niche topics where community members have specific needs or require specific interactions. Researchers who come together at conferences or in other fields after virtual chats and discussions can communicate more easily. Posting from conferences, discussing the latest research developments, providing information on journal articles, useful resources, lab projects, and

providing links to websites can introduce other scientists, students, or other interested people to valuable content and provide networking opportunities. In this way, a scientist's influence in the research world can expand. In particular, publishing articles on platforms such as Twitter and LinkedIn acts as a research filter for many scientists, making it easier for them to access studies in that field or outside of the field [5].

METHODS

This study has been prepared by taking into account the effectiveness of social media platforms of the WHEC2022 conference in the last 8 months. The studies and interactions obtained using 4 different social media platforms, namely Twitter, Facebook, Instagram, and LinkedIn, are explained. During this 8-month period, many videos and poster posts, both animated and still, were prepared and shared on social media platforms.

In addition,
- “Weekly hydrogen news” are shared in order to increase the traffic of the internet system.
- “Abstract deadline” reminders were made periodically through the conference’s social media accounts.
- Track coordinators and track titles posts were prepared and shared. Track Coordinators have been tagged in the posts to increase the interaction of the posts.
- The posts were shared on the hydrogen energy pages on the platforms in order to raise awareness, to establish new ideas, and establish the necessary contacts to strengthen connections.
- The post designs and sharing of the speakers who made special presentations at the conference were made. Speakers are tagged in posts to increase engagement.
- The posts about the “WHEC-2022 Tutorial Session” programs have been prepared.
- The posts were prepared and reminded that WHEC-2022 has a program in the form of online and onsite presentations.
- The collaboration news such as “IEA hydrogen TPC” were shared.

Table 1. Summary of WHEC-2022 Social Media Platforms activities

	Instagram		Twitter		Facebook		LinkedIn	
	Sep.- Dec.	**Jan.- Apr.**	**Sep.- Dec.**	**Jan.- Apr.**	**Sep.- Dec.**	**Jan.- Apr.**	**Sep.- Dec.**	**Jan.- Apr.**
Follower	93	124	30	40	19	15	181	302
Post	31	9	31	28	10	9	32	28
Reaction	1166	484	989	86141	173	37452	9553	8964

RESULTS AND DISCUSSION

All social media platforms have their own separate dynamics, and accordingly, their functioning and interactions differ. Our Facebook data has low values in the first months compared to other social media applications. Although this situation seems to be related to the number of posts, we cannot explain the reason for the situation with this alone. The main reason for this situation is that our stakeholders who do hydrogen studies mostly prefer other applications and there is a scarcity of Facebook sharing groups created about hydrogen energy and people do not prefer this platform for academic use.

On the other hand, in Twitter and Instagram applications, we interact with people through the "topic tags" that we use more often. It is very difficult to use these platform dynamics to provide detailed information, either visually or due to word limitations, and interact with researchers. However, it is quite easy to reach visual or verbal information and results through a hashtag. Quickly supporting a topic tag and sharing people's thoughts on the subject in an informed way allow scientific discussions.

In this study, LinkedIn is the platform with which we can quickly reach academicians, professionals, students and interested people working in the field of hydrogen energy and with which we have the most interaction. LinkedIn is due to the fact that it connects the networks in the work area, in accordance with the purpose of its establishment. Thanks to the interaction given to the shared post, the platform, which works with the logic of automatically making the post visible to the links of the interacting person, is especially effective for researchers.

CONCLUSIONS

As a result, social media platforms have a positive impact on professional networking. Each month, by adding new ones to the work done in the previous month, more people were accessed and the effectiveness of WHEC2022 in digital channels was made more visible.

REFERENCES

1. Bik HM and Goldstein MC (2013) An Introduction to Social Media for Scientists. PLOS Biology 11(4): e1001535. https://doi.org/10.1371/journal.pbio.1001535
2. Boyd DM, Ellison NB (2007) Social network sites: Definition, history and scholarship. J Comput Mediat Commun 13: 210–230.
3. Wilcox C (2012) Guest editorial: It's time to e-volve: Taking responsibility for science communication in a digital age. Biol Bull 222: 85–87.
4. Shuai X, Pepe A, Bollen J (2012) How the scientific community reacts to newly submitted preprints: Article downloads, Twitter mentions, and citations. PLoS ONE 7: e47523 .
5. Eysenbach G (2011) Can tweets predict citations? Metrics of social impact based on twitter and correlation with traditional metrics of scientific impact. J Med Internet Res 13: e123.


HOSPITALITY
MORE THAN JUST A WORD
True hospitality comes from the heart.
From a genuine desire to make sure our guests always feel totally at home.
BUSINESS CLASS
TURKISH AIRLINES
Products and services are subject to change depending on flight duration and aircraft.
STAR ALLIANCE
25 YEARS

MORE SUSTAINABLE AIR TRAVEL

Turkish Airlines has been using Sustainable Aviation Fuel (SAF) on its Istanbul-Paris route* once a week since 2/2/22 as part of its effort to provide more eco-friendly and climate-conscious air travel.

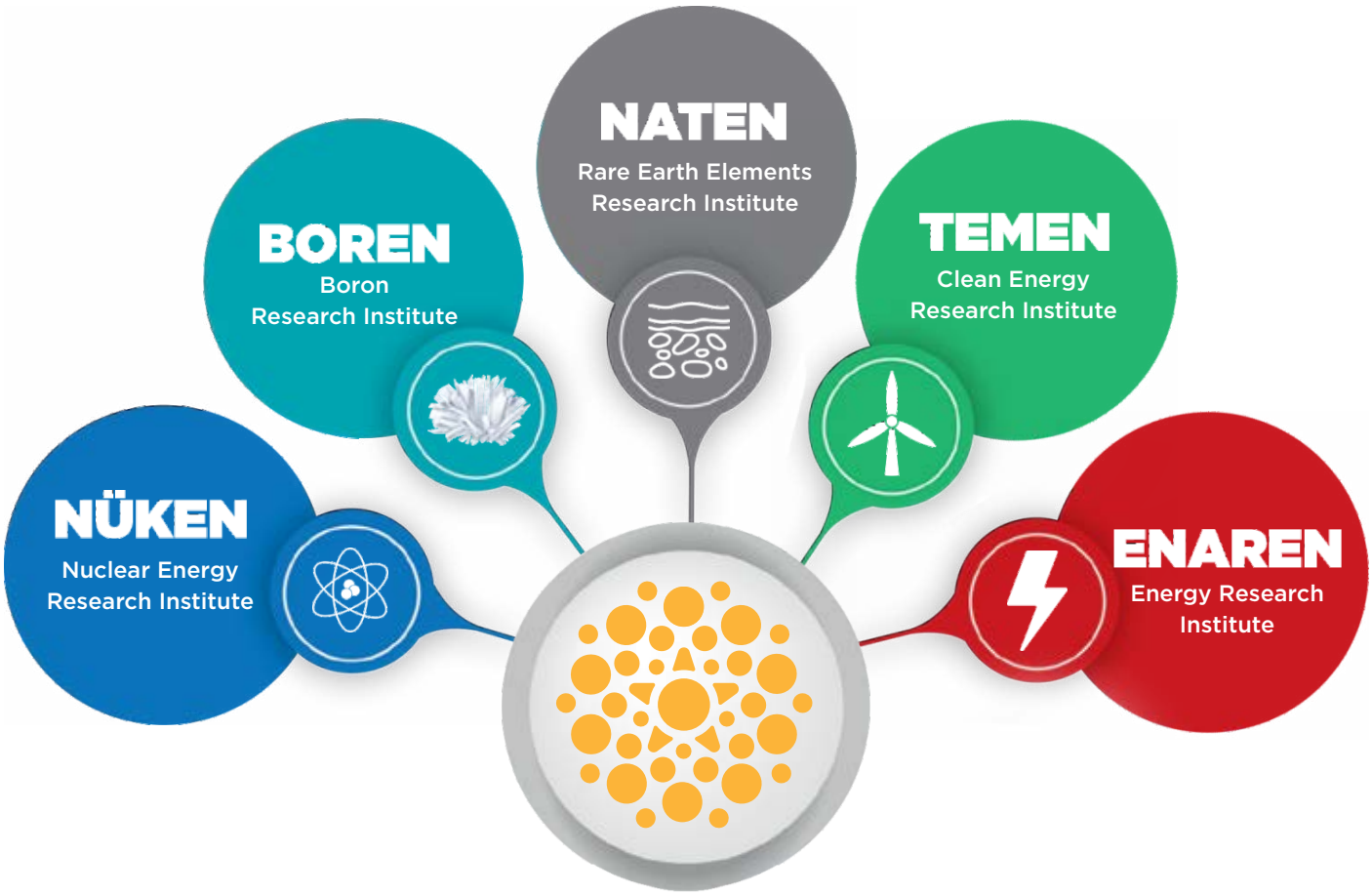


TURKISH AIRLINES

*There are already plans to expand its use to more routes.

STAR ALLIANCE | 25 YEARS

R&D INSTITUTION FOR ENERGY, NUCLEAR AND MINERALS TECHNOLOGIES



TENMAK

TURKISH ENERGY, NUCLEAR AND MINERAL RESEARCH AGENCY

tenmakbaskanlik

www.tenmak.gov.tr


BAU
Bahçeşehir University

FuelPositive
Fuel For A Mindful World

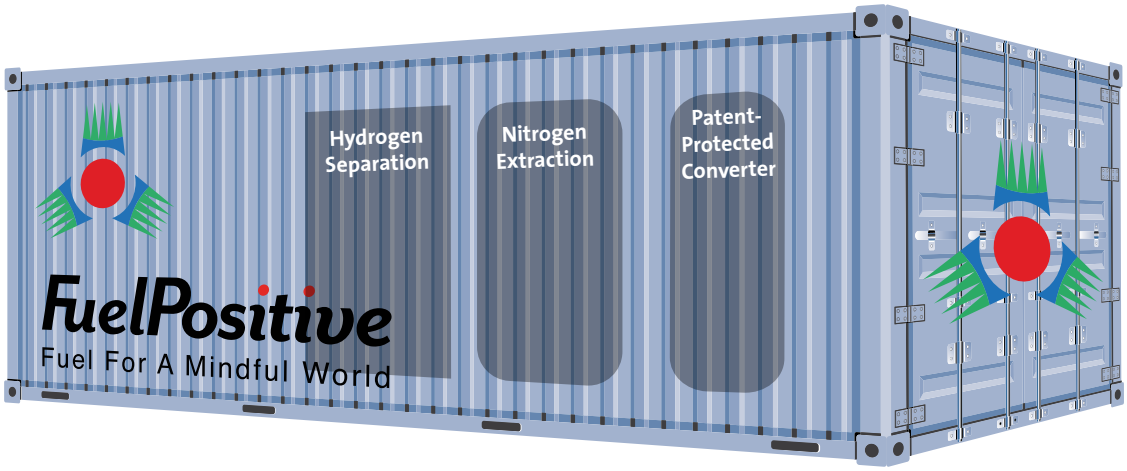


The Answer: On-Site Production

of Green H_2 and Green NH_3, where and when needed!

The question:

How do we make green hydrogen and green ammonia into practical global decarbonization solutions now?



Scan below for our website

Scan below for quick facts

Scan below to email us

TSXV: NHHH • OTCQB: NHHHF

info@fuelpositive.com

INOGEN

Knowledge Integrator



Inogen was founded in 2006 by 2 Turkish academicians as a knowledge-oriented energy company. With more than 800 employees and 4 separate companies, the Inogen Group is one of the largest renewable energy contractors in Turkey today. In line with its founding mission, Inogen carries out exemplary projects in its field such as Karapinar 1347 MW, the largest Solar Power Plant in Europe, and Kangal 50 MW, Uşak 82 MW, Sertavul 30 MW Power plants, which are the first wind-solar hybrid power plants of our country. Operating in Energy Storage, Green Hydrogen and Ammonia with many national and international collaborations, Inogen plans to become a global end-to-end solution provider in the renewable energy sector.

Wind Power Plants



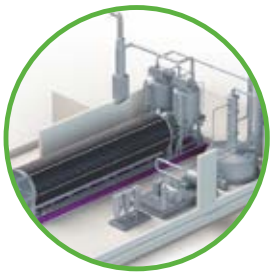
Solar Power Plants



Fuel Cell Technology



Battery Technology



Electrolize Technology







Building Integrated Photovoltaics

10th World Hydrogen Technology Convention

Hosts: International Association for Hydrogen Energy (IAHE)
China Association for Science and Technology (CAST)
China Machinery Industry Federation (CMIF)

Venue: Qiaoshan Culture Center,Nanhai District, Foshan City, Guangdong Province, P.R.China

Dates: MAY 22-26, 2023

Web: www.whtc2023.com

Contact: **Ms. Claire Tong +86 13552500706 clairtong@whtc2023.com**

Hydrogen Energy and Dual-Carbon Strategy: From Present to the Future

iyi ki ÜSKÜDAR var!

TEMSA
MOTORLU ARAÇLAR

Sabancı Üniversitesi





TEKSIS
İLERİ TEKNOLOJİLER
DESIGN - ANALYSIS • TEST - EVALUATION • MANUFACTURING • INTEGRATION • CONSULTANCY

TEKSIS was founded as a R&D executing SME to serve in Advance Energies and create new technologies for Green Future with having mission as to provide rapid, reliable, practical and cost-effective solutions. TEKSIS designs and develops products in hydrogen energy technologies and manufactures PEMFCs, electrolysers, FC test stations since 2007 in Turkey. Since its establishment, TEKSIS has gained significant experience in all rings of the hydrogen value chain.

TEKSIS contributes to the 21st Century Energy Transition and Decarbonization targets with safe, efficient and sustainable products and services with high added value that respect nature and humanity. Goals are to contribute to a more diverse and efficient energy infrastructure globally by enabling widespread commercialization of hydrogen energy and fuel cell technologies that will reduce fossil fuel usage and greenhouse gas emissions.

Hydrogen for Future


BCSMÜHENDİSLİK


Fakir
HAUSGERÄTE


İTÜ
İSTANBUL TEKNİK ÜNİVERSİTESİ
1773


Sistem Al
ALÜMİNYUM


Westfälische
Hochschule
Gelsenkirchen Bocholt Recklinghausen
University of Applied Sciences


YILDIZ TEKNİK ÜNİVERSİTESİ
1911


KUTEM


OZ
Energy


TeknoVak
INDUSTRIAL FURNACE SYSTEMS INC.

FIRAT UNIVERSITY 1975

NATIONAL HYDROGEN ASSOCIATION TURKEY

International Association for Hydrogen Energy

International Journal of Hydrogen Energy

IHTEC 2023

www.ihtec2023.org

7th International HYDROGEN TECHNOLOGIES Congress

10-12 May 2023

Fırat University, Elazığ, Turkey



Contact

Association Secretary:
Fatma Taşçı - 0 533 726 72 55 - fatma.tasci@hidrojenteknolojileri.org
www.hidrojenteknolojileri.org

Organization Secretariat

BROS Congress, Incentive and Events

Esentepe Mah. Sağlam Fikir Sok. Esen Palas Apt. A Blok No:2 D:9 Esentepe / İstanbul / Turkey
Tel: +90 212 296 66 70 / Fax: +90 212 296 66 71
www.brosgroup.net e-mail: hatice.cilek@brosgroup.net

NATIONAL HYDROGEN ASSOCIATION

TURKEY

AWARDS

Nejat Veziroğlu Special Award

This award was created on behalf of Prof. Dr. Nejat Veziroğlu, who is an international leader in hydrogen energy, the father of hydrogen technologies, and the permanent honorary president of the Hydrogen Technologies Association. It is given to people who have proven themselves in the field of hydrogen energy and technologies both domestically and internationally and have made internationally recognized contributions.

Service Award of Hydrogen Technologies Association

This award is given to the people who have dedicated themselves to hydrogen energy and have served for at least 20 years in the development and application of this field, have contributed to the communal, social, technological, and economic development of the country in this field, have been a pioneer in the education and training of youth, have made institutional contributions and are active in industrial applications.

Technology Award

This award has been created for institutions that work effectively on hydrogen energy technologies and develop technologies. It is given to institutions that develop a product for the development of hydrogen technology, establish a pilot or industrial facility in the field of hydrogen energy and technologies, have patents in the field of hydrogen energy and technologies or support technology development.

Young Researcher Award

This award has been created for researchers, who are under the age of 35 (not less than 35 years old as of the date of WHEC-2022 conference, where the award will be given) and have at least a master's degree. It is given to people who have done successful studies on hydrogen energy technologies that are recognized at the national and international levels.

Student Researcher Award

This award is given to undergraduate, graduate, or doctoral students. Candidates are expected to be under the age of 30 as of the date of the WHEC-2022 conference, where the award will be given. The candidates who will be nominated for this award or who will apply themselves, will be preferred for this award if they have developed an invention, a new application, or a unique method for hydrogen technologies

Winners of these prizes will be invited to attend the conference in which they will participate in the award ceremony, and their transportation and hotel expenses will be covered by the association.

CONTACT

+90 533 726 72 55
hidrojen@hidrojenteknolojileri.org

More information and application:
www.hidrojenteknolojileri.org

National Hydrogen Association Turkey

OntarioTech University

International Association for Hydrogen Energy

Main Sponsors

Republic of Turkey Ministry of Energy and Natural Resources

TENMAK Turkish Energy, Nuclear and Mineral Research Agency

Turkish Airlines A Star Alliance Member

Platinum Sponsors

BAU Bahçeşehir University

FuelPositive Fuel For A Mindful World

INOGEN Enerji Teknolojileri Energy Technologies

Gold Sponsors

Enerjisa Üretim

Temsa Motorlu Araçlar

Sabancı Üniversitesi

Üsküdar Belediyesi

Silver Sponsors

Kawasaki Kawasaki Gas Turbine Europe GmbH

Teksis

WHTC 2023 İNHİ

Bronze Sponsors

BCS Mühendislik

Fakir Hausgeräte

İTÜ

Sistem Alüminyum

Westfälische Hochschule Gelsenkirchen Bocholt Recklinghausen University of Applied Sciences

Other Sponsors

KUTEM

OZ Energy

TeknoVak Industrial Furnace Systems Inc.

www.whecistanbul.org
info@whecistanbul.org